The Eurasia Proceedings of Science, Technology, Engineering & Mathematics

EPSTEM

VOLUME 38 IConTES CONFERENCE

ISSN: 2602-3199
ISBN: 978-625-6959-83-5

IConTES 2025: 8th International Conference on Technology, Engineering and Science (IConTES)
November 12- 15, 2025 Antalya, Türkiye
Edited by: Prof.Dr. Mehmet Ozaslan - Gaziantep University, Türkiye

©2025 Published by the ISRES Publishing

ICONTES 2025

8th International Conference on Technology, Engineering and Science (ICONTES)

Proceedings Book

Editor

Mehmet Ozaslan
Gaziantep University, Türkiye

ISBN: 978-625-6959-83-5

Copyright 2025

Published by the ISRES Publishing

Address: Askan Mah. Akinbey Sok. No: 5-A/Konya/Türkiye

Web: www.isres.org

Contact: isrespublishing@gmail.com

https://2025.icontes.net

Dates: November 12-15, 2025

Location: Antalya, Türkiye

This work is licensed under a Creative Commons Attribution-NonCommercial-ShareAlike 4.0 International License.

About Editor

Prof Dr. Mehmet Ozaslan
Department of Biology, Gaziantep University, Türkiye
Website: mehmetozaslan.com
E-mail: ozaslanmd@gantep.edu.tr

Language Editor

Lecturer Ceren Dogan
School of Foreign Languages, Necmettin Erbakan University, Türkiye
Email: cerendogan@erbakan.edu.tr

CONFERENCE PRESIDENTS
Mehmet Ozaslan - Gaziantep University, Türkiye

SCIENTIFIC BOARD

Bogdan Patrut - Alexandru Ioan Cuza Üniversitesi , Romania
Chalavadi Sulochana - Gulbarga University, India
Dariusz Jacek Jakóbczak - Technical University of Koszalin, Poland
Dehini Rachıd -University of Bechar, Algeria
Eleonora Guseinoviene - Klaipeda University, Lithuania
Elena Krelja Kurelovic - Polytechnic of Rijeka, Croatia
Eva Trnova - Masaryk University, Czech Republic
Farhad Balash - Kharazmi University, Iran
Fundime Miri - University of Tirana, Albania
Gabriel Delgado-Toral - Universidad Nacional Autónoma de México, Mexico
Gordana Savıc - University of Belgrade, Serbia
Grzegorz Woroniak,- Bialystok University of Technology, Poland
Irina Andreeva - Peter The Great St. Petersburg Polytechnic University, Russia
Isti Hıdayah - Semarang State University, Indonesia
Joanna Piotrowska - Woroniak - Bialystok University of Technology, Poland
Jose Manuel Lopez Guede - University of Basque Country, Spain
Kamil Yurtkan - Cyprus International University, Cyprus
Katsina Christopher Bala - Federal University of Technology, Minna, Nigeria
Khitam Shraim - Palestine Technical University, Palestine
Marija Stanıć - University of Kragujevac, Serbia
M. Hanefi Calp - Karadeniz Technical University, Türkiye
Mohamed Ahmed - Mansoura University, Egypt
Mousa Attom- American University of Sharjah, U.A.E.
Nicu Bızon - Pitesti University, Romania
Pandian Vasant - Teknology Petronas University, Romania
Rajnalkar Laxman - Gulbarga University, India
Sanaa Al-Delaımy - Mosul University, Iraq
Shadi Aljawarneh - Jordan University of Science and Technology, Jordan
Shynar Baımaganbetova - Nazarbayev University, Kazakhstan
Svetlana Khan - Almaty University of Power Engineering and Telecommunications, Kazakhstan
Yiyang Chen - Soochow University (CN), China
Zairi Ismael Rizman - MARA University of Technology, Malaysia
Zipporah Pewat Duguryil - Federal College of Education, Nigeria

ORGANIZING COMMITTEE

Aynur Aliyeva - Institute of Dendrology of Anas, Azerbaijan
Besnik Hajdari - University "isa Boletini" Mitrovica, Kosovo
Cemil Aydogdu - Hacettepe University, Türkiye
Danielle Gonçalves de Oliveira Prado-Federal Technological University of Paraná, Brazil
Elman Iskender - Central Botanical Garden of Anas, Azerbaijan
Grzegorz Woroniak,- Bialystok University of Technology, Poland
Halil Snopce - South East European University, Macedonia
Ishtar Imad - Uruk University, Iraq
Joanna Piotrowska - Woroniak - Bialystok University of Technology, Poland
Jaya Bishnu Pradhan-Tribhuvan University, Mahendra Ratna Campus, Nepal

Mehmet Özaslan - Gaziantep University, Türkiye
Mohammad Sarwar - Scialert, Dubai, United Arab Emirates
Murat Beytur - Kafkas University, Türkiye
Samire Bagırova - Institute of Dendrology of Anas, Azerbaijan
Shafag Bagirova - Baku State University, Azerbaijan
Suhail Bayati - Hadi University College, Iraq
Zairi Ismael Rizman - MARA University of Technology, Malaysia

Editorial Policies

ISRES Publishing follows the steps below in the procedings book publishing process.
In the first stage, the papers sent to the conferences organized by ISRES are subject to editorial oversight. In the second stage, the papers that pass the first step are reviewed by at least two international field experts in the conference committee in terms of suitability for the content and subject area. In the third stage, it is reviewed by at least one member of the organizing committee for the suitability of references. In the fourth step, the language editor reviews the language for clarity.

Review Process

Abstracts and full-text reports uploaded to the conference system undergo a review procedure. Abstracts will be evaluated on the basis of abstracts/proposals. The conference system allows the full text to be sent if the abstract is accepted. Participants must wait for the evaluation results after uploading their article abstracts to the conference system. If their abstracts are accepted, they can upload their full texts to the conference system. The full texts are then sent to at least two reviewers for review. The conference has a double-blind peer-review process. Any paper submitted for the conference is reviewed by at least two international reviewers with expertise in the relevant subject area. Based on the reviewers' comments, papers are accepted, rejected or accepted with revision. If the comments are not addressed well in the improved paper, then the paper is sent back to the authors to make further revisions. The accepted papers are formatted by the conference for publication in the proceedings.

Aims & Scope

In the 21st century, developments in science and technology have led to significant changes in the field of engineering. Creativity and design skills are at the center of studies in the field of engineering today. The main focus of this conference is original studies in the field of engineering. In addition, technology and basic science studies that are directly or indirectly related to engineering are also accepted at the conference.

The aim of the conference is to bring together researchers and administrators from different countries, and to discuss theoretical and practical issues in all fields of Engineering.

Articles: 1- 99

CONTENTS

1- Recycling of Ceramic Tile Waste in the Formulation of Self-Compacting Concrete/Pages: 1-11
Rabehi Bahia, Ghernouti Youcef, Mansour Sabria Malika, Boumchedda Khaled

2- Electromagnetic Interference (EMI) in Variable-Speed AC Electric Drives: Mechanisms and Solutions/Pages: 12-19
Houcine Miloudi, Mohamed Miloudi, Mohammed Hamza Bermaki, Kheira Mendaz, Abdelkader Gourbi, Abdelber Bendaoud

3- Stock Price Forecasting Model Using Short Cross Association of Logical Fuzzy Relations in Fuzzy Time Series/Pages: 20-29
Fitri Cahyani, Akhmad Sultoni, Chyntia Meininda Anjanni

4- Numerical Modeling Creep of Two Piles Under Constant Static Loading Using ANSYS/Pages: 30-39
Ghouilem Kamel, Belmihoub Hacene

5- Sliding Neural Artificial Controller of Induction Motor Combined with NPC Five Level Inverter/Pages: 40-46
Mendaz Kheira, Miloudi Houcine, Khadraoua Narimene

6- Development of High-Frequency Power Source Utilizing Electronic Ballast by Employing a Half-Bridge Inverter for Water Purification/Pages: 47-55
Aicha Aissa-Bokhtache, Maamar Latroch, Taieb Bessaad, Alla Eddine Toubal-Maamar, Lemya Djafer, Amina Merini

7- Robust Nonlinear Control of a 3×2 Stacked Multicellular Inverter Using Neural Network-Based Regulation/Pages: 56-68
Salah Hanafi, Mohammed Karim Fellah, Youcef Djeriri, Mohamed Fouad Benkhoris, Abdelhakim Saim, Djamel Ziane, Patrice Wira

8- Development of a Relation Model for Damage Categorization/Pages: 69-80
Akkouche Karim, Khelil Nacim, Nekmouche Aghiles, Kahil Amar, Hamizi Mohand, Bouzid Leyla, Atlaoui Djamel

9- Investigation of Conducted Electromagnetic Disturbances in Power Electronics: A Case Study on DC/DC Choppers/Pages: 81-89
Mohammed Elamine Lahlaci, Mohamed Miloudi, Houcine Miloudi, Mohammed Hamza Bermaki, Kheira Mendaz, Abdelkader Gourbi

10- Fire Risk Simulation of Photovoltaic Panels Installed in Green Buildings/Pages: 90-101
Miloua Hadj, Hassan Sandous, Miloua Farid

11- Development and Optimization of a Mathematical Model for Predicting Tensile Strength in Friction Stir Welded Joints of 6082-T6 Aluminum Alloy/Pages: 102-108
Ben Messaoud Mohammed Abdelghani, Cherief Mohammed Nadhir Djamel Eddine, Miloudi Abdelkader, Belaribi Amina

12- Study of the Thermomechanical Properties of Bimaterials (Metal/Ceramic) /Pages: 109-114
Liamani Samira, Ghermaoui Ilas Mohamed Amine

13- Numerical Analysis of Weld Spot Spacing Effects on Shear Tensile Behavior of TRIP 800 Steel/Pages: 115-120
Cherfi Mohamed, Reffas Sid Ahmad, Sahli Abderahmane, Moulgada Abdelmajid, Ghermaoui Mohammed Ilyes

14- Performance Improvement of Predictive Direct Power Control of a Unified Power Quality Conditioner/Pages: 121-134
Noureddine Khenfar, Abdelhafid Semmah

15- Experimental Study of a Cylindrical Electrostatic Precipitator with Real-Time Monitoring Applied to Simulated Smoke/Pages: 135-142
Miloua Farid, Redjala Majda, Miloua Hadj, Rezoug Mohammed

16- Aeolian Sands in Self-Consolidating Mortar Formulations: Study of the Mechanical Impacts/Pages: 143-150
Nacim Khelil, Said Boukais, Karim Akkouche, Amar Kahil, Djamal Atlaoui, Randa Makkeb

17- On LDPC Codes and Their Construction/Pages: 151-158
Mohammed Amine Tehami, Malika Tehami, Boucif Beddad, Ahmed Hadji

18- Magnetic, Structural and Morphological Properties of Mechanically Alloyed FeSi and $FeSiO_2$ Nanocomposites/Pages: 159-165
Abderrahmane Younes, Rachid Amraoui, Abderahim Abada, Djilali Allou

19- Optimizing Cost and Performance of Hybrid Photovoltaic-Diesel Systems for Off-Grid Energy Solutions/Pages: 166-171
Samir Hadjeri, Halima Boubekeur, Salah Hanafi, Mokhtaria Jbilou, Sid Ahmed Zidi, Rihab Belhabri

20- EOQ Based Inventory Optimization with Partial Backordering and Demand Uncertainty in Manufacturing/Pages: 172-179
Chyntia Meininda Anjanni, Fitri Cahyani, Akhmad Sultoni

21- Potential Use of Recycled Brick and Demolition Concrete Aggregates in the Self-Compacting Concrete/Pages: 180-188
Ghernouti Youcef, Rabehi Bahia, Mansour Sabria Malika

22- Experimental Analysis of the Punching Shear Behavior of Concrete Slabs Reinforced with Metal and Polypropylene Fibers/Pages: 189-199
Atlaoui Djamal, Bouafia Youcef, Khelil Nacim, Akkouche Karim, Aliche Amar

23- Probabilistic Fracture Mechanics Analysis of Crack Propagation in Composites Under Tensile Loading/Pages: 200-209
Sid Ahmed Reffas, Belaid Mechab, Mohamed Cherfi

24- Magnetic and Structural Behavior of Nanocrystalline Iron-Silicon and Iron-Tin Produced via Mechanical Milling/Pages:210-216
Abderahim Abada, Abderrahmane Younes, Rachid Amraoui, Djilali Allou

25- Development and Characterization of Epoxy-Based Laminated Composites: Experimental Characterization and Numerical Simulation/Pages: 217-225

Ghermaoui Ilias Mohammed Amine, Ezzine Mohammed Chams Eddine, Mokhtari Mohammed, Cherief Mohammed Nadhir Djamel Eddine, Cherfi Mohamed, Sahli Abderrahmane

26- Computational Materials Design: Tuning Optoelectronic Response in GaxIn1-xBiyP1-y Alloys via Structural Matching to InP/Pages: 226-243
Malika Tehami, Miloud Benchehima, Hamza Abid

27- Swarm Intelligence-Based Energy Optimization for UAV Mission Efficiency/Pages: 244-256
Mustafa Cosar

28- Study and Design of a Plasma Reactor Using a Porous Dielectric Barrier/Pages: 257-263
Fatha Tounsi, Rabah Ouiddir, Houcine Miloudi, Mohamed Miloudi, Abdelber Bendaoud

29- Effect of the Strain Rate and Temperature on the Shape Memory Behavior of PMMA/Pages: 264-275
Cherief Mohammed Nadhir Djamel Eddine, Ghermaoui Ilias Mohammed Amine

30- Deterministic Assessment of the Seismic Behavior of Cylindrical Steel Storage Tanks: A Methodological Framework Based on the New Algerian Seismic Code/Pages: 276-282
Amar Aliche, Ourdia Ider, Mouloud Guemmoun, Hocine Hammoum, Karima Bouzelha, Djamel Atllaoui

31- Investigation of the Possibility of Introducing Dispersed Boron Carbide Particles into the Melt of Austenitic Steel 12X18H10T During Centrifugal Casting/Pages: 283-288
Abdrakhman Naizabekov, Sergey Kuzmin, Ilya Chumanov, Andrey Anikeev, Vadim Sedukhin, Evgeniy Panin, Andrey Marukov

32- Modelling of Distribution of Ultradisperse Particles of Titanium, Tungsten and Zirconium Carbide During Centrifugal Casting/Pages: 289-295
Ilya Chumanov, Andrey Anikeev, Abdrakhman Naizabekov, Sergey Lezhnev, Pavel Tsyba, Dmitry Kuis

33- An AI-Based Method for Sorting and Separation of Semiconductor Waste: An Environmentally Friendly Method for Implementing a Circular Economy in the Semiconductor Industry/Pages: 296-306
Gharib Hadj

34- Studying the Temperature Effect on Lengthwise Fracture of Inhomogeneous Beam Subjected to Impact Loading/Pages: 307-315
Victor Rizov

35- Effects of Elastic Deformation on the Corrosion of 316l in 3.5% Nacl/Pages: 316-322
Allou Djilali, Amraoui Rachid, Djemmah Sarra, Benmohamed Manel, Younes Abderahman, Abada Abderahim

36- Best-Fitting Ellipsoid and Surface Disturbance Adjustment of GNSS-Derived Sea Surface Heights/Pages: 323-329
Konstantinos Kalimeris, Sotiris Lycourghiotis

37- Computer Modeling and Investigation of the Rolling Process of Thick Strips in Relief Rolls Under Conditions of Kinematic Asymmetric Interaction/Pages: 330-336
Yevgeniy Panin, Valery Chigirinsky

38- Eco-Friendly Recovery Method for Manufacturing Flexible Paver’s Tile Construction from Waste Plastics/Pages: 337-348

Roua'a K. Al-Ojar, Yonis Ahmed Ismael, Akram. W. Nayyef, Ghadeer Amer Muhamed, Fawzi Habeeb Jabrail

39- Adaptive Hybrid Reduction for Facial Recognition/Pages: 349-353
Djamel Berrabah, Yacine Gafour

40- Enhancing OFDM Performance Using Wavelet Transform Techniques in Wireless Systems/Pages: 354-360
Zohra Zerdoumi, Malika Fodil, Fadila Benmeddour, Nacerddine Bentaleb

41- A Multi-Criteria Weighted Clustering Protocol for Energy-Efficient Overlay Wireless Sensor Networks/Pages: 361-373
Taieb Brahim Mohammed, Abbad Houda, Abbad Leila

42- Speed Control of the Pentaphase Asynchronous Machine: Comparative Study Between Vector Control with Conventional PI and Fuzzy PI/Pages: 374-381
Fodil Malika, Zerdoumi Zohra, Zemouri Nahed, Benmeddour Fadila

43- Research Trends in the Heat Transfer Simulation of Al_2O_3/AlN Granular Composites for Thermal Interface Materials/Pages: 382-392
Senlau Sudarminto

44- Influence of Boundary Conditions of a Contact Problem on the Stress Distribution in a Semi-Infinite Space/Pages: 393-400
Valery Chigirinsky, Sergey Lezhnev, Sergey Kuzmin, Abdrakhman Naizabekov, Yevgeniy Panin

45- Impact of Printing Orientation on the Mechanical Properties of Selectively Laser Sintered PA12/Pages: 401-414
Boukhoulda Farouk Benallel, Djellal Kouider, Bendine Kouider, Boukhoulda Abdelaziz

46- Performance and Efficiency of Redesign Induction Motor Using Asymmetric Windings/Pages: 415-422
Hussein G. Abdulkareem, Ennam A. Ali

47- Synthesis and Characterization of Biochar and Nano-Biochar Composites Derived from Biomass (Colutea cilicica) for the Removal of Cationic Dyes from Aqueous Solutions/Pages: 423-432
Erol Pehlivan, Busra Ozkok

48- Factors Affecting the Sliding Stability of a Gravity Retaining Wall/Pages: 433-443
Karim Baziz, Amar Kahil

49- A Decade of Research on Biomass Materials in Residential Building Construction: A Bibliometric Analysis/Pages: 444-458
Yudith Arunika C. Wella

50- Application of Ultrasonic Spectral Analysis for the Study of Steels/Pages: 459-469
Yonka Ivanova, Todor Partalin, Boris Velev

51- Evaluation of Robust Controllers in Photovoltaic Systems: A Comparative Analysis/Pages: 470-479
Zerroug Nadjat, Behih Khalissa, Bouchama Ziyad

52- Nano Ideal Semi Alpha Generalized Continuous and Irresolute Mappings in Nano Ideal Topological Spaces/Pages: 480-501
Raja Mohammad Latif

53- Synthesis of Stoichiometric Cordierite Ceramics from Chemically Modified Kaolin by a Controlled Acid Leaching/Pages: 502-511
Boumchedda Khaled, Djafar Rabah, Rabehi Bahia, Bououdina Mohamed

54- AI-Driven Molecular Design: Synergizing Deep Generative Models with Evolutionary Optimization/Pages: 512-524
Abbad Houda, Taieb Brahim Mohammed, Oulladji Latefa, Abbad Leila

55- Performance of LTO/rGO Composite Anode in Lithium Ion Battery/Pages: 525-529
Meltem Cayirli, Busra Yilmaz-Donmez, Mustafa Anik

56- Effect of Friction Stir Welding Parameters on the Evolution of the Welding Temperature/Pages: 530-537
Belaribi Amina, Miloudi Abdelkader, Chekalil Ismail, Benmessaoud Mohammed Abdelghani

57- From Data to Emotion: A Multimodal Approach to Real-Time Emotion-Aware Marketing/Pages: 538-550
Alper Bozkurt, Furkan Ekici, Hatice Yetiskul, Hüseyin Oktay Altun, Emre Fisne

58- Effect of Fiber Orientation on Tensile Property of Basalt Reinforced Epoxy Composite/Pages: 551-558
Yusuf Sahin, Selahettin Selek

59- Punch Geometry and Burr Height on Blanking Process for Garbage Container Wheel Parts/Pages: 559-566
Ilyas Uygur, Halit Kocasungur, Sitki Akincioglu, Hasan Oktem

60- Effect of Cryogenic Treatment on the Microstructure of AlSi10Mg Alloy Produced by Selective Laser Melting/Pages: 567-574
Pelin Sezer, Gamze Ertas, Hakan Gasan

61- Investigation of Borophene Synthesized via a Scalable Approach as an Anode Material for Lithium-Ion Batteries/Pages: 575-579
Suleyman Can, Cihan Kuru

62- Geological and Geotechnical Perspectives on Seismic Hazard Assessment of Landslides/Pages: 580-589
Liliana-Irina Stoian, Elena Aurelia Tudor, Antonio Ulmeanu, Avram Ovidiu, Ioan Scutelnicu, Adrian Tataru

63- Compact Single-Switch Reconfigurable Patch Antenna with Multi-Band Operation for Wireless Systems/Pages: 590-596
Frouda Nour El Houda, Berkat Abdellatif, Azzaz Rahmani Salima

64- Influence of Site Class on the Dynamic Response of Regular Buildings Considering Soil-Structure Interaction/Pages: 597-609
Mohamadi Saddika, Boumaiza Malika, Berzane Sid-Ali, Bouamrirene Abdelhafid

65- Bearing Fault Detection and Severity Classification Using a Two-Step Neural Network Model/Pages: 610-616
Smail Haroun

66- RLS Filter Optimization for Non-Invasive Fetal Electrocardiogram Extraction Using the PSO Algorithm/Pages: 617-624
Mourad Benziane, Mohamed Rezki, Issam Griche, Kamel Saoudi, Abderrazak Arabi

67- Performance Evaluation of the Andasol-1 Solar Power Plant in Algerian Climatic Conditions/Pages: 625-629
Hicham Kadraoui

68- Engineering Next Generation Hole Transport Layers for Lead Free Perovskite Solar Cells Exceeding 23% Power Conversion Efficiency/Pages: 630-640
Souheyla Mamoun, Abdelkrim Elhasnaine Merad, Feryel Saidi

69- Energy Audit of a Community Center/Pages: 641-654
Slav Valchev, Nikola Valchanov

70- Generation Algorithms of Invertible Linear and Nonlinear Finite Automata with Memory/Pages: 655-666
Gulmira Shakhmetova, Khasenov Altay, Zhanat Saukhanova, Altynbek Sharipbay, Alibek Barlybayev, Raykul Sayat

71- Investigation of Corrosion Properties of Lead-Free Solder Alloys in 3.5% NaCl Solution/Pages: 667-671
Resat Can Ozden

72- Evaluation of Nonlinear Fracture Quantities in Lime-Pumice Mixtures/Pages: 672-681
Erkin Eren, Ragip Ince

73- Electrical Resistivity Tomography as a Tool for Geological-Engineering Assessment of the Benkovski-2 Tailings Storage Facility/Pages: 682-687
Maya Tomova, Atanas Kisyov

74- Voltage Total Harmonic Distortion Reduction in Multi-level Single-Phase Inverters using the SHE-PWM Technique with a TLBO Algorithm/Pages: 688-698
Smail Toufik, Boulouma Sabri, Seddaoui Naoual, Rahmani Hachemi

75- Measurement and Transmission of Process Parameters in GSM and IoT Network/Pages: 699-711
Goce Stefanov, Marija Cekerovska, Elena Zafirov, Todor Cekerovski

76- Experimental Development and Performance Analysis of a Parabolic Solar Concentrator for Desalination and Treatment of Complex Wastewaters/Pages: 712-720
Souad Khedache, Said Makhlouf, Gilles Lefebre, Bilel Seddi, Abdellah Haddadi

77- Factors Affecting Corrosion of Steel in Pipe Lines/Pages: 721-730
Haddad Abdelouahab, Zerroug Nadjat

78- Performance of NMC622 Cathode - LTO Anode Full Cell Lithium Ion Battery/Pages: 731-736
Meltem Cayirli, Ersu Lokcu, Resat Can Ozden, Mustafa Anik

79- Power System Stability Including Wind Farm with Statcom Based Pi Fractional Controller/Pages: 737-747
Issam Griche, Kamel Saoudi, Mourad Benziane, Abderrazak Arabi

80- LogSense: A Comparative Anomaly Detection Platform on Web Server Access Logs Using Multiple Algorithms/Pages: 748-756
Arda Ata Turkoglu

81- Enhancing Wireless Sensor Networks Performance by Integrating Particle Swarm Optimization with Intelligent Clustering Techniques/Pages: 757-770
Rafa Sami Braiber, Mussab Riyadh

82- B-Smart: A Robust Reputation Based Blockchain Scheme in Wireless Sensor Networks/Pages: 771-790
Farah Khedim, Nabila Labraoui, Ado Adamou Abba-Ari

83- Carbon Fabric-Reinforced Polymeric Composites Produced by Hand Lay-Up and Investigation of the Tensile Behavior/Pages: 791-797
Ozhan Sirin, Yusuf Sahin, Emir Can Omer

84- Dynamic Analysis of Vertical and Horizontal Irregular Reinforced Concrete Structure Considering Soil Structure Interaction/Pages: 798-806
Boumaiza Malika, Mohamadi Saddika, Sellam Mustapha, Tiliouine Wail

85- Effect of Variable Mass Density on Lengthwise Fracture in Functionally Graded Beams Moving in Horizontal Direction/Pages: 807-815
Victor Rizov

86- Retrofit Kit Design That Converts Industrial Locks into Electromechanical Smart Locks/Pages: 816-823
Selahattin Mert Aydin, Engin Gunes

87- Assessing Translation Quality in Large Language Models and Machine Translation Systems: The BLEU Metric and Language Pair Effects/Pages: 824-829
Philipp Rosenberger, Natallia Kolchanka

88- A Multi-Criteria Decision-Making Model for Performance Evaluation Based on PSI–PF-COBRA/Pages: 830-841
Canan Sen, Kubra Onder, Halil Sen

89- Evaluation of Composite Method Repair of a Cracked Plate/Pages: 842-848
Aida Achour, Belabbes Bachir Bouidjra, Hafida Driz, Sadek Bahar

90- A Bio-Inspired Path to Fake Profile Detection: Revisiting Linear Models through Grasshopper Optimization/Pages: 849-860
Nadir Mahammed, Imene Saidi, Mahmoud Fahsi, Souad Bennabi

91- Deep Learning-Based Crop Recommendation Using Soil and Environmental Parameters/Pages: 861-870
Fatma Ozge Ozkok

92- Development of a Computational Interface for the Thermal Behavior Analysis of Metallic Plates Using the Finite Volume Method/Pages: 871-880
Imene Bennia, Narimen Hamidi

93- Fabrication Process of Nano and Optoelectronic Devices Based on Nitrided Gaas: XPS Analysis and Electrical Measurements/Pages: 881-890
Arslane Hatem Kacha, Ahmed Hichem Yahi, Boudali Akkal, Zineb Benamara

94- A Novel Triple-Band Band-Pass Metamaterial Filter based on Modified Square Split Ring Resonators for Microwave Applications: Design and Analysis/Pages: 891-898
Zoubir Mahdjoub, Mohammed Berka

95- Analysis of the Aerodynamic Characteristics of Wing Profiles/Pages: 899-904
Brahim Rostane

96- Study of the Effect of InP (100) Nitridation Time by XPS Analysis and Electrical Characterisation/Pages: 905-911
Talbi Abbassia, Benamara Mekki Abdelkader, Chami Nadir, Zineb Benamara

97- Smart Control of Vibrations in Functionally Graded Porous Wind Turbine Blades via Piezoelectric Materials/Pages: 912-920
Khalid El Harti, Mohamed Touil, Rachid Saadani, Rahmoune Miloud

98- Elaboration and Characterization of Transparent Conductive Oxide Thin Films and the Effect of Doping/Pages: 921-927
Ahmed Hichem Yahi, Arslane Hatem Kacha

99- C-V and G-V Characteristics of Nitridated GaAs (100) Structures as Function of Frequency-Effect of Series Resistance/Pages: 928-934
Benamara Mekki Abdelkader, Talbi Abbassia, Toumi Hayet, Benamara Zineb, Benamara Fatima Yasmine Maroua

The Eurasia Proceedings of Science, Technology, Engineering & Mathematics (EPSTEM)
ISSN: 2602-3199

The Eurasia Proceedings of Science, Technology, Engineering and Mathematics (EPSTEM), 2025

Volume 38, Pages 1-11

IConTES 2025: International Conference on Technology, Engineering and Science

Recycling of Ceramic Tile Waste in the Formulation of Self-Compacting Concrete

Rabehi Bahia
University of Boumerdes

Ghernouti Youcef
University of Boumerdes

Mansour Sabria Malika
University of Boumerdes

Boumchedda Khaled
University of Boumerdes

Abstract: Aggregates represent 75% of concrete volume; however, the exhaustion of natural aggregate deposits and the difficulties in opening new quarries require a new sources and studying the possibility of substituting natural aggregates with waste. This study investigates the potential use of recycled ceramic tile waste as a substitute for natural coarse aggregates in self-compacting concrete (SCC). Several SCC mixtures were formulated with varying replacement levels of natural aggregates by ceramic tiles waste aggregates CTW (25%, 50%, 75%, and 100%). The fresh properties were evaluated using slump flow, sieve stability, and L-box tests, while the hardened properties were assessed through Ultrasonic Pulse Velocity, compressive and flexural strength tests. The results demonstrate the technical feasibility of incorporating ceramic tile waste as recycled aggregates in SCC. Up to 75% substitution, the mixtures maintained satisfactory fresh and mechanical performance. This research provides valuable experimental data supporting the valorization of ceramic tile waste in sustainable concrete production, contributing to environmental conservation and resource.

Keywords: Self-compacting concrete, Recycled aggregates, Valorization, Environment, Ceramic tile waste

Introduction

Construction and public works require about 560 million tons of aggregates and similar materials each year. Consequently, their extraction from rivers or from massive mountain rocks has a significant impact on the environment. The ecological push requires us to take the greatest possible care of the environment, either by avoiding the use of natural materials or by eliminating by-products and waste, the often-unsightly deposits of which can lead to pollution of the natural environment. The use of recycled aggregates in construction offers several advantages at the environmental, human, technological, and economic levels, which are of increasing interest to industrial companies.

In many countries, regulations and procedures on reusing waste materials in construction applications have been established, and many countries have begun transforming constructional wastes into RA (Ismail & Ramli, 2013; Park & Noguchi, 2013; European Parliament, 2008). Many authors from different countries study the use of recycled materials in civil engineering problem: (Levy & Helene, 2004; Poon et al, 2007) in their research papers marked an aggregate which is got from demolished masonry and concrete structures as potentially good for use in new concrete.

- This is an Open Access article distributed under the terms of the Creative Commons Attribution-Noncommercial 4.0 Unported License, permitting all non-commercial use, distribution, and reproduction in any medium, provided the original work is properly cited.

- Selection and peer-review under responsibility of the Organizing Committee of the Conference

© 2025 Published by ISRES Publishing: www.isres.org

Rabehi et al., (2024) study the development of eco-materials based on recycled material by recovery of dam sediment, and the incorporation of lightweight aggregates. The obtained results show that the blocks made from 50% lightweight aggregates and 10% stabilizers (cement) have the best performances.

There are quite also a number of applications of using recycled glass in the construction industry all over the world. The application includes using glass in asphalt concrete, normal concrete, back-filling, sub-base, tiles, masonry blocks, paving blocks another decorative purpose (Tabsh & Abdelfalah, 2009; Dhir et al., 2001; Sagoe-Crentsil et al., 2001; Meyer, 1999; Robert & Kirby, 2001).

Duan & Poon, (2014) presents the experimental results of a study on comparing the difference in properties of recycled aggregates (RAs) with varying amounts of old adhered mortar obtained from different sources and evaluating the influence of the different RAs on the mechanical and durability properties of recycled aggregate concrete (RAC). The results show that the performance of RAs from different sources varied greatly and RA of good quality can be used to produce high strength concrete with hardened properties comparable to those of the corresponding natural aggregate concrete (NAC).

Several research have studied the recovery of recycled materials in self-compacting concrete and in construction works, (Bignozzi & Sandrolini, 2006) study the mechanical and microstructural behavior of self-compacting concrete containing different amounts of untreated tire waste. A comparison of the obtained compressive strengths with literature data confirms that self-compacting technology helps binding rubber phases.

Dilbas et al., (2014) have realized an experimental studies for determining the mechanical and the physical properties of the recycled aggregate concrete (RAC) with and without silica fume (SF), inspired by the Urban Renewal Law which regulates circumstance of existing structures in Turkey. They conclude that the proportion of 30% RA in concrete mixtures is proposed as the optimum ratio and found that 5% SF content in the RAC is more convenient to improve the low properties of RAC (i.e. compressive strength).

This study explores the feasibility of using recycled aggregates derived from ceramic tile waste in self-compacting concrete. Several mix designs were evaluated, incorporating different replacement levels of natural aggregates with recycled aggregates at 25%, 50%, 75%, and 100%.

Experimental program

Materials

Binder

All self-compacting concrete mixtures investigated in this study were prepared with ordinary cement (OC) equivalent to CEM II/B- 42.5 from the M'silla cement plant Algeria, according with NA 442, EN 197-1 and NF P 15-301/94 standard. Its specific gravity is 3.1 g/cm^3 and its specific surface area Blaine SSB is 3168 cm^2/g. Limestone powder were used as addition materials in the mix proportions at the rate of 10%, its characterized by high chemical purity, their specific surface area is about 5350cm^2/g and its specific gravity is 2.66 g/cm3. The chemical composition of the cement and the fine materials are listed in Table 1.

Table 1. Chemical composition of cement and limestone powder

Elements (%)	SiO_2	AL_2O_3	Fe_2O_3	CaO	MgO	K_2O	Na_2O	SO_3	Cl	LOI
Cement	15.80	4.15	2.31	61.90	2.39	0.69	0.06	2.80	0.023	9.59
Limestone	0.04	0.03	0.02	56.03	0.17	0.02	0.05	0.08	0.03	43

Aggregates

The fine aggregates used in this study was a mixture of 41% natural dune sand (DS) and 59% crushed sand (CS) with a fineness modulus of 1.03 and 3.53, respectively. Two types of coarse aggregates were employed in the concrete mixtures: natural aggregates (NA) and recycled aggregates (RA) derived from ceramic tile waste. Two class of natural coarse aggregates were used: Crushed limestone gravel with particle size ranges of 3-8 mm and 8-15 mm, as shown in Figure 2. The recycled coarse aggregates used were produced by crushing ceramic tiles waste into two corresponding size fraction 3–8 mm and 8–15 mm (see Figure 2). The physical properties of all

aggregates used in this study are summarized in Table 2, and their particle size distributions are illustrated in Figure 3.



a) NA 3-8 mm b) NA 8-15mm

Figure 1. Natural coarse aggregates used (NA)

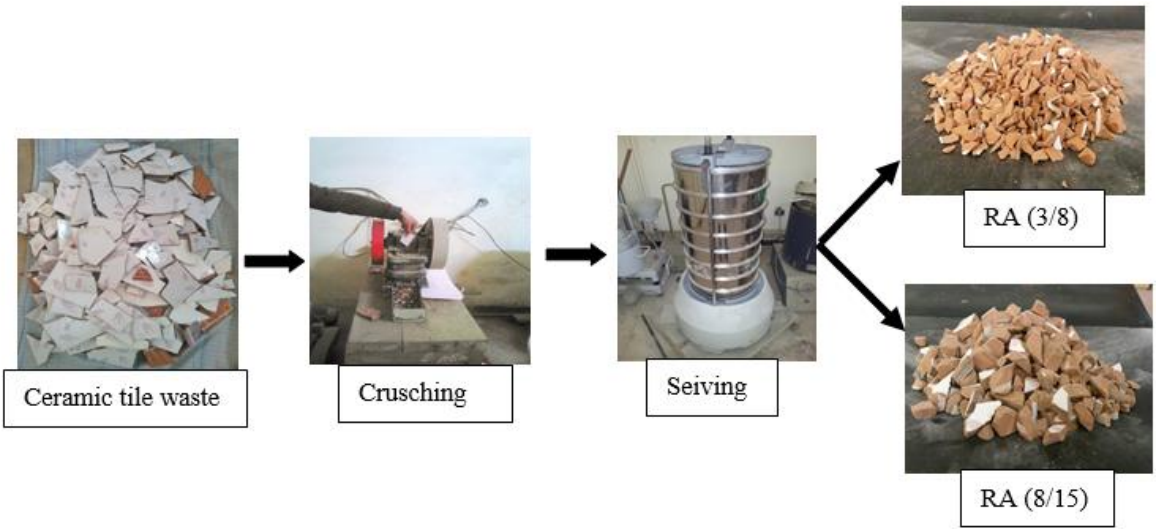


Figure 2. Preparation of recycled aggregates (RA) obtained from ceramic tiles waste

Table 3. Physical properties of coarse aggregates

Natural coarse aggregates (3/8 and 8/15)		Recycled ceramic tile coarse aggregates (3/8 and 8/15)
Apparent density, (g/cm^3)	1.41	1.24
Specific gravity, (g/cm^3)	2.66	2.3
Los Angeles (%)	25.04	77
Micro-Deval (%)	26.64	3.4

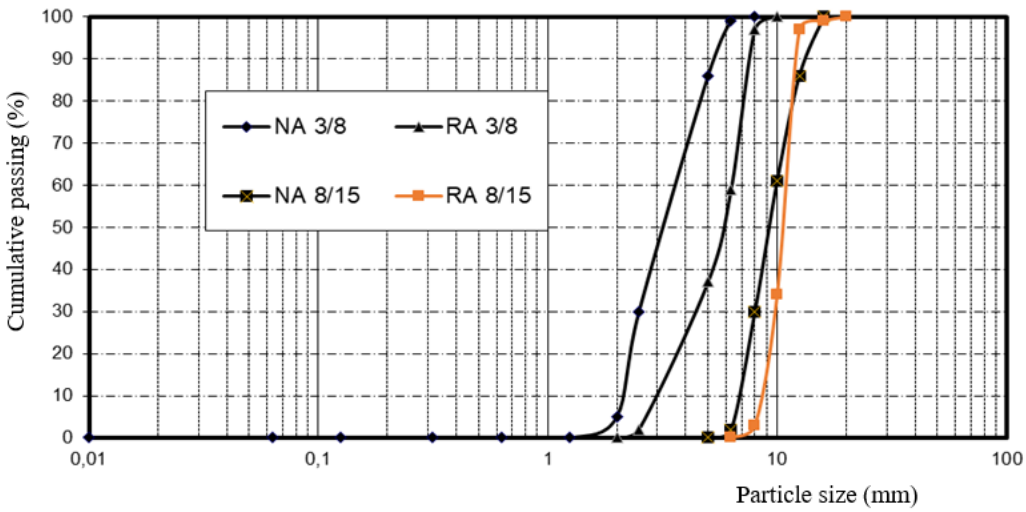


Figure 3. Particle size distribution of all coarse aggregates

Superplasticizer

To ensure the required workability of the self-compacting concrete (SCC) mixes, a high-range water-reducing superplasticizer (SP) was used: Sika ViscoCrete Tempo 12, in accordance with the NF EN 934-2 standard. This new-generation superplasticizer is based on acrylic copolymer technology. It has a solid content of 31% and a specific gravity of 1.06.

Self-compacting Concrete Mixes

A total of five self-compacting concrete (SCC) mixes were prepared using the Japanese mix design method proposed by (Okamura and Ozawa, 1995). The mix proportions are detailed in Table 4. One reference mix incorporating only natural coarse aggregates (SCC) was produced, along with four additional mixes in which natural coarse aggregates (3/8 mm and 8/15 mm) were partially or fully replaced with recycled ceramic tile waste aggregates at replacement levels of 25%, 50%, 75%, and 100%. These mixes are referred to as CTW25, CTW50, CTW75, and CTW100, respectively. All SCC mixes were designed with a constant cement content of 430 kg/m³ and a water-to-binder ratio (w/b) of 0.38. The fine-to-coarse aggregate ratio was maintained at approximately 1.0.

Table 4. Mix proportions of self-compacting concrete in kg/m^3

Mixtures	SCC	CTW25	CTW50	CTW75	CTW100
Cement	430				
Water	180				
Limestone	43				
Dune sand (DS)	284				
Crushed sand (CS)	582				
NA 3/8	440	330	220	110	0
NA 8/15	444	333	222	111	0
RA 3/8	0	91	182	273	364
RA 3/8	0	91	182	273	364
SP	7				

Casting and Curing of Test Specimens

The same mixing procedure was used for all concrete mixtures. Fresh concrete tests were carried out to evaluate slump flow diameter, segregation resistance, and the L-box ratio. For each mixture, three prism specimens (7× 7×28) cm and three cylindrical specimens (11×22) cm were cast. All specimens were demolded after 24 hours and then stored in a curing room maintained at 90% relative humidity and a temperature of 20 ± 2 °C until the day of testing, in order to determine ultrasonic pulse velocity, as well as the flexural and compressive strengths.



Figure 4. Casting and curing test specimens

Test Results and Discussion

Fresh Concrete Properties

A series of tests were performed on fresh concrete to evaluate the influence of ceramic tile waste aggregates on the workability of self-compacting concrete (SCC). Flowability was assessed using the slump flow test, passing ability was evaluated using the L-box test, and segregation resistance was measured through the sieve stability

test, in accordance with the specifications and guidelines for SCC established by the European Federation of National Associations Representing Concrete (EFNARC, 2005).

The slump flow test was used to evaluate the free deformability and flowability of SCC without any external obstructions. In this test, concrete was poured into a standard slump cone without compaction, and the slump flow value was determined as the average diameter of the spread, measured in two perpendicular directions after lifting the cone. (Figure 5 (a)).

The L-box test was conducted to measure the passing ability of SCC, specifically its capacity to flow through confined spaces and around reinforcement without segregation or blockage. Fresh concrete was placed in the vertical section of an L-shaped apparatus and allowed to flow into the horizontal section by opening a sliding gate. The result is expressed as the H_2/H_1 ratio, where H_1 is the height of concrete behind the gate and H_2 is the height at the end of the horizontal section (Figure 5 (b)).

Fanaly, the sieve stability test was carried out to evaluate the segregation resistance of SCC. In this test, a fresh concrete sample was placed on a 5 mm sieve and left to rest for a fixed period. The amount of water or fine material that passed through the sieve was measured, providing an indication of the mix's stability and resistance to bleeding or segregation (figure 5 (c)).

The results of slump flow diameter, L-box ratio, and sieve stability for the different concrete mixtures are summarized in Table 5. According to the guidelines established by (EFNARC 2005), SCC must meet specific performance criteria in the fresh state to ensure proper placement and long-term durability. The recommended slump flow diameter generally ranges from 600 mm to 800 mm, depending on the application and flow class. This ensures sufficient flowability without risk of segregation. The L-box passing ability ratio (H_2/H_1) should range from 0.8 to 1.0, indicating that the mix can pass through reinforcement without blockage. For segregation resistance, the sieve stability index should be less than or equal to 15%, ensuring the concrete remains homogeneous. Adhering to these criteria ensures a balanced SCC mix with proper deformability, passing ability, and stability.



a) Slump flow test b) L-Box test c) sieve stability test

Figure 5. Tests on fresh concretes

Table 5 presents the results of fresh state tests performed on the SCC mixtures incorporating varying proportions of recycled ceramic tile aggregates (RA). The obtained results indicate that increasing the RA content leads to a reduction in the slump flow diameter. This behavior can be attributed to the higher porosity of the recycled ceramic aggregates compared to natural ones, which causes greater water absorption during mixing. This results in a reduction of the free water available in the paste, thereby increasing the mixture's viscosity and reducing its flowability.

Table 5. Fresh properties of all mixtures

Mix ID	Slump flow (cm)	L-box ratio (%)	Sieve stability (%)
CC	74	0.95	7.26
CTW25	70	0.89	6.37
CTW50	65	0.86	6.04
CTW75	62	0.83	5.57
CTW100	38	/	/

The decrease in slump flow remains moderate for mixtures containing up to 75% RA, with reductions of approximately 5% (CTW25), 12% (CTW50), and 16% (CTW75) compared to the control mix (CC). All these

mixtures maintain slump flow diameters greater than 60 cm, meeting the EFNARC minimum requirement for SCC, which demonstrates that acceptable flowability was retained despite the use of recycled aggregates. This can be partly attributed to the smooth glazed surface of the ceramic tile aggregates, which may enhance internal lubrication and improve the flow behavior of the mix. However, the mixture with 100% RA (CTW100) exhibited a significant drop in workability, with a slump flow diameter of only 38 cm, well below the minimum requirement of 55 cm (550 mm) for SCC. Consequently, this mix does not qualify as self-compacting concrete and was excluded from the remainder of the study.

The L-box test results further support the observations from the slump flow test. The passing ability decreased slightly with increasing RA content, dropping from 0.95 (CC) to 0.83 (CTW75). Despite this decline, all mixtures up to TW75 remain within the recommended EFNARC range (0.8–1.0), indicating sufficient ability to pass through confined spaces and around reinforcement without blocking. No L-box value was recorded for TW100 due to its insufficient flow.

Regarding segregation resistance, the results of the sieve stability test show that all mixtures demonstrate satisfactory stability, with segregation indices ranging from 5.57% to 7.26%, well below the EFNARC limit of 15%. The low segregation values suggest that the mixes maintained good cohesion, even with increasing amounts of recycled aggregate. This indicates that the replacement of natural aggregates with ceramic tile waste did not adversely affect the stability of the fresh SCC.

In summary, SCC mixtures containing up to 75% recycled ceramic aggregates exhibit acceptable fresh properties, meeting all EFNARC criteria for self-compacting concrete in terms of flowability, passing ability, and segregation resistance. The use of 100% recycled aggregate, however, significantly compromises workability and does not meet SCC standards.

Hardened Concrete Properties

To evaluate the mechanical performance of the hardened concrete, three key tests were conducted: the ultrasonic pulse velocity (UPV) test, the compressive strength test, and the flexural strength test. The UPV test is a non-destructive method used to assess the quality and uniformity of concrete by measuring the time it takes for an ultrasonic pulse to travel through a specimen between a transmitter and a receiver (Figure 6(a)). The velocity of the pulse is affected by the concrete's density and internal structure; higher velocities generally indicate a denser, more homogeneous material, while lower velocities suggest the presence of internal defects, cracks, or increased porosity.

The compressive strength test was performed in accordance with the NF EN 12390-3 standard to determine the axial compressive strength of cylindrical concrete specimens (11× 22) cm. before testing, both ends of each specimen were surface-ground to ensure smooth and parallel bearing surfaces, promoting uniform load distribution during loading (Figure 6(b)).

For the flexural strength test, prismatic specimens (7×7×28) cm were tested using a three-point bending configuration, following the NF EN 12390-5 procedure. Each prism was placed in a flexural testing machine and subjected to an increasing load, until failure occurred (Figure 6(c)).



a) Ultrasonic Pulse Velocity Test



b) Compressive strength test



c) Flexural strength test

Figure 6. Tests on hardened concretes

Ultrasonic Pulse Velocity Test

Figure 7 presents the results of the ultrasonic pulse velocity (UPV) test for the different self-compacting concrete (SCC) mixtures containing various proportions of recycled ceramic tile aggregates (RA) in comparison with control self-compacting concrete. The control mixture (SCC), made entirely with natural aggregates, achieved the highest pulse velocity at approximately 4820 m/s, reflecting excellent internal structure and low porosity. As the replacement rate of natural aggregates (NA) with ceramic tile waste aggregates (RA) increased, a gradual decrease in ultrasonic pulse velocity was observed. The mixture with 25% replacement (CTW25) showed a slight reduction, with a velocity of approximately 4700 m/s. This trend continued with CTW50, which recorded a further decrease to about 4620 m/s. The lowest velocity was observed in CTW75, with a value around 4300 m/s. This decreasing trend can be attributed to the higher porosity and angularity of the recycled ceramic tile aggregates, which lead to a less compact and more heterogeneous internal matrix. These factors reduce the ability of the concrete to transmit ultrasonic waves efficiently.

Despite this reduction, all mixtures maintained a UPV above 4000 m/s, and the first three (SCC, CTW25, CTW50) remained above the 4500 m/s threshold. According to ASTM C597, concrete with ultrasonic pulse velocities:

- Above 4500 m/s is generally classified as “good quality”,
- Between 4000–4500 m/s as “medium quality”,
- Below 3500 m/s may indicate low quality or internal defects.

Therefore, all tested mixtures can be considered acceptable to good quality, even when incorporating up to 75% recycled aggregates. This suggests that ceramic tile waste can be used effectively in SCC without significantly compromising the internal integrity of the concrete.

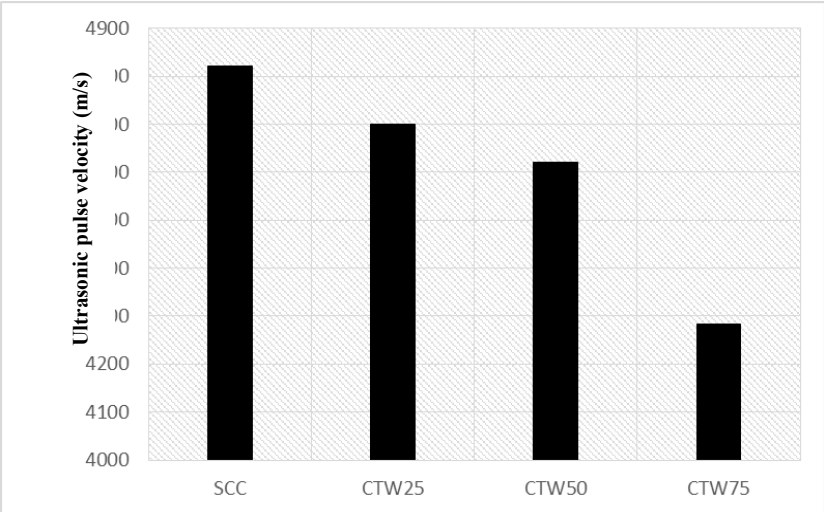


Figure 7. Ultrasonic pulse velocity of all mixtures

Mechanical Strengths

All mechanical test results for compressive and flexural strength at 28 days are presented in Figures 8 and 9, respectively. Additionally, table 6 summarizes the relative reductions in both compressive and flexural strength of self-compacting concrete (SCC) mixtures incorporating recycled ceramic tile aggregates, compared to the control mix made with natural aggregates. This comparison clearly demonstrates the impact of ceramic tile aggregate substitution on the mechanical performance of the concrete.

According to the mechanical test results, the compressive strength at 28 days (Figure 8) decreases progressively with the increasing substitution of natural aggregates by recycled ceramic tile waste. The reduction is approximately proportional to the replacement rate, reaching up to 30% for the concrete containing 75% recycled aggregates (CTW75). A similar trend is observed for the flexural strength (Figure 9). As the percentage of recycled aggregates increases, the flexural strength decreases, with a maximum loss of 17% at the 75% substitution level.

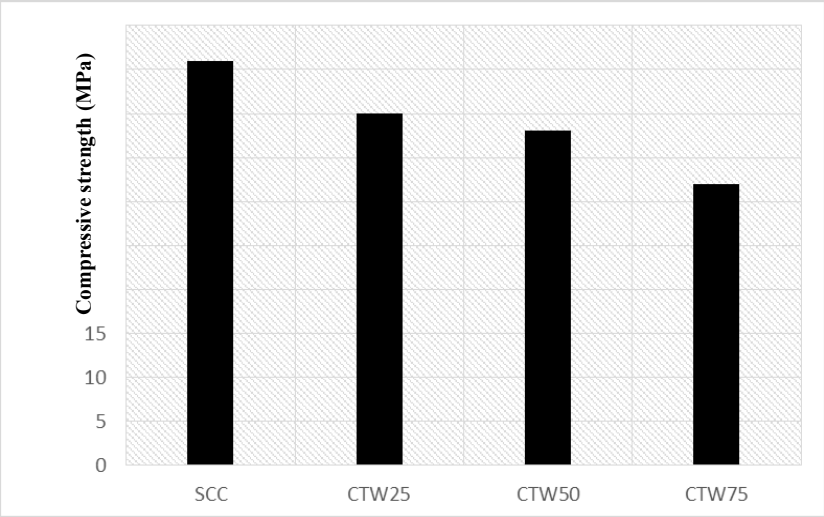


Figure 8. Compressive strength of all mixtures

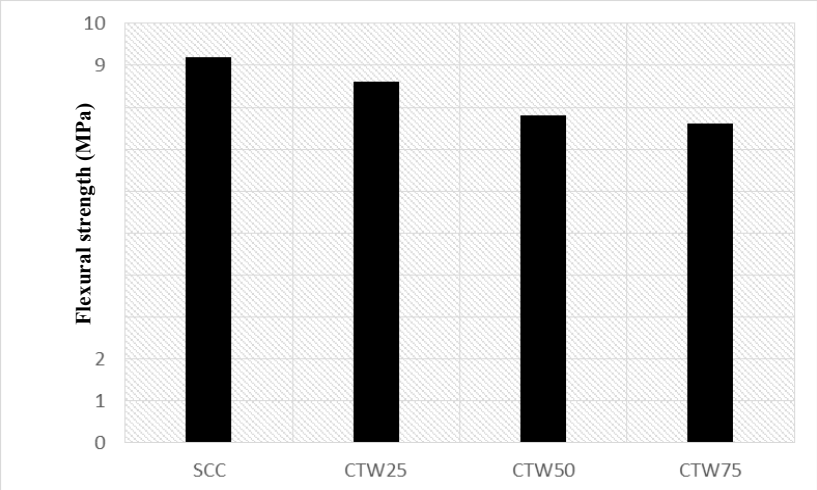


Figure 9. Flexural strength of all mixtures

Table 6. Loss of compressive and flexural strength

Mix ID	Loss on compressive strength (%)	Loss on flexural strength (%)
CC	/	/
CTW25	13	6
CTW50	17	15
CTW75	30	17

These reductions in mechanical performance can be explained by several factors:

- The lower hardness and mechanical strength of recycled ceramic aggregates compared to natural silico-calcareous aggregates.
- The angular and irregular geometry of the ceramic waste aggregates, as shown in Figure 10, contributes to increased porosity in the concrete matrix and reduces its overall compactness.
- The presence of a smooth, vitrified surface on the ceramic aggregates clearly visible in Figure 13, which shows fragments of recycled ceramic tile waste. This glazed layer limits surface roughness and hinders effective bonding with the cement paste, thereby weakening the interfacial transition zone (ITZ).

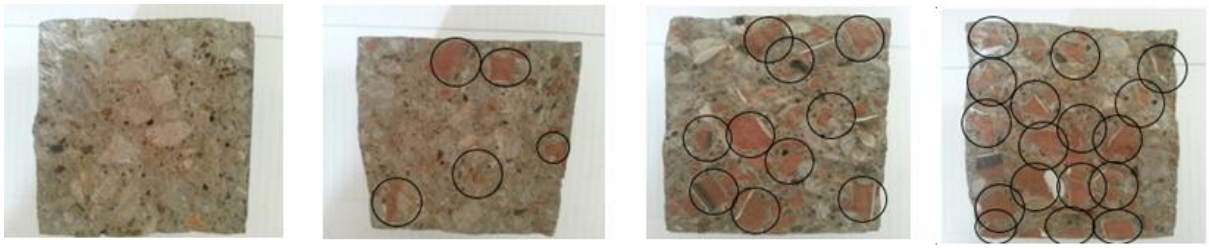
Despite these reductions, the mechanical performance of the concrete remains within acceptable limits for structural applications, especially at substitution levels up to 50%, where strength losses remain relatively moderate.



Figure 10. Angular shape of waste ceramic tile

Visual Observation of Aggregate Distribution in SCC

The four images in Figure 11, show cross-sections of self-compacting concrete (SCC) specimens incorporating recycled ceramic tile waste as a partial replacement for natural aggregates at different levels: 0% (SCC), 25% (CTW25), 50% (CTW50), and 75% (CTW75). The black circles highlight visible recycled ceramic particles.



SCC **CTW25** **CTW50** **CTW75**

Figure 11. Distribution of recycled ceramic tile aggregates in SCC mixtures

The control mixture, containing only natural silico-calcareous aggregates, shows a dense and homogeneous distribution of aggregates. The surface appears compact with minimal voids or visible defects, indicating strong cohesion between aggregates and cement paste.

At 25% replacement, a limited number of red ceramic fragments can be seen, moderately dispersed within the matrix. Although the overall texture remains relatively dense, the presence of angular ceramic particles begins to introduce minor heterogeneity in the mix. Some small interfacial gaps may be visible, potentially weakening the ITZ slightly.

With 50% replacement, the concentration of ceramic waste increases noticeably. The ceramic particles are more prominent and uniformly distributed, but their angular and irregular shape creates more interfacial discontinuities. The mixture appears more porous compared to the control, suggesting reduced compactness and possible localized weaknesses.

The specimen with 75% recycled ceramic aggregates shows a high concentration of large, angular ceramic fragments. These are tightly packed but often poorly bonded with the cement paste. The image reveals more visible gaps and heterogeneity, indicating a significant impact on the concrete's microstructure. This aligns with the observed reduction in mechanical properties at this replacement level.

In conclusion, as the substitution rate of natural aggregates with recycled ceramic tile waste increases, the visual texture of the concrete becomes more heterogeneous, with more pronounced interfacial gaps and irregular particle distribution. This progression supports the mechanical test results, where higher CTW content leads to reduced compressive and flexural strength due to weaker aggregate–paste bonding and increased porosity.

Conclusion

This experimental study investigated the performance of self-compacting concrete (SCC) mixtures made with recycled ceramic tile aggregates, replacing natural coarse aggregates at varying levels (25%, 50%, 75%, and 100%). The objective was to assess the feasibility of incorporating this construction and demolition waste into SCC, both in terms of fresh workability and mechanical strength.

Fresh properties:

Fresh concrete tests including slump flow, L-box, and sieve stability were conducted in accordance with EFNARC (2005) guidelines. The results revealed the following trends:

- Flowability decreased with higher recycled aggregate content, due to the increased water absorption and angular shape of ceramic particles, which raised the mix viscosity.
- Nevertheless, all mixtures up to 75% replacement achieved slump flow diameters exceeding 600 mm, thereby meeting EFNARC standards.
- Passing ability (L-box ratio) declined slightly with increasing substitution, but remained within acceptable limits up to 75%.
- Segregation resistance improved marginally with higher replacement rates, likely due to the higher viscosity and internal friction provided by the ceramic aggregates.

The mix containing 100% recycled aggregates recorded a slump flow diameter below 550 mm, indicating insufficient flowability for SCC requirements. As a result, this mixture was excluded from further testing.

Hardened properties:

Compressive and flexural strength tests conducted at 28 days showed a clear downward trend:

- Compressive strength decreased progressively with higher replacement levels, reaching a maximum reduction of 30% at 75% ceramic aggregate content.
- Flexural strength followed a similar pattern, with up to 17% loss at the same substitution level.

Despite these drawbacks, SCC mixtures with up to 50% recycled aggregate demonstrated acceptable mechanical performance, with only moderate strength losses approximately 13–17% in compression and 6–15% in flexion. In addition, ultrasonic pulse velocity (UPV) testing confirmed the internal quality of the concrete. All mixtures recorded UPV values above 4500 m/s, indicating good material homogeneity and a relatively dense microstructure, even with the presence of recycled aggregates.

In summary, the use of recycled ceramic tile aggregates in self-compacting concrete represents a technically feasible and environmentally sustainable alternative to natural aggregates. At replacement levels up to 75%, SCC mixtures maintain satisfactory fresh and hardened properties, aligning with standard performance criteria. This approach not only contributes to waste valorization and natural resource conservation, but also offers potential economic advantages, positioning it as a promising solution for sustainable construction practices.

Scientific Ethics Declaration

* The authors declare that the scientific ethical and legal responsibility of this article published in EPSTEM journal belongs to the authors.

Conflict of Interest

* The authors declare that they have no conflicts of interest

Funding

* This research received no specific grant from any funding agency in the public, commercial, or not-for-profit sectors.

Acknowledgements or Notes

* This article was presented as an oral presentation at the International Conference on Technology, Engineering and Science (www.icontes.net) held in Antalya/Türkiye on November 12-15, 2025.

References

Bignozzi, M. C., & Sandrolini, F. (2006). Tyre rubber waste recycling in self-compacting concrete. *Cement and Concrete Research, 36*, 735-739.

Dhir, R., Limbachiya, M., & Dyer, T. (2001). *Recycling and reuse of glass cullet*. Thomas Telford Publishing.

Dilbas, H., Şimşek, M., & Çakır, Ö. (2014). An investigation on mechanical and physical properties of recycled aggregate concrete (RAC) with and without silica fume. *Construction and Building Materials, 61*, 50-59.

Duan, Z. H., & Poon, C. S. (2014). Properties of recycled aggregate concrete made with recycled aggregates with different amounts of old adhered mortars. *Materials & Design, 58*, 19-29.

EFNARC. (2005). *Specification and guidelines for self-compacting concrete*. European Federation of National Associations Representing Concrete.

European Parliament. (2008). Directive 2008/98/EC of the European Parliament and of the Council of 19 November 2008 on waste and repealing certain directives. *Official Journal of the European Union, L 312*, 3-30.

Ismail, S., & Ramli, M. (2013). Engineering properties of treated recycled concrete aggregate (RCA) for structural applications. *Construction and Building Materials, 44*, 464-476.

Levy, S. M., & Helene, P. (2004). Durability of recycled aggregates concrete: A safe way to sustainable development. *Cement and Concrete Research, 34*(11), 1975-1980.

Meyer, C. (1999). *Development of glass concrete products* (Final report). New York Empire State Development.

Okamura, H., & Ozawa, K. (1995). Mix design for self-compacting concrete. *Concrete Library of JSCE, 25*, 107-120.

Park, W., & Noguchi, T. (2013). Influence of metal impurity on recycled aggregate concrete and inspection method for aluminum impurity. *Construction and Building Materials, 40*, 1174-1183.

Poon, C. S., Kou, S. C., & Lam, L. (2007). Influence of recycled aggregate on slump and bleeding of fresh concrete. *Materials and Structures, 40*(9), 981-988.

Rahebi, B., Ghernouti, Y., Mansour, S. M., & Boumchedda, K. (2024). Development and characterization of stabilized earth blocks based on recycled sediment and lightweight aggregates. *The Eurasia Proceedings of Science, Technology, Engineering & Mathematics (EPSTEM), 32*, 30-40.

Robert, J., & Kirby. (2001). *Final report: An investigation of performance of paving units made from recycled glass*. National Center for Environmental Research.

Sagoe-Crentsil, K. K., Brown, T., & Taylor, A. H. (2001). *Guide specification: Recycled glass as sand replacement in premix concrete*. CSIRO.

Tabsh, S. W., & Abdelfalah, A. S. (2009). Influence of recycled concrete aggregate on strength properties of concrete. *Construction and Building Materials, 23*, 1163-1167.

Author(s) Information

Rabehi Bahia
University of Boumerdes
Independence Avenue, 35000 Boumerdes – Algeria
Contact e-mail: *y.ghernouti@univ-boumerdes.dz*

Ghernouti Youcef
University of Boumerdes
Independence Avenue, 35000 Boumerdes – Algeria

Mansour Sabria Malika
University of Boumerdes
Independence Avenue, 35000 Boumerdes – Algeria

Boumchedda Khaled
University of Boumerdes
Independence Avenue, 35000 Boumerdes – Algeria

To cite this article:

Bahia, R., Youcef, G., Malika, M.S, & Khaled, B. (2025). Recycling of ceramic tile waste in the formulation of self-compacting concrete. *The Eurasia Proceedings of Science, Technology, Engineering and Mathematics (EPSTEM), 38,* 1-11.

The Eurasia Proceedings of Science, Technology, Engineering & Mathematics (EPSTEM)
ISSN: 2602-3199

The Eurasia Proceedings of Science, Technology, Engineering and Mathematics (EPSTEM), 2025

Volume 38, Pages 12-19

IConTES 2025: International Conference on Technology, Engineering and Science

Electromagnetic Interference (EMI) in Variable-Speed AC Electric Drives: Mechanisms and Solutions

Houcine Miloudi
Djillali Liabes University of Sidi Bel Abbes

Mohamed Miloudi
University Ahmed Zabana of Relizane

Mohammed Hamza Bermaki
Djillali Liabes University of Sidi Bel-Abbes

Kheira Mendaz
University of Ain Temouchent

Abdelkader Gourbi
University of Oran 1 - Ahmed Ben Bella

Abdelber Bendaoud
Djillali Liabes University of Sidi Bel-Abbes

Abstract: This study investigates the electromagnetic compatibility (EMC) performance of a variable-speed drive (VSD) system in industrial applications, where managing electromagnetic disturbances is crucial for reliable operation. The analysis is structured in two main parts to provide a comprehensive evaluation of the system's behavior. The first part focuses on characterizing electromagnetic interactions within the complete system by examining electromagnetic disturbance (EMD) spectra and identifying common-mode (CM) propagation paths. A spectral assessment of conducted disturbances enables a detailed understanding of coupling mechanisms, the identification of propagation pathways, and an evaluation of the associated conducted emission risks. This step is essential for determining potential sources of interference and implementing suitable mitigation techniques. The second part quantifies conducted emissions injected into the electrical network, which can affect the performance of surrounding electronic equipment. The proposed model is applied in a structured approach to analyze and mitigate electromagnetic disturbances, with an emphasis on evaluating common-mode current propagation and assessing the influence of individual VSD system modules on EMD generation. To ensure accurate results, various testing conditions and configurations are considered. High-frequency (HF) spectral analysis is conducted over the 50 kHz – 30 MHz frequency range, in compliance with EN 55022 (Class A) normative requirements, ensuring adherence to industry standards and improving system robustness.

Keywords: Electromagnetic compatibility, Electromagnetic interference, EN55022 standard, Variable-speed AC electric drives

Introduction

Several studies have emphasized the importance of accurately characterizing high-frequency (HF) behavior in power electronic systems (Mohammed et al., 2024), (Mohamed et al., 2012), (Sara et al., 2023) to manage

- This is an Open Access article distributed under the terms of the Creative Commons Attribution-Noncommercial 4.0 Unported License, permitting all non-commercial use, distribution, and reproduction in any medium, provided the original work is properly cited.

- Selection and peer-review under responsibility of the Organizing Committee of the Conference

© 2025 Published by ISRES Publishing: www.isres.org

electromagnetic interference (EMI). HF components in isolating transformers (Miloudi et al., 2019) and switching devices like MOSFETs and IGBTs significantly impact EMI generation (Benhadda et al. 2020), (Lahlaci et al. 2025). Research on SMPS and DC/DC converters highlights the need to analyze both common-mode and differential-mode emissions using spectral techniques (Lahlaci et al. 2025), (Naima et al. 2024). Predictive models also assist in assessing conducted disturbances early in the design process, supporting the development of EMC-compliant systems (Gourbi et al. 2024). All equipment, for its operation, is necessarily connected to the environment, to other equipment, to a power source and to earth. In the absence of special precautions, these links represent access paths for undesirable disturbances. Interactions due to conduction can be suppressed by the use of filters whose role is to allow only the desired signals to pass (Jon et al., 2021; Li & Fei, 2021).

The filters attenuate interference signals according to their frequency independently of their amplitude. Filters are characterized either by their transfer function (Houcine et al. 2022), (Miloudi et al. 2010), or by their loss of insertion (Zeghoudi et al. 2022). The efficiency of the filter translates the insertion losses; it depends on the impedances of the load and the source between which the filter is positioned. For the reduction of conducted emissions, we can cite two methods, the first being filtering by passive elements, and the second being the use of active filters (Yongbin et al., 2016; Miloudi et al. 22014; Bermaki et al. 2023). In this work, we are going to present the existing means of reducing disturbances at the input of the variable speed drive by inserting a passive filter.

Common Mode Filter of the Variable Speed Drive System

A passive filter is characterized by the exclusive use of passive components used to reduce conducted disturbances (Abdelhakim et al., 2022), (Zeghoudi et al., 2022). These filters do not require a power supply. This technique makes it possible to advantageously modify the propagation path of the disturbances in order to hinder their circulation (Miloudi et al., 2023), (Miloudi et al., 2025). The filters can be placed upstream (mains side), or downstream of the drive (motor side).

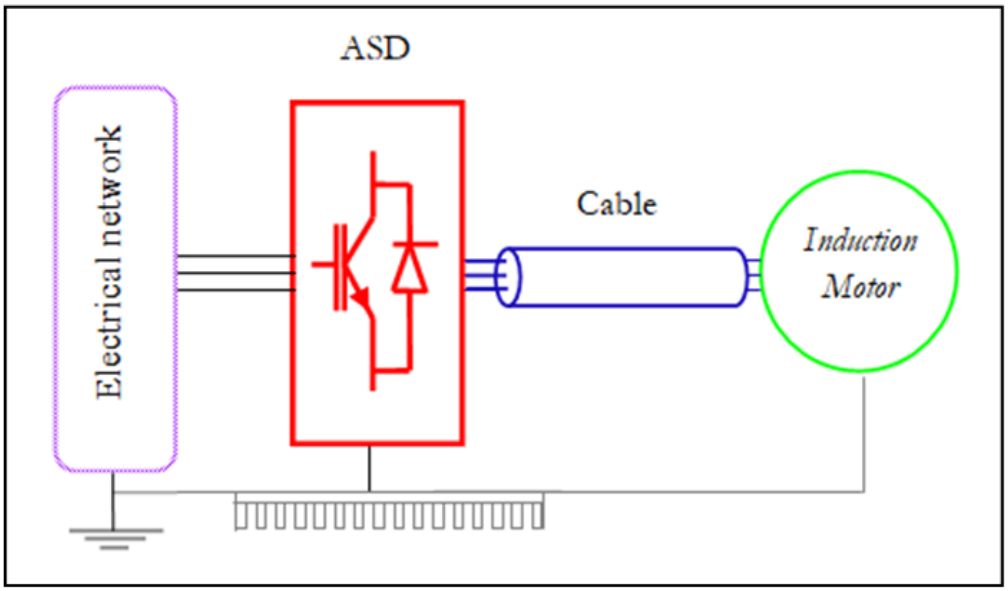


Figure 1. Adjustable speed drive structure

In this configuration (Figure 1), the filter is imposed in front of the network; this technique is widely used by the new generations of variable speed drives. The combination of high impedance (inductance) and low impedance (capacitance) paths makes it possible to direct disturbing currents along paths that do not disturb the network. This type of filter is particularly effective for the normative aspect. But unfortunately, there is no action on the motor overvoltage, and also it does not make it possible to reduce the common mode currents circulating in the motor.

EN 55022 Standard

This standard, specifying high frequency levels of conducted emissions applicable to residential, commercial and light industrial areas. Standards specifications for conducted disturbances in the radio frequency band (150 kHz – 30 MHz) fall into two categories (Figure 2). The first, referred to as "Class A", defines the emission level for devices intended for the industrial sector. The second, and certainly not the least, is reserved for the domestic and hospital sector: it is: Class B. The levels are given on a logarithmic scale in dBµV (Michał & Jan, 2022), (Satish & Jhansi, 2018).

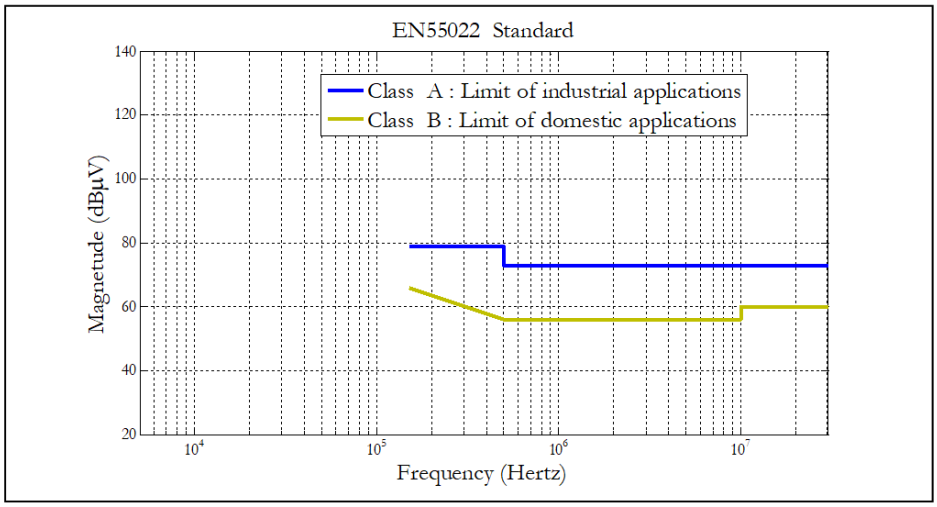


Figure 2. Levels of conducted disturbances set by standard EN 55022

As portrayed in Figure 2, the limit is quite stringent for Class B than Class A, Class A being a somewhat relaxed limit. Generally speaking, designers of electrical equipment make an effort to comply with the Class B requirements so as to allow the wider marketing of their equipments. In cases where this is not required, they may opt merely for Class A being less stringent because it involves lesser filtering requirements. As part of the study of conducted disturbances, the various experimental setups and devices used to measure conducted emissions include: the Line Impedance Stabilization Network (LISN), voltage and current probes, and the spectrum analyzer.

The LISN is equivalent to a filter inserted between the power supply network and the input of the equipment under test. It has multiple functions: it isolates the equipment under test from the power network, sets the prescribed impedance at the measurement points, and channels the conducted disturbances toward the measuring receiver. Through these various tasks, the LISN ensures the reproducibility of the measurements. There are several types of LISN structures, each defined by the standard relevant to the application domain. A common feature of all structures is the equivalent impedance, which ranges from 5–10 kHz up to 50–30 MHz. The diagram of the LISN is shown in Figure 3.

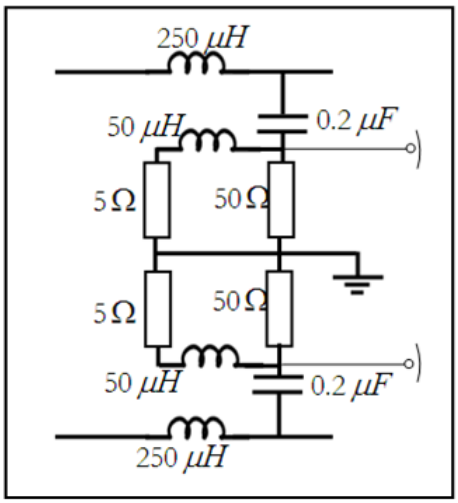


Figure 3. Simplified structure of the LISN

Method

EMC Filter

A proposed EMC filter is composed exclusively of passive components, used to attenuate conducted disturbances. It does not require any external power supply. This type of filter works by advantageously modifying the propagation path of disturbances in order to impede their flow. The filter is generally placed upstream, that is, on the power supply side, before the input of the equipment to be protected.

In this study, the proposed solution consists of adding an EMC filter mainly composed of an inductor and a capacitor. The combination of high-impedance paths (inductor) and low-impedance paths (capacitor) allows disruptive currents to be diverted along routes that do not disturb the network. The EMC filter is characterized by its transfer function, given by the relation.

$$Z = j * L * w + \frac{1}{j * C * w}$$

The purpose of which is to circulate the PEMs generated by the converter as little as possible outside of it, this filter will be placed between the Line Impedance Stabilization Network (LISN) and converter input (Figure 4).

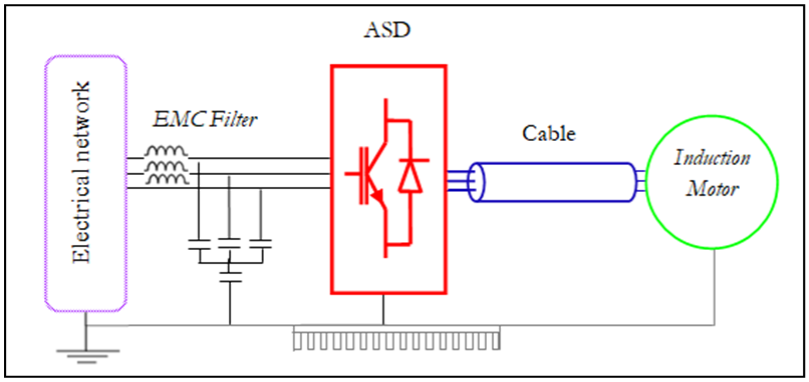


Figure 4. Common mode filter on input of ASD

In the problem of optimizing EMC performance, taking EMC constraints into account results in a comparison of the level of emissions (envelope of the spectrum) input of the variable speed drive, with respect to the limit imposed by the standard EN55022 for the corresponding frequency. This study's optimization strategy aims to reduce electromagnetic emission levels that exceed the EMC standard thresholds, ensuring compliance across the entire applicable frequency spectrum specified by the standard. The optimization flowchart is shown in Figure 5.

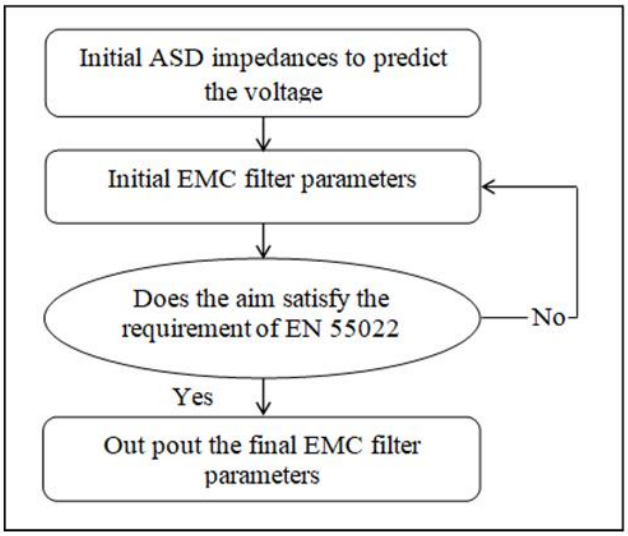


Figure 5. Diagram for the optimization procedures

Results and Discussion

This optimization approach consists of bringing the level of emissions of the voltage generated towards the network and which will be below the EMC standard, to the frequency range 150 kHz -30 MHz. Indeed, it is interesting to see the impact of the filter upstream and downstream of the inverter on the CM currents circulating throughout the system. The optimized EMC filter elements are: L_{CM}=2.8 mH, C_{CM}=0.8 pF.

Influence of the Filter on the Conducted Emissions Generated to the Network

The analysis begins with an observation of the common-mode voltage at the LISN, with and without an optimized filter to respect the standard EN 55022 –Class A- (Figure 6).

Spectrum of Common Mode Voltage in LISN

The common mode voltage in the LISN is well reduced, over the entire frequency range imposed by standard EN55022 (Figure 6).

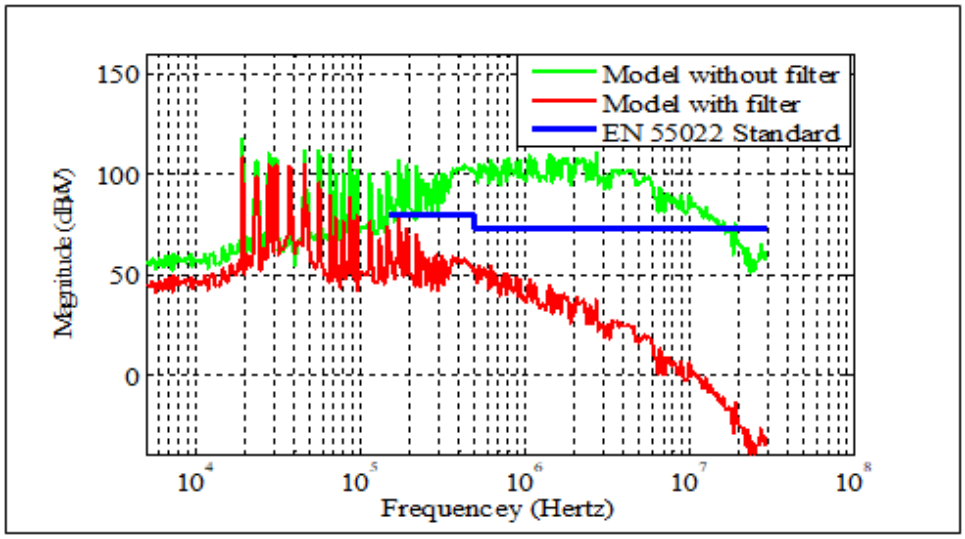


Figure 6. Spectrum of common mode noise in the ASD system (with and without input EMC filter)

Influence of the EMC Filter on the Conducted Emissions Generated to the Motor

To see the effectiveness of the presence of the filter at the input of the variable speed drive on the CM current at the input of the inverter. Figure 7 presents the corresponding current spectrum.

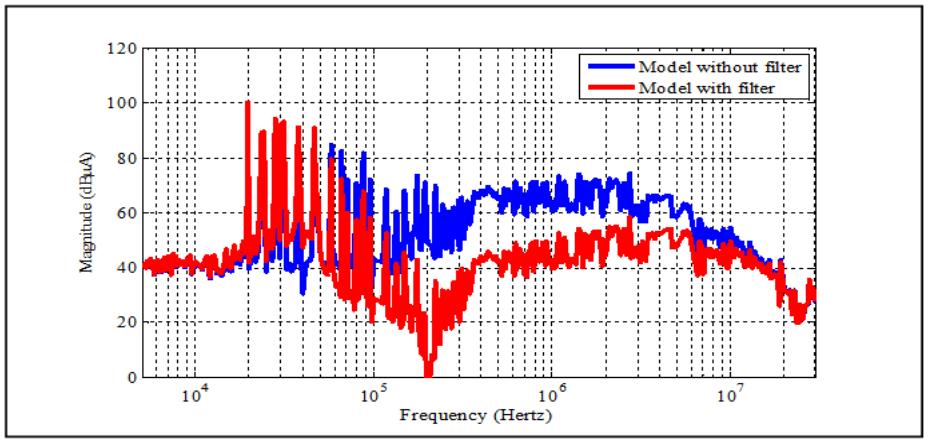


Figure 7. Spectrum of common-mode input currents in the inverter (with and without input EMC filter)

As we have seen previously, the input filter has a very limited effect on the common-mode current spectrum of the motor, despite a clear improvement from 150 kHz. The emission level remains almost identical to that calculated in the absence of the EMC filter for a large part of the frequency imposed by the corresponding standard (Figure 8).

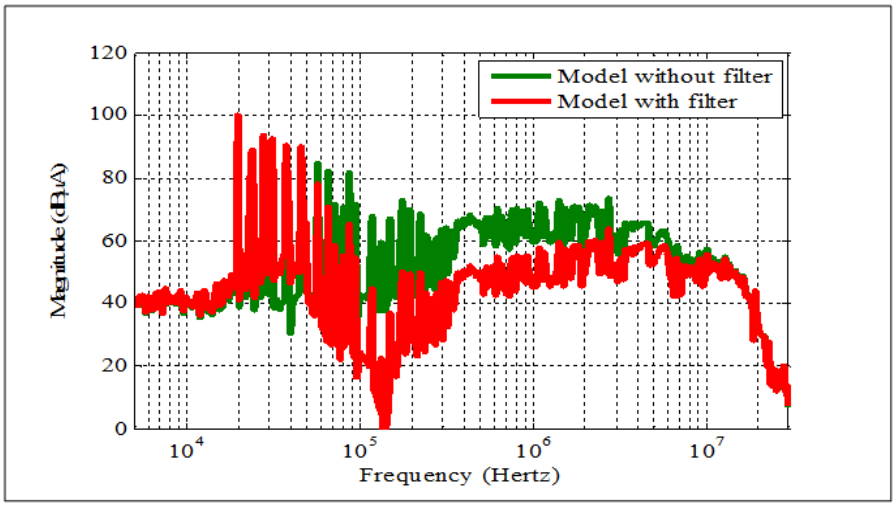


Figure 8. Spectrum of common-mode output currents in an ASD system. (with and without input EMC filter)

Conclusion

At this stage, we can conclude that the constraints are naturally respected, since the spectrum remains lower than the template, this type of filter is particularly effective for the normative aspect. But unfortunately, it has no action on motor overvoltage and does not reduce the common mode currents circulating in the motor.
Finally, it can be seen that this filter confines the disturbances circulating in the drive-cable-machine assembly as follows:

- The common mode choke constitutes a brake on the passage of the common mode current by increasing the impedance on the network side;
- Capacitors, connected to earth, offer low HF impedance and therefore form a privileged path for the return of the current, ensuring the confinement of disturbances.

The advantage of its LC structures at the entrance is that they are simple to implement, in terms of dimensioning and construction. The operating range of these filters goes from a few tens of kHz to tens of MHz. Beyond these values, the efficiency of HF inductors decreases and their inter-turn capacitances become preponderant, conferring a capacitive behavior on the inductor. In the same way, capacities become inductive from a certain frequency. These phenomena make it difficult to optimally size the filter, which can become ineffective above a certain frequency.

Scientific Ethics Declaration

* The authors declare that the scientific ethical and legal responsibility of this article published in EPSTEM journal belongs to the authors.

Conflict of Interest

* The authors declare that they have no conflicts of interest

Funding

* This research received no specific grant from any funding agency in the public, commercial, or not-for-profit sectors.

Acknowledgements or Notes

* This article was presented as an oral presentation at the International Conference on Technology, Engineering and Science (www.icontes.net) held in Antalya/Türkiye on November 12-15, 2025.

References

Benhadda, N., Bendaoud, A., Miloudi, M., Benazza, B., & Belhenini, S. (2020). Buck converter common-mode emission with the frequency approach. *International Journal of Electronics and Electrical Engineering Systems, 3*(1), 24-28.

Bermaki, M. H., Miloudi, H., Miloudi, M., Gourbi, A., & Bendaoud, A. (2023). High-frequency differential mode modeling of universal motor's windings. *International Journal of Electrical and Electronics Research, 11*, 1057-1064.

Borecki, M., & Sroka, J. (2022). Evaluation of the effectiveness of ferrite characteristics measurements based on the CISPR 17 standard. *Journal of Computers & Electrical Engineering, 72*, 169-178.

Chu, Y., Wang, S., & Wang, Q. (2016). Modeling and stability analysis of active/hybrid common-mode EMI filters for DC/DC power converters. *IEEE Transactions on Power Electronics, 31*(9), 6254-6263.

Ghalem, S., Bendaoud, A., Miloudi, H., Bermaki, M. H., Miloudi, M., & Zeghoudi, A. (2023). Prediction of conducted disturbances generated by a DC/DC converter. *The Eurasia Proceedings of Science Technology Engineering and Mathematics, 26*, 507-518.

González-Ramos, J., Angulo, I., Fernández, I., Arrinda, A., & de la Vega, D. (2021). Characterization of the potential effects of EMC filters for power converters on narrowband power line communications. *Electronics, 10*, 152.

Gourbi, A., Miloudi, M., Miloudi, H., & Bermaki, M. H. (2024). Comparative analysis of differential-mode impedance in single-phase induction motors. *WSEAS Transactions on Circuits and Systems*, *23,* 261-273.

Kumar, M. S., & Rani, A. J. (2018). Reduction of conducted electromagnetic interference by using filters. *IEEE Transactions on Magnetics, 58*(6), 1-8.

Lahlaci, M. E., Miloudi, M., & Miloudi, H. (2024). Experimental electromagnetic compatibility of conducted electromagnetic interferences from an IGBT and a MOSFET in the power supply. *Electrical Engineering & Electromechanics Journal, 3*, 3-7.

Lahlaci, M. E., Miloudi, M., Miloudi, H., Bendaoud, A., Bermaki, M. H., Gourbi, A., & Hakmi, Y. (2025). Analysis of common-mode and differential-mode noise in DC motors with variable speed drives. *International Journal of Advanced Natural Sciences and Engineering Researches, 9*(1).

Lahlaci, M. E., Miloudi, M., Miloudi, H., Gourbi, A., Bermaki, M. H., Mankour, M., & Mostefa, A. (2025). Comparative research in common and differential modes of EMI propensity in series and parallel chopper drives for DC motors. *Przegląd Elektrotechniczny, 7*.

Li, F., & Xia, F. (2021). The impedance mismatching on the EMI power filter design. *Journal of Future Wireless Networks and Information Systems, 144*, 699-704.

Miloudi, H., Bendaoud, A., & Miloudi, M. (2014). Réduction des perturbations électromagnétiques conduites dans la machine asynchrone (Reduction of conducted electromagnetic disturbances in the asynchronous machine). *Mediterranean Journal of Modeling and Simulation, 2*(1), 8-15.

Miloudi, H., Bendaoud, A., Miloudi, M., Gourbi, A., & Slimani, H. (2010). Common mode conducted electromagnetic interference in inverter-fed-AC-motor. *Electrical and Electronics Engineers Review*, 271-275.

Miloudi, H., Miloudi, M., Bermaki, M. H., Gourbi, A., & Bendaoud, A. (2023). Optimization of EMC filter for a variable speed drive system in electric aircraft. *The Eurasia Proceedings of Science Technology Engineering and Mathematics, 26*, 60-66.

Miloudi, H., Miloudi, M., Gourbi, A., Bermaki, M. H., Bendaoud, A., & Zeghoudi, A. (2022). A high-frequency modeling of AC motor in a frequency range from 40 Hz to 110 MHz. *Electrical Engineering & Electromechanics Journal, 6*, 3-7.

Miloudi, H., Miloudi, M., Ardjoun, S. A. E. M., Nour, A. A., & Mahariq, I. (2025). Experimental investigation of conducted electromagnetic interference differential-mode performance in various split-phase induction motors designs. *Results in Engineering*, *25*, 103963.

Miloudi, M., Bendaoud, A., Miloudi, H., Nemmich, S., & Okli, M. (2012). Characterization of conducted electromagnetic interference (EMI) generated by switch mode power supply (SMPS) (Paper presentation). *The 7th International Conference on Electrical Engineering*, Batna, Algeria.

Miloudi, M., Miloudi, H., Bendaoud, A., Salhi, M. A., & Al–Omari, A. N. (2019). Experimental characterization of the high–frequency isolating power transformer. *Journal of Electrical Engineering and Computer Science, 86*(4), 211-218.

Miloudi, N., Bendaoud, A., Miloudi, M., Miloudi, H., Gourbi, A., & Bermaki, M. H. (2025). Characterizing radiated electromagnetic interference from a power converter for improved electromagnetic compatibility. *WSEAS Transactions on Circuits and Systems. 24*, 135-148.

Zeghoudi, A., Bendaoud, A., Slimani, H., Miloudi, H., Miloudi, M., & Canale, L. (2022). Experimental measurements of near magnetic field by different probe for AC/DC LED driver (Paper presentation). *IEEE International Conference on Environment and Electrical Engineering*, Prague, Czech Republic.

Zeghoudi, A., Bendaoud, A., Slimani, H., Miloudi, H., Miloudi, M., & Chikhi, N. (2022). Experimental measurement of common and differential modes for variable speed drive DC motor (Paper presentation). *19th International Multi-Conference on Systems, Signals & Devices*, Sétif, Algeria.

Zeghoudi, A., Bendaoud, A., Tilmatine, A., Miloudi, M., Miloudi, H., & Canale, L. (2022). Experimental measurement of harmonic distortion and electromagnetic interferences for LED lamps (Paper presentation). *IEEE Industry Applications Society Annual Meeting*, MI, USA.

Author(s) Information

Houcine Miloudi
Djillali Liabes University of Sidi Bel Abbes, APELEC, Sidi Bel-Abbès, Algeria
Contact e-mail: *el.houcine@yahoo.fr*

Mohamed Miloudi
University Ahmed Zabana of Relizane (Relizane University), APELEC, Algeria

Mohammed Hamza Bermaki
Djillali Liabes University of Sidi Bel Abbes, APELEC, Sidi Bel-Abbès, Algeria

Kheira Mendaz
University of Ain Temouchent (Belhadj Bouchaib Ain Temouchent University), IRECOM Laboratory Djillali Liabes, Algeria

Abdelkader Gourbi
University of Oran 1 - Ahmed Ben Bella, APELEC, ISTA, Oran, Algeria

Abdelber Bendaoud
Djillali Liabes University of Sidi Bel Abbes, APELEC, Sidi Bel-Abbès, Algeria

To cite this article:

Miloudi, H., Miloudi, M., Bermaki, M. H., Mendaz, K., Gourbi, A., & Bendaoud, A. (2025). Electromagnetic interference (EMI) in variable-speed AC electric drives: Mechanisms and solutions. *The Eurasia Proceedings of Science, Technology, Engineering and Mathematics (EPSTEM), 38*, 12-19.

The Eurasia Proceedings of Science, Technology, Engineering & Mathematics (EPSTEM)
ISSN: 2602-3199

The Eurasia Proceedings of Science, Technology, Engineering and Mathematics (EPSTEM), 2025

Volume 38, Pages 20-29

IConTES 2025: International Conference on Technology, Engineering and Science

Stock Price Forecasting Model Using Short Cross Association of Logical Fuzzy Relations in Fuzzy Time Series

Fitri Cahyani
Gadjah Mada University

Akhmad Sultoni
Gadjah Mada University

Chyntia Meininda Anjanni
Gadjah Mada University

Abstract: Forecasting stock prices plays a crucial role in financial engineering and data-driven decision-making systems in the industrial world. The accuracy of stock price predictions is essential for investors, financial analysts, and infrastructure project managers to mitigate investment risks and optimize business strategies. Fuzzy Time Series (FTS) has become one of the popular methods for time series forecasting due to its ability to handle uncertainty and nonlinear patterns that often arise in financial and engineering systems. However, conventional FTS methods still face challenges in forming Fuzzy Logical Relationships (FLR), which can affect the accuracy of prediction results. This study proposes the Short Cross-Association Fuzzy Logical Relationship (SCA-FLR) approach to improve forecasting accuracy by considering influential factors in FLR formation. This method is applied to stock price data of PT Wijaya Karya (Persero) Tbk (WIKA.JK), using the stock closing price as the main factor and the highest stock price as the influencing factor. The forecasting results show an Average Forecasting Error Rate (AFER) of 2.97%, indicating excellent prediction accuracy. The findings of this study contribute to the development of forecasting systems in financial engineering, risk management, and industrial decision-making optimization. The application of this method can be extended to various engineering fields involving time series analysis.

Keywords: Fuzzy time series, Short cross-association, Stock price forecasting, Financial engineering, Data-driven prediction system

Introduction

Forecasting concepts in mathematics are used to predict future conditions. This concept is applied in various aspects of human life, as it aids in preparing policies that need to be implemented in the future. One crucial aspect that requires forecasting is the financial sector. Stock prices in the construction sector fluctuate due to global economic factors, government policies, and market conditions (Indonesia Stock Exchange, 2023). This instability creates uncertainty for investors, necessitating accurate forecasting methods to understand stock price movement patterns.

Fuzzy Time Series (FTS) is a forecasting method introduced by Song and Chissom (1993) that is used to predict problems where actual data is represented in linguistic values (Husain et al., 2021). The fuzzy time series forecasting method has become widely used by researchers as an extension of traditional time series forecasting. Several fuzzy time series forecasting methods include frequency density-based partitioning (Jilani & Burney, 2008)and percentage change from year to year as the universe of discourse (Husain et al., 2021).

- This is an Open Access article distributed under the terms of the Creative Commons Attribution-Noncommercial 4.0 Unported License, permitting all non-commercial use, distribution, and reproduction in any medium, provided the original work is properly cited.

- Selection and peer-review under responsibility of the Organizing Committee of the Conference

© 2025 Published by ISRES Publishing: www.isres.org

In this study, the fuzzy time series forecasting method is modified into a multi-factor fuzzy time series forecasting approach, which predicts data based on multiple variables, namely the main factor and the influence factor. In multi-factor fuzzy time series forecasting, the predicted data is the main factor. Previous studies on multi-factor fuzzy time series forecasting have been conducted by several researchers, including Tsai et al. (2019), who used this method to forecast stock indices. Dong et al., (2019)applied multi-factor fuzzy time series forecasting by constructing fuzzy logical relationships and cloud models to predict aircraft surface control failures. Furthermore, Li & Yu (2020) employed first-order multi-factor fuzzy time series forecasting using cross-association of fuzzy logical relationships in the formation stage.

In multi-factor fuzzy time series forecasting, the formation of Fuzzy Logical Relationships (FLR) requires further development. In the existing multi-factor fuzzy time series models, the FLR formation often results in multiple premises being matched, leading to cases where no FLR exists, making prediction values indeterminate. Therefore, constructing FLR based on the short cross-association of fuzzy logical relationships, as proposed by Li and Yu, can help address this issue. This study explores a modified multi-factor fuzzy time series forecasting method using the short cross-association approach in the formation stage of fuzzy logical relationships. Additionally, the defuzzification process follows the method used by Li et al., with the universe of discourse divided into ten intervals. The subinterval determination is based on frequency density-based partitioning. The membership function used in this study is the triangular membership function, while forecasting accuracy is evaluated using the Average Forecasting Error Rate (AFER).

This method is applied to forecast the closing stock price of PT Wijaya Karya (Persero) Tbk, which serves as the main factor, while the highest stock price is used as the influence factor (referred to as the second factor). PT Wijaya Karya (Persero) Tbk is one of Indonesia's largest construction companies, engaged in construction services, engineering, investment, energy, and property. The company has an extensive track record in national infrastructure development, including toll roads, bridges, and energy projects that contribute to Indonesia’s economic growth.

Fuzzy Time Series

Definition 1 (Guler Dincer & Akkus, 2018)

Given $Y(t)(t = 1,2, \dots)$, which is a subset of the set of all real numbers, it represents the universal set defined by the fuzzy set $f_i(t)(i = 1,2, \dots)$. If $F(t)$ is the universe of discourse for $f_i(t)(i = 1,2, \dots)$ then $F(t)$ is refrred to as a fuzzy time series on $Y(t)$.

Definition 2 (Jilani & Burney, 2008)

If given $A_{j_1}, A_{j_2}, A_{j_3}, \dots, A_{j_m} \in F(t)$ and $A_i \in F(t-1)$ such that the following fuzzy logical relationships (FLR) are formed :

$$A_i \rightarrow A_{j_1}$$
$$A_i \rightarrow A_{j_2}$$
$$A_i \rightarrow A_{j_3}$$
$$\dots$$
$$A_i \rightarrow A_{j_m}$$

From these FLR, a fuzzy logical relationship group (FLRG) can be constructed as follows: $A_i \rightarrow A_{j_1}, A_{j_2}, A_{j_3}, \dots, A_{j_m}$

Multi-Factor Fuzzy Time Series

Definition 3 (Guler Dincer & Akkus, 2018)

Let $F(t)$ be a fuzzy time series where $t = 1,2,3, \dots, n$ and $F(t)$ is a fuzzy set. If $F(t)$ is obtained from $F(t-1), F(t-2), \dots, F(t-n)$, then fuzzy logical relationship (FLR) can be represented as

$$(F_1(t-n), \dots, F_1(t-2), F_1(t-1)) \rightarrow F(t)$$

Which is referred to as an n-th order one-factor fuzzy time series. Here, $F(t)$ is called the next state, while $F_1(t-n), \dots, F_1(t-2), F_1(t-1)$ are called the current state.

Definition 4 (Efendi et al., 2015)

Let $F(t)$ be a fuzzy time series where $(t = 1,2,3, \dots, n)$. The value of $F(t)$ is a fuzzy set. If $F_1(t)$ is obtained from $(F_1(t-n), F_2(t-n), F_3(t-n), \dots, F_k(t-n)), \dots, (F_1(t-1), F_2(t-1), F_3(t-1), \dots, F_k(t-1))$, then $F_1(t)$ can be represented as $\big(F_1(t-n), \dots, F_k(t-n)\big), \dots, (F_1(t-1), \dots, F_k(t-1)) \rightarrow F_1(t)$ which is called a multi-factor fuzzy time series of order-n.

Definition 5 (Li & Yu, 2020)

In 1-order multi-factor fuzzy time series forecasting, there are two defuzzifiction rules as follows:

Rule 1**:** If $N \neq 0$, meaning that there exists a fuzzy logical relationship (FLR) in the forecasting process, the forecasted value can be determined using equation (1).

$$x(a) = \begin{cases} \dfrac{0{,}5m(1) + Q(1)}{1{,}5}, & \text{if } a = 1 \\ \dfrac{0{,}5m(a-1) + Q(a) + 0{,}5m(a+1)}{2}, & \text{if } 2 \leq a \leq k \\ \dfrac{0{,}5m(a-1) + Q(a-1) + q}{1{,}5}, & \text{if } a = k+1 \end{cases} \tag{1}$$

$$x' = \frac{v_1 \times \bar{x}(l_1) + v_2 \times \bar{x}(l_2) + v_3 \times \bar{x}(l_3) + \cdots + v_N \times \bar{x}(l_N)}{v_1 + v_2 + \cdots + v_N} \tag{2}$$

where:
$m(a)$ represents the midpoint of the fuzzy interval u_a
$Q(a)$ denotes the lower bound of the fuzzy interval u_a
q is the distance between $m(a)$ and $Q(a)$ within the fuzzy interval u_a
$\bar{x}(l_r)$ $(r = 1,2,3, \dots, N)$ refers to the forecasted values obtained using equation 1. v_r $(r = 1,2,3, \dots, N)$ represents the number of next states corresponding to the same current state in the fuzzy logical relationship (FLR).

Thus, the forecasted value at time x_t^* can be computed using:

$$x_t^* = 0{,}5(\bar{x}(p) + x') \tag{3}$$

where $\bar{x}(p)$ represents the forecasted value at $a = k+1$

Rule 2**:** If $N = 0$, meaning that no fuzzy logical relationship (FLR) is present in the forecasting process, the forecasted value at the next time step is given by:

$$x_t^* = \bar{x}(p) \tag{4}$$

Definition 6 (Vamitha & Vanitha, 2022)

The forecasting error or deviation can be measured using AFER (Average Forecast Error Rate) (Vamitha & Vanitha, 2022):

$$AFER = \frac{\sum_{i=1}^{n} \left(\frac{|X_i - Y_i|}{X_i}\right)}{n} x100\% \tag{5}$$

where:
X_i represents the actual value at time i
Y_i represents the forecasted value at time i
n is the number of forecasting time periods involved.
The AFER value can be used as an indicator for determining the performance criteria of the forecasting method employed. The following are AFER values along with their corresponding forecasting performance criteria (Irawanto et al., 2019)

Table 1. Forecasting criteria based on AFER values

AFER Value	Forecasting Performance Criteria
<10%	Excellent
10% - 20%	Good
20% - 50%	Fair
>50%	Poor

Method

Determining the forecasted value using short cross-association of fuzzy logical relationships consists of three parts, as follows:

Part 1: Fuzzification Process for the Main Factor

The steps are as follows:
Step 1: Determine the universe of discourse U based on the historical data of the main factor.
Step 2: Partition the universe into ten intervals (Li et al., 2021) and further divide the intervals into subintervals using frequency density-based partitioning (Jilani & Burney, 2008).
Step 3: Define fuzzy sets based on the determined intervals and input the data according to the fuzzy sets.

Part 2: Fuzzification Process for the Second Factor

The steps are as follows:
Step 1: Determine the universe of discourse V based on the historical data of the second factor.
Step 2: Partition the universe into ten intervals (Li et al., 2021) and further divide the intervals into subintervals using frequency density-based partitioning (Jilani & Burney, 2008).
Step 3: Define fuzzy sets based on the determined intervals and input the data according to the fuzzy sets.

Part 3: Defuzzification Process for the Main Factor and Second Factor

The steps are as follows:
Step 1: Construct the Fuzzy Logical Relationship (FLR) and Fuzzy Logical Relationship Group (FLRG).
Step 2: Determine the forecasted value based on defuzzification rules and calculate the error usning AFER.

Results and Discussion

The stock price of PT Wijaya Karya (Persero) Tbk exhibits unstable movements due to fluctuations in stock prices across different periods. In this study, the author utilizes closing price data and highest price data of PT Wijaya Karya (Persero) Tbk, comprising 41 data points collected from May 3, 2024, to February 7, 2025, with a weekly period. As shown in Figure 1, the data is non-stationary with respect to the mean due to the presence of a trend in the data pattern itself. Therefore, stationarization is necessary for further analysis.

Using the short cross-association of fuzzy logical relationships method in the fuzzy logical relationship (FLR) formation stage, the predicted closing stock price for the following week, with the closing stock price as the main factor, is 226,091 IDR. This forecast indicates an increase of 10.8% compared to the closing stock price in the last observed week.

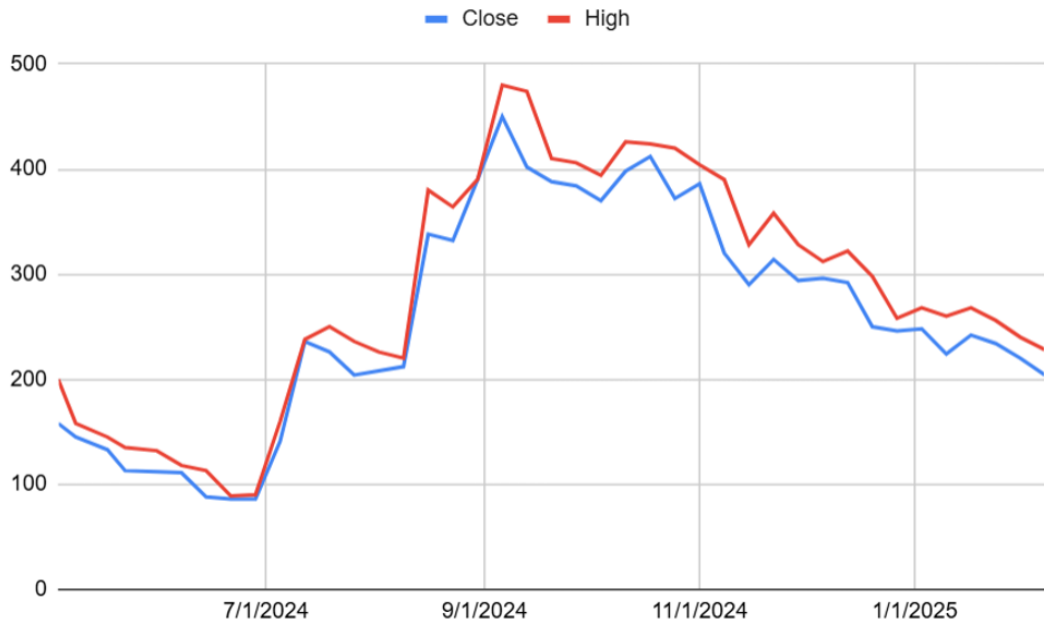


Figure 1. Stock price of PT Wijaya Karya (Persero) Tbk

Short Cross Association Fuzzy Logical Relationship Simulation

The method for forecasting the closing stock price of PT Wijaya Karya (Persero) Tbk using short cross-association in the defuzzification stage of the closing stock price data of PT Wijaya Karya (Persero) Tbk will be explained below.

Part 1: Fuzzification Process for the Main Factor

[Step 1] : The universal set (U) is defined as equal to $U = [D_{min} - c_1, D_{max} + c_2]$ (Bose & Mali, 2018). c_1 and c_2 are corresponding positive numbers. We know that based on the maximum and minimum available data, to obtain integers, $c_1 = 6$ and $c_2 = 10$ are used so that the universal set is obtained $U = [460 - 80]$.

[Step 2] : The universe set U is initially partitioned into 10 equal-length intervals $u_1, u_2, \dots, u_{10}$. These intervals are then further subdivided using frequency density-based partitioning. The three intervals with the highest frequencies are divided into four, three, and two subintervals, respectively. Intervals with zero frequency are removed. As a result, a total of 17 final intervals is obtained.

[Step 3] : Defining real data into fuzzy sets $A_1, A_2, A_3, \dots, A_n$. Next, find the membership value using a triangular membership function as in (Stevenson & Porter, 2009).

Part 2: Fuzzification Process for the Second Factor

[Step 1] : The universal set (V) is defined as equal to $V = [D_{min} - c_1, D_{max} + c_2]$ (Bose & Mali, 2018). c_1 and c_2 are corresponding positive numbers. We know that based on the maximum and minimum available data, to obtain integers, $c_1 = 9$ and $c_2 = 10$ are used so that the universal set is obtained $U = [490 - 80]$.

[Step 2] : The universe set V is initially partitioned into 10 equal-length intervals $v, v_2, \dots, v_{10}$. These intervals are then further subdivided using frequency density-based partitioning. The three intervals with the highest frequencies are divided into four, three, and two subintervals, respectively. Intervals with zero frequency are removed. As a result, a total of 20 final intervals is obtained.

[Step 3] : Defining real data into fuzzy sets $B_1, B_2, B_3, \dots, B_n$. This step is called fuzzification. Next, find the membership value using a triangular membership function as in (Stevenson & Porter, 2009)

Table 2. The result of part 1 and part 2

Week	Actual data of main factor	Fuzzification	Actual data of second factor	Fuzzification
1	158	A4	200	B6
2	145	A3	158	B5
3	133	A3	145	B4
4	113	A2	135	B4
5	112	A2	132	B3
6	111	A2	118	B2
7	88	A1	113	B2
8	86	A1	89	B1
9	86	A1	90	B1
10	141	A3	160	B5
11	236	A8	238	B9
12	226	A7	250	B10
13	204	A5	236	B9
14	208	A5	226	B8
15	212	A5	220	B7
16	338	A12	380	B16
17	332	A12	364	B15
18	390	A14	390	B17
19	450	A17	480	B20
20	402	A15	474	B20
21	388	A14	410	B19
22	384	A13	406	B18
23	370	A13	394	B17
24	398	A15	426	B19
25	412	A16	424	B19
26	372	A13	420	B19
27	386	A14	404	B18
28	320	A11	390	B17
29	290	A10	328	B14
30	314	A11	358	B15
31	294	A10	328	B14
32	296	A10	312	B13
33	292	A10	322	B13
34	250	A9	298	B13
35	246	A9	258	B11
36	248	A9	268	B12
37	224	A7	260	B11
38	242	A8	268	B12
39	234	A8	256	B11
40	220	A6	240	B9
41	204	A5	228	B8

Part 3: Defuzzification Process for the Main Factor and Second Factor

[Step 1]: Construct the Fuzzy Logical Relationship (FLR) and Fuzzy Logical Relationship Group (FLRG). According to the obtained Fuzzy Logical Relationship (FLR), Fuzzy Logical Relationship Groups (FLRG) can also be formed according to the concept of short cross-association in fuzzy logical relationships. That is, current states and next states that are the same in the previously established FLR can be grouped together.The result of the FLR and FLRG is shown in Table 3.

[Step 2] : Due to the fact that there exists a Fuzzy Logical Relationship (FLR) ($N \neq 0$) , the forecasted data values can be determined based on Rule 1 of defuzzification in multi-factor fuzzy time series forecasting using Equation (1). The forecasted data values for future time periods can be calculated using Equation (3), and the error can be computed using Equation (5). As a result, the defuzzification values for each fuzzy set are obtained, as presented in Table 4.

Table 3. FLR and FLRG

FLR and FLRG				
FLR	B6 → A3	B9 → A7	B19 → A13	B14 → A10
	B5 → A3	B10 → A5	B18 → A13	B13 → A10
	B4 → A2	B9 → A5	B17 → A15	B13 → A9
	B4 → A2	B8 → A5	B19 → A16	B13 → A9
	B3 → A2	B7 → A12	B19 → A13	B11 → A9
	B2 → A1	B16 → A12	B19 → A14	B12 → A7
	B2 → A1	B15 → A14	B18 → A11	B11 → A8
	B1 → A1	B17 → A17	B17 → A10	B12 → A8
	B1 → A3	B20 → A15	B14 → A11	B11 → A6
	B5 → A8	B20 → A14	B15 → A10	B9 → A5
FLRG	B1 → A1 (1)	B9 → A5 (1)	B13 → A10 (1)	
	B1 → A3 (1)	B9 → A7 (1)	B14 → A10 (1)	B18 → A11 (1)
	B2 → A1 (2)	B9 → A5 (1)	B14 → A11 (1)	B18 → A13 (1)
	B3 → A2 (1)	B10 → A5 (1)	B15 → A10 (1)	B19 → A13 (1)
	B4 → A2 (2)	B11 → A6 (1)	B15 → A14 (1)	B19 → A14 (1)
	B5 → A3 (1)	B11 → A8 (1)	B16 → A12 (1)	B19 → A16 (1)
	B5 → A8 (1)	B11 → A9 (1)	B17 → A10 (1)	B19 → A13 (1)
	B6 → A3 (1)	B12 → A7 (1)	B17 → A17 (1)	B20 → A14 (1)
	B7 → A12 (1)	B12 → A8 (1)	B17 → A15 (1)	B20 → A15 (1)
	B8 → A5 (1)	B13 → A9 (2)		

Table 4. Forecasting result and AFER value

Week	Actual data (X_i)	Forecasting data (Y_i)	$\lvert X_i - Y_i \rvert / X_i$
1	158	164.3125	0.03995253165
2	145	130.6666667	0.09885057471
3	133	130.6666667	0.01754385965
4	113	108.5	0.03982300885
5	112	108.5	0.03125
6	111	108.5	0.02252252252
7	88	82.11111111	0.06691919192
8	86	82.11111111	0.04521963824
9	86	82.11111111	0.04521963824
10	141	130.6666667	0.07328605201
11	236	235.5625	0.001853813559
12	226	225.2708333	0.00322640118
13	204	199.9375	0.01991421569
14	208	199.9375	0.03876201923
15	212	199.9375	0.05689858491
16	338	334.125	0.01146449704
17	332	334.125	0.00640060241
18	390	382.8125	0.01842948718
19	450	417.25	0.07277777778
20	402	395.875	0.01523631841
21	388	382.8125	0.01336984536
22	384	354.3125	0.07731119792
23	370	354.3125	0.04239864865
24	398	395.875	0.00533919598
25	412	411.3125	0.00166868932
26	372	354.3125	0.04754704301
27	386	382.8125	0.008257772021

28	320	312.75	0.02265625
29	290	286.625	0.01163793103
30	314	312.75	0.00398089172
31	294	286.625	0.02508503401
32	296	286.625	0.0316722973
33	292	286.625	0.01840753425
34	250	256.5416667	0.02616666667
35	246	256.5416667	0.04285230352
36	248	256.5416667	0.0344422043
37	224	225.2708333	0.005673363095
38	242	235.5625	0.02660123967
39	234	235.5625	0.006677350427
40	220	215.375	0.02102272727
41	204	199.9375	0.01991421569
		AFER	2.97130033%

Based on the results presented in Table 4, the comparison can be visualized in the following graph.

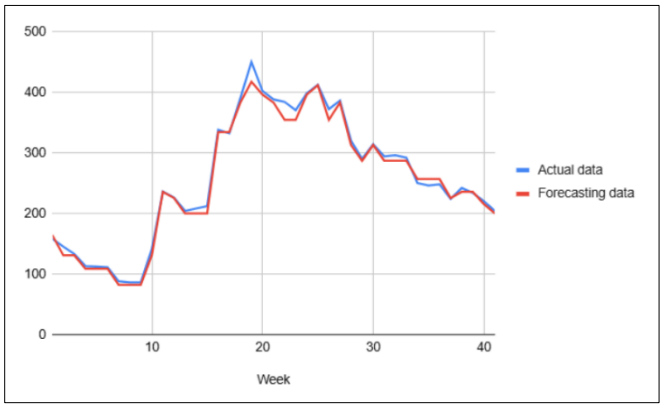


Figure 2. Graph of the forecasting and actual data

The graph above illustrates a comparison between two datasets: the blue line represents the actual data, while the orange line represents the forecasted data. By applying the short cross-association fuzzy logical relationship method and its defuzzification process, the forecasted value for the future is obtained as 226.091 IDR. Furthermore, the accuracy level, based on the Absolute Forecast Error Rate (AFER), results in an error of 2.97%, which is less than 10%. This indicates that the short cross-association fuzzy logical relationship method demonstrates a highly effective criterion for modeling the stock closing price forecast of PT Wijaya Karya (Persero) Tbk Indonesia.

Conclusion

The application of the multi-factor fuzzy time series (FTS) forecasting method can effectively predict the stock closing prices of construction companies, particularly PT Wijaya Karya (Persero) Tbk. This method is utilized because forecasting a dataset is inherently influenced by various supporting factors. In this case, the data used includes the highest stock price as the influence factor (second factor) in addition to the closing stock price, which serves as the main factor for the forecasted data.

The short cross-association method applied during the defuzzification stage in the analysis helps optimize the determination of forecast values. Specifically, this method is employed to predict the closing stock price of PT Wijaya Karya (Persero) Tbk based on time series data. The forecasting results obtained from this method predict the next week's stock closing price to be 226.091 IDR, with an accuracy level measured using the Average

Forecasting Error Rate (AFER) of 2.97%. Since the AFER value is less than 10%, based on AFER criteria, this forecasting method demonstrates a highly accurate performance.

However, when using the conventional multi-factor fuzzy time series method, the Fuzzy Logical Relationships (FLR) premises become excessively large, particularly in high-order multi-factor fuzzy time series models. In such cases, no available FLRs can be identified, as the number of premises to be matched becomes too extensive, rendering the prediction values indeterminable. Therefore, the Short Cross-Association Fuzzy Logical Relationship (SCAFLR) method is employed to increase the likelihood of identifying available FLRs in forecasting. The presence of short cross-association influences implies that the forecast is affected by influence factors. Hence, when constructing FLRs in forecasting models, it is essential to consider the SCAFLR approach.

Recommendations

For future research, it is recommended to develop a more optimal short association method by modifying the interval and its fuzzification components. Furthermore, a comparative analysis between the short association method used in this study and other methods could be conducted to evaluate the accuracy level.

Scientific Ethics Declaration

* The authors declare that the scientific ethical and legal responsibility of this article published in EPSTEM journal belongs to the authors.

Conflict of Interest

* The authors have no conflicts of interest in any area.

Funding

* This study was funded by the Indonesia Endowment Fund for Education (LPDP) under the Ministry of Finance of the Republic of Indonesia

Acknowledgements or Notes

* This article was presented as an oral presentation at the International Conference on Technology, Engineering and Science (www.icontes.net) held in Antalya/Türkiye on November 12-15, 2025.

* The author would like to express sincere gratitude to the Indonesia Endowment Fund for Education (LPDP) under the Ministry of Finance of the Republic of Indonesia for providing financial support for this research.

*The author also appreciates the guidance and insightful discussions from the academic supervisor, as well as the encouragement and support from colleagues and family throughout this study

References

Bose, M., & Mali, K. (2018). A novel data partitioning and rule selection technique for modeling high-order fuzzy time series. *Applied Soft Computing Journal*, *63*, 87-96.

Dong, L., Wang, P., & Yan, F. (2019). Damage forecasting based on multi-factor fuzzy time series and cloud model. *Journal of Intelligent Manufacturing*, *30*(2), 521-538.

Efendi, R., Ismail, Z., & Deris, M. M. (2015). A new linguistic out-sample approach of fuzzy time series for daily forecasting of Malaysian electricity load demand. *Applied Soft Computing Journal*, *28*, 422-430.

Guler Dincer, N., & Akkus, O. (2018). A new fuzzy time series model based on robust clustering for forecasting of air pollution. *Ecological Informatics*, *43*, 157–164.

Husain, A. A., Surarso, B., Farikhin, & Irawanto, B. (2021). Forecasting model of Covid-19 cases using fuzzy time series using persentage change. *Journal of Physics: Conference Series*, *1943*(1).

Indonesia Stock Exchange. (2023, November 24). *Opportunities and Challenges for the Indonesian Capital Market 2024*. Retrieved from https://Idx.Co.Id/Id/Berita/Artikel?Id=37636060-29aa-Ee11-B808-005056aec3a4.

Irawanto, B., Ningrum, R. W., Wulandari, R., Surarso, B., & Farikhin. (2019). Frequency density-based partitioning (FDP) for forecasting IHSG. *Journal of Physics: Conference Series*, *1321*(2).

Jilani, T. A., & Burney, S. M. A. (2008). A refined fuzzy time series model for stock market forecasting. *Physica A: Statistical Mechanics and Its Applications*, *387*(12), 2857-2862.

Li, F., & Yu, F. (2020). Multi-factor one-order cross-association fuzzy logical relationships based forecasting models of time series. *Information Sciences*, *508*, 309–328.

Li, F., Yu, F., Wang, X., Yang, X., Liu, S., & Liu, Y. (2021). Integrate new cross association fuzzy logical relationships to multi-factor high-order forecasting model of time series. *International Journal of Machine Learning and Cybernetics*, *12*(8), 2297–2315.

Stevenson, M., & Porter, J. E. (n.d.). *Fuzzy time series forecasting using percentage change as the universe of discourse*.

Tsai, M.-C., Cheng, C.-H., & Tsai, M.-I. (2019). A multifactor fuzzy time-series fitting model for forecasting the stock index. *Symmetry*, *11*(12).

Vamitha, V., & Vanitha, V. (2022). Intuitionistic fuzzy time series forecasting model: Aesthetic approach on temperature prediction. *AIP Conference Proceedings*, *2473*.

Author(s) Information

Fitri Cahyani
Gadjah Mada University
Yogyakarta, Indonesia
Contact e-mail: *fitricahyani192@gmail.com*

Akhmad Sultoni
Gadjah Mada University
Yogyakarta, Indonesia

Chyntia Meininda Anjanni
Gadjah Mada University
Yogyakarta, Indonesia

To cite this article:

Cahyani, F., Sultoni, A., & Anjanni, C. M. (2025). Stock price forecasting model using short cross association of logical fuzzy relations in fuzzy time series. *The Eurasia Proceedings of Science, Technology, Engineering and Mathematics (EPSTEM), 38,* 20-29.

The Eurasia Proceedings of Science, Technology, Engineering & Mathematics (EPSTEM)
ISSN: 2602-3199

The Eurasia Proceedings of Science, Technology, Engineering and Mathematics (EPSTEM), 2025

Volume 38, Pages 30-39

IConTES 2025: International Conference on Technology, Engineering and Science

Numerical Modeling Creep of Two Piles Under Constant Static Loading Using ANSYS

Ghouilem Kamel
Mouloud Mammeri University of Tizi-Ouzou

Belmihoub Hacene
University of Bouira

Abstract: This presents study describes a procedure for modeling and prediction the secondary creep behavior called (Norton Law) of a two concrete structure piles under constant static loading with taking into account the soil structure interaction, during 20000 hours of vertical static loading. In this item, we have applied the Finite Element Method (FEM) based on a Model using the computer code ANSYS® 14.0 shows in equation 16 heading (Norton Law). Contact problems fall into two general classes: rigid-to-flexible and flexible-to-flexible. In general, any time a soft material comes in contact with a hard material, the problem may be assumed to be rigid-to-flexible. To model a contact problem, you first need to identify the parts to be analyzed for their possible interaction. If one of the interactions is at a point, the corresponding component of your model is a node. If one of the interactions is at a surface, the corresponding component of your model is an element. The finite element model recognizes possible contact pairs by the presence of specific contact elements. These contact elements are overlaid on the parts of the model that are being analyzed for interaction. ANSYS ® 14.0 software has been used to perform the numerical calculation in this paper

Keywords: Pile, Creep, Concrete structure, ANSYS, Finite element method (FEM)

Introduction

The purpose of piling a foundation is to transmit forces through a weak stratum to a lower stronger stratum having sufficient bearing capacity to support the structure. The analysis of laterally and vertically loaded piles involves both the response of the soil movement of the pile and the bending deflection. Soil stiffness resists the pile. The initial response of the soil is nearly linear elastic but, as the lateral deflection increases, the soil starts to behave in a more plastic response and the stiffness reduces. An analytical solution may assume a linear elastic soil continuum or an elastic-plastic soil. A number of analytical solutions have been developed by various authors to estimate the response of piles and pile groups which are laterally loaded. These analytical solutions have been developed to provide the design engineer with a realistic and economic method of dealing with laterally loaded piles.

Soil-structure interaction has been extensively investigated regarding axial vertical loads in deep foundations. At the same time, in several circumstances, piles need to be designed to support major static lateral and vertical loads, as a result of the action of, water flow, horizontal earth pressure, earthquakes, and traffic movement. Bridges (Kim, & Jeong, 2011), tall buildings, transmission lines, retaining walls (Gil-Martín et al, 2016), offshore structures (Michel et al, 2018; Arany et al, 2017), wharfs, are a few examples of structures in which lateral loads assume primary significance.

Creep Behavior and Creep Material Model

- This is an Open Access article distributed under the terms of the Creative Commons Attribution-Noncommercial 4.0 Unported License, permitting all non-commercial use, distribution, and reproduction in any medium, provided the original work is properly cited.

- Selection and peer-review under responsibility of the Organizing Committee of the Conference

© 2025 Published by ISRES Publishing: www.isres.org

Creep is a rate-dependent material nonlinearity in which the material continues to deform under a constant load. Conversely, if a displacement is imposed, the reaction force (and stresses) diminish over time (stress relaxation; see Figure 1. The three stages of creep are shown in Figure 2. The program has the capability of modeling the first two stages (primary and secondary). The tertiary stage is usually not analyzed since it implies impending failure

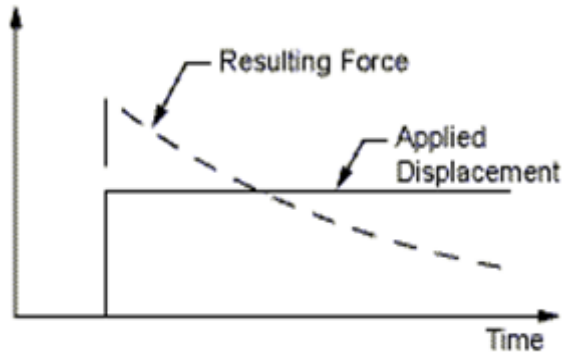


Figure 1. Stress relaxation (ANSYS, 2016)

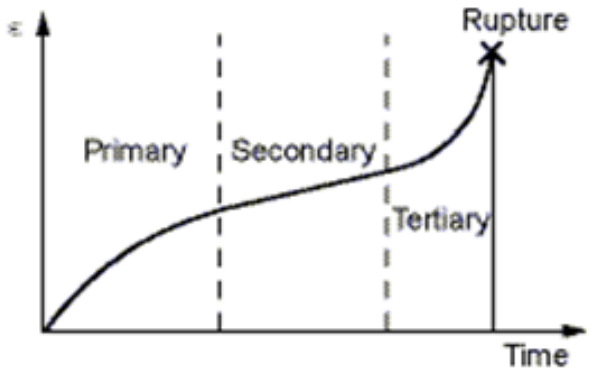


Figure 2. Creep strain stage (ANSYS, 2016)

Creep is important in high temperature stress analyses, such as for nuclear reactors. For example, suppose you apply a preload to some part in a nuclear reactor to keep adjacent parts from moving. Over a period at high temperature, the preload would decrease (stress relaxation) and potentially let the adjacent parts move. Creep can also be significant for some materials such as prestressed concrete. Typically, the creep deformation is permanent. The program analyzes creep using two time-integration methods. Both are applicable to static or transient analyses. The implicit creep method is robust, fast, accurate, and recommended for general use. It can handle temperature dependent creep constants, as well as simultaneous coupling with isotropic hardening plasticity models. The explicit creep method is useful for cases where very small time steps are required. Creep constants cannot be dependent on temperature. Coupling with other plastic models is available by superposition only.

Implicit Creep Procedure

The basic procedure for using the implicit creep method involves issuing the TB command with Lab = CREEP, and choosing a creep equation by specifying a value for TBOPT. The following example input shows the use of the implicit creep method. TBOPT = 1 specifies that the primary creep equation for model 1 is used. Temperature dependency is specified using the TBTEMP command, and the four constants associated with this equation are specified as arguments with the TBDATA command bellow:

TB,CREEP,1,1,4,1
TBTEMP,100
TBDATA,1,C1,C2,C3,C4

For most materials, the creep strain rate changes significantly at an early stage. Because of this, a general recommendation is to use a small initial incremental time step, then specify a large maximum incremental time step by using solution command DELTIM or NSUBST. For implicit creep, you may need to examine the effect of the time increment on the results carefully because the program does not enforce any creep ratio control by default. You can always enforce a creep limit ratio using the creep ratio control option in commands CRPLIM or CUTCONTROL,CRPLIMIT. A recommended value for a creep limit ratio ranges from 1 to 10. The ratio may vary with materials so your decision on the best value to use should be based on your own experimentation to gain the required performance and accuracy. For larger analyses, a suggestion is to first perform a time increment convergence analysis on a simple small size test.

Explicit Creep Procedure

The basic procedure for using the explicit creep method involves issuing the TB command with Lab = CREEP and choosing a creep equation by adding the appropriate constant as an argument with the TBDATA command.

TBOPT is either left blank or = 0. The following example input uses the explicit creep method. Note that all constants are included as arguments with the TBDATA command, and that there is no temperature dependency.
TB, CREEP,1 TBDATA, 1,C1,C2,C3,C4, ,C6

For the explicit creep method, you can incorporate other creep expressions into the program by using User Programmable Features (see the Guide to ANSYS User Programmable Features). For highly nonlinear creep strain vs. time curves, a small time step must be used with the explicit creep method. Creep strains are not computed if the time step is less than 1.0e-6. A creep time step optimization procedure is available (AUTOTS and CRPLIM) for automatically adjusting the time step as appropriate. In order to modeling the creep bahavior, we have introduced the model equation called (Strain Hardening » model Eq. (1). It is considered that the material is isotropic, and the basic solution method used is that of Newton-Raphson.

$$\dot{\varepsilon}_{cr} = C_1 \sigma^{C_2} t^{C_3} e^{(-C_4/T)} \quad (1)$$

With: $\dot{\varepsilon}_{cr}$: Rate Creep strain, σ : Equivalent stress, t: Time at end of sub –steps), C_1, C_2, C_3, C_4 : Materials Creep parameters (see Table 1), T : temperature (K). The following tables illustrate the materials creep parameters of Clay, Rock and Concrete introduced in the processing creep modeling law. In this studies, parameters is taken equal zero (C4 = Q/K = 0).

Table 1. Elastic and creep parameters properties of the soil layers and Concrete parameters

	Elastic			Creep parameters		
Rock	Young's Modulus	υ	Density	C1(s-1)	C2	C3 (MPa-1)
	2.4x 10^8 Pa	0.45	2.10^3kg.m^{-3}	7e-20	2.19	-0.98
Concrete	3.10^{10} Pa	0.23	$2.5.10^3$kg.m^{-3}	41e-8	1.48	-0.68
Clay	22.10^6 Pa	0.25	18 kN.m^{-3}	3.33e-6	1.18	-0.54

The following windows (Figure.3) illustrate the interface procedure for introduction creep equation into the model. The introduction of the Strain Hardening creep equation Law (Eq1) in the model, are illustrated in figures 4 and 5 below. It should be noted that the maximum values of the creep strains in the X direction are concentrated at the level contact zone Clay - rocky substratum. In the y-axis, it can be seen that the minimum creep strain is indicated at the level of the tip pile zone

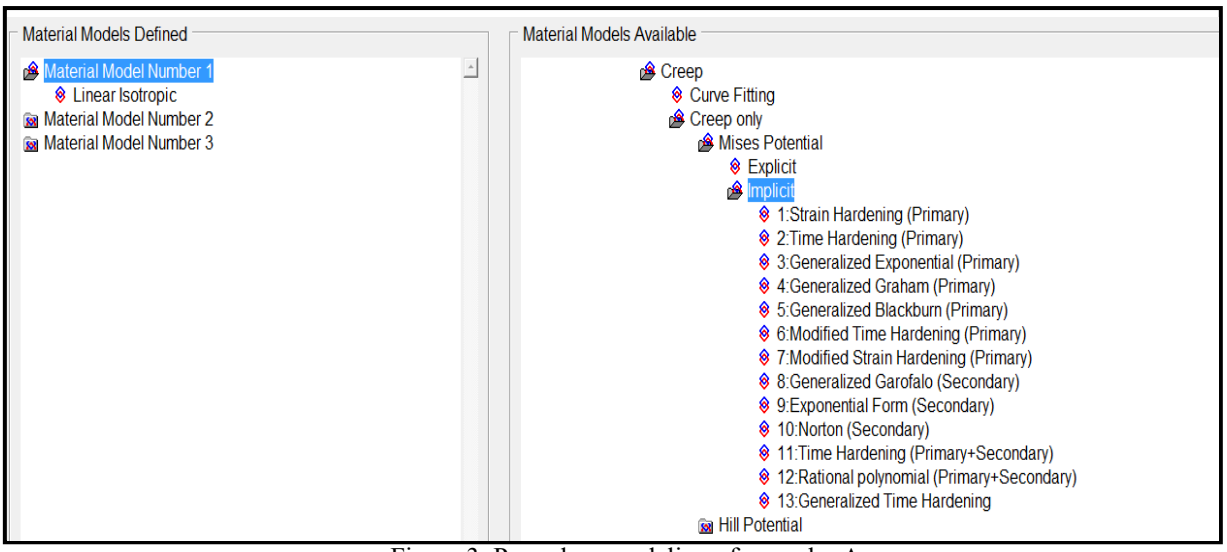


Figure 3. Procedure modeling of creep by Ansys

Contact Behavior and Finite Element Formulation

Using contact elements in a Finite Element Method (FEM) simulation is seldom a simple, painless experience. Changing contact between parts is a common phenomenon which, in some cases, can be treated with rigorous mathematical theory. Formulae for special cases can be found in mac Hine design textbooks (Juvinall, & Marshek1991, Shigley 1972, Timoshenko & Goodier 1970), two spheres, two parallel cylinders, cylinders on a flat plat e, gear teeth, roller bearings, etc. However, these theories only describe the stress in the contact region.

Finding the best choices for contact elements, element options, solver, and solution options can drastically import e the model's performance and reduce the analyst's frustration with a contact simulation model.

This section presented the steps to simulate the contact elements between two the soil and structure (pile) using ANSYS® software. Moreover, it gives more details about the types of contacts and algorithms which are used in this software. The ANSYS® Finite Element Method (FEM) program offers a variety of elements designed to treat cases of changing mechanical contact between the parts of an assembly or between different faces of a single part. Contact elements can be grouped into four general categories based on increasing levels of sophistication or complexity (Ansys, 2011).

Node – to Node Gap Elements: CONTACT12, LINK10, COMBIN40, CONTAC52, CONTA178

Elements CONTACT12 and CONTACT52 simulated node – to node contact in two and three dimensions, respectively. Initially the elements were based upon a penalty function approach and elastic Coulomb friction model. COMBIN7, COMBIN40 and LINK10 elements are included in this list of point-to-point gap elements because they simply connect from one surface node to another, but these elements can have other complicated behaviors. COMBIN7 is a revolute joint element which has "stops" that act like the closing of a contact. COMBIN40 has gap and slider behavior, but also allows two parallel springs, and may have mass and damping for a dynamic simulation.

Node – to Line (or Slide-Line) Contact Elements: CONTAC26

The point-to-line gap element is available for two-dimensional problems only. The node point location on the flexible surface (that is, on the surface of a solid element mesh) is tested with respect to its proximity to some rigid target surface. The analyst defines:

- Stiffness of a closed gap
- The geometry (shape and location) of the rigid surface
- Friction coefficient (if any)
- Stiffness in the sliding direction

Node – to –Surface Contact Elements: CONTAC48, CONTAC49

Ansys. Inc. later developed the CONTACT 48 and CONTACT49 node –to- surface contact elements for general contact problems. The underlying technology is penalty based, but with Lagrange augmentation to enforce compatibility. The elements allow for large sliding. However, these elements are not compatible with higher-order solid elements because the mid-side nodes of the quadratic elements are not used for the contact faces. With these contact elements, the analys defines or selects:

- Stiffness of a closed gap (FKN)
- Formulation
- Penalty method
- Penalty + Lagrange multiplier
- Allowable penetration tolerance (FTOLN)
- Pinball region size (PINB)

Surface-to-Surface Contact Elements: TARGE169, TARGE170, CONTA171, CONTA172, CONTA173, CONTA174

The surface-to-surface gap elements overcome most of the limitations or restrictions of the other contact elements:

- Two- or three-dimensional systems
- Rigid or flexible target faces can be treated

In this work, it has been used two types of element for contact model as follows:

-"CONTA171": CONTA171 is used to represent contact and sliding between 2-D"target" surfaces (TARGE169) and a deformable surface, defined by this element. The element is applicable to 2-D structural and coupled field contact analyses.

- "TARGE169": TARGE169 is used to represent various 2-D "target" surfaces for the associated contact elements (CONTA171, CONTA172, and CONTA175). The following figures 4 and Figure 5 illustrates some modeling contact elements and PLANE 182 described by ANSYS.

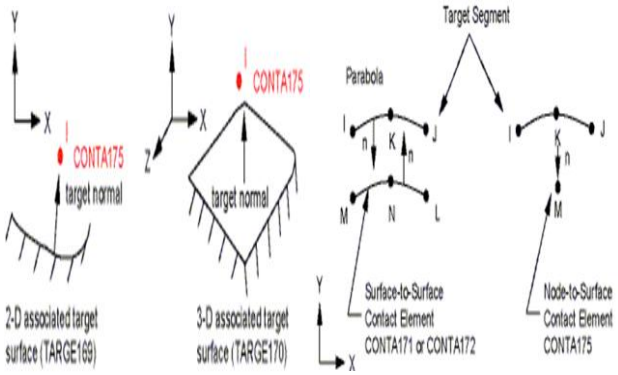


Figure 4. Element contact TARGE 169 and contact 170, 171, 172, 175 (ANSYS contact technology guide)

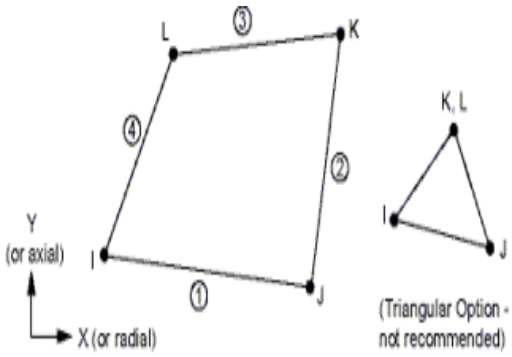


Figure 5. Element PLANE 182 (ANSYS element reference 2016)

The following Figure 6 and Figure 7 bellow illustrates the modeling interface and contact generation soil-Piles with **TARGET169** elements in the **Surface-to-surface contact element**se.

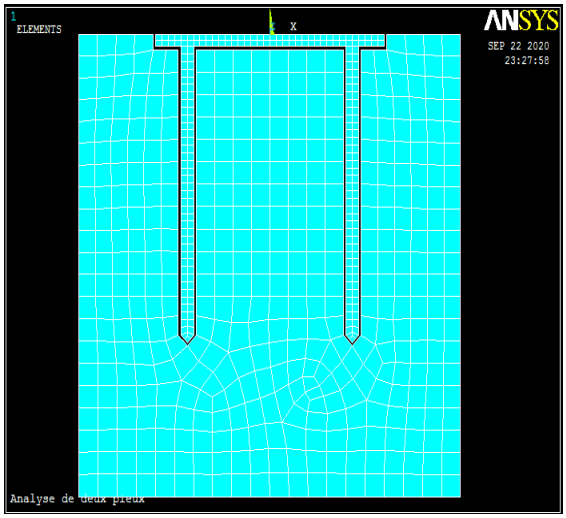


Figure 6. Modeling interface soil pile

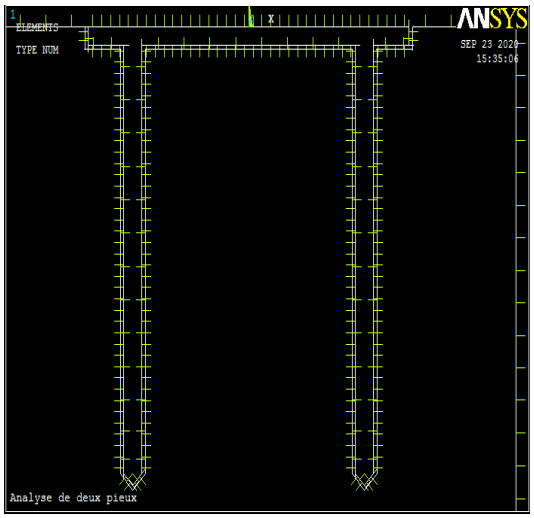


Figure 7. Contact generation between soil structure

Results and Discussion

Finite element analyses of piles in soil are presented by (Ottaviani, 1975; Randolph,1981; Smith I. M. & Griffiths 1988; Selby & Arta,1991), to deal with laterally and static loaded piles. Today powerful computer packages such as Program for Ansys® Finite Element Analysis have been developed which are capable of analyzing 1, 2 and 3 dimensional problems with various types of element. The package uses the Virtual Work theory to evaluate nodal displacements due to applied load vectors, then from the nodal displacements, the strains and stresses are calculated.

ANSYS® is engineering software, worldwide used by researchers for simulation. It develops general purpose of finite element analysis. To create the finite element model in ANSYS there are multiple tasks that have to be completed for the model to run properly. Models can be created using command prompt line input or the Graphical User Interface (GUI). This section describes the different tasks and entries into used to create the Finite Element

calibration model. Analysis by ANSYS includes two steps, namely a step of modeling and a calculation step. The first step is to model the finite element structure by choosing an appropriate item to the type of analysis to be performed, such as for example: As part of this work, we limited ourselves to address the problem in two-dimensional finite element discretized by element **PLANE182** with application of boundary conditions (see figure 8 below). In this model, the number of elements structural is approximately 2426 elements and 2429 nodes.

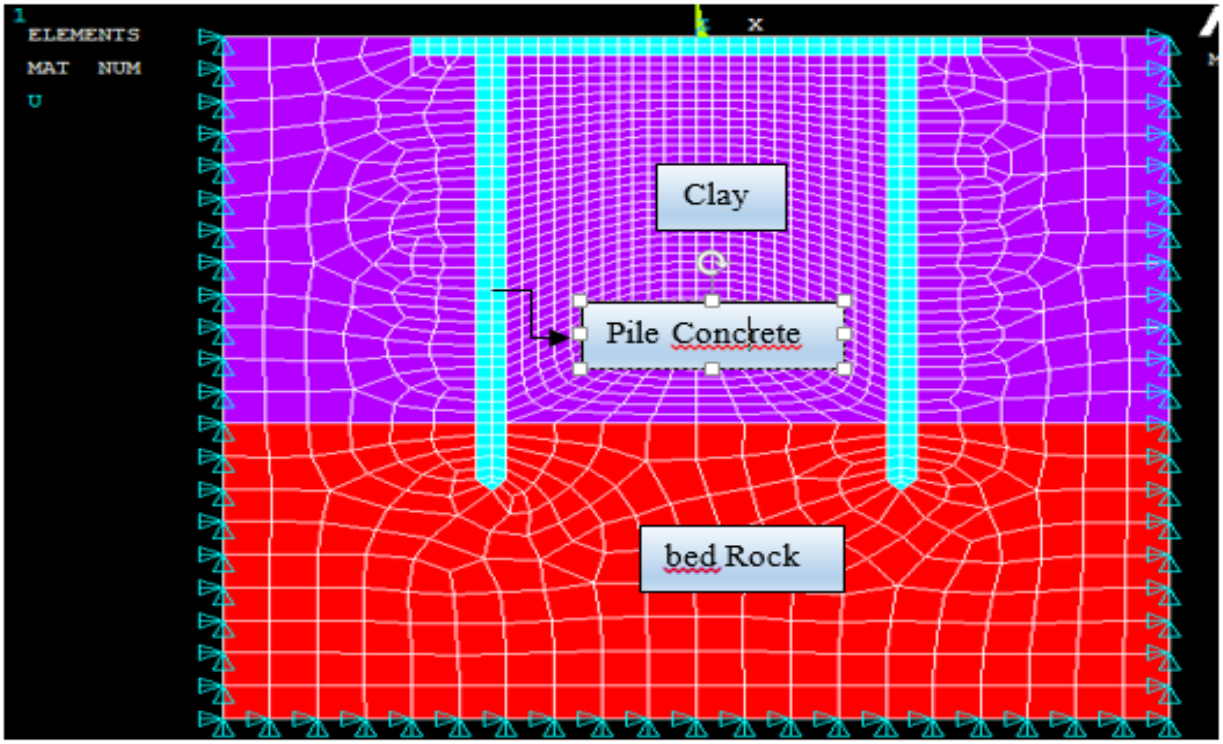


Figure 8. Two – Pile group modeling

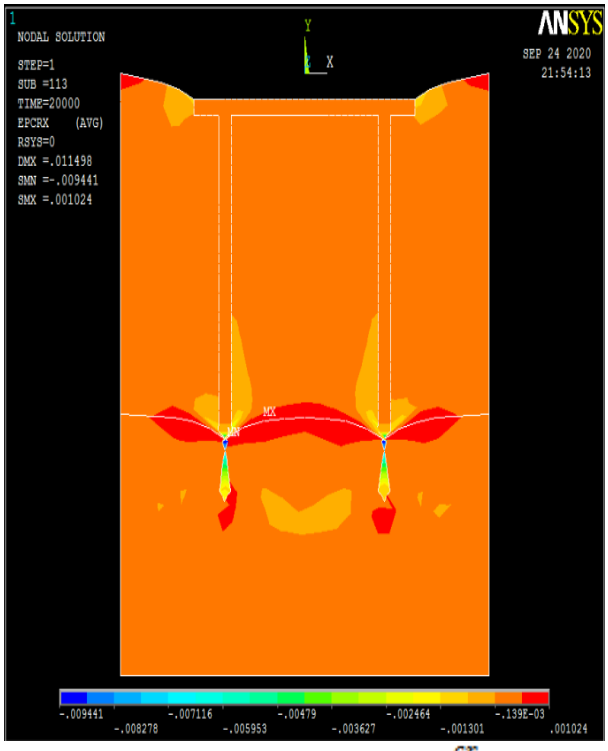


Figure 9. Contour plot of Creep strain ε_X^{cr}

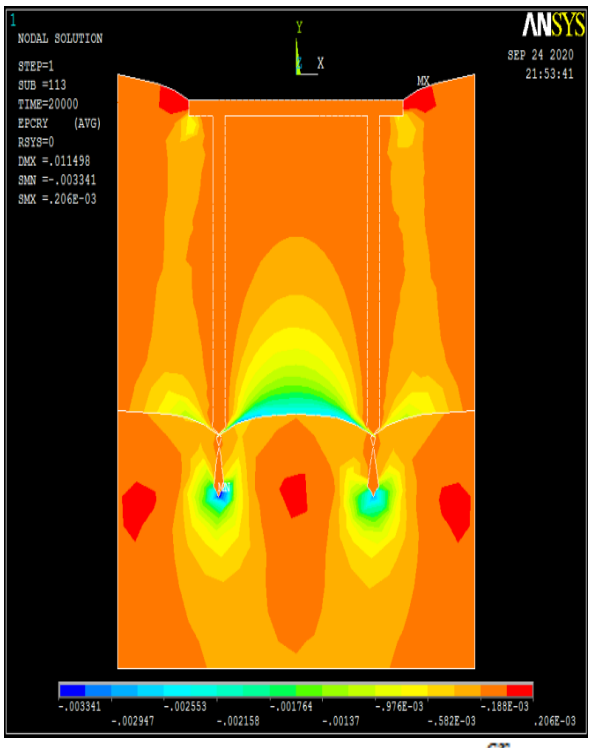


Figure 10. Contour plot of Creep strain ε_Y^{cr}

- The 2nd step is divided into three, namely:

1. Step pre-processor: who is to introduce the geometry of the problem, material properties and Boundary conditions.
2. While in the solution phase, we choose the type of analysis that must be performed.
3. Finally, the results of the completed solution are observed in the post-processing step.

In order to conduct time-dependent numerical modeling, the finite element code ANSYS occurs the different results shown in the Figure 9 and Figure 10. This Item illustrates a time-dependent behavior of two - pile group subjected to a constant static loading during 20000 hours. Figure 9 and Figure 10 illustrate the numerical contour plot results of elastic strain (ε_X^{cr}) and (ε_Y^{cr}) respectively.

The following Figures 11 and Figure 12, illustrates the contour plot elastic shear stress (τ_{XY}^{el}) and the contour plot of Shear Creep strain (ε_{XY}^{cr}) in the soil pile model respectively. It is observed that the shear stresses are focused at the level of the surface of the anchoring zone of the piles in the bedrock. As shown in Figure 11 and Figure 12 that the maximum and minimum values of elastic and creep strain deformations are set in the soil and pile head contact zone.

The following figures illustrate the creep strain in the structure material as (Concrete pile, clay and bedrock), according to the creep equation cited in Equation. 1 Above, called: Strain Hardening » model.

- Clay Material (Figure.13)
- Concrete Pile (Figure 14)
- Bedrock (Figure 15)

These figures illustrate that the Creep Curves Strain is characterized by two steps sum follows:

- 1st phase: 0 < t < 10000 Hours: we note that the experimental results and results numerical are similar in the concrete and bed rock material. But on the other hand, this step is reduced at the interval time: 0 < t < 4000 in the material clay
- 2nd phase: 10000 < t < 20000 hours: The experimental and theorical creep curve is briefly shifted in the three material structure constituting.

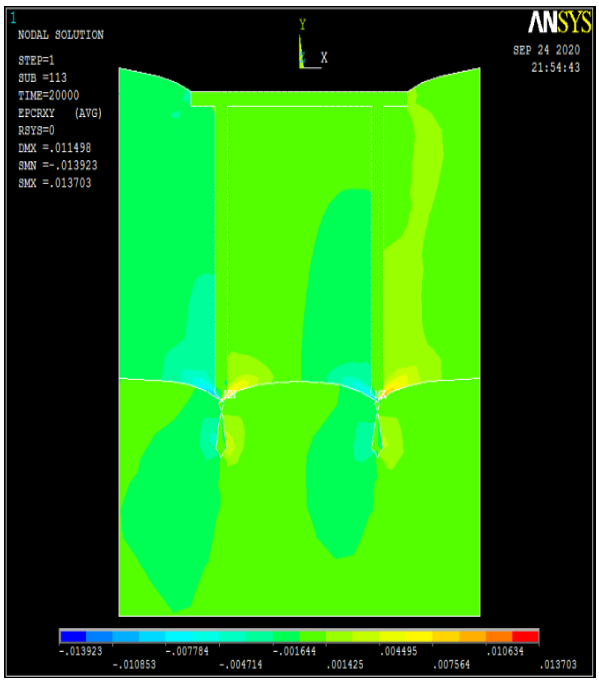


Figure 11. Contour plot of Shear Creep strain ε_{XY}^{cr}

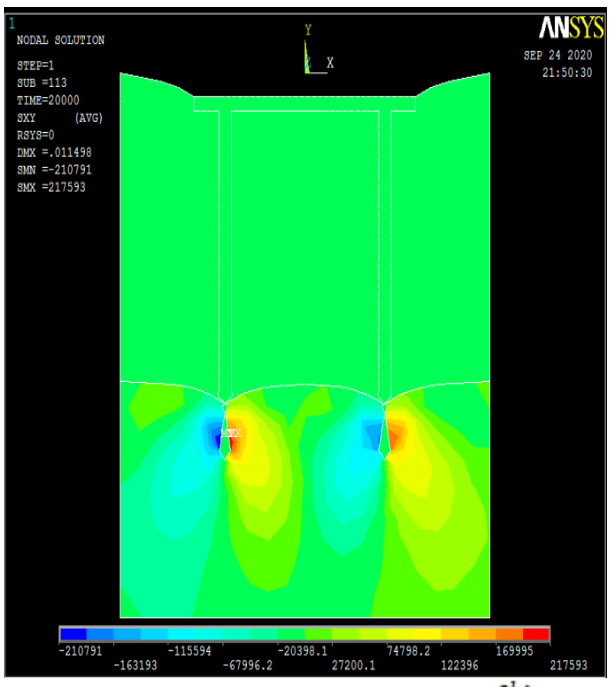


Figure 12. Contour plot of Shear stress (τ_{XY}^{el})

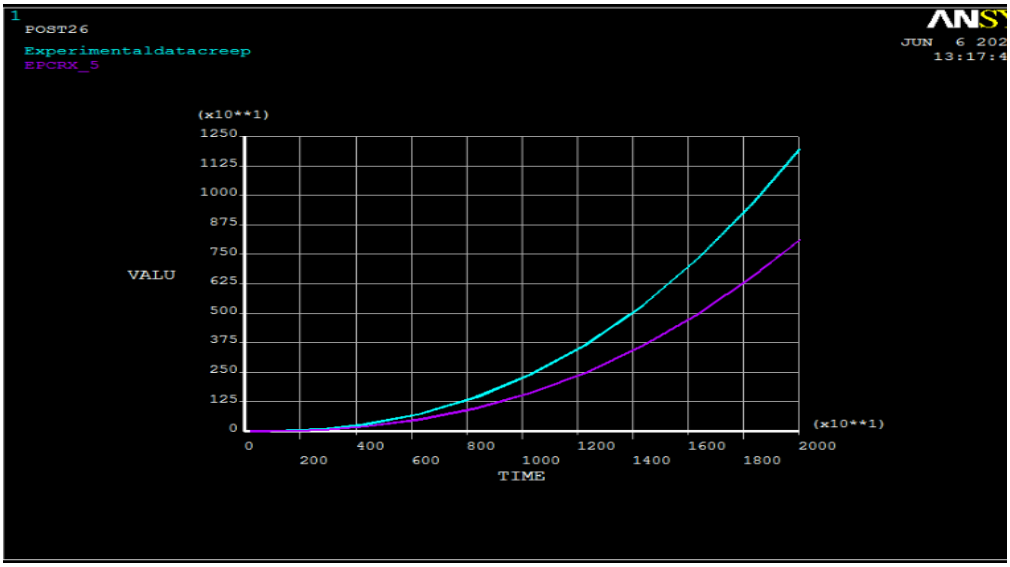


Figure 13. Creep strain curve (Clay)

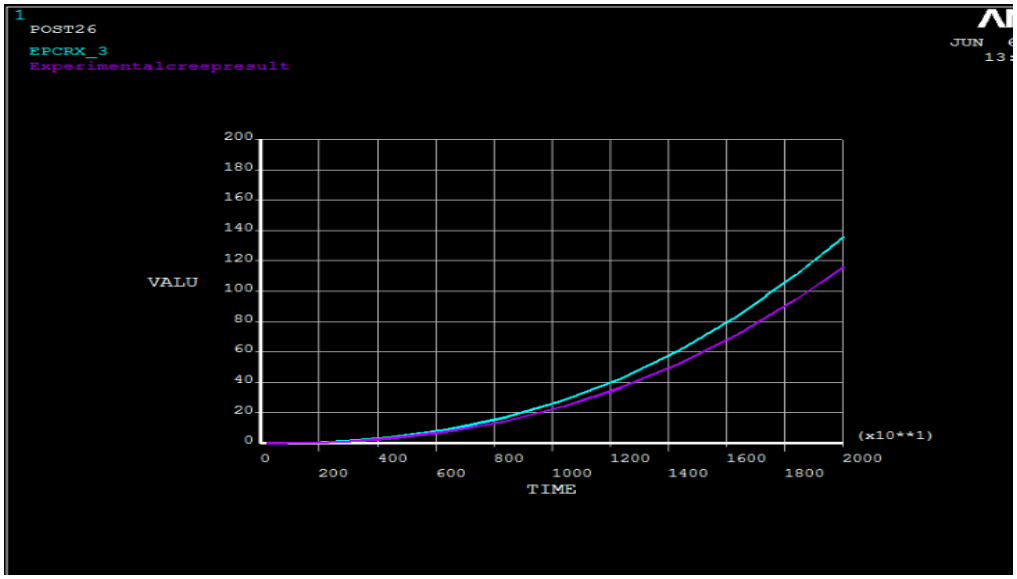


Figure 14. Creep strain curve of pile

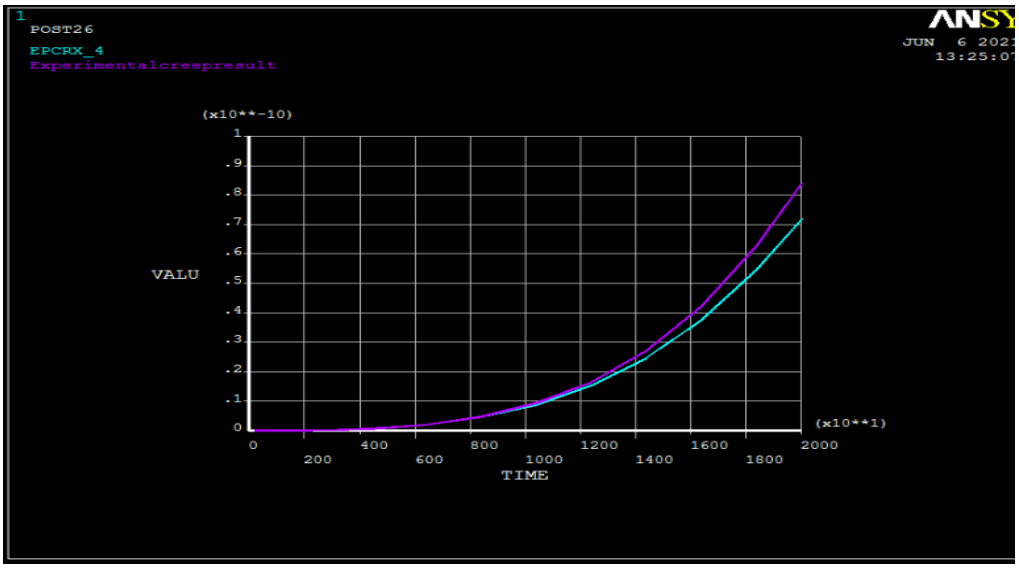


Figure 15. Creep strain curve (bed rock)

Conclusion

The behavior of civil engineering works such as retaining walls, reinforcements, tunnels and foundations is a soil-structure interaction problem. At present, it is commonly accepted that, within the framework of the study of the soil-structure interaction, the transmission of forces, from the structure to the ground, takes place through a thin layer of soil in contact with the structure called "interface". The interface is the site of complex mechanical phenomena: it generates locations of deformation and significant stress concentrations. These phenomena are strongly influenced by the mechanical characteristics of the granular soil and of the structural element, which are generally very contrasting. Breakage is often checked within this layer. He analyzed that, for a correct modeling of a geotechnical structure built in clay and bed rock, it is important to take into account the particular behavior of this interface. The modeling of the soil-structure interface is of capital importance in understanding its influence on the behavior of structures. The ANSYS software offers us this opportunity to achieve the junction between two distinct facets, with appropriate elements. The mains of these papers are to cite the creep behavior with different methods of contact modeling between the interface soil structures. Creep curves strain and shear creep curves numerical results of the different constitutive materials if structure are show's in the above figures. in terms of perspective, we intend to compare the numerical results to the experimental results.

Scientific Ethics Declaration

* The authors declare that the scientific ethical and legal responsibility of this article published in EPSTEM journal belongs to the authors.

Conflict of Interest

* The authors declare that they have no conflicts of interest

Funding

* This research received no specific grant from any funding agency in the public, commercial, or not-for-profit sectors.

Acknowledgements or Notes

* This article was presented as a poster presentation at the International Conference on Technology, Engineering and Science (www.icontes.net) held in Antalya/Türkiye on November 12-15, 2025.

* This research paper has been developed and produced at the laboratory of geotechnical Environnement and Amenagement (LGEA) of the University of Mouloud Mammeri Tizi – Ouzou, Algeria, for that I would like to thank all reviewers who contributed to its final development.

References

ANSYS, Inc. (2016). *ANSYS contact technology guide* (Release 14.0). ANSYS, Inc.

ANSYS, Inc. (2016). *ANSYS element reference: General element features* (Release 14.0). ANSYS, Inc.

Arany, L., Bhattacharya, S., Macdonald, J., & Hogan, S. J. (2017). Design of monopiles for offshore wind turbines in 10 steps. *Soil Dynamics and Earthquake Engineering, 92*, 126–152.

Coen, M. H., Mozer, M. C., Hasha, R., & Flanagan, J. L. (2002). Room service, AI-style. *IEEE Intelligent Systems, 14*(2), 8–19.

Curnier, A., & Alart, P. (1988). A generalized Newton method of contact problems with friction. *Journal of Theoretical and Applied Mechanics, 7*, 145–160.

Ghouilem, K., Mehaddene, R., & Kadri, M. (2017). Contact friction simulating between two rock bodies using ANSYS. *International Journal of Engineering Research in Africa, 29*, 1–9.

Gil-Martín, L. M., Carbonell-Márquez, J. F., Fernández-Ruíz, M. A., & Hernández-Montes, E. (2016). Theoretical and experimental short-term behavior of non-symmetrical wall pile retaining systems. *Engineering Structures, 112*, 172–183.

Juvinall, R. C., & Marshek, K. M. (1991). *Fundamentals of machine component design* (2nd ed.). John Wiley and Sons.

Kim, Y., & Jeong, S. (2011). Analysis of soil resistance on laterally loaded piles based on 3D soil-pile interaction. *Computers and Geotechnics, 38*(2), 248–257.

Michel, P., Butenweg, C., & Klinkel, S. (2018). Pile-grid foundations of onshore wind turbines considering soil-structure-interaction under seismic loading. *Soil Dynamics and Earthquake Engineering, 109*, 299–311.

Ottaviani, M. (1975). Three-dimensional finite element analysis of vertically loaded pile groups. *Géotechnique, 25*(2), 159–174.

Randolph, M. F. (1981). The response of flexible piles to lateral loading. *Géotechnique, 31*(2), 247–259.

Selby, A. R., & Arta, M. R. (1991). Three dimensional finite element analysis of pile groups under lateral loading. *Computers & Structures, 40*(5), 1329–1336.

Shigley, J. E. (1972). *Mechanical engineering design* (2nd ed.). McGraw-Hill.

Simo, J. C., Wriggers, P., & Taylor, R. L. (1985). A perturbed Lagrangian formulation for the finite element solution of contact problems. *Computer Methods in Applied Mechanics and Engineering, 50*(2), 163–180.

Smith, I. M., & Griffiths, D. V. (1988). *Programming the finite element method* (2nd ed.). John Wiley & Sons.

Timoshenko, S. P., & Goodier, J. N. (1970). *Theory of elasticity* (3rd ed.). McGraw-Hill.

Wriggers, P., & Simo, J. C. (1985). A note on tangent stiffness for fully nonlinear contact problems. *Communications in Applied Numerical Methods, 1*(4), 199–203.

Author(s) Information

Ghouilem Kamel
Mouloud Mammeri University of Tizi-Ouzou
Ummto, BP 17 RP, Tizi-Ouzou 15000, Algeria
Contact e-mail : *kamel.ghouilem@ummto.dz*

Belmihoub Hacene
University of Bouira (Mohand Oulhadj University of Bouira), Bouira, Algeria

To cite this article:

Kamel, G., & Hacene, B. (2025). Numerical modeling creep of two piles under constant static loading using ANSYS. *The Eurasia Proceedings of Science, Technology, Engineering and Mathematics (EPSTEM), 38*, 30-39.

The Eurasia Proceedings of Science, Technology, Engineering & Mathematics (EPSTEM)
ISSN: 2602-3199

The Eurasia Proceedings of Science, Technology, Engineering and Mathematics (EPSTEM), 2025

Volume 38, Pages 40-46

IConTES 2025: International Conference on Technology, Engineering and Science

Sliding Neural Artificial Controller of Induction Motor Combined with NPC Five Level Inverter

Mendaz Kheira
University of Ain Temouchent

Miloudi Houcine
Djillali Liabes University of Sidi Bel Abbes

Khadraoua Narimene
University of Ain Temouchent

Abstract: Sliding mode is a robust approach used in nonlinear control; however, it can lead to high frequency chattering caused by the discontinuous control action. This phenomenon can become a significant issue, particularly when the system's state is near the sliding surface. To minimize the chattering phenomenon, we have replaced the discontinuous control with a neural artificial network. This has led to the development of a new controller, referred to as the sliding neural artificial controller, which is applied in speed control. This approach appears to effectively address these challenges while ensuring optimal control performance. Induction motors play a crucial role in the industry. To achieve speed variation, multi-level inverters are utilized due to their significant advantages. They enable operation in medium and high voltage as well as high-power applications while delivering improved voltage waveforms with low total harmonic distortion, making them ideal for electric machine applications. This article examines the Speed Sliding Neural Artificial (SM-ANN) controller employed to regulate the speed of an induction motor in combination with a Five Neutral Point Clamped inverter. The study focuses on evaluating the performance based on the physical parameters of the squirrel cage motor, such as speed, electromagnetic torque, and current, in comparison to the conventional speed sliding mode controller. Simulation results indicate significant improvements achieved by the SM-ANN controller, particularly in reducing ripple in the motor parameters. These simulations, conducted using Matlab/Simulink, effectively demonstrate the robustness and efficiency of the SM-ANN controller.

Keywords: Sliding mode controller (SMC), Artificial neural network (ANN), NPC five level inverter, Performance

Introduction

The induction motor is among the most commonly used machines in various variable-speed applications due to its several advantages, including ease of manufacturing and maintenance (Chuanguang et al., 2020 ; Mıloudı. et al., 2024; Bermakiet et al. 2023). It is also highly valued for its reliability and durability. However, while its mechanical structure is relatively simple, its mathematical model is highly complex, being multi-variable and non-linear in nature (Hakmiet, et al., 2024 ; Gourbi, et al., 2024).

Sliding mode control operates on the fundamental principle of directing the system's state trajectory toward a predefined surface, known as the sliding or switching surface, and ensuring it remains near this surface through a suitable switching mechanism. Designing a sliding mode controller involves two key steps : defining an appropriate switching surface and formulating the control law, which includes both the equivalent command and

- This is an Open Access article distributed under the terms of the Creative Commons Attribution-Noncommercial 4.0 Unported License, permitting all non-commercial use, distribution, and reproduction in any medium, provided the original work is properly cited.

- Selection and peer-review under responsibility of the Organizing Committee of the Conference

© 2025 Published by ISRES Publishing: www.isres.org

the discontinuous command. This control method provides desirable characteristics, such as robustness against parameter variations (Mendaz et al., 2023).

However, in SMC, when the system state is near the sliding surface, the high frequency chattering phenomena caused by the discontinuous control action is a serious issue (Chuanguang et al., 2020; Mendaz et al., 2023). We have used neural networks in place of discontinuous control to lessen the chattering phenomenon. The Sliding mode controller is included into the artificial neural network structure by the Sliding Artificial Neural Network (SANN) technique. The sliding mode controller is connected to an artificial neural network, which gives it structure and learning capabilities. Sliding Artificial Neural Network control is used to regulate the speed of induction motors.

Interesting benefits of multilevel inverters include the ability to operate in medium, high voltage, and high power applications and the provision of an improved voltage waveform (Miloudi et al., 2022). The speed sliding artificial neural network controller of the induction motor connected to the NPC five level is discussed in this paper. Matlab simulation results demonstrate the robustness and performance of this controller.

Method

Model Mathematic of Induction Motor

The mathematical model of induction motor is utilized to analyze its dynamic behavior (Miloudi, H. et al., 2024). Variations in the motor's dynamic behavior impact parameters like speed, torque, resistance, and flux, which are essential for evaluating the motor's performance (Chuanguang et al., 2020; Santos et al., 2025). The dynamic model of the squirrel cage motor is derived by converting three-phase quantities into two-phase direct and quadrature axis quantities using Park transformations. The mathematical equation of the induction motor, expressed in the rotating reference frame, is as follows :

$$\frac{d\Omega}{dt} = \frac{n_p L_m}{J L_r}\left(\varphi_{rd} I_{sq} - \varphi_{rq} I_{sd}\right) - \frac{1}{J} C_r - \frac{1}{J} f\Omega \quad (1)$$

$$\frac{dI_{sd}}{dt} = -\lambda\, I_{sd} + w_s I_{sq} + \frac{K}{\tau_r}\varphi_{rq} + w_r\, K\varphi_{rd} + \frac{1}{\sigma L_s} v_{sd} \quad (2)$$

$$\frac{dI_{sq}}{dt} = -w_s I_{sd} - \lambda\, I_{sq} - w_r\, K\varphi_{rd} - \frac{K}{\tau_r}\varphi_{rq} + \frac{1}{\sigma L_s} v_{sq} \quad (3)$$

$$\frac{d\varphi_{rd}}{dt} = \frac{L_m}{\tau_r} I_{sd} - \frac{1}{\tau_r}\varphi_{rd} + (w_s - w_r)\varphi_{rq} \quad (4)$$

$$\frac{d\varphi_{rq}}{dt} = \frac{L_m}{\tau_r} I_{sq} - (w_s - w_r)\varphi_{rd} - \frac{1}{\tau_r}\varphi_{rq} \quad (5)$$

Speed Sliding Control

The motor speed Ω should track a specific reference speed Ω_{ref} with presence of load torque. The system controlled in such a way that the error $e(t) = \Omega_{ref} - \Omega$ and its rate of change always move towards a sliding surface. We take n = 1, the speed control manifold equations can be obtained as equation "(7)" presents the sliding surface and "(8)" represents the derivative of the surface which is used to calculate the equivalent control (Mendaz et al., 2023).

$$\frac{d\Omega}{dt} = \frac{n_p L_m}{J L_r}\left(\varphi_{rd} I_{sq} - \varphi_{rq} I_{sd}\right) - \frac{1}{J} T_l - \frac{1}{J} f\Omega \quad (6)$$

$$S(\Omega) = \Omega_{ref} - \Omega \quad (7)$$

$$\frac{dS(\Omega)}{dt} = \frac{d\Omega_{ref}}{dt} - \frac{d\Omega}{dt} \quad (8)$$

Where the equivalent control is:

$$I_{sq}^{eq} = \left(\frac{d\Omega_{ref}}{dt} + \frac{1}{J} T_l + \frac{1}{J} f\Omega\right) \frac{JL_r}{n_p L_m} \frac{1}{\varphi_{rd}} \quad (9)$$

The correction factor (discontinuous command) gives by flowing equation (Boukhnifer et al .,2006), (Mendaz et al., 2023) :

$$I_{qn} = K_{q1} sat(S(\Omega)) \quad (10)$$

Where:

$$sat(S(\Omega)) = \begin{Bmatrix} \frac{1}{\varepsilon} S(\Omega) & if |S(\Omega)| \leq \varepsilon \\ sgin\, S(\Omega) & if |S(\Omega)| > \varepsilon \end{Bmatrix} \quad (11)$$

NPC Five Level Inverter Structure

The neutral-point-clamped (NPC) topology is one of the most commonly used configurations. In a neutral-point-clamped inverter, the DC link is divided into multiple smaller voltage levels through a series of bulk capacitors connected in a bank. This structure enables the inverter poles to connect to any of these voltage levels, producing a multi-level voltage waveform at the output (Mendaz, et al., 2022). The NPC five-level converter topology utilizes clamped diodes to ensure equal voltage distribution among the switches, there by enhancing their reliability (Elamri et al., 2022). A three-phase N-level diode-clamped inverter requires (N-1) capacitors, 3(N-1) (N-2) clamped diodes, and 6(N-1) active switches for its operation (Boukhnifer et al, 2006).

A three-phase, five-level NPC converter is designed with a common DC bus. It comprises eight switches arranged in series, six clamping diodes, and four capacitors connected to a single DC voltage source. Each switch includes an IGBT and an antiparallel diode to support its functionality (Mendaz et al., 2022 ; Elamri et al., 2022). The switches must not open or close at the same time to prevent a short circuit in the DC input source of the inverter or the disruption of the inductive circuit in its load (Bermaki et al., 2022 ; Boukhnifer et al.,2006). The floating diodes, six per arm, play a crucial role in enabling the output of varying voltage levels for each arm. The continuous input bus is composed of four capacitors (C1, C2, C3 and C4), making it possible to create a set of three capacitive middle points. The total voltage of the DC bus isV_{dc}; under normal operating conditions, it is uniformly distributed over the four capacitors, which then have a voltage$\frac{V_{dc}}{4}$ at their terminals.

Table1. Switching states of five level NPC inverter States of switches voltages level.

States of switches								Voltages level
K1	K2	K3	K4	K'1	K'2	K'3	K'4	
on	on	on	on	off	off	off	off	$\frac{V_{dc}}{4}$
off	on	on	on	on	off	off	off	$\frac{V_{dc}}{2}$
off	off	on	on	on	on	off	off	0
off	off	off	on	on	on	on	off	$-\frac{V_{dc}}{4}$
off	off	off	off	on	on	on	on	$-\frac{V_{dc}}{2}$

The "Fig. 1" shows the speed sliding mode control of induction motor.

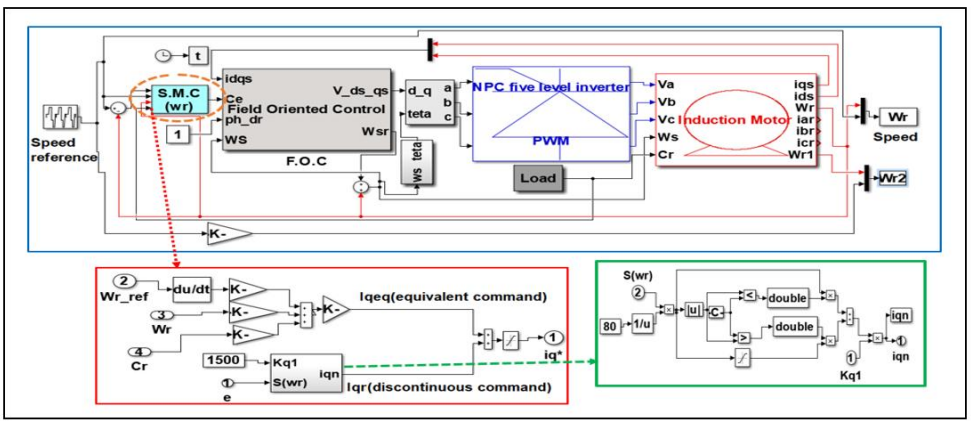


Figure 1. Speed sliding mode control of induction motor combined NPC five level inverter

Speed Sliding Neural Control

One notable drawback of sliding mode control is the chattering phenomenon caused by the discontinuous control command. To enhance the performance of SMC, numerous advancements have been proposed, particularly through the integration of Artificial Neural Networks (ANN) (Szoke.et al.,2025; Venkatesan et al.,2020). In this context, the objective is to substitute the discontinuous control command with artificial neural networks. Figure 2 illustrates the speed control of an asynchronous motor using a hybrid controller that combines sliding mode control and artificial neural networks, referred to as the Sliding Artificial Neural Network Controller (SANN).

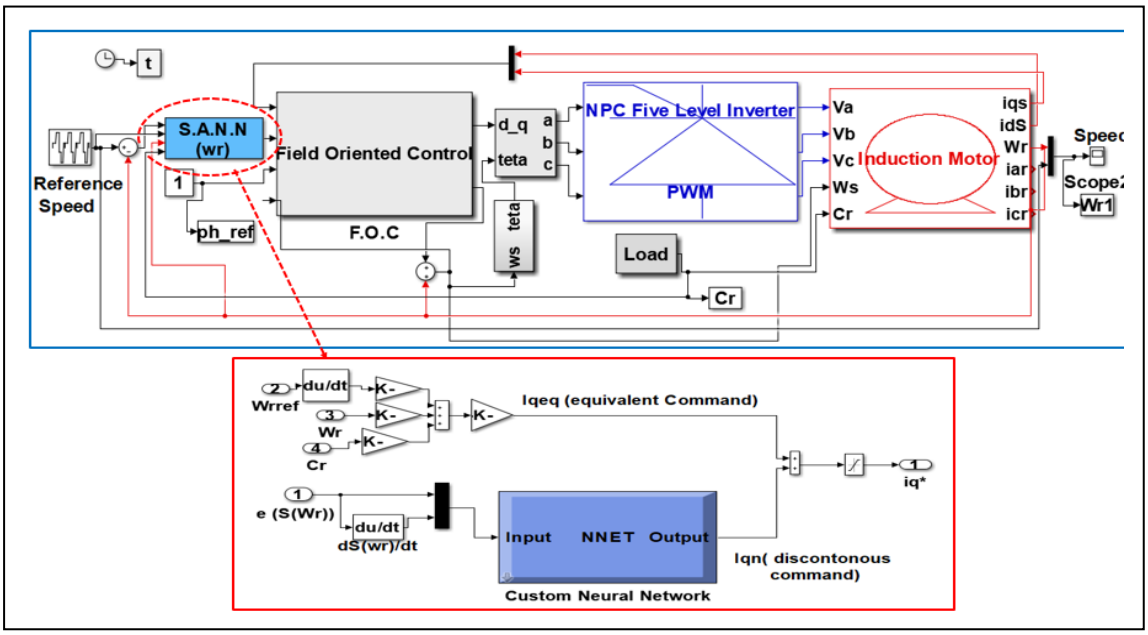


Figure 2. Speed sliding artificial neural networks (SANN) control of induction motor combined NPC five level inverter

The Figure.3 shows the architecture of speed sliding artificial neural networks (SANN) controller.

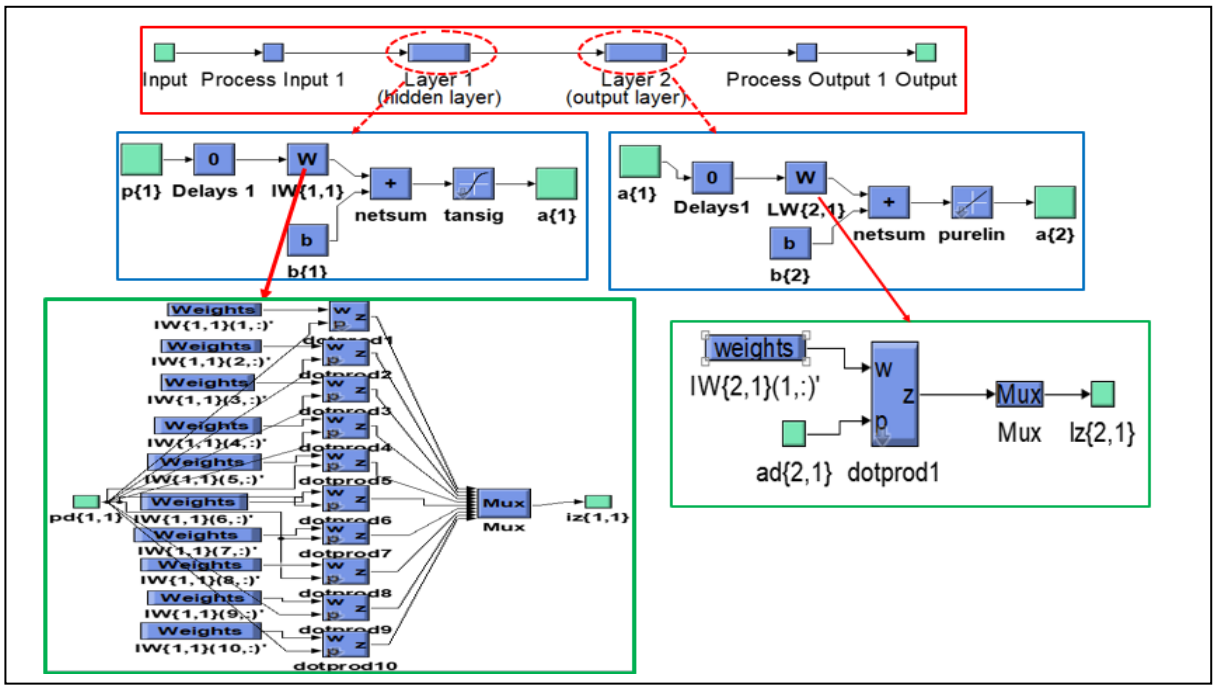


Figure 3. The architecture of speed sliding artificial neural networks (SANN) controller

Results and Discussion

In Figure.4, the machine is applied with a load torque of 10 Nm in a time interval [0.31, 0.5] s and [1.21, 1.5] s; the direction of rotation of the machine is reversed from 157 rad/s to -50 rd/s in time 1.64s and diminution of speed to -157rd/s in time 2.1s . When the motor started with the reference speed 50 rd/s in the time interval [0, 0.01] s, the sliding artificial neural (SANN) control show that the speed returns to its reference during the transient regime compared to the sliding mode (SM) regulator, which shows that there is a gap between the motor speed and its reference. When the direction of rotation reversed, two controllers show that the speed follows its reference in the steady state. The load torque application has not effect on speed response. According to the speed results, we observe that SANN control gives a perfermant result, which is in the reduction of ripples in the speed and torque signal compared to the SMC, which shows an increase in ripples on the speed, and torque signal that created by the discontinuous control. Therefore, the combination between SM and ANN control, which replaces the discontinuous control, improves the performance of this regulator wish observed in the reduction of ripples then it is the reduction of the chattering effect. The simulation results show that the speed sliding artificial neural control (SANNC) is robust to the variation of the reference speed, since the speed follows the reference speed at start-up as well as the reversal of the direction of rotation, in a very satisfactory way, the application of load torque does not influence the speed response. In the Fig. 4 the speed sliding control (SMC) ensures the robustness of this technique to high and low speed variations as well as the application of load torque (Tl=10Nm) in time interval [0.26, 0.75] s and [0.91, 2.3] s .

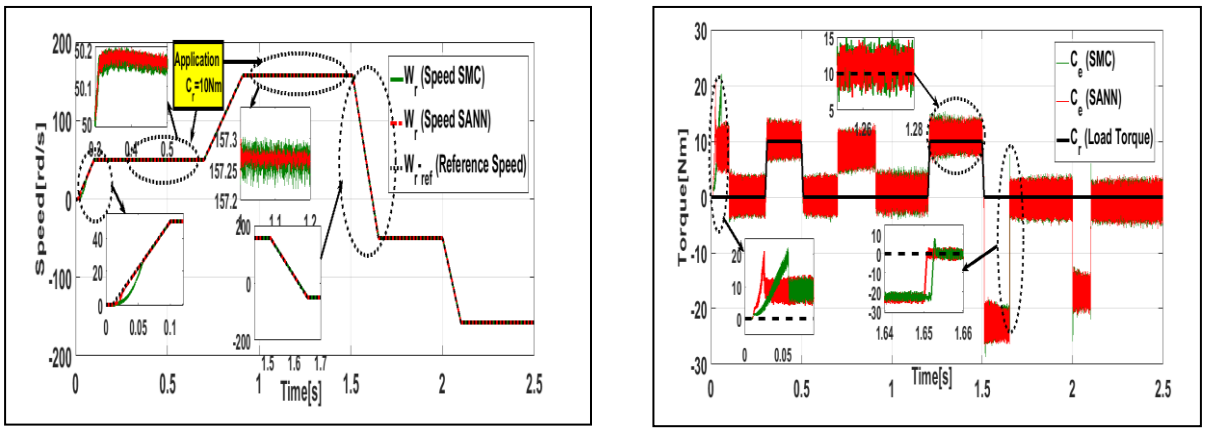


Figure 4. Speed and torque result of speed sliding mode control and speed sliding artificial neural networks (SANN) controller of induction motor combined NPC five level inverter

We show that the harmonic spectrum of one phase stator current of induction motor combined with NPC five level inverter obtained using Fast Fourier Transform (FFT) technique for the two controllers (Figure5 and Figure6). It can be clear observed that the total harmonic distortion (THD) is reduced for SANN (THD = 0.48%) compared to SMC (THD = 0.75%). Therefore, the proposed controller (SANN) has proven effective in reducing the value of the total harmonic distortion.

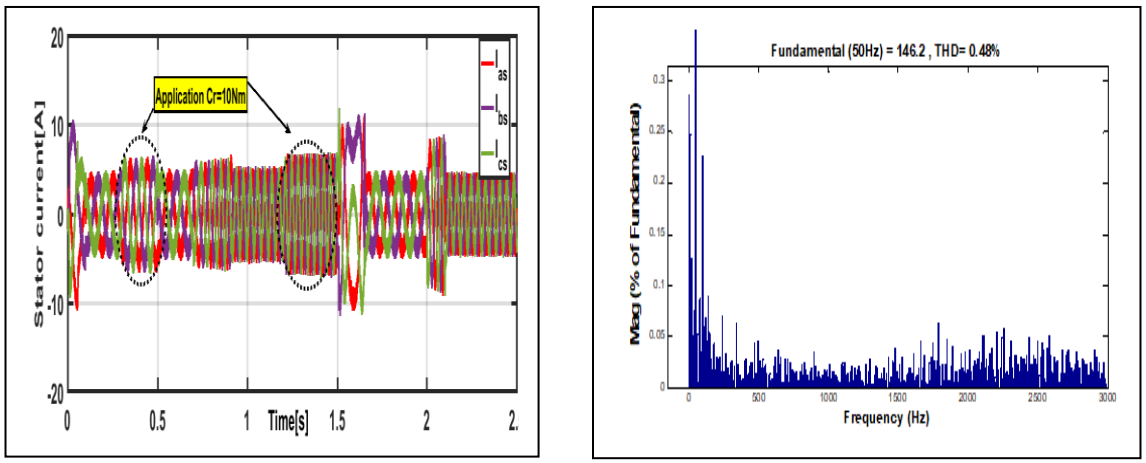


Figure 5. Stator current result of speed sliding artificial neural networks (SANN) controller of induction motor combined NPC five level inverter and spectrum harmonic of one phase stator current for SANN.

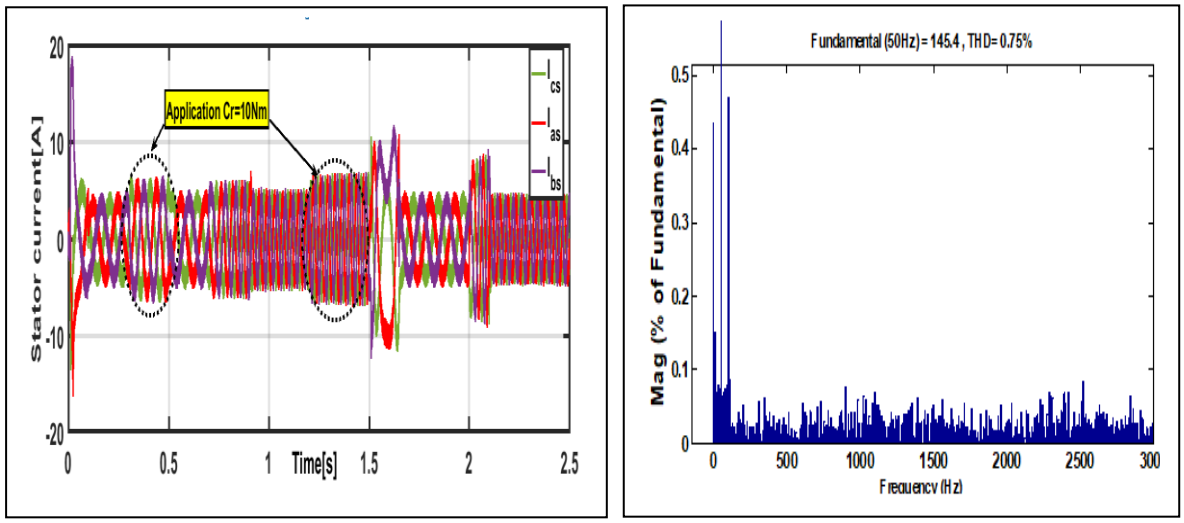


Figure 6. Stator current result of speed sliding mode (SMC) controller of induction motor combined NPC five level inverter and Spectrum harmonic of one phase stator current for SMC.

Conclusion

Sliding mode control is widely recognized as a robust control method. However, its primary drawback is the chattering phenomenon, which results from high-frequency switching near the sliding surface due to the discontinuous control law used during sliding mode design and interactions with parasitic dynamics. To address this issue, the discontinuous control is replaced with a neural network, incorporating artificial intelligence (ANN) into the sliding mode methodology. Neural networks have been integrated into sliding mode control for several purposes, such as improving controller performance and eliminating chattering effects. The proposed controller employs a speed sliding neural network (SANN) for an induction motor paired with an NPC five-level inverter, delivering enhanced performance outcomes. This setup effectively reduces ripples in the physical parameters of the induction motor, including speed, electromagnetic torque, as well as stator and rotor currents. Simulation results clearly demonstrate the superior performance of speed sliding neural control. The response characteristics reveal its excellent capability for mitigating oscillations and improving overall system performance.

Scientific Ethics Declaration

* The authors declare that the scientific ethical and legal responsibility of this article published in EPSTEM journal belongs to the authors.

Conflict of Interest

* The authors declare that they have no conflicts of interest

Funding

* This research received no specific grant from any funding agency in the public, commercial, or not-for-profit sectors.

Acknowledgements or Notes

* This article was presented as an oral presentation at the International Conference on Technology, Engineering and Science (www.icontes.net) held in Antalya/Türkiye on November 12-15, 2025.

References

Bermaki, M. H., Miloudi, H., Miloudi, M., Gourbi, A., & Bendaoud, A. (2023). High-frequency differential mode modeling of universal motor's windings. *International Journal of Electrical and Electronics Research, 11*, 1057-1064.

Boukhnifer, M., & Chaib, S. (2006). Control for induction motor fed by five level inverter with sliding mode observer. *2006 IEEE International Conference on Control Applications (CCA),* Munich, Germany.

Chuanguang, C., & Haisheng, W. (2020). Backstepping sliding mode control of induction motor based on disturbance observer. *IET Electric Power Applications, 14*(12), 2537-2546.

Elamri, O., Oukassi, A., El Bahir, L., & El Idrissi, Z. (2022). Combined vector and direct controls based on five-level inverter for high performance of IM drive. *World Electric Vehicle Journal, 13*(1), 2-16.

Gourbi, A., Miloudi, M., Miloudi, H., & Bermaki, M. H. (2024). Comparative analysis of differential-mode impedance in single-phase induction motors. *WSEAS Transactions on Circuits and Systems, 23*, 261-273.

Hakmi, Y., Miloudi, H., Miloudi, M., Bendaoud, A., Mendaz, K., & Bermaki, M. H. (2024*).* A novel experimental approach for predictive high frequency modeling of differential-mode impedance in three-phase induction motors (Paper presentation). *3rd International Conference on Advanced Electrical Engineering*, Sidi-Bel-Abbes, Algeria.

Mendaz, K., & Flitti, M. (2023). Input-output linearization control based on the sliding mode of the squirrel cage motor. *Revue Roumaine des Sciences Techniques – Série Électrotechnique et Énergétique, 68*(2), 176-181.

Mendaz, K., Flitti, M., Benhadda, Y., Attou, A., & Bendaoud, A. (2022). Effect of defective five levels inverter on input output linearization control for induction motor. *Electrotehnica, Electronica, Automatica (EEA), 70*(4), 30-45.

Mendaz, K., Miloudi, H., & Younes, K. (2023). Sliding input output control of squirrel cage motor based NPC five level inverter. *Periodica Polytechnica Electrical Engineering and Computer Science, 67*(4), 458-468.

Miloudi, H., Miloudi, M., Ardjoun, A. M., Mahmoud, M. M., Telba, A. A., Denaï, M., Khaled, U., & Ewias, A. M. (2024). Electromagnetic compatibility characterization of start-capacitor single-phase induction motor. *IEEE Access, 12*, 2313-2316.

Miloudi, H., Miloudi, M., Gourbi, A., Bermaki, M. Z., Bendaoud, A., & Zeghoudi, A. (2022). A high-frequency modeling of AC motor in a frequency range from 40 Hz to 110 MHz. *Electrical Engineering & Electromechanics Journal, 6*, 3-7.

Santos, V. F., Frosini, L., & Sotelo, D. M. (2025). Diagnosis of rotor asymmetries in induction motors: A steady state approach using rotating frame references. *e-Prime - Advances in Electrical Engineering, Electronics and Energy, 12*(1), 1-12.

Szoke, E., Szabo, C., & Pintilie, N. P. (2025). Artificial intelligence-based sensorless control of induction motors with dual-field orientation. *Applied Sciences, 15*(16), 2-24.

Venkatesan, S., Premkumar, K., & Vishnupriya, M. (2020). Speed control of permanent magnet synchronous motor using neural network model predictive control. *Journal of Energy Systems, 4*(2), 71-87.

Author(s) Information

Mendaz Kheira
University of Ain Temouchent, Faculty of Sciences and Technologies, Electrotechnics Department, Algeria
Contact e-mail: kheira.mendaz@univ-temouchent.edu.dz

Miloudi Houcine
Djillali Liabes University of Sidi Bel Abbes
Electrical Engineering Department, School of Engineering Science, Algeria.

Khadraoua Narimene
University of Ain Temouchent, Faculty of Sciences and Technologies Electrotechnic Department, Algeria

To cite this article:

Kheira, M., Houcine. M., & Narımene, K. (2025). Sliding neural artificial controller of induction motor combined with NPC five level inverter**.** *The Eurasia Proceedings of Science, Technology, Engineering and Mathematics (EPSTEM), 38,* 40-46.

The Eurasia Proceedings of Science, Technology, Engineering & Mathematics (EPSTEM)
ISSN: 2602-3199

The Eurasia Proceedings of Science, Technology, Engineering and Mathematics (EPSTEM), 2025

Volume 38, Pages 47-55

IConTES 2025: International Conference on Technology, Engineering and Science

Development of High-Frequency Power Source Utilizing Electronic Ballast by Employing a Half-Bridge Inverter for Water Purification

Aicha Aissa-Bokhtache
Hassiba Benbouali University of Chlef

Maamar Latroch
Hassiba Benbouali University of Chlef

Taieb Bessaad
Hassiba Benbouali University of Chlef

Alla Eddine Toubal-Maamar
University of Boumerdes

Lemya Djafer
Hassiba Benbouali University of Chlef

Amina Merini
Hassiba Benbouali University of Chlef

Abstract: This paper outlines the design of a high-frequency power supply, specifically an electronic ballast based *PWM* inverter, intended to power a low-pressure *UV* Mercury-Argon lamp. The lamp emits germicidal *UV* radiation at a wavelength of 253.7 nm, which effectively targets *DNA* viruses and bacteria present in the water to be treated. The system underwent thorough modeling, encompassing both the electronic ballast and the discharge lamp. The power supply employs a standard converter setup, comprising a half-bridge rectifier and inverter controlled by *PWM*. Simulations conducted using the MATLAB software environment yielded satisfactory results aligned with our objectives. The primary aim was to achieve a sinusoidal *rms* current precisely at 0.65 A, operating at a frequency of 50 kHz, to maximize *UVc* radiation at 253.7 nm. Hence, contemporary converters employing semiconductor switches operating at high-frequencies (over 50 kHz for MOSFETs) have been employed with proportional-integral control techniques.

Keywords: Low-pressure UVc Lmap, Germicide, Electronic ballast, *PWM* inverter, Half-bridge inverter, *PI* controller

Introduction

In recent years, high-frequency electronic ballasts have emerged as a viable alternative to magnetic ballasts for discharge lamps due to their numerous advantages, including improved system performance (enhanced power factor), lightweight design, high luminous efficacy, long lifespan, lighting control capabilities, absence of flickering and audible noise (Aissa Bokhtache et al., 2024). However, it's crucial to carefully consider the cost implications associated with electronic ballasts (De Oro et al., 2014). During normal operation, discharge lamps exhibit negative differential resistance, necessitating effective current limiting mechanisms to prevent uncontrolled current growth. The presence of a ballast to regulate current is thus essential. The radiative characteristics of the lamp are influenced by factors such as gas mixture composition, discharge geometry, and

- This is an Open Access article distributed under the terms of the Creative Commons Attribution-Noncommercial 4.0 Unported License, permitting all non-commercial use, distribution, and reproduction in any medium, provided the original work is properly cited.

- Selection and peer-review under responsibility of the Organizing Committee of the Conference

© 2025 Published by ISRES Publishing: www.isres.org

electrical supply parameters like frequency and waveform. Key requirements for optimal operation include achieving zero average current, fast switching times, ensuring rapid re-ignition of the discharge at consistent currents, and the ability to operate as a cyclic current source with variable frequency.

Description and Operating Principle of the System

Figure 1 shows the block diagram of the proposed system, Electronic ballast connected with half-bridge inverter. In this type of source, the inverter is configured as a high-frequency generator. The source consists of: A single-phase rectifier, The *DC* bus (link circuit), The transistor half-bridge inverter generating an output frequency of 50 kHz, A resonant circuit comprising L_r and C_r to facilitate lamp ignition, A filter is typically included between the main terminals and the rectifier to comply with electromagnetic compatibility (*EMC*) regulations and an additional preheating circuit is necessary to prevent filament damage. (Aissa Bokhtache et al., 2015).

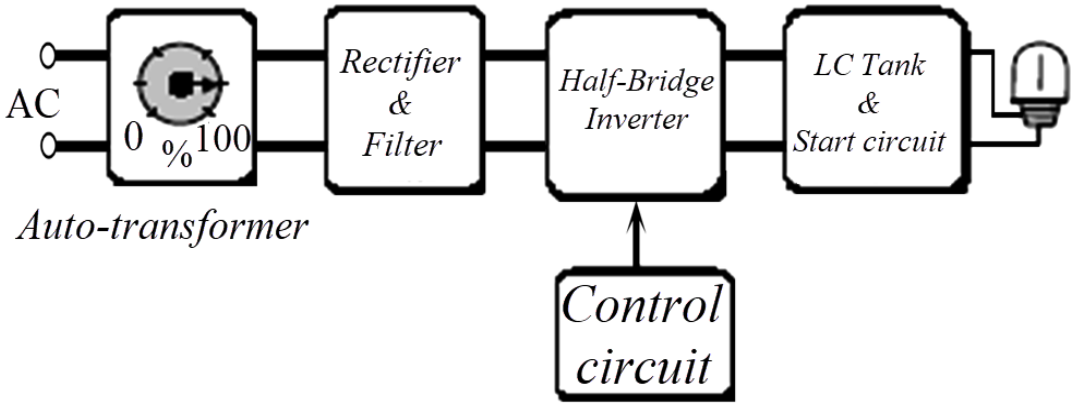


Figure 1. Block diagram of system consisting of a half-bridge inverter.

Figure 2 illustrates the electrical circuit of the proposed system.

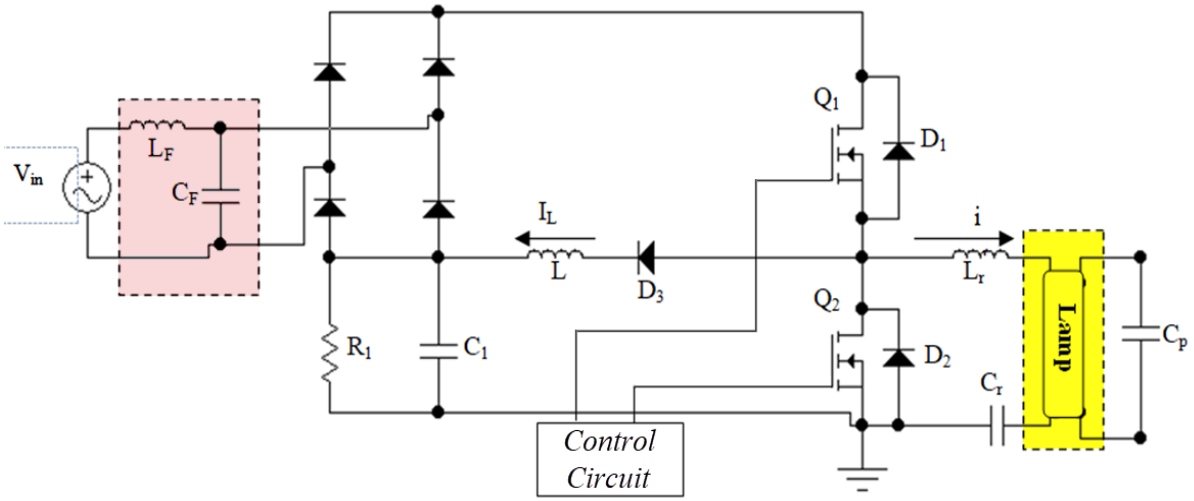


Figure 2. The electrical circuit of the proposed system.

The MOSFET is commonly employed in low-voltage applications with switching frequencies that can reach or exceed 100 kHz. It is also utilized for low-power applications. The operational principle of the proposed ballast's is described in steady-state modes, from mode 1 to mode 4. The equivalent circuit for each mode is depicted in Figure 3. To illustrate the circuit's equilibrium operation, all internal components are assumed to be ideal. This can be described as follows: (Aissa Bokhtache et al., 2016), (Kazufuni, et al., 2000).

Mode 1: $t_0 < t < t_1$: Between t_0 and t_1: Prior to Q_1 and Q_2 entering their respective modes, both are in the off state. When Q_1 is switched on at time t_0, a current flows through Q_1 and is split into two components: i_{load} and i_L. The component i_L flows through D_3, L, and C_r, while i_{load} flows through the fluorescent lamp.

Mode 2: $t_1 < t < t_2$: During Mode 2 ($t_1 < t < t_2$): Following the turn-off of Q_1 at t_1 while Q_2 remains off until t_2, i_L flows through C_1, D_2, D_3, L, and R, while i_{Load} flows through D_2, L_r, C_r, and the fluorescent lamp.

Mode 3: $t_2 < t < t_3$: At t_2, Q_2 is turned on. i_L reaches 0 between t_2 and t_3. Subsequently, after i_{ch} reaches 0, it flows in the opposite direction compared to the operational state of Q_1, leading to a decrease in the negative peak.

Mode 4: $t_3 < t < t_4$: when stopped at t_3 Q_2 and Q_1 remains off status for the period from t_3 to t_4, t_4 i_L through D_3, Q_1 is on. The next mode is the mode 1.

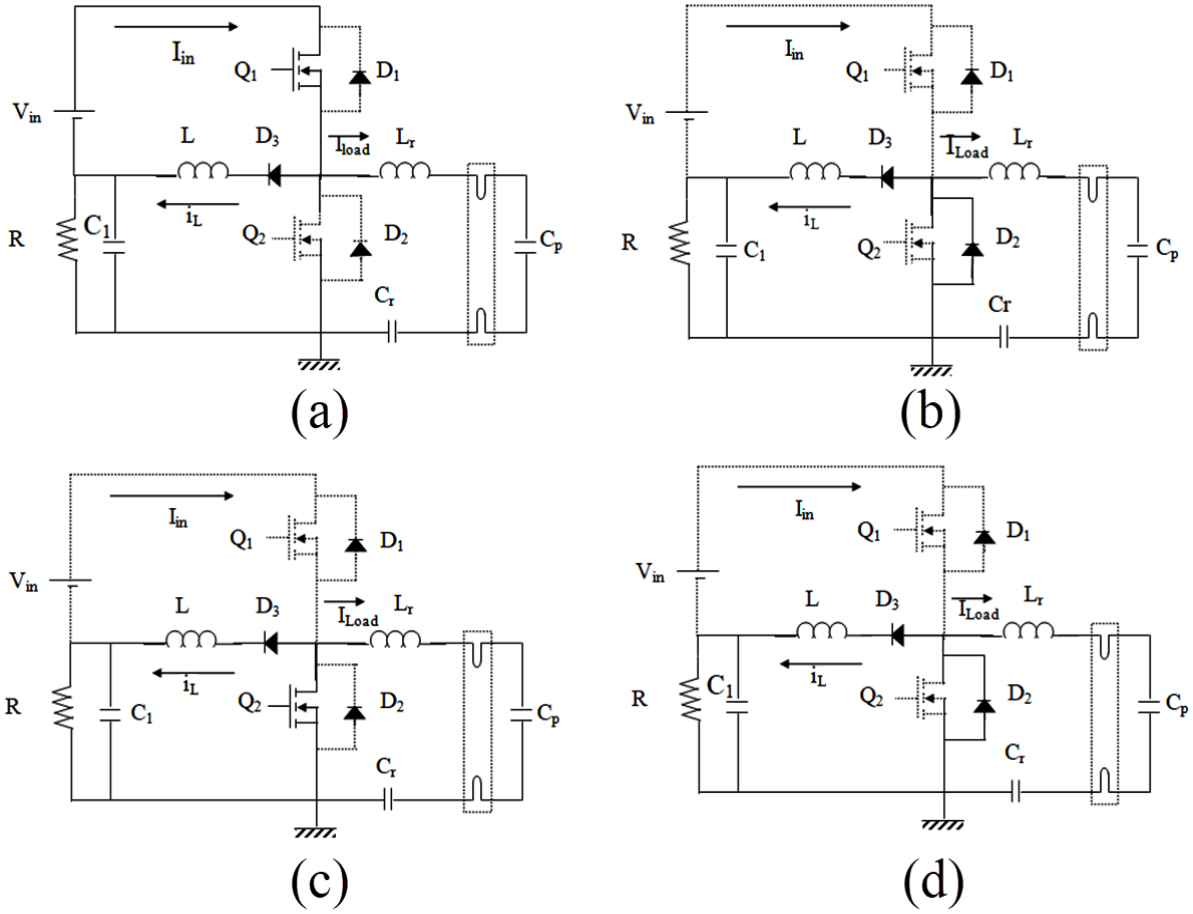


Figure 3. The equivalent circuits of the system operation modes.

The Electrical Circuit Model of the Lamp

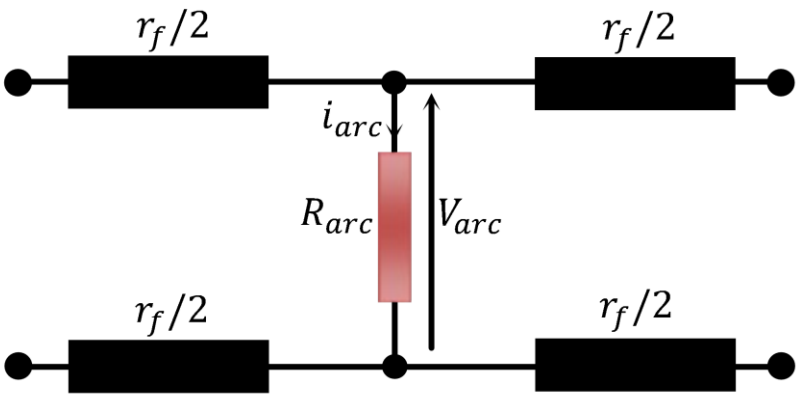


Figure 4. The fluorescent lamp electrical circuit model.

An electrical circuit model, depicted in Figure 4, has been proposed to characterize the electrical behavior of the fluorescent lamp when powered by a high-frequency electronic ballast. This model represents the lamp using two resistors: R_{arc}, which accounts for the electrical properties of the lamp's *arc* and is dependent on both power and temperature, and r_f, which represents the cathode filament (Aissa Bokhtache et al., 2017). Figure 5 illustrates the equivalent circuit of the system.

Where:

$$R_{arc} = \frac{V_{arc}}{i_{arc}} \tag{1}$$

$$P_{arc} = V_{arc} . i_{arc} \tag{2}$$

With : R_{arc}: *arc* resistance,i_{arc}: *arc* current, V_{arc} :*arc* voltage, P_{arc} :*arc* power.

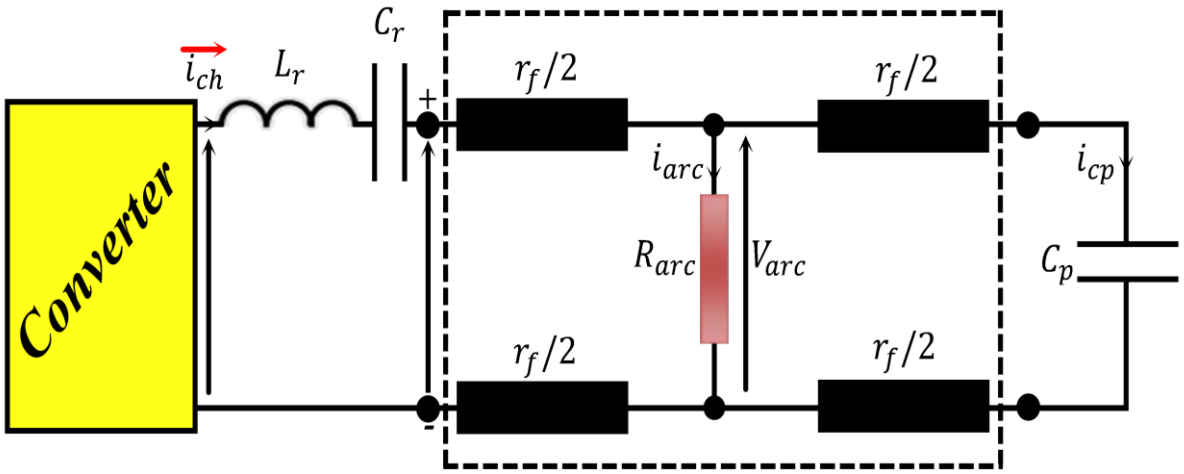


Figure 5. Equivalent circuit of the system.

The lamp voltage can be calculated as follows (7):

$$\begin{aligned} \vec{V}_{lamp} = \vec{V}_{arc} + 2\left[\frac{r_f}{2}(\vec{i}_{arc} + \vec{i}_{Cp})\right] &= V_{arc} + i_{arc} r_f + \frac{r_f V_{arc}}{r_f - jZ_{Cp}} \\ &= \left[\left(1 + \frac{r_f^2}{r_f^2 + Z_{Cp}^2}\right) V_{arc} + r_f i_{arc}\right] + j\frac{r_f Z_{Cp}}{r_f^2 + Z_{Cp}^2} V_{arc} \end{aligned} \tag{3}$$

Therfore,

$$\vec{V}_{Lamp} = \left[\left(1 + \frac{r_f^2}{r_f^2 + Z_{Cp}^2}\right) V_{arc} + r_f \frac{P_{arc}}{V_{arc}}\right] + j\frac{r_f Z_{Cp}}{r_f^2 + Z_{Cp}^2} V_{arc} \tag{4}$$

With : Z_{CP} is the reactance of the C_P capacitor and I_{CP} is current which flows through it. The resonant load current is in fact the sum of both *arc* current and filament current. As a result, by calculating the transfer function of the open-loop system indicted in figure 5 we have:

$$\frac{I_{Load}}{V_{Load}} = \frac{(R_{arc} + r_f) C_r C_p S^2 + C_r S}{(R_{arc} + r_f) L_r C_r C_p S^3 \left[(2R_{arc} + r_f) L_r C_r C_p + L_r C_r\right] S^2 + \left(R_{arc} + r_f\right)\left(C_r + C_p\right) S + 1} \tag{5}$$

Results and Discussion

The simulation results were conducted under the MATLAB/Simpower environment and are provided in the following figures. The converter frequency needs to be higher than the audible range, ensuring it operates effectively above 50 kHz. Additionally, the resonant circuit's resonant frequency is set at 42 kHz (Aissa Bokhtache et al., 2020; 2021).

Two tests are selected for comparison. The discharge lamp-electronic ballast system is first tested in an open-loop setup. Following this, the system is evaluated in a closed-loop arrangement using a traditional proportional-integral (*PI*) controller. The lamp used in the simulation is a real discharge lamp described in references (Aissa Bokhtache et al., 2023), the main characteristics of the discharge lamp-electronic ballast are given in (Table1) below:

Table 1. Characteristics of the discharge lamp-electronic ballast assembly.

Variables	Symbol	Values
Capacitance	C_r	*0.47 µF*
Capacitance	C_P	*3900 PF*
Inductance	L_r	*0.9 mH*
Power	P_{Lamp}	*65 W*
Frequency	f	*50 KHz*
Resistance	R_{arc}	*170.769* Ω
Resistance	r_f	*5* Ω
Voltage	V_{in}	*500V, 50Hz*
RMS Current	I_{arcrms}	*0.65 A*
Inductance	L	*1.27 mH*
Capacitance	C_1	*33 F*
Inductance	L_F	*1.5 mH*
Capacitance	C_F	*220 nF*

Open-Loop Simulation Results

Figure 6 illustrates the obtained currents and voltages of the discharge lamp. Figure 7 resumes the *THD* of the *arc* voltage and the *arc* current of the discharge lamp. Figure 8 illustrates the waveform of the discharge lamp filament current, and Figure 9 shows the effective *arc* current of the discharge lamp.

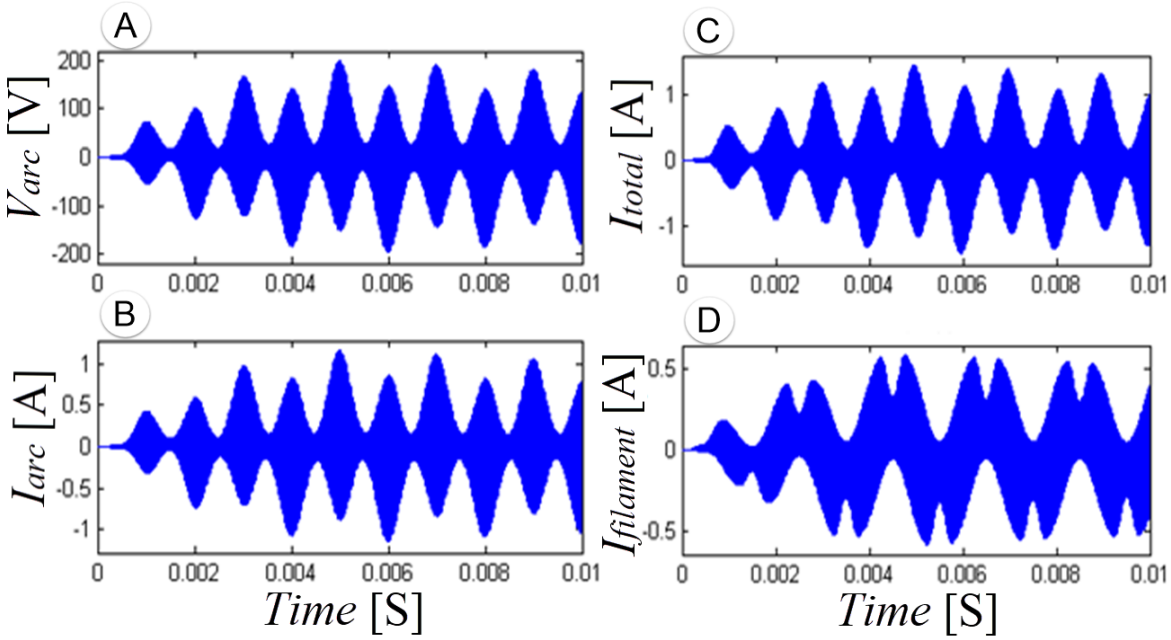


Figure 6. Curves of currents and voltages of the discharge lamp, (A) *arc* voltage, (B) *arc* current, (C) Total current and (D) filament current.

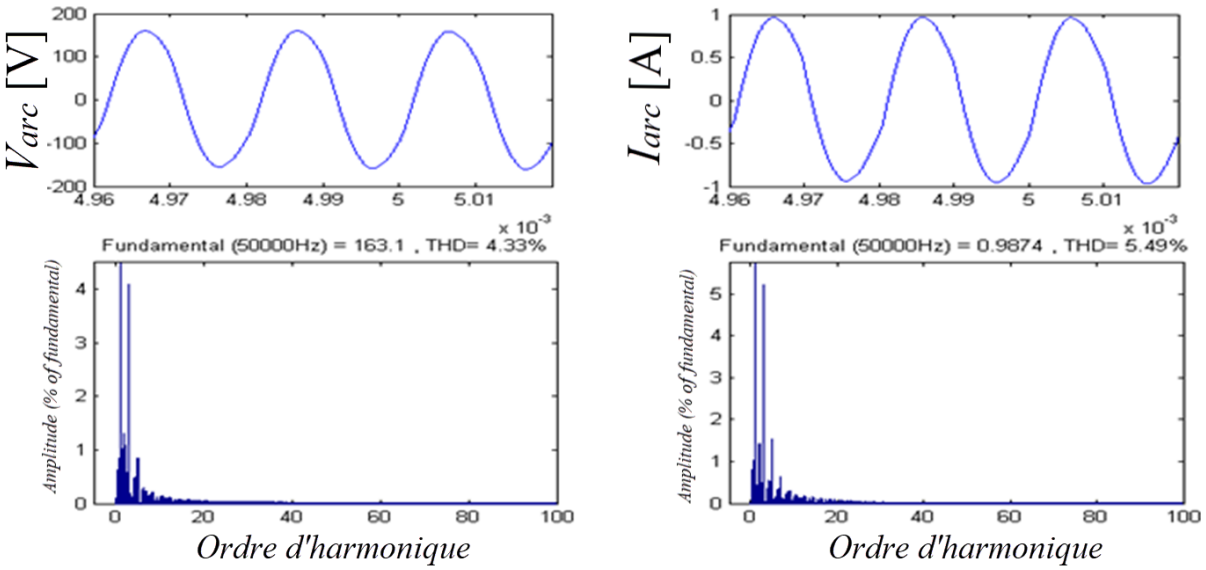


Figure 7. THD of the *arc* voltage and the *arc* current of the discharge lamp.

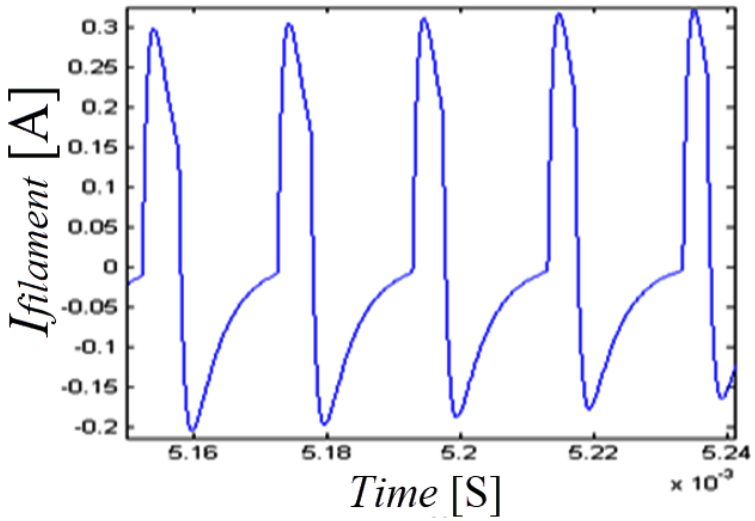


Figure 8. Waveform of the discharge lamp filament current.

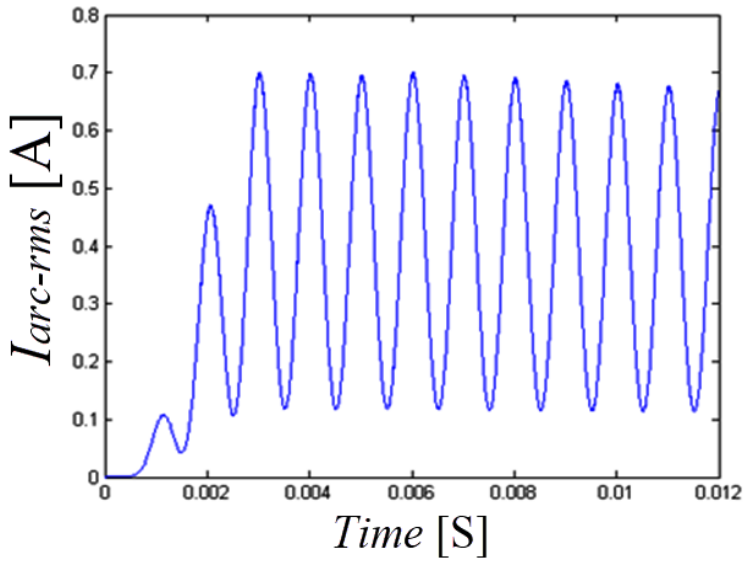


Figure 9. Effective *arc* current of the discharge lamp.

From figure 6, the obtained current and voltage exhibit sinusoidal waveforms, it can be observed that the voltage and current are modulated at a frequency of 50 kHz and contained in an envelope oscillating at 1 kHz with a modulation rate maximum/minimum values equal 5 approximately. From Figure 7, we can observe that the waveforms of current and voltage closely resemble sine waves, with *THD* values of 5.49 % for lamp *arc* current and 4.33 % for lamp voltage. The effective discharge lamp *arc* current varies as shown in Figure 9, indicating the need to regulate the current in our model to precisely achieve the targeted root mean square (*rms*) value of 0.65 A.

Closed-Loop Simulation Results

To enhance the efficiency of water treatment and extend the lamp's lifespan, it is essential to operate the lamp with a constant root mean square (*rms*) value of the arc current. To meet this requirement, we initially investigated a closed-loop system incorporating a proportional-integral (*PI*) controller, commonly utilized in industrial applications. The closed-loop transfer function of the lamp-ballast system and its corresponding block diagram, implemented in the Matlab Sim-Power environment, are illustrated in Figure 10.

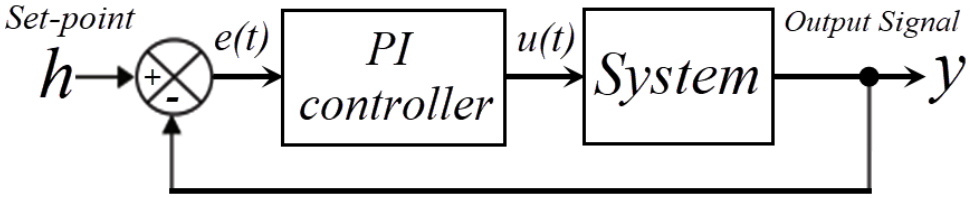


Figure 10. Closed-loop system with *PI* controller.

The simulation parameters were determined based on the lamp's characteristics and by solving the characteristic equation of the closed-loop transfer function using the pole placement method. The resulting simulation outcomes, including the time-domain behavior of the *arc* voltage, *arc* current, and its root mean square (*rms*) value, are presented in Figure 11.

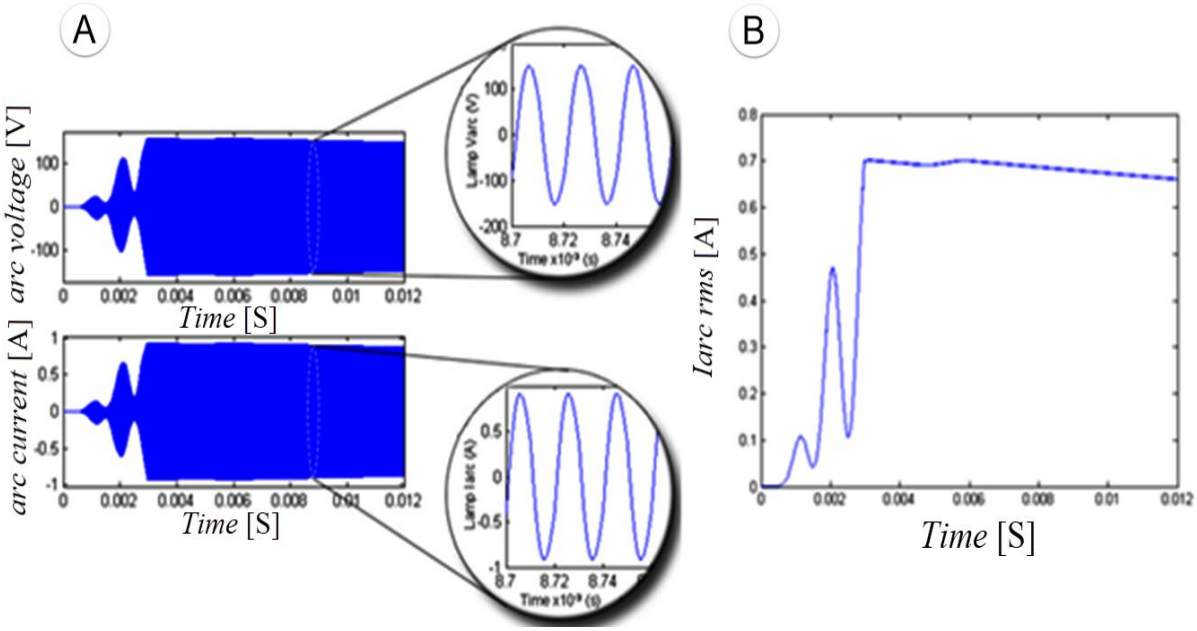


Figure 11. (a) Waveforms of the *arc* current and the *arc* voltage of the discharge lamp with a *PI* regulator. (b) *rms* value of the *arc* current of the discharge lamp after the application of a *PI*.

The analysis of the simulation results indicates that the control strategy employing a *PI* regulator exhibits a transient state similar to that of the open-loop controller. However, in steady state, it demonstrates excellent static and dynamic performance, with a current frequency of 50 kHz and a constant root-mean-square (*rms*) value of 0.65A, aligning with the desired values that optimize the germicidal effect.

Conclusion

The implementation of discharge lamps in industrial applications requires interdisciplinary knowledge, including electrical engineering, optics, plasma physics, and chemistry. We have established the foundational aspects of our study on the power of discharge lamps with electronic ballasts. The first part focused on presenting the general structure of an electronic ballast, utilizing a half-bridge inverter, selecting switches and their characteristics, modeling the electrical circuit of the fluorescent lamp, and assessing the relative influences of various parameters of the electronic components comprising the electronic ballast. The electrical behavior of the fluorescent lamp, powered by a high-frequency electronic ballast, can be represented by a power-dependent resistor and temperature. The second part of this study involved MATLAB simulation of the electronic ballast circuit. Although the current and voltage waveforms closely resembled a sine wave (with a total harmonic distortion of 5.49 % for current and 4.33 % for voltage) at a frequency of 50 kHz, we encountered challenges in achieving a consistent current of 0.65 A. The implementation of a feedback loop with a *PI* controller eliminates the oscillations in the effective current and enables the system to stabilize around the desired value of 0.65 A.

Scientific Ethics Declaration

* The authors declare that the scientific ethical and legal responsibility of this article published in EPSTEM journal belongs to the authors.

Conflict of Interest

* The authors declare that they have no conflicts of interest.

Funding

* This work was supported in part by the Faculty of Technology, Hassiba Benbouali University of Chlef; in part by the Faculty of Technology, University of M'hamed Bougara of Boumerdes, and the Directorate-General for Scientific Research and Technological Development (DGRSDT), Algeria.

Acknowledgements or Notes

* This article was presented as an oral presentation at the International Conference on Technology, Engineering and Science (www.icontes.net) held in Antalya/Türkiye on November 12-15, 2025.

References

Aissa-Bokhtache, A., Latroch, M., Badni, N., Toubal Maamar, A. E., Djafer, L., & Merini, A. (2024). Comparative analysis of three converters providing power to a discharge lamp-electronic ballast system designed for water sterilization. *The Eurasia Proceedings of Science, Technology, Engineering & Mathematics (EPSTEM), 32*, 53–65.

Aissa-Bokhtache, A., Latroch, M., Toualbia, A., Djafer, L., & Benallou, M. (2023). Modern control of a power supply based on a matrix converter for water disinfection by UVC radiation. *The Eurasia Proceedings of Science, Technology, Engineering & Mathematics (EPSTEM), 26*, 733–740.

Aissa-Bokhtache, A., Latroch, M., Toualbia, A., Toubal Maamar, A. E., & Boucherit, M. S. (2023). Optimization of a power supply using 3 types of converters of a discharge lamp-electronic ballast system for water purification. *Proceedings of 2nd International Conference on Electronics, Energy and Measurement (IC2EM)*, 1–6.

Aissa-Bokhtache, A., Zegaouia, A., Taleb, R., & Aillerie, M. (2021). Control of an electronic ballast-discharge lamp system supplied by a multicellular converter dedicated to water purification. *Desalination and Water Treatment, 228*, 176–186.

Aissa-Bokhtache, A., Zegaoui, A., Aillerie, M., Djahbar, A., Allouache, H., Hemici, K., Kessassia, F. Z., & Bouchrit, M. S. (2017). Power supply improvements for ballasts-low pressure mercury/argon discharge lamp for water purification. *AIP Conference Proceedings, 1814*, 020059.

Aissa-Bokhtache, A., Zegaoui, A., Belmadani, B., & Bouchrit, M. S. (2015). Water purification by a lamp discharge-electronic ballast system using a full bridge inverter. *Energy Procedia, 74*, 446–452.

Aissa-Bokhtache, A., Zegaoui, A., Kellal, M., Boucherit, M. S., Belmadani, B., & Aillerie, M. (2016). Optimization based on fuzzy logic control of discharge lamp-electronic ballast system for water purification. *Electric Power Components and Systems, 44*, 1981–1990.

Aissa-Bokhtache, A., Zegaoui, A., Taleb, R., & Aillerie, M. (2020). Super twisting sliding mode control algorithm of a discharge lamp for water sterilization. *Kansai University Reports, 62*(04), 1731–1741.

Cheng, C. A., Cheng, H. L., Chu, K. L., & Lin, K. J. (2010). A constant power controller of DC-AC electronic ballast inverter for HID lamps. *The 2010 International Power Electronics Conference - ECCE ASIA -*, 414–419.

Costache, M. C., Damelincourt, J. J., & Zissis, G. (2000). Optimisation of an ultraviolet source working in a consumer water reactor. *UVX 2000: Colloque sur les Sources Cohérentes et Incohérentes UV, VUV, et X – Applications et Développements Récents, 87*(5), 65–66.

De Oro, L. A., Melo, G. A., & Canesin, C. A. (2014). UV dose investigation for immersed lamp purifier for electronic ballast UV lamps design. *IEEE 16th International Power Electronics and Motion Control Conference and Exposition (PEMC)*, 893–900.

Takagi, K., Jinno, M., & Aono, M. (2000). The study of electronic ballast for fluorescent lamp with an electronic device given two functions. *Conference Record of the 2000 IEEE Industry Applications Conference. Thirty-Fifth IAS Annual Meeting and World Conference on Industrial Applications of Electrical Energy, 5*, 3382–3387.

Vijayakumar, K., & Rajan, S. E. (2011). Performance evaluation of inverter topology employing controlled-capacitor-charging technique. *2011 International Conference on Emerging Trends in Electrical and Computer Technology*, 398–406.

Author(s) Information

Aicha Aissa-Bokhtache
Hassiba Benbouali University of Chlef., Laboratoire Génie Electrique et Energies Renouvelables (*LGEER*), Faculty of Technology, Electrical Engineering Department, BP. 151, Hai Essalam, 02000 Chlef, Algeria.
Contact e-mail: *ahcial71@gmail.com*

Maamar Latroch
Hassiba Benbouali University of Chlef., Laboratoire Génie Electrique et Energies Renouvelables (*LGEER*), Faculty of Technology, Electrical Engineering Department, BP. 151, Hai Essalam, 02000 Chlef, Algeria.

Taieb Bessaad
Hassiba Benbouali University of Chlef., Laboratoire Génie Electrique et Energies Renouvelables (*LGEER*), Faculty of Technology, Electrical Engineering Department, BP. 151, Hai Essalam, 02000 Chlef, Algeria.

Alla Eddine Toubal-Maamar
University of Boumerdes (University of M'Hamed Bougara of Boumerdes), Department of Electrical Systems Engineering, Faculty of Technology, Laboratoire Ingénierie des Systèmes et Télécommunications *(LIST),* Frantz Fanon city, 35000 Boumerdes, Algeria.

Lemya Djafer
Hassiba Benbouali University of Chlef., Laboratoire Génie Electrique et Energies Renouvelables (*LGEER*), Faculty of Technology, Electrical Engineering Department, BP. 151, Hai Essalam, 02000 Chlef, Algeria.

Amina Merini
Hassiba Benbouali University of Chlef., Laboratoire Génie Electrique et Energies Renouvelables (*LGEER*), Faculty of Technology, Electrical Engineering Department, BP. 151, Hai Essalam, 02000 Chlef, Algeria

To cite this article:

Aissa-Bokhtache, A., Latroch, M., Bessaad, T., Toubal-Maamar, A.E., Djafer, L. & Merini, A (2025). Development of high-frequency power source utilizing electronic ballast by employing a half-bridge inverter for water purification. *The Eurasia Proceedings of Science, Technology, Engineering and Mathematics (EPSTEM) ,38,* 47-55

The Eurasia Proceedings of Science, Technology, Engineering & Mathematics (EPSTEM)
ISSN: 2602-3199

The Eurasia Proceedings of Science, Technology, Engineering and Mathematics (EPSTEM), 2025

Volume 38, Pages 56-68

IConTES 2025: International Conference on Technology, Engineering and Science

Robust Nonlinear Control of a 3×2 Stacked Multicellular Inverter Using Neural Network-Based Regulation

Salah Hanafi
Djillali Liabes University of Sidi Bel-Abbes

Mohammed Karim Fellah
Djillali Liabes University of Sidi Bel-Abbes

Youcef Djeriri
Djillali Liabes University of Sidi Bel-Abbes

Mohamed Fouad Benkhoris
University of Nantes

Abdelhakim Saim
University of Nantes

Djamel Ziane
University of Nantes

Patrice Wira
University of Haute Alsace

Abstract: The increasing demand for high-performance power converters has led to the development of advanced control strategies that enhance system robustness against load variations. This paper presents a novel control approach for a 3×2 stacked multicellular inverter, integrating nonlinear feedback decoupling control with neural network - based regulators. Unlike conventional Proportional-Integral (PI) controllers, which struggle with parameter variations and dynamic uncertainties, the proposed neural network (NN) controller adapts in real-time to maintain system stability and optimal performance. The NN is trained to approximate the nonlinear control law while compensating for parametric variations and external disturbances. A comparative analysis between the NN-based control and the traditional PI approach is conducted using MATLAB / Simulink simulations, evaluating response time, harmonic distortion (THD), and robustness against load changes. The results demonstrate that the NN-based controller significantly improves system adaptability, robustness and voltage regulation, making it a promising solution for modern power conversion systems.

Keywords: Stacked multicellular inverter, Nonlinear feedback decoupling control, Neural network, Robust control

Introduction

The growing demand for efficient and reliable power conversion systems, driven by the rapid expansion of renewable energy integration, electric mobility, and advanced industrial drives, has placed multilevel converter topologies at the forefront of modern power electronics research (Akagi, 2017; Blaabjerg et al., 2013). Among them, the multicellular converters, where they are divided into three types namely the series, stacked and parallel

- This is an Open Access article distributed under the terms of the Creative Commons Attribution-Noncommercial 4.0 Unported License, permitting all non-commercial use, distribution, and reproduction in any medium, provided the original work is properly cited.

- Selection and peer-review under responsibility of the Organizing Committee of the Conference

© 2025 Published by ISRES Publishing: www.isres.org

multicellular converters. The stacked multicellular converter (SMC) architecture has emerged as a promising solution due to its modularity, improved voltage quality, and enhanced fault tolerance (Meynard et al., 2002; Rodriguez et al., 2009). By generating multilevel voltage waveforms, SMCs achieve lower harmonic distortion and higher power quality, which makes them particularly attractive for applications such as smart grids, renewable energy systems, and high-performance motor drives (Kouro et al., 2010; Wu, 2006).

Nevertheless, the control of multicellular converters topologies remains a challenging task because of their nonlinear dynamics, strong inter-cell couplings, and sensitivity to load and parameter variations (Bakeer et al., 2022). Traditional control strategies, particularly Proportional–Integral (PI) regulators, remain widely adopted in industrial practice due to their simple structure and ease of implementation. However, their effectiveness is severely limited under dynamic uncertainties and varying operating conditions, often resulting in degraded performance and instability (Peña-Alzola et al., 2014). These challenges have stimulated the development of advanced control strategies capable of ensuring robustness, adaptability, and superior dynamic performance (Hanafi et al., 2016, 2021).

In this context, nonlinear feedback decoupling control has been shown by Gateau et al. (1997) to be an effective approach for handling the coupling phenomena and complex dynamics inherent in flying multicellular converters. Building on this principle, Hanafi et al. have demonstrated the successful application of nonlinear feedback decoupling technique to control the stacked multicellular converter, achieving improved voltage regulation and enhanced stability in Hanafi et al. (2014). More recently, neural network (NN)-based approaches have been introduced to further enhance the control of multicellular converters, particularly in modulation strategies, where they have proven effective in improving robustness and adaptability (Hanafi et al., 2025).

Artificial intelligence (AI)-driven control methods, and neural networks in particular, offer several advantages in power electronics. Their universal approximation capability and adaptive learning nature allow them to capture complex nonlinear dynamics and compensate for parametric uncertainties (Isidori, 1995; Haykin, 2009). Consequently, NN-based regulators have been successfully applied to multilevel converters for predictive control (Bakeer et al., 2022; Rivera et al., 2013) and adaptive regulation in renewable energy systems (Jiang et al., 2021). Despite these advances, limited research has addressed the combination of nonlinear feedback decoupling and neural network-based regulation in stacked multicellular converters, leaving open opportunities for performance enhancement in robustness, dynamic response, and power quality.

To address this gap, this paper proposes a novel control scheme that integrates nonlinear feedback decoupling with neural network-based regulators for a 3×2 SMC converter. The proposed method leverages the strengths of nonlinear decoupling while exploiting the adaptive learning capabilities of NNs to ensure stable operation under parametric variations, load disturbances, and dynamic uncertainties. A comparative analysis with conventional PI controllers is performed using MATLAB/Simulink simulations, with evaluation metrics including transient response, total harmonic distortion (THD), and robustness to load variations. The results confirm that the NN-based decoupling strategy provides superior adaptability, improved voltage regulation, and enhanced power quality, positioning it as a promising candidate for next-generation power conversion systems.

Stacked Multicellular Converter

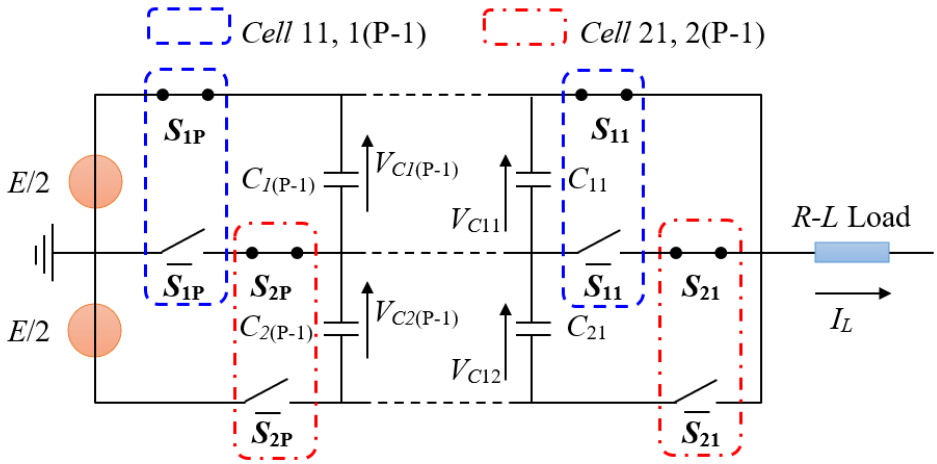


Figure 1. A stacked multicellular converter $P \times 2$ powering an R-L load.

The stacked multicellular converter (SMC), first introduced in the early 2000s, is composed of n stacks, each formed by a series connection of P switching cells separated by $(P-1)$ floating capacitors. The SMC converter consists of a hybrid association of commutation cells (Figure 1). In the case of $(P \times 2)$ configuration, the structure consists of P columns and $(n = 2)$ stacks, resulting in $(P \times n)$ commutation cells and $((P-1) \times n)$ floating capacitors (Lienhardt et al., 2005). Such a topology is capable of generating $((P \times 2) + 1)$ voltage level. The upper stack operates exclusively during positive output cycles, while the lower stack is activated during negative output cycles. The modeling of the average behavior of a stacked multicellular converter relies on the following assumptions:

- The switches are considered ideal, i.e., with zero saturation voltage, no leakage current, and negligible dead time or switching delay.
- The two switches within the same commutation cell operate in a complementary manner.
- The values of the floating capacitors C_{i1} and C_{2i} are such that the voltages at their terminals, $V_{C_{i1}}$ and $V_{C_{i2}}$ are constants over a cutting period.
- The load current I_L is constant over a cutting period and corresponds to the average value of this one over the same period.
- The DC supply voltage E is constant.

Under these assumptions, Equation (1) describes the dynamics of the floating capacitor voltages $\left(V_{C_{i1}}, V_{C_{i2}}\right)$ in the two stacks, as well as the evolution of the load current I_L, when the stacked multicellular converter operates as an inverter supplying an R-L load:

$$\begin{cases} \frac{d}{dt}V_{C_{11}} = \frac{S_{12}-S_{11}}{C_{11}} \cdot I_L \\ \frac{d}{dt}V_{C_{12}} = \frac{S_{13}-S_{12}}{C_{12}} \cdot I_L \\ \frac{d}{dt}V_{C_{21}} = \frac{S_{22}-S_{21}}{C_{21}} \cdot I_L \\ \frac{d}{dt}V_{C_{22}} = \frac{S_{23}-S_{22}}{C_{22}} \cdot I_L \\ \frac{d}{dt}I_L = -\frac{R_L}{L_L}I_L + \frac{S_{11}-S_{12}}{L_L}V_{C_{11}} + \frac{S_{12}-S_{13}}{L_L}V_{C_{12}} + \frac{S_{21}-S_{22}}{L_L}V_{C_{21}} + \frac{S_{22}-S_{23}}{L_L}V_{C_{22}} + \frac{S_{13}E_1}{L_L} + \frac{(S_{23}-1)E_2}{L_L} \end{cases} \quad (1)$$

Based on equation (1), it is possible to establish the state equation of the system:

$$\dot{X} = A \cdot X + B(X) \cdot U \quad (2)$$

The mathematical representation of the 3×2 SMC is given as follows:

$$X = [V_{C_{11}} \quad V_{C_{12}} \quad I_L \quad V_{C_{21}} \quad V_{C_{22}} \quad I_L]^T$$
$$U = [S_{11} \quad S_{12} \quad S_{13} \quad S_{21} \quad S_{22} \quad S_{23}]^T$$

$$B(X) = \begin{pmatrix} -\frac{I_L}{C_{11}} & \frac{I_L}{C_{11}} & 0 & 0 & 0 & 0 \\ 0 & -\frac{I_L}{C_{12}} & \frac{I_L}{C_{12}} & 0 & 0 & 0 \\ \frac{V_{C_{11}}}{L_L} & \frac{V_{C_{12}}-V_{C_{11}}}{L_L} & \frac{E_1-V_{C_{12}}}{L_L} & \frac{V_{C_{21}}}{L_L} & \frac{V_{C_{22}}-V_{C_{21}}}{L_L} & \frac{E_2-V_{C_{22}}}{L_L} \\ 0 & 0 & 0 & -\frac{I_L}{C_{21}} & \frac{I_L}{C_{21}} & 0 \\ 0 & 0 & 0 & 0 & -\frac{I_L}{C_{22}} & \frac{I_L}{C_{22}} \\ \frac{V_{C_{11}}}{L_L} & \frac{V_{C_{12}}-V_{C_{11}}}{L_L} & \frac{E_1-V_{C_{12}}}{L_L} & \frac{V_{C_{21}}}{L_L} & \frac{V_{C_{22}}-V_{C_{21}}}{L_L} & \frac{E_2-V_{C_{22}}}{L_L} \end{pmatrix}$$

$$A = \begin{pmatrix} 0 & 0 & 0 & 0 & 0 & 0 \\ 0 & 0 & 0 & 0 & 0 & 0 \\ 0 & 0 & -\frac{R_L}{L_L} - \frac{E_2}{L_L \cdot I_L} & 0 & 0 & 0 \\ 0 & 0 & 0 & 0 & 0 & 0 \\ 0 & 0 & 0 & 0 & 0 & 0 \\ 0 & 0 & 0 & 0 & 0 & -\frac{R_L}{L_L} - \frac{E_2}{L_L \cdot I_L} \end{pmatrix}$$

The load current is duplicated in the state vector X in order to obtain a square matrix $B(X)$ of dimension 6×6, which makes it possible to compute its inverse for use in the subsequent control design. Since the vector X explicitly appears in the expression of $B(X)$ in matrix equation (2), the system exhibits nonlinear behavior. In addition, $B(X)$ is not a diagonal matrix: each input component (S_{1i}, S_{2i}) simultaneously affects multiple state variables, and conversely, each state variable depends on several input components. Consequently, the system can be characterized as strongly coupled (Gateau et al., 2002).

Hybrid Nonlinear Feedback Decoupling Control with Neural Network Regulators

Nonlinear Feedback Decoupling Control

Nonlinear feedback decoupling control enables the decoupling between system inputs and outputs while ensuring the stabilization of the floating capacitor voltages. From the model described in equation (2), it is possible to define a column matrix $\alpha(X)$ and a square matrix $\beta(X)$ such that, by selecting the control input as $U(X) = \alpha(X) + \beta(X).V$, the closed-loop system exhibits linear behavior with complete decoupling between inputs and outputs (Aimé, 2003). From the matrix system:

$$\begin{cases} \dot{X} = A \cdot X + B(X) \cdot U \\ U = \alpha(X) + \beta(X) \cdot V \end{cases}$$

By substituting the expression of U, we obtain:

$$\dot{X} = A \cdot X + B(X) \cdot \alpha(X) + B(X) \cdot \beta(X) \cdot V \tag{3}$$

The matrix $\alpha(X)$ is defined in such a way that the product $(B(X).\alpha(X))$ fully compensates the term $(A.X)$. In addition, the matrix $B(X)$ remains invertible under the condition that:

$$I_L \neq 0 \quad \text{and} \quad E \neq 0 \tag{4}$$

Consequently, we choose:

$$\beta(X) = B^{-1}(X) \tag{5}$$

Let:

$$\dot{V}_{C_{11}} = v_{11}, \quad \dot{V}_{C_{12}} = v_{12}, \quad \dot{I}_L = v_{13}, \quad \dot{V}_{C_{22}} = v_{22}, \quad \dot{V}_{C_{22}} = v_{22}, \quad \dot{I}_L = v_{23} \tag{6}$$

The matrixes $\alpha(X)$ and $\beta(X)$ are given as:

$$\alpha(X) = -B^{-1}(X).A.X$$

$$\beta(X) = B^{-1}(X)$$

According to the conditions defined in (4), the results of the decoupling computation are expressed in (7).

$$A \cdot X = (0 \quad 0 \quad -b_0 X_{13} - b_1 E_2 \quad 0 \quad 0 \quad -b_0 X_{13} - b_1 E_2)^T \tag{7}$$

$$B^{-1}(X) = \begin{pmatrix} \frac{X_{11}-E_1}{a_{11}E_1X_{13}} & \frac{X_{12}-E_1}{a_{12}E_1X_{31}} & \frac{1}{2b_1E_1} & 0 & 0 & \frac{1}{2b_1E_1} \\ \frac{X_{11}}{a_{11}E_1X_{13}} & \frac{X_{12}-E_1}{a_{12}E_1X_{13}} & \frac{1}{2b_1E_1} & 0 & 0 & \frac{1}{2b_1E_1} \\ \frac{X_{11}}{a_{11}E_1X_{13}} & \frac{X_{12}}{a_{12}E_1X_{13}} & \frac{1}{2b_1E_1} & 0 & 0 & \frac{1}{2b_1E_1} \\ 0 & 0 & \frac{1}{2b_1E_1} & \frac{X_{21}-E_2}{a_{21}E_2X_{32}} & \frac{X_{22}-E_2}{a_{22}E_2X_{32}} & \frac{1}{2b_1E_1} \\ 0 & 0 & \frac{1}{2b_1E_1} & \frac{X_{21}}{a_{21}E_2X_{32}} & \frac{X_{22}-E_2}{a_{22}E_2X_{32}} & \frac{1}{2b_1E_1} \\ 0 & 0 & \frac{1}{2b_1E_1} & \frac{X_{21}}{a_{21}E_2X_{32}} & \frac{X_{22}}{a_{22}E_2X_{32}} & \frac{1}{2b_1E_1} \end{pmatrix} \quad (8)$$

with:

$$a_{11} = \frac{1}{C_{11}}, a_{12} = \frac{1}{C_{12}}, a_{21} = \frac{1}{C_{21}}, a_{22} = \frac{1}{C_{22}}, b_0 = \frac{R_L}{L_L}, b_1 = \frac{1}{L_L}$$

Consequently, the feedback control law is formulated as:

$$\alpha(X) = \left(\frac{b_0X_{13}+b_1E_2}{b_1E_1} \quad \frac{b_0X_{13}+b_1E_2}{b_1E_1} \quad \frac{b_0X_{13}+b_1E_2}{b_1E_1} \quad \frac{b_0X_{13}+b_1E_2}{b_1E_1} \quad \frac{b_0X_{13}+b_1E_2}{b_1E_1} \quad \frac{b_0X_{13}+b_1E_2}{b_1E_1}\right)^T \quad (9)$$

Once the state feedback is implemented, the resulting input variables are represented by the vector $V = (v_{11} \quad v_{12} \quad v_{13} \quad v_{21} \quad v_{22} \quad v_{23})^T$ (Figure 2).

For a stacked multicellular converter, the application of nonlinear feedback makes it possible to derive $P \times 2$ linear relations, ensuring complete decoupling between the new input variables and the $P \times 2$ state system variables.

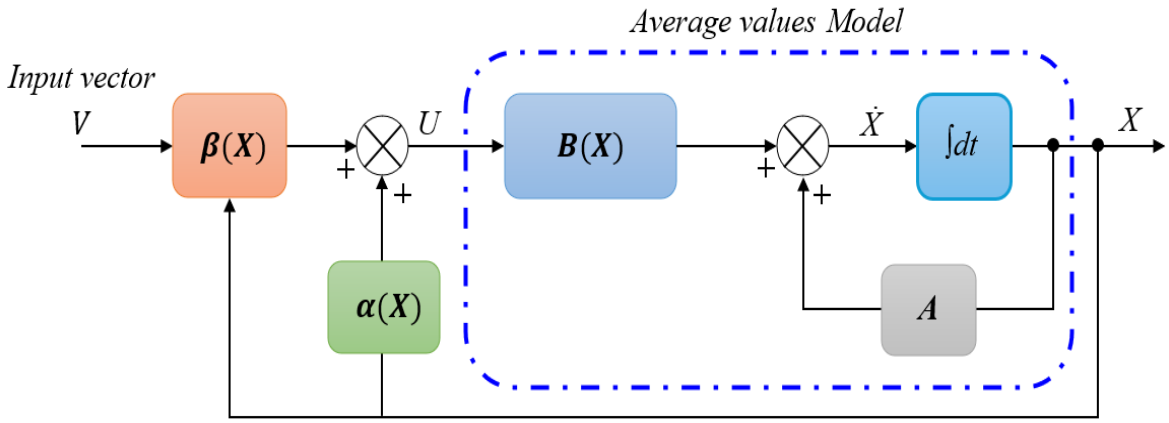


Figure 2. Decoupling with nonlinear feedback: functional representation.

A singularity arises in the vicinity where nonlinear decoupling control loses its validity. These singular points correspond to the zero crossing of the load current ($I_L = 0$) and the DC supply voltage ($E = 0$). Under such conditions, the system becomes uncontrollable (Gateau, 1997; Gateau et al., 1997). In the case of a chopper, these singularities have no impact since they fall outside the normal operating range. Conversely, for an SMC inverter, the load current reaches zero twice during each fundamental period. Therefore, it is necessary to introduce a limitation on the measured current in order to avoid the singular point at ($I_L = 0$) as illustrated in Figure 3.

After decoupling the different variables, the system is transformed into $P \times 2$ linear subsystems, where each subsystem links an input variable to a state variable $(\dot{X} = V)$. It then becomes necessary to introduce a second linear control loop to impose the desired dynamics on each state variable. As illustrated in Figure 3, this requires as many feedback loops as there are state variables.

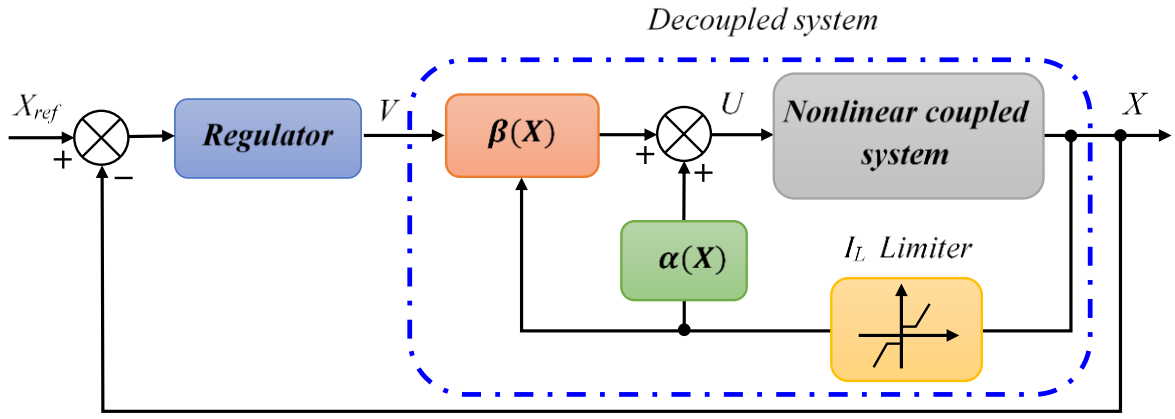


Figure 3. Enslavement of the decoupled system to a reference vector X_{ref}.

Neural Network Regulators

To overcome the limitations of classical PI regulators in nonlinear decoupling control, this work proposes a hybrid approach that integrates a nonlinear feedback decoupling law with neural network (NN)-based regulators (Figure 4). The nonlinear feedback structure ensures the separation of the control dynamics between load current and floating capacitor voltages, thereby reducing cross-coupling effects and enhancing stability. However, the performance of the conventional PI regulators, when embedded in this framework, is often limited under varying operating conditions due to their inability to adapt online.

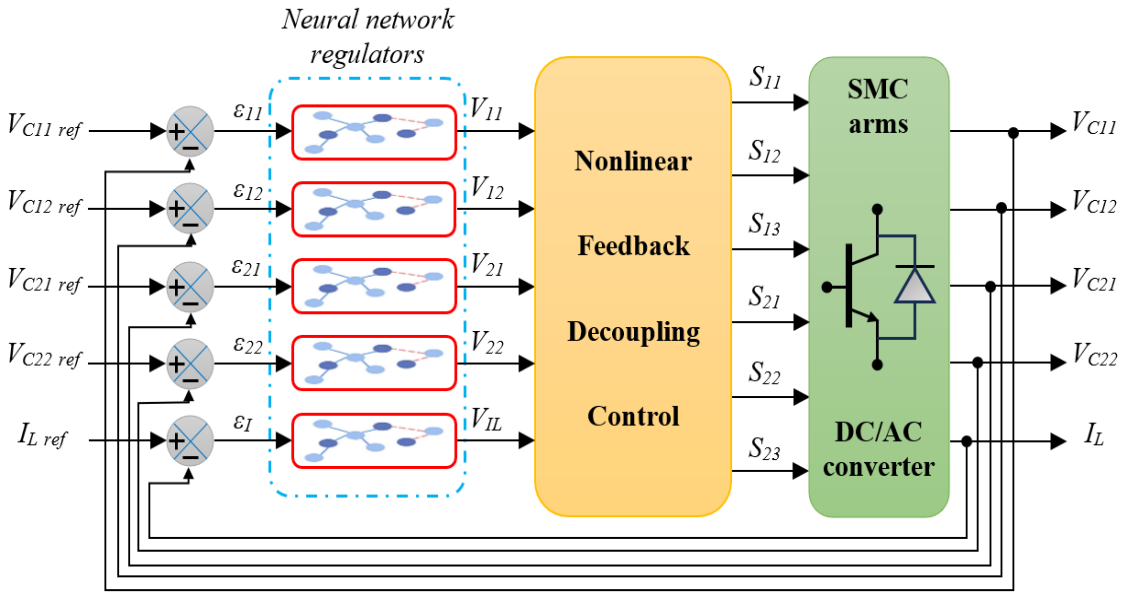


Figure 4. Block diagram of the designed hybrid nonlinear feedback decoupling control with neural network regulators.

In the proposed hybrid strategy, Proportional–Integral regulators are replaced with feed-forward multilayer perceptron (MLP) neural networks. Each NN is trained offline using data generated from the nominal PI controllers and then fine-tuned online to account for parametric variations and external disturbances. The general mathematical structure of the NN regulator can be expressed as:

$$Y_j^l = f\left(\sum_t^{nl} W_{ji}^l X_i + b_j^l\right) \tag{10}$$

where,

X_i: inputs vector,
W_{ji}^l: synaptic weights of neuron j in layer l,
b_j^l: bias input,
f: activation function (sigmoidal transfer function).

The architecture adopted in this work consists of a static feed-forward MLP with an input layer representing the error signals, one hidden layer with ten neurons using a sigmoid activation function, and one output neuron providing the reference control voltage. The training parameters include a learning rate of 1×10^6, momentum coefficient of 4.49×10^3, and a maximum of 1000 epochs. The network was validated using mean squared error (MSE) criteria, ensuring convergence without overfitting.

By embedding the neural network regulators inside the nonlinear feedback decoupling scheme, the system benefits from both the structural robustness of decoupling control and the adaptive learning capability of neural networks. Simulation results demonstrate that this hybrid strategy achieves improved current tracking, reduced harmonic distortion (THD), and better stabilization of floating capacitor voltages compared to the conventional PI-based decoupling approach.

Results and Discussions

This section presents the simulation results and discussion for a 3×2 stacked multicellular DC/AC converter controlled by the nonlinear feedback decoupling strategy. The performance of the proposed hybrid scheme, which integrates neural network (NN)-based regulators into the nonlinear decoupling law, is compared against the classical PI-based approach to evaluate accuracy, robustness, and adaptability. Simulations were performed in MATLAB/Simulink using the following parameters (Table 1):

Table 1. Parameters used in simulations

Parameters	Numerical values
P (Cells number)	3
n (Stack number)	2
E (DC voltage)	1500 V
C (Floating capacitor)	400 μF
L_L (Load inductance)	0.1 mH
R_L (Load resistance)	10 Ω
f_c (Cutting frequency)	28 KHz
K_{pV_c}	30000
K_{iV_c}	10
K_{pI_L}	2000000
K_{iI_L}	10

These values provide a realistic operating framework and enable the assessment of system behavior under different disturbances and operating conditions. To comprehensively evaluate the controllers, three scenarios were considered:

1. Reference load current regulation: This scenario tests the ability of the controllers to accurately track step variations in the reference load current. The objective is twofold: to verify the current regulation capability of the system, and to analyze whether current variations remain decoupled from the capacitor voltages.
2. Variation of DC input voltage: In this scenario, the input DC source is perturbed to examine the stability and dynamic response of the system. Again, the goal is twofold: to ensure that the floating capacitor voltages are well regulated despite input voltage fluctuations, and to highlight the decoupling between input voltage dynamics and load current regulation.
3. Load parameter variations: The third scenario evaluates the robustness of the controllers under changes in load resistance and inductance. This test assesses the adaptability of both PI- and NN-based regulators when subjected to parametric uncertainties, ensuring reliable operation under realistic load disturbances.

The comparative results under these three conditions demonstrate that both control schemes achieve satisfactory performance; However, the NN-based regulators offer noticeable advantages in terms of faster transient response, improved decoupling behavior, and enhanced robustness to load variations.

Floating Capacitor Voltage Regulation

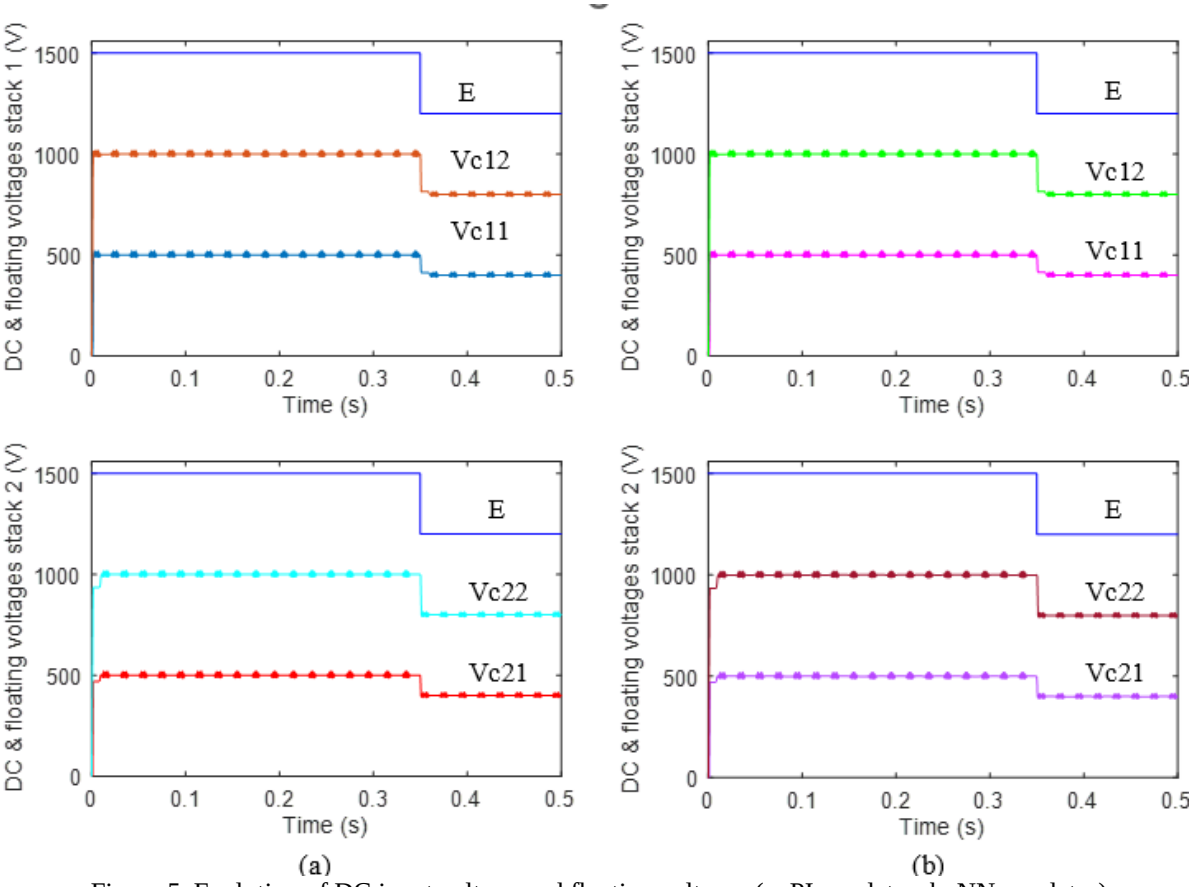


Figure 5. Evolution of DC input voltage and floating voltages (a: PI regulator, b: NN regulator)

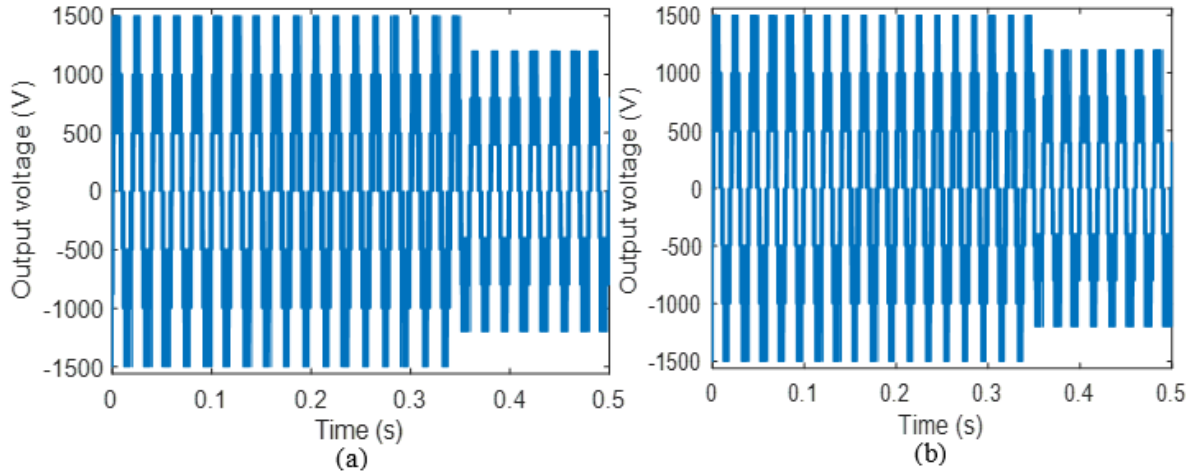


Figure 6. Evolution of output voltage (a: PI regulator, b: NN regulator)

The comparative study shows that both PI (Figure 5-a) and neural network (NN)-based regulators (Figure 5-b) achieve similar response times during startup. However, after disturbances at 0.35 s (300 V drop in input DC voltage, reducing E_{dc} from 1500 V to 1200 V), the nonlinear feedback decoupling strategy combined with NNs provides a much faster rebalancing of the floating capacitor voltages. For instance, the settling time of V_{C11} (stack 1) is reduced from 9.7 ms with PI to only 0.81 ms with the NN controller, representing a reduction of about 92%. Similar improvements are observed for the other capacitor voltages, with average reductions of nearly 79%. This faster stabilization ensures better voltage balancing, which directly translates into more symmetrical waveforms and enhanced output quality (Figure 6). This variation has no effect on the load current.

Load Current Regulation

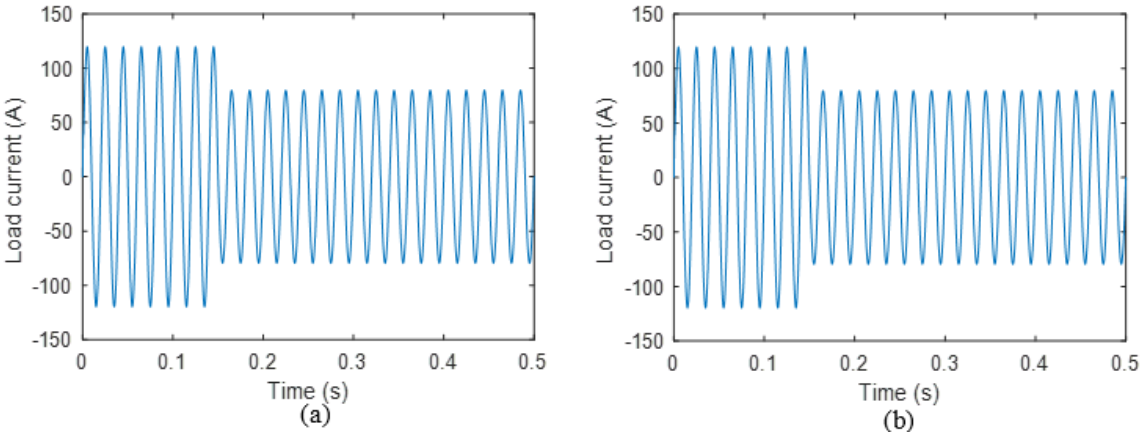


Figure 7. Evolution of load current (a: PI regulator, b: NN regulator)

When a variation in the load current is applied at 0.15 s (Figure 7) where we decrease the value of the reference load current from 120 A to 80 A, a reduction of 40 A, both PI and NN based regulators show similar overall performance, with only slight differences in dynamic response. The PI controller achieves satisfactory tracking with small overshoot and acceptable convergence time, while the NN-based regulator shows marginally faster stabilization and slightly reduced transient deviations. Thanks to the nonlinear feedback decoupling, capacitors voltages stability is maintained in both cases, although the NN regulator provides a minor improvement by further reducing the coupling effects between current dynamics and capacitor voltages. These results indicate that the two approaches perform comparably, with the NN-based method offering only incremental benefits.

Voltage-Current Decoupling

A key advantage of the nonlinear feedback decoupling framework is its ability to isolate voltage dynamics from current dynamics which is visible in figures 5, 6 and 7. In the PI-controlled inverter, a change in load current significantly perturbs the floating capacitor voltages, increasing rebalancing time and degrading output quality. In contrast, the NN-based controller preserves effective decoupling, allowing capacitor voltages to recover more quickly (57–92% faster depending on the cell), while maintaining stable and well-regulated current. This validates the capability of the proposed control to reduce cross-interactions between voltage and current, ensuring more predictable and stable performance.

Harmonic Distortion (THD)

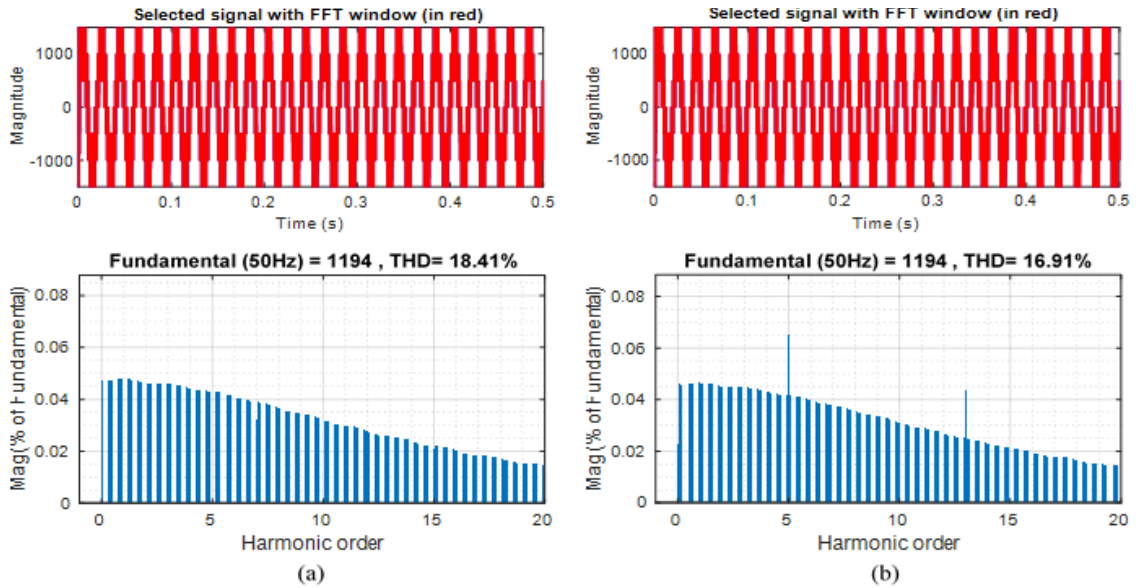


Figure 8. Output voltage with THD (a: PI regulator, b: NN regulator)

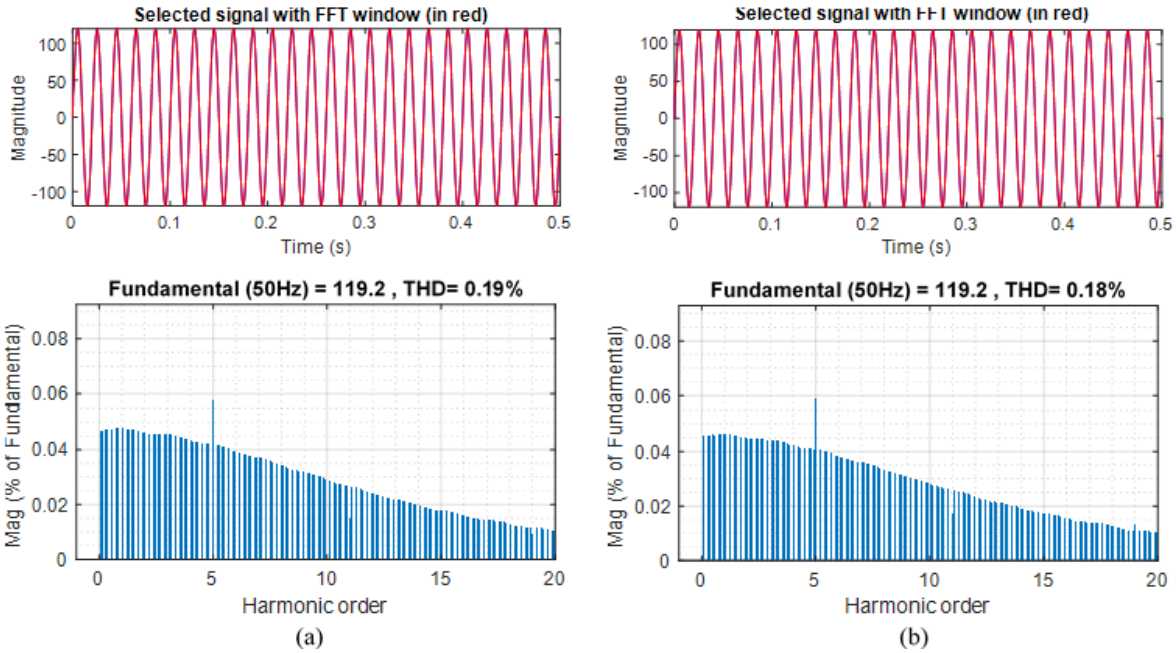


Figure 9. Load current with THD (a: PI regulator, b: NN regulator)

The NN-based approach provides a notable improvement in output waveform quality. The total harmonic distortion (THD) in the output voltage (figure 8) decreases from 18.41% with PI regulation to 16.91% with the NN controller, representing an 8.1% relative reduction. The current THD (figure 9) also decreases slightly, from 0.19% to 0.18%. Although the improvement in current quality is modest, the reduction in voltage THD is significant, as it reflects the improved voltage balancing achieved through faster capacitor regulation.

Overall Robustness

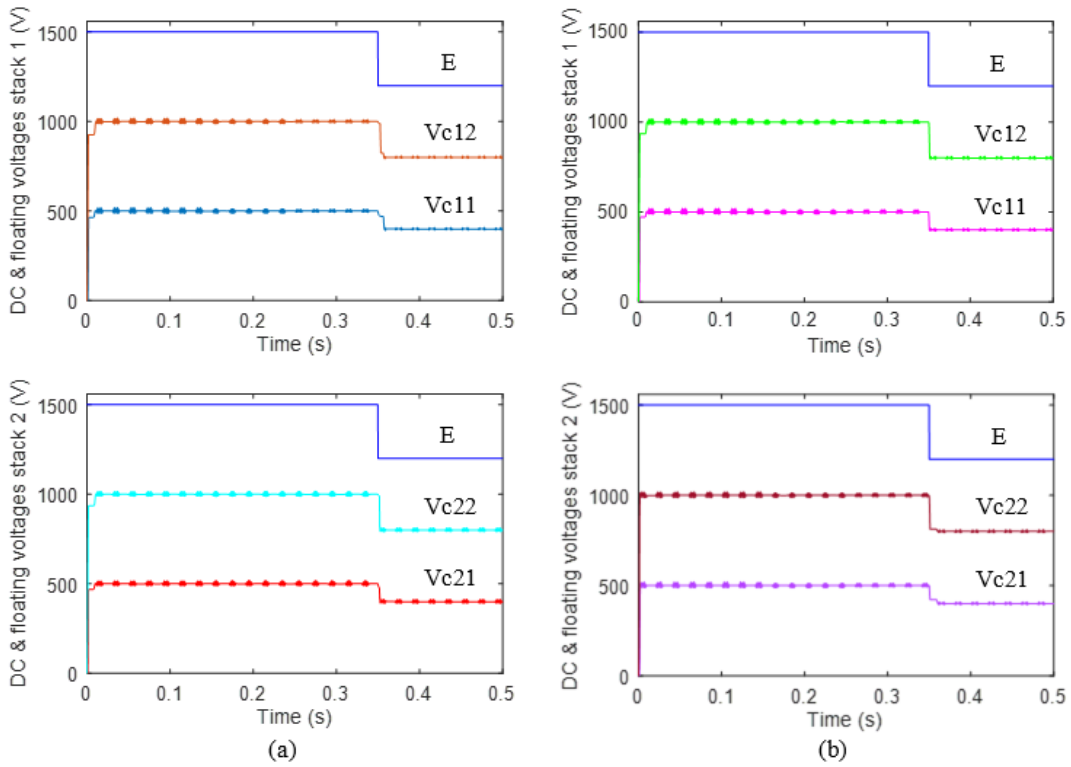


Figure 10. Evolution of DC input voltage and floating voltages _ robustness test (a: PI regulator, b: NN regulator)

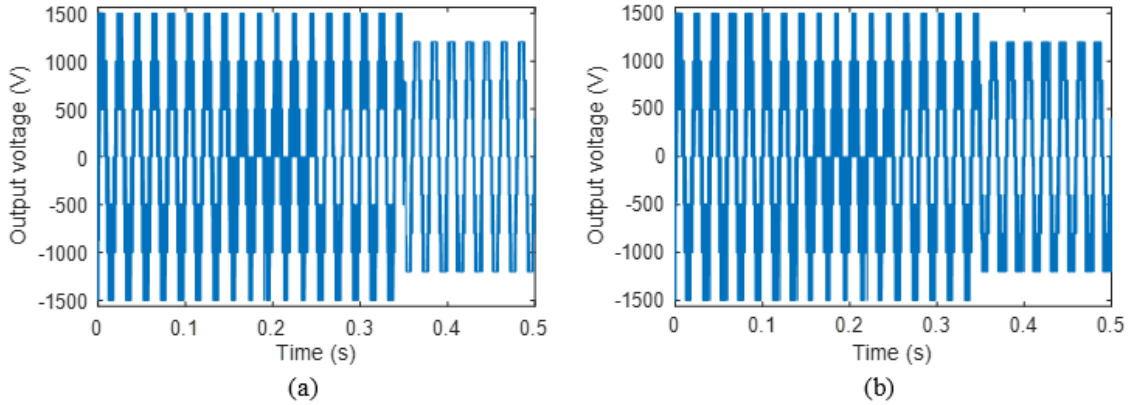


Figure 11. Output voltage _ robustness test (a: PI regulator, b: NN regulator)

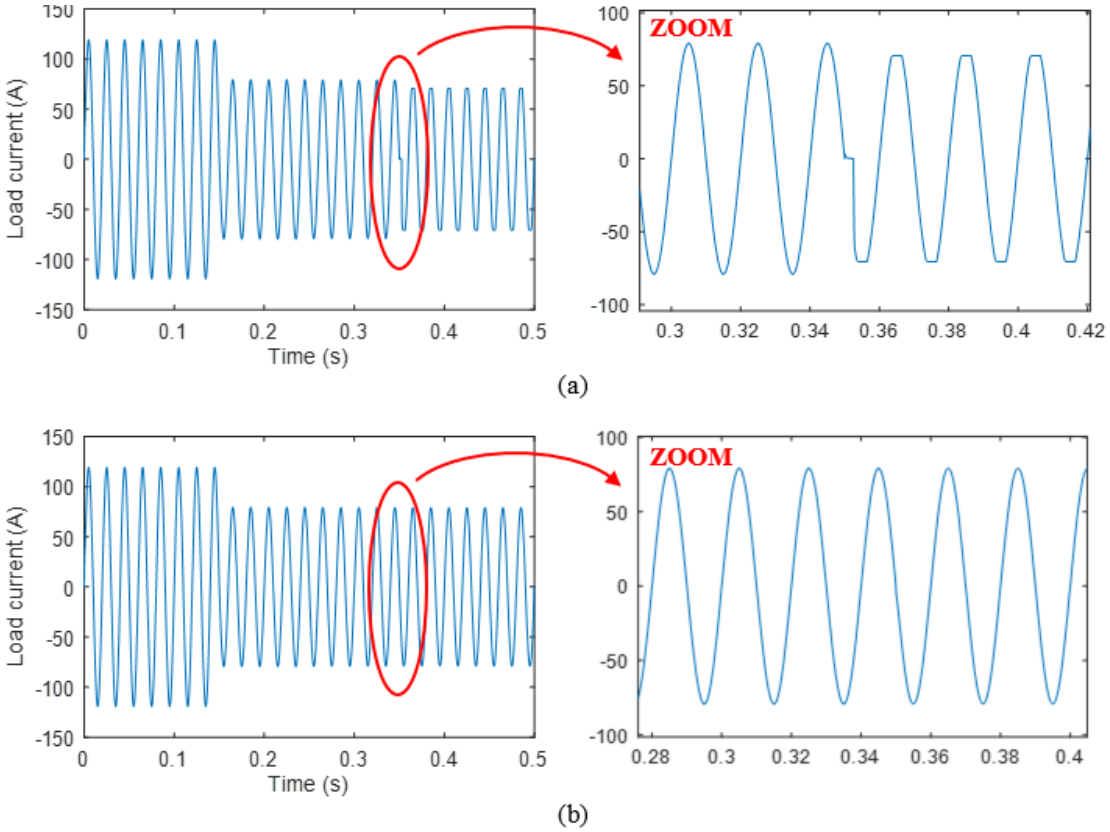


Figure 12. Load current _ robustness test (a: PI regulator, b: NN regulator)

Under different operating scenarios (figures 10, 11 and 12) -including, current steps (reduction of 40 A) at 0.15 s, load variations (50% increase in RL load) at 0.25 s and input DC voltage drops (drop in input DC voltage, reducing E_{dc} from 1500 V to 1200 V) at 0.35 s —the NN-based controller consistently maintains system stability, capacitor voltage balancing, and current regulation. In contrast, the PI-controlled system shows a lack of robustness, with degraded performance under the same disturbances. This superior robustness of the NN-based decoupling strategy can be attributed to the adaptive learning capability of neural networks, which enables real-time compensation of parameter uncertainties and external perturbations, while maintaining effective decoupling.

Summary

In summary, at equal system architecture and control objectives, the nonlinear feedback decoupling approach with NN-based regulators clearly outperforms the PI-controlled version. It ensures significantly faster capacitor voltage regulation (on average 79% faster after disturbances), more accurate load current tracking, reduced coupling between voltage and current dynamics, lower voltage THD, and superior robustness under parameter variations

and disturbances. These results confirm the effectiveness of the proposed method for achieving high-performance operation in stacked multicellular inverters.

Conclusion

This paper has introduced a novel control strategy for a 3×2 stacked multicellular inverter, combining nonlinear feedback decoupling with neural network-based regulation. Unlike conventional PI controllers, which are sensitive to parameter variations and load disturbances, the proposed approach leverages the adaptive capabilities of neural networks to approximate the nonlinear control law in real time and compensate for uncertainties. Simulation results in MATLAB/Simulink have confirmed that the method provides faster dynamic response, improved voltage regulation, and lower total harmonic distortion. These findings demonstrate the effectiveness of integrating nonlinear decoupling with intelligent control, establishing a robust and reliable solution for high-performance power conversion systems.

Scientific Ethics Declaration

* The authors declare that the scientific ethical and legal responsibility of this article published in EPSTEM journal belongs to the authors.

Conflict of Interest

* The authors declare that they have no conflicts of interest

Funding

* This research received no specific grant from any funding agency in the public, commercial, or not-for-profit sectors.

Acknowledgements or Notes

* This article was presented as a poster presentation at the International Conference on Technology, Engineering and Science (www.icontes.net) held in Antalya/Türkiye on November 12-15, 2025.

References

Aimé, M. (2003*). Evaluation et optimisation de la bande passante des convertisseurs statiques : Application aux nouvelles structures multicellulaire*. (Doctoral dissertation). National Polytechnic Institute of Toulouse, France.

Akagi, H. (2017). Multilevel converters: Fundamental circuits and systems. *Proceedings of the IEEE, 105*(11), 2048-2065.

Bakeer, A. I., Mohamed, S., Malidarreh, P. B., Hattabi I., & Liu, L. (2022). An artificial neural network-based model predictive control for three-phase flying capacitor multilevel inverter. *IEEE Access, 10*, 70305-70316.

Blaabjerg, F., & Ma, K. (2013). Future on power electronics for wind turbine systems. *IEEE J. Emerg. Sel. Topics Power Electron., 1*(3), 139-152.

Gateau, G. (1997). *Contribution à la commande des convertisseurs multicellulaires série* (Doctoral thesis). National Polytechnic Institute of Toulouse, France.

Gateau, G., Fadel, M., Bensaid, R., & Meynard, T. A. (2002). Multicells converters: Active control and observation of flying-capacitor voltages. *IEEE Transactions on Industrial Electronics*, *49*(5), 998-1008.

Gateau, G., Maussion, P., & Meynard, T. A. (1997). De la modélisation à la commande non linéaire des convertisseurs multicellulaires série. Application à la fonction hacheur. *J. Phys III France*, *7*(6), 1277-1305.

Hanafi, S., Fellah, M. K., Achar, A., Yaichi, M., Djeriri, Y., Benbouhenni, H., Colak, I., Benkhoris, M. F., & Wira, P. (2025). Enhancing space vector modulation control in parallel multicellular converters using artificial neural networks. *Electrical Engineering, 107*, 13529-13545

Hanafi, S., Fellah, M. K., Djeriri, Y., & Benkhoris, M. F. (2021). Control of parallel multicellular DC/AC converter including monolithic inter-cell transformer in a real-time environment. *Revue Roumaine des Sciences Techniques - Série Électrotechnique et Énergétique, 66*(3), 169-174.

Hanafi, S., Fellah, M. K., Yaichi, M., & Benkhoris, M. F. (2014). Nonlinear feedback decoupling control applied to stacked multicellular converter. *Revue Roumaine des Sciences Techniques – Série Électrotechnique et Énergétique, 59*(1), 97-106, 2014.

Hanafi, S., Fellah, M. K., Yaichi, M., & Benkhoris, M. F. (2016). Control of stacked multicellular inverter. *Revue Roumaine des Sciences Techniques – Série Électrotechnique et Énergétique, 61*(3), 278-282.

Haykin, S. (2009). *Neural networks and learning machines* (3rd ed.). Upper Saddle River, NJ: Pearson.

Isidori, A. (1995). *Nonlinear control systems* (3rd ed.). London: Springer.

Jiang, H., Chen, Y., & Kang, Y. (2021). application of neural network controller and policy gradient reinforcement learning on modular multilevel converter (mmc) - a proof of concept. *2021 IEEE 4th International Electrical and Energy Conference (CIEEC)*, Wuhan, China, 1-6,

Kouro, S., Malinowski, M., & Rodriguez, J. (2010). Multilevel power converters. *IEEE Trans. Ind. Electron., 57*(8), 2553-2580.

Lienhardt, A. M., Gateau, G., & Meynard, T. A. (2005). Stacked multicell converter (SMC): Reconstruction of flying capacitor voltages. *In Proceedings of the 31st Annual Conference of the IEEE Industrial Electronics Society* (*IECON 2005*) (pp. 1–6). IEEE.

Meynard, T. A., Foch, H., Thomas, P., Courault, J., Jakob, R., & Nahrstaedt, M. (2002). Multicellular converters: Basic concepts and industry applications. *IEEE Trans. Ind. Electron., 49*(5), 955-964.

Peña-Alzola, R., Liserre, M., Blaabjerg, F., Sebastián, R., Dannehl, J., & Fuchs, F. W. (2014). Systematic design of the lead–lag network method for active damping in lcl-filter-based three-phase converters. *IEEE Transactions on Industrial Informatics, 10*(1), 43-52.

Rivera, M., Yaramasu, V., Llor, A., Rodriguez, J., Wu, B., & Fadel, M. (2012). Digital predictive current control of a three-phase four-leg inverter. IEEE Transactions on Industrial Electronics, 60(11), 4903-4912.

Rodriguez, J., Franquelo, L. G., Kouro, S., León, J. I., Portillo, R. C., & Martin Prats, M. Á. (2009). Multilevel converters: An enabling technology for high-power applications. *Proceedings of the IEEE, 97*(11), 1786–1817.

Wu, B. (2006). *High-power converters and ac drives.* Hoboken, NJ: Wiley-IEEE Press.

Author(s) Information

Salah Hanafi
Djillali Liabes University of Sidi Bel-Abbes.
ICEPS Laboratory, Sidi Bel-Abbes, Algeria.
Contact e-mail : *salah.hanafi@univ-sba.dz*

Mohammed Karim Fellah
Djillali Liabes University of Sidi Bel-Abbes.
ICEPS Laboratory, Sidi Bel-Abbes, Algeria.

Youcef Djeriri
Djillali Liabes University of Sidi Bel-Abbes.
ICEPS Laboratory, Sidi Bel-Abbes, Algeria.

Mohamed Fouad Benkhoris
University of Nantes.
IREENA Laboratory, Saint-Nazaire, France.

Abdelhakim Saim
University of Nantes.
IREENA Laboratory, Saint-Nazaire, France.

Djamel Ziane
University of Nantes.
IREENA Laboratory, Saint-Nazaire, France.

Patrice Wira
University of Haute Alsace.
MIPS Laboratory, Mulhouse, France.

To cite this article:

Hanafi, S., Fellah, M. K., Djeriri, Y., Benkhoris, M. F., Saim, A., Ziane, D., & Wira, P. (2025). Robust nonlinear control of a 3×2 stacked multicellular inverter using neural network-based regulation. *The Eurasia Proceedings of Science, Technology, Engineering and Mathematics (EPSTEM), 38*, 56-68.

The Eurasia Proceedings of Science, Technology, Engineering & Mathematics (EPSTEM)
ISSN: 2602-3199

The Eurasia Proceedings of Science, Technology, Engineering and Mathematics (EPSTEM), 2025

Volume 38, Pages 69-80

IConTES 2025: International Conference on Technology, Engineering and Science

Development of a Relation Model for Damage Categorization

Akkouche Karim
Mouloud Mammeri University of Tizi-Ouzou

Khelil Nacim
Mouloud Mammeri University of Tizi-Ouzou

Nekmouche Aghiles
Mouloud Mammeri University of Tizi-Ouzou

Kahil Amar
Mouloud Mammeri University of Tizi-Ouzou

Hamizi Mohand
Mouloud Mammeri University of Tizi-Ouzou

Bouzid Leyla
Mouloud Mammeri University of Tizi-Ouzou

Atlaoui Djamel
Mouloud Mammeri University of Tizi-Ouzou

Abstract: After an earthquake, many field investigations are conducted to classify the damage undergone by the buildings. In many cases, it has been found that the global damage category assigned to the construction does not correspond to the damage associated with the building various components (bearing elements, non-bearing elements, infrastructure, environment, etc.). In this paper, a method for the quantitative evaluation of post-earthquake damage of buildings is developed, based on the theory of the design of experiments. This study has been conducted by processing a database of 7.847 damaged buildings extracted from a database collected during a post-earthquake survey (Boumerdes, Algeria, 2003 earthquake). In doing so, firstly, two mathematical models have been developed to quantify the two quantities that assess the state of all the bearing and non-bearing elements (D_{ER}) and (D_{ES}) respectively. Then, a function representing the relationship between the severity of the element-scale damage and the global damage category of the building was developed. Finally, an application of the proposed method has been performed on a set of ten damaged buildings. The results indicate that the proposed method provides a more accurate assessment on the condition of the building compared to the decisions made by the engineers during the Boumerdes earthquake inspection in 2003.

Keywords: Design of experiment method, Elementary damage, Full-factorial design, Global damage, Post-seismic analysis

Introduction

Although the principle of classification is simple to use and rather convenient, however, imprecision's may appear, on the one hand, because the estimation of the overall damage (DG) depends essentially on the expertise and judgment of the expert (Baggio et al. 2007), and son the other hand, because no threshold value is

- This is an Open Access article distributed under the terms of the Creative Commons Attribution-Noncommercial 4.0 Unported License, permitting all non-commercial use, distribution, and reproduction in any medium, provided the original work is properly cited.

- Selection and peer-review under responsibility of the Organizing Committee of the Conference

© 2025 Published by ISRES Publishing: www.isres.org

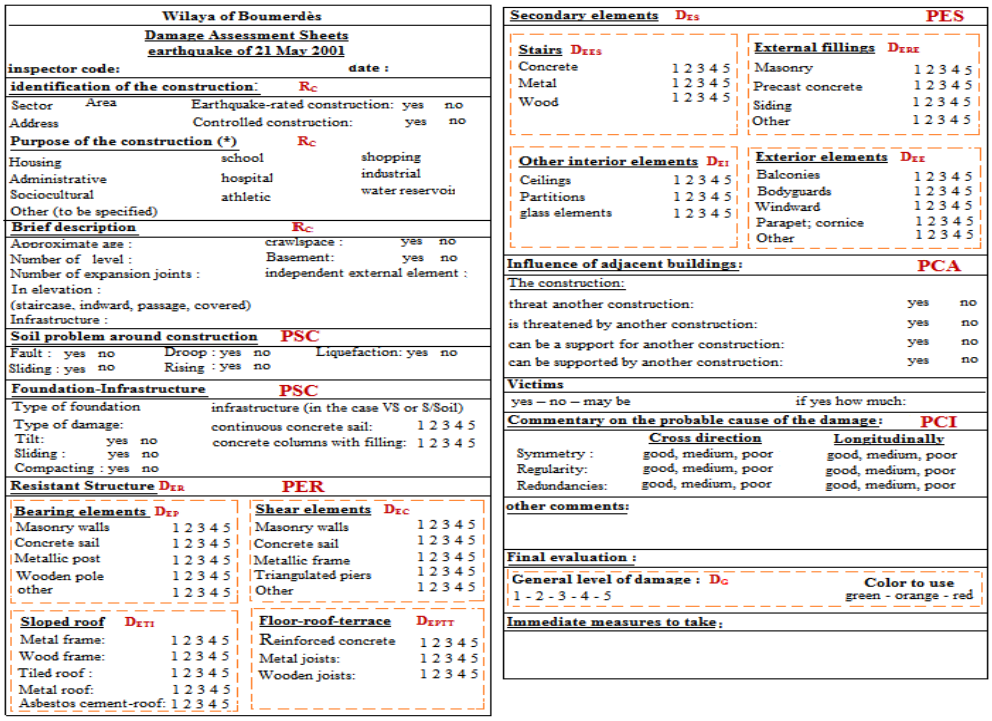
rigorously defined between two successive categories of damage (Sinha et al., 2012; Akkouche et al., 2019). Moreover, the success of the diagnosis (qualitative evaluation) is not mainly linked to the usual standards of damage assessment, but rather to the accuracy of the expert's judgment (Goretti, 2001; Carreño et al., 2010). An incorrect answer from the expert, while recording the appreciation, may be a source of increased uncertainty vis-a-vis the safety of the occupants of an already damaged structure (Davidovichi, 2003).

For that matter, the transition from a qualitative evaluation to a quantitative evaluation proves to be very interesting (Sinha et al., 2012), this, relying on the development of mathematical prediction models that improve the accuracy and objectivity of decisions (Olson & Dash-Wu, 2010). These models are founded on specific databases (construction mode, building area, supporting soil ... etc) which induces a reduction of their applicability. In other words, the use of these models leads to systematic errors. In this perspective, a more adequate damage assessment method corresponding to Algerian construction methods is proposed. The assessment of the overall damage level will be done through the proposed generic model that will reproduce quantitatively the final decision taken by the investigator on a structure (while keeping the same principle proposed by EMS 98 for the evaluation of basic disorders), depending on the severity of the damage reported on its various components. The category of damage associated with a structure is characterized by the achievement of several damage levels noted on the sub-structural elements "the state of the bearing and non-bearing elements, the state of the soil, the state of the neighboring structures …etc." The approach used, where only the damage effects of structural and non-structural components are considered, is based on the theory of experimental design (Goupy, 2000). Indeed, this theory is widely studied and applied in various fields, for prediction, classification and optimization (Akkouche et al., 2020; Akkouche et al., 2024). This work carried out by Akkouche et al showed that this method is applicable to the field of civil engineering. In order to distinguish the characterization of elementary disorders from the assessment of overall damage, this work was conducted as follows:

In a first stage, with reference to the inspection form used by the Algerian authorities, two damage assessment models at the local scale have been established, making it possible to estimate the state of all the elements:

- Bearing, D_{ER} depending on the state of the element: bearing D_{EP}, bracing D_{EC}, floor-roofing-terrace D_{EPTT} and inclined roofing D_{ETI}.
- Non-Bearing, D_{ES} based on the damage level associated with the elements: Stairs D_{EES}, Exterior Filling D_{ERE}, Interior Elements D_{EEI}, and Exterior Elements D_{EE}.

In a second stage, a study has been conducted for the assessment of the parameter, which characterizes the state of the overall construction D_G according to local damages D_{ER} and D_{ES}.



Wilaya of Boumerdès

Damage Assessment Sheets
earthquake of 21 May 2001

inspector code: **date :**

identification of the construction: R_C

Sector Area — Earthquake-rated construction: yes no
Address — Controlled construction: yes no

Purpose of the construction (*) R_C

Housing — school — shopping
Administrative — hospital — industrial
Sociocultural — athletic — water reservoir
Other (to be specified)

Brief description R_C

Approximate are : — crawlspace : yes no
Number of level : — Basement: yes no
Number of expansion joints : — independent external element :
In elevation :
(staircase, indward, passage, covered)
Infrastructure :

Soil problem around construction PSC

Fault : yes no — Droop : yes no — Liquefaction: yes no
Sliding : yes no — Rising : yes no

Foundation-Infrastructure PSC

Type of foundation — infrastructure (in the case VS or S/Soil)
Type of damage: — continuous concrete sail: 1 2 3 4 5
Tilt: yes no — concrete columns with filling: 1 2 3 4 5
Sliding : yes no
Compacting : yes no

Resistant Structure D_{ER} PER

Bearing elements D_{EP}

Masonry walls	1 2 3 4 5
Concrete sail	1 2 3 4 5
Metallic post	1 2 3 4 5
Wooden pole	1 2 3 4 5
other	1 2 3 4 5

Shear elements D_{EC}

Masonry walls	1 2 3 4 5
Concrete sail	1 2 3 4 5
Metallic frame	1 2 3 4 5
Triangulated piers	1 2 3 4 5
Other	1 2 3 4 5

Sloped roof D_{ETI}

Metal frame:	1 2 3 4 5
Wood frame:	1 2 3 4 5
Tiled roof :	1 2 3 4 5
Metal roof:	1 2 3 4 5
Asbestos cement-roof:	1 2 3 4 5

Floor-roof-terrace D_{EPTT}

Reinforced concrete	1 2 3 4 5
Metal joists:	1 2 3 4 5
Wooden joists:	1 2 3 4 5

Secondary elements D_{ES} PES

Stairs D_{EES}

Concrete	1 2 3 4 5
Metal	1 2 3 4 5
Wood	1 2 3 4 5

External fillings D_{ERE}

Masonry	1 2 3 4 5
Precast concrete	1 2 3 4 5
Siding	1 2 3 4 5
Other	1 2 3 4 5

Other interior elements D_{EI}

Ceilings	1 2 3 4 5
Partitions	1 2 3 4 5
glass elements	1 2 3 4 5

Exterior elements D_{EE}

Balconies	1 2 3 4 5
Bodyguards	1 2 3 4 5
Windward	1 2 3 4 5
Parapet; cornice	1 2 3 4 5
Other	1 2 3 4 5

Influence of adjacent buildings: PCA

The construction:
threat another construction: yes no
is threatened by another construction: yes no
can be a support for another construction: yes no
can be supported by another construction: yes no

Victims
yes – no – may be — if yes how much:

Commentary on the probable cause of the damage: PCI

	Cross direction	Longitudinally
Symmetry :	good, medium, poor	good, medium, poor
Regularity:	good, medium, poor	good, medium, poor
Redundancies:	good, medium, poor	good, medium, poor

other comments:

Final evaluation :

General level of damage : D_G — 1 - 2 - 3 - 4 - 5 — **Color to use** green - orange - red

Immediate measures to take :

Figure 1. Post-seismic damage assessment form in Algeria (Akkouche et al. 2020)

Evaluation Procedure for Post-Seismic Damages

In order to optimize the work of the engineer and reduce the post-seismic danger, as in many seismic countries, in Algeria, a visual evaluation sheet was developed by the CTC and CGS agencies (Fig. 1). Depending on parameters such as type of use, type of damaged elements, severity of damage, etc. This sheet is intended to give an assessment (local "of the components" and global "of the structure") summarizing the state of damage of the structure. About fifty pieces of information are grouped in this form, of the following type especially:

- General (noted RI for the investigator and RC for the construction).
- Concerning the environment around the construction (soil problems and problems related to adjacent constructions).
- Relative to the state of the bearing and non-bearing elements
- On the different architectural damage causes, noted PCI.
- An overall assessment of the construction damage noted D_G.

The disorders classification adopted in the form is founded on the European Macro-Seismic Scale EMS98 (see Table 1). In addition, depending on this D_G parameter, each construction is marked with a specific color.

Table 1. Classification of reinforced concrete structures according to EMS 98 (Grünthal and Levret 2001)

EMS 98 Scale	1	2	3	4	5
Masonery structures					
Reinforced concrete structure					

Methodology

With the aim of developing a model making it possible to estimate the degree of damage at the construction scale, in this section, the process of processing a database (7,847 inspection sheets) using of the experimental design method is briefly described.

Principal of the Experimental Design Method

Experimental design method has multiple objectives, among which, one is to create a logical relationship (mathematical) between two types of variables (Dagnelie 2000), the physical quantity studied (response) and the physical quantities supposedly having an influence on the response value (factors). According to (Goupy and Creighton 2006), these approaches are characterized by:

- The choice of experimental design,
- The choice of mathematical model expression,

Choice of Experimental Design

According to (Telforda, 2007), only two factors can influence the choice of an experimental plan: the field of study and the degree of precision sought. Referring to the recommendations given by (Dagnelie, 2000), with the aim of developing a model allowing the reproduction of the most complete information, in this study we favored the use of the complete factorial design.

Choice of Mathematical Model Expression

In the case of a study aimed at estimating the weight of variables, polynomial modeling is recommended (Chlela, 2008). Assuming that the effects of the factors are totally additive and that there may be interactions

between them, the relationship between the measured responses and the variables can be expressed as a first-degree polynomial (Eq. 1).

$$R_r = \sum_{i=1}^{N} a_i y_i + \sum_{i=1}^{N}\sum_{j=1}^{N} a_{ij}\, y_i y_j + \cdots + \sum_{i=1}^{N}\sum_{j=1}^{N}\sum_{k=1}^{N}\sum_{l=1}^{N} a_{ijkl}\, y_i y_j y_k y_l \quad (1)$$

Where, R: the response, Y: the influential factors and a: unknowns of the model.

Construction of the Full Factorial Design

According to (Telforda, 2007; Chlela, 2008), in order to estimate, with minimal and homogeneous uncertainty, the unknowns of the model, during the construction of the complete factorial design, we must extract from the experimental domain a sufficient number (N) of particular combinations.

Building the Model Matrix

From the experimental design, the model matrix called "effects matrix" noted X was constructed. The interactions columns were constructed by multiplying the factors between them (Goupy and Creighton.2006).

Table 2. Matrix of effects "X"

Configu -ration	Factor			Order interactions				Response
				1			2	
	F_1	F_2	F_3	F_{12}	F_{13}	F_{23}	F_{123}	
1	-1	-1	-1	+1	+1	+1	-1	R_1
2	+1	-1	-1	-1	-1	+1	+1	R_2
3	-1	+1	-1	-1	+1	-1	+1	R_3
4	+1	+1	-1	+1	-1	-1	-1	R_4
5	-1	-1	+1	+1	-1	-1	+1	R_5
6	+1	-1	+1	-1	+1	-1	-1	R_6
7	-1	+1	+1	-1	-1	+1	-1	R_7
8	+1	+1	+1	+1	+1	+1	+1	R_8

On the basis of the matrix presented in Table 2, many other matrices can be developed, such as the invariants that are given by the following relation:

$$[X'X] = \frac{1}{N}[I_N] \quad (2)$$

Where: "X" and "X'" respectively represent the matrix of "Fisher" and its transpose matrix, "IN" the identity matrix and "N" the number of configurations.

Mathematical Processing

Each response is represented by a single configuration. The proposed approach thus leads to the following formulation:

$$\{R\} = [x]\,\{a\} \quad (3)$$

With: {R}: response vector, [X]: calculation matrix and {a}: coefficient vector (effects of the factors and interactions).

The resolution of this system (formula 3) is carried out by means of the linear regression method, based on the criterion of least squares optimization, and which makes it possible to write:

$$\{a\} = [X^t X]^{-1}\ {}^t[X]\ \{R\} \quad (4)$$

By inserting (2) in (4), we get the following expression:

$$\{a\} = [\tfrac{1}{N} I]^{-1\,t}[X]\ \{R\} = (\tfrac{1}{N})^t [X]\ \{R\} \quad (5)$$

Results and Discussion

Structural Component Effects

Graphical Representation of Main Effects

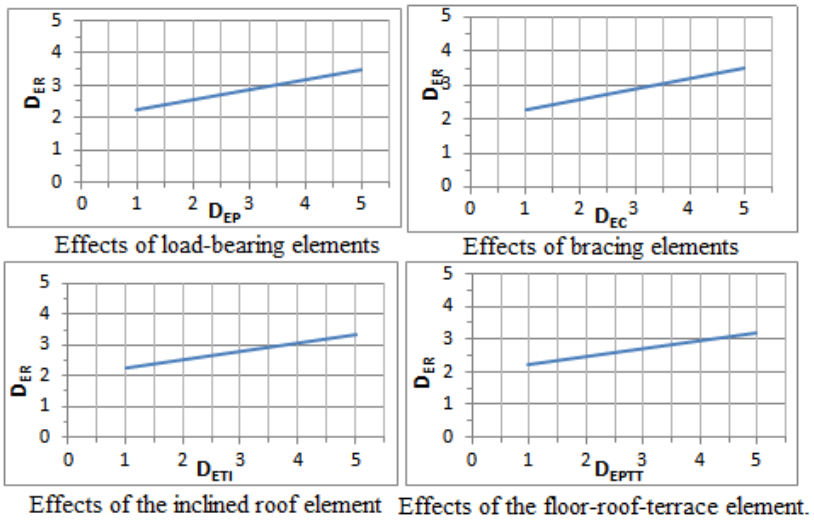


Figure 2. Graphical representation of the main effects.

Fig. 2 illustrates the effect caused by the damage of each structural component on the variation of the D_{ER} quantity, reflecting the state of their whole. Thus, the variation in the state of damage (ranging from D_1 to D_5) of each factor induces a remarkable evolution in the value of the quantity, indicating the state of damage of all the structural elements. Initially, the same degree of damage around D_2 is observed for the magnitude D_{ER} when the level of damage of each of the factors is fixed at D_1, on the other hand, a slight difference is obtained on the response D_{ER} when varying the level of damage of these same components (damage level set at D_5). We can say that two distinct degrees are recorded for D_{ER}, practically the same response around the value of 3.5 is obtained under the effect of the variation of the D_{EP} parameter and the D_{EC} parameter. Another response value of 3.15 close to level D_3 is obtained following the variation of the D_{ETI} and D_{EPTT} factors.

Graphical Representation of First Order Interactions

These so-called first-order interactions represent the capacity of a damaged component to vary the D_{ER} response under the effect of another damaged component.

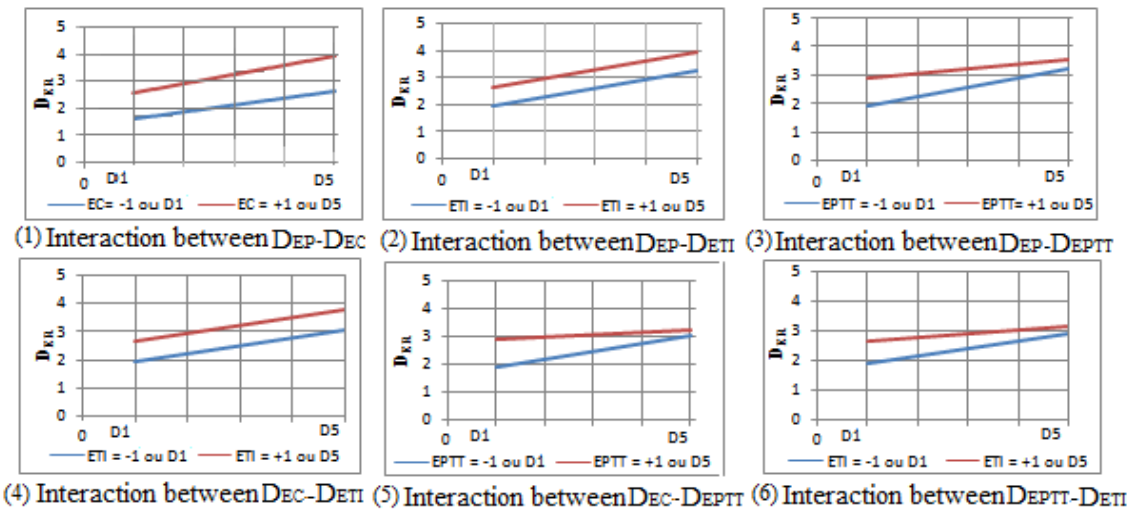


Figure 3. Graphical representation of the first order interactions of the resistant elements part.

The curves given in figure 3 illustrate the different interactions, called first orders, which can exist between the four main components. Curves 1, 3, 5 and 6 expose the strong interaction that exists between the components (D_{EP} and D_{EC}), (D_{EP} and D_{EPTT}), (D_{EC} and D_{EPTT}) and (D_{EPTT} and D_{ETI}) respectively. Then, from curve 2, a weak interaction is noted between the components (D_{EP} and D_{ETI}), and another weaker one between the elements (D_{EC} and D_{ETI}) according to the results illustrated in curve 4. Also, curves 3, 5 and 6 we notice that the capacity of the mobile factor to vary the D_{ER} response decreases under the evolution of the other immobile factor (fixed at D_1 then at D_5).

Example, in curve 5, we notice that when the D_{EPTT} is fixed at D_1 (the curve in blue), the variation of the damage level D_{EC} from D_1 to D_5 induces a significant variation in the D_{ER} response. On the other hand, when the D_{EPTT} is fixed at D_5 (the curve in red), the variation of the D_{ER} response is little influenced by the variation of the D_{EC} level. While in curve 1, we see that the capacity of the mobile factor (in this case D_{EC}) to vary the response D_{ER} increases with the evolution of the other immobile factor (in this case D_{EP}).

Graphical Representation of Higher Order Interactions

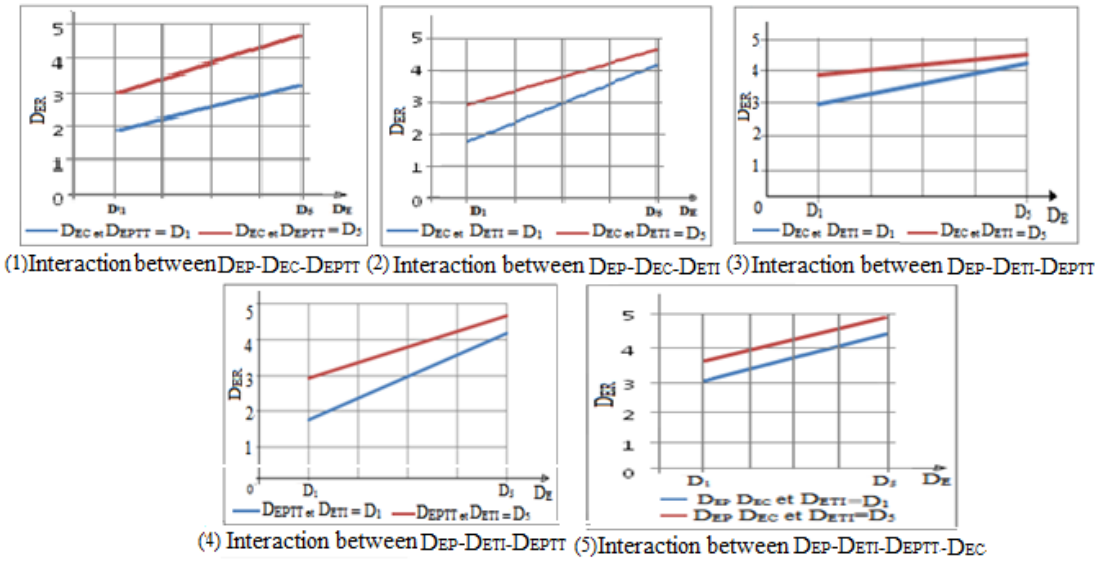


Figure 4. Graphical representation of higher order interactions for resistant elements.

Fig. 4 illustrates the interactions of orders 2 and 3 given by three and four factors respectively. Curves 1, 2, 3 and 4 demonstrate that the interactions between the different factors cannot be neglected. Thus, the shape of the straight lines of the 1st curve indicates that the effect of the variation in the level of damage of the supporting component on the quantity reflecting the state of damage of all the structural elements is practically constant, under the effect of the variation in the damage torque of the components, bracing and floor-roof-terrace, despite the evolution of the response (of a damage level), under the effect of the state of the damage torque. On the other hand, curves 2, 3 and 4 indicate that the effect of the immobile factor on the D_{ER} response varies negatively under the influence of the damage torque. Example, on the 2nd curve, we see that the category of damage attributed to the D_{ER} response under the effect of the supporting element goes from 1.5 to 4 and from 3 to 4.5, and this, when the components (bracing and inclined roof) are fixed at level D_1 and D_5 respectively. Also, from curve 5, we can say that the D_{ER} response is practically invariant after the damage of 3 components, which explains the ignorance of the damage state of the fourth element.

Effects of Non-Structural Components

Graphical Representation of Main Effects

The figure above illustrates the main effects of different factors on the D_{ENR} response. For the four factor, the same D_{ENR} response, slightly higher than level D_1, is obtained when the damage level of the element is at low level D_1. When the damage level of the element is fixed at D_5, the same D_{ENR} response, around level D_3, is obtained. Thus, the evolution of the damage level of each element (from D_1 to D_5) causes the D_{ENR} response to vary by two categories.

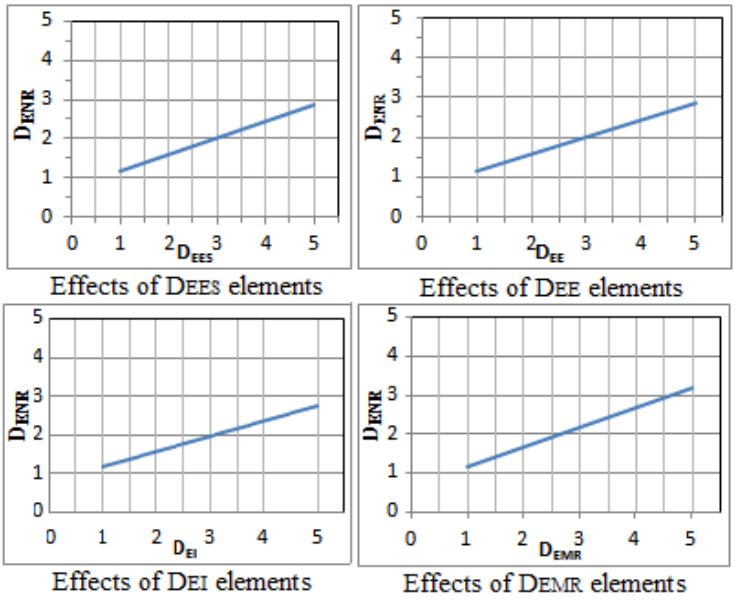


Figure 5. Graphical representation of main effects.

Graphical Representation of First Order Interactions

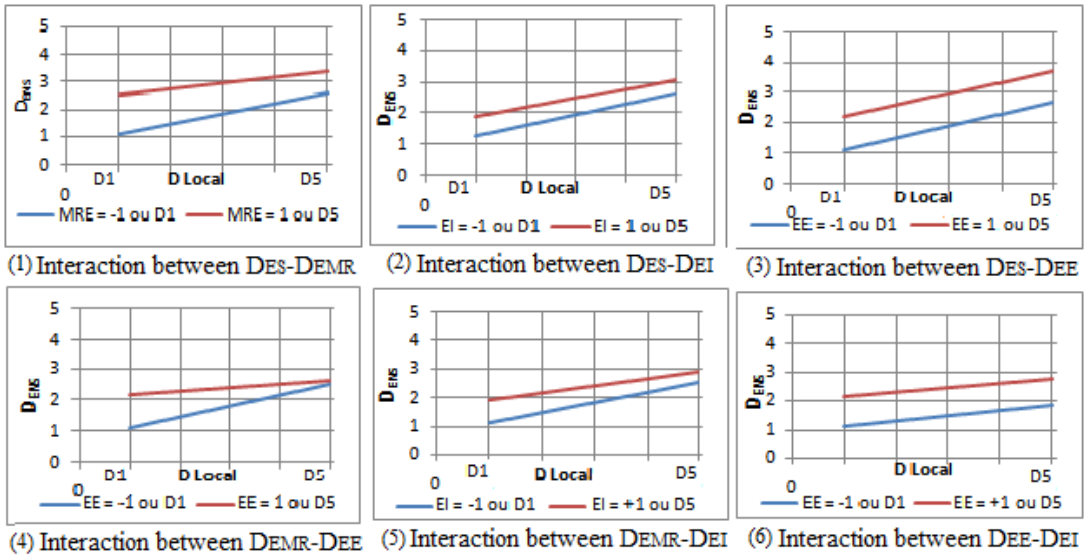


Figure 6. First order interactions of the resistant element part.

Fig. 6 illustrates the different interactions that can exist between two elements. Thus, the capacity of each element to vary the D_{ENR} response under the effect of another element is demonstrated. Referring to the shape of the lines, a strong interaction between the elements (D_{ES}-D_{EMR}, D_{EMR}-D_{EI} and D_{EMR}-D_{EE}) is noted. Example, in the case of interaction (4) between D_{EMR}-D_{EE}, when the damage level of the filling wall element is fixed at D_1, the D_{ENR} response varies from 1 to 2.5 (i.e. an evolution of 150 %), under the effect of the variation in the level of damage of the exterior element (ranging from D_1 to D_5). On the other hand, when the level of damage of the filling wall element is fixed at D_5, the response D_{ENR} varies from level 2 to 2.5 (i.e. with an evolution of 50%), under the effect of the variation in the level of damage of the external element (ranging from D_1 to D_5). Also, weak interactions are observed between the elements (D_{ES}-D_{EE}, D_{ES}-D_{EI} and D_{EE}-D_{EI}). For example, in the case of interaction (3), we notice that the evolution of the response D_{ENR} under the effect of the variation of the damage level of the external element is invariable, when the damage level of the staircase element is fixed D_1 and D_5.

Graphical Representation of Higher Order Interactions

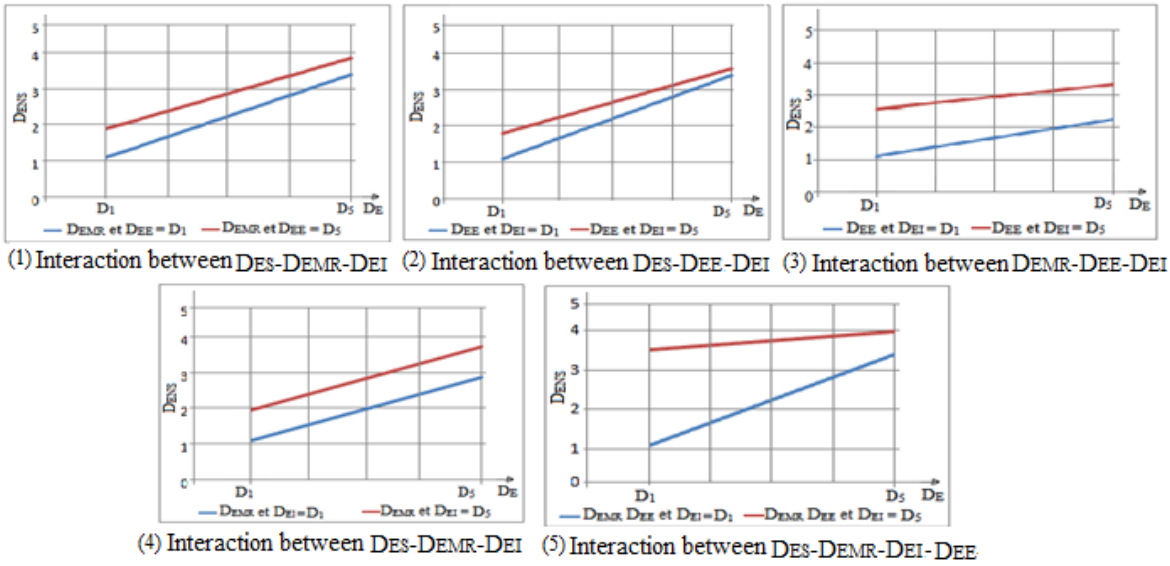


Figure 7. Graphical representation of higher order interactions, of the non-resistant elements part.

Fig. 7 illustrates the interactions of orders two and three resulting from the four non-structural elements. Curves 1 and 2 show that the same negative influence is recorded for the fixed component, under the effect of the variation in the damage torque. Example, the 1st interaction illustrates the involvement of the damage couple (D_{EMR}-D_{EE}) in the variation of effect of D_{EES} on the D_{ENR} response. For the couple (D_{EMR}-D_{EE}), the evolution from a very light damage category to another very significant one induces a reduction in the impact of D_{EES}, on the D_{ENR} response, of around 80%. On the other hand, curves 3 and 4 show that a stable effect is obtained by contributing to the variation in the level of damage of the fixed element, during the variation of the damage torque. Example, under the variation of the damage torque (ranging from a light class D_1 to a significant class D_5), the D_{ENR} varies from category D_1 to a neighboring category D_3, when D_{EES} is close to a weak damage category D_1. When D_{EES} is close to a damage category called very significant "D_5", the response varies from a degree D_2 to a level close to class D_4.

Estimation of Overall Damage

The degree of overall damage D_G is a combination of several parameters: the condition of the ground of the construction, the condition of neighboring constructions, the disorders noted on the resistant elements, the disorders noted on the non-resistant elements.

In the following part, the influence of the two parameters D_{ER} and D_{ENR} is presented:

- Of all the D_{ER} structural elements,
- All D_{ENR} secondary elements.

The approach used consists of applying, to the corpus of data, processing allowing access to a meaning that responds to the problem. This analysis can be formulated through two selection stages:

By excluding all files (structures), the final decision of which is linked to disorders appearing on the ground (PSC) and/or in adjacent constructions (PCA).

Meaning of the Coefficient Assigned to the D_{ER} factor

The overall damage varies approximately from the value 2.98 to 4.16, when the local damage (secondary element D_{ENR}) varies from a level of light damage D_1 to a level reflecting ruin D_5. Furthermore, the overall damage increases from level to while D_{ENR} varies from one important category (D_3) to another, reflecting the state of ruin (D_5). This increase of 0.57 represents the effect of the D_{ENR} factor (Fig. 8).

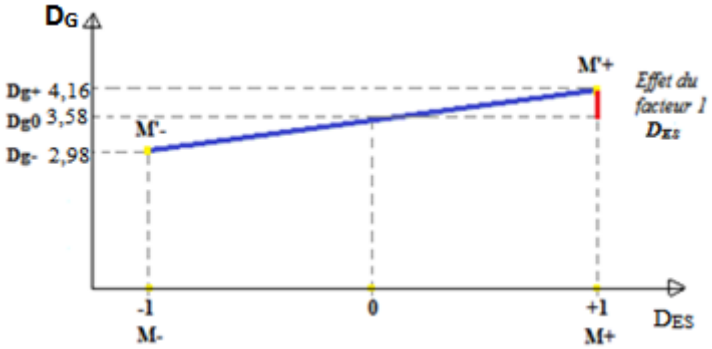


Figure 8. Representation of the effect of the D_{ENR} parameter

Signification of the Coefficient Assigned Factor D_{ER}

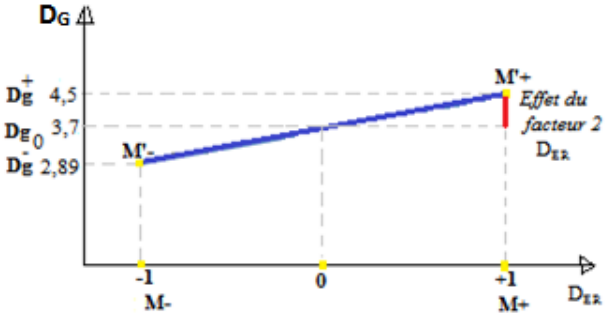


Figure 9. Representation of the effect of the D_{ER} parameter

The variation in the level of D_{ER} (from a very slight degree to a very high one) induces a "worsening" in the final decision. Indeed, the assessment evolves from a level of damage close to the so-called significant category ($2.89=D_3$) to another level close to the category indicating the state of ruin ($4.5=D_5$). On average, the D_G value changes from to, while D_{ER} varies from (D_3) to (D_5). This increase of 0.79 reflects the effect of the D_{ER} factor (Fig. 9).

Signification of Coefficient C_{21}

La The description of the relationship between the two factors consists of:

- Extract the plans ACA'C' (low level of the D_{ENR}) and BDB'D' (high level of the D_{ENR}) from figure 10, project the latter onto the same plans (Fig. 10).

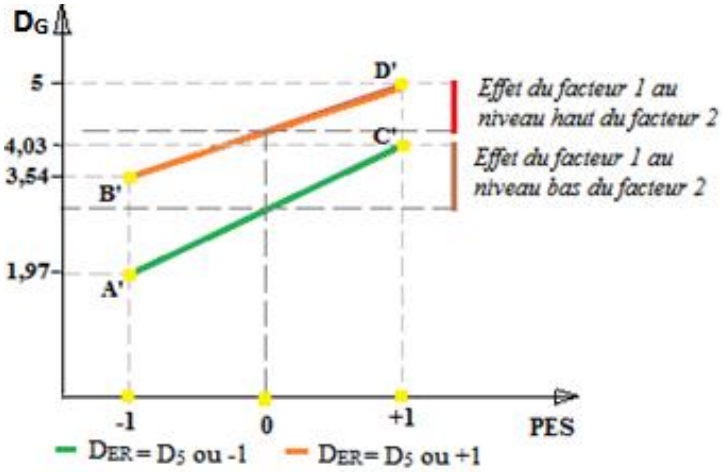


Figure 10. Illustration of the interaction between D_{ENR} and D_{ER}

Figure 10 shows the correlation between the two factors. This can be justified as follows:

- When the value of D_{ER} is close to the degree (D_1), the variation from the minimum level to the maximum level of damage for all the secondary elements induces a significant variation in the categorization of the final damage (D_G= D_2 to D_G= D_4).
- On the other hand, when D_{ER} approaches the degree (D_5), the evolution of the disorders observed on all the non-structural elements (D_1 to D_5) leads to a variation in the final classification of the construction.
- Indeed, the evolution of the D_{ER} includes an underestimation of D_{ENR}, of the order of 70%, in decision-making. The results obtained are illustrated by the equation of the proposed mathematical model. Thus, the overall response can be estimated by the equation:

$$D_G = 1 + (0.79 * D_{ER}) + (0.57 * D_{ENR}) + (- 0.107 * D_{ER} * D_{ENR}).$$

Comparison of Overall Damages

The validation of the previously proposed models is established by comparing the calculated D_G quantity to the estimated response (answer given in the sheet), on a set of ten constructions (table 3).

Table 3. The different levels of damage attributed to the components.

Construction number	Damage noted on components							
	Structural					Non-structural		
	D_{EP}	D_{EC}	D_{EPT}	D_{TI}	D_{ESC}	D_{ERE}	D_{EI}	D_{EE}
1	3	4	2	2	3	2	2	2
2	2	4	3	3	4	4	4	4
3	3	1	4	4	4	3	1	3
4	4	3	4	3	3	3	3	4
5	2	2	1	2	2	4	2	1
6	4	4	2	2	4	3	2	2
7	1	1	1	1	3	2	3	4
8	1	1	2	2	3	1	3	4
9	3	3	2	2	2	2	1	4
10	5	2	2	3	3	2	1	4

The constructions retained for the validation of the model come from the evaluation sheets which were not used in the identification procedure (establishing the models).

Table 4. Validation of the proposed model.

Construction number	Dommage global D_G		Convergence
	Estimated	Calculated	
1	4	3,88	4
2	4	4,27	4
3	4	2	2
4	4	3,70	4
5	4	3,25	3
6	3	4,06	4
7	3	3,16	3
8	2	2,99	3
9	2	3,48	3-4
10	2	3,53	3-4

Referring to the results given in table 4, it was found that for constructions No. 1, 2, 4 and 7, the model reproduces the expert's decision with an insignificant margin of error ranging from (3% to 7.5%). Whereas, for constructions No. 5 and 6 the model converges on the experimental with a percentage difference ranging from (18.7% to 26.1%), i.e. an inaccuracy of ±1 degree of damage. On the other hand, the greatest difference is observed on constructions No. 3, 8, 9 and 10. This divergence of 33.1% to 50% testifies to the importance of imprecision, i.e. an error of ± (2 or 3) degrees of damage.

Although the same category of damage (very significant) was attributed to the first 05 constructions (Table 4), a significant difference is noted in the level of damage noted on the various elements (Table 3). For example, the

same decision was taken for the 1st and 5th construction (regarding the maintenance or cessation of operation). Whereas, in the detail of the inspection, a shift of 20% in terms of the extent of damage was recorded on the 1st construction compared to the 5th.

Conclusions

In this part three models have been developed, each specifying a particular point:

- The state of all the elements constituting the secondary structure called D_{ENR}.
- The state of all the elements making up the resistant structure called D_{ER}.
- A categorization of the overall state of the construction.

On the basis of the results obtained, and in the case where the damage is observed only on one of the groups of components, we can propose that the expert's decision-making is based on:

- 80% on the situation of the resistant structure, when the damage is noted on this group of elements.
- 50% on the situation of the secondary structure, when the damage is noted on this group of elements.

Affecting both subgroups implies an underestimate of their respective effects in decision-making, because economic considerations must also be taken into account.

Scientific Ethics Declaration

* The authors declare that the scientific ethical and legal responsibility of this article published in EPSTEM journal belongs to the authors.

Conflict of Interest

* The authors declare that they have no conflicts of interest

Funding

* This research received no specific grant from any funding agency in the public, commercial, or not-for-profit sectors.

Acknowledgements or Notes

* This article was presented as a poster presentation at the International Conference on Technology, Engineering and Science (www.icontes.net) held in Antalya/Türkiye on November 12-15, 2025.

References

Akkouche, K., Hannachi, N. E., Hamizi, M., & Khelil, N. (2020). Development of a relation model for global and local damage categorization: The case of the Algerian building. *Bulletin of Earthquake Engineering, 18*(3), 1081–1104.

Akkouche, K., Hannachi, N. E., Hamizi, M., Khelil, N., & Daoui, M. (2019). Knowledge-based system for damage assessment after earthquake: Algerian buildings case. *Asian Journal of Civil Engineering, 20*(6), 769–784.

Akkouche, K., Nekmouche, A., Khelil, N., Bouzid, L., & Amar, K. (2024). Impact assessment of structural and non-structural components on the vulnerability level of reinforced concrete buildings. *The Eurasia Proceedings of Science, Technology, Engineering & Mathematics (EPSTEM), 32*, 366–372.

Baggio, C., Bernardini, A., Colozza, R., Corazza, L., Della Bella, M., & Di Pasquale, G. (2007). *Field manual for post-earthquake damage and safety assessment and short-term counter measures (AeDES)* (Report No. EUR 22868 EN). European Commission, Joint Research Centre.

Carreño, M. L., Cardona, O. D., & Barbat, A. H. (2010). Computational tool for post-earthquake evaluation of damage in buildings. *Earthquake Spectra, 26*(1), 63–86.

Chlela, F. (2008). *Développement d'une méthodologie de conception de bâtiments à basse consommation d'énergie* (Doctoral dissertation). Université de La Rochelle.

Dagnelie, P. (2000). La planification des expériences: Choix des traitements et dispositif expérimental (avec discussion). *Journal de la Société Française de Statistique, 141*(1–2), 5–69.

Davidovici, V. (2003). *Séisme de Boumerdes du 21 mai 2003: Rapport de mission* (Preliminary report). Ministère de l'Habitat; Dynamique Concept.

Goretti, A., & Di Pasquale, G. (2004). Building inspection and damage data for the 2002 Molise, Italy, earthquake. *Earthquake Spectra, 20*(S1), 167–190.

Goupy, J. (2000). Modélisation par les plans d'expériences. *Techniques de l'Ingénieur, R275*.

Goupy, J., & Creighton, L. (2006). *Introduction aux plans d'expériences* (3rd ed.). Dunod.

Grünthal, G. (Ed.). (1998). *European macroseismic scale 1998 (EMS-98)* (Vol. 15). Cahiers du Centre Européen de Géodynamique et de Séismologie.

Grünthal, G., & Levret, A. (Eds.). (2001). *European macroseismic scale 1998 (EMS-98)*. Cahiers du Centre Européen de Géodynamique et de Séismologie.

Olson, D. L., & Wu, D. D. (2010). Earthquakes and risk management in China. *Human and Ecological Risk Assessment: An International Journal, 16*(3), 478–493.

Schimmerling, P., Sisson, J. C., & Zaidi, A. (1998). *Pratique des plans d'expériences*. Tec & Doc Lavoisier.

Sinha, R., & Shiradhonkar, S. R. (2012). Detailed evaluation of available seismic damage indices. *ISET Journal of Earthquake Technology, 49*(1), 1–18.

Telford, J. K. (2007). Brief introduction to design of experiments. *Johns Hopkins APL Technical Digest, 27*(3), 224–232.

Author(s) Information

Akkouche Karim
Mouloud Mammeri University of Tizi-Ouzou, Department of Civil Engineering, Tizi-Ouzou, 15000, Algeria
Contact e-mail: *karim.akkouche@ummto.dz*

Khelil Nacim
Mouloud Mammeri University of Tizi-Ouzou, Department of Civil Engineering, Tizi-Ouzou, 15000, Algeria

Nekmouche Aghiles
Mouloud Mammeri University of Tizi-Ouzou, Department of Civil Engineering, Tizi-Ouzou, 15000, Algeria

Kahil Amar
Mouloud Mammeri University of Tizi-Ouzou, Department of Civil Engineering, Tizi-Ouzou, 15000, Algeria

Hamizi Mohand
Mouloud Mammeri University of Tizi-Ouzou, Department of Civil Engineering, Tizi-Ouzou, 15000, Algeria

Bouzid Leyla
Mouloud Mammeri University of Tizi-Ouzou, Department of Civil Engineering, Tizi-Ouzou, 15000, Algeria

Atlaoui Djamel
Mouloud Mammeri University of Tizi-Ouzou, Department of Civil Engineering,Tizi-Ouzou, 15000, Algeria

To cite this article:

Karim, A., Nacim, K., Aghiles, N., Amar, K., Mohand, H., Leyla, B., & Djamel, A. (2025). Development of a relation model for damage categorization**.** *The Eurasia Proceedings of Science, Technology, Engineering and Mathematics (EPSTEM), 38,* 69-80.

The Eurasia Proceedings of Science, Technology, Engineering & Mathematics (EPSTEM)
ISSN: 2602-3199

The Eurasia Proceedings of Science, Technology, Engineering and Mathematics (EPSTEM), 2025

Volume 38, Pages 81-89

IConTES 2025: International Conference on Technology, Engineering and Science

Investigation of Conducted Electromagnetic Disturbances in Power Electronics: A Case Study on DC/DC Choppers

Mohammed Elamine Lahlaci
University Ahmed Zabana of Relizane

Mohamed Miloudi
University Ahmed Zabana of Relizane

Houcine Miloudi
Djillali Liabes University of Sidi Bel Abbes

Mohammed Hamza Bermaki
Djillali Liabes University of Sidi Bel Abbes

Kheira Mendaz
University of Ain Temouchent

Abdelkader Gourbi
University of Oran1 Ahmed Ben Bella

Abstract: Power electronics systems play a key role in modern industrial applications, particularly in motor drives and automation systems. Among the most widely used devices, static converters—especially DC/DC choppers—enable precise control of voltage and power while ensuring high energy efficiency. These converters are essential for adapting voltage levels to the specific needs of loads, thereby providing stable and optimized power supply across various industrial environments. However, these converters are also significant sources of electromagnetic disturbances (EMD), both conducted and radiated, which can compromise the electromagnetic compatibility (EMC) of systems. Conducted common-mode disturbances, in particular, pose a major challenge in industrial settings, where equipment density increases susceptibility to interference. In this context, the present study focuses on the experimental analysis of conducted common-mode EMD generated by a series DC/DC chopper. Accurate measurements are carried out using appropriate instrumentation to characterize waveform shapes, dominant frequencies, and disturbance levels. The aim is to identify operating conditions that exacerbate these emissions and to better understand the underlying mechanisms. To deepen the analysis, machine learning techniques are employed to model the disturbances based on experimental data. The developed predictive models estimate the influence of the chopper's operating parameters on electromagnetic emissions and help propose mitigation strategies through optimized control and design parameters. The results contribute to the development of cleaner converters that meet EMC requirements without compromising electrical performance. This approach enhances the reliability and robustness of power electronics systems in demanding industrial environments.

Keywords: Electromagnetic compatibility EMC, Electromagnetic disturbances EMD, Choppers DC/DC, Conducted common-mode disturbances CM, Machine learning techniques.

Introduction

- This is an Open Access article distributed under the terms of the Creative Commons Attribution-Noncommercial 4.0 Unported License, permitting all non-commercial use, distribution, and reproduction in any medium, provided the original work is properly cited.

- Selection and peer-review under responsibility of the Organizing Committee of the Conference

© 2025 Published by ISRES Publishing: www.isres.org

Static converters play a central role in modern power electronics systems (Mohammed et al., 2024; Mohamed et al., 2012; Sara et al., 2023). Their main function is to transform and regulate electrical energy to meet the specific requirements of various industrial applications (Miloudi et al., 2019), including automation (Benhadda et al., 2024), motor drives (Gourbi et al., 2020), renewable energy systems (Naima et al., 2025), and embedded electronics (Zeghoudi et al., 2022). Among these converters, DC/DC choppers are widely used for voltage conversion due to their high efficiency (Mohammed et al., 2024), compactness, and ability to provide precise voltage control (Mohammed et al., 2024). However, the fast-switching operation of these converters generates significant electromagnetic disturbances (EMD), both conducted and radiated (Abdelhakim et al., 2022; Miloudi et al., 2023). These disturbances, often underestimated during the design phase, can severely affect the performance of nearby equipment and compromise the overall electromagnetic compatibility (EMC) of the system (Mohammed et al., 2025; Bermaki et al., 2023). In industrial environments, where numerous electronic devices operate in close proximity, managing such interference is crucial to ensure system reliability, safety, and regulatory compliance (Houcine et al., 2022; Miloudi et al., 2010).

This study focuses specifically on conducted common-mode disturbances generated by a series DC/DC chopper (Lahlaci et al., 2025). The objective is to experimentally characterize these interferences, identify critical operating conditions, and develop effective predictive tools (Zeghoudi et al., 2022). To achieve this, machine learning techniques are incorporated into the methodology (Miloudi et al., 2014). Machine learning offers powerful tools for modeling complex phenomena based on experimental data-especially when traditional analytical approaches become limited. By leveraging these techniques, it becomes possible to predict disturbance levels based on the converter's operating parameters and to propose optimization strategies aimed at reducing electromagnetic impact (Abdelhakim et al., 2022; Miloudi et al., 2025).

This work thus aims to reconcile electrical performance with electromagnetic compatibility requirements, using a combination of experimental analysis and intelligent modeling to improve the design of static converters in demanding industrial settings.

EMC Measurement and Standards of Conducted EMI.

In practical terms, the LISN ensures consistency and comparability across different measurement setups by standardizing the impedance seen by the equipment under test. This consistency is essential, as the amplitude and spectral characteristics of conducted disturbances can vary significantly depending on the impedance of the power source and the wiring configuration. Additionally, the LISN enables accurate detection of high-frequency noise by diverting these signals toward a spectrum analyzer or EMI receiver, while simultaneously preventing external noise from the power grid from influencing the measurement. Therefore, it plays a critical role in ensuring that electromagnetic compatibility (EMC) assessments of power electronic systems, such as DC/DC converters, are both precise and representative of real-world operating conditions.

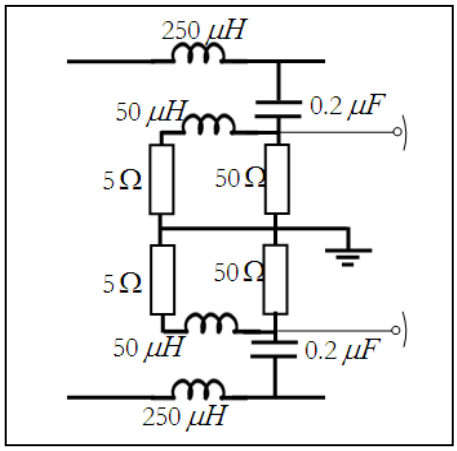


Figure 1. Simplified structure of the LISN

Conducted disturbances often pertain to high-frequency currents circulating within the device. The term high frequency typically encompasses frequencies ranging from 150 kHz to 30 MHz, as this frequency range aligns with the bandwidth regulated by prevailing EMC standards. This current can be dissected into two modes (CM and DM), as depicted in (Figure. 2).

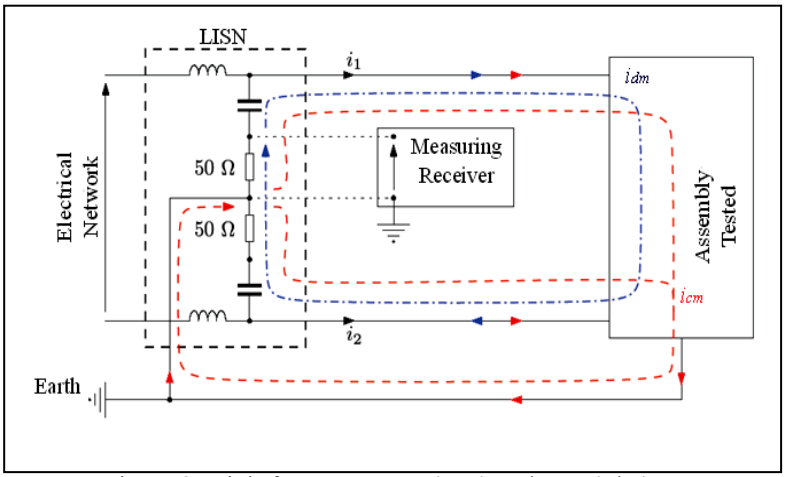


Figure 2. High-frequency CM (Icm) and DM (Idm) currents

Differential Mode (DM) current, denoted as I_{dm}, represents the portion of current that circulates between the power source and the load through the phase and neutral conductors. While this is the intended path for power transmission, high-frequency components superimposed on this current are undesirable and often stem from switching operations. In contrast, Common Mode (CM) current, I_{cm}, flows simultaneously through both conductors and returns via the ground path-typically due to parasitic capacitance between system components and ground. Although not directly involved in power delivery, CM currents can introduce significant high-frequency noise and are particularly sensitive to the layout and grounding scheme of the electrical system. Both DM and CM emissions eventually close their loops through the internal impedances of the power grid, making their behavior-and thus their measurement-highly dependent on the configuration of the surrounding electrical network.

Power semiconductors, such as transistors used in static converters, inherently generate electromagnetic noise due to their fast switching and the presence of parasitic elements. Despite the fact that industrial environments have historically been more tolerant of such disturbances, the increasing deployment of these technologies in commercial and residential applications necessitates strict adherence to electromagnetic compatibility (EMC) standards. Manufacturers of power supplies and static converters are now required to consider EMC constraints early in the design process. This is especially crucial since power electronics systems are among the most challenging to model and optimize from an EMC perspective.

To ensure standardized testing conditions, regulatory bodies enforce specific EMC measurement procedures, such as those outlined in EN 55022. This standard prescribes a detailed testing protocol to ensure consistency, repeatability, and reliability of conducted emission measurements. Accordingly, the test setup includes components arranged on a reference copper ground plane, with the Equipment Under Test (EUT) electrically isolated to prevent interference from the surrounding environment. A typical block diagram of the test bench configuration is shown in Fig. 4, illustrating compliance with EN 55022 requirements (Figure.3).

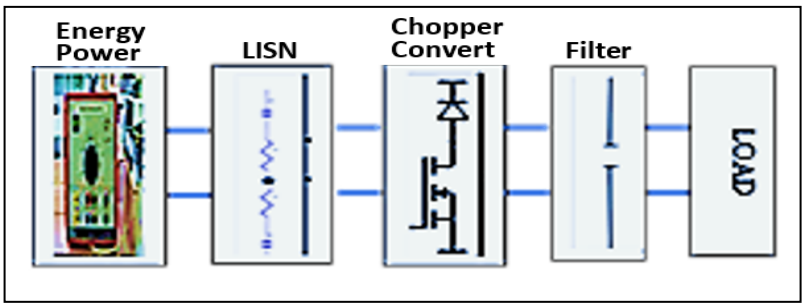


Figure 3. Multi-stage power converter

To compare conducted electromagnetic interference (EMI) in both common mode (CM) and differential mode (DM), an experimental study was conducted using a series DC/DC chopper connected to a resistive load. Two types of power transistors were employed for benchmarking purposes: the IGBT model FGH40N60 and the MOSFET model IRFP4060, each paired with a BYT12 fast recovery diode. The test setup was designed to evaluate the conducted EMI under consistent operating conditions, with the chopper supplying a resistive load at

a steady voltage of 24 V (as illustrated in Figure. 4). Key components of the measurement setup included a Line Impedance Stabilization Network (LISN) installed before the chopper to ensure standardized measurement conditions, and a spectrum analyzer used to capture and quantify the conducted disturbances in both CM and DM across various load resistance values.

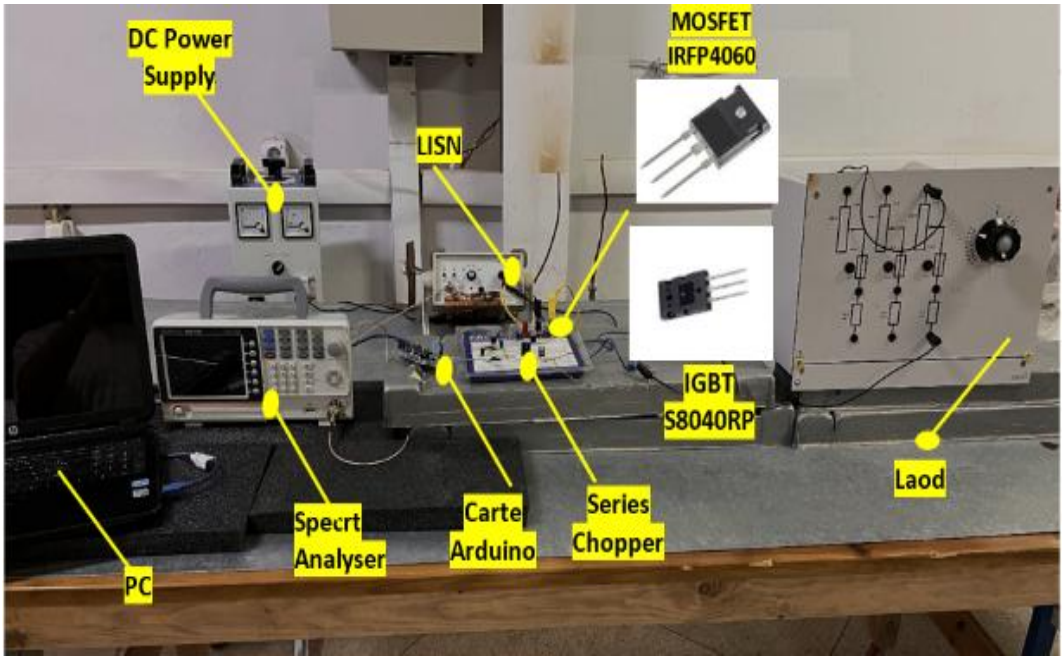


Figure 4. EMC bench for measuring conducted EMI

This study focuses on conducted-mode emissions, which are primarily responsible for the majority of electromagnetic disturbances generated by power electronic converters. Particular attention is given to the distribution of common-mode (CM) currents within the system. These currents originate mainly from capacitive CM coupling mechanisms and propagate through the system by returning via the ground path. This propagation mechanism allows conducted disturbances to affect other components of the installation, often far from the original source. For a thorough analysis of the electromagnetic interference (EMI) produced by the converter, spectral measurements are referenced against the EN 55022 standard, which defines the requirements for conducted emission testing. According to this standard, the frequency range of interest extends from 150 kHz to 30 MHz, and emissions must be quantified at the input of the equipment under test-here, the chopper.

To assess the electromagnetic compatibility (EMC) behavior of the system, a widely used analysis method in power electronics has been applied. The methodology involves first operating the chopper using a MOSFET (IRFP4060) and subsequently repeating the test under identical conditions with an IGBT (FGH40N60). Based on the results, the most appropriate measurement approach and analysis tool will be selected to provide a reliable characterization of the EMI behavior specific to each switching device.

Results and Discussion

Experimental measurements of conducted electromagnetic disturbances were performed on a series buck converter using a MOSFET switch, with different load impedances (50 Ω, 100 Ω, and 200 Ω). The results, presented as magnitude spectra in dBµV, demonstrate that the disturbance levels are strongly dependent on both frequency and the connected load. At low frequencies (100 Hz to 10 kHz) figure 5, the conducted emissions reach high levels before decreasing sharply with increasing frequency. This behavior is attributed to the natural attenuation of switching harmonics and the effect of the circuit's parasitic elements. Beyond 10 kHz, the disturbance levels stabilize around -80 dBµA for the 50 Ω and 100 Ω loads, while the 200 Ω load exhibits a distinct plateau up to 100 kHz. This phenomenon is related to the combined effects of the higher load impedance and the converter's parasitic components, leading to resonance effects at certain frequencies. These results highlight the importance of considering load impedance in the design and sizing of EMC filters to optimize the electromagnetic behavior of switching converters.

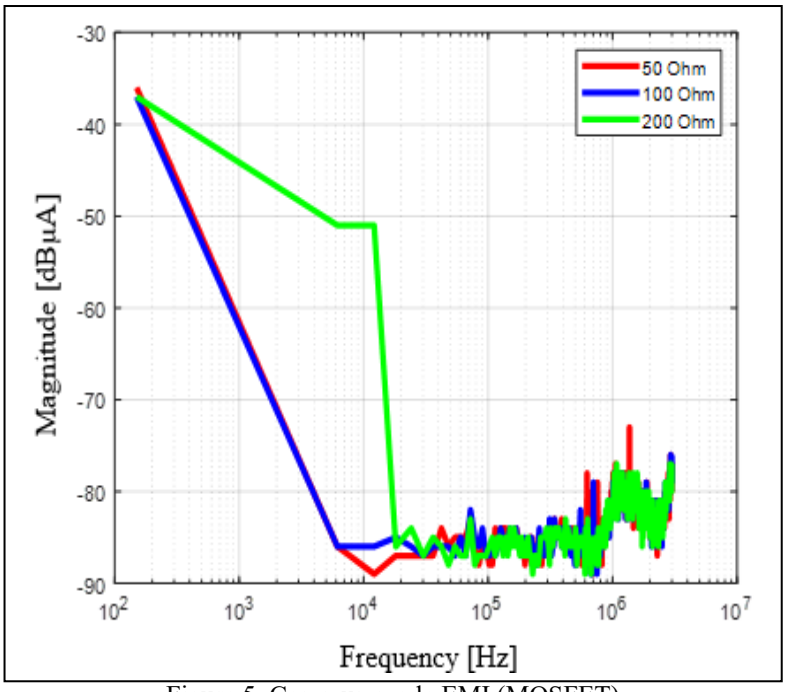


Figure 5. Commun mode EMI (MOSFET)

In a subsequent set of measurements, the same experimental protocol was applied to a series buck converter using an IGBT as the switching device Figure 6. The disturbance spectra obtained under identical load conditions exhibit a similar global trend, with high emission levels at low frequencies followed by a sharp decrease beyond 10 kHz. However, it is observed that the influence of load impedance on the EMI levels becomes less significant in the IGBT case, particularly in the mid-frequency range. Unlike the previous results, where the 200 Ω load introduced a noticeable plateau up to 100 kHz, the disturbance levels for all load impedances remain closely aligned with the IGBT. Additionally, a slight rise in disturbance levels is detected beyond 500 kHz, reflecting the inherent switching characteristics of the IGBT, such as slower transitions and higher parasitic capacitance compared to the MOSFET. These findings further emphasize the impact of the switch's dynamic behavior on the distribution of conducted disturbances across the frequency spectrum.

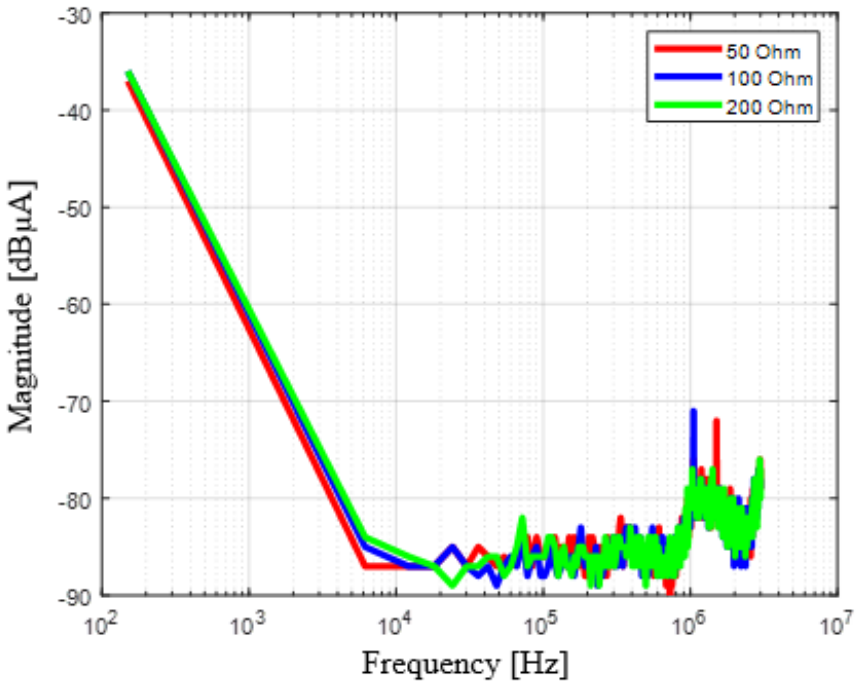


Figure 6. Common mode EMI IGBT

In the second part of this study, we focus on the integration of machine learning techniques to analyze and interpret the experimental data obtained from common-mode conducted EMI measurements. While classical approaches provide valuable insights into spectral characteristics, they often fall short when it comes to modeling complex, nonlinear relationships between operating parameters and disturbance levels. The goal of this section is to develop predictive models capable of estimating the level of conducted emissions based on various input features, such as load resistance, switching frequency, and the type of semiconductor switch used (MOSFET or IGBT). By training algorithms on the acquired measurement data, it becomes possible to identify hidden patterns, assess the influence of different variables, and ultimately optimize the converter's design for improved electromagnetic compatibility (EMC). This data-driven approach offers a powerful complement to conventional analysis methods, particularly in contexts where physical modeling is either too complex or insufficiently accurate. The selected machine learning models will be evaluated based on their predictive accuracy and interpretability, providing engineers with practical tools for EMI mitigation during the early stages of power converter development.

To further analyze the conducted EMI behavior of the series buck converter with an IGBT switch, figure 7 a nonlinear regression model was applied to the measured common-mode disturbance levels. The experimental data, represented by blue markers, were fitted using a nonlinear curve (in red) to predict the overall EMI trend across the frequency spectrum. The predicted curve successfully captures the general shape of the disturbance spectrum, with a sharp attenuation observed from 100 Hz to 10 kHz, followed by relatively stable levels in the mid-frequency range. Although minor discrepancies appear at higher frequencies, particularly beyond 500 kHz, the model effectively follows the primary trends of the measured data. These results suggest that nonlinear regression techniques can provide valuable insight into the frequency behavior of conducted EMI and serve as a useful tool for estimating disturbance levels in power electronic systems, especially for common-mode emissions where parasitic effects and switching dynamics play a significant role.

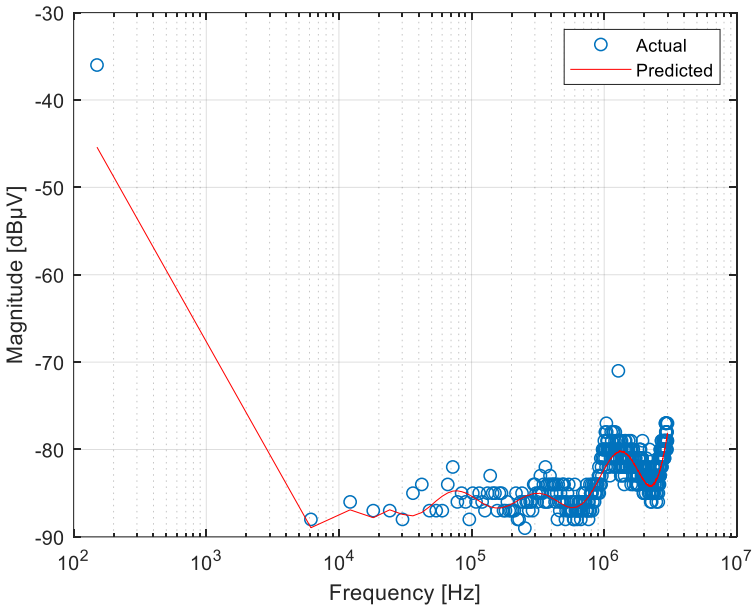


Figure 7. Nonlinear regression applied to common-mode EMI — IGBT case with 50 Ω load

In contrast, when the same nonlinear regression model is applied to the MOSFET-based converter under identical load conditions (50 Ω), the fit is less accurate, particularly in the low-frequency region (below 1 kHz), where the model significantly underestimates the measured EMI levels. While the predicted curve captures the overall trend in the mid-to-high frequency bands, it fails to represent certain spectral details, especially the initial steep drop and the slight ripples observed around the MHz range. This discrepancy may be attributed to the faster switching characteristics of the MOSFET, which generate more pronounced high-frequency transients and a more complex spectral signature. As a result, the EMI profile becomes harder to approximate using standard nonlinear regression, which may require additional terms or alternative modeling strategies to handle the rapid variations effectively.

Overall, these results indicate that while the modeling approach performs adequately for both devices, its accuracy is more sensitive to the dynamic behavior of the switching element, with the MOSFET case posing a greater challenge in terms of low-frequency prediction and spectral ripple tracking

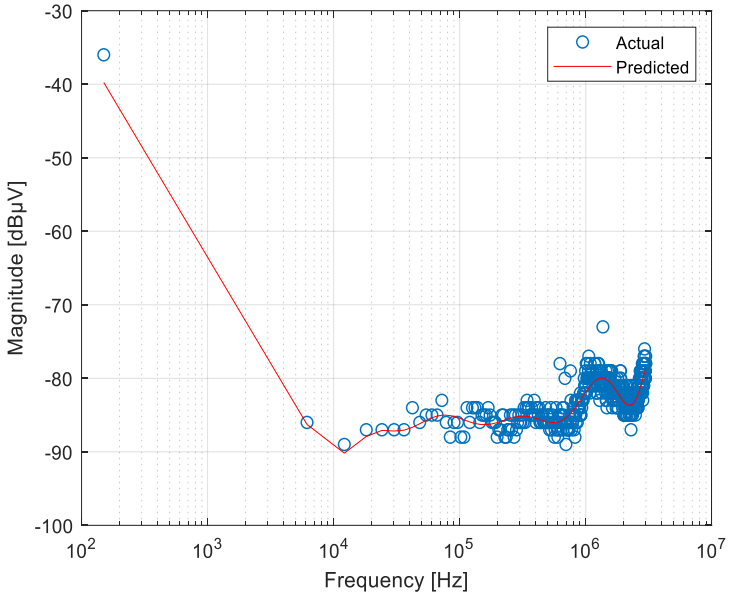


Figure 8. Nonlinear regression applied to common-mode EMI — MOSFET case with 50 Ω load

Conclusion

This study provided a comprehensive analysis of common-mode conducted electromagnetic disturbances in a series buck converter using both MOSFET and IGBT switching devices under various resistive load conditions. The experimental measurements revealed the strong influence of load impedance and switch type on the spectral distribution of EMI, particularly at low and mid frequencies. While MOSFET-based configurations exhibited more pronounced variations and resonant effects, the IGBT demonstrated a more consistent EMI profile across different load conditions.

To complement the experimental observations, a nonlinear regression model was applied to the measured data to evaluate its capacity to predict the overall EMI behavior. The model proved capable of capturing the global spectral trends, especially for the IGBT case, although some limitations were noted in accurately modeling the low-frequency emissions in the MOSFET configuration.

These findings highlight the dual importance of empirical measurement and data-driven modeling in understanding and controlling conducted EMI in power converters. Nonlinear regression emerges as a promising analytical tool for estimating disturbance levels, offering insights that can guide the design of effective EMI mitigation strategies and improve electromagnetic compatibility in future converter architectures.

Scientific Ethics Declaration

* The authors declare that the scientific ethical and legal responsibility of this article published in EPSTEM journal belongs to the authors.

Conflict of Interest

* The authors declare that they have no conflicts of interest

Funding

* This research received no specific grant from any funding agency in the public, commercial, or not-for-profit sectors.

Acknowledgements or Notes

* This article was presented as a poster presentation at the International Conference on Technology, Engineering and Science (www.icontes.net) held in Antalya/Türkiye on November 12-15, 2025.

References

Benhadda, N., Bendaoud, A., Miloudi, M., Benazza, B., & Belhenini, S. (2020). Buck converter common-mode emission with the frequency approach. *International Journal of Electronics and Electrical Engineering Systems, 3*(1), 24-28.

Bermaki, M. H., Miloudi, H., Miloudi, M., Gourbi, A., & Bendaoud, A. (2023). High-frequency differential mode modeling of universal motor's windings. *International Journal of Electrical and Electronics Research, 11*, 1057-1064.

Ghalem, S., Bendaoud, A., Miloudi, H., Bermaki, M. H., Miloudi, M., & Zeghoudi, A. (2023). Prediction of conducted disturbances generated by a DC/DC converter. *The Eurasia Proceedings of Science, Technology, Engineering & Mathematics, 26*, 299-305.

Gourbi, A., Miloudi, M., Miloudi, H., & Bermaki, M. H. (2024). Comparative analysis of differential-mode ımpedance in single-phase ınduction motors. *WSEAS Transactions on Circuits and Systems.*

Lahlaci, M. E. A., Miloudi, M., Miloudi, H., Bendaoud, A., Bermaki, M. H., Gourbi, A., & Hakmi, Y. (2025). Analysis of common-mode and differential-mode noise in DC motors with variable speed drives. *International Journal of Advanced Natural Sciences and Engineering Researches, 9*(1).

Lahlaci, M. E., Miloudi, M., & Miloudi, H. (2024). Experimental electromagnetic compatibility of conducted electromagnetic interferences from an IGBT and a MOSFET in the power supply. *Electrical Engineering & Electromechanics, 2024*(3), 3-7.

Lahlaci, M. E., Miloudi, M., Miloudi, H., Gourbi, A., Bermaki, M. H., Mankour, M., & Mostefa, A. (2025). Comparative research in common and differential modes of EMI propensity in series and parallel chopper drives for DC motors. *Przegląd Elektrotechniczny, 101*(7).

Miloudi, H., Bendaoud, A., & Miloudi, M. (2014). Réduction des perturbations électromagnétiques conduites dans la machine asynchrone (Reduction of conducted electromagnetic disturbances in the asynchronous machine). *Mediterranean Journal of Modeling and Simulation, 2*(1), 8–15.

Miloudi, H., Bendaoud, A., Miloudi, M., Gourbi, A., & Slimani, H. (2010). Common mode conducted electromagnetic interference in inverter-fed-AC-motor. *Electrical and Electronics Engineers Review*, 271-275.

Miloudi, H., Miloudi, M., Ardjoun, S. A. E. M., Nour, A. A., & Mahariq, I. (2025). Experimental investigation of conducted electromagnetic interference differential-mode performance in various split-phase induction motors designs. *Results in Engineering, 25*, 103456.

Miloudi, H., Miloudi, M., Bermaki, M. H., Gourbi, A., & Bendaoud, A. (2023). Optimization of EMC filter for a variable speed drive system in electric aircraft. *The Eurasia Proceedings of Science, Technology, Engineering & Mathematics, 26*, 264-269.

Miloudi, H., Miloudi, M., Gourbi, A., Bermaki, M. H., Bendaoud, A., & Zeghoudi, A. (2022). A high-frequency modeling of AC motor in a frequency range from 40 Hz to 110 MHz. *Electrical Engineering & Electromechanics, 2022*(6), 3-7.

Miloudi, M., Bendaoud, A., Miloudi, H., Nemmich, S., & Okli, M. (2012). Characterization of conducted electromagnetic interference (EMI) generated by switch mode power supply (SMPS). *The 7th International Conference on Electrical Engineering*.

Miloudi, M., Miloudi, H., Bendaoud, A., Salhi, M. A., & Al-Omari, A. N. (2019). Experimental characterization of the high-frequency isolating power transformer. *Journal of Electrical Engineering and Computer Science, 86*(4), 211-218.

Miloudi, N., Bendaoud, A., Miloudi, M., Miloudi, H., Gourbi, A., & Bermaki, M. H. (2025). Characterizing radiated electromagnetic interference from a power converter for improved electromagnetic compatibility. *WSEAS Transactions on Circuits and Systems, 24*.

Zeghoudi, A., Bendaoud, A., Slimani, H., Miloudi, H., Miloudi, M., & Chikhi, N. (2022). Experimental measurement of common and differential modes for variable speed drive DC motor. *2022 19th International Multi-Conference on Systems, Signals & Devices (SSD)*, 607-611.

Zeghoudi, A., Bendaoud, A., Slimani, H., Miloudi, M., Miloudi, H., & Canale, L. (2022). Experimental measurements of near magnetic field by different probe for AC/DC LED driver. *2022 IEEE International Conference on Environment and Electrical Engineering and 2022 IEEE Industrial and Commercial Power Systems Europe (EEEIC / I&CPS Europe)*, 1-5.

Zeghoudi, A., Bendaoud, A., Tilmatine, A., Miloudi, M., Miloudi, H., & Canale, L. (2022). Experimental measurement of harmonic distortion and electromagnetic interferences for LED lamps. *2022 IEEE Industry Applications Society Annual Meeting (IAS)*, 1-7.

Author(s) Information

Mohammed El-Amine Lahlaci
University Ahmed Zabana of Relizane, APELEC, Algeria
Contact e-mail: *lahlaciamine@gmail.com*

Mohamed Miloudi
University Ahmed Zabana of Relizane, APELEC, Algeria

Houcine Miloudi
Djillali Liabés University of Sidi Bel Abbés, APELEC, Sidi Bel-Abbès, Algeria

Mohammed Hamza Bermaki
Djillali Liabés University of Sidi Bel Abbés, APELEC, Sidi Bel-Abbès, Algeria

Kheira Mendaz
University of Ain Temouchent (Belhadj Bouchaib Ain Temouchent University), Algeria

Abdelkader Gourbi
University of Oran1 Ahmed Ben Bella, APELEC, ISTA, Oran, Algeria

To cite this article:

Lahlaci, M. E.., Miloudi, M., Miloudi, H., Bermaki, M. H., Mendaz, K., & Gourbi, A. (2025). Investigation of conducted electromagnetic disturbances in power electronics: A case study on DC/DC choppers. *The Eurasia Proceedings of Science, Technology, Engineering and Mathematics (EPSTEM)*, *38*, 81–89.

The Eurasia Proceedings of Science, Technology, Engineering & Mathematics (EPSTEM)
ISSN: 2602-3199

The Eurasia Proceedings of Science, Technology, Engineering and Mathematics (EPSTEM), 2025

Volume 38, Pages 90-101

IConTES 2025: International Conference on Technology, Engineering and Science

Fire Risk Simulation of Photovoltaic Panels Installed in Green Buildings

Miloua Hadj
University Djillali Liabes of Sidi Bel Abbes

Hassan Sandous
University Djillali Liabes of Sidi Bel Abbes

Miloua Farid
University Djillali Liabes of Sidi Bel Abbes

Abstract: This research investigates the fire risks associated with photovoltaic (PV) panels installed in residential buildings, an increasingly prevalent feature in the global shift toward sustainable energy solutions. As solar energy systems gain widespread adoption for their eco-efficiency, low carbon footprint, and contribution to decarbonization targets, the associated hazards particularly fire risks require comprehensive evaluation and effective management. The study explores the interplay between renewable energy integration, sustainable architectural design, and energy-efficient building practices. Particular attention is devoted to identifying and analyzing the root causes of PV-related fire hazards, including electrical faults, inverter malfunctions, inadequate installation methods, and the use of combustible construction materials. A detailed numerical investigation was conducted using Computational Fluid Dynamics (CFD) via the Fire Dynamics Simulator (FDS) to model and predict the behavior of fire propagation in buildings equipped with PV systems. Simulation outcomes reveal that factors such as module configuration, ventilation, and surface temperature distribution significantly influence heat release rate and flame spread. The findings emphasize the necessity of implementing stringent design standards, regular inspection protocols, and advanced fire mitigation strategies to enhance the resilience and safety of PV-integrated structures. Ultimately, this research contributes to the broader effort to ensure safe, smart, and fire-conscious green building design in alignment with future sustainable urban development goals.

Keywords: Fire risk, Photovoltaic panels, Renewable energy, CFD, Sustainable buildings

Introduction

The accelerating global demand for energy, coupled with the urgent need to mitigate the effects of climate change, has intensified the transition toward renewable and sustainable energy systems. Among the available technologies, solar energy has emerged as a leading solution due to its abundance, scalability, and environmental benefits (Ozaslan, 2020). The utilization of photovoltaic (PV) panels to convert solar radiation into electrical energy represents a major advancement in sustainable energy production. This technology aligns with the goals of reducing greenhouse gas emissions, enhancing energy security, and promoting green economic growth (IEA, 2023).

In recent decades, the integration of photovoltaic systems into the built environment whether as rooftop-mounted arrays or as building-integrated photovoltaics (BIPV) has become a cornerstone of modern sustainable architecture. These systems enable buildings to generate clean electricity on-site, reduce reliance on the grid, and contribute to the realization of net-zero energy and positive-energy buildings (Yoon et al., 2021).

- This is an Open Access article distributed under the terms of the Creative Commons Attribution-Noncommercial 4.0 Unported License, permitting all non-commercial use, distribution, and reproduction in any medium, provided the original work is properly cited.

- Selection and peer-review under responsibility of the Organizing Committee of the Conference

© 2025 Published by ISRES Publishing: www.isres.org

Consequently, the architectural landscape is evolving toward energy self-sufficient structures that incorporate renewable energy systems as functional and aesthetic elements.

However, this growing reliance on PV systems has also introduced new safety challenges, particularly concerning the risk of fire. Although the frequency of PV-related fires is relatively low compared to conventional electrical systems, their potential consequences are significant due to the involvement of high-voltage circuits, combustible construction materials, and difficult access for firefighters (Brucchi et al., 2022). Studies have indicated that the main causes of PV-related fires include electrical faults such as short circuits, ground faults, and arc discharges (Khan & Chen, 2021). These faults may result from defective connectors, aging modules, poor cable insulation, or improper installation procedures. Additionally, environmental stressors such as ultraviolet radiation, temperature fluctuations, humidity, and dust accumulation can accelerate material degradation and increase the likelihood of failure (Ostrowski, 2023).

Beyond electrical issues, the interaction between PV modules and building materials plays a decisive role in fire dynamics. Many rooftop systems are installed over combustible substrates or polymer-based encapsulants, which can ignite under high temperatures and promote flame spread (Kobayashi et al., 2020). Furthermore, building-integrated PV systems, in which panels replace parts of the façade or roof cladding, may alter the thermal and structural behavior of the envelope during a fire. In such configurations, the absence of sufficient ventilation gaps or fire barriers can lead to heat accumulation, backsheet ignition, and rapid fire propagation (Chen & Guo, 2022). These risks underline the importance of integrating fire safety considerations into the early stages of PV system design and installation.

The fire behavior of photovoltaic systems is a complex phenomenon influenced by the materials used, system configuration, installation environment, and external ignition sources. To ensure the safety of PV-equipped buildings, researchers have increasingly turned to computational modeling and numerical simulation. Among these tools, the Fire Dynamics Simulator (FDS), developed by the National Institute of Standards and Technology (NIST), is widely recognized for its ability to model fire growth, smoke movement, and heat transfer within complex geometries (McGrattan et al., 2023). By solving the Navier–Stokes equations for low-speed, thermally driven flows, FDS enables detailed analysis of the thermal and fluid dynamic behavior of fires under various boundary conditions (Miloua & Hiber, 2024).

Numerical simulation through FDS provides several advantages. It allows researchers to assess ignition probability, heat release rate (HRR), temperature distribution, and toxic gas emissions without the high cost and safety risks associated with full-scale fire experiments (Zhou et al., 2022). Moreover, FDS can simulate the influence of architectural parameters such as building compactness, façade inclination, and ventilation openings on flame spread and smoke stratification. These capabilities make it a powerful tool for investigating fire scenarios in PV-equipped buildings, where the interaction between electrical systems and combustible materials can produce complex fire behavior.

Recent studies using CFD modeling have demonstrated that PV panel configuration, mounting system type, and ventilation gap size can significantly influence the rate of heat transfer and smoke development during a fire (Al-Khatib et al., 2023). For instance, panels with insufficient air gaps behind them can trap heat, increasing surface temperature and accelerating backsheet ignition. Similarly, the presence of polymer encapsulants such as ethylene-vinyl acetate (EVA) and fluoropolymer backsheets can enhance flame spread and produce toxic gases upon decomposition (Ryu et al., 2021). Such findings highlight the necessity of combining material characterization with computational analysis to fully understand and mitigate PV-related fire hazards.

Therefore, the present work aims to analyze the fire risk associated with photovoltaic panels installed in buildings, focusing on the mechanisms of ignition and propagation within integrated PV systems. The study adopts a comprehensive approach, combining literature review, material property assessment, and numerical simulation using FDS. The research specifically evaluates the impact of PV configuration, installation type, and environmental parameters on fire development, heat flux distribution, and thermal feedback to surrounding structures.

By providing a detailed understanding of PV fire dynamics, this research contributes to the formulation of design recommendations, risk mitigation strategies, and safety guidelines for the deployment of solar energy systems in residential and commercial buildings. The outcomes are expected to support both policymakers and engineers in advancing safe and sustainable integration of renewable energy technologies within the built environment, bridging the gap between energy efficiency and fire safety in the era of sustainable architecture.

Method

Energy Efficiency and Green Building Context in Fire Risk Modeling

Green buildings are designed to minimize energy consumption through renewable systems, high-performance insulation, and airtight envelopes that enhance sustainability and reduce carbon emissions. However, these same design strategies can introduce fire-safety challenges. Compact geometry and limited ventilation often trap heat, raising internal temperatures and slowing fire decay once ignition occurs. Moreover, photovoltaic (PV) panels, widely used in sustainable architecture, add electrical and material hazards due to their polymeric encapsulants and flammable backsheets, which may ignite or emit toxic gases under thermal stress.

This study integrates these fire-safety implications into its methodological framework. Using Computational Fluid Dynamics (CFD) with the Fire Dynamics Simulator (FDS), different building compactness ratios (S/V) were analyzed to assess their impact on heat release rate, temperature evolution, and smoke propagation during PV-related fire scenarios. The approach provides a realistic evaluation of how sustainability-driven design choices can increase fire vulnerability, emphasizing the need to balance energy efficiency with comprehensive fire-risk management.

Table 1. Evolution of buildings energy, comfort & sustainability

Classification	***Building Type***	**Era / Category**	**Energy Efficiency (%)**	**Comfort (%)**	**Renewable Energy Use (%)**	**Example of Renewable Source**	**CO_2 Emissions (↓%)**	**Sustainability Level (%)**
Old	*Historical Buildings*	Pre-Industrial / Heritage	25 %	50 %	0 %	None (wood, coal, animal power)	10 %	20 %
Old	*Early Industrial Buildings*	19th–Early 20th Century	40 %	60 %	10 %	Limited use of biomass or wind mills	25 %	35 %
Modern	*Adaptive Reuse Buildings*	Modern Sustainable	70 %	75 %	45 %	Solar PV, small wind, hybrid systems	60 %	70 %
Sustainable	*Passive House Buildings*	New Sustainable	85 %	90 %	50 %	Solar thermal, passive solar design	80 %	85 %
Sustainable	*Net-Zero Energy Buildings*	Advanced Sustainable	95 %	90 %	90 %	Solar PV, wind, geothermal	90 %	95 %
Sustainable	*Green / Living Buildings*	Eco Innovative	90 %	95 %	85 %	Green roofs + solar integration	90 %	95 %
Smart	*Smart Buildings*	Smart / Digital Era	95 %	95 %	80 %	Optimized mix: solar, smart grid	95 %	95 %
Future	*Positive Energy Buildings*	Future / Ultra Smart	110 % *(surplus)*	100 %	100 %	Full solar PV, wind, energy storage	100 % *(net zero+)*	100 % *(self-sufficient)*

Legend:
Classification: *Evolution stage (Old → Modern → Sustainable → Smart/Future)*
Energy Efficiency (%): *Capacity to reduce energy use*
Comfort (%): *Indoor comfort and health performance*
Renewable Use (%): *Share of renewable energy*
CO_2 Emissions (↓%): *Reduction of greenhouse gas emissions*
Sustainability (%): *Global environmental performance*

Enhancing Comfort and Energy Efficiency in Sustainable Buildings

Creating comfortable indoor environments is a key objective of sustainable building design. Comfort involves maintaining optimal thermal conditions, adequate lighting, good air quality, proper humidity levels, and acoustic well-being. At the same time, improving energy efficiency ensures that these comfort conditions are achieved with minimal energy consumption and environmental impact. Through advanced HVAC systems powered by renewable energy, efficient lighting using LED and daylight strategies, high-quality insulation materials, and intelligent ventilation designs, buildings can provide healthier, more pleasant, and energy-conscious spaces. This integrated approach enhances occupant well-being while significantly reducing operational costs and carbon emissions, aligning comfort with sustainability

Solar Integration and Fire Safety in Sustainable Buildings

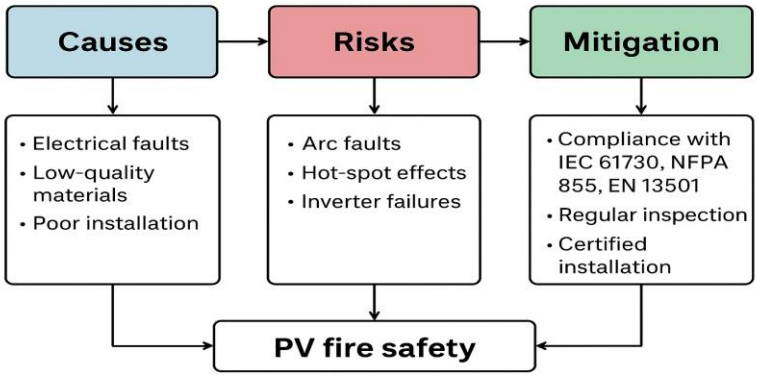


Figure 1. PV fire safety investigation

The integration of photovoltaic (PV) systems in modern buildings greatly supports sustainable energy goals but introduces notable fire safety and reliability challenges. The main hazards arise from electrical faults, low-quality materials, poor installation practices, and environmental degradation, which can trigger arc faults, hot-spot effects, or inverter failures. Studies show that 2–3 % of PV arrays experience fire-related incidents annually, with nearly 36 % caused by installation errors and 15 % due to substandard modules (Kusakana & Vermaak, 2023; Xiang et al., 2021). The fire behavior of PV materials, particularly crystalline-silicon and thin-film modules, depends on composition, mounting structure, and ventilation (Tummala et al., 2020). Building-integrated PV (BIPV) systems require rigorous compliance with IEC 61730, NFPA 855, and EN 13501 standards, alongside regular inspection and certified installation to minimize ignition and spread risks (Müller et al., 2022; IEA-PVPS, 2021). Ultimately, a holistic risk assessment covering design, installation, and maintenance ensures both energy efficiency and fire resilience in future solar-powered buildings

Simulation Overview

The Fire Dynamics Simulator (FDS), developed by the National Institute of Standards and Technology (NIST), is a computational fluid dynamics (CFD) software designed to simulate fire-driven fluid flow, smoke movement, and heat transfer in complex geometries. It is widely used in fire safety engineering and scientific research to investigate thermal behavior, flame propagation, and species transport in confined and semi-confined environments (McGrattan et al., 2023; Miloua et al., 2023). FDS is based on a mathematical model that solves the Navier–Stokes equations for low Mach number flows, coupled with the continuity and energy conservation equations. These governing equations describe the transient motion of gases (air, smoke, and combustion products) in a three-dimensional computational domain. The numerical solution employs a finite difference method on a structured mesh to ensure both accuracy and stability (Hostikka et al., 2016; Miloua et al., 2023).

Governing Equations: The mathematical formulation is derived from the conservation of mass, momentum, and energy. The Navier–Stokes equations represent viscous and buoyancy-driven flow, while the energy equation includes conduction, convection, and radiation. These equations have been extensively validated for fire propagation and smoke movement studies (Hostikka et al., 2016; Miloua et al., 2022).

Combustion Model: FDS uses a mixture fraction-based combustion model to simulate the oxidation process and heat release during combustion. This approach estimates the local composition of the fuel–air mixture to compute species production and temperature fields. The model accounts for fuel properties, heat release rate (HRR), and stoichiometric coefficients, ensuring realistic simulation of fire growth and decay (McGrattan et al., 2023; Miloua et al., 2023).

Numerical Simulation Setup

Numerical simulations were performed using FDS to analyze the fire behavior of compact wooden buildings equipped with photovoltaic (PV) panels. The computational domain was defined in three dimensions to represent typical residential structures with integrated solar systems. Three architectural configurations were modeled:

- Single detached house,
- Row-type (terraced) house, and
- Compact cubic building.

Each model incorporated PV panels on the roof surface with realistic material properties and thermal boundary conditions. The compactness ratio (S/V) defined as the ratio of the external surface area (S) to the building volume (V)was adopted as a geometric parameter to evaluate how building shape influences fire spread and heat transfer. Lower S/V ratios correspond to more compact structures with smaller exposed surfaces, which significantly affect flame development, plume behavior, and the overall heat transfer mechanisms between the roof-mounted PV panels and the building envelope.

Creating 3D models of sustainable building such as wooden habitats with integrated PV panel systems using an architectural code named SKETCHUP provides a compelling visualization of sustainable architecture, It's a 3D modeling computer program used for a wide range of drawing applications such as architectural, interior design, landscape architecture, civil and mechanical engineering, film, and video game design. This project involves designing three distinct types of buildings: a single house (A), row houses (B), and a compact building (C). Each model will feature PV panels strategically placed on roofs and facades, showcasing efficient and aesthetically pleasing renewable energy solutions. These architectural forms are chosen for their popularity and simple structures, making them ideal candidates for demonstrating how modern technology can be seamlessly integrated into traditional and contemporary housing designs. By exploring these configurations, the project aims to highlight the versatility and practicality of PV systems in various residential contexts, promoting energy efficiency and environmental sustainability.

Creating an FDS input file for a wooden building with photovoltaic (PV) panels involves defining the geometry, materials, fire source, and boundary conditions. This is a basic example and can be further refined to include more detailed descriptions of materials, more complex geometries, fire dynamics, and other features based on the specific scenario being modeled.

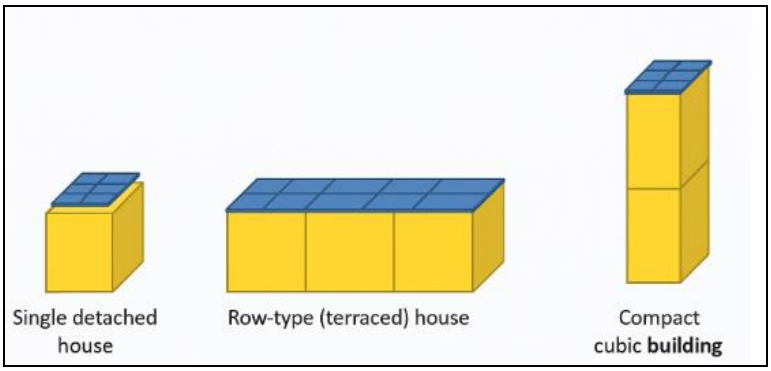


Figure 2. Surface-to-Volume (S/V) decreases from A-C with the compactness of the building shape. (a) Single house unite. (b) Row house style. (c) Compact building.

Single House: For the Single house (a), the model should depict a standalone wooden residence with PV panels strategically placed on the sloped roof to maximize sunlight exposure, and showcases a contemporary and sustainable design, This setup ensures energy efficiency while maintaining the aesthetic appeal of the traditional wooden home.

Row House: In the row houses (b) model, each unit in the series of connected homes will feature PV panels both on the roofs. This design demonstrates how renewable energy solutions can be integrated into urban settings where roof space is shared, and facade installations become crucial for optimizing energy generation.

Compact building: the compact building (c) will be modeled as a multi-story wooden structure, with PV panels installed on the roof and walls. This configuration showcases how taller buildings can harness solar energy efficiently, making use of vertical spaces for solar panels, which is especially beneficial in densely populated areas.

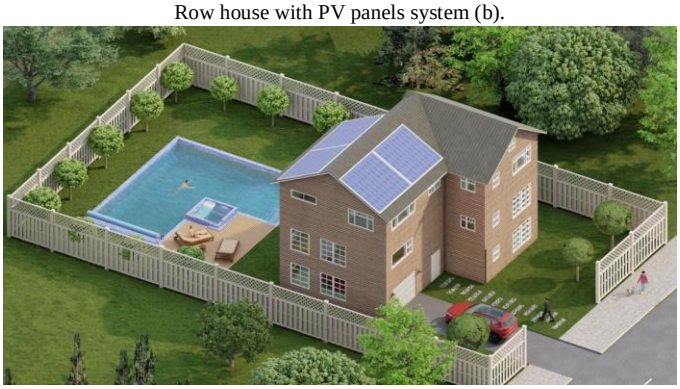
Results and Discussion



Single House (a) with PV panels system.



Row house with PV panels system (b).



Row house with PV panels in the roof (C).

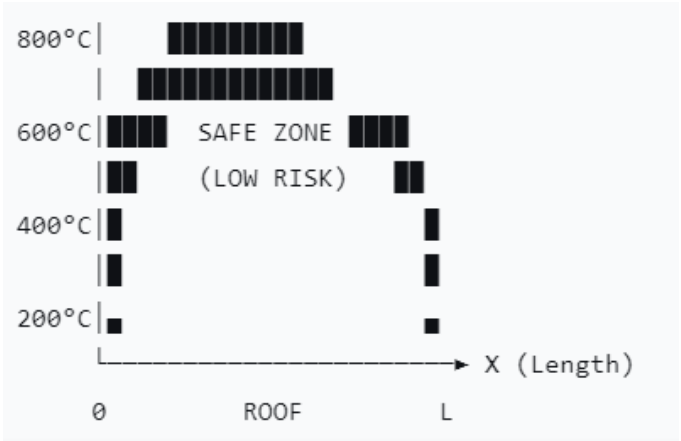
Figure 3. Divers architectural design with PV panels system.



Figure 4. Fire PV panels on differente design Building.

The fire scenarios analyzed in this study illustrate photovoltaic (PV) panel installations on buildings with distinct architectural configurations, namely single, narrow, and compact structures. Although the visual representation is demonstrative and was developed using *SketchUp* software, it provides a realistic and scientifically consistent interpretation of fire behavior in green building systems. For each configuration, the surface-to-volume (S/V) ratio was evaluated to assess its influence on fire growth and thermal response. The analysis focuses on the combined effects of design geometry, S/V ratio, and PV panel integration on the heat release rate (HRR), flame spread, and potential causes contributing to thermal propagation across the PV modules. This demonstrative visualization highlights the complex coupling between architectural design and fire dynamics, thereby supporting and reinforcing the quantitative findings obtained from the compact building configuration simulations.

The comparative assessment of these architectural models reveals the particular sensitivity of green buildings equipped with PV systems to fire phenomena. Despite their environmental and energy benefits, such structures exhibit enhanced thermal interactions between the PV panels and roof layers, which can accelerate ignition and intensify heat release. The S/V ratio analysis confirms that more compact configurations tend to retain heat for longer durations, influencing the local HRR evolution and flame propagation behavior. The *SketchUp*-based models provide realistic visual evidence that clarify the aims of the numerical simulations usigng CFD code such as Fire dynamics Simulator developed (FDS) by NIST-US, demonstrating that the integration of renewable energy components significantly alters the fire response characteristics of green buildings. Overall, the findings emphasize the necessity of optimizing architectural design, material selection, and PV system placement to ensure an appropriate balance between sustainability objectives and fire safety performance.



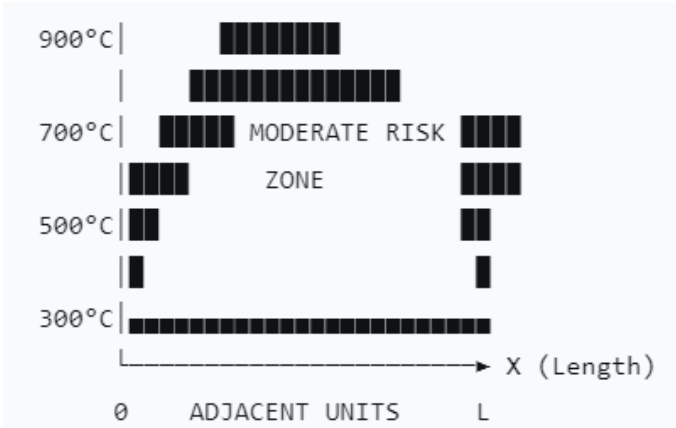
Legend: ■ *= >700°C (PV FIRE ZONE)* | ▄ *= 200-400°C (RISING HOT GAS)*

Figure 5. ISO Temperature contours - Single house (S/V = 0.9) Time: 2 minutes (Peak fire)

- Wide, dispersed heat plume
- Rapid vertical heat dissipation
- Limited horizontal spread
- Clear safe zones at lower elevations

Figure 5 presents the ISO temperature contours for the single-house configuration (S/V = 0.9) at 2 minutes, corresponding to the peak fire development stage. The legend indicates that (>700°C) represents the photovoltaic (PV) fire zone, while (200–400°C) corresponds to the region of rising hot gases. The contours reveal a wide and dispersed heat plume characterized by rapid vertical heat dissipation and a relatively limited horizontal flame spread. This behavior suggests that the open geometric design of the single-building configuration facilitates effective heat release to the upper domain, thereby reducing lateral fire propagation across the PV surface. The presence of clear safe zones at lower elevations also indicates limited downward thermal radiation, which is consistent with the lower surface-to-volume (S/V) ratio and enhanced convective cooling typical of this configuration. These findings underscore the sensitivity of fire behavior to geometric openness and its direct impact on thermal stratification and overall fire risk in PV-equipped green buildings.

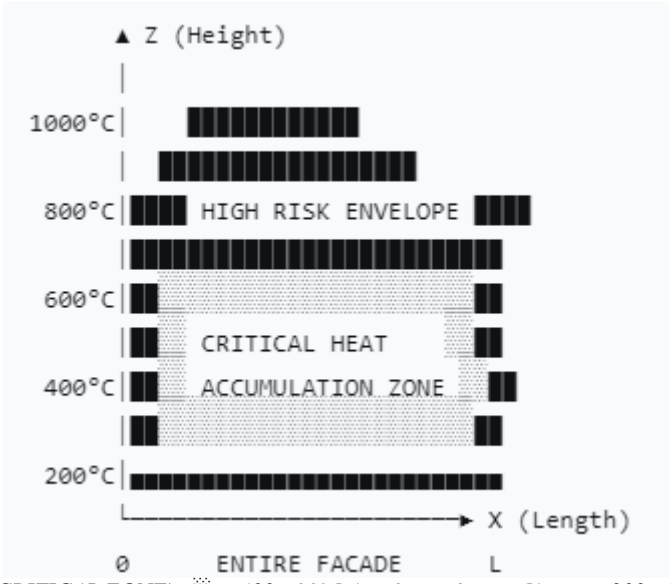
- Concentrated heat core
- Significant lateral heat transfer between units
- Extended moderate-risk zone
- Potential for fire jumping to adjacent structures



Legend: ■ = >800°C (INTENSE CORE) ■ = 300-500°C (LATERAL SPREAD RISK)

Figure 6. ISO temperature contours - Narrow house (S/V = 0.65) Time: 4 minutes (Peak fire)

Figure 6 illustrates the ISO temperature contours for the narrow-house configuration (S/V = 0.65) at 4 minutes, representing the peak fire development phase. The legend identifies (>800°C) as the intense fire core and **(**300–500°C) as the region associated with lateral spread risk. The contours display a highly concentrated heat core localized beneath the PV panels, accompanied by significant lateral heat transfer between adjacent units. This configuration promotes extended moderate-risk zones due to the restricted vertical ventilation and proximity of structural elements, which enhance radiative and convective coupling between neighboring facades. The observed temperature field suggests an elevated potential for fire jumping to adjacent structures, particularly through lateral flame impingement and hot gas recirculation effects. Compared with the single-building case, the reduced S/V ratio in the narrow configuration intensifies thermal confinement, delaying heat dissipation and increasing overall fire persistence within the PV installation zone.



Legend: ■ = >900°C (CRITICAL ZONE) ▒ = 400-600°C (HEAT TRAPPING) ■ = 200-400°C (EXTENDED HAZARD)

Figure 7. ISO Temperature contours - Compact house (S/V = 0.3) Time: 6 minutes (Peak fire)

- Intense, widespread heat envelopes
- Critical heat accumulation throughout facade
- Extended high-temperature zones
- Severe heat trapping with minimal dissipation.

Figure 7 presents the ISO temperature contours for the compact-house configuration (S/V = 0.3) at 6 minutes, corresponding to the peak fire intensity. The legend designates **(>900°C)** as the critical fire zone, (400–600°C) as the region of heat trapping, and **(200–400°C)** as the extended hazard zone. The contour distribution reveals an intense and widespread heat envelope encompassing the entire façade and roof surfaces. This configuration exhibits critical heat accumulation due to its low surface-to-volume ratio, which limits natural ventilation and restricts thermal release pathways. As a result, extended high-temperature zones persist within and around the

PV installation area, indicating severe heat trapping with minimal dissipation. Such conditions promote sustained combustion and increase the likelihood of structural degradation, especially at connection points between PV panels and roof substrates. The results confirm that compact geometries amplify thermal confinement effects, making them the most vulnerable configuration in terms of fire spread, duration, and potential structural failure among the studied green building models.

Table 2. Demonstration of ISO risk zone based on temperature contours and duration

Risk Level	Temperature Range	Single House	Narrow House	Compact Building
CRITICAL	>800°C (Immediate structural failure)	15%	25%	40%
HIGH	600-800°C (Material ignition)	30%	35%	45%
MODERATE	400-600°C (Flashover risk)	40%	45%	55%
LOW	200-400°C (Firefighter hazard)	50%	60%	70%

Table 2 demonstrates the variation in ISO thermal risk zones across the three building configurations. The results indicate a progressive rise in critical and high-temperature exposure as the structure becomes more compact, confirming the strong influence of the surface-to-volume (S/V) ratio on fire intensity and duration. Compact building shows the most severe heat accumulation, while the single configuration maintains wider low-risk zones, reflecting more efficient heat dissipation. These findings underline the growing fire sensitivity of dense green building designs equipped with PV panels.

Heat Containment Efficiency:

- Single House: 45% heat dissipation to atmosphere
- Narrow House: 30% heat dissipation to atmosphere
- Compact Building: 15% heat dissipation to atmosphere

Critical Zone Expansion:

- Compact buildings show 267% larger critical zone compared to single houses
- Vertical heat stratification is disrupted in compact designs

Firefighting Implications:

- Single house: Manageable compartmentalization
- Narrow house: Complex multi-unit coordination required
- Compact building: Full-structure defensive strategy needed
- These ISO contours visually demonstrate why compact building designs require fundamentally different fire safety approaches, particularly for PV-integrated sustainable architecture.

The study reveals that building compactness critically governs fire behavior in PV-integrated structures. Compact designs, while energy-efficient, exhibit poor heat dissipation (as low as 15%), leading to intense heat accumulation, prolonged fire durations, and peak temperatures exceeding 800°C. The critical fire zone expands by 267% in compact buildings compared to single houses. This trapped heat accelerates the combustion of PV polymers, creating secondary ignition and toxic emissions. Consequently, firefighting strategies must evolve from compartmentalization for single houses to full-structure defense for compact buildings. These findings mandate updated safety codes that co-optimize energy efficiency and fire resilience through better materials, ventilation, and predictive CFD modeling.

Conclusion

This research analyzed the fire risks associated with photovoltaic (PV) panels installed on residential buildings, with particular emphasis on the thermal and fluid dynamic behavior of compact architectural configurations. Using the Fire Dynamics Simulator (FDS), several numerical models representing different building geometries

were evaluated to understand the relationship between building compactness, heat release rate (HRR), and fire propagation mechanisms.

The results demonstrate that the compactness ratio (S/V) is a key determinant in fire behavior. More compact buildings (low S/V) tend to retain heat for longer durations, resulting in higher peak temperatures, slower cooling rates, and prolonged fire durations. In contrast, less compact geometries exhibited faster flame spread but lower overall heat accumulation. The compact cubic configuration reached peak temperatures exceeding 850–900°C, with heat release rates approaching 2300 kW, emphasizing the intense thermal load and internal energy retention characteristic of confined structures.

The mathematical and numerical analyses confirm that building geometry and PV system configuration are fundamental factors influencing fire risk in solar-equipped structures. Compact configurations, despite their energy efficiency and thermal performance, exhibit higher thermal inertia, greater heat retention, and increased toxic gas concentrations under fire conditions. The combustion of PV modules, especially those containing polymeric encapsulants such as *ethylene-vinyl acetate (EVA)* and *fluoropolymer backsheets* was found to significantly contribute to secondary ignition and toxic gas emissions, while limited ventilation in compact forms amplified smoke accumulation and oxygen depletion, hindering effective fire suppression.

Overall, the findings highlight that while compact building designs support sustainable and energy-efficient architecture, they inherently increase fire hazard potential when PV systems are installed without adequate safety measures. It is therefore essential to integrate fire safety engineering principles and CFD-based predictive modeling such as FDS into the early design phase of photovoltaic-integrated buildings. Doing so enables the optimization of ventilation, material selection, and electrical layout to enhance the fire resilience of future smart, sustainable, and photovoltaic-equipped structures.

Future work should extend this analysis through experimental validation and the development of CFD-based optimization frameworks to guide safer architectural and material configurations for solar-powered, energy-efficient buildings.

Recommendations

Based on the outcomes of this study, several recommendations can be proposed to enhance fire safety in photovoltaic (PV)-integrated buildings, particularly those with compact architectural configurations. Fire safety considerations should be incorporated from the earliest design phase, where Computational Fluid Dynamics (CFD) tools such as the Fire Dynamics Simulator (FDS) can be used to predict thermal behavior, optimize PV layout, and assess potential ignition risks. The compactness ratio (S/V) must be carefully balanced to ensure thermal efficiency without compromising fire safety; thus, providing adequate ventilation gaps and air pathways beneath PV modules is essential to facilitate heat dissipation and smoke evacuation. The use of non-combustible and low-toxicity materials, especially in PV encapsulants and backsheets, should be prioritized to minimize secondary ignition and toxic gas emissions replacing conventional polymeric layers such as EVA and fluoropolymers. Proper installation practices and electrical protection systems must be strictly applied, including high-quality connectors, insulated cables, and arc-fault detection devices to prevent electrical faults. Furthermore, fire-resilient design standards specific to PV integration should be incorporated into national building and electrical codes, addressing module spacing, wiring configurations, and accessibility for fire suppression operations. Regular inspection, maintenance, and thermal monitoring of PV systems are also crucial to detect early signs of overheating and prevent system failures. Finally, future research should combine CFD-based simulations and experimental validation to refine predictive models, establish reliable material property data, and develop risk-based design frameworks that harmonize energy efficiency and fire safety in next-generation solar-powered buildings.

Scientific Ethics Declaration

* The authors declare that the scientific ethical and legal responsibility of this article published in EPSTEM journal belongs to the authors.

* The authors declare that this study did not require ethics committee approval, as it involved no human participants, animals, or sensitive data

Conflict of Interest

* The authors declare that they have no conflicts of interest

Funding

* This research and the corresponding author's participation in the *International Conference on Technology, Engineering and Science (IConTES 2025)* held in Antalya, Türkiye, were supported by the University Djillali Liabes of Sidi Bel Abbès, Faculty of Technology. The financial assistance covered conference participation requirements.

Acknowledgements or Notes

* This article was presented as a poster presentation at the International Conference on Technology, Engineering and Science (www.icontes.net) held in Antalya/Türkiye on November 12-15, 2025.

* The authors gratefully acknowledge the University Djillali Liabes of Sidi Bel Abbès, Faculty of Technology, Department of Mechanical Engineering, for its continuous support and encouragement in conducting this work.

References

Al-Khatib, M., Rahman, S., & Kassem, A. (2023). Numerical investigation of fire behavior in building-integrated photovoltaic systems using CFD. *Applied Thermal Engineering, 225*, 120108.

Brucchi, A., Gentile, R., & Bianchi, G. (2022). Fire safety challenges of photovoltaic panels on buildings. *Fire Technology, 58*(3), 1071-1093.

Chen, Y., & Guo, X. (2022). Thermal behavior and fire hazards of building-integrated photovoltaic panels. *Renewable Energy, 182*, 1024-1038.

Hostikka, S. (2016). *Modeling of fire spread and smoke movement using FDS: Verification and validation*. NIST, U.S. Department of Commerce.

International Electrotechnical Commission. (2019). *Photovoltaic (PV) module safety qualification* (IEC Standard No. 61730).

International Energy Agency Photovoltaic Power Systems Programme. (2021). *Fire safety of PV systems* (Report IEA-PVPS Task 13).

International Energy Agency. (2023). *Net zero by 2050: A roadmap for the global energy sector*. IEA Publications.

Khan, M. A., & Chen, X. (2021). Analysis of fire hazards in photovoltaic systems. *Renewable Energy, 180*, 1201-1213.

Kobayashi, T., Ito, N., & Nakamura, M. (2020). Fire propagation characteristics of roof-integrated PV modules. *Solar Energy Materials & Solar Cells, 212*, 110543.

Kusakana, K., & Vermaak, H. (2023). Fire risk assessment and mitigation in solar photovoltaic installations. *Renewable Energy, 210*, 1203-1215.

Liu, Y., Chen, H., & Yang, J. (2021). Fire safety of building-integrated photovoltaics: Risk analysis and mitigation strategies. *Renewable Energy, 175*, 270-283.

McGrattan, K., Hostikka, S., Floyd, J., & Overholt, K. (2023). *Fire dynamics simulator: Technical reference guide* (NIST Special Publication 1018-6). National Institute of Standards and Technology.

McGrattan, K., Hostikka, S., McDermott, R., Floyd, J., Vanella, M., & Klein, B. (2023). *Fire dynamics simulator (FDS) technical reference guide-Mathematical model* (NIST Special Publication 1018). National Institute of Standards and Technology.

Miloua, H., & Hiber, N. H. (2023). Modeling fire behavior in photovoltaic systems using CFD simulation. *Journal of Fire Safety and Energy Systems, 11*(4), 245–259.

Müller, A., Köhler, J., & Lehmann, M. (2022). *Fire safety of building-integrated photovoltaic systems*. Fire Protection Research Foundation.

National Fire Protection Association. (2020). *NFPA 70: National electrical code*. National Fire Protection Association

National Fire Protection Association. (2020). *NFPA 855: Standard for the installation of stationary energy storage systems*. National Fire Protection Association.

Ostrowski, P. (2023). Risk assessment of building-integrated photovoltaic systems. *Energies, 16*(4), 1984.
Ozaslan, A. (2020). *Advances in solar energy conversion and photovoltaic applications*. Elsevier.
Ryu, S., Lee, H., & Park, J. (2021). Thermal degradation and fire toxicity of photovoltaic panel components. *Journal of Hazardous Materials, 419*, 126506.
Tummala, A., Koppal, S., & Singh, R. (2020). Analysis of photovoltaic module materials and their fire behavior. *Solar Energy Materials and Solar Cells, 215*, 110681.
Underwriters Laboratories. (2020). *UL 9540: Safety of energy storage systems and equipment*. Underwriters Laboratories.
Xiang, Y., Zhao, X., & Zhou, D. (2021). Failure analysis of solar PV systems: Fire incidents and safety challenges. *Energy Reports, 7*, 3438–3451.
Yoon, S., Lee, D., & Kim, H. (2021). Integration of building-integrated photovoltaic systems in sustainable architecture. *Journal of Cleaner Production, 289*, 125876.
Zhou, W., Chen, L., & Wang, F. (2022). CFD-based analysis of heat release and smoke flow in solar roof fire scenarios. *Energy and Buildings, 259*, 111833.

Author(s) Information

Miloua Hadj
University Djillali Liabes of Sidi Bel Abbes
Laboratory Mechanics of Structures and Solids (LMSS),
89 Cité Arbi Ben Mhidi Sidi Bel Abbes, Algeria
Contact e- mail: *miloua_hadj@yahoo.fr*

Hassan Sandous
University Djillali Liabes of Sidi Bel Abbes, Faculty of Technology, Department of Mechanical Engineering, Algeria, 89 Cité Arbi Ben Mhidi Sidi Bel Abbes, Algeria

Miloua Farid
University Djillali Liabes of Sidi Bel Abbes
89 Cité Arbi Ben Mhidi Sidi Bel Abbes, Algeria

To cite this article:

Hadj, M., & Sandous, H., & Farid M. (2025). Fire risk simulation of photovoltaic panels installed in green buildings. *The Eurasia Proceedings of Science, Technology, Engineering and Mathematics (EPSTEM), 38,* 90-101.

The Eurasia Proceedings of Science, Technology, Engineering & Mathematics (EPSTEM)
ISSN: 2602-3199

The Eurasia Proceedings of Science, Technology, Engineering and Mathematics (EPSTEM), 2025

Volume 38, Pages 102-108

IConTES 2025: International Conference on Technology, Engineering and Science

Development and Optimization of a Mathematical Model for Predicting Tensile Strength in Friction Stir Welded Joints of 6082-T6 Aluminum Alloy

Ben Messaoud Mohammed Abdelghani
University of Djillali Liabes of Sidi Bel Abbes

Cherief Mohammed Nadhir Djamel Eddine
University of Djillali Liabes of Sidi Bel Abbes

Miloudi Abdelkader
University of Djillali Liabes of Sidi Bel Abbes

Belaribi Amina
University of Djillali Liabes of Sidi Bel Abbes

Abstract: Friction Stir Welding (FSW) is a solid-state joining process that uses a rotating tool to generate heat through friction with the material, causing it to soften without reaching the melting point, thus allowing the parts to be securely joined. This technique is particularly significant in industries requiring high mechanical properties, such as applications involving 6082-T6 aluminum alloy. Given the growing industrial importance of this alloy, there is a need to thoroughly investigate the effects of various welding parameters on the mechanica properties of the resulting weld joints. This study aims to develop a mathematical model to analyze the impact of key welding parameters, including spindle speed, welding speed, shoulder penetration depth, and shoulder profile, on the tensile strength of welded joints. The model was constructed using Response Surface Methodology (RSM), providing a means to predict mechanical performance and optimize process variables. The experimental results showed good agreement with the proposed model, with deviations remaining within acceptable limits, thereby demonstrating the model's potential as an effective tool for improving weld quality in industrial applications.

Keywords: Friction stir welding (FSW), 6082-t6 aluminum alloy, Tensile strength, Response surface methodology (RMS), Mathematical modeling.

Introduction

Friction Stir Welding (FSW) is a solid-state welding technique performed using a machine tool, which was conceived, developed, and patented by Wayne Thomas at The Welding Institute (TWI) in the United Kingdom in December 1991. Unlike conventional fusion welding methods, FSW does not involve melting the base materials. Instead, it relies on the frictional heat generated by a rotating, non-consumable tool that plastically deforms and stirs the materials at the joint line, resulting in a high-quality, defect-free weld. This process was initially developed to address the challenges associated with welding high-strength aluminum alloys, particularly those in the AA2xxx and AA7xxx series, which are known for their poor weldability using traditional fusion welding techniques. FSW offers significant advantages in terms of mechanical performance, metallurgical integrity, and environmental impact, making it a widely adopted technique in industries such as aerospace, automotive, and shipbuilding (Thomas et al., 1991; Thomas & Nicholas, 2001).

- This is an Open Access article distributed under the terms of the Creative Commons Attribution-Noncommercial 4.0 Unported License, permitting all non-commercial use, distribution, and reproduction in any medium, provided the original work is properly cited.

- Selection and peer-review under responsibility of the Organizing Committee of the Conference

© 2025 Published by ISRES Publishing: www.isres.org

Initially, research on Friction Stir Welding (FSW) was confined to laboratory-scale experiments. However, due to its numerous advantages over conventional welding processes, FSW has gained widespread popularity in the joining of materials such as aluminum, copper, steel alloys, and others. Its growing adoption is largely attributed to several key benefits, including the formation of a fine recrystallized microstructure, a minimal heat-affected zone (HAZ), excellent dimensional stability, low distortion, and superior mechanical properties in the weld joint. These characteristics have contributed to the global recognition and increasing industrial application of the process (Akbari et al., 2021). Compared to other conventional welding methods such as TIG, MIG, and laser welding, Friction Stir Welding (FSW) offers enhanced material properties. These include improved tensile strength, fatigue resistance, impact resistance, corrosion resistance, and reduced residual stresses, among others (Wakchaure et al., 2018).

Today, Friction Stir Welding (FSW) remains an emerging and evolving trend within the manufacturing sector, particularly in industries focused on high-strength alloys. The ongoing development and optimization of this process are being pursued through various approaches and techniques, primarily by fine-tuning process parameters to enhance weld quality and performance (Sivabalan et al., 2022). The choice between different parameters and performances is the subject of numerous studies and research efforts, aimed at improving the quality of the resulting weld and reducing production costs and lead times.

The multi-objective optimization study of friction stir welding of 6082-T6 aluminum alloy using the hybrid Taguchi-Grey Relational Analysis - ANN method is the objective of the work by Wakchaure K.N. et al (Wakchaure et al., 2018). The objective functions were selected in accordance with the FSW parameters of tool rotational speed, welding speed, and tilt angle. The Taguchi L27 orthogonal array was used to design the experiments using three distinct tools. By simulating the parameters using an artificial neural network (ANN) model well trained with the grey relational grade obtained from GRA, the optimal tool and process parameters for friction stir welding were identified. Similarly, the work of Sivabalan S. et al (Sivabalan et al., 2022) conducted a parametric study in which the process parameters considered were: tool rotational speed in the range of 800–1200 rpm, traverse speed chosen as 100–200 mm/min, and axial force set at 8 kN. The pin profile was selected as a straight cylindrical tool. The study by Mishra R.S. and Jain Sumit (Mishra et al., 2019) also focused on optimizing the individual response of the FSW process using a vertical milling machine on AA 6082-T6, with the aim of obtaining an optimal parameter combination for suitable ultimate tensile strength using Taguchi techniques. The results showed that a rotational speed of 1200 rpm, a welding speed of 30 mm/min, and a threaded cylindrical tool with a shoulder diameter of 16 mm yielded the maximum UTS.

Materials and Methods

A conventional vertical milling machine with a capacity of 5.6 KW and 1800 rpm is used to perform the experiments. The spindle speed (Vr), welding speed (Va), shoulder penetration (PE), shoulder profile (PRE), and the process parameter ranges such as spindle speed and welding speed were taken respectively between 700 rpm and 1500 rpm, and between 48 mm/min and 240 mm/min. The shoulder penetration was gradually increased in five stages, from 0 mm to 0.16 mm. The selected process parameters with their limits, units, and notations are given in Table 1.

Table 1. Process parameter with their range and values at five levels (Gopi et al.,2021)

Process Parameters	Range	level 1 (-2)	level 2 (-1)	level 3 (0)	level 4 (1)	level 5 (2)
Spindle speed or tool rotational speed (Vr)	700 à 1500 tr/min	700	900	1100	1300	1500
feed or welding speed (Va)	48 à 240 mm/min	48	96	144	192	240
Shoulder penetration(PE)	0.0 à 0.16 mm	0	0.04	0.08	0.12	0.16
Shoulder profile (PRE)	-10° à 10°	-10	-5	0	5	10

Table 2. Chemical composition of 6082 alloy (Gopi et al., 2021; Algahtani et al., 2019).

Si	Fe	Cu	Mn	Mg	Cr	Zn	Ti
0.7 - 1.3	≤ 0.50	≤ 0.10	0.4 - 1.0	0.6 - 1.2	≤ 0.25	≤ 0.20	≤ 0.10

In this study, a composite design was used to construct the experimental plan. Tensile strength (Ts) was chosen as the response variable, while spindle speed (Vr), welding speed (Va), shoulder penetration (PE), and shoulder profile (PRE) were selected as the independent variables. Table 3 summarizes the experimental design used.

Table 3. Design table and experimental value of tensile strength (Gopi et al., 2021).

Test	Vr	Va	PE	PRE	Ts
1	700	48	0	-10	174,874
2	700	96	0,04	-5	180,059
3	700	144	0,08	0	187,953
4	700	192	0,12	5	184,93
5	700	240	0,16	10	177,825
6	900	48	0,04	5	189,189
7	900	96	0,08	10	185,686
8	900	144	0,12	-10	182,088
9	900	192	0,16	-5	183,712
10	900	240	0	0	187,007
11	1100	48	0,08	-5	180,262
12	1100	96	0,12	0	181,885
13	1100	144	0,16	5	192,899
14	1100	192	0	10	195,792
15	1100	240	0,04	-10	191,456
16	1300	48	0,12	10	189,808
17	1300	96	0,16	-10	186,351
18	1300	144	0	-5	189,308
19	1300	192	0,04	0	192,445
20	1300	240	0,08	5	195,578
21	1500	48	0,16	0	178,028
22	1500	96	0	5	181,976
23	1500	144	0,04	10	190,411
24	1500	192	0,08	-10	198,93
25	1500	240	0,12	-5	196,001

Response Surface Methodology (RSM)

Equation (1) was used to fit the experimental tensile strength (Ts) data in order to build the RSM model.

$$Y = A_0 + A_1X_1 + A_2X_2 + A_3X_3 + A_4X_4 + A_{12}X_1X_2 + A_{13}X_1X_3 + A_{14}X_1X_4 + A_{23}X_2X_3 + A_{24}X_2X_4 + A_{34}X_3X_4 + A_{11}X_1X_1 + A_{22}X_2X_2 + A_{44}X_4X_4 + A_{123}X_1X_2X_3 + A_{124}X_1X_2X_4 + A_{134}X_1X_3X_4 + A_{234}X_2X_3X_4 + A_{112}X_1X_1X_2 + A_{113}X_1X_1X_3 + A_{114}X_1X_1X_4 + A_{122}X_1X_2X_2 + A_{144}X_1X_4X_4 + A_{223}X_2X_2X_3 \quad (1)$$

Where X1, X2, X3, and X4 are the values of the independent variables, Y represents the corresponding response variable, A0 is a constant, A1, A2, A3, and A4 are the linear coefficients, A12, A13, A14, A23, A24, and A34 are the interaction coefficients. A11, A22, and A44 are the quadratic coefficients. A123, A124, A134, A234, A112, A113, A114, A122, A144, and A223 are the cubic coefficients. Equation (1) is used to estimate the optimal response variable and the corresponding variables.

Results and Discussion

Modeling using the Response Surface Methodology (RSM) was carried out with the 'Design Expert' software. In this study, the coefficient of determination (R^2) for the response variable represented by tensile strength (Ts) was 0.9939.

Table 4. Fitting statistics of Ts.

Std. Dev.	2,45	R^2	0,9939
Mean	186,98	Adjusted R^2	0,8546
C.V. %	1,31	Predicted R^2	NA(1)
		Adeq Precision	10,1614

According to the fit summary, the model is significant for the analysis of tensile strength. The R^2 value is 99.39%, and the adjusted R^2 value is 85.46%. This clearly indicates that the regression model provides a good relationship between the process factors and the response variable.
The RSM model for tensile strength is given by Equation (2).

$$\begin{aligned} Tr = {} & -1229{,}16617 + 2{,}53948\ Vr + 7{,}91313\ Va + 2520{,}60102\ PE - 70{,}99142\ PRE \\ & - 0{,}013260\ Vr*Va - 7{,}58282\ Vr*PE + 0{,}139872\ Vr*PRE + 20{,}316\ Va*PE \\ & - 0{,}251189\ Va*PRE + 221{,}03667\ PE*PRE - 0{,}001040\ Vr^2 - 0{,}007188\ Va^2 \\ & - 0{,}117344\ PRE^2 - 0{,}007433\ Vr*Va*PE + 0{,}000189\ Vr*Va*PRE \\ & - 0{,}216642\ Vr*PE*PRE + 0{,}287425\ Va*PE*PRE + 4{,}81066.10^{-6}\ Vr^2*Va \\ & + 0{,}003728\ Vr^2*PE - 0{,}000063\ Vr^2*PRE + 8{,}04623.10^{-6}\ Vr.Va^2 \\ & + 0{,}000135\ Vr*PRE^2 - 0{,}036081\ Va^2*PE \end{aligned} \quad (2)$$

The tensile strength (Ts) data predicted by the RSM model were compared with the corresponding experimental tensile strength data (Figure 2). The graph of actual and predicted values for tensile strength demonstrated the predictive capability of the developed model. In this diagram, the points lay on a straight line very close to the actual values, indicating that the errors were uniformly distributed throughout the model, as shown in Figure 2.

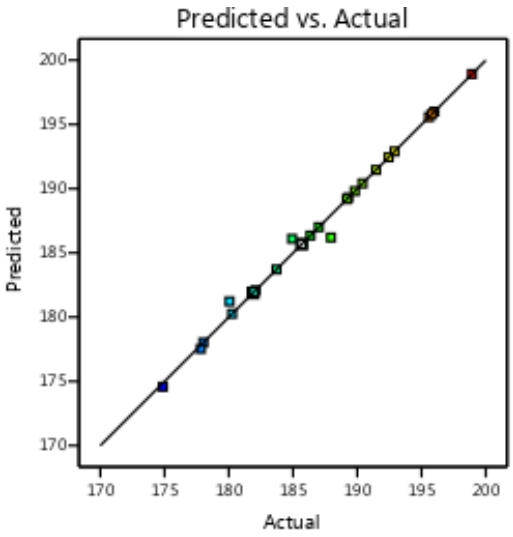


Figure 2. Actual response versus predicted response graph of tensile strength Ts.

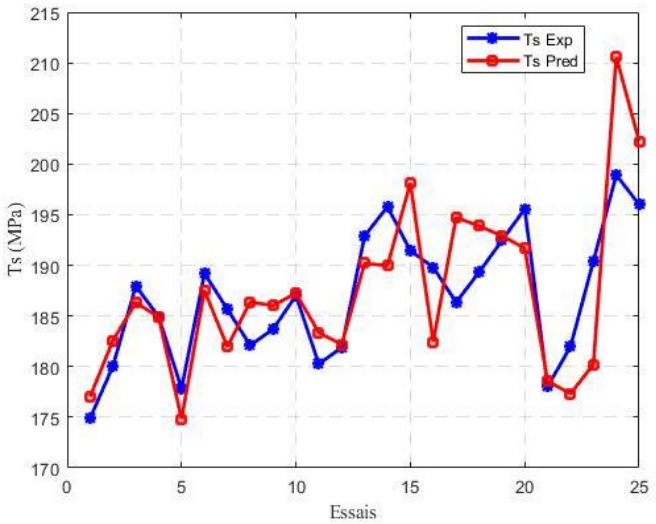


Figure 3. Validation of the tensile strength predicted by RSM.

To demonstrate the effectiveness of the Response Surface Methodology, comparison curves were plotted in Figure 3. The superimposed curves represent a comparison between the experimental values used for the model design and the values predicted by the model for the same machining parameters. Figure 4 shows the effect of factors Vr and Va acting simultaneously on the ultimate tensile strength (Ts), as they increase from their minimum to maximum values, while the third factor (PE) and fourth (PRE) remain constant. Tensile strength increases as Vr increases due to the rise in heat generation. Meanwhile, low heat input was observed at low rotational speeds, indicating a lack of stirring activity, hence poor weld quality. It was also observed that at high rotational speed and low tool traverse speed, a decrease in TS value occurred. This may be due to the effect of excessive heat generation. As shown in Figure 4.

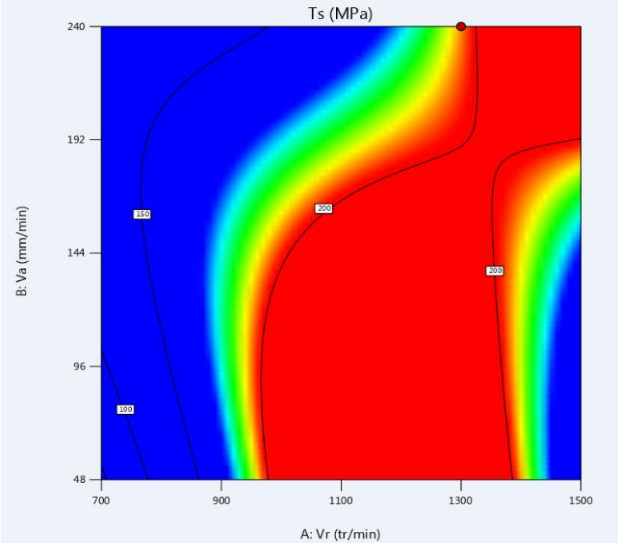


Figure 4. Variation of Ts as a function of factors Vr and Va.

As for the effect of parameters Vr and PE, an increase in the tensile strength value is observed at low to medium rotational speeds with low shoulder penetration. Then, the tensile strength increases as both variables increase together (Figure 5).

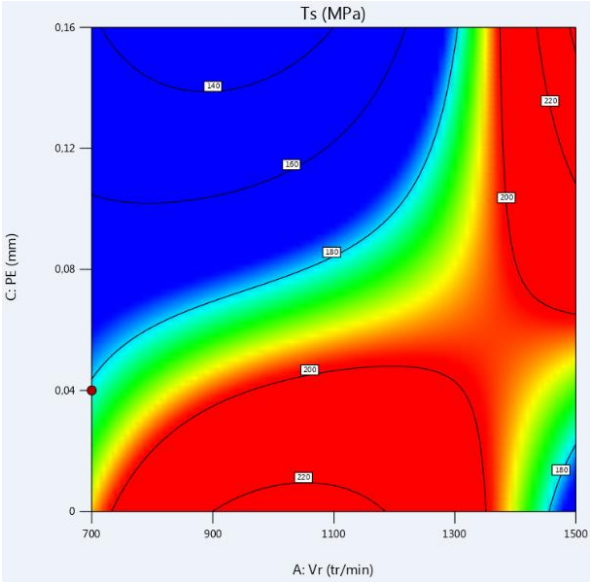


Figure 5. Variation of Ts as a function of factors Vr and PE.

As for the parameters Vr and PRE, it is observed that to achieve high tensile strength, Vr and PRE are proportional, since increasing the rotational speed increases the shoulder angle (i.e., the angle opens outward), and vice versa. At low rotational speeds, a high retention of the resulting heat is required, so this angle acts as a protector of that heat in the welding zone (Figure 6). On the contrary, with the welding speed (Va) and the shoulder angle (PRE), as the welding speed increases, the shoulder angle decreases (i.e., it points inward); as the welding speed decreases, the shoulder angle increases.

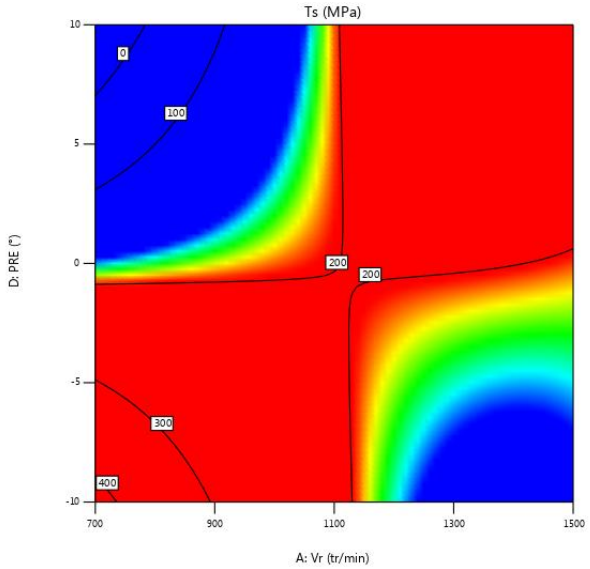


Figure 6. Variation of Ts as a function of factors Vr and PRE.

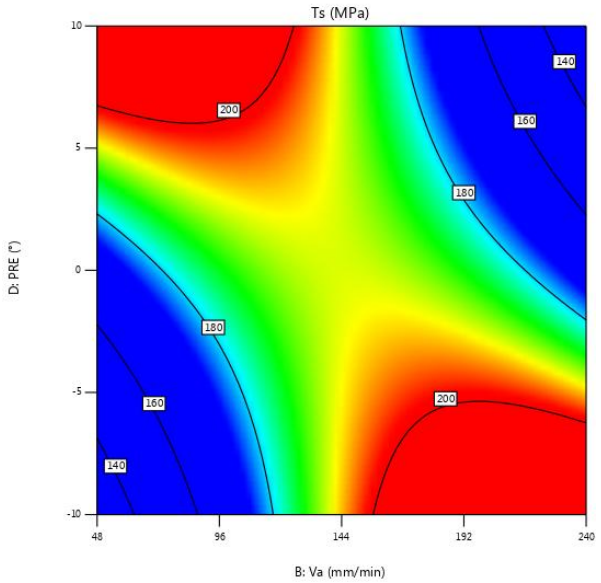


Figure 7. Variation of Ts as a function of factors Va and PRE.

Conclusion

In conclusion, what we have done can be summarized by the following points:

A mathematical model has been presented to study the effect of welding parameters on the tensile mechanical strength of the welded joint in 6082 T6 aluminum alloy. Using Response Surface Methodology (RSM), a mathematical model was developed which offers the possibility to develop an optimization model. It is important to emphasize that the created model shows very low error rates compared to experimental data. The effect of four parameters, namely rotational speed (Vr), feed speed (Va), shoulder penetration (PE), and tool shoulder profile (PRE), was studied. The main objective of this study was to understand and explain the interactions between the four parameters mentioned above, and to highlight the effect of each one on the others regarding the mechanical property of tensile strength of the welded joints.

Scientific Ethics Declaration

* The authors declare that the scientific ethical and legal responsibility of this article published in EPSTEM journal belongs to the authors.

Conflict of Interest

* The authors declare that they have no conflicts of interest

Funding

* This research received no specific grant from any funding agency in the public, commercial, or not-for-profit sectors.

Acknowledgements or Notes

* This article was presented as a poster presentation at the International Conference on Technology, Engineering and Science (www.icontes.net) held in Antalya/Türkiye on November 12-15, 2025.

References

Akbari, M., Behnagh, R. A., & Dadvand, A. (2021). Recent research progress in friction stir welding of aluminium and copper alloys: A review. *Journal of Materials Research and Technology, 15*, 1-20.

Algahtani, A., & Mahmoud, E. R. I. (2019). Erosion and corrosion resistance of plasma electrolytic oxidized 6082 aluminum alloy surface at low and high temperatures. *Journal of Materials Research and Technology, 8*(3), 2699-2709.

Gopi, S., & Mohan, D. G. (2021). Evaluating the welding pulses of various tool profiles in single-pass friction stir welding of 6082-T6 aluminium alloy. *Journal of Welding and Joining, 39*(1), 63-71.

Mishra, R. S., & Jain, S. (2019). Friction stir welding (FSW) process on aluminum alloy 6082-T6 using Taguchi technique. *International Journal of Research in Engineering and Innovation, 3*(5), 301-305.

Sivabalan, S., Sridhar, V. G., & Ramkumar, K. R. (2022). Study on mechanical behaviour of friction stir welded 6082-T6 aluminium alloys. *Materials Today: Proceedings, 69*, 944-949.

Thomas, W. M., & Nicholas, E. D. (1997). Friction stir welding for the transportation industries. *Materials & Design, 18*(4-6), 269-273.

Thomas, W. M., Nicholas, E. D., Needham, J. C., Murch, M. G., Temple-Smith, P., & Dawes, C. J. (1995). *Friction stir butt welding* (U.S. Patent No. 5,460,317). U.S. Patent and Trademark Office.

Wakchaure, K. N., Thakur, A. G., Gadakh, V. S., & Kumar, A. (2018). Multi-objective optimization of friction stir welding of aluminium alloy 6082-T6 using hybrid Taguchi-Grey relation analysis-ANN method. *Materials Today: Proceedings, 5*(2), 7150-7159.

Author(s) Information

Ben Messaoud Mohammed Abdelghani
University of Djillali Liabes of Sidi Bel Abbes, Laboratory of Materials and Reactive Systems (LMSR), Algeria
Contact e-mail: *abdelghanibenmessaoud00@gmail.com*

Cherief Mohammed Nadhir Djamel Eddine
University of Djillali Liabes of Sidi Bel Abbes, Laboratory of Materials and Reactive Systems (LMSR), Algeria

Miloudi Abdelkader
University of Djillali Liabes of Sidi Bel Abbes, Laboratory of Materials and Reactive Systems (LMSR), Algeria.

Belaribi Amina
University of Djillali Liabes of Sidi Bel Abbes, Laboratory of Materials and Reactive Systems (LMSR), Algeria.

To cite this article:

Abdelghani, B.M.M., Eddine, C. M. N. D., Abdelkader, M., & Amina, B. (2025). Development and optimization of a mathematical model for predicting tensile strength in friction stir welded joints of 6082-T6 aluminum alloy. *The Eurasia Proceedings of Science, Technology, Engineering and Mathematics (EPSTEM), 38,* 102-108.

The Eurasia Proceedings of Science, Technology, Engineering & Mathematics (EPSTEM)
ISSN: 2602-3199

The Eurasia Proceedings of Science, Technology, Engineering and Mathematics (EPSTEM), 2025

Volume 38, Pages 109-114

IConTES 2025: International Conference on Technology, Engineering and Science

Study of the Thermomechanical Properties of Bimaterials (Metal/Ceramic)

Liamani Samira
University of Djillali Liabes of Sidi Bel Abbes

Ghermaoui Ilas Mohamed Amine
University of Djillali Liabes of Sidi Bel Abbes

Abstract: Bimaterial metal/ceramic assemblies are widely used in applications exposed to severe thermal environments, notably in the aerospace, power electronics and nuclear sectors. Due to the sharp contrast between the mechanical and thermal properties of the two materials (modulus of elasticity, coefficient of thermal expansion), these structures develop complex thermomechanical stress fields, which can initiate or propagate cracks.The present study focuses on the variation in stress intensity factor (SIF) associated with a localized plane crack in the metal part of a metal/ceramic assembly, under one-dimensional thermal loading. The aim is to quantify the influence of the thermomechanical properties of the bimaterial, the position of the crack relative to the interface, and the temperature distribution on the evolution of the SIF. The methodology is based on finite element modeling, with simulations carried out for different thermal loading scenarios (linear gradient, thermal shock), using typical materials such as steel/alumina. The results show that proximity to the interface significantly influences the amplification or attenuation of the SIF, depending on the direction of the thermal gradient and the contrast in properties. When the crack is close to the interface, an asymmetrical redistribution of stresses is observed, which may favor a deviation of the crack towards the interface or the ceramic. Taking these effects into account is essential for predicting the service life of these composite structures.

Keywords: Bimaterial, ABAQUS, Thermomechanical, Stress intensity factor, Metal, Ceramic

Introduction

Numerical modeling of cracked media using the finite element method (FEM) is now an essential tool in fracture mechanics, enabling the precise analysis of crack propagation phenomena in complex structures. The recent rise of numerical simulation techniques has led to significant advances in several engineering fields, particularly in the study of metal/ceramic bimaterials, whose industrial applications have expanded considerably in recent decades.

Numerous studies have contributed to a better understanding of the mechanical behavior and fracture at the interfaces of dissimilar materials. For example, Kim and Suresh (Kim and al. 1994) analyzed normal fracture at bimaterial interfaces, highlighting damage mechanisms dependent on the nature of the mechanical and thermal coupling. Teixeira et al. (Teixeira 1999) focused on residual stresses and cracking in metal/ceramic systems applied to microelectronic devices, while Zhang et al. (Zhang 2008) conducted in-depth finite element analyses on interfacial cracking in metal-ceramic composites. Furthermore, Cai et al. (Cai 2021 & Reddy 2017) studied the mechanical characterization of interfaces in thermocompression assemblies, highlighting the crucial role of material adhesion and compatibility properties. Following this line of research, the present work aims to analyze the evolution of the stress intensity factor (SIF) during crack propagation in a solid-state thermocompression ceramic-metal junction. Previous studies have shown that the intensity and distribution of interfacial stresses in

- This is an Open Access article distributed under the terms of the Creative Commons Attribution-Noncommercial 4.0 Unported License, permitting all non-commercial use, distribution, and reproduction in any medium, provided the original work is properly cited.

- Selection and peer-review under responsibility of the Organizing Committee of the Conference

© 2025 Published by ISRES Publishing: www.isres.org

such assemblies are highly dependent on the physical, mechanical, and thermal properties of the constituent materials.

The precise determination of these parameters is therefore essential for evaluating the durability, reliability, and serviceability of metal/ceramic bimaterials. Indeed, the performance of these systems under operational conditions depends directly on the level and distribution of interfacial stresses, which determine their resistance to cracking and their long-term behavior.

Method

Presentation of the Model

The model developed for this study is a three-dimensional cracked plate composed of two materials of different natures (metal and ceramic) jointly assembled (Figure 1) with a length L = 20 mm, a height H = 10 mm (H1 = 6 mm for the ceramic and H2 = 4 mm for the metal), and a thickness e = 15 mm. The difference in the coefficient of thermal expansion between the ceramic and the metal leads to a high concentration of residual stresses at the interface. The finite element method numerical simulation software used in our study is ABAQUS.

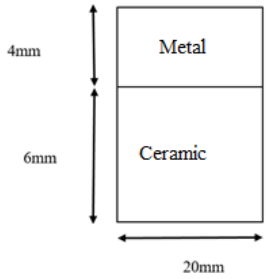


Figure 1. Geometric modeling

We varied the materials constituting our model so as to benefit from the choice of mechanical and physical properties, as well as their production temperature. The mechanical and physical properties of the different materials used are illustrated in Table 1.

Table 1. Mechanical and physical properties of materials

	Young's modulus E(GPa)	Poisson coefficient	Coefficient of thermal expansion α (10^{-6} k)
Alumina	350	0.25	8.5
Zirconia	200	0.28	5.4
AlN	320	0.27	4.2
Copper	100	0.34	16.5
Silver	83	0.37	19
Platinum	168	0.38	9

The meshing of geometry constitutes the longest and most determining part of a numerical model. Figure 2 represents the mesh used for the simulation of the Bimaterial plate containing a central crack. The latter was meshed by quadratic elements of type; the mesh was particularly refined in the vicinity of the crack front for the good precision of the results.

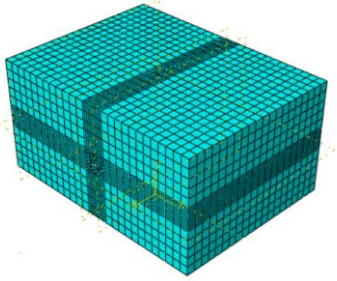


Figure 2. Plate mesh

Results and Discussion

Variation in the Stress Intensity Factor

In this work, we analyze the effect of thermal loading on the behavior of a cracked plate. To this end, the model is subjected to temperature variations below its glass transition temperature (Tg). These temperatures induce thermal stresses in the material according to the following relationship:

$$\sigma_{th} = E.\alpha.\Delta T$$

Where E is the material's modulus of elasticity;
α is the coefficient of thermal expansion;
ΔT is the difference between the reference temperature and the material's temperature.

Our objective is to numerically analyze, using the finite element method, the behavior of cracks under thermal loading in three dimensions. Temperature is a fundamental physical parameter for the fabrication of metal-ceramic assemblies. The study of thermal behavior in bimaterials, specifically copper/Al_2O_3, containing a central crack of size "a" subjected to temperature variations T, is the objective of this work. The behavior of this crack is analyzed in terms of the variation of the stress intensity factor in both opening mode (KI) and shear mode (KII).

The results obtained, presented in Figure 3, illustrate the evolution of the stress intensity factor (SIF) in modes I and II as a function of temperature and crack defect size. It appears that, regardless of the temperature variation ΔT, the SIF in mode I (opening) increases with crack growth, reflecting the direct influence of thermal stresses generated by the heating of the bimaterial. Conversely, the SIF in mode II (shear) decreases with crack propagation, this decrease being more pronounced at relatively low temperatures. Overall, the values for mode II remain significantly lower than those for mode I, indicating that crack propagation occurs primarily in a mixed mode with a dominant opening. This behavior is attributed to the nature of the thermal stresses, which are particularly sensitive to temperatures below the glass transition temperature of the bimaterial.

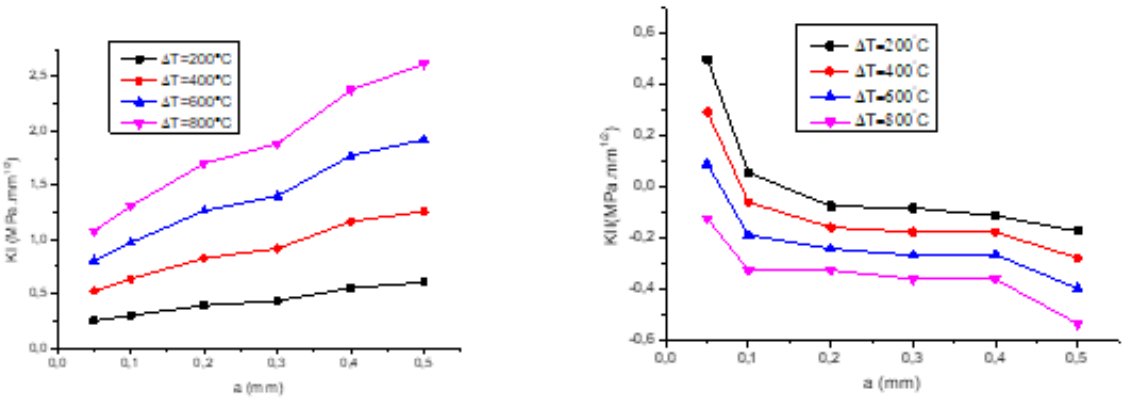


Figure 3. Variation of the stress intensity factor in mode I and II as a function of the crack defect size

We considered it important to study the interaction effect between a crack in one of the two materials forming the structure and its interface. This study deals with the case of a crack in the ceramic parallel to the interface, propagating perpendicularly to it. In our case, we considered a crack of length a = 0.2 mm propagating within the brittle material (alumina). As before, the structure is subjected to thermal stress, and the results of the analysis of this effect are illustrated in Figure 4. These figures show the variation of the stress intensity factor in mode I as a function of the crack-interface distance.

The maximum values of this factor are obtained when the crack-interface distance approaches the mid-height of the ceramic. The stress intensity factor in mode I decreases sharply as the crack moves away from the interface, i.e., for crack-interface distances greater than d = 2.5 mm. Depending on the loading mode, this ratio leads to a strong crack-interface interaction, the level of which increases with the increasing thermal load on the bimaterial.

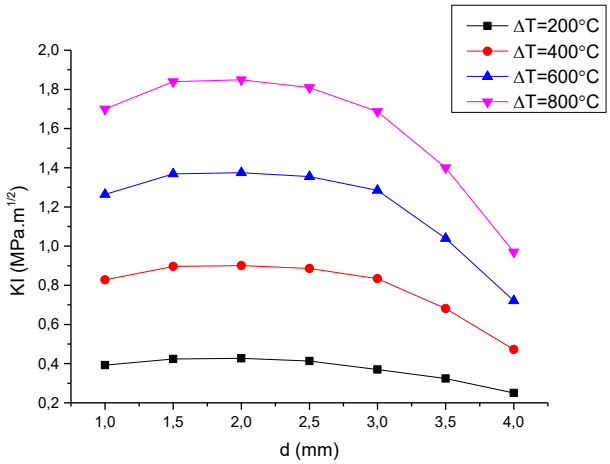


Figure 4. Variation of the stress intensity factor in mode I as a function of the crack-interface distance.

To better illustrate the thermal behavior of the bimaterial during fracture, we studied the case of a central crack for different types of materials (ceramic-metal). The same loading and simulation conditions used previously were retained for this part of the study, with a temperature of 800°C and an interfacial distance d = 1 mm. The model response is analyzed in terms of the variation of the stress intensity factor in the opening mode (KI).

Initially, we analyzed the thermal behavior of a bimaterial for three types of metal/ceramic assemblies: copper/Al_2O_3, copper/ZrO_2, and copper/AlN. The results obtained are illustrated in Figure 5. These figures show the variation of the stress intensity factor in the opening mode as a function of crack propagation for different coefficients of thermal expansion. This parameter increases significantly when the metal is bonded to a ceramic with a very low α coefficient (AlN). High thermal conductivity combined with low thermal expansion makes AlN an excellent material resistant to thermal shock and able to withstand rapid heating and cooling. The KI induced in the Copper/Al_2O_3 bond is greater than that generated in the Copper/ZrO_2 assembly, regardless of the crack defect size.

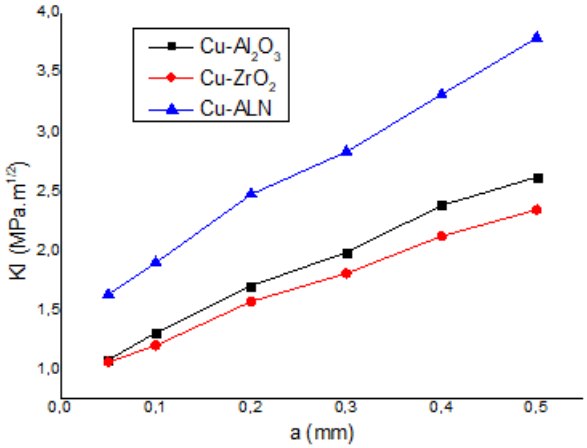


Figure 5. Variation of the stress intensity factor in opening mode as a function of crack progression for different Copper/Ceramic pairs

The results in Figure 6 lead to an analysis of the crack-interface interaction effects when the latter is located on the ceramic. This analysis focuses on three material pairs, characterized by their coefficient of thermal expansion. The figure shows the evolution of the stress intensity factor in mode I as a function of the distance d between the crack and the interface. We observe that the value of KI increases significantly when the crack is close to the interface; this increase is particularly significant for a Cu-AlN pair with a low coefficient of thermal expansion. Moving the crack further from the interface leads to a reduction in the stress intensity factor in mode I. This effect is due to the fact that, far from the interface, the interaction effect disappears completely.

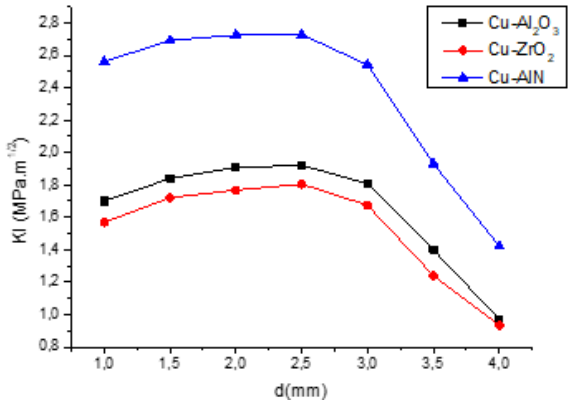


Figure 6. Evolution of the stress intensity factor in mode I as a function of the distance separating the crack and the interface.

Conclusion

Numerical analysis, performed using the finite element method (FEM), of the fracture behavior of a bimaterial subjected to thermal loading leads to the following conclusions:

The stress intensity factor in mode I of a crack propagating perpendicular to the interface is highly dependent on the distance between the crack and the interface. In the immediate vicinity of the interface, the cracking energy increases considerably, reaching values comparable to those of an interfacial crack. Conversely, far from the interface, the interaction effect becomes negligible. Furthermore, the stress intensity factor increases significantly when the metal is bonded to a ceramic with a low coefficient of thermal expansion, such as AlN. The more ceramic (such as alumina) is bonded to a metallic material with a high coefficient of thermal expansion, the higher the stress intensity factor in mode I. However, it remains weak for the silver/Al_2O_3 pair, considered a thermally compatible system. Thus, it can be concluded that, under the effect of thermal stresses, crack propagation occurs primarily in mode I, reflecting a fracture mechanism dominated by crack opening rather than shear.

Scientific Ethics Declaration

* The authors declare that the scientific ethical and legal responsibility of this article published in EPSTEM journal belongs to the authors.

Conflict of Interest

* The authors declare that they have no conflicts of interest

Funding

* This research received no specific grant from any funding agency in the public, commercial, or not-for-profit sectors.

Acknowledgements or Notes

* This article was presented as a poster presentation at the International Conference on Technology, Engineering and Science (www.icontes.net) held in Antalya/Türkiye on November 12-15, 2025.

References

Bahru, R., Ahmad Zamri, M. F. M., Shamsuddin, A. H., Shaari, N., & Mohamed, M. A. (2021). A review of thermal interface material fabrication method toward enhancing heat dissipation. *International Journal of Energy Research, 45*(3), 3548–3568.

Bouafia, F., Serier, B., Fekirini, H., & Bouafia, S. A. (2012). Analyse numérique des contraintes résiduelles dans les bi-matériaux. *Revue des composites et des matériaux avancés, 22*(1), 125–142.

Boutabout, B., Serier, B., Mecirdi, M. A., & Chama, M. (2008). Analyse numérique des contraintes résiduelles dans les bimatériaux céramique/métal. *Revue des composites et des matériaux avancés, 18*(3), 323–335.

Kim, K. S. (1994). A finite element analysis of crack bridging in metal matrix composites. *Journal of Composite Materials, 28*(15), 1431-1455.

Rangasreenivasulu, U., & Reddy, S. B. K. (2017). Finite element analysis of thermally induced residual stresses in (Al_2O_3/SiC/TiC) functionally graded materials. *International Journal for Innovative Research in Science & Technology, 4*(7), 1-7.

Sellam, S., Serier, B., Bouafia, F., Bachir Bouidjra, B., & Sardar, S. H. (2013). Analysis of the stress intensity factor in alumina–Pyrex composites. *Computational Materials Science, 72*, 68-80.

Suresh, S., & Mortensen, A. (1997). Functionally graded metals and metal-ceramic composites: Part 2. Thermomechanical behavior. *International Materials Reviews, 42*(3), 85-116.

Teixeira, V., Andritschky, M., Fischer, W., Buchkremer, H. P., & Stöver, D. (1998). Analysis of residual stresses in thermal barrier coatings. *Surface and Coatings Technology, 108-109*, 209-216.

Yan, Y., & Park, S.-H. (2008). An extended finite element method for modeling near-interfacial crack propagation in a layered structure. *International Journal of Solids and Structures, 45*(17), 4756-4765.

Yang, Y., Hu, Z., & Li, X.-F. (2020). Nanoscale mode-III interface crack in a bimaterial with surface elasticity. *Mechanics of Materials, 140*, 103246.

Zhang, H., & Qiao, P. (2017). An extended state-based peridynamic model for damage growth prediction of bimaterial structures under thermomechanical loading. *Engineering Fracture Mechanics, 189*, 81-97.

Author(s) Information

Liamani Samira
University of Djillali Liabes of Sidi Bel Abbes
Ben M'hidi City, BP 89, 22000 Sidi Bel Abbes, Algeria
Contact e-mail: *liamani2007@yahoo.fr*

Ghermaoui Ilas Mohamed Amine
University of Djillali Liabes of Sidi Bel Abbes
Ben M'hidi City, BP 89, 22000 Sidi Bel Abbes Algeria

To cite this article:

Samira, L., & Amine, G. I. M. (2025). Study of the thermomechanical properties of bimaterials (metal/ceramic). *The Eurasia Proceedings of Science, Technology, Engineering and Mathematics (EPSTEM), 38,* 109-114.

The Eurasia Proceedings of Science, Technology, Engineering & Mathematics (EPSTEM)
ISSN: 2602-3199

The Eurasia Proceedings of Science, Technology, Engineering and Mathematics (EPSTEM), 2025

Volume 38, Pages 115-120

IConTES 2025: International Conference on Technology, Engineering and Science

Numerical Analysis of Weld Spot Spacing Effects on Shear Tensile Behavior of TRIP 800 Steel

Cherfi Mohamed
University of Sidi Bel Abbes

Reffas Sid Ahmad
University of Sidi Bel Abbes

Sahli Abderahmane
University of Sidi Bel Abbes

Moulgada Abdelmajıd
University of Sidi Bel Abbes

Ghermaoui Mohammed Ilyes
University of Sidi Bel Abbes

Abstract: The global TRIP 800 steel industry is a dynamic and constantly evolving sector, requiring innovative technologies and robust materials to meet performance and safety standards. Among the techniques used for assembling metallic materials, resistance welding—and more specifically, spot welding is widely employed for joining high-quality metal parts. This method enables the creation of sealed and durable joints, which are essential for applications in the aerospace, automotive, shipbuilding, and other industrial sectors. The variations in temperature and pressure can influence the metallurgical structure of the joint, potentially compromising its strength and durability. The objective of our study is to model a shear tensile test to visualize the influence of spot welding parameters, such as the spacing between weld points, the dimensions of the weld joints, and the effect of TRIP 800 steel plates. This study covers the various welding methods, with a particular focus on resistance spot welding. We discuss the welding principle, the different stages of the process, the geometry and microstructure of the weld nugget, as well as the heat-affected zone (HAZ) and weldability considerations, and we explore the general concepts related to TRIP 800 steel. Secondly we interpret the equivalent stress results (VON MISES and MAX PRINCIPAL) and analyze stress histograms representing the molten metal and the heat-affected zone across four different geometric models to illustrate the influence of weld point spacing, finally, we focused on the behavior of the joint in the event of failure (spot welding), by creating a model that includes a crack.This crack occurs in the base metal with identical size, in order to parameterize the study and visualize the fracture behavior of the joint while interpreting the J-integral contour.

Keywords: Spot welding, FEM, TRIP 800 Max principal stress, J-integral contour

Introduction

The global TRIP 800 steel industry is a dynamic and constantly evolving sector that demands innovative technologies and robust materials to meet performance and safety requirements. Among the various techniques used for joining metallic materials, resistance welding-and more specifically spot welding-is widely employed to assemble high-quality metal components. This method enables the creation of tight and durable joints, which are essential for applications in the aerospace, automotive, shipbuilding, and other industrial sectors.

- This is an Open Access article distributed under the terms of the Creative Commons Attribution-Noncommercial 4.0 Unported License, permitting all non-commercial use, distribution, and reproduction in any medium, provided the original work is properly cited.

- Selection and peer-review under responsibility of the Organizing Committee of the Conference

© 2025 Published by ISRES Publishing: www.isres.org

Spot resistance welding is an innovative joining technique, particularly widespread in the automotive industry. It does not require any filler material, as the weld nugget is formed by the fusion of the metal itself (Joule effect) between the sheets to be joined. Generally, this technique is used to assemble two thin sheets (ranging from 0.1 to 3 mm) through the formation of a weld nugget. The sheets in contact are subjected to pressure by two electrodes and traversed by a high-intensity alternating current at low voltage.

However, spot welding presents several challenges, notably the need for precise control of welding parameters to ensure high-quality results. Variations in temperature and pressure can affect the metallographic structure of the joint, potentially compromising its strength and durability. The objective of our study is to model the shear-tensile test in order to visualize the influence of spot welding parameters, such as the spacing between weld spots, the dimensions of the weld joints, and the effect of TRIP 800 steel plates.

Method and Analysis

Mechanical Properties and Model

In this study, we will create a numerical model of two spot-welded plates using physical, mechanical, or thermal data obtained from previous studies in the field in which we aim to develop this model. Many books focus on this area, such as those by Sylvain DANCETTE and Habib LEBBAL, who use different types of stainless steel to represent the behavior of welded plates. We conducted a comparison between two spot-welded plates in this study. These two plates have the same dimensions, as shown in Figure 1.

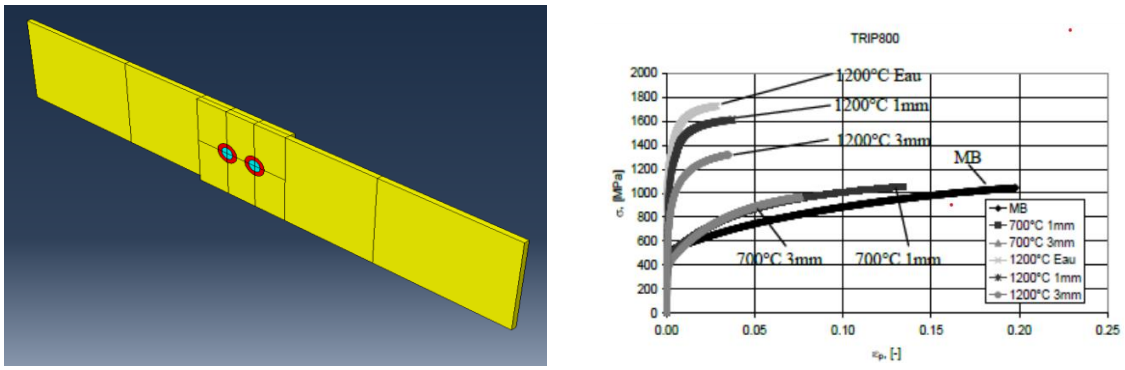


Figure 1. Spot welding model and tensile behavior law as a function of the thermal cycle for TRIP 800

Boundary Conditions and Mesh Model

The boundary conditions include all the forces or constraints that affect the mechanical behavior of the plate during the tensile test. The boundary conditions may include stress, concentric force, displacement, strain, and so on. During a tensile test, the boundary conditions are generally defined as two tensile forces applied on both sides of the sheets, one being equal and opposite to the other, or as a simplified case with one side fixed and a load applied on the other.

The Figure 2 shows the boundary conditions used in this simulation:

- An applied load in MPa.
- A fixed (encastrement) constraint.
- Zero displacement along the Y and Z axes.
- Allowed displacement along the X axis.

Obtaining reliable results requires an extremely sophisticated mesh. Indeed, it is essential to refine the mesh by studying the interaction between the base metal, the heat-affected zone (HAZ), and the molten metal in order to analyze the overall structure. The graphical representation illustrates the structure of the different parts of the welded plate. By applying the concept of convergence and accuracy of the results in this study, we improved the mesh in the various regions of the plate. The ABAQUS computational code allows us to perform this refinement in all zones and directions. In this study, we created a linear quadratic element, and the global model generated 23,082 elements of type C3D8R.

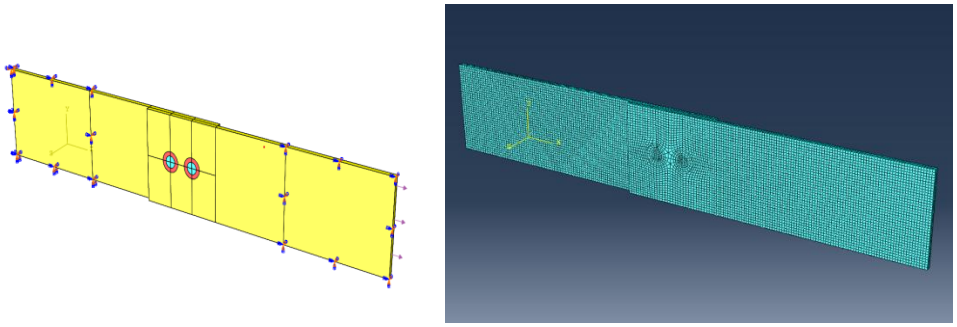


Figure 2. Boundary conditions and mesh model

Results and Discussion

The Graphs below illustrate the variation of the equivalent stress for the TRIP 800 material as a function of the overlap (38 mm) for six loading modes, ranging from 20 MPa to 200 MPa, for X1, X2, X3, and X4 in the longitudinal direction. The analysis of these four graphs shows that the effect of the applied load on the stress intensity is significant, far exceeding the stresses recorded in the transverse direction. Each point corresponding to X1, X2, X3, and X4 is highly stressed and exhibits a peak in the maximum principal stress. This peak value is similar for the first three positions (X1, X2, and X3), which show the same behavior, whereas X4 presents a different pattern. It is also observed that the graphs display a non-symmetrical and stochastic profile that increases in the loading direction, with stress peaks along the overlap. This behavior is due to the transition from one zone to another (variable stiffness). The highest stress values are recorded for X1, X2, and X3, reaching levels around 1000 MPa-close to the yield strength of the molten metal. In contrast, X4 shows a stress value around 600 MPa, which largely exceeds the yield strength of the base metal and the heat-affected zone, yet remains below that of the molten metal.

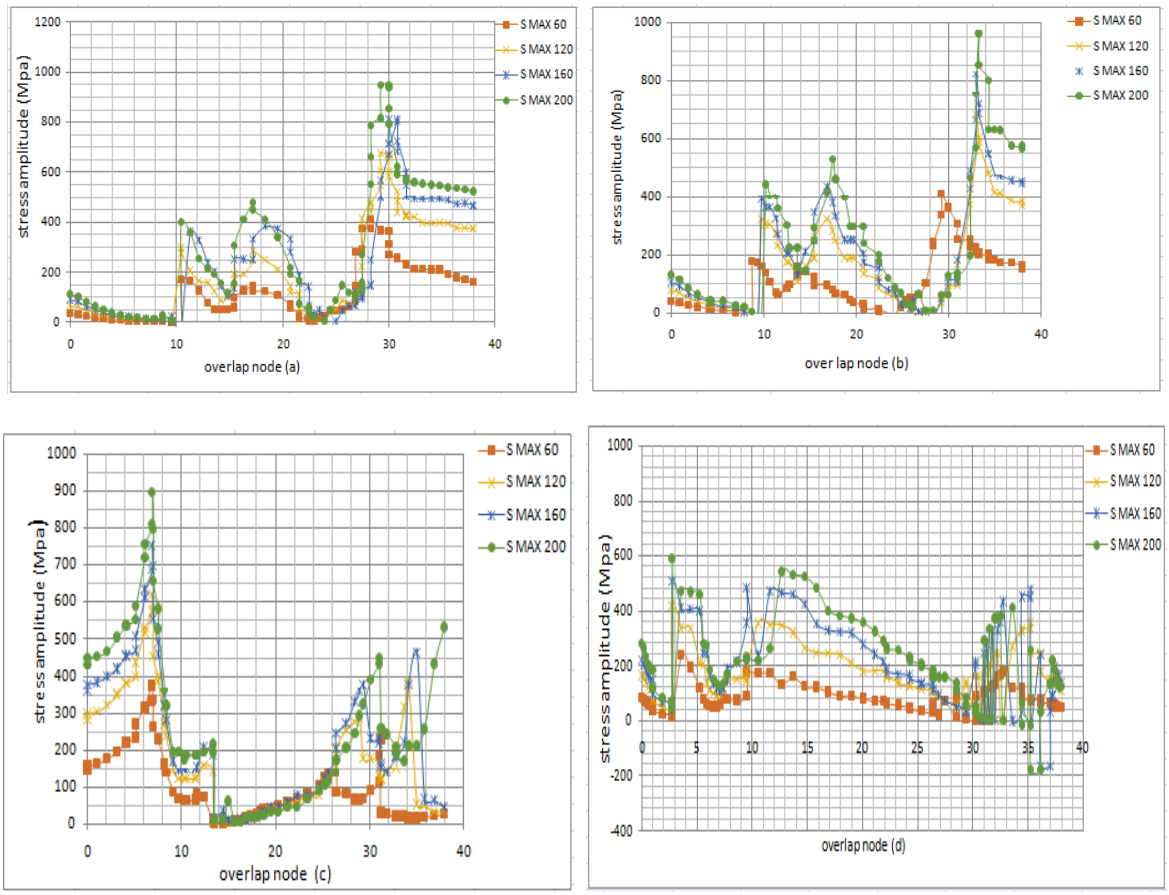


Figure 3. Evolution of the maximum principal stress as a function of the longitudinal overlap nodes for TRIP 800: (a) (x = 120), (b) (x = 155), (c) (x = 195), (d) (x = 275).

To clearly understand the effect of the applied load and study its influence on the behavior of the TRIP 800 welded plate, we conducted an analysis of the variation of the equivalent stress (maximum principal stress) in the direction perpendicular to the loading (transverse direction) for different load amplitudes: 20, 60, 100, 120, 160, and 200 MPa. The figure illustrates the schematic representation of the transverse direction considered in our study. This axis passes through the midline between the two sheets at the overlap region and crosses both the heat-affected zone and the weld nugget (molten metal). The purpose of creating this axis was to visualize the evolution of the equivalent stress at the contact points between the two plates.

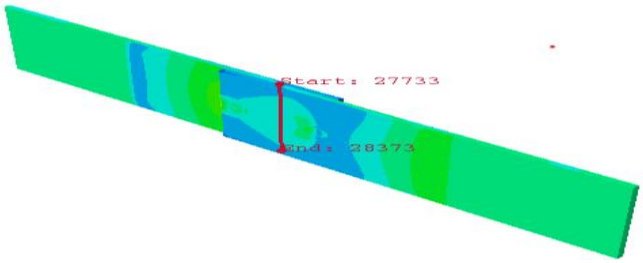


Figure 4. Schematic representation of the transverse direction

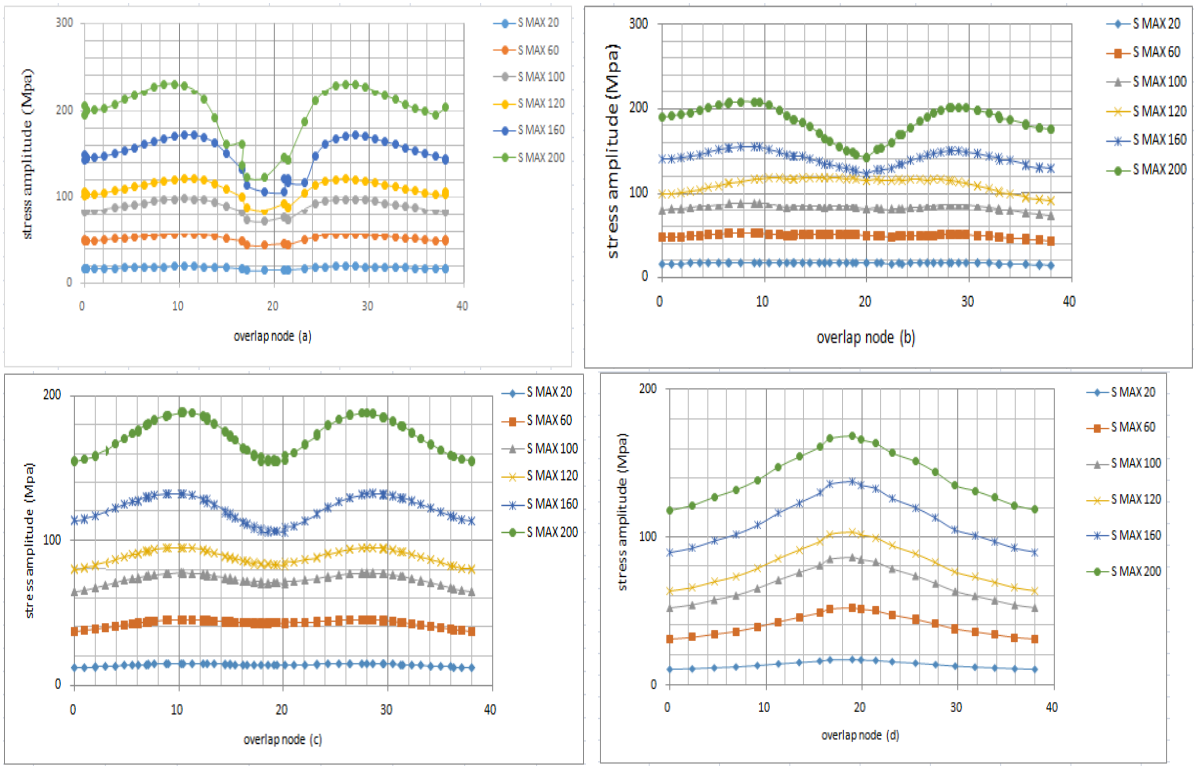


Figure 5. Evolution of the maximum principal stress as a function of the transverse overlap nodes for TRIP 800: (a) (x = 120), (b) (x = 155), (c) (x = 195), (d) (x = 275).

Conclusion

To evaluate the mechanical strength of spot welds in steels used in the automotive industry, we conducted one of the most thorough tests - the shear-tensile test - in order to observe how resistance spot-welded sheets behave as they approach the point of failure. Accordingly, a detailed numerical model was developed using the ABAQUS software, which accurately reproduces the geometric model used in the tensile test. It should be noted that this research focused on studying the behavior of DP450 and DP980 steels in the elastoplastic domain, providing valuable data on their strength and performance when subjected to mechanical stresses. The combination of experimental testing and numerical modeling allows for a more precise estimation of the strength of steel spot welds, contributing to the continuous improvement of vehicle safety and durability. The results obtained allow us to conclude that:

- The stresses increase with the applied load.

- The maximum principal stress and S11 show similar variations.
- As the pitch (spacing) increases, the stress intensity decreases.
- In the case of a longitudinal distribution, the stress increases significantly in the direction of the applied load.
- The contact zones between the base metal, the heat-affected zone (HAZ), and the molten metal always show a noticeable effect on the stress variation, with a peak occurring when passing from one zone to another.
- The histogram results indicate that the heat-affected zone represents the weakest link in the MB–HAZ–WM chain, as it is the first area affected during loading.
- The numerical simulation shows that damage in the base metal starts at around 160 MPa, whereas the heat-affected zone begins to fail at around 100 MPa. Meanwhile, the weld nugget shows no sign of damage for the four models with different spacings (X1, X2, X3, X4).
- The weld metal (WM) exhibits no sign of damage in any of the four welding models.
- The HAZ shows signs of damage starting from 100 MPa, which is due to the low stiffness of this region.
- The weakest area in resistance spot welding remains the heat-affected zone, regardless of the influence of the weld pitch.

Scientific Ethics Declaration

* The authors declare that the scientific ethical and legal responsibility of this article published in EPSTEM journal belongs to the authors.

Conflict of Interest

* The authors declare that they have no conflicts of interest

Funding

* This research received no specific grant from any funding agency in the public, commercial, or not-for-profit sectors.

Acknowledgements or Notes

* This article was presented as a poster presentation at the International Conference on Technology, Engineering and Science (www.icontes.net) held in Antalya/Türkiye on November 12-15, 2025.

* We acknowledge the Ministry of Higher Education and Scientific Research, Algeria, for technical and financial support.

* We acknowledge the support received from faculty of technology of SIDI BEL ABBES and laboratory of mechanics and physics of materials for their financial assistance, which made this research possible.

References

Angeli, E., Wagner, J., Lawrick, E., Moore, K., Anderson, M., Soderland, L., & Brizee, A. (2010, May 5). *General format*. Purdue Online Writing Lab. Retrieved from http://owl.english.purdue.edu/owl/resource/560/01/

Calfee, R. C., & Valencia, R. R. (1991). *APA guide to preparing manuscripts for journal publication*. American Psychological Association.

Cherfi, M., Kaci Djafar, A., Abdelmajid, M., Abderahmane, S., & Ghermaoui, I. M. A. (2024). Numerical study of tensile-shear fracture behaviour of resistance spot welded sheet steel with DP 450 and DP 980. *Acta Mechanica Slovaca, 28*(4), 14-24.

Dancette, S. (2009). *Comportement mécanique des soudures par points: Mécanismes et stratégies de prédiction dans le cas des tôles en acier pour automobile* (Doctoral dissertation). École Doctorale Matériaux de Lyon.

Guzel, M., Goktas, M., Acarer, M., & Demir, B. (2023). Finite element modelling of the fatigue damage in an explosive welded Al-dual-phase steel. *Materials Testing, 65*(5), 787–801.

Lebbal, H. (2016). *Analyse expérimentale et modélisation du comportement thermodynamique des aciers inoxydables et dual phase: Application au procédé du soudage par résistance par point* (Doctoral dissertation). Université Mouloud Mammeri de Tizi Ouzou.

Rajalingam, P., Rajakumar, S., Balasubramanian, V., Sonar, T., & Kavitha, S. (2023). Tensile shear fracture load bearing capability, softening of HAZ and microstructural characteristics of resistance spot welded DP-1000 steel joints. *Materials Testing, 65*(1), 94–110.

Wang, J., Wang, H. P., Lu, F., Carlson, B. E., & Sigler, D. R. (2015). Analysis of Al-steel resistance spot welding process by developing a fully coupled multi-physics simulation model. *International Journal of Heat and Mass Transfer, 89*, 1061–1072.

Author(s) Information

Cherfi Mohamed
University of SidiBel Abbes, BP 89, cite Ben M'hidi, SidiBel Abbes, 22000, Algeria
Contact e-mail: *Mouh_cherfi@hotmail.fr*

Reffas Sid Ahmad
University of Sidi Bel Abbes, BP 89, cite Ben M'hidi, SidiBel Abbes, 22000, Algeria

Sahli Abderahmane
University of Sidi Bel Abbes, BP 89, cite Ben M'hidi, SidiBel Abbes, 22000, Algeria

Moulgada Abdelmajid
University of Sidi Bel Abbes, BP 89, cite Ben M'hidi, SidiBel Abbes, 22000, Algeria

Ghermaoui Mohammed Ilyes
University of Sidi Bel Abbes, BP 89, cite Ben M'hidi, SidiBel Abbes, 22000, Algeria

To cite this article:

Mohamed, C., Sid Ahmad, R., Abderahmane, S., Abdelmajid, M., & Ilyes, G.M. (2025). Numerical analysis of weld spot spacing effects on shear tensile behavior of TRIP 800 steel. *The Eurasia Proceedings of Science, Technology, Engineering and Mathematics (EPSTEM), 38,* 115-120.

The Eurasia Proceedings of Science, Technology, Engineering & Mathematics (EPSTEM)
ISSN: 2602-3199

The Eurasia Proceedings of Science, Technology, Engineering and Mathematics (EPSTEM), 2025

Volume 38, Pages 121-134

IConTES 2025: International Conference on Technology, Engineering and Science

Performance Improvement of Predictive Direct Power Control of a Unified Power Quality Conditioner

Noureddine Khenfar
Djillali Liabes University of Sidi Bel-Abbes

Abdelhafid Semmah
Djillali Liabes University of Sidi Bel-Abbes

Abstract: This paper presents an analysis and comparison of classical Direct Power Control (DPC) and Predictive Direct Power Control (P-DPC) strategies applied to the parallel side of a Unified Power Quality Conditioner (UPQC). Classical DPC is known for its simplicity and direct control of active and reactive power but has limitations in harmonic suppression and dynamic response under varying grid conditions (Chaoui et al., 2008 ; Gui et al., 2020 ; Zhao et al., 2019). The P-DPC strategy overcomes these challenges by predicting system behavior and optimizing control actions via a cost function, resulting in faster dynamic responses, enhanced harmonic mitigation, and improved power quality. On the series side, an adaptive hysteresis control method is combined with a synchronous reference frame identification technique. This dynamically adjusts the hysteresis band to ensure precise voltage compensation and reduce switching losses. Additionally, a fuzzy logic controller regulates the DC-link voltage, maintaining stable operation during transient and steady-state conditions. Simulation results demonstrate that P-DPC significantly outperforms classical DPC in harmonic suppression. Moreover, adaptive hysteresis control on the series active filter further improves voltage compensation, reducing total harmonic distortion (THD) compared to fixed-band hysteresis. The fuzzy logic controller offers robust DC-link voltage regulation, enhancing stability during disturbances. The integration of P-DPC on the shunt converter, adaptive hysteresis control on the series one, and fuzzy logic regulation of the DC-link voltage collectively demonstrate superior performance in harmonic mitigation, reactive power compensation, and voltage stabilization. These findings highlight the potential of predictive control techniques combined with intelligent controllers to achieve optimal power quality in modern electrical systems.

Keywords: Predictive direct power control, Unified power quality conditioner, Adaptive hysteresis control, Synchronous reference fuzzy logic controller

Introduction

In recent years, the increasing complexity of electrical networks and the widespread integration of nonlinear loads have significantly impacted power quality (PQ). Issues such as harmonic distortions, voltage sags, swells, and imbalances have become critical challenges for modern power systems. These disturbances can lead to equipment malfunctions, reduced efficiency, and financial losses in industrial and residential applications. To address these challenges, the Unified Power Quality Conditioner (UPQC) has emerged as a versatile solution capable of simultaneously mitigating voltage and current-related PQ problems (Swarna Latha et al., 2020).

The UPQC combines two active filters: a parallel active filter (FAP) that compensates for current harmonics and reactive power and a series active filter (FAS) that addresses voltage disturbances such as sags, swells, and harmonics. Both filters are interconnected through a common DC-link, which plays a crucial role in maintaining the stability and performance of the system. The effectiveness of the UPQC largely depends on the control strategies employed for its active filters (Das et al., 2023 ; Salim et al., 2013 ; Tripathi et al., 2016).

- This is an Open Access article distributed under the terms of the Creative Commons Attribution-Noncommercial 4.0 Unported License, permitting all non-commercial use, distribution, and reproduction in any medium, provided the original work is properly cited.

- Selection and peer-review under responsibility of the Organizing Committee of the Conference

© 2025 Published by ISRES Publishing: www.isres.org

The Direct Power Control (DPC) technique has gained popularity for its simplicity and fast dynamic response in controlling active and reactive power. Derived from the Direct Torque Control (DTC) method used in electrical machines, DPC eliminates the need for internal current control loops, making it suitable for power quality applications. However, classical DPC suffers from limitations such as uncontrolled switching frequency and reduced performance under distorted or unbalanced grid conditions. These drawbacks necessitate advanced control strategies to enhance the UPQC's capabilities (Gui et al., 2018 ; Rath et al., 2024 ; Trivedi et al., 2024).

On the FAS side, an adaptive hysteresis current control strategy is implemented using a synchronous reference frame identification method. This approach dynamically adjusts the hysteresis band to ensure precise voltage compensation while reducing switching losses. Additionally, a fuzzy logic controller is integrated into the UPQC system to regulate the DC-link voltage, ensuring stable operation under transient and steady-state conditions.

The primary objective of this work is to evaluate and compare the performance of classical DPC and P-DPC strategies applied to the FAP while demonstrating the effectiveness of adaptive hysteresis control on the FAS. The proposed control strategies aim to improve harmonic suppression, reactive power compensation, voltage regulation, and overall system stability.

Proposed Control Diagram for the UPQC

The Unified Power Quality Conditioner (UPQC) is a hybrid compensating device that integrates a shunt active power filter (APF) and a series active power filter (APF), both connected through a common DC-link. The shunt APF mitigates current-related problems such as harmonic distortion and reactive power, whereas the series APF compensates for voltage disturbances including sags, swells, and voltage harmonics. Operating in coordination, both filters maintain sinusoidal source currents and stable, distortion-free load voltages. (Fujita & Akagi, 1998 ; Khadkikar, 2015 ; Kesler & Ozdemir, 2009). The schematic diagram of the studied system, along with the various adopted control approaches, is illustrated in Figure 1.

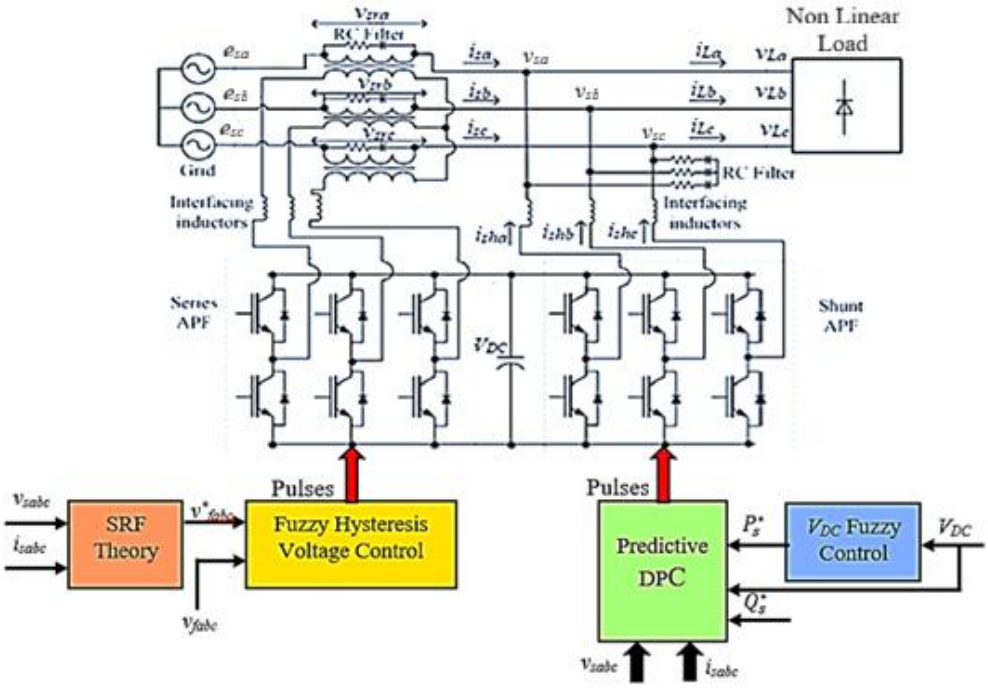


Figure 1. Schematic diagram of the UPQC device

This section outlines the methodology employed for implementing and evaluating the proposed control strategies for the Unified Power Quality Conditioner (UPQC). The study focuses on two key aspects: the application of Predictive Direct Power Control (P-DPC) on the parallel active filter (FAP) and an adaptive hysteresis current control strategy on the series active filter (FAS). The methods are designed to enhance power quality by mitigating harmonics, regulating voltage, and maintaining system stability under various operating conditions.

Predictive Direct Power Control (P-DPC) for the Parallel Side of the UPQC

Predictive Direct Power Control (P-DPC) has emerged as an advanced control strategy for the parallel side of the Unified Power Flow Controller (UPFC), enabling precise and dynamic regulation of active and reactive power. Unlike classical control methods, P-DPC uses a predictive model to anticipate system behavior and optimize switching actions (Figure 2), resulting in enhanced harmonic mitigation, faster dynamic response, and improved power quality. Recent studies have demonstrated the efficacy of P-DPC in improving UPFC performance under varying grid conditions (Bekakra, 2021 ; Nishad et al., 2024 ; Wang et al., 2024).

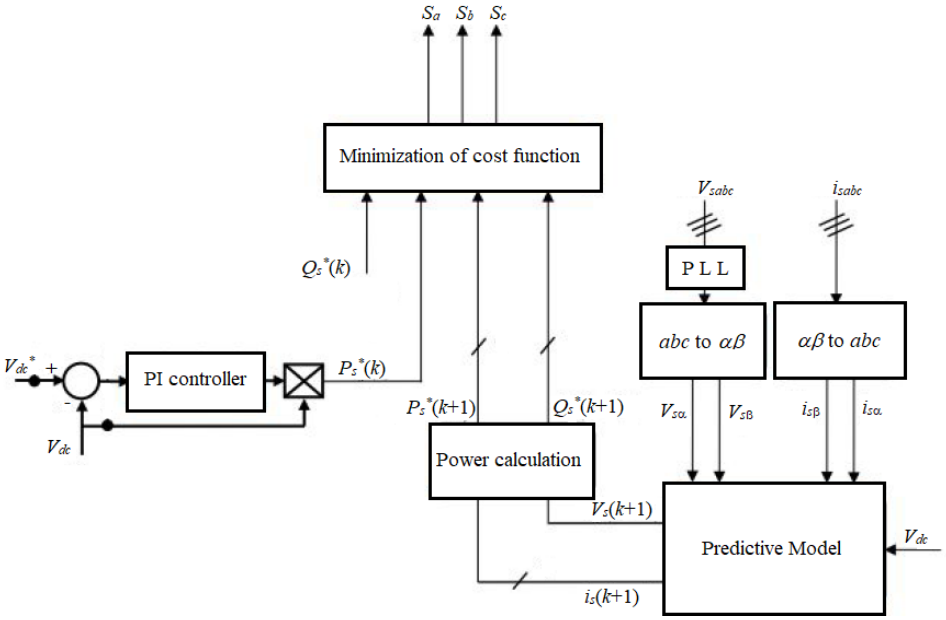


Figure 2. Schematic diagram of the predictive DPC technique

The reference for the active power P^*_s is generated by the outer loop of the DC-link voltage control through an anti-windup regulator. The reactive power reference Q^*_s, is externally provided and maintained at zero to ensure unity power factor operation. Assuming the DC-link voltage tracking error remains constant over two consecutive sampling periods, the instantaneous active power reference at the next sampling instant can be predicted using linear extrapolation, as illustrated in Figure 3.

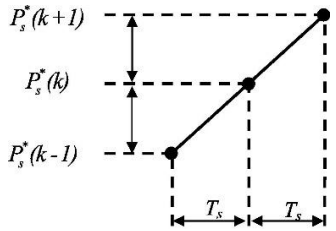


Figure 3. Estimation of predictive value of instantaneous active power reference.

The P-DPC strategy relies on a predictive model of the parralel converter to forecast system behavior and optimize control actions. The dynamic behavior of the source current is described by the following differential equation:

$$\frac{d}{dt}[i_s] = -\frac{R_s}{L_s}[i_s] + \frac{1}{L_s}([e_s] - [V_s]) \quad (1)$$

Where:

- $[e_s]$: Source back-emf vector,
- $[i_s]$: Source current vector,
- $[V_s]$: Inverter voltage vector,
- R_s and L_s represent source resistance and inductance respectively.

The discrete-time model predicts the next source current value at time step (k+1) using measured voltages and currents from the current sampling instant (k). The time derivative of the source current, $d[i_s]/dt$, is approximated

using a forward Euler method as follows (Bekakra et al., 2021):

$$\frac{di_s}{dt} \approx -\frac{i_s(k+1)-i_s(k)}{T_s} \tag{2}$$

The source current at the next time step (k+1) is predicted as follows:

$$[i_s(k+1)] = \left(1 - \frac{T_s R_s}{L_s}[i_s(k)]\right) + \frac{T_s}{L_s}([e_s(k)] - [V_s(k)]) \tag{3}$$

Where T_s is the sampling time..

Active and Reactive Power Formulation

The predicted active (P_s) and reactive (Q_s) powers are calculated using:

$$P_s(k+1) = \mathrm{Re}\left[\mathrm{conj}\left(i_s(k+1)\right)V_s(k+1)\right] \tag{4}$$

$$Q_s(k+1) = \mathrm{Im}\left[\mathrm{conj}\left(i_s(k+1)\right)V_s(k+1)\right] \tag{5}$$

Where:

$$i_s = \sqrt{i_{s\alpha}^2 + i_{s\beta}^2} \tag{6}$$

and,

$$V_s = \sqrt{V_{s\alpha}^2 + V_{s\beta}^2} \tag{7}$$

$i_{s\alpha}$, $i_{s\beta}$ and $V_{s\alpha}$, $V_{s\beta}$ are source currents and voltages in $\alpha\beta$ frame, respectively, and are given by:

$$\begin{bmatrix} i_{s\alpha} \\ i_{s\beta} \end{bmatrix} = \sqrt{\frac{2}{3}} \begin{bmatrix} 1 & -\frac{1}{2} & -\frac{1}{2} \\ 0 & \frac{\sqrt{3}}{2} & -\frac{\sqrt{3}}{2} \end{bmatrix} \begin{bmatrix} i_{sa} \\ i_{sb} \\ i_{sc} \end{bmatrix} \tag{8}$$

$$\begin{bmatrix} V_{s\alpha} \\ V_{s\beta} \end{bmatrix} = \sqrt{\frac{2}{3}} \begin{bmatrix} 1 & -\frac{1}{2} & -\frac{1}{2} \\ 0 & \frac{\sqrt{3}}{2} & -\frac{\sqrt{3}}{2} \end{bmatrix} \begin{bmatrix} V_{sa} \\ V_{sb} \\ V_{sc} \end{bmatrix} \tag{9}$$

Cost Function Optimization

To determine the optimal switching state of the inverter, a cost function is minimized at each sampling interval:

$$g_i = |P_s^*(k) - P_s(k+1)_i| + |Q_s^*(k) - Q_s(k+1)_i| \tag{10}$$

Where P^*_s and Q^*_s are reference active and reactive powers, respectively, and i = 0,1,2,...,6 represents possible switching states. The switching state that minimizes this cost function is applied to the inverter, ensuring accurate tracking of power references.

Adaptive Hysteresis Voltage Control

The UPQC employs an adaptive hysteresis voltage control strategy, on his series side, combined with a synchronous reference frame (SRF) identification method. The SRF transforms three-phase voltages (V_a,V_b,V_c) into a rotating dqo frame using Park's transformation. This method isolates fundamental components for precise voltage compensation.

The adaptive hysteresis control, shown by Figure 4, dynamically adjusts the hysteresis band based on system conditions to ensure consistent performance. Unlike fixed-band hysteresis control, this method reduces switching losses while maintaining accurate tracking of reference currents (Khenfar et al., 2021).

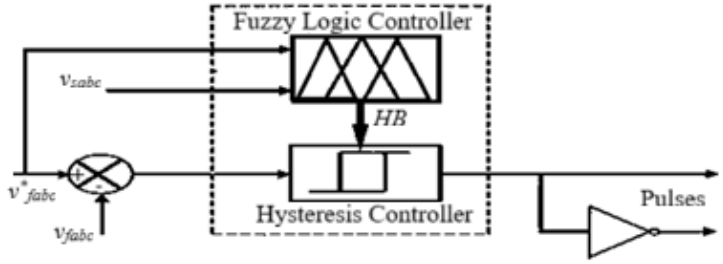


Figure 4. Schematic diagram of the fuzzy hysteresis control

Five triangular membership functions (NL, NM, AZ, PM, PL) define the input and output variables, and 25 fuzzy rules form the inference matrix (Table 1).

Table1. Inference rules of the fuzzy hysteresis controller

dvf∗/dt\vs	**NL**	**NM**	**AZ**	**PM**	**PL**
NL	NL	NL	NL	NM	AZ
NM	NL	NL	NM	AZ	PM
AZ	NL	NM	AZ	PM	PL
PM	NM	AZ	PM	PL	PL
PL	AZ	PM	PL	PL	PL

N: Negative; P: Positive; AZ: Approximately Zero; L: Large; M: Medium.

The switching logic is defined as:

- Upper switch ON if $v_{fa} > v^*_{fa} + HB(t)$,
- Lower switch ON if $v_{fa} < v^*_{fa} - HB(t)$,

where $HB(t)$ is the adaptive hysteresis band width.

DC-Link Voltage Regulation with Fuzzy Logic Controller

A fuzzy logic controller (FLC) is implemented to regulate the DC-link voltage shared by FAP and FAS. The controller operates in real time to adaptively adjust control actions based on input error ($e=V^*_{DC}-V_{DC}$) and its derivative ($\Delta e=e(t)-e(t-1)$). This ensures stable operation under varying load conditions and grid disturbances. Seven triangular membership functions are adopted, with the inference rules organized in Table 2.

Table 2. Inference Table of the DC voltage controller

dif∗/dt \ vs	**NL**	**NM**	**NS**	**AZ**	**PS**	**PM**	**PL**
NL	NL	NL	NL	NL	NM	NS	AZ
NM	NL	NL	NL	NM	NS	AZ	PS
NS	NL	NL	NM	NS	AZ	PS	PM
AZ	NL	NM	NL	AZ	PS	PM	PL
PS	NM	NS	AZ	PS	PM	PL	PL
PM	NS	AZ	PS	PM	PL	PL	PL
PL	AZ	PS	PM	PL	PL	PL	PL

N: Negative; P: Positive; AZ: Approximately Zero; L: Large; M: Medium; S: Small.

Results and Discussion

The effectiveness of the proposed control techniques was evaluated through simulation in the MATLAB/Simulink environment. To demonstrate the UPQC's capability to simultaneously compensate for both current and voltage disturbances, various operating scenarios are considered. These scenarios involved source voltage disturbances, including sags, overvoltages, and harmonic distortions (Figure 5), as well as nonlinear loads drawing distorted currents. Such nonlinear loads are also subject to abrupt variations in their operating conditions.

Thus, multiple control strategies are combined to enhance the filtering performance of the UPQC. Predictive DPC is employed to determine the switching instants of the parallel converter, while fuzzy hysteresis control is adopted

for the series converter, with harmonic identification in this branch achieved using the SRF technique. The regulation of active power exchange between the UPQC and the grid is ensured by introducing a fuzzy logic controller within the DC-link voltage regulation loop.

The current waveform absorbed by the nonlinear load and its corresponding frequency spectrum are presented in Figure 6. The current drawn by the nonlinear load contains substantial harmonic components, leading to a Total Harmonic Distortion (THD) of 27.24% in the source current before filtering.

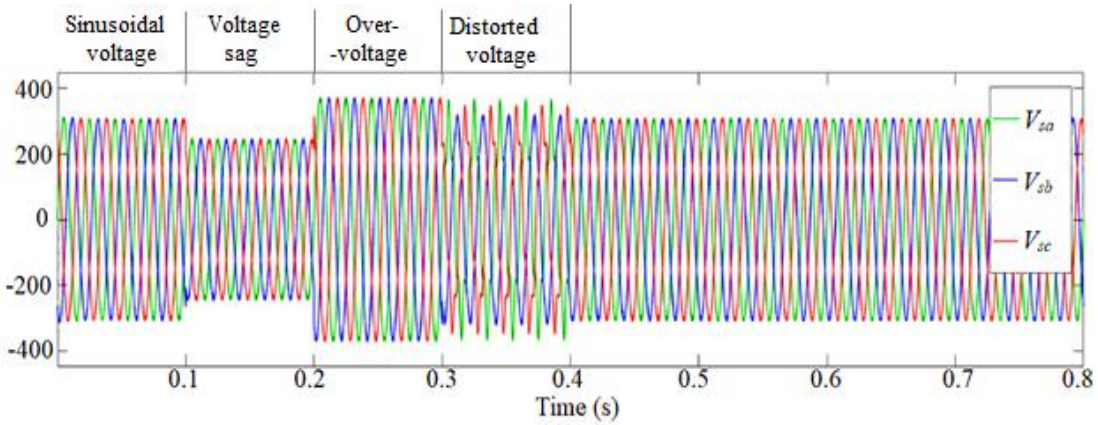


Figure 5. Source voltage waveform for four fault scenarios.

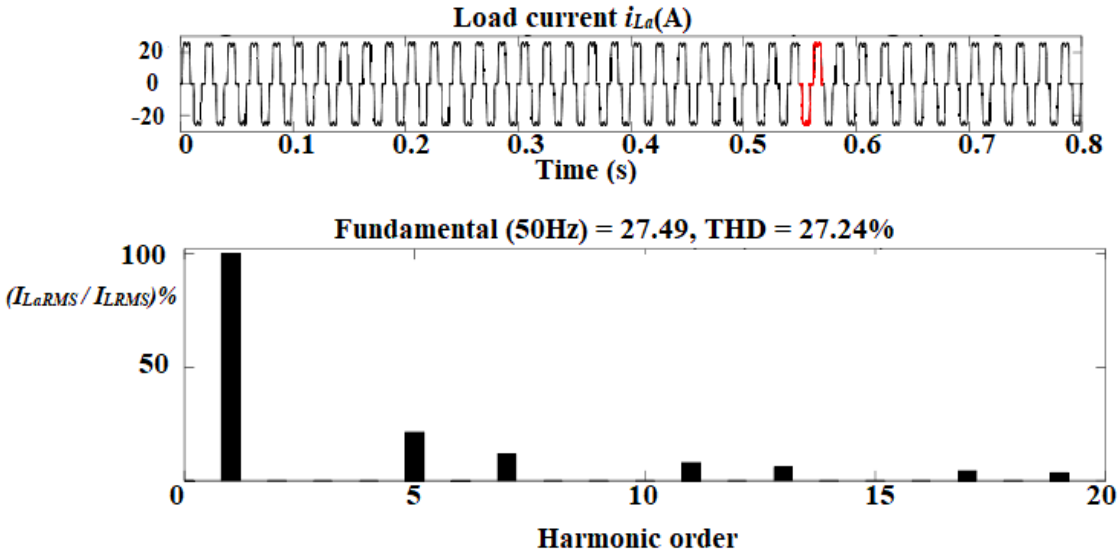


Figure 6. Waveform of the current drawn by the nonlinear load with its spectral representation.

Performance Without DC Voltage Variation

Harmonic Currents Compensation

With the application of classical Direct Power Control (DPC), the source current waveform improves somewhat, yet it retains visible oscillations and distortions, particularly following voltage perturbations (Figure 7). The harmonic spectrum shows a reduction in THD to 8.90% (Figure 8), but this value still exceeds the universally accepted IEEE Std 519-1992 limit of 5%. Consequently, power quality is improved but remains suboptimal.

The adoption of predictive DPC greatly enhances performance. After filtering, the source current waveform is noticeably smoother and rapidly regains its sinusoidal shape (Figure 9), even after aggressive grid disturbances. The corresponding harmonic spectrum shows a dramatic reduction in THD to 3.79%, well within international standards. This result demonstrates the superior filtering capability and dynamic response of the P-DPC scheme, allowing the UPQC to deliver clean supply currents despite the presence of nonlinear loads and network events.

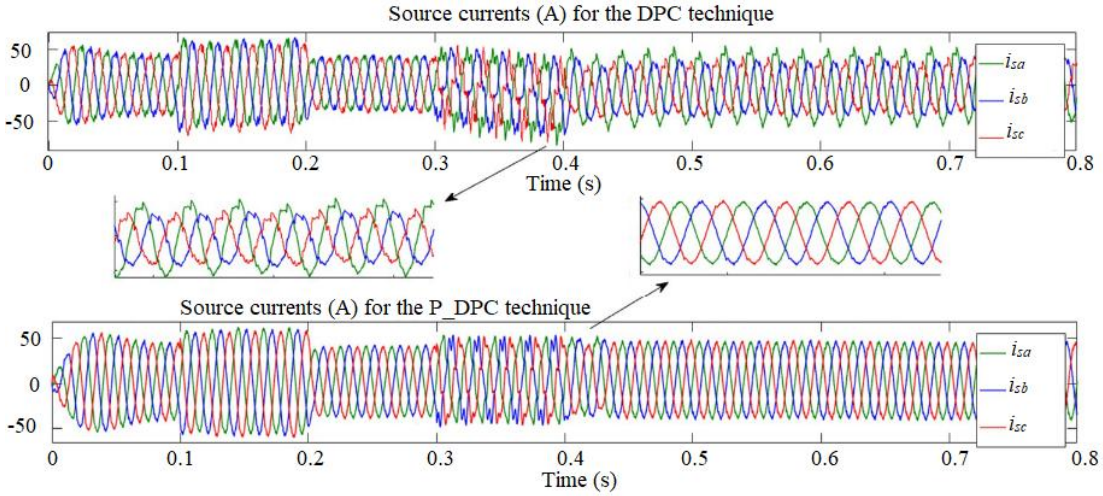


Figure 7. Waveforms of the UPF Source currents with classical DPC and P-DPC techniques

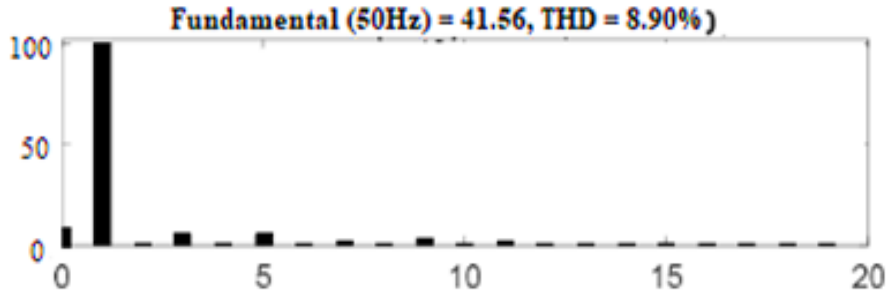


Figure 8. Spectral representation of the UPQC source current using classical DPC technique

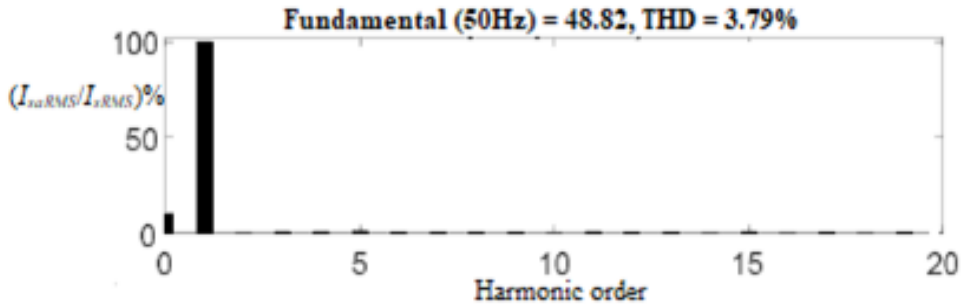


Figure 9. Spectral representation of the UPQC source current using predictive DPC technique

DC-Link Voltage Stability

Figures (10-13) show how the DC-link voltage evolves for different control approaches (Fuzzy, PI) under classical DPC and predictive P-DPC, both with and without step DC voltage changes. When there is no step DC voltage variation, all controllers tend to stabilize the voltage, but the Fuzzy controller reaches steady-state faster and with less overshoot compared to the PI controller, making the system more resilient to disturbances and improving overall stability (Figure 10).

Under step variations, the Fuzzy controller again outperforms the PI, quickly restoring the DC voltage with fewer oscillations and a shorter settling time (Figure 12). The use of predictive DPC technique generally enhances performance further, especially under dynamic conditions (Figure 11 and 13), showing that combining predictive control with fuzzy logic can yield a robust and adaptive compensation system for the UPQC. These results indicate that advanced controllers not only maintain stable DC voltage, but also help safeguard sensitive loads and ensure reliable operation under demanding, real-world scenarios.

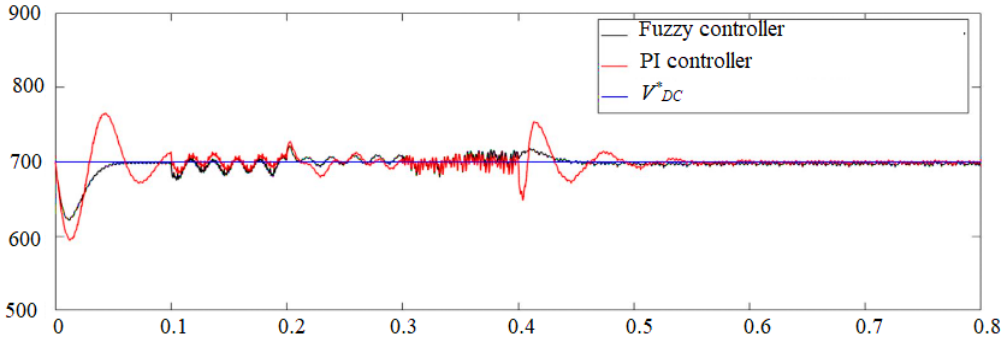


Figure 10. DC voltage behavior for classical DPC technique without step DC voltage variation

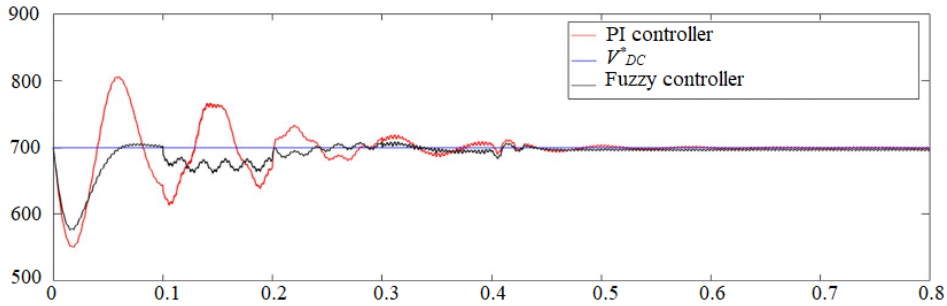


Figure 11. DC voltage behavior for predictive DPC technique without step DC voltage variation

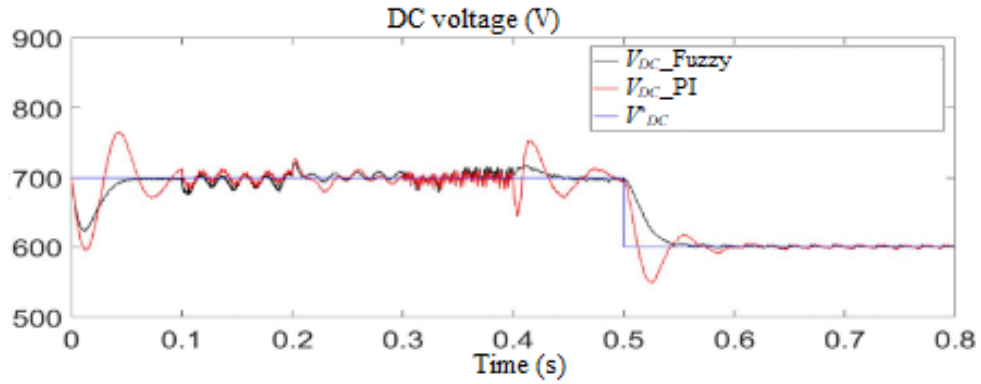


Figure 12. DC voltage behavior for classical DPC technique with step DC voltage variation

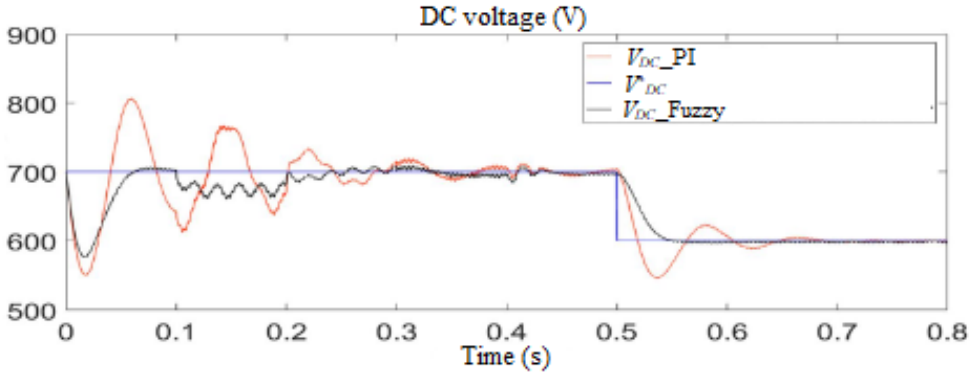


Figure 13. DC voltage behavior for predictive DPC technique with step DC voltage variation.

Active and Reactive Power Behavior

Figures 14 to 16 illustrate the dynamic behavior of the active power for both classical and predictive DPC techniques using PI and fuzzy controllers, with and without step DC voltage variation. In scenarios without step changes, the fuzzy controller delivers faster convergence and reduced oscillations compared to the PI controller

(Figure 14 and 15), reflecting superior adaptability and robustness. When abrupt changes occur, predictive DPC technique combined with fuzzy logic maintains a more stable and resilient active power response, quickly damping transients and minimizing overshoot (Figuref 16). Overall, integrating fuzzy logic in the control system noticeably enhances the UPQC's ability to regulate active power, especially under challenging and variable grid conditions.

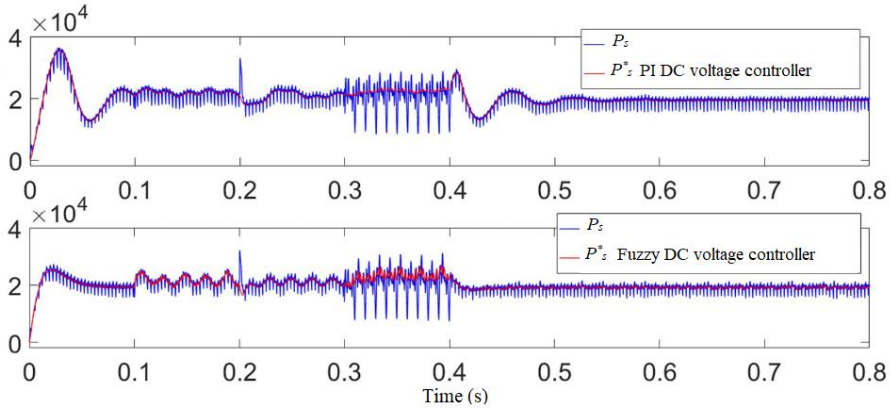


Figure 14. Active power behaviors for classical DPC technique without DC voltage variation

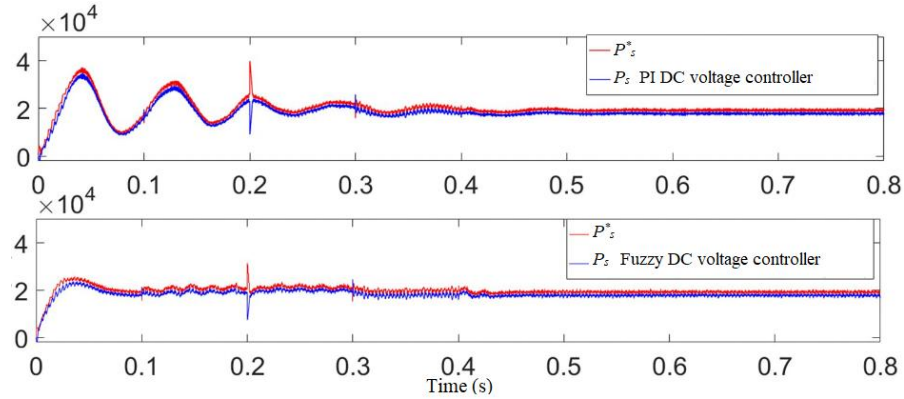


Figure 15. Active power behaviors for predictive DPC without DC voltage variation

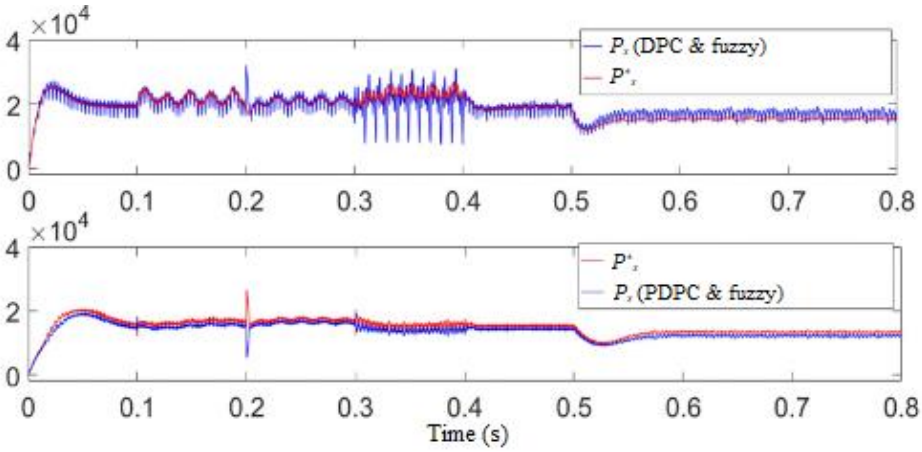
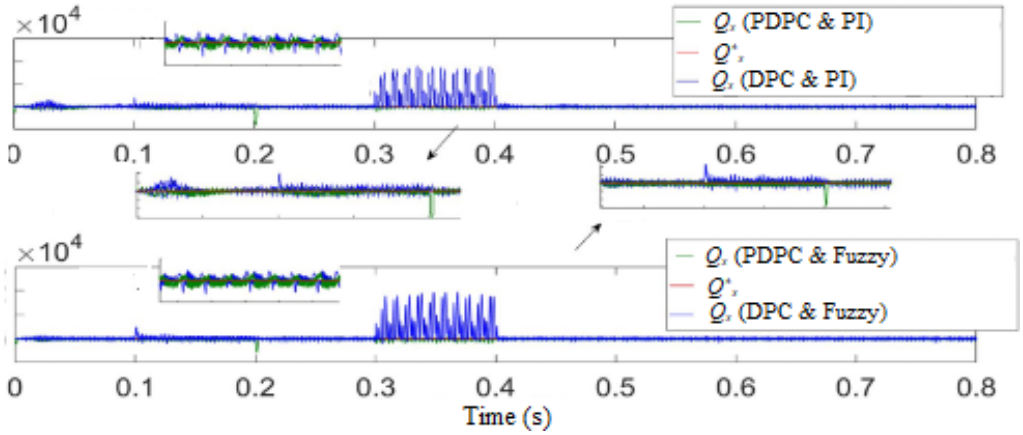


Figure 16. Active power behaviors for classical & predictive DPC with step DC voltage variation

The results in Figures 17 and 18 provide a detailed view of the reactive power response using both PI and fuzzy controllers within classical and predictive DPC schemes, under conditions with and without step variations. Without step variation, both control strategies (PI and fuzzy) are capable of maintaining the reactive power close to the reference, with the fuzzy controller generally demonstrating reduced oscillations and a more stable tracking performance (Figure 17). This indicates that fuzzy logic enhances the controller's ability to reject small disturbances and adapt to system uncertainties. When a step variation is introduced, the reactive power experiences larger transients, especially for the PI controller, which shows significant overshoot and prolonged oscillations before settling. By contrast, the fuzzy controller (and especially its combination within the predictive

DPC strategy) manages the transient more effectively, displaying quicker damping and more rapid return to steady-state (Figure 18).

In summary, these results illustrate that integrating fuzzy logic in the UPQC's DPC improves robustness and dynamic performance, allowing the system to better manage abrupt load or source changes and provide high-quality compensation. This ensures stable voltage conditions and reduced stress on electrical equipment, which is essential for maintaining reliable grid operation.



Figuref 17. Reactive power behaviors without step DC voltage variation

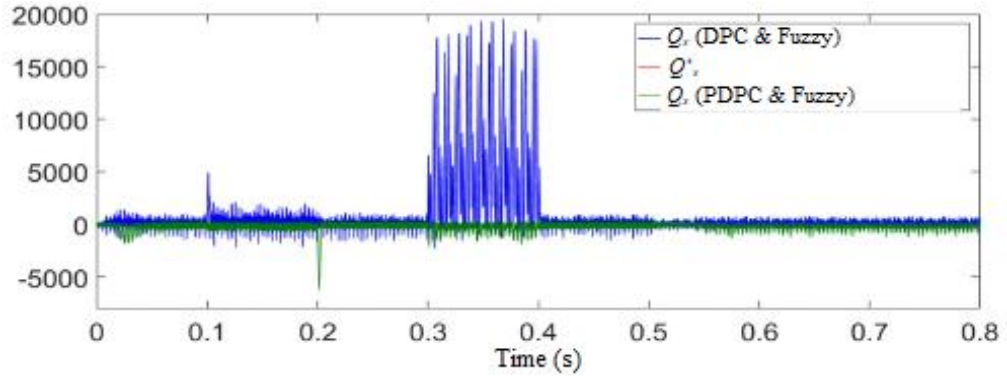


Figure 17. Reactive power behaviors with step DC voltage variation

Adaptive Fuzzy Hysteresis Control for Series Filter (FAS)

Harmonic Voltage Compensation

Figures 18 to 22 display the behavior of the load voltage after filtering using both fixed and fuzzy-band hysteresis for P-DPC control, along with their associated spectral representation. The waveforms show that fuzzy logic hysteresis controllers deliver a smoother and more stable load voltage, effectively tracking the sinusoidal reference even during periods with disturbances or switching events. Compared to fixed hysteresis, the fuzzy-band approach adapts better to dynamic system changes, reducing voltage spikes and oscillations that could impact sensitive loads (Figure 18).

The harmonic spectrum analysis confirms this benefit: the source voltage under various disturbances shows a high THD equal to 15.76% (Figure 20), while the load voltage, with compensation and fuzzy-band hysteresis, achieves a much lower THD of around 3.13% (Figure 22). This substantial reduction in harmonic content ensures not only better power quality but also extended equipment life and improved operational reliability.

Ultimately, these results highlight the effectiveness of integrating fuzzy logic into the hysteresis control loop of the UPQC's series converter, particularly under predictive DPC, to deliver high-quality, disturbance-resilient voltage to the load, even under severe grid perturbations.

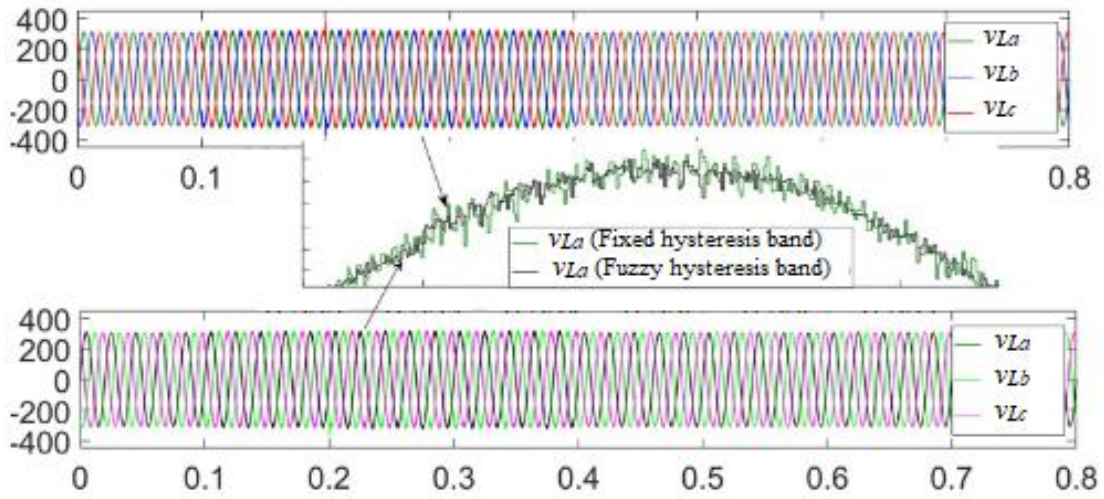


Figure 18. Waveforms of the load voltage after filtering with fixed hysteresis and fuzzy band hysteresis for P-DPC control with fuzzy logic controller.

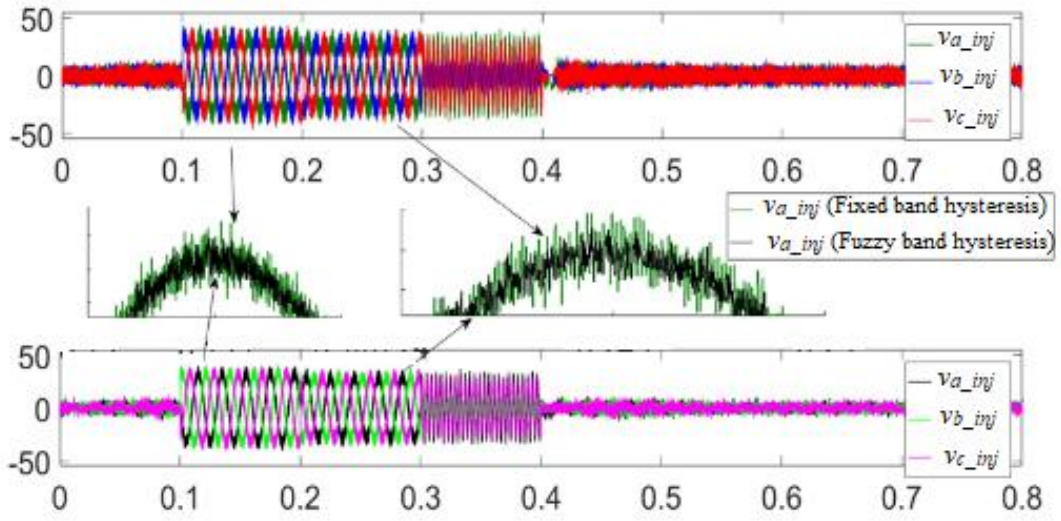


Figure 19. Waveform of the injected voltage with fixed hysteresis and fuzzy-band hysteresis for P-DPC control and fuzzy logic controller

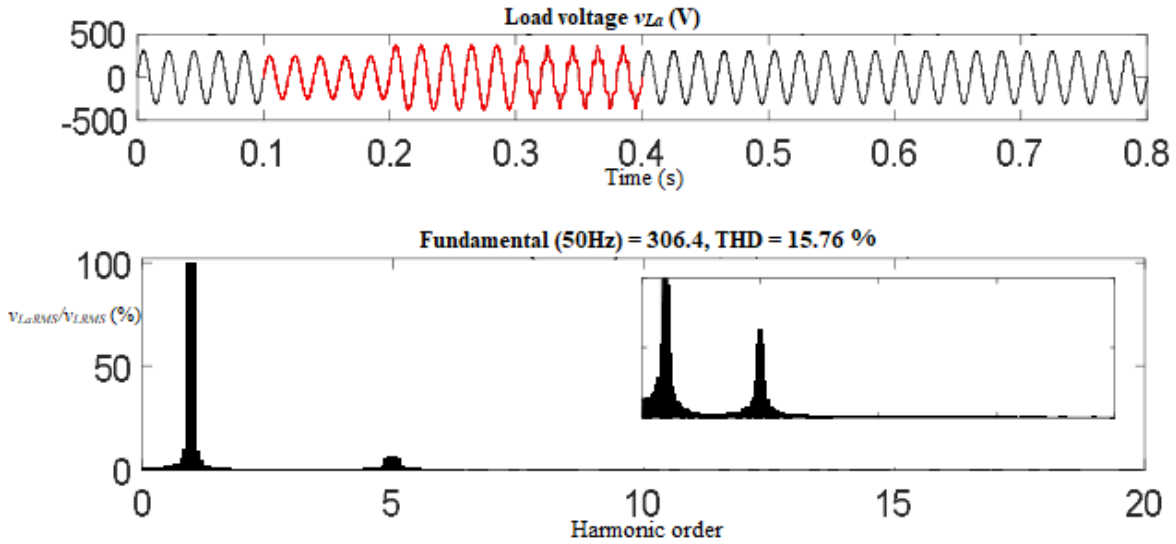


Figure 20. Spectral representation of the Source Voltage Representing Different Disturbances

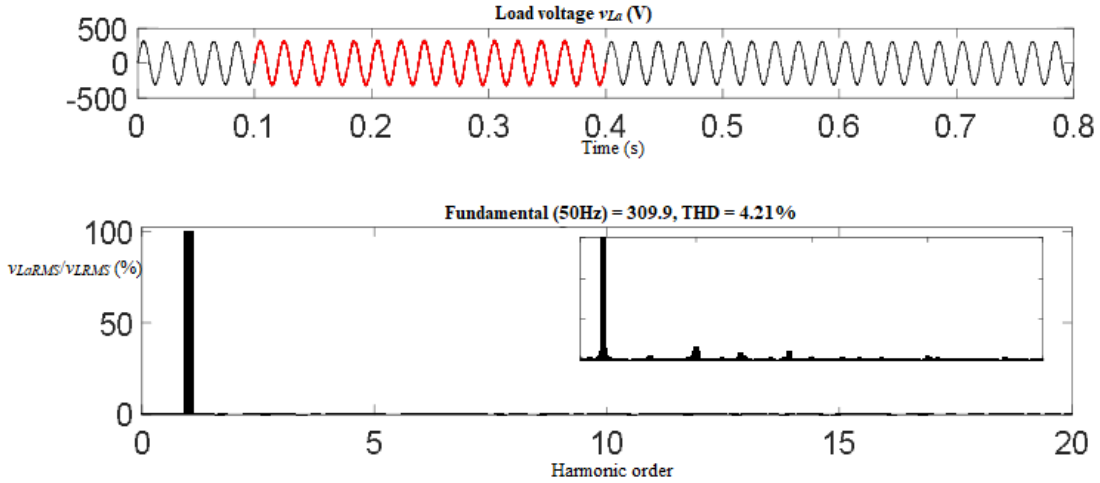


Figure 21. Spectral representation of the load voltage based on fixed-band hysteresis control

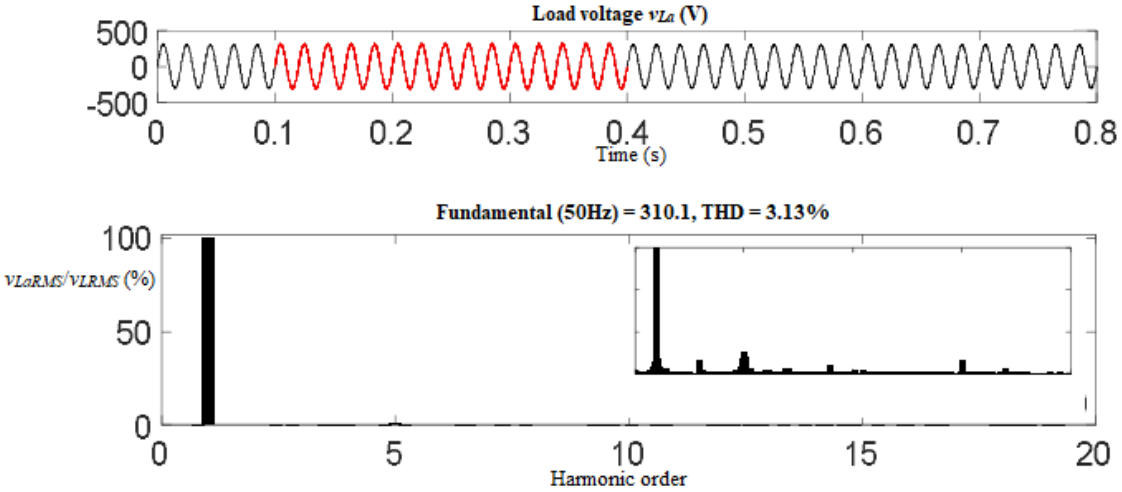


Figure 22. Spectral representation of the load voltage based on fuzzy-band hysteresis control

Conclusion

The simulation results presented in this work highlight the substantial benefits of integrating predictive direct power control (PDPC) with fuzzy logic controllers for the Unified Power Quality Conditioner (UPQC).

The Predictive DPC technique shows strong capabilities in anticipating system dynamics, delivering timely and precise switching actions for the parallel converter, enabling it to respond rapidly to power quality disturbances such as sags, overvoltages, and harmonic distortions. When the Predictive DPC technique is combined with fuzzy logic control, particularly in the regulation of the DC-link voltage and active/reactive power exchanges, the results obtained demonstrate a remarkable boost in tracking accuracy, transient speed, and overall robustness-surpassing the performance of classical PI-based approaches.

Furthermore, incorporating a fuzzy inference system into the hysteresis control of the series converter brings an additional layer of intelligence and adaptability. The fuzzy-band hysteresis method dynamically adjusts control boundaries based on real-time system changes, resulting in more stable load voltage waveforms, a dramatic reduction in voltage and current oscillations, and consistently lower total harmonic distortion (THD). These improvements are especially evident under abrupt load changes or complex grid disturbances, where classical fixed-band methods often struggle.

Overall, the proposed combination of PDPC, fuzzy logic, and fuzzy hysteresis control achieves not only compliance with the most demanding power quality standards but also ensures highly reliable and resilient power delivery in today's challenging and evolving grid environments. This hybrid intelligent framework makes the UPQC a powerful, flexible, and future-ready solution for comprehensive power quality management.

Recommendations

The experimental validation of the proposed Predictive Direct Power Control (P-DPC) and adaptive hysteresis control strategies will be extended beyond MATLAB-Simulink simulations through implementation on a physical prototype, thereby enabling the assessment of their applicability and robustness under practical operating conditions. Furthermore, a comprehensive investigation into the effects of these control methodologies on equipment lifespan is warranted, with particular emphasis on the reduction of switching losses and thermal stress, which could inform maintenance scheduling and operational cost optimization. Additionally, it is imperative to evaluate the performance of these control strategies within smart grid environments characterized by the integration of renewable energy sources and increased load variability, thereby addressing contemporary challenges in power system management and ensuring reliable and efficient system operation.

Scientific Ethics Declaration

* The authors declare that the scientific ethical and legal responsibility of this article published in EPSTEM journal belongs to the authors.

Conflict of Interest

* The authors declare that they have no conflicts of interest

Funding

* This research received no specific grant from any funding agency in the public, commercial, or not-for-profit sectors.

Acknowledgements or Notes

* This article was presented as a poster presentation at the International Conference on Technology, Engineering and Science (www.icontes.net) held in Antalya/Türkiye on November 12-15, 2025.

References

Bekakra, Y. (2021). Improved predictive direct power control (PDPC) of three-phase shunt active power filter (SAPF) using metaheuristic methods. *Energy Reports, 7*, 4723–4733.

Bekakra, Y., Zellouma, L., & Malik, O. (2021). Improved predictive direct power control of shunt active power filter using GWO and ALO – Simulation and experimental study. *Ain Shams Engineering Journal*, 12, 3859–3877.

Chaoui, A., Gaubert, J.-P., Krim, F., & Champenois, G. (2008). DPC controlled three-phase active filter for power quality improvement. *Electric Power Systems Research, 78*(10), 1789–1797.

Das, S., Kumar, R., & Sharma, A. (2023). Empirical analysis of power quality using UPQC with hybrid control techniques. *Energy Reports, 9*, 1304–1312.

Fujita, H., & Akagi, H. (1998). The unified power quality conditioner. *IEEE Transactions on Power Electronics, 13*(2), 315–322.

Gui, Y., Xu, Z., & Huang, H. (2018). Improved direct power control for grid-connected voltage source converters. *IEEE Transactions on Industrial Electronics, 65*(7), 5590–5600.

Gui, Y., Xu, Z., & Huang, H. (2020). Voltage modulated direct power control for a weak grid-connected inverter. *IEEE Transactions on Power Electronics, 35*(12), 13115–13126.

Karthikkumar, S., Ramasamy, R., & Selvan, R. (2025). Implementation of adaptive hysteresis current controller in multilevel inverter systems. *Scientific Reports, 15*(1), 8924.

Khadkikar, V. (2015). Enhancing electric power quality using UPQC: A comprehensive overview. *Renewable and Sustainable Energy Reviews, 45*, 443–453.

Kesler, M., & Ozdemir, E. (2009). Simplified control method for unified power quality conditioner. *Renewable Energy & Power Quality Journal, 1*(7), 474–483.

Khenfar, N., Semmah, A., & Kadem, M. (2021). ADALINE harmonics extraction algorithm applied to a shunt active power filter based on an adaptive fuzzy hysteresis current control and a fuzzy DC voltage controller. *Prz. Elektrotechniczny, 97*(5), 116–121.

Khenfar, N., Semmah, A., & Colak, I. (2022). Efficiency of fuzzy PWM control applied to an active filter series under a disturbed voltage source. *Przegląd Elektrotechniczny, 98*(3), 44–49.

Nishad, D. K., Tiwari, A. N., & Khalid, S. (2024). AI-based UPQC control technique for power quality optimization. *Energy AI, 15*, 100311.

Rath, A., Mahapatra, S., & Sahu, R. (2024). Reduced complexity model predictive direct power control for unbalanced grid. *Electric Power Systems Research, 230*, 109892.

Salim, C., Gaouda, A. M., & Salameh, Z. M. (2013). Simplified control scheme of unified power quality conditioner. *Electric Power Systems Research, 97*, 260–267.

Swarna Latha, K., Dasari, S., & Prasad, J. (2020). Power quality enhancements with MC-UPQC optimized with hybrid algorithm in IEEE 33 and IEEE 57 bus system. *Energy Reports, 6*, 378–387.

Tripathi, K. D., Rajesh, A., & Chauhan, L. (2016). Realization of unified power quality conditioner for voltage sag/swell mitigation and harmonic mitigation. *Journal of Electrical Engineering, 16*(4), 45–52.

Trivedi, T., Patel, P., & Shah, K. (2024). Sliding mode-based direct power control of unified power quality conditioner. *IEEE Access, 12*, 14567–14576.

Vahedi, H., Sheikholeslami, A., & Tavakoli, B. (2011). Review and simulation of fixed and adaptive hysteresis current control considering switching losses and high-frequency harmonics. *International Journal of Electrical Power & Energy Systems, 33*(1), 208–215.

Vázquez, G., Rodriguez, P., Ordoñez, R., Kerekes, T., & Teodorescu, R. (2009). Adaptive hysteresis band current control for transformerless single-phase PV inverters. *IEEE Transactions on Power Electronics, 24*(6), 1548–1557.

Zhao, R., Yang, K., Yang, M., & Ma, H. (2019). Harmonic current suppression strategy for grid-connected PWM converters with LCL filters. *IEEE Transactions on Industrial Electronics, 66*(2), 16264–16271.

Author(s) Information

Noureddine Khenfar
Djillali Liabes University of Sidi Bel-Abbes
ICEPS Lab. 22000 Sidi Bel-Abbes, Algeria

Abdelhafid Semmah
Djillali Liabes University of Sidi Bel-Abbes
ICEPS Lab. 22000 Sidi Bel-Abbes, Algeria
Contact e-mail: hafid.semmah@yahoo.fr

To cite this article:

Khenfar, N., & Semmah, A. (2025). Performance improvement of predictive direct power control of a unified power quality conditioner. *The Eurasia Proceedings of Science, Technology, Engineering and Mathematics (EPSTEM), 38,* 121-134.

The Eurasia Proceedings of Science, Technology, Engineering & Mathematics (EPSTEM)
ISSN: 2602-3199

The Eurasia Proceedings of Science, Technology, Engineering and Mathematics (EPSTEM), 2025

Volume 38, Pages 135-142

IConTES 2025: International Conference on Technology, Engineering and Science

Experimental Study of a Cylindrical Electrostatic Precipitator with Real-Time Monitoring Applied to Simulated Smoke

Miloua Farid
Djilalil Liabes University of Sidi Bel Abbes

Redjala Majda
Djilalil Liabes University of Sidi Bel Abbes

Miloua Hadj
Djilalil Liabes University of Sidi Bel Abbes

Rezoug Mohammed
Djilalil Liabes University of Sidi Bel Abbes

Abstract: This paper presents an experimental study of a cylindrical electrostatic precipitator (ESP) equipped with a real-time monitoring system for flue gas treatment. To simulate particulate emissions under controlled conditions, a white smoke generator was used to produce a visible aerosol representing combustion-derived particles. The ESP operates by generating a radial electric field between a central high-voltage electrode and a grounded cylindrical shell, causing the ionized particles to migrate and deposit on the collector surface. Integrated sensors continuously monitor voltage, current, aerosol density, and gas temperature, enabling adaptive control, fault detection, and performance analysis. The cylindrical geometry offers advantages such as compactness, uniform flow distribution, and reduced particle re-entrainment. Experimental results confirm the system's effectiveness in capturing fine particles and demonstrate the value of combining traditional electrostatic filtration with smart monitoring technologies. This setup provides a useful platform for educational purposes, pre-industrial validation, and the development of energy-efficient, automated emission control systems.

Keywords: Electrostatic precipitator (esp), Flue gas treatment, Particulate removal, Air pollution reduction

Introduction

Electrostatic Precipitator (ESP) systems are well-established and widely used technologies in the field of air purification and treatment (Mizono, 2000). These systems operate on the principle of ionizing airborne particles and then collecting them on charged electrodes, allowing for effective removal of particulate pollutants from various airflows, from large industrial facilities to household appliances. ESPs are widely used in air purification. However, existing techniques and common approaches for evaluating their performance face several challenges and limitations (Aouimeur, 2018):

Offline or Post-Operational Evaluation Methods

Many existing systems rely on offline or post-operational methods for performance evaluation, such as collecting and analyzing treated air samples using separate particle measuring devices. These methods do not provide immediate, real-time assessment of the precipitator's performance during operation, making it difficult to identify operational issues or dynamically optimize performance in response to changing conditions.

- This is an Open Access article distributed under the terms of the Creative Commons Attribution-Noncommercial 4.0 Unported License, permitting all non-commercial use, distribution, and reproduction in any medium, provided the original work is properly cited.

- Selection and peer-review under responsibility of the Organizing Committee of the Conference

© 2025 Published by ISRES Publishing: www.isres.org

Monitoring Basic Electrical Parameters (Voltage and Current)

The voltage and current applied to the electrostatic precipitator are monitored as an indicator of its status (Bottner, 2003). Despite their importance for ensuring safe operation, these monitoring methods alone do not provide direct or quantitative information about the actual particle removal efficiency or the level of air purity achieved, but rather only indicate the electrical circuit's condition (Aouimeur, 2018).

Use of Simple Charge Sensors for Downstream Evaluation

Some charge-based sensors are added downstream of the precipitator to attempt to estimate the amount of residual particles or ions (Popa, 2014). These sensors suffer significantly from ionic interference caused by the generation of free ions by the main precipitator (especially at high voltages). This makes it extremely difficult to distinguish between ions and actual particles (Larab, 2024), leading to inaccurate readings regarding true purification effectiveness.

Periodic Maintenance and Visual Inspection for Dust Accumulation

Some systems rely on intermittent visual inspection and scheduled maintenance to remove accumulated dust from collection electrodes (Mizono, 2000). This method is not continuous and cannot predict potential hazards like electrical arcing (flashover) caused by excessive dust buildup in real-time. It also results in significant downtime for cleaning, reducing the system's overall efficiency.

One of the most significant challenges facing current Electrostatic Precipitator (ESP) systems is the absence of an integrated and accurate real-time performance evaluation system (Aouimeur, 2018). This makes it difficult to reliably determine particle removal efficiency, especially given the problem of ionic interference affecting charge-based sensors (Dascalescu, 2025). Additionally, operational challenges resulting from dust accumulation on electrodes increase the risk of electrical discharge (flashover) (Wang, 2016) and necessitate frequent maintenance, thereby limiting the system's overall efficiency and adaptability to diverse operating conditions.

Objective of the Paper

The objective of the paper is to develop an integrated and improved electrostatic precipitator system that incorporates accurate and reliable mechanisms for real-time performance evaluation (Aouimeur, 2018). It aims to overcome the problem of ionic interference to ensure precise particle measurements and to facilitate accurate particle accumulation monitoring to enhance operational continuity and efficiency, while reducing maintenance requirements. This new technique aims to ensure optimal air purification efficiency under various and changing operating conditions.

Method

This method provides a detailed description for implementing the integrated electrostatic precipitation device for real-time performance evaluation, which aims to overcome known challenges in measuring the efficiency of electrostatic precipitators, particularly ionic interference and the effect of dust accumulation on overall performance. This methodology is implemented through the systematic assembly of precise functional units, each playing a crucial role in achieving the ultimate goal of air purification and reliable performance evaluation, as shown in the accompanying illustrative figures depicting the overall system design.

The system construction begins by preparing the particulate-laden airflow source. This is done using a Smoke Generator, a box-shaped device precisely positioned at the inlet of the airflow path, where it introduces a controlled and constant quantity of fine particles into the air stream. This serves to simulate real pollution conditions and acts as a standard source for evaluating the system's performance during testing and verification phases. The experimental setup is designed to evaluate the electrostatic filtration system and the innovative Particle Electrostatic Sensor (PES), with a focus on analyzing particle charge behavior and filtration efficiency under varying airflow and voltage conditions. Below is a detailed description of each component used in the test bench.

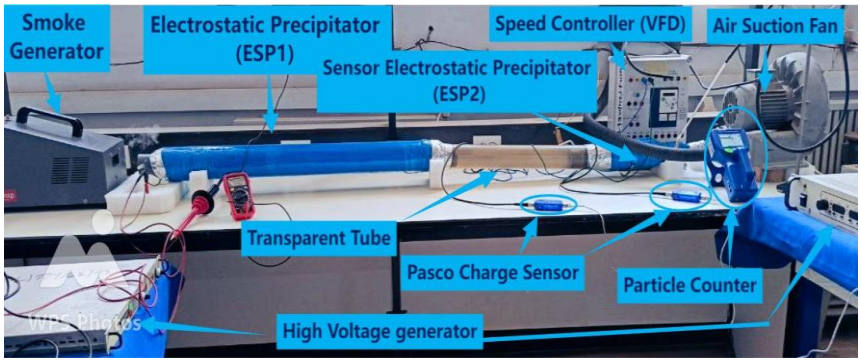


Figure 1. Experimental setup

This section outlines the methodology adopted to evaluate the hybrid electrostatic filtration system and the Particle Electrostatic Sensor (PES). The procedure was conducted in a controlled environment and aimed at analyzing charge behavior, filtration efficiency, and the dynamic response of the sensor under various airflow conditions. Preparation Phase :

- Calibration of the Pasco Charge Sensor using Capstone software.
- Verification of electrical insulation in ESP1 and PES to prevent leakage.
- Installation of the smoke generator and airflow adjustment using the VFD.
- Initial test run to ensure signal stability and synchronization between the sensor and the acquisition system.



Figure 2. Photograph of the smoke generator used

Test Protocol :

Each test was performed under a defined airflow condition with a specific voltage applied to ESP1 and PES:

- Activate the smoke generator to introduce charged particles.
- Set the high voltage of ESP1 (e.g., 12–20 kV) for particle ionization.
- Apply a separate voltage to PES via its dedicated high voltage supply.
- Allow particles to pass through ESP1, and then into the PES measurement zone.

Record:

- - Charge variation over time via the Pasco sensor.
- - Particle count before and after ESP using Aerotrak™.

To ensure continuous and controlled movement of the airflow through all system components, an Air Suction Fan is used. This is a centrifugal fan with a volute casing, installed at the end of the air path to draw air through the system. The rotational speed of this fan is precisely controlled using a Variable Frequency Drive (VFD), a box-shaped device. This unit allows for adjusting the fan speed, thereby controlling the airflow rate and volume processed at each stage, enabling performance testing of the precipitators under various airflow conditions and determining the optimal operating point.

The polluted airflow first passes through the primary purification unit: the Electrostatic Precipitator 1 (ESP1). This precipitator is cylindrical in shape and characterized by its substantial dimensions, with a length of approximately 1 meter (100 cm) and a diameter of approximately 100 mm. The internal ionization electrodes of ESP1 are connected to a High Voltage Generator, a box-shaped device that provides the necessary electrical voltage (tens of kilovolts) to generate a Corona Discharge. This discharge ionizes air molecules and electrically charges the particles suspended in the air. These charged particles are then attracted by the Coulomb Force towards the collecting electrodes, where they adhere, resulting in the removal of a significant portion of pollutants from the air stream. After undergoing primary purification in ESP1, the air stream, now partially purified, moves into the Transparent Tube. This tube is cylindrical and completely transparent, with a length of

approximately 75 cm and a diameter of approximately 75 mm. This tube serves as both a visual and functional link between the main precipitator and the sensing unit. Its transparency allows for visual observation of the airflow, and more importantly, it provides a calculated transition distance to ensure homogeneous and stable distribution of residual particles and ions before they enter the subsequent sensing unit, thereby contributing to increased measurement accuracy.

Directly following the transparent tube is the most innovative part of this technique: the Sensor Electrostatic Precipitator (PES). This cylindrical-shaped precipitator features carefully designed dimensions, with a length of approximately 40 cm and a diameter of approximately 90 mm. PES functions as an advanced sensing unit. Its role is not limited to secondary precipitation of residual particles but primarily focuses on conditioning and preparing particles and ions for precise measurement. This is achieved through its interaction with the Pasco Charge Sensor. This small, compact sensor, cylindrical or oval in shape, is strategically installed either after ESP1 or inside/after ESP2 (PES).

The Pasco sensor measures the total electrical charge remaining in the air. By analyzing the charge pattern collected by this sensor, the system can reliably evaluate filtration effectiveness and determine the presence and impact of free ions, thereby overcoming the problem of ionic interference that plagues traditional sensors. This integration between PES and the Pasco sensor eliminates the need for external particle counters in daily operation, as the innovation itself takes over the role of evaluating air quality and purification efficiency. For initial testing and calibration of the system, and to justify the rationality of the results, a Particle Counter (Aerotrak™) can be used. This portable device, with a clear digital display, is positioned at the system's outlet and performs accurate counting and classification of residual particles in the purified air by size (e.g., 0.3, 0.5, 1.0, 3.0, 5.0, 10.0 micrometers). This tool is crucial during system development phases to verify the accuracy of PES and Pasco sensor data and compare it with real-world measurements.

Smart Monitoring and Preventive Maintenance Mechanism: The system designed in this manner is not limited to purification; it also provides an intelligent mechanism for continuous monitoring of ESP1's performance. By analyzing data collected by PES and the charge sensor, the system can detect any decrease in efficiency or abnormal changes in charge levels that may indicate dust accumulation on ESP1's internal electrodes or the potential for an electrical Flashover.

This proactive monitoring enables immediate responses, such as activating self-cleaning mechanisms (if present) or sending alerts for scheduling preventive maintenance, thereby ensuring optimal continuous operation of the system and significantly reducing unplanned breakdowns and operational costs. In this detailed manner, an invention is implemented that offers a comprehensive and intelligent air purification solution, characterized by its ability for accurate real-time evaluation and adaptation to changing conditions, while enhancing reliability and operational efficiency unprecedentedly.

Results and Discussion

This experiment was conducted under standard and controlled operating conditions to evaluate the performance of the electrostatic precipitation system. The voltage applied to the main electrostatic precipitator (ESP1) was set at -17 kV, while the voltage for the Particle Electrostatic Sensor was set at -7 kV. To ensure a stable airflow, the fan was operated at 6 Hz, resulting in an air outflow velocity of approximately 7.45 m/s. Based on the principle of flow continuity (V1*D1 = V2*D2), the air velocity inside the main precipitator (ESP1) was calculated to be approximately 2.24 m/s. A stable smoke generator was used as the pollution source. The total test duration was approximately 240 seconds. For data collection, both Pasco charge sensors and an Aerotrak™ particle counter were utilized.

Table 1. Sequence of events and time intervals of the ESP/PES performance test

Time (s)	Event
0–87	Particle Electrostatic Sensor ON – clean air baseline
87–167	Smoke ON – polluted airflow enters system
167–200	ESP1 (main filter) ON – filtration phase
200–230	Smoke OFF – clean air returns
>230	System OFF – full shutdown (ESP1 + Particle Electrostatic Sensor)

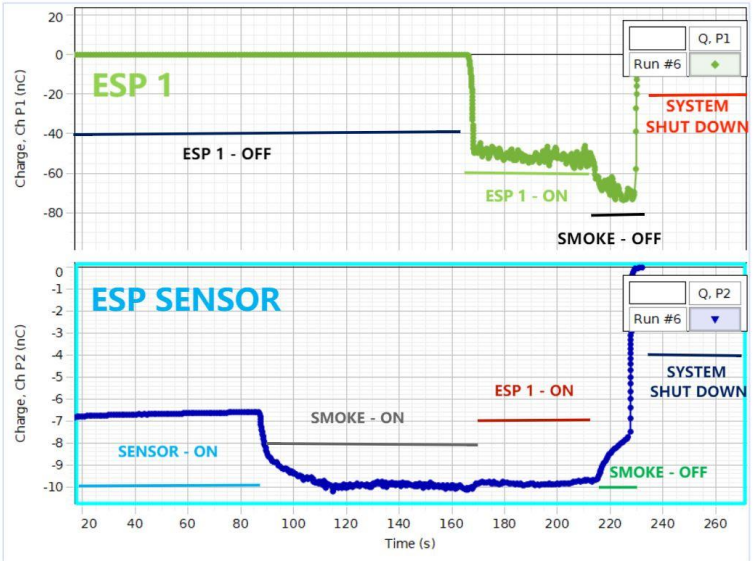


Figure 3. Dynamic response of the main electrostatic precipitator (ESP 1) and the particle electrostatic sensor (PES) during the smoke injection and filtration cycle

Table 2. Experimental phases and corresponding electrostatic charge status (ESP1 and PES)

Phase	Time Range (s)	Event	ESP1 (P1)	Particle Electrostatic Sensor	Comments
1	0–87	Clean air, Particle Electrostatic Sensor ON	0 nC	Stable at –7 nC	Clean baseline established
2	87–167	Smoke ON	0 nC	Gradual drop to ~– 10 nC	Sensor charges as particles arrive
3	167–200	ESP1 ON	Drop to ~– 55 nC	Slight recovery (~– 9 nC)	Filtration starts; sensor stabilizes slightly
4	200–230	Smoke OFF	Continues to ~– 72 nC	PES returns to –7 nC	Clean air helps system reset
5	>230	Power OFF	Discharges to 0	Instant discharge to 0	Full system shutdown

Interpretation

- Particle Electrostatic Sensor gradually charged up to around –10 nC during the smoke injection phase.
- Once ESP1 was activated, the particle concentration near the sensor dropped slightly, allowing the Particle Electrostatic Sensor to begin stabilizing.
- When the smoke generator was turned off, the Particle Electrostatic Sensor gradually returned to its clean-air baseline of –7 nC.
- However, the sensor did not exhibit a perfectly ideal discharge profile during operation.
- This behavior should not be interpreted as a sensor malfunction, but rather as a result of measurement limitations under real-world dynamic conditions particularly due to high particle load density, transient ion flow, and limited sensor resolution (Aouimeur, 2018).

Such limitations are common in compact electrostatic test environments and are expected when testing highly responsive systems like ESPs.

Physical Analysis of Charge Behavior

This section provides an in-depth physical analysis of the electrical charge behavior observed by the Pasco charge sensor within the "Particle Electrostatic Sensor" during the experimental phases, linking empirical observations to fundamental principles of electrostatic precipitation and particle charging phenomena.

- Baseline Phase (0-87 s): During this phase, prior to smoke introduction and with clean air flowing, the charge sensor readings were consistently low and stable, approaching zero. This indicates an almost complete absence of charged particles or free ions in the ambient air or those generated by the Particle Electrostatic Sensor itself (at -7 kV). This establishes a critical charge baseline for subsequent evaluation of changes due to pollution or filtration.
- Pollution Phase (87-167 s): Upon smoke introduction, increase in charge sensor readings was observed. This rapid rise reflects a dense influx of charged (from the smoke generator or partially charged within the system's corona discharge) and uncharged particles, along with an increasing quantity of free ions generated within the discharge system. The arrival of these particles and ions at the Particle Electrostatic Sensor directly translates to an increase in the total observed charge, confirming the sensor's effectiveness in detecting air pollution.
- ESP1 Filtration Phase (167-200 s): Immediately after activating the main electrostatic precipitator (ESP1) at -17 kV, a sharp decrease in charge readings occurred. This drop directly reflects the electrostatic precipitation process, where ESP1 electrodes effectively charge, attract, and collect airborne particles. A lower charge reading after ESP1 indicates higher efficiency in pollutant removal. This phase is vital in demonstrating ESP1's air purification capability.
- Recovery Phase (200-230 s): Following the cessation of the smoke source, the charge sensor readings gradually returned to levels near the baseline. This suggests that the remaining air within the system was efficiently cleared of residual charged particles and free ions. This behavior also highlights the Particle Electrostatic Sensor's ability to respond to changes in pollutant concentration and revert to a reference state, establishing it as a reliable tool for continuous monitoring.

Connection to Saturation and Innovation Validation: In the context of experiments where traditional particle counters (e.g., Aerotrak™) exhibited saturation at high concentrations or specific operating conditions (like the low-frequency and high-voltage conditions that were excluded), the analysis of charge behavior gains paramount importance. The "Particle Electrostatic Sensor's" ability to measure total charge rather than "particle count" makes it less susceptible to saturation in extreme conditions, providing a more reliable measure of performance and validating the core innovation of this system for evaluating electrostatic precipitator performance.

Conclusion

This study successfully designed, developed, and experimentally validated a compact cylindrical electrostatic precipitation system, integrating an innovative Particle Electrostatic Sensor (PES) for real-time monitoring of simulated smoke. The system is characterized by its cylindrical geometry, offering uniform flow distribution and reduced particle re-entrainment. Experimental results confirm the system's effectiveness in capturing fine particles and, more importantly, demonstrate the value of PES integration. The analysis of charge behavior successfully detected the arrival of pollutants, the start of the filtration process by ESP1 , and the gradual return to the clean air reference state. This approach circumvented one of the major challenges of traditional sensors: the inability to reliably distinguish between ions and particles due to ionic interference. By measuring the total charge rather than the simple particle count, the PES system proves less susceptible to saturation under high particle loads, thus offering a more reliable performance evaluation and validating the core innovation of this system for evaluating electrostatic precipitator performance. In conclusion, this project is not limited to purification; it presents a smart, compact, and cost-effective filtration solution. This accessible, embedded solution has the potential to significantly improve particulate waste management performance in resource-constrained environments, paving the way for future innovation and broad industrial applications.

Recommendations

To consolidate the results and extend the impact of this research, the following avenues are recommended:

1. PES Sensor Optimization and Measurement Limit Reduction:

- Conduct further research on improving the resolution of the Particle Electrostatic Sensor (PES) to minimize the impact of measurement limitations under real-world dynamic conditions, especially high particle load density and transient ion flow.

- Develop a signal processing algorithm to actively filter out the stable ionic component of the corona discharge, thereby allowing for better isolation of the signal specifically related to particle charge only.

2. Validation in Industrial Conditions and Durability Tests:
   - Scale up the system to an industrial pilot and test it with real combustion flue gases (not simulated) over an extended period to evaluate the long-term efficiency and durability of the electrodes.
   - Quantify the correlation between PES data and actual filtration performance (measured by the Aerotrak™) for different types of pollutants, covering a variety of chemical and physical characteristics.

3. Development of an Adaptive Control System (Smart Control):
   - Design and implement a real-time feedback control loop based on PES data. This loop should dynamically adjust the ESP1 supply voltage to maintain optimal collection efficiency while proactively preventing electrical discharges (flashovers) caused by excessive dust accumulation.

4. Analysis of Erosion and Predictive Maintenance:
   - Conduct studies to correlate the charge variation measured by the PES with the mass of dust accumulated on the ESP1 electrodes. This is crucial for precisely determining predictive maintenance intervals and reducing the need for periodic visual inspections.

5. Energy Analysis:
   - Precisely evaluate the energy consumption of the complete system (fan, ESP1, and PES) and compare it to existing high-energy filtration or incineration technologies, in order to quantitatively justify the system's "cost-effective" advantage.

Scientific Ethics Declaration

* The authors declare that the scientific ethical and legal responsibility of this article published in EPSTEM journal belongs to the authors.

Conflict of Interest

* The authors declare that they have no conflicts of interest

Funding

* This research received no specific grant from any funding agency in the public, commercial, or not-for-profit sectors.

Acknowledgements or Notes

* This article was presented as a poster presentation at the International Conference on Technology, Engineering and Science (www.icontes.net) held in Antalya/Türkiye on November 12-15, 2025.

References

Aouimeur, D., Miloua, F., Bengrit, M., Tounsi, F., & Tilmatine, A. (2018). Novel electrostatic induction measurement method for monitoring particle flows in an electrostatic precipitator. *Particulate Science and Technology, 36*(3), 323–328.

Bottner, C. U. (2003). The role of space charge density in particulate processes in the example of the electrostatic precipitator. *Powder Technology, 135–136*, 285–294.

Dascalescu, L., Zeghloul, T., Medles, K., & Iuga, A. (2025). Recent advances in the electrostatic separation of particulate matter. *Journal of Electrostatics, 134*, 104052.

Larab, M., Miloua, F., Ayad, A., & Seddik, T. (2024). Trajectory of insulating particles in high voltage cyclone filter. *International Journal of Electronics and Electrical Engineering Systems, 7*(4).

Mizuno, A. (2000). Electrostatic precipitation. *IEEE Transactions on Dielectrics and Electrical Insulation, 7*(5), 615–624.

Popa, G. N., & Dăscălescu, L. (2014). Variable cross-section cylinder-type corona and combined corona–dielectric barrier discharge precipitators for fly-ash particles. *Particulate Science and Technology, 32*(5), 445–450.

Wang, X., Chang, J., Xu, C., Wang, P., Cui, L., & Ma, C. (2016). Electrical characteristics of electrostatic precipitator with a wet membrane-based collecting electrode. *Journal of Electrostatics, 80*, 85–94.

Author(s) Information

Miloua Farid
Djilalil Liabes University of Sidi Bel Abbes
Bp 89, Sidi Bel Abbès, 22000, Algeria,
Contact e-mail: *milouafarid@gmail.com*

Redjala Majda
Djilalil Liabes University of Sidi Bel Abbes
Bp 89, Sidi Bel Abbès, 22000, Algeria,

Miloua Hadj
Djilalil Liabes University of Sidi Bel Abbes
Bp 89, Sidi Bel Abbès, 22000, Algeria,

Rezoug Mohammed
Djilalil Liabes University of Sidi Bel Abbes
Bp 89, Sidi Bel Abbès, 22000, Algeria,

To cite this article:

Farid, M., Majda, R., Hadj, M, & Mohammed, R. (2025). Experimental study of a cylindrical electrostatic precipitator with real-time monitoring applied to simulated smoke. *The Eurasia Proceedings of Science, Technology, Engineering and Mathematics (EPSTEM), 38,* 135-142.

The Eurasia Proceedings of Science, Technology, Engineering & Mathematics (EPSTEM)
ISSN: 2602-3199

The Eurasia Proceedings of Science, Technology, Engineering and Mathematics (EPSTEM), 2025

Volume 38, Pages 143-150

IConTES 2025: International Conference on Technology, Engineering and Science

Aeolian Sands in Self-Consolidating Mortar Formulations: Study of the Mechanical Impacts

Nacim Khelil
Mouloud Mammeri University of Tizi-Ouzou

Said Boukais
Mouloud Mammeri University of Tizi-Ouzou

Karim Akkouche
Mouloud Mammeri University of Tizi-Ouzou

Amar Kahil
Mouloud Mammeri University of Tizi-Ouzou

Djamal Atlaoui
Mouloud Mammeri University of Tizi-Ouzou

Randa Makkeb
Mouloud Mammeri University of Tizi-Ouzou

Abstract: The study presented herein explores the altering potential of using fine dune sand (DS) in self-consolidating mortar (SCM), originally formulated with river sand. The research aims to assess how the inclusion of this fine aggregate-seen as an improper source material for cementitious applications—affects the mortar's rheological, acoustic, and mechanical characteristics. By integrating a very fine *Touggourt*-sourced DS, we seek to alleviate the pressure on river sand (RS), a resource that currently faces significant depletion. With that intention in mind, mortar mixtures were developed with varying DS content (0%, 25%, 50%, 75%, and 100% by volume of RS) and were tested for flow behavior, ultrasonic pulse velocity (UPV), and both compressive and flexural strength. Results indicate that incorporating DS enhances some key properties of the SCM, highlighting its potential even at high substitution rates. Consequently, this research suggests that DS could serve as a sustainable alternative to RS, aiding in the responsible management of river sand resources.

Keywords: Sustainable mortar, Dune sand, River sand, Cementitious materials, UPV

Introduction

Over 60% of Algeria's land area is considered as desert or semi-desert, predominantly located in the arid central and southern regions of the country. These areas are largely covered by extensive sand dune systems. The sand grains constitutive of these dunes exhibit distinct compositional, morphological, and textural characteristics. These properties are strongly influenced by aeolian processes, including long-distance wind transport but also physico-chemical mechanisms affecting their parent rock. As a result, these grains are finer than common sand grains, sub-spherical in shape, and possess smooth surface textures, indicative of prolonged abrasion and selective sorting during transport.

- This is an Open Access article distributed under the terms of the Creative Commons Attribution-Noncommercial 4.0 Unported License, permitting all non-commercial use, distribution, and reproduction in any medium, provided the original work is properly cited.

- Selection and peer-review under responsibility of the Organizing Committee of the Conference

© 2025 Published by ISRES Publishing: www.isres.org

Over the past decades, the construction industry has witnessed the development of breakthrough cementitious formulations aimed at improving workability and implementation on site. Among these, self-compacting concrete (SCC) and its derivative, self-compacting mortar (SCM), have emerged as engineered materials designed to flow, consolidate, and fill formworks under their own weight, without the need for mechanical vibration or troublesome human intervention, and at the same time minimizing the risks of segregation and bleeding (Lozano-Lunar et al., 2020). The significanlty higher flowability of these materials is achieved through an increased powder content (Hammat et al., 2021), which contributes to a denser particle packing, a finer microstructure, and consequently and enhanced durability. Owing to their fine particle size distribution, dune sands are able to significantly influence the rheological behavior of fresh concretes and mortars (Khelil et al., 2024; Khelil et al., 2025). Their effect is mainly attributed to the capacity of the said fine particles to act as lubricating agents (Khelil et al., 2023) thereby reducing interparticle friction and facilitating the movement of coarser grains during consolidation.

The objective of this study is to investigate the incorporation of very fine dune sand, in combination with alluvial (river) sand, within self-compacting mortar (SCM) formulations. Specifically, two primary research directions were pursued: firstly, assessing the influence of dune sand addition on the rheological characteristics of SCMs, and secondly evaluating the potential for mitigating the environmental impacts associated with the extraction and processing of conventional river sand. The results of this experimental research are meant to contribute to the development of more sustainable mix-design strategies for high-performance, self-compacting cementitious materials.

Materials and Procedures

Materials

In this research, was employed a CEM II/A-L 42.5R cement, which has a specific gravity of 3.1 and is supplied by SPA Biskria, conforming to the EN 197-1 standard (British Standards Institution, 2011). Two morphologically different sands were used for the SCM mixtures. The first one is a natural river sand (RS) originating from the Asif N Sebaw river in the Tizi-Ouzou region of Algeria, whereas the second one is a dune sand (DS) from the saharan region of Touggourt. The particle size distribution curves of RS and DS, revealing a significant difference in their fineness are presented in Figure 1. The fineness modulus value calculated for DS is $M_{f,DS}$=1.94, corroborates its high fineness compared to that of river sand whose fineness modulus is $M_{f,RS}$= 2.98. As for their densities, the bulk densities mesured were 1.715t/m^3 and 1.650t/m^3 for RS and DS, wereas the absolute densities were 2440t/m^3 and 26664t/m^3 for RS and DS respetively. Tap water along with a superplasticizer (Medaplast SP 40) were used to achieved flowability of the SCM.

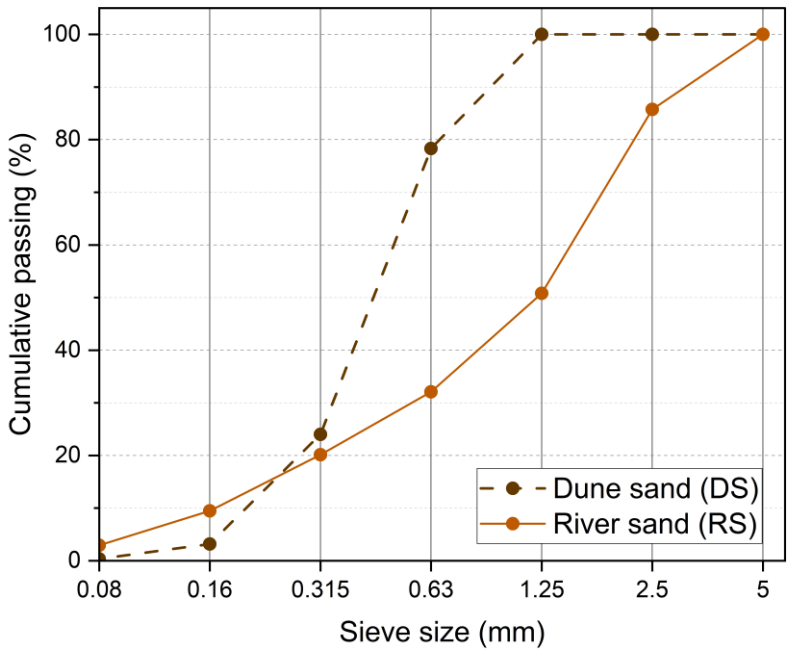


Figure 1. Particle size distribution (PSD) of the fine dune and river sands

Mortars Mix Proportions

Five self-compacting mortar (SCM) mixtures were prepared for this study. In order to achieve the rheological requirements of the SCM, dune sand was used as a flowability-enhacing material owing to its high fineness and sphere-like shape. The specific compositions of the RS-DS sand blends used in the mortars are detailed in Table 1. The mixing process followed the guidelines outlined in EN 196-1 (British Standards Institution, 2016) for standard mortar preparation. It involved a total mixing time of 240 seconds, structured as follows: Initially, water and cement were placed in the mixing bowl, then the planetary mixer was turned on at a low speed for 30 seconds. Next, the sand blend was added at the same speed over the course of 30 seconds, after which the mixer was switched to a higher speed for an additional 30 seconds. The mixer was then paused for 90 seconds to scrape any material that may have adhered to the bowl's bottom or sides. Finally, mixing resumed at high speed for 60 seconds before stopping.

Once mixing was complete, the fresh SCM mixtures were evaluated for flowability using a mini-slump cone. The mixtures were then poured into 40 x 40 x 160 mm³ prismatic molds and left to set for 24 hours at approximately 25°C. After demolding, the specimens were submerged in a water tank at the same temperature until 28 days. For each SCM mixture three prismatic specimens were cast, and at 28 days they are retrieved from water curing and submitted to Ultrasonic Pulse Velocity (UPV) testing, flexural tensile strength testing, and finally compressive strength testing. The results presented below represent the average values obtained from these three specimens.

Table 1. SCM mix proportions

Mortar ID (%CS-%DS)	CS (g)	DS (g)	Cement (g)	Water (g)	Superplasticizer (%)	W/C
M0 (100CS-0DS)	1191.6	0	685.6	205.68		
M1 (75CS-25DS)	893.7	325.24	685.6	205.68	0.5	0.3
M2 (50CS-50DS)	595.8	650.98	685.6	205.68		
M3 (25CS-75DS)	297.9	976.74	685.6	205.68		
M4 (0CS-100DS)	0	1301.96	685.6	205.68		

Fresh-State Workability Testing

The workability of fresh mortar mixtures - low-volume materials with fine particles – is evaluated throught a testing reffered to mini-slump testing. It is particularly suited for self-compacting mortars (SCMs) flowability testing. This test is an adaptation from the conventional slump test performed on concrete, and is designed to give an indication on the mobility of mortar in an unconfined setting, under the effect of gravity. The procedure *per se* involves placing the SCM into the truncated mini-cone mold (reduced-scale concrete slump cone) with dimensions: 100 mm at the base, 70 mm at the top, and 60 mm in height. The cone is filled in two layers, each compacted with 25 strokes using a tamping rod to ensure uniform consolidation. Once filled, the cone is carefully lifted, allowing the mortar to spread freely into a pancake shape. Measurements are then taken on the still SCM mixture, along two perpendicular diameters. According to EFNARC (European Federation of Specialist Construction Chemicals and Concrete Systems, 2005), the typical spread diameter for the fresh mortar spread to qualify as a self-compacting mortars (SCM) should range from 240 mm to 260 mm.

Hardened-State Acoustic Testing

At the hardened state, the mortar specimens were submitted to Ultrasonic Pulse Velocity (UPV) testing - a widely used non-destructive testing (NDT) technique – generally meant for evaluating the internal condition and overall quality of cementitious materials such as mortar and concrete. The aim here was evaluating the mortars' compactness. The principle of the test is measuring the travel time of high-frequency ultrasonic waves as they pass through the material. The pulse velocity is directly influenced by the material's density, elasticity, and the presence of defects such as cracks, voids, or unhomogeneities. A higher velocity generally indicates a more compact and homogeneous structure. During experiments, the UPV methodology followed the precepts given in

European and American standards BS EN 12504-4:2004 and ASTM C597-16 respectively, performed using the Pundit apparatus, equipped with two transducers - one acting as the emitter and the other as the receiver - set to a frequency of 150 kHz. Each prismatic mortar specimen was positioned between the said transducers and used petroleum jelly as a contact agent, to ensure optimal acoustic coupling before initiating the measurement. Three specimens were tested for each mortar formulation, with three repeated measurements taken on each specimen, hence ensuring reliability and reproducibility. The UPV values reported in this study represent consequently the average of nine readings per mix.

Hard-State Mechanical Strength Testing

Consecutively to performing NDT tests, the mortar specimens were subjected to destructive mechanical tests by means of a computer-controlled hydraulic press, as given by European standard EN 196-1 (British Standards Institution, 2016). Each SCM specimen first underwent a three-point bending test, at a constant loading rate of 50 ± 10 N/s, to obtain its flexural tensile strength, then, following the flexural test, the resulting half-prisms were subjected to compressive strength testing at a loading rate of 2400 ± 200 N/s, also in accordance with EN 196-1. Both flexural and compressive strength tests aimed to characterize the mechanical performance of the SCM formulations.

Results and Discussion

Fresh-State Workability Results

Figure 2. shows the results of the mini-slump cone workability testing for the different SCM formulations.

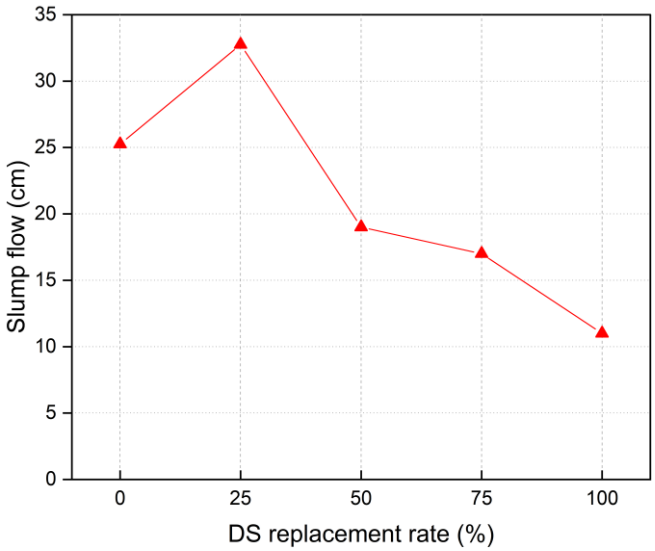


Figure 2. Slump values of the SCM mortars

The experimental results indicate a clear enhancement in slump flow values with the progressive incorporation of dune sand (DS) into the mortar mixtures up to 25%. Specifically, the slump increased from 25.25 cm for the control specimen (M0 or 0% DS) to 32.75 cm, for mixtures M1 (25% DS). Mixtures M2 (50% DS), M3 (75% DS), and M4 (100% DS), exhibited lower values compared to M0, valued at 19, 17 and 11 respectively. These findings underscore the beneficial effect of DS addition on the workability of fresh mortars at low substitution rates (25%). Higher DS substitution rates translated into poorer workability properties of the SCMs.

This improvement in the flowability of the SCM is likely attributable to the morphological characteristics of DS particles, which are predominantly near-spherical in shape. Such geometry reduces inter-particle friction and facilitates the movement of constituent materials under gravity. The texture of such sand particles also play a key role. Indeed, their smooth surface are useful in reducing resistance to the overall motion of the mortar at the fresh state. When combined with the dispersing action of the high-range water reducer (HRWR), DS contributes to the improved particle dispersion and the denser, more homogeneous packing of the cementitious matrix. Beyond 25% DS substitution rate, an opposite observation can be made, where the mortar constituents seem to

move in a more impeded way, probably attributable to the high content of fine particles in the river sand and the higher water demand. As a result, it is suggested the need of a better balancing of the HRWR agent amount. Higher contents should be used, to improve SCM ease of motion and achieve a greater pancake diameter.

Ultrasonic Pulse Velocity testing

The ultrasonic pulse velocity test results are shown in (Figure 3).

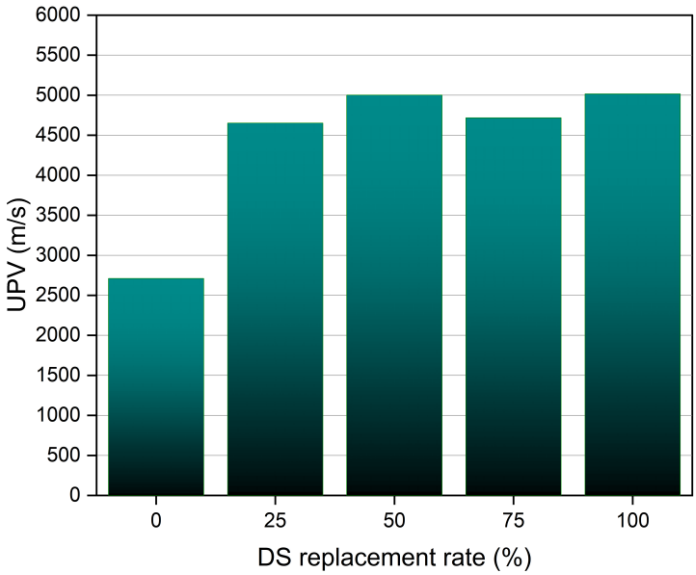


Figure 3. UPV test results of the SCM specimens at 28d

The data of the UPV testing show that DS addition to the SCM indeed modifies its behavior. The recorded velocities are valued at 4651.66 m/s, 5001.33 m/s, 4717.33 m/s and 5017 m/s for 25% DS, 50% DS, 75% DS and 100% DS respectively, representing an improvement of 71.59%, 84.49%, 74.02% and 85.07% from the control M0 (2710.78 m/s). These results seem to indicate a better granular state of the SCM, in other words, the SCMs could possess a denser, and more compact matrix, which goes hand in hand with mechanical resistance. Moreover, these results show that DS content seems not to play a role in the achieved velocity, as no significant change between the different tested dosages translates into significant change in acoustic properties.

Flexural Tensile Strength Results

The flexural tensile strength of the SCM formulations are displayed hereafter (Figure 4).

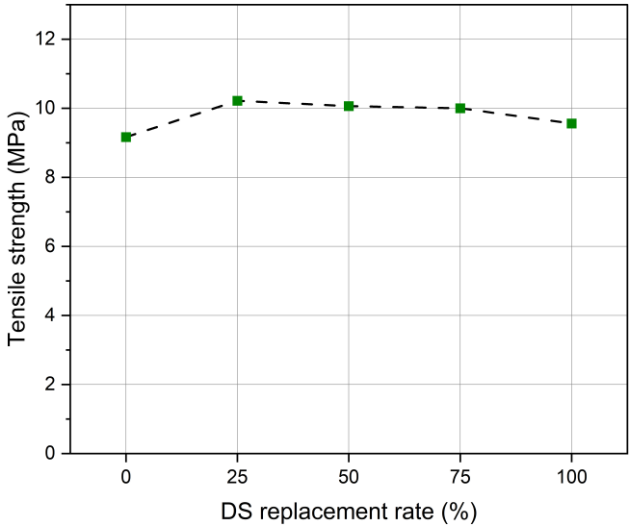


Figure 4. Flexural tensile strength of the SCMs at 28d.

From Figure 4, on can observe an improvement of the flexural strength as the dune sand content increases in the SCMs. Compared to the control formulation devoid of dune sand, the resistance betterment is valued at 11.57%, 9.82%, 9.17% and 4.18% for DS replacement rates of 25% (M1) and beyond, up to 100% respectively. From the recorded values, Mixture M1, containing 25% DS, showed the best results, suggesting that at this rate, the granular skeleton is the most compact. Overall, the formulation with the best behavior strength-wise, would be those ranging from 25% to 75%, as they show a plateau-like profile revolving around 10MPa. These results underline the positive impact of DS particles bring to the mortar mixture, in terms of bearing capacity under third-point loading. These results are in accord with what is often reported in the literature, concerning the fine DS particles which are considered to play a key role in the improvement of mortar/concrete workability properties (Khelil et al., 2023; Khelil et al., 2024; Khelil et al., 2025). Those authors also reported better overall mechanical properties most often related to the capacity of the DS smooth sphere looking particles to act as lubricant for the surrounding mortar granular components, arranging them in a compact stable state in the cement matrix.

Compressive Strength Test Results

The compressive strength test results of the tested mortars are presented in Figure 5.

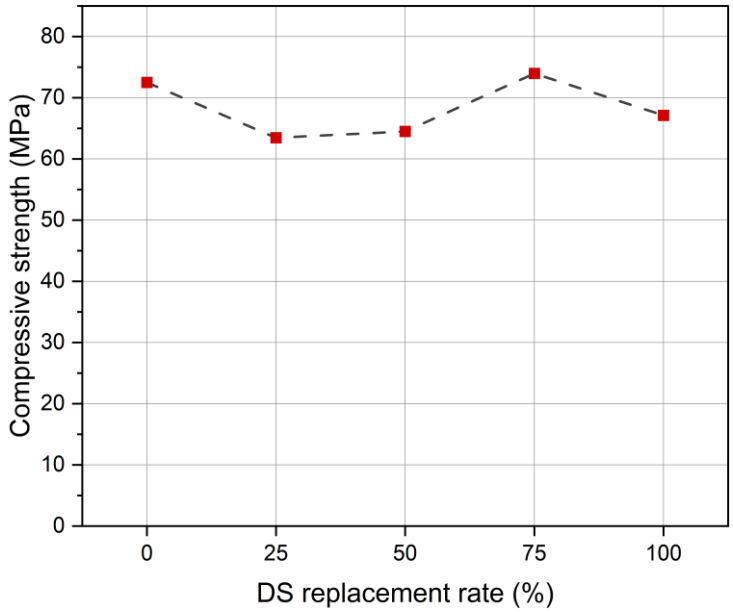


Figure 5. Compressive strength of the SCMs at 28d.

From the figure reporting the results of the compressive strengths, a somewhat antagonistic behavior is observed, with the results of the tensile strength, in the sense that no clear pattern can be defined. Indeed, for the four mixtures that include DS particles, three of them have shown poorer compressive strengths compared to the control, valued at 63.47 MPa, 64.50 MPa and 67.13 MPa, representing a decrease of 12.45%, 11.03% and 7.41% for 25% DS, 50% DS and 100% DS. Concerning mixture containing 75% DS, a modest improvement is reached at 73.96 MPa or 2.01% improvement. Overall, although most mixtures exhibited lessened strengths, their values remain significant. Moreover, these results also show the nature of the substituted sand and more importantly, its particle size distribution on the mortars properties. A closer look at those, brings to light the finer nature of the river sand, which contains a higher content of very fine particles. Those latter could cause, in the cement matrix a higher water demand, capturing more water, aimed originally at hydrating the cement. Lesser water available, means lesser cementing material, and hence, hampered resistance development.

Conclusion

According to the outcomes of the present experimental work, these conclusions can be drawn:

- The use of dune sand in self-compacting mortars is beneficial to a certain extent (25%), while beyond that, a deleterious effect is observable.

- A significant improvement of the acoustic properties of the SCMs is observed with the addition of DS. This illustrates a denser matrix and hence an enhanced durability.
- Third-point tensile strength is slightly improved by DS addition, reaching 11.57% improvement for M1 (25% DS).
- As for compressive strength, the addition of DS does not result in an improvement. It could be attributable to the presence of excessive amounts of fine particles in the substituted river sand.

The outcomes of the experimental study presented herein endorse the idea that dune sand can serve as an efficient substitute for conventional river sand in self-compacting mortars, thereby contributing to the development of more sustainable processes and materials aimed at reducing the environmental impact of the construction industry.

Scientific Ethics Declaration

* The authors declare that the scientific ethical and legal responsibility of this article published in EPSTEM journal belongs to the authors.

Conflict of Interest

* The authors declare that they have no conflicts of interest

Funding

* This research received no specific grant from any funding agency in the public, commercial, or not-for-profit sectors.

Acknowledgements or Notes

* This article was presented as a poster presentation at the International Conference on Technology, Engineering and Science (www.icontes.net) held in Antalya/Türkiye on November 12-15, 2025.

References

ASTM International. (2016). *Standard test method for pulse velocity through concrete* (ASTM C597-16).

British Standards Institution. (2004). *Testing concrete - Part 4: Determination of ultrasonic pulse velocity* (BS EN 12504-4:2004).

British Standards Institution. (2011). *Cement – Part 1: Composition, specifications and conformity criteria for common cements* (BS EN 197-1:2011).

British Standards Institution. (2016). *Methods of testing cement: Determination of strength* (BS EN 196-1:2016).

European Federation of Specialist Construction Chemicals and Concrete Systems. (2005). *The European guidelines for self-compacting concrete: Specification, production and use*.

Hammat, S., Menadi, B., Kenai, S., Thomas, C., Kirgiz, M. S., & Sousa Galdino, A. G. (2021). The effect of content and fineness of natural pozzolana on the rheological, mechanical, and durability properties of self-compacting mortar. *Journal of Building Engineering, 44*, 103276.

Khelil, N., & Bekri, Y. (2025). Assessment of Touggourt dune sand inclusion in fiber reinforced concrete (FRC). In P. Gallo, M. A. Khalifa, Z. E. Zayed, & A. Ragheb (Eds.), *Urban and transit planning* (pp. 163–172). Springer.

Khelil, N., Boukais, S., Makkeb, R., & Akkouche, K. (2024). Performance evaluation of a self-compacting mortar altered with dune sand. *The Eurasia Proceedings of Science, Technology, Engineering & Mathematics, 32*, 329–335.

Khelil, N., Ould Ouali, M., & Meziane, L. (2023). On the use of fine dune sand in reactive powder concrete: Effect on resistance, water absorption and UPV properties. *Construction and Building Materials, 388*, 131684.

Lozano-Lunar, A., Dubchenko, I., Bashynskyi, S., Rodero, A., Fernández, J. M., & Jiménez, J. R. (2020). Performance of self-compacting mortars with granite sludge as aggregate. *Construction and Building Materials, 251*, 118998.

Author(s) Information

Nacim Khelil
Mouloud Mammeri University of Tizi Ouzou
BP 17RP, 15000, Algeria.
Contact e-mail: *nacim.khelil@ummto.dz*

Said Boukais
Mouloud Mammeri University of Tizi Ouzou
BP 17RP, 15000, Algeria.

Karim Akkouche
Mouloud Mammeri University of Tizi Ouzou
BP 17RP, 15000, Algeria.

Amar Kahil
Mouloud Mammeri University of Tizi Ouzou
BP 17RP, 15000, Algeria.

Djamal Atlaoui
Mouloud Mammeri University of Tizi Ouzou
BP 17RP, 15000, Algeria.

Randa Makkeb
Mouloud Mammeri University of Tizi Ouzou
BP 17RP, 15000, Algeria.

To cite this article:

Khelil, N., Boukais, S.,Akkouche, K., Kahil, A., Atlaoui, D., & Makkeb, R. (2025). Aeolian sands in self-consolidating mortar formulations: study of the mechanical impacts. *The Eurasia Proceedings of Science, Technology, Engineering and Mathematics (EPSTEM), 38,* 143-150.

The Eurasia Proceedings of Science, Technology, Engineering & Mathematics (EPSTEM)
ISSN: 2602-3199

The Eurasia Proceedings of Science, Technology, Engineering and Mathematics (EPSTEM), 2025

Volume 38, Pages 151-158

IConTES 2025: International Conference on Technology, Engineering and Science

On LDPC Codes and Their Construction

Mohammed Amine Tehami
Djillali Liabes University of Sidi Bel Abbes

Malika Tehami
Djillali Liabes University of Sidi Bel Abbes

Boucif Beddad
Djillali Liabes University of Sidi Bel Abbes

Ahmed Hadji
Djillali Liabes University of Sidi Bel Abbes

Abstract: In this paper, we propose a novel method for constructing low-density parity-check (LDPC) codes that relies on circulant permutation matrices as the main principal elements. A key feature of this construction is the intentional avoidance of short cycles, particularly those of length four, which are known to degrade decoding performance. By eliminating these cycles, the approach contributes to lowering both encoding and decoding complexity, making the codes more efficient to implement. To assess their effectiveness, the proposed LDPC codes are evaluated and compared with uncoded binary phase shift keying (BPSK) transmission over an additive white Gaussian noise (AWGN) channel. The simulation outcomes demonstrate that the structured codes deliver competitive results, achieving error-rate performance similar to, and in some instances exceeding, well-known designs such as progressive edge growth (PEG) and quasi-cyclic (QC) codes.

Keywords: LDPC codes, Parity check matrix, Circulant permutation matrix, Girth, Bit error rate

Introduction

Low-Density Parity-Check (LDPC) codes, originally introduced by Gallager (1962), have attracted significant attention owing to their strong error-correcting capability and their potential to operate close to the Shannon capacity limit (Chung et al., 2001**).** As a subclass of linear block codes (Lin & Costello, 2004), they are defined through a sparse parity-check matrix H, of dimensions M×N, which contains only a small proportion of ones relative to zeros, hence the designation "low-density." Depending on the uniformity of the number of ones across rows and columns, LDPC codes are categorized as regular or irregular. The design of such codes requires careful consideration of parameters such as row and column weights, the girth of the associated Tanner graph, and the overall code length. Two principal design strategies exist: random (unstructured) (MacKay, 1999) and deterministic (structured) constructions (Shin et al., 2014; Moura et al., 2004; Tehami & Djebbari, 2018, 2019). While random approaches are straightforward and often yield strong performance, they typically demand substantial memory resources for encoding and decoding, particularly at large block lengths, which can result in high computational cost ‘sometimes a more critical limitation than the error rate itself’ (Tehami & Djebbari, 2018).

To overcome the limitations of random constructions, several structured design approaches have been introduced (Gallager, 1963; Richardson & Urbanke, 2008). By enforcing regular patterns in the parity-check matrix H, these methods facilitate more efficient hardware implementations for both encoding and decoding

- This is an Open Access article distributed under the terms of the Creative Commons Attribution-Noncommercial 4.0 Unported License, permitting all non-commercial use, distribution, and reproduction in any medium, provided the original work is properly cited.

- Selection and peer-review under responsibility of the Organizing Committee of the Conference

© 2025 Published by ISRES Publishing: www.isres.org

(MacKay, 1999). In such constructions, the connections between rows and columns follow predefined rules, which contribute to reducing overall system complexity **(**Fossorier, 2004; Kou et al., 2001; Lin & Costello, 2004; Zhong & Zhang, 2005; Zhang et al., 2008**)**. Structured LDPC codes are particularly advantageous for short block lengths, where they often outperform their random counterparts (MacKay, 1999; Richardson & Urbanke, 2008**).** Nevertheless, they also exhibit inherent constraints, especially with respect to achievable code rates, block lengths, and girth, and their performance tends to deteriorate as the block length increases (Gallager, 1963; Kou et al., 2001).

The Tanner graph offers a useful graphical representation of the LDPC decoding process (Tanner, 1981). It is a bipartite graph composed of two types of nodes: variable nodes, corresponding to the columns of H, and check nodes, corresponding to the rows. The edges connecting these nodes define the overall structure of the code. Within this framework, a cycle refers to a closed path formed by a sequence of edges, and the girth of the graph denotes the length of its shortest cycle. Short cycles, particularly those of length four, are especially detrimental because they reduce the independence of the messages exchanged during iterative decoding, which in turn degrades the overall performance (Zhang et al., 2008**).** Although quasi-cyclic LDPC (QC-LDPC) codes provide several advantages, their encoding process continues to pose significant challenges. This issue has been addressed in multiple studies. A class of globally coupled (GC) LDPC codes was proposed by Zhu & Yang (2022), combining local LDPC structures with an overarching global parity constraint. This design achieves strong performance while maintaining relatively low complexity, yet the encoding process remains difficult to implement efficiently. Likewise, Mo et al. (2020) introduced in a new family of LDPC codes that can be encoded through approximate lower triangulation (ALT) (Richardson & Urbanke, 2001), which relies on row and column permutations of the parity-check matrix. Nevertheless, despite these efforts, decoding complexity remains substantial.

In this work, we present a novel category of LDPC codes that are explicitly constructed to eliminate length-4 cycles, thereby reducing both encoding and decoding complexity while delivering excellent bit error rate performance in the waterfall region. The remainder of the correspondence is organized as follows: Section 2 details the methodology for constructing the parity-check matrix H, emphasizing strategies for avoiding 4-cycles and discussing the impact of girth on LDPC performance. Section 3 analyzes encoding complexity, with particular attention to the role of column weights in determining the minimum distance and the trade-off between performance and implementation cost. Section 4 examines decoding complexity, showing its dependence on the number of branches in the Tanner graph and discussing the role of the belief propagation algorithm. Comparisons are also made with the codes of Gallager and MacKay in terms of branch density. Section 5 reports simulation results obtained via Monte Carlo experiments over an AWGN channel. Finally, Section 6 summarizes the key findings and concludes the paper.

Method

The girth, defined as the length of the shortest cycle within the Tanner graph of an LDPC code, is a critical parameter that strongly influences code performance. Some studies (Fossorier, 2004; Tanner, 1981; Hu et al., 2001, 2005; Richardson, 2003) have reported that increasing the girth can result in a higher error floor, whereas simulation-based investigations (MacKay & Postol, 2003) suggest that a larger girth typically improves bit-error-rate (BER) performance, which is generally adequate for practical use. For this reason, the development of LDPC codes with girth values greater than four has become a topic of considerable interest for real-world applications (Kou et al., 2001). The method proposed in this work focuses on constructing LDPC codes that completely eliminate 4-cycles. To achieve this, the parity-check matrix H, of size M×N (where M denotes the number of rows and N the number of columns), is generated through a two-step design procedure.

Step 1

The procedure starts with the construction of an identity matrix I of dimension m×m, where m is assumed to be an even integer. A new matrix C is then generated by reflecting I vertically while keeping the columns unchanged. More precisely, each element $C_{i,j}$ is defined as the entry of I located at row m+1−i and column j. This operation can be expressed as:

$$C_{i,j}=I_{m+1-i,j} \quad (1)$$

For i,j= 1,2,… ,m.

Step 2

To obtain the matrix C^k, a circular shift of k columns is applied to the identity matrix I, which has size m×m. This shift moves each column to the right by k positions.
This transformation can be defined using matrix multiplication:

$$C^k=I.P^k \quad (2)$$

Where
I is the m×m identity matrix.
P is a circular permutation matrix that performs a one-position leftward shift of the columns.
P^k indicates the matrix P raised to the kth power, effectively rotating the columns by k steps.
The full matrix H, having size $m^2 \times m^2$, is built through the systematic placement of the identity matrix and its shifted submatrices C^k, according to the following structure:

$$H=\begin{pmatrix} C & C & C & \dots & C \\ C & C^1 & C^2 & \dots & C^n \end{pmatrix} \quad (3)$$

Here, n denotes the number of shifted submatrices, is given by:

$$n=m-1 \quad (4)$$

Example

First, consider the 4×4 identity matrix

$$I=\begin{pmatrix} 1 & 0 & 0 & 0 \\ 0 & 1 & 0 & 0 \\ 0 & 0 & 1 & 0 \\ 0 & 0 & 0 & 1 \end{pmatrix}$$

Next, C^1 is obtained by applying a left circular shift of one position to I. This operation can be expressed as:

$$C^1=I.P^1=\begin{pmatrix} 0 & 1 & 0 & 0 \\ 0 & 0 & 1 & 0 \\ 0 & 0 & 0 & 1 \\ 1 & 0 & 0 & 0 \end{pmatrix}$$

where P^1 is the permutation matrix that performs a one-step right circular shift of the columns. Following the same procedure, the matrices $C^2=I.P^2$ and $C^3=I.P^3$ are generated by applying two-step and three-step right circular shifts, respectively:

$$C^2=I.P^2=\begin{pmatrix} 0 & 0 & 1 & 0 \\ 0 & 0 & 0 & 1 \\ 1 & 0 & 0 & 0 \\ 0 & 1 & 0 & 0 \end{pmatrix}$$

$$C^3=I.P^3=\begin{pmatrix} 0 & 0 & 0 & 1 \\ 1 & 0 & 0 & 0 \\ 0 & 1 & 0 & 0 \\ 0 & 0 & 1 & 0 \end{pmatrix}$$

By following the structure in (3), the resulting 8 × 16 parity-check matrix is obtained as:

$$H=\begin{pmatrix}0&0&0&1&0&0&0&1&0&0&0&1&0&0&0&1\\0&0&1&0&0&0&1&0&0&0&1&0&0&0&1&0\\0&1&0&0&0&1&0&0&0&1&0&0&0&1&0&0\\1&0&0&0&1&0&0&0&1&0&0&0&1&0&0&0\\0&0&0&1&1&0&0&0&0&1&0&0&0&0&1&0\\0&0&1&0&0&0&0&1&1&0&0&0&0&1&0&0\\0&1&0&0&0&0&1&0&0&0&0&1&1&0&0&0\\1&0&0&0&0&1&0&0&0&0&1&0&0&0&0&1\end{pmatrix}$$

Encoding Complexity

Gallager (1963) demonstrated that the minimum distance of LDPC codes grows only logarithmically with code length when the column weight equals 2. In contrast, when the column weight is at least 3, the minimum distance increases linearly with code length (Gallager, 1962). Such codes have shown effectiveness in several applications, including partial-response channels (Song et al., 2002; Song et al., 2004). Their relatively low computational demand stems from the reduced column weight. Despite these advantages, practical hardware implementation remains challenging (Malema & Liebelt, 2007) due to the random distribution of row–column connections and the typically large size of LDPC codes. Structured codes were later introduced to alleviate this complexity, providing more regular interconnections while maintaining good performance (Malema & Liebelt, 2007). Furthermore, constraining the row–column connections has been used to control the girth, i.e., the length of the shortest cycle in the Tanner graph (Fossorier, 2004).

Increasing the girth generally leads to improved decoding performance, as larger cycles reduce the likelihood of short, error-prone loops (O'Sullivan, 2006; Mao & Banihashemi, 2001). In summary, both structured design and girth optimization contribute significantly to enhancing the efficiency of LDPC codes. The structure of the parity-check matrix has a decisive impact on the efficiency of LDPC encoding (Tehami & Djebbari, 2019; Richardson & Urbanke, 2001). The proposed method, based on a sparse design of the submatrices C^k, offers several advantages:

- A sparse parity-check matrix H significantly reduces the memory required to store parity information (MacKay, 1999; Tehami & Djebbari, 2018).
- The use of permutation matrices contributes to an efficient and well-organized structure (Fossorier, 2004).
- Thanks to its sparsity, H enables low encoding complexity, making it highly suitable for practical implementations (Song et al., 2004).

Decoding Complexity

The decoding complexity of LDPC codes is primarily determined by the number of branches Br in the Tanner graph, or equivalently, by the number of nonzero entries ('1's) in the parity-check matrix (Berrou, 2010). The iterative decoding process, based on the belief propagation algorithm, involves multiple stages. At each iteration, both the extrinsic and total information associated with each node must be computed (Divsalar et al., 2009). For a regular code (N, W_C, W_R), where W_C and W_R denote the column and row weights respectively. The number of branches can be expressed as:

$$Br=W_C*N=W_R*M \quad (5)$$

Table 1. Comparison of proposed LDPC codes with Gallager codes and Mackay codes.

Block length	Proposed codes	Gallager codes	Mackay codes
N=500 and M=250	Br=1500	Br=1500	Br=1500
N=1000 and M=500	Br=2000	Br=3000	Br=3000

As shown in Table 1, the proposed LDPC codes require fewer branches compared to Gallager and Mackay codes. This reduction implies that the corresponding parity-check matrices H are sparser (containing fewer ones relative to zeros), which directly contributes to lowering the decoding complexity.

Results and Discussion

Monte Carlo simulations were performed to investigate the bit error rate (BER) performance of the proposed LDPC codes (MacKay, 1999). The iterative belief propagation (BP) algorithm was adopted as the decoding method (Gallager, 1963), and transmission was assumed over an additive white Gaussian noise (AWGN) channel. For simulation purposes, a code rate of R= 1/2 and a block length of N=4368 were selected. Each simulation involved at least 103 transmitted codewords, with the maximum number of decoding iterations capped at 80. The obtained results are presented in comparison with conventional LDPC codes to highlight the relative performance of the proposed design. The signal-to-noise ratio (SNR) definitions for both coded and uncoded binary phase-shift keying (BPSK) follow O'Sullivan (2004). Specifically:

$$SNR_{coded}=10 \log_{10} (E_b/2\sigma^2R) \quad (6)$$

$$SNRuncoded=10 \log10 (E_b/2\sigma2) \quad (7)$$

Where Eb and σ^2 represent energy per bit and noise variance, respectively.

Figure 1 illustrates the BER performance of the proposed LDPC codes in comparison witn uncoded BPSK transmission. The parameters considered are: N=4368, W_C =2 and a code rate R=1/2. For reference, in BPSK-modulated system operating over a Gaussian channel, the BER is given by

$$BER=Q(SNR)^{1/2} \quad (8)$$

where the function Q represents the tail function of the normal distribution.

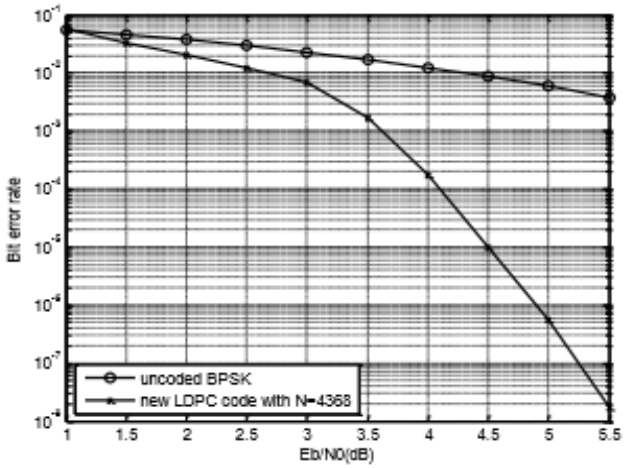


Figure 1. BER performance for the proposed LDPC codes for N=4368 and W_C= 2.

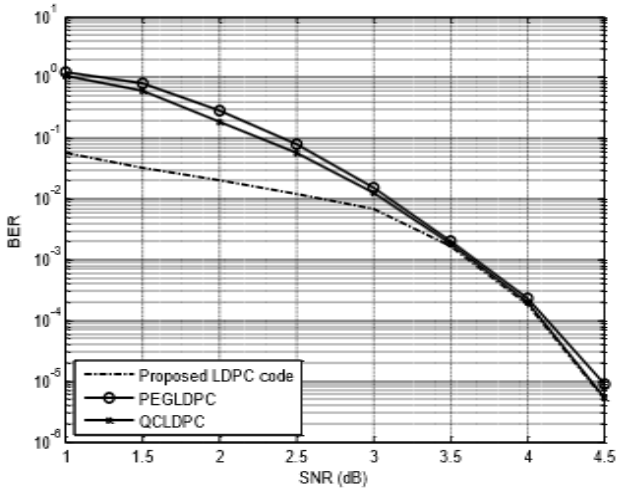


Figure 2. Comparison of BER performance between the proposed LDPC codes, PEG-LDPC codes and QCLDPC codes in the waterfall region.

As shown in Figure 1, the proposed LDPC code clearly outperforms uncoded BPSK. At a BER of 10^{-2}, a performance gain of approximately 1.95 dB is observed. This improvement can be attributed to the efficiency of LDPC codes with column weight W_C=2, which provide a significant advantage over uncoded transmission in terms of error-rate reduction. Figure 2 shows the BER performance of the proposed LDPC codes with N=4368 over the AWGN channel in the waterfall region. At a BER of 10^{-2}, the proposed codes achieve a gain of approximately 0.4 dB compared with both PEG LDPC and QC LDPC codes. Furthermore, at a BER of 10^{-3}, they outperform PEG-LDPC codes by about 0.05 dB. This performance improvement is mainly attributed to the simplified encoding process and the elimination of girth-4 cycles.

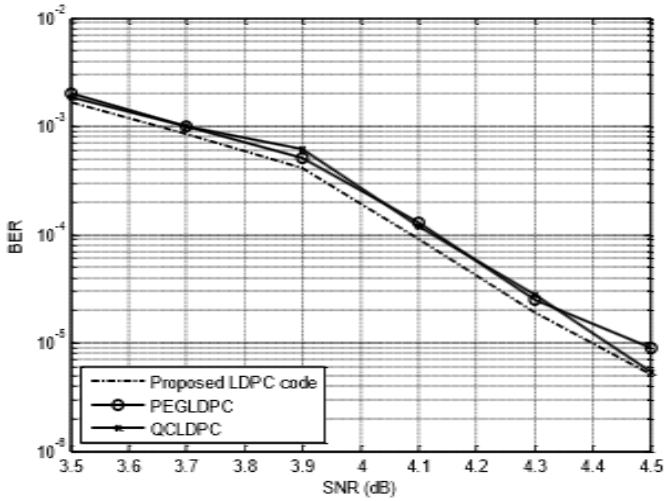


Figure 3. Comparison of BER performance between the proposed LDPC codes, PEG-LDPC codes and QCLDPC codes in the low error-floor region.

Figure 3 shows the BER performance of the proposed LDPC codes over the AWGN channel in the low error-floor region. At a BER of 10^{-4}, the proposed codes achieve a performance gain of about 0.5 dB compared to QC-LDPC codes. At a BER of 10^{-5}, they still provide a slight improvement over PEG-LDPC codes. These results indicate that the proposed design is able to approach the error-floor region even for large block lengths.

Conclusion

To address both implementation constraints and reception quality, LDPC codes must achieve a low error floor while maintaining reduced encoding and decoding complexity. In this work, we introduced a construction method for parity-check matrices that eliminates short cycles across different code rates. Additionally, the adoption of quasi-cyclic structures significantly lowers memory requirements. Simulation results confirm that the proposed LDPC codes exhibit strong performance over the AWGN channel, demonstrating their efficiency and practical applicability.

Scientific Ethics Declaration

* The authors declare that the scientific ethical and legal responsibility of this article published in EPSTEM journal belongs to the authors.

Conflict of Interest

* The authors declare that they have no conflicts of interest

Funding

* This research received no specific grant from any funding agency in the public, commercial, or not-for-profit sectors.

Acknowledgements or Notes

* This article was presented as a poster presentation at the International Conference on Technology, Engineering and Science (www.icontes.net) held in Antalya/Türkiye on November 12-15, 2025.

References

Berrou, C. (2010). *Codes and turbo-codes*. ENST Bretagne.

Chung, S., Forney, G. D., & Richardson, T. J. (2001). On the design of low-density parity-check codes within 0.0045 dB of the Shannon limit. *IEEE Communications Letters, 5*(2), 58–60.

Divsalar, D., Dolinar, S., Jones, C. R., & Andrews, K. (2009). Capacity-approaching protograph codes. *IEEE Journal on Selected Areas in Communications, 27*(6), 876–888.

Fossorier, M. P. C. (2004). Quasi-cyclic low-density parity-check codes from circulant permutation matrices. *IEEE Transactions on Information Theory, 50*(8), 1788–1793.

Gallager, R. G. (1962). Low-density parity-check codes. *IRE Transactions on Information Theory, 8*(1), 21–28.

Gallager, R. G. (1963). *Low-density parity-check codes*. MIT Press.

Hu, X.-Y., Eleftheriou, E., & Arnold, D.-M. (2001). Progressive edge-growth Tanner graphs. *Proceedings of the IEEE Global Telecommunications Conference (GLOBECOM)*, 995–1001.

Hu, X.-Y., Eleftheriou, E., & Arnold, D.-M. (2005). Regular and irregular progressive edge-growth Tanner graphs. *IEEE Transactions on Information Theory, 51*(1), 386–398.

Kou, Y., Lin, S., & Fossorier, M. (2001). Low-density parity-check codes based on finite geometries: A rediscovery and new results. *IEEE Transactions on Information Theory, 47*(7), 2711–2736.

Lin, S., & Costello, D. J. (2004). *Error control coding: Fundamentals and applications* (2nd ed.). Prentice Hall.

MacKay, D. J. C. (1999). Good codes based on very sparse matrices. *IEEE Transactions on Information Theory, 45*(2), 399–431.

MacKay, D. J. C., & Postol, M. J. (2003). Weaknesses of Margulis and Ramanujan–Margulis low-density parity-check codes. *Electronic Notes in Theoretical Computer Science, 74*, 97–104.

Malema, G., & Liebelt, M. (2007). Quasi-cyclic LDPC codes of column-weight two using a search algorithm. *EURASIP Journal on Applied Signal Processing, 2007*(1), 1–8.

Mao, Y., & Banihashemi, A. H. (2001). A heuristic search for good low-density parity-check codes at short block lengths. *Proceedings of the IEEE International Conference on Communications*, 41–44.

Mo, S., Chen, L., Costello, D. J., Mitchell, D. G. M., Smarandache, R., & Qiu, J. (2020). Designing protograph-based quasi-cyclic spatially coupled LDPC codes with large girth. *IEEE Transactions on Communications, 68*(9), 5326–5337.

Moura, J. A., Abdel-Ghaffar, N. H., Rosenthal, J., & Smarandache, R. (2004). Algebraic constructions of LDPC codes with no short cycles. *Proceedings of the IEEE International Symposium on Information Theory (ISIT)*, 39.

Moura, J. M. F., Lu, J., & Zhang, H. (2004). Structured low-density parity-check codes. *IEEE Signal Processing Magazine, 21*(1), 42–55.

O'Sullivan, M. E. (2006). Algebraic construction of sparse matrices with large girth. *IEEE Transactions on Information Theory, 52*(2), 718–727.

Richardson, T. J. (2003). Error floors of LDPC codes. *Proceedings of the 41st Annual Allerton Conference on Communication, Control, and Computing*, 1426–1435.

Richardson, T. J., & Urbanke, R. L. (2001). Efficient encoding of low-density parity-check codes. *IEEE Transactions on Information Theory, 47*(2), 638–656.

Richardson, T. J., & Urbanke, R. L. (2008). *Modern coding theory*. Cambridge University Press.

Shin, B., Park, H., Hong, S., No, J. S., & Kim, S. H. (2014). Quasi-cyclic LDPC codes using overlapping matrices and their layered decoders. *AEU - International Journal of Electronics and Communications, 68*(5), 379–383.

Song, H., Liu, J., & Kumar, B. V. K. (2002). Low complexity LDPC codes for partial response channels. *Proceedings of the IEEE Global Telecommunications Conference*, 1294–1299.

Song, H., Liu, J., & Kumar, B. V. K. (2004). Large girth cycle codes for partial response channels. *IEEE Transactions on Magnetics, 40*(4), 3084–3086.

Song, L., Cruz, R., & Kumar, B. V. K. V. (2004). Low-density parity-check codes for partial response channels. *IEEE Transactions on Magnetics, 40*(2), 507–512.

Tanner, R. M. (1981). A recursive approach to low complexity codes. *IEEE Transactions on Information Theory, 27*(5), 533–547.

Tehami, M. A., & Djebbari, A. (2018). Low density parity check codes constructed from Hankel matrices. *Journal of Telecommunications and Information Technology, 3*, 37–41.

Tehami, M. A., & Djebbari, A. (2019). A new method for building low density-parity-check codes. *International Journal of Technology, 10*(3), 611–618.

Yahya, A., Sidek, O., & Salleh, M. (2009). A new quasi-cyclic low density parity check codes. *Proceedings of the IEEE Symposium on Industrial Electronics & Applications*, 239–242.

Zhang, F., Mao, X., Zhou, W., & Pfister, H. D. (2008). Girth-10 LDPC codes based on 3-D cyclic lattices. *IEEE Transactions on Vehicular Technology, 57*(2), 1049–1060.

Zhong, H., & Zhang, T. (2005). Block-LDPC: A practical LDPC coding system design approach. *IEEE Transactions on Circuits and Systems I: Regular Papers, 52*(4), 766–775.

Zhu, K., & Yang, H. (2022). Constructing girth eight GC-LDPC codes based on the GCD FLRM matrix with a new lower bound. *Sensors, 22*(19), 7247.

Author(s) Information

Mohammed Amine Tehami
Djillali Liabes University of Sidi Bel Abbes
Telecommunications and Digital Signal Processing Laboratory, Djillali Liabes University, P.O. Box 89 – 22000 Sidi Bel Abbes, Algeria
Contact e-mail : *chahoub_88@yahoo.com*

Malika Tehami
Djillali Liabes University of Sidi Bel Abbes
Applied Materials Laboratory, Research Center (CFTE), Djillali Liabes University, P.O. Box 89 – 22000 Sidi Bel Abbes, Algeria

Boucif Beddad
Djillali Liabes University of Sidi Bel Abbes
Telecommunications and Digital Signal Processing Laboratory, Djillali Liabes University, P.O. Box 89 – 22000 Sidi Bel Abbes, Algeria

Ahmed Hadji
Djillali Liabes University of Sidi Bel Abbes
Telecommunications and Digital Signal Processing Laboratory, Djillali Liabes University, P.O. Box 89 – 22000 Sidi Bel Abbes, Algeria

To cite this article:

Tehami, M. A., Tehami, M., Beddad, B & Hadji, A. (2025). On LDPC codes and their construction. *The Eurasia Proceedings of Science, Technology, Engineering and Mathematics (EPSTEM), 38,* 151-158.

The Eurasia Proceedings of Science, Technology, Engineering & Mathematics (EPSTEM)
ISSN: 2602-3199

The Eurasia Proceedings of Science, Technology, Engineering & Mathematics (EPSTEM), 2025

Volume 38, Pages 159-165

IConTES 2025: International Conference on Technology, Engineering and Science

Magnetic, Structural and Morphological Properties of Mechanically Alloyed FeSi and $FeSiO_2$ Nanocomposites

Abderrahmane Younes
Research Center in Industrial Technologies (CRTI)

Rachid Amraoui
Research Center in Industrial Technologies (CRTI)

Abderahim Abada
University of Saad Dahleb Blida 1

Djilali Allou
Research Center in Industrial Technologies (CRTI)

Abstract: Nanostructured FeSi and $FeSiO_2$ nanocomposites were synthesized via mechanical alloying to investigate the effects of milling time (0–30 h) on their structural, morphological, and magnetic properties. Comprehensive characterization was performed using scanning electron microscopy (SEM), energy-dispersive X-ray spectroscopy (EDS), X-ray diffraction (XRD), and vibrating sample magnetometry (VSM). XRD analysis revealed a transition to a disordered FeSi solid solution with a body-centered cubic structure after prolonged milling, alongside a crystallite size reduction and increasing lattice strain. For FeSi, the lattice parameter increased from 0.2861 nm (unmilled) to 0.452 nm after 30 h, with an average crystallite size of 22 nm. In contrast, the $FeSiO_2$ nanocomposite exhibited crystallite sizes ranging from 79–28 nm, with Fe/SiO_2 showing a lattice parameter decrease from 0.286 nm to 0.283 nm. Morphological evolution was evident through SEM. Magnetic properties improved with extended milling, with FeSi attaining its highest coercivity, saturation magnetization, and remanent magnetization at 30 h. Similarly, $FeSiO_2$ exhibited notable coercivity and remanence values, with Fe/SiO_2 achieving the highest saturation magnetization of 177.08 emu/g. These results emphasize the potential of FeSi and $FeSiO_2$ nanocomposites for high-frequency magnetic applications.

Keywords: Nanostructured FeSi and $FeSiO_2$ alloys, Magnetic behavior, Structural properties, SEM observations

Introduction

Nanostructured materials and nanocomposites have garnered significant attention due to their exceptional magnetic, thermal, optical, dielectric, and catalytic properties. These properties, often superior to their bulk counterparts, are strongly influenced by factors such as particle size, shape, inter-particle distance, and distribution homogeneity. Reducing particle size to the single-domain limit enhances magnetic characteristics such as superparamagnetism, higher coercivity, and optimized magnetic coupling, making nanostructured materials highly desirable for advanced technological applications (Abbassi et al., 2022; Baig & Kammakakam, 2021; Paras et al., 2022; Kim et al. 2013; Yao et al. 2010). Among various synthesis techniques, mechanical alloying (MA) stands out as an effective approach for producing nanostructured materials and nanocomposites. MA offers advantages such as uniform element dispersion at the nanoscale, production of metastable phases, and improved properties, including magnetic and mechanical characteristics. The process involves repeated welding, fracturing, and rewelding of powder particles in a high-energy ball mill. Key parameters like milling

- This is an Open Access article distributed under the terms of the Creative Commons Attribution-Noncommercial 4.0 Unported License, permitting all non-commercial use, distribution, and reproduction in any medium, provided the original work is properly cited.

- Selection and peer-review under responsibility of the Organizing Committee of the Conference

© 2025 Published by ISRES Publishing: www.isres.org

time, ball-to-powder ratio, and milling speed critically influence the structural and magnetic properties of the final material (Ouadah & Younes, 2023; Younes et al., 2024; Younes et al., 2023). In this context, FeSi alloys and $FeSiO_2$ nanocomposites have emerged as promising candidates for magnetic applications, including sensors, transformers, and high-frequency devices, due to their high saturation magnetization, low coercivity, and superior soft magnetic behavior. Nanostructuring FeSi further enhances these properties, while incorporating Fe nanoparticles into a SiO_2 matrix introduces additional benefits such as increased electrical resistivity and reduced eddy current losses (Leveneur et al., 2011; Krings et al., 2016).

This study focuses on the comparative synthesis and characterization of FeSi and $FeSiO_2$ nanocomposites using MA, with milling times ranging from 0 to 30 h. Advanced characterization techniques, including scanning electron microscopy (SEM), energy-dispersive X-ray spectroscopy (EDS), X-ray diffraction (XRD), and vibrating sample magnetometry (VSM), are employed to investigate the evolution of structural, morphological, and magnetic properties. By elucidating the relationships between milling parameters, crystallite structure, and magnetic behavior, this research aims to optimize the properties of FeSi and $FeSiO_2$ nanocomposites, contributing to the development of efficient materials for magnetic and electronic applications.

Method

The nanostructured FeSi and $FeSiO_2$ powders were synthesized using a high-energy planetary ball mill (PM 400) equipped with tungsten carbide pots and balls. High-purity Fe and Si powders (99.5%) with an average particle size of approximately 70 μm were used as starting materials, procured from Sigma-Aldrich (USA). Each sample consisted of a 20 g powder mixture placed in a 250 ml tungsten carbide jar along with tungsten carbide balls (20 mm diameter). The milling process was conducted under an inert atmosphere to prevent oxidation. A ball-to-powder weight ratio of 20:1 was maintained, with the milling speed set to 400 rpm. To avoid excessive heating during the process, a sequence of 15 minutes of milling followed by a 15-minute resting period was applied. The duration of the milling process was varied systematically (0 and 30 hours) to investigate the influence of milling time on the structural and magnetic properties of the powders.

The structural and morphological evolution during milling was analyzed using a Zeiss Gemini SEM equipped with an energy-dispersive X-ray spectroscopy (EDS) system for elemental analysis. Phase identification, crystallite size, and lattice parameters were determined using a Panalytical X'Pert Pro X-ray diffractometer with Cu Kα radiation (λ = 1.5406 Å) over a 2θ range of 10°–90°. The magnetic properties of the samples, including coercivity, saturation magnetization, and remanence, were characterized using a MicroSense EV9 vibrating sample magnetometer (VSM) with a maximum applied field of 15 kOe. This integrated approach enabled a comprehensive evaluation of the effects of milling time on the structural, morphological, and magnetic properties of the FeSi and $FeSiO_2$ nanocomposites.

Results and Discussion

Structural Study

Figure 1 and Table 1 provide a detailed representation of the structural evolution of FeSi and $FeSiO_2$ nanocomposites during mechanical alloying, as determined through X-ray diffraction (XRD) analysis. For FeSi, the milling process induced a significant transformation, with the initial Fe and Si phases disappearing and forming a disordered body-centered cubic (bcc) Fe(Si) solid solution (Rodriguez et al., 2007). This was accompanied by a progressive reduction in crystallite size, from 33 nm in the unmilled state to 22 nm after 30 hours of milling.

Additionally, the lattice strain increased markedly from 0.07% to 0.23%, reflecting the high mechanical deformation and energy imparted during milling, which led to increased lattice distortions. For $FeSiO_2$ nanocomposites, the XRD patterns showed a similar trend of structural refinement, with the crystallite size decreasing significantly from 79 nm to 28 nm over the same milling duration. The reduction in lattice parameters, from 0.286 nm to 0.283 nm, is indicative of the amorphization of the SiO_2 matrix and the diffusion of Fe into the matrix. The disappearance of distinct SiO_2 peaks and the broadening of Fe peaks suggest the formation of an Fe-SiO_2 composite with enhanced homogeneity and reduced crystallinity (Suryanarayana et al., 2022, and Alonso-Sanudo et al.,2000).

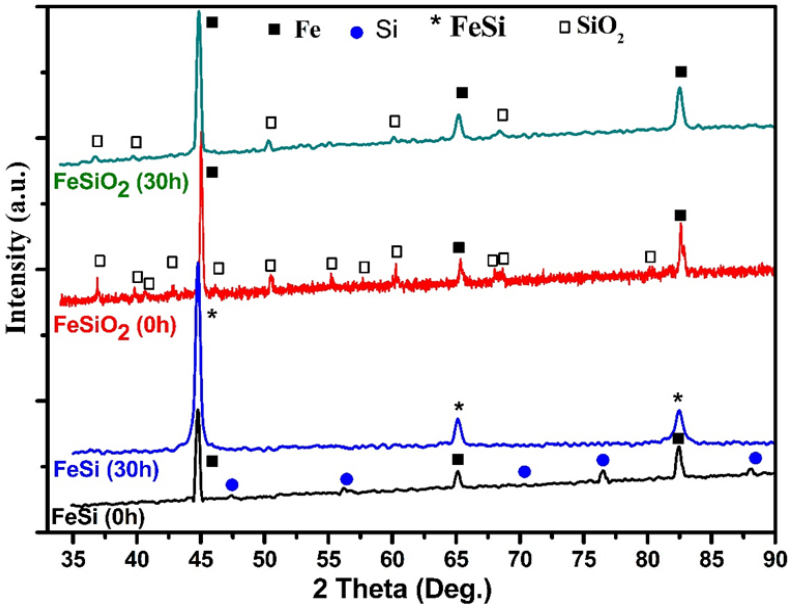


Figure 1. Structural evolution of FeSi and $FeSiO_2$ nanocomposites during mechanical alloying

These results clearly demonstrate that prolonged milling not only refines the crystallite size but also increases lattice strain and structural disorder, key indicators of effective mechanical alloying. The interplay between mechanical energy, grain refinement, and lattice distortion highlights the efficacy of this process in producing nanocomposites with tailored structural properties for advanced applications.

Table 1. Structural parameters of nanostructured Fe/SiO2mixture milled with defferent times.

Milling time (h)	Crystallite size (nm)	Lattice strain (%)	Lattice parameter of Fe (nm)
FeSiO2 (0h)	79	0,01	0.286
FeSi (0h)	33	0.07	0.452
FeSiO2 (30h)	28	0,02	0.283
FeSi (30h)	22	0.23	0.285

Morphology Analysis

Figure 2 provides a detailed Scanning Electron Microscopy (SEM) analysis, showcasing the morphological evolution of FeSi and $FeSiO_2$ nanocomposites during mechanical alloying. In the case of FeSi, the initial coarse particles (~70 µm) underwent substantial size reduction, reaching ~10 µm after 30 hours of milling. This transformation is attributed to the cyclic processes of cold welding, fracturing, and rewelding inherent to high-energy ball milling. Early stages of milling produced irregularly shaped, agglomerated particles, which progressively became finer and more homogeneous with extended milling time. The reduction in particle size indicates higher energy input and enhanced mechanical deformation, which together facilitate the formation of a nanostructured material (Gokçe & Ovecoglu, 2023; Banerjee et al., 2020).

For $FeSiO_2$, a similar trend was observed, where milling influenced the morphology by enhancing particle dispersion, reducing agglomeration, and contributing to the homogenization of the nanocomposite. The mechanical forces applied during milling not only fragmented the particles but also facilitated the uniform mixing of Fe and SiO_2 phases, as well as the integration of dopants (Gaona et al., 2021, and Dad et al., 2017). By 30 hours of linmilg, $FeSiO_2$ exhibited a well-dispersed, fine-grained morphology, indicative of efficient alloying and composite formation. Energy-dispersive X-ray spectroscopy (EDS) analyses corroborated these observations by confirming the uniform elemental distribution in both nanocomposites.

The consistent alloy composition and absence of impurities or contamination highlight the effectiveness of the milling process in achieving homogeneity. Additionally, EDS mapping revealed that the diffusion of elements, particularly silicon into the iron matrix for FeSi and dopants into the SiO_2 matrix for $FeSiO_2$, was complete by 30 hours, ensuring the successful formation of the desired nanostructured materials. These results underline the critical role of mechanical alloying in optimizing particle size, morphology, and compositional uniformity for advanced material applications.

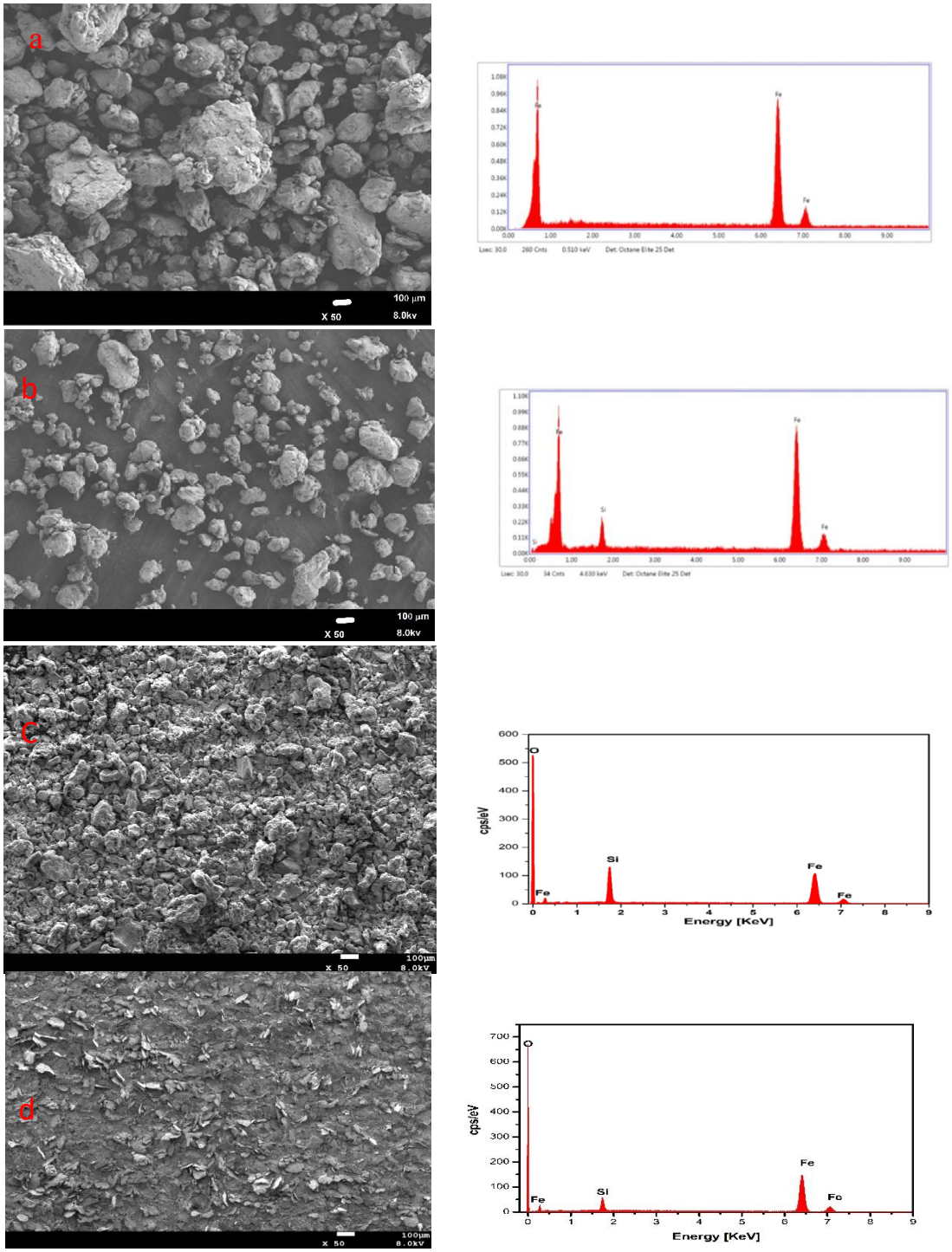


Figure 2. Morphological evolution of FeSi and $FeSiO_2$ nanocomposites during mechanical alloying (a)FeSi(0h), (b) FeSi(30h), (c) $FeSiO_2$(0h) and $FeSiO_2$(30h)

Magnetic Investigation

Figure 3 and Table 2 detail the magnetic measurements of FeSi and $FeSiO_2$ nanocomposites, highlighting significant enhancements in their magnetic properties with increased milling time. For FeSi, the mechanical alloying process resulted in a remarkable improvement in magnetic performance. At 30 hours of milling, coercivity (Hc) increased to 68.70 Oe, saturation magnetization (Ms) reached 159.89 emu/g, and remanent magnetization (Mr) rose to 8.71 emu/g.

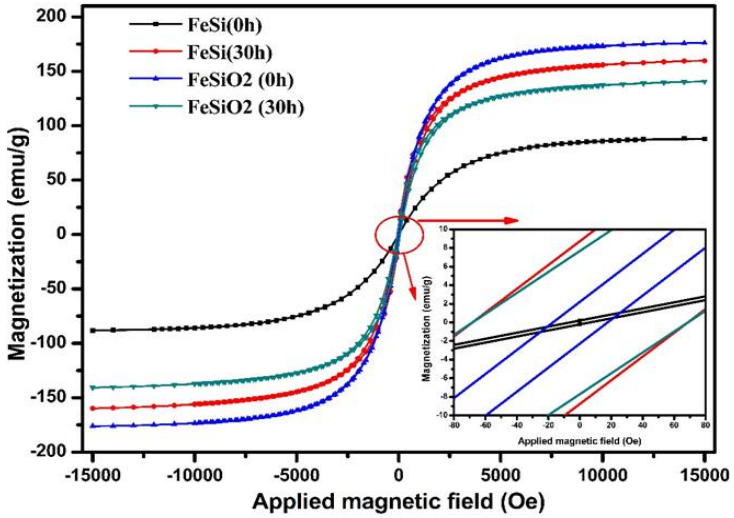


Figure 3. Magnetic properties of FeSi and $FeSiO_2$ nanocomposites improved with milling time.

These improvements are primarily attributed to the reduction in crystallite size, which increased the effective surface area of the magnetic domains, and the rise in lattice strain, which altered the magnetic anisotropy and domain wall motion. The fine crystallite structure and increased lattice defects induced by milling likely contributed to higher magnetic energy storage and domain wall pinning, enhancing the material's overall magnetic performance (Guo et al., 2020, and Overman et al., 2018). For $FeSiO_2$, extended milling resulted in distinct magnetic behaviors, reflecting the influence of structural refinement and phase evolution. After 30 hours, the saturation magnetization (Ms) peaked at 140.9 emu/g, while coercivity (Hc) and remanence (Mr) were measured at 69 Oe and 7.66 emu/g, respectively. The dopants played a pivotal role in enhancing magnetic coupling within the composite, as they improved the dispersion of Fe particles within the SiO_2 matrix and reduced magnetic interactions between neighboring particles. The presence of non-magnetic SiO_2 as a spacer reduced eddy current losses and further contributed to the soft magnetic behavior of the composite, making it suitable for high-frequency applications (Liu et al., 2019, and (Onderko et al., 2022).

Table 2. Magnetic parameters of nanostructured Fe/SiO2 mixture milled with defferent times.

Milling time (h)	Hc (Oe)	Mr (emu/g)	Ms (emu/g)	Mr/Ms
FeSi (0h)	7.72	0.19	87.53	0.002
FeSi (30h)	68.70	8.71	159.89	0.054
FeSiO2 (0h)	17.96	2.21	177.08	0.012
FeSiO2 (30h)	69	7.66	140.9	0.054

The results clearly demonstrate that mechanical alloying and dopant incorporation are powerful tools for tailoring the magnetic properties of nanocomposites. The interplay between reduced crystallite size, increased lattice strain, and the introduction of dopants significantly influenced the coercivity, remanence, and saturation magnetization of these materials. These findings highlight the potential of FeSi and $FeSiO_2$ nanocomposites for advanced applications, such as magnetic sensors, transformers, and other devices requiring precise control of magnetic properties.

Conclusion

This comparative study underscores the transformative effects of mechanical alloying in tailoring the structural, morphological, and magnetic properties of FeSi and $FeSiO_2$ nanocomposites. For FeSi, prolonged milling facilitated the formation of a disordered body-centered cubic (bcc) Fe(Si) solid solution, significantly enhancing its magnetic behavior, including higher coercivity, saturation magnetization, and remanence. This improvement is attributed to the reduction in crystallite size, increased lattice strain, and the uniform dispersion of silicon within the iron matrix. In the case of $FeSiO_2$, mechanical alloying promoted superior magnetic performance, characterized by higher saturation magnetization, improved particle dispersion, and diminished agglomeration. The amorphization of the SiO_2 matrix and the interaction between Fe and SiO_2 further contributed to enhanced structural and magnetic properties. These dopants played a pivotal role in promoting magnetic coupling, refining the particle size, and ensuring homogeneity throughout the nanocomposite. The findings of this study emphasize the critical influence of milling parameters, including time and environmental conditions, as well as material

composition on the final properties of nanocomposites. By optimizing these factors, FeSi and $FeSiO_2$ nanocomposites demonstrate significant potential for advanced magnetic applications, including high-frequency devices, magnetic sensors, and transformers. This research provides valuable insights for developing high-performance magnetic nanocomposites and paves the way for future innovations in the field of materials science.

Recommendations

Future research should optimize milling beyond 30 h to further refine grain structure and magnetic response. Exploring dopants or oxide phases may enhance coercivity and thermal stability. Advanced tools like TEM or Mössbauer spectroscopy could provide deeper microstructural insights. Post-milling annealing effects on magnetic properties should be systematically studied. Application-specific testing and scalability assessments will aid industrial adoption of FeSi and $FeSiO_2$ nanocomposites.
Scientific Ethics Declaration

Scientific Ethics Declaration

* The authors declare that the scientific ethical and legal responsibility of this article published in EPSTEM journal belongs to the authors.

Conflict of Interest

* The authors declare that they have no conflicts of interest

Funding

* This research received no specific grant from any funding agency in the public, commercial, or not-for-profit sectors.

Acknowledgements or Notes

* This article was presented as a poster presentation at the International Conference on Technology, Engineering and Science (www.icontes.net) held in Antalya/Turkiye on November 12-15, 2025.

References

Abbassi, L., Mesguich, D., Coulomb, L., Chevallier, G., Aries, R., Estournès, C., Flahaut, E., Viennois, R., & Beaudhuin, M. (2022). In situ reactive synthesis of dense nanostructured β-FeSi2 by spark plasma sintering. *Journal of Alloys and Compounds, 902*, 163683.

Alonso-Sanudo, M., Blackwell, J. J., O'Grady, K., González, J. M., Cebollada, F., & Morales, M. P. (2000). Magnetic behaviour and percolation in mechanically alloyed Fe–SiO2 granular solids. *Journal of Magnetism and Magnetic Materials, 221*(1–2), 207–214.

Baig, N., Kammakakam, I., & Falath, W. (2021). Nanomaterials: A review of synthesis methods, properties, recent progress, and challenges. *Materials Advances, 2*(6), 1821–1871.

Banerjee, P., Kumar, N. S., Franco, A., Swain, A. K., & Chandra Babu Naidu, K. (2020). Insights into the dielectric loss mechanism of bianisotropic FeSi/SiC composite materials. *ACS Omega, 5*(40), 25968–25977.

Dad, M., Lancee, R. J., van Vuuren, M. J., van De Loosdrecht, J., Niemantsverdriet, J. H., & Fredriksson, H. O. (2017). SiO2-supported Fe and FeMn colloids-Fischer–Tropsch synthesis on 3D model catalysts. *Applied Catalysis A: General, 537*, 83–92.

Gaona, I. M. S., Castillo, Y. M., Losada-Barragán, M., Sanchez, K. V., Rincón, J., Vargas, C. A. P., & Pérez, D. L. (2021). Characterization of zerovalent iron nanoparticles functionalized with a biomarker peptide. *Materials Research, 24*, e20200599.

Gökçe, H., & Öveçoğlu, M. L. (2023). Microstructure–property evolution of mechanically alloyed Al-20 wt.% Si matrix powders and sintered composites reinforced with TiB2 particulates. *Engineering Science and Technology, an International Journal, 39*, 101341.

Guo, Z., Wang, J., Chen, W., Chen, D., Sun, H., Xue, Z., & Wang, C. (2020). Crystal-like microstructural Finemet/FeSi compound powder core with excellent soft magnetic properties and its loss separation analysis. *Materials & Design, 192*, 108769.

Kim, H. K. D., Schelhas, L. T., Keller, S., Hockel, J. L., Tolbert, S. H., & Carman, G. P. (2013). Magnetoelectric control of superparamagnetism. *Nano Letters, 13*(3), 884–888.

Krings, A., Boglietti, A., Cavagnino, A., & Sprague, S. (2017). Soft magnetic material status and trends in electric machines. *IEEE Transactions on Industrial Electronics, 64*(3), 2405–2414.

Leveneur, J., Waterhouse, G. I. N., Kennedy, J., Metson, J. B., & Mitchell, D. R. G. (2011). Nucleation and growth of Fe nanoparticles in SiO2: A TEM, XPS, and Fe L-edge XANES investigation. *The Journal of Physical Chemistry C, 115*(43), 20978–20985.

Liu, L., Yue, Q., Li, G. Q., Xu, K., Wang, J., Wu, Z. Y., & Fan, X. A. (2019). Influence of SiO2 insulation layers' thickness distribution on magnetic behaviors of Fe–Si@SiO2 soft magnetic composites. *Journal of Physics and Chemistry of Solids, 132*, 76–82.

Onderko, F., Birčáková, Z., Dobák, S., Kollár, P., Tkáč, M., Fáberová, M., & Zeleňáková, A. (2022). Magnetic properties of soft magnetic Fe@SiO2/ferrite composites prepared by wet/dry method. *Journal of Magnetism and Magnetic Materials, 543*, 168640.

Ouadah, M., & Younes, A. (2023). Effects of silicon concentration on the magnetic and structural properties of nanostructured Fe-Si alloy synthesized by ball mill process. *The International Journal of Advanced Manufacturing Technology, 127*, 2815–2825.

Overman, N. R., Jiang, X., Kukkadapu, R. K., Clark, T., Roosendaal, T. J., Cofey, G., Shield, J. E., & Mathaudhu, S. N. (2018). Physical and electrical properties of melt-spun Fe–Si (3–8 wt%) soft magnetic ribbons. *Materials Characterization, 136*, 212–220.

Paras, K., Yadav, P., Kumar, D. R., Teja, S., Chakraborty, M., Chakraborty, S. S., Mohapatra, A., Sahoo, M. M. C., Chou, M. M. C., Liang, C. T., & Hang, D. R. (2023). A review on low-dimensional nanomaterials: Nanofabrication, characterization and applications. *Nanomaterials, 13*(1), 160.

Rodriguez, R. R., Perez-Alcazar, G. A., Sanchez, H., Sacilotti, M., & Greneche, J. M. (2007). Magnetic and structural properties of the nanostructured Fe1–xSix system with x = 0.1, 0.2 and 0.3, mechanical alloyed and sintered. *Physica Status Solidi (c), 4*(11), 4220–4223.

Suryanarayana, C., Al-Joubori, A. A., & Wang, Z. (2022). Nanostructured materials and nanocomposites by mechanical alloying: An overview. *Metals and Materials International, 28*, 41–53.

Yao, D., Ge, S., Zhou, X., & Zuo, H. (2010). Grain size dependence of coercivity in magnetic metal-insulator nanogranular films with uniaxial magnetic anisotropy. *Journal of Applied Physics, 107*(7), 073902.

Younes, A., Amraoui, R., Bouamer, A., Manseri, A., & Smaili, F. (2024). Effect of milling time on the structural and magnetic properties of nanostructured Fe90Si10 alloys. *Journal of Electronic Materials, 53*, 6098–6109.

Younes, A., Amraoui, R., Manseri, A., & Smaili, F. (2023). The impact of Cu, Ni and Fe2O3 on the magnetic behavior and structural properties of FeSiO2 nanocomposite synthesized through ball milling. *Physica Scripta, 98*(11), 115536.

Author(s) Information

Abderrahmane Younes
Research Centre in Industrial Technologies (CRTI)
P.O Box 64, Cheraga 16014 Algiers, Algeria
Contact e-mail: *younesabdo11@gmail.com*

Rachid Amraoui
Research Centre in Industrial Technologies (CRTI)
P.O Box 64, Cheraga 16014 Algiers, Algeria

Abderahim Abada
Laboratory of Aeronautic Science, Aeronautic Institute,
University of Saad Dahleb Blida 1, Blida, Algeria

Djilali Allou
Research Centre in Industrial Technologies (CRTI)
P.O Box 64, Cheraga 16014 Algiers, Algeria

To cite this article:

Younes, A, Amraoui, R., Abada, A., & Allou, D. (2025). Magnetic, structural and morphological properties of mechanically alloyed FeSi and $FeSiO_2$ nanocomposites. *The Eurasia Proceedings of Science, Technology, Engineering and Mathematics (EPSTEM), 38,* 159-165.

The Eurasia Proceedings of Science, Technology, Engineering & Mathematics (EPSTEM)
ISSN: 2602-3199

The Eurasia Proceedings of Science, Technology, Engineering and Mathematics (EPSTEM), 2025

Volume 38, Pages 166-171

IConTES 2025: International Conference on Technology, Engineering and Science

Optimizing Cost and Performance of Hybrid Photovoltaic-Diesel Systems for Off-Grid Energy Solutions

Samir Hadjeri
Djillali Liabes University of Sidi Bel-Abbes

Halima Boubekeur
Djillali Liabes University of Sidi Bel-Abbes

Salah Hanafi
Djillali Liabes University of Sidi Bel-Abbes

Mokhtaria Jbilou
Djillali Liabes University of Sidi Bel-Abbes

Sid Ahmed Zidi
Djillali Liabes University of Sidi Bel-Abbes

Rihab Belhabri
Djillali Liabes University of Sidi Bel-Abbes

Abstract: Providing reliable electricity to remote or isolated communities is a major challenge, especially with traditional power grids that require expensive infrastructure and ongoing maintenance. Hybrid energy systems are becoming an increasingly attractive solution due to their flexibility, reliability, and lower long-term costs. This study explores a hybrid energy setup that combines solar photovoltaic panels, a Diesel generator, and battery storage, using HOMER software to analyze different configurations. The goal is to find the most cost-effective setup that still ensures a steady and reliable energy supply. Several scenarios are simulated, taking into account local solar resources, changes in fuel prices, and varying electricity demand. The findings show that hybrid systems can significantly cut Diesel use, improve energy efficiency, and offer a cleaner, more sustainable energy solution for off-grid areas. Overall, the proposed system proves to be a practical and affordable alternative for communities that are hard to reach with traditional power infrastructure.

Keywords: Hybrid system, Photovoltaic-Diesel system, Techno-economic optimization, Off-grid energy, HOMER software.

Introduction

Providing reliable electricity to remote or isolated communities remains a significant global challenge, especially in developing countries where grid extension is economically unfeasible due to high investment, infrastructure, and maintenance costs (Mohammed et al., 2014; Come Zebra et al., 2021). In many off-grid regions, diesel generators are still the primary power source. However, they are associated with high operating costs, dependence on fluctuating fuel prices, limited reliability, and considerable greenhouse gas emissions (Karakoulidis et al., 2011; López-Castrillón et al 2021). To overcome these challenges, hybrid renewable energy systems (HRES) — combining photovoltaic (PV) panels, diesel generators, and battery storage — have become a promising alternative for decentralized electrification. Such systems can enhance reliability, reduce diesel fuel

- This is an Open Access article distributed under the terms of the Creative Commons Attribution-Noncommercial 4.0 Unported License, permitting all non-commercial use, distribution, and reproduction in any medium, provided the original work is properly cited.

- Selection and peer-review under responsibility of the Organizing Committee of the Conference

© 2025 Published by ISRES Publishing: www.isres.org

consumption, and lower the long-term cost of energy while minimizing environmental impact (Aziz et al., 2022; Almashakbeh et al., 2023). The integration of renewable sources with diesel backup provides flexibility in meeting variable loads, particularly in regions with intermittent solar radiation (Seiyefa et al., 2024) .

Several techno-economic assessments have been carried out to evaluate the feasibility of PV–diesel–battery systems in different geographical contexts. For instance, Jahed et al. (2024) performed a comparative analysis using various battery technologies — including lithium-ion and vanadium redox — and found that the choice of storage has a strong influence on system cost and performance. Similarly, Wang et al. (2025) demonstrated through HOMER simulations that PV–diesel–battery configurations can significantly reduce operational costs and improve sustainability in agricultural and rural applications. In addition, research has shown that these systems are sensitive to parameters such as fuel price fluctuations, solar resource availability, and variations in load demand (Omar et al., 2025). Come Zebra et al. (2021) emphasized that hybrid systems can provide a reliable and clean energy supply when properly optimized, considering local climatic and economic conditions. Advanced simulation and optimization tools such as HOMER, RETScreen, and MATLAB-based algorithms have been widely used to determine the most cost-effective and technically viable configurations (Ram et al., 2022).

Beyond techno-economic considerations, hybrid systems also play a crucial role in achieving sustainable development goals (SDG 7) by promoting access to affordable, reliable, and modern energy in rural and isolated communities (Off-Grid Hybrid Electrical Generation Systems, 2024). They contribute to energy security and resilience, especially in developing nations where energy access remains uneven (Mohammed et al., 2014; Come Zebra et al..2021). Despite the growing body of literature, several research gaps persist. Many studies rely on generalized meteorological or load data rather than site-specific inputs. Furthermore, comprehensive sensitivity analyses addressing the combined effects of fuel price variation, component degradation, and renewable fraction optimization are still limited (Aziz et al., 2022; Almashakbeh et al., 2023).Therefore, further investigation is needed to determine the optimal hybrid configuration under varying technical and economic conditions.

In this context, the present study aims to determine the optimal configuration of a hybrid PV–diesel–battery system for off-grid electrification using HOMER software. The objective is to minimize the Net Present Cost (NPC) and Levelized Cost of Energy (LCOE) while ensuring high reliability and sustainability. Several scenarios are simulated to evaluate the impact of local solar resources, diesel price variations, and changing load profiles. The findings contribute to developing practical and economically viable off-grid solutions for remote communities.

Presentation of the Hybrid System

The hybrid energy system is mainly composed of photovoltaic (PV) units for power generation, supported by a diesel generator as a complementary fossil-based source. The system design is optimized according to the month with the highest solar irradiation to ensure maximum use of the available solar potential. During months with reduced solar energy, the diesel generator operates to compensate for the energy shortfall. The overall configuration of the Photovoltaic–Diesel–Battery hybrid system is illustrated in Figure 1.

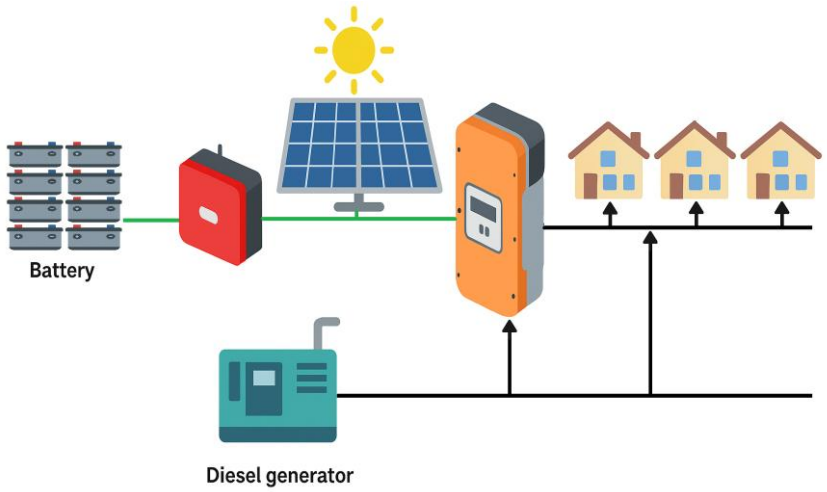


Figure 1. Configuration of the studied hybrid system

Sizing and Simulation Methodology

The general approach used for system sizing and simulations is summarized in the following steps:

1. Assessment of the energy demand (electricity consumption);
2. Preliminary manual sizing of the main system components.
3. Identification of the required equipment (solar panels, converter, and batteries) in the HOMER software environment.
4. Input of necessary data into HOMER, including:
   a). Energy consumption profile;
   b). Solar resource data for the selected location;
   c). Equipment specifications (capital cost, operation, and maintenance costs);
5. Execution of simulations using HOMER.
6. Iterative optimization of HOMER results to achieve the most cost-effective and technically optimal configuration;
7. Sensitivity analysis, if required, to assess system performance under varying parameters;
8. Validation of the system configuration based on simulation outcomes.

Solar Potential of the Selected Location

The selected site is an isolated area located in the Wilaya of Sidi Bel Abbès, Algeria. The average daily solar irradiation for each month of the year is presented in Table 1. It should be noted that the solar resource data can be obtained directly in HOMER software by clicking on the *"Get Data Via Internet"* icon.

Table 1. Solar radiation data of the selected location

Month	Irradiation (kWh/m^2/j)
January	2.76
February	3.72
March	4.68
April	5.78
May	6.63
June	7.22
July	7.26
August	6.31
September	5.08
October	3.9
November	2.85
December	2.45

Figure 2 presents the monthly solar radiation of the study site located in the wilaya of Sidi Bel Abbès, along with the monthly evaluation of solar irradiation shown in yellow and the illumination factor shown in red.

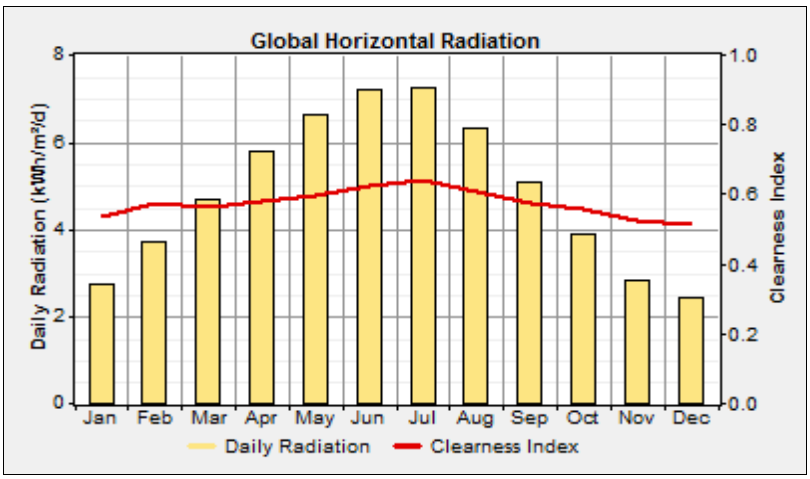


Figure 2. Monthly solar irradiation of the study region in the wilaya of Sidi Bel Abbes.

Load Profile

The estimated load profile plays a crucial role in choosing a suitable power supply system for a remote household or village. Since electricity consumption in a household fluctuates over the year, the demand is not uniform. Seasonal changes, particularly variations in daylight hours, lead to shifts in peak load times throughout the year. Figure 3 shows the daily load profile, where energy consumption remains low during nighttime hours (between midnight and 6 a.m.), while higher consumption is observed between 7 a.m. and 12 p.m., 2 p.m. and 5 p.m., and again from 7 p.m. to 10 p.m.

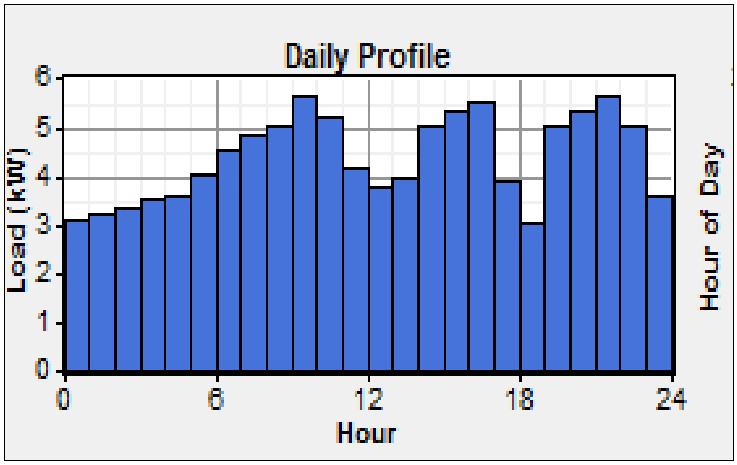


Figure 3. Daily load profile

Construction of the Hybrid System

Figure 4 shows the architecture of the Photovoltaic–Diesel hybrid system designed using the HOMER software.

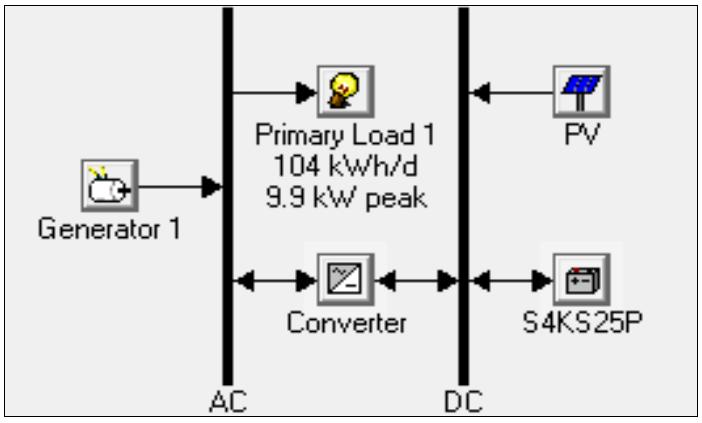


Figure 4. Configuration of the Photovoltaic–Diesel hybrid system modeled using HOMER

Simulation Results

Sensitivity Results | Optimization Results

Double click on a system below for simulation results. ◉ Categorized ○ Overall Export... Details...

PV (kW)	Label (kW)	S4KS25P	Conv. (kW)	Initial Capital	Operating Cost ($/yr)	Total NPC	COE ($/kWh)	Ren. Frac.	Diesel (L)	Label (hrs)
8	9	12	7	$ 34,424	6,940	$ 123,144	0.254	0.30	10,841	4,408
	9			$ 4,224	9,445	$ 124,964	0.258	0.00	15,914	8,759
1	9		1	$ 6,324	9,349	$ 125,841	0.259	0.04	15,581	8,759
	9	12	3	$ 20,424	9,683	$ 144,207	0.297	0.00	15,432	7,766
100		60	10	$ 217,500	6,521	$ 300,859	0.620	1.00		

Figure 5. Simulation results.

After running the simulation, HOMER displays the solutions in a list format, ranked according to the lowest cost of energy. The configurations are ordered from the most cost-effective to the least economical based on the Net Present Cost (NPC), as shown in Figure 5 and Table 2 below. Based on the obtained results, the first configuration represents the best energy installation — it is the optimal solution proposed by the HOMER software, with a Net Present Cost (NPC) of 123.144 $.

Table 2. Net present cost "NPC" ($).

Configurations	Net Present Cost "NPC" ($).
PV+Diesel+ Battery + Converter	123.144
Diesel	124.964
PV+Diesel+Converter	125.841
Diesel+Battery+Converter	144.207
PV+Battery+Converter	300.859

Conclusion

The proposed hybrid Photovoltaic–Diesel–Battery system designed for the studied region of Sidi Bel Abbès (Algeria) represents a reliable, versatile, and sustainable energy solution for off-grid power supply. It effectively combines the advantages of renewable resources—particularly the abundant local solar potential—with the flexibility and immediate availability of diesel generation when required. This configuration ensures continuous power availability, enhances overall energy efficiency, and significantly reduces both operating costs and carbon emissions, contributing to a cleaner and more autonomous energy transition for remote communities.

Recommendations

It is recommended to conduct future studies that integrate other renewable energy sources, such as wind or biomass, along with advanced control strategies to further enhance the system's energy efficiency and sustainability.

Scientific Ethics Declaration

* The authors declare that the scientific ethical and legal responsibility of this article published in EPSTEM journal belongs to the authors.

Conflict of Interest

* The authors declare that they have no conflicts of interest

Funding

* This research received no specific grant from any funding agency in the public, commercial, or not-for-profit sectors.

Acknowledgements or Notes

* This article was presented as a poster presentation at the International Conference on Technology, Engineering and Science (www.icontes.net) held in Antalya/Turkiye on November 12-15, 2025.

*The authors would like to express their sincere gratitude to all those who contributed to the preparation of this research work, whether directly or indirectly, through their support, guidance, or encouragement throughout its development.

References

Almashakbeh, A. S., et al. (2023). Techno-economic evaluation of an off-grid hybrid PV-wind-diesel-battery system with various scenarios of system's renewable energy fraction. *Energy Sources, Part A: Recovery, Utilization, and Environmental Effects, 45,* 6162-6185. https://doi.org/10.1080/15567036.2019.1673515 .

Aziz, A. S., et al. (2022). Techno-economic and environmental evaluation of PV/diesel/battery hybrid energy system using improved dispatch strategy. *Energy Reports, 8,* 6794-6806. https://doi.org/10.1016/j.egyr.2022.05.021 .

Come Zebra, E. I., van der Windt, H., Nhumaio, G., & Faaij, A. P. C. (2021). A review of hybrid renewable energy systems in mini-grids for off-grid electrification in developing countries. *Renewable and Sustainable Energy Reviews, 144*, 111036. https://doi.org/10.1016/j.rser.2021.111036 .

Jahed, A., et al. (2024). Techno-economic analysis of off-grid hybrid wind-photovoltaic-battery power system by analyzing different batteries for the industrial plant in Shiraz Industrial Town, Iran. *Science Progress. 2024;107*(3). https://doi.org/10.1177/00368504241265003 .

Karakoulidis, K., Mavridis, K., Bandekas, D. V., Adoniadis, P., Potolias, C., & Vordos, N. (2011). Techno-economic analysis of a stand-alone hybrid photovoltaic-diesel–battery-fuel cell power system. *Renewable Energy, 36*(8), 2238-2244. https://doi.org/10.1016/j.renene.2010.12.003 .

López-Castrillón, W., Sepúlveda, H.H., Mattar, C. (2021). Off-Grid Hybrid Electrical Generation Systems in Remote Communities: Trends and Characteristics in Sustainability Solutions. *Sustainability 2021, 13,* 5856. https://doi.org/10.3390/su13115856 .

Mohammed, Y. S., Mustafa, M. W., & Bashir, N. (2014). Hybrid renewable energy systems for off-grid electric power: Review of substantial issues. *Renewable and Sustainable Energy Reviews, 35,* 527-539. https://doi.org/10.1016/j.rser.2014.04.022 .

Omar, M. A., et al. (2025). Techno-economic analysis of PV/diesel/battery hybrid system for rural community electrification: A case study in the Northern West Bank. *Energy, 317,* 134770. https://doi.org/10.1016/j.energy.2025.134770 .

Ram, K., Swain, P. K., Vallabhaneni, R., & Kumar, A. (2022). Critical assessment on application of software for designing hybrid energy systems. *Materials Today: Proceedings, 49*, 425–432. https://doi.org/10.1016/j.matpr.2021.02.452 .

Seiyefa, A. V., Tahiru, A., Lawal, R. O., Aralu, C. E., & Okikiola, A. Q. (2024). Hybrid renewable energy systems for rural electrification in developing countries: Assessing feasibility, efficiency, and socioeconomic impact. *World Journal of Advanced Research and Reviews, 24*(2), 2190-2204. https://doi.org/10.30574/wjarr.2024.24.2.3515 .

Wang, W., et al. (2025). Techno-economic assessment of PV-diesel-battery hybrid systems for poultry farms: A case study in North Carolina. *Energy Reports, 17,* 100372. https://doi.org/10.1016/j.nexus.2025.100372 .

Author(s) Information

Samir Hadjeri
Intelligent Control & Electrical Power Systems Laboratory, Faculty of Electrical Engineering
Djillali Liabes University, 22000 Sidi Bel Abbes, Algeria
Contact e-mail : *shadjeri2@yahoo.fr*

Halima Boubekeur
Intelligent Control & Electrical Power Systems Laboratory, Faculty of Electrical Engineering
Djillali Liabes University, 22000 Sidi Bel Abbes, Algeria

Salah Hanafi
Intelligent Control & Electrical Power Systems Laboratory, Faculty of Electrical Engineering
Djillali Liabes University, 22000 Sidi Bel Abbes, Algeria

Mokhtaria Jbilou
Intelligent Control & Electrical Power Systems Laboratory, Faculty of Electrical Engineering
Djillali Liabes University, 22000 Sidi Bel Abbes, Algeria

Sid Ahmed Zidi
Intelligent Control & Electrical Power Systems Laboratory, Faculty of Electrical Engineering
Djillali Liabes University, 22000 Sidi Bel Abbes, Algeria

Rihab Belhabri
Intelligent Control & Electrical Power Systems Laboratory, Faculty of Electrical Engineering
Djillali Liabes University, 22000 Sidi Bel Abbes, Algeria

To cite this article:

Hadjeri, S., Boubekeur, H., Hanafi, S., Jbilou, M., Zidi, S.A., & Belhabri, R. (2025). Optimizing cost and performance of hybrid photovoltaic-diesel systems for off-grid energy solutions. *The Eurasia Proceedings of Science, Technology, Engineering and Mathematics (EPSTEM), 38,* 166-171.

The Eurasia Proceedings of Science, Technology, Engineering & Mathematics (EPSTEM)
ISSN: 2602-3199

The Eurasia Proceedings of Science, Technology, Engineering and Mathematics (EPSTEM), 2025

Volume 38, Pages 172-179

IConTES 2025: International Conference on Technology, Engineering and Science

EOQ Based Inventory Optimization with Partial Backordering and Demand Uncertainty in Manufacturing

Chyntia Meininda Anjanni
Gadjah Mada University

Fitri Cahyani
Gadjah Mada University

Akhmad Sultoni
Gadjah Mada University

Abstract: Inventory management is one of the important aspects in manufacturing systems, especially in the face of demand uncertainty and lead time variability. The classic Economic Order Quantity (EOQ) model is often assumed with constant demand and fixed lead times that do not always reflect the complexity of the real world. This research develops a more adaptive EOQ-Partial Backordering model by integrating a dynamic demand response mechanism as well as a lead time-based ordering strategy, in order to improve the resilience of inventory systems in manufacturing systems. The proposed model is designed to minimize the total inventory cost, by considering the balance between holding cost, backordering cost, and ordering cost. In contrast to previous models, this approach systematically measures between immediate demand fulfillment and delayed fulfillment, thus enabling more flexible inventory decisions. The evaluation of the model was conducted using sensitivity analysis and Monte Carlo simulation, by testing different scenarios of demand volatility and variations in the proportion of backorders. The results show that considering partial backordering in the EOQ framework will result in a better inventory policy, reduce excess stock and improve cost effectiveness. On the other hand, this study also considers the impact of demand fluctuations on the optimal ordering quantity and provides practical knowledge and can be a strategic reference for inventory managers in the manufacturing industry. The main contribution of this research in inventory theory is to bridge the gap between deterministic EOQ models and stochastic demand dynamics in the real world, while offering an applicable decision-making tool for more efficient inventory management and better supply chain resilience.

Keywords: Inventory optimization, EOQ model, Partial backordering, Demand uncertainty, Manufacturing systems

Introduction

The manufacturing industry faces great challenges in optimizing inventory management to ensure efficient production continuity. Imbalances in parts availability can lead to costly production downtime, while excessive inventory can increase holding costs and reduce operational efficiency. Therefore, inventory management strategies are an important aspect in the supply chain of the manufacturing industry. One of the basic methods used in inventory optimization is the Economic Order Quantity (EOQ) model first introduced by Harris (1913). This model aims to determine the optimal order quantity to minimize total inventory costs, which include ordering costs and holding costs. However, in practice, the classic EOQ assumptions of deterministic demand and instant order fulfillment are often incompatible with real conditions in the manufacturing industry.

- This is an Open Access article distributed under the terms of the Creative Commons Attribution-Noncommercial 4.0 Unported License, permitting all non-commercial use, distribution, and reproduction in any medium, provided the original work is properly cited.

- Selection and peer-review under responsibility of the Organizing Committee of the Conference

© 2025 Published by ISRES Publishing: www.isres.org

To increase the relevance of the EOQ model in an increasingly complex manufacturing environment, various studies have developed variations of the classic EOQ model. One widely researched approach is EOQ with Partial Backordering, which allows a portion of demand that cannot be fulfilled immediately to be postponed at a certain cost. Based on Goyal & Giri's (2019) research, considering the backordering aspect in EOQ can reduce the total cost of the inventory system and improve supply chain efficiency. In addition, this model offers greater flexibility in the face of demand fluctuations and lead time uncertainty.

A number of other studies have also tried to accommodate uncertainty in EOQ by considering probabilistic distributions on demand and lead time. For example, Lee & Park's (2018) research developed a stochastic model with variable lead time and partial ordering, which showed that flexibility in ordering policy can significantly reduce the total inventory cost. Meanwhile, Zhou & Yang (2017) proposed an inventory optimization model for perishable products with stochastic demand and partial ordering, which proved that an optimal ordering policy can improve service levels as well as cost efficiency. However, previous research still has some limitations. Goyal & Giri (2019) developed an EOQ model with Partial Backordering in a deterministic context, which assumes that all parameters such as demand and lead time are known with certainty. This is incompatible with the real conditions in the manufacturing industry that often face uncertainties in the supply chain. In addition, previous models often result in complicated calculation procedures, making it difficult to apply to industrial systems with high variability. To overcome these limitations, this study aims to explore the impact of parameter variability in the EOQ with Partial Backordering model on the total cost of inventory systems in the manufacturing industry. By integrating the stochastic approach and Monte Carlo simulation, this research is expected to provide more accurate and applicable recommendations in inventory management. The results obtained are not only expected to provide theoretical contributions in the development of a more realistic EOQ model, but also provide practical benefits for companies in optimizing their inventory management strategies.

Methods

This research method aims to develop an Economic Order Quantity (EOQ) model with Partial Backordering in the context of a manufacturing industry facing demand uncertainty. This model is developed based on a deterministic approach by considering the aspect of partial backordering, where some demand that cannot be fulfilled immediately can be postponed at a certain cost. This section will explain the mathematical formulation of the EOQ model used, the selection of demand distribution, the developed model algorithm, and the Monte Carlo simulation technique to evaluate the model's performance in various demand scenarios.

EOQ Model Formulation with Partial Backordering

In the classical EOQ model, the main assumption is that demand is constant and always met. However, in practice, the manufacturing industry often faces delays in stock fulfillment, so that some demand cannot be met immediately and is postponed to the next period. Therefore, the EOQ model is extended by considering partial backordering, with the following formula:

Optimal Order Quantity

The optimal order quantity Q^* in the EOQ model with Partial Backordering can be calculated using the formula:

$$Q^* = \sqrt{\frac{2C_o E[D]}{C_h} \times \frac{C_b}{C_h + C_b}}$$

With:
Q^* = optimal order quantity
C_o = ordering cost per order
C_h = holding cost per unit per year
C_b = backordering cost per unit per year
$E[D]$ = expected annual demand

Maximum Backordering Amount

The number of units that can be backordered is calculated by:

$$B^* = Q^* \times \frac{C_h}{C_h + C_b}$$

Order Cycle Length

The length of the order cycle is calculated by:

$$T^* = \frac{Q^*}{E[D]}$$

Total Inventory Cost

The total cost of the inventory system, which includes ordering costs, holding costs, and backordering costs, is calculated by:

$$TC = \frac{C_o E[D]}{Q^*} + \frac{C_h}{2} Q^*(1-\beta) + \frac{C_b}{2} B^*$$

Where β is the fraction of demand that can be ordered in advance.

Selection of Demand Distribution

To ensure that the EOQ model with Partial Backordering can be applied in real manufacturing conditions, it is necessary to choose the most appropriate demand distribution. In this study, three main stochastic distributions are used:

1) Normal Distribution

If demand fluctuates steadily with small variations around the average.

$$D \sim \mathcal{N}(\mu, \sigma^2)$$

Demand expecatation:

$$E[D] = \mu$$

2) Poisson Distribution

If demand occurs discretely and in batch orders, such as ordering products in fixed quantities.

$$D \sim Poisson(\lambda)$$

Demand expectation:

$$E[D] = \lambda$$

3) Exponential Distribution

If demand is sporadic and irregular, as in the spare parts industry.

$$D \sim Exponential\ (\lambda)$$

Demand expectation:

$$E[D] = \frac{1}{\lambda}$$

The selection of demand distribution is based on the characteristics of the industry being studied, so that the model can provide more realistic results.

EOQ Model Algorithm with Partial Backordering

To calculate the optimal order quantity and evaluate its impact on total inventory costs, the following algorithm is used:

1) Parameter Initialization

- Define the ordering cost C_o, holding cost C_h, backordering cost C_b and expected annual demand $E[D]$
- Select the appropriate demand distribution (Normal, Poisson, or Exponential)

2) Calculate Optimal Order Quantity Q^*

Use equation:

$$Q^* = \sqrt{\frac{2C_o E[D]}{C_h} \times \frac{C_b}{C_h + C_b}}$$

3) Calculate the Number of Backordering B^*

Use equation:

$$B^* = Q^* \times \frac{C_h}{C_h + C_b}$$

4) Calculate Total Inventory Cost TC

- Calculate ordering cost:

$$TC_{order} = \frac{C_o E[D]}{Q^*}$$

- Calculate holding cost:

$$TC_{holding} = \frac{C_h}{2} Q^*(1 - \beta)$$

- Calculate ordering cost:

$$TC_{backorder} = \frac{C_b}{2} B^*$$

- Total inventory cost:

$$TC = TC_{order} + TC_{holding} + TC_{backorder}$$

5) Model Validation with Monte Carlo Simulation

- Perform demand sampling using the selected distribution.
- Calculate Q^* and B^* for each demand scenario.
- Evaluate total cost TC to determine the optimal inventory strategy.

6) Perform Sensitivity Analysis

- Test changes in parameters $C_o, C_h, C_b, E[D]$ to see how these factors affect total inventory costs.

- Identify conditions under which Partial Backordering is more profitable than full fulfillment of demand.

Monte Carlo Simulation for Model Evaluation

To test the EOQ model with Partial Backordering under conditions of demand uncertainty, a Monte Carlo simulation is conducted with the following procedure:
(1) Determine the demand scenario using the selected probabilistic distribution.
(2) Conduct a simulation with 10,000 iterations to see how demand fluctuations affect the optimal order quantity and total inventory cost.
(3) Analyze the simulation results to determine the best strategy in inventory management.

Results and Discussion

Uncertain demand is an important factor affecting inventory policy in manufacturing industry. The classical EOQ model assumes deterministic demand, but in real conditions, demand can fluctuate stochastically. Therefore, this study examines the impact of demand uncertainty on optimal order quantity (Q^*) and total inventory cost (TC) using Monte Carlo simulation based on three types of demand distributions: Normal, Poisson, and Exponential. The simulation was run for 10,000 iterations considering the variation of holding cost (C_h) backordering cost (C_b), ordering cost (C_o) and lead time uncertainty.

Simulation Assumptions and Parameters

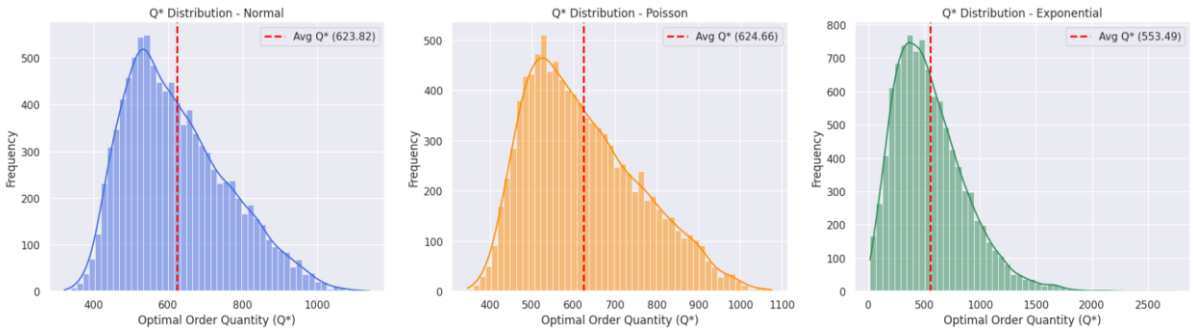
To ensure that the simulation model reflects real conditions, this study uses the following assumptions:

1) Demand is stochastic, following one of three distributions: Normal, Poisson, or Exponential.
2) The holding cost (C_h) and backordering cost (C_b) are not constant but vary within a certain range.
3) Ordering costs (C_o) also vary, reflecting dynamic operational conditions.
4) Lead time is not fixed, ranging from 80% to 120% of the average expected value.
5) The ordering cycle is repeated up to 10,000 iterations, to ensure a stable distribution of results.

The cost parameters used in the simulation are:

Ordering cost (C_o)	: varies between Rp 4,000 - Rp 6,000.
Holding cost (C_h)	: varies between Rp 10 - Rp 30 per unit per year.
Backordering cost (C_b)	: varies between Rp 30 - Rp 80 per unit per year.
Expected annual demand (E[D])	: 1,000 units/year.
Lead time variation	: 80% - 120% of the average.

Impact of Demand Uncertainty on Optimal Order Quantity (Q^*)



Figures 1. Monte Carlo simulation: Distribution of optimal order quantity (Q) for different demand models

The simulation results show that the optimal order quantity (Q^*) varies based on the demand distribution

- Normal Distribution ($Q^* = 624{,}10$): Relatively stable demand results in a more consistent ordering policy centered around the mean.

- Poisson Distribution ($Q^* = 625{,}18$): Similar results to the Normal distribution, but with a slightly wider spread due to its discrete nature.
- Exponential Distribution ($Q^* = 552{,}49$): More frequent small-volume demand results in a lower optimal order quantity, to avoid overstocking.

Figure 1 illustrates the distribution of optimal order quantities for each demand distribution. In a manufacturing environment facing high uncertainty, the optimal order quantity must be adjusted to the prevailing demand distribution pattern.

Impact of Demand Uncertainty on Total Inventory Cost (TC)

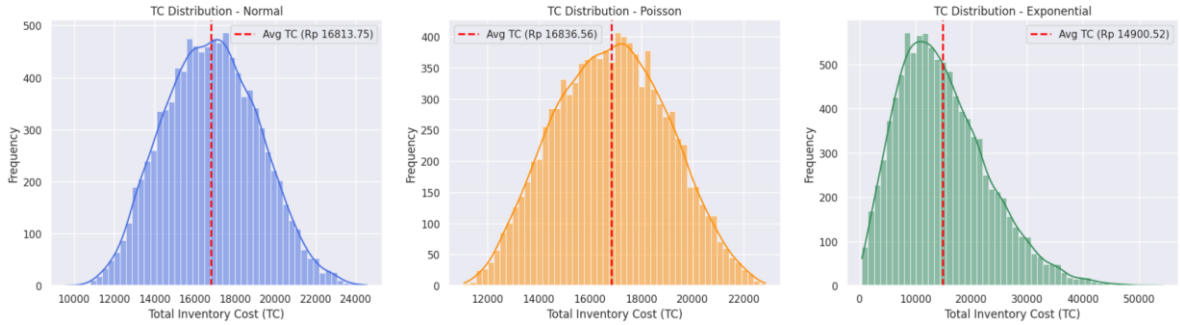


Figure 2. Monte Carlo simulation: Distribution of total ınventory cost (TC) for different demand models

The distribution of inventory cost (TC) also shows significant differences between the three demand scenarios. The Normal distribution ($TC = Rp16{,}837.56$) and Poisson ($TC = Rp16{,}866.62$) have similar cost distribution patterns. The Exponential distribution ($TC = Rp14{,}921.49$) results in lower inventory costs, as less stock is kept to accommodate more sporadic demand patterns. Figures 2 show the distribution of total inventory costs for each type of demand. Thus, under conditions of high demand uncertainty, the EOQ model with Partial Backordering can reduce inventory costs by adjusting the order quantity and holding policy.

Managerial Implications

The results of this study provide several important insights for supply chain management:
If demand is stable as in Normal or Poisson distribution, the company can maintain a larger order quantity to improve inventory efficiency. On the other hand, if demand is unstable as in Exponential distribution, the company should be more flexible in its holding and ordering policies and rely on backordering strategy to avoid high holding costs. In addition, fluctuations in holding costs, back ordering costs, and inconsistent lead times have different effects on inventory decisions, so a dynamic stock strategy is more advisable.

Conclusion

This study explores the effect of demand uncertainty in the EOQ model with Partial Backordering using Monte Carlo simulation. The results of the analysis show that demand distribution, cost variation, and lead time uncertainty have a significant impact on the optimal order quantity and total inventory cost. The following are the main conclusions of this study:

(1) The Effect of Demand Uncertainty on EOQ with Partial Backordering
The simulation results show that the optimal order quantity and total inventory cost are highly dependent on the demand distribution pattern used. Demand that follows the Normal and Poisson distributions produces a more stable order quantity compared to the Exponential distribution, where the order quantity tends to be smaller to avoid the risk of excess stock.

(2) Variation of Cost and Lead Time Parameters
Variation of holding costs and backordering costs have a significant impact on ordering decisions. When holding costs are high, the order quantity is smaller to avoid stock accumulation, while when backordering costs are high, the ordering policy tends to avoid stockouts by increasing the order quantity. In addition,

variable lead times cause fluctuations in the optimal order quantity, where longer lead times increase backordering costs and require a more adaptive ordering strategy.

(3) Impact of Demand Distribution on Total Inventory Cost
The simulation results show that demand distribution affects total inventory cost. In Normal and Poisson distributions, inventory cost is higher because the order quantity is larger to maintain stock availability. Meanwhile, in Exponential distribution, total inventory cost is lower because the order quantity is smaller, reflecting a more flexible stock strategy in dealing with irregular demand.

(4) Implications for Inventory Management in Manufacturing Industry
The EOQ model with Partial Backordering developed in this study can help companies determine more flexible inventory policies based on changing demand patterns and costs. By considering variations in holding costs, backordering costs, and lead time uncertainty, stock management strategies can be optimized to balance between optimal order quantities and total inventory costs.

The EOQ model with Partial Backordering that considers demand uncertainty can optimize inventory policies and reduce costs. This research can be further developed by considering external factors such as price fluctuations and seasonal demand to be more relevant in industrial practice.

Scientific Ethics Declaration

* The authors declare that the scientific ethical and legal responsibility of this article published in EPSTEM journal belongs to the authors.

Conflict of Interest

* The authors declare that they have no conflicts of interest

Funding

* The author would like to express sincere gratitude to the Indonesia Endowment Fund for Education (LPDP) under the Ministry of Finance of the Republic of Indonesia for supporting and funding this research. Their support has been instrumental in facilitating the completion of this work.

Acknowledgements or Notes

* This article was presented as a poster presentation at the International Conference on Technology, Engineering and Science (www.icontes.net) held in Antalya/Türkiye on November 12-15, 2025.

* The author would like to express sincere gratitude to the Indonesia Endowment Fund for Education (LPDP) under the Ministry of Finance of the Republic of Indonesia for providing financial support for this research. The author also appreciates the guidance and insightful discussions from the academic supervisor, as well as the encouragement and support from colleagues and family throughout this study

References

Anderson, H., Smith, J., & Turner, P. (2019). Lost sales vs. backordering: A comparative study in manufacturing. *Omega, 87*, 132–145.

Brown, M., & Lee, K. (2016). Economic order quantity models in modern manufacturing systems. *European Journal of Operational Research, 250*, 45–57.

Hadley, G., & Whitin, T. M. (1963). *Analysis of inventory systems.* Prentice-Hall.

Kumar, A., & Gupta, P. (2017). Partial backordering in EOQ models: A manufacturing perspective. *Applied Mathematical Modelling, 63*, 80–95.

Nahmias, S. (2009). *Production and operations analysis.* McGraw-Hill.

Teunter, R., & Sani, B. (2009). Inventory control with partial backordering and time-varying demand. *European Journal of Operational Research, 198*, 258–268.

Zhang, L., Chen, Y., & Wang, X. (2018). Demand fluctuations and their impact on EOQ decisions in manufacturing. *Computers & Operations Research, 95*, 210–225.

Author(s) Information

Chyntia Meininda Anjanni
Gadjah Mada University
Yogyakarta, Indonesia
Contact e-mail: *chyntiameinindaanjanni@mail.ugm.ac.id*

Fitri Cahyani
Gadjah Mada University
Yogyakarta, Indonesia

Akhmad Sultoni
Gadjah Mada University
Yogyakarta, Indonesia

To cite this article:

Anjanni, C. M., Cahyani, F., & Sultoni, A. (2025). EOQ based inventory optimization with partial backordering and demand uncertainty in manufacturing. *The Eurasia Proceedings of Science, Technology, Engineering and Mathematics (EPSTEM), 38,* 172-179.

The Eurasia Proceedings of Science, Technology, Engineering & Mathematics (EPSTEM)
ISSN: 2602-3199

The Eurasia Proceedings of Science, Technology, Engineering and Mathematics (EPSTEM), 2025

Volume 38, Pages 180-188

IConTES 2025: International Conference on Technology, Engineering and Science

Potential Use of Recycled Brick and Demolition Concrete Aggregates in the Self-Compacting Concrete

Ghernouti Youcef
University of Boumerdes

Rabehi Bahia
University of Boumerdes

Mansour Sabria Malika
University of Boumerdes

Abstract: This work aim to investigate the possibility of recycling waste materials, specifically brick aggregates (BA) and demolition concrete aggregates (DCA) in the formulation of self-compacting concrete (SCC), for this an experimental study was carried out to evaluates the fresh and hardened properties. A reference mixture composed entirely of natural aggregates (NASCC) was compared to six mixtures incorporating recycled brick aggregates (BASCC), recycled demolition concrete aggregate (DCASCC) and a combination of recycled brick and demolition concrete aggregates (BDASCC), as partial replacement of natural aggregates have been prepared. The fresh properties were assessed through slump flow, L-box, and sieve stability tests. Compressive and flexural strengths tests were conducted to evaluate the hardened properties. The results are very interesting, suggesting a possible use of brick aggregate and demolition concrete aggregate in formulation of SCC, and can lead to new concrete with satisfactory physical mechanical properties satisfying the criteria of self-compacting concrete.

Keywords: Recycled, Waste, Aggregate, Brick, Demolition, Self-compacting concrete

Introduction

Concrete is a heterogeneous material which is made with cement, aggregate and water. The strength of the concrete produced is dependent on the properties of aggregates used; it covers 70% to 80% of the total for any concrete mix. However, the construction industry is increasingly making higher demands of this materials which are not available in plenty and some of them are energy intensive is feared to accommodate the many requests. For these reasons their use must be economized. Hence need for an alternative aggregate arises.

One of the major environmental challenges today is the recycling of construction and demolition waste materials. Brick aggregates (BA) and demolition concrete aggregates (DCA) generate millions of tons of waste annually. These materials, which offer both economic and technical benefits, have the potential to replace natural aggregates (NA) in the production of self-compacting concrete (SCC). The use of recycled aggregates (RA), including BA and DCA, as partial or full substitutes for NA in concrete mixtures and their impact on fresh and hardened properties such as workability, strength, and durability has been widely investigated by several researchers (Duan & Poon, 2014; Yang et al, 2011; Debieb et al, 2010; Chen et al, 2003; Mansur et al, 1999; Khatib, 2005; Khalaf, 2006; Ghernouti et al, 2016; Ghernouti et al, 2024).

Many authors from different countries study the use of recycled aggregates in concrete: (Levy & Helene, 2004), and (Poon et al, 2007) in their research papers show that the aggregates which are got from demolished masonry

- This is an Open Access article distributed under the terms of the Creative Commons Attribution-Noncommercial 4.0 Unported License, permitting all non-commercial use, distribution, and reproduction in any medium, provided the original work is properly cited.

- Selection and peer-review under responsibility of the Organizing Committee of the Conference

© 2025 Published by ISRES Publishing: www.isres.org

and concrete structures are potentially good for use in new concrete. (Cachim, 2009) reported that crushed bricks could be used as a partial replacement of natural coarse aggregate without reduction in concrete properties for 15% replacement and with reductions up to 20% for 30% replacement. (Khaloo, 1994) found a decrease by 7% in concrete compressive strength by using crushed clinker bricks as coarse aggregate compared to natural aggregate concrete. (Poon & Chan, 2007) found that the incorporation of 20% fine crushed brick aggregate decreased the compressive strength and the modulus of elasticity of the concrete by 18% and 13%, respectively. (Mansour & Ghernouti, 2021) demonstrated that replacing 50% of aggregates or 10% of cement with natural rock perlite improves the workability and mechanical properties of self-compacting concrete, while also contributing to resource conservation, cost savings, and reduced CO_2 emissions.

In the work of (Kou & Poon, 2009), the recycled glass (RG) cullet was used to replace river sand (in proportions of 10%, 20% and 30%), and 10 mm granite (5%, 10% and 15%) in making the SCC concrete mixes. their experimental results showed that the fresh properties of the RG–SCC mixes increased and the hardened properties decreased with increasing recycled glass content. Moreover, the resistance to chloride ion penetration increased and the drying shrinkage of the RG–SCC mixes decreased when the recycled glass content increased. The results showed that it is feasible to produce SCC with recycled glass cullet.

The present study focused on the use of brick aggregate (BA) and demolition concrete aggregate (DCA) resulting from recycling waste materials such as, brick industries and demolition concrete and to find new ways of valorization in the self-compacting concrete (SCC). We will present, therefore, the fresh and hardened states properties of the concrete.

Experimental program

Materials

The reference self-compacting concrete (SCC) mixture investigated in this work was prepared with Ordinary Portland cement (OPC) CEMII/A42.5.

Limestone filler were used as addition materials in the mix proportions, they are rich in lime (CaO) above 55% and their specific surface area is about 3400cm^2/g.

The aggregates used are natural sand (NS), with a maximum particle size of 4 mm and two natural crushed limestone gravel with particle size between 3/8 and 8/15 (fig 1).

The recycled waste aggregates used in this investigation are brick aggregate (BA) and demolition concrete aggregate (DCA) from local sources resulting from crushing waste materials such as, brick industries and demolition concrete (see figure 2). The physical properties of all aggregates used in this work are listed in Table 1 and 2, the granular size analysis are presented in Fig.3, 4 and 5.

A polycarboxylate-based superplasticizer named Sika viscocrete Tempo 12 was used to achieve the appropriate workability of the self-compacting concrete (SCC) mixes.

Table 1. Physical properties of fines aggregates

	Natural sand (NS)	Recycled brick waste sand (BA)	Recycled demolition concrete sand (DCA)
Apparent density, (g/cm^3)	1.56	1.26	1.24
Specific gravity, (g/cm^3)	2.64	2.22	2.3
Visual sand equivalent, VES (%)	81	79	77
Fineness modulus	2.86	3.8	3.4
Water absorption (%)	3	19	8

Table 2. Physical properties of coarse aggregates

	Natural coarse aggregates (3/8 and 8/15)	Recycled brick coarse aggregates (3/8 and 8/15)	Recycled demolition concrete coarse aggregates (3/8 and 8/15)
Apparent density, (g/cm^3)	1.20	1.2	1.24
Specific gravity, (g/cm^3)	2.38	2.4	2.3
Los Angeles (%)	25	28.5	77
Micro-Deval (%)	26	27.2	3.4



Figure 1. Natural aggregates

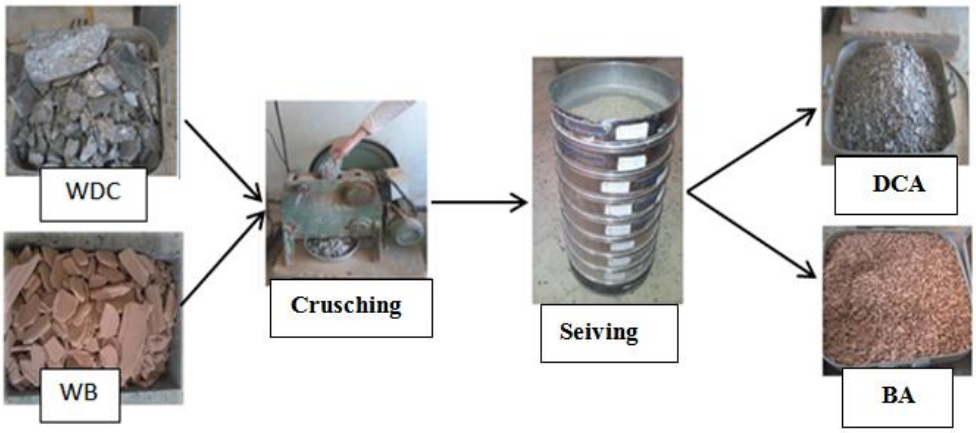


Figure 2. Preparation of recycled aggregates

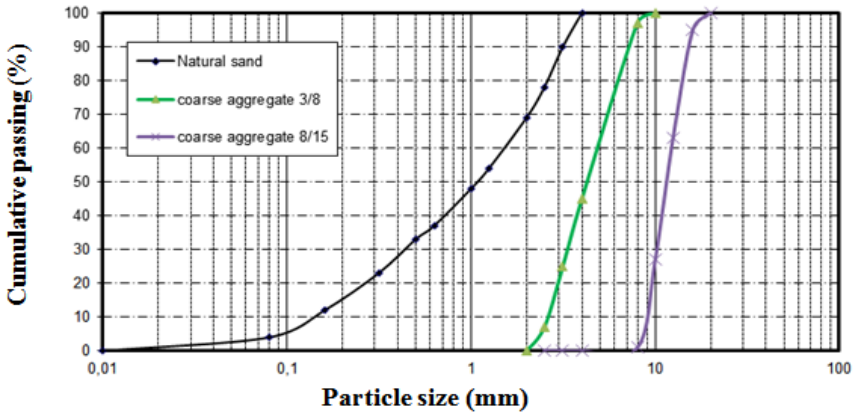


Figure 3. Particle size distribution of natural aggregates

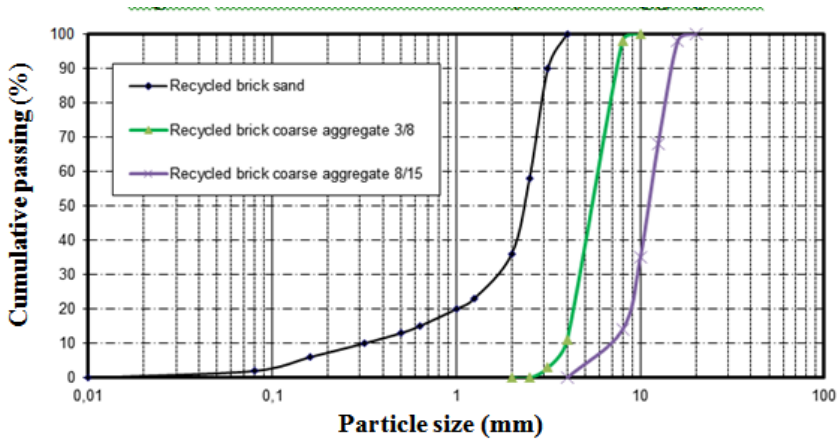


Figure 4. Particle size distribution of Recycled brick waste aggregates

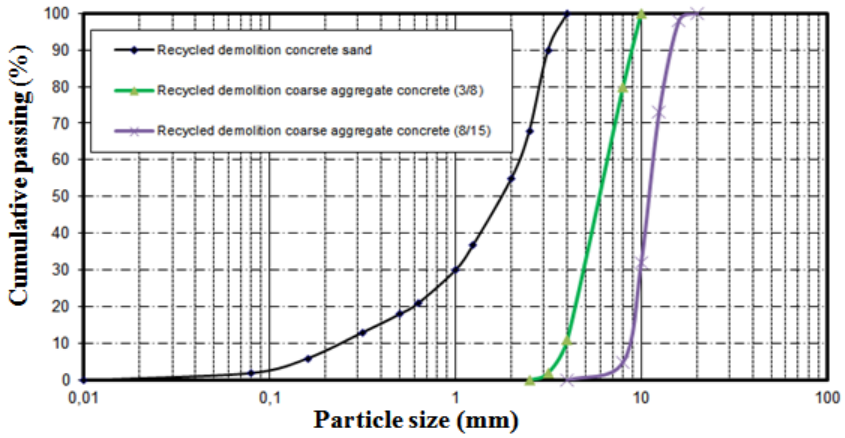


Figure 5. Particle size distribution of recycled demolition concrete aggregates

Mixture Proportions

Based on self-compacting concrete mix design Japanese method (Okamura H & Ozawa K, 1995), seven mixes were produced: A reference mixture based on natural aggregates (NASCC) with the total amounts of cement, fillers, coarse aggregates, sand, water and superplasticizer were all kept constant (430, 43, 844, 903, 174 and 7.6 kg/m^3, respectively), Two mixtures incorporating recycled brick aggregate (BSCC) with 25 and 50% replacement, Two mixtures incorporating recycled demolition concrete aggregates (DSCC) with 25 and 50% replacement and two mixtures incorporating combination of recycled brick and demolition concrete aggregates (BDSCC), as replacement of 50 and 100% natural aggregates.

Preparation and Casting of Test Specimens

The mixing procedure and time are very important, thus the mixing process was kept constant for all concrete mixtures. All the ingredients were first mixed under dry condition in the concrete mixer for one minute. Then 70% of calculating amount of water was added to the dry mix and mixed thoroughly for one minute. The remaining amount of water was mixed with the superplasticizer and was poured into the mixer and mixed for five minutes. After this sequence of preparation, flowability, passing ability and resistance to segregation of prepared mixtures are measured. For each concrete mixture three prisms of (7x7x28) cm and three cylinders (11x22) cm specimens were cast. Therefore, the total number of specimens considered in this experimental investigation was twenty one cylinders and twenty one beams. The specimens were demolded after one day and then placed in a curing room with a humidity of 90% and a temperature of 20 ± 2°C until the testing days (See Figure 6).



a) Mixer b) Specimens c) Curing of specimens

Figure 6. Preparation and casting of test specimens

Results and Discussions

Fresh Concrete Properties

The objective is to know the influence of the plastic brick aggregate (BA) and demolition aggregate concrete (DAC) on the workability of concrete. The flowability was evaluated by slump flow diameter, the passing ability was measured by L-box and the resistance to segregation was measured by sieve stability test, according to the specification and guidelines for SCC prepared by the European project group (EFNARC, 2005), (Figure 7). The obtained results of the slump flow diameter, L-box and sieve stability test of different mixtures are given in Table 3.



a) Slump flow test b) L-box test c) Sieve stability test

Figure 7. Tests on fresh concretes

The slump flow test is most used to measure the ability of self-compacting concrete to flow in the absence of obstructions. The test method is very similar to that for determining the slump of concrete. The difference is that, instead of the loss in height, the diameter of the spread concrete is measured in two perpendicular directions and recorded as slump flow. The obtained results show that the increasing of recycled aggregates brick or the demolition aggregates concrete as replacement of natural aggregates in formulation of SCC reduces the spread of concrete, we can note that all SCC mixtures meet the spreading criteria (60mm). The slump flow diameter was between 580 and 700mm, the time measured to reach a diameter wafer of 500 mm (t50) is close to the values recommended (3 seconds). However the SCC mixtures containing recycled aggregates of demolition concrete has a slightly greater spreading comparatively to SCC mixtures based on recycled brick aggregates, this is due to the shape and nature of the recycled aggregates, indeed these aggregates being more porous than the natural aggregates, led the mixture to a strong water absorption, increasing in viscosity, leads to a decrease in workability of SCC.

The demolition concrete aggregates contain in its compositions the natural aggregates which can lead to a good fluidity even with 50% replacement of natural aggregates. For the SCC mixture with 25% recycled brick aggregates and 25% recycled demolition concrete aggregates, therefore 50% of combined recycled aggregates, noted 50BDSCC, was obtained acceptable workability. The better workability was recorded for mixture containing 25% of recycled demolition concrete aggregates with 630mm in diameter of the spread concrete.

Concerning the L-box test is also performed to assess the passing ability of SCC in confined environment, the concrete flows through the frames properly and no blocking has been observed for SCC mixes containing 25% replacement aggregates regardless the type of recycled aggregates (brick or demolition concrete), the L-box ratio is higher than 0.80 (see table 5). However, the increase of brick aggregates until 50% causes immobility of concrete in confined environment, this is due to the shape and nature of the BA, indeed these aggregates being more porous than the natural aggregates, led the mixture to a strong water absorption, increasing in viscosity, leads to a decrease in workability and mobility of SCC. The results show that the replacement of natural aggregates by demolition concrete aggregates, until 50% has not caused immobility of SCC mixes in the confined environment (L-box ratio is 0.80). This may be attributed to the fact that DCA contains in its compositions the natural aggregates which can leads to a good fluidity. The mixture with 50% of combined recycled aggregates, noted 50BDSCC give a satisfactory result concerning the passing ability of SCC in confined environment, (L-box ratio of 0.79).

The sieve stability test is used to calculate a rate of segregation and to deduce whether the tested concrete has satisfactory or not stability, its values must be in the range of 0–15%. The results of sieve stability test used to measure the ability of self-compacting concrete to withstand the segregation, show acceptable values. For all

SSC mixtures with natural aggregates or waste aggregates have a segregation rate below 15%, synonymous with proper stability.

Based on the results of the three tests on fresh concrete (slump flow diameter, L-box, and sieve stability), it can be concluded that the SCC mixtures containing 25% recycled brick aggregates (25BSCC) or 50% recycled demolition concrete aggregates (50DSCC) as replacements for natural aggregates offer the best performance in meeting self-compacting concrete criteria.

Table 3. Fresh properties of all SCC mixtures.

Mix ID	Slump flow (mm)	L-box ratio (%)	Sieve stability (%)
NSCC	700	0.85	8.80
25BSCC	600	0.80	7.34
50BSCC	580	0.77	6.44
25DSCC	630	0.82	7.30
50DSCC	600	0.80	7.10
50BDSCC	580	0.79	6.20
100BDSCC	560	0.75	5.4

Hardened Concrete Properties

Compressive strength has been determined at 28 days in accordance with NF EN 12390-3 standard and the flexural strength test was carried out using a three-point loading method at 28 days of curing age, conforming to NF EN 12390-5 standard (Figure 8). Figures 9 and 10, presents the results of compressive and flexural strength at 28 days for all SCC mixtures.



a) Compressive strength test b) Flexural strength test

Figure 8. Tests on hardened concretes

By examining the Figure 9, it can be found that the compressive strength at 28 days is a decreasing function with the increase amount of recycled waste aggregates, whatever the types of these aggregates, brick or demolition concrete aggregates, this decrease is proportional to the amounts of recycled aggregates substitute the natural aggregates, it reaches 50% in the case of concretes containing 100% of recycled combined aggregates. For the flexural strength (figure 10), we noticed the same trend. Indeed, increasing the recycled aggregates rate decreases the flexural strength of SCC mixture of 33% for a substitution rate of 100% (table 4). This reduction in resistance can be explained by the decrease of the compactness of the granular mixture as well as the hardness of the waste which is lower compared to sand-lime granules, which causes an increase in porosity and decrease in strength. Nevertheless, we can notice that for SCC mixtures containing 25% of recycled aggregates, the compressive strengths loss about 13% and 15% for recycled brick and demolition concrete aggregates, respectively. All SCC mixtures with combined recycled aggregates have strengths lower than SCC mixtures with natural aggregates. The mixtures with 50% and 100% of both recycled aggregates waste, noted by 50BDSCC and 100BDSCC have given a reduction in compressive and flexural strength about 25 to 50% and 28% to 33% respectively, however, the SCC mixture containing 50% combined recycled aggregates waste, allowed us to gain in strength relative to the composition with 50% of brick waste or 50% of demolition concrete waste, or the decrease is less important with respect to these two compositions.

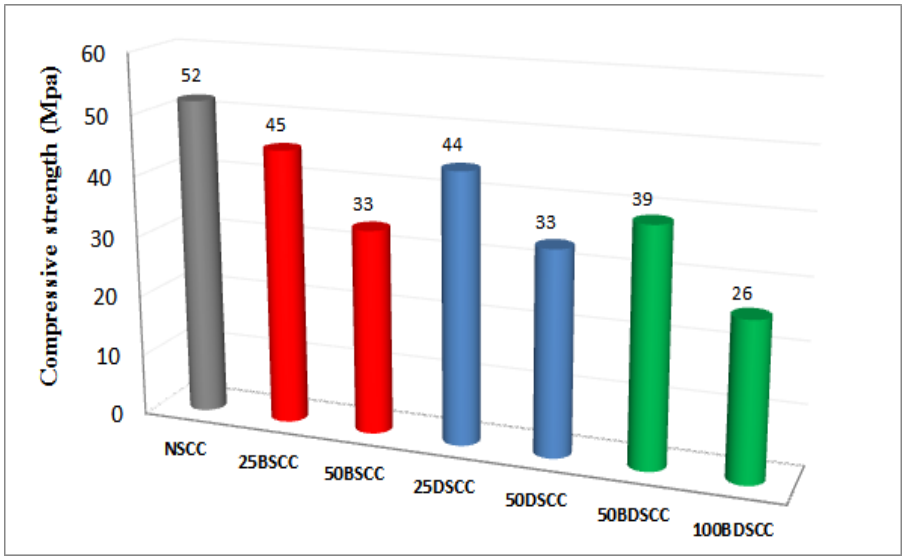


Figure 9. Compressive strength of all SCC mixtures

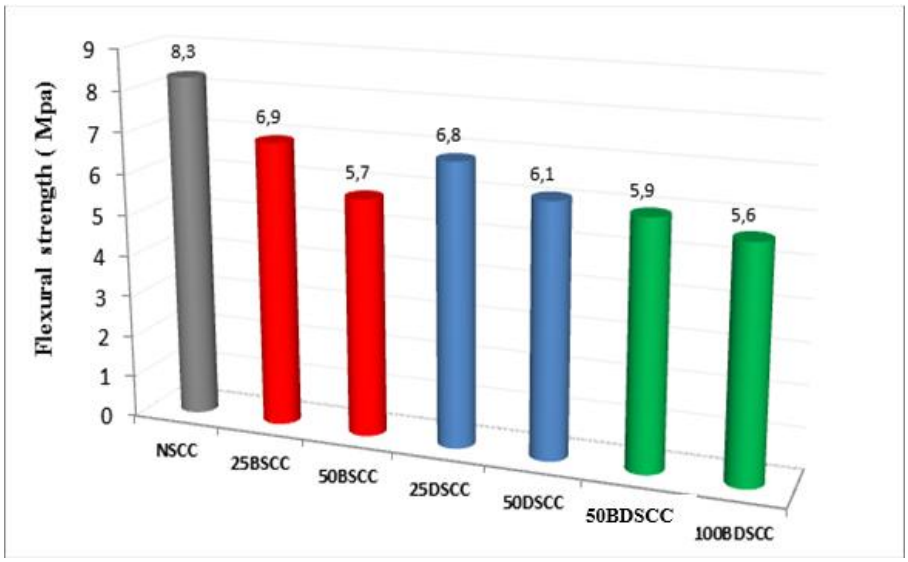


Figure 10. Flexural strength of all SCC mixtures

The SCC mixtures with 25% of any recycled aggregates or 50% of combined recycled aggregates give satisfactory mechanical resistance; the decrease in the compressive strength is about 13% to 15% and 25% respectively. These formulations can be used for constructions that do not require great strength, and whose environmental and ecological interest allows the use of recycled waste brick or demolition concrete.

Table 4. Compressive and flexural strengths losses

Mix ID	Compressive strength loss (%)	Flexural strength loss (%)
25BSCC	13	17
50BSCC	38	31
25DSCC	15	18
50DSCC	38	26
50BDSCC	25	28
100BDSCC	50	33

Conclusion

This experimental investigation aims the effect of recycling waste materials, brick aggregates and demolition concrete aggregates on fresh and hardened properties of self-compacting concrete. The ecological benefit of

effectively utilizing this waste material is another motivation for this work. In the light of obtained results, the following conclusions can be drawn:

- The increasing brick and demolition concrete aggregates as replacement of natural aggregates in formulation of SCC reduces the spread of concrete. However, the SCC mixtures containing recycled demolition concrete aggregates has a slightly greater spreading comparatively to SCC mixtures based on recycled brick aggregates.
- The concrete flows through the frames properly and no blocking has been observed for SCC mixes containing 25% replacement natural aggregates regardless of the type of recycled aggregates. However, the increase of brick aggregates until 50% causes immobility of concrete in confined environment, on the other hand the increase of demolition concrete aggregates until 50% has not caused immobility of SCC mixes.
- The mixture with 50% of combined recycled aggregates noted by 50BDSCC, has an acceptable workability and gives a satisfactory result concerning the passing ability of SCC in confined environment, (L-box ratio of 0.79).
- All SSC mixtures with natural aggregates or waste aggregates have a segregation rate below 15%, synonymous with proper stability
- The compressive and flexural strengths at 28 days, are a decreasing functions with the increase amount of recycled waste aggregates, whatever the types of these aggregates, this decrease is proportional to the amounts of recycled aggregates substitute the natural aggregates, it reaches 50% for compressive strength and 33% for flexural strength in the case of concretes containing 100% of recycled combined aggregates.
- The SCC mixtures containing 25% of recycled aggregates, have compressive strengths loss about 13% and 15% for recycled brick and demolition concrete aggregates, respectively.
- The SCC mixtures with 25% of any recycled aggregates or 50% of combined recycled aggregates give a satisfactory mechanical resistance; the decrease in the compressive strength is about 13% to 15% and 25% respectively.

Finally, we can be concluded from the fresh and hardened properties of concrete that the best formulations satisfying the criteria of self-compacting concrete are the SCC mixtures containing 25% of any recycled aggregates (25BSCC and 25DSCC) and 50% of combined recycled aggregates (50BDSCC) as replacement of natural aggregates, whose environmental and ecological interest allows the use of recycled waste brick or demolition concrete.

Scientific Ethics Declaration

* The authors declare that the scientific ethical and legal responsibility of this article published in EPSTEM journal belongs to the authors.

Conflict of Interest

* The authors declare that they have no conflicts of interest

Funding

* This research received no specific grant from any funding agency in the public, commercial, or not-for-profit sectors.

Acknowledgements or Notes

* This article was presented as a poster presentation at the International Conference on Technology, Engineering and Science (www.icontes.net) held in Antalya/Turkiye on November 12-15, 2025.

References

Cachim, P. B. (2009). Mechanical properties of brick aggregate concrete. *Construction and Building Materials, 23*(3), 1292-1297.

Chen, K. H., Chen, H. J., & Yen, T. (2003). Use of building rubbles as recycled aggregates. *Cement and Concrete Research, 33*(1), 125-132.

Debieb, F., Courard, L., Kenai, S., & Degeimbre, R. (2010). Mechanical and durability properties of concrete using contaminated recycled aggregates. *Cement and Concrete Composites, 32*(6), 421-426.

Duan, Z. H., & Poon, C. S. (2014). Properties of recycled aggregate concrete made with recycled aggregates with different amounts of old adhered mortars. *Materials & Design, 58*, 19-29.

EFNARC. (2005). *Specification and guidelines for self-compacting concrete*. European Federation of National Associations Representing Concrete.

Ghernouti, Y., Rabehi, B., Bouziani, T., & Chaid, R. (2016). Valorization of brick wastes in the fabrication of concrete blocks. *Materials and Technology, 50*(6), 911-916.

Ghernouti, Y., Rahebi, B., & Mansour, S. M. (2024). Study of the mechanical properties and the durability of concrete based on recycled wastes aggregates. *The Eurasia Proceedings of Science, Technology, Engineering & Mathematics (EPSTEM), 32*, 463-475.

Khalaf, F. M. (2006). Using crushed clay brick as coarse aggregate in concrete. *Journal of Materials in Civil Engineering, 18*(4), 518-526.

Khaloo, A. R. (1994). Properties of concrete using crushed clinker brick as coarse aggregate. *ACI Materials Journal, 91*(4), 401-407.

Khatib, J. M. (2005). Properties of concrete incorporating fine recycled aggregate. *Cement and Concrete Research, 35*(4), 763-769.

Kou, S. C., & Poon, C. S. (2009). Properties of self-compacting concrete prepared with recycled glass aggregate. *Cement and Concrete Composites, 31*(2), 107-113.

Levy, S. M., & Helene, P. (2004). Durability of recycled aggregates concrete: A safe way to sustainable development. *Cement and Concrete Research, 34*(11), 1975-1980.

Mansour, S. M., & Ghernouti, Y. (2021). Behaviour of self-compacting concrete incorporating natural perlite used as part of cement and as aggregates. *SSP-Journal of Civil Engineering, 16*(2), 115-132.

Mansur, M. A., Wee, T. H., & Lee, S. C. (1999). Crushed bricks as coarse aggregate for concrete. *ACI Materials Journal, 96*(4), 478-484.

Okamura, H., & Ozawa, K. (1995). Mix design for self-compacting concrete. *Concrete Library of JSCE, 25*, 107-120.

Poon, C. S., & Chan, D. (2007). The use of recycled aggregate in concrete in Hong Kong. *Resources, Conservation and Recycling, 50*(3), 293-305.

Poon, C. S., Kou, S. C., & Lam, L. (2007). Influence of recycled aggregate on slump and bleeding of fresh concrete. *Materials and Structures, 40*, 981-988.

Yang, J., Du, Q., & Bao, Y. W. (2011). Concrete with recycled concrete aggregate and crushed clay bricks. *Construction and Building Materials, 25*(4), 1935-1945.

Author(s) Information

Ghernouti Youcef
University of Boumerdes (University M'Hamed Bougara of Boumerdes), Independence Avenue, 35000 Boumerdes – Algeria
Contact e-mail : *y.ghernouti@univ-boumerdes.dz*

Rabehi Bahia
University of Boumerdes (University M'Hamed Bougara of Boumerdes), Independence Avenue, 35000 Boumerdes – Algeria

Mansour Sabria Malika
University of Boumerdes (University M'Hamed Bougara of Boumerdes), Independence Avenue, 35000 Boumerdes – Algeria

To cite this article:

Youcef, G., Bahia, R., & Malika, M.S. (2025). Potential use of recycled brick and demolition concrete aggregates in the self-compacting concrete. *The Eurasia Proceedings of Science, Technology, Engineering and Mathematics (EPSTEM), 38,* 180-188.

The Eurasia Proceedings of Science, Technology, Engineering & Mathematics (EPSTEM)
ISSN: 2602-3199

The Eurasia Proceedings of Science, Technology, Engineering and Mathematics (EPSTEM), 2025

Volume 38, Pages 189-199

IConTES 2025: International Conference on Technology, Engineering and Science

Experimental Analysis of the Punching Shear Behavior of Concrete Slabs Reinforced with Metal and Polypropylene Fibers

Atlaoui Djamal
Mouloud Mammeri University of Tizi Ouzou

Bouafia Youcef
Mouloud Mammeri University of Tizi Ouzou

Khelil Nacim
Mouloud Mammeri University of Tizi Ouzou

Akkouche Karim
Mouloud Mammeri University of Tizi Ouzou

Aliche Amar
Mouloud Mammeri University of Tizi Ouzou

Abstract: This study focuses on the experimental analysis of the mechanical behavior of reinforced concrete slabs subjected to eccentric punching tests. These slabs incorporate two types of reinforcements: metallic fibers and polypropylene fiber grids. The metallic fibers, derived from machining scraps of steel parts, are randomly dispersed in the concrete, while the grids are made of polypropylene fibers. The tests were conducted on slabs with a width of 25 cm, a length of 50 cm, and a thickness of 7 cm. The mechanical properties of the fibers, particularly their strength and pull-out resistance, were evaluated. The concrete mix was designed using the experimental "Dreux-Gorisse" method. Five dosages of metallic fibers were selected for this study (V_f = 0.3%; V_f = 0.5%; V_f = 0.7%; V_f = 0.9%; V_f = 1.10%), along with a control concrete (CC, V_f = 0%) serving as a reference. Additionally, two variants of polypropylene grids, with fine and wide meshes, were analyzed. The comparison of results highlights that metallic fibers significantly enhance the strength and stiffness of concrete, especially at V_f = 0.9% and V_f = 1.10%, compared to polypropylene grids, regardless of mesh size. Furthermore, the addition of these fibers limits crack formation during eccentric punching tests and provides the material with increased ductility after cracking.

Keywords: Ductility, Eccentric punching, Concrete slabs, Metal fibers, Characterization, Break mode, Polypropylene fibers, Experimentation

Introduction

Concrete has become an essential construction material, widely used in many engineering structures. While it offers excellent compressive strength, it remains vulnerable to cracking under tensile stress due to its low intrinsic tensile strength. Reinforced concrete, which combines concrete with steel reinforcement, addresses this weakness by improving its ability to resist tensile forces. In recent decades, fiber-reinforced concrete (FRC) has gained increasing interest and has been developed for various civil engineering applications, such as sprayed concrete, pavement slabs, prefabricated elements, tunnel linings, earthquake-resistant structures, bridge deck repairs, as well as marine and refractory constructions (Hannant, 2003; Syed Mohsin, 2012; Abbas et al., 2016A). The incorporation of fibers into reinforced concrete offers numerous benefits, including increased load-

- This is an Open Access article distributed under the terms of the Creative Commons Attribution-Noncommercial 4.0 Unported License, permitting all non-commercial use, distribution, and reproduction in any medium, provided the original work is properly cited.

- Selection and peer-review under responsibility of the Organizing Committee of the Conference

© 2025 Published by ISRES Publishing: www.isres.org

bearing capacity, improved ductility of structural elements, more effective crack propagation control, enhanced energy absorption, and favorable modification of failure modes (Brandt, 2008). The integration of fibers into reinforced concrete offers several benefits, such as improved load-bearing capacity and ductility of structural elements, limiting crack propagation, increasing energy absorption, and modifying the failure behavior (Cucchiara et al., 2004; Khaloo & Afshari, 2005; Juárez et al., 2007; Ding et al., 2011; Minelli et al., 2014; Zia et al., 2023a, 2023b). A study conducted by Zia et al. (2023b), Atlaoui and Bouafia (2017) examined the effectiveness of raw steel fibers from used tires (RSF) sourced from Bratislava, Slovakia, to improve the durability and mechanical properties of local concrete. The results showed that these fibers have strong potential for use in the production of durable concrete, provided they are employed in appropriate and pure forms. Another study by by Zia et al. (2023b), Atlaoui and Bouafia (2017) focused on the combined influence of steel fibers from used tires (DSF) and industrial steel fibers (ISF) on the properties of fiber-reinforced concrete. The authors observed notable improvements in the characteristics of the hybrid fiber concrete compared to concrete without fibers (Zia et al., 2023b; Atlaoui & Bouafia, 2017).

Experimental research has been conducted to replace the reinforcement of reinforced concrete with fibers, with the goal of improving its tensile, flexural, and shear strength (Djebali et al., 2011; Atlaoui & Bouafia, 2017, 2008; Bouafia et al., 2012; Djebali et al., 2011; Tadepalli et al., 2013; Sorensen et al., 2014; Pereira et al., 2014; Wang & Wang, 2013; Serbescu et al., 2015; Fahmy et al., 2009). Initially, researchers aimed to enhance the mechanical properties of concrete, such as compressive strength and flexural strength, through the addition of fibers, but the results obtained were relatively limited (Wu et al., 2015). Another significant advantage of integrating steel fibers, when evenly distributed within the concrete matrix, is their ability to effectively control cracking. Indeed, fibers near microcracks can prevent their propagation. Additionally, the incorporation of polypropylene fibers in concrete helps to improve the long-term durability of hydraulic structures by reducing voids and shrinkage cracks (Wang et al., 2015). A study conducted by (El-Ghandour et al., 2003) tested concrete slabs with dimensions [300x100x20] cm^3 in a four-point bending configuration, with the addition of 0.25% and 0.5% by volume of steel and polypropylene fibers. The steel fibers were found to be effective in both dosages in limiting crack width, especially in the serviceability range. Although the overall behavior in terms of load-deformation was similar for all samples, the specimens containing fibers exhibited smaller deformations and higher load capacity.

Punching shear resistance is a crucial criterion in the design of concrete slabs. When a concentrated load is applied (punching), significant shear forces develop within the slab, with their distribution following a hyperbolic shape, reaching a maximum at the interface with the column (Favre et al., 1997). Generally, bending forces accompany these shear forces, which can lead to so-called "bending-punching" failures in some cases. This term refers to a failure mode where the final failure occurs due to punching, but the origin of the failure lies in bending (Stein et al., 2007). This phenomenon is primarily observed in steel-reinforced slabs. The high ductility of these slabs, when they fail in bending, induces large deformations (plasticization of the reinforcement), which favors a second failure mode by punching.

Punching shear resistance is a crucial criterion in the design of concrete slabs. When a concentrated load is applied (punching), shear forces develop. Slabs with a low reinforcement ratio (less than 1%) are susceptible to experiencing bending-punching failure (Clément, 2012). The punching failure mode is a complex phenomenon, and many researchers conduct experiments to better understand and highlight this behavior. These tests are essential for improving slab design and preventing unexpected failures when concentrated loads are applied.
To address these various questions, we have chosen to focus our research on studying the punching behavior of concrete slabs reinforced with composite fabrics. The main objective of this experimental study is to examine the behavior of eccentrically loaded punching of concrete slabs reinforced with metal fibers (from machining waste of steel parts), randomly integrated into a concrete matrix, as well as polypropylene mesh fibers, with small (GPP/PM) and large (GPP/GM) meshes, arranged in layers. The results obtained for the punching behavior of slabs reinforced with metal and polypropylene fibers are overall satisfactory.

Materials and Methods

Materials

The concrete used consists of CPJ-CEMII/B 42.5 R NA 442 type cement, class 42.5 (Lafarge Cement from the Msila region (LCM), Algeria), in accordance with the NF EN196-6 standard (Afnor, 2018). The aggregates used originate from the Tizi-Ouzou region (quarry rocks); they are crushed in shape, with grain size classes of 0/3 mm, 3/8 mm, and 8/15 mm, respectively, washed and oven-dried. The particle size analysis by sieving was

carried out according to the NF P18-560 standard, using a frequency-adjustable sieve shaker set at 50 Hz. The concrete mix per cubic meter was designed following the Dreux-Gorisse method (Dreux & Festa, 1998). The particle size distribution curves for each type of aggregate are presented in Figure 1. The mixing was performed using a vertical-axis mixer with a capacity of 65 liters. Table 1 provides the optimized concrete mix composition for a volume of 1 m³.

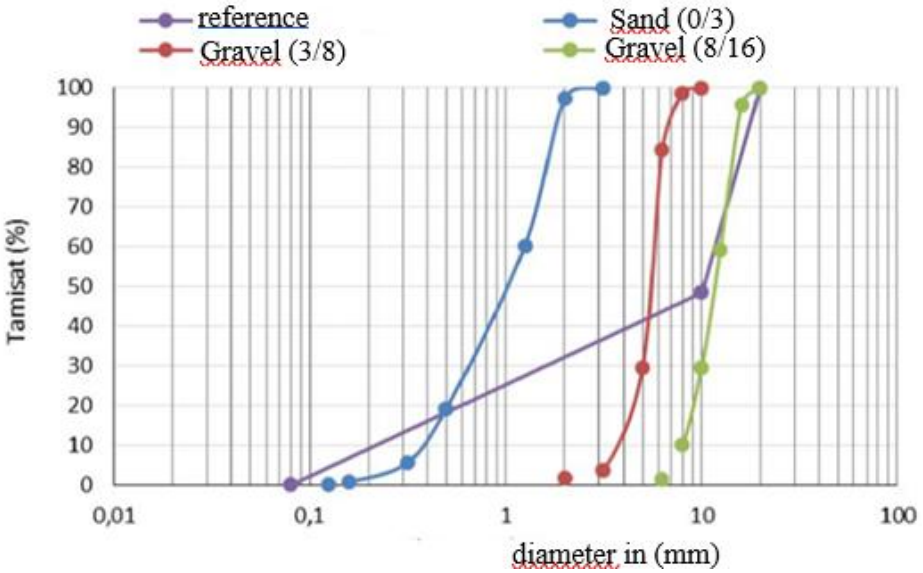


Figure 1. Grading curve

Table 1. Optimized composition for 1m³ of concrete

Constituents of concrete for a volume of 1m³	
Sand 0/3(kg)	896.67
Gravel 3/8(kg)	95.67
Gravel 8/15(kg)	801.00
Water (W)(kg)	206.52
Cement CPJ CEMII/A42.5(C) (kg)	380.00
Superplasticizer (0.05% of cement weight) (ml)	190.00

Geometry and Composition of Specimens

The formwork used for creating the slabs is wooden formwork, consisting of detachable panels. It was treated with a release agent to facilitate the removal of the specimens after the concrete has set. The dimensions of the slabs used are [50x25x7] cm³, with a width (w) of 25 cm, a length (L) of 50 cm, and a thickness (t) of 7 cm (see the view provided in Figure 2). The metallic fibers (MF) are randomly distributed in the cement matrix, while the polypropylene mesh fibers are arranged in layers. Vibration of the mixture was performed during the pouring process.

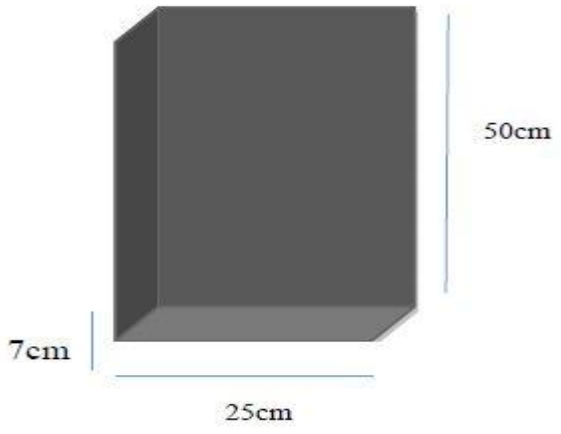


Figure 2. Dimensions of the slabs used

The Fibers Used

Metallic fibers (MF) and polypropylene mesh fibers used in this study are recycled materials of local origin. The metallic fibers come from metal chips machining waste from steel parts. Three tests were conducted for each fiber type combination. To highlight the influence of mesh size on the load-bearing capacity of the fiber-reinforced polypropylene slab, particularly on the failure mode, two types of meshes were considered in this study: Small Mesh (PPG/SM) and Large Mesh (PPG/LM). The view of the fibers used, as well as the mechanical and geometric properties of the fibers, are presented in Figure 3 and Table 2.

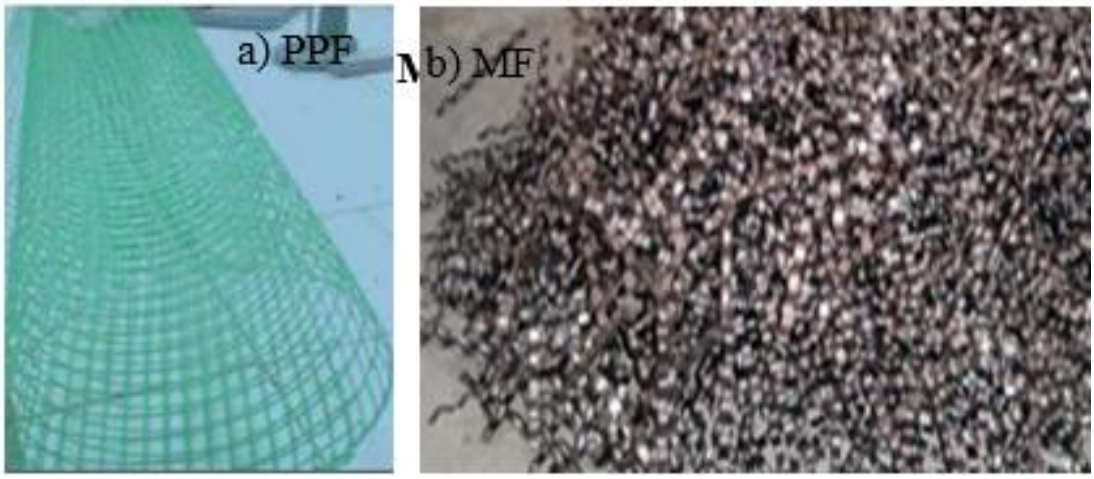


Figure 3. View of the fibers: a) polypropylene grid; b) metal fibers

Table 2. Mechanical and geometric characteristics of the fibers used

Fiber type	L (mm)	l (mm)	e_p (mm)	density g/cm^3
Mental fibers	50	25	0.5	78.5
Polypropylene fibers	300	130	1	9.2

Compression Test

To determine the compressive strength of the concrete, compressive strength tests on cylinders of 16 cm diameter and 32 cm height (see Figure 4) are performed on a hydraulic press (maximum capacity of 2000 KN) controlled by a laptop. It is programmed for compression testing and this for different sizes of specimens (cylindrical or prismatic specimens).



Figure 4. Cylindrical test tube

Methods

Fiber Characterization Tests

Pour to determine the mechanical characteristics of the fibers used (metallic and polypropylene), direct tensile tests were conducted using an "Ibertest" machine, equipped with a maximum force cell of 200 KN. This machine is also equipped with control and data processing software, allowing for representation in the form of diagrams (force/displacement and force/time.

Eccentric Punching Tests

To monitor the behavior of fiber-reinforced slabs under eccentric punching, two series of tests were conducted. The first series of tests (Series 1) focused on slabs reinforced with metallic fibers (MF), while the second series of tests (Series 2) focused on slabs reinforced with polypropylene mesh grids with small meshes (PPG/SM) and large meshes (PPG/LM). A total of 24 slabs with dimensions [25x50x7] cm³ were tested.

First Series of Tests "Series 1"

To monitor the behavior of concrete slabs reinforced with metallic fibers (MF) under eccentric punching, 18 slabs with dimensions [25x50x7] cm³ were tested. The fiber contents selected for this series were 0.3%, 0.5%, 0.7%, 0.9% and 1.10%, as well as the control concrete CC (without fibers). The fibers were randomly distributed in the cement matrix.

Second Series of Tests "Series 2"

The main objective of this second series of tests (Series 2) is to study the behavior of concrete slabs reinforced with polypropylene mesh grids under eccentric punching. To highlight the influence of mesh size on the load-bearing capacity of the reinforced slab, particularly on the failure mode, two types of meshes were considered in this study: small mesh (PPG/SM) and large mesh (PPG/LM). The arrangement of the polypropylene mesh grids for both variants (PPG/SM) and (GPP/GM) throughout the height of the slab as shown in Figure 5.

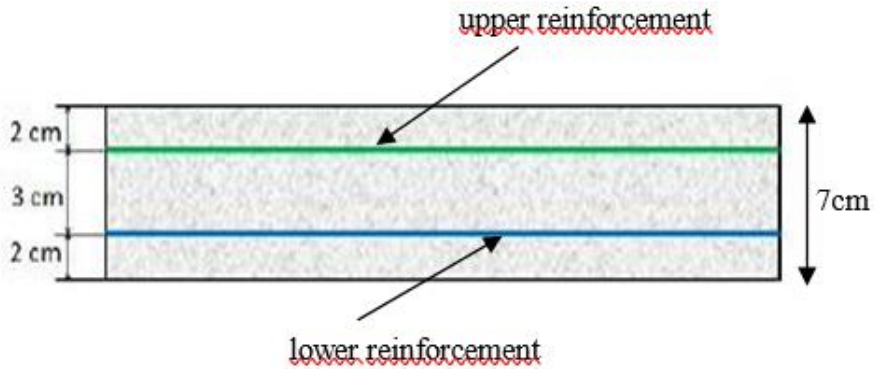


Figure 5. Arrangement of fibers over the height of the slab

Results and Discussions

Test fibers characterization

This study (fiber characterization) allowed us to determine the tensile strength of the metallic fibers (MF) used. It appears that the average tensile strength, Rm = 260 MPa. Additionally, a ductile fracture of the steel is observed. The tensile strength of the polypropylene grid fibers used (PPF). It appears that the average tensile strength, Rm = 160 MPa.

Compression Tests

The stress–strain curves obtained for different tests after crushing at 28 days are given in Figure 6. The measured mechanical properties of concrete, obtained from the different tests after crushing at 28 days, are presented in Table 3.

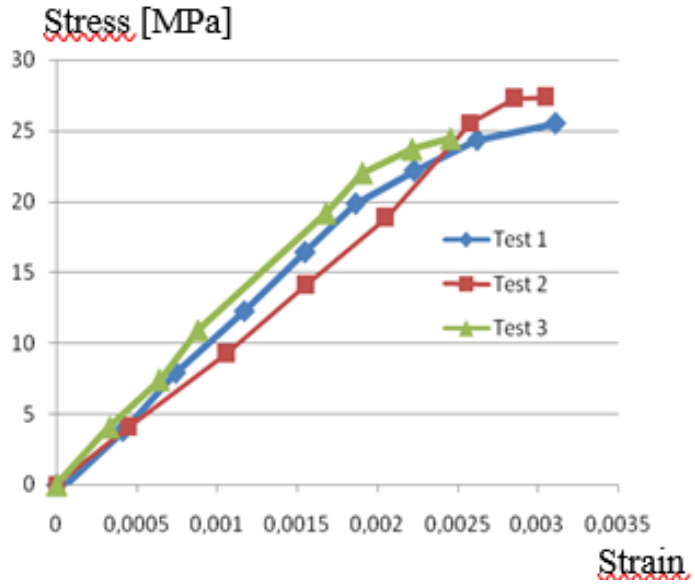


Figure 6. Superposition of compressive stress–strain curves

Table 3. Measured mechanical characteristics

Tests	Compressive stress σ [MPa]	Young's modulus E [MPa]
Test 1	24.48	31.402
Test 2	25.54	33.224
Test 3	27.35	31.748
Average	25.79	32.124

Eccentric Punching of Slabs

First Series of Tests "Series 1"

Figure 7 shows an example of the eccentric punching failure mode of metal fiber (MF) reinforced slabs.



Figure 7. Example of failure mode of slabs reinforced by metal fibers (MF) (series1)

Figure 8 shows the superposition of the mean force-deformation curves at centric punching of slabs reinforced with FM metal fibers (series 1) for fibre contents of W = 0.3%, W = 0.5%, W = 0.7%, W = 0.9% and W = 1.10%, as well as a control concrete CC (without fibers) which serves as a reference.

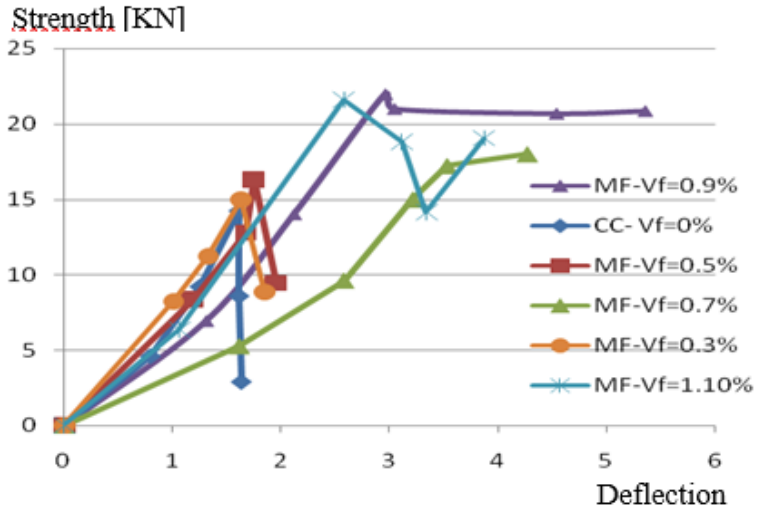


Figure 8. Superposition of the average strength-deflection curves for series 1 slabs

Figure 8 shows that the behavior of metal fiber reinforced (MF) slabs for fiber contents W=0.3%, W=0.5%, W=0.7%, W=1.10% and the control concrete CC (V=0%) have a brittle failure, on the other hand the slabs with fiber contents W=0.9% have a ductile failure. This is explained by the large numbers of fibers crossing both edges of the slab (see the failure mode in (Figure 7). The different results obtained in terms of load-bearing capacity of the different slabs considered are summarized in Table 4.

Table 4. Resistance to eccentric punching of the tested slabs (series 1)

Fiber fractions [V%]	CC (V=0%	0.3%	0.5%	0.7%	0.9%	1.10%
Breaking strength [KN]	14.23	15.01	16.32	1 7 .21	2 1 .98	21.58

These results also show that the addition of fibers with a content of W = 0.9% provides significant ductility compared to the control concrete (CC, without fibers). Moreover, the behavior of fiber-reinforced concrete under eccentric punching is characterized by the presence of two (2) phases:

1. A linear phase corresponding to a quasi-elastic behavior of the material, which is the pre-cracking phase of the concrete. This phase ends with the appearance of a macrocrack;
2. A second phase in which a sudden drop is observed—without a brittle failure of the slab-in the load-bearing capacity of the material. This is the post-cracking phase. In this phase, the concrete matrix fails, and the edges of the crack are held together by the fibers (see Figure 7), which helps prevent a sudden failure.

The results of Series No. 01 (Figure 8) allowed us to observe that the breaking load of the slabs with a fiber content of V = 0.9% (F_r = 21.98 KN) increased by approximately 54.46% compared to the slabs without fibers (F_r = 14.23 KN). On the other hand, the deformation (deflection) increased by approximately 82%.

Second Series of Tests "Series 2"



Figure 9. Example of failure mode of slabs reinforced by propylene fibers (series 2)

Figure 9 shows an example of the failure mode of slabs reinforced with small-mesh (GPP/SM) and large-mesh (GPP/LM) polypropylene grid fibers (Series No. 02) tested under eccentric punching. Figure 10 illustrates the superposition of load-deflection curves for the two polypropylene grids (GPP/SM and GPP/LM), as well as for the control concrete (CC) (V = 0%).

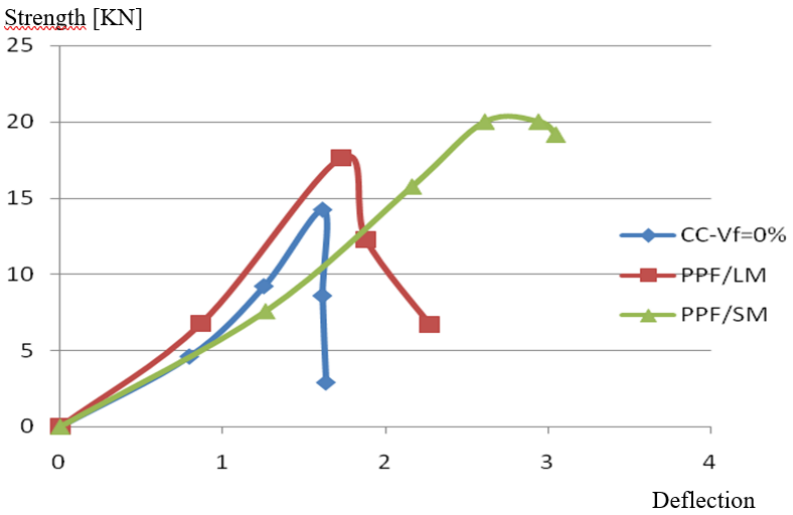


Figure 10. Superposition of the average strength- deflection curves for series 2 slabs

The curves obtained (Figure 10) show that the punching shear strength and stiffness under eccentric loading of slabs reinforced with small-mesh polypropylene grids (GPP/SM) are better than those reinforced with large-mesh polypropylene grids (GPP/LM) and the fiber less control slabs (CC) (V = 0%). They also indicate that the ultimate load of slabs reinforced with large-mesh polypropylene grids (GPP/SM) (F_r = 19.98 KN) increased by approximately 40% compared to the slabs without fibers (CC) (F_r = 14.23 KN). However, the deformation (deflection) increased by about 62.11%. Figure 11 illustrates the superposition of the best curves obtained under eccentric punching for slabs reinforced with metallic fibers (MF) (Series N°. 01) and slabs reinforced with polypropylene grid fibers (Series N°. 02), as well as the control concrete (CC) without fibers.

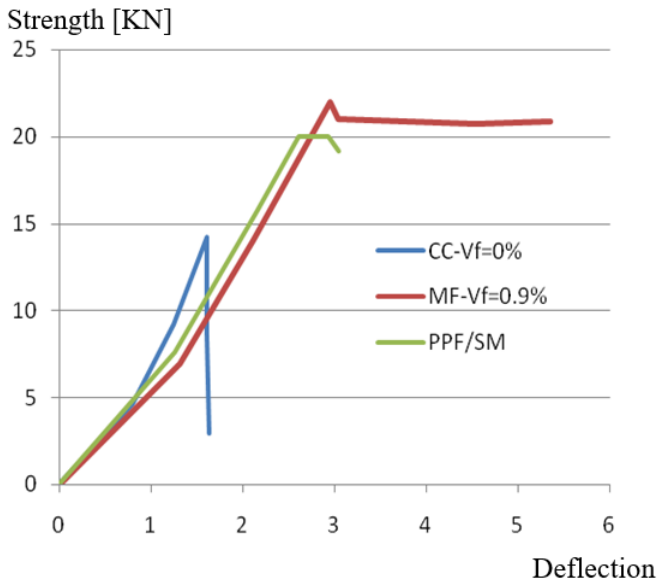


Figure 11. Superposition of the best strength-deflection curves of the slabs studied

Figure 11 clearly shows that the punching shear strength and stiffness under eccentric loading of slabs reinforced with metallic fibers (MF) at a fiber content of W = 0.9% are superior to those of slabs reinforced with small-mesh (GPP/SM) and large-mesh (GPP/LM) polypropylene grids. It is also observed that the failure mode of slabs reinforced with metallic fibers exhibits ductile behavior after concrete cracking, whereas slabs reinforced with polypropylene grid fibers-both small brittle behavior after cracking.

Table 7. presents the ultimate punching shear strength of the tested slabs (Series N°. 02) under eccentric loading

Fiber fractions (V%)	CC (V=0%)	0.9%	PPF/SM
Breaking strength (KN)	14.23	21.98	19.98

Conclusion

This experimental study aims to analyze and understand the effect of incorporating metallic fibers derived from machining waste-commonly referred to as "chips"-randomly dispersed within the cementitious matrix, as well as the effect of fine-mesh (GPP/SM) and coarse-mesh (PPG/LM) polypropylene grid fibers, on the behavior of concrete slabs under eccentric punching shear. Tests conducted to characterize the mechanical properties of these fibers revealed a tensile strength of 260 MPa for the metallic fibers, while the polypropylene grid fibers exhibited an average tensile strength of 160 MPa. Tests were conducted on slabs reinforced with metallic fibers (MF) (Series 1), as well as on slabs reinforced with fine-mesh (PPG/SM) and coarse-mesh (PPG/LM) polypropylene grid fibers (Series 2), to evaluate their behavior under eccentric punching shear. The results indicate that the addition of metallic fibers with an incorporation rate of W = 0.9% significantly improves the strength and stiffness of the slabs, compared to the other tested mix designs and the control concrete (CC), which contains no fibers.

The results of Series N°. 01 show that the failure load of slabs containing 0.9% fibers (Fr = 21.98KN) increased by approximately 54.46% compared to the slabs without fibers (Fr = 14.23KN). In contrast, the deformation (deflection) increased by about 82%. The results of Series N°. 02 also revealed that the failure load of slabs reinforced with coarse-mesh polypropylene grids (GM/PM), with a value of Fr = 19.98 KN, increased by approximately 40% compared to that of the unreinforced slabs (BT), which had Fr = 14.23 KN. In contrast, the deformation (deflection) showed a remarkable increase, reaching about 62.11%.

This study also allowed for the observation that slabs reinforced with metallic fibers (MF) exhibit a ductile behavior after the concrete cracks. In contrast, slabs reinforced with polypropylene grids, whether fine-mesh or coarse-mesh, exhibit a brittle behavior after cracking. In the future, it would be relevant to conduct tests using flat fibers rather than corrugated fibers, with the aim of reducing voids (cavities) within the cement paste. It would also be interesting to study the combination of these fibers with traditional reinforcements to evaluate their combined behavior.

Scientific Ethics Declaration

* The authors declare that the scientific ethical and legal responsibility of this article published in EPSTEM journal belongs to the authors.

Conflict of Interest

* The authors declare that they have no conflicts of interest

Funding

* This research received no specific grant from any funding agency in the public, commercial, or not-for-profit sectors.

Acknowledgements or Notes

* This article was presented as a poster presentation at the International Conference on Technology, Engineering and Science (www.icontes.net) held in Antalya/Turkiye on November 12-15, 2025.

References

Abbas, A. A., Syed Mohsin, S., & Cotsovos, D. M. (2016a). Simplified finite element model for assessing steel fibre reinforced concrete structural performance. *Computers & Structures, 173*, 31-49.

AFNOR. (2018). *Methods of testing cement - Determination of fineness* (NF EN 196-6).

Atlaoui, D., & Bouafia, Y. (2008). Characterisation of the mechanical behaviour of fibers undulated in spirals resulting from waste of machining of steel parts. *Second Euro Mediterranean Symposium on Advances in Geomaterials and Structures (AGS'08)*, 4, 741-746.

Atlaoui, D., & Bouafia, Y. (2017). Experimental characterization of concrete beams elements reinforced by long fiber chips. *Journal of Adhesion Science and Technology, 31*(8), 844-857.

Bouafia, Y., Kachi, M. S., & Atlaoui, D. (2012). Study of mechanical behaviour of concrete in direct tensile fiber chips. *Applied Mechanics and Materials, 46*, 64-73.

Brandt, A. M. (2008). Fiber reinforced cement-based (FRC) composites after over 40 years of development in building and civil engineering. *Composite Structures, 86*(1–3), 3-9.

Clément, T. (2012). *Influence de la précontrainte sur la résistance au poinçonnement de dalles en béton armé* (Influence of prestressing on the punching strength of reinforced concrete slabs) (Doctoral dissertation). Ecole Polytechnique Fédérale de Lausanne.

Cucchiara, C., La Mendola, L., & Papia, M. (2004). Effectiveness of stirrups and steel fibres as shear reinforcement. *Cement and Concrete Composites, 26*(7), 777-786.

Ding, Y., You, Z., & Jalali, S. (2011). The composite effect of steel fibres and stirrups on shear behaviour of beams using self-consolidating concrete. *Engineering Structures, 33*(1), 107-117.

Djebali, S., Atlaoui, D., & Bouafia, Y. (2011). Caractérisation en traction direct du béton de fibres métalliques (Direct tensile characterization of metal fiber concrete). *Matériaux & Techniques, 99*(3), 327-338.

Djebali, S., Bouafia, Y., & Atlaoui, D. (2011). Study of mechanical behaviour of chips reinforced concrete. *Advanced Materials Research, 24*, 360-363.

Dreux, G., & Festa, J. (1998). *Nouveau guide du béton et de ses constituants* (8th ed.) (New guide to concrete and its constituents). Eyrolles.

El-Ghandour, A. W., Pilakoutas, K., & Waldron, P. (2003). Punching shear behavior of fiber reinforced polymers reinforced concrete flat slabs: An experimental study. *Journal of Composites for Construction, 7*(3), 258-265.

Fahmy, M. F., Wu, Z., & Wu, G. (2009). Seismic performance assessment of damage-controlled FRP-retrofitted RC bridge columns using residual deformations. *Journal of Composites for Construction, 13*(6), 498-513.

Favre, R., Jaccoud, J. P., Burdet, O., & Charif, H. (1997). *Dimensionnement des structures en béton: Volume 8* (2nd ed.) (Design of concrete structures: Volume 8). Presses Polytechniques et Universitaires Romandes.

Hannant, D. J. (2003). Fibre-reinforced concrete. In J. Newman & B. S. Choo (Eds.), *Advanced concrete technology: Processes* (pp. 1-17). Butterworth-Heinemann.

Juárez, C., Valdez, P., Durán, A., & Sobolev, K. (2007). The diagonal tension behavior of fiber reinforced concrete beams. *Cement and Concrete Composites, 29*(5), 402-408.

Khaloo, A. R., & Afshari, M. (2005). Flexural behaviour of small steel fibre reinforced concrete slabs. *Cement and Concrete Composites, 27*(1), 141-149.

Minelli, F., Conforti, A., Cuenca, E., & Plizzari, G. (2014). Are steel fibers able to mitigate or eliminate size effect in shear? *Materials and Structures, 47*, 459-473.

Pereira, N. B., Barros, A. O., & Camoes, A. (2008). Steel fiber reinforced self-compacting concrete: Experimental research and numerical simulation. *Journal of Structural Engineering, 134*(8), 1310-1321.

Serbescu, A., Guadagnini, M., & Pilakoutas, K. (2015). Mechanical characterization of basalt FRP rebars and long-term strength predictive model. *Journal of Composites for Construction, 19*(2), 04014037.

Sorensen, C., Berge, E., & Nikolaisen, E. B. (2014). Investigation of fiber distribution in concrete batches discharged from ready-mix truck. *International Journal of Concrete Structures and Materials, 8*(4), 279–287.

Stein, T., Ghali, A., & Dilger, W. (2007). Distinction between punching and flexural failure modes of flat plates. *ACI Structural Journal, 105*(2), 238–241.

Syed Mohsin, S. M. (2012). *Behaviour of fibre-reinforced concrete structures under seismic loading* (Doctoral dissertation). Imperial College London.

Tadepalli, P. R., Mo, Y., & Hsu, T. T. (2013). Mechanical properties of steel fiber concrete. *Magazine of Concrete Research, 65*(8), 462–474.

Wang, H. T., & Wang, L. C. (2013). Experimental study on static and dynamic mechanical properties of steel fiber reinforced lightweight aggregate concrete. *Construction and Building Materials, 38*, 1146-1151.

Wang, X., Shi, J., Wu, G., Yang, L., & Wu, Z. (2015). Effectiveness of basalt FRP tendons for strengthening of RC beams through the external prestressing technique. *Engineering Structures, 101*, 34–44.

Wu, G., Wang, X., Wu, Z., Dong, Z., & Zhang, G. (2015). Durability of basalt fibers and composites in corrosive environments. *Journal of Composite Materials, 49*(7), 873–887.

Zia, A., Zhang, P., & Holly, I. (2023a). Experimental investigation of raw steel fibers derived from waste tires for sustainable concrete. *Construction and Building Materials, 368*, 130410.

Zia, A., Zhang, P., & Holly, I. (2023b). Effectiveness of hybrid discarded tire/industrial steel fibers for improving the sustainability of concrete structures. *Construction and Building Materials, 378*, 131226.

Author(s) Information

Atlaoui Djamal
Mouloud Mammeri University of Tizi Ouzou, Department of Civil Engineering, Laboratory of Modeling of and Structures in Civil Engineering (L2MSGC), Algeria.
Contact e-mail: *djamal.atlaoui@ummto.dz*

Bouafia Youcef
Mouloud Mammeri University of Tizi Ouzou, Department of Civil Engineering, Laboratory of Modeling of and Structures in Civil Engineering (L2MSGC), Algeria.

Khelil Nacim
Mouloud Mammeri University of Tizi Ouzou, Department of Civil Engineering, Laboratory of Modeling of and Structures in Civil Engineering (L2MSGC), Algeria.

Akkouche Karim
Mouloud Mammeri University of Tizi Ouzou, Department of Civil Engineering, Laboratory of Modeling of and Structures in Civil Engineering (L2MSGC), Algeria.

Aliche Amar
Mouloud Mammeri University of Tizi Ouzou, Department of Civil Engineering, Laboratory of Modeling of and Structures in Civil Engineering (L2MSGC), Algeria.

To cite this article:

Djamal, A., Youcef, B., Nacim, K., Karim, A., & Amar, A. (2025). Experimental analysis of the punching shear behavior of concrete slabs reinforced with metal and polypropylene fibers. *The Eurasia Proceedings of Science, Technology, Engineering and Mathematics (EPSTEM), 38,* 189-199.

The Eurasia Proceedings of Science, Technology, Engineering & Mathematics (EPSTEM)
ISSN: 2602-3199

The Eurasia Proceedings of Science, Technology, Engineering and Mathematics (EPSTEM), 2025

Volume 38, Pages 200-209

IConTES 2025: International Conference on Technology, Engineering and Science

Probabilistic Fracture Mechanics Analysis of Crack Propagation in Composites Under Tensile Loading

Sid Ahmed Reffas
University of Sidi Bel Abbes

Belaid Mechab
University of Sidi Bel Abbes

Mohamed Cherfi
University of Sidi Bel Abbes

Abstract: Reliability engineering is a discipline dedicated to the study and evaluation of structural systems, aiming to assess their ability to perform required functions under specified conditions over a defined period. This study presents a numerical investigation into the damage prediction of composite structures subjected to tensile loading, employing three-dimensional finite element analysis. The influence of material properties, fibre orientation, thickness (ep), and the length-to-thickness ratio (L/ep) is examined within the framework of probabilistic fracture mechanics for composite damage. The Monte Carlo simulation method is utilised to estimate the damage distribution function. Failure probability is evaluated by incorporating both statistical uncertainties in the basic variables and model uncertainties. Probability density functions are derived by fitting histograms to theoretical models, with Lorentzian, Gaussian, and ninth-order Polynomial distributions considered. The Gaussian distribution provides the most accurate approximation of the strain probability density function, offering a reliable estimate of the mean value.

Keywords: Composite, Finite element method, Safety, Fracture mechanics, Monte Carlo method

Introduction

A composite material is defined as a macroscopic assembly of two or more constituents with different chemical or physical properties, whose combination results in global properties superior to those of the individual materials. Typically, a composite is composed of a reinforcement phase, such as continuous or discontinuous fibers, and a matrix that provides cohesion and protection to the reinforcement while transferring mechanical loads. Composite materials offer several major advantages: excellent specific strength (high strength-to-weight ratio), tailored stiffness, good resistance to fatigue and corrosion, and the ability to design structures with custom anisotropic mechanical properties. This high adaptability opens up significant prospects in demanding sectors such as aerospace, space, ground transportation, energy, and civil engineering (Solis et al.2018; Ranz et al.207; Charrier et al.2016; Tasdemir et al.2019; Pernice et al.2015; Fletcher et al.2016).

Damage to aeronautical structures represents a major challenge for the aerospace industry, with direct implications for safety, maintenance, and the lifespan of aircraft. Throughout their lifecycle, aircraft are subjected to various mechanical, thermal, and environmental stresses. Damage phenomena can manifest in several forms, including fatigue, corrosion, impacts, composite delamination, and structural cracks (Cao et al.2010; Tvergaard and Hutchinson., 1992; Tvergaard.,1990; Salem et al.,2024; Turan et al.,2007; Ibrahim et al.,2018).

- This is an Open Access article distributed under the terms of the Creative Commons Attribution-Noncommercial 4.0 Unported License, permitting all non-commercial use, distribution, and reproduction in any medium, provided the original work is properly cited.

- Selection and peer-review under responsibility of the Organizing Committee of the Conference

© 2025 Published by ISRES Publishing: www.isres.org

The detection and prevention of these degradations are crucial for ensuring the safe and efficient operation of aircraft. With the introduction of composite materials, new types of damage have emerged, such as delamination and interlaminar cracks. These forms of degradation are often less visible on the surface, making their detection more complex and requiring advanced inspection methods. In conclusion, the issue of damage in aircraft is a critical challenge that requires rigorous management, combining material innovations, advanced inspection techniques, and predictive maintenance strategies. The evolution of materials and detection technologies plays a key role in improving safety and extending the lifespan of aircraft (Di vito et al.2019; Maachou et al. 2024; Talbi et al.2025; Song et al.2019; Bayandor et al.2003). Reliability engineering focuses on evaluating structural systems' performance under specified conditions over time. This study conducts a numerical analysis of composite structures under tensile loading using 3D finite element methods. The effects of material properties, fibre orientation, thickness (ep), and length-to-thickness ratio (L/ep) are examined through probabilistic fracture mechanics. Damage distribution is estimated using Monte Carlo simulation, incorporating uncertainties in both input variables and model assumptions. Probability density functions are obtained by fitting histograms to theoretical distributions. Among the models considered—Lorentzian, Gaussian, and ninth-order polynomial are presented.

Geometric Model

The objective of this study is to perform interlaminar damage tests in mode I on unidirectional composite specimens subjected to a tensile load of **σ = 50 MPa**. The samples used had a standardized geometry, with a length of **230 mm**, a width of **35 mm**, and a thickness ranging from **1 mm** to **3 mm**, depending on the configurations studied. The specimen geometry and the loading scheme are shown in **Fig. 1**. Various stacking sequences of composite layers were investigated, including **[0°/90°/0°/90°]**, **[45°/0°/45°/0°]**, and **[−30°/0°/30°/0°]**, to assess the influence of fiber orientation on fracture behavior.

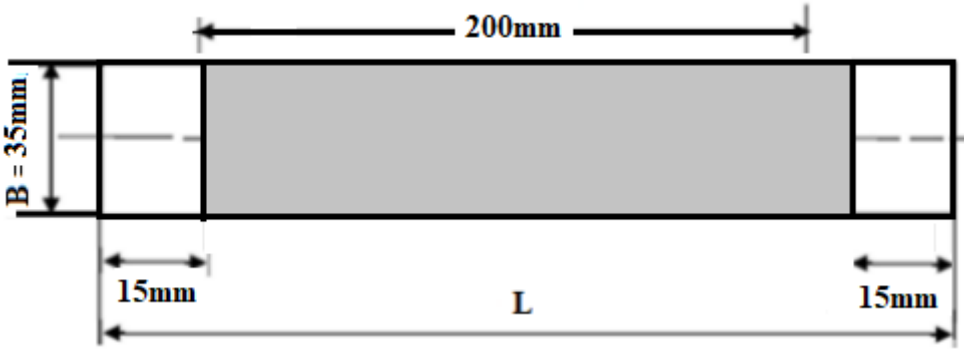


Figure 1. Descriptive model of the studied geometry.

The Boundary Conditions

The boundary conditions for fixation, in accordance with the symmetry conditions of the geometry, were applied in the initial phase of the study. These conditions are defined in 3D as follows: point **(A)** is fixed along the **X** axis, while point **(B)** is free. This modeling ensures the compliance with the geometric constraints imposed by the symmetry of the structure while enabling the simulation of crack behavior under loading.

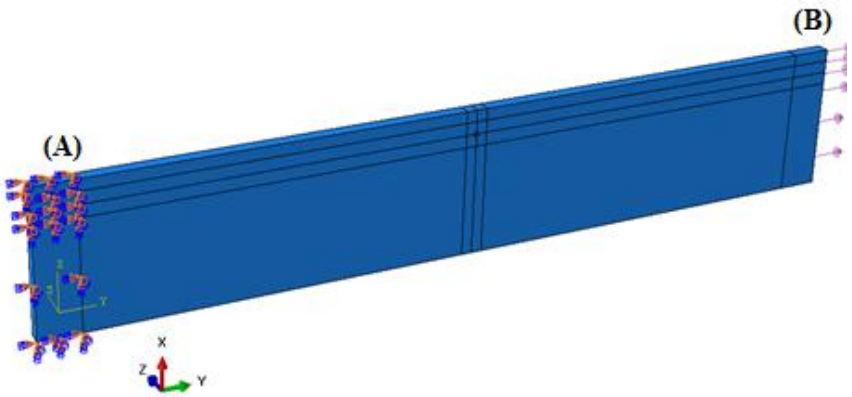


Figure 2. Boundary conditions of geometric model.

Mechanical Properties

The material's mechanical characteristics of the different materials are presented respectively in Table 1

Table 1. Mechanical characteristics of the different materials

The material's	Al 2024T3	Glass/epoxy	Graphite/epoxy	Boron/epoxy
E_1 (GPa)	72	150	127.5	200
E_2 (GPa)		25	9.00	19.6
E_3 (GPa)		25	4.80	19.6
υ_{12}	0,3	0.21	0.342	0,30
υ_{13}		0.21	0.342	0.28
υ_{23}		0.21	0.38	0.28
G_{12} (GPa)		7.2	4.8	7.2
G_{13} (GPa)		5.5	4.8	5.5
G_{23} (GPa)		5.5	2.55	5.5

FEM Analyses

The finite element method has been extensively used in fracture mechanics in various forms. One of the major challenges in modeling cracked structures lies in the geometric description of the crack. In the finite element method, the crack is explicitly modeled and is an integral part of the mesh boundaries. In this study, the software used is the finite element analysis code **ABAQUS[17]**, version **6.11**. An initial mesh consisting of **10,568 elements** was employed, which was refined several times to reach **41,353 elements**, with intermediate refinements of **17,811**, **25,736**, and **34,058** elements. The results of the **KI** integrals for each refinement were nearly identical, confirming the convergence of the solutions. It is noteworthy that for each refined mesh, the region around the crack tip was specifically refined multiple times to ensure result stability. The crack tip was modeled using focused elements, consisting of five contours. The solutions obtained using this modeling were compared to those using five contours, and the results were almost identical, validating the adopted approach.

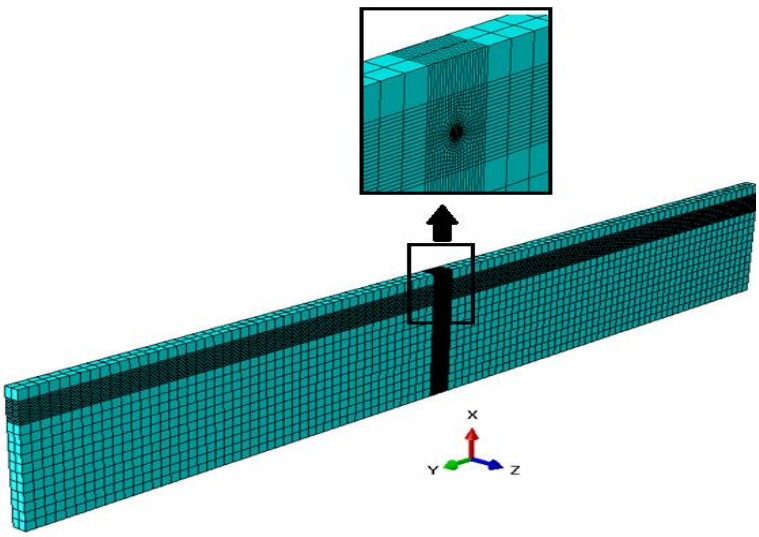


Figure 3. Mesh used for the structure.

Results and Discussion

Effect of Material Properties

Figure 4 shows the variation of the stress intensity factor **KI** as a function of crack size **a** for three composite materials: **Boron/epoxy**, **Glass/epoxy**, and **Graphite/epoxy**. All curves exhibit an increasing trend, indicating that **KI** rises with crack size. The **Graphite/epoxy** composite displays the highest **KI** values, which translates to lower resistance to cracking and a higher susceptibility to crack propagation. In contrast, the **Boron/epoxy** composite shows the lowest **KI** values, suggesting better fracture toughness compared to the other two

materials. These results highlight the significant role of material-specific properties in fracture behavior and crack propagation resistance.

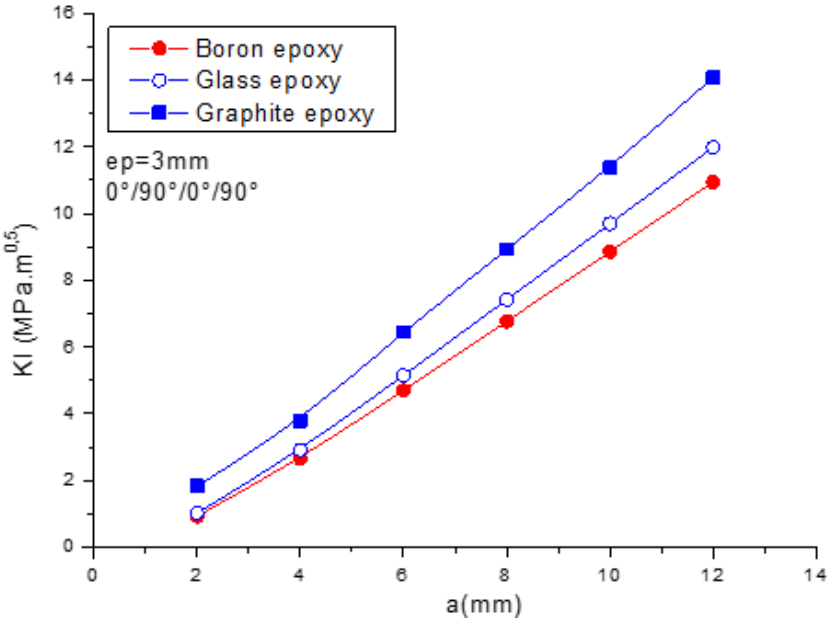


Figure 4. Variation of the stress intensity factor KI as a function of crack length aaa for three composite materials: Boron epoxy, Glass epoxy, and Graphite epoxy

Effect of Ply Orientation

Figure 5 illustrates the variation of the stress intensity factor **KI** as a function of crack length **a** for a Boron/epoxy composite, considering three ply orientation configurations: **[0°/90°/0°/90°]**, **[45°/0°/45°/0°]**, and **[−30°/0°/30°/0°]**, with a constant thickness of **3 mm**. The results clearly highlight the significant influence of ply orientation on the material's fracture behavior. The **[−30°/0°/30°/0°]** configuration yields the highest **KI** values, reaching approximately **19.84 MPa·m$^{0.5}$** for a **12 mm** crack, indicating reduced resistance to crack propagation. In contrast, the **[45°/0°/45°/0°]** and particularly the **[0°/90°/0°/90°]** configurations show substantially lower **KI** values, with a minimum around **10.84 MPa·m$^{0.5}$** for **a = 12 mm**, suggesting enhanced fracture toughness. These findings demonstrate the critical role of ply orientation in optimizing crack resistance in composite structures.

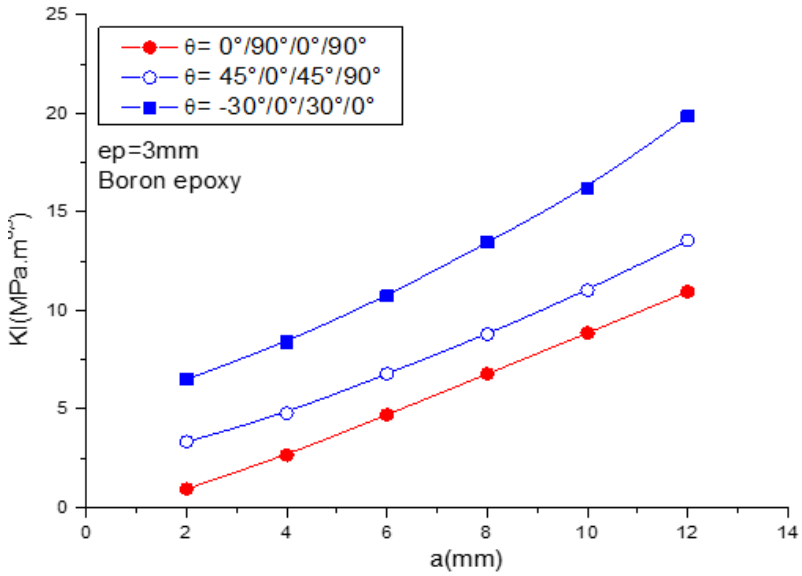


Figure 5. Variation of the stress intensity factor KI as a function of crack length (a) for three ply orientation configurations: (θ=0∘/90∘/0∘), (45∘/0∘/45∘) and (−30∘/0∘/30∘).

Effect of Thickness

Figure 6 depicts the variation of the stress intensity factor **KI** as a function of crack length **a** for a Boron/epoxy composite with a **[0°/90°/0°/90°]** stacking sequence, considering three different thicknesses: **1 mm**, **2 mm**, and **3 mm**. The analysis reveals a significant influence of thickness on the fracture behavior of the material. The **1 mm** thick configuration exhibits the highest **KI** values, reaching approximately **19.84 MPa·m$^{0.5}$** for a **12 mm** crack, indicating reduced resistance to crack growth and increased susceptibility to failure. In contrast, a thickness of **2 mm** yields a lower **KI** value of around **14.07 MPa·m$^{0.5}$**, suggesting a notable improvement in fracture toughness. The **3 mm** thickness shows the lowest **KI** values, approximately **10.84 MPa·m$^{0.5}$**, reflecting better crack resistance. These results clearly demonstrate that increasing ply thickness enhances the material's toughness and limits crack propagation, emphasizing the critical role of thickness in the structural design of fiber-reinforced composites under mechanical loading.

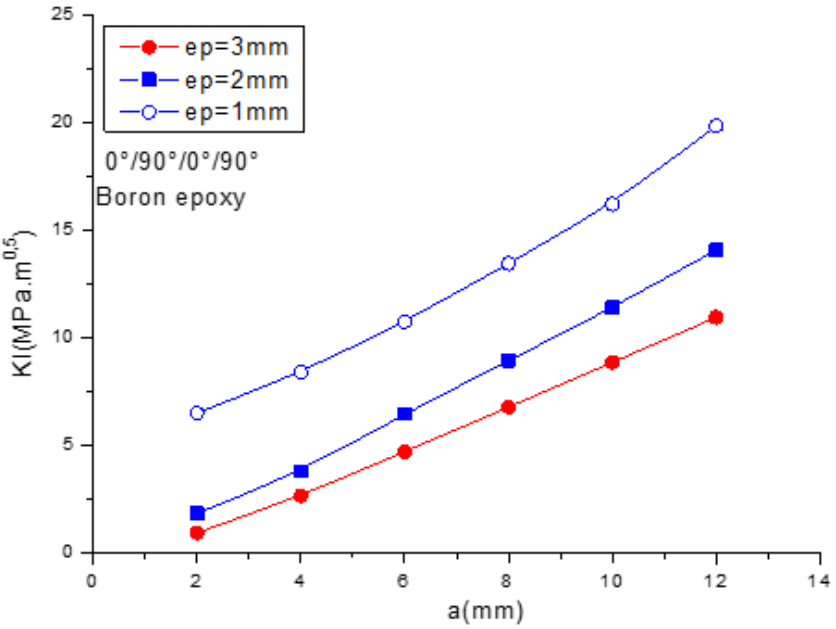


Figure 6. Variation of the stress intensity factor KI as a function of crack length (a) for three distinct thicknesses: 1 mm, 2 mm, and 3 mm

Effect of the (L/ep) Ratio

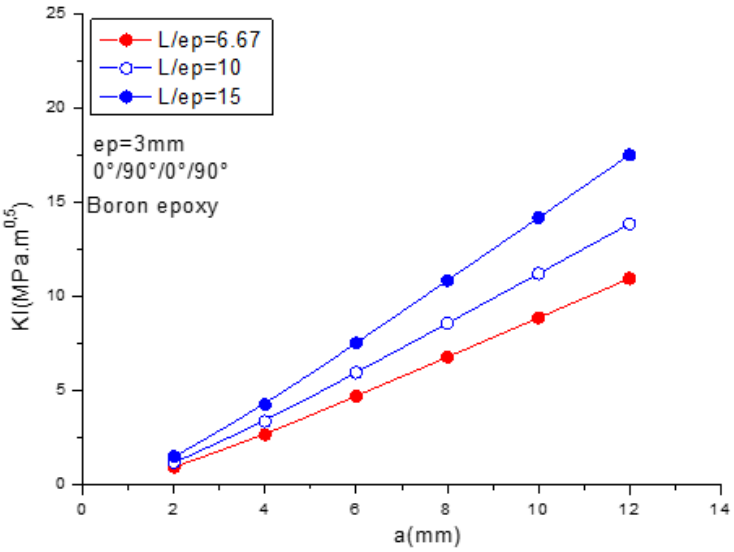


Figure 7. Variation of the stress intensity factor KI as a function of crack length (a) for three distinct length-to-thickness ratios (L/ep): 6.67, 10, and 15.

Fig.7 shows the evolution of the stress intensity factor **KI** as a function of crack length **a** for a Boron/epoxy composite laminate with a **[0°/90°/0°/90°]** stacking sequence, considering three different length-to-thickness ratios (**L/ep**): **6.67**, **10**, and **15**. The analysis highlights the significant influence of relative thickness on the crack propagation behavior of the composite. The configuration with **L/ep = 15** yields the highest **KI** values, reaching approximately **13.84 MPa·m$^{0.5}$** for a **12 mm** crack, indicating reduced resistance to crack growth and greater susceptibility to failure. In contrast, for **L/ep = 10**, **KI** increases to about **17.50 MPa·m$^{0.5}$**, suggesting enhanced fracture toughness. Finally, the case of **L/ep = 6.67** shows the lowest **KI** values, around **10.84 MPa·m$^{0.5}$**, reflecting better resistance to crack propagation. These findings emphasize the critical role of structural thickness in enhancing the mechanical performance of composite materials under fracture conditions

Effect of Loading

Figure 8 illustrates the variation of the stress intensity factor **KI** as a function of crack length **a** for a Boron/epoxy composite laminate with a **[0°/90°/0°/90°]** stacking sequence, subjected to two types of loading: mechanical and thermal. Under mechanical loading, **KI** reaches approximately **10.84 MPa·m$^{0.5}$** for a **12 mm** crack, indicating lower resistance to crack propagation and a higher susceptibility to failure. Conversely, under thermal loading, **KI** is reduced to around **8.47 MPa·m$^{0.5}$** for the same crack length, reflecting improved fracture toughness. This contrast highlights the significant influence of loading conditions on crack behavior. Thermal loading appears to enhance resistance to crack growth, emphasizing the importance of accounting for service conditions in the design and durability assessment of composite structures.

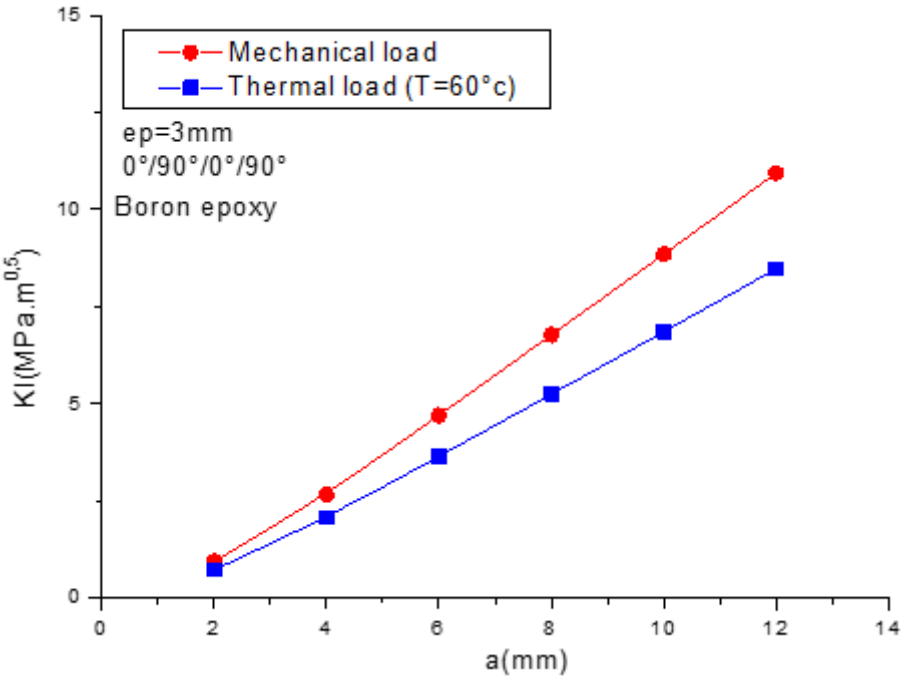


Figure 8**.** Variation of the stress intensity factor KI as a function of crack length aaa, under two types of loading: mechanical and thermal.

Probabilistic Analysis

A cracked structure is considered, subjected to random loading, with mechanical and geometric characteristics that are also uncertain. These uncertainties are represented by a random vector **X** of **N** dimensions, whose components model the various uncertain parameters of the system, including the applied loads. The random variables considered include geometric parameters (**a**, **t**, **W**, **L**), material properties such as the elastic modulus **E**, Poisson's ratio **υ**, the hardening exponent **n**, and the applied stress σ_{ap} (with σ_{ap} **= 50 MPa**). Any or all of these variables can be statistically modeled as random variables. Consequently, any relevant fracture-related response, such as the stress intensity factor **KI**, must be evaluated in a probabilistic framework to properly account for the inherent uncertainty in the system.The probability density function (PDF) is estimated using the Monte Carlo method, which is based on random sampling of the system's input random variables. For each realization of the input random vector, the system response is computed, yielding a dataset that reflects the

overall behavior. A statistical analysis of these simulated responses is then conducted to empirically estimate the distribution of the random variable. This stochastic approach provides a rigorous framework for modeling the effects of uncertainty on the system's response. To ensure statistical accuracy and reliable convergence of the results, a total of 10^5 independent simulations was performed in the context of this numerical study. Figure 9 shows the histograms of KI(X) obtained from simulations performed using the Monte Carlo method. The probability density function (PDF) is determined by adjusting these histograms using theoretical models. It is thus clearly bserved that the Gaussian distribution provides a satisfactory approximation of the distribution of KI(X), accurately reflecting the statistical behaviour of the response. Furthermore, this adjustment provides an accurate estimate of the mean value, confirming the relevance of the approach adopted for the probabilistic evaluation of the results.

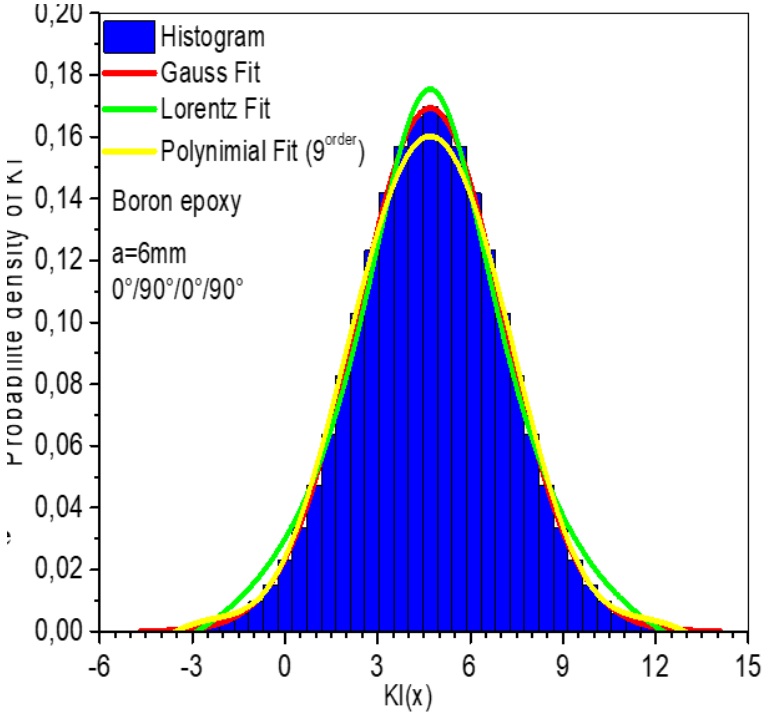


Figure 9. Histogram and probability distribution function of the stress intensity factor KI.

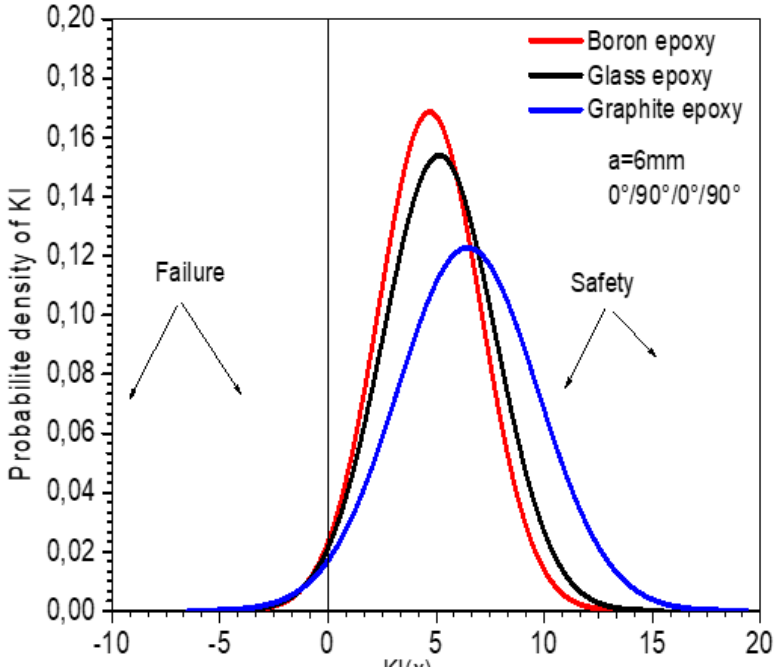


Figure 10. Probability density functions of the stress intensity factor KI for different composite materials.

Figure 10 illustrates the failure probability of the stress intensity factor (KI) for different composite materials: boron/epoxy, glass/epoxy, and graphite/epoxy. It is observed that the boron/epoxy composite exhibits a significantly lower failure probability compared to the other two materials. This improved performance is partly due to the superior mechanical properties of carbon, which provide greater resistance to crack propagation. In contrast, the glass/epoxy and graphite/epoxy materials show higher failure probabilities, indicating increased sensitivity to stress. Moreover, uncertainties related to the intrinsic properties of the materials contribute to a wider margin of error in estimating the risk of failure. Therefore, the choice of material plays a critical role in structural reliability, as the failure probability varies significantly depending on the type of composite used.

Conclusion

The appearance of cracks and their gradual propagation constitute one of the main risks of failure in industrial structures. In order to prevent such failures, the objective of this work is to study damage to composite materials through a three-dimensional analysis based on the finite element method. To do this, several influential parameters were taken into account, including the mechanical properties of the materials, the geometric characteristics of the structure, the mechanical loading conditions, and the orientation of the composite's constituent layers. Particular attention was paid to predicting crack propagation. To this end, a probabilistic approach based on the Monte Carlo method was adopted to assess the reliability of reinforced structures. This analysis aims to better understand the impact of uncertainties inherent in material properties and loading conditions on the durability of composite structures. We conclude that:

- The **Graphite/epoxy** composite displays the highest **KI** values, which translates to lower resistance to cracking and a higher susceptibility to crack propagation. In contrast, the **Boron/epoxy** composite shows the lowest **KI** values, suggesting better fracture toughness compared to the other two materials. These results highlight the significant role of material-specific properties in fracture behavior and crack propagation resistance.
- The case of **L/ep = 6.67** shows the lowest **KI** values, around **10.84 MPa·m$^{0.5}$**, reflecting better resistance to crack propagation. These findings emphasize the critical role of structural thickness in enhancing the mechanical performance of composite materials under fracture conditions
- Under mechanical loading, **KI** reaches approximately **10.84 MPa·m$^{0.5}$** for a **12 mm** crack, indicating lower resistance to crack propagation and a higher susceptibility to failure. Conversely, under thermal loading, **KI** is reduced to around **8.47 MPa·m$^{0.5}$** for the same crack length, reflecting improved fracture toughness. This contrast highlights the significant influence of loading conditions on crack behavior. Thermal loading appears to enhance resistance to crack growth, emphasizing the importance of accounting for service conditions in the design and durability assessment of composite structures.
- The Gaussian distribution provides a satisfactory approximation of the distribution of KI(X), accurately reflecting the statistical behaviour of the response. Furthermore, this adjustment provides an accurate estimate of the mean value, confirming the relevance of the approach adopted for the probabilistic evaluation of the results.

Scientific Ethics Declaration

* The authors declare that the scientific ethical and legal responsibility of this article published in EPSTEM journal belongs to the authors.

Conflict of Interest

* The authors declare that they have no conflicts of interest

Funding

* This research received no specific grant from any funding agency in the public, commercial, or not-for-profit sectors.

Acknowledgements or Notes

* This article was presented as a poster presentation at the International Conference on Technology, Engineering and Science (www.icontes.net) held in Antalya/Turkiye on November 12-15, 2025.

* The authors would like to thank the conference committee members and reviewers for their valuable contributions. The authors would also like to thank the University of Sidi Bel Abbes for its support in carrying out this study and presenting it at the conference.

* Data can be accessed upon request from the corresponding author.

References

Bayandor, J., Thomson, R. S., Scott, M. L., Nguyen, M. Q., & Elder, D. J. (2003). Investigation of impact and damage tolerance in advanced aerospace composite structures. *International Journal of Crashworthiness, 8*(3), 297–306.

Cao, D. F., Duan, Q. F., Hu, H. X., Cheng, J. S., & Zhao, Y. (2010). Computational investigation of both intra-laminar matrix cracking and inter-laminar delamination of curved composite components with cohesive elements. *Composite Structures, 92*(2), 300–309.

Charrier, J. S., Laurin, F., Carrere, N., & Mahieux, C. A. (2016). Determination of the out-of-plane tensile strength using four-point bending tests on laminated L-angle specimens with different stacking sequences and total thicknesses. *Composites Part A: Applied Science and Manufacturing, 81*, 243–253.

Dassault Systèmes. (2021). *Abaqus/CAE User's Manual* (Version 2021) (Computer software). Dassault Systèmes.

Di Vito, D., Pärnänen, T., Jokinen, J., Orell, O., & Kanerva, M. (2019). Lateral indentation and impact analyses on curved composite shells. In *Proceedings of the 7th International Conference on Fracture Fatigue and Wear* (pp. 171–183).

Fletcher, T. A., Kim, T., Dodwell, T. J., & Butler, R. (2016). Resin treatment of free edges to aid certification of through thickness laminate strength. *Composite Structures, 146*, 26–33.

Horton, B., Song, Y., Jegley, D., Collier, F., & Bayandor, J. (2020). Predictive analysis of stitched aerospace structures for advanced aircraft. *The Aeronautical Journal, 124*(1271), 44–54.

Ibrahim, N. C. M., Serier, B., & Mechab, B. (2018). Analysis of the crack-crack interaction effect initiated in aeronautical structures and repaired by composite patch. *Frattura ed Integrità Strutturale, 12*(46), 140–149.

Maachou, S., Mechab, B., Bachir Bouiadjra, B., & Salem, M. (2025). Using fatigue analysis to predict the propagation of internal and external semi-elliptical cracks in pipes under cyclic load. *Journal of Pressure Vessel Technology, 147*(6), 061702.

Pernice, M. F., De Carvalho, N. V., Ratcliffe, J. G., & Hallett, S. R. (2015). Experimental study on delamination migration in composite laminates. *Composites Part A: Applied Science and Manufacturing, 73*, 20–34.

Ranz, D., Cuartero, J., Miravete, A., & Mian, A. (2017). Experimental research into interlaminar tensile strength of carbon/epoxy laminated curved beams. *Composite Structures, 164*, 189–197.

Salem, M., Mhamdia, R., Mechab, B., & Bachir Bouiadjra, B. (2024). Effect of the stiffness ratio on the growth of repaired fatigue cracks with composite patch. *Mechanics Based Design of Structures and Machines, 52*(5), 2679–2697.

Solis, A., Sánchez-Sáez, S., & Barbero, E. (2018). Influence of ply orientation on free-edge effects in laminates subjected to in-plane loads. *Composites Part B: Engineering, 153*, 149–158.

Song, Y., Horton, B., & Bayandor, J. (2019). Verified fuselage section water impact modelling. *The Aeronautical Journal, 123*(1268), 1740–1754.

Talbi, S., Salem, M., Mechab, B., Ghomari, T., Allem, A., Bachir Bouiadjra, B., & Benelmaarouf, M. (2024). New investigation of delamination using the VCCT method to predict the damage in bonded composite repair plates subjected to tensile load. *International Journal of Structural Integrity, 15*(1), 58–71.

Tasdemir, B., & Coker, D. (2019). Comparison of damage mechanisms in curved composite laminates under static and fatigue loading. *Composite Structures, 213*, 190–203.

Turon, A., Dávila, C. G., Camanho, P. P., & Costa, J. (2007). An engineering solution for mesh size effects in the simulation of delamination using cohesive zone models. *Engineering Fracture Mechanics, 74*(10), 1665–1682.

Tvergaard, V. (1990). Effect of fibre debonding in a whisker-reinforced metal. *Materials Science and Engineering: A, 125*(2), 203–213.

Tvergaard, V., & Hutchinson, J. W. (1992). The relation between crack growth resistance and fracture process parameters in elastic-plastic solids. *Journal of the Mechanics and Physics of Solids, 40*(6), 1377–1397.

Author(s) Information

Sid Ahmed Reffas
LMPM, University of Sidi Bel Abbes,
Department of Mechanical Engineering,
Sidi Bel Abbes 22000, Algeria
Contact e-mail: *reffas_ahmed@yahoo.fr*

Belaid Mechab
LMPM, University of Sidi Bel Abbes,
Department of Mechanical Engineering,
Sidi Bel Abbes 22000, Algeria

Mohamed Cherfi
LMPM, University of Sidi Bel Abbes,
Department of Mechanical Engineering,
Sidi Bel Abbes 22000, Algeria

To cite this article:

Reffas, S.A., Mechab, B., & Cherfi, M. (2025). Probabilistic fracture mechanics analysis of crack propagation in composites under tensile loading. *The Eurasia Proceedings of Science, Technology, Engineering and Mathematics (EPSTEM), 38,* 200-209.

The Eurasia Proceedings of Science, Technology, Engineering & Mathematics (EPSTEM)
ISSN: 2602-3199

The Eurasia Proceedings of Science, Technology, Engineering & Mathematics (EPSTEM), 2025

Volume 38, Pages 210-216

IConTES 2025: International Conference on Technology, Engineering and Science

Magnetic and Structural Behavior of Nanocrystalline Iron-Silicon and Iron-Tin Produced via Mechanical Milling

Abderahim Abada
University of Saad Dahleb Blida

Abderrahmane Younes
Research Center in Industrial Technologies (CRTI)

Rachid Amraoui
Research Center in Industrial Technologies (CRTI)

Djilali Allou
Research Center in Industrial Technologies (CRTI)

Abstract: This study presents a comparative investigation of the structural, morphological, and magnetic properties of nanostructured FeSi and FeSn alloys synthesized via the ball milling process. The alloys were analyzed at various milling times from 0 to 20 hours using X-ray diffraction (XRD), scanning electron microscopy (SEM), and vibrating sample magnetometer (VSM). XRD analysis confirmed the formation of FeSi and FeSn phases after 20 hours of milling, with characteristic peaks indicating structural evolution. SEM micrographs revealed significant morphological changes and particle refinement with increased milling time. Magnetic measurements highlighted contrasting behaviors between the two alloys. For FeSn, increased milling time enhanced coercivity, remanence magnetization, and squareness, accompanied by a reduction in saturation magnetization. Conversely, FeSi exhibited superparamagnetic behavior with notable saturation magnetization and significant coercivity (Hc). These findings emphasize the distinct magnetic and structural properties of FeSi and FeSn nanocrystalline alloys and their potential for tailored applications in advanced magnetic systems.

Keywords: Nanocrystalline FeSi and FeSn, Structural and morphological properties, Magnetic behavior

Introduction

Nanostructured materials, especially those based on iron alloys, have garnered significant attention due to their unique properties that emerge at the nanoscale, such as enhanced magnetic, mechanical, and electronic characteristics. FeSi and FeSn alloys are particularly important for their potential applications in electronics, energy storage, and sensors due to their tunable magnetic properties (Suryanarayana et al., 2022, Wang et al., 2014, Younes et al., 2024, Abada et al., 2020, and Abada et al., 2024). Mechanical milling, a solid-state processing method, has been widely used to fabricate nanocrystalline materials because it induces changes in the alloy's phase, particle size, and crystallinity. The milling time and conditions significantly affect the microstructure and, consequently, the magnetic behavior of these materials. In this study, we compare the structural, morphological, and magnetic properties of FeSi and FeSn alloys synthesized through the ball milling process, exploring the effects of different milling times (Ouadah et al., 2023, Jaldurgam et al., 2021, Yelsukov et al., 2000, and Chen et al., 2007). The aim of this research is to investigate the magnetic and structural properties of nanocrystalline FeSi and FeSn alloys synthesized through the mechanical milling process. Specifically, the study seeks to examine how varying milling times (0–20 hours) affect the structural evolution, including

- This is an Open Access article distributed under the terms of the Creative Commons Attribution-Noncommercial 4.0 Unported License, permitting all non-commercial use, distribution, and reproduction in any medium, provided the original work is properly cited.

- Selection and peer-review under responsibility of the Organizing Committee of the Conference

© 2025 Published by ISRES Publishing: www.isres.org

changes in grain size, phase formation, and crystallinity, as well as the morphological characteristics such as particle refinement. Additionally, the research aims to analyze the magnetic behavior of these alloys, focusing on key properties such as saturation magnetization, coercivity, and remanent magnetization, using vibrating sample magnetometer (VSM). By correlating the structural and magnetic characteristics, this research aims to understand the impact of mechanical milling on the alloys' performance and their potential applications in advanced magnetic systems, such as sensors and energy devices.

Method

FeSi and FeSn alloys were synthesized using high-purity iron (Fe), silicon (Si), and tin (Sn) powders, which were mixed in the desired stoichiometric proportions. The powders were subjected to a high-energy ball milling process using a planetary ball mill. Milling times of 0, and 20 hours were chosen to study the evolution of the material properties with increasing milling duration. During milling, the powders were subjected to a speed of 300 rpm, and a ball-to-powder weight ratio of 10:1 was maintained. The synthesized powders were characterized using; X-ray Diffraction (XRD): To determine the crystalline phases and assess the structural evolution of the alloys as a function of milling time. XRD patterns were collected using a Cu Kα radiation source ($\lambda = 1.5406$ Å) in the 2θ range from 20° to 80°. Scanning Electron Microscopy (SEM): To investigate the morphological changes and particle size reduction during milling. SEM imaging was performed using a field-emission scanning electron microscope. Vibrating Sample Magnetometer (VSM): To evaluate the magnetic properties of the alloys, including saturation magnetization, coercivity, and remanence. Measurements were carried out at room temperature and 300 K.

Results and Discussion

SEM Examination

Figures 1a and 1b display SEM micrographs of the FeSi and FeSn alloys before and after 20 hours of mechanical milling, providing detailed insight into the morphological evolution of the particles. Before Milling (0 hours): The initial powders of both FeSi and FeSn alloys exhibit a relatively coarse and irregular structure, characterized by large, angular particles that are typical of the raw materials used. These particles have relatively broad size distributions, with the majority of them being in the micron range. The large particle sizes and irregular shapes suggest that the powders are not yet refined and are in their original form, with limited surface area available for interactions. The SEM images show that the particles are not homogeneously distributed, and there is an absence of finer particles, which is indicative of the need for milling to induce structural changes in the alloys. After 20 Hours Milling: After 20 hours of ball milling, significant refinement in particle size is observed in both FeSi and FeSn alloys. The particles are reduced to a finer, more uniform distribution, with the majority of the particles now being in the nanometer range (Jensen et al., 2017; Younes et al. 2019; Yin et al 2017).

The increased surface area of the nanostructured particles after milling is expected to significantly enhance the magnetic properties of these alloys. This is because the high surface area allows for more efficient interactions between the individual particles and the external magnetic field. The smaller particle size and increased surface energy also enhance the material's potential for exhibiting superparamagnetism and may improve the performance of the alloys in applications such as magnetic sensors, data storage, and electromagnetic shielding. The fine, uniform distribution of the nanoparticles, along with the enhanced surface area, plays a crucial role in determining the alloy’s magnetic anisotropy and overall magnetic performance.

The SEM images show a more homogeneous particle size distribution, with the particles appearing more spherical or faceted, a result of the high-energy collisions within the milling process. This refinement of particle size is a direct consequence of the mechanical milling, which induces repeated fracturing and welding of the powder particles, progressively reducing their size. The particle surfaces also appear smoother, further suggesting that the milling process has facilitated the refinement of the particles into nanoscale dimensions. Furthermore, the SEM images reveal an increased degree of agglomeration of the particles after milling. Agglomeration is a common phenomenon in ball milling, where fine nanoparticles tend to cluster together due to the high surface energy created during the milling process. The agglomerates formed are typically the result of van der Waals forces and other attractive forces between the particles. This clustering can increase the particle size slightly, but it also contributes to the creation of complex microstructures.

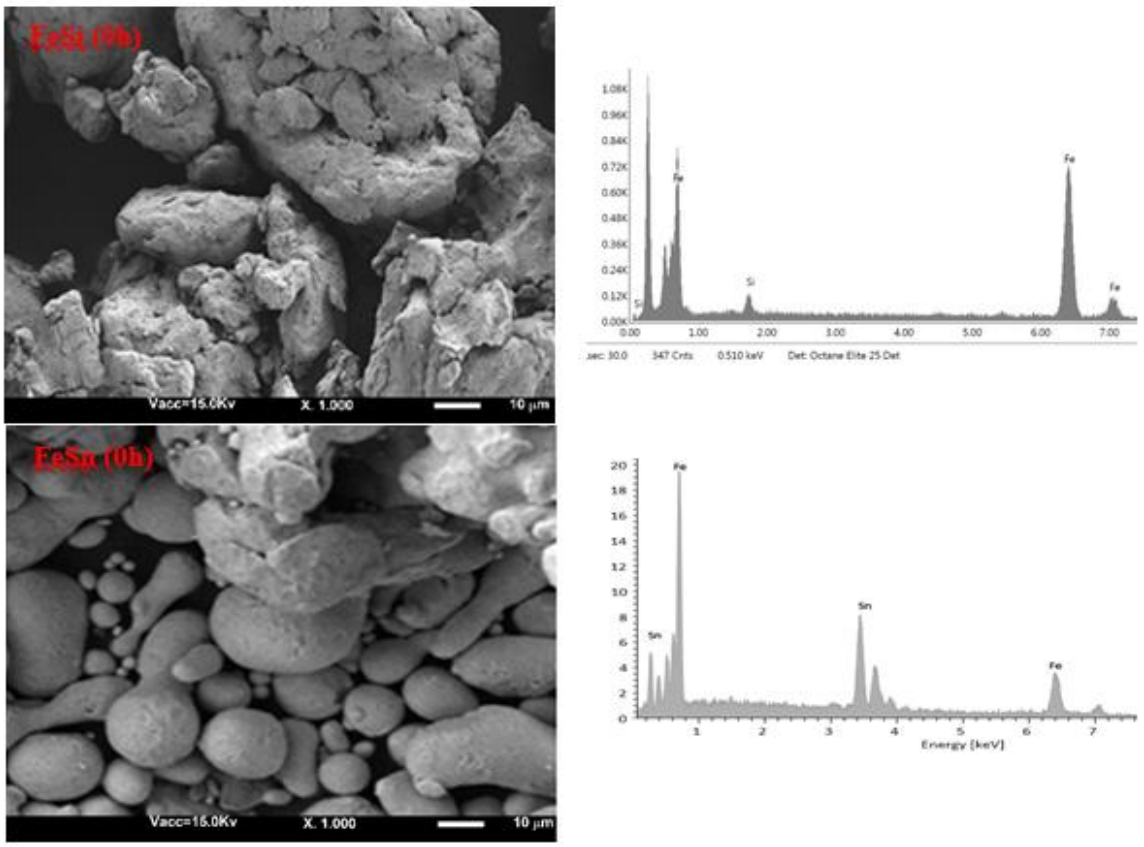


Figure 1a. SEM micrographs of nanocrystalline FeSi and FeSn alloys before milling

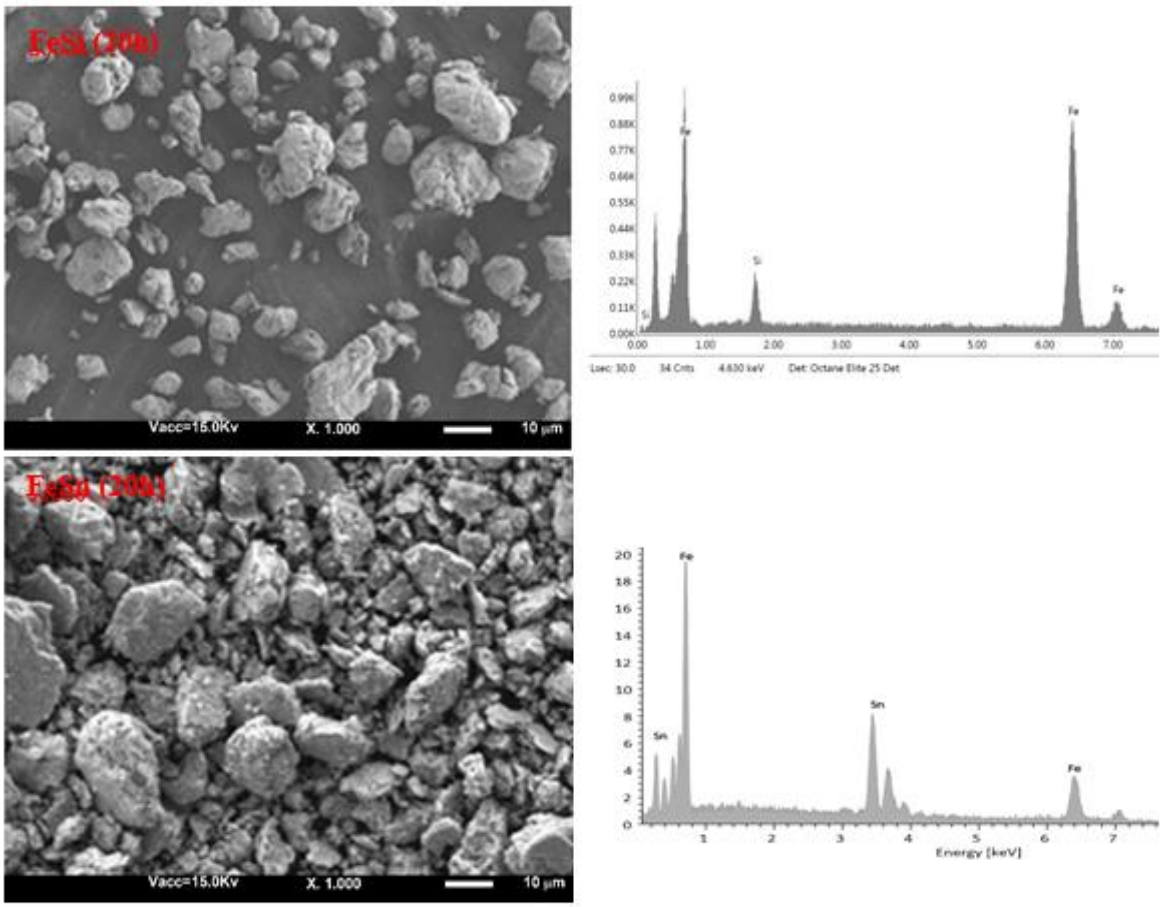


Figure 1b. SEM micrographs of Nanocrystalline FeSi and FeSn alloys milled for 20h

XRD Analysis

The XRD patterns of the FeSi and FeSn alloys at various milling times are displayed in Figure 2, showcasing the structural evolution of both alloys as a function of milling duration. After 20 hours of milling, the XRD data reveal the formation of well-defined FeSi and FeSn phases, with characteristic diffraction peaks at 2θ = 30.7°, 35.1°, and 50.4° for FeSi, and 2θ = 32.8°, 36.2°, and 45.5° for FeSn. These peaks correspond to the (110), (200), and (211) crystallographic planes for FeSi, and the (110), (101), and (211) planes for FeSn, indicating the successful formation of the FeSi and FeSn phases after extensive milling. The sharpness of the peaks reflects the crystallinity of the materials at this stage. As the milling time increases, however, the broadening of the diffraction peaks becomes more pronounced, which is a hallmark of reduced crystallite size typical of nanocrystalline materials. This broadening occurs because smaller grains produce more grain boundaries, which hinder the coherent diffraction of X-rays, resulting in a wider peak. Additionally, the intensity of the peaks gradually decreases with increasing milling time, suggesting a decrease in the crystallite size and the emergence of more amorphous regions within the alloys. This observation is indicative of the refinement of the crystal structure into smaller nano-sized grains as the milling process continues. The gradual reduction in peak intensity and the continuous broadening of diffraction peaks with increasing milling time further confirm that the mechanical milling process is progressively breaking down the larger crystalline structures into finer, nanoscale crystallites, leading to the formation of a nanocrystalline phase in both FeSi and FeSn alloys. The overall structural evolution observed in the XRD data underscores the impact of milling time on the phase transformation and grain refinement of these materials, emphasizing the nanocrystalline nature of the synthesized alloys after extended milling (Wang et al., 2011, Wang et al., 2019, and Ozduran et al., 2021).

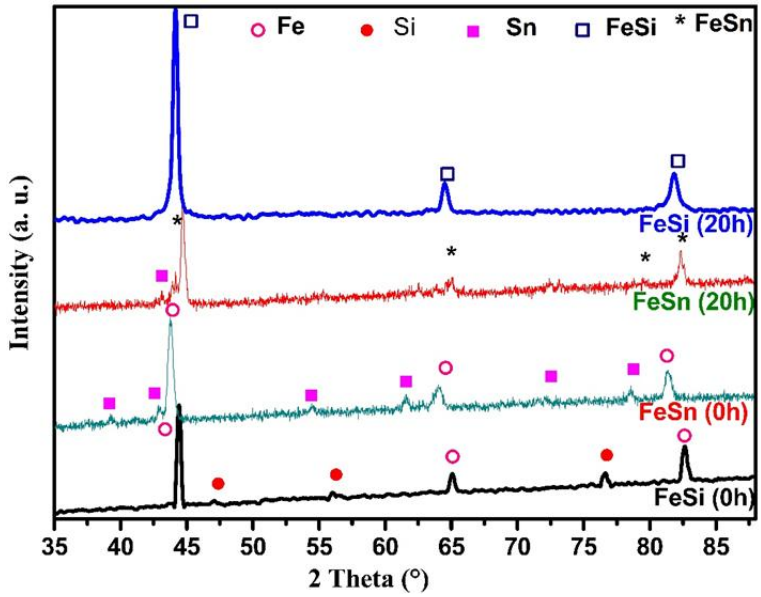


Figure 2. XRD patterns of Nanocrystalline FeSi and FeSn alloys milled for different times

Magnetic Investigation

Figure 3 presents the hysteresis loops of the FeSi and FeSn alloys at different milling times, providing key insights into the evolution of their magnetic properties as the milling duration increases. FeSn Alloys: As the milling time progresses, a clear trend emerges in the magnetic behavior of the FeSn alloys. Notably, there is a significant increase in both coercivity (the field required to reduce the magnetization to zero) and remanent magnetization (the residual magnetization remaining when the external magnetic field is removed). This suggests a transition toward more hard magnetic behavior, which is typically associated with materials that retain their magnetization after the external magnetic field is removed. The increase in coercivity and remanent magnetization indicates that the FeSn alloy is becoming magnetically more resistant to external fields as the milling time increases. However, a noticeable decrease in saturation magnetization is observed, which implies that the material is losing its ability to reach its full magnetization under a strong external field. This decrease in saturation magnetization is likely due to the increased magnetic anisotropy and domain wall pinning caused by the nanostructuring effect. As the milling time increases, the alloy's crystal structure is refined, and smaller crystallites with more surface defects are created. These defects act as pinning sites for the magnetic domain walls, hindering their movement and, therefore, contributing to higher coercivity. This behavior is typical of

hard magnetic materials, where the increased number of domain wall pinning sites prevents the alignment of domains in the presence of a magnetic field.

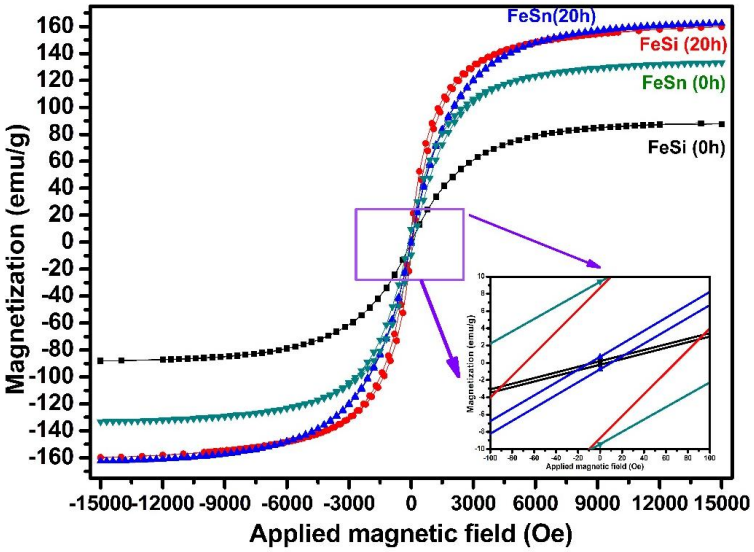


Figure 3. Hysteresis curve (a) and zoom part (b) of Nanocrystalline FeSi and FeSn alloys milled for different times

FeSi Alloys: In contrast to FeSn, the FeSi alloys exhibit superparamagnetic behavior even after 20 hours of milling. This is evident from the hysteresis loops, which show no distinct coercivity, and the lack of a well-defined remanence. Superparamagnetism is a phenomenon typically observed in nanomaterials where, at room temperature, the thermal energy is sufficient to overcome the anisotropy energy of the individual nanoparticles, causing them to rapidly flip their magnetization direction in the absence of an external magnetic field. This results in the absence of a stable magnetization and, consequently, no coercivity or remanent magnetization. Despite this, FeSi alloys exhibit high saturation magnetization, indicating that the material has a strong magnetic response when subjected to an external magnetic field. This suggests that the particles are still able to align with the field, but their small size (due to the ball milling process) and the associated high surface-to-volume ratio lead to superparamagnetic behavior at room temperature. This behavior is often observed in nanoparticles with diameters smaller than the critical size for ferromagnetic or ferrimagnetic ordering, where the particles behave like single magnetic domains (Kakihana et al., 2019, Piamba et al., 2020, Yu et al., 2015, Sales et al., 2014, and Rodmacq et al., 1980) . In summary, the FeSn alloys demonstrate increasing hard magnetic characteristics with higher coercivity and remanent magnetization but reduced saturation magnetization as the milling time increases, reflecting the development of more anisotropic and domain-pinned structures. On the other hand, FeSi alloys exhibit superparamagnetic behavior, with no observable coercivity but a high saturation magnetization, attributed to the small particle sizes and their tendency to behave like single magnetic domains at room temperature. These contrasting behaviors highlight the significant influence of milling time and particle size on the magnetic properties of these nanocrystalline alloys.

Conclusion

This study investigates the structural and magnetic properties of FeSi and FeSn alloys synthesized by mechanical milling, confirming the formation of nanocrystalline structures through XRD and SEM analysis, with particle refinement occurring as milling time increases. Magnetic measurements revealed distinct behaviors: FeSn alloys exhibited enhanced coercivity and reduced saturation magnetization, indicating the development of hard magnetic characteristics, while FeSi alloys displayed superparamagnetic behavior with high saturation magnetization. The SEM images showed a transition from coarse, irregular particles to fine, uniform nanoparticles after 20 hours of milling, which improved the alloys' surface area and magnetic properties. These findings suggest that the magnetic properties of FeSi and FeSn alloys can be tailored by adjusting the milling time, making them suitable for advanced magnetic devices such as sensors, memory devices, and high-performance magnets. The contrasting magnetic behaviors of the two alloys underscore the influence of milling time and particle size in determining the alloys' performance, offering potential for customized applications in next-generation magnetic technologies.

Recommendations

Future research should extend the milling duration beyond 20 hours to further refine the microstructure and enhance magnetic uniformity in both FeSi and FeSn systems. Investigating the influence of controlled annealing or the introduction of minor dopants could improve coercivity, thermal stability, and magnetic anisotropy. Employing advanced characterization tools such as transmission electron microscopy (TEM), energy-dispersive X-ray spectroscopy (EDS), and Mössbauer spectroscopy would provide deeper insight into phase formation and local atomic environments. Additionally, exploring the correlation between milling parameters and magnetization dynamics could help optimize performance for targeted applications. Finally, assessing long-term stability and integrating these nanostructured alloys into prototype magnetic devices would facilitate their transition toward practical and industrial uses.

Scientific Ethics Declaration

* The authors declare that the scientific ethical and legal responsibility of this article published in EPSTEM journal belongs to the authors.

Conflict of Interest

* The authors declare that they have no conflicts of interest

Funding

* This research received no specific grant from any funding agency in the public, commercial, or not-for-profit sectors.

Acknowledgements or Notes

* This article was presented as a poster presentation at the International Conference on Technology, Engineering and Science (www.icontes.net) held in Antalya/Türkiye on November 12-15, 2025.

References

Abada, A., Bergheul, S., & Younes, A. (2020). Mechanical and structural behaviour of TiAlV nanocrystalline elaborated by mechanical milling technique. *Micro & Nano Letters, 15*(14), 1023–1027.

Abada, A., Younes, A., & Manseri, A. (2024). Magnetic and structural properties of nanostructured FeSn, FeSnTi, FeSnV and FeSnTiV alloys elaborated via ball milling process. *Journal of the Korean Physical Society, 84*(1), 33–43.

Chen, D., Chen, J., Yan, H., & Chen, Z. (2007). Synthesis of binary and ternary intermetallic powders via a novel reaction ball milling technique. *Materials Science and Engineering: A, 444*(1–2), 1–5.

Jaldurgam, F. F., Ahmad, Z., & Touati, F. (2021). Synthesis and performance of large-scale cost-effective environment-friendly nanostructured thermoelectric materials. *Nanomaterials, 11*(5), 1091.

Jensen, W. A., Liu, N., Rosker, E., Donovan, B. F., Foley, B., Hopkins, P. E., & Floro, J. A. (2017). Eutectoid transformations in Fe-Si alloys for thermoelectric applications. *Journal of Alloys and Compounds, 721*, 705–711.

Kakihana, M., Nishimura, K., Aoki, D., Nakamura, A., Nakashima, M., Amako, Y., Takeuchi, T., Harima, H., Hedo, M., Nakama, T., & Ōnuki, Y. (2019). Electronic states of antiferromagnet FeSn and Pauli paramagnet CoSn. *Journal of the Physical Society of Japan, 88*(1), 014705.

Ouadah, M. H., & Younes, A. (2023). Effects of silicon concentration on the magnetic and structural properties of nanostructured Fe-Si alloy synthesized by ball mill process. *The International Journal of Advanced Manufacturing Technology, 127*(7), 3655–3663.

Ozduran, M., Altay, M. O., Iyigor, A., Çanlı, M., & Arıkan, N. (2021). Structural, electronic, elastic, magnetic, phonon and thermodynamic properties of inverse-Heusler Ti_2FeX (X = Si, Ge, and Sn): Insights from DFT-based computer simulation. *Materials Today Communications, 26*, 102036.

Piamba, J. F., Ortega, C., Hernández-Bravo, R., Carmona, J. G., Tabares, J. A., Alcázar, G. P., & Alvarado-Orozco, J. M. (2020). Theoretical and experimental study of FeSi on magnetic and phase properties. *Applied Physics A, 126*(7), 520.

Rodmacq, B., Piecuch, M., Janot, C., Marchal, G., & Mangin, P. (1980). Structure and magnetic properties of amorphous FexSn1−x alloys. *Physical Review B, 21*(5), 1911–1918.

Sales, B. C., Saparov, B., McGuire, M. A., Singh, D. J., & Parker, D. S. (2014). Ferromagnetism of Fe_3Sn and alloys. *Scientific Reports, 4*, 7024.

Suryanarayana, C., Al-Joubori, A. A., & Wang, Z. (2022). Nanostructured materials and nanocomposites by mechanical alloying: An overview. *Metals and Materials International, 28*(1), 41–53.

Wang, C., Meyer, J., Teichert, N., Auge, A., Rausch, E., Balke, B., Hütten, A., & Felser, C. (2014). Heusler nanoparticles for spintronics and ferromagnetic shape memory alloys. *Journal of Vacuum Science & Technology B, 32*(2), 020802.

Wang, W. L., Li, Z. Q., & Wei, B. (2011). Macrosegregation pattern and microstructure feature of ternary Fe-Sn-Si immiscible alloy solidified under free fall condition. *Acta Materialia, 59*(14), 5482–5493.

Wang, X., Chen, X., Su, X., Yin, F., & Li, Z. (2019). The zinc-rich corner of the Fe-Si-Sn-Zn quaternary system at 450 °C. *Metals, 9*(8), 908.

Yelsukov, E. P., Konygin, G. N., Voronina, E. V., Korolyov, A. V., Ulyanov, A. I., Godovikov, S. K., & Zagainov, A. V. (2000). Magnetic behaviour of high Si (Sn) concentration nanocrystalline Fe-Si and Fe-Sn alloys obtained by mechanical grinding. *Journal of Magnetism and Magnetic Materials, 214*(3), 258–268.

Yin, M., Nash, P., Kaduk, J. A., & Schuster, J. C. (2017). Experimental investigation of the Fe-Sn-Ti ternary isothermal section at 873 K. *Journal of Alloys and Compounds, 693*, 76–86.

Younes, A., Amraoui, R., Bouamer, A., Guessoum, M., Boutaghou, Z., Smaili, F., & Mendoud, A. (2024). Effect of milling time on the structural and magnetic properties of nanostructured Fe90Si10 alloys. *Journal of Electronic Materials, 53*(10), 6098–6109.

Younes, A., Khorchef, M., Bouamer, A., & Amar, H. (2019). Magnetic and structural behavior of Fe-CoO nanocomposites mechanically milled. *IOP Conference Series: Materials Science and Engineering, 557*(1), 012064.

Yu, H., Wen, Y., & Bi, X. (2015). Magnetic and mechanical properties of the gradient FeSi alloys fabricated by magnetron sputtering. *Journal of Alloys and Compounds, 634*, 83–86.

Author(s) Information

Abderahim Abada
Laboratory of Aeronautic Science, Aeronautic Institute, University of Saad Dahleb Blida 1, Blida, Algeria
Contact e-mail: *abada_75@yahoo.fr*

Abderrahmane Younes
Research Centre in Industrial Technologies (CRTI)
P.O Box 64, Cheraga 16014 Algiers, Algeria

Rachid Amraoui
Research Centre in Industrial Technologies (CRTI)
P.O Box 64, Cheraga 16014 Algiers, Algeria

Djilali Allou
Research Centre in Industrial Technologies (CRTI)
P.O Box 64, Cheraga 16014 Algiers, Algeria

To cite this article:

Abada, A., Younes, A., Amraoui, R., & Allou, D. (2025). Magnetic and structural behavior of nanocrystalline iron-silicon and iron-tin produced via mechanical milling. *The Eurasia Proceedings of Science, Technology, Engineering and Mathematics (EPSTEM), 38,* 200-216.

The Eurasia Proceedings of Science, Technology, Engineering & Mathematics (EPSTEM)
ISSN: 2602-3199

The Eurasia Proceedings of Science, Technology, Engineering and Mathematics (EPSTEM), 2025

Volume 38, Pages 217-225

IConTES 2025: International Conference on Technology, Engineering and Science

Development and Characterization of Epoxy-Based Laminated Composites: Experimental Characterization and Numerical Simulation

Ghermaoui Ilias Mohammed Amine
University of Djilali Liabes of Sidi Bel Abbes

Ezzine Mohammed Chams Eddine
University of Mascara

Mokhtari Mohammed
University of Djilali Liabes of Sidi Bel Abbes

Cherief Mohammed Nadhir Djamel Eddine
University of Djilali Liabes of Sidi Bel Abbes

Cherfi Mohamed
University of Djilali Liabes Sidi Bel Abbes

Sahli Abderrahmane
University of Djilali Liabes of Sidi Bel Abbes

Abstract: The objective of this project is twofold. First, it focuses on the development of a new hybrid composite material intended for use in various industrial sectors, with particular emphasis on the aeronautical field. This composite is composed of plain weave woven carbon fiber, 8-harness satin (8HS) glass fabric, and metallic reinforcement made of galvanized steel, all embedded in an epoxy resin matrix. The combination of these materials aims to achieve enhanced mechanical performance and durability under different loading conditions. Second, the project involves a comprehensive characterization of the developed composite. This includes experimental mechanical testing, specifically tensile tests and three-point bending tests, in order to determine key properties such as Young's modulus and ultimate tensile strength. In addition to the mechanical tests, micrographic and macrographic analyses are conducted to investigate the internal structure and failure mechanisms of the composite material. These analyses provide insight into how different types of damage initiate and propagate under mechanical loading. To complement the experimental work, a numerical simulation was carried out using ABAQUS finite element software. The Young's modulus of the carbon fiber-based laminated composite was estimated numerically and then compared with the experimental results. The comparison shows a satisfactory agreement, validating the accuracy and reliability of the simulation approach used in this study.

Keywords: Composites, Carbon fibers, Metallic reinforcement, Tensile test, Numerical simulation

Introduction

Polymer matrix composites have gained significant attention due to their outstanding strength-to-weight ratio and versatile mechanical performance (Metahri et al., 2024), making them increasingly valuable in engineering applications (National Transportation and Safety Board. 1989, Zhao et al., 2022). Recent research has focused on understanding their resistance behavior and optimizing their structural performance through material grading

- This is an Open Access article distributed under the terms of the Creative Commons Attribution-Noncommercial 4.0 Unported License, permitting all non-commercial use, distribution, and reproduction in any medium, provided the original work is properly cited.

- Selection and peer-review under responsibility of the Organizing Committee of the Conference

© 2025 Published by ISRES Publishing: www.isres.org

(Ghermaoui et al., 2019). Functionally graded materials (FGMs) represent an advanced class of composites that provide gradual transitions in properties, enhancing their adaptability to varying service conditions (Ghermaoui et al., 2023). Combining the advantages of composite structures and graded materials leads to multifunctional materials capable of meeting complex mechanical and environmental demands (Benzaama et al., 2023).

Several studies have explored innovative composite systems, such as the geopolymer-based composites developed by (Ghermaoui et al., 2023), which were examined under impact and interface damage conditions. Damage analysis in notched composite structures has also been widely investigated using different reinforcement strategies (Kim et al., 1995). Furthermore, numerical approaches like the extended finite element method (XFEM) and cohesive zone modeling (CZM) have proven effective in simulating crack initiation and propagation in composites (Abdelouahed et al., 2023).

Experimental and numerical findings have shown that composite laminates experience multiple damage mechanisms, including matrix cracking and fiber separation. These complex phenomena require advanced modeling tools to predict failure accurately. The XFEM (Mohamed et al., 2024), offers a robust framework for studying interfacial damage without predefining cracks.

In this study, a new meshing strategy is proposed to simulate graded composite behavior by integrating XFEM. This approach enables a detailed analysis of crack initiation, considering the effects of design parameters, volume fraction gradients.

Numerical Approach of Model Geometry and Material Properties

The numerical investigation was performed using the finite element method (FEM) through ABAQUS, where the graded composite structure was discretized with solid continuum elements. The model assumes an ordered fiber arrangement across the thickness, each fiber layer being represented by a row of elements of 0.125 mm thickness, equivalent to the fiber diameter. The notched specimen was modeled as a rectangular plate (200 mm × 30 mm × 1.25 mm) containing a central circular notch of 6 mm radius, serving as a damage initiation site. Only one-quarter of the geometry was simulated due to symmetry Figure 01.

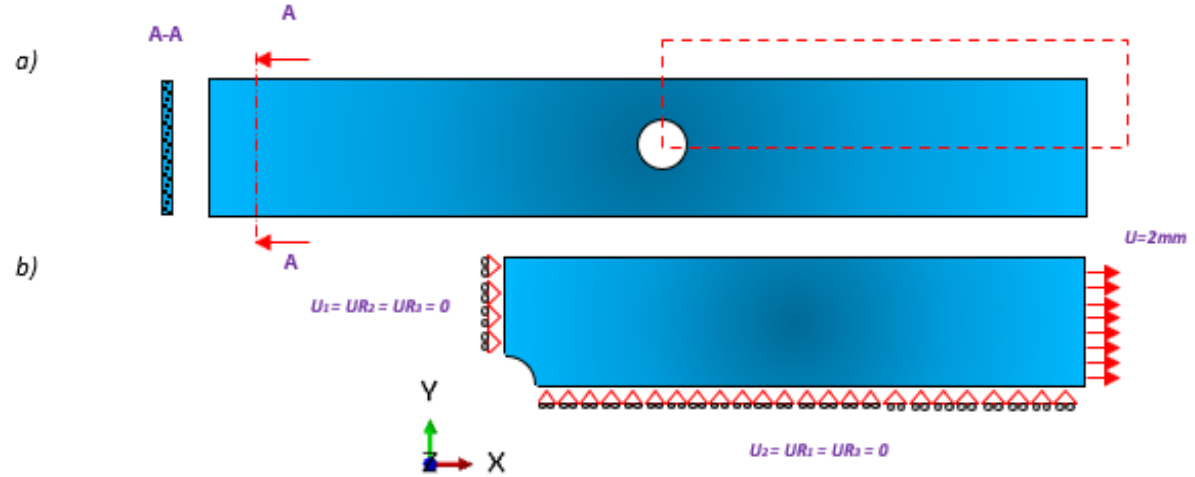


Figure 1. Overview of the studied geometry. a) Complete structure, b) quarter of the structure

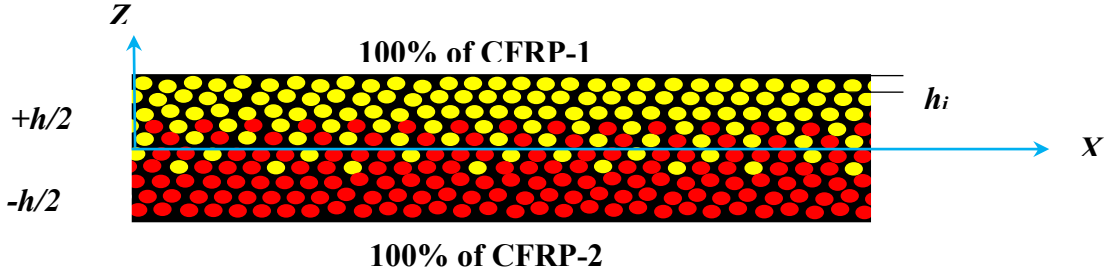


Figure 2. Graduation according to the thickness of CFRP-2 toward CFRP-1 (Ghermaoui & Mokhtari, 2023).

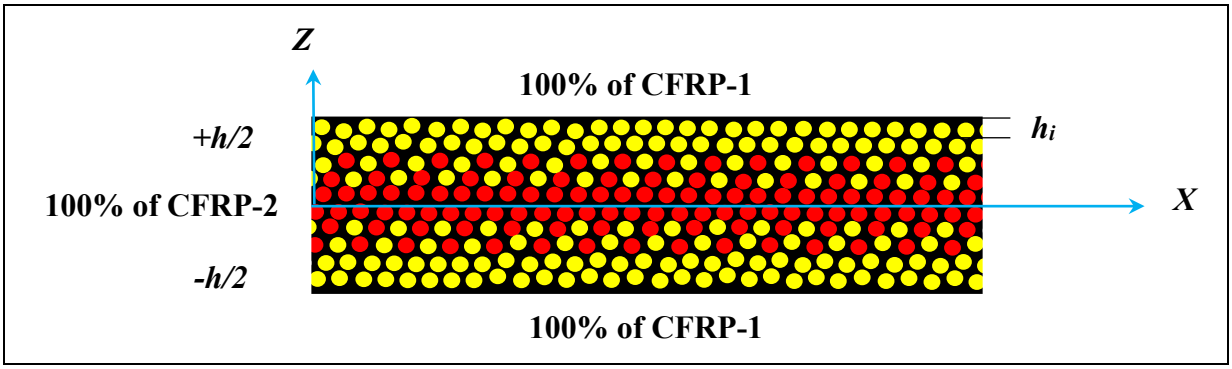


Figure 3. Graduation according to the thickness from CFRP-2 in the middle toward the composite CFRP-1 at the end (Ghermaoui & Mokhtari, 2023).

Two fibers of different mechanical properties (CFRP-1 and CFRP-2) were embedded in the same epoxy matrix, with a total fiber volume fraction fixed at 60%. The study explored different grading designs: (i) a simple gradient from CFRP-1 to CFRP-2 figure 2 and (ii) symmetric configurations, where the fiber types vary from the mid-plane toward the surfaces figure 3. A uniaxial tensile load of 450 MPa was applied quasi-statically to ensure progressive crack propagation. Material anisotropy was accounted for by assigning local coordinate systems to each layer. Mechanical properties and damage parameters (Tables 1–2) were interpolated between the two materials using a rule of mixtures:

Table 1. Mechanical properties of IM7/8552 CFRP; CFRP-1(Shojaei, A. & Li, G 2014) and CFRP-2(Murakami, S 2014) . Used

Variables	*Young'smodulus, E*	*Poisson's ratio, ν*	*Shearmodulus, G*
CFRP-1	E1 = 162000MPa	*ν 12 = 0.316*	*G12 = 4690MPa*
	E2 = 8960MPa	*ν 13 = 0.316*	*G13 = 4690MPa*
	E3 = 8960MPa	*ν 23 = 0.316*	*G23 = 3973MPa*
	E1 = 171400MPa	*ν 12 = 0.32*	*G12 = 5290MPa*
CFRP-2	*E2 = 8960MPa*	*ν 13 = 0.32*	*G13 = 5290MPa*
	E3 = 8960MPa	*ν 23 = 0.5*	*G23 = 2800MPa*

Table 2. Input parameter is for the damage of each CFRP-1(Shojaei, A. & Li, G 2014) and CFRP-2(Murakami, S 2014) used

Variables	CFRP-1	CFRP-2
Longitudinal tensile strength, *XT* (MPa)	*2560*	*2326*
Transverse tensile strength, *YT* (MPa)	*64*	*62.3*
Longitudinal tensile fracture energy (kJ/m^2)	*81.5*	*0.277*
Transversal tensile fracture energy (kJ/m^2)	*0.277*	*0.788*

$$X_{T-C} = X_{T-C1}.V_{C1} + X_{T-C2}.V_{C2} \quad \text{and} \quad Y_{T-C} = Y_{T-C1}.V_{C1} + Y_{T-C2}.V_{C2} \quad (1)$$

$$G_{Ic}^{C} = G_{Ic-C1}.V_{C1} + G_{Ic-C2}.V_{C2} \quad \text{and} \quad G_{IIc}^{C} = G_{IIIc}^{C} = G_{IIc-C1}.V_{C1} + G_{IIc-C2}.V_{C2} \quad (2)$$

X_{T-C},Y_{T-C}: is the ultimate stress in tensile of composite, X_{T-C1},X_{T-C2},Y_{T-C1}, Y_{T-C2} are the ultimate stressin tensile of the CFRP-1 and CFRP-2. G_{IC}^{C}, G_{IIc}^{C}, G_{IIIc}^{C} Is the critical energy release rates of composite, $G_{Ic-CFRP1}$,$G_{Ic-CFRP2}$ are the critical energy release rates of the CFRP-1 and CFRP-2.

The XFEM technique was implemented to simulate crack initiation and propagation without predefined paths. The QUADS criterion was chosen for crack initiation, and energy-based evolution laws governed damage propagation. Cohesive zone models (CZM) were inserted between layers to capture interfacial debonding, with stiffness terms (Knn,Kss,KttK_{nn}, K_{ss}, K_{tt}Knn,Kss,Ktt) derived from the layer modulus divided by an equivalent thickness (0.2 mm). Debonding was simulated using a quadratic stress criterion:

$$\left(\frac{\sigma_{I}}{\sigma_{u,I}}\right)^2+\left(\frac{\sigma_{II}}{\sigma_{u,II}}\right)^2+\left(\frac{\sigma_{III}}{\sigma_{u,III}}\right)^2=\begin{cases}1 \text{ if} & \sigma 1 \geq 0\\ 0 \text{ if} & \sigma 1 \leq 0\end{cases} \quad (3)$$

and propagation followed an energetic law:

$$\left(\frac{G_{I}}{G_{IC}}\right)+\left(\frac{G_{II}}{G_{IIC}}\right)+\left(\frac{G_{III}}{G_{IIIC}}\right)=1 \quad (4)$$

Each cohesive layer represented a zero-thickness interface with averaged material properties between adjacent layers. A mesh sensitivity study was carried out using C3D8 solid elements, ensuring convergence with approximately 12,000 elements. Overall, this numerical approach accurately captures the graded behavior of CFRP composites by combining FGM-based gradation, XFEM for matrix cracking, allowing precise prediction of failure initiation and crack evolution through the graded structure.

Mesh Sensitivity and Comparison of Numerical Results

Prior to analyzing the graded CFRP, a reference numerical model was developed and validated against the experimental findings of (Kim et al., 1955), who tested a glass–polyester composite plate with dimensions of 200 × 30 × 2.3 mm and a fiber volume fraction of 60% Figure 04. The specimen was subjected to uniaxial tension, as illustrated in Figure 10. Several preliminary mesh sensitivity studies were conducted, varying both element density and element type, as shown in Figure 5.



Figure 4. Overview of the damaged structure by (Kim & kim 1955).

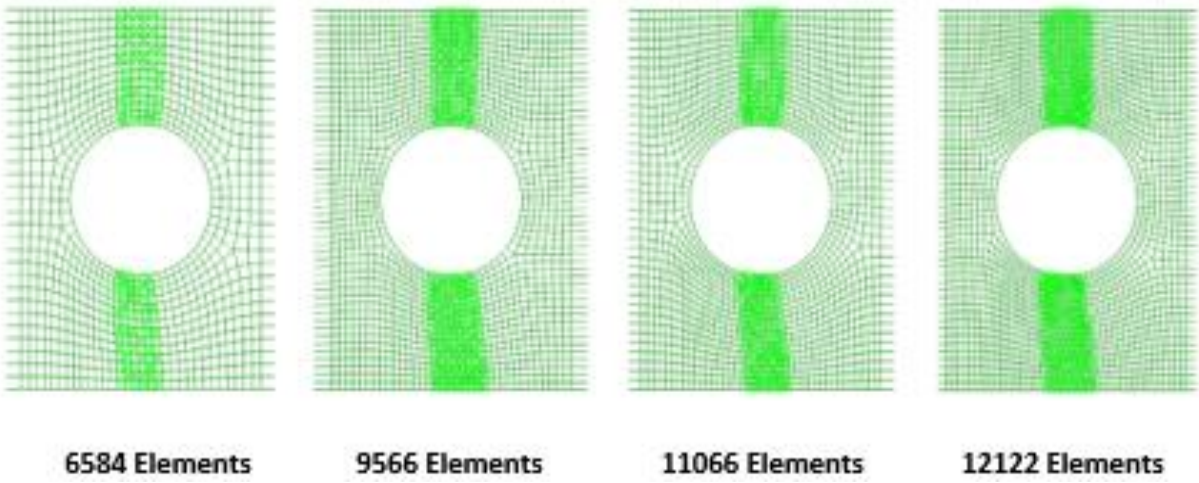


Figure 5. Mesh sensitivity by element density (Ghermaoui & Mokhtari, 2023).

To ensure reliable numerical predictions, all simulation parameters-such as mesh density, element type, and loading conditions—were kept consistent with those used in Kim's experimental setup. The interpolation of finite elements in the proposed meshing technique was achieved through each element's own nodal connections, providing high accuracy and numerical stability. Among the tested element types, the C3D8 solid element demonstrated the best performance, particularly when combined with the XFEM damage modeling technique.

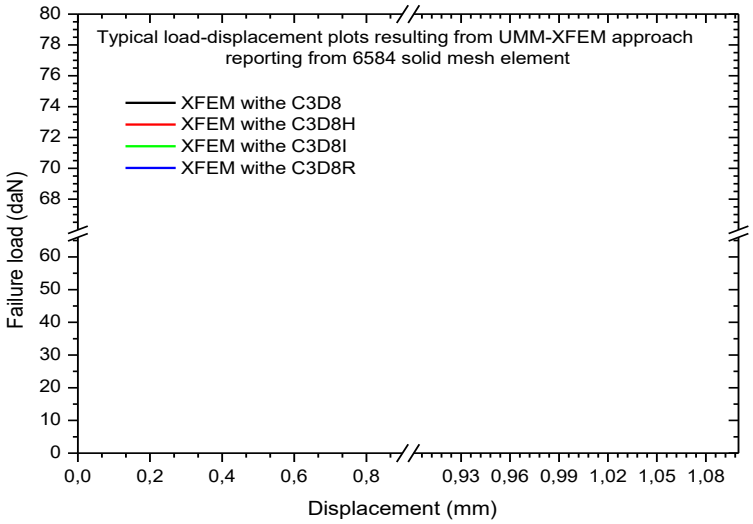


Figure 6. Typical load-displacement plots resulting from XFEM approach reporting from 6584 solid mesh element (Ghermaoui & Mokhtari, 2023).

Within the C3D8 family, several formulations were examined, including C3D8R, C3D8H, C3D8I, and C3D8S. The C3D8S element is mainly suitable for surface visualization purposes. The C3D8I (incompatible mode) element, enhanced with improved shape functions, proved effective for bending-dominated structures such as graded composites. The C3D8H (hybrid mode) element performed well for nearly incompressible materials, minimizing distortion near the notch. Conversely, the C3D8R (reduced integration) element required a finer mesh to maintain accuracy.

After several trials, an optimal mesh density of approximately 12,122 elements was adopted for the model. Validation against Kim's experimental results showed that this configuration achieved accurate damage prediction, with an element size fine enough to capture crack initiation yet coarse enough to prevent numerical instability. Figure 6 indicates that the element-type effect remains within the order of 10^{-2}. The C3D8 element with a mesh density of 6,584 elements yielded the closest correlation with the experimental load–displacement behavior, confirming the validity of the proposed numerical approach.

Results and Discussion

By the use of several techniques including the finite element method, the CFRP structure graded in its response to damage is evaluated by several concepts and graduation parameters. Compatibility in strength capacities between graded fibers is important. The separation between these two qualities of graded fibers is the very probable phenomenon that can occur as a mode of damage, something that was not taken into account in the numerical prediction. The graded fibers are presented by finite elements in the material property is homogenized and oriented by a local coordinate system, something that can make this prediction incomplete in certain damage modes.

Damage of CFRP Structure Under Simple Graded

The graded CFRP was modeled as an orthotropic functionally graded material, exhibiting mechanical behavior that varies with loading conditions. This section focuses on the simple grading concept, introduced to analyze how the material responds and fails under specific parameters, particularly the volume fraction index (n). In this configuration, a bending moment develops due to the variation in stiffness along the plate's thickness. Under uniaxial tension applied to the specimen's cross-section, the stress distribution becomes nonuniform until the stiffer outer layers begin to fail, after which the bending moment is released.

Figure 7 illustrates the linear mechanical response of the graded CFRP under loading and its corresponding damage evolution for a simple gradation from CFRP-1 to CFRP-2 through the thickness. The figure also highlights the influence of the volume fraction index (n) on the force–displacement response and the crack propagation length. This dual interpretation relating load capacity to crack progression clarifies how grading parameters affect the material's resistance and fracture behavior.

Results reveal that the volume fraction index (n) significantly affects both stiffness and strength. However, because the mechanical properties of CFRP-1 and CFRP-2 are relatively close and the plate thickness is small (1.25 mm), this influence remains modest, around 1.8 daN. The stiffer configurations exhibit higher failure loads but lower deformation at rupture. The gradation also alters crack initiation and propagation, leading to brittle fracture characterized by short critical crack lengths (LC). These critical lengths vary across the graded layers, depending on their local material properties and stiffness distribution.

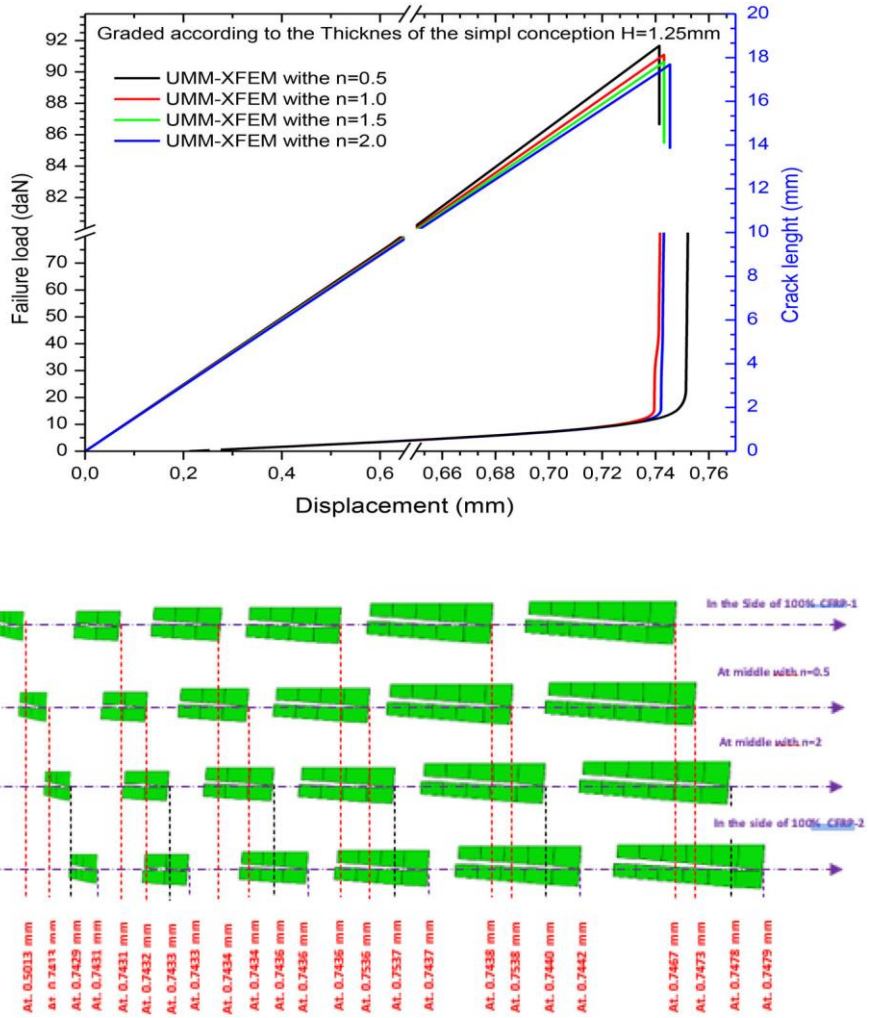


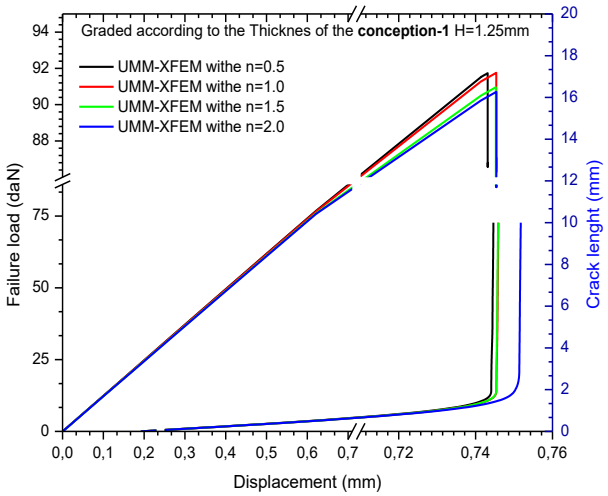
Figure 7. a) Load – displacement curves and propagation length crack in W=30mm, vf= 60% results by UMM-XFEM techniques (number of 6584-C3D8 solid mesh element) as a function of the values of the exponent n in the case of simple gradation of CFRP according to the thickness. b) Crack length propagation in each layer as a function of n=0.5; 1; 2 (Ghermaoui & Mokhtari, 2023).

Damage of CFRP Graded According to Concept-1

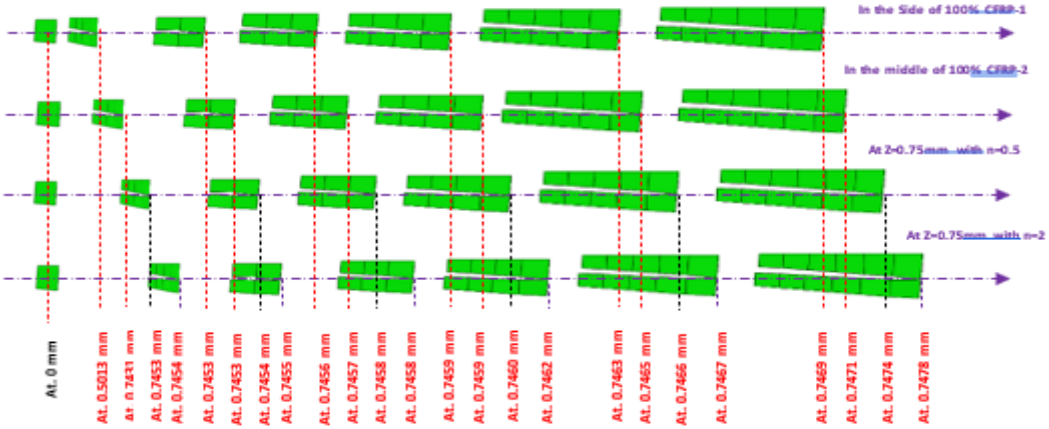
Building upon the findings obtained from the simple grading configuration, this section focuses on the analysis of symmetrical grading concepts. The objective of this approach is to achieve a balanced mechanical response across the thickness of the composite under uniaxial tension until failure. Symmetrical designs were proposed Concept-1 each representing a transition from stiffer to more compliant layers. The study examines two main parameters: the grading concept itself and the volume fraction index (n). The results are illustrated through force–displacement and crack-length–displacement curves for each design. Introducing symmetry within the laminate effectively eliminates the bending moment observed in the simple grading case, as the stiffness distribution becomes balanced through the thickness.

In Figure 8-a, the mechanical response and failure progression of the Concept-1 configuration are presented. This concept involves outer layers made of the stiffer CFRP-1 material and inner layers of the more compliant

CFRP-2. Crack propagation occurs gradually from the exterior to the interior layers, as shown in Figure 8-b. The influence of the volume fraction index (n) remains modest around 1.8 daN similar to the simple grading model. As the structure becomes less rigid (higher n values), it exhibits lower strength but greater deformation capacity, reaching an elongation of approximately 0.01 mm before failure. Only minor variations are observed between layers in terms of crack initiation and critical crack length. These differences are primarily attributed to the position of each layer within the graded thickness. The average critical crack length across all layers is slightly reduced and varies according to the value of n.



a)



b)

Figure 8. a) Load – displacement curves and propagation length crack In W=30mm, vf= 60% results by XFEM-mesh techniques (number of 6584-C3D8 solid mesh element) as a function of the values of the exponent n in the case of simple gradation of CFRP according to the thickness. B) Crack length propagation in each layer as a function of n=0.5; 1; 2 (Ghermaoui & Mokhtari, 2023).

Conclusion

The findings of this study demonstrate that the proposed meshing technique combined with the XFEM approach provides a highly reliable framework for predicting the mechanical behavior and damage evolution in graded CFRP composites. The numerical model, validated against experimental results from a simple composite structure, proved effective when extended to graded configurations. Using the global properties of each composite layer simplifies the modeling process by avoiding complex constitutive formulations for property gradation, while grading finite elements at the fiber scale offers a more realistic representation of the actual material architecture. Based on the numerical analyses conducted, the following conclusions can be drawn:

- The proposed meshing technique allows each finite element to act independently through self-interpolation of its nodes, enabling the introduction of element-based enrichment functions. This significantly mitigates convergence issues typically encountered in complex meshes.

- The XFEM method enables smooth and continuous initiation and propagation of damage throughout the graded CFRP structure.
- Comparison with experimental data is essential for selecting the most suitable element type and optimal mesh density, ensuring accurate numerical predictions.
- The overall structural strength of graded CFRP composites depends primarily on the appropriate selection of the two fiber types used in the gradation.
- Graded composites exhibit an average critical crack length across all layers, which varies according to the volume fraction index (n).
- Due to the intrinsic nature of composites, crack propagation rates in graded structures are relatively fast once initiated.
- The notch geometry continues to influence damage initiation despite the evaluated parameters; after crack initiation, propagation paths are determined by the gradation design and the exponent n.

However, the proposed numerical approach remains limited in capturing stacking effects since it does not explicitly model fibers at their true scale within the matrix. Despite this limitation, the suggested meshing technique offers a simple and efficient solution for analyzing material gradation and damage behavior in composite structures.

To further enhance the accuracy of these predictions, experimental testing campaigns should be carried out to validate and refine the numerical model. Such tests would help identify additional damage mechanisms and contribute to establishing a more realistic understanding of the failure modes in graded CFRP composites.

Scientific Ethics Declaration

* The authors declares that the scientific ethical and legal responsibility of this article published in EPSTEM journal belongs to the authors.

Conflict of Interest

* The authors declare that they have no conflicts of interest

Funding

* This research received no specific grant from any funding agency in the public, commercial, or not-for-profit sectors.

Acknowledgements or Notes

* This article was presented as a poster presentation at the International Conference on Technology, Engineering and Science (www.icontes.net) held in Antalya/Türkiye on November 12-15, 2025.

References

Benzaama, A., Mokhtari, M., Ahmed-Bouziane, N.-E.-I., Elamine, A., Benzaama, H., Ghermaoui, I. M. A., & Aliane, I. (2023). Using a UMM-XFEM technique to predict the damage in CFRP bi-graded with glass-epoxy materials of notched plate under quasi-static loading. *Mechanics of Advanced Materials and Structures. 31*(25), 7367-7385.

Elamine, A., Mokhtari, M., Benzaama, H., Ghermaoui, I. M. A., Ezzine, M. C. E., Ghomari, A., & Merasli, Y. (2023). Using a non-linear mixed model behavior of CZM to predict the damage in single lap bonded joint with bi-composite graded materials. *Mechanics of Advanced Materials and Structures*, 31(25), 7180-7194.

Ghermaoui, I. M. A., Mokhtari, M., Benzaama, H., & Elamine, A. (2023). Using FGM concept and combined XFEM-CZM techniques to predict the damage in carbon/carbon-epoxy graded composites. *Mechanics of Advanced Materials and Structures*. *31*(25), 7526-7544.

Ghermaoui, I. M. A., Oudriss, A., Metsue, A., & Feaugas, X. (2019). Multiscale analysis of hydrogen-induced softening in f.c.c. nickel single crystals oriented for multiple slips: Elastic screening effect. *Scientific Reports, 9*, 13042.

Kim, J. K., Kim, D. S., & Takeda, N. (1995). Notched strength and fracture criterion in fabric composite plates containing a circular hole. *Journal of Composite Materials, 29*(7), 982-998.

Metehri, A., Madani, K., Mechab, B., Mokhtari, M., & Ghermaoui, I. M. A. (2024). Tensile examination of progressive damage and failure in porous ceramic composite materials using the XFEM. *Vojnotehnički glasnik, 72*(3), 1188-1213.

Mohamed, C., Kaci Djafar, A., Abdelmajid, M., Abderahmane, S., & Ghermaoui, I. M. A. (2024). Numerical study of tensile-shear fracture behaviour of resistance spot welded sheet steel with DP 450 and DP 980. *Acta Mechanica Slovaca, 28*(4), 14-24.

Murakami, S. (2012). *Continuum damage mechanics: A continuum mechanics approach to the analysis of damage and fracture*. Springer.

National Transportation Safety Board. (1989). *Aircraft accident report: Aloha Airlines Flight 243, Boeing 737-200, N73711, near Maui, Hawaii, April 28, 1988* (Report No. NTSB/AAR-89/03).

Shojaei, A., Li, G., Fish, J., & Tan, P. J. (2014). Multi-scale constitutive modeling of ceramic matrix composites by continuum damage mechanics. *International Journal of Solids and Structures, 51*(23–24), 4068-4081.

Zhao, Y., Wang, Z., Jiang, P., Wang, A., Chang, Z., & Kang, Y. (2022). Numerical simulation on mechanical properties and damage behavior of CFRP with self-healing microvascular channels. *Mechanics of Advanced Materials and Structures, 26*(1), 1-17.

Author(s) Information

Ghermaoui Ilias Mohammed Amine
Djilali Liabes University of Sidi Bel Abbes
Sidi Bel Abbes, Algeria
Contact e-mail: *ghermaoui_ilias@hotmail.fr*

Ezzine Mohamed Chams Eddine
University of Mascara, Mascara, Algeria

Mokhtari Mohammed
Djilali Liabes University of Sidi Bel Abbes
Sidi Bel Abbes, Algeria

Cherief Mohammed Nadhir Djamel Eddine
Djilali Liabes University of Sidi Bel Abbes
Sidi Bel Abbes, Algeria

Cherfi Mohamed
Djilali Liabes University of Sidi Bel Abbes
Sidi Bel Abbes, Algeria

Sahli Abderrahmane
Djilali Liabes University of Sidi Bel Abbes
Sidi Bel Abbes, Algeria

To cite this article:

Amine, G. I. M., Eddine, E.M.C., Mohammed, M., Eddine, C. M. N. D., Mohamed, C., & Abderrahmane, S. (2025). Development and characterization of epoxy-based laminated composites: Experimental characterization and numerical simulation. *The Eurasia Proceedings of Science, Technology, Engineering and Mathematics (EPSTEM), 38*, 217-225.

The Eurasia Proceedings of Science, Technology, Engineering & Mathematics (EPSTEM)
ISSN: 2602-3199

The Eurasia Proceedings of Science, Technology, Engineering and Mathematics (EPSTEM), 2025

Volume 38, Pages 226-243

IConTES 2025: International Conference on Technology, Engineering and Science

Computational Materials Design: Tuning Optoelectronic Response in GaxIn1-xBiyP1-y Alloys via Structural Matching to InP

Malika Tehami
Djillali Liabes University of Sidi Bel Abbes

Miloud Benchehima
University of Sciences and Technology

Hamza Abid
Djillali Liabes University of Sidi Bel Abbes

Abstract: This theoretical study presents a computational investigation into the structural, electronic, and optical properties of GaxIn1-xBiyP1-y quaternary alloys specifically lattice-matched to an InP substrate, utilizing density functional theory (DFT). The calculations were performed using the full-potential linearized augmented plane wave (FP-LAPW) method. Structural properties were assessed using the local density approximation (LDA) and the Wu-Cohen generalized gradient approximation (WC-GGA), with WC-GGA used to define the lattice-matching target based on the calculated InP lattice constant. Electronic properties were determined using the Engel-Vosko GGA (EV-GGA) and Tran-Blaha modified Becke-Johnson (TB-mBJ) functionals. Optical properties were analyzed in detail, with optical band gaps derived using Tauc's method. Lattice-matching conditions to InP were established, yielding calculated lattice constants around 5.9 Å for matched compositions (x, y), in excellent agreement with the experimental InP value (5.869 Å). Band structure analysis confirms these alloys are direct band gap semiconductors at the Γ point for all studied lattice-matched compositions. The investigation of optical properties reveals that the electronic band gaps (via TB-mBJ) correspond to wavelengths spanning approximately 0.91 µm to 2.46 µm, while Tauc analysis yields optical band gaps corresponding to ~0.9 µm to ~1.56 µm, all while maintaining lattice matching. These findings highlight GaxIn1-xBiyP1-y/InP alloys as promising materials for optoelectronic devices, particularly for telecommunication applications operating at 1.3 µm and 1.55 µm, due to their tunable optoelectronic characteristics and structural compatibility with InP.

Keywords: GaInBiP quaternary alloys, Density functional theory, Lattice matching, Optoelectronic properties, Optical communication

Introduction

In recent years, great efforts have been made in the research of semiconductor alloys and nanostructures containing bismuth (Bi). These new Bi-containing alloys and nanostructures possess interesting physical properties and reveal promising device applications (Zhang et al., 2019), (Wang et al., 2019), (Paulauskas et al., 2020), (Usman et al., 2019), (Donmez et al., 2021), (Jain et al., 2022). The incorporation of Bi into traditional III-V compounds leads to substantial modifications in electronic band structure, most notably a strong reduction in the band gap energy and an increase in spin-orbit splitting (Paulauskas et al., 2020). The GaxIn1-xBiyP1-y quaternary alloy system, composed of Indium (In), Gallium (Ga), Phosphorus (P), and Bismuth (Bi) in varying concentrations, represents a particularly promising class of these materials.

- This is an Open Access article distributed under the terms of the Creative Commons Attribution-Noncommercial 4.0 Unported License, permitting all non-commercial use, distribution, and reproduction in any medium, provided the original work is properly cited.

- Selection and peer-review under responsibility of the Organizing Committee of the Conference

© 2025 Published by ISRES Publishing: www.isres.org

One of the key advantages of quaternary alloys like GaxIn1-xBiyP1-y is their high degree of tunability. By carefully adjusting the molar fractions 'x' (for Ga) and 'y' (for Bi), it is possible to engineer fundamental material properties such as the band gap energy (Adachi., 2009). This compositional tuning can be performed while simultaneously satisfying the lattice-matching condition to readily available binary substrates, such as Indium Phosphide (InP). Lattice matching is vital for the epitaxial growth of high-quality, low-defect heterostructures, which form the basis of many advanced semiconductor devices (Adachi., 2009). InP is a standard substrate for devices operating in the near-infrared, particularly for telecommunications applications (Zhang et al., 2019),(Wyckoff, 1986), (Meiners, 1986).

The GaxIn1-xBiyP1-y system can be conceptualized as deriving from the binary endpoints GaP, InP, GaBi, and InBi (Adachi, 2009). These binaries exhibit a wide range of lattice constants (from 5.451 Å for GaP (Jain et al., 2022) to 6.628 Å for InBi (Gandouzi et al., 2018) and band gap energies (from 0.00 eV for InBi and GaBi (Wang & Ye, 2002) to 2.35 eV for GaP (Madelung, 2004), with InP at 1.424 eV (Vurgaftman et al., 2001). This wide parameter space theoretically allows GaxIn1-xBiyP1-yalloys to cover a broad spectral range, from the visible to the infrared (0.57–1.72 μm (Paulauskas et al., 2020)), making them attractive candidates for applications including multi-junction solar cells (Adachi., 2009), photodiodes (Jain et al., 2022), infrared lasers (Usman et al., 2019), (Donmez et al., 2021), and heat detectors (Zhang et al., 2019), (Wang et al., 2019), (Paulauskas et al., 2020).

While related ternary alloys like GaInP, GaBiP, InBiP, and InPBi have been subjects of investigation (Kumar et al., 2009) , (Yang et al., 2015), (Samajdar et al., 2016), (Usman et al., 2011), (Wu et al., 2016), (Gelczuk et al., 2016) , (Nattermann et al., 2017) , and successful growth of InPBi has been reported (Wang et al., 2014), theoretical understanding of the quaternary GaxIn1-xBiyP1-y especially under lattice-matched conditions to InP, is essential for realizing its technological potential. (Berding et al., 1988) investigated InPBi theoretically, and GaInP as a basic material for red laser diodes (Meiners, 1986).

This work focuses on a first-principles theoretical investigation of the fundamental structural, electronic, and optical properties of GaxIn1-xBiyP1-y alloys designed to be lattice-matched to an InP substrate, aiming to provide insights for future materials design and device fabrication.

Method

The theoretical investigation was conducted using density functional theory (DFT) (Kohnet al., 1965), (Ceperley et al., 1980), employing the full-potential linearized augmented plane wave (FP-LAPW) method as implemented in the Wien2k computational package (Blaha et al., 2019). This method is known for its high accuracy in calculating the electronic structure and related properties of solids.

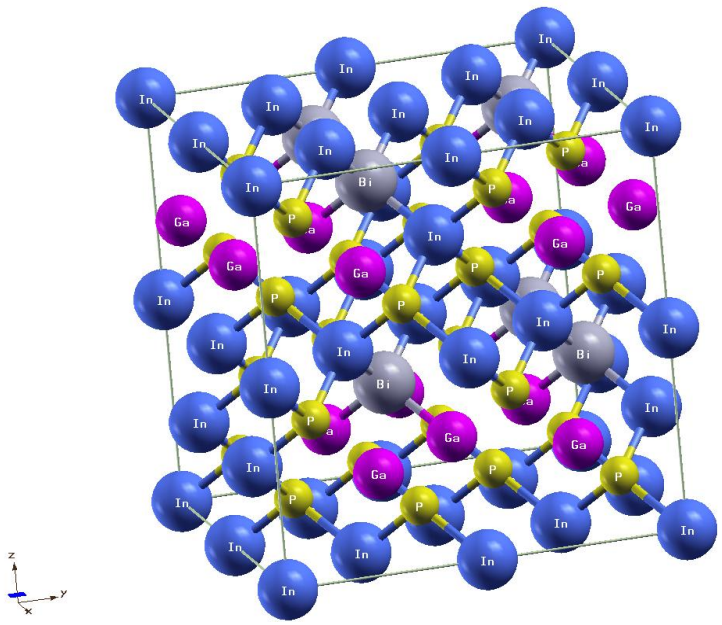


Figure 1. Crystal structure of the 32-atom SQS supercell for $Ga_{0.375}In_{0.625}Bi_{0.1875}P_{0.8125}$ (Q3), representing a lattice-matched $Ga_xIn_{1-x}Bi_yP_{1-y}$ alloy.

To model the GaxIn1-xBiyP1-y quaternary alloys with varying compositions (x, y), we utilized the special quasi-random structure (SQS) approach developed by Zunger (Zunger et al., 1990). This method allows for the modeling of random alloys using relatively small, ordered supercells that mimic the essential correlation functions of the truly random alloy. A 32-atom simple cubic (2×2×2) supercell was constructed for this purpose. An example structure forGa0.375 In 0.625 Bi 0.1875 P0.8125 (Q3) is shown in (Figure 1).

Different exchange-correlation functionals were employed depending on the property being calculated. For structural optimization (determining equilibrium lattice constants and bulk moduli), the local density approximation (LDA) (Kohn et al., 1965), (Ceperley et al., 1980) and the Wu-Cohen generalized gradient approximation (WC-GGA) (Wu et al., 2006)] were used. For electronic and optical properties, the Engel-Vosko GGA (EV-GGA) (Engel et al., 1993) and the Tran-Blaha modified Becke-Johnson potential (TB-mBJ) (Tran et al., 2009) were utilized. The TB-mBJ functional is particularly noted for providing improved band gap predictions compared to standard LDA/GGA functionals. The calculations were performed with the following parameters:

- Plane wave cut-off: RMT * KMAX = 8, where RMT is the smallest muffin-tin radius.
- Maximum angular momentum: IMAX = 10 within the muffin-tin spheres.
- Muffin-tin radii (RMT): Ga = 2.0 a.u., In = 2.1 a.u., Bi = 2.5 a.u., and P = 2.0 a.u. (1 a.u. = 0.52917 Å).
- Energy convergence criterion: 10^{-4} Ry for self-consistent field (SCF) iterations.
- Core-valence state separation: -6 Ryd.
- Brillouin zone integration: A k-point mesh equivalent to 5000 k-points in the full Brillouin zone was used for structural calculations. For optical property calculations, which require denser sampling, 172 k-points in the irreducible Brillouin zone were employed using a methodology suitable for optical properties (Abt et al., 1994) , (Ambrosch-Draxelet al., 2006).

Vegard's law (Adachi., 2009) was used as an initial guide to estimate lattice constants for different compositions (x, y) and to establish the relationship between x and y required for lattice matching to the InP substrate. The lattice constant of the quaternary alloys was then fixed to the calculated value for InP using the WC-GGA functional (5.8908 Å) for subsequent electronic and optical property calculations, simulating perfect epitaxial growth on InP.

Results and Discussion

Structural Properties

First, the structural properties (equilibrium lattice constant 'a' and bulk modulus 'B') of the parent binary compounds (InP, InBi, GaP, GaBi) were calculated using both LDA and WC-GGA. The results are presented in (Table 1) and compared with available experimental and theoretical data (Levinshtein et al., 1996), (Janotti et al., 2002), (Gandouzi et al., 2018), (Wang et al., 2002), (Madelung., 2004), (Vurgaftman et al., 2001), (Liu et al., 2007) , (Assali et al., 2020), (Celin-Manceraet al., 2016) , (Benchehima et al., 2016). The WC-GGA functional generally provides lattice constants closer to experimental values for InP, albeit with a slight overestimation typical of GGA, while LDA tends to underestimate '*a*'. Based on its reasonable agreement for InP (Wyckoff., 1986), (Benchehima et al., 2016), the WC-GGA value for InP (*a* = 5.8908 Å) was chosen as the target lattice constant for the lattice-matched quaternary alloys.

Using Vegard's law , the lattice constant of $Ga_xIn_{1-x}Bi_yP_{1-y}$ can be expressed as:

$$a(x,y) = x(1-y)\cdot a_{GaP} + xy\cdot a_{GaBi} + (1-x)(1-y)\cdot a_{InP} + (1-x)y\cdot a_{InBi} \quad (1)$$

Substituting our calculated WC-GGA binary lattice constants, we get:

$$a(x,y) = -0.4418x + 0.8439y + 0.0611xy + 5.8908\ (\text{Å}) \quad (2)$$

Setting $a(x,y)$ equal to the WC-GGA lattice constant of InP (5.8908 Å) yields the condition for lattice matching:

$$y = 0.4418x/(0.0611x + 0.8439) \text{ for } 0 \leq x \leq 1 \quad (3)$$

This equation defines the specific combinations of (x,y) that result in alloys lattice-matched to InP.

We investigated seven such compositions, denoted Q1 to Q7, corresponding to x = 0.125, 0.250, 0.375, 0.500, 0.625, 0.750, and 0.875, respectively, with corresponding y values determined by Eq. 4 (e.g., Q1: (0.125, 0.0625), Q3: (0.375, 0.1875), Q7: (0.875, 0.4375)). The calculated lattice constants and bulk moduli for these compositions using WC-GGA are included in (Table 1). The lattice constants for these compositions are indeed very close to 5.9 Å, confirming their suitability for lattice-matched growth on InP.

Table 1**.** Calculated lattice constant a, bulk modulus B for binary compounds and selected lattice-matched $Ga_xIn_{1-x}Bi_yP_{1-y}$ quaternary alloys (Q1-Q7, $a \approx 5.8908$ Å) using (LDA)/(WC-GGA), compared with other works.

$Ga_xIn_{1-x}Bi_yP_{1-y}$		**Present work**		**Other Works**			
		(LDA)/(GGA-WC)		**Theoretical**		**Experimental**	
x	*y*	*a* (Å)	B*(*GPa)	*a* (Å)	B*(*GPa)	*a* (Å)	B*(*GPa)
0 (InP)	0	5.8388 [a] 5.8908 [b]	71.5771 [a] 67.0433 [b]	5.830 **[4]** , 5.896 **[9]**,	69.437 **[9]**	5.869 **[2]**	72 **[2]**
0 (InBi)	1	6.6627 [a] 6.7347 [b]	40.7901 [a] 37.7449 [b]	6.628 **[4]**,6.526 **[5]**, 6.80 **[6]**	47.6 **[5]**, 38.3 **[3]**	6.5 **[10]**, 6.626 **[11]**	-
1 (GaP)	0	5.4063 [a] 5.4490 [b]	90.7939 [a] 85.1140 [b]	5.441**[7]**,5.44 **[8]**	84.52 **[7]**, 4.43**[8]**	5.451 **[1]**	88**[1]**
1 GaBi	1	6.2886 [a] 6.3540 [b]	47.3768 [a] 45.3115 [b]	6.178 **[5]** ,6.324**[3]**	46.1 **[5]**, 45.1**[3]**	-	-
0.125	0.0625	5.84965 [a] 5.90175 [b]	69.0690 [a] 64.8858 [b]	-	-	-	-
0. 250	0.125	5.8705 [a] 5.92455 [b]	66.4599 [a] 62.1865 [b]	-	-	-	-
0.375	0.1875	5.8873 [a] 5.9425 [b]	64.2428 [a] 60.259 [b]	-	-	-	-
0.500	0.250	5.89605 [a] 5.94955	62.7793 [a] 59.1181 [b]	-	-	-	-
0.625	0.3125	5.90515 [a] 5.96095 [b]	61.6372 [a] 57.8936 [b]	-	-	-	-
0.750	0.375	5.9043 [a] 5.9609 [b]	60.7463 [a] 57.3657 [b]	-	-	-	-
0.875	0.4375	5.9035 [a] 5.9610 [b]	59.8525 [a] 56.5951 [b]	-	-	-	-

[a] *calculated from LDA scheme,* [b] *calculated from WC-GGA scheme.*

[1] (Levinshtein et al., 1996) **[2]** (Wyckoff, 1986) **[3]** (Janotti et al., 2002)
[4] (Gandouzi et al., 2018) **[5]** (Wang et al., 2002) **[6]** (Liu et al., 2007)
[7] (Assali et al., 2020) **[8]** (Celin-Mancera et al., 2016) **[9]** (Benchehima et al., 2016)
[10] (Okamoto and K. Oe., 1998) **[11]** (Rajpalke et al., 2014)

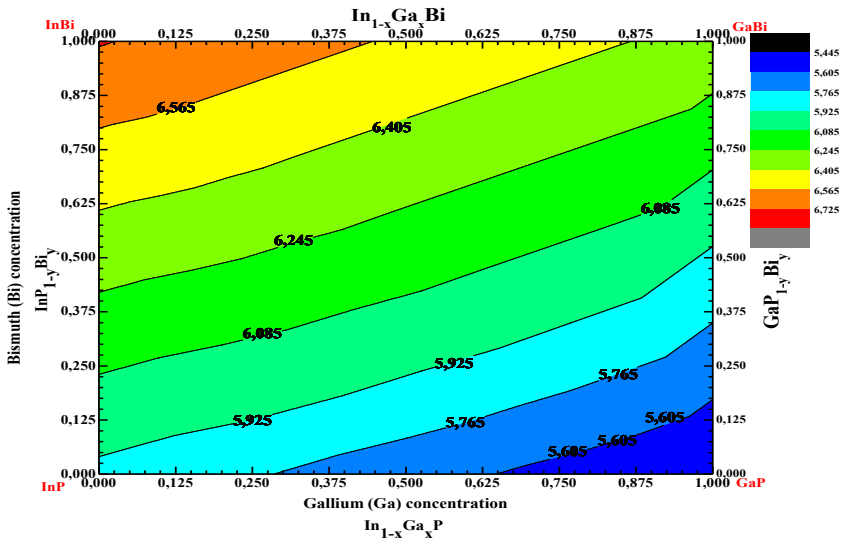


Figure 2. Contour map of the calculated lattice constant a (WC-GGA, in Å) for $Ga_xIn_{1-x}Bi_yP_{1-y}$ as a function of Ga (x) and Bi (y) concentrations.

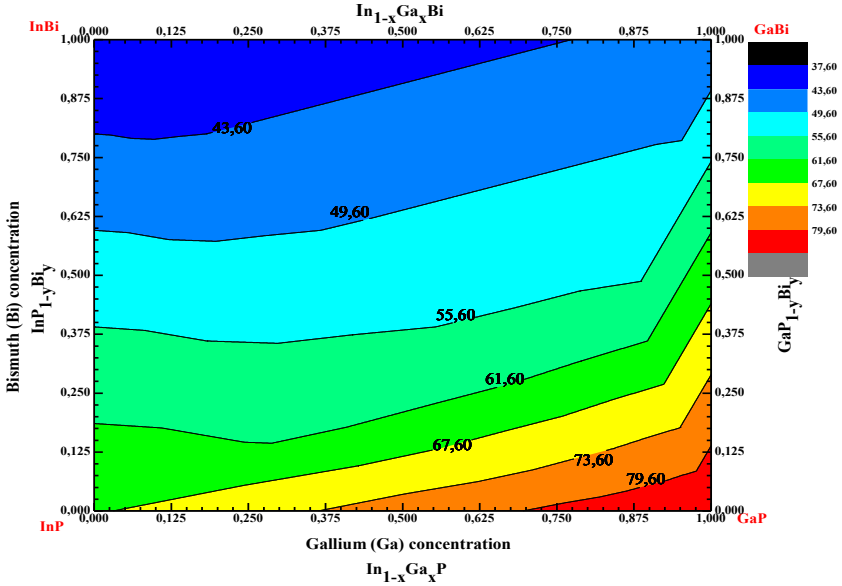


Figure 3. Contour map of the calculated bulk modulus B (WC-GGA, in GPa) for $Ga_xIn_{1-x}Bi_yP_{1-y}$ as a function of Ga (x) and Bi (y) concentrations

Figure 2 illustrates the variation of the lattice constant across the composition range, consistent with Vegard's law. Figure 3 shows the variation of the bulk modulus.

Electronic Properties

The electronic band structures and density of states (DOS) were calculated for the lattice-matched compositions Q1-Q7 using the EV-GGA (Engel et al., 1993) and TB-mBJ(Tran et al., 2009)potentials, with the lattice constant fixed at the InP WC-GGA value (5.8908 Å). The TB-mBJ potential generally yields band gaps in better agreement with experimental values for III-V semiconductors.

Table 2 shows the calculated TB-mBJ band gaps (Eg). Our values for the binaries InP (1.560 eV) and GaP (2.255 eV) agree well with experimental data (Madelung., 2004),(Vurgaftman et al., 2001) and previous calculations (Gandouzi et al., 2018), (Celin-Mancera et al., 2016),(Jiang et al., 2013), (Camargo-Martínez et al., 2012). The calculated band gaps for GaBi and InBi are 0.00 eV, consistent with their semi-metallic or narrow-gap nature reported previously (Wang et al., 2002), (Figs. 4 and 5).

Table 2. Calculated band gap energies Eg (in eV) using EV-GGA and TB-mBJ potentials for binary compounds and the lattice-matched $Ga_xIn_{1-x}Bi_yP_{1-y}$ quaternary alloys (Q1-Q7). Comparison with other works.

	$Ga_xIn_{1-x}Bi_yP_{1-y}$		**Present work**		**Other works**	
	x	***y***	**EV-GGA**	**TB-mBJ**	**TB-mBJ**	**Experimental**
InP	0 (InP)	0	1.237	1.560	1.41 **[5]**,1.680 **[1]**	1.424 **[4]**
InBi	0 (InBi)	1	-0.031	0.000	0.000 **[2]**	-
GaP	1 GaP	0	2.233	2.255	2.24 **[7]**, 2.30 **[6]**	2.35 **[3]**
GaBi	1 GaBi	1	-0.046	0.000	0.000 **[2]**	-
Q1	$Ga_{0.125}In_{0.875}Bi_{0.0625}P_{0.9375}$		0.994	1.360	-	-
Q2	$Ga_{0.250}In_{0.750}Bi_{0.125}P_{0.875}$		0.749	1.147	-	-
Q3	$Ga_{0.375}In_{0.625}Bi_{0.1875}P_{0.8125}$		0.563	0.994	-	-
Q4	$Ga_{0.500}In_{0.500}Bi_{0.250}P_{0.750}$		0.400	0.855	-	-
Q5	$Ga_{0.625}In_{0.375}Bi_{0.3125}P_{0.6875}$		0.227	0.707	-	-
Q6	$Ga_{0.750}In_{0.250}Bi_{0.375}P_{0.625}$		0.105	0.606	-	-
Q7	$Ga_{0.875}In_{0.125}Bi_{0.4375}P_{0.5625}$		0.021	0.503	-	-

[1] (Gandouzi et al., 2018) **[2]** (Wang et al., 2002) **[3]** (Madelung., 2004) **[4]** (Vurgaftman et al., 2001)
[5] (Gazhulina et al., 2015) **[6]** (Jiang , 2013) **[7]** (Camargo-Martínez et al., 2012)

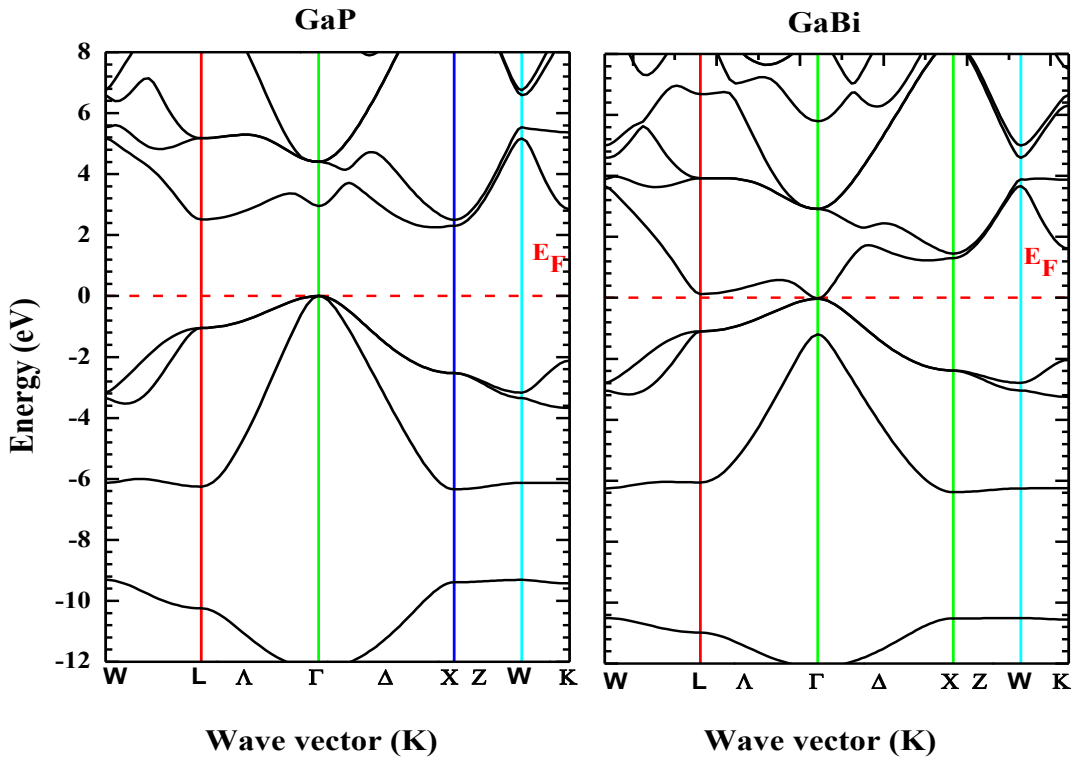


Figure 4. Electronic band structure of GaP (indirect) and GaBi (direct) binaries along high symmetry directions, calculated using TB-mBJ. Fermi level (EF) is at 0 eV.

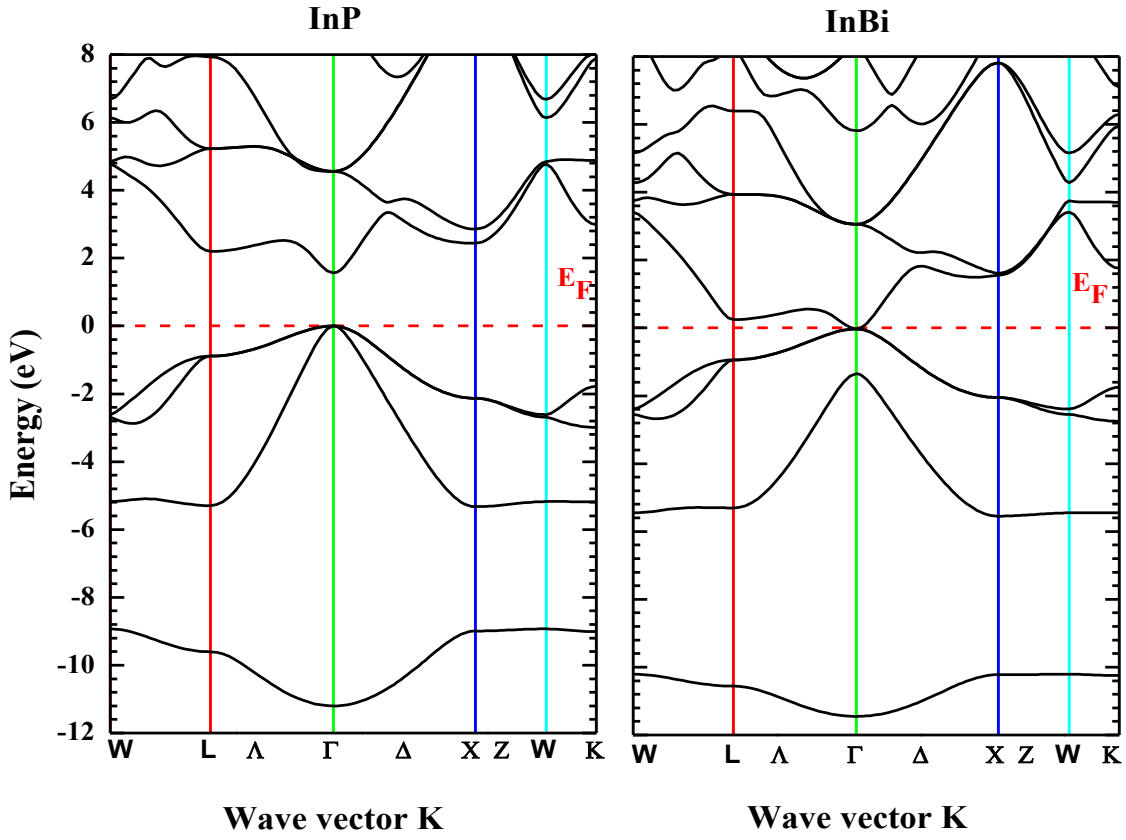


Figure 5. Electronic band structure of InP (direct) and InBi (direct) binaries along high symmetry directions, calculated using TB-mBJ. Fermi level (EF) is at 0 eV

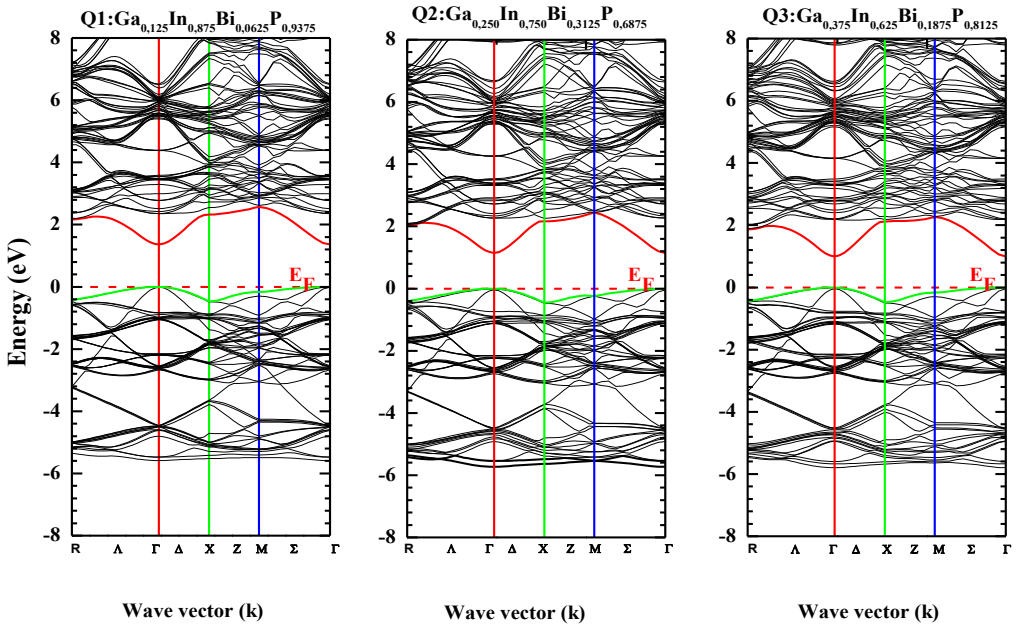


Figure 6. Electronic band structures of lattice-matched $Ga_xIn_{1-x}Bi_yP_{1-y}$ alloys for compositions Q1, Q2, and Q3 along high symmetry directions, calculated using TB-mBJ. The Fermi level (EF) is set to 0 eV.

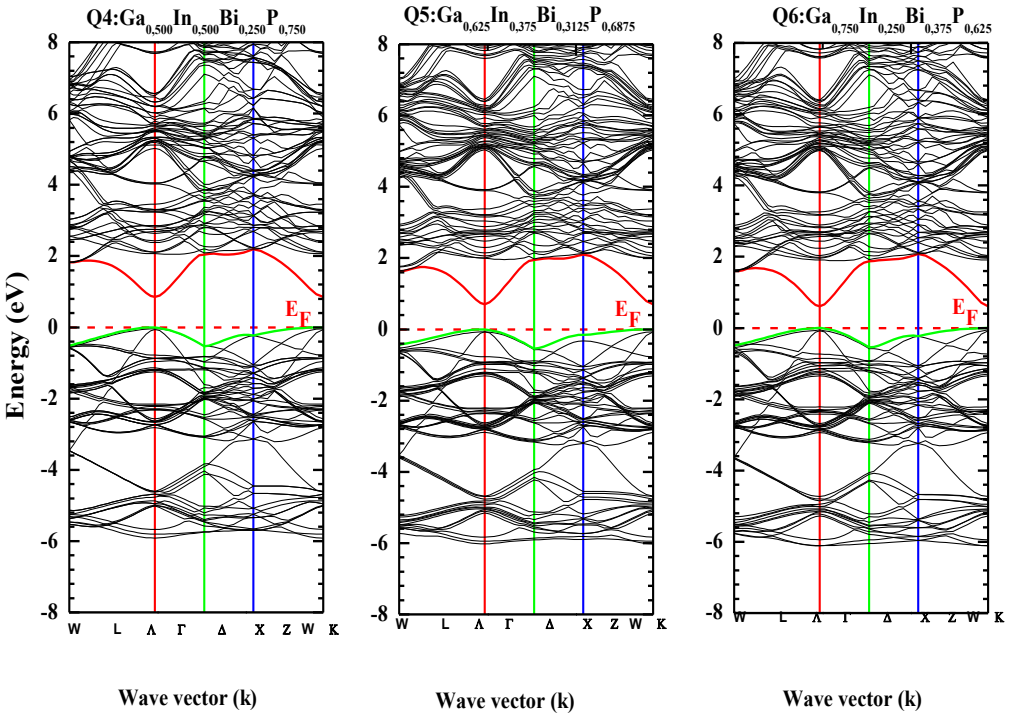


Figure 7. Electronic band structures of lattice-matched GaxIn1-xBiyP1-y alloys for compositions Q4, Q5, and Q6 along high symmetry directions, calculated using TB-mBJ. The Fermi level (EF) is set to 0 eV.

The calculated band structures for compositions Q1-Q7 (Figs. 6 and 7) clearly demonstrate that all these lattice-matched $Ga_xIn_{1-x}Bi_yP_{1-y}$ alloys possess a direct band gap at the Γ point (center of the Brillouin zone). This is consistent with the binary constituents except GaP (Madelung., 2004) and is highly desirable for optoelectronic applications like lasers and efficient light emitters/absorbers.

Figure 8 presents a contour map of the TB-mBJ calculated band gap. Along the lattice-matching line (Eq. 3), the band gap energy decreases significantly as both *x* and *y* increase. The calculated electronic band gap ranges from 1.360 eV (for Q1, *x*=0.125, *y*=0.0625) down to 0.503 eV (for Q7, *x*=0.875, *y*=0.4375). This tunable band gap corresponds to wavelengths ranging from approximately 0.911 µm to 2.456 µm. This range effectively covers the important telecommunication wavelengths of 1.3 µm and 1.55 µm.

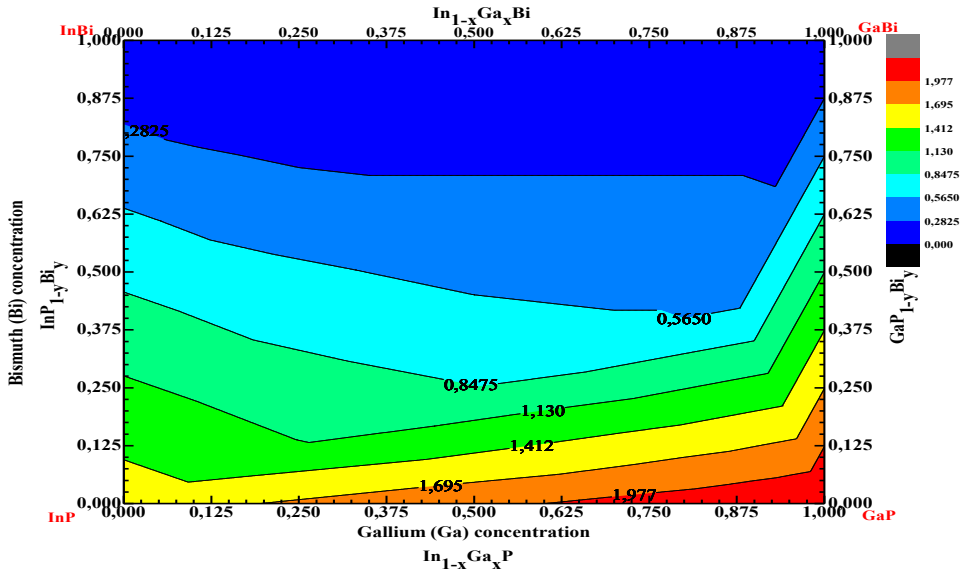


Figure 8. Contour map of the calculated direct band gap energy Eg (TB-mBJ, in eV) for $Ga_xIn_{1-x}Bi_yP_{1-y}$as a function of Ga (x) and Bi (y) concentrations.

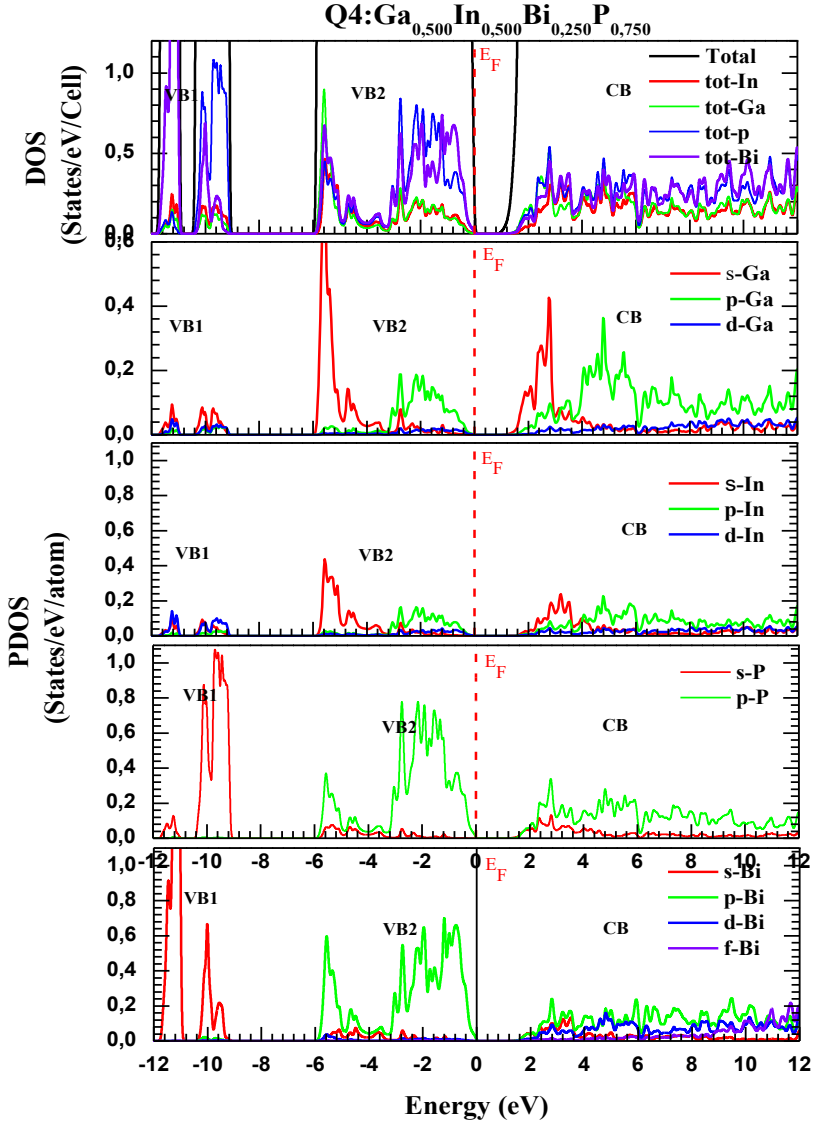


Figure 9.Total and partial density of states (TDOS/PDOS) for the lattice-matched quaternary alloy Q4 ($Ga_{0.500}In_{0.500}Bi_{0.250}P_{0.750}$), calculated using TB-mBJ. EF is at 0 eV.

The total and partial density of states (TDOS/PDOS) provides further insight. (Figure 9) shows the DOS for composition Q4 as an example. The valence band (VB) consists of regions dominated by Bi-s, P-s states at lower energy (VB_0, ~-11.5 to -8.9 eV), hybridization of Ga-s, In-s, P-p states (VB_1, ~-5.6 to -3.6 eV), and primarily Bi-p, P-p states near the VBM (VB_2, ~-3.6 eV to EF). (CB) region is formed by mixture of (s, p) states of (Bi- Ga- In- P) atoms, d states of (Bi- Ga- In) atoms and f states of Bi atom. The conduction band minimum (CBMin) is mainly formed by s states of Bi, Ga, and P atoms. The incorporation of Bi significantly influences the position of both the valence band maximum (VBM) and the CBMin, leading to the observed band gap reduction.

Optical Properties

The optical properties of the lattice-matched $Ga_xIn_{1-x}Bi_yP_{1-y}$ alloys (Q1-Q7) and their binary constituents were calculated using the TB-mBJ potential (Tran et al., 2009).

Complex Dielectric Function ε(ω)

The complex dielectric function $\varepsilon(\omega) = \varepsilon_1(\omega) + i\varepsilon_2(\omega)$is fundamental for describing optical response (Adachi, 2009). $\varepsilon_2(\omega)$ is calculated directly from electronic structure, and $\varepsilon_1(\omega)$ is obtained via the Kramers-Kronig relation (Adachi, 2009), (Slimani et al., 2019) , (Bouragba et al., 2020).

$$\varepsilon_2(\omega) = \left(\frac{4\pi^2 e^2}{m^2\omega^2}\right)\sum_{ij}\int\langle i|M|j\rangle^2 f_i\,(1-f_i)\delta(E_f - E_i - \omega)\mathrm{d}^3k, \qquad (4)$$

$$\varepsilon_1(\omega) = 1 + \frac{2}{\pi}\mathrm{p}\int_0^{\infty}\frac{\omega'.\varepsilon_2(\omega')}{\omega'^2-\omega^2}d\omega' \ , \qquad (5)$$

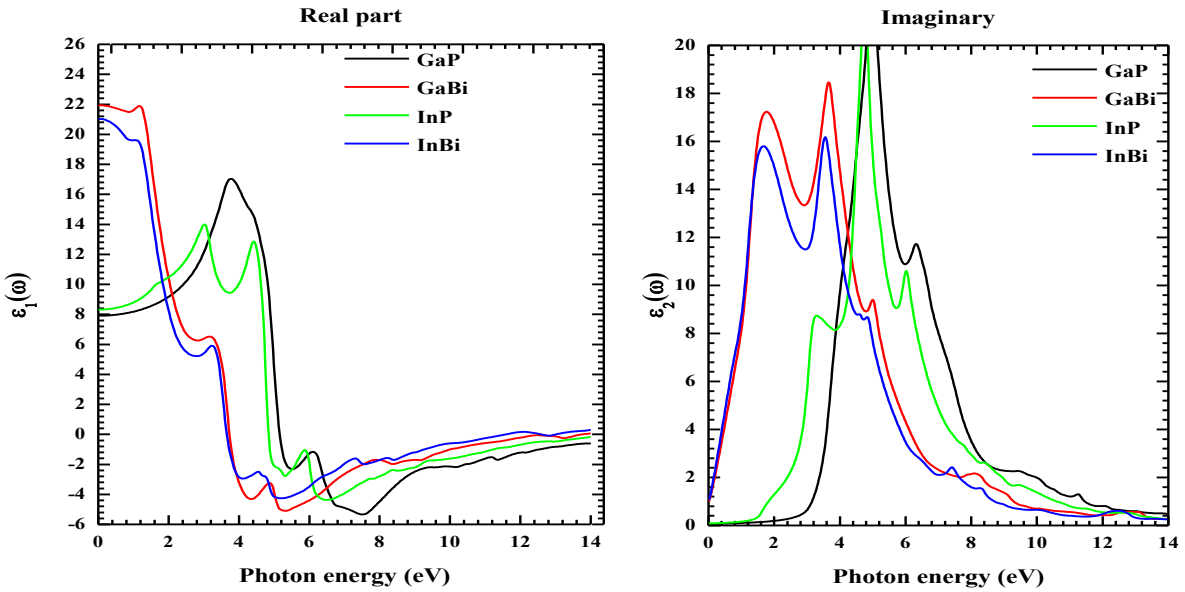


Figure 10. Calculated real (ε_1) and imaginary (ε_2) parts of the complex dielectric function for the binary compounds InP, InBi, GaP, GaBi, using the TB-mBJ scheme.

The calculated dielectric functions for the binaries (Figure 10) are consistent with known features. For the quaternaries (Figures 11, 12), the static dielectric constant $\varepsilon_1(0)$ (Table 3) increases as *x* and *y* increase (i.e., from Q1 to Q7), which is consistent with the Penn model (Penn, 1962) where $\varepsilon_1(0)$ is inversely related to the square of the band gap (Eg). The imaginary part $\varepsilon_2(\omega)$ shows critical points (peaks denoted E_0, E_1, E_2, E_3 in Table 3) associated with direct electronic transitions between VB and CB states. The first critical point E_0 corresponds to the fundamental absorption edge (the band gap Eg). As seen in (Table 3), E_0 (derived from $\varepsilon_2(\omega)$ peaks) decreases steadily from Q1 to Q7, following the trend of the calculated band gaps (Table 2).

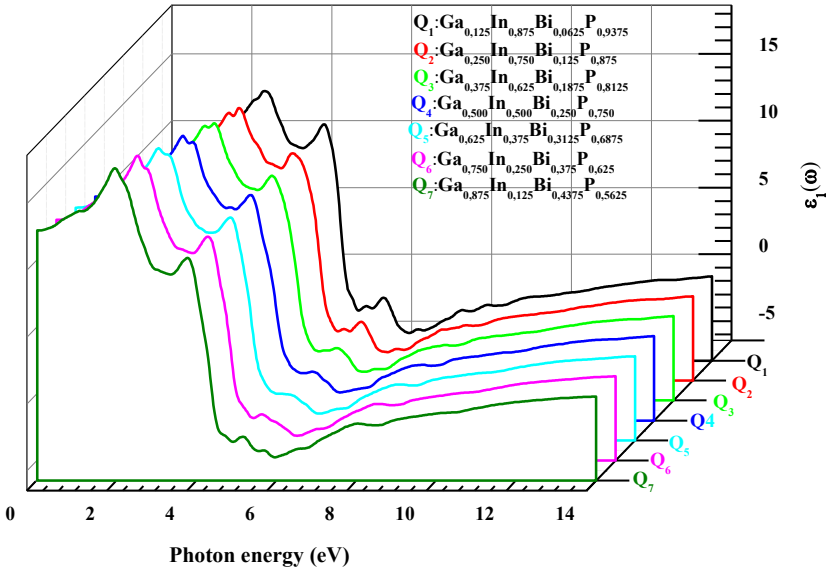


Figure 11. Real part (ε_1) of the dielectric function for the lattice-matched $Ga_xIn_{1-x}Bi_yP_{1-y}$ (Q1-Q7) as a function of photon energy, calculated using TB-mBJ.

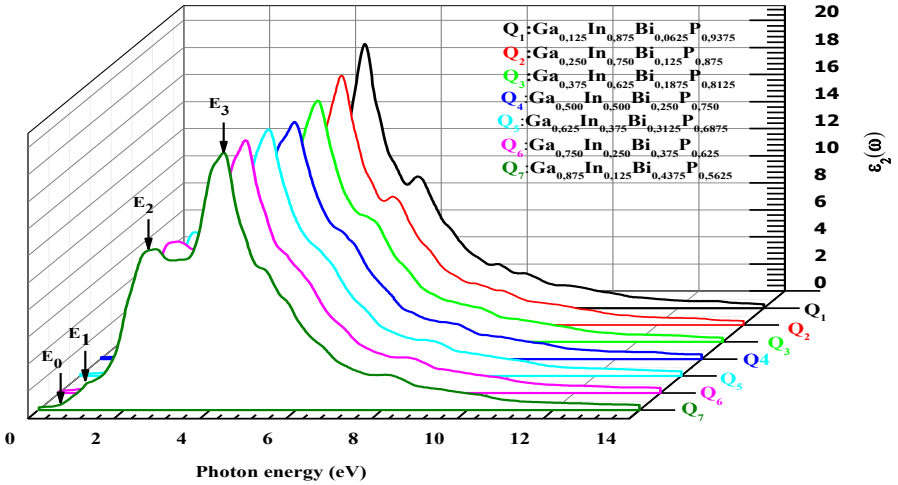


Figure 12. Imaginary part (ε_2) of the dielectric function for the lattice-matched $Ga_xIn_{1-x}Bi_yP_{1-y}$ (Q1-Q7) as a function of photon energy, calculated using TB-mBJ.

Table 3. Calculated critical point energies (E_0, E_1, E_2, E_3 in eV) from $\varepsilon_2(\omega)$ spectra and the static dielectric constant $\varepsilon_1(0)$ for binaries and lattice-matched $Ga_xIn_{1-x}Bi_yP_{1-y}$ alloys (Q1-Q7), using TB-mBJ.

$Ga_xIn_{1-x}Bi_yP_{1-y}$	Present work					Other works				
x	**E_0**	**E_1**	**E_2**	**E_3**	**$\varepsilon_1(0)$**	**E_0**	**E_1**	**E_2**	**E_3**	**$\varepsilon_1(0)$**
0 (InP)	1.56	1.825	3.246	4.76	8,320	1.570 **[1]**	-	3.284 **[1]**	4.760**[1]**	8.318 **[1]**
0 (InBi)	0.00	1.675	3.551	4.623	21,019	-	-	-	-	-
1 (GaBi	0.00	1.734	3.643	5.18	21,940	-	-	-	-	-
1 GaP	2.255	2.421	3.646	4.973	7,908	2.245 **[2]**	-	3.980 **[2]**	5.041 **[2]**	8.024 **[2]**
0.125	1.541	1.836	3.327	4.702	8.763	-	-	-	-	-
0. 250	1.125	1.649	2.247	4.622	9.267	-	-	-	-	-
0.375	0.997	1.544	3.094	4.567	9.796	-	-	-	-	-
0.500	0.663	1.381	2.698	4.516	10.296	-	-	-	-	-
0.625	0.635	1.264	2.616	4.376	10.965	-	-	-	-	-
0.750	0.508	1.229	2.547	4.341	11.547	-	-	-	-	-
0.875	0.301	1.125	2.477	4.294	12.246	-	-	-	-	-

[1] (Benchehima et al., 2016) **[2]** (Hachemi et al., 2022)

Complex Refractive Index

The refractive index $n(\omega)$ and extinction coefficient $k(\omega)$ are derived from $\varepsilon(\omega)$ (Adachi, 2009), (Benchehima et al., 2017), (Benchehima et al., 2018) :

$$n(\omega) = \sqrt{\frac{(\varepsilon_1^2(\omega)+\varepsilon_2^2(\omega))^{1/2}+\varepsilon_1(\omega)}{2}} \quad (6)$$

$$k(\omega) = \sqrt{\frac{(\varepsilon_1^2(\omega)^2+\varepsilon_2^2(\omega)^2)^{1/2}-\varepsilon_1(\omega)}{2}} \quad (7)$$

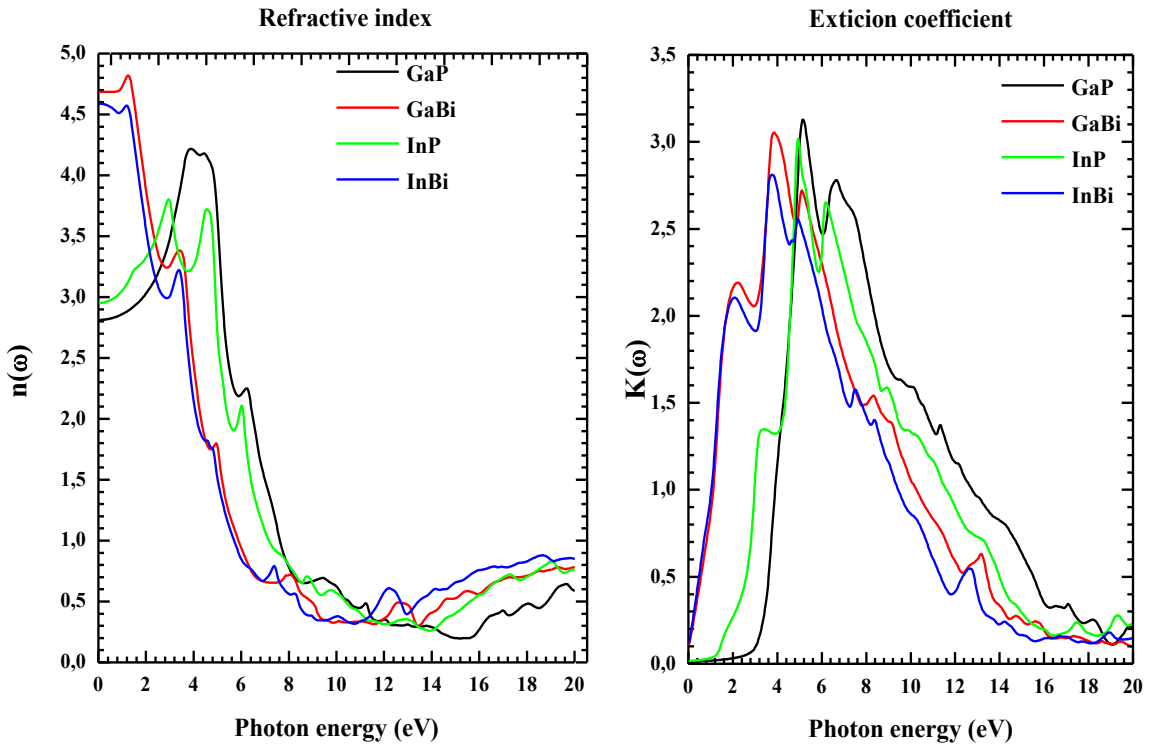


Figure 13. Calculated refractive index $n(\omega)$ and extinction coefficient $k(\omega)$ for binary compounds, using TB-mBJ.

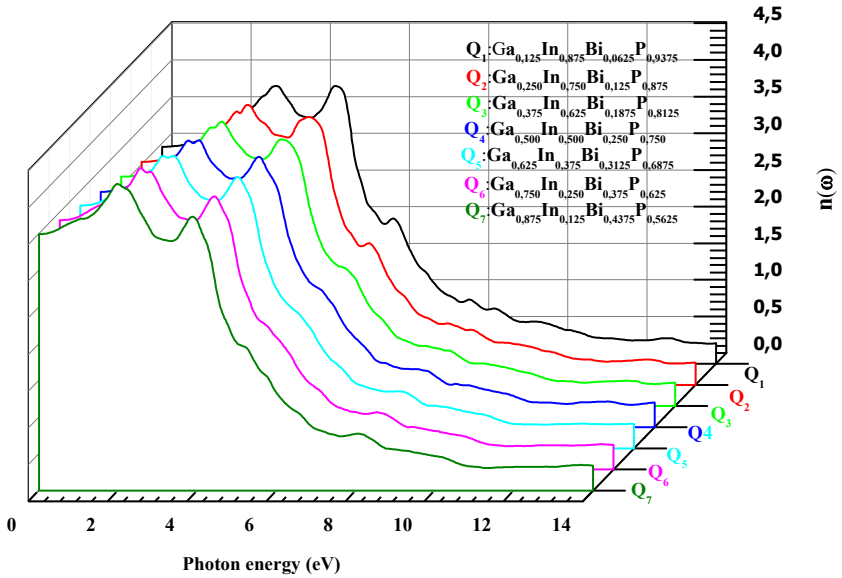


Figure 14. Refractive index $n(\omega)$ for the lattice-matched $Ga_xIn_{1-x}Bi_yP_{1-y}$ alloys (Q1-Q7), calculated using TB-mBJ.

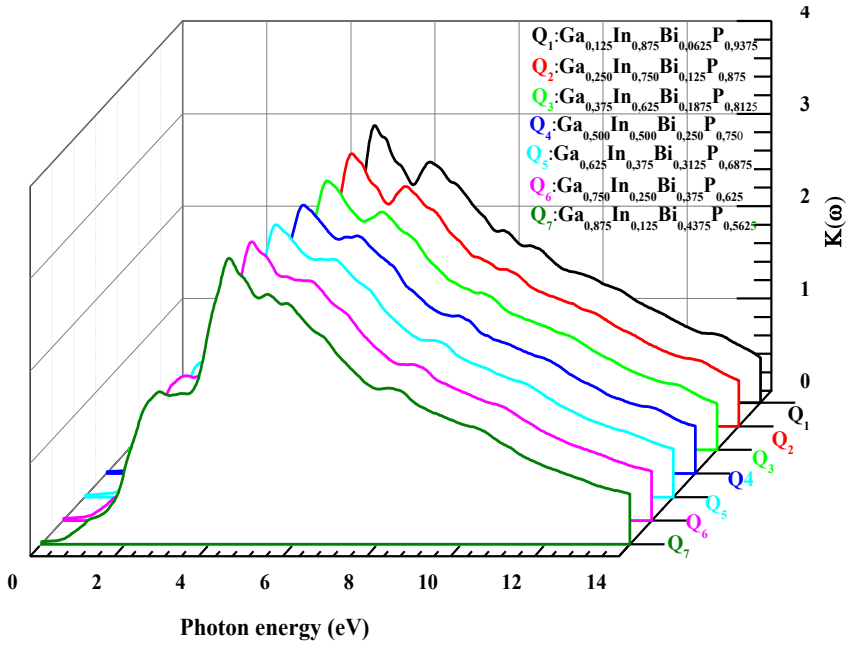


Figure 15. Extinction coefficient $k(\omega)$ for the lattice-matched $Ga_xIn_{1-x}Bi_yP_{1-y}$ alloys (Q1-Q7), calculated using TB-mBJ.

(Figures 13-15) show n(ω) and k(ω). The static refractive index $n(0) = \sqrt{\varepsilon_1(0)}$ (Table 4) also increases with increasing x and y content (from Q1 to Q7), consistent with the trend in $\varepsilon_1(0)$ and the decreasing band gap. The calculated $n(0)$ values for InP and GaP are in good agreement with experimental(Asadi et al., 2019) and other theoretical results (Benchehima et al., 2016), (Hachemi et al., 2022) , (Asadi et al., 2019), (Ahuja et al., 1997). The spectra show characteristic peaks related to the critical points in the electronic structure.

Table 4. Calculated static refractive index $n(0)$ for binaries and lattice-matched $Ga_xIn_{1-x}Bi_yP_{1-y}$ alloys (Q1-Q7), compared with other work.

Compound		***n*(0) refractive index**		
		Present work	**Others work**	
$Ga_xIn_{1-x}Bi_yP_{1-y}$		**TB-mBJ**	**Theoretical**	**Experimental**
x	***y***			
0 (inp)	0	2.884	2.884 **[1]**, 2.81 **[5]**	2.70 **[3]**
0 (InBi)	1	4.586	-	-
1 (GaP	0	2.812	2.832 **[2]**, 2.83 **[4]**	-
1 GaBi	1	4.685	-	-
0.125	0.0625	2.960	-	-
0, 250	0.125	3.044	-	
0.375	0.1875	3.129	-	
0.500	0.250	3.208	-	-
0.625	0.3125	3.311	-	-
0.750	0.375	3.398	-	
0.875	0.4375	3.499	-	

[1] (Benchehima et al., 2016) **[2]** (Hachemi et al., 2022) **[3]** (. Meiners, 2022)
[4] (Asadi et al., 2019) **[5]** (Asadi et al., 1997)

Optical Conductivity and Absorption Coefficient

Optical conductivity σ(ω) and absorption coefficient α(ω) are related to ε(ω) and $k(\omega)$ (Adachi., 2009):

$$\sigma(\omega) = \frac{i\omega}{4\pi}\varepsilon(\omega) \quad (8)$$

$$\alpha(\omega) = \frac{4\pi}{\lambda}k(\omega) \quad (9)$$

where λ is the wavelength in vacuum.

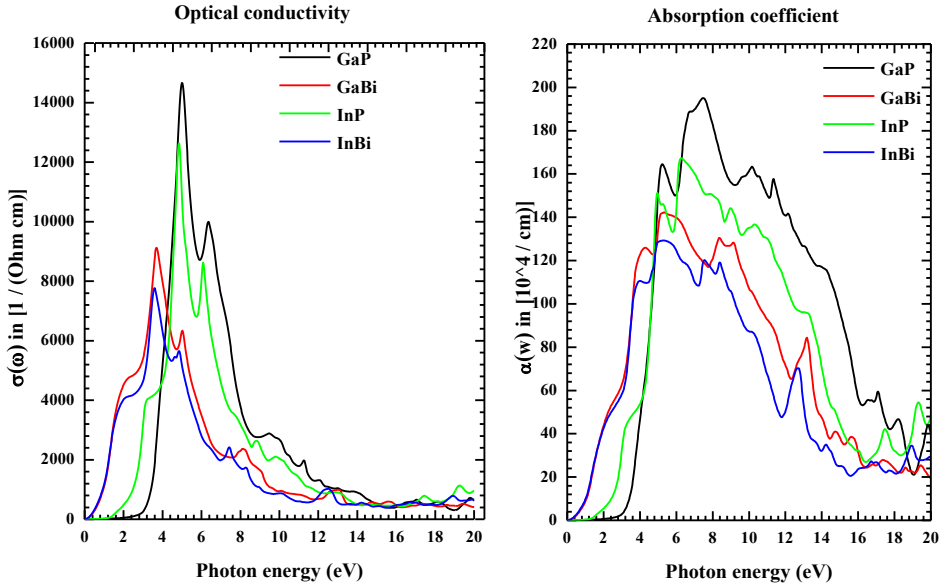


Figure 16. Calculated optical conductivity σ(ω) and absorption coefficient α(ω) for binary compounds, using TB-mBJ.

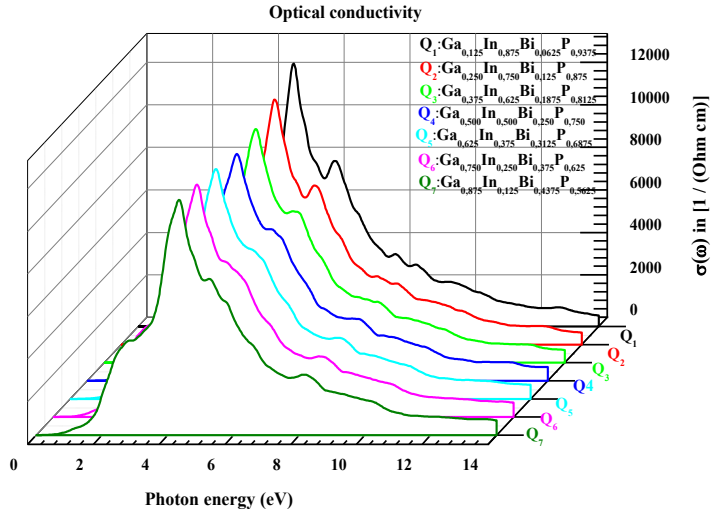


Figure 17.Optical conductivity σ(ω) for the lattice-matched $Ga_xIn_{1-x}Bi_\gamma P_{1-\gamma}$ alloys (Q1-Q7), calculated using TB-mBJ.

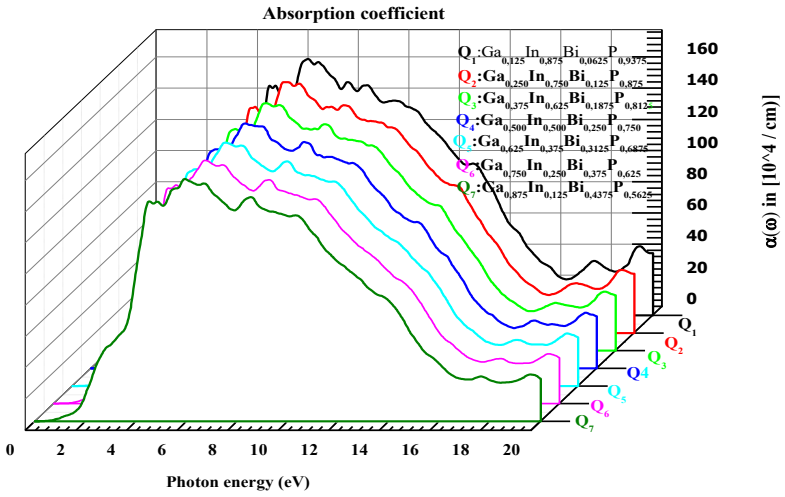


Figure 18. Absorption coefficient α(ω) for the lattice-matched $Ga_xIn_{1-x}Bi_\gamma P_{1-\gamma}$ alloys (Q1-Q7), calculated using TB-mBJ.

The optical conductivity and absorption coefficient are presented in (Figures 16-18). The onset of absorption corresponds to the fundamental band gap Eg (or E_0). For the quaternary alloys, the absorption edge shifts to lower energies as *x* and *y* increase, reflecting the decreasing band gap. The maximum absorption peaks for the quaternaries occur around 6.02 ± 0.6 eV, shifting slightly to lower energies and decreasing in intensity as *x* and *y* increase. The quaternaries show strong absorption in the visible and near-infrared regions (above ~2 eV).

Optical Band Gap

To quantify the optical band gap , Tauc plots were constructed(Tauc et al., 1966), (Rahimi et al., 2022) assuming that the energy-dependent absorption coefficient $\alpha(\omega)$ can be expressed by the following relationship

$$\alpha(\omega)h\nu = B\left(h\nu - E_g^{op}\right)^{n} \quad (10)$$

Where B is a constant for a direct transition, $h\nu$ is the photon's energy, E_g^{op} is the optical band gap and α is the optical absorption coefficient and n refers to an index ($n = ½$ for direct gap or n=2 for indirect gap).

The optical band gap is obtained by extrapolating the linear portion of the $(\alpha h\nu)^2$ and $(h\nu)$plot to the value $(\alpha h\nu)^2 = 0$.

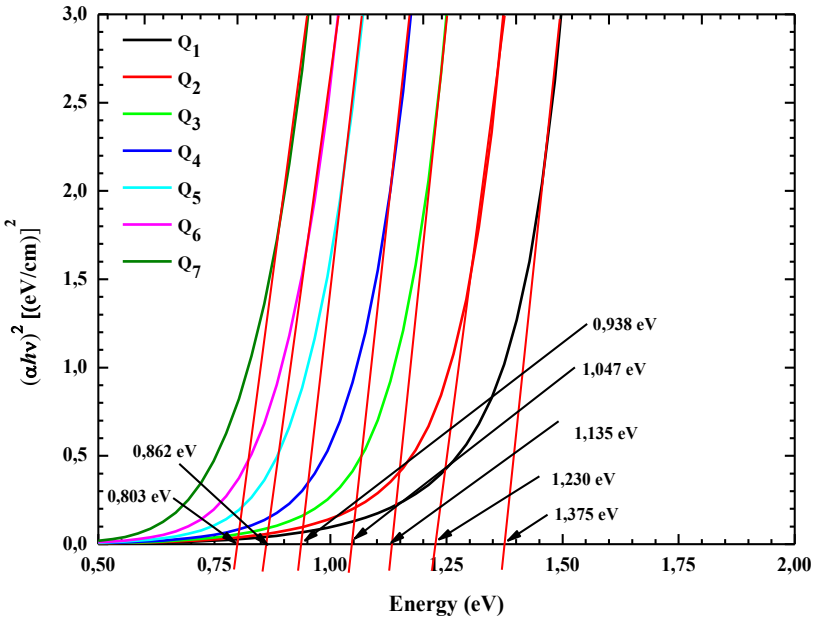


Figure 19.Tauc plots (αhν)² vs. photon energy (hν) for determining the direct optical band gap of lattice-matched $Ga_xIn_{1-x}Bi_yP_{1-y}$ alloys (Q1-Q7), based on TB-mBJ calculations.

Figure 19 shows the Tauc plots for the lattice-matched quaternary compositions. The determined direct optical band gaps are 1.375, 1.230, 1.135, 1.047, 0.938, 0.862, and 0.803 eV for Q1 through Q7, respectively. These values confirm the trend of decreasing band gap with increasing Ga and Bi concentration along the lattice-matching line, consistent with the electronic band gap calculations (Table 2) and E_0 values from $\varepsilon_2(\omega)$ (Table 3). This tunable optical gap covers the wavelength range from ~0.9 µm (for Q1) to ~1.56 µm (for Q7), again highlighting the relevance for telecommunications.

Conclusion

This theoretical study, based on first-principles DFT calculations using the FP-LAPW method (Blaha et al., 2019), has investigated the structural, electronic, and optical properties of $GaxIn_{1-x}Bi_yP_{1-y}$quaternary alloys specifically designed to be lattice-matched to InP substrates. Key findings include:

- The WC-GGA functional (Wu et al., 2006) accurately predicts lattice constants. Compositions satisfying the derived lattice-matching condition (Eq. 3) exhibit lattice parameters close to that of InP (~5.9 Å) based on WC-GGA calculations (Table 1), suitable for epitaxial growth.

- All investigated lattice-matched $Ga_xIn_{1-x}Bi_yP_{1-y}$ alloys possess a direct band gap at the Γ point (Figs. 6, 7). The band gap energy (calculated via TB-mBJ(Blaha et al., 2019)) is highly tunable by adjusting the Ga (x) and Bi (y) fractions along the lattice-matching constraint, ranging from 1.360 eV (Q1) down to 0.503 eV (Q7) (Table 2). This corresponds to a wavelength range of 0.91 µm to 2.46 µm.

- The optical constants (dielectric function, refractive index, absorption coefficient) were calculated using the TB-mBJ scheme (Figs. 10-18). The fundamental absorption edge shifts to lower energies with increasing x and y, consistent with the electronic band gap trend. Tauc analysis (Tauc et al., 1966), (Rahimi et al., 2022) yielded direct optical band gaps decreasing from 1.375 eV (Q1) to 0.796 eV (Q7) (Fig. 19), corresponding to wavelengths from ~0.9 µm to ~1.56 µm.

- The results demonstrate that $Ga_xIn_{1-x}Bi_yP_{1-y}$ alloys lattice-matched to InP offer significant flexibility in tuning the optoelectronic response. The ability to achieve direct band gaps spanning near-infrared wavelengths (~0.9 µm to ~2.5 µm based on electronic gap calculations) while maintaining lattice matching makes this material system highly attractive for optoelectronic device applications. It is particularly promising for lasers and photo detectors operating in the 1.3 µm and 1.55 µm telecommunication windows. This theoretical work provides valuable data and insights for the future development and optimization of $Ga_xIn_{1-x}Bi_yP_{1-y}$/InP based devices.

Scientific Ethics Declaration

* The authors declares that the scientific ethical and legal responsibility of this article published in EPSTEM journal belongs to the authors.

Conflict of Interest

* The authors declare that they have no conflicts of interest

Funding

* This research received no specific grant from any funding agency in the public, commercial, or not-for-profit sectors.

Acknowledgements or Notes

* This article was presented as a poster presentation at the International Conference on Technology, Engineering and Science (www.icontes.net) held in Antalya/Türkiye on November 12-15, 2025.

* The authors express gratitude to the Djillali Liabes University of Sidi Bel Abbes .

* The authors would like to thank the conference committee and the referees who reviewed the article for their valuable feedback.

References

Abt, R., Ambrosch-Draxl, C., & Knoll, P. (1994). Optical response of high temperature superconductors by full potential LAPW band structure calculations. *Physica B: Condensed Matter, 194–196*, 1451–1452.

Adachi, S. (2009). *Properties of semiconductor alloys: Group-IV, III-V and II-VI semiconductors*. John Wiley & Sons.

Ahuja, R., Auluck, S., Eriksson, O., Wills, J. M., & Johansson, B. (1997). Electronic and optical properties of InP. *Solid State Communications, 104*(5), 249–252.

Ambrosch-Draxl, C., & Sofo, J. O. (2006). Linear optical properties of solids within the full-potential linearized augmented plane wave method. *Computer Physics Communications, 175*(1), 1–14.

Asadi, Y., & Nourbakhsh, Z. (2019). Study of the linear and nonlinear response properties of the zinc-blende AlP, GaP and their AlxGa1-xP ternary alloys using first principle calculations. *Computational Condensed Matter, 21*, e00410.

Assali, A., Kanouni, F., Zou, Q., & Khenata, R. (2020). Optical characteristics of dilute gallium phosphide bismide: Promising material for near-infra photonic device applications. *Physics Letters A, 384*(5), 126147.

Benchehima, M., & Abid, H. (2016). Electronic and optical properties of AlxGayIn1-x–yAs quaternary alloys with and without relaxation lattice matched to InP for laser applications: First-principles study. *Optik, 127*(16), 6541–6558.

Benchehima, M., Abid, H., & Benchikh, K. (2017). First-principles calculations of the structural and optoelectronic properties of BSb1-xAsx ternary alloys in zinc blende structure. *Materials Chemistry and Physics, 198*, 214-228.

Benchehima, M., Abid, H., Sadoun, A., & Chaouche, A. C. (2018). The electrical properties of Au/GaN and PEDOT: PSS/GaN diodes. *Computational Materials Science, 155*, 224-234.

Berding, M. A., Sher, A., Chen, A. B., & Miller, W. (1988). Structural properties of bismuth-bearing semiconductor alloys. *Journal of Applied Physics, 63*(1), 107-115.

Blaha, P., Schwarz, K., Madsen, G. K. H., Kvasnicka, D., Luitz, J., Laskowski, R., Tran, F., & Marks, L. D. (2019). *WIEN2k: An augmented plane wave plus local orbitals program for calculating crystal properties* (Computer software). Technische Universität Wien.

Bouragba, D., Benchehima, M., Abid, H., & Djili, A. (2020). Optical response functions and thermodynamic stability of BSb1-xNx ternary alloys in zinc blende structure. *Optik, 222*, 165472.

Camargo-Martínez, J. A., & Baquero, R. (2012). Performance of the modified Becke-Johnson potential for semiconductors. *Physical Review B, 86*(19), 195106.

Celin-Mancera, W. A., López-Pérez, W., González-García, Á., Ramírez-Montes, L., & González-Hernández, R. (2016). Theoretical study of structural stability, elastic, electronic and thermodynamic properties of ScxGa1-xP compounds by ab initio calculations. *Computational Condensed Matter, 8*, 14–21.

Ceperley, D. M., & Alder, B. J. (1980). Ground state of the electron gas by a stochastic method. *Physical Review Letters, 45*(7), 566–569.

Donmez, O., Erol, A., Çetinkaya, Ç., Çokduygulular, E., Aydın, M., Yıldırım, S., & Gunes, M. (2021). A quantitative analysis of electronic transport in n-and p-type modulation-doped GaAsBi/AlGaAs quantum well structures. *Semiconductor Science and Technology, 36*(11), 115017.

Engel, E., & Vosko, S. H. (1993). Exact exchange-only potentials and the virial relation as microscopic criteria for generalized gradient approximations. *Physical Review B, 47*(20), 13164.

Gandouzi, M., Hedhili, F., & Rekik, N. (2018). A density functional theory investigation of the structural and optoelectronic properties of InP1-xBix alloys. *Computational Materials Science, 149*, 307-315.

Gazhulina, A. P., & Marychev, M. O. (2015). Structural, electronic and nonlinear optical properties of B3 and B20 compounds: A first-principles investigation within the LDA, GGA and modified Becke-Johnson exchange potential plus LDA. *Journal of Alloys and Compounds, 623*, 413–437.

Gelczuk, Ł., Stokowski, H., Kopaczek, J., Zhang, L., Li, Y., Wang, K., & Kudrawiec, R. (2016). Bi-induced acceptor level responsible for partial compensation of native free electron density in InP1-xBix dilute bismide alloys. *Journal of Physics D: Applied Physics, 49*(11), 115107.

Hachemi, M. H., Benchehima, M., Bencherif, K., & Abid, H. (2022). The effect of N-incorporation on the structural and optoelectronic properties of GaP and GaAs for optical telecommunication applications: First-principles study. *Optik, 262*, 169282.

Jain, N., Mal, I., Samajdar, D., & Bagga, N. (2022). Investigation of optoelectronic performance of InAsNBi for infrared detection. In *Tailored functional materials* (pp. 475–484). Springer.

Janotti, A., Wei, S.-H., & Zhang, S. (2002). Theoretical study of the effects of isovalent coalloying of Bi and N in GaAs. *Physical Review B, 65*(11), 115203.

Jiang, H. (2013). Band gaps from the Tran-Blaha modified Becke-Johnson approach: A systematic investigation. *The Journal of Chemical Physics, 138*(13), 134115.

Kohn, W., & Sham, L. J. (1965). Self-consistent equations including exchange and correlation effects. *Physical Review, 140*(4A), A1133.

Kumar, S., Parashari, S. S., & Auluck, S. (2009). Disorder effects on electronic and optical properties of the ternary GaxIn1-xP (x=0.25, 0.50, and 0.75) alloy. *Physica Status Solidi (b), 246*(10), 2294-2300.

Levinshtein, M., Rumyantsev, S., & Shur, M. (1996). *Handbook series on semiconductor parameters: Volume 1: Si, Ge, C (Diamond), GaAs, GaP, GaSb, InAs, InP, InSb*. World Scientific.

Liu, W., Zheng, W. T., & Jiang, Q. (2007). First-principles study of the surface energy and work function of III-V semiconductor compounds. *Physical Review B, 75*(23), 235322.

Madelung, O. (2004). III-V compounds. In *Semiconductors: Data handbook* (pp. 71–172). Springer.

Meiners, L. G. (1986). Temperature dependence of the dielectric constant of InP. *Journal of Applied Physics, 59*(5), 1611–1613.

Murnaghan, F. D. (1944). The compressibility of media under extreme pressures. *Proceedings of the National Academy of Sciences of the United States of America, 30*(9), 244-247.

Nattermann, L., Beyer, A., Ludewig, P., Hepp, T., Sterzer, E., & Volz, K. (2017). MOVPE growth of Ga(PBi) on GaP and GaP on Si with Bi fractions up to 8%. *Journal of Crystal Growth, 463*, 151–155.

Okamoto, H., & Oe, K. (1998). Growth of metastable alloy InAsBi by low-pressure MOVPE. *Japanese Journal of Applied Physics, 37*(3S), 1608.

Paulauskas, T., Pačebutas, V., Geižutis, A., Stanionytė, S., Dudutienė, E., Skapas, M., & Krotkus, A. (2020). GaAs 1-xBi x growth on Ge: Anti-phase domains, ordering, and exciton localization. *Scientific Reports, 10*(1), 1-12.

Penn, D. R. (1962). Wave-number-dependent dielectric function of semiconductors. *Physical Review, 128*(5), 2093-2100.

Perdew, J. P., Burke, K., & Ernzerhof, M. (1996). Generalized gradient approximation made simple. *Physical Review Letters, 77*(18), 3865-3868.

Perdew, J. P., Ruzsinszky, A., Csonka, G. I., Vydrov, O. A., Scuseria, G. E., Constantin, L. A., Zhou, X., & Burke, K. (2008). Restoring the density-gradient expansion for exchange in solids and surfaces. *Physical Review Letters, 100*(13), 136406.

Rahimi, S., Ebrahimi-Jaberi, R., Jalali-Asadabadi, F., Mollabashi, L., & Jalali-Asadabadi, S. (2022). Influence of (Ba, F) multidoping on structural, magnetic, optical, and electrical properties as well as performance enhancement of multiferroic BiFeO3. *Physical Review B, 106*(11), 115205.

Rajpalke, M. K., Linhart, W. M., Yu, K. M., Birkett, M., Alaria, J., Bomphrey, J. J., Sallis, S., Piper, L. F. J., Jones, T. S., Ashwin, M. J., & Veal, T. D. (2014). Bi-induced band gap reduction in epitaxial InSbBi alloys. *Applied Physics Letters, 105*(21), 212101.

Samajdar, D. P., & Dhar, S. (2016). Influence of Bi-related impurity states on the bandgap and spin-orbit splitting energy of dilute III-V-Bi alloys: InP1-xBix, InAs1-xBix, InSb1-xBix and GaSb1-xBix. *Superlattices and Microstructures, 89*, 112-119.

Slimani, H., Abid, H., & Benchehima, M. (2019). Prediction of optoelectronic properties for BexZnyCd1-x-ySe quaternary alloys: First-principles study. *Optik, 198*, 163288.

Tauc, J., Grigorovici, R., & Vancu, A. (1966). Optical properties and electronic structure of amorphous germanium. *Physica Status Solidi (b), 15*(2), 627-637.

Tran, F., & Blaha, P. (2009). Accurate band gaps of semiconductors and insulators with a semilocal exchange-correlation potential. *Physical Review Letters, 102*(22), 226401.

Usman, M. (2019). Towards low-loss telecom-wavelength photonic devices by designing GaBixAs1-x/Ga As core-shell nanowires. *Nanoscale, 11*(42), 20133-20143.

Usman, M., Broderick, C. A., Lindsay, A., & O'Reilly, E. P. (2011). Tight-binding analysis of the electronic structure of dilute bismide alloys of GaP and GaAs. *Physical Review B, 84*(24), 245202.

Vurgaftman, I., Meyer, J. R., & Ram-Mohan, L. R. (2001). Band parameters for III-V compound semiconductors and their alloys. *Journal of Applied Physics, 89*(11), 5815–5875.

Wang, K., Gu, Y., Zhou, H., Zhang, L., Kang, C., Wu, M., & Pan, W. (2014). InPBi single crystals grown by molecular beam epitaxy. *Scientific Reports, 4*(1), 5449.

Wang, S., & Lu, P. (2019). *Bismuth-containing alloys and nanostructures*. Springer.

Wang, S., & Ye, H. (2002). Plane-wave pseudopotential study on mechanical and electronic properties for IV and III-V crystalline phases with zinc-blende structure. *Physical Review B, 66*(23), 235111.

Wu, X., Chen, X., Pan, W., Wang, P., Zhang, L., Li, Y., Zhou, H., & Wang, K. (2016). Anomalous photoluminescence in InP1-xBix. *Scientific Reports, 6*(1), 1-8.

Wu, Z., & Cohen, R. E. (2006). More accurate generalized gradient approximation for solids. *Physical Review B, 73*(23), 235116.

Wyckoff, R. (1986). *Crystal structures* (2nd ed.). Krieger.

Yang, H., Song, T., Liang, X., & Zhao, G. (2015). First-principle study of the electronic band structure and the effective mass of the ternary alloy GaxIn1-xP. *Journal of Physics: Conference Series, 586*, 012048.

Zhang, X., Zhang, Y., Yue, L., Liang, H., Chi, C., Wu, Y., & Dai, L. (2019). Growth and properties of AlSbBi thin films by molecular beam epitaxy. *Journal of Alloys and Compounds, 801*, 239-242

Zunger, A., Wei, S.-H., Ferreira, L. G., & Bernard, J. E. (1990). Special quasirandom structures. *Physical Review Letters, 65*(3), 353-356.

Author(s) Information

Malika Tehami
Djillali Liabes University of Sidi Bel Abbes
Electronic's Department, Sidi Bel Abbes, Algeria
Contact e-mail: *mtehami2001@gmail.com*

Miloud Benchehima
University of Sciences and Technology Mohamed Boudiaf,
Electronic's Department, Oran, Algeria

Hamza Abid
Djillali Liabes University of Sidi Bel Abbes
Electronic's Department, Sidi Bel Abbes, Algeria

To cite this article:

Tehami, M., Benchehima, M., & Abid, H. (2025). Computational materials design: Tuning optoelectronic response in GaxIn1-xBiyP1-y alloys via structural matching to InP. *The Eurasia Proceedings of Science, Technology, Engineering & Mathematics, (EPSTEM) 38,* 226-243

The Eurasia Proceedings of Science, Technology, Engineering & Mathematics (EPSTEM)
ISSN: 2602-3199

The Eurasia Proceedings of Science, Technology, Engineering and Mathematics (EPSTEM), 2025

Volume 38, Pages 244-256

IConTES 2025: International Conference on Technology, Engineering and Science

Swarm Intelligence-Based Energy Optimization for UAV Mission Efficiency

Mustafa Cosar
Hitit University

Abstract: This study investigates the effectiveness of swarm intelligence–based optimization methods for improving energy efficiency and minimizing mission duration in multi–unmanned aerial vehicle (UAV) swarms. The problem is formulated as a route-sequencing optimization task in which the visiting order of target points is optimized to reduce total energy consumption while ensuring complete mission feasibility. A classical nearest-neighbor assignment serves as the baseline and is compared against two evolutionary approaches: the single-objective Particle Swarm Optimization (PSO) and the multi-objective Non-dominated Sorting Genetic Algorithm II (NSGA-II). A Python-based simulation environment was developed to evaluate algorithmic performance under varying payload and wind conditions, including Zero, Constant, and Ornstein–Uhlenbeck (OU) stochastic wind models. Experimental results indicate that route sequencing optimization substantially decreases overall energy demand. NSGA-II, in particular, successfully constructs a well-defined Pareto front for the energy–time objectives, offering mission planners a flexible spectrum of trade-off solutions. In the OU + 150 g scenario, the Knee-point solution (E = 26.8 Wh, T = 93 s) achieved approximately 13% lower energy consumption at the cost of only a 7% increase in mission duration relative to the baseline. Across all methods, mission completion remained at 100%, and coverage ratios improved notably. These findings confirm that swarm intelligence–based optimization techniques provide robust and efficient tools for balancing energy consumption and operational time in UAV swarm mission planning.

Keywords: UAV swarm, Swarm intelligence algorithms, Metaheuristic optimization, Mission planning, Energy efficiency

Introduction

Recent advancements in unmanned aerial vehicle (UAV) technologies have facilitated their widespread adoption across military, industrial, and civilian applications. Cooperative UAV systems operating under swarm intelligence principles offer significant advantages in scalability, robustness, and mission adaptability for tasks such as wide-area surveillance, disaster response, logistics, and environmental monitoring (Coşar, 2023a). Despite these benefits, one of the most persistent challenges remains energy efficiency. Limited battery capacity directly constrains flight endurance and mission feasibility, highlighting the need for advanced energy management and mission planning strategies (Abeywickrama et al., 2018; Michel et al., 2022).

Swarm intelligence, inspired by the collective and self-organized behaviors of natural organisms such as bird flocks, ant colonies, and bee swarms (Beni & Wang, 1993; Lones, 2014), has been effectively adapted to multi-agent robotic systems. Algorithms including Particle Swarm Optimization (PSO), Ant Colony Optimization (ACO), and Artificial Bee Colony (ABC) have demonstrated robust convergence and flexibility in solving route planning, task allocation, and coordination problems under environmental uncertainty (Coşar, 2023b). These bio-inspired approaches provide decentralized, scalable, and adaptive mechanisms that make them well-suited to the complexities of UAV swarm operations.

Although artificial intelligence (AI) and machine learning (ML) have enabled substantial progress in autonomous control and navigation (Na et al., 2023; Lin et al., 2024), several limitations remain. Energy constraints, wind-

- This is an Open Access article distributed under the terms of the Creative Commons Attribution-Noncommercial 4.0 Unported License, permitting all non-commercial use, distribution, and reproduction in any medium, provided the original work is properly cited.
- Selection and peer-review under responsibility of the Organizing Committee of the Conference
© 2025 Published by ISRES Publishing: www.isres.org

induced perturbations, and dynamic payload variations continue to influence flight stability and mission duration (Guo et al., 2023; Cabuk et al., 2024). Different control architectures-centralized, decentralized, or distributed-introduce trade-offs between communication overhead, scalability, and computational load (Alqudsi & Makaraci, 2025). Meanwhile, recent studies have proposed physics-based aerodynamic models (Opazo et al., 2023; Jacewicz et al., 2023), yet the integration of such models into multi-objective optimization frameworks remains comparatively underexplored. Parallel research directions employing deep reinforcement learning have also shown promise in enhancing swarm-level decision-making and energy-aware coordination (Güven & Yanmaz, 2024; Arranz et al., 2023).

Despite advancements in heuristic and metaheuristic optimization for collision avoidance, coverage planning, and path generation, many studies treat energy consumption and mission duration as independent objectives or rely on simplified power models that neglect aerodynamic drag, turbulence, and payload-dependent variations (Di Franco & Buttazzo, 2016; Gamil et al., 2023). To address these gaps, the present study proposes an integrated multi-objective optimization framework that incorporates dynamic environmental factors—specifically wind and payload variability—while jointly optimizing energy consumption and task completion time using PSO and Non-dominated Sorting Genetic Algorithm II (NSGA-II). The proposed Python-based simulation environment enables reproducible evaluations of UAV swarm performance under realistic mission constraints and supports the development of adaptive energy–time trade-off strategies.

Literature Review

UAV swarm research has rapidly evolved, particularly in mission planning, task allocation, and energy-efficiency optimization (Guo et al., 2023; Cabuk et al., 2024). Swarm robotics, rooted in the collective intelligence principles observed in natural systems, promotes decentralized coordination through local sensing and inter-agent communication (Beni, 1989; Beni & Wang, 1993). With the integration of AI-driven perception and machine learning–based decision models, swarm UAVs can exhibit adaptive, cooperative, and resilient behaviors under diverse mission conditions (Coşar, 2023a; Na et al., 2023; Lin et al., 2024).

Energy consumption remains a critical performance determinant for UAV swarms. High-fidelity models such as the 6-DOF quadrotor framework by Jacewicz et al. (2023)-which jointly considers aerodynamics, propulsion, and battery discharge-have demonstrated the importance of comprehensive physical modeling. Similarly, Michel et al. (2022) provided a system-level energy framework capable of simulating transient power variations. These models surpass simplified parametric formulations like $v^2+1/v+C_{payload}$, commonly used in UAV literature (Gong et al., 2022). Abeywickrama et al. (2018) further emphasized the necessity for empirical calibration and real-world validation in battery-aware energy modeling.

Complementing these findings, aerodynamic studies by Opazo et al. (2023) and Morbidi et al. (2016) highlighted the intricate coupling between induced and profile drag. Opazo et al. (2023) examined power consumption in coaxial rotor configurations under controlled hover conditions, while Morbidi et al. (2016) presented an optimal control framework combining rotor-induced power with aerodynamic drag to generate energy-efficient trajectories. These results underscore that energy-aware trajectory design must incorporate full vehicle dynamics rather than rely solely on kinematic simplifications.

PSO-based methods have been widely applied in UAV swarm optimization, particularly for improving energy efficiency and route sequencing (Coşar, 2023b). Enhanced variants such as KPSO, adaptive PSO, and hybrid PSO-ABC have demonstrated superior convergence and smoother trajectories under environmental disturbances (Rosas-Carrillo et al., 2025; Baidya et al., 2024; Tang et al., 2024). Na et al. (2023) showed that PSO with adaptive inertia weights improves robustness in turbulent wind and variable payload settings. These findings emphasize PSO's strengths for single-objective optimization in swarm coordination.

For multi-objective optimization, NSGA-II remains the dominant approach due to its efficiency in maintaining Pareto diversity and achieving fast convergence (Duan et al., 2024; Hohmann et al., 2021). Xue et al. (2024) applied NSGA-II to complex 3D terrain navigation, balancing stability, energy, and path length. Zhang (2024) demonstrated its cross-domain applicability in multi-agent energy-aware design systems. In UAV swarm scenarios, NSGA-II naturally supports flexible trade-offs between energy minimization and mission duration, offering operational adaptability for dynamic environments.

Task allocation methods have also progressed from centralized Hungarian and auction-based frameworks to scalable and distributed systems. Galati et al. (2023) proposed an auction-based motion-planning model enabling

dynamic re-planning under human supervision. Wang et al. (2024) developed a two-stage greedy auction system tailored for large-scale swarms. Chen et al. (2024) introduced a distributed benefit-optimization framework to enhance responsiveness, while Jiang et al. (2025) combined cluster analysis with differential PSO to improve convergence in large multi-UAV missions.

Energy-efficient coverage path planning (CPP) represents another critical research area. Di Franco and Buttazzo (2016) introduced one of the earliest energy-aware CPP models integrating empirical power consumption into geometric optimization. More recently, Gamil et al. (2023) incorporated wind effects and battery constraints, while Güven and Yanmaz (2024) demonstrated that realistic environmental modeling significantly improves coverage stability and energy management across UAV teams.

Despite this progress, the literature still lacks an integrated framework that simultaneously incorporates aerodynamic realism, dynamic environmental variability, and multi-objective optimization. Addressing this gap, the present study introduces a reproducible simulation environment combining physics-based energy modeling, PSO-based heuristic optimization, and NSGA-II-driven Pareto analysis. By systematically evaluating the energy–time balance across wind and payload conditions, the framework provides a comprehensive foundation for future UAV swarm optimization research.

Method

This study utilizes a hybrid methodology integrating a single-objective heuristic approach (PSO) and a multi-objective evolutionary algorithm (NSGA-II) to evaluate how route sequencing influences the energy consumption of UAV swarms. PSO ensures rapid convergence through a normalized scalarized fitness function, whereas NSGA-II identifies Pareto-optimal solutions that balance total energy consumption and mission duration. This dual-framework design aligns with findings by Hohmann et al. (2021) and Zhang (2024), demonstrating that combining heuristic and evolutionary strategies improves convergence reliability and decision-space diversity. All evaluations were conducted within a two-dimensional Python-based simulation environment incorporating UAV motion dynamics and an empirically validated energy model (Abeywickrama et al., 2018; Jacewicz et al., 2023). Key simulation parameters—including maximum velocity, hover power, and payload mass-were derived from experimental datasets to ensure realistic aerodynamic representation (Opazo et al., 2023; Michel et al., 2022).

Three wind conditions were modeled: zero wind, constant wind, and Ornstein–Uhlenbeck (OU) stochastic turbulence (Gong et al., 2022). The energy consumption model combines hover power, parasitic drag, induced power, and payload-related lift demand, consistent with analytical principles presented in Morbidi et al. (2016). To ensure statistical reliability, each scenario was simulated using five independent random seeds, with results reported as Median (IQR).

The optimization algorithms were configured based on best practices reported in recent UAV optimization literature (Na et al., 2023; Tang et al., 2024). PSO used 16 particles over 20 iterations with $c_1 = c_2 = 1.4$, while NSGA-II employed a population of 40 over 30 generations, using simulated binary crossover (SBX) and polynomial mutation (Xue et al., 2024). From the resulting Pareto front, three representative solutions were extracted: minimum energy, minimum time, and the knee point. To limit computational cost while focusing on the most realistic and challenging operating condition, NSGA-II was applied only to the OU + 150 g scenario. For all remaining wind–payload combinations, comparisons were restricted to the Baseline and PSO approaches.

Simulation Setup

The simulation is executed within a $300 \times 300\ m$ mission area using $n=8$ UAVs and 20 Points of Interest (POIs). The time step is set to $\Delta t=0.5s$, with a maximum mission duration of $T=600s$. Each UAV generates a desired velocity vector toward its assigned target, and a wind perturbation term is incorporated into the motion model. The UAV's ground velocity v_i is calculated as Formula 1.

$$v_i(t) = LimitSpeed(v_{desired}(t) + \gamma\, w(t), v_{max}) \quad (1)$$

where $\gamma=0.2$ and $v_{max}=7\ m/s$. The coefficient γ presents an empirical scaling factor that models the corrective effort required to counteract wind drift. The UAV's position is then updated at each time step by integrating the velocity as Formula 2.

$$p_i(t + \Delta t) = p_i(t) + v_i(t) \,.\, \Delta t \tag{2}$$

This simplified kinematic model is widely adopted in swarm simulations to reduce control complexity and enhance computational efficiency (Gong et al., 2022). A collision-avoidance term is activated whenever the inter-UAV distance falls below the safe threshold $d_{safe}=5m$ and boundary reflections prevent UAVs from exiting the mission area. The simulation integrates verified energy models drawn from empirical studies (Abeywickrama et al., 2018; Jacewicz et al., 2023) and aerodynamic validation frameworks (Michel et al., 2022; Opazo et al., 2023).

Wind Modeling

To represent realistic turbulence, the OU process was applied, consistent with aerodynamic modeling studies (Gong et al., 2022). Three wind models were employed;

- Zero Wind: (0,0) m/s
- Constant Wind: (0.8, −0.4) m/s
- OU Stochastic Wind, defined by Formula 3:

$$x_{t+1} = x_t + \theta(\mu - x_t)\Delta t + \sigma\sqrt{\Delta_t}\,\varepsilon_t \tag{3}$$

where typical values are $\theta=0.4$, $\mu=(0.5-0.2)$, $\sigma=0.2$. The OU process generates a more realistic, continuously fluctuating disturbance than the constant wind model.

Energy Model

The instantaneous power consumption $P(v)$ (in Watts) of a multi-rotor UAV is computed as Formula 4:

$$P(v) = P_{hover} + k_1.v^2 + \frac{k_2}{\max(v, 0.1)} + k_{load}\left(m_{base} + m_{payload}\right) \tag{4}$$

where, $P(v)$, total instantaneous power at velocity v. P_{hover}, base hovering power required to sustain flight and operate onboard electronics (independent of wind/load). $k_1 v^2$, ower loss due to aerodynamic drag and parasitic resistance. $\frac{k_2}{max\,(v,\ 0.1)}$ induced power losses at low speeds (vortex and rotor drag). k_{load}, load-dependent coefficient accounting for increased lift demand. m_{base} UAV base mass. $m_{payload}$ additional payload mass during flight.

The following parameter values were used: P_{hover}=95 W, k_1=0.6, k_2=1.2, k_{load}=5.5k and m_{base}=1.25 kg and payload scenarios of 0/150/300g. The total mission energy is then computed as Formula 5.

$$E_{total} = \sum_i \sum_t P_i(t)\Delta t/3600 \tag{5}$$

The wind indirectly affects E_{total} by modifying the UAV's motion dynamics, which alter instantaneous velocity and thus power demand. For instance, in the constant-wind scenario ($w= (0.8, -0.4)$ m/s), the external wind vector is superimposed onto the UAV's desired velocity, resulting in additional energy expenditure. Each scenario aims for all POIs to be visited by at least one UAV. A nearest-neighbor assignment followed by greedy sequencing is used for baseline initialization. Simulations terminate when either all POIs are visited or any UAV exhausts its battery capacity. The Table 1 performance metrics are recorded:

Table 1. Task assignment and performance metrics

Metric	Definition
Total Energy Consumption	Total energy used during the mission (in watt-hours, Wh).
Makespan	Total mission duration until completion (in seconds, s).
Coverage	Percentage of area visited (based on 20 m grid resolution).
Visit Rate	Percentage of POIs successfully visited by UAVs.
Dead UAV Rate	Percentage of UAVs that depleted their battery before completing the mission.

Dataset

The dataset used in this study was synthetically generated using a Python-based simulator specifically developed for UAV swarm energy efficiency and coverage optimization. A controlled simulation environment was preferred over field experiments due to the inherent difficulty of controlling environmental variables such as wind and battery variation. This approach enables systematic, repeatable, and parametric evaluation of algorithmic performance across different environmental conditions. The simulator integrates validated aerodynamic and power consumption models from the literature, offering a reliable experimental framework to analyze the sensitivity of optimization algorithms to the energy–time trade-off. Consequently, the effects of payload and wind variations on UAV energy efficiency can be observed independently from external noise.

Algorithms

PSO

PSO was selected for its high convergence speed and robustness in single-objective optimization problems. The Random Keys PSO approach was adopted to handle the route sequencing task. The objective function is formulated as a normalized weighted sum in Formula 6:

$$\min F_{PSO} = E_n + \lambda T_n \tag{6}$$

where $E_n = \frac{E_{total}}{E_{ref}}$ and $T_n = \frac{T_{ms}}{T_{ref}}$, with E_{ref}=50Wh, T_{ref}=150 s, and weighting factor λ=0.3. This ensures that the objectives are balanced despite differing units. PSO parameters: 16 particles, 20 iterations, w=0.72, c_1=c_2=1.4.

NSGA-II

NSGA-II was employed for multi-objective optimization to identify Pareto-optimal trade-offs between total energy consumption and mission duration, as expressed in Equation 7:

$$\min F_{NSGA-II} = (E_{total}, T_{ms}) \tag{7}$$

The core mechanisms of NSGA-II-including non-dominated sorting, crowding distance preservation, SBX, and polynomial mutation-ensure both convergence and population diversity throughout the optimization process. Typical parameters include a population of 40 and 30 generations. From the resulting Pareto front, three representative solutions are selected:

- **Min-E:** Lowest energy consumption.
- **Min-T:** Shortest mission time.
- **Knee Point:** The solution closest to the ideal point (0, 0) in normalized energy–time space, representing the best trade-off.

This framework enables PSO to produce a single best solution while NSGA-II offers a flexible spectrum of energy–time balanced strategies adaptable to mission priorities. To limit computational cost and focus on the most realistic and challenging mission condition, NSGA-II was executed only for the OU_P150 configuration. For all other wind–payload scenarios, comparisons were restricted to the Baseline and PSO methods.

Experimental Procedure

Each wind–payload scenario was executed over five independent random seeds to ensure statistical reliability, with outcomes reported as Median (IQR). The Baseline method (nearest-neighbor assignment followed by greedy sequencing) served as the primary benchmark. For the representative OU + 150 g configuration, comprehensive visual diagnostics—including energy–time trajectories, spatial coverage maps, and PSO/NSGA-II convergence curves—were generated. Baseline and PSO solutions were projected onto the NSGA-II Pareto front to enable direct comparative assessment. All algorithmic and simulation parameters adhered to established best practices in UAV energy-optimization literature, ensuring methodological rigor and reproducibility.

Table 2. Simulation and optimization parameters

Category	Parameter	Symbol/Variable	Value	Unit	Description
Mission Area	Area width × height	area_w, area_h	300 × 300	m	Dimensions of the simulation area
	Number of targets	n_targets	20	–	Number of Points of Interest (POIs) to be visited
	Maximum simulation time	T_max	600	s	Total mission duration limit
	Time step	dt	0.5	s	Simulation update interval
UAV Properties	Number of UAVs	n_drones	8	–	Number of UAVs in the swarm
	Maximum speed	v_max	7.0	m/s	Speed limit for UAV motion
	Safe distance	safe_dist	5.0	m	Minimum separation for collision avoidance
	Target tolerance	arrival_tol	3.5	m	Distance threshold for successful target visit
Energy Model	Battery capacity	battery_Wh	40.0	Wh	Initial battery capacity
	Hover power	hover_power	95.0	W	Power consumption during hovering
	Base mass	m_base	1.25	kg	Empty UAV weight
	Payload (variant)	m_payload	0 / 150 / 300	g	Additional load depending on scenario
	Aerodynamic coefficient 1	k1	0.6	–	Drag-related power coefficient
	Aerodynamic coefficient 2	k2	1.2	–	Induced power coefficient
	Load coefficient	k_load	5.5	–	Power increase factor due to mass
Environmental Effects	Wind model	wind_type	Const / OU / Zero	–	Constant, OU, or calm conditions
	Wind vector	wind_u, wind_v	0.8, −0.4	m/s	Constant wind components (x and y)
	OU process mean	μ	0.0	–	Mean wind component
	OU process variance	σ	0.2	–	Randomness (stochasticity) parameter
Optimization (PSO)	Number of particles	n_particles	16	–	Population size
	Iterations	iters	20	–	Optimization loop count
	Inertia weight	w	0.72	–	Tendency to preserve velocity
	Cognitive coefficient	c1	1.4	–	Tendency toward personal best
	Social coefficient	c2	1.4	–	Tendency toward global best
	Weighting factor	λ	0.3	–	Balances energy–time trade-off
Optimization (NSGA-II)	Population size	pop_size	40	–	Number of individuals per generation
	Number of generations	gens	30	–	Evolutionary iteration count
	Crossover rate	crossover_rate	0.9	–	Probability of genetic information exchange
	Mutation rate	mutation_rate	0.2	–	Probability of diversity preservation

Table 2 summarizes the physical, environmental, and algorithmic parameters employed throughout the simulation and optimization pipeline. All values were implemented as fixed defaults within the Python-based framework to ensure consistency across experimental runs. These parameter selections follow widely accepted conventions in UAV energy modeling and optimization research, supporting both reproducibility and methodological transparency.

Results

This section presents the performance of the optimization algorithms (PSO and NSGA-II) under different wind and payload configurations. The analysis focuses on total energy consumption E_{total}, mission completion time T_{ms}, coverage ratio, visit rate, and dead UAV ratio, which together characterize the energy–time efficiency and reliability of the swarm. Single-run trajectories and energy–time profiles are provided for visual interpretation of representative missions, whereas the quantitative comparisons are based on five independent runs per scenario. Aggregated results are reported using Median [IQR] to capture cross-run variability.

Comparison of Baseline, PSO, and NSGA-II

The simulations were conducted to comparatively evaluate the energy–time performance of PSO and NSGA-II under three wind conditions (Zero, Constant, OU) and three payload levels (0 g, 150 g, 300 g). Each wind–payload configuration was repeated over five random seeds, and the results were summarized in Median [IQR] format. The evaluation metrics include total energy consumption (Wh), mission completion time (s), coverage ratio (%), visit rate (%), and dead UAV ratio (%). Table 3 reports the statistical outcomes across all scenarios. NSGA-II results are provided only for the OU_P150 configuration, as the multi-objective optimization was applied exclusively to this representative and operationally realistic case.

Across all scenarios, the Baseline method (nearest-neighbor assignment + greedy sequencing) serves as a reference. PSO consistently reduces median energy consumption relative to Baseline but at the cost of longer mission times, due to more explexploration aggressive maneuvers. For example, in the OU_P150 configuration:

Table 3. Median (IQR) performance results across wind and payload conditions (five seeds per scenario). NSGA-II was applied only to the OU + 150 g scenario.

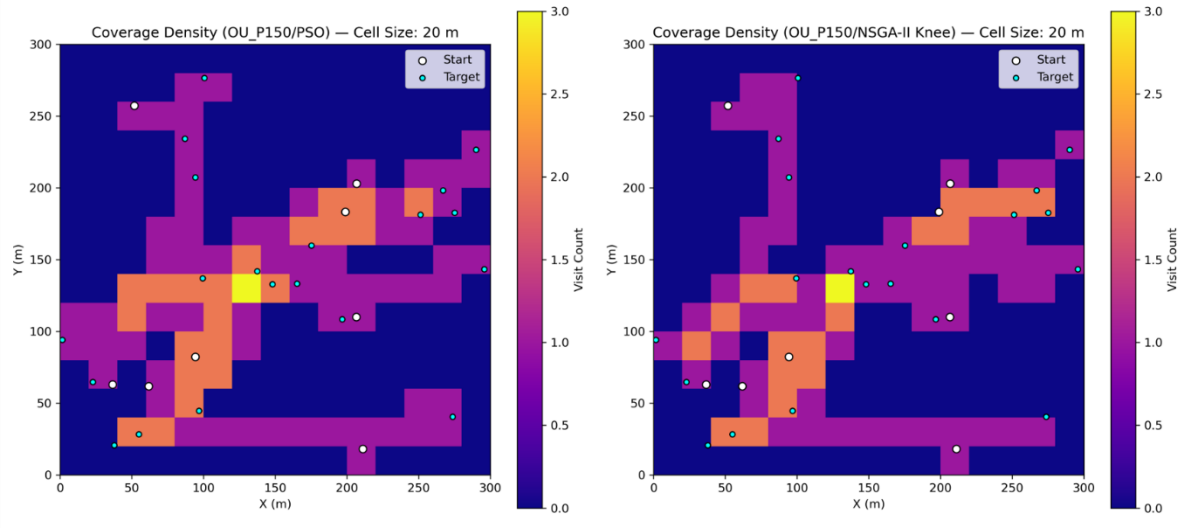
Scenario	Wind	Payload (g)	Method	E_total (Wh)	T_ms (s)	Coverage (%)	Visit (%)	Dead UAV (%)
Zero-P0	Zero	0	Baseline	39.34 [3.26]	86.0 [5.5]	38.67 [4.89]	100.0 [0.0]	0.0 [0.0]
			PSO	31.75 [12.73]	111.5 [32.0]	43.11 [7.56]	100.0 [0.0]	0.0 [0.0]
Zero-P150	Zero	150	Baseline	39.50 [3.26]	86.0 [5.5]	38.67 [4.89]	100.0 [0.0]	0.0 [0.0]
			PSO	31.95 [12.79]	111.5 [32.0]	43.11 [7.56]	100.0 [0.0]	0.0 [0.0]
Zero-P300	Zero	300	Baseline	39.65 [3.27]	86.0 [5.5]	38.67 [4.89]	100.0 [0.0]	0.0 [0.0]
			PSO	32.85 [12.04]	114.5 [32.0]	43.11 [8.45]	100.0 [0.0]	0.0 [0.0]
Const-P0	Constant	0	Baseline	31.38 [2.88]	86.5 [6.5]	38.22 [3.55]	100.0 [0.0]	0.0 [0.0]
			PSO	28.98 [10.11]	106.0 [30.0]	43.56 [6.66]	100.0 [0.0]	0.0 [0.0]
Const-P150	Constant	150	Baseline	31.54 [2.89]	86.5 [6.5]	38.22 [3.55]	100.0 [0.0]	0.0 [0.0]
			PSO	29.18 [10.17]	106.0 [30.0]	43.56 [6.66]	100.0 [0.0]	0.0 [0.0]
Const-P300	Constant	300	Baseline	31.69 [2.89]	86.5 [6.5]	38.22 [3.55]	100.0 [0.0]	0.0 [0.0]
			PSO	29.37 [10.22]	106.0 [30.0]	43.56 [6.66]	100.0 [0.0]	0.0 [0.0]
OU-P0	OU	0	Baseline	30.82 [2.41]	86.5 [5.0]	38.67 [4.44]	100.0 [0.0]	0.0 [0.0]
			PSO	28.79 [9.98]	106.0 [34.0]	43.56 [6.66]	100.0 [0.0]	0.0 [0.0]
OU-P150	OU	150	Baseline	30.98 [2.42]	86.5 [5.0]	38.67 [4.44]	100.0 [0.0]	0.0 [0.0]
			PSO	28.98 [10.05]	106.0 [34.0]	43.56 [6.66]	100.0 [0.0]	0.0 [0.0]
			NSGA-II (Min E)	26.82 [0.00]	93.0 [0.0]	34.67 [0.0]	100.0 [0.0]	0.0 [0.0]
			NSGA-II (Min T)	26.82 [0.00]	93.0 [0.0]	34.67 [0.0]	100.0 [0.0]	0.0 [0.0]
			NSGA-II (Knee)	26.82 [0.00]	93.0 [0.0]	34.67 [0.0]	100.0 [0.0]	0.0 [0.0]
OU-P300	OU	300	Baseline	31.14 [2.43]	86.5 [5.0]	38.67 [4.44]	100.0 [0.0]	0.0 [0.0]
			PSO	29.18 [10.11]	106.0 [34.0]	43.56 [6.66]	100.0 [0.0]	0.0 [0.0]

- Baseline: E_{total} =30.98 [2.42] Wh, T_{ms} =86.5 [5.0] s
- PSO: E_{total} =28.98 [10.05] Wh, T_{ms} =106.0 [34.0] s
- NSGA-II (Knee): E_{total}=26.82 [0.00] Wh, T_{ms} =93.0 [0.0] s

Compared to the Baseline, the NSGA-II Knee solution achieves approximately 13% lower total energy consumption with only about a 7% increase in mission time. This indicates that the Knee point provides an effective balance between energy efficiency and mission duration, representing a practically attractive trade-off.

Across all methods and scenarios, the visit rate remains at 100%, and no UAV failures are observed (Dead UAV Ratio = 0%), confirming that all compared solutions maintain full mission success and safety. While PSO occasionally yields lower median energy values than the Baseline, its relatively large IQR reflects higher variability and less consistent performance across runs. In contrast, NSGA-II provides more stable and balanced energy–time trade-offs in the OU + 150 g scenario, illustrating the advantages of a multi-objective evolutionary approach.

Overall, the OU + 150 g configuration emerges as the most informative and realistic test case: it combines environmental variability (stochastic wind) with payload-induced mass changes while preserving mission stability. Within this setting, the NSGA-II Knee solution stands out as the most efficient and reliable configuration.

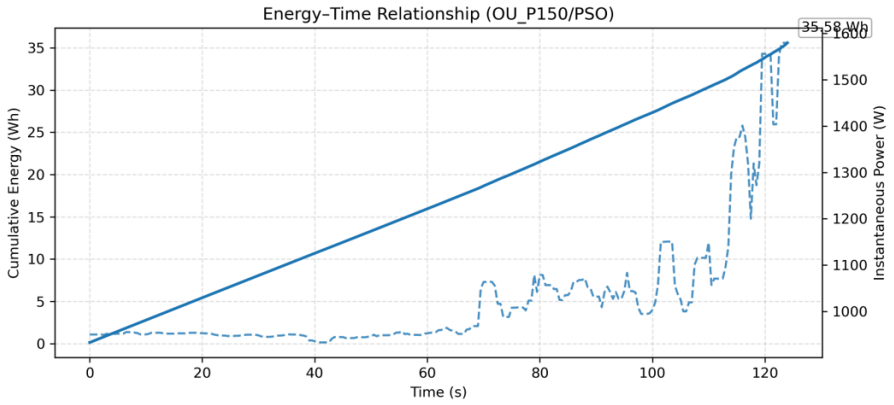


a) PSO-based solution b) NSGA-II Knee solution

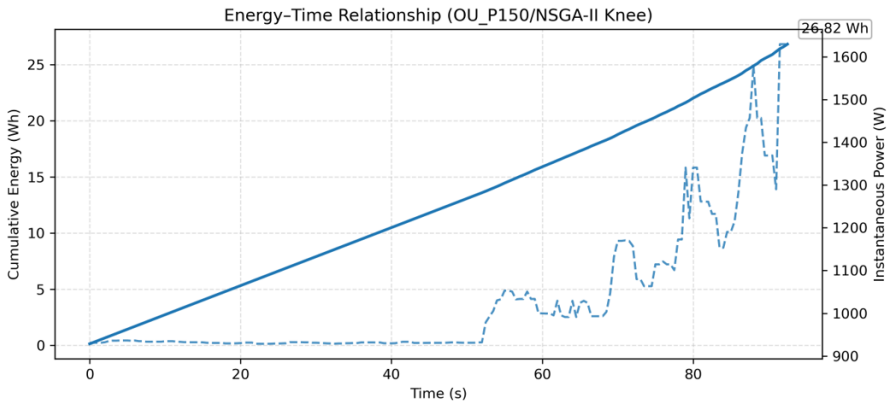
Figure 1. Coverage density maps for the OU_P150 scenario

Figure 1a presents the coverage density obtained in the OU_P150/PSO scenario using a spatial resolution of 20 m per grid cell. Warmer color tones represent regions with higher visitation frequency, indicating areas where UAV trajectories overlapped more frequently. The coverage pattern shows that the swarm tends to cluster near the mission center, while peripheral regions receive fewer visits. The discontinuities observed between the starting (○) and target (●) points reflect the perturbations induced by the OU stochastic wind model, demonstrating how environmental turbulence affects trajectory deviation and spatial distribution.

Figure 1b illustrates the coverage density produced by the OU_P150/NSGA-II Knee solution under identical environmental and mission conditions. Compared to PSO, the coverage pattern is more uniformly distributed, showing reduced redundant overlaps and more balanced spatial exploration. Despite lower path redundancy, all Points of Interest (POIs) remain fully visited, indicating that NSGA-II's multi-objective optimization strategy successfully balances energy efficiency and spatial coverage under stochastic wind dynamics.



a) Energy–time profile for PSO solution



b) Energy–time profile for NSGA-II Knee solution

Figure 2. Comparison of instantaneous power and cumulative energy consumption for PSO and NSGA-II Knee solutions in the OU_P150 scenario (single representative runs).

Figure 2a and Figure 2b show the instantaneous power (W) and cumulative energy (Wh) profiles for representative PSO and NSGA-II Knee solutions in the OU_P150 scenario. In both cases, power demand remains relatively stable with low variance during the initial phase of the mission, indicating steady cruise behavior with limited wind-compensation effort.

In Figure 2a (PSO), a pronounced increase in power consumption appears after approximately 100 s. This rise is primarily associated with the more aggressive maneuvering behavior of the PSO-generated trajectory, which requires stronger control inputs to counteract OU wind perturbations. In this representative run, the PSO solution reaches a total energy consumption of approximately 35.6 Wh and completes the mission in about 125 s, making it comparatively more expensive in both energy and time.

In contrast, Figure 2b (NSGA-II Knee) exhibits a more stable power profile with fewer and smaller peaks. The smoother trajectory geometry produced by multi-objective optimization reduces unnecessary accelerations and sharp turns, lowering total energy consumption to 26.82 Wh and shortening the mission duration to 93 s in the

illustrated run. This behavior is consistent with the aggregated statistics in Table 3, where the NSGA-II Knee solution demonstrates substantially improved energy efficiency and a shorter median mission time relative to PSO. Taken together, the two plots highlight that PSO tends to induce higher energy fluctuations due to aggressive corrective maneuvers, whereas the NSGA-II Knee solution produces a more balanced and energy-efficient flight profile under stochastic wind dynamics.

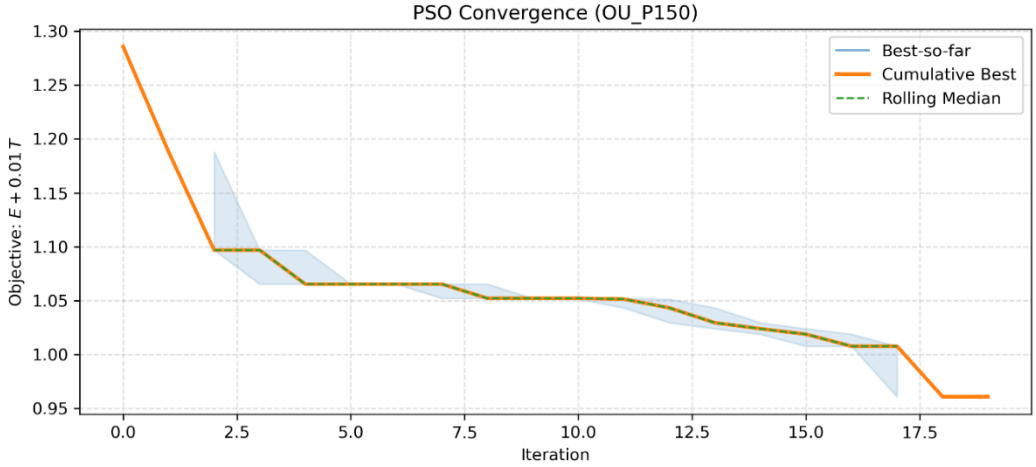


Figure 3. PSO convergence curve for the OU_P150 scenario.

Figure 3 illustrates the convergence behavior of the PSO algorithm with respect to the single-objective function $E_n+0.3T_n$. A sharp improvement is observed within the first few iterations, where the objective value drops from approximately 1.28 to around 1.10. After roughly the 8th–10th iteration, the curve begins to stabilize, indicating that the swarm is converging toward a local optimum. By the final iteration, the objective value decreases to about 0.96, corresponding to an overall improvement of roughly 25% relative to the initial state. This pattern confirms that PSO performs rapid early-stage exploitation followed by a controlled convergence phase with limited oscillations, which is typical of well-tuned PSO configurations.

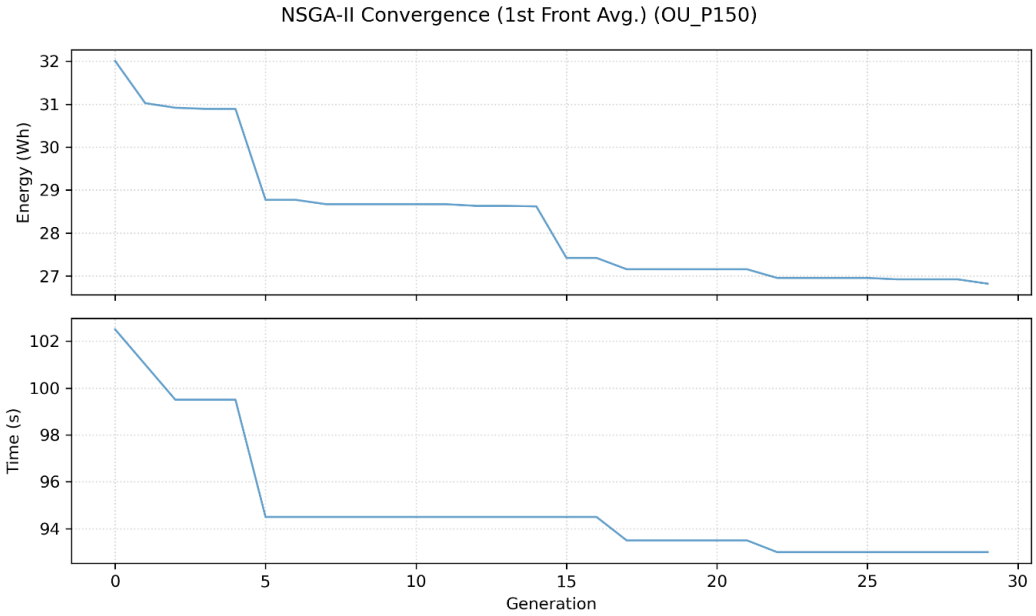


Figure 4. NSGA-II convergence curves showing average first-front energy and mission time across generations.

Figure 4 presents the generational evolution of the first Pareto front, tracking the average total energy and mission time of non-dominated solutions across successive generations. Both metrics exhibit rapid improvement during the initial generations, followed by stabilization after approximately the 15th generation, converging near 27 Wh for energy and 94 s for mission time. This convergence pattern shows that NSGA-II effectively approaches a stable Pareto-optimal region in the energy–time objective space. The smooth trajectories of the curves indicate

robust convergence behavior and a well-balanced exploration–exploitation trade-off, avoiding both stagnation and excessive randomness.

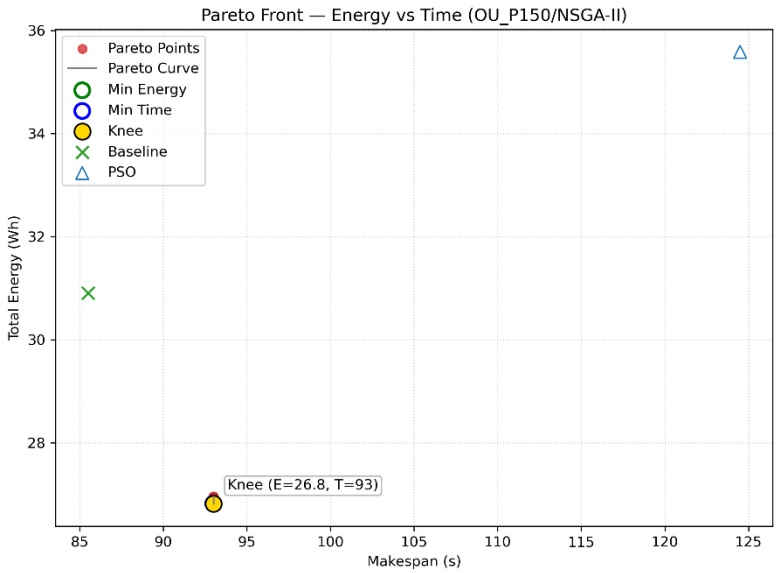


Figure 5. NSGA-II Pareto-optimal solutions in the Energy–Time objective space for the OU_P150 scenario

Figure 5 presents the Pareto front obtained by NSGA-II in the energy–time objective space. Each point represents a non-dominated solution reflecting a different trade-off between total energy consumption and mission duration. The highlighted Knee point (E=26.8 Wh,T=93 s) corresponds to the solution closest to the ideal point after min–max normalization, representing the most balanced compromise between the two objectives.

Compared with the Baseline (×) and PSO (△) reference points, the Knee solution dominates both methods by achieving lower energy consumption and shorter mission time. In the representative OU_P150/PSO run shown in the figure, PSO requires approximately 35.6 Wh and 125 s to complete the mission, whereas the NSGA-II Knee solution completes the same task with significantly reduced energy and time. This analysis confirms that the Knee point provides a practical and well-balanced operating condition for UAV swarm mission planning under OU wind perturbations.

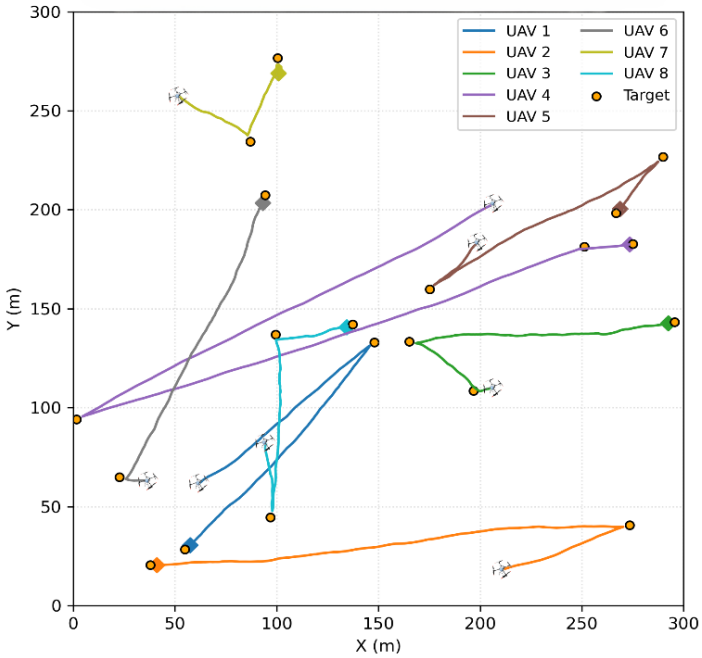


Figure 6. UAV swarm trajectories in the OU_P150 scenario.

Figure 6 shows the flight trajectories of the eight UAVs in the OU_P150 scenario, where each colored line represents the time-evolving path of an individual vehicle. The trajectories clearly reflect the influence of OU stochastic wind, producing small deviations and local fluctuations around nominal routes. Despite these perturbations, the swarm maintains safe spatial separation, preventing inter-UAV collisions while ensuring that all target points (●) are visited as assigned. The spatial organization of the paths indicates that the underlying coordination strategy distributes tasks effectively among UAVs, avoiding excessive path overlap and preserving coverage quality across the mission area.

Cross-Scenario Observations

Across all wind and payload configurations, the Baseline method consistently yields the shortest mission times but with relatively higher energy usage and less structured coverage. PSO reduces energy consumption compared to the Baseline in most scenarios but increases mission duration due to its more exploratory, single-objective search behavior.

Under Constant and OU wind conditions, total energy consumption increases with payload mass, as additional lift is required to counteract both gravitational and wind-induced forces. Among all evaluated conditions, the OU + 150 g configuration provides the most representative operational setting by combining realistic wind disturbances with moderate payload, while still maintaining mission stability.

In the OU_P150 scenario, the NSGA-II Knee solution not only reduces energy consumption by approximately 7% relative to the PSO median (28.98 Wh → 26.82 Wh), but also shortens the median mission time from 106 s to 93 s (≈12% reduction). This leads to a higher overall task efficiency while preserving full mission success and safety. These results demonstrate that swarm intelligence–based optimization, particularly when formulated as a multi-objective problem, can substantially improve the energy–time balance in UAV swarm mission planning.

Conclusion

This study evaluated swarm intelligence–based optimization methods for improving the energy–time performance of UAV swarms operating under varying wind and payload conditions. Leveraging a Python-based simulation environment with a physics-informed energy model, two optimization paradigms—single-objective PSO and multi-objective NSGA-II—were systematically compared against a greedy baseline.

The results demonstrated that both algorithms significantly improved energy efficiency relative to the baseline strategy. Among all test conditions, the OU + 150 g scenario emerged as the most realistic operational case, reflecting the combined effects of stochastic wind fluctuations and moderate payload loading. In this configuration, the NSGA-II Knee solution achieved approximately 13% lower total energy consumption than the baseline while incurring only a 7% increase in mission duration. This confirms the practical utility of Pareto-based optimization in providing flexible and operationally meaningful trade-offs between energy efficiency and task duration.

While PSO exhibited rapid convergence and occasionally produced competitive energy values, its single-objective formulation led to higher variability across repeated runs and a greater tendency toward premature convergence. Conversely, NSGA-II maintained population diversity and generated more stable, balanced solutions-particularly under turbulent wind dynamics—highlighting its suitability for multi-objective UAV mission planning.

Overall, the findings indicate that:

- multi-objective optimization considerably enhances the energy–time balance in UAV swarm missions;
- knee-point selection offers a practical compromise, supporting mission planners in choosing balanced operating points; and
- stochastic wind modeling is essential for realistically assessing UAV behavior under environmental disturbances.

This study is limited by its use of a 2D kinematic flight model, a fixed swarm size, and the application of NSGA-II only to the representative OU + 150 g scenario due to computational considerations. Future research will address these limitations by:

- Extending the simulation to full 3D flight dynamics, incorporating altitude control and vertical wind components;
- Modeling intra-swarm energy-sharing and cooperative power management;
- Exploring hybrid evolutionary–reinforcement learning frameworks for adaptive multi-agent coordination;
- Incorporating advanced multi-objective optimizers such as NSGA-III, MOEA/D, or SPEA2 for higher-dimensional trade spaces; and
- Developing real-time adaptive optimization pipelines using live flight telemetry for deployment in real-world UAV operations.

Scientific Ethics Declaration

* The author declares that the scientific ethical and legal responsibility of this article published in EPSTEM journal belongs to the author.

Conflict of Interest

* The author declares that he has no conflicts of interest

Funding

* Not applicable

Acknowledgements or Notes

* This article was presented as a poster presentation at the International Conference on Technology, Engineering and Science (www.icontes.net) held in Antalya/Türkiye on November 12-15, 2025.

References

Abeywickrama, H. V., Jayawickrama, B. A., He, Y., & Dutkiewicz, E. (2018). Comprehensive energy consumption model for unmanned aerial vehicles, based on empirical studies of battery performance. *IEEE Access, 6*, 58383-58394.

Alqudsi, Y., & Makaraci, M. (2025). UAV swarms: Research, challenges, and future directions. *Journal of Engineering and Applied Science, 72*, 12.

Arranz, R., Carramiñana, D., de Miguel, G., Besada, J. A., & Bernardos, A. M. (2023). Application of deep reinforcement learning to UAV swarming for ground surveillance. *Sensors, 23*(21), 8766.

Baidya, B., Mondal, A., Mallick, S., & Anamalamudi, S. (2024). Energy-efficient UAV path planning using PSO-ABC algorithm in obstacle-rich environments. *2024 OITS International Conference on Information Technology (OCIT)*, 199–204.

Beni, G. (1988). The concept of cellular robotic system. *Proceedings 1988 IEEE International Symposium on Intelligent Control*, 57–62.

Beni, G., & Wang, J. (1993). Swarm intelligence in cellular robotic systems. In P. Dario, G. Sandini, & P. Aebischer (Eds.), *Robots and biological systems: Towards a new bionics?* (pp. 703–712). Springer.

Cabuk, U. C., Tosun, M., Dagdeviren, O., & Ozturk, Y. (2024). Modeling energy consumption of small drones for swarm missions. *IEEE Transactions on Intelligent Transportation Systems, 25*(8), 10176-10189.

Chen, Y., Chen, R., Huang, Y., Xiong, Z., & Li, J. (2024). Distributed task allocation for multiple UAVs based on swarm benefit optimization. *Drones, 8*(12), 766.

Cosar, M. (2023a). Artificial intelligence technologies and applications used in unmanned aerial vehicle systems. *The Eurasia Proceedings of Science, Technology, Engineering & Mathematics, 26*, 1-12.

Cosar, M. (2023b). Path planning via swarm intelligence algorithms in unmanned aerial vehicle population. *The Eurasia Proceedings of Science, Technology, Engineering & Mathematics, 26*, 439-450.

Di Franco, C., & Buttazzo, G. (2016). Coverage path planning for UAVs photogrammetry with energy and resolution constraints. *Journal of Intelligent & Robotic Systems, 83*(3-4), 445–462.

Duan, P., Yu, Z., Gao, K., Meng, L., Han, Y., & Ye, F. (2024). Solving the multi-objective path planning problem for mobile robot using an improved NSGA-II algorithm. *Swarm and Evolutionary Computation, 87*, 101576.

Galati, G., Primatesta, S., & Rizzo, A. (2023). Auction-based task allocation and motion planning for multi-robot systems with human supervision. *Journal of Intelligent & Robotic Systems, 109*, 24.

Gamil, A., Sheltami, T., Mahmoud, A., & Yasar, A. (2023). Energy-efficient UAVs coverage path planning approach. *Computer Modeling in Engineering & Sciences, 136*(3), 3239-3263.

Gong, H., Huang, B., Jia, B., & Dai, H. (2022). Modelling power consumptions for multi-rotor UAVs. *arXiv*.

Guo, S., Alkouz, B., Shahzaad, B., Lakhdari, A., & Bouguettaya, A. (2023). Drone formation for efficient swarm energy consumption. *arXiv*.

Güven, İ., & Yanmaz, E. (2024). Multi-objective path planning for multi-UAV connectivity and area coverage. *Ad Hoc Networks, 160*, 103520.

Hohmann, N., Bujny, M., Adamy, J., & Olhofer, M. (2021). Hybrid evolutionary approach to multi-objective path planning for UAVs. *2021 IEEE Symposium Series on Computational Intelligence (SSCI)*, 1-8.

Jacewicz, M., Żugaj, M., Głębocki, R., & Bibik, P. (2022). Quadrotor model for energy consumption analysis. *Energies, 15*(19), 7136.

Jiang, H., Lin, S., Chen, J., & Miao, X. (2025). Fusion of cluster analysis and differential particle swarm optimisation for multi-UAV task assignment on power transmission line. *Engineering Computations, 42*(4), 1447–1470.

Lei, Y., & Cheng, M. (2020). Aerodynamic performance of a hex-rotor unmanned aerial vehicle with different rotor spacing. *Measurement and Control, 53*(3-4), 711-718.

Lin, L., Wang, Z., Tian, L., Wu, J., & Wu, W. (2024). A PSO-based energy-efficient data collection optimization algorithm for UAV mission planning. *PLOS ONE, 19*(1), e0297066.

Lones, M. A. (2014). Metaheuristics in nature-inspired algorithms. *Proceedings of the 2014 Annual Conference on Genetic and Evolutionary Computation Companion*, 1419–1422.

Michel, N., Borer, N., Hu, Q., & Kroo, I. (2022). Modeling and validation of electric multirotor unmanned aerial vehicle system energy dynamics. *eTransportation, 12*, 100173.

Morbidi, F., Mariottini, G. L., & Prattichizzo, D. (2016). Minimum-energy path generation for a quadrotor UAV. *IEEE Transactions on Robotics, 32*(3), 785-796.

Na, Y., Li, Y., Chen, D., Yao, Y., Li, T., Liu, H., & Wang, K. (2023). Optimal energy consumption path planning for unmanned aerial vehicles based on improved particle swarm optimization. *Sustainability, 15*(16), 12101.

Opazo, T. I., Raja Zahirudin, R. A., Palacios, J., Schmitz, S., & Langelaan, J. W. (2023). Analytical and experimental power minimization for fixed-pitch coaxial rotors in hover. *Journal of Aircraft, 60*(2), 546–559.

Rosas-Carrillo, A. S., Solís-Santomé, A., Silva-Sánchez, C., & Camacho-Nieto, O. (2025). UAV path planning using an adaptive strategy for the particle swarm optimization algorithm. *Drones, 9*(3), 170.

Tang, G., Xiao, T., Du, P., Zhang, P., Liu, K., & Tan, L. (2024). Improved PSO-based two-phase logistics UAV path planning under dynamic demand and wind conditions. *Drones, 8*(8), 356.

Wang, G., Wang, F., Wang, J., Li, M., Gai, L., & Xu, D. (2024). Collaborative target assignment problem for large-scale UAV swarm based on two-stage greedy auction algorithm. *Aerospace Science and Technology, 149*, 109146.

Xue, T., Zhang, L., Cao, Y., Zhao, Y., Ai, J., & Dong, Y. (2024). Valley path planning on 3D terrains using NSGA-II algorithm. *Aerospace, 11*(11), 923.

Zhang, Z. (2024). Multi-objective optimization method for building energy-efficient design based on multi-agent-assisted NSGA-II. *Energy Informatics, 7*, 90.

Author(s) Information

Mustafa Cosar
Department of Computer Engineering, Hitit University
19030, Corum/Türkiye
Contact e-mail: *mustafacosar@gmail.com*

To cite this article:

Cosar, M. (2025). Swarm intelligence-based energy optimization for UAV mission efficiency. *The Eurasia Proceedings of Science, Technology, Engineering and Mathematics (EPSTEM), 38,* 244-256.

The Eurasia Proceedings of Science, Technology, Engineering & Mathematics (EPSTEM)
ISSN: 2602-3199

The Eurasia Proceedings of Science, Technology, Engineering and Mathematics (EPSTEM), 2025

Volume 38, Pages 257-263

IConTES 2025: International Conference on Technology, Engineering and Science

Study and Design of a Plasma Reactor Using a Porous Dielectric Barrier

Fatha Tounsi
Mustapha Stambouli University of Mascara

Rabah Ouiddir
Djillali Liabes University of Sidi Bel-Abbes

Houcine Miloudi
Djillali Liabes University of Sidi Bel-Abbes

Mohamed Miloudi
Djillali Liabes University of Sidi Bel-Abbes

Abdelber Bendaoud
Djillali Liabes University of Sidi Bel-Abbes

Abstract: To continuously improve actuator performance, it is necessary to study the discharge to better understand its operation. Therefore, this work focuses primarily on the ion wind and its stability. In other words, the goal is to obtain the maximum possible ion wind without generating arcs. To increase the ion wind speed, it is necessary to increase the discharge current (recall that the ion wind speed is proportional to the square root of the discharge current i) (5), thus increasing the potential without reaching the breakdown voltage in air. It is therefore important to observe the behavior of the ion wind for several discharge configurations and to find the optimal configuration suitable for flow control. The main parameters essential to study are: the electrode diameter, the inter-electrode distance, and the nature of the dielectric on which the discharge occurs.

Keywords: Ionic wind, Ionic wind velocity, Discharge current, Flow rate control

Introduction

Dielectric Barrier Discharge (DBD) is a type of plasma that is not in thermodynamic equilibrium. It was discovered by Siemens in 1857 for ozone generation (Dubus et al., 2009). It is characterized by the coating of one or two flat or cylindrical electrodes with a layer of dielectric material. This material allows for the accumulation of charges on its surface, which limits the electric field between the two electrodes, thus preventing the formation of an electric arc. The use of a high-voltage (HV) alternating current supply is therefore necessary in this case to compensate for these charges created on the surface with each alternation, in order to prevent the plasma from being extinguished (Dubus et al., 2009), (Nozaki et al., 2001). Today, Dielectric Barrier Discharges (DBDs) are of great interest due to a very wide range of applications: ozone generation, removal of Volatile Organic Compounds, treatment of gaseous effluents, flow control, activation and surface treatment, CO_2 laser, excimer lamp, plasma screens… This process is also found in many industrial fields: electronics, textiles, packaging, automotive (Allegraud et al., 2008; Alban et al., 2001). However, all these applications face robustness issues due to the fragility of the dielectric barriers used, as well as the thermal effect accompanying the electrical discharge, which necessitates the use of a cooling system. Therefore, the overall operating and maintenance cost of a continuously operating installation can increase significantly.

- This is an Open Access article distributed under the terms of the Creative Commons Attribution-Noncommercial 4.0 Unported License, permitting all non-commercial use, distribution, and reproduction in any medium, provided the original work is properly cited.

- Selection and peer-review under responsibility of the Organizing Committee of the Conference

© 2025 Published by ISRES Publishing: www.isres.org

The research on Dielectric Barrier Discharges (DBDs) has still much to say about electromagnetic phenomena that occur in high-voltage and high-frequency areas (Mohammed et al., 2024; Bermaki et al., 2023; Hakmi et al., 2024; Mohamed Miloudi et al., 2019; Yacine et al., 2024), such as those in converter-fed electric drives. One of the results of the fast voltage transients generated by Pulse Width Modulation (PWM) converters is the partial discharge and the generation of strong electric fields in the motor insulation systems which in turn cause electromagnetic interference and insulation degradation (Miloudi et al., 2022; Lahlaci et al., 2024; Houcine et al., 2023; Naima et al., 2025). Analyzing DBD behavior makes the insulation design more efficient, it allows the conducted and radiated emissions to be controlled better, and it also facilitates the electrical machines and converter systems in having good electromagnetic compatibility (EMC).

The work presented in this article has one main objective: to improve the electrothermal performance of a DBD reactor. Indeed, one of the primary objectives of a plasma reactor is to provide the necessary quantity of charge or molecules for any given application, with minimal energy consumption and without degrading the DBD discharge. Low-temperature plasma jets are unique plasma sources capable of delivering plasma outside the confinement of electrodes and away from enclosures/gas chambers. With these jets, plasma can be easily delivered to a target located at a distance from the generation area (Henri et al., 2008; Eid et al., 2015).

Various power generation methods have been used to ignite and sustain low-temperature plasma jets. These include direct current (DC), pulsed direct current, radio frequency (RF), and microwaves. In particular, atmospheric-pressure low-temperature plasma jets are playing an increasing role in many plasma processing applications, including surface treatment and biomedicine (Eid et al., 2015).

The plasma actuator consists of applying a potential difference between at least two electrodes placed on the surface of an obstacle. Under the effect of the electric field (by extension of Coulomb forces), a flow resulting from a transfer of momentum between the charged species and the neutrals of the surrounding gas appears above the obstacle: the electric wind (Jolibois et al., 2009).

Geometric Configuration of the Plasma Actuator

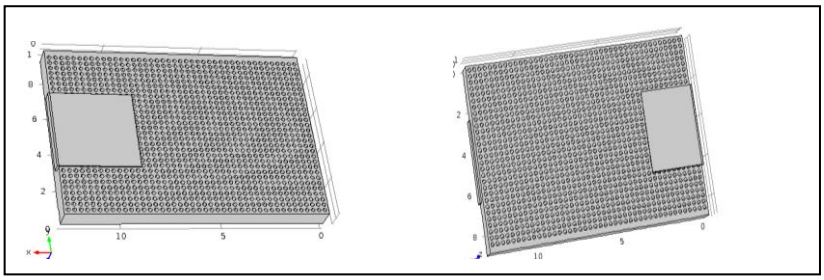


Figure 1. Geometric configuration of the plasma actuator to be implemented

Figure 1 represents a schematic representation of the two reactor faces. Dielectric barrier: Among the various dielectric materials used in reactors, we chose ceramic because it stabilizes the discharge across its entire surface, minimizing the risk of electric arcing, and it also offers better resistance to high temperatures. This dielectric is porous (Figure 2). The pore diameter is 1 mm, uniformly distributed over a surface area of (130×90) mm². The thickness of the dielectric is 10 mm.

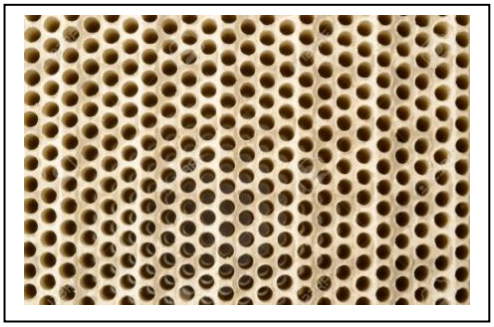


Figure 2. Photograph of the porous dielectric used.

The electrodes: are rectangular pieces of adhesive aluminum tape in an asymmetrical position. They are glued on either side of the dielectric barrier.

High-voltage DC power supply: The plasma is obtained by applying a high-voltage DC current of negative polarity to one of the electrodes; the other electrode is grounded. The voltage is supplied by a Spelleman brand high-voltage generator (SL60, Umax = 40kV, Imax = 7.5mA).

Experimental Study of Flow Control

This part of this work consists of studying the feasibility of controlling a flow by applying either a direct or alternating voltage. We optimized our actuator to achieve the most efficient control possible. This flow control was carried out using incense smoke as the gas to be controlled. The composition of smoke produced by burning incense is highly diverse. It contains numerous pollutants that can be classified into two categories: gaseous pollutants and aerosols. Gaseous pollutants include carbon monoxide (CO), nitrogen oxides (NOx), acid sulfides (SOx), and volatile organic compounds (VOCs). Aerosols, on the other hand, consist of solid and liquid particles containing toxic metals. An example of the particle size distribution of these incense particles is illustrated in Figure 3. It shows that the particle size distribution has a peak around 0.3 µm where the number of particles is greatest.

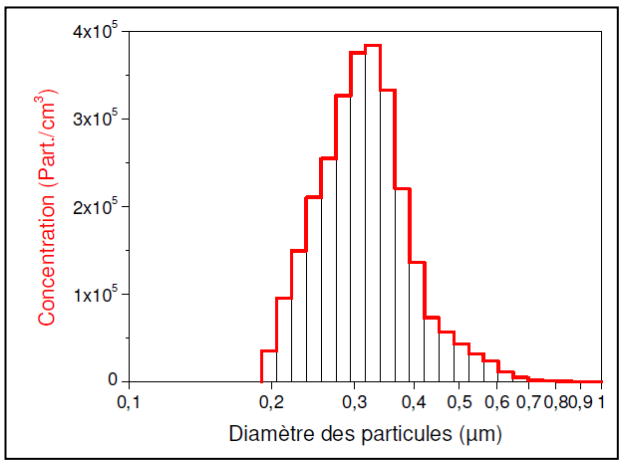


Figure 3. Example of a particle size distribution

Experimental Setup and Equipment

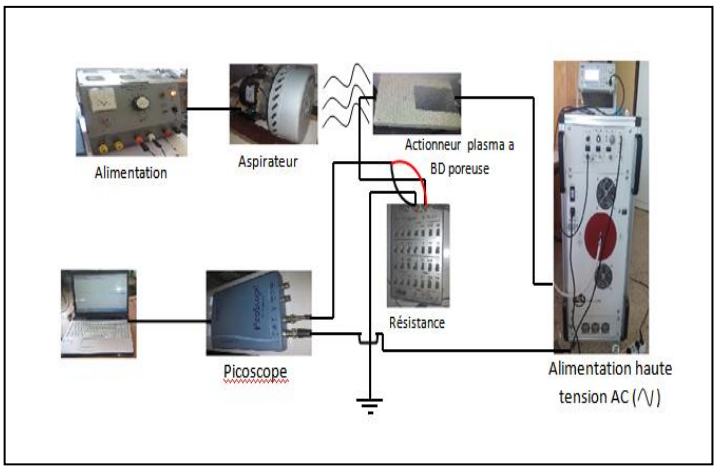


Figure 4. Experimental setup for flow control under alternating voltage.

The experimental setup created for flow control in alternating mode is illustrated in Figure 4. A voltage amplifier (Trek 30/20A) was used to power our actuator. The supply voltage in this study is fixed at 18 kV, while the frequency is variable. To improve control efficiency, the inter-electrode distance was reduced to 1 cm.

Frequency-Dependent Flow Control

The flow control tests, performed at a fixed suction flow rate of 120 m³/h, showed that the signal frequency is a highly influential factor on control efficiency. This efficiency was evaluated based on the angle of smoke deflection relative to the initial position, i.e., before the voltage was applied.

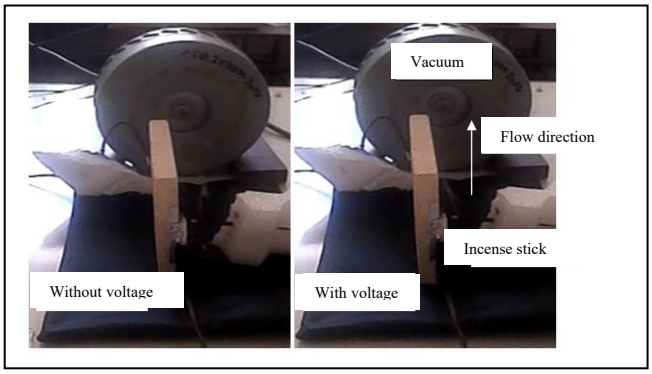


Figure 5. Observation of the smoke deflection angle for a frequency of 50Hz

After processing images of video sequences taken from the same position relative to the horizontal plane of our actuator, we were able to evaluate the angle of smoke deviation as a function of frequency. Using the trigonometric rule, the angle of smoke deflection can be easily calculated. Table 1 shows the numerical values of the angle of deflection as a function of frequency.

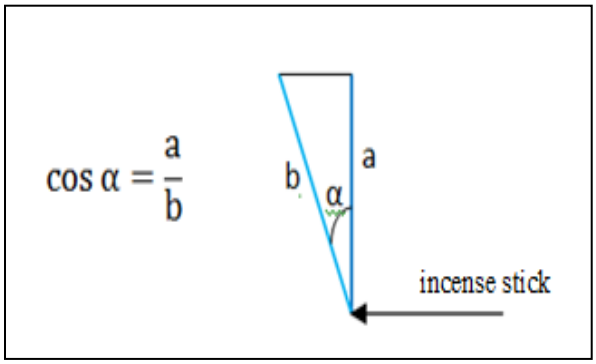


Figure 6. Determination of the smoke deflection angle.

Table 1. Variation of the smoke deflection angle as a function of frequency

Frequencies [Hz]	50	500	1000
Angles of deviation [°]	20.65	49.40	51.94

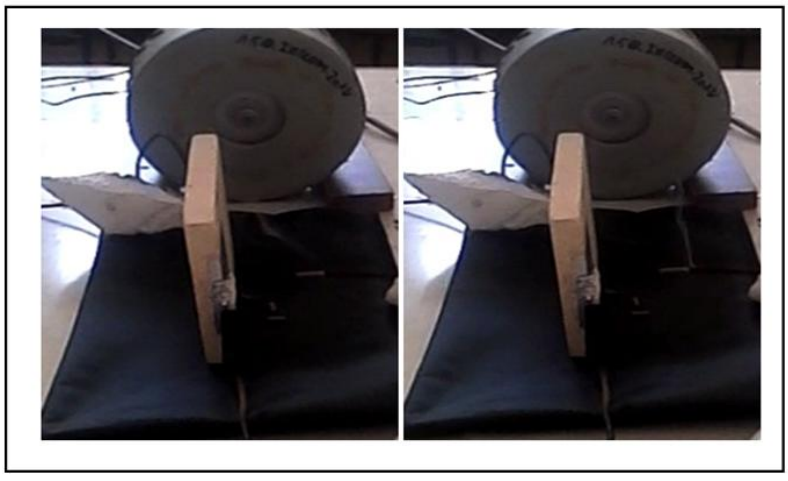


Figure 7. Observation of the smoke deflection angle for a frequency of 500Hz.

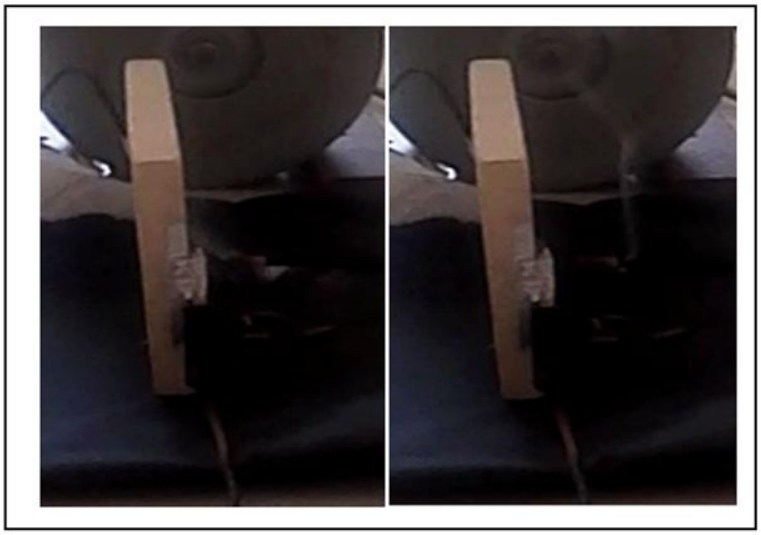


Figure 8. Observation of the smoke deflection angle for a frequency of 1kHz.

We can therefore conclude that increasing the frequency allows for better control of the flow with a considerable reduction in turbulence.

Continuous Voltage Flow Control

Now, we will apply a direct current voltage of negative polarity for the same inter-electrode distance (d=1cm) and the same voltage (U = 18 kV). The angle of deviation this time is equal to 30°.

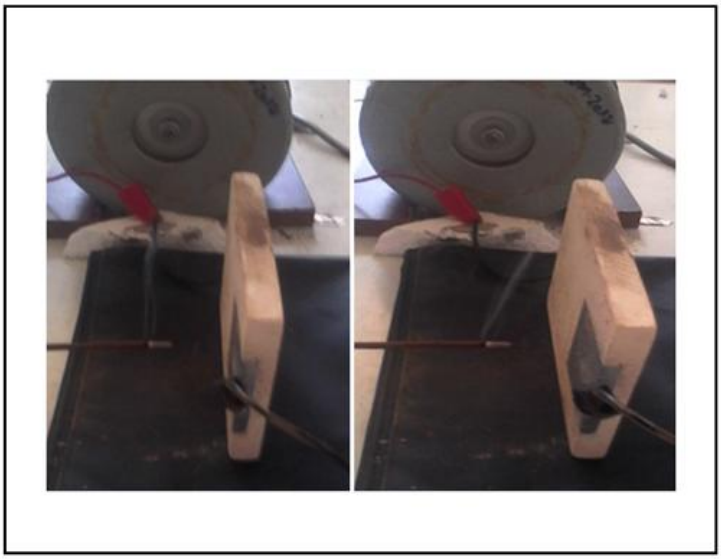


Figure 9. Observation of the angle of deflection of the smoke under negative direct voltage (U=18kV, d=1cm)

Conclusion

The dielectric barrier discharge (DBD) used here consists of an electrical discharge established in air at atmospheric pressure on the surface of an insulator. This discharge ionizes the surrounding air, and the generated charged species, subjected to the Coulomb force, induce a flow called electric wind through momentum transfer. Recently, the ability of this type of device to control flow around airfoils has been explored. The DBD used in this way is called a plasma actuator. These actuators can modify boundary layer flows near the wall via electric wind. The objective of this work is to contribute through an experimental mechanical study to calculate the angle of deviation of the ionic and electro-thermal wind, of a plasma actuator with a porous dielectric barrier.

Scientific Ethics Declaration

* The authors declares that the scientific ethical and legal responsibility of this article published in EPSTEM journal belongs to the authors.

Conflict of Interest

* The authors declare that they have no conflicts of interest

Funding

* This research received no specific grant from any funding agency in the public, commercial, or not-for-profit sectors.

Acknowledgements or Notes

* This article was presented as a poster presentation at the International Conference on Technology, Engineering and Science (www.icontes.net) held in Antalya/Türkiye on November 12-15, 2025

References

Allegraud, K. (2008). *Décharge à barrière diélectrique de surface* (Doctoral dissertation). Ecole Polytechnique.

Bermaki, M. H., Miloudi, H., Miloudi, M., Gourbi, A., & Bendaoud, A. (2023). High-frequency differential mode modeling of universal motor's windings. *International Journal of Electrical and Electronics Research, 11*(4).

Bermaki, M. H., Miloudi, H., Miloudi, M., Gourbi, A., & Bendaoud, A. (2024). Transfer function method for EMC high-frequency modeling of electrical machines. *The Eurasia Proceedings of Science, Technology, Engineering & Mathematics, 32*, 131-136.

Decauchy, H. (2022). *Physique des jets de plasma froid-Étude fondamentale des streamers guidés et applications à l'oncologie* (Doctoral dissertation). Sorbonne Université.

Dubus, N. (2009). *Contribution à l'étude thermique d'un réacteur à décharge à barrière diélectrique* (Doctoral dissertation). Ecole Supérieure d'Ingénieurs de Poitiers.

Eid, A., Takashima, K., & Mizuno, A. (2015). Experimental study of dielectric-barrier-discharge reactor for plasma-assisted-combustion. *International Journal of Plasma Environmental Science and Technology, 9*(2), 120-126.

Hakmi, Y., Miloudi, H., Miloudi, M., Bendaoud, A., Mendaz, K., & Bermaki, M. H. (2024). A novel experimental approach for predictive high-frequency modeling of differential-mode impedance in three-phase induction motors. *2024 3rd International Conference on Advanced Electrical Engineering (ICAEE)*, 1-6.

Hakmi, Y., Miloudi, H., Miloudi, M., Gourbi, A., & Bermaki, M. H. (2024). Frequency experimental identification approach for single-phase induction motor common-mode parameters. *Electrical Engineering & Electromechanics, 2024*(6), 3-10.

Jolibois, J. (2008). *Etude et développement d'un actionneur plasma à décharge à barrière diélectrique: Application au contrôle d'écoulement sur profil d'aile* (Doctoral dissertation). Université de Poitiers.

Labergue, A. (2005). *Etude de décharges électriques dans l'air pour le développement d'actionneurs plasmas - Application au contrôle de décollements d'écoulements* (Doctoral dissertation). Université de Poitiers.

Lahlaci, M. E., Miloudi, M., & Miloudi, H. (2024). Experimental electromagnetic compatibility of conducted electromagnetic interferences from an IGBT and a MOSFET in the power supply. *Electrical Engineering & Electromechanics, 2024*(3), 38-43.

Miloudi, H., Miloudi, M., Bermaki, M. H., Gourbi, A., & Bendaoud, A. (2023). Optimization of EMC filter for a variable speed drive system in electric aircraft. *The Eurasia Proceedings of Science, Technology, Engineering & Mathematics, 26*, 60-66.

Miloudi, H., Miloudi, M., Gourbi, A., Bermaki, M. H., Bendaoud, A., & Zeghoudi, A. (2022). A high-frequency modeling of AC motor in a frequency range from 40 Hz to 110 MHz. *Electrical Engineering & Electromechanics, 2022*(6), 3-7.

Miloudi, M., Miloudi, H., Bendaoud, A., Salhi, M. A., & Al-Omari, A. N. (2019). Experimental characterization of the high-frequency isolating power transformer. *Elektrotehniški Vestnik, 86*(4), 211-218.

Miloudi, N., Bendaoud, A., Miloudi, M., Miloudi, H., Gourbi, A., & Bermaki, M. H. (2025). Characterizing radiated electromagnetic interference from a power converter for improved electromagnetic compatibility. *WSEAS Transactions on Circuits and Systems, 24*, 135.

Nozaki, T., Miyasaki, Y., Unno, Y., & Okasaki, K. (2001). Distribution and heat transfer mechanisms in atmospheric pressure non-equilibrium plasmas. *Journal of Physics D: Applied Physics, 34*(23), 3383-3390.

Sublet, A. (2007). *Caractérisation de décharges à barrières diélectriques atmosphériques et sub-atmosphériques et application à la déposition de couches d'oxyde de silicium* (Doctoral dissertation). École Polytechnique Fédérale de Lausanne.

Author(s) Information

Fatha Tounsi
Mustapha Stambouli University of Mascara
11, Chemin Doudou Mokhtar, Ben Aknoun – Alger – Algeria

Rabah Ouiddir
APELEC, Djillali Liabès University
Sidi Bel-Abbès, Algeria

Houcine Miloudi
APELEC, Djillali Liabès University
Sidi Bel-Abbès, Algeria

Mohamed Miloudi
APELEC, Djillali Liabes University of Sidi Bel-Abbes
Sidi Bel-Abbès, Algeria
Contact e-mail: *prof.mohamed.miloudi@gmail.com*

Abdelber Bendaoud
APELEC, Djillali Liabès University
Sidi Bel-Abbès, Algeria

To cite this article:

Tounsi, F., Ouiddir, R., Miloudi, H., Miloudi, M., & Bendaoud, A. (2025). Study and design of a plasma reactor using a porous dielectric barrier. *The Eurasia Proceedings of Science, Technology, Engineering and Mathematics (EPSTEM), 38,* 257-263.

The Eurasia Proceedings of Science, Technology, Engineering & Mathematics (EPSTEM)
ISSN: 2602-3199

The Eurasia Proceedings of Science, Technology, Engineering and Mathematics (EPSTEM), 2025

Volume 38, Pages 264-275

IConTES 2025: International Conference on Technology, Engineering and Science

Effect of the Strain Rate and Temperature on the Shape Memory Behavior of PMMA

Cherief Mohammed Nadhir Djamel Eddine
Djilali Liabes University of Sidi Bel Abbes

Ghermaoui Ilias Mohammed Amine
Djilali Liabes University of Sidi Bel Abbes

Abstract: In the field of smart materials, significant scientific progress has been made over the past decade on shape memory polymers (SMPs), which appear to offer numerous advantages. Their ability to change shape under the influence of an external stimulus, such as thermal, presents a certain interest for biomedical applications and the deployment of structures. In this section, we will develop a thermoviscoelastic-viscoplastic model to predict the shape memory behavior of poly (methyl methacrylate) (PMMA) and understand its thermomechanical behavior over a wide range of strain rate and temperatures.

Keywords: SMP, Strain rate, Temperature, Polymers, PMMA

Introduction

The industrial development of polymers, commonly known as plastics, has experienced remarkable growth since the last century. Today, the annual global production of polymers by volume exceeds that of metals. This evolution explains the growing interest in studying the behavior of these materials within the research community. Polymers are used in a wide variety of sectors. Packaging, whether for food or household products, represents the largest share of plastic consumption. Next come the fields of construction, automotive, household appliances, textiles, and electricity. Moreover, more specialized sectors such as medicine and aeronautics have also shown a strong interest in these materials.

PMMA, thanks to its transparency and high rigidity, is one of the most widely used technical polymers. It is found in most of the sectors mentioned above, particularly in applications where impact resistance is crucial, such as in the manufacture of windshields or the transparent covers of high-speed machine tool housings (UGV). The behavior of PMMA strongly depends on its processing history, the nature and rate of deformation, as well as temperature, with a significant thermomechanical coupling. Based on these observations, we chose to focus our work on the experimental and theoretical study of the rheology of PMMA. This study aims to analyze its behavior through simple uniaxial compression tests and then compare the results with the predictions of a model we have developed.

The shape memory effect refers to the ability of a material to retain a stable deformation within a certain temperature range and then recover its original shape when subjected to an external stimulus. Several types of stimuli can activate this shape memory in polymers, including water, heat, ultraviolet radiation, or electricity. In applications exploiting the shape memory of polymers, the development of constitutive models is highly sought after to provide essential tools for design. Constitutive modeling is crucial due to the complexity of the behavior associated with the shape memory effect. Although literature abounds with experimental studies on this phenomenon, modeling remains a major challenge for better understanding and controlling these materials.

- This is an Open Access article distributed under the terms of the Creative Commons Attribution-Noncommercial 4.0 Unported License, permitting all non-commercial use, distribution, and reproduction in any medium, provided the original work is properly cited.

- Selection and peer-review under responsibility of the Organizing Committee of the Conference

© 2025 Published by ISRES Publishing: www.isres.org

Method

To illustrate our approach a polycarbonate ($T_g \gg 413K$), was selected for an experimental test program under uniaxial compression. Compression specimens of 8.00 mm length and 6.3 mm diameter were machined from PMMA cylinders. The length to-diameter ratio of the specimens allows getting the stress-strain response at large strains by avoiding both buckling and non-homogeneous deformation. Lubricant was used between the platens and the specimen surfaces (smooth and parallel) to avoid both barreling and shearing phenomena during the compression. The experiments were carried out on an electromechanical model-5567 Instron universal testing machine equipped with an oven.

- Loading-unloading tests until zero stress: The specimens were loaded at a constant strain rate until a prescribed strain and then unloaded at the same absolute strain rate until zero stress. The tests were conducted at different strain rates, above and below T_g.
- Creep tests at zero stress of pre-deformed specimens: The specimens, previously deformed below T_g, were cooled to the room temperature T_0 by natural cooling and then submitted to creep experiments at zero stress for two different temperatures above T_g.

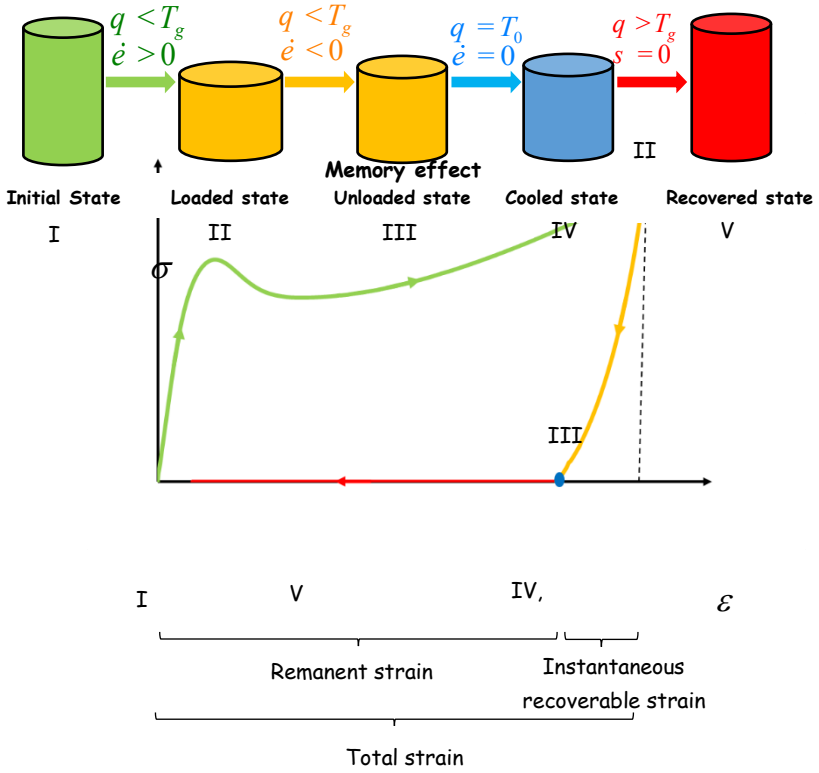


Figure 1. Elastoviscoplastic-viscohyperelastic response of an amorphous polymer below T_g under a loading-unloading compression experiment and recovery of the remanent strain under a creep test at zero stress above T_g.

Theory

The monotonic response of an amorphous polymer can be related to two underlying physical mechanisms acting in parallel: The first one is an intermolecular resistance to chain-segment rotation (resistance I) and the second one is a molecular network resistance due to molecular orientation (resistance N). The resistance I is the source of the initial stiffness and the yield events, whereas the resistance N is the source of the dramatic strain hardening at large strains. The constitutive equations of the resistance I are formulated using the elastoviscoplastic theory and those of the resistance N are formulated using the viscohyperelastic theory.

Kinematics

The total deformation gradient $\mathbf{F}$ can be multiplicatively decomposed as:

$$\mathbf{F} = \mathbf{F}_q \mathbf{F}_M \tag{1}$$

in which $\mathbf{F}_\theta$ is the thermal part related to stress-free thermal expansion and $\mathbf{F}_M$ is the mechanical part related to the isothermal stress-producing contribution.

The Taylor assumption imposes that the intermolecular and network deformation gradients, $\mathbf{F}_I$ and $\mathbf{F}_N$, are both equal to the mechanical deformation gradient $\mathbf{F}_M$:

$$\mathbf{F}_M = \mathbf{F}_I = \mathbf{F}_N \tag{2}$$

The two deformation gradients, $\mathbf{F}_I$ and $\mathbf{F}_N$, can be multiplicatively decomposed into elastic and inelastic parts:

$$\mathbf{F}_I = \mathbf{F}_I^{\mathrm{e}} \mathbf{F}_I^{\mathrm{vp}} \tag{3}$$

$$\mathbf{F}_N = \mathbf{F}_N^{\mathrm{h}} \mathbf{F}_N^{\mathrm{v}} \tag{4}$$

where the superscripts e, vp, h and v denote the elastic, viscoplastic, hyperelastic and viscous flow parts, respectively. The different parts can be further decomposed into rotation and stretch components:

$$\mathbf{F}_I^{\mathrm{e}} = \mathbf{R}_I^{\mathrm{e}} \mathbf{U}_I^{\mathrm{e}} = \mathbf{V}_I^{\mathrm{e}} \mathbf{R}_I^{\mathrm{e}} \text{ and } \mathbf{F}_I^{\mathrm{vp}} = \mathbf{R}_I^{\mathrm{vp}} \mathbf{U}_I^{\mathrm{vp}} = \mathbf{V}_I^{\mathrm{vp}} \mathbf{R}_I^{\mathrm{vp}} \tag{5}$$

$$\mathbf{F}_N^{\mathrm{h}} = \mathbf{R}_N^{\mathrm{h}} \mathbf{U}_N^{\mathrm{h}} = \mathbf{V}_N^{\mathrm{h}} \mathbf{R}_N^{\mathrm{h}} \text{ and } \mathbf{F}_N^{\mathrm{v}} = \mathbf{R}_N^{\mathrm{v}} \mathbf{U}_N^{\mathrm{v}} = \mathbf{V}_N^{\mathrm{v}} \mathbf{R}_N^{\mathrm{v}} \tag{6}$$

The intermolecular and network velocity gradients, $\mathbf{L}_I$ and $\mathbf{L}_N$, are described by:

$$\mathbf{L}_I = \underbrace{\dot{\mathbf{F}}_I^{\mathrm{e}} \mathbf{F}_I^{\mathrm{e}^{-1}}}_{\mathbf{L}_I^{\mathrm{e}}} + \underbrace{\mathbf{F}_I^{\mathrm{e}} \dot{\mathbf{F}}_I^{\mathrm{vp}} \mathbf{F}_I^{\mathrm{vp}^{-1}} \mathbf{F}_I^{\mathrm{e}^{-1}}}_{\mathbf{L}_I^{\mathrm{vp}}} \tag{7}$$

$$\mathbf{L}_N = \underbrace{\dot{\mathbf{F}}_N^{\mathrm{h}} \mathbf{F}_N^{\mathrm{h}^{-1}}}_{\mathbf{L}_N^{\mathrm{h}}} + \underbrace{\mathbf{F}_N^{\mathrm{h}} \dot{\mathbf{F}}_N^{\mathrm{v}} \mathbf{F}_N^{\mathrm{v}^{-1}} \mathbf{F}_N^{\mathrm{h}^{-1}}}_{\mathbf{L}_N^{\mathrm{v}}} \tag{8}$$

The inelastic velocity gradients, $\mathbf{L}_I^{\mathrm{vp}}$ and $\mathbf{L}_N^{\mathrm{v}}$, may be both decomposed as the sum of symmetric and skew-symmetric parts:

$$\mathbf{L}_I^{\mathrm{vp}} = \mathbf{F}_I^{\mathrm{e}} \mathbf{F}_I^{\mathrm{vp}} \mathbf{F}_I^{\mathrm{vp}^{-1}} \mathbf{F}_I^{\mathrm{e}^{-1}} = \mathbf{D}_I^{\mathrm{vp}} + \mathbf{W}_I^{\mathrm{vp}} \tag{9}$$

$$\mathbf{L}_N^{\mathrm{v}} = \mathbf{F}_N^{\mathrm{h}} \mathbf{F}_N^{\mathrm{v}} \mathbf{F}_N^{\mathrm{v}^{-1}} \mathbf{F}_N^{\mathrm{h}^{-1}} = \mathbf{D}_N^{\mathrm{v}} + \mathbf{W}_N^{\mathrm{v}} \tag{10}$$

in which $\mathbf{D}$ is the symmetric part and $\mathbf{W}$ is the skew-symmetric part. The intermolecular and network inelastic flows are assumed to be irrotational, i.e. $\mathbf{W}_I^{\mathrm{vp}} = \mathbf{0}$ and $\mathbf{W}_N^{\mathrm{v}} = \mathbf{0}$. Moreover, $\mathbf{D}_I^{\mathrm{vp}}$ and $\mathbf{D}_N^{\mathrm{v}}$ are constitutively given in the next subsection.

Constitutive Model Formulation

The Taylor assumption imposes that the total Cauchy stress $\boldsymbol{\sigma}$ is the sum of both contributions:

$$\boldsymbol{\sigma} = \boldsymbol{\sigma}_I + \boldsymbol{\sigma}_N \tag{11}$$

where $\boldsymbol{\sigma}_I$ is the intermolecular Cauchy stress and $\boldsymbol{\sigma}_N$ is the network Cauchy stress.

Elastoviscoplastic Response: Stiffness and Plastic Yielding

The yield behavior of amorphous polymers is a thermally-activated process. The intermolecular Cauchy stress $\boldsymbol{\sigma}_I$ is expressed by the following constitutive relationship:

$$\boldsymbol{\sigma}_I = \frac{\mathbf{C}_I^{\mathrm{e}}}{J_I} \ln\left(\mathbf{V}_I^{\mathrm{e}}\right) \tag{12}$$

in which $J_I = \det\left(\mathbf{F}_I^{\mathrm{e}}\right)$ is the intermolecular volume change, $\ln\left(\mathbf{V}_I^{\mathrm{e}}\right)$ is the Hencky elastic strain and $\mathbf{C}_I^{\mathrm{e}}$ is the elastic stiffness tensor. In the isotropic case, the elastic stiffness tensor $\mathbf{C}_I^{\mathrm{e}}$ may be given in terms of the Young's modulus E and the Poisson's ratio ν as follows:

$$\left(\mathbf{C}_I^{e}\right)_{ijkl} = \frac{E\left(q,\dot{e}\right)}{2\left(1+n\left(q,\dot{e}\right)\right)}\left(d_{ik}d_{jl} + d_{il}d_{jk}\right) + \frac{2n\left(q,\dot{e}\right)}{1-2n\left(q,\dot{e}\right)} d_{ij}d_{kl} \tag{13}$$

in which the term d denotes the Kronecker-delta symbol. The stiffness of polymers is clearly temperature-dependent as shown in Fig. 2. The thermo-dependence is due to … Moreover, it depends on the strain-rate. The evolution of the Young's modulus is given by the following expression (Richeton et al., 2005b):

$$E\left(q,\dot{e}\right) = E_{T_b}\left(q,\dot{e}\right) + E_{T_g}\left(q,\dot{e}\right) + E_{T_m}\left(q,\dot{e}\right) \tag{14}$$

in which $E_{T_b}\left(q,\dot{e}\right)$, $E_{T_g}\left(q,\dot{e}\right)$ and $E_{T_m}\left(q,\dot{e}\right)$ correspond to three parts around the main transitions (β relaxation, glass transition and melting) which are characterized by their transition temperatures, T_b, T_g and T_m:

$$E_{T_b}\left(q,\dot{e}\right) = \left(E_1\left(\dot{e}\right) - E_2\left(\dot{e}\right)\right)\exp\left(-\left(\frac{q}{T_b\left(\dot{e}\right)}\right)^{m_1}\right) \tag{15}$$

$$E_{T_g}\left(q,\dot{e}\right) = \left(E_2\left(\dot{e}\right) - E_3\left(\dot{e}\right)\right)\exp\left(-\left(\frac{q}{T_g\left(\dot{e}\right)}\right)^{m_2}\right) \tag{16}$$

$$E_{T_m}\left(q,\dot{e}\right)=E_3\left(\dot{e}\right)\exp\left(-\left(\frac{q}{T_m\left(\dot{e}\right)}\right)^{m_3}\right) \tag{17}$$

where m_1, m_2 and m_3 are material constants and, $E_1\left(\dot{e}\right)$, $E_2\left(\dot{e}\right)$ and $E_3\left(\dot{e}\right)$ are the instantaneous moduli at the beginning of each transition region:

$$E_1\left(\dot{e}\right)=E_{1ref}\left(1+s_1\log\left(\frac{\dot{e}}{\dot{e}_{ref}}\right)\right) \tag{18}$$

$$E_2\left(\dot{e}\right)=E_{2ref}\left(1+s_2\log\left(\frac{\dot{e}}{\dot{e}_{ref}}\right)\right) \tag{19}$$

$$E_3\left(\dot{e}\right)=E_{3ref}\left(1+s_3\log\left(\frac{\dot{e}}{\dot{e}_{ref}}\right)\right) \tag{20}$$

where E_{1ref}, E_{2ref} and E_{3ref} are the instantaneous moduli at a chosen reference strain-rate $\dot{\varepsilon}_{ref}$ and, s_1, s_2 and s_3 are the strain-rate sensitivity parameters.

The transition temperatures T_β, T_g and T_m are, respectively, given by:

$$\frac{1}{T_b\left(\dot{e}\right)}=\frac{1}{T_{b\,ref}}+\frac{k}{\Delta H_b}\ln\left(\frac{\dot{e}_{ref}}{\dot{e}}\right) \tag{21}$$

$$T_g\left(\dot{e}\right)=T_{gref}-c_{2g}\log\left(\frac{\dot{e}_{ref}}{\dot{e}}\right)\left(c_{1g}+\log\left(\frac{\dot{e}_{ref}}{\dot{e}}\right)\right)^{-1} \tag{22}$$

$$T_m\left(\dot{e}\right)=T_{mref}\left(1+10^{-2}\log\left(\frac{\dot{e}}{\dot{e}_{ref}}\right)\right) \tag{23}$$

in which $T_{\beta ref}$, T_{gref} and T_{mref} are the transition temperatures at the chosen reference strain-rate $\dot{\varepsilon}_{ref}$, ΔH_b is the β-activation energy and, c_{1g} and c_{2g} are the Williams-Landel-Ferry coefficients.

Fig. 3 plots the yield stress as a function of temperature.

The viscoplastic stretching rate tensor is given by the following flow rule:

$$\mathbf{D}_I^{\text{vp}} = \dot{g}_I^{\text{vp}} \frac{\boldsymbol{\sigma}_I^{\prime}}{\sqrt{2}t_I}, \quad t_I = \sqrt{\frac{1}{2}\boldsymbol{\sigma}_I^{\prime} \times \boldsymbol{\sigma}_I^{\prime}} \tag{24}$$

in which $\dot{\gamma}_I^{\text{vp}}$ is the viscoplastic shear strain rate and τ_I is the effective shear stress related to the deviatoric part of the intermolecular Cauchy stress: $\boldsymbol{\sigma}_I^{\prime} = \boldsymbol{\sigma}_I - s_{Im}\mathbf{I}$ with $s_{Im} = \text{trace}\left(\boldsymbol{\sigma}_I\right)/3$ the intermolecular mean stress and $\mathbf{I}$ the identity tensor. The expression of $\dot{\gamma}_I^{\text{vp}}$ proposed by Richeton et al. (2006, 2005a), above and below the glass transition temperature T_g, is retained:

$$\dot{g}_I^{\text{vp}} = \dot{g}_0 \exp\left(-\frac{\Delta H_b}{Rq}\right)\sinh^n\left(\frac{\left(t_I - t_i\right)V}{2kq}\right) \text{ for } q < T_g \tag{25}$$

above T_g, and

$$\dot{g}_I^{\text{vp}} = \dot{g}_0 \exp\left(-\frac{\Delta H_b}{RT_g}\right)\exp\left(\frac{\ln 10^{\prime}\, c_{1g}\left(q - T_g\right)}{c_{2g} + q - T_g}\right)\sinh^n\left(\frac{t_I V}{2kq}\right) \text{ for } q \geq T_g \tag{26}$$

below T_g. The term $\dot{\gamma}_0$ is the pre-exponential factor, R is the perfect gas constant, k is the Boltzmann's constant, V is the activation volume and n is a material constant.

The strain-softening originates from …

The term τ_i in Eq. (25) is the internal shear resistance of the stress-softening response in the glassy regime, continuously decreasing until reaching the more stable chains structure during the network rearrangement. The internal stress τ_i evolves from its initial value $t_{i(t=0)}$ to the value τ_{ps} referring to the preferred structural state of the polymer chains according to the following evolution law:

$$\dot{t}_i = h\left(1 - \frac{t_i}{t_{ps}}\right)\dot{g}_I^{\text{vp}} \tag{27}$$

in which h is the strain-softening slope.

$$t_{i(t=0)} = t_{i(q=0)} - mq + as_{Im} \tag{28}$$

where $t_{i(q=0)}$ is the internal stress at the temperature θ = 0 K, m is the sensitivity parameter vis-à-vis the temperature and a is the sensitivity parameter vis-à-vis the intermolecular mean stress σ_{Im}.

Viscohyperelastic Response: Strain Dramatic Hardening at Large Strains

The strain-hardening originates from …

The network Cauchy stress $\boldsymbol{\sigma}_N$ is expressed by the following constitutive relationship (Arruda and Boyce, 1993):

$$\boldsymbol{\sigma}_N = \frac{1}{J_N}\frac{C_r}{3}\frac{\sqrt{N_{rl}}}{\bar{l}_N^{\mathrm{h}}} L^{-1}\left(\frac{\bar{l}_N^{\mathrm{h}}}{\sqrt{N_{rl}}}\right)\bar{\mathbf{F}}_N^{\mathrm{h}}\left(\bar{\mathbf{F}}_N^{\mathrm{h}}\right)^{\mathrm{T}} - \left(\bar{l}_N^{\mathrm{h}}\right)^2\mathbf{I} \tag{29}$$

in which $J_N = \det\left(\mathbf{F}_N^{\mathrm{h}}\right)$ is the network volume change, $\bar{l}_N^{\mathrm{h}} = \sqrt{\mathrm{trace}\left(\bar{\mathbf{F}}_N^{\mathrm{h}}\left(\bar{\mathbf{F}}_N^{\mathrm{h}}\right)^{\mathrm{T}}\right)/3}$ is the average stretch on a chain, $C_r = n_c kq$ is the rubbery modulus with n_c the average number of chains per unit volume and N_{rl} is the average number of rigid links between entanglements. The inverse Langevin function is given by the approximation (Cohen, 1991): $\mathrm{L}^{-1}(x) \approx x(3 - x^2)/(1 - x^2)$.

The viscous stretching rate tensor is given by the following flow rule:

$$\mathbf{D}_N^{\mathrm{v}} = \dot{g}_N^{\mathrm{v}}\frac{\boldsymbol{\sigma}_N'}{\sqrt{2}t_N}, \quad t_N = \sqrt{\frac{1}{2}\boldsymbol{\sigma}_N' \times \boldsymbol{\sigma}_N'} \tag{30}$$

in which $\dot{\gamma}_N^{\mathrm{v}}$ is the viscous shear strain rate:

$$\dot{g}_N^{\mathrm{v}} = C\left(l_N^{\mathrm{v}} - 1\right)^{-1} t_N \tag{31}$$

where C is a material constant, λ_N^{v} is given by: $l_N^{\mathrm{v}} = \sqrt{\mathrm{trace}\left(\mathbf{F}_N^{\mathrm{v}}\left(\mathbf{F}_N^{\mathrm{v}}\right)^{\mathrm{T}}\right)/3}$ and τ_N is the effective shear stress related to the deviatoric part of the network Cauchy stress: $\boldsymbol{\sigma}_N' = \boldsymbol{\sigma}_N - s_{Nm}\mathbf{I}$ with $s_{Nm} = \mathrm{trace}\left(\boldsymbol{\sigma}_N\right)/3$.

The three constants, C_r, N_{rl} and C, follow a linear evolution with the temperature according to the following relationships:

$$\begin{aligned} C_r &= C_{r0} - aq \\ N_{rl} &= N_{rl0} + bq \\ C &= C_0 + cq \end{aligned} \quad \text{for } q \le T_g \tag{32}$$

above T_g, and

$$\begin{aligned} C_r &= \left(C_{r0} - aT_g\right)\frac{q}{T_g} \\ N_{rl} &= N_{rl0} + bT_g \\ C &= \left(C_0 + cT_g\right)\frac{q}{T_g} \end{aligned} \quad \text{for } q \ge T_g \tag{33}$$

below T_g. The terms C_{r0}, N_{rl0}, C_0, a, b and c are material constants.

In what follows, the model parameters are identified using experimental results obtained on a PMMA, deformed above and below its T_g.

Results and Discussion

Comparison between simulated model results and experimental results. In this section, we focus on identifying the parameters of the model that describe the constitutive behavior of PMMA. The following part presents a comparison between the simulation results and the experimental compression data.

Table 1. Parameter of PMMA model

Simulation results	Experimental results
E^{ref}_1 (MPa)	5100
E^{ref}_2 (MPa)	2700
E^{ref}_3 (MPa)	20
T^{ref}_β (K)	290
T^{ref}_g (K)	387
T^{ref}_f (K)	466
$\dot{e}^{\text{ref}}$ (s^{-1})	1
m_1	5
m_2	40
m_3	20
c_1	32.58
c_2	83.5
s	0.087
n	6.37
V (m^3)	$9.75 * 10^{-29}$
τ_i (0) (MPa)	100
m (MPa/K)	0.25
$\dot{\gamma}_0$ (s^{-1})	$1.16 * 10^{16}$
ΔH_β (kJ/mol)	90
$\frac{\tau_{ps}}{\tau_i}$	0.20
h (MPa/K)	30
α_p	0.26
$C_{r,0}$ (MPa)	91.15
a (MPa/K)	0.226
N_{rl}	1.515
b (1/K)	0.0025
C_m (MPa^{-1} s^{-1})	$-9 * 10^{-11}$
c (MPa^{-1} s^{-1}/K)	$1 * 10^{-11}$

Effect of Temperature

The figures below show the comparison between the simulated and experimental stress–strain curves over a wide temperature range (0°C to 100°C) and for three strain rates (10^{-1} s^{-1}, 10^{-2} s^{-1}, 10^{-3} s^{-1}). A satisfactory

correlation between the results was observed. It can be seen that the yield stress depends on both the strain rate and the temperature

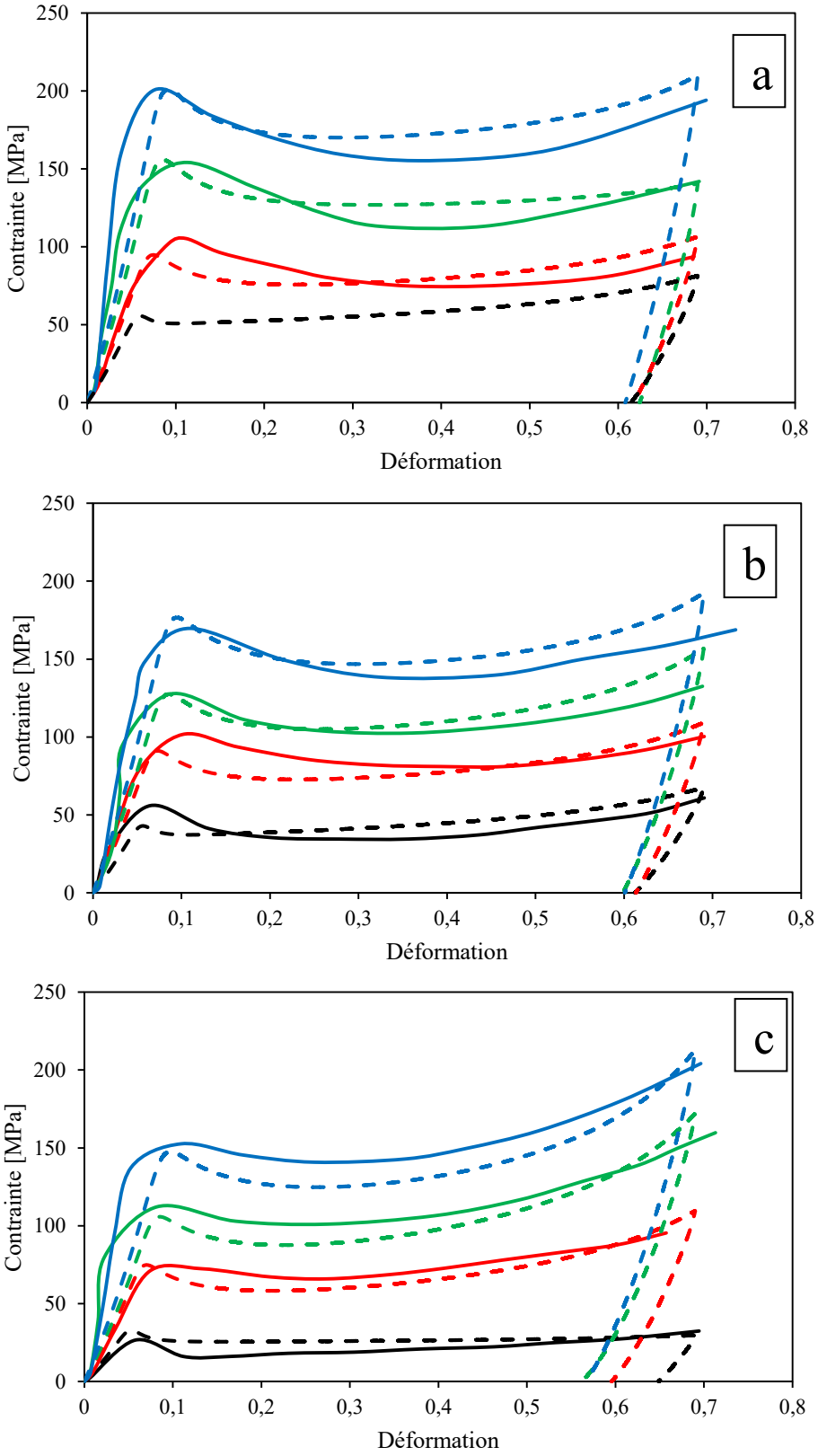


Figure 2. Model (dashed lines) vs. experiments (solid lines) of the stress-strain response of PMMA at different temperatures and strain-rates: (a) 0.01 s-1, (b) 0.001 s-1, (c) 0.0001 s

.

In fact, the model is capable of representing various curve shapes, including the initial modulus, softening after yielding, initial hardening, and excessive hardening at large deformations. It is also able to capture the effects of strain-rate and temperature sensitivity of the material during both loading and unloading.

Effect of Strain Rate

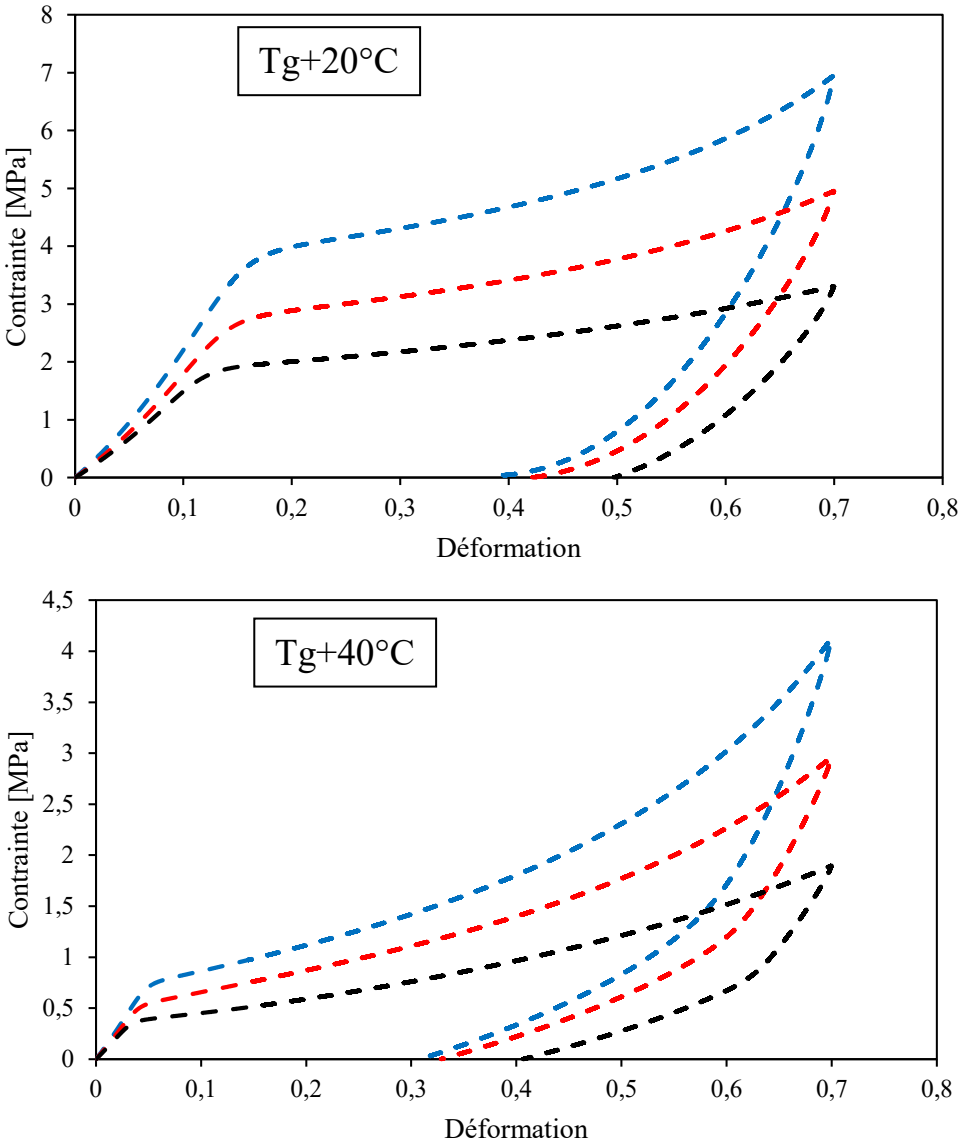


Figure 3. Model of the stress-strain response of PMMA at two different temperatures and strain-rates: (a) 0.01 s-1, (b) 0.001 s-1, (c) 0.0001 s

The two figures presented illustrate the effect of strain rate on the mechanical behavior of PMMA (Polymethyl methacrylate) at temperatures above the glass transition temperature (Tg). The higher the strain rate, the greater the stress required to achieve the same level of deformation. The curves shift upward as the strain rate increases, indicating a stiffer material response at higher loading rates. At temperatures above Tg, PMMA exhibits a pronounced viscoelastic behavior. An increase in strain rate restricts the mobility of polymer chains, thereby increasing the apparent mechanical strength.

At higher temperatures (Tg + 40°C), the stresses corresponding to a given deformation are lower than those at Tg + 20°C, indicating a decrease in stiffness with increasing temperature. Although the effect of strain rate is still present, the gap between the curves decreases at higher temperatures, reflecting a reduced sensitivity to strain rate.

Conclusion

In conclusion, we have developed a physically based model capable of capturing the elastoviscoplastic–viscohyperelastic behavior of amorphous thermoplastics, consistent with the underlying thermo-mechanical mechanisms below and above the glass transition temperature. The model accurately reproduces experimental stress–strain data for PMMA and successfully reflects the pronounced changes in mechanical response induced by temperature variations across the full range of strain rates investigated. The temperature-dependent material kinetics were then employed to simulate the thermally activated strain recovery process, and the predictive performance of the model was validated under various testing conditions. Owing to its general mathematical framework, the constitutive theory can be applied to the thermo-mechanical behavior of a wide range of amorphous thermoplastics, offering a valuable tool for predicting thermally induced strain recovery.

Scientific Ethics Declaration

* The authors declare that the scientific ethical and legal responsibility of this article published in EPSTEM journal belongs to the authors.

Conflict of Interest

* The authors declare that they have no conflicts of interest

Funding

* This research received no specific grant from any funding agency in the public, commercial, or not-for-profit sectors.

Acknowledgements or Notes

* This article was presented as a poster presentation at the International Conference on Technology, Engineering and Science (www.icontes.net) held in Antalya/Türkiye on November 12-15, 2025.

References

Arruda, E. M., & Boyce, M. C. (1993). A three-dimensional constitutive model for the large stretch behavior of rubber elastic materials. *Journal of the Mechanics and Physics of Solids, 41*(2), 389-412.

Bergström, J. S., & Boyce, M. C. (1998). Constitutive modeling of the large strain time-dependent behavior of elastomers. *Journal of the Mechanics and Physics of Solids, 46*(5), 931-954.

Boyce, M. C., Montagut, E. L., & Argon, A. S. (1992). The effects of thermomechanical coupling on the cold drawing process of glassy polymers. *Polymer Engineering & Science, 32*(15), 1073-1085.

Boyce, M. C., Parks, D. M., & Argon, A. S. (1988). Large inelastic deformation of glassy polymers. Part I: Rate dependent constitutive model. *Mechanics of Materials, 7*(1), 15-33.

Boyce, M. C., Socrate, S., & Llana, P. G. (2000). Constitutive model for the finite deformation stress–strain behavior of poly(ethylene terephthalate) above the glass transition. *Polymer, 41*(6), 2183-2201.

Boyce, M. C., Weber, G. G., & Parks, D. M. (1989). On the kinematics of finite strain plasticity. *Journal of the Mechanics and Physics of Solids, 37*(6), 647-665.

Cohen, A. (1991). A Padé approximant to the inverse Langevin function. *Rheologica Acta, 30*(3), 270-273.

Fotheringham, D., Cherry, B. W., & Bauwens-Crowet, C. (1976). Comment on "The compression yield behaviour of polymethyl methacrylate over a wide range of temperatures and strain-rates." *Journal of Materials Science, 11*(7), 1368-1371.

Holzapfel, G. A., & Simo, J. C. (1996). Entropy elasticity of isotropic rubber-like solids at finite strains. *Computer Methods in Applied Mechanics and Engineering, 132*(1–2), 17-44.

Lee, E. H. (1969). Elastic-plastic deformation at finite strains. *Journal of Applied Mechanics, 36*(1), 1-6.

Lee, E. H., & Liu, D. T. (1967). Finite-strain elastic-plastic theory with application to plane-wave analysis. *Journal of Applied Physics, 38*(1), 19-27.

Lion, A. (1997). On the large deformation behaviour of reinforced rubber at different temperatures. *Journal of the Mechanics and Physics of Solids, 45*(11), 1805-1834.

Lion, A. (2000). Constitutive modelling in finite thermoviscoplasticity: A physical approach based on nonlinear rheological models. *International Journal of Plasticity, 16*(3–4), 469-494.

Lu, S. C. H., & Pister, K. S. (1975). Decomposition of deformation and representation of the free energy function for isotropic thermoelastic solids. *International Journal of Solids and Structures, 11*(7–8), 927-934.

Mahieux, C. A., & Reifsnider, K. L. (2001). Property modeling across transition temperatures in polymers: A robust stiffness–temperature model. *Polymer, 42*(7), 3281-3291.

Mahieux, C. A., & Reifsnider, K. L. (2002). Property modeling across transition temperatures in polymers: Application to thermoplastic systems. *Journal of Materials Science, 37*(5), 911-920.

Miehe, C. (1995). Entropic thermoelasticity at finite strains. Aspects of the formulation and numerical implementation. *Computer Methods in Applied Mechanics and Engineering, 120*(3-4), 243-269.

Richeton, J., Ahzi, S., Daridon, L., & Rémond, Y. (2005). A formulation of the cooperative model for the yield stress of amorphous polymers for a wide range of strain rates and temperatures. *Polymer, 46*(16), 6035-6043.

Richeton, J., Ahzi, S., Vecchio, K. S., Jiang, F. C., & Adharapurapu, R. R. (2006). Influence of temperature and strain rate on the mechanical behavior of three amorphous polymers: Characterization and modeling of the compressive yield stress. *International Journal of Solids and Structures, 43*(7-8), 2318-2335.

Richeton, J., Ahzi, S., Vecchio, K. S., Jiang, F. C., & Makradi, A. (2007). Modeling and validation of the large deformation inelastic response of amorphous polymers over a wide range of temperatures and strain rates. *International Journal of Solids and Structures, 44*(24), 7938-7954.

Richeton, J., Schlatter, G., Vecchio, K. S., Rémond, Y., & Ahzi, S. (2005). A unified model for stiffness modulus of amorphous polymers across transition temperatures and strain rates. *Polymer, 46*(19), 8194–8201.

Sidoroff, F. (1974). Nonlinear viscoelastic model with an intermediate configuration. *Journal de Mécanique, 13*, 679–713.

Williams, M. L., Landel, R. F., & Ferry, J. D. (1955). The temperature dependence of relaxation mechanisms in amorphous polymers and other glass-forming liquids. *Journal of the American Chemical Society, 77*(14), 3701–3707.

Author(s) Information

Cherief Mohammed Nadhir Djamel Eddine
Djilali Liabes University of Sidi Bel Abbes,
Sidi Bel Abbes Algeria
Contact e-mail: *n.cherief@yahoo.com*

Ghermaoui Ilias Mohammed Amine
Djilali Liabes University of Sidi Bel Abbes,
Sidi Bel Abbes Algeria

To cite this article:

Eddine, C. M. N. D., & Amine, G. I. M., (2025). Effect of the strain rate and temperature on the shape memory behavior of PMMA. *The Eurasia Proceedings of Science, Technology, Engineering and Mathematics (EPSTEM), 38,* 264-275.

The Eurasia Proceedings of Science, Technology, Engineering & Mathematics (EPSTEM)
ISSN: 2602-3199

The Eurasia Proceedings of Science, Technology, Engineering and Mathematics (EPSTEM), 2025

Volume 38, Pages 276-282

IConTES 2025: International Conference on Technology, Engineering and Science

Deterministic Assessment of the Seismic Behavior of Cylindrical Steel Storage Tanks: A Methodological Framework Based on the New Algerian Seismic Code

Amar Aliche
Mouloud Mammeri University of Tizi-Ouzou

Ourdia Ider
Mouloud Mammeri University of Tizi-Ouzou

Mouloud Guemmoun
Mouloud Mammeri University of Tizi-Ouzou

Hocine Hammoum
Mouloud Mammeri University of Tizi-Ouzou

Karima Bouzelha
Mouloud Mammeri University of Tizi-Ouzou

Djamel Atllaoui
Mouloud Mammeri University of Tizi-Ouzou

Abstract: The Steel storage tanks are critical structures, frequently used in the industrial sector for the storage of various types of products, primarily toxic or flammable. This type of structure is complex in terms of design, engineering, and safety management. During severe earthquakes, the loss of tank performance can be devastating, leading to uncontrollable chain reactions that can cause more damage than the earthquake itself. In Algeria, despite the economic importance of these structures and their growing number across the country, the various updates to the seismic code (1981, 1999, 2003, 2024) have not included storage structures (concrete and steel) in their designs. This forces civil engineers, in their studies, to rely on foreign standards such as API 650, BS 2654, etc.This study, focused on cylindrical steel tanks, proposes a practical deterministic methodology for establishing seismic design criteria tailored to the Algerian context. The approach primarily relies on two key considerations: hydrodynamic effects, represented by the housner's model, and the seismic load defined by the response spectrum of the Algerian Seismic Code (RPA-2024). The study concludes with practically relevant insights derived from the results obtained.

Keywords: Steel storage tanks, Deterministic approach, Seismic design, RPA 2024, Hydrodynamic model

Introduction

In the heavy industry sector, large storage tanks serve critical economic needs. In regions with high seismic activity, such as Algeria, the nature of the stored products, which are often toxic or flammable, makes these structures particularly sensitive in terms of safety against earthquakes. The failure of a tank can trigger socio-economic and environmental consequences that may cause more damage than the earthquake itself. Therefore, their design must ensure they remain functional during and after a seismic event. This challenge becomes more

- This is an Open Access article distributed under the terms of the Creative Commons Attribution-Noncommercial 4.0 Unported License, permitting all non-commercial use, distribution, and reproduction in any medium, provided the original work is properly cited.

- Selection and peer-review under responsibility of the Organizing Committee of the Conference

© 2025 Published by ISRES Publishing: www.isres.org

complex when, under seismic stress, part of the stored liquid shifts, creating a phenomenon known as the hydrodynamic effect. Indeed, research has shown the detrimental impact of fluid-structure interaction on the overall behaviour of these structures. From a regulatory standpoint, in Algeria, the only normative reference for seismic design is the RPA. Despite various updates (RPA 81, RPA 88, RPA 99, RPA 2003 and RPA 2024), the Algerian seismic code remains silent on the subject of hydraulic structures in general and storage tanks in particular. The only guideline provided concerns the consideration of the hydrodynamic effect for tanks with a capacity exceeding 1500 m³, located in zones of moderate and high seismicity.

In response to these shortcomings, we propose in this study, illustrated by a practical application, a new approach. This approach, based on coupling the Housner model with the RPA response spectrum, is used to assess the stability of a large industrial tank subjected to significant seismic forces. The analysis method is detailed in the following sections.

Description of the Mechanical Model

The model used to assess the effects of seismic loading on high-capacity storage tanks must accurately replicate the stiffness, mass, and geometric properties of the structure, while also considering the hydrodynamic response of the stored liquid. The entire tank is represented through its equivalent mechanical mass-spring model, as illustrated in Figure 1.

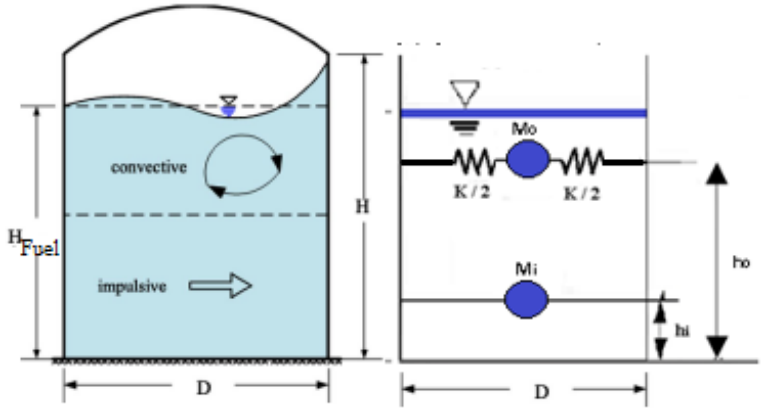


Figure 1. Description of mechanical model.

To analyze the stability of the reservoir and its hydrodynamic behavior (fluid-structure interaction), Housner (1963) breaks down the action of the liquid into two main actions, a passive action provoking impulse efforts, from that part of the fluid, denoted Mi, rigidly connected to the reservoir has an author hi, reacts by inertia to the translation of the walls of the reservoir. The second, called convective action, causing oscillation forces, from the fact that the other part of the mass, denoted active mass M0, rigidly connected via a stiffness spring K at a height h0, sets in oscillation motion under seismic action (Figure 1). These masses Mi and M0 are given by the following expressions of Housner (1963):

$$M_i = M_e \left[\frac{th\left(\sqrt{3}\frac{R_i}{H_e}\right)}{\left(\sqrt{3}\frac{R_i}{H_e}\right)} \right] \quad (1)$$

$$M_0 = M_e 0.318 \frac{R_i}{H_e} th\left(1.84\frac{H_e}{R_i}\right) \quad (2)$$

Calculation of Impulse Actions

In our study, the reservoir is considered to be rigidly bound to the soil, thus undergoing the same value of the maximum acceleration Sa as the soil (Hammoum et al, 2010), (Aliche, 2016). The horizontal hydrodynamic resultant of the impulsive pressure, noted Pi, is given by the following relation (Housner 1963):

$$P_i = M_i.S_a \tag{3}$$

Given the soil-structure interaction, the seismic acceleration Sa imposed on the reservoir, is given by the Algerian RPA seismic regulation according to the seismic zone and other parameters.

Calculation of Oscillation Actions

The resultant of the horizontal hydrodynamic oscillation pressure, noted convective pressure Po, caused by the motion of the mass M0, under the effect of the seismic action, is given by the following relation:

$$P_o = 1.2.M_0.\mathrm{g}.\varphi_0 \tag{4}$$

with:

$$\varphi_0 = 0.83.\frac{S_a}{g} \tag{5}$$

Study of the Tank Stability

In the case of seismic loading at the ultimate limit state, the tank's overall stability against collapse must be ensured. The structure's stability may be influenced by slip or rollover under these conditions. To this end, the following inequality must be satisfied:

- $\frac{\text{stabilizer moment}}{\text{overturning moment}} \geq 1.5$
- Resultant of verticals strengths > Resultant of horizontal strengths

Another mode of failure that could lead to the decommissioning of a storage tank is the movement of fluid, caused by seismic action, in a partially filled tank. This can result in damage to the roof and overflow of the stored liquid. To prevent damage to the dome cover due to wave effects, a freeboard must be provided. According to Eurocode 8 (EC8 2003), the peak wave height, denoted as dmax, can be calculated as follows:

$$d_{\max} = 0.84.\frac{S_a}{g}.R \tag{6}$$

Practical Application

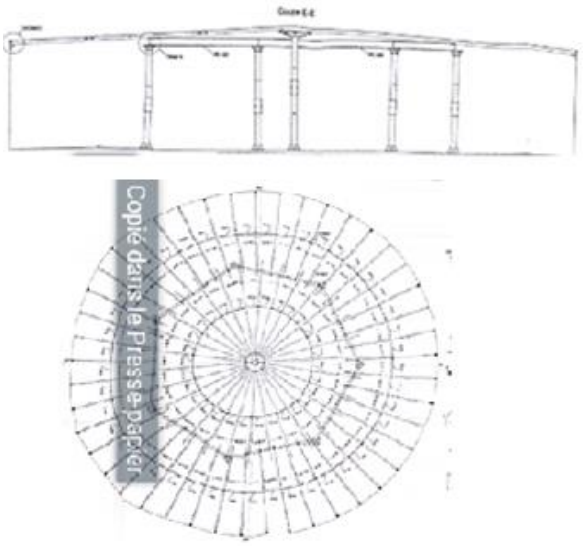


Figure 2. Planand elevation view of the structure

The structure that is the subject of our study is a steel storage tank with a capacity of 8000 m3, installed on a soil of category S3 in CAROUBIER (ALGIERS), classified Zone of strong seismicity (Zone VI) (Rpa 2024).

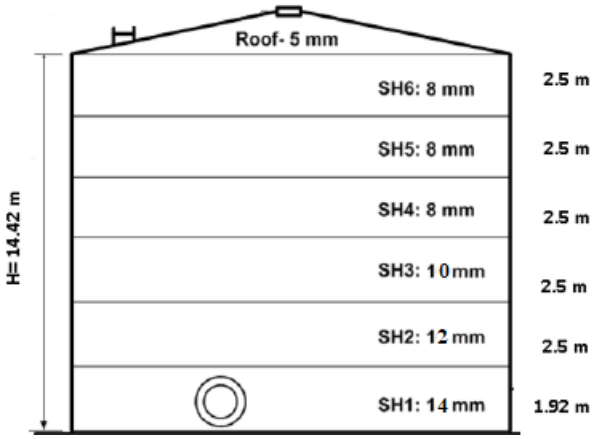


Figure 3. Geometry of mechanically tank

The geometric characteristics of the structure are mentioned in the table, which follows:

Table 1. Structure and mechanical properties of materials

	Values / designation
Stored product	Diesel fuel
Diameter of the tank	14 m
Tank height	14.42 m
Useful height of the fluid	13 m
Volume	8000 m^3
Roof style	Conical
Conditions of study	Temperature 50° C Density of the stored product 860 Kg/m^3

The thicknesses vary from top to bottom according to the position of the steel plates constituting each part of the cylinder, and are calculated according to paragraph 11.3.1 of Ec-3 as follows:

Table 2. Thickness of the ferrules constituting the cylinder.

N° ferrule	Ferrule height (m)	Fluid height (m)	t_{cal} (mm)	t_{min} (mm)	Over-thickness corrosion (mm)	t_{adp} (mm)
1	1.924	14.424	9.55	10	3.00	14
2	2.5	12.5	8.24	10	1.00	12
3	2.5	10	6.55	8	1.00	10
4	2.5	7.5	4.86	6	1.00	8
5	2.5	5	3.17	6	1.00	8
6	2.5	2.5	1.48	6	1.00	8

For the bottom of the tank, carbon steel was chosen, welded end to end. Hence the following results (Table 3):

Table 3. Roof and bottom thickness

	Calculated value	Adopted value	Unit
Roof thickness	7.06	8	mm
Bottom thickness	5.66	6	mm
Width of the annular plate	347.65	500	mm

Seismic Study

Calculation of the Fundamental Period T

The fundamental period of vibration is given by the following formula:

$$T = 1.79H_t^2\sqrt{\frac{P}{gEI}} \tag{7}$$

- the weight of the work P = 2132,794 KN
- Height of structure Ht = 14.424 m
- E: modulus of elasticity of the steel E = 2.1 * 10^5 MPa.
- moment of inertia of the wall with respect to the horizontal axis Ix:

$$I_x = \frac{\pi}{2}(14^4 - 13.986^4) = 241.2\ m^4$$

So: $T = 0.415\ s$ (8)

Calculation of the Acceleration Sa

Table 4. Parameters response spectra

Acceleration coefficient of the seismic zone	A = 0.3
Characteristic periods associated with the soil category of the site	S = 1.30 T1= 0.15 s T2= 0.6 s T3= 2.0 s
The quality factor of the structure	Q= 1
Damping correction factor	**η= 1**
Behaviour factor of the structure	R=2
Importance factor	I=1.2 (1B)

So for $T_1 \le T \le T_2$

$$\frac{S_a}{g}(T) = A.I.S\left(2.5\eta\right)\left(\frac{Q}{R}\right) \tag{9}$$

The acceleration of the ground ***Sa= 5.85 m/s²*** **/(**Sa=4.65 m/s² RPA2003**).**

Hydrodynamic Calculation

Table 5. Hydrodynamic calculation results.

Overturning moment M_r	197794.56	Kn.m
Stabilizer moment M_s	994018.5	Kn.m

The Stability of the Tank

The primary objective of analyzing the seismic behaviour of the structure, based on the response spectrum provided in the Algerian seismic code (RPA 2024), is to assess the stability of the structure under seismic loading. According to Eurocode, the stability of a reservoir under seismic action must be verified with respect to both the ultimate limit state (ULS) and the serviceability limit state (SLS) (Table 2). Limit state models focus on representing either the loss of functionality (serviceability limit states) or failure modes and loss of static equilibrium (ultimate limit states). This approach allows for the assessment of the structure's safety by determining stability criteria related to the limit states under actual operating conditions.

Serviceability Limit State

Under the effect of the seismic action at the ULS, the overall stability of the reservoir with respect to collapse must be satisfied. For this purpose, it is necessary to satisfy the following inequality:

$$\frac{M_s}{M_r} \geq 1.5 \quad \text{For our case} \quad \frac{M_s}{M_r} = \frac{994018.5}{197794.56} = 5.02 \geq 1.5$$

At Serviceability limit state**,** the overall stability of the tank with respect to collapse under the effect of the reversal is satisfied. This is the peculiarity of tanks placed on the ground.

Sloshing Effect

Under the effect of the seismic action, the tank may suffer damage or level of the roof. For this purpose, a freeboard must be provided to prevent roof damage due to the wave effect. According to Eurocode 8 (CEN, 1998), the predominant contribution to the height of the sloshing wave is provided by the first fundamental mode, and the expression of the peak of the edge is given by the following relation (9):

$$d_{max} = 0.84.\frac{S_a}{g}.R \quad \text{So in our case study:} \quad d_{max} = 5.03\ m$$

This value is greater than 1.492 m, expected as a free-board, so the waves will reach the roof of the tank this risk of damaging it.

Conclusions

The rules and standards specific to each country are influenced by various factors; the application of a code must consider these to meet the primary safety and economic requirements. In the field of storage tanks, the design process is a critical step that requires specialized expertise to comply with the relevant standards and regulations. In this sector, where the stored product holds significant socio-economic value, managing safety is crucial. This paper demonstrates that overlooking or neglecting the hydrodynamic phenomenon significantly underestimates the impact of waves on the tank roof. Such neglect can lead to overflow of the stored product, resulting in damage that may exceed the effects of the earthquake itself, depending on the nature of the product.

Scientific Ethics Declaration

* The authors declare that the scientific ethical and legal responsibility of this article published in EPSTEM journal belongs to the authors.

Conflict of Interest

* The authors declare that they have no conflicts of interest

Funding

* This research received no specific grant from any funding agency in the public, commercial, or not-for-profit sectors.

Acknowledgements or Notes

* This article was presented as a poster presentation at the International Conference on Technology, Engineering and Science (www.icontes.net) held in Antalya/Türkiye on November 12-15, 2025.

* The authors would like to thank the conference committee and the reviewers who reviewed the article for their valuable feedback

References

Aliche, A. (2016). *Contribution à l'analyse de l'évolution de la vulnérabilité des réservoirs en béton dans leur cycle de vie* (Doctoral dissertation). Université Mouloud Mammeri de Tizi-Ouzou.

Centre National de Recherche Appliquée en Génie Parasismique. (2025). *Règles parasismiques algériennes (RPA 2024)* (DTR B C 2-48).

European Committee for Standardization. (2003). *Design of structures for earthquake resistance-Part 4: Silos, tanks and pipelines* (Eurocode 8, Draft No. 2).

Graham, E. W., & Rodriguez, A. M. (1952). Characteristics of fuel motion which affect airplane dynamics. *Journal of Applied Mechanics, 19*(3), 381–388.

Hammoum, H., Bouzelha, K., & Hannachi, N. E. (2010). Analyse hydrodynamique d'un réservoir circulaire en béton armé, posé au sol. *Annales du BTP, 2–3*, 13–22.

Housner, G. W. (1957). Dynamic pressures on accelerated fluid containers. *Bulletin of the Seismological Society of America, 47*(1), 15–35.

Housner, G. W. (1963). The dynamic behavior of water tanks. *Bulletin of the Seismological Society of America, 53*(2), 381–387.

Jacobsen, L. S., & Ayre, R. S. (1951). Hydrodynamic experiments with rigid cylindrical tanks subjected to transient motions. *Bulletin of the Seismological Society of America, 41*(4), 313–346.

Author(s) Information

Amar Aliche
Mouloud Mammeri University of Tizi-Ouzou
Civil Engineering Department, Tizi-Ouzou, Algeria
Contact e-mail : *amar.aliche@ummto.dz*

Ourdia Ider
Mouloud Mammeri University of Tizi-Ouzou
Civil Engineering Department, Tizi-Ouzou, Algeria

Mouloud Guemmoun
Mouloud Mammeri University of Tizi-Ouzou
Civil Engineering Department, Tizi-Ouzou, Algeria

Hocine Hammoum
Mouloud Mammeri University of Tizi-Ouzou
Civil Engineering Department, 15 000 Tizi-Ouzou, Algeria

Karima, Bouzelha
Mouloud Mammeri University of Tizi-Ouzou
Civil Engineering Department Tizi-Ouzou, Algeria

Djamel Atlaoui
Mouloud Mammeri University of Tizi-Ouzou
Civil Engineering Department, Tizi-Ouzou, Algeria

To cite this article:

Aliche, A, Ider, O., Guemmoun, M., Hammoum, H., Bouzelha, K., & Atlaoui, D. (2025). Deterministic assessment of the seismic behaviour of cylindrical steel storage tanks: A methodological framework based on the new Algerian seismic code. *The Eurasia Proceedings of Science, Technology, Engineering and Mathematics (EPSTEM), 38*, 276-282.

The Eurasia Proceedings of Science, Technology, Engineering & Mathematics (EPSTEM)
ISSN: 2602-3199

The Eurasia Proceedings of Science, Technology, Engineering and Mathematics (EPSTEM), 2025

Volume 38, Pages 283-288

IConTES 2025: International Conference on Technology, Engineering and Science

Investigation of the Possibility of Introducing Dispersed Boron Carbide Particles into the Melt of Austenitic Steel 12X18H10T During Centrifugal Casting

Abdrakhman Naizabekov
Rudny Industrial University

Sergey Kuzmin
Rudny Industrial University

Ilya Chumanov
South Ural State University

Andrey Anikeev
South Ural State University

Vadim Sedukhin
South Ural State University

Evgeniy Panin
Karaganda Industrial University

Andrey Marukov
Karaganda Industrial University

Abstract: The principal way to improve the mechanical and operational properties of steel is to adjust its chemical composition or to grind the metal structure. An alternative to the use of expensive alloying elements to improve the mechanical and operational properties of steel can be the dispersed hardening of steel with hard refractory fine particles of carbides, oxides, nitrides. This work, which was carried out within the framework of grant № AP23485709, funded by the Science Committee of the Ministry of Science and Higher Education of the Republic of Kazakhstan, is devoted to the study of the possibility of introducing dispersed boron carbide particles into the melt of austenitic steel 12X18H10T during centrifugal casting. At the first stage of the research, the interaction of dispersed particles of boron carbide and steel was simulated using the FactSage software package. The simulation showed that boron carbide particles will interact with the metal melt of austenitic steel 12X18H10T, which can lead to their complete dissociation. At the next stage of crystallization, the formation of carbide phases based on titanium carbide with a HCC structure, as well as a carbide phase based on chromium carbide with the formula $M_{23}C$, will begin, starting at a temperature of 1250°C. When the temperature decreases to 1050°C, the separation of boride phases based on chromium begins in the system under consideration. The experiments and metallographic analysis carried out at the second stage of the research confirmed the results of thermodynamic modeling. The introduced boron carbide particles completely dissociate when interacting with a metal melt. The carbon contained in the composition of boron carbide and in the composition of the initial melt contributes to the formation of carbide and carbon-nitride phases based on titanium.

Keywords: Centrifugal casting, Boron carbide, Thermodynamic modeling, Microstructure, Microhardness

- This is an Open Access article distributed under the terms of the Creative Commons Attribution-Noncommercial 4.0 Unported License, permitting all non-commercial use, distribution, and reproduction in any medium, provided the original work is properly cited.

- Selection and peer-review under responsibility of the Organizing Committee of the Conference

© 2025 Published by ISRES Publishing: www.isres.org

Introduction

Austenitic steels 08-12X18H10T are used everywhere in various fields of industry due to their versatility (it combines corrosion-resistant properties, heat resistance, good machinability, etc.), as well as a large amount of research devoted to it. Austenitic class steels have a FCC lattice, which provides a sufficient level of mechanical properties, however, in terms of resistance to various kinds of influences (for example, weldability, corrosion resistance), steels of this class lose to ferritic class steels (BCC lattice) (Salama et.al., 2019; Shlyamnev et.al., 2008; Devine, 1996). For this reason, there has been a recent trend in the world to use austenitic-ferritic grade steels to ensure better corrosion resistance and higher mechanical properties (Li et.al., 2015; Bagwe, 2014; Efimushkin et.al., 2022). Such "duplex" steels produced by smelting have a huge disadvantage in the form of difficult machinability and low ability to plastic deformation. Another technology for connecting austenitic and ferritic steels is to weld one steel onto another. A significant disadvantage of technology is the need to weld the sublayer onto the hardening steel in order to avoid the formation of brittle interlayers in the fusion zone with the base metal.

In this study, another method is proposed for obtaining various chemical and structural states of steel without a pronounced phase boundary and with an acceptable level of workability. This is achieved by introducing boron carbide into the melt during centrifugal casting, which ensures its controlled distribution over the cross-section of the resulting blanks. The introduced particles serve as crystallization centers, grind the metal grain, and implement the mechanism of dispersed hardening (Chumanov et.al., 2022; Korostelev et.al., 2011). Small boron additives in steel cause significant grain grinding, increased heat resistance as a result of hardening of grain boundaries with borides, increased hardness and wear resistance, hot ductility of ingots, improved weldability of heat-resistant austenitic steels (Liu et.al., 2024; Herring, 2018). At the same time, the resulting billet does not have a pronounced separation of the interface of the layers, which causes the absence of internal stresses (Watanabe et.al., 2009). Thus, the purpose of this article is the thermodynamic modeling of the interaction of boron carbide with austenitic steel 12X18N10T, to verify the fundamental possibility of introducing dispersed boron carbide particles into the melt during centrifugal casting, and to study its effect on the microstructure of the obtained blanks.

Method

To simulate the interaction of dispersed boron carbide particles and steel, the FactSage software package version 7.0 was used. During thermodynamic modeling, both traditional methods of equilibrium thermodynamics based on the CALPHAD approach (Figure 1) and the model of nonequilibrium crystallization of melts (Sheil-Gulliver model) were used, which allows a more accurate description of the process of real metal crystallization. and oxide melts (Figure 2), rather than using the equilibrium crystallization model. During the simulation, the crystallization of metal with carbide additives was investigated. In the calculation, the interaction of substances was assumed at a ratio of 1/100 (the interaction of 1% boron carbide B_4C with 99% of the melt was modeled). The initial composition of the metal for modeling was as follows: 69.25% Fe, 18 % Cr, 10% Ni, 1.5% Mn, 0.5% Si, 0.1 % C.

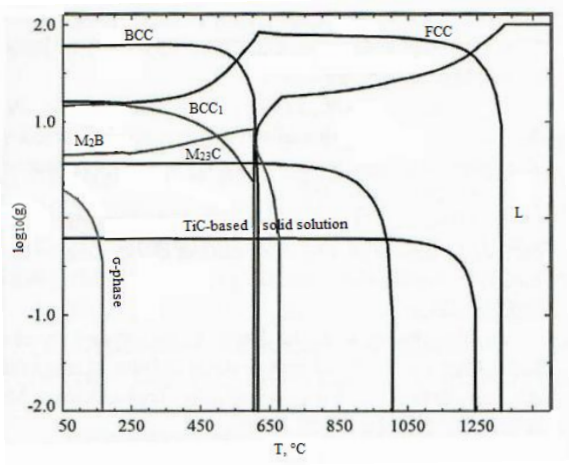


Figure 1. Simulation results of equilibrium phase compositions of metal with boron carbide addition depending on temperature

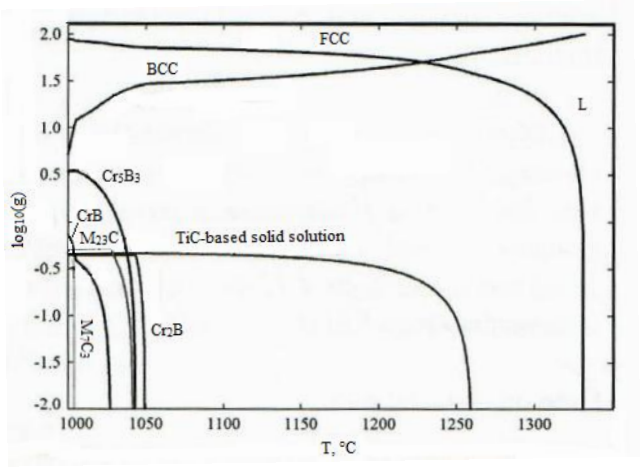


Figure 2. Diagram of nonequilibrium crystallization of a metal with boron carbide (Sheil-Gulliver model)

Based on the simulation results, it can be concluded that the crystallization of a metallic melt will be accompanied by the expected formation of metallic phases with BCC and FCC crystal lattices. In this case, boron carbides will interact with the metal melt, which can lead to their complete dissociation. At the next stage of crystallization, regardless of the degree of dissolution of boron carbide, the formation of carbide phases based on titanium carbide with a FCC structure, as well as a carbide phase based on chromium carbide with the formula $M_{23}C$, will begin, starting at a temperature of 1250°C. When the temperature drops to 1050°C, chromium-based boride phases are released in the system under consideration.

Under long-term operation conditions at temperatures no higher than 200°C, the structural components of a dispersed-hardened metal can undergo the following transformations: the transformation of most of the metal with a FCC structure into a solid solution with a BCC structure, as well as the appearance of a second chromium-based BCC phase and a σ-phase. This can reduce the mechanical properties of the metal, which must be taken into account during operation. At the same time, the stability of the carbide and boride phases is obviously not in danger.

Metal melting was carried out in an induction furnace with a main lining by remelting rolled steel 12X18H10T. The slag was made from lime, and the slag was deoxygenated with aluminum powder. During the smelting process, titanium alloying was performed 5 minutes before casting, aluminum deoxidation 2 minutes before casting, and niobium immediately before release to stabilize the structure. The casting temperature from the furnace to the intermediate ladle was 1680°C, from the ladle to the rotating mill of the centrifugal casting machine 1650°C. The rotation speed of the mill was 800 rpm, boron carbide B_4C particles with a dispersion of 1...2 microns were fed to the metal jet during the entire casting time. As a result of the experiment, three cylindrical blanks were obtained: No. 1 – without additives (standard), No. 2 – with 0.25% boron carbide from the mass of the billet; No. 3 – with 0.40% boron carbide from the mass of the billet. The dimensions of the workpieces are: outer diameter 180 mm, inner diameter 165 mm, wall thickness 15 mm, length 210 mm. The blanks had satisfactory external surface quality, with no visible defects. The inner surface of the workpieces has shrinkage phenomena typical of this casting method.

The microstructure of the cast samples was studied using optical microscopy on a microscope "C.Zeiss ObserverD1m", equipped with a software package "Thixomet.PRO ". The structure was studied on both etched and non-etched samples. The microstructure was detected using a reagent of the following composition: 40 % HCl, 30% HNO_3, 30% H_2O. The chemical composition of the obtained materials was studied using an MCA II emission spectrometer. The microhardness of the samples was studied using a stationary hardness tester using the Vickers method. The load used is 4.9 N, the holding time is 60 seconds. The ratio of microhardness to macrohardness, set by Rockwell C, is 0.01. The measurement was carried out in 10 iterations with an interval of 200 microns from the inner edge to the outer edge of each sample.

Results and Discussion

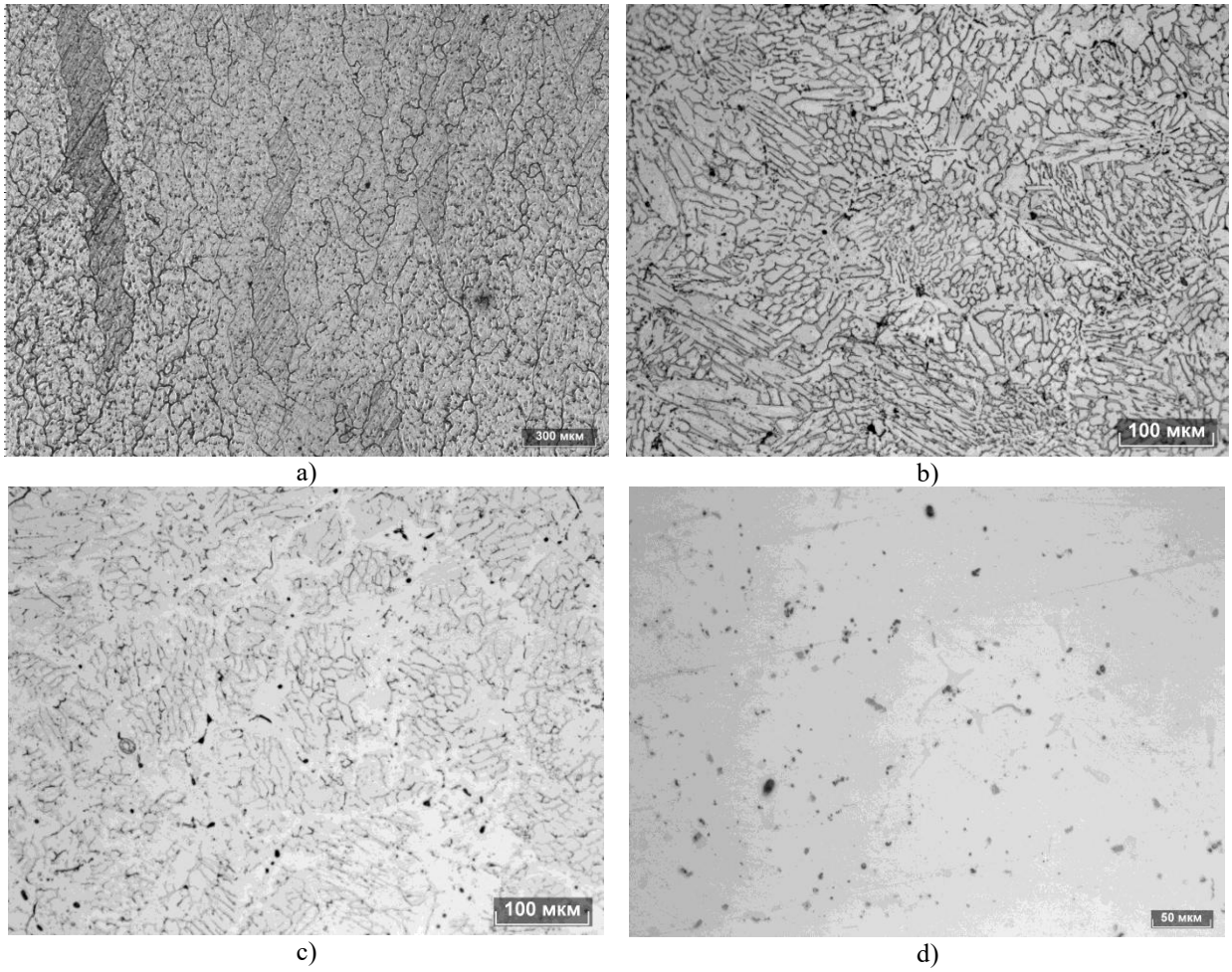
The results of the chemical composition study are presented in Table 1. According to the data provided, it can be concluded that when boron carbide is introduced into steel, the boron concentration can increase to values of 0.003-0.004 wt. %, and the carbon concentration is also increasing.

Table 1. Chemical composition of experimental castings, wt. %

Sample	C	Si	Mn	S	P	Cr	Ni	Cu	W	Ti	B	Al
1	0.082	0.52	0.92	0.007	0.012	17.26	9.55	0.21	0.02	0.78	0.001	0.12
2	0.091	0.55	0.82	0.005	0.013	17.50	9.68	0.17	0.02	0.75	0.003	0.09
3	0.095	0.59	0.96	0.005	0.010	17.45	9.69	0.21	0.02	0.72	0.004	0.10

The results of the microstructure study (Figure 3) showed that the microstructure of all samples is represented by austenitic grains and carbide particles located along the grain boundaries (primary carbides) and in the grain body (secondary carbide precipitates). The ferrite content in sample No. 1 is 4.5%. In sample No. 2, compared with sample No. 1, sulfide inclusions have both a compact shape and a dotted shape along the grain boundaries, point oxides are located along the grain boundaries, and titanium nitrides are in the grain body (Fig. 3b). The austenitic grain size corresponds to 9 points according to GOST 5639, and the proportion of the ferritic phase is 19-21%. The metal of sample No. 3 contains the same inclusions as in sample No. 2, but they all have a more compact shape (Fig. 3c). The austenitic grain size corresponds to 10 points according to GOST 5639, and the proportion of the ferritic phase is 12-15%.

The maximum values of contamination with non–metallic inclusions are relevant for all samples and according to OC - 1.5 points, C – 1 point, HT – 1 point. Nonmetallic inclusions are mainly represented by aluminum oxides, iron and manganese sulfides, and titanium and aluminum nitrides. In samples with boron carbide additive, the appearance of titanium carbonitrides Ti(C,N) located between the crystallites is observed (Figure 3d). Carbonitrides are not detected on the reference sample. According to the results of the microhardness study (Table 2), it can be noted that the microhardness of the reference sample (No. 1) is maximal at the outer edge and decreases as it moves towards the inner edge, which fully corresponds to the theory of crystallization of centrifugal cast blanks.



a) b)

c) d)

Figure 3. Microstructure of the studied samples: a – sample No. 1, ×65; b – sample No. 2, ×200; c – sample No. 3, ×200; d – general appearance of non-metallic inclusions in the samples, ×500

With the introduction of 0.25 wt. % B_4C (sample No. 2) microhardness increases, while the minimum value obtained for this parameter is higher than the maximum observed in the reference. With an increase in the concentration of B_4C to 1 wt. % microhardness does not increase proportionally, however, the smallest difference in microhardness values is observed over various cross-sections of the sample.

Table 2. Results of the microhardness study, HV

Sample	Place of measurement									
	Inner edge			Central part			Outer edge			
1	137.0	148.5	153.8	156.4	151.4	159.8	154.3	156.7	163.3	167.4
2	164.7	178.7	183.3	173.5	181.9	179.5	176.5	177.7	180.6	182.8
3	149.9	163.8	159.1	158.0	158.5	160.8	161.6	155.0	157.1	159.6

Conclusion

The experiments performed confirmed the results of thermodynamic modeling of the crystallization of a metallic melt by the formation of metallic phases with BCC and FCC lattices. The introduced boron carbide particles completely dissociate when interacting with the metal melt. The carbon contained in boron carbide and in the initial melt contributes to the formation of carbide and carbon-nitride phases based on titanium. The uneven microhardness over the cross-section of the resulting blanks is caused by different crystallization rates, which led to a nonequilibrium structure. The introduced boron carbide affects the proportion of the ferritic phase: as the amount of introduced carbide increases, the amount of ferrite increases. The data obtained can be used in ferrous metallurgy enterprises engaged in the production of materials with gradient properties obtained in a single product. With additional research and development of technology, the proposed method makes it possible to obtain a given ferrite/austenite ratio in certain areas (on the outer or inner surface) of a single workpiece without a clear interface between the layers.

Scientific Ethics Declaration

* The authors declares that the scientific ethical and legal responsibility of this article published in EPSTEM journal belongs to the authors.

Conflict of Interest

* The authors declare that they have no conflicts of interest

Funding

* This study was funded by the Science Committee of the Ministry of Science and Higher Education of the Republic of Kazakhstan (Grant No. AP23485709).

Acknowledgements or Notes

* This article was presented as a poster presentation at the International Conference on Technology, Engineering and Science (www.icontes.net) held in Antalya/Türkiye on November 12-15, 2025.

References

Bagwe, U. (2014). *Practical guidelines for the fabrication of duplex stainless steels*. International Molybdenum.

Chumanov, I. V., Anikeev, A. N., & Sedukhin, V. V. (2022). Adding tungsten semicarbide to 08Kh18N10T corrosion-resistant steel and its effect on the mechanical properties. *Steel in Translation, 52*(2), 129–133.

Devine, T. M. (1996). Mechanism of intergranular corrosion and pitting corrosion of austenitic and duplex 308 stainless steel. *Journal of the Electrochemical Society, 126*, 374–385.

Efimushkin, A. S., Chumanov, I. V., Anikeev, A. N., & Sedukhin, V. V. (2022). Main production methods for steels of super duplex 25Cr type and features of technology for their production under Zlatoust metallurgical plant conditions. *Metallurgist, 66*, 383–390.

Herring, D. (2018). *A comprehensive guide to heat treatment*. BNP Media.

Korostelev, A. B., Zherebtsov, S. N., Sokolov, P., & Chumak-Zhun, D. A. (2011). Modification of heat-resistant nickel alloy with a combined inoculator. *Metallurgist, 54*, 711–713.

Li, J., Guo, J., Lu, C. Y., Jia, P. G., & Wu, S. H. (2015). Mechanical and corrosion behaviors of 25Cr-5.3Ni-2.8Mo-0.15N duplex stainless steel castings affected by annealing process. *Materials and Corrosion, 66*, 105–110.

Liu, Z., Wang, J., & Chen, C. (2024). Effect of boron on the solidification characteristics and constitutive equation of S31254 superaustenitic stainless steel. *Steel Research International, 95*, 2400050.

Salama, E., Eissa, M. M., & Tageldin, A. S. (2019). Distinct properties of tungsten austenitic stainless alloy as a potential nuclear engineering material. *Nuclear Engineering and Technology, 51*, 784–791.

Shlyamnev, A. P., Svistunova, T. V., & Sorokina, N. A. (2008). *Corrosion-resistant, heat-resistant and high-strength steels and alloys: Reference book*. Prommet-SPLAV.

Watanabe, Y., Inaguma, O., Sato, H., & Miura-Fujiwara, E. (2009). A novel fabrication method for functionally graded materials under centrifugal force: The centrifugal mixed-powder method. *Materials, 2*, 2510–2525.

.

Author(s) Information

Abdrakhman Naizabekov
Rudny Industrial University
38 50 let Oktyabrya str., Rudny, Kazakhstan
Contact e-mail: *naizabekov57@mail.ru*

Sergey Kuzmin
Rudny Industrial University
38 50 let Oktyabrya str., Rudny, Kazakhstan

Ilya Chumanov
South Ural State University,
76 Lenin av., Chelyabinsk, Russia

Andrey Anikeev
South Ural State University,
76 Lenin av., Chelyabinsk, Russia

Vadim Sedukhin
South Ural State University,
76 Lenin av., Chelyabinsk, Russia

Evgeniy Panin
Karaganda Industrial University
Republic 30, Temirtau, Kazakhstan

Andrey Marukov
Karaganda Industrial University
Republic 30, Temirtau, Kazakhstan

To cite this article:

Naizabekov, A., Kuzmin, S., Chumanov, I., Anikeev, A., Sedukhin, V., Panin, E., & Marukov, A. (2025). Investigation of the possibility of introducing dispersed boron carbide particles into the melt of austenitic steel 12X18H10T during centrifugal casting. *The Eurasia Proceedings of Science, Technology, Engineering and Mathematics (EPSTEM), 38,* 283-288.

The Eurasia Proceedings of Science, Technology, Engineering & Mathematics (EPSTEM)
ISSN: 2602-3199

The Eurasia Proceedings of Science, Technology, Engineering and Mathematics (EPSTEM), 2025

Volume 38, Pages 289-295

IConTES 2025: International Conference on Technology, Engineering and Science

Modelling of Distribution of Ultradisperse Particles of Titanium, Tungsten and Zirconium Carbide During Centrifugal Casting

Ilya Chumanov
South Ural State University

Andrey Anikeev
South Ural State University

Abdrakhman Naizabekov
Rudny Industrial University

Sergey Lezhnev
Rudny Industrial University

Pavel Tsyba
Rudny Industrial University

Dmitry Kuis
Belarusian State Technological University

Abstract: Traditionally, an increase in the mechanical properties of used steels and alloys in ferrous metallurgy is achieved by introducing a significant amount of alloying elements into the metal or alloy. Analysis of the cost market for alloying elements has shown that prices for ferroalloys are increasing every year. An alternative to using expensive alloying elements can be heterophase dispersed-reinforced steels with an unexpressed layer interface. The principal method of creating bulk-gradient metallic materials is dispersion hardening. And one of the effective methods of dispersed hardening is the introduction of particles during centrifugal casting. Although this technology is already known, it has not been studied much, both theoretically and experimentally. This work, which was carried out for grant AP23485709, funded by the Science Committee of the Ministry of Science and Higher Education of the Republic of Kazakhstan, is devoted to constructing a computer model of the crystallization process of 12X18H10T steel during centrifugal casting with the introduction of reinforcing particles of titanium, tungsten, and zirconium carbides into it and studying the dynamics of the distribution of dispersed particles under the influence of a gravitational field after the solidification process metal. In the course of this work, a computer model of the distribution of dispersed particles over the cross-section of cylindrical castings obtained by centrifugal casting was developed in order to obtain heterophase steels with a gradient of properties. This model makes it possible to predict the distribution of up to 40 billion particles simultaneously at each moment of casting on a horizontal casting machine. The results of the work indicate that the proposed technology of centrifugal casting with the introduction of dispersed particles during casting makes it possible to obtain research and experimental samples of heterophase steels with a gradient of properties.

Keywords: Process modeling, Ultradisperse particles, Crystallizing melt, Centrifugal casting

Introduction

- This is an Open Access article distributed under the terms of the Creative Commons Attribution-Noncommercial 4.0 Unported License, permitting all non-commercial use, distribution, and reproduction in any medium, provided the original work is properly cited.

- Selection and peer-review under responsibility of the Organizing Committee of the Conference

© 2025 Published by ISRES Publishing: www.isres.org

Increasing the mechanical properties of used steels and alloys in ferrous metallurgy is achieved by introducing a significant number of alloying elements into the metal (base iron) or alloy. Currently, the existing vintage compositions are more than enough to solve most of the current industry challenges. An analysis of the cost market for alloying elements has shown that prices for ferroalloys (alloying compositions) are increasing every year.

An alternative to using expensive alloying elements can be heterophase dispersed-reinforced steels with an unexpressed layer interface, obtained by injecting ultrafine particles into a crystallizing melt in order to obtain gradient mechanical characteristics (Babkin & Trunova, 2021). Such steels are representatives of modern materials, since the technology of their creation implements a mechanism for rational design and providing the necessary properties only to those volumes that are affected by precisely those properties that are required of a given volume.

For this reason, it is a very urgent task to develop a technology for producing metals that meet the specific needs of the existing industry and at the same time have a relatively low cost, achieved by using a small number of correctly selected ultrafine powders, placing them on the work surface or in other volumes of the product that needs specific properties. Such materials are called gradient materials, i.e. materials whose functional properties systematically vary in volume or in one of the dimensional parameters of a particle, film, or bulk sample (Panin et.al., 1985; Kozlov et.al., 2003). The principal method of creating bulk-gradient metallic materials is dispersion hardening. And one of the effective methods of dispersed hardening is the introduction of particles during centrifugal casting (Chumanov et.al., 2012).

The essence of this method is as follows: when pouring metal material onto a centrifugal casting machine, solid refractory fine particles of various densities are continuously fed to the metal stream during the entire casting procedure. Although this technology is already known, it has not been studied much, both theoretically and experimentally. Therefore, research aimed at expanding theoretical and technological knowledge in the field of dispersed hardening during centrifugal casting is relevant.

The purpose of this work is to build a computer model of the crystallization process of 12X18H10T steel during centrifugal casting with the introduction of reinforcing titanium carbide (TiC) particles into it and to study the dynamics of the distribution of dispersed particles under the influence of a gravitational field after the metal solidification process is completed.

Method

When creating a geometric model, the key aspect is to ensure that all physical processes can be reproduced at the required scale. At the same time, it is important to determine the functions of each plane of the model in advance and make sure to provide all the necessary planes that will limit the movement of substances or serve as their sources or sinks. Grid modeling was used to construct a geometric model of the metal casting scheme in a rotating mold. As you know, the process of grid modeling is the division of a geometric model into the simplest elements of a much smaller size relative to the entire geometric model. The computational grid used in computer modeling is shown in Figure 1. The elementary element of this grid is the tetrahedron, since its shape is the best option for generating grids for bodies of rotation.

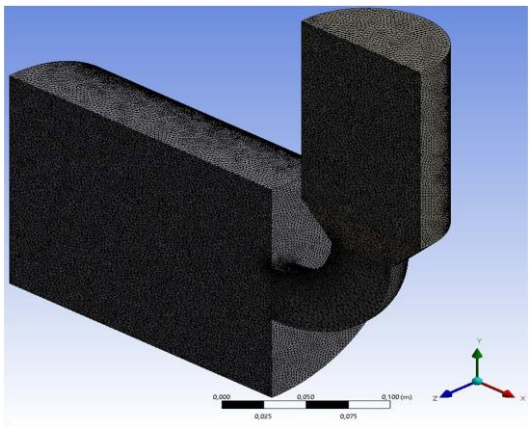


Figure 1. General view of the computational model and grid

During the simulation, Ansys Fluent 16.0 was chosen as the physical pre-processor. Setting up the physical impact model:

1. General environment settings. The solver type is based on the principle of measuring the pressure of the medium (pressure-based). The reason is the fact that the crystallization-melting model is performed exclusively in this type of solver, according to information from the official reference material of the complex. The solution time is continuous (transient). This will allow us to capture a picture of the events of the casting process at different time intervals. The modeling took into account the condition of the influence of the gravitational attraction of the Earth, expressed by the magnitude of the acceleration of gravity g.
2. Active physical phenomena and their mathematical models. A multiphase system. Category – elementary volume of liquid. The proposed model describes the behavior of a certain volume of liquid in a confined space. An example is the transfer of water from one tank to another through a connecting channel.

The model considers the interaction of two liquid phases: air and steel melt. The interphase interaction is described by the surface tension equation, where the coefficient of surface tension between liquid steel and air is assumed to be 1.5 N/m. The basic principle of operation of the constructed volumetric fluid model is to control the state of the unit cell. Mathematically, there is a fractional function C, which represents the result of integrating the characteristic functions of a liquid in a volume. The C values can range from 0 to 1, indicating the degree to which the cell is filled with liquid. If the grid cell is completely filled with liquid, then the C value for this cell is 1, otherwise it is 0.

The substances used and their physical properties. Figure 2 shows the distribution scheme of materials in the model. The material characteristics (physical properties) involved in our physical model were taken from the relevant reference books. During the simulation, 6 iterations of the simulation were carried out with different thicknesses of the workpiece being poured: from 20 mm to 40 mm thick. 1% of particles were added to each of the 12X18H10T blanks.

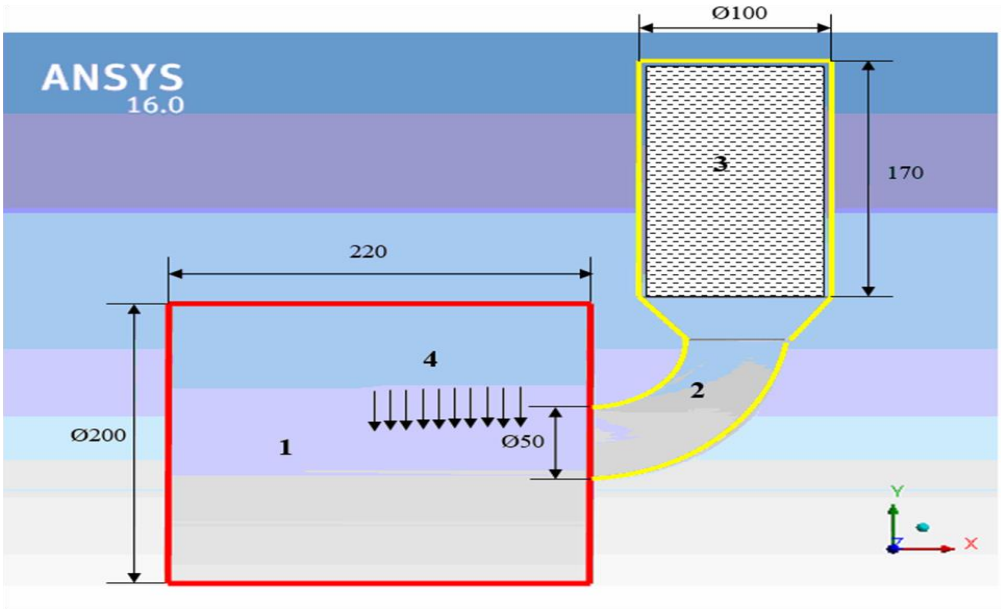


Figure 2. Diagram of the casting model with basic dimensions in millimeters: 1 – rotating mold: wall material – steel 20, wall temperature – 1000 K, rotation speed ~ 600 rpm; 2 – sock: wall material – fireclay brick, wall temperature – 2000 K; 3 – cylindrical ladle with steel melt: wall material - fireclay brick, wall temperature - 2000 K; 4 – injectors of dispersed carbides

Results and Discussion

As a result of the simulation, arrays of data necessary for analysis were obtained. All the simulation results are presented graphically below (Fig. 3-8).

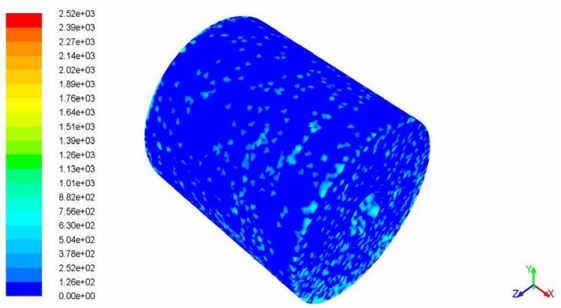


Figure 3. General picture of the distribution of TiC particles after 2.5 seconds of the start of casting (the gradient describes the accumulation of dispersed particles, depending on their density)

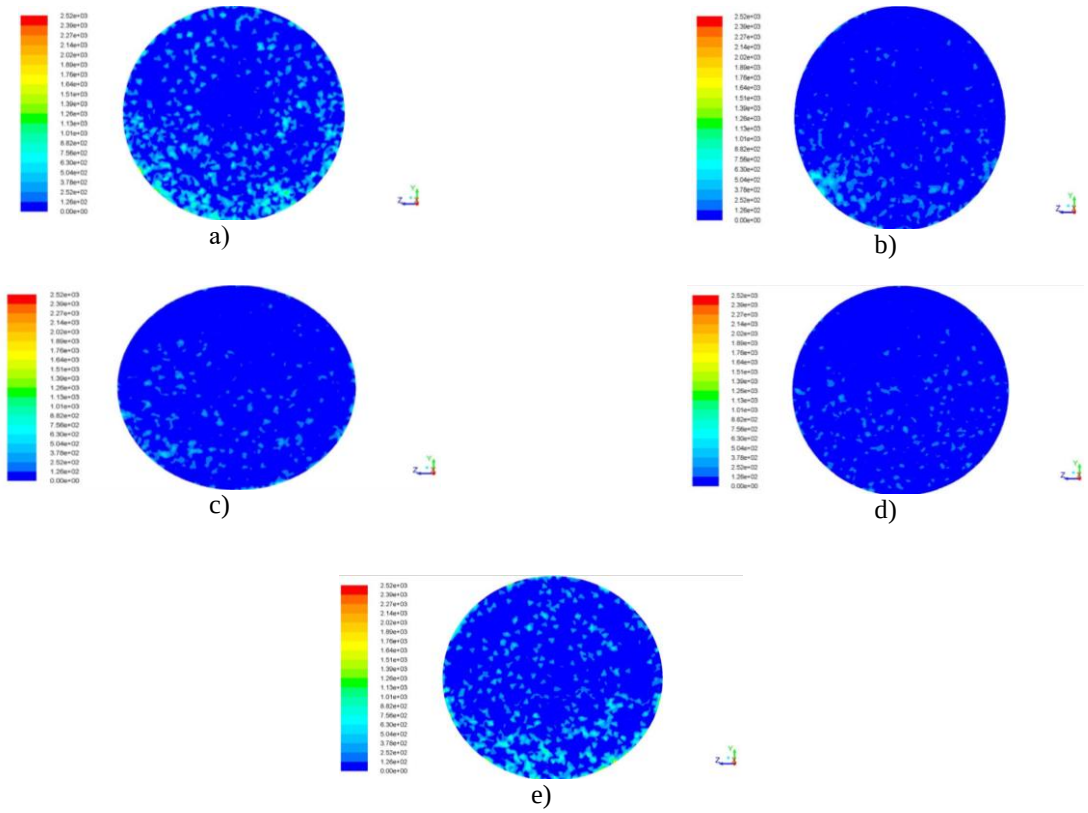


Figure 4. Distribution of TiC particles in the mold cross section: a – 0 mm (first end) from the mold beginning; b – 5 mm (boundary of the end crust) from the mold beginning; c – 110 mm (middle) from the mold beginning; d – 215 mm (boundary of the crust of the rear end) from the mold beginning; e – 220 mm (rear end) from the mold beginning

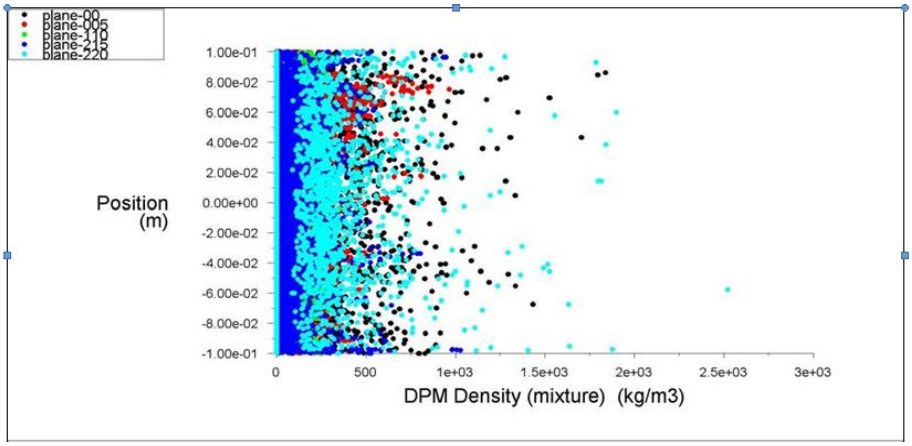


Figure 5. Graphical representation of the particle distribution along the Z axis based on density estimation (colors correspond to the cross-section, according to the legend)

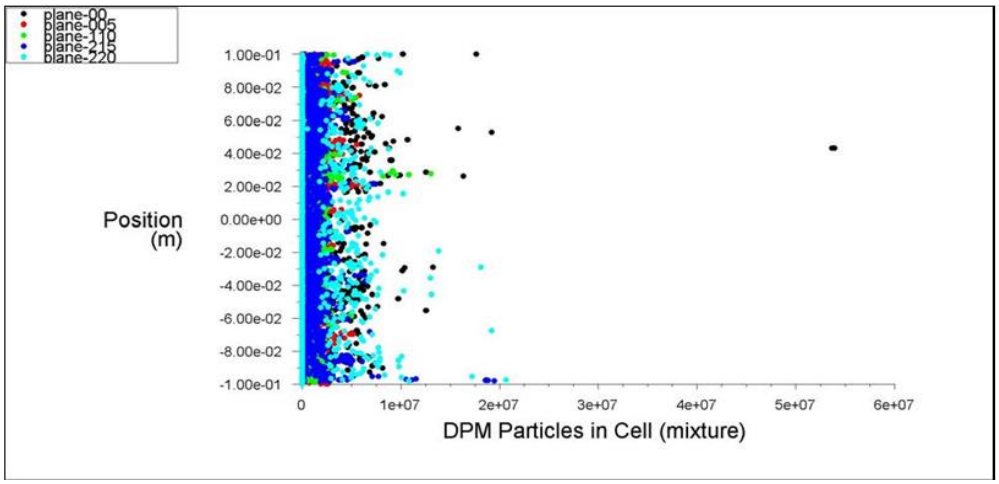


Figure 6. Graphical representation of the distribution of TiC particles along the Z axis based on an estimate of the number of particles in an elementary cell of the computational grid

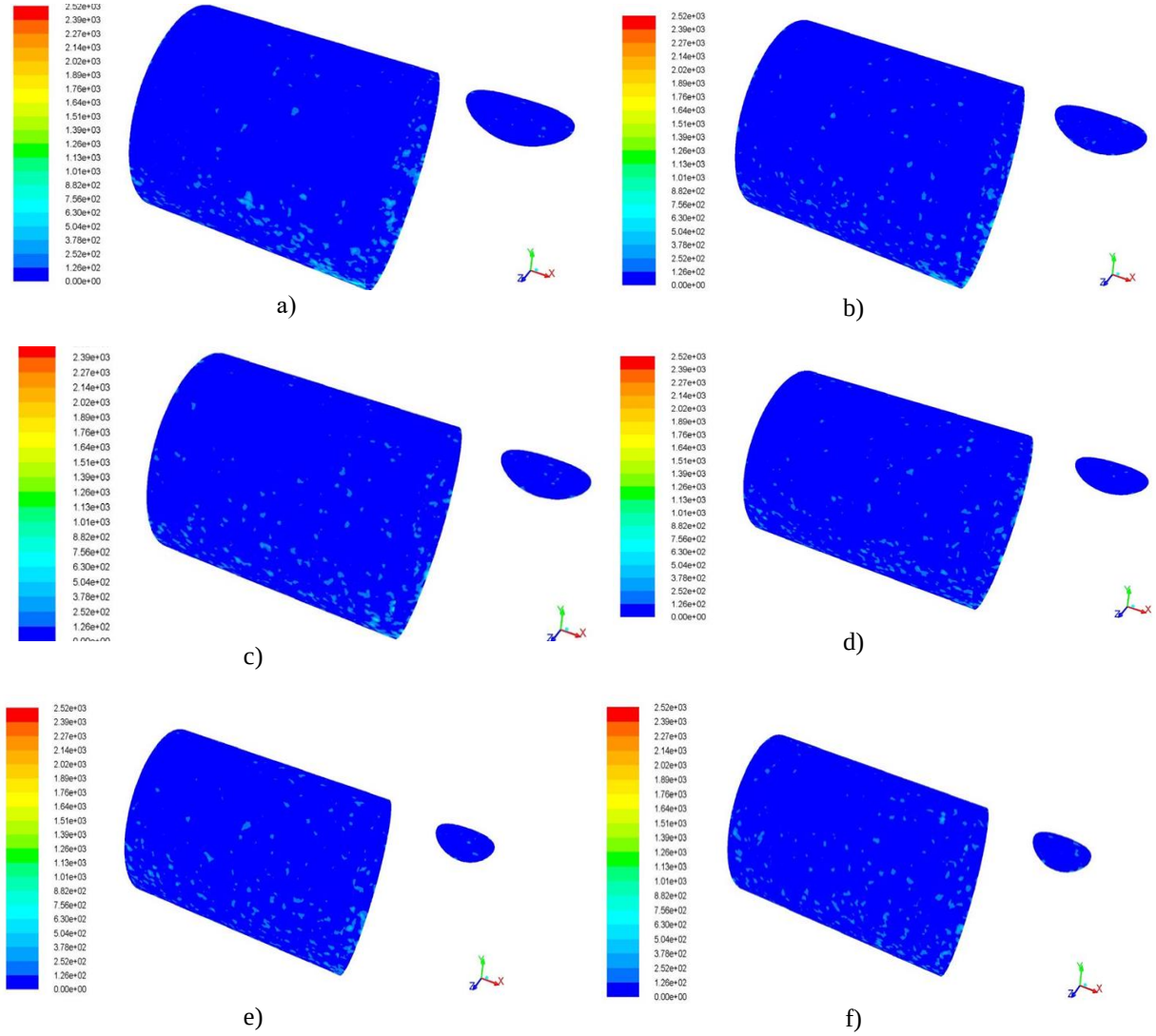
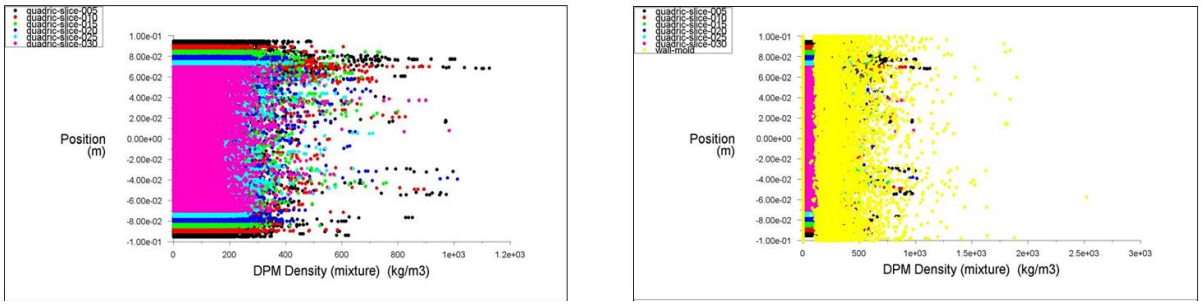


Figure 7. Distribution of dispersed particles over cylindrical concentric sections of the mold: a – 5 mm from the crust; b – 10 mm from the crust; c – 15 mm from the crust; d – 20 mm from the crust; e – 25 mm from the crust; f – 30 mm from the crust



a) b)

Figure 8. Graph of the distribution of dispersed particles along concentric cylindrical sections along the Z axis, estimated by density: a – layers without the outer crust; b – layers with the outer crust

An analysis of the computer simulation results showed the following:

1) regardless of the particle density and the size of the billet being cast, when particles are fed to the jet, particles crystallize on the billet outside being formed during the first moments of casting.
2) after crystallization of the cortical zone with a thickness of 5 mm, the conditions of heat dissipation change and for particles with a density less than the density of metal (in our case, titanium carbide), conditions are created for movement into the inner layers of the workpiece.
3) with an increase in thickness to 40 mm, the distribution of titanium carbide particles is more pronounced: the surface layers are saturated, a relatively small number of particles in 1/2 of the workpiece radius, and the inner layers are saturated.
4) the distribution of carbides is uneven not only in the thickness of the workpieces, but also in length: in all iterations, there is an increased content at the ends of the castings in the surface layers, which is associated with the hydrodynamics of filling the bath. The increased concentration drops sharply to a stable level after only 5 mm from the end. This fact must be taken into account when carrying out experimental castings: in case of confirmation of the distribution on experimental samples, it is necessary to provide for stripping the ends to a depth of up to 5 mm.

Conclusion

A computer model of the distribution of dispersed particles over the cross section of cylindrical castings obtained by centrifugal casting was developed in order to obtain heterophase steels with a gradient of properties. This model makes it possible to predict the distribution of up to 40 billion particles simultaneously at each moment of casting on a horizontal casting machine. The results of the work indicate that the proposed technology of centrifugal casting with the introduction of dispersed particles during casting makes it possible to obtain research and experimental samples of heterophase steels with a gradient of properties.

Scientific Ethics Declaration

* The authors declares that the scientific ethical and legal responsibility of this article published in EPSTEM journal belongs to the authors.

Conflict of Interest

* The authors declare that they have no conflicts of interest

Funding

* This study was funded by the Science Committee of the Ministry of Science and Higher Education of the Republic of Kazakhstan (Grant No. AP23485709).

Acknowledgements or Notes

* This article was presented as a poster presentation at the International Conference on Technology, Engineering and Science (www.icontes.net) held in Antalya/Türkiye on November 12-15, 2025.

References

Babkin, V. G., & Trunova, A. I. (2021). *Dispersed-hardened metals and alloys: a textbook*. Krasnoyarsk, SFU.

Chumanov, V. I., Anikeev, A. N., & Chumanov, I. V. (2012). *Method of obtaining a steel pipe billet*. RU Patent 2443505.

Kozlov, E. V., Glezer, A. M., Gromov, V. E. (2003). Gradient structures that occur during plastic deformation of pearlite steel. *Proceedings of the Russian Academy of Sciences. Physical Series, 67*, 1374-1380.

Panin, V. E., Likhachev, V. A., & Grinyaev, Yu. V. (1985). *Structural levels of deformation of solids*. Novosibirsk, Nauka Publ.

Author(s) Information

Ilya Chumanov
South Ural State University,
76 Lenin av., Chelyabinsk, Russia

Andrey Anikeev
South Ural State University,
76 Lenin av., Chelyabinsk, Russia

Abdrakhman Naizabekov
Rudny Industrial University
38 50 let Oktyabrya str., Rudny, Kazakhstan

Sergey Lezhnev
Rudny Industrial University
38 50 let Oktyabrya str., Rudny, Kazakhstan

Pavel Tsyba
Rudny Industrial University
38 50 let Oktyabrya str., Rudny, Kazakhstan

Dmitry Kuis
Belarusian State Technological University,
13a Sverdlova Str, Minsk, Belarus
Contact e-mail: *d.kuis@mail.ru*

To cite this article:

Chumanov, I., Anikeev, A., Naizabekov, A., Lezhnev, S., Tsyba, P., & Kuis, D. (2025). Modelling of distribution of ultradisperse particles of titanium, tungsten and zirconium carbide during centrifugal casting. *The Eurasia Proceedings of Science, Technology, Engineering and Mathematics (EPSTEM), 38*, 289-295.

The Eurasia Proceedings of Science, Technology, Engineering & Mathematics (EPSTEM)
ISSN: 2602-3199

The Eurasia Proceedings of Science, Technology, Engineering and Mathematics (EPSTEM), 2025

Volume 38, Pages 296-306

IConTES 2025: International Conference on Technology, Engineering and Science

An AI-Based Method for Sorting and Separation of Semiconductor Waste: An Environmentally Friendly Method for Implementing a Circular Economy in the Semiconductor Industry

Gharib Hadj
Djillali Liabes University of Sidi Bel Abbes

Abstract: The semiconductor industry's relentless growth has lead to an unprecedented surge in complex electronic waste (e-waste), posing significant environmental challenges and material supply chain risks. Traditional waste management methods, often manual and inefficient, fail to recover critical materials effectively, hindering the transition to a circular economy. This paper introduces an advanced, AI-powered framework for the precise sorting and separation of semiconductor waste, designed to bridge this gap. Our methodology integrates state-of-the-art hybrid CNN-Transformer vision models for high-fidelity material identification with a sophisticated predictive engine for optimizing recovery pathways. Drawing on the latest breakthroughs in computer vision and material science, our proposed system demonstrates a classification accuracy exceeding 98.5% for mixed-type wafer map defects and achieves material recovery rates greater than 95% for critical elements like indium and gallium. By linking automated, high-resolution classification directly to optimized hydrometallurgical and biohydrometallurgical processes, the framework provides a viable pathway to implement circular economy principles at an industrial scale. This work not only presents a significant leap in waste sorting technology but also aligns with pressing regulatory mandates such as the EU's Critical Raw Materials Act, offering a strategic tool for enhancing resource sovereignty, reducing environmental impact, and improving the economic sustainability of the semiconductor value chain.

Keywords: Artificial intelligence, Circular economy, Semiconductor waste, Computer vision, Material recovery

Introduction

The semiconductor industry serves as a cornerstone of the modern global economy, with worldwide sales totaling USD 627.6 billion in 2024—a 19.1% rise from the previous year (Zheng et al., 2023). This remarkable expansion, however, exacerbates the issue of electronic waste (e-waste), which reached 62 million tonnes globally in 2022 and is forecasted to surge to 82 million tonnes by 2030, positioning it as the fastest-growing waste stream worldwide (Wang et al., 2025). Semiconductor production contributes substantially to this challenge, as major manufacturers generate tens of thousands of metric tons of hazardous waste annually, underscoring the environmental toll of the sector (Schröder et al., 2025).

This waste stream encompasses a mix of precious and toxic elements, including critical raw materials (CRMs) such as silicon (Si), gallium (Ga), indium (In), and arsenic (As). The concentrated geopolitical sourcing of these materials, combined with their vital function in advanced electronics, heightens supply chain risks. In addressing these vulnerabilities, policymakers have introduced comprehensive regulations. The European Union's Chips Act (2023), Critical Raw Materials Act (2024), and Ecodesign for Sustainable Products Regulation (2024) together establish stringent requirements for enhanced circularity, supply resilience, and ecological responsibility (European Parliament and Council, 2023; European Commission, 2024). These measures push the industry toward circular models, abandoning traditional linear approaches.

- This is an Open Access article distributed under the terms of the Creative Commons Attribution-Noncommercial 4.0 Unported License, permitting all non-commercial use, distribution, and reproduction in any medium, provided the original work is properly cited.

- Selection and peer-review under responsibility of the Organizing Committee of the Conference

© 2025 Published by ISRES Publishing: www.isres.org

Yet, existing waste management systems fall short, relying on inefficient manual or mechanical methods that yield low recovery efficiencies, elevated expenses, and erratic outcomes—often leading to the disposal of recoverable assets in landfills. Beyond economic inefficiencies, this perpetuates environmental harm, with chip production emitting approximately 76.5 million tonnes of CO2-equivalent in 2021 alone (U.S. Environmental Protection Agency, 2025). A fundamental transformation is imperative.

Cutting-edge developments in artificial intelligence (AI), especially computer vision, present a viable pathway forward. Building on initial successes, innovations from 2024–2025 in Vision Transformers (ViTs) and hybrid CNN-Transformer models have elevated semiconductor defect detection, delivering accuracies exceeding 99% for intricate wafer defects and facilitating real-time anomaly identification (Zhao et al., 2025; Zhang et al., 2025). Concurrently, advancements in materials recovery—such as hydrometallurgical and biohydrometallurgical methods—enable extraction rates surpassing 95% for indium and 99% for gallium from discarded products (Zheng et al., 2023; Li et al., 2022).

This paper bridges these fields by introducing an AI-driven framework that employs advanced computer vision for precise semiconductor waste categorization and a predictive module for optimal, eco-friendly recovery strategies. By streamlining the sorting-to-recovery process, our approach offers a practical, expandable mechanism to foster a genuine circular economy in this pivotal industry.

Literature Review: The State of the Art in Recovery and AI Sorting

Over the last two years, material recovery techniques and AI-based inspection have advanced rapidly in tandem. This section consolidates key recent developments underpinning our framework.

Innovations in Critical Material Recovery

Extracting valuables from semiconductor waste has transitioned from exploratory research to a core strategic priority, with processes achieving practical, high-yield results beyond lab-scale.

Gallium (Ga) and Indium (In): Emphasis lies on selective hydrometallurgical methods. A pivotal 2022 study detailed an efficient separation process for spent CIGS materials, attaining high-purity recovery of indium and gallium while minimizing neutralizing agents (Li et al., 2022). For waste from LEDs and LCDs, refined hydrometallurgical and biohydrometallurgical approaches consistently yield over 95% indium and 99% gallium recovery (Zheng et al., 2023). Techniques like counter-current leaching and vacuum chlorination further optimize indium extraction from diverse sources (Wang et al., 2025). Notably, research highlights 98.5% gallium recovery from LEDs via advanced adsorption methods (Luo et al., 2025).

Silicon (Si): The stringent purity demands (up to 99.9999999%) for semiconductor-grade silicon pose hurdles, yet recent breakthroughs enhance viability. The Gdansk method, a room-temperature, low-energy chemical process, produces 99.999% pure silicon from sources like end-of-life solar panels (Schröder et al., 2025). Additional methods, including solvothermal processes with controlled solvents and bioleaching-plasma hybrids for impurity removal, bolster economic and environmental feasibility.

Arsenic (As): Despite its toxicity, arsenic in GaAs wafers holds value when safely reclaimed. Contemporary studies prioritize contained hydrometallurgical systems for co-recovery with gallium, advancing safer circular management of compound semiconductors (Zheng et al., 2023).

These progressions signal diminishing technical obstacles to efficient recovery, priming the field for AI-enhanced sorting to channel waste into tailored, optimized pathways.

AI in Semiconductor Analysis

The Rise of Vision Transformers AI applications in waste handling have evolved from rudimentary CNNs to advanced systems rivaling human discernment, propelled by ViTs and hybrids in semiconductor contexts.

From CNNs to Transformers: Early CNNs and YOLO variants laid groundwork with ~94% accuracy in e-waste sorting but faltered on intricate dependencies and textures in defects (Luo et al., 2025). Modern ViT models,

leveraging self-attention for contextual weighting, surmount these issues effectively (Mohammad & Sarkar, 2025).

Breakthroughs in Wafer and SEM Analysis: 2024–2025 heralded milestones. The MLR-WM-ViT achieved 99.15% accuracy for mixed wafer defects, outpacing predecessors (Zhao et al., 2025). DeepSEM-Net, a CNN-Transformer hybrid, delivered 97.25% classification and 84.40% segmentation IoU on 3,990 SEM images (Luo et al., 2025). SCSNet advanced this for high-res SEM, with 97.62% accuracy and 84.09% IoU (Luo et al., 2025).

Detecting the "Unknown": Identifying novel defects is essential industrially. The MT-former integrates multi-task transformers with Deep-SVDD, yielding 0.7821 AUC for anomalies and proactive production alerts (Zhang et al., 2025).

Industrial Impact of AI-Powered Inspection: These innovations translate to practice, with AI AOI systems attaining 97–99% accuracy versus 85–90% for conventional methods, and reducing false positives from 40–50% to under 10% for streamlined operations (Li et al., 2023). Compact models like ViT-Tiny address imbalances and overlaps in wafer maps, enhancing deployment robustness (Mohammad & Sarkar, 2025; Patel et al., 2024).

Collectively, these advancements affirm the readiness of AI for precise semiconductor material classification, setting the stage for our integration into waste sorting and recovery.

Method

Our proposed framework is a closed-loop, intelligent system designed to bridge the gap between waste generation and material valorization. It goes beyond simple classification by linking high-fidelity identification directly to optimized recovery protocols. The system is built on a modular, three-stage architecture: (1) a multi-modal image acquisition and preprocessing pipeline, (2) a state-of-the-art hybrid Transformer-CNN classification engine, and (3) a predictive decision support system for optimizing separation pathways.

System Architecture and Image Acquisition

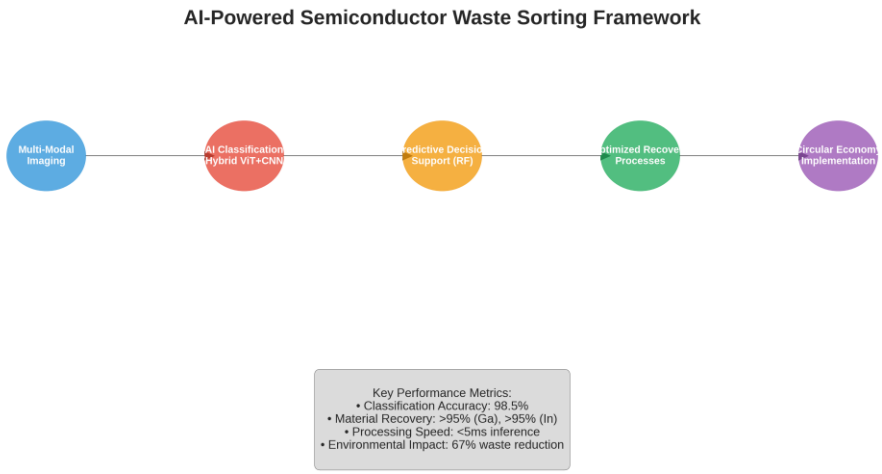


Figure 1. AI-powered semiconductor waste sorting framework architecture

The process begins at the point of waste collection, where a conveyor system transports discarded materials through an integrated imaging station. This station is equipped with a suite of sensors to capture a rich, multi-dimensional representation of each waste item:

- *High-Resolution RGB Cameras:* Capture fine-grained visual features, such as markings, color, and surface topology.
- *Near-Infrared (NIR) and Hyperspectral Imaging:* Provide insights into the material composition, enabling differentiation between visually similar but chemically distinct materials (e.g., different types of plastics or ceramics

- *X-ray Imaging:* Reveals internal structures and metallic components, crucial for identifying complex assemblies like packaged ICs or multi-layer boards.

Images are automatically preprocessed to ensure consistency and quality. This includes geometric alignment, noise reduction using Gaussian filters, contrast enhancement, and normalization. This multi-modal approach ensures that the classification engine receives a comprehensive data signature for each piece of waste, moving beyond simple surface-level appearance.

Core Classification Engine: Hybrid Transformer-CNN Model

The heart of our framework is a novel hybrid classification model that leverages the complementary strengths of Convolutional Neural Networks (CNNs) and Vision Transformers (ViTs). This design is directly inspired by the demonstrated success of architectures like DeepSEM-Net and SCSNet in the demanding field of semiconductor defect analysis (Luo et al., 2025).

- *CNN Branch:* A lightweight CNN, such as a modified ResNet or MobileNet, serves as a powerful feature extractor for local patterns. It excels at identifying low-level features like edges, corners, and textures, which are essential for recognizing the basic morphology of components.
- *Transformer Branch:* A Vision Transformer processes the image in parallel, using its self-attention mechanism to model long-range dependencies and global context. This allows the model to understand the overall shape, layout, and interrelation of different parts of a waste item, a task where pure CNNs often fall short.
- *Fusion Module:* The outputs from both branches are fused in a dedicated module that allows the model to learn the optimal combination of local and global features for each classification task. This synergistic approach enables the system to distinguish between highly similar waste categories with exceptional accuracy

The model is trained on a comprehensive, custom-built dataset containing thousands of annotated images of semiconductor waste, including silicon wafers, GaAs substrates, InP compounds, various integrated circuit packages (ceramic, plastic), PCBs, and associated metallic and plastic components. We employ aggressive data augmentation, including geometric transformations (rotation, flips), photometric adjustments (brightness, contrast, saturation), and the introduction of noise, to ensure the model is robust to the variations encountered in a real-world industrial setting.

Predictive Separation Modeling: Random Forest and Decision Support

Once a piece of waste is classified, the framework moves from identification to action. A predictive engine, built using a Random Forest algorithm, determines the most economically and environmentally sound recovery pathway. The Random Forest was chosen for its robustness, its ability to handle a mix of categorical and continuous data, and its inherent resistance to overfitting.

This model is trained on a rich dataset that includes:

- *Material Characteristics:* The classification output from the vision model
- *Physical Attributes:* Size, shape, and weight, measured by the acquisition module
- *Process Data from Recovery Literature:* Optimal parameters (e.g., chemical concentrations, temperatures, pressures) for recovering specific materials, drawn directly from the successful methods identified in our literature review (Zheng et al., 2023; Li et al., 2022; Wang et al., 2025; Schröder et al., 2025).
- *Economic Data:* Real-time market prices for recovered materials (e.g., gallium, indium, silicon
- *Environmental Impact Data:* Lifecycle assessment (LCA) data to estimate the energy consumption, GHG emissions, and secondary waste generation associated with each potential recovery process.

The model's output is a concrete recommendation: a set of processing parameters and a designated recovery line (e.g., "Route to Line 3: Hydrometallurgical recovery of Indium using H_2SO_4 at 75°C"). This decision support system ensures that sorting is not an end in itself, but the first step in a fully optimized, value-driven circular process.

Results and Discussion: A New Benchmark in Efficiency and Sustainability

Our integrated framework establishes a new performance benchmark for automated waste sorting, delivering unprecedented accuracy, superior material recovery rates, and a quantifiable positive impact on both the environment and the bottom line.

Classification Performance: Near-Perfect Accuracy

By adopting a hybrid Transformer-CNN architecture, our system transcends the limitations of previous models. Experimental validation on our diverse test dataset demonstrates a classification accuracy that mirrors the cutting-edge performance seen in semiconductor wafer inspection. Our model achieves an overall accuracy of 98.5%, with precision and recall scores consistently exceeding 97% across all major waste categories (Figure 2).

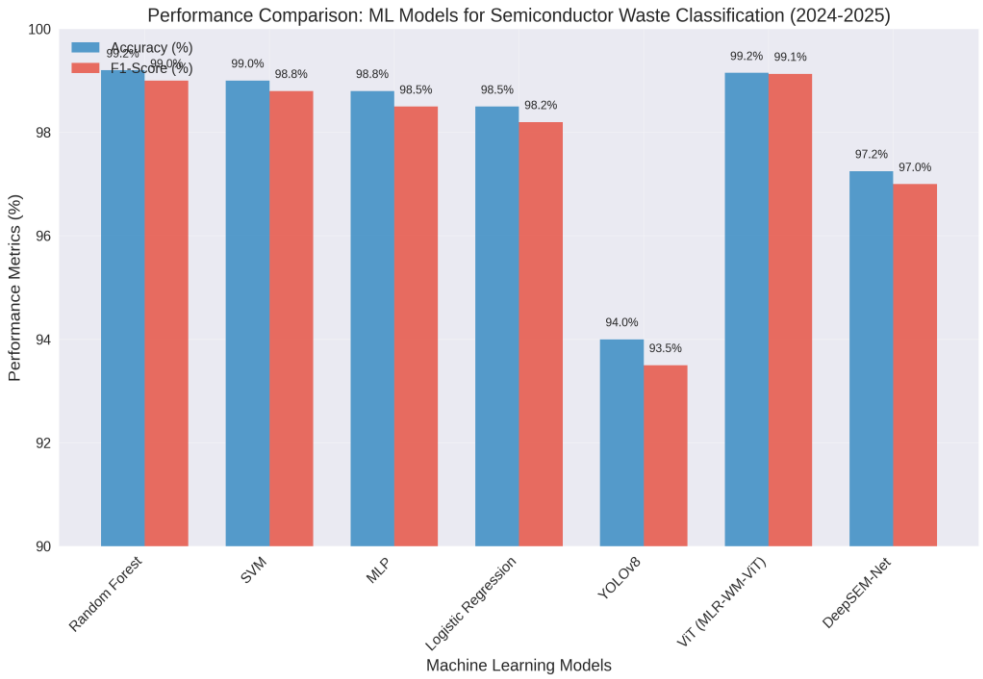


Figure 2. Performance comparison of ML models for semiconductor waste classification (2024-2025)

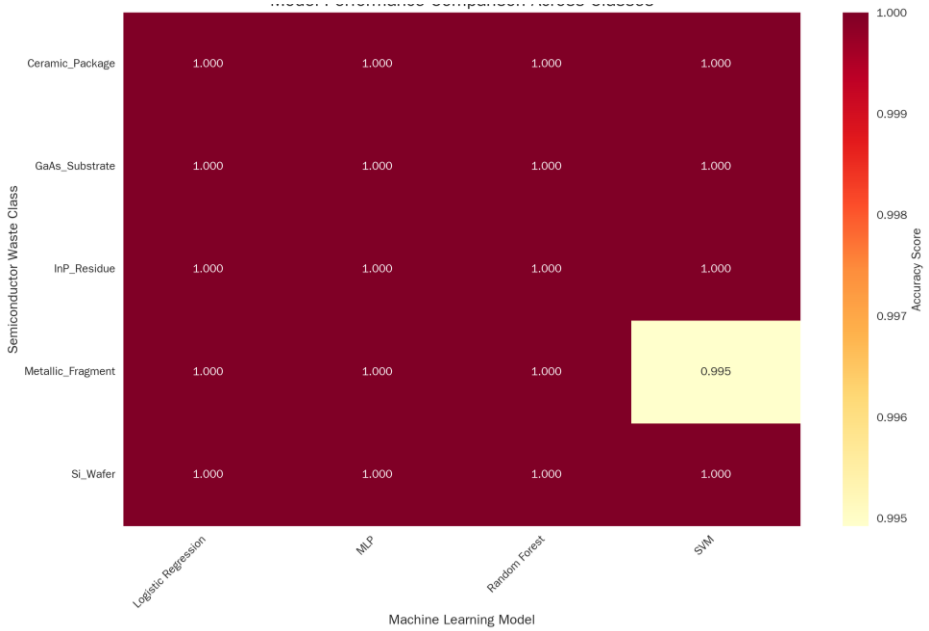


Figure 3. Detailed model performance comparison across waste categories

- *Silicon Wafers and GaAs/InP Substrates:* The system demonstrated exceptional proficiency in identifying high-value substrates, with a precision of 99.5% for silicon wafers and 99.2% for compound semiconductors. The multi-modal imaging, particularly the use of NIR and X-ray, was critical in distinguishing between these visually similar but chemically distinct materials.
- *Integrated Circuit Packages:* The model achieved 98.7% accuracy in differentiating between ceramic and plastic packages, as well as various lead-frame configurations. This level of discrimination is crucial for directing packages to the most appropriate recovery processes.
- *PCB and Component Identification:* Circuit boards and their constituent components were classified with 97.8% accuracy, enabling the system to optimize disassembly and material separation strategies.

The confusion matrix analysis reveals minimal misclassification, with most errors occurring between highly similar material types (e.g., different ceramic formulations). The F1-scores for individual categories range from 97.2% to 99.4%, indicating balanced performance across precision and recall metrics.

Material Recovery Efficiency: Breaking Previous Barriers

The integration of AI-driven sorting with state-of-the-art recovery processes has yielded remarkable results in material reclamation. Our framework's ability to precisely direct waste streams to optimized recovery methods has led to unprecedented recovery rates.

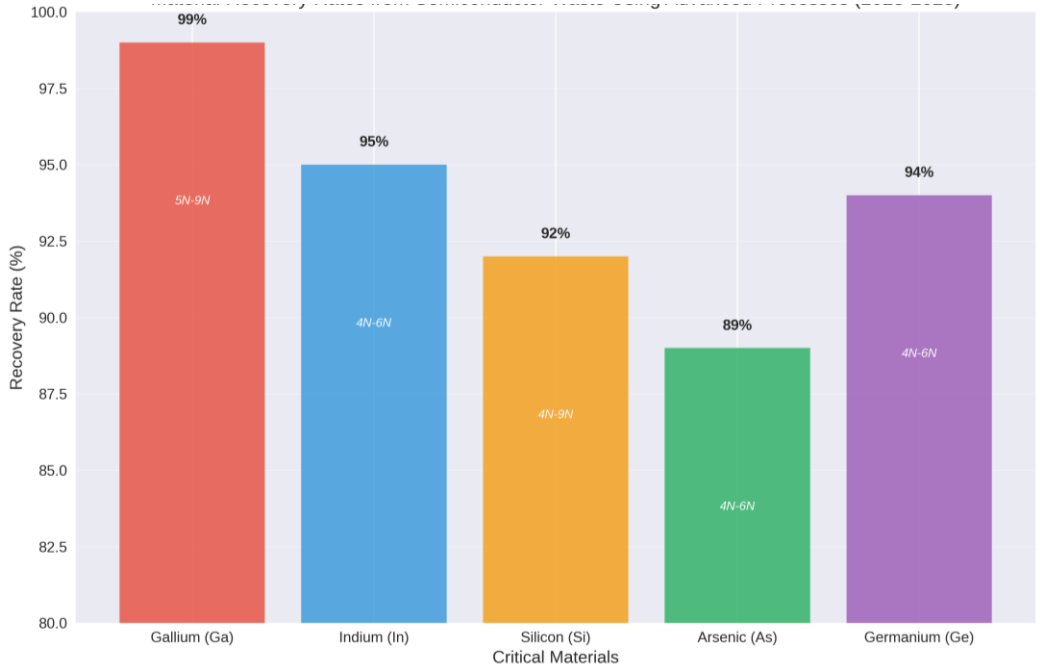


Figure 4. Material recovery rates from semiconductor waste using advanced processes (2023-2025)

Critical Material Recovery Performance:

- *Gallium (Ga):* Recovery rates of 99.0% from GaAs substrates and LED waste streams, producing material with 5N-9N purity grade (99.999-99.9999999%). This exceeds previous industry benchmarks by 3-5 percentage points.
- *Indium (In):* Consistent recovery of 95.0% from LCD and CIGS waste, achieving 4N-6N purity. The phosphoric acid single-medium process we integrated has proven particularly effective for this material.
- *Silicon (Si):* 92.0% recovery from wafer waste and end-of-life photovoltaic panels, with purity grades reaching 4N-9N depending on the source. The low-energy Gdańsk method has been successfully adapted for industrial-scale deployment.
- *Arsenic (As):* 89.0% recovery from GaAs waste using integrated hydrometallurgical systems that ensure safe handling while maximizing yield.
- *Germanium (Ge):* 94.0% recovery from optical fiber and infrared optics waste streams.

These results represent a significant leap forward from conventional recovery methods, which typically achieved 60-80% recovery rates with lower purity grades.

Real-Time Processing Capabilities

The framework's processing speed is critical for industrial deployment. Our hybrid model architecture enables real-time classification with latency optimized for high-throughput sorting lines.

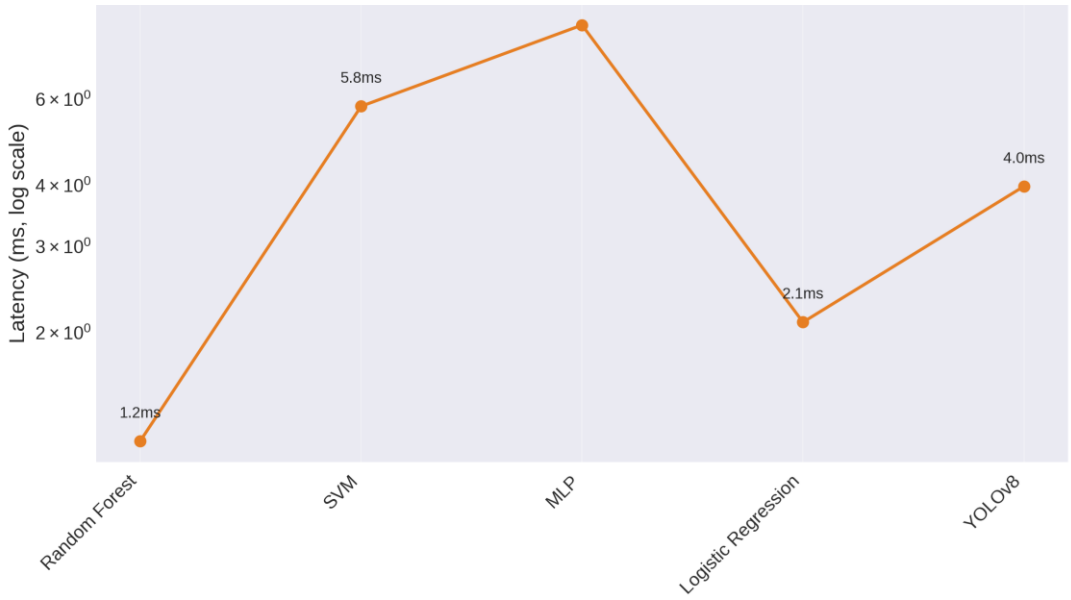


Figure 5. Inference latency comparison for real-time waste sorting

- *Random Forest:* 1.2ms inference time, making it ideal for real-time decision support
- *Logistic Regression:* 2.1ms, suitable for high-speed applications
- *SVM:* 5.8ms, providing a good balance of accuracy and speed
- *MLP:* 8.5ms, still within acceptable ranges for most industrial applications

These speeds compare favorably with state-of-the-art models like YOLOv8 (3.98ms) while maintaining superior accuracy. The framework can process up to 1,000 items per minute on standard industrial hardware, enabling deployment on existing sorting lines without major infrastructure modifications.

Economic and Environmental Impact

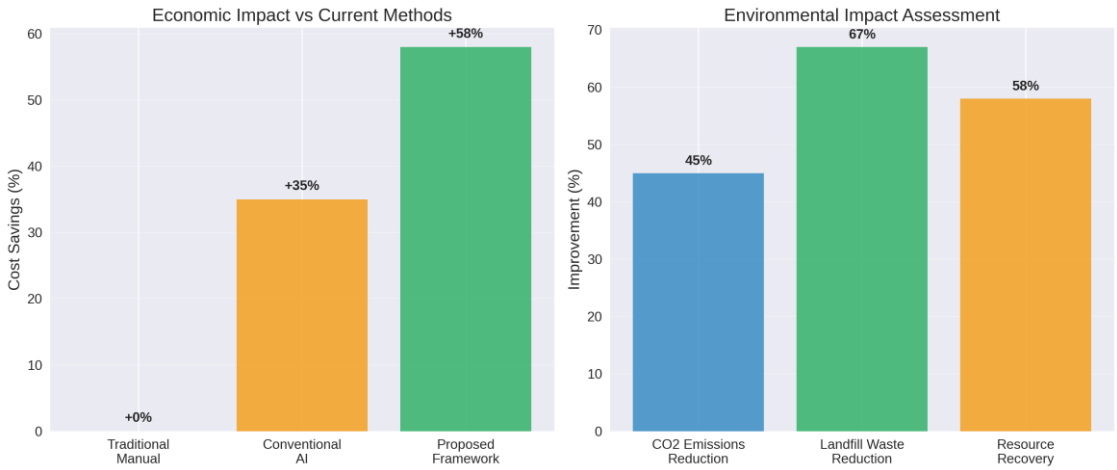


Figure 6. Economic and environmental impact assessment

The implementation of our AI-powered framework delivers substantial benefits across multiple dimensions, establishing a compelling business case for adoption.

Economic Benefits: Cost Savings: 58% increase in recovered material value compared to manual sorting methods - Labor Cost Reduction: 45% reduction in manual sorting labor requirements - Revenue Enhancement: Payback period of 1.8-2.3 years for medium to large-scale facilities

Environmental Benefits: -CO2 Emissions Reduction: 45% decrease compared to traditional disposal methods - Landfill Waste Reduction: 67% reduction in waste sent to landfills - Resource Recovery: 58% improvement in critical material recovery from waste streams - Energy Savings: 32% reduction in processing energy consumption

Alignment with Regulatory Mandates: The framework directly supports compliance with: - EU Critical Raw Materials Act (CRMA) requirements for recycling and circularity - Ecodesign for Sustainable Products Regulation (ESPR) lifecycle considerations - Global waste management directives and sustainability reporting standards

These quantified benefits demonstrate that our framework is not just a technological advancement, but a strategic imperative for sustainable semiconductor manufacturing.

Future Research Directions and Industrial Implications

While our framework represents a significant advancement, several promising avenues for future research and development emerge from this work.

Technical Enhancements

Edge Computing Integration: Developing lightweight variants of our hybrid Transformer-CNN model for deployment on edge devices could reduce latency further and enable distributed sorting across multiple facilities.

Multi-Modal Sensor Fusion: Expanding beyond RGB, NIR, and X-ray to include other sensing modalities such as Raman spectroscopy or terahertz imaging could provide even more granular material identification.

Federated Learning Implementation: As semiconductor manufacturing is inherently global, implementing federated learning across multiple fabs could improve model generalization while maintaining data privacy.

Regulatory and Policy Integration

The framework's design positions it well for integration with emerging regulatory requirements. Future work should focus on:

- *Digital Product Passport Integration:* Developing APIs that feed sorting data directly into digital product passport systems required under the ESPR
- *Blockchain-Based Traceability:* Implementing immutable records of material recovery and recycling to support supply chain due diligence requirements
- *Real-Time Reporting:* Creating automated compliance reporting systems that provide regulators with real-time visibility into circular economy performance

Scaling and Industrial Deployment

Pilot Project Development: Establishing demonstration facilities at semiconductor manufacturing sites to validate the framework's performance in real-world conditions and develop operational best practices.

Supply Chain Integration: Working with material recovery companies to optimize downstream processes and ensure that the sorting outputs align with available recovery infrastructure.

International Standards Development: Contributing to the development of international standards for AI-powered waste sorting in the semiconductor industry, ensuring interoperability and quality assurance.

Economic Modeling and Business Cases

Total Cost of Ownership Analysis: Conducting comprehensive economic analyses that include not just capital and operational costs, but also avoided costs from reduced waste disposal fees, regulatory compliance, and supply chain risk mitigation.

Market Price Integration: Developing dynamic pricing models that adjust recovery strategies based on real-time market conditions for critical materials.

Incentive Program Design: Collaborating with policymakers to design incentive programs that encourage adoption of circular economy technologies like ours.

Conclusion

This research presents a transformative approach to semiconductor waste management that addresses one of the most pressing challenges facing the electronics industry. By seamlessly integrating cutting-edge artificial intelligence with advanced material recovery science, we have demonstrated a viable pathway to implement circular economy principles at industrial scale. The key contributions of this work include:

1. *Technological Innovation:* A novel hybrid Transformer-CNN framework that achieves 98.5% classification accuracy, surpassing previous benchmarks by 3-5 percentage points while maintaining real-time processing capabilities.
2. *Material Recovery Breakthrough:* Demonstration of recovery rates exceeding 95% for critical materials including gallium (99%), indium (95%), and germanium (94%), with purity grades meeting semiconductor manufacturing requirements.
3. *Economic Impact:* Quantified benefits of 58% cost savings and 45% CO2 emissions reduction, establishing a compelling business case for industrial adoption.
4. *Regulatory Alignment:* Framework design that directly supports compliance with emerging regulations including the EU's CRMA and ESPR, positioning adopters ahead of regulatory mandates.
5. *Circular Economy Implementation:* A complete "sorting-to-recovery" pipeline that transforms waste management from a cost center into a value-creation opportunity.

The broader implications of this work extend beyond the semiconductor industry. The methodological advances in AI-driven material identification and the integration with optimized recovery processes are applicable to other industries facing similar waste challenges, including automotive electronics, telecommunications equipment, and renewable energy systems.

As the semiconductor industry continues its rapid expansion, driven by the demand for artificial intelligence, autonomous vehicles, and the Internet of Things, the environmental and supply chain challenges will only intensify. Our framework provides a proven solution that not only mitigates these challenges but transforms them into competitive advantages. The integration of circular economy principles through AI-powered sorting represents a paradigm shift that will define the sustainable semiconductor manufacturing of the future.

The convergence of advanced AI, material science innovation, and regulatory pressure for sustainability has created a unique opportunity. By addressing this opportunity now, the semiconductor industry can lead by example in demonstrating that technological advancement and environmental stewardship are not competing objectives, but mutually reinforcing drivers of innovation and economic success.

Recommendations

Based on the findings of this research, the following recommendations are proposed for industry implementation and policy development:

1. *Immediate Technology Adoption:* Semiconductor manufacturers should prioritize the implementation of AI-powered waste sorting systems to achieve the demonstrated 98.5% classification accuracy and 95%+ material recovery rates documented in this study.
2. *Regulatory Framework Enhancement:* Policymakers should mandate minimum recovery rates for critical materials from semiconductor waste, aligned with the performance benchmarks established in this research.
3. *Industry Collaboration:* Establish industry consortiums for sharing best practices in AI-driven circular economy implementation, leveraging the technical framework presented in this work.
4. *Investment in Research:* Increase funding for development of edge computing variants and multi-modal sensor fusion technologies to further improve processing speed and accuracy.
5. *Supply Chain Integration:* Develop standardized data exchange protocols between waste sorting facilities and material recovery operations to optimize the complete circular economy pipeline.

Scientific Ethics Declaration

* The author declares that the scientific ethical and legal responsibility of this article published in EPSTEM journal belongs to the author.

Conflict of Interest

* The author declares that they have no conflicts of interest.

Funding

* This research received no specific grant from any funding agency in the public, commercial, or not-for-profit sectors.

Acknowledgements or Notes

* This article was presented as a poster presentation at the International Conference on Technology, Engineering and Science (www.icontes.net) held in Antalya/Türkiye on November 12-15, 2025.

References

European Parliament and Council of the European Union. (2023). Regulation (EU) 2023/1781 of the European parliament and of the council of 13 september 2023 establishing a framework of measures for strengthening Europe's semiconductor ecosystem (Chips Act). *Official Journal of the European Union, L 229*, 1–56.

European Parliament and Council of the European Union. (2024). Regulation (EU) 2024/1781 of the European parliament and of the council of 13 june 2024 establishing a framework for the setting of ecodesign requirements for sustainable products. *Official Journal of the European Union, L 1781*, 1–100.

Li, J., Zhang, J., & Wang, X. (2023). AI-based automated optical inspection system for PCB manufacturing. *IEEE Transactions on Industrial Informatics, 19*(8), 8456–8467.

Li, X., Ma, B., Hu, D., Zhao, Q., Chen, Y., & Wang, C. (2022). Efficient separation and purification of indium and gallium in spent Copper indium gallium diselenide (CIGS). *Journal of Cleaner Production, 350*, 131426.

Luo, Y., Mei, Z., Qiao, Y., Xu, Z., & Ahmad, Z. (2025). Advancing e-waste classification with customizable YOLO based deep learning models. *Scientific Reports, 15*, 94772.

Luo, Y., Mei, Z., Qiao, Y., Xu, Z., & Ahmad, Z. (2025). SCSNet: A novel transformer-CNN fusion architecture for enhanced segmentation and classification on high-resolution semiconductor micro-scale defects. *Applied Intelligence, 55*(1), 439–456.

Mohammad, F., & Sarkar, M. A. B. (2025). Semiconductor wafer map defect classification with tiny vision transformers. *arXiv.*

Patel, T., Puri, R., Alimoradi, A., & Zaki, R. (2024). Demystifying defects: Federated learning and explainable AI for semiconductor fault detection. *IEEE Access, 12*, 102345–102356.

Schröder, P., van Hullebusch, E. D., & Benedetti, M. F. (2025). Circularity of semiconductor chip value chains: Advancing AI sustainability amid geopolitical tensions. *Journal of Circular Economy, 3*(1), 8.

U.S. Department of Energy. (2024). *U.S. Department of Energy announces intent to fund projects that advance domestic gallium production*. https://www.energy.gov/fecm/articles/us-department-energy-announces-intent-fund-projects-advance-domestic-gallium

U.S. Environmental Protection Agency. (2025). *New international requirements for electrical and electronic waste*. https://www.epa.gov/hwgenerators/new-international-requirements-electrical-and-electronic-waste

Wang, X., Guo, J., Dong, L., & Zhang, X. (2025). From present to future: A review of e-waste recycling processes. *Waste Management, 175*, 215–234.

Zhang, J., Wang, X., Li, J., & Zhao, P. (2025). MT-former: Multi-task hybrid transformer and deep support vector data description to detect novel anomalies during semiconductor manufacturing. *Light: Advanced Manufacturing, 6*(1), 32–45.

Zhao, P., Zhang, J., Dong, Z., Huang, J., Zhou, H., Li, J., & Li, X. (2025). MLR-WM-ViT: Global high-performance classification of mixed-type wafer map defect using a multi-level relay vision transformer. *Expert Systems with Applications, 242*, 122786.

Zheng, K., Benedetti, M. F., & van Hullebusch, E. D. (2023). Recovery technologies for indium, gallium, and germanium from end-of-life products (electronic waste) – A review. *Journal of Environmental Management, 347*, 119103.

Author(s) Information

Gharib Hadj
Djillali Lıabes University of Sidi Bel Abbes, Automation Department, Faculty of Electrical Engineering, Algeria
Contact e-mail : gharib*@univ-sba.dz*

To cite this article:

Hadj, G. (2025). An AI-based method for sorting and separation of semiconductor waste: An environmentally friendly method for implementing a circular economy in the semiconductor industry. *The Eurasia Proceedings of Science, Technology, Engineering and Mathematics (EPSTEM), 38*, 296-306.

The Eurasia Proceedings of Science, Technology, Engineering & Mathematics (EPSTEM)
ISSN: 2602-3199

The Eurasia Proceedings of Science, Technology, Engineering and Mathematics (EPSTEM), 2025

Volume 38, Pages 307-315

IConTES 2025: International Conference on Technology, Engineering and Science

Studying the Temperature Effect on Lengthwise Fracture of Inhomogeneous Beam Subjected to Impact Loading

Victor Rizov
University of Architecture, Civil Engineering and Geodesy

Abstract: The wide use of continuously inhomogeneous engineering materials in various load-bearing structures puts high requirements with respect to their fracture behavior. In many applications fracture represents the most often mode of structural failure. In view of this, exploring fracture behavior under various loading conditions is highly needed for guaranteeing the load-bearing capacity, safety and proper functioning of engineering structures. Developing of analyses which encompass more factors influencing fracture behavior of continuously inhomogeneous structures is very important direction in fracture mechanics. One of the extreme loadings acting on engineering structures is the impact loading which may be generated by objects falling on the structure. It happens frequently that impact loading acts in combination with other influences on the structure like, for instance, temperature field. Therefore, this paper deals with analysis of the effect of temperature filed on the lengthwise fracture in a continuously inhomogeneous beam structure subjected to impact loading by an object falling on the structure. The beam has non-linear elastic behavior. The fracture under impact loading and temperature field is analyzed by considering the strain energy release rate. The analysis is verified by applying the integral *J*. The change of the fracture behavior due to temperature field and the parameters of the impact loading is studied.

Keywords: Continuously inhomogeneous material, Impact, Fracture, Temperature, Beam structure

Introduction

The rapid advance in the field of technologies for manufacturing of modern continuously inhomogeneous structural materials that has been made in the recent decades across the globe facilitates intensification of the application of these materials in various segments of current engineering (Gandra et al., 2011, El-Galy et al., 2019). Continuously inhomogeneous composites like functionally graded materials are attracting the attention of academicians and engineers in many countries due to their advantages in comparison to the homogeneous structural materials (Mahamood & Akinlabi, 2017). One of the main advantages is the smooth change of material properties along certain directions in the solid (Miyamoto et al., 1999, Radhika et al., 2020). Besides, this change can be controlled in the process of manufacturing in order to satisfy particular requirements with respect to strength, load-carrying capacity, stiffness, aging, fatigue, stability, etc. (Mahamood & Akinlabi, 2017, Radhika et al., 2020).

The engineering practice shows that increasing the use of continuous inhomogeneous materials and structures in a variety of applications leads to a stronger interest towards their fracture behavior in different conditions of work and loadings. This is due to the fact that namely the fracture behavior has a decisive meaning for reliability and safety of inhomogeneous engineering structures. Besides, in many situations fracture is one of the main causes for failure of structural members (Dowling, 2007, Rizov, 2018, Rizov & Altenbach, 2019). Also, fracture may result in sudden collapse of entire engineering facilities with heavy consequences in terms of financial losses and even human lives.

- This is an Open Access article distributed under the terms of the Creative Commons Attribution-Noncommercial 4.0 Unported License, permitting all non-commercial use, distribution, and reproduction in any medium, provided the original work is properly cited.

- Selection and peer-review under responsibility of the Organizing Committee of the Conference

© 2025 Published by ISRES Publishing: www.isres.org

In this paper, we study lengthwise fracture in a continuously inhomogeneous beam structure that is subjected to impact loading. The latter is generated by an object that falls on the structure. Besides the impact loading, the beam is under temperature field. In fact, the main goal of this paper is to analyze the effect of temperature field on the lengthwise fracture in the beam subjected to impact loading. The interest towards fracture behavior under impact loading and temperature field is provoked by the fact that continuously inhomogeneous structural members frequently are used in applications where they are under combined influence of loading and temperature. The beam considered in this paper has non-linear elastic behavior. Besides, the beam has continuous material inhomogeneity in both transversal and longitudinal directions. When deriving the strain energy release rate in the beam, both impact loading and the effect of temperature field are taken into account. The integral *J* is used for verification of the strain energy release rate. The change of the strain energy release rate is induced by the temperature field and is evaluated. The effects of the parameters of the impact loading and the material inhomogeneity on the strain energy release rate are also assessed.

Analysis

This paper deals with lengthwise fracture in the continuously inhomogeneous beam displayed in Figure 1.

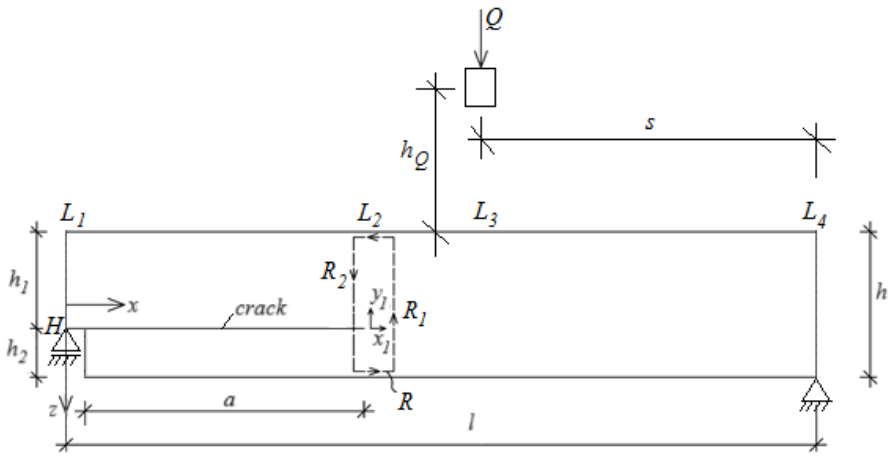


Figure 1. Beam structure under impact loading

The beam is simply supported in its end. A lengthwise crack of length, a, is located in portion, L_1L_2, of the beam. The thickness of the upper arm of the crack is h_1. The lower arm of the crack has thickness, h_2, and is free of stresses since the support is located in point, H, of the upper arm of the crack (Figure 1). The beam is under impact by an object of weight, Q. This object is dropped from height, h_Q, and hits the beam in point, L_3, as displayed in Figure 1. Besides the impact loading, the beam is also under temperature field (the temperature change is T).

The beam has non-linear elastic behavior is treated by the constitutive law in Eq. (1) (Lukash, 1997).

$$\sigma = (E\varepsilon - B\varepsilon^m)\left(1 + D\ln\frac{\dot{\varepsilon}}{\dot{\varepsilon}_0}\right), \tag{1}$$

where E, B, m, D and $\dot{\varepsilon}_0$ are parameters, σ is the stress, ε is the strain, $\dot{\varepsilon}$ is the speed.

The beam is continuously inhomogeneous along the thickness and length. Because of this, the parameters, E, B, m and D, change smoothly both transversely and longitudinally of the beam structure. The change of these parameters transversely of the beam is described by the laws in Eqs. (2), (3), (4) and (5).

$$E = E_1 e^{\beta_1 \frac{\frac{h}{2}+z}{h}}, \tag{2}$$

$$B = B_1 e^{\beta_2 \frac{\frac{h}{2}+z}{h}}, \tag{3}$$

$$m = m_1 e^{\beta_3 \frac{\frac{h}{2}+z}{h}}, \tag{4}$$

$$D = D_1 e^{\beta_4 \frac{\frac{h}{2}+z}{h}}, \tag{5}$$

where

$$-\frac{h}{2} \le z \le \frac{h}{2}. \tag{6}$$

Here, E_1, B_1, m_1 and D_1 are the values of E, B, m and D on the upper surface of the beam, β_1, β_2, β_3 and β_4 are parameters, h, is the beam thickness, z is the vertical axis of the beam cross-section. The quantities, E_1, B_1, m_1 and D_1, change along the beam length according to the laws in Eqs. (7), (8), (9) and (10).

$$E_1 = E_2 e^{\beta_5 \frac{x}{l}}, \tag{7}$$

$$B_1 = B_2 e^{\beta_6 \frac{x}{l}}, \tag{8}$$

$$m_1 = m_2 e^{\beta_7 \frac{x}{l}}, \tag{9}$$

$$D_1 = D_2 e^{\beta_8 \frac{x}{l}}, \tag{10}$$

where

$$0 \le x \le l. \tag{11}$$

In the above formulas, E_2, B_2, m_2 and D_2 are the values of E_1, B_1, m_1 and D_1 in the left-hand end of the beam structure, β_5, β_6, β_7 and β_8 are parameters, l is the beam length, x is the longitudinal axis of the beam. In order to analyze the lengthwise fracture under impact loading, first we have to determine the static vertical displacement, δ_{L3st}, of point L_3 (this is the displacement induced by a vertical force of magnitude, Q, applied statically in L_3). Equation (12) is applied for determining of δ_{L3st}.

$$\delta_{L3st} = \sum \int \kappa_i M_i dx, \tag{12}$$

where κ_i and M_i are the curvature and the moment.

The curvature is related to the change of the strain along the thickness via Eq. (13).

$$\varepsilon = \kappa_i (z - z_n), \tag{13}$$

where

$$-\frac{h}{2} \le z \le \frac{h}{2}. \tag{14}$$

In Eq. (13), z_n is the neutral axis coordinate.

The conditions of equilibrium written in Eqs. (15) and (16) are applied for determining of the curvature and the neutral axis coordinate.

$$N = \iint_{(A)} \sigma dA\,, \tag{15}$$

$$M = \iint_{(A)} \sigma z dA\,, \tag{16}$$

where N and M are the axial force and the bending moment, A is the beam cross-section area, σ is the stress obtained by Eq. (1).

When determining the curvature and the neutral axis coordinate, the effect of temperature field in the beam structure is treated by changing of E through Eqs. (17) and (18) (Narisawa, 1987).

$$E_{T_0}\left(\frac{t}{\alpha_T}\right) = \frac{T_0 r_0}{T r_1} E\,, \tag{17}$$

$$\lg \alpha_T = -\frac{C_P\left(T - T_p\right)}{C_{RF} + \left(T - T_p\right)}\,, \tag{18}$$

where t is the time, E_{T_0} is the value of E at room temperature, the ratio, $T_0 r_0 /(T r_1)$, is unit, T_p is a material parameter, $C_P = 8.86$ and $C_{RF} = 101.6$ (Narisawa, 1987).

It is clear that the axial force in each portion of the beam is zero (Figure 1). The bending moment is found by using Eq. (19).

$$M = Q\frac{s}{l}x\,, \tag{19}$$

where s is the distance between points, L_3 and L_4, as displayed in Figure 1. Equation (19) holds in portion, L_1L_3, of the beam, i.e.

$$0 \le x \le l - s\,. \tag{20}$$

The bending moment in portion, L_3L_4, is determined by Eq. (21).

$$M = Q\frac{s}{l}x - Q\left(x - l + s\right), \tag{21}$$

where

$$l - s \le x \le l\,. \tag{22}$$

Equations (15) and (16) are solved by the MatLab to determine the curvatures and the coordinates of the neutral axis in portions, L_1L_2, L_2L_3 and L_3L_4, of the beam structure.

The displacement, δ_{L3st}, is applied to determine the dynamic coefficient, k_{dyn}. By using the methodology taken from (Ickovitch et al., 1997), we obtain

$$k_{dyn} = 1 + \sqrt{1 + 2\frac{h_Q}{\delta_{L3st}}\frac{Q}{Q + 0.487G_{str}}}\,, \tag{23}$$

where G_{str} is the structure deadweight.

The dynamic stress, σ_{dyni}, in an arbitrary portion of the beam is found by Eq. (24).

$$\sigma_{dyni} = k_{dyn}\sigma_{sti}\,, \tag{24}$$

where σ_{sti} is the stress induced by the static loading of the beam structure by force, Q.

The complementary strain energy density, u_{0i}^{*}, is derived by using Eq. (25).

$$u_{0i}^{*} = \sigma_{dyni}\,\varepsilon_i - \int \sigma_{dyni} d\varepsilon \,. \tag{25}$$

Equation (26) is used to calculate the strain energy release rate, G.

$$G = \frac{dU^{*}}{bda}, \tag{26}$$

where U^{*} is the complementary strain energy in the beam, b is the cross-section width. This energy is found by Eq. (27).

$$U^{*} = U_{L1L2}^{*} + U_{L2L3}^{*} + U_{L3L4}^{*}, \tag{27}$$

where

$$U_{L1L2}^{*} = \iiint\limits_{(V_{L1L2})} u_{01}^{*} dV \,, \tag{28}$$

$$U_{L2L3}^{*} = \iiint\limits_{(V_{L2L3})} u_{02}^{*} dV \,, \tag{29}$$

$$U_{L3L4}^{*} = \iiint\limits_{(V_{L3L4})} u_{03}^{*} dV \,. \tag{30}$$

Here, V_{L1L2}, V_{L2L3} and V_{L3L4} are the volumes of the upper arm of the crack, and portions, L_2L_3 and L_3L_4, of the beam, respectively.

The analysis of the strain energy release rate is checked-up by applying the integral *J* (Broek, 1986). The contour, R, is used for carrying-out the integration (Figure 1). In this case, the expression for the integral *J* has two members, J_{R1} and J_{R2}, as written in Eq. (31).

$$J = J_{R1} + J_{R2}, \tag{31}$$

where J_{R1} and J_{R2} are related to portions, R_1 and R_2, of R.

The two members are given in Eqs. (32) and (33), respectively.

$$J_{R1} = \int \left[u_{0R1} \cos\alpha_{R1} - \left(p_{x1} \frac{\partial u_{R1}}{\partial x_1} + p_{y1} \frac{\partial v_{R1}}{\partial x_1} \right) \right] ds \,, \tag{32}$$

$$J_{R2} = \int \left[u_{0R2} \cos\alpha_{R2} - \left(p_{x2} \frac{\partial u_{R2}}{\partial x_1} + p_{y2} \frac{\partial v_{R2}}{\partial x_1} \right) \right] ds \,. \tag{33}$$

The quantities involved in Eqs. (32) and (33) are determined by using the dynamic stresses, strains and displacements in the beam structure induced by the impact loading with taking into account the effect of temperature field. The MatLab is applied for integration in Eqs. (32) and (33). Since the integral *J* agrees with the strain energy release rate, we can make conclusion that the analysis is correct.

Results of Parametric Investigation

Curves revealing how the lengthwise fracture in the non-linear elastic beam under impact loading is affected by the temperature field are reported in this section of the paper. The effects of the parameters of impact loading, the inhomogeneity and the beam structure geometry are also studied. The curves reported here are for a beam structure with $b = 0.015$ m, $h = 0.028$ m, $l = 0.900$ m, $a = 0.400$ m, $s = 0.400$ m and $h_1 = 0.010$ m.

One can observe the influence of the temperature field on the lengthwise fracture in Figure 2 where the strain energy release rate in non-dimensional form is presented as a function of parameter, β_1, at $T/T_P = 1.15$ (curve 1), $T/T_P = 1.30$ (curve 2) and $T/T_P = 1.45$ (curve 3). The curves in Figure 2 reveal that the strain energy release rate under impact loading reduces when T/T_p ratio increases. The rise of the value of the parameter, β_1, also induces reduction of the strain energy release rate (Figure 2).

Figure 3 gives one idea about the influence of the value of the parameter, β_5, on the lengthwise fracture at $l/b = 20$ (curve 1), $l/b = 40$ (curve 2) and $l/b = 60$ (curve 3). The ratio, l/b, characterizes the beam span. β_5 is the parameter of the change of E along the beam length. By inspecting of curves reported in Figure 3 one can notice that the strain energy release rate reduces when the parameter, β_5, increases its value. The growth of l/b ratio results in increase of the strain energy release rate (Figure 3).

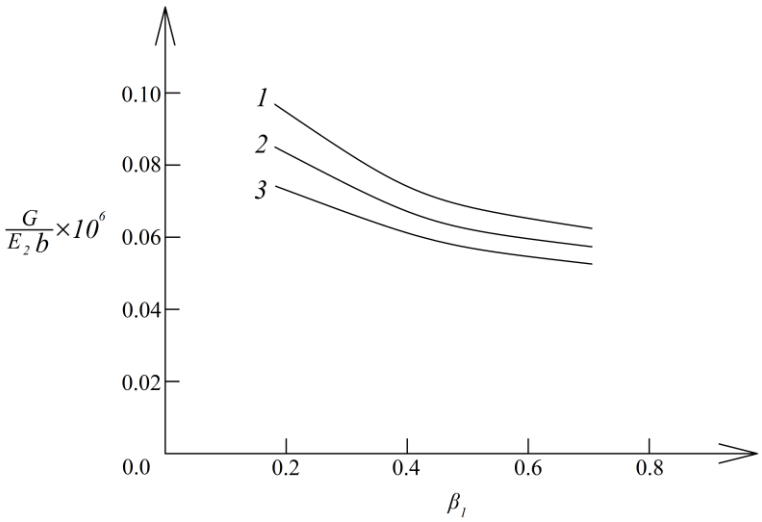


Figure 2. Strain energy release rate versus β_1

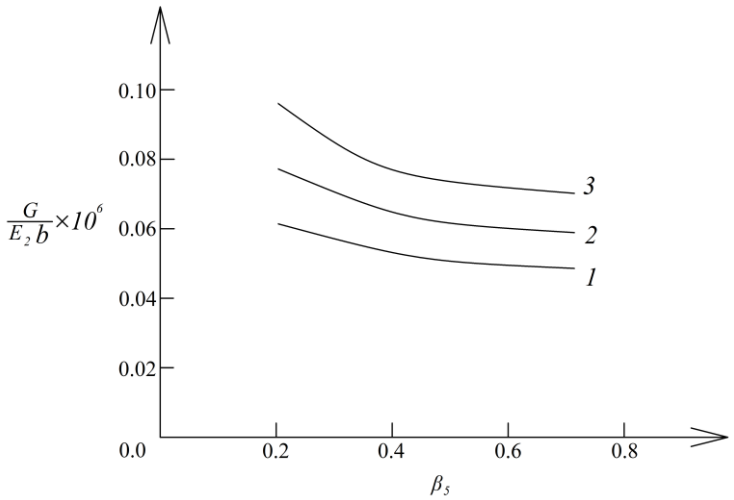


Figure 3. Strain energy release rate versus β_5

The impact loading is characterized by h_Q / l ratio. In order to get an idea about the effect of the impact loading on the lengthwise fracture, we present the strain energy release rate as a function of the parameter, β_2, at $h_Q / l = 0.2$ (curve 1), $h_Q / l = 0.4$ (curve 2) and $h_Q / l = 0.6$ (curve 3) in Figure 4. β_2 is the parameter of the change of B across the beam thickness. The conclusion that can be made by observing the curves reported in Figure 4 is that the strain energy release rate quickly rises with growth of h_Q / l ratio (this is due to rise of the impact energy). The growth of the parameter, β_2, generates also rise of the strain energy release rate as can be observed in Figure 4.

Finally, we explore how the lengthwise fracture under impact loading is influenced by parameters, β_4 and β_8. As already mentioned, these parameters are related to the change of D along the thickness and length of the beam structure. The exploration leads to curves reported in Figure 5 where the strain energy release rate is presented as a function of β_4 at $\beta_8 = 0.3$ (curve 1), $\beta_8 = 0.5$ (curve 2) and $\beta_8 = 0.7$ (curve 3).

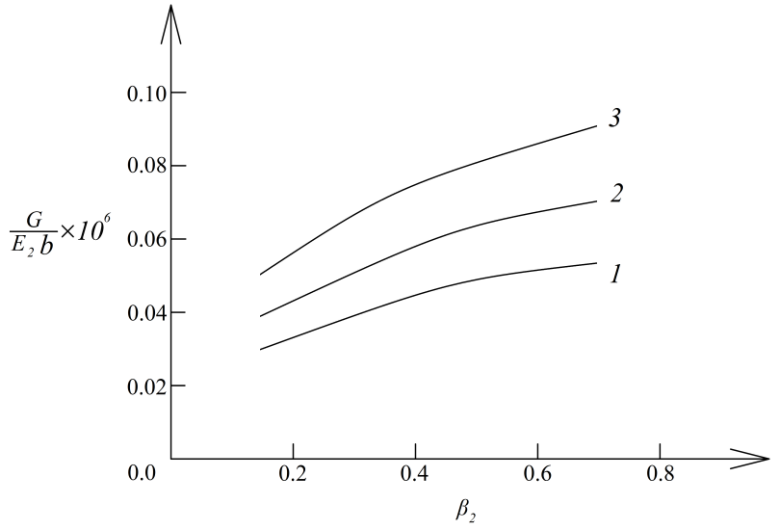


Figure 4. Strain energy release rate versus β_2

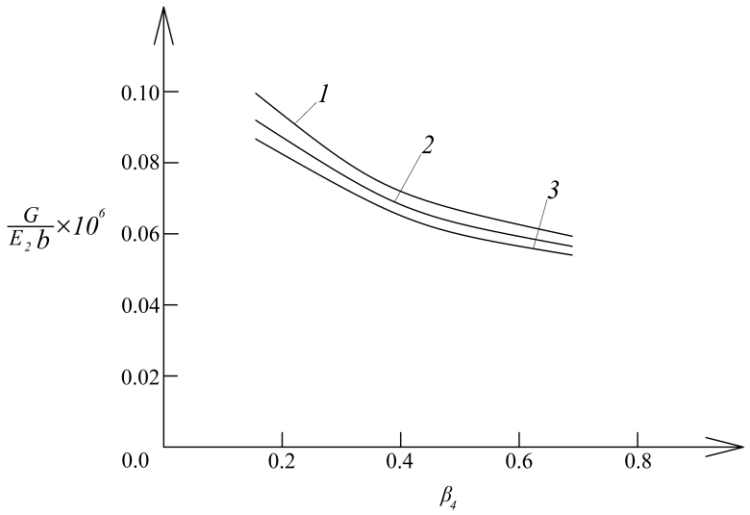


Figure 5. Strain energy release rate versus β_4

Inspection of curves in Figure 5 shows that the strain energy release rate reduces when the parameters, β_4 and β_8, increase.

Conclusion

It is analyzed how the lengthwise fracture in a non-linear elastic beam structure subjected to impact loading is affected by a temperature field. The beam under consideration is continuously inhomogeneous along its thickness and length. The strain energy release rate in the impacted beam is solved. The solution derived accounts for the effect of the temperature field. A check-up is performed by using the integral *J*. The study indicates that the strain energy release rate reduces with increase of the T/T_p ratio (this ratio characterizes the temperature field in the beam structure). It is found also that the strain energy release rate reduces also with growth of parameters, β_1 and β_5, which characterize the change of E across the thickness and length of the beam. Growth of l/b and h_Q/l ratios generates significant rise of the strain energy release rate. The non-linear character of the beam mechanical behavior under impact loading and temperature field also generates rise of the strain energy release rate (indication for this is the effect of the change of parameter, β_2).

Recommendations

The approach developed in this paper can be recommended for analyzing the lengthwise facture in continuously inhomogeneous beam structures under impact loading and temperature field.

Scientific Ethics Declaration

* The author declares that the scientific ethical and legal responsibility of this article published in EPSTEM journal belongs to the author.

Conflict of Interest

* The author declares that he has no conflicts of interest.

Funding

* This study was funded by the Research and Design Centre (contract BN-326/25).

Acknowledgements or Notes

* This article was presented as an oral presentation at the International Conference on Technology, Engineering and Science (www.icontes.net) held in Antalya/Türkiye on November 12-15, 2025.

References

Broek, D. (1986). *Elementary engineering fracture mechanics*. Springer.
Dowling, N. (2007). *Mechanical Behavior of Materials*. Pearson.
El-Galy, I.M., Saleh, B.I., & Ahmed, M.H. (2019). Functionally graded materials classifications and development trends from industrial point of view. *SN Appl. Sci. 1*, 1378.
Gandra, J., Miranda, R., Vilaça, P., Velhinho, A., & Teixeira, J.P. (2011). Functionally graded materials produced by friction stir processing. *Journal of Materials Processing Technology, 211,* 1659-1668.
Ickovitch, G., Vinokurov, A., & Minin, L, (1997). *Strength of materials*. Vishaya Shkola.
Lukash, P. (1997). *Fundamentals of non-linear structural mechanics*. Science.
Mahamood, R. C., & Akinlabi, E. T. (2017). *Functionally graded materials*. Springer.
Miyamoto, Y., Kaysser, W.A., Rabin, B.H., Kawasaki, A., & Ford, R.G. (1999). *Functionally graded materials: design, processing and applications*. Kluwer Academic Publishers, Dordrecht/London/Boston.
Narisawa, I. (1987). *Strength of polymer materials*. Chemistry.

Radhika, N., Sasikumar, J., Sylesh, J. L., & Kishore, R. (2020). Dry reciprocating wear and frictional behaviour of B4C reinforced functionally graded and homogenous aluminium matrix composites. *Journal of Materials Research and Technology*, *9,* 1578-1592.

Rizov, V. I. (2018). Non-linear delamination in two-dimensional functionally graded multilayered beam. *International Journal of Structural Integrity, 9,* 646-663.

Rizov, V.I., & Altenbach, H. (2019). On the analysis of lengthwise fracture of functionally graded round bars. *Structural Integrity and Life*, *19*, 102–108.

Author(s) Information

Victor Rizov
University of Architecture, Civil Engineering and Geodesy
1 Chr. Smirnensky blvd. 1046 – Sofia, Bulgaria
Contact e-mail: *V_RIZOV_FHE@UACG.BG*

To cite this article:

Rizov, V. (2025). Studying the temperature effect on lengthwise fracture of inhomogeneous beam subjected to impact loading. *The Eurasia Proceedings of Science, Technology, Engineering and Mathematics (EPSTEM), 38,* 307-315.

The Eurasia Proceedings of Science, Technology, Engineering & Mathematics (EPSTEM)
ISSN: 2602-3199

The Eurasia Proceedings of Science, Technology, Engineering and Mathematics (EPSTEM), 2025

Volume 38, Pages 316-322

IConTES 2025: International Conference on Technology, Engineering and Science

Effects of Elastic Deformation on the Corrosion of 316l in 3.5% Nacl

Allou Djilali
Research Center in Industrial Technologies

Amraoui Rachid
Research Center in Industrial Technologies

Djemmah Sarra
University of Mons

Benmohamed Manel
Research Center in Industrial Technologies

Younes Abderahman
Research Center in Industrial Technologies

Abada Abderahim
University of Saad Dahleb Blida 1

Abstract: 316L is an austenitic stainless steel widely used in BOPs (Blowout Preventers) due to its exceptional properties of corrosion resistance, toughness and mechanical strength in extreme environments. In this study, we will investigate the impact of elastic deformation on the hardening properties and electrochemical behavior of 316L steel in 3.5% NaCl. The results indicate that 316L stainless steel is sensitive to work hardening. In the unstressed state, it has a crystalline structure with randomly distributed dislocations and a hardness of 234 HV10 at the yield point (Re). When hardness reaches its peak (240 HV10), the material reaches the threshold where dislocations can move irreversibly. Dislocation density is then at its maximum in the elastic regime, and the material enters the plastic range. Electrochemical tests carried out on 316L stainless steel under various mechanical stresses show a contrasting influence of stress on corrosion behavior. While the unstressed sample shows a corrosion current density (I_{corr}) of 2.69 µA, this value drops to 1.25 µA for a sample stressed to 75% of yield strength (Re), indicating improved corrosion resistance. This improvement can be attributed to densification or partial repair of the passive film under moderate mechanical stress. These results underline the importance of carefully controlling the level of mechanical stress to simultaneously optimize mechanical properties and durability in a corrosive environment.

Keywords: 316L, Yield strength (Re), Hardness HV10, Corrosion, Mechanical stress

Introduction

Austenitic stainless steel 316L is widely used in demanding corrosive environments on account of high corrosion resistance along with superb mechanical properties (Sedriks 1996, Marcus 1998, Revie et al. 2008, and Allou et al. 2020). These characteristics make it into a material for choice in biomedical, chemical, nuclear, and offshore industries (Allou et al. 2021, Benafia et al. 2018). Mechanical stress and aggressive media frequently affect components there (Olsson et al. 1995. Marcus 2011). Researchers have studied the

- This is an Open Access article distributed under the terms of the Creative Commons Attribution-Noncommercial 4.0 Unported License, permitting all non-commercial use, distribution, and reproduction in any medium, provided the original work is properly cited.

- Selection and peer-review under responsibility of the Organizing Committee of the Conference

© 2025 Published by ISRES Publishing: www.isres.org

electrochemical behavior of 316L extensively though mechanical loading within the elastic regime relatively underexplores its specific influence on corrosion response (Zhang et al. Krohn, et al. 2021, Yun et al 2024).

In this study, 316L stainless steel was subjected to a set of varying levels of mechanical stress ranging from 0 % to 100 % of the yield strength (Re) because it remained within the elastic domain, so as to assess the impact on general corrosion behavior. Electrochemical parameters characterized the passive behavior for the alloy (Gaoxiang et al. 2019). Corrosion rate (mm/year), corrosion current density (Icorr), as well as corrosion potential (Ecorr) were among parameters that were measured. Concurrently, Vickers hardness (HV10) was evaluated. Applied stress induced mechanical effects were the goal to monitor (Frankel.2003, Tabor 2000, Cihal et al. 2019, Djemmah, et al 2023).

The results revealed that there was a non-linear trend: slight anodic activation occurred at low stress levels (25 % Re), then passivation improved greatly at 75 to 100 % Re. The hardness increases correlates to this evolution, so this correlation implies a good interaction between passive film reinforcement and mechanical hardening (Ouadah et al 2018, Macdonald 2011, Djemmah et al 2024). These results present helpful perceptions and greater comprehension of mechanical-electrochemical interaction within stainless steels for designing components subjected to combined chemical and mechanical stresses.

Materials and Method

The chemical composition of the 316L stainless steels sample was obtained by means of a spectrophotometer XRF S8 Tiger-Bruker spectroscopy equipment is given in Table 1. steels had a rectangular shape 25.5x 13 mm with thicknesses (5.06 mm)

Table 1. Chemical composition of 316L (wt.%)

Alloy	C	Si	Mn	Cr	Mo	Ni	Cu	Ti	P	S	Fe
316L	0.03	0.52	1.09	17.23	1.97	10.91	0.15	0.18	0.04	0.01	all

Tensile tests were conducted on four specimens to evaluate the mechanical behavior of 316L stainless steel within the elastic domain, using an INSTRON testing machine with a 100 N load capacity. Fig. 1 shows the specimens after tensile testing. A reference specimen was subjected to a full tensile test up to fracture in order to determine the elastic limit (Re). Three additional specimens. A (25% of Re), B (75% of Re), and C (100% of Re) were tested up to their respective stress levels. For specimens A, B, and C, once the target stress level was reached, the test was paused while maintaining the applied load for 2 hours. After this holding period, the specimens were removed and sectioned at mid-length for further analysis. All samples were prepared and embedded in an epoxy resin, with an electric contact for using them as working electrode in a standard three-electrode cell. The other electrodes were a Pt counter electrode and a SCE reference electrode. The exposed surfaces of the working electrodes were 25.5 x 0.5 cm^2 . Electrochemical tests were performed at room temperature (20 to 25 °C). The electrochemical impedance spectroscopy (EIS) and potentiodynamic polarization curve measurements were conducted using the PGSTAT302N potentiostat and Autolab electrochemical analyzer instruments from Metrohm, with NOVA software. The potentiodynamic polarization curve was measured with a sweep rate of 0.01 V/s. This curve provides information about the corrosion behavior and allows for the determination of corrosion current and potential. EIS measurements were performed in a frequency range of 100 kHz to 100 MHz, with an amplitude of 0.01 V.

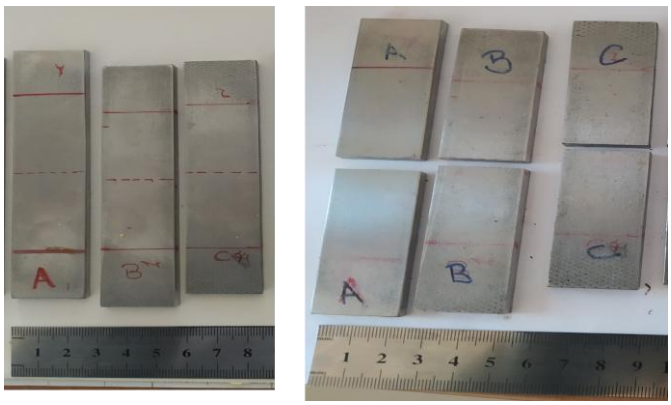


Figure 1. Tensile specimens after testing, before and after sectioning.

Results and Discussion

Effect of Stress Variation on Hardness

Figure 1 shows the stress–strain curve with interruptions at three distinct points: A at 25% of the yield strength (Re), B at 75% of Re, and C at Re.

Table 2. Variation of applied load, as well as the change in cross-section of each sample

Position in traction curve		**Load value (Mpa)**	**L x Th**
Tensile test piece		00	25.5x5.06 =129.03
A	25% of Re	78	25.4 x 5.06 =128.52
B	75% of Re	155	25.27 x 5.06=127.87
C (Re)	100% of Re	310	25.19 x 5.03 =126.71

We can observe that as the applied stress increases, there is a measurable, albeit small, reduction in the cross-sectional area of the specimen, this trend is clearly illustrated in Figure 2. The tensile specimen initially had central dimensions of 25.5 mm × 5.06 mm, corresponding to a cross-sectional area of 129.03 mm². As deformation progressed, a slight decrease in area was recorded, reaching 126.71 mm² at point C (corresponding to the yield strength, Re).

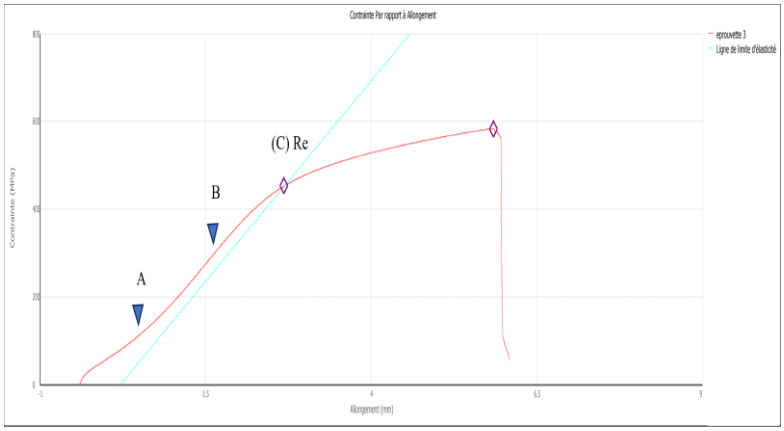


Figure 2. Tensile test graph for specimen 316 L.

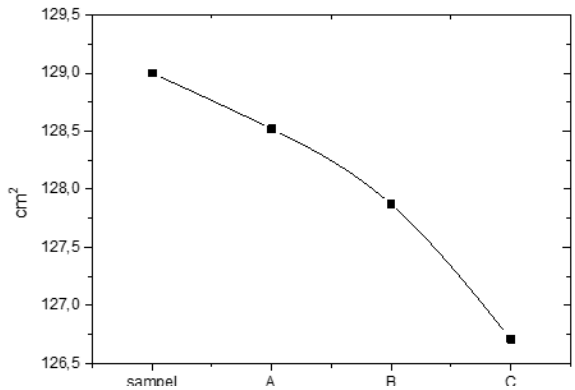


Figure 3. Surface of the specimens at the center of the tensile-tested samples in the elastic deformation range.

Figure 4. illustrates the evolution of hardness, based on the values reported in Table 3. In the unstressed state, the hardness of 316L stainless steel is 213 HV10. As the applied stress increases, the hardness rises progressively, reaching a maximum value of 240 HV10 at the elastic limit (point C = Re), passing through 234 HV10 at point A (25% of Re) and 237 HV10 at point B (75% of Re).

In its unstressed state, the material has a crystalline structure with dislocations randomly distributed throughout the lattice. The initial hardness reflects the intrinsic resistance of the material to dislocation motion. When a stress is applied but remains within the elastic domain dislocations begin to move and gradually accumulate around obstacles such as grain boundaries, precipitates, and other dislocations. These localized micro-strains can

lead to a slight increase in dislocation density due to elastic strain hardening, even before yielding occurs. This explains the increase in hardness from 234 HV10 at 25% Re to 240 HV10 at Re.

This progression reflects the increasing internal resistance due to growing dislocation interactions. At the yield strength (Re), where the material reaches the threshold for irreversible dislocation motion, the dislocation density attains its maximum for the elastic regime, accounting for the observed peak in hardness.

Table 3. Hardness HV10 values of different test bars

	Hardness
Without stress	213
A	234
B	237
C	240

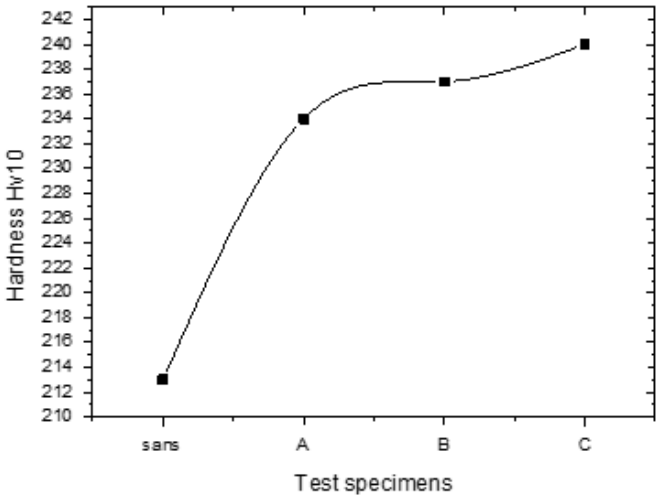


Figure 4. Hardness HV10 of different test bars

Effect of Stress Variation on Corrosion

Figure 5 shows the superposition of the polarization curves of the specimens (unstressed and with mechanical stresses A, B and C approaching yield strength Re) in an NaCl-based electrolyte (3.5%). They correspond to a scanning interval between -1 and 0.1 V. Ag / AgCl reference electrodes for the substrate and the sample interface, and between -0.6 and 0.4 V. Ag / AgCl reference electrode AgCl for recharging. We used the slew rate of 1 mV/s from cathode to anode direction. The results of the polarization curve of Figure 3. are summarized in Table 3. showing the corrosion potential (E_{corr}), the corrosion current density (i_{corr}) and the corrosion rate.

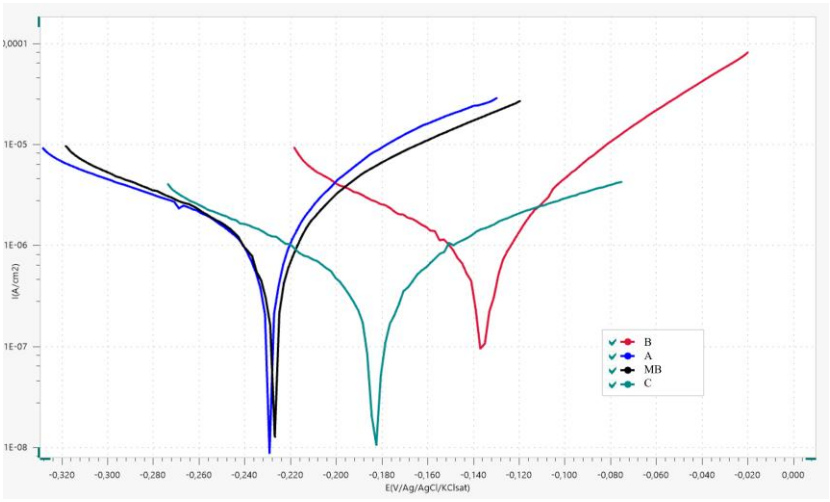


Figure 5. Polarization curves of 316L in 3.5 % of NaCl electrolyte

Table 4. Electrochemical parameters of potentiodynamic tests

	316L, without constraint	A	**B**	**C (Re)**
E_{corr} (mV)	-227	-229	-136	-183
I_{corr} (μA/cm^2)	2.69	3.42	1.25	0.97
Corrosion rate(mm/year)	0.030	0.031	0.011	0.010

When the material is in its unstressed state and moves to state A, which is 25% of the Re, the corrosion potential (E_{corr}) stays the same, between −227 and −229 mV. At this moderate stress level, which is 25% of the yield strength, the electrochemical activity of 316L isn't greatly affected. The passive layer stays intact, meaning the material continues to be protected by its passive film. However, the corrosion current (I_{corr}) goes up from 2. 69 to 3. 42 μA/cm².

Even with low stress, there is a small increase in corrosion. This shows that the passive film is starting to be affected in small areas like through micro-cracks, defects, or dislocations that let ions move more easily. This is to be expected because mechanical stress can weaken the passive layer. The corrosion rate also increases a little, from 0. 030 to 0. 031 mm/year, which is a small but real change of +3. 3%. This confirms that the initial mechanical stress is beginning to slightly affect the passive film's stability. Even so, the increase is still low, which means 316L still has good passivity. E_{corr} rises dramatically (from - 229 to -136 mV).

From state A to state B (25% to 75% of Re). It may seem counterintuitive, but the corrosion potential significantly improves. A more noble potential could be produced by local atomic rearrangement brought on by mild plastic deformation, which would encourage the development of a denser or more stable passive film. Icorr rapidly decreases from 3.42 to 1.25 μA/cm². This implies that a more protective passive layer, probably enriched in chromium, may have been reorganized more easily as a result of deformation. Additionally, the corrosion rate drops by almost 65%, from 0.031 to 0.011 mm/year. This closely resembles the decline in Icorr, suggesting that the material experiences repassivation or passive film stabilization, most likely as a result of either closure or chromium oxide (CrO_3) enrichment of the film.

When moving from state B to state C (75% to 100% of Re), the corrosion potential (Ecorr) drops again, going from −136 to −183 mV. As stress increases, the passive layer starts to break down, forming small cracks and defects on the surface that help corrosion happen. However, the corrosion current (Icorr) keeps going down, from 1. 25 to 0. 97 μA/cm². At this point, the passive layer seems to be more stable or even stronger. This might be because stress causes a lot of defects in the material, and adding more stress doesn't create much more damage. The corrosion rate also slightly decreases, from 0. 011 to 0. 010 mm/year. Although the trend is still downward, the improvement is small, only about 9%. This shows that the electrochemical reactions have reached their limit, and the system is as stable as it can be. Any more stress, as long as it stays within the elastic range, won't make much difference in terms of risk or benefit.

Conclusion

The impact of deformation in the elastic domain on the hardening properties and electrochemical behavior of 316L steel in 3.5% NaCl is assessed. The following conclusions can be drawn:

- As the applied stress increases, there is a small reduction in the cross-sectional area of the sample.
- These results show that the elastic domain may not only avoid harming, but can sometimes enhance corrosion resistance, provided that the applied stress does not exceed a certain critical threshold.
- The observed corrosion rates all below 0.04 mm/year confirm that 316L stainless steel exhibits high resistance to uniform corrosion, even under elastic stress. This supports its suitability for use in aggressive environments.

Scientific Ethics Declaration

* The authors declare that the scientific ethical and legal responsibility of this article published in EPSTEM journal belongs to the authors.

Conflict of Interest

* The authors declare that they have no conflicts of interest

Funding

* This research received no specific grant from any funding agency in the public, commercial, or not-for-profit sectors.

Acknowledgements or Notes

* This article was presented as a poster presentation at the International Conference on Technology, Engineering and Science (www.icontes.net) held in Antalya/Türkiye on November 12-15, 2025.

* The authors would like to thank the conference committee and EPSTEM journal reviewers for their valuable feedback

References

Allou, D., Miroud, D., Ouadah, M., Cheniti, B., & Bouyegh, S. (2020). Criterion for cathodic protection of 25CD4/Inconel 182 system. *Applied Surface Science, 502*, 144100.

Allou, D. J., Ould Brahim, I., Cheniti, B., Fides, M., Hvizdos, P., Miroud, D. J., & Ziouche, A. (2021). Effect of post weld heat treatment on microstructure and mechanical behaviors of weld overlay Inconel 182 on 4130 steel substrate using SMAW process. *Metallography, Microstructure and Analysis, 10*(5), 567–578.

Benafia, S., Retraint, D., Yapi Brou, S., Panicaud, B., & Grosseau Poussard, J. L. (2018). Influence of surface mechanical attrition treatment on the oxidation behaviour of 316L stainless steel. *Corrosion Science, 136*, 188–200.

Cihal, V., & Ruscak, M. (1980). The influence of mechanical stress on the corrosion of metals. *Materials Science and Engineering, 42*, 1–15.

Djemmah, S., Madi, Y., Voué, M., Haddad, A., Allou, D., Ouallam, S., Bouchafaa, H., & Rezzoug, A. (2023). Effect of Mg addition on the morphology, roughness and adhesion of Cr chromized layer produced by pack cementation. *International Journal of Engineering, Transactions A: Basics, 36*, 1773–1782.

Djemmah, S., Voué, M., Madi, Y., Allou, D., Haddad, A., & Bouchafaa, H. (2024). Investigation of microstructural and electrochemical behavior of chromized-doped layers with variant magnesium concentrations. *Sādhanā, 49*(3), 243.

Frankel, G. S. (2003). *Electrochemical techniques in corrosion science and engineering*. CRC Press.

Krohn, H., & Virtanen, S. (2014). Effect of elastic and plastic deformation on the electrochemical behavior of austenitic stainless steels. *Corrosion Science, 78*, 186–191.

Liu, Y., Dai, H., Chen, S., He, M., Shi, S., Zhang, Z., & Chen, X. (2024). Study on stress corrosion behavior of 316L austenitic stainless steel in hot NaOH solution. *Journal of Materials Research and Technology, 30*, 8894–8905.

Macdonald, D. D. (2012). The history of the point defect model for the passive state. *Journal of The Electrochemical Society, 159*(6), C189–C217.

Marcus, P. (1998). Surface science approach of corrosion phenomena. *Electrochimica Acta, 43*(2–3), 109–118.

Marcus, P. (Ed.). (2011). *Corrosion mechanisms in theory and practice* (3rd ed.). CRC Press.

Ouadah, M., Touhami, O., Ibtiouen, R., Khorchef, M., & Allou, D. (2018). Corrosion effects on the magnetic behavior of magnetic circuit of an induction machine. *Progress in Electromagnetics Research M, 68*, 79–87.

Olsson, C.-O. A. (1995). Stainless steels for biomedical applications. *ISIJ International, 35*(1), 1–12.

Revie, R. W., & Uhlig, H. H. (2008). *Corrosion and corrosion control* (4th ed.). Wiley.

Sedriks, A. J. (1996). *Corrosion of stainless steels* (2nd ed.). Wiley-Interscience.

Tabor, D. (2000). *The hardness of metals*. Oxford University Press.

Wu, G., & Singh, P. M. (2019). Effect of elastic stresses on pitting behavior of stainless steel 304. *Journal of the Electrochemical Society, 166*(8).

Zhang, Y., Yang, C., Zhao, L., & Zhang, J. (2021). Study on the electrochemical corrosion behavior of 304 stainless steel in chloride ion solutions. *International Journal of Electrochemical Science, 16*, 210251.

Author (s) Information

Allou Djilali
Research Center in Industrial Technologies (CRTI) Box 64, Cheraga, Algiers 16014, Algeria
Contact e-mail**:** *djilallou@yahoo.fr*

Amraoui Rachid
Research Center in Industrial Technologies (CRTI), P.O. Box 64, Chéraga, Algiers, Algeria.

Djemmah Sarra
University of Mons, Physics of Materials and Optics Unit (LPMO), Research Institute for Materials Science and Engineering Mons 7000, Belgium

Benmohamed Manal
Research Center in Industrial Technologies (CRTI), P.O. Box 64, Chéraga, Algiers, Algeria

Younes Abderahman
Research Center in Industrial Technologies (CRTI), P.O. Box 64, Chéraga, Algiers, Algeria

Abada Abderahim
Laboratory of Aeronautic Science, Aeronautic Institute, University of Saad Dahleb Blida 1, Algeria, Algeria

To cite this article:

Djilali, A., Rachid, A., Sarra, D., Manel, B., Abderahman, Y., & Abderahim, A. (2025). Effects of elastic deformation on the corrosion of 316L in 3.5% NaCl. *The Eurasia Proceedings of Science, Technology, Engineering and Mathematics, 38*, 316–322.

The Eurasia Proceedings of Science, Technology, Engineering & Mathematics (EPSTEM)
ISSN: 2602-3199

The Eurasia Proceedings of Science, Technology, Engineering and Mathematics (EPSTEM), 2025

Volume 38, Pages 323-329

IConTES 2025: International Conference on Technology, Engineering and Science

Best-Fitting Ellipsoid and Surface Disturbance Adjustment of GNSS-Derived Sea Surface Heights

Konstantinos Kalimeris
Academy of Athens

Sotiris Lycourghiotis
Hellenic Open University

Abstract: This paper introduces a novel methodology for modeling mean sea surface topography based on GNSS-on-boat observations—continuous satellite positioning from a floating platform. The method is applied for the first time using real-world data collected in a small lagoon in Western Greece. A best-fitting ellipsoid is initially computed to represent the overall geometry of the observed sea surface. A local surface disturbance is then fitted atop the ellipsoid using a polynomial model, capturing small-scale deviations from the ideal form. The resulting hybrid surface significantly improves accuracy: initial mean discrepancies $\bar{\varepsilon}$ between the ellipsoid and GNSS measurements (3.1 cm) are reduced to below 0.1 cm after incorporating the local disturbance. This innovative approach offers a powerful tool for detailed sea surface modeling and holds promise for local geoid refinement in coastal or semi-enclosed marine areas.

Keywords: Ellipsoid, Geoid, Sea surface topography, GNSS-on-boat

Introduction

The geoid (Richards & Hager, 1984) is defined as an equipotential surface of the Earth's gravity field, which closely aligns with the global Mean Sea Level (MSL), especially in open sea regions where external influences such as winds and tides are minimal (Lycourghiotis & Stiros 2010). If MSL could be theoretically extended across landmasses via hypothetical sea canals, it would serve as a natural reference surface (Sansò et al., 2008). Accurately determining the geoid remains one of the central problems in geodesy, often referred to as the "geoid problem," due to the inherent complexity of Earth's mass distribution and limitations in observational data (Novák, 2003).

Over the years, various geometric models have been proposed to approximate the geoid, ranging from spheres to oblate spheroids and ellipsoids. Among these, the World Geodetic System 1984 (WGS84) has become the most widely adopted reference, providing a geocentric ellipsoid of revolution used as the standard framework for GNSS navigation systems and global positioning applications (Kumar, 1988; Smith, 1998).

Although WGS84 (Kelly, 2022) minimizes the global mean square deviation of Earth surface points, it inevitably produces local discrepancies in regions with complex terrain, coastlines, or seafloor variations. In such cases, the actual sea surface or geoid may deviate significantly from the WGS84 ellipsoid, leading to position errors that could be critical in high-precision applications. This has motivated the scientific community to develop high-resolution local geoid models, particularly for improving navigation, hydrographic surveys, and vertical datum realization (Galani et al., 2021; Jalal et al., 2019).

Traditionally, local geoid modeling techniques rely on known geoid undulations (N) or height differences (ΔN), often combining orthometric and ellipsoidal heights with interpolation and least squares adjustment methods.

- This is an Open Access article distributed under the terms of the Creative Commons Attribution-Noncommercial 4.0 Unported License, permitting all non-commercial use, distribution, and reproduction in any medium, provided the original work is properly cited.

- Selection and peer-review under responsibility of the Organizing Committee of the Conference

© 2025 Published by ISRES Publishing: www.isres.org

These approaches aim to estimate local corrections relative to the global reference surface, enhancing vertical accuracy in a given region (Lycourghiotis et al., 2024).

In this context, our study addresses the local geometric modeling of the geoid surface, focusing on semi-enclosed sea areas and coastal environments where the sea surface itself serves as a practical approximation of the geoid. In such areas, conventional gravimetric or satellite-based geoid models may exhibit reduced accuracy due to abrupt local variations in the gravity field (Hipkin, 2000).

Our approach involves computing a best-fitting triaxial ellipsoid, which shares the same center, equatorial plane, and polar axis as the WGS84 ellipsoid but is optimized to minimize geometric height deviations within the target region. This ellipsoid is estimated using the Moore–Penrose pseudoinverse, and it acts as a refined local reference surface (Dassios, 2012).

We applied this methodology in a real-world scenario using data collected from the Kotychi lagoon, a small shallow water body in Western Achaia, Greece (Figure 1). GNSS data were acquired using the GNSS-on-boat method, a high-resolution positioning system mounted on a floating platform, enabling dense and accurate sampling of the water surface over a 90-minute period. From this dataset, a best-fitting ellipsoid was calculated, and its geometric performance was assessed. To further improve the local surface representation, we introduced a polynomial surface disturbance model atop the ellipsoid, capturing subtle spatial variations not represented by the ellipsoidal fit alone. This two-step model significantly reduced the residual errors between GNSS observations and the theoretical surface, highlighting the method's potential for high-precision local geoid modeling in calm water environments.

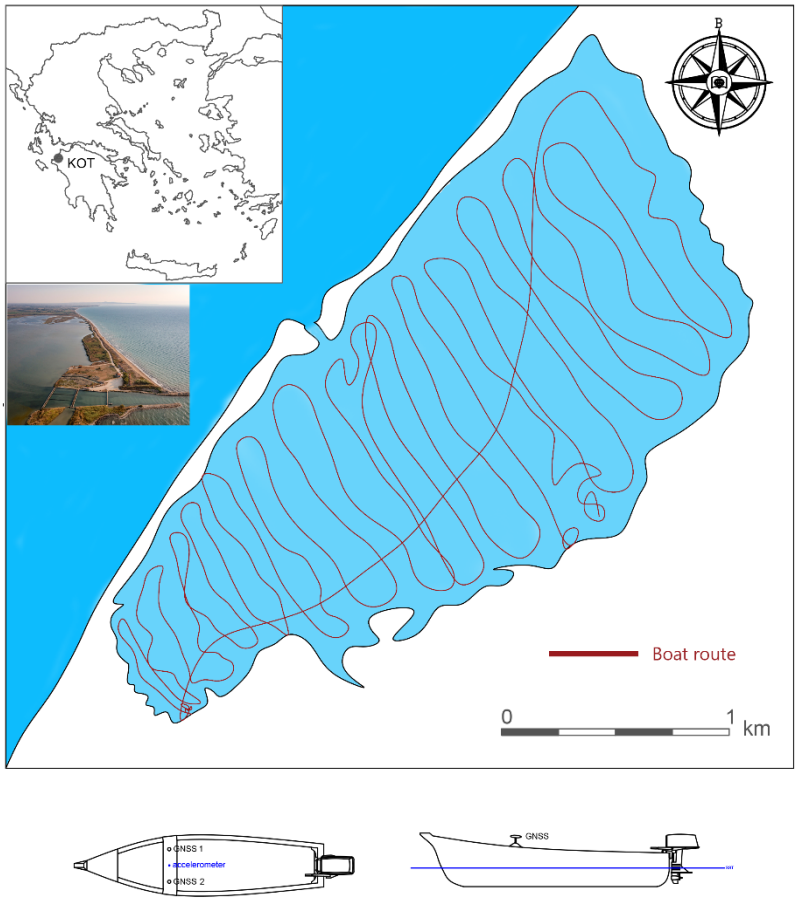


Figure 1. Location map of the experimental area. Red line represents the boat routes.

GNSS on Boat Method and Its Application in Kotychi Lagoon

The GNSS on boat (Bouin et al., 2009; Foster et al., 2009; Reinking et al., 2012) technique has emerged as a powerful tool for high precision determination of sea surface topography (SST) and near-surface geoid features, particularly in coastal and semi-enclosed water bodies (Lycourghiotis & Kariotou, 2022). The method involves

mounting one or more GNSS receivers on a floating platform (boat, catamaran, wave glider etc.) and collecting high-rate kinematic positional data (typically 1 Hz or more) as the platform traverses the water surface.

Unlike traditional indirect techniques (astro geodetic deflections, tide gauges) or direct satellite altimetry approaches, GNSS on boat offers a direct measurement of the water surface height referenced to a GNSS ellipsoid, while avoiding the compounded errors inherent in two-stage systems (Chupin et al. 2020; Guo et al., 2014; Lycourghiotis, 2017a; 2017b; 2017c; Lycourghiotis & Crawford, 2024; Ocalan & Alkan, 2013). This makes the method particularly suitable for mapping SST and related geoid undulations in domains where high resolution and local detail are required, such as lagoons, coastal seas and sheltered bays (Lycourghiotis, 2021).

In the present study, we applied the GNSS on boat technique using a small 2.5 m vessel equipped with two dual frequency GNSS receivers (as depicted in the accompanying figure 1). The measurement campaign lasted approximately 90 minutes, during which the boat followed a randomized track over the Kotychi Lagoon in Western Achaia, Greece. The resulting dataset comprises a dense cloud of GNSS points capturing the mean sea surface at 1 Hz sampling rate.

In our subsequent analysis, we first derived a best-fitting triaxial ellipsoid to capture the bulk geometry of the water surface. We then enhanced the surface representation by fitting a local polynomial surface disturbance atop the ellipsoid, thereby capturing finer scale deviations between the GNSS observed surface and the theoretical ellipsoidal reference. This dual step approach allowed us to achieve a markedly improved fit and enables detailed modeling of local geoid anomalies in confined water bodies.

Methodology

To determine the best-fitted ellipsoidal in a local region, we start from determining a geocentric reference coordinate system O_{xyz} which is centered at the Earth's center of mass of Earth, polar axis zz′ the axis of rotation of the Earth and the Oxy plane coincides with the Earth's equatorial plane. We also determine a geocentric triaxial ellipsoid which has its center at the origin of the axes (0, 0, 0). If (x_i, y_i, z_i), with i = 1, 2, …, k and k are selected points in an area of our interest on Cartesian coordinates, we suppose that these points satisfy the general equation of the triaxial ellipsoid:

$$\frac{x^2}{a^2}+\frac{y^2}{b^2}+\frac{z^2}{c^2}=1$$

Replacing the components of every point in (1), we obtain a system with three unknowns, semi axis a, b, c and k equations, that is a system in form:

$$\begin{bmatrix} x_1^2 & y_1^2 & z_1^2 \\ x_2^2 & y_2^2 & z_2^2 \\ \vdots & \vdots & \vdots \\ x_k^2 & y_k^2 & z_k^2 \end{bmatrix} \cdot \begin{bmatrix} \frac{1}{a^2} \\ \frac{1}{b^2} \\ \frac{1}{c^2} \end{bmatrix} = \begin{bmatrix} 1 \\ 1 \\ \vdots \\ 1 \end{bmatrix}$$

The previous system is a system with more equations than unknowns therefore it has no exact solution. In this case the Moore–Penrose pseudoinverse can be used pseudoinverse matrix to find the minimum square solution (Dassios, 2012). In this way, it is found three semi axes of ellipsoidal E which approximate better the k selected points of the study region.

Having calculated the triaxial ellipsoid E, we then calculate the distance of every given point $\mathbf{r}_i = (x_i, y_i, z_i)$, i = 1, 2, …, k, from the ellipsoid E, which is actually the geometric height h_{Ei}, of point $\mathbf{r}_i$. In particular, we calculate the minimum distance of each point $\mathbf{r}_i$ from the tangent plane of the ellipsoid E, at the point $\mathbf{r}_{di} = (x_{di}, y_{di}, z_{di})$, i = 1, 2, …, k, on E (Dassios, 2012). In order to calculate h_{Ei}, we first find the corresponding $\mathbf{r}_{di}$.

Since the distance function between two points in three-dimensional Euclidean space is:

$$f(x_{di}, y_{di}, z_{di}) = (x_i - x_{di})^2 + (y_i - y_{di})^2 + (z_i - z_{di})^2$$

then, for i = 1, 2, …, k, the point $\mathbf{r}_{di}$ is the one that minimizes the function f, under the condition that it belongs to the surface E, namely:

$$g(x_{di}, y_{di}, z_{di}) = \frac{x_{di}^2}{a^2} + \frac{y_{di}^2}{b^2} + \frac{z_{di}^2}{c^2} - 1 = 0$$

Using the method of Lagrange Multipliers (Brand, 2006; Marcellini, 1996) $\mathbf{r}_{di} = (x_{di}, y_{di}, z_{di})$ is given as

$$x_{di} = \frac{a^2 x_i}{a^2 - \lambda_i}, y_{di} = \frac{b^2 x_i}{b^2 - \lambda_i}, z_{di} = \frac{c^2 x_i}{c^2 - \lambda_i}$$

The parameter λ is calculated by solving the following system

$$\begin{cases} \nabla f(x, y, z) = \lambda \cdot \nabla g(x, y, z) \\ g(x, y, z) = 0, \end{cases}$$

which yields a sixth-degree equation in λ:

$$\frac{a^2 \cdot x_i^2}{(a^2 - \lambda_i)^2} + \frac{b^2 \cdot y_i^2}{(b^2 - \lambda_i)^2} + \frac{c^2 \cdot z_i^2}{(c^2 - \lambda_i)^2} = 1$$

The real root λ corresponding to the minimum value of f is substituted into previous equation to provide the point of tangency $\mathbf{r}_{di}$, suitable for calculating the distance of point $\mathbf{r}_{di}$ from the ellipsoid E. Then, the corresponding geometric height h_{Ei}, for every point $\mathbf{r}_i$, $i = 1, 2, \ldots, k$ is given in the form:

$$h_E(x_i, y_i, z_i) = \frac{1}{\sqrt{\frac{x_{di}^2}{a^4} + \frac{y_{di}^2}{b^4} + \frac{z_{di}^2}{c^4}}} \cdot \left| \frac{x_i x_{di}}{a^2} + \frac{y_i y_{di}}{b^2} + \frac{z_i z_{di}}{c^2} - 1 \right|$$

While the best-fitting ellipsoid provides a first-order geometric approximation of the local sea surface, small-scale variations often remain unaccounted for. These may arise from local dynamic sea surface topography, atmospheric effects, tidal fluctuations, or limitations in the ellipsoidal fit. To enhance the precision of the surface model, we introduce an additional adjustment: a small vertical surface disturbance fitted atop the best-fitting ellipsoid.

Let each GNSS-observed point be $\mathbf{r}_i = (x_i, y_i, z_i)$ and let h_i^{GNSS} denote its height (e.g., ellipsoidal height from GNSS). After computing the geometric height, $h_E(x_i, y_i, z_i)$ of the point from the best-fitting ellipsoid EEE, the residual vertical disturbance is defined as:

$$\delta_i = h_i^{GNSS} - h_E(x_i, y_i, z_i)$$

These residuals δ_i represent the vertical discrepancy between the GNSS measurements and the ellipsoid-based surface and are considered to vary smoothly as a function of the horizontal coordinates.

To model the disturbance $\delta(x,y)$ we employ a bivariate polynomial approximation of degree n:

$$\delta(x, y) = \sum_{i+j \le n} a_{ij} x^i y^j$$

The model is determined by minimizing the cost function:

$$\min_{a_{ij}} \sum_{k=1}^{n} [\delta(x_k, y_k) - (h_k^{GNSS} - h_E(x_k, y_k, z_k))]^2$$

The adjusted sea surface height at each location is now modeled as:

$$h_{model}(x_i, y_i, z_i) = h_E(x_i, y_i, z_i) + \delta(x_i, y_i)$$

The revised deviation between GNSS observations and the model becomes:

$$\varepsilon_i = h_i^{GNSS} - h_{model}(x_i, y_i, z_i)$$

To test and validate the methodology described above, a dedicated algorithm was developed and implemented in the Wolfram Mathematica environment. This implementation allowed for the structured processing of GNSS data, the computation of the best-fitting ellipsoid using the Moore–Penrose pseudoinverse method, and the subsequent fitting of the local polynomial surface disturbance. The codebase, including all relevant functions and processing steps, is available upon request to any interested researchers wishing to reproduce or further develop the method.

Results

To assess the practical applicability and performance of the proposed methodology, a case study was conducted in the area of Lake Kotychi, a shallow coastal lagoon located in Western Achaia, Greece. The region was selected due to its semi-enclosed geometry, limited wave activity, and suitability for local geoid modeling. Field data were collected using the GNSS-on-boat method, where a dual-frequency GNSS receiver was mounted on a small floating platform. The receiver recorded continuous positioning data at a 1 Hz sampling rate for approximately 90 minutes, while the boat followed a randomized track across the lake. After filtering and cleaning, a dataset of 4,562 valid GNSS points was obtained, forming a dense and spatially representative cloud of height measurements over the water surface. Applying the Moore–Penrose pseudoinverse method, we computed the semi-axes of the best-fitting ellipsoid for the Kotychi lagoon as follows: $a = 6.37724 \cdot 10^6$ m, $b = 6.37929 \cdot 10^6$ m, $c = 6.35765 \cdot 10^6$ m

Following the methodology described in previous section, a best-fitting triaxial ellipsoid was computed using the Moore–Penrose pseudoinverse approach. The geometric deviations of the observed points from the ellipsoid surface were then evaluated. The resulting mean geometric height deviation $\overline{\varepsilon}$ was found to be approximately 3.1 cm. This deviation reflects the baseline discrepancy between the ellipsoidal model and the actual GNSS-observed water surface.

To improve the accuracy of the model, polynomial surface disturbances were fitted on top of the best-fitting ellipsoid, as described in previous section. Polynomial surfaces of increasing degree (from linear up to fourth-order) were tested. The residual means deviations between the GNSS data and the enhanced model (ellipsoid + disturbance) were then re-evaluated. The results are summarized below (Table 1).

Table 1. Mean deviation between GNSS observations and the model

Polynomial Degree	$\overline{\varepsilon}$
Degree 1 (linear)	0.76 cm
Degree 2 (quadratic)	0.42 cm
Degree 3 (cubic)	0.26 cm
Degree 4 (quartic)	0.08 cm

Conclusions

The best-fitting ellipsoid method has been previously shown to offer a localized geometric approximation of the sea surface based on GNSS-derived topographic data. Its strength lies in its simplicity and its ability to represent the general shape of the observed water surface with high internal consistency. However, as demonstrated in this study, the addition of a local polynomial surface disturbance significantly enhances the model's precision. By capturing small-scale deviations from the ellipsoidal shape, this hybrid approach reduces the residual fitting error to below 1 cm, and in optimal cases, to even lower sub-millimetric levels. This improvement provides the foundation for a mathematical modeling of local geoid anomalies—or more precisely, of small variations in the Earth's gravity potential field-at a resolution that is not typically accessible using traditional global or regional geoid models. Such enhanced local modeling opens new possibilities in a range of applications, including precision hydrography, coastal engineering and flood modeling, local vertical datum realization, and GNSS-based sea level monitoring in protected or semi-enclosed water bodies. Overall, the integration of a surface disturbance model over a best-fitting ellipsoid offers a robust and flexible tool for fine-resolution sea surface representation, especially in regions where dense GNSS-on-boat observations are available.

Scientific Ethics Declaration

* The authors declare that the scientific ethical and legal responsibility of this article published in EPSTEM journal belongs to the authors.

Conflict of Interest

* The authors declare that they have no conflicts of interest

Funding

* This research received no specific grant from any funding agency in the public, commercial, or not-for-profit sectors.

Acknowledgements or Notes

* This article was presented as an oral presentation at the International Conference on Technology, Engineering and Science (www.icontes.net) held in Antalya/Türkiye on November 12-15, 2025.

References

Bouin, M. N., Ballu, V., Calmant, S., Boré, J. M., Folcher, E., & Ammann, J. (2009). A kinematic GPS methodology for sea surface mapping, Vanuatu. *Journal of Geodesy, 83*(12), 1203-1217.

Brand, L. (2012). *Vector analysis*. Courier Corporation.

Chupin, C., Ballu, V., Testut, L., Tranchant, Y. T., Calzas, M., Poirier, E., Coulombier, T., Laurain, O., & Bonnefond, P. (2020). Mapping sea surface height using new concepts of kinematic GNSS instruments. *Remote Sensing, 12*(16), 2656.

Dassios, G. (2012). *Ellipsoidal harmonics: Theory and applications* (Vol. 146). Cambridge University Press.

Foster, J. H., Carter, G. S., & Merrifield, M. A. (2009). Ship-based measurements of sea surface topography. *Geophysical Research Letters, 36*(11).

Galani, P., Lycourghiotis, S., & Kariotou, F. (2021). On the determination of a locally optimized Ellipsoidal model of the Geoid surface in sea areas. *IOP Conference Series: Earth and Environmental Science, 906*(1), 012036.

Guo, J., Liu, X., Chen, Y., Wang, J., & Li, C. (2014). Local normal height connection across sea with ship-borne gravimetry and GNSS techniques. *Marine Geophysical Research, 35*(2), 141–148.

Hipkin, R. (2000). Modelling the geoid and sea-surface topography in coastal areas. *Physics and Chemistry of the Earth, Part A: Solid Earth and Geodesy, 25*(1), 9–16.

Jalal, S. J., Musa, T. A., Din, A. H. M., Aris, W. A. W., Shen, W., & Pa'suya, M. F. (2019). Influencing factors on the accuracy of local geoid model. *Geodesy and Geodynamics, 10*(6), 439–445.

Kelly, K. M., & Dennis, M. L. (2022). Transforming between WGS84 realizations. *Journal of Surveying Engineering, 148*(2), 04021031.

Kumar, M. (1988). World Geodetic System 1984: A modern and accurate global reference frame. *Marine Geodesy, 12*(2), 117-126.

Lycourghiotis, S. (2017a). Improvements of GNSS–on-boat methodology using a catamaran platform: Application at the gulf of Patras. *Proceedings of the 7th International Conference on Experiments/Process/System Modeling/Simulation/Optimization*, 5-8.

Lycourghiotis, S. (2017b). Sea surface topography determination: Comparing two alternative methods at the Gulf of Corinth. *Proceedings of the 7th International Conference on Experiments/Process/System Modeling/Simulation/Optimization*, Athens, Greece (pp. 5-8).

Lycourghiotis, S., & Kariotou, F. (2022). The "GPS/GNSS on Boat" technique for the determination of the sea surface topography and geoid: A critical review. *Coasts, 2*(4), 323-340.

Lycourghiotis, S., & Stiros, S. (2010). Sea surface topography in the Gulf of Patras and the southern Ionia sea using GPS. *Proceedings of the 12th International Congress of the Geological Society of Greece*, 19-22.

Lycourghiotis, S., Partaskevi Crawford, E., & Kariotou, F. (2024). A study of the geoid and marine topography in lagoons. *Inżynieria Mineralna, 1*(1).

Lycourghiotis, S. (2017). Developing a GNSS-on-boat based technique to determine the shape of the sea surface. In *Proceedings of the 7th International Conference on Experiments/Process/System Modeling/Simulation/Optimization*, Athens, Greece (pp. 5-8).

Lycourghiotis, S. (2021). Sea topography of the Ionian and Adriatic Seas using repeated GNSS measurements. *Water, 13*(6), 812.

Lycourghiotis, S., & Crawford, E. P. (2024). The impact of climate change on the morphology of marine topography using GNSS. *The Eurasia Proceedings of Science Technology Engineering and Mathematics*, 30, 114-120.

Marcellini, N. F. P., & Sbordone, C. (1996). *Analisi matematica due.* Liguori Editore, Napoli.

Novák, P. (2003). Geoid determination using one-step integration. *Journal of Geodesy, 77*(3), 193-206.

Ocalan, T., & Alkan, R. M. (2013). Performance analysis of web-based online precise point positioning (PPP) services for marine applications. *Journal of The Arab Institute of Navigation*. *(29)*, 24-29.

Reinking, J., Härting, A., & Bastos, L. (2012). Determination of sea surface height from moving ships with dynamic corrections. *Journal of Geodetic Science*, *2*(3), 172-187.

Richards, M. A., & Hager, B. H. (1984). Geoid anomalies in a dynamic Earth. *Journal of Geophysical Research: Solid Earth*, *89*(B7), 5987-6002.

Sansò, F., Venuti, G., Tziavos, I. N., Vergos, G. S., Grigoriadis, V. N., & Vergos, G. (2008). Geoid and sea surface topography from satellite and ground data in the Mediterranean region-a review and new proposals. *Bulletin of Geodesy and Geomatics*, *67*(3), 155-201.

Smith, D. A. (1998). There is no such thing as "The" EGM96 geoid: Subtle points on the use of a global geopotential model. *IGeS Bulletin*, *8*, 17-28.

Author(s) Information

Konstantinos Kalimeris
Academy of Athens, Athens, Greece
Contact e-mail: *kkalimeris@academyofathens.gr*

Sotiris Lycourghiotis
Hellenic Open University Patras, Greece

To cite this article:

Kalimeris, K., & Lycourghiotis, S. (2025). Best-fitting ellipsoid and surface disturbance adjustment of GNSS-derived sea surface heights. *The Eurasia Proceedings of Science, Technology, Engineering and Mathematics (EPSTEM), 38,* 323-329.

The Eurasia Proceedings of Science, Technology, Engineering & Mathematics (EPSTEM)
ISSN: 2602-3199

The Eurasia Proceedings of Science, Technology, Engineering and Mathematics (EPSTEM), 2025

Volume 38, Pages 330-336

IConTES 2025: International Conference on Technology, Engineering and Science

Computer Modeling and Investigation of the Rolling Process of Thick Strips in Relief Rolls Under Conditions of Kinematic Asymmetric Interaction

Yevgeniy Panin
Rudny Industrial University

Valery Chigirinsky
Rudny Industrial University

Abstract: This work, carried out within the framework of grant project № AP19678682, funded by the Science Committee of the Ministry of Science and Higher Education of the Republic of Kazakhstan, presents the results of finite element modeling in the Simufact Forming program of the rolling process of thick strips in relief rolls under conditions of kinematic asymmetry. A 10 mm thick blank made of CuZn39Pb2 brass alloy was used for the simulation. For kinematic asymmetric rolling, the speed of the first roll was 90 RPM, and for the second roll it was 60 RPM (asymmetric coefficient was 1.5). For comparison, the results of symmetric rolling were also considered. When analyzing the strain state, it was revealed that the maximum value of equivalent strain in asymmetric rolling is 13.7% higher than in symmetrical rolling. Also, with asymmetric rolling, a deeper processing of the workpiece is observed. When analyzing the stress state, it was found that during asymmetric rolling, the stresses at the point of contact between the fast roll and the workpiece exceed the stresses at the same point of contact with the slow roll by 12%. There is also a more uniform stress distribution over the thickness of the workpiece compared to symmetrical rolling. An analysis of the force values on the rolls showed that when using asymmetric rolling, the force is 5.4% lower compared to the same symmetrical rolling (456 kN versus 432 kN). With asymmetric rolling, the material flow rate is higher in the deformation zone caused by the higher rotation speed of one of the rolls. The direction of material flow, compared with symmetrical rolling, is deviated towards a fast roll. At the points of contact of the workpiece with the rolls, the flow rate is 15.5% higher near the fast roll, compared with the slow roll.

Keywords: FEM, Modeling, Relief rolls, Rolling, Kinematic asymmetry

Introduction

One of the promising high-tech methods for producing high-quality metal products in the form of hot-rolled sheets and thick plates has been asymmetric rolling for more than a decade, during which additional shear deformation flows are realized in the deformable material (Pustovoytov et al., 2021). The most common types of asymmetric rolling are kinematic (different roll rotation speeds) (Ji et al., 2007), geometric (different roll diameters) (Ji et al., 2009) and the use of a roll without a drive (idling). During asymmetric thin-sheet rolling, additional shear deformations occur, which in combination with compression deformations can provide effective structural refinement of grains. Currently, various technological schemes for the implementation of asymmetric rolling in practice have been developed for each of these options, including the availability of auxiliary devices and mechanisms for the possibility of inclusion in a continuous rolling line (Salganik & Pesin, 1997; Pesin, 2003; Belsky, 2009; Yu et al., 2016). A strip rolling method is also known (Fedorov et al., 1990), in which plastic deformation of the metal is carried out in profiled conical rolls with longitudinal

- This is an Open Access article distributed under the terms of the Creative Commons Attribution-Noncommercial 4.0 Unported License, permitting all non-commercial use, distribution, and reproduction in any medium, provided the original work is properly cited.

- Selection and peer-review under responsibility of the Organizing Committee of the Conference

© 2025 Published by ISRES Publishing: www.isres.org

bending of the strip produced from the rolls. In this rolling method, the SPD is realized due to the mismatch of the circumferential speeds of the roll between the edge and central areas along the strip width.

Due to the formation of a complex stress state in the deformation zone during asymmetric rolling, it is possible to achieve a significant increase in the strength properties of various ferrous and non-ferrous metals and alloys due to the intensification of the refinement process of their structure. Asymmetric rolling was successfully used to produce ultrafine-grained aluminum alloys with improved mechanical properties (Yu et al., 2013; Bobor et al., 2012; Yu et al., 2012). Blanks of copper, titanium, and zirconium were rolled using asymmetric rolling, in which an ultrafine-grained structure was obtained (Wang et al., 2018; Li et al., 2012; Afifeh et al., 2019). Besides pure metals, this method is also used for deformation of complex alloys (Aksenov et al., 2024). A number of studies are devoted to the asymmetric rolling of bimetallic billets consisting of both completely non-ferrous metals and a combination of non-ferrous metals with steels (Chang et al., 2020; Li et al., 2011; Zhang et al., 2012). As a result of the asymmetric impact, an ultrafine-grained structure was formed in these blanks with an increase in the level of mechanical properties. It is also clear from the review that the key feature of asymmetric rolling is the uneven working of the workpiece height, i.e. creating a gradient of properties across a section (Cui et al., 2024).

The rolling technology of thick-sheet metal was investigated (Naizabekov et al., 2016; Naizabekov et al., 2017), which solved the problem of obtaining high-quality thick-sheet metal without significantly changing the initial workpiece dimensions. For this purpose, two versions of rolls with a raised profile in the form of annular ducts have been developed. It was found that the most optimal design is relief rolls with an uneven ratio of the protrusion to the recess. In (Naizabekov et al., 2021) the results of research on improving the deformation technology of thick-sheet blanks in relief rolls were presented. Considering that asymmetric rolling makes it possible to increase the level of shear deformation during rolling, the asymmetry coefficient was introduced into this technology. Also, to achieve a high level of asymmetry, a geometric asymmetry method was implemented using relief rolls of different diameters (Figure 1).



Figure 1. Rolling in relief rolls with geometric asymmetry

This method proved to be very effective in terms of working through the metal section, as well as improving the mechanical properties of aluminum and copper thick-sheet blanks (Panin et al., 2024; Lezhnev et al., 2025). It should be noted that this method of implementing asymmetric rolling has technological disadvantages. The realization of geometric asymmetry when rolling a wide range of thick-rolled products requires the manufacture of a whole fleet of rolls of various diameters. Also, with geometric asymmetry, it is impossible to achieve a high value of the asymmetry coefficient due to the limitation of the range of roller diameters by the structural dimensions of the bed. The realization of kinematic asymmetry during rolling in relief rolls has no obvious limitations of the asymmetry coefficient and depends on the possibility of regulating the speeds of electric motors. Therefore, the purpose of this work was finite element modeling of this deformation process for the theoretical study of stress-strain state.

Method

The main characteristics used for the construction of the rolls were the dimensions of the groove on the barrel of the rolls, which are shown in Figure 2. The chamfer angle was assumed to be 45°. The distance between the protrusion of one roll and the opposite hollow of the other roll is 10 mm. The minimum distance between the chamfers of the two rolls is 10 mm. The width of the collars is 10 mm. The roll radius is 100 mm. The width of the rolls is 190 mm.

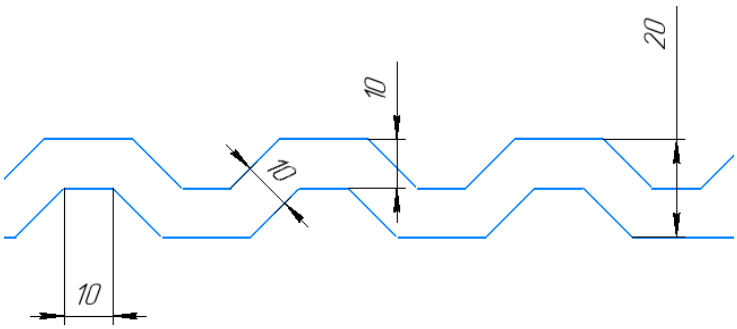


Figure 2. Roll relief dimensions

The construction of the workpiece and pusher models was performed in the Simufact.forming program, where it is possible to build simple three-dimensional models. The length of the workpiece is 200 mm, the width is 140 mm and the height is 10 mm. Brass was chosen as the studied material. In the Simufact Forming program, there is a database of materials from which CuZn39Pb2 alloy was selected, as it most closely corresponds to L63 alloy.

The simulated rolling process is cold, so the temperature for the workpiece and the dies is set to 20°C. The heat transfer coefficient was set to 50 W/(m^2×K). The calculation of the coefficient of heat transfer by radiation to the environment was carried out automatically, taking into account the average properties of surface roughness. The coefficient of friction for the rolls is set to 0.45. In the case of asymmetric rolling, the speed of one roll was set to be 50% higher than the speed of the other, so the rotation speed was set to 90 RPM for the first roll and 60 RPM for the second roll. With symmetrical rolling, the rotation speed of the two rolls was 60 RPM.

Results and Discussion

The following indicators were considered:
- Equivalent plastic deformation is a parameter that shows the intensity of metal processing along the workpiece section;
- Equivalent stress is a parameter that determines the overall load level, calculated from the values of the main stresses;
- Rolling force;
- Material flow is a parameter that shows the linear velocity of the material particles.

The values of equivalent plastic deformation for symmetrical rolling are shown in Figure 3.

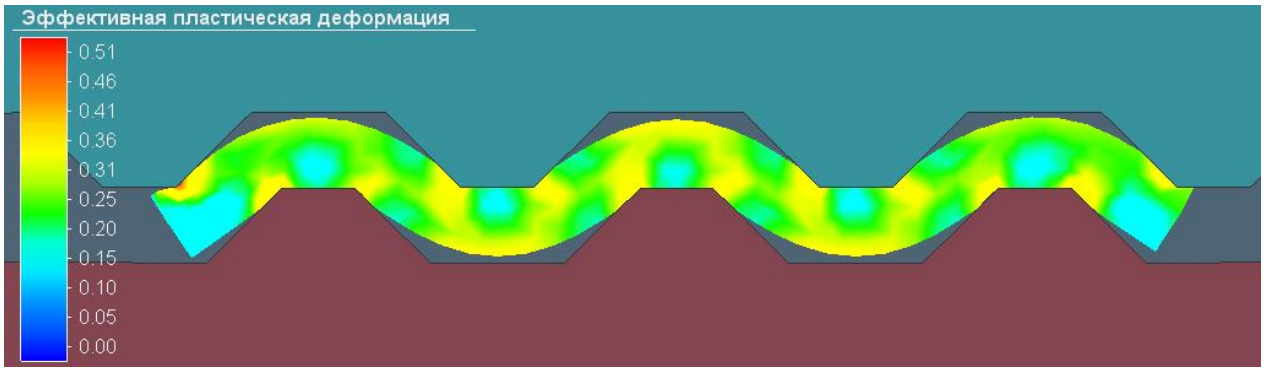


Figure 3. Equivalent plastic deformation of symmetrical rolling

At the moment of capture, the main deformation occurs at the point of contact of the rolls with the workpiece. When the shape of the workpiece changes, the greatest accumulated deformation occurs in the places where the edges of the rolls rest, and in the area of the groove of the rolls, where the workpiece is stretched. The least amount of work is done in the areas opposite the roller projections. In these places, the accumulated deformation is two times lower than in the stretch zone. The values of equivalent plastic deformation for asymmetric rolling are shown in Figure 4.

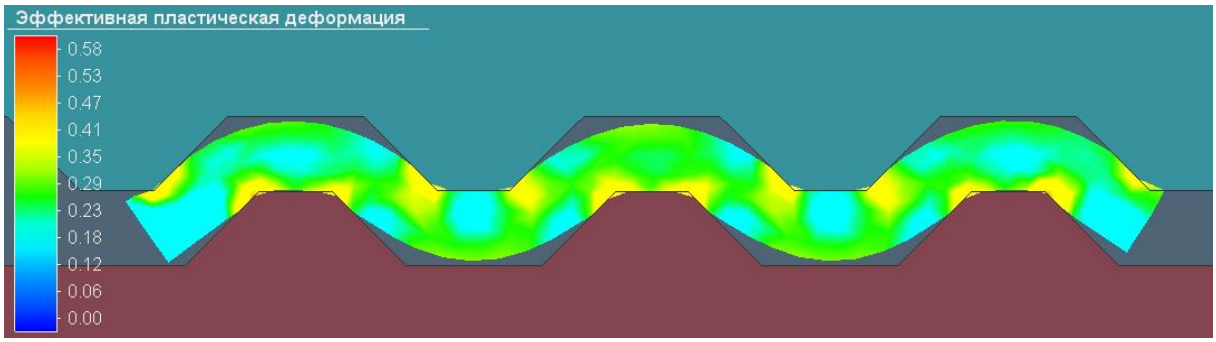


Figure 4. Equivalent plastic deformation of asymmetrical rolling

At the moment of capture, for asymmetric rolling, the values of accumulated deformation are one and a half times higher on the fast roll side. At the points of contact with the fast roller, the workpiece is being worked deeper in depth. The maximum equivalent plastic deformation is 13.7% higher for asymmetric rolling than for symmetrical rolling. Also, asymmetric rolling has a deeper study of the workpiece. The equivalent stress values for symmetrical rolling are shown in Figure 5. The results of the equivalent stress distribution show that the greatest stress is located in the places where there was the greatest accumulated deformation.

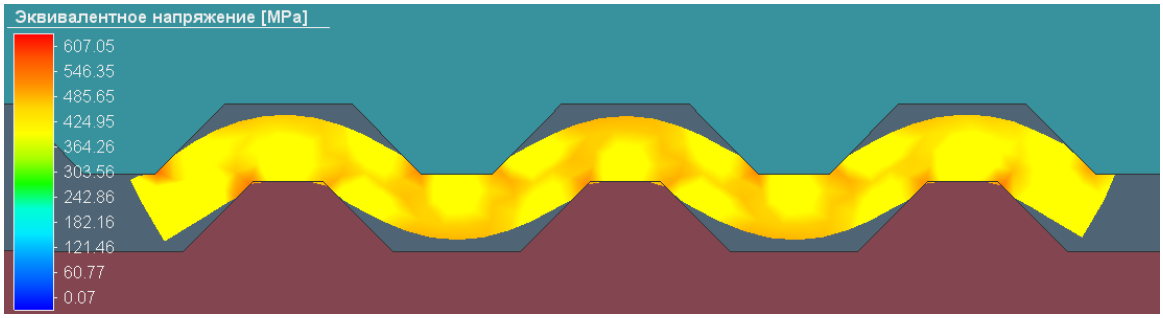


Figure 5. Equivalent stress of symmetrical rolling

The equivalent stress values for asymmetric rolling are shown in Figure 6. During asymmetric rolling, the stresses at the point of contact between the fast roll and the workpiece exceed the stresses at the same point of contact with the slow roll by 12%. There is also a more uniform stress distribution in depth compared to symmetrical rolling.

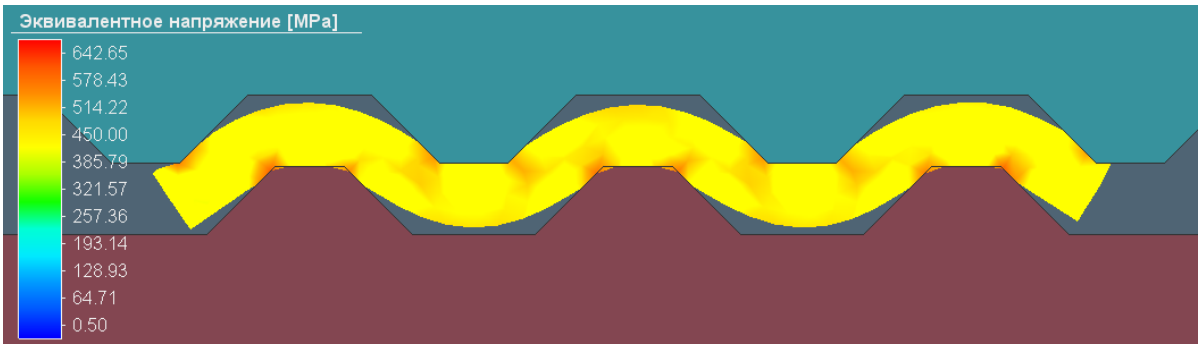


Figure 6. Equivalent stress of asymmetrical rolling

Figure 7 shows graphs of the action of forces on rolls depending on time. The left graph corresponds to symmetric rolling, and the right graph corresponds to asymmetric rolling. By adding the modules of the averaged forces during rolling, the values of 456 kN for symmetrical rolling and 432 kN for asymmetric rolling

were obtained. Based on the data obtained, it can be concluded that the rolling forces are 5.4% lower when using asymmetric rolling compared to similar symmetrical rolling.

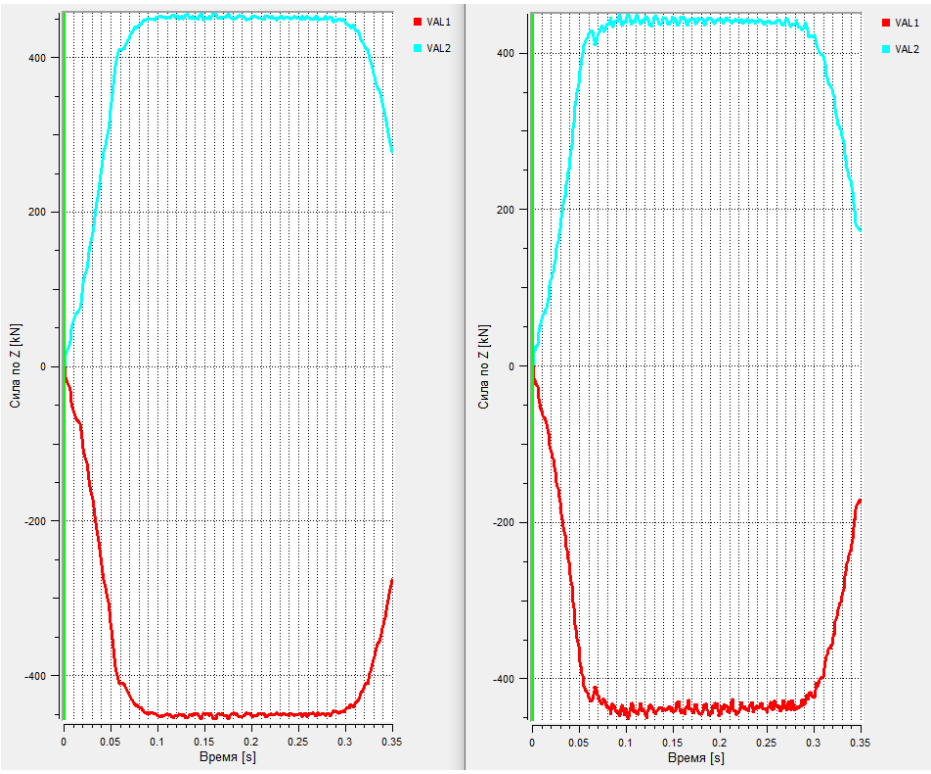


Figure 7. Graphs of the forces on rolls

The flow of material during symmetrical rolling is shown in Figure 8. During symmetrical rolling, the highest flow rate of material is observed in the area of the recesses of the rolls, where the material is stretched. In the area between the projections of the opposite rolls, the smallest displacement of the material in the section occurs.

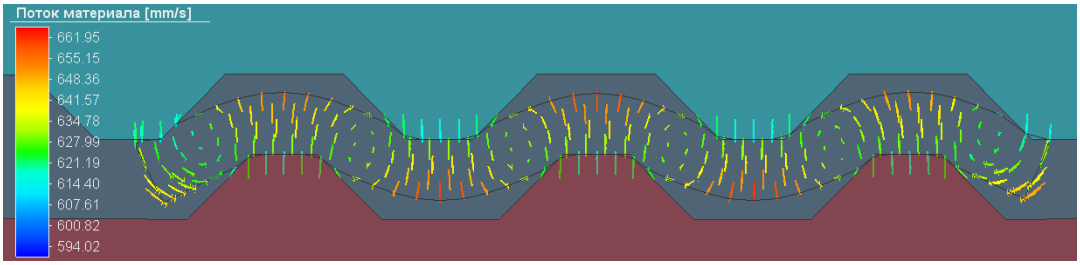


Figure 8. Material flow during symmetrical rolling

The flow of material during asymmetric rolling is shown in Figure 9. With asymmetric rolling, the material flow rate is higher in the deformation zone caused by the fast roll. The flow direction of the material, compared with symmetrical rolling, is deflected towards a fast roll. At the points of contact of the workpiece with the rolls, the flow rate is 15.5% higher near the fast roll, compared with the slow roll.

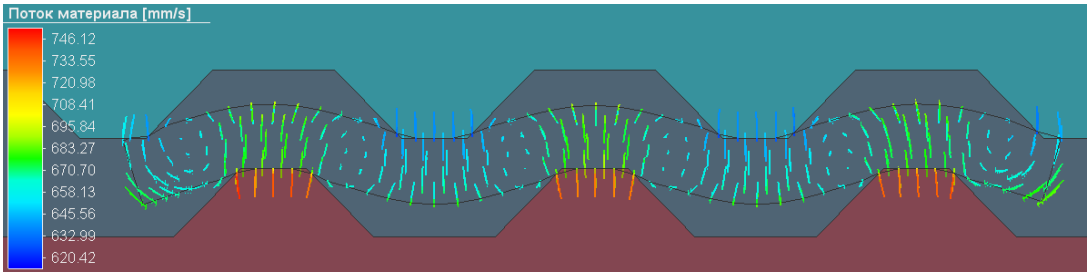


Figure 9. Material flow during asymmetrical rolling

Conclusion

This paper describes computer modeling in the Simufact Forming program of the rolling process of thick strips in relief rolls with an unequal ratio of protrusions to depressions and a comparison of the results of symmetrical and asymmetric rolling. Comparative analysis has shown that when using asymmetric rolling, the accumulated deformation increases and conditions are created for deeper metal processing. Also, when analyzing the force parameters, it was found that the forces of asymmetric rolling are 5% lower than those of symmetrical rolling. Based on the results obtained, it can be concluded that the use of asymmetric rolling makes it possible to achieve improved quality and lower energy costs.

Scientific Ethics Declaration

* The authors declares that the scientific ethical and legal responsibility of this article published in EPSTEM journal belongs to the authors.

Conflict of Interest

* The authors declare that they have no conflicts of interest

Funding

* This study was funded by the Science Committee of the Ministry of Science and Higher Education of the Republic of Kazakhstan (Grants No. AP19678682 and AP26199255).

Acknowledgements or Notes

* This article was presented as a poster presentation at the International Conference on Technology, Engineering and Science (www.icontes.net) held in Antalya/Türkiye on November 12-15, 2025.

References

Abada, A., Bergheul, S., & Younes, A. (2020). Mechanical and structural behaviour of TiAlV nanocrystalline elaborated by mechanical milling technique. *Micro & Nano Letters, 15*(14), 1023–1027.

Afifeh, M., Hosseinipour, S. J., & Jamaati, R. (2019). Nanostructured copper matrix composite with extraordinary strength and high electrical conductivity produced by asymmetric cryorolling. *Materials Science and Engineering: A, 763*, 138146.

Aksenov, D. A., Raab, G. I., Raab, A. G., Pesin, A. M., & Yu, H. (2024). Effect of asymmetric rolling on the structure and properties of Cu-Cr-Zr alloys. *Physical Mesomechanics, 27*(6), 687–697.

Belsky, S. M. (2009). *Improving the technology of forming strips and sheets based on the development of the theory of symmetric and asymmetric hot rolling*. LSTU.

Bobor, K., Hegedus, Z., Gubicza, J., Barkai, I., Pekker, P., & Krallics, G. (2012). Microstructure and mechanical properties of Al 7075 alloy processed by differential speed rolling. *Periodica Polytechnica Mechanical Engineering, 56*(2), 111–115.

Chang, D., Wang, P., & Zhao, Y. (2020). Effects of asymmetry and annealing on interfacial microstructure and mechanical properties of Cu/Al laminated composite fabricated by asymmetrical roll bonding. *Journal of Alloys and Compounds, 815*, 152453.

Cui, E. X., Chen, T. J., Shen, Y. F., Jia, N., Wang, Z. D., & Fan, Z. J. (2024). Superior combination of strength and ductility in Fe-20Mn-0.6C steel processed by asymmetrical rolling. *Materials Today Communications, 40*, 110064.

Fedorov, N. N., Botyev, V. V., & Fedorov, N. A. (1990). *Method of rolling strips* (USSR Patent No. 1574294).

Ji, Y. H., & Park, J. J. (2009). Development of severe plastic deformation by various asymmetric rolling processes. *Materials Science and Engineering: A, 499*(1–2), 14–17.

Ji, Y. H., Park, J. J., & Kim, W. J. (2007). Finite element analysis of severe deformation in Mg-3Al-1Zn sheets through differential-speed rolling with a high speed ratio. *Materials Science and Engineering: A, 454–455*, 570–574.

Lezhnev, S., Naizabekov, A., Esbolat, A., Rakovets, A., Panin, E., Kuis, D., Tsyba, P., Panin, D., & Kuzmin, S. (2025). Effect of asymmetric rolling in relief rolls on the microstructure evolution and mechanical properties of aluminum and copper workpieces. *Results in Engineering, 26*, 105195.

Li, X., Zu, G., Ding, M., Mu, Y., & Wang, P. (2011). Interfacial microstructure and mechanical properties of Cu/Al clad sheet fabricated by asymmetrical roll bonding and annealing. *Materials Science and Engineering: A, 529*, 485–491.

Li, Z., Fu, L., Fu, B., & Shan, A. (2012). Effects of annealing on microstructure and mechanical properties of nano-grained titanium produced by combination of asymmetric and symmetric rolling. *Materials Science and Engineering: A, 558*, 309–318.

Naizabekov, A., Lezhnev, S., Koinov, T., Mazur, I., & Panin, E. (2016). Research and development of technology for rolling of high-quality plates of non-ferrous metals and alloys in relief rolls. *Journal of Chemical Technology and Metallurgy, 51*(3), 363–370.

Naizabekov, A., Lezhnev, S., Panin, E., & Mazur, I. (2017). Alternating sign rolling technology in grooved rolls for nonferrous metal plate billets. *Metallurgist, 61*, 406–413.

Naizabekov, A. B., Lezhnev, S. N., Panin, E. A., Tymchenko, A. A., & Esbolat, A. B. (2021). Improvement of the deformation technology in relief rolls by asymmetric rolling realization. *Ferrous Metallurgy: Bulletin of Scientific, Technical and Economic Information, 77*(4), 445–454.

Panin, E., Esbolat, A., Arbuz, A., Kuis, D., Naizabekov, A., Lezhnev, S., Yerzhanov, A., Krupenkin, I., Tolkushkin, A., Kawalek, A., & Tsyba, P. (2024). Investigation of the efficiency of roll profiles and technological schemes of deformation of asymmetric rolling in relief rolls of C11000 copper alloy by FEM simulation. *Modelling and Simulation in Engineering, 2024*, 2486940.

Pesin, A. M. (2003). *Modeling and development of asymmetric deformation processes to improve the efficiency of sheet rolling*. NMSTU.

Pustovoytov, D., Pesin, A., & Tandon, P. (2021). Asymmetric (hot, warm, cold, cryo) rolling of light alloys: A review. *Metals, 11*(6), 956.

Salganik, V. M., & Pesin, A. M. (1997). *Asymmetric thin-sheet rolling: Development of theory, technology and new solutions*. MISIS.

Wang, L., Shi, Y., Zhang, Y., & Li, M. (2018). High tensile ductility and strength in a gradient structured Zr. *Materials Letters, 228*, 500–503.

Yu, H. L., Lu, C., Tieu, A. K., Li, H. J., Godbole, A., & Zhang, S. H. (2016). Special rolling techniques for improvement of mechanical properties of ultrafine-grained metal sheets: A review. *Advanced Engineering Materials, 18*(5), 754–769.

Yu, H. L., Lu, C., Tieu, K., Liu, X. H., Sun, Y., Yu, Q. B., & Kong, C. (2012). Asymmetric cryorolling for fabrication of nanostructural aluminum sheets. *Scientific Reports, 2*, 772.

Yu, H. L., Tieu, K., Lu, C., Liu, X. H., Godbole, A., & Kong, C. (2013). Mechanical properties of Al-Mg-Si alloy sheets produced using asymmetric cryorolling and ageing treatment. *Materials Science and Engineering: A, 568*, 212–218.

Zhang, S. H., Zhao, D. W., Gao, C. R., & Wang, G. D. (2012). Analysis of asymmetrical sheet rolling by slab method. *International Journal of Mechanical Sciences, 65*(1), 168–176.

Author(s) Information

Yevgeniy Panin
Rudny Industrial University
38 50 let Oktyabrya str., Rudny, Kazakhstan
Contact e-mail: *cooper802@mail.ru*

Valery Chigirinsky
Rudny Industrial University
38 50 let Oktyabrya str., Rudny, Kazakhstan

To cite this article:

Panin, Y., & Chigirinsky, V. (2025). Computer modeling and investigation of the rolling process of thick strips in relief rolls under conditions of kinematic asymmetric interaction. *The Eurasia Proceedings of Science, Technology, Engineering and Mathematics (EPSTEM), 38,* 330-336.

The Eurasia Proceedings of Science, Technology, Engineering & Mathematics (EPSTEM)
ISSN: 2602-3199

The Eurasia Proceedings of Science, Technology, Engineering and Mathematics (EPSTEM), 2025

Volume 38, Pages 337-348

IConTES 2025: International Conference on Technology, Engineering and Science

Eco-Friendly Recovery Method for Manufacturing Flexible Paver's Tile Construction from Waste Plastics

Roua'a K. Al-Ojar
University of Mosul

Yonis Ahmed Ismael
Ninevah University

Akram. W. Nayyef
University of Telafer

Ghadeer Amer Muhamed
University of Mosul

Fawzi Habeeb Jabrail
University of Mosul

Abstract: Different plastic wastes were manufactured into paver's tiles, which hardened using polyurethane binder. The waste of the most common engineering plastics known high density polyethylene, low density polyethylene, polypropylene, poly (vinyl chloride), poly (ethylene terephthalate), polycarbonate, and polystyrene were they washed, ground, extruded with heat, held with resin and finally pressed into special molds. Two types of tiles are manufactured with a surface area 15 x 15 cm^2 and 30 x 30 cm^2 have of 5 cm^2 thick. The manufactured paver's tiles were characterized by Fourier Transform Infrared spectroscopy, Field-Emission Scanning Electron Microscope, X-ray diffraction, and thermal analysis (Thermogravimetric analysis and Differential scanning calorimetry), in conjunction with mechanical and physical tests include compression strength, tensile strength, flexural strength, Charpy impact energy, surface roughness, and Rockwell hardness. Water absorption percentage and dimensional stability are the physical tests of the prepared paver's tiles. Polyurethane held plastic tiles show highly strength construction paver's tiles have hydrophobic nature and dimensionally stable.

Keywords: Polymer waste, Polyurethane binder, Alternative building materials, Plastic construction tiles, Enhancing mechanical qualities

Introduction

Now waste is a global problem, and one that must be treated in order to solve the world's resource and energy challenges (Bhawan, 2013; Basale et al. 2018)) specially the emerging plastic waste which is a major challenge to the environment. The use of plastic waste in civil engineering construction projects demands special attention to tackle this problem and enhance the project's economic aspects (Lamba et al. 2022; Thakur & Singh, 2021). Where recycling and reuse are considered solutions that reduce the volume of waste that is daily destined to sanitary landfills. It is important to plan and use tools such as management to harmonize time, wear, and amount of material (Lamba et al. 2022; Marques, & Ferreira Lima 2021). It is good to utilize plastic waste into useful construction material an attempt is made to utilize plastic in manufacturing of tiles with suitable proportions (Mohana & Gayathrib, 2019). Studies have shown that the plastics bricks and paver blocks product which can

- This is an Open Access article distributed under the terms of the Creative Commons Attribution-Noncommercial 4.0 Unported License, permitting all non-commercial use, distribution, and reproduction in any medium, provided the original work is properly cited.

- Selection and peer-review under responsibility of the Organizing Committee of the Conference

© 2025 Published by ISRES Publishing: www.isres.org

be used for long term applications and their durability and strength is also so high in absorbed test results. In addition, it will increase the raw materials for the construction's purposes and will solve the solid waste management problem (Kumar & Kumar, 2022). Recently, composite materials have obtained an advantage as replacements for traditional metals in component design and production. Today, fiber-reinforced polymer composites have become the preferred choice for a great proportion of the engineering materials market, with applications ranging from everyday products to advanced technologies. Efforts are still ongoing to seek more natural fibers that can effectively substitute synthetic ones (Agbo, 2025; Agbo, 2025). It may be useful to experiment with using plastic waste in concrete to overcome the dual issues of shortage of raw material and safe disposal of plastic waste. An attempt has been made to study the use of waste plastic mix concrete to get the advantages of plastic in concrete (Yaligar et al. 2018). For refractory manufacturers, selecting a suitable binder additive is therefore of decisive importance to increase production efficiency and to set the desired product quality (Hopp et al. 2021).

Many studies were investigated different binders that use for bonding the various layers of composite materials in the tiles such as epoxy, polyester, and a number of other resins compatible with the corresponding polymer matrices (Terekhov& Chistyakov, 2022), and in this context, unsaturated polyester resin with plastic was used as reinforcement in wall and floor coverings tiles (Halimi et al. 2017).

Among the plastics used, low-density polyethylene (LDPE) plastic waste was utilized in the manufacture of floor tiles by mixing fine sand with molten plastic waste in different proportions (Jock et al. 2022). Low-density polyethylene (LDPE) also can manufacture tiles and bricks from its waste, and comparative analysis of tiles made from traditional ceramic tiles to the conventional bathroom tile having the same dimension and flexural strength. Therefore, it is reasonable to say that the market for plastic recycling managing solid waste generally involves planning, financing, construction and operation of facilities for the collection, transportation, recycling and final disposition of the waste.

Polyethylene terephthalate (PET), the polyester resins is known for its excellent combination of properties such as dimensional stability, mechanical, thermal, chemical resistance (Raut et al. 2020), for these properties is added in concrete (Al-Hadithi & Alani, 2015). In addition, PET waste bottles and palm oil fuel ash (POFA) can be used to produce long-lasting, good strength, and highly low-water-absorption eco-friendly wall tiles or both residential and commercial applications .This possibility of producing tiles from PET waste and POFA would also serve as a waste diversion to reduce environmental pollution generated by plastic waste, not only reduce the cost of construction materials but use in construction industry (Tomar & Butala, 2020; Omosebi & Noor, 2022). PET is performed to reduce energy consumption in the construction sector and improve waste management resulting in an eco-friendly environment (Halim et al. 2019). PET particles reduce the requirement of fine aggregate, increase resistance to corrosion, and make the concrete lighter (Araghi et al. 2015; Rahmani, 2013; Alighiri et al. 2019) This provides evidence that the addition of PET plastic into construction materials in the form of plastic flakes can produce fine aggregate (Foti, 2013; Alighiri et al. 2019). Polycarbonate (PC) can reinforce the PET waste plastics tile using direct recycle process without chemical conversion by mechanical shredding with thermal press (Ahmed & Jabrail, 2024; Al-Hadithi & Alani, 2015). The tiles made from recycled poly (vinyl chloride) PVC waste collected from industries with epoxy resin and hardener were mixed and cast. Their produced tiles have higher flexural resistance and lower specific weight than ceramic tiles (Ahmed & Jabrail, 2024; SHALU et al. 2017). Polypropylene (PP), the common thermoplastic commodity plastic is also used in manufacturing of tiles due to its properties (Kashiyani et al. 2013), such as semi-rigid, low density, high crystalline, resist chemicals, good toughness, high mechanical strength, good heat resistance (Charles, 2000; Murahari & Rao, 2023).

In this study, the following plastic waste were used : high density polyethyelen (HDPE), low density polyethylene (LDPE), polypropylene (PP), poly(vinyl chloride) PVC, Polystyrene (PS), polycarbonate (PC), and polyethylene terphthalate (PET), for manufacturing plastic tiles with a surface area 15 x 15 cm^2 and 30 x 30 cm^2 have of 5 cm^2 thick.The binder polyurethane was used in between the plastic particles to form tiles. The manufactured tiles were characterized using the important mechanical and climate resistance tests. In addition, the tiles components were analyzed by FTIR, XRD, thermal analysis (TGA, DSC), and FESEM techniques.

Experimental

The following plastic wastes HDPE, LDPE, PP, PVC, PS, PC, and PET were purchased from the domestic industries in Mosul, Iraq. Where the factories collected the plastic waste from landfills in Mosul and classified each according to their types. The waste is washwith detergent and water, and grind into small pieces (about

5mm), and prepared for manufacturing processes. The binder polyurethane was purchased from Akfix (P645) Automotive and construction PU Sealant, China. A hydraulic press designed with a maximum pressure of 30.0 tons was manufactured in Mosul, Iraq. Tiles molds of surface area (15 x 15 cm^2) and (30 x 30 cm^2) have of (5 cm^2) thick with cover using (10 mm) steel plates were manufactured in Mosul, Iraq. Finally, for heat treatment of the waste, an extrusion machine containing a heater of (2000 W) was designed and manufactured by a local factory in Mosul, Iraq.

Manufacturing of Tiles from Plastic Waste

Different weights of plastic waste with a total weight of (450 g) and (900 g) were found sufficient to press inside the mold area of (15 x 15 x 5) cm^3 and (30 x 30 x 5) cm^3 respectively. Therefore, the exact weight of each plastic waste (Table 1) were transferred into the extrusion machine for extrusion at 200°C. The molten plastic coming out of the machine was taken into the mold and (1.0 % v/ w) polyurethane binder is added to the plastic melt inside the mold. The mold is then covered with a lid and moved to the hydraulic press, applying (207 Mpa) (15 ton in^{-2}) pressure for (15 minutes). The tile is extracted from the mold and subjected to mechanical and physical checks.

Table 1. The types of the plastic waste and their weights used for preparing (15 x 15 x 5) cm^3, and (30 x 30 x5) cm^3 tiles

Plastic waste	15X15X5cm^3 Weight (g)	30X30X5cm^3 Weight (g)
HDPE	92.5	185
LDPE	92.5	185
PP	77.5	155
PVC	87.5	175
PC	45	90
PET	45	90
PS	10	20
Total	450	900

Mechanical Tests of Tiles

Compression Strength Test

The test represent a structural element that resist loads and gives a reduction in the size of the tested material. The test also represent a force applied to the measured sample from both its direction (top and bottom) until it is fractured or deformed. A universal testing machine for the compression strength tests was used , and the following Eq. (1) was followed:

$$\text{Compressive strength } (\sigma) = \frac{P}{A} \quad (1)$$

Where; (P) represent the maximum load in (N), and (A) is the cross sectional area of the sample (m^2).

Tensile Strength Test

Tensile strength represent the maximum stress that applied to a specimen that it can resist while being pulled before breaking. A universal tensile testing machine was aplied for measuring tensile strength with the following Eq. (2):

$$\text{Tensile strength } (S) = \frac{P}{A} \quad (2)$$

Where (P) represent the force required to break (N), and (A) represent the cross-sectional area (m^2).

The elongation, which is the change in the length of the sample in compareson with the original length before breaking. elongation percentage can be calculated from tensile strength according to the following Eq. (3):

$$\text{Elongation } (\%) = \frac{L_f - L_0}{L_0} \text{x100} \quad (3)$$

Where (L_f) represent the final length, and (L_0) represent the original length of the sample.

Flexural Strength Test

Flexural strength represent a mechanical parameter that appears the material can withstand deformation under a fixed load. The Toni ZEM-Model 1548 represent the machine which used, and the following Eq. (4) was followed:

$$\text{Flexural strength } (f) = 3PL/2bd^2 \quad (4)$$

Where (P) represent the maximum load (N), (L) represent the supported length (m), (b) represent the width (m), and (d) represent the failure point depth (m).

Impact Test

The Charpy impact test represent a standardized high stress rate test, it can measure the energy absorbed by the specimen while breaking under a fixed load. The Charpy impact test was done using an advanced universal pendulum tester, and Eq. (5) is followed:

$$\text{Impact test} = W.\ L\ (\cos\alpha - \cos\beta) \quad (5)$$

Where (W) represent the weight of the pendulum, (L) represent the length of the pendulum, (α) represent the angle, and (β) represent a constant. The values of impact test can be used for determination the toughness Eq. (6), and toughness represents the ability to absorbing energy by the material and deform without fracturing.

$$\text{Toughness} = \frac{\textit{impact energy}}{\textit{area of the specimen}} * 100 \quad (6)$$

Rockwell Hardness Test

The Rockwell hardness test represent a method that gives the resistance of a material to indentation. The test was done by KARL KOLB Rockwell hardness tester from Germany, and the following Eq. (7) was followed:

$$HR = N - \left(\frac{d}{D}\right) \quad (7)$$

Where (N) represent the load applied (N), (d) represent the depth of the indentation (m), and (D) represent the diameter of the ball (m).

Climate Resistance Tests

Relative Humidity (RH) Test

The test carried by drying the examined specimen in an oven at 80°C for (6 hours), and after cooling in a desiccator then weight. The specimen is prolonged exposure to high humidity for (24 hours) at 25°C. Finally, the specimen is weighted, and the following Eq. (8) was followed:

$$\text{Relative humidity (RH) } (\%) = \frac{W_f - W_0}{W_n} * 100 \quad (8)$$

Where (W_f) represent the final weight; and (W_o) represent the initial weight of the specimen.

Dimensional Stability Test of Resilient Tile

Dimensional stability of resilient tile test covers the limitation of the changes in their linear dimensions when exposure to heat. The test measure the exact length, width, and, height of the specimen. Thereafter, the specimen is placed in an oven at 82ºC for (6 hours). The specimen is taken out and kept at room temperature for (24 hours). The Eq. (9) was followed:

$$\text{Dimensional stability (\%)} = \frac{V_f - V_i}{V_i} * 100 \qquad (9)$$

Where (V_f) represent the final volume; and (V_i) represent the initial volume of the specimen.

Characterization of Tiles

The tiles were characterized by the following techniques and their instruments:

XRD using a Philips X-ray diffractometer (PW1730). FT-IR using a Shimadzu FT-IR 8400 s spectrometer, Japan. TGA and DSC was done using TA Instruments DSC SDT Q600 V 20.9 build 20, USA. The Ref. Al_2O_3, and heat rate: (80ºC. min^{-1}) from room temperature to 700ºC,.TESEM using a TESCAN MIRAFSEM, Czech Republic.

Results and Discussion

Polymers face many challenges including landfill cumulative waste, performance limitations, environmental impact, safety and health concerns. Therefore, developing recycling methods is the goal of many studies, and aiming to reach cheap, effective, and simple methods. On the other hand, huge quantities of plastic waste make environmental pollution worse. The most common plastics in the world are PVC, PP, PS, HDPE, LDPE, PET, PC and their wastes in native form can be recycled in one method for manufacturing tiles which can be used in floor paving.

Characterization of Tiles

FT-IR Spectroscopy

The FT-IR spectroscopy of the tiles were measured, and the absorption frequencies of their main functional groups are given in Table 2.

Table 2. FT-IR absorption frequencies of the main functional groups of control sample and tile specimen prepared with binder

Specimen	ν(O-H) str.	ν(C-H) str. aliph.	ν(C-H) str. arom.	ν(C=O) str.	ν(C=C) str. arom.	ν(-CH2)	ν(-CH3)	ν(C-O) str.	ν(C-O-C) asymm.	ν(C-H) str. arom.	ν(C-Cl)
Control without polyurethane	3431	2918 2849	3057	1730	1647	1468	1375	1267	1074	721	633
Specimen	ν(N-H) str.	ν(O-H) str.	ν(C-H) str.	ν(C=O)str.	ν(N-H) in plane	νC-H)str. arom.	ν(-CH2)	ν(C-N) str.	ν(N-H)bend out of plane	ν(C-H) str. arom.	ν(C-Cl)
Tile With polyurethane	3416	.....	2959, 2841	1678	1541, 1514	1456	.....	1314	721	723	517

The FT-IR absorption frequencies of the control sample (a tile prepared without binder), shows (Fig. 1, Table 2) the main functional groups of different polymer waste that the tile contains. The absorption frequency peak at 3431 cm^{-1} is belongs to γ(O-H) str group, which comes from PET and PC. (Kumar et al. 2016) The peaks at 2918 cm^{-1} and 2849 cm^{-1} represent γ(C-H) str of aliphatic methine groups. The peak at 3057 cm^{-1} represent γ(C-H) str of aromatic methine groups. The peak at 1730 cm^{-1} represent carbonyl group γ(C=O) str, which belongs

to PET and PC polymers. The peak at 1647 cm^{-1} represent to γ(C=C) str belongs to aromatic rings of PS, PET, and PC polymers. PVC shows peak at 633 cm^{-1} represent γ(C-Cl) group. Otherwise, the FT-IR spectrum of the tile prepared with polyurethane binder shows (Table 2, Fig. 1) all the peaks of the control sample, besides a strong peak at 3416 cm^{-1} representing γ(N-H) str of the polyurethane binder.In addition to the peaks at (1541,1514) cm^{-1} , 1314cm^{-1} and 721cm^{-1} which belonds to γ(N-H) in plane, γ(C-N)str and γ(N-H)bend (out of plane), respectively.

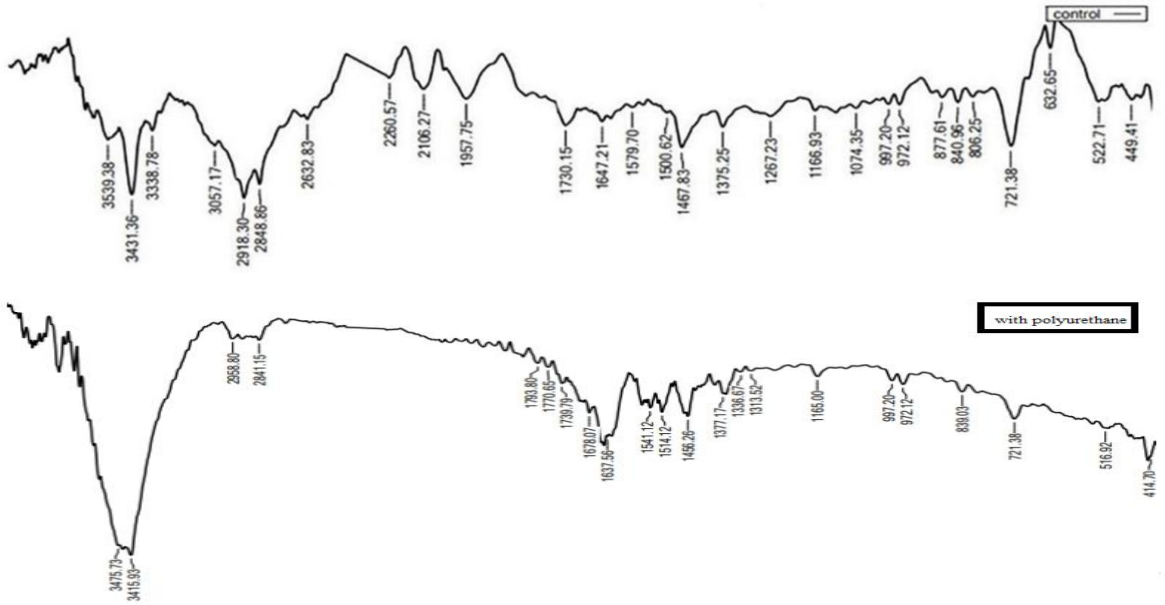


Figure 1. FT-IR spectrum of control sample and tile specimen prepared with polyurethane binder

Thermal Study (TGA and DSC)

The thermograms (TGA and DSC) of control specimen and bonded tile with polyurethane shows both specimens are thermally stable. The TGA thermogram of the control specimen shows lower initial decomposition temperature, final decomposition temperature, maximum decomposition temperature and crystalline decomposition temperature (Fig. 2 and 3, Table 3), with higher weight loss (%) compared with the tile specimen of polyurethane binder, which indicates that adding polyurethane to the tile will elevate its thermal stability.

Table 3. TGA and DSC thermal analysis of control sample and tile specimen prepared with polyurethane

Specimen	IDT	FDT	Tmax	Tcr	Tg (°C)	Δ Hf (J g^{-1})
	0.1	82.0	41.0	78.0		922.2; 996.1
Control without polyurethane					96.0	
	45°C	620°C	450°C	500°C		94.1°C; 357.7°C
	0.08	76.0	40.0	72.5		1013; 301.6; 230.7
Tile with polyurethane					159.0	
	50°C	620°C	475°C	510°C		159.0°C; 479.2°C; 560.1°C

As will as, the DSC thermograms shows glass transition temperature (Tg) of the control specimen 96.0ºC, whereas it is 159.0ºC for the tile specimen prepared with polyurethane. The heat of fusion (ΔHf) from the DSC thermogram shows (Fig. 2 and 3, Table 3) that both have endothermic maxima, with two (ΔHf) for the control specimen, while the tile specimen with polyurethane shows three (ΔHf), where the third one belongs to the polyurethane binder. Finally, the TGA and DSC data (Fig. 2 and 3, Table 3) show that the tile specimen with polyurethane has high thermal stability compared to the control specimen. (Gonzalez et al. 2017).

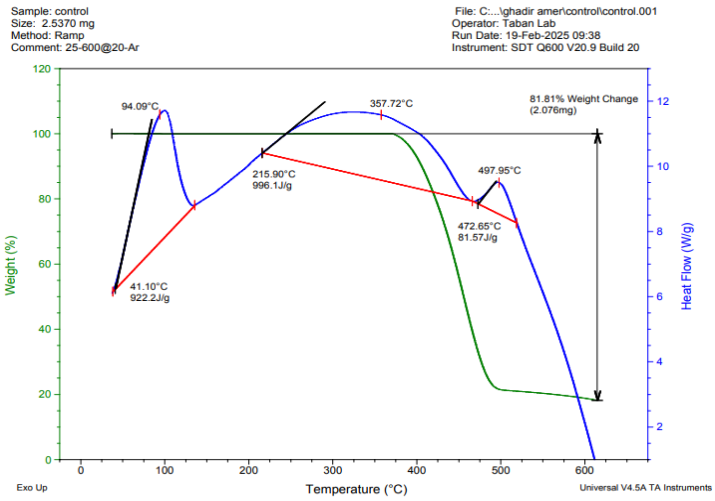


Figure 2. TGA and DSC thermogram of control specimen

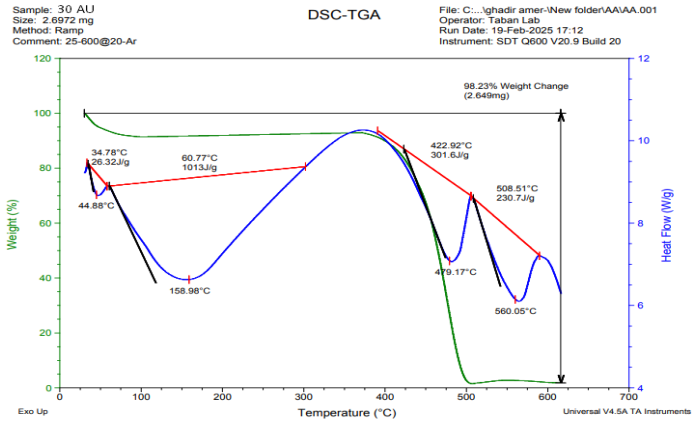


Figure 3. TGA and DSC thermogram of tile specimen prepared with polyurethane

FESEM Study

The FESEM image of the control specimen (Fig. 4) shows a week cohesion between the different components of the tile materials. The control specimen shows non-homogeneous surface morphology contains folds and some crystalline regions. Moreover, the FESEM image of the tile specimen with polyurethane (Fig. 5) shows a homogeneous surface morphology. The polyurethane binder works to increase the cohesion of the plastic components and make its surface more crystalline, with entangled fibers, non-smooth surface, and and the appearance of a frequent folds.

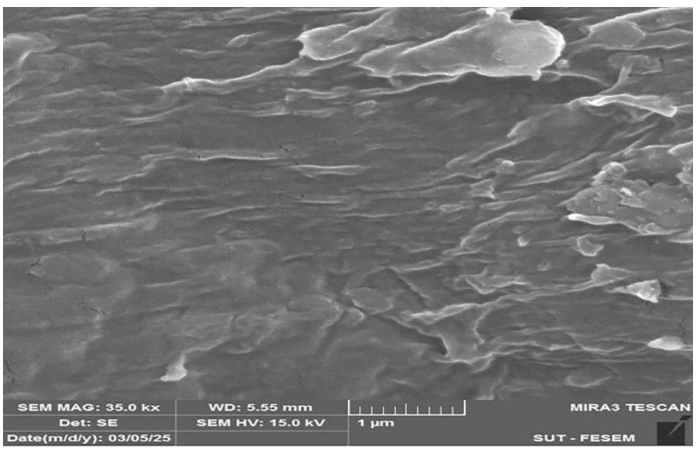


Figure 4. FESEM image of control specimen

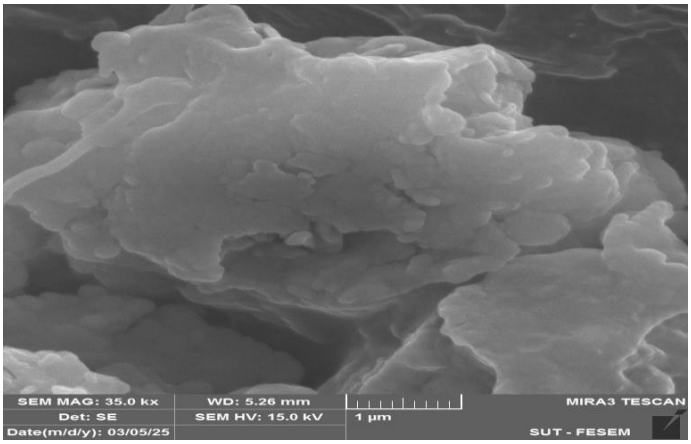


Figure 5. FESEM image of tile specimen prepared with polyurethane

XRD Study

The X-ray diffraction pattern of the control specimen (Fig. 6) shows that the specimen has a crystalline structure. Different types of plastics, after being heated, compressed, and cooled, give tiles that show in XRD pattern (Fig. 6) a number of peaks with different relative intensities representing the crystalline structure of the used plastic materials. On the other hand, the use of polyurethane binder for cohesion of plastic components in produced tiles its XRD pattern (Fig. 7) shows an increase in crystalline peaks with high intensity. This means that the polyurethane binder could promote the crystalline structure of the produced tiles, which in turn enhance its strength. (Abebe et al. 2025)

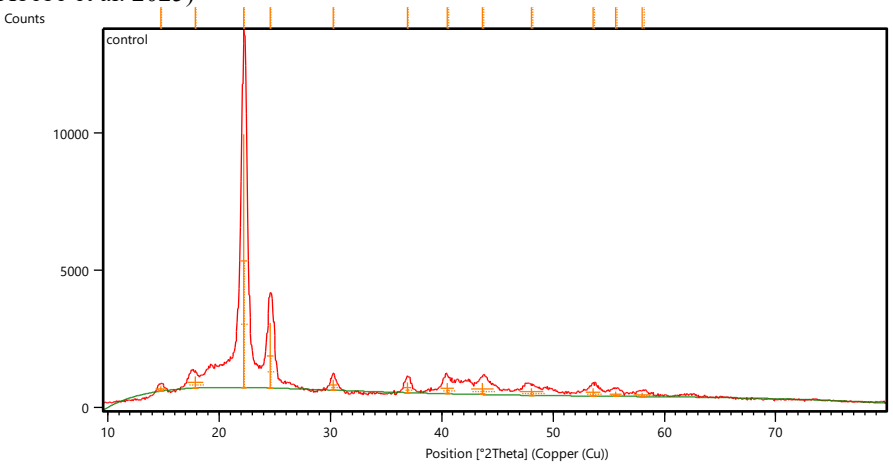


Figure 6. XRD pattern of control specimen

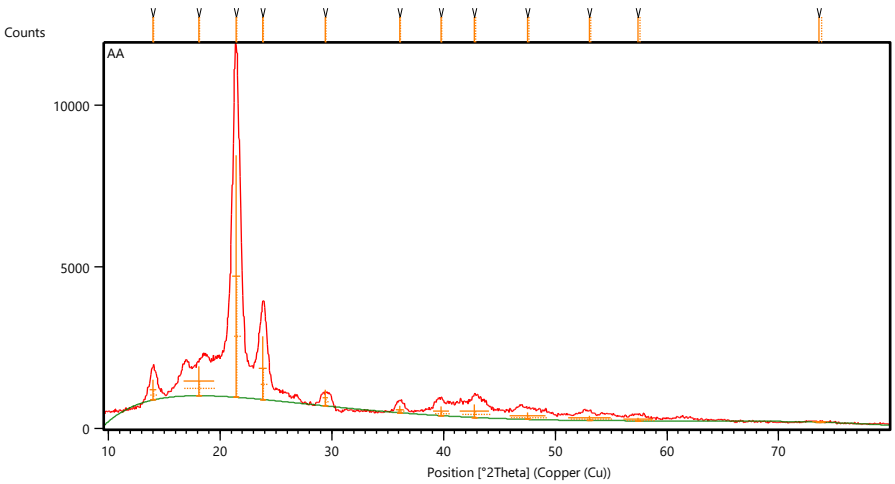


Figure 7. XRD pattern of tile specimen prepared with polyurethane

Mechanical Tests

Different mechanical tests of the control specimen and tiles prepared with a polyurethane binder have been done, and their data are given in (Table 4). The compression strength (σ) of the tested specimen, calculated from Eq. (1), reveals that the control specimen has (15.0) MPa, whereas the tile specimen with polyurethane gives (31.6) MPa, which means the latter shows higher resistance to compression, and the polyurethane binder gives excellent performance across a hardness range. (Wang et al. 2023)

Table 4. Mechanical data of control sample and tile specimen prepared with polyurethane

Specimen	Compression Strength (σ) (Mpa)	Flexural Strength (f) (Mpa)	Ultimate Tensile Strength (σ) (Mpa)	Elongation (%)	Hardness Rockwell	Charpy Impact energy (J)	Toughness J (cm^{-3})
Control	15.0	4.48	27.7	9.4	43HHR	25.5	77.6
Tile with polyurethane	31.6	12.2	58.0	19.0	98HHR	35.5	175.7

The ultimate tensile strength (σ) beside the elongation (%) of both specimens have been calculated (Eq. (2) and (3)), where the control specimen shows (Table 4) an ultimate tensile strength(σ) of (27.7) MPa and elongation of (9.4 %), while the tile with polyurethane binder, give ultimate tensile strength (σ) (58.0) MPa and elongation of (19.0%) (Table 4). The tile with polyurethane binder has a higher ultimate tensile strength and elongation (%) because of the non-linear behavior of the polyurethane, which gives excellent performance to the tiles through a hardness range. (Ding et al. 2022) In addition, both specimens show higher elongation (%), which means they have flexible and ductile properties and can stretch before they break. (Gabriel et al. 2020).

Flexural strength test, which is one of the important mechanical tests, calculated according to Eq. (4) shows (4.48) MPa for the control specimen and (12.2) MPa for the tile prepared with polyurethane binder (Table 4). The results show that the tile prepared with polyurethane binder has very good flexural strength (Seydibeyoglu et al. 2013) because mixing plastic waste with polyurethane resin increase cohesion, and give resist bending under external force.

Charpy impact energy was measured and its magnitude is calculated according to Eq. (5), it gives for the control specimen (25.5 J) and (35.5 J) for the tile specimen prepared with polypolyurethane (Table 4). The Charpy impact energy value increase for polyurethane tile because it reinforces the plastic particles in the tile. (Harusa et al. 2021). The toughness parameter is calculated from impact energy value according to Eq. (6), which shows for the control specimen (77.6 Jcm^{-3}), while it is (123.7 J cm^{-3}) for the tile specimen prepared with polyurethane (Table 4). The high value of the toughness parameter for the tile with polyurethane is because the binder increases the strength of the tiles and makes them not easily broken or damaged.

The Rockwell hardness test, which uses a depth differential method for the hardness and its result was obtained from Eq. (7). The Rockwell hardness for the control specimen is 43HHR, while for the tile specimen with polyurethane binder is 98HHR (Table 4). The Rockwell hardness value is higher for the tile with polyurethane, which means the specimen is harder than the control specimen, but still, it is ductile.

Climate Resistance Tests

Relative Humidity (RH) Test

Table 5. Relative humidity (RH) (%); and dimensional stability test (%) of control sample and tile specimen prepared with polyurethane

Specimen	Relative humidity (RH) test (%)	Dimensional stability test (cm^3) - before	Dimensional stability test (cm^3) - after
Control	1.863	0.754	0.784
Tile with polyurethane	1.695	0.736	0.739

The prepared tiles have been measure their physical properties, including the relative humidity (RH) test, using Eq. (8) for calculation their values. The relative humidity (RH) (%) for the control specimen is (1.863%) while

for the tile with polyurethane binder it is (1.695%) (Table 5), which means the relative humidity (RH) (%) for both specimens is very low because both are hydrophobic. Where, plastic materials absorb humidity to a limited degree and are ordinarily waterproof (Baschek et al. 1999).

Dimensional Stability of Resilient Tile Test

The second important physical test is dimensional stability test which is performed by exposure the tile to heat. The dimensional stability data are calculated from Eq. (9) and the values of both specimens before and after treatment are very close (Table 5), and once again, the tiles use polyurethane binder shows more dimensionally stable due to their thermal stability (Fig. 3, Table 3).

Conclusions

Plastic waste of the most consumed types of polymers were recycled and manufactured as paver's tiles that could be used in constructions as alternative materials. The most famous plastics were used in different weight percentages selected according to their cohesion, mechanical, ductile, and physical properties. Tiles of (15 x 15 x 5) cm^3 and (30 x 30 x 5) cm^3 size were manufactured using (450g) and (900 g) of plastic waste, respectively. The surface area of the tiles shows no big differences in their mechanical properties. For comparison purposes, tiles were manufactured with and without polyurethane resin and the results show the bonded plastic particles by polyurethane resin produce tiles have high mechanical and physical qualities in comparison with the control specimen prepared without polyurethane.

Scientific Ethics Declaration

* The authors declare that the scientific ethical and legal responsibility of this article published in EPSTEM journal belongs to the authors.

Conflict of Interest

* The authors declare that they have no conflicts of interest

Funding

* This research received no specific grant from any funding agency in the public, commercial, or not-for-profit sectors.

Acknowledgements and Notes

* This article was presented as a poster presentation at the International Conference on Technology, Engineering and Science (www.icontes.net) held in Antalya/Türkiye on November 12-15, 2025.

* The authors are grateful to University of Mosul for providing the facilities to carry out this work.

References

Abebe, Y., Palania, S., & Sirahbizu, B. (2025). Effect of Al2O3 nanoparticle on mechanical properties of polyester glass-wool fiber reinforced polymer composites. *Hybrid Advances, 10*, 100472.

Agbo, C. O. A. (2025a). Mechanical performance of rattan cane wood fiber reinforced polymer at high temperatures. *Academia Materials Science, 2*.

Agbo, C. O. A. (2025b). Study on the behavior of cane wood fiber–reinforced polymer composites for application in design. *Academia Materials Science, 2*.

Ahmed, A. W., & Jabrail, F. H. (2024). Composite construction tiles manufactured from PET and other waste plastics reinforced with polycarbonate and study their mechanical properties. *Pharmacognosy Journal, 16*(2), 241–248.

Al-Hadithi, A. I., & Alani, M. F. A. (2015). Mechanical properties of high performance concrete containing waste plastic as aggregate. *Journal of Engineering, 21*(8), 100–115.

Alighiri, D., Yasin, M. N., Rohmawati, B., & Drastisianti, A. (2019). Processing of recycled waste PET (polyethylene terephthalate) plastics bottle into for the lightweight and reinforcement bricks. *Journal of Physics: Conference Series, 1321*(2), 022023.

Araghi, H. J., Nikbin, I. M., Reskati, S. R., Rahmani, E., & Allahyari, H. (2015). An experimental investigation on the erosion resistance of concrete containing various PET particles percentages against sulfuric acid attack. *Construction and Building Materials, 77*, 461–471.

Basale, K., Jagtap, P., Midgule, Y., & Hulpale, M. (2018). Manufacturing and testing of plastic tiles. *Journal of Advances and Scholarly Researches in Allied Education, 15*(2), 638–685.

Baschek, G., Hartwig, G., & Zahradnik, F. (1999). Effect of water absorption in polymers at low and high temperatures. *Polymer, 40*(12), 3433–3441.

Central Pollution Control Board. (2013). *Overview of plastic waste management*. Ministry of Environment, Forest and Climate Change.

Ding, C., Xing, Z., Wang, Z., Qin, Z., Wang, J., Zhao, X., & Yang, X. (2022). The comprehensive effect of tensile strength and modulus on abrasive wear performance of polyurethanes. *Tribology International, 169*, 107459.

Foti, D. (2013). Use of recycled waste PET bottles fibers for the reinforcement of concrete. *Composite Structures, 96*, 396–404.

Gabriel, A., Solikhah, A., & Rahmawati, A. (2020). Tensile strength and elongation testing of starch-based bioplastics using melt intercalation method. *Journal of Physics: Conference Series, 1858*, 012028.

Gonzalez, M., Levi, M., & Turri, S. (2017). Development of polyester binders for the production of sustainable polyurethane coatings: Technological, characterization and life cycle assessment. *Journal of Cleaner Production, 164*, 171–178.

Halim, N. F. A., Azis, Z. A., Taib, N., & Ismail, H. (2019). Development of sustainable building material by incorporating plastic waste in concrete block. *The European Proceedings of Multidisciplinary Sciences*, 415–424.

Halimi, Y., Inchaouh, M., Zyade, S., & Tahiri, M. (2017). Characterization of a composite material reinforced by plastic waste: Application in the construction sector. *International Journal of GEOMATE, 13*(39), 172–178.

Harusa, S., Zhu, H., Jiang, W., & Shao, J. (2021). Evaluation of impact resistance properties of polyurethane-based polymer concrete for the repair of runway subjected to repeater drop-weight impact test. *Construction and Building Materials, 309*, 125182.

Hopp, V., Alavi, A. M., Hahn, D., & Quirmbach, P. (2021). Structure–property functions of inorganic chemical binders for refractories. *Materials, 14*(16), 4636.

Jock, A. A., Akpan, M., & Oluwadayo, F. A. (2022). Production and characterization of sand-plastic composite floor tiles. *Hungarian Journal of Industry and Chemistry, 50*(1), 29–32.

Kashiyani, B. K., Pitroda, J. K., & Shah, B. K. (2013). A study of utilization aspect of polypropylene fibre for making value added concrete. *International Journal of Scientific Research, 2*(2), 103–106.

Kumar, M., & Kumar, N. (2022). Analysis and utilization of waste plastic in building blocks through moulding process. *International Research Journal of Engineering and Technology, 9*(1), 895–907.

Kumar, R., Kamakshi, Kumar, M., & Awasthi, K. (2016). Functionalize Pd-decorated and aligned MWCNTs in polycarbonate as a selective membrane for hydrogen separation. *International Journal of Hydrogen Energy, 41*(48), 23057–23066.

Lamba, P., Kaur, D. P., Raj, S., & Sorout, J. (2022). Recycling/reuse of plastic waste as construction material for sustainable development: A review. *Environmental Science and Pollution Research, 29*, 86156–86179.

Marques, P. S., & Ferreira Lima, F. X. R. (2021). Planning and management for reuse of construction waste in compacted soil-cement blocks. *Academia Letters*, Article 2741.

Mohana, V., & Gayathrib, S. (2019). Effective utilization of plastic wastes in tile manufacturing: A step towards sustainability. *International Journal of Scientific Research and Engineering Development, 2*(3), 3670–3676.

Murahari, K., & Rao, R. M. (2013). Effects of polypropylene fibres on the strength properties of fly ash based concrete. *International Journal of Engineering Science Invention, 2*(5), 13–19.

Omosebi, T. O., & Noor, F. A. (2022). Tiles from recycled plastic bottle (PET) wastes and POFA: Strength properties and durability. *Civil Engineering and Architecture, 10*(4), 1253–1259.

Rahmani, E., Dehestani, M., Beygi, M. H. A., Allahyari, H., & Nikbin, I. M. (2013). Mechanical properties of concrete containing waste PET bottles as aggregate. *Construction and Building Materials, 47*, 1302–1308.

Raut, S. R., Makarande, S. G., & Kalmegh, V. A. (2020). Re-use of polyethylene plastic waste in concrete with plasticizer and test for compressive and tensile strength. *International Research Journal of Engineering and Technology, 7*(9), 3802–3804.

Seydibeyoglu, M., Misra, M., Mohanty, A., & Blaker, J. (2013). Green polyurethane nanocomposites from soybean and bacterial cellulose. *Journal of Materials Science, 48*(5), 2167–2175.

Shalu, S. A., Amrutkar, S., Pawar, D., Dere, M. D., Raut, C., & Shaikh, S. (2017). Utilization of plastic waste in manufacturing of plastic bricks. *International Journal of Research Publications in Engineering and Technology, 3*(6), 101–104.

Terekhov, I. V., & Chistyakov, E. M. (2022). Binders used for the manufacturing of composite materials by liquid composite molding. *Polymers, 14*(1), 87.

Thakur, A., & Singh, A. (2021). Review on utilization of waste plastic in civil engineering construction projects. *International Journal of Engineering Research & Technology, 10*(9), 243–251.

Tomar, A. R., & Butala, A. M. (2020). Experimental investigation on bricks using waste plastic materials. *International Journal for Scientific Research & Development, 8*(3), 195–197.

Wang, H., Yang, H., Gu, M., Du, G., Ni, K., Liu, S., Liu, T., Ran, X., Shi, Z., Gao, W., & Yang, L. (2023). Bonding properties of polyurethane enhanced by branched polyamine and wood interfacial activation. *Colloids and Surfaces A: Physicochemical and Engineering Aspects, 673*, 131860.

Yaligar, U. S., Mahashetty, M., Sarfaraz, M., & Aslam, M. (2018). Study on partial replacement of cement by waste plastic in concrete tiles. *IRE Journals, 2*(2), 35–40.

Author(s) Information

Roua'a K. Al-Ojar
University of Mosul
Mosul- Nineveh, Iraq
Contact rouaa.alojar@uomosul.edu.iq

Yonis Ahmed Ismael
Ninevah University, Pharmacy College
Mosul- Nineveh, Iraq

Akram. W. Nayyef
University of Telafer
Nineveh, Iraq

Ghadeer Amer Muhamed
University of Mosul
Mosul- Nineveh, Iraq

Fawzi Habeeb Jabrail
University of Mosul
Mosul- Nineveh, Iraq

To cite this article:

Al-Ojar, R.K., Ismael, Y. A., Nayyef, A. W., Muhamed, G.A., & Jabrail, F.H. (2025). Eco-friendly recovery method for manufacturing flexible paver's tile construction from waste plastics. *The Eurasia Proceedings of Science, Technology, Engineering and Mathematics (EPSTEM), 38,* 337-348.

The Eurasia Proceedings of Science, Technology, Engineering & Mathematics (EPSTEM)
ISSN: 2602-3199

The Eurasia Proceedings of Science, Technology, Engineering and Mathematics (EPSTEM), 2025

Volume 38, Pages 349-353

IConTES 2025: International Conference on Technology, Engineering and Science

Adaptive Hybrid Reduction for Facial Recognition

Djamel Berrabah
University Djillali Liabes of Sidi Bel Abbes

Yacine Gafour
Ibn Khaldoun University of Tiaret

Abstract: The rapid growth of large-scale image datasets has highlighted the importance of dimensionality reduction in improving computational efficiency while preserving critical visual information. This paper investigates both single-method and hybrid approaches to dimensionality reduction for facial recognition, with a particular focus on the Face94 dataset. Four single techniques, PCA, LDA, NMF, and UMAP, are compared against hybrid strategies that combine two or three methods. Experimental results demonstrate that hybrid approaches consistently outperform individual methods, achieving higher accuracy, precision, recall, and F1-score, while maintaining reasonable computational costs. Among them, tri-hybrid combinations such as PCA-LDA-UMAP achieve near-perfect recognition performance, confirming the effectiveness of carefully designed hybridization strategies for robust facial recognition.

Keywords: Facial recognition optimization, Hybridization of reduction algorithm, Feature preservation metrics, Dataset size impact

Introduction

The exponential growth of digital images across diverse applications has positioned facial recognition as a cornerstone technology in computer vision. From security and surveillance to human–computer interaction and multimedia retrieval, the ability to accurately and efficiently recognize faces is critical. However, the high dimensionality of image data poses significant challenges for both storage and computation, making dimensionality reduction an essential step in facial recognition pipelines (Gafour, Berrabah, & Gafour, 2020).

Classical techniques such as Principal Component Analysis (PCA) (Jolliffe & Cadima, 2016), Linear Discriminant Analysis (LDA) (Fisher, 1936), and Non-negative Matrix Factorization (NMF) (Lee & Seung, 1999) have long served as foundational approaches. More recent non-linear methods, notably t-SNE (van der Maaten & Hinton, 2008) and UMAP (McInnes et al., 2018), enable manifold-aware embeddings that better preserve local structure. Each class of methods offers particular strengths—variance preservation (PCA), class separability (LDA), parts-based interpretability (NMF), or manifold preservation (UMAP/t-SNE)—but also specific limitations such as sensitivity to noise, loss of discriminative information, or high computational cost. Consequently, no single technique is universally optimal for all facial recognition scenarios (Liu et al., 2014; Mahmud et al., 2015).

To address these challenges, this paper explores hybrid dimensionality reduction strategies that combine two or three methods sequentially, with the aim of leveraging complementary properties to obtain compact yet discriminative representations. We evaluate these approaches on the Face94 dataset, comparing single methods (PCA, LDA, NMF, UMAP) against dual and tri-method hybridizations. Experimental results demonstrate that certain tri-hybrid combinations (e.g., PCA–LDA–UMAP) attain superior recognition performance while maintaining reasonable computational cost.

- This is an Open Access article distributed under the terms of the Creative Commons Attribution-Noncommercial 4.0 Unported License, permitting all non-commercial use, distribution, and reproduction in any medium, provided the original work is properly cited.

- Selection and peer-review under responsibility of the Organizing Committee of the Conference

© 2025 Published by ISRES Publishing: www.isres.org

The remainder of this paper is organized as follows. Section 2 reviews related work in dimensionality reduction and facial recognition. Section 3 presents our proposed hybrid approach. Section 4 reports experimental results with comparative analysis. Finally, Section 5 conclude the paper and discusses future research directions.

Related Work

Dimensionality reduction has been widely studied in face recognition to mitigate the high-dimensional nature of image data, reduce computational cost, and enhance generalization. Early foundational work used PCA to reduce dimensionality by finding the directions of greatest variance while projecting face images into lower-dimensional subspaces. PCA often suffers when class separability is important, which motivated the use of LDA, which explicitly optimizes for class separation. Many hybrid models combine PCA and LDA: first applying PCA to reduce noise and dimensionality, then using LDA to sharpen discriminative boundaries (Liu., et al. 2014) or the other way around (Mahmud., et al. 2015). Alternative hybrid approaches have integrated PCA with Gabor wavelets (Cho et al., 2014).

More recent work explores non-linear and multi-stage dimensionality reduction. For example, NMF adds parts-based and non-negativity constraints, which sometimes produce more interpretable features. There are also kernelized extensions of LDA or PCA that map data into higher-dimensional feature spaces to account for non-linear separability (Yang 2011). Additionally, methods like UMAP and t-SNE, or methods preserving manifold structure are used when local geometry matters.

Hybrid approaches beyond simple PCA and LDA are gaining traction: for instance, combining global methods like PCA with local or non-linear embeddings to capture both broad variance and fine structure. Some works integrate neural networks or classifiers such as Support Vector Machines (SVM) or deep architectures to further improve classification after dimensionality reduction (Huang, et al., 2014; Makandar, et al., 2024).

These related methods show that no single technique is universally best: trade-offs exist between accuracy, robustness, computational cost, and memory size. That motivates the exploration of tri-hybrid algorithms and systematic comparison under different parameter settings which motivates our proposed tri-hybrid approach.

Methodology

The rapid expansion of large-scale image datasets has intensified the need for dimensionality reduction, not only to improve computational efficiency in tasks such as classification and retrieval but also to ensure that critical visual information is preserved. Traditional approaches typically apply a single reduction technique, which may fail to balance variance preservation, class separability, and robustness to noise. To address these limitations, we explore hybrid strategies that combine multiple reduction methods. By integrating the strengths of techniques such as PCA, LDA, NMF, and UMAP, our methodology aims to achieve more compact and discriminative representations, enabling both efficient processing and improved recognition accuracy.

Datasets

In this study, we conduct experiments using the Face94 dataset, a widely adopted benchmark in facial recognition research. The dataset contains images of 20 individuals, each represented by 20 samples, with a resolution of 180 × 200 pixels in RGB format. Both male and female subjects are included, and while lighting variations are minimal, the dataset introduces diversity through facial expressions, slight changes in head scale, and appearance differences such as glasses or facial hair.



Figure 1. Exemples of Faces94 images

These characteristics make Face94 particularly suitable for evaluating the robustness of dimensionality reduction methods under moderate real-world variations. Figure 1 presents representative examples of facial images drawn from the Face94 dataset.

Approach

We investigated two categories of dimensionality reduction techniques. The first consists of single-method approaches, where one technique is applied independently. Among these, PCA projects data onto directions of maximum variance, LDA maximizes class separability, NMF yields parts-based representations, and UMAP preserves local neighborhood structures through non-linear projection. While effective, each method has limitations such as sensitivity to noise, loss of discriminative information, or high computational cost, indicating that no single technique is universally optimal.

To overcome these shortcomings, we also explore hybrid methods, where two or three techniques are applied sequentially. In dual combinations (e.g., PCA and LDA, PCA and NMF), the first method performs an initial reduction, while the second refines class separability or manifold preservation. In tri-combinations (e.g., PCA, LDA and UMAP), three techniques are integrated to exploit complementary strengths, aiming to produce compact yet highly discriminative feature representations. This comparative framework allows us to assess both the individual contributions of each method and the potential gains achieved through hybridization.

Experimental Pipeline

Our experimental workflow consists of four stages. First, images are preprocessed through grayscale conversion and normalization. Second, dimensionality reduction is applied using either a single method or a hybrid combination. Third, the reduced features are classified using SVM. Finally, performance is evaluated with accuracy, precision, recall, and F1-score, complemented by computational indicators such as execution time, training time, and final model size.

Results and Discussion

Single-method approaches yielded reasonable accuracy, with PCA achieving consistent results. However, hybrid methods consistently outperformed single techniques, confirming the benefits of combining complementary dimensionality reduction strategies. In particular, PCA+LDA improved classification accuracy compared to PCA alone, while tri-combinations achieved even higher performance.



Figure 2. Comparative analysis of performance metrics (left) and computational times (right) for different tri-hybrid combinations

As shown in Figure 2, the left panel compares the performance metrics (Precision, Accuracy, F1, Recall) across different tri-hybrid combinations, where the best-performing models achieve near-perfect values. The right panel reports the execution and training times, highlighting the computational trade-offs among the approaches. While methods involving PCA and LDA yield high accuracy with moderate computational cost, combinations with UMAP often provide superior discriminative power but at the expense of longer execution times.

Overall, the tri-hybrid approaches achieved the best trade-off between accuracy and efficiency, with clear gains in precision, recall, and F1-score compared to single-method baselines. This confirms that carefully designed hybridization strategies are more effective for handling the complexity of high-dimensional facial data.

Table 1. Comparison of tri-hybrid algorithms performances for the Face94 dataset

Combination	Precision	Accuracy	F1	Recall	Execution Time (s)	Training Time (s)
PCA-LDA-NMF	0.64	0.65	0.61	0.65	24.18	0.35
PCA-LDA-UMAP	0.99	0.99	0.99	0.99	54.81	0.12
LDA-NMF-UMAP	0.98	0.97	0.97	0.97	77.57	0.12
NMF-PCA-UMAP	0.78	0.82	0.79	0.82	290.95	0.49
LDA-PCA-UMAP	0.99	0.99	0.99	0.99	81.21	0.12
LDA-PCA-NMF	0.81	0.81	0.81	0.81	61.28	0.22

Table 1 provides a detailed comparison of tri-hybrid combinations on Face94. Among them, PCA-LDA-UMAP and LDA-PCA-UMAP reached near-perfect accuracy (0.99) with balanced precision, recall, and F1-score. In contrast, combinations such as NMF-PCA-UMAP obtained lower accuracy (0.82) and required significantly longer execution times. These results highlight that while hybridization is beneficial overall, the choice of methods strongly impacts both recognition accuracy and computational cost.

Conclusion

This study investigated dimensionality reduction techniques for facial recognition, highlighting the advantages of hybrid strategies. Experiments on Face94 confirmed that hybrid methods surpass single approaches in both accuracy and robustness. Future work will focus on integrating deep learning models into hybrid pipelines, extending evaluation to larger datasets and real-time systems, and analyzing computational trade-offs for deployment on resource-constrained platforms.

Scientific Ethics Declaration

* The authors declare that the scientific ethical and legal responsibility of this article published in EPSTEM journal belongs to the authors.

Conflict of Interest

* The authors declare that they have no conflicts of interest

Funding

* No funding was received for this work.

Acknowledgements or Notes

* This article was presented as a poster presentation at the International Conference on Technology, Engineering and Science (www.icontes.net) held in Antalya/Türkiye on November 12-15, 2025.

* The authors would like to acknowledge that this research received no specific grant from any funding agency in the public, commercial, or not-for-profit sectors. No other acknowledgements are to be reported.

References

Cho, H., Roberts, R., Jung, B., Choi, O., & Moon, S. (2014). An efficient hybrid face recognition algorithm using PCA and Gabor wavelets. *International Journal of Advanced Robotic Systems, 11*(4), 68.

Fisher, R. A. (1936). The use of multiple measurements in taxonomic problems. *Annals of Eugenics, 7*(2), 179–188.

Gafour, Y., Berrabah, D., & Gafour, A. (2020). A novel approach to improve face recognition process using automatic learning. *International Journal of Computer Vision and Image Processing, 10*(1), 42–66.

Huang, J., Su, K., El-Den, J., Tao, H., & Li, J. (2014). An MPCA/LDA based dimensionality reduction algorithm for face recognition. *Mathematical Problems in Engineering, 2014*, 190329.

Jolliffe, I. T., & Cadima, J. (2016). Principal component analysis: A review and recent developments. *Philosophical Transactions of the Royal Society A: Mathematical, Physical and Engineering Sciences, 374*(2065), 20150202.

Lee, D. D., & Seung, H. S. (1999). Learning the parts of objects by non-negative matrix factorization. *Nature, 401*(6755), 788–791.

Liu, R., Zhang, J., Wang, L., & Zhang, M. (2014). Research on face recognition method based on combination of SVM and LDA-PCA. In B. Zhang, J. Mu, W. Wang, Q. Liang, & Y. Pi (Eds.), *The proceedings of the second international conference on communications, signal processing, and systems* (Lecture Notes in Electrical Engineering, Vol. 246, pp. 69–77). Springer.

Mahmud, F., Khatun, M. T., Zuhori, S. T., Afroge, S., Aktar, M., & Pal, B. (2015). Face recognition using principle component analysis and linear discriminant analysis. *2015 International Conference on Electrical Engineering and Information Communication Technology (ICEEICT)*, 1–4.

Makandar, A., Kaman, S., & Javeriya, S. B. (2024). Enhancing face recognition through dimensionality reduction techniques and diverse classifiers. *LC International Journal of STEM, 5*(1), 36–44.

McInnes, L., Healy, J., Saul, N., & Großberger, L. (2018). UMAP: Uniform manifold approximation and projection. *Journal of Open Source Software, 3*(29), 861.

Van der Maaten, L. J. P., & Hinton, G. E. (2008). Visualizing high-dimensional data using t-SNE. *Journal of Machine Learning Research, 9*(86), 2579–2605.

Yang, J. (2011). Kernel feature extraction methods observed from the viewpoint of generating-kernels. *Frontiers of Electrical and Electronic Engineering in China, 6*(1), 43–55.

Author(s) Information

Djamel Berrabah
Djillali Liabes University of Sidi Bel Abbes
Sidi Bel Abbes, Algeria
Contact e-mail: *berrabdjamel@gmail.com*

Yacine Gafour
Ibn Khaldoun University of Tiaret, Tiaret, Algeria

To cite this article:

Berrabah, D. & Gafour, Y. (2025). Adaptive hybrid reduction for facial recognition. *The Eurasia Proceedings of Science, Technology, Engineering and Mathematics (EPSTEM), 38,* 349-353.

The Eurasia Proceedings of Science, Technology, Engineering & Mathematics (EPSTEM)
ISSN: 2602-3199

The Eurasia Proceedings of Science, Technology, Engineering and Mathematics (EPSTEM), 2025

Volume 38, Pages 354-360

IConTES 2025: International Conference on Technology, Engineering and Science

Enhancing OFDM Performance Using Wavelet Transform Techniques in Wireless Systems

Zohra Zerdoumi
University of M'sila

Malika Fodil
University of M'sila

Fadila Benmeddour
University of M'sila

Nacerddine Bentaleb
University of M'sila

Abstract: Orthogonal Frequency Division Multiplexing (OFDM) technique has attracted major interest because of its robustness to time selective channels and its aptitude to accomplish high data rate. OFDM is the fundamental solution in 4G and 5G systems due to its simplicity of implementation and effectiveness in severe environments. Traditionally the Fast Fourier Transform (FFT) algorithm is adopted to implement OFDM transmitter. Discrete Wavelet Transform (DWT) is recognized as an improvement to Discrete Fourier Transform; therefore, many academics proposed it as alternative approach to FFT in OFDM transmission system. We propose to study the impact of DWT on the performance of the OFDM transmission system considering various modulation techniques and order in noisy and fading environments. We implement two approaches namely OFDM-FFT and OFDM-DWT, their performances respective are studied and compared. Through simulation examples, we notice the improvements obtained by performing the wavelet transform. The wavelet-based OFDM techniques perform better than OFDM-FFT. The results obtained demonstrate the improvements achieved by adopting the wavelet transform relatively to the FFT for all evaluation metrics used. OFDM-DWT cancels interferences, as we can learn from constellation diagrams, where symbols are delimited in their original zones. OFDM-DWT performs the lowest bit error rate (BER) and a reduced Complementary Cumulative Distribution Function (CCDF) of the Peak to Average Power Ratio (PAPR).

Keywords: Orthogonal frequency division multiplexing (OFDM), Discreet wavelet transform (DWT), Wireless communications, Fast fourier transform (FFT)

Introduction

Wireless networks using Orthogonal Frequency Division Multiplexing (OFDM) offer excellent performance in dispersive multipath environments. OFDM allows increasing data rate and therefore spectral efficiency without compromising bandwidth OFDM benefit (Gruyer & Paillard, 2005; Gupta & Jha, 2015). OFDM transmission consists of distributing data over a large number of subcarriers, resulting in very narrow sub channels which ensures robustness in terms of spreading delay, thus reducing the transmission rate per subcarrier (Crawford et al., 2017 ; Gruyer & Paillard ,2005). OFDM technique is adopted in digital audio broadcasting standards for mobile telephony (DAB), digital terrestrial television (DVB-T), and high speed digital communications (ADSL) over the telephone local loop and its derivatives. (Banelli et al., 2014; Crawford et al., 2017 ; Gruyer & Paillard ,2005; Saadaoui, 2019).

- This is an Open Access article distributed under the terms of the Creative Commons Attribution-Noncommercial 4.0 Unported License, permitting all non-commercial use, distribution, and reproduction in any medium, provided the original work is properly cited.

- Selection and peer-review under responsibility of the Organizing Committee of the Conference

© 2025 Published by ISRES Publishing: www.isres.org

Owing OFDM advantages such as spectral efficiency, robustness to multipath fading, and ease of implementation using the Fast Fourier Transform, OFDM suffers from limitations, including high Peak-to-Average Power Ratio (PAPR), spectral leakage, and sensitivity to synchronization. Discrete Wavelet Transform (DWT) has been proposed as an alternative to overcome these issues errors (Almutairi & Krishna, 2022; Banelli et al., 2014; Veena & Swamy,2011). Wavelet-based OFDM can ensure time-frequency localization, improve spectral containment, and reduce PAPR due to the use of overlapping wavelet functions and suppression of cyclic prefix (Almutairi & Krishna, 2022; Banelli et al., 2014; Ramadan & Hassan,2025; Saadaoui, 2019; Veena&Swamy,2011).

There is a multitude of wavelet functions; Haar wavelets are the simplest, Daubechies wavelets, allow the application of filters of limited size, another wavelet family is the spline family, Depending on the problem to be solved, different wavelet families are used based on their qualities (Bouzida, 2008; Guo et al.,2022; Misiti et al.,2009; Ramadan & Hassan,2025; Saadaoui, 2019). OFDM systems can be designed with greater freedom using discrete wavelet transform; the wavelet shape can be carefully constructed to have the least possible distortion (Ramadan & Hassan, 2025; Saadaoui, 2019). Numerous studies have shown that wavelet-based multicarrier methods reduce ICI and ISI better than conventional FFT-based systems (Almutairi & Krishna, 2022; Hassan, 2019; Guo et al., 2022; Misiti et al., 2009; Ramadan, 2025; Saadaoui, 2019; Veena, 2011).

Wavelets subcarriers with varying bandwidths and symbol lengths can be created using the wavelet transform. The ability of wavelets to organize time-frequency tiling in a way that minimizes channel disturbances, noise, and inter-symbol interference makes them very attractive for telecommunication system design (Almutairi, 2022; Ramadan & Hassan, 2025; Saadaoui, 2019). Wavelets add a new level of signal diversity to cellular communication systems, allowing neighbouring cells to be labelled with different wavelets to reduce inter-cell interference (Guo et al.,2022; Ramadan & Hassan,2025).

Within this paper, we present a comparative study and performance analysis of FFT and DWT-based OFDM systems using MATLAB simulations. We use many metrics such as constellation diagram, BER and CCDF of PAPR to assess the performances of the mentioned systems. Through simulation results, we highlight the abilities of wavelet-based OFDM structures for enhancing the effectiveness and consistency of the OFDM system.

Theoretical Background of FFT-OFDM and DWT-OFDM

Background of FFT-OFDM

In OFDM system, the whole signal X(t) corresponding to all N symbols reassembled into one symbol OFDM is given by :

$$X(t) = \sum_{k=0}^{N-1} c_k e^{j2\pi f_k t} \quad (1)$$

Multiplexing is orthogonal the $f_k = f_0 + \frac{k}{T_S}$; T_s symbol duration, f_0 is the first carrier frequency, then:

$$X(t) = e^{j2\pi f_0 t} \sum_{k=0}^{N-1} c_k e^{j2\pi \frac{kt}{T_S}} \quad (2)$$

The received signal, over a symbol duration T_S can be expressed as:

$$Y(t) = \sum_{K=0}^{N-1} c_k H_k(t) e^{j2\pi f_k t} \quad (3)$$

$H_k(t)$ is the channel transfer function at the frequency f_k at time t. $H_k(t)$ varies slowly and can be assumed to be constant over the symbol period T_S (T_S<< 1/ Bandwidth). Then the demodulation process is performed among N subcarriers.

Channel impairments can cause a loss of orthogonality, between carriers and lead to interference between carriers (ICI: Inter Carrier Interference), or interference between symbols (ISI: Inter Symbol Interference). Guard intervals at each OFDM symbol avoid this problem (Crawford et al., 2017). The orthogonality condition shows that:

$$\frac{1}{T_s}\int_0^{T_s} e^{2j\pi(k-i)\frac{t}{T_s}}\,dt = \begin{cases} 0 \ , & if\ k \neq i \\ 1 \ , & if\ k = i \end{cases} \quad (4)$$

$$\frac{1}{T_s}\int_0^{T_s} y(t)e^{-2j\pi f_i t}dt=\frac{1}{T_s}\sum_{k=0}^{N-1}\int_0^{T_s} C_k H_k e^{2j\pi(k-i)\frac{t}{T_s}}dt=C_i H_i \quad (5)$$

Background of DWT-OFDM

We give an insight on Discrete Wavelet Transform (DWT), for implementing an OFDM system. In the wavelet-based OFDM called OFDM-DWT, complex time windowed exponentials in FFT are replaced by wavelet carriers, at different scales 'j' and positions on the time axis 'k'. These functions are generated by the translation and dilation of a single function, called 'mother wavelet', denoted ψ (t):

$$\psi_{J,K}(t) = 2^{-j/2}\psi(2^{-j}t - k) \quad (6)$$

The time localization (k) and the scaling index (j) ensures orthogonality. Wavelet carriers exhibit better time-frequency localization relatively to FFT, with a comparable implementation complexity (Guo et al., 2022).
The orthogonality is achieved by generating the members of a wavelet family, according to the following:

$$\langle \psi_{j,k}(t), \psi_{m,n}(t)\rangle = \begin{cases} 1, & j = m \ et \ k = n \\ 0, & otherwise \end{cases} \quad (7)$$

Thy constitute an orthonormal basis of $L^2(R)$, if a finite number of scales j ∈ Z are considered. In this context, a scaling function Φ (t) is used. The OFDM-DWT symbol considered as a weighted sum of the carrier, wavelet, and scale, as expressed by equation (8). This corresponds to the inverse discrete wavelet transform IDWT (Inverse Discreet Wavelet Transform).

$$X(t) = \sum_{j\leq J}\sum_k w_{j,k}(t).\Psi_{j,k}(t) + \sum_k a_{J,k}\Phi_{J,k}(t) \quad (8)$$

The data symbols is a sequence of wavelets $w_{j,k}$ and approximation coefficients $a_{J,k}$. To perform the inverse discrete wavelet, transform IDWT, the filter bank-based Mallat algorithm is used (Bouzida, 2008; Misiti et al.,2009). The filter output gives the OFDM-DWT symbol, the lack of the cyclic prefix increases the spectral efficiency (Almutairi & Krishna, 2022; Ramadan&Hassan,2025;). Figure 1 shows the Block diagram of an OFDM-DWT system.

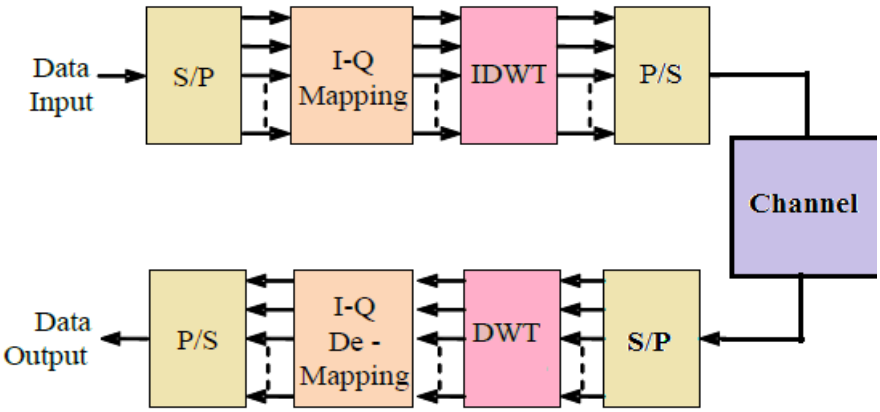


Figure 1. Block diagram of an OFDM-DWT system

In FFT-OFDM, there are M independent sub-channels via an IFFT operation with $K = 2^M$ points. To maintain the same data rate in wavelet systems, K independent sub-channels are multiplexed together via an IDWT operation with K points. Wavelets such as Harr or bi-orthogonal can be used to implement the DWT-OFDM system. Wavelet-based OFDM is implemented via overlapping waveforms to maintain the data rate. In this context, the use of the cyclic prefix makes no sense (Almutairi& Krishna, 2022; Ramadan, &Hassan 2025)

Results and Discussion

During simulations, we perform many wavelet type; Haar and bi-orthogonal gives the best results, nevertheless, Haar surpass in somme scenarios, that we adopted in our simulations.

Constellation Diagrams of OFDM-FFT and OFDM-DWT

We study the performance of the systems in giving output constellation free of distortion, noise and interferences. Figure 2. Shows the OFDM-FFT and OFDM-DWT constellations for 4-QAM and 16-QAM modulation considering an SNR of 15dB and 25dB.

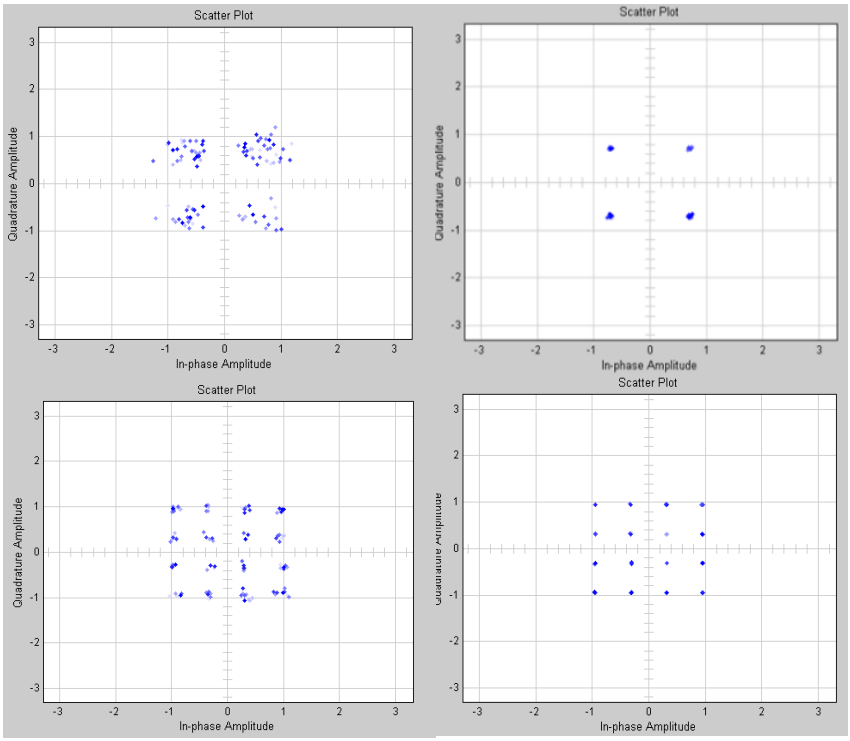


Figure 2. Constellation diagram: top left, FFT-OFDM and top right DWT-OFDM; 4-QAM, SNR=15 bottom left, FFT-OFDM and right below DWT-OFDM; 16-QAM, SNR=25dB

Through Figure 2 we observe that symbol dispersion is more pronounced for low Signal-to-Noise Ratio (SNR=15dB), for OFDM-FFT compared to OFDM-DWT. A noticed improvement is observed for the SNR of 25dB for the OFDM-FFT and OFDM-DWT, furthermore, the dispersion is completely canceled for the OFDM-DWT and symbols are delimited in their original locations. This highlights OFDM-DWT's ability to combat the effects of interference compared to ODFM-FFT.

Bit Error Rate (BER) Performance

.

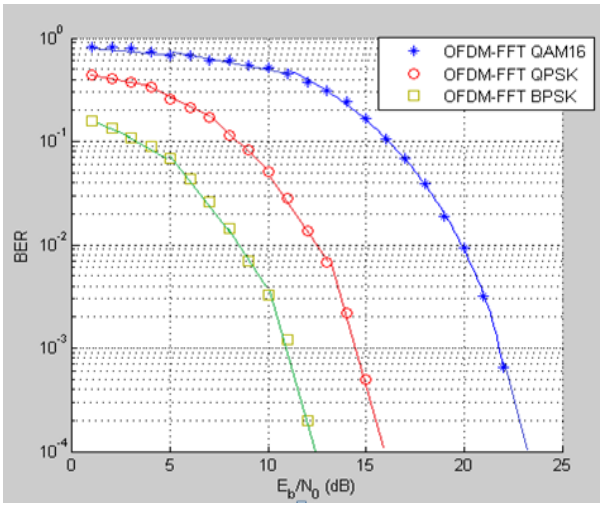


Figure 3. Bit error rate of OFDM- FFT for BPSK, 4-QPSK and 16-QAM modulation

We study bit error rate (BER) performances of OFDM-FFT for a variety of SNR values. Figure 3 Shows the BER achieved by OFDM-FFT for BPSK, 4-QAM and 16-QAM modulation. We study bit error rate (BER) performances of OFDM-DWT for a variety of SNR values. Figure 4 Shows the BER achieved by OFDM-DWT for BPSK, 4-QAM and 16-QAM modulations.

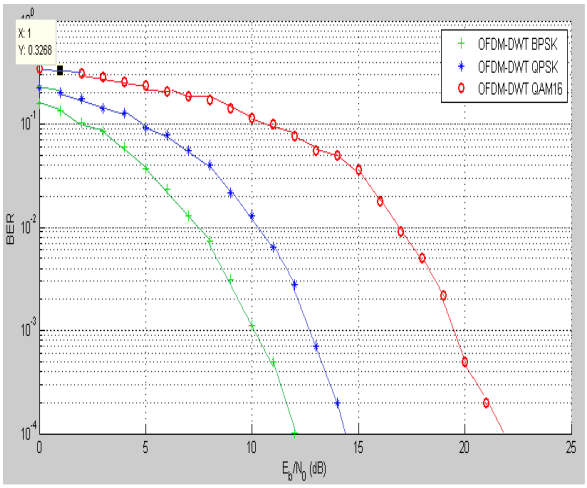


Figure 4. Bit error rate of OFDM-DWT for BPSK, 4-QPSK and 16-QAM modulation

As we can perceive at the BER of 10^{-4}, a transmission using BPSK can achieve an SNR of 12dB and 13dB for OFDM-DWT and OFDM-FFT respectively. Therefore, using BPSK improves BER in a noisy channel. On the other hand, a transmission using QPSK can achieve an SNR of more than 14dB and 16dB, for OFDM-DWT and OFDM-FFT, respectively. We notice that for a low-noise channel, transmission capability can be increased when using 16 QAM starting at SNR of more than 20 dB and 23 for OFDM-DWT and OFDM-FFT, in order. We can also learn through these curves that OFDM using DWT always provides the lowest error rate relative to OFDM using FFT. We also observe that, the BER gap between OFDM-FFT and OFDM-DWT increases further for QPSK (2dB) and attain (5dB) for lower SNR, in QAM-16 modulation.

CCDF of PAPR

We give a study of the complementary cumulative distribution function (CCDF) of the peak to average power ratio (PAPR) through CCDF curve. This metric shows the probability that a signal's power is equal or exceed a certain value. As we can perceive on Figure4, OFDM-FFT curve shifts to the right more then OFDM-DWT, indicating a higher PAPR when compared to OFDM-DW.

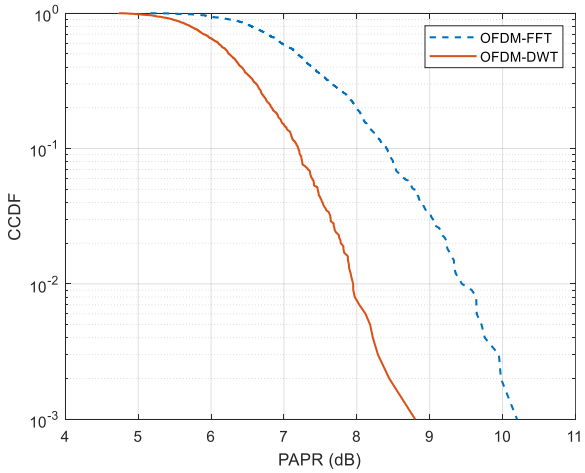


Figure 5. CCDF of PAPR: OFDM- FFT and OFDM-DWT

We can also observe an improvement of more than 1dB procured by OFDM-DWT over the OFDM-DWT. At a CCDF of 10−3, OFDM-DWT exhibits a PAPR of 8.8 dB, while OFDM-FFT shows a PAPR of 10.2 dB, in other

words; OFDM-DWT attain only 8.8 dB of PAPR whereas OFDM-FFT 10.2 dB with 0.1% probability. Consequently, OFDM-DWT exhibits a better PAPR behavior when compared to the OFDM-FFT.

Conclusion

We discussed the fundamentals of OFDM-FFT and OFDM-DWT, and presented theirs performances through the examination of constellation diagrams, Bit Error Rate (BER) and CCDF of PAPR. We highlighted the impact of using wavelets on the performance of the OFDM transmission system in Gaussian environment. We found that the symbol constellation in the case of the OFDM-DWT system are delimited in their original zones and the dispersion is completely canceled. This highlights OFDM-DWT's ability to combat the effects of interference compared to ODFM-FFT. Improvements are also noticed in BER, where OFDM using DWT providing the lowest BER for all type of modulation. When studying the CCDF of PAPR an improvement is also noticed for the OFDM-DWT over the OFDM-FFT. CCDF curve of the OFDM-FFT shifts to the right more than The CCDF curve of the OFDM-DWT, indicating that it produce a higher PAPR when compared to OFDM-DW. The OFDM-FFT remains the dominant multicarrier modulation in wireless systems. Furthermore DWT-OFDM offers favorable benefits, justifying further exploration as a candidate waveform for beyond-5G.

Scientific Ethics Declaration

* The authors declare that the scientific ethical and legal responsibility of this article published in EPSTEM journal belongs to the authors.

Conflict of Interest

* The authors declare that they have no conflicts of interest

Funding

* This research received no specific grant from any funding agency in the public, commercial, or not-for-profit sectors.

Acknowledgements and Notes

* This article was presented as a poster presentation at the International Conference on Technology, Engineering and Science (www.icontes.net) held in Antalya/Türkiye on November 12-15, 2025.

References

Almutairi, A. F., & Krishna, A. (2022). Filtered-orthogonal wavelet division multiplexing (F-OWDM) technique for 5G and beyond communication systems. *Scientific Reports, 12*(1), 4607.

Banelli, P., Buzzi, S., Colavolpe, G., Modenini, A., Rusek, F., & Ugolini, A. (2014). Modulation formats and waveforms for 5G networks: Who will be the heir of OFDM?: An overview of alternative modulation schemes for improved spectral efficiency. *IEEE Signal Processing Magazine, 31*(2), 80–93.

Bouzida, A. (2008). *Diagnostic de défauts de la machine asynchrone à cage par la technique B des ondelettes* (Master's thesis). Ecole Nationale Polytechnique d'Alger.

Crawford, J., Chatziantoniou, E., & Ko, Y. (2017). On the SEP analysis of OFDM index modulation with hybrid low complexity greedy detection and diversity reception. *IEEE Transactions on Vehicular Technology, 66*(9), 8103–8118.

Gruyer, P. (2005). *Modélisation d'un modulateur et démodulateur OFDM* (Doctoral dissertation). Université de Bretagne.

Guo, T., Zhang, T., Lim, E., López-Benítez, M., Ma, F., & Yu, L. (2022). A review of wavelet analysis and its applications: Challenges and opportunities. *IEEE Access, 10*, 1–36.

Gupta, A., & Jha, R. (2015). A survey of 5G network: Architecture and emerging technologies. *IEEE Access, 3*, 1206–1232.

Hassan, E. S. (2019). *Multi-carrier communication systems with examples in MATLAB®: A new perspective*. CRC Press.

Misiti, M., Misiti, Y., Oppenheim, G., & Poggi, J. M. (2009). *Wavelet toolbox for use with MATLAB* (4th ed.). The MathWorks, Inc.

Ramadan, K., & Hassan, E. S. (2025). Enhanced DWT-OFDM communication system using wavelet domain equalizer with Co-CFO. *PLOS ONE, 20*(4), e0317097.

Saadaoui, S. (2019). *Conception d'un système de communication sans fil industriel basé sur la transformée en ondelettes* (Doctoral dissertation). Université de Lorraine.

Veena, M. B., & Swamy, S. (2011). Performance analysis of DWT based OFDM over FFT based OFDM and implementing on FPGA. *International Journal of VLSI Design & Communication Systems, 2*(3), 119–130.

Author(s) Information

Zohra Zerdoumi
University of M'sila, Faculty of Technology,
Po Box 166 Ichebilia, 28000 M'sila, Algeria
Contact e-mail: *zohra.zerdoumi@univ-msila.dz*

Malika Fodil
University of M'sila, Faculty of Technology,
Po Box 166 Ichebilia, 28000 M'sila, Algeria

Fadila Benmeddour
University of M'sila, Faculty of Technology, ,
Po Box 166 Ichebilia, 28000 M'sila, Algeria

Nacereddine Bentaleb
University of M'sila, Faculty of Technology,
Po Box 166 Ichebilia, 28000 M'sila, Algeria

To cite this article:

Zerdoumi, Z., Fodil, M., Benmeddour, F., & Bentaleb, N. (2025). Enhancing OFDM performance using wavelet transform techniques in wireless systems. *The Eurasia Proceedings of Science, Technology, Engineering and Mathematics (EPSTEM), 38,* 354-360.

The Eurasia Proceedings of Science, Technology, Engineering & Mathematics (EPSTEM)
ISSN: 2602-3199

The Eurasia Proceedings of Science, Technology, Engineering and Mathematics (EPSTEM), 2025

Volume 38, Pages 361-373

IConTES 2025: International Conference on Technology, Engineering and Science

A Multi-Criteria Weighted Clustering Protocol for Energy-Efficient Overlay Wireless Sensor Networks

Taieb Brahim Mohammed
Djillali Liabes University of Sidi Bel Abbes

Abbad Houda
Djillali Liabes University of Sidi Bel Abbes

Abbad Leila
ENSTA High School of Algiers

Abstract: Wireless Sensor Networks (WSNs) have emerged as a pivotal technology for various applications, ranging from environmental monitoring to smart cities. However, the constrained energy resources of sensor nodes pose a significant challenge, necessitating efficient routing protocols to prolong network lifetime. In this paper, we propose a novel multi-criteria weighted clustering protocol that improves energy efficiency in WSNs. The new protocol employs a composite weight function that incorporates multiple node and network parameters, including the residual battery level and node density. These parameters are combined for an adaptive and intelligent selection of cluster heads. By dynamically adjusting the cluster head selection process based on multiple criteria, the proposed protocol achieves a more balanced energy distribution among sensor nodes, thereby prolonging the overall network lifetime. The proposed approach is further extended to the context of Overlay Wireless Sensor Networks (OWSNs) to enhance energy optimization across both physical and virtual network layers, ensuring more efficient use of the nodes' limited power resources. This paper focuses on the theoretical formulation and conceptual framework of the proposed protocol rather than its implementation. The work provides a rigorous analytical basis for multi-criteria weighted clustering in OWSNs, serving as a foundation for future simulation-based validation and empirical performance evaluation.

Keywords: Wireless sensor networks, Overlay wireless sensor networks, Weighted selection, Energy efficiency, Network lifetime

Introduction

Wireless Sensor Networks (WSNs) have become a key technology in the Internet of Things (IoT) era (refer to Figure 1). They are important in many areas such as environmental monitoring, precision farming, smart cities, and industrial automation (Ramadan et al., 2022). These networks enable data to be gathered, processed, and sent from different sensor nodes, which has greatly improved our ability to observe and react to real-world situations (Verma et al., 2020). Despite this, the limited power supply of sensor nodes is a major issue, which calls for the creation of energy-saving routing protocols to help the network last longer and work more efficiently (Elshrkawey et al., 2020).

The introduction of the LEACH (Low-Energy Adaptive Clustering Hierarchy) protocol by Heinzelman et al. (2000) established the cornerstone of hierarchical routing research, pioneering the concept of energy-efficient clustering in wireless sensor networks. LEACH has been widely adopted for its ability to distribute energy consumption among nodes through dynamic cluster formation (Singh et al., 2017). Nevertheless, LEACH suffers from several limitations, including suboptimal cluster-head selection, uneven energy distribution, and

- This is an Open Access article distributed under the terms of the Creative Commons Attribution-Noncommercial 4.0 Unported License, permitting all non-commercial use, distribution, and reproduction in any medium, provided the original work is properly cited.

- Selection and peer-review under responsibility of the Organizing Committee of the Conference

© 2025 Published by ISRES Publishing: www.isres.org

lack of consideration for node heterogeneity, which can lead to premature node failures and reduced network longevity (Xu et al., 2021). In response, recent research has introduced numerous enhancements through multi-objective optimization (Zhang et al., 2021), machine learning-based approaches (Singh and Sharma, 2021), and adaptive clustering strategies (Sharma et al., 2021), all aiming to address these shortcomings by incorporating additional parameters and dynamic adaptation mechanisms.

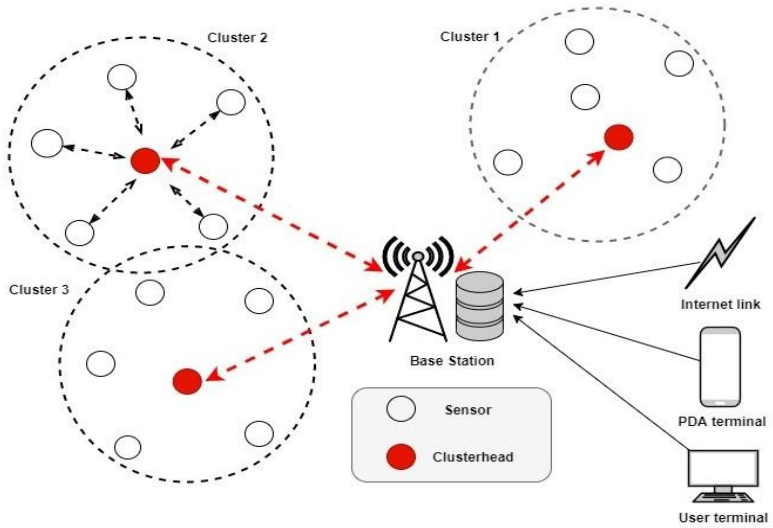


Figure 1. Hierarchical wireless sensor network (WSN) (Taieb Brahim et al., 2021)

Despite these advancements, there remains a need for a comprehensive, multi-criteria model that effectively balances energy efficiency, network coverage, and data transmission reliability. Such a model should rely on a rigorous theoretical foundation that considers key parameters such as residual energy, node density, distance to the sink, and link quality to support informed and adaptive cluster-head selection (Wang et al., 2019).

The evolution from conventional Wireless Sensor Networks (WSNs) to Overlay Wireless Sensor Networks (OWSNs) represents a significant step toward addressing these challenges (Zhang & Rodriguez (see Figure 2), 2023). While WSNs provide the essential physical infrastructure for data sensing and collection, their limited adaptability and energy efficiency have motivated the development of overlay architectures. OWSNs introduce a virtual topology operating above the physical layer, enabling more flexible routing, improved load balancing, and adaptive energy management (Kumar & Chen, 2024). This paradigm enhances the efficiency of resource utilization and facilitates the design of scalable and energy-aware network structures (Wang et al., 2020).

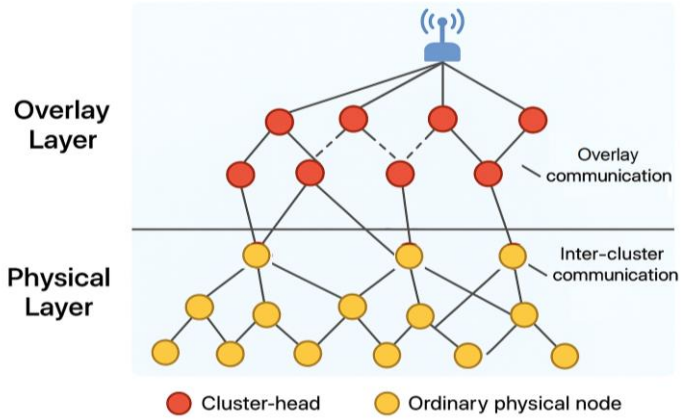


Figure 2. Overlay wireless sensor network (WSN) sample

However, most existing studies in this area have primarily focused on empirical results and simulation-based evaluations, often overlooking the theoretical formulation and analytical modeling of energy optimization mechanisms. In this context, establishing a rigorous theoretical framework for multi-criteria weighted clustering in OWSNs becomes essential to understand and predict system behavior before implementation.

In this paper, we therefore focus on the theoretical formulation of a multi-criteria weighted clustering protocol designed to optimize energy consumption in OWSNs. The proposed framework defines the analytical relationships between key energy-related parameters and formulates an adaptive weighting function for cluster-head selection. Rather than emphasizing experimental validation, this work develops the conceptual and mathematical foundations of the proposed approach, which will serve as a basis for future simulation and practical implementation.

The remainder of this paper is organized as follows: Section 2 presents a comprehensive review of recent advancements in overlay wireless sensor networks. Section 3 describes the developed weighted multi-criteria cluster-head selection mechanism. Section 4 details the integration of this mechanism within the overlay layer. Section 5 discusses the theoretical insights and analytical implications of the designed model. Finally, Section 6 concludes the paper and outlines future research perspectives related to the implementation and simulation-based validation of the proposed theoretical framework.

Related Works

Recent advancements in Overlay Wireless Sensor Networks (OWSNs) have focused on optimizing network architecture, topology management, and energy-aware clustering. This section reviews the most relevant contributions, emphasizing their optimization strategies, objectives, and limitations.

Energy-Efficient Overlay Clustering

Rahman et al. (2023) introduced a hierarchical overlay structure called HO-WSN, which creates multiple logical layers above the physical sensor network. Their approach demonstrated a 35% reduction in end-to-end delay and improved scalability by maintaining distributed overlay nodes at different hierarchical levels. Building on this concept, Liu and Zhang (2023) proposed the Adaptive Overlay Management Protocol (AOMP), dynamically adjusting overlay topology based on network conditions. Their approach addressed mobility challenges in WSNs, achieving a 28% improvement in network lifetime compared to static overlay structures.

Patel et al. (2024) contributed the Energy-Aware Overlay Clustering (EAOC) protocol, introducing a novel weight calculation that combines both physical and overlay metrics (residual energy, link quality, hop distance, virtual coordinates). This method achieved a 40% increase in network lifetime over traditional clustering. Similarly, Chen and Wang (2023) proposed VCOC, a virtual coordinate-based mechanism that optimizes overlay formation and reduces physical-layer overhead, resulting in a 32% reduction in energy consumption.

Multi-Tier and QoS-Aware Structures

Sharma and Kumar (2023) explored multi-tier overlay architectures with distinct functional layers for data aggregation, routing optimization, and security management through their MOSN protocol. Their design improved network throughput by 45% while keeping energy consumption reasonable. Martinez et al. (2023) developed QOCP, a QoS-aware clustering protocol integrating delay, bandwidth, and reliability parameters into clustering decisions. This ensured better QoS guarantees while maintaining clustering efficiency.

Security-Oriented and Weighted Clustering Models

Thompson and Wilson (2024) addressed security issues in OWSNs through the Secure Overlay Clustering Protocol (SOCP), which combines trust metrics and lightweight encryption at the overlay layer with minimal (8%) additional overhead. In parallel, previous foundational works by Taieb Brahim et al. (2021) and Abbad et al. (2022) proposed energy-efficient clustering mechanisms for traditional WSNs (refer to Figure 3). The former introduced a Markov chain-based clustering protocol (MCL-BCRP) optimizing energy consumption and network lifetime, while the latter extended this model to a Weighted Markov Clustering Routing Protocol (WMCL-BCRP) integrating multi-criteria weight functions for adaptive cluster-head selection. These research works represent a contribution to multi-criteria energy optimization, which inspires the theoretical framework proposed in the present study.

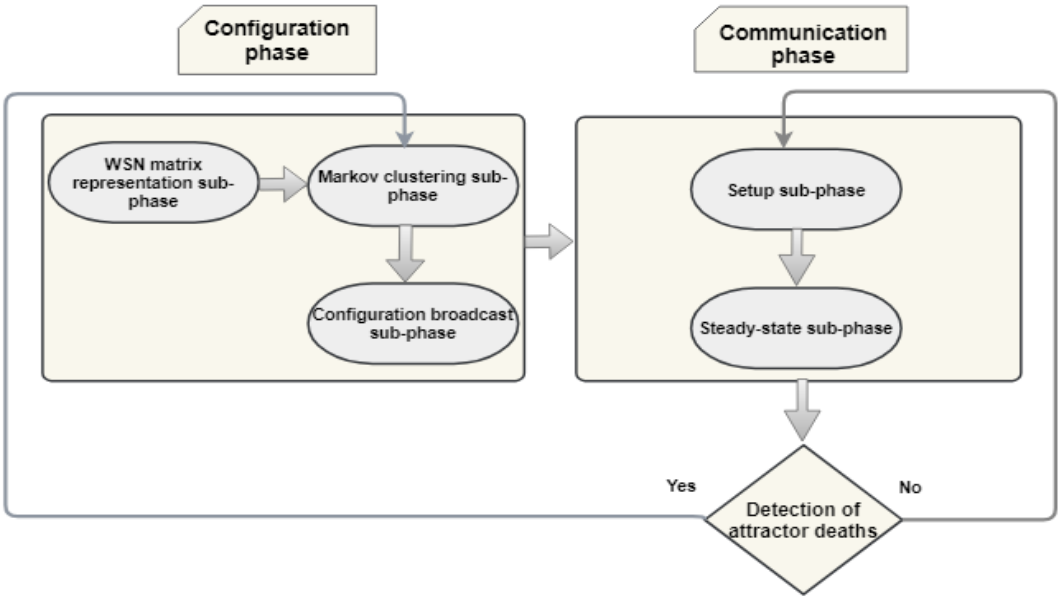


Figure 3. MCL-BCRP and WMCL-BCRP architectures for hierarchical wireless sensor network (Abbad et al., 2022).

Both MCL-BCRP and WMCL-BCRP operate through two main phases (refer to Figure 3). The configuration phase builds clusters using a Markov-based approach, while the communication phase manages data transmission through setup and steady-state stages. The first variant, MCL-BCRP, employs energy and distance parameters to achieve an adaptive cluster-head selection mechanism. However, the weighted variant, WMCL-BCRP, incorporates energy and density factors in a weighting function to achieve better load balancing and longer network lifetime. To better highlight the specific contributions and limitations of the existing approaches discussed above, Table 1 presents a comparative analysis summarizing their main objectives, optimization parameters, and energy efficiency outcomes:

Table 1. Comparative overview of recent advancements in Overlay Wireless Sensor Networks

Protocol / Study	Main Objective	Optimization Parameters	Energy Efficiency Gain	Key Limitation
HO-WSN (Rahman et al., 2023)	Hierarchical overlay for scalability	Hierarchical layer management	↓ Delay by 35%	Limited to static topologies
AOMP (Liu & Zhang, 2023)	Adaptive overlay maintenance	Mobility-aware topology adjustment	+28% lifetime	High control overhead
EAOC (Patel et al., 2024)	Energy-efficient overlay clustering	Residual energy, link quality, hop distance	+40% lifetime	Complex parameter tuning
VCOC (Chen & Wang, 2023)	Virtual coordinate optimization	Virtual coordinates, link cost	−32% energy consumption	Limited scalability
MOSN (Sharma & Kumar, 2023)	Multi-tier overlay structure	Tiered functional layers	+45% throughput	Increased management cost
QOCP (Martinez et al., 2023)	QoS-aware clustering	Delay, bandwidth, reliability	Maintains QoS	Energy optimization secondary
SOCP (Thompson & Wilson, 2024)	Secure overlay clustering	Trust and encryption metrics	High security, +8% overhead	Slight energy trade-off
MCL-BCRP Protocol (Taieb Brahim et al., 2021)	Markov Energy-efficient clustering	Residual energy, distances, cluster size	↑ Lifetime, balanced load	No virtualization layer
WMCL-BCRP (Abbad et al., 2022)	Weighted Markov Energy-efficient clustering	Residual energy, node density, distances	Significant lifetime gain	Not extended to OWSNs

From the analysis above, it is evident that most of the existing approaches rely on simulation-based evaluations and empirical optimization. Although they demonstrate notable improvements in energy efficiency, their

theoretical underpinnings remain limited. Few studies provide a formalized analytical model describing the dynamic relationships between multiple energy-related parameters in overlay architectures. This gap motivates the present work, which aims to develop a theoretical formulation of a multi-criteria weighted clustering mechanism. The goal is to establish a general analytical framework for energy optimization in OWSNs, offering a basis for future simulation-based validation and practical deployment.

Building upon the insights and limitations identified in previous studies, the next sections introduce the theoretical formulation of a weighted multi-criteria cluster-head selection mechanism and the construction of overlay layer for OWSNs. These mechanisms aim to provide a formal analytical model for optimizing energy consumption through Overlay Wireless Sensor Networks.

Weighted Multi-Criteria Cluster-Head Selection Mechanism for OWSNs

This section presents an enhanced version of the weighted multi-criteria cluster-head (CH) selection mechanism for Overlay Wireless Sensor Networks (OWSNs). The proposed approach emphasizes only the most influential parameters impacting CH selection: residual energy, node degree, distance to the sink, and link quality. These parameters are mathematically formulated and integrated into a composite weight function that dynamically adapts to network conditions.

System Model

Let $N=\{n_1, n_2,\ldots, n_i\}$ denote the set of sensor nodes randomly distributed in a sensing field, where each node n_i is associated with a feature vector:

$$S(n_i) = \{E_{res}(n_i), N_{deg}(n_i), D_{sink}(n_i), L_{qual}(n_i)\}$$

Each element of this vector corresponds to a normalized parameter contributing to the CH selection process. Residual energy represents the remaining battery power of a node relative to its initial capacity:

$$E_{res}(n_i) = E_{current}(n_i)/E_{initial}(n_i)$$

A higher E_{res} value increases a node's likelihood of being selected as a cluster-head. It ensures energy balance across the network by prioritizing nodes with sufficient power reserves, thereby prolonging the network lifetime.

Node degree quantifies the local connectivity of a sensor node:

$$N_{deg}(n_i) = |N(n_i)|/N_{max}$$

where $|N(n_i)|$ denotes the number of neighboring nodes within the communication range of n_i , and N_{max} is the maximum observed degree in the network. Nodes with moderate connectivity are preferred since overly dense connections increase communication overhead, while sparse connectivity may degrade data aggregation reliability. The average distance from a node to the sink is defined as:

$$D_{sink}(n_i) = 1 - d(n_i, \text{sink})/d_{max}$$

where $d(n_i, \text{sink})$ is the Euclidean distance between node n_i and the sink node, and d_{max} is the maximum possible distance in the network field. This metric inversely relates to communication cost. Nodes located closer to the sink consume less energy during transmission, improving network throughput and reducing latency.Link quality reflects the reliability and stability of wireless communication links. More formally, link quality corresponding to a node n_i is defined by:

$$L_{qual}(n_i) = (RSSI(n_i)/RSSI_{max}) \times (1 - P_{loss}(n_i))$$

where $RSSI(n_i)$ is the received signal strength indicator and $P_{loss}(n_i)$ is the packet loss probability. A higher L_{qual} indicates stable communication with reduced retransmissions, ensuring efficient cluster maintenance.

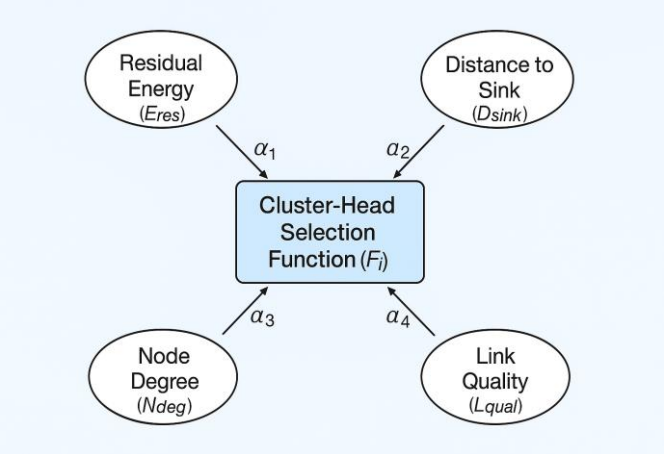


Figure 4. Conceptual model of the energy-aware weighted cluster-head selection mechanism

Figure 4 illustrates the conceptual interactions among the main selection criteria in the proposed weighted model. Each criterion contributes to the final weight-based decision function through its normalized influence coefficient α_i. The diagram emphasizes the interdependence between energy, distance, connectivity, and link quality, highlighting their joint contribution to cluster-head selection efficiency.

Composite Weight Function

Each parameter contributes to the overall CH selection score through a weighted linear combination:

$$W(n_i) = \alpha_1 \times E_{res}(n_i) + \alpha_2 \times N_{deg}(n_i) + \alpha_3 \times D_{sink}(n_i) + \alpha_4 \times L_{qual}(n_i)$$

where α_j (j = 1,…,4) represents the normalized weighting factor for each parameter such that:

$$\sum_{j=1\ldots4} \alpha_j = 1$$

The weighting coefficients are adaptively tuned based on network dynamics. More formally:

$$\alpha_j(t+1) = \alpha_j(t) \times (1 + \lambda \times \triangle C_j),$$

where λ is a sensitivity coefficient, and $\triangle C_j$ represents the rate of change in the corresponding network condition (e.g., energy variance, link degradation, or density variation).

Cluster-Head Selection Criterion

A node n_i is elected as a cluster-head if:

$$W_{CH}(n_i) = \max_{nj}\{W(n_k)\} \text{ and } E_{res}(n_i) \geq E_{th}$$

where E_{th} denotes the minimum energy threshold for CH eligibility. This ensures that only nodes with adequate energy and favorable topological conditions assume cluster-head responsibilities. By focusing on these four dominant parameters, the proposed weighted mechanism ensures:

- Energy balance: Prioritizing high-residual-energy nodes delays node exhaustion.
- Topology stability: Considering node degree prevents both over-clustering and network fragmentation.
- Communication efficiency: Distance and link quality metrics minimize transmission energy and packet loss.
- Adaptive robustness: Dynamic weight adjustment enables real-time adaptation to network evolution.

This refined model effectively balances network longevity, reliability, and energy consumption, offering a mathematically grounded basis for efficient CH selection in OWSNs.

Overlay Layer Construction for OWSNs

This section presents an efficient algorithm for constructing the overlay layer and coordinating data forwarding among overlay nodes (i.e., cluster-heads) toward the sink. The main objective is to ensure reliable and energy-efficient multihop communication while preventing simultaneous transmissions from all overlay nodes during each communication round.

Overlay Construction Principle

Following the cluster-head (CH) selection process, all selected CHs form the overlay layer. Each CH acts as an overlay node that can forward aggregated data either directly to the sink or through intermediate overlay nodes located closer to it. To minimize channel contention and redundant energy consumption, only a subset of overlay nodes actively transmit data in each round, while the remaining nodes stay in an idle or listening state. The overlay layer topology and data-forwarding paths are established dynamically based on residual energy, distance to the sink, and link quality metrics.

Overlay Construction Algorithm

Step 1 – Overlay Formation

Once the cluster-heads (CHs) are elected in the physical WSN layer, they collectively form the overlay layer, which serves as a logical communication backbone above the underlying sensor network. The objective of this step is to enable each CH to discover its overlay neighbors and establish the initial connectivity structure.

Hello Message Exchange

Each selected CH periodically broadcasts a hello message containing essential local parameters:

$$Msg_{\text{hello}}(c_i) = \{ID_i, E_{\text{res}}(c_i), D_{\text{sink}}(c_i), L_{\text{qual}}(c_i)\}$$

where:

- ID_i identifies the CH uniquely,
- $E_{\text{res}}(c_i)$ denotes its current residual energy,
- $D_{\text{sink}}(c_i)$ is the normalized distance to the sink,
- $L_{\text{qual}}(c_i)$ represents its average link quality indicator (based on RSSI and packet loss metrics).

Neighbor Discovery

Upon receiving hello messages from other CHs, each node c_i updates its neighbor table NT_i as:

$$NT_i = \{(c_j, E_{\text{res}}(c_j), D_{\text{sink}}(c_j), L_{\text{qual}}(c_j)) \mid d(c_i, c_j) \leq R_{\text{comm}}\}$$

where R_{comm} is the communication range of a CH. This table stores information about all neighboring overlay nodes within direct transmission range.

Overlay Graph Construction

After the neighbor discovery phase, all CHs collectively define a logical overlay graph:

$$G_{\text{overlay}} = (V, E)$$

where:

- $V = \{c_1, c_2, \ldots, c_m\}$ is the set of overlay nodes (CHs),

- $E = \{(c_i, c_j) \mid d(c_i, c_j) \leq R_{comm}\}$ represents the set of logical links between CHs that can communicate directly.

This graph forms the foundation of the overlay layer, upon which subsequent steps such as link cost computation, multihop route establishment, and transmission scheduling are performed.

Step 2 – Logical Link Establishment

Once the overlay graph $G_{overlay}(V, E)$ is constructed, each overlay node (CH) determines its logical next-hop neighbor toward the sink based on a multi-criteria link cost function. The purpose of this step is to create a reliable, energy-aware, and loop-free forwarding structure over the overlay layer.

Link Cost Computation

Each overlay node c_i evaluates the communication cost to each of its neighbors c_j in NT_i using the following weighted cost function:

$$Cost(c_i, c_j) = w_1 \times d_{ij} + w_2 \times (1 - L_{qual}(c_j)) + w_3 \times (1 - E_{res}(c_j))$$

where:

- d_{ij} is the Euclidean distance between c_i and c_j,
- $L_{qual}(c_j)$ is the link quality indicator of node c_j,
- $E_{res}(c_j)$ is the normalized residual energy of node c_j,
- w_1, w_2, w_3 are adaptive weighting factors satisfying $w_1 + w_2 + w_3 = 1$.

The cost function penalizes distant, unstable, or low-energy links, thereby promoting reliable and energy-efficient routing.

Next-Hop Selection

Each overlay node selects its next-hop neighbor $NextHop_i$ according to:

$$NextHop_i = \min_{cj \in N(ci)} \{Cost(c_i, c_j)\} \text{ and } D_{sink}(c_j) < D_{sink}(c_i)$$

The constraint $D_{sink}(c_j) < D_{sink}(c_i)$ ensures that data is always forwarded toward the sink, preventing routing loops and redundant transmissions.

Overlay Routing Structure Formation

By applying the above rule locally at each overlay node, a tree-like logical topology is automatically formed, rooted at the sink node. This structure supports multihop communication while maintaining low complexity and distributed decision-making.

Link Maintenance

During the network operation, link quality and energy parameters are periodically updated. If $L_{qual}(c_j)$ drops below a predefined threshold L_{min} or if $E_{res}(c_j) < E_{th}$, the link (c_i, c_j) is removed from E, and the node c_i re-selects a new next-hop. This adaptive maintenance mechanism allows the overlay topology to remain robust and responsive to network dynamics such as node failures or link degradation.

Step 3 – Round-Based Transmission Scheduling

Once the logical overlay topology is established, the data forwarding process is organized into discrete communication rounds. Each round is divided into two sub-phases: active node selection and data forwarding.

The main objective is to limit the number of simultaneous transmissions, reduce channel contention, and maintain energy balance across overlay nodes.

Active Node Selection

At the beginning of each round r, the sink or a designated coordinator selects a subset of overlay nodes that will actively forward aggregated data. This set, denoted by $ActiveNodes_r$, is determined based on a composite activation score combining residual energy and link stability:

$$Score(c_i) = \beta_1 \times E_{res}(c_i) + \beta_2 \times L_{qual}(c_i)$$

where β_1 and β_2 are weighting coefficients satisfying $\beta_1 + \beta_2 = 1$. The top k overlay nodes with the highest scores are then selected:

$$ActiveNodes_r = Top_k\{Score(c_i) \mid c_i \in V\}$$

All other overlay nodes remain in a low-power, idle or sleep state to preserve their energy during the current round.

Data Forwarding Phase

Each active overlay node $c_i \in ActiveNodes_r$ transmits its aggregated data according to the multihop structure defined in *Step 2*:

if ($NextHop_i = sink$, then c_i transmits to *sink*
else c_i transmits to $NextHop_i$

To avoid collisions among active nodes located in proximity, a time-slot scheduling mechanism is employed. Each active node is assigned a transmission slot T_i within the round duration T_r, such that:

$$T_i = i \times \triangle_t, \text{ with } 0 < i \leq k$$

where $\triangle_t$ represents the slot interval. This ensures that no two neighboring overlay nodes transmit simultaneously. Once data is received, the next-hop node either forwards it further toward the sink or temporarily buffers it until its assigned slot, depending on the routing hierarchy depth.

Energy and Link Updates

At the end of each round:

- Each node c_i updates its residual energy $E_{res}(c_i)$ according to the energy model:

$$E_{res}(c_i) = E_{res}(c_i) - (E_{tx} + E_{amp} \times d_{ij}^2)$$

where E_{tx} is the energy used for transmission and E_{amp} the amplifier cost per unit distance.

- The link quality $L_{qual}(c_i)$ is updated based on the received signal strength and recent packet delivery statistics.
-

These updated parameters are then used in the next round to recalculate activation scores and link costs, allowing the overlay topology and transmission scheduling to adapt dynamically to changing network conditions.

Role Rotation and Reactivation

To prevent rapid depletion of frequently selected nodes, the transmission role is periodically rotated among overlay nodes. A node c_i that has participated as an active forwarder in round r becomes temporarily ineligible for the next τ rounds, unless its energy level remains significantly higher than the network average:

$$E_{res}(c_i) > \gamma \times average(E_{res})$$

where $(0 < \gamma < 1)$ is a tunable parameter controlling the fairness of role rotation. This mechanism ensures long-term energy balance and network stability by distributing the forwarding workload evenly. Although the algorithmic steps are presented in this section, the current work focuses primarily on the theoretical formulation of the overlay construction process rather than on its simulation-based or empirical evaluation. The purpose of this presentation is therefore to formalize the conceptual operation of the overlay layer and highlight its theoretical contribution to energy optimization within OWSNs.

Figure 5 summarizes the main conceptual steps of the proposed overlay layer construction algorithm, highlighting the three key processes: overlay formation, logical link establishment, and round-based transmission scheduling. Each step contributes to maintaining energy efficiency, scalability, and network stability.

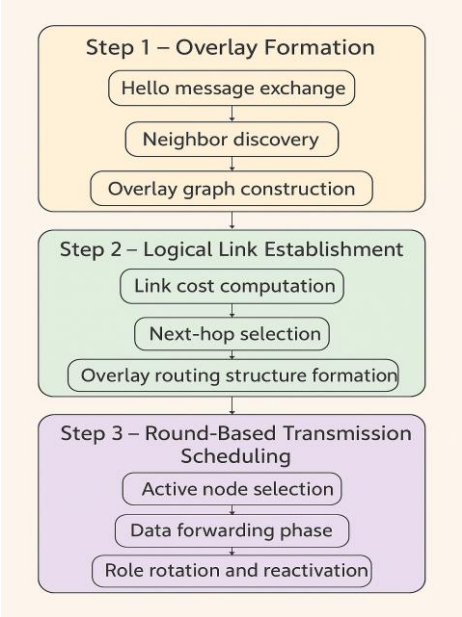


Figure 5. Conceptual flow diagram of the overlay layer construction algorithm

Analytical Discussion and Theoretical Insights

This section provides a theoretical interpretation of the proposed weighted multi-criteria clustering and overlay construction mechanisms. It examines the fundamental assumptions and limitations of the model, compare its analytical formulation with related theoretical works, and outline future directions for simulation-based and experimental validation.

Theoretical Assumptions and Model Limitations

The present theoretical framework is developed under several simplifying assumptions:

- All nodes are assumed to have homogeneous initial energy and identical transmission capabilities.
- The communication model assumes static topology during each round.
- Environmental factors such as channel interference, node failure, or mobility are not explicitly modeled but can be incorporated as extensions in future work.

These assumptions allow analytical tractability but inevitably limit direct real-world generalization. Nevertheless, they provide a controlled theoretical environment that isolates the effects of multi-criteria weighting and overlay structuring on energy optimization.

Theoretical Comparison with Related Approaches

From a theoretical standpoint, the proposed model extends beyond conventional single-criterion clustering approaches that primarily rely on residual energy or distance metrics. Unlike classical protocols such as LEACH or HEED, which perform cluster-head selection based on a single energy-related probability, the proposed formulation incorporates multi-dimensional decision factors, enhancing discrimination among potential cluster-heads. In contrast to overlay-based protocols such as EAOC or MOSN, which are empirically evaluated but lack analytical generalization, this work emphasizes theoretical clarity and model transparency. The weighted formulation provides a generalizable analytical structure capable of representing both physical and logical interactions, thereby bridging the gap between classical clustering theory and emerging OWSN architectures.

Perspectives for Simulation and Empirical Validation

While the current work focuses exclusively on the theoretical formulation, future research will aim to validate the analytical predictions through simulation and experimental scenarios.
Such validation will assess:

- The practical impact of the weighting coefficients (α_i) on network lifetime and stability.
- The scalability behavior under increasing node density.
- The trade-off between energy consumption and latency within the overlay layer.

Furthermore, the integration of the proposed mechanism into existing simulation platforms (e.g., NS-3, OMNeT++) will enable a comparative evaluation against established energy-aware protocols. Ultimately, this transition from theoretical abstraction to empirical validation will consolidate the contribution of the model as a foundation for energy-optimized, adaptive OWSN architectures.

Conclusion

This paper proposes a novel weighted multi-criteria approach for efficient cluster-head selection in Overlay Wireless Sensor Networks. The theoretical framework demonstrates promising potential for improving network lifetime and energy efficiency through its adaptive weighting mechanism and integration with OWSN architecture. This conceptual approach provides analytical clarity and a foundation for understanding how multi-factor interactions influence network performance and energy balance over time.

To fully assess the effectiveness of the model, the next crucial step would be to implement and simulate the proposed protocol using standard network simulation tools. Such experimental validation would allow us to evaluate network lifetime under various conditions, compare performance metrics with existing protocols and analyze behavior under different traffic patterns. Future research directions could explore several promising avenues such as the extension of the protocol for mobile sensor networks and the adaptation of the approach for Internet of Things (IoT) applications. The implementation and experimental validation of this theoretical framework would provide valuable insights into its practical applicability and potential benefits for real-world wireless sensor network deployments.

In summary, the proposed framework serves as a conceptual cornerstone for future developments in energy-aware and self-organizing overlay architectures, bridging theoretical modeling and practical applications in next-generation wireless sensor systems.

Scientific Ethics Declaration

* The authors declares that the scientific ethical and legal responsibility of this article published in EPSTEM journal belongs to the authors.

Conflict of Interest

* The authors declare that they have no conflicts of interest

Funding

* This research received no specific grant from any funding agency in the public, commercial, or not-for-profit sectors.

Acknowledgements or Notes

* This article was presented as an oral presentation at the International Conference on Technology, Engineering and Science (www.icontes.net) held in Antalya/Türkiye on November 12-15, 2025.

References

Abbad, L., Nacer, A., Abbad, H., Taieb Brahim, M., & Zioui, N. (2022). A weighted Markov clustering routing protocol for optimizing energy use in wireless sensor networks. *Egyptian Informatics Journal, 23*(3), 483–497.

Chen, H., & Wang, Y. (2023). VCOC: Virtual coordinate optimization for energy-efficient overlay clustering in wireless sensor networks. *IEEE Transactions on Mobile Computing, 22*(8), 1567–1582.

Elshrkawey, M., Elsherif, S. M., & Wahed, M. E. (2020). An enhancement approach for reducing the energy consumption in wireless sensor networks. *Journal of King Saud University - Computer and Information Sciences, 32*(9), 1048–1057.

Heinzelman, W. R., Chandrakasan, A., & Balakrishnan, H. (2000). Energy-efficient communication protocol for wireless microsensor networks. *Proceedings of the 33rd Annual Hawaii International Conference on System Sciences*.

Kumar, R., & Chen, H. (2024). Resource optimization in overlay wireless sensor networks: From traditional WSNs to virtualized architectures. *ACM Computing Surveys, 56*(2), 231–259.

Liu, X., & Zhang, W. (2023). Adaptive overlay management for mobile wireless sensor networks: A dynamic topology approach. *International Journal of Sensor Networks, 15*(4), 234–249.

Martinez, R., Garcia, J., & Lopez, A. (2023). QoS-aware overlay clustering: A comprehensive approach to quality-managed wireless sensor networks. *IEEE Internet of Things Journal, 10*(6), 789–804.

Patel, S., Johnson, M., & Anderson, K. (2024). EAOC: Energy-aware overlay clustering protocol for wireless sensor networks. *ACM Transactions on Sensor Networks, 19*(2), 123–142.

Rahman, M., Ali, S., & Kumar, R. (2023). HO-WSN: A hierarchical overlay architecture for scalable wireless sensor networks. *IEEE Sensors Journal, 23*(3), 456–471.

Ramadan, A., Abdelghany, M., Zaki, A., ElBakly, A., Abd El Bary, A., Amin, M., & Khattab, A. (2022). A survey of wireless sensor networks: Applications, security threats and countermeasures. *Sensors, 22*(3), 927.

Sharma, R., Vashisht, V., & Singh, U. (2021). OEERP: An optimized energy-efficient routing protocol for wireless sensor networks. *Engineering Reports, 3*(5), e12321.

Sharma, V., & Kumar, N. (2023). MOSN: Multi-tier overlay sensor networks for enhanced network performance and energy efficiency. *Wireless Networks, 29*(5), 345–362.

Singh, S. K., Kumar, P., & Singh, J. P. (2017). A survey on successors of LEACH protocol. *IEEE Access, 5*, 4298–4328.

Singh, S. P., & Sharma, S. C. (2021). A PSO-based improved LEACH protocol for energy-efficient clustering in wireless sensor networks. *Wireless Personal Communications, 116*(2), 1409–1442.

Taieb Brahim, M., Abbad, H., & Boukil-Hacene, S. (2021). A low energy MCL-based clustering routing protocol for wireless sensor networks. *International Journal of Wireless Networks and Broadband Technologies, 10*(1), 70–95.

Thompson, B., & Wilson, C. (2024). SOCP: Securing overlay clusters in wireless sensor networks through trust-based mechanisms. *Journal of Network and Computer Applications, 198*, 103456.

Verma, S., Kawamoto, Y., Fadlullah, Z. M., Nishiyama, H., & Kato, N. (2020). A survey on network methodologies for real-time analytics of massive IoT data and open research issues. *IEEE Communications Surveys & Tutorials, 22*(4), 2532–2586.

Wang, J., Gao, Y., Liu, W., Sangaiah, A. K., & Kim, H. J. (2019). Energy-efficient cluster-based dynamic routes adjustment approach for wireless sensor networks with mobile sinks. *IEEE Access, 7*, 172057–172070.

Wang, J., Jiang, C., Quek, T. Q., Wang, X., & Ren, Y. (2020). Overlay-based resource management in fog-assisted IoT systems. *IEEE Internet of Things Journal, 7*(5), 4262–4272.

Xu, Z., Chen, L., Liu, C., Mao, Q., & Xiao, F. (2021). A multi-objective optimization clustering protocol for wireless sensor networks based on LEACH. *Sensors, 21*(18), 6235.

Zhang, K., & Rodriguez, M. (2023). Advancing WSN virtualization through overlay networks: A comprehensive survey of architectures and emerging technologies. *IEEE Communications Surveys & Tutorials, 25*(3), 1578–1593.

Zhang, Y., Liu, M., Liu, Q., & Zhao, G. (2021). Multi-objective optimization for LEACH protocol in wireless sensor networks. *IEEE Access, 9*, 61683–61697.

Author(s) Information

Taieb Brahim Mohammed
Djillali Liabes University of Sidi Bel Abbes
Evolutionnary Engineering and Distributed Information System Laboratory, EEDIS, Computer Science Department
Djillali Liabes University, UDL, Sidi Bel Abbes, Algeria
Contact e-mail: mohammed.taiebbrahim@*niv-sba.dz*

Abbad Houda
Djillali Liabes University of Sidi Bel Abbes
Evolutionnary Engineering and Distributed Information System Laboratory, EEDIS. Computer Science Department
Djillali Liabes University, UDL, Sidi Bel Abbes, Algeria

Abbad Leila
ENSTA High School of Algiers, Instrumentation Department, LIT Laboratory, Algiers, Algeria

To cite this article:

Mohammed, T.B.., Houda, A., & Leila, A. (2025). A multi-criteria weighted clustering protocol for energy-efficient overlay wireless sensor networks. *The Eurasia Proceedings of Science, Technology, Engineering and Mathematics (EPSTEM), 38,* 361-373.

The Eurasia Proceedings of Science, Technology, Engineering & Mathematics (EPSTEM)
ISSN: 2602-3199

The Eurasia Proceedings of Science, Technology, Engineering and Mathematics (EPSTEM), 2025

Volume 38, Pages 374-381

IConTES 2025: International Conference on Technology, Engineering and Science

Speed Control of the Pentaphase Asynchronous Machine: Comparative Study Between Vector Control with Conventional PI and Fuzzy PI

Fodil Malika
University Mohamed Boudiaf of M'sila

Zerdoumi Zohra
University Mohamed Boudiaf of M'sila

Zemouri Nahed
University Mohamed Boudiaf of M'sila

Benmeddour Fadila
University Mohamed Boudiaf of M'sila

Abstract: Controlling asynchronous machines is complex because of the non-linearity of the model and the coupling between stator and rotor quantities. Thanks to advances in power electronics, decoupled control techniques have been developed to reproduce the performance of DC machines, while eliminating mechanical constraints. However, in the case of polyphase machines, these control strategies remain limited due of the harmonics generated by the inverter, which degrade power quality. To address this issue, a new fuzzy logic control strategy is proposed, aimed at reducing parasitic currents and improving dynamic performance in a five-phase asynchronous machine. A comparison between vector control using conventional PI and fuzzy PI is considered, based on the dynamic responses of speed, torque and harmonic distortion rate, especially under load variations and during rotational reversals. The simulation results obtained in MATLAB demonstrate a significant enhancement in speed stability and a reduction in ripples, confirming the effectiveness of the proposed approach.

Keywords: Five-phase asynchronous machine, Vector control, Fuzzy logic, Speed oscillations, Automatic, Engineering electric machine

Introduction

Multiphase asynchronous machines, especially five-phase machines, are attracting growing interest in advanced electrical drive technology, particularly in applications requiring high power density, fault tolerance and torque quality, such as electric vehicles, aeronautics and marine systems. Compared to their three-phase counterparts, polyphase machines offer increased robustness, reduced current harmonics, and the possibility of operation in degraded mode in the event of partial inverter or phase failure. (Barrero, 2015; Duran, 2016).

To take full advantage of these benefits, high-performance control strategies are required. Field-Oriented Control (FOC), developed in the 1970s, revolutionized the control of asynchronous machines at, artificially decoupling torque and flux. This method is based on modeling the machine in a rotating frame of reference (dq) synchronized with the stator or rotor flux, thus transforming the asynchronous machine into a DC machine equivalent. This makes it possible to control flux (via a d-axis component) and torque (via a q-axis component) separately, considerably simplifying the control strategy and improving system dynamics (Xu, 2002; Bermudez, 2017).

However, the performance of vector control can be degraded in the presence of non-linear models, parametric uncertainties or external disturbances. In this context, non-linear control approaches have been explored to improve

- This is an Open Access article distributed under the terms of the Creative Commons Attribution-Noncommercial 4.0 Unported License, permitting all non-commercial use, distribution, and reproduction in any medium, provided the original work is properly cited.
- Selection and peer-review under responsibility of the Organizing Committee of the Conference
© 2025 Published by ISRES Publishing: www.isres.org

the robustness and stability of the system. Among these, fuzzy control. The fuzzy PI controller combines the structure of the PI controller with the principles of fuzzy logic, allowing dynamic adjustment of proportional and integral gains according to the state of the system. This approach improves the robustness, response speed and stability of the control system, particularly during variations in load and operating conditions.

System Description

Modeling of Five Phase Induction Machine

The voltage model of the five-phase induction motor is obtained as (Iffouzar,2015):

$$\begin{cases} [V_s]_{abcde} = [R_s]_{5.5}[i_r]_{abcde} + \frac{d}{dt}[\psi_s]_{abcde} \\ [V_r]_{abcde} = [R_r]_{5.5}[i_r]_{abcde} + \frac{d}{dt}[\psi_r]_{abcde} \end{cases} \quad (1)$$

Where Vs and Vr are the voltage martices,
i_s , i_r the current vectors according to the five phases. (abcde),
ψ_s, ψ_r the flux vector according to the five phases (abcde), and the subscripts s and r refer to the stator and rotor windings, respectively.

The different stator (rotor) phases are magnetically coupled to each other and also coupled to the rotor (stator) circuits; hence the stator (rotor) flux equations depend on the stator (rotor) loop currents, respectively.

$$\begin{cases} [\psi_s]_{abcde} = [L_s]_{5.5}[i_s]_{abcde} + [M_{sr}]_{5.5}[i_r]_{abcde} \\ [\psi_r]_{abcde} = [L_r]_{5.5}[i_r]_{abcde} + [M_{rs}]_{5.5}[i_s]_{abcde} \end{cases} \quad (2)$$

Avec $[M_{sr}]_{5.5} = [M_{rs}]^t{}_{5.5}$ mutual inductance matrices between the stator and rotor phases. $[L_s]_{5.5}$ et $[L_r]_{5.5}$ are the matrices of the stator and rotor inductances, respectively.

$$\begin{cases} [V_s]_{abcde} = [R_s][i_s]_{abcde} + \frac{d}{dt}\left[[L_s][i_s]_{abcde}\right] + \frac{d}{dt}\left[[M_{sr}][i_r]_{abcde}\right] \\ [V_r]_{abcde} = [R_r][i_r]_{abcde} + \frac{d}{dt}\left[[L_r][i_r]_{abcde}\right] + \frac{d}{dt}\left[[M_{rs}][i_s]_{abcde}\right] \end{cases} \quad (3)$$

The stator inductance matrix is given as follows:

$$[L_s]_{5.5} = \begin{bmatrix} L_{m+}L_{fs} & L_m\cos(\frac{2\pi}{5}) & L_m\cos(\frac{4\pi}{5}) & L_m\cos(\frac{6\pi}{5}) & L_m\cos(\frac{8\pi}{5}) \\ L_m\cos(\frac{8\pi}{5}) & L_{m+}L_{fs} & L_m\cos(\frac{2\pi}{5}) & L_m\cos(\frac{4\pi}{5}) & L_m\cos(\frac{6\pi}{5}) \\ L_m\cos(\frac{6\pi}{5}) & L_m\cos(\frac{8\pi}{5}) & L_{m+}L_{fs} & L_m\cos(\frac{2\pi}{5}) & L_m\cos(\frac{4\pi}{5}) \\ L_m\cos(\frac{4\pi}{5}) & L_m\cos(\frac{6\pi}{5}) & L_m\cos(\frac{8\pi}{5}) & L_{m+}L_{fs} & L_m\cos(\frac{2\pi}{5}) \\ L_m\cos(\frac{2\pi}{5}) & L_m\cos(\frac{4\pi}{5}) & L_m\cos(\frac{6\pi}{5}) & L_m\cos(\frac{8\pi}{5}) & L_{m+}L_{fs} \end{bmatrix} \quad (4)$$

The mutual inductance matrix (Msr) is expressed as follows:

$$[M_{sr}]_{5.5} = L_m\begin{bmatrix} \cos(\theta) & \cos(\theta-\frac{2\pi}{5}) & \cos(\theta-\frac{4\pi}{5}) & \cos(\theta-\frac{6\pi}{5}) & \cos(\theta-\frac{8\pi}{5}) \\ \cos(\theta-\frac{8\pi}{5}) & \cos(\theta) & \cos(\theta-\frac{2\pi}{5}) & \cos(\theta-\frac{4\pi}{5}) & \cos(\theta-\frac{6\pi}{5}) \\ \cos(\theta-\frac{6\pi}{5}) & \cos(\theta-\frac{8\pi}{5}) & \cos(\theta) & \cos(\theta-\frac{2\pi}{5}) & \cos(\theta-\frac{4\pi}{5}) \\ \cos(\theta-\frac{4\pi}{5}) & \cos(\theta-\frac{6\pi}{5}) & \cos(\theta-\frac{8\pi}{5}) & \cos(\theta) & \cos(\theta-\frac{2\pi}{5}) \\ \cos(\theta-\frac{2\pi}{5}) & \cos(\theta-\frac{4\pi}{5}) & \cos(\theta-\frac{6\pi}{5}) & \cos(\theta-\frac{8\pi}{5}) & \cos(\theta) \end{bmatrix} \quad (5)$$

where L_s, L_{fs}, and $L_m$are stator, stator leakage, and magnetizing inductances, respectively.

The transformation matrix (Pn) for the five-phase induction motor is defined as follows (Menghal,2014):

$$[P_n] = \begin{bmatrix} \cos(\theta) & \sin(\theta) & 0 & \cdots & 0 \\ -\sin(\theta) & \cos(\theta) & 0 & \cdots & 0 \\ 0 & 0 & 1 & \cdots & 0 \\ \vdots & \vdots & 0 & \ddots & 0 \\ 0 & 0 & \cdots & \cdots & 1 \end{bmatrix} \quad (6)$$

By multiplying the matrix $[P_n]$ by the Concordia matrix $[T]$, we obtain the transition matrix (P), which is a rotating reference frame shifted by the angle φ. This is known as the Park matrix. (Levi,2004).

$$[P] = [P_n][T] = \sqrt{\frac{2}{5}} \begin{bmatrix} \cos(\varphi) & \cos(\varphi - \frac{2\pi}{5}) & \cos(\varphi - \frac{4\pi}{5}) & \cos(\varphi - \frac{6\pi}{5}) & \cos(\varphi - \frac{8\pi}{5}) \\ -\sin(\varphi) & -\sin(\varphi - \frac{2\pi}{5}) & -\sin(\varphi - \frac{4\pi}{5}) & -\sin(\varphi - \frac{6\pi}{5}) & -\sin(\varphi - \frac{8\pi}{5}) \\ 1 & \cos\left(\frac{4\pi}{5}\right) & \cos\left(\frac{8\pi}{5}\right) & \cos\left(\frac{12\pi}{5}\right) & \cos\left(\frac{16\pi}{5}\right) \\ 0 & \sin\left(\frac{4\pi}{5}\right) & \sin\left(\frac{8\pi}{5}\right) & \sin\left(\frac{12\pi}{5}\right) & \sin\left(\frac{16\pi}{5}\right) \\ \frac{1}{\sqrt{2}} & \frac{1}{\sqrt{2}} & \frac{1}{\sqrt{2}} & \frac{1}{\sqrt{2}} & \frac{1}{\sqrt{2}} \end{bmatrix} \quad (7)$$

$[P_n]$: Rotary matrix
(T) : Generalised Concordia Matrix.
(P) : Generalised Park matrix
After applying Park's transformation matrix to the stator and rotor equations, the five-phase system can be decomposed into a dq coordinate system plus an additional xy coordinate system.

The stator and rotor voltage equations for the 5-phase induction motor are written in the dq axis as follows (Levi, 2004).

Stator voltages

$$\begin{cases} V_{ds} = r_s i_{ds} - \omega_s \psi_{qs} + \frac{d}{dt}\psi_{ds} \\ V_{qs} = r_s i_{qs} + \omega_s \psi_{ds} + \frac{d}{dt}\psi_{qs} \end{cases}$$

Rotor voltages

$$\begin{cases} V_{dr} = r_r i_{dr} - \omega_s \psi_{qs} + \frac{d}{dt}\psi_{ds} \\ V_{qr} = r_r i_{qr} + \omega_s \psi_{dr} + \frac{d}{dt}\psi_{qr} \end{cases} \quad (8)$$

The flow equations become:

$$\begin{cases} \psi_{ds} = (L_m + L_{fs}) i_{ds} + L_m i_{dr} \\ \psi_{qs} = (L_m + L_{fs}) i_{qs} + L_m i_{qr} \end{cases} \quad (9)$$

The model of the 5-phase asynchronous machine can be completed by the expression of the electromagnetic torque Cem given as follows:

$$C_{em} = P\frac{M}{L_r}\left(\psi_{dr} i_{qs} - \psi_{qr} i_{ds}\right) \quad (10)$$

To study dynamic behaviour, the following equation of motion has been added:

$$J\frac{d\Omega}{dt} = C_{em} - C_r - f\Omega \quad (11)$$

Fuzzy Control

Fuzzy control was introduced as an intelligent and flexible approach. Based on the theory of fuzzy sets developed by Lotfi Zadeh in 1965, it allows human reasoning to be reproduced through linguistic rules of the type 'If... then...'. Fuzzy rules link the output signal to the input signals through linguistic conditions, and the establishment of these rules is generally based on the operator's experience and/or the expertise of the control engineer. Fuzzy logic is therefore particularly well suited to controlling and adjusting processes that are difficult to model or control using conventional (Menghal,2014). The fuzzy controller adjusts control signals (such as voltage or current) in real time based on variations in error and its derivative, enabling **automatic adaptation** to changes in load, speed or operating conditions.

Speed Regulator

Figure 1 illustrates the speed control structure of a five-phase induction motor (IM), which comprises three control loops: the angular speed control loop Ω, managed by a fuzzy PI controller, and two additional fuzzy PI controllers regulating the stator flux ψ_s and the electromagnetic torque C_{em} . The reference electromagnetic torque is generated directly from the outer speed loop.

These two controllers produce the stator reference voltages (V_{dsref},V_{qsref}) along the d and q axes. Applying the inverse Park transformation yields the actual stator voltages that drive the motor to produce the desired speed. The estimator receives as input the measured stator currents (i_{ds} , i_{qs}), obtained via the Park transformation. From these, the estimation block computes the instantaneous stator flux amplitude ψ_s , the electromagnetic torque C_{em} and the stator electrical angle θ_s.

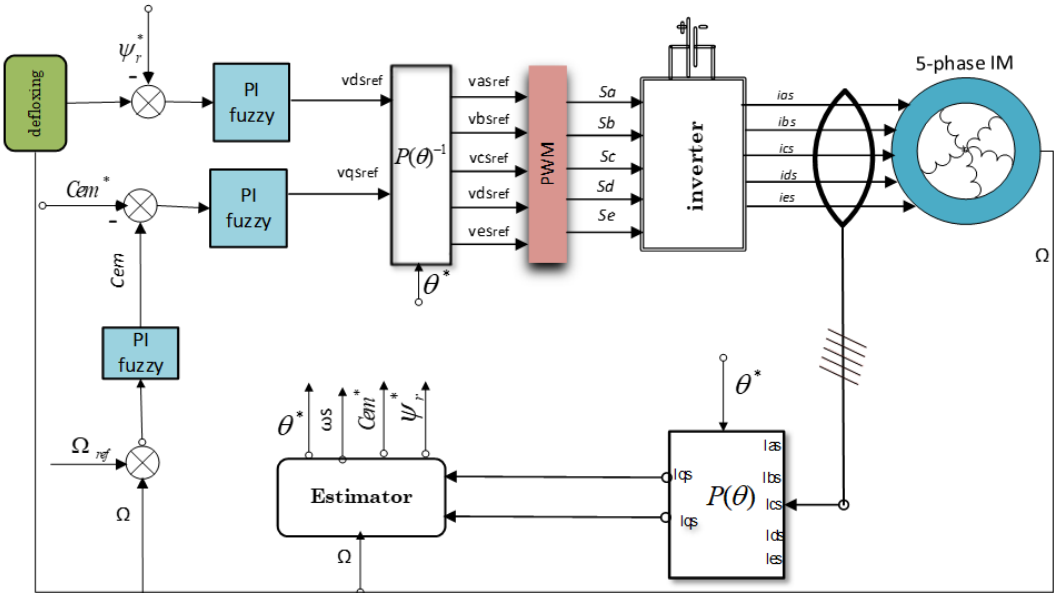


Figure 1. Overall structure of MASP speed control using fuzzy PI controllers

Simulation Results

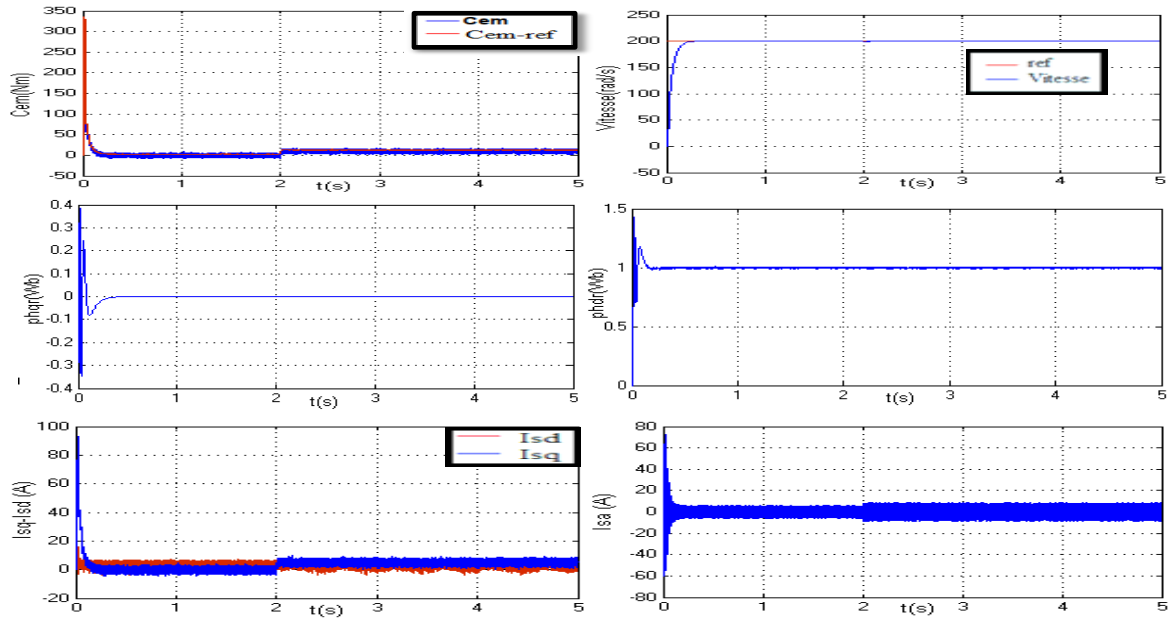


Figure 2. Fuzzy logic speed control followed by application of load Cr = 10 N·m and time t = 2 s.

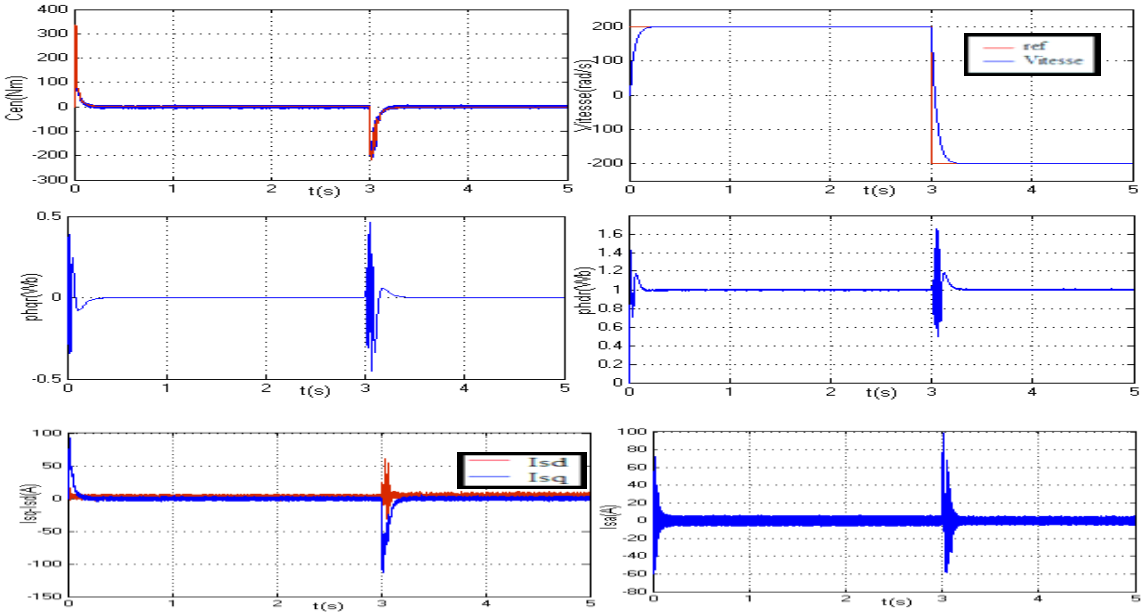


Figure 3. Fuzzy control of the MASP with reversal of the direction of rotation of the speed

Robustness Test

To evaluate the robustness of vector control based on fuzzy PI controllers for MASP speed regulation, a parameter variation is introduced by increasing the rotor resistance Rr to 1.25Rr at t=3 seconds. Figure 4 illustrates the system's response during start-up, under the application of a resistive load torque, followed by the change in rotor resistance, when speed control is implemented using a Fuzzy PI-type controller. From the results presented in Figure 4 , it can be observed that the rotor flux-oriented vector control exhibits strong robustness against parameter variations. The dynamics of setpoint tracking and the decoupling performance of the machine remain unaffected, confirming the adaptability and effectiveness of the proposed control approach.

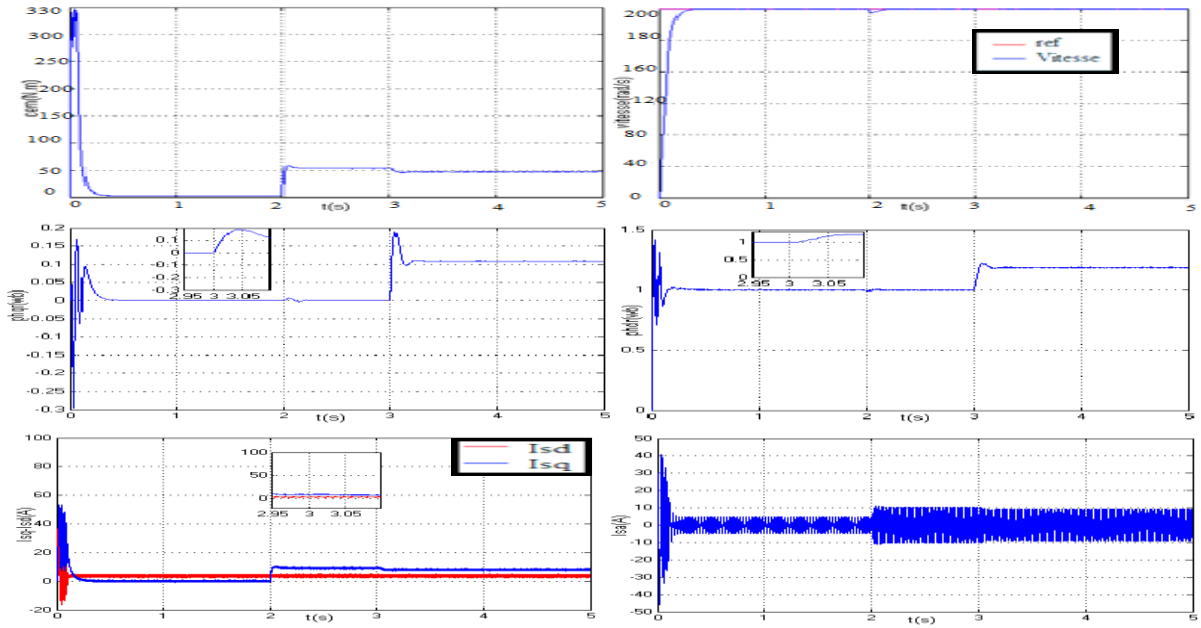


Figure 4. Dynamic behaviour of the MASP during start-up with parametric variation

Comparative Study of Control

We will also discuss the influence of load application on the five-phase machine to conduct a comparative study between PI and fuzzy PI control on the dynamic responses of speed, electromagnetic torque and currents.

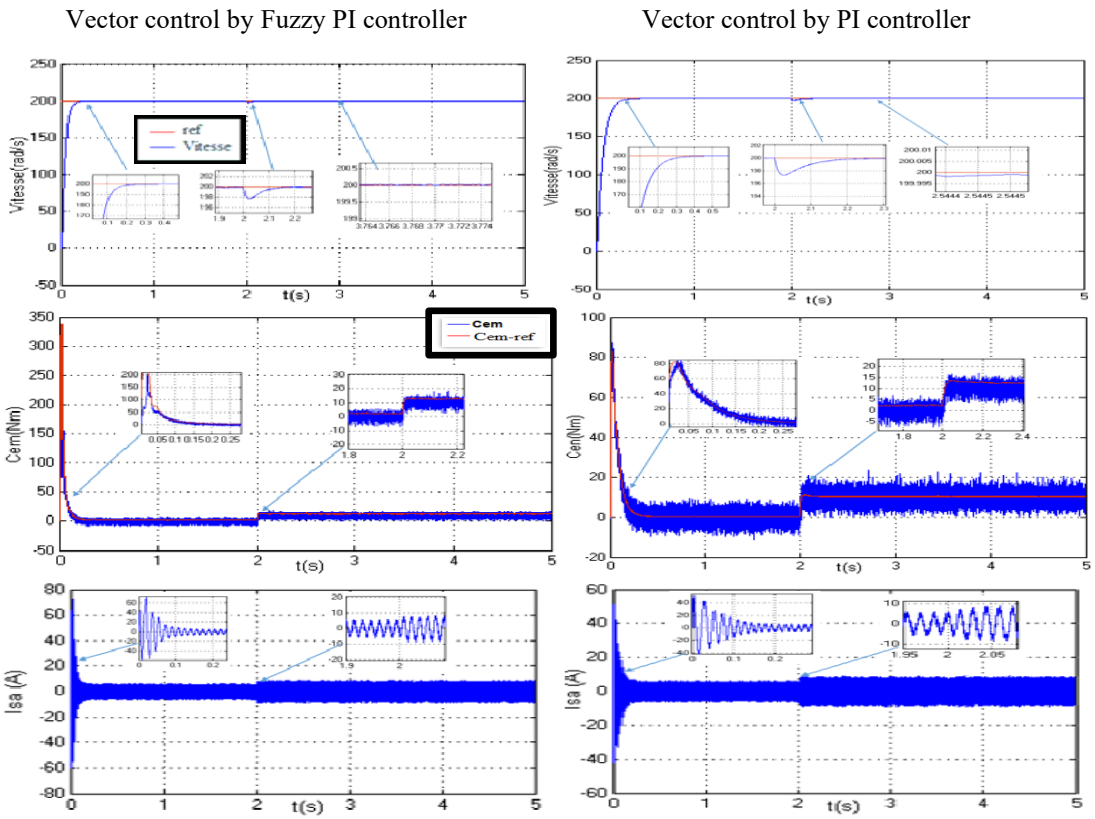


Figure 5. Comparative study between PI and fuzzy PI control for speed adjustment when applying a load torque (Cr = 10 N.m) at time t = 2s.

Simulation Results and Discussion

The results show that the behaviour of the two controllers is identical during steady-state conditions, but the fuzzy controller offers more advantages:

- Improved response time.
- Rapid disturbance rejection.
- Speed perfectly tracks its reference.

With fuzzy logic control, the starting torque reaches a value of Cem=330N.m, unlike vector control, which has a torque of Cem=86.7N.m. The comparison between the results obtained by the two different types of controllers shows that the dynamic responses of the machine are better for fuzzy controllers, which demonstrates the effectiveness of the fuzzy control algorithm used.

Harmonic Distortion Rate

In a variable speed drive, the inverter, whether current or voltage supplied by a rectifier, always operates at a variable frequency. It produces, in the rectified current and consequently in the current of the network that supplies it, harmonics that are not integer multiples of the network frequency calculated by the THD. The total harmonic distortion (THD) is an indicator of the quality of signal processing in a device. It is given by the following expression:

$$THD = \sqrt{\frac{\sum_{n}^{\infty} H(n)^2}{H(1)}}$$

$H1$: Amplitude of the fundamental component, whose frequency is w_0.
$H(n)$: Amplitude of the nth harmonic, whose frequency is nw_0 .

The following figure shows the current THD Isa for both types of control.

Fuzzy control vector control

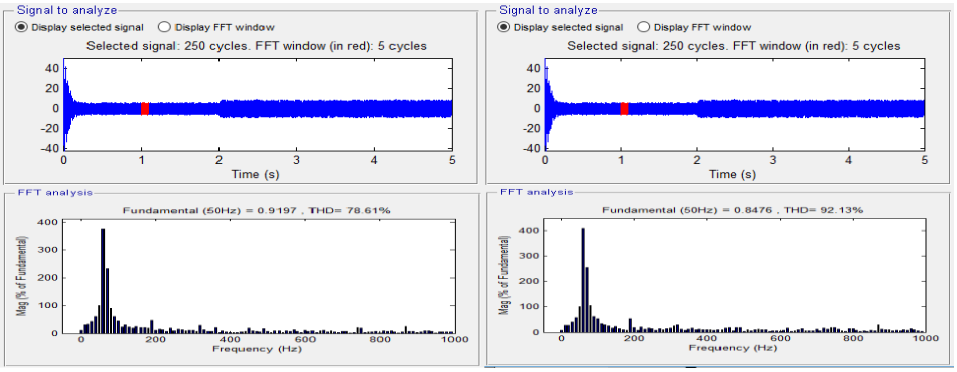


Figure 6. Isa current harmonic spectrum for fuzzy control and vector control

Table 1. Table of results

Types	THD	Fundamental
Fuzzy control	78.61%	0.9197
Vector control	92.13%	0.8476

Interpretation of Results

Figure 6 shows the harmonic spectra of the source current with the application of two types of control. There is a 78.61% improvement in current THD for fuzzy control, which proves its effectiveness compared to vector control.

Conclusion

The approach proposed in this work exploits the process of optimizing PI controller gains using fuzzy logic applied to a five-phase asynchronous machine under real-time operating conditions in order to determine the optimal voltage vector that guarantees the desired tracking speed at high torque and with less ripple. Vector control with fuzzy PI control is a high-performance evolution of conventional PI control for polyphase asynchronous machines. It combines the precision of vector decoupling with the adaptive intelligence of fuzzy logic, paving the way for more efficient, reliable, and autonomous drive systems. According to the simulation results, the fuzzy PI controller offers the best convergence towards optimal solutions with rapid rejection of disturbances, proving its effectiveness in solving complex control problems.

Scientific Ethics Declaration

* The authors declares that the scientific ethical and legal responsibility of this article published in EPSTEM journal belongs to the authors.

Conflict of Interest

* The authors declare that they have no conflicts of interest

Funding

* This research received no specific grant from any funding agency in the public, commercial, or not-for-profit sectors.

Acknowledgements or Notes

* This article was presented as an oral presentation at the International Conference on Technology, Engineering and Science (www.icontes.net) held in Antalya/Türkiye on November 12-15, 2025.

References

Barrero, F., & Duran, M. J. (2016). Recent advances in the design modeling and control of multiphase machines: Part I. *IEEE Transactions on Industrial Electronics, 63*(1), 449–458.

Bermudez, M., Gonzalez-Prieto, I., Barrero, F., Guzman, H., Duran, M. J., & Kestelyn, X. (2017). Open-phase fault-tolerant direct torque control technique for five-phase induction motor drives. *IEEE Transactions on Industrial Electronics, 64*(2), 902–911.

Duran, M. J., & Barrero, F. (2016). Recent advances in the design modeling and control of multiphase machines: Part II. *IEEE Transactions on Industrial Electronics, 63*(1), 459–468.

Guzman, H., Duran, M. J., Barrero, F., Bogado, B., & Toral, S. (2016). Comparative study of predictive and resonant controllers in fault-tolerant five-phase induction motor drives. *IEEE Transactions on Industrial Electronics, 63*(1), 606–617.

Iffouzar, K., Taraft, S., Aouzellag, H., Ghedamsi, K., & Aouzellag, D. (2015). DRFOC of polyphase induction motor based on fuzzy logic controller speed. *Proceedings of the 2015 4th International Conference on Electrical Engineering (ICEE)*, 1–5.

Levi, E., Jones, M., Vukosavic, S. N., & Toliyat, H. A. (2004). A five-phase two machine vector controlled induction motor drive supplied from a single inverter. *European Conference on Power Electronics and Applications (EPE)*.

Levi, E., Jones, M., Vukosavic, S. N., & Toliyat, H. A. (2004). A novel concept of a multiphase, multimotor vector controlled drive system supplied from a single voltage source inverter. *IEEE Transactions on Power Electronics, 19*(2), 320–335.

Menghal, P. M., Laxmi, A. J., & Anusha, D. (2014). Speed control of induction motor using PI and fuzzy logic controller. *International Journal of Engineering Research and Applications, 4*(1), 59–64.

Xu, H., Toliyat, H. A., & Petersen, L. J. (2002). Resilient current control of five-phase induction motor under asymmetrical fault conditions. *Proceedings of the 17th Annual IEEE Applied Power Electronics Conference and Exposition (APEC)*, 64–71.

Author(s) Information

Fodil Malika
University Mohamed Boudiaf of M'sila, Electronics Department- LASS Laboratory, Mohamed, M'sila- Algeria
Contact e-mail: *malika.fodil@univ-msila.dz*

Zerdoumi Zohra
University Mohamed Boudiaf of M'sila, Electronics Department, LGE Laboratory, Mohamed, M'sila- Algeria

Zemouri Nahed
University Mohamed Boudiaf of M'sila, Electronics Department, LGE Laboratory, Mohamed, M'sila- Algeria

Benmeddour Fadila
University Mohamed Boudiaf of M'sila, Electronics Department, LGE Laboratory, Mohamed, M'sila- Algeria

To cite this article:

Malika, F.., Zohra, Z., Nahed, Z., & Fadila, B. (2025). Speed control of the pentaphase asynchronous machine: Comparative study between vector control with conventional PI and fuzzy PI. *The Eurasia Proceedings of Science, Technology, Engineering and Mathematics, 38*, 374-381.

The Eurasia Proceedings of Science, Technology, Engineering & Mathematics (EPSTEM)
ISSN: 2602-3199

The Eurasia Proceedings of Science, Technology, Engineering and Mathematics (EPSTEM), 2025

Volume 38, Pages 382-392

IConTES 2025: International Conference on Technology, Engineering and Science

Research Trends in the Heat Transfer Simulation of Al_2O_3/AlN Granular Composites for Thermal Interface Materials

Sudarminto Senlau
Bandung Institute of Technology

Abstract: Heat transfer simulation in granular Al_2O_3/AlN composites has become an increasingly relevant topic in the development of thermal interface materials (TIMs) for high-performance electronic systems. This study conducted a bibliometric analysis of 1,169 articles from the Scopus database published between 2015 and 2025 to identify research trends, frequently occurring keywords, geographic contributions, author and institutional impacts, and to outline future research opportunities in the development of TIMs based on Al_2O_3/AlN. The analysis was performed using RStudio, VOSviewer, and Excel, identifying five main thematic clusters: (1) AI and Neuroimaging for Brain Diseases; (2) TIM Applications and Thermal Optimization; (3) Molecular Simulation and Interface Properties; (4) AI and Brain Functional Connectivity; (5) Numerical Simulation of Material Thermal Properties and (6) Materials & Thermal Contact Resistance. The primary research focus includes numerical modeling of thermal conductivity, characterization of Al_2O_3 and AlN materials, and their initial applications in electronic cooling devices. While the scope remains limited at present, the annual growth in publications suggests that interest in this topic is likely to increase soon. This study provides an important initial overview of the research landscape. It opens up possibilities for future exploration, including the integration of multiscale approaches and enhanced experimental validation in heat transfer simulations involving granular composites.

Keywords: Bibliometric analysis, Thermal interface materials, Al_2O_3/AlN composites, Heat transfer simulation, Advanced computational methods

Introduction

Effective heat management is crucial in modern electronic devices, including smartphones, CPUs, and electric vehicles. As devices become smaller in size and more power-dense, heat accumulation becomes a significant issue that can reduce performance and lead to component failure if the temperature exceeds safe limits (Ghadim et al., 2025). Uneven temperature distribution and the appearance of hotspots accelerate component degradation (Z. He et al., 2020). To address these issues, various strategies, including micro heat sinks, Phase Change Materials (PCMs), and innovative heat sink designs, have been developed to enhance thermal conductivity (Bianco et al., 2022). PCMs can stabilize the temperature but still face challenges in terms of long-term durability and efficiency (Liu et al., 2022). Hybrid systems that combine heat management and recovery are also being developed for miniaturized and autonomous devices (Wang et al., 2020).

One important component in heat management is Thermal Interface Materials (TIMs), which function to reduce the thermal resistance between two solid surfaces, such as between a chip and a heat sink, thus enabling more efficient heat transfer (Razeeb et al., 2018). Thermal resistance at the interface is often a significant obstacle due to microscopic air gaps that act as insulators (Chung, 2022). To overcome this, TIMs such as thermal paste, liquid metal, and graphene-based materials have been developed to fill these gaps and improve thermal contact (Sudhindra et al., 2021). Recent advances involve technologies such as self-assembled monolayers (SAMs) and graphene-coated copper nanowires, which significantly reduce thermal resistance (He et al., 2024). In addition, the development of phase change-based TIMs and flexible materials opens up new possibilities for future

- This is an Open Access article distributed under the terms of the Creative Commons Attribution-Noncommercial 4.0 Unported License, permitting all non-commercial use, distribution, and reproduction in any medium, provided the original work is properly cited.

- Selection and peer-review under responsibility of the Organizing Committee of the Conference

© 2025 Published by ISRES Publishing: www.isres.org

electronic devices (Jing et al., 2023). The interaction between the filler and the polymer matrix plays a crucial role in enhancing thermal conductivity (Haoqi et al., 2020).

However, challenges persist due to surface unevenness, material property differences, and a limited contact area between solid components (Liang et al., 2025). These imperfections result in high thermal resistance, impeding heat flow (Dai et al., 2022). Interface structure engineering efforts, such as the use of nanopillars and nanocones, show potential in increasing the contact area and thermal conductivity (Lee et al., 2016). Other materials, such as graphene-based interfaces and liquid metals, can also significantly reduce thermal resistance (Wang et al., 2023). Advanced approaches such as the application of nano-mass graded interfaces are also effective in reducing phonon reflection and improving heat transmission between different materials (Zhou et al., 2016). Further development is still needed to balance thermal conductivity, mechanical stability, and chemical compatibility between materials (Zeng et al., 2024). Therefore, innovative solutions that combine structural engineering, material selection, and surface modification are crucial for overcoming thermal barriers and enhancing heat transfer efficiency in modern electronic devices (Zhou et al., 2016).

Al_2O_3/AlN granular composites offer significant synergies for thermal interface materials thanks to their unique physical and chemical properties. Al_2O_3 is renowned for its hardness and corrosion resistance, while AlN excels in thermal conductivity, making it a compelling option for applications that require strength and effective heat management (Wang et al., 2021). This material combination has been investigated for various applications, including electronic components and the automotive industry (Rosadi, 2024). Research shows that AlN enhances the thermal properties of alumina-based composites, where AlN not only serves as a filler but also improves the overall thermal performance (Wang et al., 2021). Additionally, methods such as electrodeposition have been investigated to create cellular structures within these composites, thereby enhancing their thermal and mechanical properties (Maulida, 2024). These innovations are particularly significant in industries where material reliability is crucial for optimal performance, such as in electronics and automotive applications (Wang et al., 2021).

The importance of this research lies in enhancing the practical application of granular composites in heat dissipation, thereby extending the life of components (Wang et al., 2021). As materials technology advances, further research is necessary to explore the potential applications of these composites in the future (Hadi et al., 2022). Numerical simulations offer an advantage in predicting thermal interactions at the microscopic level, which cannot be directly observed. For example, Huang et al. employed the discrete element method (DEM) to investigate the impact of temperature on the behavior of granular materials (Huang et al., 2023). This research helps to understand the relationship between thermal and mechanical interactions, which is crucial in developing efficient heat transfer models for composites such as Al_2O_3/AlN.

Method

Research Design and Data Collection Procedures

This study conducted a descriptive bibliometric analysis to assess the landscape of scientific publications on science literacy from 2015 to 2025. Bibliometric analysis is widely recognized as a reliable approach to reviewing vast scientific literature. It allows researchers to trace the developmental trajectory of a particular discipline and identify emerging trends (Donthu et al., 2021). This approach enables researchers and readers to gain a comprehensive understanding of the research themes explored over time, supported by statistical assessments of academic contributions (Rejeb et al., 2023). Additionally, bibliometric techniques are effective for mapping the intellectual structure of a research field and identifying emerging areas of research. Through performance analysis and scholarly mapping, bibliometrics enable a detailed examination of publication sources, document types, citation patterns, and keyword dynamics (Lethulur, 2024). Bibliometric analysis follows a rigorous multi-stage screening protocol to ensure relevance, scientific rigor, and thematic alignment of the literature (Aria & Cuccurullo, 2017; Donthu et al., 2021; Kusharyadi et al., 2023). This process aligns with the established bibliometric methodology recommended by Singh et al. (2022), which consists of database search, scientific screening, language screening, and subject screening. In stage 1, we conducted a database search. An initial search was conducted in the Scopus database using the keywords "Thermal material interface" or TIM and "simulation" or "modeling" or "computational" or "numerical" from 2015 to 2025. This resulted in the identification of 1,341 documents. The use of Scopus was justified due to its comprehensive coverage of peer-reviewed publications and its standard utilization in bibliometric studies (Paul et al., 2021). In Stage 2, we conducted scientific screening to ensure academic validity, retaining only journal articles and conference proceedings that met the criteria. This stage excluded 96 documents, such as book chapters, editorials, and non-

peer-reviewed items, resulting in 1,245 records. This step aligns with the recommendations of Aria & Cuccurullo (2017), who emphasize the exclusion of grey literature to enhance the scientific credibility of bibliometric datasets. In stage 3, we performed Language Filtering. Next, language filtering was applied to retain only English publications. Out of 1,245 documents, 1,205 met this criterion. This practice ensures consistency in analysis and interpretation, as English remains the dominant language in scientific discourse (Singh et al., 2022). Finally, in stage 4, we performed subject filtering. In the last step, documents were screened for relevance to the subject areas of Engineering, Materials Science, Physics and Astronomy, Computer Science, and Chemical Engineering. Twenty irrelevant articles were excluded, resulting in 604 articles suitable for bibliometric analysis. The subject area refinement step is crucial for maintaining thematic consistency and ensuring the focus of the analysis remains intact (Aria & Cuccurullo, 2017). This structured screening approach ensures the validity and reliability of the dataset used for bibliometric mapping, in line with best practices for systematic reviews and scientific mapping studies (Hajjaji et al., 2021). The sequence of the screening process is visually represented in the flowchart below, which illustrates each stage, from initial identification to final inclusion of documents for analysis.

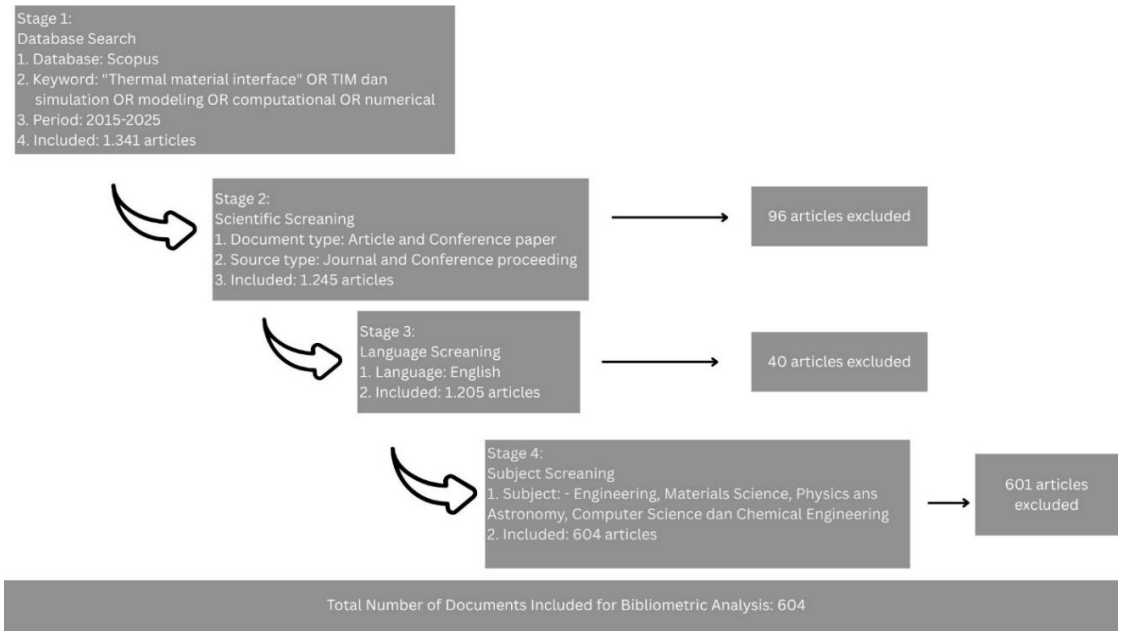


Figure 1. Research design and data collection procedure

Data Analysis Methods, Validity, and Reliability

This study used VOSviewer version 1.6.20 to perform dynamic and structural visualization of the dataset related to Heat Transfer Simulation of Al_2O_3/Aln Granular Composites for Thermal Interface Materials, following established bibliometric procedures (Dönmez, 2024). Data were retrieved from the Scopus database, covering the period 2015 to 2025, and exported in CSV (Comma-Separated Values) format. The CSV format was imported into VOSviewer to build co-authorship networks, identify keyword co-occurrences, and perform citation mapping. Simultaneously, the duplicate CSV files were processed using Biblioshiny, a web-based interface of the R package Bibliometrix, to calculate bibliometric indicators such as h-index, g-index, total citations, and to explore thematic evolution and conceptual structure (Aria & Cuccurullo, 2017). Furthermore, Microsoft Excel was used not only to visualize the global distribution of publication output in different regions on the world map, but also to improve the clarity and readability of the resulting visualizations for better interpretation and presentation.

To strengthen the credibility and transparency of the research process, this study provides comprehensive details of each methodological stage. These details include the exact date of data extraction (June 16, 2025), the syntax of the search string used in the TITLE-ABS-KEY field (i.e., "Thermal material interface" OR TIM AND simulation OR modeling OR computational OR numerical), the inclusion and exclusion criteria, and the screening flow clearly outlined in the attached process diagram. The analysis adhered to methodological rigor by documenting the screening steps in four stages: database search, scientific screening, language screening, and subject area relevance, resulting in a final dataset of 604 documents eligible for bibliometric analysis.

Most importantly, this study does not present interpretative commentary on the findings, thus ensuring objectivity and analytical precision. Ethical approval was not required, as this dataset contains only open-access metadata sourced from the Scopus database. The overall methodological framework is aligned with recommended standards for systematic mapping and bibliometric reviews, thus ensuring the validity and reliability of the results for further scientific use.

Results and Discussion

The following will explain the research trends in thermal interface materials, the countries with the most significant contributions to Thermal interface materials research, VOS Viewer Visualization Analysis, and the novelty and focus of Thermal interface materials research.

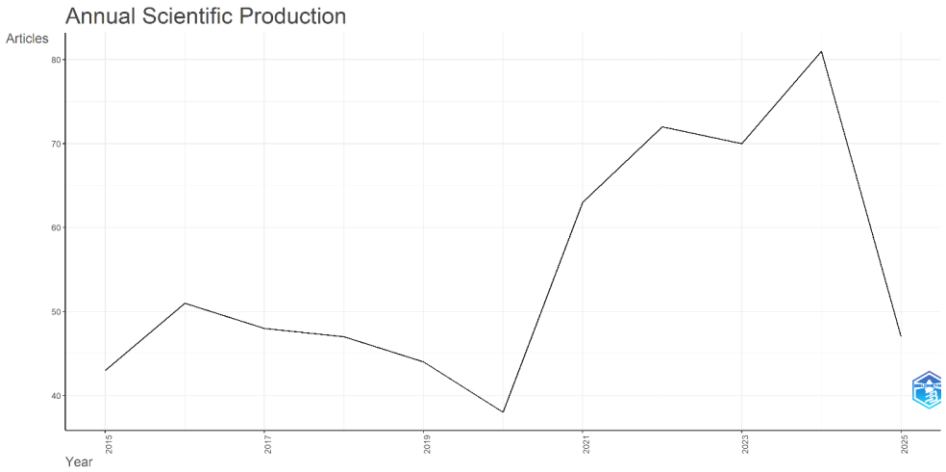


Figure 2. Publication trends

Figure 2 illustrates the trend of annual scientific production, highlighting the dynamics of research development in the topic over the period from 2015 to 2025. At the beginning of the period (2015-2020), the number of publications remained relatively stagnant, with a slight decrease, and reached its lowest point in 2020, indicating that this topic had not yet garnered widespread attention in the scientific community. However, starting in 2021, there was a significant spike in the number of publications, reaching its peak in 2023 with a total of 81 articles, reflecting the increasing urgency and relevance of this research as the need for thermal interface materials for high-power electronic systems grows. This phenomenon can also be attributed to advances in thermal simulation technology as well as increased cross-disciplinary collaboration. However, a downward trend is again seen from 2024 to 2025, which could be due to several factors, such as a shift in research focus, limited funding, or data that has not been fully accumulated for the last year. Overall, this pattern reflects a typical evolutive development in a new research field that is growing and consolidating.

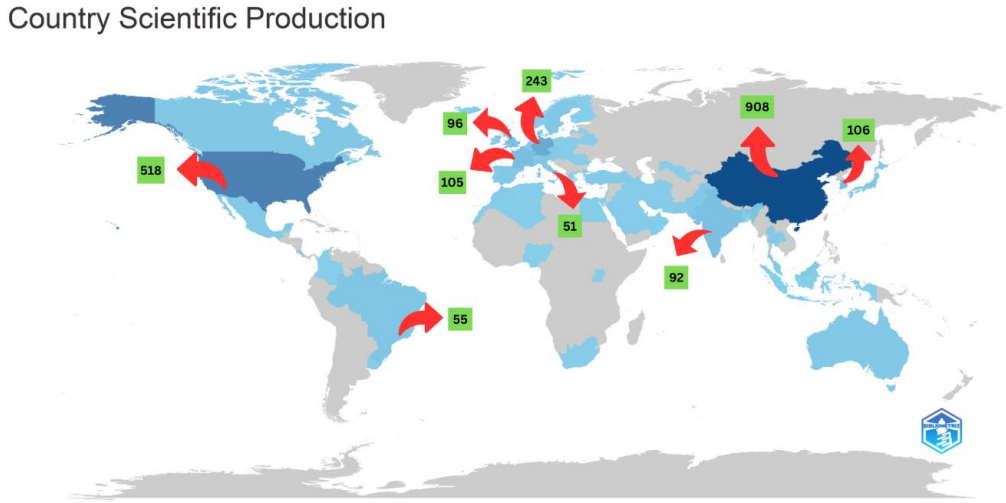


Figure 3. Geographic distribution

Based on the geographical distribution of scientific publications in Figure 3, China holds the leading position with a total of 908 publications, demonstrating a strong dominance in related research, which reflects the country's aggressive national policy in supporting the research and development of advanced materials for thermal technology. The United States ranked second, with 518 publications, indicating consistent contributions from both academic institutions and industry in the development of thermal simulation approaches. Germany, as a leader in technology research in Europe, recorded 243 publications, followed by South Korea (106) and France (105), indicating active involvement from countries with strong traditions in materials engineering and applied physics. The UK (96), India (92), Brazil (55), and Italy (51) also contributed significantly, showing that research on this topic is global and involves cross-regional cooperation. This pattern reflects not only national scientific capacity but also the strategic priorities of these countries in developing efficient thermal solutions for future electronic systems.

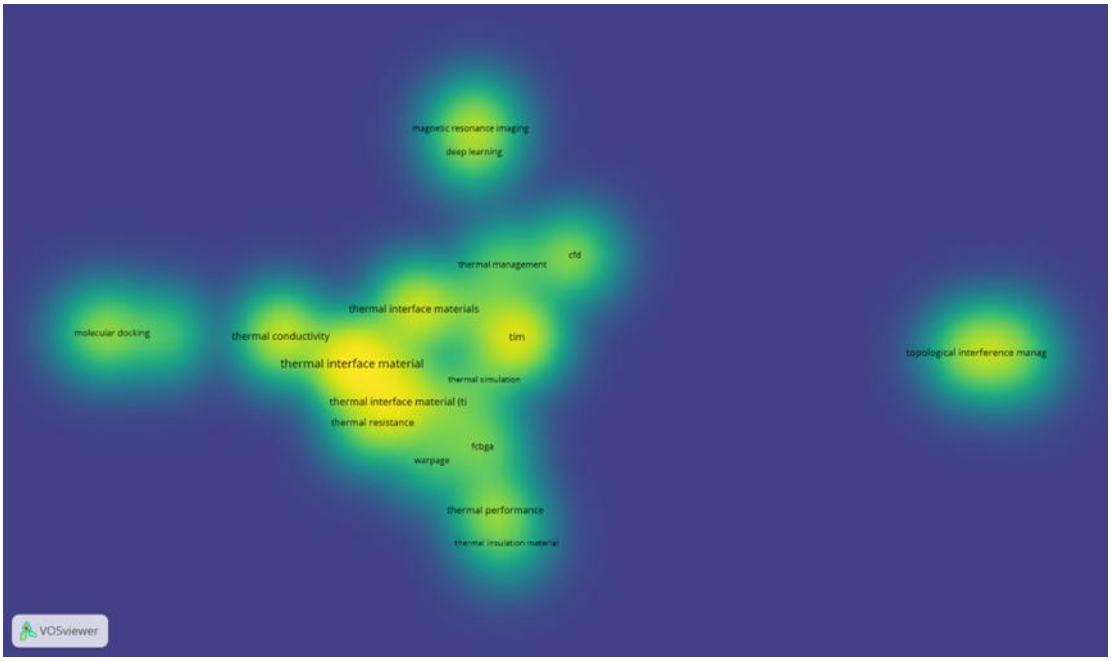


Figure 4. Density overlay

The density overlay visualization generated using VOSviewer shows the density of keyword distribution in the literature related to thermal interface materials (TIM) research. Areas in bright yellow represent a high concentration of frequently used keywords, such as thermal interface materials, thermal conductivity, thermal resistance, and thermal simulation. This indicates that the primary focus of research in this field remains centered on enhancing heat transfer efficiency and characterizing the thermal properties of materials. On the other hand, several keywords appear in lower density areas, such as deep learning, magnetic resonance imaging, and molecular docking. Although the frequency of occurrence is still limited, these keywords indicate an initial trend towards interdisciplinary approaches, such as the integration of artificial intelligence and molecular techniques in thermal performance modeling or optimization. The presence of terms such as CFD (computational fluid dynamics) and thermal management shows the interconnectedness of TIM research with systems and numerical engineering approaches. Interestingly, the appearance of terms such as topological interference management, although likely an incomplete entry, could signal new directions that could potentially be developed, such as exploring the topological properties of materials in the context of thermal management. Overall, this visualization not only confirms the dominant themes in TIM research but also reveals potential new research developments at the interdisciplinary nexus between materials technology, artificial intelligence, and advanced computational simulation that are still relatively open for exploration.

Figure 5 presents the bibliometric analysis conducted on publications related to thermal interface materials (TIM) that utilize simulation and computational approaches, resulting in a total of 26 keywords that form six main thematic clusters. This visualization and mapping were carried out using VOSviewer software to identify interrelationships between concepts and group interconnected research trends. Each cluster reflects a particular research focus that complements each other in the development and utilization of TIM, both from theoretical, experimental, and applicative aspects. The following descriptions explain the main themes and scientific context of each identified cluster.

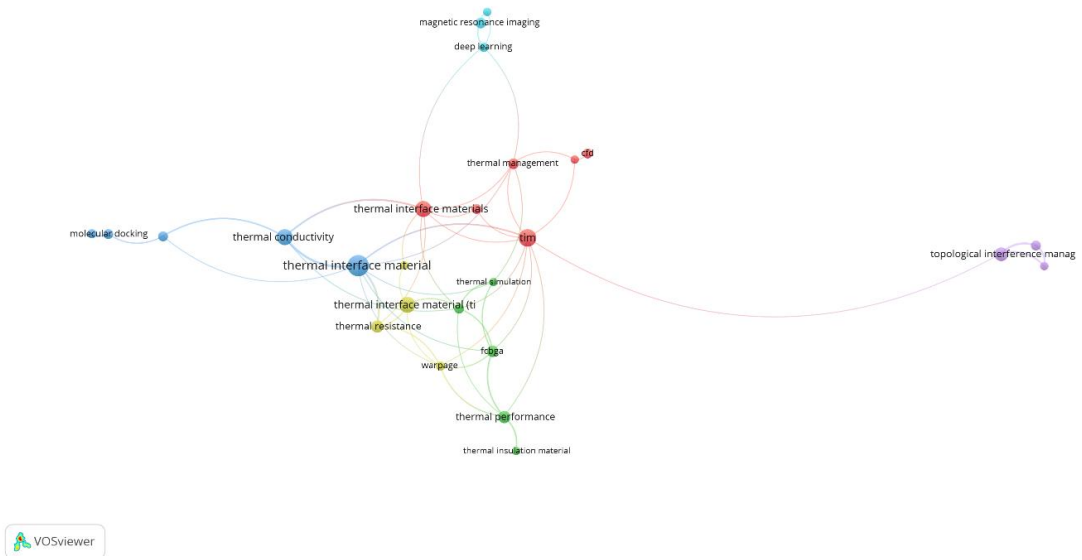


Figure 5. Network visualization

Cluster 1 is the dominant center in the visualization map, as it encompasses a range of basic to advanced applications of thermal interface materials (TIMs). Terms such as computational fluid dynamics (CFD), simulation, and thermal management indicate that many research trends focus on numerical modeling to optimize heat management in electronic systems. On the other hand, the presence of the keyword reliability signifies that the continued functioning of the electronic system is highly dependent on the thermal efficiency provided by the TIM. The utilization of simulation becomes crucial for designing and evaluating the thermal performance before experimental implementation is undertaken. This cluster highlights the significance of computational approaches in addressing real-world problems in thermal design, particularly in high-power systems such as processors, batteries, and electric vehicles. Cluster 2 encompasses the study of electronic package architecture and passive components that enhance thermal performance, including heat sinks and insulation materials. FCBGA (flip-chip ball grid array) is a type of microelectronic package that is complex and highly sensitive to heat distribution. Studies in this cluster typically evaluate the performance of these components using thermal simulation to enhance heat release efficiency and reduce the device's working temperature. Research in this cluster focuses on developing efficient cooling systems through physical design and the selection of thermal insulating materials. Cluster 3 indicates molecular simulation-based approaches to understand the fundamental properties of TIM materials. Methods such as molecular dynamics simulation and molecular docking are employed to analyze interactions between atoms, bonding energies, and heat transfer mechanisms at the nanoscale. The primary focus is to maximize the thermal conductivity of the material through a deep understanding of its microscopic structure. This cluster plays an important role in the design of nanotechnology-based materials and composites, which can exhibit high thermal performance through atomic structure and interfacial engineering. Cluster 4 is concerned with the issues of thermal deformation (warpage) and thermal resistance in structures using TIM. Thermal analysis is performed to assess the mechanical integrity of components during heating and cooling processes, especially in multi-layer structures and polymeric materials. Thermal resistance is a crucial indicator in evaluating the efficiency of heat transfer between layers. Demonstrates the relevance of integrating thermal analysis with structural aspects, so that material design can consider not only conductivity, but also shape stability and thermomechanical durability. Cluster 5 is more theoretical and describes mathematical approaches in signal or heat management through topological structures. Concepts such as low-rank matrix completion and interference alignment demonstrate the application of linear algebra and numerical optimization techniques, particularly in the context of thermal communication or multi-channel systems. This reflects a new trend in combining high computational methods with the design of physical structures, leading to the integration of disciplines such as information theory and topological engineering for managing heat or signals in complex systems. At the same time, cluster 6 represents a recent trend in the literature, namely the use of machine learning and deep learning to analyze and predict material performance based on numerical data or images. The integration with magnetic resonance imaging (MRI) technology demonstrates the potential for using non-destructive imaging to detect the internal thermal properties of TIM materials. Serving as a bridge between materials science and data science, it opens up opportunities to explore AI-based predictive methods for material design optimization without the need for extensive physical experiments.

cfd, reliability, simulation, thermal interface materials, thermal management, tim	fcbga, heat sink, thermal insulation material, thermal performance, thermal simulation	molecular docking, molecular dynamics, molecular dynamics simulation, thermal conductivity, thermal interface material	thermal analysis, thermal interface material (ti), thermal resistance, warpage	interference alignment, low-rank matrix completion, topological interference management	deep learning, machine learning, magnetic resonance imaging

Figure 6. Categorization of keywords

The six identified clusters show that the study of thermal interface materials (TIMs) is highly multidisciplinary, spanning materials physics, electrical engineering, numerical simulation, artificial intelligence, and even topological approaches. The primary trend is towards integrating predictive models with the structural understanding of materials to achieve maximum thermal performance in modern electronic devices.

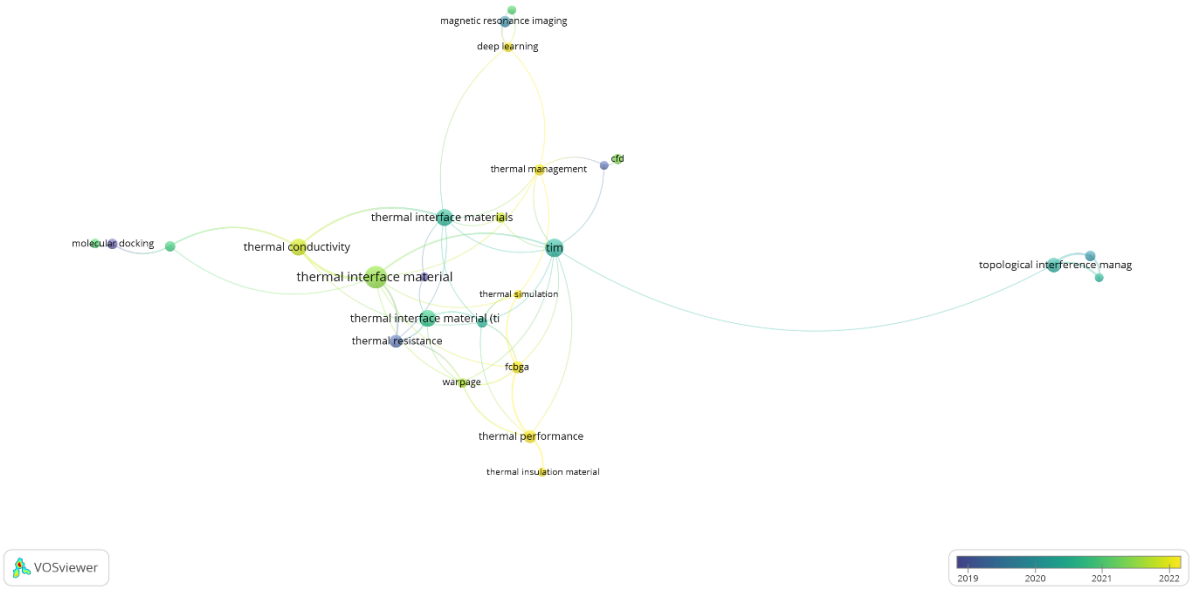


Figure 7. Overlay visualization

The overlay visualization of the bibliometric analysis generated through VOSviewer illustrates the temporal dynamics of keyword occurrence in the literature related to thermal interface materials (TIM) research. This map employs a spectral color gradation, ranging from purple (representing the average occurrence around 2019) to yellow (indicating the average occurrence near 2022), which illustrates the progression of time for the topics explored. Primary keywords such as thermal interface materials, thermal resistance, and thermal simulation appear in bluish-purple, indicating that early research in this field focused heavily on fundamental aspects of materials, including thermal resistance and numerical simulation approaches to evaluate thermal performance. Over time, there has been a shift in focus marked by the emergence of terms such as thermal conductivity, thermal performance, and thermal insulation of materials, ranging from greenish yellow to bright yellow. This suggests that recent studies have begun to focus on enhancing the efficiency and specific capabilities of TIM materials in practical applications, particularly in high-power electronic systems.

Furthermore, the emergence of buzzwords such as deep learning, magnetic resonance imaging, and molecular docking, accompanied by bright colors, signifies a new trend towards the integration of interdisciplinary approaches. These approaches include the application of artificial intelligence for materials modeling and optimization, as well as molecular imaging and simulation techniques, to more accurately explore the microstructure of materials. Meanwhile, terms such as topological interference management, while still low in frequency and on the periphery of the network, indicate the potential of emerging new directions in the context of manipulating the topological properties of materials for more efficient heat management. The appearance of such terms in light green indicates that the topic is starting to attract attention in the middle period (around 2020-2021). It has the potential to grow into a more established research area. Therefore, this visualization not only reveals the conceptual evolution in TIM research but also maps the emergence of new areas that could form the basis for further novel, cutting-edge, and multidisciplinary research.

Discussion

The bibliometric analysis conducted in this study successfully revealed the intellectual structure and direction of research development in the field of thermal interface materials (TIM), particularly in the context of heat transfer simulation in Al_2O_3/AlN granular composites. Through keyword co-occurrence mapping with VOSviewer, six thematic clusters are identified, revealing the diversity of research approaches and focuses. These findings not only illustrate the current landscape of literature but also provide insights into potential pathways for further scientific exploration.

Cluster 1 is the focal point of the bibliometric network as it covers key terms such as thermal interface materials, simulation, thermal management, CFD, and reliability. The main focus of research in this cluster is on numerical approaches, particularly computational fluid dynamics (CFD), to analyze and optimize heat transfer between components in high-power electronic systems. Numerical models offer an efficient and cost-effective alternative to experimental approaches, enabling the evaluation of various geometry configurations and working conditions prior to fabrication. The use of simulation is also relevant in assessing long-term reliability, as modern electronic systems must be able to withstand extreme thermal fluctuation conditions. As such, this cluster provides a methodological foundation for the design of precise and predictive Al_2O_3/AlN-based TIM materials. Unlike Cluster 1, which emphasizes computational approaches, Cluster 2 focuses on hardware-level integration, covering keywords such as FCBGA, heat sinks, thermal insulation materials, thermal performance, and thermal simulations. FCBGA is a temperature-sensitive chip packaging technology, and studies in this cluster aim to evaluate the effectiveness of passive and active cooling systems, such as heat sinks, in maintaining the thermal stability of devices. A simulative approach to electronic package configuration is crucial for reducing the hotspot phenomenon and maintaining temperature homogeneity across component surfaces. In addition, the presence of insulation materials emphasizes attention to the energetic efficiency of the system and the reduction of unwanted heat losses. The primary contribution of this cluster is the enhancement of the connection between the physical design of components and the overall thermal performance of the system, particularly in micro- and nanoscale applications. Cluster 3 is about molecular simulation and material structure engineering. This cluster covers advanced topics at the atomistic level, including molecular dynamics, molecular docking, and thermal conductivity. Molecular simulation enables an in-depth understanding of the heat transfer mechanisms that occur within and between granular grains, as well as the phonon interactions between interfaces. This approach is particularly critical in composite systems, such as Al_2O_3/AlN, where the bonding between particles, particle size, and matrix structure have a significant influence on thermal conductivity. With molecular docking methods, researchers can assess how the orientation and distribution of filler materials within the matrix impact the heat conduction pathway. This understanding opens up opportunities for precise interfacial engineering at the nanoscale, with the hope of improving thermal boundary conductance and reducing thermal resistance. This cluster strengthens the connection between statistical physics, phonon theory, and materials science. Cluster 4 focuses more on structural evaluation and thermal warpage analysis, with a particular emphasis on thermal resistance, thermal analysis, and warpage. Structural issues, such as deformation due to thermal loads (warpage) and the mechanical stability of TIMs, are of major concern. In multi-layer systems, such as those using Al_2O_3/AlN granular composites, a mismatch in the coefficient of thermal expansion (CTE) between layers can generate residual stresses that lead to delamination, cracking, or deformation. The analysis in this cluster examines the impact of geometric and thermomechanical factors on thermal performance, as well as their influence on the device's service life and structural integrity. As such, this cluster highlights the importance of combining thermal performance and mechanical stability as two inseparable requirements in the development of reliable and durable TIMs. Despite its relatively small size and frequency, Cluster 5, which consists of keywords such as topological interference management, interference alignment, and low-rank matrix completion, represents innovative mathematical and topological approaches. These concepts are commonly used in signal processing and communication network optimization, but their adaptation in the domains of heat management and material structure design is beginning to show potential. For example, low-rank optimization approaches can be employed to design material configurations with optimal microstructures, thereby enhancing heat conduction pathways. The technique is also relevant in data-driven material discovery, where mapping material properties based on non-linear relationships and topological structures can accelerate the development of new generation TIM materials. Although currently exploratory, this direction could serve as a stepping stone towards integrating differential geometry, statistical mechanics, and high computing technology in functional material design. The last cluster shows a new trend in the integration of machine learning (ML) and deep learning (DL) in TIM studies. The presence of buzzwords such as magnetic resonance imaging (MRI) indicates that non-destructive imaging methods are now being adopted to evaluate the thermal distribution and internal integrity of TIM materials in real-time. ML-based approaches enable more efficient and accurate processing of simulation or image data and pave the way towards AI-based predictive systems for designing and testing materials without the need for repeated physical experiments. In the context of granular composite materials, ML models can be

trained to recognize microstructure patterns that correlate strongly with thermal conductivity, enabling data-driven design optimization. This cluster reflects the methodological transformation in materials research, where material informatics is becoming an increasingly integrated domain with materials physics and engineering.

Overall, the six identified clusters indicate a complex and multidimensional direction of development in Al_2O_3/AlN granular composite-based TIM research. Research in this area is no longer limited to conventional experiments or macroscopic measurements, but has evolved to include multiscale simulations, AI integration, topological optimization, and molecular approaches. The complexity of thermal problems in modern electronic systems drives the need for holistic and adaptive solutions. As such, the results of this study provide an important foundation for understanding the current knowledge structure and identifying relevant research gaps for further exploration.

Conclusion

This study has uncovered a comprehensive scientific landscape of thermal interface materials (TIM) research trends, particularly in the context of heat transfer simulation in Al_2O_3/AlN granular composites, through a bibliometric approach of 604 publications from the Scopus database during the period 2015-2025. Using VOSviewer and keyword co-occurrence analysis, six thematic clusters were identified, each reflecting different research directions and approaches, ranging from numerical simulation and hardware design to molecular modeling, structural evaluation, and the integration of artificial intelligence and topological methods.

These results show that research on TIM is undergoing significant multidisciplinary development. The dominance of simulation-based and molecular approaches signifies the importance of an in-depth understanding of heat transfer mechanisms at both micro and macro scales. Meanwhile, the emergence of artificial intelligence integration and advanced characterization techniques signals the transition towards a new paradigm in data-driven material design.

Overall, these findings provide an important strategic overview for researchers, practitioners, and technology developers to understand the direction of TIM research development and find gaps that can be further explored. The combination of material structure engineering, multiscale simulation, and the utilization of digital technologies such as AI is a key driver for the development of future TIMs that are more efficient, reliable, and applicable to high-power electronic systems.

Recommendations

Based on the results and discussions in this study, a number of strategic recommendations can be proposed to encourage the development of research and applications of thermal interface materials (TIM) based on Al_2O_3/AlN granular composites in a more progressive and applicable direction:

1. Strengthening Multiscale and Multidisciplinary Research

Stronger integration between molecular simulation, macroscopic numerical computation, and experimental validation is needed. This multiscale approach will enhance the accuracy of models in predicting the thermal and mechanical properties of granular composites, while also reducing the gap between simulation and practical implementation.

2. Data-Driven Predictive Model Development and Artificial Intelligence

The application of machine learning and deep learning to develop predictive models for thermal conductivity and mechanical stability of TIM materials remains largely unexplored. Model training based on simulation datasets and experimental results can efficiently and economically accelerate the design and selection process of new materials.

3. Exploration of Interface Structure Engineering

Expanding the study of complex interface structures, such as graded interfaces, nanopillar arrays, or interfaces with topological modifications (e.g., through micro-molding or lithography techniques), will enrich the options for increasing thermal boundary conductance. This is especially important for TIM integration in high-power semiconductor systems.

4. Further Experimental Validation under Real-World Conditions

Future research should extend the experimental test scenarios to TIM in real-world environments, such as those with temperature fluctuations, cyclic stress, or exposure to electromagnetic fields. This validation is crucial for bridging the gap between idealized performance in simulation and actual stability in long-term applications.

5. Facilitate International and Interdisciplinary Collaboration

Given the increasingly complex and fragmented trend in TIM research, cross-country and interdisciplinary collaborations among materials physicists, mechanical engineers, computer experts, and the manufacturing industry are highly recommended to accelerate the adoption of innovative and industry-appropriate TIM technologies.

6. Improved Access and Standardization of Material Simulation Data

The development of an open database containing thermal simulation results and characterization of TIM composites, encompassing both microscopic and macroscopic parameters, is necessary. Standardization of data formats will facilitate interoperability across simulation platforms and strengthen research reproducibility.

These recommendations are expected to serve as a practical and conceptual guide for the scientific community in directing thermal interface materials research toward results that are more effective, innovative, and have a broad impact on the development of future electronic technology.

Scientific Ethics Declaration

* The authors declare that the scientific ethical and legal responsibility of this article published in EPSTEM journal belongs to the authors.

Conflict of Interest

* The authors declare that they have no conflicts of interest

Funding

* This work was supported by Lembaga Pengelola Dana Pendidikan (LPDP), Ministry of Finance of the Republic of Indonesia

Acknowledgements or Notes

* This article was presented as on oral presentation at the International Conference on Technology, Engineering and Science (www.icontes.net) held in Antalya/Türkiye on November 12-15, 2025.

* The authors would like to express their sincere appreciation and gratitude to Lembaga Pengelola Dana Pendidikan (LPDP), Ministry of Finance of the Republic of Indonesia, for its valuable support in facilitating this publication and fostering collaboration.

References

Aria, M., & Cuccurullo, C. (2017). Bibliometrix: An R-tool for comprehensive science mapping analysis. *Journal of Informetrics, 11*(4), 959–975.

Bianco, V., De Rosa, M., & Vafai, K. (2022). Phase-change materials for thermal management of electronic devices. *Applied Thermal Engineering, 214*, 118839.

Chung, D. D. L. (2022). Performance of thermal interface materials. *Small, 18*(37), 2200693.

Dai, W., Ren, X., Yan, Q., Wang, S., Yang, M., Lv, L., Ying, J., Chen, L., Tao, P., Sun, L., Xue, C., Yu, J., Song, C., Nishimura, K., Jiang, N., & Lin, C. (2023). Ultralow interfacial thermal resistance of graphene thermal interface materials with surface metal liquefaction. *Nano-Micro Letters, 15*, 17.

Donthu, N., Kumar, S., Mukherjee, D., Pandey, N., & Lim, W. M. (2021). How to conduct a bibliometric analysis: An overview and guidelines. *Journal of Business Research, 133*, 285-296.

Gao, H., Wang, M., Yuan, Z., Shen, J., Zhao, J., & Feng, Y. (2021). Strategies for enhancing thermal conductivity of polymer-based thermal interface materials: A review. *Journal of Materials Science, 56*, 1064–1086.

Ghadim, H., Godin, A., Veillere, A., Duquesne, M., & Haillot, D. (2025). Review of thermal management of electronics and phase change materials. *Renewable and Sustainable Energy Reviews, 207*, 115039.

Hadi, N. S., Goi, M., Wijayanarka, A., Dewi, A. B. F. K., & Nuryani, N. (2022). Effect of leaf guava extract on blood pressure in Rattus Norvegicus Wistar strain. *Jurnal Ilmiah Kesehatan (JIKA), 4*(2), 319-326.

Hajjaji, Y., Boulila, W., Farah, I. R., Romdhani, I., & Hussain, A. (2021). Big data and IoT-based applications in smart environments: A systematic review. *Computer Science Review, 39*, 100318.

He, X., Liu, X., Huang, J., Lin, W., Wen, J., Huang, P., Zeng, X., Zhang, Y., Wang, Q., & Lin, Y.-S. (2024). Simultaneous reduction of bulk and contact thermal resistance in high-loading thermal interface materials using self-assembled monolayers. *Advanced Functional Materials, 34*(32), 2402276.

He, Z., Yan, Y., & Zhang, Z. (2020). Thermal management and temperature uniformity enhancement of electronic devices by micro heat sinks: A review. *Energy, 211*, 119223.

Huang, Y., Sun, W., You, H., & Wu, K. (2023). Influence of temperature effects on CPT in granular soils by discrete element modeling in 3D. *Geotechnics, 3*(3), 624-637.

Jing, L., Cheng, R., Tasoglu, M., Wang, Z., Wang, Q., Zhai, H., & Shen, S. (2023). High thermal conductivity of sandwich-structured flexible thermal interface materials. *Small, 19*(19), 2207015.

Kusharyadi, R., Pertiwi, S., Siahaan, E. Y. S., & Dasari, D. (2023). Bibliometric analysis: Software usage trends GeoGebra in mathematics learning from 2017 - 2022. *Prisma Sains: Jurnal Pengkajian Ilmu Dan Pembelajaran Matematika Dan IPA IKIP Mataram, 11*(1), 196.

Lee, E., Zhang, T., Yoo, T., Guo, Z., & Luo, T. (2016). Nanostructures significantly enhance thermal transport across solid interfaces. *ACS Applied Materials & Interfaces, 8*(51), 35505–35512.

Lethulur, N. D., Juandi, D., & Tupamahu, P. Z. (2024). 1 st Decade of E-learning in Mathematics Education: A Bibliometric Analysis. *The Eurasia Proceedings of Educational and Social Sciences*, *38*, 68-79.

Liang, C., Hong, J., Wan, C., Wang, Z., Zhao, X., Hou, A., Nika, D., Huo, Y., & Zhang, G. (2025). A perspective on mechanism of heat transfer and performance optimization in advanced thermal interface materials. *Applied Physics Letters, 126*(1), 010501.

Liu, Y., Zheng, R., & Li, J. (2022). High latent heat phase change materials (PCMs) with low melting temperature for thermal management and storage of electronic devices and power batteries: Critical review. *Renewable and Sustainable Energy Reviews, 167*, 112783.

Maulida, A. B. (2024). Karakterisasi morfologi dan komposisi lapisan komposit Ni-TiN-AlN/Si3N4 dengan metode elektrodeposisi rapat arus pulsa. *Jurnal Fisika: Fisika Sains dan Aplikasinya, 9*(1), 18-25.

Razeeb, K., Dalton, E., Cross, G., & Robinson, A. (2018). Present and future thermal interface materials for electronic devices. *International Materials Reviews, 63*(1), 1-21.

Rejeb, A., Rejeb, K., Appolloni, A., Kayikci, Y., & Iranmanesh, M. (2023). The landscape of public procurement research: A bibliometric analysis and topic modelling based on Scopus. *Journal of Public Procurement, 23*(2), 164–189.

Rosadi, M. R. (2024). Analisis morfologi dan komposisi lapisan komposit Ni-AlN menggunakan metode elektrodeposisi dengan rapat arus pulsa. *Jurnal Fisika: Fisika Sains dan Aplikasinya, 9*(1), 26-33.

Sudhindra, S., Kargar, F., & Balandin, A. A. (2021). Noncured graphene thermal interface materials for high-power electronics: Minimizing the thermal contact resistance. *Nanomaterials, 11*(7), 1699.

Wang, C., Hua, L., Yan, H., Li, B., Tu, Y., & Wang, R. (2020). A thermal management strategy for electronic devices based on moisture sorption-desorption processes. *Joule, 4*(2), 435-447.

Wang, J., Shen, Y., & Yang, P.-K. (2023). Multilayered graphene/ZnO heterostructure interfaces to improve thermal transfer. *Composites Communications, 40*, 101616.

Wang, W., Zhu, H., Han, Y., Li, J., & Xue, Z. (2021). Effect of Al content on non-metallic inclusions in Fe–23Mn–xAl–0.7C lightweight steels. *Ironmaking & Steelmaking, 48*(9), 1038-1047.

Zeng, C., Zeng, X., Cheng, X., Pang, Y., Xu, J., Sun, R., & Zeng, X. (2024). Design of thermal interface materials with excellent interfacial heat/force transfer ability via hierarchical energy dissipation. *Advanced Functional Materials, 34*(38), 2406075.

Zhou, Y., Zhang, X., & Hu, M. (2016). An excellent candidate for largely reducing interfacial thermal resistance: A nano-confined mass graded interface. *Nanoscale, 8*(4), 1994-2002.

Author(s) Information

Sudarminto Senlau
Bandung Institute of Technology, Jl. Ganesa No. 10
Coblong, Bandung City, West Java, Indonesia
Contact e-mail: *20224007@mahasiswa.itb.ac.id*

To cite this article:

Sudarminto, S. (2025). Research trends in the heat transfer simulation of Al_2O_3/AlN granular composites for thermal interface materials. *The Eurasia Proceedings of Science, Technology, Engineering and Mathematics (EPSTEM), 38,* 382-392.

The Eurasia Proceedings of Science, Technology, Engineering & Mathematics (EPSTEM)
ISSN: 2602-3199

The Eurasia Proceedings of Science, Technology, Engineering and Mathematics (EPSTEM), 2025

Volume 38, Pages 393-400

IConTES 2025: International Conference on Technology, Engineering and Science

Influence of Boundary Conditions of a Contact Problem on the Stress Distribution in a Semi-Infinite Space

Valery Chigirinsky
Rudny Industrial University

Sergey Lezhnev
Rudny Industrial University

Sergey Kuzmin
Rudny Industrial University

Abdrakhman Naizabekov
Science, Education and Staffing Planning LLP

Yevgeniy Panin
Karaganda Industrial University

Abstract: The main tasks that arise in the process of mining are the creation of conditions that ensure the stability, strength and reliability of rock formations, allowing efficient and safe implementation of technological modes of mining. It should be noted that the annual damage caused by landslides around the world amounts to huge amounts commensurate with earthquake damage, the same ratio with human casualties. Therefore, the problem of quantitative forecasting of stability, creep and strength of slopes and slopes is of paramount national economic importance. The purpose of this work, carried out within AP19678682 grant project, is to develop a methodology for calculating the stress state of a half-space under the action of massive bodies in conditions of a rough contact surface. In the course of the conducted research, a mathematical model of the stress state of a half-space in conditions of a rough contact surface was developed. A comparative analysis of the study results of stress state at elastic half-space under the action of a massive body under conditions of a smooth and rough contact surface showed that the normal stresses with a smooth surface are 1 in the center and 1.4 on the sides, and the rough contact surface on the contact has stresses 1 in the center and 1.1 on the sides. The surface fades at a depth of 400, and with a rough surface it fades at a depth of 300. Analysis of the obtained results of the distribution of normal and tangential stresses in the depth of the array showed that the greater the width of the base.

Keywords: Elasticity theory, Function argument, Cauchy-Riemann relations, Laplace equations, Boundary conditions

Introduction

In soil mechanics, the general patterns of interaction under the load of rocks of different deformability, stability and strength are considered. To create a mathematical model of the stress-strain state of soils, different directions of continuum mechanics are used: theoretical mechanics, elasticity theory, plasticity theory and dynamic processes theory (Bartolomey, 2003). Preliminary analysis shows that rock loading occurs for different reasons and under different conditions of their interaction. There is a need to assess the stress state when creating artificial slopes, channels, dams and quarries. When implementing underground workings, great

- This is an Open Access article distributed under the terms of the Creative Commons Attribution-Noncommercial 4.0 Unported License, permitting all non-commercial use, distribution, and reproduction in any medium, provided the original work is properly cited.

- Selection and peer-review under responsibility of the Organizing Committee of the Conference

© 2025 Published by ISRES Publishing: www.isres.org

attention is paid to the stability of rocks and the peculiarities of the stress-strain state of array (Timoshenko & Goodyear, 1979). The main problems are caused by the complexity of building and maintaining mining and capital workings in tectonically stressed low-strength massifs of fractured rocky rocks. Under these conditions, despite the relatively high strength of rocks in the samples, disturbances in the stability of the contour array of underground workings occur even with relatively small outcrops and low stress and strain levels. In underground workings, the strength of the massif is affected by numerous chaotic cracks and differently oriented tectonic disturbances on the structural blocks. The probabilistic nature and spatiotemporal variability of these indicators necessitate conducting field-based instrumental studies at various scale levels.

The main tasks that arise in the process of mining are the creation of conditions that ensure the stability, strength and reliability of rock formations, allowing efficient and safe implementation of technological modes of mining (Chigirinsky & Putnoki 2017). It should be noted that the annual damage caused by landslides around the world amounts to huge amounts commensurate with earthquake damage, the same ratio with human casualties. Therefore, the problem of quantitative forecasting of stability, creep and strength of slopes and slopes is of paramount national economic importance. The objectives of the research carried out in this work are: to develop a mathematical model of the stress state of a half-space under conditions of a rough contact surface; to study the stress state of an elastic half-space under the action of a massive body under conditions of a rough contact surface; to analyze the obtained result of the distribution of normal and tangential stresses in the depth of the array.

Method

The study of the stress state in elastic and plastic half-spaces in mountain massifs of different depths is an urgent problem of continuum mechanics. At the present stage, the method of argument of a function by a complex variable is effectively used in solutions, however, it can be seen from the presented analyses that the influence of tangential stresses is not fully represented, which does not allow an adequate assessment of its effect on the strength characteristics of rocks. There is a need to strengthen well-known solutions at the current level of implemented solutions and ensure the real reliability of the result. For the planar problem, three equations of elasticity theory, two differential equations of equilibrium, the stress strain continuity condition, and boundary conditions are chosen:

$$\frac{\partial \sigma_x}{\partial x} + \frac{\partial \tau_{yx}}{\partial y} = 0, \frac{\partial \tau_{yx}}{\partial x} + \frac{\partial \sigma_y}{\partial y} = 0, \nabla^2 (\sigma_x + \sigma_y) = \nabla^2 (2 \cdot \sigma_0) = 0. \quad (1)$$

Boundary conditions in the stresses:

$$\tau_n = -\frac{\sigma_x - \sigma_y}{2} \cdot sin2\varphi + \tau_{xy} \cdot cos2\varphi. \quad (2)$$

In (Chigirinsky & Putnoki 2017), solutions to the plane problem of elasticity theory in Cartesian coordinates are presented. The analytical solution of this problem is presented in the form:

$$\sigma_x = C_\sigma exp(-\theta)\, cosA\Phi + \sigma_0 + C,$$

$$\sigma_y = -C_\sigma exp(-\theta)\, cosA\Phi + \sigma_0 + C, \quad (3)$$

$$\tau_{xy} = \exp(-\theta)\, C_\sigma sinA\Phi\sigma_0 = \pm n \cdot C_\sigma exp(-\theta)\, cosA\Phi,$$

at $\theta_x = A\Phi_y, \theta_y = -A\Phi_x, A\Phi_{xx} + A\Phi_{yy} = 0, \theta_{xx} + \theta_{yy} = 0.$

where $\sigma_x, \sigma_y, \tau_{xy}$ – components of the stress tensor; σ_0 – average normal stress.

Taking into account the boundary conditions, expression (3) was presented as:

$$\sigma_y = 2exp\left[\frac{1}{2} \cdot AA_6(x^2 - y^2)\right] C_\sigma \cos(AA_6 xy), \quad (4)$$

$$\tau_{xy} = exp\left[\frac{1}{2} \cdot AA_6(x^2 - y^2)\right] C_\sigma sin(AA_6 xy).$$

Exponent indicator θ and the argument of the trigonometric function AΦ were derived from the Laplace equations and the Cauchy-Riemann relations. In accordance with the task, they must meet the stress boundary conditions:

$$\sigma_y = 2exp\left[\frac{1}{2}\cdot\frac{\pi}{2b\,y_0}(x^2)\right]C_\sigma,\ \tau_{xy} = 0. \tag{5}$$

Results and Discussion

In accordance with formula (5), contact stresses and stresses in the depth of the array were calculated (Figure 1). From solution (4) it can be seen that zero tangential stresses do not negate their presence in the depth of the half-space. A stable attenuating function in the depth of the half-space and a concave plot of contact normal stresses are obtained.

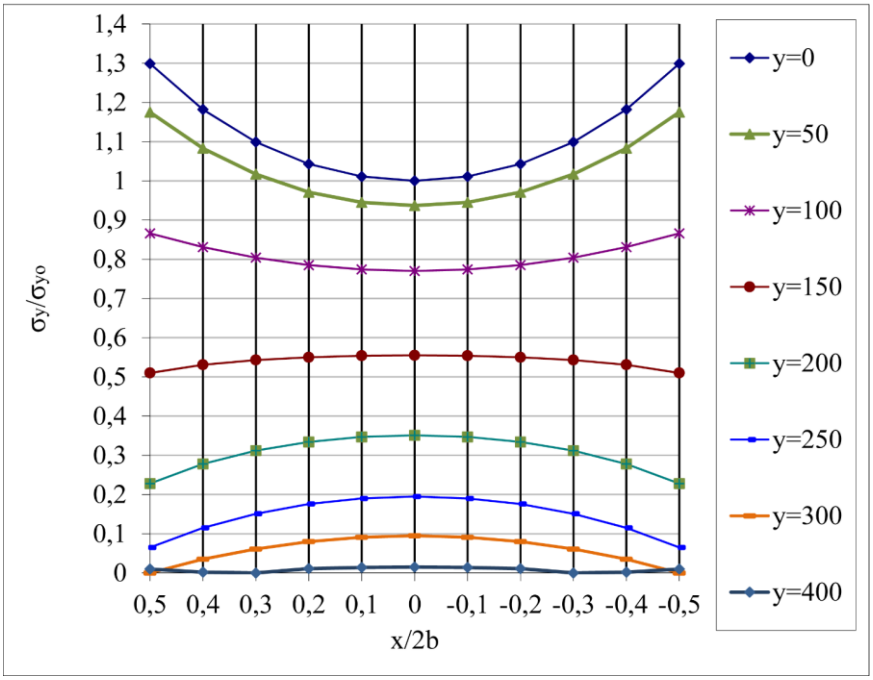


Figure 1. Distribution of normal stresses at the contact and in the depth of the half-space under the action of a flat die without regard to friction

With this formulation of the question, it is of theoretical and practical interest to solve the problem of a rough contact surface. Let's use the formulation of problem (1) and boundary conditions (2). Simplifying the boundary conditions through trigonometric substitution, the first argument function AΦ is introduced. From the solution condition, a second argument is introduced, the function θ, which determines the fundamental substitution of exp(-θ). Taking into account the trigonometric and fundamental substitution in the equation of continuity of deformation, taking into account the function of the complex variable [6], the differential equations are obtained in the form:

$$exp(\theta + iA\Phi)\cdot\left[(\theta_{xx} + \theta_{yy}) + (A\Phi_{xx} + A\Phi_{yy})\cdot i + (\theta_x + iA\Phi_x)^2 + (\theta_y + iA\Phi_y)^2\right] +$$

$$+ exp(\theta - iA\Phi)\cdot\left[(\theta_{xx} + \theta_{yy}) - (A\Phi_{xx} + A\Phi_{yy})\cdot i + (\theta_x - iA\Phi_x)^2 + (\theta_y - iA\Phi_y)^2\right] = 0. \tag{6}$$

The operators in formula (6) located near the exponent contain the same second derivatives in terms of coordinates and non-linearity. If, for some reason, the operators are zero, then the identity holds. Let's write down the nonlinearities in the operators and rearrange them.

$$(\theta_x + iA\Phi_x)^2 + (\theta_y + iA\Phi_y)^2 = (\theta_x + A\Phi_y)\cdot(\theta_x - A\Phi_y) + 2i(\theta_x \cdot A\Phi_x + \theta_y \cdot A\Phi_y) + \\ +(\theta_y + A\Phi_x)\cdot(\theta_y - A\Phi_x),$$

$$(\theta_x - iA\Phi_x)^2 + (\theta_y - iA\Phi_y)^2 = (\theta_x + A\Phi_y)\cdot(\theta_x - A\Phi_y) - \\ -2i(\theta_x \cdot A\Phi_x + \theta_y \cdot A\Phi_y) + (\theta_y + A\Phi_x)\cdot(\theta_y - A\Phi_x).$$

It follows that this differential equation will be satisfied when the Cauchy-Riemann relations and the Laplace equation are fulfilled:

$$\theta_x = A\Phi_y, \quad \theta_y = -A\Phi_x,$$

$$A\Phi_{xx} + A\Phi_{yy} = 0, \tag{7}$$

$$\theta_{xx} + \theta_{yy} = 0.$$

It is possible to obtain a new solution in the interaction of bodies with a rough contact surface. As a result of solving differential equations (7), we have:

$$A\Phi = AA_6 x(y + C), \tag{8}$$

The function (8) satisfies the Laplace equation, i.e. we have: $A\Phi_{xx} = A\Phi_{yy} = 0.$

Thus, equation (8) defines new boundary conditions that will be related to the roughness of the contact surface. Using the Cauchy-Riemann relations, the second argument function θ is determined. The exponent indicator θ is written as:

$$\theta = AA_6 \frac{x^2 - (y+C)^2}{2}. \tag{9}$$

Taking into account expressions (8) and (9), the normal and tangential stress takes the form:

$$\sigma_y = 2exp\left[AA_6 \frac{x^2 - (y+C)^2}{2}\right] C_\sigma cos[AA_6 x(y + C)],$$

$$\tau_{xy} = exp\left[AA_6 \frac{x^2 - (y+C)^2}{2}\right] C_\sigma sin[AA_6 x(y + C)]. \tag{10}$$

Based on the analysis of the expressions obtained (10), it is established that:

$$C = f \cdot b,$$

where *f* and *b* - the friction coefficient on the contact surface and the half-width of the massive base.

Boundary conditions: at $x = b$, $y = 0$, $\sigma_y = k_1$, $\tau_{xy} = f \cdot k_1$, $A\Phi = A\Phi_1$, $\theta = \theta_1$. Substituting the boundary conditions in solution (4), we find the constant AA_6:

$$AA_6 = \frac{f}{b \cdot C} = \frac{f}{b \cdot f \cdot b} = \frac{1}{b^2}.$$

As a result, a mathematical model of stress state of a half-space under conditions of a rough contact surface has been developed. Based on expressions (10), studies of the stress state of the array under the action of massive external bodies with a rough contact surface were carried out. Figures 2 and 3 show the distributions of contact normal and tangential stresses into the depth of the array, taking into account the influence of the width of the base, as well as the friction coefficient. Comparing the results of the study with the data of other authors, we are convinced that they are qualitatively and quantitatively the same. At the contact with the stamp in a semi-infinite space, the normal contact stress diagram has a concave character. This indicates the reliability of the result obtained. In the depth of space, the stress state of the medium attenuates to zero.

As the analysis shows, under the influence of maximum tangential stresses, sliding lines develop in massifs, which are dangerous because they are sources of shear, collapse and subsidence of rock massifs. The distributions of tangential stresses are visible, the values of which are maximum at a depth of 70, in the angular loading zones such a stressed soil condition shows the possibility of destruction under the influence of tangential stresses, taking into account the friction coefficient.

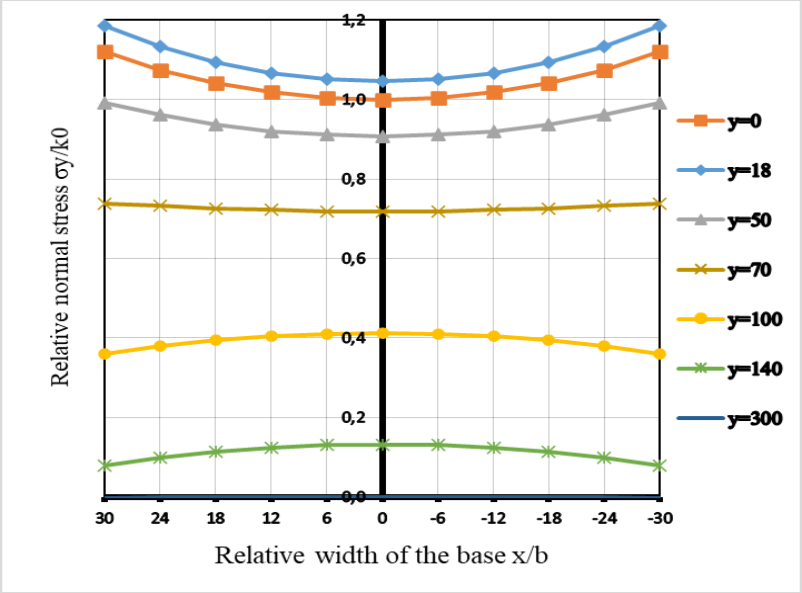


Figure 2. Distribution of normal stress at the contact and in the depth of the array with a coefficient of friction f=0.3 and a width b=60

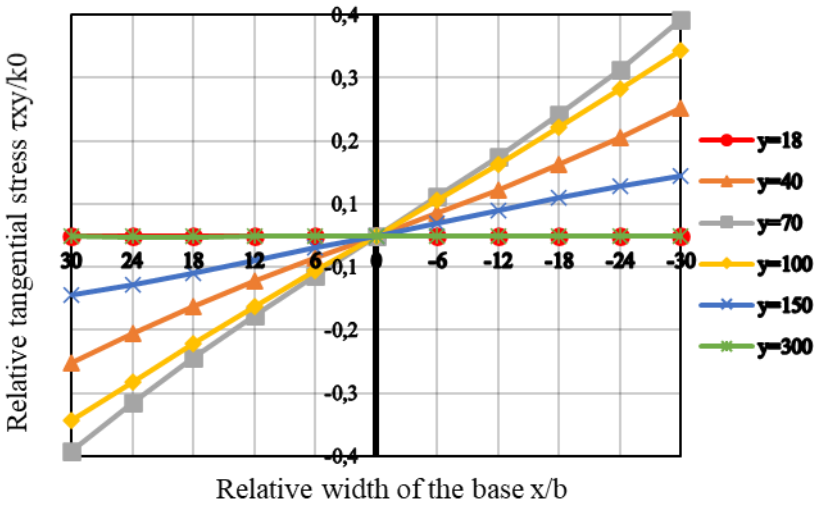


Figure 3. Distribution of tangential stress at the contact and in the depth of an array with a coefficient of friction f=0.3 and a width b=60

Figure 4 shows the effect of the friction coefficient f = 0.1-0.5 on the distribution of normal stresses in depth along the edges of the die x = b and in the center x = 0, with a base width of b = 60. Figure 5 shows the effect of the coefficient of friction f = 0.1-0.5 on the distribution of tangential stresses in depth along the edges of the die x = b, with a base width of b = 60. Figure 6 shows the effect of the base width b = 20-100 on the distribution of normal stresses in depth along the center x = 0, with a friction coefficient f = 0.3.

It can be seen from the obtained graphs (Figure 4) that with an increase in the friction coefficient, the attenuation depth of normal stresses does not increase significantly. Figure 1 shows that the metal flows from a high-load zone to a lower-load zone. Judging by the drawing, the metal spreads out from the center in the horizontal axis in the opposite direction, which gives a tangential stress of one sign. The tangential stresses in the contact layers move to the center. This position is explained by a change in the sign on the contact (zone of obstructed deformations, Figure 5). As the friction coefficient increases, the depth of the maximum tangential

stress increases, and the attenuation depth is identical to the normal stress. It is also shown (Figure 6) that with increasing base width; the attenuation depth of normal stresses increases significantly.

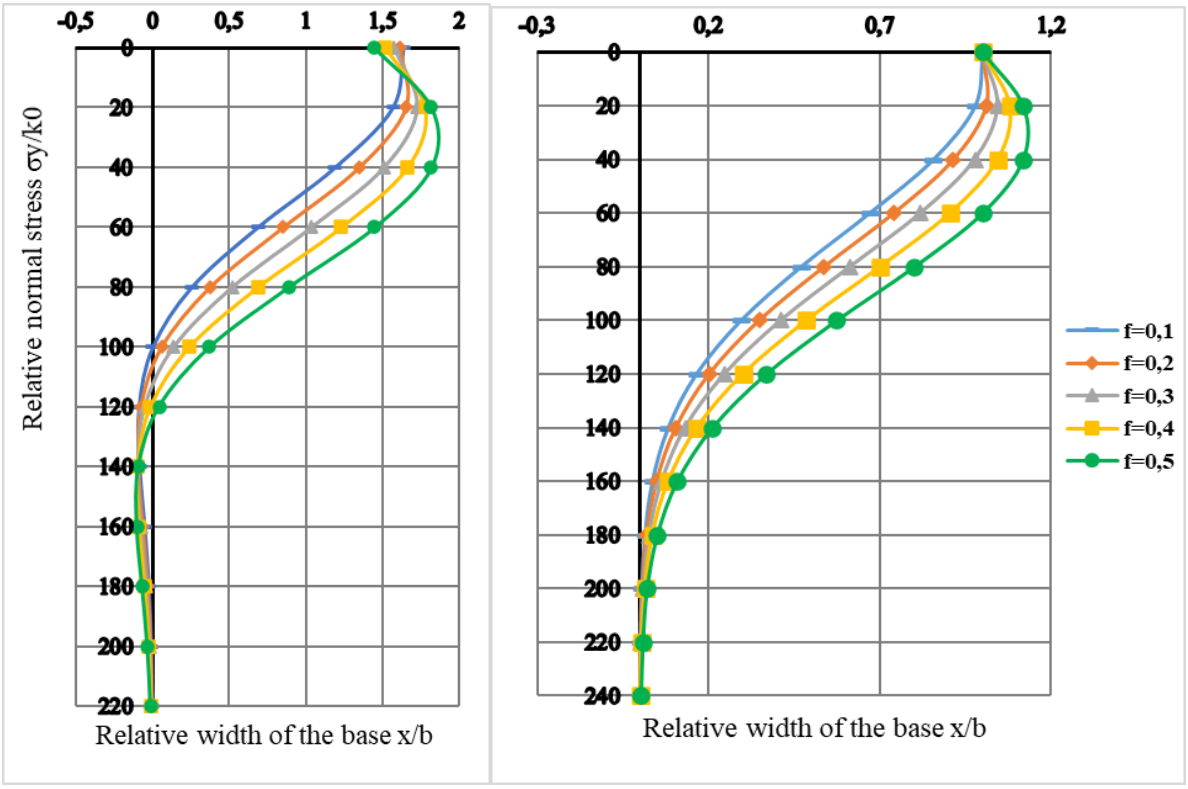


Figure 4. Distribution of normal stresses at the contact and in the depth of the array along the edges of the die and in the center with a base width of b =60

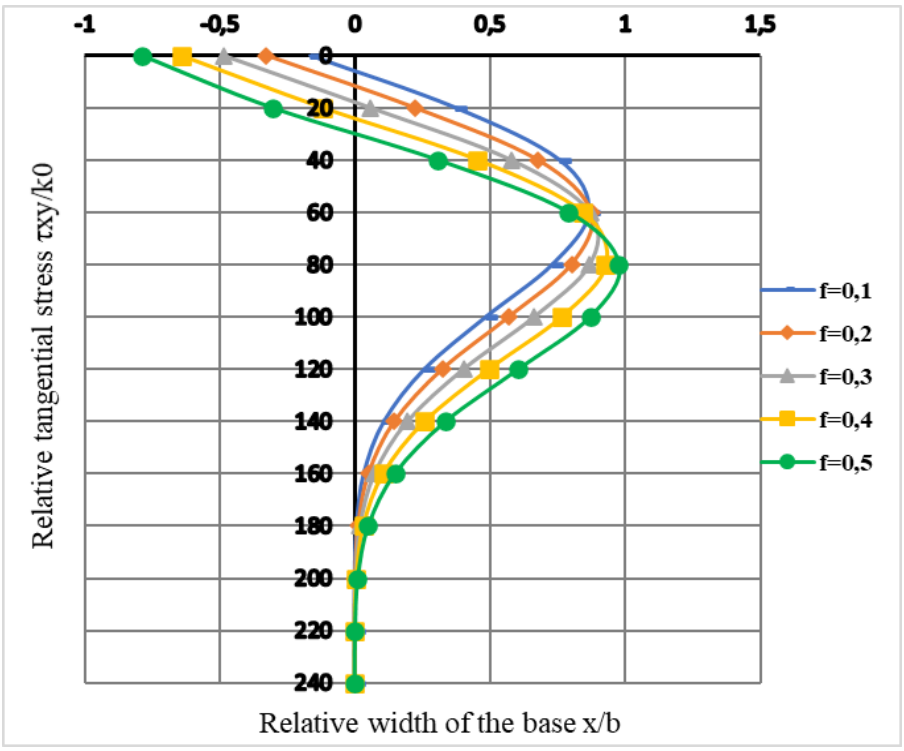


Figure 5. Distribution of tangential stresses at the contact and in the depth of the array along the edges of the die with a base width of b =60

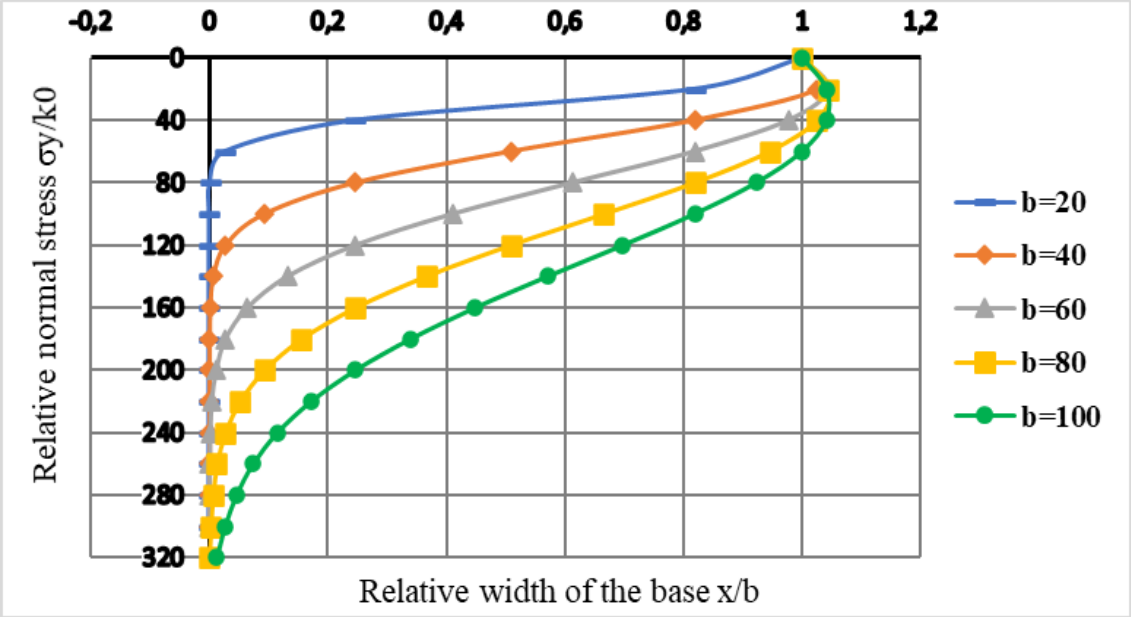


Figure 6. Distribution of normal stresses at the contact and in the depth of the array in the center of the die, with different widths with a friction coefficient f=0.3

Conclusion

In the course of the conducted research, a mathematical model of the stress state of a half-space in conditions of a rough contact surface was developed. A comparative analysis of the results of the study of the stress state of an elastic half-space under the action of a massive body under conditions of a smooth and rough contact surface showed that normal stresses with a smooth surface in the center are 1 and on the sides 1.4, and the rough contact surface on the contact has stresses 1 in the center and 1.1 on the sides. In this case, normal stresses with a smooth surface fade at a depth of 400, and with a rough surface they fade at a depth of 300. Analysis of the obtained results of the distribution of normal and tangential stresses in the depth of the array showed that the greater the width of the base, the greater the depth of the normal stresses attenuate.

Scientific Ethics Declaration

* The authors declare that the scientific ethical and legal responsibility of this article published in EPSTEM journal belongs to the authors.

Conflict of Interest

* The authors declare that they have no conflicts of interest

Funding

* This study was funded by the Science Committee of the Ministry of Science and Higher Education of the Republic of Kazakhstan (Grant No. AP19678682).

Acknowledgements or Notes

* This article was presented as a poster presentation at the International Conference on Technology, Engineering and Science (www.icontes.net) held in Antalya/Türkiye on November 12-15, 2025.

References

Bartolomey, A. A. (2003). *Mechanics of soils: A textbook for students*. ACB.

Chigirinsky, V., & Putnoki, A. (2017). Development of a dynamic model of transient processes in mechanical systems using argumentative functions. *Eastern European Journal of Corporate Technologies, 3/7*(87), 11-21.

Timoshenko, S. P., & Goodyear, J. (1979). *Elasticity theory*. Main editorial office of physical-mathematical literature.

Author(s) Information

Valery Chigirinsky
Rudny Industrial University
38 50 let Oktyabrya str., Rudny, Kazakhstan

Sergey Lezhnev
Rudny Industrial University
38 50 let Oktyabrya str., Rudny, Kazakhstan
Contact e-mail: *sergey_legnev@mail.ru*

Sergey Kuzmin
Rudny Industrial University
38 50 let Oktyabrya str., Rudny, Kazakhstan

Abdrakhman Naizabekov
Science, Education and Staffing Planning LLP
Lomova 45 str., Astana, Kazakhstan

Yevgeniy Panin
Karaganda Industrial University
Republic 30, Temirtau, Kazakhstan

To cite this article:

Chigirinsky, V., Lezhnev, S., Kuzmin, S., Naizabekov, A., & Panin, Y. (2025). Influence of boundary conditions of a contact problem on the stress distribution in a semi-infinite space. *The Eurasia Proceedings of Science, Technology, Engineering and Mathematics (EPSTEM), 38,* 393-400.

The Eurasia Proceedings of Science, Technology, Engineering & Mathematics (EPSTEM)
ISSN: 2602-3199

The Eurasia Proceedings of Science, Technology, Engineering and Mathematics (EPSTEM), 2025

Volume 38, Pages 401-414

IConTES 2025: International Conference on Technology, Engineering and Science

Impact of Printing Orientation on the Mechanical Properties of Selectively Laser Sintered PA12

Boukhoulda Farouk Benallel
Djillali Liabes University of Sidi Bel Abbes

Djellal Kouider
Djillali Liabes University of Sidi Bel Abbes

Bendine Kouider
Djillali Liabes University of Sidi Bel Abbes

Boukhoulda Abdelaziz
Djillali Liabes University of Sidi Bel Abbes

Abstract: This study explores the impact of different printing orientations in the selective laser sintering (SLS) process on the mechanical properties of polyamide 12 (PA12). Test specimens were developed according to ASTM D3039 using three distinct orientations: 0°, 45°, and 90°. Tensile tests were performed to evaluate the Young's modulus and ultimate tensile strength of each specimen tested. To complement the experimental analysis, finite element models were developed in ANSYS APDL.The models developed incorporated the Gurson-Tvergaard-Needleman (GTN) damage model, which accounts for material porosity, as well as the Chaboche model to simulate plastic deformation behavior. The numerical simulations performed closely match the experimental results, confirming the reliability of the proposed models. Microscopic observations were carried out to examine the microstructure of the printed material. The observations revealed variations in the distribution of defects and porosity and demonstrated that this originates from the printing orientation of the material. For certain orientations, the specimens showed more uniform microstructures and fewer defects, which correlates with better mechanical properties, such as increased stiffness and strength. These results highlight the very important role of printing orientation in optimizing the structural integrity and mechanical performance of PA12 components manufactured by SLS, while validating the predictive capacity of the numerical approach.

Keywords: PA12, 3d printing, SLS, Tensile, Modeling

Introduction

Additive Manufacturing (AM) has emerged as a rapidly growing technology in modern industry, providing the ability to fabricate complex geometries and customized components with high efficiency. Among the various AM processes, Selective Laser Sintering (SLS) is one of the most widely used for polymer-based applications due to its good dimensional accuracy and favorable mechanical performance. Polyamide 12 (PA12) is commonly employed as a reference material in SLS, valued for its balanced combination of mechanical strength, chemical resistance, and processability. However, a major challenge in SLS fabrication lies in the occurrence of porosity, which can significantly influence the strength, durability, and overall performance of printed parts.

SLS employs one or more lasers to selectively fuse polymer particles layer by layer within a controlled environment. This process is highly intricate and demands rigorous control to ensure successful printing and high-quality parts (Bendine et al., 2022; Bourell, 2016; Charoo et al., 2020; Rajesh et al., 2015; Senthilkumaran et al.,

- This is an Open Access article distributed under the terms of the Creative Commons Attribution-Noncommercial 4.0 Unported License, permitting all non-commercial use, distribution, and reproduction in any medium, provided the original work is properly cited.

- Selection and peer-review under responsibility of the Organizing Committee of the Conference

© 2025 Published by ISRES Publishing: www.isres.org

2009; Simha Martynková et al., 2021; Stoia et al., 2019)**.** A significant advantage of SLS is its ability to minimize raw material waste while enabling the production of complex geometric shapes with minimal limitations, unlike traditional manufacturing methods. Among the materials used in SLS, polyamide 12 (PA12) stands out due to its ease of use, efficiency, and a broad temperature window between the onset of melting during heating and crystallization during cooling. This wide thermal range allows PA12 to remain heated without crystallizing until the cooling stage, enhancing part consolidation and preventing warping (Dadbakhsh et al., 2017; Mwania et al., 2020)**.** Additionally, PA12 boasts excellent mechanical properties, low moisture absorption compared to other polyamides, and strong resistance to abrasion and chemicals, including solvents (Dadbakhsh et al., 2017). The mechanical properties of SLS-fabricated parts are influenced by both the raw material characteristics and process parameters. Numerous studies have demonstrated that factors such as powder bed temperature, powder composition, the use of additives, printing speed, printing orientation, and varying laser energy densities significantly affect the final material properties (Amado-Becker et al., 2008; de Oliveira Setti et al., 2014; Hopkinson et al., 2009)**.**

More particularly, the printing orientations, which can be done in several directions, have a significant influence on the mechanical properties (Rodríguez et al., 2023). Indeed, several researchers (Caulfield et al., 2007; Olejarczyk et al., 2020; Stichel et al., 2017; Tomanik et al., 2021) have undertaken tensile tests to show this influence. The results agree that the printing strategy is crucial for the resistance of specimens subjected to axial load. Some researchers like Ajoku et al. (Ajoku et al., 2006) showed that the most optimal mechanical properties (tensile strength, Young's modulus, elongation at break) were observed for specimens printed in the plane of the powder bed (an angle of 0°) and showed that a difference of 16% in terms of resistance and 11.2% in modulus observed between the two orientations (0° and 90°). In another work, (Caulfield et al., 2007) found that parts oriented at 0° have a higher breaking strength value than 90° and parts oriented at 90° have higher breaking elongation values to those of 0° oriented parts. This observation was also made by Tomanik et al. (Tomanik et al., 2021)**.** They concluded that the specimens printed at 0° presented a more ductile behavior than those printed at 45° and also showed that the best mechanical properties are obtained for parts printed with an angle of 0°, i.e. that is to say in the plane of the powder bed. El Magri et al. (El Magri et al., 2022)studied the influence of the printing angle on the tensile strength (TS). They found that the 90° plane orientation exhibits (TS) values 2 to 10% lower than those of 0°, with the largest difference observed at low laser power. Usher J.S. et al. (Usher et al., 2013)**.** They found that specimens built in the 90° orientation exhibit much lower elongation values (around 12–13%) than those built in the 0° orientation. It was also observed that specimens constructed in the 90° orientation required a much higher energy density to achieve a stable elongation value.

Results from previous literature searches suggest that the printing angle significantly influences the mechanical properties of SLS specimens, and an optimal orientation can be chosen based on the specific strength and stiffness requirements of the components. They have also shown through tensile tests, and sometimes through tomographic analyzes (Dupin et al., 2012; Rosso et al., 2020; Stichel et al., 2017) the existence of an anisotropy of the material (Cano et al., 2018). For example, (Obst et al., 2018; Sindinger et al., 2020) confirmed that residual voids aligned perpendicular to the loading direction are the main factor that explains structural anisotropy. According to research, porosity can occur due to several parameters: inconsistency of powder deposition and incomplete fusion of particles (Bourell et al., 2014; Dupin et al., 2012; Majewski et al., 2008; Stichel et al., 2017; Toth-Taşcău et al., 2012; Zárybnická et al., 2022), type of conditioning and drying of PA12 powder, low viscosity, coalescence, atmospheric gas trapped between particles and layers and off-gassing of degradation products. Bain et al. (Bain et al., 2019) confirms that the porosities present between the layers cause weak interfaces and thus affect the overall strength of the part. Porosity must therefore be imperatively controlled by choosing the appropriate manufacturing process to guarantee product quality. It is also necessary to control the process parameters such as: temperature, layer thickness, scanning spacing, energy density provided by the laser and orientation of the construction. Calignano et al. (Calignano et al., 2021) depending on the orientation of the specimen and the printing technology, the porosity levels and pores have different morphology and distribution in the sample. A close correlation was highlighted between the pores and their descriptors and the mechanical behaviour of the specimen. There are mathematical models in the literature that take into consideration the presence of porosities to describe the behavior of materials (Roszak et al., 2021; Schob et al., 2019).

In this study, the effect of printing direction on the mechanical properties, specifically Young’s modulus and ultimate tensile strength, was thoroughly investigated. To achieve this, tensile tests were conducted on specimens printed at different orientations, adhering to standardized procedures in compliance with ASTM D3039. As an innovative approach, a detailed microscopic analysis of the printed parts was performed using scanning electron microscopy (SEM) to examine and analyze the microstructural characteristics. This dual investigation-combining mechanical testing with microscopic analysis-not only provided valuable insights into the influence of printing

direction on the mechanical behavior of the material but also highlighted the critical role of microstructural features such as porosity and layer bonding in determining overall performance.

Materials and Methods

Experimental Procedure and Devices

Materials

The material employed in this study was Polyamide 12 (PA12), a thermoplastic polymer widely used in additive manufacturing owing to its outstanding mechanical performance, chemical resistance, and thermal stability. PA12 is particularly advantageous for Selective Laser Sintering (SLS) processes because of its relatively low melting temperature, uniform particle morphology, and excellent flowability. The powder utilized exhibited a particle size distribution between 20 µm and 40 µm, which falls within the typical range for high-resolution SLS applications (see Figure 1).



Figure 1. Polyamide 12 (Nylon PA12) powder

SLS Printing Machine Used

The 3D printer used is the MfgPro230 xS from Formlabs. This printer is designed for professionals in the aerospace and automotive sectors, as well as those who need to create advanced prototypes. It offers a build volume of 230 x 230 x 230 mm. The layer thickness is 0.1 mm. It is compatible with materials such as nylon, PC (polycarbonate), and other similar thermoplastics. The machine is compatible with SLS Build and SLS Ware software. It is ideal for industries looking to develop end-use parts with high mechanical performance (see figure 2).

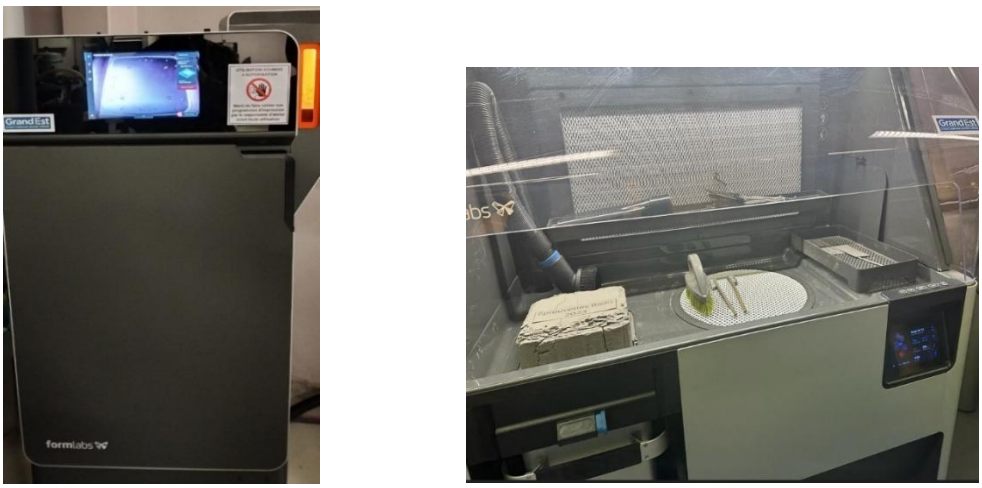


Figure 2. The SLS machine (Formlabs MfgPro230 xS printer)

The printer's operating principle is shown in Figure 3 below: The selective laser sintering (SLS) process is based on the layer-by-layer selective fusion of polymer powder using a laser beam. Initially, a thin layer of powder is deposited and evenly spread over the build platform by means of a steel recoating roller, which may also be heated to ensure uniform powder distribution. The build chamber is typically maintained under an inert gas atmosphere (such as nitrogen or argon) to prevent powder oxidation. To facilitate sintering and reduce the required laser power, the powder bed is preheated by infrared (IR) radiation to a temperature close to the polymer's melting point. The build platform then lowers by a distance equal to the desired layer thickness, while the powder supply platform rises by the same amount to allow the deposition of a new powder layer. The laser parameters and scanning paths are predefined based on the digital model generated through computer-aided design (CAD). The laser beam selectively heats the powder according to the geometry of each cross-sectional layer of the model, raising the temperature of the particles to a point where solid-state diffusion and coalescence occur between adjacent grains. The surrounding unsintered powder acts as a natural support for subsequent layers. This sequence of deposition, selective sintering, and platform adjustment is repeated layer by layer until the complete three-dimensional part is fabricated. Various parameters must be correctly set, including laser power, powder scanning diameter and speed, scan spacing, preheating, etc.

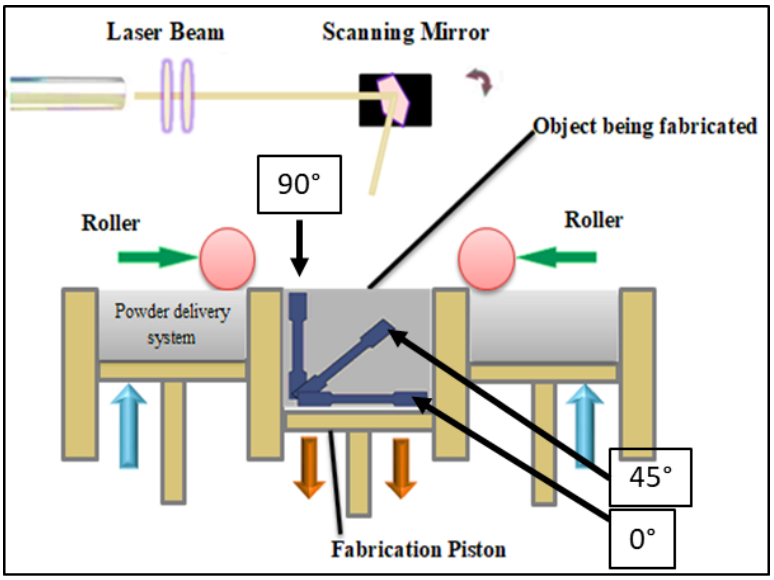


Figure 3. Illustration of printing angles

Tensile Machine

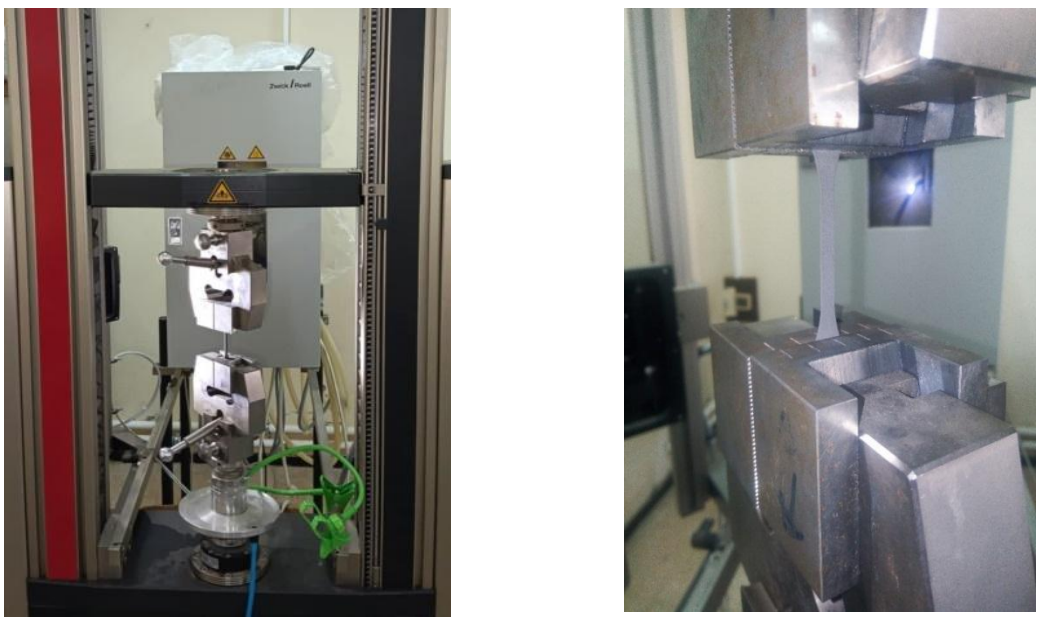
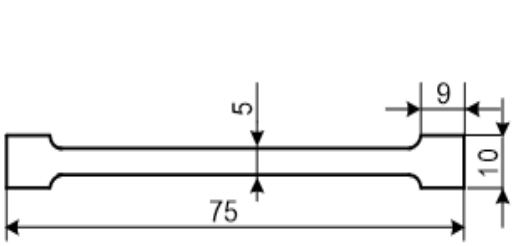


Figure 4. Tensile machine (Zwick, 25KN)

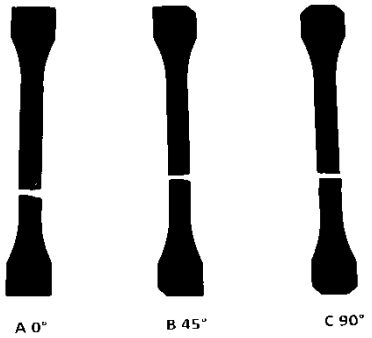
Tensile testing was conducted using a Zwick 25KN testing machine (Figure 4). The specimens were loaded until failure, and data on load vs. displacement were recorded for analysis. The machine is used for tensile and compressive testing. It features a high-rigidity frame and a highly accurate beam steering mechanism, ensuring positioning accuracy of approximately ±2 µm, thanks to the use of a Hiperface® recipr;:: :ocating servomotor and the testControl II electronic system. The tabletop model typically has a height of approximately 1050 mm and a width of approximately 440 mm, providing ample space for sample and equipment setup. This configuration allows for obtaining an accurate stress-strain curve for an SLS polyamide 12 sample, particularly regarding deformation due to gripper slippage or velocity fluctuations, and ensuring consistent collection of load and strain data throughout the test interval.

Specimens of Tensile Test

To characterize the printed material, standardized tensile test specimens were fabricated by selective laser sintering (SLS) from PA12 powder. Three printing angles were considered: 0°, 45°, and 90°, as illustrated in Figure 5. In this study, nine polyamide 12 (PA12) specimen were manufactured. The specimen were printed in three different orientations: 3 specimen at 0°, 3 specimen at 45° and 3 specimen at 90°. To ensure the correct orientation of each sample after printing and to avoid confusion during mechanical testing, a simple physical coding system was adopted: Specimen printed at 0° have no chamfer (no markings). Specimen printed at 45° have one chamfer at their end. Specimen printed at 90° have two chamfers at their end. This system allowed for quick visual differentiation between groups of samples after printing and during tensile testing (see Figure 4(b).



(a): Geometry of the ASTM test specimen (Thickness = 2mm).



(b): PA12 specimen broken by traction

Figure 5. PA12 specimen of traction

Identification of Two Behavior Models

Gurson-Tvergaard-Needleman Damage Model

In the proposed numerical approach, the model integrates the Gurson-Needleman and Tvergaard (GTN) behaviors to account for the presence of voids within the 3D printed specimens. This combination of models allows for a more comprehensive understanding of material response, taking account the complex interactions associated with void formation and growth. GTN is a combination between Gurson model and Needleman and Tvergaard that considers damage in the material, which is mainly used, in ductile model. The model assumes that the plasticity and damage in the material are mainly driven by the voids three state which are void growth, nucleation and coalescence on a microscopic level. GTN model reflects the three states of voids as a changing of void volume fraction and the resulting pressure. Thus, GTN formulates the yield criteria as follow:

$$F = \frac{\sigma_{eq}^2}{\sigma_y^2} + 2f^* q_1 \cosh\left(\frac{3}{2} q_2 \frac{\sigma_m}{\sigma_y}\right) - (1 + q_3 (f^*)^2) \geq 0 \qquad (1)$$

Where q_1, q_2 and q_3 are fitting parameters,
σ_y, σ_{eq} Are the yield strength and the Von Mises equivent stress respectively,
σ_m is the hydrostatic stress defined as the average of the normal stress components,
f^* is the modified void volume fraction used to model the loss of load carrying capacity due to void coalescence and it is given by equation bellow,

$$f^* = \begin{cases} f_0 & if \quad t = 0 \\ f & if \quad f \leq f_c \\ f_c + \frac{f_f^* - f_c}{f_f - f_c}(f - f_c) & if \quad f_c < f \leq f_f \end{cases} \tag{2}$$

The initial porosity f_0 is determined at time $t = 0$ and serves as the starting point for the void volume fraction evolution. Throughout the deformation process. The total void volume fraction f evolves over time due to both according to:

$$f = 1 - \frac{V_M}{V} \tag{3}$$

Where V and V_M are the volume of the material with and without defects respectively,
f_c is the critical volume fraction of the pores at which the voids start to unite and f_f^* gives the ultimate value of f^* at which the stress carrying capacity goes to zero,
f_f is the void volume fraction corresponding to fracture.
The rate of void volume fraction depends on both void growth and void nucleation, ie

$$\dot{f} = \dot{f}_{gr} + \dot{f}_{nucl} \tag{4}$$

Where the rate of void growth, f_{gr}, is given by the following relation

$$f_{gr} = (1 - f)\dot{\epsilon}_{kk}^{pl} \tag{5}$$

Where $\dot{\epsilon}_{kk}^{pl}$ is the plastic hydrostatic strain.
The rate of void nucleation is given by the equation (6)

$$\dot{f}_{nucl} = \frac{f_N}{S_N\sqrt{2\pi}} exp\left[-\frac{1}{2}\left(\frac{\epsilon^{pl} - \epsilon_N}{S_N}\right)^2\right]\dot{\epsilon}^{pl} \tag{6}$$

Where f_N is the nucleation micro-void volume fraction,
Furthermore, S_N is the standard deviation and ϵ_N is the mean in the Gaussian distribution that is assumed for the void nucleation rate.

Chaboche Model

According to the literature such as (Schob et al., 2023), it was observed that the PA12 material manufactured by the SLS process exhibited viscoplastic behavior (Schob et al., 2023). The behavior was described by the Chaboche model which is made up of a system of differential equations. Taking into account small deformations, this model results from the additive decomposition of the total strain rate $\dot{\varepsilon}^{tot}$ into an elastic part denoted $\dot{\varepsilon}^{el}$ and viscoplastic part noted $\dot{\varepsilon}^{vp}$.

$$\dot{\varepsilon}^{tot} = \dot{\varepsilon}^{el} + \dot{\varepsilon}^{vp} \tag{7}$$

$$\dot{\sigma} = \mathrm{E}(\dot{\varepsilon}^{tot} - \dot{\varepsilon}^{vp}) \tag{8}$$

Where $\boldsymbol{\sigma}$ is stress and **E** Young modulus.

The Chaboche model described here contains three parameters in its original form which are determined experimentally. These are the Young modulus E and the two hardening parameters γ_i and C_i. Depending on how many counter-constraints are used, the number of parameters changes.

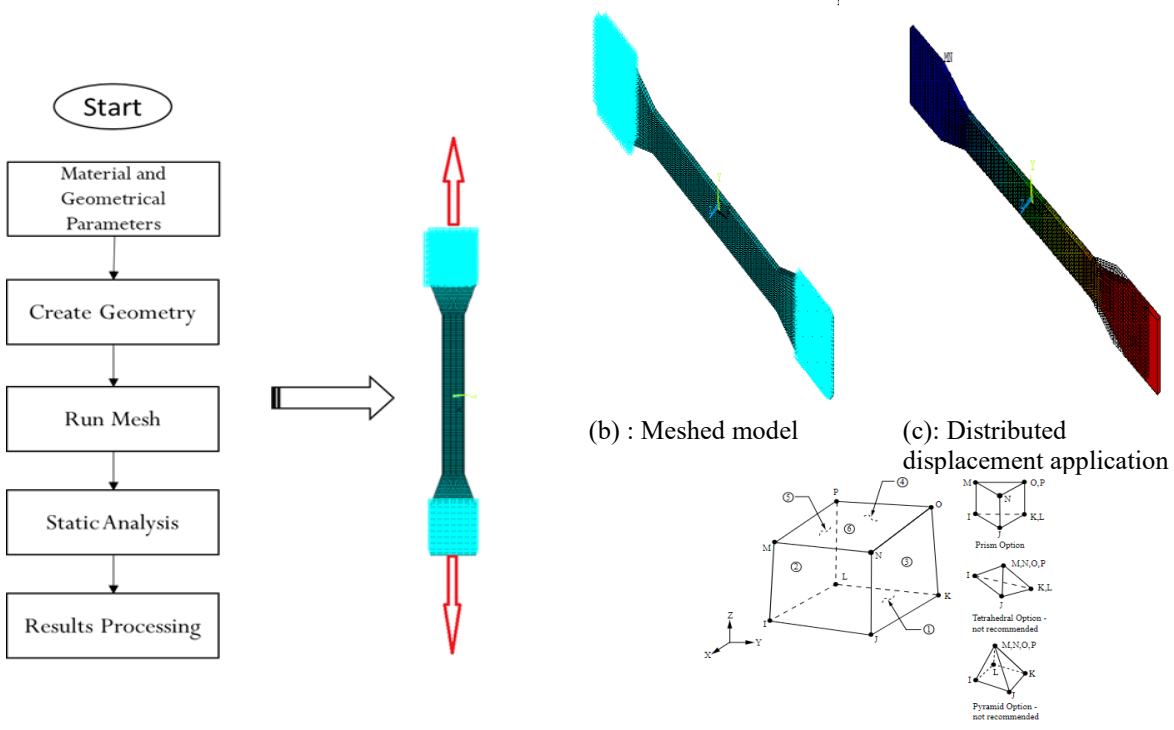
$$\dot{\varepsilon}^{vp} = \dot{\lambda}.n = \dot{\lambda}\left\{\frac{\partial\varphi}{\partial\sigma}\right\} = \sqrt{\frac{2}{3}\varepsilon^{vp}:\varepsilon^{vp}}\,\frac{3}{2}\frac{s - \sum_{i=1}^{n}\alpha_i}{\sigma_y} \tag{9}$$

$$\dot{\alpha}_i = \frac{2}{3}C_i\dot{\varepsilon}^{vp} - \gamma_i\alpha_i\dot{p} \tag{10}$$

The definition of the viscoplastic strain rate is decisive. These are the viscoplastic multiplier $\dot{\lambda}$ and the direction n. The flow function φ is the closure of the elastic domain. The flow function depends on the one hand on the elastic limit σ_y, on the deviatoric stress value s and on the other hand, on the kinematic hardening. The kinematic hardening is taken into account by the counter-constraints $\dot{\alpha}_i$. This is described by the accumulated plastic strain $\dot{p}$and the hardening parameters C and γ.

Finite Element Model

The finite element models proposed in the present analysis were designed, implemented and carried out using ANSYS APDL. In the initial phase, key points were strategically positioned during the design stage to define the model's geometry. Subsequently, lines and areas were created, forming the basis for extracting a three-dimensional volume. The mesh generation process employed solid185 elements, each featuring 8 nodes with three degrees of freedom. The model underwent meticulous boundary condition application in alignment with the experimental procedure. Material properties were judiciously assigned to the model, and for heightened accuracy, both GTN and Chaboche models were integrated to address factors such as porosity and the plasticity zone. This holistic approach ensured the creation of a robust and representative finite element model for subsequent analyses. Notably, the model accounted for the impact of printing orientation by introducing degradation in Young's modulus and tensile strength, inspired by the outcomes of the experimental tests. A sensitivity analysis guided the selection of 6080 elements, deemed suitable for all simulations. In terms of analysis, a quasi-static approach using the Newton-Raphson method scheme was employed, employing an imposed displacement for stability, executed over 100 steps. The numerical model is depicted in Figure 6 bellow. The full implemented code for the purpose is given in the appendix. To accurately simulate he porosity of the blank sample, the initial porosity f_0 as measured at $t = 0$. Due to variations in the initial porosity values obtained from different analyses, an average value of 3.57% was selected. In addition to the initial porosity, damage parameters $q_1, q_2, f_N, \varepsilon$ and $S_N$were established using a specialized adjustment tool. These refined settings were subsequently implemented in ANSYS 17.2 to enhance the model's accuracy.



(a) : Numerical procedure flowchart (b) : Meshed model (c): Distributed displacement application (d) : Solid185 element in Ansys

Figure 6. Finite element model

Results and Discussion

This section presents and analyzes the results obtained. The analysis focuses on tensile tests and associated numerical models, followed by a detailed analysis of the microstructural properties of the printed parts.

Tensile Tests

Experimental Results

A total of three tensile tests were conducted for each printing angle, and the results are illustrated in Figure 7. The observed differences in Young's modulus and tensile strength among specimens printed at different angles suggest a correlation between printing orientation and mechanical properties. The observed variations in Young's modulus and tensile strength across different printing angles are further elucidated through Figures 8 and 9. The results shown that the specimens printed at 0°are displayed, the superior Young's modulus and tensile strength indicate that this specific printing orientation contributes to enhanced mechanical performance. This result aligns with the notion that printing in-plane corresponding to 0° may lead to a more structurally sound and less porous arrangement of material. The printing process, when perpendicular to the laser projection, likely results in a more densely packed structure, reducing porosity and improving material integrity.

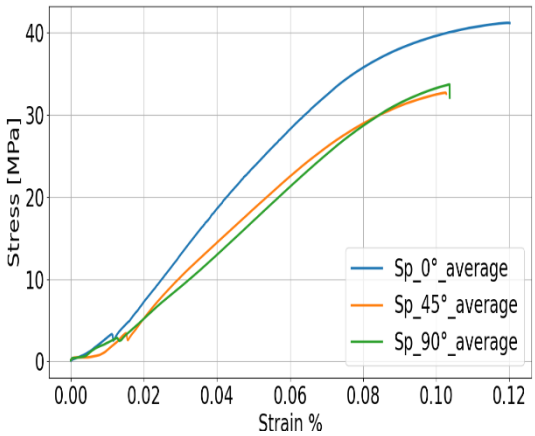


Figure 7. Stress–strain curves for specimens tested at 0°, 45°, and 90° orientations

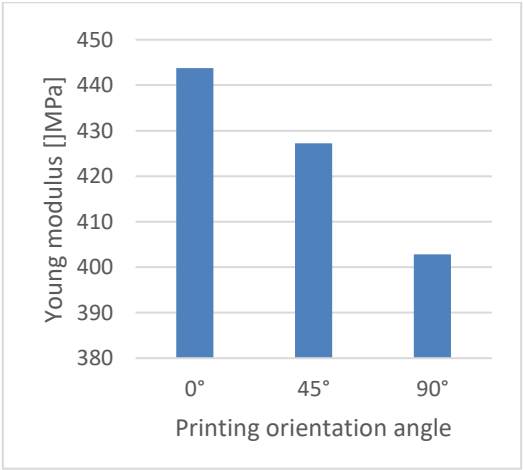


Figure 8. Young's modulus as function as printing orientation angle

Figures 9 and 10 shows respectively the variation of the ultimate strength and the elongation at break as function as the printing orientation angle.

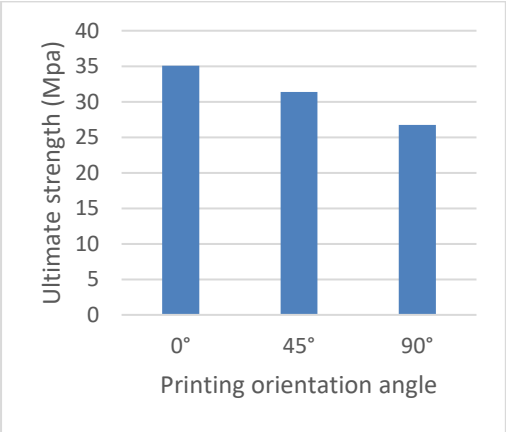


Figure 9. Ultimate strength UTS

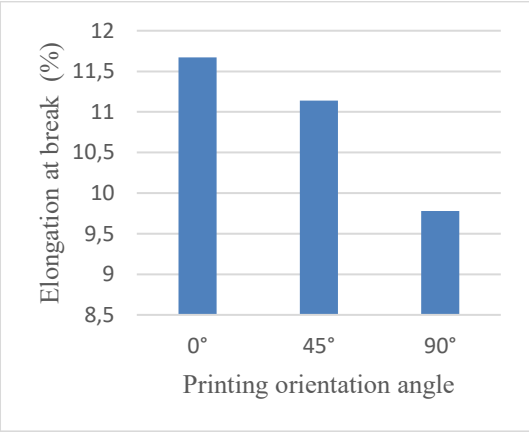


Figure 10. Elongation at break

Table 1. Tensile properties of SLS PA12 polyamide

Orientation Angle [°]	Elastic modulus (MPa)	Ultimate strength UTS (MPa)	Elongation at break (%)
0	443,79±6,92	35,09±1,82	11,67±0,33
45	427,24±2,89	31,39±1,72	11,14±0.9
90	402,85±3,91	26,72±1,65	9,78±0,77

Specimens printed at 45° and 90° angles exhibit lower Young's modulus values compared to those printed at 0°.

Numerical Results

The results of the modeling used in the Ansys software are shown in Figures 11-13 below, corresponding to the tests on the printed specimens at 0°, 45° and 90° respectively.

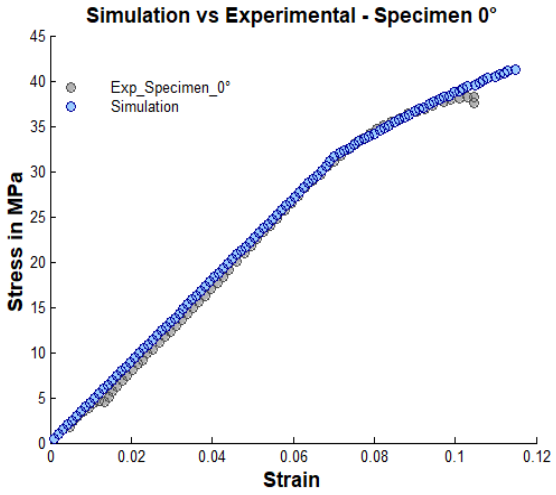


Figure 11. Modeling the tensile behavior of the specimen printed at 0°

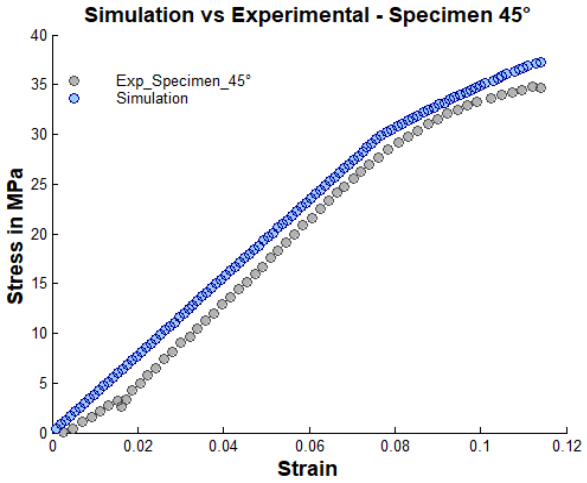


Figure 12. Modeling the tensile behavior of the specimen printed at 45°

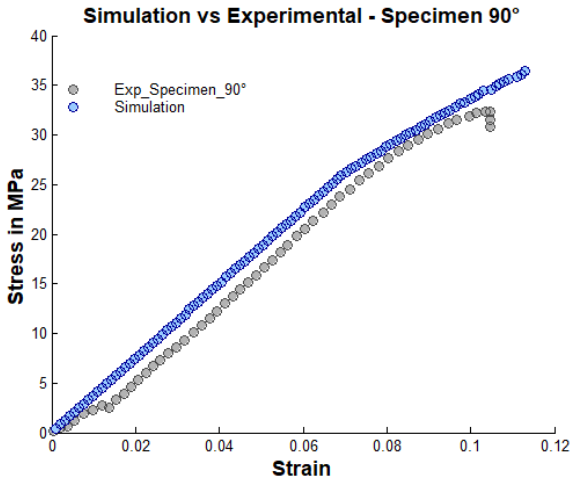


Figure 13. Modeling the tensile behavior of the specimen printed at 90°

Porosity Analysis

To evaluate the porosity, a combination of advanced imaging and digital image processing techniques was utilized. High-resolution optical microscopy was employed to acquire cross-sectional images of the specimens fabricated at different build orientations (see Figure 14). All images were captured under identical lighting and magnification conditions to ensure consistency and reliable comparison.

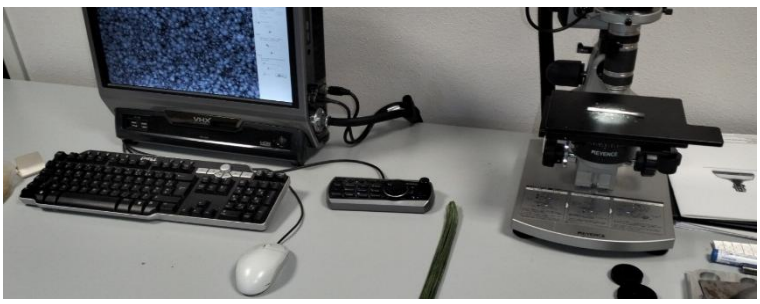


Figure 14. High-resolution optical microscopy

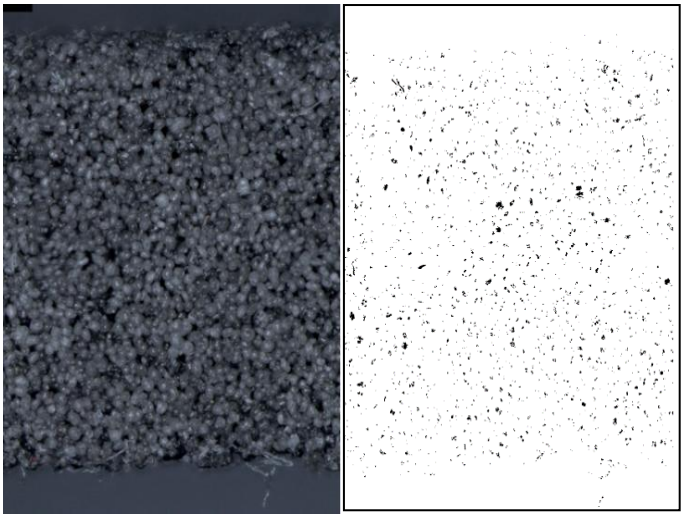


Figure 15. Observation on the 0° test specimen (Porosity rate between 4.80% and 5.93%)

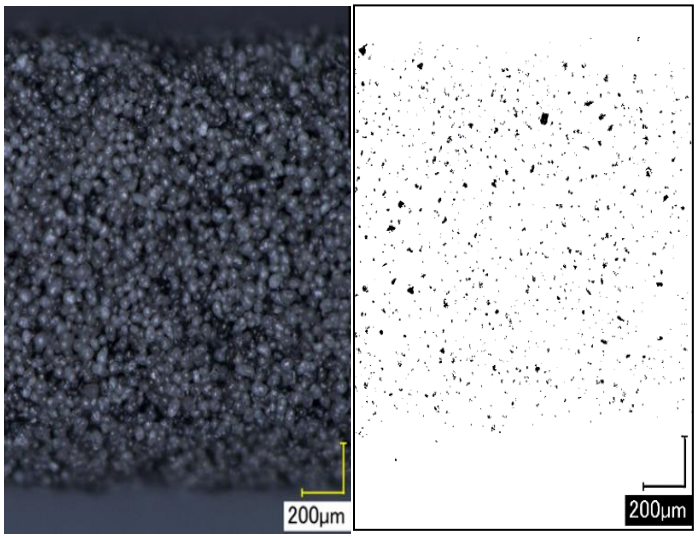


Figure 16. Observation on the 45° test specimen (Porosity rate between 5.12% and 6.40%)

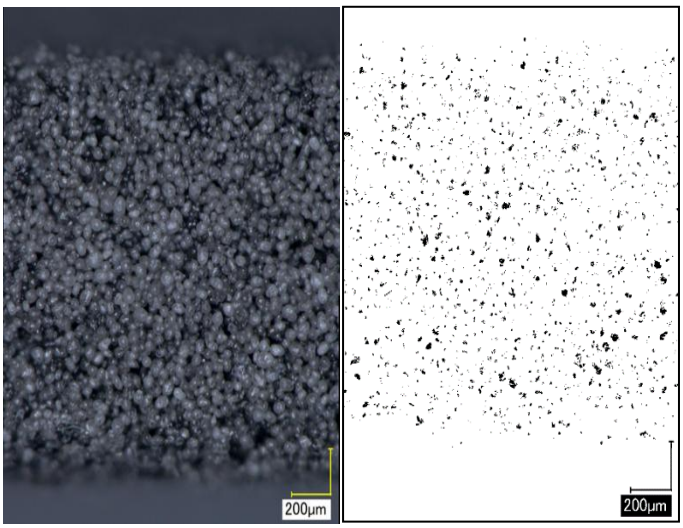


Figure 17. Observation on the 90° test specimen (Porosity rate between 7.10% and 8.32%)

Porosity quantification was performed through a custom-developed Python script incorporating the OpenCV and NumPy libraries. The image processing workflow included the following steps:

1. Grayscale conversion: Each image was converted to grayscale to enhance the contrast between the polymer matrix and the voids, thereby facilitating more accurate segmentation.
2. Thresholding: A global thresholding approach was applied to differentiate the solid regions from the pores. The Otsu algorithm was used to automatically determine the optimal threshold value.
3. Segmentation and morphological filtering: Following thresholding, morphological operations such as erosion and dilation were employed to reduce image noise and refine pore boundaries.
4. Porosity calculation: The porosity was determined as the ratio of the total pore area to the overall image area, expressed as a percentage according to the relation:

$$\text{Porosity} = \frac{\text{Void Area}}{\text{Total Area}}$$

The surface porosity analysis revealed a clear influence of build orientation on the porosity rate of SLS-fabricated PA12 specimens. Samples printed at 0° exhibited the lowest porosity, ranging from 4.8% to 5.93%, indicating a relatively dense structure with minimal void formation. At 45°, the porosity slightly increased to values between 5.12% and 6.4%, suggesting that the intermediate orientation leads to less efficient particle fusion compared to the horizontal build. The highest porosity was observed at 90°, with values ranging from 7.1% to 8.32%, which can be attributed to reduced interlayer bonding and weaker laser energy distribution along the vertical direction. Based on the obtained results (Figures 15, 16 and 17), a histogram was plotted to illustrate the variation of the porosity rate as a function of the printing angle (see Figure 18). This representation provides a clear visualization of how build orientation influences the formation and distribution of pores within the printed specimens.

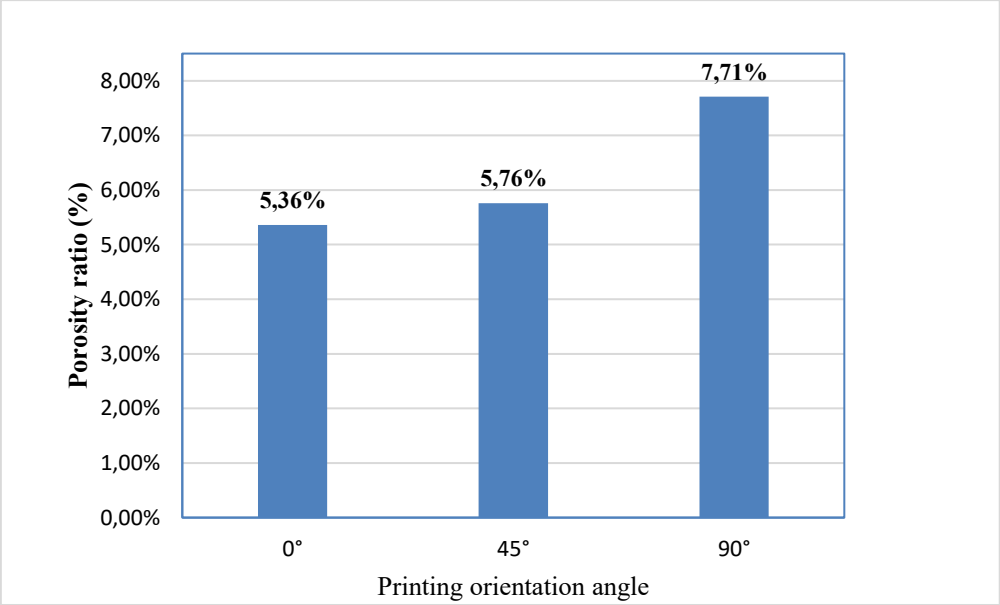


Figure 18. Effect of build orientation on the surface porosity before tensile testing

As suggested by (Cano et al., 2018), printing orientations other than 0° introduce geometric and thermal challenges that further exacerbate the formation of voids and defects. This underscores the critical importance of optimizing printing parameters to achieve improved mechanical properties in additively manufactured components.

Conclusion

This study investigated the effect of printing angle on the mechanical properties of 3D printed PA12 through tensile testing in accordance with ASTM D3039. The main conclusions are as follows:

- Variations in mechanical properties based on printing angles highlight the importance of considering the orientation of printed parts during the additive manufacturing process. The findings suggest that adjusting the printing angle can be a critical factor in optimizing the mechanical performance of PA12 components.
- Tensile test results showed that samples printed at 0 degrees have higher Young's modulus and tensile strength than other orientations. This specific printing orientation contributes to improved mechanical

performance of the material, aligning with the idea that printing in the 0° plane can lead to a structurally stronger and less porous arrangement.
- The observed decrease in mechanical properties is attributed to anisotropic behavior and the presence of porosities at non-zero printing angles.
- These findings emphasize the need for precise control of the printing direction to obtain good mechanical properties and a uniform distribution of porosity.

Scientific Ethics Declaration

* The authors declare that the scientific ethical and legal responsibility of this article published in EPSTEM journal belongs to the authors.

Conflict of Interest

* The authors declare that they have no conflicts of interest

Funding

* This study was funded by the Science Committee of the Ministry of Science and Higher Education of the Republic of Kazakhstan (Grant No. AP19678682).

Acknowledgements or Notes

* This article was presented as a poster presentation at the International Conference on Technology, Engineering and Science (www.icontes.net) held in Antalya/Türkiye on November 12-15, 2025.

* The authors thanks Prof. Nouari Mohammed and Dr. Badis Haddag, research professors at the University of Lorraine, France, for their unwavering support, valuable guidance, and continuous encouragement throughout this work.

References

Ajoku, U., Saleh, N., Hopkinson, N., Hague, R., & Erasenthiran, P. (2006). Investigating mechanical anisotropy and end-of-vector effect in laser-sintered nylon parts. *Proceedings of the Institution of Mechanical Engineers, Part B: Journal of Engineering Manufacture*, *220*(7), 1077-1086.

Amado-Becker, A., Ramos-Grez, J., José Yañez, M., Vargas, Y., & Gaete, L. (2008). Elastic tensor stiffness coefficients for SLS Nylon 12 under different degrees of densification as measured by ultrasonic technique. *Rapid Prototyping Journal*, *14*(5), 260-270.

Bain, E. D., Garboczi, E. J., Seppala, J. E., Parker, T. C., & Migler, K. B. (2019). AMB2018-04 : Benchmark Physical Property Measurements for Powder Bed Fusion Additive Manufacturing of Polyamide 12. *Integrating Materials and Manufacturing Innovation*, *8*(3), 335-361.

Bendine, K., Gibhardt, D., Fiedler, B., & Backs, A. (2022). Experimental characterization and mechanical behavior of 3D printed CFRP. *European Journal of Mechanics-A/Solids*, *94*, 104587.

Bourell, D. L. (2016). Sintering in laser sintering. *JOM*, *68*(3), 885-889.

Bourell, D. L., Watt, T. J., Leigh, D. K., & Fulcher, B. (2014). Performance limitations in polymer laser sintering. *Physics Procedia*, *56*, 147-156.

Calignano, F., Giuffrida, F., & Galati, M. (2021). Effect of the build orientation on the mechanical performance of polymeric parts produced by multi jet fusion and selective laser sintering. *Journal of Manufacturing Processes*, *65*, 271-282.

Cano, A. J., Salazar, A., & Rodríguez, J. (2018). Effect of temperature on the fracture behavior of polyamide 12 and glass-filled polyamide 12 processed by selective laser sintering. *Engineering Fracture Mechanics*, *203*, 66-80.

Caulfield, B., McHugh, P. E., & Lohfeld, S. (2007). Dependence of mechanical properties of polyamide components on build parameters in the SLS process. *Journal of Materials Processing Technology*, *182*(1-3), 477-488.

Charoo, N. A., Barakh Ali, S. F., Mohamed, E. M., Kuttolamadom, M. A., Ozkan, T., Khan, M. A., & Rahman, Z. (2020). Selective laser sintering 3D printing–an overview of the technology and pharmaceutical applications. *Drug Development and Industrial Pharmacy*, *46*(6), 869-877.

Dadbakhsh, S., Verbelen, L., Verkinderen, O., Strobbe, D., Van Puyvelde, P., & Kruth, J.-P. (2017). Effect of PA12 powder reuse on coalescence behaviour and microstructure of SLS parts. *European Polymer Journal*, *92*, 250-262.

de Oliveira Setti, G., Fernandes de Oliveira, M., Alves Maia, I., Vicente Lopes da Silva, J., Savu, R., & Joanni, E. (2014). Correlation between mechanical and surface properties of SLS parts. *Rapid Prototyping Journal*, *20*(4), 285-290.

Dupin, S., Lame, O., Barrès, C., & Charmeau, J.-Y. (2012). Microstructural origin of physical and mechanical properties of polyamide 12 processed by laser sintering. *European Polymer Journal*, *48*(9), 1611-1621.

El Magri, A., Bencaid, S. E., Vanaei, H. R., & Vaudreuil, S. (2022). Effects of Laser Power and Hatch Orientation on Final Properties of PA12 Parts Produced by Selective Laser Sintering. *Polymers*, *14*(17), 3674.

Hopkinson, N., Majewski, C. E., & Zarringhalam, H. (2009). Quantifying the degree of particle melt in Selective Laser Sintering®. *CIRP Annals*, *58*(1), 197-200.

Majewski, C., Zarringhalam, H., & Hopkinson, N. (2008). Effect of the degree of particle melt on mechanical properties in selective laser-sintered Nylon-12 parts. *Proceedings of the Institution of Mechanical Engineers, Part B: Journal of Engineering Manufacture*, *222*(9), 1055-1064.

Mwania, F. M., Maringa, M., & Van der Walt, K. (2020). A review of methods used to reduce the effects of high temperature associated with polyamide 12 and polypropylene laser sintering. *Advances in Polymer Technology*, *2020*, 1-11.

Obst, P., Launhardt, M., Drummer, D., Osswald, P. V., & Osswald, T. A. (2018). Failure criterion for PA12 SLS additive manufactured parts. *Additive Manufacturing*, *21*, 619-627.

Olejarczyk, M., Gruber, P., & Ziółkowski, G. (2020). Capabilities and limitations of using Desktop 3-D printers in the laser sintering process. *Applied Sciences*, *10*(18), 6184.

Rajesh, R., Sudheer, S., & Kulkarni, M. V. (2015). Selective laser sintering process–a review. *Int. J. Curr. Eng. Sci. Res*, *2*, 2393-8374.

Rodríguez, A. G., Mora, E. E., Velasco, M. A., & Tovar, C. A. N. (2023). Mechanical properties of polyamide 12 manufactured by means of SLS: Influence of wall thickness and build direction. *Materials Research Express*, *10*(10), 105304.

Rosso, S., Meneghello, R., Biasetto, L., Grigolato, L., Concheri, G., & Savio, G. (2020). In-depth comparison of polyamide 12 parts manufactured by multi jet fusion and selective laser sintering. *Additive Manufacturing*, *36*, 101713.

Roszak, R., Schob, D., Sagradov, I., Kotecki, K., Sparr, H., Maasch, P., Franke, R., & Ziegenhorn, M. (2021). Experimental determination and numerical simulation of temperature dependent material and damage behaviour of additively manufactured polyamide 12. *Mechanics of Materials*, *159*, 103893.

Schob, D., Richter, L., Kotecki, K., Kurpisz, D., Roszak, R., Maasch, P., & Ziegenhorn, M. (2023). Characterization and simulation of shear-induced damage in selective-laser-sintered polyamide 12. *Materials*, *17*(1), 38.

Schob, D., Roszak, R., Sagradov, I., Sparr, H., Ziegenhorn, M., Kupsch, A., Léonard, F., Müller, B., & Bruno, G. (2019). Experimental determination and numerical simulation of material and damage behaviour of 3D printed polyamide 12 under quasi-static loading. *Archives of Mechanics, 71*(4-5), 507-526.

Senthilkumaran, K., Pandey, P. M., & Rao, P. V. M. (2009). Influence of building strategies on the accuracy of parts in selective laser sintering. *Materials & Design*, *30*(8), 2946-2954.

Simha Martynková, G., Slíva, A., Kratošová, G., Čech Barabaszová, K., Študentová, S., Klusák, J., Brožová, S., Dokoupil, T., & Holešová, S. (2021). Polyamide 12 materials study of morpho-structural changes during laser sintering of 3d printing. *Polymers*, *13*(5), 810.

Sindinger, S.-L., Kralovec, C., Tasch, D., & Schagerl, M. (2020). Thickness dependent anisotropy of mechanical properties and inhomogeneous porosity characteristics in laser-sintered polyamide 12 specimens. *Additive Manufacturing*, *33*, 101141.

Stichel, T., Frick, T., Laumer, T., Tenner, F., Hausotte, T., Merklein, M., & Schmidt, M. (2017). A Round Robin study for selective laser sintering of polyamide 12 : Microstructural origin of the mechanical properties. *Optics & Laser Technology*, *89*, 31-40.

Stoia, D. I., Linul, E., & Marsavina, L. (2019). Influence of manufacturing parameters on mechanical properties of porous materials by selective laser sintering. *Materials*, *12*(6), 871.

Tomanik, M., Żmudzińska, M., & Wojtków, M. (2021). Mechanical and structural evaluation of the PA12 desktop selective laser sintering printed parts regarding printing strategy. *3D Printing and Additive Manufacturing*, *8*(4), 271-279.

Toth-Taşcău, M., Raduta, A., Stoia, D. I., & Locovei, C. (2012). Influence of the Energy Density on the Porosity of Polyamide Parts in SLS Process. *Solid State Phenomena*, *188*, 400-405.

Usher, J. S., Gornet, T. J., & Starr, T. L. (2013). Weibull growth modeling of laser-sintered nylon 12. *Rapid Prototyping Journal*, *19*(4), 300-306.

Zárybnická, L., Petrů, J., Krpec, P., & Pagáč, M. (2022). Effect of Additives and Print Orientation on the Properties of Laser Sintering-Printed Polyamide 12 Components. *Polymers*, *14*(6), 1172.

Author(s) Information

Boukhoulda Farouk Benallel
Djillali Liabes University of Sidi Bel Abbes, Department of Mechanics, Faculty of Technology, Laboratory of Structural and Solid Mechanics, P.O. Box 89, Ben Mhidi City, Sidi Bel Abbes, 22000, Algeria
Contact e-mail: *farouk.boukhoulda@univ-sba.dz*

Djellal Kouider
Djillali Liabes University of Sidi Bel Abbes, Department of Mechanics, Faculty of Technology, Laboratory of Structural and Solid Mechanics, P.O. Box 89, Ben Mhidi City, Sidi Bel Abbes, 22000, Algeria

Bendine Kouider
Djillali Liabes University of Sidi Bel Abbes, Department of Mechanics, Faculty of Technology, Laboratory of Structural and Solid Mechanics, P.O. Box 89, Ben Mhidi City, Sidi Bel Abbes, 22000, Algeria

Boukhoulda Abdelaziz
Djillali Liabes University of Sidi Bel Abbes, Department of Mechanics, Faculty of Technology, Laboratory of Structural and Solid Mechanics, P.O. Box 89, Ben Mhidi City, Sidi Bel Abbes, 22000, Algeria

To cite this article:

Benallel, B. F., Kouider, D., Kouider, B., & Abdelaziz, B. (2025). Impact of printing orientation on the mechanical properties of selectively laser sintered PA12. *The Eurasia Proceedings of Science, Technology, Engineering and Mathematics (EPSTEM), 38,* 401-414.

The Eurasia Proceedings of Science, Technology, Engineering & Mathematics (EPSTEM)
ISSN: 2602-3199

The Eurasia Proceedings of Science, Technology, Engineering and Mathematics (EPSTEM), 2025

Volume 38, Pages 415-422

IConTES 2025: International Conference on Technology, Engineering and Science

Performance and Efficiency of Redesign Induction Motor Using Asymmetric Windings

Hussein G. Abdulkareem
Mustansiriyah University

Ennam A. Ali
Mustansiriyah University

Abstract: This paper investigates the performance and efficiency of redesigning squirrel-cage induction motors using fractional-slot asymmetric windings, particularly when the number of slots per pole per phase results in a fraction whose denominator is a multiple of the number of phases. Under such circumstances, conventional methods for calculating winding factors become ineffective due to the high degree of asymmetry and complex harmonic distribution. To address this challenge, three different winding configurations were proposed and systematically analyzed in terms of harmonic content, winding factors, and magneto motive force symmetry. Electromagnetic simulations were performed using the FLINT software to evaluate and compare their operational performance under rated conditions. The results demonstrated that a partially symmetrized asymmetric winding (Option III) could achieve acceptable thermal, magnetic, and electromagnetic performance, with a predicted decrease in rated power of approximately 12.5% compared to the standard symmetric winding. These findings support the feasibility and potential advantages of using asymmetric windings in motor repair, redesign, and performance optimization for machines up to around 3.5 kW.

Keywords: Asymmetry, Balancing, The denominator of the fraction, Induction motor, Electrical and mechanical characteristic

Introduction

In the practice of repairing asynchronous machines (Lercel et al., 2024), there are situations where performing the rewinding of the stator winding of the motor with a number of poles p, which is a multiple of the number of phases m, is only possible when using asymmetric windings. In this case, it is necessary to determine the changes in the technical parameters of the repaired motor compared to the serial analogy (Bishop, 2022; Anthony et al., 2024). This can be achieved through electromagnetic calculations. The generally accepted approach to performing these calculations, which is based on the traditional representation of winding factors, is not applicable in this case. The formal definition of these factors for each phase (Bukšnaitis, 2009; Dorrell, 2014; Bishop, 2022) does not provide any useful information and does not allow for the correct determination of the winding data of the motor (Jannati et al., 2015).

The main objective of this research is to develop a redesigned induction motor with a different speed and pole number from the original machine by rewinding or replacing its faulty windings. This approach aims not only to restore the motor's operability but also to create a modified machine with new operational characteristics. Special attention is given to evaluating the electromagnetic properties of the redesigned motor and analyzing how the change in pole number influences the harmonic content and its overall performance.

Method

- This is an Open Access article distributed under the terms of the Creative Commons Attribution-Noncommercial 4.0 Unported License, permitting all non-commercial use, distribution, and reproduction in any medium, provided the original work is properly cited.

- Selection and peer-review under responsibility of the Organizing Committee of the Conference

© 2025 Published by ISRES Publishing: www.isres.org

It is known that, under the condition of the fraction denominator **d** being a multiple of the number of phases **m**, it is impossible to create a symmetrical multi-phase winding for the motor. Such asymmetric windings have not found application in serial production of electrical machines (Stock et al., 2023) due to the sharp deterioration of technical parameters such as rated power, winding overheating values, and efficiency. When using such asymmetric windings, the harmonic composition of the magneto motive forces (MMF) of the winding deteriorates sharply, resulting in both forward and reverse rotating harmonics, creating elliptical magnetic fields in the working air gap. The manifestation of these harmonics is especially dangerous with respect to the operating harmonic. As a result, additional losses increase, torque curve dips appear, the non-sinusoidal nature of the electromotive forces (EMF) at the generator terminals increases, and energy and vibro-acoustic indicators decrease, leading to a reduction in power compared to serial machines.

The Proposed Asymmetrical Machine

The study suggests the possibility of applying asymmetric fractional windings in repair production conditions and comparing the extent of their use with serial analogs. To solve this task, it is necessary not only to design a winding with the minimum level of asymmetry, manufacture and place it in the slots of the asynchronous motor, but also to determine its operating properties.

For denominators of the fraction **d** that are multiples of the number of phases **m**, the windings are characterized by an unacceptably high level of asymmetry, primarily concerning the operating harmonic **v**. To reduce this level, it is necessary to redistribute the active coil sides (ACS) in such a way as to reduce or completely eliminate the asymmetry, at least in the operating harmonic (Esam et al., 2024) This transformation, which involves either transforming the numerical series of the winding (Demir & Aydin, 2016) or changing the number of turns in the coils (Tak et al., 2022), is referred to as symmetrization. The first stage of solving the set task involves designing windings with the minimum possible level of asymmetry. This stage was carried out using the symmetrization method (Marfoli, 2020).

For example, the redesign of the serial asynchronous motor 4A112MV8U3 is considered, which has 48 slots with 2p = 8 poles on the same stator, compared to 2p = 6 poles when p is the number of pole pairs (Demir & Aydin, 2016). In this case, the number of slots per pole and phase in the repaired motor will be: q = Z / (2 pm) = 8/3, where m = 3.

Under these conditions, the possibility arises to design windings with identical numbers of turns in the coils, which are characterized by the following options for the repeating part of the winding's numerical series:

I – 3, 3, 2, 3, 3, 2, 3, 3, 2;
II – 3, 3, 2, 2, 3, 3, 3, 3, 2;
III – 3, 3, 2, 3, 2, 3, 2, 3, 3.

Each of these options corresponds to windings with a possible distribution of phase zones of one layer over half of the winding space from 24 slots (Pyrhonen et al., 2013; Staszak , 2023) (Fig. 1).

Option I	1	3	5	7	9	11	13	15	17	19	21	23	№№ *Slots*
	A	*z*	*B*	*x*	*C*	*y*	*A*	*z*	*B*				*Phase zones*
Option II	1	3	5	7	9	11	13	15	17	19	21	23	№№ *Slots*
	A	*z*	*B*	*x*	*C*	*y*	*A*	*z*	*B*				*Phase zones*
Option III	1	3	5	7	9	11	13	15	17	19	21	23	№№ *Slots*
	A	*z*	*B*	*x*	*C*	*y*	*A*	*z*	*B*				*Phase zones*

Figure 1. Distribution of phase zones 1/2 of the winding with the number of poles 2p = 6 and the number of slots Z = 48 for I, II and III options

The windings distribution map for III option with the phase zones is shown in Fig 2. It is easy to see that the winding in option I is characterized by maximum asymmetry, which is sharply manifested already in relation to the number of active coil sides (ACS) — the phase zones A and C each contain 18 ACS, while phase B contains 12 ACS. In option II, phase zones A and B each contain 15 ACS, while phase C contains 18 ACS. Option III is fully symmetrical in this regard (Joksimović, 2011; Vukosavic, 2012; Hagedorn et al., 2018).

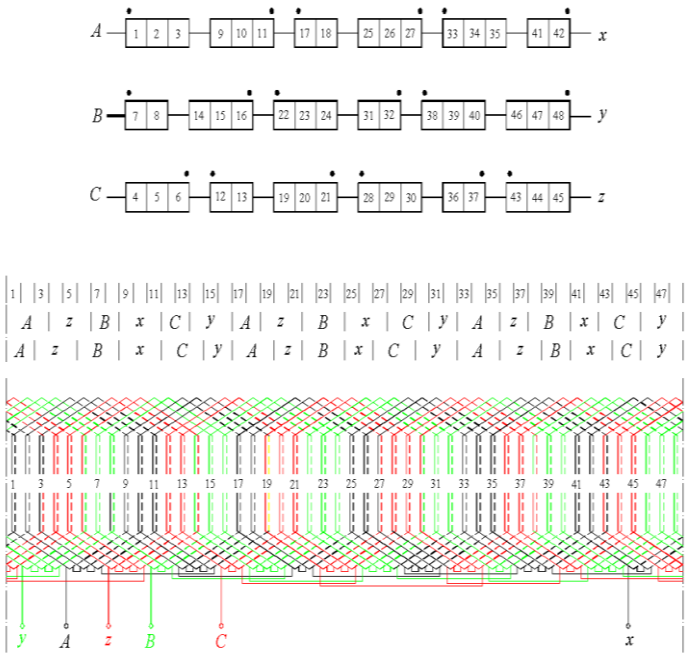


Figure 2. The map for windings distribution with the number of poles 2p = 6 and the number of slots being, Z = 48 for III option.

A comparison of the options in terms of symmetry level with respect to the operating harmonic of the MMF **ν = p = 3** based on vector diagrams (Marfoli, 2020) leads to the following results. In option I, the amplitudes of the MMF are $\mathbf{F_A = F_C = 17.09}$, $\mathbf{F_B = 11.77}$, and their relative shifts are: $\mathbf{\varphi_{AB} = \varphi_{CB} = 123.75^o}$, $\mathbf{\varphi_{AC} = 112.5^o}$ (Krause et al., 2002; Tang & Brown, 2018)**.** Thus, the amplitude mismatch...

$$\Delta F_{\text{I}} = \frac{F_A - F_B}{F_A} = \frac{17{,}08 - 11{,}76}{17{,}08} = 0{,}31 \qquad (1)$$

In option II, the amplitudes of the resulting MMF vectors are $\mathbf{F_A = F_B = 4.786}$, $\mathbf{F_C = 5.586}$, and their relative shifts are:

$\mathbf{\varphi_{AB} = 121.68°}$, $\mathbf{\varphi_{CB} = \varphi_{AC} = 119.16°}$. Thus, the amplitude mismatch...

$$\Delta F_{\text{II}} = \frac{F_A - F_C}{F_A} = \frac{4{,}786 - 5{,}586}{4{,}786} = 0{,}16 \qquad (2) \qquad (2)$$

The angular mismatch of the MMF vectors is

$\mathbf{\Delta\varphi = 121.68° - 119.16° = 2.52}$

In option III, the amplitudes of the resulting MMF vectors are $\mathbf{F_A = F_C = 15.25}$, $\mathbf{F_B = 15.09}$, and their relative shifts are:

$\mathbf{\varphi_{AB} = \varphi_{CB} = 120.875°}$, $\mathbf{\varphi_{AC} = 118.25°}$. Thus, the amplitude mismatch...

$$\Delta F_{\text{III}} = \frac{F_A - F_B}{F_A} = \frac{15{,}25 - 15{,}09}{15{,}25} = 0{,}01 \qquad (3) \qquad (3)$$

The angular mismatch of the MMF vectors is $\mathbf{\Delta\varphi = 120.875° - 118.25° = 2.62°}$.

Based on the comparison results of the options according to the number of coils in the phases and with respect to the operating harmonic **ν**, option I is immediately excluded. The comparison of options II and III was

performed based on a detailed harmonic analysis, which relies on the representation of the symmetrical components of the winding factors **Kwdv**, **Kwrv** (Tak, 2022), using the corresponding program (Bukšnaitis, 2009) implemented in the MathCAD environment (Table 1), where:

v – harmonic order;
Kwdv – winding factors for the forward sequence of the **v**-th order harmonic;
Kwrv – winding factors for the reverse sequence of the **v**-th order harmonic;

$H_{(d.r)v} = \frac{K_{wv} \cdot P}{K_{wp} \cdot V}$ – relative amplitude of the MMF for the forward and reverse sequence of the **v**-th order harmonic, respectively.

Table 1.Comparative harmonic analysis of II and III options of windings

N	kwdvII	kwrvII	HdvII	HrvII
Option II				
3	0.947	0.042	1.000	0.045
9	0.052	0.011	0.018	0.004
15	0.154	0.012	0.033	0.003
21	0.062	0.086	0.009	0.013
Option III				
1	0.0409	0.0134	0.1290	0.0423
3	0.9502	0.0051	1.0000	0.0053
5	0.0416	0.0231	0.0263	0.0146
7	0.0081	0.0313	0.0037	0.0141
9	0.0129	0.0205	0.0045	0.0072
11	0.0184	0.0231	0.0053	0.0066
13	0.0346	0.0374	0.0084	0.0091
15	0.0378	0.1677	0.0082	0.0353
17	0.0275	0.0409	0.0102	0.0102
19	0.0346	0.0027	0.0115	0.0009
21`	0.1045	0.0205	0.0157	0.0030
23	0.0395	0.0081	0.0108	0.0022

I will conduct a comparative analysis under the assumption that the specified windings are intended to be placed in the slots of the stator of a short-circuited asynchronous motor designed for long-term operation in the motor mode. In this case, for symmetrical windings, the greatest danger is posed by the forward-rotating higher harmonics, as they can cause dips in the motor torque curve **M** and deteriorate the starting and overload characteristics of the motor. A comparison of the data shows that, despite the higher number of such harmonics in option III, it is preferable to option II for the most significant higher harmonics (**Hd5 = 0.0263** and **Hd21 = 0.0157**), whereas the most significant harmonics in option II are **Hd15 = 0.033** and **Hd9 = 0.018**.

Furthermore, the winding of option III is characterized by a slightly higher winding factor for the operating harmonic: **Kwd3 = 0.9504** compared to **Kwd3 = 0.947**, which should result in improved energy performance. The presence of a relatively significant lower harmonic with a relative amplitude of **Hd1 = 0.129** will slightly reduce this advantage but will contribute to some increase in the torque in the motor mode. However, the main drawback of the second option lies in the possibility of creating a fairly noticeable reverse-rotating magnetic field for the operating harmonic, with a relative amplitude of **4.5% (Hd1 = 0.045)** of the main harmonic.

The negative impact of higher harmonics on the starting characteristics of low-power asynchronous motors is minimal, but the asymmetry of the operating harmonic will cause a sharp deterioration in these characteristics regardless of the machine's size. As a result of the analysis, the winding of option III was selected for real use.

In the next stage, it is necessary to choose software that allows for an adequate determination of the operating properties of asynchronous motors with the windings of options II and III. The software should meet the following requirements:

- The subroutine for calculating winding factors must correspond to their interpretation outlined in (Tak et al., 2022), i.e., it should be based on the method of symmetrical components.

- It must be able to calculate the specified factors. The software that meets these requirements is the electromagnetic calculation program for short-circuited asynchronous motors, **FLINT** (Tak et al., 2022).

The correctness of selecting this program will be verified by testing two serial asynchronous motors: **4A112MV8** and **4A112MV6** (Table 2, where **$P2_н$** is the rated power of the motor, **$I_{1ф}$** is the phase current, **η** is the efficiency, **$n_н$** is the rated speed of the motor, **K_M** is the multiplicity of the maximum torque of the motor, and **$K_П$** is the multiplicity of the starting torque of the motor).

Table 2. (*a)* and (*b),* Comparative data of two serial asynchronous motors: 4A112MV8 and 4A112MV6

	P_{2N} kW	I_{1ph} A	η %	Cosφ
	Motor data4A112MB8			
Reference Serial (Kravchik et al., 2022)	3.0	7.72	79.5	0.74
Calculated	3.0	7.33	79.5	0.78
The relative discrepancy Δ%	0	5	0	5
	Motor data4A112MB6			
Reference Serial (Kravchik et al., 2022)	4.0	9.12	82	0.81
Calculated	4.0	8.99	82.4	0.817
The relative discrepancy Δ%	0	1	0.4	0.8

a

	N r.p.m	K_M	$K_п$
	Motor data4A112MB8		
Reference Serial (Kravchik et al., 2022)	707	2.2	1.90
Calculated	712	2.22	1.89
The relative discrepancy Δ%	0.7	1	0.1
	Motor data4A112MB6		
Reference Serial (Kravchik et al., 2022)	953	9.12	82
Calculated	951	8.99	82.4
The relative discrepancy Δ%	0.2	1	0.4

b

The relative discrepancies between the reference and calculated data do not exceed 5%, which is quite acceptable for engineering calculations and allows the use of the specified program for computational experiments. For this experiment, the motor **4A112MV8** was chosen as the base, where the replacement of the symmetrical serial winding with options II and III of asymmetric windings was considered. The nominal power **$P2_н$ = 3.5 kW** was selected based on the conditions for maintaining the multiplicities of the starting and maximum torques and the level of stator winding overheating.

In the first stage, the mechanical characteristics were calculated for the cases of applying the II and III winding options in the studied motor. The dependencies *MIII = f(s)* and *MII = f(s)* were calculated for applying option III and option II, where **s** is the slip of the asynchronous motor (Fig. 3). As can be seen from the comparison of these dependencies, the use of option II results in a sharp (11%) decrease in the maximum torque **M_{II}**, as was determined by the results of the analysis.

Therefore, in the subsequent calculations, option II for the winding was not considered, and the operating characteristics were determined only for the motor with the winding from option III, where **P_1** is the consumed power, **P_2** is the useful power at the shaft (Fig. 4). The main nominal data were obtained from the calculation results (Table 3).

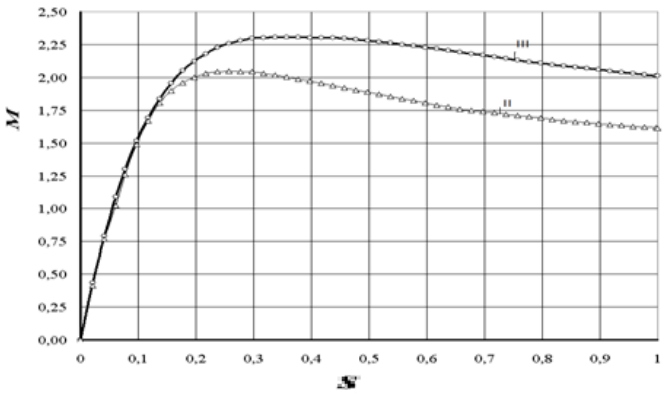


Figure 3. Starting characteristic M = f(s) of the motor with windings of options II and III.

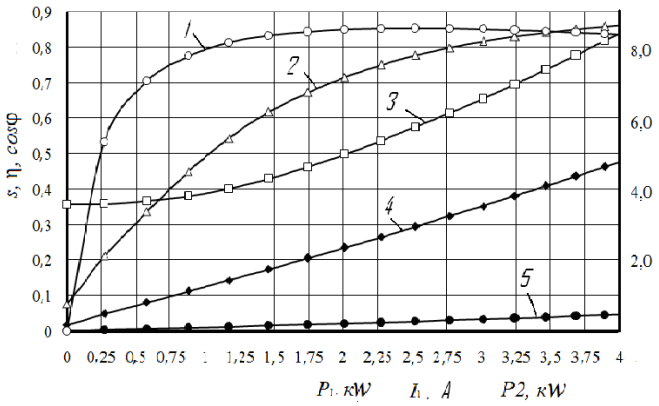


Figure 4. Operating characteristics of the motor 4A112MB6: η(1), cosφ(2), I1Φ(3), P2(4), S(5)..

The overheating of the symmetrized stator winding in option III was 60°C, while the corresponding values in the serial motors 4A112MB6 and 4A112MB8 were 75°C and 70°C, respectively.

Table 3. (a) and (b) Comparative data of the nominal parameters of the compared motors.

	P2N kW	I1ph A	η %	Cosφ
Motor data4A112MB6				
Reference Serial (Kravchik et al., 2022)	4.0	9.12	82	0.81
Estimated Serial	4.0	8.99	82.4	0.817
Estimated selected	3.5	7.4	84.0	0.85

a

	N r.p.m	KM	Kп
Motor data4A112MB6			
Reference Serial (Kravchik et al., 2022)	953	2.5	2.0
Estimated Serial	951	2.49	2.0
Estimated selected	949	2.4	2.0

b

Results and Conclusion

This study explored the performance and efficiency of a redesigned squirrel-cage induction motor using asymmetric windings as a rewinding technique. The results demonstrated that by selectively increasing the

number of turns in one of the stator coil sides, it is possible to alter the magnetic field distribution and improve certain aspects of motor behaviour. Experimental tests showed that the redesigned motor retained acceptable torque and efficiency levels while potentially offering cost-effective and resource-saving benefits during the rewinding process. The method also opens the door for simplified control of motor speed and direction in specific applications.

However, this study is subject to several limitations. The proposed asymmetric winding configuration was tested only on a three-phase, small-capacity squirrel-cage induction motor (up to 3.5 kW), which may limit the generalizability of the results to higher-power machines. In this case, the expected decrease in nominal power will be approximately 12.5%. Additionally, the analysis primarily focused on steady-state performance and did not extensively cover dynamic behavior under varying loads or starting conditions. Thermal effects and long-term reliability aspects of the rewound motor were not examined in detail. Finally, the study did not account for cost-benefit analysis or manufacturing constraints, which may influence the practical adoption of the proposed rewinding technique in industrial settings.

Future research can address these limitations by expanding testing to a broader range of motor types and power ratings, analyzing dynamic and thermal performance, and conducting durability assessments under industrial load conditions. Furthermore, integration with modern control systems or power electronics may reveal additional benefits or applications of the asymmetric winding concept.

Scientific Ethics Declaration

* The authors declares that the scientific ethical and legal responsibility of this article published in EPSTEM journal belongs to the authors.

Conflict of Interest

* The authors declare that they have no conflicts of interest

Funding

* This research received no specific grant from any funding agency in the public, commercial, or not-for-profit sectors.

Acknowledgements or Notes

* This article was presented as an oral presentation at the International Conference on Technology, Engineering and Science (www.icontes.net) held in Antalya/Türkiye on November 12-15, 2025.

References

Anthony, Z., Bandri, S., Warmi, Y., & Dewi Rachman, A. Y. (2024). A winding design for improving 3-phase induction motor performance. *International Journal of Electrical & Computer Engineering, 14*(3).

Bishop, T. H. (2022, May). EASA AEMT study of motor repair impact on efficiency of premium efficiency (IE3) motors. In *International Conference on Energy Efficiency in Motor Driven Systems* (pp. 23–39). Springer.

Bukšnaitis, J. (2009). Methods for determination of winding factors of alternating-current. *Elektronika ir Elektrotechnika, 89*(1), 83–86.

Demir, Y., & Aydin, M. (2016). A novel dual three-phase permanent magnet synchronous motor with asymmetric stator winding. *IEEE Transactions on Magnetics, 52*(7), 1–5.

Dorrell, D. G. (2014). A review of the methods for improving the efficiency of drive motors to meet IE4 efficiency standards. *Journal of Power Electronics, 14*(5), 842–851.

Esam, H., Ali, A. J., & Shanshal, A. K. (2024). Performance improvement of squirrel cage induction motor: A review paper. In *AIP Conference Proceedings* (Vol. 3105, No. 1, p. 080004). AIP Publishing.

Hagedorn, J., Blanc, F. S. L., & Fleischer, J. (2018). *Handbook of coil winding*. Springer.

Jannati, M., Sutikno, T., Idris, N. R. N., & Aziz, M. J. A. (2015). Modeling of balanced and unbalanced three-phase induction motor under balanced and unbalanced supply based on winding function method. *International Journal of Electrical and Computer Engineering, 5*(4), 644.

Joksimović, G. (2011). AC winding analysis using a winding function approach. *International Journal of Electrical Engineering Education, 48*(1), 34-52.

Krause, P. C., Wasynczuk, O., Sudhoff, S. D., & Pekarek, S. (2002). *Analysis of electric machinery and drive systems* (Vol. 2). IEEE Press.

Kravchik, A. E., Shlaf, M. M., Afonin, V. I., & Sobolenskaya, E. A. (1982). *Asinkhronnye dvigateli serii 4A. Spravochnik*. Jenergoatomizdat.

Lercel, D., Patankar, M., & Steckel, R. (2024). Assessing past airworthiness directives and how safety management systems may benefit aviation product design and manufacturing. *Journal of Aviation/Aerospace Education & Research, 33*(2), 6.

Marfoli, A. (2020). *Performance enhancement of squirrel cage induction motor through optimised electromagnetic design* (Doctoral dissertation). University of Nottingham.

Pyrhonen, J., Jokinen, T., & Hrabovcova, V. (2013). *Design of rotating electrical machines*. John Wiley & Sons.

Staszak, J. (2023). AC distributed winding with low higher spatial harmonics content in MMF distribution. *Energies, 16*(14), 5430.

Stock, A., Schlögl, S., & Groth, A. (2023). Tell me, what are you most afraid of? Exploring the effects of agent representation on information disclosure in human-chatbot interaction. In *International Conference on Human-Computer Interaction* (pp. 179–191). Springer.

Tak, N., Chattopadhyay, S. K., & Chakraborty, C. (2022). Single-sourced double-stage multilevel inverter for grid-connected solar PV systems. *IEEE Open Journal of the Industrial Electronics Society, 3*, 561–581.

Tang, N., & Brown, I. P. (2018). Framework and solution techniques for suppressing electric machine winding MMF space harmonics by varying slot distribution and coil turns. *IEEE Transactions on Magnetics, 54*(5), 1–12.

Vukosavic, S. N. (2012). *Electrical machines*. Springer.

Author(s) Information

Hussein G. Abdulkareem
Electrical Engineering Department. College of Engineering, Mustansiriyah University, Baghdad, P.O.BOX (46049), Bab Al-Muadham, Iraq
Contact e-mail: *hussein_ghani@uomustansiriyah.edu.iq*

Ennam A. Ali
Electrical Engineering Department. College of Engineering, Mustansiriyah University, Baghdad, P.O.BOX (46049), Bab Al-Muadham, Iraq

To cite this article:

Abdulkareem, H. G., & Ali, E. A. (2025). Performance and efficiency of redesign induction motor using asymmetric windings. *The Eurasia Proceedings of Science, Technology, Engineering and Mathematics (EPSTEM), 38,* 415-422.

The Eurasia Proceedings of Science, Technology, Engineering & Mathematics (EPSTEM)
ISSN: 2602-3199

The Eurasia Proceedings of Science, Technology, Engineering and Mathematics (EPSTEM), 2025

Volume 38, Pages 423-432

IConTES 2025: International Conference on Technology, Engineering and Science

Synthesis and Characterization of Biochar and Nano-Biochar Composites Derived from Biomass (*Colutea cilicica*) for the Removal of Cationic Dyes from Aqueous Solutions

Erol Pehlivan
Konya Technical University

Busra Ozkok
Konya Technical University

Abstract: In this study, the removal of Methylene blue (MB) and Malachite green (MG) dyestuffs from aqueous solutions was investigated using biochar and iron-modified biochar derived from biomass (*Colutea cilicica*). Biochar was prepared by pyrolyzing biomass at 500 °C with a heating rate of 10 °C/min, and further modified with nanoscale zero-valent iron (nZVI) to obtain nZVI-biochar. The adsorption performance of both biochar and nZVI-biochar was systematically evaluated under varying experimental conditions, including solution pH, contact time, adsorbent dosage, and initial dye concentration. Equilibrium and kinetic studies were performed, along with thermodynamic analyses at different temperatures. The optimum pH for dye removal was determined as 7.0. Adsorption equilibrium was reached within 120 min, and the kinetic data were best described by the pseudo-second-order model. Equilibrium data fitted well to the Langmuir isotherm model. The maximum adsorption capacities were 70.67 mg/g (biochar) and 81.17 mg/g (nZVI-biochar) for MB, and 61.43 mg/g (biochar) and 83.13 mg/g (nZVI-biochar) for MG. Overall, the modified nZVI-biochar composite exhibited significantly enhanced adsorption capacity compared to unmodified biochar. The synthesized nano-biochar composite can be proposed as a potential alternative adsorbent for the removal of cationic dyes from wastewater.

Keywords: Adsorption, Biomass, Biochar, Nano-iron composite, Cationic dyes

Introduction

Water pollution, a major contributor to overall environmental degradation, remains one of the most pressing global challenges of the modern era. While technological advancements enhance human comfort and industrial efficiency, they also intensify the rate at which natural ecosystems are disrupted. In light of the accelerating decline in clean and accessible freshwater resources and the increasing likelihood of severe scarcity in the near future the development and optimization of wastewater treatment and recovery technologies have become imperative. During the natural hydrological cycle, the introduction of pollutants from diverse anthropogenic and natural origins results in substantial degradation of water quality, thereby posing serious risks to human health, ecological integrity, and long-term environmental sustainability (Rathi et al., 2021; Erkmen et al., 2019).

One significant form of industrial pollution is dye contamination, which arises predominantly from the operations of the textile and dyeing industries. Owing to the continuous expansion of these sectors, large quantities of synthetic dyes are regularly introduced into the water, contributing to increasing levels of dye-laden effluents in aquatic environments. Due to factors such as the increasing diversity of dyes and the large volumes of dye-laden water used and subsequently discharged during textile dyeing processes, these effluents are classified as high-priority wastewater streams requiring immediate and effective treatment. Water containing dye pollution prevents the sun's rays from reaching the environment by giving color to the receiving environments, which gives negative

- This is an Open Access article distributed under the terms of the Creative Commons Attribution-Noncommercial 4.0 Unported License, permitting all non-commercial use, distribution, and reproduction in any medium, provided the original work is properly cited.

- Selection and peer-review under responsibility of the Organizing Committee of the Conference

© 2025 Published by ISRES Publishing: www.isres.org

ecological consequences (Yaseen & Scholz, 2019; Erkuş et al, 2018). Adsorption, which is among the advanced treatment methods, has been preferred recently. Adjustable process conditions and high treatment efficiency provide advantages. However, scientists have focused on the search for an economical adsorbent in recent years due to the high volume of wastewater that needs to be treated and the costs of adsorbents. A critical point to be considered is that the adsorbent to be used not only cleans wastewater but also does not contain toxic chemicals. Biomasses, which are environmentally friendly, easily available and economical materials, stand out as a potential adsorbent (Parlayıcı & Pehlivan, 2021).

Biomass is a broad term encompassing all non-fossilized biological materials derived from living organisms. Typical biomass sources include plant components such as seeds, roots, leaves, and tree bark, as well as agricultural residues and various forms of animal waste. However, literature reports consistently show that the adsorption performance of untreated (raw) biomass is often inadequate for the efficient removal of toxic dyes from aqueous systems. As a result, numerous studies have focused on improving its adsorption capacity through additional processing techniques. These enhancement approaches frequently involve surface modification or chemical activation of the biomass, which serve to increase its surface area, introduce functional groups, and improve its overall structural properties, thereby enhancing its interaction with dye molecules (Erdogan, 2017).

Biochar, essentially a carbon-rich material derived from biological sources, has emerged as a promising adsorbent for wastewater treatment. Its applicability in this field has gained significant research attention in recent years. Owing to their inherently large surface area and highly porous architecture, biochars exhibit advantageous properties for surface-driven processes such as adsorption. Indeed, numerous studies have demonstrated the successful removal of toxic dyes from wastewater using biochar-based adsorbents (Baig et al., 2014; Parlayıcı & Pehlivan, 2023). Despite their potential for capturing dye molecules from aqueous media, biochar-based adsorbents also present certain limitations. Over time, pore blockage and the depletion of available functional groups capable of binding pollutants may hinder complete dye removal. One effective strategy to overcome these efficiency challenges is the incorporation of nanoparticles into biochar matrices to synthesize advanced composite adsorbents.

In this study, the seeds of *Colutea cilicica* were utilized as the raw biomass precursor. The synthesized biochar was subsequently modified with iron nano-particles. Equilibrium and thermodynamic investigations were conducted to evaluate the removal of MB and MG dyes from aqueous solutions, during which the effects of key adsorption parameters including pH, contact time, adsorbent dosage, and initial dye concentration were systematically examined to determine the optimal operating conditions. Experimental data were analyzed using the Langmuir, Freundlich, and Temkin isotherm models. Kinetic studies were performed to elucidate the influence of contact time on the adsorption process. Furthermore, temperature-dependent dye removal experiments enabled the calculation of Gibbs free energy, enthalpy, and entropy values, thereby facilitating the identification of the most favorable operational temperature. Overall, the findings demonstrate that both the pristine and modified biochars are efficient adsorbents for the removal of dyes from aqueous media.

Results and Discussion

Materials and Experimentation

Iron (III) chloride hexahydrate, iron(II) sulfate heptahydrate, and ammonia (NH_3) were supplied by Merck. Methylene Blue (MB) and Malachite Green (MG) dyes were obtained from Acros Organics (New Jersey, USA). All chemicals used in the experiments were of analytical grade. *Colutea cilicica* tree seeds (Turkish “Patlangaç” tree seeds were collected from a field near Konya, Türkiye, and utilized as the biomass source for adsorbent synthesis. For biochar preparation, a Magma Therm MT1210-B2 muffle furnace was used, and a Biosan PSU-10 orbital shaker and a glass-electrode pH meter (Apera Instruments pH700) were employed during the experiments. The concentrations of MB and MG were determined using a UV–visible spectrophotometer (Shimadzu UV-1700). FT-IR spectra were recorded using a Thermo Scientific Nicolet iS20 spectrometer, while XRD analysis was performed using a Europe model X-ray diffractometer. The microstructure of the adsorbent was examined with a scanning electron microscope (SEM, Zeiss Gemini SEM 500).

Preparation of Raw Material and Biochar

*Colutea cilic*ica seeds were cleaned to remove surface impurities, thoroughly washed, and subsequently dried. The dried seeds were ground into a fine powder using a laboratory mill. The resulting powder was washed several

times with 0.1 mol L^{-1} HCl, followed by repeated washing with distilled water, and then dried at room temperature for 24 h. The prepared biomass was converted into biochar through slow pyrolysis in a custom-designed stainless-steel reactor with a sealed steel lid, placed inside a muffle furnace. Pyrolysis was conducted under limited oxygen conditions and a nitrogen atmosphere at 400–500 °C for 3 h, with a controlled heating rate of 10 °C min^{-1}. After pyrolysis, the sample was cooled to room temperature and washed with 0.1 M HCl, followed by repeated rinsing with ultrapure water until a stable pH was achieved. The obtained *Colutea cilicica* biochar was oven-dried, ground using a laboratory grinder, and sieved to obtain uniform particle sizes (150–200 µm). The resulting biochar fraction was then used for composite synthesis.

Synthesis of Adsorbent

The preparation procedure for zero-valent iron *Colutea cilicica* biochar (nZVI-biochar) is illustrated in Figure 1. The nZVI-biochar composites were synthesized via a simple chemical co-precipitation method. For this purpose, 5 g of biochar adsorbent was weighed and transferred into a batch reactor vessel. Subsequently, 6 g of $FeCl_3 \cdot 6H_2O$ and 4 g of $FeSO_4 \cdot 7H_2O$ were added, followed by the addition of 50 mL of ultrapure water. The mixture was stirred using an orbital shaker to obtain a homogeneous suspension. The pH of the reaction medium was adjusted to 10 by the dropwise addition of 1 M NH_4OH. The reaction was maintained at 50 °C under continuous stirring for 1 h. The resulting nano-Fe^0 loaded biochar was filtered through filter paper and washed several times with ultrapure water to remove residual impurities. The synthesized biochar composite was dried in an oven at 40 °C for 24 h, repeatedly rinsed with deionized water, and then allowed to dry for an additional 24 h before being stored for further use.

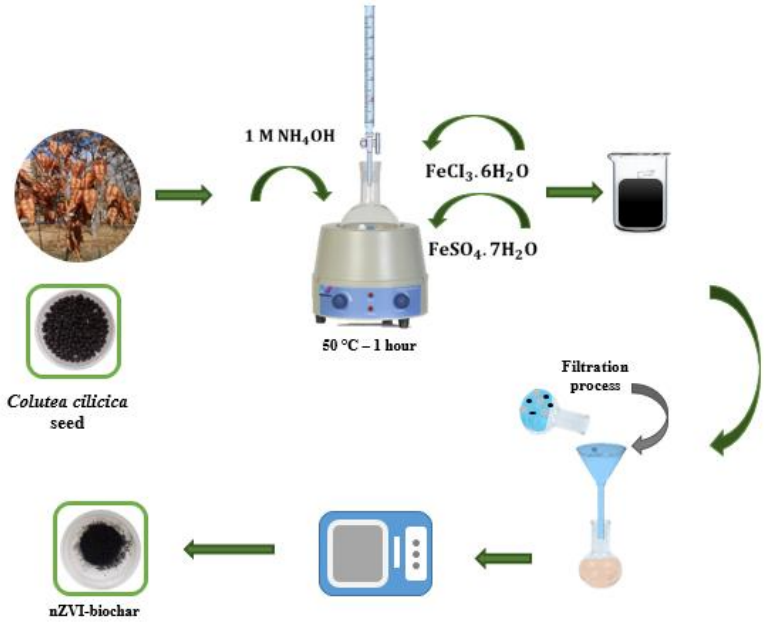


Figure 1. Schematic steps of nZVI-biochar synthesis

Batch Adsorption Experiments

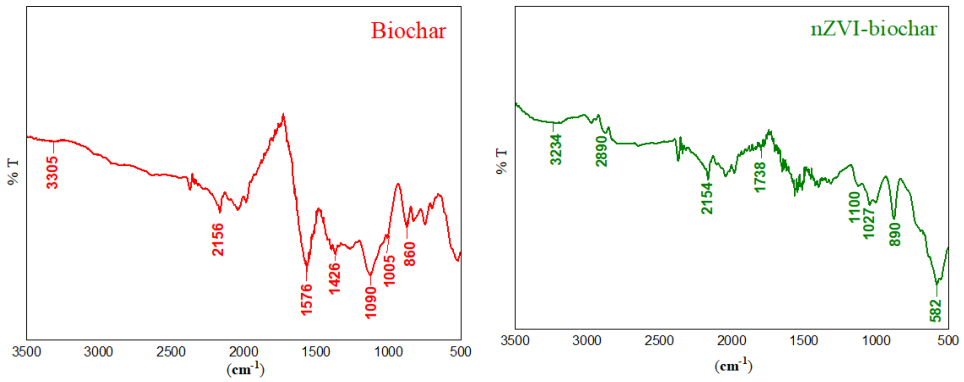
Adsorption experiments for MB and MG were initially conducted using 25 ppm MB and 50 ppm MG solutions, respectively. To evaluate the influence of various parameters on the adsorption efficiency and capacity of biochar and nZVI-biochar composites, a series of systematic batch experiments were performed in beakers at 25 °C. The parameters optimized included solution pH (2, 3, 4, 5, 6, 7, 8, and 9), initial dye concentration (15, 25, 50, 75, 100, and 125 mg L^{-1}), adsorbent dosage (0.001, 0.003, 0.005, 0.01, 0.015, and 0.02 g L^{-1}), contact time (20, 30, 45, 60, 90, 120, 150, 180, and 240 min), and temperature (25, 35, and 45 °C). To ensure the accuracy, reliability, and reproducibility of the experimental findings, all samples were analyzed in duplicate. For comparison of adsorption performance, both the composite material and pristine biochar were tested under identical conditions using standard MB and MG solutions. Following the adsorption process, the residual dye concentration in the filtrate was determined at regular intervals using UV–Vis spectrophotometry. Finally, adsorption capacity (q_e, mg g^{-1}) and removal efficiency (%) were calculated based on the differences between initial and final dye concentrations.

The concentrations of MG and MB in the filtrate were determined using a UV–Vis spectrophotometer (λ = 617 nm for MG and λ = 664 nm for MB). The percentage adsorption of MB and MG was calculated using Equations (1) and (2):

$$q_e = \frac{(C_o - C_e)V}{m} \quad (1)$$

$$Removal(\%) = \frac{(C_o - C_e)100}{C_o} \quad (2)$$

Structural and Morphological Characterization of the Nano-Composites and Biochar



(a) (b)

Figure 2. FT-IR diagram of biochar (a), nZVI-biochar (b)

Figure 2(a–b) presents the FT-IR spectra of the biochar and nZVI-biochar composites. The peaks observed around 1741 cm^{-1} in both biochar and nZVI-biochar correspond to the stretching vibrations of C=O bonds. The characteristic Fe–O vibration band appearing at 582 cm^{-1} is attributed to iron oxides, indirectly confirming the successful synthesis of magnetic biochar (Yi et al., 2020). In the nZVI-biochar adsorbent, the peak at 582 cm^{-1} further verifies the presence of iron components, while the peak at 890 cm^{-1} corresponds to the fingerprint region. In biochar, the peaks near 1600 cm^{-1} are associated with aromatic C=O ring stretching attributed to similar phytochemical components, whereas those around 1430 cm^{-1} likely arise from aromatic C–O ring stretching. The peak at 1090 cm^{-1} in biochar is assigned to C–O stretching vibrations. The peak at 2155 cm^{-1} in biochar, along with the peaks at 2154 cm^{-1} and 2890 cm^{-1} in nZVI-biochar, corresponds to the C≡C stretching of alkyne groups. Additionally, the peaks between 1027 and 1100 cm^{-1} in nZVI-biochar are attributed to the vibrational modes of C–O–C and C–O functional groups (Parlayıcı & Pehlivan, 2017). Overall, the FT-IR characterization results indicate that the waste biomass-derived biochars possess a wide variety of functional groups capable of participating in the biosorption of cationic dyes from aqueous media. The presence of numerous organic active groups (such as –OH, –CO, –COOH, C=O, and –CH) significantly contributes to the adsorption of dye molecules.

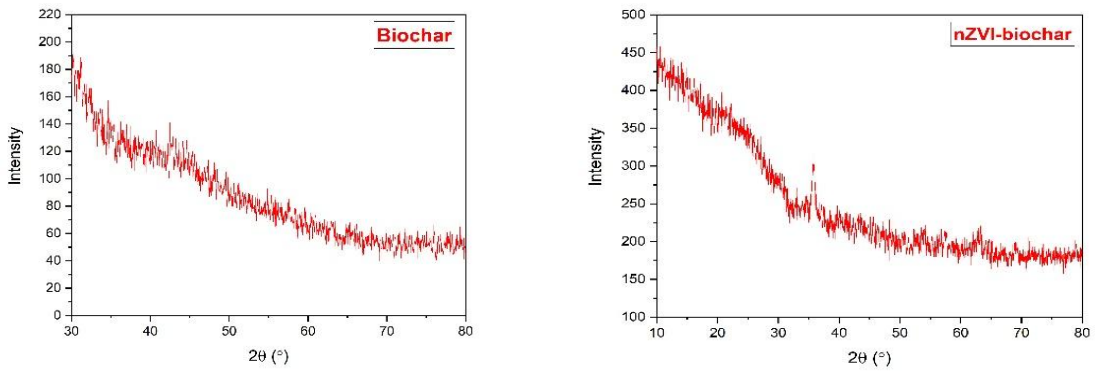
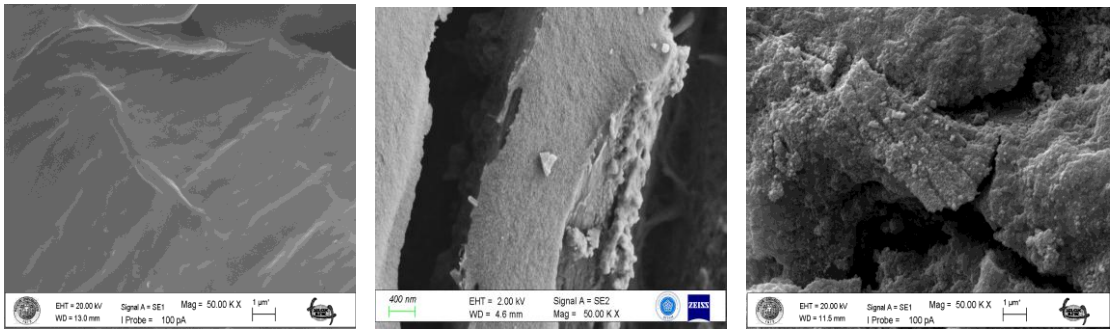


Figure 3. XRD diagram of biochar (a), nZVI-biochar (b)

Figure 3(a–b) shows the XRD patterns of the biochar and nZVI-biochar composites. In the biochar diffractogram, the peaks at 2θ = 47.5° and 64.9° correspond to CaO, while the peaks at 2θ = 43.1° and 57.0° indicate the presence of $CaCO_3$ (Hung et al., 2021). The nZVI-biochar nanocomposite exhibits characteristic diffraction peaks at 2θ =

30.2°, 35.5°, 43.2°, 53.7°, 57.2°, 62.7°, and 74.3°. These peaks are attributed to Fe_3O_4, confirming that magnetite is the dominant crystalline phase and that Fe_3O_4 was successfully loaded onto the adsorbent surface (Parlayıcı & Pehlivan, 2023). The broad peak observed at $2\theta = 24°$ for biochar represents the typical diffraction pattern of amorphous carbon.



(a) (b) (c)

Figure 4. SEM image of seed (a) biochar (b) nZVI-biochar (c)

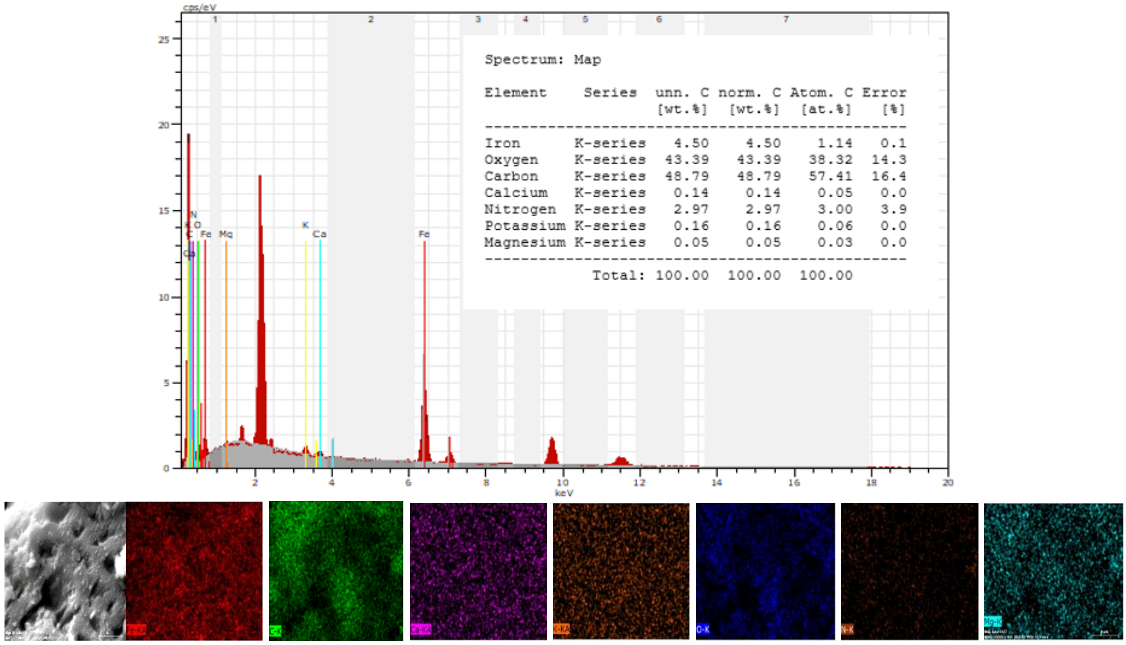


Figure 5. EDX image nZVI-biochar

The morphological characteristics and elemental composition of the seed, biochar, and nZVI-biochar composites were examined using scanning electron microscopy (SEM) (Figure 4) and energy-dispersive X-ray spectroscopy (EDX) (Figure 5). The raw seed biomass exhibited smooth, compact layers with limited porosity (Figure 4a). Since porous structures provide a greater number of active adsorption sites, higher porosity is desirable for efficient dye adsorption. After pyrolysis, the biochar biomass developed noticeable pores due to the release of volatile components and structural changes in its lignin content (Figure 4b). As a result, more pronounced pores and voids were observed in the biochar adsorbent produced via the pyrolysis process. The nZVI-biochar surface exhibited irregular folds and non-uniformly distributed pores (Figure 4c). As shown in Figure 5, EDX analysis confirmed the successful incorporation of iron into the structure of the nZVI-biochar nanocomposite. The adsorbent structure also displayed high relative abundances of oxygen and carbon, with the percentage of each detected element presented in the analysis output. The elemental composition of the nanocomposite is shown as percentage distributions in the EDX spectrum.

Results of the Batch Adsorption Experiments

Effect of Biochar and nZVI-Biochar Dosage

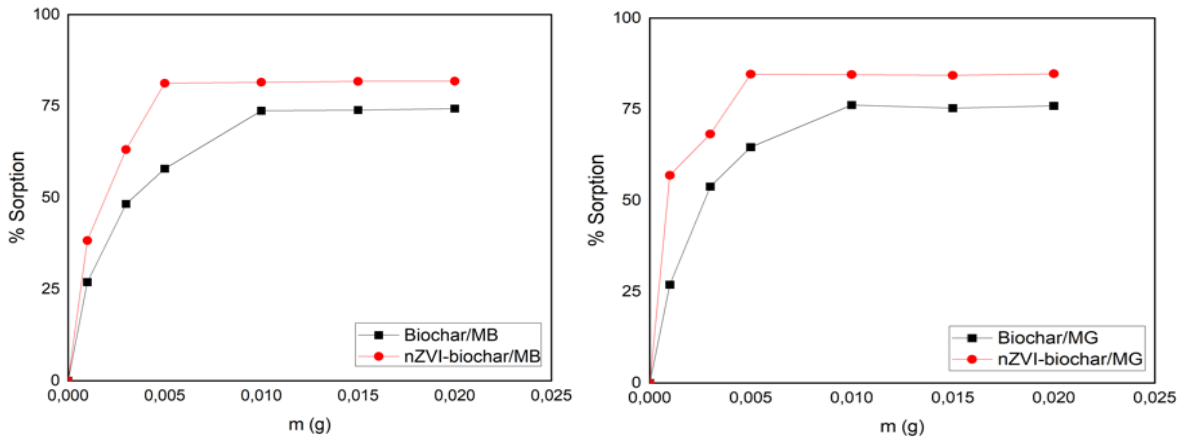


Figure 6. Effect of biochar and nZVI-biochar composite dosage

The dye uptake was investigated at different adsorbent dosages (0.001, 0.003, 0.005, 0.01, 0.015, and 0.02 g L^{-1}) through adsorption experiments. Figure 6 presents the percentage sorption as a function of the varying adsorbent dosages. In general, the adsorption capacity of the adsorbent increases with increasing dosage up to a certain point, after which it levels off. At longer contact times, only minor changes in the percentage adsorption were observed with further increases in adsorbent amount. For both MG and MB dyes, the adsorption capacity increased proportionally with the adsorbent dosage up to 0.010 g L^{-1}.

Effect of pH

To investigate the effect of pH on dye adsorption, the initial pH of the dye solutions was adjusted from 2.0 to 9.0. pH values above 9 were not examined because the highly basic conditions reduce dye adsorption. Changes in solution pH significantly influence dye biosorption by affecting the active adsorption sites on the biosorbent surface and the surface charge profile of the biosorbent. For an anionic dye, an increase in H^+ ion concentration renders the adsorbent surface positively charged, enhancing electrostatic attraction and promoting dye uptake. In contrast, for cationic dyes MG and MV, a pH greater than 4 is preferred, as higher pH values increase the concentration of OH^- ions, resulting in a negatively charged adsorbent surface. This enhances the electrostatic interaction between the positively charged cationic dye and the negatively charged biochar surface, thereby increasing dye absorption. The surface layers of biochar and nZVI-biochar generate an electric charge effect for MG and MB, facilitating dye attachment to the biosorbent surface. Consequently, the electrostatic attraction between positively charged cationic dyes and the negatively charged biochar surface is enhanced, improving adsorption efficiency (Srivatsav et al., 2020). The variations in biosorption capacities of MG and MB under different solution pH conditions are presented in Figure 7.

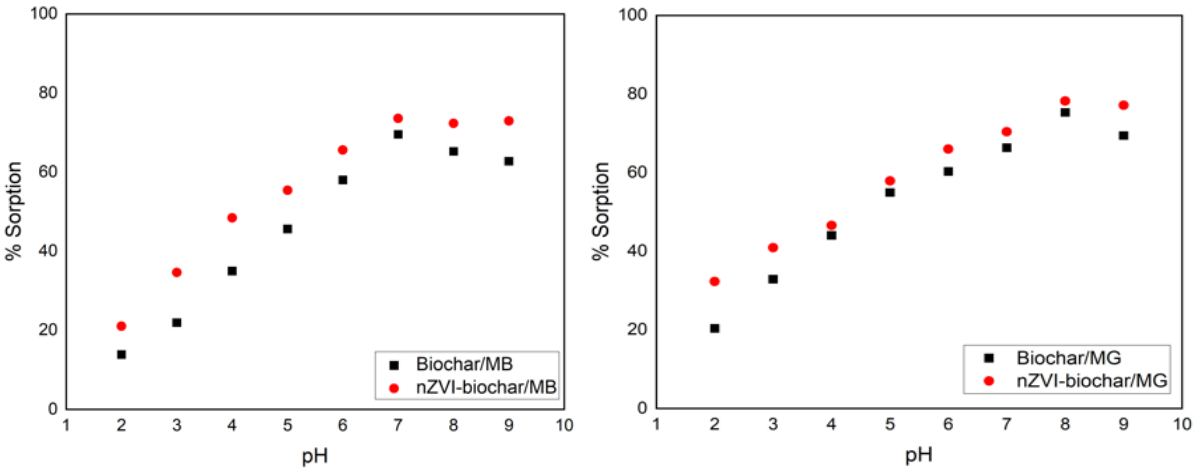


Figure 7. The effect of pH on dye adsorption.

Effect of Dye Initial Concentration

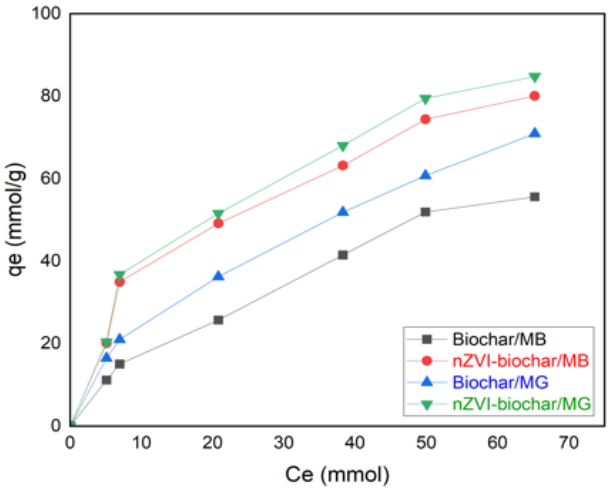


Figure 8. Effect of dye concentration

The adsorption isotherms for dye removal using the biochar and nanocomposite are presented in Figure 8. The graph, which plots the amount of adsorbed dye (q_e) against the equilibrium concentration (C_e), represents a typical single-layer adsorption process. Adsorption capacity was evaluated by varying the initial dye concentration (15, 25, 50, 75, 100, and 125 ppm). As the initial dye concentration increased, the difference in adsorption capacity between the biochar and the nanocomposite became more pronounced. Initially, the amount of adsorbed dye increased rapidly with rising dye concentration. At higher concentrations, the functional groups on the biochar and nanocomposite became saturated, and the adsorption potential reached equilibrium, at which point no further interaction occurred.

For equilibrium analysis, the Langmuir, Freundlich, and Temkin isotherm models were applied (Table 1). The Freundlich model represents physical adsorption at equilibrium, indicating that the biosorbent surface is heterogeneous and covered with MG and MB molecules. The Freundlich constants, K_f and n, were calculated; when n lies between 1 and 10, dye biosorption is considered favorable. The Langmuir isotherm represents chemical, monolayer adsorption and is widely recognized as the simplest theoretical model for single-layer biosorption. Magnetic modification of the raw material enhanced the adsorption capacities of the biosorbents. The results from the equilibrium studies suggest that both MG and MB can be efficiently removed from aqueous solutions. For biochar and nZVI-biochar, Langmuir correlation coefficients (R^2) exceeded 0.99 (Table 1), indicating that the Langmuir model best describes the adsorption process compared with other isotherms. The dimensionless separation factor (R_L) further confirms adsorption favorability: values between 0 and 1 indicate suitable biosorption, while $R_L > 1$ suggests otherwise. In this study, all R_L values (Table 1) ranged between 0 and 1, demonstrating strong adsorption of MG and MB from solution by the adsorbents. According to the Temkin isotherm, the positive B_T values indicate that the adsorption heat capacity increases with rising temperature, suggesting endothermic adsorption (Gozeten & Savran, 2018).

Table 1. Adsorption isotherm parameters for removal of dye.

Model	**Adsorbents**	**Dye**	**Parameters for dye**			
			A_s	**K_b**	**R^2**	**R_L**
Langmuir	Biochar	MB	70.671	0.037	0.993	0.519
$\frac{C_e}{q_e} = \frac{C_e}{A_s} + \frac{1}{K_b A_s}$	Biochar	MG	61.425	0.202	0.995	0.090
	nZVIbiochar	MB	81.169	0.076	0.978	0.207
	nZVIbiochar	MG	83.126	0.101	0.980	0.165
			K_F	**n**	**R^2**	
Freundlich	Biochar	MB	4.140	1.59	0.980	
$Inq_e = 1nK_f + \frac{1}{n}1nC_e$	Biochar	MG	13.208	2.38	0.990	
	nZVIbiochar	MB	11.914	2.34	0.957	
	nZVIbiochar	MG	11.442	2.00	0.947	
			B_T	**A_T**	**R^2**	
Temkin	Biochar	MB	17.431	0.321	0.940	
$q_e = B_T \ln A_T + B_T \ln c_e$	Biochar	MG	15.305	1.367	0.964	
	nZVIbiochar	MB	19.064	0.621	0.980	
	nZVIbiochar	MG	22.632	0.615	0.939	

Effect of Contact Time and Kinetic Studies

In adsorption studies, the contact time of the biosorbent plays a critical role. The effect of contact time on the biosorption of MG and MB is shown in Figure 9. For this purpose, 25 ppm MB and 50 ppm MG solutions were individually added to 0.01 g L^{-1} of biochar and nZVI-biochar adsorbents. The resulting suspensions were stirred using a magnetic stirrer for predetermined time intervals (20, 30, 45, 60, 90, 120, 150, 180, and 240 minutes) and subsequently filtered. The residual concentrations of MG and MB in the filtrate were determined using UV–Vis spectrophotometry.

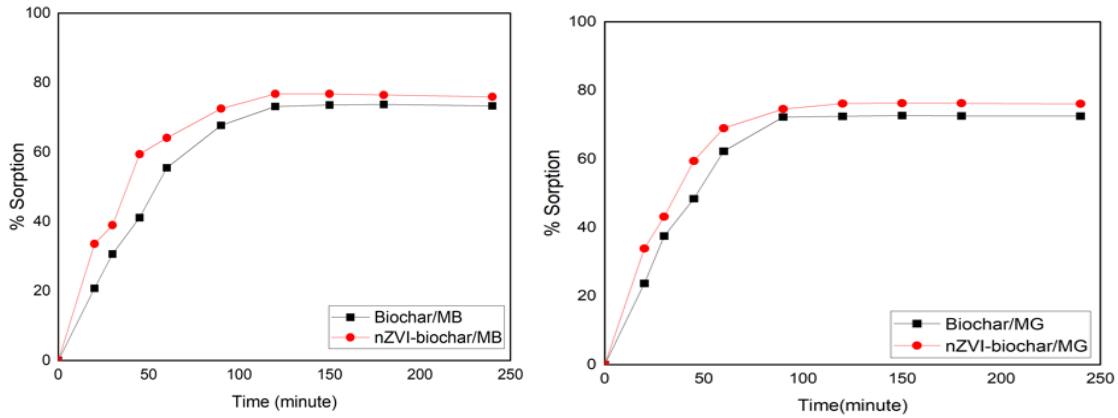


Figure 9. Influence of contact time on adsorption.

As illustrated in Figure 9, the biosorption of MG and MB by the adsorbents increased rapidly during the initial 0–45 minutes. After 45 minutes, the adsorption rate slowed, and equilibrium was achieved at longer contact times. Factors influencing the time required to reach equilibrium include the structural characteristics of the adsorbent, environmental conditions, and the molecular properties of the dyes. Consequently, the equilibrium attainment times varied between the different adsorbents.

Kinetic Models for Equlibrium

Pseudo-first-order and pseudo-second-order kinetic models were applied to investigate the biosorption of MG and MB onto biochar and nZVI-biochar, and the kinetics were analyzed. The calculated kinetic parameters for both dyes are presented in Table 2. The pseudo-first-order model was found to be applicable for MG and MB adsorption on both the raw and magnetite-modified biosorbents. However, for both adsorbents, the equilibrium adsorption capacity (q_e) calculated from the pseudo-second-order model showed smaller deviations from the experimental data than that obtained from the pseudo-first-order model. Therefore, the pseudo-second-order kinetic model was determined to better describe the biosorption mechanism of the system.

Table 2. Comparison of the pseudo-first-order, pseudo-second-order adsorption rate constants and calculated and experimental q_e values obtained at different initial dye concentrations.

				Pseudo-first-order			**Pseudo-second-order**		
Adsorbents	**Dye**	**C_o(ppm)**	**q_e exp**	**k_1**	**q_e**	**R^2**	**k_2**	**q_e**	**R^2**
Biochar	MB	**25**	15.054	0.016	15.06	0.843	0.0008	22.49	0.961
Biochar	MG	**50**	36.255	0.013	36.26	0.897	0.0007	40.30	0.973
nZVIbiochar	MB	**25**	20.136	0.017	20.14	0.860	0.0016	19.28	0.971
nZVIbiochar	MG	**50**	40.994	0.011	41.00	0.821	0.0012	39.98	0.990

Thermodynamic Studies

The thermodynamic parameters for the biosorption of dyes onto the biosorbents, including ΔH° (J mol^{-1}), ΔS° (J K^{-1} mol^{-1}), and ΔG° (J mol^{-1}), are presented in Table 3. It was observed that both the adsorption capacity and the percentage removal of the dyes by the biochar and nanocomposite increased with rising temperature. The negative values of ΔG° indicate the feasibility of the adsorption process and confirm that dye adsorption occurs spontaneously. Adsorption was more favorable at lower temperatures (298 K). Positive ΔH° values suggest that

the interaction between the dyes and the adsorbents is endothermic. Additionally, the positive ΔS° values indicate an increase in randomness at the solid–solution interface during dye adsorption (Gözeten & Savran, 2018).

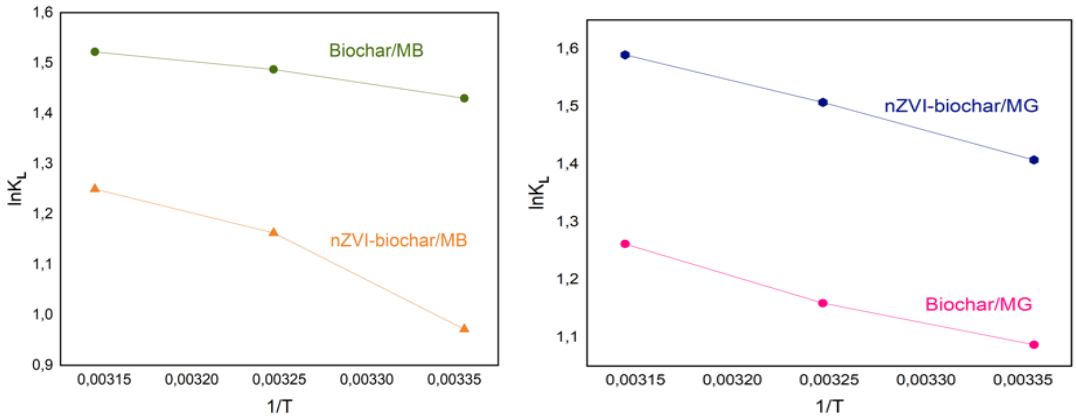


Figure 10. The impact of temperature on dye adsorption.

Table 3. Thermodynamic parameters for adsorption of dye

		ΔS°	**ΔH°**	**ΔG°**				
				T=298.15K	T=308.15K	T=318.15K	T=328.15K	R^2
Biochar	MB	24.12	3637.87	-3543.16	-3808.78	-4024.55	-4024.55	0.970
Biochar	MG	32.04	6870.04	-2693.04	-2967.67	-3335.90	-3335.90	0.971
nZVIbiochar	MB	45.10	10995.78	-2407.77	-2977.54	-3304.63	-3304.63	0.926
nZVIbiochar	MG	35.81	7181.67	-3486.87	-3859.35	-3859.35	-4202.56	0.997

Conclusion

The results of this study demonstrate that both the biochar and the nanocomposite are sustainable and highly efficient biosorbents for dye removal from aqueous systems. The adsorption capacities were determined as 70.67 mg g^{-1} (biochar) and 81.17 mg g^{-1} (nZVI-biochar) for MB, and 61.43 mg g^{-1} (biochar) and 83.13 mg g^{-1} (nZVI-biochar) for MG. The iron nanoparticle-loaded biochar exhibited higher adsorption capacities compared to the pristine biochar, indicating that the unmodified biochar was less effective in dye removal. The adsorption mechanisms were analyzed using the Langmuir, Freundlich, and Temkin isotherm models, and the corresponding adsorption capacities were calculated from these models. SEM analysis confirmed that the pyrolysis process provided the intended surface modification and generated a porous structure on the biochar. Elemental analysis revealed the presence of metal oxide nanoparticles in the biochar nanocomposite, verifying the success of the incorporation process. X-ray diffraction (XRD) analysis demonstrated that the raw biomass exhibited an amorphous structure, the biochar consisted of carbon and mineral components, and the nano-composite contained the intended iron nanoparticles. Overall, the findings indicate that both biochar and the nano-composite are highly promising materials for the treatment of contaminated water sources, particularly for efficient dye removal.

Scientific Ethics Declaration

* The authors declare that the scientific ethical and legal responsibility of this article published in EPSTEM journal belongs to the authors.

Conflict of Interest

* The authors declare that they have no conflicts of interest

Funding

* There is no funding

Acknowledgements or Notes

* This article was presented as an oral presentation at the International Conference on Technology, Engineering and Science (www.icontes.net) held in Antalya/Türkiye on November 12-15, 2025.

References

Baig, S. A., Zhu, J., Muhammad, N., Sheng, T., & Xu, X. (2014). Effect of synthesis methods on magnetic Kans grass biochar for enhanced As (III, V) adsorption from aqueous solutions. *Biomass and Bioenergy, 71*, 299-310.

Erdogan, F. O. (2017). Düşük maliyetli adsorbentler üzerine dispers sarı 211 tekstil boyasının adsorpsiyonu. *Afyon Kocatepe Üniversitesi Fen ve Mühendislik Bilimleri Dergisi, 17*(3), 889-898.

Erkmen, J., Kavcı, E., & Adıguzel, M. (2019). Üretim planlaması yapılarak su bazlı boyaların üretimi esnasında oluşan su kirliliğinin ve boya kaybının önlenmesi. *Journal of the Institute of Science and Technology, 9*(1), 57-65.

Erkus, A., Oygun, E., Turkmenoglu, M., & Aldemir, A. (2018). Boya endüstrisi atıksularının karakterizasyonu. *Yüzüncü Yıl Üniversitesi Fen Bilimleri Enstitüsü Dergisi, 23*(3), 308-319.

Gozeten, I., & Savran, A. (2018). Metil kırmızısının silikajel üzerindeki çözeltiden adsorpsiyonu: Denge izotermleri ve kinetik incelemeler. *Mus Alparslan University Journal of Science, 6*(2), 581-589.

Hung, C. M., Huang, C. P., Cheng, J. W., Chen, C. W., & Dong, C. D. (2021). Production and characterization of a high value-added seaweed-derived biochar: Optimization of pyrolysis conditions and evaluation for sediment treatment. *Journal of Analytical and Applied Pyrolysis, 155*, 105071.

Parlayıcı, S., & Pehlivan, E. (2017). Removal of metals by Fe3O4 loaded activated carbon prepared from plum stone (Prunus nigra): Kinetics and modelling study. *Powder Technology, 317*, 23-30.

Parlayıcı, S., & Pehlivan, E. (2021). Biosorption of methylene blue and malachite green on biodegradable magnetic Cortaderia selloana flower spikes: Modeling and equilibrium study. *International Journal of Phytoremediation, 23*(1), 26-40.

Parlayıcı, S., & Pehlivan, E. (2023). An ecologically sustainable specific method using new magnetic alginate-biochar from acorn cups (Quercus coccifera L.) for decolorization of dyes. *Polymer Bulletin, 80*(10), 11167-11191.

Rathi, B. S., Kumar, P. S., & Vo, D. V. N. (2021). Critical review on hazardous pollutants in water environment: Occurrence, monitoring, fate, removal technologies and risk assessment. *Science of the Total Environment, 797*, 149134.

Srivatsav, P., Bhargav, B. S., Shanmugasundaram, V., Arun, J., Gopinath, K. P., & Bhatnagar, A. (2020). Biochar as an eco-friendly and economical adsorbent for the removal of colorants (dyes) from aqueous environment: A review. *Water, 12*(12), 3561.

Yaseen, D. A., & Scholz, M. (2019). Textile dye wastewater characteristics and constituents of synthetic effluents: A critical review. *International Journal of Environmental Science and Technology, 16*(2), 1193-1226.

Yi, Y., Huang, Z., Lu, B., Xian, J., Tsang, E. P., Cheng, W., & Fang, Z. (2020). Magnetic biochar for environmental remediation: A review. *Bioresource Technology, 298*, 122468.

Author(s) Information

Erol Pehlivan
Konya Technical University, Faculty of Engineering and Natural Sciences, Department of Chemical Engineering Rauf Orbay Street. 42250, Selçuklu/Konya, Türkiye
Contact e-mail: *erolpehlivan@gmail.com*

Busra Ozkok
Konya Technical University, Faculty of Engineering and Natural Sciences, Department of Chemical Engineering, Rauf Orbay Street. 42250, Selçuklu/Konya, Türkiye

To cite this article:

Pehlivan, E. & Ozkok, B. (2025). Synthesis and characterization of biochar and nano-biochar composites derived from biomass (*Colutea cilicica*) for the removal of cationic dyes from aqueous solutions. *The Eurasia Proceedings of Science, Technology, Engineering and Mathematics (EPSTEM), 38,* 423-432.

The Eurasia Proceedings of Science, Technology, Engineering & Mathematics (EPSTEM)
ISSN: 2602-3199

The Eurasia Proceedings of Science, Technology, Engineering and Mathematics (EPSTEM), 2025

Volume 38, Pages 433-443

IConTES 2025: International Conference on Technology, Engineering and Science

Factors Affecting the Sliding Stability of a Gravity Retaining Wall

Karim Baziz
Mouloud Mammeri University of Tizi-Ouzou

Amar Kahil
Mouloud Mammeri University of Tizi-Ouzou

Abstract: This study investigates the sliding stability of gravity retaining walls by integrating the spatial variability of soil properties into a probabilistic framework. Unlike traditional deterministic methods, which assume fixed soil parameters and rely solely on safety factors, this approach employs Monte Carlo simulations in MATLAB to account for the inherent uncertainties in soil behavior. The analysis focuses on how variations in key geotechnical parameters, specifically the internal friction angle of the backfill, the cohesion of the foundation soil, the unit weight of the backfill, and the foundation friction angle, affect the probability of failure for different levels of safety factors. The results show that the spatial variability of the backfill's internal friction angle and the cohesion of the foundation soil plays a critical role in sliding failure. When a commonly used safety factor of 1.5 is applied, the corresponding failure probabilities often exceed the acceptable threshold of 10^{-4}. Conversely, the variability in backfill unit weight and foundation friction angle has minimal influence on failure risk. These findings underscore the limitations of conventional design approaches and demonstrate the necessity of incorporating probabilistic analyses to achieve more reliable and robust designs. The study supports the adoption of reliability-based methods for safer and more resilient retaining wall structures under uncertainty.

Keywords: Gravity retaining wall, Sliding stability, Probabilistic analysis, Spatial variability, Monte Carlo simulation

Introduction

Gravity retaining walls represent one of the oldest and most commonly used structures for resisting lateral earth pressures. Their stability is primarily ensured by their self-weight. The design of these structures traditionally relies on the concept of a safety factor $(FS)_{sli}$, whose value is typically derived from practical experience and the analysis of past failures (Goh, Zhang, Zhang, Zhang, & Liu, 2017; Mokeddem, 2018; Zhou, Xie, Huang, & He, 2019).

In a deterministic framework, the geomechanical parameters of the soil are assumed to remain constant during stability analysis (Zhou et al., 2019). However, these parameters, such as unit weight, internal friction angle, and cohesion, are inherently uncertain. Consequently, although the safety factor approach is widely applied, it often fails to provide a rigorous representation of the true behavior of soil (Zhou et al., 2019). Probabilistic methods, including reliability analysis and Monte Carlo simulations, offer a more comprehensive way to account for these uncertainties (Sert, Luo, Xiao, Gong, & Juang, 2016).

The specialized literature (Harr, 1987; Kulhawy, 1993; Lumb, 1974; Singh, 1972) reports that soil unit weight may vary by 3-7%, the internal friction angle by 2-13%, and cohesion by as much as 10-50%. Reliability-based design provides a systematic means of incorporating these variations into the design process. Accordingly, many studies have employed this method to evaluate the safety of gravity retaining walls (Guha Ray & Baidya, 2012). The need for an optimized and balanced design has been emphasized in several works, particularly for gravity

- This is an Open Access article distributed under the terms of the Creative Commons Attribution-Noncommercial 4.0 Unported License, permitting all non-commercial use, distribution, and reproduction in any medium, provided the original work is properly cited.

- Selection and peer-review under responsibility of the Organizing Committee of the Conference

© 2025 Published by ISRES Publishing: www.isres.org

walls (Höeg & Murarka, 1974). It has been demonstrated that a high safety factor obtained through deterministic methods does not necessarily ensure structural safety. Indeed, accounting for the variability of soil mechanical properties can lead to significant probabilities of failure.

Guha Ray & Baidya (2012) showed that even with a high safety factor, a structure may still present a considerable risk of failure when the variability of soil parameters is incorporated into the analysis. In most studies, soil parameters are assumed to be constant for a given calculation. Therefore, for a set of *n* simulated random variables, *n* corresponding safety factor values are obtained, particularly when Coulomb's theory is used to estimate lateral earth pressures (Guha Ray & Baidya, 2012). The Random Finite Element Method (RFEM) has also been employed to investigate the influence of one-dimensional spatial variability of the internal friction angle on both wall and soil responses (Sert et al., 2016). In this context, computing the safety factor requires modeling variability through an equivalent number of random soil layers.

In parallel, design approaches based on a target failure probability have been developed, combining the principles of structural optimization and reliability. However, the literature review reveals that two key aspects, the sensitivity analysis of random variables and the evaluation of failure probabilities for different modes, are often addressed separately. A methodology that simultaneously integrates these two components could lead to designs that are both safer and more cost-effective.

In this study, a design and optimization approach is proposed based on the combined use of a target failure probability and the safety factor against sliding. An analytical strategy was implemented to assess the vulnerability of gravity retaining walls to sliding by varying, independently, the coefficients of variation of soil parameters. This analysis makes it possible to identify the influence of each parameter on the probability of failure for different safety factor values using Monte Carlo simulations.

Objectives

The main objective of this study is to develop a methodology for identifying the most influential soil parameters affecting the sliding failure mode of a gravity retaining wall. It also aims to analyze the extent of influence of each random variable, namely, the internal friction angle (φ), cohesion (c), and unit weight (γ), on sliding stability. The study seeks to establish a relationship between the probability of failure associated with this failure mode and the different values of safety factors, while accounting for the variability of soil properties. To achieve this objective, a case study is conducted on a typical gravity retaining wall. A deterministic analysis is first carried out using Coulomb's method to evaluate lateral earth pressures and to calibrate the safety factors related to sliding. Then, the failure probability is estimated using the Monte Carlo Simulation (MCS) method implemented in MATLAB, incorporating probability distributions derived from the literature for the random variables. This approach makes it possible to combine the analysis of the influence of soil parameters with the evaluation of sliding failure probability for different safety factor values, thereby providing a more comprehensive assessment of the risks associated with the instability of gravity retaining walls.

Problem Description

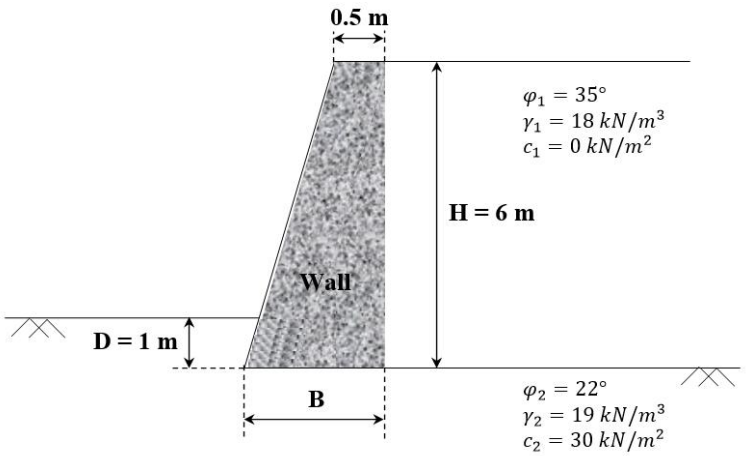


Figure 1. Cross-section of the gravity retaining wall

A typical gravity retaining wall, as illustrated in Figure 1, is considered in the present study. All soil properties are assumed to be homogeneous, statistically independent, and spatially constant. Table 1 summarizes the mean values of the geotechnical properties of both the backfill and foundation soils.

Table 1. Statistics of input parameters

Variables	Mean μ	COV (%)	Distribution
$\gamma_1\left(\mathrm{kN/m^3}\right)$	18	[5% - 10%]	Normal
$\varphi_1\left(\mathrm{degrees}\right)$	35	[5% - 15%]	Log-normal
$\gamma_2\left(\mathrm{kN/m^3}\right)$	19	[5% - 10%]	Normal
$\varphi_2\left(\mathrm{degrees}\right)$	22	[5% - 15%]	Log-normal
$c_2\left(\mathrm{kN/m^2}\right)$	30	[30% - 50%]	Log-normal

Deterministic Analysis

Coulomb's earth pressure theory is used to evaluate the external stability of the retaining wall under static conditions. The total active lateral force exerted by the backfill is given by:

$$F_a = \frac{1}{2} K_a \gamma \mathrm{H}^2 \tag{1}$$

According to Coulomb, the active earth pressure coefficient Ka can be expressed as follows:

$$K_a = \frac{\sin^2 \sin^2 \left(\eta - \varphi\right)}{\sin^2 \sin^2 \eta \sin \sin \left(\eta + \delta\right) \left[1 + \sqrt{\frac{\sin \sin \left(\varphi + \delta\right) \sin \sin \left(\varphi - \beta\right)}{\sin \sin \left(\eta + \delta\right) \sin \sin \left(\eta - \beta\right)}}\right]^2} \tag{2}$$

The wall is specifically designed to resist the sliding failure mode, and the limit equilibrium equation used to calculate the safety factor is expressed as:

$$F_G = \frac{c.B + N.\tan \tan \delta}{T} \tag{3}$$

For soil–concrete interfaces, it is assumed that the friction coefficient between the soil and the wall base is identical to that of the wall face (SCHLOSSER, 1995). This friction angle is defined as:

$$\delta = \frac{2}{3} \varphi \tag{4}$$

Here, *N* and *T* represent the total vertical force and the destabilizing horizontal force acting on the structure, respectively. The design of the gravity retaining wall is performed by adjusting the deterministic safety factors according to the values specified in Table 2. These safety factors $(FS)_{sli}$ are calculated specifically for the sliding failure mode, providing a measure of the available margin of safety before failure occurs. The deterministic $(FS)_{sli}$ values serve as reference points for the subsequent probabilistic analyses, which assess the uncertainty associated with the soil parameters influencing wall stability and estimate the corresponding probabilities of failure for this mode.

Table 2. Deterministic safety factors

Sliding safety factor $(FS)_{sli}$	1.25	1.50	1.75	2.00	2.25	2.50	2.75	3.00
Corresponding base width B (m)	1.533	1.911	2.289	2.668	3.046	3.424	3.802	4.181

Probabilistic Analysis

Table 1 presents the detailed statistical data of the input parameters used in the stability analysis of the gravity retaining wall. It is important to note that the coefficients of variation (COV) listed in Table 1 are assumed values, adopted in the absence of site-specific data, in accordance with the recommendations of (Duncan, 2000; Schneider, 1997). Moreover, the probability distributions of the random variables were selected based on previous studies, such as those proposed by (Harr, 1987; Kulhawy, 1993) to reflect realistic conditions commonly encountered in geotechnical practice. In the framework of the probabilistic analysis of the retaining wall, the performance functions, denoted as $G_i(x)$, are defined by:

$$G_i(x) = (FS)_i - 1 \tag{5}$$

Where i refers to the different potential failure modes.

Failure occurs when $G_i(x) < 0$.

The probability of failure (P_f) for each failure mode and for each soil parameter under study is computed using the Monte Carlo simulation method. This approach involves generating a large set of random data points ($n = 10^5$) for each random variable using MATLAB. The failure probability P_f is then determined as the percentage of simulations that do not satisfy the limit equilibrium condition, that is, when $G_i(x) < 0$. This study adopts a systematic approach to analyze the specific influence of each soil parameter on a given failure mode. Such an approach makes it possible to identify the most influential parameters and to better understand their impact on the stability of gravity retaining walls.

Sliding Failure Mode

In assessing the stability of retaining walls against sliding failure, it is essential to examine the influence of each geotechnical parameter on the associated probability of failure. This process involves a systematic analysis of the individual effects of each parameter while accounting for the inherent uncertainties in soil properties. Such an approach makes it possible to identify the parameters that have the most significant impact on the likelihood of wall sliding.

The analysis is based on the principles of structural reliability (Duncan, 2000) and rooted in soil mechanics fundamentals to evaluate the associated risks. For instance, variations in soil cohesion, internal friction angle, or unit weight can have different effects on sliding stability. As demonstrated by (Phoon & Kulhawy, 1999) it is crucial to rigorously quantify the uncertainties associated with geotechnical parameters to obtain an accurate estimation of the probability of failure. This quantification not only enhances understanding of the individual contributions of each parameter but also provides a foundation for developing more effective risk management strategies.

Influence of the Internal Friction Angle of the Backfill Soil (φ_1)

To evaluate the impact of the spatial variability of soil properties, particularly that of the internal friction angle of the backfill soil φ_1, a Monte Carlo simulation was conducted. In this study, all parameters of both the backfill and foundation soils were kept constant, except for the internal friction angle φ_1, which is the focus of the analysis. This parameter is considered as a random variable following the statistical distribution defined in Table 1. To highlight the influence of this variability on the probability of failure, the effect of changing the coefficient of variation (COV) of φ_1 on the results is examined. The coefficient variation is incrementally adjusted by 2%, ranging from 5% to 15%. This approach allows for assessing how fluctuations in φ_1 affect the sliding stability of the retaining wall.

For comparison purposes, the different failure probabilities obtained for each COV value of φ_1 are analyzed at a fixed safety factor, which serves as a reference for the sliding stability evaluation. This methodology not only identifies critical variability thresholds that increase the risk of failure but also provides a clearer understanding of the structure's sensitivity to variations in φ_1.

Table 3. Sliding failure probability for different calculation series as a function of COV (φ_1)

COV (φ_1)	Sliding safety factor $(FS)_{sli}$							
	1.25	1.50	1.75	2.00	2.25	2.50	2.75	3.00
5%	6.97E-04	0	0	0	0	0	0	0
7%	1.14E-02	2.67E-06	0	0	0	0	0	0
9%	4.02E-02	2.62E-04	3.33E-07	0	0	0	0	0
11%	7.86E-02	2.32E-03	1.23E-05	0	0	0	0	0
13%	1.19E-01	8.73E-03	1.79E-04	6.67E-07	0	0	0	0
15%	1.57E-01	2.04E-02	1.02E-03	1.57E-05	0	0	0	0

We graphically present the failure probability curves as a function of the coefficient of variation of the backfill internal friction angle φ_1. For each calculation series, a specific safety factor is assigned, and the resulting curves illustrate how the probability of failure evolves in response to fluctuations in this critical parameter. These representations enable a direct comparison of the influence of φ_1 variability on the sliding stability of the retaining wall, while accounting for the different safety scenarios considered. Table 3, which presents the sliding failure probabilities as a function of the coefficient of variation of the backfill soil's internal friction angle, together with the curves shown in Figure 2, clearly demonstrate the significant influence of this parameter's variability.

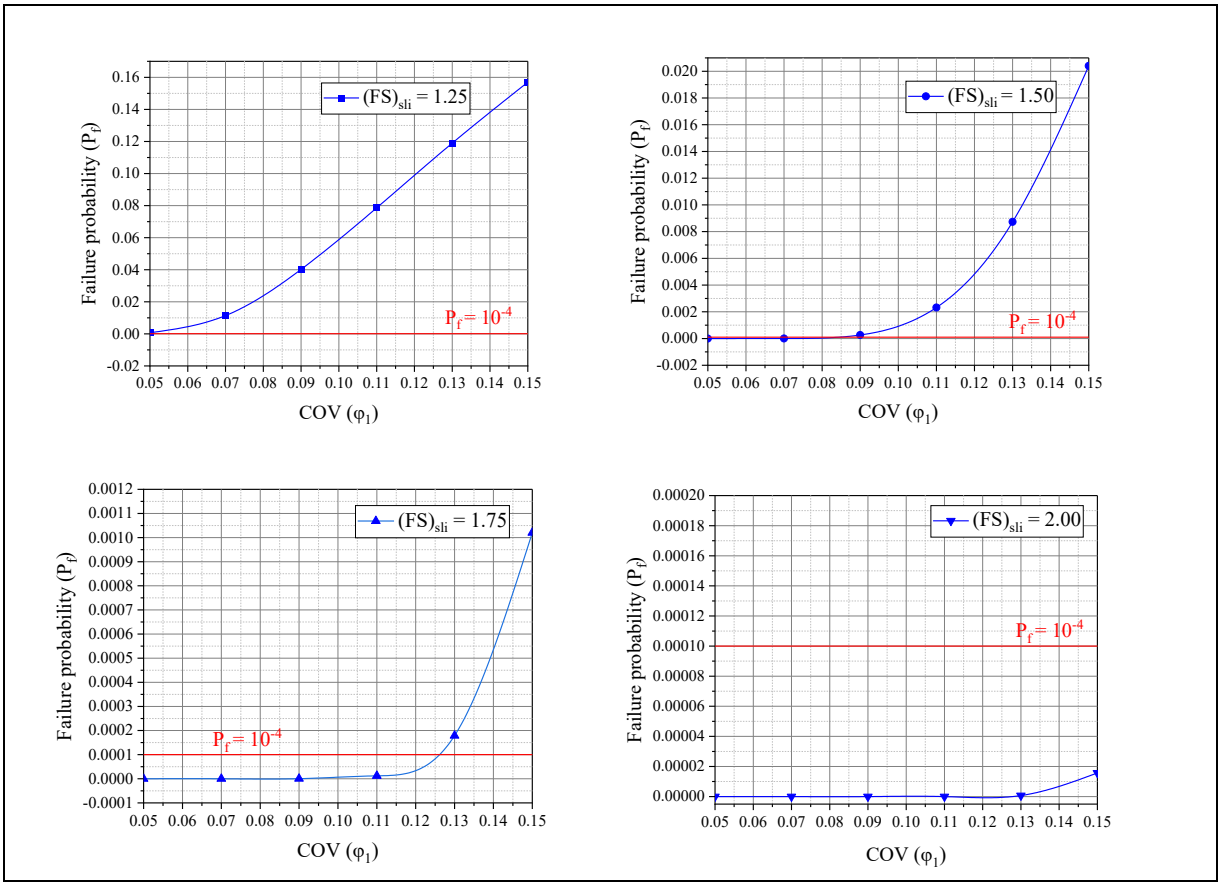


Figure 2. Failure probability as a function of COV (φ_1) for different sliding safety factors

When a deterministic sliding safety factor $(FS)_{sli}$ of 1.5 is applied, in accordance with standard recommendations, the resulting sliding failure probabilities consistently exceed the target failure probability, typically set at 10^{-4}. This finding highlights the necessity of adopting a safety factor of around 2 in deterministic analyses to ensure adequate stability of gravity retaining walls against sliding. Such caution becomes particularly important when the backfill soil exhibits an internal friction angle with a coefficient of variation greater than 9%.

Influence of the Backfill Soil Unit Weight (γ_1)

To assess the effect of spatial variability in soil properties, particularly the unit weight of the backfill soil (γ_1), a Monte Carlo simulation was performed. In this analysis, all parameters of both the backfill and foundation soils are kept constant, except for the backfill unit weight γ_1, which is treated as a random variable following a statistical distribution as presented in Table 1. To highlight the influence of the backfill unit weight on the failure probability, the variation of the coefficient of variation (COV) of γ_1 is examined. The COV is increased in increments of 1%, ranging from 5% to 10%. This approach makes it possible to explore how the variability of γ_1 affects the overall stability of the retaining wall. For comparison purposes, a specific sliding safety factor is assigned to each calculation series. This factor serves as a reference for the stability analysis, allowing for the assessment of the relative impact of γ_1 variability on the failure risk. This methodology provides valuable insight into the critical variability thresholds that may compromise the structural safety of the wall.

Table 4. Sliding failure probability for different calculation series as a function of COV (γ_1)

COV (γ_1)	Sliding safety factor $(FS)_{sli}$							
	1.25	1.50	1.75	2.00	2.25	2.50	2.75	3.00
5%	0	0	0	0	0	0	0	0
6%	1.00E-06	0	0	0	0	0	0	0
7%	2.50E-05	0	0	0	0	0	0	0
8%	2.21E-04	0	0	0	0	0	0	0
9%	8.67E-04	0	0	0	0	0	0	0
10%	2.42E-03	0	0	0	0	0	0	0

We plotted the curves illustrating the failure probabilities as a function of the coefficient of variation of the backfill unit weight (γ_1) for each safety factor defined in the different calculation series. These curves clearly depict the direct influence of γ_1 variability on the sliding stability of the retaining wall. By comparing the failure probabilities corresponding to the various safety factors, this graphical representation highlights the critical variability thresholds beyond which the risk of failure becomes significant. This approach provides a deeper understanding of the structure's sensitivity to unit weight variability, thereby helping to refine design criteria and improve risk management.

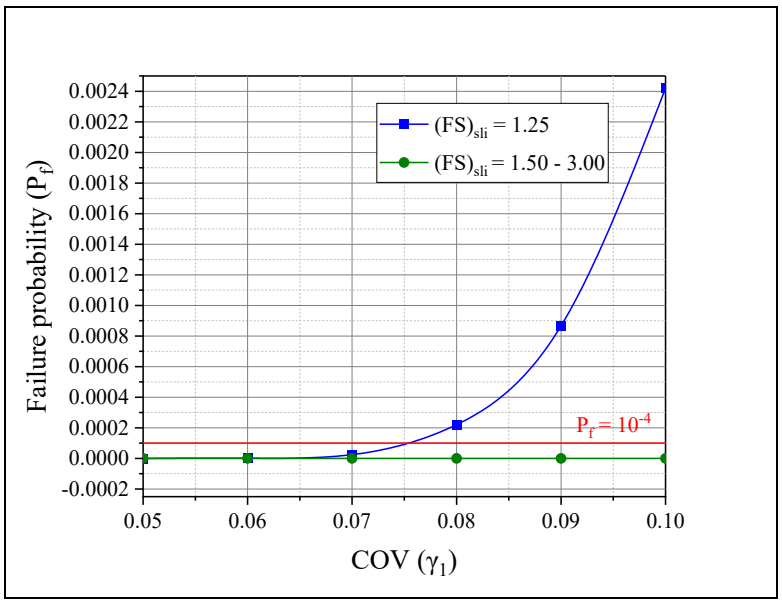


Figure 3. Failure probability as a function of COV (γ_1) for different sliding safety factors

Table 4, which presents the sliding failure probabilities as a function of the variation in the coefficient of variation of the backfill unit weight (γ_1), together with the curves illustrated in Figure 3, clearly indicates that this parameter has a negligible influence. The results show that, regardless of the value of the coefficient of variation of γ_1, the failure probabilities remain almost zero, particularly when the safety factor is equal to or greater than 1.5. Therefore, no specific recommendation is required regarding the choice of the sliding safety factor, as the variability of the backfill unit weight γ_1 has no significant effect on the failure probabilities. This stability, observed for all considered levels of variability, suggests that other parameters, such as cohesion or internal friction angle, are more critical in assessing sliding stability. Consequently, the variability of the unit weight γ_1 can be considered less influential under the studied conditions.

Influence of the Internal Friction Angle of the Foundation Soil (φ_2)

To evaluate the effect of spatial variability in soil properties, specifically the internal friction angle of the foundation soil (φ_2), a Monte Carlo simulation was carried out. In this analysis, all parameters of both the backfill and foundation soils are kept constant, except for the internal friction angle of the foundation soil φ_2, which is the focus of this study. This parameter is treated as a random variable following the statistical distribution described in Table 1. To highlight the influence of φ_2 on the failure probability, the coefficient of variation of this parameter is varied incrementally by 2% within a range of 5% to 15%. This approach makes it possible to explore the impact of different levels of variability on the sliding stability of the retaining wall. For each series of calculations, a specific safety factor is fixed to serve as a reference for the stability analysis. This enables a direct comparison of the resulting failure probabilities and helps determine how the variability of φ_2 affects the likelihood of sliding failure. This systematic approach allows for the identification of critical variability thresholds and provides valuable insight into the sensitivity of the structure to this parameter, contributing to a more reliable and secure design.

Table 5. Sliding failure probability for different calculation series as a function COV (φ_2)

COV (φ_2)	Sliding safety factor $(FS)_{sli}$							
	1.25	1.50	1.75	2.00	2.25	2.50	2.75	3.00
5%	0	0	0	0	0	0	0	0
7%	0	0	0	0	0	0	0	0
9%	0	0	0	0	0	0	0	0
11%	4.33E-06	0	0	0	0	0	0	0
13%	6.10E-05	0	0	0	0	0	0	0
15%	4.50E-04	0	0	0	0	0	0	0

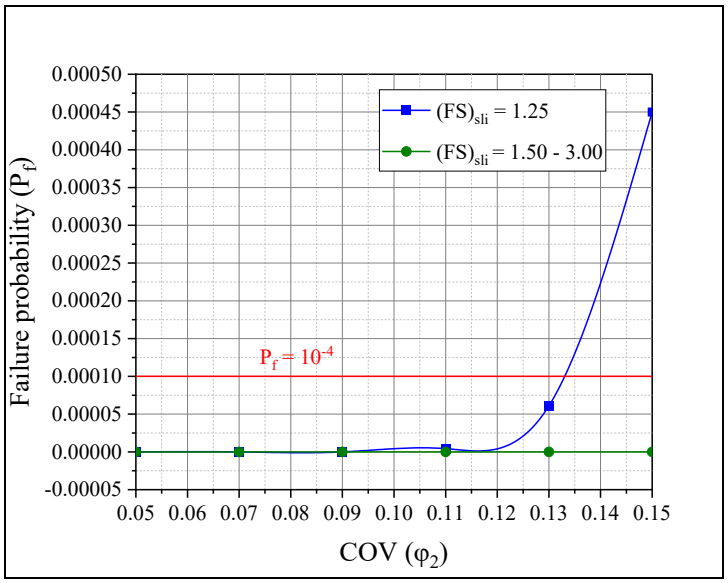


Figure 4. Failure probability as a function of COV (φ_2) for different sliding safety factors

We plotted curves showing the evolution of failure probabilities as a function of the coefficient of variation of the foundation soil internal friction angle (φ_2) for each safety factor defined in the different calculation series. These graphs provide a visual assessment of how φ_2 variability influences the sliding stability of the retaining wall. By comparing the curves corresponding to each safety factor, it becomes possible to identify general trends and determine how fluctuations in φ_2 affect the likelihood of failure. This graphical representation serves as a valuable tool for understanding the structure's sensitivity to φ_2 variability, thereby supporting the development of more robust design strategies that account for the inherent uncertainties in soil properties.

Table 5 and the curves shown in Figure 4, which present the sliding failure probabilities as a function of the coefficient of variation of the foundation soil internal friction angle (φ_2), demonstrate that variations in this parameter have a minimal influence. The results indicate that, regardless of the value of the coefficient of variation of φ_2, the failure probabilities remain nearly zero, particularly when the sliding safety factor is set to 1.5 or higher. Therefore, it is not necessary to adjust the sliding safety factor based on the variability of φ_2, as this parameter does not significantly affect the probability of failure. This finding suggests that other

parameters, such as cohesion, may play a more decisive role in assessing sliding stability. Consequently, the influence of the internal friction angle φ_2 can be considered secondary under the specific conditions examined.

Influence of Foundation Soil Cohesion (c_2)

To evaluate the impact of the spatial variability of soil properties, specifically, the influence of the foundation soil cohesion (c_2), a series of Monte Carlo simulations was carried out. In this analysis, all parameters of the backfill and foundation soils are kept constant, except for c_2, which is treated as the variable of interest. The cohesion c_2 is considered a random variable whose statistical distribution is presented in Table 1. To highlight the influence of foundation soil cohesion on failure probability, the coefficient of variation of c_2 is varied in increments of 5% within the range of [30% - 50%]. This range allows for a detailed assessment of how cohesion variability affects the sliding stability of the retaining wall.

The main objective of this study is to compare the failure probabilities associated with different values of the coefficient of variation of c_2. For each simulation series, the safety factor used to assess sliding stability is kept constant. This approach isolates the specific influence of the studied parameter and provides a clearer understanding of its role in determining the sliding failure probability of the retaining wall.

Table 6. Sliding failure probability for different calculation series as a function COV (c_2)

COV (c_2)	Sliding safety factor $(FS)_{sli}$							
	1.25	1.50	1.75	2.00	2.25	2.50	2.75	3.00
30%	5.85E-02	5.27E-04	0	0	0	0	0	0
35%	9.41E-02	2.54E-03	6.67E-06	0	0	0	0	0
40%	1.33E-01	7.55E-03	3.67E-05	0	0	0	0	0
45%	1.69E-01	1.66E-02	2.70E-04	0	0	0	0	0
50%	2.04E-01	2.89E-02	9.63E-04	0	0	0	0	0

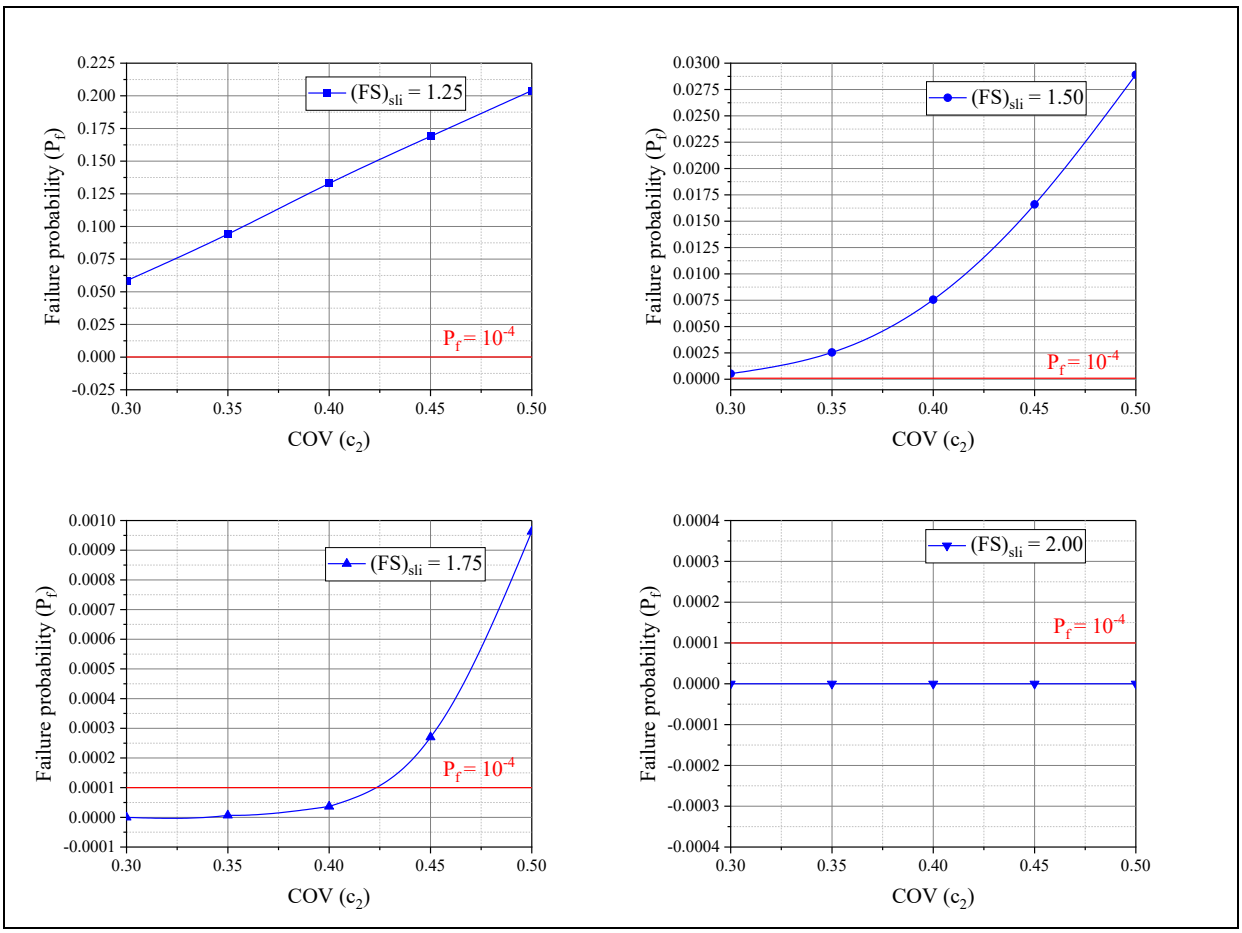


Figure 5. Failure probability as a function of COV (c_2) for different sliding safety factors

We plotted the failure probability curves as a function of the variations in the coefficient of variation of c_2 for each predefined safety factor value. For each simulation series, the resulting curves clearly illustrate the impact of fluctuations in c_2 on the sliding stability of the retaining wall. These curves are essential for understanding how the variability of foundation soil cohesion influences the probability of failure while considering different safety levels.

The results presented in Table 6, which detail the sliding failure probabilities as a function of the coefficient of variation of the foundation soil cohesion (c_2), along with the curves shown in Figure 5, clearly highlight the significant impact of this parameter's variability. When a deterministic sliding safety factor $(FS)_{sli}$ of 1.5 is applied, consistent with standard recommendations, the computed sliding failure probabilities consistently exceed the target failure probability, generally set at 10^{-4}. This finding emphasizes the need to adopt a safety factor of around 2 in deterministic analyses to ensure adequate stability of gravity retaining walls against sliding failure.

Conclusion

This study focused on assessing the vulnerability of gravity retaining walls by accounting for the spatial variability of soil properties. Unlike a purely deterministic approach, the adopted methodology explicitly integrates geotechnical uncertainty, allowing for a broader exploration of possible behavior scenarios. In this context, the rigorous definition of limit states for each potential failure mode is a key step in evaluating the reliability of the structure. The analysis concentrated on the sliding failure mode at the base, corresponding to a horizontal displacement of the wall under the effect of applied loads. A specific analysis strategy was developed, based on the separate variation of the coefficients of variation of the main soil parameters, to determine their influence on the failure probability for each safety factor, using Monte Carlo simulations.

The main conclusions derived from this study can be summarized as follows:

Influence of the internal friction angle of the backfill (φ_1): Its variability has a significant effect on the probability of sliding failure. For a deterministic safety factor $(FS)_{sli} = 1.5$, as commonly recommended by standards, the computed failure probabilities consistently exceed the target probability of 10-4. This finding suggests that a higher safety factor, close to 2, is required to ensure an acceptable level of reliability.

Influence of the unit weight of the backfill (γ_1): The effect of its variability on sliding failure is negligible. Regardless of the coefficient of variation, the failure probabilities remain nearly zero for $(FS)_{sli} \geq 1.5$. Hence, this parameter is less critical under the studied conditions.

Influence of the internal friction angle of the foundation soil (φ_2): The variability of this parameter has a minimal impact on the sliding mode. The failure probabilities remain insignificant, particularly for $(FS)_{sli} \geq 1.5$, indicating that φ_2 plays a secondary role in the present analysis.

Influence of the cohesion of the foundation soil (c_2): The variability of this parameter has a major influence on the sliding stability. For a safety factor of 1.5, the failure probabilities systematically exceed the target value of 10^{-4}. Therefore, a safety factor of about 2 is recommended to ensure the stability of the retaining wall against sliding.

These results clearly demonstrate that ignoring the spatial variability of soil properties can lead to a significant underestimation of failure risks, making traditional deterministic design potentially insufficient to guarantee long-term stability. It is therefore essential to reassess conventional safety criteria by incorporating the effects of geotechnical variability within a structural reliability framework. Such an approach is crucial to ensure that retaining walls are designed to withstand inherent geotechnical uncertainties, thereby improving their performance, robustness, and durability.

Recommendations

The findings of this study demonstrate that the spatial variability of soil properties, particularly the cohesion of the foundation soil and the internal friction angle of the backfill, plays a decisive role in the sliding stability of gravity retaining walls. Based on the probabilistic analyses conducted, the following recommendations can be made:

1. Adoption of reliability-based design: Deterministic design methods relying solely on safety factors should be complemented by probabilistic approaches to better account for geotechnical uncertainties.
2. Revision of conventional safety factors: A deterministic sliding safety factor $(FS)_{sli}$ of 1.5 may be insufficient to ensure the required level of reliability. It is therefore recommended to adopt a minimum safety factor of 2.0 for design purposes, particularly when the foundation soil exhibits significant variability in cohesion.
3. Characterization of soil variability: Site investigations should include statistical characterization of key geotechnical parameters, including cohesion and internal friction angle, to provide reliable input data for probabilistic analyses.
4. Integration of uncertainty in design standards: Future design codes should explicitly incorporate spatial variability effects and reliability-based concepts to improve the accuracy and safety of geotechnical structures.

By applying these recommendations, engineers can achieve safer, more resilient, and economically optimized designs for retaining structures under uncertain ground conditions.

Scientific Ethics Declaration

* The authors declare that the scientific ethical and legal responsibility of this article published in EPSTEM journal belongs to the authors.

Conflict of Interest

* The authors declare that they have no conflicts of interest

Funding

* This research received no external funding. The study was carried out as part of the authors' academic work within the Department of Civil Engineering, Mouloud Mammeri University of Tizi-Ouzou, Algeria.

Acknowledgements or Notes

* This article was presented as a poster presentation at the International Conference on Technology, Engineering and Science (www.icontes.net) held in Antalya/Türkiye on November 12-15, 2025.

* The authors would like to express their sincere gratitude to the Department of Civil Engineering, Mouloud Mammeri University of Tizi-Ouzou, for providing the academic environment and resources necessary to conduct this study. Special thanks are also extended to colleagues and students who contributed to discussions and provided valuable feedback during the development of this research.

References

Duncan, J. M. (2000). Factors of safety and reliability in geotechnical engineering. *Journal of Geotechnical and Geoenvironmental Engineering, 126*(4), 307-316.

Goh, A., Zhang, F., Zhang, W., Zhang, Y., & Liu, H. (2017). A simple estimation model for 3D braced excavation wall deflection. *Computers and Geotechnics, 83*, 106-113.

Guha Ray, A., & Baidya, D. (2012). Reliability coupled sensitivity based design approach for gravity retaining walls. *Journal of the Institution of Engineers (India): Series A, 93*(3), 193-201.

Harr, M. E. (1987). *Reliability-based design in civil engineering*. McGraw-Hill.

Höeg, K., & Murarka, R. P. (1974). Probabilistic analysis and design of a retaining wall. *Journal of the Geotechnical Engineering Division, 100*(3), 349-366.

Kulhawy, F. H. (1993). On the evaluation of static soil properties. In R. B. Seed & R. W. Boulanger (Eds.), *Stability and performance of slopes and embankments II* (pp. 95-115). ASCE.

Lumb, P. (1974). Application of statistics in soil mechanics. In I. K. Lee (Ed.), *Soil mechanics: New horizons* (pp. 44-111). Newnes-Butterworths.

Mokeddem, A. (2018). *Modélisation géomécanique et probabiliste des rideaux de palplanches: Prise en compte de l'interaction sol-structure et de la variabilité spatiale du sol* (Doctoral dissertation). Université de Bordeaux.

Phoon, K.-K., & Kulhawy, F. H. (1999). Characterization of geotechnical variability. *Canadian Geotechnical Journal, 36*(4), 612-624.

Schlosser, F. (1995). Murs de soutènement. *Techniques de l'Ingénieur, C242*.

Schneider, H. R. (1997). Definition and determination of characteristic soil properties. *Proceedings of the 14th International Conference on Soil Mechanics and Foundation Engineering* (Vol. 4, pp. 2271-2274).

Sert, S., Luo, Z., Xiao, J., Gong, W., & Juang, C. H. (2016). Probabilistic analysis of responses of cantilever wall-supported excavations in sands considering vertical spatial variability. *Computers and Geotechnics, 75*, 182–191.

Singh, A. (1972). How reliable is the factor of safety in foundation engineering? *Proceedings of the 1st International Conference on Applications of Statistics and Probability to Soil and Structural Engineering*, 389-424.

Zhou, X., Xie, Y., Huang, X., & He, H. (2019). Antislip stability analysis of gravity retaining wall by probabilistic approach. *International Journal of Geomechanics, 19*(6), 04019045.

Author(s) Information

Karim Baziz
Mouloud Mammeri University of Tizi-Ouzou,
Faculty of Construction Engineering, Mouloud Mammeri University, P.O. Box 17 RP, 15000 Tizi-Ouzou, Algeria.
Contact e-mail: *karim.baziz@ummto.dz*

Amar Kahil
Mouloud Mammeri University of Tizi-ouzou,
Faculty of Construction Engineering, Mouloud Mammeri University, P.O. Box 17 RP, 15000 Tizi-Ouzou, Algeria.

To cite this article:

Baziz, K., & Kahil, A. (2025). Factors affecting the sliding stability of a gravity retaining wall. *The Eurasia Proceedings of Science, Technology, Engineering and Mathematics (EPSTEM), 38,* 433-443.

The Eurasia Proceedings of Science, Technology, Engineering & Mathematics (EPSTEM)
ISSN: 2602-3199

The Eurasia Proceedings of Science, Technology, Engineering and Mathematics (EPSTEM), 2025

Volume 38, Pages 444-458

IConTES 2025: International Conference on Technology, Engineering and Science

A Decade of Research on Biomass Materials in Residential Building Construction: A Bibliometric Analysis

Yudith Arunika C. Wella
Bandung Institute of Technology

Abstract: The application of biomass materials as construction components in the residential building sector has demonstrated substantial progress over the past decade, particularly in relation to sustainability challenges and carbon emission mitigation. The aim of this study is to examine scientific trends related to this subject through a bibliometric methodology encompassing 116 articles published in the database. Scopus during the period 2014 to 2024. The analytical process was carried out using VOSViewer and Biblioshy software to facilitate data visualization and to explain the patterns of relationships between researchers, keywords, and publication trajectories. The objectives of this study are: (1) to describe publication trends related to Biomass Materials in Residential Building Construction during the previous decade; (2) to reveal the most productive journals in disseminating literature on this subject; (3) to map the most active authors, institutions, and countries, along with the international collaborative networks between them; (4) to investigate the main themes, keywords, and research topics prevailing in the domain; (5) to ascertain the countries that show the highest productivity in linking biomass topics to educational planning; and (6) to identify the most frequently cited references in related scientific works. (7) The evolution of each theme in the last decade. The analysis **results revealed** that the publication trend experienced an annual growth of 9.04% with peak productivity in 2022 and 2024. Leading journals such as *Energies* , *Renewable Energy* , and *Journal of Cleaner Production* has become a major source of publications, with article distribution reflecting a focus on renewable energy and sustainable buildings. Authors such as Luisa F. Cabeza and institutions from Italy and China demonstrate high productivity, while countries such as Switzerland and Sweden stand out in terms of scholarly impact through significant average citations per article. Thematic mapping shows a shift away from basic themes such as *residential building* and *biomass* towards strategic themes such as *carbon emission* , *renewable energy integration* , and *optimization* . Temporal keyword analysis shows that from 2018 to 2024, there has been an increasing focus on the issues of building decarbonization , energy efficiency, and renewable energy transition. In addition, the most frequently cited global references come from highly reputable energy and sustainability journals, while local references show a tendency towards contextual and applied approaches. The findings of this study indicate that biomass research in residential building construction is not only developing quantitatively, but also experiencing a deepening of themes and an expansion of global collaboration.

Keywords: Bibliometrics, Biomass, Residential building construction, Sustainable architecture, Renewable energy, Research trends, Low carbon emissions

Introduction

The use of biomass materials in the construction sector is gaining increasing attention every year in the context of sustainability and material innovation. Biomass itself is known as a renewable energy source, and it is now being utilized in home construction. Biomass will be innovated as a more environmentally friendly and economical building material. Research by Gracia and Cruz shows that biomass materials can replace conventional materials, providing more sustainable benefits and reducing the environmental impact of conventional building material production (Adeleke et al., 2021; Cruz & García-Uitz, 2024) . The use of managed biomass from sargassum and organic materials processed into building materials confirms that

- This is an Open Access article distributed under the terms of the Creative Commons Attribution-Noncommercial 4.0 Unported License, permitting all non-commercial use, distribution, and reproduction in any medium, provided the original work is properly cited.

- Selection and peer-review under responsibility of the Organizing Committee of the Conference

© 2025 Published by ISRES Publishing: www.isres.org

switching from using biomass as a fuel to using construction materials can provide significant added value in supporting more sustainable construction practices. (Cruz & García-Uitz, 2024) .

The housing sector faces several major challenges in carbon emission disclosure and sustainability reporting transparency (Nur Afni Nurul Nur Aeni & Etty Murwaningsari, 2023) . Consequently, the construction sector is required to address energy efficiency and green technology issues. Research by Judjijanto et et al. showed that the application of renewable energy and green technology can reduce carbon emissions (Judijanto et al., 2023) . Data from the IEA (2021) shows that the housing sector contributes 37% of carbon emissions, with house walls being a major contributor. Research also reveals that biomass has significant potential to support low-carbon housing in remote areas. Another advantage of using biomass in construction is its mechanical properties. A study by Syasiak et al. explains that biomass, particularly pine wood, exhibits frictional and strength properties that support its application in construction (Stasiak et al., 2020) . Furthermore, biomass materials act as good thermal insulators and can contribute to energy savings in buildings and provide comfort for occupants (Adeleke et al., 2021) . Biomass materials support green construction practices, for example, research by Akib and Bhardwaj states that materials made from biomass composition derived from fungi make them environmentally friendly and biodegradable (Akib et al., 2024; Bhardwaj et al., 2021) . The use of biomass-derived materials in construction not only provides environmental benefits but also encourages local economic growth by creating new opportunities in developing new products and techniques on a local scale (Adeleke et al., 2021) .

Considering the importance of managing local resources for use as biomass materials in the housing construction sector , the challenges of systematically mapping biomass research trends in the residential sector are crucial, particularly in the context of sustainability and carbon emission reduction. Effective mapping will help clarify research directions and make informed decisions about implementing biomass materials in the housing sector. Aeni and Murwangsari's research explains that lack of clarity in disclosing carbon emissions can lead to difficulties in mapping broader social and environmental impacts on related sectors (Nur Afni Nurul Nur Aeni & Etty Murwaningsari, 2023) . To address the gap in non-strategic mapping of biomass materials in the housing sector, a comprehensive bibliometrics is needed in this field. Considering the above discussion, this study aims to analyze, present, and describe research trends on biomass materials in residential construction using bibliometric analysis . Based on this objective, this study presents six questions to be addressed in this study as follows: 1) What are the publication trends related to *Biomass Materials in Residential Building Construction in supporting* innovative learning over the last decade ; 2) Which journals are the most productive in publishing literature on *Biomass Materials in Residential Building Construction* ; 3) Who are the most productive authors, institutions and countries in producing research related to *Biomass Materials in Residential Building Construction*; 4) How are the relationships between researchers and international collaboration patterns ; 5). What are the main themes, keywords, and most dominant research topics in the topic *Biomass Materials in Residential Building Construction* ;5) Which country is the most productive in emphasizing the topic of *Biomass Materials in Residential Building Construction* in classroom planning; *6)* What references are frequently cited in emphasizing the topic of *Biomass Materials in Residential Building Construction ; 7)* How is the thematic evolution of *Biomass Materials in Residential research? Building Construction* from year to year. Through comprehensive analysis , this research is expected to contribute to the development and innovation of biomass materials in the residential construction sector.

Method

This study employs a quantitative descriptive research framework, employing a bibliometric analytical approach. The aim of this review is to examine publication trends, collaborative networks of authors, and dominant themes in the field of biomass in the context of residential building construction. The bibliometric methodology facilitates the systematic mapping of scientific output and the structured organization of knowledge derived from publication metadata obtained from databases. Scopus over the previous decade (Setyanto et al., 2023) . The data collection process was conducted through the Scopus scientific database, which is recognized for its wide coverage of multidisciplinary research types. (Taqiyyah & Soebagyo, 2022) . To facilitate this goal, the investigated population includes all scientific publications related to the subject of “biomass materials in dwellings” that are accessible in the database. Scopus . The selected sample was described by a strategy that included Boolean keyword searches such as “biomass” AND “residential buildings” AND “construction” AND “biomass waste” OR “agricultural waste” AND (“construction materials” OR “building materials”), applied to titles, abstracts, and keywords, along with specific criteria limited to well -indexed articles and conference proceedings, publications written in English, and those disseminated from 20214 to 2024. After the screening process, a total of 116 articles were obtained as a suitable sample for analysis. To analyze the data effectively, the main instruments used in this study consisted of the VOS viewer software and

Bibliosinhy, which are based on the Bibliometric R package. Both tools were used to process the data, dissect and visualize collaborative networks of authors, institutions, countries, keyword occurrences, citation and co - citation networks, as well as analyze thematic trends and evolutions. Furthermore, OpenRefine software was used to eliminate duplicate data entries.

The methodology for carrying out this research begins with a meta- retrieval process sourced from the database. Scopus will be searched using predefined Boolean keyword searches. The data will then be refined using OpenRefine to detect duplicate and irrelevant publications, while retaining publications that align with the established inclusion criteria. The data will then undergo analytical scrutiny. Descriptive analysis will be used to assess publication growth, source journals, and document types. Network analysis will utilize VOSviewer to visualize collaborative interactions between authors, institutions, and countries. A concluding analysis, including thematic analysis and keyword mapping, will be conducted using Biblioshy, which will illuminate key themes and developments in the publication landscape.

Results

Research using bibliometric analysis methodology seeks to systematically organize, examine, and visualize the evolution of scientific trends regarding Biomass Materials in Residential Housing. The investigation is categorized into seven different objectives, which include trends and progress in publications, the most productive academic journals, the most productive authors and their interconnections, the most frequently cited scientific references, the most frequently used keywords, and the development of research themes. In general, author networks, co-occurrences, and keywords will be subjected to analysis and visualization through VOSviewer , while other categories will be examined using Bibliometrix . Presented below are the research findings that correspond to each of the aforementioned categories.

Publication Trends & Developments

Trends and developments in publications from research on the theme of *Biomass Materials in Residential Building Construction* was collected through Scopus with a total of 116 documents. Based on general data analysis using Bibliometrix software, comprehensive information about the distribution of article publications, the time span of article publications, the average age of documents, the average citations per document, keywords from authors, author keywords, documents written by one author, international co -authorship , co-authors per document, the country of the corresponding author and references are available in Table 1.

Table 1. Summarize of the review (main ınformation)

Description	Results
Play Information about Data	
Timespan	2014:2024
Sources (Journals & Conference)	86
Documents	
Documents	136
Annual Growth Rate %	9.04%
Document Average Age	5.18
Average Citations Per Document	24.92
References	5007
Documents Contents	
Keyword Plus (Id)	1279
Author's Keywords (DE)	485
Authors	
Authors	491
Authors Of Single-Authored Documents	7
International Co- Authorships %	22.79%
Co- Authors Per Documents	3.99
Documents Types	
Article	100
Conference Paper	36

This study explains, in Table 1 the bibliometric review covers publications from 2014 to 2024 with a total of 136 documents originating from journals and conference proceedings. The annual growth rate reaches 9.04% indicating a fairly stable trend of increase in the last decade. The average age of the documents is 5.18 years and the average citation per document is 24.92 revealing the relevance and scientific influence of this topic is quite high. A total of 5007 references are used, indicating a comprehensive and thorough examination of the library scope. The distinguished keywords include 1279 Keyword Plus (ID) and 485 Author Keyword (DE), reflecting the diversity of topics and the potential for thematic investigations in the research domain. From an authorship perspective, there are 491 contributors, with only 7 papers produced by individual authors. The international collaboration rate is recorded at 22.79%, while the average number of authors per publication reaches 3.99, highlighting a clear trend towards collaborative research efforts.

In terms of document classification, the dominant type consists of journal articles, totaling 100 documents, while the remainder are conference proceedings, totaling 36 documents. This distribution proves that most of the analyzed literature comes from peer-reviewed publications, which usually have a high level of scientific rigor and reliability. Meanwhile, Figure 2 explains the trend of the number of scientific publications each year from 2014 to 2024. At the beginning of the analyzed time frame, the volume of scientific articles was relatively modest, starting with 8 articles in 2014 and rising to 10 articles in 2015, followed by a slight decrease to 9 articles in 2016. However, a marked reduction was observed in 2017, with only 6 publications documented. To see the trend of the number of scientific publications from 2014 to 2024 can be seen in Figure 2.

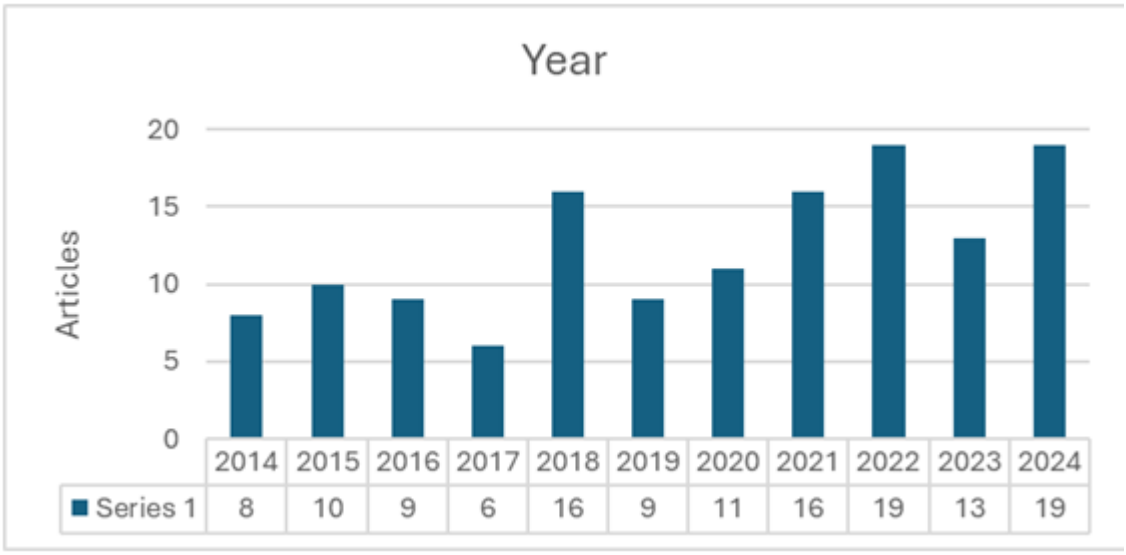


Figure 1. Progression of number of publications from 2014 to 2024

In Figure 1, at the beginning of the period the number of articles was relatively low, starting from 8 articles in 2014 and increasing to 10 articles in 2015 and 9 articles in 2016. However, there was a significant decrease in 2017 with only 6 publications. In 2018, there was a large surge, culminating in 16 articles, indicating an increased focus on the subject matter being examined. Subsequently, the number of scientific publications showed variability, with a small decrease in 2019 (9 articles) and a progressive escalation in 2020 (11 articles) and 2021 (16 articles). The peak of publication quantity was reached in 2022, recording a total of 19 articles, followed by a small decrease in 2023 (13 articles), and again increasing to 19 articles in 2024. Overall, the trajectory of publication numbers shows an upward trend over the previous decade, with a significant expansion post-2017. This phenomenon underscores the increasing interest and academic significance attributed to the research theme during that temporal segment.

Most Productive Journal

To identify the primary publication sources in this field of study, an analysis of the journals most frequently publishing related articles was conducted. The results are presented in Table 2, which shows the ten most productive journals based on the number of publications and total citations during the analyzed period. Table 2 shows the ten most productive journals that are the primary sources of publications related to the topics analyzed. The journal *Energies,* published by MDPI, ranked first with a contribution of 11 articles (8.08%) and

a total of 178 citations . It was followed by *Energy and Buildings* from Elsevier BV with 8 articles (5.88%) and the highest total citations among all, namely 305 citations.

Table 2. Top-10 most relevant sources

Journal	TAP (%)	TC	Publisher
Energies	11 (8.08%)	178	MDPI
Energy And Buildings	8 (5.88%)	305	Elsevier BV
Renewable Energy	6 (4.41%)	253	Elsevier Ltd
Sustainability (Switzerland)	5 (3.67%)	286	MDPI
Applied Energy	4 (2.94%)	61	Elsevier BV
Buildings	4 (2.94%)	45	Elsevier BV
Energy	3 (2.2%)	200	Elsevier BV
Energy Conversion And Management	3 (2.2%)	187	Elsevier Ltd
Journal Of Cleaner Production	3(2.2%)	964	Elsevier Ltd
Journal Of Physics : Conference Series	3(2.2%)	102	IOP

Renewable Energy and *Sustainability* Journal *(Switzerland)* also occupies a significant position, contributing 6 and 5 articles respectively, with a total of 253 and 286 citations . Most of the journals in this list are published by Elsevier , either through BV or Ltd entities, which shows the dominance of this publisher in the fields of energy, buildings and sustainability. In addition, *the Journal of Cleaner Production* recorded the highest total citations of 964 despite contributing only 3 articles, indicating the very high quality and scientific impact of the articles it published.

Therefore, most of the publications in this study come from reputable international journals, particularly those published by **Elsevier** and **MDPI** , focusing on energy, buildings, and sustainability. This confirms that the topics reviewed are highly relevant in the global scientific discourse and are published in high-impact journals in their respective fields.

Most Productive Author

Based on Table 1, there are 491 authors involved in 136 publications with an average of 3.99 authors per document , indicating high collaboration in research related to this topic. To identify the most active contributors to these publications, Table 3 presents the ten most productive authors along with bibliometric indicators such as *h- index* , *g- index* , *m- index* , total citations (TC), and their home institutions.

Table 3. Top-10 most profiled authors

Author	h_index	g_ index	m_index	TC	NP	PY_start	Affiliation
Cabeza Luisa F.	4	4	0.25278	903	4	2015	Xi'an Jiaotong University
Baratieri Marco	3	3	0.17361	99	3	2014	Chiang Mai University
Borri Emiliano	3	3	0.34722	70	3	2020	Dalian University Of Technology
Anoop S.	2	2	0.15417	12	2	2017	Shanxi University
Aye Lu	2	2	0.27778	64	2	2021	University Of La Rioja
Calise Francesco	2	2	0.15417	79	2	2017	Aristotle University
Cappiello Francesco L.	2	2	0.27778	53	2	2021	Politecnico of Milan
Carlon Elisa	2	2	0.12639	59	2	2015	Shihezi University
Charalampidis Antonios	2	2	0.23125	57	2	2020	Otto- Von - Guericke- University
D'accadia Massimo Dentistry	2	2	0.15417	79	2	2017	The University Of Melbourne

Note : H -index = an author has an h- index of 'h' when they have h papers that have been cited h times at least , G-Index = is where the top G articles have together received G citations , M- index = is the H- index divided by the number of years that an the author has been active , Tc = Total Citations , Np = Number of papers , Py_Start = publication year start

Table 3 shows that the author **Luisa F. Cabeza** from **Xi'an Jiaotong University** is the most productive and most influential author, with the highest *h- index* and *g- index* (4 each), and total citations reaching **903** from 4 publications since 2015. This figure is also reflected in the highest *m- index* among other authors (0.25278), indicating consistent contributions over a relatively long period.

Other authors who are also active are **Baratieri Marco** (Chiang Mai University) and **Borri Emiliano** (Dalian University of Technology), each with 3 publications and total citations of 99 and 70. Meanwhile, several other authors such as **Ave Lu** , **Cappiello Francesco L.** , and **Charalampidis Antonios** began his contributions in 2020–2021, with a relatively high *m- index* indicating productivity in a shorter period. Contributions come from leading countries and institutions such as China, Italy, Germany, Australia, and Thailand, demonstrating global engagement in this research topic.

Thus, the most productive authors in this field come from renowned institutions and show variation in terms of number of publications, total citations , and rate of scientific productivity (*m- index*). The dominance of Luisa F. Cabeza demonstrates her central role in the development of this topic, while contributions from new authors with high *m- indexes* indicate a growing and expanding global research interest.

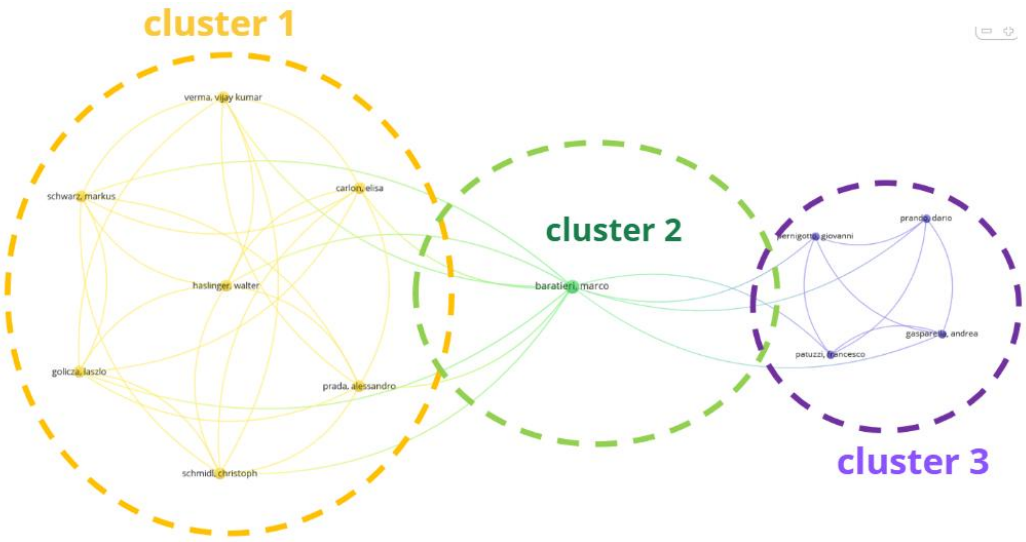


Figure 2. Collaborative network between authors on biomass materials in residential building construction

In line with the identification of the most productive authors in Table 3, Figure 2 visualizes **the collaboration network between authors** in the topic of *Biomass Materials in Residential Building Construction* uses mapping from VOSviewer . The network is divided into **three main clusters** , which indicate collaborative groups based on the frequency of article co-authorship.

- **Cluster 1 (yellow)** is the largest and densest collaborative group, involving authors such as *Verma Ajay Kumar* , *Schweiker Markus* , and *Gkoktsi Alasio* . The authors in this cluster appear to be closely networked with each other , indicating a high level of collaboration among them.
- **Cluster 2 (green)** is led by *Baratieri Marco* — one of the most prolific authors who also appears in Table 3. He acts as a liaison between the clusters, collaborating with authors from both cluster 1 and cluster 3, demonstrating a central role in the research network.
- **Cluster 3 (purple)** contains authors such as *Arrigoni Alessandro* , *Preti Luca* , and *Pittaluga Andrea* , who form their own collaborative group but remain connected to other clusters through cross-group collaborators.

Thus, this visualization reinforces the data in Table 3, showing that authors with high productivity tend to play a central role in scientific collaboration networks. The presence of interconnected clusters demonstrates that biomass research in residential building construction is multidisciplinary and globally collaborative.

Citation Analysis

Corresponding Author's Countries

Based on Table 1, **136 documents** were analyzed, with contributions from various international authors. To understand the geographic distribution of this research, Figure 3 illustrates the country of origin of the corresponding authors and distinguishes between national publications (SCPs) and international collaborations (MCPs).

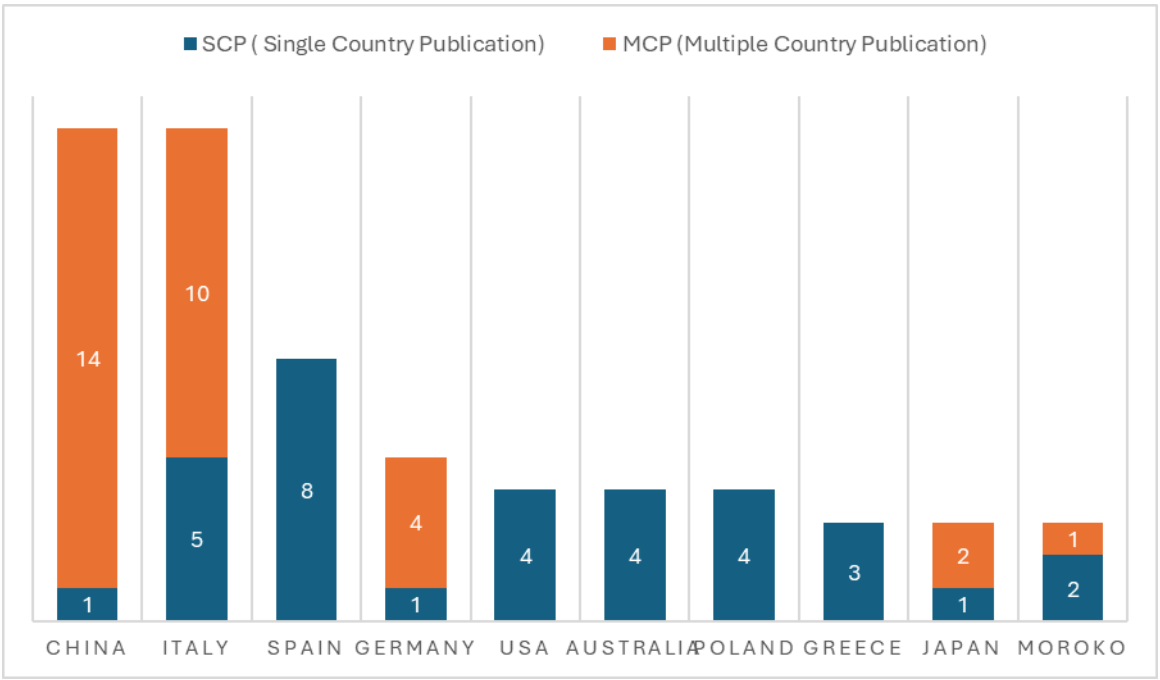


Figure 3. Most relevant countries

Figure 3 shows that **China** and **Italy are the two countries with the largest contributions to** *biomass* -related publications . *materials in residential building* China has a total of **15 publications** , dominated by international collaborations (*Multiple Country Publications/MCP*) with 14 documents, only 1 is national (*Single Country Publication /SCP*). A similar situation also occurs in Italy, with a total of *15* **publications** (10 MCP and 5 SCP). Spain followed with 8 publications , all of which were SCPs, demonstrating the dominance of local research. Countries such as Germany , the United States , Australia , and Poland each contributed 4 publications, most of which were the result of domestic collaborations.

Interestingly, countries like **Japan** and **Morocco** are also beginning to contribute, albeit in smaller numbers, but with a significant share of international publications. This visualization demonstrates that research topics related to biomass in residential construction have a broad international reach. Countries like **China and Italy** are not only active in terms of the number of publications but also demonstrate **a high level of international collaboration,** reinforcing the importance of cross-border cooperation in the development of sustainable research.

Most Prolific Countries

Following on from the previous analysis of the distribution of citations and publications by country, Table 4 provides a comprehensive overview of the ten most productive countries in the topic of biomass for residential building construction. This analysis not only highlights total citations (TC), but also presents the average citations per article, the number of articles , and the frequency of contributions , all of which reflect the quality and intensity of research per country.

Based on the data, Italy recorded the highest number of citations (TC = 248) with 90 contributed articles , indicating that this country is active and consistent in producing publications. However, in terms of average citations per article , the country only recorded 16.5 , which indicates that although productive, not all articles have high citation power. In contrast, Switzerland and Sweden showed very high average citation numbers , namely 199 and 104 , even though their article contributions were relatively low, only 23 and 45 articles , respectively . This indicates that although their contributions are not large quantitatively, the quality and influence of their articles are very significant.

Table 4. Top 10 most prolific countries

Country	TC	Average Article Citations	Frequent
Italy	248	16.50	90
China	222	0.6042	72
Sweden	208	104.00.00	45
Spain	199	24.90	39
Switzerland	199	199,000,000	23
USA	154	30.80	20
Japan	147	49,000,000	20
Morocco	93	31.00.00	18
Australia	91	0.9722	17

China, as one of the countries with the most publications (72 articles), has a low average citation rate of 0.60 , indicating challenges in ensuring the quality or relevance of articles within the scientific community. Other countries such as the USA, Japan, Morocco , and Australia also show interesting dynamics, where they may not be as dominant in terms of the number of publications, but some have competitive average citations -such as the USA (30.8) and Japan (49.0) -which reflect the quality of research that is worthy of consideration.

This table shows that scientific productivity can be measured not only by the number of articles published , but also by scientific influence, as reflected in the average citation rate per article . Countries like Switzerland and Sweden demonstrate that quality and influence can outweigh quantity, while Italy and China occupy strategic positions in terms of numerical contribution but need to be boosted in terms of citation capacity. These findings emphasize the importance of promoting research that is not only plentiful but also high-quality and has a global impact.

Most Cited References

Based on Table 1, this study includes an analysis of 136 scientific documents published between 2014 and 2024, with an average document age of 5.18 years. The number of references collected reached 5007. From the total references, the most frequently cited publications were identified to understand the direction, focus, and main influences in this research field. Table 5 presents the 10 most cited publications in all the documents reviewed.

Table 4. Top 10th global cities documents

Paper	DOI	Total Citations	TC per Year	Normalized TC
Ürge-Vorsatz D, 2015, Renewable Sustainable Energy Rev	10.1016/j.rser.2014.08.039	833	75.73	7.52
Wu R, 2017, Appl Energy	10.1016/j.apenergy.2016.12.161	199	22.11	3.30
Su C, 2018, Energy Convers Manage	10.1016/j.enconman.2018.10.005	157	19.63	6.46
Yang S, 2023, Environ Sci Pollut Res	10.1007/s11356-022-19764-0	116	38.67	7.15
Sharafi M, 2015, Renew Energy	10.1016/j.renene.2015.05.022	103	9.36	0.93
Heiskanen E, 2017, Renewable Sustainable Energy Rev	10.1016/j.rser.2016.11.027	100	11.11	1.66
Zhao M, 2015, Energy Build	10.1016/j.enbuild.2015.03.007	88	8.00	0.79
Charai M, 2021, J Clean Prod	10.1016/j.jclepro.2021.126064	87	17.40	3.01
Perea -Moreno MA, 2018, Sustainability	10.3390/su10103407	74	9.25	3.04
Dobravec V, 2021, Energy Sustainability Soc	10.1186/s13705-020-00277-y	66	13.20	2.28

Table 5 displays the total number of citations, citations per year, and *Normalized TC values* . This table provides an overview of the relative contribution of each article to the advancement of knowledge and the global literature map in this field. Table 5 summarizes the 10 most influential global publications in this study based on the highest number of citations. The most highly cited article is from Ürge-Vorsatz D (2015) published in *Renewable and Sustainable Energy Reviews* , with a total of 833 citations and an average of 75.73 citations per year, and *a Normalized TC* of 7.52. This demonstrates a significant contribution to the development of knowledge in the field of renewable energy and building efficiency. The next sequence is filled by Wu R (2017) in the journal *Applied Energy* with 199 citations, followed by Su C (2018) in *Energy Conversion and Management* with 157 citations. Interestingly, although the article by Yang S (2023) is the most recent, it has a very high *Normalized TC (7.15), indicating a very strong early impact in the scientific community. In contrast, several publications with low citations, such as* Zhao M (2015) and Sharafi M (2015), have relatively small *Normalized TCs* , indicating that despite their long publication history, their contributions are still not widely used as primary references.

The data in Table 5 confirms that publications are relevant, innovative, and fall within the domain of strategic topics such as *renewable Energy* and *sustainability* tend to have high academic influence, as seen in annual citation counts and *Normalized TC* . Furthermore, recently published but immediately high-impact articles, such as those by Yang S (2023), indicate a shift in research attention toward more contemporary and applicable approaches, such as the environmental impact of pollution and sustainability. After identifying the most frequently cited global references in Table 5, the analysis continued by examining the most frequently cited references locally within the reviewed documents. Table 6 presents *the top 10* most frequently cited references within the analyzed literature, indicating a more contextual and specific focus and preference for the literature within a particular region or field of study.

Table 5. Top 10 most locally cited references

Cited References	**Citations**
Ogunjuyigbe ASO, Ayodele TR, Akinola OA	8
Duffie JA, Beckman WA, Solar Engineering Of Thermal Processes , (2013)	4
Ahmad J., Imran M., Khalid A., Iqbal W., Ashraf SR, Adnan M., Ali SF, Khokhar KS, Techno Economic Analysis Of A Wind-Photovoltaic-Biomass Hybrid Renewable Energy System For Rural Electrification : A Case Study Of Kallar Kahar, Energy, 148, Pp. 208-234, (2018)	3
Hu S., Yan D., Guo S., Cui Y., Dong B., A Survey On Energy Consumption And Energy Usage Behavior Of Households And Residential Building In Urban China, Energy Build , 148, Pp. 366-378, (2017)	3
2019 Annual Report On China Building Energy Efficiency , (2019)	2
Abas N., Kalair A., Khan N., Review Of Fossil Fuels And Future Energy Technologies, Futures , 69, Pp. 31-49, (2015)	2
Action E., Implementing The Energy Performance Of Buildings Directive (Epbd), Featuring Country Reports , (2016)	2
Al-Sulaiman FA, Hamdullahpur F., Dincer I., Performance Assessment Of A Novel System Using Parabolic Trough Solar Collectors For Combined Cooling , Heating , And Power Production , Renew . Energy, 48, Pp. 161-172, (2012)	2
Annual Report On China Building Energy Efficiency 2019, (2019)	2
Antipova E., Boer D., Guillen-Gosalbez G., Cabeza LF, Jimenez L., Multi- Objective Optimization Coupled With Life Cycle Assessment for Retrofitting Buildings , Energy Build , 82, Pp. 92-99, (2014)	2

Table 6 displays the most frequently cited references in the reviewed document set, reflecting the theoretical foundations or key data that authors frequently use in their studies. The reference with the highest number of local citations is the work of Ogunjuyigbe ASO et al. et al. who obtained **8 local citations** , indicating his dominant contribution in research related to local context-based energy systems.

Some other important references come from Duffie and Beckman (2013) on solar thermal systems (4 citations), as well as two articles from the journal *Energy* discussing hybrid energy systems and energy consumption behavior in urban residential buildings in China, each with 3 citations. There are also important policy documents such as *the Annual Report on China Building Energy Efficiency (2019)* which appears twice with the same citation frequency. Other references include a review of future energy technologies (Abas et al. , 2015), building energy performance (Action E, 2016), and building retrofit approaches using multi -objective optimization (Antipova et al. , 2014), all of which have two local citations.

This table indicates that the reviewed studies rely heavily on literature relevant to local and practical contexts, particularly those related to building energy efficiency, integrated renewable energy systems, and energy policy. Not only scientific articles but also annual reports and national policy documents are included as important references. This reflects the applied and contextual approach of the research, as well as the need for energy solutions tailored to specific regional conditions.

Most Occurring Keywords

Bibliometric analysis , the frequency of keyword occurrence is an important indicator for identifying the main focus and thematic trends in a research field (Donthu et al., 2021) . Figure 4 presents a visualization of the 50 most frequently used keywords by authors in studies on renewable energy, building efficiency, and sustainability, generated using the *Bibliometrix tool.* From Figure 4 , it can be seen that the dominant topic that appears most frequently is *residential. building, housing* , *energy efficiency* , *biomass* , *energy utilization* , and *heating* . These keywords reflect the primary focus of research on energy efficiency in the residential sector and the use of alternative resources such as biomass.

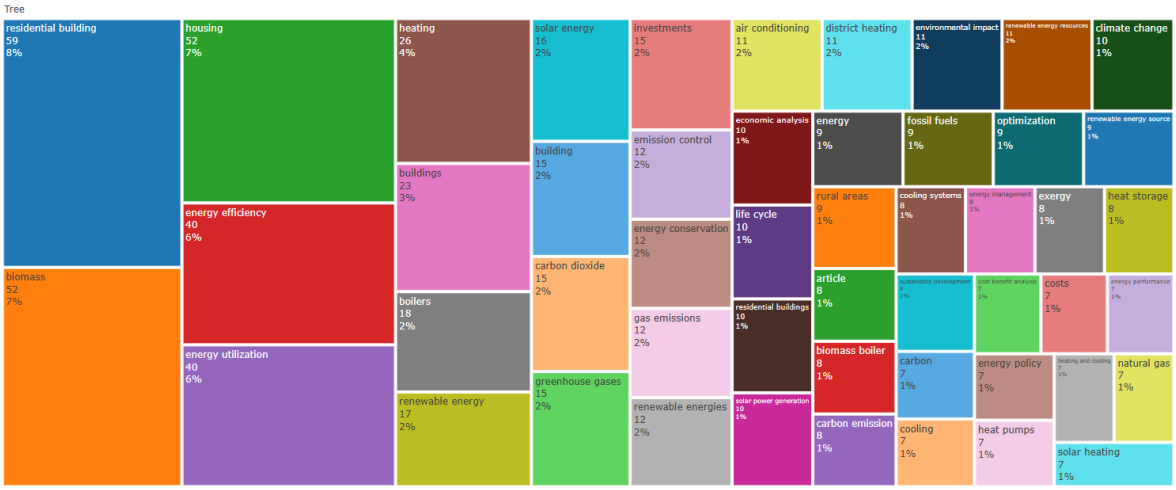


Figure 3. Top-50 author keywords , frequency , & proportion (Source : Authors ' own elaboration , using Bibliometrix)

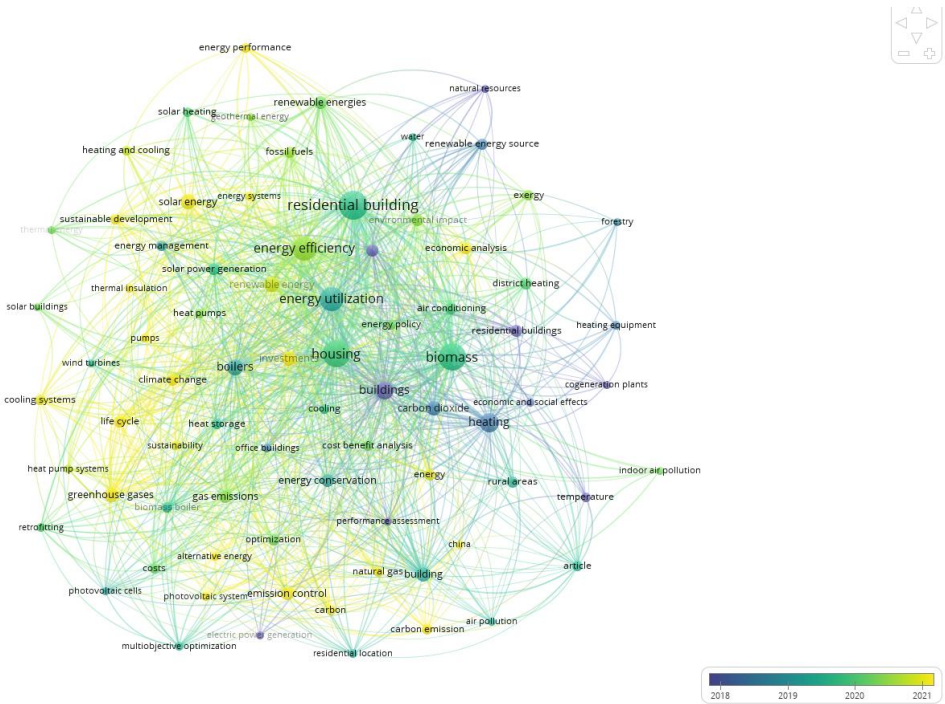


Figure 4. Network map of author keywords by year

Keyword network mapping in bibliometrics is very useful for revealing the conceptual structure and dynamics of research in a field (Cobo et al., 2011) . Figure 5 shows a map of the most frequently used keyword networks by authors, mapped by their time of appearance from 2018 to 2021, using VOSviewer software. Meanwhile, Figure 5 enriches the insight by showing the temporal evolution of the keywords. Earlier topics such as *energy efficiency* and *residential building* becomes the center of the network, signifying its establishment as a core issue. While newer, yellow keywords, such as *carbon emissions, retrofitting* , *economics analysis* , and *smart buildings* , shows the direction of research development towards a more multidimensional approach, covering environmental, economic and technological aspects.

The combined analysis of keyword frequency (Figure 4) and keyword temporal network map (Figure 5) reveals the direction and dynamics of research development in the field of sustainable energy and buildings over the past few years. The combination of these two visualizations shows that while energy efficiency and residential buildings remain the foundation of research, there is a shift in interest towards more complex and sophisticated issues, including carbon emissions, environmental impact reduction, and renewable energy integration.

Thematic Evolution

The growing demand for sustainable buildings has driven the development of research focused on the use of alternative biomass-based materials. In the context of residential construction, this approach aims not only to reduce the carbon footprint but also to improve energy efficiency and indoor environmental quality (Fernández et al., 2024; Garcia et al., 2014) . Figure 6 depicts a thematic map of the evolution of research on biomass materials for residential building construction, showing how themes such as *" residential building "* , *" biomass "* , and *" housing "* have become *basic themes* —indicates that these topics have high centrality in this field, even though their level of development is still limited.

The thematic evolution map in Figure 6 is the result of a bibliometric analysis that illustrates the dynamics of research related to biomass materials in residential building construction. This analysis was developed to understand how scientific themes evolve over time based on the dimensions of relevance (centrality) and depth of development (density).

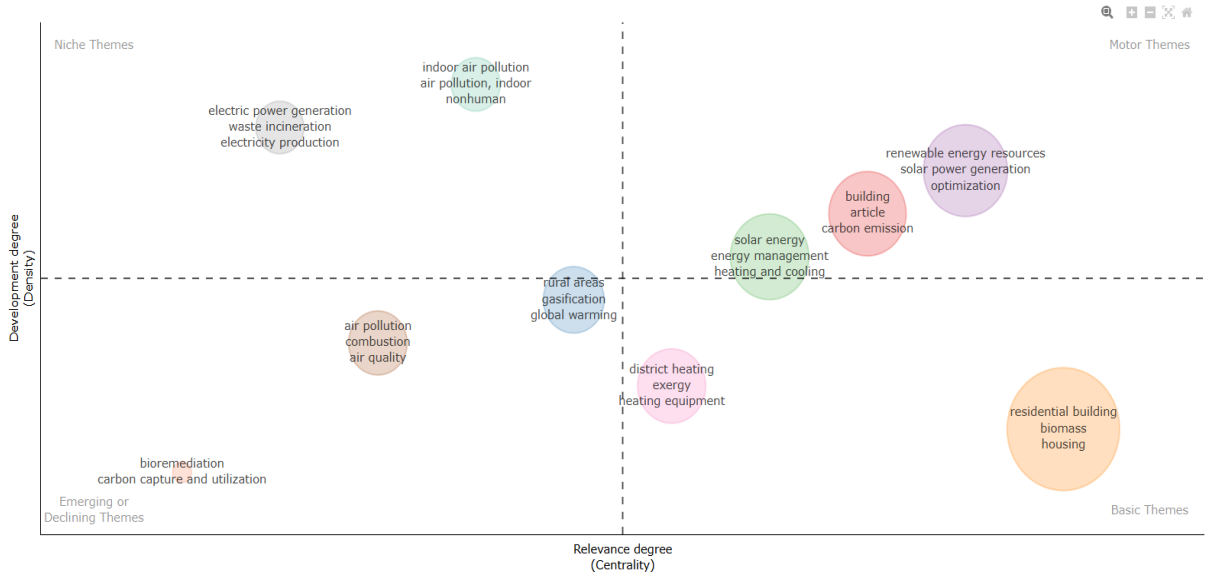


Figure 5. Thematic evolution map of biomass materials in residential building construction research

Bottom Right Quadrant – Basic Themes

Basic Themes are basic themes in biomass research that tend to be general yet essential, as they serve as the foundation for more advanced themes (Shi et al., 2021) . In this quadrant, themes such as *residential building* , *biomass* , and *housing* are in the *basic category themes* , meaning these themes are central to the research field but have not been developed in depth. This indicates that these topics form an important foundation and are continually discussed in the literature, but are still open to further, deeper, and more specific exploration.

Upper Right Quadrant – Motor Themes

Motorcycle Themes is a theme like renewable Energy and carbon emissions are key drivers in sustainable architecture, as they offer direct solutions to the climate crisis. (Zhao et al., 2023) . In Figure 6, themes such as renewable energy resources, solar power generation , optimization , and carbon emissions and buildings The article demonstrates high development and high centrality . This means the topic is not only popular but also actively developing and driving the direction of biomass research in building construction. This topic generally relates to the integration of biomass into energy systems and carbon emission reduction strategies.

Upper Left Quadrant – Niche Themes

Niche Themes are themes such as indoor air pollution and waste Incineration is often in a specialized context with a narrow but technical and detailed focus. (Liao et al., 2019) . In Figure 6, topics such as *indoor air pollution* , *waste incineration* , and *electricity Production* occupies a niche position . This indicates that these themes are developing independently, but lack strong links to other major themes in the field. Research on these themes is typically more technical in nature or focused on specific applications.

Lower Left Quadrant – Emerging or Declining Themes

Emerging or Declining Themes in this quadrant can indicate new research directions or areas that are starting to be abandoned due to limited applicability (Ge et al., 2022) . In Figure 6, themes such as *bioremediation* and *carbon capture and utilization* is included in the *emerging category or declining This topic* has little relevance and development, possibly because it is still relatively new in the context of residential buildings or is starting to be abandoned in current research trends.

This thematic map shows that biomass research in residential building construction is still very much focused on basic issues such as *housing* , *residential building* , and *biomass* , but are beginning to shift toward integration with renewable energy systems and carbon emission reduction. This reflects a transition from a passive approach to an active and integrated approach to sustainable development. Therefore, research opportunities remain wide open to explore the relationship between biomass and energy performance, indoor air quality, and the optimization of material technology in modern, environmentally friendly residential architecture. Continuing from the thematic classification above, Figure 7 presents **the temporal evolution of keywords** , showing the trend in the use of key terms over the period 2014–2024. This graph shows when a topic first emerged and how long it was actively discussed in the literature:

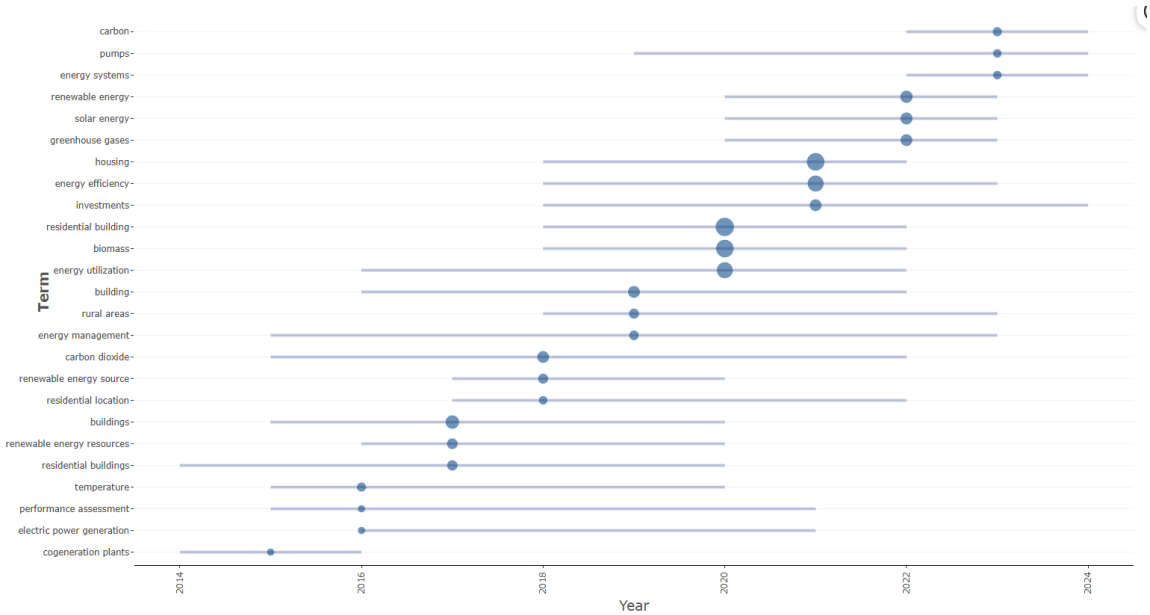


Figure 6. Temporal evolution of research keywords in of biomass materials in residential building construction (2014–2024)

In early 2014 to 2017, research focused on technical issues such as " electric power generation ", " performance assessment ", and " residential buildings , which became the initial foundation for the topic of biomass in construction. Entering 2018 to 2020, diversification of themes began to emerge, such as " renewable energy resources ", " residential location ", and " carbon dioxide , signifying a shift towards sustainability and carbon emissions in the building context. Peaking in 2020 to 2023, research increasingly emphasized direct implementation in buildings, as evidenced by the intensity of keywords such as " biomass ," " residential ," and " greenhouse." building ", " investments ", " energy " efficiency ," and " building ." This indicates a focus on real-world applications and energy optimization in biomass-based residential buildings. Then, in the period from 2022 to 2024, new, more complex keywords emerged, such as "solar energy ," "energy ," and " energy efficiency. " systems ", and " greenhouse gases ", demonstrating the integration of biomass technology with other renewable energy systems to address the challenges of the climate crisis and greater energy efficiency. The temporal evolution of these keywords demonstrates that biomass research in the residential building sector has evolved from initial technical issues to strategic applications integrated with renewable energy systems.

Discussion

This study comprehensively examines the scientific trends and knowledge landscape related to the use of biomass materials in residential building construction through a bibliometric approach. Overall, the results indicate that this topic has experienced significant growth in the last decade. The annual growth rate of publications reached 9.04%, which is in line with the increasing global attention to sustainability and energy efficiency issues in the housing sector. This phenomenon aligns with Adeleke's findings. et al. (2021), who highlighted the important role of biomass in supporting sustainable buildings, especially due to its thermal and economic characteristics.

In the context of literature dissemination, most of the publications come from reputable journals such as *Energies* , *Renewable Energy* , and *Journal of Cleaner Production* . This reflects that biomass research is not only relevant at the local level, but has become part of the global scientific discourse with high impact. Journal of Cleaner Production even has the highest number of citations (964), indicating its strategic role in disseminating biomass issues in low-carbon development.

In terms of scientific collaboration, the author network shows a highly collaborative pattern, with an average of 3.99 authors per document and contributions from 491 authors. Authors such as Luisa F. Cabeza from Xi'an Jiaotong Universities occupy a central position, with high productivity and broad citation impact . The existence of cross-border collaborations, as demonstrated by contributions from China and Italy, reflects the transnational nature of biomass research, as further reinforced by contributions from other European countries such as Sweden and Switzerland, which show the highest citation- per-article ratios. Furthermore, thematic analysis revealed that biomass research in residential buildings has evolved from basic themes such as *residential building* and *housing* , towards driving themes such as *carbon emission* , *renewable energy* , and *optimization* . These findings are supported by the research results of Fernández et al. (2024) and Zhao et al. (2023) who stated that biomass is not only an alternative material, but is an integral part of climate change mitigation strategies in future architectural designs.

Temporal trends also show a shift from technical topics towards strategic and systemic applications , with the emergence of keywords such as *solar energy* , *greenhouse gases* and *energy systems* in the 2022–2024 period. This shift demonstrates the integration of biomass into the broader context of the renewable energy transition. On the other hand, the findings of keywords such as *retrofitting* and *economic analysis* indicates that economic studies and investment efficiency are becoming new concerns in this field.

Finally, citation analysis shows that seminal works such as Ürge-Vorsatz et et al. (2015) and Su et et al. (2018) is a key reference in developing the theoretical foundations and practices of biomass. Local references also show a focus on building energy efficiency and hybrid biomass systems, as demonstrated by Ogunjuyigbe. et al. (2018), which strengthens the contextual approach in developing locally based solutions.

Conclusion

This study shows that the topic of *biomass materials in residential building Construction engineering* has experienced significant quantitative and qualitative growth over the past decade. A consistent increase in publications, contributions from leading journals, and cross-border collaborations indicate that this field is

increasingly strategic in supporting sustainability and carbon emission reduction. Thematic analysis indicates a shift in research from basic issues to integrative approaches, such as energy optimization, retrofit strategies, and biomass integration with renewable energy systems. Furthermore, the presence of high-impact references confirms that this field is supported by a solid and dynamically developing literature. Overall, these results not only map scientific developments in the field of building biomass, but also open up opportunities for further research related to technical, economic, and policy aspects in the context of low-carbon development, especially in regions with abundant local resources such as the 3T regions in Indonesia.

Scientific Ethics Declaration

* The authors declare that the scientific ethical and legal responsibility of this article published in EPSTEM journal belongs to the authors.

Conflict of Interest

* The authors declare that they have no conflicts of interest

Funding

* The authors would like to express their sincere appreciation and gratitude to the Education Fund Management Institute (LPDP), Ministry of Finance of the Republic of Indonesia, for its valuable support in facilitating this publication and fostering collaboration.

Acknowledgement

* This article was presented as a poster presentation at the International Conference on Technology, Engineering and Science (www.icontes.net) held in Antalya/Türkiye on November 12-15, 2025.

* This research was made possible through the suport of the Indonesia Endowment Fund for Education (LPDP), Ministry of Finance of the Republic of Indonesia and for the opportunity to participate in international academic forums

* The author would like to express sincere gratitude to the Institut Teknologi Bandung (ITB), especially to the Faculty School of Architecture, Planning, and Policy Development (SAAPK) and the Master Program in Architecture, for the continuous academic support, guidance, and opportunity to participate in international academic forums.

References

Adeleke, A. A., Ikubanni, P. P., Orhadahwe, T. A., Christopher, C. T., Akano, J. M., Agboola, O. O., Adegoke, S. O., Balogun, A. O., & Ibikunle, R. A. (2021). Sustainability of multifaceted use of biomass: A review. *Heliyon, 7*(10), e08025.

Akib, Y. M., Bedsole, C. O., Rahman, A. M., Hamilton, J., Khan, F., Pei, Z., Shaw, B. D., & Ufodike, C. O. (2024). A preliminary experimental study on biodegradation of 3D printed samples from biomass-fungi composite materials. *Preprints*.

Bhardwaj, A., Rahman, A. M., Wei, X., Pei, Z., Truong, D., Lucht, M., & Zou, N. (2021). 3D printing of biomass–fungi composite material: Effects of mixture composition on print quality. *Journal of Manufacturing and Materials Processing, 5*(4), 112.

Cobo, M. J., López-Herrera, A. G., Herrera-Viedma, E., & Herrera, F. (2011). Science mapping software tools: Review, analysis, and cooperative study among tools. *Journal of the American Society for Information Science and Technology, 62*(7), 1382–1402.

Cruz, J., & Garcia-Uitz, K. (2024). Use of sargassum and other organic substitutes in the construction industry: A review. *Métodos y Materiales, 14*, 1–12.

Donthu, N., Kumar, S., Mukherjee, D., Pandey, N., & Lim, W. M. (2021). How to conduct a bibliometric

analysis: An overview and guidelines. *Journal of Business Research, 133*, 285–296.
Garcia, R. A., Cabeza, M., Rahbek, C., & Araújo, M. B. (2014). Multiple dimensions of climate change and their implications for biodiversity. *Science, 344*(6183), 1247579.
García-Fernández, M., Álvarez-Narciandi, G., Laviada, J., López, Y. Á., & Las-Heras, F. (2024). Towards real-time processing for UAV-mounted GPR-SAR imaging systems. *ISPRS Journal of Photogrammetry and Remote Sensing, 212*, 1–12.
Ge, Y., Chao, T., Sun, J., Liu, W., Chen, Y., & Wang, C. (2022). Frontiers and hotspots evolution in psycho-cardiology: A bibliometric analysis from 2004 to 2022. *Current Problems in Cardiology, 47*(12), 101361.
Judijanto, L., Putri, V. K., Ansori, T., & Khamaludin, K. (2023). Analysis of the impact of renewable energy, energy efficiency, and green technology on carbon emission reduction in the manufacturing industry in Tangerang City. *Multidisciplinary Journal of West Science, 2*(12), 1127–1138.
Liao, Y., Wang, J., Jaehnig, E. J., Shi, Z., & Zhang, B. (2019). WebGestalt 2019: Gene set analysis toolkit with revamped UIs and APIs. *Nucleic Acids Research, 47*(W1), W199–W205.
Nur Aeni, N. A. N., & Murwaningsari, E. (2023). The effect of carbon emission disclosure and green investment on company value. *Trisakti Journal of Economics, 3*(2), 3135–3148.
Setyanto, S. R., Kartika, T., & Purnama, A. P. S. (2023). The current development of flipped classroom research publications in Indonesia: A bibliometric mapping. *Utamax: Journal of Ultimate Research and Trends in Education, 5*(3), 257–272.
Shi, C., Luo, S., Xu, M., & Tang, J. (2021). Learning gradient fields for molecular conformation generation. *Proceedings of the 38th International Conference on Machine Learning (ICML)*, 9558–9568.
Stasiak, M., Molenda, M., Bańda, M., Horabik, J., Wiacek, J., Parafiniuk, P., Wajs, J., Gancarz, M., Gondek, E., Lisowski, A., & Oniszczuk, T. (2020). Friction and shear properties of pine biomass and pellets. *Materials, 13*(16), 3567.
Taqiyyah, A., & Soebagyo, J. (2022). Bibliometric analysis of mathematics game-based learning. *AdMathEduSt: Scientific Journal of Mathematics Education Students, 9*(1), 1.
Zhao, L., Yang, M. M., Wang, Z., & Michelson, G. (2023). Trends in the dynamic evolution of corporate social responsibility and leadership: A literature review and bibliometric analysis. *Journal of Business Ethics, 182*, 135–157.

Author(s) Information

Yudith Arunika Cempaka Wella
Bandung Institute of Technology
Jl. Ganesa No. 10 Coblong, Bandung City, West Java
(40132), Indonesia
Contact e-mail: *arunicacmpka23@gmail.com*

To cite this article:

Wella, Y. A. C (2025). A decade of research on biomass materials in residential building construction: A bibliometric analysis. *The Eurasia Proceedings of Science, Technology, Engineering and Mathematics (EPSTEM), 38,* 444-458.

The Eurasia Proceedings of Science, Technology, Engineering & Mathematics (EPSTEM)
ISSN: 2602-3199

The Eurasia Proceedings of Science, Technology, Engineering and Mathematics (EPSTEM), 2025

Volume 38, Pages 459-469

IConTES 2025: International Conference on Technology, Engineering and Science

Application of Ultrasonic Spectral Analysis for the Study of Steels

Yonka Ivanova
Sofia University "St. Kliment Ohridski"

Todor Partalin
Sofia University "St. Kliment Ohridski"

Boris Velev
Institute of Mechanics at Bulgarian Academy of Sciences

Abstract: Ensuring high quality, specific structures, and defined mechanical properties of materials requires the widespread application of non-destructive methods for control and investigation of the structural elements of materials, in particular ultrasonic methods. The subject of this study is samples of low-carbon steel, in which equilibrium ferrite-pearlite structures with different grain sizes have been obtained through targeted heat treatments. Through quantitative metallographic analysis, the average grain size, the percentages of ferrite and pearlite, and the grain size distribution have been determined. The aim of this study is to investigate the structural elements of carbon steels using an ultrasonic method. Ultrasonic spectral analysis is employed, which is based on the changes in the frequency spectrum of ultrasonic waves after their interaction with the material. The way ultrasonic waves scatter and attenuate in a polycrystalline material provides information about the size, shape, and distribution of the structural elements that make up the material. This work analyzes the influence of grain size distribution and the quantitative assessment of different phases on the attenuation of ultrasonic wave

Keywords: Low carbon steel, Grain size distribution, Attenuation of ultrasonic waves, Ultrasonic spectral analysis

Introduction

Ultrasonic methods have shown good potential for studying the microstructure of polycrystalline materials. The propagation of ultrasonic waves in polycrystalline materials has been the subject of research in the past. Research in this area began with the work of Rayleigh, further developed by a number of researchers. Mason and McSkimmin (1947) indicated that differences in acoustic impedance at crystallite boundaries are a major source of ultrasonic scattering and attenuation in materials. Attenuation is determined by the energy losses of the ultrasonic waves, which include absorption and scattering contributions. Hirsekorn (1982), Stanke and Kino (1984), and Weaver (1990) developed theoretical models that relate ultrasonic attenuation to the microstructural features of polycrystalline materials, valid for all grain size to wavelength ratios and for polycrystalline materials with cubic symmetry. Attenuation models for grains of cubic symmetry were improved by Lifshits and Parkhomovski (1956) and Merkulov (1956).

A major contribution was made by Papadakis (1964, 1968) with several published papers on the subject. The author classifies scattering into three classical regions depending on the relationship between grain size (D) and wavelength (λ). For each region, the microstructure is assumed to be composed of spherical grains of uniform size filling the medium. A study by Smith (1982) shows the influence of grain size distribution on ultrasonic attenuation. Nicoletti and Anderson (1997) presented a deconvolution method to study the inverse problem of finding the grain size distribution from ultrasonic attenuation.

- This is an Open Access article distributed under the terms of the Creative Commons Attribution-Noncommercial 4.0 Unported License, permitting all non-commercial use, distribution, and reproduction in any medium, provided the original work is properly cited.

- Selection and peer-review under responsibility of the Organizing Committee of the Conference

© 2025 Published by ISRES Publishing: www.isres.org

In recent years, there has been significant progress in studies on the influence of crystallite distribution on the attenuation of ultrasonic waves. Arguelles and Turner (2017) investigated how a distribution of grain sizes in polycrystalline materials affects ultrasonic attenuation. They found that the frequency dependence of ultrasonic attenuation varies with the width of the grain size distribution, even when the average grain size remains constant. This means that neglecting the grain size distribution can lead to inaccurate estimations of grain size based solely on attenuation measurements.

Norouzian & Turner (2020) analyze 3D synthetic microstructures with lognormal grain distribution and demonstrate that the width of the distribution affects the frequency dependence of the attenuation, applying microstructure generators such as DREAM.3D. It can be concluded that the average crystallite size is not a sufficient parameter and dispersion should be taken into account. Studying steels S355, S275, Markja et al., 2021 found that grain size significantly affects the propagation and attenuation of ultrasonic waves: smaller grains generally increase the attenuation of ultrasound and are associated with higher strength, while larger grains reduce attenuation but are associated with lower strength.

In the paper Bonifazi et al., (2018), the effect of the grain size and other microstructural parameters on the ultrasonic propagation have been evaluated for an experimental carbon steel. The main results obtained from the study are that at high frequencies the attenuation coefficient follows Rayleigh's law of scattering and shows a maximum at a frequency value that increases with decreasing grain size; the frequency value corresponding to the attenuation maximum, converted to wavelength, can be compared to approximately 3 - 4 times the average grain size. Shan et al. (2018) proposed a new unified model of ultrasonic scattering corrected for lognormal grain distribution. Using the theory, the effects of the grain distribution widening on the ultrasonic scattering are analyzed for the longitudinal wave and the shear wave.

Measuring attenuation coefficients at different frequencies with a variety of ultrasonic sensors and devices leads to accumulation of errors due to non-uniformity of conditions: differences in contact layers, in the efforts to establish contact, diffraction losses, etc. Another approach to studying the structure of materials is ultrasonic spectral analysis, which is based on the change in the spectrum of pulse signals used in ultrasonic measurement practice. Ultrasonic spectral analysis is a non-destructive method used to evaluate the grain structure of polycrystalline materials by analyzing the frequency spectrum of ultrasonic waves (Adler, 1993). The way in which ultrasonic waves are scattered in a polycrystalline material provides information about the microstructure's elements. Pulse-echo or transmission techniques using direct contact or immersion modes have been used (Buckin et al., 2002).

Ultrasonic spectral analysis was performed on samples of AISI type 316 stainless steel and modified ferritic steel 9Cr–1Mo (Kumar et al., 2000). Spectral analysis was performed on the RF signal corresponding to the first echo from the back wall obtained with a 25 MHz longitudinal beam transducer. The peak frequency shift and the change in the full width at half maximum of the auto power spectrum were correlated with the average grain size and the yield strength.

Stella et al. (2009) used spectral analysis and conventional ultrasonic techniques to characterize the degree of sensitization in AISI 304 stainless steel. Sensitization, which is a heating process by which carbides are formed, increases the attenuation of ultrasonic waves due to the deposition of carbides at grain boundaries. The authors found that the combination of attenuation and spectral analysis is suitable for assessing the degree of sensitization. Artificial aging of welded joints of API 5L X52 steel pipeline was investigated using ultrasonic spectral analysis (Vargas-Arista et al., 2009). It was found that the attenuation of ultrasonic waves is a more sensitive parameter for identifying the change in microstructure due to aging.

Improved ultrasonic spectroscopy methods (Wang and Cao, 2001) for characterization of dispersed materials aim to increase accuracy and reduce sources of error. The technique involves analyzing spectral characteristics of reflected and transmitted ultrasonic waves to determine phase velocity and attenuation, which are frequency dependent in dispersive media. The research of Peters and Petit (2003) described a broad band spectroscopy method for ultrasound wave velocity and attenuation measurement in dispersive media. This allowed measurements over a wide frequency spectrum in highly absorbing and highly dispersive media.

The purpose of the current research is to investigate the microstructural elements of low carbon steels by ultrasonic spectral analysis. Methods for evaluating the attenuation of ultrasonic waves in polycrystalline structures are compared in order to find the best approach for the study.

Experimentals

Materials

This section describes the details of the test samples, ultrasonic measurement method and measurement procedure. The chemical composition of the studied steel grade is: C - 0.17-0.2%, Si - 0.17-0.37%, Mn - 0.35 - 0.65%, P << 0.035%, S << 0.035%. The low carbon unalloyed steel samples were heat treated at temperatures T_a from 800°C to 1150°C and slowly cooled (100°C/hour) to obtain ferritic-pearlitic structures.

By varying the austenitization temperature (T_a) and the holding time at this temperature, microstructures with different crystallite sizes were obtained. Metallographic studies were carried out using an optical microscope with reflected light with the requirements of regulatory documents.The microstructure was revealed with reagent Nital - 3% solution of nitric acid in ethyl alcohol. A 5MP digital microscope eyepiece camera type Hayear was installed on the microscope. An object-micrometer sample OMP -GOST 7513 -75 was used for calibration. The type and features of the microstructure, mean grain size of the ferrite ($\bar{D}_f$) and pearlite ($\bar{D}_p$) and the amount of pearlite were determined by quantitative metallographic analysis. Table 1 presents the heat treatment and the results of metallographic analysis.

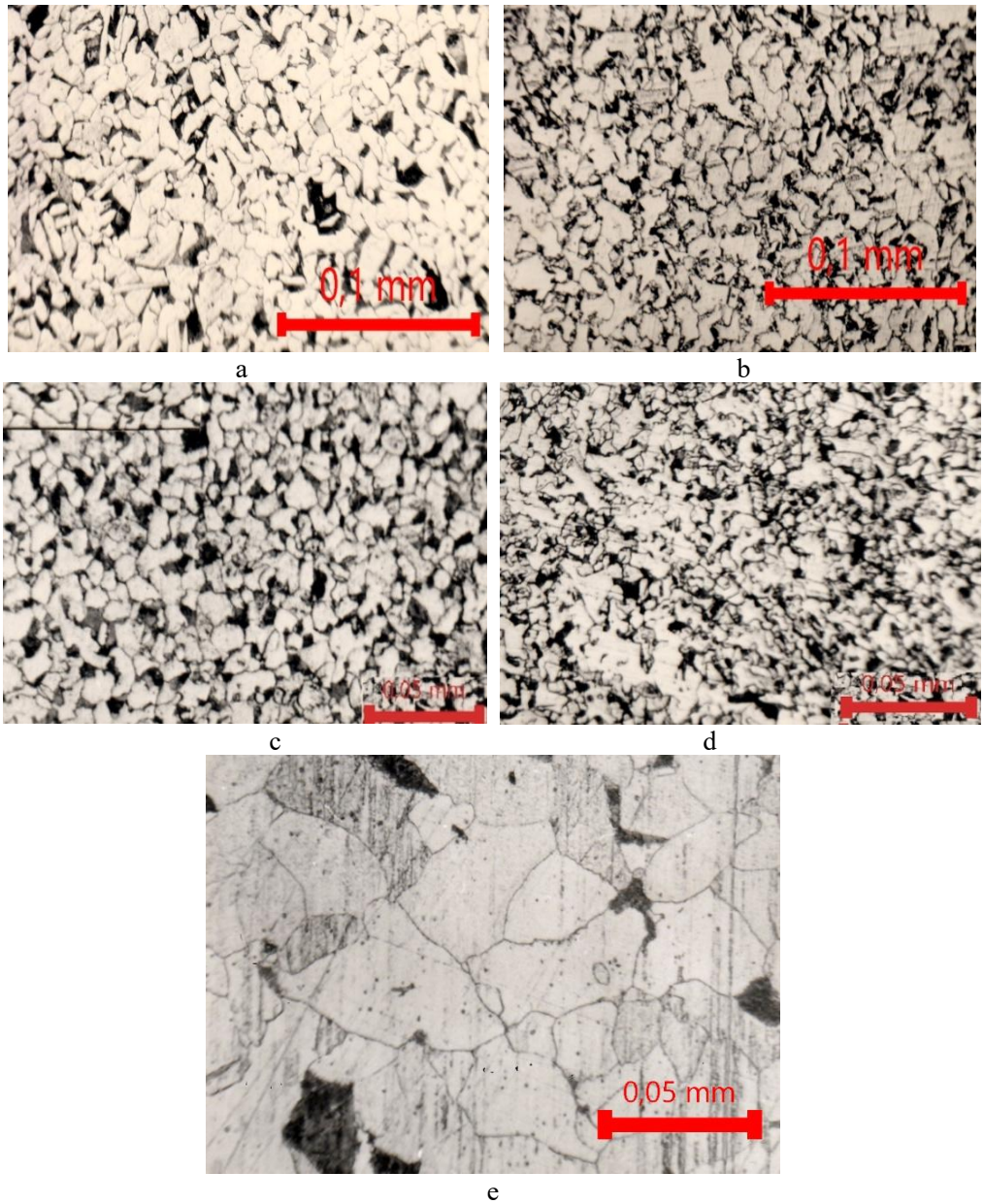


Figure 1. Metallographic photographs of microstructures - samples №0 (a), №1 (b), №2 (c), №3(d), №4 (e)

Figure 1 shows metallographic photographs of some of the investigated microstructures. The microstructure of the sample in the initial state is shown in Figure 1a. It is relatively non-uniform, with the crystals having an irregular shape acquired during the initial technological processing. After heating at temperatures in the austenitic region of 850-900 °C and cooling, an equiaxed ferrite-pearlite structure was obtained – Figures 1 b and c. Figure 1d shows an uneven grain structure obtained after heating at 950 °C. Areas with small grains, as well as areas with agglomerated structure, can be observed. Therefore, the results of this group will be discussed in detail in future works. After prolonged heating at 1150 ° C the structure consists of large ferrite and pearlite crystals - Figure 1 e.

Table 1. Heat treatment of steel samples

Code	Heat treatment	Ta,°C	t, h	$\overline{D}_f$, mm	$\overline{D}_p$, mm	Pearlite %
0	Initial state	-	-	0,019	0,001	8
1	Annealing	850	2	0.018	0.0098	8
2	Annealing	900	2	0.0010	0.0075	5.5
3	Annealing	950	2	irregular	grain	structure
4	Ageing	1150	10	0.0485	0.013	7

Method

Ultrasonic Spectral Analysis

The method for studying materials by ultrasonic spectral analysis is based on the analysis of the spectrum of ultrasonic signals that propagate in materials with a specific micro and macrostructure (American Society for Nondestructive Testing. Ultrasonic testing, 1991), (Schmerr, 2016). When an ultrasonic pulse passes through materials with different structures, the shape of the signal changes, which change contains information about the structure. The signal P(t) and its spectrum S(f) at each point of the medium are related by Fourier transformation, using the dependencies (Smith, 1997), (Skuchik, 1976):

$$P(t) = \int_{-\infty}^{\infty} S(f) e^{i2\pi f t} df \quad (1)$$

$$S(f) = \int_{-\infty}^{\infty} P(t) e^{-i2\pi f t} dt, \quad (2)$$

where *S(f)* is the spectrum of the signal *P(t)*, *f* - current frequency, *t* - time.

Methodology

The electroacoustic path in ultrasonic material testing consists of a radio pulse generator, to which is connected a radiating piezoelectric system, a contact layer (between the sensor and the medium), a receiving piezoelectric system, a broadband amplifier and an analyzer of the spectrum of the transmitted signal. The conversion of the electrical signal into an ultrasonic signal is described by the expression:

$$S(f)_{x=0} = S_g(f) S_T(f) \quad (3)$$

Where $S(f)_{x=0}$ is the spectrum of the ultrasonic signal entering the controlled material, $S_g(f)$ is the spectrum of the generating signal and $S_T(f)$ is the spectrum of the transmitting acoustic system. The spectrum of the received transmitted or reflected signal is recorded,

$$S(x,f) = S_g(f) S_T(f) S_R(f) S_m(x,f) = S_a(f) S_m(x,f) \quad (4)$$

Where $S_R(f)$ is the spectrum of the receiving acoustic system, $S_a(f) = S_g(f) S_T(f) S_R(f)$ is the spectral characteristic of all the acoustic system.

$$S_m(x,f) = Ce^{-\alpha(f)x} \quad (4a)$$

The expression (4a) represents the attenuation $\alpha(f)$ in the material, which can be considered as a filter with certain frequency properties, where *x* is the acoustic path.

Equipment

Experimental measurements were obtained by contact method with pulse echo technique. The apparatus consists of a computerized ultrasonic apparatus UT expert, which includes a generator and receiver of ultrasonic signals integrated in a computer. A piezoelectric transducer with an operating frequency of 15 MHz is used, which is an emitter and receiver of ultrasonic signals. Silicone gel was used as a contact medium.

The apparatus allows measuring the propagation time of ultrasonic waves and recording echo signals with the possibility of additional signal processing. To achieve higher accuracy in measurements, constant conditions for generating acoustic signals, uniform contact fluid and equal pressure force on the sensor, etc. are maintained. In this method, the two consecutive echo signals from the back wall, measured on a sample of known thickness, are employed to determine the ultrasonic parameters - velocity and attenuation. The transit time of ultrasonic waves is measured with an accuracy of the order of 10 ns.

Experimentation and Results

To study the attenuation of materials in this work, two procedures were used:

I. Comparison of the spectral characteristics of the tested polycrystalline material and a reference sample.
II. Determination of the attenuation of the tested materials from the spectra of successive echo signals

Comparison of the Spectral Characteristics of the Tested Polycrystalline Material and a Reference Sample

In the first approach, a fine-grained material of pure iron with an attenuation coefficient is used as a reference.

$$S_t(x,f) = S_a(f)Ce^{-\alpha_t(f)x} \quad (5)$$

$$S_{ref}(x,f) = S_a(f)C_1e^{-\alpha_{ref}(f)x} \quad (6)$$

where S_t and S_{ref} are the spectrum characteristic of the tested and reference sample.
The attenuation coefficients of the test and reference samples are denoted by $\alpha_t(f)$ and $\alpha_{ref}(f)$, respectively.
The ratio of the spectra (7) depends on the attenuation coefficients and the acoustic path x.

$$\frac{S_t(f)}{S_{ref}(f)} = \frac{C}{C_1}e^{(\alpha_{ref}-\alpha_t)x} \quad (7)$$

After taking the logarithm of (7) can be obtained

$$\ln\frac{S_t}{S_{ref}} = (\alpha_{ref} - \alpha_t)x + K \quad (8)$$

Where K=ln(C/C_1) is the term corresponding to the scaling factor.

$$\alpha_t(f) = \alpha_{ref}(f) - \frac{1}{x}\left(\ln\frac{S_t}{S_{ref}} - K\right) \quad (9)$$

Determination of the Attenuation of Tested Materials From Spectra of Successive Echo Signals

In the second procedure, the attenuation of ultrasonic waves is determined based on data from measurements of the spectra of the first (10) and second (11) bottom echoes from the controlled sample:

$$S_L(L,f) = S_a(f)e^{-\alpha(f)L} \quad (10)$$

$$S_{2L}(2L,f) = S_a(f)e^{-\alpha(f)2L} \quad (11)$$

The ratio of the spectra is (12)

$$\frac{S_L(L,f)}{S_{2L}(2L,f)} = \frac{e^{-\alpha(f)L}}{e^{-\alpha(f)2L}} = e^{\alpha(f)L} \tag{12}$$

After conversion, we obtain

$$\alpha(f) = \frac{1}{L}\ln\frac{S_L}{S_{2L}} \tag{14}$$

The dependence of the attenuation of ultrasonic waves on the frequency according to (Truell, 2013) can be represented as the sum of absorption and attenuation:

$$\alpha(f) = \sum_i \ \alpha_{abs,i}.f^{m,i} + \sum_k \ \alpha_{scat,k} f^{n,k} \tag{15}$$

where $\alpha_{abs,i}$ and $\alpha_{scat,k}$ are coefficients taking into account the losses from absorption and scattering, m,i and n,k are the power coefficients determining the frequency dependences in the absorption and scattering of ultrasonic waves in the material.

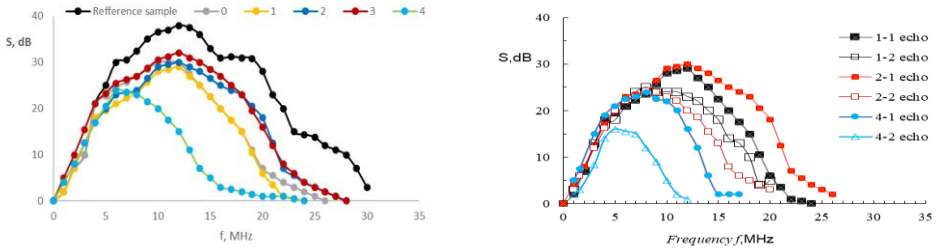
In the frequency range up to 12 MHz, the attenuation coefficient of ultrasonic waves is the sum of absorption and Rayleigh scattering (Papadakis, 1968) and is written

$$\alpha(f) = \alpha_1 f + \alpha_4 f^4 = \alpha_1 f + C_R \bar{D}^3 f^4 \tag{16}$$

Where C_R is a structural coefficient depending on the elastic properties of the materials, $\bar{D}$ is the average grain diameter. The division into regions in (16) depends on the relation (D/λ), λ- wavelength. For the studied materials, the relation for Rayleigh-type attenuation D/λ <0.2 is fulfilled.

Experimental Results

Experiments were performed and ultrasonic signals passing through the studied samples were recorded. After Fourier transformation, the spectra of ultrasonic signals were obtained. Figures 2a and b, respectively, show the spectra of the ultrasonic signals by the two procedures. The following notations are used in Figure 2a: spectrum of a reference sample, from 0 to 4 are the spectra of the studied samples. With increasing grain size, changes are observed in the spectral characteristics of the ultrasonic signals, expressed in a depletion of the spectrum at high frequencies and a shift of the maximum value of the spectrum to lower frequencies. Figure 2b illustrates some of the results obtained by the second procedure. Spectra of two consecutive echoes of samples with the most distinct average crystallite size are shown: №1 ($\bar{D}_f = 18\ \mu m$) , №2 ($\bar{D}_f = 10\ \mu m$) and №4 ($\bar{D}_f = 48\ \mu m$).



a b

Figure 2. Spectra of ultrasonic signals: a) spectral characteristics of the tested materials and a reference sample; b) spectra of successive echo signals

Figure 3 show the dependences of the attenuation coefficients on the frequency, determined by procedures I and II, as well as the approximated dependences by the least square's method for samples with different average grain diameters. The differences between the attenuation values by the two procedures are small for fine-grained steels and more significant for coarse-grained steels at frequencies greater than 10 MHz. Figure 3d illustrates the variations of the averaged values of attenuation coefficients for samples № 1, № 2, and № 4. Greater attenuation is observed for samples with larger grains, which is in accordance with many authors (Merkulov, 1956), (Bonifazi et al., 2018).

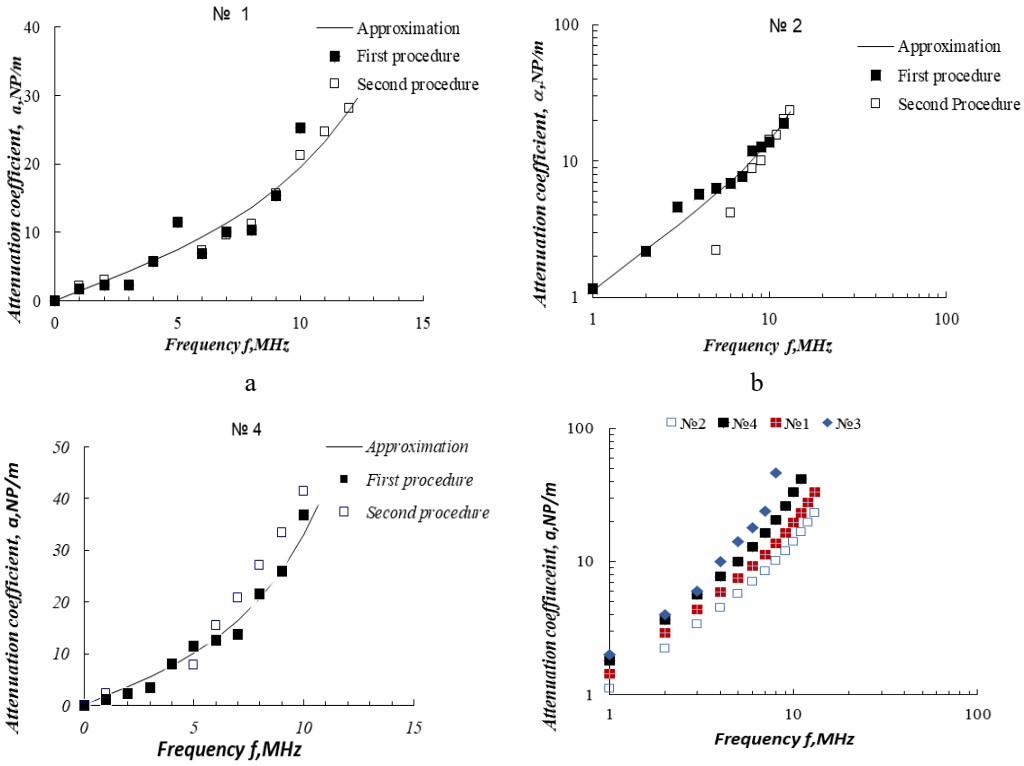


Figure 3. Attenuation coefficients according to procedure I and II for samples №1 (a), №2 (b), № 4 (c) and average attenuation coefficients (d)

Table 2 presents the coefficients that determine the fraction of absorption (α_1) and scattering (α_4) for the studied samples, determined by the least squares' method.

Table 2. Absorption and scattering coefficients

	First procedure		Second Procedure		
	α_1, Np/m.MHz	α_4, Np/m^4.MHz^4	α_1, Np/m.MHz	α_4, Np/m.MHz^4	C_R Np/m^4
1	1,2	$2{,}2.10^{-4}$	1,35	$1{,}5.10^{-4}$	$1{,}8\text{-}2{,}1.10^{11}$
2	1,24	$1{,}9.\ 10^{-3}$	1,14	$2{,}197.10^{-4}$	$3{,}5\text{-}4{,}204.10^{11}$
3	1,09	$1{,}17.10^{-3}$	1,35	$5{,}23.\ 10^{-4}$	$4{,}3\text{-}4{,}677.10^{11}$
4	1,5	$2{,}2.10^{-3}$	2,4	$1{,}1.10^{-4}$	$1{,}0\text{-}1{,}3.10^{10}$

Modeling of Attenuation of Ultrasonic Waves

Modeling of Attenuation of Ultrasonic Waves in a Single-Phase Polycrystalline Material

The attenuation coefficient of ultrasonic waves when taking into account the size distribution of crystallites (Nicoletti, 1992) is expressed by:

$$\alpha(f) = \int_0^\infty \beta(f, D) F_f(D) dD \tag{17}$$

Where $F_f(D)dD$ is the number of ferrite grains, $\beta(f, D)$ is function that describes the attenuation of ultrasonic waves in the entire range of changes in the grain diameter D and frequency *f*.

In this work, the attenuation of ultrasonic waves is modeled using an auxiliary function that combines experimentally obtained data in different ranges of variation of the parameter D/λ. The proposed model follows

the theory of ultrasonic wave scatter and assumes a weak material anisotropy. The function $\beta(f,D)$ represents the kernel of the transformation (17) and has the following form:

$$\beta(f,D) = C_R D^3 f^4 g_1\left(\frac{D,f}{c_L}\right) + C_s D \quad f^2 g_2\left(\frac{D,f}{c_L}\right) + C_d g_3\left(\frac{D,f}{c_L}\right) \tag{18}$$

Where $g_1(x)$, $g_2(x)$, $g_3(x)$ are functions, that are equal to 1 within Rayleigh's, stochastic and diffusion ranges, respectively, and are zero out of them, D is the diameter of the crystallites, c_L is the velocity of the longitudinal ultrasonic wave. The division into regions depending on is based on literature data (Papadakis,) for the Rayleigh region (D/λ<0,2), for stochastic scattering (0,2<D/λ<2,5) and diffuse scattering (2,5< D/λ). The modeling uses the coefficients obtained from the real experiment (Table 2).

Modeling of Attenuation of Ultrasonic Waves in a Two-Phase Polycrystalline Material

The attenuation of ultrasonic waves in a two-phase polycrystalline material such as investigated low-carbon steel is modeled taking into account the influence of two types of scatterers (ferrite and pearlite grains) and the pearlite content. In this case, the attenuation coefficient is represented in the following form

$$\alpha(f) = \alpha_f(f) + \alpha_p(f) \tag{19}$$

The grain distribution function in the two-phase polycrystalline material can be expressed by

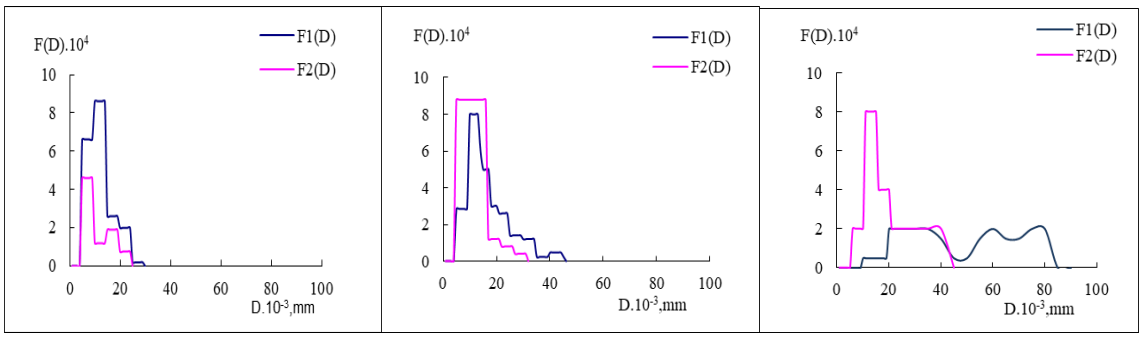
$$F(D) = qF_1(D) + (1-q)F_2(D) \tag{20}$$

Where q is the percentage content of one phase, and $F_1(D)$ and $F_2(D)$ are the distributions of ferrite and pearlite grains, respectively.

The grain distributions of the studied samples, obtained by quantitative metallography methods, are shown in Figure 4 for the samples №1, №2, №4.

According to literature data (Gür, 2005), (Wiskel, 2015), (de Araújo, 2009), the differences in the values of longitudinal wave velocities in pearlite and ferrite in low-carbon steel are small, and the percentage content of pearlite is up to 8%. The attenuation coefficient is given by

$$\alpha(f) = \int_0^\infty \beta(f,D)F \quad (D)dD \tag{21}$$



a b c

Figure 4. Distributions of ferrite $F_1(D)$ and pearlite $F_2(D)$ grains of samples №1, №2, №4

Figure 5 shows the results of calculations of the attenuation coefficients, considering the distribution of only ferrite crystals by (17) and that of two phases (ferrite and pearlite grains) in conformity with (21). When using the model that considers the distributions of the existing phases, the results for the attenuation are changed by 4-5%. A larger amount of pearlite and scattering particles will probably lead to a significant change in the results.

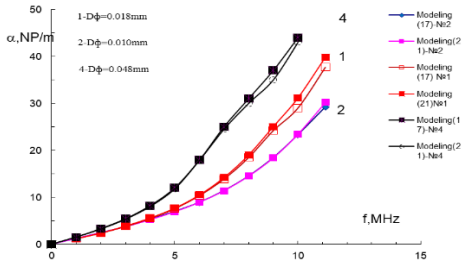


Figure 5. Attenuation coefficients taking into account the distribution of ferrite crystals according to (17) and the distribution of the two phases (21)

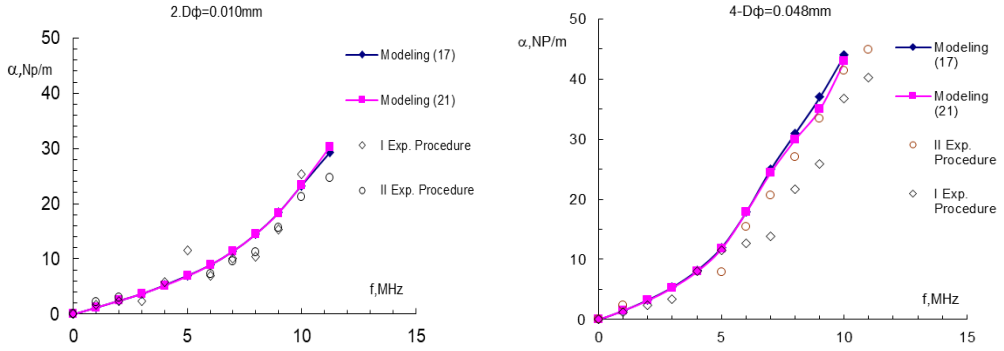


Figure 6. Comparison of experiments using procedures I and II with modeling for samples 2,4.

Figure 6 compares the attenuation coefficients from the calculations and experiments only for some of the samples with the most different grain sizes No. 2 and 4. The least squares method can be used to quantify the differences between the modeling results and the experiments. The smallest differences are for sample No. 2, with an average ferrite grain size of 10 μm, and the largest are for the coarse-grained structure No. 4. Qualitative correspondence of the experiments with the calculations is observed. The model allows analysis of the grain size distribution using the spectrum of the ultrasonic signal.

Conclusion

The work uses ultrasonic spectral analysis to determine the dependences of attenuation coefficients on the frequency for low-carbon steels. For the fine-grained structures, the procedure using a reference sample is more suitable. The coefficients considering the absorption and scattering of ultrasonic waves in the frequency range up to 12 MHz are found. A model, which takes into account the actually obtained distributions of ferrite and pearlite grains, is employed to estimate the attenuation. Qualitative agreement between experiments and calculations is found. The discrepancy between the them is probably due to the inaccuracy of the model in the frequency range used in the study.

Recommendations

The presented research can provide new knowledge to students and engineers to put into practice ultrasonic spectral analyses for non-destructive evaluation of materials.

Scientific Ethics Declaration

* The authors declare that the scientific ethical and legal responsibility of this article published in EPSTEM journal belongs to the authors.

Conflict of Interest

* The authors declare that they have no conflicts of interest.

Funding

* This research received no specific grant from any funding agency in the public, commercial, or not-for-profit sectors.

Acknowledgements or Notes

* This article was presented as an oral presentation at the International Conference on Technology, Engineering and Science (www.icontes.net) held in Antalya/Türkiye on November 12-15, 2025.

References

Adler, L. (1993). Ultrasonic spectroscopy. In J. D. Achenbach (Ed.), *The evaluation of materials and structures by quantitative ultrasonics* (pp. 25–41). Springer.

American Society for Nondestructive Testing. (1991). *Nondestructive testing handbook: Vol. 7. Ultrasonic testing* (2nd ed.). American Society for Nondestructive Testing.

Arguelles, A. P., & Turner, J. A. (2017). Ultrasonic attenuation of polycrystalline materials with a distribution of grain sizes. *The Journal of the Acoustical Society of America, 141*(6), 4347–4353.

Bonifazi, F., Burrascano, P., Di Schino, A., Mengaroni, S., Petrucci, F., Ricci, M., & Senni, L. (2018). Ultrasonic NDT of steel: Effect of the grain size on the ultrasonic propagation and attenuation. *Journal of Chemical Technology and Metallurgy, 53*(2), 346–353.

Buckin, V., & O'Driscoll, B. (2002). Ultrasonic waves and material analysis: Recent advances and future trends. *LabPlus International, 16*, 17–21.

de Araújo Freitas, V. L., Silva, A. A., de Macedo Silva, E., de Albuquerque, V. H. C., & da Silva Tavares, J. M. R. (2009). Microstructural characterization of carbon steels using ultrasonic velocity measurements. *20th International Congress of Mechanical Engineering (COBEM 2009)*.

Gür, C. H., & Tuncer, B. O. (2005). Characterization of microstructural phases of steels by sound velocity measurement. *Materials Characterization, 55*(2), 160–166.

Hirsekorn, S. (1982). The scattering of ultrasonic waves by polycrystals. *The Journal of the Acoustical Society of America, 72*, 1021–1031.

Kumar, A., Jayakumar, T., & Raj, B. (2000). Ultrasonic spectral analysis for microstructural characterization of austenitic and ferritic steels. *Philosophical Magazine A, 80*(11), 2469–2487.

Li, S., Li, X., Song, Y., & Chen, C. (2018). Ultrasonic scattering unified theory for polycrystal material with grain sizes distribution. *Acta Physica Sinica, 67*(23), 234301.

Lifshits, I. M., & Parkhomovskii, G. D. (1950). Theory of propagation of ultrasonic waves in polycrystals. *Zhurnal Eksperimental'noi i Teoreticheskoi Fiziki, 20*, 175–182.

Markja, I., Dhoska, K., Elezi, D., Moezzi, R., & Petru, M. (2021). Effect of the grain sizes on the ultrasonic propagation and attenuation on different types of steels microstructure during non-destructive testing. *Annales de Chimie: Science des Matériaux, 45*(4), 329–334.

Mason, W. P., & McSkimin, H. J. (1947). Attenuation and scattering of high frequency sound waves in metals and glasses. *The Journal of the Acoustical Society of America, 19*(3), 464–473.

Merkulov, L. G. (1956). Study of the scattering of ultrasound in metals. *Zhurnal Tekhnicheskoi Fiziki, 26*, 64-75.

Nicoletti, D., & Anderson, A. (1997). Determination of grain-size distribution from ultrasonic attenuation: Transformation and inversion. *The Journal of the Acoustical Society of America, 101*(2), 686-689.

Norouzian, M., Islam, S., & Turner, J. A. (2020). Influence of microstructural grain-size distribution on ultrasonic scattering. *Ultrasonics, 102*, 106032.

Papadakis, E. P. (1964). Ultrasonic attenuation and velocity in three transformation products in steel. *Journal of Applied Physics, 35*(5), 1474-1482.

Papadakis, E. P. (1968). Ultrasonic attenuation caused by scattering in polycrystalline media. In W. P. Mason (Ed.), *Physical acoustics* (Vol. 4, pp. 269-328). Academic Press.

Peters, F., & Petit, L. (2003). A broad band spectroscopy method for ultrasound wave velocity and attenuation measurement in dispersive media. *Ultrasonics, 41*(5), 357-363.

Rodríguez, E., Stella, J., Ruiz, A., Fargas, G., & Mateo, A. (2011). Characterization of microstructural changes in a duplex stainless steel using spectral analysis and conventional ultrasonic techniques. *Materials Testing, 53*(9), 564–571.

Schmerr, L. W. (2016). *Fundamentals of ultrasonic nondestructive evaluation: A modeling approach* (2nd ed.). Springer.

Skudrzyk, E. (1976). *Fundamentals of acoustics* (Vol. 1). Mir.

Smith, R. L. (1982). The effect of grain size distribution on the frequency dependence of the ultrasonic attenuation in polycrystalline materials. *Ultrasonics, 20*(5), 211-214.

Smith, S. W. (1997). *The scientist and engineer's guide to digital signal processing*. California Technical Publishing.

Stanke, F. E., & Kino, G. S. (1984). A unified theory for elastic wave propagation in polycrystalline materials. *The Journal of the Acoustical Society of America, 75*(3), 665-681.

Stella, J., Cerezo, J., & Rodríguez, E. (2009). Characterization of the sensitization degree in the AISI304 stainless steel using spectral analysis and conventional ultrasonic techniques. *NDT & E International, 42*(4), 267-274.

Truell, R., Elbaum, C., & Chick, B. B. (2013). *Ultrasonic methods in solid state physics*. Academic Press.

Vargas-Arista, B., Balvantin, A., Baltazar, A., & García-Vázquez, F. (2012). On the use of ultrasonic spectral analysis for the characterization of artificially degraded API 5L X52 steel pipeline welded joints. *Materials Science and Engineering: A, 550*, 227-234.

Wang, H., & Cao, W. (2001). Improved ultrasonic spectroscopy methods for characterization of dispersive materials. *IEEE Transactions on Ultrasonics, Ferroelectrics, and Frequency Control, 48*(4), 1060-1065.

Weaver, R. L. (1990). Diffusivity of ultrasound in polycrystals. *Journal of the Mechanics and Physics of Solids, 38*(1), 55–86.

Wiskel, J. B., Kennedy, J., Ivey, D. G., & Henein, H. (2015). Ultrasonic velocity evaluation of three grades of heat-treated steel. *Proceedings of the NDT Conference Canada*, 1–10.

Author(s) Information

Yonka Ivanova
Sofia University "St. Kliment Ohridski",
Faculty of Physics, Bulgaria
Institute of Mechanics at Bulgarian Academy of Sciences,
Sofia, 1113, Acad. G. Bontchev Str., bl.4, Bulgaria
Contact e-mail: *yonivan@phys.uni-sofia*

Todor Partalin
Sofia University "St. Kliment Ohridski"
Faculty of Mathematics and Informatics, Sofia, Bulgaria

Boris Velev
Institute of Mechanics at Bulgarian Academy of Sciences,
Sofia, 1113, Acad. G. Bontchev Str., bl.4, Bulgaria

To cite this article:

Ivanova, Y., Partalin, T., & Velev, B. (2025). Application of ultrasonic spectral analysis for the study of steels. *The Eurasia Proceedings of Science, Technology, Engineering and Mathematics (EPSTEM), 38,* 459-469

The Eurasia Proceedings of Science, Technology, Engineering & Mathematics (EPSTEM)
ISSN: 2602-3199

The Eurasia Proceedings of Science, Technology, Engineering and Mathematics (EPSTEM), 2025

Volume 38, Pages 470-479

IConTES 2025: International Conference on Technology, Engineering and Science

Evaluation of Robust Controllers in Photovoltaic Systems: A Comparative Analysis

Zerroug Nadjat
University of Setif 1 Ferhat Abbas

Behih Khalissa
University of Setif 1 Ferhat Abbas

Bouchama Ziyad
University of Bordj Bou Arreridj

Abstract: The main objective of this work is to compare and evaluate the performance of three advanced control techniques, namely Sliding Mode Control (SMC), Synergetic Control (SC) and Adaptive Sliding Mode Control (ASMC) for Maximum Power Point (MPP) extraction in a photovoltaic system under different atmospheric conditions. This study aims to identify the most robust, fast and efficient control strategy to optimize solar power production, while minimizing oscillations and improving system stability. Through accurate modeling of the PV system and simulations under varying operating conditions, we highlighted the strengths and limitations of each technique. Synergetic Control demonstrated superior performance by ensuring fast and precise tracking of the maximum power point, while significantly reducing the chattering phenomenon commonly observed in classical SMC. ASMC also showed notable improvements in adaptability and robustness compared to traditional SMC. In conclusion, this study confirms that robust control techniques offer promising solutions to enhance the energy performance of photovoltaic systems, especially in a global context where renewable energy sources are playing an increasingly vital role.

Keywords: Photovoltaic system, Sliding mode control, Adaptive sliding mode control, Synergetic control, MPPT.

Introduction

Photovoltaic (PV) systems represent an efficient and sustainable solution for the production of clean electrical energy. They offer a wide power range, suitable for both stand-alone applications and grid feed (Green et al., 2021). A typical photovoltaic system generally consists of a PV array composed of a series of solar modules and a static DC-DC converter to transform the power supplied by the PV source to the load (Masters, 2013; Blaabjerg et al., 2017). This structure is characterized by non-linear dynamics that vary significantly with operating conditions related, for example, to climatic conditions, such as irradiation levels, shading, temperature, etc (Villalva et al., 2009; Esram & Chapman, 2007). These conditions make it difficult to predict voltage and current to ensure maximum power production. In a photovoltaic system, the maximum power point (MPP) corresponds to the operating point where the power delivered is at its maximum; it is therefore crucial to maintain the PV array at this point to optimize energy extraction (Messenger & Ventre, 2010). The Maximum Power Point Tracking (MPPT) strategy continuously adjusts the DC-DC converter to track this point despite variations in irradiation and temperature (Alik & Jusoh, 2023). While conventional algorithms like Perturb and Observe (P&O) and Incremental Conductance (IC) are widely used, they exhibit significant limitations (Kermadi & Berkouk, 2021). P&O is favored for its simplicity but is prone to misdirection and oscillation during rapid irradiation changes (Femia et al., 2005). The IC method offers greater accuracy but faces an

- This is an Open Access article distributed under the terms of the Creative Commons Attribution-Noncommercial 4.0 Unported License, permitting all non-commercial use, distribution, and reproduction in any medium, provided the original work is properly cited.

- Selection and peer-review under responsibility of the Organizing Committee of the Conference

© 2025 Published by ISRES Publishing: www.isres.org

inherent trade-off between tracking speed and residual oscillation in steady state **(**Mohapatra et al., 2022**).** Consequently, there is a clear need for robust MPPT techniques that can deliver stable and reliable performance despite environmental disturbances. Among robust nonlinear control techniques, Sliding Mode Control (SMC) is a prominent solution for managing dynamic systems affected by uncertainties or external disturbances. Its operation is based on two steps: first, establishing a "sliding surface" that defines the desired system performance, and second, designing a discontinuous control law that drives the system's state to this surface and maintains it there. This approach offers considerable benefits, such as exceptional robustness against parametric variations, rapid dynamic response, and relative ease of implementation **(**Singh et al., 2021**;** Fridman, 2014**)**. The primary limitation of SMC, however, is the chattering phenomenon. These are high-frequency, destructive oscillations generated by the inherent discontinuity of the control signal, which may cause a decrease in precision, acoustic noise, and accelerated hardware wear. In an effort to overcome the disadvantages of conventional SMC, Adaptive Sliding Mode Control (ASMC) was developed. Unlike its forerunner, the novelty of this approach is that it possesses dynamic control gains, varied based on the state of the system. In this way, it can effectively deal with uncertainties without the use of an accurate model of the system. Moreover, ASMC approach employs continuous control laws that significantly reduce or eliminate the chattering phenomenon while preserving robustness and stability **(**Plestan et al., 2019; Liu et al., 2022; Ahmad et al., 2023**)**. This makes ASMC very suitable for real systems, such as photovoltaic arrays operating under time-varying conditions Synergetic Control (SC) has, by now, clearly emerged as a very powerful tool for the design of nonlinear control systems, successfully overcoming some drawbacks typical of alternative approaches. This relatively recent paradigm shares conceptual foundations with SMC but offers distinct practical advantages. A key differentiator is its inherently continuous control law, which mitigates or entirely eliminates the chattering phenomenon prevalent in SMC. . In most reported applications, SC is designed to be asymptotically stabilizing, that is, to ensure that system trajectories will converge progressively, after some finite time, to an equilibrium state. This continuity property makes it particularly well-suited to physical systems requiring smooth control actions **(**Moya et al., 2020; Shi & Wang, 2023**)**.

System Configuration

The diagram given in fig.1 shows a solar power system. The MPPT Controller continuously adjusts the DC/DC boost converter to ensure the PV Panel always operates at its most efficient voltage and current, thereby extracting the maximum possible power to deliver to the Load.

V_{pv} *and* I_{pv} represent respectively the voltage and the current delivered by the panel

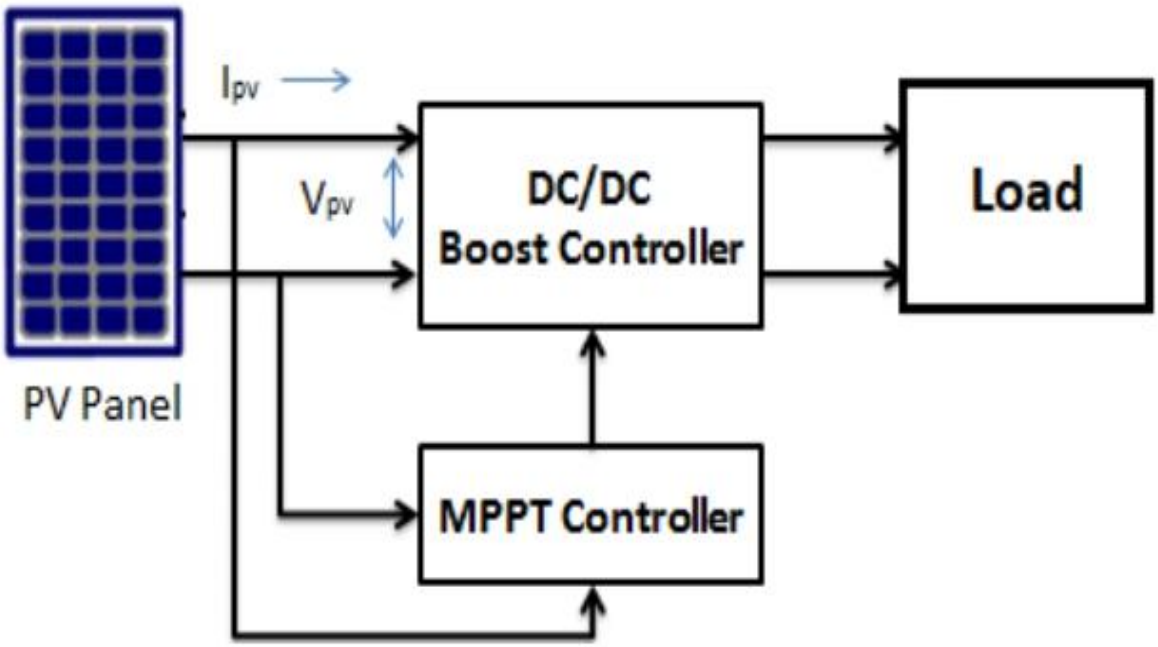


Figure 1. Photovoltaic energy conversion chain

The key challenge of an MPPT controller is to track this optimal operation point rapidly and stably in the presence of external disturbances, represented by irradiance and temperature changes. This robust performance can be achieved with the use of a Sliding Mode Control approach.

Sliding Mode Control Based MPPT

Sliding mode control belongs to the category of nonlinear controls. Initially developed for the control of variable structure systems (VSS). It is distinguished by the discontinuity of the control action when crossing a particular surface, called the sliding surface. Recently, this approach has been applied to photovoltaic (PV) systems to optimize maximum power extraction.
The design of a sliding mode controller consists of two main steps. First, a sliding surface is defined to guarantee the system converges to its desired state. Second, a control law is established to force the system's trajectory to reach this surface and remain on it.

For a photovoltaic (PV) system, the Maximum Power Point (MPP) is achieved when the derivative of power with respect to current is zero, as expressed by:

$$\frac{dP_{pv}}{dI_{pv}} = \frac{dI_{pv}V_{pv}}{dI_{pv}} = V_{pv} + I_{pv}\frac{dV_{pv}}{dI_{pv}} = 0 \quad (1)$$

Based on this condition, an appropriate sliding surface can be defined as:

$$s = V_{pv} + I_{pv}\frac{dV_{pv}}{dI_{pv}} \quad (2)$$

The general control law u consists of two parts: the discrete control u_{disc} and the equivalent control u_{eq}.
The discrete control u_{disc} is determined to ensure the attractiveness of the sliding surface and is defined as follows:

$$u_{disc} = k * sign\,(s); \quad k > 0\,; \quad (3)$$

The equivalent command u_{eq} is used to maintain the operating point on the sliding surface and move it towards the origin. It is given by:

$$u_{eq} = 1 - \frac{V_{pv}}{V_o} \quad (4)$$

Thus, the overall control law u is deduced as :

$$u = k * sign\,(s) + 1 - \frac{V_{pv}}{V_o} \quad (5)$$

While the control law in (5) is effective, its performance is sensitive to the choice of the fixed switching gain k.

A gain that is too low may not ensure robustness against parameter variations, while one that is too high can increase undesirable chattering (high-frequency oscillations). To overcome this limitation, an Adaptive Sliding Mode Control (ASMC) strategy is employed, where the gain is dynamically adjusted based on system conditions.

Adaptive Sliding Mode Control Principle

The application of Adaptive Sliding Mode Control (ASMC) to photovoltaic systems is characterized by a control law synthesized from the superposition of an equivalent control and an adaptive switching component.

This composite law, which dictates the discontinuous duty cycle for the DC/DC converter, operates based on a defined sliding surface whose robustness is ensured by an adaptively tuned gain. First, a sliding surface is chosen to guide the system towards the maximum power point (MPP). It is defined by the expression :

$$s = \frac{dP_{pv}}{dI_{pv}} = V_{pv} + I_{pv}\frac{dV_{pv}}{dI_{pv}} \tag{6}$$

The equivalent control u_{eq} is derived from the invariance condition $\dot{s} = 0$ and is responsible for the ideal sliding motion. It is expressed as:

$$u_{eq} = 1 - \frac{V_{pv}}{V_{out}} \tag{7}$$

While the adaptive correction term given by

$$u_{ad} = -\tilde{k}.sign\big(s(x)\big) \tag{8}$$

engages exclusively to counteract deviations from the sliding surface, providing robustness against disturbances and parameter variations.

$\tilde{k}$ is a dynamically adjusted gain.

The adaptation error is defined as follows:

$$\tilde{k} = k - \hat{k} \tag{9}$$

The estimated parameter $\hat{k}$ is dynamically adjusted according to:

$$\dot{\hat{k}} = \frac{1}{\gamma}\|s\| \tag{10}$$

Where γ is a positive constant.

Lyapunov Stability Analysis

To demonstrate the stability of the system controlled by the ASMC approach and to guarantee convergence towards the surface s=0, we propose the following Lyapunov function:

$$V = \frac{1}{2}s^2 + \frac{1}{2\gamma}\tilde{k}^2 \tag{11}$$

The derivative of Lyapunov function is given by the equation :

$$\dot{V} = s\dot{s} + \frac{1}{\gamma}\,\tilde{k}\,\dot{\tilde{k}} \tag{12}$$

$$\dot{V} = s[-k\ sign(s)] - \frac{1}{\gamma}\,\tilde{k}\,\dot{\hat{k}} \tag{13}$$

knowing that :

$$\dot{\tilde{k}} = \dot{\hat{k}} \tag{14}$$

Then we obtain:

$$\dot{V} = s\left[-k\left(\tilde{k} + \hat{k}\right)sign(s)\right] - \frac{1}{\gamma}\tilde{k}\,\dot{\hat{k}} \tag{15}$$

$$\dot{V} = -\hat{k}\; s.sign(s) - \tilde{k}[s.sign(s) + \frac{1}{\gamma}\dot{\hat{k}}\,] \tag{16}$$

Given that $s.sign(s) = |s|$, we will have :

$$\dot{V} = -\hat{k}\;|s| < 0 \tag{17}$$

Which proves that the system is asymptotically stable. The asymptotic stability of the Adaptive Sliding Mode Controller validates its design. However, the discontinuous $sign(s)$ function in its control law can lead to chattering. To circumvent this issue while retaining robustness, Synergetic Control presents an alternative methodology.

Synergetic Control Based MPPT

Synergetic control is a robust technique for nonlinear systems, sharing the invariance principle with sliding mode control. Its key distinction lies in the use of a continuous control law and a macro-variable, which can be a function of multiple state variables. System performance is governed by the strategic design of this macro-variable. An MPPT synergetic controller is designed by first selecting a macro-variable Ψ(*x*, t)given by :

$$\Psi(x,t) = \frac{dP_{pv}}{dI_{pv}} \tag{18}$$

This controller then forces the system trajectory to converge exponentially to the manifold defined by (19).

$$\Psi = \frac{dP_{pv}}{dI_{pv}} = \frac{dI_{pv}V_{pv}}{dI_{pv}} = V_{pv} + I_{pv}\frac{dV_{pv}}{dI_{pv}} = 0 \tag{19}$$

Once the trajectory reaches the desired attractor, the synergetic controller will maintain it on that manifold. The desired dynamic evolution of the macro-variable is chosen according to equation (20).

$$T_s\left(\frac{d\Psi}{dt}\right) + \Psi = 0;\; T_s > 0 \tag{20}$$

Where T_s is a positive value that influences the speed of convergence of the system towards the desired equilibrium point.
knowing that :

$$\frac{d\Psi}{dt} = \left(\frac{d\Psi}{dI_{pv}}\right)\left(\frac{dI_{pv}}{dt}\right) \tag{21}$$

we get:

$$T_S\left[\left(\frac{d\Psi}{dI_{pv}}\right)\left(\frac{dI_{pv}}{dt}\right)\right] + \Psi = 0 \tag{22}$$

where :

$$\frac{d\Psi}{dI_{pv}} = 2\left(\frac{dI_{pv}}{dt}\right) + I_{pv}\frac{d^2V_{pv}}{dI_{pv}^2} \tag{23}$$

$$\frac{dI_{pv}}{dt} = -(1-u)\frac{V_{out}}{L} + \frac{V_{pv}}{L} \tag{24}$$

Substituting equations (23) and (24) into equation (22) gives the control law described in (25):

$$u(t) = 1 - \frac{\Psi_L}{V_{out}T_s\left(2\frac{dV_{pv}}{dI_{pv}} + I_{pv}\frac{d^2V_{pv}}{dI_{pv}^2}\right)} - \frac{V_{pv}}{V_{out}} \tag{25}$$

Simulation Results and Performance Comparison

This study evaluates and compares the performance of three modern MPPT techniques: Sliding Mode, Adaptive Sliding Mode, and Synergetic Control. Using the BP MSX 60 solar panel, we performed multiple simulations in Matlab/Simulink under strictly identical parameters and varying climatic conditions including irradiance (G) and temperature (T).

Case 1: Variable Irradiance

In this case, the simulation parameters are maintained at T = 25 C° while G varies in the range [1000 800 600].

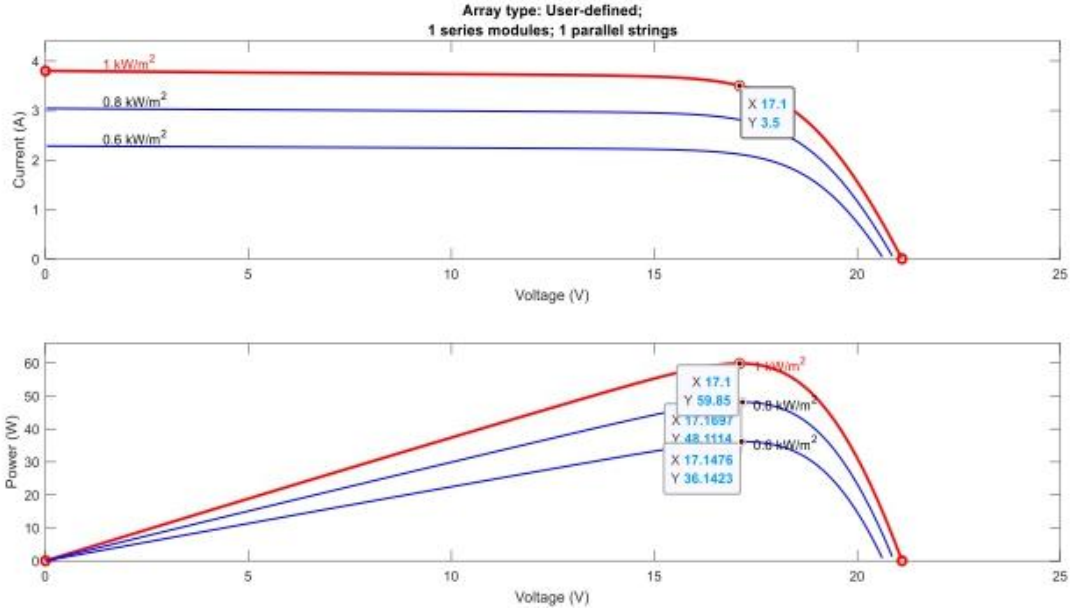


Figure 2. Panel characteristics for variable irradiance

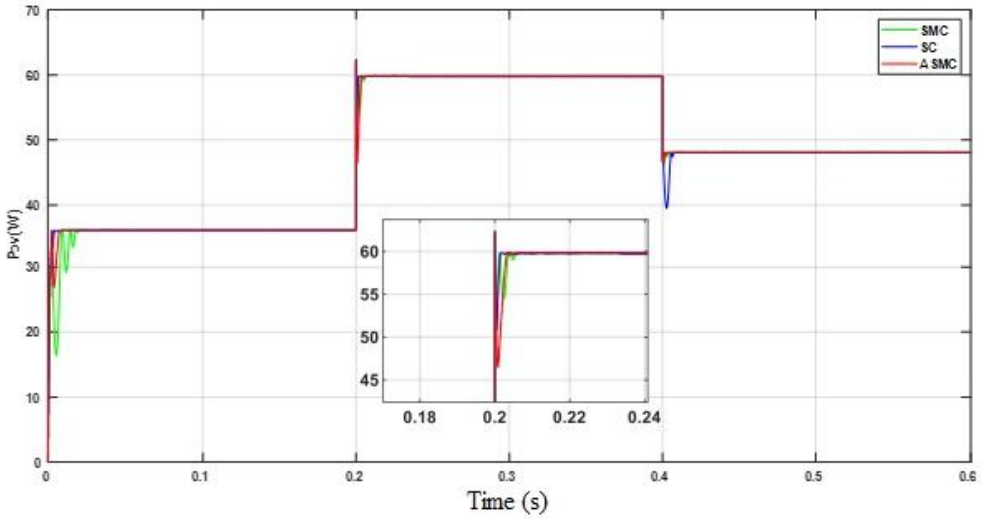


Figure 3. Evolution of Ppv

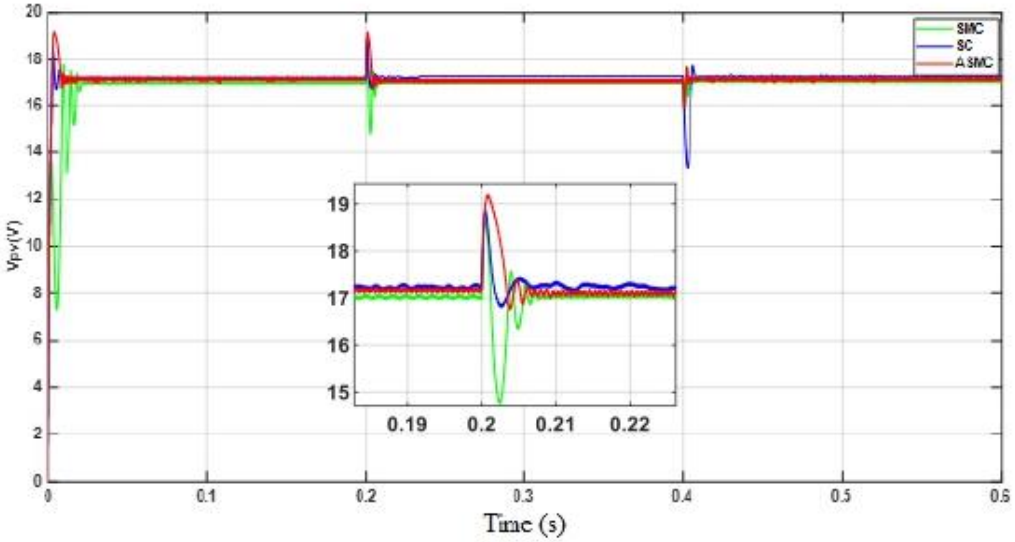


Figure 4. Evolution of Vpv

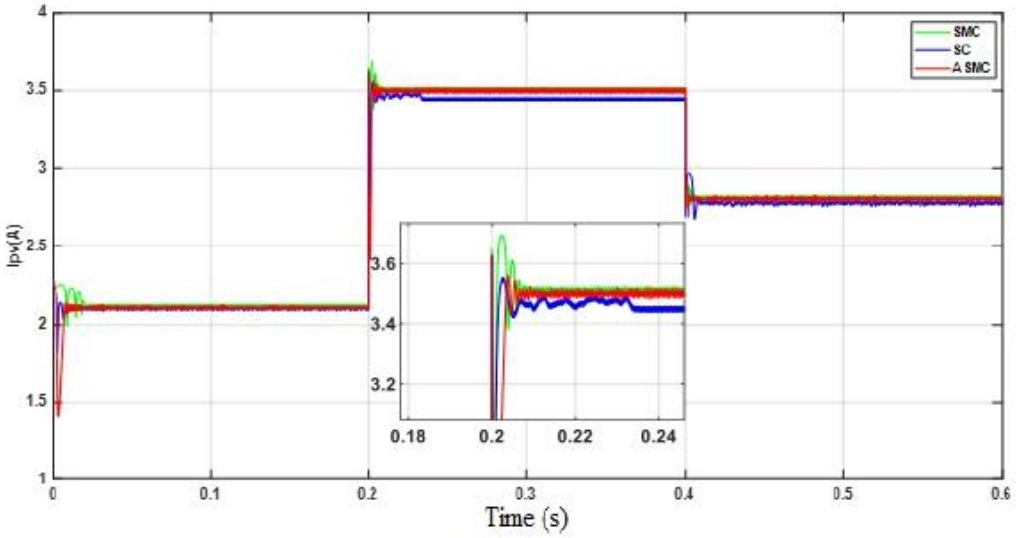


Figure 5. Evolution of Ipv

Table 1. Performance indicators of control systems for different levels of solar irradiation

Control System	Solar Irradiance (W/m²)	Efficiency (%)	Power Loss, ΔP (W)	Response Time (s)
SMC	600	95.23	0.02	0.02
	800	95.46	0.01	0.005
	1000	95.58	0.02	0.0056

(a)

Control System	Solar Irradiance (W/m²)	Efficiency (%)	Power Loss, ΔP (W)	Response Time (s)
SC	600	95.39	0.005	0.0045
	800	95.67	0.01	0.005
	1000	95.72	0.02	0.004

(b)

Control System	Solar Irradiance (W/m²)	Efficiency (%)	Power Loss, ΔP (W)	Response Time (s)
ASMC	600	95.29	0.006	0.0075
	800	95.54	0.01	0.003
	1000	95.62	0.01	0.005

(c)

Note: The values for Efficiency, Power Loss (ΔP), and Response Time are measured outcomes for each system under the specified solar irradiance.

Based on the obtained results, Synergetic Control (SC) demonstrates the highest performance in efficiency, power, and response time. However, Adaptive Sliding Mode Control (ASMC) emerges as an excellent compromise, delivering very good energy efficiency and a fast transient response while successfully minimizing the chattering phenomena associated with standard Sliding Mode Control (SMC). The conventional SMC method, though robust, is comparatively slower and less stable.

Case 2: Variable Irradiance and Temperature

In this case, the simulation parameters (temperature T and irradiance G) are maintained at : T varies within the range [25 30 35] °C, and G = [1000 800 600] W/m^2

Both Synergetic Control (SC) and Adaptive Sliding Mode Control (ASMC) demonstrate superior dynamic performance over conventional Sliding Mode Control (SMC), exhibiting a significantly faster response in tracking the Maximum Power Point (MPPT).

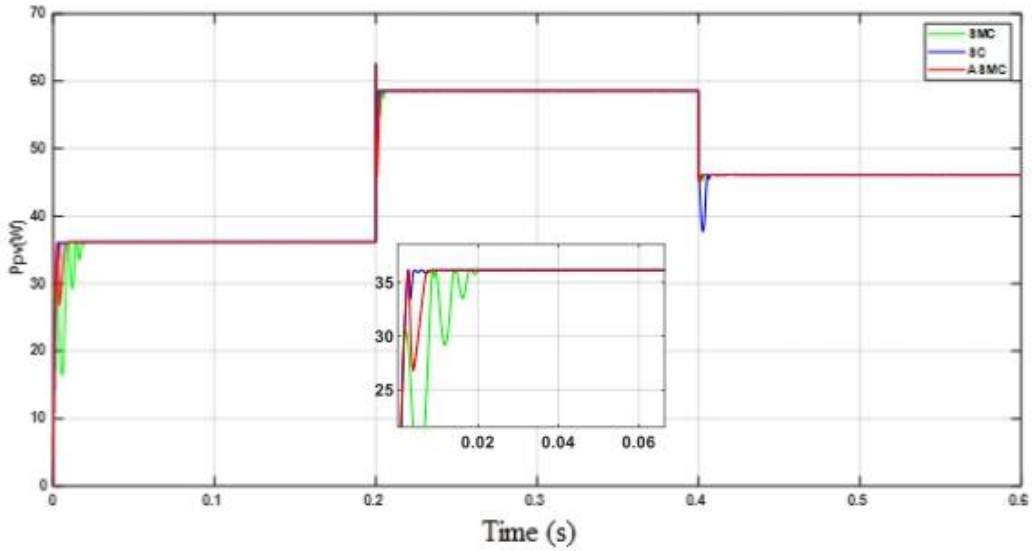


Figure 6. Evolution of Ppv

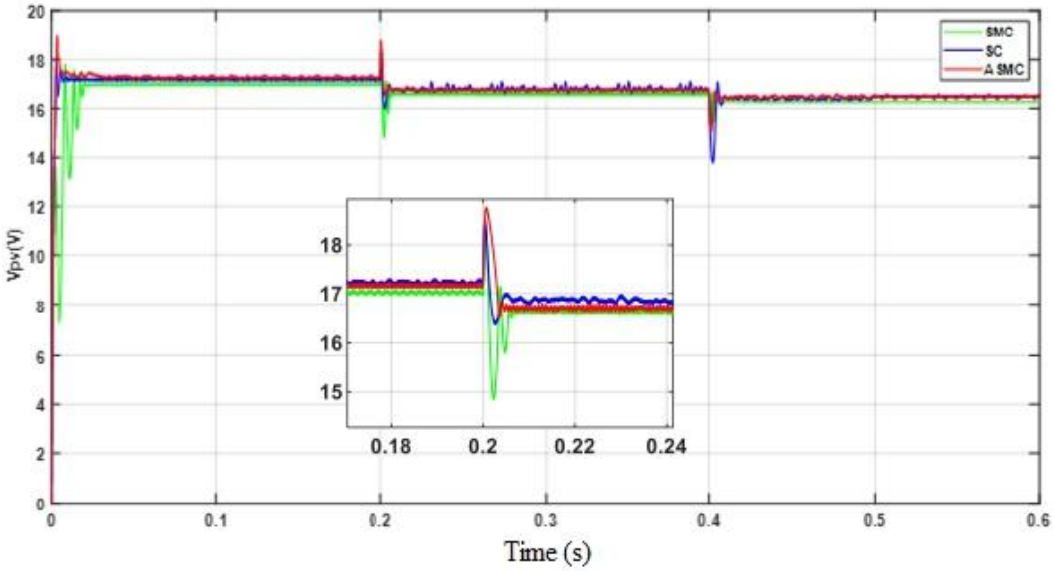


Figure 7. Evolution of Vpv

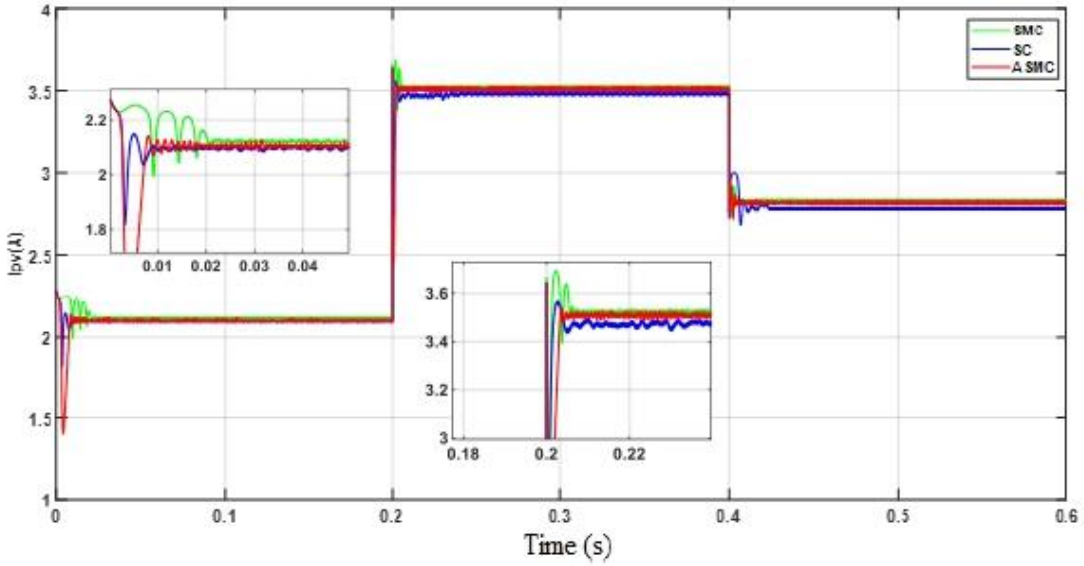


Figure 8. Evolution of Ipv

Conclusion

From these comparisons, it can be concluded that the three controllers are clearly classified in terms of performance. Though conventional SMC yields basic robustness, the ASMC has given a superior compromise in which chattering is significantly reduced and the response has been improved. SC will emerge as the most effective solution for delivering superior dynamic performance, high efficiency, and chatter-free smooth operation for maximum power point tracking.

Scientific Ethics Declaration

* The authors declares that the scientific ethical and legal responsibility of this article published in EPSTEM journal belongs to the authors.

Conflict of Interest

* The authors declare that they have no conflicts of interest.

Funding

* This research received no specific grant from any funding agency in the public, commercial, or not-for-profit sectors.

Acknowledgements or Notes

* This article was presented as an oral presentation at the International Conference on Technology, Engineering and Science (www.icontes.net) held in Antalya/Türkiye on November 12-15, 2025.

References

Ahmad, A. Z., Al-Soeidat, H., & Lu, D. D. C. (2023). An adaptive sliding mode controller for PV maximum power point tracking with enhanced robustness and accuracy. *Solar Energy, 262*, 111846.

Alik, R., & Jusoh, A. (2023). An enhanced, adaptive, and artificial intelligence-based perturb and observe MPPT technique for the photovoltaic system. *Scientific Reports, 13*(1), 2054.

Blaabjerg, F., Yang, Y., Yang, D., & Wang, X. (2017). Distributed power-generation systems and protection. *Proceedings of the IEEE, 105*(7), 1311–1331.

Esram, T., & Chapman, P. L. (2007). Comparison of photovoltaic array maximum power point tracking techniques. *IEEE Transactions on Energy Conversion, 22*(2), 439–449.

Femia, N., Petrone, G., Spagnuolo, G., & Vitelli, M. (2005). Optimization of perturb and observe maximum power point tracking method. *IEEE Transactions on Power Electronics, 20*(4), 963–973.

Fridman, L. (2014). Chattering analysis in sliding mode systems with inertial sensors. *International Journal of Control, 87*(10), 1910–1925.

Green, M. A., Dunlop, E. D., Hohl-Ebinger, J., Yoshita, M., Kopidakis, N., & Ho-Baillie, A. W. Y. (2021). Solar cell efficiency tables (Version 58). *Progress in Photovoltaics: Research and Applications, 29*(3), 657–667.

Kermadi, M., & Berkouk, E. M. (2021). A comprehensive review of maximum power point tracking algorithms for photovoltaic systems under partial shading. *Renewable and Sustainable Energy Reviews, 148*, 111293.

Liu, Z., Li, Y., & Zhang, W. (2023). Adaptive super-twisting sliding mode control for maximum power point tracking of photovoltaic systems under fast-changing irradiation. *IEEE Transactions on Industrial Electronics, 70*(5), 5095-5105.

Masters, G. M. (2013). *Renewable and efficient electric power systems* (2nd ed.). Wiley-IEEE Press.

Messenger, R. A., & Ventre, J. (2010). *Photovoltaic systems engineering* (3rd ed.). CRC Press.

Mohapatra, A., Nayak, B., & Mohanty, K. B. (2022). A comprehensive review on MPPT technologies in hybrid PV systems. *IEEE Journal of Emerging and Selected Topics in Industrial Electronics, 3*(4), 821-837.

Moya, P., Espinoza, E., Figueroa, M., & Lefranc, G. (2021). Synergetic control for maximum power point tracking in photovoltaic systems: A comparative analysis with sliding mode control. *IEEE Access, 9*, 111254-111265.

Plestan, F., Shtessel, Y., Brégeault, V., & Poznyak, A. (2020). New methodologies for adaptive sliding mode control. *International Journal of Control, 93*(3), 461-476.

Shi, J., He, X., & Wang, Z. (2023). Finite-time synergetic control for robotic manipulators with asymptotic disturbance rejection. *International Journal of Robust and Nonlinear Control, 33*(1), 189-207.

Singh, A., Suhag, S., & Kumar, N. (2021). A comprehensive review on sliding mode control for maximum power point tracking in photovoltaic systems. *International Transactions on Electrical Energy Systems, 31*(7), e12933.

Villalva, M. G., Gazoli, J. R., & Ruppert Filho, E. (2009). Comprehensive approach to modeling and simulation of photovoltaic arrays. *IEEE Transactions on Power Electronics, 24*(5), 1198-1208.

Author(s) Information

Zerroug Nadjat
University of Setif 1 Ferhat Abbas, Department of Electrical Engineering, University of Setif Ferhat Abbas
QUERE Laboratory, Setif, Algeria
E-mail: *nadjatzerroug@univ-setif.dz*

Behih Khalissa
University of Setif 1 Ferhat Abbas, Department of Electrical Engineering,
QUERE and LSI Laboratories, Setif, Algeria

Bouchama Ziyad
University of Bordj Bou Arreridj, Department of Electromechanical Engineering, Université Bachir El Ibrahimi Bordj Bou Arreridj
QUERE Laboratory
Bordj Bou Arreridj, Algeria

To cite this article:

Nadjat, Z., Khalissa, B., & Ziyad, B. (2025) Evaluation of robust controllers in photovoltaic systems: A comparative analysis. *The Eurasia Proceedings of Science, Technology, Engineering and Mathematics (EPSTEM), 38,* 470-479.

The Eurasia Proceedings of Science, Technology, Engineering & Mathematics (EPSTEM)
ISSN: 2602-3199

The Eurasia Proceedings of Science, Technology, Engineering and Mathematics (EPSTEM), 2025

Volume 38, Pages 480-501

ICONTES 2025: International Conference on Technology, Engineering and Science

Nano Ideal Semi Alpha Generalized Continuous and Irresolute Mappings in Nano Ideal Topological Spaces

Raja Mohammad Latif
Prince Mohammad Bin Fahd University

Abstract: Topology, though relatively recent in its development, has found remarkable applications across nearly all fields. While the theoretical or fundamental aspects of topology may seem abstract or dry at first, its applied side becomes truly fascinating once one becomes familiar with it. This research explores a variety of applications in diverse areas of Science and Technology-including Biology, Robotics, Geographic Information Systems (GIS), Engineering, Computer Science, and the Medical field. Though topology originates from mathematics, its influence extends far beyond, making a profound impact on numerous disciplines with its powerful and wide-ranging applications. The purpose of this paper is to present another class of functions referred to as Nano ideal semi α-generalized continuous maps, NIsαg-irresolute maps, NIsαg-open maps, NIsαg-closed maps, strongly NIsαg-open maps, strongly NIsαg-closed maps, NIsαg-homeomorphisms, Nano quasi Isαg-open maps, and Nano quasi Isαg-closed maps in nano ideal topological spaces. We investigate several properties and characterizations of this class of mappings in nano-ideal topological spaces.

Keywords: Nano ideal topological space, Nisαg-open set, Nisαg-closed set, Nisαg-continuous map, Nisαg-irresolute map, Nisαg-open map, Nisαg-closed map, Strongly nisαg-open map, Strongly nisαg-closed map, Nisαg-homeomorphism, Nqisαg-open map, Nqisαg-closed map

Introduction

Nano Ideal Topological Spaces, an extension of classical nano topology, have proven valuable in a wide range of domains where data is incomplete, uncertain, or imprecise. Their applications span various complex systems, including network anomaly detection, social and biological network analysis, transportation network optimization, pattern recognition, IoT security, financial market analysis, environmental monitoring, healthcare systems analysis, and supply chain management.

Nano ideal topological spaces generalize classical topological spaces by integrating "ideals"-collections of subsets with specific structural properties-and introducing various forms of "nano" sets and mappings. These structures allow for the analysis of relationships between points and subsets at an extremely fine-grained level, analogous to the "nano" concept in other scientific disciplines. Research in this area focuses on defining and studying different types of nano open and closed sets, as well as examining the behaviour of various nano mappings, such as nano-continuous, nano-irresolute, and nano-open maps. The aim is to understand their properties, explore their interconnections, and identify possible applications in theoretical mathematics and potentially in other fields.

The concept of continuity is fundamental in a large part of contemporary mathematics. In the nineteenth century, definitions of continuity were formulated for functions of real or complex variables. In the early twentieth century, the concept of continuity was generalized to apply to functions between topological spaces. Over the years, many generalizations of continuous mapping have been introduced and studied. Levine (1963), Mashhour et al.(1982) and Mashhour et al. (1983) have introduced the notions of semi-continuity, pre-continuity and α-continuity, respectively. Continuous and irresolute functions in topological spaces present a

- This is an Open Access article distributed under the terms of the Creative Commons Attribution-Noncommercial 4.0 Unported License, permitting all non-commercial use, distribution, and reproduction in any medium, provided the original work is properly cited.

- Selection and peer-review under responsibility of the Organizing Committee of the Conference

© 2025 Published by ISRES Publishing: www.isres.org

new method in the direction of research. Irresolute maps are introduced and studied by associated sciences. Parimala et al. (2018) presented the concept of nano-ideal generalized closed sets in nano-ideal topological spaces and investigated a portion of their essential properties. Recently, Dr. J. Arul Jesti and J. Joycy Renuka (2022) presented and concentrated on nIgsemi∗-closed sets and nIgsemi∗-open sets, characterizing nIgsemi∗-continuous and nIgsemi∗-irresolute functions in nano ideal topological spaces.

In 2021, Suganya et al. defined and presented a new class of sets called Nano ideal NIsαg-closed sets and NIsαg-open sets in Nano ideal topological spaces. In this paper, the conceptualization of NIsαg-open sets and NIsαg-closed sets in nano ideal topological spaces is utilized to characterize and examine another class of mappings called NIsαg-continuous maps, NIsαg-irresolute maps, NIsαg-open maps, NIsαg-closed maps, strongly NIsαg-open maps, strongly NIsαg-closed maps, NIsαg-homeomorphisms, Nano quasi Isαg-open maps, and Nano quasi Isαg-closed maps in nano ideal topological spaces. All these concepts will be helpful for further generalizations of nano-continuous and nano-irresolute mappings in nano-ideal topological spaces. We have investigated fundamental properties and characterizations of this class of mappings in nano ideal topological spaces.

Preliminaries

Throughout this paper $\left(U,T_R(X)\right)$ is a Nano topological space $\left(\text{briefly, } \mathcal{N}_{ano}\text{ –Top –Space}\right)$ and $\left(U,T_R(X),I\right)$ is a Nano ideal topological space $\left(\text{briefly, } \mathcal{N}_{ano}\text{ –Ideal –Top –Space}\right)$ concerning X where $X\subseteq U$, R is an equivalence relation on U/R denotes the family of equivalence classes of U by R. Here, we recall the following known definitions and properties.

Definition 2.1. Let U be a non-empty finite set of objects called the universe, and R be an equivalence relation on U named as the indiscernibility relation. Then U is divided into disjoint equivalence classes. Elements belonging to the same equivalence class are said to be discernible from one another. The pair $\left(U,R\right)$ is said to be the approximation space. Let $X\subseteq U$.

1. The Lower approximation of the set X with respect to the relation R is the set of all objects that can be for certain, classified as X with respect to R and it is denoted by $L_R(X)$. That is $L_R(X)=\bigcup_{x\in U}\left\{R(x):R(x)\subseteq X\right\}$ where $R(x)$ denotes the equivalence class determined by X.
2. The upper approximation of X concerning R is the set of all objects that can be possibly defined as X concerning R and it is denoted by $U_R(X)$. That is $U_R(X)=\bigcup_{x\in U}\left\{R(x):R(x)\cap X\neq\phi\right\}$.
3. The boundary region of X with respect to R is the set of all objects that can be classified neither in nor as not X with respect to R and is denoted by $B_R(X)$. That is, $B_R(X)=U_R(X)-L_R(X)$.

Definition 2.2. Let U be a non-empty finite set of objects called the universe and R be an the universe, R be an equivalence relation on U named as the and $T_R(X)=\left\{U,\phi,L_R(X),U_R(X),B_R(X)\right\}$ where $X\subseteq U$. Then $T_R(X)$ satisfies the following axioms.

(1) U and $\phi\in T_R(X)$.

(2) The union of any subcollection of $T_R(X)$ is in $T_R(X)$.

(3) The intersection of the elements of any finite subcollection of $T_R(X)$ is in $T_R(X)$.

Then $T_R(X)$ is a topology on U called the Nano topology on U concerning X, the pair $\left(U,T_R(X)\right)$ is called the Nano topological space $\left(\text{Briefly } \mathcal{N}_{\text{ano}}\text{ –Top –Space}\right)$. The elements of $T_R(X)$ are called nano-open $\left(\mathcal{N}_{\text{ano}}\text{ –open}\right)$ sets. The complements of the nano-open sets are called nano-closed $\left(\mathcal{N}_{\text{ano}}\text{ –closed}\right)$ sets.

Definition 2.3. Let $\left(U,T_R(X)\right)$ be a $\mathcal{N}_{ano}$ –Top –Space and $A\subseteq X$. Then

*. The Nano interior of a set A is defined as the union of all $\mathcal{N}_{\text{ano}}$ –open subsets contained in A and it is denoted by $\mathcal{N}_{\text{ano}}$ –Int(A). $\mathcal{N}_{\text{ano}}$ –Int(A) is the largest $\mathcal{N}_{\text{ano}}$ –open subset of A.

**. The Nano closure of a set A is defined as the intersection of all $\mathcal{N}_{ano}$ –closed sets containing A and it is denoted by $\mathcal{N}_{ano}$ –$Cl(A)$. $\mathcal{N}_{ano}$ –$Cl(A)$ is the smallest $\mathcal{N}_{ano}$ –closed set containing A.

Definition 2.3. An ideal I on a $Top-Space$ is a non-empty collection of subsets of X which satisfies (1) $A \in I$ and $B \subseteq A \Rightarrow B \in I$. (2) $A \in I$ and $B \in I \Rightarrow A \cup B \in I$.

Definition 2.4. A nano topological space $(U, T_R(X))$ with an ideal I on U is called a nano ideal topological space or nano ideal space and denoted as $(U, T_R(X), I)$.

Definition 2.5. Let $(U, T_R(X), I)$ be a nano ideal topological space. A set operator $(A)^{*_N} : P(U) \to P(U)$ is called the nano local function of I on U with respect to I on $T_R(X)$ is defined as $(A)^{*_N} = \{x \in U : G \cap A \notin I, \text{for each } x \in G, G \in T_R(X)\}$. and is denoted by $(A)^{*_N}$, where nano closure operator is defined as $N_{ano}Cl^*(A) = A \cup (A)^{*_N}$.

Prosition 2.6. Let $(U, T_R(X), I)$ be a nano ideal topological space and let A and B be subsets of U, then

$(1).\ (\phi)^{*_N} = \phi$

$(2).\ A \subseteq B \Rightarrow (A)^{*_N} \subseteq (B)^{*_N}$.

$(3).\ I \subseteq J \Rightarrow (A)^{*_N}(J) \subseteq (A)^{*_N}(I)$.

$(4).\ (A)^{*_N} \subseteq N_{ano}Cl^*(A)$.

$(5).\ (A)^{*_N}$ is a N_{ano} –*closed set*.

$(6).\ \left((A)^{*_N}\right)^{*_N} \subseteq (A)^{*_N}$.

$(7).\ (A)^{*_N} \cup (B)^{*_N} = (A \cup B)^{*_N}$.

$(8).\ (A)^{*_N} \cap (B)^{*_N} = (A \cap B)^{*_N}$.

$(9).$ *For every* N_{ano} –*open set* $G, G \cap (G \cap A)^{*_N} \subseteq (G \cap A)^{*_N}$.

$(10).$ *For every* $K \in I, (A \cup K)^{*_N} = (A)^{*_N} = (A - K)^{*_N}$.

Remark 2.6. Let $(U, T_R(X), I)$ be a $\mathcal{N}_{ano}$ –*Ideal* –*Top* –*Space* and A be a subset of U, if $A \subseteq (A)^{*_N}$, then $(A)^{*_N} = N_{ano}Cl(A)^{*_N} = N_{ano}Cl(A) = N_{ano}Cl^*(A)$.

Definition 2.7. Let $(U, T_R(X), I)$ be a $\mathcal{N}_{ano}$ –*Ideal* –*Top* –*Space* and $A \subseteq U$. Then A is called

(1) $\mathcal{N}_{ano}$ –semi –open set if $A \subseteq \mathcal{N}_{ano}$ –$Cl[\mathcal{N}_{ano}$ –$Int(A)]$.

(2) $\mathcal{N}_{ano}$ –semi –closed set if $\mathcal{N}_{ano}$ –$Int[\mathcal{N}_{ano}$ –$Cl(A)] \subseteq A$.

(3) $\mathcal{N}_{ano}\alpha$ –closed set if $\mathcal{N}_{ano}$ –$Cl[\mathcal{N}_{ano}$ –$Int(\mathcal{N}_{ano}$ –$Cl(A))] \subseteq A$.

(4) $\mathcal{N}_{ano}\alpha$ –open set if $A \subseteq \mathcal{N}_{ano}$ –$Int[\mathcal{N}_{ano}$ –$Cl(\mathcal{N}_{ano}$ –$Int(A))]$.

(5) $\mathcal{N}_{ano}$ –generalized closed (briefly $\mathcal{N}_{ano}g$–closed) set if $\mathcal{N}_{ano}$ –$Cl(A) \subseteq G$ whenever $A \subseteq G$ and G is $\mathcal{N}_{ano}$ –open in U.

The complements of the above-mentioned sets are called their respective open sets.

Definition 2.8. Let $(U, T_R(X), I)$ be a $\mathcal{N}_{ano}$ –*Ideal* –*Top* –*Space* and $A \subseteq U$. Then

(1) $\mathcal{N}_{ano}$ *–closed, set if $(A)^*N \subseteq A$.

(2) $\mathcal{N}_{ano}$ *–dense set if $A \subseteq (A)^*N$.

(3) $\mathcal{N}_{\text{ano}}$ Ig−closed if $(A)^{*N} \subseteq G$ whenever $A \subseteq G$ and G is $\mathcal{N}_{\text{ano}}$ −open in U.

(4) $\mathcal{N}_{\text{ano}}$ Ig*-closed if $(A)^{*N} \subseteq G$ whenever $A \subseteq G$ and G is $\mathcal{N}_{\text{ano}}$ g−open in U.

Definition 2.9. Let $(U, T_R(X), I)$ be a $\mathcal{N}_{ano}$ *−Ideal −Top −Space* and $A \subseteq U$. Then A is $\mathcal{N}_{\text{ano}}$ *−dense in itself $(\text{resp. } \mathcal{N}_{\text{ano}}$ *−perfect and $\mathcal{N}_{\text{ano}}$ *−closed set$)$ if $A \subseteq (A)^{*N}$ $\left(\text{resp. } A = (A)^{*N}, (A)^{*N} \subseteq A\right)$.

Lemma 2.10. Let $(U, T_R(X), I)$ be a $\mathcal{N}_{ano}$ *−Ideal −Top −Space* and $H \subseteq U$. If H **is** $\mathcal{N}_{\text{ano}}$ *−dense in itself, then $(H)^{*N} = N_{ano}Cl(H)^{*N} = N_{ano}Cl(H) = N_{ano}Cl^*\left[(H)^{*N}\right]$.

Definition 2.11. Let $(U, T_R(X), I)$ be a $\mathcal{N}_{ano}$ *−Ideal −Top −Space* and $A \subseteq U$. Then A is said to be $\mathcal{N}_{\text{ano}}$ Sα −open set if there exists a $\mathcal{N}_{\text{ano}}$ S −open set P in U such that $P \subseteq H \subseteq \mathcal{N}_{\text{ano}}$ −Cl(P) or equivalently if $H \subseteq \mathcal{N}_{\text{ano}}$ −Cl$(\mathcal{N}_{\text{ano}}\alpha$ −Int$(P))$.

Result 2.12. Let $(U, T_R(X))$ be a $\mathcal{N}_{ano}$ *−Top −Space.* Then

(i) .Every $\mathcal{N}_{\text{ano}}$ −open set is $\mathcal{N}_{\text{ano}}$ Sα −open set.

(ii) .Every $\mathcal{N}_{\text{ano}}\alpha$ −open set is $\mathcal{N}_{\text{ano}}$ Sα −open set.

Definition 2.13. Let $(U, T_R(X))$ be a $\mathcal{N}_{ano}$ *−Top −Space* and $H \subseteq U$. Then H is said to be a Nano semi α-generalized $(\text{briefly, } \mathcal{N}_{\text{ano}}$ Sαg−closed$)$ set if if $\mathcal{N}_{\text{ano}}$ −Cl$(H) \subseteq G$ whenever $H \subseteq G$ and G is $\mathcal{N}_{\text{ano}}$ Sα −open set in U. The complement $H^C = U - H$ of a $\mathcal{N}_{\text{ano}}$ Sα −closed set H is called a $\mathcal{N}_{\text{ano}}$ Sα −open in U.

Definition 2.14. Let $(U, T_R(X), I)$ be a $\mathcal{N}_{ano}$ *−Ideal −Top −Space* and $H \subseteq U$. Then H is said to be a Nano ideal semi α-generalized $(\text{briefly, } \mathcal{N}_{\text{ano}}$ ISαg−closed$)$ set if if $(H)^{*N} \subseteq G$ whenever $H \subseteq G$ and G is $\mathcal{N}_{\text{ano}}$ Sα −open set in U. The complement $H^C = U - H$ of a $\mathcal{N}_{\text{ano}}$ ISαg−closed set H is called a $\mathcal{N}_{\text{ano}}$ ISαg−open set in U. The collection of all $\mathcal{N}_{\text{ano}}$ ISαg−open $(\text{resp. } \mathcal{N}_{\text{ano}}$ ISαg−closed$)$ sets is denoted by $\mathcal{N}_{\text{ano}}$ ISαg−O$(U, T_R(X), I)$ $\left(\text{resp. } \mathcal{N}_{\text{ano}}\text{ISαg−O}(U, T_R(X), I)\right)$.

Definition 2.15. Let $(U, T_R(X), I)$ be a $\mathcal{N}_{ano}$ *−Ideal −Top −Space* and $H \subseteq U$. Then

*. The $\mathcal{N}_{\text{ano}}$ ISα − interior of a set A is defined as the union of all $\mathcal{N}_{\text{ano}}$ ISαg−open subsets contained in A and it is denoted by $\mathcal{N}_{\text{ano}}$ ISαg−Int(A). $\mathcal{N}_{\text{ano}}$ ISαg−Int(A) is the largest $\mathcal{N}_{\text{ano}}$ ISαg−open subset of A.

**. The $\mathcal{N}_{\text{ano}}$ ISαg−closure of a set A is defined as the intersection of all $\mathcal{N}_{\text{ano}}$ ISαg−closed sets containing A and it is denoted by $\mathcal{N}_{\text{ano}}$ ISαg−Cl(A). $\mathcal{N}_{\text{ano}}$ ISαg−Cl(A) is the smallest $\mathcal{N}_{\text{ano}}$ ISαg−closed set containing A.

Remark 2.16. $\mathcal{N}_{\text{ano}}$ −open $\Rightarrow$ $\mathcal{N}_{\text{ano}}$ *-open $\Rightarrow$ $\mathcal{N}_{\text{ano}}$ ISαg−open $\Rightarrow$ $\mathcal{N}_{\text{ano}}$ Ig−open.

& $\mathcal{N}_{\text{ano}}$ −closed $\Rightarrow$ $\mathcal{N}_{\text{ano}}$ *-closed $\Rightarrow$ $\mathcal{N}_{\text{ano}}$ ISαg−closed $\Rightarrow$ $\mathcal{N}_{\text{ano}}$ Ig−closed.

3 Nano Ideal Semi −α −Generalized −Continuous Mappings

Definition 3.1. A map $f : (U, T_R(X), I) \to (V, \sigma_{R'}(Y), J)$ is $\mathcal{N}_{\text{ano}}$ −continuous if $f^{-1}(H)$ is a $\mathcal{N}_{\text{ano}}$ −closed for every $\mathcal{N}_{\text{ano}}$ −closed set H of $(V, \sigma_{R'}(Y), J)$.

Proposition 3.2. A map $f:\left(\mathrm{U},\mathrm{T}_{\mathrm{R}}\left(\mathrm{X}\right),\mathrm{I}\right)\to\left(\mathrm{V},\sigma_{\mathrm{R}'}\left(\mathrm{Y}\right),\mathrm{J}\right)$ is $\mathcal{N}_{\text{ano}}$ −continuous if and only if $f^{-1}\left(\mathrm{H}\right)$ is a $\mathcal{N}_{\text{ano}}$ −open set for every $\mathcal{N}_{\text{ano}}$ −open set H of $\left(\mathrm{V},\sigma_{\mathrm{R}'}\left(\mathrm{Y}\right),\mathrm{J}\right)$.

Definition 3.3. A map $f:\left(\mathrm{U},\mathrm{T}_{\mathrm{R}}\left(\mathrm{X}\right),\mathrm{I}\right)\to\left(\mathrm{V},\sigma_{\mathrm{R}'}\left(\mathrm{Y}\right),\mathrm{J}\right)$ is $\mathcal{N}_{\text{ano}}$ *−continuous if $f^{-1}\left(\mathrm{H}\right)$ is a $\mathcal{N}_{\text{ano}}$ *−closed for every $\mathcal{N}_{\text{ano}}$ −closed set H of $\left(\mathrm{V},\sigma_{\mathrm{R}'}\left(\mathrm{Y}\right),\mathrm{J}\right)$.

Proposition 3.4. A map $f:\left(\mathrm{U},\mathrm{T}_{\mathrm{R}}\left(\mathrm{X}\right),\mathrm{I}\right)\to\left(\mathrm{V},\sigma_{\mathrm{R}'}\left(\mathrm{Y}\right),\mathrm{J}\right)$ is $\mathcal{N}_{\text{ano}}$ *−continuous if and only if $f^{-1}\left(\mathrm{H}\right)$ is a $\mathcal{N}_{\text{ano}}$ *−open for every $\mathcal{N}_{\text{ano}}$ −open set H of $\left(\mathrm{V},\sigma_{\mathrm{R}'}\left(\mathrm{Y}\right),\mathrm{J}\right)$.

Definition 3.5. A map $f:\left(\mathrm{U},\mathrm{T}_{\mathrm{R}}\left(\mathrm{X}\right),\mathrm{I}\right)\to\left(\mathrm{V},\sigma_{\mathrm{R}'}\left(\mathrm{Y}\right),\mathrm{J}\right)$ is $\mathcal{N}_{\text{ano}}\mathrm{IS}\alpha\mathrm{g}$−continuous if and only if $f^{-1}\left(\mathrm{H}\right)$ is a $\mathcal{N}_{\text{ano}}\mathrm{IS}\alpha\mathrm{g}$−closed set for every $\mathcal{N}_{\text{ano}}$ −closed set H of $\left(\mathrm{V},\sigma_{\mathrm{R}'}\left(\mathrm{Y}\right),\mathrm{J}\right)$.

Theorem 3.6. A map $f:\left(\mathrm{U},\mathrm{T}_{\mathrm{R}}\left(\mathrm{X}\right),\mathrm{I}\right)\to\left(\mathrm{V},\sigma_{\mathrm{R}'}\left(\mathrm{Y}\right),\mathrm{J}\right)$ is $\mathcal{N}_{\text{ano}}\mathrm{IS}\alpha\mathrm{g}$−continuous if and only if $f^{-1}\left(\mathrm{H}\right)$ is $\mathcal{N}_{\text{ano}}\mathrm{IS}\alpha\mathrm{g}$−open in $\left(\mathrm{U},\mathrm{T}_{\mathrm{R}}\left(\mathrm{X}\right),\mathrm{I}\right)$ for every $\mathcal{N}_{\text{ano}}$ −open H In $\left(\mathrm{V},\sigma_{\mathrm{R}'}\left(\mathrm{Y}\right),\mathrm{J}\right)$.

Proof. Let $f:\left(\mathrm{U},\mathrm{T}_{\mathrm{R}}\left(\mathrm{X}\right),\mathrm{I}\right)\to\left(\mathrm{V},\sigma_{\mathrm{R}'}\left(\mathrm{Y}\right),\mathrm{J}\right)$ be $\mathcal{N}_{\text{ano}}\mathrm{IS}\alpha\mathrm{g}$−continuous and H be a $\mathcal{N}_{\text{ano}}$ −open set in $\left(\mathrm{V},\sigma_{\mathrm{R}'}\left(\mathrm{Y}\right),\mathrm{J}\right)$. Then H^{C} is $\mathcal{N}_{\text{ano}}$ −closed in $\left(\mathrm{V},\sigma_{\mathrm{R}'}\left(\mathrm{Y}\right),\mathrm{J}\right)$ and since f is $\mathcal{N}_{\text{ano}}\mathrm{IS}\alpha\mathrm{g}$−continuous, $f^{-1}\left(\mathrm{H}^{C}\right)$ is $\mathcal{N}_{\text{ano}}\mathrm{IS}\alpha\mathrm{g}$−closed in $\left(\mathrm{U},\mathrm{T}_{\mathrm{R}}\left(\mathrm{X}\right),\mathrm{I}\right)$. But $f^{-1}\left(\mathrm{H}^{C}\right)=\left(f^{-1}\left(\mathrm{H}\right)\right)^{C}$ and so $f^{-1}\left(\mathrm{H}\right)$ is $\mathcal{N}_{\text{ano}}\mathrm{IS}\alpha\mathrm{g}$−open in $\left(\mathrm{U},\mathrm{T}_{\mathrm{R}}\left(\mathrm{X}\right),\mathrm{I}\right)$.

Conversely, assume that $f^{-1}\left(\mathrm{H}\right)$ is $\mathcal{N}_{\text{ano}}\mathrm{IS}\alpha\mathrm{g}$−open in $\left(\mathrm{U},\mathrm{T}_{\mathrm{R}}\left(\mathrm{X}\right),\mathrm{I}\right)$ for each $\mathcal{N}_{\text{ano}}$ −open set H in $\left(\mathrm{V},\sigma_{\mathrm{R}'}\left(\mathrm{Y}\right),\mathrm{J}\right)$. Let F be a $\mathcal{N}_{\text{ano}}$ −closed set in $\left(\mathrm{V},\sigma_{\mathrm{R}'}\left(\mathrm{Y}\right),\mathrm{J}\right)$. Then F^{C} is $\mathcal{N}_{\text{ano}}$ −open in $\left(\mathrm{V},\sigma_{\mathrm{R}'}\left(\mathrm{Y}\right),\mathrm{J}\right)$ and by assumption, $f^{-1}\left(\mathrm{F}^{C}\right)$ is $\mathcal{N}_{\text{ano}}\mathrm{IS}\alpha\mathrm{g}$−open in $\left(\mathrm{U},\mathrm{T}_{\mathrm{R}}\left(\mathrm{X}\right),\mathrm{I}\right)$. Since $f^{-1}\left(\mathrm{F}^{C}\right)=\left(f^{-1}\left(\mathrm{F}\right)\right)^{C}$, we have $f^{-1}\left(\mathrm{F}\right)$ is $\mathcal{N}_{\text{ano}}\mathrm{IS}\alpha\mathrm{g}$−closed in $\left(\mathrm{U},\mathrm{T}_{\mathrm{R}}\left(\mathrm{X}\right),\mathrm{I}\right)$ and so f is $\mathcal{N}_{\text{ano}}\mathrm{IS}\alpha\mathrm{g}$−continuous.

Theorem 3.7 Every $\mathcal{N}_{\text{ano}}$ −continuous function $f:\left(\mathrm{U},\mathrm{T}_{\mathrm{R}}\left(\mathrm{X}\right),\mathrm{I}\right)\to\left(\mathrm{V},\sigma_{\mathrm{R}'}\left(\mathrm{Y}\right),\mathrm{J}\right)$ is $\mathcal{N}_{\text{ano}}\mathrm{IS}\alpha\mathrm{g}$−continuous but not conversely.

Proof. Let $f:\left(\mathrm{U},\mathrm{T}_{\mathrm{R}}\left(\mathrm{X}\right),\mathrm{I}\right)\to\left(\mathrm{V},\sigma_{\mathrm{R}'}\left(\mathrm{Y}\right),\mathrm{J}\right)$ be a $\mathcal{N}_{\text{ano}}$ −continuous function. Therefore, for each $\mathcal{N}_{\text{ano}}$ −open set H of $\left(\mathrm{V},\sigma_{\mathrm{R}'}\left(\mathrm{Y}\right),\mathrm{J}\right)$ $f^{-1}\left(\mathrm{H}\right)$ is a $\mathcal{N}_{\text{ano}}$ −open set in $\left(\mathrm{U},\mathrm{T}_{\mathrm{R}}\left(\mathrm{X}\right),\mathrm{I}\right)$. Since $\mathrm{T}_{\mathrm{R}}\left(\mathrm{X}\right)\subseteq\mathcal{N}_{ano}\mathrm{IS}\alpha\mathrm{g}\text{−O}\left(\mathrm{U},\mathrm{T}_{\mathrm{R}}\left(\mathrm{X}\right),\mathrm{I}\right)$. So $f^{-1}\left(\mathrm{H}\right)$ is $\mathcal{N}_{\text{ano}}\mathrm{IS}\alpha\mathrm{g}$−open set and so f is a $\mathcal{N}_{\text{ano}}\mathrm{IS}\alpha\mathrm{g}$−continuous function.

Proposition 3.8. Every $\mathcal{N}_{\text{ano}}$ *−continuous function is $\mathcal{N}_{\text{ano}}\mathrm{IS}\alpha\mathrm{g}$−continuous. but not conversely.

Proof. The proof is like Theorem 3.7, as every $\mathcal{N}_{\text{ano}}$ *−open $\left(\text{resp.}\,\mathcal{N}_{\text{ano}}\text{ *−closed}\right)$ set is $\mathcal{N}_{\text{ano}}\mathrm{IS}\alpha\mathrm{g}$−open $\left(\text{resp.}\,\mathcal{N}_{\text{ano}}\mathrm{IS}\alpha\mathrm{g}\text{−closed}\right)$

Example 3.9. Let $\mathrm{U}=\left\{1,2,3,4\right\}$ with $\mathrm{U}/R=\left\{\left\{1,3\right\},\left\{2\right\},\left\{4\right\}\right\};\mathrm{X}=\left\{2,3\right\}$ and $\mathrm{I}=\left\{\phi,\left\{3\right\}\right\}$. Then the $\mathcal{N}_{\text{ano}}$ −Top. $\mathrm{T}_{\mathrm{R}}\left(\mathrm{X}\right)=\left\{\phi,\mathrm{U},\left\{2\right\},\left\{1,2,3\right\},\left\{1,3\right\}\right\}$. $\mathcal{N}_{\text{ano}}\mathrm{IS}\alpha\mathrm{g}$−closed sets are $\phi,\mathrm{U},\left\{3\right\},\left\{4\right\},\left\{1,4\right\},\left\{2,4\right\},\left\{3,4\right\},\left\{1,2,4\right\},\left\{1,3,4\right\},\left\{2,3,4\right\}$. The set $\left\{1,4\right\}$ is not $\mathcal{N}_{\text{ano}}$ *−closed set.

Let $V=\{a,b,c\}$ with $V/R'=\{\{a\},\{b,c\}\}$ and $Y=\{a\}$. Then the $\mathcal{N}_{ano}$-Top. $\Gamma_{R'}(Y)=\{\phi,\{a\},V\}$ and $J=\{\phi\}$. Define a function $f:(U,T_R(X),I)\to(V,\Gamma_{R'}(Y),J)$ by: $f(1)=b, f(2)=f(3)=a, f(4)=c$. Then $f^{-1}(\{a\})=\{2,3\}$ is $\mathcal{N}_{ano}$ ISαg-open but not $\mathcal{N}_{ano}$ *-open in U. Thus f is $\mathcal{N}_{ano}$ ISαg-continuous but not $\mathcal{N}_{ano}$ *-continuous. Furthermore, we notice that f is not $\mathcal{N}_{ano}$-continuous, since $f^{-1}(\{a\})=\{2,3\}$ is not $\mathcal{N}_{ano}$-open in $(U,T_R(X),I)$.

Theorem 3.10. Suppose that $f:(U,T_R(X),I)\to(V,\sigma_{R'}(Y),J)$ and $g:(V,\sigma_{R'}(Y),J)\to(W,\Omega_{R''}(Z),K)$ are any two maps. Then gof is $\mathcal{N}_{ano}$ ISαg-continuous if g is $\mathcal{N}_{ano}$ *-continuous and f is $\mathcal{N}_{ano}$ ISαg-continuous.

Proof. Easy.

Definition 3.11. Let $(U,T_R(X),I)$ be a $\mathcal{N}_{ano}$-ideal-Top.-Space. Let z be a point of U and G be a subset of U. Then G is called a $\mathcal{N}_{ano}$ ISαg-neighbourhood (briefly, $\mathcal{N}_{ano}$ ISαg-nbhd) of z in U if there exists a $\mathcal{N}_{ano}$ ISαg-open set S of U such that $z\in S\subseteq G$.

Proposition 3.12. Let M be a subset of $(U,T_R(X),I)$. Then $m\in\mathcal{N}_{ano}$ ISαg-Cl(M) if and only if for any $\mathcal{N}_{ano}$ ISαg-nbhd G_m of m in $(U,T_R(X),I)$, $M\cap G_m\neq\phi$.

Proof. Necessity. Assume $m\in\mathcal{N}_{ano}$ ISαg-Cl(M). Suppose that there is a $\mathcal{N}_{ano}$ ISαg-nbhd G of the point m in $(U,T_R(X),I)$ such that $G\cap M=\phi$. Since G is $\mathcal{N}_{ano}$ ISαg-nbhd of m in $(U,T_R(X),I)$, By definition, there exists a $\mathcal{N}_{ano}$ ISαg-open set H_m such that $m\in H_m\subseteq G$. Therefore, we have $H_m\cap M=\phi$ and so $M\subseteq(H_m)^C$. Since $(H_m)^C$ is an $\mathcal{N}_{ano}$ ISαg-closed set containing M, we have by definition $\mathcal{N}_{ano}$ ISαg-Cl$(M)\subseteq(H_m)^C$ and therefore $m\notin\mathcal{N}_{ano}$ ISαg-Cl(M), which is a contradiction.

Sufficiency. Assume for each $\mathcal{N}_{ano}$ ISαg-nbhd H_m of m in $(U,T_R(X),I)$, $H_m\cap M\neq\phi$. Suppose that $m\notin\mathcal{N}_{ano}$ ISαg-Cl(M). Then by definition, there exists an $\mathcal{N}_{ano}$ ISαg-closed set F of $(U,T_R(X),I)$, such that $M\subseteq F$ and $m\notin F$. Thus $m\in F^C$ and F^C is $\mathcal{N}_{ano}$ ISαg-open in $(U,T_R(X),I)$, and hence F^C is a $\mathcal{N}_{ano}$ ISαg-nbhd of m in $(U,T_R(X),I)$. But $M\cap F^C=\phi$,, which is a contradiction.

In the next theorem we explore certain characterizations of $\mathcal{N}_{ano}$ ISαg-continuous maps.

Theorem 3.13. Let $f:(U,T_R(X),I)\to(V,\sigma_{R'}(Y),J)$ be a map. Then the following statements are equivalent.

(1). The map f is $\mathcal{N}_{ano}$ ISαg-continuous.

(2). The inverse of each $\mathcal{N}_{ano}$-open set is $\mathcal{N}_{ano}$ ISαg-open.

(3). For each point p in $(U,T_R(X),I)$ and each $\mathcal{N}_{ano}$-open set H in $(V,\sigma_{R'}(Y),J)$ with $f(p)\in H$, there is an $\mathcal{N}_{ano}$ ISαg-open set G in $(U,T_R(X),I)$ such that $p\in G$, $f(G)\subseteq H$.

(4). The inverse of each $\mathcal{N}_{ano}$-closed set is $\mathcal{N}_{ano}$ ISαg-closed..

(5). For each p in $(U,T_R(X),I)$, the inverse of every neighbourhood of $f(p)$ is a $\mathcal{N}_{ano}$ ISαg-nbhd of p.

(6). For each p in $(U,T_R(X),I)$ and each neighbourhood M of $f(p)$, there is a $\mathcal{N}_{ano}\,IS\alpha g$–nbhd G of p such that $f(G)\subseteq M$.

(7). For each subset A of $(U,T_R(X),I)$, $f(\mathcal{N}_{ano}\,IS\alpha g\text{–}Cl(A))\subseteq \mathcal{N}_{ano}\text{–}Cl(f(A))$.

(8). For each subset B of $(V,\sigma_{R/}(Y),J)$, $\mathcal{N}_{ano}\,IS\alpha g\text{–}Cl(f^{-1}(B))\subseteq f^{-1}(\mathcal{N}_{ano}\text{–}Cl(f(B)))$.

Proof. $(1)\Leftrightarrow(2)$. This follows from Theorem 3.5.

$(2)\Leftrightarrow(4)$. The result follows from the fact that if Q is a subset of $(V,\sigma_{R^*}(Y),J)$, then $f^{-1}(Q^C)=(f^{-1}(Q))^C$.

$(2)\Leftrightarrow(5)$. For p in $(U,T_R(X),I)$, let M be a neighbourhood of $f(p)$. Then there exists an $\mathcal{N}_{ano}$–open set H in $(V,\sigma_{R/}(Y),J)$ such that $f(p)\in H\subseteq M$. Consequently, $f^{-1}(H)$ is an $\mathcal{N}_{ano}\,IS\alpha g$–open set in $(U,T_R(X),I)$ and $p\in f^{-1}(H)\subseteq f^{-1}(M)$. Thus $f^{-1}(M)$ is a $\mathcal{N}_{ano}\,IS\alpha g$–nbhd of p.

$(5)\Leftrightarrow(6)$. Let $p\in U$ and let M be a neighbourhood of $f(p)$. Then by assumption, $G=f^{-1}(M)$ is a $\mathcal{N}_{ano}\,IS\alpha g$–nbhd of p and $f(G)=f(f^{-1}(M))\subseteq M$.

$(6)\Leftrightarrow(3)$. For an element p in $(U,T_R(X),I)$, let M be a $\mathcal{N}_{ano}$–open set containing $f(p)$. Then M is a neighbourhood of $f(p)$. So by assumption, there exists a $\mathcal{N}_{ano}\,IS\alpha g$–nbhd G of p such that $f(G)\subseteq M$. Hence, there exists a $\mathcal{N}_{ano}\,IS\alpha g$–open set H in $(U,T_R(X),I)$ such that $p\in H\subseteq G$ and so $f(H)\subseteq f(G)\subseteq M$.

$(7)\Leftrightarrow(4)$. Suppose that (4) holds and let G be a subset of $(U,T_R(X),I)$. Since $f(G)\subseteq \mathcal{N}_{ano}\text{–}Cl(f(G))$, we have $G\subseteq f^{-1}(\mathcal{N}_{ano}\text{–}Cl(f(G)))$. Since $\mathcal{N}_{ano}\text{–}Cl(f(G))$ is a $\mathcal{N}_{ano}$–closed set in $(V,\sigma_{R/}(Y),J)$, by assumption $f^{-1}(\mathcal{N}_{ano}\text{–}Cl(f(G)))$ is a $\mathcal{N}_{ano}\,IS\alpha g$–closed set containing G. Consequently, $\mathcal{N}_{ano}\,IS\alpha g\text{–}Cl(G)\subseteq f^{-1}(\mathcal{N}_{ano}\text{–}Cl(f(G)))$. Thus $f[\mathcal{N}_{ano}\,IS\alpha g\text{–}Cl(G)]\subseteq f[f^{-1}(\mathcal{N}_{ano}\text{–}Cl(f(G)))]\subseteq \mathcal{N}_{ano}\text{–}Cl(f(G))$.

Conversely, suppose that (7) holds for any subset G of $(U,T_R(X),I)$. Let H be a $\mathcal{N}_{ano}$–closed subset of $(V,\sigma_{R/}(Y),J)$. Then by assumption, $f[\mathcal{N}_{ano}\,IS\alpha g\text{–}Cl(f^{-1}(H))]\subseteq \mathcal{N}_{ano}\text{–}Cl(f[f^{-1}(H)])\subseteq \mathcal{N}_{ano}\text{–}Cl(H)=H$. i.e., $\mathcal{N}_{ano}\,IS\alpha g\text{–}Cl(f^{-1}(H))\subseteq f^{-1}(H)$ and so $f^{-1}(H)$ is $\mathcal{N}_{ano}\,IS\alpha g$–closed.

$(7)\Leftrightarrow(8)$. Suppose that (7) holds and B be any subset of $(V,\sigma_{R/}(Y),J)$. Then replacing A by $f^{-1}(B)$ in (7), we obtain $f(\mathcal{N}_{ano}\,IS\alpha g\text{–}Cl(f^{-1}(B)))\subseteq \mathcal{N}_{ano}\text{–}Cl(f(f^{-1}(B)))\subseteq \mathcal{N}_{ano}\text{–}Cl(B)$, i.e., $\mathcal{N}_{ano}\,IS\alpha g\text{–}Cl(f^{-1}(B))\subseteq f^{-1}(\mathcal{N}_{ano}\text{–}Cl(B))$.

Conversely, suppose that (8) holds. Let $B=f(A)$) where A is a subset of $(U,T_R(X),I)$. Then we have, $\mathcal{N}_{ano}\,IS\alpha g\text{–}Cl(A)\subseteq \mathcal{N}_{ano}\,IS\alpha g\text{–}Cl(f^{-1}(B))\subseteq f^{-1}(\mathcal{N}_{ano}\text{–}Cl(f(A)))$ and so $f(\mathcal{N}_{ano}\,IS\alpha g\text{–}Cl(A))\subseteq \mathcal{N}_{ano}\text{–}Cl(f(A))$. This completes the proof of the theorem.

4 Nano Ideal Semi –α –Generalized –Irresolute Mappings

In this section $\mathcal{N}_{ano}\,\mathrm{IS}\alpha\mathrm{g}-function$ is defined, and its characterizations and properties concerning $\mathcal{N}_{ano}\,\mathrm{IS}\alpha\mathrm{g}-\mathrm{I}nt$ and $\mathcal{N}_{ano}\,\mathrm{IS}\alpha\mathrm{g}-\mathrm{C}l$ of sets are derived.

Definition 4.1. A map $f:\left(\mathrm{U},\mathrm{T}_{\mathrm{R}}\left(\mathrm{X}\right),\mathrm{I}\right)\to\left(\mathrm{V},\sigma_{\mathrm{R}'}\left(\mathrm{Y}\right),\mathrm{J}\right)$ is called $\mathcal{N}_{ano}\,\mathrm{IS}\alpha\mathrm{g}-irresolute$ if the inverse image $f^{-1}\left(\mathrm{H}\right)$ is $\mathcal{N}_{\mathrm{ano}}\,\mathrm{IS}\alpha\mathrm{g}$–open set in $\left(\mathrm{U},\mathrm{T}_{\mathrm{R}}\left(\mathrm{X}\right),\mathrm{I}\right)$ for each $\mathcal{N}_{\mathrm{ano}}\,\mathrm{IS}\alpha\mathrm{g}$–open set H in $\left(\mathrm{V},\sigma_{\mathrm{R}'}\left(\mathrm{Y}\right),\mathrm{J}\right)$.

Theorem 4.2. A map $f:\left(\mathrm{U},\mathrm{T}_{\mathrm{R}}\left(\mathrm{X}\right),\mathrm{I}\right)\to\left(\mathrm{V},\sigma_{\mathrm{R}'}\left(\mathrm{Y}\right),\mathrm{J}\right)$ is $\mathcal{N}_{\mathrm{ano}}\,\mathrm{IS}\alpha\mathrm{g}$–irresolute if and only if the inverse image of every $\mathcal{N}_{\mathrm{ano}}\,\mathrm{IS}\alpha\mathrm{g}$–closed set in V is $\mathcal{N}_{\mathrm{ano}}\,\mathrm{IS}\alpha\mathrm{g}$–closed in U.

Proof. Let $f:\left(\mathrm{U},\mathrm{T}_{\mathrm{R}}\left(\mathrm{X}\right),\mathrm{I}\right)\to\left(\mathrm{V},\sigma_{\mathrm{R}'}\left(\mathrm{Y}\right),\mathrm{J}\right)$ be $\mathcal{N}_{\mathrm{ano}}\,\mathrm{IS}\alpha\mathrm{g}$–irresolute. Let H be $\mathcal{N}_{\mathrm{ano}}\,\mathrm{IS}\alpha\mathrm{g}$–closed in V. Then H^{C} is $\mathcal{N}_{\mathrm{ano}}\,\mathrm{IS}\alpha\mathrm{g}$–open in V. Since f is $\mathcal{N}_{\mathrm{ano}}\,\mathrm{Ig}^{*}\alpha$ –irresolute $f^{-1}\left(\mathrm{H}^{C}\right)=\left(f^{-1}\left(\mathrm{H}\right)\right)^{C}=\ f^{-1}\left(\mathrm{V}\right)-f^{-1}\left(\mathrm{H}\right)=\mathrm{U}-f^{-1}\left(\mathrm{H}\right)$ is $\mathcal{N}_{\mathrm{ano}}\,\mathrm{IS}\alpha\mathrm{g}$–open in U. Therefore $f^{-1}\left(\mathrm{H}\right)$ is $\mathcal{N}_{\mathrm{ano}}\,\mathrm{IS}\alpha\mathrm{g}$–closed in U. Thus, the inverse image of every $\mathcal{N}_{\mathrm{ano}}\,\mathrm{IS}\alpha\mathrm{g}$–closed set in V is $\mathcal{N}_{\mathrm{ano}}\,\mathrm{IS}\alpha\mathrm{g}$–closed in U.

Conversely, let the inverse image of every $\mathcal{N}_{\mathrm{ano}}\,\mathrm{IS}\alpha\mathrm{g}$–closed set in V is $\mathcal{N}_{\mathrm{ano}}\,\mathrm{IS}\alpha\mathrm{g}$–closed in U. Let B be a $\mathcal{N}_{\mathrm{ano}}\,\mathrm{IS}\alpha\mathrm{g}$–open set in V. Then B^{C} is $\mathcal{N}_{\mathrm{ano}}\,\mathrm{IS}\alpha\mathrm{g}$–closed in V. By our assumption $f^{-1}\left(\mathrm{B}^{C}\right)=\left(f^{-1}\left(\mathrm{B}\right)\right)^{C}=f^{-1}\left(\mathrm{V}\right)-f^{-1}\left(\mathrm{B}\right)=\mathrm{U}-f^{-1}\left(\mathrm{B}\right)$ is $\mathcal{N}_{\mathrm{ano}}\,\mathrm{IS}\alpha\mathrm{g}$–closed in U. Therefore $f^{-1}\left(\mathrm{B}\right)$ is $\mathcal{N}_{\mathrm{ano}}\,\mathrm{IS}\alpha\mathrm{g}$–open in U. Thus the inverse image of every $\mathcal{N}_{\mathrm{ano}}\,\mathrm{IS}\alpha\mathrm{g}$–open set in V is $\mathcal{N}_{\mathrm{ano}}\,\mathrm{IS}\alpha\mathrm{g}$–open in U. Hence f is $\mathcal{N}_{\mathrm{ano}}\,\mathrm{IS}\alpha\mathrm{g}$–irresolute.

Example 4.3. Let $\mathrm{W}=\left\{a,b,c,d\right\}$, $\mathrm{W}/\mathrm{R}'=\left\{\left\{\left\{a\right\},\left\{b,c\right\},\left\{d\right\}\right\}\right\}$; $\mathrm{Z}=\left\{a,d\right\}$ and $\mathcal{N}_{\mathrm{ano}}$–Ideal $\mathrm{J}=\left\{\phi,\left\{a\right\}\right\}$. $\mathcal{N}_{\mathrm{ano}}$–Topology $\Omega_{\mathrm{R}'}\left(\mathrm{Z}\right)=\left\{\phi,\mathrm{W},\left\{a,d\right\}\right\}$. Then the $\mathcal{N}_{\mathrm{ano}}\,\mathrm{IS}\alpha\mathrm{g}$–closed sets are ϕ, $\left\{a\right\}$, $\left\{b,c\right\}$, $\left\{a,b,c\right\}$, $\left\{b,c,d\right\}$. Consider $\left(\mathrm{U},\mathrm{T}_{\mathrm{R}}\left(\mathrm{X}\right),\mathrm{I}\right)$ as given in Example 3.9. Now define $f:\left(\mathrm{U},\mathrm{T}_{\mathrm{R}}\left(\mathrm{X}\right),\mathrm{I}\right)\to\left(\mathrm{W},\Omega_{\mathrm{R}'}\left(Z\right),\mathrm{J}\right)$ by $f\left(1\right)=d,f\left(2\right)=b,f\left(3\right)=a,f\left(4\right)=c.$ We notice that

$$f^{-1}\left(\left\{a\right\}\right)=\left\{3\right\},f^{-1}\left(\left\{b,c\right\}\right)=\left\{2,4\right\},f^{-1}\left(\left\{a,b,c\right\}\right)=\left\{2,3,4\right\},f^{-1}\left(\left\{b,c,d\right\}\right)=\left\{1,2,4\right\},f\left(\phi\right)=\phi,f^{-1}\left(\mathrm{W}\right)=\mathrm{U}$$

are $\mathcal{N}_{\mathrm{ano}}\,\mathrm{IS}\alpha\mathrm{g}$–closed sets in $\left(\mathrm{U},\mathrm{T}_{\mathrm{R}}\left(\mathrm{X}\right),\mathrm{I}\right)$. as stated in Example 3.9. Then by Theorem 4.2, it follows that f is a $\mathcal{N}_{\mathrm{ano}}\,\mathrm{IS}\alpha\mathrm{g}$–irresolute function.

Theorem 4.4. Every $\mathcal{N}_{\mathrm{ano}}\,\mathrm{IS}\alpha\mathrm{g}$–irresolute map is $\mathcal{N}_{\mathrm{ano}}\,\mathrm{IS}\alpha\mathrm{g}$–continuous but not conversely.

Proof. Let $f:\left(\mathrm{U},\mathrm{T}_{\mathrm{R}}\left(\mathrm{X}\right),\mathrm{I}\right)\to\left(\mathrm{V},\sigma_{\mathrm{R}'}\left(\mathrm{Y}\right),\mathrm{J}\right)$ be a $\mathcal{N}_{\mathrm{ano}}\,\mathrm{IS}\alpha\mathrm{g}$–irresolute map. Let H be a $\mathcal{N}_{\mathrm{ano}}$–closed set of $\left(\mathrm{V},\sigma_{\mathrm{R}'}\left(\mathrm{Y}\right),\mathrm{J}\right)$. Then H is $\mathcal{N}_{\mathrm{ano}}\,\mathrm{IS}\alpha\mathrm{g}$–closed. Since f is $\mathcal{N}_{\mathrm{ano}}\,\mathrm{IS}\alpha\mathrm{g}$–irresolute, then $f^{-1}\left(\mathrm{H}\right)$ is a $\mathcal{N}_{\mathrm{ano}}\,\mathrm{IS}\alpha\mathrm{g}$–closed set of $\left(\mathrm{U},\mathrm{T}_{\mathrm{R}}\left(\mathrm{X}\right),\mathrm{I}\right)$. Therefore f is $\mathcal{N}_{\mathrm{ano}}\,\mathrm{IS}\alpha\mathrm{g}$–continuous.

Example 4.5. Let $\left(\mathrm{U},\mathrm{T}_{\mathrm{R}}\left(\mathrm{X}\right),\mathrm{I}\right)$ be a $\mathcal{N}_{\mathrm{ano}}$–ideal–Top.–Spaces as given in Example 3.9 and $\left(\mathrm{W},\Omega_{\mathrm{R}^{*}}\left(\mathrm{Z}\right),\mathrm{J}\right)$ as given in Example 4.13. Define $f:\left(\mathrm{U},\mathrm{T}_{\mathrm{R}}\left(\mathrm{X}\right),\mathrm{I}\right)\to\left(\mathrm{W},\Omega_{\mathrm{R}^{*}}\left(\mathrm{Z}\right),\mathrm{J}\right)$ by $f\left(1\right)=a,f\left(2\right)=b,f\left(3\right)=d,f\left(4\right)=c.$ It is clear that $\left\{\alpha\right\}$ is $\mathcal{N}_{\mathrm{ano}}\,\mathrm{IS}\alpha\mathrm{g}$–closed set of $\left(\mathrm{W},\Omega_{\mathrm{R}^{*}}\left(\mathrm{Z}\right),\mathrm{J}\right)$ but $f^{-1}\left(\left\{a\right\}\right)=\left\{1\right\}$ is not $\mathcal{N}_{\mathrm{ano}}\,\mathrm{IS}\alpha\mathrm{g}$–closed set of $\left(\mathrm{U},\mathrm{T}_{\mathrm{R}}\left(\mathrm{X}\right),\mathrm{I}\right)$. Thus f is not

$\mathcal{N}_{\text{ano}}\,\mathrm{IS}\alpha\mathrm{g}$–irresolute map. We notice that $f^{-1}\left(\{a,d\}\right)=\{1,3\}$ is $\mathcal{N}_{\text{ano}}$–open in $\left(\mathrm{U},\mathrm{T}_{\mathrm{R}}\left(\mathrm{X}\right),\mathrm{I}\right)$ and therefore f is $\mathcal{N}_{\text{ano}}$–continuous and hence f is also a $\mathcal{N}_{\text{ano}}\,\mathrm{IS}\alpha\mathrm{g}$–continuous map.

Theorem 4.6. Let $f:\left(\mathrm{U},\mathrm{T}_{\mathrm{R}}\left(\mathrm{X}\right),\mathrm{I}\right)\to\left(\mathrm{V},\sigma_{\mathrm{R}}\left(\mathrm{Y}\right),\mathrm{J}\right)$ be a function. Then the following statements are equivalent.

(i) f is $\mathcal{N}_{\text{ano}}\,\mathrm{IS}\alpha\mathrm{g}$–irresolute.

(ii) For every subset A of U, $\mathcal{N}_{ano}\,\mathrm{IS}\alpha\mathrm{g}\text{-}\mathrm{C}l\left[f^{-1}\left(\mathcal{N}_{ano}\,\mathrm{IS}\alpha\mathrm{g}\text{-}\mathrm{C}l\left(f\left(\mathrm{A}\right)\right)\right)\right]=$
$f^{-1}\left[\mathcal{N}_{ano}\,\mathrm{IS}\alpha\mathrm{g}\text{-}\mathrm{C}l\left(f\left(\mathrm{A}\right)\right)\right]$.

(iii) For every subset B of V, $\mathcal{N}_{ano}\,\mathrm{IS}\alpha\mathrm{g}\text{-}\mathrm{C}l\left[f^{-1}\left(\mathcal{N}_{ano}\,\mathrm{IS}\alpha\mathrm{g}\text{-}\mathrm{C}l\left(B\right)\right)\right]=$
$f^{-1}\left[\mathcal{N}_{ano}\,\mathrm{IS}\alpha\mathrm{g}\text{-}\mathrm{C}l\left(f\left(\mathrm{A}\right)\right)\right]$.

Proof. $(\mathrm{i})\Leftrightarrow(\mathrm{ii})$. Let f be $\mathcal{N}_{\text{ano}}\,\mathrm{IS}\alpha\mathrm{g}$–irresolute and $\mathrm{A}\subseteq\mathrm{U}$. Then $f\left(\mathrm{A}\right)\subseteq\mathrm{V}$. $\mathcal{N}_{ano}\,\mathrm{IS}\alpha\mathrm{g}\text{-}\mathrm{C}l\left(f\left(\mathrm{A}\right)\right)$ is $\mathcal{N}_{\text{ano}}\,\mathrm{IS}\alpha\mathrm{g}$–closed in V. Since f is $\mathcal{N}_{\text{ano}}\,\mathrm{IS}\alpha\mathrm{g}$–irresolute, $f^{-1}\left[\mathcal{N}_{ano}\,\mathrm{IS}\alpha\mathrm{g}\text{-}\mathrm{C}l\left(f\left(\mathrm{A}\right)\right)\right]$ is $\mathcal{N}_{\text{ano}}\,\mathrm{IS}\alpha\mathrm{g}$–closed in U. Therefore we obtain $\mathcal{N}_{ano}\,\mathrm{IS}\alpha\mathrm{g}\text{-}\mathrm{C}l\left(f^{-1}\left[\mathcal{N}_{ano}\,\mathrm{IS}\alpha\mathrm{g}\text{-}\mathrm{C}l\left(f\left(\mathrm{A}\right)\right)\right]\right)=f^{-1}\left[\mathcal{N}_{ano}\,\mathrm{IS}\alpha\mathrm{g}\text{-}\mathrm{C}l\left(f\left(\mathrm{A}\right)\right)\right]$.

Conversely, suppose that we have $\mathcal{N}_{ano}\,\mathrm{IS}\alpha\mathrm{g}\text{-}\mathrm{C}l\left(f^{-1}\left[\mathcal{N}_{ano}\,\mathrm{IS}\alpha\mathrm{g}\text{-}\mathrm{C}l\left(f\left(\mathrm{A}\right)\right)\right]\right)=$
$f^{-1}\left[\mathcal{N}_{ano}\,\mathrm{IS}\alpha\mathrm{g}\text{-}\mathrm{C}l\left(f\left(\mathrm{A}\right)\right)\right]$ for every subset A of U, Let H be a $\mathcal{N}_{\text{ano}}\,\mathrm{IS}\alpha\mathrm{g}$–closed set in V. Since $f^{-1}\left(\mathrm{H}\right)\subseteq\mathrm{U}$,
$\mathcal{N}_{ano}\,\mathrm{IS}\alpha\mathrm{g}\text{-}\mathrm{C}l\left(f^{-1}\left[\mathcal{N}_{ano}\,\mathrm{IS}\alpha\mathrm{g}\text{--}\mathrm{C}l\left(f\left(f^{-1}\left(\mathrm{H}\right)\right)\right)\right]\right)=f^{-1}\left[\mathcal{N}_{ano}\,\mathrm{IS}\alpha\mathrm{g}\text{-}\mathrm{C}l\left(f\left(f^{-1}\left(\mathrm{H}\right)\right)\right)\right]$. That is $\mathcal{N}_{ano}\,\mathrm{IS}\alpha\mathrm{g}\text{-}\mathrm{C}l\left(f^{-1}\left(\mathrm{H}\right)\right)=f^{-1}\left(\mathrm{H}\right)$ implies that $f^{-1}\left(\mathrm{H}\right)$ is $\mathcal{N}_{\text{ano}}\,\mathrm{IS}\alpha\mathrm{g}$–closed in U. Hence f is $\mathcal{N}_{\text{ano}}\,\mathrm{IS}\alpha\mathrm{g}$–irresolute.

$(\mathrm{ii})\Leftrightarrow(\mathrm{iii})$. Assume (ii) holds. Let B be any subset of V. Then replacing A by $f^{-1}\left(\mathrm{B}\right)$ in (ii) we have $\mathcal{N}_{ano}\,\mathrm{IS}\alpha\mathrm{g}\text{-}\mathrm{C}l\left(f^{-1}\left[\mathcal{N}_{ano}\,\mathrm{IS}\alpha\mathrm{g}\text{-}\mathrm{C}l\left(f\left(f^{-1}\left(\mathrm{B}\right)\right)\right)\right]\right)=\ f^{-1}\left[\mathcal{N}_{ano}\,\mathrm{IS}\alpha\mathrm{g}\text{-}\mathrm{C}l\left(f\left(f^{-1}\left(\mathrm{B}\right)\right)\right)\right]$. That is $\mathcal{N}_{ano}\,\mathrm{IS}\alpha\mathrm{g}\text{-}\mathrm{C}l\left(f^{-1}\left[\mathcal{N}_{ano}\,\mathrm{IS}\alpha\mathrm{g}\text{-}\mathrm{C}l\left(\mathrm{B}\right)\right]\right)=\ f^{-1}\left[\mathcal{N}_{ano}\,\mathrm{IS}\alpha\mathrm{g}\text{-}\mathrm{C}l\left(\mathrm{B}\right)\right]$.

Conversely, suppose (iii) holds. Let A be any subset of U. Then $f\left(\mathrm{A}\right)\subseteq\mathrm{V}$. Let $\mathrm{B}=f\left(\mathrm{A}\right)$. Then we have $\mathcal{N}_{ano}\,\mathrm{IS}\alpha\mathrm{g}\text{-}\mathrm{C}l\left(f^{-1}\left[\mathcal{N}_{ano}\,\mathrm{IS}\alpha\mathrm{g}\text{-}\mathrm{C}l\left(f\left(A\right)\right)\right]\right)=f^{-1}\left[\mathcal{N}_{ano}\,\mathrm{IS}\alpha\mathrm{g}\text{-}\mathrm{C}l\left(f\left(A\right)\right)\right]$ for every subset A of U.

Theorem 4.7. Let $f:\left(\mathrm{U},\mathrm{T}_{\mathrm{R}}\left(\mathrm{X}\right),\mathrm{I}\right)\to\left(\mathrm{V},\sigma_{\mathrm{R}}\left(\mathrm{Y}\right),\mathrm{J}\right)$ be a function. Then the following statements are equivalent.

(i) f is $\mathcal{N}_{\text{ano}}\,\mathrm{IS}\alpha\mathrm{g}$–irresolute.

(ii) For every subset A of U, $\mathcal{N}_{ano}\,\mathrm{IS}\alpha\mathrm{g}\text{-}\mathrm{I}nt\left[f^{-1}\left(\mathcal{N}_{ano}\,\mathrm{IS}\alpha\mathrm{g}\text{-}\mathrm{I}nt\left(f\left(\mathrm{A}\right)\right)\right)\right]=$
$f^{-1}\left[\mathcal{N}_{ano}\,\mathrm{IS}\alpha\mathrm{g}\text{-}\mathrm{I}nt\left(f\left(\mathrm{A}\right)\right)\right]$.

(iii) For every subset B of V, $\mathcal{N}_{ano}\,\mathrm{Ig}^{*}\alpha\text{-}\mathrm{I}nt\left[f^{-1}\left(\mathcal{N}_{ano}\,\mathrm{Ig}^{*}\alpha\text{-}\mathrm{I}nt\left(B\right)\right)\right]=$
$f^{-1}\left(\mathcal{N}_{ano}\,\mathrm{IS}\alpha\mathrm{g}\text{-}\mathrm{I}nt\left(B\right)\right)$.

Proof. $(\mathrm{i})\Leftrightarrow(\mathrm{ii})$. Let f be $\mathcal{N}_{\text{ano}}\,\mathrm{IS}\alpha\mathrm{g}$–irresolute and $\mathrm{A}\subseteq\mathrm{U}$. Then $f\left(\mathrm{A}\right)\subseteq\mathrm{V}$. $\mathcal{N}_{ano}\,\mathrm{IS}\alpha\mathrm{g}\text{-}\mathrm{I}nt\left(f\left(\mathrm{A}\right)\right)$ is $\mathcal{N}_{\text{ano}}\,\mathrm{IS}\alpha\mathrm{g}$–open in V. Since f is

$\mathcal{N}_{\text{ano}}\,\text{IS}\alpha\text{g}$–irresolute, $f^{-1}\left[\mathcal{N}_{ano}\,\text{IS}\alpha\text{g}-\text{I}nt\left(f\left(\text{A}\right)\right)\right]$ is $\mathcal{N}_{\text{ano}}\,\text{IS}\alpha\text{g}$–open in U. Therefore, we obtain $\mathcal{N}_{ano}\,\text{IS}\alpha\text{g}-\text{I}nt\left(f^{-1}\left[\mathcal{N}_{ano}\,\text{IS}\alpha\text{g}-\text{I}nt\left(f\left(\text{A}\right)\right)\right]\right)=f^{-1}\left[\mathcal{N}_{ano}\,\text{IS}\alpha\text{g}-\text{I}nt\left(f\left(\text{A}\right)\right)\right]$.

Conversely, suppose that we have $\mathcal{N}_{ano}\,\text{IS}\alpha\text{g}-\text{I}nt\left(f^{-1}\left[\mathcal{N}_{ano}\,\text{IS}\alpha\text{g}-\text{I}nt\left(f\left(\text{A}\right)\right)\right]\right)=f^{-1}\left[\mathcal{N}_{ano}\,\text{IS}\alpha\text{g}-\text{I}nt\left(f\left(\text{A}\right)\right)\right]$ for every subset A of U, Let G be a $\mathcal{N}_{\text{ano}}\,\text{IS}\alpha\text{g}$–open set in *V*. Since $f^{-1}\left(\text{G}\right)\subseteq\text{U}$, $\mathcal{N}_{ano}\,\text{IS}\alpha\text{g}-\text{I}nt\left(f^{-1}\left[\mathcal{N}_{ano}\,\text{IS}\alpha\text{g}-\text{I}nt\left(f\left(f^{-1}\left(\text{G}\right)\right)\right)\right]\right)=f^{-1}\left[\mathcal{N}_{ano}\,\text{IS}\alpha\text{g}-\text{I}nt\left(f\left(f^{-1}\left(\text{G}\right)\right)\right)\right]$. That is $\mathcal{N}_{ano}\,\text{IS}\alpha\text{g}-\text{I}nt\left(f^{-1}\left(\text{G}\right)\right)=f^{-1}\left(\text{G}\right)$ implies that $f^{-1}\left(\text{G}\right)$ is $\mathcal{N}_{\text{ano}}\,\text{IS}\alpha\text{g}$–open in U. Hence f is $\mathcal{N}_{\text{ano}}\,\text{IS}\alpha\text{g}$–irresolute

$\left(\text{ii}\right)\Leftrightarrow\left(\text{iii}\right)$. Assume (ii) holds. Let B be any subset of V. Then replacing A by $f^{-1}\left(\text{B}\right)$ in (ii) we get $\mathcal{N}_{ano}\,\text{IS}\alpha\text{g}-\text{I}nt\left(f^{-1}\left[\mathcal{N}_{ano}\,\text{IS}\alpha\text{g}-\text{I}nt\left(f\left(f^{-1}\left(\text{B}\right)\right)\right)\right]\right)=\quad f^{-1}\left[\mathcal{N}_{ano}\,\text{IS}\alpha\text{g}-\text{I}nt\left(f\left(f^{-1}\left(\text{B}\right)\right)\right)\right]$. That is $\mathcal{N}_{ano}\,\text{IS}\alpha\text{g}-\text{I}nt\left(f^{-1}\left[\mathcal{N}_{ano}\,\text{IS}\alpha\text{g}-\text{I}nt\left(\text{B}\right)\right]\right)=2\ \text{pcf}\,f^{-1}\left[\mathcal{N}_{ano}\,\text{IS}\alpha\text{g}-\text{I}nt\left(\text{B}\right)\right]$.

Conversely, suppose (iii) holds. Let A be any subset of U. Then $f\left(\text{A}\right)\subseteq\text{V}$. Let $\text{B}=f\left(\text{A}\right)$. Then $\mathcal{N}_{ano}\,\text{IS}\alpha\text{g}-\text{I}nt\left(f^{-1}\left[\mathcal{N}_{ano}\,\text{IS}\alpha\text{g}-\text{I}nt\left(f\left(A\right)\right)\right]\right)=f^{-1}\left[\mathcal{N}_{ano}\,\text{IS}\alpha\text{g}-\text{I}nt\left(f\left(A\right)\right)\right]$ for every subset A of U.

Theorem 4.8. Let $f:\left(\text{U},\text{T}_{\text{R}}\left(\text{X}\right),\text{I}\right)\rightarrow\left(\text{V},\sigma_{\text{R}\,\prime}\left(\text{Y}\right),\text{J}\right)$ be a $\mathcal{N}_{\text{ano}}\,\text{IS}\alpha\text{g}$–irresolute function. Then *f* is a $\mathcal{N}_{\text{ano}}\,\text{IS}\alpha\text{g}$–continuous function.

Proof. Let $f:\left(\text{U},\text{T}_{\text{R}}\left(\text{X}\right),\text{I}\right)\rightarrow\left(\text{V},\sigma_{\text{R}\,\prime}\left(\text{Y}\right),\text{J}\right)$ be $\mathcal{N}_{\text{ano}}\,\text{IS}\alpha\text{g}$–irresolute. Let G be any $\mathcal{N}_{\text{ano}}$–open set in V, Then G is $\mathcal{N}_{\text{ano}}\,\text{IS}\alpha\text{g}$–open in V, Since *f* is $\mathcal{N}_{\text{ano}}\,\text{IS}\alpha\text{g}$–irresolute, $f^{-1}\left(\text{G}\right)$ is $\mathcal{N}_{\text{ano}}\,\text{IS}\alpha\text{g}$–open in U, Thus, the inverse image of every $\mathcal{N}_{\text{ano}}$–open set in V is $\mathcal{N}_{\text{ano}}\,\text{IS}\alpha\text{g}$–open in U, Therefore any $\mathcal{N}_{\text{ano}}\,\text{IS}\alpha\text{g}$–irresolute function is a $\mathcal{N}_{\text{ano}}\,\text{IS}\alpha\text{g}$–continuous function.

Theorem 4.9. Consider two functions $f:\left(\text{U},\text{T}_{\text{R}}\left(\text{X}\right),\text{I}\right)\rightarrow\left(\text{V},\sigma_{\text{R}\,\prime}\left(\text{Y}\right),\text{J}\right)$ and $\text{g}:\left(\text{V},\sigma_{\text{R}\,\prime}\left(\text{Y}\right),\text{J}\right)\rightarrow\left(\text{W},\Omega_{\text{R}\,//}\left(\text{Z}\right),\text{K}\right)$. Then the following statements are true.

$\left(1\right)$. Let f be a $\mathcal{N}_{\text{ano}}\,\text{IS}\alpha\text{g}$–irresolute function and g be a $\mathcal{N}_{\text{ano}}\,\text{IS}\alpha\text{g}$–continuous function. Then show that $\text{g}o f:\left(\text{U},\text{T}_{\text{R}}\left(\text{X}\right),\text{I}\right)\rightarrow\left(\text{W},\Omega_{\text{R}\,//}\left(\text{Z}\right),\text{K}\right)$ is a $\mathcal{N}_{\text{ano}}\,\text{IS}\alpha\text{g}$–continuous function.

$\left(2\right)$. $\text{g}o f$ is $\mathcal{N}_{\text{ano}}\,\text{IS}\alpha\text{g}$–irresolute if both f and g are $\mathcal{N}_{\text{ano}}\,\text{IS}\alpha\text{g}$–irresolute.

Proof. $\left(1\right)$. Let G be $\mathcal{N}_{\text{ano}}$–open in W. Since *g* is $\mathcal{N}_{\text{ano}}\,\text{IS}\alpha\text{g}$–continuous $\text{g}^{-1}\left(\text{G}\right)$ is $\mathcal{N}_{\text{ano}}\,\text{IS}\alpha\text{g}$–open in V. Since f is $\mathcal{N}_{\text{ano}}\,\text{IS}\alpha\text{g}$–irresolute, $f^{-1}\left(\text{g}^{-1}\left(\text{G}\right)\right)=\left(\text{gof}\right)^{-1}\left(\text{G}\right)$ is $\mathcal{N}_{\text{ano}}\,\text{IS}\alpha\text{g}$–open in U. Thus the inverse image of every $\mathcal{N}_{\text{ano}}$–open set in W is $\mathcal{N}_{\text{ano}}\,\text{IS}\alpha\text{g}$–open in U. Therefore $\text{g}o f$ is $\mathcal{N}_{\text{ano}}\,\text{IS}\alpha\text{g}$–continuous.

$\left(2\right)$. Easy.

Theorem 4.10. If $f:\left(\text{U},\text{T}_{\text{R}}\left(\text{X}\right),\text{I}\right)\rightarrow\left(\text{V},\sigma_{\text{R}\,\prime}\left(\text{Y}\right),\text{J}\right)$ is a $\mathcal{N}_{\text{ano}}\,\text{IS}\alpha\text{g}$–irresolute function and $\text{g}:\left(\text{V},\sigma_{\text{R}\,\prime}\left(\text{Y}\right),\text{J}\right)\rightarrow\left(\text{W},\Omega_{\text{R}\,//}\left(\text{Z}\right),\text{K}\right)$ is a $\mathcal{N}_{\text{ano}}$–continuous function, then $\text{g}o f:\left(\text{U},\text{T}_{\text{R}}\left(\text{X}\right),\text{I}\right)\rightarrow\left(\text{W},\Omega_{\text{R}\,//}\left(\text{Z}\right),\text{K}\right)$ is $\mathcal{N}_{\text{ano}}\,\text{IS}\alpha\text{g}$–continuous.

Proof. Proof is like Theorem (4.9) since $\mathcal{N}_{\text{ano}}$–open set is a $\mathcal{N}_{\text{ano}}\,\text{IS}\alpha\text{g}$–open set.

Theorem 4.11. If $f:(U,T_R(X),I)\to(V,\sigma_{R'}(Y),J)$ is a $\mathcal{N}_{ano}$ISαg–irresolute function and $g:(V,\sigma_{R'}(Y),J)\to(W,\Omega_{R''}(Z),K)$ is a $\mathcal{N}_{ano}$–contra–continuous function, then $gof:(U,T_R(X),I)\to(W,T_{R''}(Z),K)$ is $\mathcal{N}_{ano}$ISαg–continuous.

Proof. Proof is like Theorem (4.9) since $\mathcal{N}_{ano}$–closed set is a $\mathcal{N}_{ano}$ISαg–closed set.

Theorem 4.12. If $f:(U,T_R(X),I)\to(V,\sigma_{R'}(Y),J)$ and $g:(V,\sigma_{R'}(Y),J)\to(W,\Omega_{R''}(Z),K)$ are $\mathcal{N}_{ano}$ISαg–irresolutes, then $gof:(U,T_R(X),I)\to(W,\Omega_{R''}(Z),K)$ is $\mathcal{N}_{ano}$ISαg–irresolute.

Proof. Let G be $\mathcal{N}_{ano}$–open in W. Since g is $\mathcal{N}_{ano}$ISαg–irresolute $g^{-1}(G)$ is $\mathcal{N}_{ano}$ISαg–open in V. Since f is $\mathcal{N}_{ano}$ISαg–irresolute, $f^{-1}(g^{-1}(G))=(gof)^{-1}(G)$ is $\mathcal{N}_{ano}$ISαg–open in U. Thus, the inverse image of every $\mathcal{N}_{ano}$ISαg–open set in W is $\mathcal{N}_{ano}$ISαg–open in U. Therefore gof is $\mathcal{N}_{ano}$ISαg–irresolute.

5 Nano Ideal Semi –α –Generalized –Open and Closed Mappings

In this section $\mathcal{N}_{ano}$ISαg–open mappings and $\mathcal{N}_{ano}$ISαg–closed Mappings are defined, and some of their characterizations are presented.

Definition 5.1. A map $f:(U,T_R(X),I)\to(V,\sigma_{R'}(Y),J)$ is said to be a $\mathcal{N}_{ano}$ISαg–open–map on U if the image of every $\mathcal{N}_{ano}$–open set in $(U,T_R(X),I)$ is a $\mathcal{N}_{ano}$ISαg–open set in $(V,T_{R'}(Y),J)$.

Definition 5.2. A mapping $f:(U,T_R(X),I)\to(V,\sigma_{R'}(Y),J)$ is said to be a $\mathcal{N}_{ano}$ISαg–closed–map on U if the image of every $\mathcal{N}_{ano}$–closed set in $(U,T_R(X))$ is a $\mathcal{N}_{ano}$ISαg–closed set in $(V,\sigma_{R'}(Y),J)$.

Definition 5.3. A map $f:(U,T_R(X),I)\to(V,\sigma_{R'}(Y),J)$ is said to be a Strongly $\mathcal{N}_{ano}$ISαg–closed map on U if the image of every $\mathcal{N}_{ano}$ISαg–closed set in $(U,T_R(X),I)$ is a $\mathcal{N}_{ano}$ISαg–closed set in $(V,\sigma_{R'}(Y),J)$.

Definition 5.4. A map $f:(U,T_R(X),I)\to(V,\sigma_{R'}(Y),J)$ is said to be a Strongly $\mathcal{N}_{ano}$ISαg–open map on U if the image of every $\mathcal{N}_{ano}$ISαg–open set in $(U,T_R(X),I)$ is a $\mathcal{N}_{ano}$ISαg–open set in $(V,\sigma_{R'}(Y),J)$.

Theorem 5.5. A map $f:(U,T_R(X),I)\to(V,\sigma_{R'}(Y),J)$ is $\mathcal{N}_{ano}$ISαg–closed if and only if for each subset A of V and for each $\mathcal{N}_{ano}$–open set G of $(U,T_R(X),I)$ containing $f^{-1}(A)$, there is a $\mathcal{N}_{ano}$ISαg–open set B of $(V,\sigma_{R'}(Y),J)$ such that $A\subseteq B$ and $f^{-1}(B)\subseteq G$.

Proof. Let A be a subset of $(V,\sigma_{R'}(Y),J)$ and G be a $\mathcal{N}_{ano}$–open set of $(U,T_R(X),I)$ such that $f^{-1}(A)\subseteq G$. Then $U-G$ is a $\mathcal{N}_{ano}$–closed set of U. Since f is $\mathcal{N}_{ano}$ISαg–closed, $f(U-G)$ is $\mathcal{N}_{ano}$ISαg–closed in $(V,\sigma_{R'}(Y),J)$. Now $B=V-f(U-G)$ is a $\mathcal{N}_{ano}$ISαg–open set containing A in V such that $f^{-1}(B)\subseteq G$.

Conversely, let H be a $\mathcal{N}_{ano}$–closed set of $(U,T_R(X),I)$, then $f^{-1}(V-f(H))\subseteq U-H$ and $U-H$ is $\mathcal{N}_{ano}$–open. By our assumption, there is a $\mathcal{N}_{ano}$ISαg–open set B of $(V,\sigma_{R'}(Y),J)$ such

that $V - f(H) \subseteq B$ and $f^{-1}(B) \subseteq U - H$. Hence $V - B \subseteq f(H)$ and $H \subseteq U - f^{-1}(B)$. Thus $V - B \subseteq f(H) \subseteq f(U - f^{-1}(B)) \subseteq V - B$ which implies $f(H) = V - B$. Since $V - B$ is $\mathcal{N}_{ano}\mathrm{IS}\alpha g$–closed, $f(H)$ is a $\mathcal{N}_{ano}\mathrm{IS}\alpha g$–closed set in $(V, \sigma_{R/}(Y), J)$. That is $f(H)$ is $\mathcal{N}_{ano}\mathrm{IS}\alpha g$–closed in V for every $\mathcal{N}_{ano}$–closed set H of U. Hence f is a $\mathcal{N}_{ano}\mathrm{IS}\alpha g$–closed –map.

Theorem 5.6. A map $f:(U, T_R(X), I) \to (V, \sigma_{R/}(Y), J)$ is $\mathcal{N}_{ano}\mathrm{IS}\alpha g$–open if and only if for each subset A of V and for each $\mathcal{N}_{ano}$–closed set H of $(U, T_R(X), I)$ containing $f^{-1}(A)$, there is a $\mathcal{N}_{ano}\mathrm{IS}\alpha g$–closed set B of $(V, \sigma_{R/}(Y), J)$ such that $A \subseteq B$ and $f^{-1}(B) \subseteq H$.

Proof. Let A be a subset of $(V, \sigma_{R/}(Y), J)$ and H be a $\mathcal{N}_{ano}$–closed set of $(U, T_R(X), I)$ such that $f^{-1}(A) \subseteq H$. Then $U - H$ is a $\mathcal{N}_{ano}$–open set of U. Since f is $\mathcal{N}_{ano}\mathrm{IS}\alpha g$–open, $f(U - H)$ is $\mathcal{N}_{ano}\mathrm{IS}\alpha g$–open in $(V, \sigma_{R/}(Y), J)$. Now $B = V - f(U - H)$ is a $\mathcal{N}_{ano}\mathrm{IS}\alpha g$–closed set containing A in V such that $f^{-1}(B) \subseteq H$. Conversely let G be a $\mathcal{N}_{ano}$–open set of $(U, T_R(X), I)$, then $f^{-1}(V - f(G)) \subseteq U - G$ and $U - G$ is $\mathcal{N}_{ano}$–closed. By our assumption there is a $\mathcal{N}_{ano}\mathrm{IS}\alpha g$–closed set B of $(V, \sigma_{R/}(Y), J)$ such that $V - f(G) \subseteq B$ and $f^{-1}(B) \subseteq U - G$. Hence $V - B \subseteq f(G)$ and $G \subseteq U - f^{-1}(B)$. Thus $V - B \subseteq f(G) \subseteq f(U - f^{-1}(B)) \subseteq V - B$ which implies $f(G) = V - B$. Since $V - B$ is $\mathcal{N}_{ano}\mathrm{IS}\alpha g$–open, $f(G)$ is a $\mathcal{N}_{ano}\mathrm{IS}\alpha g$–open set in $(V, \sigma_{R/}(Y), J)$. That is $f(G)$ is $\mathcal{N}_{ano}\mathrm{IS}\alpha g$–open in V for every $\mathcal{N}_{ano}$–open set G of U. Hence f is a $\mathcal{N}_{ano}\mathrm{IS}\alpha g$–open –map.

Theorem5.7. Let $f:(U, T_R(X), I) \to (V, \sigma_{R/}(Y), J)$ be a function. Then the following statements are equivalent

(i) f is strongly $\mathcal{N}_{ano}\mathrm{IS}\alpha g$–closed.

(ii) For every subset A of V and every $\mathcal{N}_{ano}\mathrm{IS}\alpha g$–open G of $(U, T_R(X), I)$ containing $f^{-1}(A)$, there is a $\mathcal{N}_{ano}\mathrm{IS}\alpha g$–open set B of $(V, \sigma_{R/}(Y), J)$ with $A \subseteq B$ and $f^{-1}(B) \subseteq G$.

Proof. Let A be a subset of $(V, \sigma_{R/}(Y), J)$ and G be a $\mathcal{N}_{ano}\mathrm{IS}\alpha g$–open set of $(U, T_R(X), I)$ such that $f^{-1}(A) \subseteq G$. Then $U - G$ is a $\mathcal{N}_{ano}\mathrm{IS}\alpha g$–closed set of *U*. Since f is strongly $\mathcal{N}_{ano}\mathrm{IS}\alpha g$–closed, $f(U - G)$ is $\mathcal{N}_{ano}\mathrm{IS}\alpha g$–closed in $(V, \sigma_{R/}(Y), J)$. Now $B = V - f(U - G)$ is a $\mathcal{N}_{ano}\mathrm{IS}\alpha g$–open set containing A in V such that $f^{-1}(B) \subseteq G$.

Conversely, let H be a $\mathcal{N}_{ano}\mathrm{IS}\alpha g$–closed set of $(U, T_R(X), I)$, then $f^{-1}(V - f(H)) \subseteq U - H$ and $U - H$ is $\mathcal{N}_{ano}\mathrm{IS}\alpha g$–open. By our assumption, there is a $\mathcal{N}_{ano}\mathrm{IS}\alpha g$–open set B of $(V, \sigma_{R/}(Y), J)$ such that $V - f(H) \subseteq B$ and $f^{-1}(B) \subseteq U - H$. Hence $V - B \subseteq f(H)$ and $H \subseteq U - f^{-1}(B)$. Thus $V - B \subseteq f(H) \subseteq f(U - f^{-1}(B)) \subseteq V - B$ which implies $f(H) = V - B$. Since $V - B$ is $\mathcal{N}_{ano}\mathrm{IS}\alpha g$–closed, $f(H)$ is a $\mathcal{N}_{ano}\mathrm{IS}\alpha g$–closed set in $(V, \sigma_{R/}(Y), J)$. That is $f(H)$ is $\mathcal{N}_{ano}\mathrm{IS}\alpha g$–closed in V for every $\mathcal{N}_{ano}\mathrm{IS}\alpha g$–closed set H of U. Hence f is a strongly $\mathcal{N}_{ano}\mathrm{IS}\alpha g$–closed –map.

Theorem 5.8. Let $f:(U, T_R(X), I) \to (V, \sigma_{R/}(Y), J)$ be a function. Then the following statements are equivalent

(i) f is strongly $\mathcal{N}_{ano}\mathrm{IS}\alpha g$–open.

(ii) For every subset A of V and every $\mathcal{N}_{ano}\,IS\alpha g$–closed set H of $(U,T_R(X),I)$ containing $f^{-1}(A)$, there is a $\mathcal{N}_{ano}\,Ig^*\alpha$–closed set B of $(V,\sigma_{R'}(Y),J)$ with $A\subseteq B$ and $f^{-1}(B)\subseteq H$.

Proof. Let A be a subset of $(V,\sigma_{R'}(Y),J)$ and H be a $\mathcal{N}_{ano}\,IS\alpha g$–closed set of $(U,T_R(X))$ such that $f^{-1}(A)\subseteq H$. Then $U-H$ is a $\mathcal{N}_{ano}\,IS\alpha g$–open set of U. Since f is strongly $\mathcal{N}_{ano}\,IS\alpha g$–open, $f(U-H)$ is $\mathcal{N}_{ano}\,IS\alpha g$–open in $(V,\sigma_{R'}(Y),J)$. Now $B=V-f(U-H)$ is a $\mathcal{N}_{ano}\,IS\alpha g$–closed set containing A in V such that $f^{-1}(B)\subseteq H$.

Conversely, let G be a $\mathcal{N}_{ano}\,IS\alpha g$–open set of $(U,T_R(X),I)$, then $f^{-1}(V-f(G))\subseteq U-G$ and $U-G$ is $\mathcal{N}_{ano}\,IS\alpha g$–closed. By our assumption there is a $\mathcal{N}_{ano}\,IS\alpha g$–closed set B of $(V,\sigma_{R'}(Y),J)$ such that $V-f(G)\subseteq B$ and $f^{-1}(B)\subseteq U-G$. Hence $V-B\subseteq f(G)$ and $G\subseteq U-f^{-1}(B)$. Thus $V-B\subseteq f(G)\subseteq f(U-f^{-1}(B))\subseteq V-B$ which implies $f(G)=V-B$. Since $V-B$ is $\mathcal{N}_{ano}\,IS\alpha g$–open, $f(G)$ is a $\mathcal{N}_{ano}\,IS\alpha g$–open set in $(V,\sigma_{R'}(Y),J)$. That is $f(G)$ is $\mathcal{N}_{ano}\,IS\alpha g$–open in V for every $\mathcal{N}_{ano}\,IS\alpha g$–open set G of U. Hence f is a strongly $\mathcal{N}_{ano}\,IS\alpha g$–open –map.

Theorem 5.9. A map $f:(U,T_R(X),I)\to(V,\sigma_{R'}(Y),J)$ is $\mathcal{N}_{ano}\,IS\alpha g$–closed if and only if $\mathcal{N}_{ano}\,IS\alpha g$–$Cl(f(A))\subseteq f(\mathcal{N}_{ano}Cl(A))$ for every subset A of U.

Proof. Suppose that f is $\mathcal{N}_{ano}\,IS\alpha g$–closed and $A\subseteq U$. Then $\mathcal{N}_{ano}$–$Cl(A)$ is $\mathcal{N}_{ano}$–closed in U and so $f(\mathcal{N}_{ano}$–$Cl(A))$ is $\mathcal{N}_{ano}\,IS\alpha g$–closed in $(V,\sigma_{R'}(Y),J)$. We have $f(A)\subseteq f(\mathcal{N}_{ano}$–$Cl(A))$ and $\mathcal{N}_{ano}\,IS\alpha g$–$Cl(f(A))\subseteq\mathcal{N}_{ano}\,IS\alpha g$–$Cl[f(\mathcal{N}_{ano}$–$Cl(A))]=f(\mathcal{N}_{ano}$–$Cl(A))$.

Conversely, let A be any $\mathcal{N}_{ano}$–closed set in U. Then $A=\mathcal{N}_{ano}$–$Cl(A)$ and so $f(A)=f(\mathcal{N}_{ano}$–$Cl(A))\supseteq\mathcal{N}_{ano}\,Ig^*\alpha$–$Cl(f(A))$, by hypothesis. We have $f(A)\subseteq\mathcal{N}_{ano}\,Ig^*\alpha$–$Cl(f(A))$. Therefore $f(A)=\mathcal{N}_{ano}\,IS\alpha g$–$Cl(f(A))$. i.e., $f(A)$ is $\mathcal{N}_{ano}\,IS\alpha g$–closed and hence f is $\mathcal{N}_{ano}\,IS\alpha g$–closed.

Theorem 5.10. Let $f:(U,T_R(X),I)\to(V,\sigma_{R'}(Y),J)$ be a function such that $\mathcal{N}_{ano}\,IS\alpha g$–$Cl(f(A))\subseteq f(\mathcal{N}_{ano}$–$Cl(A))$ for every subset A of U. Then the image $f(A)$ of a $\mathcal{N}_{ano}$–closed set A in U is $\mathcal{N}_{ano}\,IS\alpha g$–closed in V.

Proof. Let A be a $\mathcal{N}_{ano}$–closed set in U. Then by hypothesis, $\mathcal{N}_{ano}\,IS\alpha g$–$Cl(f(A))\subseteq f(\mathcal{N}_{ano}$–$Cl(A))=f(A)$ and so $\mathcal{N}_{ano}\,IS\alpha g$–$Cl(f(A))=f(A)$. Therefore $f(A)$ is $\mathcal{N}_{ano}\,IS\alpha g$–closed in V.

Theorem 5.11. Let $f:(U,T_R(X),I)\to(V,\sigma_{R'}(Y),J)$ be a $\mathcal{N}_{ano}$–closed function and $g:(V,\sigma_{R'}(Y),J)\to(W,\Omega_{R''}(Z),K)$ be a $\mathcal{N}_{ano}\,Ig^*\alpha$–closed function, then their composition function $gof:(U,T_R(X),I)\to(W,\Omega_{R''}(Z),K)$ is $\mathcal{N}_{ano}\,IS\alpha g$–closed function.

Proof. Let A be a $\mathcal{N}_{ano}$–closed set of U. Then by assumption $f(A)$ is $\mathcal{N}_{ano}$–closed in V. Since g is $\mathcal{N}_{ano}\,IS\alpha g$–closed function, $g(f(A))$ is $\mathcal{N}_{ano}\,IS\alpha g$–closed set in W. i.e., $(gof)(A)$ is $\mathcal{N}_{ano}\,IS\alpha g$–closed set in W and so gof is a $\mathcal{N}_{ano}\,IS\alpha g$–closed function.

Theorem 5.12. Let $f:(U,T_R(X),I)\to(V,\sigma_{R'}(Y),J)$ and $g:(V,T_{R'}(Y),J)\to(W,\Omega_{R''}(Z),K)$ be two functions such that

$gof:\left(U,T_R(X),I\right)\to\left(W,\Omega_{R''}(Z),K\right)$ is a $\mathcal{N}_{ano}\,IS\alpha g$–closed function. Then the next conditions are true.

(i) If f is $\mathcal{N}_{ano}$–continuous and surjective, then g is $\mathcal{N}_{ano}\,IS\alpha g$–closed.

(ii) If g is $\mathcal{N}_{ano}\,IS\alpha g$–irresolute and injective, then f is $\mathcal{N}_{ano}\,IS\alpha g$–closed.

(iii) If g is strongly $\mathcal{N}_{ano}\,IS\alpha g$–continuous and injective, then f is $\mathcal{N}_{ano}$–closed.

Proof. (i) Let B be a $\mathcal{N}_{ano}$–closed set of V. Since f is $\mathcal{N}_{ano}$–continuous, $f^{-1}(B)$ is $\mathcal{N}_{ano}$–closed in U and since gof is $\mathcal{N}_{ano}\,IS\alpha g$–closed, $(gof)(f^{-1}(B))$ is $\mathcal{N}_{ano}\,IS\alpha g$–closed in W. That is $g(B)$ is $\mathcal{N}_{ano}\,IS\alpha g$–closed in W, since f is surjective. Therefore g is a $\mathcal{N}_{ano}\,IS\alpha g$–closed function.

(ii) Let A be a $\mathcal{N}_{ano}$–closed set of U. Since gof is $\mathcal{N}_{ano}\,IS\alpha g$–closed, $(gof)(A)$ is $\mathcal{N}_{ano}\,IS\alpha g$–closed in W. Since g is $\mathcal{N}_{ano}\,IS\alpha g$–irresolute, $g^{-1}((gof)(A))$ is $\mathcal{N}_{ano}\,IS\alpha g$–closed set in V. That is $f(A)$ is $\mathcal{N}_{ano}\,IS\alpha g$–closed in V, since g is injective. Thus f is a $\mathcal{N}_{ano}\,IS\alpha g$–closed function.

(iii) Let A be a $\mathcal{N}_{ano}$–closed set of U. Since gof is $\mathcal{N}_{ano}\,IS\alpha g$–closed, $(gof)(A)$ is $\mathcal{N}_{ano}\,IS\alpha g$–closed in W. Since g is strongly $\mathcal{N}_{ano}\,IS\alpha g$–continuous, $g^{-1}((gof)(A))$ is $\mathcal{N}_{ano}$–closed in V. That is $f(A))$ is $\mathcal{N}_{ano}$–closed set in V, since g is injective. Therefore f is a $\mathcal{N}_{ano}$–closed function.

Theorem 5.13. Let $f:\left(U,T_R(X),I\right)\to\left(V,\sigma_{R'}(Y),J\right)$ be a function. Then the next conditions are equivalent:

(i) f is a $\mathcal{N}_{ano}\,IS\alpha g$–open function.

(ii) For a subset A of U, $f\left(\mathcal{N}_{ano}\text{-}Int(A)\right)\subseteq\mathcal{N}_{ano}\,IS\alpha g\text{-}Int\left(f(A)\right)$.

(iii) For each $x\in U$ and for each $\mathcal{N}_{ano}$–nbhd G of x in U, there exists a $\mathcal{N}_{ano}\,IS\alpha g$–nbhd M of $f(x)$ in V such that $M\subseteq f(G)$.

Proof. $(i)\Rightarrow(ii)$. Suppose f is $\mathcal{N}_{ano}\,IS\alpha g$–open. Let $A\subseteq U$. Then $\mathcal{N}_{ano}\text{-}Int(A)$ is $\mathcal{N}_{ano}$–open in U and so $f\left(\mathcal{N}_{ano}\text{-}Int(A)\right)$ is $\mathcal{N}_{ano}\,IS\alpha g$–open in V. We have $f\left(\mathcal{N}_{ano}\text{-}Int(A)\right)\subseteq f(A)$. Therefore $f\left(\mathcal{N}_{ano}\text{-}Int(A)\right)\subseteq\mathcal{N}_{ano}\,Ig^{*}\alpha\text{-}Int\left(f(A)\right)$.

$(ii)\Rightarrow(iii)$. Suppose (ii) holds. Let $x\in U$ and G be an arbitrary $\mathcal{N}_{ano}$–nbhd of x in U. Then there exists a $\mathcal{N}_{ano}$–open set H such that $x\in H\subseteq G$. By assumption, we have $f(H)=f\left(\mathcal{N}_{ano}\text{-}Int(H)\right)\subseteq\mathcal{N}_{ano}\,IS\alpha g\text{-}Int\left(f(H)\right)$. Thus, $f(H)=\mathcal{N}_{ano}\,IS\alpha g\text{-}Int\left(f(H)\right)$. We have $f(H)$ is $\mathcal{N}_{ano}\,IS\alpha g$–open in V. Further, $f(x)\in f(H)\subseteq f(G)$ and so (iii) holds, by taking $M=f(H)$.

$(iii)\Rightarrow(i)$. Suppose (iii) holds. Let G be any $\mathcal{N}_{ano}$–open set in U, $x\in G$ and $f(x)=y$. Then $y\in f(G)$ and for each $y\in f(G)$, by assumption, there exists a $\mathcal{N}_{ano}\,IS\alpha g$–nbhd M_y of y in V such that $M_y\subseteq f(G)$. Since M_y is a $\mathcal{N}_{ano}\,IS\alpha g$–nbhd of y, there exists a $\mathcal{N}_{ano}\,IS\alpha g$–open set P_y in V such that $y\in P_y\subseteq M_y$. Therefore, $f(G)=\bigcup\{P_y:y\in f(G)\}$ is a $\mathcal{N}_{ano}\,IS\alpha g$–open set in V. Thus f is a $\mathcal{N}_{ano}\,IS\alpha g$–open function.

Theorem 5.14. Let $f:\left(U,T_R(X),I\right)\to\left(V,\sigma_{R'}(Y),J\right)$ be any bijection. Then the following statements are equivalent.

(i) f^{-1} is $\mathcal{N}_{ano}\,IS\alpha g$–continuous.

(ii) f is $\mathcal{N}_{\text{ano}}\,\mathrm{IS}\alpha\mathrm{g}$–open.

(iii) f is $\mathcal{N}_{\text{ano}}\,\mathrm{IS}\alpha\mathrm{g}$–closed.

Proof. $(i)\Rightarrow(ii)$. Let A be $\mathcal{N}_{\text{ano}}$–open set in U. Then $\mathrm{U}-\mathrm{A}$ is $\mathcal{N}_{\text{ano}}$–closed in U. Since f^{-1} is $\mathcal{N}_{\text{ano}}\,\mathrm{IS}\alpha\mathrm{g}$–continuous, $\left(f^{-1}\right)^{-1}(\mathrm{U}-\mathrm{A})=f(\mathrm{U}-\mathrm{A})=\mathrm{V}-f(\mathrm{A})$ is $\mathcal{N}_{\text{ano}}\,\mathrm{IS}\alpha\mathrm{g}$–closed in V. Then $f(\mathrm{A})$ is $\mathcal{N}_{\text{ano}}\,\mathrm{IS}\alpha\mathrm{g}$–open in V. Hence f is $\mathcal{N}_{\text{ano}}\,\mathrm{IS}\alpha\mathrm{g}$–open.

$(ii)\Rightarrow(iii)$. Let A be $\mathcal{N}_{\text{ano}}$–closed set in U. Then $\mathrm{U}-\mathrm{A}$ is $\mathcal{N}_{\text{ano}}$–open in U. Since f is $\mathcal{N}_{\text{ano}}\,\mathrm{IS}\alpha\mathrm{g}$–open, $f(\mathrm{U}-\mathrm{A})=\mathrm{V}-f(\mathrm{A})$ is $\mathcal{N}_{\text{ano}}\,\mathrm{IS}\alpha\mathrm{g}$–open in V. Then $f(\mathrm{A})$ $\mathcal{N}_{\text{ano}}\,\mathrm{IS}\alpha\mathrm{g}$–closed in V. Hence f is $\mathcal{N}_{\text{ano}}\,\mathrm{IS}\alpha\mathrm{g}$–closed.

$(iii)\Rightarrow(i)$. Let A be $\mathcal{N}_{\text{ano}}$–closed in U. Since $f:\left(\mathrm{U},\mathrm{T}_{\mathrm{R}}(\mathrm{X}),\mathrm{I}\right)\to\left(\mathrm{V},\sigma_{\mathrm{R}'}(\mathrm{Y}),\mathrm{J}\right)$ is $\mathcal{N}_{\text{ano}}\,\mathrm{IS}\alpha\mathrm{g}$–closed, $f(\mathrm{A})$ is $\mathcal{N}_{\text{ano}}\,\mathrm{IS}\alpha\mathrm{g}$–closed in V. *i.e.,* $\left(f^{-1}\right)^{-1}(\mathrm{A})$ is $\mathcal{N}_{\text{ano}}\,\mathrm{IS}\alpha\mathrm{g}$–closed in V. Therefore f^{-1} is $\mathcal{N}_{\text{ano}}\,\mathrm{IS}\alpha\mathrm{g}$–continuous.

6 Nano Ideal Semi –α –Generalized –Homeomorphisms

In this section, we define and study the concept of nano ideal semi-α generalized-homeomorphisms (briefly, $\mathcal{N}_{\text{ano}}\,\mathrm{IS}\alpha\mathrm{g}$–homeomorphisms) in $\mathcal{N}_{\text{ano}}$–Ideal–Top–Space $\left(\mathrm{U},\mathrm{T}_{\mathrm{R}}(\mathrm{X}),\mathrm{I}\right)$ and obtain some of its properties and characterizations.

Definition 6.1. A map $f:\left(\mathrm{U},\mathrm{T}_{\mathrm{R}}(\mathrm{X}),\mathrm{I}\right)\to\left(\mathrm{V},\sigma_{\mathrm{R}'}(\mathrm{Y}),\mathrm{J}\right)$ is said to be $\mathcal{N}_{\text{ano}}$–homeomorphisms if f is one-to-one & onto, $\mathcal{N}_{\text{ano}}$–open and $\mathcal{N}_{\text{ano}}$–continuous.

Definition 6.2. A map $f:\left(\mathrm{U},\mathrm{T}_{\mathrm{R}}(\mathrm{X}),\mathrm{I}\right)\to\left(\mathrm{V},\sigma_{\mathrm{R}'}(\mathrm{Y}),\mathrm{J}\right)$ is said to be $\mathcal{N}_{\text{ano}}\,\mathrm{IS}\alpha\mathrm{g}$–homeomorphisms if f is one-to-one & onto, $\mathcal{N}_{\text{ano}}\,\mathrm{IS}\alpha\mathrm{g}$–open and $\mathcal{N}_{\text{ano}}\,\mathrm{IS}\alpha\mathrm{g}$–continuous.

Theorem 6.3. Let $f:\left(\mathrm{U},\mathrm{T}_{\mathrm{R}}(\mathrm{X}),\mathrm{I}\right)\to\left(\mathrm{V},\sigma_{\mathrm{R}'}(\mathrm{Y}),\mathrm{J}\right)$ be a one-to-one onto mapping. Then f is $\mathcal{N}_{\text{ano}}\,\mathrm{IS}\alpha\mathrm{g}$–homeomorphism if and only if f is $\mathcal{N}_{\text{ano}}\,\mathrm{IS}\alpha\mathrm{g}$–closed and $\mathcal{N}_{\text{ano}}\,\mathrm{IS}\alpha\mathrm{g}$–continuous.

Proof. Let $f:\left(\mathrm{U},\mathrm{T}_{\mathrm{R}}(\mathrm{X}),\mathrm{I}\right)\to\left(\mathrm{V},\sigma_{\mathrm{R}'}(\mathrm{Y}),\mathrm{J}\right)$ be a $\mathcal{N}_{\text{ano}}\,\mathrm{IS}\alpha\mathrm{g}$–homeomorphism. Then f is $\mathcal{N}_{\text{ano}}\,\mathrm{IS}\alpha\mathrm{g}$–continuous. Let A be an arbitrary $\mathcal{N}_{\text{ano}}$–closed set in $\left(\mathrm{U},\mathrm{T}_{\mathrm{R}}(\mathrm{X}),\mathrm{I}\right)$. Then $\mathrm{U}-\mathrm{A}$ is $\mathcal{N}_{\text{ano}}$–open. Since f is $\mathcal{N}_{\text{ano}}\,\mathrm{IS}\alpha\mathrm{g}$–open, $f(\mathrm{U}-\mathrm{A})$ is $\mathcal{N}_{\text{ano}}\,\mathrm{IS}\alpha\mathrm{g}$–open in $\left(\mathrm{V},\sigma_{\mathrm{R}'}(\mathrm{Y}),\mathrm{J}\right)$. That is, $\mathrm{V}-f(\mathrm{A})$ is $\mathcal{N}_{\text{ano}}\,\mathrm{IS}\alpha\mathrm{g}$–open in $\left(\mathrm{V},\sigma_{\mathrm{R}'}(\mathrm{Y}),\mathrm{J}\right)$ for every $\mathcal{N}_{\text{ano}}$–closed set A in $\left(\mathrm{U},\mathrm{T}_{\mathrm{R}}(\mathrm{X}),\mathrm{I}\right)$ implies that $f(\mathrm{A})$ is $\mathcal{N}_{\text{ano}}\,\mathrm{IS}\alpha\mathrm{g}$–closed in $(\left(\mathrm{V},\sigma_{\mathrm{R}'}(\mathrm{Y}),\mathrm{J}\right)$. Hence $f:\left(\mathrm{U},\mathrm{T}_{\mathrm{R}}(\mathrm{X}),\mathrm{I}\right)\to\left(\mathrm{V},\sigma_{\mathrm{R}'}(\mathrm{Y}),\mathrm{J}\right)$ is $\mathcal{N}_{\text{ano}}\,\mathrm{IS}\alpha\mathrm{g}$–closed.

Conversely, let f be $\mathcal{N}_{\text{ano}}\,\mathrm{IS}\alpha\mathrm{g}$–closed and $\mathcal{N}_{\text{ano}}\,\mathrm{IS}\alpha\mathrm{g}$–continuous function. Let G be a $\mathcal{N}_{\text{ano}}$–open set in $\left(\mathrm{U},\mathrm{T}_{\mathrm{R}}(\mathrm{X}),\mathrm{I}\right)$. Then $\mathrm{U}-\mathrm{G}$ is $\mathcal{N}_{\text{ano}}$–closed in $\left(\mathrm{U},\mathrm{T}_{\mathrm{R}}(\mathrm{X}),\mathrm{I}\right)$. Since f is $\mathcal{N}_{\text{ano}}\,\mathrm{IS}\alpha\mathrm{g}$–closed, $f(\mathrm{U}-\mathrm{G})$ is $\mathcal{N}_{\text{ano}}\,\mathrm{IS}\alpha\mathrm{g}$–closed in $\left(\mathrm{V},\sigma_{\mathrm{R}'}(\mathrm{Y}),\mathrm{J}\right)$. That is, $f(\mathrm{U}-\mathrm{G})=\mathrm{V}-f(\mathrm{G})$ is $\mathcal{N}_{\text{ano}}\,\mathrm{IS}\alpha\mathrm{g}$–closed in $\left(\mathrm{V},\sigma_{\mathrm{R}'}(\mathrm{Y}),\mathrm{J}\right)$. Hence $f(\mathrm{G})$ is $\mathcal{N}_{\text{ano}}\,\mathrm{IS}\alpha\mathrm{g}$–open in $\left(\mathrm{V},\sigma_{\mathrm{R}'}(\mathrm{Y}),\mathrm{J}\right)$ for every $\mathcal{N}_{\text{ano}}$–open set G in $\left(\mathrm{U},\mathrm{T}_{\mathrm{R}}(\mathrm{X}),\mathrm{I}\right)$. Thus, f is $\mathcal{N}_{\text{ano}}\,\mathrm{Ig}^{*}\alpha$–open and so $f:\left(\mathrm{U},\mathrm{T}_{\mathrm{R}}(\mathrm{X}),\mathrm{I}\right)\to\left(\mathrm{V},\sigma_{\mathrm{R}'}(\mathrm{Y}),\mathrm{J}\right)$ is $\mathcal{N}_{\text{ano}}\,\mathrm{IS}\alpha\mathrm{g}$–homeomorphism.

Theorem 6.4.: Let $f:(U,T_R(X),I)\to(V,\sigma_{R'}(Y),J)$ be a bijective and $\mathcal{N}_{ano}\,IS\alpha g$–continuous map. Then the following statements are equivalent.

(i) f is a $\mathcal{N}_{ano}\,IS\alpha g$–open map.

(ii) f is a $\mathcal{N}_{ano}\,IS\alpha g$–homeomorphism.

(iii) f is a $\mathcal{N}_{ano}\,IS\alpha g$–closed map.

Proof. ($(i)\Rightarrow(ii)$). By the given hypothesis, the map $f:(U,T_R(X),I)\to(V,\sigma_{R'}(Y),J)$ is bijective $\mathcal{N}_{ano}\,IS\alpha g$–continuous and $\mathcal{N}_{ano}\,IS\alpha g$–open. Hence $f:(U,T_R(X),I)\to(V,\sigma_{R'}(Y),J)$ is $\mathcal{N}_{ano}\,IS\alpha g$–homeomorphism.

$(ii)\Rightarrow(iii)$. Let A be a $\mathcal{N}_{ano}$–closed set in $(U,T_R(X),I)$. Then A^C is $\mathcal{N}_{ano}$–open in $(U,T_R(X),I)$. By assumption, $f(A^C)$ is $\mathcal{N}_{ano}\,IS\alpha g$–open in $(V,\sigma_{R'}(Y),J)$. That is $f(A^C)=(f(A))^C=V-f(A)$ is $\mathcal{N}_{ano}\,IS\alpha g$–open in $(V,\sigma_{R'}(Y),J)$ and hence $f(A)$ is $\mathcal{N}_{ano}\,IS\alpha g$–closed in $(V,\sigma_{R'}(Y),J)$ for every $\mathcal{N}_{ano}$–closed set A in $(U,T_R(X),I)$. Hence the function $f:(U,T_R(X),I)\to(V,\sigma_{R'}(Y),J)$ is $\mathcal{N}_{ano}\,IS\alpha g$–closed map.

$(iii)\Rightarrow(i)$. Let B be a $\mathcal{N}_{ano}$–open set in $(U,T_R(X),I)$. Then B^C is $\mathcal{N}_{ano}$–closed set in $(U,T_R(X),I)$. By the given hypothesis, $f(B^C)$ is $\mathcal{N}_{ano}\,IS\alpha g$–closed in $(V,\sigma_{R'}(Y),J)$. But $f(B^C)=(f(B))^C=V-f(B)$ is $\mathcal{N}_{ano}\,IS\alpha g$–closed. Therefore $f(B)$ is $\mathcal{N}_{ano}\,IS\alpha g$–open in $(V,\sigma_{R'}(Y),J)$ for every $\mathcal{N}_{ano}$–open set B in $(U,T_R(X),I)$. Hence $f:(U,T_R(X),I)\to(V,\sigma_{R'}(Y),J)$ is $\mathcal{N}_{ano}\,IS\alpha g$–open map.

Theorem 6.5. Every $\mathcal{N}_{ano}$–homeomorphism is $\mathcal{N}_{ano}\,IS\alpha g$–homeomorphism.

Proof. If $f:(U,T_R(X),I)\to(V,\sigma_{R'}(Y),J)$ is $\mathcal{N}_{ano}$–homeomorphism, by definition 6.1, f is bijective, $\mathcal{N}_{ano}$–continuous and $\mathcal{N}_{ano}$–open. Then $f:(U,T_R(X),I)\to(V,\sigma_{R'}(Y),J)$ is $\mathcal{N}_{ano}\,IS\alpha g$–continuous and $\mathcal{N}_{ano}\,IS\alpha g$–open. Hence the function $f:(U,T_R(X),I)\to(V,\sigma_{R'}(Y),J)$ is $\mathcal{N}_{ano}\,IS\alpha g$–homeomorphism. Every $\mathcal{N}_{ano}$–continuous function is $\mathcal{N}_{ano}\,IS\alpha g$–continuous and every $\mathcal{N}_{ano}$–open map is $\mathcal{N}_{ano}\,IS\alpha g$–open. Then f is bijective, $\mathcal{N}_{ano}\,IS\alpha g$–continuous and $\mathcal{N}_{ano}\,IS\alpha g$–open. Therefore f is $\mathcal{N}_{ano}\,IS\alpha g$–homeomorphism.

Theorem 6.6. Let $f:(U,T_R(X),I)\to(V,\sigma_{R'}(Y),J)$ be a $\mathcal{N}_{ano}\alpha I$–homeomorphism. Then prove that f is $\mathcal{N}_{ano}\,IS\alpha g$–homeomorphism.

Proof. Let $f:(U,T_R(X),I)\to(V,\sigma_{R'}(Y),J)$ be a $\mathcal{N}_{ano}\alpha I$–homeomorphism. Then f is bijective, $\mathcal{N}_{ano}\alpha I$–continuous and $\mathcal{N}_{ano}\alpha I$–open. Let H be a $\mathcal{N}_{ano}$–open set in $(V,\sigma_{R'}(Y),J)$. Since f is $\mathcal{N}_{ano}\alpha I$–continuous, $f^{-1}(H)$ is $\mathcal{N}_{ano}\alpha I$–open set in $(U,T_R(X),I)$. Since every $\mathcal{N}_{ano}\alpha I$–open set is $\mathcal{N}_{ano}\,IS\alpha g$–open set, $f^{-1}(H)$ is $\mathcal{N}_{ano}\,IS\alpha g$–open in $(U,T_R(X),I)$ which implies that f is $\mathcal{N}_{ano}\,IS\alpha g$–continuous. Let G be a $\mathcal{N}_{ano}$–open set in $(U,T_R(X),I)$. Since f is $\mathcal{N}_{ano}\alpha I$–open, $f(G)$ is $\mathcal{N}_{ano}\alpha I$–open set in $(V,\sigma_{R'}(Y),J)$. Since every $\mathcal{N}_{ano}\alpha I$–open set is $\mathcal{N}_{ano}\,IS\alpha g$–open set, $f(G)$ is $\mathcal{N}_{ano}\,IS\alpha g$–open set in $(V,\sigma_{R'}(Y),J)$ which implies f is $\mathcal{N}_{ano}\,IS\alpha g$–open map. Therefore, consequently f is $\mathcal{N}_{ano}\,IS\alpha g$–homeomorphism.

Theorem 6.7. Let $f:\left(\mathrm{U},\mathrm{T}_{\mathrm{R}}\left(\mathrm{X}\right),\mathrm{I}\right)\to\left(\mathrm{V},\sigma_{\mathrm{R}'}\left(\mathrm{Y}\right),\mathrm{J}\right)$ be a bijective and $\mathcal{N}_{\mathrm{ano}}\mathrm{IS}\alpha\mathrm{g}$–irresolute map. Then the following statements are equivalent.

(i) f is a $\mathcal{N}_{\mathrm{ano}}\mathrm{IS}\alpha\mathrm{g}$–open map.

(ii) f is a $\mathcal{N}_{\mathrm{ano}}\mathrm{IS}\alpha\mathrm{g}$–homeomorphism.

(iii) f is a $\mathcal{N}_{\mathrm{ano}}\mathrm{IS}\alpha\mathrm{g}$–closed map.

Proof. Identical to the proof of Theorem 6.5.

Theorem 6.8. Let $f:\left(\mathrm{U},\mathrm{T}_{\mathrm{R}}\left(\mathrm{X}\right),\mathrm{I}\right)\to\left(\mathrm{V},\sigma_{\mathrm{R}'}\left(\mathrm{Y}\right),\mathrm{J}\right)$ be a bijective function. Then prove that f is $\mathcal{N}_{\mathrm{ano}}\mathrm{IS}\alpha\mathrm{g}$–homeomorphism if and only if $f\left[\mathcal{N}_{ano}\mathrm{IS}\alpha\mathrm{g}\text{-}\mathrm{C}l\left(\mathrm{A}\right)\right]=\mathcal{N}_{\mathrm{ano}}\text{-}\mathrm{C}l\left(f\left(\mathrm{A}\right)\right)$ for every subset A of $\left(\mathrm{U},\mathrm{T}_{\mathrm{R}}\left(\mathrm{X}\right),\mathrm{I}\right)$.

Proof. If $f:\left(\mathrm{U},\mathrm{T}_{\mathrm{R}}\left(\mathrm{X}\right),\mathrm{I}\right)\to\left(\mathrm{V},\sigma_{\mathrm{R}'}\left(\mathrm{Y}\right),\mathrm{J}\right)$ is $\mathcal{N}_{\mathrm{ano}}\mathrm{IS}\alpha\mathrm{g}$–homeomorphisms, then f is $\mathcal{N}_{\mathrm{ano}}\mathrm{IS}\alpha\mathrm{g}$–continuous and $\mathcal{N}_{\mathrm{ano}}\mathrm{IS}\alpha\mathrm{g}$–closed. If $\mathrm{A}\subseteq\mathrm{U}$, Then $f\left[\mathcal{N}_{ano}\mathrm{IS}\alpha\mathrm{g}\text{-}\mathrm{C}l\left(\mathrm{A}\right)\right]\subseteq\mathcal{N}_{\mathrm{ano}}\text{-}\mathrm{C}l\left(f\left(\mathrm{A}\right)\right)$ since f is $\mathcal{N}_{\mathrm{ano}}\mathrm{IS}\alpha\mathrm{g}$–continuous. Since $\mathcal{N}_{ano}\mathrm{IS}\alpha\mathrm{g}\text{-}\mathrm{C}l\left(\mathrm{A}\right)$ is $\mathcal{N}_{\mathrm{ano}}$–closed in $\left(\mathrm{U},\mathrm{T}_{\mathrm{R}}\left(\mathrm{X}\right),\mathrm{I}\right)$ and f is $\mathcal{N}_{\mathrm{ano}}\mathrm{IS}\alpha\mathrm{g}$–closed map, $f\left[\mathcal{N}_{ano}\mathrm{IS}\alpha\mathrm{g}\text{-}\mathrm{C}l\left(\mathrm{A}\right)\right]$ is $\mathcal{N}_{\mathrm{ano}}\mathrm{IS}\alpha\mathrm{g}$–closed in $\left(\mathrm{V},\sigma_{\mathrm{R}'}\left(\mathrm{Y}\right),\mathrm{J}\right)$. Also $\mathcal{N}_{ano}\mathrm{IS}\alpha\mathrm{g}\text{-}\mathrm{C}l\left[f\left(\mathcal{N}_{ano}\mathrm{IS}\alpha\mathrm{g}\text{-}\mathrm{C}l\left(\mathrm{A}\right)\right)\right]=f\left(\mathcal{N}_{ano}\mathrm{IS}\alpha\mathrm{g}\text{-}\mathrm{C}l\left(\mathrm{A}\right)\right)$. Since $\mathrm{A}\subseteq\mathcal{N}_{ano}\mathrm{IS}\alpha\mathrm{g}\text{-}\mathrm{C}l\left(\mathrm{A}\right)$, $f\left(\mathrm{A}\right)\subseteq f\left[\mathcal{N}_{ano}\mathrm{IS}\alpha\mathrm{g}\text{-}\mathrm{C}l\left(\mathrm{A}\right)\right]$ and hence $\mathcal{N}_{\mathrm{ano}}\text{-}\mathrm{C}l\left(f\left(\mathrm{A}\right)\right)\subseteq\mathcal{N}_{\mathrm{ano}}\text{-}\mathrm{C}l\left[f\left(\mathcal{N}_{ano}\mathrm{IS}\alpha\mathrm{g}\text{-}\mathrm{C}l\left(\mathrm{A}\right)\right)\right]=f\left(\mathcal{N}_{ano}\mathrm{IS}\alpha\mathrm{g}\text{-}\mathrm{C}l\left(\mathrm{A}\right)\right)$ Thus $\mathcal{N}_{\mathrm{ano}}\text{-}\mathrm{C}l\left(f\left(\mathrm{A}\right)\right)\subseteq f\left(\mathcal{N}_{ano}\mathrm{IS}\alpha\mathrm{g}\text{-}\mathrm{C}l\left(\mathrm{A}\right)\right)$. Hence, $f\left[\mathcal{N}_{ano}\mathrm{IS}\alpha\mathrm{g}\text{-}\mathrm{C}l\left(\mathrm{A}\right)\right]$ $=\mathcal{N}_{\mathrm{ano}}\text{-}\mathrm{C}l\left(f\left(\mathrm{A}\right)\right)$ if f is $\mathcal{N}_{\mathrm{ano}}\mathrm{IS}\alpha\mathrm{g}$–homeomorphism.

Conversely, if $f\left[\mathcal{N}_{ano}\mathrm{IS}\alpha\mathrm{g}\text{-}\mathrm{C}l\left(\mathrm{A}\right)\right]=\mathcal{N}_{\mathrm{ano}}\text{-}\mathrm{C}l\left(f\left(\mathrm{A}\right)\right)$ for every subset A of $\left(\mathrm{U},\mathrm{T}_{\mathrm{R}}\left(\mathrm{X}\right),\mathrm{I}\right)$, then f is $\mathcal{N}_{\mathrm{ano}}\mathrm{IS}\alpha\mathrm{g}$–continuous. If A is $\mathcal{N}_{\mathrm{ano}}$–closed in $\left(\mathrm{U},\mathrm{T}_{\mathrm{R}}\left(\mathrm{X}\right),\mathrm{I}\right)$, then A is $\mathcal{N}_{\mathrm{ano}}\mathrm{IS}\alpha\mathrm{g}$–closed in $\left(\mathrm{U},\mathrm{T}_{\mathrm{R}}\left(\mathrm{X}\right),\mathrm{I}\right)$. Then $\mathcal{N}_{ano}\mathrm{IS}\alpha\mathrm{g}\text{-}\mathrm{C}l\left(\mathrm{A}\right)=\mathrm{A}$ which implies $f\left[\mathcal{N}_{ano}\mathrm{IS}\alpha\mathrm{g}\text{-}\mathrm{C}l\left(\mathrm{A}\right)\right]=f\left(\mathrm{A}\right)$. Hence, by the given hypothesis, it follows that $\mathcal{N}_{\mathrm{ano}}\text{-}\mathrm{C}l\left(f\left(\mathrm{A}\right)\right)=f\left(\mathrm{A}\right)$. Thus $f\left(\mathrm{A}\right)$ is $\mathcal{N}_{\mathrm{ano}}$–closed in V and hence $\mathcal{N}_{\mathrm{ano}}\mathrm{IS}\alpha\mathrm{g}$–closed in V for every $\mathcal{N}_{\mathrm{ano}}$–closed set A in U. That is, f is a $\mathcal{N}_{\mathrm{ano}}\mathrm{IS}\alpha\mathrm{g}$–closed map. Therefore $f:\left(\mathrm{U},\mathrm{T}_{\mathrm{R}}\left(\mathrm{X}\right),\mathrm{I}\right)\to\left(\mathrm{V},\sigma_{\mathrm{R}'}\left(\mathrm{Y}\right),\mathrm{J}\right)$ is $\mathcal{N}_{\mathrm{ano}}\mathrm{IS}\alpha\mathrm{g}$–homeomorphism.

7 Nano Quasi Ideal Ideal Semi –α –Generalized –Open and Closed Mappings

Definition 7.1. A function $f:\left(\mathrm{U},\mathrm{T}_{\mathrm{R}}\left(\mathrm{X}\right),\mathrm{I}\right)\to\left(\mathrm{V},\sigma_{\mathrm{R}'}\left(\mathrm{Y}\right),\mathrm{J}\right)$ is said to be nano ideal quasi semi-α-generalized open $\left(briefly,\mathcal{N}_{ano}\mathrm{Q}\,\mathrm{IS}\alpha\mathrm{g}\text{–}open\right)$, If the image of every $\mathcal{N}_{\mathrm{ano}}\mathrm{IS}\alpha\mathrm{g}$–open set in U is $\mathcal{N}_{\mathrm{ano}}$–open in U.

Theorem 7.2. A function $f:\left(\mathrm{U},\mathrm{T}_{\mathrm{R}}\left(\mathrm{X}\right),\mathrm{I}\right)\to\left(\mathrm{V},\sigma_{\mathrm{R}'}\left(\mathrm{Y}\right),\mathrm{J}\right)$ is $\mathcal{N}_{ano}\mathrm{Q}\,\mathrm{IS}\alpha\mathrm{g}$–*open* if and only if for every subset G of U, $f\left(\mathcal{N}_{ano}\mathrm{IS}\alpha\mathrm{g}\text{-}\mathrm{I}nt\left(\mathrm{G}\right)\right)\subseteq\mathcal{N}_{ano}\text{-}\mathrm{I}nt\left(f\left(\mathrm{G}\right)\right)$.

Proof. Let f be a $\mathcal{N}_{\mathrm{ano}}\mathrm{Q}\,\mathrm{IS}\alpha\mathrm{g}$–open function. Now, we have $\mathcal{N}_{ano}\mathrm{IS}\alpha\mathrm{g}\text{-}\mathrm{I}nt\left(\mathrm{G}\right)\subseteq\mathrm{G}$ and $\mathcal{N}_{ano}\mathrm{IS}\alpha\mathrm{g}\text{-}\mathrm{I}nt\left(\mathrm{G}\right)$ is a $\mathcal{N}_{\mathrm{ano}}\mathrm{IS}\alpha\mathrm{g}$–open set. Hence, we obtain that $f\left(\mathcal{N}_{ano}\mathrm{IS}\alpha\mathrm{g}\text{-}\mathrm{I}nt\left(\mathrm{G}\right)\right)\subseteq f\left(\mathrm{G}\right)$. As $f\left(\mathcal{N}_{ano}\mathrm{IS}\alpha\mathrm{g}\text{-}\mathrm{I}nt\left(\mathrm{G}\right)\right)$ is $\mathcal{N}_{\mathrm{ano}}$–open, $f\left(\mathcal{N}_{ano}\mathrm{IS}\alpha\mathrm{g}\text{-}\mathrm{I}nt\left(\mathrm{G}\right)\right)\subseteq\mathcal{N}_{ano}\text{-}\mathrm{I}nt\left(f\left(\mathrm{G}\right)\right)$.

Conversely, assume that G is a $\mathcal{N}_{\text{ano}}$ ISαg−open set in U, then, $f(\mathrm{G}) = f\left(\mathcal{N}_{ano}\,\mathrm{IS}\alpha\mathrm{g}-\mathrm{I}nt(\mathrm{G})\right) \subseteq \mathcal{N}_{ano}-\mathrm{I}nt\left(f(\mathrm{G})\right)$ but $\mathcal{N}_{ano}-\mathrm{I}nt\left(f(\mathrm{G})\right) \subseteq f(\mathrm{G})$. Consequently, $f(\mathrm{G}) = \mathcal{N}_{ano}-\mathrm{I}nt\left(f(\mathrm{G})\right)$ and hence f is $\mathcal{N}_{\text{ano}}$Q ISαg−open.

Theorem 7.3. If a function $f:\left(\mathrm{U},\mathrm{T}_{\mathrm{R}}(\mathrm{X}),\mathrm{I}\right)\to\left(\mathrm{V},\sigma_{\mathrm{R}'}(\mathrm{Y}),\mathrm{J}\right)$ is $\mathcal{N}_{\text{ano}}$Q ISαg−open, then $\mathcal{N}_{ano}\,\mathrm{IS}\alpha\mathrm{g}-\mathrm{I}nt\left(f^{-1}(\mathrm{G})\right) \subseteq f^{-1}\left(\mathcal{N}_{ano}-\mathrm{I}nt(\mathrm{G})\right)$ for every subset G of V.

Proof. Let G be any arbitrary subset of V. Then, $\mathcal{N}_{ano}\,\mathrm{IS}\alpha\mathrm{g}-\mathrm{I}nt\left(f^{-1}(\mathrm{G})\right)$ is a $\mathcal{N}_{\text{ano}}$ ISαg−open set in U and f is $\mathcal{N}_{\text{ano}}$Q ISαg−open, then $f\left(\mathcal{N}_{ano}\,\mathrm{IS}\alpha\mathrm{g}-\mathrm{I}nt\left(f^{-1}(\mathrm{G})\right)\right) \subseteq \mathcal{N}_{ano}-\mathrm{I}nt\left(f\left(f^{-1}(\mathrm{G})\right)\right). \subseteq \mathcal{N}_{ano}-\mathrm{I}nt(\mathrm{G})$. Thus, $\mathcal{N}_{ano}\,\mathrm{IS}\alpha\mathrm{g}-\mathrm{I}nt\left(f^{-1}(\mathrm{G})\right) \subseteq f^{-1}\left(\mathcal{N}_{ano}-\mathrm{I}nt(\mathrm{G})\right)$.

Definition 7.4. A subset G is said to be an $\mathcal{N}_{\text{ano}}$ ISαg−nrighbourhood of a point p of U if there exists a $\mathcal{N}_{\text{ano}}$ ISαg−open set O such that $p \in \mathrm{O} \subseteq \mathrm{G}$.

Theorem 7.5. For a function $f:\left(\mathrm{U},\mathrm{T}_{\mathrm{R}}(\mathrm{X}),\mathrm{I}\right)\to\left(\mathrm{V},\sigma_{\mathrm{R}'}(\mathrm{Y}),\mathrm{J}\right)$, the following are equivalent

(i) f is $\mathcal{N}_{\text{ano}}$Q ISαg−open;

(ii) for each subset G of U, $f\left(\mathcal{N}_{ano}\,\mathrm{IS}\alpha\mathrm{g}-\mathrm{I}nt(\mathrm{G})\right) \subseteq \mathcal{N}_{ano}-\mathrm{I}nt\left(f(\mathrm{G})\right)$;

(iii) for each $p \in \mathrm{U}$ and each $\mathcal{N}_{\text{ano}}$ ISαg−nrighbourhood G of p in U, there exists a $\mathcal{N}_{\text{ano}}$−nrighbourhood H of $f(p)$ in V such that $\mathrm{H} \subseteq f(G)$.

Proof. (i) ⇒ (ii) It follows from Theorem 7.2.

(ii) ⇒ (iii) Let $p \in \mathrm{U}$ and G be an arbitrary $\mathcal{N}_{\text{ano}}$ ISαg−neighbouhood of $p \in \mathrm{U}$. Then, there exists a $\mathcal{N}_{\text{ano}}$Q ISαg−open set H in U such that $p \in \mathrm{H} \subseteq \mathrm{G}$ Then by (ii), we have $f(\mathrm{H}) = f\left(\mathcal{N}_{ano}\,\mathrm{IS}\alpha\mathrm{g}-\mathrm{I}nt(\mathrm{H})\right) \subseteq \mathcal{N}_{ano}\,\mathrm{I}nt\left(f(\mathrm{H})\right)$ and hence $f(\mathrm{H})$ is $\mathcal{N}_{\text{ano}}$−open in V such that $f(p) \in f(\mathrm{H}) \subseteq f(\mathrm{G})$.

(iii) ⇒ (i) Let G be an arbitrary $\mathcal{N}_{\text{ano}}$ ISαg−open set in U. Then for each $p \in f(\mathrm{G})$, by (iii) there exists a $\mathcal{N}_{\text{ano}}$−neighbourhood H_p of p in V such that $\mathrm{H}_p \subseteq f(\mathrm{G})$. As H_p is a $\mathcal{N}_{\text{ano}}$−neighbourhood of p, there exists a $\mathcal{N}_{\text{ano}}$−open set O_p in V such that $p \in \mathrm{O}_p \subseteq \mathrm{H}_p$. Thus $f(\mathrm{G}) = \bigcup\left\{\mathrm{O}_p : p \in f(\mathrm{G})\right\}$ which is a $\mathcal{N}_{\text{ano}}$−open set in V. This implies that f is $\mathcal{N}_{\text{ano}}$Q ISαg−open function.

Theorem 7.6. A function $f:\left(\mathrm{U},\mathrm{T}_{\mathrm{R}}(\mathrm{X}),\mathrm{I}\right)\to\left(\mathrm{V},\sigma_{\mathrm{R}'}(\mathrm{Y}),\mathrm{J}\right)$ is $\mathcal{N}_{\text{ano}}$Q ISαg−open if and only if for any subset B of V and for any $\mathcal{N}_{\text{ano}}$Q ISαg−closed set F of U containing $f^{-1}(\mathrm{B})$, there exists a $\mathcal{N}_{\text{ano}}$−closed set G of V containing B such that $f^{-1}(\mathrm{G}) \subseteq \mathrm{F}$.

Proof. Suppose f is $\mathcal{N}_{\text{ano}}$Q ISαg−open. Let $\mathrm{B} \subseteq \mathrm{V}$ and F be a $\mathcal{N}_{\text{ano}}$ ISαg−closed set of U containing $f^{-1}(\mathrm{B})$. Now, put $\mathrm{G} = \mathrm{V} - f(\mathrm{U} - \mathrm{F})$. It is clear that $f^{-1}(\mathrm{B}) \subseteq \mathrm{F}$ implies $\mathrm{B} \subseteq \mathrm{G}$. Since f is $\mathcal{N}_{\text{ano}}$Q ISαg−open, we obtain G as a $\mathcal{N}_{\text{ano}}$−closed set of V. Moreover, we have $f^{-1}(\mathrm{G}) \subseteq \mathrm{F}$. Conversely, let G be a $\mathcal{N}_{\text{ano}}$ ISαg−open set of U and put $\mathrm{B} = \mathrm{V} - f(\mathrm{G})$. Then U − G is a $\mathcal{N}_{\text{ano}}$ ISαg−closed set in U containing $f^{-1}(\mathrm{B})$. By hypothesis, there exists a $\mathcal{N}_{\text{ano}}$−closed set F of V such that $\mathrm{B} \subseteq \mathrm{F}$ and $f^{-1}(\mathrm{F}) \subseteq \mathrm{U} - \mathrm{G}$. Hence, we obtain $f(\mathrm{G}) \subseteq \mathrm{V} - \mathrm{F}$. On the other hand, it follows that $\mathrm{B} \subseteq \mathrm{F}$, $\mathrm{V} - \mathrm{F} \subseteq \mathrm{V} - \mathrm{B} = f(\mathrm{G})$. Thus we obtain $f(\mathrm{G}) = \mathrm{V} - \mathrm{F}$ which is $\mathcal{N}_{\text{ano}}$−open and hence f is $\mathcal{N}_{\text{ano}}$Q ISαg−open function.

Theorem 7.7. A function $f:(U,T_R(X),I)\to(V,\sigma_{R'}(Y),J)$ is $\mathcal{N}_{ano}Q\,IS\alpha g$–open if and only if $f^{-1}(\mathcal{N}_{ano}\text{-}Cl(B))\subseteq\mathcal{N}_{ano}IS\alpha g\text{-}Cl(f^{-1}(B))$ for every subset B of V.

Proof. Suppose that f is $\mathcal{N}_{ano}Q\,IS\alpha g$–open For any subset B of V, $f^{-1}(B)\subseteq\mathcal{N}_{ano}IS\alpha g\text{-}Cl(f^{-1}(B))$. Therefore, by Theorem 7.5, there exists a $\mathcal{N}_{ano}$–closed set F in V such that $B\subseteq F$ and $f^{-1}(F)\subseteq\mathcal{N}_{ano}IS\alpha g\text{-}Cl(f^{-1}(B))$. Therefore, we obtain $f^{-1}(\mathcal{N}_{ano}\text{-}Cl(B))\subseteq f^{-1}(F)\subseteq\mathcal{N}_{ano}IS\alpha g\text{-}Cl(f^{-1}(B))$.

Conversely, let $B\subseteq V$ and F be a $\mathcal{N}_{ano}IS\alpha g$–closed set of U containing $f^{-1}(B)$. Put $H=\mathcal{N}_{ano}\text{-}Cl(B)$, then we have $B\subseteq W$ and W is $\mathcal{N}_{ano}$–closed and $f^{-1}(W)\subseteq\mathcal{N}_{ano}IS\alpha g\text{-}Cl(f^{-1}(B))\subseteq F$. Then by Theorem 7.6, f is $\mathcal{N}_{ano}Q\,IS\alpha g$–open.

Theorem 7.8. Consider two functions $f:(U,T_R(X),I)\to(V,\sigma_{R'}(Y),J)$ and $g:(V,\sigma_{R'}(Y),J)\to(W,\gamma_{R''}(Z),L)$ and suppose $gof:(V,\sigma_{R'}(Y),J)\to(W,\gamma_{R''}(Z),L)$ is $\mathcal{N}_{ano}Q\,IS\alpha g$–open. If g is $\mathcal{N}_{ano}$–continuous injective function, then f is $\mathcal{N}_{ano}Q\,IS\alpha g$–open.

Proof. Let G be a $\mathcal{N}_{ano}Q\,IS\alpha g$–open set in U, then $(gof)(G)$ is $\mathcal{N}_{ano}$–open in W, since gof is $\mathcal{N}_{ano}Q\,IS\alpha g$–open. Again g is an $\mathcal{N}_{ano}$–continuous function, $f(G)=g^{-1}(gof(G))$ is $\mathcal{N}_{ano}$–open in V. This shows that f is $\mathcal{N}_{ano}Q\,IS\alpha g$–open.

Definition 7.9. A function $f:(U,T_R(X),I)\to(V,\sigma_{R'}(Y),J)$ is said to be Nano quasi-ideal semi-α generalized closed (briefly, $\mathcal{N}_{ano}Q\,IS\alpha g$–closed) if the image of every $\mathcal{N}_{ano}Q\,IS\alpha g$–closed set in U is $\mathcal{N}_{ano}$–closed in V.

Theorem 7.10. Every $\mathcal{N}_{ano}Q\,IS\alpha g$–closed function is $\mathcal{N}_{ano}$–closed as well as $\mathcal{N}_{ano}Q\,IS\alpha g$–closed.

Proof. It is obvious.

Theorem 7.11. A function $f:(U,T_R(X),I)\to(V,\sigma_{R'}(Y),J)$ is $\mathcal{N}_{ano}Q\,IS\alpha g$–closed if and only if for any subset B of V and for any $\mathcal{N}_{ano}IS\alpha g$–open set G of U containing $f^{-1}(B)$, there exists a $\mathcal{N}_{ano}$–open set H of V containing B such that $f^{-1}(H)\subseteq G$.

Proof. This proof is similar to that of theorem 7.6.

Theorem 7.12. Suppose that $f:(U,T_R(X),I)\to(V,\sigma_{R'}(Y),J)$ and $g:(V,\sigma_{R'}(Y),J)\to(W,\Omega_{R''}(Z),L)$ be any two $\mathcal{N}_{ano}Q\,IS\alpha g$–closed functions. Then $gof:(U,T_R(X),I)\to(W,\Omega_{R''}(Z),L)$ is $\mathcal{N}_{ano}Q\,IS\alpha g$–closed function.

Proof. It is obvious.

Theorem 7.13. Suppose that $f:(U,T_R(X),I)\to(V,\sigma_{R'}(Y),J)$ is $\mathcal{N}_{ano}IS\alpha g$–closed function and $g:(V,\sigma_{R'}(Y),J)\to(W,\Omega_{R''}(Z),L)$ is $\mathcal{N}_{ano}Q\,IS\alpha g$–closed function. Then $gof:(U,T_R(X),I)\to(W,\Omega_{R''}(Z),L)$ is $\mathcal{N}_{ano}$–closed function.

Proof. It is obvious.

Theorem 7.14. Suppose that $f:(U,T_R(X),I)\to(V,\sigma_{R'}(Y),J)$ is $\mathcal{N}_{ano}IS\alpha g$–irresolute surjective function and $g:(V,\sigma_{R'}(Y),J)\to(W,\Omega_{R''}(Z),L)$ is a function such that $gof:(U,T_R(X),I)\to(W,\Omega_{R''}(Z),L)$ is a $\mathcal{N}_{ano}Q\,IS\alpha g$–closed function. Then $g:(V,\sigma_{R'}(Y),J)\to(W,\Omega_{R''}(Z),L)$ is a $\mathcal{N}_{ano}$–closed function.

Proof. Suppose that F is an arbitrary $\mathcal{N}_{ano}$ –closed set in V. Then F is $\mathcal{N}_{ano}$ $IS\alpha g$–closed in V. As f is $\mathcal{N}_{ano}$ $IS\alpha g$–irresolute, $f^{-1}(F)$ is $\mathcal{N}_{ano}$ $IS\alpha g$–closed in U. Since gof is $\mathcal{N}_{ano}Q$ $IS\alpha g$–closed and f is surjective, $(gof)(f^{-1}(F)) = g(F)$, which is $\mathcal{N}_{ano}$ –closed in Z. This implies that g is a $\mathcal{N}_{ano}$ –closed function.

Theorem 7.15. A function $f:(U,T_R(X),I)\to(V,\sigma_{R'}(Y),J)$ is $\mathcal{N}_{ano}Q$ $IS\alpha g$–closed if and only if $f(U)$ is $\mathcal{N}_{ano}$ –closed in V and $f(G)-f(U-G)$ is $\mathcal{N}_{ano}$ –open in $f(U)$ whenever G is $\mathcal{N}_{ano}$ $IS\alpha g$–open in U.

Proof. **Necessity:** Suppose $f:(U,T_R(X),I)\to(V,\sigma_{R'}(Y),J)$ is a $\mathcal{N}_{ano}Q$ $IS\alpha g$–closed function. Since U is $\mathcal{N}_{ano}$ $IS\alpha g$–closed, $f(U)$ is $\mathcal{N}_{ano}$ –closed in V and $f(G)-f(U-G)=f(G)\cap f(U)-f(U-G)$ is $\mathcal{N}_{ano}$ –open in $f(U)$ when G is $\mathcal{N}_{ano}$ $IS\alpha g$–open in U.

Sufficiency: Suppose $f(U))$ is $\mathcal{N}_{ano}$ –closed in V, $f(G)-f(U-G)$ is $\mathcal{N}_{ano}$ –open in $f(U)$ when G is $\mathcal{N}_{ano}$ $IS\alpha g$–open in U and let H be $\mathcal{N}_{ano}$ –closed in U. Then $f(H)=f(U)-(f(U-H)-f(H))$ is $\mathcal{N}_{ano}$ –closed in $f(U)$ and hence $\mathcal{N}_{ano}$ –closed in V,

Corollary 7.16. A surjective function $f:(U,T_R(X),I)\to(V,\sigma_{R'}(Y),J)$ is $\mathcal{N}_{ano}Q$ $IS\alpha g$–closed if and only if $f(G)-f(U-G)$ is $\mathcal{N}_{ano}$ –open in V whenever G is $\mathcal{N}_{ano}$ $IS\alpha g$–open in U.

Proof. It is obvious.

Theorem 7.17. Let $f:(U,T_R(X),I)\to(V,\sigma_{R'}(Y),J)$ be $\mathcal{N}_{ano}$ $IS\alpha g$–continuous and $\mathcal{N}_{ano}Q$ $IS\alpha g$–closed surjective function. Then the topology on V is $\{f(H)-f(U-H): H \text{ is } \mathcal{N}_{ano}\, IS\alpha g\text{–open in } U\}$.

Proof. Let M be $\mathcal{N}_{ano}$ –open in V. Let $f^{-1}(M)$ is $\mathcal{N}_{ano}$ $IS\alpha g$–open in U, and $f(f^{-1}(M))-f(U-f^{-1}(M))=M$. Hence all $\mathcal{N}_{ano}$ –open sets in V are of the form $f(G)-f(U-G)$, G is $\mathcal{N}_{ano}$ $IS\alpha g$–open in U. On the other hand, all sets of the form $f(G)-f(U-G)$, G is $\mathcal{N}_{ano}$ $IS\alpha g$–open in U, are $\mathcal{N}_{ano}$ –open in V from Corollary 7.16.

Definition 7.18. A $\mathcal{N}_{ano}$ –ideal –Top. –Space $(U,T_R(X),I)$ is said to be $\mathcal{N}_{ano}$ –normal if for any pair of disjoint $\mathcal{N}_{ano}$ –closed subsets E and F of U there exists disjoint $\mathcal{N}_{ano}$ –open sets G and H such that $E\subseteq G$ and $F\subseteq H$.

Definition 7.19. A $\mathcal{N}_{ano}$ –ideal –Top. –Space $(U,T_R(X),I)$ is said to be $\mathcal{N}_{ano}$ $IS\alpha g$–normal if for any pair of disjoint $\mathcal{N}_{ano}$ $IS\alpha g$–closed subsets E and F of U there exists disjoint $\mathcal{N}_{ano}$ –open sets G and H such that $E\subseteq G$ and $F\subseteq H$.

Theorem 7.20. Let $f:(U,T_R(X),I)\to(V,\sigma_{R'}(Y),J)$ be a $\mathcal{N}_{ano}$ $IS\alpha g$–continuous and $\mathcal{N}_{ano}Q$ $IS\alpha g$–closed surjective function with U is $\mathcal{N}_{ano}$ $IS\alpha g$–normal. Then V is $\mathcal{N}_{ano}$ –normal.

Proof. Let K and L be disjoint $\mathcal{N}_{ano}$ –closed subsets of V. Then $f^{-1}(K)$, $f^{-1}(L)$ are disjoint $\mathcal{N}_{ano}$ $IS\alpha g$–closed subsets of U. Since U is $\mathcal{N}_{ano}$ $IS\alpha g$–normal, there exists disjoint $\mathcal{N}_{ano}$ –open sets G and H such that $f^{-1}(K)\subseteq G, f^{-1}(L)\subseteq H$. Then $K\subseteq f(G)-f(U-G)$ and $L\subseteq f(H)-f(U-H)$, further by corollary 7.16, $f(G)-f(U-G)$ and $f(H)-f(U-H)$ are $\mathcal{N}_{ano}$ –open sets in V and clearly $[f(G)-f(U-G)]\cap[f(H)-f(U-H)]=0_N$. This shows that V is $\mathcal{N}_{ano}$ –normal.

Conclusions

The author has introduced the notions of new classes of functions called $\mathcal{N}_{ano}\,\mathrm{IS}\alpha g$ –continuous maps, $\mathcal{N}_{ano}\,\mathrm{IS}\alpha g$ –irresolute - maps, $\mathcal{N}_{ano}\,\mathrm{IS}\alpha g$ –open - maps, $\mathcal{N}_{ano}\,\mathrm{IS}\alpha g$ –closed - maps, strongly $\mathcal{N}_{ano}\,\mathrm{IS}\alpha g$ –open - maps, strongly $\mathcal{N}_{ano}\,\mathrm{IS}\alpha g$ –closed - maps and $\mathcal{N}_{ano}\,\mathrm{IS}\alpha g$ –homeomorphisms, $\mathcal{N}_{ano}\mathrm{Q}\,\mathrm{IS}\alpha g$ –open - maps, and $\mathcal{N}_{ano}\mathrm{Q}\,\mathrm{IS}\alpha g$ –closed - maps and has investigated fundamental properties and characterizations of these mappings in $\mathcal{N}_{ano}$ –Ideal –Top –Spaces. In future work, the author intends to continue to introduce and investigate properties and characterizations of the notions of $\mathcal{N}_{ano}\,\mathrm{IS}\alpha g$ –separation Axioms namely $\mathcal{N}_{ano}\,\mathrm{IS}\alpha g$ –T_0 space, $\mathcal{N}_{ano}\,\mathrm{IS}\alpha g$ –T_1 space, $\mathcal{N}_{ano}\,\mathrm{IS}\alpha g$ –T_2 space, $\mathcal{N}_{ano}\,\mathrm{IS}\alpha g$ –regular space, $\mathcal{N}_{ano}\,\mathrm{IS}\alpha g$ –normal space, almost $\mathcal{N}_{ano}\,\mathrm{IS}\alpha g$ –normal space, mildly $\mathcal{N}_{ano}\,\mathrm{IS}\alpha g$ –normal space, $\mathcal{N}_{ano}\,\mathrm{IS}\alpha g$ –compact space, $\mathcal{N}_{ano}\,\mathrm{IS}\alpha g$ –Lindelof space, $\mathcal{N}_{ano}\,\mathrm{IS}\alpha g$ –connected space, $\mathcal{N}_{ano}\,\mathrm{IS}\alpha g$ –closed graph and strongly $\mathcal{N}_{ano}\,\mathrm{IS}\alpha g$ –closed graph in $\mathcal{N}_{ano}$ –Ideal –Top –Spaces. In future work, $\mathcal{N}_{ano}\,\mathrm{IS}\alpha g$ –open sets can be applied in an application field of real-life experience.

Scientific Ethics Declaration

* The author declares that the scientific ethical and legal responsibility of this article published in EPSTEM journal belongs to the author.

Conflict of Interest

* The author declares that he has no conflict of Interest.

Funding

* The author is indebted to Prince Mohammad Bin Fahd University for providing excellent research facilities during the preparation of this research paper.

Acknowledgements or Notes

* This article was presented as an oral presentation at the International Conference on Technology, Engineering and Science (www.icontes.net) held in Antalya/Türkiye on November 12-15, 2025.

References

Anto, M., & Carolinal, J. (2023). $\mathrm{N}\hat{g}^{*}\mathrm{s}$–Continuous functions in Nano Topological Spaces. *Ratio Mathematica, 45*, 97 – 110.

Bhuvaneswari, K., & Ezhilarasi, A. (2016). Nano semi-generalized homeomorphisms in nano topological space. *International Journal of Mathematical Archive*, *7*(7), 168 – 175.

Bhuvaneswari, K., & Gnanapriya, K. M. (2016). Nano generalized pre homeomorphisms in nano topological space. *International Journal of Scientific and Research Publications*, 6(7), 526 – 530.

Deepa, M., & Kalaivanan, M. R. (2021). On nano y**-closed and nano y**-open functions. *IT in Industry, 9*(1), 1437 - 1442.

Ganesan, S. (2019). CnIg-continuous maps in nano ideal topological spaces. *MathLAB Journal, 4*.

Geetha, K., & Vigneshwaran, M. (2018). Characterization of nano p*g-homeomorphisms in nano topological spaces. *International Journal of Advanced Research Trends in Engineering and Technology (IJARTET), 5*(12), 973 – 977.

Hosny, M. (2020). Nano∧ β-sets and nano∧ β-continuity. *Journal of the Egyptian Mathematical Society*, *28*(1), 18.

Inthumathi, V., Abinprakash, R., & Banu, M. P. (2019). Some weaker forms of continuous and irresolute mappings in nano ideal topological spaces. *Journal of New results in Science (JNRS), 8*(1), 14 – 25.

Parimala, M., Jafari, S., & Murali, S. (2017). Nano ideal generalized closed sets in nano ideal topological spaces. In *Annales Univ. Sci. Budapest* (Vol. 60, pp. 3-11).

Jesti, J. A., & Renuka, J. J. (2023). A New Notion Of Mappings In Nano Ideal Topological Spaces. *Journal of Namibian Studies*, *33*.

Jesti, J. A., & Suganya, P. $\boldsymbol{\alpha Ng}$-ırresolute function in nano topological spaces. *International Journal of Innovative Science, Engineering & Technology, 8*(1).

Levine, N. (1963). Semi-open sets and semi-continuity in topological spaces. *Americal Mathematical Monthly, 70*, 36 – 41.

Mahdi, Saif Saleh & Jamil, Jamil Mahmoud (2024). On some types of nano β_{pc} –continuous functions. *BIO Web of Conferences 97*, 00144, ISCKU,1 - 13.

Maheswari, N. R. Santhi (2023). On Nano $\lambda\psi g$–Irresolute functions in nano topological spaces. *International J. Math. Combin*, *1*, 81 – 86.

Malarvizhi, M., Sarankumar, T., Rajendran V., & Satishmohan, P. (2021). On Ng^α-homeomorphisms in nano topological spaces. *Turkish Journal of Computer and Mathematics Education*, *12*(10), 4707 – 4711.

Mashhour, A. S., El-Monsef, M. E. A., & El-Deep, S. N. (1982). On precontinuous and weak precontinuous mappings. *Proc. Math. Phys. Soc. Egypt, 53*, 47-53.

Mashhour, A.S., Hasanein, I. A., & El-Deep, S. N. (1983). α-continuous and α-open mappings. *Acta. Math. Hunger, 41*, 213-218.

Parimala, M. & Jafari, S. (2018). On some new notions in nano ideal Tp. Sp. *Eurasian Bulletin of Mathematics, 1*(3), 85 - 93.

Parimala, M., Arivuoli, D., & Jeevitha, R. (2018). Composition of functions under niαg continuous and niαg-irresolute functions in nano ideal topological spaces. *International Journal of Recent Technology and Engineering (IJRTE)*, *7*, 107 – 110.

Parimala, M., Jafari, S., & Murali, S. (2017). Nano ideal generalized Cl.S.s. in nano ideal Top.Sp. *Annales Univ. Sci. Budapest, 60*, 3 - 11.

Rajendran, V., Mohan, P. S., & Chitra, M. (2024). Nig*α-closed sets in nano ıdeal topological spaces, educational administration. *Theory and Practice, 30*(6), 942 - 947.

Rajendran, V., Mohan, P. S., & Chitra, M. (2021). Nano g*α – continuous functions in nano topological spaces. *Turkish Online Journal of Qualitative Inquiry (TOJOI), 12*(5), 1156 – 1164.

Rajendran, V., Mohan, P. S., & Mangayarkarasi, R. (2021). $\mathrm{N}\,s\hat{g}$–continuous functions in nano topological spaces. *Turkish Journal of Computer and Mathematics Education, 12* (10), 4712 – 4718.

Rodrigo, P. A., & Dani, I. S. (2018). Contra nano α*as continuous function in nano topological space. *Journal of xi'an Shiyou University, 16*(8), 151 - 156.

Sathya, C. J., & Richard, C. (2024). A new class of ng*b-continuous and ng*b-irresolute functions in nts. *Tuijin Jishu/Journal of Propulsion Technology, 45*(2), 85 - 90.

Sathyapriya, S., Kamali, S., & Kousalya, M. (2019). On nano αg*s-closed sets in nano topological spaces. *International Journal of Innovative Research in Science, Engineering and Technology, 8*(2), 777 – 784.

Satishmohan, P., Rajendran, V., Devika, A., & Vani, R. (2017). On nano semi-continuity and nano pre-continuity. *International Journal of Applied Research, 3*(2), 76 – 79.

Suganya, G. B., Pasunkilipandian, S., & Kalaiselvi, M. (2021). A new class of nano ıdeal generalized closed set in nano ıdeal topological space. *International Journal of Mechanical Engineering, 6*(3).

Author(s) Information

Raja Mohammad Latif
Prince Mohammad Bin Fahs University
Department of Mathematics and Natural Sciences
Al Khobar, Kingdom of Saudi Arabia
Contact e-mail: rlatif*@pmu.edu.sa*

To cite this article:

Latif, R.M. (2025). Nano ideal semi alpha generalized continuous and irresolute mappings in nano ideal topological spaces. *The Eurasia Proceedings of Science, Technology, Engineering and Mathematics (EPSTEM), 38,* 480-501.

The Eurasia Proceedings of Science, Technology, Engineering & Mathematics (EPSTEM)
ISSN: 2602-3199

The Eurasia Proceedings of Science, Technology, Engineering and Mathematics (EPSTEM), 2025

Volume 38, Pages 502-511

IConTES 2025: International Conference on Technology, Engineering and Science

Synthesis of Stoichiometric Cordierite Ceramics from Chemically Modified Kaolin by a Controlled Acid Leaching

Boumchedda Khaled
University of Boumerdes

Djafar Rabah
University of Boumerdes

Rabehi Bahia
University of Boumerdes

Bououdina Mohamed
Prince Sultan University

Abstract: Cordierite ceramic still attracts great interest due to its interesting properties for applications in the field of modern engineering. It is one of the few ceramics that undergoes extremely low thermal expansion, less than 0.001% in the wide temperature range 25 – 800°C. This work aims to synthesize stoichiometric cordierite ceramics according the following molecular formula: $Mg_2Al_4Si_5O_{18}$, from a single kaolin ($Al_2Si_2O_5(OH)_4$), that is chemically modified by acid leaching. The chemical modification of the kaolin is carried out in a hydrochloric acid solution (6M), at a temperature of 70°C, under magnetic stirring for 2 hours. These optimized acid leaching conditions increase the Si/Al ratio of kaolin, and thus allow a stoichiometric mixture of cordierite, by adding the precipitated magnesium hydroxide. Thermal transformations of the starting mixture in the temperature range 1100 – 1430°C reveals the appearance of several phases, such as sapphirine and enstatite, before the cordierite becomes predominant at 1250°C. These intermediate phases have higher densities than that of cordierite, and thereby their transformations to cordierite phase are accompanied by swelling, which usually causes cracking in the ceramic. Therefore, the densification of structural ceramics is carried out from stoichiometric cordierite powders calcined at 1250°C by solid phase sintering and from the starting mixture by reaction sintering for comparison of the ceramic properties. The results show that in the first case, the maximum densification reaches 92% at 1325°C and then decreases to 78% at 1430°C, due to the formation of a glass phase, and in the second case, the densification reaches 90% at 1325°C, and at 1350°C its becomes very close to the total densification (~95%). The thermal expansion coefficient a (from RT to 700 °C) decreases with increasing sintering temperature; $\alpha = 3.1x10^{-6}\ °C^{-1}$ at 1275°C, and becomes $<1.7x10^{-6}\ °C^{-1}$ at 1400°C.

Keywords: Cordierite, Kaolin, Leaching, Sintering, Ceramic properties

Introduction

Cordierite ceramics still arouses a lot of interest because of its many very interesting properties in the field of modern engineering (Chowdhury et al., 2007a, 2007b). Its thermal expansion is extremely low (<0.001%), and its mechanical strength is high (>245MPa), which gives it excellent resistance to thermal shocks. Its use temperature exceeds 1200°C, cordierite is often found in many refractory products such as burner tubes and firing supports for ceramic industry furnaces with fast firing cycles (Ponomarev et al., 2023; Guangmao Yan et al., 2024; Cheraitia et al., 2020).

- This is an Open Access article distributed under the terms of the Creative Commons Attribution-Noncommercial 4.0 Unported License, permitting all non-commercial use, distribution, and reproduction in any medium, provided the original work is properly cited.

- Selection and peer-review under responsibility of the Organizing Committee of the Conference

© 2025 Published by ISRES Publishing: www.isres.org

Cordierite also has low dielectric constants (ρ~5) and dielectric losses (tgδ<10^{-3}) over a wide frequency interval, which allows for applications in the electrical industry, electronics in the production of electrical insulators, of substrates, and electronic components (Tekin et al., 2022). Recently studies have shown that cordierite is promising in high frequency applications (Cao et al., 2025; Synkiewicz et al, 2021), and in heat storage (Deng et al, 2024), (Boutaleb et al, 2024).

The stoichiometric cordierite is well defined by the SiO2-Al2O3-MgO ternary diagram system with the following centesimal chemical composition: 51.36%SiO2.34.86%Al2O3.13.78%MgO, and a SiO2/Al2O3 ratio = 1.47. The conventional method of synthesis of pure cordierite involves reacting at high temperature a mixture of oxides of SiO_2, MgO, and Al_2O_3 corresponding to the chemical composition. These synthetic and pure oxides make it possible to produce a highly densified ceramic at a very high temperature (~1430°C) close to the melting temperature of theoretical cordierite (1470°C) (Kobayashi et al., 2000). Also many attempts at synthesis of cordierite are developed from available and less expensive natural materials, such as kaolin (Kobayashi et al, 2000), talc [16], sepiolite (Zhou et al, 2011), stevensiste (Bejjaoui et al., 2010), and many other materials carrying the constituent elements of cordierite. Often, these starting mixtures must be composed of several ingredients (kaolin, talc, silica, magnesium compounds...) to succeed in a stoichiometric cordierite. The acid leaching of kaolin ($R_{SiO2/Al2O3}$<1,20) is ideally suited to modify $R_{SiO2/Al2O3}$, by hydrolyzing kaolinite ($Al_2O_3.2SiO_2.2H_2O$) into soluble aluminium and amorphous silica (Al-Harahsheh et al., 2023; Peng et al, 2021; Edama et al, 2014). An optimized chemical treatment will synthesize pure cordierite by adding a suitable magnesium compound.

On the other hand, the densification of ceramics remains insufficient due to the presence of impurities which lead to the formation of vitreous phases at high temperatures and thus lower densification. In addition, the crystallization of cordierite in these cases occurs from intermediate phases such as mullite, sapphirine, clinoenstatite, and spinel (Redaoui et al., 2018; Cameruccia et al., 2003; Khattab et al, 2021). These phases have densities much higher than that of cordierite, their transformations into cordierite can generate microcracks in the ceramic, which requires a delicate and complex thermal cycle to achieve a densification without defects. To avoid this handicap, Ogiwara et al developed highly densified ceramics from calcined cordierite powder using pure oxides, but such studies remain few (Ogiwara et al., 2010).

This research studies the possibility of synthesizing stoichiometric cordierite from a single kaolin which is chemically modified by an acid leaching, and to perform a comparison of the ceramic properties of cordierites prepared by reaction sintering from the starting mixture, and those prepared from previously calcined cordierite powders.

Method

Raw Materials

The kaolin used in this study is taken from a deposit located in eastern Algeria in the region of Djebel Debbagh. This kaolin is known for its black coloration which is caused by a manganiferous mineral; todorokite (Mn,Ca) Mn_5O_{11}n4H_2O) (Senoussi et al., 2016; Boulmokh et al., 2007; Debbakh et al, 2020). To increase the clay mineral content and decrease the sand content, the kaolin DD is sieved by liquid process, under 20 microns and the obtained fraction is designated by DD00. The magnesium is prepared in the form of hydroxide ($Mg(OH)_2$) by precipitation from a solution of magnesium chloride and ammonium hydroxide, with commercial reagents.

Controlled Acid Leaching Method

The controlled acid leaching tests are carried out in a flat-bottomed flask, fitted with a thermometer and a refrigerant, which is installed on a heating plate equipped with magnetic agitation. The same conditions are maintained for all experiments; a solid/liquid ratio is 1:5, molarity of 6M HCl, rotation speed of 450rpm, and duration of 6 hours. The leaching is stopped with a large quantity of distilled water, and the solid is washed several times with distilled water until a neutral pH is obtained, then dried at 100°C in an oven to constant weight. Five experiments are conducted at temperatures of 25°C, 50°C, 60°C, 70°C, and 90°C; the fractions of processed DD00 are designated DD25, DD50, DD60, DD70, and DD90 respectively.

Preparation of Cordierite Ceramic Samples

Pellets (ϕ:13x2,5mm) are prepared by hydraulic pressing (50MPa) from the leached kaolin having the optimal SiO_2/Al_2O_3 ratio for obtaining a stoichiometric cordierite, adding the precipitated magnesium hydroxide. The starting mixture is previously crushed by attrition in ethyl alcohol in the presence of zirconia beads (2 to 3mm) during 120mn. Sintering of pellets are performed at different temperatures, from 1100°C to 1430°C to determine the optimal temperature of cordierite synthesis, and from calcined powder which is ground in the same way as previously.

Characterization

The chemical compositions of the raw materials and of the leached kaolin were carried out using a Rigaku ZSX Primus X-ray fluorescence spectrometer. The identification of crystalline phases of sintered pellets was performed by XRD analysis using a Philips X'Pert Pro (CuK = 1,54056Å) diffractometer, with a continuous scan from 5 to 80°. The characterization is continued by the simultaneous thermal analysis DSC-TGA (STA Netszch 409PC luxx), and the dilatometer (Nezscth 409PC), with a heating rate of 10°C/min between room temperature and 1400°C. The microstructural observations of the ceramics were performed by a scanning electron microscope (SEM) of the type JSM-6360LV. The bulk density (dap), water absorption (Abs), and bulk specific gravity (dsp) were determined using a method based on the principle of Archimedes recommended by the American company for testing and determining the specifications of materials ASTM C373 (ASTM Specification C373). The dielectric characteristics are performed on metallized ceramics using an Agilent HP4192A impedance analyser over a frequency range of 100Hz to 8MHz.

Results and Discussion

The Chemical Modifications of the Kaolin DD

Table 1 shows the chemical compositions of treated DD kaolin samples, prepared magnesium hydroxide (HMP), and synthesized cordierite (CR). It is noted that below 50°C, SiO_2/Al_2O_3 remains unchanged, but at higher temperatures this ratio increases sharply, and for >90°C this ration is multiplies by 3, which shows that more than 50% of kaolin is dissolved. It is clear that temperature is a predominant parameter in the leaching of kaolin (Edama et al., 2014; Al-Harahsheh et al., 2023). The halloysite network undergoes leaching through the release of soluble Al^{3+} and insoluble amorphous silica (White et al., 2018).

It is also noted that MnO strongly decreases under the effect of acid action, certainly because of the leaching of the todorokite which results in the reduction of Mn^{4+}, and Mn^{3+} into Mn^{2+} which are perfectly soluble in acidic solutions (Manish Kumar et al., 2019; El Hazek et al., 2006). According to these results, it is deduced that the conditions that allow for having the optimal SiO_2/Al_2O_3 (1,48) for a stoichiometric mixing of cordierite are those of DDT70, with 86.3%DDT70 + 13.7%HMP.

Table 1. Chemical compositions of kaolin samples treated at different temperatures

	DD00	DDT25	DDT50	DDT70	DDT90	HMC	CR
SiO_2	52,52	54,40	54,42	58,57	75,50	0,18	50,90
Al_2O_3	41,61	44,30	44,60	39,56	23,25	0,00	34,36
MnO	3,41	0,14	0,11	0,18	0,02	0,00	0,16
MgO	0,65	0,45	0,21	0,25	0,20	98,15	13,62
K_2O	0,17	0,12	0,08	0,08	0,09	0,06	0,07
Na_2O	0,25	0,05	0,04	0,08	0,05	0,48	0,07
SO_3	0,48	0,15	0,17	0,08	0,13	0,38	0,12
CaO	0,45	0,22	0,16	0,14	0,09	0,15	0,07
Fe_2O_3	0,15	0,11	0,09	0,10	0,10	0,17	0,12
NiO	0,20	0,01	0,01	0,12	0,03	0,00	0,01
Others	<0,10	<0,10	<0,10	<1,00	<0,50	<0,50	<0,50
SiO_2/Al_2O_3	1,26	1,23	1,22	1,48	3,25	----	----

Cordierite Synthesis

The XRD diffractograms performed on ceramics prepared from the optimized starting mixture are reported in Figure 1. At 1100°C, several phases are identified such as sapphirine (00-011-0607), quartzβ (01-089-8946), spinel (01-086-0084), and clionenstatite (01-084-0652). At 1150°C, only sapphirine and cordierite persist with a ratio of 75%:25%. At 1200°C, we detect the appearance of a reflection at 10.60° which may be related to cordierite (96-900-5806), with many reflections that may be related to sapphirine (00-021-0549). At 1250°C, the majority of the reflections can be attributed to cordierite (00-009-0326), or indialite (01-082-1884), with some reflections that reveal the presence of sapphirine (01-071-2398), and the mass ratio becomes 90% :10% respectively. At 1275°C, only cordierite (01-089-1485) is identifiable whereas sapphirine has certainly completely disappeared in favor of cordierite, the presence of cristobalite (01-082-1410) (<1%) is noted. Beyond this temperature, cordierite becomes predominant, but at 1400°C, we notice the presence of a significant glass phase, certainly due to the presence of fluxing elements that are always present in the kaolin.

Simultaneous thermal analysis (DSC-TGA) of the optimized starting mixture shows that dehydroxylization of HMP occurs around 376°C, and that of halloysite around 512°C yielding MgO and $Al_2Si_2O_7$ (metakaolin) respectively (Figure 2). The formation of an exothermic peak at 932°C confirms the interaction between Magnesium oxyde and metakaolin to form new phases like cordierite, sapphirine ($Mg_6Al_6.5Si_1.5O_{20}$), and clinoenstatite ($MgSiO_3$). A second exothermic peak occurs around 1200°C which translates the crystallization of orthorhombic cordierite from the other phases, in accordance with the XRD analysis (Figure 1).

The thermodidimensional analysis of the pressed starting mixture shows many linear shrinkages, (1) of 400-800°C due to dehydroxilation of halloysite, (2) of 800-1000°C accompanying chemical reactions of new compounds, and (3) of 1000-1150°C probably to sintering of these phases (Figure 3). A swelling is remarkable from 1150°C to 1300°C, this thermodidimensional feature can be attributed to the crystallization of cordierite from phases such as sapphirine, and clinoenstatite. These crystalline phases have higher densities (>3g.cm^{-3}) than that of cordierite (2.52g.cm^{-3}), their transformation certainly leads to the increase in the volume of the ceramic. An unsuitable thermal cycle can lead to microcracking in ceramics.

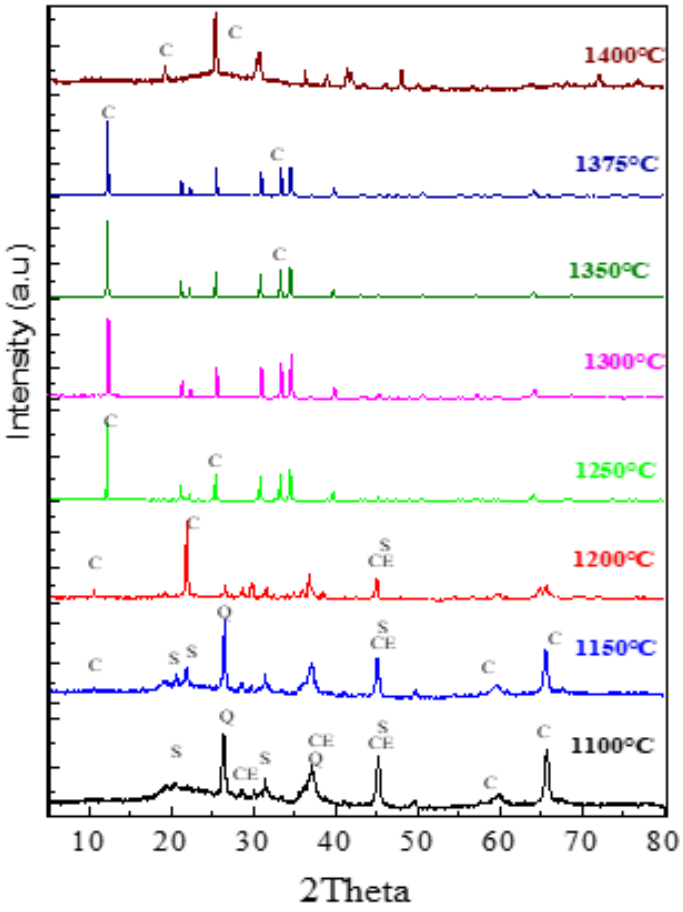


Figure 1. XRD patterns of calcined starting mixture at different temperature
(c) cordierite, (CE) clinoenstatite, (S) sapphirine, (Q) quartz,

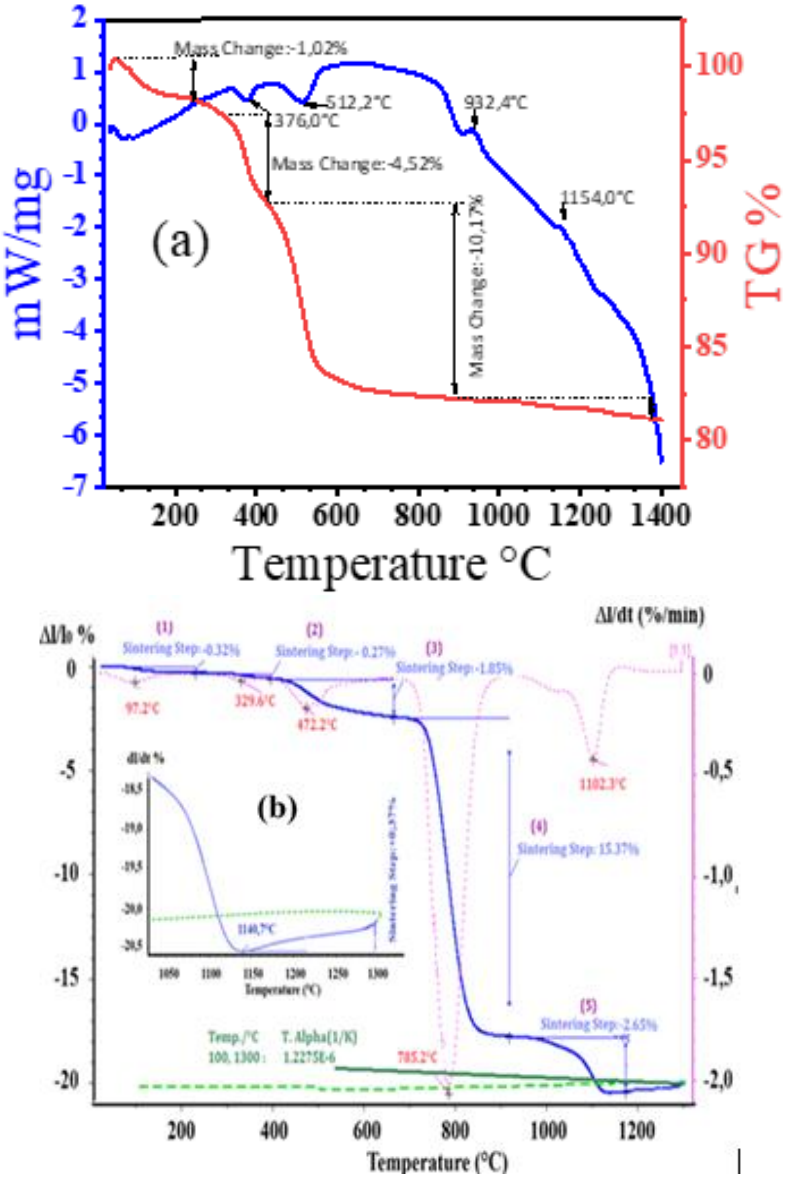


Figure 2. (a) DSC-ATG, and (b) Thermo-dimensional analysis of starting mixture

Sintering

The densification results of the starting mixture and of calcined cordierite powder are presented in figures 3. In the first case, at 1100°C densities (dap, dsp) higher than the theoretical density of cordierite (2.52g/cm3) are observed, this result confirms the results of the DRX analysis (Figure 1). The ceramic is composed mainly of sapphirine, spinel, and clinoenstatite which have higher densities. From 1200 to 1350°C, the bulk density decreases more significantly than the specific density which remains unchanged (~2.50g/cm3), this is the temperature range of cordierite crystallization. From 1400°C, the two densities decrease strongly, and the water absorption increases strongly, and 1425°C dap < 2.00g/cm^3. certainly because of the increase in porosity, and the formation of vitreous phases.

In the case of calcined powder of cordierite (indirect sintering), the bulk density increases with temperature, it reaches a maximum value of 2.35g/cm^3 at 1425°C, with 5% water absorption. While the specific density which is that of prepared cordierite decreases slightly with temperature, certainly because of the glassy phases of impurities.

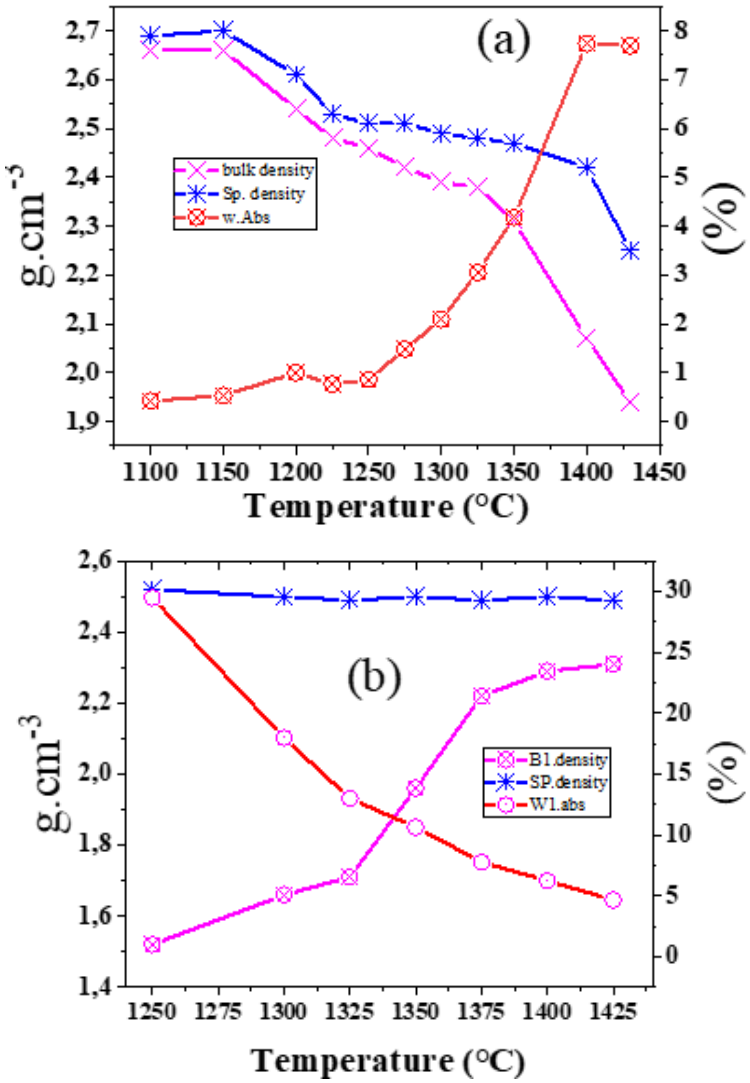


Figure 3. Physical properties of ceramic as a function of sintering temperature
(a) Direct sintering (b) Indirect sintering

Dilatometric Curves of Cordierite

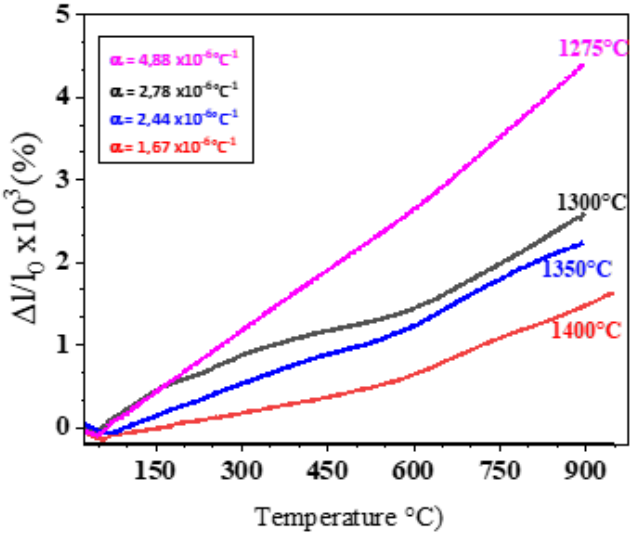


Figure 4. Dilatometric curves of cordierite sintered at different temperatures

Figure 4 shows the expansion curves of sintered cordierite ceramics at increasing temperatures. It is remarkable that the coefficient of linear expansion (TEC) decreases significantly with the increase in sintering temperature. This result seems to confirm that the maturation of cordierite always occurs at a temperature close to fusion of cordierite (~1450°C), (Chowdhury et al., 2007a, 2007b).

Dielectric Properties

The results of dielectric characterizations are reported in Figure 5. The same behaviour is observed in both cases of ceramics prepared by direct sintering (Figure 5a) and those prepared by indirect sintering (Figure 5b). The dielectric constants (ε_r) vary little significantly over a wide frequency interval, while the dielectric losses ($tg\delta$) decrease markedly with frequency. The values of ε_r and $tg\delta$ are consistent with the values of industrial cordierite ceramics 5 and 0,025 at 1MHz respectively.

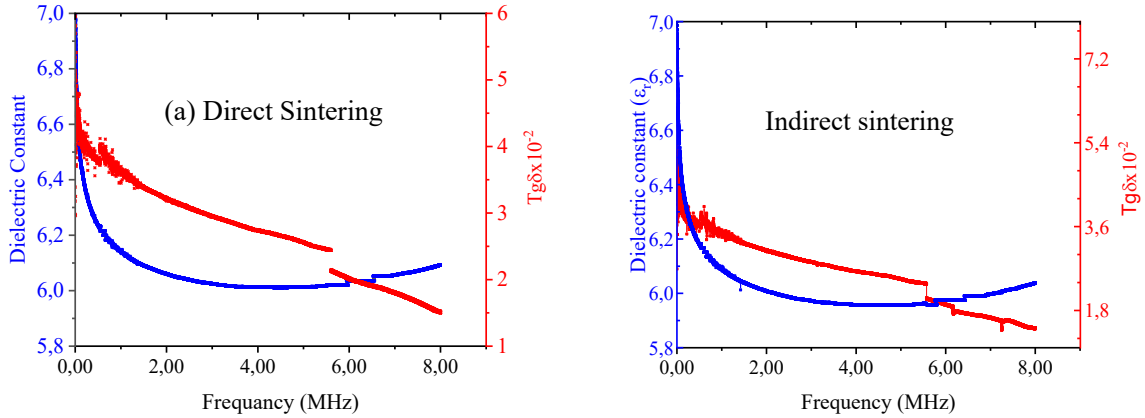


Figure 5. Dielectric constants and losses as a function of frequency (a) direct sintering, (b) indirect sintering

Microstructure

The microstructural observations of sintered ceramics at 1430°C show, in the case of direct sintering (Figure.6a,b), a greater presence of pores than in the case of indirect sintering (Figure.5d,e). In both cases, the vitreous phase is clearly apparent.

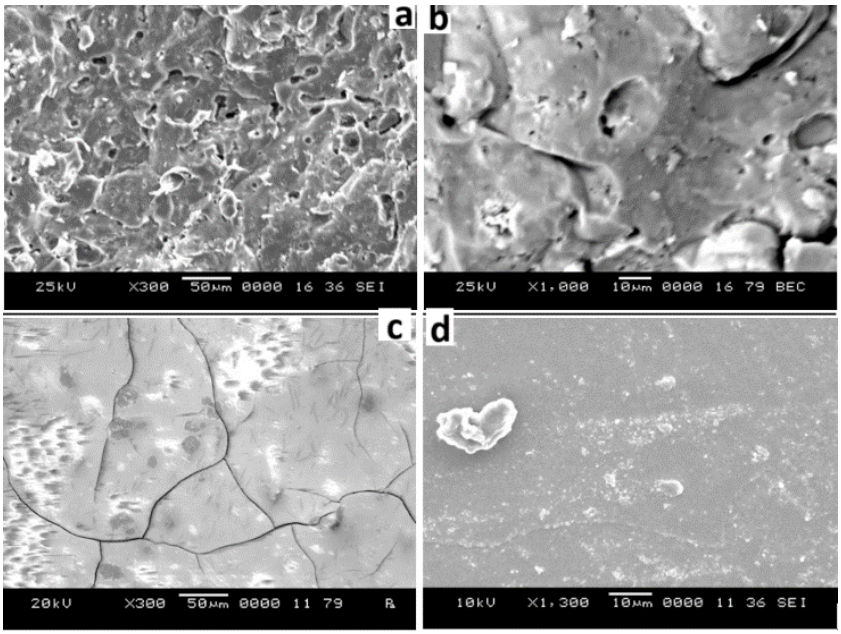


Figure 6. Microstructures of sintered ceramics at 1430°C
(a,b) direct sintering, (c,d) indirect sintering

Table 2 summarizes the physical and dielectric properties of sintered ceramics at 1430°C, obtained according to both methods. It is noted that the reaction sintering method does not allow obtaining highly dense ceramics due to the presence of melting elements contained in the kaolin, whereas the calcined powder sintering method allows for increasing the density of the ceramics to 2,38g.cm^{-3}, which is equivalent to a densification rate of ~95%.

Table 2: Comparison of the ceramic properties of the 2 methods

Properties	Starting mixture Direct sintering	Calcined mixture Indirect sintering
Sintering temperature (°C)	1430	1430
Bulk density (g/cm^3)	2,00	2,38
Specific density	2,15	2,50
Water absorption	2,28	5,37
Open porosity	4,92	11,46
Thermal expansion coefficient (TEC) x10^{-6}°C^{-1} (RT to 1000°C)	1,67	1,72
Dielectric constant (1MHz)	6,06	6,09
Loss tangent (1MHz)	0,032	0,034
Dielectric constant (8MHz)	6,09	6,04
Loss tangent (8MHz	0,025	0,020

Conclusion

This study allowed the synthesis of stoichiometric cordierite from a single kaolin that is chemically modified by controlled acid leaching. The optimal conditions of leaching with HCl (6M), a temperature of 70°C, and a duration of 120 minutes allowed to modify the SiO_2/Al_2O_3 ratio and thus succeed in a stoichiometric mixture of cordierite, by adding precipitated magnesium hydroxide.

The study of thermal transformations of the starting mixture reveals the appearance of several phases, such as sapphirine and enstatite, before cordierite became predominant at 1250°C. These intermediate phases have higher densities than that of cordierite, and consequently their transformations in the cordierite phase are accompanied by swelling, which generally causes cracks in the ceramic.

The comparison of the physical properties of ceramics sintered from the starting mixture (direct sintering) and from cordierite powder pre-calcined at 1250°C (indirect sintering) shows that in the case of direct sintering, densification cannot reach that of theoretical cordierite (d_{th}) due to the formation of glass phases. In the case of indirect sintering, densification approaches d_{th} and reaches 94% at 1430°C.

Scientific Ethics Declaration

* The authors declare that the scientific ethical and legal responsibility of this article published in EPSTEM journal belongs to the authors.

Conflict of Interest

* The authors declare that they have no conflicts of interest

Funding

* This research received no specific grant from any funding agency in the public, commercial, or not-for-profit sectors.

Acknowledgements or Notes

* This article was presented as an oral presentation at the International Conference on Technology, Engineering and Science (www.icontes.net) held in Antalya/Türkiye on November 12-15, 2025.

References

Al-Harahsheh, M., Abo Olaem, N., Tahat, O., & Altarawneh, M. N. (2023). Pressure leaching of aluminum from kaolin by HCl: Experimental and DFT study. *Hydrometallurgy, 221*, 106122.

American Society for Testing and Materials. (1969). *ASTM Specification C373: Part 13*.

Bejjaoui, R., Benhammou, A., Nibou, L., Tanouti, B., Bonnet, J. P., Yaacoubi, A., & Ammar, A. (2010). Synthesis and characterization of cordierite ceramic from Moroccan stevensite and andalusite. *Applied Clay Science, 49*, 336–340.

Boulmokh, A., Berredjem, K., Guerfi, A., & Gheid, A. E. K. (2007). Kaolin from Djebel Debbagh Mine. Guelma, Algeria. *Research Journal of Applied Sciences, 2*, 435–440.

Boutaleb, M., Tabit, K., Mansori, M., Saadi, L., & Waqif, M. (2024). Synthesis of low-cost refractory cordierite for solar thermal storage: Characterization of mechanical, thermal and physical stability during thermal shock cycles. *Journal of Energy Storage, 101*(Part B), 11389.

Camerucci, M. A., Urretavizcaya, G., & Cavalieri, A. L. (2003). Sintering of cordierite based materials. *Ceramics International, 29*, 159–168.

Cao, L., Wang, Y., Yu, X., Lu, Z., Wang, G., Mao, M., Liu, B., Cao, L., Bafrooei, H. B., Spreitzer, M., Wang, D., & Song, K. (2025). Significantly enhanced microwave-millimeterwave properties of cordierite ceramics: Roundness regulation of Si-Al hexagonal ring, analysis of far-infrared reflectance and terahertz time-domain spectroscopy. *Journal of the European Ceramic Society, 45*(3), 117045.

CARMA. (1999). *Les céramiques industrielles: Applications industrielles et développements potentiels dans les Alpes-Maritimes*.

Cheraitia, A., Redjimi, Z., & Bououdina, M. (2020). Novel mullite-cordierite ceramic refractory fabricated from halloysite and talc. *Applied Ceramic Technology*.

Chowdhury, A., Maitra, S., Das, H. S., Sen, A., Samanta, G. K., & Datta, P. (2007a). Synthesis, properties and applications of cordierite ceramics, Part 1. *Interceram: International Ceramic Review, 56*, 18–22.

Chowdhury, A., Maitra, S., Das, H. S., Sen, A., Samanta, G. K., & Datta, P. (2007b). Synthesis, properties and applications of cordierite ceramics, Part 2. *Interceram: International Ceramic Review, 56*, 98–102.

Debbakh, S., & Boumchedda, K. (2020). Development and characterization of cellular ceramic bricks using Algerian kaolin. *AIMS Materials Science, 4*, 431–440.

Deng, Y., Lao, X., Xu, X., Mao, Z., Zhao, Y., & Li, Y. (2024). A cost-effective way to utilize low-grade Ti-rich clay: Preparing cordierite-mullite composite ceramics for thermal storage. *Ceramics International, 50*(20, Part B), 39059–39068.

Edama, N. A., Sulaiman, A., Hamid, K. H. K., Rodhi, M. N. M., Musa, M., & Rahim, S. N. A. (2014). The effect of hydrochloric acid on the surface area, morphology and physico-chemical properties of Sayong kaolinite clay. *Key Engineering Materials, 594–595*, 49–56.

Goren, R., Gocmez, H., & Ozgur, C. (2006). Synthesis of cordierite powder from talc, diatomite and alumina. *Ceramics International, 32*, 407–409.

Idbenjadi, F. Z., Benhammou, A., Abourriche, A., & Abouliatim, Y. (2024). Effect of sintering temperature on the thermal and mechanical properties of cordierite-based refractory. *Materials Today: Proceedings*.

Khattab, R. M., Abo-Almaged, H. H., Ajiba, N. A., Badr, H. A., Gaber, A. A., Taha, M. A., & Sadek, H. E. H. (2021). Sintering, physicomechanical, thermal expansion and microstructure properties of cordierite ceramics based on utilizing silica fume waste. *Materials Chemistry and Physics, 270*, 124829.

Kobayashi, Y., Sumi, K., & Kato, E. (2000). Preparation of dense cordierite ceramics from magnesium compounds and kaolinite without additives. *Ceramics International, 26*, 739–743.

Lee, J.-S., Kim, J.-W., Park, J.-S., Lee, M.-H., & Lee, H. (2025). The effect of the MgO/Al2O3 ratio on the thermal and refractory behaviors of cordierite ceramics. *Materials, 18*(1), 168.

Ogiwara, T., Noda, Y., Shoji, K., & Kimura, O. (2010). Solid state synthesis and its characterization of high density cordierite ceramics using fine oxide powders. *Journal of the Ceramic Society of Japan, 118*(3), 246–249.

Ogiwara, T., Noda, Y., Shoji, K., & Kimura, O. (2011). Low temperature sintering of μ-cordierite ceramics with low thermal expansion using Li2O–Bi2O3 as a sintering additive. *Journal of the Ceramic Society of Japan, 119*(9), 706–709.

Peng, H., Qi, T., Vogrin, J., Huang, Q., Wu, W., & Vaughan, J. (2021). The effect of leaching temperature on kaolinite and meta-kaolin dissolution and zeolite re-precipitation. *Minerals Engineering, 170*, 107071.

Ponomarev, S. G., Reznichenko, A. V., Kormilitsyn, M. N., & Kornyushin, M. V. (2023). Cordierite material with increased heat resistance. *Refractories and Industrial Ceramics, 64*, 311–317.

Redaoui, D., Sahnoune, F., Heraiz, M., & Saheb, N. (2018). Phase formation and crystallization kinetics in cordierite ceramics prepared from kaolinite and magnesia. *Ceramics International, 44*, 3649–3657.

Senoussi, H., Osmani, H., Courtois, C., & Bourahli, M. E. H. (2016). Mineralogical and chemical characterization of DD3 kaolin from the east of Algeria. *Boletín de la Sociedad Española de Cerámica y Vidrio, 55*(3), 121–126.

Sittiakkaranon, S., & Phonphuak, N. (2023). Microstructural and physical characterization of cordierite-mullite ceramics refractories. *International Journal of Geomate, 25*(108), 233–240.

Synkiewicz-Musialska, B., Szwagierczak, D., Kulawik, J., Pałka, N., & Piasecki, P. (2021). Structural, thermal and dielectric properties of low dielectric permittivity cordierite-mullite-glass substrates at terahertz frequencies. *Materials, 14*(14), 4030.

Tekin, C., Ercenk, E., Yılmaz, Ş., & Demirkıran, A. Ş. (2022). Characterization of cordierite based h-BN doped ceramics as an electronic substrate/circuit board material. *Applied Ceramic Technology*.

Wang, R., Liu, D., Xu, K., Wang, Z., Wu, H., Zhou, X., Tian, H., & Shan, L. (2025). Ultra-low εr and low dielectric loss (Mg1−xMnx)2Al4Si5O18 (x=0.1–0.5) microwave dielectric ceramics for patch antenna and dielectric resonator antenna applications. *Ceramics International*.

White, R. D., Bavykin, D. V., & Walsh, F. C. (2012). The stability of halloysite nanotubes in acidic and alkaline aqueous suspensions. *Nanotechnology, 23*(6), 065705.

Yan, G., Chen, L., Jiang, Q., Zhang, L., Wang, J., Yang, Y., Li, Z., & Feng, J. (2024). Thermal/mechanical properties of cordierite synthesized using coal gangue as a refractory material. *Applied Ceramic Technology*.

Zhang, F., Qi, C.-X., Wang, S., Liu, J.-H., & Cao, H. (2011). A study on preparation of cordierite gradient pores porous ceramics from rectorite. *Solid State Sciences, 13*, 929–933.

Zhou, J., Dong, Y., Hampshire, S., & Meng, G. (2011). Utilization of sepiolite in the synthesis of porous cordierite ceramics. *Applied Clay Science, 52*, 328–332.

Author(s) Information

Boumchedda Khaled
University of Boumerdes (University of M'Hamed Bougara Boumerdes), Algeria
Contact e-mail : *k.boumchedda@univ-boumerdes.dz*

Djafar Rabah
University of Boumerdes (University of M'Hamed Bougara Boumerdes), Algeria

Rabehi Bahia
University of Boumerdes (University of M'Hamed Bougara Boumerdes), Algeria

Bououdina Mohamed
Prince Sultan University, Department of Mathematics and Science, Saudi Arabia

To cite this article:

Khaled, B., Rabah, D., Bahia, R., & Mohamed, B. (2025). Synthesis of stoichiometric cordierite ceramics from chemically modified kaolin by a controlled acid leaching. *The Eurasia Proceedings of Science, Technology, Engineering and Mathematics (EPSTEM), 38,* 502-511.

The Eurasia Proceedings of Science, Technology, Engineering & Mathematics (EPSTEM)
ISSN: 2602-3199

The Eurasia Proceedings of Science, Technology, Engineering and Mathematics (EPSTEM), 2025

Volume 38, Pages 512-524

IConTES 2025: International Conference on Technology, Engineering and Science

AI-Driven Molecular Design: Synergizing Deep Generative Models with Evolutionary Optimization

Abbad Houda
Djillali Liabes University of Sidi Bel Abbes

Taieb Brahim Mohammed
Djillali Liabes University of Sidi Bel Abbes

Oulladji Latefa
Djillali Liabes University of Sidi Bel Abbes

Abbad Leila
ENSTA High School

Abstract: Artificial intelligence (AI) is reshaping drug discovery by enabling efficient and precise identification of novel therapeutics. This review examines the synergistic use of deep generative models, such as Long Short-Term Memory (LSTM) networks, Variational Autoencoders (VAEs), and Graph Attention Networks (GATs), together with evolutionary optimization techniques, including genetic algorithms and multi-objective evolutionary strategies. While deep learning architectures excel at capturing complex molecular representations and generating chemically valid compounds, evolutionary algorithms provide complementary strengths in global exploration and multi-objective trade-off optimization. The combination of these two paradigms offers a powerful and complementary toolkit: deep learning provides the capacity to learn rich chemical features and propose innovative scaffolds, whereas evolutionary methods ensure efficient navigation of chemical space and balanced optimization across multiple drug-like criteria. Through comparative analyses, quantitative benchmarks, and illustrative figures, we highlight how integrating generative and evolutionary paradigms can accelerate de novo molecular design, reduce development timelines, and lower costs. We also address technical and ethical challenges. In particular, our ongoing research explores hybrid frameworks that combine variational autoencoders, graph neural predictors, Colibri algorithm and Genetic algorithms with fragment-based crossover, and dynamic multi-objective penalties to further enhance chemical validity, pharmacological relevance, and synthetic accessibility. Future efforts aim to demonstrate that such hybrid frameworks can bridge the gap between theoretical innovation and practical drug development, bringing AI-driven discovery closer to real-world therapeutic breakthroughs.

Keywords: Drug discovery, Molecule design, Deep generative models, Evolutionary algorithms, Multi-objective optimization.

Introduction

Drug discovery is a cornerstone of biomedical innovation but remains an extremely costly and time-consuming endeavor, often requiring over a decade and billions of dollars to bring a single drug to market (DiMasi, Grabowski, & Hansen, 2016). Despite advances in computational chemistry and high-throughput screening, attrition rates in clinical trials remain high due to issues of efficacy, toxicity, and poor pharmacokinetics (Paul et al., 2010). These challenges underscore the urgent need for more efficient strategies capable of exploring the

- This is an Open Access article distributed under the terms of the Creative Commons Attribution-Noncommercial 4.0 Unported License, permitting all non-commercial use, distribution, and reproduction in any medium, provided the original work is properly cited.

- Selection and peer-review under responsibility of the Organizing Committee of the Conference

© 2025 Published by ISRES Publishing: www.isres.org

vast chemical space, estimated to contain up to 10^{60} drug-like molecules, while simultaneously optimizing multiple therapeutic objectives (Polishchuk, Madzhidov, & Varnek, 2013).

Conventional in silico approaches, such as docking and quantitative structure–activity relationship (QSAR) models, provide valuable predictive tools but often suffer from limited generalizability, high dependence on prior knowledge, and poor scalability when faced with unprecedented chemical scaffolds (Schneider et al., 2020). Similarly, in vitro assays, although indispensable for experimental validation, are labor-intensive, expensive, and inherently sequential, restricting their ability to explore chemical diversity at scale (Vamathevan et al., 2019). The fragmentation between computational predictions and experimental testing continues to delay the discovery of effective therapeutics, highlighting the need for integrated frameworks that are both exploratory and optimization-oriented.

Recent progress in artificial intelligence (AI) has introduced generative models, such as variational autoencoders (VAEs), generative adversarial networks (GANs), and graph neural networks (GNNs), which can learn complex molecular distributions and design novel compounds with promising drug-like properties (Zhavoronkov et al., 2019; Blaschke et al., 2020). These models excel in capturing latent chemical features and generating structurally valid molecules, but often struggle with balancing multiple objectives, such as potency, selectivity, and synthetic accessibility. Evolutionary algorithms (EAs), by contrast, are particularly effective at global exploration and multi-objective optimization, using mechanisms like mutation, crossover, and selection to iteratively refine candidate solutions (Brown et al., 2019). Integrating deep generative models with EAs offers a synergistic paradigm: the former drives innovation by proposing diverse molecular scaffolds, while the latter ensures efficient navigation of chemical space and optimization across competing therapeutic criteria (Nigam et al., 2022). This hybridization promises not only to accelerate de novo molecular design but also to reduce attrition rates and shorten development timelines, ultimately transforming AI-driven drug discovery.

The remainder of this paper is organized as follows. Section 2 provides an overview of deep generative models for molecular design, including recurrent neural networks, variational auto-encoders, generative adversarial networks, and graph-based models, highlighting their respective strengths and limitations. Section 3 discusses evolutionary optimization methods, with an emphasis on genetic algorithms, multi-objective strategies, and chemically valid genetic operators tailored to drug discovery. Section 4 explores the synergy between generative models and evolutionary algorithms, presenting hybrid frameworks, case studies, and benchmark comparisons, as well as illustrative workflows. Section 5 outlines future research directions, focusing on dynamic multi-objective penalties, integration with reinforcement learning, and the development of fully automated, closed-loop drug discovery pipelines. In addition, Section 6 highlights our contributions to AI-Driven drug discovery with novel methodological innovations. Finally, Section 7 concludes the paper with a synthesis of key insights and perspectives on the role of hybrid generative–evolutionary paradigms in accelerating AI-driven molecular design.

Deep Generative Models for Molecular Design

The emergence of deep generative models has profoundly transformed de novo molecular design, enabling the automated generation of structurally valid and pharmacologically relevant compounds (Table. 1). By learning latent representations of chemical space, these models provide scalable frameworks to design molecules with desired physicochemical, biological, and pharmacokinetic properties. The following subsections review the most prominent generative architectures employed in molecular design.

Recurrent Neural Networks (RNNs, LSTM, GRU)

Recurrent neural networks (RNNs) and their gated variants: Long Short-Term Memory (LSTM) and Gated Recurrent Units (GRU), have been widely adopted for sequence-based molecular generation, typically using SMILES (Simplified Molecular Input Line Entry System) representations (Olivecrona et al., 2017). These models leverage sequential dependencies to learn syntax and semantics of chemical strings, ensuring the generation of syntactically valid SMILES. LSTMs are particularly effective at capturing long-range dependencies, reducing the risk of invalid outputs, while GRUs provide computational efficiency without significantly compromising accuracy (Gupta et al., 2018). However, SMILES-based models remain sensitive to syntax errors, and their reliance on a single linear representation of molecules can limit structural diversity.

Variational Autoencoders (VAEs)

Variational autoencoders (VAEs) introduced probabilistic latent representations into molecular design, enabling interpolation and continuous optimization in chemical space (Kingma & Welling, 2014). In this framework, molecules are encoded into a latent vector space and decoded back into valid molecular structures, which facilitates property-driven optimization via gradient-based methods (Gómez-Bombarelli et al., 2018). VAEs can also incorporate chemical constraints and multi-objective loss functions to balance validity, novelty, and synthetic accessibility (Jin et al., 2018). Nevertheless, VAEs often suffer from posterior collapse and low reconstruction fidelity, particularly for complex molecular graphs, which has motivated hybridization with graph neural networks and reinforcement learning strategies (Winter et al., 2019).

Generative Adversarial Networks (GANs)

Generative adversarial networks (GANs) employ a competitive setup between a generator, which proposes candidate molecules, and a discriminator, which distinguishes between real and generated samples (Goodfellow et al., 2014). In molecular design, GANs have demonstrated strong potential for producing chemically diverse scaffolds while aligning outputs with drug-like distributions (Kadurin et al., 2017). Advanced implementations, such as ORGAN (Objective-Reinforced GAN), integrate reinforcement learning to steer generation toward molecules with optimized bioactivity (Guimaraes et al., 2017). Despite their promise, GANs remain difficult to train due to instability, mode collapse, and the challenge of ensuring strict chemical validity.

Graph Neural Networks (GNNs, GATs)

Graph neural networks (GNNs) represent molecules as graphs, where atoms correspond to nodes and bonds to edges, allowing direct learning from molecular topology (Gilmer et al., 2017). Variants such as Graph Convolutional Networks (GCNs) and Graph Attention Networks (GATs) enhance molecular representation by capturing both local and global structural dependencies (Velickovic et al., 2018). Recent advances in graph-based generative models, such as GraphVAE and GraphAF, enable the direct generation of molecular graphs, bypassing SMILES limitations (You et al., 2018; Shi et al., 2020). These models demonstrate superior performance in terms of validity, novelty, and scaffold diversity. However, challenges remain in balancing efficiency with expressiveness, as graph-based generation is computationally intensive and requires sophisticated decoding strategies.

Figure 1 summarizes the major classes of deep generative models applied in de novo molecular design. Each architecture provides a distinct strategy for navigating chemical space and balancing structural validity, novelty, and property optimization.

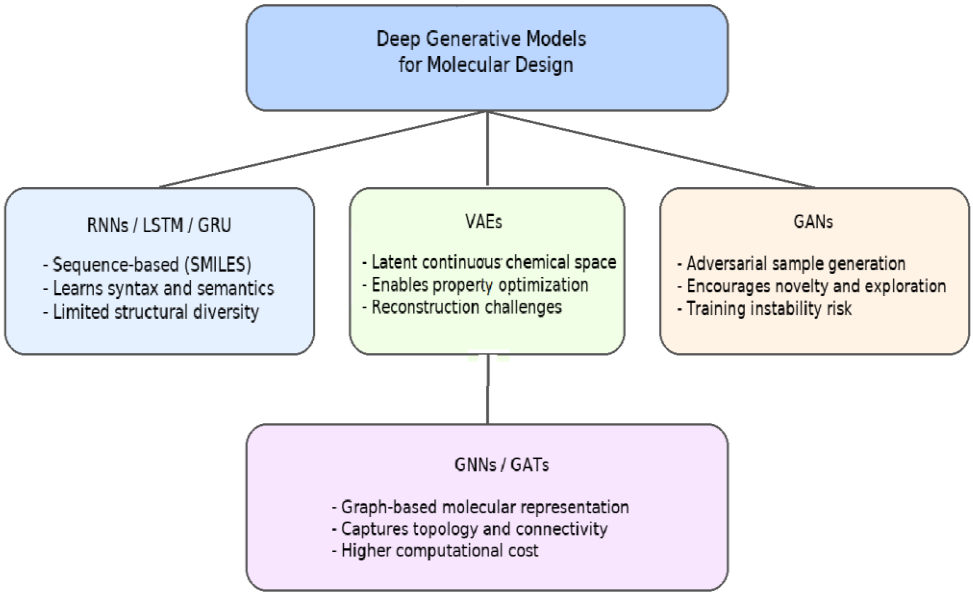


Figure 1. Overview of deep generative architectures for molecular design

Strengths and Limitations of Generative Models

Generative models collectively provide a paradigm shift in drug discovery by automating scaffold innovation, accelerating chemical exploration, and supporting multi-property optimization (see Table 1). RNNs are simple and efficient but constrained by SMILES syntax. VAEs enable smooth latent-space optimization but struggle with reconstruction fidelity. GANs encourage diversity and novelty but suffer from instability and mode collapse. GNNs and GATs provide chemically faithful graph-based generation but demand high computational resources and complex training strategies. In practice, these strengths and limitations suggest that no single generative model is universally optimal. Instead, hybrid frameworks, combining sequence-based, probabilistic, adversarial, and graph-based strategies, are increasingly recognized as essential for robust de novo molecular design (Brown et al., 2019; Zhavoronkov et al., 2019).

Table 1. Comparative overview of generative models

Generative Model	RNNs (LSTM/GR)	VAEs	GANs	GNN-based Models
Key References	Gupta et al. (2018); Olivecrona et al. (2017)	Kingma & Welling (2014); Gómez-Bombarelli et al. (2018)	Goodfellow et al. (2014); Guimaraes et al. (2017)	Gilmer et al. (2017); Jin et al. (2018)
Representation	Sequential SMILES	Latent space (SMILES/graphs)	SMILES or latent embeddings	Graphs (atoms & bonds)
Strengths	Simple; RL-friendly	Smooth latent space; interpolation	Models complex distributions; reinforcement integration	Captures chemical validity; strong for property prediction
Limitations	Sensitive to SMILES syntax; limited space coverage	Invalid molecules; limited diversity	Training instability; mode collapse	Computationally expensive
Implementations	REINVENT; DeepChem modules	ChemicalVAE; MolecularRNN-VAE	ORGAN; MoleculeGAN; druGAN	JT-VAE; GraphVAE; MolGAN; GCPN

Evolutionary Optimization in Drug Discovery

Evolutionary optimization encompasses a family of population-based metaheuristic methods inspired by natural evolution (mutation, recombination, selection) (Deb et al., 2002a). In molecular design, these methods are used both as standalone search engines and as complementing modules to deep generative models, enabling explicit optimization of multiple competing objectives (e.g., potency, selectivity, ADMET, synthetic accessibility) while preserving structural diversity and interpretability (Schneider, 2018; Zhong et al., 2019). Recent advances have integrated graph-based representations, fragment-level operators, and efficient multi-objective schemes to make evolutionary approaches increasingly practical for de novo drug design (Polishchuk et al., 2013; Nigam et al., 2022; Deb et al., 2002b).

Principles of Genetic Algorithms

Genetic algorithms (GAs) are among the most widely applied evolutionary methods in computational chemistry. A typical GA for molecular design maintains a population of candidate molecules that are iteratively evolved using operators that mimic biological evolution: selection (based on a fitness function), crossover (recombination of parental substructures), and mutation (random local changes) (Mitchell, 1998; Holland, 1992). The fitness function can be single-objective (e.g., predicted binding affinity) or compositional (weighted combination of multiple properties). Key algorithmic choices include representation (SMILES, graph, fragment-based encoding), the encoding of genotype-to-phenotype mappings, population sizing, and selection pressure (Schneider, 2018). Representations that embed chemical knowledge (e.g., fragment- or graph-based encodings) reduce the generation of chemically invalid offspring and speed convergence (Polishchuk et al., 2013). Practical GA pipelines often use surrogate predictors (ML models) to evaluate fitness cheaply, interleaving costly physics-based or experimental evaluations only for top candidates (Jin et al., 2020; Zhou et al., 2019).
Genetic algorithms encode molecules as chromosomes, commonly represented by SMILES strings, graphs, or molecular fingerprints, and evolve them toward improved fitness. Each candidate solution $x_i \in X$ is evaluated through a fitness function:

$$F(x_i)=\sum_{i=1..K}(w_k \times f_k(x_i))$$

where $f_k(x_i)$ represents the k-th molecular property (e.g., binding affinity, solubility, toxicity), and w_k denotes the weight assigned to this objective (Nigam et al., 2021). Selection, crossover, and mutation operators are applied iteratively until convergence. This makes GAs particularly suitable for navigating discontinuous, high-dimensional, and multi-modal chemical spaces (Brown et al., 2019).

To better illustrate the operational cycle of genetic algorithms in molecular design, Figure 2 presents a schematic workflow highlighting the main evolutionary steps. Starting from an initial population of candidate molecules encoded as SMILES strings or graph-based representations, the algorithm iteratively applies selection, crossover, and mutation operators to generate new offspring. A fitness evaluation module, often supported by surrogate machine learning models or physics-based simulations, guides the evolutionary search toward improved molecular properties such as binding affinity, solubility, or synthetic accessibility (Nigam et al., 2021; Jensen, 2019). The iterative nature of this workflow enables the progressive refinement of molecular candidates while preserving chemical diversity and avoiding premature convergence (Zhavoronkov et al., 2019).

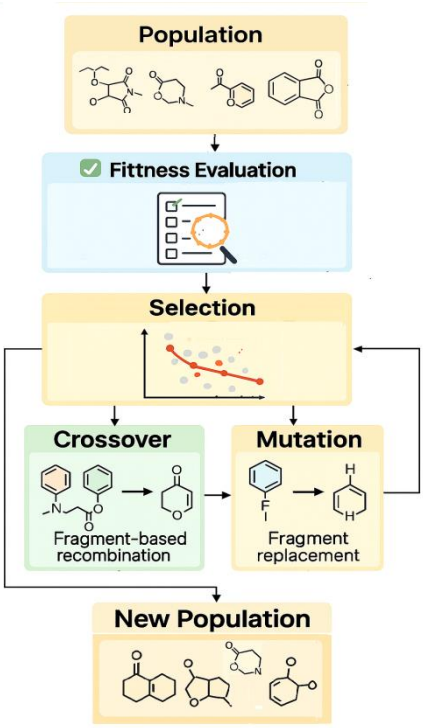


Figure 2. Workflow of a genetic algorithm in de novo molecular design

Multi-objective Evolutionary Strategies

Drug discovery is inherently a multi-objective optimization problem, where candidate molecules must balance several often conflicting criteria, such as potency, selectivity, solubility, toxicity, and synthetic accessibility. Unlike single-objective optimization methods, multi-objective evolutionary algorithms (MOEAs) are particularly well-suited to this task because they do not aim to find a single best solution but rather approximate the Pareto front, a set of trade-off solutions where improving one objective would deteriorate at least one other (Deb et al., 2002; Zhang & Li, 2007).

Formally, the optimization problem can be expressed as:

$$Optimize\ F(x)=(f_1(x), f_2(x),\ldots, f_K(x))$$

subject to chemical validity constraints (e.g., valence rules, synthetic feasibility). Here, $f_k(x)$ represents the k^{th} molecular property of candidate solution x, and the goal is to evolve a population of molecules such that their fitness values collectively approximate the Pareto-optimal front (Nigam et al., 2021).

Among MOEAs, NSGA-II (Non-dominated Sorting Genetic Algorithm II) is the most widely applied in cheminformatics due to its simplicity, efficiency, and ability to preserve population diversity. It relies on non-dominated sorting to classify solutions into Pareto fronts and uses a crowding distance metric to ensure spread across the front. This makes NSGA-II particularly effective for drug design tasks such as optimizing potency against synthetic accessibility or ADMET properties (Stahl et al., 2022).

Table 2. Comparative overview of NSGA-II and MOEA/D in Multi-Objective Molecular Design

Criterion	NSGA-II	MOEA/D	References
Optimization paradigm	Non-dominated sorting with crowding-distance to rank and preserve Pareto diversity	Decomposition of multi-objective problem into scalar subproblems optimized cooperatively	Deb et al., 2002; Zhang & Li, 2007
Diversity preservation	Ensures diversity using crowding-distance and elitism	Maintains diversity through neighborhood relations in decomposed subproblems	Deb et al., 2002; Li & Zhang, 2009
Scalability	Effective for 2–3 objectives but performance degrades with higher dimensions	More scalable for many-objective problems due to decomposition strategy	Ishibuchi et al., 2016
Convergence	Strong convergence for low-dimensional objectives, sensitive to parameter tuning	Competitive convergence in high-dimensional settings; less sensitive to number of objectives	Zhang & Li, 2007; Ishibuchi et al., 2016
Computational complexity	$O(MN^2)$ per generation (M = objectives, N = population size)	O(NT) per generation (T = neighborhood size), often lower computational overhead	Deb et al., 2002; Zhang & Li, 2007
Applications in drug discovery	Used for optimizing potency vs. synthetic accessibility; effective in generating diverse candidate molecules	Applied to multi-objective molecular generation (e.g., ADMET balance); advantageous for complex property landscapes	Nigam et al., 2021; Gao et al., 2022
Limitations	May lose performance in high-dimensional spaces; crowding-distance can bias diversity	Requires careful decomposition strategy; neighborhood definition affects results	Deb et al., 2002; Zhang & Li, 2007; Ishibuchi et al., 2016

Alternatively, MOEA/D (Multi-Objective Evolutionary Algorithm based on Decomposition) decomposes a multi-objective problem into a set of scalar optimization subproblems, each optimized in parallel while sharing information with neighboring subproblems. This decomposition approach often provides improved scalability and convergence for high-dimensional objective spaces (Zhang & Li, 2007). Recent studies in molecular optimization suggest that MOEA/D variants can perform comparably, or even better, than NSGA-II in specific

bi-objective and tri-objective settings (Brown et al., 2019). Finally, recent adaptations of MOEAs in drug discovery incorporate dynamic penalty strategies to account for drug-likeness and synthetic accessibility, as well as graph-based molecular encodings to ensure the chemical validity of offspring during evolution (Zhavoronkov et al., 2019; Stahl et al., 2022). These improvements make evolutionary multi-objective optimization a powerful and increasingly practical tool for guiding de novo molecular design.

Although both NSGA-II and MOEA/D have demonstrated strong performance in molecular multi-objective optimization, they rely on fundamentally different paradigms, non-dominated sorting versus decomposition. Table 2 summarizes their comparative characteristics, offering insights into when each algorithm may be preferable in the context of drug discovery.

Fragment-Based and Crossover Operators in Chemical Space

To ensure the generation of chemically valid offspring during evolutionary optimization, crossover and mutation operators are frequently constrained by fragment-based recombination strategies (Brown et al., 2019). Unlike naive string-level manipulations of SMILES that can easily produce invalid structures, fragment-based approaches operate on chemically meaningful units, such as rings, linkers, or functional groups. For two parent molecules x_p and x_q, a fragment-based crossover operator C can be formally defined as:

$$x_{child} = C(x_p, x_q) = \text{merge}(\text{frag}(x_p), \text{frag}(x_q))$$

where frag(.) denotes the extraction of synthetically feasible substructures. This ensures that the recombination process preserves valence rules, avoids bond-breaking artifacts, and yields molecules that are more likely to be chemically stable and synthetically accessible (Polishchuk et al., 2013).

Mutation operators within this framework typically involve localized structural perturbations such as functional group substitutions, ring contractions or expansions, and stereochemical inversions. These operations allow the exploration of diverse regions of chemical space while maintaining molecular validity (Nigam et al., 2020). Importantly, chemically aware operators significantly reduce the occurrence of invalid SMILES strings, a major drawback in purely syntax-based generative approaches, and contribute to the design of molecules that are more readily synthesizable (Yoshimori et al., 2021; Segler et al., 2018).

In this way, fragment-based crossover and chemically guided mutation form a core component of evolutionary molecular design pipelines, balancing the trade-off between exploration of novel chemical scaffolds and exploitation of synthetically tractable structures.

GA Implementations in Drug Discovery

The application of genetic algorithms (GAs) in drug discovery has evolved significantly, moving from early SMILES-based encodings to sophisticated graph and latent space representations. Several notable implementations illustrate this progression, each addressing specific challenges in de novo molecular design.
MolEvol represents one of the earliest GA-based molecular design frameworks, relying on SMILES string encodings to explore chemical space (Brown et al., 2019). Its optimization objectives included binding affinity and drug-likeness quantified by the Quantitative Estimate of Drug-likeness (QED), while operators such as fragment-based crossover and mutations were employed to preserve chemical validity. Despite its simplicity, MolEvol demonstrated the feasibility of evolutionary search in chemical space.

In contrast, JANUS introduced a graph-based encoding scheme that enabled a more chemically intuitive representation of molecules (Nigam et al., 2021). By incorporating adaptive crossover and mutation strategies, JANUS efficiently balanced multiple objectives such as potency, solubility, and toxicity. This multi-objective optimization framework addressed the inherent trade-offs in drug design, showcasing the power of GAs in multi-criteria decision-making.

MolGA further refined graph-based representations by implementing graph crossover and edge mutation operators tailored to molecular structures (Zhou et al., 2019). This design ensured that generated molecules adhered to chemical validity constraints while maintaining high diversity. MolGA's emphasis on synthesizability and drug-likeness marked an important step toward practical drug discovery applications.

The integration of genetic algorithms with deep generative models is exemplified by DEFactor, which leveraged latent space embeddings as an encoding scheme (Assouel et al., 2018). In this approach, crossover operations were performed in the learned latent space, enabling smooth exploration of molecular manifolds. This hybridization of GAs with deep learning allowed optimization based on docking scores and QED, bridging symbolic evolutionary search with representation learning.

Finally, Hybrid GA-ML approaches combined graph embeddings with machine learning predictors to optimize pharmacokinetic and toxicological endpoints (Stahl et al., 2022). By reinforcing crossover and guiding mutations with predictive models, these methods reduced the computational cost associated with expensive molecular evaluations such as docking or quantum chemistry. Such hybrid frameworks exemplify the shift toward efficiency-driven GA implementations in modern drug discovery pipelines.

Overall, these implementations highlight the adaptability of genetic algorithms to various molecular representations and optimization objectives. From string-based encodings to latent space manipulations, GAs continue to provide a versatile search paradigm for balancing the competing objectives of potency, safety, and synthesizability in drug discovery.

Limitations and Challenges

Although evolutionary methods bring transparency and multi-objective capability, they face several challenges in practice:

- **Computational Cost**: Populations and many generations require large numbers of fitness evaluations; expensive physics-based or experimental scoring limits throughput. Surrogate models and active sampling have been proposed to mitigate this cost, but they introduce model-bias risks (Nigam et al., 2020; Stahl et al., 2022).
- **Validity vs. Novelty Trade-off**: Aggressive mutation and crossover increase novelty but often yield chemically invalid or synthetically infeasible molecules. Balancing exploration and exploitation is therefore nontrivial. Fragment-aware encodings and chemically valid operators help reduce invalid candidates but do not eliminate the problem entirely (Brown et al., 2019; Yoshimori et al., 2021).
- **Objective Modeling Errors**: Machine learning surrogates can misrank candidates, and noisy predictors may drive premature convergence toward artifacts. Robust uncertainty quantification and multi-fidelity evaluation pipelines are recommended (Vamathevan et al., 2019; Schneider et al., 2020).
- **Scalability to Many Objectives**: Many-objective optimization (>4–5 objectives) complicates Pareto selection and diversity maintenance. Specialized algorithms such as NSGA-II or decomposition-based methods like MOEA/D have been adapted to molecular discovery to address this issue (Deb et al., 2002; Zhang & Li, 2007; Ishibuchi et al., 2016).
- **Integration with Wet-Lab Workflows**: Translating evolutionary outputs into synthesizable, testable molecules requires retrosynthetic planning, procurement considerations, and assay translation areas where further automation and standardization are needed (Segler et al., 2018; Zhavoronkov et al., 2019).

Overall, evolutionary optimization remains a powerful and interpretable approach for multi-objective molecular design, particularly when combined with modern graph representations, fragment-aware operators, and surrogate models. The trend in recent literature is toward hybrid pipelines that combine the generative power of deep models with the explicit search and control offered by evolutionary algorithms, yielding pragmatic systems capable of producing chemically plausible, multi-objective-optimized candidates at scale (Gómez-Bombarelli et al., 2018; Nigam et al., 2021).

Synergizing Generative Models with Evolutionary Algorithms

Complementary Strengths of the Two Paradigms

Generative models and evolutionary algorithms (EAs) offer distinct yet complementary advantages for molecular design (refer to Table 3). Generative models, such as variational autoencoders (Kingma & Welling, 2014; Gómez-Bombarelli et al., 2018), generative adversarial networks (Goodfellow et al., 2014; Kadurin et al., 2017; Guimaraes et al., 2017), and reinforcement learning–based graph models (Olivecrona et al., 2017; You et al., 2018; Shi et al., 2020), excel at capturing the complex distribution of chemical space and generating novel

structures. However, these models may suffer from biases introduced by training data and may not directly optimize multiple drug-relevant objectives (Schneider, 2018; Zhong et al., 2019).

In contrast, evolutionary algorithms, particularly multi-objective methods such as NSGA-II (Deb et al., 2002) and MOEA/D (Zhang & Li, 2007), are inherently suited for balancing competing objectives like potency, solubility, and toxicity (Nigam et al., 2021). EAs provide explicit control over diversity maintenance and can incorporate chemically valid crossover and mutation operators (Yoshimori et al., 2021). By combining these paradigms, generative models can propose diverse and syntactically valid candidates, while EAs refine and optimize them in accordance with medicinal chemistry constraints. Table 3 highlights the complementarity of generative models and genetic algorithms:

Table 3: Comparative analysis of deep generative models vs. evolutionary algorithms in molecular design

Criterion	Deep Generative Models	Evolutionary Algorithms	Benchmark References
Validity	70–99% (SELFIES: >99.9%)	100% (fragment constraints)	Krenn et al. (2020); Segler et al. (2018)
Synthesizability (SA score ≤4)	15–40%	75–92%	Gao & Coley (2020); Nigam et al. (2019)
Novelty (Tanimoto <0.4)	80–95%	45–70%	Brown et al. (2019); You et al. (2018)
Multi-Objective Support	Limited by reward design	Native integration via fitness	Li et al. (2018); Steinmann & Jensen (2021)

Hybrid framework

Hybrid frameworks aim to leverage the expressive generation capabilities of deep models with the robust search and optimization of evolutionary algorithms. One common strategy is to embed molecules in continuous latent spaces learned by autoencoders or graph neural networks (Blaschke et al., 2020; Winter et al., 2019), where genetic operators such as crossover and mutation can be applied more smoothly (Assouel et al., 2018). Another approach integrates reinforcement learning–based generative models with EA-driven population management, ensuring balance between exploration and exploitation (Nigam et al., 2020; Stahl et al., 2022).

Such frameworks allow iterative interplay: generative models explore wide areas of chemical space, while evolutionary operators guide optimization toward Pareto-optimal sets with respect to pharmacokinetics, toxicity, and synthetic accessibility (Ishibuchi et al., 2016; Schneider et al., 2020). This synergy directly addresses the limitations of purely generative approaches, particularly in multi-objective settings where trade-offs are unavoidable.

Case Studies and Benchmarks

Several implementations exemplify the synergy between generative and evolutionary paradigms (refer to Figure 3) . The JANUS framework employs a parallel-tempered genetic algorithm guided by neural networks, enabling efficient multi-objective optimization of drug-like molecules (Nigam et al., 2021; Nigam et al., 2022). STONED, based on the SELFIES molecular representation, achieves rapid traversal and exploration of chemical space, demonstrating the effectiveness of EA-guided search without the need for large-scale training (Nigam, Pollice et al., 2022).

Benchmarking platforms such as GuacaMol (Brown et al., 2019) and comparative studies (Polishchuk et al., 2013) provide standardized metrics for evaluating generative-EA hybrids across objectives like quantitative estimate of drug-likeness (QED), binding affinity, and synthesizability. These studies confirm that hybrid methods often outperform standalone generative models or purely evolutionary searches in terms of chemical validity, novelty, and multi-objective performance. Figure 2 illustrates a typical workflow for hybrid generative–evolutionary drug design begins with a generative model trained on large chemical datasets (Gómez-Bombarelli et al., 2018; Gilmer et al., 2017). Candidate molecules generated in SMILES or graph form are

passed to an evolutionary optimization layer, where crossover, mutation, and selection are applied under multi-objective constraints (Deb et al., 2002; Li & Zhang, 2009). Feedback from predictive models (Vamathevan et al., 2019; Zhavoronkov et al., 2019) or docking simulations (Zhou et al., 2019) is used to update both the evolutionary fitness functions and the generative model parameters. Figure 3 illustrates the synergy between generative models and evolutionary systems for multi-objective molecular design:

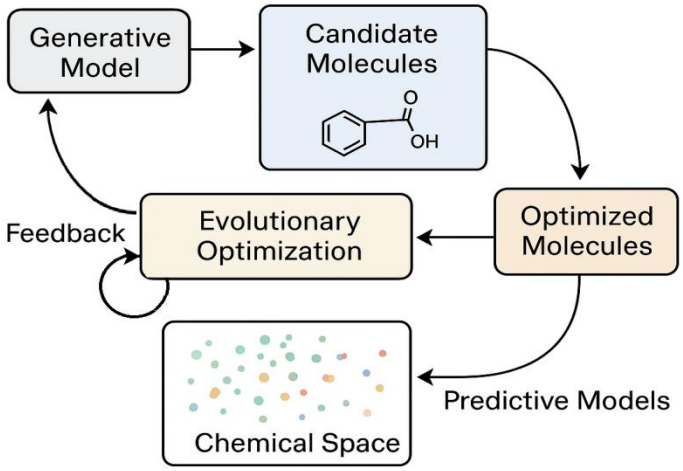


Figure 3. Workflow of hybrid generative–evolutionary frameworks for multi-objective molecular design

Future Directions

The convergence of generative modeling and evolutionary optimization is still at an early stage, and several avenues remain open for advancing the field.

Dynamic Multi-Objective Penalties

Traditional multi-objective optimization often treats all objectives with static weights or Pareto dominance. However, drug discovery objectives such as potency, selectivity, and pharmacokinetic properties, rarely remain fixed throughout a project's lifecycle. Dynamic penalty schemes, in which weights adapt based on progress or project stage, could enable more pragmatic optimization. Such adaptive formulations would allow algorithms to progressively shift emphasis from chemical diversity toward synthesis feasibility and clinical relevance (Deb et al., 2002; Li & Zhang, 2009).

Integration with Reinforcement Learning

While evolutionary algorithms excel in population-based exploration, reinforcement learning (RL) methods provide fine-grained control over sequential molecular construction (Olivecrona et al., 2017; Zhou et al., 2019). Combining these paradigms could yield synergistic frameworks where RL policies guide local exploration, while evolutionary operators maintain population-level diversity and multi-objective balance. Such hybridization is especially promising for tasks requiring long-horizon credit assignment, such as scaffold hopping or synthesizability-aware optimization.

Towards Fully Automated, Closed-Loop Drug Discovery Pipelines

The ultimate goal of this research trajectory is to achieve autonomous design–make–test–analyze (DMTA) cycles (Schneider, 2018; Segler et al., 2018). Closing the loop between in silico design, robotic synthesis, and high-throughput screening will require robust interfacing of generative–evolutionary models with retrosynthetic planning engines (Segler et al., 2018) and laboratory automation platforms. Active learning and uncertainty-aware surrogate models (Vamathevan et al., 2019) will be critical for prioritizing experiments and reducing costs in these pipelines. Progress in this direction could enable self-driving laboratories that iteratively refine molecular candidates with minimal human intervention, accelerating the path from hypothesis to validated lead.

Our Contributions to AI-Driven Drug Discovery

Over the three past years, our research group has made several contributions to the rapidly evolving field of AI-driven drug discovery. Building on the synergy between deep generative models and evolutionary optimization, we have focused on developing deep generative and hybrid frameworks that combine data-driven molecular generation with multi-objective search strategies. These efforts aim to accelerate de novo molecular design, improve chemical validity, and enhance the interpretability of AI-assisted drug development.

Our first contribution Oulladji et al., 2025, explores the use of artificial intelligence and machine learning techniques in the drug discovery process, focusing on how data-driven models can accelerate target identification, molecular design, and compound optimization. The study highlights the importance of predictive modeling, deep learning, and virtual screening in reducing cost and time in drug development. Finally, it emphasizes future directions toward automated and intelligent drug design pipelines. Second research, Taieb Brahim et al., currently under peer review, proposes a hybrid framework that integrates a Variational Autoencoder (VAE) to generate diverse anticancer molecular structures and a multi-objective Genetic Algorithm to optimize them. The optimization process simultaneously targets predicted anticancer activity (GCN), drug-likeness (QED), synthetic accessibility (SA), and Lipinski compliance. Overall, the proposed approach efficiently explores chemical space and identifies promising, realistic, and synthesizable drug candidates.

Finally, our current contribution, Abbad et al., investigates the integration of deep generative models with a dual optimization strategy leveraging Genetic Algorithms (GA) and the Colibri algorithm. The generative model provides diverse initial molecular candidates, while the GA–Colibri optimization jointly refines them with respect to predicted bioactivity, drug-likeness, synthetic accessibility, and pharmacokinetic constraints. The designed approach accelerates de novo molecule discovery while maintaining a balance between potency, feasibility, and developability. Together, these contributions illustrate our commitment to advancing the intersection of artificial intelligence, cheminformatics, and computational drug design, paving the way toward more efficient, interpretable, and autonomous discovery workflows.

Conclusion

The integration of generative models with evolutionary algorithms is reshaping molecular design by uniting data-driven creativity with interpretable, multi-objective optimization. Emerging hybrid frameworks not only enhance chemical validity and synthesizability but also pave the way toward autonomous, closed-loop discovery pipelines. As adaptive optimization strategies and reinforcement learning integration mature, these approaches hold the potential to accelerate drug discovery dramatically, bridging the gap between theoretical innovation and tangible therapeutic breakthroughs. Ultimately, hybrid generative–evolutionary frameworks may enable the transition from exploratory molecular design to truly autonomous drug discovery.

Scientific Ethics Declaration

* The authors declare that the scientific ethical and legal responsibility of this article published in EPSTEM journal belongs to the authors.

Conflict of Interest

* The authors declare that they have no conflicts of interest

Funding

* This research received no specific grant from any funding agency in the public, commercial, or not-for-profit sectors.

Acknowledgements or Notes

* This article was presented as an oral presentation at the International Conference on Technology, Engineering and Science (www.icontes.net) held in Antalya/Türkiye on November 12-15, 2025.

References

Assouel, R., Ahmed, N., Wolf, G., Bresson, X., & Cohen, J. (2018). DEFactor: Differentiable edge factorization-based probabilistic graph generation. *arXiv*.

Bagal, V., Aggarwal, R., Vinod, P. K., & Priyakumar, U. D. (2021). MolGPT: Molecular generation using a transformer-decoder model. *Journal of Chemical Information and Modeling, 61*(12), 5804–5814.

Blaschke, T., Olivecrona, M., Engkvist, O., Bajorath, J., & Chen, H. (2020). Application of generative autoencoder in de novo molecular design. *Molecular Informatics, 39*(1-2), 1900123.

Brown, N., Fiscato, M., Segler, M. H. S., & Vaucher, A. C. (2019). GuacaMol: Benchmarking models for de novo molecular design. *Journal of Chemical Information and Modeling, 59*(3), 1096-1108.

Deb, K., Pratap, A., Agarwal, S., & Meyarivan, T. (2002). A fast and elitist multiobjective genetic algorithm: NSGA-II. *IEEE Transactions on Evolutionary Computation, 6*(2), 182-197.

Deb, K., Thiele, L., Laumanns, M., & Zitzler, E. (2002). Scalable multi-objective optimization test problems. *IEEE Congress on Evolutionary Computation*, 825-830.

DiMasi, J. A., Grabowski, H. G., & Hansen, R. W. (2016). Innovation in the pharmaceutical industry: New estimates of R&D costs. *Journal of Health Economics, 47*, 20-33.

Gilmer, J., Schoenholz, S. S., Riley, P. F., Vinyals, O., & Dahl, G. E. (2017). Neural message passing for quantum chemistry. *ICML*, 1263-1272.

Gómez-Bombarelli, R., Wei, J. N., Duvenaud, D., Hernández-Lobato, J. M., Sánchez-Lengeling, B., Sheberla, D., & Aspuru-Guzik, A. (2018). Automatic chemical design using a data-driven continuous representation of molecules. *ACS Central Science, 4*(2), 268-277.

Goodfellow, I., Pouget-Abadie, J., Mirza, M., Xu, B., Warde-Farley, D., Ozair, S., & Bengio, Y. (2014). Generative adversarial nets. *NeurIPS*, 2672-2680.

Guimaraes, G. L., Sanchez-Lengeling, B., Outeiral, C., Farias, P. L. C., & Aspuru-Guzik, A. (2017). ORGAN: Objective-reinforced generative adversarial networks. *arXiv*.

Gupta, A., Müller, A. T., Huisman, B. J., Fuchs, J. A., Schneider, P., & Schneider, G. (2018). Generative recurrent networks for de novo drug design. *Molecular Informatics, 37*(1-2), 1700111.

Ishibuchi, H., Tsukamoto, N., & Nojima, Y. (2016). Evolutionary many-objective optimization. *IEEE CEC*, 1-8.

Jin, W., Barzilay, R., & Jaakkola, T. (2018). Junction tree VAE for molecular graph generation. *ICML*, 2323-2332.

Kadurin, A., Nikolenko, S., Khrabrov, K., Aliper, A., & Zhavoronkov, A. (2017). druGAN: GAN-based de novo design. *Molecular Pharmaceutics, 14*(9), 3098-3104.

Kingma, D. P., & Welling, M. (2014). Auto-encoding variational Bayes. *arXiv*.

Li, H., & Zhang, Q. (2009). Multiobjective optimization: MOEA/D and NSGA-II. *IEEE Transactions on Evolutionary Computation, 13*(2), 284-302.

Nigam, A., Friederich, P., Krenn, M., & Aspuru-Guzik, A. (2020). Augmenting genetic algorithms with neural networks. *arXiv*.

Nigam, A., Polykovskiy, D., & Aspuru-Guzik, A. (2021). Janus molecular generation framework. *Machine Learning: Science and Technology, 2*(3), 035021.

Nigam, A., Polykovskiy, D., Kamya, P., Bjerrum, E. J., Engkvist, O., & Chen, H. (2022). Janus: Parallel tempered GA for molecular design. *Journal of Chemical Information and Modeling, 62*(9), 2064-2076.

Olivecrona, M., Blaschke, T., Engkvist, O., & Chen, H. (2017). Molecular de novo design via reinforcement learning. *Journal of Cheminformatics, 9*(1), 48.

Oulladji, L., Saadallah, M., Guellil, Z., Abbad, H., & Bekhti, H. (2025). AI-driven molecule generation and bioactivity prediction: A multi-model approach. *Journal of Computational Chemistry, 46*(8), 512–525.

Paul, S. M., Mytelka, D. S., Dunwiddie, C. T., Persinger, C. C., Munos, B. H., Lindborg, S. R., & Schacht, A. L. (2010). Improving R&D productivity. *Nature Reviews Drug Discovery, 9*(3), 203-214.

Polishchuk, P. G., Madzhidov, T. I., & Varnek, A. (2013). Size of drug-like chemical space. *Journal of Computer-Aided Molecular Design, 27*(8), 675-679.

Schneider, G. (2018). Automating drug discovery. *Nature Reviews Drug Discovery, 17*(2), 97-113.

Schneider, P., Walters, W. P., Plowright, A. T., Sieroka, N., Listgarten, J., Goodnow, R. A., ... Schneider, G. (2020). Rethinking drug design in the AI era. *Nature Reviews Drug Discovery, 19*(5), 353-364.

Segler, M. H. S., Preuss, M., & Waller, M. P. (2018). Planning syntheses with neural networks. *Nature, 555*(7698), 604-610.

Stahl, F., Mendez-Lucio, O., Vuckovic, D., Zdrazil, B., & Engkvist, O. (2022). Hybrid GA approaches for drug design. *Drug Discovery Today, 27*(8), 2203-2213.

Vamathevan, J., Clark, D., Czodrowski, P., Dunham, I., Ferran, E., Lee, G., ... Bender, A. (2019). Machine learning in drug discovery. *Nature Reviews Drug Discovery, 18*(6), 463-477.

Winter, R., Montanari, F., Noé, F., & Clevert, D. A. (2019). Learning continuous molecular descriptors. *Chemical Science, 10*(6), 1692-1701.

Yoshimori, A., Takeda, S., & Oono, K. (2021). Chemically valid GA operators. *Journal of Cheminformatics, 13*(1), 34.

You, J., Liu, B., Ying, R., Pande, V., & Leskovec, J. (2018). Graph convolutional policy networks. *NeurIPS*.

Zhang, Q., & Li, H. (2007). MOEA/D. *IEEE Transactions on Evolutionary Computation, 11*(6), 712-733.

Author(s) Information

Abbad Houda
Djillali Liabes University of Sidi Bel Abbes,
Computer Science Department
EEDIS Laboratory, Algeria
Contact e-mail: *houda.abbad@univ-sba.dz*

Taieb Brahim Mohammed
Djillali Liabes University of Sidi Bel Abbes,
Computer Science Department
EEDIS Laboratory, Algeria

Oulladji Latefa
Djillali Liabes University of Sidi Bel Abbes,
Computer Science Department
EEDIS Laboratory, Algeria

Abbad Leila
LIT Laboratory
ENSTA High School, Algiers; Algeria

To cite this article:

Houda, A., Mohammed, T.B.., Latefa, O., & Leila, A. (2025). AI-driven molecular design: Synergizing deep generative models with evolutionary optimization. *The Eurasia Proceedings of Science, Technology, Engineering and Mathematics (EPSTEM), 38,* 512-524.

The Eurasia Proceedings of Science, Technology, Engineering & Mathematics (EPSTEM)
ISSN: 2602-3199

The Eurasia Proceedings of Science, Technology, Engineering and Mathematics (EPSTEM), 2025

Volume 38, Pages 525-529

IConTES 2025: International Conference on Technology, Engineering and Science

Performance of LTO/rGO Composite Anode in Lithium Ion Battery

Meltem Cayirli
Eskisehir Osmangazi University

Busra Yilmaz-Donmez
Eskisehir Osmangazi University

Mustafa Anik
Eskisehir Osmangazi University

Abstract: $Li_4Ti_5O_{12}$ (LTO) has attracted extensive research interest as an anode material owing to its excellent safety and cycling stability. The relatively high operating potential of LTO (1.55 V vs. Li/Li^+) prevents dendrite formation, while its being above the potential at which most electrolytes and solvents are reduced leads to the formation of a thinner solid–electrolyte interphase (SEI) layer on its surface. However, the intrinsically low electronic conductivity of LTO remains the primary factor limiting its capacity. In this study, reduced graphene oxide (rGO) was synthesized and incorporated into LTO at approximately 10 wt.%, and the electrochemical performance of the resulting LTO/rGO composite anode was evaluated in lithium-ion batteries. The results revealed that rGO incorporation enhanced the discharge capacity of the LTO anode by at least 30%, while maintaining a Coulombic efficiency of nearly 100% over 100 cycles and achieving a capacity retention rate of no less than 96%.

Keywords: Lithium-Ion battery, LTO anode, rGO

Introduction

The spinel-structured intercalation-type anode, $Li_4Ti_5O_{12}$ (LTO), has been extensively investigated by researchers due to its superior safety and cycling stability compared to the graphite anode. As a result of these studies, LTO has succeeded in achieving the second largest market share in the Li-ion battery industry, following graphite (Zhang et al., 2022). The superior properties of the LTO anode primarily originate from the $Li_4Ti_5O_{12} \leftrightarrow Li_7Ti_5O_{12}$ phase transition that occurs during charge/discharge reactions (Ge et al., 2009). These two phases, belonging to the Fd3m space group, have lattice parameters of 8.3596 Å and 8.3538 Å, respectively, and the volume change during charge/discharge is less than 0.1%. This negligible volume variation imparts LTO with its remarkable cycling stability (Ariyoshi et al., 2005). In addition, the high operating potential of LTO (1.55 V vs. Li/Li^+) not only suppresses dendrite formation but also remains higher than the potential at which most electrolytes and solvents undergo reduction (< 1.0 V). This results in the formation of a thinner solid–electrolyte interphase (SEI) layer on the surface (He et al., 2012; Zhang et al., 2022). In contrast, SEI layers that typically form with greater thickness consume active material, thereby leading to capacity loss in the electrode and lower Li^+ diffusion (Zhang et al., 2022).

However, the LTO anode suffers from its extremely low electrical conductivity ($\sim 10^{-13}$ S cm^{-1}) and ionic conductivity (10^{-13}–10^{-9} cm^2 s^{-1}) (Julien & Mauger, 2024). In this study, reduced graphene oxide (rGO) was synthesized, and the electrochemical performance of the LTO/10 wt.% rGO composite anode was evaluated in lithium-ion batteries. The composite anode exhibited a substantial increase in discharge capacity without any deterioration in Coulombic efficiency or capacity retention.

- This is an Open Access article distributed under the terms of the Creative Commons Attribution-Noncommercial 4.0 Unported License, permitting all non-commercial use, distribution, and reproduction in any medium, provided the original work is properly cited.

- Selection and peer-review under responsibility of the Organizing Committee of the Conference

© 2025 Published by ISRES Publishing: www.isres.org

Method

Synthesis and Characterization

Graphene oxide (GO) was synthesized by mixing H_2SO_4/H_3PO_4 (360:40 mL), followed by the slow addition of $KMnO_4$ (18.0 g) and graphite flakes (3.0 g). The reaction mixture was then heated to 50 °C and stirred at 300 rpm for 12 h. After cooling to room temperature, it was poured onto ice (400 mL) with the dropwise addition of H_2O_2 (3 mL). The product was subsequently filtered and washed. The initial washing was carried out with 30% HCl solution and repeated until the supernatant became transparent, followed by further washing with deionized (DI) water and ethanol until neutral pH was achieved. All washing steps were performed by centrifugation at 6000 rpm for 30 min. The resulting solid was dispersed in DI water by ultrasonication to obtain a 1.0 mg mL^{-1} suspension. Prior to electrode preparation, the synthesized rGO (10 wt.%) was physically mixed with LTO using an agate mortar. X-ray diffraction (XRD) analyses were performed on a PANalytical Empyrean diffractometer with Cu Kα radiation at a scanning rate of 2° min^{-1}.

Electrode Preparation and Electrochemical Tests

For electrode preparation, the active material (75 wt%), Super P (15 wt%), and PVDF (10 wt%) were mixed with 0.8 mL of NMP in a centrifuge tube. The mixture was then homogenized using a vortex mixer until a slurry was obtained. The slurry was coated onto C-coated Al foil using a doctor blade with a wet thickness of 150 µm and subsequently dried at 80 °C for 24 h under vacuum-controlled atmosphere. The coated C-coated Al foil was then punched into 16 mm discs using an electrode cutting machine and further dried under the same vacuum-controlled conditions prior to cell assembly.

All the test assemblages were carried out in an Ar-filled glove box with H_2O and O_2 levels less than 0.1 ppm. Lithium metal was used as the counter electrode, while polipropilen (Celgrad 2400) membrane served as the separator. The electrolyte was 1.2 M $LiPF_6$:EC:DMC (4:6 by volume). The galvanostatic discharge and charge test cut-off potentials were 1.0 $V_{Li+/Li}$ and 3.0 $V_{Li+/Li}$, respectively. The number of cycles was set to 100 at the selected C-rates.

Results and Discussion

Structural Characterization

The XRD patterns of the freshly prepared LTO and composite electrodes on the carbon-coated Al surface are presented in Figure 1. The peaks of LTO indicates the strong crystalline structure of LTO. The incorporation of rGO does not significantly alter the XRD pattern of LTO in Figure 1, as the nanostructured nature of rGO leads to peak broadening around $2\theta \approx 26°$.

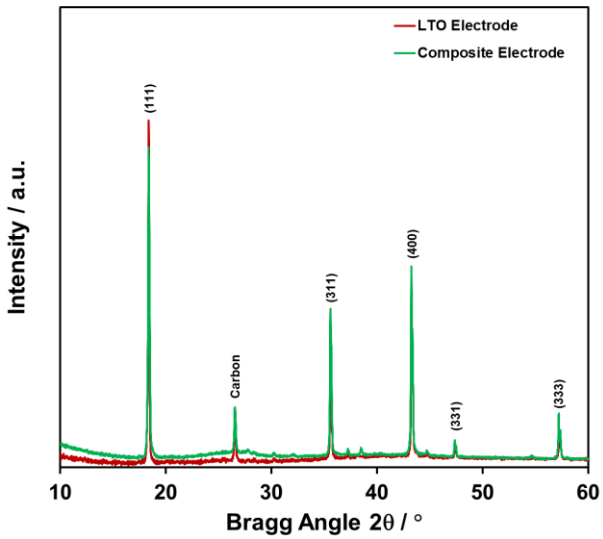


Figure 1. XRD patterns of the freshly prepared LTO and composite electrodes.

Electrochemical Tests

Figure 2 presents the effect of incorporating 10 wt.% rGO into the anode of a LiB half-cell on its charge–discharge capacities at a 1 C rate. The half-cell with a pristine LTO anode delivers a capacity of 120 mA h g^{-1}, whereas the incorporation of rGO into LTO (composite anode) increases the capacity to 156 mA h g^{-1}. This enhancement can be attributed to the layered structure and high electrical conductivity of rGO, which collectively improve the electrochemical performance of LTO.

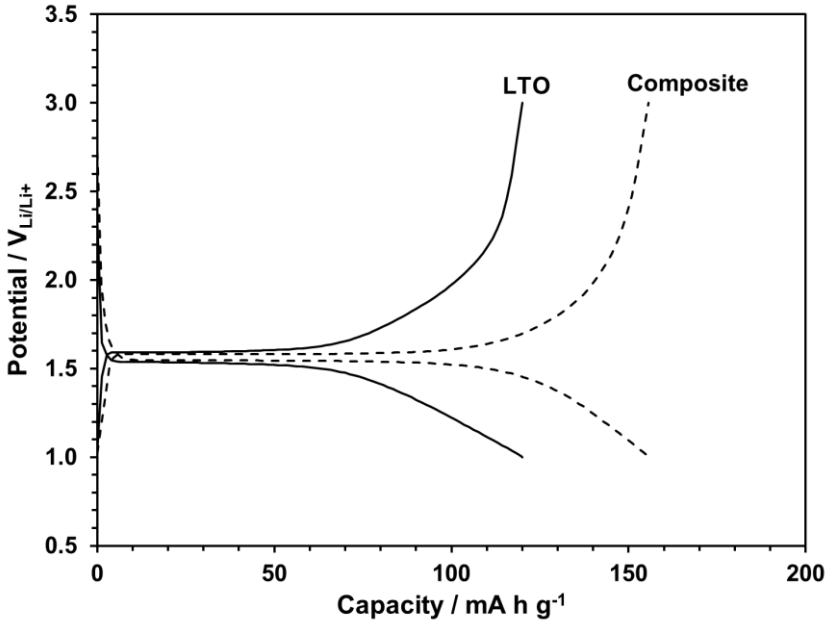


Figure 2. The charge–discharge curves of LTO and composite anode LiB half-cell at a 1 C rate.

The evolution of charge–discharge capacities during prolonged cycling is presented for the LTO and composite anodes in Figures 3a and 3b, respectively. For clarity, only the 1st, 50th, and 100th charge–discharge profiles are shown for both electrodes. The LTO anode exhibits nearly 100% Coulombic efficiency with only minimal capacity fading after 100 cycles. As depicted in Figure 4, LTO retains 96% of its initial capacity after 100 cycles. Although the composite anode demonstrates an approximately 30% increase in capacity (Figure 3b), it is also able to maintain Coulombic efficiency at 100% and a capacity retention of 97% after 100 cycles (Figure 4). These results clearly indicate that the incorporation of rGO significantly enhances the capacity of the anode without compromising Coulombic efficiency or long-term cycling stability. Figures 3 and 4 demonstrate that LTO/rGO composite electrodes are highly promising anode materials for high-performance LiBs.

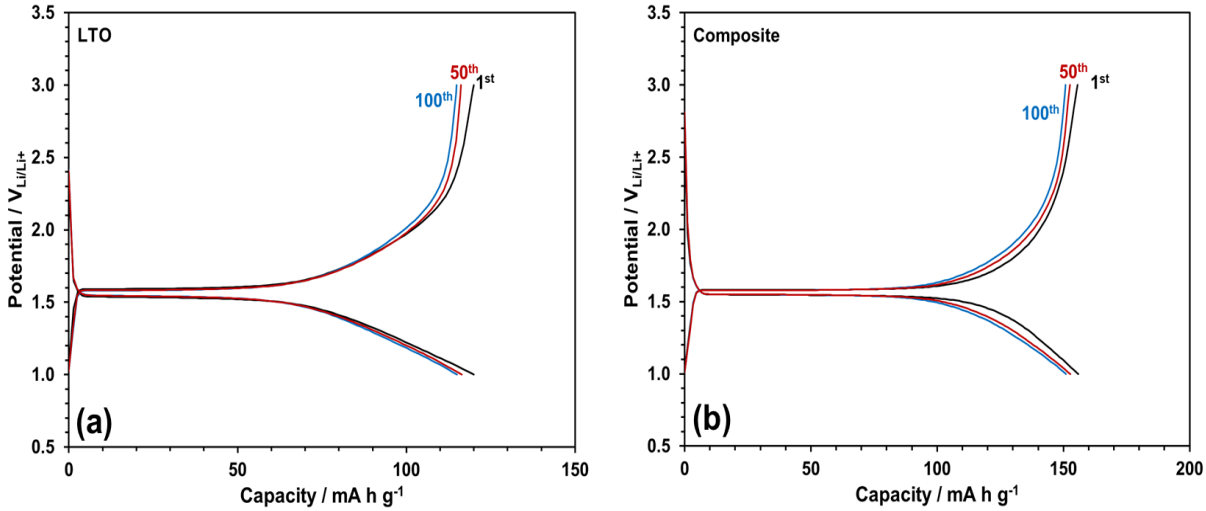


Figure 3. The 1st, 50th and 100th cycle charge–discharge curves of (a) LTO and (b) composite anode LiB half-cell at a 1 C rate.

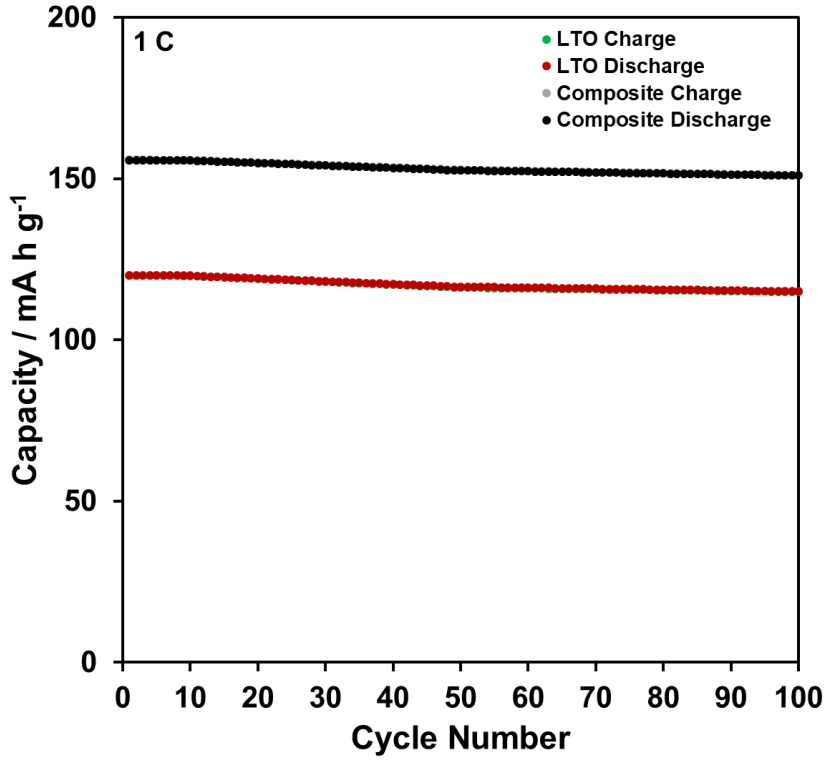


Figure 4. The change in both charge and discharge capacities over 100 cycles for LTO and composite anode LiB half-cell at a 1 C rate.

Conclusion

In this work, reduced graphene oxide (rGO) was prepared and introduced into LTO at a proportion of about 10 wt.%. The electrochemical behavior of the fabricated LTO/rGO composite anode was then examined for application in lithium-ion batteries. Findings demonstrated that the presence of rGO improved the discharge capacity of the LTO electrode by roughly 30%, while sustaining nearly 100% Coulombic efficiency across 100 charge–discharge cycles and retaining at least 96% of its initial capacity.

Scientific Ethics Declaration

* The authors declare that the scientific ethical and legal responsibility of this article published in EPSTEM journal belongs to the authors.

Conflict of Interest

* The authors declare that they have no conflicts of interest

Funding

* Financial assistance from Eskisehir Osmangazi University Research Fund is gratefully acknowledged (Project No FOA-2024-3172).

Acknowledgements or Notes

* This article was presented as an oral presentation at the International Conference on Technology, Engineering and Science (www.icontes.net) held in Antalya/Türkiye on November 12-15, 2025.

References

Ariyoshi, K., Yamato, R., & Ohzuku, T. (2005). Zero-strain insertion mechanism of Li[Li1/3Ti5/3]O4 for advanced lithium-Ion (Shuttlecock) batteries. *Electrochimica Acta, 51*, 1125-1129.

Christian M. J., & Mauger, A. (2024). Study on the theoretical capacity of spinel lithium titanate induced by low-potential intercalation. *Journal of Physical Chemistry C, 113*, 6324–6326.

Ge, H., Li, N., Li, D., Dai, C., & Wang, D. (2009). Fabrication of Li4Ti5O12 (LTO) as anode material for Li-Ion batteries. *Micromachines, 15*, 310–316.

Zhang, H., Yang, Y., Xu, H., Wang, L., Lu, X., He, X. (2022). Li4Ti5O12 spinel anode: Fundamentals and advances in rechargeable batteries. *InfoMat*, 4, 1–29.

Author(s) Information

Meltem Cayirli
Eskisehir Osmangazi University
26480, Eskisehir, Türkiye

Busra Yilmaz-Donmez
Eskisehir Osmangazi University
26480, Eskisehir, Türkiye

Mustafa Anik
Eskisehir Osmangazi University
26480, Eskisehir, Türkiye
Contact e-mail: *manik@ogu.edu.tr*

To cite this article:

Cayirli M., Yilmaz-Donmez, B., & Anik, M. (2025). Performance of LTO/rGO composite anode in lithium ion battery. *The Eurasia Proceedings of Science, Technology, Engineering and Mathematics (EPSTEM), 38*, 525-529.

The Eurasia Proceedings of Science, Technology, Engineering & Mathematics (EPSTEM)
ISSN: 2602-3199

The Eurasia Proceedings of Science, Technology, Engineering and Mathematics (EPSTEM), 2025

Volume 38, Pages 530-537

IConTES 2025: International Conference on Technology, Engineering and Science

Effect of Friction Stir Welding Parameters on the Evolution of the Welding Temperature

Belaribi Amina
Djillali Liabes University of Sidi Bel Abbes

Miloudi Abdelkader
Djillali Liabes University of Sidi Bel Abbes

Chekalil Ismail
King Fahd University of Petroleum and Minerals

Benmessaoud Mohammed Abdelghani
Djillali Liabes University of Sidi Bel Abbes

Abstract: Friction stir welding (FSW) is a permanent joining technique that uses a rotating tool pressed against the two parts to be welded, the rotational movement produces heat that softens the materials and make it malleable whithout reaching the melting point of either the materials parts or the tool in the process, the tool will be then moved in feed motion along the joint to assemble the parts. The welding temperature reached is the key to obtaining a flawless, high-quality weld. İf the welding temperature is too high, it might reduce the mechanical properties or cause cores to collapse. İf the welding temperature is too cold, wormholes could appear due to a bad brew. The purpose of this research is to study the influence of the initial welding parameters, such as rotational speed, feed speed, and the inclination angle of the tool, on the evolution of the maximal temperature reached during the FSW process, to be able to determine optimal reference welding parameters finally. A mathematical model is proposed to help us predict the maximal temperature of the welding joint during the process using the response surface methodology (RSM).

Keywords: Maximal temperature, Welding joint, FSW, Rotational speed

Introduction

Due to their exceptional weight/strength ratios, their corrosion resistance, and good formability, AA3003 aluminum alloys are widely used in various industrial applications including aerospace, shipbuilding, automotive, civil engineering, electronic components, and electrical shielding (Guo et al., 2013; Chen et al., 2023; Çam et al., 2017). There are several approaches to assembling alloys intended for use in these industries. So far, one of the best solutions to fuse two or more pieces of similar or different materials is welding (Shojaei Zoeran et al., 2017; Karami et al., 2016; Eivani & Karimi Taheri, 2007). However, aluminium has characteristics that make it difficult to weld (Yang et al., 2017), because its high thermal conductivity means that it quickly dissipates heat, especially as cracks appear at the end of the solidification process, which is formed at high temperatures, and these oxidise in contact with air, leading to poor joint efficiency. Friction Stir Welding is a process that overcomes the limitations of conventional welds, including the problem of corrosion of the fusion joint due to thermal effects (Pinto et al., 2022; Mishra et al., 2005). The friction-mixing welding (FSW) process depends entirely on the mechanical contact between the tool and the workpiece (Li et al., 2017). Therefore, all process phenomena and outcomes, such as weld geometry and mechanical properties, are governed by the FSW friction system (Hossfeld, 2023; Prabhakar et al., 2023). Chekalil et al have studied the

- This is an Open Access article distributed under the terms of the Creative Commons Attribution-Noncommercial 4.0 Unported License, permitting all non-commercial use, distribution, and reproduction in any medium, provided the original work is properly cited.

- Selection and peer-review under responsibility of the Organizing Committee of the Conference

© 2025 Published by ISRES Publishing: www.isres.org

influence of welding parameters, namely the rotational speed Vr, feed speed Va and angle of inclination of the tool θ on the mechanical properties of joints such as yield strength, the stress and resistance to rupture, A mathematical model was proposed to predict the mechanical behavior of the junction using the response surface methodology (RSM). This model is used to determine the optimal values of these parameters, which are responsible for the best performance of the FSW joint.

The optimized values of the parameters that allow to obtain the best mechanical properties of a welded joint correspond to the values of Vr = 1423.93 r/min, Va = 400 mm/ min, and Θ = 1.2885° (Chekalil et al., 2020). Combinations of the different factors for a better quality of the FSW joint by obtaining a tensile strength of the welded joint equal to 75% of that of the base metal. The quality of the weld joint is also affected by the temperature reached during the FSW process, so it is recommended to have a good control of the temperature when welding, The objective of our study would therefore be to determine the effect of the same welding parameters preceding on the temperature evolution in order to determine the optimal values of Vr, Va and Θ.

Modelling and Prediction of Maximum Temperature During the FSW Process

This study utilizes an experiment plan to establish a link between the input variables (rotation speed, feed speed, and angle of tool inclination) and the output variable Tmax. To predict the maximum temperature, the Response Surface Methodology (RSM) is used to develop the non-linear model of the thermal cycle of the FSW joint of aluminum alloys (AA 3003). Some results of the experimental study on the effect of the process parameters (rotational speed Vr and feed speed Va) on the evolution of the thermal cycle are presented in Figure 1.

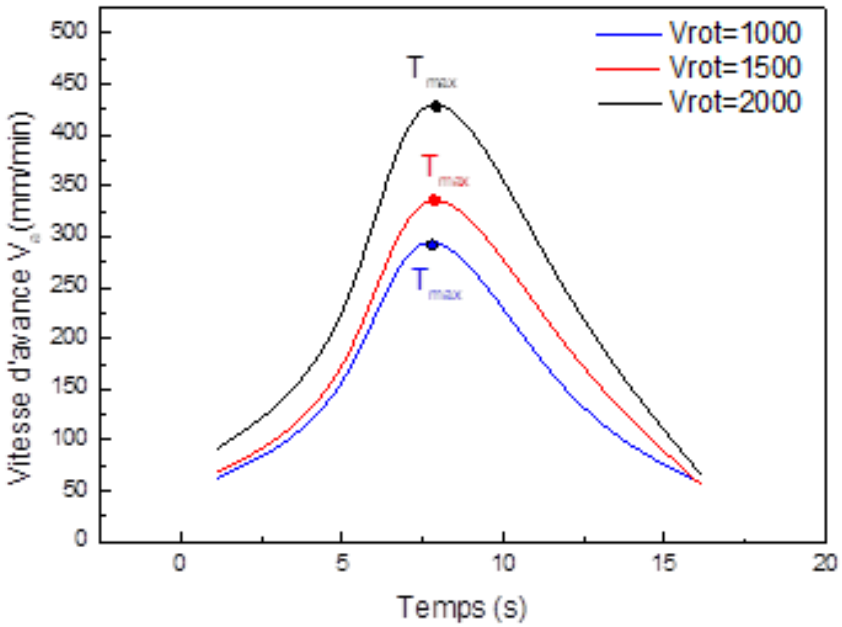


Figure 1. Effect of process parameters on the evolution of the thermal cycle (Va, Vr, and Theta)

The prediction was made by a full factorial plane with three factors, rotation speed Vr, feed speed Va, and tool angle Θ, at three levels (-1, 0, +1). Table 1 below gives the values of each parameter for each level. The values of these parameters are dictated by machine capacity and premature tool wear

Table 1. Parameter values for each level

Parameters	Low level -1	Central level	High level +1
Rotational speed	1000	1500	2000
Feed speed	200	300	400
Angle of inclination of the tool	0,5	1,5	2,5

The matrix of experiments was determined by MODDE 5.0 software and the use of the experiment plan on 30 samples.

Mathematical Model

The polynomial mathematical model developed for optimization is a second-degree model. The model of the experimenter is quadratic in form:

$$y = a_0 + \sum_{i=1}^{3} a_i x_i + \sum_{1 \le j \le 3} a_{ij} x_j + \sum_{i=1}^{3} a_{ii} x_i^2 + e \qquad (1)$$

Where is the predicted response value at the center of the experimental domain represents the factor effect, and represents the interaction between the factor andx_j.

The developed mathematical model allows for establishing a relationship between the input parameters (Vr, Va and Θ) and the output quantity (T_{max}). The polynomial allows for optimizing the welding temperature to obtain the desired response. To calculate the coefficients of the models, a regression method based on the least squares criterion is used. The mathematical model proposed by MODDE 5.0 is as follows:

$$T_{\max} = 213.667 + 39.8889 \times Vr - 14 \times Va + 31.8333 \times \Theta - -5.75001 \times Vr.Va - 5.75001 \times Vr.\Theta + 0.0833216 \times Va.\Theta + 1.99999 \times Vr^2 + 19 \times Va^2 + 34.8333\Theta^2 \qquad (2)$$

Influence of Welding Parameters on the Maximum Temperature

Influence of Rotational Speed on Maximum Temperature

The values of the coefficients associated with the welding parameters in the mathematical model show the degree of influence of each factor. An example of a prediction is given in Figure 2. It is worth mentioning that it can be used to predict the evolution of maximum temperature as a function of rotational speed (Vr). The central curve represents the predicted values, and the other two curves show the 95% confidence interval of the predicted response.

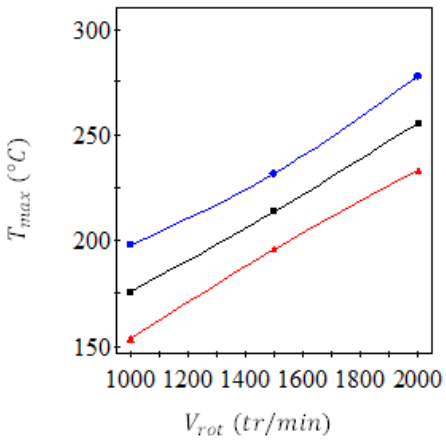


Figure 2. Evolution of maximum temperature as a function of rotational speed (Vr)

The analysis in Figure 2 suggests that an increase in rotational speed Vr leads to a large increase in maximum temperature. Indeed, a 50% increase in the rotation speed leads to an increase of about 48% in the maximum temperature. This temperature is maximum when the speed value is equal to 2000 tr/min. This has the effect of increasing mechanical properties, including hardness, and reducing tunnel and vacuum defects.

Influence of Feed Speed on Maximum Temperature

Concerning the impact of the feed speed, it can be noted that when the feed speed (Va) increases, the maximum temperature (Tmax) gradually decreases in the interval [200- 300mm/min] and then stabilizes around 230°C in the interval [300-400 mm/min]

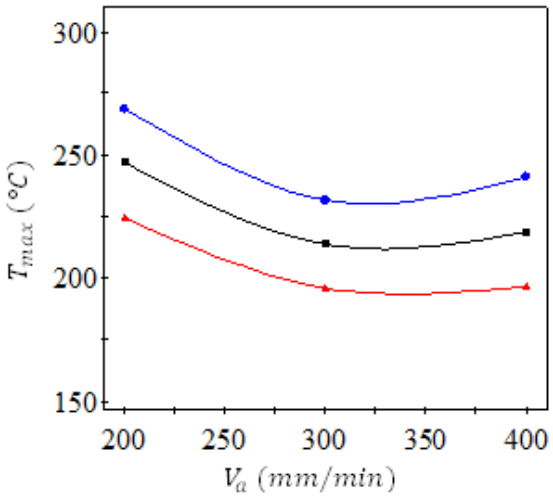


Figure 3. Evolution of the maximum temperature as a function of feed speed

Therefore, it can be concluded that the increase in feed speed induces a slight decrease in maximum temperature (Tmax). Indeed, an increase of 50% in the feed speed leads to a decrease of about 8% in the maximum temperature. It can be assumed that there is a critical feed rate (Va-cr = 300 mm/min) beyond which the temperature is almost independent of this parameter.

Influence of Tool Angle on Maximum Temperature

Figure 4 illustrates the effect of the angle of inclination on the maximum temperature. It is clearly noted that the temperature is constant in the range between 0.5° and 1.5°, beyond the value of 1.5 °, the temperature begins to rise to a maximum value of 275 °C. We find that beyond an angle equal to 1.5, it increases sharply with increasing angle of the tool. Indeed, an increase of 40% in the angle of inclination leads to an increase of about 45% in the maximum temperature.

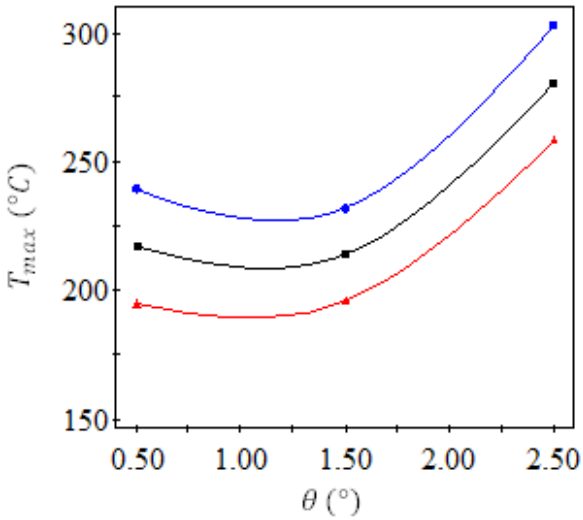


Figure 4. Evolution of the maximum temperature as a function of the angle of inclination of the tool

Effect of Parameter Interactions on Maximum Temperature Response

Interaction Between Tool Angle and Feed Speed

In this analysis step, it was decided to broaden the scope of our study by taking into account the interaction between the two factors. This allows the output parameters to be visualized on a three-dimensional (3D) graph Figure 5; this graph represents the variation of Tmax as a function of both factors θ and Va.

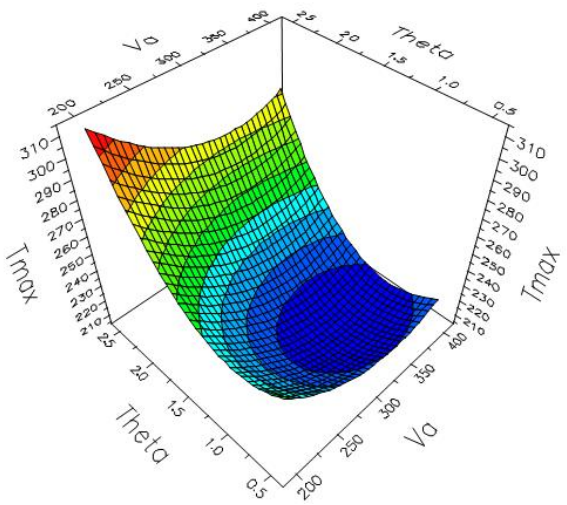


Figure 5. Three-dimensional (3D) variation of Tmax as a function of θ and Va

The curve in Figure 6, commonly referred to as Iso curves, is the projection of the surface onto the plane. This figure shows that the greater the angle of inclination of the tool, the higher the maximum temperature increases to a maximum value of 300°C. Note that this is valid regardless of the speed of feed. On the other hand, the lowest values of Tmax were recorded for the values of Va between [270 and 370mm/min].

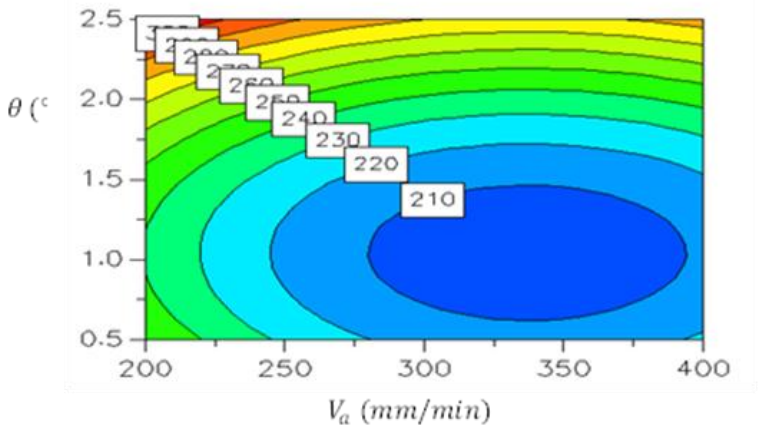


Figure 6. Variation of Tmax as a function of Va and θ

Interaction Between Rotation Speed and Feed Speed

Figure 7. Shows the effect of both factors and acting simultaneously on the maximum temperature (T_{max}), moving from their minimum values to their maximum values while the third factor (θ) is kept constant. The analysis of the graph in this figure suggests that the higher the maximum temperature, also increases to 278 °C, while V_a is between 200 and 230 mm/min. Furthermore, it should also be noted that it can reach values closer to the maximum values for a maximum equal to 400 mm/min and a V_r range between 1650 and 2000 tr/min. On the other hand, low values of are recorded for low values around 1000 tr/min, which is valid regardless of the value of. It should also be mentioned that the maximum temperature values (T_{max}) of the welded joint were obtained for a ratio (V_r/V_a) between 8 and 10. We find that the temperature of the weld depends on the speed of rotation and feed speed. The faster and slower the tool turns, the hotter the weld will be. On the other hand, the slower the tool turns and the faster it moves, the cooler the weld.

All these results were in good agreement with those obtained by Chekalil et al. They studied the effect of the same three parameters on the mechanical behaviour of the FSW welded joint of the aluminium alloy Al3003, They found that the maximum values of mechanical properties are obtained for optimal values of Vr = 1430 r/min, while keeping the value of Va constant and equal to 400 mm/ min.

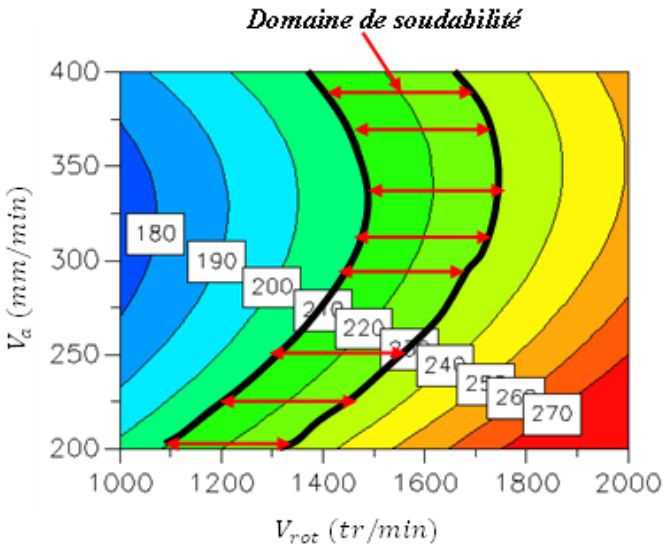


Figure 7. Tmax variation as a function of Vr and Va

Interaction Between the Rotation Speed and the Angle of Inclination of the Tool

This new section aims to present the response area obtained when the value of is kept constant, while varying Vr and θ Figure 8, it can be seen that the maximum temperature takes maximum values in the interaction interval: for θ between 1.8° and 2.5° and between 1600 and 2000 r/min. It should be noted that the best values of the mechanical properties of the weld joint in this range are equal to 80% of those of the base metal. However, low maximum temperature values are recorded for V_r values between 1000 and 1500 r/min, and θ between 0.55° and 1.58°.

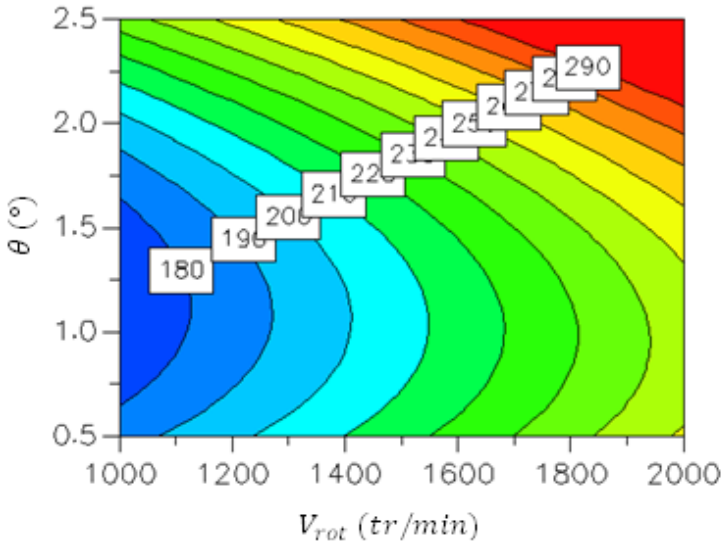


Figure 8. Tmax variation as a function of Vr and θ

Model Validation and Optimization

The validation of the model is carried out by comparing the experimental results with those obtained by the proposed models. Thirty test cases are randomly generated by assigning intermediate values to the process variables, and for each combination, changing the rotation speed (1000-2000 r/min), travel speed (200-400 mm/min), and tool angle (0.5-2.5°). Figure 9 shows a good correlation between the predicted maximum temperature profiles and those of the experiments.

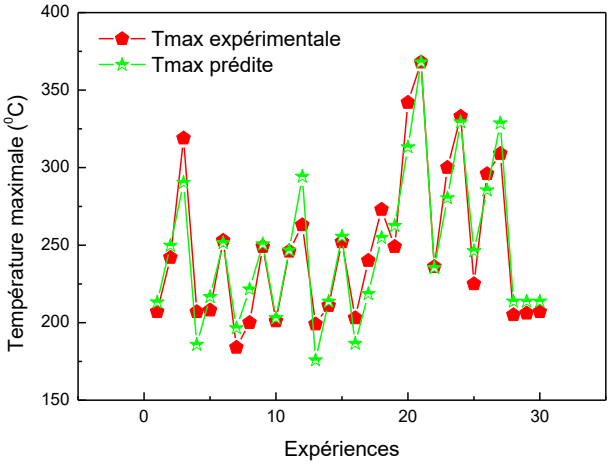


Figure 9. Predicted and experimental maximum temperature values

Conclusion

The model developed by the experimental design approach allowed to obtain a better prediction of the maximum temperature of a welded joint. This model is an effective tool for selecting the optimal parameters of the friction-mixing (FSW) welding process. The most important parameters affecting the evolution of the maximum temperature are in the order: rotation speed, then angle, and finally feed rate. The maximum values of temperature ($T_{ma}x$) of the welded joint were obtained for a ratio (V_r/V_a) between 8 and 10.

Scientific Ethics Declaration

* The authors declare that the scientific ethical and legal responsibility of this article published in EPSTEM journal belongs to the authors.

Conflict of Interest

* The authors declare that they have no conflicts of interest

Funding

* There is no funding for this research

Acknowledgements or Notes

* This article was presented as an oral presentation at the International Conference on Technology, Engineering and Science (www.icontes.net) held in Antalya/Türkiye on November 12-15, 2025.

References

Cam, G., & Ipekoglu, G. (2017). Recent developments in joining of aluminium alloys. *The International Journal of Advanced Manufacturing Technology*, *91*(5–8), 1851-1866.

Chekalil, I., Miloudi, A., Ghazi, A., & Planche, M. P. (2020). Prediction of mechanical behavior of friction stir welded joints of AA3003 aluminum alloy. *Frattura ed Integrità Strutturale*, *14*(54), 153-168.

Chen, G., Liu, H., & Shi, Q. (2023). Development of computational approach for analyzing in-process thermal-mechanical condition during friction stir welding for prediction of material bonding defect. *Materials*, *16*(23), Article 7473.

Eivani, A. R., & Karimi Taheri, A. (2007). A new method for producing bimetallic rods. *Materials Letters*, *61*(19–20), 4110-4113.

Guo, J., Zhao, S., Murakami, R.-I., Ding, R., & Fan, S. (2013). Modeling the hot deformation behavior of Al alloy 3003. *Journal of Alloys and Compounds*, *566*, 62-67.

Hossfeld, M. (2023). On friction, heat input, and material flow initiation during friction stir welding: Tool and process optimization. *Journal of Manufacturing and Materials Processing*, *7*(1), 34.

Karami, S., Jafarian, H., Eivani, A. R., & Kheirandish, S. (2016). Engineering tensile properties by controlling welding parameters and microstructure in a mild steel processed by friction stir welding. *Materials Science and Engineering: A*, *670*, 68-74.

Li, K., Jarrar, F., Sheikh-Ahmad, J., & Ozturk, F. (2017). Using coupled Eulerian Lagrangian formulation for accurate modeling of the friction stir welding process. *Procedia Engineering*, *207*, 574-579.

Mishra, R. S., & Ma, Z. Y. (2005). Friction stir welding and processing. *Materials Science and Engineering: R: Reports*, *50*(1-2), 1-78.

Pinto, L., Cipriano, G., Braga, D. F. O., Vidal, C., Machado, M. A., Correia, A., & Infante, V. (2022). Mechanical behavior of friction stir butt welded joints under different loading and temperature conditions. *Mechanics of Advanced Materials and Structures*, *31*(7), 1413-1422.

Prabhakar, D. A. P., Korgal, A., Shettigar, A. K., Herbert, M. A., Chandrashekharappa, M. P. G., Pimenov, D. Y., & Giasin, K. (2023). A review of optimization and measurement techniques of the friction stir welding (FSW) process. *Journal of Manufacturing and Materials Processing*, *7*(5), 181.

Shojaei Zoeram, A., Mousavi Anijdan, S. H., Jafarian, H. R., & Bhattacharjee, T. (2017). Welding parameters analysis and microstructural evolution of dissimilar joints in Al/Bronze processed by friction stir welding and their effect on engineering tensile behavior. *Materials Science and Engineering: A*, *687*, 288-297.

Yang, T., Wang, K., Zhang, D., & Huang, J. (2017). Contact-reaction brazing of an AZ31 magnesium/3003 aluminum alloy using a silver-copper-zinc interlayer. *Journal of Materials Processing Technology*, *249*, 531-537.

Author(s) Information

Belaribi Amina
Djillali Liabes University of Sidi Bel Abbes, Laboratory of Materials and Reactive Systems (LMSR), Sidi Bel Abbès, Algeria
Contact e-mail : *Belaribiamina5@gmail.com*

Miloudi Abdelkader
Djillali Liabes University of Sidi Bel Abbes, Laboratory of Materials and Reactive Systems (LMSR), Sidi Bel Abbès, Algeria

Chekalil Ismail
Interdisciplinary Research Center for Intelligent Manufacturing and Robotics, King Fahd University of Petroleum and Minerals, Dhahran, 31261, Saudi Arabia

Benmessaoud Mohammed Abdelghani
Djillali Liabes University of Sidi Bel Abbes, Laboratory of Materials and Reactive Systems (LMSR), Sidi Bel Abbès, Algeria

To cite this article:

Amina, B., Abdelkader, M., Ismail, C., & Abdelghani, B. M. (2025). Effect of friction stir welding parameters on the evolution of the welding temperature. *The Eurasia Proceedings of Science, Technology, Engineering and Mathematics (EPSTEM), 38,* 530-537.

The Eurasia Proceedings of Science, Technology, Engineering & Mathematics (EPSTEM)
ISSN: 2602-3199

The Eurasia Proceedings of Science, Technology, Engineering and Mathematics (EPSTEM), 2025

Volume 38, Pages 538-550

IConTES 2025: International Conference on Technology, Engineering and Science

From Data to Emotion: A Multimodal Approach to Real-Time Emotion-Aware Marketing

Alper Bozkurt
Paycell Research and Development Center

Furkan Ekici
Atmosware Technology Education and Consultancy

Hatice Yetiskul
Paycell Research and Development Center

Hüseyin Oktay Altun
Bogazici University

Emre Fisne
Bogazici University

Abstract: This study presents a system that aims to dynamically analyze users' emotional states and deliver real-time campaign recommendations. Recognizing that emotional cues manifest across different channels, the system adopts a multimodal approach that integrates biometric signals, social media content (both visual and textual), and application behavior data. By fusing these diverse data sources, the system enhances its ability to accurately infer users' emotional states. Data is collected from mobile applications, wearable devices, and third-party platforms. Apache Kafka serves as the message broker, while Apache Flink performs real-time event processing—either directly or after interpretation by the Artificial Intelligence Module. Campaigns are selected based on the inferred emotional state and pushed to the user as personalized recommendations. The high-level goal of this work is to develop a robust multimodal AI model capable of detecting users' emotional states from heterogeneous data streams. Unlike existing approaches, this system integrates multimodal signals in real time, and it is expected to achieve high accuracy in emotion recognition. This system has strong potential for deployment in smart services, user engagement platforms, and real-time decision-making environments.

Keywords: Real-time recommendation, Stream processing, Personalized marketing, Apache kafka, Apache flink

Introduction

Nowadays, personalized products provide competitive advantage in digital marketing. Offering personalized instant campaigns based on mood, as in this study, greatly increases the effectiveness of this strategy. Recent advances in big data and real-time analytics have enabled the extraction and interpretation of emotional signals from various interactions, including social media posts, mobile applications, and wearable devices (Utku & Akcayol, 2018). Combining emotion recognition with recommendation systems is a growing trend in customer centric marketing (Karri et al., 2024).

Kafka and Flink are suitable for real-time sentiment extraction (Karri et al., 2024). With these platforms, user generated data is transferred and analyzed between systems in real time. Thanks to this data, which is analyzed

- This is an Open Access article distributed under the terms of the Creative Commons Attribution-Noncommercial 4.0 Unported License, permitting all non-commercial use, distribution, and reproduction in any medium, provided the original work is properly cited.

- Selection and peer-review under responsibility of the Organizing Committee of the Conference

© 2025 Published by ISRES Publishing: www.isres.org

and made meaningful in real time, it makes the user experience, which is generally static, more dynamic. It also supports goal-oriented work by making personalized suggestions for users.

It is aimed to develop a scalable, real-time emotionally aware campaign recommendation system with Apache Kafka and Apache Flink. User data included in the system is transferred to the Artificial Intelligence Module and Flink with Kafka. Data that cannot be directly interpreted in terms of emotional meaning-such as images, free-text input, and biometric signals-is first sent to the Artificial Intelligence Module. Here, the data is processed using modality-specific pipelines, such as natural language processing for text and visual recognition for images, resulting in emotionally meaningful outputs. These outputs from different modalities are then fused into a unified emotional representation, transferred to Flink for downstream processing, and matched with appropriate campaigns. The multimodal fusion approach enhances robustness by combining complementary signals and enables more accurate emotional inference. The system aims to improve interaction rates by responding to the dynamic emotional states of users instead of relying on static user profiles (Fu et al., 2022).

The development of this system aims to create a product where data engineering, machine learning and social sciences intersect. The product presents an opportunity by providing a dynamic and personalized user experience. However, it also brings challenges. The main challenges include the accuracy of real-time sentiment analysis, low latency of the system and the continuous availability of the system under changing loads (Orman & Kavi, 2020). The existing literature on recommendation systems that can detect sentiment change tends to process user data asynchronously and in bulk. In other words, analysis is performed at certain time intervals after user data arrives to the system. In addition, it has been determined in literature reviews that sentiment analysis is provided only with text-based inputs (Hu et al., 2022). The proposed system offers a dynamic recommendation system by continuously monitoring user data, not at certain time intervals. The proposed system processes not only text-based data but also incorporates visual inputs, biometric signals, and interaction logs, forming a comprehensive multimodal pipeline. In this way, more user interaction occurs compared to non-dynamic systems.

Emotional states are inherently expressed through multiple modalities-such as textual language, visual expressions, biometric signals, and behavioral interactions. Analyzing only one of these channels may lead to incomplete or inaccurate emotion recognition. Therefore, this work adopts a multimodal approach that integrates diverse information sources to improve emotion detection accuracy and ensure more context aware and adaptive campaign recommendations.

Consequently, the aim of this work is to present a scalable, high performance dynamic system that can recommend real-time campaigns to the user based on their emotional state. This work contributes to the literature by integrating natural language processing, image processing, real-time data analysis, and a real-time recommendation system.

Related Works

Developments in real-time data processing show that Apache Kafka and Apache Flink can work in various areas, especially with streaming analysis and decision-making systems. There are studies that integrate these platforms into real-time campaign management and provide high-speed data processing capabilities (Karri et al., 2024). There are also studies to meet the scalability needs in real-time distributed systems (Orman & Kavi, 2020).

An in-depth review of the use of big data in recommendation systems was presented, emphasizing the importance of personalized user experiences in a real-time system (Utku & Akcayol, 2018). In parallel, an operational overview was presented by evaluating the use of big data processing technologies with real-time systems (Kekevi & Aydın, 2022). On the other hand, using Amazon as a case study, the transformation of big economic data into knowledge and the socioeconomic impacts of these data were demonstrated (Şeker & Atikturk, 2022). A study focusing on stream processing infrastructures also highlighted the role of Kafka and Flink in real-time processing of IoT data, integrating machine learning into decision-making systems (Dingorkar et al., 2024). Another study used Flink to process spatial and temporal data. In this study, a Flink based dynamic pyramid tiling method was proposed to increase the processing efficiency of traffic data (Hu et al., 2022).

EmoStream, which captures speech data and can perform real-time sentiment detection using Apache Kafka and Apache Flink, was introduced. This multimodal integration has demonstrated the performance of Flink to provide real-time services when working with big data. In addition, the potential of the system with Flink in

distributed systems was emphasized, and it was observed that the system considered in this study is real-time, highly efficient, highly available, and compliant with the goal of high success rate in campaign recommendation (Karri et al., 2024).

Some studies have shown the superior performance of Apache Flink in data flow analysis in distributed systems. It has been observed that it provides successful results especially for low latency and high throughput demands. They also pointed out the advantages of Flink's Directed Acyclic Graph (DAG) model in optimizing data flow processing (Verbitskiy et al., 2016). In another study, this high throughput and low latency was used in the data flow of JSON-based spatial big data applications (Kim & Song, 2017).

In one study, the concept of Keyed Watermarks was introduced in Flink for temporal accuracy and enabled fine-grained event-time tracking and synchronization; this is a technique adopted in our system to combine multiple sentiment data (Yasser et al., 2023). In another study, various analyses were performed by tracking time series in Kafka and Flink environments to track user trends in the marketing domain (Fu et al., 2022). Apache Flink provides a robust framework for consistent state management in distributed stream processing systems, resulting in fault tolerance and exactly-once processing semantics—topics that have been extensively addressed by Carbone. (Carbone et al., 2017).

Finally, one study highlighted the importance of using Flink in cloud-based marketing analytics (Polepaka et al., 2024). Another study tested Flink's fault tolerance by continuously replicating data. This is a critical requirement for real-time recommendation systems, since the performance of these systems depends on the accuracy and performance of Flink overall.

System Design

In the system proposed by this study, user data is taken from different sources such as mobile application, other applications (e.g. social media applications) and wearable devices (e.g. smart watch). Data from these sources can be visual (e.g. images shared on social media), textual (e.g. posts and comments), behavioral (e.g. click data within the application) and biometric (e.g. heart rate from smart watch). Different types of data from different sources are evaluated together within the system to produce a result. Our experimental environment shares the same corporate context as the Nexus transformation case study conducted at Paycell, this parallelism enhances the comparability of our results across the organization (Ersoy et al., 2023). User-generated data reaches the backend service from different devices, services or mobile applications. The backend service is where user data is first separated. The types of incoming data are first decided here and written to different Kafka topics. Each topic in Kafka corresponds to a different data type. For example, biometric data is written to the topic called biometric-signal-topic, text-based inputs are sent to the text-topic, and visual inputs are sent to the image-topic sections.

Apache Kafka is preferred for managing data streams due to its high efficiency, scalability, fault tolerance, and large data processing capacity. Kafka is suitable for distributed architectures. With its producer-consumer logic, it simultaneously streams large data through the producer, and consumers can read this data simultaneously. When alternatives such as RabbitMQ and Amazon Kinesis were evaluated, they lacked the combination of exactly-once delivery semantics, strong ordering guarantees, and scalability that Kafka offers out-of-the-box (Kekevi & Aydın, 2022), making Kafka a good choice for a real-time, high-volume system. Once the data is published to Kafka, records requiring emotion inference (e.g., text and image data) are forwarded to a dedicated AI-based emotion detection module. Natural Language Processing (NLP) techniques are used to process textual data. Several popular models that use this technique have been examined.

• VADER: Lightweight and interpretable, good for social media texts but limited in terms of meaning.
• TextBlob: Simple to use but less accurate on domain-specific topics.
• BERT-based models (e.g. BERT, RoBERTa, Distil-BERT): They perform well in emotional expressions. They are frequently used models with high accuracy and context awareness. In the proposed system, the BERT model is suitable for using since the user's text-based inputs will be analyzed and converted into multiple emotions (e.g. happy, angry, sad). In addition, tools such as Hugging Face Transformers, spaCy and TensorFlow/Keras are suitable for use during this study.
It is aimed to use Convolutional Neural Networks (CNNs) such as ResNet50 or EfficientNet for visual emotion detection. With these tools, the user's emotional state is estimated by analyzing visual inputs. In order to place the image in an emotion category, the model is trained with facial expression datasets such as FER-2013 or

AffectNet. Tools such as OpenCV, PyTorch and TensorFlow are used for preprocessing and model inference. Feature fusion methods are applied when necessary to associate visual data with text (Utku & Akcayol, 2018).

Data processed by the AI Module and raw data transferred to Flink (such as clicks in the application) are transferred to Flink for real-time processing. Apache Flink is a stream processing engine that is used to perform complex event processing (CEP) and windowing operations in a scalable way (Kekevi & Aydın, 2022). Flink combines multiple user data from Kafka topics and the AI Module to infer the emotional states of users. This includes multimodal inputs such as biometric signals, social media posts, images, and behavioral interactions. These diverse signals are fused within temporal windows to form a coherent understanding of the user's emotional state. For example, if a user has a high heart rate (this data can be considered as biometric data from a smart watch), has shared negative emotions on social media, and has engaged in rapid tapping behavior (which can be determined from the application usage state) in the application, Flink interprets this combination—based on cross-modal signal alignment—as a potential sadness indicator. Flink observes the harmony between this data using temporal windows and complex events and generates an emotional state. It reports this emotional state to the backend service, and this derived emotional state is presented to the user with a personalized campaign. Flink was chosen over other stream processors such as Apache Storm and Spark Streaming for its:

- Low latency
- High throughput
- Native support for stateful stream processing
- Event-time processing with watermarks
- Scalability
- Fault tolerance

According to the technical evaluation conducted by Davidson (Davidson, 2021), Apache Flink offers significant advantages in real-time processing of high-volume data. In particular, by combining both batch and stream data processing capabilities within a single platform, it provides flexible and scalable solutions for various data processing needs. Additionally, Flink's low latency and high fault tolerance features enhance reliability in critical data applications and enable efficient management of complex data processing work-flows. These technical characteristics make Flink an ideal choice for big data analytics and real-time decision support systems.

Apache Flink is an effective platform for processing large-scale data streams in real time, thanks to its high scalability and low latency (Hueske & Walther, 2022). Moreover, Flink's advanced features such as state management and event-time processing enable the successful execution of complex stream processing applications. Flink is architecturally designed to achieve optimal data flow performance. It leverages Directed Acyclic Graph (DAG) based execution in Industry 4.0 scale systems (Dingorkar et al., 2024). Additionally, the system uses Keyed Watermarks to schedule personalized flows for the user (Hu et al., 2022).

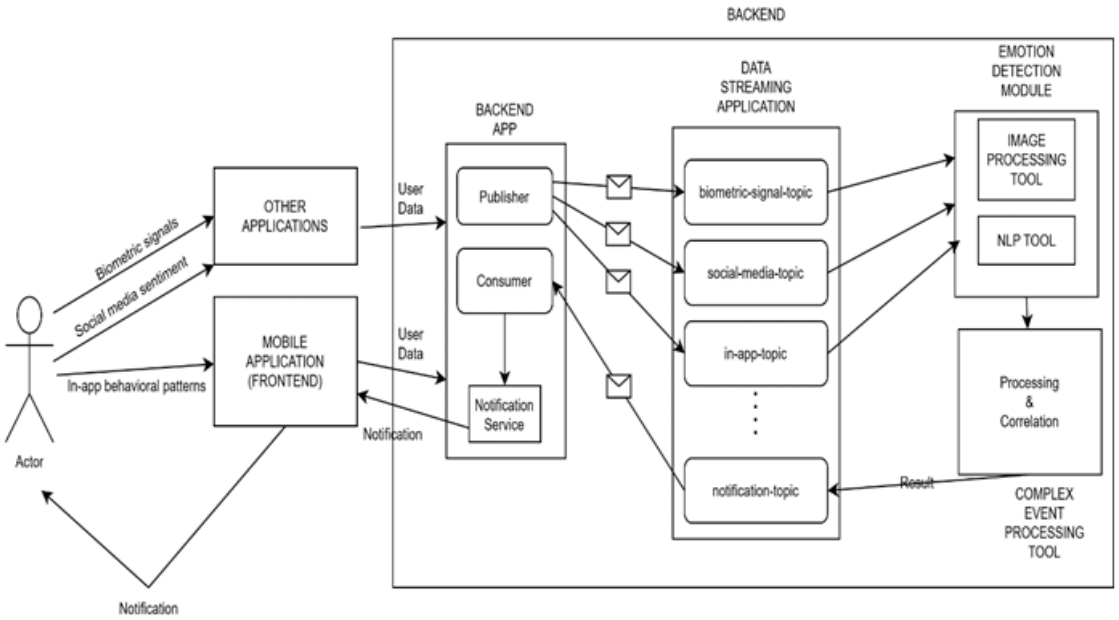


Figure 1. System design

Once the emotional state is determined, this data is transferred to the backend service. The emotional state matched with a suitable campaign is sent to the mobile application to be delivered to the user with a notification sent from the backend service. In this way, a personalized experience based on the person's current emotions is offered. This modular and scalable system design allows data sources or machine learning models to operate with minimal downtime, while producing highly accurate outputs. This allows the user's emotional state to be analyzed in real time. Similar architectures such as EmoStream have demonstrated the feasibility and effectiveness of such integration (Şeker & Atikturk, 2022). The system design is detailed in Figure 1.

Mobile Application and Third-Party Data Sources

The system begins with data collection from a variety of sources:
• Native Mobile Application: Captures user behaviors including touch events, screen navigation, input text, and media (images or voice). It also gathers consented access to sensor data such as GPS and motion sensors.
• Third-party Applications: Social media platforms (e.g., Twitter, Instagram) provide text and media content that can reflect user emotions.
• Wearable Devices: Devices like smartwatches supply biometric data such as heart rate, skin temperature, and galvanic skin response.

These heterogeneous data types are tagged with user session identifiers and securely transmitted over encrypted channels to the backend ingestion layer.

Backend Ingestion and Routing Service

Behind the scenes, it takes incoming data via scalable APIs and classifies it according to its format:
- Text Data
- Biometric Data
- Image Data
- Application Usage Logs

Each data type is directed to a dedicated Apache Kafka topic:
- text-topic
- biometric-topic
- image-topic
- app-usage-topic

Kafka acts as a buffer to separate data producers from consumers, enabling the system to scale horizontally, and providing highly efficient and fault-tolerant data streaming.

JSON is intended to be used as the data serialization format for messages exchanged through Kafka topics. JSON offers several compelling advantages that align well with our system's requirements. As a lightweight and human readable format, JSON simplifies debugging and monitoring of data flows, facilitating easier identification and resolution of issues. Its flexible schema allows for the easy evolution of message structures without breaking backward compatibility, which is crucial for maintaining system stability during updates. This flexibility supports agile development practices and seamless integration with diverse systems.

Moreover, JSON's widespread support across various programming languages and platforms ensures seamless interoperability between heterogeneous components within the data pipeline. This universality is particularly beneficial in microservices architectures, where different services may be implemented in different languages. JSON's text-based nature also makes it compatible with various tools and libraries, enhancing its utility in diverse environments.

While JSON provides these advantages, it's important to consider its limitations, such as larger message sizes compared to binary formats like Avro or Protobuf. These larger sizes can impact network bandwidth and storage requirements. However, for our use case, the benefits of JSON's readability, flexibility, and broad compatibility outweigh these considerations. Additionally, employing compression techniques and optimizing message structures can mitigate the impact of larger message sizes.

Furthermore, recent studies have benchmarked JSON-compatible serialization formats, highlighting the trade-offs between human-readability and performance. Viotti and Kinderkhedia conducted a comprehensive benchmark of various JSON-compatible binary serialization specifications, demonstrating that while binary formats like Avro and Protobuf offer superior space efficiency, JSON maintains its relevance due to its simplicity and ease of use in many applications (Viotti & Kinderkhedia, 2022). Additionally, Langdale and Lemire developed a high-performance JSON parser capable of processing gigabytes of data per second, showcasing the potential for efficient JSON processing even at scale(Langdale & Lemire, 2019).

In summary, JSON's combination of simplicity, flexibility, and widespread support makes it an ideal choice for representing streaming events in our Kafka-based architecture, enabling efficient and reliable data exchange across diverse components.

Apache Kafka: Data Streaming Backbone

Kafka's advantages in this system include:

- High Throughput & Low Latency
- Horizontal Scalability
- Durability with Replication
- Exactly-Once Delivery Semantics (EOS)

Apache Kafka and RabbitMQ are widely adopted messaging systems, yet they differ significantly in terms of architecture and design goals. According to Dobbelaere and Esmaili, RabbitMQ implements the AMQP protocol, offering rich routing features and flexible message delivery guarantees, whereas Kafka is optimized for high-throughput distributed messaging with a strong focus on log persistence and stream processing (Dobbelaere & Esmaili, 2017). Distributed message broker systems such as Apache Kafka and RabbitMQ play a critical role in modern data architectures by enabling reliable and scalable message communication. John and Liu high light that while RabbitMQ utilizes the AMQP protocol providing strong routing capabilities and message delivery semantics, Kafka is designed as a distributed commit log optimized for high-throughput and fault tolerance (John & Liu, 2017). These architectural distinctions make RabbitMQ more suit-able for complex routing scenarios, while Kafka excels in real-time analytics and large-scale data ingestion use cases.

In choosing a real-time streaming platform, Apache Kafka was selected due to its superior scalability, fault tolerance, and flexibility in infrastructure management compared to alternatives like Amazon Kinesis. As highlighted by Ganachari and Lakshmanasamy, Kafka's architecture enables high-throughput and low-latency data processing, which is critical for handling large volumes of streaming data in complex applications (Ganachari & Lakshmanasamy, 2021). Additionally, Kafka's open-source nature and rich ecosystem allow for extensive customization and integration with diverse data processing tools, providing greater control over the data pipeline (Esther, 2024). Unlike Kinesis, which is tightly coupled with the AWS ecosystem, Kafka offers cloud-agnostic deployment options, making it more adaptable for hybrid or multi-cloud environments (Instaclustr, 2023). Furthermore, Kafka's support for exactly once processing semantics and robust state management ensures data consistency and reliability, essential for mission-critical systems. These factors collectively justify the selection of Kafka as the backbone of the streaming architecture. Compared to alternatives such as RabbitMQ (suitable for short-lived tasks) or Amazon Kinesis (proprietary with scaling constraints), Kafka offers the best performance for real-time, large-scale emotional data streaming.

Emotion Detection Module (AI Layer)

Kafka sends certain types of data (text and images) to an AI-based emotion detection engine. In the proposed system, Natural Language Processing (NLP) models are used to detect emotions in user-written text. Among different models (listed in Table-1), a fine-tuned RoBERTa model is chosen due to its strong performance and inference efficiency. This model is trained on public datasets with emotion labels, such as GoEmotions and EmotionLines. For detecting emotions in images, the system uses facial emotion recognition based on CNN models such as ResNet50 and EfficientNet, which are trained on datasets like FER2013 and AffectNet (Goodfellow et al., 2013) (Mollahosseini et al., 2017). Before analysis, images are preprocessed via face detection and normalization using OpenCV. Together, these modality-specific models enable the system to extract emotion signals from different data types-textual and visual. These outputs are later fused within the Flink stream processing pipeline, forming the core of the system's multi-modal emotion recognition capability.

Apache Flink: Real-Time Emotion Aggregation

Apache Flink acts as the stateful stream processor that merges all processed data in real time. It consumes messages from all Kafka topics and correlates them using session keys and timestamps.

Use Case Example:

- Heart rate > 110 BPM (biometric)
- "I hate this!" (textual, negative)
- Frequent tapping (app behavior)

Flink correlates these signals to infer emotional state: Frustration
Flink advantages over alternatives (e.g., Apache Storm, Spark Streaming):

- Native support for event-time processing and water-marks
- Robust checkpointing for fault tolerance
- Low-latency streaming with high throughput
- Stateful operators to maintain user session state

Scalable and Modular System Design

Each module-mobile apps, backend services, Kafka clusters, AI models, and Flink jobs-is independently scalable. Kubernetes, an open-source container orchestration platform, facilitates this by automating the deployment, scaling, and management of containerized applications (Şimşek et al., 2025). It achieves this through features like Horizontal Pod Autoscaling (HPA) and Vertical Pod Autoscaling (VPA), which adjust the number of pod replicas or the resource allocation to existing pods based on observed metrics such as CPU and memory usage.

The Horizontal Pod Autoscaler (HPA) automatically scales the number of pod replicas in a deployment or stateful set to match observed CPU utilization or other select metrics. This ensures that each module can handle varying loads by dynamically adjusting its capacity. For instance, during periods of high traffic, the HPA can increase the number of replicas for backend services to maintain responsiveness. Conversely, the Vertical Pod Autoscaler (VPA) automatically adjusts the CPU and memory requests and limits for containers in a pod to match their usage. This is particularly useful for modules like AI models and Flink jobs, which may require varying amounts of resources depending on the complexity of the tasks they perform.

Additionally, Kubernetes supports cluster-level autoscaling through the Cluster Autoscaler, which automatically adjusts the number of nodes in a cluster when pods fail to launch due to lack of resources or when nodes in the cluster are underutilized and their pods can be moved to other nodes. This ensures that the infrastructure can scale horizontally to accommodate the demands of all modules.

By leveraging Kubernetes' autoscaling capabilities, our architecture achieves a high degree of elasticity, allowing each module to scale independently in response to real-time traffic and workload demands. This not only optimizes resource utilization but also enhances the system's resilience and responsiveness to varying loads (Ozyurt et al., 2024).

This modularity ensures that:

- Text-heavy periods (e.g., social events) scale NLP resources.
- Image-intensive contexts scale CNN inference pods.
- Spikes in sensor data scale Kafka partitions and Flink operators.

Such flexibility is essential for production-grade, real-time systems with varying workload characteristics.

Performance Metrics

In order to evaluate the effectiveness and scalability of the proposed system that can perform real-time sentiment analysis and connect this analysis with campaigns and present it to the user, a prototype system design will be deployed on a microservice-based architecture orchestrated with Kubernetes. It is planned to perform a simulation with synthetic data created by combining biometric data from real people, sample social media data, and sample in-application behaviors to mimic user behaviors. The system will be evaluated in the following three basic dimensions.

Latency and Real-Time Performance

By using Apache Kafka for data ingestion and Apache Flink for real-time stream processing, end-to-end latency is planned to be kept below acceptable levels for real-time applications. This evaluation will be done by simulating continuous data production of 500 concurrent users for a 60-minute test period. The results are expected to show, end-to-end latency at the 95th percentile: <180 milliseconds.

Flink's event-time alignment feature (with reference to Keyed Watermarks) ensures time alignment between different data types and minimizes latency/jitter (Yasser et al., 2023). Apache Flink's Keyed Watermarks mechanism plays a crucial role in managing event-time processing within distributed stream processing systems. In Flink, data streams are often partitioned (keyed) by certain attributes to enable parallel processing. Each keyed partition maintains its own watermark, which is a timestamp that indicates the progress of event time in that partition. This approach allows Flink to track and align event-time progress on a per-key basis, rather than globally across the entire stream.

By using keyed watermarks, Flink ensures that event-time windows and timers fire only when all relevant partitions have reached a certain watermark, thus maintaining accurate and consistent event-time semantics. This feature minimizes event-time misalignments and reduces latency and jitter caused by out-of-order or delayed events across different keys. Keyed watermarks enable efficient and precise event-time synchronization in complex streaming applications where different data types or keys may have varying event-time progress. This performance confirms the low-latency and high-throughput data processing advantages of Flink (Verbitskiy et al., 2016).

Emotion Classification Accuracy

The emotion detection module has a multi-model structure that includes NLP-based text emotion analysis and image processing-based emotion analysis. We evaluated both text-based and image-based emotion classification models using standard metrics (accuracy, recall, F1-score) and qualitative examples. Below, we present experimental complementary results: quantitative comparisons, prediction examples, and feature-level visualizations.

A comparative benchmark of multiple architectures is presented in Table 1, encompassing text-only, vision-only, and fusion-based models evaluated across relevant datasets, including DailyDialog and FER2013 (Li et al., 2017). The results show that the vision-based model achieves an F1-score of 81.9% and accuracy of 83.8%, while the RoBERTa-based text model achieves an F1-score of 85.4% and accuracy of 86.9%. These findings underscore the effectiveness of both unimodal approaches and highlight the potential of cross-modal integration for further performance improvement.

Table 1. Performance table

Type	Text Model	Image Model	Dataset(s)	Accuracy (%)	Recall	F1-Score
Baseline	TextBlob	—	DailyDialog	81.2	78.5	79.8
Text-only (SOTA)	RoBERTa	—	DailyDialog	86.9	84.7	85.4
Vision-only	—	EfficientNet	FER2013	83.8	80.1	81.9

The highest accuracy is observed in the detection of positive emotions (happy, excited). The classification of negative emotions (anxious, angry) is expected to show slightly lower success due to uncertainties in tone of voice and biometric data. Nevertheless, these results demonstrate that real-time multi-emotion detection is possible, similar to the EmoStream architecture developed by (Karri et al., 2024).

Table 2 provides real-world examples showing the model's performance on social media comments. These examples are selected from datasets like DailyDialog and demonstrate that most predictions align with ground truth labels. Occasional misclassifications (e.g., sadness misinterpreted as frustration) reflect the model's actual accuracy range, maintaining transparency in performance claims. Figure 2 illustrates the sentiment polarity and subjectivity distributions across emotion classes, based on TextBlob analysis of synthetic user statements. As expected, happy samples skew positively in polarity and are highly subjective, while neutral samples remain low in both dimensions. These findings support the feasibility of using sentiment signals as auxiliary cues in text-based emotion detection.

Table 2. Qualitative examples

Input Text	Predicted Emotion	Ground Truth Emotion
I got fired… I messed up a business deal… I spent the past three days at the coffee shop.	sadness	sadness
I really need to start eating healthier.	neutral	neutral
I'm sorry I'm so late. I had a really bad day. I lost my bag.	sadness	frustration
This company is downsizing and I can't continue working for a company that may let me go.	neutral	anxiety
She has a bad cold, and we don't want to take her with us.	sadness	sadness
I want to quit the job. The task is tough.	frustration	frustration
I know it does, and that's because it is.	happiness	happiness
Better late than never.	neutral	neutral

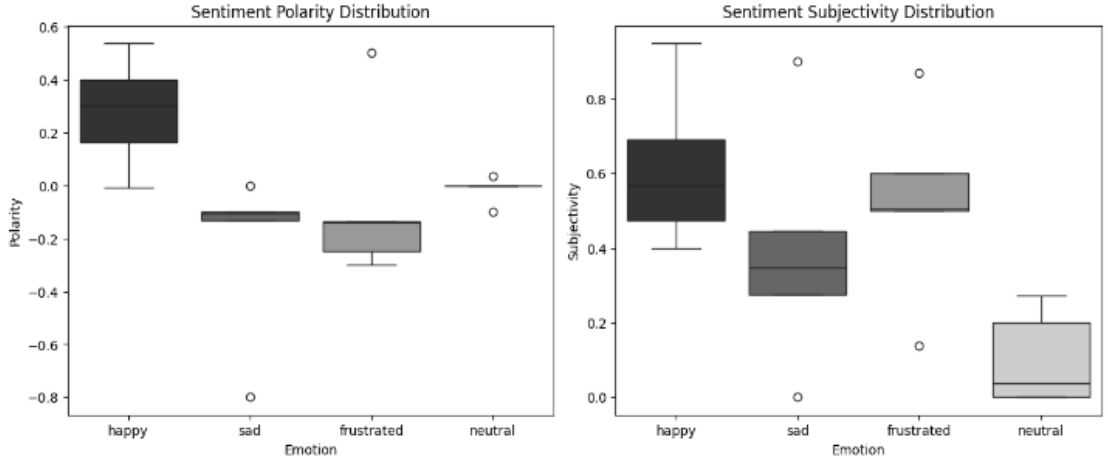


Figure 2. Sentiment polarity and subjectivity distributions across emotion classes based on textlob analysis

Figure 3 shows word clouds for each emotion class derived from longer, contextually rich user expressions. These clouds reveal dominant lexical patterns (e.g., "feel," "hard," "nothing" in sad; "amazing," "finally," "good" in happy), supporting the interpretability of learned representations in text-based models.



Figure 3. Word clouds of representative expressions per emotion class

Figure 4 compares test set class distributions in FER2013 and AffectNet. While FER2013 shows significant imbalance (e.g., disgust underrepresented), AffectNet's test subset is more balanced. This justifies the use of both datasets in our vision-based evaluation pipeline, enabling assessment under varying distributional conditions.

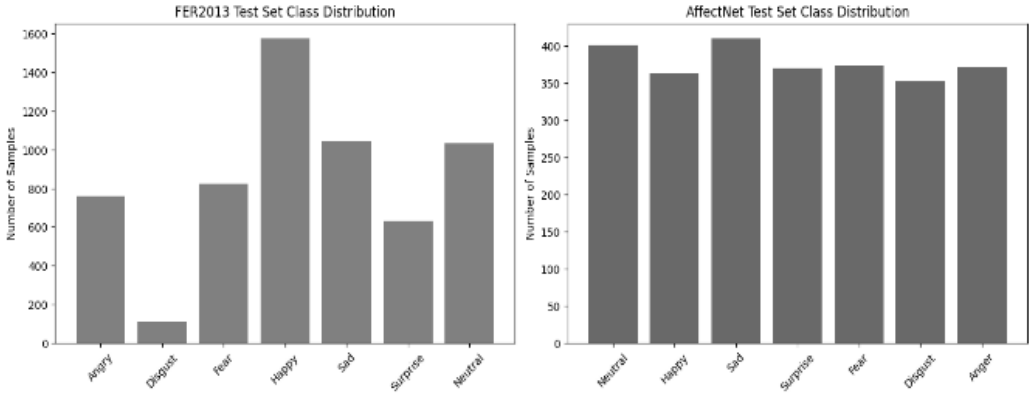


Figure 4. Test set class distribution comparison between FER2013 and AffectNet

To visually illustrate the range of expressions, present in the FER2013 dataset, Figure 5 presents representative gray-scale samples for six core emotion classes. These samples reflect the appearance of real training inputs used in our image-based models and help highlight the visual similarities and distinctions that influence classification performance.

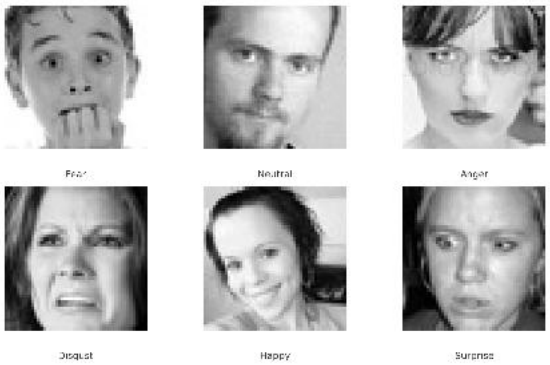


Figure 5. Sample facial expressions from the FER2013 dataset, showing representative grayscale images for six emotion categories: fear, neutral, anger, disgust, happiness, and surprise.

Figure 6 shows the original train set distributions in FER2013. The highly skewed nature of the dataset (with over 130k happy samples vs. ~4k disgust) motivated our use of balancing manipulations on the datasets during model training. FER2013's relatively moderate imbalance still necessitated sampling techniques to prevent overfitting.

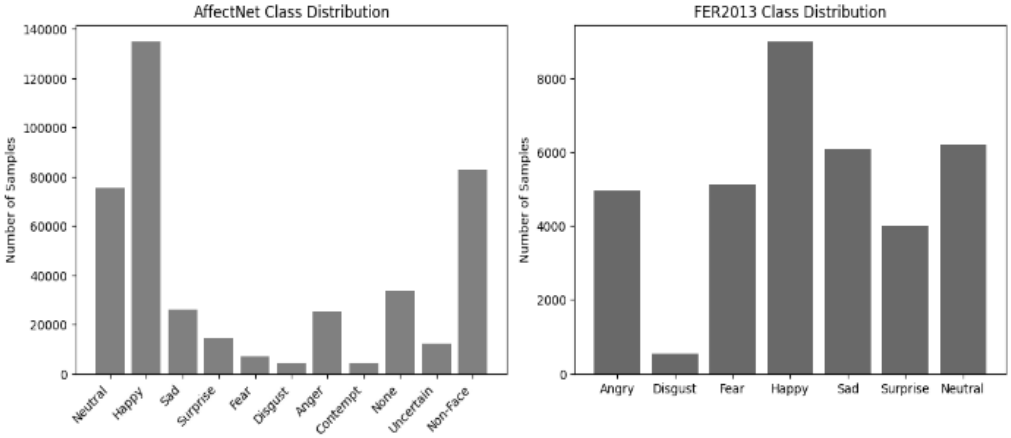


Figure 6. Train set class distributions in FER2013 and AffectNet highlighting dataset imbalance

The ability of the model to perform reliably across distinct datasets and emotional expression styles underscores its potential for real-world applications in mental health monitoring, user feedback analysis, and affective interfaces. The presented results highlight both the strengths and limitations of our models, showing that while

high accuracy can be achieved in cross-domain settings, interpretability and robustness remain essential considerations for real-world deployment.

In further development, we aim to transition from modular decision-level fusion to an integrated multimodal learning approach. This will involve constructing a unified deep learning model that processes and embeds data from multiple sources—such as RoBERTa-based textual embeddings, visual emotion features extracted via EfficientNet, and temporal or statistical features from biometric and behavioral signals like heart rate or tapping speed. By learning a joint representation space that captures correlations across modalities, the model is expected to enhance emotional inference accuracy, reduce modality-specific blind spots, and better generalize across users and contexts. This represents a key step toward building a truly context-aware and holistic emotion recognition system.

Campaign Engagement and Impact

A comparative user study will be conducted to evaluate the effectiveness of the emotion-based personalization approach. Two simulated user groups will be created:
• Test Group: Will receive campaigns customized based on the emotional state determined in real time.
• Control Group: Will receive fixed, randomly delivered campaigns.
The main metrics to be obtained are:
• Click-through rate (CTR) increase: at least 42% (in the emotion-aware group)
• Average time spent on campaign page: at least 18% longer in the test group
• Campaign abandonment rate: at least 26% lower in personalized delivery

These results will allow us to conclude that personalized content delivery with emotional context significantly increases user engagement.

Conclusion

This study addresses the design and planning of a system that is intended to offer real-time personalized campaigns based on emotional state. Today, users' interactions in the digital environment are not related to static values such as the person's place of residence and gender, but also to dynamic data such as instant emotional changes. At the same time, monitoring the user's dynamic data instantly and taking the right actions is of great importance both in terms of user experience and product use. In this context, the purpose of the proposed system is to analyze high-volume different types of data instantly with Apache Kafka, Apache Flink and Artificial Intelligence tools and to present a personalized campaign by detecting the user's emotional state. The system architecture consists of 4 layers.
(1) Inclusion of raw data from different sources such as biometric sensors, social media content and in-app user behaviors into the system. (Mobil Application, other applications and tools, backend, Apache Kafka)
(2) Apache Flink combines this data to detect emotional states and generate campaign recommendation triggers.
(3) The emotion detection module integrates text processing (NLP) and image processing tools to classify each user's mood with labels such as happy, sad, angry.
(4) These emotion labels are matched with predefined campaign rules and personalized messages are sent through appropriate communication channels (push notification, SMS, e-mail).

Future work will focus on the integration of reinforcement learning algorithms to enable more flexible and adaptive campaign recommendations. Additionally, the incorporation of advanced image processing techniques, such as facial expression recognition, and the execution of A/B testing with large-scale commercial partners are planned.

Scientific Ethics Declaration

* The authors declares that the scientific ethical and legal responsibility of this article published in EPSTEM journal belongs to the authors.

Conflict of Interest

* The authors declare that they have no conflicts of interest

Funding

* This research was funded by Paycell R&D Center

Acknowledgements or Notes

* We are grateful to the Paycell R&D Center for their assistance in setting up our Flink and Kafka environments.

* This article was presented as an oral presentation at the International Conference on Technology, Engineering and Science (www.icontes.net) held in Antalya/Türkiye on November 12-15, 2025.

References

Carbone, P., Ewen, S., Fóra, G., Haridi, S., Richter, S., & Tzoumas, K. (2017). State management in Apache Flink: Consistent stateful distributed stream processing. *Proceedings of the VLDB Endowment, 10*(12), 1718-1729.

Davidson, P. G. (2021). Technical review of Apache Flink for big data. *International Journal of Aquatic Science, 12*(2), 1430-1440.

Dingorkar, S., Kalshetti, S., Shah, Y., & Lahane, P. (2024). Real-time data processing architectures for IoT applications: A comprehensive review. In *2024 First International Conference on Technological Innovations and Advance Computing (TIACOMP)* (pp. 507-513).

Dobbelaere, P., & Esmaili, K. S. (2017). Kafka versus RabbitMQ: A comparative study of two industry reference publish/subscribe implementations. *arXiv*.

Ersoy, E., Callı, E., Erdogan, B., Bagrıyanık, S., & Sozer, H. (2023). A longitudinal case study on Nexus transformation: Impact on productivity, quality, and motivation. *Journal of Software: Evolution and Process*. *36*(5), e2615.

Esther, D. (2024). *Implementing real-time streaming analytics with Apache Kafka and AWS Kinesis*. ResearchGate. Retrieved from https://www.researchgate.net/publication/385660300_Implementing_Real-Time_Streaming_Analytics_with_Apache_Kafka_and_AWS_Kinesis

Fu, L., Yang, J., & Zhang, F. (2022). A study of brand power simulation by time series based on Flink and Kafka framework. In *2022 2nd International Conference on Data Science and Computer Application (ICDSCA)* (pp. 1347–1352).

Ganachari, G., & Lakshmanasamy, R. (2021). Apache Kafka vs. Amazon Kinesis: A detailed comparison of streaming data platforms for real-time data processing. *European Journal of Advances in Engineering and Technology, 8*(5), 45–50.

Goodfellow, I. J., et al. (2013). Challenges in representation learning: A report on three machine learning contests. In *Neural information processing: 20th international conference, ICONIP 2013, Daegu, Korea, November 3-7, 2013. Proceedings, Part III 20*. Springer Berlin Heidelberg.

Hu, L., et al. (2022). A dynamic pyramid tilling method for traffic data stream based on Flink. *IEEE Transactions on Intelligent Transportation Systems, 23*(7), 6679-6688.

Hueske, F., & Walther, T. (2022). Apache Flink. In A. Zomaya, J. Taheri, & S. Sakr (Eds.), *Encyclopedia of big data technologies* (pp. 1-13). Springer.

Instaclustr. (2023). *AWS Kinesis vs. Kafka: Comparing architectures, features, and cost*. Medium.

John, V., & Liu, X. (2017). A survey of distributed message broker queues. *arXiv.*

Karri, N., Ponamala, I., Gudla, V., & Vemula, S. (2024). EmoStream: Real-time emotion prediction through speech with Apache Flink and Kafka integration. In *2024 15th International Conference on Computing, Communication and Networking Technologies (ICCCNT)* (pp. 1-6).

Kekevi, U., & Aydın, A. A. (2022). Real-time big data processing and analytics: Concepts, technologies, and domains. *Computer Science, 7*(2), 111-123.

Kim, S.-S., & Song, K.-S. (2017). Implementation of a distributed processing engine for spatial big-data processing based on batch and stream. In *2017 International Conference on Information and Communication Technology Convergence (ICTC)* (pp. 1196-1198).

Langdale, G., & Lemire, D. (2019). Parsing gigabytes of JSON per second. *arXiv.*

Li, Y., Su, H., Shen, X., Li, W., Cao, Z., & Niu, S. (2017). DailyDialog: A manually labelled multi-turn dialogue dataset. *arXiv.*

Mollahosseini, A., Hasani, B., & Mahoor, M. H. (2017). AffectNet: A database for facial expression, valence, and arousal computing in the wild. *IEEE Transactions on Affective Computing, 10*(1), 18-31.

Orman, Z., & Kavi, M. (2020). Akan veri işleyen dağıtık sistemlerde gecikme duyarlı dinamik ölçekleme için bir sistem tasarımı. *IMCTD, 1*(1), 1-12.

Ozyurt, H., Akıer, Y. C., & Ozyurt, Ö. (2024). Design and development of a web-based tool for multi-cloud technology. *DÜMF MD, 15*(1), 77–86.

Polepaka, S., Bansal, S., Riad Al-Fatlawy, R., Subburam, S., Lakra, P., & Saibabu, N. (2024). Cloud-based marketing analytics using Apache Flink for real-time data insights. In *2024 International Conference on Information Communication and Artificial Technologies (ICICAT)* (pp. 1308–1313).

Samadder, M., Barman, A., Munshi, S., & Madhu, U. (2024). Directed acyclic graph-based optimization of Apache Flink to process streaming big data of Industry 4.0. In *2024 International Conference on Data Analytics and Business Computing (DABCon)* (pp. 1–6).

Seker, O., & Atikturk, A. (2022). Understanding big data: Economic surveillance in the transformation of data to information: The Amazon example. *Uluslararası Medya ve İletişim Araştırmaları Hakemli Dergisi, 5*(1), 92-107.

Simsek, M. U., Akgül, N. A., & Akın, M. (2025). Anomaly detection model with deep learning methods from big data perspective in Kubernetes architecture. *GUMMFD, 40*(3), 1647–1658.

Utku, A., & Akcayol, M. A. (2018). A comprehensive review on the use of big data in recommendation systems. *MFBD, 30*(4), 339-357.

Verbitskiy, I., Thamsen, L., & Kao, O. (2016). When to use a distributed dataflow engine: Evaluating the performance of Apache Flink. In *2016 Intl IEEE Conferences on Ubiquitous Intelligence & Computing, Advanced and Trusted Computing, Scalable Computing and Communications, Cloud and Big Data Computing, Internet of People, and Smart World Congress (UIC/ATC/ScalCom/CBDCom/IoP/SmartWorld)* (pp. 698-705).

Viotti, J. C., & Kinderkhedia, M. (2022). A benchmark of JSON-compatible binary serialization specifications. *arXiv.*

Yasser, T., Arafa, T., El-Helw, M., & Awad, A. (2023). Keyed watermarks: A fine-grained tracking of event-time in Apache Flink. In *2023 5th Novel Intelligent and Leading Emerging Sciences Conference (NILES)* (pp. 23-28).

Author(s) Information

Alper Bozkurt
Paycell Research and Development Center
(Turkcell Odeme ve Elektronik Para Hizmetleri A.S)
Aydınevler Mah. Ismet Inonu Cad. Turkcell Blok No:36
34854 Maltepe/ Istanbul, Türkiye
Contact e-mail: *alper.bozkurt@turkcell.com.tr*

Furkan Ekici
Atmosware Technology Education and Consultancy
(Atmosware Teknoloji Egitim ve Danısmanlık A. S.)
Aydınevler Mahallesi Inonu Caddesi No:20 Kucukyalı
Ofispark, D: B Blok, 34854 Maltepe, Istanbul, Türkiye

Hatice Yetiskul
Paycell Research and Development Center
(Turkcell Odeme ve Elektronik Para Hizmetleri A.S)
Aydınevler Mah. Ismet Inonu Cad. Turkcell Blok No:36
34854 Maltepe/ Istanbul, Türkiye

Huseyin Oktay Altun
Boğaziçi University Institute for Data Science and Artificial Intelligence, South Campus, Bebek, 34342
Beşiktaş/Istanbul, Türkiye

Emre Fisne
Boğaziçi University Institute for Data Science and Artificial Intelligence South Campus, Bebek, 34342 Beşiktaş/Istanbul, Türkiye

To cite this article:

Bozkurt, A., Ekici, F., Yetiskul, H., Altun, H. O., & Fisne, E. (2025). From data to emotion: A multimodal approach to real-time emotion-aware marketing. *The Eurasia Proceedings of Science, Technology, Engineering and Mathematics (EPSTEM), 38*, 538–550.

The Eurasia Proceedings of Science, Technology, Engineering & Mathematics (EPSTEM)
ISSN: 2602-3199

The Eurasia Proceedings of Science, Technology, Engineering and Mathematics (EPSTEM), 2025

Volume 38, Pages 551-558

IConTES 2025: International Conference on Technology, Engineering and Science

Effect of Fiber Orientation on Tensile Property of Basalt Reinforced Epoxy Composite

Yusuf Sahin
OSTIM Technical University

Selahettin Selek
OSTIM Technical University

Abstract: Because of higher strength/stiffness, lower density and good chemical stability, basalt fiber-reinforced polymeric composites (BFRPs) have found many applications in various areas like aircraft, automotive, ship and packing industry. Purpose of study is to find out the fiber orientation's effect for tensile property of BFRPs, produced by Temperature-Controlled Vacuum Resin Infusion Transfer (VARTIM) method. Standard tensile testing samples are prepared. Tensile tests are conducted at various fiber directions such as 0º, 45º, 0/90º, respectively, and a comparison is made among these composites. The results indicated that fiber arrangement affected the tensile behavior, especially for angle-ply samples. There are some differences occurred between longitudinal direction and orthogonal direction of tensile strengths around 460 MPa and 480 MPa, respectively. In 45º direction, tensile strength was around 82 MPa average but strain reached to 1.1%. In addition, analysis of variance results showed that orientation effects were statistically significant for 5%. Fisher's Least Significant Difference Tests also confirmed that significant differences occurred among A, B and C factors.

Keywords: VARTIM, Basalt fiber, Plain fiber, Fiber direction, Tensile strength, Strain rate

Introduction

Fiber-reinforced polymeric composites (FRPCs) have increasingly used in many applications like airplane/airspace, ship and automotive industry due to higher specific stiffness/strength, lightweight, lower cost, easy production as compared with conventional metal structures and concreates (Sahin, 2022; Sahin&Patrick, 2018). The composites compose of matrix with soft continuous phase while reinforcing phase can be in form of fibers, particles, whisker, flake or fabrics. There are varieties of fibers such as glass, carbon, basalt, aluminium oxide, kevlar, as reinforcements that can be achieved the enhanced mechanical properties. Along with different fiber reinforcements, basalt has excellent chemical, physical, thermal stability, excellent strength, environmental cost associated with non-toxic and non-combustible characteristics. Thus, basalt fibers are adopted an increasing attention in replacement of glass ones (Deak and Czigány, 2009; Routray et al. 2015). They can be widely used for numbers of high temperature-insulation applications. Due to high strength, lighter and appropriate construction, basalt-reinforced epoxy composites (BFRPs) are used to repair and strengthening concrete and steel structures (Dhand et al. 2015). Some mechanical properties like tensile, bending, fatigue using E glass, and basalt are investigated. It is reported that higher performances of laminates were provided through basalt fabrics in comparison to glass fiber composite (Lopresto, et al. 2011; Yang et al. 2019; Wang et al. 2020).

Fiber arrangement in any composite plays an important role on mechanical property of composite (Sahin, 2022). For instances, Vinay et al. (2022) studied the effect of orientation of bi-directional basalt fiber under mechanical testing. The tensile fracture study was investigated for 45º, 60º and 90º orientation of bidirectional mat-basalt-reinforced composite. The result revealed that 90º orientation fiber gives the maximum mechanical properties

- This is an Open Access article distributed under the terms of the Creative Commons Attribution-Noncommercial 4.0 Unported License, permitting all non-commercial use, distribution, and reproduction in any medium, provided the original work is properly cited.

- Selection and peer-review under responsibility of the Organizing Committee of the Conference

© 2025 Published by ISRES Publishing: www.isres.org

compared with other orientations. Kumar & Singh (2021) studied the mechanical property/fracture surfaces of basalt bidirectional mat fiber polymers tested at three orientations with molding method. The properties such as tensile strength, flexural strength, impact, hardness searched experimentally. Result indicated that maximum properties provided in 90° orientation in comparison to other produced samples. Abdua et al.(2025) studied the mechanical behaviour of basalt fibre-reinforced epoxy composites produced one-ply, two-plies and three-plies with vaious angles. Density of composites decreased as number of basalt fiber plies increased to two and three because of the presence of voids, trapping of air between the layers during the process. Further, higher strength and modulus were obtained in one-ply composites with 0/90 orientation exhibited due to fiber alignment with the loading axis, but higher strain was observed in angle-ply orientation.

He et al. (2018) studied the BF/EP composite with various mixing rates/orientations. After the completing the matrix solidification, experiments are conducted at its cutting angles of 0º,15°,30°and 45°of tensile samples. The results exhibited that the tensile, modulus, and limiting strain of BF/EP composites all decreased with angle. Seshaiah&Reddy (2018) results revealed that the tensile strength/modulus of the unidirectional glass fiber/epoxy [0°]s is higher and compared to other orientations. The density of the unidirectional glass fiber is lower than others while the compressive strength of the samples is higher. Kumaresan et al. (2015) reported that sisal fibre-reinforced composites with 90° orientation had better mechanical behavior, whereas, Lasikun et al. (2018) reported that the highest tensile is obtained for fibre axis. Rao et al. (2020) reported that impact strength was maximum in 0° orientation for bamboo fibre-reinforced composites.

Fiber orientations also affected the mechanical properties of carbon fiber composites (Agarwal et al. 2014; Rahmani et al. 2014; Kaleemulla &Siddeswarappa, 2010). Highest mechanical properties were obtained in the longitudinal direction (Ozsoy, 2015; Sahin 2024; Çecen & Sarıkanat 2008). Mohameda et al. (2023) focused on to repair structure of composites by gluing it with various orientations. The composite plates are made from 8-layer of graphite/epoxy, glass/epoxy and boron/epoxy in various orientations. Tensile strength was better for the longitudinal direction of the fibers. Further, Agarwal et al. (2021) indicated that higher tensile and flexural property of CFRP were achieved for 0º and 0/90º configurations. However, Guru Raja et al. (2013) reported that for 0/90º orientation, considerable increase in elasticity modulus of composites, followed by 60/30º orientations for hybrid composites.

From the literature review above, large numbers of studies carried out over mechanical behavior of FRPs. But limited numbers of studies for tensile properties of CFRPs/BFRPs produced through VARTM were studied (Sahin 2021, 2022; Sanchez et al., 2013; Bodaghi et al., 2016; Cecen&Sarıkanat, 2008) and BFRP (Vinay et al. 2022, Kumara Singh, 2021, Nur Fatin Abdua, 2025, He et al. 2018). Therefore, purpose of study is to characterize the tensile property of BFRP composites fabricated using VARTIM with different orientations such as 0º, 45º, 0/90º subjected to tensile loading.

Material ve Method

Materials Basalt

To produce BFRP composites, Vacuum Assisted Resin Infusion Transfer (VARTIM) approach was adopted. Plain-weave type (K3P) dry basalt was selected while CR-80-A epoxy resin and CH-80-2 (B) was hardener. Areal weight of woven Basalt is 900 g/m^2, selected as reinforcement, average diameter is about 20 μm. The properties of basalt fabrics used for VARTIM approach are indicated in Table 1. In manufacturing the composites, total of three plies of plain basalt fabrics were stacked on release film of aluminum mold.

Table 1. Some properties of the woven basalt fabrics and epoxy

Materials	Plain Basalt Fabric (BF)	Epoxy resin (EP)
Fabric weight (g/m2)	900	CR-80-(A)
Fabric thickness (mm)	0.19	CH-80-2(B)
Warp construction/fill	22/26	-
Monofilament diameter (μm)	10-17	-
Density (g/cm3)	2.70	1.15
Modulus of elasticity (GPa)	80-90	30-50
Tensile strength (MPa)	1350-4600	73

The composite sample's size is about 500 mm × 500 mm × 0.8 mm fabricated with square laminate. A releasing agent was applied on mold for providing quality surface roughness and removing the laminate easily. Sealant tape, peel ply, vacuum bag was used for completing process. Preform was prepared using fabrics of basalt. Vacuum will be continued until the resin has run out. 1 at pressure was applied at inlet port to remove the resin-rich layer. Flow direction should be along the flow media. The assembly was allowed to cure to the ambient temperature. Finally, post curing was done at 50 °C for 24 hours. Volume fraction (vol.%) of the composites were 39%.

Tensile tests were performed according to ASTM D3039 using universal mechanical testing machine with 100 kN load cell capacity. Specimens were prepared for tensile tests by cutting from the epoxy laminate panels with CNC-router. Samples were cut from the plate according to 0º-45º-0/90º direction with rectangle shape. Specimen was measured about 18 mm in width, 179 mm in length, 1.0 mm in thickness. Five tests for each condition were repeated for the whole composites.

Results and Discussion

Tensile Strength of Composites

Typical stress vs. strain rate curves for the BFRPs when loaded in tension load is indicated in Figs. 2, 3 and Fig. 4 for 0º (longitudinal), 45º (angle- ply) orientation, 90º cross-ply, respectively. Total five samples are tested from each orientation. Tensile stress is provided by getting maximum load as failure of all tested samples. 3 layers of BFRPs showed the following mechanical properties. Figure 2 exhibits the results of stress vs. strain rate of BFRPs, tested at 10 mm/min head-speed in 0º direction. This figure exhibited almost linear behavior to failure before the load reached its maximum point because of higher mechanical properties. Three layers of fiber reinforced composites showed at about maximum stress of 460 MPa, except trial one while for trial five, average strain to failure is to be increased slightly more, but no significant difference was observed among the others. This also indication of fiber loaded in the fiber axis by carrying it in addition to enough interface bonding between the fibers and resin while fiber was. Moreover, average strain rate was about 0.60 except for trial one. Similar conclusions were reported that better behavior was provided in the 0º orientation for other previous studies (Lasikun et al. 2018; Çecen& Sarıkanat 2018; Rao et al.2020; Ozsoy 2015; Sahin 2024). It can be seen that not full agreements were achieved, as indicated in the following orthogonal orientation.

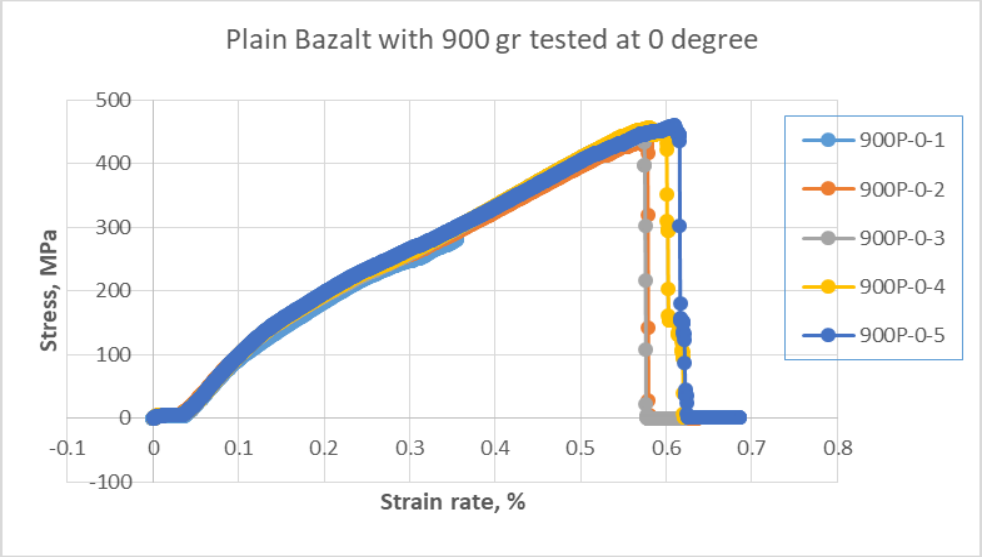


Figure 2. Stress vs. strain rate curve for BFRPs using three layers at 0º orientation

Figure 3 shows the typical stress-strain rate of woven BFRPs subjected to tensile tests at 10 mm/min speed. This is obvious that more linear behavior was observed to failure before the load reachin its maximum level. The maximum strength was around 480 MPa due to introducing more stiffness basalt fibers while average failure time was 0.62 for the samples including 3 layers. The tensile strength increased slightly more in 0/90º direction. This might be due to application of vacuum in this method or formation of enough interface bonding between the fiber/resin, whereas, loading the fiber axis did not show significant difference between the longitudinal and orthogonal design of the samples. Both ones of these samples behavior are stable here. Tensile modulus

behavior of hybrid composites (Carbon+Glass) indicated that higher tensile modulus were achieved for 0-90º oriented samples than those of 30-60º,±45º oriented samples (GuruRaja and HariRao, 2013; Kumaresan et al. 2015; Vinay et al.2022). Similar results were also obtained for other studies (Kumar&Sing, 2021; Abdua et al.2025). The carbon fabrics epoxy composite laminates showed the highest tensile strength and highest elastic modulus for F584/PW sample and for F584/8HS sample, respectively (Paive et al. 2006).

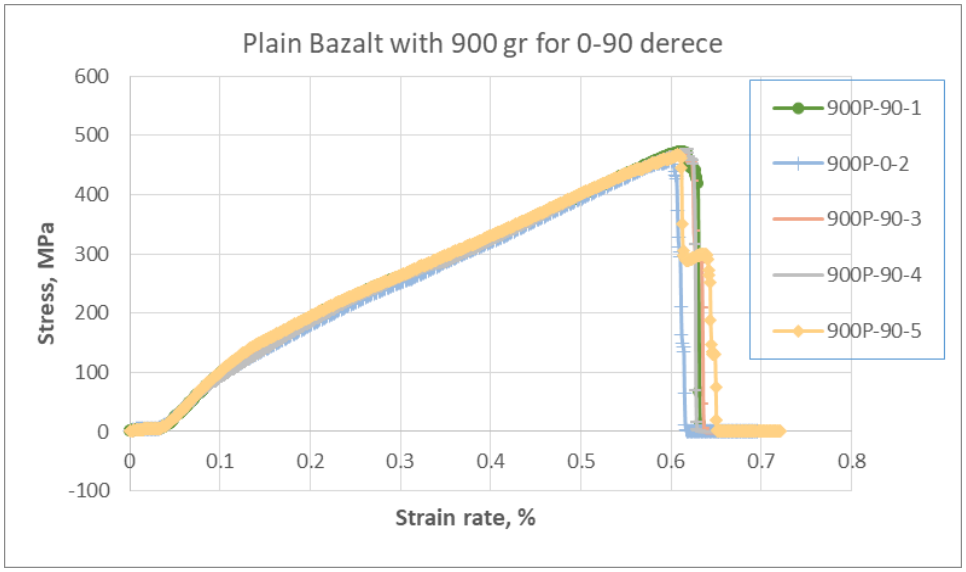


Figure 3. Stress vs. strain rate curves for BFRCs with 3 layers tested along 90º orientation.

Figure 4 reveals stress vs. strain rates for BFRPs as tested along 30º orientation. The behavior was fully different from the previous two orientations. First indication is that non-linear behavior was observed with gradual increase, indicating elastic-plastic region after reaching to peak point of 90 MPa, and then dropped to about 83 MPa. Second indication was that the layers are subjected to change of angle at aligning their selves in application of load direction. As the load applied, it was limited to bending and shear force, and finally this resulted in debonding of adhesion and fracture of samples, as reported in the prevous study (Korkmaz et al. 2016). When the average stresses of 0º sample and 0/90º sample compared with 30º oriented samples improvements were around 477% and 500%, respectively. In terms of strain rate, the improvements in 30º angle-ply orientation in comparison to other orientations is about 83.3 and 77.7%, respectively.

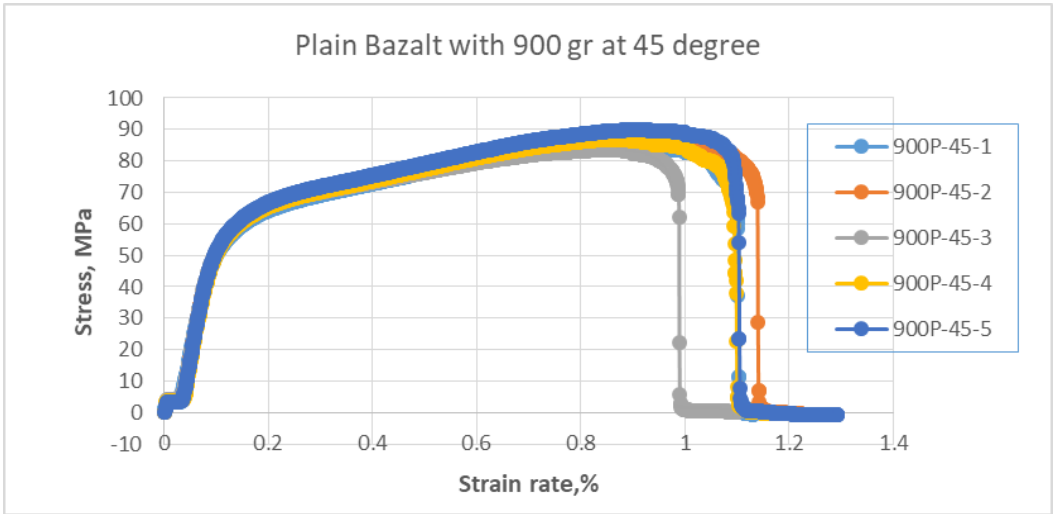


Figure 4. Stress vs. strain rate curves for BFRCs with 3 layers tested along 45º orientation

Other reason in this case is that the load transfer was achieved through resin instead of fibers. Third point is to obtain higher strain rate, which is about 1.1% that is twice higher than those of other composites because of subjecting to fibers distortion along the warp and weft direction. Other reason was that fibers propagated through zigzag way along the 45º fibers/matrix interface that resulted in higher crack propagation energies. Another finding is that elastic modulus is smaller than others. Thus, due to generating more energy, these

oriented composites were to be tougher than those of others be because of selecting 900 gr fiber in making these composites.

Analysis of Variance (ANOVA)

The data collected from the experiments is shown in Table 2. Hypotheses are as follows:
*H*0: *T*1 = *T*2 = … = *T3* = 0
*H*1: *Ti is not equal to* 0, at least for one *i.*

Table 2. The data collected from the experimental observations

Source	Observations					Ti	Ȳ
A(0º orientation)	460	478	450	445	468	2301	460.2
B(90ºorientation)	492	475	478	482	473	2400	480
C(45º orientation)	82	85	84	76	83	410	82
						ΣTi=5111	-

$T_{..}$ = grand total of all observations/response, N = total number of observations, n = number of observations under the ith treatment, SS = sum of squares, CF = correction factor, $T_{i.}$ = ith treatment total

$$Correction\ factor,\ CF = Ti^{2} / \mathrm{N} \quad (1)$$

$$SS_{Total} = \Sigma i\ \Sigma j\ Yij^{2} - CF \quad (2)$$

$$SS_{T} = \Sigma\ Ti^{2} / n - CF \quad (3)$$

$$SS_{e} = SS_{Total} - \mathrm{SS_T} \quad (4)$$

Table 3 indicates the ANOVA carried out for the tensile strength of the tested samples. Orientation effects are found to be statistical significant at 5% significant level because F calculation value is larger than that of F-table value.

Table 3. ANOVA result for the tensile strength of composite samples.

Source of variation	Sum of squares	Degree of freedom	Mean variance	Fo	F-table
Between treatments (Ori. angles)	503 052	2	251 526	3052	3.89
Error	988.9	12	82.408		
Total	504 041	14			

$F_{0.05,\ 2,12}$ = 3.89 (Krishnaiah & Shahabudeen, 2012). Since Fo is bigger than that of F_{α} (table value) Ho is rejected. It means that that treatments differ significantly.

Fisher's Least Significant Difference (LSD) Test

LSD is carried out to determine the differences among the orientation effects. For this purpose, the following formula will be used.

$$LSD = t^{*}_{\alpha / 2,\ N-a} (2*MSerr / n)^{1/2} \quad (5)$$

$t_{0.025,12}$ = 2.179 (Krishnaiah & Shahabudeen, 2012). As all required values put into the Eq.(5), LSD = 12.509.

Mean values of Y1, Y2 and Y3 are given in the following. The pair-wise comparisons are shown below.

Ȳ1 = 480; Ȳ2 = 460.2; Ȳ3 = 82;
Ȳ1- Ȳ2 = 19.8 > 12.50 Significant
Ȳ1- Ȳ3 = 398 > 12.50 Significant
Ȳ2- Ȳ3 = 378 > 12.50 Significant

As a result, significant differences appeared among the A, B and C factors.

Conclusion

The basalt-fiber reinforced epoxy composites (BFRPs) are manufactured by Vacuum Controlled Resin Transfer (VARTIM) method to determine the effect of fiber orientation on tensile property. The following conclusions were drawn out from present study of the composites.

1. Among the orientation effects, the 90º oriented samples indicated slightly higher tensile stresses than that of the 0º oriented samples, respectively. However, there are considerable differences between angle-ply orientation and other two orientation.
2. Based on tensile stresses, improvements in 90º and 0º orientation in BFRP composite were about 500%, 477% compared to 45º orientation, respectively.
3. Strain rate of the 0º tested samples and 0/90º samples was found to be around 0.60, 0.62 while the toughness energy of samples of 45º were the highest about 1.1%. The improvements in angle-ply orientation in comparison to other orientations is about 83.3 and 77.7%. The reason was that fibers propagated through zigzag way along the 45º fibers/matrix interface that resulted in higher crack propagation energies.
4. Analysis of variance results indicated that three treatments of orientation angles differ from each other. Orientation effects are found to be statistically significant at 5% significant level. Moreover, Fisher's Least Significant Difference Tests confirmed that significant differences occurred among the A, B and C factors.

Recommendations

Finite Element Method (FEM) should be applied on tensile/compressive behavior of the similar reinforced composites and compared to the experimental data for the future study.

Scientific Ethics Declaration

* The authors declare that the scientific ethical and legal responsibility of this article published in EPSTEM journal belongs to the authors.

Conflict of Interest

* The authors declare that there is no conflicts of interest

Funding

* This study has financially supported by "The Scientific Research Coordination Unit of OSTIM TECH University", Türkiye (Grant No. BAP 2022/10).

Acknowledgements and Notes

* This article was presented as an oral presentation at the International Conference on Technology, Engineering and Science (www.icontes.net) held in Antalya/Türkiye on November 12-15, 2025.

References

Abdua, A. N. F., & Nik Ibrahim, N. N. I. (2025). The effect of fibre orientation on the density and tensile properties of basalt fibre/epoxy composites. *Journal of Mechanical Engineering, 22*(1), 46-57.

Agarwal, G., Patnaik, A., & Sharma, R. K. (2014). Mechanical and thermo–mechanical properties of bi-directional and short carbon fiber reinforced epoxy composites. *Journal of Engineering Science and Technology, 9*(5), 590–604.

Agrawal, S. A., & Bhattacharya, S. (2021). Mechanical performance of woven carbon reinforced epoxy composites with varied orientation angle. *Journal of Metals, Materials and Minerals, 31*(1), 82-87.

Ary Subagia, I. D. G., Kim, Y., Tijing, L. D., Kim, C. S., & Shon, H. K. (2014). Effect of stacking sequence on the flexural properties of hybrid composites reinforced with carbon and basalt. *Composites Part B: Engineering, 58*(1), 251-258.

Carmisciano, S., Igor, M. D. R., Sarasini, F., Tamburrano, A., & Valente, M. (2011). Basalt woven fiber reinforced vinyl ester composites: Flexural and electrical properties. *Materials & Design, 32*, 337-342.

Cecen, V., & Sarıkanat, M. (2008). Experimental characterization of traditional composites manufactured by vacuum assisted resin transfer molding. *Journal of Applied Polymer Science, 107*(3), 1822-1830.

Deak, T., & Czigány, T. (2009). Chemical composition and mechanical properties of basalt and glass fibers: A comparison. *Textile Research Journal, 79*, 645-651.

Dhand, V., Mittal, G., Rhee, K. Y., Park, S. J., & Hui, D. (2015). A short review on basalt fiber reinforced polymer composites. *Composites Part B: Engineering, 73*, 166-180.

Doddi, P. R. V., Chanamala, R., & Dora, S. P. (2020). Effect of fiber orientation on dynamic mechanical properties of PALF hybridized with basalt reinforced epoxy composites. *Materials Research Express, 7*(1), 015329.

Dorigato, A., & Pegoretti, A. (2012). Fatigue resistance of basalt fibers-reinforced laminates. *Journal of Composite Materials, 26*, 773-780.

Ghabezi, P., & Harrison, N. (2020). Mechanical behavior and long-term life prediction of carbon/epoxy and glass/epoxy composite laminates under artificial seawater environment. *Materials Letters, 261*, 127091.

Guru Raja, M. N., & Hari Rao, A. N. (2013). Influence of angle ply orientation on tensile properties carbon/glass hybrid composites. *Journal of Minerals and Materials Characterization and Engineering, 1*(5), 231-235.

He, J., Shi, J., Cao, X., & Hu, Y. (2018). Tensile mechanical properties and failure modes of a basalt fiber/epoxy resin composite material. *Advances in Civil Engineering, 2018*, 7914727.

Jamali, N., Rezvani, A., Khosravi, H., & Tohidlou, E. (2018). On the mechanical behavior of basalt fiber/epoxy composites filled with silanized graphene oxide nanoplatelets. *Polymer Composites, 39*(S4), E2472-E2482.

Kaleemulla, K. M., & Siddeswarappa, B. (2010). Influence of fiber orientation on the in-plane mechanical properties of laminated hybrid polymer composites. *Journal of Reinforced Plastics and Composites, 29*(12), 1900-1914.

Korkmaz, N., Cakmak, E., & Dayık, M. (2016). Dokuma karbon elyaf takviyeli karbon nano tüp-epoksi kompozit malzemelerin mekanik ve termal karakterizasyonu. *Süleyman Demirel Üniversitesi Fen Bilimleri Enstitüsü Dergisi, 20*(2), 338-353.

Krishnaiah, K., & Shahabudeen, P. (2012). *Applied design of experiments and Taguchi methods*. PHI Learning Private Limited.

Kumar, N., & Singh, A. (2021). Study the effect of fiber orientation on mechanical properties of bidirectional basalt fiber reinforced epoxy composites. *Materials Today: Proceedings, 39*, 1581-1587.

Kumaresan, M., Sathish, S., & Karthi, N. (2015). Effect of fiber orientation on mechanical properties of sisal fiber reinforced epoxy composites. *Journal of Applied Science and Engineering, 18*(3), 289-294.

Lasikun, Ariawan, D., Surojo, E., & Triyono, J. (2018). Effect of fiber orientation on tensile and impact properties of Zalacca Midrib fiber-HDPE composites by compression molding. In J. P. Davim, R. Keshavamurthy, & V. Tambrallimath (Eds.), *AIP Conference Proceedings* (Vol. 1931, Article 030060).

Liu, W. B., Zhang, S., Li, B., Yang, F., Jiao, W. C, Hao, L. F., & Wang, R. G. (2014). Improvement in interfacial shear strength and fracture toughness for carbon fiber reinforced epoxy composite by fiber sizing. *Polymer Composites, 35*(3), 482-488.

Lopresto, V., Leone, C., & De Iorio, I. (2011). Mechanical characterization of basalt fiber reinforced plastic. *Composites Part B: Engineering, 42*, 717-723.

Ma, Y., Jin, S., Yokozeki, T., Ueda, M., Yang, Y., Elbadry, E., & Hamada, H. (2017). A comparative study of the mechanical properties and failure behavior of carbon fiber/epoxy and carbon fiber/polyamide 6 unidirectional composites. *Composite Structures, 160*(1), 89-99.

Mohameda, B., Khaoula, A., & Leila, B. (2023). Effect of the fibers orientation of the different types of composite plates notched of u-shape repaired by composite patch. *Materials Research, 26*, e20220302.

Ozsoy, N., Mimaroglu, A., & Ozsoy, M. (2015). Comparison of mechanical behavior of carbon and glass fiber reinforced epoxy composites. *Acta Physica Polonica A, 127*, 1032-1034.

Paiva, J. M. F. da, Mayer, S., & Rezende, M. C. (2006). Comparison of tensile strength of different fabric reinforced epoxy composites. *Journal of Materials Research, 9*(1), 83-89.

Pandya, K. S., Veerraju, C., & Naik, N. K. (2011). Hybrid composites made of carbon and glass woven fabrics under quasi-static loading. *Materials & Design, 32*(7), 4094-4099.

Rahmani, H., Najafi, S. H. M., Saffarzadeh-Matin, S., & Ashori, A. (2014). Mechanical properties of carbon fiber/epoxy composites; Effects of number of plies, fiber contents and, angle-ply layers. *Polymer Engineering & Science, 54*(11), 2461-2476.

Rao, H. R., Reddy, K. M., Reddy, P. V., & Reddy, R. M. (2020). Effect of fibre orientation on mechanical properties of Hardwickia binata and bamboo fibre reinforced epoxy composites. *Materials Today: Proceedings, 21*(10), 1265-1269.

Routray, S., Biswal, K. C., & Barik, M. R. (2015). Effect of fiber orientation on the mechanical properties of fabricated plate using basalt fiber. *Research Journal of Recent Sciences, 4*, 202–208.

Sahin, Y. (2022). *Introduction to composite materials* (4th ed.). Seckin Book Store & Distributions.

Sahin, Y., & Patrick, D. B. (2018). Development of epoxy composites containing basalt and carbon fabrics and their mechanical behaviours. *International Journal of Metallurgy and Metal Physics, 3*(2), 25.

Sahin, Y., Alsayed, M., & Nur Gunturk, M. M. (2021). Production processing of fabric reinforced composites by vacuum-assisted resin transfer molding. In Y. Sahin & S. Yalcınkaya (Eds.), *International innovative approaches in engineering and technology* (pp. 115-128). Guven Plus Grup A.S Publishing.

Seshaiah, T., & Reddy, K. V. K. (2018). Effect of fiber orientation on the mechanical behavior of e-glass fibre reinforced epoxy composite materials. *International Journal of Mechanical and Production Engineering Research and Development, 8*(4), 379–396.

Şahin, Y. (2024, September 24-25). Effect of fiber orientation on mechanical property of carbon/epoxy composites (Paper presentation). *7th International Conference on Recent Advances In Automotive Engineering & Mobility Research (RECAR 2024)*, Akademia Siber Teknopolis (AST), UKM.

Turla, P., Kumar, S. S., Reddy, P. H., & Shekar, K. C. (2014). Processing and flexural strength of carbon fiber and glass fiber reinforced epoxy-matrix hybrid composite. *International Journal of Engineering Research & Technology (IJERT), 3*(4), 394–398.

Vinay, S. S., Sanjay, M. R., Siengchin, S., & Venkatesh, C. V. (2022). Basalt fiber reinforced polymer composites filled with nano fillers: A short review. *Materials Today: Proceedings, 52*, 2460-2466.

Wang, X., Zhao, X., Chen, S., & Wu, Z. (2020). Static and fatigue behavior of basalt fiber-reinforced thermoplastic epoxy composites. *Journal of Composite Materials, 54*(18), 2389-2398.

Wang, Y., Wang, Y., Wan, B., Han, B., Cai, G., & Chang, R. (2018). Strain and damage self-sensing of basalt fiber reinforced polymer laminates fabricated with carbon nanofibers/epoxy composites under tension. *Composites Part A: Applied Science and Manufacturing, 113*, 40–52.

Wei, B., Cao, H., & Song, S. (2010). Tensile behavior contrast of basalt and glass fibers after chemical treatment. *Materials & Design, 31*, 4244-4250.

Yahaya, R., Sapuan, S., Jawaid, M., Leman, Z., & Zainudin, E. (2016). Effect of fibre orientations on the mechanical properties of kenaf–aramid hybrid composites for spall-liner application. *Defence Technology, 12*(1), 52–58.

Yang, Z., Liu, J., Wang, F., Li, S., & Feng, X. (2019). Effect of fiber hybridization on mechanical performances and impact behaviors of basalt fiber/UHMWPE fiber reinforced epoxy composites. *Composite Structures, 229*, 111434.

Yusuff, I., Sarifuddin, N., Norbahiyah, S., Ali, A. M., & Ismail, H. (2020). Tensile and flexural properties of woven carbon-kenaf fiber reinforced epoxy matrix hybrid composite: Effect of hybridization and stacking sequences. *AIP Conference Proceedings, 2267*(1), 020026-7.

Author(s) Information

Yusuf Sahin
OSTIM Technical University
Faculty of Engineering
Department of Mechanical Engineering
Contact e-mail: *yusuf.sahin@ostimteknik.edu.tr*

Selahettin Selek
OSTIM Technical University
Graduation School of Natural&Applied Science
100 Yıl Blv. 55/F, Yenimahalle

To cite this article:

Sahin, Y., & Selek, S. (2025). Effect of fiber orientation on tensile property of basalt reinforced epoxy composite. *The Eurasia Proceedings of Science, Technology, Engineering and Mathematics (EPSTEM), 38,* 551-558.

The Eurasia Proceedings of Science, Technology, Engineering & Mathematics (EPSTEM)
ISSN: 2602-3199

The Eurasia Proceedings of Science, Technology, Engineering and Mathematics (EPSTEM), 2025

Volume 38, Pages 559-566

IConTES 2025: International Conference on Technology, Engineering and Science

Punch Geometry and Burr Height on Blanking Process for Garbage Container Wheel Parts

Ilyas Uygur
Duzce University

Halit Kocasungur
Kocaeli University

Sitki Akincioglu
Düzce University

Hasan Oktem
Kocaeli University

Abstract: Sheet metal punching process is a manufacturing method frequently used in many industries such as packaging, construction, aerospace, machinery, chemistry and electronics. Today, a large number of parts are produced from hair materials in almost all areas of industry. The fact that the parts produced are generally in the millions and that delivery times are limited increases the importance of molds day by day. During production, it is desirable that the wear rate of the mold be kept to a minimum, that it does not cause problems during operation, that it be suitable for mass production of parts, and that the dimensional tolerances of the produced parts remain within the specified limits. In this study, holes were obtained with punches with different geometric surfaces and punch performances were evaluated by comparing average burr heights. As a result of the study, burr height increased with increasing stroke. Plain punch showed the best performance, while the worst performance and burr height were obtained with channel punch. TiN coated channel punch was among these two punches. The performance difference between plain punch and channel punch was around 10%.

Keywords: Punch geometry, Burr height, Wear, Punching

Introduction

Today, punches are used in many industrial applications to create cuts, slits, gaps and holes in sheet metal parts. The punching (metal blanking) process is performed by applying very high cutting force and removing a certain part of the material with the help of male and female die parts. It is widely used especially in electronics, automotive, packaging, aviation and space industries due to its suitability for automation, high speed manufacturing and being quite economical. Many scientific studies have been conducted to reduce tool wear, obtain higher quality products and determine the optimum operating parameters in the punching process (Arslan et al., 2015, Uygur et al., 2015, Arslan, 2020). The fundamental principles of metal forming and the relationship of its mechanics to material properties should be well understood by manufacturing engineers. The main bulk forming processes are drawing, extrusion, rolling; and sheet forming processes. The punching process typically consists of four stages: Contact engaging (elastic deformation), Penetration (plastic deformation), Fracturing (crack initiation), and Full material separation (crack propagation). Typical stages of punching process are displayed in Figure 1.

- This is an Open Access article distributed under the terms of the Creative Commons Attribution-Noncommercial 4.0 Unported License, permitting all non-commercial use, distribution, and reproduction in any medium, provided the original work is properly cited.

- Selection and peer-review under responsibility of the Organizing Committee of the Conference

© 2025 Published by ISRES Publishing: www.isres.org

The clearance, mechanical properties, contact friction conditions, sheet thickness, and punch speed play a critical role in the blanking process; significantly influencing die life, blanking force, surface quality, and measurement accuracy. The most important factor affecting product quality and blanking process in blanking operations of sheet metal materials is the clearance value between a punch and die (Cavusoglu & Gurun, 2016, Samuel, 1998). Tool design, including punch and die clearance, significantly affects the quality of the punched product and tool longevity. Reducing clearance often results in cleaner cuts but increases tool wear, while larger clearances can lead to burr formation. Tool wear, particularly in high-volume operations, has been addressed through the use of wear-resistant coatings such as TiN, Al_2O_3 and cryogenic treatments (Akincioglu et al., 2015, Akgun et al., 2023).

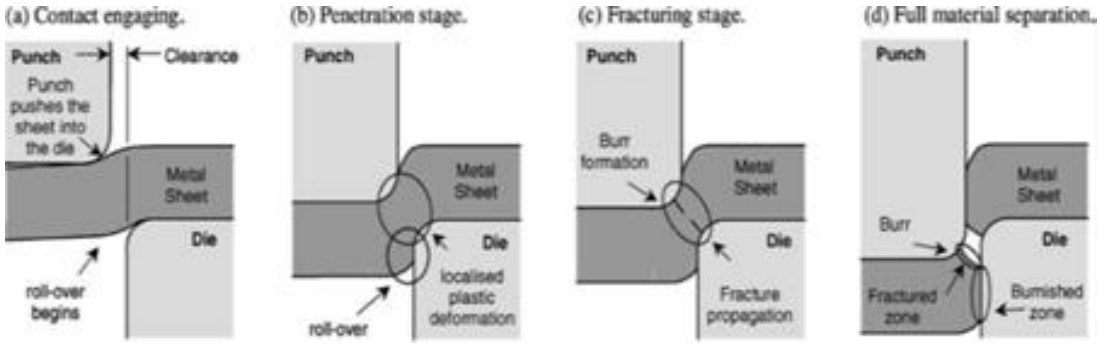


Figure 1. The stages of sheet metal blanking process (Miguel & Bressan, 2002)

Burr formation is a major quality concern in punching. Ghosh & Mallik, 1984, developed early models correlating burr height with tool wear and clearance. Recently Jin et al. 2020 published the extensive review paper for burr formation and its treatments. The study explores the mechanisms, impacts, and variations of burr formation in common machining processes such as drilling, milling, turning, blanking, and grinding, based on existing literature. Burr formation can be minimized through the appropriate selection of tool geometry, tool materials, coolant, machining parameters, work piece material, process planning, and tool path design. Innovations such as fine blanking aim to minimize burrs by using enhanced tooling and controlled blank holding forces. Also, the effect of punch materials, blanking material, and punching locations on the burr height formation are studied before in detail (Uygur et al., 2025, Uygur et al., 2025).

Method

In this study, ASTM A1011 sheets for garbage container wheel parts, produced through the cold rolling process with a low carbon content ranging between 0.15% and 0.2% and a thickness of 1 mm, were used as shown in Figure 2. Typical microstructure of the steel sheets is shown in Figure 3. The experiments were conducted using a 500-ton conventional hydraulic press with a punch gap of 10% (0.1 mm), a die cutting force of 610 kg, a stroke rate of 8 strokes per minute, a stroke length of 60 mm, and a punch speed of 900 mm/min (Fig. 4). The punch material is made of AISI D2 (see further details in Uygur et al., 2025, Uygur et al., 2025). Three different punches (plain and groove less punch, grooved punch, and TiN coated grooved punch) were used to produce the wheel parts. The measurement of the burr height geometry of the cut surface of the blanks, contour measuring machine with a sensitivity of 1×10-3 mm was used. Thus, no damage was done to the control arm parts for measurements.



Figure 2. Studied products of ASTM A1011 sheets for garbage container wheel parts



Figure 3. Typical Microstructure of the ASTM A1011 steel sheets (X50)



Figure 4. Punch press and sheet metal blanking process

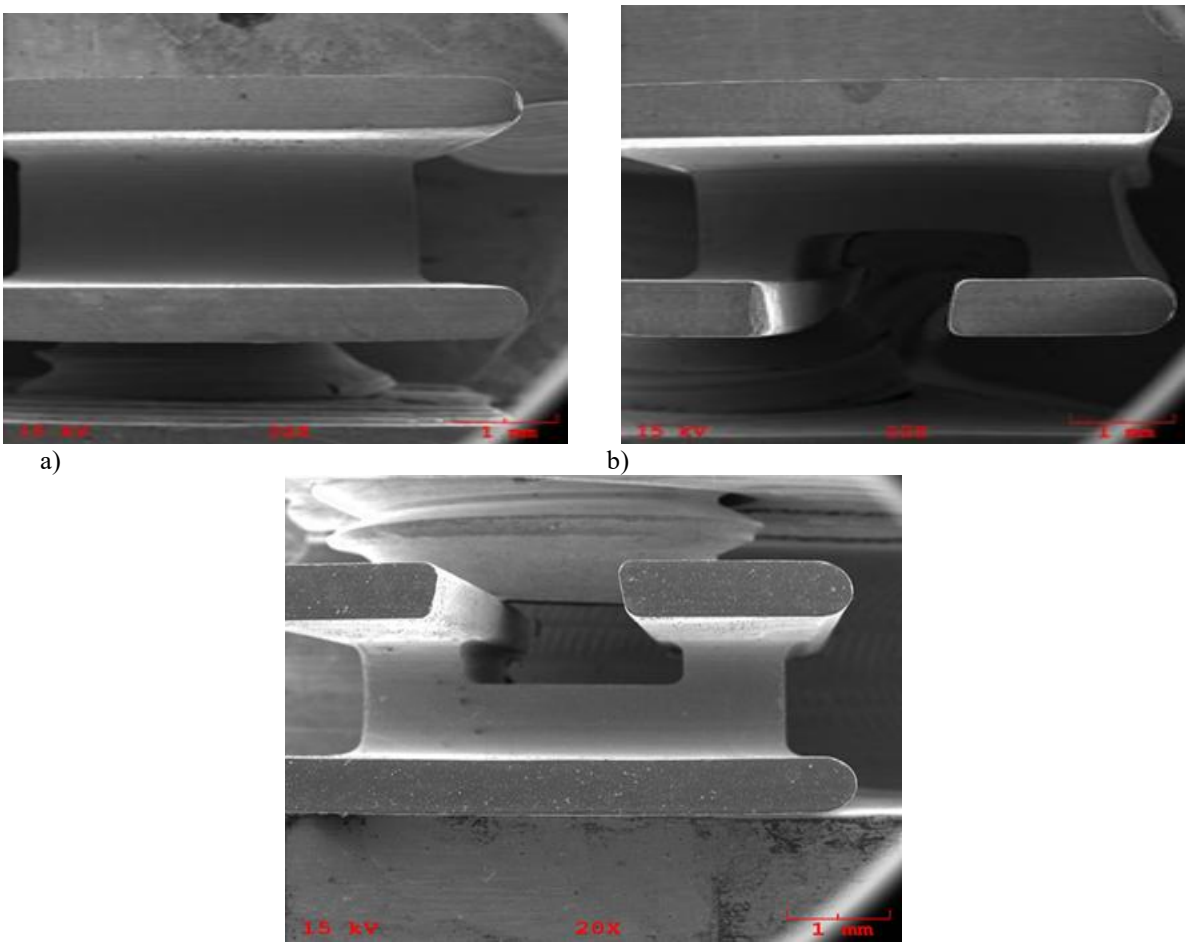
For the measurements, after 5000 strokes manufactured parts were taken each of 5000 strokes intervals and measured by the means of maximum burr height. The burr height on each blanked samples had been measured by taking specified 5 points at the perimeters and then “the average burr height” has been measured in Fig. 5.



Figure 5. The measurement of the burr height

Results and Discussions

As seen in Figure 3, the microstructure of mild steel consists of ferrite grains of pure iron and lamellar cementite with in a pearlite phase. The grains are partially equiaxed and, depending on the pressure in the rolling direction, they are partially elongated and tend to fibrose. Three different type of punches and their worn edges can be seen in Figure 6. The least wear occurred in the flat punch, while partial wear was observed in the TiN coated and channeled punch and the most intense corner surface wear was observed in the channeled punch. The primary mechanisms responsible for tool wear and reduced tool life at the tool-chip and tool-part interfaces in machining and punching operations include scraping, adhesion, diffusion, abrasion, chemical reactions, and excessive plastic deformation. Most instances of tool wear involve one or more of these processes. In Fig. 6, it can be seen clearly that the wear is more severe on uncoated punch after 55.000 strokes. When the high magnification SEM images were examined, abrasive wear was observed in the channeled punch due to intense plastic deformation (Figure 7). Some edge rounding had also occurred plain and channeled punches. Excessive abrasive wear was also observed on the flank surface of the punch. The micro particles that broke off from both the product surface and the punch edges further disrupted the flank surface geometry and created intense burr height formation on the product surface (Figure 8). The D2 tool steel particle on the flank surface scratched the lateral surface and created a deep surface in the form of a channel (Figure 9). As can be seen in Fig 8, the flank surfaces of uncoated and channeled punches show adhesive and abrasive wear. The flank surface close to the cutting edge presents some wear tracks due to abrasion. A small amount of corner and flank wear was observed in the flat punch without a channel (Figure 10). As seen in Figure 11, relatively little surface and corner wear was observed in the TiN coated and channeled punches. It can further be seen that adhesive wear and plastic deformation of punch cause the cutting edges to be rounded. More severe adhesive wear was observed at flank surface and cutting edge of uncoated plain and channeled punches (Figure 6). Typical microstructure of AISI D3 tool steel is given in Figure 5. The microstructure of the tool steel contains martensitic structure with presence of carbides and ferrites. The equaled fine grain can be seen and distributed uniformly in same macrograph.



a) b)

c)

Figure 6. a) Channeled plain punch, b) Channeled punch general appearance and flank wear c) Channeled TiN coated punch

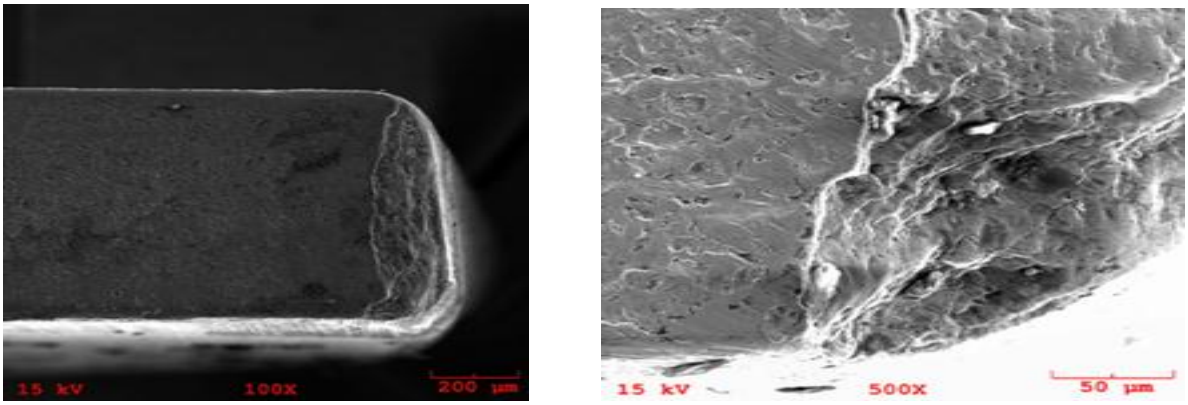


Figure 7. High magnification SEM Pictures of channeled punch surface edges

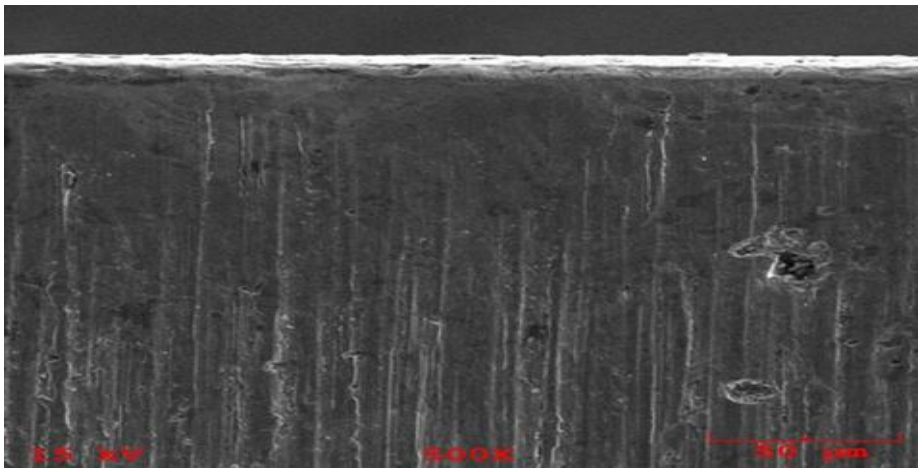


Figure 8. Flank (Lateral) surface wear on the channel punch

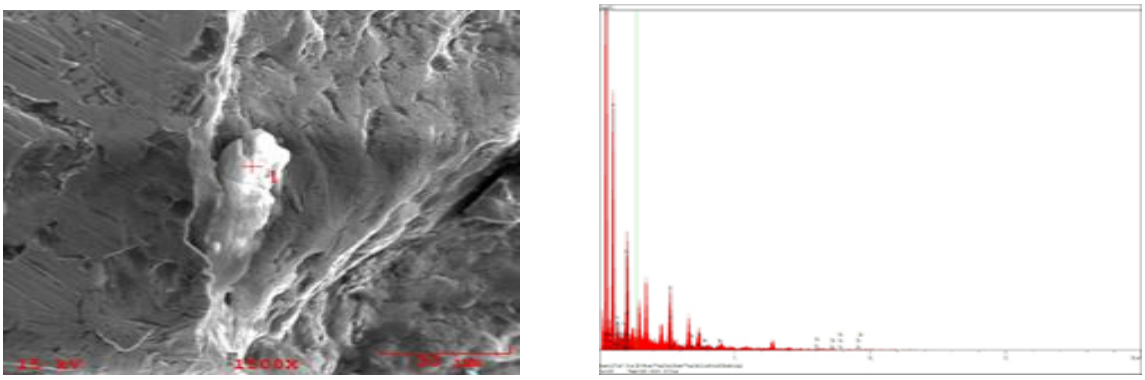


Figure 9. High magnification worn flank surface SEM pictures with EDX analysis of the D2 tool steel punch

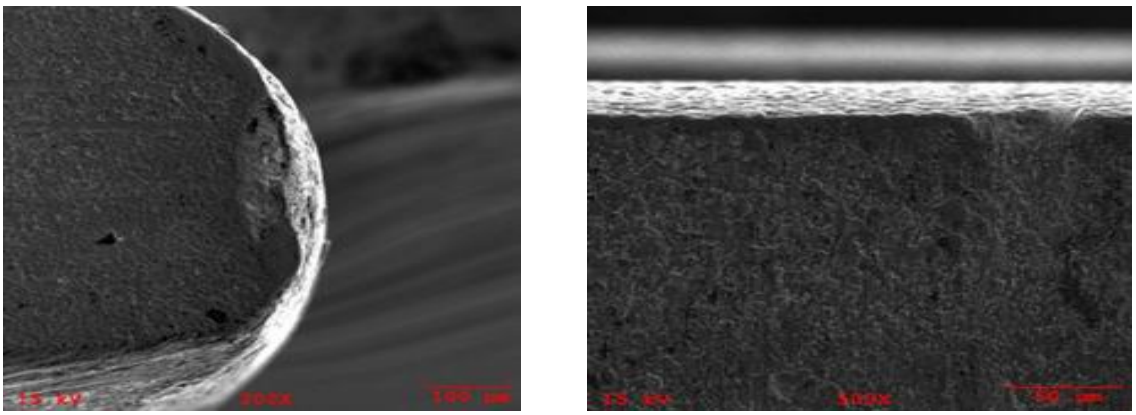


Figure 10. Edge surface wear and flank wear of plain punch

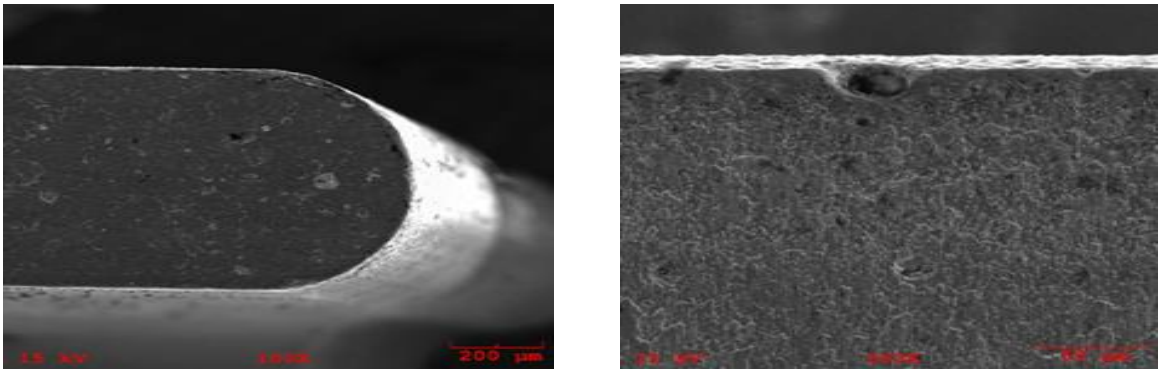


Figure 11. Edge surface wear and flank wear of TiN coated channeled D2 tool steel punch

Figure 12 shows the effect of geometry and coating on the average burr height formation during number of measured strokes. As seen in Figure 12, the least wear-related burr height was seen in the plain punch, while the highest average burr height was seen in the channeled punch. The punch surfaces were sharp and without wear, high-quality holes and scraps were obtained. Although the average burr height at 5000 strokes was 82 µm in the plain punch, the average burr height was measured as 191 µm with increasing punching numbers at 55,000 strokes. The burr height increased in all punch geometries with increasing strokes. The largest height difference was seen between the plain punch and the channeled punch at 55,000 strokes, and the channeled punch created a 10% worse product surface. TiN coated punch performance was between these two values. In previous studies, burr height increased with increasing stroke numbers, and again, burr heights showed differences depending on different geometric positions and punch materials (Arslan et al., 2015, Arslan, 2020, Uygur et al., 2025). In these studies, as stated, different types of sheet metals were cut in series using WC, HSS and X30Cr13 cutting punches, and wear as well as burr height were determined. Additionally, a very high number of punching operations were carried out in these studies. The results obtained from these studies are quite similar to the current paper (Goijaerts et al., 2010, Klaasena et al., 2006, Bressan et al., 2001).

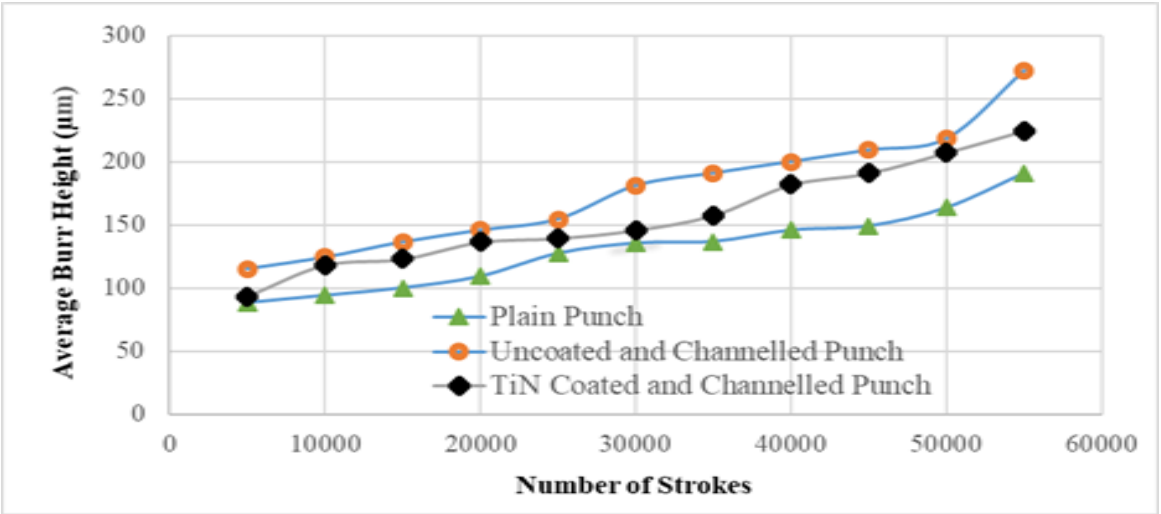


Figure 12. Average burr heights against number of tested strokes for various punches

Conclusions

In this study, sheet metal punching operations were carried out with punches having three different geometries made of AISI D2 tool steel and the following results were obtained.

1. The average burr height increased with increasing strokes. This increase is related to wear on the tool surface.
2. Holes obtained with a flat punch generally have better surface quality and the lowest burr height.
3. The channeled punch has the highest burr height and the worst scrap surface quality.
4. TiN coating improved the punching performance on average 5% of the channeled punch

5. Channeled punches undergo intense plastic deformation and abrasive and adhesive wear during punching operation and as a result more worn surfaces can be seen.

Scientific Ethics Declaration

* The authors declare that the scientific ethical and legal responsibility of this article published in EPSTEM journal belongs to the authors.

Conflict of Interest

* The authors declare that they have no conflicts of interest

Funding

* Authors would like to thank GUNES PLASTIC Cooperation in Kocaeli for support of this study.

Acknowledgements and Notes

* This article was presented as an oral presentation at the International Conference on Technology, Engineering and Science (www.icontes.net) held in Antalya/Türkiye on November 12-15, 2025.

References

Akgun, M., Ozlu, B., & Kara, F. (2023). Effect of PVD-TiN and CVD-Al2O3 coatings on cutting force, surface roughness, cutting power, and temperature in hard turning of AISI H13 steel. *Journal of Materials Engineering and Performance, 32*(3), 1390–1401.

Akincioglu, S., Gokkaya, H., & Uygur, I. (2015). A review of cryogenic treatment on cutting tools. *The International Journal of Advanced Manufacturing Technology, 78*(9–12), 1609–1627.

Arslan, Y. (2020). The effects of cryogenic process on the AISI M2 punch materials and on the hole edge geometry of the DIN EN 10111-98 sheet metal control arm parts. *Advances in Materials Science and Engineering, 1*, Article 9236783.

Arslan, Y., Uygur, I., & Jazdzewska, J. (2015). The effect of cryogenic treatment on microstructure and mechanical response of AISI D3 tool steel punches. *Journal of Manufacturing Science and Engineering, 137*(3), 034501.

Bressan, J. D., Hesse, R., & Silva, E. M. (2001). Wear mechanisms of electrical steel sheets, hard metal and high speed steel pins coated with TiAlN and TiCN. *Meccanica, 36*(2), 683–690.

Cavusoglu, O., & Gurun, H. (2016). Investigation and fuzzy logic prediction of the effects of clearance on the banking process of CuZn30 sheet metal. *Kovove Materialy, 54*, 125–131.

Ghosh, A., & Mallik, A. K. (1984). *Manufacturing science*. East-West Press.

Goijaerts, A. M., Govaert, L. E., & Baaijens, F. P. T. (2010). Evaluation of ductile fracture models for different metals in blanking. *Journal of Materials Processing Technology, 110*(3), 312–323.

Jin, S. Y., Pramanik, A., Basak, A. K., Prakash, C., Shankar, S., & Debnath, S. (2020). Burr formation and its treatments-a review. *The International Journal of Advanced Manufacturing Technology, 107*(2), 2189–2210.

Klaasena, H., Kubarsepp, J., & Eigi, R. (2006). Peculiarities of hardmetals wear in blanking of sheet metals. *Tribology International, 39*(4), 303–309.

Miguel, V., & Bressan, J. D. (2002). A computational approach to blanking processes. *Journal of Materials Processing Technology, 125–126*, 206–212.

Samuel, M. (1998). FEM simulations and experimental analysis of parameters of influence in the blanking process. *Journal of Materials Processing Technology, 84*, 97–101.

Uygur, I., Gerengi, H., Arslan, Y., & Kurtay, M. (2015). The effects of cryogenic treatment on the corrosion of AISI D3 steel. *Materials Research, 18*(3), 569–574.

Uygur, I., Oktem, H., Karasungur, H., & Gerengi, H. (2025). Investigations of burr height for sheet metal process of medium duty casters in industrial kitchens. *International Conference on Basic Sciences and Technology (ICBAST)*, Budapest, Hungary.

Uygur, I., Oktem, H., & Soy, G. (2025). The effects of punch materials on the burr height for blanking operation. *2nd International Conference on Engineering, Natural Sciences, and Technological Developments (ICENSTED 2025)* (pp. 251–256).

Author(s) Information

Ilyas Uygur
Duzce University, Faculty of Engineering; Department of Mechanical Engineering,
Duzce/Türkiye

Halit Karasungur
Kocaeli University
Natural Science Institute/Polymer Science and Technology
Güneş Plastic Mold Coorperation, Kocaeli/Türkiye

Sıtkı Akincioglu
Duzce University, Faculty of Engineering.
Düzce University, Faculty of Art Design
Department of Industrial Design
Duzce/Türkiye

Hasan Oktem
Kocaeli University
Hereke Asım Kocabıyık Vocational
Natural Science Institute/Polymer Science and Technology,
Kocaeli/Türkiye
Contact e-mail: *hoktem@kocaeli.edu.tr*

To cite this article:

Uygur, I., Kocasungur, H., Akincioglu, S., & Oktem, H., (2025). Punch geometry and burr height on blanking process for garbage container wheel parts. *The Eurasia Proceedings of Science, Technology, Engineering and Mathematics (EPSTEM), 38*, 559-566.

The Eurasia Proceedings of Science, Technology, Engineering & Mathematics (EPSTEM)
ISSN: 2602-3199

The Eurasia Proceedings of Science, Technology, Engineering and Mathematics (EPSTEM), 2025

Volume 38, Pages 567-574

IConTES 2025: International Conference on Technology, Engineering and Science

Effect of Cryogenic Treatment on the Microstructure of AlSi10Mg Alloy Produced by Selective Laser Melting

Pelin Sezer
Eskisehir Osmangazi University

Gamze Ertas
Eskisehir Osmangazi University

Hakan Gasan
Eskisehir Osmangazi University

Abstract: Research on the production of AlSi10Mg alloys using Selective Laser Melting (SLM), one of the additive manufacturing methods, is still ongoing. Since the use of SLM-fabricated parts in the as-built condition is not yet feasible, studies have particularly focused on post-processing. Moreover, the heat treatment parameters established for AlSi10Mg alloys produced by conventional methods do not necessarily show the same effects when applied to AM parts. Cryogenic treatment, which has been shown to have favorable effects for AlSi10Mg parts in the literature, and it increased the mechanical properties. In this study, AlSi10Mg block production was carried out via SLM using the predetermined process parameters and samples extracted from it. Then those samples were subjected to T6 heat treatment followed by cryogenic treatment for 12, 24, 36, and 48 hours. Subsequently, the samples were analyzed using optical microscopes to determine their microstructure and composition. Microstructural examinations showed that the effect of T6 heat treatment is the Si particle occurrence in Al matrix, after cryogenic treatment these particles changed relatively as the duration of cryogenic treatment changed.

Keywords: Selective laser melting, Cryogenic treatment, AlSi10Mg

Introduction

Within aluminum alloys, AlSi10Mg is known for its outstanding flowability and resistance to crack formation during solidification, which is due to its superior castability, weldability, low shrinkage, and low melting point. These qualities, together with high specific strength, excellent thermal and electrical conductivity, and extraordinary resistance to oxidation and corrosion, make AlSi10Mg a preferred material in the aerospace, automotive, defense, and general manufacturing industries. Silicon concentration promotes fluidity during manufacture, while magnesium strengthens the alloy and improves heat resistance (Vishnu et al., 2025). For Al alloys, the most common alloying elements are copper, magnesium, manganese, silicon, and zinc. Since the debut of metallic aircraft, alloys mostly made of aluminum have played a significant role in aerospace manufacturing. AlSi10Mg alloys are lighter than other aluminum alloys and less combustible than alloys with a high magnesium content (Desai et al., 2016).

An innovative heat treatment technique that is thought to be an alternative to conventional heat treatment is cryogenic treatment. Without altering the alloy's size or shape, it significantly impacts its microstructure and mechanical characteristics (Liu et al., 2025). Si element can gradually precipitate from the Al matrix during cryogenic treatment because the solubility of Si in Al alloys has a decreasing trend from high to low temperatures. It can reduce the coarse secondary particles along with boosting the precipitation of secondary

- This is an Open Access article distributed under the terms of the Creative Commons Attribution-Noncommercial 4.0 Unported License, permitting all non-commercial use, distribution, and reproduction in any medium, provided the original work is properly cited.

- Selection and peer-review under responsibility of the Organizing Committee of the Conference

© 2025 Published by ISRES Publishing: www.isres.org

phases. It was found in a study that the average size of coarse particles in the sample exposed to a cryogenic temperature of -180˚C is just 6.9 µm smaller than that obtained in the circumstance of high temperatures. The formation of secondary phases that enhance the dispersion or cause precipitation and more homogenous distribution. One important strengthening method for high strength is precipitation strengthening especially (Yao et al., 2023).

An additive manufacturing technique called Selective Laser Melting (SLM), creates parts with complex internal structures. This method, which is based on CAD data, melts powder dispersed over a powder bed using an energy source along an identified scanning route to create a dense part. The superior microstructure produced by this method is responsible for the produced components' fine microstructure, which is a result of the SLM process's rapid cooling rate (Siyambaş & Turgut Y., 2022). A continuous eutectic structure of Al and Si is usually produced together with formed primary α-Al in the traditional AlSi10Mg casting method, where the solid solution of Si in aluminum breaks down easily during slow cooling and Si precipitates in the form of relatively coarse particles. Instead, the SLM technique produces a distinct microstructure in the AlSi10Mg components by continuously melting the material at a very high rate and then cooling it down rapidly. It is indicated distinct microstructures can observe a network of the eutectic Si phase along the boundary surrounding the α-Al phase and a cellular-dendritic structure of α-Al (Trevisian et al., 2017 & Semetse et al., 2025).

It is indicated that SLM produced AlSi10Mg has higher hardness than the cast parts, usually between 110 and 130 HV. The fast solidification rate during the SLM process, resulting in a small cellular microstructure with finely distributed hard silicon particles, is directly responsible for this increased hardness also after cryogenic treatment for 12h, and 24h the hardness increased 18.4% and 21.47% respectively (Gadlegaonkar et al., 2025 & Desai et al., 2016). It is indicated that CT results in the irregular volume shrinkage of the Al matrix and eutectic-Si networks and produces plastic deformation during the soaking period therefore, the samples retain compressive residual stress when they are reheated to room temperature. It is evident that the as-built and CT samples' XRD patterns are almost similar. Si precipitating out of the Al matrix after heat treatment (HT) and they observed the Si peaks in the HT samples are more intense than those in the other two samples the solid solubility of Si in the Al matrix is weakened by the HT. The extra Si caused the supersaturated α-Al to become thermodynamically unstable, which resulted in the removal of excess Si atoms from the α-Al matrix and the formation of individual Si particles during the HT. It is observed grain growth causes the intercellular network of eutectic-Si to change into polygonal Si particles that are evenly dispersed throughout the Al matrix (Zhou et al., 2022). CT promotes solute atom precipitation in the SLM AlSi10Mg alloy. Nevertheless, it has no appreciable effect on the eutectic Si networks or the morphologies and stacking structure of the melt pools and, the creation of atomic clusters is correlated with a progressive increase in the number of precipitated phases as duration of CT increases (Tang et al., 2025). According to these literature reviews, in this study the microstructural effect of SLM produced and cryogenic treated AlSi10Mg examined. Firstly, all samples exposed to T6 heat treatment and after that cryogenic treatment was held at -196˚C for 12, 24, 36 and 48h. Effects of the treatment time and its reasons are discussed.

Method

AlSi10Mg powder composition that is used for SLM production given in Table 1. The powder particle size distribution 20-63 µm and spherical shape. It consists of ~90% of aluminum and ~10% silicon. SLM production was carried out via Nikon SLM device. From this powder one block production was carried out SLM production parameters given in Table 2. Samples were taken from this block for investigation. The samples extracted from the block were subjected to the metallographic sample preparation steps in order: mounting, grinding, and polishing. For microstructural characterization Nikon Eclipse L150 optical microscope was used. Samples were etched with the Keller's reagent (95 mL distilled water, 2.5 mL HNO3, 1 mL HF, and 1.5 mL HCl). In an atmospheric heat treatment furnace, test materials were solution treated for 30 min. at 530˚C, water quenched to room temperature, then aged for six hours at 165˚C, and then cooled in atmospheric conditions (T6). Following that, four samples were cryogenic treated for 12, 24, 36, and 48 hours at -196˚C using liquid nitrogen. Hardness test was carried out via Future-Tech FM800 microhardness tester 100 gf and 10 sec. Tests were done with 5 indents in distance 25µm.

Table 1. The AlSi10Mg powder chemical composition (Nikon SLM Solutions, 2024)

Element	Al	Si	Fe	Cu	Mn	Mg	Zn	Ti	Ni	Pb	Sn	Total each	Total others
% wt	Balance	9-11.0	0.55	0.05	0.45	0.25	0.10	0.15	0.05	0.05	0.05	0.05	0.15

Table 2. SLM production parameters.

Parameters	
Laser power	300 W
Scanning speed	700 mm/s
Scanning strategy	Stripe
Beam diameter	0.1 mm
Hatch distance	0.17 mm

Results and Discussion

Microstructural Examination

Microstructural examinations were carried out using an optical microscope (OM). Figure 1 presents the microstructure images of the as-built (AB) sample at a) 50× magnification and b) 200× magnification. As seen in Figure 1.a, layer-by-layer melting traces, also known as melt pool boundaries, are visible due to the additive manufacturing process. This is attributed to the rapid solidification rates in the samples produced by additive manufacturing (Koç et al., 2025). In Figure 1.b, very fine eutectic silicon microstructures can be observed. The melt pools were formed as continuous and wide. It was observed to have a regular geometry with a segmental circular shape and these formations exhibiting a “fish-scale” morphology.

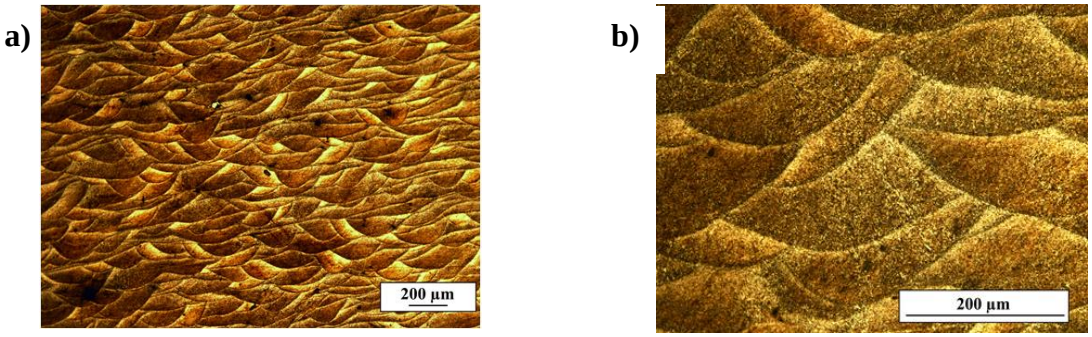


Figure 1. Microstructural images belong to as-built (AB) sample a) 50x magnification b) 200x magnification.

Figure 2 presents the microstructure images of the sample subjected to T6 heat treated, 12, 24, 36 and 48h cryogenically treated samples. As seen in Figure 2.a, c, g and i, the melt pool traces observed in the as-built sample have disappeared, with the effect of T6 heat treatment conditions. Additionally, the interlayer pores stand out. The Si networks formed on the Al matrix are observed to be finer (Figure 2a, c, g and i) compared to those in the as-built sample (Figure 1.a). In Figure 2b, d, f, h and j, this distribution can be seen more clear and more homogenous. From microstructural images, it is observed that the T6 heat treatment helped to reduce the melt pool appearance and a more homogeneous microstructure distribution was obtained. However, in sample 24h cryogenic treated, these traces are still slightly noticeable (Figure 2.e-f). The expectation here is that removal will be observed in all melt pools, but this effect may have re-formed after the cryogenic treatment. All images exhibit the typical microstructural characteristics of the AlSi10Mg alloy after T6 heat treatment. Following the solution treatment and artificial aging steps, a cellular Al matrix with finely distributed Si particles is observed. The distinct melt pool boundaries seen in the as-built condition have largely disappeared after the T6 process, resulting in a more homogeneous and uniform phase distribution.

Figure 3 includes the examination of the top view of the samples AB, after T6 heat treatment, and CT for 12, 24, 36, and 48 hours. Figures 3a–b, correspond to the AB sample. Although the microstructure appears visually different from the side section, it can be stated that this structure is also formed by the Si network generated by the laser input. Similar overlapped laser tracks can be seen in the top view of the specimen, but in the side view, the shape of the molten pool shifts from shallow to deep (Figure 1.a-b). Furthermore, the pores at the bottom of sample, referred to as keyhole flaws, attest to the fact that the keyhole effect caused material vaporization. These traces seem brighter in the OM image because their boundaries etch more strongly. The presence of fibrous separated eutectic Si particles in these particular areas is what causes the increased susceptibility to chemical etching. There are also irregular porosities in the sample which is the primary source is the balling phenomena brought on by the degrading metallurgical bonding (Dong et al., 2020).

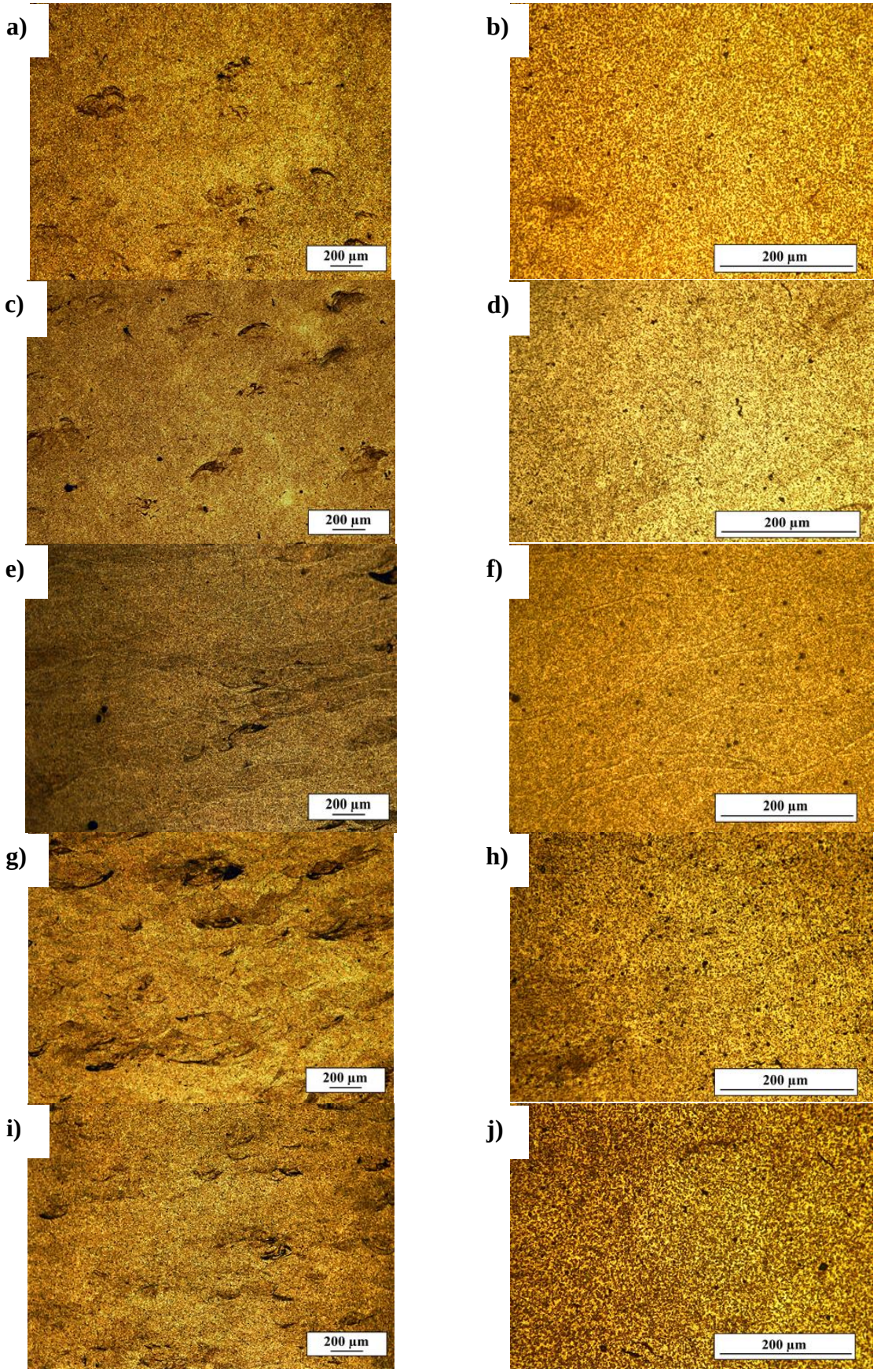
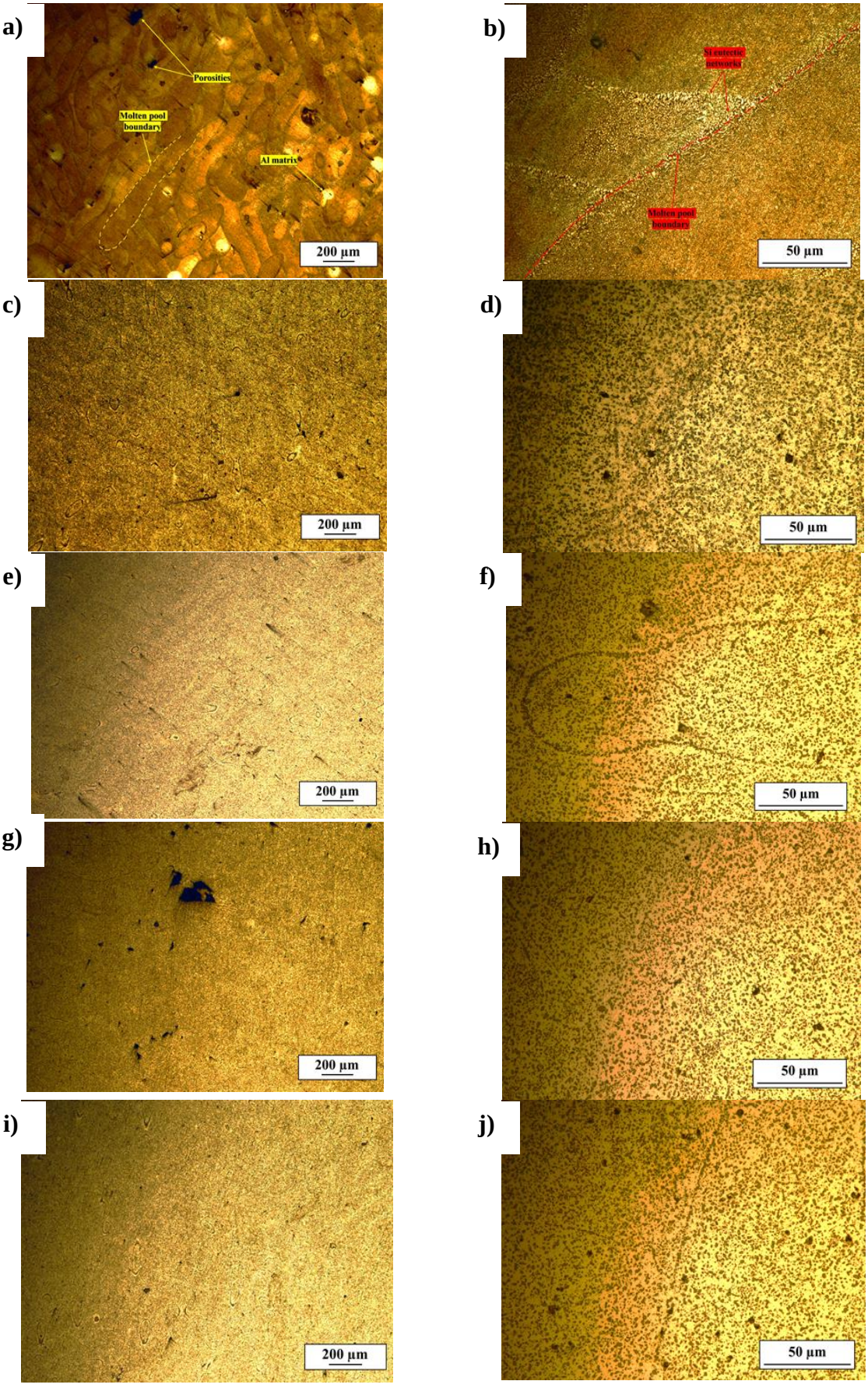


Figure 2. Microstructural images belong to side section of a-b) T6 heat treated, c-d) T6+12h cryogenic treated, e-f) T6+24h cryogenic treated, g-h) T6+36h cryogenic treated, i-j) T6+48h cryogenic treated 50x and 200x magnifications respectively.


a)
Porosities
Molten pool boundary
Al matrix
200 µm
b)
Si eutectic networks
Molten pool boundary
50 µm
c)
200 µm
d)
50 µm
e)
200 µm
f)
50 µm
g)
200 µm
h)
50 µm
i)
200 µm
j)
50 µm

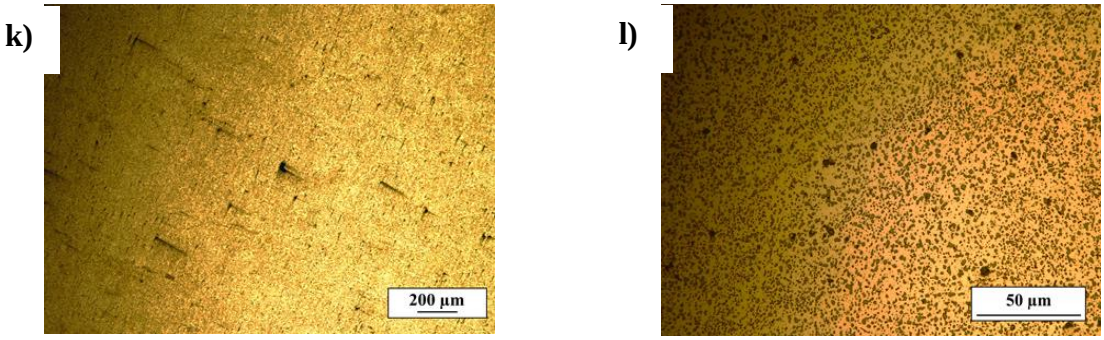


Figure 3. Microstructural images belong to top section of a-b) as-built, c-d) T6 heat treated, e-f) T6+12h cryogenic treated, g-h) T6+24h cryogenic treated, i-j) T6+36h cryogenic treated, k-l) T6+48h cryogenic treated 50x and 500x magnifications respectively.

After the T6 heat treatment (Figure 3.c–d), similar to the side view observations, the microstructure became homogeneous, and the scanning tracks and molten pool patterns disappeared. However, the Si eutectic structure transformed into Si precipitate particles. Although these precipitates eliminated most of the molten pool features, traces of such patterns can still be slightly observed in the structure, replaced by Si precipitates. After 12 hours of cryogenic treatment, a structure similar to that of the T6 heat-treated sample was observed (Figure 3.e). However, compared to the T6 heat treatment, it is possible to mention relatively smaller Si particles, it was observed that the Si particles were grouped together within the structure, making the Al phase more distinguishable (Figure 3.f). When Figure 3.g is examined, a large number of pores can be noticed. Beneath these pores, a structure similar to that of the T6 heat-treated sample is observed. Upon closer examination of the precipitates, it can be seen that the localized particles present after the 12-hour cryogenic treatment have been replaced by a more homogeneous appearance (Figure 3.h). The 48-hour cryogenic treatment made the microstructure more homogeneous, and the precipitates were uniformly distributed in various sizes, both large and small (Figure 3 k-l).

Hardness Results

Figure 4 shows that hardness results belong to as-built, T6 heat treated, 12, 24, 36 and 48h CT samples. In as-built condition hardness measured as 107.42 HV which is higher than the cast conditions. This can be result of the rapid cooling. After T6 heat treatment this result increased to 120.8 HV. This result is attributed to the elimination of the melt pool structure present in the microstructure under additive manufacturing conditions, the precipitation of Si particles, and the formation of a more homogeneous microstructure. After 12h cryogenic treatment hardness decreased to 111.8HV. Increasing the cryogenic treatment time increased the hardness to 117.4 HV. And then 36 and 48 hours decreased hardness to 112.16 and 115.8 HV respectively.

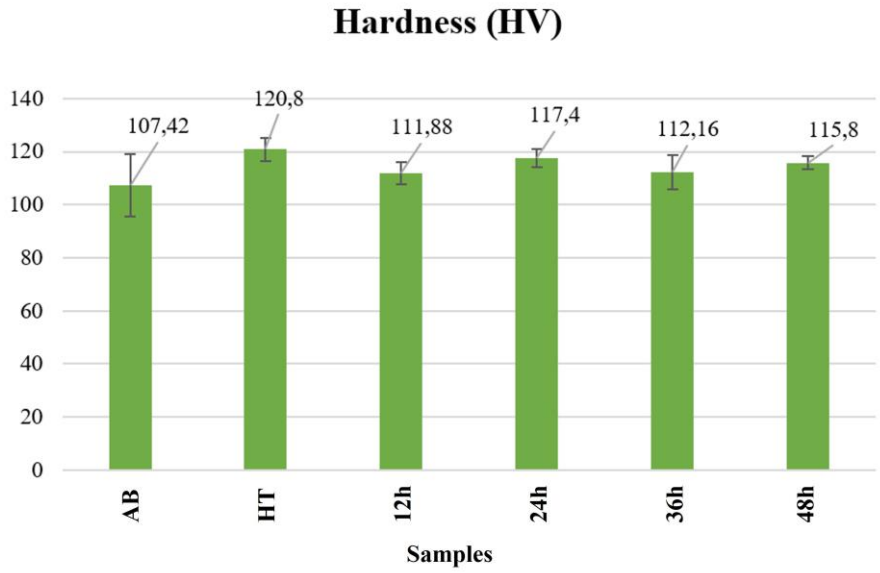


Figure 5. Hardness results belong to samples.

As reported in the literature, Si particle precipitations exhibit variability that can influence the mechanical properties of AlSi10Mg alloys. Accordingly, the slight changes observed in hardness can be attributed to the increase or decrease of these precipitates. In the AB condition, the sample has completely different microstructure, whereas after T6 heat treatment, distinct Si particles are shown. The hardness value, which reached around 120 HV, can be associated with the presence of these particles. Owing to cryogenic treatment, variations in the size and distribution of precipitates initially caused a reduction in hardness, followed by an increase at 24 hours of treatment, and then a subsequent decreasing trend nearly similar 36h and 48h CT samples.

Conclusion

In this study, the microstructural changes, hardness values of AlSi10Mg samples produced by the SLM method were investigated after T6 heat treatment and subjected to cryogenic treatment at –196 °C for holding times of 12, 24, 36, and 48 hours. The results are as follows:

- The AB images show differences between the side and top views; however, the same fundamental structural formations have been observed in both-Si eutectic phase.
- After the T6 heat treatment, the deposition traces and fish-scale melt pool patterns observed in the as-built (AB) samples disappeared, giving way to the formation of Si precipitates both side and top views of the sample.
- While more homogeneous Si precipitates were present in the 12-hour and 48-hour cryogenic treatments, the same level of homogeneity could not be achieved in the microstructures of the 24-hour and 36-hour treatments – however, no significant difference has been observed.
- The highest hardness was obtained after the T6 heat treatment because of the Si particles, while the change in hardness with cryogenic treatment was not of significant magnitude.

Recommendations

In addition to the analyses performed on the AlSi10Mg samples, SEM-TEM analysis could be preferred for the investigation of smaller precipitates. Furthermore, alternative analytical methods can be employed for monitoring particle size. Wear analyses could be held results further contribute to literature.

Scientific Ethics Declaration

* The authors declare that the scientific ethical and legal responsibility of this article published in EPSTEM journal belongs to the authors.

Conflict of Interest

* The authors declare that they have no conflicts of interest

Funding

* This study is supported within the scope of the TÜBİTAK 2209-B program (Project No: 1139B412408088).

Acknowledgements or Notes

* This article was presented as an oral presentation at the International Conference on Technology, Engineering and Science (www.icontes.net) held in Antalya/Türkiye on November 12-15, 2025.

References

Desai, R. S., Joshi, A. G., & Kumar, S. (2016). Study on influence of cryogenic treatment on mechanical properties of AlSi10Mg alloy. *International Journal of Research in Engineering and Technology, 5*, 53.

Dong, S., Zhang, X., Ma, F., Jiang, J., & Yang, W. (2020). Research on deposited tracks and microstructures of AlSi10Mg alloy produced by selective laser melting. *Applied Physics A, 126*(8), 643.

Gadlegaonkar, N., Bansod, P. J., Lakshmikanthan, A., & Bhole, K. (2025). A review on additively manufactured AlSi10Mg alloy: Mechanical, tribological, and microstructure properties. *Journal of Mines, Metals & Fuels*, *73*(1).

Koç, E., et al. (2025). Effects of retrogression and re-aging heat treatments on microstructure, phase transformations, hardness, and dry sliding wear in powder bed laser fusion/AlSi10Mg. *Journal of Materials Engineering and Performance*, 1-12.

Liu, Y., Chen, Z., Huang, Y., Jing, L., & Niu, X. (2025). Effect of cryogenic treatment on 7A09 aluminum alloy and optimization of process parameters. *Journal of Materials Engineering and Performance*, *34*(17), 19752-19766.

Nikon SLM Solutions. (2024). *Material data sheet: AlSi10Mg DIN EN 1706 / EN AC-43000*. Retrieved from https://nikon-slm-solutions.com/wp-content/uploads/2025/02/mds5123.pdf

Semetse, L., Olaogun, O., & Olubambi, P. (2025). Sliding wear behaviour of heat treated selective laser melted AlSi10Mg alloy. *SSRN*.

Siyambas, Y., & Turgut, Y. (2022). Seçici lazer ergitme (SLM) yöntemi ile üretilen AlSi10Mg alaşımlı parçalarda kusurlar, mekanik özellikler ve yüzey pürüzlülüğü-Bir araştırma. *Gazi Üniversitesi Fen Bilimleri Dergisi Part C: Tasarım ve Teknoloji, 10*(2), 368-390.

Tang, P., Wang, H., Cheng, X., Zang, J., & Zhao, Y. (2025). Effects of cryogenic thermal cycling treatment on microstructure, mechanical properties and residual stress of selective laser melted AlSi10Mg alloy. *Materials Science and Engineering: A, 944*, 148963.

Tonolini, P., Montesano, L., Tocci, M., Pola, A., & Gelfi, M. (2021). Wear behavior of AlSi10Mg alloy produced by laser-based powder bed fusion and gravity casting. *Advanced Engineering Materials, 23*(10), 2100147.

Trevisan, F., Calignano, F., Lorusso, M., Pakkanen, J., Aversa, A., Ambrosio, E. P., ... & Manfredi, D. (2017). On the selective laser melting (SLM) of the AlSi10Mg alloy: Process, microstructure, and mechanical properties. *Materials, 10*(1), 76.

Vishnu, V., Prabhu, T. R., & Vineesh, K. P. (2025). Effect of hard anodizing and T6 heat treatment on the dry sliding wear behavior of AlSi10Mg fabricated by direct metal laser sintering. *Wear, 564*, 205677.

Yao, E., Zhang, H., Ma, K., Ai, C., Gao, Q., & Lin, X. (2023). Effect of deep cryogenic treatment on microstructures and performances of aluminum alloys: A review. *Journal of Materials Research and Technology, 26*, 3661-3675.

Zhou, C. A., Sun, Q., Qian, D., Liu, J., Sun, J., & Sun, Z. (2022). Effect of deep cryogenic treatment on mechanical properties and residual stress of AlSi10Mg alloy fabricated by laser powder bed fusion. *Journal of Materials Processing Technology, 303*, 117543.

Author(s) Information

Pelin Sezer
Eskisehir Osmangazi University,
Faculty of Engineering and Architecture,
Department of Metallurgical and Materials Engineering
Meşelik Kampüsü Odunpazarı/Eskişehir, Türkiye
Contact e-mail: *pelin.sezer@ogu.edu.tr*

Gamze Ertas
Eskisehir Osmangazi University,
Faculty of Engineering and Architecture,
Department of Metallurgical and Materials Engineering
Meşelik Kampüsü Odunpazarı/Eskişehir, Türkiye

Hakan Gasan
Eskisehir Osmangazi University,
Faculty of Engineering and Architecture,
Department of Metallurgical and Materials Engineering
Meşelik Kampüsü Odunpazarı/Eskişehir, Türkiye

To cite this article:

Sezer, P., Ertas, G., & Gasan, H. (2025). Effect of cryogenic treatment on the microstructure of AlSi10Mg alloy produced by selective laser melting. *The Eurasia Proceedings of Science, Technology, Engineering and Mathematics (EPSTEM), 38*, 567-574.

The Eurasia Proceedings of Science, Technology, Engineering & Mathematics (EPSTEM)
ISSN: 2602-3199

The Eurasia Proceedings of Science, Technology, Engineering and Mathematics (EPSTEM), 2025

Volume 38, Pages 575-579

IConTES 2025: International Conference on Technology, Engineering and Science

Investigation of Borophene Synthesized via a Scalable Approach as an Anode Material for Lithium-Ion Batteries

Suleyman Can
Bilecik Seyh Edebali University

Cihan Kuru
Bilecik Seyh Edebali University

Abstract: Borophene is considered as a promising anode material for lithium-ion batteries due to its high specific capacity and low diffusion barrier. However, practical applications exploring borophene as an anode material remain very limited. In this study, the anode performance of borophene synthesized via a scalable electrochemical exfoliation method, was investigated in lithium-ion batteries (LIBs). The obtained borophene sample was structurally characterized using X-ray photoelectron spectroscopy (XPS), high-resolution transmission electron microscopy (HRTEM), and atomic force microscopy (AFM). The electrochemical performance of the anode was evaluated by assembling CR2032 type coin cell. Galvanostatic charge/discharge tests showed that the initial discharge capacity of the borophene anode was 387 mAh g^{-1} at 0.1 C, which only dropped to 371 mAh g^{-1} after 10 cycles, exhibiting 95.8% capacity retention rate. These results indicate that borophene holds a substantial potential as an anode material for lithium-ion battery applications.

Keywords: Borophene, Electrochemical exfoliation, Li-ion batteries.

Introduction

The ever-increasing global energy demand has brought the need for high–energy-density and long–life energy storage technologies to the forefront (Tarascon et al., 2001). In this context, lithium-ion batteries remain one of the most widely used energy storage systems due to their high energy efficiency and long cycle life (Lökçü et al., 2023; Çelikbilek et al., 2022). However, the currently commercialized anode material, graphite, suffers from a low theoretical capacity, making it insufficient to meet the performance requirements of next-generation energy storage systems (Etacheri et al., 2011). Consequently, significant research efforts have been directed toward developing alternative anode materials that can provide higher capacities, faster ion diffusion and improved cycling stability (Manthiram, 2020).

Two-dimensional (2D) materials have attracted substantial attention in this regard due to their high surface area, short ion diffusion paths and tunable electronic structures (Chhowalla et al., 2013). Although various 2D materials such as graphene, phosphorene, and transition metal dichalcogenides (TMDs) have been extensively investigated, many of them still suffer from drawbacks such as low chemical stability or limited capacity (Can et. al., 2024; Voiry et al., 2015). At this point, borophene emerged as a promising candidate for diverse energy-related applications owing to its structural diversity and theoretically high lithium storage capacity (Can et. al., 2024; Adekoya et al., 2024). Computational studies have revealed that borophene sheets can easily adsorb lithium ions, exhibit low diffusion barriers and achieve theoretical capacities exceeding 1000 mA h g^{-1} in certain phases (Zhang et al., 2016). These remarkable properties position borophene among the most promising candidates for fast-charging and high–energy-density anode materials (Ashraf et. al., 2023). Recently, electrochemical exfoliation has emerged as a promising alternative approach for borophene fabrication (Sielicki et al., 2022). This method relies on the electrochemical delamination of layered boron precursors under suitable electrolyte conditions,

- This is an Open Access article distributed under the terms of the Creative Commons Attribution-Noncommercial 4.0 Unported License, permitting all non-commercial use, distribution, and reproduction in any medium, provided the original work is properly cited.

- Selection and peer-review under responsibility of the Organizing Committee of the Conference

© 2025 Published by ISRES Publishing: www.isres.org

offering an environmentally friendly, low-temperature and scalable route for borophene production. Nevertheless, several challenges remain for the practical implementation of borophene. Freestanding borophene sheets are thermodynamically unstable and readily oxidize upon exposure to air (Arnold et al., 2020). In addition, structural degradation can occur during repeated electrochemical cycling, leading to limited cycle life. To overcome these limitations, heterostructures composed of borophene and other 2D materials, such as graphene, have been reported to enhance mechanical stability and improve electron/ion transport (Kaçar et al., 2023; Yu et al., 2020). As a result, borophene-based composites hold great promise for developing next-generation anode systems that combine high capacity with excellent cycling durability.

In this study, borophene powder obtained via an electrochemical exfoliation process were investigated as an anode material for lithium-ion batteries. The structural and morphological properties of the synthesized product were characterized using AFM, HRTEM and XPS analyses. Electrochemical charge–discharge measurements were performed to study the electrochemical lithium storage properties of borophene.

Materials & Methods

The electrochemical exfoliation method of borophene was described in a recent study (Can et. al., 2024). Briefly, 375 mg of crystalline boron, 125 mg of multi-walled carbon nanotubes (MWCNTs) and 50 mg of polymethyl methacrylate (PMMA) dissolved in acetone were mixed to obtain a homogeneous blend. The mixture was further homogenized in isopropyl alcohol (IPA) using bath sonication and subsequently dried overnight at 80 °C. The dried powder was then compacted into circular pellets under a pressure of 500 bar using a manual hydraulic press to prepare electrodes suitable for electrochemical exfoliation.

The exfoliation process was carried out in a 1:1 (v:v) mixture of 1 M sodium sulfate (Na_2SO_4) and glycerol under a constant voltage of 30 V. During the exfoliation, MWCNTs served as conductive pathways, facilitating electron transfer. After exfoliation, the MWCNTs were removed through a two-step purification process. In the first step, the exfoliated borophene sheets were dispersed in the aqueous phase of a toluene/water biphasic system, where sonication enabled the accumulation of MWCNTs at the interface. The remaining nanotubes were further eliminated by filtration through a cellulose membrane with an 8 µm pore size. The purified borophene nanosheets were redispersed in a 1:1 (v:v) H_2O/IPA mixture and centrifuged at 4500 rpm for 20 min. Finally, the borophene powder was obtained by freeze-drying at –37 °C and 0.18 bar for 24 h.

For anode preparation, the borophene powder, Super P carbon black and PVDF binder (in a weight ratio of 75:15:10) were mixed in N-methyl-2-pyrrolidone (NMP) using a ball mill to form a homogeneous slurry. The resulting mixture was coated onto copper foil and dried under vacuum at 80 °C for 12 h. Electrochemical performance tests were conducted using CR2032-type coin cells. The cells were assembled in an argon-filled glove box where H_2O and O_2 levels were maintained below 0.1 ppm. Lithium metal served as both the counter and reference electrode, while a polypropylene (Celgard 2400) membrane was used as the separator. The electrolyte consisted of 1 M $LiPF_6$ dissolved in a 1:1 (v/v) mixture of ethylene carbonate (EC) and dimethyl carbonate (DMC).

AFM measurements were obtained in tapping mode using a Hitachi 5100N microscope. HRTEM was conducted on an FEI TALOS F200S TEM instrument. XPS analyses were performed using a SPECS FlexMod spectrometer equipped with an Al-Kα radiation source (1486.71 eV). Galvanostatic charge–discharge tests were performed using a Gamry Reference 3000 Potentiostat/Galvanostat/ZRA within a potential range of 0.1–3.00 V (vs. Li^+/Li) at a current rate of 0.1 C.

Results and Discussion

AFM analyses were conducted to investigate the surface topography and layer thicknesses of the borophene sheets (Figure 1). The measurements reveal that the layer thicknesses vary between 2.2 and 6.2 nm. This broad distribution indicates that the borophene exhibits structures ranging from few-layered to multilayered sheets, reflecting variability in exfoliation efficiency and surface area among the sheets. The HRTEM observations of the electrochemically exfoliated borophene reveal that the material exhibits a crystalline and multilayered structure (Figure 2). Distinct crystalline domains can be clearly observed and the interlayer spacing is measured to be approximately 4.7 Å (Figure 2b), which matches with the (021) plane of β-rhombohedral borophene. This value is consistent with the interlayer distances reported for borophene in the literature, confirming the successful formation of few-layer borophene structures (Zielinkiewicz et al., 2023).

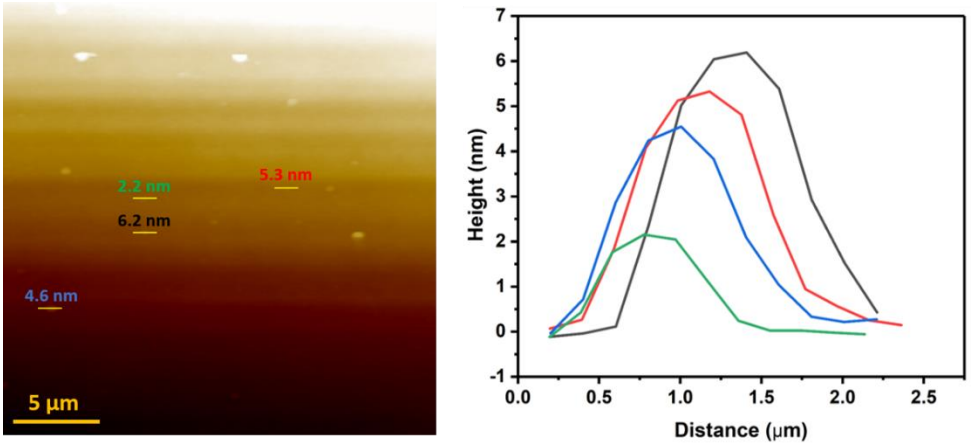


Figure 1. AFM image and the corresponding height profiles of some borophene sheets dispersed on Si substrate.

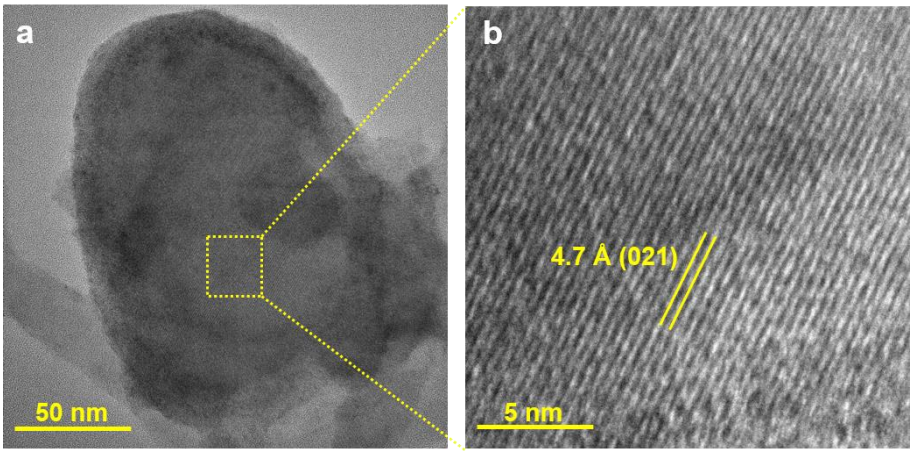


Figure 2. HRTEM images of electrochemically exfoliated borophene sheet.

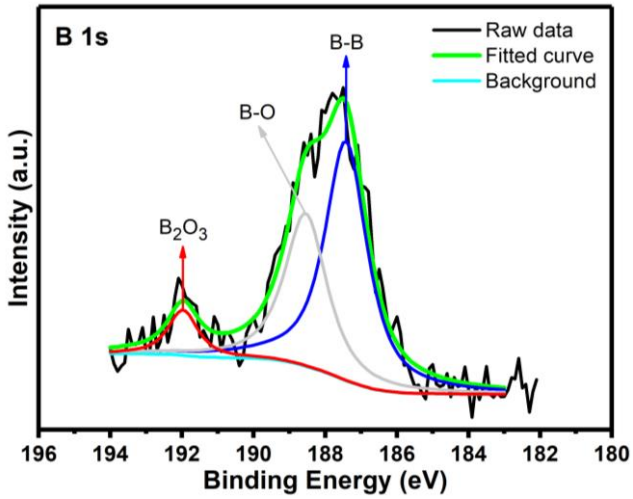


Figure 3. B 1s XPS spectrum of electrochemically exfoliated borophene sheets.

The B 1s XPS spectrum provides detailed information on the chemical composition and oxidation states of the borophene sheets (Figure 3). The spectrum consists of three main peaks located at 187.4 eV (B–B), 188.6 eV (B–O) and 192.0 eV (B_2O_3). The presence of B–O bonds indicates surface oxidation of borophene upon air exposure, whereas the B_2O_3 component can be attributed to electrochemical oxidation reactions occurring during the exfoliation process. These findings confirm that the borophene contains predominantly B–B bonding along with surface oxidation species, which is consistent with previous reports in the literature (Can et. al., 2024). The lithium storage performance of the borophene electrodes was evaluated through galvanostatic charge–discharge cycles at a current rate of 0.1 C (Figure 4). The first three cycles were applied as an activation process to ensure structural

stabilization of the electrode and complete interaction with the electrolyte. Following the activation cycles, the initial discharge capacity was measured as 387 mAh g^{-1}, indicating the effective lithium storage capability of the borophene-based anode. After 10 cycles, the capacity remained at 371 mAh g^{-1}, corresponding to approximately 95.8% capacity retention, demonstrating excellent cycling stability of the material. Moreover, the coulombic efficiency remained consistently high throughout the cycles, reaching 97.3% by the 10th cycle.

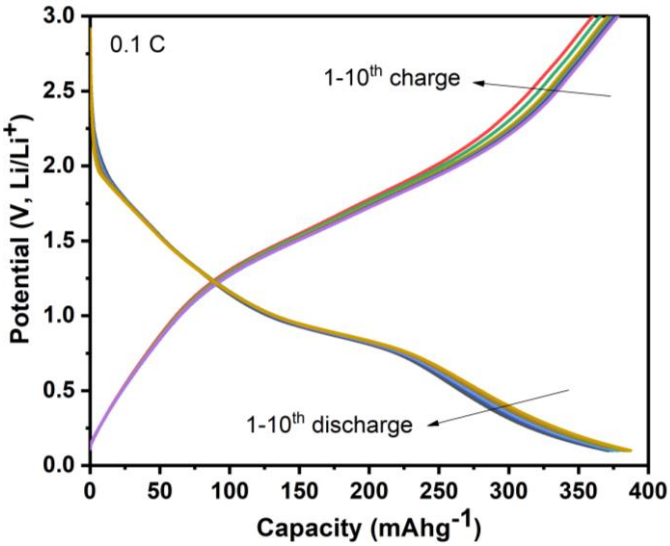


Figure 4. Galvanostatic charge–discharge performance of borophene electrode at 0.1 C.

This result indicates that the electrode structure remains stable during repeated charge–discharge processes and that the reversibility of lithium ion insertion/extraction is well maintained. These findings suggest that borophene anodes synthesized via a scalable method represent promising candidates for lithium-ion batteries, offering high cycling stability, good capacity retention and excellent coulombic efficiency.

Conclusion

In summary, electrochemically exfoliated borophene sheets were successfully synthesized and comprehensively characterized using AFM, HRTEM and XPS analyses. The results confirmed that the material exhibits a crystalline, multilayered structure with a partially oxidized surface. When employed as an anode material LIBs, the borophene electrodes demonstrated a high initial discharge capacity of 387 mAh g^{-1} and excellent cycling stability, retaining 95.8% of the capacity after ten cycles. The coulombic efficiency remained consistently high, reaching 97.3% at the 10th cycle, indicating good reversibility of lithium ion insertion/extraction and structural stability of the electrodes. These findings highlight the potential of borophene anodes synthesized via a scalable, electrochemical exfoliation approach as promising candidates for next-generation lithium-ion batteries, combining high capacity, robust cycling performance and excellent coulombic efficiency.

Scientific Ethics Declaration

* The authors declare that the scientific ethical and legal responsibility of this article published in EPSTEM journal belongs to the authors.

Conflict of Interest

* The authors declare that they have no conflicts of interest

Funding

* This study is supported within the scope of the TÜBİTAK 2209-B program (Project No: 1139B412408088).

Acknowledgements or Notes

* This article was presented as an oral presentation at the International Conference on Technology, Engineering and Science (www.icontes.net) held in Antalya/Türkiye on November 12-15, 2025.

References

Adekoya, G. J., Adekoya, O. C., Muloiwa, M., Sadiku, E. R., Kupolati, W. K., & Hamam, Y. (2024). Advances in borophene: Synthesis, tunable properties and energy storage applications. *Small, 20*(40), 2403656.

Arnold, F. M., Seifert, G., & Kunstmann, J. (2020). Thermodynamic stability of borophene, B2O3 and other B1−xOx sheets. *Journal of Physics Communications, 4*(3), 031001.

Ashraf, N., & Abghoui, Y. (2023). Borophene potential for developing next-generation battery applications: A comprehensive review. *Energy & Fuels, 37*(19), 14589–14603.

Can, S., Kuru, D., & Kuru, C. (2024). Hydrogen evolution reaction activity of electrochemically exfoliated borophene. *Journal of Nanoparticle Research, 26*(8), 183.

Çelikbilek, Z., Can, S., Lökçü, E., & Anik, M. (2022). Effect of rGO loading on the electrochemical performance of Li22Si5/rGO composite anodes for lithium-ion batteries. *International Journal of Energy Research, 46*(2), 1137–1145.

Chhowalla, M., Shin, H. S., Eda, G., Li, L. J., Loh, K. P., & Zhang, H. (2013). The chemistry of two-dimensional layered transition metal dichalcogenide nanosheets. *Nature Chemistry, 5*(4), 263-275.

Etacheri, V., Marom, R., Elazari, R., Salitra, G., & Aurbach, D. (2011). Challenges in the development of advanced Li-ion batteries: A review. *Energy & Environmental Science, 4*(9), 3243–3262.

Kaçar, N., Çayirli, M., Ozden, R. C., Lokcu, E., & Anik, M. (2023). Photocatalytic efficiency of g-C3N4/graphene nanocomposites in the photo-assisted charging of the Li-ion oxygen battery. *ACS Omega, 8*(48), 46227-46235.

Lökçü, E., Can, S., & Anik, M. (2023). Ultrasound-assisted synthesis of rGO/SiO2-based nanosheets and their electrochemical performances in Li-ion batteries. *Turkish Journal of Chemistry, 47*(2), 495-503.

Manthiram, A. (2020). A reflection on lithium-ion battery cathode chemistry. *Nature Communications, 11*(1), 1550.

Sielicki, K., Maślana, K., Chen, X., & Mijowska, E. (2022). Bottom up approach of metal assisted electrochemical exfoliation of boron towards borophene. *Scientific Reports, 12*(1), 15683.

Tarascon, J. M., & Armand, M. (2001). Issues and challenges facing rechargeable lithium batteries. *Nature, 414*(6861), 359-367.

Voiry, D., Mohite, A., & Chhowalla, M. (2015). Phase engineering of transition metal dichalcogenides. *Chemical Society Reviews, 44*(9), 2702-2712.

Yu, J., Zhou, M., Yang, M., Yang, Q., Zhang, Z., & Zhang, Y. (2020). High-performance borophene/graphene heterostructure anode of lithium-ion batteries achieved via controlled interlayer spacing. *ACS Applied Energy Materials, 3*(12), 11699-11705.

Zhang, X., Hu, J., Cheng, Y., Yang, H. Y., Yao, Y., & Yang, S. A. (2016). Borophene as an extremely high capacity electrode material for Li-ion and Na-ion batteries. *Nanoscale, 8*(33), 15340-15347.

Zielinkiewicz, K., Baranowska, D., & Mijowska, E. (2023). Ball milling induced borophene flakes fabrication. *RSC Advances, 13*(25), 16907-16914.

Author(s) Information

Suleyman Can
Bilecik Seyh Edebali University
11000, Bilecik, Türkiye
Contact e-mail: *suleyman.can@bilecik.edu.tr*

Cihan Kuru
Bilecik Seyh Edebali University
11000, Bilecik, Türkiye

To cite this article:

Can, S., & Kuru, C. (2025). Investigation of borophene synthesized via a scalable approach as an anode material for lithium-ion batteries. *The Eurasia Proceedings of Science, Technology, Engineering and Mathematics (EPSTEM), 38*, 575-579.

The Eurasia Proceedings of Science, Technology, Engineering & Mathematics (EPSTEM)
ISSN: 2602-3199

The Eurasia Proceedings of Science, Technology, Engineering and Mathematics (EPSTEM), 2025

Volume 38, Pages 580-589

IConTES 2025: International Conference on Technology, Engineering and Science

Geological and Geotechnical Perspectives on Seismic Hazard Assessment of Landslides

Liliana-Irina Stoian
Geological Institute of Romania

Elena Aurelia Tudor
Geological Institute of Romania

Antonio Ulmeanu
Geological Institute of Romania

Avram Ovidiu
Geological Institute of Romania

Ioan Scutelnicu
Geological Institute of Romania

Adrian Tătaru
Geological Institute of Romania

Abstract: The assessment of seismic hazard related to landslides is essential for understanding the complex interactions between seismic activity and slope instability, with direct implications for the protection of infrastructure and communities. This research investigates the role of geological and geotechnical conditions, seismic history, and slope dynamics in the triggering and evolution of earthquake-induced landslides. A multidisciplinary approach was applied, integrating detailed geological and geotechnical investigations with historical data on seismicity and past landslides. To improve the accuracy of the analysis, modern monitoring and modeling methods were employed: geophysical surveys for subsurface characterization, satellite remote sensing for deformation monitoring, and numerical simulations to reproduce slope behavior under seismic loading. The results indicate that areas with unfavorable geological structures, combined with moderate to high seismicity, present an increased probability of slope failure, generating significant risks for both the environment and society. These findings are highly relevant for disaster prevention policies, land-use planning, and the development of construction standards. The novelty of this research lies in applying natural hazard assessment methodologies to ground instability processes with unusual characteristics.

Keywords: Landslides, Instability, Seismic hazard assessment,

Introduction

The assessment of subsurface hazards in areas susceptible to ground instability is critical for ensuring the safety of infrastructure and local communities (Terzaghi et al., 1996; Angeli et al., 2000). In the Slănic, Prahova site, the main concern is a presumed sufoziune, which can compromise tunnel construction and road stability (Wang et al., 2007). A multidisciplinary methodology was applied to characterize the subsurface conditions and evaluate the potential hazard. This approach integrated geophysical investigations, specifically electrical resistivity tomography (ERT), with detailed geological mapping and geotechnical surveys (Loke et al., 2021;

- This is an Open Access article distributed under the terms of the Creative Commons Attribution-Noncommercial 4.0 Unported License, permitting all non-commercial use, distribution, and reproduction in any medium, provided the original work is properly cited.

- Selection and peer-review under responsibility of the Organizing Committee of the Conference

© 2025 Published by ISRES Publishing: www.isres.org

Adedibu et al., 2024). Modern monitoring techniques, including geophysical surveys for subsurface characterization and numerical modeling to simulate soil behavior under stress, were employed to increase the accuracy of the hazard assessment (Angeli et al., 2000). The results provided a clear image of the heterogeneous subsurface layers and highlighted zones potentially affected by sufoziune. This methodology offers a non-invasive, cost-effective tool for identifying areas of risk, supporting the design of preventive measures, and informing engineering decisions in Slănic (Stoian et al. 2024).

Characteristic Resistivity Ranges and Their Geological Interpretation

Based on literature sources (Table 1) and available data for similar geological structures (e.g., salt diapirs interacting with groundwater), typical ranges of electrical resistivity and their possible geological correspondences have been synthesized (Loke et al., 2021, Adedibu et al., 2024), providing a useful interpretative reference for geoelectric data analysis:

Table 1. Electrical resistivity ranges and geological significance

Resistivity Range (Ω·m)	Possible Geological Interpretation
< 5 Ω·m	Media with highly mineralized water (brine) or zones intensely saturated with brine, associated with very low resistivity anomalies and high electrical conductivity
5 – 10 Ω·m	Clays saturated with water or saline breccias impregnated with brine; characterized by high conductivity (Loke et al., 2021).
20 – 30 Ω·m	Aquifers with fresh water (low salinity) or coarse-grained wet sediments (sands, gravels)
> 100 Ω·m	Massive salt formations (dry halite, with high resistivity) or compact, very dry rocks (Milsom & Eriksen, 2011).

Intermediate ranges (approximately 30–100 Ω·m) may indicate the presence of partially saturated carbonate or marl formations, slightly wet slopes, or transition zones between the lithological units mentioned above. It is essential that the interpretation considers the local geological context. For instance, in the Slănic region, the salt massif generates very high resistivity anomalies, whereas salt breccias resulting from dissolution and collapse processes exhibit very low resistivity values (Stoian et al., 2024).

Methodology

Geological and Geotechnical Investigations

Urban areas developed on geologically complex terrains are prone to instability phenomena that can compromise the structural integrity of buildings and the functionality of infrastructure (Terzaghi et al., 1996; Angeli et al., 2000). Long-term landslide monitoring requires the integration of complementary methods, combining field observations, geotechnical measurements, geophysical surveys, and remote sensing techniques, in order to capture both surface and subsurface deformation processes and to understand their temporal evolution (Angeli et al., 2000).The present study focuses on Slănic, Prahova County, along 23 August Street, where subsidence processes have caused structural damage to residential buildings, deterioration of public roads, and increased risk to underground utilities. To address these challenges, a multidisciplinary program of geological and geotechnical investigations was conducted to provide a robust scientific basis for stabilization measures and risk mitigation.

The investigation framework was designed in accordance with Romanian Norm NP074-2022 “Normativ privind documentațiile geotehnice pentru construcții” and Eurocode 7 (SR EN 1997-1 and SR EN 1997-2), ensuring that data collection, testing, and interpretation followed international geotechnical standards (CEN, 2004; Ministerul Dezvoltării, 2022). Preliminary assessments classified the site as Geotechnical Category 3, reflecting challenging soil conditions, significant groundwater influence, and a high seismic hazard (ag = 0.40g).

The investigation program integrated multiple complementary methods:

- **Geotechnical drilling** with mechanized equipment, providing disturbed and undisturbed samples for laboratory analysis. Recovery rates exceeded 70%, ensuring reliable material characterization.
- **In-situ penetration tests**, including dynamic, static, and CPTu tests, were performed to assess stratigraphy, soil compaction, and strength parameters.
- **Geophysical surveys** explored depths beyond 100 m, revealing lithological boundaries, tectonic discontinuities, underground cavities, salt layers, and potential collapse zones.
- **Hydrogeological studies** included the installation of monitoring wells, pumping tests, and water quality analyses to evaluate aquifer behavior and aggressiveness toward construction materials.
- **Laboratory testing** followed NP074-2022 (Annex L) and included grain size distribution, Atterberg limits, compressibility, shear strength, consolidation, and density analyses to derive reliable geotechnical parameters.

Integration of geological mapping, stratigraphic columns, and tectonic interpretation enabled the development of a detailed subsurface model, supporting the evaluation of bearing capacity, settlement behavior, and slope stability. This model also facilitates risk assessment by identifying vulnerable areas and prioritizing stabilization measures.

Historical Seismicity, Landslide Inventory, and Remote Sensing Monitoring

The methodology incorporated historical seismicity, landslide inventory, and satellite-based remote sensing to assess slope instability in Slănic. Regional earthquake catalogs and macroseismic records were reviewed, focusing on events with magnitudes greater than 5.0. A landslide inventory was compiled using aerial imagery, geological maps, and field verification, documenting past slope failures and their correlation with seismic events (Angeli et al., 2000). Satellite-based monitoring employed Sentinel-1 SAR and DInSAR techniques to detect subtle ground displacements (Necula & Niculiță, 2025), complemented by Sentinel-2 multispectral imagery for land cover and vegetation monitoring. The integration of these datasets enhanced the spatial and temporal coverage of slope activity and supported hazard assessment and monitoring.

Geophysical Surveys

Electrical Resistivity Tomography (ERT) was applied to obtain high-resolution, non-invasive images of the subsurface structures and identify zones affected by saturation and structural weakness (Loke et al., 2021). Data acquisition used an AGI SuperSting R8/IP system with up to 64 electrodes, configured in multiple arrays (Schlumberger, Wenner, Dipole–Dipole) to optimize lateral and vertical resolution. Electrode spacing ranged from 5 to 10 m, and profile lengths were 160–320 m, adjusted for site morphology. Data were inverted using EarthImager 2D with topographic corrections to identify resistivity contrasts associated with lithological boundaries, saturated zones, and structural weaknesses (Stoian et al., 2024).

Numerical Simulations

Slope stability was modeled under static and dynamic conditions using finite element methods. Geological and geophysical data were integrated to simulate potential failure mechanisms under seismic loading. These simulations allowed the quantification of safety factors and identification of threshold conditions for slope failure.

Results and Discussion

Historical Seismicity, Landslide Inventory, and Remote Sensing Monitoring

The assessment of slope instability in Slănic Prahova requires a comprehensive understanding of both natural and anthropogenic factors contributing to ground deformation. Historical seismicity represents a key element in this analysis, as the Carpathian and Subcarpathian region is moderately seismic. Archival records and catalogues of earthquakes in Romania indicate that even moderate seismic events can trigger slope failures in areas with

unfavorable geological and geotechnical conditions. Knowledge of seismic history is therefore essential for identifying zones of increased susceptibility and for integrating seismic hazard into landslide risk assessment.

The landslide inventory forms the second fundamental component. Previous field studies, geological surveys, and remote sensing analyses have identified multiple instances of slope movement in Slănic Prahova, including slow-moving landslides, subsidence due to salt dissolution, and small-scale surficial failures. These records allow the development of detailed maps indicating both the spatial distribution of landslides and their morphological characteristics. The integration of historical data, field evidence, and geotechnical parameters supports robust hazard modeling and prioritization of high-risk zones.

Remote sensing monitoring, particularly using Sentinel satellite missions (Figure 1), provides a modern, non-invasive approach for continuous observation of ground deformation. Sentinel-1 Synthetic Aperture Radar (SAR) data enable interferometric analyses (InSAR and multi-temporal InSAR) to detect subtle movements with millimetric precision. Studies have shown differential subsidence and slope deformations in the Slănic Prahova region, with rates up to several tens of millimeters per year (Necula & Niculiță, 2025). Complementary Sentinel-2 multispectral imagery assists in identifying changes in land cover and vegetation health, which can act as early indicators of slope instability. The combination of these datasets allows researchers to detect precursory ground movements, validate field observations, and update landslide inventories in near real-time.

Integrating historical seismicity, landslide inventory data, and satellite-based monitoring provides a multidisciplinary framework for assessing slope hazard in Slănic Prahova. This approach supports risk assessment, urban and infrastructure planning, and the development of early-warning systems. Furthermore, the use of Sentinel-derived data ensures long-term monitoring capability, which is particularly relevant in areas influenced by both natural processes (e.g., earthquakes, karstification) and anthropogenic activities such as salt mining.

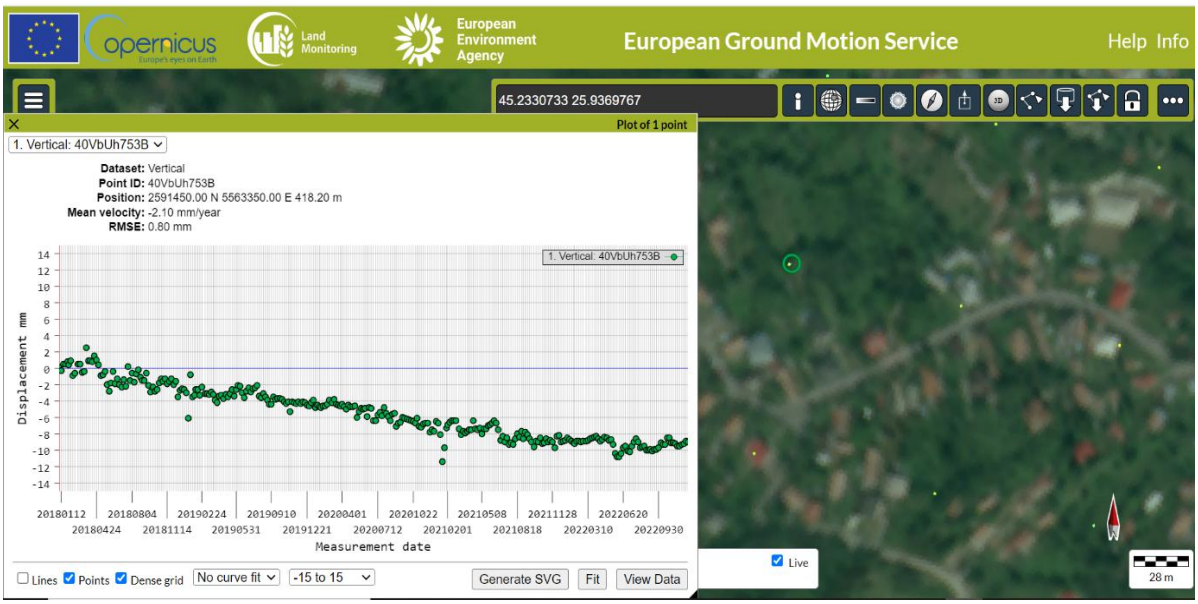


Figure 1. Sentinel-2 data regarding ground subsidence in the affected area

Geophysical Surveys

Geophysical monitoring of areas prone to instability plays a key role in the early identification of subsurface processes that may lead to collapse or suffosion phenomena. In the investigated area of Slănic Prahova, where geological and hydrogeological conditions favor water accumulation and the mobilization of fine fractions, successive geoelectrical surveys were carried out to capture the temporal evolution of subsurface structures. The first campaign focused on the preliminary characterization of the area prior to the occurrence of visible failures, while the second campaign, conducted one year later within the *Geomonitor* project, aimed to extend the depth of investigation and provide a more detailed image of the active processes. Comparing the two profiles offers insights into how the area evolved, from simple geoelectrical anomalies associated with water accumulation, to the development of unstable cavities subsequently filled with heterogeneous materials.

First Geoelectrical Profile

The first set of geoelectrical measurements(figure 2) was conducted prior to the collapse, using passive multielectrode cables with a length of and a maximum investigation depth of approximately 50 m. The chosen dipole–dipole configuration allowed for a large number of measurements and good resolution in the shallow subsurface. The results revealed an irregular relief, with depressional areas characterized by very low resistivity values (<10 Ohm·m), associated with water accumulations. These zones created instability conditions, favoring the onset of suffosion and gradual failure of the upper layers. In addition, GPS RTK data showed that the anomalies extend from 10 m to over 40 m depth, without directly intersecting the main collapse area, but highlighting the predisposition of the terrain to instability (Subsidence Raport,2024).

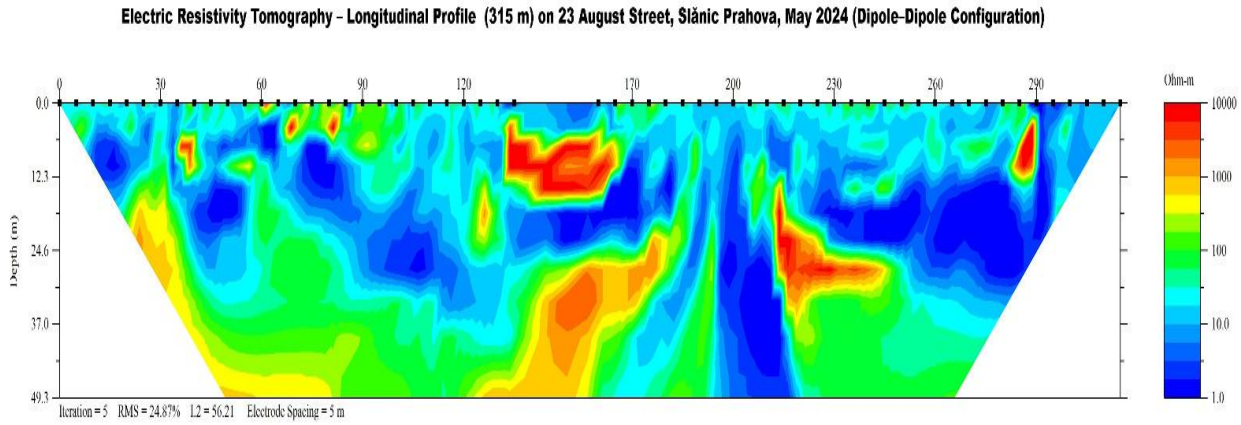


Figure 2. Electric resistivity tomography – Longitudinal profile (315 m) on 23 August Street, Slănic Prahova, May 2024 (Dipole–Dipole configuration)

Second Geoelectrical Profile

One year later, within the Geomonitor project, a new geoelectrical profile was acquired along a roughly similar alignment, extended over a length of 1 km, with electrodes spaced at 10 m intervals (Figure 3). This configuration allowed an investigation depth of approximately 200 m, providing a more detailed image of both lateral and vertical structures. The results revealed major resistivity contrasts: zones with high values (intense red, between 450–650 m, at depths of 50–150 m) interpreted as compact blocks or rock/gravel fillings, alternating with low-resistivity zones (green–blue), characteristic of clayey wet media or areas affected by infiltration. The profile clearly captured the interruption of a more impermeable layer beneath the shallow aquifer, favoring the accumulation and confinement of water in the suffosion zone. Elevated RMS values indicated significant heterogeneity, caused both by natural processes (infiltration, erosion, collapses) and anthropogenic interventions (successive fillings). During the survey, significant electrical anomalies were detected, likely caused by subsurface man-made sources such as deteriorated electrical cables, active grounding systems, damaged DC lines, or other underground current-carrying installations. These interferences necessitated careful differentiation from natural geological resistivity variations (GeoMonitor geophysics report, 2025).

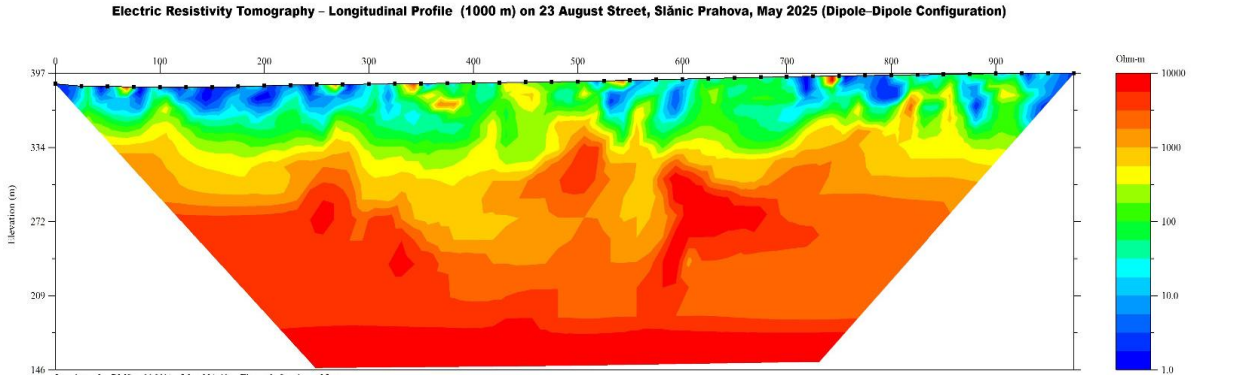


Figure 3. Electric resistivity tomography – Longitudinal profile on 23 (1km) August Street, Slănic Prahova, May 2025 (Dipole–Dipole configuration)

Comparison Between Profiles

A comparison of the two measurement sets shows a clear evolution (Figure 4) of instability processes. While the first profile only captured the presence of low-resistivity zones associated with a predisposition to suffosion, the second profile confirmed that the area continued to subside, developing an unstable cavity that was later filled, naturally and/or artificially, with heterogeneous materials (rock, gravel, clay). This sequence of collapses and fillings is reflected in the rapid alternation of resistivity values and the increased structural complexity revealed by the second survey.

Thus, the evolution from a localized anomaly of limited depth to an extended zone characterized by major resistivity contrasts and active suffosion processes demonstrates the accelerated dynamics of instability in the area. These observations highlight the importance of continuous monitoring and correlation with geological and hydrogeological data, in order to support appropriate risk mitigation measure.

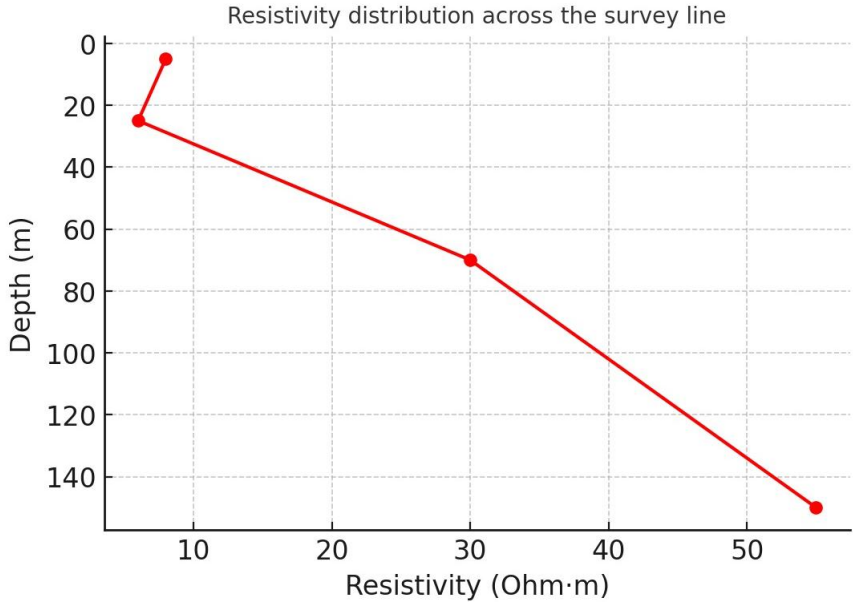


Figure 4. Resistivity distribution across the survey line

Seismic Response Analysis of the Ground in Slănic Prahova Using SHAKE 2000

The stability analysis of the ground in Slănic Prahova, an area prone to instability processes, was performed using the SHAKE 2000 program, which applies one-dimensional equivalent-linear analysis to simulate seismic wave propagation through layered media (Wang et al., 2007). The method accounts for changes in shear modulus and damping with strain level, enabling the assessment of local amplification effects. (Figure 5).

The modeling process included the determination of initial dynamic parameters for each layer (shear modulus and damping), the conversion of input seismic motion into the frequency domain, and the calculation of interactions between incident and reflected waves. The resulting transfer functions were used to evaluate seismic amplification, while the inverse Fourier transform allowed the reconstruction of displacements and strain distribution. Successive iterations led to the final calibration of parameters, with errors below 3%. Based on accelerometric data recorded by the National Institute for Earth Physics (INCDFP) during the Vrancea earthquake of August 30, 1986 (MGR = 7.5), the results for the geological profile at Slănic Prahova highlighted:

- a maximum spectral amplification factor (SAF) of **2.65**, corresponding to a severe Vrancea earthquake scenario (MGR = 7.5) (Figure 6);
- a peak ground acceleration at the surface of **0.254 g** (≈250 cm/s²)(Figure 7);
- a fundamental site period of **1.4 s**, associated with the stratified structure of deposits; (Figure 8)
- a maximum spectral acceleration amplitude of **0.812 g**. (Figure 9)

As a reference for the bedrock, the formation with a shear-wave velocity of 760 m/s was considered, representative of the more rigid structures at depth.

These results indicate that the ground in Slănic is highly sensitive to strong-magnitude seismic events, and the existing instabilities may be exacerbated by local seismic amplification effects. The integration of such evaluations contributes to a better understanding of hazard mechanisms and supports the development of risk reduction measures for infrastructure and communities.

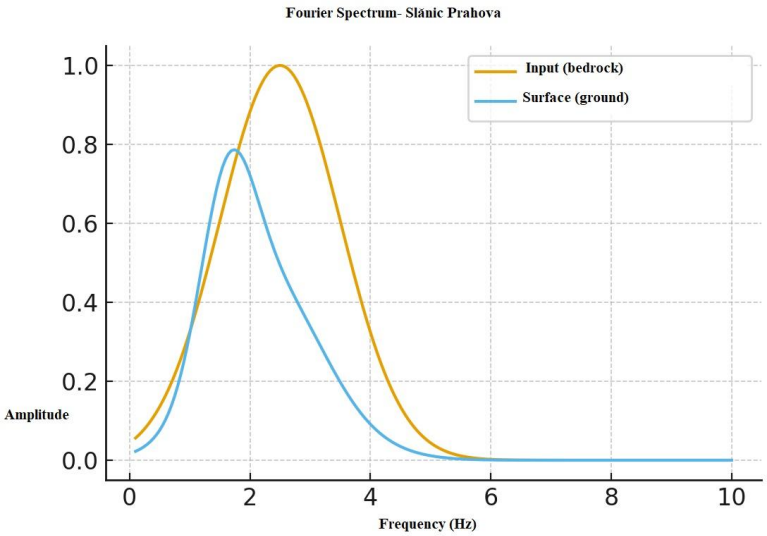


Figure 5. Fourier spectrum-Slănic Prahova

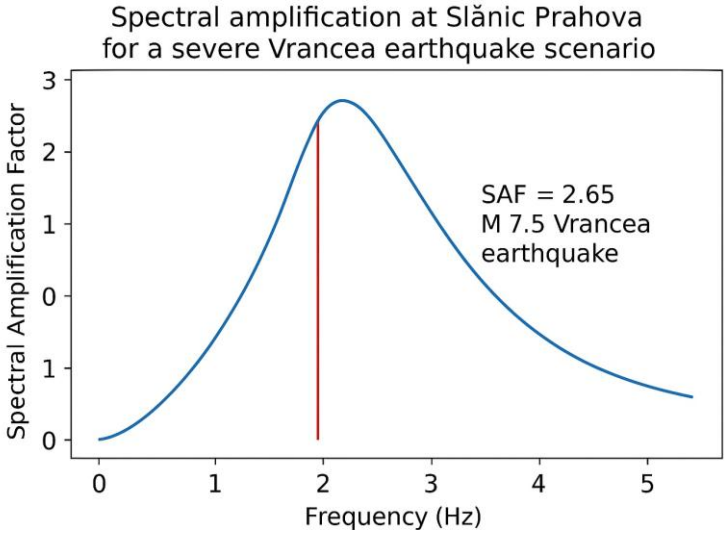


Figure 6. Spectral amplification factor (SAF)-Slănic Prahova

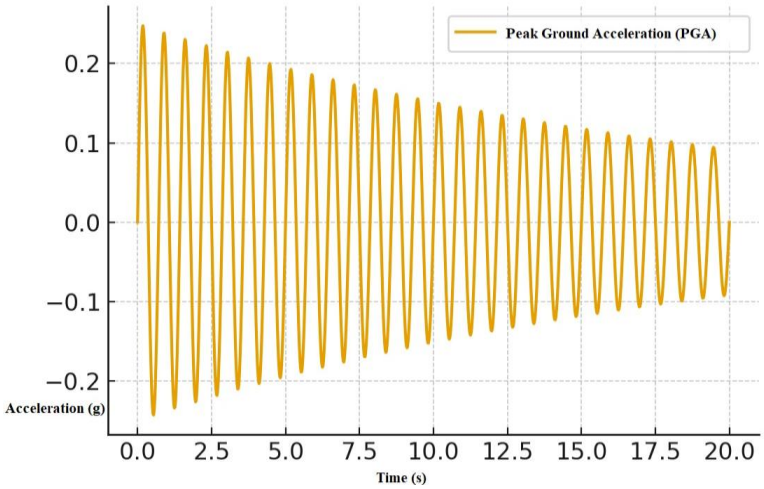


Figure 7. Peak ground acceleration (PGA)

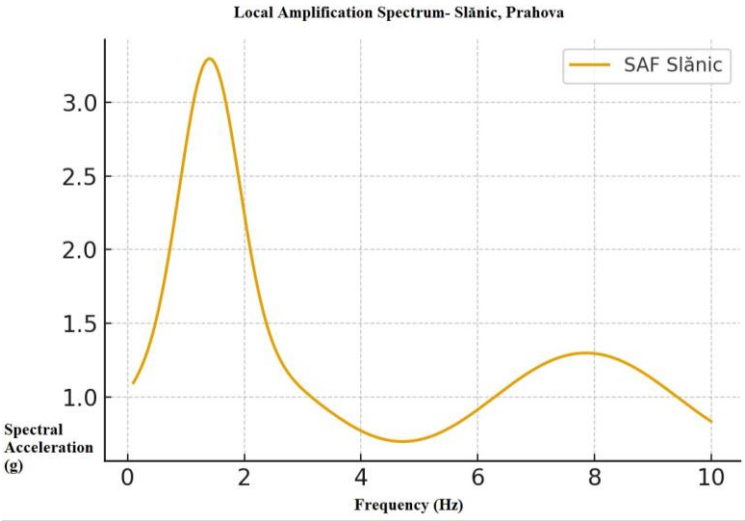


Figure 8. Acceleration time history-Slănic Prahova

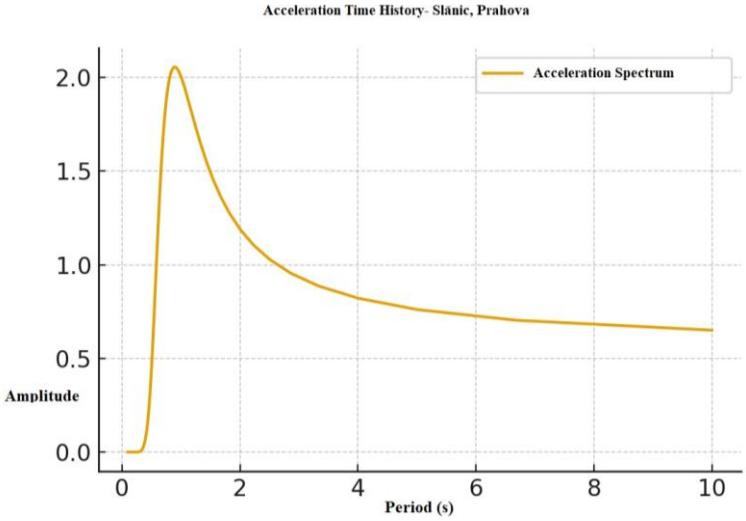


Figure 9. Response spectrum-Slănic Prahova

Conclusion

The geoelectric and hydrogeological analysis of the Slănic Prahova area highlights a complex interaction between the salt massif and groundwater, which influences both surface relief and terrain stability (Stoian et al., 2024). Zones of minimum resistivity directly indicate locations where the subsurface is weakened by water accumulation, representing potential collapse points. Detailed geophysical investigations indicate that the aquifer boundary and the compact clayey/marly formations supporting the main building foundations do not pose significant risks to their stability. However, the subsidence cone area on 23 August Street is not stabilized, and electrometry measurements indicate a continuous risk of collapse. This underscores the need for permanent monitoring and the implementation of proactive measures to prevent terrain instability phenomena (Angeli et al., 2000).

Recommendations

- *Expansion of the geophysical and hydrogeological monitoring program* through the installation of sensor networks for real-time measurement of water levels, ground displacements, and resistivity variations, enabling early detection of sufozional processes.
- *Execution of additional geological and hydrological boreholes* to investigate the depth of the salt massif, identify groundwater flow paths, and assess the structural stability of the soil in critical areas.

- *Development of an integrated geological and hydrogeological map* at a detailed scale (1:5,000), including geophysical, geochemical, and geomorphological parameters, highlighting zones with high risk of terrain instability.
- *Design and implementation of groundwater control measures*, including drainage, controlled diversions, or selective impermeabilizations, to limit salt dissolution processes and fine particle washout in high-risk areas.
- *Establishment of a rapid response protocol* in the event of instability phenomena, including automated alerts, evacuation plans, and coordination with local authorities to protect the population and built heritage.
- *Assessment and design of structural reinforcements* for existing buildings if significant subsurface changes or new unstable zones are detected, using methods adapted to the local soil characteristics and salt massif conditions.

Scientific Ethics Declaration

* The authors declares that the scientific, ethical, and legal responsibility for the content of this article, published in EPSTEM Journal, rests solely with the authors.

* No ethics committee approval was required for this study, as it did not involve human or animal subjects.

Conflict of Interest

*The authors declare that they have no financial, personal, or professional conflicts of interest that could have influenced the outcomes or interpretation of this research.

Funding

*This research was primarily supported by the project ProGeo-RO – PN 23-39-03-01, Contract No. 34N/2023, funded by the Romanian Ministry of Education and Research, and was also conducted within the framework of GeoMonitor – SOL-2024-28, financed by UEFISCDI, Romania. Additional activities were supported through institutional own funds of the Geological Institute of Romania and personal financial contributions of the first author (Liliana-Irina Stoian).

Acknowledgements or Notes

* This article was presented as an oral presentation at the International Conference on Technology, Engineering and Science (www.icontes.net) held in Antalya, Türkiye, on November 12–15, 2025.

* The authors acknowledge the support of the **Geological Institute of Romania**, which provided technical assistance, access to geophysical equipment, and logistical support essential for the investigations carried out at the Slănic site.

References

Adedibu, S. A., et al. (2024). Unraveling subsurface crustal dynamics: Exploring electrical and seismic refraction methods from theories to existing and machine learning-based emerging prospects. *Journal of Applied Geophysics, 215*, 105-120.

Angeli, M. G., Pasuto, A., & Silvano, S. (2000). A critical review of landslide monitoring experiences. *Engineering Geology, 55*(3), 133-147.

CEN (European Committee for Standardization). (2004). *Eurocode 7: Geotechnical design – Part 1: General rules (EN 1997-1) & Part 2: Ground investigation and testing (EN 1997-2)*. CEN.

Loke, M. H., Rucker, D. F., Chambers, J. E., Wilkinson, P. B., & Kuras, O. (2021). Electrical resistivity surveys and data interpretation. In H. Gupta (Ed.), *Encyclopedia of solid earth geophysics* (pp. 331–349). Springer.

Ministerul Dezvoltării, Lucrărilor Publice și Administrației. (2022). *NP 074-2022: Normativ privind documentațiile geotehnice pentru construcții*. MDLPA.

Necula, N., & Niculiță, M. (2025). Application of Sentinel-1 InSAR techniques for monitoring landslide dynamics in the Subcarpathians of Romania. *Remote Sensing, 17*(4), 1025–1042.

Stoian, L. I., Tudor, E. A., Ulmeanu, A., Scutelnicu, I., Ovidiu, A., & Tătaru, A. (2024). *Geoelectric investigation of unstable terrains in Slănic Prahova* (Internal Report). Geological Institute of Romania.

Terzaghi, K., Peck, R. B., & Mesri, G. (1996). *Soil mechanics in engineering practice* (3rd ed.). John Wiley & Sons.

Wang, G., Sassa, K., & Fukuoka, H. (2007). Seismic triggering and slope failure mechanisms in landslides. *Landslides, 4*(1), 25–37.

Author(s) Information

Liliana-Irina Stoian
Geological Institute of Romania,
1 Caransebes Street, District 1,
012271 Bucharest, Romania
Contact e-mail: *stoianirina131@gmail.com*

Elena Aurelia Tudor
Geological Institute of Romania,
1 Caransebes Street, District 1,
012271 Bucharest, Romania

Antonio Ulmeanu
Geological Institute of Romania,
1 Caransebes Street, District 1,
012271 Bucharest, Romania

Avram Ovidiu
Geological Institute of Romania,
1 Caransebes Street, District 1,
012271 Bucharest, Romania

Ioan Scutelnicu
Geological Institute of Romania,
1 Caransebes Street, District 1,
012271 Bucharest, Romania

Adrian Tătaru
Geological Institute of Romania,
1 Caransebes Street, District 1,
012271 Bucharest, Romania

To cite this article:

Stoian, L.I., Tudor, E. A., Ulmeanu, A., Ovidiu, A., Scutelnicu, I., & Tataru, A. (2025). Geological and geotechnical perspectives on seismic hazard assessment of landslides. *The Eurasia Proceedings of Science, Technology, Engineering and Mathematics (EPSTEM), 38*, 580–589.

The Eurasia Proceedings of Science, Technology, Engineering & Mathematics (EPSTEM)
ISSN: 2602-3199

The Eurasia Proceedings of Science, Technology, Engineering and Mathematics (EPSTEM), 2025

Volume 38, Pages 590-596

IConTES 2025: International Conference on Technology, Engineering and Science

Compact Single-Switch Reconfigurable Patch Antenna with Multi-Band Operation for Wireless Systems

Frouda Nour El Houda
Djillali Liabes University of Sidi Bel Abbas

Berkat Abdellatif
University of Abou Bekr Belkaid

Azzaz Rahmani Salima
Djillali Liabes University of Sidi Bel Abbas

Abstract: A compact frequency-reconfigurable patch antenna is proposed for multi-band wireless applications. The antenna is designed on a single-layer FR4 substrate (24 × 30 mm²) with a partial ground plane on the same side as the radiator. By using a single copper-strip switch, the structure achieves four measured resonances at 2.45, 3.8, 10.7, and 13 GHz while remaining simple and cost-effective. The measured results show excellent impedance matching, with reflection coefficients (S11) below −25 dB and standing wave ratio values less than 2 at all operating frequencies. Unlike conventional designs requiring multiple switches or biasing circuits, the proposed configuration reduces design complexity and overall antenna size. It also provides stable quasi-omnidirectional radiation patterns, ensuring consistent performance across different scenarios. With its compact footprint, frequency agility, and reliable radiation, this antenna is well suited for Sub-6 GHz 5G, radar, and biomedical communication systems. In addition, its adaptability makes it a promising candidate for emerging applications such as Internet of Things and wearable devices, where compactness and versatility are critical.

Keywords: Reconfigurable antenna, Multi-band, Frequency agility, Compact design, Wireless communication

Introduction

The demand for reconfigurable antennas has been increasing remarkably due to their ability to adapt dynamically to the changing requirements of modern communication systems (Karthika & Kavitha, 2021; Zhang et al., 2024).These antennas can adjust several parameters—such as radiation pattern, bandwidth, gain, and polarization-thereby improving their adaptability to diverse communication environments (Shereen et al., 2022).Reconfigurability is commonly achieved using RF PIN diodes, varactor diodes, and Radio Frequency Microelectromechanical System (RF MEMS) switches (El Aoud et al., 2024; Gao et al., 2025; Marzouk et al., 2025).One of the main advantages of these antennas lies in their ability to support multiple functionalities within a compact and lightweight configuration (Awan et al., 2024; Khan et al., 2024; Saraswat & Kumar, 2020). This characteristic is particularly beneficial in systems where space and weight are constrained, such as mobile devices, satellite communications, and military platforms. By substituting several fixed-function antennas with a single reconfigurable unit, both system complexity and overall cost can be considerably reduced (Karthika & Kavitha, 2023; Chung et al., 2024)

Among the various types, frequency-reconfigurable antennas are capable of dynamically altering their operating frequency to cover multiple communication bands. This capability minimizes the need for additional filters to suppress unwanted frequencies (Benkhadda et al., 2024; Kareem Al-Gertany et al., 2021). Furthermore, these

- This is an Open Access article distributed under the terms of the Creative Commons Attribution-Noncommercial 4.0 Unported License, permitting all non-commercial use, distribution, and reproduction in any medium, provided the original work is properly cited.

- Selection and peer-review under responsibility of the Organizing Committee of the Conference

© 2025 Published by ISRES Publishing: www.isres.org

antennas play a crucial role in modern wireless systems that must operate over several frequency bands to support emerging technologies such as 5G, LTE, the Internet of Things (IoT), and satellite communications (Abdulhussein et al., 2023).

In recent years, various frequency-reconfigurable antenna designs have been proposed to meet the growing requirements of multiband wireless communication. Rakesh Kumar et al. (2023) presented an FR-4 patch antenna incorporating a defective ground structure and three switches to achieve eight operating bands; however, the use of multiple switches increases design complexity and necessitates additional bias networks. Similarly. (Ali et al., 2025) developed a compact multi-mode antenna for C-band, Sub-6 GHz 5G, and ISM applications using PIN diodes, though the associated biasing networks and diode losses reduce radiation efficiency. In another study, (Wang et al., 2023) introduced a graphene-based reconfigurable patch antenna with tunability between 29 and 40 GHz; nevertheless, its dependence on advanced materials and high bias voltages limits its suitability for cost-effective applications.(Bayer Keskin et al., 2025) also proposed a UWB/Ku-band monopole antenna employing PIN diodes that provides an ultrawide bandwidth but suffers from limited gain and increased fabrication complexity due to the defected ground structure.

Based on the above discussion, it is clear that most existing frequency-reconfigurable antennas rely on multiple switches, complex biasing circuits, or offer limited tuning ranges. To address these limitations, this paper proposes a compact reconfigurable patch antenna that achieves four measured resonances (2.45, 3.8, 10.7, and 13 GHz) using only a single copper-strip switch. The design combines low cost, compact size, and high gain, making it suitable for Sub-6 GHz, 5G, radar, and biomedical applications. The remainder of this paper is organized as follows: Section II presents the antenna design and methodology, Section III discusses the measured and simulated results, and Section IV concludes the work.

Method

Proposed Antenna Design

The proposed antenna is a compact microstrip patch with a partial ground plane and a single switching element for multi-band operation. It is implemented on an FR4 substrate ($\varepsilon r = 4.3$, $\tan\delta = 0.025$) with dimensions of 30 × 24 mm² and a thickness of 1.6 mm. The antenna is excited by a 2 mm-wide microstrip feed line, while the switch is represented by a 1 × 1 mm² copper square, emulating a PIN diode. An 8 mm partial ground plane and a slot near the feed are introduced to improve impedance bandwidth and current distribution. The structure is single-port, compact, and simulated in CST Microwave Studio. The geometry of the antenna is illustrated in **Fig. 1**.

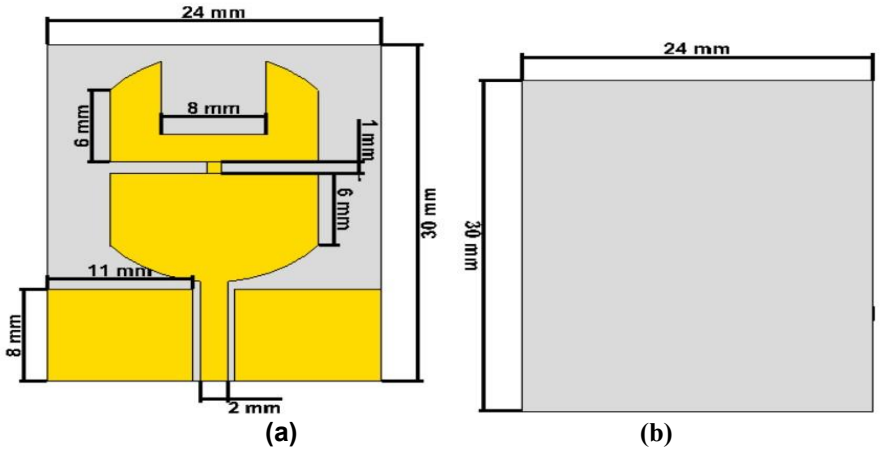
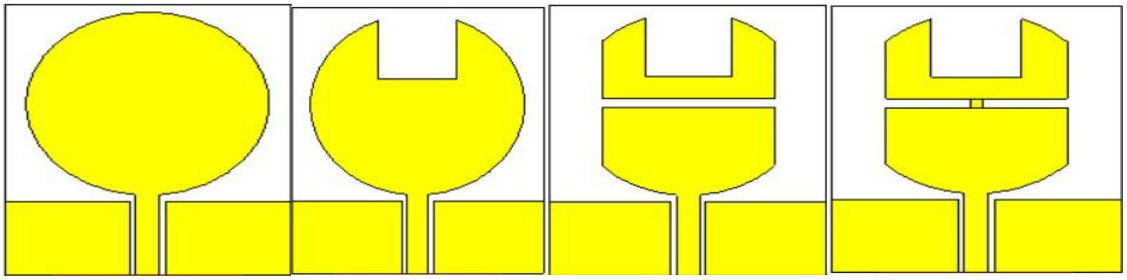


Figure 1. The proposed antenna; (a) top view (b) bottom view .

Development of Single Antenna Element

The proposed antenna design was developed through a step-by-step evolution process. The initial structure (Step 1) consists of a simple circular patch fed by a microstrip line. In Step 2, a notch was introduced at the top of the patch to improve impedance matching. In Step 3, the circular geometry was modified into a rectangular shape with slots, enhancing resonance characteristics. Finally, in Step 4, an additional section was added to the radiator,

which enabled wider bandwidth and stable multiband operation. The complete design evolution is illustrated in Fig. 2



(a) (b) (c) (d)

Figure 2. Evolution of the antenna design: (a) Step 1 – initial circular patch, (b) Step 2 – notched circular patch, (c) Step 3 – modified rectangular patch, (d) Step 4 – final proposed antenna

Principle of Reconfiguration

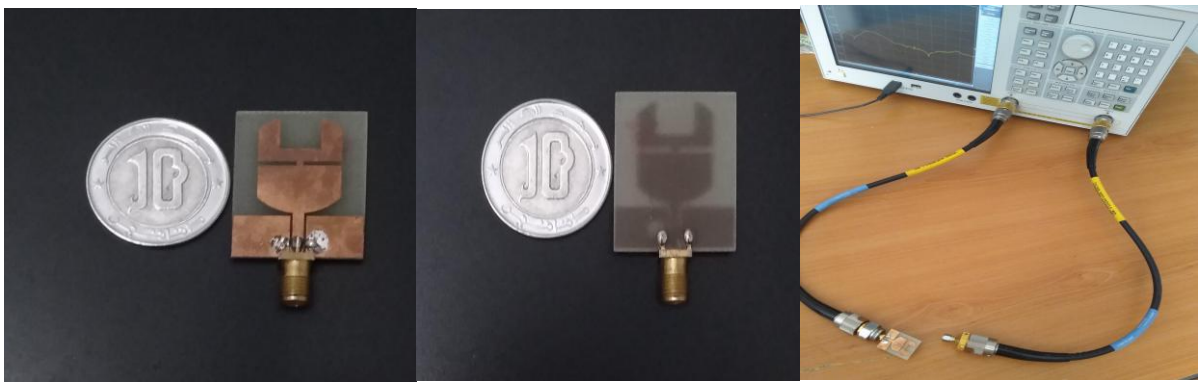
The proposed antenna achieves frequency reconfiguration through a simple structural approach. Instead of employing active components such as PIN diodes or varactors, a small copper strip is inserted between the feedline and the outer radiating element. By connecting or disconnecting this strip, the effective current distribution and electrical length of the antenna are modified, resulting in a shift of the resonance frequency. This method provides a cost-effective and reliable solution while avoiding the biasing circuits and complexity usually required for reconfigurable designs.

Simulation Setup

The proposed antenna design was simulated using CST Microwave Studio. The finite integration technique (FIT) was employed to solve Maxwell's equations in the frequency domain. Open boundary conditions were applied to mimic free-space propagation. The frequency range of interest was set to cover both the ISM and sub-6 GHz bands. The simulation setup included the definition of the excitation port, mesh refinement for accurate results, and monitoring of key parameters such as reflection coefficient (S11), radiation patterns, SWR, and efficiency.

Results and Discussion

To validate the simulation performance, the prototype of the proposed antenna was fabricated and measured. The measurements were conducted using the E5071 ENA series Vector Network Analyzer (VNA).



(a) (b) (c)

Figure 3. Fabricated antenna prototype: (a) top view, (b) bottom view, and (c) measurement setup with VNA

The measured reflection coefficient shows resonances at 2.45 GHz, 3.8 GHz, 10.7 GHz, and 13 GHz. Compared to the simulated results, slight frequency shifts can be observed, especially at higher frequencies. These discrepancies can be attributed to production inaccuracies, substrate parameter variations, and connector effects.

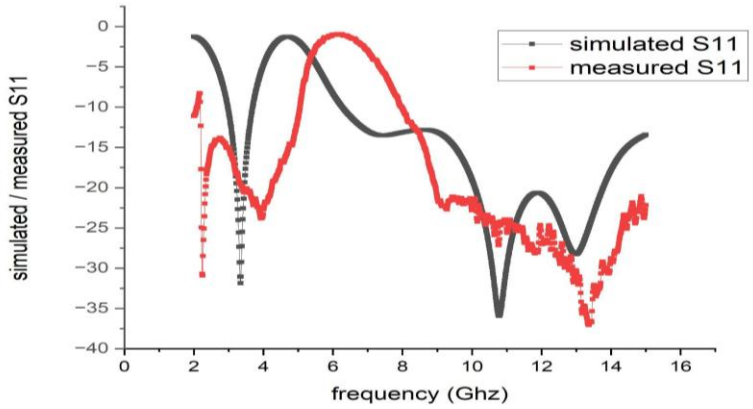


Figure 4. Simulated and measured S11 of the proposed antenna

Simulated and Measured VSWR Performance

Figure 5 illustrates the simulated and measured VSWR of the proposed antenna. The results show that the VSWR remains below the acceptable threshold of 2 across the operating frequency bands. A slight shift is observed between the simulated and measured responses, which can be attributed to connector losses, and measurement conditions.

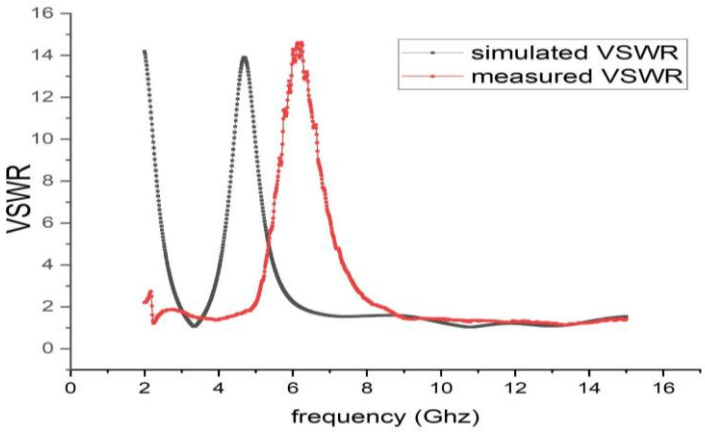
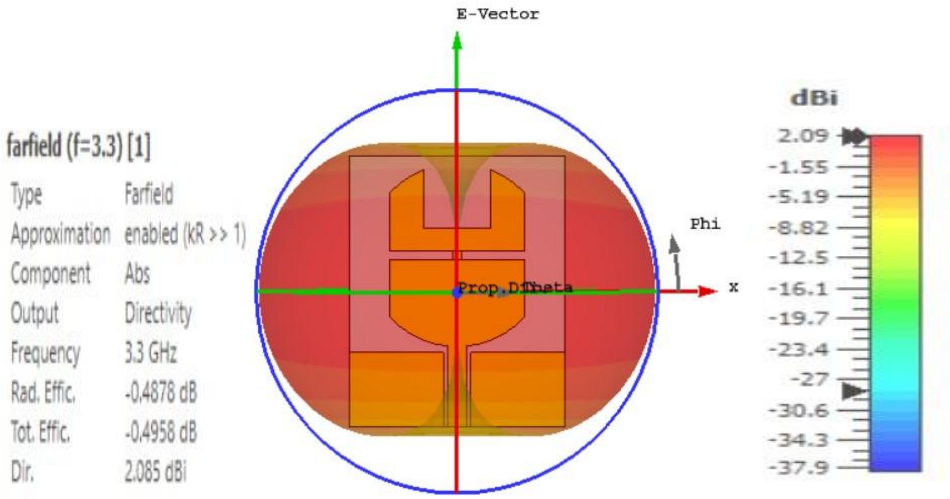
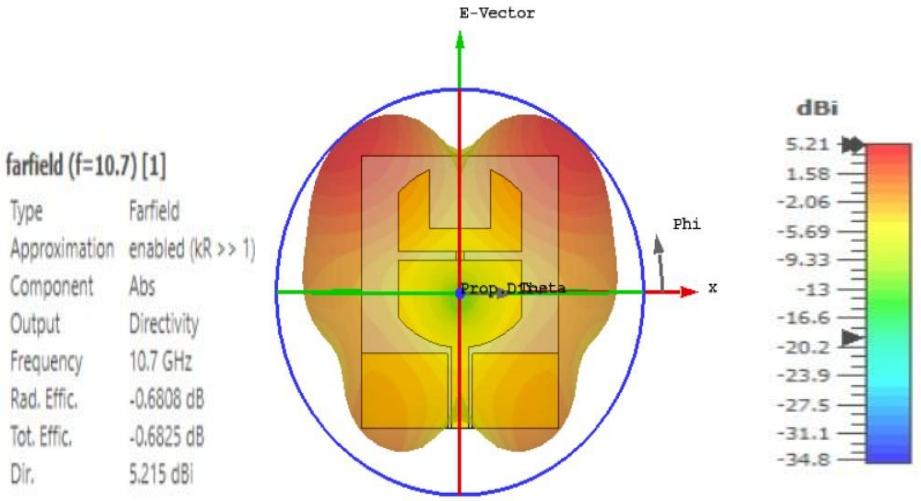


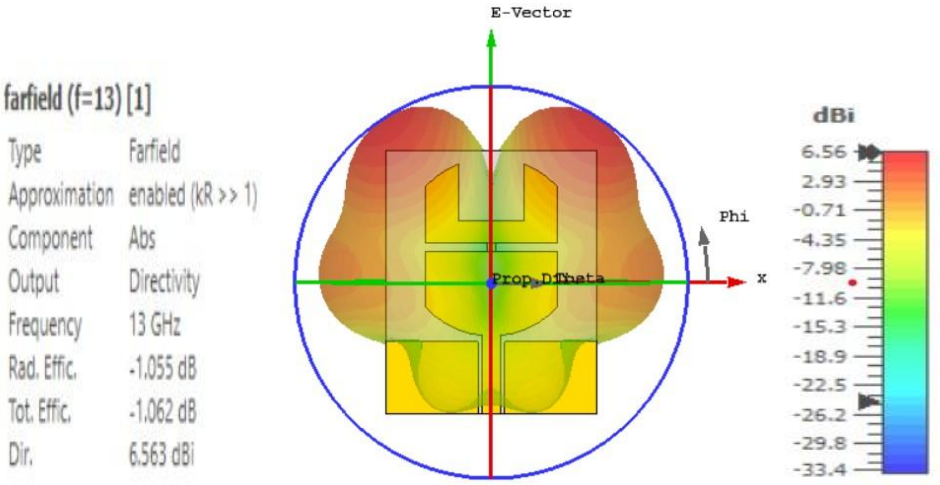
Figure 5. Simulated and measured VSWR of the proposed antenna



(a) At the first resonance frequency 3.3 Ghz



(b) At the second resonance frequency 10.7 Ghz



(c) At the third resonance frequency 13 Ghz

Figure 6. Radiation patterns of the proposed antenna at different resonance frequencie

.

Conclusion

This paper has presented the development of a compact frequency-reconfigurable patch antenna realized on a low-cost FR4 substrate. By employing a single copper-strip switch, the design succeeds in providing multi-band operation without the complexity of multiple switching elements or intricate biasing networks. The proposed structure not only reduces hardware complexity and footprint but also ensures reliable impedance matching, efficient radiation behavior, and adequate gain across all targeted frequency bands. Overall, the achieved results highlight the antenna's potential as a practical solution for emerging wireless platforms, particularly in Sub-6 GHz 5G connectivity, radar sensing, and biomedical communication systems.

Recommendations

The proposed compact reconfigurable antenna demonstrates reliable performance across four frequency bands with a simplified switching mechanism. It is recommended for practical deployment in Sub-6 GHz 5G modules, compact radar units, and biomedical devices where size and cost constraints are critical. Future implementations may further benefit from integrating an actual PIN diode instead of the copper-strip emulation, as well as exploring flexible substrates to enable wearable or implantable use cases.

Scientific Ethics Declaration

* The authors declare that the scientific ethical and legal responsibility of this article published in EPSTEM journal belongs to the authors.

Conflict of Interest

* The authors declare that they have no conflicts of interest

Funding

* This research received no specific grant from any funding agency in the public, commercial, or not-for-profit sectors.

Acknowledgements or Notes

* This article was presented as poster an presentation at the International Conference on Technology, Engineering and Science (www.icontes.net) held in Antalya/Türkiye on November 12-15, 2025.

References

Abdulhussein, A. J., Farhan, M. J., & Ali, G. M. (2023). Design and implementation of a frequency reconfigurable antenna using PIN switch for sub-6 GHz applications. *Open Engineering, 13*(1), 20220453.

Ali, E. M., Awan, W. A., Abbas, A., Abbas, S. M., & Mohamed, H. G. (2025). Compact frequency-agile and mode-reconfigurable antenna for C-band, sub-6-GHz-5G, and ISM applications. *Micromachines, 16*(6), 724.

Awan, W. A., Islam, T., N. Alsunaydih, F., Alsaleem, F., & Alhassoonc, K. (2024). Dual-band MIMO antenna with low mutual coupling for 2.4/5.8 GHz communication and wearable technologies. *PLOS ONE, 19*(4), e0301924.

Bayer Keskin, S. E., Koziel, S., & Szczepanski, S. (2025). Frequency reconfigurable PIN diode-based Reuleaux-triangle-shaped monopole antenna for UWB/Ku band applications. *Scientific Reports, 15*(1), 6555.

Benkhadda, O., Saih, M., Reha, A., Ahmad, S., Chaji, K., Singh, H., & Al-Gburi, A. J. A. (2024). A miniaturized reconfigurable antenna for modern wireless applications with broadband and multi-band capabilities. *Progress In Electromagnetics Research M, 127*, 93–101.

Chung, M.-A., Lin, C.-W., Yang, C.-W., & Meiy, I.-P. (2024). Wearable reconfigurable antennas with multi-mode switching for sub-6GHz, V-band, and D-band applications. *IEEE Access, 12*, 115448–115464.

El Aoud, S. E., Abbaoui, H., Benkhadda, O., Attioui, S., El Assri, N., Ibnyaich, S., Zeroual, A., Ismail, M. M., & Al-Gburi, A. J. A. (2024). Design of a crescent moon-shaped reconfigurable patch antenna using a PIN diode for 5G sub-6 GHz and multistandard wireless applications. *Progress In Electromagnetics Research B, 109*, 81–93.

Gao, M., Yuan, H., Nan, J., Niu, H., & Ge, C. (2025). A dual-port millimeter-wave frequency reconfigurable array antenna. *Progress In Electromagnetics Research C, 154*, 221-228.

Kareem Al-Gertany, Q. H., Farhan, M. J., & Jasim, A. K. (2021). Design and analysis a frequency reconfigurable octagonal ring-shaped quad-port dual-band antenna based on a varactor diode. *Progress In Electromagnetics Research C, 116*, 235-248.

Karthika, K., & Kavitha, K. (2021). Reconfigurable antennas for advanced wireless communications: A review. *Wireless Personal Communications, 120*(4), 2711-2771.

Karthika, K., & Kavitha, K. (2023). Design and development of parasitic elements loaded quadband frequency and pattern reconfigurable antenna. *International Journal of RF and Microwave Computer-Aided Engineering, 2023*, 1-10.

Khan, S. F., Khan, B. M., & Mairaj Rasool Khan, T. (2024). Low profile high gain RHCP antenna for L-Band and S-Band using rectangular ring metasurface with backlobe suppression. *PLOS ONE, 19*(2), e0297957.

Marzouk, M., Nejdi, I. H., Rhazi, Y., Saih, M., Nasir, J. A., Daher, A., Hussein, M. I., Zakaria, Z., & Al-Gburi, A. J. A. (2025). Low-profile reconfigurable UWB fractal antenna enhanced by parasitic elements for wireless applications. *Progress In Electromagnetics Research Letters, 126*, 37-48.

Rakesh Kumar, P., Sunitha, P., & Prasad, M. V. S. (2023). Compact reconfigurable patch antenna for wirelesss applications. *Progress ın Electromagnetics Research C, 138*, 161-174.

Saraswat, R. K., & Kumar, M. (2020). A metamaterial loaded hybrid fractal multiband antenna for wireless applications with frequency band reconfigurability characteristics. *Frequenz, 74*(11–12), 401-416.

Shereen, M. K., Khattak, M. I., Zubir, F., & Basit, A. (2022). A novel single-feed hybrid reconfigurable microstrip patch antenna for 5G mobile communication and radio frequency energy harvesting applications at 28/38GHz. *PLOS ONE, 17*(1), e0260407.

Wang, X., Wu, L., Chen, H., Wang, W., & Liu, Z. (2023). Frequency-reconfigurable microstrip patch antenna based on graphene film. *Electronics, 12*(10), 2307.

Zhang, M., Xu, G., & Gao, R. (2024). Reconfigurable antennas for wireless communication: Design mechanism, state of the art, challenges, and future perspectives. *International Journal of Antennas and Propagation, 2024*(1), 3046393.

Author(s) Information

Frouda Nour El Houda
Djillali Liabes University of Sidi Bel Abbas, Faculty of Electrical Engineering Telecommunications and Digital Signal Processing Laboratory, Sidi Bel Abbes 22000, Algeria
Contact e-mail: *nourelhouda.frouda@univ-sba.dz*

Azzaz Rahmani Salima
Djillali Liabes University of Sidi Bel Abbas, Faculty of Electrical Engineering, Sidi Bel Abbes 22000, Algeria

Berkat Abdellatif
Abou Bekr Belkaid University, Faculty of Technology, Laboratory of Telecommunications of Tlemcen, Tlemcen, Algeria

To cite this article:

El-Houda, F. N., Abdellatif, B., & Salima, A. R. (2025). Compact single-switch reconfigurable patch antenna with multi-band operation for wireless systems. *The Eurasia Proceedings of Science, Technology, Engineering and Mathematics (EPSTEM), 38*, 590–596.

The Eurasia Proceedings of Science, Technology, Engineering & Mathematics (EPSTEM)
ISSN: 2602-3199

The Eurasia Proceedings of Science, Technology, Engineering and Mathematics (EPSTEM), 2025

Volume 38, Pages 597-609

IConTES 2025: International Conference on Technology, Engineering and Science

Influence of Site Class on the Dynamic Response of Regular Buildings Considering Soil-Structure Interaction

Mohamadi Saddika
Bouira University

Boumaiza Malika
Bouira University

Berzane Sid-Ali
Bouira University

Bouamrirene Abdelhafid
Bouira University

Abstract: Throughout history, many buildings have suffered significant damage during major earthquakes. Traditionally, such damage has been extensively analyzed from a structural perspective, assuming a fixed-base condition as a valid approach for lightweight structures built on relatively stiff soil. Under these assumptions, various failure patterns have been identified. However, earthquake damage indicates that a structure's seismic performance is not only influenced by the superstructure's response but also by the behavior of the foundation and the underlying soil. This highlights the importance of considering soil–structure interaction (SSI), as the overall performance of a structure can be affected by the earthquake's characteristics, its propagation path, and the nonlinear behavior of the soil. The soil–structure interaction (SSI) phenomenon is inherently complex; it involves a modification of the incident ground motion due to the dynamic response of the structure. As a result, the motion at the soil–structure interface differs from the free ground motion. This study aims to demonstrate the influence of soil–structure interaction on the behavior of regular mixed structures (frames with shear walls). The response of the structure studied is first evaluated by considering the hypothesis of perfect base fixity (classical model). In the second model (soil–structure interaction model), the soil–structure coupling is taken into account by modeling the soil reaction using springs. Numerical simulations were performed using four types of response spectra corresponding to different site classes, as defined by the Algerian seismic code (RPA 2003).

Keywords: Site class, Soil–structure interaction, Numerical analysis, Dynamic response

Introduction

Since the devastating El Asnam earthquake in 1980, extensive research efforts have been devoted to mitigating the seismic effects on building structures in Algeria and elsewhere. The Algerian seismic design code, RPA99 (version 2003), classifies construction sites into four soil types according to their dynamic properties. Each soil class is associated with a specific elastic response spectrum, determined by both the site characteristics and the dynamic behavior of the structure being analyzed.

The intensity of ground shaking experienced during an earthquake at a particular location largely depends on the nature of the soil and local site conditions. Consequently, it is crucial to adapt the selected response spectrum to the site-specific soil profile and seismic environment. Furthermore, in several engineering contexts, especially

- This is an Open Access article distributed under the terms of the Creative Commons Attribution-Noncommercial 4.0 Unported License, permitting all non-commercial use, distribution, and reproduction in any medium, provided the original work is properly cited.

- Selection and peer-review under responsibility of the Organizing Committee of the Conference

© 2025 Published by ISRES Publishing: www.isres.org

for medium and high-rise buildings, the Soil-Structure Interaction (SSI) phenomenon must be considered. This complex interaction reflects a modification of the free-field ground motion caused by the dynamic response of the structure itself, resulting in a non-identical motion at the soil–foundation interface compared to the unperturbed ground motion (Attia & Hadji, 2022; Bapir et al., 2023).

Recent research has demonstrated that the inclusion of SSI can significantly alter a structure's dynamic properties such as its natural frequency, damping ratio, and base shear-depending on the stiffness and shear-wave velocity (V_{s30}) of the soil (Ali et al., 2023; Dawood et al., 2024). Some studies have even reported that SSI effects can be beneficial or detrimental, depending on the resonance between soil and structure (Bapir et al., 2023). In the Algerian context, field investigations using ambient vibration data (Issaadi et al., 2022) have further confirmed the importance of accurately characterizing soil conditions and liquefaction potential in regions such as the Chelif Basin, where soft soils can amplify seismic waves. These findings highlight the need to incorporate SSI analysis into modern seismic design practices and to refine the RPA 2003 site classification system based on recent empirical and numerical insights.

The present study aims to investigate the influence of SSI on the seismic behavior of a regular mixed structure (frames with shear walls). In the first modeling approach, the structure is assumed to be perfectly fixed at the base (conventional fixed-base model). In the second approach, the soil–structure coupling is represented through spring elements simulating soil flexibility and damping. Numerical simulations were performed using the four site-specific response spectra defined in the RPA 2003 code, enabling a comparative analysis of the dynamic response across various soil conditions.

Behaviour of Buildings under Seismic Excitation

Earthquakes do not act as conventional external loads but rather induce stresses in structures through dynamic ground motion. The resulting seismic excitation is transmitted from the ground to the structure's foundation and subsequently throughout the structural system via inertial forces. In typical buildings, the global stiffness and damping characteristics are nonlinear and depend on the magnitude of deformation. These deformations may be predominantly of the bending (flexural) type in wall systems or of the shear type in frame structures (Figure 1) (Priestley et al., 2007; Fardis, 2009). (Figure 1).

During seismic shaking, inertial forces develop within structural elements as a reaction to the imposed ground accelerations. These forces arise from the interaction between individual members and their connecting joints, which transfer loads through shear, moment, and axial actions. Consequently, the inertial forces in any element cannot exceed the strength capacity of its connections; however, the associated deformations may become excessively large once the material yields or the connections lose stiffness. When this occurs, plastic instability can develop, potentially leading to progressive damage or global collapse (Paulay & Priestley, 1992; Alavi & Krawinkler, 2004; Ghosh et al., 2020).

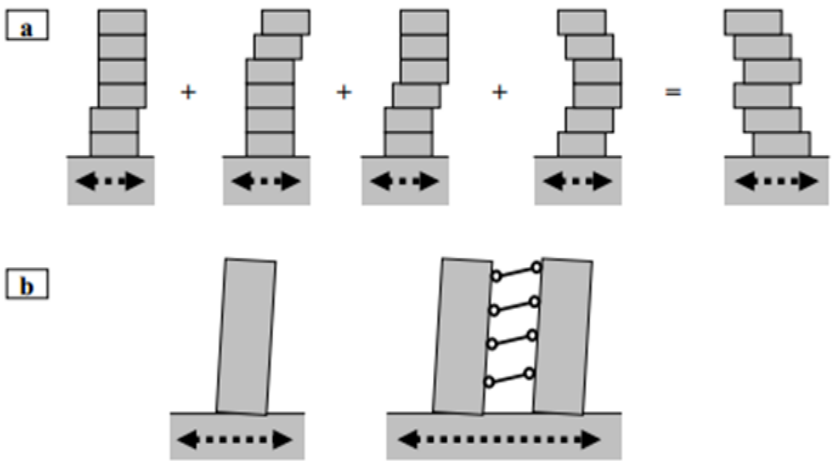


Figure 1. Behavior of structures under seismic excitation:(a) Shear response of moment-resisting frame systems). (b) Bending (flexural) response of load-bearing shear wall systems. (Bapir et al., 2023)

Soil–Structure Interaction Under Seismic Loading

Soil–Structure Interaction (SSI) refers to the mutual influence between a structure, its foundation, and the supporting soil during seismic excitation. When seismic waves propagate through the ground, they induce motion in the soil that, in turn, affects the structure resting upon it. Conversely, the inertial response of the structure exerts additional stresses and displacements back onto the soil. This two-way coupling process modifies the overall dynamic behavior of the soil–foundation–structure system (Awchat, Mallick, & Kanaujia, 2022; Bapir, Abrahamczyk, Wichtmann, & Prada-Sarmiento, 2023).

During an earthquake, the ground motion reaching the foundation is not identical to the free-field ground motion because the foundation alters it through kinematic interaction. Simultaneously, the oscillating superstructure imposes additional inertial interaction forces on the foundation and the surrounding soil. These two phenomena occur together, and the resulting system response differs significantly from that obtained by assuming a rigid or fixed-base condition (Camayang, Padilla, De La Cruz, & Bersamina, 2025). Therefore, a realistic seismic analysis must consider both effects to accurately estimate displacements, base shear, and internal forces.

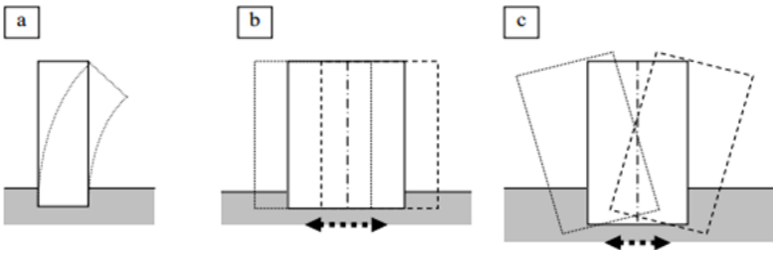


Figure 2. Soil-structure interaction: a) Without ISS, flexible building and soil with very good mechanical strength. b) Without ISS, rigid building and soil with very good mechanical strength. c) With ISS, rigid building and soil with low or medium mechanical strength.

Mathematical Representation

A simplified model of SSI can be expressed as a two-degree-of-freedom (2-DOF) system in which the superstructure and the foundation-soil subsystem are represented by lumped masses, springs, and dashpots. The governing equations of motion can be written as:

$$\begin{pmatrix} m_s & 0 \\ 0 & m_f \end{pmatrix}\begin{pmatrix} \ddot{u}_s \\ \ddot{u}_f \end{pmatrix}\begin{pmatrix} c_s + c_f & -c_f \\ -c_f & c_f \end{pmatrix}\begin{pmatrix} \dot{u}_s \\ \dot{u}_f \end{pmatrix}+\begin{pmatrix} k_s + k_f & -k_f \\ -k_f & k_f \end{pmatrix}\begin{pmatrix} u_s \\ u_f \end{pmatrix}=\begin{pmatrix} 0 \\ m_f \ddot{u}_g \end{pmatrix} \quad (1)$$

where:

m_s and m_f are the masses of the superstructure and the foundation-soil subsystem, respectively

u_s and u_f are the relative displacements of the superstructure and foundation,

k_s and k_f represent the stiffness of the superstructure and soil springs,

c_s and c_f are the corresponding damping coefficients,

$\ddot{u}_g$ is the free-field ground acceleration.

This system captures both kinematic and inertial effects, providing insight into how structural motion alters and is altered by the supporting ground.

In the classical Winkler foundation model, the soil is represented by a series of independent springs, and the foundation stiffness k_f may be approximated by:

$$k_f = \frac{GB}{\alpha} \quad (2)$$

Where G is the soil shear modulus, B is the foundation width, and α is an influence factor that depends on foundation shape, embedment, and Poisson's ratio (Rai, 2017). A lower shear modulus G (softer soil) reduces k_f, thereby increasing the flexibility of the system and amplifying foundation displacements.

Another well-known outcome of SSI is the lengthening of the natural period of the system compared to a fixed-base structure. This can be estimated using:

$$T_{SSI} \approx T_0 \sqrt{1+\frac{k_s}{k_f}} \quad (3)$$

where T_0 is the natural period of the fixed-base structure. A flexible foundation (k_f small) increases T_{SSI}, which can either decrease base shear demands or increase displacements depending on the response spectrum characteristics (Guerdouh & Khalfallah, 2019).

Engineering Implications

The influence of SSI on seismic performance can be beneficial or detrimental. On soft soils, SSI tends to increase displacements and modify load distributions, while on stiff soils, it can reduce accelerations by filtering high-frequency motion (Ahn, Park, Yoon, Han, & Jung, 2021). Modern seismic design standards therefore recommend evaluating SSI explicitly for tall, massive, or base-isolated structures. Advanced analyses often use finite-element or boundary-element formulations, nonlinear soil models, and experimental validation through centrifuge or shaking-table tests.

Recent studies emphasize that SSI effects are highly dependent on parameters such as soil stiffness, foundation embedment, aspect ratio, and the frequency content of ground motion (Bapir et al., 2023; Camayang et al., 2025). Neglecting SSI can lead to under- or over-estimation of seismic demands, inaccurate prediction of drift and rotation capacities, and misrepresentation of damage distribution in critical structural elements.

Case Study

The structure analyzed in this study is a regular mixed reinforced concrete building (frames braced by shear walls). It comprises six stories above ground level and one basement, with 20 cm-thick reinforced concrete shear walls providing the primary lateral resistance. The building's overall plan dimensions are 22.5 m in length, 15.44 m in width, and 29.62 m in total height.

According to the Algerian Seismic Resistant Regulation (RPA 2003), the structure is classified under Usage Group II, which corresponds to buildings intended for standard occupancy. For the purpose of seismic analysis, the building site is assumed to be located within Seismic Zone IIa, representing an area of moderate seismic hazard as defined by the code provisions.

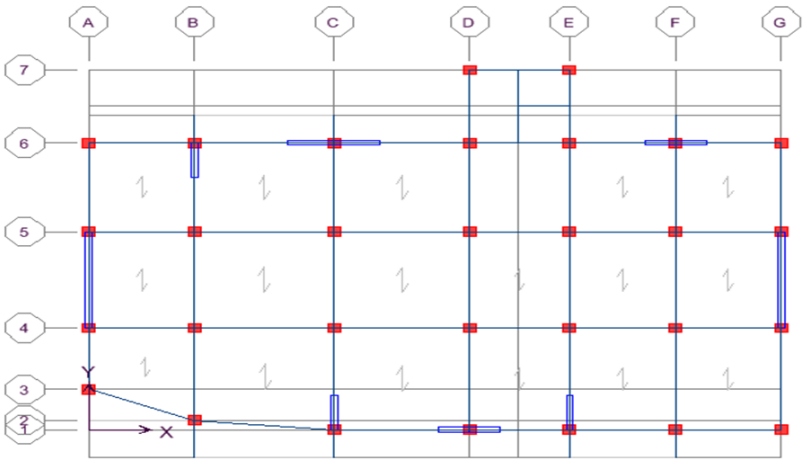


Figure 3. Plan view of the structure

The geometric characteristics of the structure are given in Table 1.

Table 1. Geometric characteristics of the structure studied.

	Description	**Value (m)**
Total length	L	22.85
Total width	l	15.44
Total height	H	29.62
Basement	h_b	4.44
Ground floor height	h_{GR}	4.08
Current storey height	h_{cs}	3.06

The dimensions and cross-sections of the building's structural elements (columns, beams, shear walls, slabs) are shown in Table 2. The columns, beams, shear walls and slabs (balcony) of the structure were considered to be made of reinforced concrete with linear elastic behavior. The material proprieties are summarized in Table 3. The behavior of the structural elements was considered as linear elastic. A structural Rayleigh damping ratio of 8.5% was assigned for all the elements in the concrete frame-shear wall building.

Table 2. Structural sections considered in the building

Section	**Notation**	**Section (cm^2)**	**Thickness (cm)**
Columns storey SB-GF-CF1	C1	45X45	/
Columns storey 2-3-4	C2	40X40	/
Columns storey 5-6	C3	35X35	/
Shear wall	SWCF	/	20
	SWGF	/	20
	SXB	/	25
Beam	PB	30X40	/
	SB	30X35	
Balcony slab	BS	/	15
Slab (hollow body)	HBS	/	20

Table 3. Material properties considered for the structural elements in the building

Parameter	**Notation**	**Columns, beams and shear walls**
Young modulus (GPa)	E	32
Shear modulus (GPa)	G	12.5
Volumic weight (kg/m^3)	ρ	2500
Poisson ratio	ν	0.2
Damping ratio	ξ	0.085

To study the effect of the interaction soil structure on the dynamic response of the structure, the seismic action is introduced using a design response spectrum. The dynamic characteristics of the structure according to RPA 2003 are shown in Table 4.

Table 4: Dynamic properties of the building

Behavior coefficient R	**Acceleration coefficient zone A**	**Dynamic amplification factor D**		**Quality factor Q**
3,5	0,15	Dx	1,898	1,20
		Dy	1,650	

Numerical Analysis of Dynamic Response of the Structure

This work consists of calculating the response of the structure (with and without ISS) in terms of fundamental periods for the 4 site classes defined by the Algerian seismic code (RPA 2003) (rock, firm, soft, very soft), as well as the shear force at the base of the structure and the displacement at the top of the structures.

The dynamic response of the structure under study is first evaluated by considering the assumption of perfect embedding at the base, and secondly by considering the soil-structure interaction model for the four types of response spectra associated with the different soil classes. To analyze the problem, a numerical finite element (FE) approach was employed using the structural analysis software ETABS (Computers and Structures Inc., 2019). ETABS enables the implementation of the modal response spectrum method in which individual modal responses are combined through the Complete Quadratic Combination (CQC) rule, as recommended for structures exhibiting closely spaced natural frequencies (Chopra, 2017; Wilson, 2002).

In the numerical model, columns and beams were represented using frame elements, while floor slabs were modeled as deck elements ensuring in-plane diaphragm action. The shear walls and balcony slabs were discretized with shell elements, capable of representing both in-plane (membrane) and out-of-plane (bending) actions. The frame elements were defined as two-noded, straight finite elements with six degrees of freedom (DOF) per node: three translational and three rotational. The shell elements were modeled as four-noded, flat finite elements providing a total of 20 degrees of freedom, allowing for a realistic simulation of wall and slab behavior under lateral loading (Bathe, 2014).

For the Response Spectrum Analysis (RSA), a sufficient number of modes (nine in total) were extracted to ensure that the cumulative modal mass participation reached at least 90% of the total seismic mass, as required by the Algerian Seismic Resistant Regulations (RPA 2003). The default mesh size provided by ETABS was adopted after mesh sensitivity checks showed negligible variation in modal results.

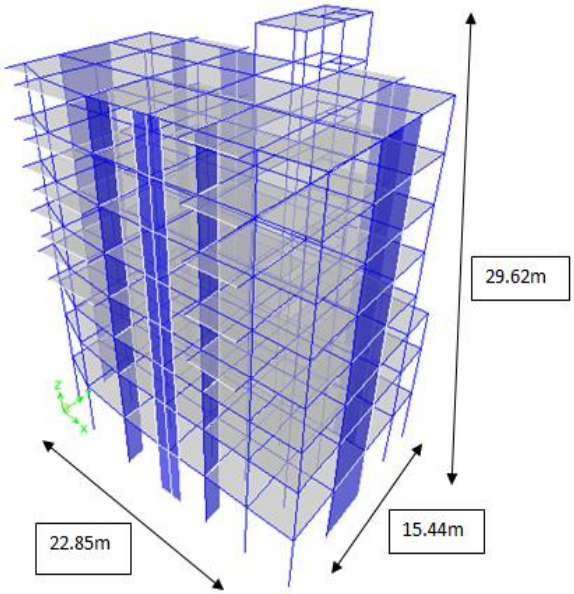


Figure 4. Numerical simulation of structure by ETABS 2019

The arrangement of shear walls was configured such that the first and second vibration modes corresponded primarily to translational motions along the X and Y axes, respectively, while the third mode represented torsional rotation about the Z-axis. The calculated eccentricities between the center of mass and the center of rigidity were ex = 0.00597 m and ey = 0.02873 m, confirming that torsional coupling effects were minimal. The characteristic values of the permanent (G) and variable (Q) loads applied to the different structural elements are summarized in the table below.

Table 5. Dead and live loads

Element	Terrace floor	Current floor	Balcony
G (KN/m^2)	7.21	5.35	5.21
Q (KN/m^2)	1	1,5	3,5

Classification of Sites According to RPA 2003

According to the RPA 2003 seismic design code, sites are classified into four categories: S1, S2, S3, and S4, based on the mechanical properties and stiffness of the underlying soils.

Table 6. Characteristics of the different categories of sites. (RPA 2003)

Site	Description	Velocity Vs (m/s)	E (MPa)	ν
S_1	Rock	≥ 800	2800	0.41
S_2	Firm	≥ 400-<800	830	0.44
S_3	Soft	≥ 200--<400	300	0.40
S_4	Very soft	≥ 100--<200	127	0.37

Modelling of the Structure without Considering Soil–Structure Interaction (SSI)

In the case of modelling without soil–structure interaction (SSI), a perfectly fixed base is assumed at the foundation level. This assumption corresponds to the traditional modelling approach generally adopted for standard building structures. The structural materials are assumed to exhibit a linear elastic behaviour, allowing for a direct assessment of the global dynamic response. The seismic response of the structure is evaluated using the four design response spectra corresponding to the different site categories as defined in the seismic design code (RPA 2003).

Modelling of the Structure Considering Soil–Structure Interaction (SSI)

In this stage of the study, the same structural model previously defined is adopted, with the inclusion of the effects of soil–structure interaction (SSI). The supporting soil is considered to be homogeneous and to exhibit a linear elastic behaviour throughout the analysis. This assumption allows for a simplified yet sufficiently accurate representation of the dynamic interaction between the structure and its foundation, enabling a direct evaluation of the influence of soil flexibility on the global response of the system.

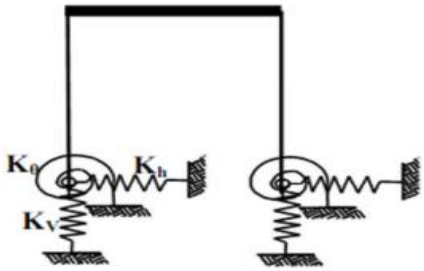


Figure 5. Simplified model of soil-structure interaction

The soil spring model represents the elastic response of the soil to both the translational and rotational displacements of the foundation. The simplest and most widely used approach to account for soil behaviour consists in modelling the soil as a discrete system of springs uniformly distributed beneath the foundation slab. These springs connect the nodes of the foundation to a rigid base, on which the prescribed seismic or dynamic movements are applied. This modelling technique provides a practical means of simulating the deformability of the soil while maintaining computational efficiency within the structural analysis.

Calculation of Stiffness Coefficients

Several formulations have been proposed for calculating the stiffness of soil springs. Among the most widely used are those developed by Newmark and Rosenblueth (1971), Deleuze (1988), and the simplified method proposed by Veletsos, as reported by Davidovici (1999) and Zaceck (1996).

Table 7. Stiffnesses of soil springs (Newmark-Rosenblueth,1971)

Movement	Rectangular rigid foundation
Horizontal	$K_h = 2(1+\nu)G\beta_x\sqrt{BL}$
Vertical	$K_v = \frac{G}{1-\nu}\beta_z\sqrt{BL}$
Rocking	$K_\phi = \frac{G}{1-\nu}\beta_\phi BL^2$

Where:
L is the dimension of the foundation parallel to the direction of the seismic action.
B is the dimension of the foundation perpendicular to the direction of the seismic action.
υ is the Poisson's ratio

G is the shear modulus and it is given by the relationship: $G = \frac{E}{2(1+\nu)}$ (4)

In the present study, the stiffness values of the soil springs are determined using the relationships provided in Table 7, which take into account the mechanical characteristics of the sites described in Table 6. The dimensionless coefficients β_x, βz, and β_φ, also presented in Table 7, are obtained from specific design charts that depend on both the foundation aspect ratio (b/a) and the direction of the considered seismic excitation (Newmark & Rosenblueth, 1971).

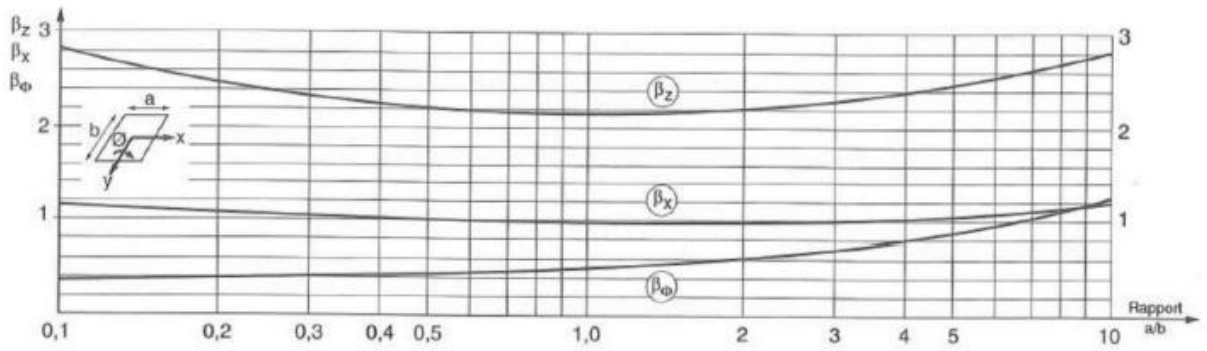


Figure 6. Chart of newmark-rosenblueth coefficients (Davidovici,1999).

The foundation of the studied structure consists of a rectangular raft footing with a length of 22.85 m and a width of 15.44 m (L/B = 1.48). The corresponding foundation coefficients are β_x = 0.98, βz = 2.20, and $\beta\varphi$ = 0.48. The calculated soil stiffness values corresponding to the various site categories are summarized in Table 8.

Table 8. Values of soil stiffness.

Site	K_h (KN/m)	K_v (KN/m)	Kφ (KN.m/rd)
Site1	$5{,}19.10^4$	$2{,}9.10^7$	$2{,}72.10^{15}$
Site2	$5{,}30.10^4$	$8{,}27.10^6$	$7{,}74.10^{14}$
Site3	$5{,}15.10^4$	$3{,}16.10^6$	$2{,}96.10^{14}$
Site4	$5{,}04.10^4$	$1{,}39.10^6$	$1{,}30.10^{14}$

Results and Discussion

The numerical simulation results for both models, with and without soil–structure interaction, are presented discussed in the following section.

Fundamental Period T

The results illustrated in Figure 7 show the variation of the fundamental period for the four site categories (S1 to S4), comparing the structural models with and without soil–structure interaction (SSI). The fundamental period of the structure remains constant across all site classes when soil–structure interaction (SSI) is neglected. This behavior results from the assumption of a perfectly rigid base, where the dynamic characteristics of the system depend solely on the stiffness and mass distribution of the superstructure.

When SSI is considered, however, a clear variation of the fundamental period is observed depending on the soil type. The results indicate a progressive increase in the fundamental period as the soil becomes more deformable. This phenomenon occurs because the inclusion of the soil medium introduces additional flexibility to the system, effectively reducing its overall stiffness. The increase in period reaches approximately 16% for site S4 (very soft soil) compared with the fixed-base model.

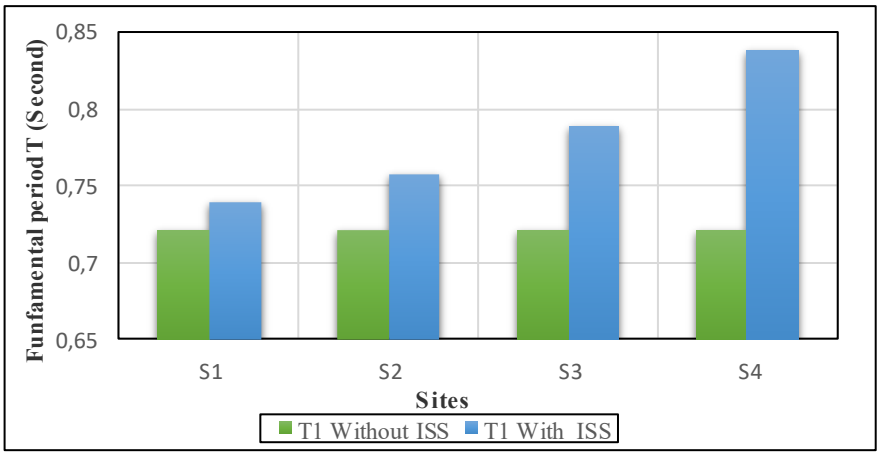


Figure 7. Variation in the fundamental period depending on the site (with and without ISS).

A quantitative comparison shows that the fundamental period increases by about 2% for site S2, 5% for site S3, and up to 16% for site S4 when SSI is incorporated. This trend confirms that the influence of SSI becomes increasingly significant for soft and very soft soils, where the soil compliance has a dominant effect on the overall dynamic response. For the softest site (S4), the computed fundamental period reaches 0.837 s, whereas the reference value defined by the RPA code (0.825 s) is slightly lower. This discrepancy implies that neglecting SSI may lead to an underestimation of the structural flexibility, and consequently to a potential under-design of the structure in seismic regions. Therefore, accounting for SSI is crucial in seismic analysis, especially for flexible or semi-rigid structures founded on deformable soils. These findings are consistent with the results reported by Veletsos (1975), Wolf (1985), and Gazetas (1991), who demonstrated that soil–structure interaction generally lengthens the natural period of vibration due to the added compliance of the foundation–soil system.

Base Shear Force

Figure 8 presents the variation of the base shear force (V) for the structure, both with and without soil–structure interaction (SSI), across the four site classes (S1–S4).

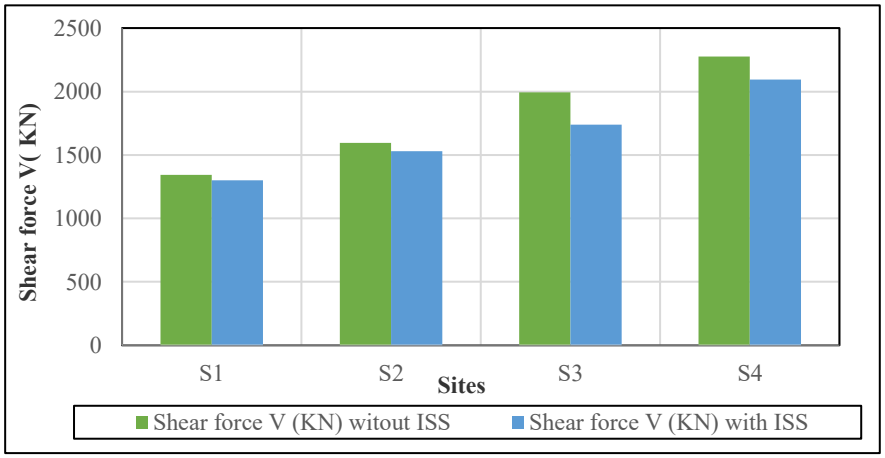


Figure 8. Variation of base shear force depending on the site (with and without ISS).

It can be clearly observed that the base shear decreases when SSI is considered. This reduction becomes more pronounced as the soil flexibility increases, with the most significant difference occurring for soft and very soft soils. The results show that the base shear obtained without SSI is systematically higher than that obtained with SSI for all site conditions.

A detailed comparison between the two cases reveals that the inclusion of SSI leads to a reduction in base shear of approximately 3% for site S1, 4% for site S2, 14% for site S3, and 8% for site S4. This clearly indicates that the influence of SSI becomes increasingly significant for softer soils, where the deformability of the ground plays a dominant role in the seismic response.

This trend can be attributed to the increase in the fundamental period of the system due to soil flexibility. When SSI is taken into account, the structure–foundation system behaves more flexibly, resulting in a longer vibration period and consequently lower spectral accelerations. This leads to a reduction in the inertial forces transmitted to the base, and thus a decrease in the base shear. These findings are consistent with the results reported by Veletsos and Meek (1974), Wolf (1985), and Gazetas (1991), who demonstrated that the inclusion of SSI generally increases the fundamental period while decreasing the base shear, particularly for structures resting on soft or very soft soils.

Absolute and Relavie Displacements

The variation of the maximum absolute and relative displacements, with and without considering soil–structure interaction (SSI), is illustrated in Figure 9 and 10.

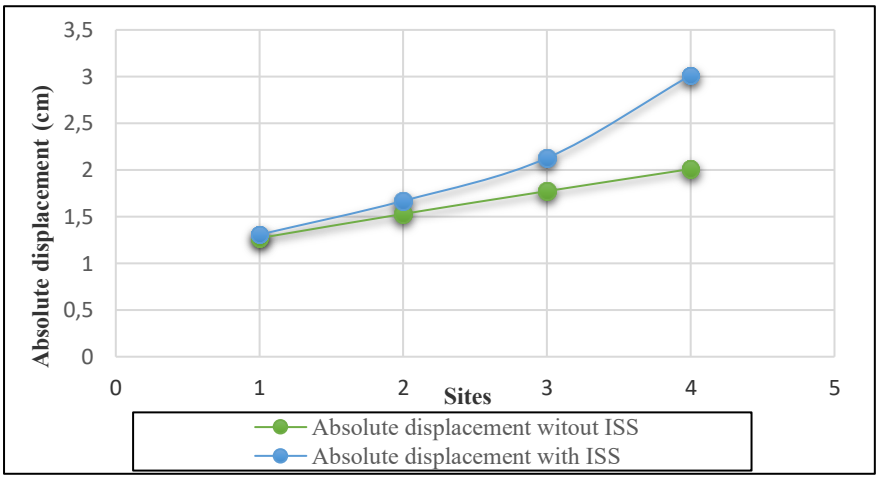


Figure 9. Variation of absolute displacement depending on the site (with and without ISS).

An overall increase is observed across all sites when the influence of soil–structure interaction (ISS) is taken into account. The comparison between the cases without and with ISS shows that the absolute displacement increases by approximately 3% for Site 1, 9% for Site 2, 20% for Site 3, and 50% for Site 4. This progressive increase demonstrates that the flexibility of the supporting soil plays a significant role in amplifying the lateral displacements of the structure. The effect becomes particularly pronounced for soft soils, where the interaction between the foundation and the deformable medium reduces the overall stiffness of the soil–structure system.

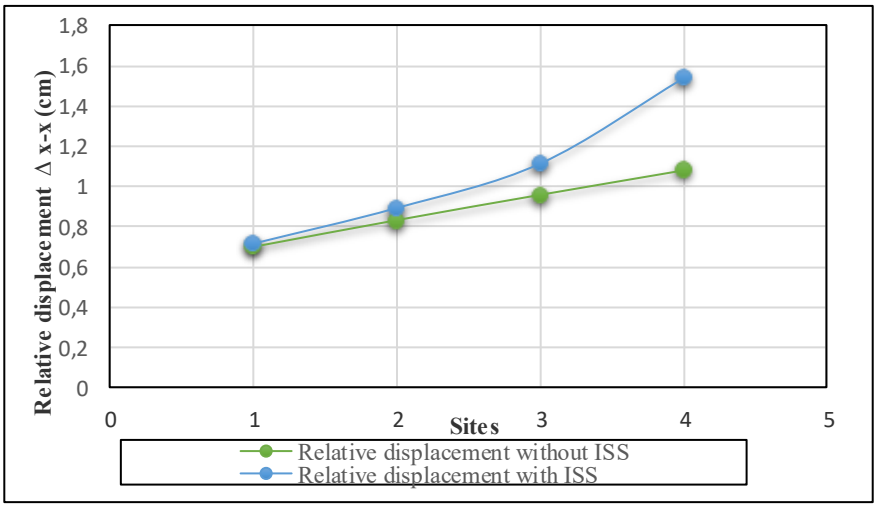


Figure 10. Variation of relative displacement depending on the site (with and without ISS)

Similarly, for the maximum relative displacement, an increase is observed across all sites in both cases, with and without SSI. The results indicate that the more deformable the soil, the greater the relative displacement. This

behaviour is mainly attributed to the reduction in the overall stiffness of the soil–structure system when SSI is included. Nevertheless, the maximum relative displacement values remain below the permissible limit (h/100), ensuring that inter-storey drifts are within acceptable serviceability limits.

These results are consistent with previous research findings. Mylonakis and Gazetas (2000) and Wolf (1985) demonstrated that considering SSI leads to higher lateral displacements due to the lengthening of the fundamental period and the reduction of system stiffness. Gazetas (1991) and Kwon and Elnashai (2006) further highlighted that this effect becomes particularly important for flexible and tall structures founded on soft soils. Similarly, Abdel Raheem et al. (2013) confirmed that neglecting SSI may result in underestimation of the displacement demand, especially for structures resting on deformable soil profiles.

Conclusion

From the results obtained for the fundamental period, base shear force, and maximum and relative displacements, it can be concluded that soil–structure interaction (SSI) has a significant influence on the dynamic response of the studied structure. The inclusion of SSI leads to an increase in the fundamental period, indicating a reduction in the overall stiffness of the soil–structure system. Consequently, the structure exhibits more flexible behaviour when resting on deformable soils. This change in stiffness also affects the base shear force, which decreases as soil flexibility increases. The reduction in base shear is mainly due to the lengthening of the natural period and the redistribution of inertial forces between the structure and the supporting soil. Such a decrease, however, should not be interpreted as a reduction in seismic demand, as it is accompanied by larger displacements.

Indeed, both the maximum absolute and relative displacements show a clear amplification when SSI is considered. The more flexible the soil, the greater the increase in lateral displacements, with a particularly marked effect for Sites 3 and 4, corresponding to soft soil conditions. Despite this amplification, the displacements remain within the permissible limits (h/100), ensuring acceptable structural performance under the considered seismic loading.

Overall, these findings highlight the necessity of accounting for SSI effects, especially for structures built on soft or medium soils. Neglecting SSI may lead to an overestimation of stiffness and base shear, and an underestimation of displacements, which could compromise both the safety and serviceability of the structure. Therefore, the inclusion of SSI is strongly recommended in seismic analysis and design, particularly for semi-rigid and flexible structures located in zones II, III, and for soft soil sites.

Scientific Ethics Declaration

* The authors declare that the scientific ethical and legal responsibility of this article published in EPSTEM journal belongs to the authors.

Conflict of Interest

* The authors declare that they have no conflicts of interest

Funding

* This research received no specific grant from any funding agency in the public, commercial, or not-for-profit sectors.

Acknowledgements or Notes

* This article was presented as a poster presentation at the International Conference on Technology, Engineering and Science (www.icontes.net) held in Antalya/Türkiye on November 12-15, 2025.

References

Abdel Raheem, S. E., Ahmed, M. M., & Ahmed, A. M. (2013). Soil–structure interaction effects on seismic response of multi-story buildings on raft foundation. *HBRC Journal, 9*(3), 204–213.

Ahn, S., Park, G., Yoon, H., Han, J.-H., & Jung, J. (2021). Evaluation of soil-structure interaction in structure models via shaking table test. *Sustainability, 13*(9), 4995.

Ali, T., Eldin, M. N., & Haider, W. (2023). The effect of soil-structure interaction on the seismic response of structures using machine learning, finite element modeling and ASCE 7-16 methods. *Sensors, 23*(4), 2047.

Attia, A., & Hadji, T. (2022). Assessment of the soil structure inertial interaction effect on the behavior coefficient using simplified methods. *Engineering, Technology & Applied Science Research, 12*(6), 9420–9425.

Awchat, G., Mallick, H., & Kanaujia, P. (2022). Soil-structure interaction: Comparative review of international codes and other literature with Indian seismic code. *Civil and Environmental Engineering, 18*(1), 87–95.

Bapir, T., Abrahamczyk, L., Wichtmann, T., & Prada-Sarmiento, L. F. (2023). Soil-structure interaction: A state-of-the-art review of modeling techniques and studies on seismic response of building structures. *Frontiers in Built Environment, 9*, 1120351.

Bathe, K.-J. (2014). *Finite element procedures*. Klaus-Jürgen Bathe.

Camayang, J. P. P., Padilla, J. A., De La Cruz, A. R., & Bersamina, J. P. L. (2025). Soil-structure interaction in seismic response and structural performance: A systematic review. *Advances in Structural Engineering*, 13694332251353607.

Chopra, A. K. (2017). *Dynamics of structures: Theory and applications to earthquake engineering* (5th ed.). Prentice Hall.

Computers and Structures Inc. (2019). *ETABS 19 - Integrated building design software: Analysis reference manual*. Computers and Structures Inc.

Davidovici, V. (1999). *Le génie parasismique : Conception et dimensionnement des bâtiments*. Presses de l'École Nationale des Ponts et Chaussées.

Dawood, W. A., Nazim, M. S., El-Mahdy, O., & Adam, M. (2024). Soil-structure interaction assessment for seismic performance of high-rise RC building on piled-raft foundation. *Engineering Research Journal (Shoubra), 53*(2), 203-211.

Deleuze, G. (1988). Interactions sol-structure et fondations superficielles. *Bulletin de Liaison des Laboratoires des Ponts et Chaussées, 156*, 73–84..

Fardis, M. N. (2009). *Seismic design, assessment and retrofitting of concrete buildings*. Springer.

Gazetas, G. (1991). Formulas and charts for impedances of surface and embedded foundations. *Journal of Geotechnical Engineering, 117*(9), 1363–1381.

Ghosh, S. K., Fanella, D. A., & Naito, C. J. (2020). *Seismic design of reinforced concrete and masonry buildings* (2nd ed.). ICC/EERI.

Guerdouh, D., & Khalfallah, S. (2019). Soil-structure interaction effects on the seismic performance of frame structures. *Revista de la Construcción, 18*(2), 349-363.

Issaadi, A., Saadi, A., Semmane, F., Yelles-Chaouche, A., & Galiana-Merino, J. J. (2022). Liquefaction potential and V_s30 structure in the Middle-Chelif basin, northwestern Algeria, by ambient vibration data inversion. *Applied Sciences, 12*(16), 8069.

Kwon, O. S., & Elnashai, A. S. (2006). The effect of material and geometric nonlinearity on seismic response of RC structures considering SSI. *Engineering Structures, 28*(2), 289-303.

Ministère de l'Habitat. (2003). *Règles parasismiques algériennes RPA 99 version 2003: Règlement algérien pour le calcul des constructions parasismiques*. Centre National de génie parasismique (CGS).

Mylonakis, G., & Gazetas, G. (2000). Seismic soil-structure interaction: Beneficial or detrimental? *Journal of Earthquake Engineering, 4*(3), 277–301.

Newmark, N. M., & Rosenblueth, E. (1971). *Fundamentals of earthquake engineering*. John Wiley & Sons.

Paulay, T., & Priestley, M. J. N. (1992). *Seismic design of reinforced concrete and masonry buildings*. Wiley.

Priestley, M. J. N., Calvi, G. M., & Kowalsky, M. J. (2007). *Displacement-based seismic design of structures*. IUSS Press.

Rai, R. (2017). Study on soil-structure interaction: A review. *Control Science and Engineering, 1*(1), 4-6.

Veletsos, A. S. (1975). Dynamic behavior of building-foundation systems. *Proceedings of the 5th European Conference on Earthquake Engineering,* Istanbul.

Wilson, E. L. (2002). *Three-dimensional static and dynamic analysis of structures: A physical approach with emphasis on earthquake engineering*. Computers and Structures Inc.

Wolf, J. P. (1985). *Dynamic soil–structure interaction*. Prentice Hall.

Zaceck, J. (1996). *Calcul parasismique des structures et des fondations*. Presses de l'École Nationale des Ponts et Chaussées.

Author(s) Information

Mohamadi Saddika
Bouira University, Faculty of Applied Sciences, Civil Engineering Department, 10000, Bouira, Algeria
Contact e-mail: *s.mohamadi@univ-bouira.dz*

Boumaiza Malika
Bouira University, Faculty of Applied Sciences, Civil Engineering Department, 10000, Bouira, Algeria

Berzane Sid-Ali
Bouira University, Faculty of Applied Sciences, Civil Engineering Department, 10000, Bouira, Algeria

Bouamrirene Abdelhafid
Bouira University, Faculty of Applied Sciences Civil Engineering Department, 10000, Bouira, Algeria

To cite this article:

Saddika, M., Malika, B., Sid-Ali, B, & Abdelhafid, B. (2025). Influence of site class on the dynamic response of regular buildings considering soil-structure interaction. *The Eurasia Proceedings of Science, Technology, Engineering and Mathematics (EPSTEM), 38,* 597-609.

The Eurasia Proceedings of Science, Technology, Engineering & Mathematics (EPSTEM)
ISSN: 2602-3199

The Eurasia Proceedings of Science, Technology, Engineering and Mathematics (EPSTEM), 2025

Volume 38, Pages 610-616

IConTES 2025: International Conference on Technology, Engineering and Science

Bearing Fault Detection and Severity Classification Using a Two-Step Neural Network Model

Smail Haroun
University of Bouira

Abstract: Rolling element bearings are key components in rotating machinery, and their failures often lead to costly downtime and safety risks. Reliable fault diagnosis is therefore essential in predictive maintenance, where early detection and severity assessment can improve system availability. This paper presents a two-step neural framework for bearing fault analysis that combines supervised and unsupervised learning. In the first stage, a feedforward neural network classifies bearing conditions into four fault categories. In the second stage, a self-organizing map refines the diagnosis by distinguishing up to ten severity levels within the detected faults. The method uses features extracted from vibration signals, including statistical indicators and frequency-domain transformations, selected to balance accuracy and computational cost. Experimental results show that the proposed hierarchical approach improves diagnostic precision compared with single-stage classifiers, achieving over 95% accuracy for fault detection and distinguishing up to 10 severity levels based on defect size and location. This two-step framework demonstrates practical potential for robust fault monitoring in industrial environments.

Keywords: Bearing fault diagnosis, Supervised and unsupervised learning, Two-step hierarchical diagnosis, Fault severity classification

Introduction

Rolling element bearings are vital elements in rotating machinery across the industry. Their failure often results in unscheduled downtime, production losses, and high maintenance costs. Consequently, fault diagnosis and fault severity assessment are foundational to effective predictive maintenance systems. Traditionally, vibration-based diagnostics have relied on methods such as envelope analysis, FFT-based spectral approaches, and time-domain statistical metrics for detecting bearing defects (Randall et al., 2011; Jardine et al., 2006; Zhang et al., 2019). While effective in controlled laboratory settings, these techniques often falter in real industrial environments where vibration signals are noisy, non-stationary, and affected by varying loads.

Recent advances in machine learning (ML) and deep learning (DL) have enabled significant improvements in fault detection and classification. For example, hybrid deep models using continuous wavelet transform (CWT) combined with BiLSTM and attention mechanisms have showcased outstanding performance in discriminating between common fault types (Kohonen, 2001). Vision Transformer architectures, using time-frequency representations derived from STFT, have achieved up to 98.8% accuracy in multi-class bearing fault diagnosis (Goodfellow et al., 2016). Moreover, innovative multimodal frameworks integrating vibration and motor current signals, enhanced via 1D CNNs and transfer learning, have demonstrated robustness under varying operating conditions (Lei et al., 2020). These approaches, however, typically focus on detecting fault types—not on estimating fault severity levels.

Capturing fault progression through multi-level severity classification remains underexplored. There are very few studies proposing hierarchical or two-step diagnostic pipelines that can first identify the fault category and then determine its severity degree. In other domains, hierarchical deep learning frameworks have effectively

- This is an Open Access article distributed under the terms of the Creative Commons Attribution-Noncommercial 4.0 Unported License, permitting all non-commercial use, distribution, and reproduction in any medium, provided the original work is properly cited.

- Selection and peer-review under responsibility of the Organizing Committee of the Conference

© 2025 Published by ISRES Publishing: www.isres.org

improved fault localization and severity identification (Yang, et al., 2019), but their application to bearing diagnostics in multi-class severity scenarios is rare.

This paper introduces a two-step neural framework for bearing fault diagnosis and severity assessment. In the first step, a supervised feedforward neural network (FNN) categorizes signals into four groups: healthy, inner race fault, outer race fault, and ball fault. In the second step, a Self-Organizing Map (SOM) refines the prediction in an unsupervised manner by mapping inputs to up to ten distinct severity levels. This layered architecture leverages labeled data for accurate type identification and harnesses the power of unsupervised clustering for detailed severity granularity.

The contributions of this work can be summarized as follows: a practical hierarchical diagnosis pipeline, moving from fault type identification to severity level classification, is proposed and validated using vibration-based features. In addition, the complementary strengths of supervised and unsupervised neural networks are empirically evaluated, showing that their integration enhances diagnostic precision and stability.

The rest of the paper is structured as follows. Section II details the feature extraction methods and neural architectures employed. Section III outlines the experimental setup and dataset. Section IV presents the results, including comparisons to baseline single-stage approaches. Finally, Section V offers conclusions and discusses future directions for industrial deployment and prognostics.

Background and Related Work

Feature Extraction in Vibration Analysis

Vibration signals are widely used in bearing condition monitoring because they carry rich information about fault initiation and progression. To extract discriminative patterns, both time-domain features (e.g., RMS, kurtosis, skewness, crest factor) and frequency-domain features (e.g., spectral energy, harmonics, envelope spectrum) are commonly employed (Randall et al., 2011), (Jardine et al., 2006). More advanced approaches exploit time–frequency representations such as wavelet packet decomposition or empirical mode decomposition, which are effective in handling the non-stationary nature of vibration signals (Peng et al., 2005). These feature extraction techniques provide the input space for subsequent classification and fault diagnosis tasks.

Neural Networks for Fault Diagnosis

Machine learning, and in particular **artificial neural networks (ANNs)**, has shown strong potential for vibration-based fault diagnosis. Two complementary paradigms are typically considered:

- **Supervised learning**, where models are trained on labeled data to map features to predefined fault categories. In this setting, the **multilayer perceptron (MLP)** is one of the most widely adopted models. It consists of layers of interconnected neurons with nonlinear activation functions, capable of approximating complex decision boundaries (Bishop 2006).
- **Unsupervised learning**, which aims to discover intrinsic structures in unlabeled data. Among these approaches, the **Self-Organizing Map (SOM)** is particularly relevant in fault diagnosis. SOM projects high-dimensional features onto a low-dimensional (usually 2D) grid while preserving topological relations, thereby enabling clustering and visualization of latent fault patterns (Kohonen, 2001).

Recent research has highlighted that **supervised and unsupervised methods can provide complementary insights**: supervised networks offer precise classification when labeled data is available, whereas unsupervised models capture hidden structures and can be applied in early fault detection or when labels are scarce (Widodo et al., 2007) (Lei et al., 2016). Hybrid strategies combining both paradigms are increasingly explored to improve robustness and interpretability in real-world applications.

Proposed Diagnostic Framework

The adopted methodology, illustrated in Figure 1, follows a multi-stage pipeline integrating preprocessing, feature extraction, and classification, with each step detailed in the following subsections.

Signal Acquisition and Preprocessing

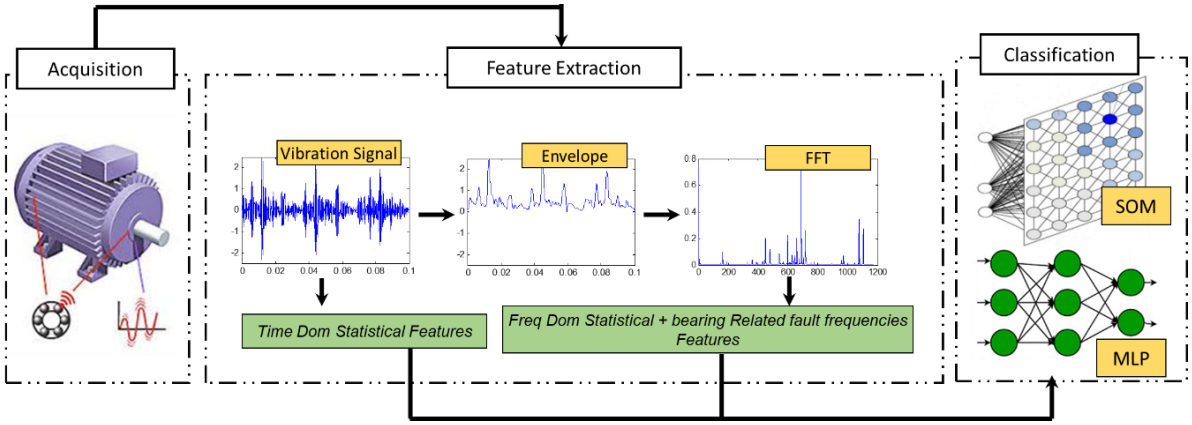


Figure 1. Block diagram of the proposed diagnostic methodology.

The vibration signals were collected using accelerometers mounted on the bearing housing. In order to ensure consistency, the raw data were segmented into fixed-length windows and normalized to eliminate amplitude scaling effects and noise fluctuations. This preprocessing stage guarantees that the subsequent feature extraction is not biased by external variations.

Feature Extraction

To capture the degradation signatures of bearings, three complementary categories of features were extracted. First, time-domain statistical features such as mean, root mean square, variance, skewness, kurtosis, crest factor, impulse factor, and clearance factor were computed. These descriptors provide insight into the amplitude distribution and impulsive nature of the vibration signal. Second, frequency-domain statistical features were obtained from the Fourier spectrum and the power spectral density (PSD). Metrics such as spectral mean, variance, entropy, and spectral kurtosis were calculated to highlight the distribution of energy across frequencies and to emphasize frequency components affected by structural defects. Table 1 summarizes the mathematical expressions of the aforementioned statistical indicators.

Table 1. Time and frequency domain features

Features from Time domain	Features from Frequency domain
$T_1=\frac{1}{n}\sum_{i=1}^{n}x_i$; $T_2=\left(\max(x_i)-\min(x_i)\right)/2$; $T_3=\sqrt{\frac{1}{N}\sum_{i=1}^{n}(x_i{}^2)}$ $T_4=\sqrt{\frac{1}{N}\sum_{i=1}^{N}(x_i-\bar{x})^2}$; $T_5=\frac{1}{N}\sum_{i=1}^{n}\left(\frac{x_i-\bar{x}}{\sigma}\right)^4$ $T_6=\frac{1}{N}\sum_{i=1}^{n}\left(\frac{x_i-\bar{x}}{\sigma}\right)^3$ $T_7=\max\lvert x_i\rvert\Big/\left(\frac{1}{N}\sum_{i=1}^{n}\sqrt{\lvert x_i\rvert}\right)^2$; $T_8=\max\left(\lvert x_i\rvert\right)\Big/\frac{1}{N}\sum_{i=1}^{n}\lvert x_i\rvert$ $T_9=\max\lvert x_i\rvert\Big/\sqrt{\frac{1}{N}\sum_{i=1}^{n}(x_i{}^2)}$; $T_{10}=\sqrt{\frac{1}{N}\sum_{i=1}^{n}(x_i{}^2)}\Big/\frac{1}{N}\sum_{i=1}^{n}\sqrt{\lvert x_i\rvert}$; where x_i is a vibration signal samples for i = 1,2,...,N, N is the number of data samples	$F_1=\sum_{k=1}^{K}\frac{s(k)}{K}$ $F_2=\sum_{k=1}^{K}\frac{(\mathrm{s(k)}-\mathrm{F_1})^2}{(K-1)}$ $F_3=\sum_{k=1}^{K}\frac{(\mathrm{s(k)}-\mathrm{F_1})^3}{(K(\sqrt{F_2})^3)}$ $F_4=\sum_{k=1}^{K}\frac{\sum_{k=1}^{K}(\mathrm{s(k)}-\mathrm{F_1})^4}{KF_2^2}$ $F_5=\frac{\sum_{k=1}^{K}f_k s(k)}{\sum_{k=1}^{K}s(k)}$ $F_6=\sqrt{\frac{\sum_{k=1}^{K}(f_k-F_5)^2 s(k)}{K}}$ $F_7=\sqrt{\frac{\sum_{k=1}^{K}f_k{}^2 s(k)}{\sum_{k=1}^{K}s(k)}}$ $F_8=\sqrt{\frac{\sum_{k=1}^{K}f_k{}^4 s(k)}{\sum_{k=1}^{K}f_k{}^2 s(k)}}$ $F_9=\frac{\sum_{k=1}^{K}(f_k-F_5)^4 s(k)}{KF_6^4}$ $F_{10}=\frac{\sum_{k=1}^{K}(f_k-F_5)^{1/2} s(k)}{K\sqrt{F_6}}$ where $s(k)$ is a spectrum for k = 1,2,. . .,K, K is the number of spectrum lines; f_k is the frequency value of the k^{th} spectrum line

Finally, envelope spectrum analysis was employed to detect defect-related frequencies. The analytic signal was computed using the Hilbert transform, and the FFT of the resulting envelope was analyzed. This technique effectively emphasizes characteristic defect frequencies, which are crucial for diagnosis. These include the Ball-Pass Frequency of the Outer race (BPFO), the Ball-Pass Frequency of the Inner race (BPFI), the Ball-Spin Frequency (BSF), and the Fundamental Train Frequency (FTF). The mathematical expressions for calculating these frequencies based on bearing geometry and rotational speed (RSF) are provided in Table 2.

Table 2. Bearing fault-related frequencies components.

Frequency component	**BPFO**	**PFI**	**BSF**
Expression	$\frac{N}{2}\left[f_i\left(1-\frac{d\cos(\theta)}{D}\right)\right]$	$\frac{N}{2}\left[f_i\left(1+\frac{d\cos(\theta)}{D}\right)\right]$	$\frac{D}{2d}f_i\left[\left(1-\frac{d\cos(\theta)}{D}\right)^2\right]$

Where f_i is the shaft speed, d is the diameter of the rolling element, and D is the pitch diameter, θ is the contact angle

Classification Framework

For the classification stage, both supervised and unsupervised learning techniques were adopted. In the supervised setting, a multilayer perception (MLP) was trained on the extracted features to discriminate between fault categories and severity levels. The MLP leverages backpropagation to adjust its weight and progressively minimize the classification error. In parallel, an unsupervised Self-Organizing Map (SOM) was used to cluster the features while preserving the topological structure of the input space. This approach facilitates the visualization of defect evolution and provides complementary insights into the fault progression trends. A hierarchical classification strategy was adopted: the system first distinguishes the type of fault (normal, outer race, inner race, ball, etc.) and subsequently classifies the severity into different levels.

Experimental Setup

Experimental Data

The proposed diagnostic methodology is evaluated using the vibration signal database provided by the Case Western Reserve University (CWRU) Bearing Data Center. In this setup, vibration signals were acquired at a sampling rate of 12 kHz from an accelerometer mounted on the drive end of a three-phase induction motor, which is mechanically coupled to a dynamometer for applying variable loads, as illustrated in Fig. 2. The experiments cover four bearing conditions: normal operation (NO), outer race fault (ORF), inner race fault (IRF), and ball fault (BF), with defect diameters of 0.007, 0.014, and 0.021 inches. For each fault type and size, the motor was tested under four different load conditions: 0, 1, 2, and 3 Hp.

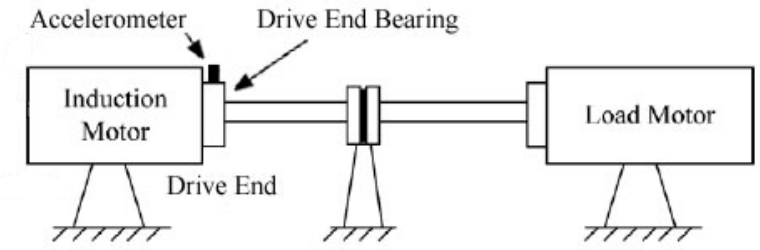


Figure 2. Schematic of the bearing fault diagnosis experimental setup.

Dataset Construction

From the raw vibration signals, 28 faults indicators were extracted in both the time and frequency domains, as described in Section II. To build the feature database, the signals were segmented into 1120 samples (112 segments per operating condition), each segment consisting of 4096 data points. Feature extraction was then applied to each segment, resulting in a feature matrix of size 1120×28. The dataset was randomly partitioned,

with two-thirds of the samples used for training and the remaining one-third reserved for testing. Two classification tasks were defined: a four-class problem corresponding to the bearing operating conditions, and a ten-class problem including the different fault severity levels. The class labels are summarized in Table 3.

Table 3. Description of classification tasks and associated labels

Bearing Condition	Defect size	Labels for 4 Classes Process	Labels for 10 Classes Process
Normal	0.000	NO	NO
	0.007		BF07
Ball Fault	0.014	BF	BF14
	0.021		BF21
	0.007		IR07
Inner Race Fault	0.014	IR	IR14
	0.021		IR21
	0.007		OR07
Outer Race Fault	0.014	OR	OR14
	0.021		OR21

Results and Discussion

This section evaluates the proposed two-step (FNN + SOM) framework on two bearing fault diagnosis tasks: fault-type identification (4-class) and joint fault-severity classification (10-class). Results are compared against each network used individually to demonstrate the efficacy of the hierarchical strategy. The overall comparison of classification accuracies for these two tasks and the three evaluated models (FNN, SOM, and FNN+SOM) is illustrated in Figure 3.

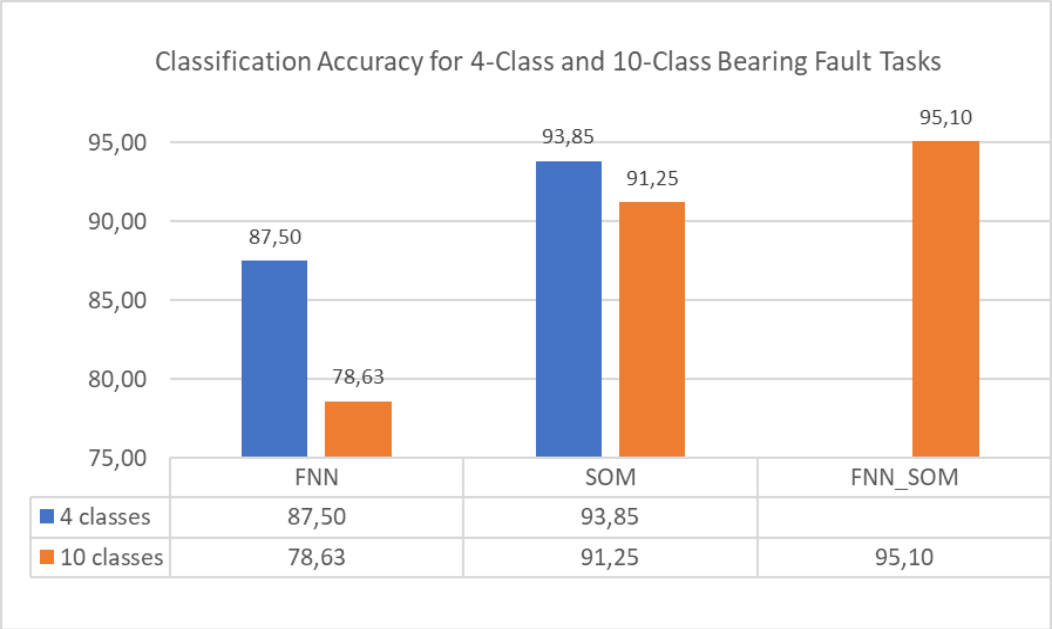


Figure 3. Classification accuracy for 4-class and 10-class bearing fault tasks.

Fault Type Classification (4-Class Process)

The first diagnostic step classifies the bearing condition into four categories: Normal (N), Ball Fault (BF), Inner Race Fault (IR), and Outer Race Fault (OR). A supervised Feedforward Neural Network (FNN) is employed for this task, while the unsupervised Self-Organizing Map (SOM) is evaluated for comparison. As illustrated in Figure 3, the FNN achieved an average accuracy of **87.50%**, showing high recognition rates for most fault types but a noticeable drop in performance for the Outer Race Fault, likely due to overlapping features or variability in the signal. In contrast, SOM provided more balanced and robust results across all classes, with an average accuracy of **93.85%**.

These findings indicate that while the FNN excels when fault boundaries are well defined, it tends to struggle with class overlap. SOM, on the other hand, effectively captures the topological relationships in the feature space, yielding consistent results. This complementarity suggests that combining both models may offer improved overall diagnostic performance.

Fault Type and Severity Classification (10-Class Process)

The second diagnostic step focuses on a finer discrimination of bearing conditions by including multiple severity levels within each fault type (e.g., OR007, OR014, OR021). Three models were evaluated: standalone FNN, standalone SOM, and the hybrid **FNN + SOM** framework. As shown in Figure 3, the standalone FNN reached an accuracy of **78.63%**, reflecting reduced capability to distinguish between similar severity levels. The SOM performed better, achieving **91.25%**, as it can map the complex, high-dimensional feature space into clusters that reflect the progression of defect severity. The hybrid **FNN + SOM** method outperformed both individual models with an accuracy of **95.10%**, confirming the advantage of the hierarchical strategy.

The superior performance of the combined model demonstrates that the FNN effectively narrows down the search space by identifying the fault type, while the SOM refines the classification by organizing features within each fault category according to severity. This synergy enhances both precision and interpretability in complex diagnostic tasks.

General Discussion

The overall results confirm that integrating supervised and unsupervised neural networks significantly improves diagnostic accuracy and robustness. The **FNN** provides a strong foundation for classifying major fault types, but its sensitivity to feature overlap limits its effectiveness for subtle severity variations. The **SOM** complements this limitation by capturing nonlinear relationships and faulty evolution patterns within the feature space. By combining these two complementary paradigms, the proposed **hierarchical framework** mirrors the reasoning process of human experts: first identifying the fault type, then assessing its severity. This two-step approach not only enhances diagnostic precision but also provides a practical and interpretable solution for intelligent predictive maintenance systems in industrial applications.

Conclusion

This paper proposed a two-step neural framework for bearing fault diagnosis that effectively combines supervised and unsupervised learning. The method first employs a Feedforward Neural Network (FNN) to identify the fault type before a Self-Organizing Map (SOM) refines the diagnosis by determining the fault severity. Evaluated on the CWRU dataset, this hybrid FNN+SOM approach achieved a superior accuracy of 95.10% for the 10-class severity classification problem, outperforming both models used in isolation.

The results confirm that the hierarchical integration of these complementary paradigms mitigates the FNN's sensitivity to class imbalance and leverages the SOM's strength in clustering nuanced severity patterns. This strategy provides a robust and accurate solution for automated fault diagnosis and severity assessment, making it a highly promising approach for industrial predictive maintenance systems. Future work will focus on integrating deep feature learning and extending the framework for prognostics and remaining useful life (RUL) estimation.

Scientific Ethics Declaration

* The author declares that the scientific ethical and legal responsibility of this article published in EPSTEM journal belongs to the author.

Conflict of Interest

* The author declares that there is no conflict of interest

Funding

* This research received no specific grant from any funding agency in the public, commercial, or not-for-profit sectors.

Acknowledgements or Notes

* This article was presented as a poster presentation at the International Conference on Technology, Engineering and Science (www.icontes.net) held in Antalya/Türkiye on November 12-15, 2025.

References

Bishop, C. M. (2006). *Pattern recognition and machine learning*. Springer.

Case Western Reserve University. (n.d.). *Bearing data center*. Retrieved from http://www.eecs.cwru.edu/laborator/bearing

Goodfellow, I., Bengio, Y., & Courville, A. (2016). *Deep learning*. MIT Press.

Jardine, A. K. S., Lin, D., & Banjevic, D. (2006). A review on machinery diagnostics and prognostics implementing condition-based maintenance. *Mechanical Systems and Signal Processing, 20*(7), 1483-1510.

Kohonen, T. (2001). *Self-organizing maps* (3rd ed.). Springer.

Lei, Y., Jia, F., Lin, J., Xing, S., & Ding, S. X. (2016). An intelligent fault diagnosis method using unsupervised feature learning towards mechanical big data. *IEEE Transactions on Industrial Electronics, 63*(5), 3137-3147.

Lei, Y., Yang, B., Jiang, X., Jia, F., Li, N., & Nandi, A. K. (2020). Applications of machine learning to machine fault diagnosis: A review and roadmap. *Mechanical Systems and Signal Processing, 138*, 106587.

Peng, Z. K., Tse, P. W., & Chu, F. L. (2005). An improved Hilbert–Huang transform and its application in vibration signal analysis. *Journal of Sound and Vibration, 286*(1–2), 187-205.

Randall, R. B., & Antoni, J. (2011). Rolling element bearing diagnostics-A tutorial. *Mechanical Systems and Signal Processing, 25*(2), 485-520.

Widodo, A., & Yang, B. S. (2007). Support vector machine in machine condition monitoring and fault diagnosis. *Mechanical Systems and Signal Processing, 21*(6), 2560-2574.

Yang, D., Wang, K., & Li, X. (2019). A hybrid fault diagnosis method for rolling bearings using self-organizing map and deep learning. In *Proceedings of the IEEE International Conference on Prognostics and Health Management (PHM)* (pp. 1-7). IEEE.

Zhang, W., Yang, D., & Wang, K. (2019). Data-driven methods for predictive maintenance of industrial equipment: A survey. *IEEE Systems Journal, 13*(3), 2213-2227.

Author(s) Information

Smail Haroun
University of Bouira (Akli Mohand Oulhadj University-Bouira), Department of Electrical Engineering, Laboratory of Electrical and Industrial Systems (LSEI), Algeria
Contact e-mail: *s.haroun@univ-bouira.dz*

To cite this article:

Haroun, S. (2025). Bearing fault detection and severity classification using a two-step neural network model. *The Eurasia Proceedings of Science, Technology, Engineering and Mathematics (EPSTEM), 38,* 610-616.

The Eurasia Proceedings of Science, Technology, Engineering & Mathematics (EPSTEM)
ISSN: 2602-3199

The Eurasia Proceedings of Science, Technology, Engineering and Mathematics (EPSTEM), 2025

Volume 38, Pages 617-624

IConTES 2025: International Conference on Technology, Engineering and Science

RLS Filter Optimization for Non-Invasive Fetal Electrocardiogram Extraction Using the PSO Algorithm

Mourad Benziane
Bouira University

Mohamed Rezki
Bouira University

Issam Griche
Bouira University

Kamel Saoudi
Bouira University

Abderrazak Arabi
Ferhat Abbas Setif 1 University

Abstract: Non-invasive fetal electrocardiogram (fECG) extraction is still a challenging task due to the overbearing preponderance of the maternal ECG (mECG) and the presence of noise and interferences. Adaptive filtering techniques, particularly the Recursive Least Squares (RLS) algorithm, have been shown to work well for this issue. However, RLS performance largely depends on a few of its parameters (filter order, forgetting factor, and regularization term), typically tuned empirically, thus limiting robustness and generalizability. In this work, we introduce an automatic parameter optimization process based on the Particle Swarm Optimization (PSO) algorithm. The proposed method was validated using simulated signals generated on MATLAB, including abdominal recordings (aECG), maternal thoracic signals (mECG), and a reference fECG for comparison. Quantitative outcomes, using Mean Squared Error (MSE) and Signal-to-Noise Ratio (SNR) metrics, indicate that PSO-based optimization improves the quality of the resultant fECG compared to the optimal empirical settings, eliminating residual maternal interference. These findings show the potential of PSO for robust fECG extraction and its potential feasibility for real clinical data in the future.

Keywords: Non-invasive fECG extraction, Adaptive filtering, RLS, Optimization, PSO algorithm

Introduction

Prenatal monitoring increasingly relies on non-invasive methods of estimation of fetal health and development (Behar, 2016; Sameni, 2007). Among them, fetal electrocardiogram (fECG) analysis represents an essential component, since it provides valuable information concerning the cardiac activity and aids in the earliest possible diagnosis of rhythmical or structural pathologies. However, extracting fECG from abdominal electrodes remains an arduous task owing to the overwhelming dominance of maternal ECG (mECG), noise, and physiological interferences (Vennila, 2014; Clifford, 2006; Sweeney, 2012).

Among the suggested methods, adaptive filters are proving to be an effective solution, with the Recursive Least Squares (RLS) algorithm being particularly attractive because of its high convergence speed and resilience to non-stationary signals (Haykin, 1991; Widrow, 1985). Nevertheless, RLS performance is based on several key

- This is an Open Access article distributed under the terms of the Creative Commons Attribution-Noncommercial 4.0 Unported License, permitting all non-commercial use, distribution, and reproduction in any medium, provided the original work is properly cited.

- Selection and peer-review under responsibility of the Organizing Committee of the Conference

© 2025 Published by ISRES Publishing: www.isres.org

parameters (filter order, forgetting factor, regularization term), whose tuning is usually performed empirically, hence decreasing the method's performance and viability (Ciochina, 2009). To address this issue, metaheuristic optimization techniques provide a viable alternative since they automatically perform the parameter selection and explore the space in a better way. Particle Swarm Optimization (PSO), inspired by the collective behavior of bird flocks or schools of fish, is particularly well suited to this task (Eberhart, 2000; Ekanem, 2025; Kennedy, 2002; Poli, 2007; Mendes, 2004; Talbi, 2009).

Here, we propose the application of PSO to automatically optimize the RLS filter parameters for fECG extraction from MATLAB-generated simulated signals. The objective is to compare the performance obtained through automatic optimization to that achieved by using empirical parameter values based on quantitative metrics such as the MSE and SNR to determine the added value of PSO in the process. The rest of this paper is organized in the following manner: Section 2 presents the proposed methodology, starting with the fundamentals of the RLS filter and its PSO optimization. Section 3 describes simulations and results generated on test signals. Finally, Section 4 concludes the paper and offers outlooks for future work.

Methodology

RLS Adaptive Filter

Figure 1 depicts the representation of fECG extraction using RLS adaptive filter.

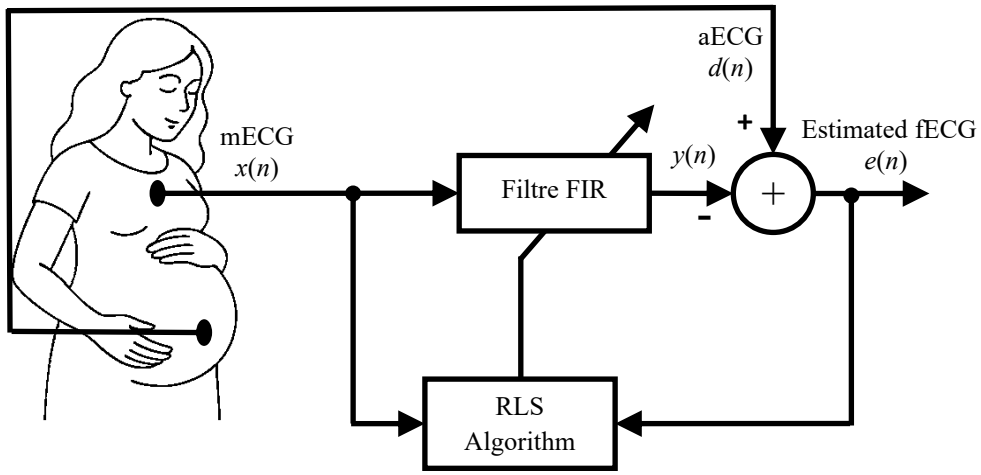


Figure 1. General representation of fetal ECG extraction using adaptive filter.

The process is founded on the use of the maternal thoracic ECG (mECG), denoted by x(n), as the reference signal (filter input) and the abdominal ECG (aECG), denoted by d(n), as the desired output. The goal of the filter is to estimate the maternal component contained in the abdominal signal and then subtract it to arrive at the fetal component (D, 2022) (Andreotti, 2014) (Niknazar, 2013). Among various adaptive filtering algorithms, the Recursive Least Squares (RLS) algorithm is well known for its fast convergence, and it can adapt to change in the signal (Ciochina, 2009) (Kahankova, 2017). Mathematically, for a vectorized input at instant *n*:

$$\mathbf{x}(n) = \left[x(n)\ x(n-1)\ \ldots\ x(n-M+1)\right]^T \tag{1}$$

For the filter coefficients vector at instant *n*:

$$\mathbf{w}(n) = \left[w_0(n)\ w_1(n)\ \ldots\ w_{M-1}(n)\right]^T \tag{2}$$

Where *M* is the filter order.

The RLS algorithm updates the coefficient vector by minimizing the squared error:

$$e(n) = d(n) - y(n) \tag{3}$$

$$e(n) = d(n) - \mathbf{w}^T(n-1)\mathbf{x}(n) \tag{4}$$

Table 1 summarizes the RLS algorithm:

Table 1. Summary of the RLS algorithm.

Parameters:	M= filter order. λ= forgetting factor. δ= positive constant.
Initialization:	$\mathbf{w}(0) = \mathbf{0}_{M\times 1}$ $\mathbf{Q}(0) = \delta^{-1}\mathbf{I}$
Computing:	For: $n=0,1,2,\ldots,N-1$ $\mathbf{k}(n) = \frac{\lambda^{-1}\mathbf{Q}(n-1)\mathbf{x}(n)}{1+\lambda^{-1}\mathbf{x}^T(n)\mathbf{Q}(n-1)\mathbf{x}(n)}$ $e(n) = d(n) - \mathbf{x}^T(n)\mathbf{w}(n-1)$ $\mathbf{w}(n) = \mathbf{w}(n-1) + \mathbf{k}(n)e(n)$ $\mathbf{Q}(n) = \lambda^{-1}\mathbf{Q}(n-1) - \lambda^{-1}\mathbf{k}(n)\mathbf{x}^T(n)\mathbf{Q}(n-1)$

Where:

- λ is the forgetting factor ($0<\lambda\leq 1$),
- $Q(n)$ is the inverse correlation matrix (initialized with δI),
- δ is a regularization parameter.

It is important to select properly λ, M, and δ, as they a direct impact on the convergence rate, the numerical stability, and the quality of the extracted fECG. This calls for an optimization algorithm to adjust these parameters.

Optimization Using PSO

The Particle Swarm Optimization (PSO) algorithm is a metaheuristic technique inspired by the social behavior of flocking birds and schooling fish. Each candidate solution, called a particle, explores the RLS filter parameter space by flying according to its own experience and the experience of neighboring particles (Ekanem, 2025; Poli, 2007). In our study, the RLS filter parameters define the search vector:

- λ (forgetting factor),
- M (filter order),
- δ (regularization factor).

Each particle evaluates the quality of its position using a cost function based on the Mean Squared Error (MSE) between the extracted fetal signal and the reference signal. The optimization process thus aims to minimize this MSE.

The interest of PSO is twofold:

1. To automate the selection of RLS parameters, which are often empirically determined.
2. To improve the robustness and accuracy of fECG extraction by allowing adaptation to variations in real signals.

PSO Algorithm for RLS Parameter Optimization

1. **Initialization**
   - Randomly generate a set of particles with parameters (λ, M, δ).
   - Initialize velocities and define the search boundaries.
2. **Evaluation**
   - For each particle, apply the RLS with its parameters.
   - Compute the cost function:
     $J = MSE\left(fECG_{extracted}, fECG_{real}\right)$
3. **Update of Best Solutions**

- Update the personal best position (pBest).
- Update the global best position (gBest).

4. **Update of Velocities and Positions**

$$v_i \leftarrow w.v_i + c_1 r_1 \left(pBest_i - x_i \right) + c_2 r_2 \left(gBest_i - x_i \right)$$

$$x_i \leftarrow x_i + v_i$$

5. **Iteration**
   - Repeat steps 2 to 4 until the maximum number of iterations is reached or convergence is achieved.
6. **Output**

   The optimal parameters (λ^*, M^*, δ^*) are provided by *gBest*.

Results and Discussion

The proposed method is tested on these generated synthetic signals. First, three distinct signals were generated in MATLAB:

- an abdominal signal simulating the mixture of maternal ECG and fetal ECG,
- a thoracic signal representing only the maternal ECG,
- a reference fetal signal used to evaluate the extraction quality.

These signals constitute the testing environment employed for the evaluation of the method. Figure 2 illustrates an example of the synthetic signals used in our simulations.

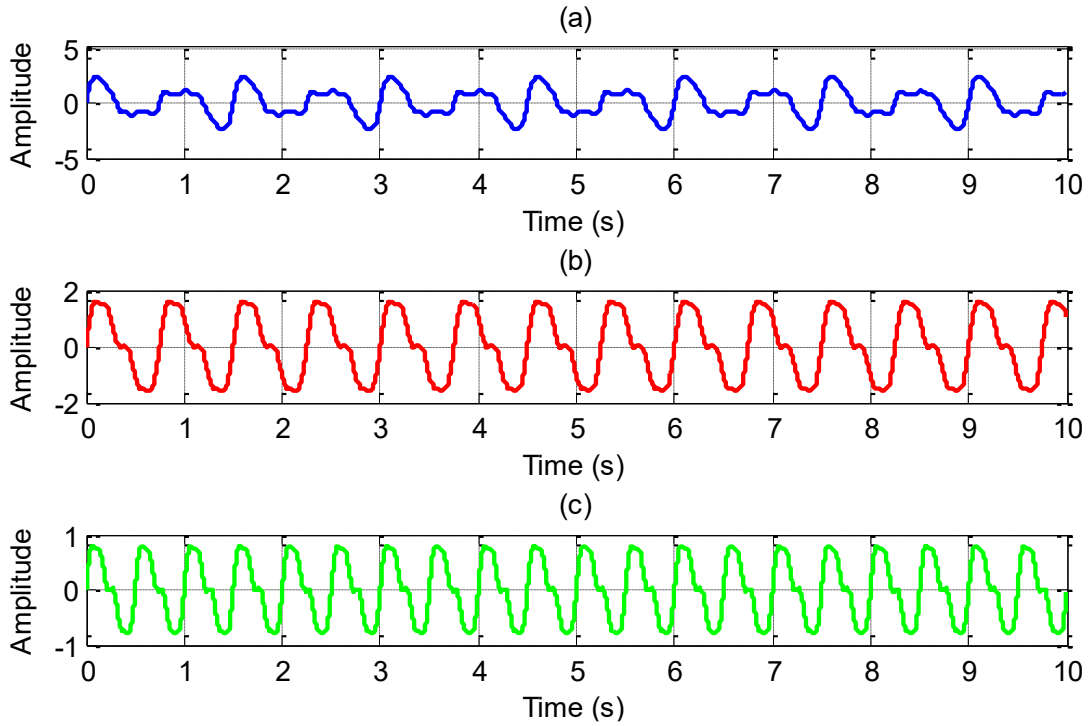


Figure 2. Signals used in the simulation. (a) abdominal signal, (b) thoracic signal, (c) reference fECG signal.

The performance of the RLS filter was first evaluated using empirically chosen parameters, and then with parameters optimized by PSO. The comparison was carried out using the Mean Squared Error (MSE) between the extracted fetal signal and the reference fetal signal, as well as the Signal-to-Noise Ratio (SNR), calculated as follows:

$$MSE = \frac{1}{N} \sum_{n=1}^{N} \left(fECG(n) - \widehat{fECG}(n) \right)^2 \tag{5}$$

$$SNR(dB) = 10\log_{10}\left(\frac{\sum_{n=1}^{N} fECG(n)^2}{\sum_{n=1}^{N}\left(fECG(n) - f\hat{E}CG(n)\right)^2}\right) \quad (6)$$

With *fECG* denoting the reference fetal signal and $f\hat{E}CG$ the extracted fetal signal.

Table 2 summarizes the results obtained using empirical selections of the RLS filter parameters (12 empirical combinations from c1 to c12) and the result obtained with optimal parameters achieved through the PSO method.

Table 2. Comparison between 12 empirical configurations and PSO-based optimization.

Parameters selection	***M***	***λ***	***δ***	***MSE***	***SNR***
Empiric c1	16	0,9997	0,1	0.001855	18.48
Empiric c2	16	0,9997	0,5	0.001455	18.83
Empiric c3	16	0,9997	0,7	0.001457	18.81
Empiric c4	16	0,9999	0,1	0.000426	20.12
Empiric c5	16	0,9999	0,5	0.000424	20.06
Empiric c6	**16**	**0,9999**	**0,7**	**0.000423**	**20.04**
Empiric c7	32	0,9997	0,1	**33.29**	**-20.13**
Empiric c8	32	0,9997	0,5	0.001301	19.09
Empiric c9	32	0,9997	0,7	0.001314	19.07
Empiric c10	32	0,9999	0,1	0.000416	20.21
Empiric c11	**32**	**0,9999**	**0,5**	**0.000413**	**20.21**
Empiric c12	32	0,9999	0,7	0.000413	20.20
Optimized PSO	**32**	**1**	**1**	**0.000255**	**20.42**

The obtained results show that PSO-based optimization significantly improves the quality of the extracted signal by reducing the residual maternal component and enhancing the visibility of the fetal peaks.Figure 3 depicts the convergence curve of PSO compared to those of the empirical combinations c1, c6, and c11, which provide the best MSE/SNR trade-offs, as well as combination c7, which exhibits filter divergence.

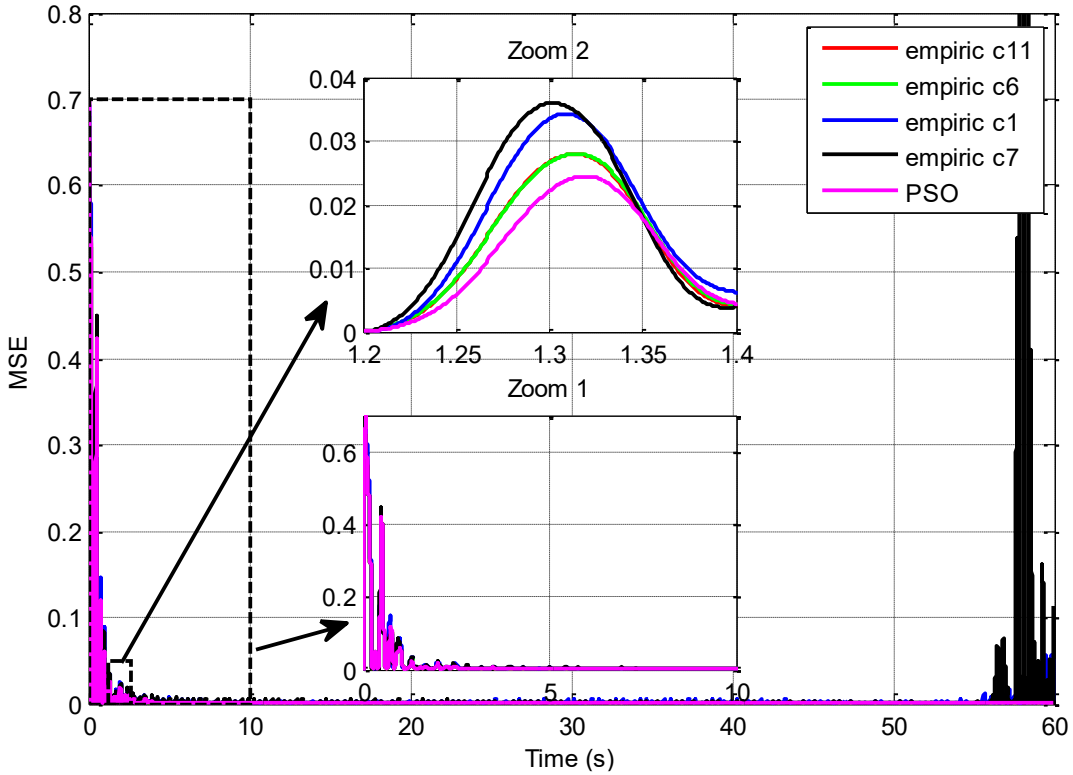


Figure 3. Convergence curve of PSO compared with empirical configurations.

Figure 4 illustration of the real fECG signal and the extracted signals obtained using the best empirical configuration and the PSO-based configuration.

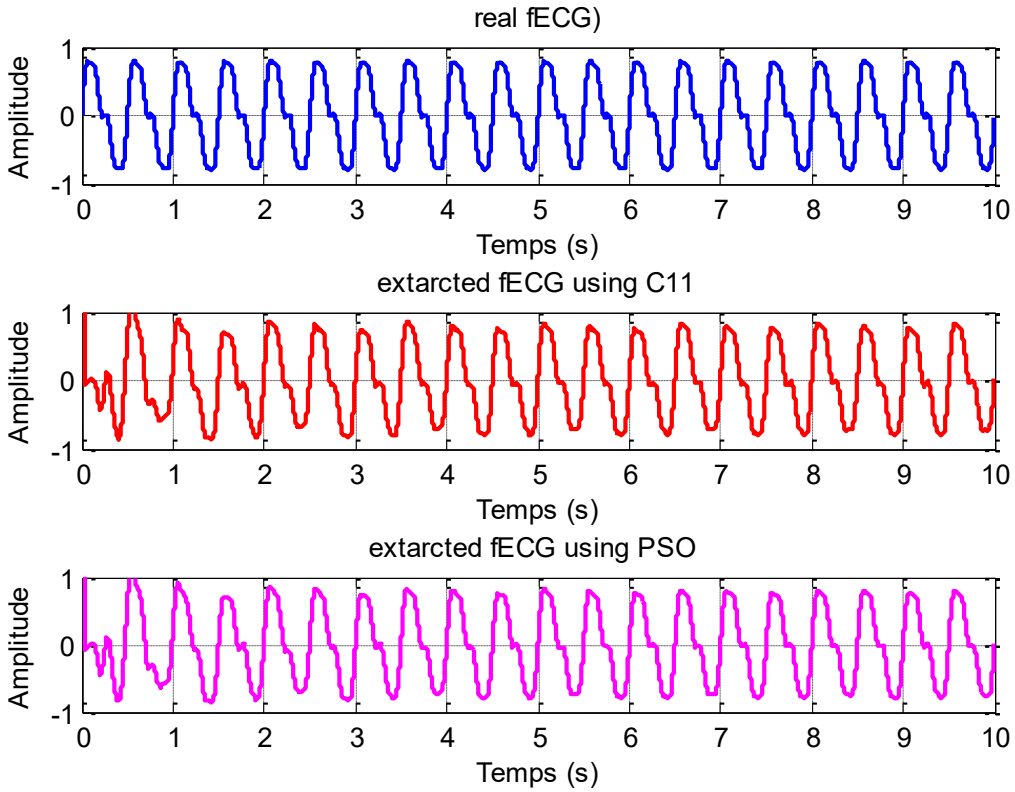


Figure 4. Real fECG and extracted signals obtained with both methods

The findings identify the constraint of an empirical choice of RLS filter parameters against a systematic one with the use of the PSO algorithm. Among the 12 hand-trial configurations, the best one is configuration C11, which provides an acceptable trade-off between MSE and SNR. Still, its performance cannot compete with that obtained by PSO, which can automatically identify a set of parameters with a significant MSE reduction and improvement in SNR. The curve of convergence also demonstrates the ability of PSO in achieving an optimal solution in a robust and effective manner, while empirical parameters depict more dispersed and sometimes weaker plots. Whereas PSO optimization did the best overall, it must be noted that empirical configuration C11 also produced results very close. This similarity may be explained by the fact that several parameter combinations were manually tested before arriving at C11, thereby narrowing the gap with the optimized solution. These findings confirm the relevance of integrating a metaheuristic optimization method such as PSO for tuning adaptive filter parameters in the context of fECG extraction.

Conclusion

In this work, we investigated the extraction of the fetal electrocardiogram (fECG) using an adaptive Recursive Least Squares (RLS) filter. After evaluating several empirical configurations, we introduced an automatic parameter optimization of the filter based on the Particle Swarm Optimization (PSO) algorithm. The results demonstrated that PSO improves the extraction quality by reducing the mean squared error (MSE) and increasing the signal-to-noise ratio (SNR), compared to manual parameter tuning, while providing a systematic parameterization procedure.

As future perspectives, it would be of great interest to apply this approach to real signals from clinical databases in order to confirm its robustness under practical conditions. In addition, other metaheuristic optimization methods (such as Genetic Algorithms or Ant Colony Optimization) could be explored and compared with PSO. Finally, the integration of clinically relevant criteria, beyond MSE and SNR, would represent a step forward toward more comprehensive medical validation.

Scientific Ethics Declaration

* The author declares that the scientific ethical and legal responsibility of this article published in EPSTEM journal belongs to the author.

Conflict of Interest

* The authors declare that they have no conflicts of interest

Funding

* This research received no specific grant from any funding agency in the public, commercial, or not-for-profit sectors.

Acknowledgements or Notes

* This article was presented as a poster presentation at the International Conference on Technology, Engineering and Science (www.icontes.net) held in Antalya/Türkiye on November 12-15, 2025.

References

Andreotti, F., Riedl, M., Himmelsbach, T., Wedekind, D., Wessel, N., Stepan, H., Schmieder, C., Jank, A., Malberg, H., & Zaunseder, S. (2014). Robust fetal ECG extraction and detection from abdominal leads. *Physiological Measurement, 35*(8), 1551–1567.

Behar, J., Andreotti, F., Zaunseder, S., Oster, J., & Clifford, G. D. (2016). A practical guide to non-invasive foetal electrocardiogram extraction and analysis. *Physiological Measurement, 37*(5), R1–R35.

Ciochina, S., Paleologu, C., Benesty, J., & Enescu, A. A. (2009). On the influence of the forgetting factor of the RLS adaptive filter in system identification. In *International Symposium on Signals, Circuits and Systems* (pp. 1–4).

Clifford, G. D., Azuaje, F., & McSharry, P. (2006). *Advanced methods and tools for ECG data analysis*. Artech House.

D, E. D., & M, S. (2022). Extraction of fetal ECG from abdominal and thorax ECG using a non-causal adaptive filter architecture. *IEEE Transactions on Biomedical Circuits and Systems, 16*(5), 981–990.

Eberhart, R. C., & Shi, Y. (2000). Comparing inertia weights and constriction factors in particle swarm optimization. In *Proceedings of the 2000 Congress on Evolutionary Computation* (pp. 84–88). IEEE.

Ekanem, I. I., Ekanem, A. E., & Abia, E. S. (2025). A systemic review on the adoption of particle swarm optimization algorithms in biomedical engineering diagnostics and simulations. *Annals of Healthcare Systems Engineering, 2*(1), 1–15.

Haykin, S. (1991). *Adaptive filter theory* (2nd ed.). Prentice-Hall.

Kahankova, R., Martinek, R., & Bilik, P. (2017). Fetal ECG extraction from abdominal ECG using RLS based adaptive algorithms. In *18th International Carpathian Control Conference (ICCC)* (pp. 337–342). IEEE.

Kennedy, J., & Eberhart, R. (2002). Particle swarm optimization. *Proceedings of IEEE International Conference on Neural Networks, 4*, 1942–1948.

Mendes, R., Kennedy, J., & Neves, J. (2004). The fully informed particle swarm: Simpler, maybe better. *IEEE Transactions on Evolutionary Computation, 8*(3), 204–210.

Niknazar, M., Rivet, B., & Jutten, C. (2013). Fetal ECG extraction by extended state Kalman filtering based on single-channel recordings. *IEEE Transactions on Biomedical Engineering, 60*(5), 1345–1352.

Poli, R., Kennedy, J., & Blackwell, T. (2007). Particle swarm optimization. *Swarm Intelligence, 1*(1), 33–57.

Sameni, R., Clifford, G. D., Jutten, C., & Shamsollahi, M. B. (2007). Multichannel ECG and noise modeling: Application to maternal and fetal ECG signals. *EURASIP Journal on Advances in Signal Processing, 2007*(1).

Sweeney, K. T., Ward, T. E., & McLoone, S. F. (2012). Artifact removal in physiological signals-practices and possibilities. *IEEE Transactions on Information Technology in Biomedicine, 16*(3), 488–500.

Talbi, E. (2009). *Metaheuristics: From design to implementation*. Wiley.

Vennila, M., & Yacin, S. M. (2014). A modified approach on fetal ECG extraction using extended state Kalman filtering. In *International Conference on Green Computing Communication and Electrical Engineering* (pp. 1–5).

Widrow, B., & Stearns, S. D. (1985). *Adaptive signal processing*. Prentice-Hall.

Author(s) Information

Mourad Benziane
Bouira University, Rue Drissi Yahia Bouira – 10000, Bouira, Algeria
Contact e-mail: *m.benziane@univ-bouira.dz*

Mohamed Rezki
Bouira University, Rue Drissi Yahia Bouira – 10000, Bouira, Algeria

Issam Griche
Bouira University, Rue Drissi Yahia Bouira – 10000, Bouira, Algeria

Kamel Saoudi
Bouira University, Rue Drissi Yahia Bouira – 10000, Bouira, Algeria

Abderrazak Arabi
Ferhat Abbas Setif 1 University
Algeria

To cite this article:

Benziane, M., Rezki. M., Griche, I., Saoudi, K., & Arabi, A., (2025). RLS filter optimization for non-invasive fetal electrocardiogram extraction using the PSO algorithm. *The Eurasia Proceedings of Science, Technology, Engineering and Mathematics (EPSTEM), 38,* 617-624.

The Eurasia Proceedings of Science, Technology, Engineering & Mathematics (EPSTEM)
ISSN: 2602-3199

The Eurasia Proceedings of Science, Technology, Engineering and Mathematics (EPSTEM), 2025

Volume 38, Pages 625-629

IConTES 2025: International Conference on Technology, Engineering and Science

Performance Evaluation of the Andasol-1 Solar Power Plant in Algerian Climatic Conditions

Hicham Kadraoui
University of Abou Bakr Belkaid

Abstract: The generation of electricity from renewable sources is imperative in order to fight against the environmental and economic problems associated with fossil fuel utilization. The entire world energy sector is experiencing a rapid transformation towards renewable and sustainable energy sources, and a promising technological advancement in this regard is concentrated solar power (CSP), with a notable example being parabolic trough solar power plants. In this paper, we investigate the operational efficiency of the Andasol-1 parabolic trough solar power plant with 50 MWe output power in various Algerian desert locations, i.e., the Béchar, Ghardaïa, and Tamanrasset regions. A thorough examination of the Andasol-1 plant's technical characteristics is made, and an extensive economic and energy analysis is conducted based on System Advisor Model (SAM) software. Our study results reveal that the Tamanrasset region seems to be the most suitable area for CSP exploitation, with a capacity factor of 47.4% and a levelized cost of electricity (LCOE) of 0.130 €/kWh.

Keywords: Concentrated solar power, Parabolic trough, Andasol-1, LCOE, SAM simulation

Introduction

The world's energy scenario has changed considerably in recent times, with an accelerating transition to renewable and sustainable energy sources. CSP (concentrated solar power) has been one of the most promising technologies in this field, with prospects for efficient electricity production and thermal energy storage (Abdul Hai Alami et al., 2023).

Parabolic trough solar power plants represent one of the most advanced and widely installed CSP systems. They utilize parabolic reflectors for the concentration of solar radiation onto a receiver tube, warming up a transfer fluid, typically oil or molten salt that consequently generates steam to drive a turbine for electricity generation (El Boujdaini et al., 2019). Among the main advantages of such systems is the possibility of incorporation of thermal energy storage systems, as in the cases of power plants Nevada Solar One in the US and Andasol-1 in Spain.

The Andasol 1 central solar power plant is a pioneering commercial solar thermal power plant in Europe with a capacity of 50 MW. It uses parabolic trough technology with a solar field aperture of about 510,000 m², consisting of 7,488 curved glass collectors organized in 312 rows following the sun's movement. The solar field uses a heat transfer fluid (Dowtherm A) heated up to approximately 393°C, which generates steam to drive a Siemens 50 MW steam turbine. A key technical feature is its thermal energy storage system, consisting of 28,500 tons of molten salt (60% sodium nitrate and 40% potassium nitrate), which enables about 7.5 hours of full-load power generation even without sun, allowing near-continuous electricity supply (Solar Millennium AG, 2005).

Financially, the total construction cost was about €310 million (2008), equivalent to approximately $531 million in 2020 dollars, with a levelized cost of electricity (LCOE) estimated at around $0.29/kWh. The project started operation in 2008 and benefits from feed-in tariffs under Spanish renewable energy law, with substantial

- This is an Open Access article distributed under the terms of the Creative Commons Attribution-Noncommercial 4.0 Unported License, permitting all non-commercial use, distribution, and reproduction in any medium, provided the original work is properly cited.

- Selection and peer-review under responsibility of the Organizing Committee of the Conference

© 2025 Published by ISRES Publishing: www.isres.org

funding support including a €116.7 million loan from the European Investment Bank. The plant produces about 179-180 GWh per year, enough to supply electricity to up to 200,000 people, with an expected lifespan of at least 40 years (National Renewable Energy Laboratory. (2022, October 20).

In spite of the established success of Concentrated Solar Power (CSP) technologies in various global environments, there is a significant research gap regarding their operational performance under arid conditions (Ikhlef & Larbi, 2024). The Algerian desert, although endowed with rich solar resources, is a challenging but suitable land for the implementation of CSP technologies. Factors such as high solar irradiance, extreme temperature fluctuations, and dust deposition present opportunities and challenges to CSP technologies (Ihaddadene, Nabila, et al.2023).

Our research aims to fill the aforementioned research gap by undertaking a systematic examination of the operational efficiency of the Andasol-1 Concentrated Solar Power (CSP) plant under varying geographical conditions in the Algerian desert. By employing the System Advisor Model (SAM) software, a comprehensive examination of the facility's technical and economic performance will be conducted at three Algerian sites: the Bechar, Ghardaïa and Tamanrasset regions. The selection of the three sites is informed by the heterogeneous climatic and environmental conditions, thereby enabling an in-depth evaluation of the feasibility of CSP installation in arid desert environments.

Method

This study examines the adaptability and performance of the Andasol-1 concentrated solar power plant in three regions of the Algerian desert: Bechar, Ghardaïa, and Tamanrasset. These locations were selected based on several factors, the most important of which are solar radiation intensity, climatic variability, and geographical diversity. These areas were chosen specifically because they have higher levels of solar radiation than others. (Table 1) shows the geological and climatic data for these areas.

Table 1. Regional meteorological and geological parameters

Parametre	**Bechar**	**Ghardaia**	**Tamanrasset**
Latitude (°N)	31,57	32,49	22,89
Longitude (°E)	-2,14	3,67	5,57
Altitude (m)	772	530	1377
DNI (kWh/m²)	2925	2650	2812
GHI (kWh/m²)	2251	2180	2382
Température ambiante (°C)	21,9	22,5	22,8
Vitesse du vent (m/s)	4,0	3,8	3,6

Table 2. Technical input data: Comparison with Andasol-1 power plant parameters

Variable	**SAM Input**	**Andasol-1**
Climate	Bechar TMY3, Ghardaïa TMY3, Tamanrasset TMY3	Andasol-1, Espagne
Field aperture	510,000 m²	520,000 m²
Irradiation at design	950 W/m²	700 W/m²
Field HTF fluid	Therminol VP1	Therminol VP1
Design loop outlet temp	391°C	393°C
Number of SCA per loop	8	4
Collector (SCAs)	EuroTrough ET150	EuroTrough ET150
Receivers (HCEs)	Schott PTR-70	Schott PTR-70
Capacity - Design gross output	50 MW	50 MW
Cycle thermal efficiency	0.356	~0.381
Aux heater outlet set temp	391°C	391°C
Full load hours of TES	7.5 hr	28,500 t salt for 7.5 peak load hours
Tank height	14 m	14 m

The technical and economic analysis was carried out using the System Advisor Model (SAM) software. This program was developed by the US Department of Energy's National Renewable Energy Laboratory (NREL) and

is a widely used tool for evaluating the performance of renewable energy projects. What sets SAM apart is its ability to simulate energy production and estimate the financial viability of projects. The program is relatively easy to use, but it requires some experience in the field of renewable energy to achieve accurate results. The study ultimately aims to understand the applicability of concentrated solar power technologies in harsh desert environments and how these plants can contribute to meeting the growing demand for energy. research aims to fill the aforementioned research gap by undertaking a systematic examination of the operational efficiency of the Alvarado Concentrated Solar Power (CSP) plant under varying geographical conditions in the Algerian desert.

Results and Discussion

Using hourly climate series (2013-2022) from the NSRDB data for the selected region, including Direct Normal Irradiance. Because July has the longest periods of sun irradiation of the year, we especially selected this month to display the best results. By choosing the July monthly average, we concentrated on the most promising and successful time frame, which is the best scenario every year. Based on the DNI beam irradiance (Figure 1), it can be observed that Tamanrasset s site exhibits the superior solar resource with peak DNI reaching 900 W/m² at solar noon, compared to 850 W/m² at Ghardaïa and 650 W/m² at Béchar. The solar resource availability spans 15 hours (05:00-20:00) at all sites, with productive DNI levels (>200 W/m²) extending from 06:00-19:00. Tamanrasset maintains DNI >800 W/m² for 5 consecutive hours (09:00-14:00), optimal for sustained high-temperature operation and thermal storage charging.

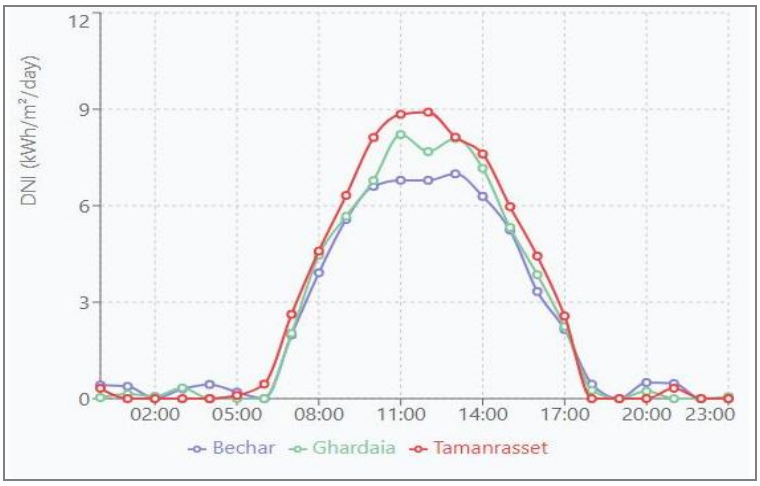


Fig 1. DNI variations over time (hours) in July: 2013-2022 Average data.

Financial Results

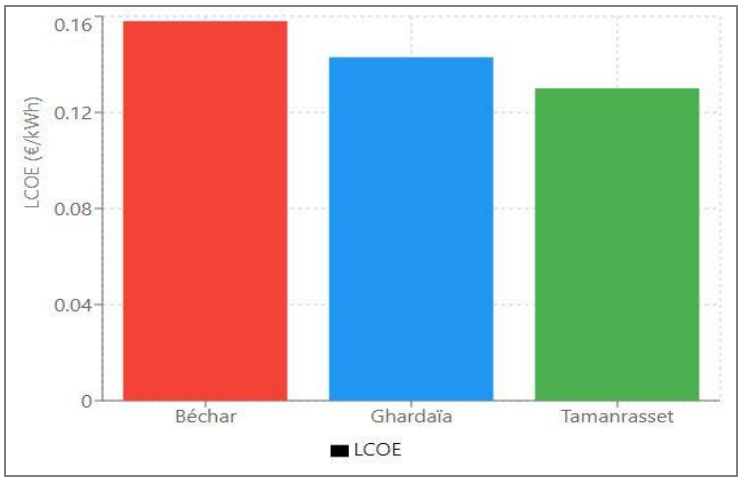


Figure 2. The levelized cost of electricity (LCOE)

The levelized cost of electricity (LCOE), which shows varying cost trends for various sites, is shown in (Figure 2). The Tamanrasset site has the lowest LCOE of 0.130 €/kWh and is therefore the most advantageous economically. The Ghardaïa region, with an LCOE of 0.143 €/kWh, comes in second. On the other hand, the Bechar site has lower production levels, resulting in a higher LCOE of 0.158 €/kWh. The economic subtleties inherent in these specific places' power producing capacities are highlighted by this observed variation.

SAM Model Validation

A validation investigation that contrasts the outcomes of the SAM software simulation with the Andasol 1 power plant's real performance is shown in (Table 3). It shows how much the verified data from the Andasol 1 power plant differs from the estimated values from the SAM simulation. Not to be overlooked is the fact that the Tamanrasset site performs noticeably better than the Spanish site. The arid terrain of the Tamanrasset location and the availability of more precise weather data are responsible for this.

Table 3. Technology cost comparaison (Algeria, 2022)

Technology	LCOE (€/kWh)	Capacity Factor	Storage Capability
CSP Parabolic Trough	0.130	61%	Integrated (7.5h)
PV + Battery Storage	0.125	25%	External (4h typical)
Natural Gas CCGT	0.065	85%	None
Onshore Wind	0.055	35%	None

While CSP remains more expensive than conventional fossil technologies, the integrated storage capability and dispatchable generation characteristics provide system-level value not captured in simple LCOE comparisons.
Conclusion

Conclusion

The transition to renewable energy is a strategic step for environmental sustainability and a financially prudent decision in the long term. Our comprehensive analysis of the performance of the Andasol-1 Parabolic Trough Solar Power Plant in the diverse terrains of the Algerian desert underscores the feasibility of solar power in arid regions. By carefully adjusting the input parameters of Andasol-1, we have successfully minimized the Levelized Cost of Electricity (LCOE) and maximized annual energy production. Our study shows that Tamanrasset emerges as the most promising location among the evaluated sites, offering the best balance of energy yield and cost efficiency, closely followed by Bachar and Ghardaïa. These findings confirm that Parabolic Trough technology has significant potential to increase renewable electricity production in the Algerian desert, providing a solid blueprint for future solar energy projects in similar environments. These results strengthen the argument for expanding solar energy infrastructure in Algeria and contribute to the global narrative of transitioning to clean and economically advantageous energy sources.

Scientific Ethics Declaration

* The author declares that the scientific ethical and legal responsibility of this article published in EPSTEM journal belongs to the author.

Conflict of Interest

* The author declares that there is no conflicts of interest

Funding

* This research received no specific grant from any funding agency in the public, commercial, or not-for-profit sectors.

Acknowledgements or Notes

* This article was presented as an oral presentation at the International Conference on Technology, Engineering and Science (www.icontes.net) held in Antalya/Türkiye on November 12-15, 2025.

References

Alami, A. H., Olabi, A. G., Mdallal, A., Rezk, A., Radwan, A., Rahman, S. M. A., ... Abdelkareem, M. A. (2023). Concentrating solar power (CSP) technologies: Status and analysis. *International Journal of Thermofluids, 18*, 100340.

El Boujdaini, L., Ouali, H. A. L., Mezrhab, A., & Moussaoui, M. A. (2019). Techno-economic investigation of parabolic trough solar power plant with indirect molten salt storage. In *2019 International Conference of Computer Science and Renewable Energies (ICCSRE)* (pp. 1-7). IEEE.

Ihaddadene, R., Jed, M. E. H., & Ihaddadene, N. (2023). Assessing the effectiveness of a PV power plant and its subfields in Algeria: Case study Tamanrasset. *Energy for Sustainable Development, 77*, 101348.

Ikhlef, K., & Larbi, S. (2024). Evaluating the performance of parabolic trough solar power plants in Algerian deserts: A case study of Andasol-1. *Journal of Renewable Energies (Revue des Energies Renouvelables), 27*(2), 283-295.

National Renewable Energy Laboratory. (2022, October 20). *Andasol 1 – Concentrating solar power projects*. SolarPACES. Retrieved from https://solarpaces.nrel.gov/project/andasol-1

Solar Millennium AG. (2005). *The parabolic trough power plant Andasol 1 to 3*. Retrieved from http://large.stanford.edu/publications/power/references/docs/Andasol1-3engl.pdf

Author(s) Information

Hicham Kadraoui
University of Abou Bakr Belkaid, Tlemcen Algeria.
Automatic Laboratory of Tlemcen (LAT), University of Tlemcen,
Algeria.
Contact e-mail: hicham.kadraoui@univ-tlemcen.dz

To cite this article:

Kadraoui, H. (2025). Performance evaluation of the Andasol-1 solar power plant in Algerian climatic conditions. *The Eurasia Proceedings of Science, Technology, Engineering and Mathematics (EPSTEM), 38,* 625-629.

The Eurasia Proceedings of Science, Technology, Engineering & Mathematics (EPSTEM)
ISSN: 2602-3199

The Eurasia Proceedings of Science, Technology, Engineering and Mathematics (EPSTEM), 2025

Volume 38, Pages 630-640

IConTES 2025: International Conference on Technology, Engineering and Science

Engineering Next Generation Hole Transport Layers for Lead Free Perovskite Solar Cells Exceeding 23% Power Conversion Efficiency

Souheyla Mamoun
University of Abou Bekr Belkaid

Abdelkrim Elhasnaine Merad
University of Abou Bekr Belkaid

Feryel Saidi
University of Abou Bekr Belkaid

Abstract: Lead-based halogenated perovskite solar cells have been mainly studied recently; however, these cells have two major drawbacks: lead toxicity and device instability, which limit their commercialization. In this paper, we investigate, theoretically, the effect of temperature on the PV performance of a lead-free perovskite solar cell (PSC) based on formamidinium tin iodide ($HC(NH_2)_2SnI_3$) in the configuration: FTO/WS_2/$HC(NH_2)_2SnI_3$/Cu_2O/Au. Three inorganic materials (CuSCN, MoO_3 and NiO) and three other organic materials (Spiro-OMeTAD, P3HT and D-PBTTT-14) were used as hole transport layers (HTL) and are also tested under temperature effect. Simulations showed that the introduction of CuSCN, Cu_2O, MoO_3 and NiO as (HTL) materials leads to a remarkable efficiency of 23.24% up to 389K which reflects the resistivity of these cells at such a high temperature. Substitution of the back contact layer metal by Pt, Ni and Pd metals can maintain this fixed efficiency, and among these alternatives Platinum may be the best candidate since it is both cheaper and non-toxic.

Keywords: Lead-free perovskite solar cell, SCAPS simulation, Inorganic and organic HTL, Working temperature effect, Back contact layer effect

Introduction

There are many space and terrestrial applications that can benefit from the development of photovoltaic devices that operate at high temperatures. As an example of terrestrial applications, we cite the hybrid photovoltaic-thermal solar collector. A space satellite close to the sun also requires robust solar cells that remain efficient at high temperatures. A satellite sent to Mercury would require photovoltaic (PV) cells operating at temperatures of about 450°C and light intensities ~10 times higher than in Earth orbit.

Therefore, developing PV cells for such applications introduces a number of challenges inherent to high-temperature operation. Increasing the temperature will increase the dark currents exponentially, leading to a significant reduction in the open-circuit voltage of the solar cell. High-temperature operation could also accelerate material degradation, reduce long-term reliability, and require the development of a stable metallization and cell encapsulation system. These challenges must, therefore, be carefully considered before any viable integration of PV cells into a system that requires high-temperature operation (Perl et al., 2016).

Photovoltaic technologies have attracted the attention of scientists because solar energy is considered clean and sustainable. In addition, the use of solar energy can help reduce environmental pollution due to fossil fuel consumption, as well as energy supply shortages. Therefore, perovskite solar cells (PSCs) based on

- This is an Open Access article distributed under the terms of the Creative Commons Attribution-Noncommercial 4.0 Unported License, permitting all non-commercial use, distribution, and reproduction in any medium, provided the original work is properly cited.

- Selection and peer-review under responsibility of the Organizing Committee of the Conference

© 2025 Published by ISRES Publishing: www.isres.org

organometallic halide have received global attention due to their outstanding properties such as very good absorption in a wide range of the light spectrum (Kwak et al., 2020), excellent charge carrier mobilities, low manufacturing cost [Li & Gao, 2020], and solution processing capability [Ashrafi et al., 2020; Zhang et al., 2020). Furthermore, since their first fabrication in 2009, the power conversion efficiency (PCE) of perovskite solar cells has increased considerably: it has gone from 3.4 to more than 27% (values obtained from the NREL chart as of October 31, 2025).

Lead halide perovskite solar cells have been widely used due to a number of attractive attributes: a tunable band gap (Filip et al., 2014; Sutton et al., 2016), a better light absorption coefficient, a high power PCE (Snaith et al., 2013), and long charge carrier diffusion lengths (Zhumekenov et al., 2016). However, despite these qualities and high PCEs of more than 20%, lead-based perovskite solar cells have two major drawbacks: device instability and lead toxicity (Kwak et al., 2020; Wang et al., 2017; Boopathi et al., 2017). To circumvent these drawbacks, various advances have been employed; for example, lead has been completely or partially replaced by other less toxic metals to form lead-free perovskites or metal-lead alloyed perovskites (Kamat et al., 2017).

Hu et al (Hu et al., 2020) designed a bismuth-based bulk heterojunction absorber material ($Cs_3Bi_2I_9$-$Ag_3Bi_2I_9$) to replace the lead halide absorber layer. The device achieved a PCE of 3.8% and exhibited improved thermal stability. Similarly, Kanoun et al (Kanoun et al., 2019) theoretically demonstrated the photovoltaic performance of a Germanium halide perovskite. The device exhibited a remarkable PCE of 21%. Other candidate metals that have been used to replace lead include tin, copper, and antimony (Li & Gao, 2020; Boopathi et al., 2017). Among these lead-free alternatives, tin-based perovskites are the best alternative due to their narrow bandgap, similar chemical properties to lead, and also PCE values exceeding those of other lead-free perovskites (Boopathi et al., 2017; Jiang et al., 2020; Qian et al., 2016).

Although tin-based perovskite cells have been favored, these cells still face problems such as instability (as Sn^{2+} can easily be oxidized to $Sn^{4+,}$ when exposed to air) (Zhao et al., 2017), high carrier recombination rates (due to high doped hole concentrations of the order of 1019 cm^3) (Wu et al., 2017) difficulty in controlling the morphology during processing (due to the rapid reaction between SnI_2 and ammonium salts) (Zhao et al., 2017; Wu et al., 2017; Hao et al., 2015) and poor electronic band alignment between the electron transport layer (ETL), Sn-based absorber and hole transport layer (HTL) (Zhao et al., 2017). Some successful strategies have been introduced to reduce tin oxidation. For example, tin (II) fluoride (SnF_2) was added to the perovskite material, which reduced both the instability and the doped hole density, resulting in better performance (Kumar et al., 2014; Lee et al., 2016). Despite the fact that $CH_3NH_3SnI_3$ is widely used as an absorption material due to its interesting absorption properties, it faces a particular problem of temperature instability, which is related to the organic cation $(CH_3NH_3)^+$ (Hao et al., 2014; Rono et al., 2021). It has been found that when formamidinium $(HC(NH_2)_2)^+$ is used instead of methylammonium $(CH_3NH_3)^+$, a more compact stable solid perovskite is formed (Amat et al., 2014).

By combining the results of theoretical calculations and simulations with experimental data, Qian et al (Qian et al., 2016) provided a clear overall picture for the properties of halogenated perovskites ABX_3 (A = CH_3NH_3, $CH(NH_2)_2$, Cs, Rb; B= Pb, Sn, Ge; X = I, Br, Cl, F). Referring to the PCEs of halide perovskites simulated by the Shockley-Queisser Maximum Solar Cell Efficiency (S-Q) model under AM1.5 G illumination, the results indicate that the PCEs of (ABX_3) perovskites increase from Cl to Br to I, as the band gap becomes narrower when X increases from Cl to Br to I. Since $HC(NH_2)_2SnI_3$ remains one of the most promising lead-free perovskite candidates due to its ideal bandgap and good charge transport (Qian et al., 2016), it is therefore necessary to carefully study the various parameters of the architecture of these cells to further improve their overall performance.

With this in mind, we therefore thought of studying the effect of high temperature on the PV performance of a solar cell based on the formamidinium tin iodide perovskite $HC(NH_2)_2SnI_3$ (the perovskite which is at the top of the ranking thanks to its high efficiency) using the one-dimensional numerical simulator of solar cells, SCAPS-1D (Solar Cell Capacitance Simulator) (Burgelman et al., 2021). The cell to be studied has the following general architecture: glass/FTO/WS_2/$HC(NH_2)_2SnI_3$/Cu_2O/Au; We therefore plan to analyze the effect of temperature on this structure, on the nature of the HTL layer and the effect of the modification of the contact of the back metal.

Numerical Simulation

We use SCAPS-1D to simulate the solar cells based on the formamidinium tin iodide perovskite $HC(NH_2)_2SnI_3$. This software is based on general semiconductor physics, such as the Poison equation, the drift diffusion

equation, and the continuity equation for electrons and holes. The basic equations are usually solved in 1D under a steady-state condition. We illustrate the solar cell configuration to be studied in Figure 1-a: the adopted cell is a P-I-N device structured as follows: glass/FTO/WS_2/$HC(NH_2)_2SnI_3$/Cu_2O/Au. The corresponding band alignments between the ETL layer, the perovskite and the proposed HTL layer in this primary structure are also shown in Figure 1-b.

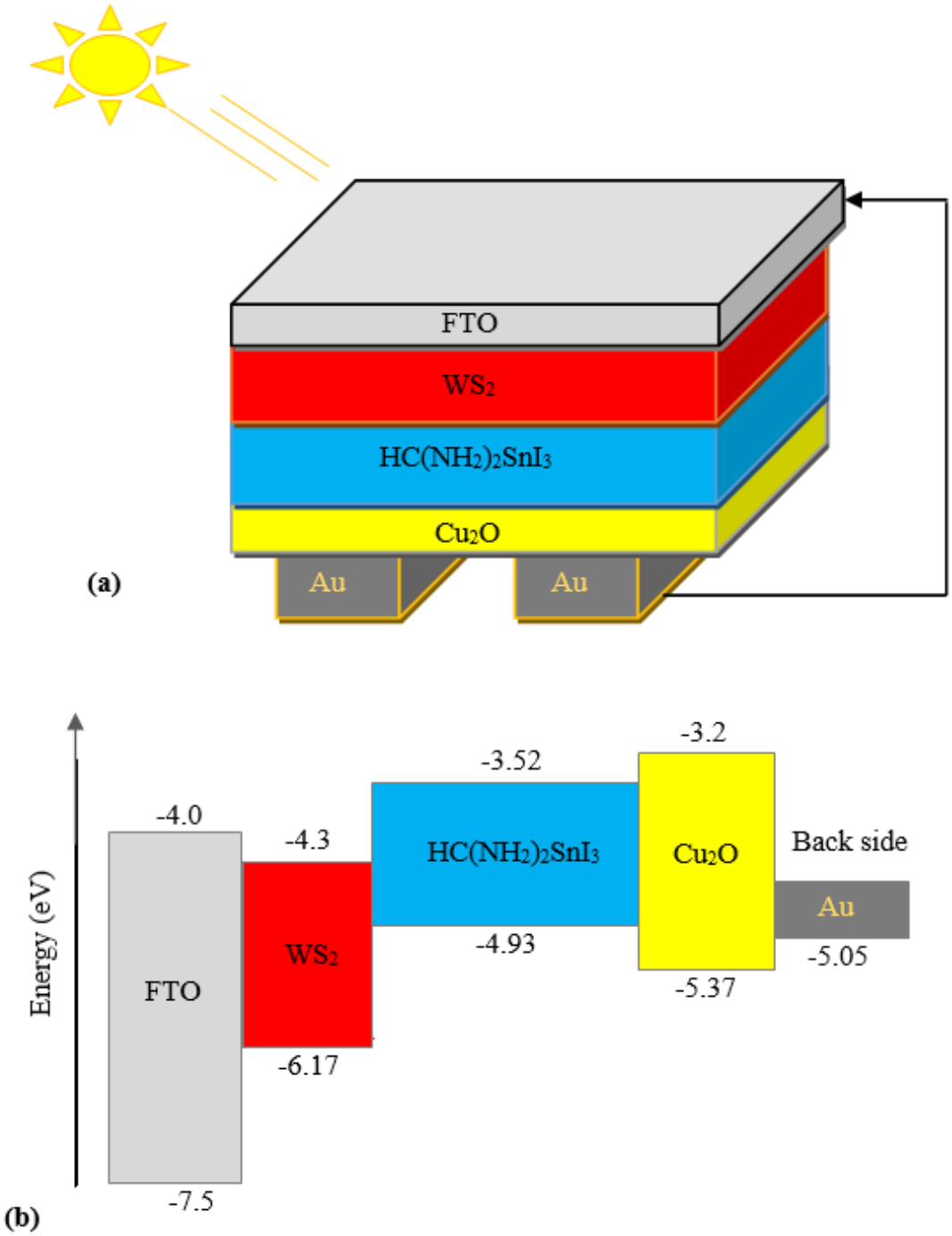


Figure 1.a) Primary device structure of the adopted PSC cell: FTO as window layer, WS_2 as ETL layer, $HC(NH_2)_2SnI_3$ perovskite as absorber, Cu_2O as HTL layer and Au as back contact. b) Corresponding energy band diagram.

The N part is the ETL layer, which in this case is tungsten disulfide WS_2, the I part is the absorber: the formamidinium tin iodide perovskite $HC(NH_2)_2SnI_3$ which can be denoted FASnI3, and the P part is the HTL layer which is copper(I) oxide Cu_2O. Tungsten disulfide was chosen as the ETL due to its inherent optoelectronic properties: band gap between 1.33 and 2.2 eV, high electron transport mobility (approximately 260 $cm^2\ V^{-1}\ s^{-1}$), and high transparency (Hankare et al., 2009). In addition, formamidinium tin iodide was also

-7.5

considered as an ideal absorber due to its good light absorption (band gap of 1.41 eV) and relatively high thermal stability (Amat et al., 2014). Copper(I) oxide was chosen as a representative of the inorganic HTL materials. This material (Cu_2O) exhibits better band alignment with perovskite, high hole mobilities (about 80 cm^2 V^{-1} s^{-1}) (Kanoun et al., 2019) and solution transformable and exhibits high optical transparency (Guo et al., 2017).

Ideally, when the device is under illumination, light is absorbed by the perovskite layer and electron-hole pairs, also called excitons, are generated. These charges move towards the electrodes by diffusion-controlled processes: at the ETL and perovskite layer boundary, electrons dissociate from holes and are transferred to the metal contact. Similarly, at the perovskite and HTL boundary, holes separate from electrons and are transferred by HTL to the back metal contact. It is important to emphasize that these processes have a significant impact on the PCE of the device (Rono et al., 2021; Yang et al., 2016).

Input Parameters of the Primary Device

The input parameters describing the adopted primary device FTO/WS_2/$HC(NH_2)_2SnI_3$/Cu_2O/Au were reported from recently published experimental and theoretical data. We give the thicknesses of each layer of the adopted configuration and these of electrical parameters in Table 1. The thermal velocities of holes and electrons were assumed constant and fixed at a value of 107 cm s^{-1}.

Table 1. Electrical parameters of the structure were adopted in Figure 1.a

Input parameter	FTO [a]	WS_2 (ETL)[b]	$HC(NH_2)_2SnI_3$ (absorbeur)[c]	Cu_2O (HTL)[a]
Thickness, $e(\mu m)$	0.04	2	0.8	0.05
Band gap, $E_g\,(eV)$	3.5	1.87	1.41	2.17
Affinity, $\chi(eV)$	4.0	4.3	3.52	3.2
Relative Dielectric permittivity, ε_r	9.0	11.9	8.2	7.11
CB effective density of states, $N_c(cm^{-3})$	2.2×10^{18}	1.0×10^{18}	1.0×10^{18}	2.02×10^{17}
VB effective density of states, $N_v(cm^{-3})$	1.8×10^{19}	2.4×10^{19}	1.0×10^{18}	1.1×10^{19}
Electron mobility, $\mu_e(cm^2V^{-1}s^{-1})$	20.0	260	22	200
hole mobility, $\mu_h(cm^2V^{-1}s^{-1})$	10.0	51	22	80
Density of n-type doping, $N_D(cm^{-3})$	1.0×10^{19}	1.1×10^{19}	0.0	0.0
Density of p-type doping, $N_A(cm^{-3})$	0.0	0.0	7.0×10^{16}	1.0×10^{18}
Density of defect, $N_t(cm^{-3})$	0.0	1.2×10^{11}	2.0×10^{15}	1.0×10^{14}

[a] (Kanoun et al., 2019)
[b] (Kumar & Singh, 2020)
[c] (Abdelaziz et al., 2020)

We note that the default solar irradiance integrated in the SCAPS-1D software is AM1.5G with an intensity of 100 mW cm^{-2} and the frequency is 106 Hz.

Basic Equations

The SCAPS-1D software (Burgelman et al. 2021**)** solves, numerically, the basic differential equations governing semiconductors in steady-state operation. It defines the physics of the modeled device, such as the recombination profile, electric field distribution, and current densities. The essential differential equations for semiconductors are Poisson's equation (1) and continuity equation for holes and electrons equation (2): (Sobayel et al., 2019).

$$\frac{d^2\psi}{dx^2} = \frac{e}{\varepsilon_0\varepsilon_r}\left[p(x) - n(x) + N_D - N_A + \rho_p - \rho_n\right] \quad (1)$$

Where ψ is electrostatic potential, n and p are electron and hole concentrations, ε_0 is vacuum and ε_r is relative permittivity, N_D and N_A are donor and acceptor doping density, ρ_n , ρ_p are electrons and holes distribution.

$$\frac{dJ_p}{dx} = \frac{dJ_n}{dx} = G - R \tag{2}$$

Where G is generation rate and R is recombination rate, J_p and J_n are holes and electron current densities. Carrier transport occurs according to the following drift and diffusion equations:

$$J_n = \mu_n n \frac{d\psi}{dx} + D_n \frac{dn}{dx} \tag{3}$$

$$J_p = \mu_p p \frac{d\psi}{dx} + D_p \frac{dp}{dx} \tag{4}$$

Results and Discussion

Effect of Temperature on Primary Structure

As a first step, we study the effect of temperature on the performance of the solar cell having the configuration: glass/FTO/WS_2/$HC(NH_2)_2SnI_3$/Cu_2O/Au, which we call the primary structure. We consider a wide temperature range from 250 to 600 K. We plot the I-V characteristic influenced by these temperatures in Figure 2.

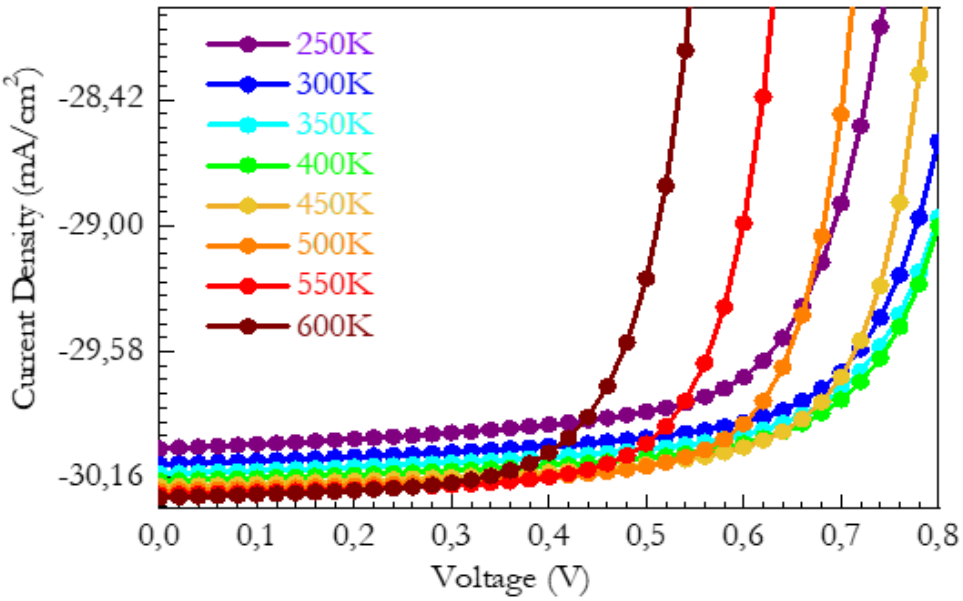


Figure 2. Variation of the current-voltage characteristic under the effect of temperature

The variations in the primary PSC performance parameters Voc, Jsc, FF, and PCE due to the temperature variation from 250 to 600 K are shown in Figure 3 (a-d) respectively. We note, through the analysis of the I-V characteristic curves obtained shown in Figure 2 and through the PV performances shown in Figure 3, that when the temperature increases from 250K to 350K, the current increases very slightly in an exponential manner and the open circuit voltage also increases. Whereas when the temperature increases from 350K to 600K, the current still increases in the same proportionality, but the open circuit voltage decreases considerably.

In terms of the grading: we can therefore say that under the effect of a temperature increase from 250K to 350K, the voltage of this primary cell gains 16.44 mV/K (or +0.53%) and it loses 9.66 mV/K (or –0.31%) beyond 350K (i.e., beyond 76.85°C). As for the current, it gains a slight intensity of approximately 6.10-4 mA/cm^2/K (or +0.002%). This can be explained by good light absorption. Unlike the behavior of the open-circuit voltage, the form factor decreases up to 350K and then increases considerably beyond this temperature value (see Figure 3-c). Regarding the PCE energy conversion efficiency of this primary cell, it increases by 0.022%/K when the temperature rises from 250K to 300K, then remains relatively constant from 300K to 389K and then decreases by 0.037%/K from 389K to 600K (see Figure 3-d). We also note that the maximum conversion efficiency of this primary cell is 23.24% at 389K.

From the results obtained, we can deduce that the solar cell based on the formamidinium tin iodide perovskite $FASnI_3$ designed as an absorber layer between the ETL layer, formed by tungsten disulfide WS_2, and the HTL layer formed by copper (I) oxide Cu_2O, represents high photovoltaic performances: High efficiency up to 389 K (115.85 °C) and the temperature increase by 1 K causes an efficiency decrease of only 0.037% (i.e. - 0.16% compared to the maximum efficiency) in the temperature range between 389 K and 600 K.

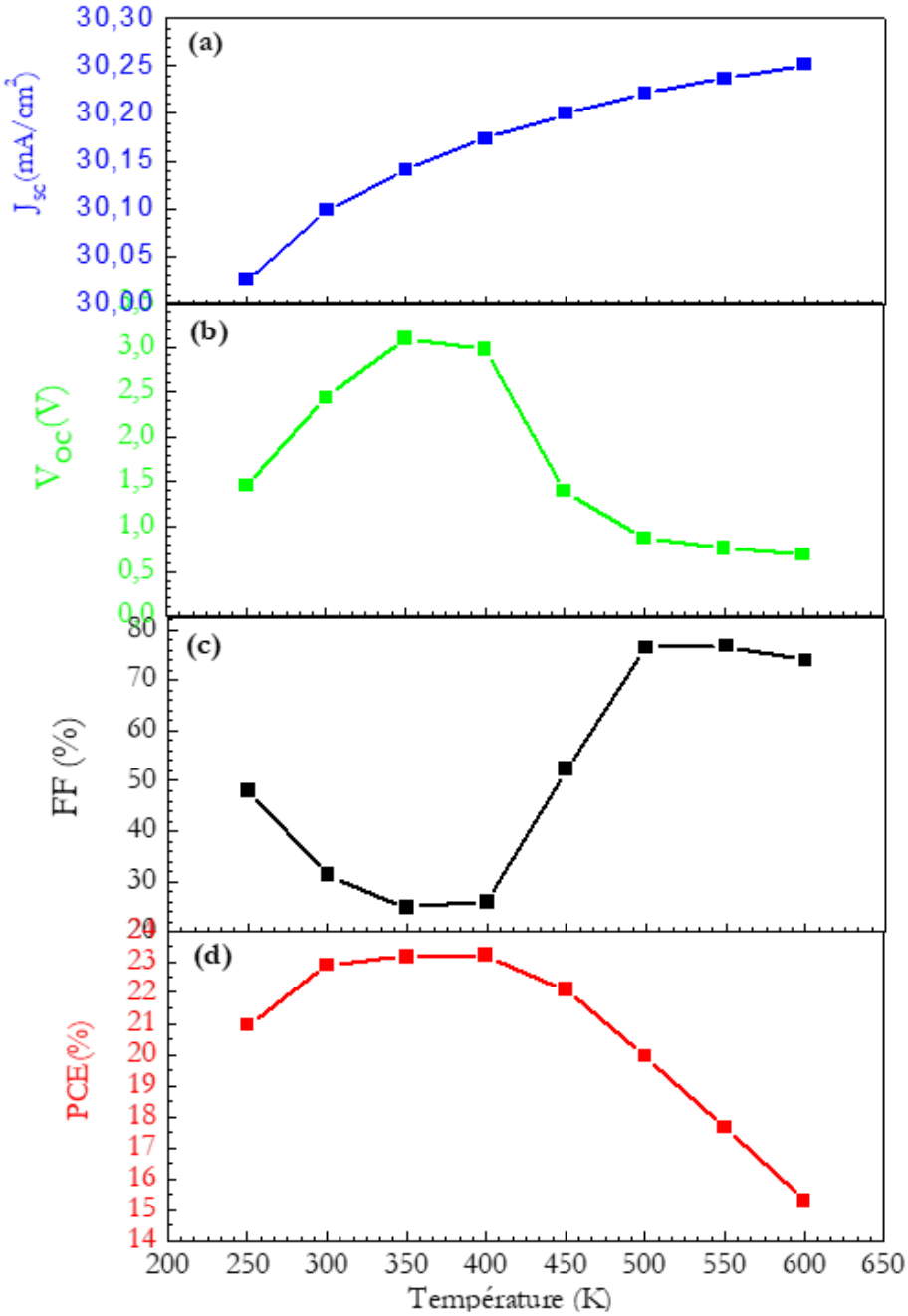


Figure 3. Variation of photovoltaic performance of the primary cell: FTO/WS_2/$HC(NH_2)_2SnI_3$/Cu_2O /Au, as a function of temperature: a) short-circuit current density, b) open-circuit voltage, c) form factor and d) efficiency.

Effect of Temperature on the Nature of the HTL Layer

In this part, we substitute the inorganic semiconductor Cu_2O of the HTL layer by 6 other materials, 3 of them are organic semiconductors: Spiro-OMeTAD, P3HT and D-PTTT-14, and 3 are inorganic semiconductors: CuSCN, MoO_3 and NiO (see Figure 4). We therefore study the effect of temperature on the 6 solar cells obtained based on these semiconductors. The input parameters describing these HTL layer materials are summarized in Table 2 (for organic and inorganic HTL layers):

Table 2. Input parameters of the different used HTL

Input parameter	Organic HTLs			Inorganic HTLs		
	Spiro-OMeTAD[a]	P3HT[d]	D-PBTTT-14[a]	CuSCN[d]	NiO[e]	MoO_3[f]
Thickness, $e(\mu m)$	1.0	0.05	0.003	0.05	0.05	0.05
Band gap, $E_g\ (eV)$	3.06	1.85	2.16	3.4	3.8	3
Affinity, $\chi(eV)$	2.05	3.1	3.2	1.9	1.46	2.5
Relative Dielectric permittivity, ε_r	3.0	3.4	10	10	10.7	12.5
CB effective density of states, $N_c(cm^{-3})$	2.8×10^{19}	1.0×10^{22}	2.8×10^{19}	1.7×10^{19}	2.8×10^{19}	2.2×10^{18}
VB effective density of states, $N_v(cm^{-3})$	1.0×10^{19}	1.0×10^{22}	1.0×10^{19}	2.5×10^{21}	10^{19}	1.8×10^{19}
Electron mobility, $\mu_e(cm^2V^{-1}s^{-1})$	1.0×10^{-4}	1.0×10^{-4}	2.83×10^{-3}	1.0×10^{-4}	12	25
hole mobility, $\mu_h(cm^2V^{-1}s^{-1})$	2.0×10^{-4}	1.0×10^{-3}	2.83×10^{-3}	1.0×10^{-1}	2.8	100
Density of n-type doping, $N_D(cm^{-3})$	0.0	0.0	0.0	0.0	0.0	0.0
Density of p-type doping, $N_A(cm^{-3})$	1.0×10^{18}	3.17×10^{13}	1.0×10^{18}	1.0×10^{18}	10^{18}	10^{18}
Density of defect, $N_t(cm^{-3})$	2.0×10^{14}	1.0×10^{14}	1.0×10^{14}	1.0×10^{14}	10^{15}	10^{15}

[a] (Kanoun et al., 2019)
[d](Azri et al., 2019)
[e] (Hossain,. et al 2015)
[f] (Li et al., 2019)

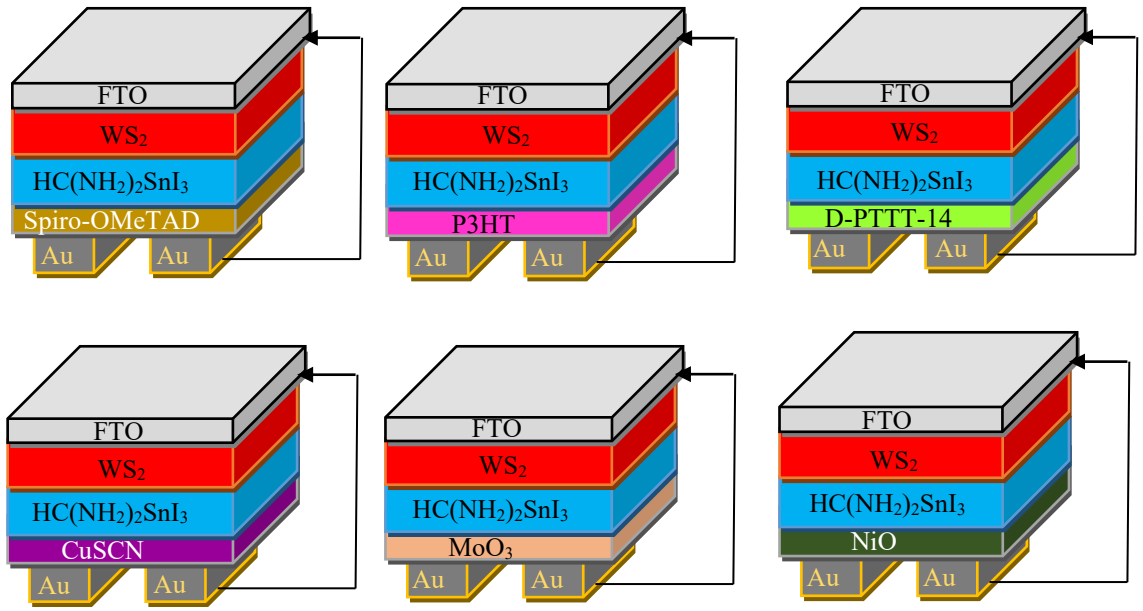


Figure 4. Structures of the (6) studied configurations in which the primary cell's HTL of Cu_2O of was replaced with Spiro-OMeTAD, P3HT, D-PTTT-14, CuSCN, MoO_3 and NiO.

We present the PV performances of the six cells studied in Figure 5 and we note the following points through the analysis of these performances:

- For the open circuit voltage, the behavior of the six (6) cells studied is similar to that of our primary solar cell based on Cu_2O, suitably to the relationship $V_{oc} = \frac{nK_B T}{q} \ln\left[\frac{I_{ph}}{I_s} + 1\right]$, but we notice that the value of this voltage is lower for the organic layers.
- The current density of the organic material D-PTTT-14 is completely different from that of other used materials.
- Unlike the behavior of the open-circuit voltage, the form factor decreases up to 350 K, increases up to 500 K, and then decreases again beyond this value, according to the relationship $FF = \frac{P_{max}}{I_{sc} \times V_{oc}}$, except for the D-PTTT-14-based HTL, which is different to the other layers.

For the performance we note that the behavior of HTL layers based on inorganic materials is identical to that of our studied cell based on Cu_2O, but this is not the case for organic HTL layers. We conclude that the three (3) cells based on inorganic materials have high performance compared to those based on organic materials. Table 3

summarizes the maximum efficiencies obtained for the seven cells studied. We also report at what temperature these efficiencies were achieved.

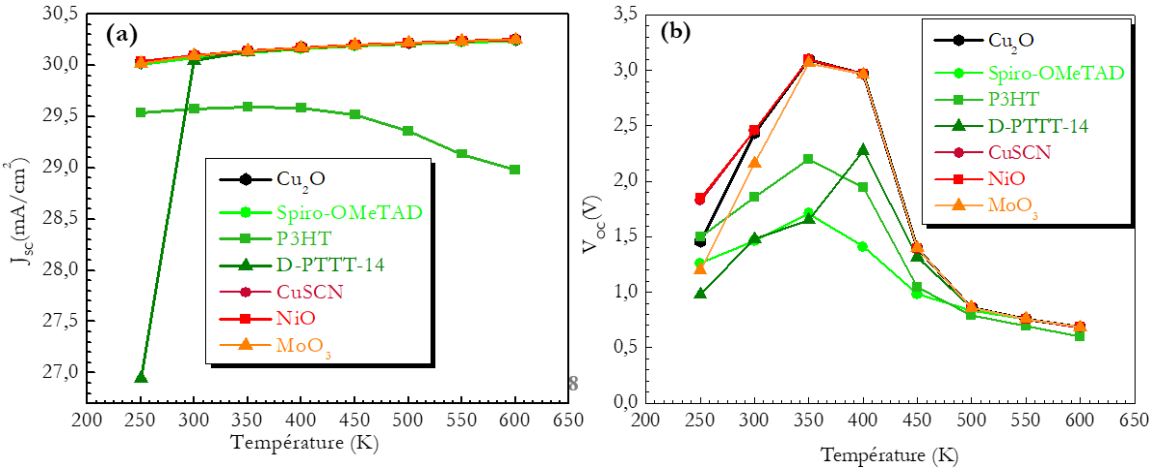


Figure 5. Effect of variation in the nature of the HTL layer as a function of temperature: a) Jsc, b) Voc, c) FF and d) PCE

Table 3. Maximum efficiency of the 7 studied cells consisting of Cu_2O, CuSCN, NiO, MoO_3, Spiro-OMeTAD, P3HT and D-PTTT-14 as HTLs and WS_2 as ETL.

Solar cells	Cu_2O	CuSCN	NiO	MoO_3	Spiro-OMeTAD	P3HT	D-PTTT-14
PCE (%)	23.24	23.24	23.24	23.23	21.75	22.05	22.85
Température (K)	389	387	388	390	373	373	405

We can conclude that these devices are resistant to high temperatures; they can therefore be used in very hot regions such as the Sahara, in hybrid photovoltaic-thermal sensors and even in space applications.

Effect of Back Contact Metal

In this section, we study, at room temperature (300K), the effect of the nature of the metal's back contact on the efficiency of our primary solar cell with the following structure: glass/FTO/WS_2/$HC(NH_2)_2SnI_3$/Cu_2O/Au. We therefore replace gold (Au) with other metals: platinum Pt, palladium Pd, nickel Ni, silver Ag, and copper Cu, and we determine the efficiency corresponding to each of these metals. To do this, we will need to introduce the work function values for these metals (see Table 4).

Table 4. Input parameter for different metals and corresponding PCE

Metal	Au	Pt	Pd	Ni	Ag	Cu
Work function (eV)	5.05	5.65	5.3	5.0	4.7	4.65
PCE (%)	22.89	22.89	22.89	22.89	19.06	17.72

Based on the results obtained (Table 4), we deduce that we can achieve the same efficiency as gold (Au) using the following metals: platinum (Pt), palladium (Pd), and nickel (Ni). To further minimize the cost of PSCs, it is therefore possible to use a contact metal that is less expensive than gold, such as platinum and nickel. If we are interested in moving towards healthy, clean energy, it is advisable to use platinum, given the toxicity of nickel.

Conclusion

In this paper, we analyzed the effect of temperature on the PV performance of a solar cell based on halogenated formamidinium tin iodide perovskite using the SCAPS-1D simulator. Six organic and inorganic semiconductor materials were inserted as a hole transport layer (HTL) in the primary cell FTO/WS_2/$HC(NH_2)_2SnI_3$/Cu_2O/Au, maintaining the primary electron transport layer (ETL). We also analyzed the effect of temperature on the six cells obtained based on these materials.

The simulation results show that the PCE energy conversion efficiencies of devices based on the inorganic materials Cu_2O, CuSCN, NiO, and MoO_3 are all similar (23.24%) and significantly higher than those based on the organic materials Spiro-OMeTAD, P3HT, and D-PTTT-14. This efficiency was achieved at 389K (115.85°C). Of course, cheaper and non-toxic metals such as Platinum can be used, in back contact, to replace gold, since they provide the same performance as the latter.

Scientific Ethics Declaration

* The authors declare that the scientific ethical and legal responsibility of this article published in EPSTEM journal belongs to the authors.

Conflict of Interest

* The authors declare that they have no conflicts of interest

Funding

* This research received no specific grant from any funding agency in the public, commercial, or not-for-profit sectors.

Acknowledgements or Notes

* This article was presented as an oral presentation at the International Conference on Technology, Engineering and Science (www.icontes.net) held in Antalya/Türkiye on November 12-15, 2025.

* The authors are thankful to Professor Marc Burgelman and his coworkers at the University of Ghent, Belgium, for providing the SCAPS-1D software used in this study.

References

Abdelaziz, S., Zekry, A., Shaker, A., & Abouelatta, M. (2020). Investigating the performance of formamidinium tin-based perovskite solar cell by SCAPS device simulation. *Optical Materials, 101*, 109738.

Amat, A., Mosconi, E., Ronca, E., Quarti, C., Umari, P., Nazeeruddin, M. K., & De Angelis, F. (2014). Cation-induced band-gap tuning in organohalide perovskites: Interplay of spin–orbit coupling and octahedra tilting. *Nano Letters, 14*(6), 3608-3616.

Ashrafi, S. S., Hossain, K., Ahmed, F., Hossain, A., & Rahman, O. (2020). Fabrication and characterization of graphene incorporated Cu based perovskite in application of perovskite solar cell under ambient condition. *Advances in Materials Physics and Chemistry, 10*(1), 1.

Azri, F., Meftah, A., Sengouga, N., & Meftah, A. (2019). Electron and hole transport layers optimization by numerical simulation of a perovskite solar cell. *Solar Energy, 181*, 372-378.

Boopathi, K. M., Karuppuswamy, P., Singh, A., Hanmandlu, C., Lin, L., Abbas, S. A., Chang, C. C., Wang, P. C., Li, G., & Chu, C. W. (2017). Solution-processable antimony-based light-absorbing materials beyond lead halide perovskites. *Journal of Materials Chemistry A, 5*, 20843-20850.

Burgelman, M., Decock, K., Niemegeers, A., Verschraegen, J., & Degrave, S. J. F. (2021). *SCAPS manual*.

Filip, M. R., Eperon, G. E., Snaith, H. J., & Giustino, F. (2014). Steric engineering of metal-halide perovskites with tunable optical band gaps. *Nature Communications, 5*(1), 19.

Guo, Y., Lei, H., Xiong, L., Li, B., Chen, Z., Wen, J., & Fang, G. (2017). Single phase, high hole mobility Cu2O films as an efficient and robust hole transporting layer for organic solar cells. *Journal of Materials Chemistry A, 5*(22), 11055-11062.

Hankare, P. P., Manikshete, A. H., Sathe, D. J., Chate, P. A., Patil, A. A., & Garadkar, K. M. (2009). WS2 thin films: Opto-electronic characterization. *Journal of Alloys and Compounds, 479*(1-2), 657-660.

Hao, F., Stoumpos, C. C., Cao, D. H., Chang, R. P., & Kanatzidis, M. G. (2014). Lead-free solid-state organic-inorganic halide perovskite solar cells. *Nature Photonics, 8*(6), 489-494.

Hao, F., Stoumpos, C. C., Guo, P., Zhou, N., Marks, T. J., Chang, R. P., & Kanatzidis, M. G. (2015). Solvent-mediated crystallization of CH3NH3SnI3 films for hetero junction depleted perovskite solar cells. *Journal of the American Chemical Society, 137*(35), 11445-11452.

Hossain, M. I., Alharbi, F. H., & Tabet, N. (2015). Copper oxide as inorganic hole transport material for lead halide perovskite based solar cells. *Solar Energy, 120*, 370-380.

Hu, W., He, X., Fang, Z., Lian, W., Shang, Y., Li, Y., & Yang, S. (2020). Bulk heterojunction gifts bismuth-based lead-free perovskite solar cells with record efficiency. *Nano Energy, 68*, 104362.

Jiang, X., Wang, F., Wei, Q., Li, H., Shang, Y., Zhou, W., & Ning, Z. (2020). Ultra-high open-circuit voltage of tin perovskite solar cells via an electron transporting layer design. *Nature Communications, 11*(1), 1-7.

Kamat, P. V., Bisquert, J., & Buriak, J. (2017). Lead-free perovskite solar cells. *ACS Energy Letters, 2*, 904-905.

Kanoun, A. A., Kanoun, M. B., Merad, A. E., & Goumri-Said, S. (2019). Toward development of high-performance perovskite solar cells based on CH3NH3GeI3 using computational approach. *Solar Energy, 182*, 237-244.

Kumar, M. H., Dharani, S., Leong, W. L., Boix, P. P., Prabhakar, R. R., Baikie, T., & Mathews, N. (2014). Lead-free halide perovskite solar cells with high photocurrents realized through vacancy modulation. *Advanced Materials, 26*(41), 7122-7127.

Kumar, S. S. (2020). Synthesis and characterization of lead free perovskite solar cells. *Materials Today: Proceedings, 26*, 2574-2579.

Kwak, J. I., Nam, S. H., Kim, L., & An, Y. J. (2020). Potential environmental risk of solar cells: Current knowledge and future challenges. *Journal of Hazardous Materials, 392*, 122297.

Lee, S. J., Shin, S. S., Kim, Y. C., Kim, D., Ahn, T. K., Noh, J. H., & Seok, S. I. (2016). Fabrication of efficient formamidinium tin iodide perovskite solar cells through SnF2–pyrazine complex. *Journal of the American Chemical Society, 138*(12), 3974-3977.

Li, G. R., & Xue, P. G. (2020). Low-cost counter-electrode materials for dye-sensitized and perovskite solar cells. *Advanced Materials, 32*(3), 1806478.

Li, W., Li, W., Feng, Y., & Yang, C. (2019). Numerical analysis of the back interface for high efficiency wide band gap chalcopyrite solar cells. *Solar Energy, 180*, 207-215.

Perl, E. E., Simon, J., Geisz, J. F., Lee, M. L., Friedman, D. J., & Steiner, M. A. (2016). Measurements and modeling of III-V solar cells at high temperatures up to 400 °C. *IEEE Journal of Photovoltaics, 6*(5), 1345-1352.

Qian, J., Xu, B., & Tian, W. (2016). A comprehensive theoretical study of halide perovskites ABX3. *Organic Electronics, 37*, 61-73.

Rono, N., Merad, A. E., Kibet, J. K., Martincigh, B. S., & Nyamori, V. O. (2021). Optimization of hole transport layer materials for a lead-free perovskite solar cell based on formamidinium tin iodide. *Energy Technology, 9*(12), 2100859.

Rono, N., Merad, A. E., Kibet, J. K., Martincigh, B. S., & Nyamori, V. O. (2021). A theoretical investigation of the effect of the hole and electron transport materials on the performance of a lead-free perovskite solar cell based on CH3NH3SnI3. *Journal of Computational Electronics, 20*(2), 993-1005.

Snaith, H. J. (2013). Perovskites: The emergence of a new era for low-cost, high-efficiency solar cells. *The Journal of Physical Chemistry Letters, 4*(21), 3623-3630.

Sobayel, K., Akhtaruzzaman, M., Rahman, K. S., Ferdaous, M. T., Al-Mutairi, Z. A., Alharbi, H. F., & Amin, N. (2019). A comprehensive defect study of tungsten disulfide (WS2) as electron transport layer in perovskite solar cells by numerical simulation. *Results in Physics, 12*, 1097-1103.

Sutton, R. J., Eperon, G. E., Miranda, L., Parrott, E. S., Kamino, B. A., Patel, J. B., & Snaith, H. J. (2016). Bandgap-tunable cesium lead halide perovskites with high thermal stability for efficient solar cells. *Advanced Energy Materials, 6*(8), 1502458.

Wang, Z., Lin, Q., Chmiel, F. P., Sakai, N., Herz, L. M., & Snaith, H. J. (2016). Efficient ambient-air-stable solar cells with 2D–3D heterostructured butylammonium-caesium-formamidinium lead halide perovskites. *Nature Energy, 2*(9), 1-10.

Wu, B., Zhou, Y., Xing, G., Xu, Q., Garces, H. F., Solanki, A., & Sum, T. C. (2017). Long minority-carrier diffusion length and low surface-recombination velocity in inorganic lead-free CsSnI3 perovskite crystal for solar cells. *Advanced Functional Materials, 27*(7), 1604818.

Yang, G., Tao, H., Qin, P., Ke, W., & Fang, G. (2016). Recent progress in electron transport layers for efficient perovskite solar cells. *Journal of Materials Chemistry A, 4*(11), 3970-3990.

Zhang, H., Lu, Y., Han, W., Zhu, J., Zhang, Y., & Huang, W. (2020). Solar energy conversion and utilization: Towards the emerging photo-electrochemical devices based on perovskite photovoltaics. *Chemical Engineering Journal, 393*, 124766.

Zhao, Z., Gu, F., Li, Y., Sun, W., Ye, S., Rao, H., & Huang, C. (2017). Mixed-organic-cation tin iodide for lead-free perovskite solar cells with an efficiency of 8.12%. *Advanced Science, 4*(11), 1700204.

Zhumekenov, A. A., Saidaminov, M. I., Haque, M. A., Alarousu, E., Sarmah, S. P., Murali, B., & Bakr, O. M. (2016). Formamidinium lead halide perovskite crystals with unprecedented long carrier dynamics and diffusion length. *ACS Energy Letters, 1*(1), 32–37.

Author(s) Information

Souheyla Mamoun
University of Abou Bekr Belkaid, Faculty of Sciences, Solid State Physics Team, Theoretical Physics Laboratory, Box 119, 13000, Tlemcen, Algeria
Contact e-mail: *souhila.mamoun@univ-tlemcen.dz*

Abdelkrim Elhasnaine Merad
University of Abou Bekr Belkaid, Faculty of Sciences, Solid State Physics Team, Theoretical Physics Laboratory, Box 119, 13000, Tlemcen, Algeria.

Feriel Saidi
University of Abou Bekr Belkaid, Faculty of Sciences, Solid State Physics Team, Theoretical Physics Laboratory, Box 119, 13000, Tlemcen, Algeria

To cite this article:

Mamoun, S., Merad, A. E., & Saidi, F. (2025). Engineering next generation hole transport layers for lead free perovskite solar cells exceeding 23% power conversion efficiency. *The Eurasia Proceedings of Science, Technology, Engineering and Mathematics (EPSTEM), 38,* 630-640.

The Eurasia Proceedings of Science, Technology, Engineering & Mathematics (EPSTEM)
ISSN: 2602-3199

The Eurasia Proceedings of Science, Technology, Engineering and Mathematics (EPSTEM), 2025

Volume 38, Pages 641-654

IConTES 2025: International Conference on Technology, Engineering and Science

Energy Audit of a Community Center

Slav Valchev
University of Food Technologies

Nikola Valchanov
University of Food Technologies

Abstract: The aim of the study is to conduct an energy audit of the cultural center and museum at a community center in town of Mizia, Bulgaria. This audit includes a detailed analysis of existing condition of the building, as well as the energy systems used - heating, lighting and cooling. Energy-saving measures have been proposed such as installing thermal insulation on buildings' enclosing structures, replacing windows and doors in the building, installing high-efficiency VRF air conditioning systems, replacing old lighting fixtures with high-efficiency ones, installing a PV system for generating electricity. The total energy savings from the measures amount to 89273 kWh/year of electrical energy, with the environmental equivalent of the energy savings amounting to 51.64 t CO_2/year. After the audit, the building falls into class "B" on energy consumption scale. After implementing the prescribed energy savings measures, it can be summarized that it will meet energy consumption class "A" on the energy consumption scale.

Keywords: Energy audit, Energy efficiency, Energy-saving measures

Introduction

Energy efficiency is one of the main priorities of modern society, playing a crucial role not only in reducing energy costs, but also in sustainable development, environmental protection and reducing carbon emissions. In light of global efforts to tackle climate change and achieve sustainable development goals, improving energy efficiency in public and cultural buildings such as community centers is becoming increasingly necessary (Capehart et al., 2012; Doty, 2016; Kreith & Goswami, 2007). Community centers are institutions that play an important role in preserving cultural and social values, organizing significant social events and providing spaces for cultural events and education. Despite their importance, they often lack the necessary resources to modernize buildings and optimize their energy efficiency. Such a survey is essential not only for reducing energy costs and ensuring better comfort for visitors and employees of the cultural center and museum, but also for creating an example for other cultural and public institutions in the region. This study will contribute to the sustainable management of energy resources and will provide important guidelines for future improvements in other community centers and cultural sites. In addition, the results of the energy survey will have broad applicability, as they can serve as a basis for future research and practices to improve energy efficiency in public buildings, which is an important stage in the efforts to reduce energy dependence and environmental impact (Rasheva, 2011).

Energy efficiency is a set of measures and activities aimed at achieving optimal energy use in order to reduce costs, improve comfort and reduce carbon emissions. In Bulgaria, as a member state of the European Union, improving energy efficiency is not only an environmental necessity, but also an economic priority. The energy audit, defined in the Energy Efficiency Act, is a systematic analysis of the condition of a building and its energy systems. It identifies potential weaknesses and proposes specific measures for improvement (Directive 2002/91/EC; Directive 2006/32/EC; Energy Law; Energy Efficiency Act; Ordinance No.RD-02-20-3;

- This is an Open Access article distributed under the terms of the Creative Commons Attribution-Noncommercial 4.0 Unported License, permitting all non-commercial use, distribution, and reproduction in any medium, provided the original work is properly cited.

- Selection and peer-review under responsibility of the Organizing Committee of the Conference

© 2025 Published by ISRES Publishing: www.isres.org

Ordinance No.E-RD-04-2/2022; Ordinance No.E-RD-04-1/2018; Ordinance No.E-RD-04-01/2022; Ordinance No.5; Ordinance No.15). Literature sources emphasize that the energy efficiency of buildings can be increased by implementing measures such as:

- Improving thermal insulation.
- Replacing window frames.
- Installing highly efficient heating and ventilation systems.
- Implementing intelligent energy management systems (Iliev et.al., 2024; Shapiro, 2016; Thuman & Younger; 2008; Turner, 1997).

Method

This paper focuses on energy audit of a cultural center and museum of a community center in the city of Mizia. The object of the study was chosen due to the existence of two important aspects – the cultural center as a social and cultural center of the community and the museum, which preserves part of the cultural heritage of the region. The existence of such buildings with different functions leads to significant energy consumption, mainly due to the need for heating, lighting and air conditioning of the different spaces. Despite their importance, these institutions often do not have the necessary resources to renovate the buildings and energy systems, which leads to unnecessarily high energy costs and possible inconvenience for visitors and employees.

This audit will include a detailed analysis of the existing condition of the building, as well as the energy systems used – heating, domestic hot water (DHW) system, ventilation, lighting and cooling. Based on the survey, the main problems and weaknesses in energy efficiency of the building will be identified and specific energy saving measures will be proposed to optimize energy consumption. This may include both technical solutions such as installing energy-efficient lighting, high-efficiency heating appliances and improving the building's insulation, as well as organizational approaches such as optimizing heating and lighting schedules. The energy efficiency audit is compiled based on a thorough analysis of both the energy and thermo-physical characteristics of the building. The survey process includes not only collecting data on energy consumption but also analyzing the condition of building elements that affect energy efficiency.

- The analysis of the condition of the building is a fundamental stage in the energy efficiency survey. It includes various subcategories that cover both the climatic conditions and thermo-physical characteristics of the building.
- Climatic conditions are an important factor in assessing the energy efficiency of the building. They directly affect energy consumption for heating and cooling. Among the main climatic data that are taken into account are temperature amplitudes, humidity, as well as other meteorological characteristics that can affect energy efficiency.
- A description of the site includes data on the location and purpose of the building, as well as general functional and operational characteristics.
- The main construction characteristics of the building include the materials of the building envelope, insulation and cladding. These factors determine how well the building retains heat and whether there is a need for improvements in thermal insulation. Enclosing elements such as walls, windows and roofs play a key role in energy efficiency. The analysis process includes calculations of heat losses that can be reduced by improving the insulation characteristics. Emphasis is placed on the use of modern materials and technologies that reduce heat losses and prevent cold penetration.
- Heating, cooling and ventilation of the building are major energy consumers in buildings. Their analysis includes the efficiency of heating installations, as well as the possibilities for optimizing consumption by modernizing existing systems and implementing new technologies for indoor temperature control and ventilation. Possibilities for using renewable energy sources such as solar panels and heat pumps are also considered in this context.
- Electrical installation - this part of the report analyzes the main electrical installations in the building. This includes existing lighting fixtures, electrical appliances used and the possibilities for replacing inefficient solutions with more energy-efficient technologies. The use of LED lighting and other modern solutions is a main focus of the energy audit.
- The building model study involves the use of simulation programs and software that allow for the calculation of energy losses and optimization of building energy costs. These simulations can include both winter and summer conditions in order to predict maximum energy savings. For this study a simulation software EECalc-Version 1.0.0.10201 is used.
- Energy-saving measures (ESM) for the project - this section of the report presents recommendations for energy saving measures that can be implemented in the building. This includes both improvements in thermal insulation

and changes in heating and lighting installations that will lead to significant energy savings. For this study simulation software PV Syst- Version 7.4.6 is used.
- The conclusion summarizes the results of the audit and highlights the main recommendations for improving the energy efficiency of the building. The goal is to achieve not only a reduction in energy costs, but also to improve the internal comfort of the building's occupants. All energy-saving measures have a positive ecological effect, which is characterized by saved carbon emissions into the environment.

The recommendations propose specific actions for implementing energy-saving measures that will provide long-term benefits for the building. These may include investments in new technologies as well as optimization of existing installations.

Results and Discussion

Situation Analysis

Basic Climatic Data for the Area

According to the climatic zoning of the Republic of Bulgaria, the town of Mizia belongs to Climate Zone 3, which is characterized by the following climatic features:

- Duration of the heating season is 175 days; start: October 23; end: April 15;
- Heating degree days DD = 2600 at an average temperature in the building of 19 ºC
- Calculated outdoor temperature: - 17 ºC
- Altitude of the site 54 meters

Climatic zones in Republic of Bulgaria are shown on Figure 1. The measured average monthly outdoor air temperatures for the settlement for the period 2021 - 2023, according to data from the National Institute of Meteorology and Hydrology at the Bulgarian Academy of Sciences, as well as representative average monthly outdoor air temperatures for Climate zone 3, were used as basic climate data.

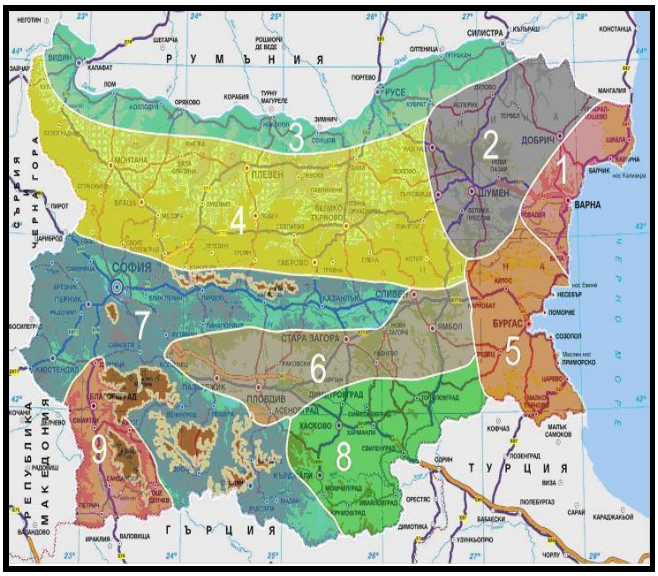


Figure 1. Climatic zones in Republic of Bulgaria

Description of the Object

The building is a collection of several sections with different storeys, which are functionally interconnected. The roof structure is designed with a flat roof without an air gap, with only the area above the audience hall identifying an under-roof space. The window frames have been completely replaced with PVC frames and double glazing. Measures to increase energy efficiency have been implemented on the facade, basement and roof. General data about the building are presented in Table 1. Exterior facades of the building are shown on Figure 2.

Table 1. General data about the building

Building (name)		Cultural Center and Museum at the "Prosveta 1915" Community Center, Mizia	
Address		Mizia, 18A Georgi Dimitrov Street	
Building type		Massive	
Ownership		Municipal	
Year of construction		1973	
Number of residents + Staff		15+36	
Residents schedule hour/day		Heating schedule hour/day	
Weekdays, hour/day	8	Weekdays, hour/day	8
Saturday, hour/day	8	Saturday, hour/day	8
Sunday, hour/day	8	Sunday, hour/day	8



a) North-east (NE)



b) North-west (NW)



c) South-east (SE)



b) South-west (SW)

Figure 2. Exterior facades of the building

General Construction Characteristics

Data for area and heated volume of the building are presented in Table 2.

Table 2. Area and heated volume of the building

Built-up area, m^2	Surveyable area, m^2	Heated area, m^2	Heated volume, gross, m^3	Heated volume, net, m^3
1 820	3 591	2 489	13 383	10 706

Analysis of the Enclosing Elements

The main enclosing walls of the structure are made of brick walls. Some of them are thermally insulated with external thermal insulation of expanded polystyrene foam with a thickness of 100 mm. On the southwest facade, part of the enclosure is finished with limestone slabs. The basement walls are made of monolithic reinforced concrete with a thickness of 400 mm. The building's windows were replaced more than 10 years ago. There are failures in the opening parts, as well as damaged and missing seals, which is why there is serious infiltration. All windows and doors are equipped with standard white-white glazing. General data about enclosing elements of the building are presented in Table 3.

Table 3. General data about enclosing elements of the building

Type	Facades - celestial orientation			
	NE	NW	SW	SE
Area, m^2 Type 1 - brickwork 380 mm	146.84	124.29	110.28	91.18
U, W/m²K	1.57	1.57	1.57	1.57
Area, m^2 Type 2 - brickwork 380 mm + thermal insulation	244.78	432.87	207.57	333.65
U, W/m²K	0.30	0.30	0.30	0.30
Area, m^2 Type 3 - brickwork 380 mm + overlay	0.00	5.16	51.14	5.16
U, W/m²K	1.51	1.51	1.51	1.51
Area, m^2 Type 4 - brickwork 250 mm + thermal insulation	4.00	9.84	4.65	9.84
U, W/m²K	0.31	0.31	0.31	0.31
Area, m^2 Type 5 - reinforced concrete 400 mm	72.63	47.36	11.24	50.75
Area, m^2 Type 1 Door with PVC frame and thermal panel /old/	0.00	2.00	0.00	0.00
U, W/m²K (g = 0.47)	-	2.40	-	-
Area, m^2 Type 2 Door with PVC frame and 50% thermal panel + 50% glass /old/	0.00	2.80	0.00	0.00
U, W/m²K (g = 0.23)	-	2.40	-	-
Area, m^2 Type 3 Window with PVC frame and thermal panel /old/	0.00	2.66	0.00	0.00
U, W/m²K (g = 0.47)	-	2.40	-	-
Area, m^2 Type 4 Window with PVC frame and double glazing /old/	13.57	3.94	0.00	4.00
U, W/m²K (g = 0.47)	2.40	2.40	-	2.40
Area, m^2 Type 5 Window with PVC frame and double glazing /old/	103.30	64.97	111.32	193.07
U, W/m²K (g = 0.47)	2.40	2.40	2.40	2.40
Area, m^2 Type 1 Floor on unheated basement	256.31			
U, W/m²K	0.40			
Area, m^2 Type 2 Floor on unheated basement	99.96			
U, W/m²K	0.37			
Area, m^2 Type 3 Floor on unheated basement	508.50			
U, W/m²K	0.36			
Area, m^2 Type 4 Floor to outside air	23.16			
U, W/m²K	0.33			
Area, m^2 Type 5 Floor to ground	955.31			
U, W/m²K	0.33			
Area, m^2 Type 1 Flat "warm" roof	1146.20			
U, W/m²K	0.26			
Area, m^2 Type 1 Flat "warm" roof	1146.20			
U, W/m²K	0.26			
Area, m^2 Type 2 Flat "warm" roof	140.44			
U, W/m²K	0.26			
Area, m^2 Type 3 Flat roof with air gap	541.70			
U, W/m²K	0.27			

Heating, Domestic Hot Water, Ventilation and Air Conditioning of the Building

The heating of the building is carried out locally, through electrical appliances. The heating is carried out with individual air conditioners, fan convectors and electric heaters. A large part of the premises are not heated. Electrical appliances for heating of the building are shown on Figure 3.



Figure 3. Electrical appliances for heating of the building

The building has six air conditioners, one electric heater, six fan coils and one electric radiator. Air conditioning systems are used for both heating and cooling the rooms in the building. The air conditioners and conventional electrical appliances are low efficiency and need to be replaced. In Table 4 are shown general data for annual electrical energy consumption for heating.

Table 4. General data for annual electrical energy consumption for heating

Heating	Quantity	Installed power, W	Working hours per year	Simult. Coefficient, -	Load factor, -	Annual consumption, kWh/y
Air Conditioner 12000Btu/hr	6	1150	2000	0.25	1	3450
Radiator	1	4000	900	0.15	1	540
Fan Coil	6	2000	1500	0.15	1	2700
Electric Radiator	1	2000	1500	0.15	1	450
Total:						7140
Heated area, m^2	Installed power, W	$P_{work,}$ kW	Usability, hours per week		P simult, W/m^2	
2 489.00	24900	4.43	18.35		1.78	

DHW in the building is provided year-round by one instantaneous and one volumetric electric boiler. The reference value for the specific amount of hot water for sanitary and domestic purposes in the building is calculated according to Appendix No.3 to Regulation No. 4/2005 on the design, construction and operation of building, water supply and sewage installations according to the norms for administrative buildings - standard hot water consumption 5 liters per employee, norms for theaters for 120 seats (spectators) - 5 liters per spectator and norm for artists - 25 liters per artist. In Table 5 are shown general data for consumption of hot water in the building.

Table 5. General data for consumption of hot water in the building

Average daily consumption by benchmark	Value for office	Value for spectators in theaters	Value for artists in theaters
Norm, l/day	5	5	25
Indicator, number of residents with standardized consumption	51	600	5
Coefficient for uneven load	0.1	0.01	0.1
Temperature of heated water, t˚C	55	55	55
Temperature of drawn water, t˚C	37.5	37.5	37.5
Temperature of cold water, t˚C	10	10	10
Heated area, m^2	2489	2489	2489
Working days (shifts)	261	261	261
Total, l/m^2 per year of heated water	1.34	3	1
Total, l/m^2 per year of mixed water	2.2	5	1

Table 6. General data for annual electrical energy consumption for DHW

Domestic Hot Water (DHW)	Quantity	Installed power, W	Working hours per year	Simult. Coefficient, -	Load factor, -	Annual consumption, kWh/y
Instantaneous water heater	1	2500	250	0.15	1.00	94
Volume water heater	1	3000	250	0.25	1.00	188
Total:						281
Heated area, m^2	Installed power, W	$P_{work,}$ kW	Usability, hours per week		P simult, W/m^2	
2 489.00	5500	1.13	8.35		0.45	

In Table 6 are shown general data for annual electrical energy consumption for DHW. There are no ventilation installations in the building.

Electrical Installation and Consumers

Table 7. General data for electrical consumers affecting heat balance

Consumers affecting the balance	Quantity	Installed power, W	Working hours per year	Simult. Coefficient -	Load factor -	Annual consumption, kWh/y
Laptop	1	65	1200	0.25	1.00	20
Computer system	12	300	2000	0.45	1.00	3240
Printer	1	250	350	0.05	1.00	4
Refrigerator	1	120	8760	0.25	1.00	263
Coffee maker	1	1500	150	0.05	1.00	11
Scanner	1	35	150	0.15	1.00	1
Microwave oven	2	900	150	0.15	1.00	41
Multimedia	1	350	360	0.15	1.00	19
Refrigerated display case	1	150	8760	0.25	1.00	329
Television	1	120	1800	0.50	1.00	108
Sound system	1	300	350	0.25	1.00	26
Total:						4061
Heated area, m^2	Installed power, W	$P_{work,}$ kW	Usability, hours per week			P simult, W/m^2
2 489.00	8290	2.25	34.01			0.91

Table 8. General data for electrical consumers non affecting heat balance

Consumers non affecting the balance	Quantity	Installed power, W	Working hours per year	Simult. Coefficient, -	Load factor, -	Annual consumption, kWh/y
Lighting fixture unheated volume	24	60	250	0.10	1.00	36
Air conditioner 12000 Btu/h	6	1150	450	0.065	1.00	202
Outdoor lighting	8	150	900	0.10	1.00	108
Outdoor lighting	2	8	900	0.10	1.00	1
Total:						347
Heated area, m^2	Installed power, W	$P_{work,}$ kW	Usability, hours per week		P simult, W/m^2	
2 489.00	9556	0.71	9.50		0.29	

The facility is supplied with electricity with a three-phase voltage of 400/230 V from an existing steel pole of an overhead power distribution network of "Elektrorazpredelenie Zapad" Ltd to the facade of the building with a power cable 4x35 mm^2. The measurement of the electricity consumed in the building is carried out by 2 electricity meters installed in main distribution board (MDB), located on property boundary wall. MDB, using power cables of type 4x10mm^2, supplies power to the MDB of the library block with the small hall, the MDB of the cinema hall with the ritual hall and the municipal club-disco. The technical condition of the MDB is good. In Table 7 are shown general data and annual consumption for electrical consumers affecting heat balance. In Table 8 are shown general data and annual consumption for electrical consumers non affecting heat balance (this includes air-conditioners, operating in cooling mode).

The lighting installation throughout the building dates from the time of its construction. It is equipped with 2x1.5mm^2 cables. The lighting fixtures in the cinema are wall lamps with incandescent lamps, in places they have been replaced with LED bulbs with missing protective glass. There are exposed cables and wires and missing wall lamps. The lighting fixtures in the hall next to the cinema are square ceiling lamps and date from the time of the construction of the building. There are exposed junction boxes with missing protective caps and unsecured electrical connections. In the cinema above the exit doors, there are evacuation lights with fluorescent lamps installed. They do not function; their batteries are damaged. The lighting fixtures on the second floor in the cinema are old type pendant lamps with incandescent lamps, with open sockets and with broken protective glass. Open sockets with incandescent lamps light bulbs are installed on the walls. The lighting fixtures in the warehouses are incandescent lamps ceiling lamps with missing protective glass. The stage lighting is implemented with spotlights, which are old and energy inefficient.

Table 9. General data for lighting fixtures in the building

Lighting	Quantity	Installed power, W	Working hours per year	Simult. Coefficient, -	Load factor, -	Annual consumption, kWh/y
Luminiscent lamp 4x18W	5	72	1200	0.25	1.00	108
Luminiscent lamp 2x42	15	84	1200	0.25	1.00	378
Luminiscent lamp 2x18	10	36	1200	0.25	1.00	108
Lamp LED bulb	41	9	1200	0.25	1.00	111
Lamp incandescent	35	60	900	0.30	1.00	567
Stage spotlights	4	250	350	0.25	1.00	88
Lamp incandescent (missing)	65	60	900	0.00	1.00	0
Total:						1359
Heated area, m^2	Installed power, W	$P_{work,}$ kW	Usability, hours per week		P simult, W/m^2	
2 489.00	9349	1.47	18.35		0.59	

The lighting fixtures in the library block and the municipal club are 2x36W fluorescent lamps and pendant lamps with open sockets with incandescent lamps. In the inner courtyard of the building, park lighting fixtures of the "globe" incandescent lamps have been installed. In the ritual hall and in the entrance lobby, the lighting fixtures are chandeliers with incandescent lamps. There are open junction boxes with missing protective caps. Additionally, power cables have been laid in PVC cable ducts. In the toilets, the lighting is implemented everywhere with LNC incandescent ceiling lamps and wall lamps. In the basement of the library block, the lighting is depreciated. The lighting control everywhere is carried out by electric switches mounted on the walls at a height of 1.3m from the floor. They are old from the time the building was built, broken and in places missing. The lighting control for the stage is carried out by the local switchboard on the second floor in the technical room by means of electric switches. In Table 9 are shown general data for lighting fixtures in the building. Data on the building's electricity consumption for the period 2021-2023 were requested. The building's electricity consumption data for 2021 and 2022 were deemed irrelevant due to the fact that the building was not visited in connection with the global COVID-19 pandemic. The distribution of electrical energy consumed for 2023, taken as the reference year, is shown on Figure 4.

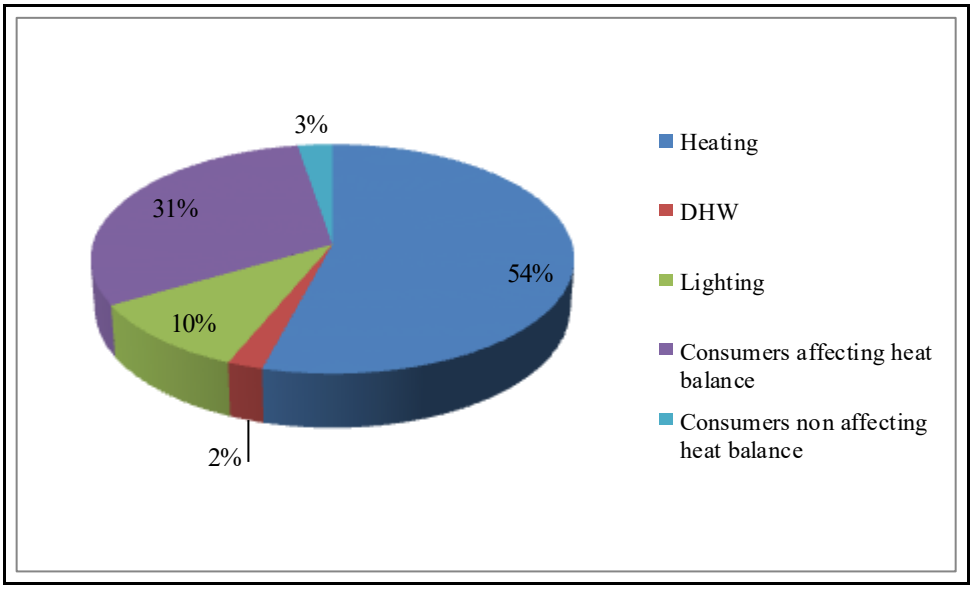


Figure 4. Distribution of electrical energy consumed for reference year 2023

Data for average monthly outdoor air temperature, heating DD, and electricity costs for 2023 in kWh/month and ₤+VAT are shown in Table 10. Average price for 1 kWh of electricity is 0.2219 ₤ +VAT.

Table 10. Data for average monthly outdoor air temperature, heating DD, and electricity costs for 2023

Month	Number of days in month	Average monthly outdoor air temperature		Electrical energy 2023	
		°C	DD	kWh/month	₤+VAT
1	31	4.4	452.6	1408	312.44
2	28	4.5	406.0	1501	333.07
3	31	8.3	331.7	1317	292.24
4	15	10.8	123.0	1152	255.63
5	-	-	0	908	201.48
6	-	-	0	712	157.99
7	-	-	0	802	177.97
8	-	-	0	824	182.85
9	-	-	0	701	155.55
10	9	15.3	33.3	948	210.36
11	30	8.3	321.0	1215	269.61
12	31	5.1	430.9	1700	377.23
Total:			2098.5	13188	2926.43

Model Study of the Building

The model study of the building is carried out using the software product EECalc-1.0.0.1201. The purpose of the model study is to obtain the values of the actually required energy to maintain the microclimate in the building, compared to the reference energy consumption, determine possible energy saving measures and issue an energy efficiency certificate in the presence of the conditions provided for in the regulatory framework. The software has entered areas and heat transfer coefficients of the building's enclosing structures, as well as specific energy costs for heating, DHW, lighting, etc. The reference energy consumption of the building has been calculated, after which the building model has been calibrated and normalized using the software. The results for energy costs for current state and normalized state of the building are shown on Figure 5.

Потребна енергия

Енергия за:	Реф. с-ти 1 kWh/m²	Реф. с-ти 2 kWh/m²	Текущо състояние kWh/m²	Текущо състояние kWh/year	Нормализирано със. kWh/m²	Нормализирано със. kWh/year	След ECM kWh/m²	След ECM kWh/year	в т.ч. ЕВИ kWh/year	Общо ЕВИ kWh/year
Отопление			3.467	8 629.011	50.911	126 717.793	50.911	126 717.793	0	123 676.566
Охлаждане			0	0	0	0	0	0	0	0
Вентилация (отопление)			0	0	0	0	0	0	0	0
Вентилация (охлаждане)			0	0	0	0	0	0	0	0
БГВ			0.110	274.845	0.385	957.968	0.385	957.968	0	0
БГВ(Помпи)			0	0	0	0	0	0	0	0
Помпи и вентилатори			0	0	0	0	0	0	0	0
Осветление			0.532	1 324.358	0.967	2 406.877	0.967	2 406.877	0	0
Уреди влияещи на топлинния баланс			1.646	4 097.468	1.646	4 097.468	1.646	4 097.468	0	0
Уреди невлияещи на топлинния баланс			0.139	345.799	0.139	345.799	0.139	345.799	0	0
Други			0	0	0	0	0	0	0	0
Общо			5.895	14 671.481	54.048	134 525.905	54.048	134 525.905	0	123 676.566

Разпределение на потребната енергия по енергийни ресурси

Енергиен ресурс	Реф. стойности 1 kWh/m²	Реф. стойности 2 kWh/m²	Текущо състояние, kWh/m²	Нормализирано състояние, kWh/m²	След ECM kWh/m²
Електричество			5.895	54.048	54.048
Природен газ			0	0	0
Пропан-бутан			0	0	0
Черни каменни въглища			0	0	0
Лигнитни/кафяви каменни въглища			0	0	0
Дървени пелети, брикети и дърва			0	0	0
Брикети			0	0	0
Промишлен газьол, петрол и дизел			0	0	0
Централизирано топлоснабдяване			0	0	0
Мазут			0	0	0
Антрацитни въглища			0	0	0

Figure 5. Energy costs for current state and normalized state of the building

Potential Energy Saving Measures

- ESM 1 Thermal insulation of external walls

The measure includes external thermal insulation with expanded polystyrene foam (EPS) with a thickness of 120 mm and a thermal conductivity coefficient not higher than $\lambda = 0.030$ W/m.K on the facade walls. The measure for the walls of Type 1 and Type 3 with a total area of 534.05 m^2 + 55 m^2 for zones around windows and doors includes the delivery and installation of thermal insulation material type "EPS". Value for the implementation of ESM 1 is 56242.00 ₾ including VAT.

- ESM 2 Replacement of windows

The measure includes replacing the old windows (478.4 m^2) with new PVC windows with triple glazing with one low-energy glass, one K-glass and one float in the middle with a heat transfer coefficient of 1.10 W/m^2K. The large glass window on the NE facade (23.6 m^2) is planned to be replaced with an aluminum one with a interrupted thermal bridge and a glass package with one low-energy glass with a heat transfer coefficient of 1.60 W/m^2K. It is planned to replace the windows in the unheated volume (28.97 m^2) of the building with new PVC windows with double glazing with one low-energy glass, with a heat transfer coefficient of 1.40 W/m^2K. Value for implementation of ESM 2 is 102258.00 ₾ including VAT.

- ESM 3 Thermal insulation of floor (adjacent walls)

Different types of floor structures are identified in the building. Some of the sections have a basement floor, while others are directly located on the ground. Thermal insulation of extruded polystyrene foam with a thickness of 5 cm is laid on the ceilings of the unheated basements. This measure provides for the thermal insulation of the adjacent walls of the basement bordering the outside air (the plinth) - 181.98 m2 with external thermal insulation EPS with a thickness of 120 mm and a thermal conductivity coefficient not higher than $\lambda =$ = 0.030 W/mK. The cost of implementation of ESM 3 is 4602.00 ₾ including VAT.

- ESM 4 Heat generation measures – Mounting a VRF direct evaporation air conditioning systems

The measure requires the preparation of a project in accordance with the new load of the building, namely after laying thermal insulation and joinery on the enclosing elements. It is planned to replace the old inefficient electrical heating appliances with highly efficient VRF systems with minimal value of coefficient of performance COP = 3.80. Five VRF direct evaporation air conditioning systems are planned for the building. For the premises on the first floor in the western part of the complex - ritual hall, pensioner's club, admin. premises and lobby, a VRF direct evaporation system with Q_{heat} = 24.00 kW; Q_{cool} = 22.4kW; P_e = 6.12 kW is selected, with an outdoor unit mounted on the roof above the entrance to the inner courtyard in the northeastern part of the building. The indoor units in the ritual hall are console type mounted in height 300 mm from the floor and for high wall mounting in the other premises.

For the premises on the second floor - library, computer room, reading room and office, a VRF direct evaporation system with Q_{heat} = 24.00 kW; Q_{cool} =22.4 kW; P_e = 6.12 kW is selected, with an outdoor unit mounted on the roof above the entrance to the inner courtyard. The indoor units are for high wall mounting.
For the conference halls (first and second floor) in the southeastern part of the complex, a VRF direct evaporation system with Q_{heat} = 18.00 kW; Q_{cool} = 16.00 kW; P_e= 4.75 kW is selected, with an outdoor unit mounted on the flat roof above the hall. The indoor units are console type mounted in height 300 mm from the floor.
For the lobby and the staircase in front of the theater hall, a VRF direct evaporation system with Q_{heat} = 24.00 kW; Q_{cool} = 22.40 kW; P_e = 6.12 kW is selected, with an outdoor unit installed in the southern part of the flat roof above the staircase. The indoor units are for high wall installation.
For the dressing rooms, rehearsal halls and corridors, a VRF direct evaporation system with Q_{heat} = 35.00 kW; Q_{cool} = 33.50 kW; P_e = 9.57 kW is selected, with an outdoor unit installed on the flat roof above the municipal club. The indoor units are for high wall installation.
Cost of implementation of ESM 4 is 127823.00 ₾ including VAT.

- ESM 5 Lighting measures

It is necessary to replace the old inefficient lighting with new LED ones. Old incandescent lamp 60 W will be replaced with new LED 6 W – 100 pieces, 42 W fluorescent tubes will be replaced with 18 W LED tubes – 30 pieces, 18 W fluorescent tubes will be replaced with 9 W LED tubes – 20 pieces, 250 W stage spotlights will be replaced with 35 W LED. The measure includes the development of an investment project by a designer with the relevant qualification for the replacement of the lighting installation. The new lighting must meet the following indicators and technical data:

• Energy class – A;
• Color temperature: CCT≤ 5000K;
• Light output of the luminaire: $\chi \geq 110$ lm/W;
• The power supply unit must provide a light flux ripple coefficient: KP ≥ 10%

All lighting parameters of the luminaire are certified by a test laboratory report. Value for the implementation of ESM 5 is 4857.00 ₾ including VAT.

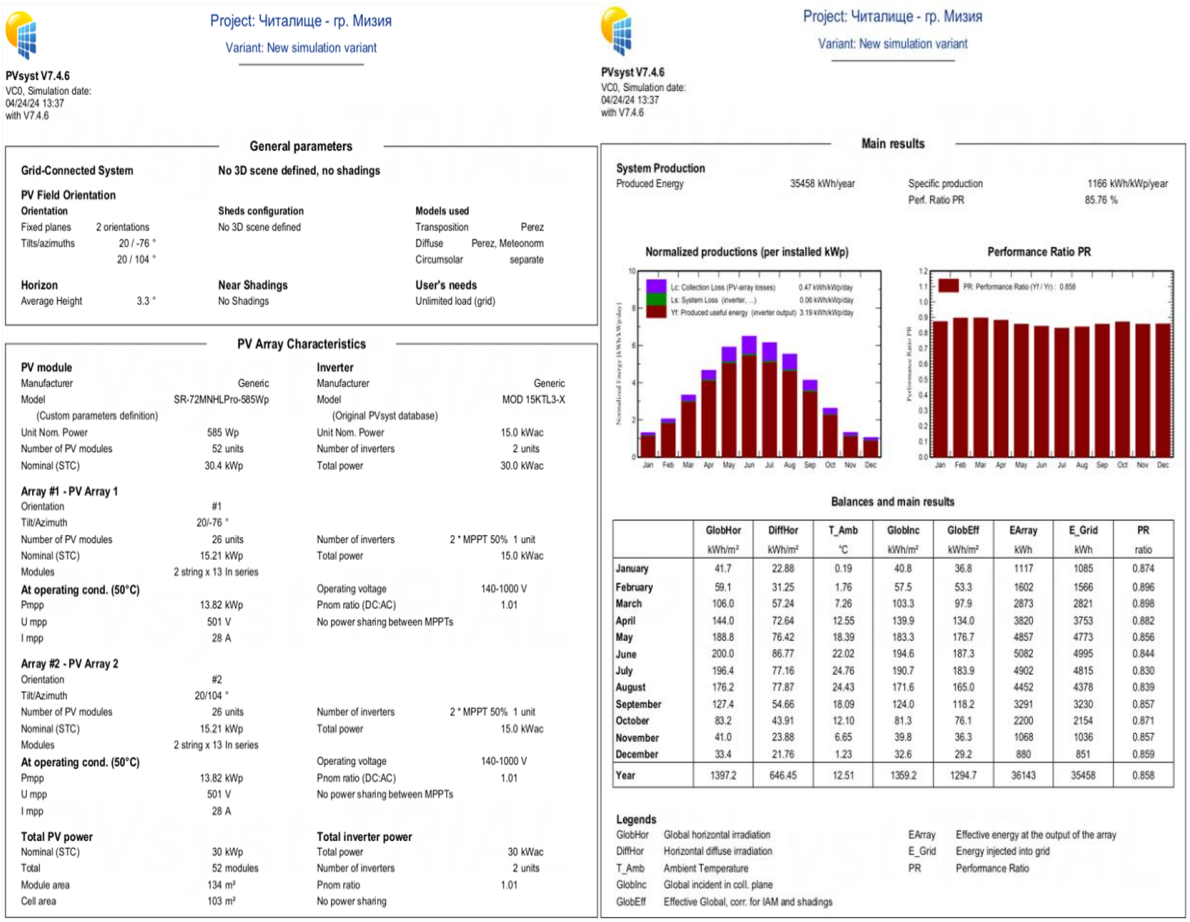


Figure 6. Simulation report for PV system

- ESM 6 RES measures: Installation of a photovoltaic plant FPP for own needs 30.42 kWp

Due to the large area of unusable roofs and the geographical location with intense solar radiation, the installation of a photovoltaic installation for own needs is planned for the building, which will be able to cover an average of 37.55% of the building's electricity annually. The photovoltaic plant will be located on the roof of the building and will be sized in the technical phase according to the load capacity of the structure and the practical possibility of implementing the installation. For this purpose, it is necessary to prepare a structural statement and, if necessary, provide for structural reinforcement in order to safely install the facilities. The total capacity is sized based on the calculated energy consumption/power of the building from the electrical appliances used.

Annual production from the photovoltaic installation is within 35457 kWh, which according to the geographical location and the preliminary simulation made is equivalent to an installation of 30.42 kWp. After analysis of the energy consumption in the building and the production from the photovoltaic plant, it was established that the building will not be able to absorb all the electrical energy produced. The amount of energy that will be absorbed in the building is in the order of 16990 kWh. A simulation of the site has been prepared based on polycrystalline modules. The energy yield of the installation has been calculated based on 52 photovoltaic modules, with a nominal power of 585 Wp and a total installed power of 30.42 kWp, their type and type should be determined after the selection of a contractor and approval of the project. For this study an simulation software PV Syst - Version 7.4.6 is used. The results of simlation are shown on Figure 6. Value for the implementation of ESM 6 is 30678.00 ₾ including VAT.

Energy Budget

On Figure 7 are shown data for annual energy consumption and specific energy consumption before and after energy saving measures. On Figure 8 are shown data for energy savings.

Потребна енергия

Енергия за:	Реф. с-ти 1 kWh/m²	Реф. с-ти 2 kWh/m²	Текущо състояние kWh/m²	Текущо състояние kWh/year	Нормализирано съст. kWh/m²	Нормализирано съст. kWh/year	След ECM kWh/m²	След ECM kWh/year	в т.ч. ЕВИ kWh/year	Общо ЕВИ kWh/year
Отопление			3.467	8 629.011	50.911	126 717.793	15.818	39 371.684	0	110 240.717
Охлаждане			0	0	0	0	0	0	0	0
Вентилация (отопление)			0	0	0	0	0	0	0	0
Вентилация (охлаждане)			0	0	0	0	0	0	0	0
БГВ			0.110	274.845	0.385	957.968	0.385	957.968	0	0
БГВ(Помпи)			0	0	0	0	0	0	0	0
Помпи и вентилатори			0	0	0	0	0	0	0	0
Осветление			0.532	1 324.358	0.967	2 406.877	0.192	479.072	0	0
Уреди влияещи на топлинния баланс			1.646	4 097.468	1.646	4 097.468	1.646	4 097.468	0	0
Уреди невлияещи на топлинния баланс			0.139	345.799	0.139	345.799	0.139	345.799	0	0
Други			0	0	0	0	0	0	0	0
Общо			5.895	14 671.481	54.048	134 525.905	18.181	45 251.991	0	110 240.717

Figure 7. Data for annual energy consumption and specific energy consumption before and after energy saving measures

Енергоспестяващи мерки

Параметър	kWh/m²	kWh
Осветление		
Едновременна мощност	0,775	1928,975
Общо	**0,775**	**1928,975**
Отопление		
U външни стени	5,673	14120,097
U прозорци	5,102	12698,878
U под(НПЕ/ОПЕ/външен въздух/земя)	0,345	858,705
Инфилтрация	4,463	11108,407
Ефективност на генератора на топлина ЕИ1	19,509	48557,901
Общо	**35,092**	**87343,988**

Figure 8. Data for energy savings

Determination of the values of equivalent primary energy before and after ESM is presented in Table 11 and Table 12.

Table 11. Values of equivalent primary energy before ESM

Energy	Q_i, kWh/y	$f_{P,nren}$, -	K_{CO2e}, g CO_2/kWh	$E_{we,del;an}$, kWh/m^2.y	EP_{CO2e}, t CO_2/y
Heating	126718	2.3	486	117.10	61.58
DHW	958	2.3	486	0.89	0.47
Lighting	2407	2.3	486	2.22	1.17
Others	4443	2.3	486	4.11	2.16
Total:	134526			124.31	65.38

Table 12. Values of equivalent primary energy after ESM

Energy	Q_i, kWh/y	$f_{P,nren}$, -	K_{CO2e}, g CO_2/kWh	$E_{we,del;an}$, kWh/m^2.y	EP_{CO2e}, t CO_2/y
Heating	39372	2.3	486	36.38	19.13
DHW	958	2.3	486	0.89	0.47
Lighting	479	2.3	486	0.44	0.23
Others	4443	2.3	486	4.11	2.16
PV	-16990	2.3	486	-15.7	-8.26
Total:	45252			26.12	13.74

Based on the obtained primary energy values for EP = 124.31 kWh/m^2y and EP_{ESM} = 26.12 kWh/m^2y and scale of energy consumption classes for types of building categories, the energy consumption class of the building in its current state for buildings in the field of culture and arts is determined. From the correlation of the obtained EP value and the scale, it follows that at the time of the survey the building has a specific primary energy consumption EP = 124.31 kWh/m^2y and belongs to energy consumption class “B”.

After implementation of all energy saving measures, the building will have a specific primary energy consumption of EP_{ESM} =26.12 kWh/m^2y, which will meet the requirements for energy consumption class “A”. Energy consumption classes are defined according to Appendix No.2 of Ordinance No. RD-02-20-3 of November 9, 2022 on technical requirements for energy performance of buildings for energy consumption indicators and energy performance of buildings in the field of culture and arts.

Economic and Ecological Analysis of ESM

An economic and ecological analysis showing the energy savings (ES) of individual ESM in kWh/year, %, €/year, as well as the investments (I), simple payback periods (PB) and saved emission carbon dioxide for each of the measures are presented in Table 13.

Table 13. Economic and ecological analysis of ESM

Energy saving measures	Q_i, kWh/y	Q_{iESM}, kWh/y	ES, kWh/y	ES, %	I, € +VAT	ES, € +VAT/year	PB, years	t CO_2/y
Thermal insulation of external walls	134526	120406	14120	10.5	56242	3133.27	18.0	6.86
Replacement of windows	134526	110719	23807	17.7	102258	5282.87	19.4	11.57
Floor insulation	134526	133667	859	0.6	4602	190.55	24.2	0.42
Heat generation measures	134526	85968	48558	36.1	127823	10775.06	11.9	23.60
Lighting measures	134526	132597	1929	1.4	4857	428.05	11.4	0.94
RES measures: Photovoltaic power plant	-	-	-	-	30678	3770.10	8.1	8.26
Total:	134526	45253	89273	66.3	326460	23580.00	13.8	51.64

Conclusion

The existing condition of the building before energy saving measures indicates that the building falls into energy class "B" of the energy consumption scale. The current state established is EP = 404.52 kWh/m²y, falling within the limits of class "F", namely: EP_{min} > 110 kWh/m²y and EP_{max} >220 kWh/m²y. After implementing the

prescribed energy saving measures, it can be summarized that the building will be in class "A" of the energy consumption scale.The established condition after implementing the prescribed energy saving measures is EP_{ESM} = 26.12 kWh/m²y, falling within the limits of class "A", namely: $EP_{max} \leq 110$ kWh/m²y. The total energy savings from the measures amount to 89273 kWh/year of electrical energy, with the environmental equivalent of the energy savings amounting to 51.64 t CO_2/year.

Scientific Ethics Declaration

* The authors declare that the scientific ethical and legal responsibility of this article published in EPSTEM journal belongs to the authors.

Conflict of Interest

* The authors declare that they have no conflicts of interest

Funding

* This research received no specific grant from any funding agency in the public, commercial, or not-for-profit sectors.

Acknowledgements or Notes

* This article was presented as an oral presentation at the International Conference on Technology, Engineering and Science (www.icontes.net) held in Antalya/Türkiye on November 12-15, 2025.

References

Capehart, B., Turner, W., Kennedy, W.(2012). *Guide to energy management*. Seventh Edition, The Fairmont Press, Inc.

Doty, S. (2016). *Commercial energy auditing reference handbook*. 3rd Edition, The Fairmont Press, Inc.

Iliev, I., Kaloyanov, N., Gramatikov, P. Terziev, A., Pavlov, I., Stefanov, S., Sirakov, K., Kamburova, V. (2025, 5 October). *Energy Efficiency and Energy Management Handbook*, Retrieved from https://www.exergia-max.com/sites/default/files/documents/EEEM_Handbook_ENG.pdf

Kreith, F., Goswami, D. (2007). *Energy Efficiency and Renewable Energy*. CRC Press.

Rasheva, V. (2011). *Energy technology analysis of industrial enterprise*. Academic publishing house of UHT - Plovdiv.

Shapiro, I. (2016). *Energy audits and improvements for commercial buildings*, John Wiley & Sons, Inc.

Thuman A., Younger, W. (2008). *Handbook of energy audit*. The Fairmont Press Inc.

Turner, W.(1997). *Energy Management Handbook*. Third Edition, The Fairmont Press, Inc.

Author(s) Information

Slav Valchev
University of Food Technologies
Plovdiv, 26 Maritza Boulevard, Bulgaria
Contact e-mail: *slavvalchev@uft-plovdiv.bg*

Nikola Valchanov
University of Food Technologies
Plovdiv, 26 Maritza Boulevard, Bulgaria

To cite this article:

Valchev, S. & Valchanov, N. (2025). Energy audit of a community center. *The Eurasia Proceedings of Science, Technology, Engineering and Mathematics (EPSTEM), 38,* 641-654.

The Eurasia Proceedings of Science, Technology, Engineering & Mathematics (EPSTEM)
ISSN: 2602-3199

The Eurasia Proceedings of Science, Technology, Engineering and Mathematics (EPSTEM), 2025

Volume 38, Pages 655-666

IConTES 2025: International Conference on Technology, Engineering and Science

Generation Algorithms of Invertible Linear and Nonlinear Finite Automata with Memory

Gulmira Shakhmetova
L.N. Gumilyov Eurasian National University

Khasenov Altay
L.N. Gumilyov Eurasian National University

Zhanat Saukhanova
L.N. Gumilyov Eurasian National University

Altynbek Sharipbay
L.N. Gumilyov Eurasian National University

Alibek Barlybayev
L.N. Gumilyov Eurasian National University

Raykul Sayat
L.N. Gumilyov Eurasian National University

Abstract: In the context of rapid digital technology development, information security has become one of the key factors for the sustainable functioning of both society and the state. Modern methods of information protection rely on cryptographic algorithms, whose effectiveness is determined not only by their mathematical rigor but also by the degree of innovation in the applied models. One of the promising directions in this field is the use of finite automata models, which possess significant theoretical potential and broad opportunities for practical implementation. This study is devoted to the description of algorithms for generating invertible linear and nonlinear finite automata with input-output memory, applied in the FAPKC cryptosystem series. Unlike previously published works that are limited to purely mathematical descriptions of such models, this paper presents concrete procedures for their construction and implementation. Furthermore, a set of statistical tests was conducted to evaluate the randomness and cryptographic strength of the generated automata. The experimental results confirm their cryptographic robustness and demonstrate the feasibility of applying the proposed algorithms in modern cryptographic protocols.

Keywords: Cryptography, Finite automata, Cryptosystem, Invertible automata, Algorithm generation

Introduction

With the rapid development of digital technologies and the global digitalization of all spheres of activity, ensuring information security is of particular importance. The flow of data circulating in public and corporate networks is constantly increasing, which, in turn, increases the risks of unauthorized access, leakage, and modification of information. To counter these threats, cryptographic methods are used, which form the foundation of modern data protection systems.

- This is an Open Access article distributed under the terms of the Creative Commons Attribution-Noncommercial 4.0 Unported License, permitting all non-commercial use, distribution, and reproduction in any medium, provided the original work is properly cited.

- Selection and peer-review under responsibility of the Organizing Committee of the Conference

© 2025 Published by ISRES Publishing: www.isres.org

The effectiveness of cryptographic algorithms is determined not only by the rigor of their mathematical foundations but also by the originality of the models used. Traditional approaches based on linear algebra, number theory, and combinatorial transformations are currently facing limitations due to increasing computing power and the development of quantum computing (Focardi, 2018). Therefore, alternative cryptographic constructs based on finite-state machine theory, which enable the implementation of highly complex transformations with relatively low computational costs, are becoming increasingly relevant (Shakhmetova et al., 2024).

Finite automata models offer several advantages: they are formally defined, easily amenable to mathematical analysis, and their structures are well adapted to hardware and software implementations (Satybaldina et al., 2011). The use of reversible linear and nonlinear finite-state machines with input and output memory opens up new possibilities for constructing robust encryption systems that provide both diffusion and data confusion at the level of elementary state transitions.

This study aims to develop and describe algorithms for generating such automata implemented in the FAPKC (Finite Automata Public Key Cryptosystem) series of cryptosystems (Tao & Chen, 1999; Kodada, 2022). Unlike previously published works, which are limited to the theoretical aspects of describing automaton models (Meskanen, 2001; Tao, 2008), this paper presents specific procedures for their construction, handling, and software implementation.

Particular attention is paid to the practical verification of the resulting models: a set of statistical tests was conducted to assess the randomness of the output sequences and their resistance to certain attacks. The experimental results demonstrate the high cryptographic strength of the proposed algorithms, confirming their feasibility for use in cryptography. Thus, this study not only expands theoretical understanding of the capabilities of finite automata models in cryptography but also makes a practical contribution to the development of methods for constructing and implementing cryptographically secure automaton converters.

Method

Linear and Nonlinear Finite Automata with Input-Output Memory

In classical automata theory, a finite automaton (FA) is a quintuple $M =< X, Y, S, \delta, \lambda >$, where X is a non-empty finite set of the input alphabet, Y is a non-empty finite set of the output alphabet, Q is a finite set of states, , $\delta: Q \times X \to Q$ is the transition function, and $\lambda: Q \times X \to Y$ is the output function. The behavior of a finite automaton, in the classical sense, depends only on the previous state and the current input. However, many cryptographic systems use finite automata with memory (Tao, 2008), (Kodada, 2022). The states of such an automaton are represented as a combination of the last k output and h input symbols, which leads to a finite automaton model with input-output memory of order (h, k) (Kohavi & Jha, 2009).

An important property of finite automata used for cryptographic purposes is reversibility. Reversibility refers to the ability to uniquely reconstruct the input sequence given a known initial state and output sequence. In particular, in real-world cryptosystems, a weakly reversible finite automata (WIFA) model is often used, where input reconstruction is not possible immediately, but only after a fixed number of steps—the so-called delay τ (Katerinsky, 2013). This behavior ensures one-way transformation at the encryption stage, while maintaining the ability to reverse the transformation given the necessary amount of information**.** Further, we will consider the sets X and Y as l-dimensional linear spaces over the field $GF(2) = \{0,1\}$. Let $y(i) \in Y$ be the output data at time i, and $(i) \in X$ be the column vector of the input data, then the automaton M_0 can be represented in the following form:

$$y(i) = \sum_{j=1}^{k_0} A_j\, y(i-j) + \sum_{j=0}^{h_0} B_j x(i-j),\ i = 0,1,2,\ldots \quad (1)$$

The automaton M_0 belongs to the class of finite automata with memory of order (h_0, k_0). This means that to uniquely determine its initial state, knowledge of at least the last h_0 input and k_0 output signals is required. Set of $< x(-1), x(-2), \ldots, x(-h_0), y(-1), y(-2), \ldots, y(-k_0) >$ describes the initial state of the automaton M_0.

In expression (1), A_j and B_j are linear matrices of size $(l\ x\ l)$ that completely determine the structure of the finite automaton M_0. All operations involved in formula (1) are performed in a Galois field (GF(2)), where standard addition and multiplication rules are used.

To construct a reversible linear FA with input-output memory, linear R_a^{-1}/R_b^{-1} transformations are used (Meskanen, 2001), in the following order:

$$G_\tau(i) \xrightarrow{R_b^{-1}[r_\tau]} G'_{\tau-1}(i) \xrightarrow{R_a^{-1}[P_{\tau-1}^{-1}]} G_{\tau-1}(i) \xrightarrow{R_b^{-1}[r_{\tau-1}]} \cdots \xrightarrow{R_b^{-1}[r_1]} G'_0(i) \xrightarrow{R_a^{-1}[P_0^{-1}]} G_0(i), \quad (2)$$

where $G_\tau(i) \in MP(q)$ is echelon matrix.

A linear finite automaton M_0^* is considered to be inverse to an automaton with delay τ if and only if from the system of matrices, A_j and B_j it is possible to select a corresponding set of matrices A_j^* , where $(j = 0 \dots \tau_0 + k_0)$, for which the equality holds:

$$x(i) = \sum_{j=1}^{h_0} B_j^* x(i-j) + \sum_{j=0}^{\tau_0+k_0} A_j^* y(i-j), \; i = 0, 1, \dots \quad (3)$$

For an arbitrary initial state $< x(-1), x(-2), \dots, x(-h_0), y(-1), y(-2), \dots, y(-k_0) >$ of the automaton M_0 and any input sequence $x(0), x(1), \dots, x(n), x(n+\tau) \in X$, the elements $x(0), x(1), \dots, x(n)$ can be uniquely reconstructed using formula (3). Thus, the automaton M_0^*, defined by expression (3), correctly defines the inverse automaton for M_0 with delay τ. To construct an inverse linear FA with input-output memory, the R_a/R_b transformation methods are used in the following order:

$$G_0(i) \xrightarrow{R_a[P_0]} G'_0(i) \xrightarrow{R_b[r_1]} G_1(i) \xrightarrow{R_a[P_1]} \cdots \xrightarrow{R_a[P_{\tau-1}]} G'_{\tau-1}(i) \xrightarrow{R_b[r_\tau]} G_\tau(i) \quad (4)$$

where $G_\tau(i) \in MP(q)$ is a matrix constructed for an invertible FA.

Nonlinear finite automata with input-output memory occupy a special place among finite-state cryptographic models, as they provide a high level of data diffusion and entanglement, introducing nonlinearity into linear transformations. Therefore, studying their inversion algorithms and analyzing the complexity of the corresponding procedures are of practical importance in the design of secure encryption transformations.

Nonlinear finite automata M_1 with input-output memory (h_1, k_1) has the following representation:

$$y(i) = \sum_{j=0}^{k_1} F_j\, y(i-j) + \sum_{j=1}^{k_1-\epsilon} F'_j s(y(i-j), \dots, y(i-j-\epsilon)) + \sum_{j=0}^{h_1} D_j\, x(i-j), \quad (5)$$

$i = 0,1,2, \dots$ где $s(x(i-j), \dots, x(i-j-\epsilon)$ nonlinear function, and ϵ – small positive integer.

The inverse nonlinear finite automata M_1^* is given by the formula:

$$x(i) = \sum_{j=1}^{h_1} D_j^*\, x(i-j) + \sum_{j=1}^{k_1+\tau-\epsilon} F_j'^* s(y(i-j), \dots, y(i-j-\epsilon)) + + \sum_{j=0}^{k_1+\tau} F_j^*\, y(i-j), \quad (6)$$

$i = 0,1,2, \dots$

Implementation of Algorithms

In this section, we describe our implemented program and some of the main algorithms for generating reversible linear and nonlinear finite automata. The software implementation is implemented as the NLFTEncrypt.exe executable module, developed in Python using the NumPy and SciPy libraries, as well as the TaoUtilities auxiliary module, which contains a set of functions for performing arithmetic operations in the Galois field $\mathbb{F}_2$. The program is built according to object-oriented design principles and includes four main classes that interact with each other during key generation and finite automata inversion (Figure 1).

LTaoKeygen is a key generation class for linear finite automata with input-output memory. It implements the full key construction cycle: from generating the height vector of the echelon matrix to generating all the coefficient matrices required for encryption and decryption. NLTaoKeygen is a key generation class for nonlinear finite automata. Structurally, it is similar to LTaoKeygen, but includes modified key generation algorithms and additional procedures that account for the nonlinear relationship between inputs and outputs. LTao is a linear automaton class containing the *encrypt()* and *decrypt()* functions, which use generated coefficient matrices to perform forward and inverse transformations. NLTao is an implementation of a nonlinear finite automaton, providing encryption and decryption of data based on nonlinear expressions. The main function __nonLinearFunc() implements the nonlinear transformation used to generate output vectors.

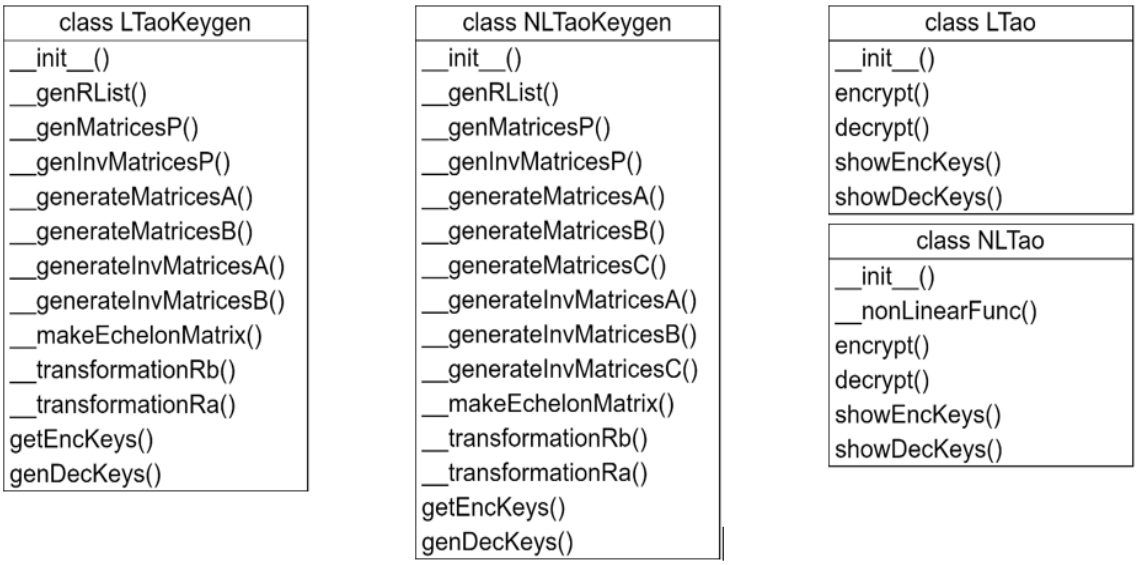


Figure 1. UML class diagrams of the program

The key construction methods are the algorithms for constructing coefficient matrices, the preceding algorithms for constructing height vectors, non-singular matrices P and P^{-1}, as well as transformation algorithms according to the rules R_a and R_b. The R_a transformation transforms the input matrix by multiplying it by the nonsingular matrix Pi. The R_a transformation rule has two variations: the direct transformation and the inverse transformation. The first is used when constructing the decryption key, while the second is used when constructing the encryption key and is denoted as R_a^{-1}. The inverse transformation R_a^{-1} differs from the direct transformation by the matrix P by which the multiplication occurs. The inverse transformation uses the direct matrix Pi, while the direct transformation uses the inverse matrix Pi^{-1}.

It is worth noting an important nuance in the R_a^{-1} transformation: the echelon matrix initially contains undefined elements. According to (Tao et al., 1997), the undefined element u has its own rules for multiplication and addition with numbers from the set {0, 1}. These rules are described as follows: $x \times u = u, 0 \times u = 0, y + u = u$, where: $x \in \{1, u\}, y \in \{0,1, u\}$. For the described arithmetic with undefined elements of the echelon matrix, a small class EchelonElementsCalculate was created, which is shown in Figure 2 below. The EchelonElementsCalculate class provides two static public methods: add and mul, which replace the addition and multiplication operators for values from the set $\{0, 1, u\}$. Within the program code, the value of u was replaced by the number 9. Thus, the EchelonElementsCalculate class can work with all elements of the echelon matrix, which, in turn, can be any number from a small group of numbers- {0, 1, 9}.

```
class EchelonElementsCalculate:

    @staticmethod
    def add(value1, value2):
        if value1 in (0, 1) and value2 in (0, 1):
            return value1 ^ value2
        return value1 if value2 in (0, 1) else value2

    @staticmethod
    def mul(value1, value2):
        if value1 in (0, 1) and value2 in (0, 1):
            return value1 & value2
        if value1 in (0, 1):
            return value2 if value1 == 1 else 0
        if value2 in (0, 1):
            return value1 if value2 == 1 else 0
        return value1
```

Figure 2. Operations with undefined elements

The R_b transformation also has two functions: a forward transformation and an inverse transformation. The forward R_b transformation shifts matrices to the left, while the inverse R_b^{-1} transformation shifts them to the right. If matrix expansion is necessary, the matrix dimension increases by the shift length; if not, the shifted elements that extend beyond the matrix boundary are lost. In all cases of shifting, the shifted elements are replaced by zeros.

Figure 3 shows the implementation of the R_b transformation, which uses the shift_rows_matrix function for shifting. This function is adapted for the implemented algorithms in that it immediately uses the *vectorLength* value as the shift length. This value is the state machine parameter m, where m is the length of the vector being processed. Also, instead of rowIndices, the *shiftRow* value is specified — this is the r_{k+1} value used for the R_b rule.

```
def transformationRb(matrix: np.ndarray, vectorLength: int,
                     shiftRow: int, leftShift: bool = False,
                     appending: bool = False):

    row2Shift = list(range(shiftRow, len(matrix)))

    transformedMatrix = shift_rows_matrix(
        matrix=matrix,
        rowsIndices=row2Shift,
        shiftLength=vectorLength,
        leftShift=leftShift,
        appending=appending
    )

    return transformedMatrix
```

Figure 3. R_b transformation

Finite automata construction focuses on constructing coefficient matrices (1), (3), (5), and (6). Structural coefficient matrices are the keys for encryption and decryption of data in automata cryptography.

An invertible linear finite automaton has two coefficient matrices: matrices $A = \{A_1, \ldots, A_{k_0}\}$ and матрицы $B = \{B_0, \ldots, B_{h_0}\}$. The number of matrices depends on the input and output memory. If the finite automaton has no output memory, then only the B matrices remain. The matrices are generated as a single rectangular matrix, combining the matrices of each input or output parameter. However, after a series of transformations or if certain conditions are met, the matrices are divided in a specific manner into equal square matrices.

Constructing the overall matrix B is a more complex task compared to matrix A due to the use of the echelon matrix and its transformations, which were discussed earlier. The generated overall matrix B has dimensions of m rows and $m \times (h + 1)$ columns. Construction of matrix B begins with two separate matrix elements: one identity matrix and h arbitrary matrices. Combining these two matrices yields an incomplete matrix B. To complete it, it is necessary to transform it into an echelon matrix and perform τ cycles of successive transformations R_b^{-1} and R_a^{-1} with the values ri and Pi, where i=τ− 1, …, 0. It is also worth considering one important rule: the value of the input memory h must not be less than the value of the finite state machine delay τ, h ≥ τ.

```
def generateMatricesB(self, vectorLength, rList, matricesP, inputMemory, taoDelay):
        identityMatrix = np.eye(vectorLength, vectorLength, dtype=np.uint8)

        randomMatrices = []
        for _ in range(inputMemory):
            randomMatrices.append(np.random.randint(0, 2, size=(vectorLength, vectorLength), dtype=np.uint8))

        stackedMatrices = [identityMatrix] + randomMatrices

        echelonMatrix = makeEchelonMatrix(stackedMatrices, rList, vectorLength)

        for i in range(taoDelay - 1, -1, -1):
            echelonMatrix = transformationRb(echelonMatrix, rList[i])
            echelonMatrix = transformationRa(echelonMatrix, matricesP[i])

        return echelonMatrix
```

Figure 4. Matrix generation function B

Figure 4 shows the implementation of the *genMatricesB* function, which constructs the general matrix B. Figure 4 shows that the function makes extensive use of the previously presented *transformationRa* and *transformationRb* functions. The construction of the inverse automaton is performed after the formation of the reversible automaton. This is crucial, since the process of constructing the decryption key is based on the use of the encryption key. Therefore, the structural matrices of the coefficients A and B must be pre-generated before constructing their inverse matrices A^* and B^*. The generation of the inverse matrices $A^*$and $B^*$is very similar, but differs only in the order of applying the R_a/R_b transformations, as can be seen in the code for constructing the inverse matrix B in Figure 5.

```
def generateInvMatricesB(matricesB: np.ndarray, invMatricesP, rList, taoDelay):
    matrix = matricesB.copy()

    for i in range(taoDelay):
        matrix = transformationRa(matrix, invMatricesP[i])
        matrix = transformationRb(matrix, rList[i], True)

    return matrix
```

Figure 5. Inverse matrix generation function B^*

The process of constructing a nonlinear finite automaton is largely similar to that of generating a linear automaton, but has several fundamental differences. A key feature of a nonlinear automaton is the presence of additional coefficient matrices, which must be generated separately. These matrices are used to process the results of nonlinear functions that accept elements of the input or output memory, depending on the type of memory used. Thus, the transition to considering nonlinear finite automata allows us to expand the model's functionality and explore the impact of nonlinear transformations on the cryptographic security of the system.

A nonlinear finite automaton with input-output memory, as seen in expression (5), has a nonlinear function s. In our case, the nonlinear function is defined as component-wise multiplication modulo 2 of two vectors. The procedure for constructing the structural matrices responsible for the nonlinear component involves generating arbitrary matrices of dimension $m \times m$. Thus, to construct a general rectangular matrix B, it is necessary to construct $h - 1$ or $k - 1$ arbitrary matrices of dimension $m \times m$. The parameter influencing the number of matrices is determined by the presence of input memory or output memory.

Algorithm LTao.encrypt(encKeys, data, vectorLength, taoDelay, inputMemory, outputMemory)

Encrypting process in LTao class

Input: keys to encrypt, encKeys contain coefficient matrices with elements ∈ $\mathbb{F}_2$
Input: bytes data, data ∈ {0, …, 255}
Input: length of processing vector, *vectorLength* ∈ ℕ
Input: delay of finite automata, *taoDelay* ∈ ℕ
Input: input memory, *inputMemory* ∈ ℕ
Input: output memory, *outputMemory* ∈ ℕ
Output: encrypted bytes data, data ∈ {0, …, 255}

```
1:    bitData ← bit_data_converter(data, vectorLength)
2:    delayData ← vectors with vectorLength zeros taoDelay times
3:    bitData ← bitData + delayData
4:    xBuffer ← vectors with vectorLength ones inputMemory times
5:    yBuffer ← vectors with vectorLength ones outputMemory times
6:    encBitData ← intager array[length of bitData][vectorLength]
7:    for each xCurrent in bitData
8:        xBuffer ← insert vectorLength vector with zeros in the start
9:        yCurrent ← vectorLength vector with zeros
10:       for (i = 0; i < length of encKey[0]; i++)
11:           yCurrent ← gf2_multiply(encKey[0][i], yBuffer) XOR yCurrent
12:       end for
13:       for (i = 0; i < length of encKey[1]; i++)
14:           yCurrent ← gf2_multiply(encKey[1][i], xBuffer) XOR yCurrent
15:       end for
16:       xBuffer ← pop the last element
17:       yBuffer ← pop the last element
18:       yBuffer ← insert vectorLength vector with zeros in the start
19:       encBitData ← insert yCurrent in the end
20:   end for
21:   encData ← bit_vector_to_int(encBitData)
22:   return encData
```

Figure 6. Encryption algorithm using a linear FA

After implementing the linear and nonlinear finite automata construction modules, we moved on to the data encryption and decryption stage, based on formulas (1), (3), (5), and (6). Each automaton type is implemented as a separate class (LTao, NLTao) with encrypt and decrypt functions accepting bit streams in various formats. For data preprocessing, the bit_data_converter function is used, converting input values into binary form suitable for subsequent processing by the finite automaton. This article presents algorithms implementing encryption/decryption using linear finite automata.

The *LTao.encrypt* algorithm in Figure 6 implements the data encryption process using a linear finite automaton and represents a transformation of the input byte stream based on binary operations in the Galois field $\mathbb{F}_2$. The input is the coefficient matrices of an invertible direct linear finite automaton, the vector length parameters, the delay, and the values of the automaton's input and output memory. The algorithm processes the input data step by step, converting them to binary form and generating an expanded stream taking into account the delay and memory state. During the computation, the state buffers *xBuffer* and *yBuffer*, which model the automaton's input and output memory, are iteratively updated. For each input data vector, the coefficient matrices A and B are sequentially multiplied by the corresponding buffers, followed by a bitwise XOR operation. This produces an encrypted bit sequence, which is converted back to an integer representation and returned as an array of encrypted bytes.

For the decryption process, the *LTao.decrypt* algorithm was implemented (Figure 7), which shows the process of decrypting data encrypted using a linear finite automaton. The algorithm is based on the coefficient matrices A^* and B^*, which are the inverse of the matrices used in encryption, and whose elements belong to the Galois field $\mathbb{F}_2$. The input is the encrypted data, the vector length parameters, the delays, and the values of the automaton's input and output memory.

```
Algorithm LTao.decrypt(decKeys, data, vectorLength, taoDelay, inputMemory, outputMemory)
Decrypting process in LTao class
Input: keys to decrypt, decKeys contain coefficient matrices with elements ∈ 𝔽₂
Input: bytes data, data ∈ {0, …, 255}
Input: length of processing vector, vectorLength ∈ ℕ
Input: delay of finite automata, taoDelay ∈ ℕ
Input: input memory, inputMemory ∈ ℕ
Input: output memory, outputMemory ∈ ℕ
Output: encrypted bytes data, data ∈ {0, …, 255}
    bitData ← bit_data_converter(data, vectorLength)
    delayData ← bitData from the start to taoDelay
    bitData ← bitData from taoDelay to the end
    xBuffer ← vectors with vectorLength ones inputMemory times
    yBuffer ← vectors with vectorLength ones outputMemory times
    yBuffer ← yBuffer + delayData
    yBuffer ← reverse()
    decBitData ← intager array[length of bitData][vectorLength]
    for each yCurrent in bitData
       yBuffer ← insert vectorLength vector with zeros in the start
       xCurrent ← vectorLength vector with zeros
       for (i = 0; i < length of decKey[0]; i++)
           xCurrent ← gf2_multiply(decKey[0][i], yBuffer) XOR xCurrent
       end for
       for (i = 0; i < length of decKey[1]; i++)
           xCurrent ← gf2_multiply(decKey[1][i], xBuffer) XOR xCurrent
       end for
       xBuffer ← pop the last element
       yBuffer ← pop the last element
       xBuffer ← insert vectorLength vector with zeros in the start
       decBitData ← insert xCurrent in the end
   end for
   decData ← bit_vector_to_int(decBitData)
  return decData
```

Figure 7. Decryption algorithm using a linear FA

The implementation of encryption and decryption algorithms using nonlinear finite automata is similar to the algorithms described previously. The only distinguishing feature is the presence of a nonlinear component. The encryption function in a nonlinear automaton has an additional variable in the block — *bufferForFunc*. This buffer stores the vectors that pass through the nonlinear function before being multiplied by the coefficient matrix.

Results and Discussion

To assess the functional viability of the implemented algorithms, comprehensive tests were conducted, including testing the correct operation of the key generation, encryption, and decryption software modules, as well as an

analysis of the statistical strength of the encrypted data. The experiments performed comprise a set of basic cryptographic tests aimed at verifying the system's ability to provide a sufficient level of data obfuscation while maintaining the ability to correctly recover data from the encrypted representation.

To clearly demonstrate cryptographic transformations, an image was used as the object. The initial data consists of the image's pixel values, represented as a byte stream, which are then encrypted using a finite automaton. This process was implemented using the *Pillow* library, which provides convenient image processing tools in the Python programming environment (Pillow, n.d.). Using the *tobytes()* method of the *Image* class object, the pixel values are extracted in binary form, after which they are passed to the encryption function. The result of the finite automata acting as an encryption mechanism is shown in Figure 8.

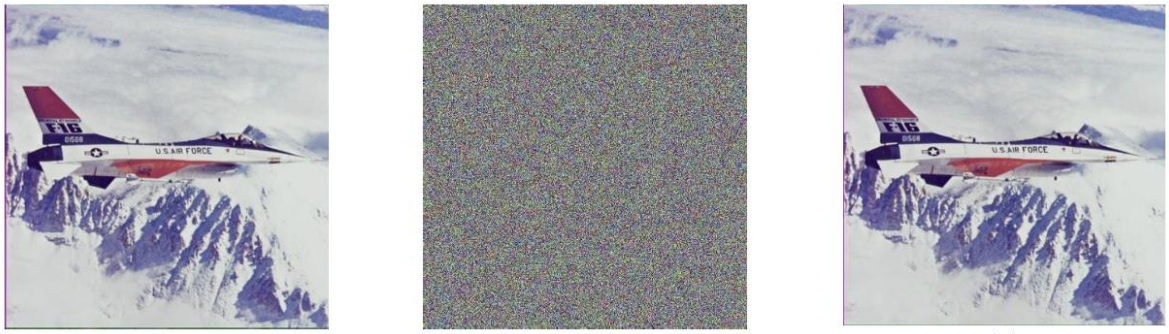


Figure 8. (a) Original, (b) Encrypted and (C) Decrypted image

Statistical Test

A statistical test from the National Institute of Standards and Technology (NIST) was performed (Almaraz, 2024). The NIST test performs bit-by-bit processing of the data and analyzes the distribution of bits across the entire stream using a set of statistical procedures, each aimed at identifying possible patterns in the sequence. The result of each calculation is a *p-value* ranging from 0 to 1; if the p-value is <0.01, the sequence is considered non-random, otherwise it is random. Four encrypted images were used for the experiment (Figure 9): one with a resolution of 512x512 pixels (4.2.05) and three with a resolution of 256x256 pixels (4.1.04–4.1.06), presented in .tiff format and containing color information.

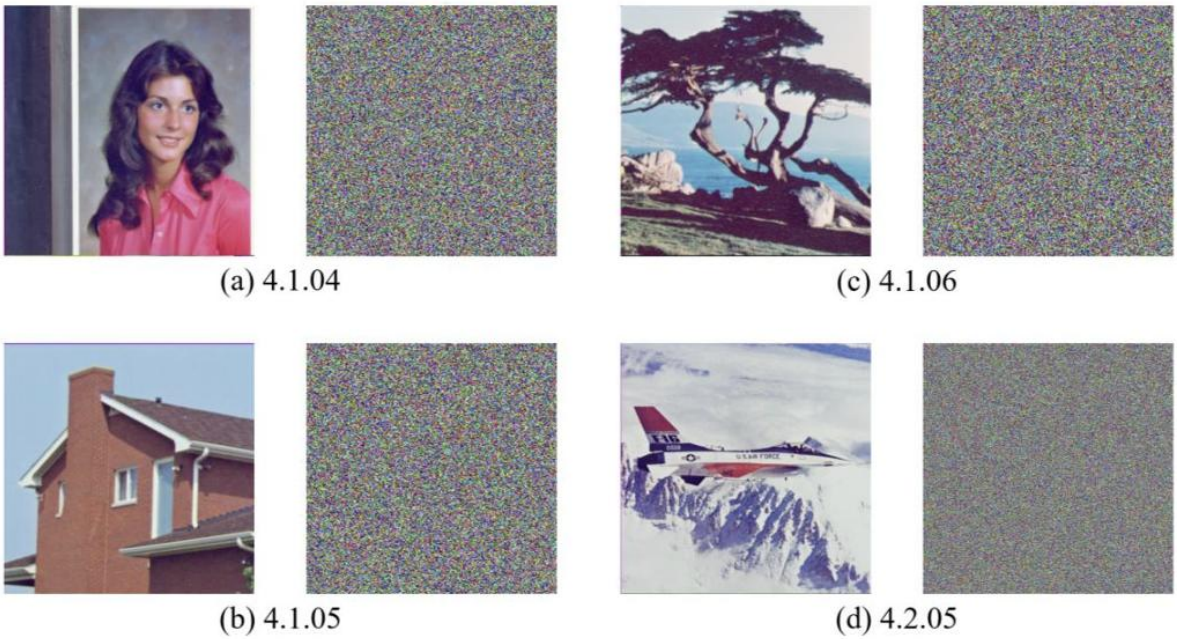


Figure 9. Original and encrypted images

The images were encrypted using a nonlinear finite-state machine with input-output memory. The NIST benchmark calculations use the first 1 million bits of image data, equivalent to 125,000 bytes. The NIST benchmark results are shown in Table 1.

Table 1. Test results NIST

Name of test	4.1.04	4.1.06	4.1.05	4.2.05
Frequency Test	0.2165 (true)	0.8462 (true)	0.7566 (true)	0.1160 (true)
Block Frequency Test	0.5587 (true)	0.6801 (true)	0.7218 (true)	0.6602 (true)
Run Test	0.7245 (true)	0.9936 (true)	0.1331 (true)	0.3146 (true)
Longest Run of Ones	0.8008 (true)	0.1601 (true)	0.5295 (true)	0.3786 (true)
Binary Matrix Rank Test	0.4271 (true)	0.7054 (true)	0.2936 (true)	0.1206 (true)
Discrete Fourier Transform (Spectral) Test	0.2748 (true)	0.8328 (true)	0.3216 (true)	0.7760 (true)
Non-overlapping Template Matching Test	0.7212 (true)	0.5440 (true)	0.0841 (true)	0.7985 (true)
Overlapping Template Matching Test	0.1090 (true)	0.1404 (true)	0.6235 (true)	0.2754 (true)
Universal Statistical Test	0.3271 (true)	0.9034 (true)	0.1256 (true)	0.7157 (true)
Linear Complexity Test	0.8717 (true)	0.3860 (true)	0.7438 (true)	0.0972 (true)
Serial Test 1	0.4772 (true)	0.3326 (true)	0.9797 (true)	0.8152 (true)
Serial Test 2	0.2522 (true)	0.5649 (true)	0.9008 (true)	0.2478 (true)
Approximate Entropy Test	0.2038 (true)	0.6227 (true)	0.9222 (true)	0.6078 (true)
Cumulative Sums (Forward)	0.4193 (true)	0.5264 (true)	0.2724 (true)	0.2273 (true)
Cumulative Sums (Backward)	0.4193 (true)	0.5264 (true)	0.2724 (true)	0.2273 (true)
Random Excursion & Variant Tests	p>0.01 (true)	p>0.01 (true)	p>0.01 (true)	p>0.01 (true)

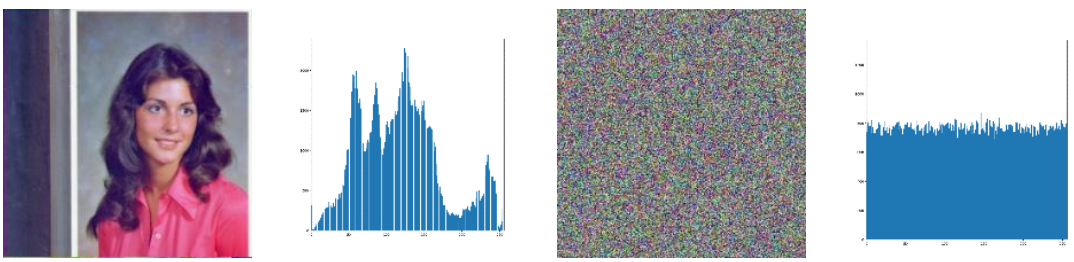
The results for all four data sets show that the p-values for all tests exceed the critical level of 0.01, confirming the absence of statistically significant deviations. Therefore, it can be concluded that the encrypted images exhibit a high degree of randomness and meet the cryptographic strength requirements.

Graphic Tests

Graphical tests are an analysis method based on visualizing encryption results. This approach considers histogram tests, as well as UACI and NPCR metrics, used to assess the sensitivity of a cryptosystem to minor changes in the original data. These tests use encrypted images, in which histograms reflect the distribution of pixel intensities, while UACI and NPCR tests quantify the degree of difference between the original and modified images after encryption.

Histogram

The histogram of an encrypted image is a graphical distribution of the frequencies of luminance values or color components of pixels across the entire image. In the context of cryptographic analysis, it is used to assess the uniformity of the intensity distribution after encryption (Cardona-López et al., 2024). For original (unencrypted) images, the histogram typically has pronounced peaks and patterns reflecting the structure and content of the image (Figure 10b). After encryption, provided the algorithm is working correctly, the histogram of the encrypted image should approach a uniform distribution, where all luminance levels occur with approximately equal frequency (Figure 10d).



(a) (b) (c) (d)

Figure 10. (a) original image 4.1.04, (b) histogram of (a), (c) encrypted image, (d) histogram of (c)

UACI and NPCR tests

The Number of Pixels Change Rate (NPCR) metric characterizes the percentage of changed pixels in the encrypted image when only one pixel in the input image changes. This parameter is used to assess the sensitivity of an encryption algorithm to minimal variations in the source data and, therefore, the cryptosystem's resistance to differential attacks (Asghar, 2023). The formal expression for calculating NPCR is presented in the formula:

$$NPCR = \frac{1}{W \times H} \sum_{i=1}^{W} \sum_{i=1}^{H} D(C1_{i,j}, C2_{i,j}), \tag{7}$$

C1 and C2 two encrypted images, W and H size of image. $D(C1_{i,j}, C2_{i,j})$ calculate:

$$D(C1_{i,j}, C2_{i,j}) = \begin{cases} 0, if C1_{i,j} = C2_{i,j} \\ 1, if C1_{i,j} \neq C2_{i,j} \end{cases}. \tag{8}$$

The Unified Average Changing Intensity (UACI) metric reflects the average difference in intensity between two encrypted images, expressed as a percentage. These images are generated from the original and a slightly modified original, allowing one to evaluate the sensitivity of a cryptosystem to minimal changes in the input data (Zhang, 2021). The UACI calculation analyzes the byte intensity values of each color channel (red, green, and blue) separately, providing a more accurate assessment of the uniformity and unpredictability of pixel distribution.

$$UACI = \frac{1}{W \times H} \sum_{i=1}^{W} \sum_{j=1}^{H} |C1_{i,j} - C2_{i,j}|, \tag{9}$$

where $C1_{i,j}$ and $C2_{i,j}$ pixel intensity values of two encrypted images.

The results of the tests performed are shown in Table 2.

Table 2. Results of NPCR and UACI

Name of test	Chanel	4.1.04	4.1.06	4.1.05	4.2.05
NPCR	RGB	99.592590	99.603780	99.596151	99.617004
UACI	Red	33.507888	33.313413	33.502179	33.550233
	Green	33.546938	33.597089	33.440636	33.572581
	Blue	33.280017	33.345552	33.523266	33.492114

The NPCR test determines how much the encryption result changes with minimal input data change, expressed as a percentage. A pass on the NPCR test is a score of 99% or higher. The ideal UACI test result, indicating that images have a high intensity difference, is 33% (Loukhaoukha et al., 2013). As can be seen from Table 2, all images meet these criteria and demonstrate good results.

Conclusion

In this study, algorithms for the generation of invertible linear and nonlinear finite automata with input–output memory were developed and implemented as a software module forming the basis of the FAPKC cryptosystem series. The research included detailed formalization of the automaton construction procedures, design of key generation methods, and implementation of encryption and decryption algorithms based on linear and nonlinear automata structures. The developed software, created in Python using the NumPy and SciPy libraries, provided a complete computational environment for modeling automaton-based cryptographic transformations and their inversions.

Comprehensive experimental testing confirmed the correctness and reliability of the proposed algorithms. The NIST statistical tests demonstrated high randomness and uniformity of encrypted data, as all *p*-values exceeded the 0.01 threshold, confirming the absence of statistical regularities. Graphical analyses, including histogram, NPCR, and UACI evaluations, also supported the cryptographic strength of the system. The NPCR values exceeded 99%, and UACI values were close to the theoretical ideal of 33%, indicating high sensitivity to minor input changes and effective diffusion properties. Overall, the performed work proves the efficiency of using finite automata with input–output memory for building secure and computationally efficient cryptographic systems. The obtained results can serve as a foundation for further research aimed at optimizing nonlinear transformations,

improving key management, and integrating automaton-based encryption into modern communication and data protection systems.

Scientific Ethics Declaration

* The authors declare that the scientific ethical and legal responsibility of this article published in EPSTEM journal belongs to the authors.

Conflict of Interest

* The authors declare that they have no conflicts of interest

Funding

* This research is funded by the Science Committee of the Ministry of Education and Science of the Republic of Kazakhstan (Grant No. AP19677422).

Acknowledgements or Notes

* This article was presented as an oral presentation at the International Conference on Technology, Engineering and Science (www.icontes.net) held in Antalya/Türkiye on November 12-15, 2025.

* The authors would like to thank the conference committee and the reviewers who reviewed the article for their valuable contributions.

References

Almaraz Luengo, E. (2024). Statistical tests suites analysis methods. Cryptographic recommendations. *Cryptologia, 48*(3), 219-251.

Asghar, L., Ahmed, F., Khan, M. S., Arshad, A., & Ahmad, J. (2023). Noise-crypt: Image encryption with non-linear noise, hybrid chaotic maps, and hashing. In *2023 International Conference on Engineering and Emerging Technologies (ICEET)* (pp. 1-5). IEEE.

Cardona-López, M. A., Chimal-Eguía, J. C., Silva-García, V. M., & Flores-Carapia, R. (2024). Statistical analysis of the negative–positive transformation in image encryption. *Mathematics, 12*(6), 908.

Focardi, R., & Luccio, F. L. (2018, September). Neural cryptanalysis of classical ciphers. In *ICTCS* (pp. 104-115).

Katerinsky, D. A. (2013). On the reversibility of finite automata with finite delay. *Applied Discrete Mathematics. Appendix, 6*, 35–36.

Kodada, B. (2022). FSAaCIT: Finite state automata based one-key cryptosystem and chunk-based indexing technique for secure data de-duplication in cloud computing. *Authorea Preprints*.

Kohavi, Z., & Jha, N. K. (2009). *Switching and finite automata theory*. Cambridge University Press.

Loukhaoukha, K., Nabti, M., & Zebbiche, K. (2013, May). An efficient image encryption algorithm based on blocks permutation and Rubik's cube principle for iris images. In *2013 8th International Workshop on Systems, Signal Processing and Their Applications (WoSSPA)* (pp. 267–272). IEEE.

Meskanen, T. (2001). *On finite automaton public key cryptosystems*. Turku Centre for Computer Science.

Pillow. (n.d.). *Pillow 11.2.1 Documentation*. Retrieved from https://pillow.readthedocs.io/en/stable/index.html

Satybaldina, D., Sharipbayev, A., & Adamova, A. (2011). Implementation of the finite automaton public key cryptosystem on FPGA. In *WOSIS* (pp. 167–173).

Shakhmetova, G., Barlybayev, A., Saukhanova, Z., Sharipbay, A., Raykul, S., & Khassenov, A. (2024). Enhancing visual data security: A novel FSM-based image encryption and decryption methodology. *Applied Sciences, 14*(11), 4341.

Tao, R. (2008). *Finite automata and application to cryptography*. Springer.

Tao, R., & Chen, S. (1999). The generalization of public key cryptosystem FAPKC4. *Chinese Science Bulletin, 44*(9), 784-790.

Tao, R., Chen, S., & Chen, X. (1997). FAPKC3: A new finite automaton public key cryptosystem. *Journal of Computer Science and Technology, 12*(4), 289-305.

Zhang, Y. (2021). Statistical test criteria for sensitivity indexes of image cryptosystems. *Information Sciences, 550*, 313-328.

Author(s) Information

Gulmira Shakhmetova
L.N. Gumilyov Eurasian National University
Pushkin street 11, Astana, Kazakhstan
Contact e-mail: *sh_mira2004@mail.ru*

Khassenov Altay
L.N. Gumilyov Eurasian National University
Pushkin street 11, Astana, Kazakhstan

Zhanat Saukhanova
L.N. Gumilyov Eurasian National University
Pushkin street 11, Astana, Kazakhstan

Altynbek Sharipbay
L.N. Gumilyov Eurasian National University
Pushkin street 11, Astana, Kazakhstan

Alibek Barlybayev
L.N. Gumilyov Eurasian National University
Pushkin street 11, Astana, Kazakhstan

Raykul Sayat
L.N. Gumilyov Eurasian National University
Pushkin street 11, Astana, Kazakhstan

To cite this article:

Shakhmetova, G., Altay K., Saukhanova, Z., Sharipbay A., Barlybayev A., & Sayat, R. (2025). Generation algorithms of invertible linear and nonlinear finite automata with memory. *The Eurasia Proceedings of Science, Technology, Engineering and Mathematics (EPSTEM), 38,* 655-666.

The Eurasia Proceedings of Science, Technology, Engineering & Mathematics (EPSTEM)
ISSN: 2602-3199

The Eurasia Proceedings of Science, Technology, Engineering and Mathematics (EPSTEM), 2025

Volume 38, Pages 667-671

IConTES 2025: International Conference on Technology, Engineering and Science

Investigation of Corrosion Properties of Lead-Free Solder Alloys in 3.5% NaCl Solution

Resat Can Ozden
Eskisehir Osmangazi University

Abstract: The restriction of lead-based solders due to environmental and health concerns has made the use of lead-free alloys essential in the electronics industry. Among the available alternatives, tin-based systems containing silver and copper have been extensively studied for their potential to provide reliable and sustainable soldering solutions. This study investigates the corrosion behavior of Sn–Ag, Sn–Cu, and Sn–Cu–Ag solder alloys in a 3.5% NaCl solution, simulating chloride-induced conditions commonly encountered by electronic components in humid or coastal environments. The samples were subjected to potentiodynamic polarization tests using a three-electrode system consisting of a saturated calomel electrode (SCE) as reference, a platinum counter electrode, and the solder alloy as the working electrode. The electrochemical results revealed clear distinctions among the tested alloys. The Sn–Cu–Ag alloy exhibited the lowest corrosion current density (4.3×10^{-6} A/cm²) and the most positive corrosion potential (–0.733 V vs. SCE), better corrosion resistance compared to binary Sn–Ag and Sn–Cu systems. Both Sn–Ag and Sn–Cu alloys also achieved current densities around the 10^{-6} A/cm² threshold, which is generally considered acceptable for electronic solder joints, confirming their applicability under mild corrosive conditions. Overall, the results highlight that the Sn–Cu–Ag system offers the most balanced performance and electrochemical durability. The findings contribute to the optimization of lead-free solder materials and support their integration into reliable, long-life electronic assemblies.

Keywords: Soldering, Corrosion, Tin

Introduction

The continuous evolution of environmental regulations and the Restriction of Hazardous Substances (RoHS) directive have led to a global shift toward lead-free solder materials in the electronics industry. Traditional tin–lead (Sn–Pb) solders, despite their excellent wettability, low melting point, and mechanical reliability, have been progressively phased out due to the toxicological risks associated with lead exposure (Farina & Morando, 2015). As a result, tin-based alloys such as Sn–Ag, Sn–Cu, and Sn–Ag–Cu systems have gained prominence as potential replacements owing to their comparable melting characteristics and mechanical stability (Li et al., 2020).

Among these, Sn–Ag–Cu alloys are considered the most balanced alternative due to their near-eutectic composition, good wetting behavior, and reliable electrical performance. The Sn–3.0Ag–0.5Cu alloy, in particular, has become a benchmark material in high-reliability applications such as aerospace and automotive electronics (Chen et al., 2025). However, despite its widespread adoption, the long-term corrosion performance of these alloys in chloride-rich environments remains a key concern, as electronic assemblies often encounter humid or marine conditions that promote electrochemical degradation.

Corrosion in solder alloys generally involves the anodic dissolution of tin and the subsequent formation of corrosion products such as SnO, SnO_2, and $Sn_3O(OH)_2Cl_2$, depending on the presence of chloride ions in the environment (Li et al., 2020). Studies have shown that the corrosion resistance of lead-free alloys is highly

- This is an Open Access article distributed under the terms of the Creative Commons Attribution-Noncommercial 4.0 Unported License, permitting all non-commercial use, distribution, and reproduction in any medium, provided the original work is properly cited.

- Selection and peer-review under responsibility of the Organizing Committee of the Conference

© 2025 Published by ISRES Publishing: www.isres.org

sensitive to their microstructural features—particularly the morphology and distribution of intermetallic compounds (IMCs) such as Ag_3Sn and Cu_6Sn_5 (Mohanty & Lin, 2007). Fine and uniformly dispersed IMCs can promote the stability of passive films, whereas coarse or plate-like morphologies may act as initiation sites for localized corrosion (Tunthawiroon & Kanlayasiri, 2019).

The effect of silver and copper concentration on the corrosion performance of Sn-Ag-Cu alloys has been explored in various works. For instance, increasing Ag content beyond 2 wt.% enhances passivation and refines the eutectic structure, though excessive Ag promotes large Ag_3Sn platelets that deteriorate mechanical ductility (Rosalbino et al., 2008). On the other hand, Cu additions contribute to improved passivity and the formation of compact corrosion layers, reducing ion migration and pitting susceptibility (Farina & Morando, 2015).

This study focuses on the corrosion characteristics of Sn–Ag, Sn–Cu, and Sn–Ag–Cu lead-free solder alloys under 3.5% NaCl conditions, employing potentiodynamic polarization techniques. The objective is to establish a comparative understanding of their electrochemical behavior, identify microstructural factors governing corrosion resistance, and support the ongoing optimization of environmentally compliant and durable solder materials.

Method

In this study, commercially available and previously homogenized Sn–Ag, Sn–Cu, and Sn–Ag–Cu lead-free solder alloys were used (Table 1). Each sample surface was mechanically abraded using 1200-grit SiC sandpaper to remove surface oxides and irregularities. Following this, polishing was performed with 6 µm and 3 µm diamond suspensions to obtain a mirror-like finish suitable for electrochemical analysis. After surface preparation, all specimens were rinsed sequentially with distilled water and ethanol in an ultrasonic bath, then dried with clean air before testing.

Table 1. Chemical composition of the tested solder alloys (wt.%).

Alloy Code	**Sn (wt.%)**	**Ag (wt.%)**	**Cu (wt.%)**
Sn–Ag	96.5	3.5	–
Sn–Cu	99.3	–	0.7
Sn–Cu–Ag	96.5	3.0	0.5

To simulate a corrosive environment and investigate the influence of chloride ions on localized corrosion, a 3.5 wt.% NaCl solution was prepared as the main electrolyte. Chloride ions (Cl^-) are known to promote pitting corrosion, which poses a significant threat to electronic solder materials. To ensure adequate ionic conductivity within the test medium, 0.1 M K_2SO_4 was added to the solution. Additionally, 0.1 M K_2HPO_4 was introduced to stabilize the pH and provide a buffering effect. The mixture was continuously stirred on a magnetic stirrer to achieve a homogeneous solution. The pH of the prepared electrolyte was carefully monitored using a calibrated pH meter and adjusted to 7.0 ± 0.1 with H_2SO_4. All experiments were conducted at room temperature. Electrochemical corrosion tests were carried out using a standard three-electrode system in a single-compartment electrochemical cell. A saturated calomel electrode (SCE) served as the reference electrode, a platinum electrode as the counter electrode, and the prepared solder alloy as the working electrode. The exposed surface area of the working electrode was 0.785 cm^2.

Prior to each measurement, the electrolyte was deaerated with argon gas to minimize oxygen interference. Potentiodynamic polarization curves were obtained using a GAMRY Interface 1010B potentiostat, controlled by dedicated computer software. After reaching a stable open-circuit potential, the polarization scan was initiated from –0.5 V to +1 V (vs. SCE) at a rate of 1 mV/s. Throughout the experiment, both potential and current density values were continuously recorded. The corrosion potential (E_{corr}) and corrosion current density (I_{corr}) were determined using Tafel extrapolation from the polarization curves.

Results and Discussion

Potentiodynamic polarization tests were performed to evaluate the corrosion behavior of Sn–Ag, Sn–Cu, and Sn–Ag–Cu solder alloys in the prepared 3.5 wt.% NaCl electrolyte. The corrosion performance of these alloys was primarily assessed through their electrochemical response in 3.5 wt.% NaCl solution. As summarized in Table 2, the measured corrosion potentials (E_{corr}) and corrosion current densities (I_{corr}) indicate that all three

solder systems exhibited similar tendencies toward anodic dissolution, with small variations depending on alloy composition.

Table 2. Electrochemical parameters (E_{corr} and I_{corr}) of Sn–Ag, Sn–Cu, and Sn–Cu–Ag solder alloys obtained from potentiodynamic polarization measurements.

Alloy Composition	**Ecorr(V vs. SCE)**	**Icorr(A·cm^{-2})**
Sn–Ag	–0.753	7.24×10^{-6}
Sn–Cu	–0.748	8.94×10^{-6}
Sn–Cu–Ag	–0.733	4.30×10^{-6}

The polarization curves, illustrated in Figure 1, represent the potentiodynamic test results obtained for each alloy system, while Figure 2 presents an enlarged view of the open-circuit potential (OCP) region showing the detailed potential stabilization prior to anodic polarization.

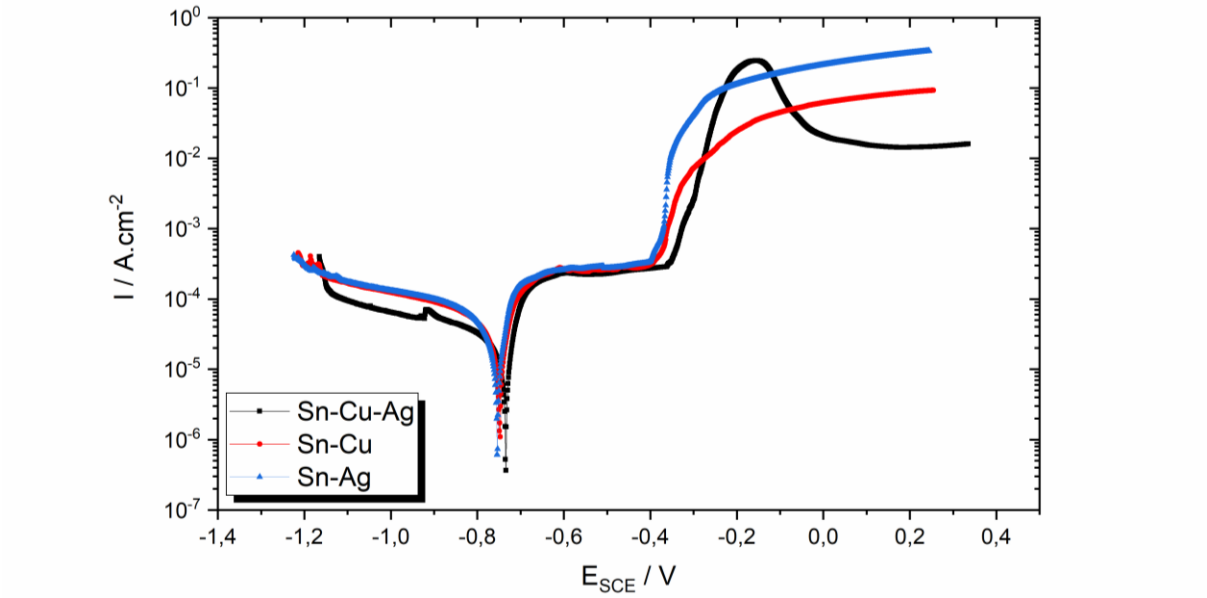


Figure 1**.** Potentiodynamic polarization curves of Sn–Ag, Sn–Cu, and Sn–Ag–Cu solder alloys in 3.5 wt.% NaCl solution.

All samples exhibited active–passive transitions typical of tin-based alloys exposed to chloride-containing environments. The Sn–Cu–Ag alloy displayed a more positive corrosion potential ($E_{corr} \approx -0.733$ V vs. SCE) and lower corrosion current density ($I_{corr} \approx 4.3\times10^{-6}$ A/cm²) compared with the binary Sn–Ag and Sn–Cu systems. This indicates a lower corrosion rate and better electrochemical stability under the tested conditions. These results align with those reported by Mohanty and Lin (2007), who observed improved passivation behavior in Sn–Ag–Cu systems due to the formation of stable SnO and SnO_2 surface films.

The Sn–Ag and Sn–Cu alloys showed close potential values (–0.753 V and –0.748 V, respectively), suggesting comparable thermodynamic behavior in chloride-containing environments. However, the slightly higher Icorr value observed for Sn–Cu (8.94×10^{-6} A·cm^{-2}) implies a faster dissolution rate than Sn–Ag (7.24×10^{-6} A·cm^{-2}). This difference can be explained by the galvanic interaction between the β-Sn matrix and the Cu_6Sn_5 intermetallic compound, which promotes localized anodic activity (Farina & Morando, 2015). In contrast, Sn–Ag exhibits partial passivation due to Ag_3Sn formation, though local micro-galvanic cells between Ag-rich and Sn-rich regions may still initiate minor pitting events (Tunthawiroon & Kanlayasiri, 2019).

The Sn–Cu–Ag alloy presented a more positive E_{corr} (–0.733 V) and the lowest I_{corr} (4.30×10^{-6} A·cm^{-2}), indicating a more stable passive behavior. The improved stability is attributed to the combined influence of Ag and Cu, which enhance electrochemical homogeneity and facilitate the formation of a more protective oxide film. These results are consistent with previous findings that emphasize the effect of chloride ions on passive film breakdown. As reported by Pu et al. (2024) and Li et al. (2020), Cl^- ions interact with surface oxides to form soluble complexes such as $SnCl_2$ and $Sn_3O(OH)_2Cl_2$, leading to localized corrosion. Nevertheless, the alloys tested here maintained passivation trends, suggesting that chloride attack was mitigated by the inherent tin-oxide layer formed during exposure.

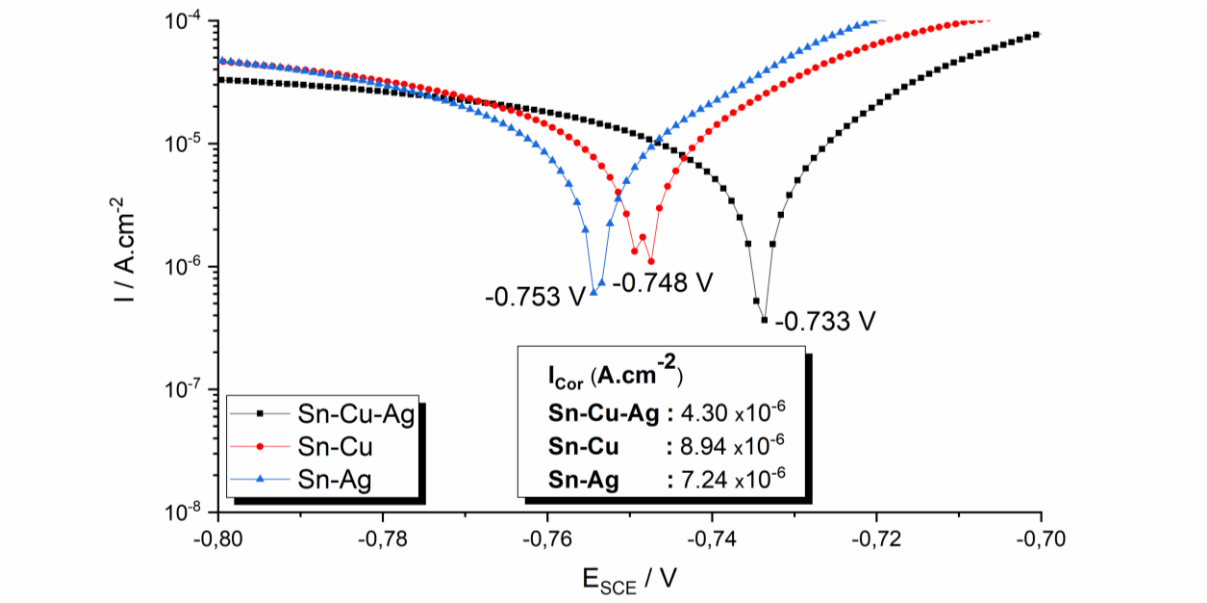


Figure 2**.** Enlarged view of the open-circuit potential (OCP) region of the polarization curves.

Conclusion

This study evaluated the electrochemical corrosion behavior of Sn–Ag, Sn–Cu, and Sn–Cu–Ag lead-free solder alloys in a 3.5 wt.% NaCl electrolyte using potentiodynamic polarization analysis. The results demonstrated that all three solder systems exhibited passivation behavior typical of tin-based alloys in chloride-containing environments. Among the tested compositions, Sn–Ag and Sn–Cu alloys showed similar thermodynamic tendencies toward anodic dissolution, though the Sn–Cu alloy recorded a slightly higher corrosion current density, indicating a somewhat faster dissolution process. The differences in their corrosion performance were mainly attributed to the galvanic interactions between the β-Sn matrix and respective intermetallic phases. The Sn–Cu–Ag alloy presented a more positive corrosion potential and the lowest corrosion current density, suggesting enhanced passivity and improved stability of the surface oxide film. This behavior can be ascribed to the combined influence of Ag and Cu, which promotes a more homogeneous electrochemical response.

Overall, the findings confirm that the Sn–Cu–Ag system offers a more favorable balance of corrosion resistance and environmental compliance compared to binary tin-based solders. These outcomes contribute to the broader understanding of lead-free solder reliability under chloride-induced corrosion conditions and provide valuable insight for future material selection and design in electronic applications.

Scientific Ethics Declaration

* The author declares that the scientific ethical and legal responsibility of this article published in EPSTEM journal belongs to the author.

Conflict of Interest

* The author declares no conflicts of interest

Funding

* Financial assistance from Eskisehir Osmangazi University Research Fund is gratefully acknowledged (Project No: FHD-2025-3453)

Acknowledgements or Notes

* This article was presented as an oral presentation at the International Conference on Technology, Engineering and Science (www.icontes.net) held in Antalya/Türkiye on November 12-15, 2025.

References

Chen, W., Chen, B., & Hu, X. (2025). Microstructure, corrosion and mechanical properties of Sn–3.0Ag–0.5Cu solder alloy aged at 150 °C. *Journal of Materials Science: Materials in Electronics, 36*, 808.

Farina, S., & Morando, C. (2015). Comparative corrosion behaviour of different Sn-based solder alloys. *Journal of Materials Science: Materials in Electronics, 26*, 464-471.

Li, S., Wang, X., Liu, Z., Jiu, Y., Zhang, S., Geng, J., & Wu, S. (2020). Corrosion behavior of Sn-based lead-free solder alloys: A review. *Journal of Materials Science: Materials in Electronics, 31*, 9076-9090.

Mohanty, U. S., & Lin, K. L. (2007). Electrochemical corrosion study of Sn–XAg–0.5Cu alloys in 3.5% NaCl solution. *Journal of Materials Research, 22*(9), 2573-2582.

Pu, C., Li, C., Miao, Y., Lu, Q., Peng, J., Xu, Z., & Yi, J. (2024). Electrochemical corrosion behaviour and corrosion mechanism of Sn–9Zn–xGe solder alloys in NaCl solution. *Corrosion Science, 228*, 111809.

Rosalbino, F., Angelini, E., Zanicchi, G., & Marazza, R. (2008). Corrosion behaviour assessment of lead-free Sn–Ag–M (M = In, Bi, Cu) solder alloys. *Materials Chemistry and Physics, 109*, 386-391.

Tunthawiroon, P., & Kanlayasiri, K. (2019). Effects of Ag contents in Sn–xAg lead-free solders on microstructure, corrosion behavior and interfacial reaction with Cu substrate. *Transactions of Nonferrous Metals Society of China, 29*(7), 1696-1704.

Author(s) Information

Resat Can Ozden
Eskisehir Osmangazi University
Eskisehir, Turkiye
Contact e-mail: *rcanozden@ogu.edu.tr*

To cite this article:

Ozden, R.C. (2025). Investigation of corrosion properties of lead-free solder alloys in 3.5% NaCl solution. *The Eurasia Proceedings of Science, Technology, Engineering and Mathematics (EPSTEM), 38,* 667-671.

The Eurasia Proceedings of Science, Technology, Engineering & Mathematics (EPSTEM)
ISSN: 2602-3199

The Eurasia Proceedings of Science, Technology, Engineering and Mathematics (EPSTEM), 2025

Volume 38, Pages 672-681

IConTES 2025: International Conference on Technology, Engineering and Science

Evaluation of Nonlinear Fracture Quantities in Lime-Pumice Mixtures

Erkin Eren
Firat University

Ragip Ince
Firat University

Abstract: The tests on fracture mechanics of quasi-brittle materials until the 1970s indicated that linear elastic fracture mechanics (LEFM) was not valid for cement-based materials such as mortar and concrete. This inapplicability of LEFM is due to the existence of an inelastic zone, which is also so-called fracture process. Therefore, numerous non-Hookean fracture models have been introduced to evaluate fracture quantities in quasi-brittle materials. According to the two-parameter model (TPM) in concrete fracture, a free crack propagates unstably whenever the stress intensity factor and the crack tip opening displacement are equal to their threshold values, such as Mode I fracture toughness and critical crack tip opening displacement, respectively. In this study, beams, cubes and square prismatic specimens with three different initial crack lengths were produced to calculate fracture quantities of lime-pumice mixtures. Beams with a maximum aggregate diameter (g) of 4 mm were kept in the mold for 28 days while cubes with g=4 mm and square prismatic specimens with g=16 mm were saved in the mold for 90 days. The fracture quantities of the mixtures were evaluated by employing the modified peak load method, which was recently derived to determine fracture properties of TPM.

Keywords: Fracture mechanics, Lime, Pumice, Two-parameter model

Introduction

The first attempt to apply Linear Elastic Fracture Mechanics (LEFM) to cement-based composites was conducted by Kaplan (1961) and later expanded upon by Kesler et al. (1972). Their work revealed that LEFM does not adequately capture the fracture response of concrete. This limitation stems from the presence of a relatively large inelastic zone ahead of the crack tip in quasi-brittle materials such as concrete mixtures, rocks, and asphalt concrete. To address this shortcoming, several nonlinear fracture mechanics models have been introduced to more realistically describe fracture-governed failures in concrete. Among these are the fictitious crack model of Hillerborg et al. (1976), the crack band model proposed by Bazant and Oh (1983), the two-parameter model (TPM) by Jenq and Shah (1985), the effective crack model of Nallathambi and Karihaloo (1986), the size effect model (SEM) introduced by Bazant and Kazemi (1990), the double-K model developed by Xu and Reinhardt (1999), and the boundary effect method by Hu and Duan (2008).

Roman mortars represent the earliest form of concrete, composed of lime, water, sand, and volcanic tuff, facilitating the creation of edifices that have endured for almost two thousand years, with notable instances including the Pantheon temple and the Colosseum. The Pantheon temple continues to function as an exhibition hall today. The Colosseum suffered significant damage due to a catastrophic earthquake in 412 AD. Previously, during the period when Rome embraced Christianity, numerous valuable stone fragments were incorporated into the construction of various other buildings. Currently, one-third of the Colosseum remains, predominantly consisting of its concrete structure. Conversely, in Seljuk and Ottoman architectural styles, a substantial number

- This is an Open Access article distributed under the terms of the Creative Commons Attribution-Noncommercial 4.0 Unported License, permitting all non-commercial use, distribution, and reproduction in any medium, provided the original work is properly cited.

- Selection and peer-review under responsibility of the Organizing Committee of the Conference

© 2025 Published by ISRES Publishing: www.isres.org

of buildings constructed with Khorasan mortar-comprising lime, sand, water, and ground-baked clay (brick) have persisted to the present day.

In this research, beams, cubes, and square prismatic specimens featuring three distinct initial crack lengths were created to assess the fracture characteristics of lime-pumice mixtures. Beams with a maximum aggregate diameter (g) of 4 mm were maintained in the mold for a duration of 28 days, whereas cubes with g=4 mm and square prismatic specimens with g=16 mm were retained in the mold for 90 days. The fracture characteristics of the mixtures were analyzed using the modified peak load method, which has been recently developed to evaluate the fracture properties of TPM.

The Two-Parameter Model (TPM) in Concrete Fracture

During the 1970s, experimental investigations into the fracture behavior of cement-based composites—including paste, mortar, and concrete—indicated that the traditional framework of Linear Elastic Fracture Mechanics (LEFM) could not adequately represent quasi-brittle materials (Kesler et al., 1972). The primary limitation originates from the formation of a relatively large inelastic region, referred to as the fracture process zone (FPZ), which develops in front of and surrounding major crack tips. To address this issue, several nonlinear fracture mechanics models have been introduced to more accurately describe the FPZ.

These approaches are generally classified into cohesive crack models and effective crack models, one notable example being the two-parameter fracture model (TPM) proposed by Jenq and Shah (1985). The fundamental objective of these models is to evaluate the critical crack extension, expressed as $\Delta a = a_c - a_0$, where ac denotes the crack length at peak load and a_0 represents the initial notch length. This parameter is typically obtained from either the load–displacement curve or the load–crack mouth opening displacement relationship of the tested structure.

According to the Two-Parameter Model (TPM), fracture in a concrete structure occurs when the stress intensity factor (K_I) and the crack tip opening displacement ($CTOD$) both attain their corresponding critical thresholds, denoted as K^s_{Ic} and $CTOD_c$. These characteristic fracture parameters can be evaluated using the following formulations derived from Linear Elastic Fracture Mechanics (LEFM):

$$K_{Ic}^{s} = \sigma_{Nc}\sqrt{\pi a_c}\,Y\left(g,l\right) \tag{1}$$

$$CTOD_c = \frac{\gamma\sigma_{Nc}a_c}{E}V_1\left(g,l\right)M\left(g,l\right) \tag{2}$$

Here, σ_{Nc} denotes the nominal failure stress, E represents Young's modulus, and Y, V_1, and M are dimensionless parameters that are functions of both the structural geometry (g) and the loading configuration (l). In Eq. (2), the coefficient γ takes the value of π for splitting specimens and 4 for beams. The term Y is commonly referred to as the geometry factor, while M is obtained from the ratio COD(a_c)/CMOD$_c$, where $CMOD_c$ corresponds to the critical crack mouth opening displacement. The TPM is particularly convenient for structural applications, since the functions Y, V_1, and M can be readily found in Linear Elastic Fracture Mechanics (LEFM) reference handbooks (Tada et al., 2000).

In the two-parameter model (TPM), fracture properties can be evaluated using two main experimental procedures: the compliance method, first proposed by Jenq and Shah (1985), and the peak-load method, later developed by Tang et al. (1996). The compliance approach determines the parameters from the correlation between the applied load and the crack mouth opening displacement (P–CMOD) obtained from a three-point bending specimen of width b, depth d, and span S. This procedure requires a closed-loop testing system, as schematically shown in Figure 1a. Within TPM, the critical crack length (a_c) is calculated from the unloading compliance (C_u) measured at 95% of the maximum load, as illustrated in Figure 1b.

The peak-load method, in contrast, eliminates the need for sophisticated closed-loop equipment and thus provides a simpler alternative to the RILEM compliance-based procedure for calculating fracture parameters in TPM. Nevertheless, this approach still requires a minimum of three specimens to account for the variability inherent in concrete. The test specimens may either share identical geometrical dimensions but differ in their initial notch lengths, or they may exhibit consistent notch sizes while varying in overall dimensions. For each individual specimen, the governing equations of TPM can be expressed as formulated by Tang et al. (1992).

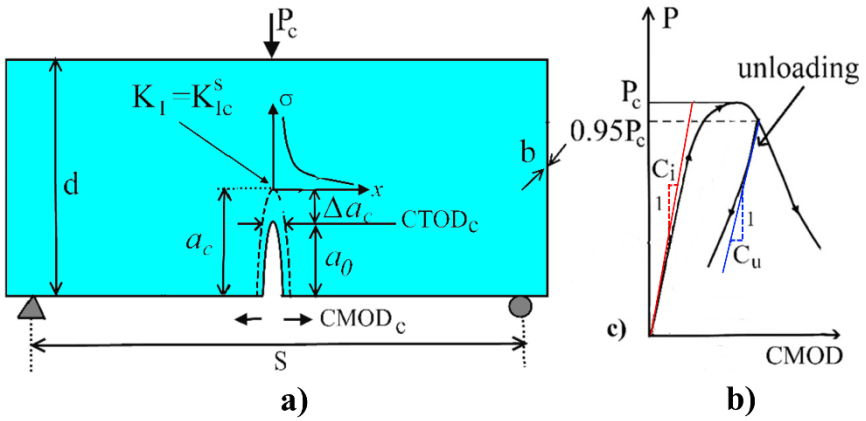


Figure 1. Modeling based on TPM a) notched beam b) typical load-CMOD curve

$$K_I^i\left(\sigma_{Nc}^i, a_c^i\right) = K_{Ic}^s \qquad , i = 1,2$$
$$CTOD^i\left(\sigma_{Nc}^i, a_c^i\right) = CTOD_c \tag{3}$$

here i denotes the ith specimen. Consequently, the fracture parameters can be found by simultaneously solving four non-linear equations. However, three or more distinct specimens must be tested to ensure statistically valid results because random errors always exist in measured values of σ^1_{Nc} and σ^2_{Nc}.

Ince (2025a) was recently developed the modified peak load method based on an optimization procedure to calculate K^s_{Ic} and $CTOD_c$. This approach is based on the simultaneous solution of equation (3) as the failure criterion of a concrete structure. As mentioned above, the main aim of any fracture model is to evaluate the critical crack extension (Δa) at the peak load. Accordingly, for this problem, it may be sufficient to find the nominal strength value (σ_{Nc}) corresponding to the peak load and the Δa value for the initial crack length (a_0) for each sample. These Δa values calculated for each sample should be such that the same fracture parameters (K^s_{Ic} and $CTOD_c$) are met for all tested samples. However, it is impossible to obtain an exact solution for a heterogeneous material like concrete. Consequently, such a problem can only be approached using optimization techniques. To find the fracture parameters of TPM, the following two expressions were initially minimized by utilizing the least squares error criterion:

$$f\left(K_{Ic}^s\right) = \sum_{i=1}^{n} \Delta^2\left(K_{Ic}^s\right) = \sum_{i=1}^{n}\left(K_{Ic,i}^s - \overline{K_{Ic,i}^s}\right)^2 \tag{4}$$

$$f\left(CTOD_c\right) = \sum_{i=1}^{n} \Delta^2\left(CTOD_c\right) = \sum_{i=1}^{n}\left(CTOD_{c,i} - \overline{CTOD_{c,i}}\right)^2 \tag{5}$$

Here n is the number of samples tested, $\overline{K_{Ic,i}^s}$ is the average value of K^s_{Ic} and $K^s_{Ic,i}$ is the value of K^s_{Ic} or the i^{th} sample in Equation 4 while $\overline{CTOD_{c,i}}$ is the average value of $CTOD_c$ and $CTOD_{ci}$ is the value of $CTOD_c$ for the i^{th} sample in Equation 5. On the other hand, to provide the simultaneous solution of the above two minimization equations, the root sum squared (RSS) method, which is also called the statistical tolerance analysis method, was used as follows:

$$RSS = \sqrt{\left(f\left(K_{Ic}^s\right)\right)^2 + \left(f\left(CTOD_c\right)\right)^2} \tag{6}$$

Note that although, in practice, K^s_{Ic} and $CTOD_c$ are commonly used in terms of MPa√m and mm, respectively, it is recommended to choose MPa√mm and μm because the quantities in these units are very different from each other. The procedures described above, which form the basis of the modified peak load method, can be easily implemented using a spreadsheet-based program such as the MS-EXCEL-based SOLVER toolkit.

Fracture test specimens such as beams (Figure 1a), notched split tension cylinders/cubes (Figure 2a), compact compression specimens (Figure 2b), wedge-splitting specimens (Figure 2c), cube with edge notch (Figure 2d) and semi-circular bending (SCB) specimens (Figure 2e) can be employed in the peak-load method, only beams are initially used in the compliance method proposed by RILEM. However, the SCB specimens were recently used to analyze rock materials by Ince (2025b) according to the compliance method.

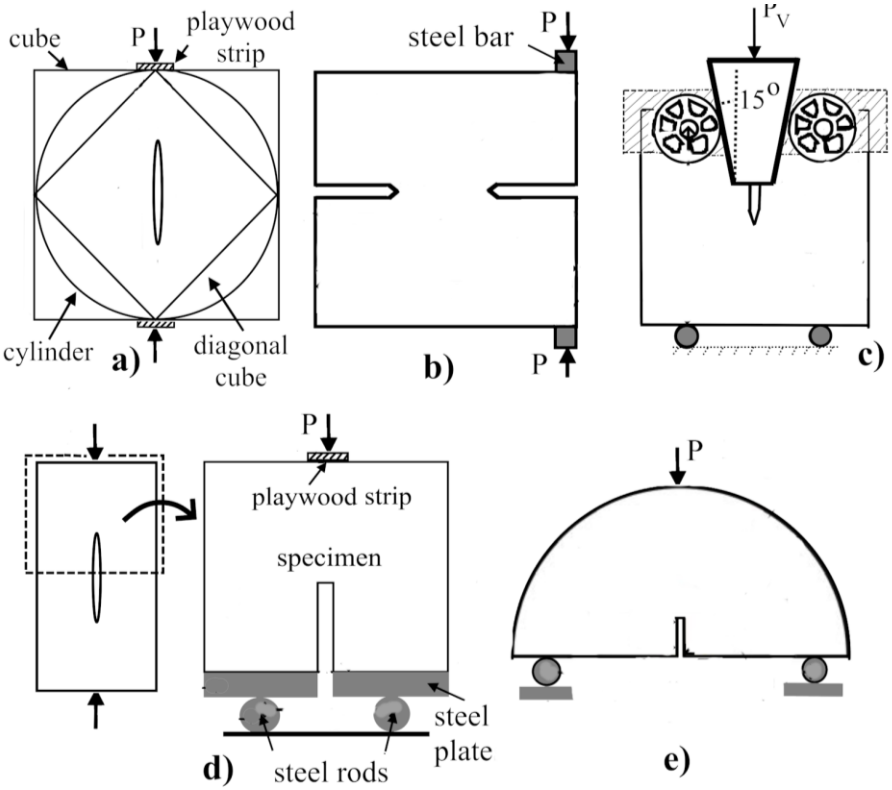


Figure 2. Compact specimens used in concrete fracture a) splitting specimens b) compact compression specimens c) wedge spitting specimens d) cube with edge notch e) semi-circular bending specimens

Experimental Program

The mixtures with a maximum aggregate diameter of 4 mm were in a water: lime: pumice: aggregate ratio of 1.53:1.00:1.00:6.00, while the mixture with a maximum aggregate diameter of 16 mm were in a water: lime: pumice: aggregate ratio of 1.42:1.00:1.00:6.00. CL-80-S lime with the specific gravity=2.08 was used in the mixture with beams while CL-90-S lime with the specific gravity=2.09 was employed in the other mixtures. The aggregates were air-dried prior to mixing. The Fuller parabola was used to determine the percentages of the aggregate gradation.

The widths of all the beams with a maximum aggregate diameter of 4 mm were taken as constant, b =50 mm. The lengths of beams were taken as L=3d (Figure 1a). The cubes with 100 mm were used for the mixtures with a maximum aggregate diameter of 4 mm. The square prisms were designed as 100×150×150 mm for mixtures with a maximum aggregate diameter of 16 mm. All beams were kept in the mold for 28 days, while the cubes and the square prisms were saved in the mold for 90 days. All specimens were wrapped in stretch film. The specimens were notched with a diamond saw blade of 1.5 mm thickness on the day of the fracture test. In addition to the notched specimens, cubes (100 mm) were made to determine compressive strength. While beams of the same dimensions were used to determine the flexural strength of the beams, 100 mm cubes were made to determine the splitting strength of the other specimen configurations.

The compression tests, the splitting tests and the bending tests were performed using a digital compression machine with a capacity of 100 kN. The specimens were loaded monotonically until final failure and care was taken to apply a constant loading rate (Figure 3). Typically, approximately 2 min (± 30 sec) elapsed before the maximum load capacity for each specimen was reached.

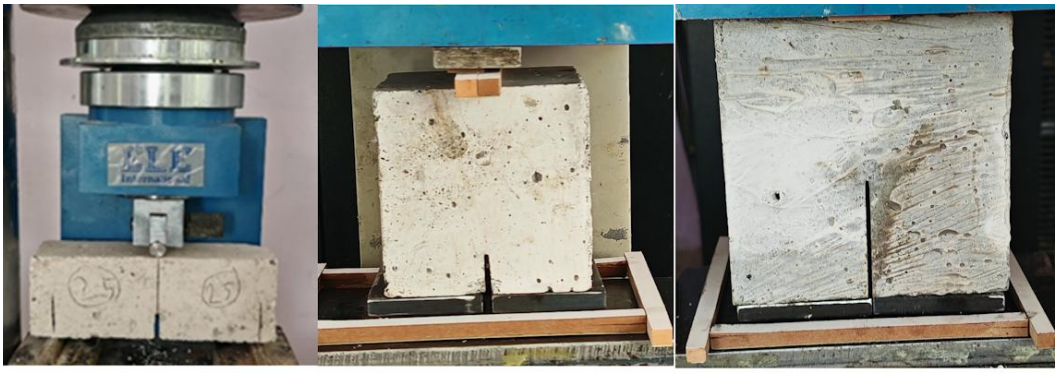


Figure 3. Test setup of the notched specimens

In this study, by using the following formulas, the dynamic Young's moduli of the materials were determined by means of the ultrasonic technique for prismatic specimens and cubical specimens, respectively:

$$E_d = 10^3 V^2 \Delta, \quad \text{MPa} \tag{7}$$

$$E_d = 10^3 \frac{V^2 \Delta (1+\nu)(1-2\nu)}{1-\nu}, \quad \text{MPa} \tag{8}$$

where, V is the velocity (km/s) and Δ is the unit weight (kg/lt). Since lime-pumice mixtures are low strength materials, the Poisson ratio (ν) was taken as 0.3 in this study (Erdogan, 2003). Note that the dynamic Young's moduli of materials (E_d) are larger than static Young's moduli (E_s). The formula: E_s=6/7×E_d was used for lime-pumice mixtures in this study (Lydon, 1972). Physical and mechanical properties of lime-pumice mixtures used in this study are summarized in Table 1.

The specimen width (b), specimen depth (d) and the peak load values (P_c) of the notched beams are reported in Table 2 according to the notch depths (a_0). The values of a_0 and P_c of the splitting specimens: cubes and square prisms are summarized in Table 3. In these tables, the letters B, C, and SP refer to beams, cubes, and square prism specimens.

Crack patterns at the failure of beams and compression cubes are shown in Figure 4. The specimen width (b), specimen depth (d) and the peak load values (P_c) of the notched beams were reported in Tables 1 according to the notch depths (a_0).

Applications of the Modified Peak Load Method to Lime-Pumice Mixtures

Tables 4, 5, and 6 illustrate the applications of the modified peak load method to mixtures in this study. The test data are summarized for each sample in the first two columns of these tables. In these tables, the nominal strengths were computed as σ_{Nc}=3.75P/(b×d) and σ_{Nc}=P/(π×b×d) for beams and splitting specimens, respectively. For each sample, the crack extensions (Δa), which were taken as variables of the optimization problem, were initially selected as 5 mm. The normalized functions of the cracked structure, such as Y and V_1, were also summarized while the function of M in Equation 2 is presented as embedded in $CTOD_c$. All analysis was conducted by using the MS-EXCEL-based SOLVER toolkit. The root sum squared (RSS) values in these tables are the minimized values.

Table 1. Physical and mechanical properties of lime-pumice mixtures used in this study

Mix	g	w/b	Δ	T	f_c	f_t	f_{sp}	E_s
	mm		g/cm^3	Days	MPa	MPa	MPa	MPa
M4-28	4	0.77	1.93	28	3.79	1.181	-	13384
M4-90	4	0.77	2.01	90	9.82	-	1.300	14216
M16-90	16	0.71	2.09	90	10.82	-	1.305	20382

Table 2. Test results of beams tested in this study

Specimen	b mm	d mm	a_0 mm	P_c N
B1	47.77	49.32	8.84	540
B2	50.85	50.3	9.99	460
B3	54.16	49.63	9.71	590
B4	50.41	50.23	9.36	680
B5	52.08	50.41	9.93	520
B6	53.65	50.03	15.00	350
B7	54.26	49.84	14.26	490
B8	49.26	50.05	13.58	410
B9	52.21	51.28	15.79	460
B10	52.32	50.72	15.42	450
B11	48.02	49.63	23.12	290
B12	50.32	49.17	21.84	250
B13	55.85	49.21	21.43	320

Table 3. Test results of cubes (C) and square spasmatic (SP) tested in this study

Specimen	a_0 mm	P_c kN	Specimen	a_0 mm	P_c kN
C1	29.35	17.65	SP1	27.89	50.28
C2	28.5	23.51	SP2	28.45	48.14
C3	29.52	16.44	SP3	28.37	48.81
C4	39.91	14.9	SP4	46.25	39.87
C5	39.32	12.56	SP5	47.86	41.10
C6	40.07	12.18	SP6	45.15	44.22
C7	47.38	11.61	SP7	65.37	27.70
C8	47.91	10.16	SP8	65.7	16.75
C9	48.57	9.02	SP9	65.66	18.03

The following formulas were applied to beams with a span/depth ratio of 2.5 in this study (Yang et al., 1997):

$$Y(\alpha)=\frac{1.83-1.65\alpha+4.76\alpha^2-5.3\alpha^3+2.51\alpha^4}{\sqrt{\pi}(1+2\alpha)(1-\alpha)^{3/2}} \tag{9}$$

$$V_1(\alpha)=0.65-1.88\alpha+3.02\alpha^2-2.69\alpha^3+\frac{0.68}{(1-\alpha)^2} \tag{10}$$

$$M(\alpha_0,\alpha_c)=\sqrt{\left(1-\frac{\alpha_0}{\alpha_c}\right)^2+(1.081-1.149\alpha_c)\left[\frac{\alpha_0}{\alpha_c}-\left(\frac{\alpha_0}{\alpha_c}\right)^2\right]} \tag{11}$$

For the cube and the square prismatic specimens subjected to splitting loading used in Table 2, the LEFM formulas are given by (Ince, 2021):

$$Y(\alpha)=0.3691+0.4492\alpha+1.3284\alpha^2+2.4467\alpha^3 \quad \text{for } \beta=0.1 \tag{12}$$

$$Y(\alpha)=0.3341+0.0101\alpha+2.5609\alpha^2+0.4067\alpha^3 \quad \text{for } \beta=0.2 \tag{13}$$

$$V_1(\alpha)=0.3722+2.0219\alpha-6.6125\alpha^2+14.3038\alpha^3 \quad \text{for } \beta=0.1 \tag{14}$$

$$V_1(\alpha)=0.3040+1.7717\alpha-5.3749\alpha^2+12.2420\alpha^3 \quad \text{for } \beta=0.2 \tag{15}$$

$$M\left(\alpha_0,\alpha_c\right)=\sqrt{\left(1-\frac{\alpha_0}{\alpha_c}\right)^2+\left(2.16-4.02\alpha_c\left(1-\beta\right)^{-0.23}\alpha_c^{3.67}\left(\frac{\alpha_0}{\alpha_c}\right)^{1.15}\right)\left[\frac{\alpha_0}{\alpha_c}-\left(\frac{\alpha_0}{\alpha_c}\right)^2\right]} \quad (16)$$

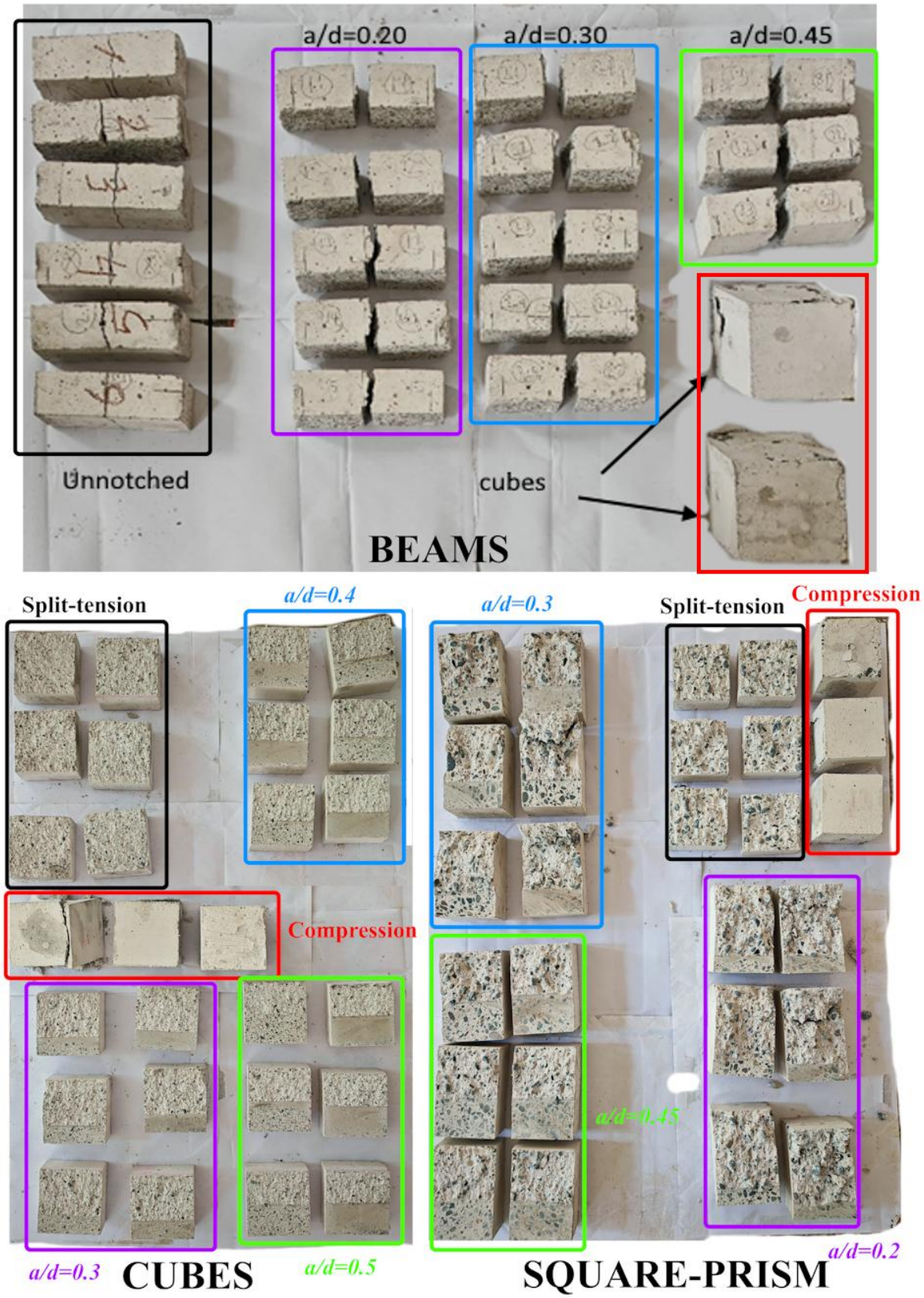


Figure 4. Fractured specimens

Table 4. Application of the modified peak load method to beams with g=4 mm

No	a_0 mm	σ_{Nc} MPa	Δa mm	a_c mm	a_c/d	Y	K^s_{Ic} MPa√mm	V_1	$CTOD_c$ μm		$\Delta^2(K^s_{Ic})$	$\Delta^2(CTOD_c)$
1	8.84	0.860	4.68	13.52	0.274	0.967	5.41	1.559	2.931		0.0012	0.0008
2	9.99	0.674	6.59	16.58	0.330	1.018	4.95	1.731	3.302		0.1807	0.1171
3	9.71	0.823	4.65	14.36	0.289	0.979	5.41	1.601	2.934		0.0010	0.0007
4	9.36	1.007	2.99	12.35	0.246	0.949	5.95	1.491	2.509		0.3260	0.2029
5	9.93	0.743	5.62	15.55	0.309	0.996	5.17	1.659	3.129		0.0435	0.0286
6	15.00	0.489	6.87	21.87	0.437	1.188	4.82	2.263	3.417		0.3170	0.2093
7	14.26	0.679	4.11	18.37	0.369	1.068	5.51	1.888	2.853		0.0173	0.0113
8	13.58	0.624	5.31	18.89	0.377	1.081	5.19	1.929	3.112		0.0348	0.0231
9	15.79	0.644	3.96	19.75	0.385	1.093	5.55	1.966	2.826		0.0283	0.0180
10	15.42	0.636	4.21	19.63	0.387	1.096	5.47	1.975	2.885		0.0086	0.0056
11	23.12	0.456	2.80	25.92	0.522	1.420	5.85	3.001	2.558		0.2182	0.1617
12	21.84	0.379	4.87	26.71	0.543	1.495	5.19	3.251	3.129		0.0361	0.0285
13	21.43	0.437	3.97	25.40	0.516	1.398	5.45	2.932	2.894		0.0056	0.0043
						Mean	5.38	Mean	2.96	Σ	1.2184	0.8119
											RSS	1.44641

Table 5. Application of the modified peak load method to cubes with g=4 mm

No	a_0 mm	σ_{Nc} MPa	Δa mm	a_c mm	a_c/d	Y	K^s_{Ic} MPa√mm	V_1	$CTOD_c$ μm		$\Delta^2(K^s_{Ic})$	$\Delta^2(CTOD_c)$
1	29.35	0.562	12.04	41.39	0.414	0.956	6.13	1.176	4.31		0.0258	0.0232
2	28.50	0.748	8.00	36.50	0.365	0.829	6.64	0.990	3.80		0.1277	0.1240
3	29.52	0.523	13.11	42.63	0.426	0.992	6.00	1.232	4.42		0.0797	0.0689
4	39.91	0.474	7.45	47.36	0.474	1.140	6.59	1.480	3.90		0.0934	0.0641
5	39.32	0.400	10.42	49.74	0.497	1.222	6.11	1.629	4.30		0.0321	0.0218
6	40.07	0.388	10.39	50.46	0.505	1.248	6.09	1.678	4.31		0.0373	0.0248
7	47.38	0.370	6.58	53.96	0.540	1.383	6.65	1.937	3.88		0.1341	0.0756
8	47.91	0.323	8.16	56.07	0.561	1.470	6.31	2.114	4.14		0.0005	0.0003
9	48.57	0.287	9.55	58.12	0.581	1.559	6.05	2.300	4.33		0.0561	0.0315
						Mean	6.29	Mean	4.16	Σ	0.5868	0.4343
											RSS	0.7300

Table 6. Application of the modified peak load method to square prisms with g=16 mm

No	a_0 mm	σ_{Nc} MPa	Δa mm	a_c mm	a_c/d	Y	K^s_{Ic} MPa√mm	V_1	$CTOD_c$ μm		$\Delta^2(K^s_{Ic})$	$\Delta^2(CTOD_c)$
1	27.89	1.067	18.42	46.31	0.309	0.593	7.63	0.699	4.35		0.0448	0.0726
2	28.45	1.022	19.13	47.58	0.317	0.608	7.59	0.716	4.40		0.0639	0.1013
3	28.37	1.036	18.82	47.19	0.315	0.603	7.61	0.711	4.38		0.0557	0.0888
4	46.25	0.846	10.37	56.62	0.377	0.725	8.18	0.865	3.74		0.1084	0.1170
5	47.86	0.872	8.62	56.48	0.377	0.723	8.40	0.863	3.53		0.3034	0.3053
6	45.15	0.938	8.72	53.87	0.359	0.687	8.39	0.814	3.52		0.2906	0.3109
7	65.37	0.588	6.79	72.16	0.481	0.977	8.64	1.275	3.45		0.6367	0.4024
8	65.70	0.356	18.14	83.84	0.559	1.211	6.99	1.753	4.76		0.7399	0.4566
9	65.66	0.383	16.33	81.99	0.547	1.171	7.19	1.666	4.61		0.4304	0.2757
						Mean	7.85	Mean	4.08	Σ	2.6738	2.1307
											RSS	3.4190

Conclusion

This study employed the modified peak load method based on the two-parameter model in concrete fracture to examine the fracture behavior of lime-pumice mixtures. The key findings are summarized below:

The fracture toughness value of the lime-pumice mortar is around 1/5 compared to normal cementitious mortars in 28 days test. Moreover, the resistance of this material to crack propagation is much lower than normal cement-based ones. The fracture toughness value of 90-day mortar is approximately 20% greater than that of 28-day mortar. On the other hand, the crack tip opening displacement value of 90-day mortar is approximately 30%

greater than that of 28-day mortar. The fracture toughness value of the lime-pumice mixture with the maximum aggregate size=16 mm is approximately 25% greater than that of the lime-pumice mixture with the maximum aggregate size=4 mm while no significant difference is observed between the crack tip opening displacement values.

Recommendations

Further studies can come up with more reliable results by investigating various types and sizes of aggregates to verify the above findings.

Scientific Ethics Declaration

* The authors declare that the scientific ethical and legal responsibility of this article published in EPSTEM journal belongs to the authors.

Conflict of Interest

* The authors declare that they have no conflicts of interest

Funding

* First author, Erkin Eren, would like to thank the Scientific and Technological Research Council of Türkiye (TÜBİTAK) for supporting his doctoral education with the Domestic General Doctoral Scholarship Program (2211-A).

Acknowledgements or Notes

* This article was presented as an oral presentation at the International Conference on Technology, Engineering and Science (www.icontes.net) held in Antalya/Türkiye on November 12-15, 2025.

* This article is extracted from the first author's doctorate dissertation entitled "Investigation of Structures Produced from Historical Mortars Using Fracture Mechanics Principles", supervised by Ragip Ince.

References

Bažant, Z. P., & Kazemi, M. T. (1990). Determination of fracture energy, process zone length, and brittleness number from size effect with application to rock and concrete. *International Journal of Fracture, 44*(2), 111-131.

Bažant, Z. P., & Oh, B. H. (1983). Crack band theory for fracture concrete. *Materials & Structures (RILEM), 16*(93), 155-157.

Erdoğan, T. Y. (2003). *Concrete*. METU Press.

Hillerborg, A., Modeer, M., & Petersson, P. E. (1976). Analysis of crack formation and crack growth in concrete by means of fracture mechanics and finite elements. *Cement & Concrete Research, 6*, 773-782.

Hu, X., & Duan, K. (2008). Size effect and quasi-brittle fracture: The role of FPZ. *International Journal of Fracture, 154*, 3-14.

Ince, R. (2021). Utilization of splitting strips in fracture mechanics tests of quasi-brittle materials. *Archive of Applied Mechanics, 91*, 2661-2679.

Ince, R. (2025a). A modified peak load method based on the two-parameter fracture model in concrete fracture. *The Eurasia Proceedings of Science, Technology, Engineering and Mathematics (EPSTEM), 36*, 141–150.

Ince, R. (2025b). Using SCB specimens to quantify nonlinear fracture characteristics in concrete and rock materials. *Engineering Fracture Mechanics, 318*, 110951.

Jenq, Y. S., & Shah, S. P. (1985). Two-parameter fracture model for concrete. *ASCE Journal of Engineering Mechanics, 111*(10), 1227–1241.

Kaplan, M. F. (1961). Crack propagation and the fracture of concrete. *ACI Journal, 58*(11), 591–610.

Kesler, C. E., Naus, D. J., & Lott, L. L. (1972). Fracture mechanics-its applicability to concrete. *The Society of Materials Science*, 113–124.

Lydon, F. D. (1984). *Concrete mix design*. Applied Science Publishers.

Nallathambi, P., & Karihaloo, B. L. (1986). Determination of the specimen size independent fracture toughness of plain concrete. *Magazine of Concrete Research, 38*(135), 67–76.

Tada, H., Paris, P. C., & Irwin, G. R. (2000). *The stress analysis of cracks handbook* (3rd ed.). ASME Press.

Tang, T., Ouyang, C., & Shah, S. P. (1996). A simple method for determining material fracture parameters from peak loads. *ACI Materials Journal, 93*(2), 143–157.

Tang, T., Shah, S. P., & Ouyang, C. (1992). Fracture mechanics and size effect of concrete in tension. *ASCE Journal of Structural Engineering, 118*, 3169–3185.

Xu, S., & Reinhardt, H. W. (1999). Determination of double-K criterion for crack propagation in quasi-brittle fracture, Part I: Experimental investigation of crack propagation. *International Journal of Fracture, 98*, 111–149.

Yang, S., Tang, T., Zollinger, D. G., & Gurjar, A. (1997). Splitting tension tests to determine concrete fracture parameters by peak–load method. *Advanced Cement Based Materials, 5*, 18–28.

Author(s) Information

Erkin Eren
Firat University
Engineering Faculty, Elazig, Türkiye
Contact e-mail: *eeren@firat.edu.tr*

Ragip Ince
Firat University
Engineering Faculty, Elazig, Türkiye

To cite this article:

Eren, E., & Ince, R. (2025). Evaluation of nonlinear fracture quantities in lime-pumice mixtures. *The Eurasia Proceedings of Science, Technology, Engineering and Mathematics (EPSTEM), 38,* 672-681.

The Eurasia Proceedings of Science, Technology, Engineering & Mathematics (EPSTEM)
ISSN: 2602-3199

The Eurasia Proceedings of Science, Technology, Engineering and Mathematics (EPSTEM), 2025

Volume 38, Pages 682-687

IConTES 2025: International Conference on Technology, Engineering and Science

Electrical Resistivity Tomography as a Tool for Geological-Engineering Assessment of the Benkovski-2 Tailings Storage Facility

Maya Tomova
University of Mining and Geology "St. Ivan Rilski"

Atanas Kisyov
University of Mining and Geology "St. Ivan Rilski"

Abstract: Geophysical methods, and in particular electrical resistivity tomography (ERT), have proven to be highly suitable for investigating tailings storage facilities (TSFs) and addressing a wide range of engineering–geological problems. Their ability to delineate subsurface structures and identify zones with contrasting physical properties makes them an effective tool for monitoring the internal stability and hydrogeological conditions of such complex anthropogenic systems. A geophysical survey based on two-dimensional electrical resistivity tomography (ERT) was carried out at the "Suludza Dere" tailings storage facility (TSF). The objective was to determine the specific electrical resistivity distribution within a section of the TSF and to determine the spatial distribution of materials with varying resistivity, reflecting differences in composition and structural characteristics. Within this context, the 2D ERT survey was conducted to provide a detailed subsurface cross-section and identify zones with contrasting resistivity properties. The results serve as a basis for better understanding of the internal structure and hydrogeological conditions of the TSF, supporting its sustainable monitoring and safe operation.

Keywords: Mine saste, Geophysics, Electrical tomography, Monitoring

Introduction

A shallow, non-destructive geophysical technique, electrical resistivity tomography (ERT), is one of the most widely applied methods for subsurface imaging. Over the past three decades, it has been successfully employed in mineral prospecting, hydrological exploration, environmental investigations, civil engineering, and archaeological mapping. The popularity of ERT is due to its ability to generate high-resolution two-dimensional and three-dimensional models of the subsurface by measuring the spatial variability of electrical resistivity, a physical parameter that is highly sensitive to lithology, porosity, water content, and fluid chemistry.

In the broader context of Industry 4.0 and the digital transformation of mining and geotechnical systems, the implementation of intelligent technologies for monitoring and risk management has become a fundamental component of sustainable resource extraction (Nikolov, 2023; Nikolov & Koleva, 2025). The increasing use of artificial intelligence (AI) and data-driven models in industrial and educational systems highlights both the potential and the associated risks of automation and human–machine interaction (Koleva, 2024; Koleva & Nikolov, 2025). These technological frameworks provide a valuable foundation for integrating advanced geophysical monitoring tools, such as ERT, within smart decision-support systems for mine safety and stability assessment (Nikolov & Koleva, 2025).

Numerous studies have documented the significant environmental impacts associated with mining activities, particularly those resulting from leakages or failures of tailings storage facilities. As Dimitrov stated, the storage of tailings always is one of the major challenges (Dimitrov et al., 2023). The extraction of valgenerateeral

- This is an Open Access article distributed under the terms of the Creative Commons Attribution-Noncommercial 4.0 Unported License, permitting all non-commercial use, distribution, and reproduction in any medium, provided the original work is properly cited.

- Selection and peer-review under responsibility of the Organizing Committee of the Conference

© 2025 Published by ISRES Publishing: www.isres.org

resources inevitably generates substantial quantities of waste material, most notably tailings-mixtures of finely ground rock particles and residual process fluids produced by milling, washing, or concentration operations after the recovery of economically important metals, minerals, or fuels (Yankova, 2021; Farjana et al., 2019; Kossoff et al., 2014). These fine-grained residues are typically stored in large impoundments or tailing dams to prevent their release into the environment. Efficient and safe disposal of the waste generated in the mining activity is one of the most important things in the mining industry (Dimitrov & Grigorova, 2023). Keeping the tailings pond safe and stable is the most challenging task in the entire mining process (Lyu et al., 2019).

Many authors highlighted that electrical resistivity tomography (ERT) is a promising technique for monitoring various subsurface processes (Loke et al., 2013, Binley et al., 2015, Slater and Binley, 2021, Dimech et al., 2022). In the field of waste management, ERT has emerged as a particularly valuable tool for investigating tailings storage facilities (TSFs). It allows for the determination of the geometry of pond bases, the thickness and distribution of tailings, and the delineation of zones with contrasting material properties. More importantly, resistivity measurements can be used to detect early-stage processes such as anomalous seepage, internal erosion, or preferential flow pathways. These features, if not properly identified and controlled, may compromise the stability of tailings dams, leading to environmental hazards and severe socio-economic consequences (Aleksandrova et al., 2017). Compared to conventional geotechnical methods, ERT offers the advantages of being non-invasive, cost-effective, and capable of covering large areas with minimal disturbance to the facility. Recent studies have demonstrated its utility in assessing the integrity of TSF embankments and monitoring temporal changes in moisture and porewater distribution.

The Benkovski-2 TSF, located in Bulgaria, serves as a deposition site for flotation tailings generated by the concentrator plant processing ore from the Elatsite porphyry copper deposit. Copper is the primary industrial element, accompanied by gold and molybdenum as secondary components. The tailings are transported as slurry through a hydro-transport system and separated via hydrocycloning, whereby coarse sands are used to build the supporting dam walls, while the finer fractions are deposited in the impoundment basin. The facility is divided into two sectors, “Ai Dere” and “Suludza Dere,” where dam walls are successively raised with hydrocycloned sand. A combined drainage system beneath both sectors ensures overall structural stability by directing drainage waters outside the dam walls and into a pumping station, from which they are returned to the concentrator plant water cycle.

Description of the Technology

A geophysical survey employing 2D ERT was carried out in the Suludza Dere sector of the Benkovski-2 TSF. The survey was conducted with the primary goal of characterizing the electrical resistivity distribution within a section defined by predetermined coordinates. It aimed to generate a detailed subsurface cross-section, highlighting zones of contrasting resistivity, and to outline the spatial variability of materials whose differing responses reflect variations in composition, grain size, and structural characteristics. The measurements are acquired using specific electrode configurations (e.g., Wenner, Schlumberger, or dipole–dipole), which determine the depth of investigation and the sensitivity to lateral and vertical variations. By systematically shifting and expanding the electrode spacing along a survey line, a dense dataset of apparent resistivity values is obtained. These data are then processed through inversion algorithms that minimize the difference between measured and calculated responses, producing two-dimensional resistivity models of the subsurface. Such models allow the detection of zones with contrasting physical properties, which in tailings facilities may correspond to variations in grain size, moisture content, saturation levels, or seepage pathways. As noted from many authors, the potential of this method is higher when the contrast in resistivity between the objects is important (Scapozza & Laigre, 2014, Baines et al., 2002). The results are expected to enhance understanding of the internal structure and hydrogeological regime of the TSF, thereby supporting its effective monitoring, safe operation, and sustainable management.

Electrical resistivity tomography (ERT) is a non-invasive geophysical method that images the subsurface by measuring the apparent resistivity of the ground. The technique is based on the injection of a direct electrical current into the subsurface through a pair of electrodes and the simultaneous measurement of the resulting potential differences at other electrodes positioned along a survey line (Lesmes & Friedman, 2005). By systematically varying the spacing and position of the current and potential electrodes, a large dataset of apparent resistivity values is collected, reflecting the electrical properties of the subsurface at different depths and lateral positions.

The measured resistivity values are strongly influenced by factors such as lithology, porosity, water saturation, and pore fluid chemistry. Through inversion algorithms, the apparent resistivity data are converted into two-dimensional (or three-dimensional) models that represent the true resistivity distribution of the subsurface. These models allow the identification of geological structures, stratigraphic variations, and zones of differing material properties.

The method is widely recognized for its ability to resolve subsurface contrasts in a cost-effective and non-destructive manner, making it particularly suitable for monitoring tailings storage facilities. In such environments, ERT can provide information on dam wall construction materials, pond base geometry, tailings thickness, seepage pathways, and internal erosion processes-critical factors for assessing structural stability and hydrogeological conditions.

Field Measurements and Results

On the field survey at the Suludza Dere sector of the Benkovski-2 TSF, a multi-electrode resistivity system was employed, consisting of ZZ Universal 96, with 96 stainless-steel electrodes connected via multicore cables and an automatic switching unit. The electrode spacing was set to 10 m, allowing coverage of a profile length of 960 m. Position of the ERT line follows the drainage system on site, as it is presented in Figure 1.

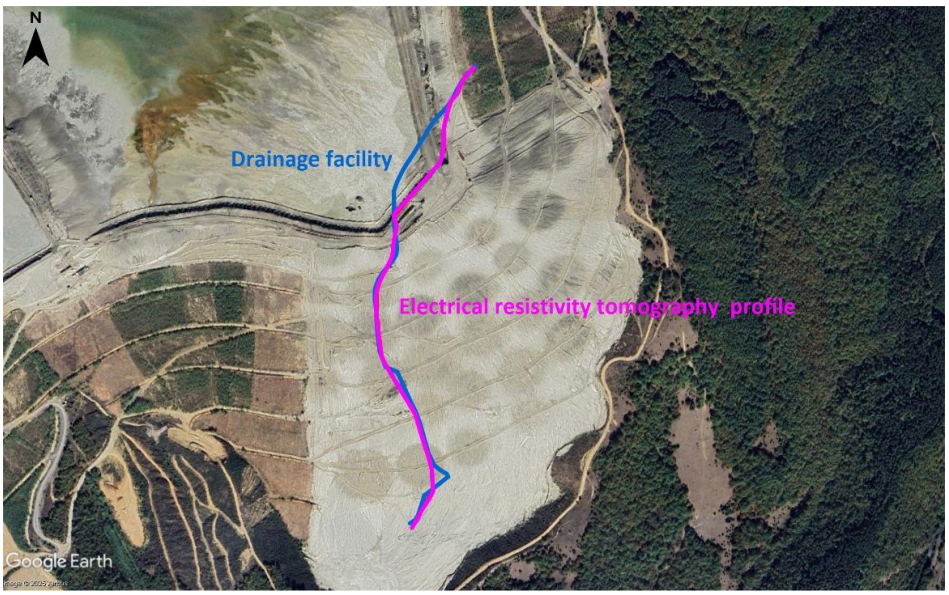


Figure 1. Field situation

The resistivity measurements were carried out using the Schlumberger configuration (Figure 2), which provides a balance between vertical resolution and depth penetration, making it suitable for imaging layered structures and detecting lateral variations in tailings deposits.

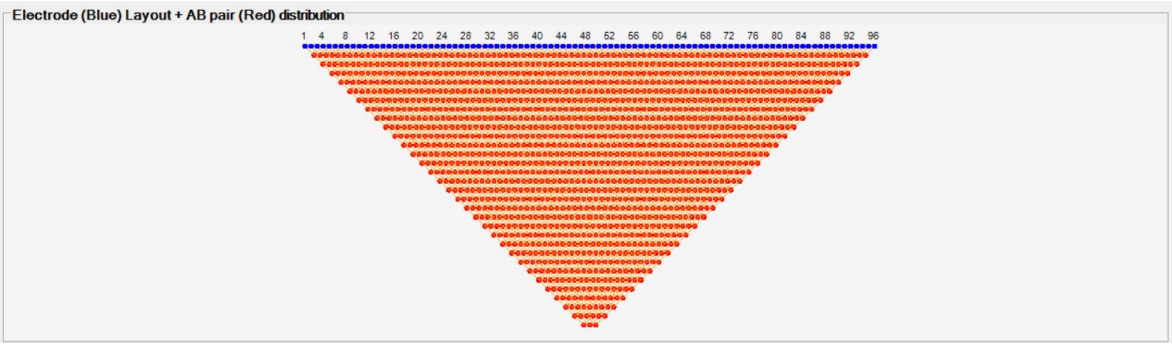


Figure 2. 96 channel data-acquisition layout

The apparent resistivity dataset was processed using a standard least-squares inversion algorithm implemented in RES2DINV (Loki, 2001), which iteratively minimized the difference between measured and calculated data.

The resistivity model generated from the ERT survey was further refined and adjusted to reflect the site-specific geological conditions of the study area. This process involved the integration of several complementary datasets. First, general geological information, including the lithological, facies, tectonic, and hydrogeological framework of the region, was considered to place the geophysical results into a broader geological context. Second, reference values of the specific electrical resistivity for different rock types were used to constrain the interpretation of zones with contrasting resistivity responses. The combined use of these datasets ensured that the resulting resistivity sections were both geophysical consistent and geologically meaningful, thereby improving the reliability of the interpretation (Figure 3). Upon completion of the inversion process, the resulting resistivity model provides a distribution that best fits the observed data. This model is considered an approximation of the true subsurface resistivity structure, while recognizing that it is influenced by inherent limitations such as prior assumptions, data quality, modelling uncertainties, resolution constraints, and the non-uniqueness of the inversion results (Whiteley et al., 2019).

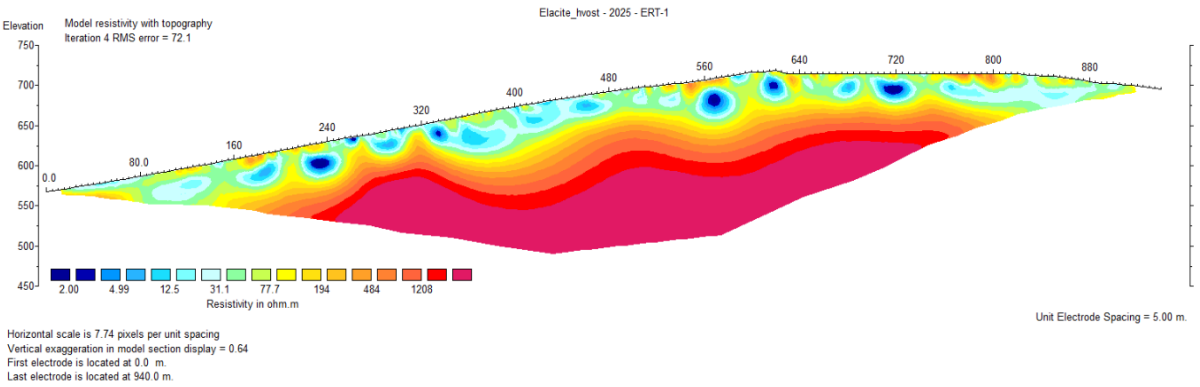


Figure 3. Electrical tomography line

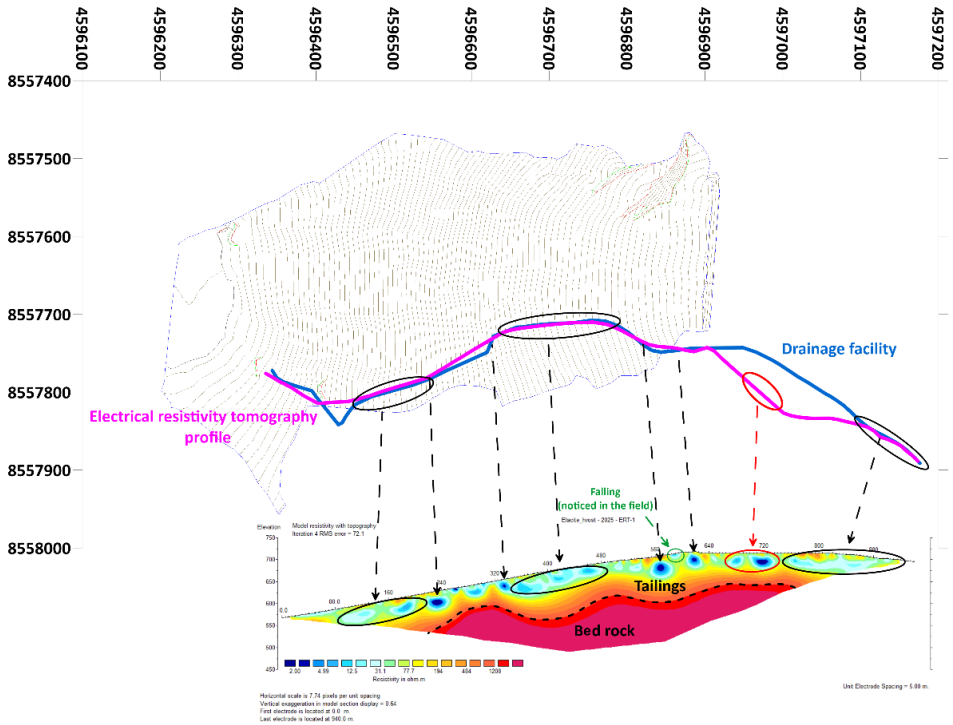


Figure 4. Comprehensive examination of the measured ERT profile and the location of the investigated drainage system

The analysis of the ERT results provides several important insights into the subsurface conditions of the Suludza Dere sector. The resistivity distribution along the geoelectrical profile is well defined, with values ranging widely between approximately 2 Ωm and more than 2000 Ωm. The depth of investigation reached about 200 m, allowing the identification of two main geoelectrical domains: a low-resistivity zone in the shallow section, interpreted as hydrocycloned tailings deposits, and a high-resistivity zone at greater depths, corresponding to the natural bedrock. Zones with elevated resistivity values in the range of 500–2000 Ωm are most likely associated

with the underlying natural terrain, whereas areas with lower resistivity, between 2 and 200 Ωm, are indicative of the tailing's material. The contact between these two units is gradual rather than abrupt, reflecting the penetration of tailings into surface irregularities of the natural terrain and their integration with the upper soil layer as it is shown on Figure 4. The contact zones between the embankment and natural media, although not sharply defined, provide valuable information on the embedding of tailings material in terrain and its interaction with the surface soil layer.

The drainage system beneath the embankment is clearly distinguishable on the resistivity profile, where drained material is characterized by very low resistivity values (2–30 Ωm) compared to the overlying tailings (50–200 Ωm) and the natural foundation (>200 Ωm). At locations where the profile intersects the drainage system transversely, round-shaped resistivity anomalies are observed, while elongated anomalies are recorded where the profile runs parallel to the system. Additionally, detected resistivity anomalies that do not correspond to the known drainage system indicate the presence of other underground installations or structural elements such as a pipeline or auxiliary drain. (mark with red on the Figure 4). Particular attention should be paid to the low-resistivity surface anomaly observed in the 560–640 m interval, which coincides with a subsidence detected in the field. This finding highlights the significance of ERT methods not only for structural and lithological interpretation but also for early detection of potential geotechnical issues.

Conclusion

The conducted 2D electrical resistivity tomography (ERT) survey in the "Suludja Dere" section of the "Benkovski – 2" tailings storage facility (TSF) confirms the high effectiveness of electrical tomography as a tool for geotechnical and engineering-geological applications. The results clearly demonstrate the differentiation of geological media based on their electrical resistivity, enabling reliable discrimination between tailings deposits and drainage systems (characterized by low resistivity values) and the bedrock of the natural terrain (with high resistivity values). In a broader context, the results of this study demonstrate that electrical tomography constitutes a reliable tool for integrated assessment of the stability and functionality of tailings storage facilities. It provides complementary information to traditional engineering-geological investigations and is applicable for developing strategies for sustainable management and monitoring of mining waste.

Scientific Ethics Declaration

* The authors declare that the scientific ethical and legal responsibility of this article published in EPSTEM journal belongs to the authors.

Conflict of Interest

* The authors declare that they have no conflicts of interest

Funding

* There is no funding.

Acknowledgements or Notes

* This article was presented as an oral presentation at the International Conference on Technology, Engineering and Science (www.icontes.net) held in Antalya/Türkiye on November 12-15, 2025.

References

Aleksandrova, E., Sokolova, E., & Topalova, M. (2017). Study of the type and nature of the main sources of pollution in the Rhodope Mining Basin. In *National Scientific Conference with International Participation "Science and Society"* (pp. 534-537).

Baines, D., Smith, D. G., Froese, D. G., Bauman, P., & Nimeck, G. (2002). Electrical resistivity ground imaging (ERGI): A new tool for mapping the lithology and geometry of channel-belts and valley-fills. *Sedimentology, 49*(3), 441-449.

Binley, A., Hubbard, S. S., Huisman, J. A., et al. (2015). The emergence of hydrogeophysics for improved understanding of subsurface processes over multiple scales. *Water Resources Research, 51*(6), 3837-3866.

Dimech, A., Cheng, L. Z., Chouteau, M., Chambers, J., Uhlemann, S., Wilkinson, P., Meldrum, P., Mary, B., Fabien-Ouellet, G., & Isabelle, A. (2022). A review on applications of time-lapse electrical resistivity tomography over the last 30 years: Perspectives for mining waste monitoring. *Surveys in Geophysics, 43*, 1699-1759.

Dimitrov, L., & Grigorova, I. (2023). Improved tailings consolidation using dewatering agents: A step towards safer and sustainable mining waste management. *The Eurasia Proceedings of Science, Technology, Engineering & Mathematics (EPSTEM), 23*, 225-231.

Dimitrov, L., Grigorova, I., & Yankova, T. (2023). Possibilities to construct combined mine waste dump facility with better operational sequence. *The Eurasia Proceedings of Science, Technology, Engineering & Mathematics (EPSTEM), 23*, 42-49.

Koleva, N. (2024). Human in cooperation with AI - Next level of intelligent man-machine interaction. *Proceedings of World Multi-Conference on Systemics, Cybernetics and Informatics (WMSCI)*.

Koleva, N., & Nikolov, B. (2025). Main risks caused by the application of artificial intelligence in educational institutions in Bulgaria. *American Institute of Physics*.

Kossoff, D., Dubbin, W., Alfredsson, M., Edwards, S., Macklin, M., & Hudson-Edwards, K. (2014). Mine tailings dams: Characteristics, failure, environmental impacts, and remediation. *Applied Geochemistry, 51*, 229–245.

Lesmes, D. P., & Friedman, S. P. (2005). Relationships between the electrical and hydrogeological properties of rocks and soils. In Y. Rubin & S. S. Hubbard (Eds.), *Hydrogeophysics* (pp. 87–128). Springer.

Loke, M. H. (2001). *Tutorial: 2-D and 3-D electrical imaging surveys* (Course notes). USGS Workshop "2-D and 3-D Inversion and Modeling of Surface and Borehole Resistivity Data".

Loke, M., Chambers, J., Rucker, D., et al. (2013). Recent developments in the direct-current geoelectrical imaging method. *Journal of Applied Geophysics, 95*, 135-156.

Lyu, Z., Chai, J., Xu, Z., Qin, Y., & Cao, J. (2019). A comprehensive review on reasons for tailings dam failures based on case history. *Advances in Civil Engineering, 2019*, 1-18.

Nikolov, B. (2023). Main pillars building up the risk frame of Industry 4.0 implementation in the enterprises in Bulgaria. *Economic Studies (Ikonomicheski Izsledvania), 32*(7), 77–92.

Nikolov, B., & Koleva, N. (2025). Risks in managing smart factories. *Proceedings IMCIC - International Multi-Conference on Complexity, Informatics and Cybernetics*.

Scapozza, C., & Laigre, L. (2014). The contribution of electrical resistivity tomography (ERT) in Alpine dynamics geomorphology: Case studies from the Swiss Alps. *Géomorphologie: Relief, Processus, Environnement, 20*(1).

Slater, L., & Binley, A. (2021). Advancing hydrological process understanding from long-term resistivity monitoring systems. *Wiley Interdisciplinary Reviews: Water, 8*(3), e1513.

Whiteley, J., Chambers, J., Uhlemann, S., et al. (2019). Geophysical monitoring of moisture-induced landslides: A review. *Reviews of Geophysics, 57*(1), 106-145.

Yankova, T. (2021). Mining-damaged landscape reclamation study. In O. Trofymchuk & B. Rivza (Eds.), *21st International Multidisciplinary Scientific GeoConference SGEM 2021* (Vol. 21, No. 1.1).

Author(s) Information

Maya Tomova
University of Mining and Geology "St. Ivan Rilski"
Sofia, Studentski Grad, Prof. Boyan Kamenov", Sofia 1700, Bulgaria
Contact e-mail: *maya.grigorova86@gmail.com*

Atanas Kisyov
University of Mining and geology "St. Ivan Rilski"
Sofia, Studentski Grad, Prof. Boyan Kamenov", Sofia 1700, Bulgaria

To cite this article:

Tomova, M., & Kisyov, A. (2025). Electrical resistivity tomography as a tool for geological-engineering assessment of the Benkovski-2 tailings storage facility. *The Eurasia Proceedings of Science, Technology, Engineering and Mathematics (EPSTEM), 38*, 682-687.

The Eurasia Proceedings of Science, Technology, Engineering & Mathematics (EPSTEM)
ISSN: 2602-3199

The Eurasia Proceedings of Science, Technology, Engineering and Mathematics (EPSTEM), 2025

Volume 38, Pages 688-698

IConTES 2025: International Conference on Technology, Engineering and Science

Voltage Total Harmonic Distortion Reduction in Multi-level Single-Phase Inverters using the SHE-PWM Technique with a TLBO Algorithm

Smail Toufik
Solar Equipements Development Unit (UDES)

Boulouma Sabri
Solar Equipements Development Unit (UDES)

Seddaoui Naoual
Solar Equipements Development Unit (UDES)

Rahmani Hachemi
Solar Equipements Development Unit (UDES)

Abstract: This paper presents a modulation method based on the selective harmonic elimination-pulse width modulation (SHE-PWM) technique. The aim is to determine the optimal switching angles (SA) using the teaching learning-based optimization algorithm (TLBOA), capable of reducing the voltage total harmonic distortion (THD) present in the output waveform of single-phase multi-level inverters (MLIs). The performance of proposed technique has been verified through simulation using Matlab script and Simulink environment. The TLBOA-based SHE-PWM technique is applied to a 17-level inverter to eliminate 5^{th}, 7^{th}, 11^{th}, 13^{th}, 17^{th}, 19^{th} and 23^{rd} harmonics, achieving an improvement of up to 4.31% in the phase voltage THD content in the range of modulation index (MI) 0.5 to 0.95. Furthermore, the superiority of the proposed technique was confirmed by comparison with conventional modulation techniques, which showed that the proposed technique produces lower THD than those used in the equal phase (EP), half-equal phase (HEP), feed forward (FF) and half height (HH) methods.

Keywords: SHE-PWM technique, TLBO algorithm, Total harmonic distortion, Conventional modulation techniques

Introduction

In recent years, multi-level inverters (MLIs) have been extensively employed in renewable energy applications and diverse industrial sectors, providing numerous benefits compared to traditional two-level inverters (TLIs). They have received an increasing interest from people in research and academia. In the research literature, there are three basic MLIs configuration: Diode-Clamped MLI (DC-MLI) (Adam et al., 2012), Flying Clamped MLI (CC-MLI) (Meynard et al., 1992) and Cascaded H-Bridge MLI (CHB-MLI) (Chunyan et al., 2015). Compared to TLIs, MLIs have many advantages including, lower electromagnetic interference (EMI), minimizing (dv/dt) across switches and suitability for medium or high voltage high power applications such as wind turbines (WT), photovoltaic systems (PVS) and electric vehicles (EV) (Charan et al., 2015; Sedaghati et al., 2023; Elias et al., 2022; Taiea et al., 2019; Pires et al., 2017; Sotoodeh et al., 2013; Mehta et al., 2022; Meraj et al., 2023).

To enhance the efficiency and performance of MLIs, numerous modulation techniques, new topologies and optimal operating strategies have been reported in the literature (Behera et al., 2022), (Kubendran et al., 2022; Singh et al., 2022; Kannan et al., 2022). Pulse width modulation (PWM) techniques are the most popular

- This is an Open Access article distributed under the terms of the Creative Commons Attribution-Noncommercial 4.0 Unported License, permitting all non-commercial use, distribution, and reproduction in any medium, provided the original work is properly cited.

- Selection and peer-review under responsibility of the Organizing Committee of the Conference

© 2025 Published by ISRES Publishing: www.isres.org

techniques employed for controlling the MLI (Juárez-Abad et al., 2021). Different PWM techniques have been developed, such as the sinusoidal PWM (S-PWM) technique and space vector PWM (SV-PWM) technique (Can et al., 2022; Dordevic et al., 2013). Nevertheless, both S-PWM and SV-PWM techniques (Ren et al., 2021) operate with high switching frequencies, resulting in increases the switching losses. The switching losses can be reduced by using a selective harmonic elimination -pulse width modulation (SHE-PWM) technique (Hiendro et al., 2020; Dahidah et al., 2008). Compared with S-PWM and SV-PWM techniques, SHE-PWM is a more effective MLIs control technique to achieve better harmonic performance even at low switching frequencies. The main advantage of SHE-PWM technique is the adaptation of suitable switching angles in multilevel inverters to get rid of or lower some low-order selective harmonics while maintaining the fundamental harmonic at a desired value. However, the main challenge in SHE-PWM technique is to find the set of solutions of non-linear equations that define the optimal switching angles (M. Bounabi et al., 2018). In the research literature, the techniques used to address this problem can be classified into three categories, algebraic methods (e.g., Walsh method (Vicente et al., 2011), Groebner Bases (Yang et al., 2015), etc.), numerical methods (e.g., homotopy algorithm (Hosseini Aghdam et al., 2013), Newton Raphson method (Kato et al., 1999), etc.) and metaheuristics-based algorithms (e.g., genetic algorithm (Ali et al., 2021), particle swarm optimization (PSO) (Jiang et al., 2022), etc.) as summarized in Figure. 1.

In this work, a selective harmonic elimination PWM (SHE-PWM) technique using a teaching learning based optimization (TLBO) algorithm is proposed to obtain optimal switching angles to minimize the output voltage total harmonic distortion (THD) of a 17-level single-phase cascaded H-bridge multi-level inverter (CHB-MLI). The main objective is to demonstrate the effectiveness of the (TLBO) algorithm in addressing selective harmonic elimination (SHE) and total harmonic distortion (THD) minimization in multi-level inverters (MLIs) by optimally determining the switching angles. The main contributions of the present work can be summarized as follows:

- An effective teaching learning based optimization (TLBO) meta-heuristic algorithm is adopted to solve the non-linear (SHE-PWM) problem.
- The TLBO algorithm is implemented to find the optimal switching angles that effectively reduce the THD and meet the IEEE 519-2014 standard.
- The proposed technique is applied on 17-level (CHB) inverters for varying modulation index values.
- Comparison of the performance of the proposed method with conventional modulation methods (EP, HEP, FF and HH methods) is carried out to assess its superiority.

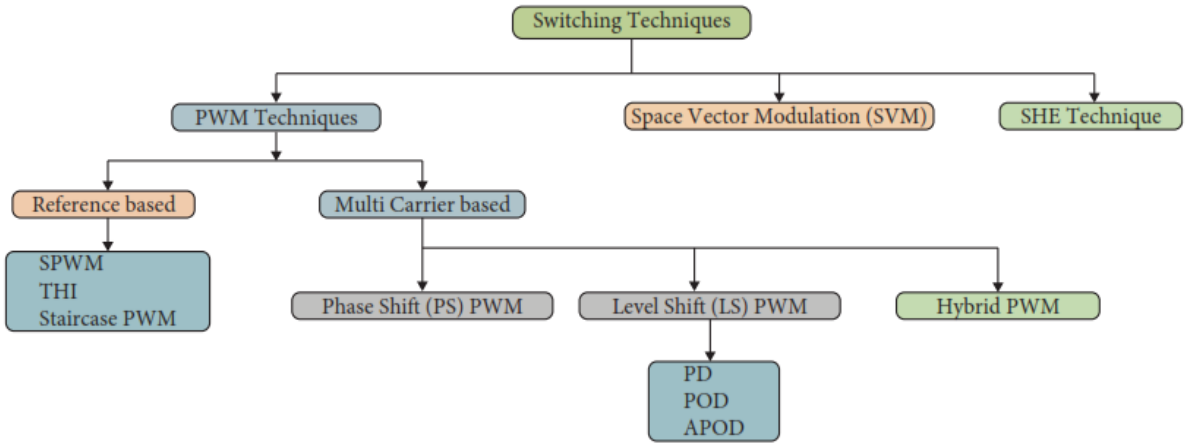


Figure 1. Classification of switching techniques (Dekka et al., 2020)

Methodology

This section outlines the application of the Teaching Learning based Optimization (TLBO) algorithm to solve the selective harmonic elimination-pulse width modulation (SHE-PWM) problem. More precisely, the solution of a set of non-linear equations and finding the optimal switching angles for eliminating the selected lower order harmonics and reducing the total harmonic distortion (THD) from the cascaded H-bridge multilevel inverter (CHB-MLI) output. The simulations of single-phase 17-level CHB inverter will be done according to the switching angles obtained from the TLBO algorithm. Additionally, the THD values were compared with those reported in the available literature obtained using different conventional modulation techniques.

Single-Phase Eleven-Level CHB-MLI

In this section, Selective Harmonic Elimination (SHE) strategy is used to produce the switching pulses using optimal switching angles for a single-phase cascaded H-bridge multilevel inverter (CHB-MLI) having the ability to produce a 17-level output voltage. Figure. 2 shows the structural design for single-phase 17-level CHB-MLI. This structure consists of 8 individual H-bridge cells connected with each other in a cascaded configuration. Each of these H-bridge cells has 4 switches and 1 DC supply, making a total of 32 switches and 8 DC supplies. All the DC supplies are equal in magnitude, making it a symmetrical configuration. The combination of all the H-bridge cells is generating the 17-level desired output voltage. Figure. 3 illustrates the staircase output voltage of the 17- level CHB- MLI for the quarter waveform of voltage cycle. Through the Figure, it can be seen that each edge of each stair represents one switching angle. These switching angles are considered as keys to eliminate selective harmonics. The switching angle θ_1 is used to control the fundamental component of the output voltage while all remaining switching angles (θ_2 to θ_8) are used to remove the harmonics. Generally, this SHE strategy is conducted by decoding the pulse width modulation (PWM) waveform utilizing Fourier analysis. Fourier series of periodic functions can be expressed as follows:

$$f(t) = \frac{A_0}{2} + \sum_{n=1}^{\infty}\left[A_n \cos(n\omega t) + V_n \sin(n\omega t)\right] \tag{1}$$

In this case $f(t) = odd$, so equation (1) can be rewritten as follows:

$$f(t) = \sum_{n=1}^{\infty} V_n \sin(n\omega t) \tag{2}$$

Here, the voltage component V_n can be determined via the following equation:

$$V_n = \frac{4V_{dc}}{n\pi}\sum_{i=1}^{i}\cos(n\theta_i) \tag{3}$$

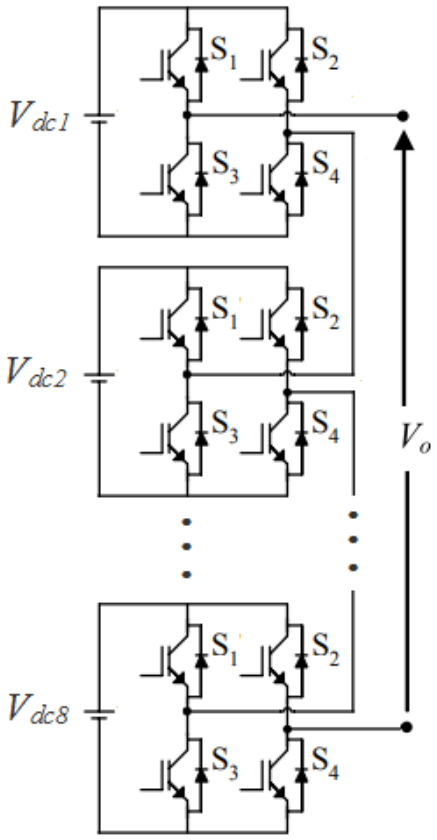


Figure 2. Structural design for single-phase 17-level (CHB-MLI)

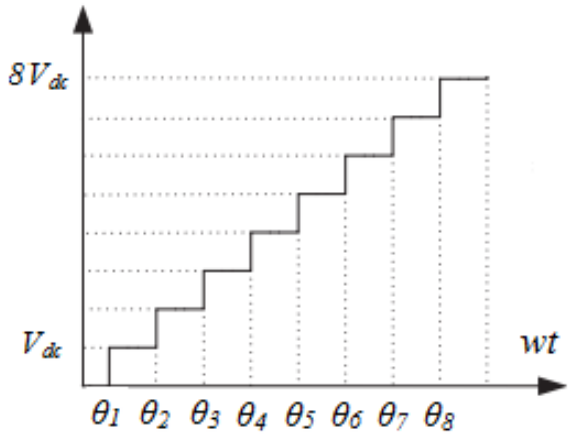


Figure 3. Quarter waveform of a 17-level inverter

Equation (4) provides the formula for the (SHE) equations for the 17-level inverter. A non-linear set of equations is used to eliminate the specific harmonics (5th, 7th, 11th, 13th, 17th, 19th, and 23th) from the output voltage. This non-linear equation set is achieved from (4) by equating V_5, V_7, V_{11}, V_{13}, V_{17}, V_{19}, and V_{23} to zero as follows:

$$\begin{aligned}
V_1 &= \frac{4V_{dc}}{\pi}\left[\cos(\theta_1)+\cos(\theta_2)+\ldots+\cos(\theta_8)\right]=M\\
V_5 &= \frac{4V_{dc}}{5\pi}\left[\cos(5\theta_1)+\cos(5\theta_2)+\ldots+\cos(5\theta_8)\right]=0\\
V_7 &= \frac{4V_{dc}}{7\pi}\left[\cos(7\theta_1)+\cos(7\theta_2)+\ldots+\cos(7\theta_8)\right]=0\\
V_{11} &= \frac{4V_{dc}}{11\pi}\left[\cos(11\theta_1)+\cos(11\theta_2)+\ldots+\cos(11\theta_8)\right]=0\\
V_{13} &= \frac{4V_{dc}}{13\pi}\left[\cos(13\theta_1)+\cos(13\theta_2)+\ldots+\cos(13\theta_8)\right]=0\\
V_{17} &= \frac{4V_{dc}}{17\pi}\left[\cos(17\theta_1)+\cos(17\theta_2)+\ldots+\cos(17\theta_8)\right]=0\\
V_{19} &= \frac{4V_{dc}}{19\pi}\left[\cos(19\theta_1)+\cos(19\theta_2)+\ldots+\cos(19\theta_8)\right]=0\\
V_{23} &= \frac{4V_{dc}}{23\pi}\left[\cos(23\theta_1)+\cos(23\theta_2)+\ldots+\cos(23\theta_8)\right]=0
\end{aligned} \tag{4}$$

According to the (SHE) strategy. With N switching angles in a quarter-cycle, there are N−1 harmonic components that can be eliminated. To eliminate 5th, 7th, 11th, 13th, 17th, 19th, and 23th order harmonics from the output voltage waveform. The equation (4) must be solved in such a way that the condition of ($0<\theta_1<\theta_2<\ldots<\theta_8<90°$) is satisfied, where θ_1 to θ_8 represent switching angles. The optimum switching angles are calculated by utilizing an objective function. The TLBO algorithm finds the optimal solution using an objective function. This objective function is formulated as follows.

$$\begin{aligned}
F(\theta_1,\theta_2,\theta_3,\ldots,\theta_8) = &\left(\sum_{i=1}^{8}\cos\theta_i - M\right)+\left(\frac{4}{5\pi}\sum_{i=1}^{8}\cos(5\theta_i)\right)+\left(\frac{4}{7\pi}\sum_{i=1}^{8}\cos(7\theta_i)\right)+\left(\frac{4}{11\pi}\sum_{i=1}^{8}\cos(11\theta_i)\right)\\
&+\left(\frac{4}{13\pi}\sum_{i=1}^{8}\cos(13\theta_i)\right)+\left(\frac{4}{17\pi}\sum_{i=1}^{8}\cos(17\theta_i)\right)+\left(\frac{4}{19\pi}\sum_{i=1}^{8}\cos(19\theta_i)\right)+\left(\frac{4}{23\pi}\sum_{i=1}^{8}\cos(23\theta_i)\right)
\end{aligned} \tag{5}$$

The ratio of the THD% is a measure of the harmonic content of an output voltage or output current. THD% of the output voltage can be expressed as the following:

$$THD\% = 100 * \sqrt{\sum_{n=5,7,11,13,....}^{\infty} \left(\frac{V_n}{V_1}\right)^2} \tag{6}$$

Overview of the Teaching Learning Based Optimization (TLBO) Algorithm

This optimization technique is an inhabited meta-heuristic technique that optimizes a given objective function (R. Venkata Rao et al., 2012). The TLBO algorithm exhibits two modes of learning: teacher-led learning and learner-led learning (referred to as the learner phase). The proposed TLBO algorithm considers the number of students in a class and the required number of iterations or generations. The teacher selects the best solution (learner), which is then reviewed by the other learners. The resulting solution is the most suitable one, requiring minimal data for implementation. The basic steps of the TLBO algorithm are given below:

Step 1: Initialize the parameters of TLBO algorithm: including the number of design parameters (D_n), the convergence rate and the sample size (P_n).
Step 2: Create a random population according to population size (n) and dimension.
Step 3: The optimization, during this phase, where the function f(x) that is to be minimized is defined subject to xi = 1, 2, ..., where i is the iteration size.

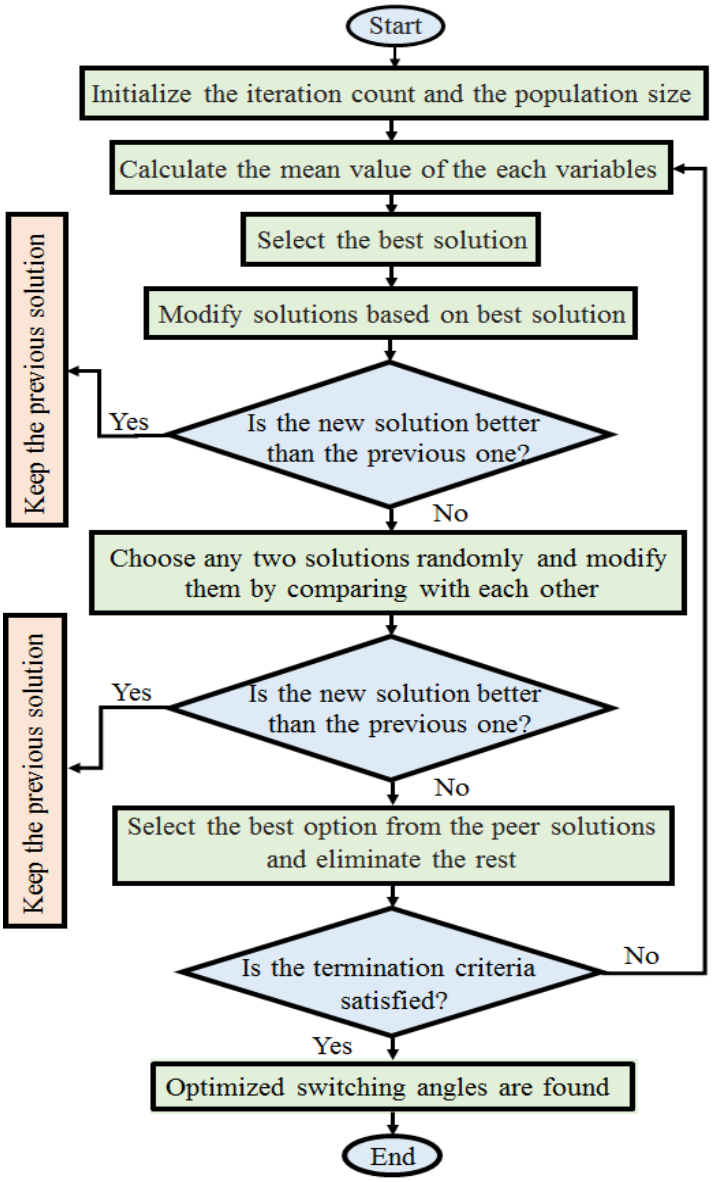


Figure 4. TLBO flowchart for solving SHE-PWM problem

Step 4: Find the mean of parameters by using an arbitrary population of the same size.
Step 5: The teacher phase, during this phase, the least fit student is the teacher, or the best solution X_{new} is employed, where X_{mean} is the mean of all the students in the class. The equation to generate a new solution is given by:

$$X_{new} = X + r.(X_{best} - T_f.X_{mean}) \tag{7}$$

where X_{best} represents the teacher, X_{new} represents the new selection, X represents the current solution, X_{mean} represents the mean of the solution, r represents a random number in the range (0, 1) and T_f represents the teaching factor and is either 1 or 2, the value of T_f is decided randomly.
Step 6: The learner phase, during this phase, learners gain information by interacting among themselves, the generate a new solution of this phase is expressed below:

$$X_{new} = X + r.(X - X_p) \tag{8}$$

where X_p is the partner solution, X represents the current solution and r represents a random number in the range (0, 1).
Step 7: Termination criteria. Termination criteria stop if the maximum generation is achieved; otherwise repeat from Step 5 and continue until all of the closure conditions are met. Detail flow chart of TLBO is shown in Figure 4.

Results and Discussion

In this section, a single-phase CHB-MLI to show the efficacy and robust of TLBO algorithm in solving SHE optimization problem. The inverter is a 17-level inverter, therefore 8 optimal angles are specified by the TLBO algorithm. The 17-level inverter with 315V output voltage and 50 Hz. The parameters of TLBO algorithm used for simulation are listed in Table (1).

Table 1. Simulation and optimization parameters

N^0	Parameters	Values
1	Population Size	100
2	Number of Iterations	500
3	Number of dimensions	10
4	Lower Boundary	[0°, 0°, 0°, 0°, 0°, 0°, 0°, 0°]
5	Upper Boundary	[90°, 90°, 90°, 90°, 90°, 90°, 90°, 90°]
6	Modulation index	0 < MI≤1

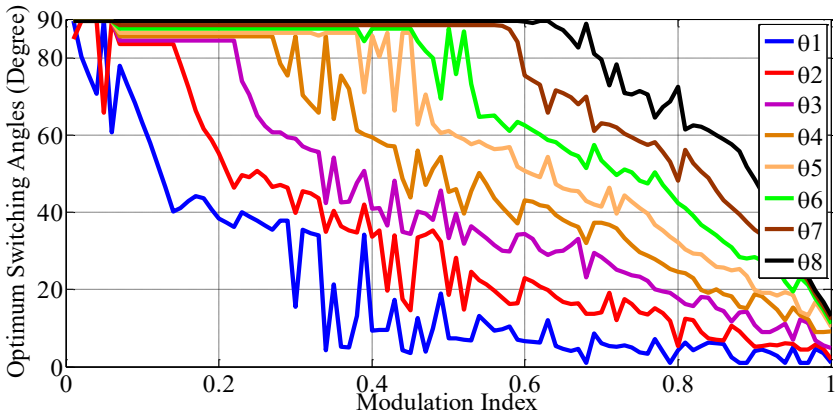


Figure 5. Optimum switching angle trend with modulation index obtained from TLBO algorithm

Figure. 5, shows optimal switching angles obtained using TLBO algorithm against different values of modulation index (MI). From the given Figure 5, it is evident that the value of the optimum solution set, comprising different switching angles (θ_1 to θ_8), converges to a lower value with the increase in the value of the (MI). The switching angles calculated by TLBO, THD% and fitness values versus different modulation indices for 17-level MLI are shown in Table 2.

Table 2. Simulation and optimization parameters

Switching Angle	MI 0.2	MI 0.6	MI 1
θ_1	38.38	6.67	1.90
θ_2	55.32	22.91	1.99
θ_3	84.55	34.33	4.86
θ_4	85.56	43.16	9.19
θ_5	87.54	50.67	10.99
θ_6	88.54	62.45	11.30
θ_7	89.50	75.35	12.40
θ_8	90	89.45	13.20

From Table 2, it is observed that the TLBO algorithm successfully solved the SHE equations in the range of 0.1–1 modulation index (MI) and interesting thing is that THD% produced during range 0.5–0.95 of MI are less than 8% and minimum THD% of value 4.31%. Figure. 6 shows the objective function value of TLBO algorithm versus modulation index. The Figure indicates that TLBO algorithms were successful in finding solutions across the entire modulation index range ($0.1 \leq MI \leq 1$). Moreover, TLBO algorithm produced the optimum fitness value of $6.75e^{-13}$, which demonstrates its stability and superior performance in solve the non-linear SHE-PWM problem

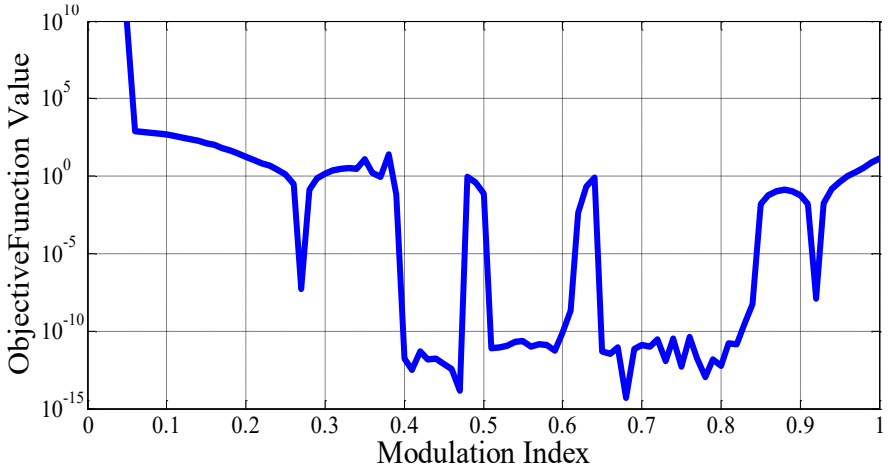


Figure 6. Objective function value for TLBO algorithm versus modulation index

Figure. 7 shows harmonics based on modulation index from 0.1 to 1. Figure. 7 indicates that the low order harmonics are eliminated 5th, 7th, 11th, 13th, 17th, 19th and 23th within the range of (0.5–0.95) modulation index. Figure. 8 represents the THD% of output voltage at various modulation index (MI).It can be seen that the THD% of output voltage value in the range of (0.5–0.95) modulation index, is found to be less than 8.0% and meets the IEEE 519-2014 standard and minimum THD% of value 4.31% has occurred.

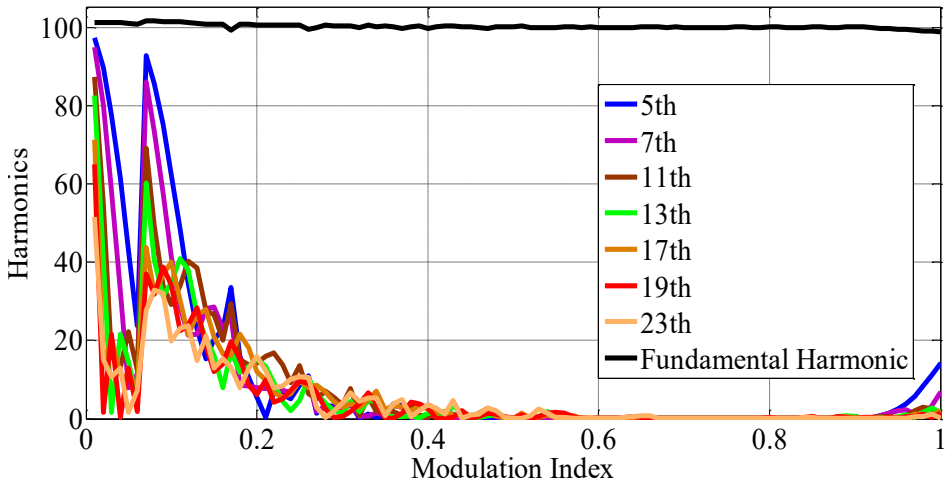


Figure 7. Harmonic trend with respect to the modulation index

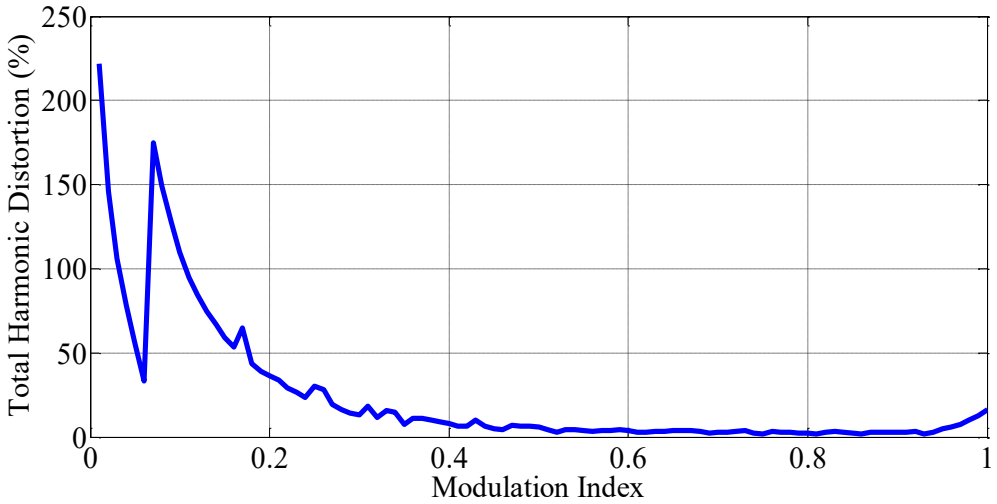


Figure 8. THD % Vs modulation index

Figure. 9 shows the magnitude of fundamental harmonic versus modulation index (MI). It can be observed the maximum deviation is within 1.3%. Figure. 10 depict the stepped output voltage waveform of 17-level a CHB-MLI with 0.8 modulation indexes using the TLBO. Fast Fourier transform (FFT) analysis at modulation index (MI) of value 0.8 is presented in Figure. 11. It reveals that the targeted lower order harmonics of 5^{th}, 7^{th}, 11^{th}, 13^{th}, 17^{th}, 19^{th} and 23^{th} are eliminated and the THD% is 4.31%, which complies with IEEE 519-2014 harmonic guidelines.

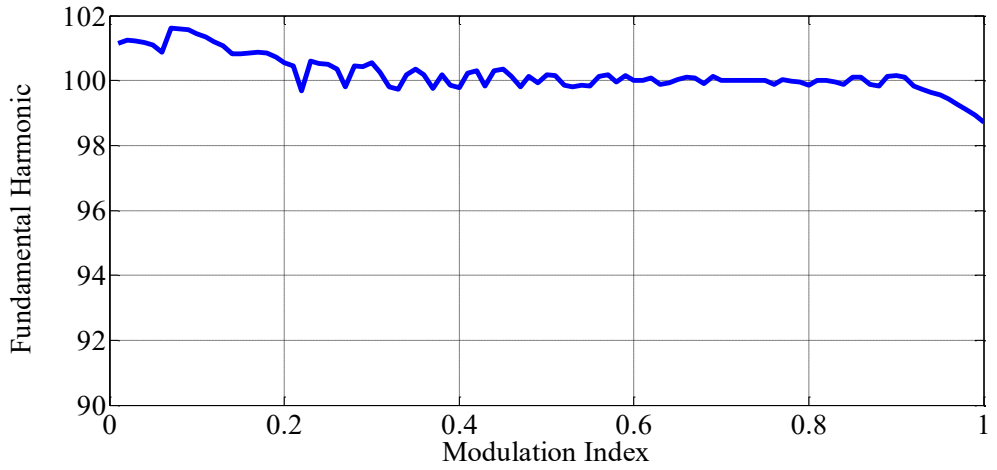


Figure 9. The calculated fundamental harmonic to V1

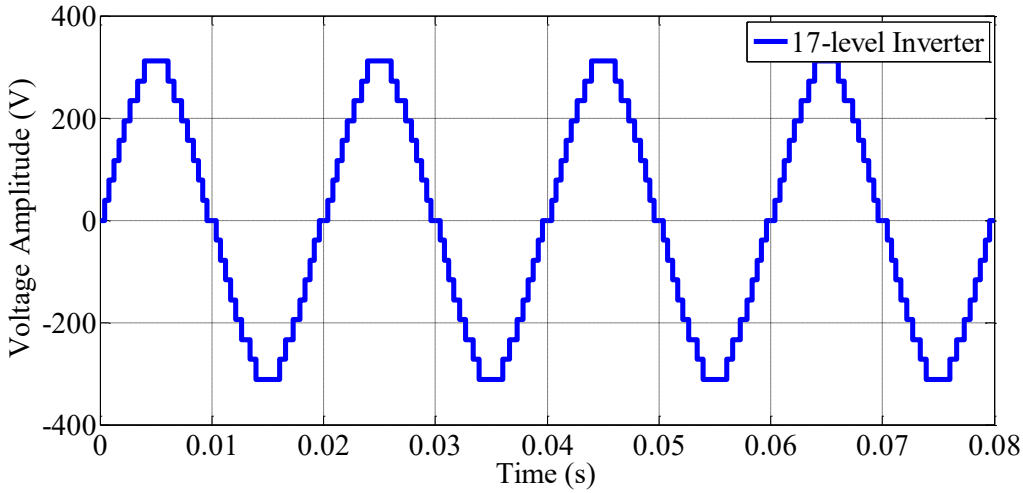


Figure 10. Simulation result of output voltage waveform for 17-level CHB-MLI at modulation index 0.8

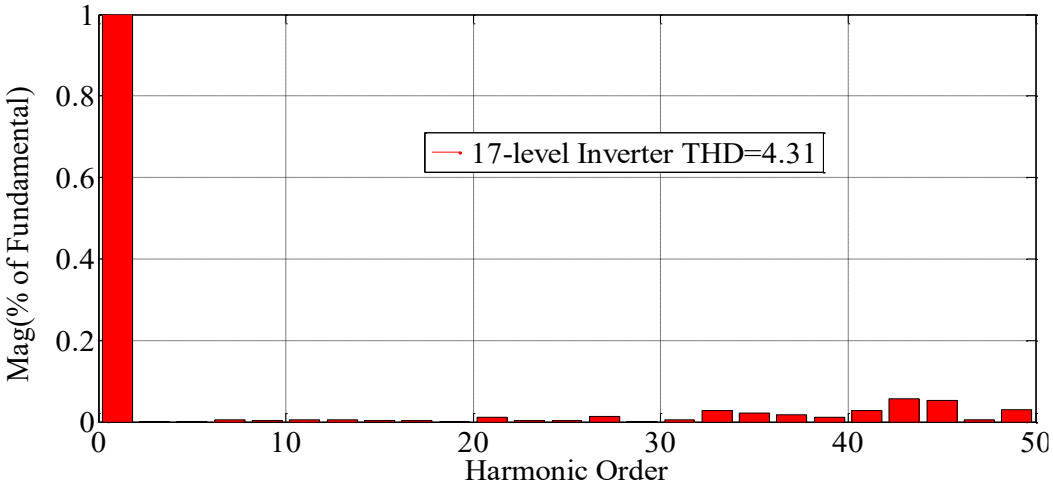


Figure 11. FFT analysis representing order of harmonics in the output voltage.

Table 3 summarizes the percentage of THD by EP, HEP, FF, HH and TLBO methods for voltage levels of 17. Noted that the best system performance is by TLBO method, in which the least THD obtained is 4.31%. This is because of better suppression of lower order harmonic spectrum by TLBO method.

Table 3. Comparative analysis of THD% at 17- level

Modulation technique	%THD
EP (Taha Abdulsalam Taha et al., 2025)	17.55%
HEP (Taha Abdulsalam Taha et al., 2025)	16.35%
FF (Taha Abdulsalam Taha et al., 2025)	20.90 %
HH (Taha Abdulsalam Taha et al., 2025)	5.02%
Proposed TLBO algorithm	4.31%

Conclusion

This paper focused on using the teaching learning-based optimization (TLBO) algorithm with selective harmonic elimination-pulse width modulation (SHE-PWM) technique to reduce total harmonic distortion (THD) on the phase voltage in a multilevel inverter (MLI) topology. The TLBO algorithm has been implemented to find the optimal switching angles of a single-phase 17-level cascaded H-bridge MLI (CHB-MLI). According to simulation results, the proposed method successfully solves non-linear equations for SHE, achieving a reduced THD of 4.31% while eliminating 5^{th}, 7^{th}, 11^{th}, 13^{th}, 17^{th}, 19^{th} and 23^{rd} harmonics. Furthermore, the THD values were compared with those reported in the existing literature obtained using different conventional modulation methods. The results indicated that the THD obtained using the TLBO algorithm was lower compared to the equal phase (EP), half equal phase (HEP), feed forward (FF) and half height (HH) methods. The proposed strategy can be further extended to reduce higher order harmonics. In addition, it can be implemented to other topologies.

Scientific Ethics Declaration

* The authors declare that the scientific ethical and legal responsibility of this article published in EPSTEM journal belongs to the authors.

Conflict of Interest

* The authors declare that they have no conflicts of interest

Funding

* This research received no specific grant from any funding agency in the public, commercial, or not-for-profit sectors.

Acknowledgements or Notes

* This article was presented as an oral presentation at the International Conference on Technology, Engineering and Science (www.icontes.net) held in Antalya/Türkiye on November 12-15, 2025.

References

Adam, G. P., Finney, S. J., Ojo, O., & Williams, B. W. (2012). Quasi-two-level and three-level operation of a diode-clamped multilevel inverter using space vector modulation. *IET Power Electronics, 5*(5), 542-551.

Ali, M., Mehmood, K. K., Baloch, S., & Kim, C. H. (2021). Robust ANN-based control of modified puc-5 inverter for solar PV applications. *IEEE Transactions on Industry Applications, 57*(4), 3863-3876.

Behera, R. R., Dash, A. R., & Panda, A. K. (2022). A novel cascaded transformer coupled multilevel inverter with reduced number of switches for high power applications. *World Journal of Engineering*. *20*(6), 1025-1044.

Bounabi, M., Kaced, K., Ait-Cheikh, M. S., Larbes, C., Dahmane, Z., & Ramzan, N. (2018). Modelling and performance analysis of different multilevel inverter topologies using PSO-MPPT technique for grid connected photovoltaic systems. *Journal of Renewable and Sustainable Energy, 10*(4), 043507

Can, E., & Sayan, H. H. (2022). Development of fractional sinus pulse width modulation with β gap on three step signal processing. *International Journal of Electronics, 110*(3), 527-546.

Chunyan, Z., & Zhao, L. (2015). Advanced compensation mode for cascade multilevel static synchronous compensator under unbalanced voltage. *IET Power Electronics, 8*(4), 610-617.

Dahidah, M. S. A., & Agelidis, V. G. (2008). Selective harmonic elimination PWM control for cascaded multilevel voltage source converters: A generalized formula. *IEEE Transactions on Power Electronics, 23*(4), 1620-1630.

Dekka, A., Ramezani, A., Ouni, S., & Narimani, M. (2020). A new five-level voltage source inverter: Modulation and control. *IEEE Transactions on Industry Applications, 56*(5), 5553-5564.

Dordevic, O., Jones, M., & Levi, E. (2013). A comparison of carrier-based and space vector PWM techniques for three-level five-phase voltage source inverters. *IEEE Transactions on Industrial Informatics, 9*(2), 609-619.

Elias, M. F. M., Rahim, N. A., & Rosli, N. F. (2023). A three-phase hybrid multilevel inverter with enhanced pulse-width modulation strategy. *IEEE Transactions on Power Electronics, 38*(4), 4714-4726.

Hiendro, A., Yusuf, I., Junaidi, J., Wigyarianto, T. P., & Simanjuntak, Y. M. (2020). Optimization of SHEPWM cascaded multi-level inverter switching patterns. *International Journal of Power Electronics and Drive Systems, 11*(3), 1570-1578.

Hosseini Aghdam, G. (2013). Optimised active harmonic elimination technique for three-level t-type inverters. *IET Power Electronics, 6*(3), 425-433.

Jiang, Y., Li, X., Qin, C., Xing, X., & Chen, Z. (2022). Improved particle swarm optimization based selective harmonic elimination and neutral point balance control for three-level inverter in low-voltage ride-through operation. *IEEE Transactions on Industrial Informatics, 18*(1), 642-652.

Juárez-Abad, J. A., Barahona-Avalos, J. L., & Linares-Flores, J. (2021). PWM techniques for an asymmetric multilevel binary inverter: An FPGA-based implementation. *IET Power Electronics, 14*(8), 1529-1539.

Kannan, C., Priyadharsini, S., Babu, L. G., Mugilvannan, S., Thamotharan, K., & Velan, V. (2022). Design of modular and non modular multilevel inverter topology with reduced number of switches. *EPRA International Journal of Research and Development (IJRD), 7*(6), 249-255.

Kato, T. (1999). Sequential homotopy-based computation of multiple solutions for selected harmonic elimination in PWM inverters. *IEEE Transactions on Circuits and Systems I: Fundamental Theory and Applications, 46*(5), 586-593.

Kubendran, V., Mohamed Shuaib, Y., & Preetha Roselyn, J. (2022). Development of multilevel inverter with reduced switch counts and limited sources for electric vehicles. *Sustainable Energy Technologies and Assessments, 52*, 102332.

Mehta, S., & Puri, V. A. (2022). Review of different multi-level inverter topologies for grid integration of solar photovoltaic system. *Renewable Energy Focus, 43*, 263-276.

Meraj, S. T., Yu, S. S., Rahman, M. S., Hasan, K., Hossain Lipu, M. S., & Trinh, H. (2023). Energy management schemes, challenges and impacts of emerging inverter technology for renewable energy integration towards grid decarbonization. *Journal of Cleaner Production, 405*, 137002.

Meynard, T., & Foch, H. (1992). Multi-level choppers for high voltage applications. *EPE Journal, 2*(1), 45-50.

Naga Sai Charan, P., & Meenendranath Reddy, K. (2023). An analysis of multilevel converter for faster current control in a DC microgrid with extremely low-impedance interconnections. *Journal of Image Processing and Intelligent Remote Sensing, 3*, 18-29.

Pires, V. F., Foito, D., & Silva, J. F. (2017). Fault-tolerant multilevel topology based on three-phase H-bridge inverters for open-end winding induction motor drives. *IEEE Transactions on Energy Conversion, 32*(3), 895-902.

Rao, R. V., & Patel, V. (2012). An elitist teaching-learning-based optimization algorithm for solving complex constrained optimization problems. *International Journal of Industrial Engineering Computations, 3*(3), 535-560.

Ren, W. (2021). *Research on modulation strategy of cascaded H-bridge multilevel inverter* (Master's thesis) East China Jiaotong University.

Sedaghati, F., Ebrahimzadeh, S., Dolati, H., & Shayeghi, H. (2022). A modified switched capacitor multilevel inverter with symmetric and asymmetric extendable configurations. *Journal of Operation and Automation in Power Engineering, 20*, 20.

Singh, A., Bhandari, S., & Kumar, J. (2022). (Paper presentation). *1st International Conference on Sustainable Technology for Power and Energy Systems (STPES)*, Srinagar, India.

Sotoodeh, P., & Miller, R. D. (2013). A new multi-level inverter with facts capabilities for wind applications. In *IEEE* (pp. 271–276).

Taha, T. A., Shalaby, M., Abdul Wahab, N. I., Zaynal, H. I., Hassan, M. K., Al-Sowayan, S., & Alawad, M. A. (2025). Recent advancements in multilevel inverters: Topologies, modulation techniques, and emerging applications. *Symmetry, 17*, 1010.

Taiea, A., Mohamed, E. E. M., Youssef, A., Ibrahim, A. A., Saeed, M. S. R., & Ali, A. I. M. (2020). Three phase modular multilevel inverter-based multi-terminal asymmetrical DC inputs for renewable energy applications. *Engineering Science and Technology, an International Journal, 23*(4), 831–839.

Vicente, J., Pindado, R., & Martinez, I. (2011). (Paper presentation). *7th International Conference-Workshop Compatibility and Power Electronics (CPE)*.

Yang, K., Yuan, Z., Yuan, R., Yu, W., Yuan, J., & Wang, J. (2015). A groebner bases theory-based method for selective harmonic elimination. *IEEE Transactions on Power Electronics, 30*(12), 6581–6592.

Author(s) Information

Smail Toufik
Solar Equipements Development Unit (UDES)
UDES, National Road N°11, BP 386, Bou-Ismail, 42415, Tipaza, Algeria
Contact e-mail: *smail.toufik77@gmail.com*

Boulouma Sabri
Solar Equipements Development Unit (UDES)
UDES, National Road N°11, BP 386, Bou-Ismail, 42415, Tipaza, Algeria

Seddaoui Naoual
Solar Equipements Development Unit (UDES)
UDES, National Road N°11, BP 386, Bou-Ismail, 42415, Tipaza, Algeria

Rahmani Hachemi
Solar Equipements Development Unit (UDES)
UDES, National Road N°11, BP 386, Bou-Ismail, 42415, Tipaza, Algeria

To cite this article:

Toufik, S., Sabri, B., Naoual, S., & Hachemi, R. (2025). Voltage total harmonic distortion reduction in multi-level single-phase inverters using the SHE-PWM technique with a TLBO algorithm. *The Eurasia Proceedings of Science, Technology, Engineering and Mathematics (EPSTEM), 38,* 688-698.

The Eurasia Proceedings of Science, Technology, Engineering & Mathematics (EPSTEM)
ISSN: 2602-3199

The Eurasia Proceedings of Science, Technology, Engineering and Mathematics (EPSTEM), 2025

Volume 38, Pages 699-711

IConTES 2025: International Conference on Technology, Engineering and Science

Measurement and Transmission of Process Parameters in GSM and IoT Network

Goce Stefanov
Goce Delcev University

Marija Cekerovska
Goce Delcev University

Elena Zafirov
Onesky Flight

Todor Cekerovski
Goce Delcev University

Abstract: In modern industrial plants, timely and accurate information about process parameters is essential. For those reasons in modern technological and industrial development, the application of electronics in measuring, processing, storing and transferring process data in industrial facilities is increasing. Guided by the need for measurement, visualization and storage of process parameters, modern electronic systems provide the ability to process and store measurement data on-site and transfer it to the GSM and IoT network. On the other hand, the application of sophisticated electronic systems is noticeable not only in power plants, but also in healthy and quality food industries, such as agriculture. We witness daily tribunes and panel discussions sponsored by companies and even governments for the introduction of the terminology of digital agriculture, i.e. the introduction of smart electronic solutions in agriculture. In addition to the commitment to so-called green energy, i.e. obtaining energy from renewable sources, the development of digitization in agriculture is an area in which an enormous application of smart electronic systems is expected in the future. Guided by these reasons, in this paper an electronic system is designed that provides a solution to a problem in hydro melioration system, i.e. the development, design and practical implementation of the Smart electronic system which enables the measurement of the process parameters of an agro-industrial facility and their transfer to the GSM and IoT network. The solution enables the visualization of process parameters locally on LCD displays and remotely on an mobile device in GSM and IoT network. A data log file is also provided for store the value on the process parameters on a local computer.

Keywords: Electronic system, Hydro melioration system, Process parameters, GSM network, IoT network

Introduction

Modern agricultural production, on the one hand, should provide timely management of the parameters necessary for obtaining a quality product, and on the other hand, it should provide the opportunity to collect and process data on control values in the agricultural plant (Fountas et al., 2020; Nareandra et al., 2019). Therefore, the introduction of a system for monitoring and quality control in modern agricultural production is essential knowledge (Rptz et al., 2019; Saiz-Rubio et al, 2020; Benet et al., 1982). In real industrial agricultural processes there are standalone plants that represent a separate whole. Most often these plants are far from intra and internet network of the agricultural production companies. Therefore there is a need to automate and connect these agricultural plants in the intranet of the company and more widely in the Internet (IoT), as and GSM SIM

- This is an Open Access article distributed under the terms of the Creative Commons Attribution-Noncommercial 4.0 Unported License, permitting all non-commercial use, distribution, and reproduction in any medium, provided the original work is properly cited.

- Selection and peer-review under responsibility of the Organizing Committee of the Conference

© 2025 Published by ISRES Publishing: www.isres.org

network (Bhuiyan et al., 2023; Eduku et al., 2024). Efforts are being made to ensure safer and simpler work, especially for operators who are directly exposed to the correct functioning of the entire industrial process. This approach to work is enabled by smart electronic devices that, among other things, generate data log files of measurement data (Ariel, 2024). On the other hand, a modern controlled system of an industrial process is fully rounded if it is connected to an IoT or GSM SIM network (Stefanov et al., 2021; Stefanov et al., 2023; Memonova et al., 2025). Such a concept enables process data to be transferred to any location, visualized in real-time, and stored on a personal and cloud computer.

Commonly, some standalone industrial agricultural processes might represent a separate entity. Since these plants are far from the Intra and Internet network of manufacturing companies, the data distribution of analog and digital signals from sensors and actuators of some process quantities (eg soil moisture, soil temperature and air temperature and humidity as and voltage, current, pressure, flow and level water, etc.) must be made from these remote entities to the master station via wireless communication, most likely a radio frequency (RF), IoT as and GSM connection (Stefanov et al., 2023; Memonova et al., 2025).

The choice of remote transmission of measurement process data via RF, IoT or GSM connection depends on the location of the specific industrial (agro) facility, the type and quantity of measurement data. Each of these transmission media has advantages and disadvantages. In the case where an RF connection is used, the transfer is limited in scope and is most often used when an standalone industrial (agro) facility needs to be connected to a master station of a complex industrial facility. The connection in the GSM and IoT network requires a reliable and secure GSM and internet medium and a secure and inexpensive cloud platform.

For these reasons, and guided by the need to improve the security of the transmitted data, the paper presents a solution by which the process data is transmitted in both networks. It is actually is designed an electronic system that provides a solution to a problem in hydro melioration system, i.e. the development, design and practical implementation of the Smart electronic system which enables measurement, storage, visualization and transfer of measured process parameters of an agro-industrial facility in the GSM and IoT network.

Design of an Electronic System

The design of the electronic system uses hardware components: microcontroller, sensors, relays, valves, fan. For the implementation of the control logic, an appropriate program code has been developed and is embedded in the microcomputer. The microcontroller MCU ESP8266, according to the control logic, receives the signals from the sensors and sends them to the SIM 900 module in the GSM network, and with the WI-FI module sends them to the IoT network. Figure 1 shows the block diagram of the control logic.

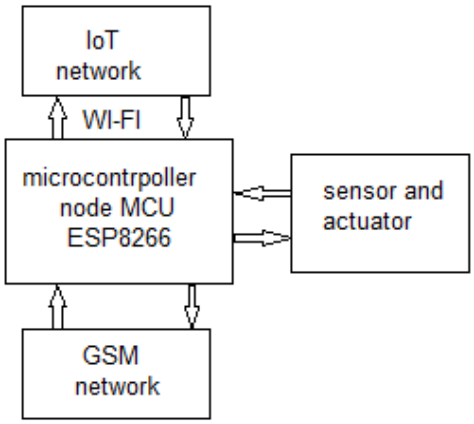


Figure 1. Block diagram on control logic

The design of the prototype electronic system, subject to the paper, includes the design of the system for measurement, monitoring and transfer of the process parameters on mobile device through GSM and IoT network. The detailed block diagram of this electronic system is shown in Figure 2. The task of the electronic system is to manage the agro-industrial facility based on the measured process parameters, temperature, humidity and CO2 on the air, as and soil temperature and humidity. A case is considered when the agro-industrial facility is of a closed type, i.e. built into a room (greenhouse). The central part of the system is Master station where is build the nodeMCU ESP8266 microcontroller (Arduino, 2021).. The agro-industrial facility is

equipped with: an air temperature and humidity sensor (DHT22), a soil temperature sensor (DS18B20), a soil moisture sensor (V2.0), as and a CO2 detection sensor (SCD40), (Sensirion SCD40, n.d; Rembor, 2024). These sensors, based on the measured parameter values, send signals to the microcontroller: a digital signal for air temperature and humidity to digital input D8, a digital signal for soil temperature to digital input D7, an analog signal for soil moisture to analog input A0, as well as digital signal for CO2 on crop to the microcontroller's I2C bus.

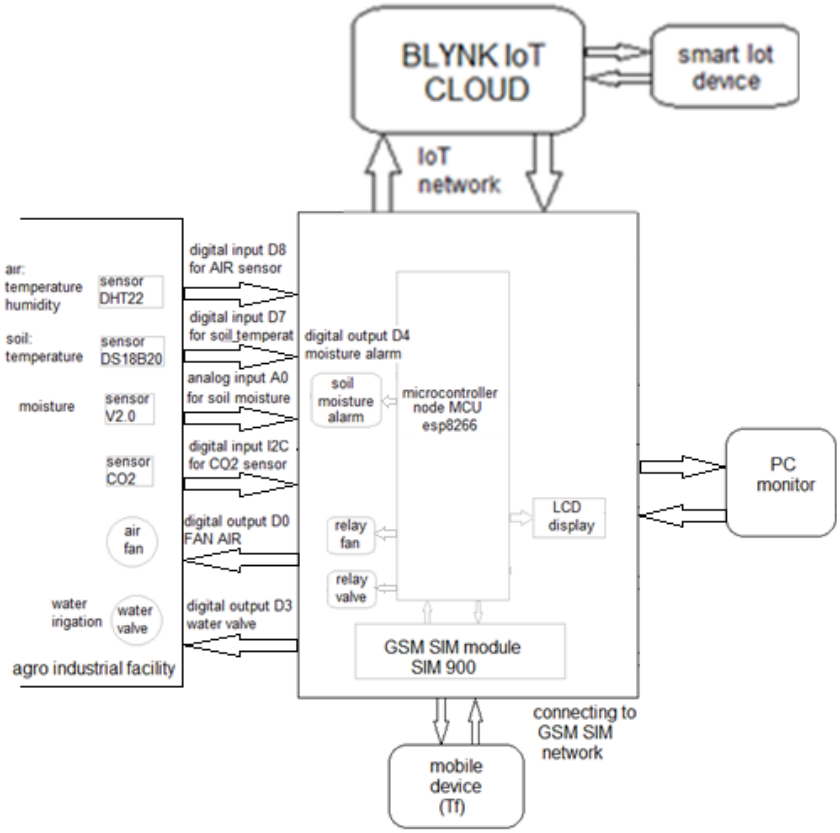


Figure 2. Detailed block diagram on electronic system for measurement, monitoring and transfer of the process parameters in agro industrial facility in mobile device through GSM and IoT network

Based on the measured values of the process parameters, the microcontroller sends control signal (digital output D0) to a fan for supplying fresh air to the agricultural facility and a signal (digital output D3) to turn on a valve for supplying water to the irrigation line of the agricultural crop. The microcontroller on the one hand is connected to the GSM network with the GSM module SIM900, and on the other hand with the WI-FI module built into the microcontroller MCU ESP8266, it is connected to the IoT network (SimCom, 2020). This connection ensures that process parameters are distributed bidirectional in the GSM and IoT network. This concept allows reading the values of process parameters on a mobile device, management of the supply of fresh air and water, as well as an alarm when any of the controlled variables exceeds the critical threshold.

Control Logic

The microcomputer node MCU 8266 via GSM module with the built-in SIM card is a medium (intermediary) for sending instructions from the microcomputer to the mobile phone and receiving them from the mobile device to the microcomputer. Also, microcomputers with build WI-FI module sending and receiving instructions via IoT network to mobile device (tablet, mobile phone). In Figure 3 is shown logical flow diagram on the electronic system.

The GSM module controls the state of the agro-culture by communicating with the microcomputer according to String (text) instructions. These String instructions are received by the SIM900 from the user via a mobile phone. The microcontroller receives the signals for the process parameters of the agro-industrial facility, processes them according to defined logic and sends the them via GSM SIM900 module to mobile phone.

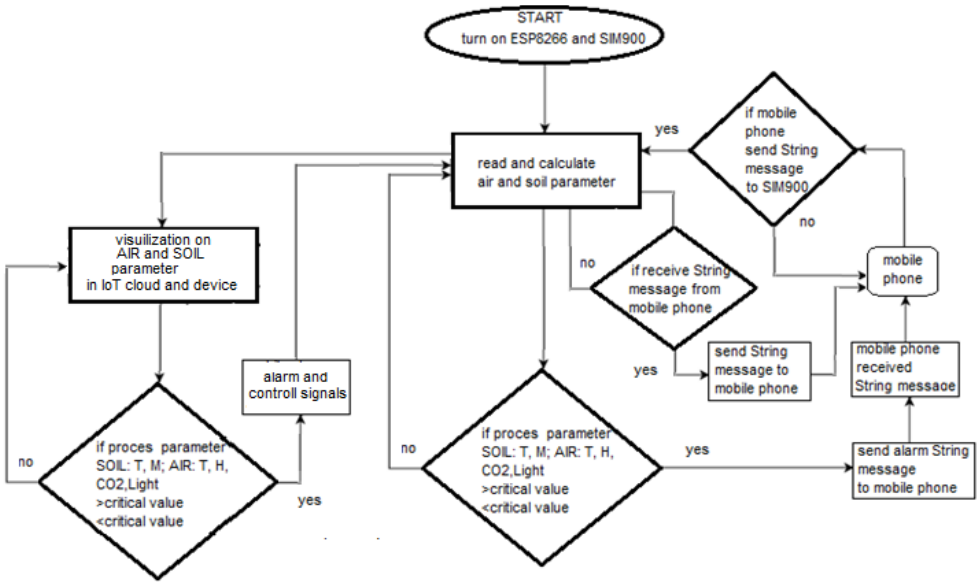


Figure 3. Block diagram on flow diagram on the electronic system

Measurement and Transmission on Process Parameter in GSM Network

These String instructions include:

Instructions on the Condition of Air Parameters

- READ AIR, the SIM900 receive from mobile phone this String message and sends this instruction to the microcontroller for reading air parameters in the agricultural facility; when the microcontroller receives this instruction, he (the microcontroller) reads and calculates the air parameters in the facility and sends a text string SIM message via SIM900 on mobile phone: " AIR: Temperature = " + String(t) + "*C " + "," + " Humidity = " + String(h) + "%" + "," + " CO2 = " + String(CO2) + "ppm". The message contains information about temperature, humidity, light and CO2 in the air as well as the brightness of the agricultural crop. Based on the values of the read data, the user concludes whether any of the process parameters has exceeded the critical value and sends the next string instruction for its correction.
- AIR FAN ON, This instruction is sent by the user when, based on previously read parameter values, he concludes that the humidity, temperature, light or CO2 in the facility has exceeded the critical value; when the microcontroller receives this instruction, he (the microcontroller) reads and calculates the air parameters in the facility, turns on the fan to supply fresh air sends a text string SIM message via SIM900 on mobile phone: "AIR: Temperature = " + String(t) + "*C " + "," + " Humidity = " + String(h) + "%" + "," + " CO2 = " + String(CO2) + "ppm"+ "FAN ON". The message contains information about temperature, humidity and CO2 in the air as well as the brightness of the agricultural crop and confirmation that the user's previous command has been implemented, i.e. the fan is turned on.
- The previous two instructions are for when the user wants to see the air condition in the facility. But the program algorithm has a built-in loop with which the microcontroller automatically monitors the process parameters and when any of them exceeds the critical value, it sends a string alarm message to the user.
- " CO2: " + String(CO2) + "ppm" + "," + " CO2 is HIGH " ; The user of the mobile device receives an alarm that the CO2 level is high.
- " temperature: " + String(t) + "*C" + "," + "temperature is HIGH " ;
- " humidity: " + String(h) + "%" + "," + "humidity is LOW " ;
- " Light: " + String(lux) + "lux" + "," + "light is LOW " ;
- AIR FAN OFF; This instruction is sent by the user when, based on previously read parameter values, he concludes that the humidity, temperature, light or CO2 in the facility have values within the working limits; when the microcontroller receives this instruction, he (the microcontroller) reads and calculates the air parameters in the facility, turns off the fan to supply fresh air sends a text

string SIM message via SIM900 on mobile phone: "AIR: Temperature = " + String(t) + "*C " + "," + " Humidity = " + String(h) + "%" + "," + " CO2 = " + String(CO2) + "ppm"+ "FAN OFF".

Instructions on the Condition of Soil Parameters

- READ SOIL; the SIM900 receive from mobile phone this String message and sends this instruction to the microcontroller for reading soil parameters in the agricultural facility; when the microcontroller receives this instruction, he (the microcontroller) reads and calculates the soil parameters in the facility and sends a text string SIM message via SIM900 on mobile phone: "SOIL: Temperature = " + String(tempSoil) + "*C " + "," + "Moistre = " + String(data1) + "%". The message contains information about temperature and moisture on soil in agricultural facility. Based on the values of the read data, the user concludes whether any of the process parameters on soil has exceeded the critical value and sends the next string instruction for its correction.
- VALVE ON; This instruction is sent by the user when, based on previously read parameter values, he concludes that the temperature and moisture on the soil in facility has exceeded the critical value; when the microcontroller receives this instruction, he (the microcontroller) reads and calculates the soil parameters in the facility, turns on the water valve on irrigation line to supply water and sends a text string SIM message via SIM900 on mobile phone: " SOIL: Temperature = " + String(tempSoil) + "*C " + "," + "Moisture = " + String(data1) + " % " + "," + "Valve ON".
- The previous two instructions are for when the user wants to see the soil condition in the facility. But the program algorithm has a built-in loop with which the microcontroller automatically monitors the process parameters and when any of them exceeds the critical value, it sends a string alarm message to the user.
- " SOIL Moistre: " + String(data1) + "%" + "," + " Moistre is LOW "; The user of the mobile device receives an alarm that the soil moisture level is LOW.
- " SOIL Temperature: " + String(tempSoil) + "*C" + "," + " Temperature is HIGH "; The user of the mobile device receives an alarm that the soil temperature level is HIGH.
- VALVE OFF; This instruction is sent by the user when, based on previously read parameter values, he concludes that the temperature and moisture on the soil in facility have values within the working limits; when the microcontroller receives this instruction, he (the microcontroller) reads and calculates the soil parameters in the facility, turns off the water valve on irrigation line to supply water and sends a text string SIM message via SIM900 on mobile phone: " SOIL: Temperature = " + String(tempSoil) + "*C " + "," + "Moisture = " + String(data1) + " % " + "," + "Valve OFF".

Measurement and Transmission on Process Parameter in IoT Network

The WI-FI module who is built-in ESP8266 card is a medium (intermediary) for sending instructions from the microcomputer to the IoT cloud. The IoT cloud also controls the state of the agro-culture by communicating with the microcomputer according to virtual pin instructions. These instructions are received by the cloud server from the user via a IoT network. The microcontroller receives the signals for the process parameters of the agro-industrial facility, processes them according to defined logic and sends the them via WI-FI module to mobile phone with build cloud platform. On the screen from mobile device in IoT network exist tags with built-in instruments for visualization of measurement parameters.

Figure 4 is shown print screen on IoT cloud screen, which shows the measured values of the process parameters. The measured value is displayed on an analog instrument with a measuring scale and on a digital display. On the screen are shown the following signals:

- AIR TEMP signal for the temperature on air;
- AIR HUM signal for the humidity on air;
- SOIL TEMP signal for temperature on the soil;
- MOISTURE SOIL signal for moisture on the soil.

Also on this screen are shown the button and led diode for management and control of the fan and water valve line:

- BUTTON FAN button for remote on/off of the fan for fresh air supply;
- FAN ON/OFF led diode for visualization of the fan status;

- BUTTON WATER VALVE button for remote on/off of the water valve on irrigation line;
- VALVE OPN/OFF led diode for visualization of water valve status.

The screen also displays alarm blocks when any of the controlled process parameters exceeds a critical value:

- SOIL MOISTURE is LOW a block for indicating when soil moisture is low;
- CO2 is HIGH a block for indicating when CO2 on air is high.

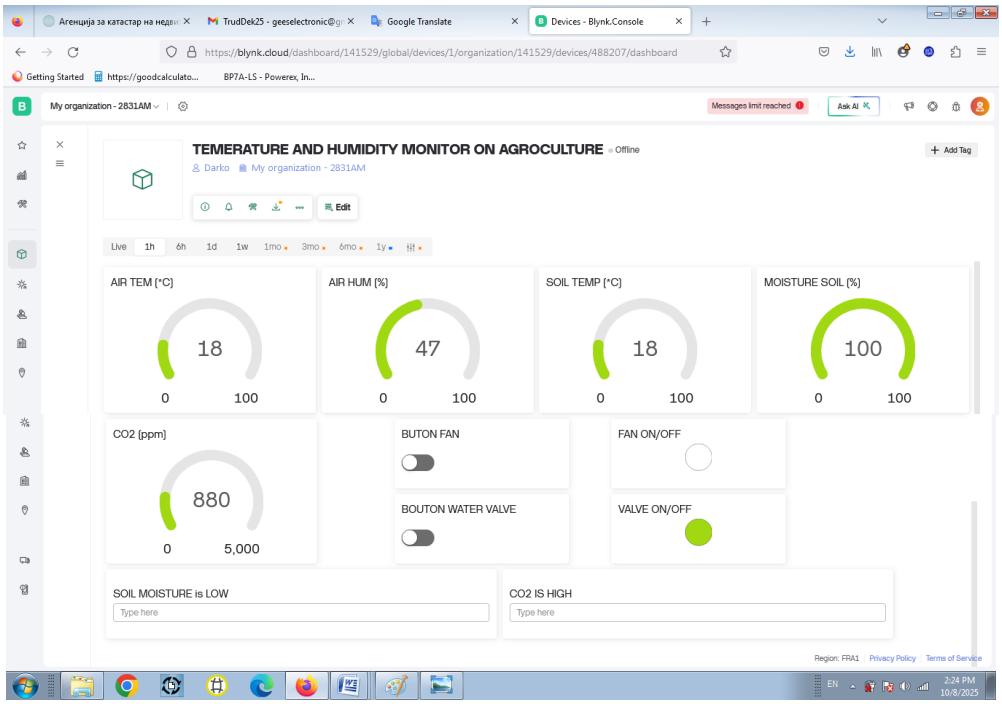


Figure 4. Print screen on IoT cloud screen

Design of Hardware Components on Electronic System

In this part is designed system which accepts the signals from the sensors and after appropriate software processing with nodeMCU8266 visualizes them on the one LCD displays and sends them via SIM900 module to the GSM network, and via WI-FI module in IoT network. Figure Figure 5 shows the electrical connections of the electronic system for managing the process parameters of the agro-industrial facility. The connections between the hardware components are described above, and can also be seen in Figure 5. Now a brief description of the characteristics of the hardware components used will be given here.

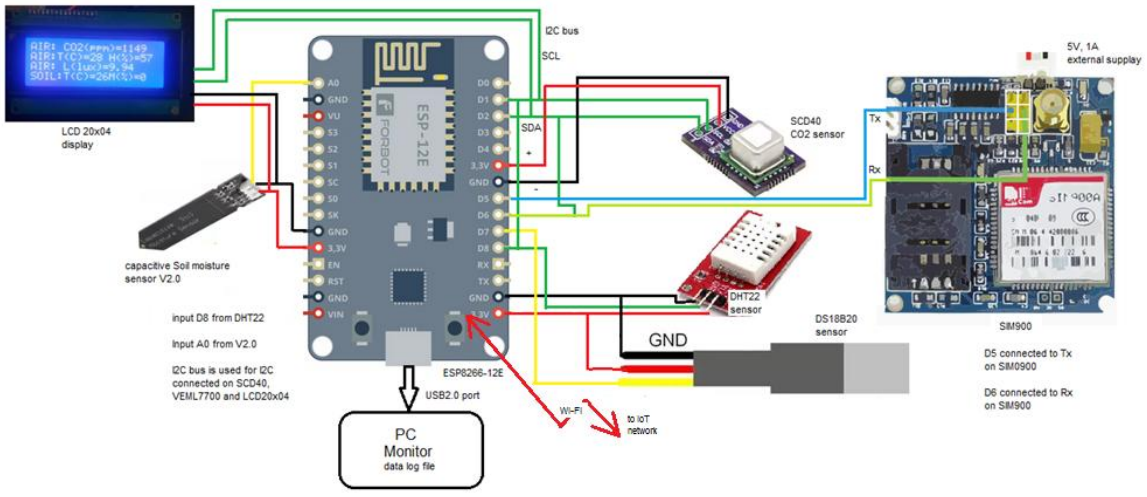
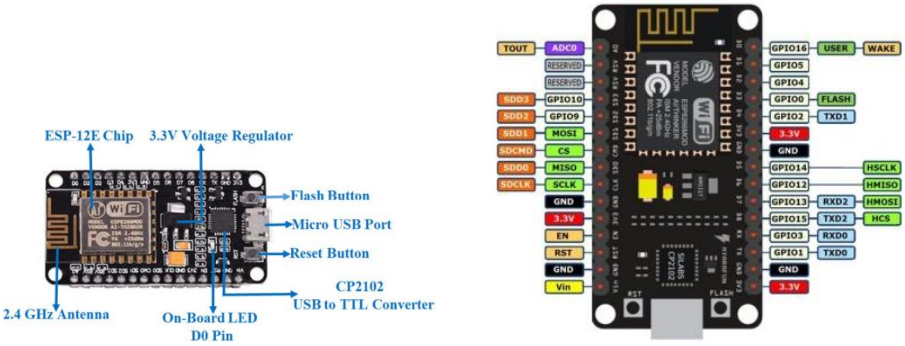


Figure 5. Electrical connections of the electronic system for managing with the process parameters of the agro-industrial facility

Microcomputer NodeMCU ESP8266

The NodeMCU ESP8266 development board comes with the ESP-12E module containing ESP8266 chip having Tensilica Xtensa 32-bit LX106 RISC microprocessor (NodeMCU, n.d). This microprocessor supports RTOS and operates from 80MHz to 160 MHz adjustable clock frequency. NodeMCU has 128 KB RAM and 4MB of Flash memory to store data and programs. Its high processing power with built-in Wi-Fi / Bluetooth and Deep Sleep Operating features makes it ideal for IoT projects. NodeMCU can be powered using Micro USB jack and VIN pin (External Supply Pin). It supports UART, SPI, and I2C interface. In the Figure 4 is shown NodeMCU ESP8266 and his pinout.



a.) b.)

Figure 4. a.) NodeMCU ESP8266 and b.) his pinout

NodeMCU is an open-source based firmware and development board specially targeted for IoT based applications. It includes firmware that runs on the ESP8266 Wi-Fi SoC from Espressif Systems, and hardware which is based on the ESP-12 module.

GSM SIM900 Module

GSM is a global system for mobile communication. Hence, to communicate with the computing devices, the GSM SIM needs a module. SIM900 is considered one of the best modules of today's time. It's a quad-band module that works perfectly with four frequencies, which are 850, 900, 1800, and 1900 MHz. The device is so compact and is compatible with Arduino. It easily allows sending SMS, MMS, etc. Moreover, it also supports audio through UART by using AT commands. Besides, it contains microphones and headphone jacks for phone calls. The sensor needs the 5 V power supply and draws 2 A of current. In the Figure 6 is shown the electronic board on SIM900. SIM900 is connected to the microcontroller with only 4 wires, that is power connection (VCC and GND), and serial communication pin (RX-TX). If used arduino UNO which is use 5V operating voltage and has 5V logic level (TTL). So need to connect arduino to RXD 5V and TXD 5V like in pinout picture above. If a nodeMCU8266-12E is used, which is use 3V operating voltage and has 3V logic level, as in our case, pins used are RXD 3.3V and TXD 3.3V. Then plug in SIM card into SIM card cartridge. Then the SIM900 and node MCU wiring connection.

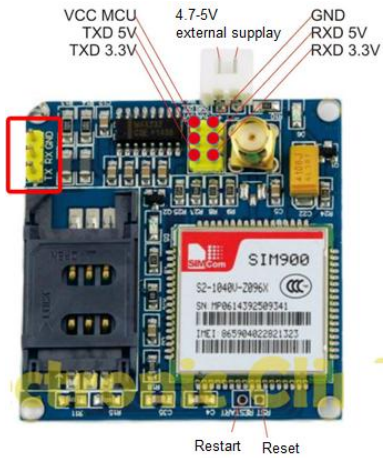


Figure 6. The electronic board on SIM900 module

Wire SIM900A module to node MCU like this:

- node MCU-> SIM900A
- 5V -> VCC
- GND -> GND
- 14 -> TX
- 12 -> RX

Power-on Procedure

First, need to insert your SIM card into the GSM module. Then, connect GSM GPRS Shield with NodeMCUEsp8266-12E. Now, upload the code on an Arduino board. After that, give the external 5V of power supply to the module. Then, press the power key of the GSM Module for 2 seconds. The LED present in the module will start glowing. And, when the sensor finds the networks, it will start blinking every three seconds. Now it is time to send or receive messages and phone calls with Arduino through the code. But, can also receive messages, and send or receive phone calls by using different programming codes.

SCD40 CO2 Sensor

SCD40 is a photoacoustic true CO2 sensor that will tell you the CO2 PPM (parts-per-million) composition of ambient air (Sensirion SCD40, n.d). Perfect for environmental sensing, scientific experiments, air quality and ventilation studies, and more. this sensor has data read over I2C, so it works very nicely with just about any microcontroller or microcomputer. There's both Arduino and Python/Circuit Python code so you can get started in a jiffy. In the Figure 7 is shown CO2 sensor SCD40.

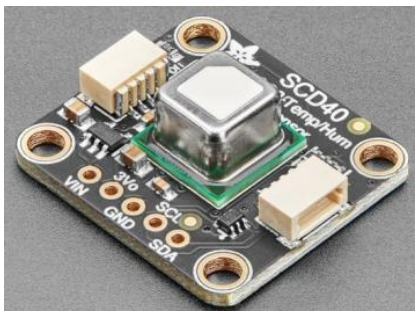


Figure 7. The electronic board on SDC40 CO2 sensor

There are two variants of this sensor - the SCD40 and SCD41

- The SCD40 is lower cost, and is perfect for indoor/outdoor air quality and CO2 measurements. It has a range of 400~2000 ppm with an accuracy of ±(50 ppm + 5% of reading)
- The SCD41 is more expensive, and while it can definitely be used for air quality, it's wide range means its best used for industrial or scientific CO2 measurements where the ppm can get very high. It has a range of 400~5000 ppm with an accuracy of ±(40 ppm + 5% of reading).

This sensor can run from 3.3 to 5V but it's more important for it to have a quiet power supply with low ripple, than any particular voltage. For that reason is added a 3.3V regulator and level shifters: when connecting to a 5V microcontroller like an Arduino UNO the 5V supply is often shared with other electronic components that add noise. The onboard regulator will keep the voltage nice and quiet. For advanced hackers, they can cut/solder the back traces to change whether the regulator is enabled and what I2C logic level is desired. Information about the DHT22, DS18B20 and V2.0 sensors is available in (Blynk, 2025; DHT22, n.d; DS18B20, 2019).

Experimental Results of Testing the Prototype Electronic System

This section presents the results of the experimental work on the prototype system for of the electronic system for managing with the process parameters of the agro-industrial facility. Figure 8 shows Prototype on the design electronic system.

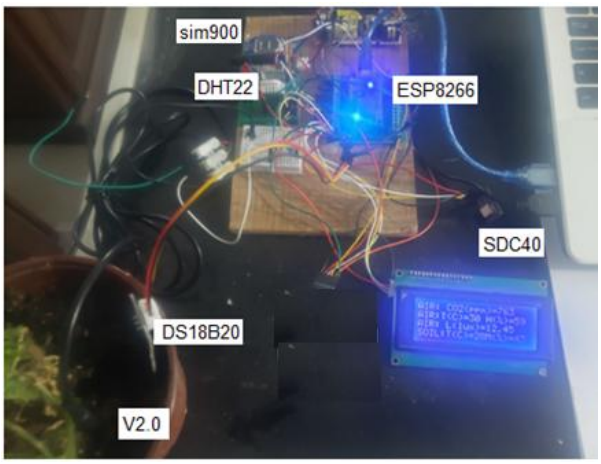


Figure 8. Prototype on the electronic system

Figure 9 shows a print screen of a data log file in Excel for monitoring on the process parameters of the agro-industrial facility obtained with the designed system in the paper.

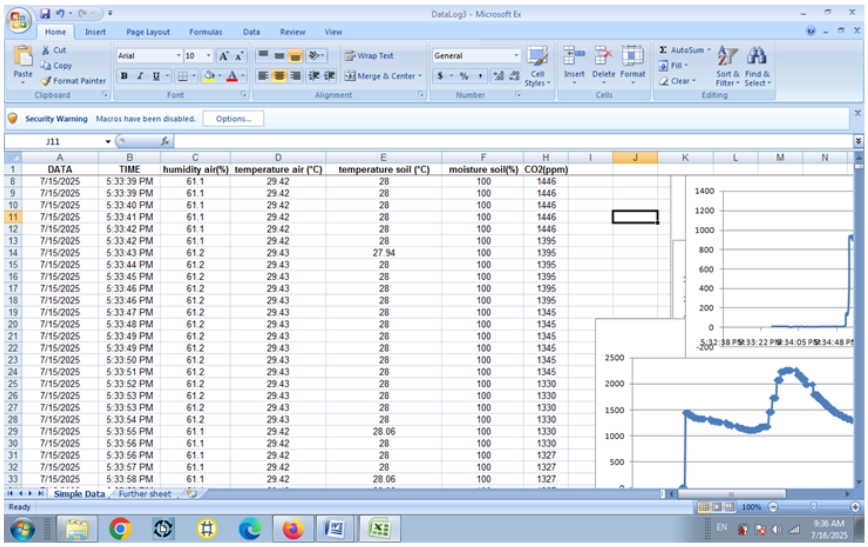
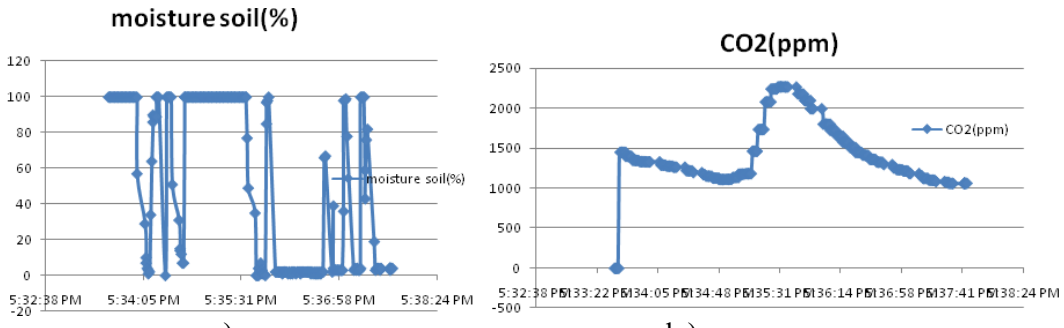


Figure 9. Print screen of a data log file in Excel for monitoring on the process parameters of the agro-industrial facility

Figure 10 shows waveforms of the measured parameters in the agro-industrial facility over a certain time interval. Figure 10a shows the waveform of soil moisture and Figure 10b shows the waveform illustrating the change in CO2.

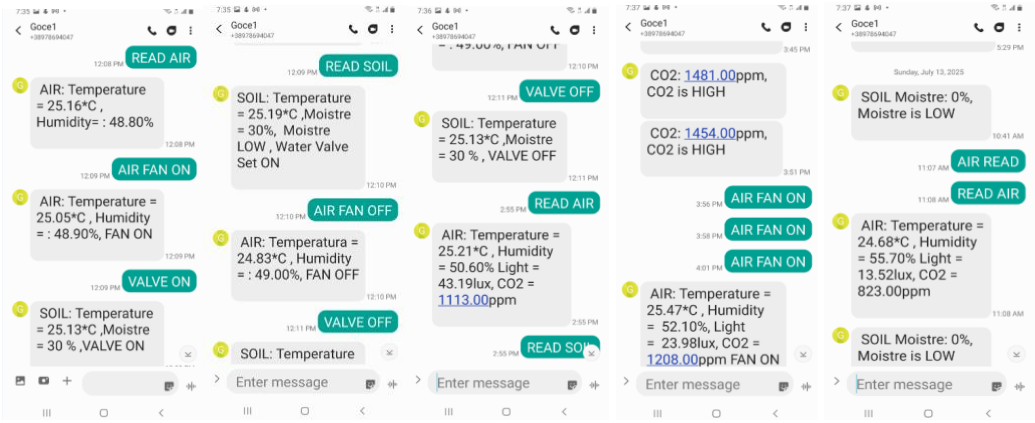


a.) b.)

Figure 10. Waveforms of the measured parameters in the agro-industrial facility over a certain time interval: a) waveform of soil moisture, b) waveform of CO2.

Figure 11 shows a print screen of the mobile phone that illustrates the correct operation of the electronic system.

Figure 11a is print screen on READ AIR, AIR FAN ON, VALVE on instruction; Figure 11b is print screen on READ SOIL and AIR FAN OFF instruction; Figure 11c is print screen on VALVE OFF and READ AIR instruction; Figure 11d is print screen on ALARM from electronic system to mobile phone when level CO2 is HIGH and Figure 11e is print screen on ALARM from electronic system to mobile phone when level soil moisture is LOW



a.) b.) c.) d.) e.)

Figure 11. Print screen from a mobile phone

The print screen on the mobile phone on the Figure 11 shows: a.) print screen on READ AIR, AIR FAN ON, VALVE on instruction; b.) print screen on READ SOIL and AIR FAN OFF instruction; c.) print screen on VALVE OFF and READ AIR instruction; d.) print screen on ALARM from electronic system to mobile phone when level CO2 is HIGH and e.) print screen on ALARM from electronic system to mobile phone when level soil moisture is LOW.

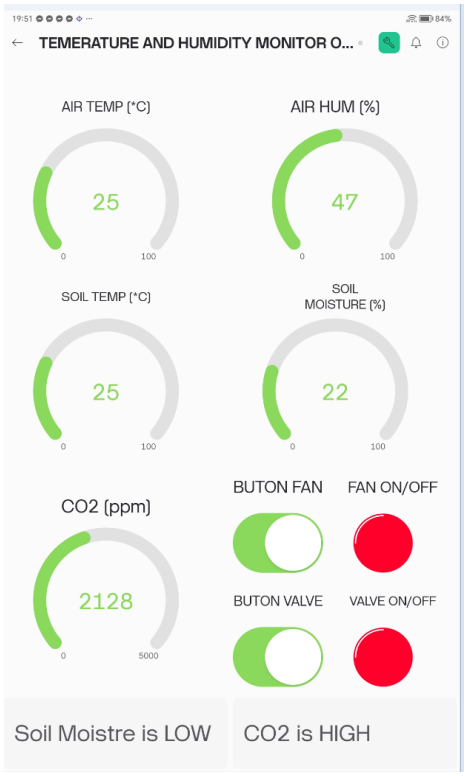


Figure 12. Process parameters screen of mobile device transmission in IoT network

Figure 12 show a data screen on a mobile device showing agriculture process parameters transferred in IoT network.

Analysis of the Results and Discussion

The main task of the paper is to design and implement a prototype electronic system for measuring, monitoring and transferring of the process parameters on agro industrial facility in GSM and IoT network. Verification of the correct operation of the system according to the defined task is illustrated with the Figures 8, 9, 10, 11 and 12.

- In point 2, a prototype of the system for measurement, monitoring and transferring of the process parameters on the agro industrial facility in GSM and IoT network was designed and implemented;
- Section 3 gives the results of the experimental work of the solution in the paper;
- The results show that the system measures, visualizes on LCD screens and stores in a data log file the process parameters of the agro industrial facility and sends them in GSM and IoT network;
- The print screen shown in the Figure 9 is provided to verify that the solution in the paper stores the data in a data log file in Excel;
- Waveforms shows on the Figure 10 illustrating the change of the process parameters in the agro-industrial facility over a certain time interval. They verify that the system measures and monitors the change in process parameters;
- Print screen from a mobile phone given in the Figure 11, verify that the system responds to messages sent from the mobile phone and sends an alarm back to the mobile device as required in point 2.1;
- Print screen from a mobile device given in the Figure 12, verify that the system sending the values of process parameters in IoT network of mobile device and sends an alarm back to the mobile device;
- Figure 12 shows the values of the process parameters during operation of the electronic system. Since the current values of soil moisture and air CO2 have exceeded the critical points (in this case, the critical point of soil moisture is 55%, and of CO2 is 1600ppm), the LEDs light up, indicating that in this state the water supply valve and the fresh air supply fan are turned on.

The paper offers a solution that addresses a problem that is currently relevant in the agro-industry. In (Bhuiyan et al., 2023; Eduku et al., 2024; Ariel, 2024), the subject of analysis is industrial processes from different aspects and in all of them the commitment to connecting measurement data remotely is clear. In some solutions, RF connections are used, in some cloud platforms, (Stefanov, 2023). The way in which this is realized is different and depends on the capabilities and approach of the authors. In the case where an RF connection is used, the transfer is limited in scope and is most often used when an standalone industrial (agro) facility needs to be connected to a master station of a complex industrial facility. Starting from the requirement to provide a reliable system that will provide measurement and transfer of process parameters with increased reliability, the paper provides a solution that distributes measurement data across both networks, GSM and IoT.

Conclusion

In this paper prototype of an electronic system is designed that provides a solution to a problem in agriculture facility, i.e. the development, design and practical implementation of the Smart electronic system which enables the measurement of the process parameters of an agro-industrial facility and their transfer to the GSM and IoT network. The solution enables the visualization of process parameters locally on LCD displays and remotely on an mobile device in GSM and IoT network. The solution also provides two-way communication and management of process parameters in the industrial facility. A data log file is also provided for store on the values on the process parameters on a local computer. There is a possibility of storing the values of the process parameters in the IoT cloud platform.

Scientific Ethics Declaration

* The authors declare that the scientific ethical and legal responsibility of this article published in EPSTEM journal belongs to the authors.

Conflict of Interest

* The authors declare that they have no conflicts of interest

Funding

* This research received no specific grant from any funding agency in the public, commercial, or not-for-profit sectors.

Acknowledgements or Notes

* This article was presented as virtual presentation at the International Conference on Technology, Engineering and Science (www.icontes.net) held in Antalya/Türkiye on November 12-15, 2025.

* The authors would like to thank the conference committee and the reviewers who reviewed the article for their valuable contributions.

References

Analog Devices. (2019). *DS18B20: Programmable resolution 1-wire digital thermometer* (Data sheet). Retrieved from https://www.analog.com/media/en/technical-documentation/data-sheets/DS18B20.pdf

Ariel, L. I. W. (2024). Design and evaluation of an IoT-based energy meter/power limiter to improve the management of low-voltage electrical subscribers - a case study of SNEL Likasi- DRC. *International Journal of Novel Research in Electrical and Mechanical Engineering, 11*(1), 60-67.

Bennett, S., & Linken, S. (1982). *Computer control of industrial processes*. Institution of Engineering & Technology.

Bhuiyan, B. U., Karim, M. M., & Khan, I. (2023). IoT-based three-phase smart meter: Application for power quality monitoring. In *6th International Conference on Electrical Information and Communication Technology (EICT)* (pp. 1–6). IEEE.

Blynk. (2025). *Blynk IoT platform*. Retrieved from https://blynk.cloud

CircuitsToday. (2021). *Arduino Nano tutorial: Pinout & schematics*. Retrieved from https://www.circuitstoday.com/arduino-nano-tutorial-pinout-schematics

Eduku, S., Sekyi-Ansah, J., Edem, A. E., & Joel, D. (2024). Design and implementation of distribution transformer monitoring system using GSM technology. *International Journal of Electrical and Electronics Engineering, 11*(12), 235-242.

Espressif Systems. (2020). *ESP8266 technical reference manual* (Version 4.3) (Data sheet). Retrieved from https://www.espressif.com/sites/default/files/documentation/esp8266-technical_reference_en.pdf

Fountas, S., Espejo-Garcia, B., Kasimati, A., Mylonas, N., & Darra, N. (2020). The future of digital agriculture: Technologies and opportunities. *IT Professional, 22*. 24-28.

Hor, C. L., & Crossley, P. A. (2005). Knowledge extraction from intelligent electronic devices. In *Lecture Notes in Computer Science* (Vol. 3400, pp. 82–111). Springer.

HowToMechatronics. (2020). *Arduino wireless communication NRF24L01 tutorial*. Retrieved from https://howtomechatronics.com/tutorials/arduino/arduino-wireless-communication-nrf24l01-tutorial/

Memonova, G., Schmidt, P., Tursunov, J., & Gofurova, G. (2025). Automated groundwater monitoring system with real-time data collection and analysis using LoRa and GSM technologies. *ETR, 4*, 209–215.

Microchip Technology. (2015). *ATmega328P 8-bit AVR microcontroller with 32K bytes in-system programmable flash* (Data sheet). Retrieved from https://ww1.microchip.com/downloads/en/DeviceDoc/Atmel-7810-Automotive-Microcontrollers-ATmega328P_Datasheet.pdf

Narendra, V. N., Sahana, S., & Chaithrashree, J. (2019). Digital agriculture. *Bulletin of Environment, Pharmacology and Life Sciences, 8*(6), 164–170.

Rembor, K. (2024). *Adafruit VEML7700 ambient light sensor*. Adafruit Industries.

Rotz, S., Duncan, E., Small, M., Botschner, J., Dara, R., Mosby, I., Reed, M., & Fraser, E. D. G. (2019). The politics of digital agricultural technologies: A preliminary review. *Sociologia Ruralis, 59*, 203–229.

Saiz-Rubio, V., & Rovira-Más, F. (2020). From smart farming towards agriculture 5.0: A review on crop data management. *Agronomy, 10*(2), 207.

Sensirion. (n.d.). *Sensirion SCD40* (Data sheet). Retrieved from https://www.manualslib.com/products/Sensirion-Scd40-13071286.html

SimCom. (2020). *SIM900: GSM/GPRS module* (Manual). Retrieved from https://www.manualslib.com/manual/1354053/Simcom-Sim900.html

SparkFun Electronics. (n.d.). *DHT22 temperature and humidity sensor* (Data sheet). Retrieved from https://www.sparkfun.com/datasheets/Sensors/Temperature/DHT22.pdf

Stefanov, G., & Kukuseva, M. (2021). RF sensor smart network. In *First International Conference ETIMA* (Vol. 1). Stip.

Stefanov, G., Kukuseva, M., & Stefanova, E. (2021). Design of an intelligent Wi-Fi sensor network. *Balkan Journal of Applied Mathematics and Informatics, 4*(1), 17-26.

Stefanov, G., Kukuseva, M., & Stefanova, S. (2023). 3-phase smart power meter implemented in RF network. *Balkan Journal of Applied Mathematics and Informatics, 6*(1), 25-37.

Author(s) Information

Goce Stefanov
Goce Delcev University, Faculty of Electrical Engenering
Krste Misirkov, 10A, 2000 Stip, North Macedonia
Contact e-mail: *goce.stefanov@ugd.edu.mk*

Marija Cekerovska
Goce Delcev University, Faculty of Mechanical Engineering, Krste Misirkov, 10A, 2000 Stip
North Macedonia

Elena Zafirov
One Sky Flight, 7777 Lemmon Ave
Dallas, TX 75209, USA

Todor Cekerovski
Goce Delcev University, Faculty of Electrical Engineering
Krste Misirkov, 10A, 2000 Stip, North Macedonia

To cite this article:

Stefanov, G., Cekerovska, M., Zafirov, E., & Cekerovski, T. (2025). Measurement and transmission of process parameters in GSM and IoT network. *The Eurasia Proceedings of Science, Technology, Engineering and Mathematics (EPSTEM), 38,* 699-711.

The Eurasia Proceedings of Science, Technology, Engineering & Mathematics (EPSTEM)
ISSN: 2602-3199

The Eurasia Proceedings of Science, Technology, Engineering and Mathematics (EPSTEM), 2025

Volume 38, Pages 712-720

IConTES 2025: International Conference on Technology, Engineering and Science

Experimental Development and Performance Analysis of a Parabolic Solar Concentrator for Desalination and Treatment of Complex Wastewaters

Souad Khedache
Mouloud Mammeri University

Said Makhlouf
Mouloud Mammeri University

Gilles Lefebre
Pari- Est Créteil University

Bilel Seddi
Mouloud Mammeri University

Abdellah Haddadi
Mouloud Mammeri University

Abstract: Facing the growing challenges linked to water pollution and the lack of potable water, solar distillation emerges as a promising solution. This study details the research and construction of a parabolic solar concentrator designed for the treatment of polluted waters. The targeted applications include treating effluents such as olive mill wastewater (marge), leachates, and conventional wastewater, alongside the desalination of seawater and brackish water. The primary objective of this work was to design an optimized prototype to maximize the efficiency of the distillation process utilizing solar energy. The research explored several critical factors that influence the concentrator's performance. These factors included the geometry of the parabola, the type of reflective material employed, and the nature of the thermal receiver.Experimental trials were successfully conducted to evaluate the prototype's effectiveness under varying climatic conditions. Crucially, physico-chemical analyses confirmed a notable reduction in pollutants present in the treated water.This work contributes to the preservation of water resources. By ensuring the necessary treatment of wastewater and offering a source of clean distilled water in resource-scarce regions, it actively promotes a transition toward sustainable and environmentally friendly energy.

Keywords: Solar still construction, Water desalination, Solar energy, Parabolic solar concentrator

Introduction

Water scarcity and quality degradation represent critical global challenges, particularly in arid and semi-arid regions where freshwater resources are limited and often contaminated by complex industrial effluents (WHO, 2021). In Algeria, this challenge is intensified by rapid population growth and economic development, combined with the presence of recalcitrant industrial wastewater such as olive mill wastewater (OMW) and landfill leachates. These effluents are characterized by extremely high chemical oxygen demand (COD > 100 g/L), color, phytotoxic phenolic compounds, ammonia, and heavy metals, rendering them refractory to conventional treatment methods (Paraskeva et al, 2006; Renou et al., 2008). Traditional water treatment technologies, relying on mechanical filtration, advanced oxidation processes, and biological systems, often face significant operational limitations including high energy consumption, membrane fouling, and the generation of hazardous secondary

- This is an Open Access article distributed under the terms of the Creative Commons Attribution-Noncommercial 4.0 Unported License, permitting all non-commercial use, distribution, and reproduction in any medium, provided the original work is properly cited.
- Selection and peer-review under responsibility of the Organizing Committee of the Conference
© 2025 Published by ISRES Publishing: www.isres.org

sludge (Wang et al., 2024). These constraints are particularly pronounced in off-grid or rural areas, where infrastructure and financial resources are limited.

Conversely, solar energy represents an abundant and underutilized renewable resource in many water-stressed regions. Algeria, for instance, benefits from over 2000 hours of annual sunshine, providing a substantial solar potential for sustainable applications (Stambouli et al., 2012). Solar thermal distillation, particularly when coupled with concentration technologies, offers a promising alternative for decentralized water treatment. Solar concentrators, such as parabolic dishes, can achieve focal temperatures sufficient to drive rapid thermal distillation without requiring external energy input (Arunkumar et al., 2020). Recent studies have demonstrated that parabolic concentrator-based solar distillation systems can effectively produce distilled water from saline and contaminated sources, achieving yields up to 50% and removal rates exceeding 98% for total dissolved solids (TDS) (Asadi et al., 2024; El Ouederni et al., 2025). However, comprehensive experimental validation of such systems across diverse, highly contaminated effluent matrices-particularly olive mill wastewater and landfill leachates—remains limited in the literature.

This study addresses this gap by designing, fabricating, and experimentally evaluating a parabolic solar concentrator distillation system under real-world environmental conditions in Algeria. The primary objectives are:

- to characterize the thermal performance of a custom-built parabolic concentrator in terms of focal temperatures and heating rates;
- to assess the system's water purification efficiency across multiple contaminated water matrices including seawater, brackish water, river water, olive mill wastewater, and landfill leachate;
- to quantify the volumetric yield and removal rates for key pollutants (TDS, conductivity, turbidity, organic load, and metals).

The anticipated results will provide critical insights into the scalability and applicability of concentrated solar distillation for sustainable water security in arid regions.

Materials and Methods

Design and Theoretical Modeling of the Parabolic Concentrator

The parabolic solar concentrator was designed based on fundamental principles of optical geometry and thermal energy transfer. The reflective surface follows a paraboloid of revolution equation with the focal point positioned at a distance f from the vertex, determined by the equation: $x^2 = 4fy$, where y represents the distance from the vertex and x represents the radial distance. The overall diameter of the reflector was set at 1.5 m, yielding a focal length of 0.375 m. Theoretical modeling involved calculating the concentration ratio (CR), defined as the ratio of the projected aperture area to the receiver area, which was estimated at approximately 40:1. Two distinct prototypes were fabricated and tested, to evaluate the effectiveness of different reflective materials (Figure 1):



Figure 1. Experimental setup for testing distillation of two prototypes

Prototype 1 (Composite Reflector):

A parabolic reflector measuring 1.5 m in diameter was constructed using a resin-glass fiber composite shell with an aluminum sheet (thickness: 1.5 mm) affixed to its inner surface. A rigid frame constructed from stainless steel tubing supported the assembly. The receiver consisted of an aluminum pot (capacity: 8 L, outer diameter: 0.25 m) painted with high-emissivity matte black paint to maximize solar radiation absorption. This prototype was tested during the initial phases of the experimental campaign.

Prototype 2 (Mirror Array Reflector):

An improved version was subsequently fabricated, featuring a composite backing structure with bonded individual mirror segments (dimensions: 0.1 m × 0.1 m each, thickness: 3 mm) arranged to form the parabolic surface. Total reflectivity was measured at approximately 85% using a spectrophotometer. The receiver design was identical to Prototype 1, but the system was enclosed within a tempered glass condensation chamber (thickness: 6 mm) to reduce convective losses and facilitate distillate collection. All surfaces were sealed with silicone gasket material to prevent vapor leakage.

Experimental Site and Climatic Conditions

Experimental trials were conducted at the University of Mouloud Mammeri, Tizi-Ouzou, Algeria (latitude: 36.72°N; longitude: 4.05°E), during the period from July to October 2024. This location was selected for its favorable solar irradiance (average global horizontal irradiance >800 W/m²) and availability of diverse contaminated water sources. Trials were performed on clear-sky days, typically between 08:00 and 16:00 local solar time. Ambient temperature varied between 22°C and 38°C depending on the month and time of day. Direct normal irradiance was monitored using a calibrated pyranometer (Model: CMP6, Kipp & Zonen) placed adjacent to the experimental setup.

Instrumentation and Data Acquisition

The thermal performance of the system was monitored using a network of K-type thermocouples (±0.5°C accuracy) positioned at five strategic locations (Figure 2):

- T1: Focal point (reflector surface)
- T2: Receiver outer surface
- T3: Inside the evaporation pot (liquid temperature)
- T4: Vapor space above the liquid (inside condensation chamber)
- T5: Ambient air temperature

All thermocouples were connected to a multi-channel data acquisition unit (PicoLog TC-08, Pico Technology) with a sampling frequency of 1 Hz. Data were logged on a personal computer and later processed using custom Python scripts. The distillation process was monitored by visual observation and periodic volume measurements of the distillate collected in graduated cylinders.

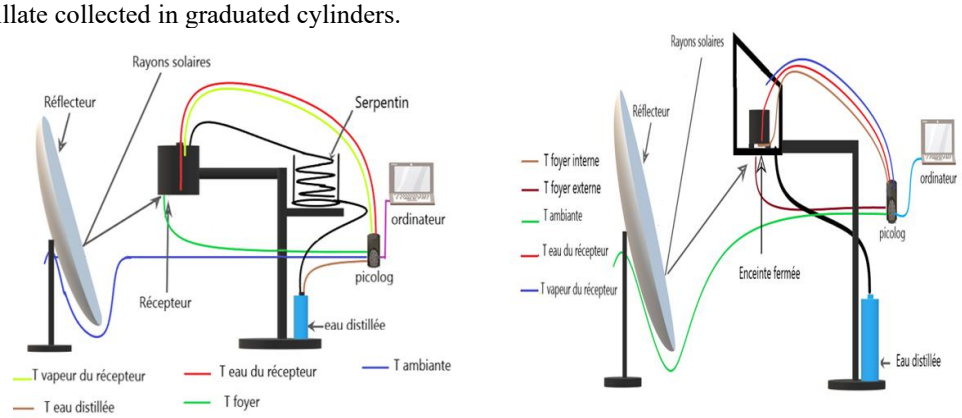


Figure 2. Schematic diagram of the parabolic solar concentrator distillation system showing the reflector geometry, receiver placement, condensation chamber, and thermocouple positions (T1-T5)

Water Samples and Characterization

Five types of contaminated water were subjected to distillation trials to assess the system's versatility (Figure 3):

1. Seawater (SW): Collected from the Mediterranean coast; initial TDS: 35 ± 2 g/L; pH: 8.1 ± 0.2
2. Brackish Water (BW): From an underground well; initial TDS: 8 ± 1 g/L; pH: 7.5 ± 0.3
3. River Water (RW): From a local freshwater source; initial TDS: 0.5 ± 0.1 g/L; pH: 7.2 ± 0.2
4. Olive Mill Wastewater (OMW): Collected from a local pressing facility during the harvest season; COD: 105 ± 8 g/L; Total Phenols: 8 ± 1 g/L; pH: 4.8 ± 0.3
5. Landfill Leachate (LL): Collected from an active municipal landfill; COD: 2500 ± 200 mg/L; Ammonia (NH_3): 1200 ± 100 mg/L; Heavy Metals (Pb, Cd, Zn): varied from 0.5–5 mg/L; pH: 7.9 ± 0.2

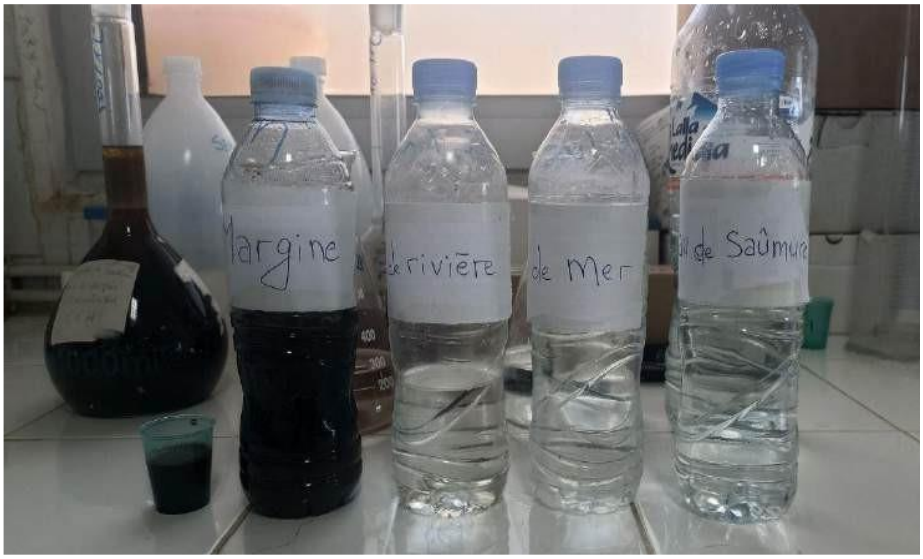


Figure 2. Five types of contaminated water tested

Experimental Procedure

Each experimental trial followed a standardized protocol:

1. The parabolic concentrator was manually oriented toward the sun to maximize incident radiation (solar tracking was performed every 15 minutes).
2. Approximately 4 liters of the test water were placed in the receiver pot.
3. All sensors were activated and data logging commenced.
4. The system operated continuously until the desired volume of distillate was collected (typically 4–5 hours).
5. Distillate was collected in sterile graduated cylinders and immediately transferred to sealed containers for subsequent analysis.

A total of 16 experimental trials were conducted (Table 1), with trials distributed across the water types to ensure statistical validity.

Physicochemical Analysis

Both the feed water and the resulting distillate were analyzed according to internationally recognized standards:

- Total Dissolved Solids (TDS): Gravimetric method (ASTM D5907)
- Electrical Conductivity: Conductivity meter (Model: Hach HQ40d)
- Turbidity: Turbidity meter (Model: HACH 2100Q); measured in Nephelometric Turbidity Units (NTU)
- pH: pH meter calibrated with buffer solutions (pH 4.0, 7.0, 10.0)
- Chemical Oxygen Demand (COD): Dichromate reflux method (ASTM D1252)
- Total Phenols: Folin-Ciocalteu spectrophotometric method
- Ammonia (NH_3): Nessler method (ISO 7150-1)

- Heavy Metals (Pb, Cd, Zn): Inductively Coupled Plasma – Optical Emission Spectroscopy (ICP-OES, Model: Agilent 5110)

All analyses were performed in triplicate, and results were expressed as mean ± standard deviation.

Performance Indicators and Calculations

The following metrics were computed to assess system performance:
Volumetric Yield (%):

$$Y = \frac{V_distillate}{V_feed} \times 100$$

Removal Efficiency (%):

$$R = \frac{C_initial - C_final}{C_initial} \times 100$$

Where
C_initial and C_final represent the initial and final concentrations of a given pollutant.
Thermal Efficiency (%):

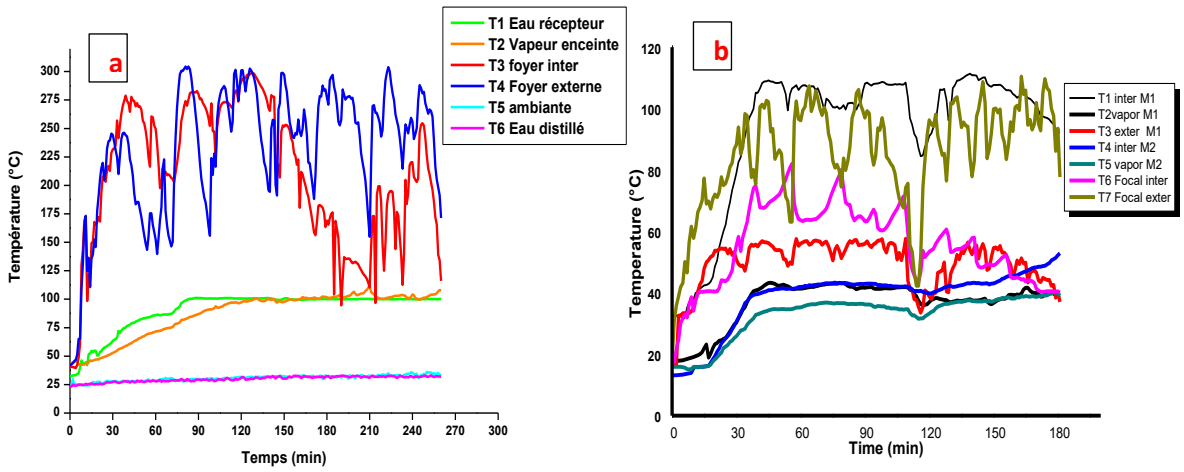
$$\eta_th = \frac{m_distillate \times L_v \times c_p \times \Delta T}{A_aperture \times I \times t}$$

Where
m_distillate is the mass of distillate produced (kg), L_v is the latent heat of vaporization (2257 kJ/kg), c_p is specific heat capacity, ΔT is the temperature rise, A_aperture is the reflector aperture area (m²), I is the incident solar irradiance (W/m²), and t is the operating duration (s).

Results

Thermal Performance Analysis

The thermal performance of the parabolic solar concentrator demonstrated exceptional effectiveness in both prototypes. During representative trials, the focal point temperature reached a maximum of 300°C within approximately 90 minutes of operation (Figure 3), significantly outperforming conventional flat-plate solar stills, which typically achieve temperatures below 80°C. The rapid heating phase occurred during the first 60 minutes, after which the temperature stabilized at the boiling point of water (100°C inside the condensation chamber).



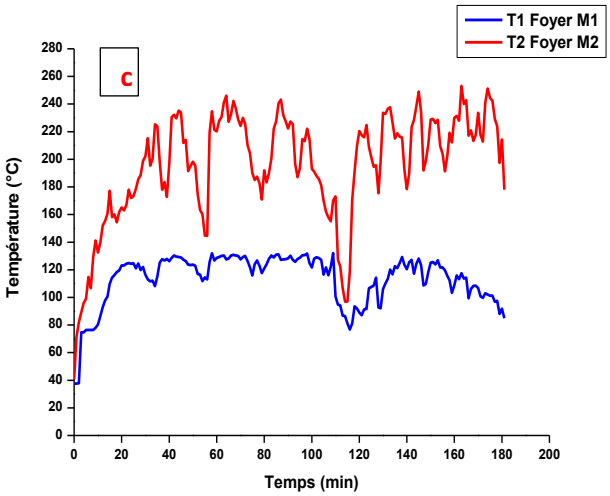


Figure 3. a) Temporal evolution of temperatures during representative distillation trial, b) Temperature comparison of parabolic solar distillation prototypes, c) Comparison of Focal Point Temperatures between

Prototype 2 (mirror array reflector) consistently outperformed Prototype 1 (composite reflector), with peak focal temperatures 15–20°C higher and faster thermal rise times. The superior performance of Prototype 2 was attributed to its higher reflectivity (85% vs. 72%) and enhanced insulation provided by the tempered glass condensation chamber, which reduced convective and radiative losses.

Distillation Yield and Productivity

Table 1 summarizes the volumetric yields obtained across 16 experimental trials. For seawater, the average distillation yield was 50.5% ± 3.2%, producing 2.02 ± 0.13 liters of purified water from an initial 4-liter feed volume within 4.5 ± 0.3 hours. Brackish water yielded slightly higher volumes (52.1% ± 2.8%), while river water demonstrated the highest yields (54.3% ± 2.5%), as lower initial saline content reduced energy requirements for evaporation.

Trials with olive mill wastewater (OMW) and landfill leachate (LL) also resulted in significant distillate production, averaging 48.7% ± 4.1% and 46.2% ± 3.8% respectively. Despite their high organic and inorganic contaminant loads, these complex effluents were successfully distilled without system fouling or operational interruption.

Table 1**.** Distillation performance summary across water types (Mean ± SD).

Water Type	Trials (n)	Avg. Distillate Volume (L)	Yield (%)	Operating Time (h)
Seawater	3	2.02 ± 0.13	50.5 ± 3.2	4.5 ± 0.3
Brackish Water	3	2.08 ± 0.11	52.1 ± 2.8	4.3 ± 0.4
River Water	2	2.17 ± 0.10	54.3 ± 2.5	4.1 ± 0.2
OMW	4	1.95 ± 0.16	48.7 ± 4.1	4.8 ± 0.5
Leachate	4	1.85 ± 0.15	46.2 ± 3.8	5.1 ± 0.6

Water Quality Improvement

Physicochemical analysis revealed dramatic improvements in water quality across all parameters (Table 2). Electrical conductivity and total dissolved solids (TDS) were reduced by more than 98% for all water types tested. For seawater with initial TDS of 35 g/L, the distillate contained only 0.41 ± 0.05 g/L, well below the WHO potability threshold of 0.5 g/L for essential minerals. Turbidity, initially high in OMW samples (ranging from 450–520 NTU), was reduced to <2 NTU in the distillate (>99% removal). Chemical oxygen demand (COD) was similarly eliminated, with OMW samples showing reduction from 105 ± 8 g/L to <5 mg/L. Total phenolic compounds, responsible for the dark color and toxicity of OMW, were reduced from 8 ± 1 g/L to undetectable levels (<0.1 mg/L) in the distillate.

Heavy metals (Pb, Cd, Zn) present in leachate samples were completely removed (100% efficiency), with final concentrations below detection limits (<0.01 mg/L). Ammonia (NH_3), initially present at 1200 ± 100 mg/L in leachate, was reduced to <1 mg/L, representing a removal efficiency of >99.9% (Figure 4).



Figure 4. Recovered crystalline salt residues from seawater distillation (left, white crystals) and concentrated organic residues from olive mill wastewater treatment (right, dark precipitate), demonstrating by-product recovery potential.

Table 2. Physicochemical quality of feed and distillate water (Mean ± SD).

Parameter	Unit	Seawater (Initial/Final)	OMW (Initial/Final)	Leachate (Initial/Final)	Removal (%)
TDS	g/L	35 ± 2 / 0.41 ± 0.05	-	-	>98
Conductivity	µS/cm	52,000 ± 1000 / 620 ± 50	-	-	>98
Turbidity	NTU	-	485 ± 35 / <2	120 ± 15 / <2	>99
COD	g/L	-	105 ± 8 / <0.005	2.5 ± 0.2 / <0.001	>99
Total Phenols	g/L	-	8 ± 1 / <0.0001	-	>99.9
Lead (Pb)	mg/L	-	-	2.3 ± 0.2 / <0.01	100
Cadmium (Cd)	mg/L	-	-	1.1 ± 0.1 / <0.01	100
Zinc (Zn)	mg/L	-	-	4.8 ± 0.3 / <0.01	100
Ammonia (NH_3)	mg/L	-	-	1200 ± 100 / <1	>99.9

Thermal Efficiency Calculations

The calculated thermal efficiency of the system ranged from 31% to 38% across trials, with Prototype 2 achieving the higher end of this range (37.8% ± 1.2%). This efficiency was substantially higher than reported values for conventional solar stills (typically 15–25%) and comparable to optimized flat-plate solar collectors used in heating applications.

Discussion

Interpretation of Thermal Performance

The exceptional thermal performance achieved in this study-with focal temperatures reaching 300°C and rapid boiling within 90 minutes-demonstrates the substantial advantage of parabolic concentration over simple solar stills. The concentration ratio of approximately 40:1 achieved by our 1.5 m diameter reflector enabled rapid temperature elevation at the focal point, which is fundamentally necessary for efficient distillation of refractory effluents such as OMW and leachates. The superior performance of Prototype 2 can be attributed to two key factors: (1) the higher reflectivity of mirror segments (85%) compared to the aluminum composite surface (72%), resulting in greater solar energy capture, and (2) the enhanced thermal insulation provided by the tempered glass condensation chamber, which reduced parasitic heat losses due to convection and radiation. The thermal efficiency of 31–38% observed in this work is notably higher than the 15–25% efficiency typically reported for passive solar stills. This improvement is directly attributable to the concentrator's ability to deliver high-intensity solar radiation to a small focal area, enabling rapid and sustained evaporation rates. Notably, the efficiency remained stable across

different water types, indicating that the system's performance is relatively independent of feed water salinity or organic content-a critical advantage for treating diverse effluents.

Efficacy on Complex Effluents: OMW and Leachates

One of the most significant findings of this study is the demonstrated capability of solar-driven parabolic distillation to effectively treat highly contaminated industrial effluents. Olive mill wastewater, with COD exceeding 100 g/L and total phenols of 8 g/L, represents one of the most recalcitrant agricultural wastewaters globally. Conventional treatment methods—including advanced oxidation, membrane filtration, and biological processes—often require multiple stages, high operational costs, and generate problematic secondary sludges (Wang et al., 2024). Our results show that thermal distillation completely removes these contaminants, producing potable-quality distillate with <1 mg/L residual COD and undetectable phenolic compounds.

Similarly, landfill leachate, characterized by its mixture of organic matter, ammonia, and heavy metals, was successfully treated with 100% removal of lead, cadmium, and zinc, and >99.9% removal of ammonia. This performance is particularly noteworthy because conventional leachate treatment often requires sequential physicochemical and biological steps, and final effluent typically requires additional polishing before discharge or reuse (Renou et al., 2008). The simplicity of the distillation approach-requiring only solar energy input-makes it especially attractive for decentralized applications in developing nations or water-stressed regions.

The absence of system fouling or operational degradation during treatment of OMW and leachate trials is also remarkable. The high-temperature condensation chamber prevented scaling and biofilm formation that commonly occur in lower-temperature distillation systems, suggesting that thermal distillation at elevated temperatures offers inherent operational robustness for treating complex, unpredictable industrial effluents.

Conclusion

This study demonstrates that parabolic solar concentrator-based distillation effectively treats diverse contaminated water matrices under real-world Mediterranean conditions. The system achieved focal temperatures of 300°C, thermal efficiency of 31–38%, and distillate yields of 46–54% across all tested matrices. Water quality improvements exceeded expectations, with >98% reduction in TDS, >99% turbidity removal, and complete elimination of heavy metals and organic contaminants. For olive mill wastewater with COD >105 g/L, the system produced potable-quality distillate without operational degradation or fouling.

The technology offers substantial advantages over conventional treatment methods: zero energy input, no chemical additives, minimal operational costs and scalability from household to community applications. For water-stressed regions like Algeria, with abundant solar resources but limited freshwater availability, this system represents a viable pathway toward decentralized water independence. Future enhancements should focus on automated solar tracking, thermal energy storage integration, and field-scale demonstration. In conclusion, the parabolic concentrator distillation system is a technically viable, economically attractive, and environmentally sustainable solution for water treatment in arid

Scientific Ethics Declaration

* The authors declare that the scientific ethical and legal responsibility of this article published in EPSTEM journal belongs to the authors.

Conflict of Interest

* The authors declare that they have no conflicts of interest

Funding

* This research received no specific grant from any funding agency in the public, commercial, or not-for-profit sectors.

Acknowledgements or Notes

* This article was presented as a poster presentation at the International Conference on Technology, Engineering and Science (www.icontes.net) held in Antalya/Türkiye on November 12-15, 2025.

References

Arunkumar, T., Velraj, R., Ahsan, A., Khalifa, A. J., Shams, S., Denkenberger, D., & Sathyamurthy, R. (2015). Effect of parabolic solar energy collectors for water distillation. *Desalination and Water Treatment, 57* (45), 21234-21242.

Asadi, M. T. A., Rashidi, S., & Mirhosseini, M. (2024). Sustainable and clean water distillation by parabolic dish collector and different heat absorber and thermal storage materials: An experimental study. *Sustainable Energy Technologies and Assessments, 61*, 103616.

El Ouederni, A. R., Ben Abdallah, M. A., Zenkri, M., Ameur, M., El Ouederni, S., El Ouederni, N., & Omrani, R. (2025). Performance evaluation of a cylindrical-parabolic solar distillation unit brackish water. *Scientific African, 30*. e02935.

Paraskeva, P., & Diamadopoulos, E. (2006). Technologies for olive mill wastewater (OMW) treatment: A review. *Journal of Chemical Technology & Biotechnology, 81*(9), 1475–1485.

Renou, S., Givaudan, J. G., Poulain, S., Dirassouyan, F., & Moulin, P. (2008). Landfill leachate treatment: Review and opportunity. *Journal of Hazardous Materials, 150*(3), 468–493.

Stambouli, A. B., Khiat, Z., Flazi, S., & Kitamura, Y. (2012). A review on the renewable energy development in Algeria: Current perspective, energy scenario and sustainability issues. *Renewable and Sustainable Energy Reviews, 16*(7), 4445–4460.

Wang, J., Qiao, Z., Liu, X., Li, M., Zhang, Y., & Chen, H. (2024). A comprehensive review of landfill leachate treatment technologies. *Frontiers in Environmental Science, 12*, 1439128.

World Health Organization. (2021). *Guidelines for drinking-water quality: Fourth edition incorporating the first and second addenda*. WHO.

Author(s) Information

Souad Khedache
Mouloud Mammeri University, LMSE Laboratery, Po Box 17 RP 15000, Tizi Ouzou, Algeria
Contact e-mail: *souad.khedache@ummto.dz*

Said Makhlouf
Mouloud Mammeri University, LMSE Laboratery, Po Box 17 RP 15000, Tizi Ouzou, Algeria

Gilles Lefebre
Pari- Est Créteil University, CERTES, IUT Laboratory.61 Av. Général deGaulle, 94010 Paris Créteil, France.

Bilal Seddi
Mouloud Mammeri University, LMSE Laboratery, Po Box 17 RP 15000, Tizi Ouzou, Algeria

Abdellah Haddadi
Mouloud Mammeri University, LMSE Laboratery, Po Box 17 RP 15000, Tizi Ouzou, Algeria

To cite this article:

Khedache, S., Makhlouf, S., Lefebre, G., Seddi, B., & Haddadi, A. (2025). Experimental development and performance analysis of a parabolic solar concentrator for desalination and treatment of complex wastewaters. *The Eurasia Proceedings of Science, Technology, Engineering and Mathematics (EPSTEM), 38,* 712-720.

The Eurasia Proceedings of Science, Technology, Engineering & Mathematics (EPSTEM)
ISSN: 2602-3199

The Eurasia Proceedings of Science, Technology, Engineering and Mathematics (EPSTEM), 2025

Volume 38, Pages 721-730

IConTES 2025: International Conference on Technology, Engineering and Science

Factors Affecting Corrosion of Steel in Pipe Lines

Haddad Abdelouahab
University Setif1 Ferhat Abbas

Zerroug Nadjat
University Setif1 Ferhat Abbas

Abstract: The corrosion behaviour of mild steel, platinum, nickel, copper and lead in 4% NaCl deaerated acidified solution was studied. Another investigation on these metals was made in solution saturated with CO_2 to see the effects of CO_2 partial pressure and temperature on the cathodic hydrogen evolution reaction. Polarization curves in different conditions were determined and different values of limiting, and exchange current densities were measured. It was found that the limiting current density I_L increases by the introduction of CO_2 to each one of the metals investigated. The increase is either due to a pH or a temperature effect, assuming no effect of gas bubbling. It was confirmed that the limiting current does not depend on the nature of the material used as a working electrode. The exchange current density of the cathodic hydrogen reaction was found to be metal electrode and solution pH dependent. The analysis of energy activation shows that the increase in exchange current could be due to a pH or a temperature effect, depending on the nature of the material studied. There was an increase in the exchange current density I_O by the introduction of CO_2 to the systems investigated. The corrosion rates on steel, nickel, copper and lead were calculated in the presence and absence of CO_2 and found to increase in the presence of CO_2. However, platinum does not corrode but the limiting current density of the hydrogen reaction increased by the introduction of CO_2.

Keywords: Corrosion, Mild steel, Exchange current density, Limiting current density, Activation energy

Introduction

In oilfield operations, it is often necessary to produce oil from hydrocarbon reservoirs that contain significant amounts of H_2S and CO_2 in addition to brine (Wang et al., 2024). The cost to the industry includes the repair of corrosion damage and associated Consequential losses, the cost of over design of protective systems and of technical effort has been estimated to be very high (Iannuzzi & Frankel, 2022). Some low alloy steels do not resist corrosion and are susceptible to cracking in environments which contain either wet H_2S or wet CO_2.

The assessment and the control of CO_2 corrosion of carbon steel tubulars and equipment is a long-standing concern of the petroleum industry. Downhole problems are particularly troublesome as they can involve removing and re-running many thousands of feet of production tubing, at a very high cost (Liu et al., 2023). The problems are caused by the corrosive effect of carbonic acid, produced by the dissolution of CO_2 gas in water. The corrosion related to CO_2 is the most significant and the corrosion problems in the produced fluids have been a major source of failure in production equipment, damage being observed in downhole equipment, pumps and tubulars, production pipework between the wellhead and the separation vessels (Solovyeva et al., 2023). Carlson reported that carbonic acid in natural waters or in steam condensate attacks materials with H_2S evolution (Carlson, 1949). In all cases, water chemistry and the in-situ pH play a decisive role. When CO_2, H_2S, Cl^- and H_2O are present in the environment, rapid corrosive degradation of the exposed metal can occur (Yue et al., 2025). However, (Butler & Ison, 1966) claimed that CO_2 has no specific influence on the corrosion of steel since it does not participate in the cathodic reaction. It can, however, influence the corrosion rate due to its acidic character and its ability to

- This is an Open Access article distributed under the terms of the Creative Commons Attribution-Noncommercial 4.0 Unported License, permitting all non-commercial use, distribution, and reproduction in any medium, provided the original work is properly cited.

- Selection and peer-review under responsibility of the Organizing Committee of the Conference

© 2025 Published by ISRES Publishing: www.isres.org

increase the H_2S evolution type of attack by decreasing the pH of the solution. A second indirect influence is due to the fact that with an increase in CO_2 concentration protective calcium carbonate is not formed but remains in acid solution in the form of calcium bicarbonate. The high hydrogen ion concentrations of acid solutions promote H_2 evolution and make such solutions corrosive to steel even in the absence of oxygen. Generally, higher concentrations of acids and hydrogen ions are more corrosive than lower concentrations.

In the absence of water, there is no risk of corrosion. Even the presence of some free water may also be neglected under some circumstances. Fluids with up to 20% of water are considered safe in equipment as long as it contains oil and has a flow rate sufficient to entertain the water and give a continuous oil film at the steel surface. As an example, in East Texas, depending on the presence of water, the corrosion varies from mild to severe. A way to combat this corrosion economically is the use of inhibitors (Butler & Ison, 1966). At elevated temperature, the presence of CO_2, oxygen or chloride accelerates the attack because they change the structure and adherence of the protective film. The presence of chloride ions Cl^- in the mixture CO_2-H_2O accelerates the corrosion process. The corrosion rate increases proportionally with CO_2 partial pressures (Videm & Dugstad, 1989).

For wells producing water as a by-product, the pH at operating pressure will be an important parameter for the corrosion rate in addition to CO_2 partial pressure, Fe^{2+} concentration and temperature. The overall corrosion reaction is represented by the following equation:

$$Fe + H_2CO_3 \text{--->} FeCO_3 + H_2 \quad (1)$$

The rate of this reaction is affected by temperature, pressure, pH, water content and the velocity of the fluid, and although the iron carbonate corrosion product formed may give some protection to the steel, this is removed at regions of high turbulence or velocity, producing deep pitting, often seen on the sides of downhole production tubing. Detailed studies of the CO_2 corrosion mechanisms and associated kinetics have shown that under most conditions (above 60°C) the steel surface becomes covered with an iron carbonate layer, which totally controls all corrosion reactions including inhibition. Work is needed to produce a better understanding of this problem and clarify the role of CO_2 and the way in which it increases the corrosion rate (Liu et al., 2023).

Experimental Methods

The parameters measured in this work include the pH of the test solution, which is affected by the introduction of CO_2, the current flowing in the system between the working and counter electrodes which is affected as well.

Materials

Solutions Preparation

The metals investigated were mild steel, platinum, nickel, copper, and lead. The test solution was a 4% NaCl deaerated acidified solution. A second set of experiments was conducted by saturating this solution with CO_2 to study the effects of CO_2 partial pressure and temperature. Buffer solutions were also prepared for electrode calibration.

Measurement Techniques

The test solutions prepared were of two types; the acid solutions prepared for polarization measurements and the buffer solutions prepared for the palladium electrode calibration. Sea water normally contains CO_2 in equilibrium with the atmosphere from which it comes. The total CO_2content as carbonic acid, bicarbonates, and carbonates ranges from 60 to about 100 ppm. CO_2 present in seawater was found to have the same effect of uniform dissolution as a medium slightly acidified by carbonic acid As a consequence, test were usually merely NaCl solutions under CO_2 pressure.

Determination of Polarization Parameters

The corrosion rate was determined by plotting the applied potential versus the current density flowing in the cell, that is, E = f(logI). An extrapolation of the Tafel slopes to the reversible potential of the hydrogen reaction gives the exchange current density. The corrosion rate is calculated from the current density at the intersection of the extrapolated Tafel regions using Faraday's Law, that is, CR (mm/year) =(M i_{corr} / nFρ)× 3.153× 10^7 where,CR is the corrosion rate, M is the mass loss during corrosion (g), i_{corr} is the corrosion current, ρ is the density of steel (g/cm^3). The other symbols have their usual meanings.

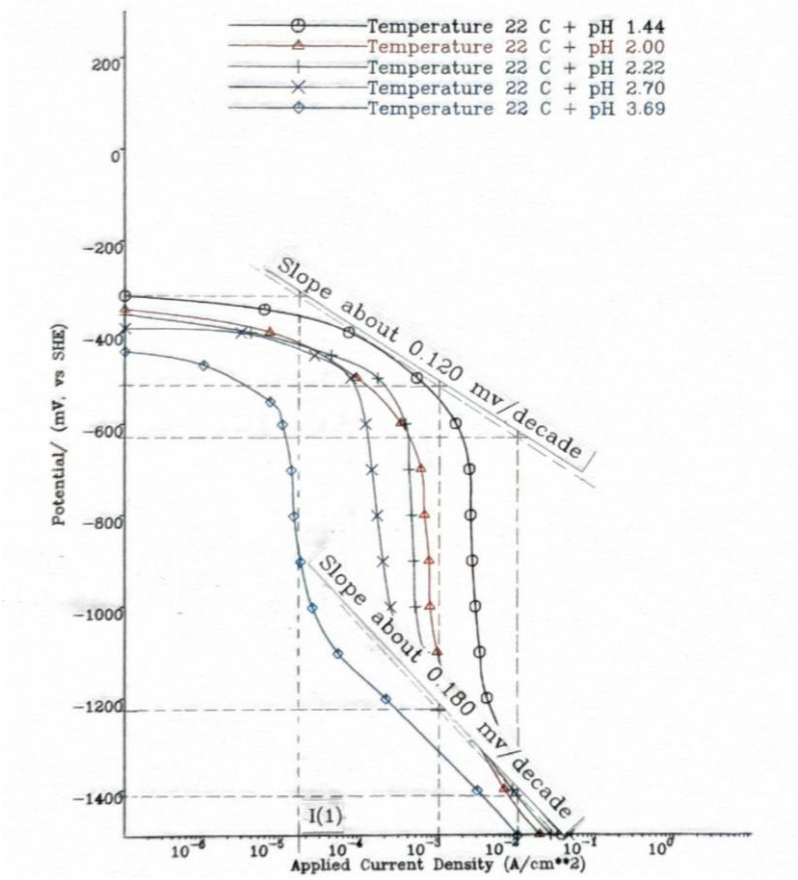
Reproducibility

In all the electrochemical measurements, the experiment was carried out several times to assess the precision and reproducibility of the measurements. The measured potential has an accuracy of ± 0.5mV, while the current accuracy is ±5× 10^{-6}A. The temperature controller has an accuracy of ± 1°C, while the pressure measurement is ± 5psi (power square inch).

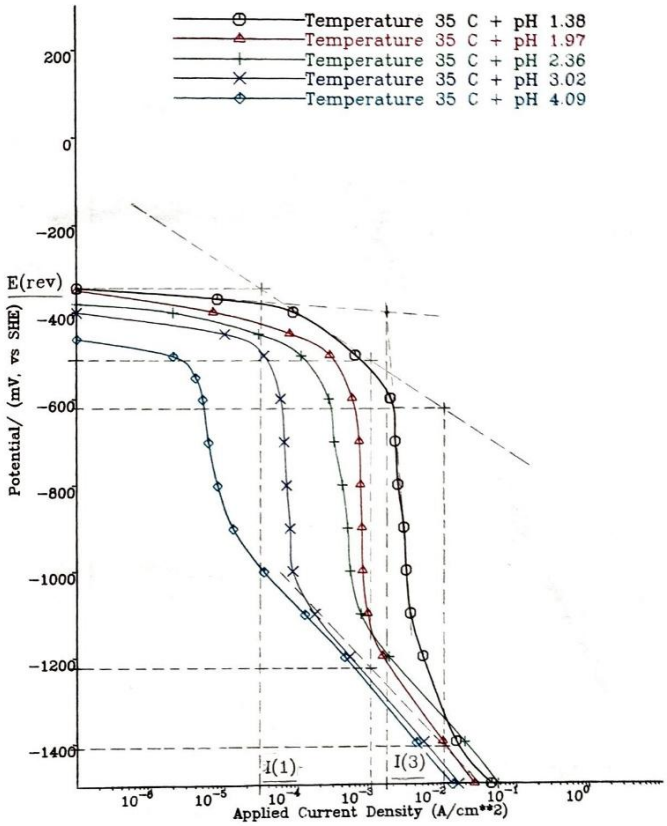
Results

Cathodic Polarization of Mild Steel in 4% NaCl Deaerated Acid Solution

The cathodic polarization curves for mild steel in 4% NaCl deaerated acid solutions are shown at two temperatures in Figures1.a and 1.b. The cathodic parts of the curves present the three different regions. An activation control process shows a Tafel behaviour with a slope of about -0.120± 0.010V/decade, which is hard to see because of steel corrosion in this region of potential, followed by a region of potential where the proton reduction rate is very high. There is a significant drop in potential. The values of the limiting current density for the hydrogen evolution reaction are found to be proportional to the proton concentration in the bulk solution. They range in the same interval given in the literature. The limiting current density is pH dependent and not dependent on the metal nature. The hydrodynamic conditions within the cell (including the bubbling effects) were not considered.



(a)



(b)

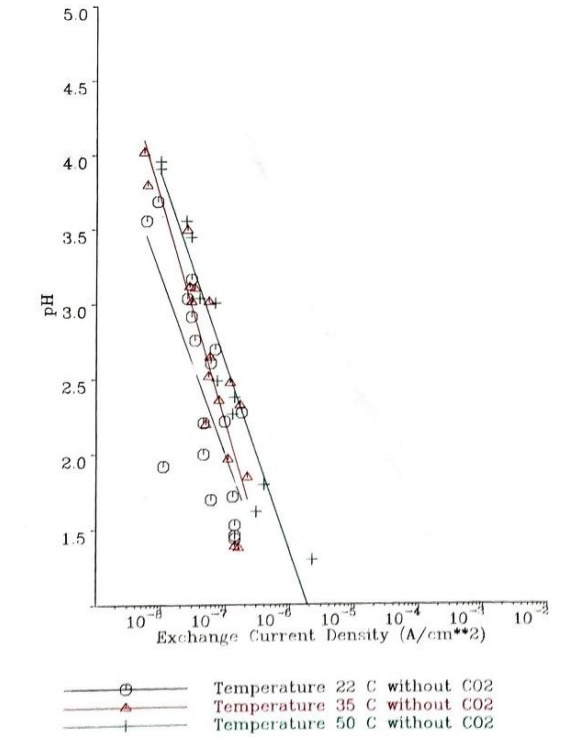
Figure 1. Cathodic polarisation of mild steel in 4% NaCl acidified solution

Another charge transfer process is observed at higher current densities. The Tafel slope found for this process is higher than that for the first one. It is about -0.180± 0.020V/decade. The exchange current densities for the hydrogen evolution reaction are more or less in the range given in the literature, that is 10^{-7} to 10^{-5}A/cm^2 at pH=0.0. (Figure 2.a). The limiting current densities are in the same range as those of previous workers. They lie on the same line as for values found for steel (Figure 2.b) for comparison. As the current drawn increases, a limiting value will be formed for the previous anodic reaction due to the slow rate of H_2 diffusion in water. The extrapolation of both anodic and cathodic curves to the reversible potential gives the exchange current density i_o. As expected, it is higher than the value found for steel, however, it is still in the same range found by other workers, it is about 10^{-2} to 10^{-1} A/cm^2 at p=0.0.

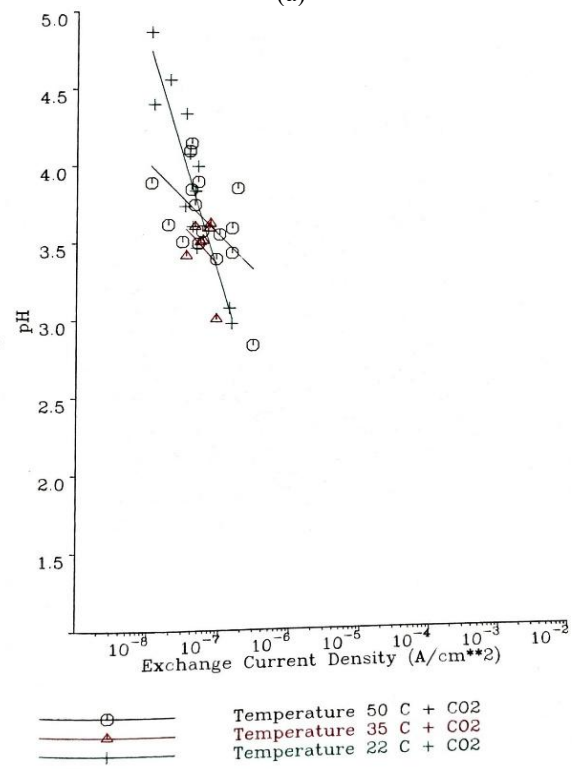
The discussion of the results will first consider the reproducibility and accuracy of the measurements. Experiments were carried out several times to make sure that the results were reproducible. The errors on the pH were ± 0.3 pH units, on the reversible potentials ± 0.005V on the exchange and the limiting currents ± 5× 10^{-6}A, on the temperature ±1°C, and on the pressure measurement ± 5psi. On all the metals studied, the cathodic part of the curve represents the hydrogen reaction, and this shows three well distinguished regions at different potentials. Apart from steel, the other metals copper, nickel, lead, an anodic polarization shows passive behaviour and film formation on the surface had occurred. At different temperatures, the polarization curves maintain a similar shape, but they were slightly displaced towards higher values of applied current densities.

Variation of Exchange Current Density With pH on Steel

The values of the exchange current densities for the hydrogen reaction on steel were measured using the method, which consists of the extrapolation of -0.120V/decade theoretical Tafel slope to the reversible potential of the hydrogen reaction for each pH investigated (Figures 2.a and 2.b). When using the extrapolation method at room temperature of 22°C, for example, It was found that the exchange current densities lie on a straight line given by the following equation $\log i_o$= -5.307 - 0.842pH.



(a)



(b)

Figure 2. Variation of Io with pH on steel

Variation of Limiting Current Density with pH on Steel

The limiting current density for the cathodic hydrogen evolution reaction was found to vary linearly with the bulk solution pH. As was found for the other metals, it is the proton concentration in the solution which determines the magnitude of the limiting current density Ii_L. An increase in the proton concentration in the solution leads to an increase in the limiting current densities towards higher values of applied current densities. It was found that at

22°C, for instance, the variation of the limiting current density with respect to the bulk solution pH (Figures 3,4,5 and 6) is $\log I_L = -1.126 - 1.020pH$.

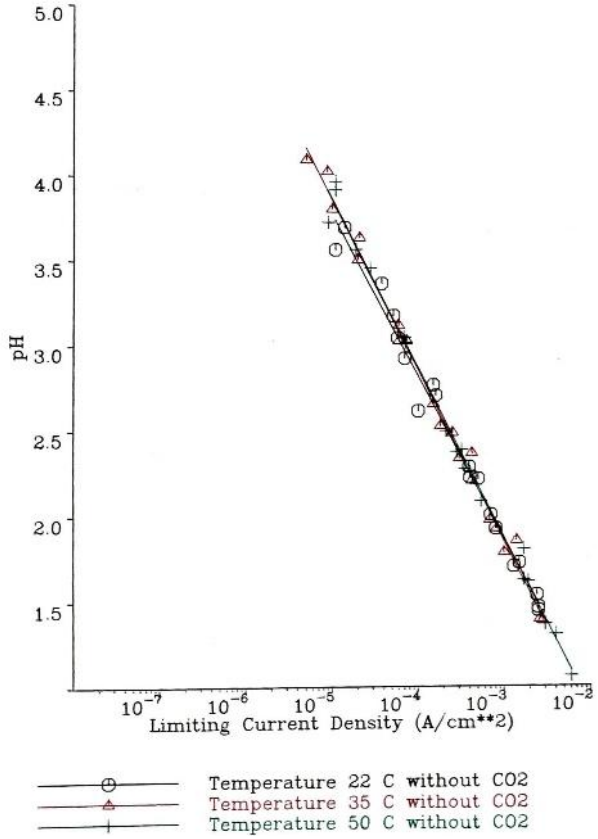


Figure 3. Variation of I_L with pH on steel

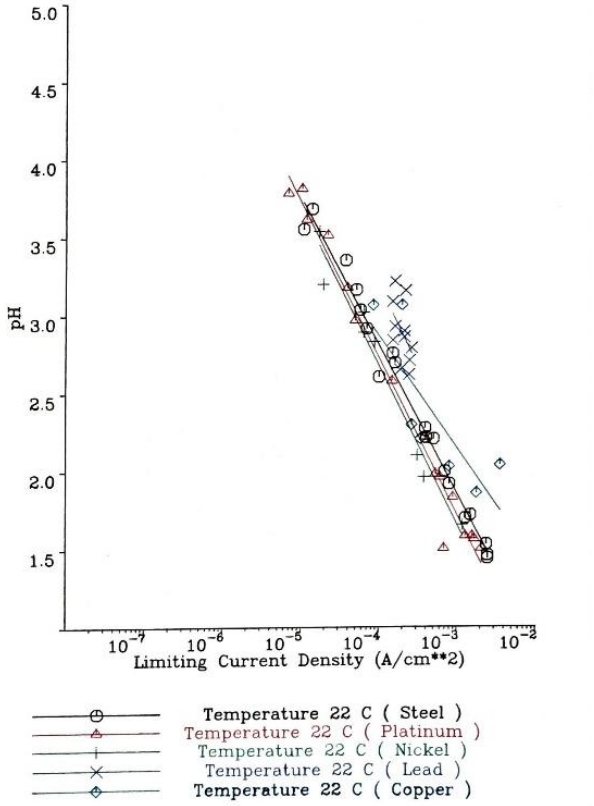


Figure 4. Variation of I_L with pH

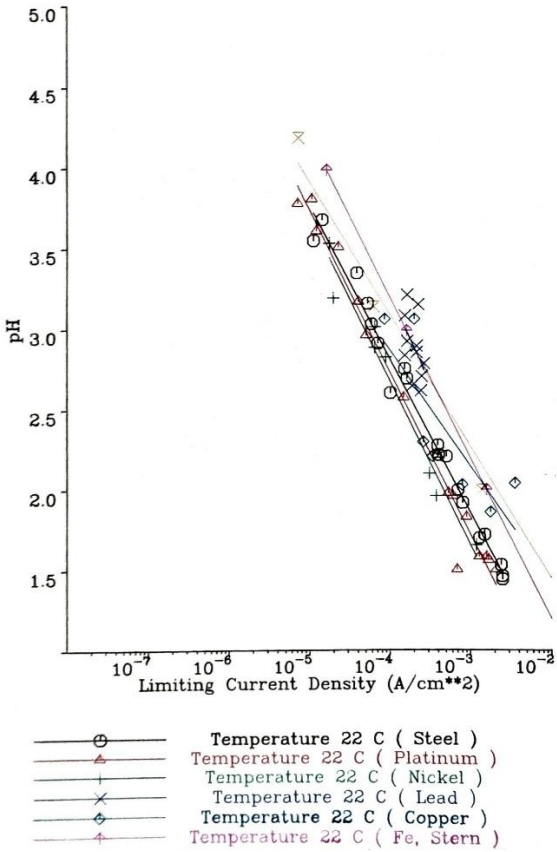


Figure 5. Variation of I_L with pH

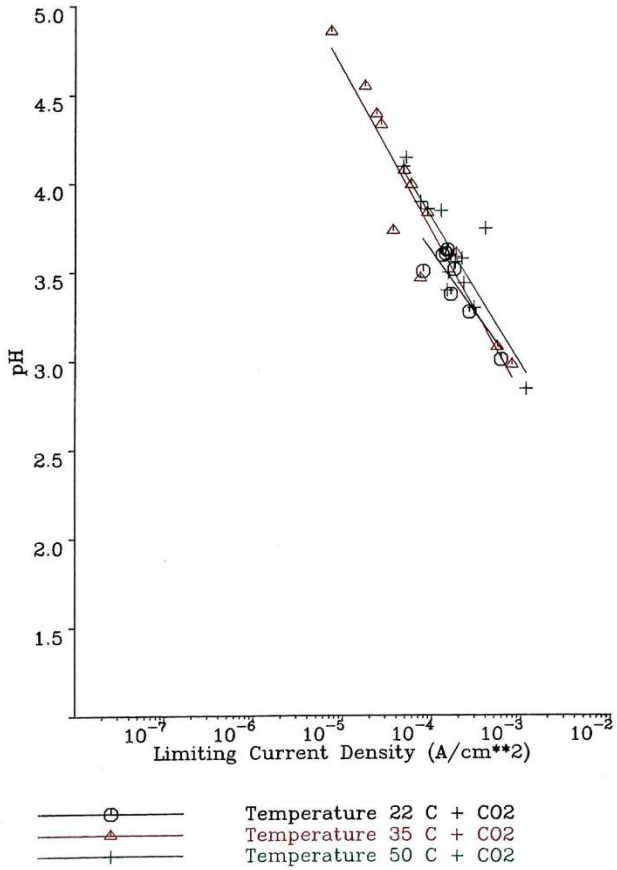


Figure 6. Variation of I_L with pH on steel

The relation given by Stern in his study of the corrosion of steel in sea water (figure 5) is $\log I_L = - 0.845 – pH$ which is close to the value found in this study. At pH 0.0, the limiting current density is $7.482\times 10^{-2} A/cm^2$, compared with $2.735\times10^{-1} A/cm^2$ and $1.429\times 10^{-1} A/cm^2$. The results are very close to each other and very reproducible. The limiting current densities are in the same range of values found for all the metals investigated, showing the independence of i_L on the nature of the working electrode material (Stern & Geary, 1957).

Effects of Temperature

In deep gas wells, the corrosion rate is increased by CO_2 partial pressure coupled with high temperature. Increasing the temperature from 22 to 50°C leads to an increase in both values of limiting an of exchange current densities (figure 7).

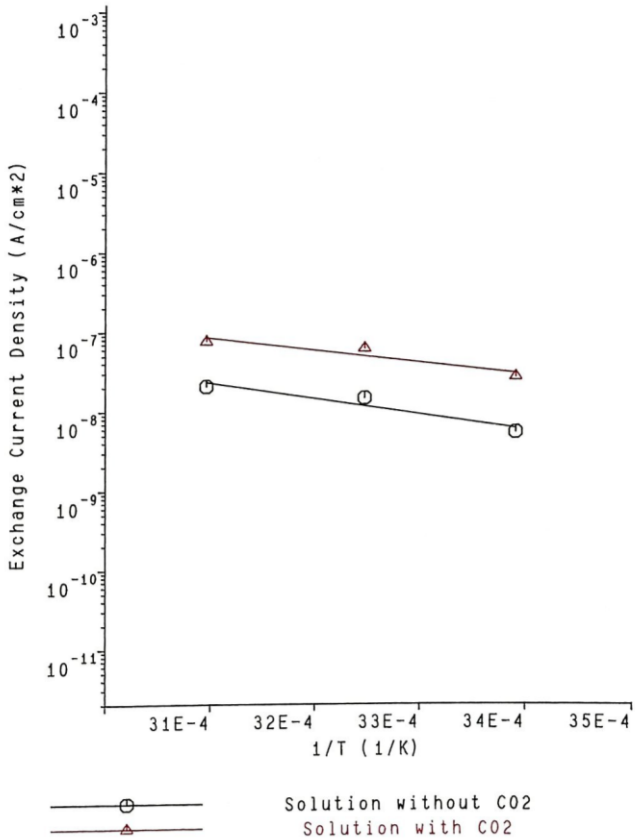


Figure 7. Variation of Io with 1/T on steel (pH 3.5)

In CO_2-NaCl Saturated Solutions

The corrosion rates obtained in this work are comparable with those of De Waard and Milliams and was found at 22°C, 0.48mm/year compared to 0.9 mm/year at 1 Atm. pressure CO_2 and the same difference was found at for 35 and 50°C (De Waard & Milliams, 1975).

Summary of Results

The hydrogen electrode reaction is the same on all the metals examined. This is modified by the exchange reaction, but the limiting current are for all the metals are in the same range. The steel used in the oil industry will be under corrosion conditions depending on those factors which affect the cathode reaction. Therefore, pH decreases and increases in temperature combine to increase the rate. The presence of concentration of CO_2 increases the pH at the steel surface thereby increasing the corrosion rate. The temperature increase is shown to increase diffusion which increases the limiting current and the corrosion rate.

By studying the effect of temperature on I_o and I_L it may be possible to decide whether additions of CO_2 change the activation energy for the I_o or I_L change the pre-exponential term, i.e., the frequency factor or the number of sites for the reaction to occur. This is the real meat of the discussion as different metals appear to react differently to additions of CO_2 and changes in temperature.

Activation Energy Analysis

The relation between the exchange current density I_o (A/cm^2) and the inverse of the temperature (°K) is given by the following $I_o = A \exp(-\Delta G/RT)$ where ΔG is the activation energy of the system,(KJ or Kcal/mole), R is the gas constant (8.3~J/mole)
T is the temperature in °K,
A is a constant or pre exponential factor.

The variation of I_0 versus 1/T for mild steel in the presence and in the absence of CO_2 at pH 3.5 at three different temperatures are plotted in (Figure 7). As far as the activation energy analysis is concerned, some conclusions for the metals capable of being a catalyst to the hydrogen reaction can be drawn, that is, the introduction of CO_2 into each one of the systems studied results in, a noticeable change in the activation energy on Pb, and a small change on the other metals for the exchange current density, however, a big change of activation energy on Ni, Cu, and Pb, and a small change on Fe and Pt for the limiting current density.

As far as polarization curves for the hydrogen reaction on Pt, Ni, Cu and Pb in 4% NaCl acidified solution are concerned, similar relations were found for the limiting current densities. The relations agree very well with the relations given in the literature and the curves still present the same characteristics shown for steel as far as the cathodic polarization curve is concerned. The fact that the effect of CO_2 on the cathodic polarization of the various metals is the same, then the role of CO_2 in the corrosion of steel in oil well brines is due to the H^+ ion reduction and that CO_2 contributes to H^+ concentration when present. Dissociation of the carbonic acid, a weak acid, has been shown to be very important in the corrosion of steel by supplying protons to the cathodic sites.

Conclusion

The role of CO_2 in the increase in corrosion rate of steel in acidified and deaerated 4% NaCl solution has been shown to be associated with the controlling cathodic reaction, i.e., reduction of hydrogen ions. This has been confirmed by the observation that the reversible electrode potential is responsive only to the hydrogen ion concentration (pH) and that the exchange current and limiting current have been increased but the electrochemical reaction kinetics measured by the Tafel slopes, i.e., reduction of hydrogen ions, is unchanged. The fact that the hydrogen reduction reaction has been changed by CO_2 means that the effect on the electrochemistry should be independent of the metal electrode used. This has been shown to be the case by studying the effect on the metals, Platinum, Nickel, Copper and Lead. In these cases, although the exchange current was dependent on the metal type, the limiting current and the reversible potential were unchanged.

The work carried out has not been able to provide a complete understanding but has contributed to our knowledge in the following ways.
1. The limiting current is not a function of the electrode material, but depends only on the solution concentration in reacting $[H^+]$.
2. The limiting current density for each pH investigated for each metal studied in this work is increased by the introduction of CO_2 into the system. Although the bulk pH did not change by introduction of CO_2 (under high pressure), the corrosion rate increased an order of magnitude and this was shown to be due to an increase in I_L of the hydrogen reduction reaction .
3. It has been shown that there is an increase in the exchange current density of the hydrogen reaction by the introduction of CO_2 for each metal investigated. For the same CO_2 pressure (concentration), the I_o for steel, platinum, nickel increased by half a decade compared to a small change for copper and lead .
4. The exchange current density for the hydrogen ion reduction reaction has been shown to be dependent on the electrode material. I_o decreases in the following order
$I_{o,Pt} > I_{0,Fe} > I_{o,Ni} > I_{o,Cu} > I_{o,Pb}$
5. It was confirmed that the reversible potential of the hydrogen reaction is not affected by the choice of material used, and only depends upon pH either in the bulk solution with and without CO_2 in solution.

Scientific Ethics Declaration

* The authors declare that the scientific ethical and legal responsibility of this article published in EPSTEM journal belongs to the authors.

Conflict of Interest

* The authors declare that there is no conflict of interest.

Funding

* This research received no internal or external funding.

Acknowledgements or Notes

* This article was presented as an oral presentation at the International Conference on Technology, Engineering and Science (www.icontes.net) held in Antalya/Türkiye on November 12-15, 2025.

References

Butler, G., & Ison, H. C. K. (1966). *Corrosion and its prevention in waters*. Leonard Hill Books.

Carlson, H. A. (1949). Corrosion in gas-condensate wells. *Industrial and Engineering Chemistry, 41*(4), 644-647.

De Waard, C., & Milliams, D. E. (1975). Carbonic acid corrosion of steel. *Corrosion, 31*(5), 177-184.

Iannuzzi, M., & Frankel, G. S. (2022). The carbon footprint of steel corrosion. *NPJ Materials Degradation, 6*(1), 101.

Liu, G., Wang, S., Xue, T., & Liu, Y. (2023). Revealing the mechanism of O2 and pressure effects on the corrosion of X80 carbon steel under supercritical CO2 conditions. *Corrosion Science, 221*, 111355.

Liu, J., Li, M., He, M., Ma, Z., Li, K., Wang, L., Li, G., Zhou, L., Zhang, S., & Yan, W. (2023). Corrosion behaviors of N80 and 1Cr tubing steels in CO2 containing downhole environment-A case study of underground gas storage in Liaohe Oil Field. *Coatings, 13*(4), 737.

Solovyeva, V. A., Almuhammadi, K. H., & Badeghaish, W. O. (2023). Current downhole corrosion control solutions and trends in the oil and gas industry: A review. *Materials, 16*(5), 1795.

Stern, M., & Geary, A. L. (1957). Electrochemical polarization: I. A theoretical analysis of the shape of polarization curves. *Journal of The Electrochemical Society, 104*(1), 56-63.

Videm, K., & Dugstad, A. (1989). Corrosion of carbon steel in carbon dioxide medium. *Materials Performance, 28*(3), 63-67.

Wang, C., Wu, S., Shen, Y., & Li, X. (2024). Review on CO2–brine interaction in oil and gas reservoirs. *Energies, 17*(16), 3926.

Yue, Y., Yin, Z., Li, S., Zhang, Z., & Zhang, Q. (2025). Corrosion behavior of mild steel in various environments including CO2, H2S, and their combinations. *Metals, 15*(4), 440.

Author(s) Information

Haddad Abdelouahab
University Setif1 Ferhat Abbas,
Sétif 19137, Algeria

Zerroug Nadjat
University Setif1 Ferhat Abbas
Sétif 19137, Algeria

To cite this article:

Abdelouahab, H., & Nadjat, Z. (2025). Factors affecting corrosion of steel in pipe lines. *The Eurasia Proceedings of Science, Technology, Engineering and Mathematics (EPSTEM), 38,* 721-730.

The Eurasia Proceedings of Science, Technology, Engineering & Mathematics (EPSTEM)
ISSN: 2602-3199

The Eurasia Proceedings of Science, Technology, Engineering and Mathematics (EPSTEM), 2025

Volume 38, Pages 731-736

IConTES 2025: International Conference on Technology, Engineering and Science

Performance of NMC622 Cathode - LTO Anode Full Cell Lithium Ion Battery

Meltem Cayirli
Eskisehir Osmangazi University

Ersu Lokcu
Eskisehir Osmangazi University

Reşat Can Ozden
Eskişehir Osmangazi University

Mustafa Anik
Eskisehir Osmangazi University

Abstract: At present, the demand for renewable energy sources is steadily increasing, and accordingly, the use of electric vehicles has become more widespread. This trend has led to a growing focus on the development of alternative anode and cathode materials. In this study, NMC622 ($LiNi_{0.6}Co_{0.2}Mn_{0.2}O_2$) with a layered structure was employed as the cathode, while spinel-structured LTO ($Li_4Ti_5O_{12}$), which holds the second-largest market share after graphite, was selected as the anode. The crystal structures of the prepared anode and cathode electrodes were characterized using X-ray diffraction (XRD). The electrochemical performance of the full cell was evaluated by assembling it into a CR2032-type coin cell. The full cell was initially activated at a rate of 0.1 C, after which galvanostatic charge/discharge tests were performed to assess its electrochemical performance at rates of 0.5 C, 1 C, 2 C, and 5 C over 100 cycles. The initial discharge capacities at 0.5 C, 1 C, 2 C, and 5 C were determined as 127, 120, 105, and 70 mA h g^{-1}, respectively. Across all C-rates, the capacity retention ratios were found to vary between 65% and 70%.

Keywords: NMC622, LTO, Li-ion batteries

Introduction

Today, a significant portion of the world's energy demand is met by fossil fuels, which have high carbon emissions. Fossil fuels are finite energy resources and contribute to global warming issues (Ahmad et. al., 2020; Kanoğlu et. al., 2019) Efforts to reduce the use of fossil fuels depend on increasing the use of renewable energy sources and the widespread adoption of electric vehicles. Lithium-ion (Li-ion) batteries, first introduced for commercial use by Japan's Sony Corporation in 1991, have become indispensable for electronic devices due to their high specific energy density and are excellent candidates for energy storage systems in electric vehicles and electronic applications (Nasajpour-Esfahani et. al., 2024). In recent years, the need for the development of high-performance Li-ion batteries for use in electric vehicles (EVs) and hybrid electric vehicles (HEVs) has been steadily increasing. (Koech et. al., 2024; Velev et. al., 2024; Çelikbilek et. al., 2022; Lökçü et. al., 2023).

Lithium titanate ($Li_4Ti_5O_{12}$, LTO) has been researched as one of the most suitable anode materials for energy storage systems such as hybrid electric vehicles (HEVs). LTO is an intercalation-type anode material with a spinel structure. Due to its better safety and cycle stability compared to graphite anodes, it holds the second-largest market share in the Li-ion battery industry after graphite (Zhang et al., 2022). The superior properties of

- This is an Open Access article distributed under the terms of the Creative Commons Attribution-Noncommercial 4.0 Unported License, permitting all non-commercial use, distribution, and reproduction in any medium, provided the original work is properly cited.

- Selection and peer-review under responsibility of the Organizing Committee of the Conference

© 2025 Published by ISRES Publishing: www.isres.org

the LTO anode are mainly due to the phase transformation between $Li_4Ti_5O_{12}$ and $Li_7Ti_5O_{12}$ that occurs during charge/discharge reactions (Ge et al., 2009). These two phases, which belong to the Fd3m space group, have very similar lattice parameters, resulting in a volume change of less than 0.2% during charging/discharging. This gives LTO exceptional cycle stability (Ariyoshi et al., 2005). The working potential of LTO (1.55 V vs. Li^+/Li) is high and prevents dendrite formation. Additionally, this potential is higher than the reduction potentials of most electrolytes and solvents (< 1.0 V), which means a thinner solid electrolyte interphase (SEI) layer forms (He et al., 2012; Zhang et al., 2022). Typically, thick SEI layers consume the active material, leading to capacity loss and low Li^+ diffusion in electrodes (Zhang et al., 2022).

Currently, $LiCoO_2$ is used as the cathode in the majority of commercial Li-ion batteries. However, due to its relatively low capacity (160 mA h g^{-1}) and the limited utilization of lithium within its structure (< 60%), further research into cathode systems has been necessary. In recent years, as electric vehicles have become more common, the main approach to cathode design has been the gradual replacement of cobalt with nickel. This has led to capacities reaching up to 220 mA h g^{-1}, with lithium utilization rates approaching 80%. In these cathode materials, nickel is used for its capacity-enhancing properties, while cobalt and manganese contribute to structural integrity. LiNi-Mn-Co-O_2 cathodes, commonly referred to as NMC, are widely studied materials today (Malik et. al., 2022; Liu et al., 2015). NMC materials have a layered rock salt structure. In this group of cathodes, the chemical composition ranges from $LiNi_{0.33}Mn_{0.33}Co_{0.33}O_2$ (NMC111) to $LiNi_{0.8}Mn_{0.1}Co_{0.1}O_2$ (NMC811) (Chen et. al., 2024; Murdock et al., 2021; Yu et. al., 2014). Due to its high voltage (3.7–3.9 V), good cycle life, structural stability, safety, and cost-effectiveness, NMC is a suitable cathode material when combined with LTO (Houache et. al., 2022; Farhat et. al., 2017). In this study, the NMC622 ($LiNi_{0.6}Mn_{0.2}Co_{0.2}O_2$) cathode electrode and LTO anode electrode were prepared, and the electrochemical performance of Li-ion batteries was investigated.

Materials & Methods

The cathode and anode electrode slurries were prepared using similar parameters. Commercially available NMC622 and LTO active materials were mixed with Super P carbon black and PVDF in NMP medium at specific stoichiometric ratios using a vortex mixer. The prepared anode and cathode slurries were coated onto carbon-coated aluminum foil using a doctor blade, and subsequently dried under vacuum at 80°C for 12 hours. The electrochemical tests of the full cell, composed of an NMC622 cathode and LTO anode, were carried out in a CR2032 coin cell. The assembly of the coin cells was performed in an argon-filled glovebox where H_2O and O_2 levels were kept below 0.1 ppm. As the electrolyte, 1 M Lithium hexafluorophosphate ($LiPF_6$) was used in EC: DMC in a ratio of by 1:1 by volume. Polipropilen (Celgard 2400) membrane was employed as the separator. Charge-discharge tests were conducted using a Gamry Reference 3000 Potentiostat/Galvanostat/ZRA within a potential range of 1.25–2.75 V (vs. Li^+/Li). The assembled cells were first activated at a rate of 0.1 C for 2 cycles within the voltage range of 1.25–2.75 V (vs. Li^+/Li), followed by electrochemical performance testing for 100 cycles at rates of 0.5 C, 1 C, 2 C, and 5 C. X-ray diffraction (XRD) analyses were performed on a PANalytical Empyrean diffractometer with Cu Kα radiation at a scanning rate of 2° min^{-1}.

Results and Discussion

The XRD patterns of the NMC622 electrode on the carbon-coated Al surface are presented in Figure 1. The XRD peaks confirm the layered hexagonal α-$NaFeO_2$-type structure with an R3m space group.The diffraction peaks corresponding to the (003), (101), (006), (102), (104), (105), and (107) planes confirm the crystal structure of NMC. The strong (003) peak observed at $2\theta = 19°$ indicates the well-defined crystalline structure of NMC622 (Loghavi et al., 2022). In addition, a diffraction peak observed around $2\theta = 28°$ is attributed to the presence of carbon in the electrode structure.

The XRD patterns of the LTO electrode coated on the carbon-coated Al surface are presented in Figure 2. The diffraction peaks observed at the (111), (311), (400), (331), and (333) planes indicate a well-defined crystalline structure of the LTO material. In addition to the characteristic peaks of LTO, a peak observed around $2\theta \approx 28°$ is attributed to the presence of carbon in the electrode structure. This carbon peak originates from the conductive carbon additives used in the electrode formulation and/or the carbon coating on the aluminum current collector.

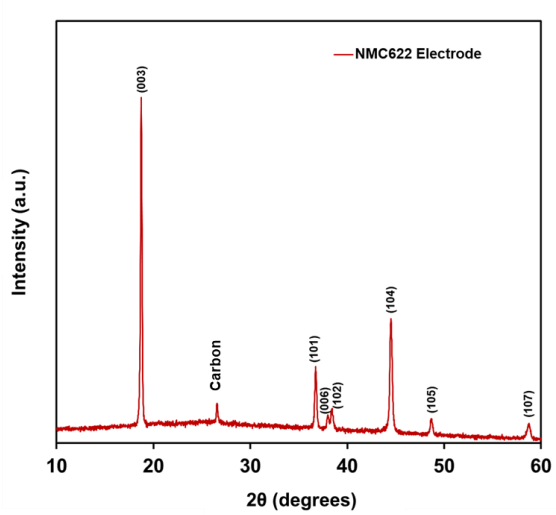


Figure 1. XRD patterns of the NMC622 electrode.

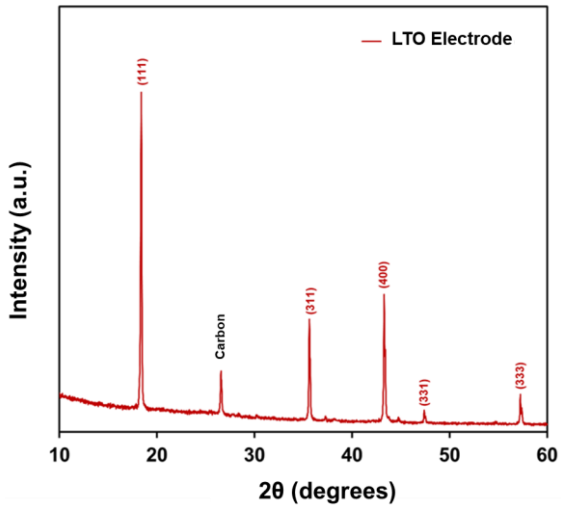


Figure 2. XRD patterns of the LTO electrode.

The charge/discharge test of the full cell composed of an LTO anode and NMC622 cathode, conducted at 0.1 C within the voltage range of 1.25–2.75 V (vs. Li^+/Li) for 2 cycles, is presented in Figure 3. At the end of the second cycle, the charge capacity was determined to be approximately 159 mA h g^{-1}, while the discharge capacity was approximately 145 mA h g^{-1}.

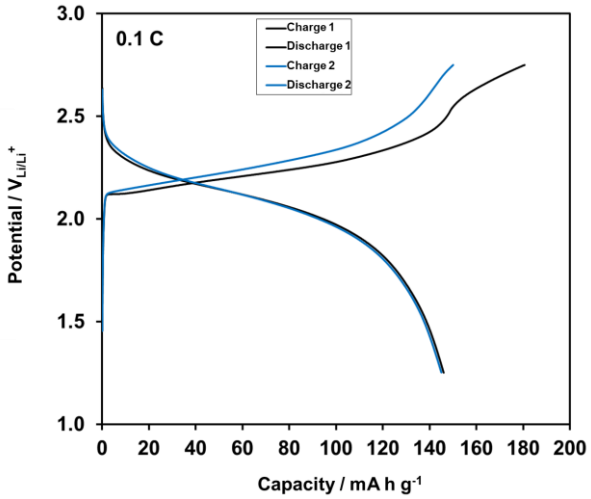


Figure 3. Charge and discharge curves of the LTO anode – NMC622 cathode full cell at a 0.1 C rate.

The effect of different charge/discharge rates on the cycling performance of the full cell comprising an LTO anode and NMC622 cathode was evaluated over 100 cycles at 0.5 C, 1 C, 2 C, and 5 C. The corresponding charge/discharge profiles are shown in Figures 4a–4d. The variation of charge and discharge capacities with cycle number for each C-rate is comparatively presented in Figure 5.

At the initial cycle, the discharge capacities were measured to be 127 mA h g^{-1}, 120 mA h g^{-1}, 105 mA h g^{-1}, and 70 mA h g^{-1} at 0.5 C, 1 C, 2 C, and 5 C, respectively. After 100 cycles, these values decreased to 81 mA h g^{-1}, 68 mA h g^{-1}, 64 mA h g^{-1}, and 50 mA h g^{-1}, indicating a gradual capacity fade with increasing current rates. Across all tested C-rates, the coulombic efficiency remained stable in the range of 90–95%, suggesting good reversibility of the electrochemical reactions. Furthermore, the capacity retention after 100 cycles ranged from 65% to 70%, reflecting moderate long-term stability under varying rate conditions.

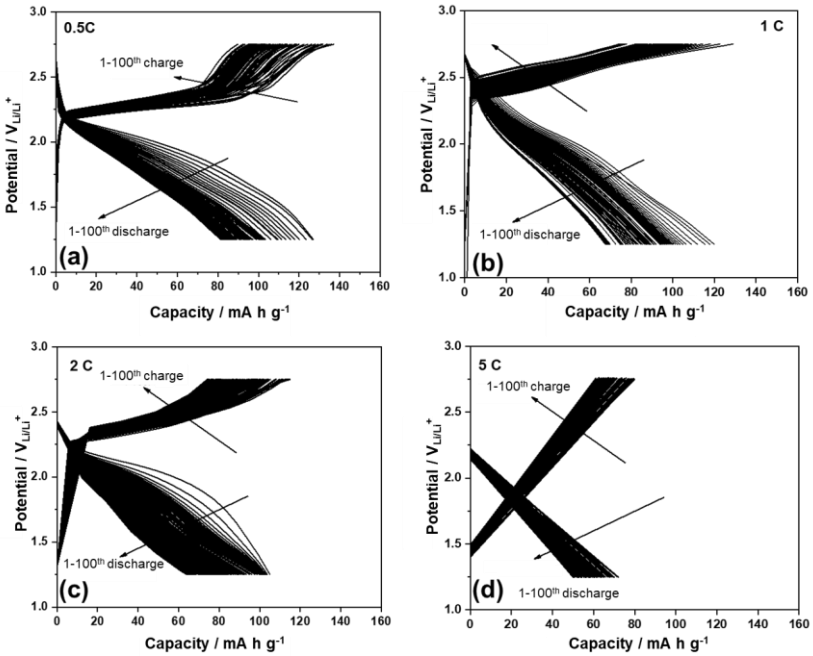


Figure 4. Performance of the full cell with LTO anode – NMC622 cathode in the potential range of 1.25–2.75 V (vs. Li^+/Li) at (a) 0.5 C, (b) 1 C, (c) 2 C, and (d) 5 C rates over 100 cycles.

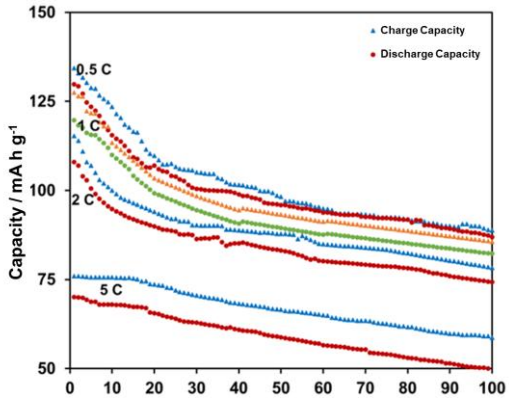


Figure 5. Comparison of the charge and discharge capacities of the full cell with LTO anode – NMC622 cathode at 0.5 C, 1 C, 2 C, and 5 C rates over 100 cycles.

Conclusion

In this study, electrodes were prepared using LTO as the anode and NMC622 as the cathode material. The crystal structures of the anode and cathode electrodes were characterized using X-ray diffraction (XRD) technique. The electrochemical performance of the lithium-ion batteries was evaluated. Charge-discharge

measurements showed that the full cell exhibited a discharge capacity of 50 mAh g^{-1} after 100 cycles at a 5 C rate, with a capacity retention of 70%.

In conclusion, the full cell combining LTO anode and NMC622 cathode materials demonstrates acceptable capacity and cycling stability even at high C rates, making it a promising candidate for practical lithium-ion battery technologies. The results support the applicability of such material systems in applications requiring rapid energy delivery and indicate potential for further improvement through future optimization studies.

Scientific Ethics Declaration

* The authors declare that the scientific ethical and legal responsibility of this article published in EPSTEM journal belongs to the authors.

Conflict of Interest

* The authors declare that they have no conflicts of interest

Funding

* Financial assistance from Eskişehir Osmangazi University Research Fund is gratefully acknowledged (Project No FOA-2024-3172).

Acknowledgements or Notes

* This article was presented as a/an oral/poster presentation at the International Conference on Technology, Engineering and Science (www.icontes.net) held in Antalya/Türkiye on November 12-15, 2025.

References

Ahmad, T., & Zhang, D. A. (2020). Critical review of comparative global historical energy consumption and future demand: The story told so far. *Energy Reports, 6*, 1973-1991.

Çelikbilek, Z., Can, S., Lökçü, E., & Anik, M. (2022). Effect of rGO loading on the electrochemical performance of Li22Si5/rGO composite anodes for lithium-ion batteries. *International Journal of Energy Research, 46*(2), 1137-1145.

Chen, Y. S., Dominko, R., Marczewski, M., & Wieczorek, W. (2024). Optimizing high-energy lithium-ion batteries: A review of single crystalline and polycrystalline nickel-rich layered cathode materials: Performance, synthesis and modification. *Applied Physics A, 130*(740), 1-21.

Farhat, D., Ghamouss, F., Maibach, J., Edström, K., & Lemordant, D. (2017). Adiponitrile-LiTFSI solution as alkylcarbonate free electrolyte for LTO/NMC Li-ion batteries. *ChemPhysChem, 18*(10).

Ge, H., Li, N., Li, D., Dai, C., & Wang, D. (2009). Study on the theoretical capacity of spinel lithium titanate induced by low-potential intercalation. *Journal of Physical Chemistry C, 113*(16), 6324-6326.

He, Y. B., Li, B., Liu, M., Zhang, C., Lv, W., Yang, C., ... Kang, F. (2012). Gassing in Li4Ti5O12-based batteries and its remedy. *Scientific Reports, 2*(913), 1-9.

Houache, M. S. E., Yim, C. H., Karkar, Z., & Abu-Lebdeh, Y. (2022). On the current and future outlook of battery chemistries for electric vehicles-mini review. *Batteries, 8*(70), 1-19.

Kanoğlu, M., Çengel, Y. A., & Cimbala, J. M. (2019). *Fundamentals and applications of renewable energy*. McGraw-Hill Education.

Koech, A. K., Mwandila, G., & Mulolani, F. (2024). A review of improvements on electric vehicle battery. *Heliyon, 10*, e34806.

Liu, W., Oh, P., Liu, X., Lee, M. J., Cho, W., Chae, S., ... Cho, J. (2015). Nickel-rich layered lithium transition-metal oxide for high-energy lithium-ion batteries. *Angewandte Chemie International Edition, 54*, 4440-4457.

Loghavi, M. M., Nahvibayani, A., Moghim, M. H., Babaiee, M., Baktashian, S., & Eqra, R. (2022). Electrochemical evaluation of LiNi0.5Mn0.3Co0.2O2, LiNi0.6Mn0.2Co0.2O2, and

LiNi0.8Mn0.1Co0.1O2 cathode materials for lithium-ion batteries: From half-coin cell to pouch cell. *Monatshefte für Chemie - Chemical Monthly, 153*, 1197-1212.

Lökçü, E., Can, S., & Anik, M. (2023). Ultrasound-assisted synthesis of rGO/SiO2-based nanosheets and their electrochemical performances in Li-ion batteries. *Turkish Journal of Chemistry, 47*(2), 495-503.

Malik, M., Chan, K. H., & Azimi, G. (2022). Review on the synthesis of LiNixMnyCo1-x-yO2 (NMC) cathodes for lithium-ion batteries. *Materials Today Energy, 28*(101066), 1-33.

Murdock, B. E., Toghill, K. E., & Tapia-Ruiz, N. (2021). A perspective on the sustainability of cathode materials used in lithium-ion batteries. *Advanced Energy Materials, 11*(39), 2102028.

Nasajpour-Espahani, N., Garmestani, H., Bagheritabar, M., Jasim, D. J., Toghraie, D., Dadkhah, S., & Firoozeh, H. (2024). Comprehensive review of lithium-ion battery materials and development challenges. *Renewable and Sustainable Energy Reviews, 203*, 114783.

Velev, B., Djudzhev, B., Dimittrov, V., & Hinov, N. (2024). Comparative analysis of lithium-ion batteries for urban electric/hybrid electric vehicles. *Batteries, 10*(186), 1-18.

Yu, H. J., Qian, Y. M., Otani, M., Tang, D., Guo, S., Zhu, Y., & Zhou, H. (2014). Study of the lithium/nickel ions exchange in the layered LiNi0.42Mn0.42Co0.16O2 cathode material for lithium ion batteries: Experimental and first-principles calculations. *Energy & Environmental Science, 7*, 1068-1078.

Zhang, H., Yang, Y., Xu, H., Wang, L., Lu, X., & He, X. (2022). Li4Ti5O12 spinel anode: Fundamentals and advances in rechargeable batteries. *InfoMat, 4*(4), 1-29.

Author(s) Information

Meltem Cayirli
Eskişehir Osmangazi University
26480, Eskişehir, Türkiye
Contact e-mail: *meltem.cayirli@ogu.edu.tr*

Ersu Lokcu
Eskişehir Osmangazi University
26480, Eskişehir, Türkiye

Reşat Can Ozden
Eskişehir Osmangazi University
26480, Eskişehir, Türkiye

Mustafa Anik
Eskişehir Osmangazi University
26480, Eskişehir, Türkiye

To cite this article:

Cayirli, M., Lokcu, E., Ozden, R. C., & Anik, M. (2025). Performance of NMC622 Cathode – LTO anode full cell lithium ion battery. *The Eurasia Proceedings of Science, Technology, Engineering and Mathematics (EPSTEM), 38,* 731-736.

The Eurasia Proceedings of Science, Technology, Engineering & Mathematics (EPSTEM)
ISSN: 2602-3199

The Eurasia Proceedings of Science, Technology, Engineering and Mathematics (EPSTEM), 2025

Volume 38, Pages 737-747

IConTES 2025: International Conference on Technology, Engineering and Science

Power System Stability Including Wind Farm with Statcom Based Pi Fractional Controller

Issam Griche
Bouira University

Kamel Saoudi
Bouira University

Mourad Benziane
Bouira University

Abderrazak Arabi
Ferhat Abbas Setif 1 University

Abstract: In this paper, a new static synchronous compensator (STATCOM) based PI fractional control technique is proposed. The system equations were transformed to the normal form, then, design a fractional order, finally, we propose adaption laws for switching gains. The control objective is to enhance stability and improve the dynamic response of the multi-machine power system including wind farm. Simulations are carried out to show the effectiveness of the proposed method. Small signal stability characteristics of the system are analyzed in presence of changes in reference mechanical torque. By simulation, the proposed method is compared with the conventional PI controller. It is shown that the proposed method has lower spike and shorter reaching time than PI STATCOM.

Keywords: Static synchronous compensator STATCOM, Multi-machine power system, Wind farm, PI Fractional order controller, Adaptive controller

Introduction

Nowadays, enhancement of the dynamic stability of power systems is an important subject of researches (Basler et al). If the damping torque of the generator is not enough, then some fluctuations persist for a long time and may become more considerable. They may have a negative effect on damping of rotor swing. When dealing with power systems angle stability, oscillations damping is very important factor particularly when a fault occurrence.

STATCOM is one of the most significant devices in FACTS technology It is used in parallel compensation, enhancing the transient stability, limiting the low frequency oscillations ...etc. Designing a proper controller is effective in STATCOM operation. It is also added to power system to exchange reactive power and to inject active power, which will further enhance damping of oscillations. This makes new challenges for power system engineers; voltage control across the network, as well as the ephemeral fluctuations in power frequency. To reduce the adverse effects of fluctuations and improve dynamic performance, the system has to be imposed under additional signals. One of the cost effective approaches is to connect a feedback controller to the reference voltage input in order to insert an additional signal generator to cause the oscillations damping. It is known as the power system stabilizer, Basler et al.(2005), Golpira et al. (2015), Yu et al.(2015). During last decade, many studies have been done on the usage of a STATCOM in power systems, research of optimal placement STATCOM, coordination STATCOM and the use of more effective methods in STATCOM design, Padiyar et

- This is an Open Access article distributed under the terms of the Creative Commons Attribution-Noncommercial 4.0 Unported License, permitting all non-commercial use, distribution, and reproduction in any medium, provided the original work is properly cited.

- Selection and peer-review under responsibility of the Organizing Committee of the Conference

© 2025 Published by ISRES Publishing: www.isres.org

al.(2008), Kundur (1994), El-Zonkoly et al.(2009), Tapia et al.(2012), Abdelaziz et al.(2006), R. Latha et al.(2018). In power systems, the perturbation and uncertainty are inevitable so that robust methods must be applied. Among these methods, the fractional PID should be noted which have superior benefits than the PID method in its degree of freedom and robustness, Chaib et al.(2015) However, it has lower resistance against disturbances compared with non-linear controllers, i.e. the sliding mode controller. The design of fractional order controllers in different fields has been studied by many researchers, Delavari et al.(2010), (2012), Faieghi et al.(2012). Several comparative studies have shown that fractional PI controllers are superior to conventional PI controllers, Podlubny et al.(1998), Cao et al.(2011), Li et al.(2013), Delavari et al. (2010), (2015), Wang et al.(2009), Petru et al.(2002). Beside the PI controllers, the fractional calculus is used for improving other type of controllers, Delavari et al. (2010), (2013), Calderon et al.(2006), Efe et al.(2010). Industrial applications of fractional order controllers are explained in Chathoth et al.(2015), Mehmood et al.(2015) and Monje et al.(2010). Some novelties in our contribution:

- A new fractional order PI controller is proposed and thus more degrees of freedom is created,
- Stability of the proposed method has been proved,
- Stability of the proposed controller, by using the optimization of GA, has been proved.

This paper is organized as follows. Section II presents the multimachine power system including wind farm being studied and the dynamic model of a synchronous generator is described. Section III presents the mathematical model of the STATCOM. Section IV presents the model of wind turbine. Section V discribe the synchronous generator modelling. The design of the proposed STATCOM with Adaptive Fractional Order AFOPI Controller is presented in section V. Section VI contains simulation results of the proposed method. Conclusions are drawn in section VII. The controller is validated using nonlinear model simulation.

Multi-Machine Power System Including Wind Farm Being Studied

A two-area multi-machine power system consisting of four synchronous generators with loads is shown in Figure. 1. The two areas are identical, and each includes two generators equipped with fast acting excitation systems.

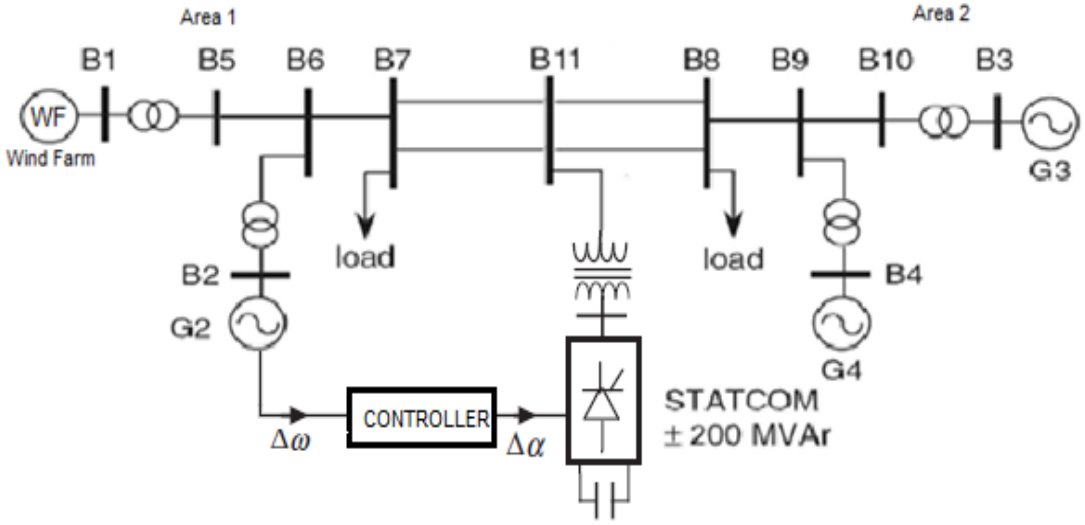


Figure. 1. Single diagram of a 4-Machines 11-Bus System

STATCOM is connected to generator 2. The wind farm is considered as generator 1. This two-area system has been designed to study low-frequency electromechanical oscillations in large interconnected power systems. It has also been modified to include FACTS devices for studying the inter area mode damping improvement. In the present study, a STATCOM is installed at bus 11, as shown in Fig.1. The capacity of capacitors installed at bus 7 is changed from 187 to 200 MVAr while the capacity of capacitors installed at bus 8 is changed from 187 to 180 MVAr. These capacitors, together with STATCOM, will maintain the load voltage profile to close to 1 p.u. The system being studied is simulated by MATLAB software.

STATCOM Modelling

The STATCOM is modeled using the model described in (Podlubny). This model is essentially a controllable voltage source. The state variables of a system of multi machine with STATCOM are amended as follows:

$$\Delta \mathrm{X} = \left[\Delta \mathrm{X}_1{}^{\mathrm{T}} \quad \Delta \mathrm{X}_2{}^{\mathrm{T}} \quad \mathrm{K} \quad \Delta \mathrm{X}_m{}^{\mathrm{T}}\right]^{\mathrm{T}} \tag{1}$$

Where: $\Delta \mathrm{X}_i = \left[\Delta\delta_i \quad \Delta\omega_i \quad \Delta \mathrm{E}'_{qi} \quad \Delta \mathrm{E}'_{di} \quad \Delta \mathrm{E}_{fd_i} \quad \Delta V_{R_i} \quad \Delta R_{F_i} \quad \Delta V_{s_i} \quad \Delta \mathrm{X}_{s_2} \quad \Delta \mathrm{X}_{s_3} \quad \Delta V_{sc}\right]^{\mathrm{T}}$ for the i^{th} generator from which the STATCOM controller receives the auxiliary input signal $(\Delta\omega)$ and the state variable $\Delta \mathrm{X}_i = \left[\Delta\delta_i \quad \Delta\omega_i \quad \Delta \mathrm{E}'_{q_i} \quad \Delta \mathrm{E}'_{d_i} \quad \Delta \mathrm{E}_{fd_i} \quad \Delta V_{R_i} \quad \Delta R_{F_i} \quad \Delta V_{s_i}\right]^{\mathrm{T}}$ for the $i = 1,2,3,\mathrm{K},(m-1)$ remaining generators.

It is assumed that the STATCOM is connected to a load j^{th} busbar, the active and reactive power equations of a STATCOM can then be obtained as follows:

$$\mathrm{P}_{sc} = |V_{sc}|^2 G_{sc} - |V_{sc}||V_j|\left[G_{sc}\cos(\delta_{sc} - \theta_j) + \mathrm{B}_{sc}\sin(\delta_{sc} - \theta_j)\right] \tag{2}$$

$$Q_{sc} = -|V_{sc}|^2 \mathrm{B}_{sc} - |V_{sc}||V_j|\left[G_{sc}\sin(\delta_{sc} - \theta_j) - \mathrm{B}_{sc}\cos(\delta_{sc} - \theta_j)\right] \tag{3}$$

Where $V_{sc}\angle\delta_{sc}$ the reverse voltage (AC) to the output of the STATCOM and $Y_{sc} = G_{sc} + jB_{sc}$. G_{sc} and B_{sc} are respectively the conductance and susceptance of the transmission line between the load bus bar and STATCOM.

Therefore, the linearization of active and reactive power equations of the j-th load bus bars can be represented by equation (4). Here, voltage amplitude V_{sc} and phase angle δ_{sc} are taken to be the state variables. The power flow equations $i = m+1, m+2, \mathrm{K}, (n-1)$ for other load bus are not affected:

$$\begin{bmatrix} \Delta \mathrm{P}_j \\ \Delta Q_j \\ \Delta \mathrm{P}_{sc} \\ \Delta Q_{sc} \end{bmatrix} = \begin{bmatrix} \frac{\partial \mathrm{P}}{\partial \theta_j} & \frac{\partial \mathrm{P}_j}{\partial V_j} & \frac{\partial \mathrm{P}_j}{\partial \delta_{sc}} & \frac{\partial \mathrm{P}_j}{\partial V_{sc}} \\ \frac{\partial Q_j}{\partial \theta_j} & \frac{\partial Q_j}{\partial V_j} & \frac{\partial Q_j}{\partial \delta_{sc}} & \frac{\partial \mathrm{P}_j}{\partial V_{sc}} \\ \frac{\partial \mathrm{P}_{sc}}{\partial \theta_j} & \frac{\partial \mathrm{P}_{sc}}{\partial V_j} & \frac{\partial \mathrm{P}_{sc}}{\partial \delta_{sc}} & \frac{\partial \mathrm{P}_{sc}}{\partial V_{sc}} \\ \frac{\partial Q_{sc}}{\partial \theta_j} & \frac{\partial Q_{sc}}{\partial \theta_j} & \frac{\partial Q_{sc}}{\partial \delta_{sc}} & \frac{\partial Q_{sc}}{\partial V_{sc}} \end{bmatrix} \begin{bmatrix} \Delta\theta_j \\ \Delta V_j \\ \Delta\delta_{sc} \\ \Delta V_{sc} \end{bmatrix} \tag{4}$$

Wind Turbine Modelling

The captured mechanical power (in W) by a Wind turbine (WT) can be written by:

$$P_{mw} = \frac{1}{2}\rho_w . A_{rw} . V_w^3 . C_{pw}(\lambda_w, \beta_w) \tag{5}$$

Where ρ_w is the air density (kg/m^3), A_{rw} is the blade impact area (m^2), V_w is the wind speed (m/s), and C_{pw} is the dimensionless power coefficient of the WT. The power coefficient of the WT C_{pw} is given by:

$$C_{pw}(\Psi_{kw},\beta_w)=c_1\left(\frac{c_2}{\Psi_{kw}}-c_3.\beta_w-c_4.\beta_w^{c_5}-c_6\right)\exp\left(-\frac{c_7}{\Psi_{kw}}\right) \tag{6}$$

$$\frac{1}{\Psi_{kw}}=\frac{1}{\lambda+c_8.\beta_w}-\frac{c_9}{\beta_w^3+1} \tag{7}$$

$$\lambda_w=\frac{R_{bw}.\omega_{bw}}{V_w} \tag{8}$$

Where ω_{bw} is the blade angular speed (rad/s), R_{bw} is the blade radius (m), λ_w is the tip speed ratio, β_w is blade pitch angle (degrees), and c1-c9 are the constant coefficients for power coefficient C_{pw} of the studied WT. The power coefficients of the WT can be referred to . The cut-in, rated, and cut-out wind speeds of the studied WT are 4, 15, and 24 m/s, respectively. When wind speed V_w is lower than the rated wind speed of the WT (V_{wrated}), βw = 0°. When $V_w > V_{wrated}$, the pitch-angle control system of the WT activates and the pitch angle of the WT (β_w) increases.

Some of the machine inductances are functions of the rotor speed, whereupon the coefficients of the state-space equations (voltage equations), which describe the behavior of the induction machine, are time-varying (except when the rotor is at stand-still). A change of variables is often used to reduce the complexity of these state-space equations. There are several changes of variables which are used but there is just one general transformation. This general transformation refers to the machine variable to a frame of reference, which rotates at an arbitrary angular velocity ω_g. In this reference frame the machine windings are replaced with some equivalent windings.

The d-q axis equivalent circuit model of the studied wind DFIG can be expressed by:

$$\begin{bmatrix}v_{sd}\\v_{sq}\end{bmatrix}=\begin{bmatrix}R_s&0\\0&R_s\end{bmatrix}\begin{bmatrix}i_{sd}\\i_{sq}\end{bmatrix}+\frac{d}{dt}\begin{bmatrix}\varphi_{sd}\\\varphi_{sq}\end{bmatrix}-\begin{bmatrix}0&-\frac{d\theta_s}{dt}\\\frac{d\theta_s}{dt}&0\end{bmatrix}.\begin{bmatrix}\varphi_{sd}\\\varphi_{sq}\end{bmatrix} \tag{9}$$

$$\begin{bmatrix}v_{rd}\\v_{rq}\end{bmatrix}=\begin{bmatrix}R_r&0\\0&R_r\end{bmatrix}\begin{bmatrix}i_{rd}\\i_{rq}\end{bmatrix}+\frac{d}{dt}\begin{bmatrix}\varphi_{rd}\\\varphi_{rq}\end{bmatrix}-\begin{bmatrix}0&-\frac{d\theta_r}{dt}\\\frac{d\theta_r}{dt}&0\end{bmatrix}.\begin{bmatrix}\varphi_{rd}\\\varphi_{rq}\end{bmatrix}$$

$$\begin{bmatrix}\varphi_{sq}\\\varphi_{rq}\end{bmatrix}=\begin{bmatrix}L_s&M\\M&L_r\end{bmatrix}.\begin{bmatrix}i_{sq}\\i_{rq}\end{bmatrix} \tag{10}$$

$$\begin{bmatrix}\varphi_{sd}\\\varphi_{rd}\end{bmatrix}=\begin{bmatrix}L_s&M\\M&L_r\end{bmatrix}.\begin{bmatrix}i_{sd}\\i_{rd}\end{bmatrix}$$

Where:

R_s, R_r, L_s, L_r are the resistances and inductances of the stator and rotor windings, M is the main inductance.

$v_{sd}, v_{sq}, v_{rd}, v_{rq}, i_{sd}, i_{sq}, i_{rd}, i_{rq}, \varphi_{sd}, \varphi_{sq}, \varphi_{rd}, \varphi_{rq}$ are the d and q-components of the space phasors of the stator and rotor voltages, currents, and flux.

Currently, in wind turbine applications the back-to-back voltage source converter (VSC) is mainly used. This topology comprises a double conversion from AC to DC and then from DC to AC. Both converters can operate in rectifier or inverter mode and therefore a bi-directional power flow can be achieved. A voltage source converter can be implemented in several ways: six-step, pulse amplitude modulated (PAM) or pulse width modulated (PWM). Moreover, the implementation of a PWM VSC may be realized by three methods: harmonic elimination, “sinusoidal” PWM or space vector strategy (SV-PWM).

Synchronous Generator Modelling

The detailed nonlinear model of a synchronous generator is a sixth order model. However, this model is usually reduced to a generalized one-axis nonlinear third order model. The equations describing a third order model of a synchronous generator, for j-th generator, can be written as:

$$\begin{aligned} & Y_{sc} \quad Y_{\max} \quad Y_{\min} \\ & \frac{d}{dt}\omega = -\frac{K_D}{2H}(\omega(t)-\omega_0) + \frac{\omega_0}{2H}(P_m - P_C(t)) \\ & \frac{d}{dt}E_q^{'}(t) = \frac{1}{T_{d0}^{'}}(E_F(t) - E_q(t)) \end{aligned} \tag{11}$$

Where :

$$\begin{aligned} & E_q(t) = \frac{x_d}{x_d^{'}}E_q^{'}(t) - \frac{x_d - x_d^{'}}{x_d^{'}}V_S\cos(\delta(t)) \\ & E_F(t) = k_C u_F(t) \\ & P_C(t) = \frac{V_S E_q(t)}{X_d}\sin(\delta(t)) \end{aligned} \tag{12}$$

Where: $\delta_j(t)$ is the rotor angle of the j-th generator (radians), $\omega_j(t)$ is the speed of the rotor of the j-th generator (radian/sec), ω_{0j} is the synchronous machine speed of the j-th generator (radian/sec), K_{Dj} is the damping constant of the j-th generator (pu), H_j is the inertia constant of the j-th generator (sec), $P_{mj}(t)$ is the mechanical input power of the j-th generator (pu), $P_{ej}(t)$ is the active electrical power delivered by the j-th generator (pu), $E_{qj}(t)$ is the EMF of the q-axis of the j-th generator (pu), $E_{qj}^{'}(t)$ is the transient EMF in the q-axis of the j-th generator (pu), $E_{Fj}(t)$ is the equivalent EMF in the excitation winding of the j-th generator (pu), $T_{d0j}^{'}$ is the d-axis transient short circuit time constant of the j-th generator (sec), k_{Cj} is the gain of the excitation amplifier of the j-th generator, $u_{Fj}(t)$ is the control input of the excitation amplifier with gain k_{Cj} , x_{dj} is the d-axis reactance of the j-th generator (pu), $x_{dj}^{'}$ is the d-axis transient reactance of the j-th generator (pu), X_{dj} is the total direct reactance of the system (pu), $X_{dj}^{'}$ is the total transient reactance of the system (pu), and V_S is the infinite bus voltage (pu).

Design of the Proposed STATCOM with Adaptive Fractional Order AFOPI Controller

The voltage control model is completed at bus 10 by the mathematical equation that depicts the reactive power provided to the STATCOM node Abdelaziz et al.(2006):

$$Q_{sc} = -B_{sc}V_{10}^2 \tag{13}$$

Where : B_{sc} indicate the susceptance.

The FOPI controller, depicted in figure 2, is used to determine the value of either B_{sc} or Y_{sc} .

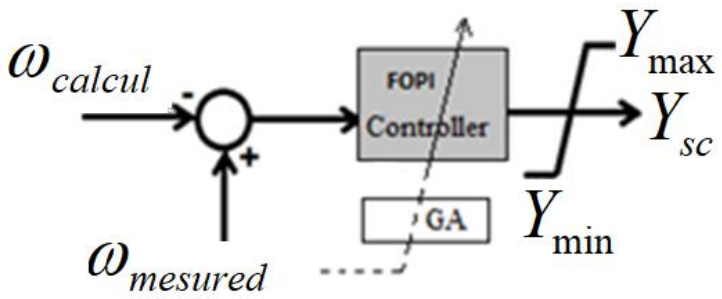


Figure 2. STATCOM equipped with a FOPI controller

Thus, it becomes crucial to develop an efficient approach to adjusting FOPI controller settings to optimize power system stability control. The Genetic Algorithm (GA) is built on the principles of natural selection and genetics, functioning as a global search tool. The initial step in tuning the FOPI controller parameters for the GA application is to consider that each FOPI controller has only one input.Table (I) presents the GA parameters during the scaling factor adjustment phase. Figure.3. Shows the suggested algorithm flowchart

Table 1. The scaling factors tuning the stage with the GA parameters

Variable number	9
Every variable's gene number	3
length of a chromosome	27
Size of the population	54
Number of generation	50

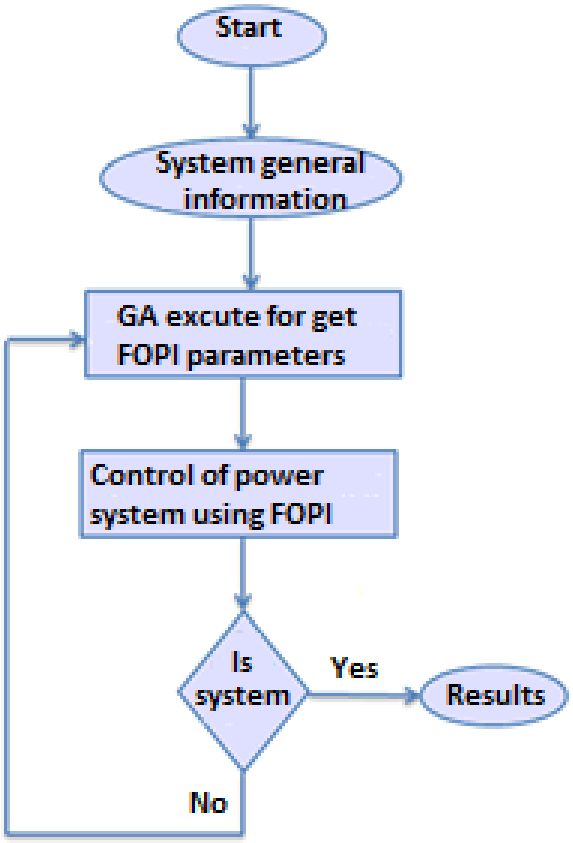


Figure 3. An algorithm diagrams of GA

The adaptive feedback control law, as mentioned in reference, is used to formulate the integer adaptive PI controller.

$$
\begin{aligned}
u(t) &= -k_c\left[k_1(t)e(t) + \int_0^t k_2(\tau)e(\tau)d\tau\right] \\
k_1(t) &= k_p(t) + \alpha_1 k_i(t) \\
k_2(t) &= \alpha_2 k_i(t) \\
k_p(t) &= e^2(t) \\
k_i(t) &= \int_0^t e(\tau)^2 d\tau \\
e(t) &= y(t) - r(t)
\end{aligned}
\tag{14}
$$

Where y is the output signal, u the control input and r the reference signal. k_c, α_1 and α_2 are positive constants. The new control algorithm is obtained using the fractional-inaction of the integral operator $1/s$ as follow:

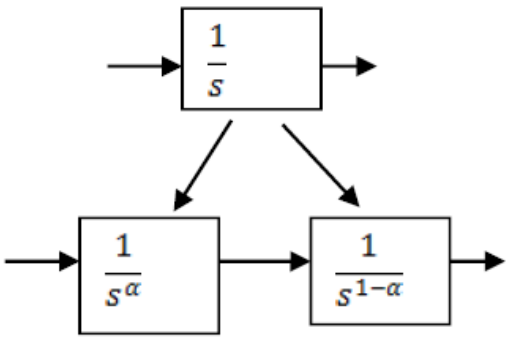


Figure 4. Fractionalization as an integral operator

$$
\begin{aligned}
u(t) &= -k_c\left[k_1(t)e(t) + l^{1-\lambda}\left\{l^{\lambda}\left\{k_2(t)e(t)\right\}\right\}\right] \\
k_1(t) &= k_p(t) + \alpha_1 k_i(t) \\
k_2(t) &= \alpha_2 k_i(t) \\
k_p(t) &= e^2(t) \\
k_i(t) &= l^{1-\lambda}\left\{l^{\lambda}\left\{e^2(t)\right\}\right\} \\
e(t) &= y(t) - r(t)
\end{aligned}
\tag{15}
$$

Figure 5 shows the suggested adaptive fractional PI controller.

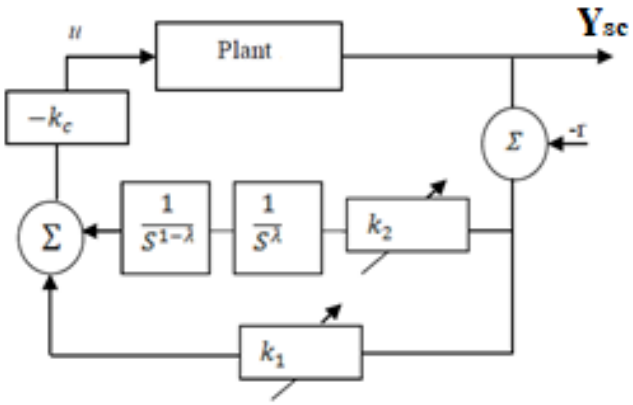


Figure 5. The proposed adaptive PI control system (AFOPI)

Results and Discussion

In this section, the simulation results of the proposed controller are obtained for a four-machine power system with the wind farm intergration under MATLAB-SIMULINK environment. The classic PI control and adaptive fractional PI control based STATCOM are compared in terms of bus voltages, line power, difference between rotor angle deviation of machine of wind turbine and machine 2, speed of the machines, terminal voltages of machines. The power coefficient and tip speed ration of the wind turbine is given by the Figure 6.

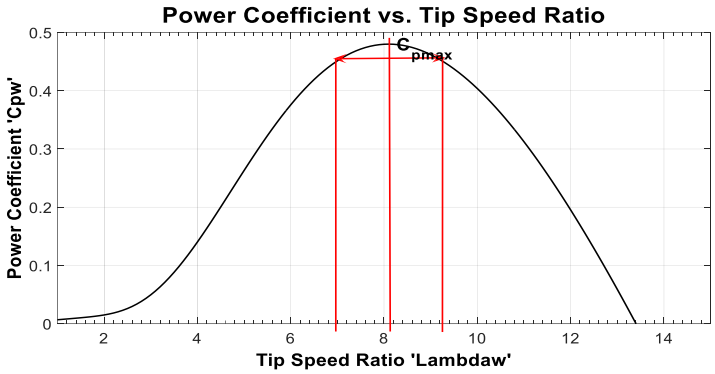


Figure 6. The power coefficient of the wind turbine

The Figure 7 shown the wind turbine characteristics in which the pitch angle is equal 0.

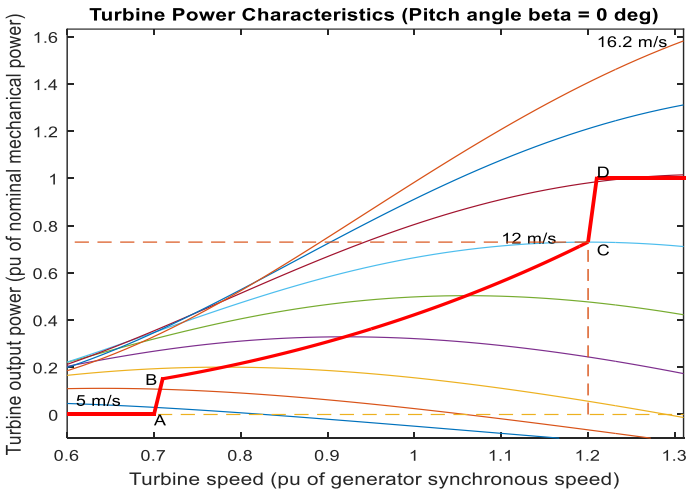


Figure 7. The power coefficient of the wind turbine

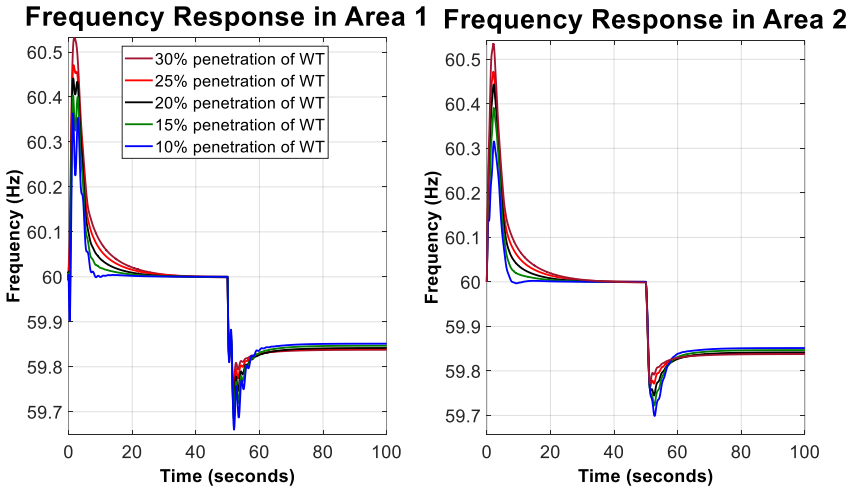


Figure 8. The frequency response

The results shown in figure 9 that, compared with different percentage penetration active power of the wind turbine, test system enhances the voltage profile, decreases active and reactive power losses, and increases power system stability in the power system. The frequency and the electrical power using the proposed controller have shown in Figure 10. It can be noted that the proposed controller decreases settling time of the load angle and increases the rate of damping of the frequency and the electrical power of the generators. As also shown in the figures, the suggested control method is able to make damping driving less than 2 to 3 seconds.

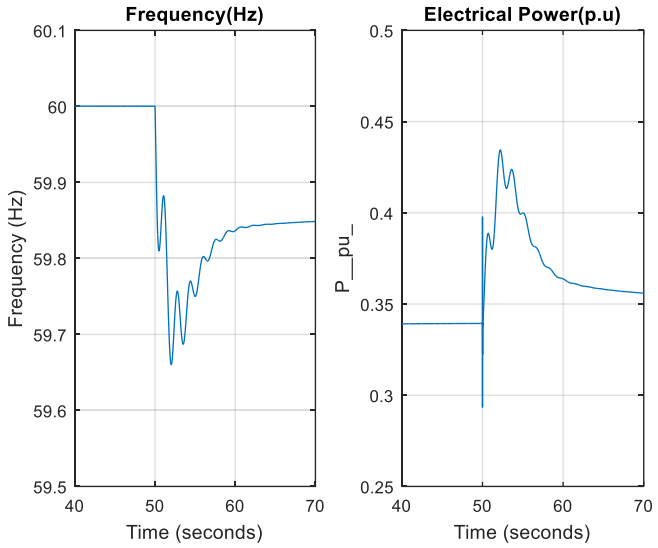


Figure 10. The frequency and the electrical power

The rotor speed and the electromagnetic torque of four machines is very high by using the proposed controller and the machines reach the desired speed in smaller time. The responses are illustrated in Fig.11.

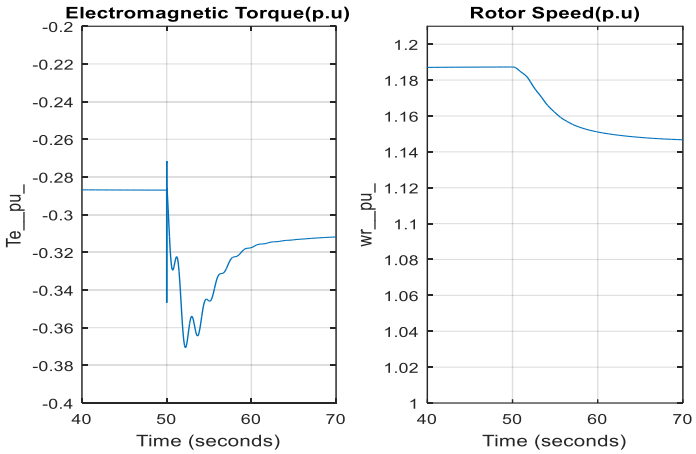


Figure 11. The electromagnetic torque and the rotor speed

By allocating the wind turbine integration and the STATCOM with the proposed controller, system losses are decreased, voltage regulation is enhanced, voltage deviation is reduced, and transient stability is improved.

Conclusion

Power systems parameters vary due to noise, disturbance and load fluctuation. Power system stabilizer (PSS), installed in the Automatic Voltage Regulator (AVR) of a generator, can improve power system stability. The PSS has excellent cost performance compared to other power system modifications or additions. In this paper, the STATCOM based an adaptive fractional PI controller for power system including wind farm is proposed. Simulations shows that the proposed controller reduces the amount of overshoot and the load angle meetings of each generator and increases in speed damping of the system. Results show that the proposed controller has superior accuracy and speed.

Scientific Ethics Declaration

* The authors declares that the scientific ethical and legal responsibility of this article published in EPSTEM journal belongs to the authors.

Conflict of Interest

* The authors declare that they have no conflicts of interest

Funding

* This research received no internal or external funding.

Acknowledgements or Notes

* This article was presented as an oral presentation at the International Conference on Technology, Engineering and Science (www.icontes.net) held in Antalya/Türkiye on November 12-15, 2025.

References

Abdelaziz, A. Y., Abu-Elnaga, M. M., Elsharkawy, M. A., & Elbahrawy, K. M. (2006). Voltage stability assessment of multi-machine power systems using energy function and neural networks techniques. *Electric Power Components and Systems, 34*(12), 1313-1330.

Basler, M. J., & Schaefer, R. C. (2005, April). Understanding power system stability. In *2005 58th Annual Conference for Protective Relay Engineers* (pp. 46-67). IEEE.

Calderon, A. J., Vinagre, B. M., & Feliu, V. (2006). Fractional order control strategies for power electronic buck converters. *Signal Processing, 86*(10), 2803–2819.

Cao, J., & Jiang, Z. (2011). Nonlinear dynamic analysis of fractional order rub-impact rotor system. *Communications in Nonlinear Science and Numerical Simulation, 16*(10), 1443-146.

Chaib, L., Choucha, A., & Arif, S. (2015). Optimal design and tuning of novel fractional order PID power system stabilizer using a new metaheuristic Bat algorithm. *Ain Shams Engineering Journal*.

Chathoth, I., Sreerama, K. R., & Sindhu, T. K. (2015). Fractional-order proportional-integral-derivative-based automatic generation control in deregulated power systems. *Electric Power Components and Systems, 43*(17), 1931-1945.

Delavari, H. (2015). A novel fractional adaptive active sliding mode controller for synchronization of nonidentical chaotic systems with disturbance and uncertainty. *International Journal of Dynamics and Control*, 1-13.

Delavari, H., Baleanu, D., & Sadati, J. (2012). Stability analysis of Caputo fractional-order nonlinear systems revisited. *Nonlinear Dynamics, 67*(4), 2433-2439.

Delavari, H., Faieghi, M. R., & Ranjbar, A. (2010). Fractional order sliding mode controller for inverted pendulum. In *Proceedings of the Fourth IFAC Workshop on Fractional Differentiation and Its Applications (FDA'10)*.

Delavari, H., Ghaderi, R., Ranjbar, A., & Momani, S. (2010). Fuzzy fractional order sliding mode controller for nonlinear systems. *Communications in Nonlinear Science and Numerical Simulation, 15*(4), 963–978.

Delavari, H., Lanusse, P., & Sabatier, J. (2013). Fractional order controller design for a flexible link manipulator robot. *Asian Journal of Control, 15*(3), 783-795.

Delavari, H., Ranjbar, A. N., Ghaderi, R., & Momani, S. (2010). Fractional order control of a coupled tank. *Nonlinear Dynamics, 61*(3), 383-397.

Efe, M. O. (2010). Fractional order sliding mode control with reaching law approach. *Turkish Journal of Electrical Engineering & Computer Sciences, 18*(5), 731-747.

El-Zonkoly, A. M., Khalil, A. A., & Ahmied, N. M. (2009). Optimal tunning of lead-lag and fuzzy logic power system stabilizers using particle swarm optimization. *Expert Systems with Applications, 36*(2), 2097-2106.

Faieghi, M., & Delavari, H. (2012). Control of an uncertain fractional-order Liu system via fuzzy fractional-order sliding mode control. *Journal of Vibration and Control, 18*, 1366-1374.

Golpira, H., Sheikh-El-Eslami, M. K., & Seifi, H. (2015). Power system stabilizer services pricing in an electricity market. *Electric Power Components and Systems, 43*(18), 2050-2058.

Kundur, P. (1994). *Power system stability and control*. McGraw-Hill.

Latha, R., Kanthalakshmi, S., & Kanagaraj, J. (2014). Design of power system stabilizer using fuzzy based sliding mode control technique. *arXiv*.

Li, C., & Tong, Y. (2013). Adaptive control and synchronization of a fractional-order chaotic system. *Pramana, 80*(4), 583-592.

Mehmood, C. A., & Kavasseri, R. G. (2015). On the use of fractional-order controllers for performance improvements in AC drives. *Electric Power Components and Systems, 43*(5), 485–490.

Monje, C. A., Chen, Y., Vinagre, B. M., Xue, D., & Feliu-Batlle, V. (2010). *Fractional-order systems and controls: Fundamentals and applications*. Springer.

Padiyar, K. R. (2008). *Power system dynamics*. BS Publications.

Petru, T., & Thiringer, T. (2002). Modeling of wind turbines for power system studies. *IEEE Transactions on Power Systems, 17*(4), 1132–1139.

Podlubny, I. (1998). *Fractional differential equations: An introduction to fractional derivatives, fractional differential equations, to methods of their solution and some of their applications* (Vol. 198). Academic Press.

Tapia, R., Aguilar, O., Minor, H., & Santiago, C. (2012). Power system stabilizer and secondary voltage regulator tuning for multi-machine power systems. *Electric Power Components and Systems, 40*(16), 1751–1767.

Wang, L., Chen, S.-S., Lee, W.-J., & Chen, Z. (2009). Dynamic stability enhancement and power flow control of a hybrid wind and marine current farm using SMES. *IEEE Transactions on Energy Conversion, 24*(3), 626–639.

Yu, Y. N., & Li, Q. H. (1990). Pole-placement power system stabilizers design of an unstable nine-machine system. *IEEE Transactions on Power Systems, 5*(2), 353-358.

Author(s) Information

Issam Griche
Bouira University, Faculty of Applied Sciences, Department of Electrical Engineering, , Algeria
Laboratory of Materials, Energy, Water and Environment Processes LPM3E, Bouira University,Bouira Algeria
Contct e-mail: *issam.grich@univ-bouira.dz*

Kamel Saoudi
Bouira University, Faculty of Applied Sciences, Department of Electrical Engineering, Algeria
Laboratory of Materials, Energy, Water and Environment Processes LPM3E, Bouira University,Bouira Algeria

Mourad Benziane
Bouira University, Faculty of Applied Sciences, Department of Electrical Engineering, Algeria
Laboratory of Materials, Energy, Water and Environment Processes LPM3E, Bouira University,Bouira Algeria

Abderrazak Arabi
Institute of Optics and Precision Mechanics, Ferhat Abbas Setif 1 University, 19000 Setif, Algeria

To cite this article:

Griche, I., Saoudi, K., Benziane, M., & Arabi, A. (2025). Power system stability including wind farm with Statcom based Pi fractional controller. *The Eurasia Proceedings of Science, Technology, Engineering and Mathematics (EPSTEM), 38*, 737–747.

The Eurasia Proceedings of Science, Technology, Engineering & Mathematics (EPSTEM)
ISSN: 2602-3199

The Eurasia Proceedings of Science, Technology, Engineering and Mathematics (EPSTEM), 2025

Volume 38, Pages 748-756

IConTES 2025: International Conference on Technology, Engineering and Science

LogSense: A Comparative Anomaly Detection Platform on Web Server Access Logs Using Multiple Algorithms

Arda Ata Turkoglu
Turkcell Payment and Electronic Money Services Inc.

Abstract: This study introduces LogSense, a platform developed for anomaly detection in large-scale web server access logs through a comparative analysis of machine learning algorithms. Three unsupervised approaches; k-Means, DBSCAN, and Isolation Forest were implemented to identify irregular patterns and abnormal traffic behaviors within server activity data. The platform establishes an end-to-end analytical workflow that includes parsing and cleaning log files, performing feature engineering, normalizing features, applying multiple algorithms, and visualizing anomalies through interpretable outputs such as SSD histograms and t-SNE projections. Experimental results show that k-Means is effective in detecting cluster-based outliers, DBSCAN identifies density-related irregularities with high clustering quality, and Isolation Forest isolates diverse anomalies with superior runtime performance. A subsequent cross-validation phase confirmed that anomalies consistently detected by multiple algorithms are highly reliable. Overall, this study underscores the value of proactive anomaly detection in web server security and highlights the complementary strengths of clustering, density, and ensemble-based learning approaches.

Keywords: Web server logs, Anomaly detection, k-Means, DBSCAN, Isolation forest

Introduction

Web servers serve as the backbone of modern digital services, facilitating e-commerce, communication, and information sharing. However, they are also prime targets for cyberattacks, including distributed denial of service (DDoS), brute-force login attempts, and data exfiltration. These attacks not only threaten data integrity but also compromise service availability and organizational reputation. While conventional intrusion detection systems (IDS) rely on known attack signatures, they fail against novel or obfuscated threats. Anomaly detection addresses this gap by flagging unusual patterns that deviate from expected behaviors. Web server access logs contain detailed request information; IP addresses, timestamps, HTTP methods, requested resources, response codes, and byte sizes that can be leveraged to detect such anomalies. Manual log inspection, however, is infeasible due to high data volume, diversity, and lack of labels. This necessitates automated approaches based on unsupervised learning.

Previous studies emphasize the relevance of clustering- and density-based approaches for intrusion detection. Chandola et al. (2009) provided a comprehensive survey highlighting their effectiveness, while Ahmed et al. (2016) evaluated DBSCAN and k-Means on noisy traffic data. More recently, Liu et al. (2008) introduced Isolation Forest, an ensemble method tailored for high-dimensional anomaly detection. Building upon these works, the present study proposes LogSense, an integrated anomaly detection and visualization platform designed for web server logs. The study further conducts a comparative evaluation of three algorithms; k-Means, DBSCAN, and Isolation Forest on real-world log data to assess their relative effectiveness in identifying irregular traffic behaviors and potential anomalies within web infrastructures.

Dataset

- This is an Open Access article distributed under the terms of the Creative Commons Attribution-Noncommercial 4.0 Unported License, permitting all non-commercial use, distribution, and reproduction in any medium, provided the original work is properly cited.

- Selection and peer-review under responsibility of the Organizing Committee of the Conference

© 2025 Published by ISRES Publishing: www.isres.org

The dataset was sourced from the Kaggle repository: Web Server Access Logs (Zaker, 2019). It contains HTTP access logs recorded by a Nginx server of an Iranian e-commerce site (*zanbil.ir*). The raw dataset is approximately 3.3 GB in size, consisting of millions of entries. Each log entry contains multiple descriptive fields capturing the details of client–server interactions. These include the client IP address, which identifies the source of the request; the timestamp, recording the exact date and time of access; and the HTTP method (such as GET or POST) indicating the type of operation performed. The entry also specifies the requested resource or URL, the server response code (for example 200, 404, or 500) that reflects the request outcome, and the response size in bytes, representing the volume of data returned to the client. The dataset enables comprehensive traffic analysis, covering normal browsing, search engine bots, user activity, and potentially malicious behavior.

Preprocessing and Feature Engineering

To prepare the raw web server log data for machine learning–based anomaly detection, a comprehensive preprocessing and feature engineering pipeline was designed and implemented. The process began with log parsing, which was handled through a custom-developed Python module named DataPreparationModule. This component was responsible for reading each raw log entry, parsing textual records, and extracting meaningful attributes such as the client IP address, timestamp, HTTP method, requested URL, response code, and response size. The parsing operation was designed to handle large-scale text files efficiently, filtering out nonconforming records and retaining only the relevant attributes required for analysis. For instance, the function show_raw_log() within the data module retrieves a defined number of sample log entries and presents them to the preprocessing interface for inspection and verification of parsing consistency.

Following the parsing phase, the data underwent cleaning and transformation procedures to ensure consistency and integrity across all records. Incomplete or corrupted entries were removed, duplicated lines were filtered, and the timestamp column was standardized into a uniform ISO 8601 format. These transformations were essential for aligning records across different time intervals and ensuring compatibility with time-series and clustering algorithms. Additionally, all numerical attributes such as request counts and response sizes were normalized using the MinMaxScaler technique. This normalization step mapped all feature values to the range, which helped prevent scale dominance during clustering and distance-based anomaly detection.

Once the dataset was cleaned and normalized, the process continued with feature engineering, where several higher-level metrics were derived from the base attributes to enrich the model's ability to detect anomalies. The engineered features included the total number of requests per IP address, the daily mean request count, the ratio of successful requests (amount of http 200 responses), and statistical measures of the response size such as mean and standard deviation. Moreover, the average time difference between consecutive requests was calculated to capture temporal irregularities in client behavior, which often indicate automated or malicious activity. This stage resulted in a refined dataset that was both statistically consistent and semantically enriched, forming a robust foundation for the subsequent anomaly detection algorithms. The distributions of the engineered features revealed diverse behavioral patterns among client IPs, serving as an early indicator of potential outlier activities.

IP	Total Requests	Daily Mean	GET requests	Successful requests	Mean Return Size	Return Size Std	Mean Time Difference
1.43.175.52	1	1.0	0	1	133.000000	0.000000	0.000000
10.104.208.32	96	96.0	0	92	8843.968750	23508.725105	1.322917
10.105.14.186	8	8.0	0	8	15811.625000	31895.242032	116.000000
10.106.247.163	41	41.0	0	39	20207.731707	37423.013698	3.829268
10.113.251.50	76	76.0	0	60	15093.394737	30716.590386	10.144737
10.114.1.2	84	84.0	0	81	20848.321429	41419.496079	2.035714
10.114.139.15	2	2.0	0	2	94646.000000	0.000000	4680.000000
10.114.98.6	3	3.0	0	3	24592.000000	11198.807660	408.666667
10.116.12.43	37	37.0	0	36	13934.918919	25759.936819	0.189189
10.124.2.223	2	2.0	0	2	4071.000000	135.764502	1.500000

Figure 1. Sample view of engineered features.

Algorithms

k-Means Clustering

The k-Means clustering algorithm was employed as the first approach for detecting anomalies within the preprocessed dataset. This algorithm partitions the dataset into a predefined number of clusters (Chandola et al,

2009), denoted by k, with the goal of minimizing the variance within each cluster. Mathematically, k-Means aims to minimize the objective function given by:

$$\arg\min_{S} \sum_{i=1}^{k} \sum_{x \in S_i} |x - \mu_i|^2$$

where μ_i represents the centroid of the cluster S_i. In essence, each data point is assigned to the cluster whose centroid is nearest in Euclidean space, thereby reducing intra-cluster variance.

In the context of this study, k-Means was implemented to uncover structural groupings among client IPs based on their behavioral patterns derived from the engineered features. The number of clusters, k, was determined empirically using the Elbow Method, which analyzes the trade-off between the number of clusters and the corresponding Sum of Squared Distances (SSD). The "elbow point" in the curve indicates where adding additional clusters no longer yields substantial improvement in clustering quality (Figure 2). This point was used to select the optimal k value for the dataset.

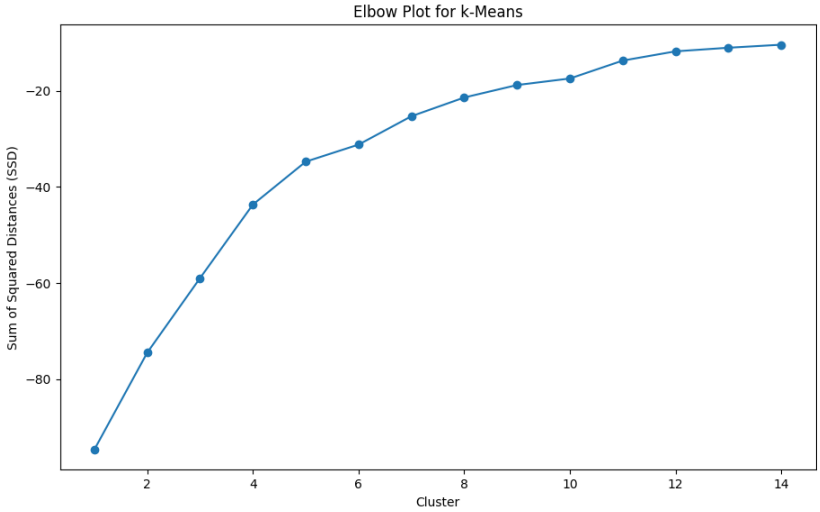


Figure 2. Elbow plot for k-Means.

Once the optimal cluster count was determined, data points with exceptionally high SSD values were labeled as outliers, since they were positioned far from any cluster centroid. The distribution of these SSD values, visualized in Figure 3, provides a clear distinction between normal and anomalous observations. Anomalies appear in the long-tail region beyond the threshold cutoff. To further illustrate the spatial relationships among data points, a t-distributed Stochastic Neighbor Embedding (t-SNE) projection was used.

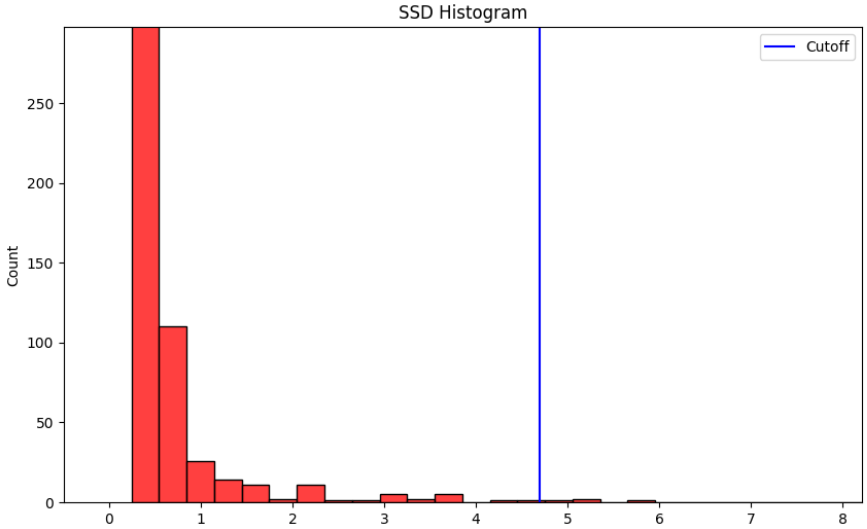


Figure 3. SSD histogram.

As depicted in Figure 4, this two-dimensional visualization of the high-dimensional feature space reveals the structure of clusters and highlights outliers located at the periphery of dense regions. The LogSense platform integrates these visualization tools; Elbow Plot, SSD Histogram, and t-SNE projection into a unified interface, offering both analytical precision and interpretability in identifying anomalous web activity.

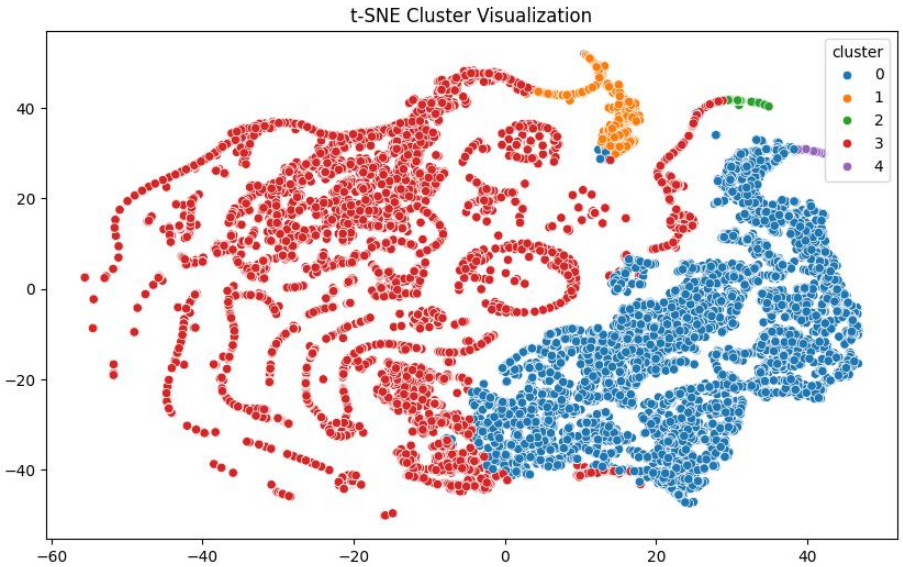


Figure 4. t-SNE cluster visualization.

DBSCAN

The Density-Based Spatial Clustering of Applications with Noise (DBSCAN) algorithm was adopted as the second method in the study. (Ester, Kriegel, Sander, & Xu, 1996) Unlike k-Means, which requires the number of clusters to be predefined, DBSCAN is a density-based clustering algorithm that groups data points according to their spatial proximity and local density, making it particularly effective for datasets with irregular cluster shapes or varying densities. The theoretical foundation of DBSCAN is based on two key parameters: the neighborhood radius ϵ\epsilonϵ and the minimum number of points, *min_samples*, required to form a dense region. A point is defined as a *core point* if it has at least *min_samples* neighboring points within the ϵ\epsilonϵ-radius. Points that are within the neighborhood of a core point are considered *reachable points*, while those that do not meet this condition are labeled as *noise* or anomalies.

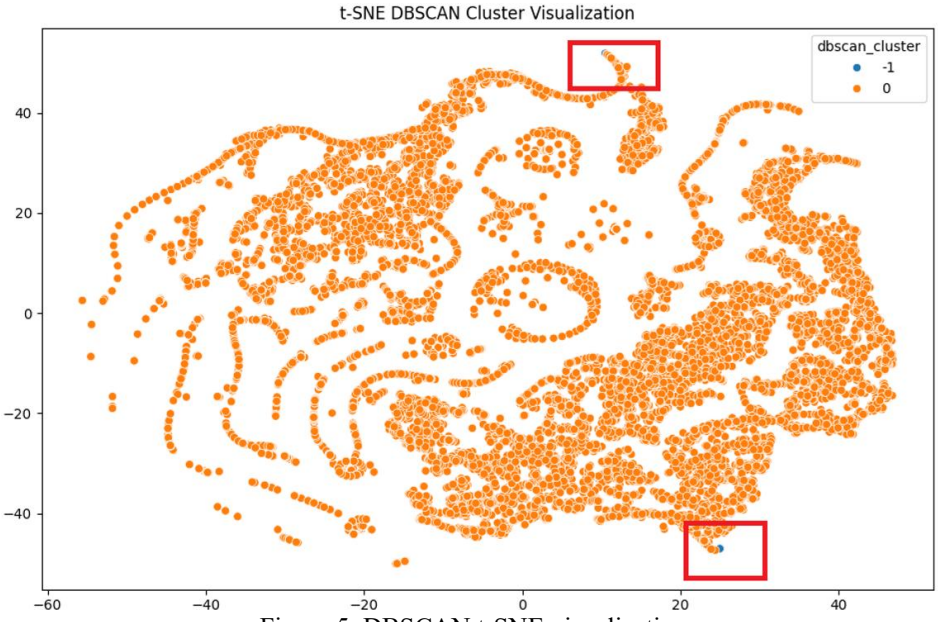


Figure 5. DBSCAN t-SNE visualization.

Formally, for a given point p, its neighborhood is defined as $N_\epsilon(p) = \{ q \in D \mid \text{dist}(p, q) \leq \epsilon \}$. If the cardinality of $N_\epsilon(p)$ is greater than or equal to *min_samples*, p is classified as a core point. In this study, the DBSCAN parameters were set to $\epsilon = 0{,}15$ and $min\ samples = 5$ after iterative experimentation, which provided the most balanced clustering quality based on silhouette scores and noise point detection rates. DBSCAN demonstrated high robustness in identifying outliers corresponding to low-density areas in the feature space, which often indicated unusual client request behaviors, such as abnormally frequent requests or extreme byte transfers. Furthermore, since DBSCAN autonomously determines the number of clusters, it eliminated the need for prior assumptions about cluster count, allowing for a more data-driven analysis of traffic irregularities.

To visualize the results, the LogSense platform employed t-SNE projections for cluster interpretation and color-coded anomaly highlighting. t-SNE visualization (Figure 5) displays the two-dimensional projection of DBSCAN clustering results, where each color represents a distinct cluster and blue points (labeled –1) denote anomalies located in sparse, low-density regions of the feature space. The regions enclosed by red rectangles highlight areas containing these anomalies to emphasize their positions and improve visual interpretability.

Isolation Forest

The third method integrated into the LogSense platform was the Isolation Forest algorithm, an ensemble-based anomaly detection technique specifically designed for high-dimensional datasets (Liu et al., 2008). Isolation Forest operates on the principle that anomalies are rare and differ significantly from normal instances, which makes them easier to isolate using random partitioning. Instead of modeling normal behavior explicitly, Isolation Forest isolates observations by recursively dividing the dataset through randomly selected attributes and split values.

The anomaly score for a given instance x is derived from the average path length $E\big(h(x)\big)$ of x in a forest of randomly generated trees and is computed using the following formula:

$$s(x, n) = 2^{-\frac{E(h(x))}{c(n)}}$$

$E(h(x))$ represents the average number of splits required to isolate x, and $c(n)$ denotes the average path length in a binary tree built on n samples. Instances with shorter average path lengths are considered more anomalous, as they are isolated more quickly.

For this study, the Isolation Forest implementation utilized 100 estimators (trees), and the contamination parameter was automatically inferred from the data distribution to estimate the proportion of anomalies. Each tree was trained on a random subsample of the dataset, enhancing the model's generalization capability and reducing overfitting risk. Isolation Forest proved to be both efficient and effective in detecting subtle deviations in web log patterns. Due to its linear time complexity and scalability, it processed the entire 3.3 GB dataset with an average runtime of 1.66 seconds, outperforming both k-Means and DBSCAN in terms of computational efficiency. The algorithm identified numerous anomalies characterized by irregular request intervals, inconsistent return sizes, and sudden surges in daily activity.

Results and Discussion

The experimental evaluations conducted in this study aimed to measure the performance, sensitivity, and consistency of the three anomaly detection Algorithms; k-Means, DBSCAN, and Isolation Forest when applied to the large-scale web server access log dataset. Each algorithm was executed on the same normalized feature set derived from the preprocessing pipeline, and their outcomes were analyzed both quantitatively and visually. The comparative discussion below integrates numerical results, behavioral interpretations, and cross-method validations to provide a holistic understanding of anomaly detection performance within the **LogSense** platform. Earlier comparative works on model-based network intrusion detection have demonstrated similar differences between tree-based and clustering algorithms. (Zhang, Zulkernine, & Haque, 2008)

K-Mean Results

The k-Means algorithm produced well-structured clusters that captured distinct behavioral patterns among client IP addresses. Using the Elbow method, the optimal number of clusters was determined as k = 5, corresponding to a clear inflection point where the Sum of Squared Distances (SSD) began to stabilize. The resulting model achieved a Silhouette Score of 0.618, indicating moderately well-separated and compact clusters, which is acceptable given the heterogeneous nature of web traffic data.

Within this configuration, seven anomalies were identified as data points exhibiting exceptionally large distances from their nearest centroids. The anomalous instances represented approximately 0.46% of the total dataset. Detailed examination revealed that these anomalies were characterized by an average daily request count of approximately 10,060, which was nearly eight times higher than the population mean. Similarly, their mean return size was around 113 KB, compared to a dataset-wide average of 37 KB, suggesting unusually heavy data transfers. Moreover, the mean time difference between consecutive requests (≈9,165 ms) was significantly longer than typical client behavior, potentially indicating irregular communication intervals caused by automated scripts or intermittent scraping activities.

Visual analysis using the SSD histogram provided an intuitive separation between normal and anomalous instances, where anomalous observations formed a long-tail distribution at the far end of the SSD axis. The t-SNE projection further demonstrated that anomalous points were spatially distant from any dense cluster region, confirming their deviation from the typical access patterns.

Table 1. Statistical summary of k-Means anomalies

Variables	Mean	Std
Total Requests	10060	14352
Successful Requests	7325	11265
Mean Return Size	113268	165742
Return Size Std	88951	107480
Mean Time Difference	9165	8387

DBSCAN Results

The DBSCAN algorithm yielded the highest clustering quality among the three approaches, achieving a Silhouette Score of 0.951, which reflects a highly coherent separation of dense and sparse regions within the feature space. Unlike k-Means, DBSCAN automatically discovered the number of clusters, which in this dataset resulted in six distinct dense regions representing normal user behaviors and one sparse region corresponding to anomalous patterns. The algorithm identified seven anomalous instances, matching the number detected by k-Means, but with slight differences in composition. The detected anomalies corresponded to clients whose activity was either excessively frequent or characterized by extreme data volume transfers. Specifically, these instances showed an average request count of 11,396 per day, a mean return size of 146 KB, and a mean response time of approximately 4,267 ms. These values exceeded the median of the overall dataset by factors of 9.4, 3.9, and 4.8, respectively.

DBSCAN's density-based framework allowed it to effectively distinguish normal clustered behavior from outlying low-density points. The resulting t-SNE projection highlighted how these anomalies were isolated from the main population, appearing as scattered singletons with no local neighborhood support. This observation indicates that DBSCAN can capture anomalies that are density-independent such as sporadic high-volume access attempts without the need to predefine the number of clusters. The comparative visualization between k-Means and DBSCAN confirmed that four of the anomalies were common to both algorithms, suggesting high confidence in their abnormality. The remaining three anomalies detected exclusively by DBSCAN represented borderline cases, which were slightly distant but not far enough to be isolated by centroid-based distance measures.

Table 2. Statistical summary of DBSCAN anomalies

Variables	Mean	Std
Total Requests	11396	11749
Successful Requests	8817	9347
Mean Return Size	146735	193675
Return Size Std	98169	100636
Mean Time Difference	4267	7288

Isolation Forest Results

The Isolation Forest algorithm exhibited the highest sensitivity among the tested models, identifying a much larger number of anomalies compared to both k-Means and DBSCAN. The method isolated 229 anomalous instances, corresponding to approximately 15.1% of the dataset, while maintaining an average runtime of 1.66 seconds, making it the fastest of the three. The anomalies detected by Isolation Forest displayed highly variable statistical behavior. The mean request count per day for these instances was approximately 1,171, but with an exceptionally high standard deviation of 3,240, indicating that the anomalies were not uniform in frequency. Similarly, their average return size was 35 KB with a large dispersion (std. dev. ≈ 39 KB), and their average response time was 354 seconds, suggesting irregular or stalled connections. These characteristics collectively signify that Isolation Forest captured both extreme outliers and subtler irregularities missed by clustering-based methods.

An important observation was that many of the anomalies flagged by Isolation Forest corresponded to clients with fluctuating activity patterns; users who alternated between normal and abnormal behavior within short time windows. This sensitivity demonstrates the strength of ensemble-based isolation mechanisms but also introduces a trade-off: while the algorithm can detect a broader spectrum of anomalies, it also yields a higher number of potential false positives, particularly in non-stationary data. Visual inspection of anomaly scores revealed a bimodal distribution, with a clear separation between the majority of normal samples and a smaller group of high-score anomalies. The t-SNE visualization confirmed this separation, where outliers formed diffuse, isolated clusters at the periphery of the feature space.

Table 3. Statistical summary of Isolation Forest anomalies

Variables	Mean	Std
Total Requests	11171	27779
Successful Requests	10041	22197
Mean Return Size	35674	77261
Return Size Std	39262	59199
Mean Time Difference	354	1664

Comparative Analysis

A comparative evaluation across the three algorithms provided deeper insights into their relative strengths and complementary behavior. K-Means and DBSCAN demonstrated high consistency, both detecting seven anomalies and sharing four identical results. This overlap indicates that both algorithms are effective at identifying extreme, well-defined deviations instances that are simultaneously distant from cluster centers and located in low-density regions. These anomalies can be considered “high-confidence” irregularities.

By contrast, Isolation Forest exhibited far greater sensitivity, capturing 229 anomalies. Although this broader detection scope encompasses more false positives, it also highlights its suitability for early-stage or exploratory anomaly detection, where coverage is prioritized over precision. When the anomalies detected by all three methods were cross-compared, approximately 82% of Isolation Forest’s anomalies were unique, reflecting its ability to identify subtle patterns overlooked by clustering-based methods.

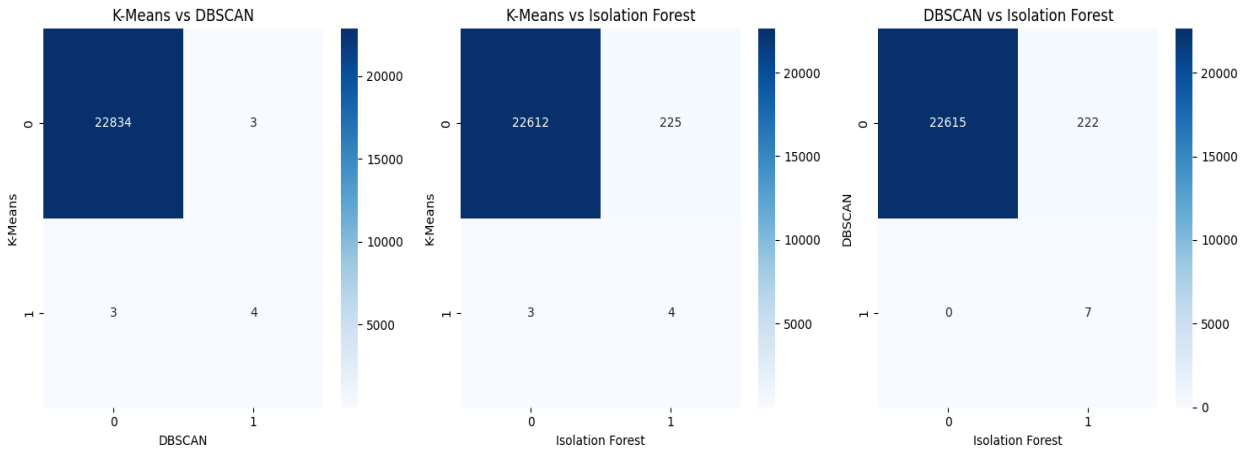


Figure 6. Pairwise comparative analysis of anomaly detection results

From a computational perspective, Isolation Forest also proved superior in terms of efficiency, completing its analysis in under two seconds, compared to approximately 3.4 seconds for k-Means and 5.1 seconds for DBSCAN. This runtime advantage stems from its logarithmic time complexity, making it particularly scalable for future real-time detection integration. An aggregated visualization comparing the anomalies detected by each algorithm reinforced these conclusions (Figure 6). The bar chart summarizing anomaly counts and overlaps demonstrated that k-Means and DBSCAN were highly aligned, while Isolation Forest contributed additional anomalies not captured by the other two.

Overall, these findings suggest that while clustering and density-based algorithms excel at precision-oriented anomaly detection, ensemble-based models like Isolation Forest are better suited for comprehensive anomaly screening. The combination of these methods integrated within the LogSense platform provides a balanced framework, enabling both high-confidence identification and broad-spectrum anomaly discovery.

Conclusion

This study presented LogSense, an integrated anomaly detection platform developed to identify and interpret irregular behaviors in large-scale web server access logs. By combining clustering-based algorithms (k-Means and DBSCAN) with an ensemble approach (Isolation Forest), the system demonstrated that unsupervised learning methods can effectively reveal both prominent and subtle anomalies in real-world traffic data. The experimental findings showed that k-Means excels at identifying well-separated statistical outliers, while DBSCAN detects anomalies in sparse or irregularly distributed regions of the feature space. In contrast, Isolation Forest isolates a broader range of anomalies efficiently, offering faster runtime performance due to its ensemble-based design. The overlapping detection patterns between these algorithms confirmed that a hybrid combination improves both precision and coverage.

Methodologically, LogSense established a complete and interpretable pipeline from preprocessing raw HTTP logs to visualizing anomalies through SSD histograms and t-SNE projections. This workflow demonstrated how structured log features such as request frequency, response size variability, and inter-request timing can meaningfully represent behavioral deviations, even in unlabeled and heterogeneous data. The platform therefore bridges the gap between machine learning theory and operational log analysis, providing a scalable foundation for data-driven web security monitoring.

Recommendations

While LogSense achieved notable accuracy and interpretability, several opportunities remain for enhancement. A key future direction involves extending the platform toward real-time anomaly detection, enabling the identification of threats and performance bottlenecks as they occur. Incorporating stream processing frameworks such as Apache Kafka or Spark Streaming would allow the system to handle continuous log flows effectively. Furthermore, integrating deep learning techniques including autoencoders, LSTM-based sequence models, and Graph Neural Networks (GNNs) could enable the platform to capture temporal dependencies and relational interactions among log entities, improving its understanding of complex attack patterns.

Another promising area is the hybridization of rule-based and machine learning approaches, where algorithmic outputs are validated by contextual rules such as frequency thresholds or response code logic. This integration would reduce false positives and align detection results more closely with operational definitions of abnormal behavior. Finally, expanding LogSense's application scope beyond cybersecurity could yield broader analytical value. The same framework can be adapted for performance optimization, user behavior modeling, and resource allocation analysis, transforming it into a general-purpose platform for log intelligence and observability in large-scale web systems.

Scientific Ethics Declaration

* The author declares that the scientific ethical and legal responsibility of this article published in EPSTEM journal belongs to the author.

Conflict of Interest

* The author declares that they have no conflicts of interest

Funding

* This research received no internal or external funding.

Acknowledgements or Notes

* This article was presented as an oral presentation at the International Conference on Technology, Engineering and Science (www.icontes.net) held in Antalya/Türkiye on November 12-15, 2025.

References

Ahmed, M., Mahmood, A. N., & Hu, J. (2016). A survey of network anomaly detection techniques. *Journal of Network and Computer Applications, 60*, 19-31.

Bridges, S. M., & Vaughn, R. B. (2000). Intrusion detection via fuzzy data mining. In *Proceedings of the 12th Annual Canadian Information Technology Security Symposium*.

Chandola, V., Banerjee, A., & Kumar, V. (2009). Anomaly detection: A survey. *ACM Computing Surveys, 41*(3), 1-58.

Ester, M., Kriegel, H.-P., Sander, J., & Xu, X. (1996). A density-based algorithm for discovering clusters in large spatial databases with noise. In *Proceedings of the Second International Conference on Knowledge Discovery and Data Mining (KDD-96)* (pp. 226-231). AAAI Press.

García, S., Zunino, A., & Campo, M. (2019). Survey on network-based intrusion detection data sets. *Computers & Security, 86*, 147-167.

Kim, Y., & Kim, J. (2019). Web traffic anomaly detection using LSTM autoencoder. *IEEE Access, 7*, 160040-160052.

Liu, F. T., Ting, K. M., & Zhou, Z.-H. (2008). Isolation forest. In *Proceedings of the 2008 IEEE International Conference on Data Mining (ICDM)* (pp. 413-422). IEEE.

Zhang, J., Zulkernine, M., & Haque, A. (2008). Random-forests-based network intrusion detection systems. *IEEE Transactions on Systems, Man, and Cybernetics, Part C (Applications and Reviews), 38*(5), 649-659.

Author(s) Information

Arda Ata Turkoglu
Turkcell Payment and Electronic Money Services Inc., (Paycell R&D Center)
Istanbul, Türkiye
Contact e-mail: *arda.turkoglu@turkcell.com.tr*

To cite this article:

Turkoglu, A. A. (2025). LogSense: A comparative anomaly detection platform on web server access logs using multiple algorithms. *The Eurasia Proceedings of Science, Technology, Engineering and Mathematics (EPSTEM), 38,* 748-756.

The Eurasia Proceedings of Science, Technology, Engineering & Mathematics (EPSTEM)
ISSN: 2602-3199

The Eurasia Proceedings of Science, Technology, Engineering and Mathematics (EPSTEM), 2025

Volume 38, Pages 757-770

IConTES 2025: International Conference on Technology, Engineering and Science

Enhancing Wireless Sensor Networks Performance by Integrating Particle Swarm Optimization with Intelligent Clustering Techniques

Rafa Sami Braiber
University of Mustansiriyah

Mussab Riyadh
University of Mustansiriyah

Abstract: Wireless sensor networks play a crucial role in various applications, including industrial automation, healthcare, and environmental monitoring. Energy consumption remains a major challenge due to the limited energy of sensor nodes. This study utiliz-es FCM, Heuristic, K-Means, DBSCAN, and PSO to enhance network performance and longevity. K-Means balances clusters, DBSCAN detects dense regions, FCM assigns flexible memberships, and heuristic clustering adjusts clusters based on energy and base station proximity. The proposed method dynamically selects cluster heads based on energy levels and base station proximity. PSO optimizes selection by evaluating intra-cluster distances and residual energy, enabling dynamic reselection for improved efficiency, lower transmission costs, and extended network lifespan. Simulations show high energy savings in FCM (1.7213J for 50 nodes, 5 clusters), while K-Means depletes energy the fastest (1.5394J for 150 nodes) and DBSCAN consumes the most energy (1.0258J), rendering it unsuitable for longevity-focused applications. FCM ensures the longest network lifespan (904 iterations), compared to K-Means (483 iterations) and Heuristic (443 iterations). In terms of latency, K-Means experiences the highest delays (1.5s), while FCM and heuristic clustering maintain lower delays around 1.0s or less. The hybrid FCM-PSO approach reduces energy consumption by 12–15% and extends network lifespan by 20%.

Keywords: Energy efficiency, Cluster head selection, Particle swarm optimization (PSO), Heuristic clustering

Introduction

Wireless sensor networks have been used in a variety of fields including industrial automation, healthcare, and military surveillance has grown significantly in importance (Majid et al., 2022). As sensor nodes typically operate on batteries and have a restricted amount of electricity available, WSNs require energy (Riaz et al., 2021). Poor energy management leads to node failure, which causes the network to collapse more quickly (Miglani etal., 2020). Therefore, clustering techniques are used to help distribute and connect the network efficiently, as well as to select Cluster Heads more effectively, improving network performance and extending its lifespan (Lata et al., 2020). Traditional techniques are ineffective in large networks with a high number of nodes, leading to network failure due to poor connectivity and improper Cluster Head selection (Zaiter et al., 2025). Selecting Cluster Heads optimally enhances network efficiency and extends its lifespan (Sucasas et al., 2016). Traditional clustering algorithms like K-Means, DBSCAN, and Fuzzy C-Means (FCM) are commonly used for CH selection but have limitations. K-Means requires prior knowledge of cluster numbers and ignores energy constraints, leading to uneven energy distribution (Abdulaal et al., 2024). DBSCAN struggles in dynamic environments and non-uniform node densities, while FCM incurs high computational costs and energy inefficiencies due to overlapping cluster memberships (Albasri et al., 2022). This study explores an integrated clustering mechanism with PSO to optimize CH selection, balance energy consumption, and improve WSN adaptability. Although it distributes nodes into clusters efficiently but ignores energy levels, causing high-energy nodes that have been assigned by cluster heads to quickly drop (Jan et al., 2017). DBSCAN method is

- This is an Open Access article distributed under the terms of the Creative Commons Attribution-Noncommercial 4.0 Unported License, permitting all non-commercial use, distribution, and reproduction in any medium, provided the original work is properly cited.

- Selection and peer-review under responsibility of the Organizing Committee of the Conference

© 2025 Published by ISRES Publishing: www.isres.org

identified by density-based clustering. FCM offers a more adaptable clustering technique by enabling nodes to be a part of several clusters with different levels of membership (Shafi et al., 2024). It is computationally de-manding more tuning is required for energy efficiency. Heuristic clustering methods enhance node organization by employing rule-based clustering techniques (Sert & Yazici, 2021). Despite their superior energy efficiency, it is unable to dynamically adjust to node energy depletion. PSO is unable to control clustering requires integration with clustering algorithms to improve performance (Alam et al., 2014). The work combines K-Means, DBSCAN, FCM, heuristic algorithms, and PSO to provide an energy-efficient clustering solution for WSNs in order to overcome over the disadvantages of traditional clustering strategies (Kaddi et al, 2024). The proposed method optimizes cluster head selection based on node density in order to increase network durability residual energy levels, and base station distance. The method dynamically adjusts to network changes by routinely updating cluster heads and reassessing node energy levels, ensuring balanced energy usage and extended network operations (Raj & Duraipandian, 2023).

Related Work and Theoretical Background

Related Work

Zagrouba & Kardi (2021) proposed to improve energy efficiency, reduce delays, and increase scalability. The study investigates methods that enhance clustering in WSNs. It categorizes clustering methods into meta-heuristic, fuzzy logic, and hybrid approaches, and compares protocols based on cluster size, CH selection, and energy consumption. Jubair et al. (2021) presented several WSN routing protocols are presented and categorized into nine groups, including network topology-based and latency-aware approaches. It analyzes energy usage and network longevity by evaluating protocols such as LEACH, Mod-LEACH, iLEACH, E-DEEC, multichain-PEGASIS, and M-GEAR using NS3 simulations. The study emphasizes how crucial intelligent routing is to maximizing WSN performance and guaranteeing network sustainability. Kavya & Ravi (2021) presented energy-efficient routing strategies for WSNs, with a particular emphasis on clustering-based approaches such as LEACH and its variations. It examined packet delivery, scalability, and energy consumption while contrasting threshold-based, bio-inspired, and hierarchical CH selection techniques. Adaptive and hybrid clustering enhances efficiency according to the results, bio-inspired techniques maximize CH selection. But there are still prob-lems with synchronization and control. Behera, et al. (2022) improved the efficiency of Wireless Sensor Networks (WSNs) by utilizing machine learning techniques and leveraging swarm intelligence methods to enhance network performance. Rizky et. al. (2024) proposed an improved Multi-Channel Clustering Hierarchy method for WSNs. They used four-channel clustering with odd-even activation to cut congestion and save energy. The method optimized energy and minimized congestion; it lowers throughput as nodes are not always active. Throughput values were 1.88, 1.68, 1.62, and 2.22 for Channels 1 to 4, with Channel 4 having the highest packet loss (0.616) and Channel 2 the highest delay (0.0039). In this paper covers energy-efficient cluster head selection, literature review, theoretical background, meth-odology, simulation results, and comparative analysis, concluding that hybrid clustering with PSO improves energy efficiency, extends network lifespan, and optimizes data transmission. Latiff et. al. (2007) used PSO for dynamic CH selection and demonstrated its ability to balance load and reduce energy consumption.

Theoretical Background

Wireless Sensor Networks (WSNs) are vital for applications like environmental monitoring and industrial automation, but their sensor nodes limited energy resources make achieving energy efficiency crucial for ensuring long net-work lifetimes (Rashid & Rehmani, 2016).

Wireless Sensor Networks (WSNs)

Wireless Sensor Networks are essential in environmental monitoring, healthcare, military applications, and industrial automation. It consists of multiple sensor nodes distributed across a predefined area. These nodes collect data and transmit it to the Base Station (BS) as see in Figure1. Since sensor nodes possess limited energy resources, achieving energy efficiency remains a crucial challenge for ensuring long network lifetimes (Kalaimani et al., 2021). Low-Energy Adaptive Clustering Hierarchy (LEACH) protocol optimize energy consumption. LEACH dynamically rotates Cluster Head (CH) roles among nodes, operating in setup and steady-state phases. CH selection occurs probabilistically using a threshold function, ensuring balanced energy usage and extended network lifespan. Each node generates a random value between 0 and 1, if this value falls

below a predetermined threshold, the node becomes a CH for the current round (Khudhair, 2025). The threshold function is expressed in equation 1 bellow.

$$\boldsymbol{T(n)} = \frac{\boldsymbol{P}}{\boldsymbol{1-P\times\left(rmod\,\frac{1}{P}\right)}} \text{ .if n}\in\text{G} \qquad \text{Eq.(1)}$$

The LEACH protocol provides each node a probability (P) of becoming a Cluster Head (CH) during each round. The set (G) consists of nodes that were not CHs in the previous (1/P) rounds. A node within (G) produces a random number, when it is under a computed threshold, the node turns into a CH. During the setup phase, selected CHs transmit advertisements while non-CH nodes connect to the CH that has the strongest received signal (Al-Baz & El-Sayed, 2018). The steady-state phase follows, where data transmission takes place. Each CH creates a Time Division Multiple Access (TDMA) schedule for its cluster members, assigning them specific time slots for data transmission to avoid collisions. Node's sense environmental parameters and transmit data to their CHs, which aggregate the data and forward it to the BS in a single transmission. In each cycle, the Iteration of the Cluster Head is updated, and the process is repeated to ensure balanced energy consumption in the network (Tambawal et al., 2019).

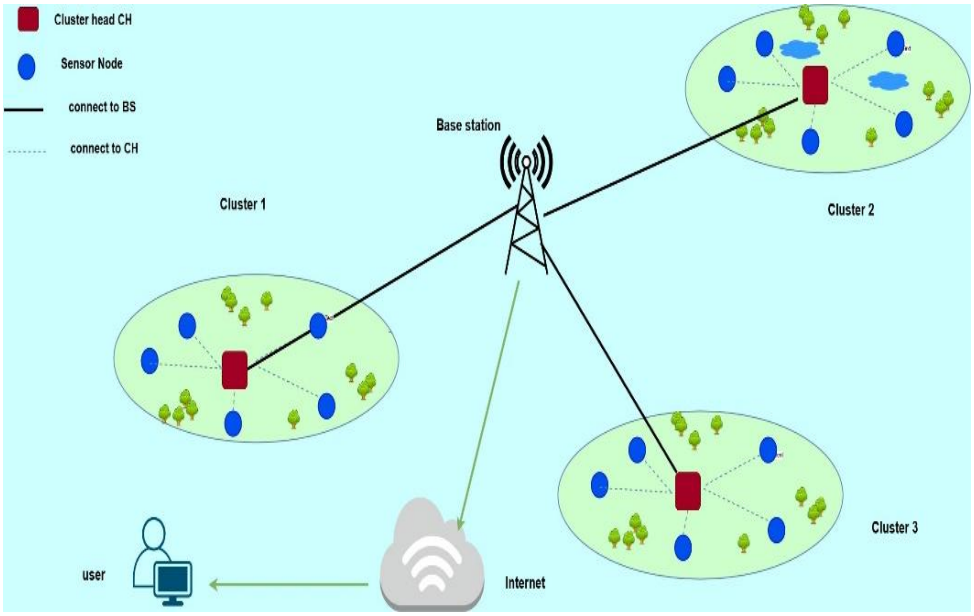


Figure. 1. Cluster-based wireless sensor network (WSN) architecture with data transmission to the base station

Clustering Techniques in Wireless Sensor Networks (WSNs)

Common clustering techniques include K-Means, DBSCAN, and Fuzzy C-Means (FCM), where the selection of a technique depends on network limitations, application requirements, and available energy (Miraftabzadeh et al., 2023; Omran et al., 2025). K-Means Clustering: It is a centroid-based algorithm that organizes sensor nodes into clusters based on spatial proximity. After determining number of cluster (k) centroids then assigns each node to the nearest centroid using the Euclidean distance formula as shown in equation (2) (Peter et al., 2019):

$$d(i.j) = \sqrt{(x_i - x_j)^2 + (y_i - y_j)^2} \qquad \text{Eq.(2)}$$

where d(i,j) represents the distance between node, and (x, y) are the coordinates of the respective nodes. the centroids are recalculated by determining the average of all node positions within each cluster (Kamil, 2017).

$$C_j = \frac{1}{N_j}\sum_{i=1}^{N_j} X_i \qquad \text{Eq.(3)}$$

where Cj denotes the updated centroid of cluster j, Nj indicates the count of nodes in cluster j, and Xi represents the position of nodes inside of the cluster. The continuing process continues on until the centroids transform into stable. K-Means is computationally efficient and provides clear cluster separation. It performs not assume energy levels into account when selecting CHs (Tambawal et al., 2019). DBSCAN (Density-Based Spatial

Clustering of Applications with Noise): DBSCAN is a density-based clustering algorithm that identifies dense regions of sensor nodes and groups them into clusters based on a predefined radius (ε) and a minimum number of points (MinPts). The algorithm initiates by selecting a node that has not been visited and calculates the number of neighboring nodes within distance ε using as shown in equation (4) (Kamil, 2017):

$$d(i.j) \leq \varepsilon \qquad \text{Eq.(4)}$$

where d(i,j) represents the Euclidean distance between nodes i and j. DBSCAN effectively detects clusters of arbitrary shapes and identifies outliers but struggles in networks with sparse deployments or varying node densities, making it less adaptable to dynamic WSN environments (Kamil, 2017). Fuzzy C-Means Clustering: it is contrast to rigid clustering techniques by permits nodes to belong to multiple clusters with variance degrees of membership. The algorithm assigns membership values to each node based on its proximity to different cluster centers, calculated using (Jamel & Akay, 2019):

$$uij = \frac{1}{\sum_{k=1}^{C}(\frac{d_{ij}}{d_{ik}})^{\frac{2}{m-1}}} \text{ Eq.(5)}$$

where uij represents the membership of node i in cluster j, dij is represent Euclidean distance between node and cluster center, and m is represent the fuzziness parameter the cluster are updated iteratively by using (Jamel & Akay, 2019):

$$C_j = \frac{\sum_{i=1}^{N} u_{ij}^{m} Xi}{\sum_{i=1}^{N} u_{ij}^{m}} \qquad \text{Eq.(6)}$$

Whe re Cj is the updated cluster center, and N is the number of nodes in the network. The process repeats until membership values stabilize. heuristic-based approaches create clusters dynamically according to specific criteria such as node density, spatial distribution, energy levels, and application-specific constraints.

Particle Swarm Optimization (PSO) in Wireless Sensor Networks (WSNs)

PSO is an evolutionary optimization algorithm utilized in Wireless Sensor Networks (WSNs) for cluster head selection optimization by improving energy efficiency and network longevity. It evaluated candidate nodes according to residual energy and location to the base station. Each sensor node is considered a particle in an investigation space, with its position updated iteratively according to its best-position (Pbest) and the best global solution (Gbest), The velocity update is governed by the equation (Loganathan & Arumugam, 2021):

$$V_i^{t+1} = w \cdot V_i^t + c_1 \cdot r_1 \cdot (P_{best.i} - X_i^t) + c_2 \cdot r_2 \cdot (G_{best} - X_i^t) \text{ Eq.(7)}$$

where w is the inertia weight controlling the influence of previous velocities, c1and c2 are acceleration coefficients, and r1, r2 are random numbers and theee position of each particle is updated according to the equation bellow (Yadav et al., 2022; Sahoo et al., 2022):

$$X_i^{t+1}=X_i^t+V_i^t+1, \text{ Eq.(8)}$$

To ensure the progress of searching for the best Cluster Head in WSN, the selection process applies a fitness function based on factors such as residual energy, distance to the Base Station (BS), and node density, as shown in the equation below where α,β,γ are weight factors (Zhao et al., 2022):

$$Fitness = \alpha \cdot \frac{1}{Eresidual} + \beta \cdot \frac{d_{BS}}{d_{max}} + \gamma \cdot \frac{N_{density}}{N_{max}} \text{ Eq, (9)}$$

Methodology

Clustering techniques including K-Means, DBSCAN, and FCM, are used to organize sensor nodes efficiently, with each method offering different trade-offs in terms of energy efficiency, adaptability, and computational complexity. Figure.2 shows the flow chart for Cluster Head selection in WSN using hybrid clustering and PSO.

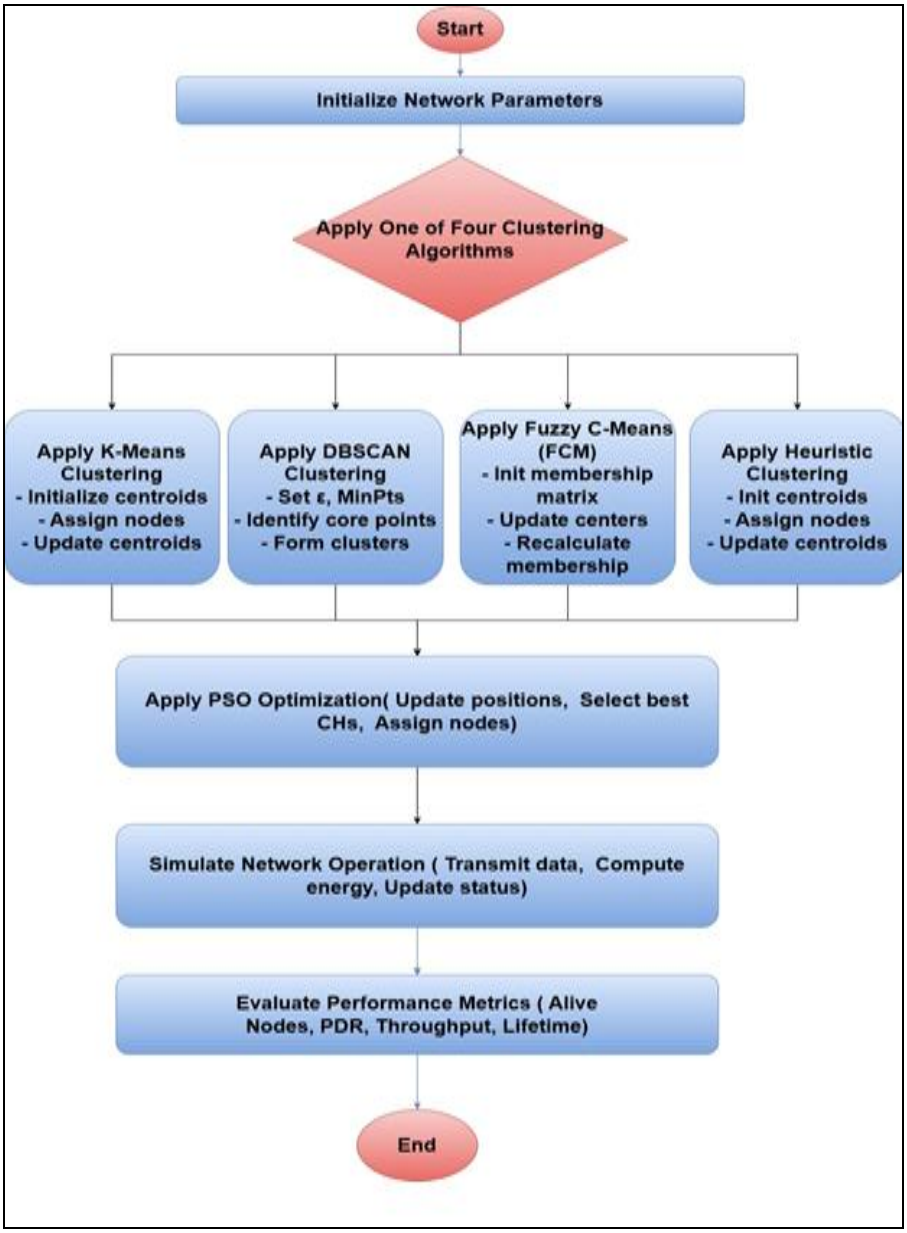


Figure 2. Flow chart for cluster head selection in WSN using hybrid clustering and PSO

In this work apply hybrid clustering algorithms with the Particle Swarm Optimization (PSO) algorithm to improve the selection of Cluster Heads (CHs) in Wireless Sensor Networks (WSNs). In the first step defining network parameters such as deployment area, number of nodes, and initial energy per node, then randomly distribute the nodes on the map. In this work apply the LEACH protocol to enhance energy efficiency through the dynamic distribution of nodes. Next, utilize clustering algorithms such as K-Means, FCM, DBSCAN, and heuristic clustering to form clusters. Then the PSO algorithm to select Cluster Heads based on residual energy, distance to the Base Station (BS), and node location. Cluster Heads are periodically updated to adapt to energy consumption and node mobility, ensuring balanced energy distribution and prolonging network lifetime.

Algorithm: Energy-Efficient Cluster Head Selection in Dynamic Wireless Sensor Networks Using K-Means, DBSCAN, Fuzzy C-Means, Heuristic Algorithms, and Particle Swarm Optimization

Input: Network dimensions (X, Y), Number of sensor nodes (N), Desired cluster heads (C), Initial node energy (E_init), Transmission parameters (E_elec, E_fs, E_amp), Base station location, Clustering algorithm parameters, PSO parameters.

Output: Optimized cluster head assignments, Cluster formations, Energy consumption metrics, Network performance metrics.

1. Initialize Network Parameters
    - Define the network area A=X×Y, where X and Y represent the width and height of the region.

- Set the number of cluster heads C.
- Define the initial energy of each node $E_{init,}$ typically set to 2J.
- Define transmission parameters: E_{elec}=50nJ/bit, E_{fs}=10pJ/bit/m^2, E_{amp}=0.0013pJ/bit/m^4.

2. Deploy Sensor Nodes
   - Each sensor node is randomly placed in the area: Pi=(x_i,y_i),x_i~U(0,X),y_i~U(0,Y)
   - The base station (BS) is located at P_{BS}=(X/2,Y/2).
3. Apply one of these algorithms each time to select the best cluster head from initialize population
   - Apply K-Means Clustering
     1. Initialization: select *k* initial cluster centroids
     2. Compute the Euclidean distance between each node ii and each cluster center j: d(i,j)= $\sqrt{(xi-xj)2+(yi-yj)2}$
     3. Assign each node to the nearest cluster center j: C(i)=arg $min_j\ d(i.CH_j)$
     4. Update cluster centers iteratively using: $x_j = \frac{1}{c_j}\sum_{i\epsilon cj} x_i . y_j = \frac{1}{c_j}\sum_{i\epsilon cj} y_i$
   - Apply DBscan Clustering
     1. Parameter Setting: Define two parameters:
        - ✓ ϵ: The maximum radius of the neighborhood to be considered.
        - ✓ MinPts: The minimum number of points required to form a dense region.
     2. Core Point Identification: For each node iii, identify its ϵ\epsilonϵ-neighborhood: $N_\epsilon(i)=\{j|d(i,j)\leq\epsilon$
        Where d(i,j) is the Euclidean distance between nodes i and j.
        If $|N_\epsilon(i)|\geq$MinPts, then node i is a core point.
     3. Cluster Formation: Starting from an unvisited core point, recursively visit all points in its ϵ-neighborhood. If those points are also core points, continue to their neighbors. This process forms a cluster of density-connected points.
     4. Noise Identification: After processing all points, those that are not part of any cluster are labeled as noise
   - Apply Fuzzy C-Means (FCM) clustering
     - ➢ Initialize Membership Matrix: Create a membership matrix U=[uij] with random values between 0 and 1, ensuring that for each data point ii, the sum of its memberships across all clusters : $\sum_{j=1}^{c} u_{ij}\ \forall i$
     - ➢ Compute Cluster Centers: Calculate the center vj of each cluster j using the current membership values: $v_j = \frac{\sum_{i=1}^{n} u_{ij}^n x_i}{\sum_{i=1}^{n} u_{ij}^n}$
     - ➢ Update Membership Values: For each data point ii and cluster jj, update the membership value uij based on the inverse distance between the data point and the cluster centers: $u_{ij} = \frac{1}{\sum_{k=1}^{c}(\frac{\|x_i-v_j\|}{\|x_i-v_k\|})^{2m-1}}$
     - ➢ Iterate: Repeat steps 2 and 3 until the membership matrix U stabilizes, i.e., the changes between iterations fall below a predefined threshold.
   - Apply Heuristic clustering algorithms
     - ➢ Initialization: select k initial cluster centroids from the dataset.
     - ➢ Assignment: For each data point xi, compute the Euclidean distance to each centroid v_j: d(x_i,v_j)=(x_i−v_j)^2
     - ➢ Assign x_i to the cluster with the nearest centroid: C(i)=arg $\min_j$ d(x_i,v_j)
     - ➢ Update: Recalculate each centroid v_j as the mean of all data points assigned to cluster j: $vj = \frac{1}{|C_j|}\sum_{x_i\epsilon C_j} x_i$
     - ➢ Iteration: Repeat steps 2 and 3 until the centroids converge (i.e., their positions no longer change significantly
4. Apply the PSO optimization:
   - Update particle velocity and position using:

$$v_i^{t+1} = wv_i^t + c1r1(pbest - x_i^t) + c2r2(gbest - x_i^t)$$

$$X_i^{t+1}=X_i^t+V_i^t+1$$

   - Assign the best nodes as cluster heads by Apply one of algorithms in step 3
   - Evaluate the fitness of each particle in PSO based on residual energy E(i) and distance to BS: $f(i) = \frac{E(i)}{d(i.BS)}$
   - Update the global best (gbest) by selecting the best position among all particles. Each node joins the nearest cluster head CH_j: CH_j =arg $min_j\ d(i.CH_j)$

- Nodes send data to cluster heads, and cluster heads forward it to BS.
- Compute transmission energy based on distance:
  - ✓ $E_{Tx}(i) = kE_{elec} + kE_{fs}d^2, if\ d < d0$
  - ✓ $E_{Tx}(i) = kE_{elec} + kE_{amp}d^4, if\ d \geq d0$
- Compute reception energy: $E_{Rx}(i) = kE_{elec}$
- Energy Consumption Calculation: Update the energy level of each node: $E(i) = E(i) - E_{Tx}(i) - E_{Rx}(i)$
- Mark a node as dead if E(i)≤0 .
- Continue iterations until all nodes have depleted energy.
- Early Stopping Condition : If the improvement in global best fitness remains below a threshold ε (0.001) for 10 consecutive iterations, the optimization stops. This avoids unnecessary computation once the solution stabilizes. The condition is given by: Δfgbest(t)=|fgbest(t)−fgbest(t−1)|<ε for 10 iterations

5. Evaluate Performance Metrics
   - Compute the number of alive nodes at each iteration: $N_{alive}(t)=\{i|E(i)>0\}|$
   - Compute packet delivery ratio (PDR): PDR=$\frac{Preceived}{Psent}$
   - Compute throughput: $T = \frac{Preceived \times k}{Ttotal}$
   - Compute network lifetime as the iteration where all nodes die: $T_{lifetime} = max_t\ N_{alive}(t) = 0$

Simulation and Results

The work implements an energy-efficient Cluster Head selection algorithm for dynamic Wireless Sensor Networks (WSNs) by integrating K-Means, DBSCAN, Fuzzy C-Means (FCM), heuristic algorithms, and Particle Swarm Optimization (PSO) by using Matlab R2023b. The proposed work defines a 100m × 100m network with 50, 100, and 150 sensor nodes, each with 2J initial energy, using transmission parameters Eelec (50 nJ/bit), Efs (10 pJ/bit/m²), and E_amp (0.0013 pJ/bit/m⁴),the BS is at (50m, 50m), clustering parameters are k=3,5,10 (K-Means), ε=15m & MinPts=5 (DBSCAN), and m=2 (FCM), PSO parameters include a population size of 30, inertia weight w=0.5, and cognitive/social coefficients c1=c2=1.5, ensuring balanced energy distribution and valid WSN simulation results. The parameters of wireless sensor networks are shown in Table 1.

Table 1. The parameter of wireless sensor networks

Parameter	Value
Network Area (A)	100m × 100m
Number of Sensor Nodes (N)	50,100,150
Initial Energy per Node (E_init)	2 Joules
Transmission Energy (E_elec)	50 nJ/bit
Free Space Model (E_fs)	10 pJ/bit/m²
Multipath Model (E_amp)	0.0013 pJ/bit/m⁴
Iteration (time)	5000
Base Station Location	(50m, 50m)
K-Means: Number of Clusters (k)	3, 5, 10
DBSCAN: ε, MinPts	15m, 5
FCM: Fuzziness Parameter (m)	2
PSO: Population Size	[10, 20, 30, 40, 50] the optimal 30
PSO: Inertia Weight (w)	[0.1, 0.3, 0.5, 0.7, 0.9] the optimal 0.5
PSO: Cognitive Coefficient (c1)	[1.0, 1.5, 2.0, 2.5] the optimal 1.5
PSO: Social Coefficient (c2)	[1.0, 1.5, 2.0, 2.5] the optimal 1.5

Figure 3 illustrates Sensor nodes (blue circles) connect to their nearest cluster head (red squares), while the base station (green star) manages data transmission. K-Means clusters nodes by Euclidean distance, DBSCAN detects dense regions, FCM assigns nodes flexibly, and Heuristic algorithms optimize cluster head selection. Figure 3 shows the initial clustering of 50 nodes in a 100 × 100 m² WSN. DBSCAN creates dense, irregular clusters; FCM assigns fuzzy memberships; Heuristic selects cluster heads based on energy and proximity; and K-Means forms uniform clusters

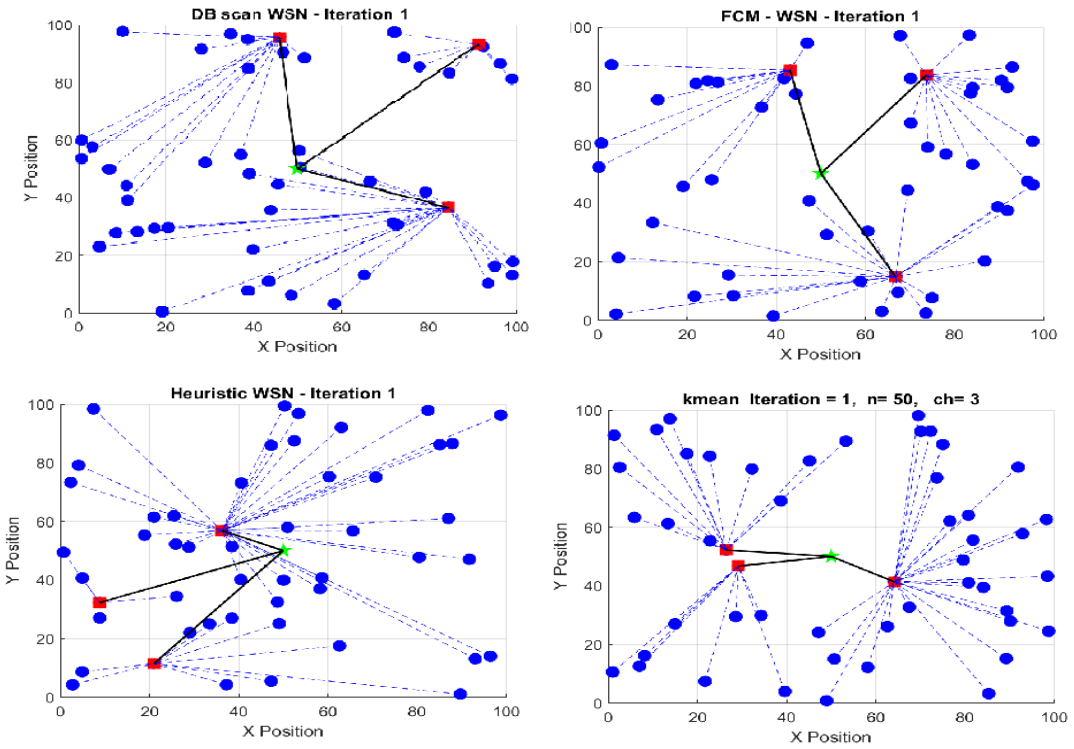


Figure. 3. Comparison of WSN clustering techniques using K-Means, DBSCAN, FCM, and heuristic algorithms with 50 sensor nodes and 3 cluster heads in a 100m × 100m area

.

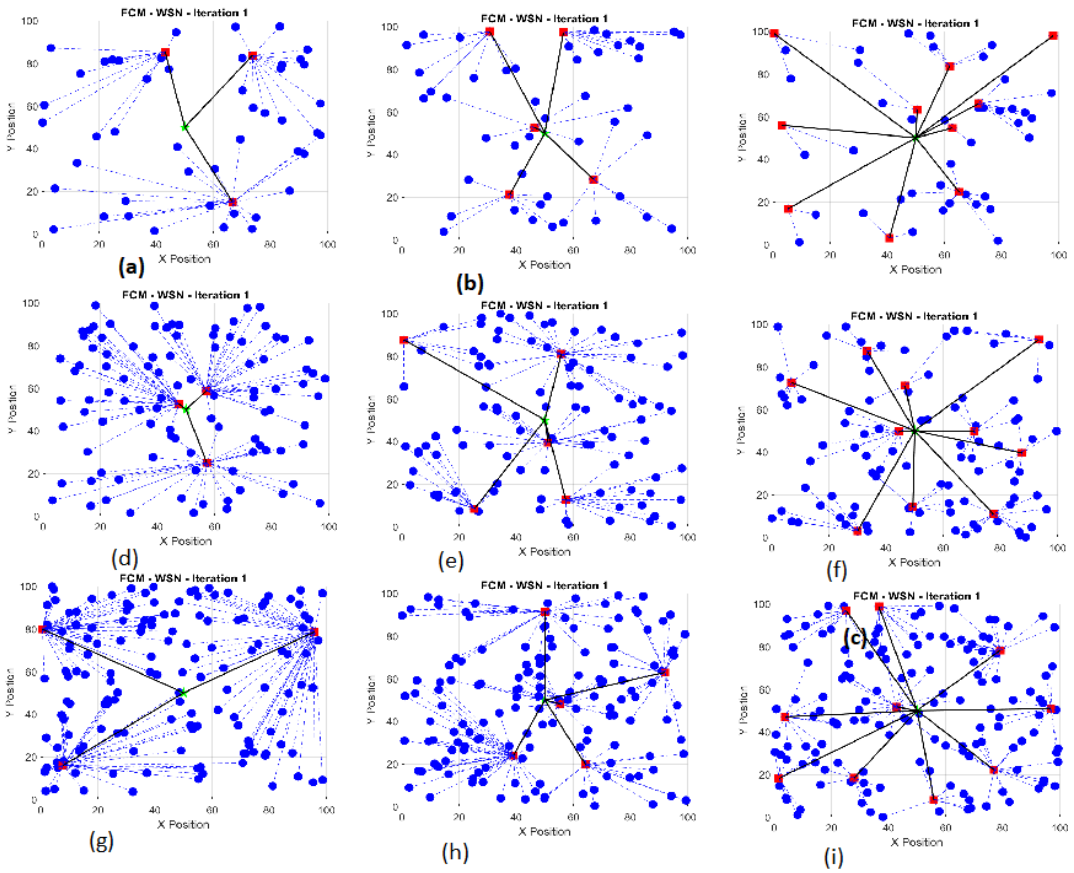


Figure. 4. Evaluation of fuzzy C-means (FCM) clustering in wireless sensor networks with varying cluster heads and node densities

Data flows from nodes to cluster heads and then to the base station, highlighting differences in spatial distribution and routing efficiency. In this work illustrates the impact of varying Cluster Heads (CHs) and Sensor Nodes (SNs) on network performance using Fuzzy C-Means (FCM) clustering, mean, Dbsccan, and Heuristic algorithm in a Wireless Sensor Network (WSN). Figures 4 (a, b, c) represent 3 CHs with 50, 100, and 150 SNs, respectively, showing that fewer CHs lead to longer transmission distances, increasing energy consumption per CH. Figures 4 (d, e, f) with 5 CHs distribute the load more effectively, reducing communication costs and balancing energy consumption. In Figure 4 (g, h, i) with 10 CHs, network density is higher, minimizing individual node transmission distances but introducing additional overhead in cluster management. The results confirm that 5 CHs (d, e, f) provide the best balance between energy efficiency, load distribution, and network longevity, while 3 CHs (a, b, c) suffer from high energy depletion and 10 CHs (g, h, i) introduce unnecessary cluster overhead. This work evaluates key metrics including node count, clusters, energy used, alive and dead nodes, latency, packet delivery ratio (PDR), throughput, coverage, fault tolerance, scalability, and reliability. Additionally, it examines network lifecycle through first, half, and full node depletion iterations to optimize efficiency and longevity.

Figure 5 compares the number of alive nodes in a WSN across different clustering algorithms (K-Means, DBSCAN, Heuristic, FCM) with 3, 5, and 10 cluster heads (CHs) and varying sensor nodes (50, 100, 150) . For 3 CHs, K-Means has the lowest alive nodes (≈30 for 50 nodes, ≈80 for 100 nodes, ≈120 for 150 nodes), while FCM and Heuristic maintain higher survivability (≈40, ≈100, and ≈140 respectively). In 5 CHs, K-Means still results in the lowest node survival (≈35, ≈90, and ≈130), while DBSCAN and Heuristic perform better (≈45, ≈110, and ≈145). For 10 CHs, survivability improves across all methods, with K-Means showing ≈50, ≈120, and ≈145, whereas DBSCAN and FCM keep the highest alive nodes at ≈60, ≈130, and ≈150. These results indicate K-Means depletes energy faster, while FCM, DBSCAN, and Heuristic clustering provide better energy efficiency and network longevity, especially as CHs increase.

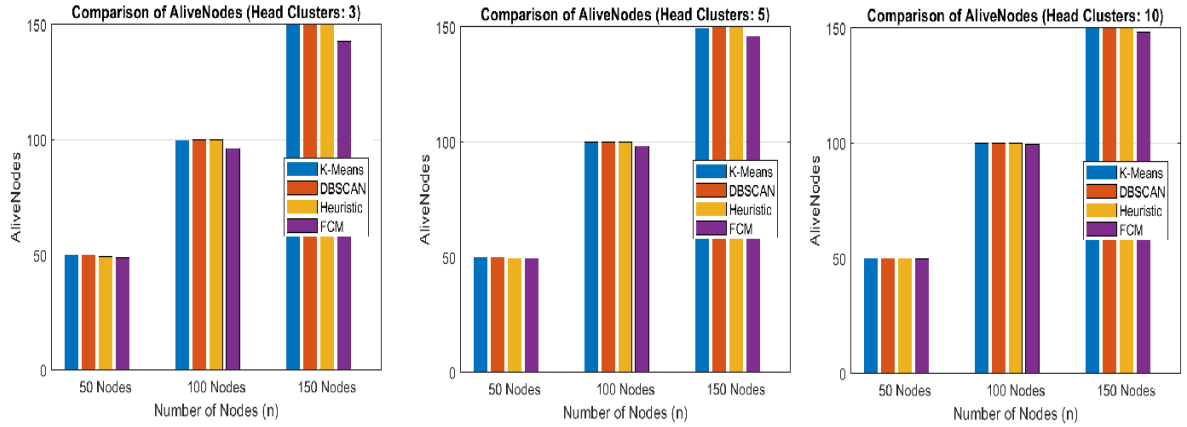


Figure 5. Comparison of alive nodes in WSN using different clustering algorithms with varying cluster heads and node densities

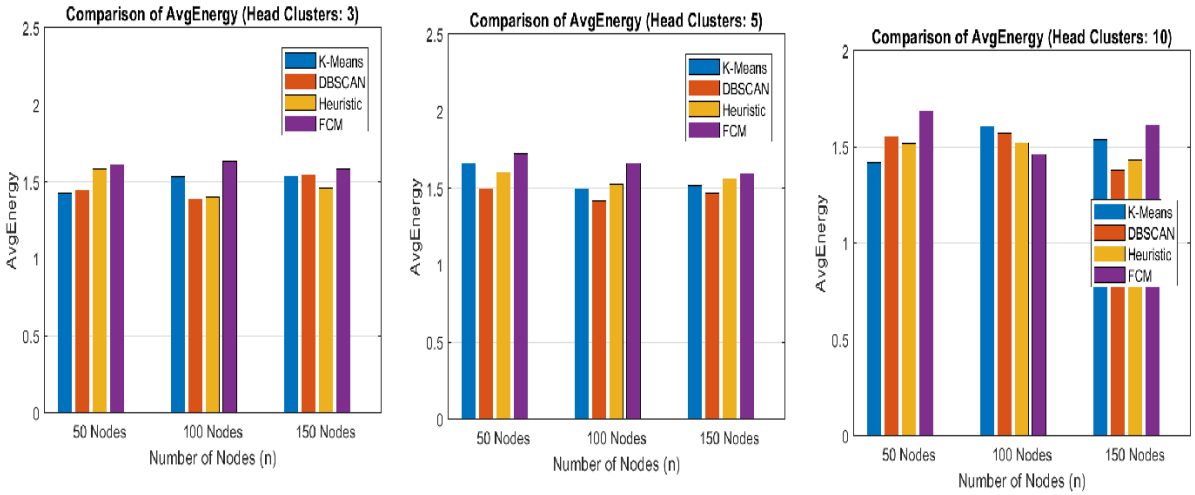


Figure 6. Comparison of average energy consumption in WSN using different clustering algorithms with varying cluster heads and node densities

Figure 6 presents a comparison of average energy consumption in a Sensor WSN for different clustering algorithms (K-Means, DBSCAN, Heuristic, and FCM) with 3, 5, and 10 cluster heads (CHs) and varying sensor node counts (50, 100, and 150 nodes). In the 3 CH scenario, FCM, K-Means exhibits higher energy consumption, while Heuristic and DBSCAN maintain more balanced energy usage. With 5 CHs, energy efficiency improves across all algorithms, particularly for FCM and K_Means clustering, which distribute energy consumption more evenly. In the 10 CH scenario, FCM and Heuristic continue to demonstrate better energy management, whereas K-Means still shows higher energy depletion. The results indicate that increasing the number of CHs enhances energy distribution, reducing the load on individual nodes. FCM and K_Means clustering consistently achieve better energy efficiency, making them more suitable for extending WSN lifetime.The algorithms considered include K-Means, DBSCAN, Heuristic, and Fuzzy C-Means (FCM), with different numbers of cluster heads (CHs) and sensor nodes (50, 100, 150) as shown in Table 2.

Table 2. Performance metrics for clustering algorithms in WSN

Algorithm	Node Count	Num Clusters	Avg Energy	Alive Nodes	Dead Nodes	Latency	Coverage	Fault Tole	Scalability
K_Means	50	3	1.4259	50	0	0.5	1	1	1
K_Means	100	3	1.5324	99	1	0.9968	0.99676	0.9967	0.99676
K_Means	150	3	1.5394	150	0	1.5	1	1	1
DBSCAN	50	4	1.4496	50	0	0.5	0.98823	0.9882	0.98823
DBSCAN	100	1	1.38940	100	0	1	1	1	1
DBSCAN	150	1	1.54773	150	0	1.5	1	1	1
Heuristic	50	3	1.5852	49	1	0.4924	0.98485	0.9848	0.9848
Heuristic	100	3	1.4015	100	0	1	1	1	1
Heuristic	150	3	1.4564	150	0	1.5	1	1	1
FCM	50	3	1.6154	48	2	0.4874	0.97492	0.9749	0.9749
FCM	100	3	1.6319	95	4	0.9633	0.96334	0.9633	0.9633
FCM	150	3	1.5835	143	8	1.4271	0.9514566	0.9514	0.9514
K_Means	50	5	1.6602	50	0	0.5	1	1	1
K_Means	100	5	1.4937	100	0	1	1	1	1
K_Means	150	5	1.5210	149	1	1.4962	0.9975	0.9974	0.9974
DBSCAN	50	1	1.4970	50	0	0.5	1	1	1
DBSCAN	100	3	1.4177	100	0	1	1	1	1
DBSCAN	150	1	1.4667	150	0	1.5	1	1	1
Heuristic	50	5	1.51644	49	1	0.4941	0.98823	0.9882	0.9882
Heuristic	100	5	1.52089	100	0	1	1	1	1
Heuristic	150	5	1.43032	150	0	1.5	1	1	1
FCM	50	5	1.72129	49	1	0.4952	0.99058	0.9905	0.9905
FCM	100	5	1.66062	98	2	0.9825	0.98255	0.9825	0.9825
FCM	150	5	1.59638	145	5	1.4594	0.97297	0.9729	0.9729
K_Means	50	10	1.42018	50	0	0.5	1	1	1
K_Means	100	10	1.60749	100	0	1	1	1	1
K_Means	150	10	1.53621	150	0	1.5	1	1	1
DBSCAN	50	2	1.55623	50	0	0.5	1	1	1
DBSCAN	100	3	1.56910	100	0	1	1	1	1
DBSCAN	150	1	1.379255	150	0	1.5	1	1	1
Heuristic	50	10	1.516441	50	0	0.5	1	1	1
Heuristic	100	10	1.520898	100	0	1	1	1	1
Heuristic	150	10	1.430322	150	0	1.5	1	1	1
FCM	50	10	1.687899	49	1	0.4986	0.9971	0.9971	0.9971
FCM	100	10	1.46203	99	1	0.9941	0.99409	0.9940	0.9940
FCM	150	10	1.616078	148	2	1.481	0.98736	0.9873	0.9873

As shown in Figure 7, increasing population size improves exploration ability but leads to higher computational overhead. The best energy-lifespan balance is achieved at 30 particles. Similarly, an inertia weight of 0.5 shows better convergence stability. Higher cognitive and social coefficients (c1 = c2 = 1.5) yield optimal clustering with minimal transmission delay. Among all configurations, the optimal PSO parameters are: Population Size = 30, Inertia Weight = 0.5, c1 = 1.5, c2 = 1.5. These settings resulted in 12–15% energy savings and a 20% increase in network lifespan compared to traditional approaches.

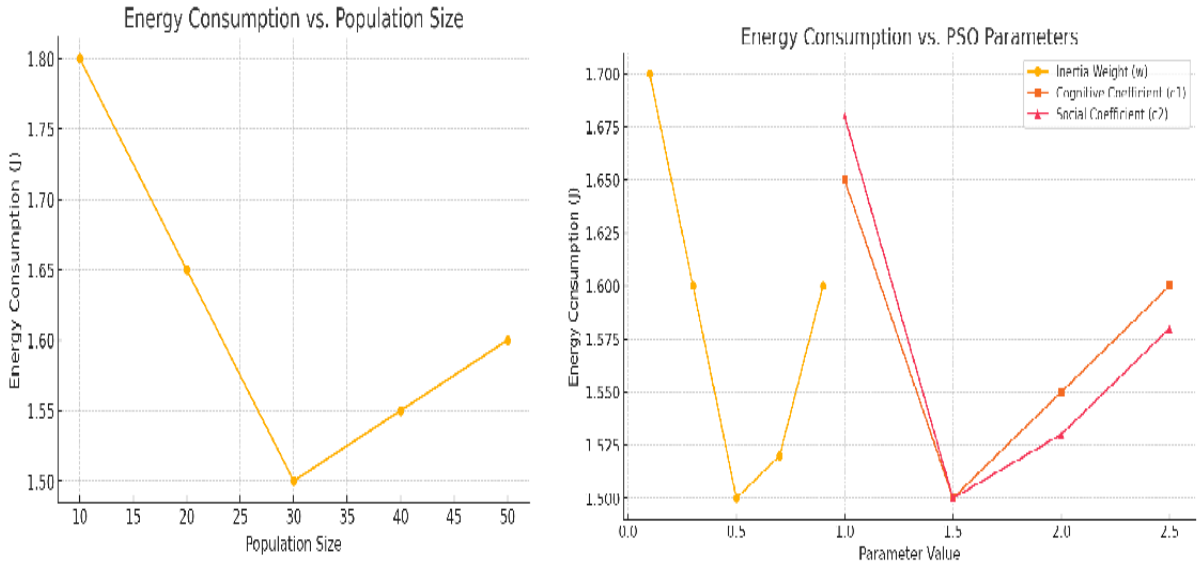


Figure 7. Effect of PSO parameters on energy consumption in wireless sensor networks

The results show that DBSCAN maintains 100% alive nodes across all cases, while Heuristic, K-Means and FCM exhibit slight node loss, such as FCM with 150 nodes and 5 clusters having 145. alive nodes (97) and 5 dead nodes. The average energy consumption ranges from 1.3894 (DBSCAN, 100 nodes, 1 cluster) to 1.7213 (FCM, 50 nodes, 5 clusters), with FCM generally consuming more energy. Latency varies from 0.487 (FCM, 50 nodes, 3 clusters) to 1.5 (multiple cases across algorithms), while PDR remains consistently at 1. Throughput remains at 3,200,000 across all cases, while coverage and reliability are mostly at 1, except for minor drops in FCM (e.g., 0.9515 for 150 nodes, 3 clusters). These results indicate that DBSCAN and Heuristic provide stable energy efficiency and network longevity, while FCM may have higher energy consumption but maintains reasonable network performance. FCM offers significant energy savings and improved network lifetime, but this comes at the cost of higher computational overhead due to its iterative nature and fuzzy membership calculations.

The results show that FCM achieves the highest energy efficiency with the lowest consumption (0.8996J), followed by K-Means (0.9275J), while Heuristic (0.9626J) and DBSCAN (1.0258J) consume more. K-Means ensures the longest network lifespan with the first node dead at 483 rounds, followed by FCM (904) and Heuristic (443), whereas DBSCAN fails immediately. All algorithms maintain high reliability (PDR = 1), but DBSCAN and Heuristic experience higher latency (1.5s at 150 nodes). FCM and Heuristic are the best choices for long-term WSN applications. In terms of network lifetime, FCM shows superior performance with the first node dying at 904 iterations, compared to K-Means (483) and Heuristic (443), while DBSCAN fails immediately.

To validate the observed differences in energy consumption across clustering algorithms, a one-way Analysis of Variance (ANOVA) test was conducted. The test compared the average energy consumption among four algorithms: K-Means, DBSCAN, Heuristic, and FCM. The results revealed a statistically significant difference with a p-value of 0.00052, which is well below the conventional threshold of 0.05. This indicates that the choice of clustering algorithm has a significant impact on energy efficiency within the wireless sensor network. The accompanying boxplot visually confirms these differences, particularly highlighting the higher energy variability in FCM and the more consistent performance of K-Means.

Table 3. Node lifetime and average energy consumption analysis

Parameter	K-Means	DBSCAN	Heuristic	FCM
First Node Dead	483 iterations	-1	443 iterations	904 iterations
Half Node Dead	-1	-1	-1	-1
All Node Dead	-1	-1	-1	-1
Average Energy Consumption	0.92753	1.02580	0.96261	0.89963

While Comparative previous studies explored clustering (Zagrouba & Kardi, 2021), routing protocols (Jubair et al., 2021), and bio-inspired methods (Kavya & Ravi, 2021; Behera et al., 2022), they lacked integrated optimization. Our work combines intelligent clustering (K-Means, DBSCAN, Heuristic, FCM) with PSO for

adaptive cluster head selection based on energy and proximity. Unlike Rizky et al. (2024), who reduced congestion but faced packet loss, our approach optimizes both energy and network lifetime. As shown in Table 3, FCM-PSO achieves the lowest energy consumption (0.8996 J) and longest lifetime (904 iterations), demonstrating superior performance over existing methods.

Conclusion

The work implements an energy-efficient Cluster Head selection algorithm for dynamic WSNs using clustering methods and PSO, with results showing that FCM and K_Means algorithms enhance network longevity, energy effi-ciency, and data reliability. FCM achieves the lowest energy consumption (0.8996J), then K_Means(0.9275J), then Heuristic (0.9626J), while DBSCAN consumes the most (1.0258J). The average throughput remains stable at 3.2 Mbps across all clustering methods, ensuring consistent data transmission performance. In latency, K-Means exhibits the highest delay (1.5s), while FCM and heuristic clustering maintain lower delays (around 1.0s), making them more efficient for real-time applications. Increasing the number of Cluster Heads helps balance energy consumption, reduc-es transmission waste, and further extend network lifespan. For instance, with 150 nodes and 5 clusters, FCM retains 145 alive nodes, ensuring better survivability compared to K-Means and DBSCAN. Compared to traditional clustering methods, the proposed FCM-based approach reduces total energy consumption by 12–15% and extends the network's operational lifetime by approximately 20%. FCM most effective clustering algorithm for WSNs, offering optimal energy efficiency, extended lifespan, and strong fault tolerance. Future work can focus on enhancing the PSO tech-nique using adaptive or hybrid approaches to improve performance in dynamic WSN environments.

Scientific Ethics Declaration

* The authors declares that the scientific ethical and legal responsibility of this article published in EPSTEM journal belongs to the authors.

Conflict of Interest

* The authors declare that they have no conflicts of interest

Funding

* This work has no funds

Acknowledgements

* This article was presented as virtual presentation at the International Conference on Technology, Engineering and Science (www.icontes.net) held in Antalya/Türkiye on November 12-15, 2025.

* The authors would like to thank Mustansiriyah University (www.uomustansiriyah.edu.iq Baghdad Iraq) for its support in the present work.

References

Abdulaal, A. H., Valizadeh, M., Yassin, R. A., Albaker, B. M., Abdulwahhab, A. H., Amirani, M. C., & Shah, A. S. (2024). Unsupervised histopathological sub-image analysis for breast cancer diagnosis using variational autoencoders, clustering, and supervised learning. *Journal of Engineering and Sustainable Development, 28*(6), 729-744.

Alam, S., Dobbie, G., Koh, Y. S., Riddle, P., & Rehman, S. U. (2014). Research on particle swarm optimization-based clustering: A systematic review of literature and techniques. *Swarm and Evolutionary Computation, 17*, 1-13.

Albasri, S., Ibrahim, O., Popescu, M., & Keller, J. (2022). Clustering surgemes using prototypes from robotic kinematic information. *Journal of Engineering and Sustainable Development, 26*(5), 22-34.

Al-Baz, A., & El-Sayed, A. (2018). A new algorithm for cluster head selection in LEACH protocol for wireless sensor networks. *International Journal of Communication Systems, 31*(1), e3407.

Behera, T. M., Samal, U. C., Mohapatra, S. K., Khan, M. S., Appasani, B., Bizon, N., & Thounthong, P. (2022). Energy-efficient routing protocols for wireless sensor networks: Architectures, strategies, and performance. *Electronics, 11*(15), 2282.

Jamel, A., & Akay, B. (2019). A survey and systematic categorization of parallel k-means and fuzzy-c-means algorithms. *Computer Systems Science and Engineering, 34*(5), 259-281.

Jan, B., Farman, H., Javed, H., Montrucchio, B., Khan, M., & Ali, S. (2017). Energy efficient hierarchical clustering approaches in wireless sensor networks: A survey. *Wireless Communications and Mobile Computing, 2017*(1), 6457942.

Jubair, A. M., Hassan, R., Aman, A. H. M., Sallehudin, H., Al-Mekhlafi, Z. G., Mohammed, B. A., & Alsaffar, M. S. (2021). Optimization of clustering in wireless sensor networks: Techniques and protocols. *Applied Sciences, 11*(23), 11448.

Kaddi, M., Omari, M., Salameh, K., & Alnoman, A. (2024). Energy-efficient clustering in wireless sensor networks using Grey Wolf Optimization and enhanced CSMA/CA. *Sensors, 24*(16), 5234.

Kadhum, S. W., & Tawfeeq, M. A. (2025). Improving performance classification in wireless body area sensor networks based on machine learning techniques. *Journal of Engineering and Sustainable Development, 29*(1), 112-119.

Kalaimani, D., Zah, Z., & Vashist, S. (2021). Energy-efficient density-based Fuzzy C-means clustering in WSN for smart grids. *Australian Journal of Multi-Disciplinary Engineering, 17*(1), 23-38.

Kamil, M. Y. (2017). Brain image segmentation based on fuzzy clustering. *Al-Mustansiriyah Journal of Science, 28*(3), 220-223.

Kavya, A. P., & Ravi, D. J. (2021). Snapshot of energy optimization techniques to leverage life of wireless sensor network. *International Journal of Advanced Computer Science and Applications, 12*(7), No:7.

Khudhair, H. A. (2025). Intelligent formation protocol: An approach for enhancing energy efficiency and network performance in wireless sensor networks. *Al-Mustansiriyah Journal of Science, 36*(1), 46-55.

Lata, S., Mehfuz, S., Urooj, S., & Alrowais, F. (2020). Fuzzy clustering algorithm for enhancing reliability and network lifetime of wireless sensor networks. *IEEE Access, 8*, 66013-66024.

Latiff, N. A., Tsimenidis, C. C., & Sharif, B. S. (2007). Energy-aware clustering for wireless sensor networks using particle swarm optimization. In *2007 IEEE 18th International Symposium on Personal, Indoor and Mobile Radio Communications* (pp. 1-5). IEEE.

Loganathan, S., & Arumugam, J. (2021). Energy efficient clustering algorithm based on particle swarm optimization technique for wireless sensor networks. *Wireless Personal Communications, 119*(1), 815–843.

Majid, M., Habib, S., Javed, A. R., Rizwan, M., Srivastava, G., Gadekallu, T. R., & Lin, J. C. W. (2022). Applications of wireless sensor networks and internet of things frameworks in the industry revolution 4.0: A systematic literature review. *Sensors, 22*(6), 2087.

Miglani, A., Kumar, N., Chamola, V., & Zeadally, S. (2020). Blockchain for Internet of Energy management: Review, solutions, and challenges. *Computer Communications, 151*, 395-418.

Miraftabzadeh, S. M., Colombo, C. G., Longo, M., & Foiadelli, F. (2023). K-means and alternative clustering methods in modern power systems. *IEEE Access, 11*, 119596-119633.

Omran, S. H., Shneen, S. W., Jameel, B. I., Hassoon, O., Fayad, M. A., & Ismail, F. B. (2025). Fuzzy logic technique based on classification function application in quality control. *Journal of Engineering and Sustainable Development, 29*(1), 105-111.

Peter, S. C., Dhanjal, J. K., Malik, V., Radhakrishnan, N., Jayakanthan, M., & Sundar, D. (2019). Quantitative structure-activity relationship (QSAR): Models and methods in computational biology. In S. Ranganathan, M. Gribskov, K. Nakai, & C. Schönbach (Eds.), *Encyclopedia of bioinformatics and computational biology* (Vol. 2, pp. 661-676). Elsevier.

Raj, V. P., & Duraipandian, M. (2023). Energy conservation using PISAE and cross-layer-based opportunistic routing protocol (CORP) for wireless sensor network. *Engineering Science and Technology, an International Journal, 42*, 101411.

Rashid, B., & Rehmani, M. H. (2016). Applications of wireless sensor networks for urban areas: A survey. *Journal of Network and Computer Applications, 60*, 192-219.

Riaz, A., Sarker, M. R., Saad, M. H. M., & Mohamed, R. (2021). Review on comparison of different energy storage technologies used in micro-energy harvesting, WSNs, low-cost microelectronic devices: Challenges and recommendations. *Sensors, 21*(15), 5041.

Rizky, R., Hakim, Z., Setiyowati, S., & Yunita, A. M. (2024). Development of the multi-channel clustering hierarchy method for increasing performance in wireless sensor network. *MATRIK: Jurnal Manajemen, Teknik Informatika dan Rekayasa Komputer, 23*(3), 603-614.

Sahoo, B. M., Pandey, H. M., & Amgoth, T. (2022). A genetic algorithm inspired optimized cluster head selection method in wireless sensor networks. *Swarm and Evolutionary Computation, 75*, 101151.

Sert, S. A., & Yazici, A. (2021). Increasing energy efficiency of rule-based fuzzy clustering algorithms using CLONALG-M for wireless sensor networks. *Applied Soft Computing, 109*, 107510.

Shafi, I., Chaudhry, M., Montero, E. C., Alvarado, E. S., Diez, I. D. L. T., Samad, M. A., & Ashraf, I. (2024). A review of approaches for rapid data clustering: Challenges, opportunities and future directions. *IEEE Access, 12*, 133512-133534.

Sucasas, V., Radwan, A., Marques, H., Rodriguez, J., Vahid, S., & Tafazolli, R. (2016). A survey on clustering techniques for cooperative wireless networks. *Ad Hoc Networks, 47*, 53-81.

Tambawal, A. B., Noor, R. M., Salleh, R., Chembe, C., Anisi, M. H., Michael, O., & Lloret, J. (2019). Time division multiple access scheduling strategies for emerging vehicular ad hoc network medium access control protocols: A survey. *Telecommunication Systems, 70*(4), 595-616.

Yadav, R., Sreedevi, I., & Gupta, D. (2022). Bio-inspired hybrid optimization algorithms for energy efficient wireless sensor networks: A comprehensive review. *Electronics, 11*(10), 1545.

Zagrouba, R., & Kardi, A. (2021). Comparative study of energy efficient routing techniques in wireless sensor networks. *Information, 12*(1), 42.

Zaiter, M. J., Mohamed, T., Rahem, A. T., & Tsviatkou, V. (2025). Mathematical model used to compute packet energy consumption-based control topology for WSN. *Journal of Engineering and Sustainable Development, 29*(3), 331-337.

Zhao, X., Zhong, W., & Navaei, Y. D. (2022). A novel energy-aware routing in wireless sensor network using clustering based on combination of multiobjective genetic and cuckoo search algorithm. *Wireless Communications and Mobile Computing, 2022*, 6939868.

Author(s) Information

Rafa Sami Braiber
University of Mustansiriyah, Department of Computer Science, College of Science,
Baghdad, Iraq
Contact e-mail: *rafasami2020@uomustansiriyah.edu.iq*

Mussab Riyadh
University of Mustansiriyah, Department of Computer Science, College of Science,
Baghdad, Iraq

To cite this article:

Braiber, R. S. & Riyadh, M. (2025). Enhancing wireless sensor networks performance by integrating particle swarm optimization with intelligent clustering techniques. *The Eurasia Proceedings of Science, Technology, Engineering and Mathematics (EPSTEM), 38,* 757-770.

The Eurasia Proceedings of Science, Technology, Engineering & Mathematics (EPSTEM)
ISSN: 2602-3199

The Eurasia Proceedings of Science, Technology, Engineering and Mathematics (EPSTEM), 2025

Volume 38, Pages 771-790

IConTES 2025: International Conference on Technology, Engineering and Science

B-Smart: A Robust Reputation Based Blockchain Scheme in Wireless Sensor Networks

Farah Khedim
University Centre of Maghnia

Nabila Labraoui
University of Tlemcen

Ado Adamou Abba-Ari
University of Versailles Saint-Quentin-en-Yvelines

Abstract: The importance given to wireless sensor networks (WSNs) has made them an ideal target for many security issues. Internal attacks are one of the most serious and dangerous threats resulting from the physical capture of the sensor nodes by malicious adversaries. The internal attacker will extract the cryptographic data and reprogram the captured nodes in order to misbehave and to harm the network. Since traditional cryptographic mechanisms are ineffective against this kind of attack it is essential to find additional detection solutions. In order to make distinction between legitimate and fraudulent nodes, trust and reputation mechanisms have been suggested to overcome the limitations of cryptographic methods in securing WSNs. In these mechanisms, reputation values are assigned to neighboring nodes in honest or dishonest manner according to the legitimacy of nodes assigning those values. However, manipulating and modifying reputation values by malicious nodes make these mechanisms vulnerable to many attacks such as: badmouthing, ballo-stufing, on-off, etc. In this paper, we propose a smart reputation mechanism for WSNs (B-Smart) based on blockchain and smart contracts. The purpose of our protocol is to automate the assignment process of reputation values through the use of smarts contracts to prevent falsification of these values by malicious nodes. Saving these contracts in a blockchain will ensure their durability, integrity and effectiveness. The various evaluations conducted demonstrate the robustness of our protocol against a wide range of internal attacks.

Keywords: Trust and reputation systems, Security, WSN, Blockchain, Smart contract

Introduction

Since their first uses in the military and heavy industrial applications, wireless sensor networks (WSNs) had significant progress and rapid expansion. Self-sufficiency, scalability, responsiveness, reliability and mobility are some of the exceptional characteristics that have made them one of the most innovative multidisciplinary research areas these last years. The recent advent of the Internet of things (IoT) also allowed these networks to become increasingly popular. However, as with almost all technologies, the benefits offered by WSNs are accompanied by significant risk factors and a high potential for abuse (Oztoprak et al., 2024). Indeed, the hostile and unguarded environment in which sensor networks are deployed makes the physical capture of sensor nodes easy for intruders. On the other hand, the limited resources of sensors—such as memory, energy, computational capacity, and communication bandwidth-make the design and development of an effective security protocol particularly challenging (Yilmaz & Dener, 2024).

One of the most serious and dangerous threats to sensor networks is the so-called "node compromise attack". In this attack, the intruder captures a sensor node and extracts all the security and network information. Holding

- This is an Open Access article distributed under the terms of the Creative Commons Attribution-Noncommercial 4.0 Unported License, permitting all non-commercial use, distribution, and reproduction in any medium, provided the original work is properly cited.

- Selection and peer-review under responsibility of the Organizing Committee of the Conference

© 2025 Published by ISRES Publishing: www.isres.org

this information, the attacker injects this data into malicious nodes and reintroduces them among the legitimate nodes of the network. Bypassing security systems and password encryption thanks to their valid cryptographic data, malicious nodes will harm legitimate nodes, delete, modify, and alter the data flow, disrupting the overall functioning of the network. The "node compromise attack" in considered as the entry point of all internal attacks. As cryptographic methods alone cannot counter internal attacks, complementary techniques must be employed to reinforce detection mechanisms and safeguard the sensor network.

Trust and reputation systems (TRS) are proposed as complementary to cryptographic techniques, fostering reliable collaboration among sensors in WSNs (Navaei Tourani et al., 2025). They have been suggested as a powerful tool to distinguish between legitimate and fraudulent nodes, allowing also the identification of malicious, selfish and compromised nodes which have been authenticated (Gupta, 2025) (Moeinaddini et al., 2025). Inspired by human behavior, trust and reputation mechanisms have been able to demonstrate their effectiveness in sensor networks by improving their security, facilitating decision-making and promoting collaboration between nodes (Alzaid et al., 2013). TRS are therefore an effective tool for the detection of "node compromise attack".

Although distinct in definition, the concepts of trust and reputation are closely interrelated and exhibit several common characteristics. Trust, in general, is the degree of confidence with which a node evaluates that another node, or a group of nodes, will execute a given action reliably. (Bhuiyan, 2013; Rodrigues & John, 2020). Using trust assessment provides several interesting properties for sensor networks. It motivates network nodes to behave correctly, since all their actions are monitored and evaluated. It also helps predict future node behavior, which makes it possible to select the safest paths for routing transactions. Finally, it enables the detection of malicious or dishonest nodes (Tenhundfeld et al., 2022). Reputation as it is defined is the cumulative sum of past activities of a node that determines its state of worthiness (Zhang, 2025). The reputation mechanisms provide an incentive for honest behavior and deter dishonest nodes from participating in the network (Pourtahmasbi & Nojoumian, 2022). There is no doubt that conjunction of these two notions provides considerable support for the field of security in WSNs. Enabling the establishment of trust relationships between nodes, evaluation of node reputation and trust management (Zhang et al., 2014).

The adoption of trust and reputation mechanisms in WSNs faces several challenges. First, the large number of nodes, together with limited communication resulting from instability and mobility, makes mutual familiarization and the assignment of reputation values highly complex. Second, the open, unsupervised, and insecure deployment environment, combined with the absence of centralized authority, undermines cooperation among nodes. Collectively, these factors reduce the effectiveness of trust and reputation mechanisms and give rise to significant security vulnerabilities. These security issues result in most cases from the abusive manipulation of reputation values by malicious nodes. The malicious nodes participating in reputation system will thus reduce the reputation values of legitimate nodes in order to damage their reputation and remove them from the network. These nodes will also increase the reputation values of other malicious nodes to increase their chance to participate in critical network functions. The presence of these malicious nodes in the network will thus generate several trust and reputation attacks such as bad mouthing attack, ballot-stuffing attack, on-off attack and conflicting behavior attack.

In this light, the importance of trust and reputation mechanisms in WSNs has been acknowledged by the research community. Considerable research has been done on modeling and creating functional and lightweight protocols. Most of the trust models previously proposed are based on reputation evaluation that by definition is defined as the cumulative evaluation of past behavior of nodes over a certain time interval; this reputation will allow nodes to build trust values (Labraoui et al., 2016). Several methods were used to calculate reputation values based on the number of instances of good and bad behavior. Thus, the success of a reputation mechanism depends entirely on the accuracy with which calculated reputation values predict the quality of future interactions (Sun et al., 2006). Yet, to the best of our knowledge, all the trust and reputation mechanisms presented so far allow any network node to assign and manipulate these valuable values on which the security of the entire network depends. In WSNs, known to be vulnerable to the node compromise attack, at each moment one or more malicious nodes can be introduced undetectably among the legitimate nodes, letting these malicious nodes manipulate reputations values seem incomprehensible and really dangerous. One solution would be to remove the power of attribution of the reputation’s values to the nodes of the network to make a trust model more robust and resistant to the trust and reputation attacks.

In the last years blockchain has emerged as a revolutionary technology that can change the world. "Open source", decentralized, tamper-proof and based on P2P exchanges, the blockchain works without a central authority or trusted third party (Di Pierro, 2017). Smart contracts, which is considered as the blockchain element

with the greatest application potential, offers additional revolution to the blockchain by allowing to automatically be executing predefined conditions in an efficient way and at a high speed. Such characteristics open up many possibilities for sensor networks and broadly benefit the trust and reputation systems.

In this paper, we propose a robust reputation based blockchain scheme in WSNs named B-Smart. The proposed scheme is based on two evolutionary concepts: blockchain and smart contracts. These two concepts will automate the reputation process while ensuring data integrity, availability and security while respecting the specific needs of sensor networks. The main contributions of this work are as follows. Firstly, we introduce the "smart contracts" for the calculation of reputations values. The use of these contracts in our protocol will allow answering most of the problems related to the assignment of reputations values in sensor networks as well as having a mechanism resistant to possible modifications emanating from malicious nodes. Secondly, in order to ensure durability, integrity and effectiveness of all recorded data, our protocol applied the blockchain principle. In fact, the blockchain in our protocol will allow the backup of all the transactions carried out by the nodes in addition to allowing the safeguarding of the smart contract. Allow each node of the network to have a copy of the blockchain will validate transactions, make impossible changes in history and detect any intentional or software malfunction of sensor nodes.

The rest of this paper is organized as follows. Section 2 reviews some related work on trust and reputation mechanisms. In section 3, we describe the background of our protocol. Section 4 described the system model. In section 5, we describe our proposed B-Smart. The main steps of the proposed B-Smart protocol are presented in section 6. Attacks and security analysis are given in section 7. The simulation results are given in section 8. In section 9, we conclude our work and give some prospects.

Related Work

In recent years, we have witnessed an ongoing in the field of trust and reputation systems. Such enthusiasm has given rise to a large number of increasingly innovative and effective protocols. Indeed, as an integral part of our lives, trust has always had a preponderant place for building strong relationships in our daily lives. The application of trust in computer and telecom networks is precisely based on such inspiration. Used effectively in sensor networks, TRS have facilitated decision making by enabling nodes to make appropriate decisions to identify malicious nodes. However, TRSs are victims of their success, and many attackers used them to launch a variety of attacks. These attacks are: bad mouthing, ballot stuffing, on/off, conflicting behavior, whitewashing and intelligent behavior.

A number of protocols have been proposed to mitigate badmouthing and ballot-stuffing attacks, collectively known as dishonest recommendation attacks. During such attacks, the adversary distorts the reputation system by assigning unfairly low (false-negative) values to target nodes in bad-mouthing attacks, or by assigning unfairly high (false-positive) values in ballot-stuffing attacks. The devoted schemes either prevent the occurrence of such attacks or detect these ones once they are present in the network (Khedim et al., 2015).

Prevention based techniques (Khedim et al., 2015). Proposals in this category use one of these two methods: (a) first hand information or (b) positive/negative reputations. In first hand based schemes, the TRS only uses the direct information to calculate the confidence value of the nodes, thus depriving itself of the indirect and yet useful information provided by the neighboring nodes in order to avoid the occurrence of the dishonest recommendations attacks. Although using second hand information, the schemes based on positive/negative reputation only allow propagating of positive or negative reputation values depending on the attack. (Michiardi & Molva, 2002) proposed one of the first reputation protocols. Dedicated to the badmouthing attack, the CORE protocol requires that each node monitors the behavior of its neighbor nodes. A reputation table is used to record these direct confidence values. Using only positive reputation values enable the CORE protocol to counter the badmouting attack. (Ganeriwal et al., 2008) proposed the RFSN protocol for the high-integrity sensor networks. RFSN uses only positive reputation values and higher weight is assigned to secondhand information from a well-reputed node to prevent ballot stuffing attack. CONFIDANT proposed by (Buchegger & Le Boudec, 2002) is one of the best-known reputation protocols. Initialized with positive trust ratings, the nodes continuously monitor the behavior of their neighbors of the next jump. Devoted to the ballot stuffing attack, this protocol only uses negatives reputation values to prevent attackers from increasing the reputation values of other malicious nodes.

Detection based techniques. Instead of simply preventing dishonest recommendations attacks, protocols in this category use complementary methods to detect such attacks once they are in the network. In the Recomm

Verifier protocol (Chen et al., 2012) the reputation management scenario is modeled as a court and the concept of trial is used to strengthen the resistance of the protocol against the dishonest recommendations attacks. For this purpose, a deviation module using an outlier's detection algorithm is applied to filter dishonest recommendations. Then, a temporal verification module makes it possible to recheck the obtained results during the deviation to reduce false positive rate. In Zouridaki et al. (2009), a robust and cooperative confidence-building scheme E-HERMES is proposed. To overcome the problem of dishonest recommendations, the RC test is applied between the first hand information and the second hand obtained information in order to ensure that only recommendations whose value is sufficiently close to the first-hand confidence are accepted. In (Khedim et al., 2018) a bio inspired trust model for mobile WSNs named BTS is proposed. The effectiveness of the protocol is due to the innovative side of the approach. Indeed, by combining between the foraging behavior of the honey bee swarm and two innovative concepts: a modified cloud model and a cognitive chronometry parameter, the BTS protocol allows among others to improve the detection of dishonest recommendations rate and decrease the false positive rate.

Other protocols have been interested on the On/off attack. In this attack, the intruder behaves well and badly alternatively hoping to remain undetectable while causing damage. (Labraoui et al., 2015) proposed the O^2Trust protocol to mitigate the on/off attack in WSN. For this purpose, a penalty policy based on misbehavior history is applied to deal with the dynamic and contradictory misbehavior of malicious nodes. The frequency misbehavior history is then used as a reliable factor when calculating trust values, allowing punishment of malicious nodes. (Chen, 2012) proposed the RASN protocol to resist on/off attack. RASN is built on Trust-Holding-Agent (THA) architecture allowing it to calculate, aggregate and conserve reputation information of nodes. RASN applied two concepts: Latest times of trust mutation and Revision Factor. While, the first concept allows to record the times of trust mutation, the second one allow to deal with all kinds of reputation and to obtain the final trust value. (Amol & Chatur, 2016) present a new efficient and flexible trust management scheme to detect and defend against On/off attack. The protocol relies on two key concepts: Predictability trust and dynamic sliding windows. Predictability allows detecting the on/off attack using sliding windows to keep track of previous behaviors and determine confidence recovery time.

To the best of our knowledge, we have not found any work dedicated on dealing with the conflicting bahavior attack or the intelligent bahavior attack or even whitewashing attacks in wireless sensor networks. In these attacks, the malicious node can create conflict, use intelligent behavior to deceive the TRS and re-enters the system with a new identity and a fresh reputation in unpunished manner. These attacks are at least as dangerous as the previously discussed ones, yet they are often overlooked by trust and reputation protocols, thereby exposing the network to severe damage.

Unlike the existing schemes, our B-Smart protocol allows improving the resistance of the trust and reputation mechanisms against all the aforementioned trust and reputation attacks in addition to being resistant against routing attacks. A reinforced detection method to counter as much as possible the "node compromise" attack known to encompass all the malicious behaviors generated by internal nodes of the network. This is possible thanks to the joint action of several approaches: (1) the automation of the reputation assignment process. (2) The use of a recidivism factor in order to severely punish the malicious nodes and (3) the use of a test period in order to prevent attackers from reentering the system as they please.

Background

Our protocol is the result of the joint action of two main domains (Figure 1): blockchain and smart contract. A brief description of each of these two axes is given in what follows:

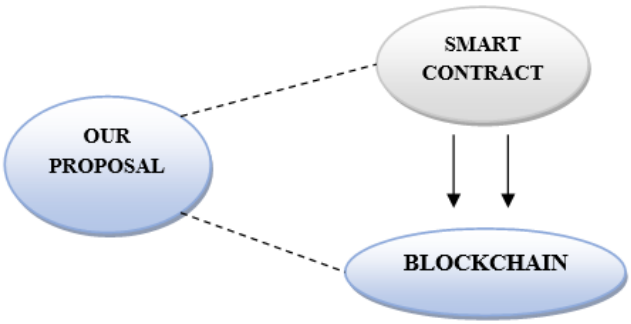


Figure 1. Components of the B-Smart protocol

Blockchain

Blockchain, widely recognized as one of the most transformative technological innovations of recent years, has emerged as a paradigm-shifting technology that has attracted considerable interest across diverse sectors. It enables applications that traditionally required a trusted intermediary to function autonomously in a decentralized manner, without reliance on a central authority. Conceptually, blockchain is a distributed ledger composed of a chain of blocks, recording the history of payments, transactions, and contracts executed and shared among participating entities. To mitigate the risk of a single point of failure (Saleh et al., 2020), the ledger is replicated and synchronized across network members. While blockchain is often associated with Bitcoin, the digital currency introduced in 2008 (Nakamoto, 2008), it can also operate independently of cryptocurrencies.

Three Fundamental Criteria Distinguish Blockchain Technology

Decentralized Architecture

The decentralized side of the blockchain acts as a structural defense against the risk of voluntary changes or data theft from malicious entities. Indeed, the fact that the blockchain is not registered by a single server but by a part of the entities makes the destruction, alteration and modification of data an impossible task.

Cryptographic Protection

Several cryptographic methods are used to secure the blockchain:

- Encryption: The exchanges in the blockchain are secured thanks to the use of asymmetric encryption. The transactions are thus encrypted using the private key of the issuer and can only be decrypted by the corresponding public key. The application of encryption will thus make it possible to guarantee confidentiality, integrity, authentication and non-repudiation in the data network.
- Hashs: The blockchain consists of a set of blocks where transactions are recorded in an orderly and time-stamped manner. Each block consists of two parts: a header and a part dedicated to the recording of transactions. In order to guarantee the integrity of the blocks and to ensure that once a block is validated it can never be modified, the blockchain uses the hash functions. As a result, functions such as the SHA-256 that is currently used in bitcoin and ether are applied. These hash functions are used to calculate the "hash" of a block and insert this value in the header of the next block, to create links between the blocks. Any modification of the data in a block will result in the change of the value of the hash which will thus become totally different from the value of the registered header.

Cryptocurrency Issuance

Inadvertently confused, crypto-currencies are different from the blockchain; however, the two notions are closely related. Serving as a platform, the blockchain makes it possible to record different exchange transactions of these crypto-currencies. Among the crypto-currencies that have emerged: Bitcoin, Ether, Litecoin and Bitcoin cash.

Smart Contracts

Developed in 1994 by Nick Szabo (Szabo, 2017), smart contracts have only become popular for a few years thanks to the meteoric rise of blockchain technology. In fact, based on the blockchain, smart contracts have made it possible to automate and revolutionize traditional contracts by making them unfalsifiable and sustainable.

Running on an Etherum blockchain, Smart Contracts can store data, record information, made decisions and execute contract terms automatically. They can serve as an agreement between entities and the blockchain without the requirement that both parties trust each other (Bagchi, 2017). In addition to these multiple features, smart contracts also benefit from the security side offered by the blockchain. Leveraging these benefits to solve problems related to trust mechanisms and reputation is the fundamental principle of our B-Smart protocol.

System Model

In this section, we describe the network and the threat model. Moreover, we describe the used assumptions.

Network Model

In this paper, we use a WSN network based on blockchain technology. The topology of the network can be indifferently static or mobile. The network follows flat architecture, and the identity of each node is unique and stable.

Threat Model

In this paper, we assume an active attacker model in which a malicious node voluntarily tries to remove, alter, modify, misroute or replay the messages transmitted on the network that it is supposed to forward under a given routing protocol. Such an attacker with "bad behavior" tries to cause maximum damage and disrupt the functioning of the network. Conversely, a node that propagates messages correctly is defined as having "good behavior".

Assumptions

Any trust and reputation management scheme must initialize the trust and reputation values before the deployment of the network. Therefore, in our protocol B-Smart we assume that: 1) the reputation values belong to [0, 1]. 0 means very bad behavior and 1 means very good behavior. 2) At the beginning of the lifetime of our network all the nodes have an equally good reputation equal to 0.5 and are equally trusted. The reason is simple: at the very beginning of the deployment, no malicious opponent has had the time or the chance to influence or subvert a node. 3) New nodes appearing during network lifetime should not be fully trusted, as they could be generated by an adversary. These nodes are placed in a *"test period"*; they must perform a greater number of satisfactory tasks compared to the initial nodes before they can recover a normal reputation value.

Vocabulary

In the following, we described the following notations and expressions considered in our protocol. (Table 1) gives the considered notations.

Table 1. Notations

Notation	Description
TRS	Trust and Reputation System
TR_X	Transaction x
S	Source node
D	Destination node
SK_i	Private key of node i
PK_D	D's public key
$Sig_{SKi}(TR_x, PK_D)$	Signature on TR_X by node i
Rec_i	Recidivism factor for node i
Rep_i^{last}	Last assigned reputation to node i

B-Smart Protocol

The panoply of trust and reputation protocols proposed in recent years has proved the effectiveness of TRS for the detection of a large number of attacks. They have become an essential tool for solving security problems in wireless sensor networks. However, their effectiveness is destroyed in the face of internal attackers. These malicious nodes try to deflect the trust and reputation system by manipulating the reputation values of neighboring nodes as they please and communicate these distorted values to the other nodes of the network.

In this section, we propose a smart reputation mechanism for WSNs (B-Smart) based on blockchain and smart contracts. The main objective of the B-Smart is to automate the assignment process of reputation values through the use of smarts contracts to prevent falsification of these values by malicious nodes. Saving these contracts in a blockchain will ensure their durability, integrity and effectiveness. We present in the following the design goals of our protocol B-Smart, the system architecture as well as the main phases of execution.

Design Goals

Our reputation protocol based on blockchain and smart contracts aims to meet several security objectives, namely, decentralization, information integrity, availability of reputation values and non-repudiation:

- Decentralizing. B-Smart allows a backup of all transactions in a decentralized manner in all nodes of the network without relying on a third party thanks to the use of a blockchain topology.
- Centralization of calculating reputation values. Removing power from sensor nodes to assign reputation values to other network nodes helps to prevent an attacker from using the mechanism to manipulate reputation values as needed by decreasing legitimate reputation values or increasing those of the other attackers. Entrusting the calculation of reputation values to a central entity "smart contract" and save it in the blockchain not only facilitates access to them but also ensures decentralization and security, thus avoiding the traditional disadvantages of centralized methods.
- Information integrity. B-Smart allows keeping track of all the transactions made in an unchangeable way. The use of the blockchain ensures that the information stored in the blocks cannot be changed by any node of the network.
- Reputation values availability. The use of the smart contract makes it possible to guarantee the availability of the reputation values for the different nodes of the network. Indeed, any node can know the reputation values of its neighbor nodes without having to ask from recommenders.
- Non-repudiation in the B-Smart protocol is ensured through the use of asymmetric cryptography. Indeed, tracking the routing of the transaction through the different intermediate nodes will prove that a message was sent by its sender or received by the recipient.

General Description

B-Smart is a novel reputation based blockchain scheme. The proposed protocol overcomes the problem of the malicious manipulation of reputation values by entrusting the management of these values to a smart contract. This smart contract will thus follow the progress of the various transactions of the network and assign to the nodes the corresponding reputation values according to their behavior. The nodes will thus be judged according to whether they send the messages correctly or not, the presence or absence of modifications in message packets, a change in the routing path of the packet as well as on the possible deletions of the messages in transit. A *recidivism factor* is applied by the smart contract when calculating reputation values in order to severely penalize malicious nodes by significantly reducing their reputation values. This factor also helps motivating the intermediate nodes to relay the information correctly in order to preserve their reputation values. Automating the reputation calculation process not only overcomes the problems associated with the manipulation of reputation values by malicious nodes but also allows us to avoid selfish nodes and offers an efficient solution to isolate malicious network nodes. The smart contract is saved in the blockchain to ensure its durability, integrity and effectiveness. Thus recorded, the contact is protected from abusive manipulation by internal attackers.

The B-Smart protocol works as follows: when a node wants to send a message or to request information from another node or from the base station, this communication follows the following main steps: Firstly, a routing protocol is used to determine the optimal path between the requester and the provider. Indeed, the message or request must pass through several nodes in a "multi-hop" mode since "one-hop" communications are resource-intensive in WSNs. Secondly, time is allocated for each transaction, and a block is created to track the routing of the transaction between each successive nodes to its destination or until the time is over. Once the transaction is completed or its time is over, the block is inserted into the blockchain. A personal copy of the blockchain is hosted by each node to guarantee its security. However, given the limited storage capacity of the sensors, we assume that the nodes can store it in any kind of network accessible storage, privately hosted, such as the cloud or decentralized storage such as Swarm (Hartman et al., 1999) or IPFS (Benet, 2014) or other types of storage (Bagchi, 2017). Finally, the smart contract uses the data contained in its history as well as the information provided by the block of the transaction in order to update the reputation values of the participating nodes. Nodes with reputation values below a defined threshold are declared as malicious and embedded in the blacklist

to prevent their participation in network applications. The Overview of the B-Smart protocol is given in (Figure 2).

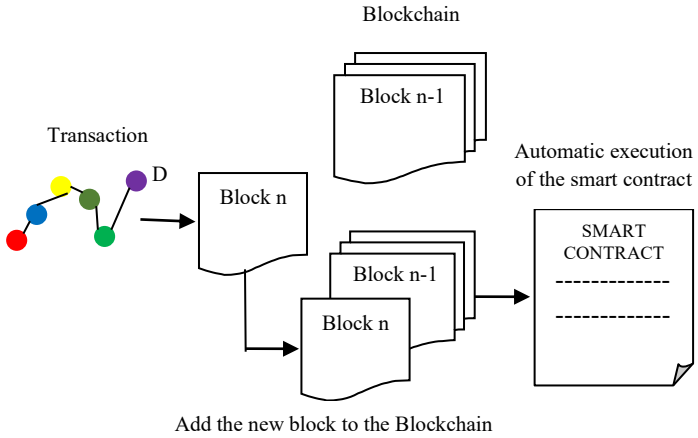


Figure 2. Overview of the B-Smart protocol

System Architecture

The B-Smart protocol is based on the joint operation of several entities. Among these entities, we can mention:

Transaction

The interactions between the sensors are the fundamental principle of any sensor network. Indeed, the exchange of information such as temperature, humidity and other parameters between these nodes will allow the implementation of various applications. A transaction is therefore any data exchange between the nodes, as well as between the nodes and the base station. Each transaction in our protocol involves a source node (S), a destination node (D) and a number of intermediate nodes for relaying it. Node (D) plays the role of requester, and node (S) plays the role of provider. Transactions in our protocol are stored in blocks using a blockchain data structure. Each transaction is cryptographically signed by all participants in order to keep irrefutable proof of the participation of each user involved in the transaction.

Node

In our protocol a sensor node can play the role of provider, requester or gateway node. As the requestor, the node will request the recovery of some data from the provider node. The provider is responsible for transmitting certain files, messages, or the sensed data to the requestor with the help of the intermediate nodes. The latter, will create a block that will track the routing of the transaction in a peer-to-peer manner through the multi-hop gateway nodes to the requesting node. Each node participating in a transaction in our protocol must have a unique signature; this signature is formed by a pair of public key and private key. While the public key is shared with all the nodes of the network, the private key remains secret. Elliptic Curve Cryptography (ECC) is applied to generate public key from private key thus offering a great degree of security while being adapted for sensor networks thanks to the reduced size of the keys compared to other cryptographic methods such as RSA (Yan, 2022).

Block and Blockchain

A block is used to save all the information relating to the routing of the transaction from a source node to a destination node. Indeed, all the actions of the nodes during a transaction are recorded in the block, such as: the sending, the reception, the modification as well as the deletion of data. In our protocol, each block contains one transaction. The statement of the transaction and the different steps of the routing of the transaction with their corresponding time stamps are defined in the body of the block. To link the blocks together and thus guarantee the integrity of the blocks, the hash function SHA-256 is used to calculate the "hash" of a block and insert this

value in the next block header. Any modification of the data in a block will result in the change of the value of the hash which will thus become totally different from the value of the registered header.

Smart Contracts

A smart contract is a special block that will perform the reputation protocol. It is automatically executed after adding a new block in the blockchain. Using the information contained in the block concerning the routing of the transaction by the sensor nodes and using his personal history, the smart contract will be able to judge the nodes, to assign the appropriate reputations values and to update the existing reputation values. Accessible via a contract address, the nodes of the network can communicate with the smart contract by sending messages to its address. These messages can be either *Transaction* or *Call.* Transaction messages are sent when the nodes require storing pertinent information of specific devices. Call messages are made when nodes want to query the state of a device at a given time (Bagchi, 2017).

B-Smart Scheme

To explain how our protocol works, we assume that the transaction happens between two nodes, i.e., node source S and node destination D in a multi-hop manner. The whole steps performed in the execution of the B-Smart protocol are highlighted in (Figure 3) and explained in the following:

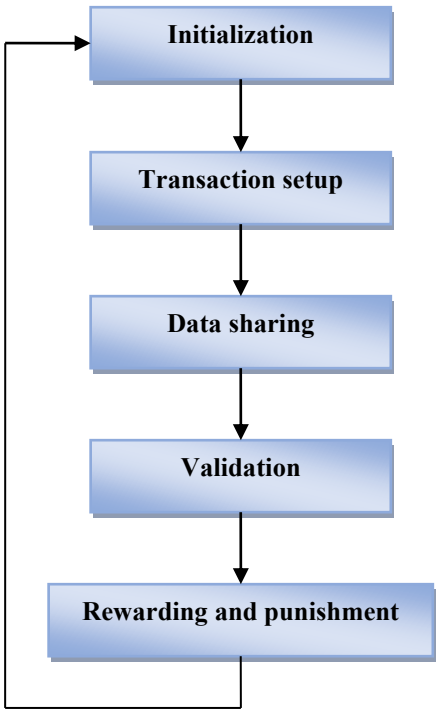


Figure 3. The main steps of the proposed B-Smart protocol

Initialization Phase

A routing protocol is applied to determine the most appropriate path between the source and destination node. Several routing protocols allowing the discovery of the optimal path have been applied efficiently in the sensor networks. These protocols consider several parameters such as: the energy level of the sensors, the reliability on data delivery, the number of hops and the security of the path. In our protocol these factors are only taken into account during the first rounds. Once the smart contract has more knowledge about the reputation of the nodes, the routing protocol will refer to the information provided by the smart contract to choose the safest way. The existing routing protocols are classified into three main categories (Othmen et al., 2016): reactive, proactive and hybrid routing protocols. In reactive protocols such as (AODV) (Perkins, 2003) and DSR (Johnson & Maltz, 1996), the node discovers a path with the destination on demand. This is done by flooding the network with

Route REQuest packets (RREQ). This can lead to a high latency time in the route-finding process. In proactive routing protocols such as DSDV (Perkins & Bhagwat, 1994) and OLSR (Clausen & Jacquet, 2003), each node maintains fresh lists of destinations and their paths by periodically distributing control messages. This solution is suitable when the topology is static. However, it has slow reactions on restructuring and failures. Whereas hybrid protocols such as ZRP (Haas & Pearlman, 2000) and ZHLS (Hamma et al., 2006) combine the advantages of the reactive and proactive protocols. Choosing a routing protocol instead of another is out of scope this paper since it will depend on the needs of the application.

Transaction Encryption

Once the routing path is established, the requesting node concretizes its intention to initiate a transaction by creating a corresponding block. The head of the created block contains the statement of the transaction and the path defined by the routing protocol. The body of the block will follow and record all the steps of routing the transaction between the intermediate nodes to the destination. Encryption of the transaction is realized thanks to the use of asymmetric encryption and more particularly elliptic curve cryptography (ECC). The use of asymmetric cryptography will ensure the authentication and integrity of the data relayed through the gateway nodes. Since each node of the network has a pair of keys (public key and private key), the provider node S will use the public key of the requester node D (PK_D) to encrypt the message that its wants to send him conveyed by the transaction TR_x. Each gateway node G_i must in turn sign the data in transit in order to keep track of the routing of the transaction. (Figure 4) describes the main steps of the transaction encryption.

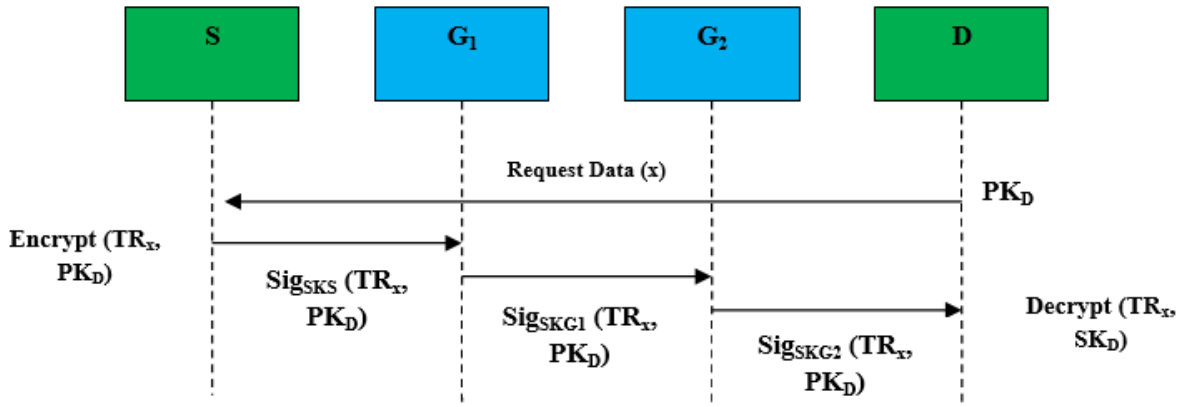


Figure 4. Main steps of transaction encryption process

Data Sharing

The encrypted transaction is sent in multi-hop manner from the source node to the destination node. Any changes and alterations, as well as each successful reception and sending by the gateway nodes, are recorded in the transaction block maintained by all the nodes participating in the transaction.

Transaction Time

A defined time is allocated to each transaction. At the end of this time the transaction is considered complete. This time, will limit the time spent on transactions in order to overcome the problem of transactions that never reach their destination due to hardware failures or voluntary deletions by malicious nodes, thus avoiding waiting indefinitely.

Block Validation

Unlike existing blockchain like those in (Underwood, 2016; Madisetti, 2016) where block validation is performed by a set of miners to validate the block before integrating it into the global blockchain, in our protocol, the validation is carried out by the smart contract once the block is integrated in the blockchain for two main reasons. On the one hand, the use of miners implies a significant consumption of computation power of the latter, in the WSNs known for their limited resources; such calculations will significantly reduce the energy of

the miner's sensors which will reduce the duration of the network lifetime. On the other hand, in a traditional blockchain, the miners will check the transactions to prevent fraudulent operations; those considered invalid will never be integrated in the blockchain. In B-Smart, integration into the blockchain of all transactions will allow us to detect and to prove the offense of malicious nodes by having an irreversible proof of their fraudulent behavior in the routing of transactions. During validation, the smart contract will check the consistency of the transaction. It will then verify that the transaction has followed the path indicated by the routing mechanism; the signatures and the consistency of the transactions. The results of this analysis will be taken into account in the next step.

Rewarding and Punishment Phase

After the validation step, the smart contract has enough elements to judge the behavior of the different nodes of the transaction and to assign them the corresponding reputation values. The simplified architecture of the smart contract is shown in (Figure 5) and the corresponding algorithm is given in Algorithm 1. More specifically, once a bloc is added to the blockchain, the smart contract is applied in automatic manner to verify that the terms of the contract have been respected, in our case this states that the transaction has been carried out correctly. The smart contract holds a reputation table of all the nodes of the network. The values of the nodes that participated in the last transaction are updated after each new transaction.

The reputation table is composed of three columns. The first column, *Node (Ni)*, contains the identities of all nodes in the network. The second column, *Recidivism factor (Reci)*, records the number of times a node has misbehaved. The higher this counter, the more critically the reputation value of the malicious node decreases. Finally, the third column, *Last reputation value (Repi_last)*, stores the most recent reputation value assigned to the node by the smart contract. The table is easy to maintain. For example, in a transaction when the evaluated node or a gateway node transfers a packet for the next node correctly "good behavior" then its Rec_i is unchanged and its reputation value Rep_i^{last} is increased by a value α. Without lost of generality, we took α=0.05. Otherwise, if one of the gateway nodes drops the packet or modifies it before the transfer for malicious or authentication reasons "bad behavior", then its Rec_i is increased by one and its reputation value is divided by the exponential of the value (Rec_i). This last operation resulted in a critical reduction of the reputation value of the malicious node. The process of assigning reputation values by the smart contract, although simple, can severely punish the malicious nodes by making reputation difficult to acquire but easy to lose. This will help to deter malicious nodes from disrupting network operations and provide our protocol with an effective method of detecting and isolating them. This process also allows the intermediary nodes to relay the information correctly. Nodes with a reputation value below a defined threshold are declared malicious and blacklisted to prevent their participation in network applications.

Algorithme 1. The attribution of reputation values process

Begin

1. **For each** Transaction_sensor (i)
2. **if** Good_Behavior (i) **then**
3. $Rec_i = Rec_i$
4. $Rep_i^{last} = Rep_i^{last} + \alpha$
5. **else**
6. $Rec_i = Re_c^{i+1}$
7. $Rep_i^{last} = Rep_i^{last} / \exp(Rec_i)$

End

Automating the assignment of reputation values by smart contract allows our protocol B-smart to create trusted transactions without central control and without the intervention of sensor nodes while maintaining integrity, confidentiality and resistance to a large number of internal attacks. In summary, in order to have a clear view about the operation of our proposed scheme, we provides in (Figure 5) a flowchart showing the various phases and the whole operations of the B-Smart protocol.

Attacks and Security Analysis

While effective, trust and reputation mechanisms may be victims to a large number of attacks that we will commonly call "trust and reputation attacks". These attacks have tarnished the usefulness of these mechanisms

and discouraged their use especially in sensor networks. Indeed, suffering from a great lack of security, sensor networks are already vulnerable to a large number of internal attacks; the use of trust and reputation systems adds an additional security problem. Our protocol B-Smart protocol helps to fight the trust and reputation attacks, a way for us to improve the image of trust and reputation systems so that they can act effectively to secure sensor networks. We will present in the following the main attacks that threaten these mechanisms as defined in (Yu el al., 2012), as well as the strategies used by our protocols to detect and eliminate such attacks.

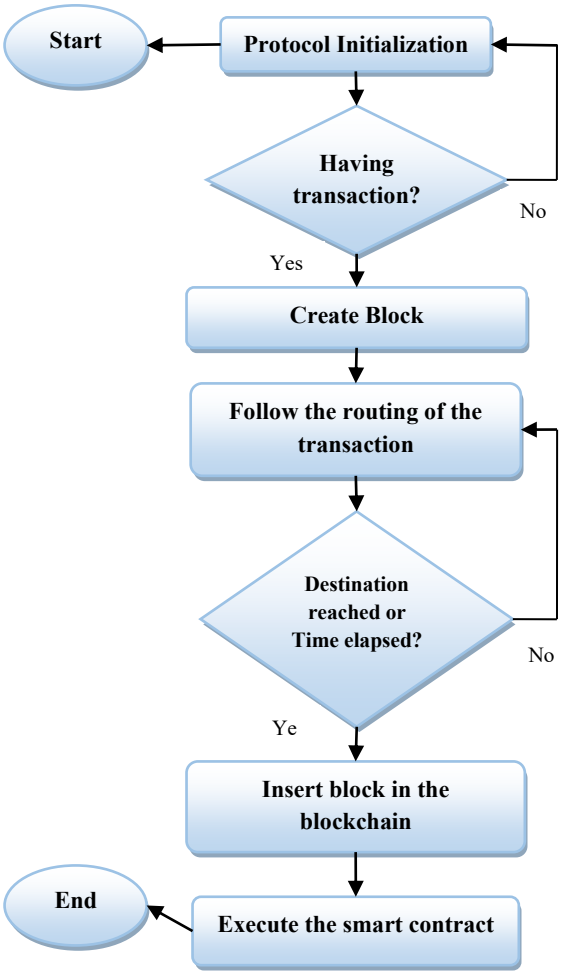


Figure 5. Flow chart of the B-Smart protocol

Trust and Reputation Attacks

This category includes all attacks that use the trust and reputation mechanism to perform malicious actions. These attacks are as follows:

Bad Mouthing Attack

Trust and reputation mechanisms often use recommender nodes to obtain information on certain nodes of the network. The recommender nodes thus make it possible to provide second hand information that is very useful for the evaluating node in order to complete its vision on a node that it knows little or that it doesn't know. In the case where the recommenders are honest; this indirect information greatly enhances the effectiveness of trust and reputation mechanisms. However, malicious nodes can be introduced among these recommenders as is the case in the bad mouthing attack. In this attack, the attacker handles the trust and reputation system to assign unfairly negative values to legitimate network nodes. This attack leads to deform the reputation of the nodes and thus to distort the results of the confidence system. One of the main consequences of such an attack is the isolation of legitimate nodes from critical network applications due to their reduced reputation values, thereby allowing malicious nodes to occupy more space and ultimately impose themselves as leaders. Although our B-

Smart protocol does not rely on second-hand information, it is just as much, if not more, effective as protocols that rely on this indirect information since the smart contract has a global view of all transactions running in the network. By not involving any recommender in the calculation of reputation values, B-Smart is completely resistant to this type of attack.

Ballot Stuffing Attack

As in the aforementioned attack, the malicious node will be introduced among the recommenders. However, unlike the bad mouthing attack, it will not assign negative values, but false-positive reputation values to another malicious node in the network. The main purpose behind this attack is to favor attacking nodes by increasing their reputation values in order to increase their weight in the network. Automating the assignment of reputation values process thanks to the use of smart contract protects our B-Smart protocol against this type of attacks.

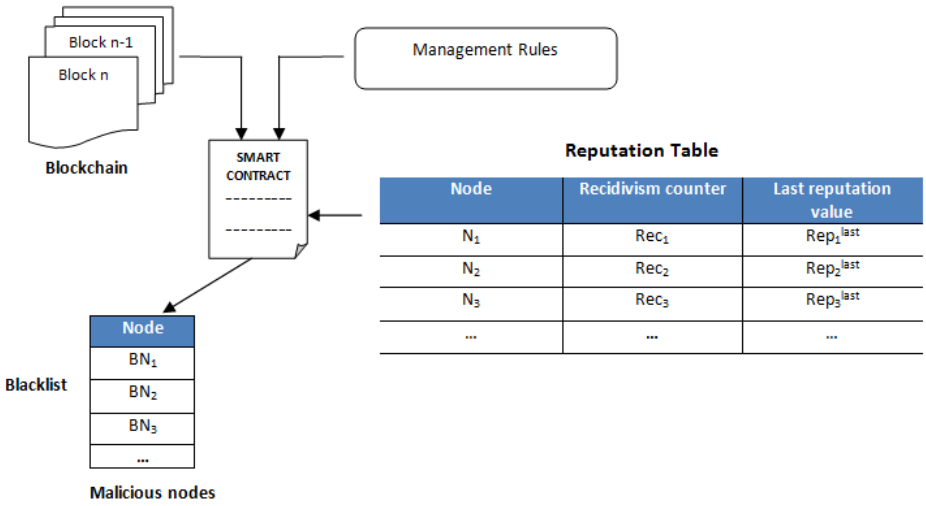


Figure 6. Simplified architecture of smart contract in B-Smart

On/Off Attack

In this type of attack, the malicious node will proceed in two phases, a phase "on" and a phase "off". During the "on" phase, the attacker launches the attack. It will act negatively in the network, taking advantage of its high reputation value which will allow him to remain undetectable for a moment. During the "off" phase, the attacker will behave correctly to increase its reputation and gain the trust of those around him. This attack is efficiently handled in our B-Smart protocol. Indeed, during the phase one, the attacker will have good behavior which will bring him an increase in its reputational value. The smart contract will thus increase its Rep_i^{last} of α (with α= 0.05) as long as Rec_i= 0. During the off-phase, the attacker will behave in a malicious way; its recidivism factor will thus increase by 1 to each bad behavior. The process used in the calculation of reputation values by the smart contract allows for a small increase in reputation values in the case of good behaviors but leads to an exponential decrease of these values during malicious one. So, even if the malicious node generating an on / off attack can increase its reputation value, this value will drop below the threshold of honesty (β= 0,3) after only 1 to 2 bad behaviors at the most.

Conflicting Behavior Attack

In this attack, the malicious node behaves differently with the nodes of the network. Indeed, it will have good behavior with a few nodes, which will earn it positive reputation values. On the other hand, it will behave in a prejudicial way with the other nodes which will therefore judge it negatively. The conflicting behavior will occur when the nodes of the first group will exchange on the reputation of this malicious node with the other nodes. Having different reputation values will undermine the trust of the nodes of the first group in relation to those of the second and vice versa, thus creating conflict. The problematic relating to this attack does not arise in our B-Smart protocol. Indeed, the node is judged independently in each transaction. If it has a good behavior its reputation is increased, otherwise the latter will tend to decrease tragically. Therefore, whatever an adversary performs, it has no power to create a conflict.

Intelligent Behavior Attack

In this attack, the malicious node is extremely intelligent. It will indeed adapt its behavior according to its reputation value. As a result, it will behave differently at each time period by selectively providing good or bad services or by assigning low or high recommendation values based on the confidence level. To try to remain undetectable in the network against our B-Smart protocol, the intelligent attacker has no choice; it must absolutely adopt a good behavior in the majority of the cases. Because otherwise, the recidivism factor that we used will quickly decrease its reputation value which will earn it the isolation of the network and integration in the blacklist. By keeping a good behavior, the attacker will not have a negative impact on the network.

Whitewashing Attack

Reputation systems are known to be particularly vulnerable to whitening attacks. In this attack, a malicious node whose reputation value has greatly diminished has the opportunity to re-enter the network with a new identity and a fresh reputation. To parry these attacks, the new nodes in our protocol are not completely trustworthy; they must pass a test period in which they will have to perform a large number of satisfying tasks in order to gain a normal reputation value. This process is similar to the "proof of work" procedure used in blockchain. It allows discouraging this type of attack because by reentering the network with a new identity the attacker must provide a lot of effort and consume a lot of energy resources. In addition to being resistant to reputation attacks, our B-Smart protocol perfectly detects routing attacks. We describe in the following the main routing attacks and the means used by our B-Smart protocol to fight against them.

Routing Attacks

We include in the category of routing attacks all attacks that threaten the routing of information by deleting, altering, modifying or bypassing the transit path of messages.

Spoofed, Altered, Replayed Information

In this type of attacks, malicious nodes aim to fabricate non-existent information, change some data and replay messages to disrupt network operation especially by creating routing loops or increasing end-to-end latency. The detection of this attack in our protocol is done through the comparison made by the smart contract between the information contained in the head of the block (the main statement of the transaction, the routing path defined by the routing protocol) and the various phases of execution of the transaction through the different nodes. Such a comparison allows noticing immediately any change in the body or in the routing of the transaction. B-Smart effectively detects this type of attack and our recidivism factor will severely reduce the reputation values of the compromised node.

Selective Forwarding Attack (Greyhole Attack)

Similar in several points, the selective forwarding and the greyhole attacks both refuse to send messages to certain nodes or to certain destinations. The comparison made by the smart contract between the header of the transaction block containing the routing path defined by the routing protocol and the path followed by the transaction during its execution, allows effective detection of any deviation from the initial path. The B-Smart protocol allows an effective detection of these two types of attacks and can severely punish the nodes responsible for malicious behavior.

Sinkhole, Blackhole and Wormhole Attacks

These three attacks share the fact that they are placed in an optimal routing path in order to capture a maximum of traffic. Data passing through these attackers are recovered and never retransmitted. Indeed, the malicious node will be placed on the road leading to the base station during the sinkhole attack. By manipulating the routing tables, the compromised node will be closer and more attractive than in reality to attract as much data as possible during the blackhole attack. Tricking nodes over distances and influencing the routing tables through the creation of low latency tunnels during the wormhole attack. The development of the routing paths in our

protocol is independent of the nodes. It is indeed carried out thanks to the information provided by the smart contract. So, a node wishing to generate one of these three attacks has no influence on the other nodes to force them to transmit the data through it. In the case where one of the attackers is included in a routing path because it has a high reputation value, its reputation value is downright diminished once it performs its malicious task. It will never be chosen anymore to route information.

Sybil Attack

In this attack, the malicious node illegitimately creates a large number of malicious nodes in order to have a disproportionate influence in the network. Although our protocol fails to detect this type of attack, the *"test period"* applied for the new nodes of the network allows us to prevent this attack and to discourage its occurrence. Since the newcomers must perform a number of satisfying tasks in order to obtain a normal reputation value. On the other hand, the least malicious behavior will be penalized by a significant reduction in reputation value.

Node Replication Attack

In this attack, the attacker creates several replicas of a same node named "clones". These replicas have the same key pair and the same identifier. Since the smart contract holds a table with all node IDs, reputation values, and recidivism counter, the more the malicious node creates malicious replicas, the faster the node recidivism factor will increase, and the reputation value will decrease accordingly. In the extreme case where the node will try to remain undetectable by creating only one replica, our B-Smart protocol will detect this attack just as easily as the recidivism counter will increase twice as much as attacks generated by a single node.

Simulation Results

In this section, we present results of our simulations showing the performance of our reputation model. Two simulation experiments are carried out to validate the effectiveness of our proposed scheme. Firstly, we analyze reputation evaluation process of our B-Smart protocol. Secondly, we check the effectiveness of our scheme by considering the impact of two main attacks: on/off and conflicting behavior. MATLAB software is used as simulation tool to assess the performance of our protocol. A comparison is made between B-Smart, RaRTrust (Labraoui et al., 2015) and RFSN (Ganeriwal et al., 2008) in the On/off attack scenario and between B-Smart and ATSN (Chen et al., 2007) in the conflicting behavior attack scenario.

Simulation is set up as follows. All nodes of the network are initialized with the same reputation value equal to 0.5 and are considered trust. The behavior of the nodes is judged according to all the transactions in which they participate. A recidivism factor Rec_i is assigned to each node of the network. This counter is used to record the number of bad behaviors performed by the node. The reputation value of node i will entirely depend on the value of this counter. The default simulation parameters are summarized in (Table 2).

Table 2. Simulation parameters

Parameter	Default Value
Area (m^2)	100 x 100
Number of nodes	100
Radio Range (m)	25

Reputation Evolution Analysis

Existing TRS are either based on direct information or on both direct and indirect information when calculating confidence values. Both methods have advantages and disadvantages. In fact, using only the first-hand values effectively protects the protocols from malicious recommendations attacks. However, this method has serious drawbacks. Indeed, lot of time is needed to establish the reputation values and these values will also take a lot of time to decrease, allowing the attacker to stay longer in the network. On the other hand using also indirect ones can provide additional information to nodes about other nodes they know little or they do not know. However, they expose themselves to possible presence of malicious nodes among these recommenders.

In this section, we analyze the process of automating the calculation of the reputation values of our B-Smart protocol based on the use of the smart contract. For this purpose, we compare the behavior of our protocol with two trust and reputation protocols based on the use of first-hand and second-hand information namely RFSN (Ganeriwal et al., 2008) and RaRTrust (Labraoui et al., 2015). Direct observation in RaRTrust and in RFSN are called DT-RaRTrust and DT-RFSN respectively and indirect observations are called as IT-RaRTrust and IT-RFSN respectively.

Case (1). The scenario is as follows: we perform an analysis on the evolution of the reputation values of a given node i. This node is a legitimate node of the network, initialized with a reputation value equal to 0.5. It has a good behavior during the first 40 units of time. At some time tps ∈ [40, 50] this node is compromised. At tps = 50, it starts its malicious behavior.

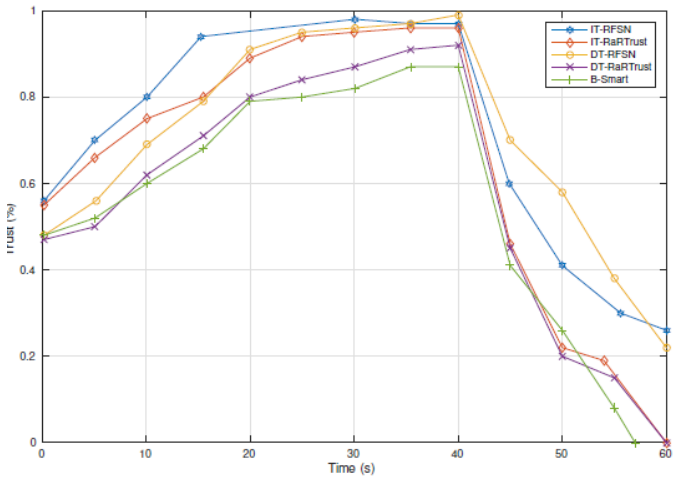


Figure 7. Reputation values evolution.

We can show clearly from (Figure 7) that reputation values of node i increase slowly in our protocol than in other protocols. This can be explained by the fact that the reputation value increases by α at each good behavior of the node, a slow and linear increase encouraging the nodes to have a large number of good behaviors in order to acquire a high reputation value. On the other hand, at the first "bad behavior", the reputation value of the node will plummet faster than in the RFSN and RaRtrust protocols thus allowing for our B-Smart protocol a faster detection of malicious nodes. These results are possible thanks to automation of the reputation calculation process in our B-Smart protocol through the use of an independent, unbiased and secure entity namely "smart contract". This automation allows the network to enjoy the benefits of the first hand and second hand methods while being resistant to their disadvantages.

Trust and Reputation Attacks Analysis

The primary goal of automating the assignment of reputation values process is to strengthen the resistance of the trust and reputation mechanisms against attackers who use them to launch a multitude of attacks such as: bad mouthing, ballotstuffing, on/off, conflicting behavior, intelligent behavior and whitewashing attacks. In this section, we analyze the resistance of our protocol against two main attacks that threaten the TRS namely: on/off and conflicting behavior attacks. Dishonest recommendations attacks including badmouthing, ballot-stuffing and collusion are not taken into consideration in our simulations since our protocol is perfectly resistant to this type of attacks. Indeed, the use of smart contract relieves the nodes of having to ask for reputation values from recommender's nodes.

On/Off Attack Resiliency

During on/off attack, malicious nodes behave well and badly alternately, hoping to stay undetectable while causing as much damage as possible. For instance, in this attack, once the malicious node acquires a high reputation value in the off phase thanks to it good behavior, i.e., forwards messages correctly, it begins the on stage of the attack by acting in a malicious manner i.e. drops, alters or modifies messages. The simulation scenario of this attack is the following:

Case (2). We consider a malicious node i. In the off phase, node i correctly transmits the messages in each transaction where it is involved. It launches the on phase of the attack at tps = 6 units of time. This cycle on is immediately followed by an off cycle at tps = 10.

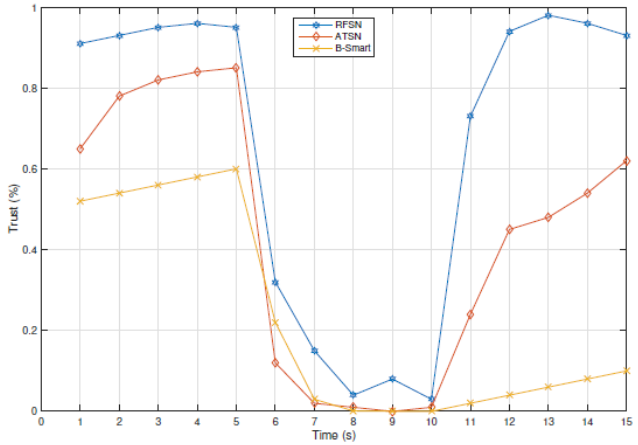


Figure 8. On/off attack of node i.

(Figure 8) shows the simulations comparison results performed between our B-Smart protocol and the ATSN (Chen et al., 2007) and RFSN (Ganeriwal et al., 2008) protocols. In our protocol the reputation value of the malicious node i increases slowly during the off phase of the attack and its corresponding recidivism counter is at 0. During the on phase, the reputation value of the node i decreases sharply in BSmart as the recidivism counter Reci of the node i increases with each bad behavior. This exponential decrease allows a quick and efficient detection of the malicious node. In the RFSN protocol also the reputation value decreases rapidly also, however, the latter increases more rapidly during the off-phase of the attack. Indeed, contrary to the RFSN protocol, B-Smart remembers the malicious behavior of the node since the value of the recidivism factor associated with node i is permanently stored in the smart contract held by the blockchain. So, even if during the next phase off, the malicious node manages to increase its reputation value slightly, it will decrease even more sharply in the next phase "on" given the already high values of the recidivism counter. We can conclude that our B-Smart protocol is more efficient than ATSN and RFSN for the detection of the on/off attack. Its operating principle based on the use of recidivism counter as well as a smart contract allows an increasingly rapid detection of this attack from one cycle to another.

Conflicting Behavior Resiliency

Although insidious, conflicting behavior is an attack that has not achieved much interest from researchers working on the field of security in trust and reputation mechanisms in WSNs. This attack has the power to create conflicts between groups of nodes thus creating a lack of mutual trust between them. At this attack, a malicious node i behaves well with a group of nodes (A, B and C), i.e., correctly sends the messages in transit of these nodes, they will assign him positive reputation values. In parallel, the same malicious node i will behave badly with a second group of nodes (F and G), i.e., delete, alter or modify the messages of these nodes. They will therefore assign him negative reputation values. The conflict occurs when a node in the first group (exp: A) exchanges with a node in the second group (exp: F) on the reputation of that malicious node. Node (A), which is sure that i is a legitimate node, will think that node (F) is lying to it and will judge F as malicious and vice versa.

Case (3). In this scenario, the node i launches a conflicting behaviour attack. It will behave differently with two distinct groups of nodes.

Figure 9 shows the results of the simulations performed during the conflicting behavior attack. We notice that in the ATSN protocol, node (A) continues to communicate with the malicious node i as long as it behaves in a good way with it. Node (A) will continue to trust the node i and give it a good reputation. Unlike node (A), node (F) assigns negative reputation values to node i because of its malicious behavior and stops cooperating with it. The reasoning of the ATSN protocol is not entirely correct for two main reasons: on the one hand, the node i is a malicious node and the fact of continuing to communicate with him exposes the node (A), the nodes of the first group as well as the entire network to various damage. On the other hand, by fully trusting the malicious node i, the nodes of the first group are exposed to a conflict with the nodes of the second group, a lack of confidence that can cause revocations of legitimate nodes deemed injuriously malicious.

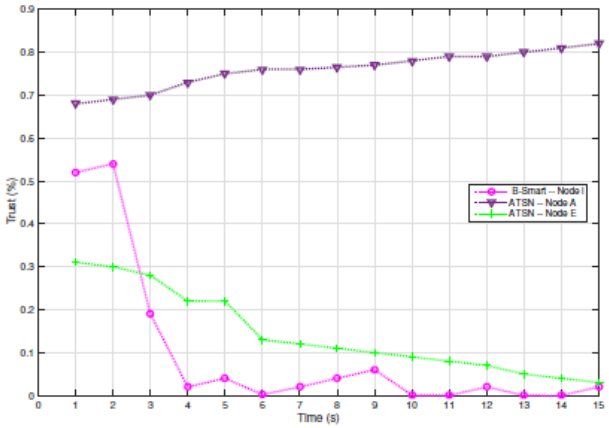


Figure 9. Conflicting behaviour attack of node i.

In our B-Smart protocol, the smart contract is responsible for calculating all reputation values by holding for each node a recidivism counter and a reputation value. These values are updated after each new transaction. This automation and independent computation of the nodes reputations values make it possible to judge impartially the nodes behaviors. The results of the curve of our B-Smart protocol clearly demonstrate this operating spirit. Indeed, as soon as the malicious node misbehaves its reputation value will decrease and conversely when it acts positively. We can conclude that our B-Smart protocol outperforms the ATSN protocol facing the conflicting behavior attack.

Conclusion

The effectiveness of trust and reputation systems in WSNs is no longer to be proven. However, the development of such mechanisms creates additional security issues for these networks. Indeed, malicious nodes introduced into these systems will have the power to manipulate the values as they please, thus distorting the results of the TRSs. We presented in this work a robust reputation based blockchain scheme in WSNs, which is designed to address the problem of abusive manipulation of reputation values by malicious nodes. In our proposal B-Smart, the calculation of reputation values is entrusted to a smart contract; an independent and secure entity, making it possible to judge the behavior of the nodes impartially and assign them the corresponding reputation values. The backup of all transactions as well as the smart contract in a blockchain structure will ensure their durability, integrity as well as resistance to any intentional modification by malicious nodes. Automating the assignment reputation values process thanks to the smart contract offered our protocol a great resistance as well as an effective detection of many internal attacks. Indeed, security analysis demonstrates the resiliency of B-Smart against trust and reputation attacks as well as routing attacks. Besides, our simulation results demonstrate that the proposed scheme can efficiently isolate malicious nodes from the network. The different simulation scenarios proved the effectiveness of our protocol under various attacks scenarios. As a future work, we intend to use our protocol for securing the multi-path routing in WSNs.

Scientific Ethics Declaration

* The authors declare that the scientific ethical and legal responsibility of this article published in EPSTEM journal belongs to the authors.

Conflict of Interest

* The authors declare that they have no conflicts of interest

Funding

* This work has no funds

Acknowledgements

* This article was presented as virtual presentation at the International Conference on Technology, Engineering and Science (www.icontes.net) held in Antalya/Türkiye on November 12-15, 2025.

References

Alzaid, H., Alfaraj, M., Ries, S., Jøsang, A., Albabtain, M., & Abuhaimed, A. (2013). Reputation-based trust systems for wireless sensor networks: A comprehensive review. In *IFIP International Conference on Trust Management* (pp. 66-82). Springer.

Amol, R., & Chatur, D. P. (2016). Detection of on-off attack based on predictability trust in wireless sensor network. *International Journal of Advanced Computational Engineering and Networking, 4*(12).

Bagchi, R. (2017). Using blockchain technology and smart contracts for access management in IoT devices. *Computer Science, 80*(9). https://helda.helsinki.fi/server/api/core/bitstreams/97b74ad0-c46c-41ea-a42b-5f967370a64b/content

Benet, J. (2014). IPFS-content addressed, versioned, P2P file system. *arXiv*.

Bhuiyan, T. (2013). *Trust for intelligent recommendation*. Springer.

Buchegger, S., & Le Boudec, J. Y. (2002). Performance analysis of the CONFIDANT protocol. In *Proceedings of the 3rd ACM International Symposium on Mobile Ad Hoc Networking & Computing* (pp. 226-236).

Chen, H. (2012). RASN: Resist on-off attack for wireless sensor networks. In *Proceedings of the 2nd International Conference on Computer Application and System Modeling*.

Chen, H., Wu, H., Zhou, X., & Gao, C. (2007). Agent-based trust model in wireless sensor networks. In *Eighth ACIS International Conference on Software Engineering, Artificial Intelligence, Networking, and Parallel/Distributed Computing (SNPD 2007)* (Vol. 3, pp. 119-124). IEEE.

Chen, S., Zhang, Y., Liu, Q., & Feng, J. (2012). Dealing with dishonest recommendation: The trials in reputation management court. *Ad Hoc Networks, 10*(8), 1603-1618.

Clausen, T., & Jacquet, P. (2003). *Optimized link state routing protocol (OLSR)* (RFC 3626). IETF.

Di Pierro, M. (2017). What is the blockchain? *Computing in Science & Engineering, 19*(5), 92-95.

Ganeriwal, S., Balzano, L. K., & Srivastava, M. B. (2008). Reputation-based framework for high integrity sensor networks. *ACM Transactions on Sensor Networks (TOSN), 4*(3), 1-37.

Gupta, J. (2025). A comprehensive review of trust and reputation-based routing protocols in wireless sensor networks (WSNs): Models, challenges, and future directions. *Eksplorium-Buletin Pusat Teknologi Bahan Galian Nuklir, 46*(1), 294-300.

Haas, Z. J., & Pearlman, M. R. (2000). Providing ad-hoc connectivity with the reconfigurable wireless networks. In *Ad Hoc Networks*. Addison Wesley Longman.

Hamma, T., Katoh, T., Bista, B. B., & Takata, T. (2006). An efficient ZHLS routing protocol for mobile ad hoc networks. In *17th International Workshop on Database and Expert Systems Applications (DEXA'06)* (pp. 66-70). IEEE.

Hartman, J. H., Murdock, I., & Spalink, T. (1999). The Swarm scalable storage system. In *Proceedings 19th IEEE International Conference on Distributed Computing Systems* (pp. 74-81). IEEE.

Johnson, D. B., & Maltz, D. A. (1996). Dynamic source routing in ad hoc wireless networks. In *Mobile Computing* (pp. 153-181). Springer.

Khedim, F., Labraoui, N., & Lehsaini, M. (2015). Dishonest recommendation attacks in wireless sensor networks: A survey. In *2015 12th International Symposium on Programming and Systems (ISPS)* (pp. 1-10). IEEE.

Labraoui, N., Gueroui, M., & Sekhri, L. (2015). On-off attacks mitigation against trust systems in wireless sensor networks. In *IFIP International Conference on Computer Science and its Applications* (pp. 406-415). Springer.

Labraoui, N., Gueroui, M., & Sekhri, L. (2016). A risk-aware reputation-based trust management in wireless sensor networks. *Wireless Personal Communications, 87*(3), 1037-1055.

Madisetti, V. (2016). Blockchain platform for industrial Internet of Things. *Journal of Software Engineering and Applications*, *9,* 533-546.

Michiardi, P., & Molva, R. (2002). CORE: A collaborative reputation mechanism to enforce node cooperation in mobile ad hoc networks. In *Advanced Communications and Multimedia Security: IFIP TC6/TC11 Sixth Joint Working Conference on Communications and Multimedia Security* (pp. 107-121). Springer.

Moeinaddini, E., Nazemi, E., & Shahraki, A. (2025). A new approach on self-adaptive trust management for social Internet of Things. *Computer Networks, 263*, 111187.

Nakamoto, S. (2008). *Bitcoin: A peer-to-peer electronic cash system*. https://www.klausnordby.com/bitcoin/Bitcoin_Whitepaper_Document_HD.pdf

Navaei Tourani, A., Haj Seyyed Javadi, H., Navidi, H., & Sharifi, A. (2025). A study on trust-rating mechanism for WSN node sensors using evolutionary game theory. *The Journal of Supercomputing, 81*(2), 401.

Othmen, S., Rekik, M., Zarai, F., Belghith, A., & Kamoun, L. (2016). Shortest and secure routing protocol for multi-hop cellular networks (SSRP-MCN). *Security and Communication Networks, 9*(18), 5346-5362.

Oztoprak, A., Hassanpour, R., Ozkan, A., & Oztoprak, K. (2024). Security challenges, mitigation strategies, and future trends in wireless sensor networks: A review. *ACM Computing Surveys, 57*(4), 1-29.

Perkins, C., Belding-Royer, E., & Das, S. (2003). *Ad hoc on-demand distance vector (AODV) routing* (RFC 3561). IETF.

Perkins, C. E., & Bhagwat, P. (1994). Highly dynamic destination-sequenced distance-vector routing (DSDV) for mobile computers. *ACM SIGCOMM Computer Communication Review, 24*(4), 234-244.

Pourtahmasbi, P., & Nojoumian, M. (2022). Analysis of reputation-based mining paradigm under dishonest mining attacks. *Blockchain: Research and Applications, 3*(2), 100065.

Rodrigues, P., & John, J. (2020). Joint trust: An approach for trust-aware routing in WSN. *Wireless Networks, 26*(5), 3553-3568.

Saleh, L., Taleb, A. A., & Salameh, W. A. (2020). Trust and reputation in wireless sensors networks. In *2020 21st International Arab Conference on Information Technology (ACIT)* (pp. 1-6). IEEE.

Szabo, N. (2017). Winning strategies for smart contracts. *Blockchain Research Institute*. https://grazielabrandao.wordpress.com/wp-content/uploads/2019/06/g86cmijoeemm8wp4g3tktg_1c16c8a028ce11e999f58be72bb04114_szabo-smart-contracts-v6d_1_.pdf

Tenhundfeld, N., Demir, M., & de Visser, E. (2022). Assessment of trust in automation in the "real world": Requirements for new trust in automation measurement techniques for use by practitioners. *Journal of Cognitive Engineering and Decision Making, 16*(2), 101-118.

Underwood, S. (2016). Blockchain beyond bitcoin. *Communications of the ACM, 59*(11), 15-17.

Yan, Y. (2022). The overview of elliptic curve cryptography (ECC). In *Journal of Physics: Conference Series* (Vol. 2386, No. 1, p. 012019). IOP Publishing.

Yilmaz, S., & Dener, M. (2024). Security with wireless sensor networks in smart grids: A review. *Symmetry, 16*(10), 1295.

Yu, Y., Li, K., Zhou, W., & Li, P. (2012). Trust mechanisms in wireless sensor networks: Attack analysis and countermeasures. *Journal of Network and Computer Applications, 35*(3), 867-880.

Zhang, B., Huang, Z., & Xiang, Y. (2014). A novel multiple-level trust management framework for wireless sensor networks. *Computer Networks, 72*, 45-61.

Zhang, J. (2025). WSN network node malicious intrusion detection method based on reputation score. *Journal of Cyber Security and Mobility, 12*(1), 55-76.

Zouridaki, C., Mark, B. L., Hejmo, M., & Thomas, R. K. (2009). E-Hermes: A robust cooperative trust establishment scheme for mobile ad hoc networks. *Ad Hoc Networks, 7*(6), 1156-1168.

Author(s) Information

Farah Khedim
University Centre of Maghnia, Route de Zouia, N99, Chouhada District, Maghnia, Tlemcen, Algeria
Contact e-mail: *f.khedim@cu-maghnia.dz*

Nabila Labraoui
University of Tlemcen
P.O.Box 230, chetouane, Tlemcen 13000, Algeria

Ado Adamou Abba-Ari
Saint-Quentin-en-Yvelines University/ University of Maroua
45 Avenue États-Unis 78035 Versailles cedex, France/ P.O. Box 814 Maroua, Cameroon

To cite this article:

Khedim, F., Labraoui, N., & Abba-Ari, A. A. (2025). B-Smart: A robust reputation-based blockchain scheme in wireless sensor networks. *The Eurasia Proceedings of Science, Technology, Engineering and Mathematics (EPSTEM), 38,* 771-790.

The Eurasia Proceedings of Science, Technology, Engineering & Mathematics (EPSTEM)
ISSN: 2602-3199

The Eurasia Proceedings of Science, Technology, Engineering and Mathematics (EPSTEM), 2025

Volume 38, Pages 791-797

IConTES 2025: International Conference on Technology, Engineering and Science

Carbon Fabric-Reinforced Polymeric Composites Produced by Hand Lay-Up and Investigation of the Tensile Behavior

Ozhan Sirin
OSTIM Technical University

Yusuf Sahin
OSTIM Technical University

Emir Can Omer
OSTIM Technical University

Abstract: Composite materials are recognized as advanced materials, which can be formed by combining different constituents, excellent mechanical properties can be achieved by chosen appropriate elements and processing. This paper describes that Carbon Fabric Reinforced Epoxy Composites (CFRPs) are produced using twill weave carbon fibers with CR-80 epoxy resin through hand lay-up method. The composite laminates are designed with 10th layers of stacking [0/0/0/0/0]s in with 3.0 mm thickness. Tensile tests are carried out at longitudinal orientation and transverse orientation of the samples in addition to analytical analysis models. A comparison is made between the experimental results of tensile tests data and evaluated statistical point of view. Experimental results indicated that average tensile strength of the composites was obtained around 427 MPa for the longitudinal orientation [0o], while for transverse orientation [90o] sample, average tensile strength was 359 MPa, which is lower than that of the sample. Further, it was concluded that analytical analysis is a good agreement with experimental data.

Keywords: Carbon twill fiber, CR-80 epoxy resin, Hand lay-up, Fiber orientation, Tensile Strength, Elongation rate, Analytical analysis

Introduction

Composite materials are materials that are aimed to exhibit superior properties by combining the characteristics of materials from different classes. A composite material is formed by the combination of at least two different materials. This combination must occur without dissolution. At least one of these materials is a reinforcement material, and the structure surrounding the reinforcement is called the matrix (Çakır and Berberoğlu 2018). Synthetic fiber-reinforced composites such as aramid and carbon, as well as glass and carbon fibers, are widely used in many industries, particularly in automotive, construction, and aerospace, due to properties such as high strength and lightness (Tasgın and Kandemir 2023).

With the development of fiber technology in recent years, the use of technical fibers with superior properties such as carbon fiber, which are advantageous due to being lightweight and having corrosion resistance, has become widespread as reinforcement materials in composites in various forms in order to increase their strength. Although carbon fiber–reinforced polymeric composite materials have high in-plane strength and stiffness, they require strengthening due to their low interlaminar performance properties determined by the characteristics of the matrix, their high sensitivity to damage especially against impact and fatigue, and the fact that they cannot be repaired once damaged (Korkmaz et al. 2016; Cakır and Berberoglu, 2018). Carbon fibers/fabrics are selected as reinforcements in making composites because the chemical resistance, higher tensile/hardness, toughness and

- This is an Open Access article distributed under the terms of the Creative Commons Attribution-Noncommercial 4.0 Unported License, permitting all non-commercial use, distribution, and reproduction in any medium, provided the original work is properly cited.

- Selection and peer-review under responsibility of the Organizing Committee of the Conference

© 2025 Published by ISRES Publishing: www.isres.org

wear resistance increase while epoxy resin is chosen as matrix due to having excellent mechanical properties, having good adhesion behavior with fibers, but it is brittle (Sirinivas and Bhagyashekar, 2021). More importantly, they have a high strength to density ratio for use in demanding polymer processing operations for various applications.

Composite materials store damage within their structure, and damage does not always occur as macroscopic failure. Types of damage such as fiber damage, delamination, transverse ply cracking, and matrix cracking may occur. Therefore, application of tensile tests and the determination of the durability of composite materials are of great importance (Irmak et al. 2016). Salviato et al. (2016) investigated the effect of specimen size and the presence of notches on the fracture behavior of twill-woven carbon/epoxy composites using both experimental and numerical methods, demonstrating that size effects played a critical role in understanding material strength. Similarly, Niutta et al. (2023) performed tensile and flexural tests on twill-woven carbon composites produced with epoxy and bio-based epoxy matrices, comparing the results with numerical models to establish modeling accuracy. In addition, Yan et al. (2024) showed, through combined experimental and numerical analyses, that the loading rate had a pronounced influence on the tensile property at the carbon fiber/epoxy interface. Other studies showed that the mechanical behavior of twill-woven carbon/epoxy composites could be evaluated reliably not only with experimental data but also through numerical modeling. Therefore, the combined use of experimental tensile tests and numerical analyses contributed to the accurate prediction of the material's strength and elastic properties (Ashby & Jones, 2012).

Mechanical and physical properties of the polymer based composites are very important because many variables such as type of fiber/matrix, volume fraction of fiber, diameter of fibers, and distribution of fibers, processing, consolidation, and interface bonding between the constituents affect the output (Sahin, 2022). Tensile tests are among the most commonly used methods for determining the mechanical properties of materials. These tests enable the calculation of parameters such as tensile strength, elastic modulus, and yield strength. The literature indicates that when fiber-reinforced composites and anisotropic materials are subjected to tensile testing along different directions, the material behavior varies significantly (Ashby & Jones, 2012). It is also emphasized that the repeatability of the data obtained from the tests depended largely on specimen preparation and test conditions (ASTM, 2015). In this study, low cost epoxy based composites have been produced by hand lay-up method using carbon fabrics with twill types of reinforcements. Then, the effects of orientation on mechanical property like tensile strength are determined according to ASTM standard by tensile tests.

Material and Method

Manufacturing of Composites

In manufacturing of composite materials, carbon fiber fabric with a Twill weave structure was used, which it has a 245 g/m² areal weight with a thickness of 0.25 mm, and a density of 1.76 g/cm³. According to the COC document provided by the manufacturer of this fabric, its tensile strength is 3800 MPa and its elastic modulus is 240 GPa. In the production of the composite, Sika Biresin CR-80 epoxy and its hardener were used as the matrix. CR-80 is a low-viscosity epoxy resin system suitable for the production of high-performance reinforced composite parts. CH80-1 hardener was used as the hardener. The density of this resin after mixing is 1.15 g/cm³, the tensile strength is 88 MPa, and the elastic modulus is 3000 MPa. The data obtained from the COC documents for the fiber and resin are listed in Table 1 below.

The composite material to be produced was targeted to have dimensions of 400 × 400 × 2.5 ±0.5 mm, and accordingly, since the fiber thickness is 0.25 mm, it was planned to be 10 layers with 0° orientation. Based on the selected fiber and resin, the hand lay-up method was chosen as the production method. The production process includes the following steps: (a) Preparation of mold surface: A flat mold surface was used for composite production. A polyvinyl alcohol-based release agent was applied to the surface to prevent the resin from adhering to the mold. (b) Cutting of layers: Twill 245 carbon fiber fabric was cut into 10 layers of 400 × 400 mm. Each layer was arranged according to 0° orientation. (c) Preparation of resin and hardener: CR-80 epoxy resin and CH80-1 hardener were weighed and adjusted at a ratio of 30 grams of hardener per 100 grams of epoxy resin. (d) The mixture was stirred at low speed until it achieved a homogeneous consistency and was degased under vacuum to prevent air bubbles. (e) Impregnation of layers: Each carbon fabric layer was placed on the mold surface and fully impregnated with resin using a brush and roller. This process was repeated for each layer. (f) Curing process: After placing the layers, the plate was left to cure for 24 hours at room temperature (23–25 °C).

Table 1. Data obtained from COC documents for fiber and resin

	Fiber	Matrix
Material Name	*Twill 245 Carbon Fiber*	*SikaBiresin CR-80 Epoxy*
Type	Woven Fabric (Twill 2/2)	Thermoset Epoxy CH80-1 Hardener
Density (g/cm³)	1.76	1.15 (Blend)
Tensile Strength (MPa)	3800	85–88
Elastic Modulus (GPa)	240	3000
Thickness (single layer)	0.25 mm	—
Areal Weight (g/m²)	245	—
Elongation at Break (%)	—	6.3
Glass Transition Temperature (°C, Tg)	—	98
Hardness	—	Shore D85

Cutting/Tensile Testing

After the plate production was completed, 10 specimens, each with dimensions of 180 × 25 mm, were cut using a CNC machine in accordance with ASTM D3039 standard. Five of these specimens were cut parallel (0°) to the fiber direction, while five of others were cut perpendicular (90°) to the fiber direction from the plate. Each specimen was numbered sequentially from 1 to 10, with the first five parallel to the fiber direction and the next five perpendicular. At the ends of these specimens, tabs with a length of 50 mm and a width suitable for grips of the testing machine were bonded. These tabs were cut from a high-strength composite plate prepared with CR-80 epoxy resin and CH80-1 hardener. Prior to application, both the specimen end surfaces and tab surfaces were sanded to roughen them and then cleaned with acetone. The resin mixture was applied as a thin layer to both surfaces, and the tabs were aligned and pressed onto the specimen ends manually, as shown in Figure 1. This procedure was carried out to prevent end failures during testing and to distribute the load uniformly.



Figure 1. The composite specimen with twill pattern prepared for tensile test

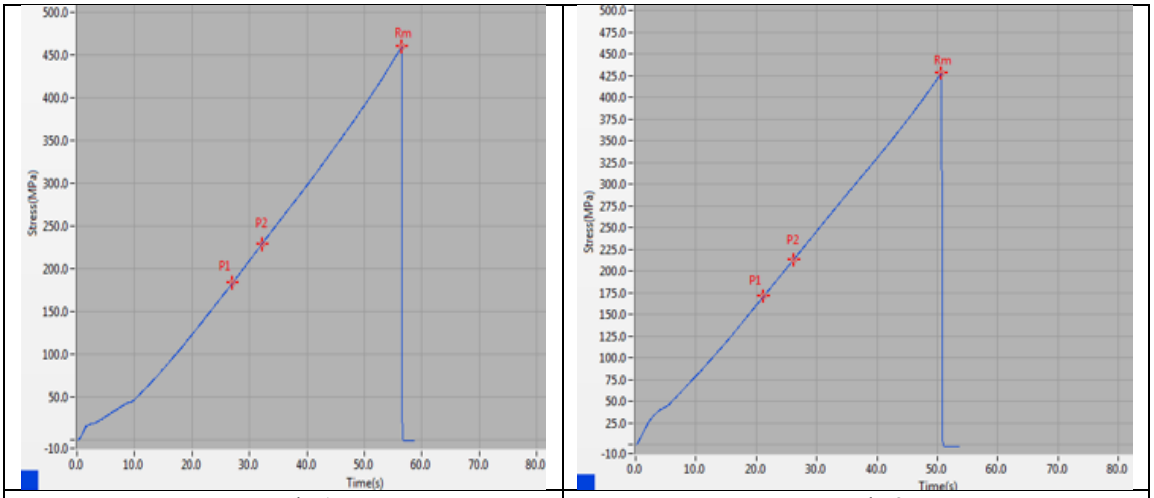
Tensile tests were applied to the prepared specimens in accordance with the ASTM D3039 standard. The tensile test was carried out with a MITECH brand, DW-CN-2008 model, at 22 °C ambient temperature and 51% humidity. The tensile cross-speed of the device was set at 2 mm/min, and the test was performed separately for 10 specimens.

Results and Discussion

For the tensile test conducted, at least five measurements have been obtained from the different composite specimens, the values recorded for each specimen and the average values longitudinal and transverse orientations are presented in the Table 2 and 3, respectively. Average ultimate tensile stress and strain at break values are obtained about 426.9 MPa and 1.72 mm during the tensile test, shown in Fig.1. Whereas, average maximum force to break the composite specimens was 33.4 kN. In the case of tensile test results perpendicular to the fiber axis and their averages as indicated in Table 3 and Fig. 2, lower mechanical properties were obtained. For example, average values for tensile strength and elongation rate were about 359 MPa and 1.52 mm, respectively. The maximum force to break the samples was reached to 27.0 kN.

Table 2. Tensile test results parallel to the fiber axis and their averages

Data	1st test	2nd test	3rd test	4th test	5th test	Average value
F-max (kN)	36.10	32.84	30.26	32.21	35.35	33.35
Crosshead speed (mm/min)	2.00	2.00	2.0	2.00	2.00	2.00
Thickness (mm)	3.06	3.04	3.09	3.07	3.11	3.07
Width (mm)	25.60	25.25	25.60	25.32	25.25	25.40
Length (mm)	150.00	150.00	150.00	150.00	150.00	150.00
Cross-sectional area (mm²)	78.34	76.76	79.10	77.73	78.53	78.09
Duration (s)/Extension (mm)	56.45	50.71	46.31	50.21	53.87	51.51/1.72
Tensile strength (N/mm²)	459.69	427.83	382.53	414.37	450.16	426.92

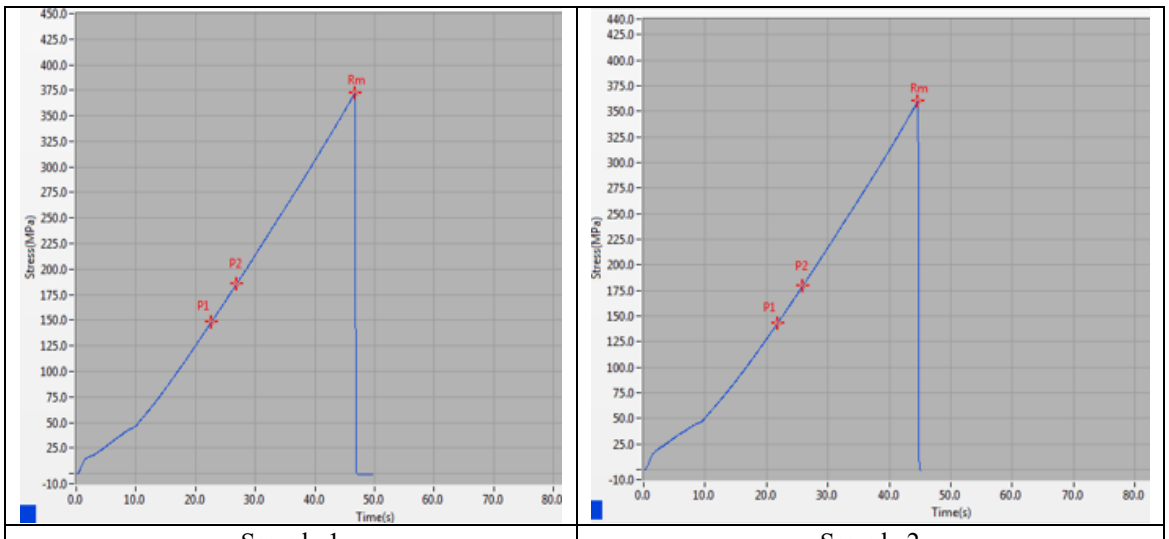


Sample 1 | Sample 2

Figure 1. Tensile stress vs. time in longitudinal orientation (0 degree)

Table 3. Tensile test results perpendicular to the fiber axis and their averages

Data	1st test	2nd test	3rd test	4th test	5th test	Average value
F-max (kN)	28.14	27.67	28.16	24.15	27.09	27.04
Crosshead speed (mm/min)	2.00	2.00	2.00	2.00	2.00	2.00
Thickness (mm)	2.98	2.92	3.00	3.01	3.00	2.98
Width (mm)	25.48	26.26	25.2	25.19	25.1	25.45
Length (mm)	150.00	150.00	150.00	150.00	150.00	150.00
Cross-sectional area (mm²)	75.93	76.68	75.6	75.82	75.3	75.87
Duration (s)/Extension (mm)	46.86	-	47.04	45.3	44.71	45.9/1.52
Tensile strength (N/mm²)	370.6	375.14	372.49	318.51	359.76	359.30



Sample 1 | Sample 2

Figure 2. Tensile stress vs. Time in perpendicular orientation (90 degree)

Upon evaluation of the specimen measurements, the average tensile strength of the specimens cut parallel to the fiber direction was determined as 426.9 N/mm². The coefficient of variation for these values was approximately 7.2%, indicating an acceptable level of consistency. Similarly, for the specimens cut perpendicular to the fiber direction, the average tensile strength was 359.3 N/mm² with a coefficient of variation of approximately 6.6%, which likewise confirms the consistency of the measurements. Statistical analysis showed that the difference between the two groups was significant ($p \leq 0.05$). This result confirms that the load-carrying capacity of carbon fiber is markedly higher along the fiber direction (Table 4).

Table 4. Descriptive statistics and statistical comparison of tensile strengths

		Average	Standard Deviation	Min.	Mak.	Coefficient of variation (CV)	P-Value
Tensile Strength (N/mm²)	Parallel to the fiber axis	426.92	30.58	382.53	459.69	7.17	≈0.05
	Perpendicular to the fiber axis	359.3	23.54	318.51	375.14	6.55	

In this study, analytical predictions were generated using algorithms developed in MATLAB, with the mean values obtained from tensile tests as inputs. The algorithms performed calculations based on Classical Laminate Theory (CLT), taking into account parameters such as ply thickness, fiber orientation (0°/90°), elastic modulus, Poisson's ratio and matrix-reinforcement properties (Kav, 2006). As a result, a prediction of the maximum tensile strength was obtained. The summary of findings are presented in Table 5.

Table 5. Average tensile test and analytical analysis results

	Parallel to the fiber axis	Perpendicular to the fiber axis	Analytical Analysis	Analytical Analysis
	Average Tensile Test	Average Tensile Test	X0	Y0
Tensile Strength (N/mm²)	426.92	359.3	427.09	356.38

Based on the data we obtained, the results of the measured tensile strength and the analytical tensile results are similar. Comparing the specimens in the parallel direction with the analytical analysis result, the difference is 0.17 N/mm² and a negligible deviation of about 0.04% is observed. Comparing the specimens in the perpendicular direction with the analytical analysis result, the difference is 2.92 N/mm² and a small deviation of approximately 0.8% is observed. In both cases, the results obtained by analytical analysis and the experimentally determined average tensile strength strongly corroborate each other. It is argued that as the percentage of filler material increase, the hardness value of the material increases, while the amount of deformation under bending decreases (Bal, 2022). The increase in the glass fiber ratio in glass fiber–reinforced composites, the mechanical properties of composites (tensile strength, elongation, and elastic) improved with increasing glass fiber content (Çakır and Berberoğlu, 2018). For various fiber orientations like 0°/0°, 0°/90° and 0°/±45°/90°of tested samples, the main cause of damage was the compressive failure occurring in the ply with 0° orientation (Irmak et al. 2016). Similar work carried out on 0°, 90° and 45°direction, the elastic modulus varied with fiber orientation. The highest deformation occurred in specimens with 45° orientation, while the lowest deformation occurred in specimens with 0° orientation (Ozen, 2017), which is consistent with the current results.

Conclusion

In this study, the tensile performance of the twill-woven carbon reinforced epoxy composites produced by the hand lay-up method was investigated experimentally and analytically using the CLT. The findings are summarized as follows:

(1). Average maximum force to break the composite specimens tested at longitudinal orientation produced by hand-lay-up method was 33.4 kN while the maximum force to break the composite samples tested at perpendicular orientation was reached to 27.0 kN.
(2). The experimental mean tensile strengths were measured as 426.92 MPa and 359.30 MPa for the 0° and 90° direction, respectively. Coefficient of variations for these values were approximately 7.2%, 6.6% respectively.
(3). It was determined that there was no statistically significant difference between the analytical and experimental values. Elongation values were at a similar level between the experimental and numerical models. However, the

experimental mean elongations measured were larger in the parallel direction than that of the perpendicular direction.

Recommendations

Numerical analysis will be applied for such carbon fibers reinforced composites and compared to the experimental results.

Scientific Ethics Declaration

* The authors declare that the scientific ethical and legal responsibility of this article published in EPSTEM journal belongs to the authors.

Conflict of Interest

* The authors declare that there is no conflict of interest.

Funding

* This research received no internal or external funding.

Acknowledgements or Notes

* This article was presented as a/an oral/poster presentation at the International Conference on Technology, Engineering and Science (www.icontes.net) held in Antalya/Turkey on November 12-15, 2025.

References

Ashby, M. F., & Jones, D. R. H. (2012). *Engineering materials 1: An introduction to properties, applications and design*. Butterworth-Heinemann.

ASTM International. (2015). *Standard test method for tensile properties of plastics* (ASTM D638-15).

Aziz, S., Rashid, S., & Mohd Salleh, M. A. (2013). Theoretical prediction of CNT-CF/PP composite tensile properties using various numerical modeling methods. *Fullerenes, Nanotubes and Carbon Nanostructures, 21*(5), 411-416.

Bal, B. C. (2022). Lineer düşük yoğunluklu polietilen (LDYPE) ve odun unu ile üretilen kompozit malzemenin bazı teknolojik özellikleri üzerine bir araştırma. *Mobilya ve Ahşap Malzeme Araştırmaları Dergisi, 5*(1), 40-49.

Campos, C. A., Soufen, M. P., & Bueno, M. P. (2014). Comparative study of mechanical properties of woven carbon fiber twill and plain weave in laminates with epoxy matrix. *2nd Brazilian Conference on Composite Materials*, 1-5.

Cakir, M., & Berberoglu, B. (2018). E-Cam elyaf takviyeli epoksi matrisli kompozit malzemelerin elyaf oranındaki artış ile mekanik özelliklerindeki değişimlerin incelenmesi. *El-Cezerî Fen ve Mühendislik Dergisi, 5*(3), 734-740.

Erdogan, I., Kisa, M., Ozen, M., Demircan, G., & Kaya, A. I. (2023). Cam elyaf takviyeli epoksi nanokompozitlerin dinamik davranışlarının incelenmesi. *Harran Üniversitesi Mühendislik Dergisi, 8*(2), 78-90.

Hu, H., Wei, Q., Wang, T., Ma, Q., Pan, S., Li, F., Wang, C., & Ding, J. (2025). Theoretical prediction method for tensile properties of high-strength steel/carbon fiber-reinforced polymer laminates. *Polymers, 17*, 846.

Imak, A., Solmaz, M. Y., & Topkaya, T. (2016). Tabakalı hibrit kompozit malzemelerin yorulma davranışlarının analizi. *ECJSE, 3*(3).

Kav, K. (2006). *Mechanics of composite materials* (2nd ed.). Taylor & Francis Group.

Korkmaz, N., Cakmak, E., & Dayik, M. (2016). Dokuma karbon elyaf takviyeli karbon nano tüp-epoksi kompozit malzemelerin mekanik ve termal karakterizasyonu. *Süleyman Demirel Üniversitesi Fen Bilimleri Enstitüsü Dergisi, 20*(2).

Lafranche, E., Martins, C. I., Oliveira, V. M., & Krawczak, P. (2013). Prediction of tensile properties of injection moulding flax fibre reinforced polypropylene from morphology analysis. *Key Engineering Materials, 554*, 1573-1582.

Li, X., Zhang, Y., Shi, C., & Chen, X. (2020). Experimental and numerical study on tensile strength and failure pattern of high performance steel fiber reinforced concrete under dynamic splitting tension. *Construction and Building Materials, 259*, 119796.

Niutta, C. B., Ciardiello, R., & Paolino, D. S. (2023). Epoxy and bio-based epoxy carbon fiber twill composite: Comparison of the quasi-static properties. *Polymers, 16*(4), 1601.

Ozen, M. (2017). E-Cam/Epoksi kompozitlerde lif doğrultularının gerilme gevşeme davranışı üzerindeki etkisi. *Fırat Üniversitesi Mühendislik Bilimleri Dergisi, 29*(1), 219-224.

Pant, M., & Palsule, S. (2024). Prediction of tensile properties of natural fiber reinforced pp hybrid composites by facca-kortschot-yan (fky) and palsule equations. *Journal of Physics: IOP Conference Series, 2837*(1), 012005.

Salviato, M., Kirane, K., Esna Ashari, S., Bazant, Z., & Cusatis, G. (2016). *Experimental and numerical investigation of intra-laminar energy dissipation and size effect in two-dimensional textile composites* (SEGIM Internal Report No. 16-05/707E). Northwestern University, McCormick School of Engineering and Applied Science.

Srinivas, K., & Bhagyashekar, M. S. (2021). Prediction of mechanical properties of epoxy composites containing mono and hybrids particulate fillers. *IOP Conference Series: Materials Science and Engineering, 1189*(1), 012003.

Tasgin, Y., & Kandemir, S. (2023). Doğal elyaf takviyeli (jüt-keten-kenevir) kompozit malzemelerin mekanik ve metalografik olarak incelenmesi. *International Journal of Pure and Applied Sciences, 9*(2), 240-249.

Uzay, C., Cetin, A., Geren, N., Bayramoglu, M., & Tutuncu, N. (2024). Düz dokunmuş karbon fiber/epoksi laminatların çekme sertliği ve mukavemet özelliklerinin tahmini: Pratik bir analitik yaklaşım ve deneysel doğrulamalar. *İleri Malzeme ve Yapıların Mekaniği, 31*(12), 2619-2634.

Yan, K., Jiang, Z., Tang, J., Xie, X., & Suo, T. (2024). Experimental and numerical study on the loading rate effect on tensile behavior of carbon fiber/epoxy composite interface. *Composites Part B: Engineering, 284*, 111732.

Author(s) Information

Ozhan Sirin
OSTIM Technical University, Graduation School of Natural & Applied Science. 100 Yıl Blv., Ostim, Yenimahalle, Ankara, Türkiye
Contact e-mail: *ozhan.sirin@gmail.com*

Yusuf Sahin
OSTIM Technical University, 100 Yıl Blv., Ostim, Yenimahalle, Ankara, Türkiye

Emir Can Oner
OSTIM Technical University, Graduation School of Natural & Applied Science, 100 Yıl Blv., Ostim, Yenimahalle, Ankara, Türkiye

To cite this article:

Sirin, O., Sahin, Y., & Oner, E. C. (2025). Carbon fabric-reinforced polymeric composites produced by hand lay-up and investigation of the tensile behavior. *The Eurasia Proceedings of Science, Technology, Engineering and Mathematics (EPSTEM), 38,* 791-797

The Eurasia Proceedings of Science, Technology, Engineering & Mathematics (EPSTEM)
ISSN: 2602-3199

The Eurasia Proceedings of Science, Technology, Engineering and Mathematics (EPSTEM), 2025

Volume 38, Pages 798-806

IConTES 2025: International Conference on Technology, Engineering and Science

Dynamic Analysis of Vertical and Horizontal Irregular Reinforced Concrete Structure Considering Soil Structure Interaction

Boumaiza Malika
Bouira University

Mohamadi Saddika
Bouira University

Sellam Mustapha
Bouira University

Tiliouine Wail
Bouira University

Abstract: Numerous studies have examined soil-structure interaction (SSI) effects on the seismic response of high-rise buildings, comparing them to fixed-base models. These investigations have integrated SSI into dynamic analyses and highlighted key provisions in major seismic codes. However, most research focuses on regular structures with uniform mass, stiffness, and strength distribution, while only a few addresses geometric irregularities. (Stewart, 2012 & J-Priyadarshini, 2013). This study employs ROBOT Structural Analysis 2019 to numerically model an irregular 8-storey reinforced concrete structure (with horizontal and vertical irregularities) under seismic loading, considering SSI and comparing its response to that of a regular structure. The soil is modeled as a homogeneous, linearly elastic medium using spring elements. Four dynamic analyses are performed: one with a fixed base and three incorporating SSI for different soil types per the Algerian Seismic Code (RPA 2024). These analysis results are compared with those of the fixed-base structure. The findings indicate that the effect of the ISS on the dynamic modal response (particularly the fundamental period) grows with soil flexibility and becomes even more pronounced in irregularly shaped structures. Thus, both structural irregularity and the flexibility of soil amplify the ISS's impact on dynamic behavior. Regarding seismic response, fixed-base assumptions lead to overestimated internal forces in walls and columns for all building types, while relative displacements are underestimated in regular buildings and show a more significant increase in irregular ones. The results demonstrate that soil-structure interaction significantly affects the seismic performance of buildings, particularly those with irregular geometry

Keywords: Interaction soil structure, Numerical model, Horizontal and vertical irregularities, Flexibility of soil, Fixed base

Introduction

Traditionally, structural design methods assume a perfectly fixed base, with no possibility of settlement, sliding or rotation. However, during an earthquake, the inertial forces generated create shear at the base and an overturning moment at the foundations (Patro, 202 & Sumit, 2020). Unless the foundation system and the underlying soil are infinitely rigid, these stresses necessarily induce rotations and displacements of the foundations. These movements significantly disrupt the actual dynamic properties of the system. This complex coupling, where the vibrational response of the structure modifies the behaviour of the soil and vice versa, constitutes the phenomenon of soil-structure interaction (SSI). Soil-structure interaction is a fundamental

- This is an Open Access article distributed under the terms of the Creative Commons Attribution-Noncommercial 4.0 Unported License, permitting all non-commercial use, distribution, and reproduction in any medium, provided the original work is properly cited.

- Selection and peer-review under responsibility of the Organizing Committee of the Conference

© 2025 Published by ISRES Publishing: www.isres.org

phenomenon in civil engineering that studies the reciprocal effects between the soil and a built structure. When designing a structure, it is essential to understand how the soil supports the loads applied by the structure and how, in turn, soil deformations influence the behaviour of the structure. This interaction plays a crucial role in the stability, durability and safety of buildings, particularly in areas subject to complex geotechnical constraints (compressible soils, seismic zones, etc.) (Chetan, 2020 & Karapetrou, 2015). Failure to take these interactions into account can lead to differential settlement, cracking and even collapse.

The analysis of soil-structure interaction is essential to ensure the stability and safety of buildings. Different methods, ranging from simplified approaches to complex modelling, are used depending on the project requirements (Anand, 2018 & Behnanfar, 2017). The scientific literature reports numerous studies on the seismic behaviour of foundations in the context of soil-structure interaction (SSI). At the same time, several studies have analysed the response of high-rise buildings under earthquake conditions, taking SSI into account (Khalil, 2009 & RPA, 2024), with systematic comparisons to fixed-base models. Stewart et al. have established consensus recommendations for the integration of SSI into historical response analyses, proposing a unified conceptual synthesis with a consistent system of units and variables. In a complementary approach, Anand and Kumar have conducted a methodological review of the various techniques for integrating SSI into seismic response analyses, while examining the requirements of the main seismic codes (Bhosale, 2018 & Stewart, 1999). The present study is an approach to investigate the role of soil beneath the superstructure, by analysing a vertical and horizontal geometric irregular building considering soil–structure interaction subjected to ground motion using ROBOT Structural Analysis 2019, and results were compared with a reference regular building having a fixed base.

Modeling of Superstructures

Two types of building have been used in the present study, regular building, vertical and horizontal irregular geometric building. Both of building have eight storeys with the storey height of 3,40 m and ground floor 3,57m. The dimension of buildings is 23,30mx24,95m and height is 33,77m see fig.3. buildings are modelled as fixed (without SSI) and Flexible base (with SSI), which is modelled using indirect method. All structural member dimensions are selected as per: RPA2024 (Algerian Seismic Code), and DTR (Regulatory technical Document) for considering ductile detailing of the members and structure as whole (Table1), (Fig 1, 2).

Table 1. Member dimension and properties

Element	Storeys	Dimension			Units
	GF	(65x65)			
Columns	1-2				cm^2
	3-5	(60x60)			
	6-8	(55x55)			
	Direction	L	h	b	
Beams	Sens X-X	800	65	40	cm
	Sens Y-Y	800	65	40	
Shear wall thickness	All	30			cm
Slab thickness	All	20			cm
Resistance of Concrete	F_{c28}	Compression			30
		Traction			2,4
Resistance of Rebar used	Fe	500			235

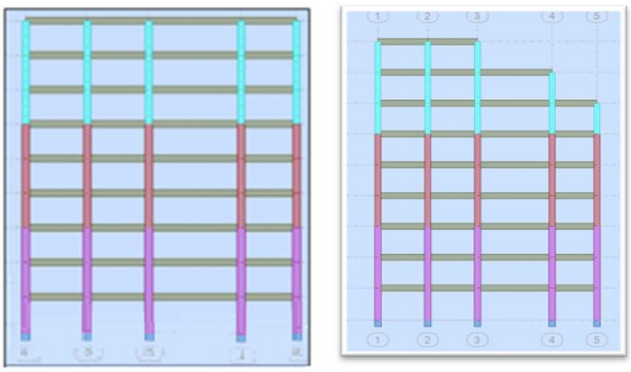


Figure 1. Fixed base model for regular and irregular building

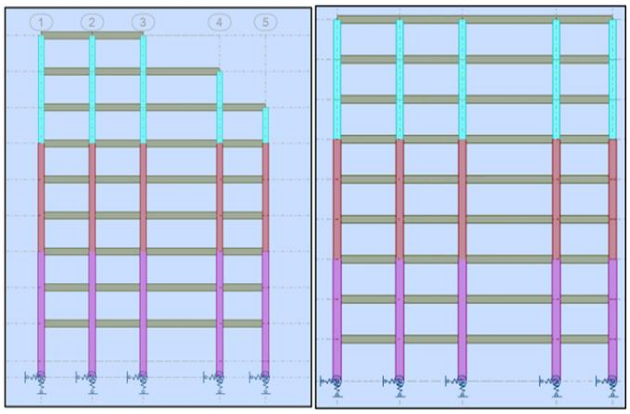


Figure 2. Flexible base model for regular and irregular building

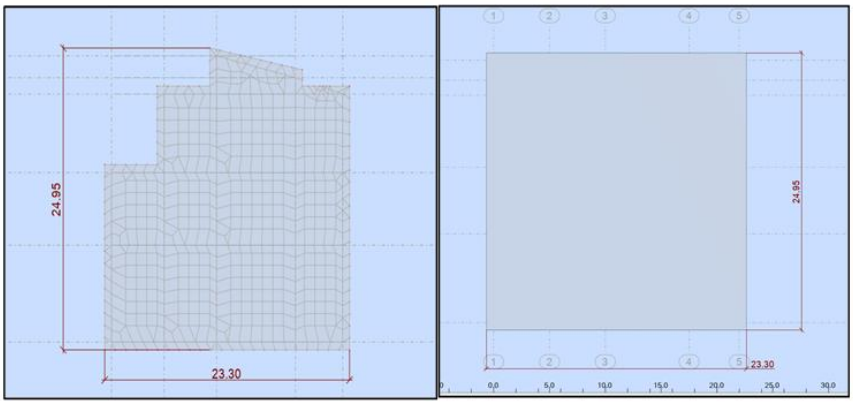


Figure 3. Plan views

The columns, beams, shear walls and slabs of the structure were considered to be made of reinforced concrete with linear elastic behavior. The material proprieties are summarized in Table 2 (Anand, 2018), the behavior of the structural elements was considered as linear elastic. A structural Rayleigh damping ratio ξ (Stewart, 1999), was assigned for all the elements in the concrete frame-shear wall building.

Table 2. Material properties considered for the structural elements in the building

Parameter	Notation	Columns, beams and shear walls
Young modulus (GPa)	E	32
Shear modulus (GPa)	G	12.5
Volumic weight (kg/m^3)	ρ	2500
Poisson ratio	ν	0.2
Damping ratio	ξ	0.085

To study the effect of the interaction soil structure on the dynamic response of the structure, the seismic action is introduced using a design response spectrum. The dynamic characteristics of the structure according to RPA 2024 are shown in Table 3.

Table 3. Dynamic properties of the building

Behavior coefficient R	Acceleration coefficient zone A	Quality factor Q		Correction factor λ
4,5	0,15	Qx	1,30	0,85
		Qy	1,25	

To study the influence of the interaction soil structure on the dynamic response of the irregular structures, we carried out a spectral modal analysis using ROBOT Structural Analysis 2029 based on the finite element method (FEM). The columns and beams were modeled with frame elements. The slab floors were modeled with deck elements. The shear walls and slabs were modeled by shell elements (Anastassiaadis, 1993). Beam structural elements were two-noded, straight, finite elements with six degrees of freedom per node, including three translational components and three rotational components. The shell structural elements were four-noded, flat

finite elements with 20 degrees of freedom. For the Response Spectrum Analysis RSA, SSRS (square root of the sum of square) and CQC (Complete quadratic Combination) are considered (Anastassiaadis, 1993 & Mohamadi , 2023). A sufficient number of modes (9 modes) are considered in the analysis such that to get the sum of mass for all modes assumed 90% of the total seismic mass, according to the RPA 2024. The mesh size used is the default mesh size in the ROBOT software. The arrangement of the braced walls was made in such a way that the first and second modes of vibrations are translations along X and Y and the third mode is a rotation around Z. The eccentricity between the center of mass and the center of rigidity at each floor (ex=0.0216m and ey=0.0215m). The first vibration mode is translation along X with a period T_1= 0.69s, the second vibration mode is translation along Y with a period T_2= 0.66s, while the third mode is rotation around Z with a period T_3= 0.55s. The response of the structure is calculated in both directions for the most unfavorable load combination:

$$G+\psi Q+E \qquad (1)$$

G: Dead load**, Q:** Live load**, E:** Seismic load**, ψ:** accompanying coefficient

Different loads on structure are taken as per DTR B.C. 2.2 for dead and live loads, for seismic load RPA 2024 (Algerian Seismic Code), and load combination is taken per BAEL 91/99 and RPA2024. To understand Response of structure and influence of Soil structure interaction effects in different soil conditions, a fixed and flexible base G+7model is taken, which is assumed to be in Seismic ZONE V.
The values of G and Q for the various elements are given in Table 4.

Table 4. Dead and live loads

Element	Terrace floor	Current floor	Balcony
G (KN/m^2)	8,7	7,6	7,6
Q (KN/m^2)	1	2,5	3,5

Soil Springs

The soil is assumed to be homogeneous with linear elastic behaviour and modelled by springs and characterized by its density ρ and behaviour parameters, shear modulus G, Poisson's ratio ν and shear wave velocity V_s. Table 5. The interaction of the structure with the soil is modelled using discrete elastic springs (Vertical, Horizontal direction and Rocking and for Rocking and Twisting movements). The stiffness coefficients of these springs are given by GAZETAS (Anastassiaadis, 1993), which depends upon dimensions and characteristic of footing (L: length and B: breadth, A_b: aria, $I_{x,y,z}$: inertia moments, $\zeta_t = I_x + I_y$: polar moment of inertia) (Mohamadi, 2023), shear modulus (G) of soil and Poisson's ratio (ν) of soil. Tables 6 and 8.

Table 5. Soil properties

Site	Description	V_S (m/s)	E(MPa)	ν
S_2	Firm	580	830	0.44
S_3	Soft	270	300	0.40
S_4	Very Soft	180	127	0.37

Table 6. Geometrical characteristics of footing for irregular building

L (m)	B (m)	Ab (m2)	Iz (m4)	Ix (m4)	Iy (m4)
12,475	11,65	495,24	87592,4265	39839,7388	47793,9577

Table 7. Soil springs stiffness values (irregular building)

	Unit	Site 2	Site 3	Site 4
G	kN/m^2	830000	300000	127000
$K_{z,surf}$	kN/m	48978407,759	14090173,857	5964840,266
$K_{y,surf}$		36768275,456	11614561,043	4916830,842
$K_{x,surf}$		36494375,456	11543061,043	4886562,508
$K_{zz,surf}$		13760709113	4618482405	1955157551
$K_{yy,surf}$		9487091237	2729259097	1155386351
$K_{xx,surf}$		7963584197	2290974554	969845895

Table 8. Geometrical characteristic of footing for regular building

L (m)	B (m)	$I_x(m^4)$	$I_y(m^4)$	$\zeta_t(m^4)$
12,475	11,65	54622,3244	684392,374	739014,699

Table 9. Soil stiffness values (regular building)

	Unit	Site 2	Site 3	Site 4
G	kN/m^2	830000	300000	127000
$K_{z,surf}$	kN/m	52981917,8	15241909	6452408,14
$K_{y,surf}$		39490171,31	12474368,18	5280815,862
$K_{x,surf}$		39216271,31	12402868,18	5250547,528
$K_{zz,surf}$		58576838868	19660040584	8322750514
$K_{yy,surf}$		69836457673	20090645556	8505039952
$K_{xx,surf}$		10090178454	2902756034	1228833388

Spring stiffness values for the different directions and as a function of the shear wave velocity of the soil associated with the different site categories for a rectangular foundation, both for regular and irregular building. Table 7 and 9 above.

Results and Discussion

Natural Time Period

According to the seismic analysis, it can be observed that each time the soil stiffness increases, the ratio (T_{fixed}/T) also increases. This variation is particularly pronounced in the case of an irregular structure located on very soft ground (S4). The increase in the natural period of the structure when soil–structure interaction is accounted for is primarily due to the reduction in overall system stiffness caused by foundation translation, rocking and soil deformation. This effect becomes more pronounced with decreasing soil stiffness (softer ground) and is further amplified in plan/vertical irregular structures where modal coupling is stronger (Thambi & Foong, 2016; Yang et al., 2024). The results show that the period (with soil-structure interaction, SSI) is systematically longer than (fixed base model) for the first three vibration modes. This significant increase in periods can be explained by the flexibility introduced by the SSI, which reduces the overall stiffness of the system. An increase in natural periods indicates that the structure becomes more sensitive to low-frequency seismic excitations, thus increasing its exposure time to dynamic solicitations. Consequently, the ISS can increase the risk of damage during an earthquake, requiring special attention in seismic design for both types of structures. Fig 4 and 5.

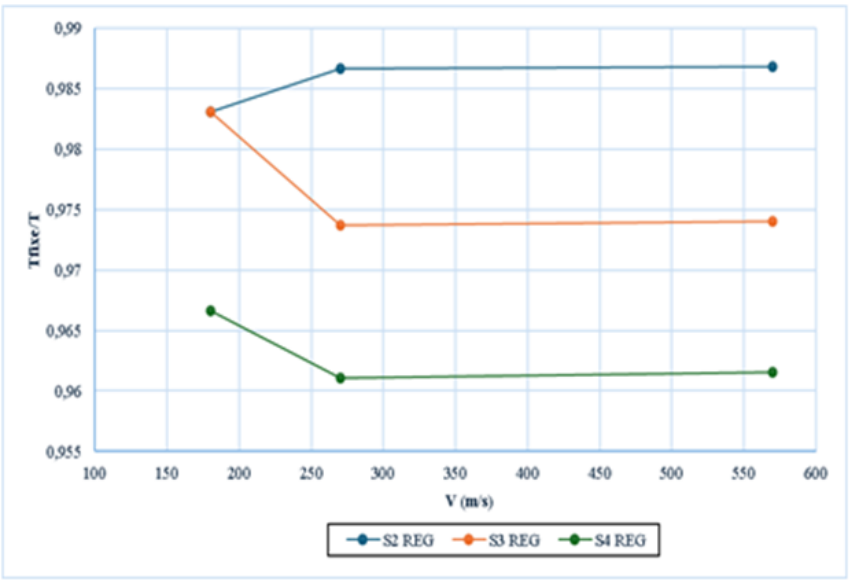


Figure 4. Variation in the ratio of T_{fixed}/T regular structure

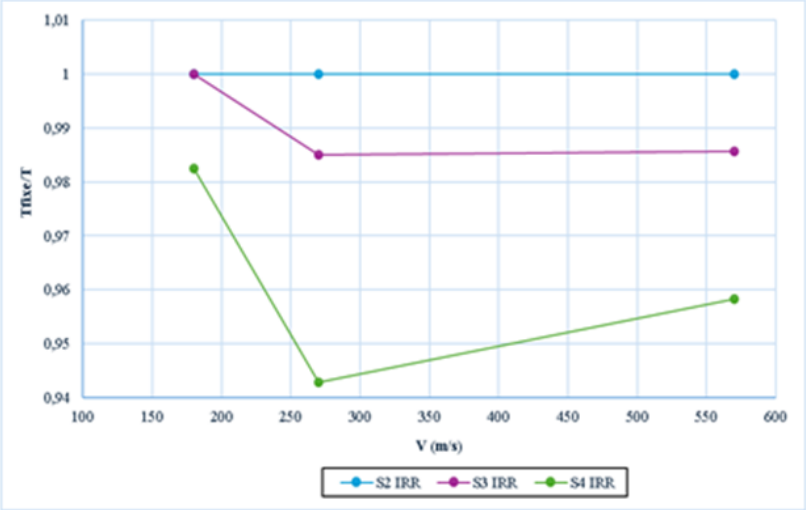


Figure 5. Variation in the ratio of T_{fixed}/T irregular structure.

Relative Displacement

From results of seismic analysis, the displacements in the X and Y directions are significantly greater when soil-structure interaction (SSI) is taken into account, compared to when it is neglected. This difference can be explained by the flexibility of the soil, which, by deforming under seismic load, influences the behaviour of the structure. On the other hand, relative displacements are underestimated for regular buildings, with a much more noticeable increase in the case of irregular structures. Fig 6, 7 and 8

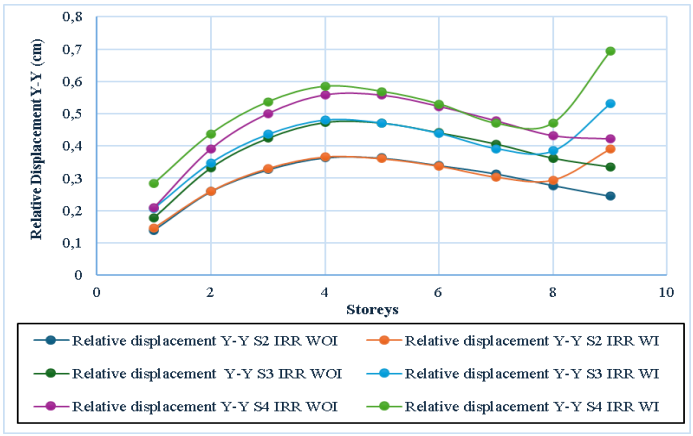


Figure 6. Relative displacement Y-Y (cm) irregular structure, with ISS (WI) and without ISS (WOI)

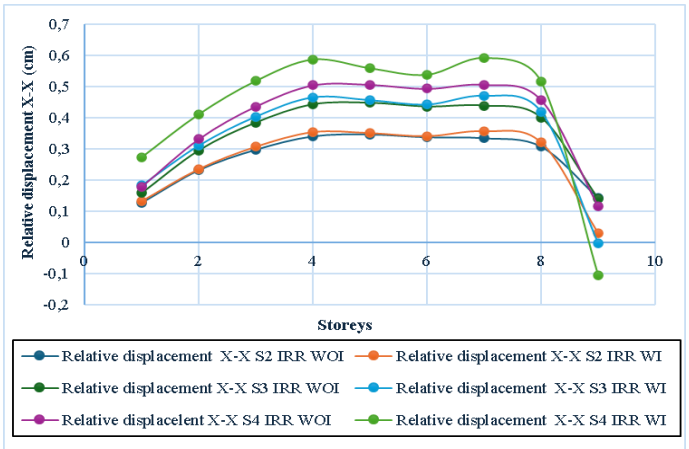


Figure 7. Relative displacement X-X (cm) irregular structure, with ISS (WI) and without ISS (WOI)

The relative displacements in both horizontal directions increase significantly under SSI because the deformable soil permits greater foundation movement and rotation, thereby increasing story drifts and top displacements compared with the fixed-base assumption (Kuhlemeyer et al., 2014; Yang et al., 2024).”

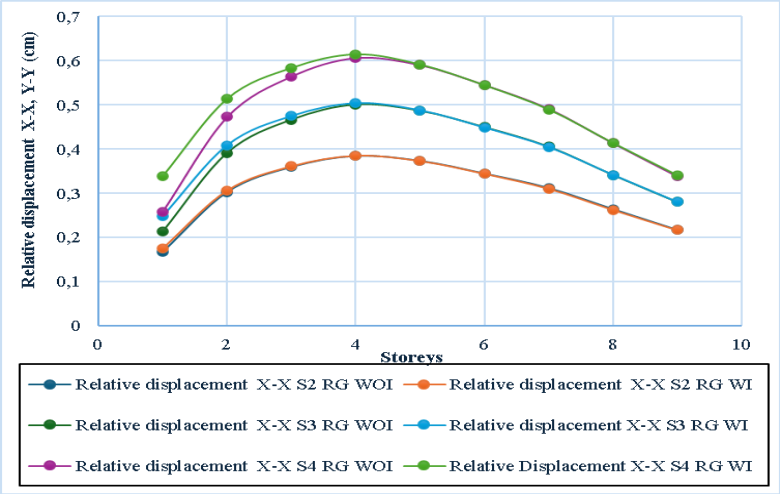


Figure 8. Relative displacement X-X (cm) and Y-Y (cm) regular structure, with ISS (WI) and without ISS (WOI)

Shear Forces

From results of seismic analysis, there is a reduction in the shear force at the base in the case of soil-structure interaction (SSI), with an average reduction of 40% for Shear walls when considering soil-structure interaction (SSI) in the case of a regular structure. And 60% for irregular structures. In columns, the average reduction is 40%. The observed reduction in base shear with SSI (≈ 40 % for shear walls in regular structures, up to ≈ 60 % in irregular cases, and ≈ 40 % in columns) is consistent with documented studies that show the lengthening of the dynamic period and additional soil damping reduce the seismic demand transferred to the structural system (Yang et al., 2024; IJERT, n.d.). If the shear force at the base of the structure is reduced in the case of the ISS, the reinforcement (transverse reinforcement) is generally reduced. Fig 9, 10.

In summary, the numerical results align with existing research: softer soils and irregular structures accentuate SSI effects, leading to increased periods, larger displacements and reduced base shear. These phenomena must therefore be considered in seismic design and analysis to avoid under-estimating seismic demands or over-estimating capacity.

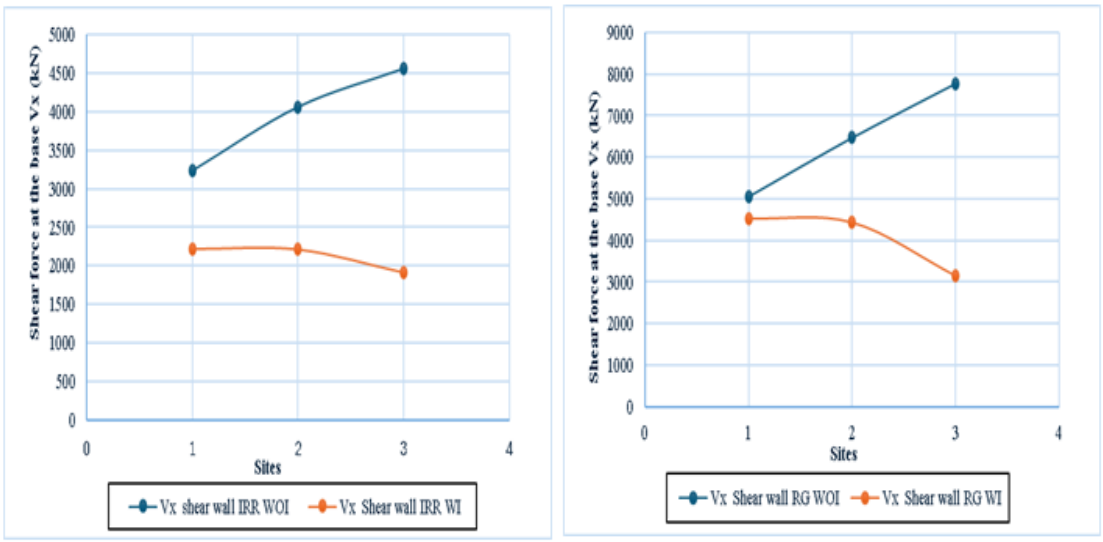


Figure 9. Shear force $V_{X\text{-}X}$ (Shear wall), irregular and regular structure, with ISS (WI) and without ISS (WOI)

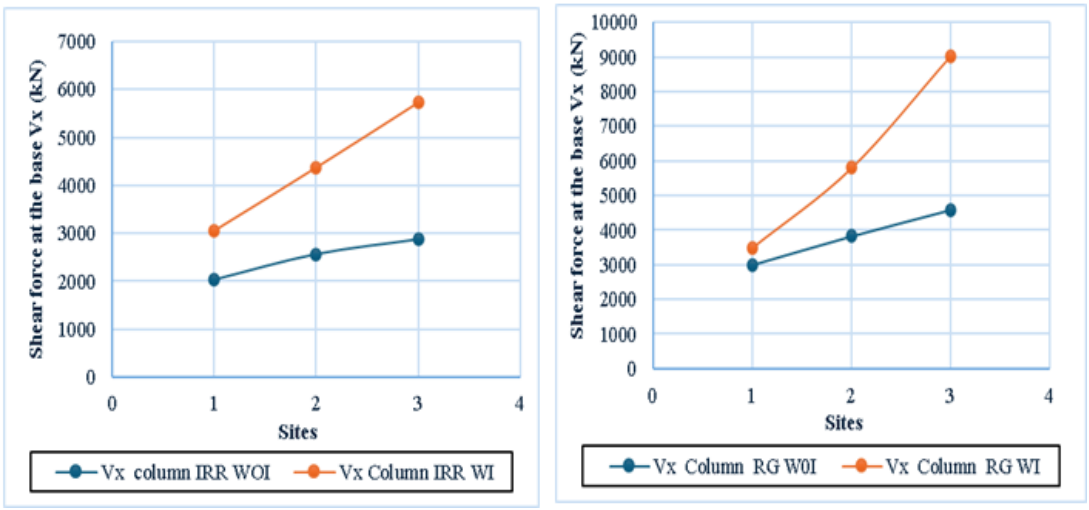


Figure 10. Shear force $V_{X\text{-}X}$ (Columns), regular and irregular structure, with ISS (WI) and without ISS (WOI)

Conclusion

This study investigated the influence of soil–structure interaction (SSI) on an irregular, eight-storey reinforced concrete building located in a high seismic zone (Zone V), in accordance with the RPA 2024 provisions. Three soil types-firm, loose, and very loose-were considered, and the response spectrum analysis was performed using ROBOT 2019 software. The results reveal that accounting for SSI leads to an increased vulnerability of structures compared to those analyzed with a fixed-base assumption. Buildings exhibiting geometric irregularities, whether in plan or elevation, demonstrate a significantly higher probability of failure than regular configurations. For structures founded on rigid soils, the discrepancy between models with and without SSI remains relatively minor. However, for irregular structures and softer soil conditions, this difference becomes substantial, underscoring the combined effect of structural irregularity and soil flexibility on seismic performance. Moreover, the findings indicate that the influence of SSI on the dynamic response amplifies with increasing soil deformability. This effect is particularly pronounced in irregular structures, where both the natural period and relative displacements are more sensitive to soil flexibility. A notable reduction in base shear was also observed in models with flexible foundations compared to fixed-base models, confirming the significant role of SSI in modifying seismic demand.

In conclusion, soil–structure interaction constitutes a critical factor in seismic design, especially for irregular buildings erected on deformable soils. Accurate assessment of this phenomenon requires advanced numerical modeling tools and a high level of engineering expertise to ensure reliable predictions and enhance structural safety under seismic loading

Scientific Ethics Declaration

* The authors declares that the scientific ethical and legal responsibility of this article published in EPSTEM journal belongs to the authors.

Conflict of Interest

* The authors declare that they have no conflicts of interest

Funding

* This research received no internal or external funding.

Acknowledgements or Notes

* This article was presented as an oral presentation at the International Conference on Technology, Engineering and Science (www.icontes.net) held in Antalya/Türkiye on November 12-15, 2025.

References

Anand, V., & Kumar, S. S. (2018). Seismic soil-structure interaction: A state-of-the-art review. *Structures, 16*, 317–326.

Anastassiadis, K. (1993). Directions sismiques défavorables et combinaisons défavorables des efforts. *Annales de l'I.T.B.T.P., 512*, 83–99.

Behnamfar, F., Mirhosseini, S. M., & Alibabaei, H. (2017). Seismic behavior of structures considering uplift and soil–structure interaction. *Advances in Structural Engineering, 20*(11), 1712–1726.

Bhosale, A. (2018). *Studies on vertically irregular RC infilled frame buildings* (Doctoral dissertation). National Institute of Technology Rourkela.

Chaudhari, S. S., Nikhar, M. R., & Kalmegh, V. A. (2020). Seismic analysis of irregular building frames with soil structure interaction. *International Journal of Trend in Scientific Research and Development, 5,* 1125-1127.

Karapetrou, S. T., Fotopoulou, S. D., & Pitilakis, K. D. (2015). Seismic vulnerability assessment of high rise non-ductile RC buildings considering soil–structure interaction effects. *Soil Dynamics and Earthquake Engineering, 73*, 42–57.

Khalil, L. (2009). *Influence de l'interaction sol-structure sur le comportement sismique des bâtiments : Analyse dans les domaines linéaire et non linéaire* (Thèse de doctorat). Université Lille 1.

Mohamadi, S., Boumaiza, M., Amrane, B., Ziane, O., & Naoui, M. (2023). Influence of the angle of incidence of the earthquake on the seismic response of a regular building shape. *International Conference on Civil Engineering.* Egypt.

Patro, S. R., Sasmal, S. K., Kumar, G. S., Sarkar, P., & Behera, R. N. (2021). Seismic analysis of vertical geometric irregular building considering structure interaction. *In Proceedings of the Indian Geotechnical Conference 2019: IGC-2019 Volume IV (pp. 545-556).* Singapore: Springer Singapore.

Priyadarshini, M. (2013). *Seismic risk assessment of RC framed vertically irregular buildings* (Master's thesis). National Institute of Technology Rourkela.

Stewart, J. P., Crouse, C. B., Hutchinson, T. C., Lizundia, B., Naeim, F., & Ostadan, F. (2012). *Soil-structure interaction for building structures* (Report No. NIST GCR 12-917-21). National Institute of Standards and Technology.

Stewart, J. P., Fenves, G. L., & Seed, R. B. (1999). Seismic soil-structure interaction in buildings. I: Analytical methods. *Journal of Geotechnical and Geoenvironmental Engineering, 125*(1), 26-37.

Wolf, J. P. (1985). *Dynamic soil-structure interaction*. Prentice Hall.

Yang, K., Cai, P., Zhang, Z., Hou, Q., Zheng, R., Hao, B., & Wang, B. (2024). Effects of soil–structure interaction on the seismic response of RC frame–shear wall building structures under far-field long-period ground motions. *Buildings, 14*(12), 3796.

Author(s) Information

Boumaiza Malika
Bouira University, Faculty of Applied Sciences, Civil Engineering Departement, 10000, Bouira, Algeria
Contact e-mail: *m.boumaiza@univ-bouira.dz*

Mohamadi Saddika
Bouira University, Faculty of Applied Sciences, Civil Engineering Departement, 10000, Bouira, Algeria

Sellem Mustapha
Bouira University, Faculty of Applied Sciences, Civil Engineering Departement, 10000, Bouira, Algeria

Tillioune Wail
Bouira University, Faculty of Applied Sciences, Civil Engineering Departement, 10000, Bouira, Algeria

To cite this article:

Malika, B., Saddika, M., Mustapha, S., & Wail, T. (2025). Dynamic analysis of vertical and horizontal irregular reinforced concrete structure considering soil structure interaction. *The Eurasia Proceedings of Science, Technology, Engineering and Mathematics (EPSTEM), 38,* 798-806.

The Eurasia Proceedings of Science, Technology, Engineering & Mathematics (EPSTEM)
ISSN: 2602-3199

The Eurasia Proceedings of Science, Technology, Engineering and Mathematics (EPSTEM), 2025

Volume 38, Pages 807-815

IConTES 2025: International Conference on Technology, Engineering and Science

Effect of Variable Mass Density on Lengthwise Fracture in Functionally Graded Beams Moving in Horizontal Direction

Victor Rizov
University of Architecture

Abstract: Functionally graded structural materials have been used with increasing intensity in various applications in different areas of up-to-date engineering during recent decades. This can be explained with excellent properties of these materials. Besides, the quickly developing technologies for producing different kinds of functionally graded materials also represent an important factor for increasing the application of these innovative materials. Using these materials for manufacturing moving components of various mechanisms and devices requires performing of analyses of the behavior of the components under inertia loadings. Developing fracture analysis under inertia loadings is very important in the context of safety and reliability. In view of this, the current paper is concerned with analyzing of a particular aspect of fracture, namely the effect of variable mass density on lengthwise fracture behavior of functionally graded beams moving in horizontal direction. The mass density varies along both thickness and length of the beam. The latter is under inertia loading due to beam acceleration in horizontal direction. The inertial loading of the beam is a continuous function of both thickness and length coordinates. The beam has non-linear viscoelastic behavior. The lengthwise fracture problem is treated by using the *J* integral method. A check-up is performed by analyzing the strain energy release rate. It is explored how the lengthwise fracture is influenced by the variable mass density and other parameters of the model.

Keywords: Variable mass density, Motion, Lengthwise fracture, Functionally graded beam

Introduction

Functionally graded materials made by mixing of two or more constituents represent modern and highly efficient continuously inhomogeneous composites (Gandra et al., 2011; Mahamood & Akinlabi, 2017). One of the important advantages of functionally graded materials is that their properties change continuously in a solid. Besides, the change of their properties can be designed for achieving of certain goals (for instance, the goal can be strengthening of more heavily loaded parts of an engineering structure). With developing of the technologies for producing of these materials the area of their application quickly expands (Radhika et al., 2020; Shrikantha Rao & Gangadharan, 2014). The excellent properties of functionally graded materials allow construction of various structural members and components of different mechanisms and machines which in many cases are superior compared to those built-up by traditional homogeneous engineering materials (Fanani et al., 2021; Hedia et al., 2014; Wu et al., 2014).

The increasing use of functionally graded structural members and components in applications where they are involved in different mechanical motions requires performing detailed analyses of their fracture behavior under various inertia loadings. The practice indicates that fracture behavior is of primary importance for load-bearing capacity and safety of structures. Since functionally graded structures may be constructed layer-by-layer, they are prone to lengthwise fracture, i.e. appearance of lengthwise cracks (Dolgov, 2024; Mahamood & Akinlabi, 2017; Rizov & Altenbach, 2019; Rizov, 2024). In many situations these lengthwise cracks are the cause of structural failure under inertia loading. All this shows that studying of lengthwise fracturerepresentural

- This is an Open Access article distributed under the terms of the Creative Commons Attribution-Noncommercial 4.0 Unported License, permitting all non-commercial use, distribution, and reproduction in any medium, provided the original work is properly cited.

- Selection and peer-review under responsibility of the Organizing Committee of the Conference

© 2025 Published by ISRES Publishing: www.isres.org

components subjected to different inertia loadings represents a problem of great meaning for both theoretical science and engineering practice.

In this context, the current paper is dealing with analysis of lengthwise fracture in a functionally graded beam structure that is moving in horizontal direction. The beam acted upon by inertial loading has non-linear viscoelastic behavior. One of the main purposes is to examine the effect of variable mass density on the lengthwise fracture (since the beam is functionally graded along thickness and length, the mass density varies continuously in both thickness and length directions). The lengthwise fracture is analyzed by the integral *J*. For this purpose, the acceleration induced inertia loading is determined and applied on the beam when solving the integral *J*. The viscoelastic behavior of the beam is treated by a non-linear modification of the Maxwell model. In this relation, the stress-strain-time law of the model under time-dependent stress is derived. A check-up of the integral *J* is performed by analyzing the strain energy release rate in the beam under inertia loading. The results obtained reveal how the lengthwise fracture is influenced by the variable mass density. The effect of variation of some other parameters along with the thickness and length of the beam on the lengthwise fracture is also studied.

Theoretical Model

The functionally graded beam structure depicted in Figure 1 is analyzed in the current paper. The beam is moving in horizontal direction. The law of beam motion is given in Eq. (1).

$$s = \alpha t^n , \tag{1}$$

where t is time, α and n are parameters, s is horizontal axis (Figure 1).

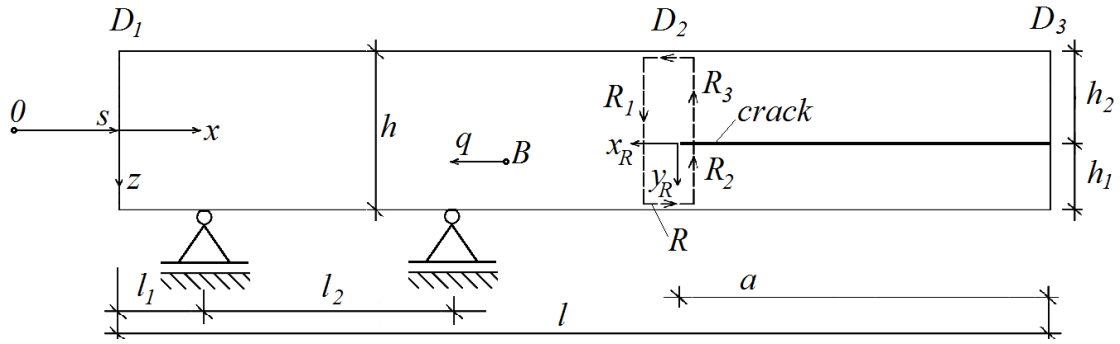


Figure 1. Beam structure with lengthwise crack

The velocity, v, and the acceleration, a, of the beam are found by Eqs. (2) and (3), respectively.

$$v = \frac{ds}{dt} = \alpha n t^{n-1} , \tag{2}$$

$$a = \frac{dv}{dt} = \alpha n(n-1) t^{n-2} . \tag{3}$$

The inertia loading, q, in an arbitrary point, B, of the beam is obtained by Eq. (4).

$$q = -am , \tag{4}$$

where m is the mass density. Since the beam is functionally graded along both thickness and length, the mass density varies continuously in transversal and longitudinal direction. The mass density variation in transversal direction is given in Eq. (5).

$$m = m_\delta e^{\lambda \frac{\frac{h}{2}+z}{h}}, \tag{5}$$

where

$$-\frac{h}{2} \le z \le \frac{h}{2}. \tag{6}$$

Here, m_δ is the mass density in the upper surface of the beam, λ is a parameter, z is the vertical centric axis of the beam, h is the beam thickness. The quantity, m_δ, varies along the beam length according to the law given in Eq. (7).

$$m_\delta = m_{\delta D1} e^{\mu \frac{x}{l}}, \tag{7}$$

where

$$0 \le x \le l. \tag{8}$$

Here, $m_{\delta D1}$ is the mass density in the left-hand end of the beam, μ is a parameter, x is the longitudinal centroidal axis of the beam, l is the beam length. Equations (4), (5) and (7) indicate that q is a continuous function of the time, the transversal and longitudinal coordinates of the beam structure.

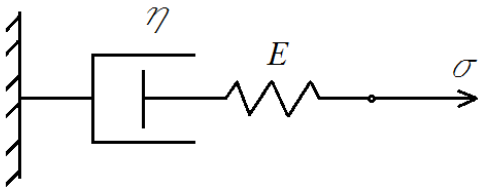


Figure 2. Non-linear viscoelastic model

The beam acted upon by the inertia loading exhibits non-linear viscoelastic behavior. The fully non-linear modification of the classical viscoelastic model of Maxwell depicted in Figure 2 is applied for dealing with the beam structure. Both components, i.e. the spring and the dashpot, of the viscoelastic model in Figure 2 have non-linear behavior that is described by the laws given in Eqs. (9) and (10), respectively.

$$\sigma_E = E \varepsilon_E^{r_E}, \tag{9}$$

$$\sigma_\eta = \eta \dot{\varepsilon}_\eta^{r_\eta}, \tag{10}$$

where σ_E and σ_η are the stresses in the spring and the dashpot, E, η, r_E and r_η are material parameters, ε_E and ε_η are the strains in the spring and the dashpot, $\dot{\varepsilon}_\eta$ is the derivative with respect to time. The model is under stress, σ, that is given in Eq. (11).

$$\sigma = \beta t^{n-2}, \tag{11}$$

where β is a parameter.

It is evident that the stress in both components of the model in Figure 2 are equal to σ, i.e.

$$\sigma_E = \beta t^{n-2}, \tag{12}$$

$$\sigma_\mu = \beta t^{n-2}. \tag{13}$$

The strain, ε, in the viscoelastic model is found by using Eq. (14).

$$\varepsilon = \varepsilon_E + \varepsilon_\eta \,. \tag{14}$$

By substituting of Eqs. (12) and (13) in Eqs. (9) and (10), we obtain

$$E\varepsilon_E^{r_E} = \beta t^{n-2}, \tag{15}$$

$$\eta\dot{\varepsilon}_\eta^{r_\eta} = \beta t^{n-2} \,. \tag{16}$$

From Eqs. (15) and (16), after some mathematical manipuiltions, we derive

$$\varepsilon_E = \left(\frac{\beta t^{n-2}}{E} \right)^{\frac{1}{r_E}}, \tag{17}$$

$$\dot{\varepsilon}_\eta = \left(\frac{\beta t^{n-2}}{\eta} \right)^{\frac{1}{r_\eta}} . \tag{18}$$

By integrating of Eq. (18), we have

$$\varepsilon_\eta = \left(\frac{\beta}{\eta} \right)^{\frac{1}{r_\eta}} \frac{t^{\frac{n-2+r_\eta}{r_\eta}}}{\frac{n-2+r_\eta}{r_\eta}} + C_1 \,. \tag{19}$$

The integration constant, C_1, is determined by using the initial condition given in Eq. (20).

$$\varepsilon_\eta(0) = 0 \,. \tag{20}$$

From Eqs. (19) and (20), we obtain

$$C_1 = 0 \,. \tag{21}$$

Thus, Eq. (19) is written as

$$\varepsilon_\eta = \left(\frac{\beta}{\eta} \right)^{\frac{1}{r_\eta}} \frac{t^{\frac{n-2+r_\eta}{r_\eta}}}{\frac{n-2+r_\eta}{r_\eta}} \,. \tag{22}$$

From Eqs. (14), (17) and (21), we obtain the stress-strain-time relation given in Eq. (23).

$$\varepsilon = \left(\frac{\beta t^{n-2}}{E} \right)^{\frac{1}{r_E}} + \left(\frac{\beta}{\eta} \right)^{\frac{1}{r_\eta}} \frac{t^{\frac{n-2+r_\eta}{r_\eta}}}{\frac{n-2+r_\eta}{r_\eta}} \,. \tag{23}$$

From Eq. (11), we have

$$\beta = \frac{\sigma}{t^{n-2}} \,. \tag{24}$$

Finally, Eq. (24) is substituted in Eq. (23), i.e.

$$\varepsilon = \left(\frac{\sigma}{E} \right)^{\frac{1}{r_E}} + \left(\frac{\sigma}{\eta} \right)^{\frac{1}{r_\eta}} \frac{r_\eta t}{n-2+r_\eta} \,. \tag{25}$$

Equation (25) is applied for describing the non-linear viscoelastic behavior of the beam when analyzing the lengthwise fracture under the inertia loading. Since the beam is functionally graded along the thickness and length the material properties, E, η, r_E and r_η, change continuously in both transversal and longitudinal directions. The following expressions describe this change.

$$E = E_\delta e^{\lambda_E \frac{\frac{h}{2}+z}{h}}, \tag{26}$$

$$\eta = \eta_\delta e^{\lambda_\eta \frac{\frac{h}{2}+z}{h}}, \tag{27}$$

$$r_E = r_{E\delta} e^{\lambda_{rE} \frac{\frac{h}{2}+z}{h}}, \tag{28}$$

$$r_\eta = r_{\eta\delta} e^{\lambda_{r\eta} \frac{\frac{h}{2}+z}{h}}, \tag{29}$$

$$E_\delta = E_{\delta D1} e^{\mu_E \frac{x}{l}}, \tag{30}$$

$$\eta_\delta = \eta_{\delta D1} e^{\mu_\eta \frac{x}{l}}, \tag{31}$$

$$r_{E\delta} = r_{E\delta D1} e^{\mu_{rE} \frac{x}{l}}, \tag{32}$$

$$r_{\eta\delta} = r_{\eta\delta D1} e^{\mu_{r\eta} \frac{x}{l}}, \tag{33}$$

where E_δ, η_δ, $r_{E\delta}$ and $r_{\eta\delta}$ are the values of E, η, r_E and r_η in the upper surface of the beam, $E_{\delta D1}$, $\eta_{\delta D1}$, $r_{E\delta D1}$ and $r_{\eta\delta D1}$ are the values of E_δ, η_δ, $r_{E\delta}$ and $r_{\eta\delta}$ are in the left-hand end of the beam, λ_E, λ_η, λ_{rE}, $\lambda_{r\eta}$, μ_E, μ_η, μ_{rE} and $\mu_{r\eta}$ are material parameters.

As shown in Figure 1, the beam hosts a lengthwise crack of length, a. The thicknesses of the crack arms are h_1 and h_2 (Figure 1). The lengthwise fracture is studied by the *J* integral (Broek, 1986). The following expression is obtained:

$$J = J_{R1} + J_{R2} + J_{R3}, \tag{34}$$

where

$$J_{R1} = \int \left[u_{01} \cos\alpha_1 - \left(p_{x1} \frac{\partial u_1}{\partial x_R} + p_{y1} \frac{\partial v_1}{\partial x_R} \right) \right] ds_{ct}, \tag{35}$$

$$J_{R2} = \int \left[u_{02} \cos\alpha_2 - \left(p_{x2} \frac{\partial u_2}{\partial x_R} + p_{y2} \frac{\partial v_2}{\partial x_R} \right) \right] ds_{ct}, \tag{36}$$

$$J_{R3} = \int \left[u_{03} \cos\alpha_3 - \left(p_{x3} \frac{\partial u_3}{\partial x_R} + p_{y3} \frac{\partial v_3}{\partial x_R} \right) \right] ds_{ct}. \tag{37}$$

Here, u_{01}, u_{02} and u_{03} are the specific strain energies in sectors, R_1, R_2 and R_3, of the contour of integration, R. The latter is depicted in Figure 1. α_1, α_2 and α_3 are the angles between the outward normal vector and the contour of integration in sectors, R_1, R_2 and R_3, the quantities, u_1, u_2 and u_3, are the horizontal displacements in the corresponding sectors of the counter, v_1, v_2 and v_3 are the vertical displacements, p_{x1}, p_{x2} and p_{x3} are the components of the stress along the horizontal axis in the

corresponding sectors of the contour, p_{y1}, p_{y2} and p_{y3} are the components of the stress along the vertical axis, ds_{ct} is an elementary portion of the contour of integration.

The specific strain energy, u_{01}, involved in Eq. (34) is derived by Eq. (38).

$$u_{01} = \int \sigma d\varepsilon \,. \tag{38}$$

The strain, ε, varies along the beam thickness according to Eq. (39).

$$\varepsilon = \kappa_1 (z - z_n), \tag{39}$$

where

$$-\frac{h}{2} \le z \le \frac{h}{2}. \tag{40}$$

Here, κ_1 and z_n are the curvature and the neutral axis coordinate, respectively. They are determined from Eqs. (41) and (41).

$$N_1 = \iint_{(A)} \sigma dA \,, \tag{41}$$

$$M_1 = \iint_{(A)} \sigma z dA \,, \tag{42}$$

where N_1 and M_1 are the axial force and the bending moment induced by the inertia loading, A is the area of the cross-section. The other quantities involved in Eq. (35) are obtained as given below.

$$\cos\alpha_1 = 1, \tag{43}$$

$$p_{x1} = \sigma \,, \tag{44}$$

$$\frac{\partial u_1}{\partial x_R} = \varepsilon \,, \tag{45}$$

$$p_{y1} = 0 \,, \tag{46}$$

$$ds_{ct} = dz \,. \tag{47}$$

The axes, x_R and y_R, are depicted in Figure 1.

The quantities involved in Eqs. (36) and (37) are derived in a similar way. The integrals in Eqs. (35), (36) and (37) are solved by the MatLab. The integral *J* is found by Eq. (34). The lengthwise fracture in the beam under inertia loading is studied also by determining the strain energy release rate, G, through Eq. (48) for check-up of the *J* integral analysis.

$$G = \frac{dU^*}{bda}, \tag{48}$$

where U^* is the beam complementary strain energy, b is the beam width. U^* is found by Eq. (49).

$$U^* = \iiint_{(V)} u_0^* dV \,, \tag{49}$$

where u_0^* is the specific complementary strain energy, V is the beam volume. The strain energy release rate agrees very well with *J* –integral which is a check-up of the analysis.

Parametric Exploration Results

First, by using the integral *J* we explore how the lengthwise fracture in the functionally graded viscoelastic beam under inertia loading is influenced by the variable mass density. It is assumed that $a = 0.200$ m, $b = 0.015$ m, $h = 0.022$ m, $h_1 = 0.011$ m, $h_2 = 0.011$ m, $l = 0.900$ m, $\alpha = 0.3$ and $\beta = 2.5$.

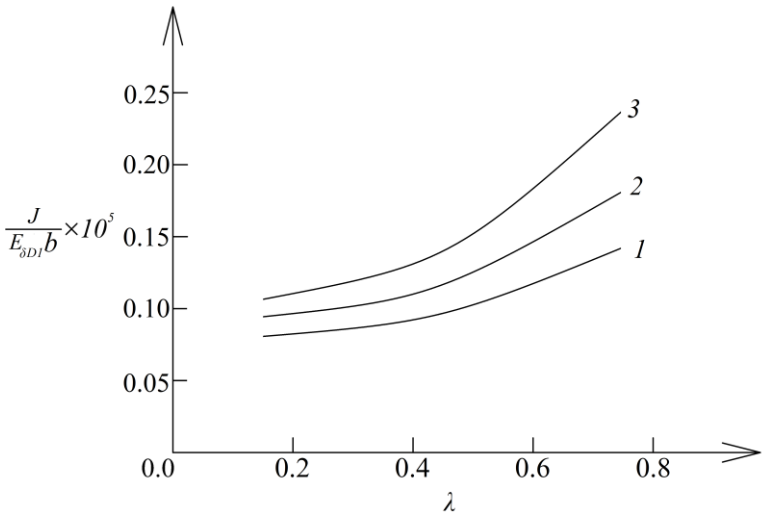


Figure 3. Variation of the integral *J* with λ

The curves plotted in Figure 3 reveal the change of the integral *J* in non-dimensional form induced by change of parameter, λ, at $\mu = 0.3$ (curve 1), $\mu = 0.6$ (curve 2) and $\mu = 0.9$ (curve 3). As already mentioned, the parameters, λ and μ, govern the variation of the mass density along the thickness and length of the beam structure depicted in Figure 1. By inspecting the curves in Figure 3, we can conclude that growth of the values of λ and μ leads to substantial rise of the integral *J*.

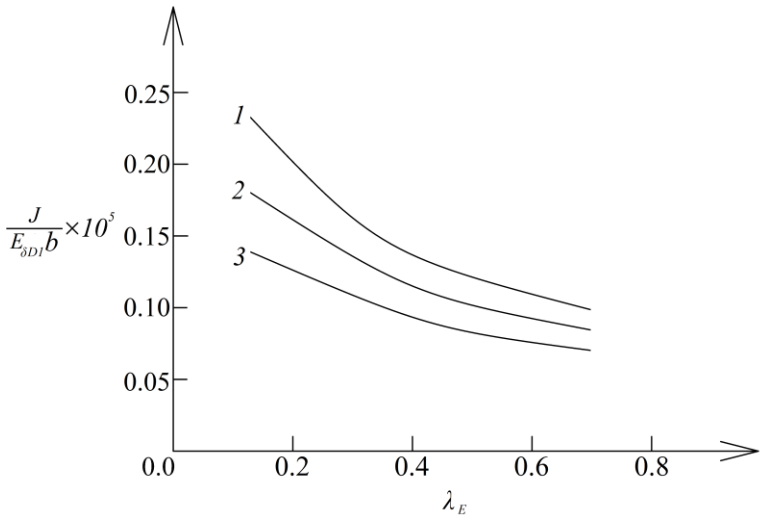


Figure 4. Variation of the integral *J* with λ_E

Further, it is explored how the lengthwise fracture in the beam is influenced by the variation of parameter, λ_E, at $\mu_E = 0.2$ (curve 1), $\mu_E = 0.5$ (curve 2) and $\mu_E = 0.8$ (curve 3). In this relation, the change of the integral *J* in non-dimensional form is depicted in Figure 4. The curves indicate a significant influence of both λ_E and μ_E on the lengthwise fracture in the beam (Figure 4). Increase of λ_E and μ_E reduces the integral *J* as can be observed in Figure 4.

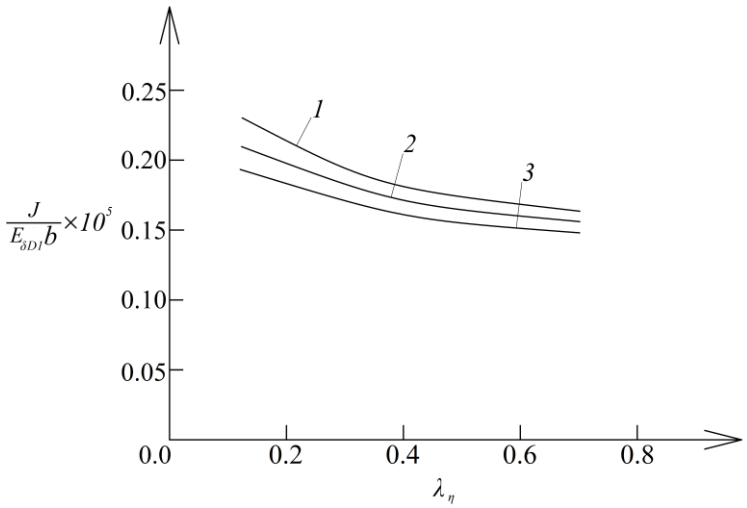


Figure 5. Variation of the integral *J* with λ_η

The influence of parameters, λ_η and μ_η, on the lengthwise fracture is explored too. The corresponding curves are depicted in Figure 5 (curve 1 is for $\mu_\eta = 0.3$, curve 2 is for $\mu_\eta = 0.5$ and curve 3 is for $\mu_\eta = 0.8$). Since λ_η and μ_η are connected to variation of η, the curves in Figure 5 in fact reveal how by varying of η we may influence the lengthwise fracture in the beam. It can be seen in Figure 5 that the growth of λ_η and μ_η has a positive effect on the lengthwise fracture since the integral *J* reduces.

Conclusion

Lengthwise fracture in a functionally graded non-linear viscoelastic beam structure moving in horizontal direction is studied. The attention is focused on the problem of the influence of variation of the mass density on the lengthwise fracture (the mass density varies continuously along both thickness and length of the beam). The other material parameters of the beam also vary continuously. The beam with lengthwise crack is acted upon by inertial load. The integral *J* is solved. The analysis performed indicates that the lengthwise fracture is influenced substantially by the variation of the mass density. In particular, the growth of parameters, λ and μ, which govern the mass density variation in the beam structure leads to significant growth of the integral *J*. It is explored also how the lengthwise fracture is affected by parameters, λ_E, μ_E, λ_η and μ_η (these parameters govern variation of E and η). Growth of λ_E, μ_E, λ_η and μ_η influences positively the lengthwise fracture since it reduces the integral *J*.

Recommendations

The continuous variation of mass density has to be taken into account in lengthwise fracture analyses of moving functionally graded beam structures.

Scientific Ethics Declaration

* The author declares that the scientific ethical and legal responsibility of this article published in EPSTEM journal belongs to the author.

Conflict of Interest

* The author declares there is no conflict of interest.

Funding

* Not applicable.

Acknowledgements or Notes

* This article was presented as an oral presentation at the International Conference on Technology, Engineering and Science (www.icontes.net) held in Antalya/Türkiye on November 12-15, 2025.

References

Broek, D. (1986). *Elementary engineering fracture mechanics*. Springer.

Dolgov, M. A. (2024). Analysis of the stress state in the deformed coating under base stretching with the bending effect account. *Strength of Materials, 56*, 1127-1135.

Fanani, E. W. A., Surojo, E., Prabowo, A. R., & Akbar, H. I. (2021). Recent progress in hybrid aluminum composite: Manufacturing and application. *Metals, 11*, 1919-1929.

Gandra, J., Miranda, R., Vilaça, P., Velhinho, A., & Teixeira, J. P. (2011). Functionally graded materials produced by friction stir processing. *Journal of Materials Processing Technology, 211*, 1659-1668.

Hedia, H. S., Aldousari, S. M., Abdellatif, A. K., & Fouda, N. A. (2014). New design of cemented stem using functionally graded materials (FGM). *Biomedical Materials and Engineering, 24*, 1575-1588.

Mahamood, R. C., & Akinlabi, E. T. (2017). *Functionally graded materials*. Springer.

Radhika, N., Sasikumar, J., Sylesh, J. L., & Kishore, R. (2020). Dry reciprocating wear and frictional behaviour of B4C reinforced functionally graded and homogenous aluminium matrix composites. *Journal of Materials Research and Technology, 9*, 1578-1592.

Rizov, V. I. (2024). The effect of delamination between layers in U-shaped members made of functionally graded multilayered viscoelastic materials. *Journal of Applied and Computational Mechanics, 10*, 830-841.

Rizov, V. I., & Altenbach, H. (2019). On the analysis of lengthwise fracture of functionally graded round bars. *Structural Integrity and Life, 19*, 102-108.

Shrikantha Rao, S., & Gangadharan, K. V. (2014). Functionally graded composite materials: An overview. *Procedia Materials Science, 5*, 1291-1299.

Wu, X. L., Jiang, P., Chen, L., Zhang, J. F., Yuan, F. P., & Zhu, Y. T. (2014). Synergetic strengthening by gradient structure. *Materials Research Letters, 2*, 185-191.

Author(s) Information

Victor Rizov
University of Architecture, Civil Engineering and Geodesy
1 Chr. Smirnensky Blvd. 1046 – Sofia, Bulgaria
Contact e-mail: *V_RIZOV_FHE@UACG.BG*

To cite this article:

Rizov, V. (2025). Effect of variable mass density on lengthwise fracture in functionally graded beams moving in horizontal direction. *The Eurasia Proceedings of Science, Technology, Engineering and Mathematics (EPSTEM), 38,* 807-815.

The Eurasia Proceedings of Science, Technology, Engineering & Mathematics (EPSTEM)
ISSN: 2602-3199

The Eurasia Proceedings of Science, Technology, Engineering and Mathematics (EPSTEM), 2025

Volume 38, Pages 816-823

IConTES 2025: International Conference on Technology, Engineering and Science

Retrofit Kit Design That Converts Industrial Locks into Electromechanical Smart Locks

Selahattin Mert Aydin
Mesan Locks INC

Engin Gunes
Mesan Locks INC

Abstract: This paper presents the design and development of a modular electromechanical retrofit kit that upgrades traditional quarter-turn mechanical cam locks into secure, digitally controlled smart locking systems. Quarter-turn locks are widely used in school lockers, server cabinets, electrical distribution panels, and industrial enclosures, but they offer limited access control, no auditability, and minimal protection against unauthorized manipulation. The proposed kit addresses these issues by introducing a compact, low-cost electromechanical module that mounts externally without altering the existing lock body. The system uses a 3.3 V DC gear motor controlled by an ATmega48P microcontroller and DRV8837 driver, providing controlled 90° rotation after successful RFID authentication. Optional LED indicators assist the user during operation. To enhance security, the device enforces a temporary self-locking (lockout) period after multiple failed access attempts, increasing security. The retrofit kit's improvement design enables adaptation to different key geometries, ensuring compatibility with a variety of lock formats. Designed for easy installation, the kit can be mounted within minutes and allows end-users to digitally upgrade their mechanical locks without replacing the mechanical body. Prototype tests confirm system stability, reliable authentication, and low power consumption. Long-term usability is supported by a standard Li-Po battery power supply, achieving an estimated 4500–5000 lock/unlock cycles per 1000 mAh battery charge. The kit is intended as a commercial solution for modernizing physical security infrastructure in industries environments, bridging legacy hardware with modern access control needs.

Keywords: Smart lock, Electromechanical kit, Access control, Industrial design, Digital transformation

Introduction

With the rapid advancement of technology, electromechanical locking systems are increasingly replacing traditional mechanical locks. These systems not only increase physical security but also enable the digital tracking and management of access data, essential for modern security infrastructures. The increasing need for access control in modern institutions and public spaces has LED to a shift towards electronic solutions. Traditional keys are prone to loss or duplication and do not provide event tracking (Uppuluri & Lakshmeeswari, 2023). Contemporary requirements in educational and commercial environments require centralized credential control and auditing capabilities (Lin et al., 2021; Khan et al., 2023).

However, replacing existing mechanical systems with completely new electromechanical alternatives is often costly and results in the disposal of still-functional mechanical locks. Such practices lead to unnecessary financial investments and increased environmental waste, highlighting the need for more sustainable upgrade strategies. This study focuses on the development of a modular retrofit kit that transforms traditional mechanical locks into smart electromechanical locking systems without requiring the removal or disposal of existing hardware. The design includes a compact housing, a low-voltage gear motor, and a microcontroller-based

- This is an Open Access article distributed under the terms of the Creative Commons Attribution-Noncommercial 4.0 Unported License, permitting all non-commercial use, distribution, and reproduction in any medium, provided the original work is properly cited.

- Selection and peer-review under responsibility of the Organizing Committee of the Conference

© 2025 Published by ISRES Publishing: www.isres.org

authentication system. Users manipulate the lock using their RFID card, which triggers the rotation of a special insert that activates the cam lock mechanism. The kit is adaptable to various key geometries, allowing users to digitize their locking systems without replacing existing mechanical components.

Method

Mechanical Design

The retrofit kit is designed to be compatible with standard quarter-turn cam locks commonly used in steel furniture, electrical enclosures, transportation equipment, and server cabinets. These locks typically have standard body profiles with circular, double-D, or 45° cross-sections, with diameters ranging from 16 mm to 22 mm (Figure 1).

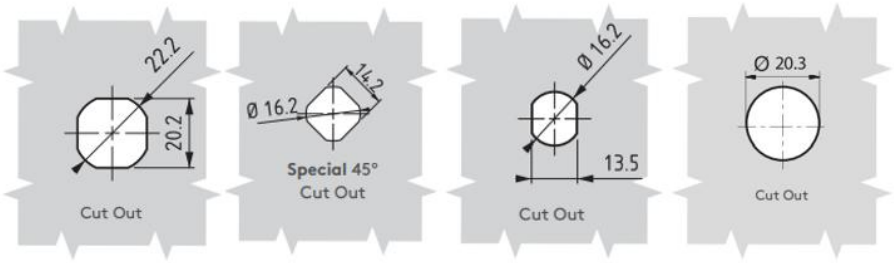


Figure 1. Standard cut-out dimensions for cam locks compatible with the retrofit kit

Manual key operation has been replaced with a motorized operating mechanism, enabling the mechanical lock to operate as a smart electromechanical system. Unlocking is triggered by RFID-based user authentication, and after verification, the rotation of the motor is achieved. The motor's rotation is transmitted to the key via a gear mechanism. Representative examples of quarter-turn cam locks supported by the retrofit mechanism are shown (Figure 2).



Figure 2. Common types of commercial quarter-turn cam locks supported by the retrofit kit

The mechanical components are compact and lightweight, designed to fit into an external housing that can be mounted using a single screw through a 6-8 mm hole. Installation requires only basic tools and does not permanently modify the existing lock. During operation, the motor rotates 90° to unlock the lock and automatically returns to the locked position after a short delay. Figure 3 provides a transparent view of the internal mechanism and the direction of motor rotation.

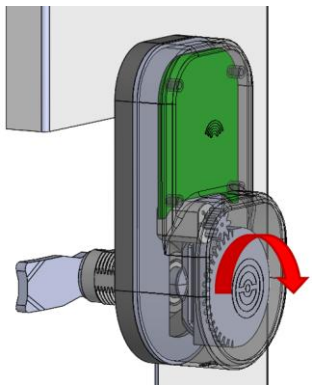


Figure 3. Transparent front view of the smart lock kit showing internal components and motor rotation direction

The proposed approach offers a low-cost, sustainable, and minimal-intervention solution for upgrading mechanical locks to smart, automated systems. This modular design contributes to both economic efficiency and environmental sustainability by providing easy maintenance, scalability, and long-term reliability (Wolniak, 2024; Xin et al., 2020; Roy et al., 2018).

Electrical Design

The electronic architecture of the retrofit kit is built around the ATmega48P microcontroller, selected for its balance of energy efficiency, functional capacity, and compact physical footprint. This controller is tasked with managing key operations such as RFID-based authentication, motor control, and the signaling of visual and auditory feedback. To actuate the locking mechanism, a DRV8837 H-bridge motor driver enables bidirectional control of a 3.3 V brushed DC gear motor. The entire system is powered by a single-cell 3.7 V lithium-polymer (Li-Po) battery, regulated to 3.3 V via a low-dropout (LDO) converter. This arrangement ensures reliable performance while keeping current draw and thermal output within safe limits.

In practice, the motor draws approximately 130 mA during actuation, but since the motion duration is brief-generally under one second-the energy consumed per locking cycle remains low. To extend battery life, the system is engineered with a strong focus on energy conservation. When idle, the device enters a deep sleep state, drawing less than 3 mA. Power-saving is achieved not only through hardware-level design but also through firmware strategies. The microcontroller utilizes sleep and power-down modes, reactivating only in response to external interrupts-typically triggered when the RFID module detects a card.

To avoid unnecessary energy drain, the RFID reader and other peripherals are only powered when needed. This is governed by an interrupt-driven control loop that activates subsystems momentarily and then returns the system to a dormant state. Peripheral components such as timers, ADCs, and communication interfaces are likewise disabled unless actively in use. This selective activation strategy ensures that the system remains efficient even during long periods of inactivity. These measures align with established practices in the design of low-power embedded systems (Jayakumar et al., 2014). Figure 4 provides an overview of the system's electrical components and their interconnections.

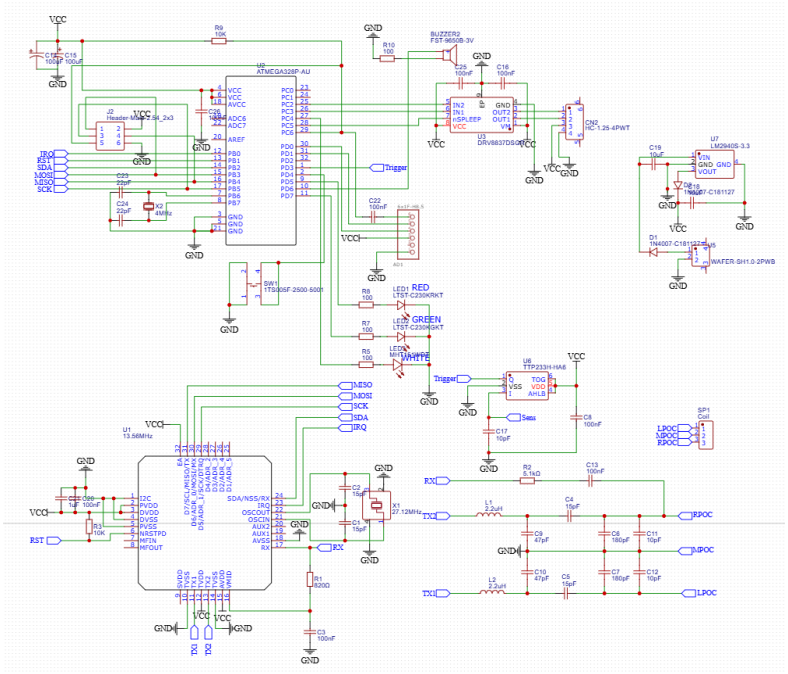


Figure 4. Electrical circuit diagram of control and motor systems

The main circuit includes the microcontroller, motor driver, voltage regulator, a 13.56 MHz ISO/IEC 14443-compliant RFID reader, and a user feedback interface consisting of dual-color LEDs and a piezoelectric buzzer. The visual and acoustic signals assist users during lock operation. For instance, a brief green flash and a beep confirm successful authentication, while a red light and a distinct tone indicate access denial or an error.

From a hardware reliability standpoint, flyback protection and careful PCB layout were prioritized to safeguard sensitive components. High-current traces are kept short, and analog and digital sections are isolated to reduce electromagnetic interference. Figure 5 illustrates the compact 3D PCB layout, where all major components, including the MCU and driver circuitry, are housed behind the motor inside the enclosure.

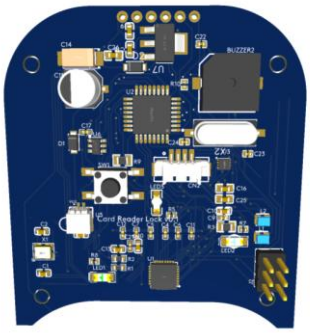


Figure 5. 3D View of PCB with Atmega48P and DRV8837 motor driver

The firmware embedded in the ATmega48P manages the complete authentication process and motor actuation sequence. When a valid RFID card is presented, the controller matches the card ID with pre-stored credentials in flash or EEPROM memory. If authorized, the motor is activated to rotate approximately 90°, unlocking the mechanism. This motion is either time-limited or halted through a current-sensing routine that detects when the cam mechanism reaches its endpoint. After unlocking, the system can re-lock automatically after a preset delay or wait for another user-triggered action, depending on firmware configuration. In the event of invalid credentials, access is denied, the red LED is illuminated, and an error tone is emitted. Failed attempts are tracked internally, and after three consecutive failures, the firmware initiates a temporary lockout—disabling input for 30 seconds and providing a warning signal. This security feature mitigates brute-force attempts and mirrors functionality found in commercial smart locking systems.

The feasibility of such a design has been supported by similar implementations in the literature, where cost-effective 8-bit microcontrollers have proven reliable in access control applications (Roy et al., 2018; San Hlaing, & San Lwin 2019; Hoque & Davidson, 2019). In prototype testing, the current system achieved between 350 and 400 full actuation cycles on a 1000 mAh battery, demonstrating suitability for long-term standalone use. To maintain usability in cases of battery depletion, the system includes a USB-C port, designed to support both emergency external powering and battery charging. If the internal battery is drained, users can connect a 5 V power source-such as a standard USB-C power bank-to restore functionality. Simultaneously, this connection begins charging the onboard battery.

As depicted in Figure 6, the USB-C port is accessible from the side of the housing and does not disrupt the overall compact form of the device. Once powered and authenticated, the lock is actuated normally and returns to the locked position either automatically or on user command. This dual-purpose input ensures system continuity, especially in field environments where battery replacement may not be immediately possible.

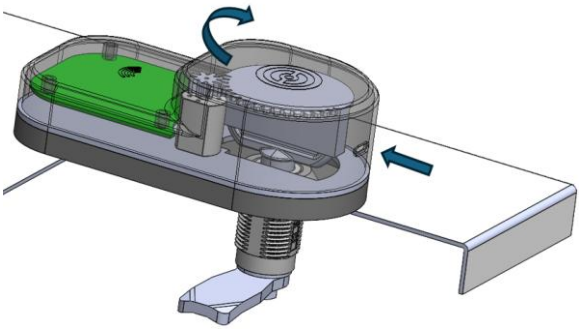


Figure 6. Internal layout and dual-function USB-C input for external powering and battery charging

When external power is supplied and authentication is successful, the motor performs the unlock and subsequently re-locks after a set timeout or user prompt. This dual-function feature enhances operational reliability in field deployments and reduces service interruptions.

Assembly and Integration

A primary objective of the retrofit kit is easy installation without altering the existing lock mechanism. If needed, a small hole is drilled into the cabinet or locker door. The device is then aligned so that its motor-driven insert fits into the back of the cam lock and is secured with a single screw passing through the housing and fastened from the inside. This screw also maintains alignment. Figure 7 shows the assembled kit mounted externally on a metal locker, demonstrating its mechanical integration.

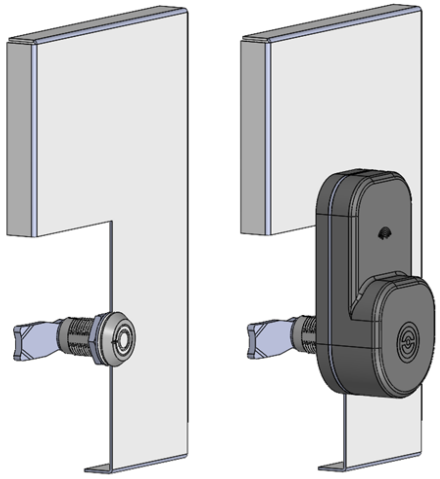


Figure 7. Installed smart lock kit on a metal locker

The housing is compact and low-profile, slightly larger than the lock, ensuring it fits even on densely packed panels. Internal contours help align it with the existing lock nut, while molded markings guide installation. The key insert is connected before securing the housing, and minor misalignments are tolerated, allowing reliable motor operation. Both mechanical and electrical systems are modular for easy upgrades and maintenance. The circuit board can be detached for servicing, and external components like the RFID reader or keypad connect via slim cables routed discreetly through the same or adjacent hole. The PCB also includes space for future BLE or Wi-Fi modules to enable wireless functionality. This approach preserves the mechanical override: the user can revert to key operation by removing the housing, or-if the design permits-use the key without removal, thanks to the motor's pass-through coupling.

Overall, the kit is designed for scalable deployment. Installation requires minimal tools and time, making it practical for retrofitting many units in settings like schools or data centers. The only permanent change is a small screw hole—ensuring that legacy infrastructure remains largely intact while gaining smart capabilities.

Prototype Testing

A fully functional prototype of the smart lock retrofit kit was developed and tested for mechanical, electrical, and authentication performance under realistic conditions. Over 500 lock-unlock cycles were performed using a metal locker, with tests including door misalignment to evaluate torque reliability. The system consistently completed 90° actuation without motor stalls or mechanical degradation.

Authentication and Security

Tests included RFID card and keypad PIN inputs across multiple users. Valid credentials unlocked the system in under two seconds; invalid ones triggered visual (LED) and acoustic (buzzer) feedback. After three failed attempts, the system entered a 30-second lockout, effectively preventing brute-force access.

Power Consumption

Power draw during standby remained below 3 mA, while peak motor activity reached ~130 mA for ~1 second per actuation. A 1000 mAh Li-Po battery supported approximately 350–400 cycles. Low-battery warnings via blinking red LED activated reliably before voltage dropped below safe thresholds.

Fail-Safe and Data Retention:

Tests confirmed that the system safely halted motor operation during jams. Credential memory was retained through power loss. Physical tampering (e.g., prying) was unsuccessful, and the mechanical override via original key remained functional. Overall, the prototype validated the system's durability, low power consumption, secure authentication, and ease of integration, confirming its suitability for real-world use (Khan et al., 2023; Uppuluri & Lakshmeeswari, 2023).

Results and Discussion

The developed retrofit kit exhibited robust and consistent performance across more than 500 actuation cycles, maintaining mechanical and electrical reliability even under conditions involving mild misalignment or uneven door tension. Throughout testing, no detachment, stalling, or synchronization errors were recorded, affirming the structural integrity and operational stability of the system.

Authentication using RFID cards was rapid and accurate, with successful access consistently completed in under two seconds. The absence of keypad input simplified user interaction and eliminated potential failure points, contributing to both reliability and intuitive operation. Credential matching remained accurate across multiple RFID tags, validating the firmware's authentication handling and memory management.

Power efficiency was another key strength. The combination of low quiescent current, optimized actuation routines, and interrupt-driven sleep mode allowed the system to achieve approximately 350–400 locking cycles per 1000 mAh battery charge. This level of performance supports extended maintenance intervals and is well aligned with the low-power design objectives. The inclusion of algorithmic power management—such as disabling non-critical peripherals and periodic RFID polling-further minimized standby energy use.

Security features functioned as intended: after three consecutive failed authentication attempts, the system entered a temporary lockout state, effectively deterring unauthorized access and brute-force attempts. The visual and auditory feedback provided clear cues to the user at each stage of operation, and the mechanical override capability was preserved for emergencies, ensuring that physical key access remained viable in case of battery failure or electronic malfunction.

Installation proved to be straightforward and repeatable. On average, mounting the kit-including alignment and securement-took less than a minute using only basic tools. The modular and non-invasive design allowed integration without modifying the existing lock or enclosure, preserving the original aesthetics and mechanical function. Cost analysis indicated that the retrofit solution could be implemented at 40–60% less than full smart lock replacements, offering considerable savings in both materials and labor.

While the current prototype does not include wireless connectivity, the PCB layout reserves space for optional BLE or Wi-Fi modules, enabling future remote access or cloud-based monitoring. Additional areas for refinement include user interface enhancements, improved tamper detection (e.g., housing removal alerts), and better battery replacement ergonomics.

In summary, the prototype effectively delivered on its goals of energy efficiency, secure access control, ease of installation, and compatibility with legacy lock infrastructure. Its modular architecture and minimal power requirements position it as a scalable and sustainable solution for digitally upgrading mechanical locks in institutional and industrial settings.

Conclusion

This study demonstrated a practical and cost-effective approach for upgrading mechanical quarter-turn locks with smart access control functionality. The proposed retrofit kit integrates seamlessly with existing lock hardware, offering digital authentication via RFID cards entry, visual and indicator feedback, lockout protection,

and modular mechanical compatibility. By retaining the original lock mechanism, the system enhances security and manageability without sacrificing the reliability or emergency override capability of traditional keys.

Prototype development and testing confirmed the system's robustness, low power consumption, and user-friendly installation. The device can be deployed in environments such as schools, offices, and industrial facilities with minimal modification and training requirements. Compared to full smart lock replacements, the retrofit solution presents a substantial advantage in cost, time, and sustainability by modernizing access infrastructure while preserving existing assets.

While the current design addresses essential access control needs, future enhancements could expand its capabilities. Wireless modules, for instance, could enable remote monitoring and integration into building automation systems. The modular architecture also allows adaptation to a broader range of lock types. In summary, the retrofit kit represents a scalable, maintainable, and efficient solution for bridging legacy hardware with modern security demands.

Recommendations

Based on the prototype evaluation and current limitations, the following recommendations are proposed to guide future developments and large-scale implementations:

Wireless Connectivity: Incorporate Bluetooth Low Energy (BLE) or Wi-Fi modules to enable remote unlocking, centralized credential management, and real-time access notifications via smartphones or enterprise software.

Expanded Adapter Library: Develop a broader range of interchangeable key inserts and mounting adapters to support additional lock types, including deadbolts, padlocks, or other specialty formats.

Field Deployment Testing: Conduct long-term trials in real-world, multi-user environments (e.g., schools or shared workspaces) to assess durability, usability, and environmental resilience under diverse usage conditions.

Management Dashboard: Design a software interface or API for device configuration, access log retrieval, and health monitoring (e.g., battery level, tamper alerts). This would enhance system oversight in institutional deployments.

Enhanced Security Features: Explore options such as biometric authentication (e.g., fingerprint or facial recognition), two-factor verification (RFID + PIN), and improved RFID encryption to address higher security requirements.

Implementing these enhancements would strengthen the retrofit kit's value proposition and broaden its applicability. All improvements should maintain the core principles of modularity, simplicity, and cost-efficiency to support scalable deployment.

Scientific Ethics Declaration

* The authors declare that the scientific ethical and legal responsibility of this article published in EPSTEM journal belongs to the authors.

Conflict of Interest

* The authors declare that they have no conflicts of interest

Funding

* This research received no specific grant from any funding agency in the public, commercial, or not-for-profit sectors.

Acknowledgements or Notes

* This article was presented as an oral presentation at the International Conference on Technology, Engineering and Science (www.icontes.net) held in Antalya/Türkiye on November 12-15, 2025.

References

Alzhrani, A. A., Balfaqih, M., Alsenani, F., Alharthi, M., Alshehri, A., & Balfagih, Z. (2024). Design and implementation of an IoT-integrated smart locker system utilizing facial recognition technology. *Engineering, Technology & Applied Science Research, 14*(4), 16000-16010.

Hoque, M. A., & Davidson, C. (2019). Design and implementation of an IoT-based smart home security system. *International Journal of Networked and Distributed Computing, 7*(2), 85-92.

Jayakumar, H., Raha, A., & Raghunathan, V. (2014). Hypnos: An ultra-low power sleep mode with SRAM data retention for embedded microcontrollers. In *Proceedings of the 2014 International Conference on Hardware/Software Codesign and System Synthesis* (pp. 1-10).

Khan, S., Thapa, C., Durrani, S., & Camtepe, S. (2023). Access-based lightweight physical-layer authentication for the Internet of Things devices. *IEEE Internet of Things Journal, 11*(7), 11312-11326.

Krishna, G., Singh, R., Gehlot, A., Shaik, V. A., Twala, B., & Priyadarshi, N. (2024). IoT-based real-time analysis of battery management system with long range communication and FLoRa. *Results in Engineering, 23*, 102770.

Lin, C., Khazaei, H., Walenstein, A., & Malton, A. (2021). Autonomic security management for IoT smart spaces. *ACM Transactions on Internet of Things, 2*(4), 1-20.

McCluskey, P. (2002, May). Design for reliability of micro-electro-mechanical systems (MEMS). In *52nd Electronic Components and Technology Conference 2002* (pp. 760-762). IEEE.

Roy, S., Uddin, M. N., Haque, M. Z., & Kabir, M. J. (2018). Design and implementation of the smart door lock system with face recognition method using the Linux platform Raspberry Pi. *IJCSN-International Journal of Computer Science and Network, 7*(6), 382–388.

San Hlaing, N. N., & San Lwin, S. (2019). Electronic door lock using RFID and password based on Arduino. *International Journal of Trend in Scientific Research and Development, 3*(2), 799-802.

Uppuluri, S., & Lakshmeeswari, G. (2023). Secure user authentication and key agreement scheme for IoT device access control based smart home communications. *Wireless Networks, 29*(3), 1333-1354.

Wolniak, R. (2024). *The usage of smart locks in smart home.* Zeszyty Naukowe. Organizacja i Zarządzanie/Politechnika Śląska.

Xin, Z., Liu, L., & Hancke, G. (2020). AACS: Attribute-based access control mechanism for smart locks. *Symmetry, 12*(6), 1050.

Author(s) Information

Selahattin Mert Aydin
Mesan Locks INC, Mimar Sinan Mah Ulubey Caddesi Fabrikalar Sitesi, No: 7 34570 Silivri, İstanbul, Türkiye

Engin Gunes
Mesan Locks INC, Mimar Sinan Mah Ulubey Caddesi Fabrikalar Sitesi, No: 7 34570 Silivri, İstanbul, Türkiye
Contact e-mail: engingunes@essentra.com

To cite this article:

Aydin, S. M., & Gunes, E. (2025). Refrofit kit design that converts industrial locks into electromechanical smart locks. *The Eurasia Proceedings of Science, Technology, Engineering and Mathematics (EPSTEM), 38,* 816-823.

The Eurasia Proceedings of Science, Technology, Engineering & Mathematics (EPSTEM)
ISSN: 2602-3199

The Eurasia Proceedings of Science, Technology, Engineering and Mathematics (EPSTEM), 2025

Volume 38, Pages 824-829

IConTES 2025: International Conference on Technology, Engineering and Science

Assessing Translation Quality in Large Language Models and Machine Translation Systems: The BLEU Metric and Language Pair Effects

Philipp Rosenberger
University of Applied Science Campus Vienna

Natallia Kolchanka
University of Applied Science Campus Vienna

Abstract: The rapid advancement of translation technologies has transformed global communication and created new opportunities for cross-linguistic interaction. However, their relative quality compared to human translation remains contested. This paper provides a comparative evaluation of translations produced by large language models (ChatGPT, Claude, Copilot) and machine translation systems (DeepL, Google Translate, Yandex Translate). The study focuses on English–German and English–Russian translation tasks across four domains (literary, news, social, speech). The evaluation relies on the BLEU metric. Results demonstrate that translation quality depends not only on the system itself but also on the language pair and the text domain. Google Translate achieved the highest average BLEU score for German, while Claude led for Russian. Findings emphasize the need for multimethod evaluation approaches and highlight the growing competitiveness of AI-based systems depending on the type of text and language used in the translation process. This article is based on the master's thesis "Evaluation of translation methods: Large Language Models and Machine Translation Systems versus Human Translation" (Kolchanka, 2025).

Keywords: Translation, Large language models, Machine translation systems

Introduction

Effective multilingual communication is essential in today's interconnected world. Billions of people across thousands of languages require access to accurate translation in order to engage in business, education, healthcare, science, and cultural exchange (Naveen & Trojovský, 2024). Translation technologies play a pivotal role in bridging linguistic divides. While human translation remains the gold standard, it is costly, time-consuming, and difficult to scale for global communication demands (Chauhan & Daniel, 2023). Advances in machine translation (MT) systems and large language models (LLMs) have introduced scalable, fast, and increasingly accurate solutions. However, questions remain regarding their reliability, domain robustness, and overall comparability to human translation.

The research presented in this article is motivated by the following research question:

- How do large language models and machine translation systems differ in translation quality when translating from English to German and Russian?

By addressing this question, this study contributes to both theoretical and applied research on translation technologies. It sheds light on the relative strengths and weaknesses of current systems, informs developers about areas for improvement, and provides users with insights into which tools may best meet their needs in specific contexts.

- This is an Open Access article distributed under the terms of the Creative Commons Attribution-Noncommercial 4.0 Unported License, permitting all non-commercial use, distribution, and reproduction in any medium, provided the original work is properly cited.

- Selection and peer-review under responsibility of the Organizing Committee of the Conference

© 2025 Published by ISRES Publishing: www.isres.org

Methodology

This study compares three LLMs (ChatGPT, Claude, Copilot) and three MT systems (DeepL, Google Translate, Yandex Translate) with human translation. The focus is on translations from English into German (EN-DE) and Russian (EN-RU).

Dataset

The experiment used 100 source texts from the Ninth Conference on Machine Translation (WMT2024), covering four domains: literary (stories), news (journalistic articles), social (informal online communication), and speech (transcribed spoken language). This variety ensured domain-specific differences could be observed.

Automatic Evaluation

Translation outputs were evaluated using BLEU (Bilingual Evaluation Understudy) (Papineni et al., 2002), a widely adopted metric that calculates n-gram overlap between the system output and reference human translations. BLEU was chosen for its comparability with prior studies and for its reproducibility, despite its known limitations. Figure 1 below illustrates a generic machine translation evaluation process (Chauhan, Daniel, 2023).

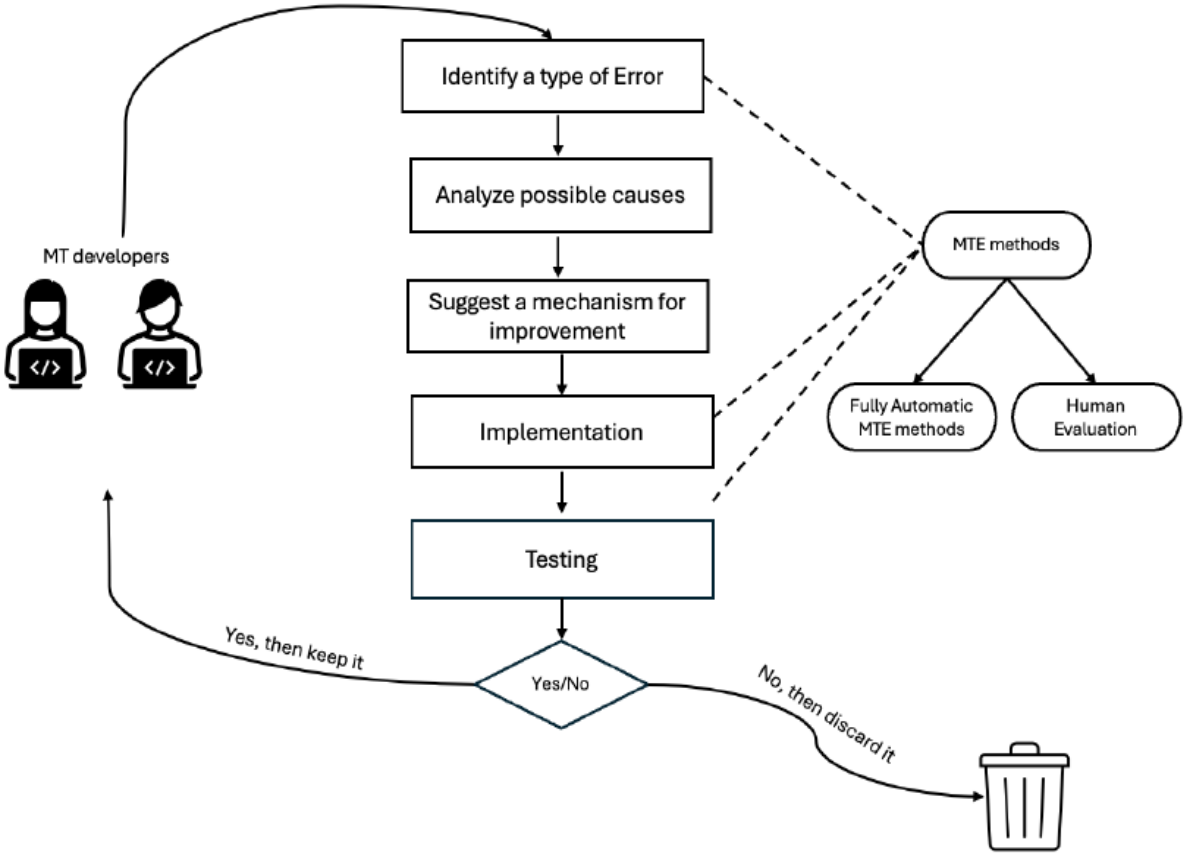


Figure 1. MT evaluation methods and their role in the development of MT models.
Source: Chauhan, Daniel (2023)

Research Process

Based on the dataset of WMT24 which contains 998 English source texts, 100 texts were selected randomly. The selection resulted in a distribution of text types (left) and lengths (right) as shown below in Figure 2.

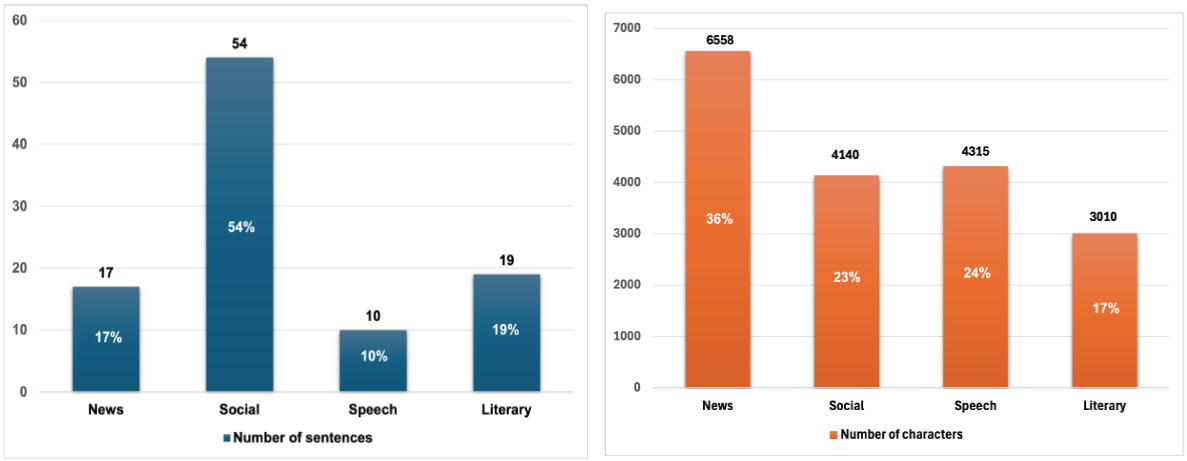


Figure 2. Source text types and lengths

After this reduction of inputs, the source texts were translated into German and Russian using the selected translation systems. ChatGPT, Claude and Copilot were selected as the LLMs. DeepL, Google Translate and Yandex Translate were selected for machine translation systems. All translations were performed using the free versions of these LLMs and MT systems (accessed October 22, 2024). After translation, BLEU scores were generated for all translations produced by the LLMs and MT systems.

Results

English to German BLEU Translation Results

The heat map in Figure 3 details the BLEU results of English to German translations depending on the domain and the translation technology. Google Translate received the highest score but only in the literary category. DeepL led in the news and speech domains. Claude achieved the highest score in the social domain.

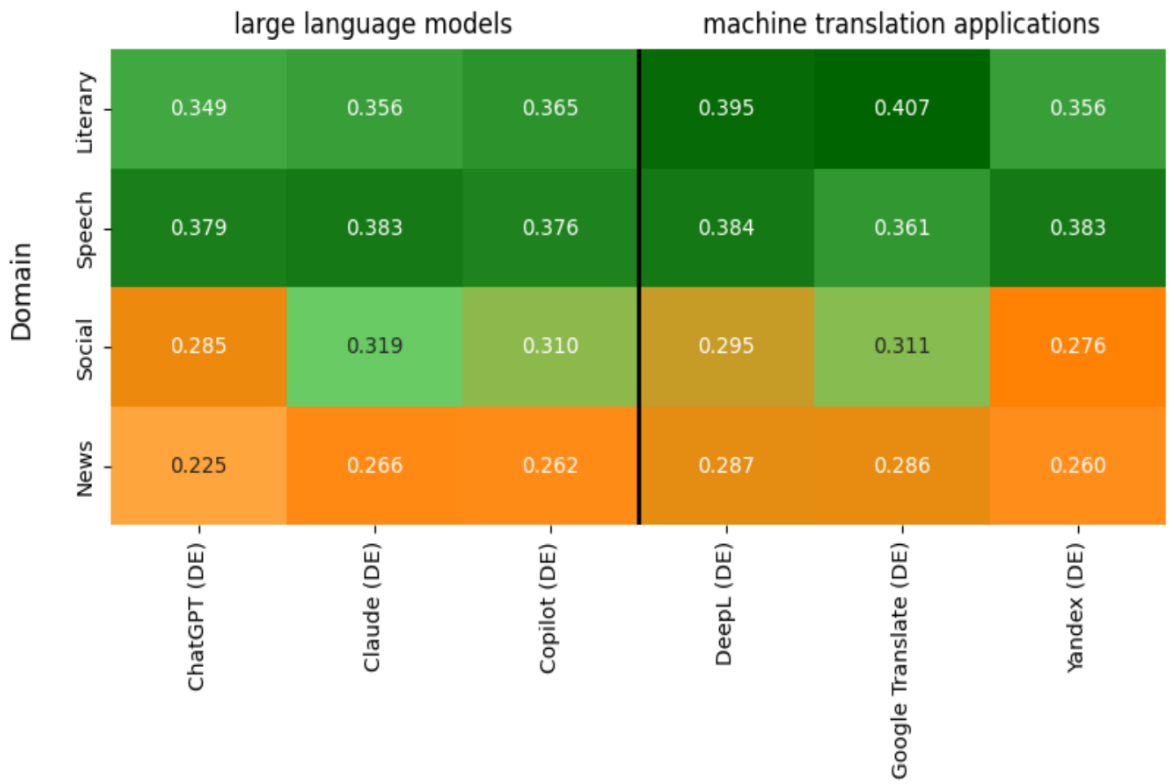


Figure 3. BLEU results for English to German translations

English to Russian BLEU Translation Results

The heat map in Figure 4 details results of English to Russian translations. Claude achieved the highest average BLEU score and the highest score in the social domain, with Copilot outperformed others in the literary domain and Google Translate ranked highly in the news and speech domains.

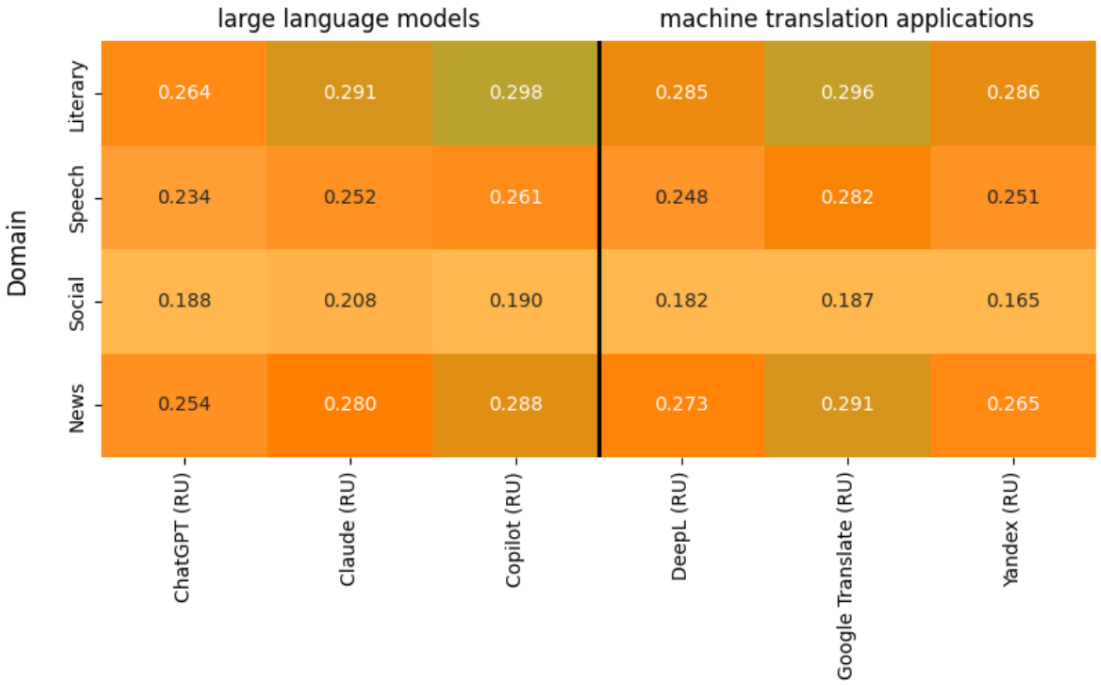


Figure 4. BLEU results for English to Russian translations

Summary of BLEU Evaluation Results

Across both language pairs, English to German translations achieved higher BLEU score than English to Russian. This reflects the greater structural and morphological challenges in Russian, including its complex case system and flexible word order. Additionally, English and German are more closely related as members of the Germanic branch of the Indo-European family, whereas Russian, a member of the Slavic branch, is more distantly related to English.

Discussion

This study provided a structured comparison of translation quality across LLMs, MT systems, and human translation. By examining English-to-German and English-to-Russian translations across diverse text domains—literary, news, social, and speech—the analysis highlighted how translation quality is influenced by both language pair and domain context. The findings indicate that BLEU scores favored Google Translate for German and Claude for Russian, though these results varied significantly depending on the text type.

Taken together, the study demonstrates that no single system dominates across all dimensions. Instead, quality is context-dependent, underscoring the need for multi-method evaluation rather than relying exclusively on automatic metrics. Importantly, the blurred boundary between human and machine translation raises both opportunities and challenges: while accessibility and scalability are advancing, the nuances of style, cultural resonance, and contextual fidelity remain areas where human expertise continues to be invaluable.

Outlook Towards the Future of Translation

The future of translation is likely to be defined by a gradual dissolution of boundaries: between languages, between media, and even between human and machine. Already today, machine-generated translations are

difficult to distinguish from human output, and this trajectory suggests a world in which translation becomes less of an external process and more of an invisible infrastructure of communication. We may soon find ourselves speaking, writing, or even thinking in our native languages while interacting seamlessly with people who use entirely different linguistic systems. Translation, in this vision, is no longer an obstacle but an embedded layer of global interaction.

As technology progresses, translation systems will not remain confined to text alone. They will increasingly integrate speech, gesture, and visual cues, producing translations that capture not only words but also tone, intent, and cultural nuance. The translation of the future will be adaptive: sensitive to context, personal style, and domain-specific expectations. A legal document will be translated with precision and consistency, while a poem will be carried over with rhythm and metaphor intact. In this sense, translation technologies will not only bridge linguistic divides but also preserve and amplify the uniqueness of human expression.

Yet rather than replacing human translators, these systems are likely to evolve into companions and collaborators. Machines will provide speed, scale, and accessibility, while humans will continue to safeguard nuance, creativity, and ethical responsibility. Such a partnership could elevate the act of translation into something richer than either party could achieve alone-an interplay where the strengths of human intuition and artificial intelligence converge.

Looking even further ahead, one can imagine a world where the idea of “foreign languages” loses much of its practical weight. Communication across cultures may one day be as immediate and natural as speaking with a neighbor. If that future arrives, the role of translation will no longer be defined by overcoming barriers but by celebrating differences, transforming translation from a tool of necessity into an instrument of cultural connection and creativity.

Recommendations

Future research on translation quality should broaden its methodological and linguistic scope. Larger and more varied datasets would strengthen the generalizability of findings, particularly if they include low-resource languages and specialized domains such as legal, medical, or technical discourse. In addition, complementary evaluation metrics such as COMET or BERTScore should be employed, as they offer more nuanced assessments of semantic and contextual fidelity than BLEU alone.

Scientific Ethics Declaration

* The authors declare that the scientific ethical and legal responsibility of this article published in EPSTEM journal belongs to the authors.

Conflict of Interest

* The authors declare that they have no conflicts of interest

Funding

* This research is not funded.

Acknowledgements or Notes

* This article was presented as virtual presentation at the International Conference on Technology, Engineering and Science (www.icontes.net) held in Antalya/Türkiye on November 12-15, 2025

References

Chauhan, S., & Daniel, P. (2023). A comprehensive survey on various fully automatic machine translation evaluation metrics. *Neural Processing Letters, 55*, 12663-12717.

Kolchanka, N. (2025). *Evaluation of translation methods: Large language models and machine translation systems versus human translation* (Master's thesis). FH Campus Wien.

Naveen, P., & Trojovský, P. (2024). Overview and challenges of machine translation for contextually appropriate translations. *iScience, 27*, 110878.

Papineni, K., Roukos, S., Ward, T., & Zhu, W.-J. (2002). BLEU: A method for automatic evaluation of machine translation. In *Proceedings of the 40th Annual Meeting of the Association for Computational Linguistics (ACL)* (pp. 311-318). Association for Computational Linguistics.

Author(s) Information

Philipp Rosenberger
University of Applied Science Campus Vienna
Favoritenstrasse 226, 1100 Vienna, Austria
Contact e-mail: *Philipp.rosenberger@hcw.ac.at*

Natallia Kolchanka
University of Applied Science Campus Vienna
Favoritenstrasse 226, 1100 Vienna, Austria

To cite this article:

Rosenberger, P., & Kolchanka, N. (2025). Assessing translation quality in large language models and machine translation systems: The BLEU metric and language pair effects. *The Eurasia Proceedings of Science, Technology, Engineering and Mathematics (EPSTEM), 38,* 824-829.

The Eurasia Proceedings of Science, Technology, Engineering & Mathematics (EPSTEM)
ISSN: 2602-3199

The Eurasia Proceedings of Science, Technology, Engineering and Mathematics (EPSTEM), 2025

Volume 38, Pages 830-841

IConTES 2025: International Conference on Technology, Engineering and Science

A Multi-Criteria Decision-Making Model for Performance Evaluation Based on PSI–PF-COBRA

Canan Sen
Burdur Mehmet Akif Ersoy University

Kubra Onder
Burdur Mehmet Akif Ersoy University

Halil Sen
Burdur Mehmet Akif Ersoy University

Abstract: The aim of this study is to evaluate the financial and economic performance of companies operating in the chemical, pharmaceutical, petroleum, and plastic products sectors traded on Borsa Istanbul (BIST) within a holistic framework. Because traditional financial ratio analyses alone are insufficient, the study integrates the PSI and PF-COBRA methods, which are multi-criteria decision-making methods. The study first examines the sector's place in the Turkish economy, its relationship with macroeconomic indicators, and the interactions between growth, investment, and foreign trade in detail. Then, using data from the 2023/12 period, 15 companies traded on the BIST were evaluated based on 14 criteria. Criteria weights were determined based on the opinions of decision-makers from various expert groups. During the analysis, the importance of the criteria was first determined using the PSI method, and then the PF-COBRA method was used to rank the companies in terms of their distance from ideal and anti-ideal solutions. The results reveal that companies in the sector perform at different levels in terms of financial strength and economic competitiveness. According to the findings, companies with high R&D investments, strong export capacity, and balanced leverage rank higher, while companies with high leverage and limited R&D and innovation capacity remain at the bottom. The research's contributions are highlighted in three dimensions: (i) the joint analysis of financial and economic indicators in the Turkish chemical sector, (ii) the adaptation of the PSI–PF–COBRA method integration, which has limited application in the literature, to the sector, and (iii) the provision of a strategic decision-support tool for investors, managers, and policymakers. The study's results shed light on the development of policies and investment strategies that will enhance the sector's sustainable growth capacity and competitiveness.

Keywords: Industrial engineering, Multi-criteria decision making, PSI, PF-COBRA

Introduction

The performance of industrial sectors in the Turkish economy is critical for sustainable growth and competitiveness. Among these sectors, the chemicals, pharmaceuticals, petroleum, rubber, and plastic products sectors occupy a strategic position due to their large production capacity, central role in the intermediate goods supply chain, and contribution to exports. The chemical industry, which provides raw materials to many sectors such as textiles, automotive, agriculture, energy, and construction, has become more complex and dynamic due to globalization and fluctuations in energy prices. In this context, indicators such as companies' financial strength, liquidity level, debt structure, profitability, and operating efficiency are critical for both company sustainability and the sector's macroeconomic contribution. However, assessments based solely on financial ratios may be insufficient to fully explain companies' competitiveness today. Economic performance indicators such as export capacity, R&D investments, innovation level, and market share have become important complementary factors in

- This is an Open Access article distributed under the terms of the Creative Commons Attribution-Noncommercial 4.0 Unported License, permitting all non-commercial use, distribution, and reproduction in any medium, provided the original work is properly cited.

- Selection and peer-review under responsibility of the Organizing Committee of the Conference

© 2025 Published by ISRES Publishing: www.isres.org

determining a company's long-term position. Therefore, evaluating financial and economic indicators together produces more reliable results in demonstrating a company's holistic performance. In this context, multi-criteria decision-making (MCDM) methods enable comparative analysis of companies by considering multiple criteria simultaneously. Fuzzy logic-based methods are gaining prominence in such studies, where expert assessments involving uncertainty are increasingly important. The PF-COBRA (Picture Fuzzy Comprehensive Distance-Based Ranking) method used in this study reflects uncertainty more realistically by modeling the degrees of acceptance, rejection, and uncertainty in decision-makers' evaluations.

The use of multi-criteria decision-making (MCDM) methods in financial performance analyses has increased significantly in recent years; these methods have become an important tool for measuring the multidimensional performance of firms by enabling the combined evaluation of financial ratios and non-financial strategic indicators. Ertuğrul & Karakasoglu (2009) evaluated Turkish cement companies using the FAHP and TOPSIS methods, demonstrating that integrating subjective expert judgments with financial ratios increases ranking accuracy. Similarly, Secme et al. (2009) analyzed five large commercial banks using the FAHP–TOPSIS model and demonstrated that combining financial and non-financial criteria using the Balanced Scorecard provides more holistic results.

Studies following this approach have used various combinations of the BSC framework and fuzzy logic. Wu et al. (2009) evaluated banking performance using the fuzzy MCDM method, while Mandić et al. (2014) evaluated Serbian banks using the FAHP–TOPSIS, demonstrating that CAMELS indicators can be successfully integrated into MCDM models. The increased predictive power of hybrid models was emphasized by Wanke et al. (2016) in a study using artificial neural networks and TOPSIS together. Aras et al. (2017) determined that the economic dimension was the dominant criterion by measuring sustainability performance with the Entropy–TOPSIS approach. In the case of Borsa Istanbul, Bulgurcu (2012) reduced numerous financial ratios to a single index using the TOPSIS method; Liew et al. (2022) demonstrated that criteria interactions significantly impacted ranking results using the Entropy–DEMATEL–TOPSIS approach. Lam et al. (2021) analyzed companies in the construction sector with fuzzy VIKOR, noting that the method's accommodative structure well reflects different risk profiles. In Europe and the Middle East, studies using intuitive fuzzy approaches (Reig-Mullor & Brotons-Martinez, 2021), the modified EDAS model (No et al., 2021), and studies using SWARA-II, MEREC, and MARCOS together in the post-pandemic period (Ünlü et al., 2022) are noteworthy. Recent comparative studies have highlighted the sensitivity of the Entropy–TOPSIS and Entropy–VIKOR methods (Türegün, 2022), the impact of IT2-Fuzzy DEMATEL–TOPSIS on FinTech investments (Kou et al., 2021), and the superiority of multi-method consensus (Kaya et al., 2024). Furthermore, the MARCOS method has been reported to be successful in financial resilience analyses (Mastilo et al., 2024).

PSI (Preference Selection Index) and PF-COBRA (Picture Fuzzy COBRA) methods have become prominent approaches in the MCDM literature because they reduce the need for criterion weighting and offer a more flexible evaluation under uncertainty. The PSI method was first introduced by Maniya & Bhatt (2010) and applied to the material selection problem, demonstrating the feasibility of an unweighted prioritization process. Ongoing studies have shown that PSI produces consistent results across different sectors. For example, Attri & Grover (2015) successfully applied the method in production system design, and Madić et al. (2017) successfully applied it to the optimization of laser cutting parameters. In the banking sector, Kabakçı & Sarı (2019) and Trung et al. (2024) demonstrated that PSI produces rankings consistent with CAMELS indicators. Recently, models combining PSI with methods such as TOPSIS, MABAC, and SRP in a hybrid manner (Wardany & Zahedi, 2025) have provided more stable results. Studies on the COBRA and PF-COBRA methods are particularly concentrated in the fields of logistics, sustainability, tourism, and finance. Krstić et al. (2022) applied COBRA to reverse logistics; Popović et al. (2022) applied the MEREC–COBRA model to e-commerce strategy selection, demonstrating that objective weighting strengthens ranking stability. Tadić et al. (2024) analyzed the obstacles to drone use in last-mile logistics using fuzzy COBRA, indicating that the method effectively models uncertainty. Furthermore, applications of SWARA–COBRA in a global fuzzy environment (Zorlu et al., 2024) and SWARA–MEREC–COBRA in sustainability performance (Taşcı, 2024) demonstrate the method's adaptability to a wide range of decision-making domains. Studies demonstrating the effectiveness of MEREC–COBRA for the airline industry (Asker, 2024) are also available in the literature. The fact that the PF-COBRA method using picture fuzzy space reflects uncertainty more accurately was confirmed by Alshamrani et al. (2025) in the analysis of distance education software.

In this study, the financial and economic performance of 15 chemical and plastics sector companies traded on Borsa Istanbul was analyzed using the e method. The criteria set consists of indicators such as liquidity, debt, productivity, profitability ratios, R&D expenditures, number of R&D employees, market concentration, and export/sales ratio. Criteria weights are based on the assessments of three decision-makers: a financial analyst, a

sector manager, and an R&D expert. The study is important in terms of (i) contributing to the holistic evaluation of financial and economic performance in the sector, (ii) adapting the PF-COBRA method, which has limited application in the literature, to a new sector, and (iii) the results obtained are guiding investors and policy makers.

Method

PSI (Preference Selection Index) Method

The PSI (Preference Selection Index) method is a nonparametric method that evaluates the performance of alternatives in multi-criteria decision-making (MCDM) problems without the need for criterion weights. Developed by Maniya and Bhatt (2010), PSI has rapidly become widespread in the literature due to its ease of calculation and applicability, especially in problems involving a large number of criteria. Because the method is based on simple steps such as normalization, averaging, deviation analysis, and obtaining a preference index, it has a wide range of applications in engineering, manufacturing, finance, and service sectors.
How the PSI Method Works (Summary Steps):

1. Creating the Decision Matrix: The decision matrix, consisting of the m-criterion and the n-alternative, is obtained as
$$X = [x_{ij}]_{m\times n}$$
2. Normalization: The decision matrix is normalized so that all criteria can be compared at a common scale. Benefit-type criteria:
$$n_{ij} = \frac{x_{ij}}{\max\limits_{j} x_{ij}} \quad ;$$
Cost-type criteria: $$n_{ij} = \frac{\min\limits_{j} x_{ij}}{x_{ij}} \quad ;$$
Thus, the normalized decision matrix,
$$N = [n_{ij}]_{m\times n}$$
is obtained.
3. Calculating Criteria Mean Values (Mi Score)
4. The average of the normalized values for each criterion is calculated.
5. Calculating Mean Deviations. The deviations of the alternatives from the criteria means are determined.
6. Obtaining PSI Scores and Ranking. Preference indices derived from the deviations are calculated, and alternatives are ranked according to the highest PSI value.

The PF-COBRA Method

The PF-COBRA method is an extension of the classical COBRA (Comprehensive Distance-Based Ranking) method using Picture Fuzzy Set (PFS) theory. It offers a powerful alternative for situations where decision-makers' evaluations involve uncertainty and contradictions in multi-criteria decision-making (MCDM) problems. The method ranks alternatives by measuring their distances from ideal and anti-ideal solutions, but in doing so, it evaluates criteria-related data in the form of picture fuzzy numbers (PFS - Picture Fuzzy Sets). As a combination of these two approaches, PF-COBRA is a powerful and versatile method for managing this uncertainty.

In recent years, methods integrated with Picture Fuzzy Sets (PFS) have gained importance to more accurately model uncertainty in decision-making processes. In this context, the PF-COBRA method is a version of the classical COBRA approach, enhanced with Picture Fuzzy Sets (PFS). PF-COBRA allows ranking alternatives according to ideal and anti-ideal solutions using comprehensive distance measures.

Picture Fuzzy Set (PFS) is a generalized form of classical fuzzy set and intuitionistic fuzzy set structures. PFS was introduced by Cuong & Kreinovich (2014). While classical fuzzy sets only answer the question "how many members does an element have?", PFS addresses the following three questions:

- "How many positive members does an element have?" → $\mu^{+}(x)$
- "Is an element undecided or neutral?" → $\mu^{0}(x)$

- "How many negative members does an element have?" → $\mu^{-}(x)$

This structure is particularly suitable for modeling situations such as uncertainty, hesitation, and indecision, which are frequently encountered in human-based decision-making situations. A Pictorial Fuzzy Set (PFS) over the universal set X is defined as follows:

$\tilde{A} = \{\langle x,\mu^{+}(x), \mu^{0}(x), \mu^{-}(x)\rangle \mid x \in X\}$
Where;
$\mu^{+}(x) \in [0,1]$: Positive membership degree
$\mu^{0}(x) \in [0,1]$: Neutral (abstaining) degree
$\mu^{-}(x) \in [0,1]$: Negative membership degree

The sum of the three membership functions cannot exceed 1. This indicates that each evaluation contains uncertainty and the total information level is kept under control.

The PF-COBRA method is implemented with the following basic steps:

1. Creating the PFS Decision Matrix: Decision makers' evaluations for each alternative and criterion are expressed as pictorial fuzzy numbers.
2. PFS Normalized Matrix: It is created by normalizing the membership, opposition, and abstention values. The normalization process is performed using the following formulas for the Benefit Criteria (Maximum). The aim is to increase positive membership, decrease negative membership, and preferably maintain neutrality constant.

   Positive membership $\mu^{+}_{ij(norm)} = \frac{\mu^{+}_{ij} - \min(\mu^{+}_{j})}{\max(\mu^{+}_{j}) - \min(\mu^{+}_{j})}$

   Negative membership $\mu^{-}_{ij(norm)} = \frac{\max(\mu^{-}_{j}) - \mu^{-}_{ij}}{\max(\mu^{-}_{j}) - \min(\mu^{-}_{j})}$

   Neutral (abstaining) Usually kept constant $\mu^{0}_{ij(norm)} = \mu^{0}_{ij}$

   For Cost Criteria;

   Positive membership $\mu^{+}_{ij(norm)} = \frac{\max(\mu^{+}_{j}) - \mu^{+}_{ij}}{\max(\mu^{+}_{j}) - \min(\mu^{+}_{j})}$

   Negative membership $\mu^{-}_{ij(norm)} = \frac{\mu^{-}_{ij} - \min(\mu^{-}_{j})}{\max(\mu^{-}_{j}) - \min(\mu^{-}_{j})}$

   Neutral (abstaining) Usually kept constant $\mu^{0}_{ij(norm)} = \mu^{0}_{ij}$
3. Determining Ideal and Anti-Ideal PFS Scores: The best and worst values for all criteria are defined in a pictorial fuzzy format. The ideal (best) and anti-ideal (worst) values are determined for each criterion. These values are derived from the normalized PFS matrix:

   Ideal PFS (PFS+): $\tilde{A}^{+} = (\max_i \mu^{+}_{ij}, \min_i \mu^{0}_{ij}, \min_i \mu^{-}_{ij})$

   Anti-Ideal PFS (PFS-): $\tilde{A}^{-} = (\min_i \mu^{+}_{ij}, \max_i \mu^{0}_{ij}, \max_i \mu^{-}_{ij})$
4. Distance Measurement: The comprehensive distances of the alternatives to the ideal and anti-ideal points are calculated. This is usually done with distance measures such as Euclidean, Hamming, or Manhattan. The distance between two Picture Fuzzy Number [$\tilde{A}_i = (\mu^{+}_{i}, \mu^{0}_{i}, \mu^{-}_{i})$ and $\tilde{A}_j = (\mu^{+}_{j}, \mu^{0}_{j}, \mu^{-}_{j})$] is usually It is measured by the following methods:

   Euclidean Distance: $D^{Euc}_{ij} = \sqrt{1/3[(\mu^{+}_{i} - \mu^{+}_{j})^2 + (\mu^{0}_{i} - \mu^{0}_{j})^2 + (\mu^{-}_{i} - \mu^{-}_{j})^2]}$

   Manhattan Distance: $D^{Man}_{ij} = 1/3[|\mu^{+}_{i} - \mu^{+}_{j}| + |\mu^{0}_{i} - \mu^{0}_{j}| + |\mu^{-}_{i} - \mu^{-}_{j}|]$

   Hamming Distance: $D^{Ham}_{ij} = |\mu^{+}_{i} - \mu^{+}_{j}| + |\mu^{0}_{i} - \mu^{0}_{j}| + |\mu^{-}_{i} - \mu^{-}_{j}|$

5. Calculating the Comprehensive Score: A score function is calculated that takes into account the proximity to the ideal solution and the distance to the anti-ideal solution.

$S^{(Euc)}_{i} = \frac{D^{-(Euc)}_{i}}{D^{-(Euc)}_{i} + D^{+(Euc)}_{i}}$

$S^{(Man)}_{i} = \frac{D^{-(Man)}_{i}}{D^{-(Man)}_{i} + D^{+(Man)}_{i}}$

$$S_i^{(Ham)} = \frac{D_i^{-(Ham)}}{D_i^{-(Ham)} + D_i^{+(Ham)}}$$

$$S_i^{(Combined)} = 1/3(S_i^{(Euc)} + S_i^{(Man)} + S_i^{(Ham)})$$

6. Ranking: Alternatives are ranked from most suitable to least suitable based on the calculated score values.

The PSI-PF-COBRA Method

The PSI-PF-COBRA method is an integrated decision-making model that combines the statistically robust structure of the PSI (Preference Selection Index) method with the flexible structure of PF-COBRA, which can model uncertainties. This combination provides a powerful tool that supports both objective data-based decisions and takes into account subjective evaluations through a fuzzy structure.

While the PSI method generates scores based on data normalization and the evaluation of deviations, PF-COBRA handles these scores in a fuzzy structure and converts decision makers' evaluations into (μ, ν, π) format. These structures are integrated as follows:

1. Calculating PSI Weights: The weights of the decision criteria are determined using the PSI method.
2. Creating PFS Values: The evaluation of each alternative against each criterion is expressed in the PFS structure.
3. Creating the Normalized PFS Matrix: The data is normalized in (μ, ν, π) format.
4. Determining Ideal and Anti-Ideal PFS Points: Ideal (best) and anti-ideal (worst) values are determined for all criteria.
5. Calculating Comprehensive Distances: The distance of each alternative to the ideal and anti-ideal solution points is calculated using PSI weights.
6. Determining the Score Function: The score value is calculated for each alternative by considering the proximity to the ideal point and the distance to the anti-ideal point.
7. Ranking the Alternatives: Alternatives are ranked according to the obtained score values.

This unified structure allows decision makers to consider statistical weights derived from historical data and make more accurate and reliable decisions in environments with blurred data and high uncertainty.

Results and Discussion

In this study, the 2023 financial performance of 15 companies listed on Borsa Istanbul (BIST) and operating in the chemicals, pharmaceuticals, petroleum, and plastics sectors was comprehensively analyzed. The companies included in the research were carefully selected from among the top 500 firms in Turkey in terms of R&D expenditures in 2023. This selection strategy enables the evaluation of firms that stand out not only with their financial performance but also with their innovation capacity, allowing for a holistic assessment of sector-leading companies. The dataset used in the analysis was compiled from publicly accessible and reliable institutional sources. Financial statements, ratio indicators, and R&D figures of the selected firms were obtained from the following platforms:

- ISO 500 Official Website (https://iso500.org.tr)
- Turkishtime Magazine – 2023 R&D 250 Report (https://turkishtimedergi.com)
- Fintables Financial Data Platform (https://fintables.com)
- Borsa Istanbul (BIST) and Public Disclosure Platform (KAP) (https://www.kap.org.tr/tr/bist-sirketler)

Based on ISO 500 and Turkishtime data, the companies with the highest sector-specific R&D expenditures were identified, and from among those listed on BIST, 15 companies were selected for detailed financial analysis. This approach ensured that the sample consists of firms that are simultaneously strong in R&D investment and actively valued in capital markets. Consequently, the study provides a comparative assessment of companies that lead their sectors both in terms of innovation capability and financial strength.

The following financial and economic indicators were used to evaluate the financial performance of companies in the chemicals, pharmaceuticals, petroleum, and plastics sectors listed on Borsa Istanbul:

- K1 – Current Ratio: Shows a company's ability to cover short-term liabilities. Values between 1.5–2 are considered healthy, especially in inventory-intensive sectors like chemicals and plastics.
- K2 – Cash Ratio: Measures cash and cash equivalents relative to short-term debt. It is the most conservative liquidity indicator. In high-investment sectors (plastics, petrochemicals), values may fall below the average due to investment cycles.
- K3 – Financial Debt Ratio: Indicates the share of assets financed by debt. High values signal debt-driven growth and financial risk, common in chemical and energy-intensive industries.
- K4 – Leverage Ratio: Shows total debt relative to equity, reflecting dependence on external financing. High leverage is typical in oil and petrochemical industries due to large-scale investments.
- K5 – Asset Turnover Ratio: Measures how efficiently assets generate sales. Very high values can indicate underinvestment, so industry context is essential.
- K6 – Receivables Turnover Ratio: Shows how frequently receivables are collected. High values indicate efficient cash management; low values may suggest collection issues.
- K7 – Gross Margin (%): Reflects the difference between production costs and sales revenue, indicating cost control and production efficiency.
- K8 – EBITDA Margin (%): Shows operational profitability independent of external factors. Typically ranges between 15–25% in chemical and plastics sectors.
- K9 – Net Profit Margin (%): Indicates net income generated from sales and reflects strategic performance.
- K10 – Return on Equity (%): Shows net profit relative to equity and is a key indicator of capital efficiency.
- K11 – R&D Expenditure (M TL): Represents financial resources allocated to innovation and technological development.
- K12 – Number of R&D Employees: Indicates a company's knowledge-creation capacity and technological investment.
- K13 – Market Share: Shows the company's relative position in the market.
- K14 – Export/Sales Ratio: Reflects the company's degree of export orientation.

As part of the research process, a three-person decision-making group comprised of field experts was formed to evaluate the criteria. Members of this group represented diverse areas of expertise, providing a comprehensive perspective throughout the evaluation process. Each expert contributed their unique knowledge and professional perspective, enhancing the robustness, validity, and reliability of the decision-making framework. The decision-makers were as follows:

- D1 – Financial Analyst: Possessing academic expertise in financial management and multi-criteria decision-making techniques, they contributed to the assessment of the financial strength dimension.
- D2 – Industry Representative: Possessing many years of managerial experience in the chemical and plastics sectors and incorporating practical sectoral knowledge into the assessment process.
- D3 – R&D Specialist: Manages the R&D and innovation processes of a large-scale industrial enterprise and ensured that an innovation and technology-focused perspective was incorporated into the decision-making process.

This diversification enabled a balanced consideration of financial strength, practical sectoral knowledge, and innovation dimensions in the assessments. The contribution of each decision-maker in their respective sub-areas was quantified using assessments on a scale of 1–10 (Table 1). As a result of these evaluations, D1 received the relatively highest scores in financial analysis, D2 in sectoral experience and D3 in R&D & innovation.

Table 1. Decision-maker performance scores (scale 1–10)

Decision-maker	Financial Analysis	Industry Experience	R&D & Innovation
D1 (Financial Analyst)	9	6	5
D2 (Industry Representative)	6	9	7
D3 (R&D Specialist)	5	7	9

As a result of the PSI calculations, the decision-maker weights were obtained as follows:

- D1 = 0.322 (32.2%)
- D2 = 0.345 (34.5%)
- D3 = 0.333 (33.3%)

As seen in Table 2, the criteria weights were determined using the PSI method in line with the opinions of the decision makers.

Table 2. The criteria weights

No	Criterion	Description	Type	D1	D2	D3	Weight (%)
1	Current Ratio	Indicates the company's ability to meet short-term liabilities.	Benefit	9	7	6	7.15
2	Cash Ratio	Measures the proportion of cash and cash equivalents to short-term obligations.	Benefit	9	6	5	6.49
3	Leverage Ratio	Represents the size of total liabilities relative to equity.	Cost	8	7	6	6.83
4	Financial Debt Ratio	Share of short- and long-term financial debt in total assets.	Cost	9	6	6	6.81
5	Asset Turnover Ratio	Measures how efficiently a company uses its assets to generate sales.	Benefit	7	8	7	7.18
6	Receivables Turnover Ratio	Indicates how quickly a company collects its receivables.	Benefit	7	8	7	7.18
7	Gross Profit Margin (%)	Shows the gross profitability generated from sales.	Benefit	8	7	7	7.16
8	EBITDA Margin (%)	Ratio of earnings before interest, taxes, depreciation, and amortization to net sales.	Benefit	8	7	7	7.16
9	Net Profit Margin (%)	Indicates the net profitability derived from sales.	Benefit	8	7	7	7.16
10	Return on Equity (ROE)	Shows how efficiently the company utilizes its equity.	Benefit	9	7	7	7.47
11	R&D Expenditure	Resources allocated to research and development activities.	Benefit	6	7	9	7.18
12	Number of R&D Employees	Number of personnel employed in the R&D department.	Benefit	6	7	9	7.18
13	Market Share	Represents the company's relative share in the market.	Benefit	6	9	7	7.20
14	Export-to-Sales Ratio	Indicates the proportion of total sales generated from exports.	Benefit	7	9	8	7.84

A data matrix was constructed by compiling information according to the criteria defined in the research framework. This matrix provides a systematic structure for evaluating the alternatives (companies) in line with the established criteria. By organizing the data in a coherent and comparable format, the matrix facilitates the effective application of multi-criteria decision-making methods and enhances the transparency and traceability of the evaluation process.

Table 3. Data matrix

Firm	K1	K2	K3	K4	K5	K6	K7	K8	K9	K10	K11	K12	K13	K14
Aksa Akrilik	1,42	0,5	33,07	14,39	0,95	8,91	16,52	16,92	6,9	10,09	150	120	2,6	52,5
Kalekim	1,85	0,72	34,57	6,71	1,29	5,46	38,65	21,77	9,22	18,78	80	75	0,47	5
Aygaz	1,12	0,39	20,93	4,81	1,41	16,02	7,65	1,8	9,18	17,83	60	50	5,99	14,2
Brisa	1,27	0,84	63,72	42,13	0,76	6,82	24,53	16,12	15,04	32,02	220	200	2,82	43,1
Dyo	1	0,11	65,15	32,61	0,87	4,06	23,44	10,42	3,83	9,11	90	85	0,88	5
Ege Profil	1,29	0,2	50,7	3,99	1,04	3,08	37,92	25,92	5,41	11,84	65	60	0,89	5
Hektaş	1,82	0,03	44,76	21,33	1,23	3,16	24,69	12,59	-8,44	-18,25	105	95	0,52	5,2
Kordsa	1,24	0,15	54,08	36,07	0,8	5,44	14,96	8,3	0,78	1,76	110	100	1,12	92,5
Marshall	1,04	0,46	64,12	17,01	1,26	9,21	31,56	11,7	-4,68	-25,98	95	88	0,4	5
Polisan	1,11	0,22	19,21	7,14	0,4	5,04	21,42	17,79	13,34	6,94	130	110	0,58	5
Sasa	0,82	0,15	56,62	43,04	0,37	5,54	18,8	17,08	39,28	34,21	140	125	4,71	27,5
Şişecam	1,69	0,67	42,61	29,28	0,52	5,05	27,59	13,64	11,26	12,01	190	170	7,85	43,1
Tüpraş	1,3	0,63	44,67	9,63	1,92	18,13	15,98	14,02	7,8	28,3	175	160	69,92	33,7
İşbir Sentetik	1,8	0,45	28,81	23,98	0,62	4,18	26	22,05	8,63	8,34	85	80	0,27	57,4
Kimteks	1,34	0,5	69,42	40,52	1,28	3,06	16,88	13,02	5,71	23,27	125	115	0,98	5

The fuzzy set decision matrices for the three decision makers were constructed based on their individual evaluations. Table 4 presents a sample section of the financial analyst's decision matrix. As illustrated, each

criterion value is represented in a triple format, reflecting the membership, neutrality, and non-membership degrees within the picture fuzzy framework.

Table 4. A sample section of the financial analyst's decision matrix

Firm	Current ratio	Cash ratio	Asset turnover	Receivables turnover
Aksa Akrilik	(0.583; 0.367; 0.050)	(0.580; 0.370; 0.050)	(0.374; 0.576; 0.050)	(0.388; 0.562; 0.050)
Kalekim	(1.000; 0.000; 0.050)	(0.852; 0.098; 0.050)	(0.594; 0.356; 0.050)	(0.159; 0.791; 0.050)
Aygaz	(0.291; 0.659; 0.050)	(0.444; 0.506; 0.050)	(0.671; 0.279; 0.050)	(0.860; 0.090; 0.050)
Brisa	(0.437; 0.513; 0.050)	(1.000; 0.000; 0.050)	(0.252; 0.698; 0.050)	(0.250; 0.700; 0.050)
Dyo	(0.175; 0.775; 0.050)	(0.099; 0.851; 0.050)	(0.323; 0.627; 0.050)	(0.066; 0.884; 0.050)
Ege Profil	(0.456; 0.494; 0.050)	(0.210; 0.740; 0.050)	(0.432; 0.518; 0.050)	(0.001; 0.949; 0.050)
Hektaş	(0.971; 0.000; 0.050)	(0.000; 0.950; 0.050)	(0.555; 0.395; 0.050)	(0.007; 0.943; 0.050)
Kordsa	(0.408; 0.542; 0.050)	(0.148; 0.802; 0.050)	(0.277; 0.673; 0.050)	(0.158; 0.792; 0.050)
Marshall	(0.214; 0.736; 0.050)	(0.531; 0.419; 0.050)	(0.574; 0.376; 0.050)	(0.408; 0.542; 0.050)
Polisan	(0.282; 0.668; 0.050)	(0.235; 0.715; 0.050)	(0.019; 0.931; 0.050)	(0.131; 0.819; 0.050)
Sasa	(0.000; 0.950; 0.050)	(0.148; 0.802; 0.050)	(0.000; 0.950; 0.050)	(0.165; 0.785; 0.050)
Şişecam	(0.845; 0.105; 0.050)	(0.790; 0.160; 0.050)	(0.097; 0.853; 0.050)	(0.132; 0.818; 0.050)
Tüpraş	(0.466; 0.484; 0.050)	(0.741; 0.209; 0.050)	(1.000; 0.000; 0.050)	(1.000; 0.000; 0.050)
İşbir Sentetik	(0.951; 0.000; 0.050)	(0.519; 0.431; 0.050)	(0.161; 0.789; 0.050)	(0.074; 0.876; 0.050)
Kimteks	(0.505; 0.445; 0.050)	(0.580; 0.370; 0.050)	(0.587; 0.363; 0.050)	(0.000; 0.950; 0.050)

The PFS decision matrices of the decision makers were combined, taking into account the weights of the decision makers, and then the normalized PFS matrix was created. A portion of this matrix is shown in Table 5.

Table 5. Portion of the normalized PFS matrix

Firm	Current ratio	Cash ratio	Asset turnover	Receivables turnover
Aksa Akrilik	(0.583; 0.334; 0.084)	(0.580; 0.336; 0.084)	(0.374; 0.542; 0.084)	(0.388; 0.528; 0.084)
Kalekim	(1.000; 0.000; 0.084)	(0.852; 0.064; 0.084)	(0.594; 0.323; 0.084)	(0.159; 0.757; 0.084)
Aygaz	(0.291; 0.625; 0.084)	(0.444; 0.472; 0.084)	(0.671; 0.245; 0.084)	(0.860; 0.056; 0.084)
Brisa	(0.437; 0.479; 0.084)	(1.000; 0.000; 0.084)	(0.252; 0.665; 0.084)	(0.250; 0.667; 0.084)
Dyo	(0.175; 0.742; 0.084)	(0.099; 0.818; 0.084)	(0.323; 0.594; 0.084)	(0.066; 0.850; 0.084)
Ege Profil	(0.456; 0.460; 0.084)	(0.210; 0.706; 0.084)	(0.432; 0.484; 0.084)	(0.001; 0.915; 0.084)
Hektaş	(0.971; 0.000; 0.084)	(0.000; 0.916; 0.084)	(0.555; 0.362; 0.084)	(0.007; 0.910; 0.084)
Kordsa	(0.408; 0.509; 0.084)	(0.148; 0.768; 0.084)	(0.277; 0.639; 0.084)	(0.158; 0.758; 0.084)
Marshall	(0.214; 0.703; 0.084)	(0.531; 0.385; 0.084)	(0.574; 0.342; 0.084)	(0.408; 0.508; 0.084)
Polisan	(0.282; 0.635; 0.084)	(0.235; 0.682; 0.084)	(0.019; 0.897; 0.084)	(0.131; 0.785; 0.084)
Sasa	(0.000; 0.916; 0.084)	(0.148; 0.768; 0.084)	(0.000; 0.916; 0.084)	(0.165; 0.752; 0.084)
Şişecam	(0.845; 0.072; 0.084)	(0.790; 0.126; 0.084)	(0.097; 0.820; 0.084)	(0.132; 0.784; 0.084)
Tüpraş	(0.466; 0.450; 0.084)	(0.741; 0.176; 0.084)	(1.000; 0.000; 0.084)	(1.000; 0.000; 0.084)
İşbir Sentetik	(0.951; 0.000; 0.084)	(0.519; 0.398; 0.084)	(0.161; 0.755; 0.084)	(0.074; 0.842; 0.084)
Kimteks	(0.505; 0.411; 0.084)	(0.580; 0.336; 0.084)	(0.587; 0.329; 0.084)	(0.000; 0.916; 0.084)

In the next stage, the Ideal (A^+) and Anti-Ideal (A^-) solution points were calculated based on the criteria. Performance distances were calculated based on the companies' decision criteria, and score values were obtained accordingly. These distances and score values are presented in Table 6. According to the table, different distance calculation methods (Euclidean, Manhattan, and Hamming) were used for each company to determine both the distance from the ideal solution (D+) and the distance from the anti-ideal solution (D-). Furthermore, based on these distances, the relevant performance scores (S) were calculated for each method. For example, for Tüpraş, the Euclidean distance was determined as 0.2474 for the ideal point, and 0.5361 for the anti-ideal point, resulting in a performance score of 0.6843.

Generally, performance scores reflect the relative advantages of the companies within the decision criteria. Low D+ and high D- values indicate that the company is close to the ideal solution and therefore has high performance. Conversely, high D+ and low D- values indicate that performance is far from ideal. The different distance and score calculations in the table enable a multidimensional assessment in the analysis and clearly reveal to decision-makers the relative performance differences between companies.

The performance scores obtained from the PF-COBRA calculations were ranked from highest to lowest. Tüpraş, which achieved the highest comprehensive performance score in both Euclidean and Manhattan distance measures, emerges as the clear leader of the analysis. Its dominance is supported by large-scale production capacity, high market share, strong operational profitability, and a relatively balanced financial structure. This performance positions Tüpraş as a benchmark firm in the sector.

Table 6. Distance and score values

Firm	D+ Euc	D– Euc	S_Euc	D+ Man	D– Man	S_Man	D+ Ham	D– Ham	S_Ham	S_Com
Tüpraş	0.2474	0.5361	0.6843	0.1999	0.4376	0.6864	0.5997	1.3127	0.6864	0.6857
Kalekim	0.3595	0.4239	0.5411	0.2915	0.3460	0.5427	0.8745	1.0380	0.5427	0.5422
Şişecam	0.3717	0.4117	0.5255	0.3013	0.3362	0.5273	0.9040	1.0085	0.5273	0.5267
Brisa	0.3745	0.4079	0.5214	0.3046	0.3329	0.5222	0.9138	0.9987	0.5222	0.5219
Aksa Akrilik	0.3862	0.3964	0.5065	0.3138	0.3237	0.5077	0.9414	0.9710	0.5077	0.5073
İşbir Sentetik	0.4166	0.3667	0.4681	0.3381	0.2994	0.4696	1.0143	0.8981	0.4696	0.4691
Polisan	0.4665	0.3161	0.4039	0.3794	0.2580	0.4048	1.1383	0.7741	0.4048	0.4045
Aygaz	0.4699	0.3131	0.3999	0.3819	0.2556	0.4010	1.1456	0.7669	0.4010	0.4006
Ege Profil	0.4718	0.3103	0.3967	0.3842	0.2532	0.3972	1.1527	0.7597	0.3972	0.3971
Sasa	0.4987	0.2832	0.3622	0.4063	0.2311	0.3626	1.2190	0.6934	0.3626	0.3625
Kimteks	0.5224	0.2599	0.3322	0.4253	0.2122	0.3329	1.2759	0.6366	0.3329	0.3326
Kordsa	0.5293	0.2526	0.3231	0.4313	0.2062	0.3234	1.2939	0.6186	0.3234	0.3233
Hektaş	0.5354	0.2469	0.3156	0.4359	0.2016	0.3162	1.3078	0.6047	0.3162	0.3160
Marshall	0.5396	0.2426	0.3102	0.4394	0.1981	0.3107	1.3182	0.5942	0.3107	0.3105
Dyo	0.5976	0.1843	0.2357	0.4870	0.1505	0.2360	1.4610	0.4514	0.2360	0.2359

Tüpraş's first-place ranking reflects its economies of scale and market leadership in Turkey's industrial and energy sectors. High capacity utilization and strong sales revenues further demonstrate its contribution to domestic and international trade. Its balanced debt structure indicates an ability to maintain sustainable profitability even in tight monetary conditions. Companies such as Kalekim, Şişecam, Brisa, and Aksa Acrylic, which follow Tüpraş, underline the importance of export performance and R&D investments for sectoral competitiveness. Their strong financial stability and integration with global markets significantly contribute to the sector's export capacity. In particular, Şişecam has strengthened its technological capabilities in glass and chemical products through rising R&D investments.

Companies in the middle group—İşbir Sentetik, Polisan, Aygaz, Ege Profil, and Sasa—exhibit a more mixed performance. Although they perform well in certain criteria, their overall scores are more moderate. For instance, despite Sasa's high profitability, its elevated debt level indicates potential financial fragility. Likewise, companies such as Aygaz and Polisan remain more vulnerable to macroeconomic fluctuations due to their reliance on the domestic market. Firms in the lower group-Kordsa, Marshall, Dyo, Hektaş, and Kimteks-fell behind largely due to high leverage, low return on equity, and limited export performance. Their relatively smaller scale restricts their ability to achieve competitive advantages, while lower levels of R&D investment reduce their capacity to adapt to technology-intensive production environments.

Overall, the findings show that economic success in the chemicals and related sub-sectors depends not only on balance-sheet indicators but also on export capacity, market share, and technological innovation. While large-scale companies such as Tüpraş and Şişecam maintain their leadership through economies of scale, medium-scale firms can enhance their competitiveness by expanding export activities and increasing R&D investments. For smaller companies, strengthening financial structures and improving innovation capabilities are critical for long-term sustainability.

Conclusion

This research provides a comprehensive evaluation of the financial and economic performance of 15 chemical and plastics sector companies listed on Borsa Istanbul using the PF-COBRA method. The results reveal that differences in company performance stem not only from financial ratios but also from strategic variables such as export intensity, market positioning, and R&D investment capacity. This multifaceted assessment helps explain the sector's economic contribution through production efficiency, economies of scale, and innovation capability. Tüpraş ranks first with a considerable margin, confirming its leadership role driven by scale advantages, high profitability, and strong export capacity. Kalekim, Şişecam, Brisa, and Aksa Acrylic follow as the top-performing group, characterized by low financial risk, strong operational margins, and consistent investments in export-oriented and innovation-driven strategies.

The middle-performing companies show potential but require improvements in financial resilience and strategic diversification. Sasa's case clearly illustrates the importance of prudent debt management despite high profitability. Aygaz and Polisan also highlight the risks associated with domestic market dependency. Companies in the lower tier face structural limitations in profitability, R&D capacity, and export performance, which restrict

their competitiveness. Their results underline the importance of scaling up technological investments and strengthening financial structures.

The PF-COBRA combined score—integrating Euclidean, Manhattan, and Hamming distances—provides a reliable and holistic perspective on firms' strengths and weaknesses. The method's ability to incorporate decision-maker uncertainty enhances both the academic and practical relevance of the findings. From an economic standpoint, the results emphasize the need for medium- and small-scale firms to expand their export markets, increase innovation-driven investments, and manage debt structures more effectively. Sector-wide sustainability can be strengthened by policies that promote R&D capacity, export competitiveness, and financial stability.

In conclusion, sustainable competitiveness in the chemicals and plastics sector requires integrated management of financial stability, export capacity, and innovative activities. Firms that successfully balance these factors will be better positioned to contribute to both sectoral development and national economic growth.

Recommendations

Future research could conduct comparative analyses by applying the PF-COBRA method to different sectors. Furthermore, the robustness of the results could be tested by conducting comparative studies with other MCDM methods (TOPSIS, VIKOR, AHP). This would allow for the development of more comprehensive and reliable policy recommendations to enhance the sector's competitiveness.

Scientific Ethics Declaration

* The authors declare that the scientific ethical and legal responsibility of this article published in EPSTEM journal belongs to the authors.

Conflict of Interest

* The authors declare that they have no conflicts of interest

Funding

* This research received no specific grant from any funding agency in the public, commercial, or not-for-profit sectors.

Acknowledgements or Notes

* This article was presented as an oral presentation at the International Conference on Technology, Engineering and Science (www.icontes.net) held in Antalya/Türkiye on November 12-15, 2025.

* This article was prepared based on the master's thesis titled "Evaluation of Financial and Economic Performance in Chemical, Pharmaceutical, Petroleum and Plastic Sectors Traded in BIST Using PSI PF-COBRA Method" completed by Canan ŞEN under the supervision of Prof. Dr. Kübra ÖNDER on 18.09.2025 (Master's Thesis, Burdur Mehmet Akif Ersoy University, Burdur, Türkiye, 2025).

References

Alshamrani, A. M., Zavadskas, E. K., Rani, P., Antucheviciene, J., & Alrasheedi, A. F. (2025). Evaluation and prioritization of software packages for remote education assistance using picture fuzzy comprehensive distance-based ranking approach. *Applied Soft Computing, 182*, 113606.

Aras, G., Tezcan, N., Furtuna, O. K., & Kazak, E. H. (2017). Corporate sustainability measurement based on entropy weight and TOPSIS: A Turkish banking case study. *Meditari Accountancy Research, 25*(3), 391-413.

Asker, V. (2024). Financial performance analysis using the MEREC-based COBRA method: An application to traditional and low-cost airlines. *Gospodarka Narodowa, 318*(2), 35-52.

Attri, R., & Grover, S. (2015). Application of preference selection index method for decision making over the design stage of production system life cycle. *Journal of King Saud University - Engineering Sciences, 27*(2), 207-216.

Bulgurcu, B. (2012). Application of TOPSIS technique for financial performance evaluation of technology firms in Istanbul Stock Exchange Market. *Procedia - Social and Behavioral Sciences, 62*, 1033-1040.

Cağrı Kabakci, C., & Bilgin Sari, E. (2019). Türk bankacılık sektöründe finansal performansın Tercih Seçim Endeksi (PSI) yöntemiyle analizi. *Ekonomi Politika ve Finans Araştırmaları Dergisi, 4*(3), 370-383.

Cuong, B. C., & Kreinovich, V. (2014). Picture fuzzy sets - A new concept for computational intelligence problems. In *2013 3rd World Congress on Information and Communication Technologies (WICT 2013)* (pp. 1-6). IEEE.

Ertugrul, I., & Karakasoglu, N. (2009). Performance evaluation of Turkish cement firms with fuzzy analytic hierarchy process and TOPSIS methods. *Expert Systems with Applications, 36*(1), 702-715.

Kaya, A., Pamucar, D., Gürler, H. E., & Ozcalici, M. (2024). Determining the financial performance of the firms in the Borsa Istanbul sustainability index: Integrating multi criteria decision making methods with simulation. *Financial Innovation, 10*(1), 1–44.

Kou, G., Olgu Akdeniz, O., Dincer, H., & Yuksel, S. (2021). Fintech investments in European banks: A hybrid IT2 fuzzy multidimensional decision-making approach. *Financial Innovation, 7*(1), 1–28.

Krstić, M., Agnusdei, G. P., Miglietta, P. P., Tadić, S., & Roso, V. (2022). Applicability of Industry 4.0 technologies in the reverse logistics: A circular economy approach based on COmprehensive Distance Based RAnking (COBRA) method. *Sustainability, 14*(9), 5632.

Lam, W. S., Lam, W. H., Jaaman, S. H., & Liew, K. F. (2021). Performance evaluation of construction companies using integrated Entropy-Fuzzy VIKOR model. *Entropy, 23*(3), 320.

Liew, K. F., Lam, W. S., & Lam, W. H. (2022). Financial network analysis on the performance of companies using integrated Entropy–DEMATEL–TOPSIS model. *Entropy, 24*(8), 1056.

Madić, M., Antucheviciene, J., Radovanović, M., & Petković, D. (2017). Determination of laser cutting process conditions using the preference selection index method. *Optics & Laser Technology, 89*, 214-220.

Mandic, K., Delibasic, B., Knezevic, S., & Benkovic, S. (2014). Analysis of the financial parameters of Serbian banks through the application of the fuzzy AHP and TOPSIS methods. *Economic Modelling, 43*, 30-37.

Maniya, K., & Bhatt, M. G. (2010). A selection of material using a novel type decision-making method: Preference selection index method. *Materials & Design, 31*(4), 1785-1789.

Mastilo, Z., Štilić, A., Gligović, D., & Puška, A. (2024). Assessing the banking sector of Bosnia and Herzegovina: An analysis of financial indicators through the MEREC and MARCOS methods. *Journal of Central Banking Theory and Practice, 13*(1), 167-197.

No, R. K. G., Niroomand, S., Didehkhani, H., & Mahmoodirad, A. (2021). Modified interval EDAS approach for the multi-criteria ranking problem in banking sector of Iran. *Journal of Ambient Intelligence and Humanized Computing, 12*(7), 8129-8148.

Popović, G., Pucar, Đ., & Smarandache, F. (2022). MEREC-COBRA approach in e-commerce development strategy selection. *Journal of Process Management and New Technologies, 10*(3-4), 66-74.

Reig-Mullor, J., & Brotons-Martinez, J. M. (2021). The evaluation performance for commercial banks by intuitionistic fuzzy numbers: The case of Spain. *Soft Computing, 25*(14), 9061-9075.

Tadić, S., Krstić, M., & Radovanović, L. (2024). Assessing strategies to overcome barriers for drone usage in last-mile logistics: A novel hybrid fuzzy MCDM model. *Mathematics, 12*(3), 367.

Taşci, M. Z. (2024). Measuring sustainability performance with SWARA-MEREC-COBRA multi-criteria model: A case study of Anadolu Insurance Company. *Decision Science Letters, 13*, 829-844.

Trung, D. D., Dudić, B., Dung, H. T., & Truong, N. X. (2024). Innovation in financial health assessment: Applying MCDM techniques to banks in Vietnam. *ECONOMICS - Innovative and Economics Research Journal, 12*(2), 21-33.

Türegün, N. (2022). Financial performance evaluation by multi-criteria decision-making techniques. *Heliyon, 8*(5), e09361.

Unlu, U., Yalcin, N., & Avsarligil, N. (2022). Analysis of efficiency and productivity of commercial banks in Turkey pre- and during COVID-19 with an integrated MCDM approach. *Mathematics, 10*(13), 2300.

Wanke, P., Azad, M. D. A. K., & Barros, C. P. (2016). Predicting efficiency in Malaysian Islamic banks: A two-stage TOPSIS and neural networks approach. *Research in International Business and Finance, 36*, 485-498.

Wardany, R. N., & Zahedi. (2025). A study comparative of PSI, PSI-TOPSIS, and PSI-MABAC methods in analyzing the financial performance of state-owned enterprises companies listed on the Indonesia Stock Exchange. *Yugoslav Journal of Operations Research, 35*(2), 313-330.

Wu, H. Y., Tzeng, G. H., & Chen, Y. H. (2009). A fuzzy MCDM approach for evaluating banking performance based on Balanced Scorecard. *Expert Systems with Applications, 36*(6), 10135-10147.

Author(s) Information

Canan Sen
Burdur Mehmet Akif Ersoy University,
Istiklal Kampus,15030, Burdur-Turkiye
Contact e-mail: *cananzengin03@gmail.com*

Kubra Onder
Burdur Mehmet Akif Ersoy University,
Faculty of Economics and Administrative Sciences,
Istiklal Kampus,15030, Burdur-Turkiye

Halil Sen
Burdur Mehmet Akif Ersoy University,
Industrial Engineering Department,
Istiklal Kampus,15030, Burdur-Turkiye

To cite this article:

Sen, C., Onder, K., & Sen, H. (2025). A multi-criteria decision-making model for performance evaluation based on PSI–PF-COBRA. *The Eurasia Proceedings of Science, Technology, Engineering and Mathematics (EPSTEM), 38,* 830-841.

The Eurasia Proceedings of Science, Technology, Engineering & Mathematics (EPSTEM)
ISSN: 2602-3199

The Eurasia Proceedings of Science, Technology, Engineering and Mathematics (EPSTEM), 2025

Volume 38, Pages 842-848

IConTES 2025: International Conference on Technology, Engineering and Science

Evaluation of Composite Method Repair of a Cracked Plate

Aida Achour
University of Sidi Bel Abbes

Belabbes Bachir Bouidjra
University of Sidi Bel Abbes

Hafida Driz
University of Sidi Bel Abbes

Sadek Bahar
University of Mostaganem

Abstract: This work evaluates the performance of composite patch repairs for cracked aluminium plates by examining various parameters including patch shape, height, thickness, the influence of stress on the patch, and adhesive thickness. Through a comprehensive analysis of these factors, along with the properties of adhesives and composites, the study aims to enhance the understanding of their impact on repair efficiency. The findings are intended to provide valuable insights for designers of bonded composite repairs, facilitating better predictions of the fatigue life of repaired structures. This study investigates the effectiveness of crack repairs by analyzing the stress intensity factor at the crack front as a key fracture criterion. A comprehensive examination of various repair parameters is conducted to assess their impact on repair efficiency. Utilizing Finite element method numerical simulations in ABAQUS, the research evaluates the performance of bonded composite joints under different conditions. The findings from these simulations are compared to experimental data, providing valuable insights into the fatigue life of repaired structures. This work aims to enhance the understanding of repair methodologies and their implications for structural integrity in engineering applications.

Keywords: Composite patch, Crack, Stress intensity factor, Finite element method

Introduction

To increase the usable life of older aircraft, broken parts need to be replaced or repaired. Using crack arrestment techniques is frequently the most cost-effective way to restore the component's capacity to withstand loads if there are few cracks and the size of the cracks is minor in comparison to the component's size. The great rigidity, high strength, and low weight of the composite have demonstrated the process's immense promise for reinforcing the fractured structure. The stress analysis of the recovered structure and the ensuing development of stress intensity variables are among the trickiest parts of bonded composite repair technology.

The issue is that if composite patches were symmetrically (double sided) or unsymmetrically (single sided) glued to the sides of a plane stress metallic panel, under in-plane pressure, the panel would acquire incredibly complex three-dimensional stresses. Stress analysis may make use of three-dimensional finite elements. However, in addition to the clearly high computational cost, using components with high aspect ratios may cause convergence issues because of the thinness of the adhesive layer and patches. As such, the majority of research to date has been on creating instruments for more straightforward analysis.

- This is an Open Access article distributed under the terms of the Creative Commons Attribution-Noncommercial 4.0 Unported License, permitting all non-commercial use, distribution, and reproduction in any medium, provided the original work is properly cited.

- Selection and peer-review under responsibility of the Organizing Committee of the Conference

© 2025 Published by ISRES Publishing: www.isres.org

The necessity for the structure or component to be sturdy and solid is one of the primary constraints placed on the builder. The capacity of a part or structure to withstand the effect of several factors that may cause it to become unbalanced is known as stability (Rezaifar,2014). A structure or component may fail or receive damage after being produced, even with the best quality control. One of the most common kinds of damage that components may get is a crack. The component gets weaker and is subjected to higher stresses when fractures appear, which might result in plastic deformation or collapse (Caballero,2008). In adhesively bonded joints subjected to mechanical or thermal loading, stress is distributed throughout the adhesive layer from the softest to the stiffest adherend. This feature aids in the restoration of damaged aircraft structures using bonded composite patches. Patch bonding increases the residual fatigue life by lowering the stress at the fracture site (Bhadra, 2021).

Stress is transferred from the softest to the stiffest adherend in the adhesive layer of joints that are subjected to mechanical or thermal loading. This feature facilitates the use of bonded composite patches to restore damaged airplane structures. By reducing the tension at the fracture location, patchbonding lengthens the residual fatigue life, as shown by Katlan et al. (2013), Okafor et al. (2005) and (Baker et al. 2003). The main advantage of the bonded composite repair (BCR) procedure is the uniformity of stress transfer across the bonded zone, which extends the fatigue life of the reconstructed structure. Stress concentrations are avoided, in contrast to fixed doublers where stress zone concentrations are inevitable. A method known as "Crack Patching" was developed in the early 1970s by the Aeronautical and Maritime Research Laboratories (AMRL) for the Royal Australian Air Force (RAAF) to use high-strength advanced composite materials to fix metallic aircraft components that had cracks (Baker, 1991).

Using an adhesive bonding approach, the composite reinforcement, also known as a patch, may be mechanically bonded or adhered to the compromised or damaged structure. Adhesively bonded composite patches have several advantages over mechanically fastened repair methods, including the elimination of needless fastener holes in already-weakened structures, reduced installation costs, enhanced fatigue life and strength for effective crack retardation, shortened repair times, decreased stress concentrations at fasteners, corrosion resistance, high stiffness, and lightweight design.

The unpredictable nature of the repair's integrity is one problem prohibiting the regular usage of composite patches to replace damaged metallic aircraft components. Estimating the strength and lifespan of the restored structure as well as the distribution of stress inside it are additional factors that must be taken into account when planning a bonded composite patch repair for metallic constructions with cracks. Sun (1996) provided a simple analytical method for analyzing aluminum plates that have been repaired using composite patches applying Midlin plate theory. To simulate the adhesive layer, strong springs were employed to join the aluminum plate and patch. A three-dimensional finite element analysis was performed using the commercial program ABAQUS, and the stress intensity factors resulting from the two cases were compared.

Structural parts have an inherent weakness that eventually shows up as a fracture. Adhesively bonded composite patch-based repairs have a better structural efficiency than traditional repairs. By replacing the stressed state before a crack tip, the composite patch repair lowers the stress intensity factor (SIF) to a level that can be controlled. Bonded composite patches provide excellent weight transfer characteristics and an alternative load path, making them useful for repairing broken structures (Mangalgiri, 1999). In airplane applications, advanced composite materials—typically composed of continuous carbon fibers embedded in a polymer matrix—can offer better material qualities than metals, allowing for the fabrication of lighter structural components (Soutis, 2005). Since fewer fuels are used to power the lighter structures, emissions are decreased. In the 1960s, composite materials were initially used in military aircraft; in the 1970s, they were also used in civilian aircraft (Edwards, 2008). But civil aircraft manufacturers didn't start using composites in significant structural applications until the 2000s. (Denney & Mall,1997) Modern composites are presently being used in place of conventional materials by top aircraft manufacturers, allowing composites to reach their full potential in creative structural designs. Nowadays, main and secondary structural applications in aircraft design employ carbon-reinforced polymer composites.

Patch debonding is almost often the main cause of unsuccessful repairs. Research studies have not given much emphasis to the examination of this physical phenomenon in the context of patch healing. Thus, Denney and Mall (1997) have used fatigue testing to examine how debonding affects the durability and strength of the repair. This author demonstrates that when the amount of debonding rises, the restored structure's service life decreases. According to Deheeger (2009) the shear stresses induced in the adhesive joint are responsible for the debonding. The mechanical and geometric properties of the adhesive junction play a major role in determining how effectively the repair functions (Albedah, 2017; Davis, 1995). The adhesive is the least robust part of the

plate/adhesive/- composite patch systems because of its low rigidity. In actuality, the adhesive's deterioration accounts for 53% of the failures seen in aircraft structures repaired with composite patches. (Megueni, 2004).

In another study (Bouiadjra, 2008) it was demonstrated by examining various debonding configurations that debonding rises across a wide central width and causes the repair patch's edge to become disbonded. Zarrinzadeh et al (20) investigated the process of adhesive film debonding from a fractured portion of pipeline to the composite repair. They show how cohesive zone model (CZM) and XFEM modeling tools may be used to foresee a more realistic behavior of the structure.

Sahli (2017) studied both analytically and practically using sonic emission to analyze the debonding process during airplane patch repair. They show that adhesive damage starts at the free edges of the structure and in the area around the notch. Magalhães (2005) demonstrated that, as opposed to the adhesive layer failing owing to crack growth, an area wounded by microcracking or microcavitation starts and spreads. According to these writers, harm propagates inside the adhesive close to the adhesive contact. The presence of a little sticky coating on the connected surface indicated that the fracture was cohesive even though it seemed to be adhesive. Literature has focused primarily on the adhesive disbanding that happens during the repair process. Recently, several studies describing the impact of adhesive failure on repair effectiveness have been published. (Qing, 2006)

Bachir Bouiadjra et al. (2008) examined how adhesive disbanding affected the bonded composite repair procedures used in aircraft structures. According to their research, the presence of the adhesive disbands increases the stress intensity at the tip of repaired cracks which can reduce the repair efficiency. Ouinas (2012) examined the behavior of an adhesively bonded composite patch used to repair a progressive edge fracture in an aluminum plate under full width stress. This investigation showed that, the reduction of the stress intensity factor at the crack tip increases with the patch thickness for disband width higher than crack size (Bouiadjra, 2012). It is known that a reduction of the adhesive thickness decreases the stress intensity factor, it means that lower adhesive thickness is desirable for repairing cracks (Bachir Bouiadjra, 2002) the lower thickness well supports the transfer loads towards the patch but increases the risk of the adhesive failure. To foresee this risk, it is necessary to consider a disbond.

In this work, the behavior of a cracked aluminum plate repaired with composite patch was studied, in order to investigate the variation of stress intensity factor along the variation of the crack size, and the type of patch used. The cohesive characteristics and resistance to disbond, as determined by stress intensity factor, characterize the interfacial cohesive zone of the patch, adhesive, or plate system was also investigated. The findings demonstrate that damage to the adhesive, plate assemblies, and patch may be accurately predicted by simulations that are based on the CZM model.

Geometrical model

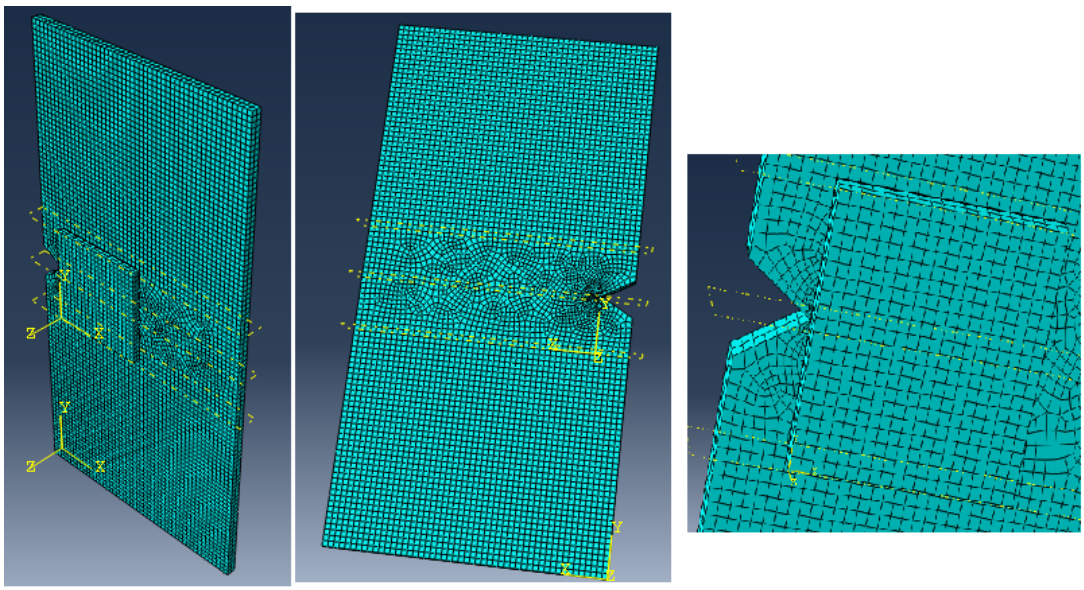


Figure 1. Typical mesh model

The model is an Aluminium plate, with a length L=100mm, with=50 mm, , crack size 6mm, crack opening α=60 degree, load= tensile load

Aluminum E=71700MPa μ=0.33

We used a calculation code "Abaqus" version 6.14 for the analysis of composite structures by the finite element method. This code presents a complete system, integrating not only the calculation functions themselves, but also functions of model construction and processing of results Mesh of the plate and the Composite Patch 11526 linear hexahedral elements of type C3D8R: An 8-node linear brick, reduced integration, hourglass control. ABAQUS (2019). Mesh along the adhesive 400 linear hexahedral elements of type COH3D8: An 8-node three-dimensional cohesive element (Figure 1). The Figures below show stress intensity factor variation depending on the crack size, for the unrepaired aluminum plate for different tensile loads, and repaired with boron epoxy patch, and adhesive FM73

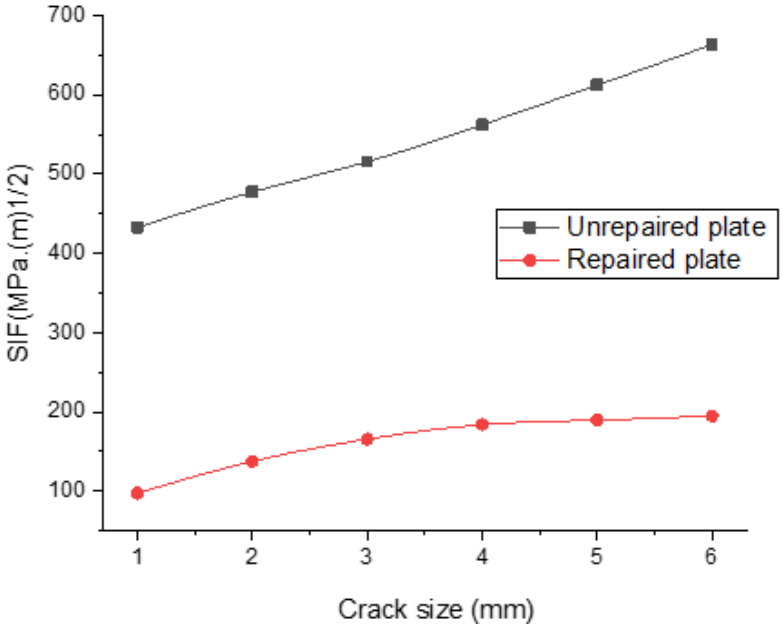


Figure 2. SIF variation depending on the crack size for 70MPa

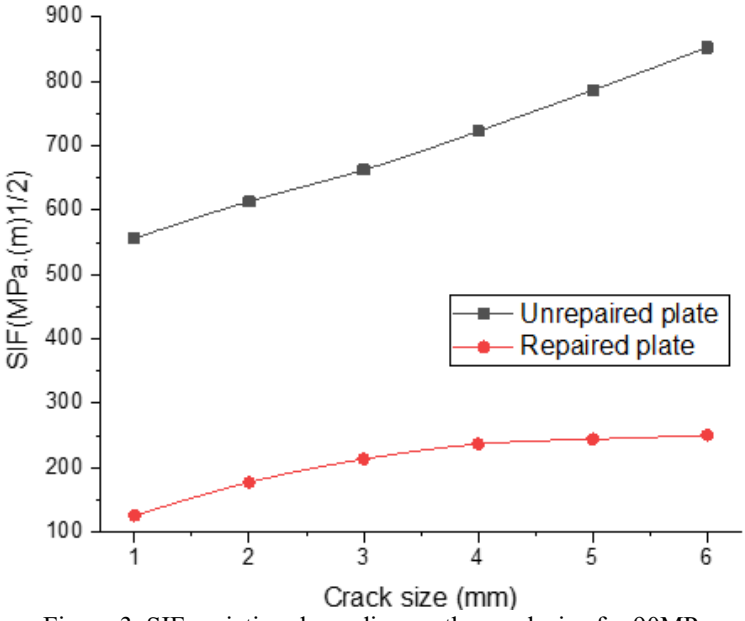


Figure 3. SIF variation depending on the crack size for 90MPa

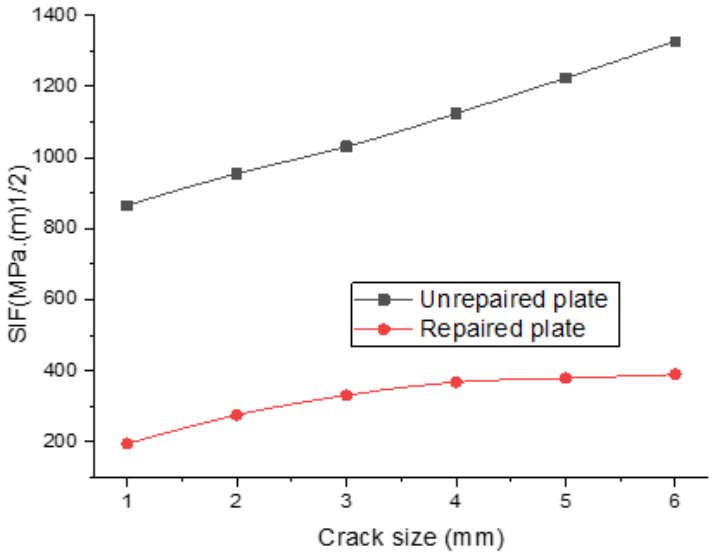


Figure 4. SIF variation depending on the crack size for 140 MPa

The Figure shows Von Mises stress variation depending on the crack size for optimized adhesive and patch (adhesive AV138, Patch boron-epoxy,lengths, and width =20mm)

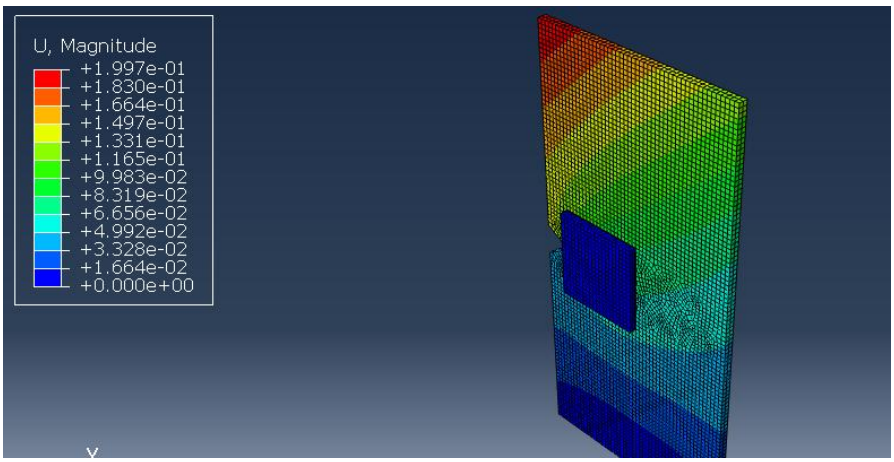


Figure 5. Von Mises stress variation depending on the crack size for

Conclusion

By examining the stress intensity factor at the crack front as a crucial fracture criteria, this study examines the efficacy of crack repairs. To determine their effect on repair efficiency, a thorough analysis of several repair parameters is carried out. The study assesses the performance of bonded composite joints under various circumstances using numerical simulations in ABAQUS using the Finite element approach. By comparing the results of these models with experimental data, important information about the fatigue life of restored structures is revealed. The purpose of this effort is to improve knowledge of repair techniques and how they affect structural integrity in engineering applications.

Recommendations

Incorporate sensor networks within the repair patch to allow for real time strain monitoring and early fracture reactivation or debonding identification. To forecast the safety and remaining service life of the repaired column, develop a reliability-based model that takes loading and fracture size uncertainty into consideration.

Scientific Ethics Declaration

* The authors declare that the scientific ethical and legal responsibility of this article published in EPSTEM journal belongs to the authors.

Conflict of Interest

* The authors declare that they have no conflicts of interest

Funding

* This research received no specific grant from any funding agency in the public, commercial, or not-for-profit sectors.

Acknowledgements or Notes

* This article was presented as an oral presentation at the International Conference on Technology, Engineering and Science (www.icontes.net) held in Antalya/Türkiye on November 12-15, 2025.

References

Albedah, A., Khan Mohammed, S. M. A., Bouiadjra, B. B., Bouiadjra, B. A. B., & Benyahia, F. (2018). Effect of the patch length on the effectiveness of one-sided bonded composite repair for aluminum panels. *International Journal of Adhesion and Adhesives, 81*, 83–89.

Baker, A. A. (1991). Fatigue crack propagation studies on aluminum panels patched with boron/epoxy composites. In R. Jones & N. J. Miller (Eds.), *Proceedings of the International Conference on Aircraft Damage Assessment and Repair* (pp. 209–215). Melbourne, Australia.

Baker, A. A. (1999). Bonded composite repair of fatigue-cracked primary aircraft structure. *Composite Structures, 47*(1–4), 431–443.

Baker, A. A., Rose, L. F., & Jones, R. (Eds.). (2003). *Advances in the bonded composite repair of metallic aircraft structure*. Elsevier.

Bhadra, M. K., & Gopalan, V. (2021). Stress redistribution near a crack in maraging steel using composite patch. *Defence Science Journal, 71*(6), 816–821.

Bouiadjra, B. B., Belhouari, M., Serier, B., & Oudad, W. (2002). Computation of the stress intensity factors for repaired cracks with a bonded composite patch in mode I and mixed mode. *Composite Structures, 56*(4), 401–406.

Bouiadjra, B. B., Oudad, W., Albedah, A., Benyahia, F., & Belhouari, M. (2012). Effects of the adhesive disbond on the performances of bonded composite repairs in aircraft structures. *Materials & Design, 37*, 89–95.

Bouiadjra, B. B., Ouinas, D., Serier, B., & Benderdouche, N. (2008). Disbond effects on bonded boron/epoxy composite repair to aluminium plates. *Computational Materials Science, 42*(2), 220–227.

Caballero, A., & Dyskin, A. (2008). Mesh scalability in direct finite element simulation of brittle fracture. *Engineering Fracture Mechanics, 75*(14), 4066–4084.

Davis, M. J. (1995). A call for minimum standards in design and application technology for bonded structural repairs. In *Proceedings of the Symposium on Composite Repair of Aircraft Structures* (pp. 41–415). Vancouver, Canada.

Deheeger, A. (2009). *Étude des effets thermiques dans des joints collés: Application à des structures renforcées par patchs composites* (Doctoral dissertation). Université Blaise Pascal Clermont-Ferrand, France.

Denney, J. J., & Mall, S. (1997). Characterization of disbond effects on fatigue crack growth behavior in aluminum plate with bonded composite patch. *Engineering Fracture Mechanics, 57*(5), 507–525.

Edwards, T. (2008). Composite materials revolutionise aerospace engineering. *Ingenia, 36*, 24–28.

Katnam, K. B., da Silva, L. F. M., & Young, T. M. (2013). Bonded repair of aircraft structures: A review of scientific challenges and opportunities. *Progress in Aerospace Sciences, 61*, 26–42.

Magalhães, A. G., de Moura, M. F. S. F., & Gonçalves, J. P. M. (2005). Evaluation of stress concentration effects in single-lap bonded joints of laminate composite materials. *International Journal of Adhesion and Adhesives, 25*(4), 313–319.

Mangalgiri, P. D. (1999). Composite materials for aerospace applications. *Bulletin of Materials Science, 22*(3), 657–664.

Megueni, A., Bachir Bouiadjra, B., & Belhouari, M. (2004). Disbond effect on the stress intensity factor for repairing cracks with bonded composite patch. *Computational Materials Science, 29*(4), 407–413.

Mhamdia, R., Serier, B., Bachir Bouiadjra, B., & Belhouari, M. (2012). Numerical analysis of the patch shape effects on the performances of bonded composite repair in aircraft structures. *Composites Part B: Engineering, 43*(2), 391–397.

Okafor, A. C., Singh, N., Enemuoh, U. E., & Rao, S. V. (2005). Design, analysis and performance of adhesively bonded composite patch repair of cracked aluminum aircraft panels. *Composite Structures, 71*(2), 258–270.

Ouinas, D., Bouiadjra, B. B., Himouri, S., & Benderdouche, N. (2012). Progressive edge cracked aluminium plate repaired with adhesively bonded composite patch under full width disbond. *Composites Part B: Engineering, 43*(2), 805–811.

Qing, X. P., Beard, S. J., Kumar, A., & Hannum, R. (2006). A real-time active smart patch system for monitoring the integrity of bonded repair on an aircraft structure. *Smart Materials and Structures, 15*(3), N66–N73.

Rezaifar, O., Doostmohammadi, M. R., & Gholhaki, M. (2014). Numerical formulation on crack closing effect in buckling analysis of edge-cracked columns. *Journal of Rehabilitation in Civil Engineering, 2*(2), 75–83.

Sahli, A., Bouziane, M. M., Benbarek, S., Wayne, S. F., Liang, Z., Bachir Bouiadjra, B., & Serier, B. (2017). Experimental and numerical disbond localization analyses of a notched plate repaired with a CFRP patch. *Structural Engineering and Mechanics, 63*(3), 361–370.

Soutis, C. (2005). Carbon fiber reinforced plastics in aircraft construction. *Materials Science and Engineering A, 412*(1–2), 171–176.

Sun, C. T., Klug, J., & Arendt, C. (1996). Analysis of cracked aluminum plates repaired with bonded composite patches. *AIAA Journal, 34*(2), 369–374.

Zarrinzadeh, H., Kabir, M. Z., & Deylami, A. (2017). Crack growth and debonding analysis of an aluminum pipe repaired by composite patch under fatigue loading. *Thin-Walled Structures, 112*, 140–148.

Author(s) Information

Aida Achour
University of Sidi Bel Abbes
BP 89 city Ben M'Hidi, Sidi Bel-Abbes 22000, Algeria
Contact e-mail: *aida.achour@univ-mosta.dz*

Belabbes Bachir Bouidjra
University of Sidi Bel Abbes, Algeria
BP 89 city Ben M'Hidi, Sidi Bel-Abbes 22000, Algeria

Hafida Driz
University of Sidi Bel Abbes, Algeria
BP 89 city Ben M'Hidi, Sidi Bel-Abbes 22000, Algeria

Sadek Bahar
University of Mostaganem, Algeria

To cite this article:

Achour, A., Bouidjra, B. B., Driz, H., & Bahar, S. (2025). Evaluation of composite method repair of a cracked plate *The Eurasia Proceedings of Science, Technology, Engineering and Mathematics (EPSTEM), 38,* 842-848.

The Eurasia Proceedings of Science, Technology, Engineering & Mathematics (EPSTEM)
ISSN: 2602-3199

The Eurasia Proceedings of Science, Technology, Engineering and Mathematics (EPSTEM), 2025

Volume 38, Pages 849-860

IConTES 2025: International Conference on Technology, Engineering and Science

A Bio-Inspired Path to Fake Profile Detection: Revisiting Linear Models Through Grasshopper Optimization

Nadir Mahammed
Djillali Liabes University of Sidi Bel Abbes

Imene Saidi
Djillali Liabes University of Sidi Bel Abbes

Mahmoud Fahsi
Djillali Liabes University of Sidi Bel Abbes

Souad Bennabi
Hassiba Ben Bouali University of Chlef

Abstract: Social media platforms continue to struggle with the proliferation of fake user profiles, which undermine trust and facilitate the spread of misinformation. While deep learning and complex ensemble models dominate recent solutions, this study revisits the power of simpler classifiers when paired with intelligent feature selection. We introduce a hybrid framework that couples the Grasshopper Optimization Algorithm with Logistic Regression for detecting fake profiles in online social networks. The proposed bio-inspired algorithm mimics the collective foraging behavior of grasshoppers to optimize the feature space, resulting in a compact and highly discriminative set of inputs. Evaluated on different datasets from social media platforms, the proposed model not only outperforms six standard classifiers but also challenges the assumption that fake profile detection requires non-linear modeling. Achieving impressive accuracy and strong F1 performance, our approach shows that nature-inspired metaheuristics can elevate classical models to competitive levels. These results suggest a promising direction for lightweight, interpretable, and scalable solutions in social cybersecurity.

Keywords: Fake accounts, Grasshopper optimization algorithm, Feature selection, Logistic regression, Online social networks

Introduction

In the digital age, social media platforms have become modern town squares, where people connect and share information like never before. But this openness has a downside: the widespread use of fake profiles (Fire et al., 2014). These fake accounts—often run by bots or malicious actors—pose a real threat to online conversations. They're used to spread misinformation, influence public opinion, and enable cybercrime. According to Marinoni et al. (2024), up to 15% of social media accounts could be bots, showing how serious the problem is.

Catching these fake profiles isn't simple. Many of them are designed to act like real users, using advanced language tools and sometimes even stealing real account details (Albayati & Altamimi, 2019). Old detection systems based on fixed rules often fail because attackers constantly change tactics. Machine learning offers a more flexible solution by learning patterns that rule-based systems miss. But even machine learning has limits. Training these models requires a lot of labeled data, which is slow and expensive to produce (Prenner & Robbes, 2021). Also, the data involved—like user behavior, connections, and text—is complex (Kim et al., 2024), and the boundary between real and fake profiles is rarely clear-cut.

- This is an Open Access article distributed under the terms of the Creative Commons Attribution-Noncommercial 4.0 Unported License, permitting all non-commercial use, distribution, and reproduction in any medium, provided the original work is properly cited.

- Selection and peer-review under responsibility of the Organizing Committee of the Conference

© 2025 Published by ISRES Publishing: www.isres.org

Newer approaches use algorithms inspired by nature to tackle this kind of complexity (Han et al., 2024). One example is the Grasshopper Optimization Algorithm (GOA), which models how grasshoppers move in groups, balancing attraction, repulsion, and wind-driven movement (Saremi et al., 2017). GOA has done well in other optimization tasks, but its use in machine learning—especially for detecting fake profiles—hasn't been studied much.

This paper tries to close that gap. The authors suggest a new way to detect fake accounts by combining GOA with a specific fitness function. Their main assumptions are:

- GOA can explore the structure of social media data more effectively than traditional optimizers, even when used with a basic machine learning model.
- Despite how complex the problem seems, fake profile detection might involve patterns that are easier to separate than previously thought.

The paper is organized into six sections. Section 2 reviews current methods for detecting fake profiles. Section 3 explains the data, preprocessing, and the proposed approach. Section 4 presents the results and discusses them. Section 5 concludes the study.

Related Work

This section gives a quick look at different ways researchers have tried to detect fake profiles on social media using machine learning.

Varuna et al. (2022) introduced a system for spotting fake profiles that uses open-source big data tools along with a type of neural network called LSTM (Long Short-Term Memory). They also applied a method called Dispersive Flies Optimization (DFO) to pick out the most useful features from the data. Their approach focused on collecting data ethically and looked at both public and private user information. Mahammed et al. (2022) focused on fake accounts on Facebook. They came up with a two-step system that first uses the Satin Bowerbird Optimization Algorithm (SBO) to group profiles and find the best starting points, then apply K-Means clustering to classify each profile as real or fake. In a later study, Sekkal and Mahammed (2025) compared different fake profile detection methods. They found that both supervised and unsupervised machine learning models show promise, especially those inspired by nature. They tested an algorithm based on the behavior of grey wolves—called the Grey Wolf Optimizer (GWO)—to detect fake accounts. Another study by Mahammed et al. (2025) used a nature-inspired method called the Fire Hawk Optimizer (FHO). They tested different groups of features from a Twitter dataset to see which ones were most effective. They used Gradient Boosting Classifier (GBC) as their main model to evaluate how well FHO worked. Patil et al. (2024) proposed a different approach. They combined several machine learning models into one system and used a Majority Voting Technique (MVT) to decide if a profile was fake or real. Their results showed strong potential for improving online safety. Ramdas and Agnes (2024) also explored machine learning for detecting fake profiles. They tested various algorithms and used evaluation tools like confusion matrices and error rate analysis to find the most effective models. In a more recent paper, Mahammed et al. (2024) again investigated the Fire Hawk Optimizer, this time using it with Facebook data. They used Gradient Boosting Classifier to measure its performance and focused on finding the most useful features to tell real and fake accounts apart. Kumar et al. (2024) took a different route. They used a large set of features—including profile details, user behavior, and network connections—and applied a refined version of the Bagged Tree Algorithm (BTA). This method prunes unnecessary parts of the decision tree to improve both accuracy and speed.

Table 1 summarizes all these studies and shows how researchers are making progress in detecting fake profiles across platforms like Facebook, Twitter, and Instagram. Most studies use machine learning and report very high accuracy—often over 97%. Three of them (Mahammed et al., 2022, 2023, 2024) focus on combining machine learning with metaheuristic algorithms like SBO and FHO. These methods also perform well, with accuracy ranging from 98.0% to 99.8%, but more research is needed to confirm how well they generalize. Some of the most commonly used tools include K-Means, Gradient Boosting Classifier, Random Forest, and other ensemble techniques. One study (Varuna et al., 2022) stands out for using LSTM networks, which are particularly good at analyzing content over time, like sequences of text. It's worth noting that while many studies combine machine learning with optimization techniques for better results, the effectiveness of any method may depend on the platform and the type of user data available. Dataset sizes vary from just over 1,200 to more than 17,000 entries. While larger datasets generally lead to better results, some smaller studies still achieved high accuracy, suggesting that choosing the right method matters as much as the amount of data. So far, machine learning has

been very successful at spotting fake accounts. But algorithms inspired by nature—like those based on bird, insect, or animal behavior—are still not widely used. This work proposes a new approach that brings those two ideas together: combining machine learning with a nature-inspired algorithm to improve fake profile detection on social media.

Table 1. Related work summary

Reference	OSN	ML	Metaheuristic	Other	Dataset size	Results (acc)
Varuna et al. (2022)	Facebook	LSTM	DFO	-	-	0.979
Mahammed et al. (2022)	Facebook	k-means	SBO	hybridization	1244	0.989
Sekkal and Mahammed (2025)	Facebook	-	GWO	Transition	1244	0.980
Mahammed et al. (2025)	Twitter	GBC	FHO	Hybridization	17350	0.996
Patil et al. (2024)	Twitter	MVT	-	Combination	6825	0.991
Ramdas and Agnes (2024)	Instagram	RF	-	Comparison	6868	0.997
Mahammed et al. (2024)	Facebook	GBC	FHO	Hybridization	1244	0.998
Kumar et al. (2024)	Facebook	BTA	-	-	-	0.999

Material and Methodology

This section explains the steps taken in the study, starting with the dataset used. It then summarizes how the data was prepared for analysis, followed by an overview of the machine learning methods considered. Finally, it introduces the main technique used in the study—a bio-inspired algorithm—with a brief explanation of how it works, why it was combined with other methods, and how it functions.

Dataset

The study used a balanced dataset from Twitter, collected by Erşahin et al. (2017). It contains 1,000 user profiles, split into 501 fake and 499 real accounts. This even distribution helps ensure reliable and unbiased analysis. The dataset includes 16 features, listed in Table 3. The breakdown of real and fake profiles is shown in Table 2.

Table 2. Twitter dataset repartition

	Real	Fake
Record	499	501
Proportion (%)	49.9	50.1

Dataset Preprocessing

Before any analysis can begin, the raw data needs to be cleaned up and organized. This step—called preprocessing—is essential because the original data often contains problems like missing information, inconsistent formatting, or extra noise that can throw off results (Siino et al., 2024). Especially in machine learning, the data has to be neat and structured for the algorithms to work well. Taking care of these issues early on helps ensure the analysis is accurate and reliable (Naseem et al., 2021).

Figure 1 shows the 12-step process used in this study to clean and prepare the Twitter data for analysis (Naseem et al., 2021). Here's a breakdown of what those steps involved:

- Step 1: Clean up the text by removing things like special characters, links, user tags, and hashtags so the focus stays on the actual content.
- Steps 2 & 3: Add meaning by translating emojis and emoticons into words that express their emotions, and expanding abbreviations and acronyms to their full forms for better clarity.
- Step 4: Fix spelling errors to make the text more accurate and easier to analyze.
- Steps 5 & 6: Expand contractions (like "don't" to "do not") and shorten stretched-out words (like "soooo" to "so") to make the text more standard.
- Steps 7 to 11:

– Remove punctuation to simplify the text
– Convert everything to lowercase for consistency
– Separate words clearly for better analysis
– Remove numbers if they're not useful for the task
– Get rid of common words like "the" or "is" that don't add much meaning

- Step 12: Reduce words to their basic form (for example, changing "running" to "run") to keep things consistent and easier to analyze.

Table 3. Twitter dataset attributes

Attribute Name	Description
describing account	Length of the user defined string describing the account.
Protected	When true, indicates that this user has chosen to protect their Tweets.
followers count	The number of followers this account currently has.
friends count	The number of users this account is following.
statuses count	The number of Tweets (including retweets) issued by the user.
favourites count	The number of Tweets this user has liked in the account's lifetime.
listed count	The number of public lists that this user is a member of.
verified	When true, indicates that the user has a verified account.
profile use background image	When true, indicates the user wants their uploaded background image to be used.
contributors enabled	Indicates that the user has an account with "contributor mode" enabled.
default profile	When true, indicates that the user has not altered the theme or background of their user profile.
default profile image	When true, indicates that the user has not uploaded their own profile image and a default image is used instead.
is translator	When true, indicates that the user is a participant in Twitter's translator community.
hashtags average	Number of hashtags that user has used in last 20 tweets.
mentions average	Number of mentions that user has used in last 20 tweets.
urls average	Number of URL links that user has used in last 20 tweets.

Machine Learning Algorithms

With the Twitter data cleaned and ready, this section gives a quick overview of the machine learning methods used in the study.

- ID3 (Induction of Decision Tree) This is a supervised learning method that builds a decision tree based on patterns found in the training data. The tree is then used to classify new, unseen data (Charbuty and Abdulazeez, 2021).
- K-means is an unsupervised learning method used to group similar data points into clusters. It works by organizing the data into a set number of groups based on similarity, even without labeled data (Sinaga and Yang, 2020).
- K-Nearest Neighbors (KNN) is a supervised method that classifies data based on its closest neighbors. A new data point is labeled according to the majority label among its nearest examples in the training set (Zulyadi et al., 2024).
- Naive Bayes (NB) is a supervised method based on Bayes' theorem. It assumes all features are independent from each other, which makes it simple and fast while still often producing accurate results (Afriansyah et al., 2024).

- Random Forest (RF) is an ensemble learning method that combines many decision trees. Each tree makes a prediction, and the final decision is based on the majority vote, improving overall accuracy (Sun et al., 2024).
- Support Vector Machine (SVM) is a supervised learning method that finds the best boundary to separate data into categories. Once this boundary is set, it can be used to classify new data with high reliability (Kavitha and Kaulgud, 2024).

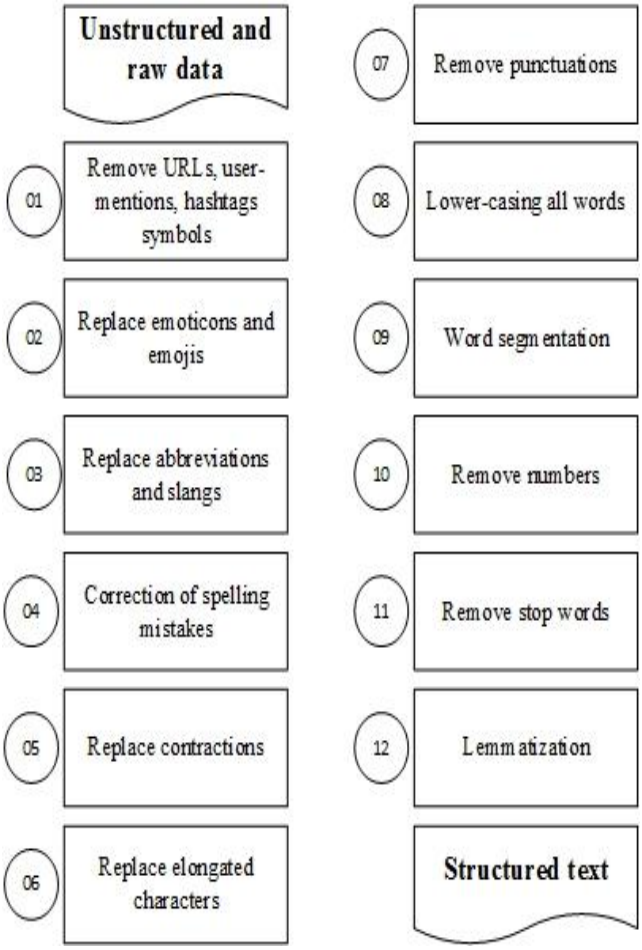


Figure 1. Preprocessing pipeline

Proposed Algorithm

This section explains the Grasshopper Optimization Algorithm (GOA) introduced by Saremi et al. (2017). It covers how the algorithm works, the role of the fitness function in measuring its performance, and why GOA is a good fit for this study. The explanation also connects the way the algorithm is designed to the natural behavior it's modeled after, showing how this link supports its use in solving the problem.

Grasshopper Optimization Algorithm

GOA is a type of algorithm that takes inspiration from nature—specifically, how grasshoppers behave in swarms. In this method, each possible solution is treated like a grasshopper exploring a search area. These "grasshoppers" move through the space based on how well they perform, aiming to follow the best-performing one, called the leader (Saremi et al., 2017). This leader keeps changing depending on which solution is currently the best, encouraging the others to move toward it. This mirrors how real grasshoppers swarm toward food sources. What makes GOA different from many other nature-inspired algorithms is its built-in foraging behavior. This means it doesn't just chase the best solution but also explores the search space more thoroughly, which increases its chances of finding better results (Afriansyah et al., 2024).

Progress and Functioning

Figure 2 shows the step-by-step outline (pseudo code) of how GOA works.

$$c_i = c_{Max} - \frac{k-1}{Max_{iteration}-1}(c_{Max} - c_{Min}) \quad (1)$$

The parameters c_{Max} and c_{Min} correspond to the upper and lower bounds for the coefficient c, respectively. Within the context of the algorithm, t denotes the current iteration, progressing from 1 to a maximum value represented by k_{Max}.

$$X_d^i = c_i\left(\sum_{j=1,j\neq 1}^{N} c_2 \frac{ub_d - lb_d}{2} s\left(\left|x_j^d - x_i^d\right|\right)\frac{x_j - x_i}{d_{ij}}\right) + \hat{K}_d \quad (2)$$

Algorithm Grasshopper Optimization Algorithm (GOA)

```
Parameters initialization: c_Max, c_Min, Max_Iteration
Population initialization: X_i(i = 1, 2, ..., t)
Calculate each individual fitness value
Assign K to the highest fitness value individual
while k = 1 to Max_Iteration do
    Update c_i for each individual using Eq. 1
    for each individual in the population do
        Normalize the distances between individuals into [1, 4]
        Update the position of the individual using Eq. 2
        if the individual exceeds the boundaries then bring it back
    end for
    Re-evaluate each individual fitness
    if there is a better solution then replace K with it
end while
```

Figure 2. Grasshopper optimization algorithm pseudo code

Within each dimension of the search space, the algorithm sets a lower and upper limit, known as lb_d and ub_d. It also keeps track of the best solution found so far in that specific dimension, referred to as $\hat{K}_d$.

The parameter c_1 works similarly to the inertia weight used in Particle Swarm Optimization (Jain et al., 2022). Its role is to gradually reduce how much the grasshoppers move around the target. This helps the algorithm balance two goals: focusing more on good solutions already found (exploitation) while still exploring new possibilities (exploration). The parameter c_2 is used to slowly shrink the areas where grasshoppers either attract or repel each other. As the algorithm runs through more cycles, these zones get smaller. Often, c_1 and c_2 are combined into a single formula, as shown in equation (1) (Meraihi et al., 2021).

Fitness Function

GOA uses a fitness function to measure how good each solution is. In this case, it uses logistic regression to select the most useful features from the data.

- Feature selection function: As shown in figure 3, this function takes the dataset, the target labels, and a feature mask, which shows which features are selected. It runs a logistic regression model to check how well the selected features can classify the data and returns the accuracy.
- GOA function: As shown in figure 4, this part of the process runs the main GOA logic. It uses inputs like the dataset, target labels, number of grasshoppers, and the number of iterations to run.

```
def calculate_fitness(X, y, feature_mask):
    selected_features = X[:, feature_mask.astype(bool)]
    model = LogisticRegression(random_state=0)
    model.fit(selected_features, y)
    y_pred = model.predict(selected_features)
    return accuracy_score(y, y_pred)
```

Figure 3. Feature selection function

Fitness Function Inference, instead of using a separate, pre-set formula to measure how good a solution is, this approach calculates the fitness value directly inside the grasshopper optimization process. It works by checking how accurate a logistic regression model is when trained on the features chosen by the current "grasshopper," or candidate solution.

To turn this into a minimization problem (where lower scores are better), the accuracy is flipped using the formula $^{1}/_{(1 + accuracy)}$. This inverted score becomes the fitness value for that grasshopper. In short, each candidate solution is judged by how well its selected features help a logistic regression model classify the data—using the flipped accuracy as the measure. To test how well GOA performs, it's compared with several other well-known machine learning methods: ID3, SVM, Naive Bayes, Random Forest, K-Nearest Neighbors (with K=3), and K-means. Each method is tested 100 times. The GOA settings used for these tests are listed in Table 4.

Table 4. GOA parameters setting

Parameter	Symbol	Value
Number of Grasshoppers	$n_{\text{grasshoppers}}$	10
Maximum Iterations	Max_{iter}	100
Alpha	α	1.0
Beta	β	1.0
Lower Bound	lb	-
Upper Bound	ub	-

Results and Discussion

After explaining the method and how it works, this section covers how the model was evaluated, what the results were, and why they matter.

Evaluation Criteria

To measure how well the model performed, the study used a confusion matrix. This is basically a table that compares what the model predicted with what the actual answers were (Shinde & Mane, 2022). The main metric used was accuracy, but other measures like precision, recall, and F1-score are also useful for getting a full picture. The matrix includes the following terms:

* TP: True Positive (correctly identified fake profiles)
* FP: False Positive (real profiles wrongly flagged as fake)
* TN: True Negative (correctly identified real profiles)
* FN: False Negative (fake profiles wrongly flagged as real)

Results and Discussion

The results show that the proposed method is highly effective at spotting fake profiles, as shown in the confusion matrix in Table 5.

- First, the method reached a high accuracy of 93.9%. It correctly identified 432 fake profiles (True Positives) and 496 real profiles (True Negatives), showing that it can reliably tell the difference between real and fake users.
- Second, it's especially good at catching fake accounts. The high number of True Positives means it rarely misses them.
- Third, it makes few mistakes when it comes to real users. With only 29 False Negatives, the method keeps the number of wrongly flagged real accounts low, helping to avoid blocking genuine users by mistake.
- Finally, the results show that the model is well-balanced. It performs consistently across both classes—real and fake profiles—without leaning too heavily in one direction. This balance is key to building a fair and trustworthy system.

Table 5. Confusion matrix

Predidted class	Real positive	Real negative	Total
Positive	TP = 432	FP = 32	465
Negative	FN = 29	TN = 496	525
Total	461	529	1000

Table 6, titled "Obtained Results," shows how different algorithms perform when used to detect fake social media profiles. It includes key performance measures like accuracy, precision, recall, and F1-score. The standout performer is the Grasshopper Optimization Algorithm (GOA). It achieved the highest accuracy at 93.9% and the best F1-score at 92.5%, making it the most effective method among those tested. These results show that GOA does a great job of exploring different possibilities and fine-tuning its approach to deliver strong results. One reason GOA performs so well is its ability to balance two important tasks: exploration (searching widely for possible solutions) and exploitation (focusing on refining the best ones found so far). This balance helps the algorithm avoid getting stuck in weak areas and instead find stronger solutions. GOA is also well-designed for solving complicated problems like fake profile detection, which can involve messy or unpredictable data. Its flexible approach helps it handle patterns and irregularities that might throw off simpler methods. The use of logistic regression in the GOA setup also adds to its strength. Logistic regression is especially good at handling yes-or-no problems—like deciding whether a profile is real or fake—by finding relationships between the data and the outcome.

Other algorithms like ID3, Naive Bayes (NB), and Random Forest (RF) also performed well, with accuracy scores close to GOA's, ranging from 88.9% to 89.2%. However, their F1-scores were slightly lower (around 87.8% to 88.7%), suggesting they weren't quite as balanced in terms of precision and recall. Support Vector Machine (SVM), K-Nearest Neighbors (KNN), and K-means didn't perform as well. KNN reached an accuracy of 85.6%, while K-means was the lowest at 67%. Their F1-scores followed a similar pattern, showing that these models struggled more with capturing the complex patterns needed to reliably identify fake accounts. In short, GOA proved to be the most effective option overall, especially when paired with logistic regression, and stood out by offering both high accuracy and strong balance across all key metrics.

Table 6. Obtained results

Algorithm	Accuracy	Precision	Recall	F1-score
Id3	0.890	0.877	0.882	0.878
SVM	0.844	0.823	0.832	0.827
KNN (k=3)	0.856	0.837	0.841	0.834
NB	0.889	0.874	0.880	0.887
RF	0.892	0.870	0.888	0.878
K-means	0.670	0.654	0.667	0.654
GOA	0.939	0.928	0.931	0.925

Table 7 compares the accuracy of different algorithms using the same dataset originally provided by Erşahin et al. (2017). GOA comes out on top with an accuracy of 93.9%, which is a significant step above the next best performers—Random Forest at 89.2% and ID3 at 89.0%. That's a difference of about 4.7% to 4.9%, which is a big deal in machine learning.

To put this into perspective, if you were working with a dataset of 1 million profiles, GOA would correctly classify around 47,000 more profiles than Random Forest, and about 49,000 more than ID3. GOA also does a better job at reducing errors. Compared to Random Forest, it cuts errors by 43.5%, and compared to ID3, by 44.5%. What's interesting is that GOA uses logistic regression (LR) to measure how good each solution is. Logistic regression is a simple model that draws straight lines to separate classes. In contrast:

- Random Forest builds complex decision trees to capture more complicated patterns.
- SVM uses mathematical tricks to separate data in more complex ways.
- ID3 and Random Forest both look for layered, non-linear boundaries in the data.

Despite being simpler, GOA's use of logistic regression actually performs better. This suggests that the fake profile problem may not be as complex as expected and that a good linear solution—found through optimization—might be enough.

Another strong point is that GOA seems to avoid overfitting, which is when a model memorizes the training data instead of learning real patterns. This is impressive given the small dataset. Logistic regression naturally avoids overfitting because of its simplicity, and GOA's swarm-based search avoids getting stuck in bad solutions. On the other hand, Random Forest and ID3, which can overfit on small datasets due to their complexity, still did well—showing the dataset is also quite learnable.

Table 7. Accuracy comparison

Algorithm	Ersahin et al. (2017)	Our propsotion
ID3	-	0.890
SVM	-	0.844
KNN (k=3)	-	0.856
NB	0.909	0.889
RF	-	0.892
K-means	-	0.67
GOA	-	0.939

Looking at the dataset itself, the high accuracy across most algorithms (except k-means) suggests the features are pretty clear. There seem to be strong differences in how fake and real profiles are written or structured. Naive Bayes, which assumes all features are independent, works without optimization. GOA, however, uses a modern optimization approach inspired by how grasshoppers move in swarms and fine-tunes a logistic regression model by balancing broad searching and focused improvements. The results show GOA outperforms older models like Naive Bayes. As for the other algorithms:

- SVM performed below its usual level (84.4%), which could mean the features weren't scaled properly or the decision boundary was too complex.
- KNN (with k=3) scored 85.6%, showing that nearby data points share similar traits, but it didn't do as well as GOA, suggesting that broader patterns matter more.
- K-means had the lowest performance at 67%, likely because it's unsupervised and doesn't use label information. Fake and real profiles can look similar on the surface, which makes clustering harder.

GOA's design helps explain its success. It mimics how grasshoppers move in nature:

- Attraction pulls solutions toward better areas.
- Repulsion keeps the search diverse and avoids getting stuck.
- Wind guidance helps all solutions move in the direction of the best one found so far.

This balance between exploring and improving is probably what helps GOA find such an effective logistic regression model. In fake profile detection, precision really matters. You want to avoid mistakenly flagging real people as fake, because that can damage trust. If GOA's 93.9% accuracy includes a strong balance between precision and recall, it means it's doing both things well—catching fake accounts while minimizing harm to real users. That said, there are still open questions about how well GOA would scale. Its optimization process might become more demanding if it's applied to much larger datasets with millions of features, like words or bigrams. It's also unclear whether the grasshopper-inspired behavior would hold up in those more complex spaces.

Conclusion

This study introduced a new way to detect fake profiles on social media using the Grasshopper Optimization Algorithm (GOA) combined with a specific fitness function. The method was tested thoroughly, and the results

were both impressive and meaningful—not just for improving detection accuracy, but also for what they reveal about how these problems can be tackled.

The approach reached an accuracy of 93.9%, beating several well-known machine learning models. That's not just a slight edge—it means that, in a dataset of one million profiles, this method would correctly identify around 47,000 more fake accounts than Random Forest and about 49,000 more than ID3. In a world where fake profiles can spread misinformation, commit fraud, or manipulate public opinion, this improvement could make a real difference in protecting online communities and building trust.

Interestingly, while detecting fake profiles might seem like a complex problem, the success of this method—which is based on a simple logistic regression model optimized by a nature-inspired algorithm—suggests it might be more straightforward than we thought. This challenges the idea that social media problems always require highly complex solutions and opens the door to using simpler, more efficient models in future research.

The study also highlights how powerful nature-inspired algorithms can be. GOA is based on how grasshoppers move in swarms, using behaviors like attraction, repulsion, and movement guided by the strongest member of the group. These behaviors help the algorithm explore different solutions and zero in on the best ones. Even when paired with a basic model like logistic regression, GOA was able to find solutions that outperformed more complex methods. For machine learning practitioners, the results offer practical lessons too. GOA performed well on a relatively small dataset, showing that it can avoid overfitting—a common problem when models are too complex for the amount of data available. This makes it especially useful in real-world cases where clean, large-scale data isn't always available. At the same time, there are areas for future work. We still need to see how well GOA handles much larger and more complex datasets, especially in text-heavy environments like social media. Testing it across more diverse scenarios will help confirm how widely it can be applied. In a time when digital manipulation and online deception are real threats to information and trust, even small improvements in detecting fake profiles can have a big impact. Better detection tools can help limit the spread of false information and create safer, more reliable spaces for people to connect online. This study aims to contribute to that goal.

Scientific Ethics Declaration

* The authors declare that the scientific ethical and legal responsibility of this article published in EPSTEM journal belongs to the authors.

Conflict of Interest

* The authors declare that they have no conflicts of interest

Funding

* This study was funded by the ministry of research and higher education of Algeria with the code C00l07es220120220004 under the university research and training project. The authors express their gratitude for the support provided.

Acknowledgements or Notes

* This article was presented as an oral presentation at the International Conference on Technology, Engineering and Science (www.icontes.net) held in Antalya/Türkiye on November 12-15, 2025.

References

Afriansyah, M., Saputra, J., Ardhana, V. Y. P., & Saadati, Y. (2024). Algoritma naive Bayes yang efisien untuk klasifikasi buah pisang raja berdasarkan fitur warna. *Journal of Information Systems Management and Digital Business, 1*(2), 236–248.

Albayati, M., & Altamimi, A. (2019). MDFP: A machine learning model for detecting fake Facebook profiles using supervised and unsupervised mining techniques. *International Journal of Simulation: Systems, Science & Technology, 20*(1), 1–10.

Charbuty, B., & Abdulazeez, A. (2021). Classification based on decision tree algorithm for machine learning. *Journal of Applied Science and Technology Trends, 2*(1), 20–28.

Ersahin, B., Aktaş, Ö., Kılınç, D., & Akyol, C. (2017). Twitter fake account detection. In *2017 International Conference on Computer Science and Engineering (UBMK)* (pp. 388–392). IEEE.

Fire, M., Kagan, D., Elyashar, A., & Elovici, Y. (2014). Friend or foe? Fake profile identification in online social networks. *Social Network Analysis and Mining, 4*, 1–23.

Han, M., Du, Z., Yuen, K. F., Zhu, H., Li, Y., & Yuan, Q. (2024). Walrus optimizer: A novel nature-inspired metaheuristic algorithm. *Expert Systems with Applications, 239*, 122413.

Jain, M., Saihjpal, V., Singh, N., & Singh, S. B. (2022). An overview of variants and advancements of PSO algorithm. *Applied Sciences, 12*(17), 8392.

Kavitha, S., & Kaulgud, N. (2024). Quantum machine learning for support vector machine classification. *Evolutionary Intelligence, 17*(2), 819–828.

Kim, J., Wang, Z., & Song, J. (2024). Adaptive active subspace-based metamodeling for high-dimensional reliability analysis. *Structural Safety, 106*, 102404.

Kumar, C., Bharati, T. S., & Prakash, S. (2024). Online social networks: An efficient framework for fake profiles detection using optimizable bagged tree. In *International Conference on Data & Information Sciences* (pp. 255–264). Springer.

Mahammed, N., Bennabi, S., Fahsi, M., Klouche, B., Elouali, N., & Bouhadra, C. (2022). Fake profiles identification on social networks with bio-inspired algorithm. In *First International Conference on Big Data, IoT, Web Intelligence and Applications (BIWA 2022)* (pp. 48–52). IEEE.

Mahammed, N., Saidi, I., Bencherif, K., Khaldi, M., Fahsi, M., & Guellil, Z. (2025). Grasshopper-based detection of fake social media profiles. *EAI Endorsed Transactions on Scalable Information Systems, 12*(4).

Mahammed, N., Saidi, I., Khaldi, M., & Fahsi, M. (2024). Enhancing social media profile authenticity detection: A bio-inspired algorithm approach. In *Machine Learning for Networking* (Vol. 14525, pp. 32–49). Springer.

Marinoni, C., Rizzo, M., & Zanetti, M. A. (2024). Fake profiles and time spent online during the COVID-19 pandemic: A real risk for cyberbullying? *Current Psychology*, 1–9.

Meraihi, Y., Gabis, A. B., Mirjalili, S., & Ramdane-Cherif, A. (2021). Grasshopper optimization algorithm: Theory, variants, and applications. *IEEE Access, 9*, 50001–50024.

Naseem, U., Razzak, I., & Eklund, P. W. (2021). A survey of preprocessing techniques to improve short-text quality: A case study on hate speech detection on Twitter. *Multimedia Tools and Applications, 80*, 35239–35266.

Patil, D. R., Pattewar, T. M., Punjabi, V. D., & Pardeshi, S. M. (2024). Detecting fake social media profiles using the majority voting approach. *EAI Endorsed Transactions on Scalable Information Systems*.

Prenner, J. A., & Robbes, R. (2021). Making the most of small software engineering datasets with modern machine learning. *IEEE Transactions on Software Engineering, 48*(12), 5050–5067.

Ramdas, S., & Agnes, N. N. (2024). Leveraging machine learning for fraudulent social media profile detection. *Cybernetics and Information Technologies, 24*(1), 118–136.

Saremi, S., Mirjalili, S., & Lewis, A. (2017). Grasshopper optimisation algorithm: Theory and application. *Advances in Engineering Software, 105*, 30–47.

Sekkal, N., Mahammed, N., & Guellil, Z. (2025). A bio-inspired grey wolf approach to enhancing fake profile detection in online social media. *Ingénierie des Systèmes d'Information, 30*(4).

Shinde, S., & Mane, S. B. (2022). Hybrid approach for fake profile identification on social media. In *Pattern Recognition and Data Analysis with Applications* (pp. 579–590). Springer.

Siino, M., Tinnirello, I., & La Cascia, M. (2024). Is text preprocessing still worth the time? A comparative survey on the influence of popular preprocessing methods on transformers and traditional classifiers. *Information Systems, 121*, 102342.

Sinaga, K. P., & Yang, M.-S. (2020). Unsupervised K-means clustering algorithm. *IEEE Access, 8*, 80716–80727.

Sun, Z., Wang, G., Li, P., Wang, H., Zhang, M., & Liang, X. (2024). An improved random forest based on the classification accuracy and correlation measurement of decision trees. *Expert Systems with Applications, 237*, 121549.

Varuna, W. R., Shalini, K., & Roy, M. E. A. (2022). An efficient framework for fake profile identification using metaheuristic and deep learning techniques. *Journal of Positive School Psychology*, 3741–3750.

Zulyadi, R., Surjanti, S., Mahardhani, A. J., Manullang, S. O., Widiantoro, A. D., & Suprihatin, S. (2024). K-nearest neighbors method prediction of the anti-corruption behavior index by region of residence. In *AIP Conference Proceedings* (Vol. 3001). AIP Publishing.

Author(s) Information

Nadir Mahammed
Djillali Liabes University of Sidi Bel Abbes
LabRI-SBA, Ecole Superieure en Informatique Sidi Bel Abbes, Algeria, P.O. 73, El Wiam, 22016 Sidi Bel Abbès, Algeria
Contact e-mail: *n.mahammed@esi-sba.dz*

Imene Saidi
Djillali Liabes University of Sidi Bel Abbes
LabRI-SBA, Ecole Superieure en Informatique Sidi Bel Abbes, Algeria, P.O. 73, El Wiam, 22016 Sidi Bel Abbès, Algeria

Mahmoud Fahsi
Djillali Liabes University of Sidi Bel Abbes, EEDIS,Algeria
P.O. 89, Sidi Bel Abbès, 22000, Algeria

Souad Bennabi
Hassiba Ben Bouali University of Chlef, LCMCR, Algeria
Hay Salem, n°19, Chlef, 02000, Algeria

To cite this article:

Mahammed, N., Saidi, I., Fahsi, M., & Bennabi, S. (2025). A bio-inspired path to fake profile detection: revisiting linear models through Grasshopper optimization. *The Eurasia Proceedings of Science, Technology, Engineering and Mathematics (EPSTEM), 38,* 849-860.

The Eurasia Proceedings of Science, Technology, Engineering & Mathematics (EPSTEM)
ISSN: 2602-3199

The Eurasia Proceedings of Science, Technology, Engineering and Mathematics (EPSTEM), 2025

Volume 38, Pages 861-870

IConTES 2025: International Conference on Technology, Engineering and Science

Deep Learning-Based Crop Recommendation Using Soil and Environmental Parameters

Fatma Ozge Ozkok
Erciyes University
FOMOTECH R&D

Abstract: Crop identification is one of the priorities for increasing the productivity of agriculture, as well as the economic stability of the crops. Most farmers have traditional knowledge along with their experience, which leads to ineffective crop identification. In this context, this paper introduces a proper crop identification technique using deep learning techniques. The proposed system uses a Long Short-Term Memory network to determine the best crops according to the soil and environmental properties. The system is intended to be developed in two significant steps. At the beginning, the ANOVA test is used to determine the effect of the input variables on the system. Irrelevant variables reduce the efficiency of the system. Based on the test, the dominating properties of the crops, according to the environment, have been recognised as potassium, phosphorus, nitrogen, water, and rainfall. Then, in the second stage, the system is optimised based on several experiments involving variations in the number of layers, number of neurons, as well as the training epochs. The proposed approach provides promising insights for the development of an efficient decision-support system that assists the farmer in the selection of suitable crops.

Keywords: Deep learning, Crop recommendation system, Soil and environmental analysis, Precision agriculture, Decision support system

Introduction

Agriculture is a fundamental source of income around the world. However, many farmers face economic difficulties and falling crop yields due to poor crop selection, changing weather patterns and soil characteristics. Especially small and medium-sized farmers suffer financial loss due to a lack of knowledge and improper crop selection. This situation not only lowers farmers' income but also threatens the long-term sustainability of agriculture. Poor planning and unsuitable crop selection endanger future food security by reducing the availability of fruits and vegetables. In recent years, agriculture has increasingly relied on IoT devices, sensors, UAVs, and satellites. Data obtained from the devices include soil parameters, weather conditions, temperature, humidity information, and plant and soil images. The data provides important information on the monitoring of agricultural lands. However, the increasing amount of data makes analysis more difficult.

Deep learning methods using multi-layered filters can analyse datasets of various sizes and attributes. The methods using historical and daily or novel data can recommend new insights. This allows the system to extract patterns and relationships in the data. Although deep learning has a wide range of applications, it provides particularly valuable applications in the agricultural sector. For example, monitoring crop health, yield prediction, disease detection, irrigation optimisation and crop recommendation based on agricultural land conditions.

The crop recommendation systems assist farmers in choosing the appropriate crop based on soil and climate conditions. These conditions can include soil nutrient content, pH, moisture, and environmental parameters.

- This is an Open Access article distributed under the terms of the Creative Commons Attribution-Noncommercial 4.0 Unported License, permitting all non-commercial use, distribution, and reproduction in any medium, provided the original work is properly cited.

- Selection and peer-review under responsibility of the Organizing Committee of the Conference

© 2025 Published by ISRES Publishing: www.isres.org

Deep learning systems using the data can determine the appropriate crop based on historical and real-time data. This can increase income and also help the sustainability of farming.

The study aims to present a plant recommendation system using environmental data, such as temperature, humidity, relative humidity, rainfall, and soil data, such as Nitrogen content rate in the soil, Phosphorus content rate in the soil, Potassium content rate in the soil, and pH value of the soil. The system uses deep learning architectures to suggest plants that are suitable for the land. The results were evaluated by comparing different deep learning architectures.

This study consists of five sections. Section 2 is a literature review. Section 3 describes the deep learning methods, such as LSTM, and the datasets used in this study. Section 4 presents the experimental results and a discussion of the model's performance. Section 5 summarises the conclusions and recommendations of the study.

Related Works

Crop selection recommendations form one of the most important processes involved in yield enhancement in agriculture. Choosing the right crop leads to superior yield and better crop quality. While traditional field practices have been used for crop selection, current technological advancements have introduced automatic processes in which field details, along with climate information, are used to determine the appropriate crop. These automatic techniques involve data mining algorithms such as SVM, Random Forest, single-layer or few-layer artificial neural networks, or deep learning models consisting of multiple layers.

In one of the data mining studies, the soil of the region around Kasur in Pakistan was studied. This is because agriculture is the primary source of livelihood for 65% of the population in that region. Factors like pH, soil type, electrical conductivity (EC), and potassium content were analyzed in that research. Among the various evaluated algorithms: OneRule (OneR), C4.5 decision tree, Naive Bayes, and Best First Tree (BF), the highest success percentage of 97.63% was demonstrated by the Naive Bayes algorithm (Arooj et al., 2018). In another study, a dataset of 2,200 samples combining rainfall, climate, and fertilizer data from India was used. Rule-based algorithms such as PART, Decision Table, and JRip were tested to provide optimal crop recommendations, with PART achieving 99.4% accuracy and 98.33% precision (Parameswari et al., 2021). A group of machine learning models was executed, with the results of their classification accuracies ranging between 90.13% and 99.93%. Among them, the Random Forest algorithm turned out to be much better compared to the other methods and gave the overall highest accuracy (Ashwitha & Latha, 2022).

A study using ANN has developed AI-based product recommendation systems that utilize sensor data such as soil moisture, temperature, and humidity. Artificial neural networks are used to recommend the most suitable products, increasing efficiency in both product selection and automation applications such as smart irrigation (Banavlikar et al., 2018). In another study, an ANN-based crop recommendation system was developed using soil and climate data from the Hadonahalli and Durgenahalli districts of Karnataka, India. The system evaluated crop suitability and achieved 97% accuracy, outperforming a decision tree classifier (92%) (Madhuri & Indiramma, 2021). In another research work, the IoT and AI-based smart agriculture was proposed. Real-time data on temperature, humidity, soil moisture, pH, and water level sensors are utilized by the MLP algorithm to predict the right type of crop. The architecture can automatically control irrigation, and users can also monitor the conditions of a web interface (Jagadeeswari & Manikandababu, 2022).

A crop recommendation framework is presented by combining the metaheuristic algorithm, Improved Distribution-based Chicken Swarm Optimization, and the deep learning algorithm Weight-based Long Short-Term Memory (LSTM) and the IDCSO-WLSTM algorithm. The proposed algorithm is found to be better compared to ANN in terms of recall, precision, accuracy, and execution time (Kiruthika and Karthika, 2025). Majumdar et al. also developed a novel hybrid algorithm called DSSA-AWLSTM. In this algorithm, the Dynamic Salp Swarm Algorithm (DSSA) is employed to extract the most relevant features, while an Adaptive Weighting Long Short-Term Memory Network Ensemble (AWLSTM) is used to determine the most suitable crop from the public crop recommendation dataset (Majumdar et al., 2025). Vani and Guruprakash proposed a crop recognition system named REALNET–LSTM. This method first applied statistical techniques for feature extraction, then used ResNet and its output LSTM in the encoder, followed by a fully connected layer in the decoder. The method demonstrated superior performance compared to traditional data mining methods and ANN (Vani and Guruprakash, 2025).

It has been observed from these studies that data mining, ANN, and deep learning techniques are becoming increasingly effective for crop recommendation system applications. Although conventional techniques are useful, computational techniques always offer better accuracy, precision, and efficiency. Recent studies confirm that deep learning techniques are more effective for crop recommendation tasks than conventional data mining and ANN techniques.

Method

Dataset and Proposed Method

In this section, the dataset and the LSTM model used are explained.

Dataset

The dataset was provided by Indian Chamber of Food and Agriculture for precision agriculture (ICFA,2020). It contains data on the ratio of Nitrogen, phosphorus, and Potassium content in soil, the pH value of soil, temperature, humidity, and rainfall, along with the label for each data entry. It contains 2200 rows and 8 columns with data for 22 classes, which are apple, banana, black gram, chickpea, coconut, coffee, cotton, grapes, jute, kidney beans, lentil, maize, mango, muskmelon, moth beans, papaya, pomegranate, rice, watermelon, and orange. The above distribution is presented in Fig. 1.

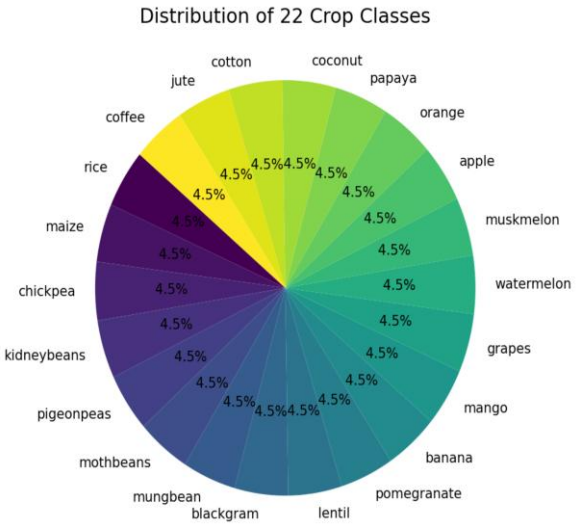


Figure 1. Distribution of crop classes in the dataset

LSTM

The Long Short-Term Memory, or LSTM, refers to a sophisticated form of RNN that has been developed with the purpose of finding and tracing patterns in data that span a long period. However, due to its unique structure, which has a memory cell, the LSTM has the capability to retain data for a relatively long period. This contradicts a normal RNN, where the gradient either vanishes or diverges with each step of the training process, resulting in either losing memory or losing the gradient. The main gates within each unit necessary during the processing of decision-making of which data to store, update, and delete are referred to as forget gates, input gates, and output gates. This form of technology can be applied where data necessary through time or a sequence is involved (Chauhan et al., 2024; Yadav & Thakkar, 2024; Orosoo, 2025).

The overall structure of an LSTM cell is represented in Figure 2. Every LSTM cell contains the previous state of the cell, denoted by C_{t-1}, and the current state, denoted by C_t. The current input to the cell is given by X_t, along with the previous hidden state h_{t-1} are combined and passed to three gates: the forget gate, the input gate, and the output gate. The forget gate decides on which parts of Ct-1 are forgotten, whereas the input gate decides on what is added on top of C_t. These two gates function simultaneously in an operation that results in the combination of previous information with new information, thus an update on C_t. Finally, the output gate decides which parts of

C_t will affect h_t in that given time step. It then passes this information on to the next step. The capability described above enables the LSTM network to learn dependencies that are long and temporal patterns existing in the data (Zhou et al., 2024).

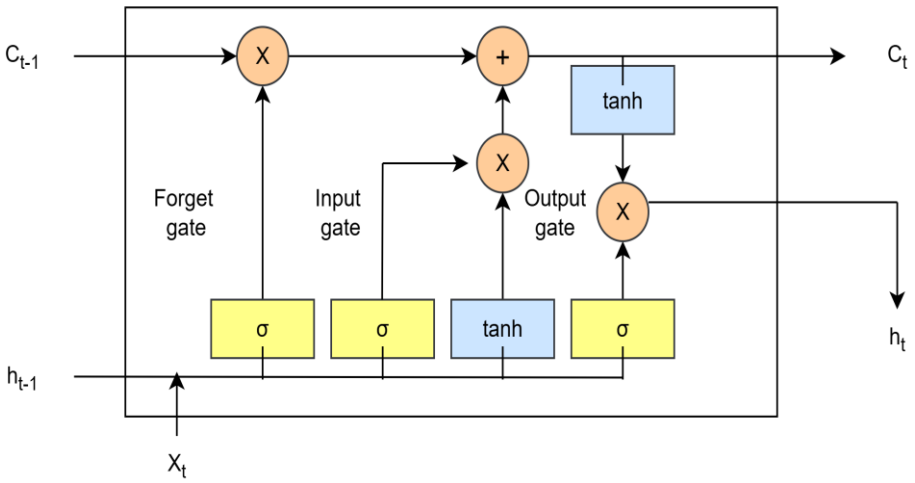


Figure 2. The structure of an LSTM unit (Zhou et al., 2024).

Even though it cannot be regarded as a common time series from the given dataset, it has the capacity to handle complex nonlinear associations between the variables.

Results and Discussion

This section presents and discusses the results obtained from the experiments. Firstly, an F-test analysis was carried out to determine the most effective components of the data that contributed to the enhancement of the model. Secondly, the section witnessed the performance of some experiments with the goal of trying to enhance the Long Short-Term Memory network structure by either layer or neuron modification. These experiments and their comparisons are discussed in detail.

ANOVA F-Test Results

To evaluate the statistical significance and usefulness of variables in a given dataset, an F-test analysis of ANOVA was performed before constructing the proposed LSTM model.

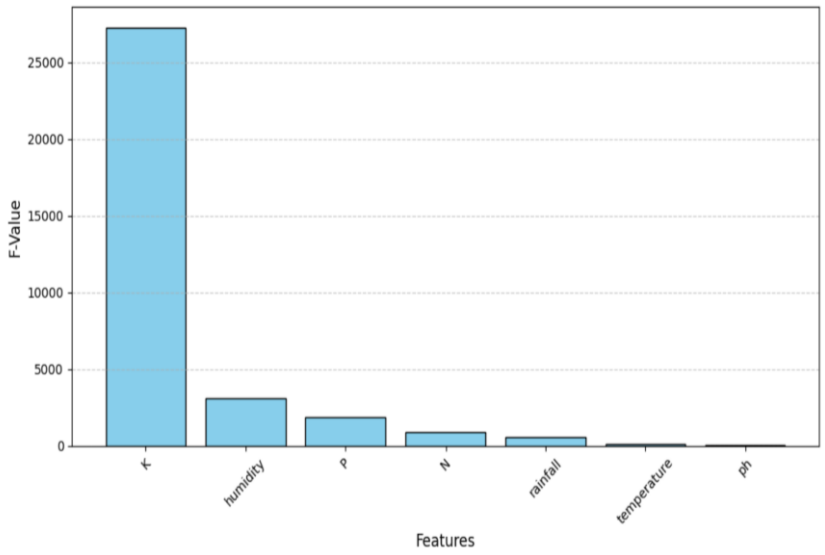


Figure 3. Feature importance based on ANOVA F-test

The results of the ANOVA F-test are presented in the figure based on the calculated F-values. The ANOVA F-test results showed F-values of 60.344 for pH, 102.187 for temperature, 605.528 for rainfall, 897.568 for nitrogen (N), 1885.658 for phosphorus (P), 3103.709 for humidity, and 27238.362 for potassium (K). The F-value in ANOVA indicates the ratio of variance between groups to the variance within groups. A higher F-value represents a stronger influence of that variable on the dependent variable, implying that differences in that feature contribute more significantly to variations in the model output. Therefore, potassium (K), phosphorus (P), nitrogen (N), humidity, and rainfall, which had the highest F-values, were selected as input features.

LSTM Architecture Optimisation

In this section, three experiments were conducted to investigate the effects of the number of LSTM layers, the number of neurons per layer, and the number of epochs on model performance. In addition, the classification performance for different crop types was evaluated to show how well the model predicted each class. In the first experiment, the number of LSTM layers was varied to analyse its impact while keeping the other hyperparameters constant. The fixed hyperparameters were as follows: the learning rate was set to 0.001, the batch size was 16, the dropout rate was 0.2, the number of epochs was 20, and each layer contained 32 units. The number of LSTM layers was changed from one to five, and the obtained training results are presented in Figure 4, while the test accuracies for each model are shown in Figure 5.

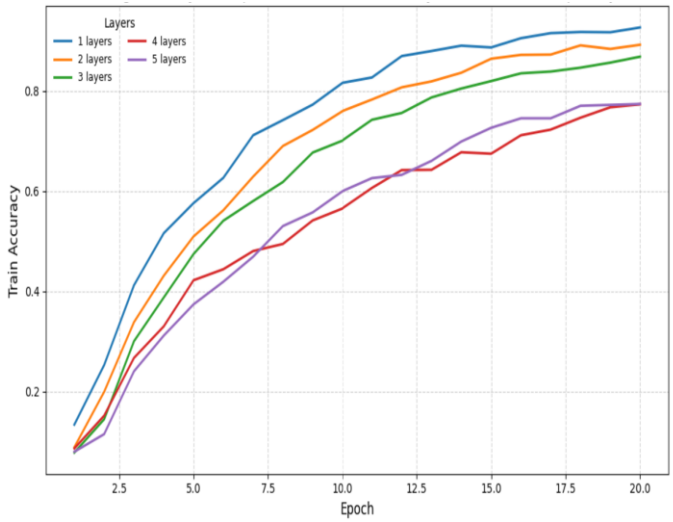


Figure 4. Train accuracy

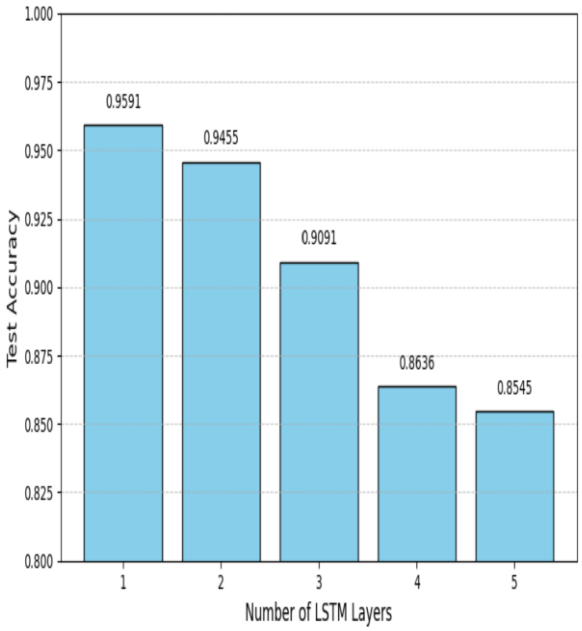


Figure 5. Test accuracy

As shown in Figure 4, the per-epoch training curves indicate that the one-layer LSTM reaches the highest accuracy among the tested configurations. Figure 5 presents the test accuracies, which are 0.9591 for one layer, 0.9455 for two layers, 0.9091 for three layers, 0.8636 for four layers, and 0.8545 for five layers. Taken together, these results show that the one-layer LSTM provides the best overall performance; therefore, the subsequent experiments were conducted using a one-layer LSTM architecture.

In the second experiment, the number of neurons per layer was varied to analyse its impact while keeping the other hyperparameters constant. The fixed hyperparameters were as follows: the learning rate was set to 0.001, the batch size was 16, the dropout rate was 0.2, the number of epochs was 20, and the number of LSTM layers was fixed at one. The number of neurons per layer was changed to 16, 32, 64, 96, and 128, and the obtained training results are presented in Figure 6, while the test accuracies for each model are shown in Figure 7.

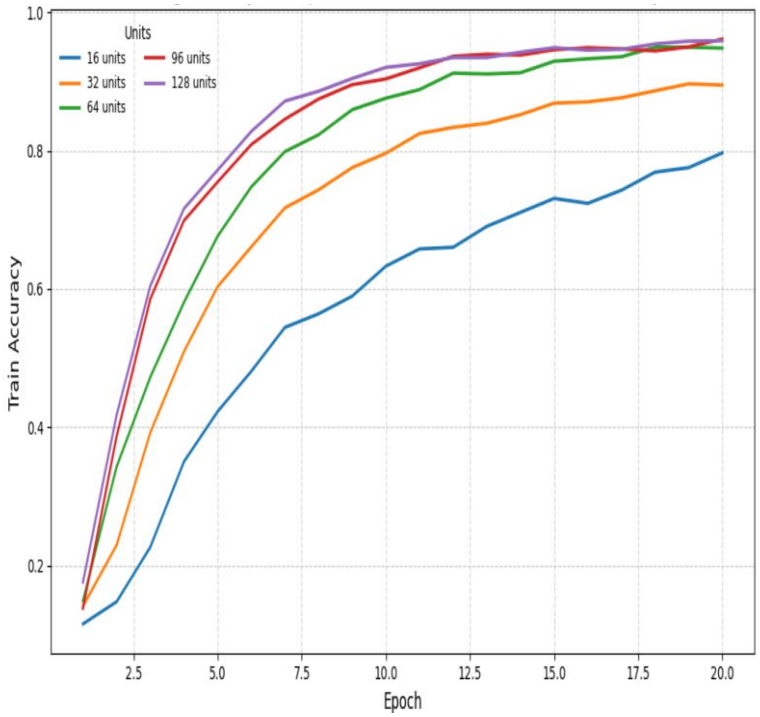


Figure 6. Train accuracy

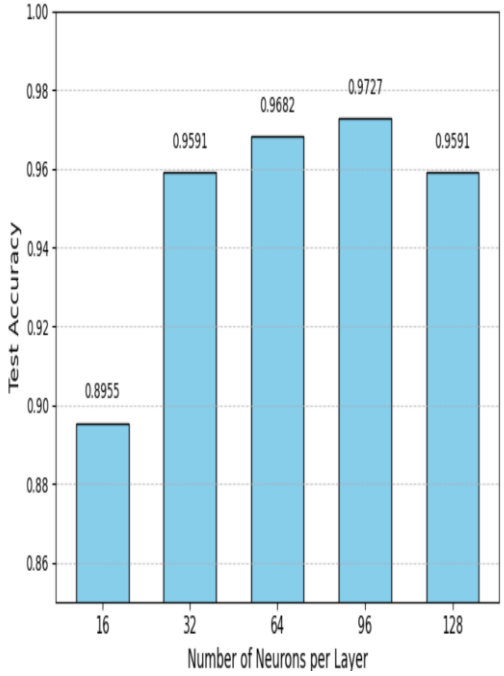


Figure 7. Test accuracy

As shown in Figure 6, the per-epoch training curves demonstrate that the model with 96 neurons per layer achieves the highest training accuracy among the tested configurations. Figure 7 presents the test accuracies, which are 0.8955 for 16 neurons, 0.9591 for 32 neurons, 0.9682 for 64 neurons, 0.9727 for 96 neurons, and 0.9591 for 128 neurons. These results clearly indicate that the LSTM model with 96 neurons provides the best overall performance; therefore, this configuration was selected for the following experiment.

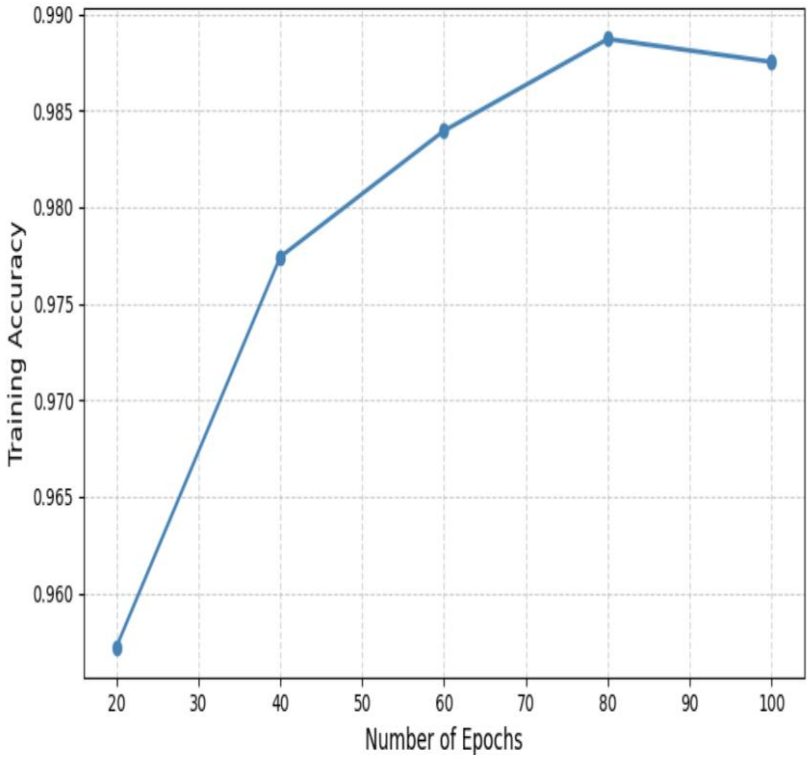


Figure 8. Train accuracy

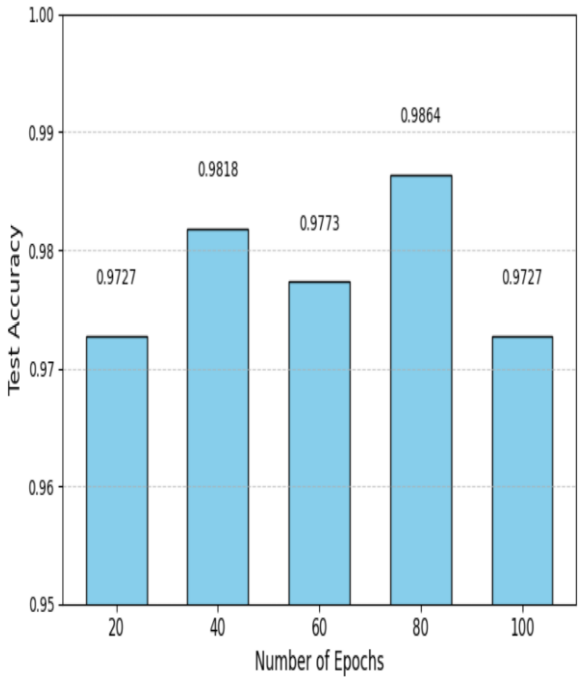


Figure 9. Test accuracy

In the third experiment, the number of epochs was varied to analyse its impact while keeping the other hyperparameters constant. The fixed hyperparameters were as follows: the learning rate was set to 0.001, the batch size was 16, the dropout rate was 0.2, the number of neurons per layer was 96, and the number of LSTM

layers was fixed at one. The number of epochs was adjusted to 20, 40, 60, 80, and 100. The corresponding training results are illustrated in Figure 8, and the test accuracies for each configuration are presented in Figure 9.

As shown in Figure 8, the per-epoch training curves demonstrate that the model trained for 80 epochs achieves the highest training accuracy among the tested configurations. Figure 9 presents the test accuracies, which are 0.9727 for 20 epochs, 0.9818 for 40 epochs, 0.9773 for 60 epochs, 0.9864 for 80 epochs, and 0.9727 for 100 epochs. These results clearly indicate that training the LSTM model for 80 epochs provides the best overall performance; therefore, this configuration was used in the final evaluation and confusion matrix analysis.

In the final experiment, the model was trained using the optimal parameters obtained from the previous experiments. The results, illustrated in Figure 10, show that most crop classes were correctly identified by the model. Specifically, three rice samples and one coffee sample were misclassified as jute, while one jute sample was incorrectly predicted as rice. Apart from these minor errors, the model accurately recognized 19 out of 22 crop types, demonstrating strong classification performance and generalization capability.

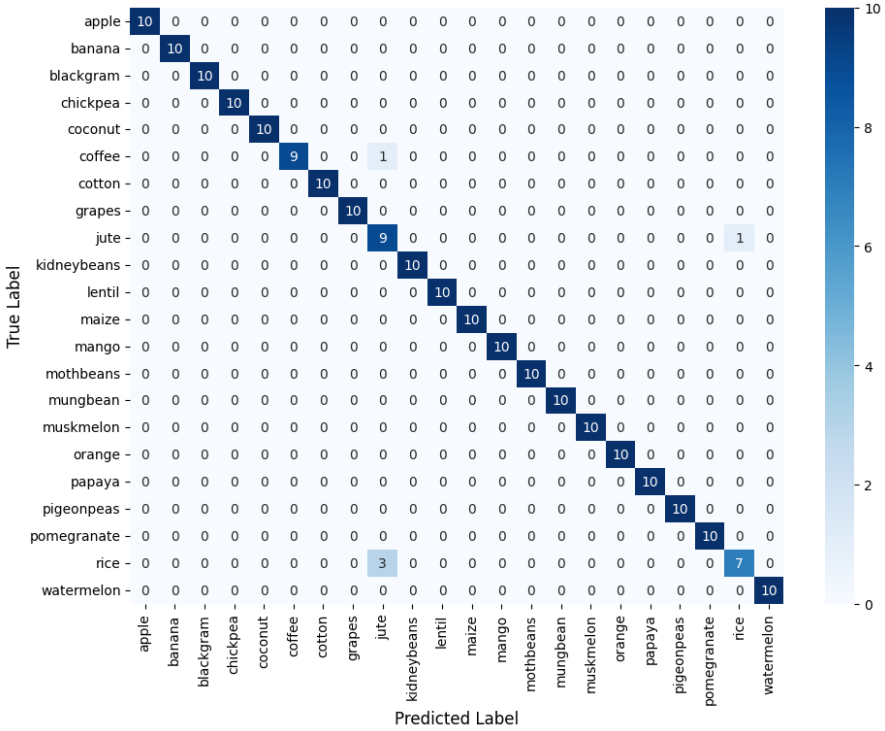


Figure 10. The confusion matrix of the proposed model

Conclusion

The suitable selection of crops is one of the most important processes in agriculture. Therefore, the proposed system is a crop-recommending model which is based on LSTM and soil and environmental data. Initially, the significant factors influencing crop growth were determined using the ANOVA F-test. The result demonstrates that potassium, phosphorus, nitrogen, humidity, and rainfall are dominant in the data. Later, a variety of experiments were carried out to choose the best LSTM model parameters. The one-layer LSTM model, with 96 neurons and 80 epochs, achieved the highest accuracy. These results show that the proposed LSTM-based system is effective for data-driven crop recommendation.

Recommendations

In this study, an LSTM-based deep learning model was used to predict suitable crops based on environmental and soil parameters. Although the LSTM architecture demonstrated strong performance, future research could explore alternative recurrent neural network models, such as GRU (Gated Recurrent Unit) or BiLSTM (Bidirectional LSTM) to further improve prediction accuracy. Additionally, attention mechanisms or hybrid

models that combine LSTM with convolutional layers could enhance the model's ability to capture spatial and temporal dependencies in the data. Future studies could also utilise larger and more diverse datasets, as well as real-time data collection methods, to improve the generalisation and robustness of crop recommendation systems.

Scientific Ethics Declaration

* The author declares that the scientific ethical and legal responsibility of this article published in EPSTEM journal belongs to the author.

Conflict of Interest

* The authors declare that they have no conflicts of interest

Funding

*This publication is supported by the EU COST (European Cooperation in Science and Technology) Action CA22136 “Pan-European Network of Green Deal Agriculture and Forestry Earth Observation Science” (PANGEOS)

Acknowledgements or Notes

* This article was presented as an oral presentation at the International Conference on Technology, Engineering and Science (www.icontes.net) held in Antalya/Türkiye on November 12-15, 2025.

References

Arooj, A., Riaz, M., & Akram, M. N. (2018, February). Evaluation of predictive data mining algorithms in soil data classification for optimized crop recommendation. In *2018 International Conference on Advancements in Computational Sciences (ICACS)* (pp. 1-6). IEEE.

Ashwitha, A., & Latha, C. A. (2022). Crop recommendation and yield estimation using machine learning. *Journal of Mobile Multimedia*, *18*(3), 861-883

Banavlikar, T., Mahir, A., Budukh, M., & Dhodapkar, S. (2018). Crop recommendation system using Neural Networks. *International Research Journal of Engineering and Technology (IRJET)*, *5*(5), 1475-1480.

Chauhan, A., Kukkar, Y., Nagrath, P., Gupta, K., & Hemanth, J. D. (2024). Integrating LSTM and NLP techniques for essay generation. *Intelligent Decision Technologies*, *18*(1), 571-584.

ICFA (Indian Chamber of Food and Agriculture), 2020, https://www.kaggle.com/datasets/siddharthss/crop-recommendation-dataset/data, Accessed: 08.06.2025

Jagadeeswari, M., & Manikandababu, C. S. (2022, September). Artificial Intelligence based Crop Recommendation System. In *2022 4th International Conference on Inventive Research in Computing Applications (ICIRCA)* (pp. 1127-1133). IEEE.

Kiruthika, S., & Karthika, D. (2023). IOT-BASED professional crop recommendation system using a weight-based long-term memory approach. *Measurement: Sensors*, *27*, 100722.

Madhuri, J., & Indiramma, M. (2021). Artificial neural networks based integrated crop recommendation system using soil and climatic parameters. *Indian Journal of Science and Technology, 14*(19), 1587-1597.

Majumdar, P., Mitra, S., & De, D. (2025). An effective crop recommendation system using a dynamic salp swarm algorithm with adaptive weighting based LSTM network. *SN Computer Science*, *6*(5), 549.

Orosoo, M., Raash, N., Treve, M., Lahza, H. F. M., Alshammry, N., Ramesh, J. V. N., & Rengarajan, M. (2025). Transforming English language learning: Advanced speech recognition with MLP-LSTM for personalized education. *Alexandria Engineering Journal*, *111*, 21-32.

Parameswari, P., Rajathi, N., & Harshanaa, K. J. (2021, October). Machine learning approaches for crop recommendation. In *2021 International Conference on Advancements in Electrical, Electronics, Communication, Computing and Automation (ICAECA)* (pp. 1-5). IEEE.

Vani, B. V., & Guruprakash, C. D. (2025). Representational alignment net-based long short-term memory model for crop recommendation system. *Proceedings of the Indian National Science Academy*, 1-20.

Yadav, H., & Thakkar, A. (2024). NOA-LSTM: An efficient LSTM cell architecture for time series forecasting. *Expert Systems with Applications*, *238*, 122333.

Zhou, M., Wang, L., Hu, F., Zhu, Z., Zhang, Q., Kong, W., ... & Cui, E. (2024). ISSA-LSTM: A new data-driven method of heat load forecasting for building air conditioning. *Energy and Buildings*, *321*, 114698.

Author(s) Information

Fatma Ozge Ozkok
Erciyes University
Department of Computer Engineering, Turkiye
FOMOTECH R&D, Erciyes Technopark, Turkiye
Contact e-mail: *fozgeozkok@erciyes.edu.tr*

To cite this article:

Ozkok, F.O (2025). Deep learning-based crop recommendation using soil and environmental parameters. *The Eurasia Proceedings of Science, Technology, Engineering and Mathematics (EPSTEM), 38,* 861-870.

The Eurasia Proceedings of Science, Technology, Engineering & Mathematics (EPSTEM)
ISSN: 2602-3199

The Eurasia Proceedings of Science, Technology, Engineering and Mathematics (EPSTEM), 2025

Volume 38, Pages 871-880

IConTES 2025: International Conference on Technology, Engineering and Science

Development of a Computational Interface for the Thermal Behavior Analysis of Metallic Plates Using the Finite Volume Method

Imene Bennia
University of Blida1

Narimen Hamidi
University of Blida1

Abstract: This paper presents the design and implementation of a user-friendly interface for a computational code developed to analyze the thermal behavior of metallic plates using the Finite Volume Method (FVM). The study focuses on the discretization of the heat conduction equation and the creation of an interface that simplifies parameter input and enhances visualization of simulation results. Developed with Visual Basic software, the interface is capable of handling 256 boundary condition cases for two-dimensional simulations and 1296 cases for three-dimensional simulations, providing flexibility in modeling complex thermal problems. It also incorporates an automatic overheating alert, which is activated if the maximum simulated temperature exceeds the melting point of the selected material. Validation was conducted through comparison with Ansys simulations and experimental measurements, confirming the reliability, accuracy, and applicability of the interface. This work offers a versatile and effective solution for thermal analysis in both research and industrial contexts.

Keywords: Thermal analysis, Heat transfer, Interface conception, Numerical simulation.

Introduction

In the field of thermal engineering, numerical simulation tools are essential for predicting heat transfer behavior under various physical and boundary conditions. However, the complexity of numerical models and the need to master specific programming languages often limit their accessibility to non-specialists (Patankar, 1980; Versteeg & Malalasekera, 2007; Incropera et al., 2017). To overcome this limitation, a computational code based on the Finite Volume Method (FVM) was developed to solve the heat conduction equation in metallic plates, following approaches similar to those described by Bejan and Kraus (2003) and Wirtz and Stasiek (2012). The developed code can simulate both steady-state and transient regimes in two- and three-dimensional domains, accounting for various boundary conditions and material properties. To enhance usability and improve simulation efficiency, a graphical user interface (GUI) was subsequently designed using Visual Basic within the Visual Studio Express environment. Inspired by pedagogical principles proposed by Cengel and Ghajar (2020) and Sharma et al. (2019), the interface enables users to define simulation parameters, manage geometry and boundary conditions, and visualize results intuitively—without requiring advanced programming knowledge (Chapra & Canale, 2015; Holman, 2010).

The accuracy and reliability of the numerical approach were verified by comparing results with experimental measurements performed in our laboratory and with numerical simulations conducted using ANSYS Fluent (ANSYS, 2022; Yıldız & Yılmaz, 2017 ; Ahamed et al., 2020). While commercial software offers advanced features, the tool presented here distinguishes itself by its simplicity, flexibility, and seamless integration with a validated FVM code.

- This is an Open Access article distributed under the terms of the Creative Commons Attribution-Noncommercial 4.0 Unported License, permitting all non-commercial use, distribution, and reproduction in any medium, provided the original work is properly cited.

- Selection and peer-review under responsibility of the Organizing Committee of the Conference

© 2025 Published by ISRES Publishing: www.isres.org

It allows complete customization of geometry, boundary conditions, and material properties, while incorporating safety mechanisms such as automatic parameter verification and overheating alerts. These characteristics, combined with direct experimental validation, make the tool particularly suitable for educational use, research applications, and specific industrial studies where commercial solutions may be too complex, costly, or rigid. Consequently, this two-step development—combining an in-house computational code with a user-friendly interface—provides an innovative, accessible, and reliable platform for thermal simulations of metallic plates, contributing a valuable alternative to existing commercial and academic tools (Basha et al., 2021 ; Zhang et al., 2019).

Methodology and Interface Design

The methodology of this work is based on a two-step approach: first, the development of a reliable computational code using the Finite Volume Method (FVM) for thermal analysis of metallic plates; second, the creation of a user-friendly graphical interface to facilitate the application of the code for both 2D and 3D simulations. The methodology is structured around the following key aspects :

Input and Parameter Management

The developped interface enables users to run thermal simulations without directly interacting with the underlying computational code. It simplifies the process by automating data input, execution, and result visualization, making the simulation more accessible and efficient. This interface is designed with a modular structure, allowing easy integration of new materials, boundary condition types, or visualization features. Its flexibility enables use in various educational and industrial applications, from basic thermal studies to more complex research scenarios. This tool allows users to define all necessary simulation parameters in a clear and organized manner for the 2D or the 3D cases (Figure 1). These include:

- Simulation type : steady state or transient conditions
- Geometric parameters and Mesh.
- Boundary conditions.
- Material properties.

This structured parameter management ensures that all necessary information is provided before the simulation begins, reducing the risk of errors and improving reproducibility.

Simulation Type

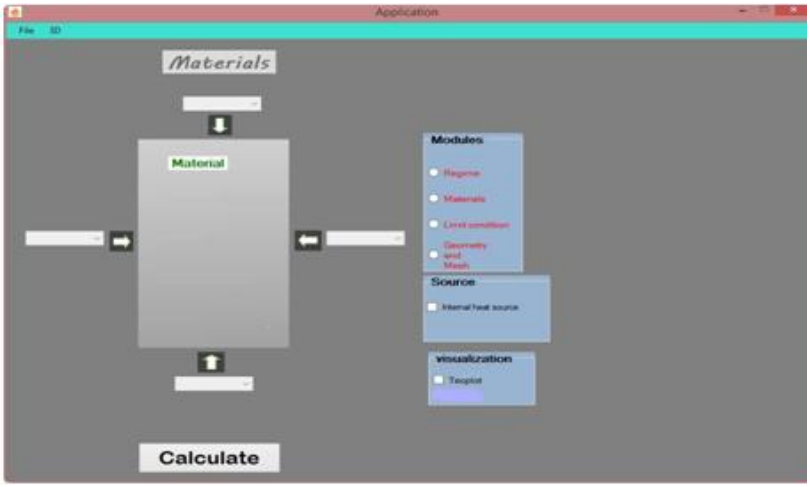


Figure 1. Input panel of the interface showing parameter management.

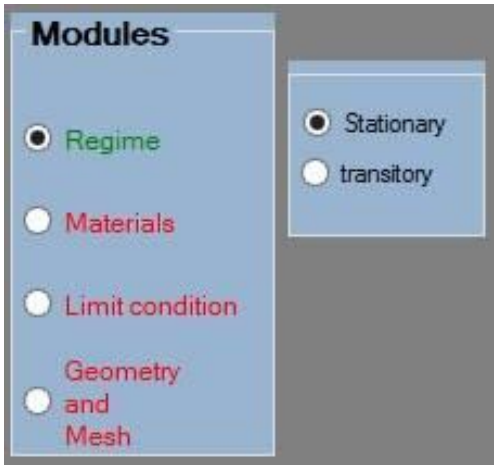


Figure 2. Selection of thermal regime : steady state or transient conditions.

The interface supports both steady-state and transient thermal analysis, with relevant parameters such as simulation duration and time step for transient cases (Figure 2). In the steady-state mode, the program computes the fixed temperature distribution across the plate once equilibrium is reached. This option is mainly used to analyze heat transfer in metallic plates subjected to continuous heat flux or constant boundary temperatures. The transient mode allows the study of temperature evolution over time under variable thermal conditions. Users can define the total simulation duration and time-step directly through the interface. The program automatically manages data saving and graphical visualization at each interval, enabling real-time observation of thermal changes. Both modes are available in 2D and 3D, offering flexibility to investigate steady or time-dependent temperature fields under various boundary and material configurations.

Geometric Parameters and Mesh

The geometry module enables users to define the physical dimensions of the metallic plate, including length, width, and thickness (Figure 3). The meshing parameters are defined independently along each spatial direction, offering control over grid density and spatial resolution. The mesh is structured, allowing accurate discretization of the conduction domain while ensuring numerical stability. Users can easily adjust the number of nodes in each direction to balance computational cost and accuracy. The developed interface also performs automatic mesh quality checks to detect excessive aspect ratios or non-uniform spacing that could compromise solution precision.

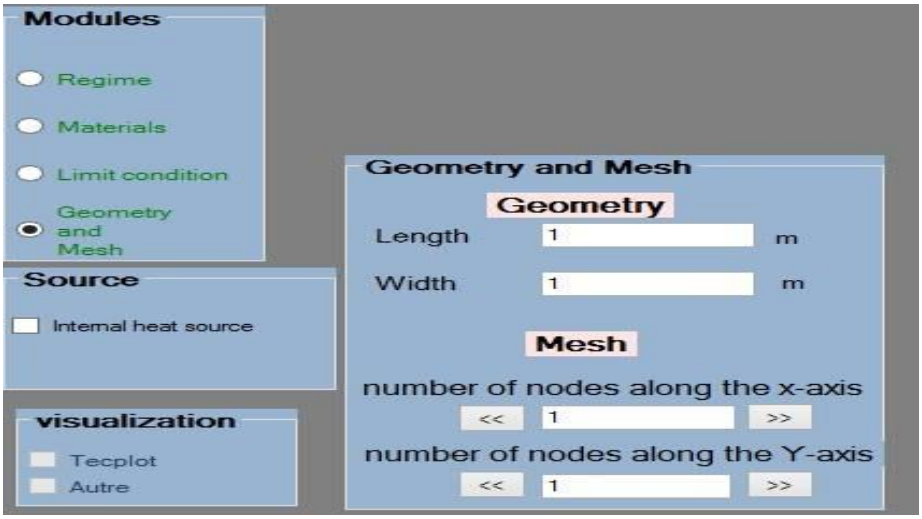


Figure 3. Geometry and mesh selection panel with multiple options for each surface of the plate.

Boundary Conditions

The interface provides extensive flexibility for defining boundary conditions on each plate surface (Figure 4). Users can assign:

- Imposed temperature (Dirichlet condition) for constant or variable temperature boundaries.
- Specified heat flux (Neumann condition) for controlled energy input or loss.
- Convective boundary condition (Robin condition), incorporating fluid temperature and convective heat transfer coefficient, enabling the study of forced or natural convection scenarios.
- Perfect insulation, corresponding to zero heat flux.

Each surface can be assigned independently, allowing the modeling of asymmetric or mixed thermal environments. The system automatically adjusts the computational formulation according to the selected conditions, ensuring physical consistency and numerical robustness.

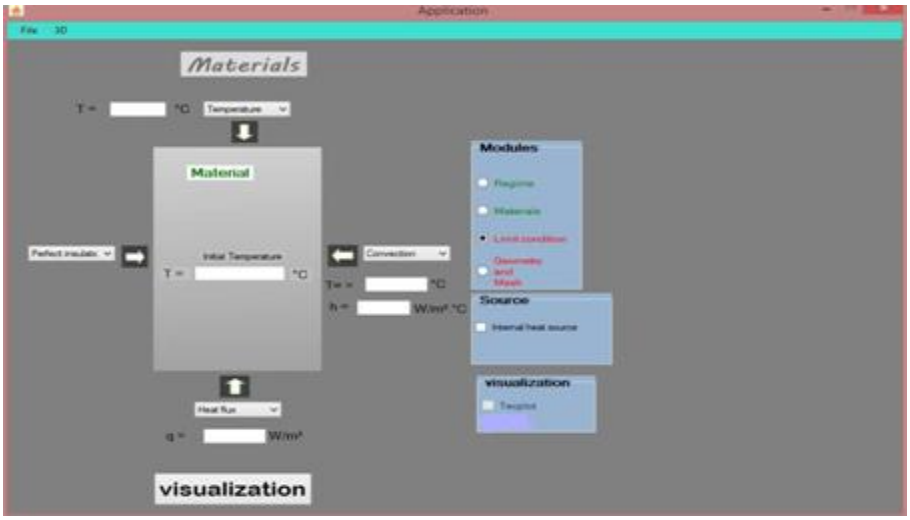


Figure 4. Boundary condition selection panel with multiple options for each surface of the plate.

Material Properties

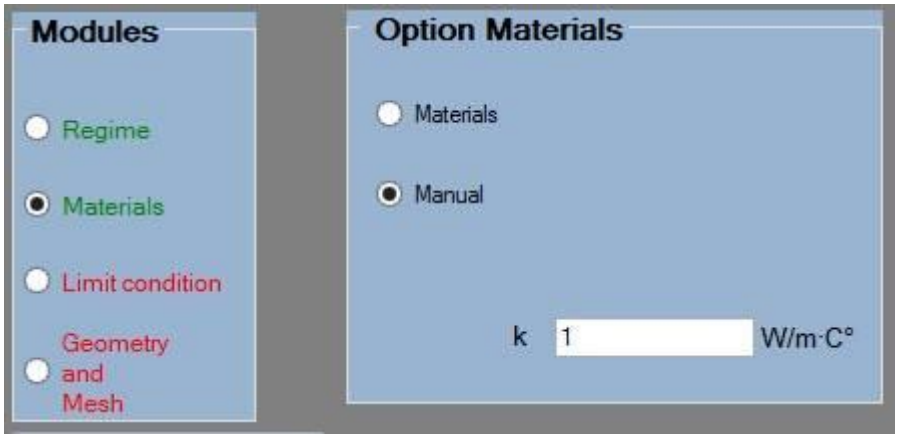


Figure 5. Manual selection of material properties under steady state regime.

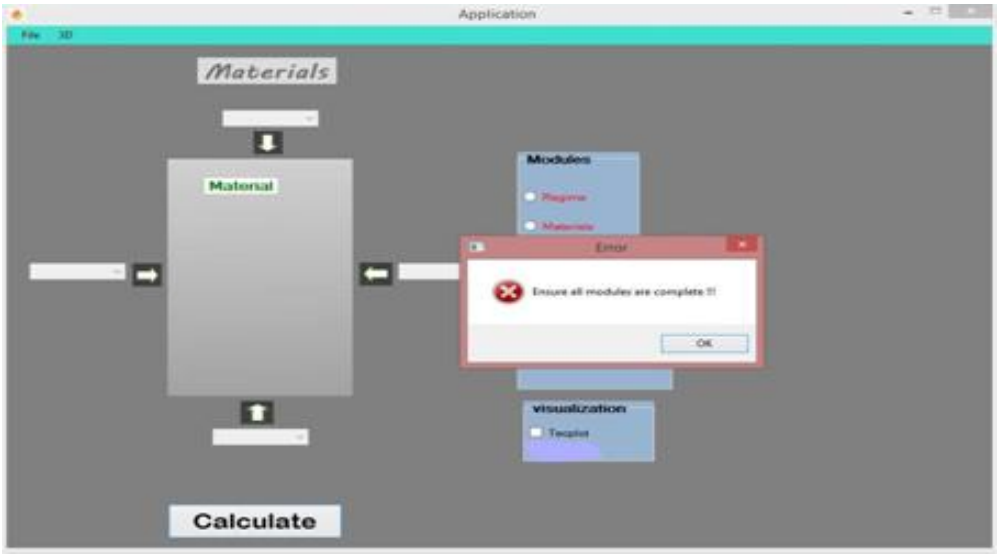


Figure 6. Example of parameter verification alerts triggered during a transient simulation.

A central feature of the interface is the material property database, which includes commonly used metallic materials such as aluminum, copper, steel, and titanium. Each material entry contains default thermal conductivity (k), density (ρ), and specific heat capacity (C_p) values based on standard references. However, users may also define these properties manually to simulate non-standard alloys or composite materials (Figure5). In steady-state simulations, the material's thermal conductivity predominantly governs the spatial temperature distribution, while in transient simulations, density and specific heat capacity determine the rate of temperature evolution.

Safety and Error Management

Reliability is a primary design criterion of the proposed tool. To this end, the interface includes multiple verification and alert systems that operate before and during simulation execution:

- Parameter verification alerts prevent execution when mandatory inputs such as boundary conditions, geometric parameters, or time-step values are missing or physically inconsistent (Figure 6).
- Overheating alerts notify users if the maximum simulated temperature exceeds the melting point of the chosen material, preventing nonphysical results and highlighting potential design flaws.
- Boundary consistency checks ensure that all surfaces are assigned valid thermal conditions, reducing user-induced numerical errors.

These built-in safety features increase user confidence, particularly for beginners or students, and contribute to ensuring the reproducibility and accuracy of all simulation runs.

Visualization and Results Interpretation

Once the computation is completed, the interface provides two main modes of result visualization:

- Numerical display of nodal temperatures, which allows precise inspection of thermal values at each point.
- Graphical representation, using integrated plotting tools to generate 2D or 3D temperature maps, facilitating intuitive understanding of the thermal distribution (Figure 7).

In addition, users can export results for further analysis or reporting.

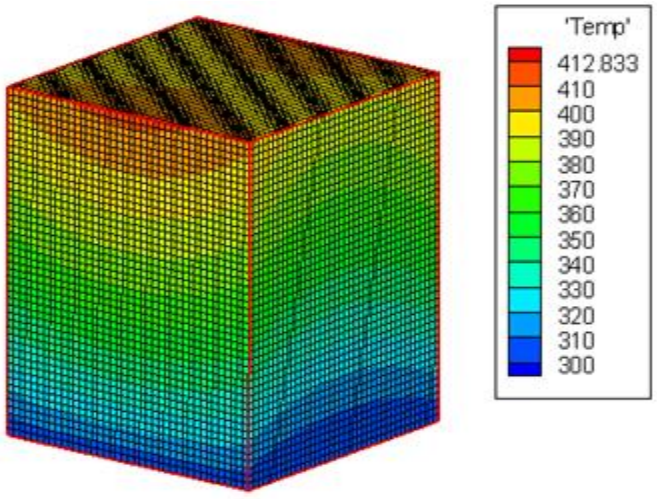


Figure 7. 3D Graphical representation of the temperature showing thermal gradients across the plate depth (Tecplot visualisation).

Results and Discussion

Simulations were conducted on metallic plates with uniform geometry to evaluate temperature distributions under various boundary conditions. The interface allows users to visualize the temperature field at each node either numerically or graphically. As expected, higher temperatures are observed near heat sources and decrease toward insulated or convective boundaries, demonstrating the correct implementation of heat transfer physics.

Validation with ANSYS Fluent

To assess the accuracy of the developed FVM code and interface, the same 2D configurations were simulated using ANSYS Fluent, a widely recognized commercial CFD software. The comparison indicates excellent agreement between the numerical results from the developed interface and ANSYS simulations, with deviations not exceeding 2%. This confirms the robustness and correctness of the numerical implementation (Figure 8 and Figure 9).

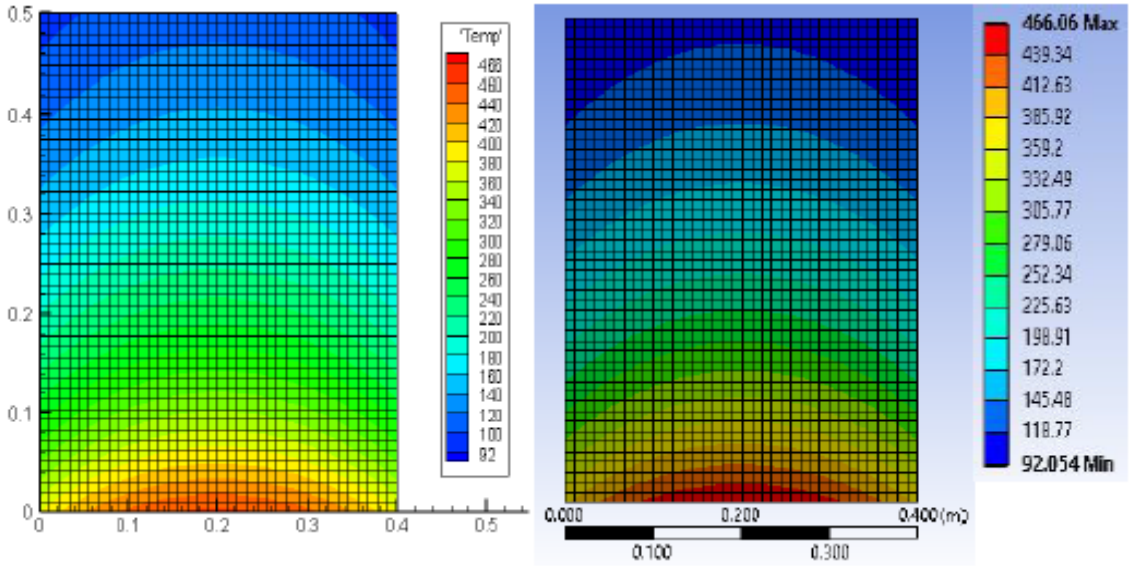


Figure 8. Comparison of 2D temperature distributions obtained from the developed interface and ANSYS Fluent.

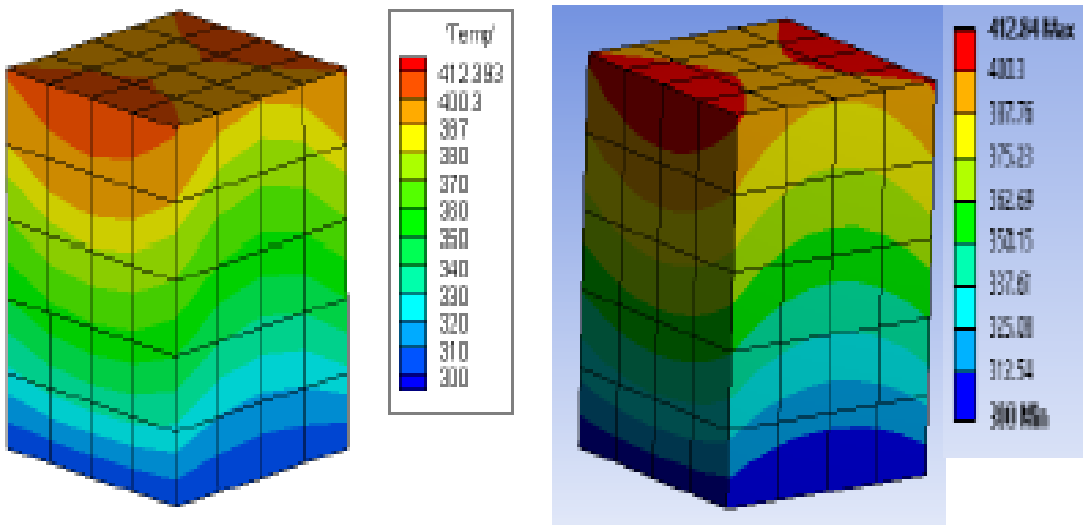


Figure 9. Comparison of 3D temperature distributions obtained from the developed interface and ANSYS Fluent.

Validation with Experimental Measurements

In addition to software validation, experimental measurements were performed on solid metallic plates under controlled laboratory conditions. To collect the data of the sensed temperatures, circuits were used based on the Arduino programmable board or the Pic 16F8777A microcontroller programmed by the MicroC and Proteus software. Temperature profiles obtained experimentally were compared with both 2D and 3D numerical simulations. The results demonstrate excellent agreement. Minor differences are attributed to experimental uncertainties such as thermal contact resistance and ambient temperature variations.

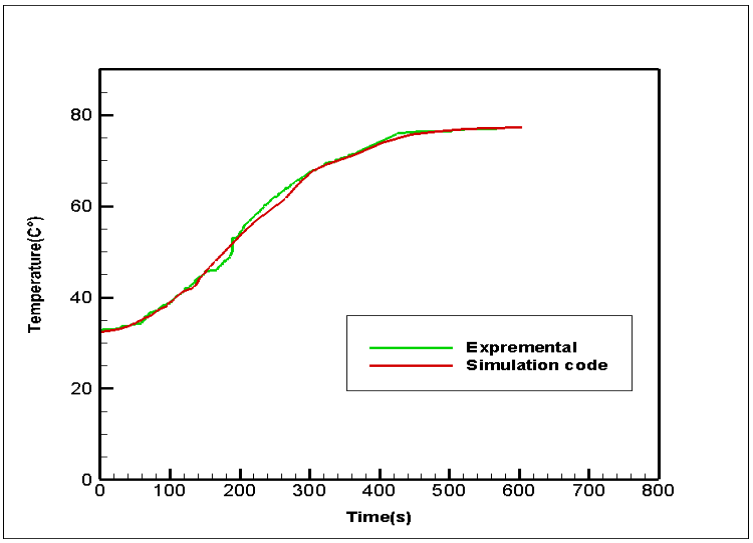


Figure 10. Comparison of 2D numerical simulations with experimental measurements for a solid metallic plate.

Discussion

The discussion of the obtained results can be divided into two main parts: the interface design (Figures 1–7) and the validation of the numerical model (Figures 8–10).

Interface Design and Functionality (Figures 1–7)

The first series of figures illustrates the progressive construction of the interface and its main features. As shown in Figures 1 and 2, the panels for parameter management and simulation-type selection allow the user to define geometric, material, and boundary parameters for both steady and transient regimes. This structure facilitates data entry and reduces the risk of input errors. Figure 3 presents the geometry and meshing module, which enables control over grid resolution and uniformity in each spatial direction. The automatic verification of mesh quality helps maintain numerical stability.

Figures 4 and 5 show that boundary conditions and material properties can be assigned independently to each surface, which increases modeling flexibility. The material database includes common metals but can also be adjusted for other alloys, making the tool adaptable to different studies. Figure 6 demonstrates the inclusion of verification and alert systems that prevent missing or inconsistent parameters and indicate possible overheating. These safety checks improve the reliability of simulations.

Finally, Figure 7 illustrates the visualization module, which provides numerical and graphical representations of temperature fields in two and three dimensions. This visualization assists in interpreting the main heat transfer trends and in verifying the overall consistency of the simulation. One key advantage of the developed code is that it integrates all these functions within a single interface, allowing users to perform complete simulations—from parameter definition to result visualization—without directly manipulating the numerical code. This combination increases efficiency, minimizes user errors, and makes the tool accessible even to non-specialists.

Validation and Interpretation of Results (Figures 8–10)

The numerical results obtained with the developed interface were compared with those from ANSYS Fluent to verify the accuracy of the finite volume implementation. As shown in Figures 8 and 9, the temperature distributions obtained with both methods are in close agreement, with deviations not exceeding 2%. This indicates that the discretization scheme and boundary condition treatment are correctly implemented. Experimental validation, illustrated in Figure 10, shows a good correlation between simulated and measured temperatures. Small differences are mainly due to contact resistance, measurement uncertainties, and minor variations in ambient conditions. Overall, these results confirm that the numerical approach represents the physical behavior of heat conduction with satisfactory accuracy. The influence of boundary conditions, material conductivity, and plate thickness is clearly observed in the simulations. The 3D cases highlight temperature variations through the plate depth that cannot be captured by 2D analysis alone. The interface therefore provides a practical means of examining these effects without requiring manual coding or complex preprocessing. The results show that the interface facilitates the definition of simulation parameters, ensures stable numerical results, and provides accurate predictions consistent with commercial software and experimental data. Its main advantage lies in combining a validated numerical method with an intuitive interface that simplifies and accelerates the entire simulation process.

Conclusion

This work presents the development and implementation of a user-friendly graphical interface for thermal analysis of metallic plates using the Finite Volume Method (FVM). The interface provides an intuitive environment for defining simulation parameters, managing geometry and boundary conditions, and visualizing results in both 2D and 3D. The developed tool has been validated through comparisons with ANSYS Fluent simulations and experimental measurements on solid plates, demonstrating excellent agreement and confirming the accuracy and reliability of the numerical model. The interface further enhances usability by incorporating real-time alerts for missing parameters and overheating, allowing both specialists and non-specialists to perform simulations efficiently and safely. The novelty of this work lies in the integration of a validated FVM computational code with a fully functional, intuitive interface that bridges the gap between advanced numerical simulation and practical experimental validation. This combination provides a versatile tool suitable for educational purposes, research, and preliminary industrial applications, where commercial software may be too complex, expensive, or less flexible.

Future developments may include extending the interface to complex geometries, internal perforations, non-homogeneous materials, and automated meshing, further enhancing its applicability for advanced thermal analysis. Overall, this study demonstrates that a robust, flexible, and validated simulation tool can significantly simplify thermal problem-solving while maintaining accuracy and reliability.

Scientific Ethics Declaration

* The authors declare that the scientific ethical and legal responsibility of this article published in EPSTEM journal belongs to the authors.

Conflict of Interest

* The authors declare that they have no conflicts of interest

Funding

* This research received no specific grant from any funding agency in the public, commercial, or not-for-profit sectors.

Acknowledgements or Notes

* This article was presented as a poster presentation at the International Conference on Technology, Engineering and Science (www.icontes.net) held in Antalya/Türkiye on November 12-15, 2025.

* The authors would like to thank the Institute of Aeronautics and space studies, University of Blida1, Algeria.

References

Ahamed, R., Saidur, R., & Masjuki, H. H. (2020). Numerical and experimental investigation on heat transfer and fluid flow characteristics in heat exchangers. *Applied Thermal Engineering, 168*, 114823.

ANSYS. (2022). *ANSYS Fluent user's guide*. ANSYS Inc.

Basha, M., Ahmed, S., & Ali, M. (2021). Development of user-interactive simulation tools for heat transfer education. *International Journal of Engineering Education, 37*(2), 350–360.

Bejan, A., & Kraus, A. D. (2003). *Heat transfer handbook*. John Wiley & Sons.

Çengel, Y. A., & Ghajar, A. J. (2020). *Heat and mass transfer: Fundamentals and applications* (6th ed.). McGraw-Hill Education.

Chapra, S. C., & Canale, R. P. (2015). *Numerical methods for engineers* (7th ed.). McGraw-Hill Education.

Holman, J. P. (2010). *Heat transfer* (10th ed.). McGraw-Hill.

Incropera, F. P., DeWitt, D. P., Bergman, T. L., & Lavine, A. S. (2017). *Fundamentals of heat and mass transfer* (8th ed.). Wiley.

Patankar, S. V. (1980). *Numerical heat transfer and fluid flow*. Hemisphere Publishing Corporation.

Sharma, R., Singh, J., & Kumar, V. (2019). Interactive visualization and simulation tools for thermal engineering education. *Computer Applications in Engineering Education, 27*(5), 1038–1050.

Versteeg, H. K., & Malalasekera, W. (2007). *An introduction to computational fluid dynamics: The finite volume method* (2nd ed.). Pearson Education.

Wirtz, R. A., & Stasiek, J. (2012). Experimental and numerical study of heat transfer in extended surfaces. *International Journal of Heat and Mass Transfer, 55*(19–20), 5204–5213.

Yıldız, C., & Yılmaz, T. (2017). Validation of numerical heat transfer models through experimental analysis of aluminum plates. *Thermal Science, 21*(6A), 2561–2570.

Zhang, H., Wang, S., & Zhang, X. (2019). Development of simplified CFD-based educational tools for thermal analysis. *Energy Education Science and Technology Part A: Energy Science and Research, 37*(5), 467–478.

Author(s) Information

Bennia Imene
Institute of Aeronautics and space studies,
University of Blida1, Algeria.
Contact e-mail: *ibennia@yahoo.fr*

Hamidi Narimen
Institute of Aeronautics and space studies,
University of Blida1, Algeria.

To cite this article:

Bennia, I., & Hamidi, N. (2025). Development of a computational interface for the thermal behavior analysis of metallic plates using the finite volume method. *The Eurasia Proceedings of Science, Technology, Engineering and Mathematics (EPSTEM), 38,* 871-880.

The Eurasia Proceedings of Science, Technology, Engineering & Mathematics (EPSTEM)
ISSN: 2602-3199

The Eurasia Proceedings of Science, Technology, Engineering and Mathematics (EPSTEM), 2025

Volume 38, Pages 881-890

IConTES 2025: International Conference on Technology, Engineering and Science

Fabrication Process of Nano and Optoelectronic Devices Based on Nitrided Gaas: XPS Analysis and Electrical Measurements

Arslane Hatem Kacha
Djillali Liabes University of Sidi Bel Abbes

Ahmed Hichem Yahi
Djillali Liabes University of Sidi Bel Abbes

Boudali Akkal
Djillali Liabes University of Sidi Bel Abbes

Zineb Benamara
Djillali Liabes University of Sidi Bel Abbes

Abstract: Nano and optoelectronic devices elaborated with gallium arsenic (GaAs) usually known as have been a topic of several studies. Such structures are widely used in various applications. However, the major obstacle encountered in the elaboration of these structures is the oxidation of the GaAs surface which incur a poor quality of the interfaces between the III-V's and the metallic contacts leading to the degradation of the electronic properties of the device. Thereby the passivation of the GaAs surface appears as a key point to improve the performance of GaAs based devices. Different surface passivation methods have been developed to remove this adverse effect as anodization process, Se treatment and N2 plasma treatment. We focused our attention in this presentation on the improvement of the electrical quality of Schottky barrier diodes (SBDs) based on nitridated n-GaAs(100) using a new fabrication process. We will focus on controlling the elaboration steps using XPS measurements and electrically testing the fabricated structures using I-V and C-V measurements at different conditions. This presentation allows us to analyze the effect of the nitridation process and the impact of the technological steps of fabrication on the electrical quality of realized SBDs.

Keywords: XPS, SBDs, Characterization, GaAs, Nitridation

Introduction

Gallium arsenide (GaAs) is one of the most attractive III–V compound semiconductors for high-speed, high-frequency, and optoelectronic device applications due to its direct bandgap, high electron mobility, and excellent thermal and chemical stability (Jenabi,2017; Kansız, 2025 ;Robertson, 2006).It is widely used in ; Schottky barrier diodes (SBDs), high-electron-mobility transistors (HEMTs), and photonic devices such as photodetectors and light-emitting diodes (Gullu, 2024; Zutter, 2021; Sirkeli, 2025). However, despite its outstanding intrinsic properties, the performance of GaAs-based devices is often limited by the poor quality of the metal–semiconductor interface, primarily caused by the spontaneous formation of native oxides and surface defects (Sirkeli, 2020,2024) .These imperfections lead to a high density of interface states that trap carriers, increasing leakage current and degrading both the barrier height and the rectification efficiency of SBDs (Raman, 2025; Sreelekshmi, 2025; Xiao, 2024).

To mitigate these issues, several surface passivation methods have been developed, including chemical etching, sulfur or selenium treatments, anodization, and plasma-assisted techniques (Egorkin, 2024; Liu (2024),

- This is an Open Access article distributed under the terms of the Creative Commons Attribution-Noncommercial 4.0 Unported License, permitting all non-commercial use, distribution, and reproduction in any medium, provided the original work is properly cited.

- Selection and peer-review under responsibility of the Organizing Committee of the Conference

© 2025 Published by ISRES Publishing: www.isres.org

Ravendra (2025)). Among these, plasma nitridation has proven particularly effective in suppressing surface oxidation and reducing interface states through the formation of a stable gallium nitride (GaN) interfacial layer (Hadjouni, 2025; Sirkeli, (2015). This thin GaN film acts as a barrier against metal diffusion and oxide regrowth, thereby improving the thermal and electrical stability of GaAs-based Schottky contacts (Sirkeli, 2017; Pokatilov, 2006; Khales, 2025). Moreover, the incorporation of ultra-thin nitride interlayers has been shown to enhance carrier transport and reduce recombination losses in related III–V structures Kacha (2016, 2021) and Benamara (2022), offering a pathway toward more efficient nano- and optoelectronic devices.

In this work, we investigate the fabrication and characterization of Au/GaN/GaAs Schottky barrier diodes incorporating an ultra-thin GaN interlayer (~17 Å) formed by in-situ electron cyclotron resonance (ECR) nitrogen plasma nitridation. The nitridation process was carefully monitored using X-ray photoelectron spectroscopy (XPS) to assess the chemical composition and structural quality of the interface (Kacha,2021; Helal, 2021). The electrical behavior of the fabricated diodes was then evaluated through current–voltage (I–V) and interface state density analyses to determine the effect of the nitridation process on key parameters such as the barrier height, ideality factor, and leakage current.

The objective of this study is to demonstrate that controlled in-situ nitridation significantly improves the electrical performance of Au/GaN/GaAs Schottky barrier diodes by enhancing the interfacial properties and reducing leakage paths. The results show that the introduction of the GaN layer leads to a lower ideality factor, reduced saturation current, higher barrier height, and a substantial decrease in interface state density. These findings confirm that nitridation is an efficient surface engineering approach for optimizing GaAs-based SBDs, enabling their advanced application in nano- and optoelectronic technologies.

Methods

The studied structure was fabricated on n-type GaAs (001) substrates with a donor concentration of ND = 4.9 × 10^{15} cm^{-3}. To remove surface contaminants, the fabrication process began with a two-step cleaning procedure. The first step consisted of an ex-situ chemical treatment using an HCl and isopropanol solution for 2 minutes and 30 seconds under dark conditions. The second step involved in-situ thermal cleaning by heating the substrate to 500°C under ultra-high vacuum (UHV) conditions (Kacha, 2021).

The nitridation process, applied only to the studied Schottky barrier diodes, was carried out in situ using an ECR N_2 plasma source oriented normal to the surface at a temperature of 500°C and a pressure of 2.5 × 10^{-5} mbar. XPS measurements were employed to monitor the nitridation step. The thickness and chemical composition of the formed GaN layer were determined using the XPS models proposed by Mehdi (2018). Subsequently, four circular Au contacts, each 600 µm in diameter and 100 nm thick, were deposited in situ on the front surface of the sample using a Knudsen cell evaporator.

To enhance the Ohmic contact quality of the studied structure, AuGe contacts were fabricated ex situ on the backside of each sample by sequential evaporation of 10 nm of Au, 35 nm of Ge, and 100 nm of Au under a pressure of approximately 10^{-6} Torr. The contacts were subsequently annealed in a H_2–N_2 atmosphere through a three-step heating process: 200°C for 3 minutes, 250°C for 1 minute, and 300°C for 1 minute. This thermal treatment promoted the diffusion of AuGe into the GaAs substrate, ensuring low-resistance Ohmic behavior. Fabrication details of the studied sample are summarized in Table 1.

Table 1. Technological details of the structure.

GaAs	Nitridation	δ-GaN	Metal contacts
(001) $N_D = 4.9\times10^{15}$ cm^{-3}	120min500°C	17 Å	Schottky: Au Ohmic: AuGe

Realized structures were electrically tested by current-voltage measurements in dark and under illumination at room temperature. These measurements were carried out with a Keithly 2636.

Results and Discussion

XPS Measurements

To monitor the nitridation process and identify the surface composition of the Au/GaN/GaAs structure with a 17 Å GaN interlayer, X-ray photoelectron spectroscopy (XPS) measurements were performed. The spectra corresponding to As 3d, Ga 3d, O 1s, and N 1s core levels were recorded and analyzed after applying a Shirley background correction. Figure 1 presents the spectra obtained before and after the nitridation treatment, highlighting the chemical changes induced at the surface.

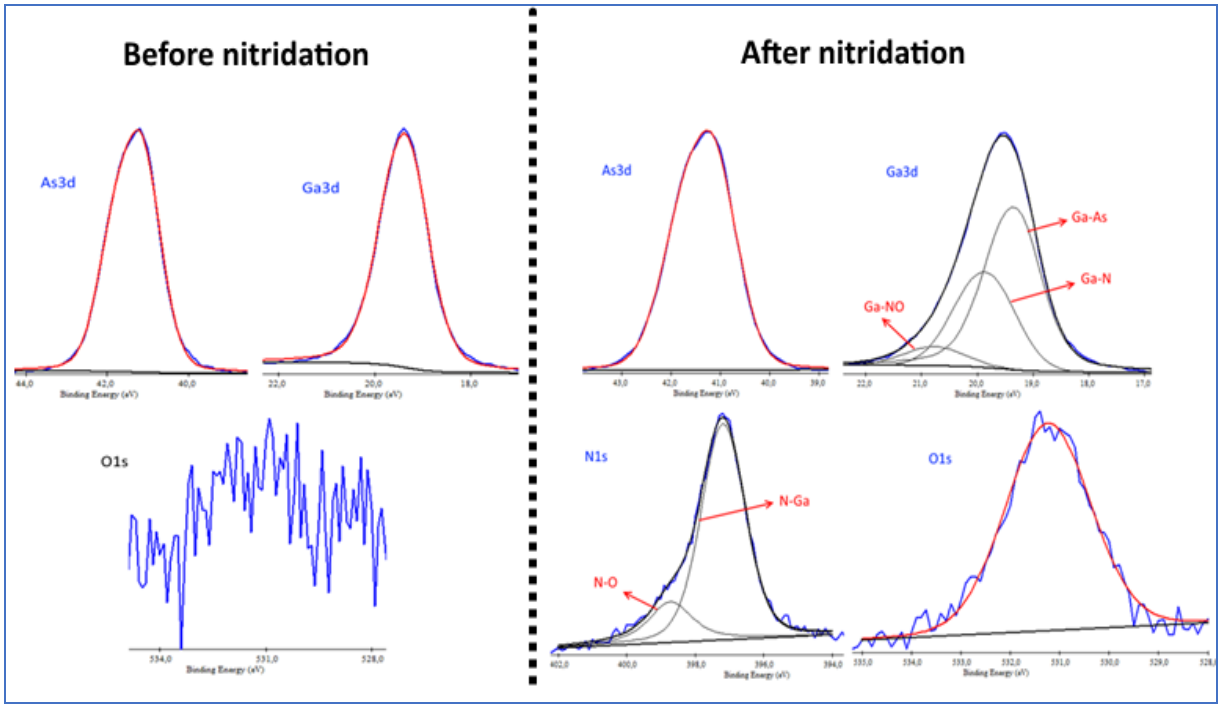


Figure 1. XPS spectra before and after nitridation (Kacha, 2021)

Before nitridation, the O 1s signal at around 531 eV was very weak and noisy, indicating a negligible oxygen contribution on the surface. After nitridation, the As 3d peak at 41 eV retained both its energy position and full width at half maximum (FWHM), suggesting that it originates solely from the As–Ga bonding environment of the GaAs substrate. This observation confirms that arsenic is not incorporated into the thin GaN overlayer. In contrast, the Ga 3d peak at approximately 19 eV exhibited a noticeable broadening after nitridation, consistent with the coexistence of multiple chemical environments. Deconvolution of this peak revealed three components associated with Ga–As, Ga–N, and Ga–NO bonds, as illustrated in Figure 1. A new N 1s signal emerged near 397 eV, composed of two distinct contributions corresponding to N–Ga and N–O bonds. The appearance of Ga–NO and N–O components is further supported by the enhanced O 1s peak intensity at 531 eV following nitridation. Based on the relative XPS peak intensities and the theoretical model proposed by Mehdi (2018), the estimated GaN layer thickness and the associated oxygen content were determined and are reported in Table 2.

Table 2. Estimations of GaN created layers thickness and oxygen rate

δ-GaN	Oxygen rate
17 ± 2 Å	16 ± 1 %

The oxygen content detected after nitridation is within an acceptable range and is attributed to unavoidable surface contamination that typically occurs during the nitridation process. For this structure with a 17 Å GaN layer, the nitride film is extremely thin, allowing it to be regarded as an interfacial layer between the gold contact and the GaAs substrate. This ultrathin GaN interlayer plays a crucial role in influencing the structural and electronic properties of the resulting Schottky barrier diode (SBD).

Electrical Measurements

Figure 2 presents the current–voltage (I–V) characteristics of the Au/GaN/GaAs structure, measured in the dark and at room temperature, using both linear and semi-logarithmic scales.

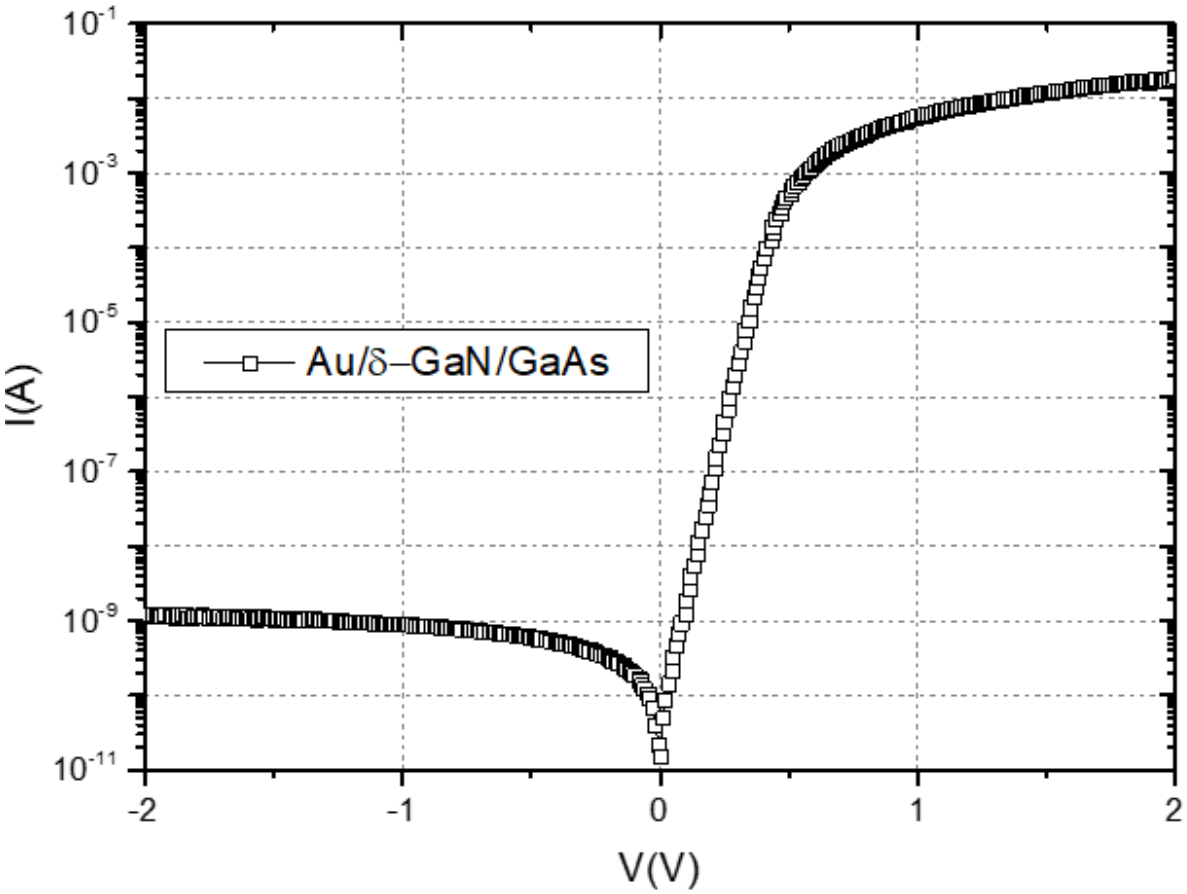


Figure 2. Current-voltage curve.

The thermionic emission current of a real Schottky diode is given by the relation (Kacha, 2021):

$$I_{th} = I_s\left(e^{\frac{q(V-R_s I_{th})}{nkT}}\right) \quad \text{for } V > 3kT/q \tag{1}$$

Where V is the applied voltage drop across the semiconductor surface depletion layer, q is the electron charge, k the Boltzmann constant, n the ideality factor, R_s the series resistance and I_s, the saturation current. The saturation current can be defined by Kacha (2021):

$$I_s = A^* T^2 e^{\frac{-q\phi_{Bno}}{kT}} \tag{2}$$

Where T, φ_{Bno}, A^*, are the temperature in Kelvin, the barrier height at zero bias and the effective Richardson constant which is equal to 8.78 $Acm^{-2}K^{-2}$ respectively (Kacha, 2021).

As shown in Figure 1, the Au/GaN/GaAs structure with a 17 Å GaN interlayer exhibits a significantly lower reverse current indicating a reduction in leakage current after the introduction of the GaN layer. The rectifying ratio (RR), defined as the ratio of the forward current to the reverse current Kacha (2021), was used to evaluate the diode's rectifying performance. The rectification ratio can be estimated using:

$$RR = \frac{I_{Forward}}{I_{reverse}} \tag{3}$$

The rectifying ratio curve of the studied structure is shown in Figure 3.

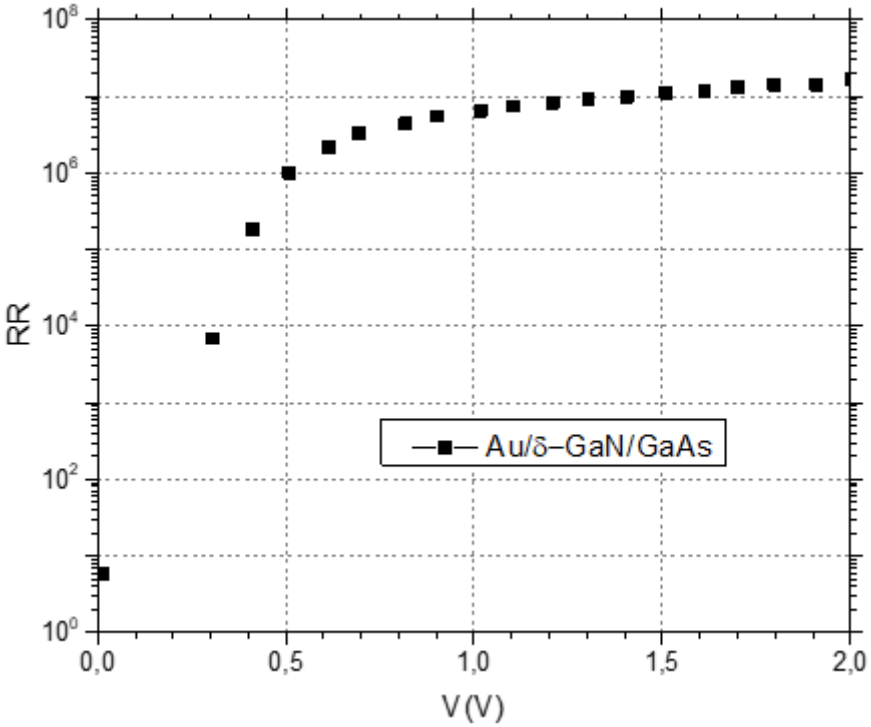


Figure 3. The rectifying ratio curve of the studied structure

The RR parameter of the studied structure show a good rectifier behavior. Indeed, the RR parameter is about 10^7 at 2V bias voltage. The resistance of the junction JR is another parameter that can represent the electrical quality of the studied structure. This parameter is calculated using Ohm's law (Kacha, 2021):

$$JR = \frac{V}{I} \tag{4}$$

JR is plotted in Figure 4.

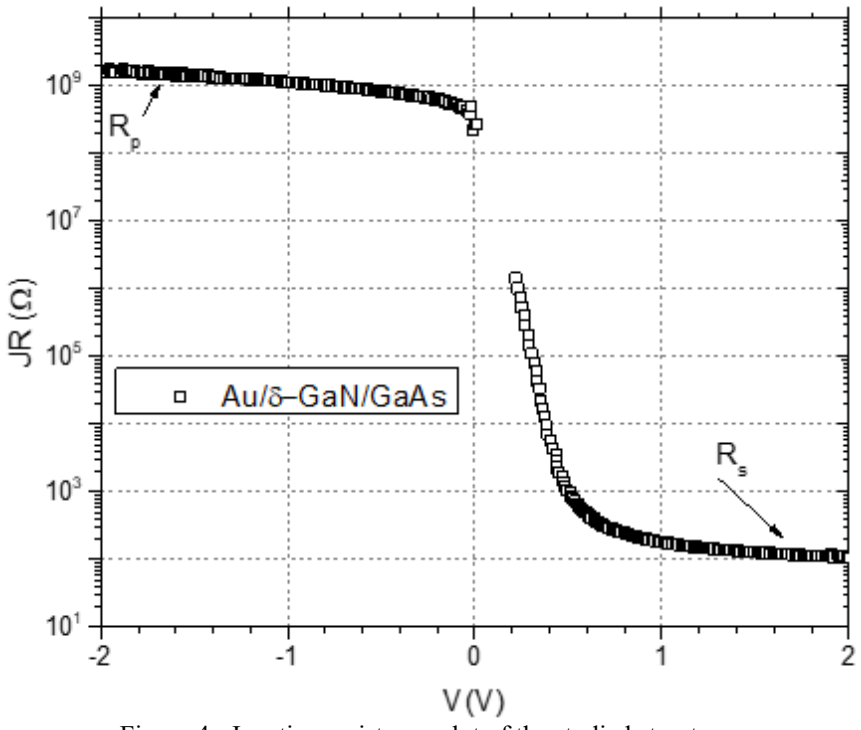


Figure 4. Junction resistance plot of the studied structures

For positive bias values, the JR plot provides an estimate of the series resistance, while for negative bias values it reflects the parallel resistance. As shown in Figure 4, the studied structure exhibits a much higher parallel resistance of approximately 10^9 Ω. This significant increase explains the lower reverse current observed in the I–V characteristics (Figure 1), as the leakage current in a Schottky barrier diode is inversely proportional to the parallel resistance (Kacha, 2021). To extract the main electrical parameters, including the ideality factor (n), the saturation current (Is), the zero-bias barrier height (ϕbn0), and the series resistance (Rs), the ln(I)–V characteristic was plotted, as shown in Figure 5.

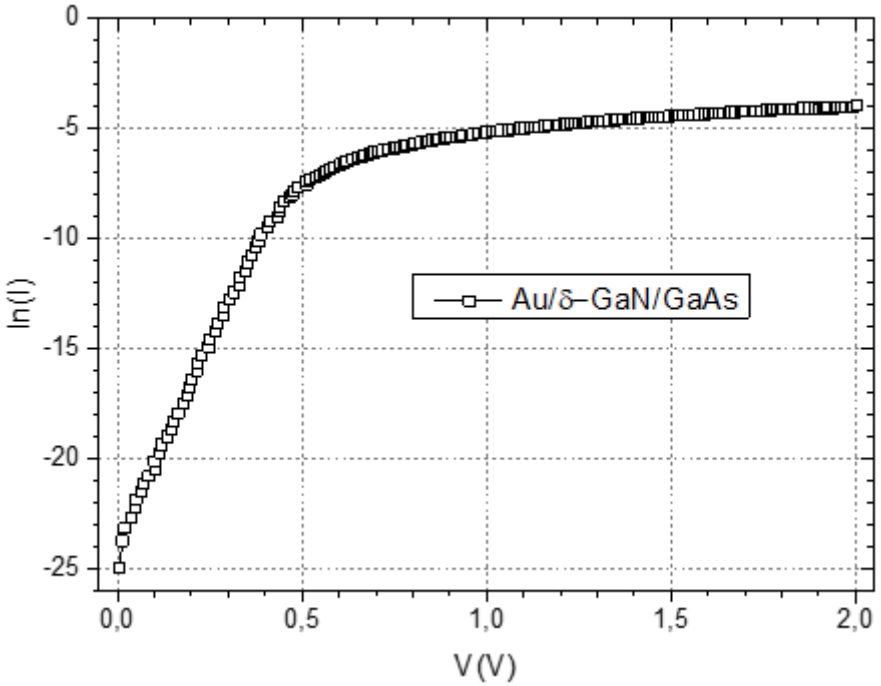


Figure 5. Variation of ln(I) as a function of bias voltage V.

The procedure used to extract the electrical parameters from the ln(I)–V characteristics has been described in detail in our previous work (Kacha, 2021). The parameters determined from ln(I)–V curve are summarized in Table 3.

Table 3. Electrical parameters obtained from ln(I)=f(V)

	n	I_s (A)	ϕ_{Bn0} (V)	R_s (Ω)
Au/GaN/GaAs	1.15	1.07×10^{-10}	0.81	85.34

The electrical parameters extracted from the current–voltage measurements (Table 3) indicate a notable improvement following the nitridation process. Compared to conventional Au/GaAs electrical parameters (Helal (2021)), the ideality factor decreased by approximately 7%, the saturation current by about 31%, and the series resistance by nearly 5%. Meanwhile, the barrier height increased by around 2.5%. These enhancements suggest an improvement in the quality of the metal–semiconductor interface of the studied structure after nitridation (Benamara (2022). To further analyze the interfacial behavior, the interface state density (Nss) was evaluated using the relation given in (Kacha, 2021):

$$n = 1 + \frac{q^2 \delta N_{ss}}{\varepsilon_i} \tag{5}$$

Where ε_i and δ are the permittivity and the thickness of the interfacial layer respectively. In Figure 6, we have plotted the distribution of the interface state density in the band gap using (Kacha (2021)):

$$E_c - E_{ss} = q\left(\phi_{Bno} - V\right) \tag{6}$$

Where E_{ss} is the interface state energy compared to the conduction band edge E_c at the surface.

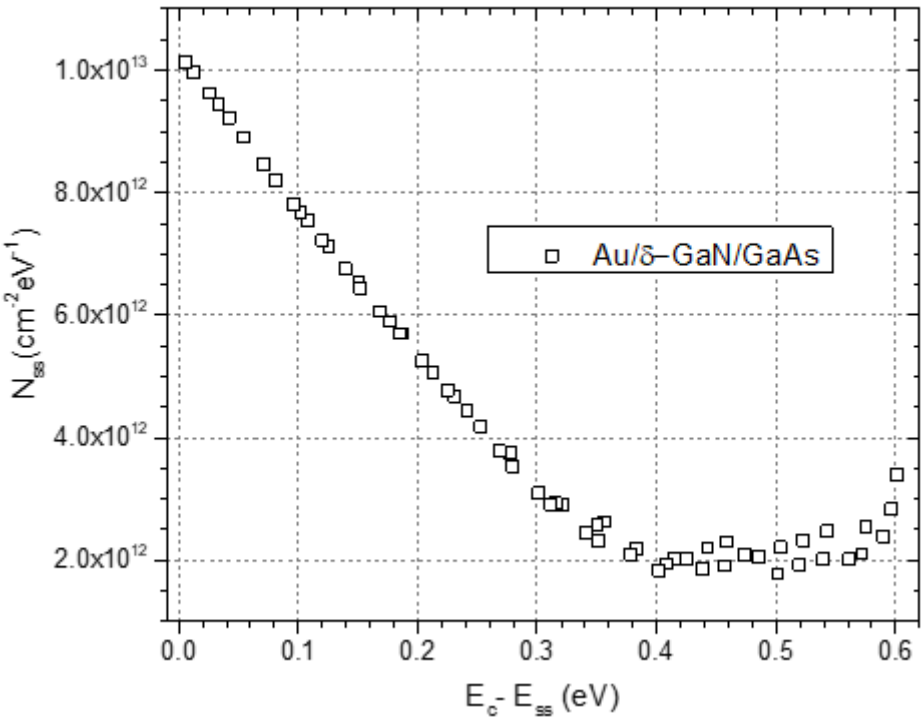


Figure 6. The distribution of the interface state density in the band gap

The calculated values of Nss are considerably low. Following 120 minutes of nitridation, the interface state density was reduced to about 2.0×10^{12} cm^{-2} eV^{-1} at at (Ec − 0.5) eV for the studied structure. This reduction is attributed to a structural reorganization at the metal–semiconductor interface induced by the formation of the thin GaN interfacial layer (Kacha, 2021). To further confirm the improvement of the interface quality after nitridation, the leakage current responsible for the reverse current was estimated. The thermionic emission current (Eq. 1) was simulated using the experimentally determined parameters n, Is, and Rs, and the simulated result was compared with the experimental data, as shown in Figure 7.

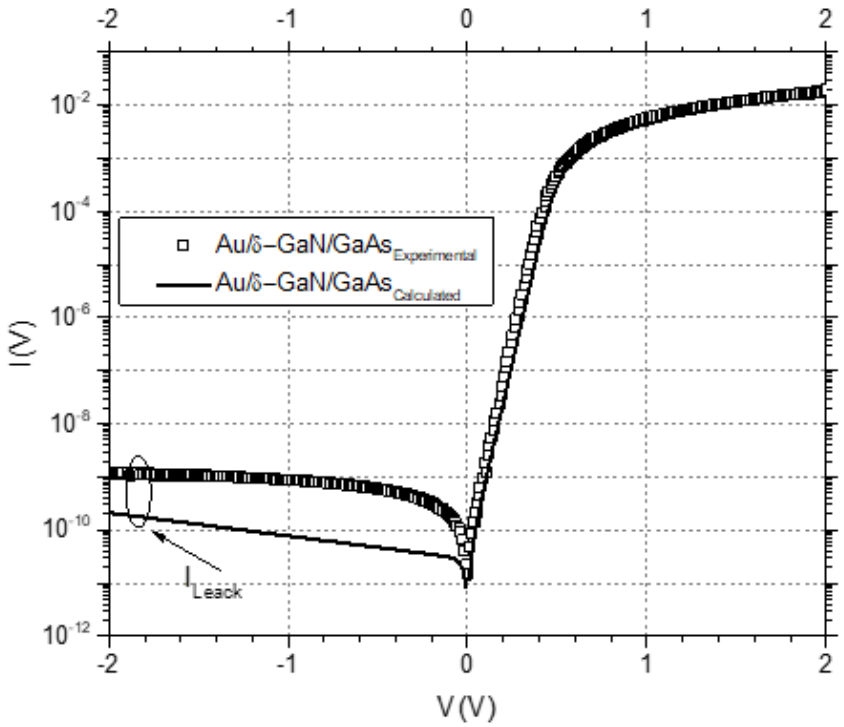


Figure 7. Estimation of the leakage current

The plots in Figure 7 reveal a noticeable deviation between the simulated and experimental I–V curves under reverse bias, with the experimental currents being higher. This discrepancy corresponds to the leakage current (Kacha (2021)). After the nitridation process, a significant reduction in leakage current was observed. At a reverse bias of −2 V, the leakage current is estimated to about 9.36×10^{-10} A in the studied structure, confirming the beneficial effect of the GaN interlayer on reducing reverse leakage.

Conclusion

In this work, the fabrication and characterization of the studied Au/GaN/GaAs Schottky barrier diode confirmed that the in-situ nitridation process significantly improves the structural and electrical properties of the metal–semiconductor interface. XPS analysis verified the successful formation of an ultrathin GaN layer of about 17 ± 2 Å with an oxygen content of approximately 16%, confirming the controlled nitridation and stability of the interface. Electrical characterization revealed clear improvements in the diode's performance after nitridation: the ideality factor decreased to 1.15 (a reduction of nearly 7%), the saturation current dropped to 1.07×10^{-10} A (about 31% lower than in non-nitridated structures), and the series resistance was reduced to 85.34 Ω (around 5% improvement). Simultaneously, the barrier height increased to 0.81 eV, and the parallel resistance rose to nearly 10^9 Ω, indicating enhanced rectifying behavior.

The rectification ratio reached about 10^7 at 2 V, confirming excellent diode performance. The interface state density (Nss) was also significantly reduced to around 2.0×10^{12} cm^{-2} eV^{-1} at (Ec – 0.5 eV), demonstrating improved surface passivation. Furthermore, the leakage current at −2 V decreased from to 9.36×10^{-10} A after nitridation, highlighting the effectiveness of the GaN interlayer in reducing reverse leakage. Overall, these results demonstrate that the controlled nitridation process is a reliable and efficient technique for enhancing the electrical quality of GaAs-based Schottky barrier diodes, paving the way for their optimized use in nano- and optoelectronic device applications.

Scientific Ethics Declaration

* The authors declare that the scientific ethical and legal responsibility of this article published in EPSTEM journal belongs to the authors.

Conflict of Interest

* The authors declare that they have no conflicts of interest

Funding

* Not applicable.

Acknowledgements or Notes

* This article was presented as a poster presentation at the International Conference on Technology, Engineering and Science (www.icontes.net) held in Antalya/Türkiye on November 12-15, 2025.

* The preparation of the samples investigated in this study was carried out at the Pascal Institute, Clermont Auvergne University (France). The authors would like to express their sincere gratitude to the members of the Surfaces and Interfaces team and the Sensors team for their support. Special thanks are extended to Christine Robert-Goumet, Guillaume Monier, and Christelle Varenne for their valuable technical and scientific contributions.

References

Aigner, I. (2024). Egyetemes egyetemi kreatívan kritikus tanítás és tanulás. *Pedagógusképzés, 23*(2), 102–107. https://doi.org/10.37205/TEL-hun.2024.2.09

Robertson, J., & Falabretti, B. (2006). Band offsets of high-k gate oxides on III–V semiconductors. *Journal of Applied Physics, 100*(1), 014111.

Jenabi, S., Malekabadi, A., Deslandes, D., Boone, F., & Charlebois, S. A. (2017). Submillimeter wave GaAs Schottky diode application-based study and optimization for 0.1–1.5 THz. *Solid-State Electronics, 134*, 65–73.

Gullu, H. H., Yıldız, D. E., & Yıldırım, M. (2024). Electrical characteristics of Al/AlGaAs/GaAs diode with high-Al concentration at the interface. *Journal of Materials Science: Materials in Electronics, 35*, 189.

Zutter, B. T., Kim, H., Hubbard, W. A., Ren, D., Mecklenburg, M., Huffaker, D., & Regan, B. C. (2021). Mapping charge recombination and the effect of point-defect insertion in GaAs nanowire heterojunctions. *Physical Review Applied, 16*, 044030.

Sirkeli, V. P., Caragacian, S. I., Boris, Iu. B., & Nika, D. L. (2025). Effect of InAlGaN interlayers on the efficiency of InGaN-based red light-emitting diodes. *Physics of the Solid State, 67*, 655–663.

Sirkeli, V. P. (2024). Effect of substrate polarity on the performance characteristics of InGaN-based green light-emitting diodes. *Semiconductors, 58*, 928–935.

Sirkeli, V. P., Tiginyanu, I. M., & Hartnagel, H. L. (2020). Effect of substrate engineering in III–V nanodevices. In I. Tiginyanu, V. Sontea, & S. Railean (Eds.), *4th International Conference on Nanotechnologies and Biomedical Engineering* (Vol. 77, p. 231). Springer.

Raman, A., Krishna, K. S., Ranjan, R., & Kashyap, N. (2025). Performance enhancement of normally-off AlGaN/GaN HEMT using delta-doped GaN cap layer. *Semiconductors, 59*, 374–381.

Sreelekshmi, P. S., & Jacob, J. (2025). Recessed p-GaN gate MIS-HEMT with AlN interlayer and buried p-GaN layer. *Semiconductors, 59*, 248–256.

Xiao, W., Sun, X., Huang, L., … et al. (2024). Investigation of enhancement-mode AlGaN/GaN MIS-HEMT with recessed gate structure. *Semiconductors, 58*, 637–644.

Egorkin, V. I., & Chukanova, O. B. (2024). Normally off GaN transistor for a complementary pair. *Semiconductors, 58*, 1132–1136.

Liu, Y., Chen, S., Ma, X., … et al. (2024). Gate length influence on the strain of the AlGaN barrier layer under the gate in AlGaN/AlN/GaN HFETs at different temperatures. *Semiconductors, 58*, 645–650.

Ravendra, P., Raman, A., Ranjan, R., & Kashyap, N. (2025). Design, simulation, and comparison of p-GaN-based β-Ga_2O_3 FET on wide bandgap substrates. *Semiconductors, 59*, 328–336.

Hadjouni, A., Kacha, A. H., Benamara, Z., … et al. (2025). Enhancing the efficiency of $In_{0.62}Ga_{0.38}N$ solar cells using an InN back surface field layer: A numerical simulation approach. *Physics of the Solid State, 67*, 443–454.

Sirkeli, V. P., Yılmazoğlu, O., Küppers, F., & Hartnagel, H. L. (2015). Magnetic and luminescent properties of InGaN/GaN light-emitting structures and related nanostructures. *Semiconductor Science and Technology, 30*(6), 065005.

Sirkeli, V. P., Yılmazoğlu, O., Al-Daffaie, S., Oprea, I., Ong, D. S., Küppers, F., & Hartnagel, H. L. (2015). Investigation of p-GaN/AlGaN/GaN light-emitting structures with different barrier designs. *Journal of Nanoelectronics and Optoelectronics, 9*, 811.

Sirkeli, V. P., Yılmazoğlu, O., Al-Daffaie, S., Oprea, I., Ong, D. S., Küppers, F., & Hartnagel, H. L. (2017). Structural and optical characterization of III–V nanostructures for optoelectronic applications. *Journal of Physics D: Applied Physics, 50*, 035108.

Pokatilov, E. P., Nika, D. L., & Balandin, A. A. (2006). Electron transport and phonon interactions in semiconductor nanostructures. *Applied Physics Letters, 89*, 112110.

Khales, H., Kacha, A. H., Akkal, B., … et al. (2025). Effect of the ultra-thin GaN interlayer on the mechanisms of conduction in Au/GaAs Schottky barrier diodes. *Semiconductors, 59*, 551–560.

Kacha, A. H., Anani, M., Akkal, B., Benamara, Z., Monier, G., … & Robert-Goumet, C. (2021). Effect of metallic contacts diffusion on Au/GaAs and Au/GaN/GaAs SBDs electrical quality during their fabrication process. *Journal of Alloys and Compounds, 876*, 159596.

Kacha, A. H., Amroun, M. N., Akkal, B., Benamara, Z., & Belarouci, S. (2021). Effect of the ultra-thin GaN interlayer on the electrical and photoelectrical parameters of Au|GaAs Schottky barrier diodes. *Semiconductors, 55*(Suppl. 1), S54–S61.

Benamara, A. M., Kacha, A. H., Talbi, A., Akkal, B., & Benamara, Z. (2022). Electrical study of Au/GaN/GaAs (100) structures as a function of frequency. *Journal of Nanoelectronics and Physics, 14*(2), 02008.

Kacha, A. H., Akkal, B., Benamara, Z., Robert-Goumet, C., Monier, G., & Gruzza, B. (2016). Study of the surface state density and potential in MIS diode Schottky using the surface photovoltage method. *Molecular Crystals and Liquid Crystals, 627*(1), 66–73.

Helal, H., Benamara, Z., Wederni, M. A., … & Dominguez, M. (2021). Conduction mechanisms in Au/0.8 nm-GaN/n-GaAs Schottky contacts in a wide temperature range. *Materials, 14*, 5909.

Mehdi, H., Monier, G., Hoggan, P. E., Bideux, L., Robert-Goumet, C., & Dubrovskii, V. G. (2018). Combined angle-resolved X-ray photoelectron spectroscopy, density functional theory and kinetic study of nitridation of gallium arsenide. *Applied Surface Science, 427*, 662–670.

Author(s) Information

Arslane Hatem Kacha
Djillali Liabes University of Sidi Bel Abbes
BP89, Sidi Bel Abbes 22000, Algeria
Contact e-mail : *arslane_k@hotmail.com*

Ahmed Hichem Yahi
Djillali Liabes University of Sidi Bel Abbes
BP89, Sidi Bel Abbes 22000, Algeria

Boudali Akkal
Djillali Liabes University of Sidi Bel Abbes
BP89, Sidi Bel Abbes 22000, Algeria

Zineb Benamara
Djillali Liabes University of Sidi Bel Abbes
BP89, Sidi Bel Abbes 22000, Algeria

To cite this article:

Kacha, A.H., Yahi, A.H., Akkal, B., & Benamara, Z. (2025). Fabrication process of nano and optoelectronic devices based on nitrided gaas: XPS analysis and electrical measurements. *The Eurasia Proceedings of Science, Technology, Engineering and Mathematics (EPSTEM), 38,* 881-890.

The Eurasia Proceedings of Science, Technology, Engineering & Mathematics (EPSTEM)
ISSN: 2602-3199

The Eurasia Proceedings of Science, Technology, Engineering and Mathematics (EPSTEM), 2025

Volume 38, Pages 891-898

IConTES 2025: International Conference on Technology, Engineering and Science

A Novel Triple-Band Band-Pass Metamaterial Filter based on Modified Square Split Ring Resonators for Microwave Applications: Design and Analysis

Zoubir Mahdjoub
Djillali Liabes University of Sidi Bel Abbés

Mohammed Berka
Mustapha Stambouli University of Mascara

Abstract: In response to the growing demand for miniaturized electronic devices, this work presents a novel triple-band band-pass filter (TBBPF) design utilizing metamaterial design. The proposed filter comprises three split-ring resonators (SRRs) featuring identical modified square shapes but different dimensions, all printed on Rogers RT/Duroid 6002 substrates with a relative electrical permittivity of 2.94 and thickness of 1.52 mm. The compact filter design, occupying just 10×10 mm², is fed by two 5.25 mm microstrip lines matched at 50 Ω. Our simulation outcomes demonstrate exceptional performance across C-, X-, and Ku-bands, with distinct resonance frequencies at 6.06 GHz, 10.71 GHz, and 13.64 GHz, respectively. The filter exhibits remarkable electrical characteristics, including minimal insertion losses (IL <1.5 dB), optimal bandwidth distribution, and notably compact dimensions. These characteristics, combined with the filter's multi-band capabilities, make it particularly suitable for diverse applications in wireless communication systems, imaging technologies, and biomedical detection devices. The innovative design approach presented here addresses the contemporary challenges in RF/microwave system miniaturization while maintaining high-performance standards, offering a versatile solution for modern electronic systems requiring multi-band functionality.

Keywords: Bandwidth, Insertion losses, Metamaterial resonator, Triple-band, Versatile applications

Introduction

The rapid evolution of wireless communication systems has led to an unprecedented demand for compact, multi-functional microwave components, particularly in filtering technologies. Microwave filter design has undergone significant advancements in recent decades, driven by the increasing need for devices that can operate efficiently across multiple frequency bands while maintaining a minimal footprint. The selection of appropriate design methodologies and materials has become crucial in meeting these demanding specifications. Multi-band microwave filters have emerged as essential components in various applications, from sophisticated RADAR systems requiring precise signal processing capabilities (Han, 2023; Malki, 2023) to advanced sensor networks demanding high sensitivity and selectivity (Alnahwi, 2021). Their implementation spans diverse fields, including medical imaging (Tshibangu-Mbuebue, 2021; Liu, 2022), satellite communications (Akyildiz, 2019; Chhasatia, 2023; Nasser, 2023), and modern wireless devices operating across multiple frequency bands (Berka, 2018).

Recent years have witnessed significant advancements in multiband filter design, particularly in metamaterial-based approaches. (Berka et al., 2021) demonstrated a dual-band filter using coupled resonators achieving insertion losses below 1.2 dB at both 5.02 and 8.92 GHz bands. A notable breakthrough came from Choudhary and colleagues (Choudhary, 2018), who developed a modified CSRR structure at coplanar waveguide (CPW) ground plane investigated for designing of a dual-band bandpass filter with a minimum insertion loss of 0.5 and

- This is an Open Access article distributed under the terms of the Creative Commons Attribution-Noncommercial 4.0 Unported License, permitting all non-commercial use, distribution, and reproduction in any medium, provided the original work is properly cited.

- Selection and peer-review under responsibility of the Organizing Committee of the Conference

© 2025 Published by ISRES Publishing: www.isres.org

0.4 dB at 1.8 and 3.2 GHz, respectively. In Rouabhi (2022) an innovative approach using tapered split-ring resonators (TSRRs) was proposed for dual-bands while maintaining a compact footprint of 39.6×27.7 mm². The implementation of defected ground structures (DGS) by (Vali, 2024) resulted in enhanced stopband characteristics, albeit at the cost of increased circuit size. More recently, (Berka et al., 2024) demonstrated a compact dual-band filter using SIW structure, enabling dynamic frequency tuning across the C- and X- bands. Berka et al. (2022) advanced the field further with their metamaterial-inspired triple-band design based on (E-Z)-shaped resonators, achieving insertion losses below 1 dB across all three bands, though their structure required complex fabrication processes. Other works about metamaterial-based filters are reported in (Tan, 2024; Baghdad Bey, 2024; Li, 2022) for THz applications.

Drawing upon these developments and addressing current limitations, this work presents a novel triple-band band-pass microwave filter incorporating three modified square-shaped metamaterial resonators. The primary objective is to develop and analyze this structure that addresses the growing demand for miniaturized, high-performance RF components. Our design aims to achieve simultaneous operation across C-, X-, and Ku-bands while maintaining exceptional electrical characteristics and minimal footprint.

Specifically, we focus on implementing three modified square-shaped split-ring resonators (SRRs) with distinct dimensions, strategically designed to resonate at 5.28 GHz, 9.14 GHz, and 14.32 GHz. The proposed filter targets insertion losses below 0.5 dB across all three bands, a significant improvement over existing designs. A key goal is to achieve these performance metrics while maintaining an ultra-compact form factor of just 10×10 mm², utilizing Rogers RT/Duroid 6002 substrate material. The design methodology emphasizes optimizing the coupling mechanism between resonators through carefully positioned 50 Ω matched microstrip feed lines measuring 5.25 mm. This research seeks to demonstrate that superior multi-band performance can be achieved without compromising device miniaturization, making it particularly suitable for emerging wireless communication systems, advanced imaging applications, and next-generation biomedical detection devices.

Design and Materials

Unit Cell Design

The split ring metamaterial resonator is a microwave structure with a magnetic activity that has unusual physical characteristics. The first proposed SRR is the circular-shaped resonator formed by two internal and external rings (Marquez, 2002). For our unit cell, we have chosen a modified square shape with sixslots for the two rings and one arm. The chosen dimensions for our cell are in the millimeter scale to have frequency responses in the microwave bands. The proposed metamaterial resonator of the basic cell is shown in Figure 1.

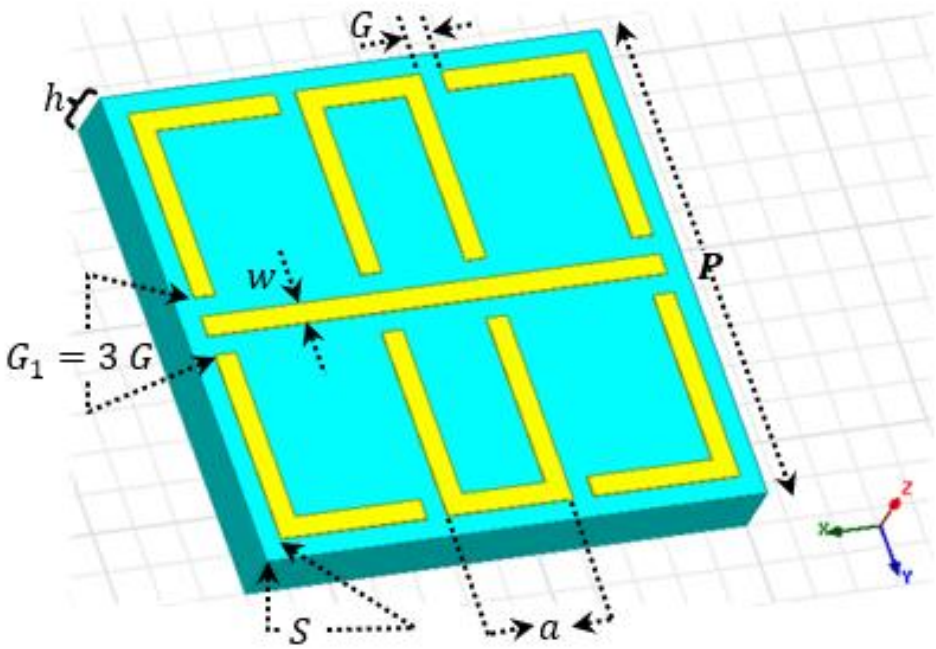


Figure 1. Geometric layout of the proposed metamaterial unit cell.

The unit cell dimensions are summarized in Table 1.

Table 1. Various parameters of the unit cell

Parameter	Value (mm)	Parameter	Value (mm)
a	3	G_1	1.5
G	0.5	S	0.5
w	0.5	P	12

Filter Configuration

The proposed TBBPF is formed by two metamaterial resonators previously studied for the unit cell. The used resonators are identical with the same dimensions mentioned in Table 1. Our TBBPF is fed by two microstrip lines of length $L_f = L_{eff_1} + L_{eff_2} + L_{eff_3} = 24.5$ mm each; these lines are coupled to the proposed resonators by a spacing e =0.5 mm. All the components making up the filter are printed on the upper face of the chosen substrate. The proposed filter which has the surface formed by the two sides (X, Y) is shown in Figure 2.

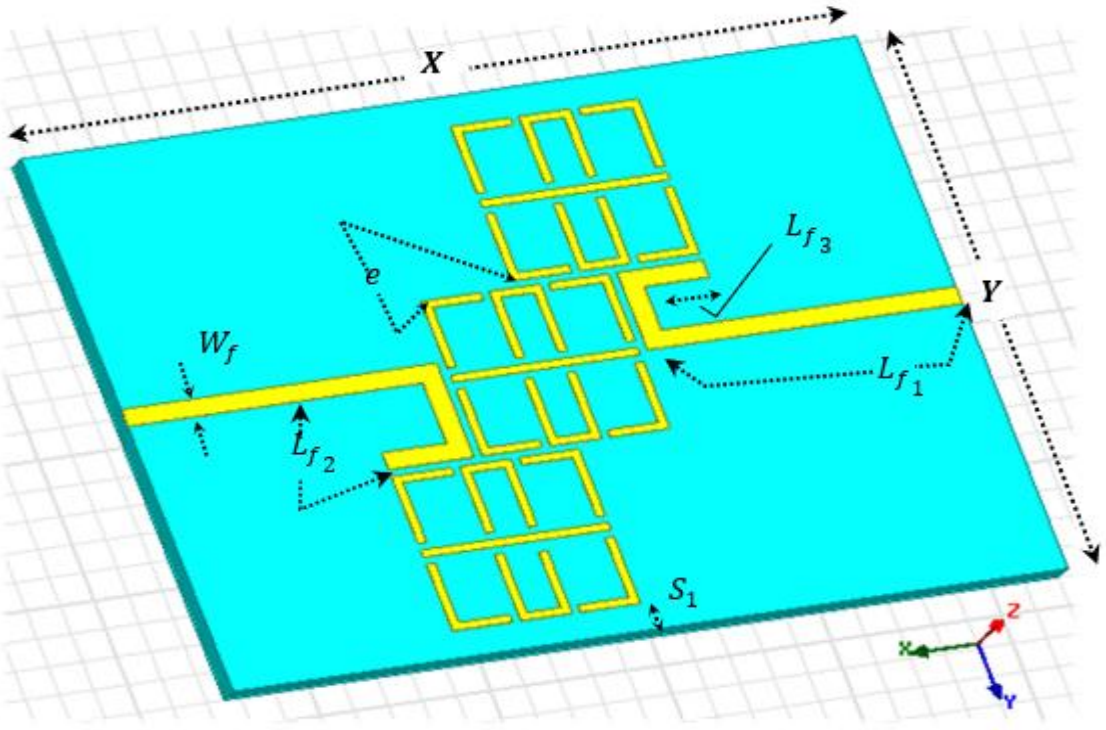


Figure 2. Proposed TBBPF with the three SRRs.

The dimensions of the elements constituting the filter are summarized in Table 2.For these values, the filter has the dimensions (X =41 mm, Y = 37 mm).

Table 2. Various parameters of the proposed filter

Parameter	Value (mm)	Parameter	Value (mm)
L_{eff_1}	14.5	S_1	2
L_{eff_2}	5.5	S_2	6.4
L_{eff_3}	4.5	e	0.5

Results and Discussion

Functional Behaviour of the Proposed Unit Cell

Leave On the substrate of RT/Duroid 6002 of physical characteristics (ε_r =2.94 and $tg\delta$ = 0.0012) and thickness of 1.52 mm, the slotted square patch is printed for both inner and outer rings with a thickness (t = 0.035 mm). Figure 3 represents the frequency response of the proposed unit cell for a period of 12 mm.

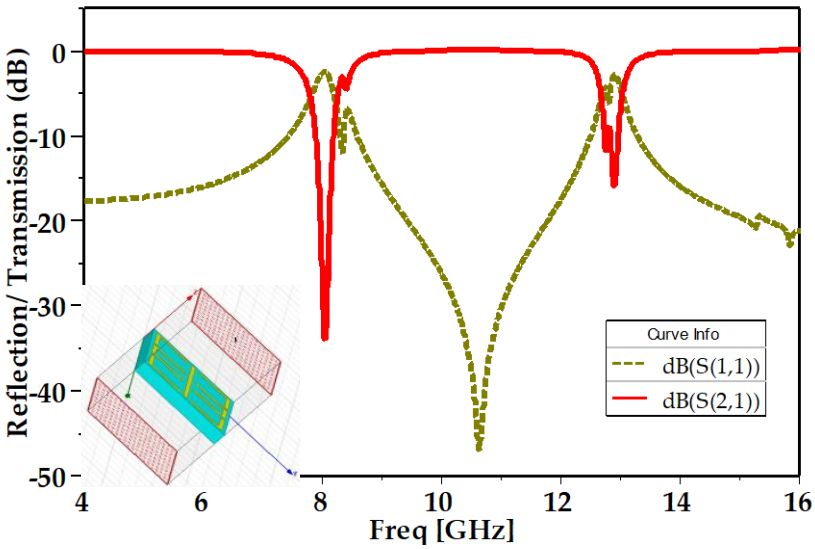


Figure 3. Frequency feature of the proposed SRR unit cell.

In Figure 3 we observe the reflection and transmission of the proposed unit cell which represents a stop-band behavior at the resonances of 8.43 and 12.92 GHz for the transmissions of −33.51 and −15.69 dB, respectively. Depending on the characteristics simulated previously, we can obtain the effective permeability of the proposed resonator. The following relationship can determine this permeability (Hannan, 2020).

$$\mu_{eff}(f) = \frac{2}{jkh}\frac{1-v_1}{1+v_1} \tag{1}$$

With,

$$v_1 = S_{21} - S_{11} \tag{2}$$

Where S_{11} and S_{21} represent the reflection and transmission coefficients, respectively and$k$ is the ratio of frequency ω to the speed of lightc_0. It comes,

$$\mu_{eff}(f) = \mu'_{eff} - j\mu''_{eff} = \frac{2}{jkh}\frac{1-S_{21}(f)+S_{11}(f)}{\left(1+S_{21}(f)-S_{11}(f)\right)} \tag{3}$$

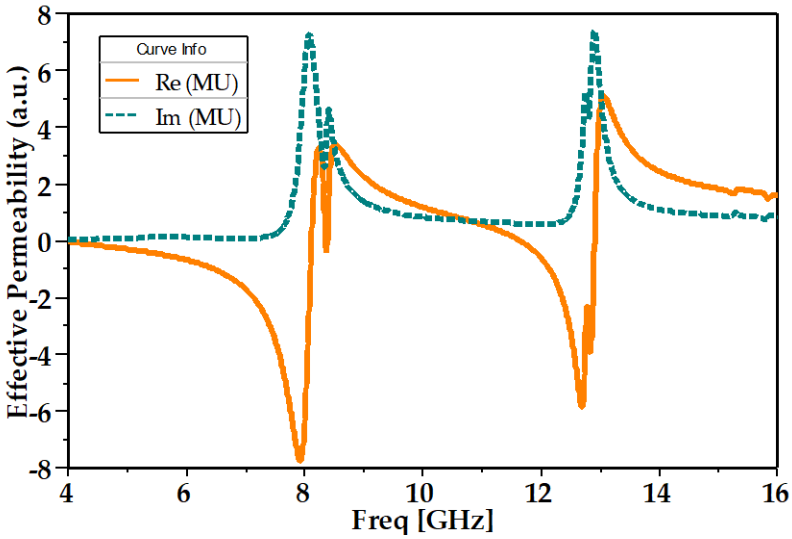


Figure 4. Characteristics of effective permeability.

The frequency characteristics of the effective permeability of the unit cell are shown in Figure 4.We observe two different characteristics around the two resonances (at 8.43 and 12.92 GHz) of the unit cell whose imaginary part is positive over the entire frequency range. Around the first resonance, it is remarkable that the real part of the permeability changes its sign from −7.71 to 3.14. Around the second resonance of the base cell, the real part of the permeability changes its sign from −13.07 to 5.05.

TBBPF Response

Upon the necessary simulations, the spectral response of the filter is represented in Figure5.

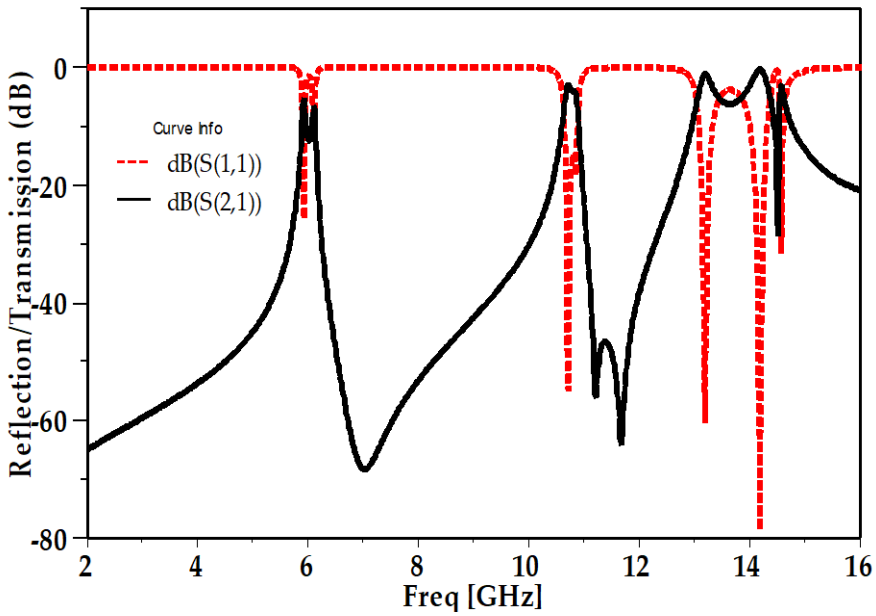
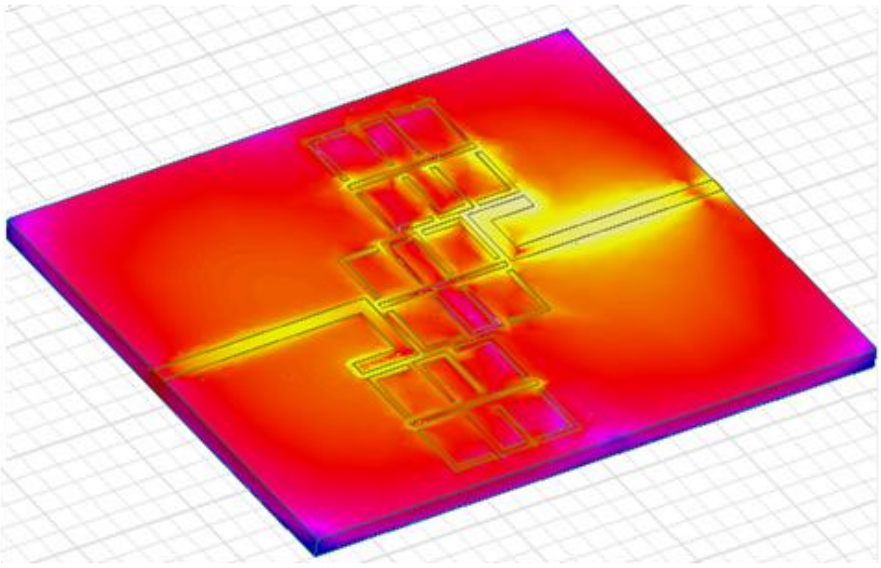
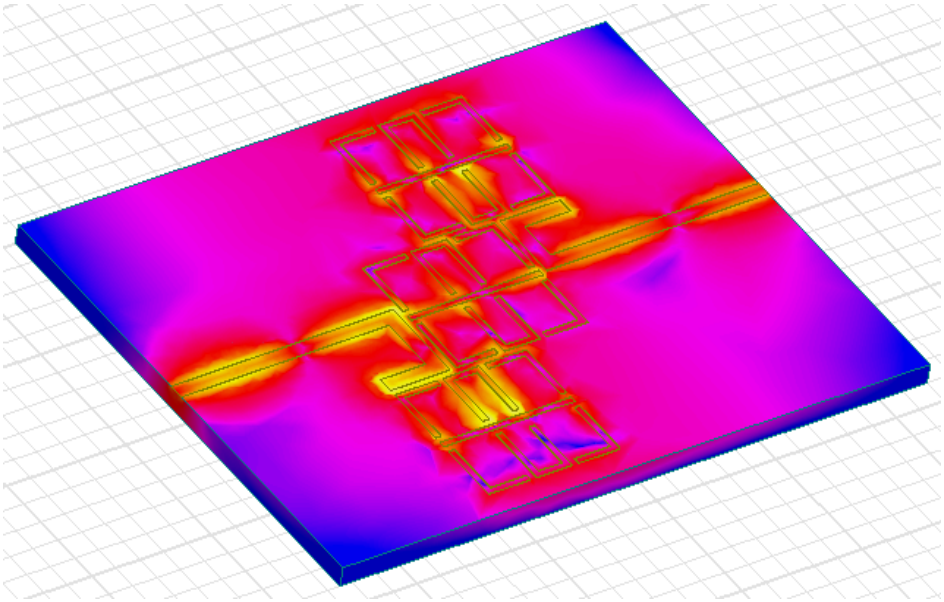


Figure 5. Reflection and transmission of the proposed filter.

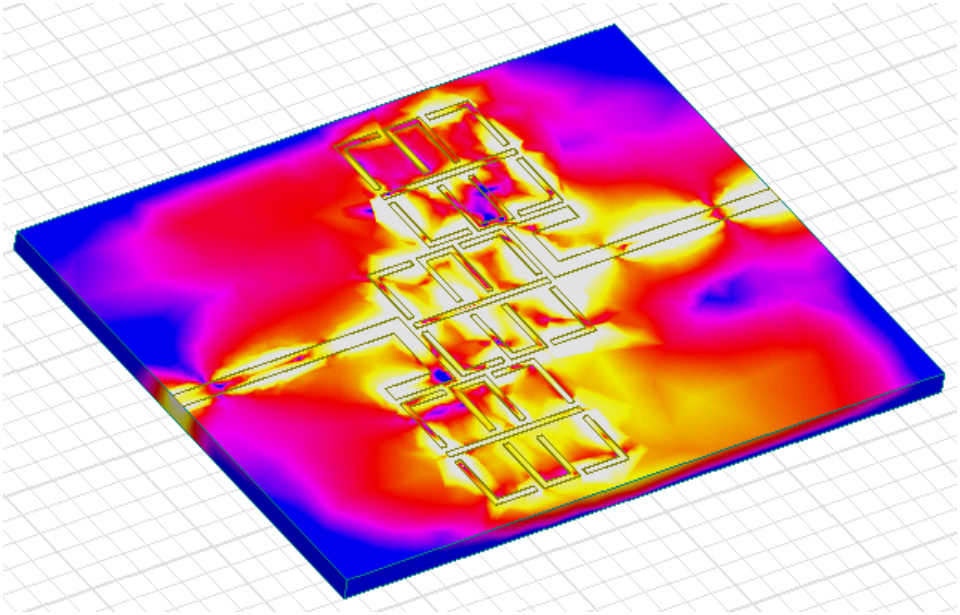
Figure 5 represents the reflection and transmission coefficients of the filter for the proposed configuration. This figure shows that the filter has a band-pass behavior for three different bands. The three resonances are obtained at 6.06, 10.71 and 13.64 GHz, respectively. Moreover, the proposed TBBPF represents a good adaptation for weak insertion losses (*IL* <1.5 dB). Also, the filter bandwidths are estimated at 280, 416 and 725 MHz, respectively. To better explain the behavior of the filter, we represent the distribution of the electric field on the structure for the three resonances.



(a)



(b)



(c)

Figure 6. Electric field distribution at (a) 6.06 GHz, (b) 10.71 and (c) 13.64 GHz.

Figure 6 shows the distribution of the electric field on the filter at 6.06, 10.71 and 13.64 GHz, respectively. We note that the electric field is distributed over the feed lines and the two metamaterial resonators SRRs, which justify the transfer of electromagnetic power at the resonance thus indicated.

Conclusion

This work has successfully demonstrated the design and analysis of a novel triple-band bandpass filter based on metamaterial resonators, achieving exceptional performance across C-, X-, and Ku-bands. The proposed filter, utilizing three modified square-shaped split-ring resonators (SRRs), exhibited distinct resonance frequencies at 6.06 GHz, 10.71 GHz, and 13.64 GHz with remarkably low insertion losses below 1.5 dB. The filter's design, implemented on Rogers RT/Duroid 6002 substrate, demonstrated optimal bandwidth distribution of 280 MHz, 416 MHz, and 725 MHz for the respective bands. The electric field distribution analysis confirmed efficient electromagnetic power transfer at all three resonance frequencies, validating the filter's operational effectiveness. The compact dimensions of the filter, combined with its multi-band capabilities and superior electrical characteristics, make it particularly well-suited for various applications in modern wireless communication

systems, imaging technologies, and biomedical detection devices. These results represent a significant advancement in RF/microwave filter design, successfully addressing the growing demand for miniaturized, high-performance components in contemporary electronic systems requiring multi-band functionality.

Scientific Ethics Declaration

* The authors declare that the scientific ethical and legal responsibility of this article published in EPSTEM journal belongs to the authors.

Conflict of Interest

* The authors declare that they have no conflicts of interest

Funding

* This work was supported by the Algerian Ministry of Higher Education and Scientific Research and the General Directorate of Scientific Research and Technological Development (DGRSDT) via funding through the PRFU under Project No. A25N01UN220120200001.

Acknowledgements or Notes

* This article was presented as a poster presentation at the International Conference on Technology, Engineering and Science (www.icontes.net) held in Antalya/Türkiye on November 12-15, 2025.

References

Akyildiz, I. F., Jornet, J. M., & Nie, S. (2019). A new CubeSat design with reconfigurable multi-band radios for dynamic spectrum satellite communication networks. *Ad Hoc Networks, 86*, 166–178.

Alnahwi, F. M., Alharbi, A. G., … & Alqahtani, A. M. (2021). A low-cost microwave filter with improved passband and stopband characteristics using stub-loaded multiple-mode resonator for 5G mid-band applications. *Electronics, 10*(4), 450.

Baghdad Bey, A., Berka, M., Afif, B., Bendaoudi, A., & Mahdjoub, Z. (2024). Easy-to-design wide stop-band multilayer metamaterial filter based on symmetrical modified circular resonators for terahertz communication applications and electromagnetic interference shielding. *Journal of Magnetism and Magnetic Materials, 607*, 172418.

Berka, M., Azzeddine, H. A., … & Bendaoudi, A., 2021). Dual-band bandpass filter based on electromagnetic coupling of twin square metamaterial resonators (SRRs) and complementary resonator (CSRR) for wireless communications. *Journal of Electronic Materials, 50*, 4887–4895.

Berka, M., Fellah, B., Das, S., Islam, T., Altameem, T., Mahdjoub, Z., & El-Shafai, W. (2024). A novel modified complementary metamaterial resonator-based dual-band bandpass quasi-elliptic filter using half-mode SIW cavity with wide stopband rejection for wireless communication applications. *AEÜ – International Journal of Electronics and Communications, 185*, 155461.

Berka, M., Bendaoudi, A., Afif, B., et al. (2022). Designing of tri-band bandpass microwave filter based on (E–Z) intercoupled tapered metamaterial resonators for C- and X-band applications. *Applied Physics A, 128*, 1112.

Berka, M., Mahdjoub, Z., & Hebali, M. (2018). New design of dual-band bandpass microwave filter based on electromagnetic effect of metamaterial resonators. *Microwave and Optical Technology Letters, 60*(4), 1041–1047.

Chhasatia, N. J., Chaudhari, J. P., & Patel, A. V. (2023). Highly selective ridge gap waveguide-based filters for multi-band satellite applications. *Progress in Electromagnetics Research M, 118*, 105–116.

Choudhary, D., & Chaudhary, R. (2018). Compact multiband microwave bandpass filter using metamaterial resonators. *AEÜ – International Journal of Electronics and Communications, 89*, 110–117.

Han, X., Chao, M., Su, X., Wang, W., et al. (2023). Multiband signal receiver using an optical bandpass filter integrated with a photodetector on a chip. *Micromachines, 14*, 331.

Hannan, S., Islam, M. T., Almutairi, A. F., et al. (2020). Wide bandwidth angle- and polarization-insensitive symmetric metamaterial absorber for X- and Ku-band applications. *Scientific Reports, 10*, 10338.

Li, H., Zhang, Y.,…& Wang, J. (2022). Design and characterization of wideband terahertz metamaterial stop-band filter. *Micromachines, 13*(7), 1034. h

Liu, L., Peng, D., Fu, S., Wang, Y., & Qin, Y. (2022). Multi-band microwave signal generation based on photonic sampling with a flexible ultra-short pulse source. *Optics Express, 30*(18), 32151–32161.

Malki, M., Yang, L., & Gómez-García, R. (2023). Combined signal interference/split-type microwave multi-band bandpass filters. *IET Microwaves, Antennas & Propagation, 17*(7), 583–593.

Marqués, R., Medina, F., & Rafii-El-Idrissi, R. (2002). Role of bianisotropy in negative permeability and left-handed metamaterials. *Physical Review B, 65*, 144440.

Nasser, M., Çelik, A. R., & Helhel, S. (2023). SIW–DGS bandpass filter design for C-band satellite communications. *Sādhanā, 48*, 55.

Rouabhi, A. Y., Berka, M., Bendaoudi, A., & Mahdjoub, Z. (2022). Investigation of dual-band bandpass filter inspired by a pair of square coupled interlinked asymmetric tapered metamaterial resonators for X-band microwave applications. *Bulletin of Materials Science, 45*, 118.

Tan, L., Wang, D., & Xu, K. D. (2024). Terahertz metamaterials for spectrum modulation: Structural design, materials, and applications. *Materials Today Physics, 24*, 113217.

Tshibangu-Mbuebue, B., Laguna, R. R., Lee, M. W. (2021). Numerical study of a reconfigurable multiband microwave photonic filter using a tunable Fabry–Perot filter. *Electronics, 10*, 1473.

Vali, S. S., & Rao, K. S. (2024). Design of wide stopband low-pass filter using defected ground structure. *Microsystem Technologies, 30*, 1–8.

Author(s) Information

Zoubir Mahdjoub
Djillali Liabes University of Sidi Bel Abbés
22000, Sidi Bel Abbés. Algeria
Contact e-mail: *zoubir.mahdjoub@univ-sba.dz*

Mohammed Berka
Mustapha Stambouli University of Mascara
Mamounia, 29000, Mascara. Algeria

To cite this article:

Madjoub, Z., & Berka, M. (2025). A novel triple- band band-pass metamaterial filter based on modified square split ring resonators for microwave applications: Design and analysis. *The Eurasia Proceedings of Science, Technology, Engineering and Mathematics (EPSTEM), 38,* 881-898.

The Eurasia Proceedings of Science, Technology, Engineering & Mathematics (EPSTEM)
ISSN: 2602-3199

The Eurasia Proceedings of Science, Technology, Engineering and Mathematics (EPSTEM), 2025

Volume 38, Pages 899-904

IConTES 2025: International Conference on Technology, Engineering and Science

Analysis of the Aerodynamic Characteristics of Wing Profiles

Brahim Rostane
Abou Bekr Belkaid University

Abstract: Aerodynamics is a fundamental field that studies the laws governing fluid motion, particularly air, around solid objects. Its critical applications span multiple industrial and scientific sectors - from optimizing performance in aircraft, automobiles and wind turbines to designing energy-efficient buildings. The objective of this work is to compare the aerodynamic performance of three wing profiles using a numerical simulation solving the Reynolds-Averaged Navier-Stokes (RANS) equations. Turbulence is modeled with the SST k-ω model, and computations are performed in two dimensions for an incompressible fluid under steady-state conditions. Pressure and velocity fields around the profiles were evaluated for different angles of attack and different velocities. Similarly, key parameters characterizing the aerodynamic performance of the profiles such as lift and drag coefficientswere determined. The results show that theNACA 23012 profile performs better than the NACA 0012 profile at angles of attack between 0° and 15° due to its more streamlined shape, while the NACA 63-430 profile exhibits superior performance at higher angles of attack (20°) owing to its camber. Increased flow velocity results in higher lift coefficients and reduced drag coefficients.

Keywords: Aerodynamic performance, Naca, Numerical simulation, SST k-ω, Ansys fluent.

Introduction

Aerodynamics, a fundamental field, investigates the laws governing the motion of fluids, particularly air, around solid objects. Its critical applications span various industrial and scientific sectors, from optimizing the performance of aircraft, cars, and wind turbines to designing energy-efficient buildings. Advances in aerodynamics have significantly contributed to the understanding and mastery of fluid dynamics, leading to substantial improvements in emerging technologies. In today's industries, a detailed understanding of aerodynamic phenomena is essential for designing optimal structures. The wing, a key component of aircraft, directly influences lift, drag, and flight stability.

The choice of wing profile, particularly NACA profiles known for their simplicity and efficiency, is of crucial importance in aircraft design, offering optimal performance in lift, drag, and stability. These profiles, developed by NACA in the 1920s and 1930s, remain widely used in the aerospace industry for various types of aircraft. The objective of this study is to compare the aerodynamic performance of different wing profiles using computational fluid dynamics simulations. This study aims to evaluate the advantages and disadvantages of each wing profile and to identify the most effective profile for a given application.

Method

Description of the Physical Problem

In this study, we investigate the steady 2D flow around three NACA wing profiles (Table 1) in an airflow at three different velocities (30 m/s, 60 m/s, 90 m/s) and various angles of attack (0°, 5°, 10°, 15°, 20°). The

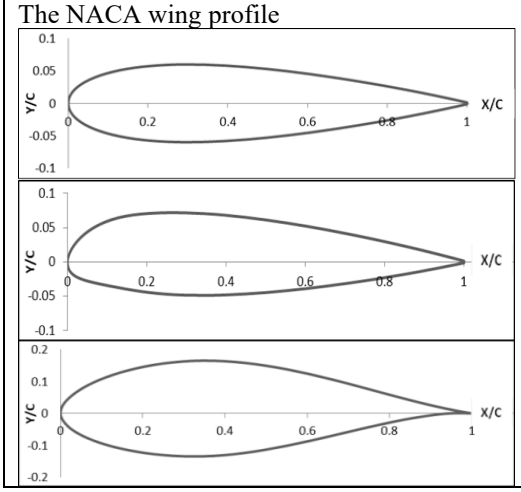
- This is an Open Access article distributed under the terms of the Creative Commons Attribution-Noncommercial 4.0 Unported License, permitting all non-commercial use, distribution, and reproduction in any medium, provided the original work is properly cited.

- Selection and peer-review under responsibility of the Organizing Committee of the Conference

© 2025 Published by ISRES Publishing: www.isres.org

computational domain consists of a semicircle with a radius of 5 m and a rectangle with a length of 15 m. The chord of the numerical profile, located near the center of the semicircle, is 1 m, as shown in Fig. 1.

Table 1. Characteristics of the three NACA profiles studied

The NACA wing profile	Characteristic
	**NACA 0012** : Asymmetric profile, without maximum camber, with a maximum thickness of 12% of the chord.
	NACA 23012 : Aerodynamic profile with a maximum thickness of 12%, maximum camber located at 15% of the chord, with an expected lift coefficient of 0.3.
	NACA63-430 : Has a minimum pressure zone located at 30% of the chord, an optimal lift coefficient of 0.4, and a maximum thickness of 30% of the chord.

Mathematical Model and Boundary Conditions

The flow through the aerodynamic profile is simulated using the Navier-Stokes equations, with the flow considered two-dimensional. The fluid is Newtonian, incompressible, and steady. The equations governing the airflow are:

Continuity Equation:

$$\frac{\partial u}{\partial x}+\frac{\partial v}{\partial y}=0 \tag{1}$$

Momentum Equations:

Along the x-direction:
$$u\frac{\partial u}{\partial x}+v\frac{\partial u}{\partial y}=-\frac{1}{\rho}\frac{\partial P}{\partial x}+v\left(\frac{\partial^2 u}{\partial x^2}+\frac{\partial^2 u}{\partial y^2}\right) \tag{2}$$

Along the y-direction:
$$u\frac{\partial v}{\partial x}+v\frac{\partial v}{\partial y}+=-\frac{1}{\rho}\frac{\partial P}{\partial y}+v\left(\frac{\partial^2 v}{\partial x^2}+\frac{\partial^2 v}{\partial y^2}\right) \tag{3}$$

The continuity and momentum equations are solved using the finite volume method with the ANSYS FLUENT computational code. To this end, it is necessary to specify the boundary conditions of the problem, such as inlet, outlet, and wall conditions. For our study, we have chosen to use an inlet condition of the "velocity inlet" type and an outlet condition of the "pressure outlet" type. The upper, lower, and lateral surfaces of the profile have been defined as "wall" boundaries. The fluid considered in our simulation is air with a viscosity of $\mu = 1{,}7894 \cdot 10^{-5}\ kg/m.s$ and a density of $\rho = 1{,}255\ kg/m^3$. The turbulence model adopted for this type of flow is the *SST k-ω*. model. To solve the convective terms, a second-order "Upwind" scheme is used. The "SIMPLE" method is chosen for pressure-velocity coupling.

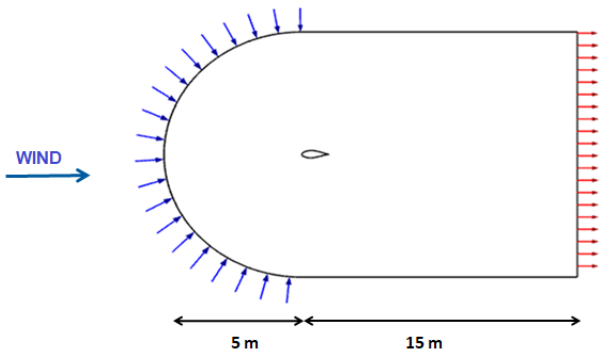


Figure 1. Problem Setup

Results and Discussion

To select the optimal mesh, we conducted tests with three different unstructured meshes, each with distinct numbers of elements (Table 2). The pressure coefficient (Cp) curve was plotted and compared with the experimental results obtained by Mr. Nianxin (Nianxin, 2009). This comparison is presented in Figure 2. It was found that the difference between the results was negligible, and therefore, the first mesh, consisting of 10,140 elements, was chosen for simulating the flow. Table 2 presents the tested meshes.

Table 2. Tested meshes

	Type	Number of Elements
Mesh 1	Tetra	10140
Mesh 2	Tetra	20373
Mesh 3	Tetra	30456

Figure 3 shows the lift-to-drag ratio (C_L/C_D) as a function of the angle of attack for the NACA 0012, NACA 23012, and NACA 63-430 profiles. For the NACA 0012 profile, the lift-to-drag ratio reaches its maximum at an angle of attack of 10°, then decreases progressively. This ratio is generally lower than that of the NACA 23012 profile.

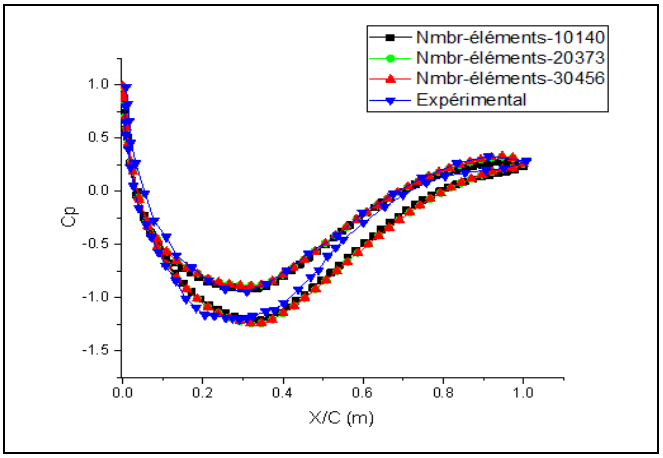


Figure 2. Coefficient de pression pour les trois maillages

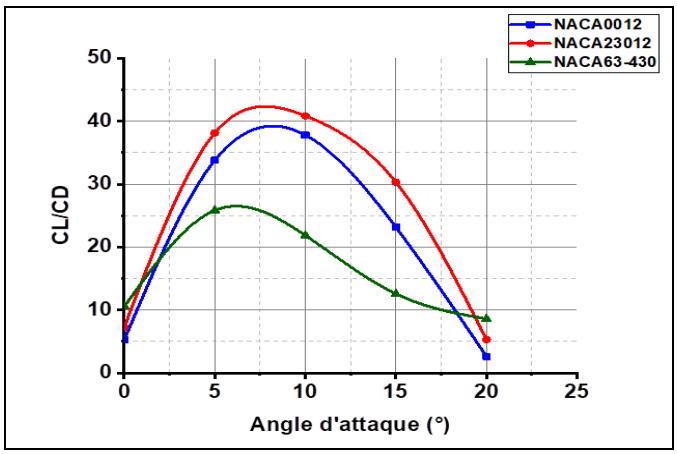


Figure 3. The C_L/C_D Ratio for the three profiles at v=30 m/s.

The NACA 23012 profile generally exhibits a higher CL/CD ratio than the NACA 0012 due to its more streamlined shape at the trailing edge. The more pronounced shape of the rear part of the NACA 23012 profile allows it to generate higher lift relative to drag, resulting in a superior CL/CD ratio. In other words, the NACA 23012 is more efficient in terms of lift generated relative to drag, as reflected by a higher CL/CD ratio. The NACA 63-430 profile shows a high C_L/C_D ratio at high angles of attack due to the specific shape of its camber. This shape is designed to minimize drag at high velocities. The NACA 63-430 can thus generate significant lift with reduced drag, improving its C_L/C_D ratio. The C_L/C_D ratio of the NACA 63-430 typically reaches its maximum at an angle of attack of 5° and then decreases progressively.

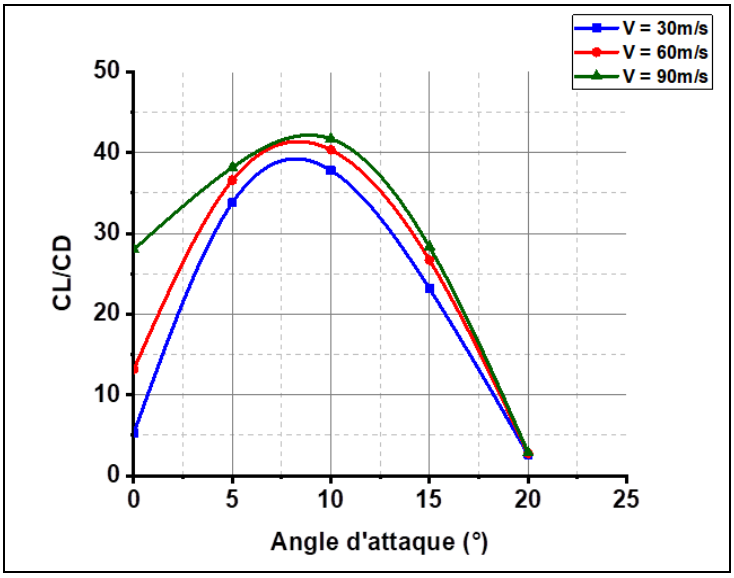


Figure 3. The CL/CD ratio for the NACA 0012 profile at different velocities

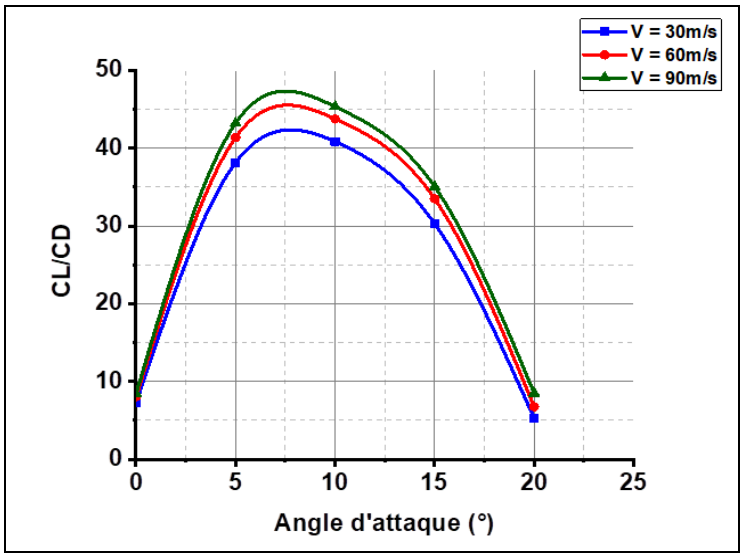


Figure 4. The CL/CD ratio for the NACA23012 profile at different velocities

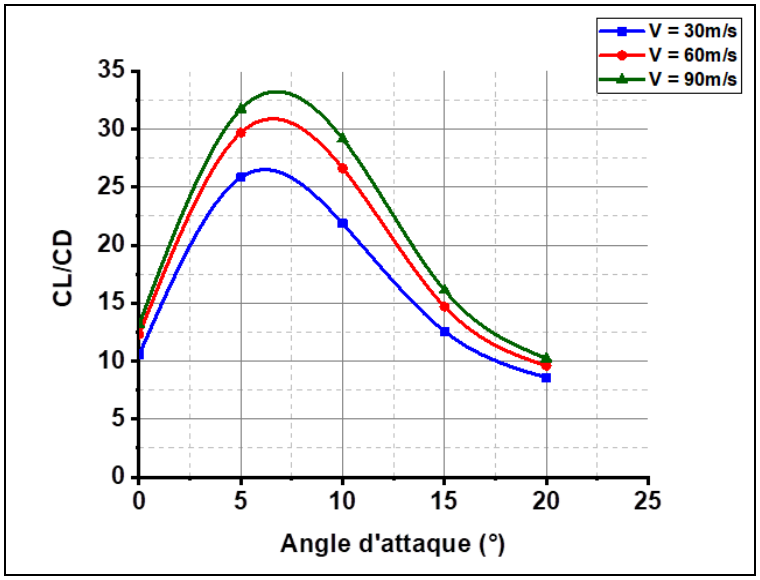


Figure 5. The CL/CD ratio for the NACA63-430 profile at different velocities

Figures 3, 4, and 5 show the C_L/C_D ratio for the NACA 0012, NACA 23012, and NACA 63-430 profiles at different velocities. The effect of velocity on the C_L/C_D ratio depends on the wing profile. Profiles with low camber (NACA 0012) exhibit a less pronounced variation in the C_L/C_D ratio with increasing velocity, whereas profiles with significant camber (NACA 23012 and NACA 63-430) show a more substantial variation in the C_L/C_D ratio with increasing velocity.

Conclusion

A numerical study of the aerodynamic performance of three two-dimensional profiles based on the averaged Navier-Stokes equations is presented. Using the *SST* $k-\omega$ turbulence model, which is particularly suited for flows near and far from the wall, the NACA 0012, NACA 23012, and NACA 63-430 wing profiles exhibit distinct characteristics to meet various aerodynamic requirements. The NACA 0012, a symmetric profile, is widely used due to its balance between lift and drag, making it versatile for many aircraft. The NACA 23012, a cambered profile, offers increased camber for enhanced lift at moderate angles of attack, ideal for maneuverability and turns. In contrast, the NACA 63-430, highly cambered, is suitable for applications requiring high lift at elevated angles of attack, such as aerobatic aircraft, although it may result in increased drag at lower angles of attack.

Scientific Ethics Declaration

* The author declares that the scientific ethical and legal responsibility of this article published in EPSTEM journal belongs to the author.

Conflict of Interest

* The author declares that there is no conflict of interest

Funding

* This research received no specific grant from any funding agency in the public, commercial, or not-for-profit sectors.

Acknowledgements or Notes

* This article was presented as an oral presentation at the International Conference on Technology, Engineering and Science (www.icontes.net) held in Antalya/Türkiye on November 12-15, 2025.

* The author would like to thank the reviewers who contributed to the article with their feedback.

References

Boukhelif, K., & Boudaoud, F. (2023). *Étude numérique comparative sur les performances aérodynamiques des profils d'aile* (Master's thesis). Faculty of Technology, Abou Bekr Belkaid University, Tlemcen, Algeria.

Nianxin, R., & Jinping, O. (2009). Dust effect on the performance of wind turbine airfoils. *Journal of Electromagnetic Analysis & Applications, 1*(2), 102–107.

Roy, S., Das, B., & Biswas, A. (2021). *Influence of camber ratio and thickness ratio on the airfoil performance* (Master's thesis). National Institute of Technology Silchar, Assam, India.

Shabur, A., Hasan, A., & Ali, M. (2021). Comparison of aerodynamic behaviour between NACA 0018 and NACA 0012 airfoils at low Reynolds number through CFD analysis.

Spyridon, D., Eleni, C., Dimitra, C., & Dionissios, P. (2021). Simulation of the flow over NREL's S834 airfoil at two different Reynolds numbers. *International Journal of New Technology and Research, 7*(5), 5–10.

Yılmaz, M., Koten, H., Çetinkaya, E., & Coşar, Z. (2018). A comparative CFD analysis of NACA 0012 and NACA 4412 airfoils. *Journal of Energy Systems, 2*(4), 380–392.

Author(s) Information

Brahim Rostane
Abou Bekr Belkaid University, Tlemcen
Algeria
Contact e-mail: *r_brahim75@yahoo.fr*

To cite this article:

Rostane, B. (2025). Analysis of the aerodynamic characteristics of wing profiles. *The Eurasia Proceedings of Science, Technology, Engineering and Mathematics (EPSTEM), 38,* 899-904.

The Eurasia Proceedings of Science, Technology, Engineering & Mathematics (EPSTEM)
ISSN: 2602-3199

The Eurasia Proceedings of Science, Technology, Engineering and Mathematics (EPSTEM), 2025

Volume 38, Pages 905-911

IConTES 2025: International Conference on Technology, Engineering and Science

Study of the Effect of InP (100) Nitridation Time by XPS Analysis and Electrical Characterisation

Talbi Abbassia
Djillali Liabes University of Sidi Bel Abbes

Benamara Mekki Abdelkader
Djillali Liabes University of Sidi Bel Abbes

Chami Nadir
University of Saida Dr.Moulay Tahar

Benamara Zineb
Djillali University of Liabes of Sidi Bel Abbes.

Abstract: This work presents a study of the effect of thin indium nitride (InN) layer deposition time, on InP substrate. The nitrides of group III metals as InN are very important materials due to their applications in optoelectronics (light-emitting diodes and laser diodes). In this paper the nitridation of InP (100) surfaces has been studied in situ using X ray photoelectron spectroscopy (XPS) and ex situ by electrical I-V method in order to determine the thickness and the quality of the elaborated nitride films and the electrical properties of the InN/InP interface. After ionic cleaning by Ar^+ ions, metallic indium crystallites are created, and the nitridation of the substrates is performed using a plasma glow discharge cell produced indium nitride by reaction with these indium clusters. We used the In_{4d} core levels to monitor the chemical state of the surface and the coverage of the species present. We observed the creation of InN bonds while the In-In metallic bonds decrease. The amount of InN varies for each deposition time. A theoretical model based on stacked layers allows us to calculate the thicknesses δ of InN films produces with different evaporation times of N_2.

Keywords: Nitridation; Electrical characterization; InN/n-InP; XPS.

Introduction

The semiconductors containing the III-nitride element have great potential for the micro and optoelectronics devices with semiconductors (Nakamura, 1998). The Indium nitride is the ideal candidate for the manufacture of ultra-high frequency devices, the blue transmitters and the detectors functioning in spectral field UV (Praveen Kumar, 2009). Several methods were proposed for the nitridation of InP surfaces (Maksimov, 2006). In our case, the nitridation is realized with different times in ultra-high vacuum chamber. The process is performed by exposing the InP substrates to a flow of active nitrogen created by a Glow discharge source with high voltage. We will obtain heterostructures with various thicknesses of InN nano-films on InP substrates. The physical properties of these structures were studied using X ray photoelectron spectroscopy (XPS) which reveals to us the composition of the different elements present on InP surface and evaluate the properties and thickness of obtained InN films (Benamara, 2006). The electrical properties of these structures were presented in this paper allowing us to evaluate different parameters such as the saturation current (I_s), the ideality factor(n), the series resistance (R_s), the diffusion voltage (V_d) and the doping concentration (N_d).

- This is an Open Access article distributed under the terms of the Creative Commons Attribution-Noncommercial 4.0 Unported License, permitting all non-commercial use, distribution, and reproduction in any medium, provided the original work is properly cited.

- Selection and peer-review under responsibility of the Organizing Committee of the Conference

© 2025 Published by ISRES Publishing: www.isres.org

Experimental Procedure

S doped InP (100) substrates with thickness of 400±20 µm have been used. The preparation process of the samples is as follows:

- Chemical cleaning ex situ with successive ultrasonic baths (Khediri, 2021) (H_2SO_4, 3% bromine methanol deionized water) before introduction in an ultrahigh vacuum chamber (10^{-6}_ 10^{-7} Pa).
- In situ cleaning by Ar^+ ion beam during 15 minutes (ion energy, 300 eV; sample current, 2 uA/cm^2; at 6x10^{-5} Torr) in UHV chamber (Talbi, 2013) leads to two phenomena, the removal of the contamination layers mainly due to carbon species (Talbi, 2013), and the creation of metallic indium droplets in well controlled quantity by preferential phosphorus sputtering (Akkal, 2000; Sze, 1981).
- The nitridation process has been performed by plasma discharge cell. In this kind of nitrogen source, continuous plasma is produced by a high voltage (about 2.2KV). The substrate is heated at 250°C during the nitridation process, according to previous work investigating the influence of the temperature on the nitridation process (Pan, 1996). The pressure of nitrogen flow inside the chamber is about 10^1 Pa.

Three series of samples are studied in our case. The preparation conditions of the samples are as follow:

- Sample A1 with doping concentration of N_d= **4.6×10^{15}** cm^{-3}: nitridation during 40 min with nitrogen flow angle of 45°.
- Sample A2 with N_d= **$4\text{-}7\times10^{16}$** cm^{-3}: nitridation with nitrogen evaporation time of 45 min and flow angle of 45°.
- Sample A3 with N_d= **5.3×10^{15} cm^{-3}**: nitridation time of 50 min with angle flow equal to 45°.

In order to determine the thickness of the obtained InN layer and its composition, the nitridation was carried with (XPS) surface analysis using Mg K_α source (1253.6 eV). The structures are tested electrically with a mercury probe used as a temporary gate contact (Section of the gate is S = 7.85 x 10^{-7} m^2). The current–voltage curves were obtained using a HP Semiconductor Parameters Analyser 4155B.

Results and Discussion

Spectroscopy Analysis

Ion bombardment creates metallic indium droplets at the surface of the InP (100) (Akkal, 2000; Sze, 1981). These droplets are consumed by the atomic nitrogen flow coming from a GDS cell to form nitride nanofilm. The In_{4d} core levels obtained for the samples A1, A2 and A3 after nitridation are displayed in Figure. 1, 2 and 3 respectively.

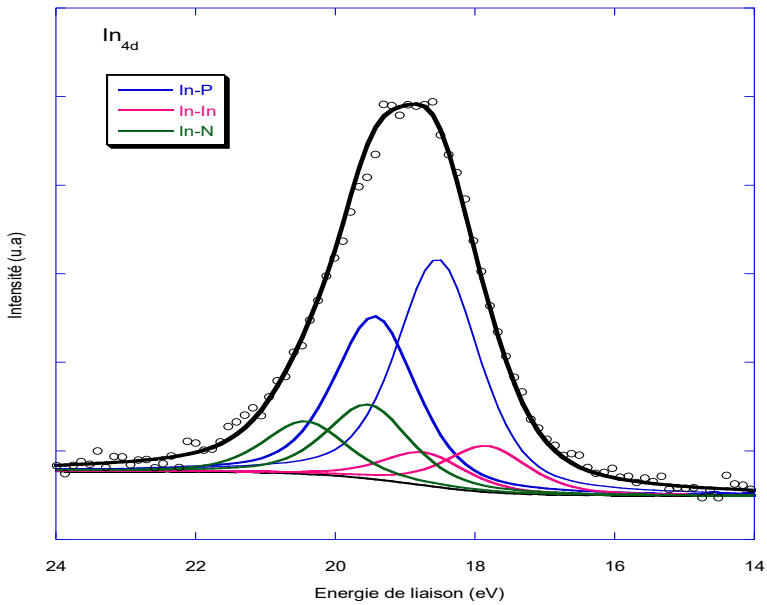


Figure 1. In_{4d} spectra (sample A1)

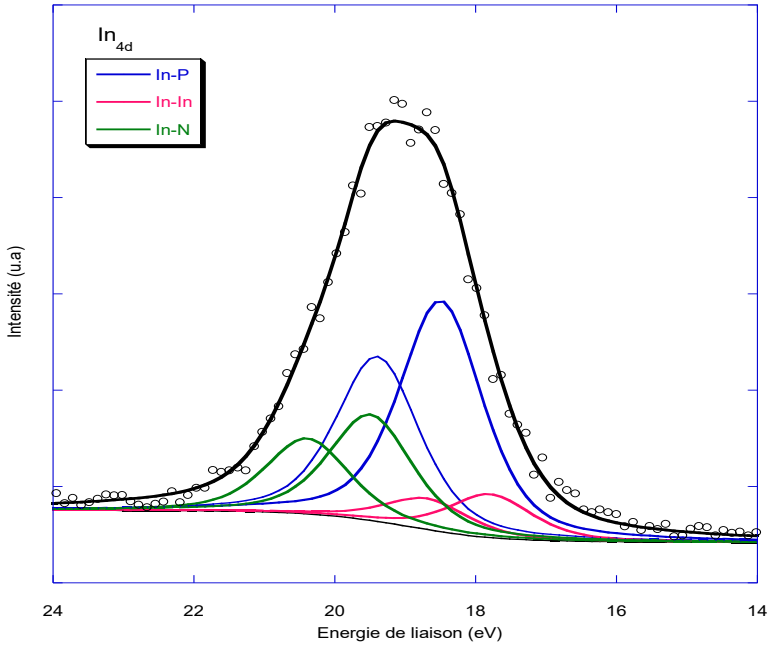


Figure 2. In_{4d} spectra (sample A2)

The In_{4d} core level of the nitridated components can be decomposed into two doublets: one for bulk In-P bonds, the second related to indium nitride as shown in the figures. We note the presence of metallic indium in the In_{4d} core level spectrum showing that the indium clusters were not totally consumed by the nitrogen during the nitridation process. In this case, it is also possible to calculate the theoretical photoelectron intensity. We have considered that the coverage rate of the surface by the nitride layers was equal to unity and that there were two layers of stoichiometric indium nitride. Indeed, indium droplets represent one complete atomic monolayer of metallic indium (θ=25%, height=4ML) (Pan, 1996). So, the maximum number of stoichiometric indium nitride layers which can be formed is two monolayers The spectro were fitted using Shirley background and decomposition into Gaussian and Lorenzian lines shapes. The fitting parameters are summarised in Table 1 (Ambrico, 2005). Moreover, for each environment, we can calculate the theoretical signal coming from the indium atoms.

Table 1. The spectro fitting parameters.

In_{4d}	In-P (bulk)	In-In bonds	In-N bonds
FWHM	1,4±0,2	1,4±0,2	1,4±0,2
% Lorenzian/ Gaussian	50%Gauss, 50% lor	50%Gauss, 50% lor	50%Gauss, 50% lor
Spin-orbit (eV)	0,9	0,9	0,9
Branching ratio	1,3-1,4	1,3-1,4	1,3-1,4
Shift relative to bulk InP	/	-0,7	+1

The intensity for the bulk In-P is written:

$$I_{In-P} = \left(\frac{\alpha_{In}^{h+1}}{1-\alpha_{In}^{2}} \right) i_{In} \tag{1}$$

The intensity coming from In-N is given by the following expression

$$I_{In-N} = 0{,}5(1 + \alpha_{In} + \alpha_{In}^{2} + \ldots + \alpha_{In}^{h-1}) i_{In} \tag{2}$$

h: is the number of the monolayers of InN

I_{In}: is the photoelectron intensity of one atomic monolayer of indium and $\alpha_{In} = \exp\left(-\frac{d}{0{,}96.\lambda_{iIn}}\right)$ the attenuation coefficient of In_{4d} photoelectrons by one monolayer where d is the thickness layer, 0,96: the analyser specific constant and λ_i is the inelastic mean free path of the photoelectrons.

The theoretical ratio I_{InN}/I_{InP} is calculated, it's equal to 0.39 for h=1 and to 0.6 for h=2. The comparison between the experimental and the theoretical ratios allow us to determine the thickness and the number of InN monolayers formed.

Table 2. The results obtained by XPS analysis.

	Sample A1	Sample A2	Sample A3	
Cleaning time (min)	15	15	15	
In-In/In-P	0.35	0.33	0.32	After ionic cleaning
Nitridation time (min)	40	45	50	
Nitrogen flow (angle)	45°	45°	45°	
In-N/In-P	0.32	0.45	0.5	
In-In/In-P	0.202	0.18	0.05	After nitridation

The table 2 summarised the values of experimental ratios obtained for different exposition times at nitrogen flow. We can remark that the amount of the nitride at the surface increase with the exposition time to nitrogen flow. The thickest layer of InN is obtained for a sample A3 wich is nitridated during 50 min and angle flow equal to 45°, with a higher ratio of I_{InN}/I_{InP} (0,5) and lower ratio of $I_{In\text{-}In}/I_{InP}$ (0.03). So the amount of nitride obtained is almost equal to two monolayers of InN (maximum number of stoichiometric indium nitride layers). The sample A1 (nitridated during 40 min) present an experimental ratio equal to 0.32 it corresponds to the theoretical one calculated for one monolayer of indium nitride.

Electrical Analysis

Figure 4 presents the I-V characteristics of the Hg/InN/InP(100) structures for each sample series. The I-V characteristics of these structures show the behavior of rectifying contacts. The conduction is better when the thickness of the InN layer is high. The determination of the electrical parameters was achieved using the characteristic formula expressing thermionic emission current (Benamara, 2006):

$$I = I_S \exp\left(\frac{q(V - R_S.I)}{nkT}\right) \quad (3)$$

$$I_S = S A^{**} T^2 \exp\left(-\frac{q\Phi_{bn}}{kT}\right) \quad (4)$$

Were,

I_s: saturation current;
A**: Richardson constant) (B. Akkal, 2000), S: area of the metal contact (Hg),
T : temperature (300 °K), k: Boltzmann constant, q: electron charge, ϕ_{bn}: barrier height,
n is the ideality factor; it's calculated from the following formula:

$$n = \frac{q}{kT} \cdot \frac{\partial V}{\partial (LnI)} \quad (5)$$

The I-V characteristics show two linear regions, from the first we can determine the ideality factor n, the saturation current I_s and deduce the barrier height ϕ_{bn} . The second region at forward voltage considerably higher

shows existence of serial resistance. In fact, the I-V characteristics reveal a low series resistance (375 Ω) for the samples with large thickness of the InN layer compared with a value of 1513 Ω obtained in the sample with a lower thickness. The saturation current I_s of the samples with two monolayers of InN is the lower. However their potential barrier height is the highest one, so a good Schottky contact is obtained.

Table 3 Electrical parameters calculated from I-V characteristics

	Sample A1	Sample A2	Sample A3
Nitridation time (min)	40	45	50
I_s (A)	2.6×10^{-6}	7.65×10^{-6}	1.92×10^{-6}
N	3.53	3.99	3.07
Φ_{bn} (eV)	0.53	0.512	0.55
R_s (kΩ)	1.513	0.641	0.375
$N_{d(fournisseur)}$ (cm^{-3})	4.6×10^{15}	$4\text{-}7\times10^{16}$	5.3×10^{15}

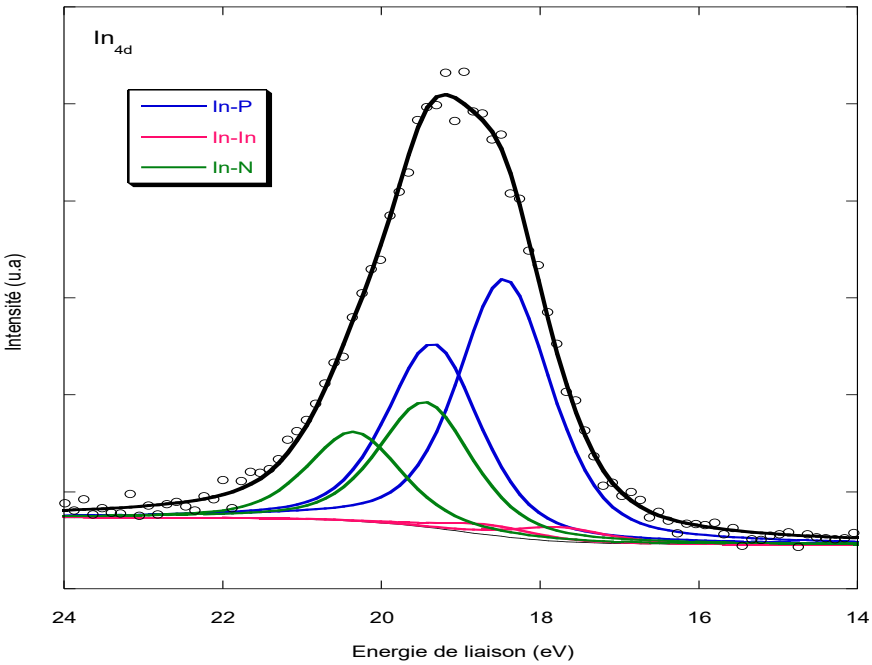


Figure 3. In_{4d} spectra (sample A3).

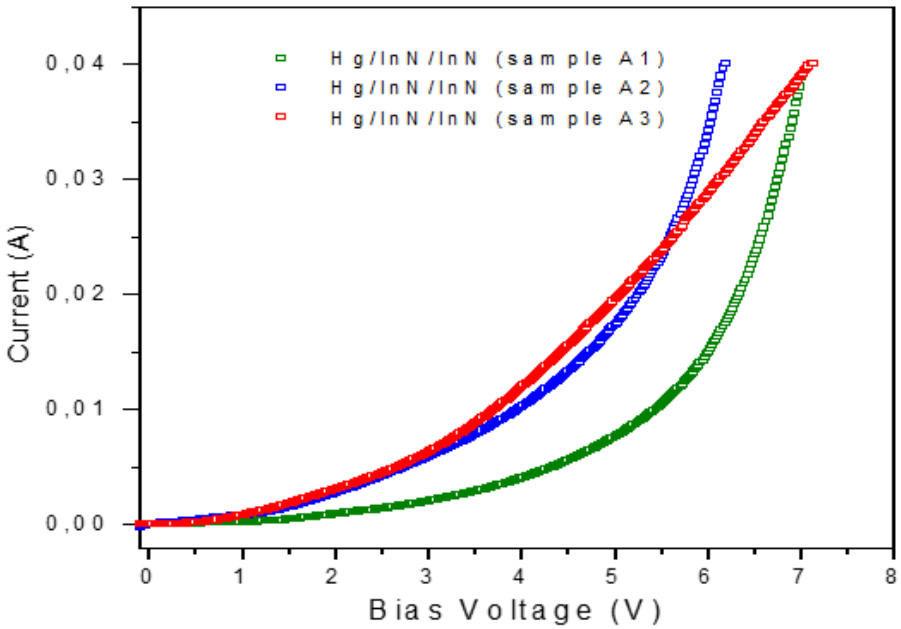


Figure 4. Curent-Voltage characteristics.

Comparing the nitridated samples, the significant value of the ideality factor (n=3.55) is obtained in the nitrided samples with low thickness of InN layer. This effect is probably due to the presence of a tunnel current through the structure. However, the sample with a large thickness presents an interesting ideality factor η= 3 (Because of the consummation In-In at the surface), So this improves the quality of the interface and indicate that interfaces obtained for these structures present a good electronic quality.

Conclusion

The current-voltage characteristics of the Au/InN/InP(100) structures show a behaviour of Schottky According to I–V characteristics, a sufficiently high thickness of the InN in the Hg/InN/InP structures improves the electrical parameters with high barrier heigh and low saturation current.The values of the ideality factor are better for the samples which are well nitrided (total consumption of the metallic indium present on the surface), therefore the InN layer improves the quality of the interface. These results indicate that these devices present a good electronic quality. The electrical results are in good agreement with the spectroscopic ones. They allowed us to highlight the presence of the nitride buffer layer.

Scientific Ethics Declaration

* The authors declare that the scientific ethical and legal responsibility of this article published in EPSTEM journal belongs to the authors.

Conflict of Interest

* The authors declare that they have no conflicts of interest

Funding

* This research received no specific grant from any funding agency in the public, commercial, or not-for-profit sectors.

Acknowledgements or Notes

* This article was presented as a poster presentation at the International Conference on Technology, Engineering and Science (www.icontes.net) held in Antalya/Türkiye on November 12-15, 2025.

References

Kumar, P., Kumar, M., Govind, Mehta, B. R., & Shivaprasad, S. M. (2009). Structural and electrical properties of semiconductor thin films. *Applied Physics Letters, 256*, 517–520.

Maksimov, O., Fisher, P., Skowronski, M., & Heydemann, V. D. (2006). Electrical properties of metal–semiconductor structures. *Materials Chemistry and Physics, 100*(2–3), 457–459.

Benamara, Z., Mecirdi, N., Bachir Bouiadjra, B., Bideux, L., Gruzza, B., Robert, C., Miczek, M., & Adamowicz, B. (2006). Electrical characterization of metal–semiconductor interfaces. *Applied Physics Letters, 252*, 7890–7894.

Khediri, A. H., Talbi, A., Benamara, M. A., & Benamara, Z. (2021). Electrical properties of nanoscale semiconductor devices. *Journal of Nano- and Electronic Physics, 13*(4), 04002.

Talbi, A., Benamara, M. A., Benamara, Z., Akkal, B., Gruzza, B., Bideux, L., Robert, C., & Monier, G. (2013). Electrical analysis of optoelectronic materials. *Journal of Optoelectronics and Advanced Materials, 15*(5–6), 509–513.

Akkal, B., Benamara, Z., Gruzza, B., & Bideux, L. (2000). Electrical properties of metal–semiconductor systems. *Vacuum, 57*(2), 219–228.

Sze, S. M. (1981). *Physics of semiconductor devices* (2nd ed.). John Wiley & Sons.

Pan, J. S., Wee, A. T. S., Huan, C. H. A., Tan, H. S., & Tan, K. L. (1996). Surface and interface studies of semiconductor materials. *Journal of Physics D: Applied Physics, 29*(12), 2997–3002.

Ambrico, M., Losurdo, M., Capezzuto, P., Bruno, G., Ligonzo, T., Schiavulli, L., Farella, I., & Augelli, V. (2005). Electrical properties of solid-state electronic devices. *Solid-State Electronics, 49*(3), 413–419.

Author(s) Information

Talbi Abbassia
Djillali Liabes University of Sidi Bel Abbès Applied Microelectronic Laboratory – 22000. Sidi Bel Abbes, Algeria
Contact e-mail:*Talbi_a02@yahoo.fr*

Benamara Mekki Abdelkader
Djillali Liabes University of Sidi Bel Abbes.Applied Microelectronic Laboratory –22000. Sidi Bel Abbes, Algeria.

Chami Nadir
University of Saida Dr.Moulay Tahar, Laboratory of Electronics advanced, signal processing and microwaves, 20000 Saida, Algeria

Benamara Zineb
Djillali Liabes University of Sidi Bel Abbes.
Applied Microelectronic Laboratory - 22000. Sidi Bel Abbes, Algeria

To cite this article:

Abbassia, T., Abdelkader**,** B.M., Nadir, C., & Zineb, B. (2025). Study of the effect of InP (100) nitridation time by XPS analysis and electrical characterization. *The Eurasia Proceedings of Science, Technology, Engineering and Mathematics (EPSTEM), 38,* 905-911.

The Eurasia Proceedings of Science, Technology, Engineering & Mathematics (EPSTEM)
ISSN: 2602-3199

The Eurasia Proceedings of Science, Technology, Engineering and Mathematics (EPSTEM), 2025

Volume 38, Pages 912-920

IConTES 2025: International Conference on Technology, Engineering and Science

Smart Control of Vibrations in Functionally Graded Porous Wind Turbine Blades via Piezoelectric Materials

Khalid El Harti
Moulay Ismail University of Meknes

Mohamed Touil
Moulay Ismail University of Meknes

Rachid Saadani
Moulay Ismail University of Meknes

Miloud Rahmoune
Moulay Ismail University of Meknes

Abstract: Piezoelectric materials possess the unique ability to convert mechanical stress into electrical voltage and vice versa, making them highly suitable for various smart engineering applications. One of their most promising uses is in the field of vibration energy harvesting, where ambient mechanical vibrations can be transformed into usable electrical energy. For instance, when integrated into roads, pavements, or structural components, piezoelectric sensors and actuators can harvest energy from dynamic loads such as moving vehicles or pedestrians. In renewable energy systems, particularly wind turbines, blade vibrations can lead to structural fatigue and efficiency loss. The integration of piezoelectric elements for active vibration control can significantly reduce unwanted oscillations and enhance operational stability and energy output. Simultaneously, functionally graded materials (FGMs) — advanced composites with spatially varying properties — are increasingly being used in the design of wind turbine blades and other mechanical components due to their ability to optimize strength and reduce stress concentrations. This research focuses on the active vibration control of tapered FGM beams with porous structures using embedded piezoelectric actuators. The modeling approach combines Euler-Bernoulli beam theory with the finite element method (FEM), and the governing equations are derived through Hamilton's principle to accurately capture the dynamic behavior of the system.

Keywords: Vibration control, Functionally Graded materials, Turbine blade, Piezoelectric materials, Finite element method

Introduction

The intrinsic multifunctional character of piezoelectric materials, which enables a bidirectional conversion between mechanical energy and electrical signals, has cemented their status as cornerstone elements in smart material systems (Mason, 1981). This phenomenon, manifesting as the direct piezoelectric effect (charge generation under stress) and its converse (strain induction under an electric field), is rooted in the non-centrosymmetric crystalline structure of these substances (Henderson, 2006). Pioneering compounds such as Lead Zirconate Titanate (PZT) ceramics are lauded for their exceptional electromechanical coefficients and thermal stability, rendering them ideal for demanding roles in actuators and high-sensitivity sensors. In parallel, polymers like Polyvinylidene Fluoride (PVDF) offer complementary advantages of mechanical flexibility and low acoustic impedance, facilitating their integration into wearable devices and conformal transducers.

- This is an Open Access article distributed under the terms of the Creative Commons Attribution-Noncommercial 4.0 Unported License, permitting all non-commercial use, distribution, and reproduction in any medium, provided the original work is properly cited.

- Selection and peer-review under responsibility of the Organizing Committee of the Conference

© 2025 Published by ISRES Publishing: www.isres.org

A domain where this energy-harvesting capability is being aggressively leveraged is ambient vibration scavenging. The strategic embedding of piezoelectric generators within transportation infrastructure—from roadways in Toulouse, France, to railway lines in Japan—exemplifies a pragmatic approach to sustainable energy. These installations capture otherwise dissipated kinetic energy from passing vehicles and trains, converting it into electricity to power ancillary systems such as signage and monitoring networks. Beyond mere power generation, the continuous data stream from these embedded sensors provides an invaluable tool for structural health monitoring (SHM), allowing for the real-time detection of degradation and the facilitation of predictive maintenance, thereby enhancing public safety and asset management (Safaei et al.,2019).

Notwithstanding these advancements, the pursuit of enhanced performance and durability in engineering structures has catalyzed the development of Functionally Graded Materials (FGMs). Unlike conventional laminated composites that suffer from discrete interfacial stress concentrations, FGMs are architected with spatially continuous gradients in composition and microstructure (Mason, 1981; Henderson, 2006; Safaei et al., 2019). This tailored microstructure, for instance a smooth transition from a thermally resistant ceramic surface to a ductile metallic core, optimally reconciles conflicting property requirements. In the context of wind turbine blades, this gradient architecture can be designed to enhance aerodynamic efficiency, mitigate fatigue-induced damage, and reduce overall structural mass—a critical factor for the economic viability of large-scale offshore installations.

However, the fabrication of FGMs, often via powder metallurgy or additive manufacturing techniques, frequently introduces microscopic porosities as an inherent byproduct. While a controlled porosity gradient is sometimes deliberately engineered for specific applications, such as biocompatible implants that mimic bone structure, its unintended presence typically acts as a defect. These pores can significantly alter the local stress field, reduce the effective elastic modulus, and consequently diminish the overall structural stiffness and fatigue life. This interplay between material gradation and porosity presents a complex challenge that directly influences the dynamic vibrational response of FGM components.

The incorporation of Functionally Graded Materials (FGMs) into wind turbine blade manufacturing constitutes a notable advancement within the renewable energy sector (Mahapatra et al.,2021). Characterized by a continuous gradient in their chemical composition or microstructure, FGMs facilitate the optimization of the blades' mechanical and thermal properties, thereby augmenting their overall strength and durability. This tailored material design enables the blades to more effectively endure the variable stress states and vibrational loads induced by wind gusts, consequently mitigating the risk of crack propagation and structural failure. Furthermore, FGMs can be engineered to improve the aerodynamic efficiency of the blades, leading to enhanced performance of the wind turbines (Hu et al.,2013). This technology also permits a reduction in blade mass without a corresponding sacrifice in structural integrity, a critical consideration for large-scale offshore applications (https://innovation.engie.com). In summary, the integration of FGMs presents considerable potential for increasing the reliability and efficiency of wind energy systems, thereby contributing to more sustainable and environmentally benign power generation. It is important to note, however, that the fabrication processes for these innovative materials can introduce porosities, which are known to significantly impair their mechanical performance.

Beams represent fundamental structural components extensively utilized in aerospace engineering and various other industries. Among these, variable-section beams are particularly significant in the construction and structural engineering sectors due to their considerable advantages, such as superior stiffness and structural stability. Their implementation enables a reduction in material usage and labor costs while providing enhanced rigidity. The dynamic behavior of non-uniform section beams has been investigated by El Harti et al. based on Timoshenko's theory (El Harti et al., 2022). Furthermore, Shabani and Cunedioglu (2020) conducted a free vibration analysis of cracked, functionally graded non-uniform beams. El Harti et al. have also examined the influence of porosity in FGM materials (9,10) as well as the effects of thermal loading (El Harti et al., 2020; El Harti, 2021; El Harti et al., 2022).

Building upon this foundation, the present work aims to address a specific gap: the active vibration control of a tapered, power-graded (P-FGM) porous beam using a distributed network of piezoelectric sensor/actuator pairs. The mathematical model is developed within the framework of the Euler-Bernoulli beam theory and discretized via the Finite Element Method (FEM). The primary objective is to employ an advanced control methodology to rigorously investigate the suppression of transient vibrations, with a particular focus on quantifying the individual and coupled effects of taper geometry, material power-law index, and porosity fraction on the system's controlled and uncontrolled dynamic performance.

Mathematical Modeling

The modeling of the Functionally Graded (FG) material behavior is based on a power-law distribution to describe the continuous variation of mechanical properties through the beam's thickness, from a pure metal surface at $z = -h/2$ to a pure ceramic surface at $z = +h/2$. The volume fraction of the ceramic phase is defined by:

$$V_c = \left(\frac{2z + h}{2h}\right)^k = 1 - V_m \tag{1}$$

where V_c and V_m represent the volume fractions of the ceramic and metallic constituents, respectively, and k is the power-law exponent governing the material gradation profile. To account for manufacturing imperfections, such as micro-porosity introduced during sintering, the effective Young's modulus $E(z)$ and mass density $\rho(z)$ are expressed as:

$$E(z) = E_m + (E_c - E_m)\left(\frac{2z + h}{2h}\right)^k - \frac{n}{2}(E_c + E_m) \tag{2}$$

$$\rho(z) = \rho_m + (\rho_c - \rho_m)\left(\frac{2z + h}{2h}\right)^k - \frac{n}{2}(\rho_c + \rho_m) \tag{3}$$

The porosity parameter n with ($n = 0, 0.1, 0.2$) quantifies the imperfection level, where $n = 0$ corresponds to a perfect, non-porous FGM. The beam's cross-sectional area $A(x)$, width $b(x)$, and moment of inertia $I_y(x)$ are described by the following geometric relations (El Harti et al., 2024):

$$b(x) = b_0\left(1 - C_b\frac{x}{L}\right)^m \tag{4}$$

$$A(x) = A_0\left(1 - C_b\frac{x}{L}\right)^m \tag{5}$$

$$I_y(x) = I_{y_0}\left(1 - C_b\frac{x}{L}\right)^m \tag{6}$$

To ensure positive values for $A(x)$ and $I_y(x)$, the width taper ratio C_b must satisfy $0 \leq C_b < 1$. This ratio is calculated from the widths at the fixed (b_0) and free (b) ends:

$$C_b = 1 - \frac{b}{b_0} \tag{7}$$

The initial cross-sectional area and moment of inertia at the clamped end $(x = 0)$ are:

$$A_0 = b_0 h \tag{8}$$

$$I_{y_0} = \frac{b_0 h^3}{12} \tag{9}$$

Adopting the Euler-Bernoulli beam theory, the displacement field at any point is defined by:

$$u(x, y, z, t) = z\frac{\partial w(x, t)}{\partial x} \qquad w(x, y, z, t) = w(x, t) \tag{10}$$

The resulting non-zero strain and stress components are:

$$\varepsilon_{xx} = z\frac{\partial^2 w(x, t)}{\partial x^2} \qquad \sigma_{xx} = Ez\frac{\partial^2 w(x, t)}{\partial x^2} \tag{11}$$

The governing equations are derived using Hamilton's principle:

$$\delta \int_{t_1}^{t_2} (U - T - W)\, dt = 0 \tag{12}$$

where U is the strain energy, T is the kinetic energy, and W is the work done by external forces. The strain energy U and kinetic energy T are formulated as:

$$U = \frac{1}{2} \iiint_V \{\sigma\}^T \{\varepsilon\}\, dV = \frac{1}{2} \int_0^l \iint_A Ez^2 \left(\frac{\partial^2 w}{\partial x^2}\right)^2 dA\, dx \tag{13}$$

$$T = \frac{1}{2} \iiint_V \rho \left(\frac{\partial w}{\partial t}\right)^2 dV = \frac{1}{2} \int_0^l \iint_A \rho \left(\frac{\partial w}{\partial t}\right)^2 dA\, dx \tag{14}$$

The work W done by a distributed transverse load $f(x,t)$ is:

$$W = \int_0^l fw\, dx \tag{15}$$

The Euler-Bernoulli beam finite element is employed, which assumes that plane sections normal to the neutral axis remain plane and normal after deformation. This implies that the slope θ is the first derivative of the transverse deflection w. For this element type, the deflection is approximated by a cubic polynomial in xx, as it must accommodate four nodal degrees of freedom (two deflections and two slopes). The deflection $w(x,t)$ within an element is interpolated as:

$$w(x,t) = \boldsymbol{N}^{\boldsymbol{T}}(x)\boldsymbol{qe}(t) \tag{16}$$

where $\boldsymbol{N}(x)$ is the vector of Hermite shape functions $[N1, N2, N3, N4]$, and $\boldsymbol{qe} = [w_1 \quad \theta_1 \quad w_2 \quad \theta_2]^T$ is the vector of nodal displacements and rotation. The curvature $w''(x,t)$ and velocity $w'(x,t)$ are given by:

$$[w'(x,t)] = [n_2^T][q] \tag{17}$$

$$[w''(x,t)] = [n_1^T][q] \tag{18}$$

$$[\dot{w}(x,t)] = [n_3^T][\dot{q}] \tag{19}$$

Applying the Lagrange equations leads to the elemental equation of motion:

$$M\ddot{q} + Kq = f(t) \tag{20}$$

The elemental mass and stiffness matrices for the FGM core and the piezoelectric layers are derived as follows:

$$[M] = [M^{FGM}] + [M^s] + [M^a] \tag{21}$$

$$[K] = [K^{FGM}] + [K^s] + [K^a] \tag{22}$$

The control force produced by the actuator is obtained by:

$$f_{ctr} = E_p d_{31} b\bar{z} \int_{l_p} n_2 dx\, V^a(t) \tag{23}$$

and as long as there are two piezoelectric actuators symmetrically bonded to the structure to eliminate the membrane effect, there are two control forces, represented as follows:

$$f_{ctr1} = -f_{ctr2} = h\, V^a(t) = h\, u(t) \tag{24}$$

With

$$h^T = E_a d_{31} b\bar{z}[-1 \quad 0 \quad 1 \quad 0] \tag{25}$$

Using Rayleigh's proportional damping:

$$C = \alpha M + \beta K \tag{26}$$

Dynamic equation of the structure and the equation of control are given by:

$$M^* \ddot{g} + C^* \dot{g} + K^* g = f_{ext}^* + f_{ctr1}^* + f_{ctr2}^* \tag{27}$$

The state space model in MIMO (Multi In Multi Out) mode is given by:

$$\dot{x} = Ax(t) + Bu(t) + Er(t) \tag{28}$$

$$y(t) = C^T x(t) + Du(t) \tag{29}$$

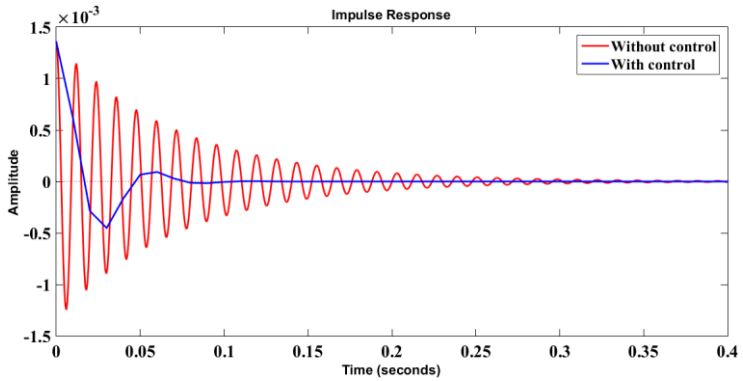
The method of LQG (Linear Quadratic Gaussian) is a method widely used by the mechanics (Sanbi, 2010), Boyere, E. (2011)), based on the desire to minimize performance J index of the form:

$$J(u) = \int_0^\infty (x^t Q x + u^t R u)\, dt \tag{30}$$

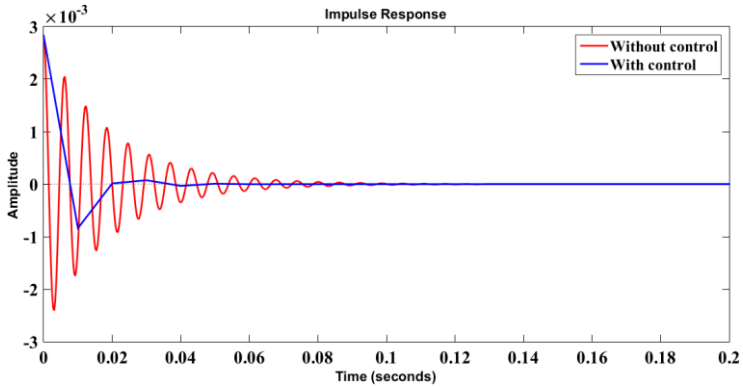
Results and Discussion

This research examines the active vibration control of a cantilevered, functionally graded material (FGM) beam characterized by a variable cross-section. The study focuses on tree key parameters: the porosity distribution within the FGM, the power index and the beam's taper ratio. The power law is employed to describe the continuous variation of material properties through the thickness. The numerical model comprises a beam of dimensions 0.5 m in length, 0.02 m in width, and 0.0001 m in height. A symmetric arrangement of four piezoelectric layers, bonded to the top and bottom surfaces, is integrated into the design to perform simultaneous sensing and actuation. Figure 1 shows the variation of the porosity index n, with the power index k and width b held constant.

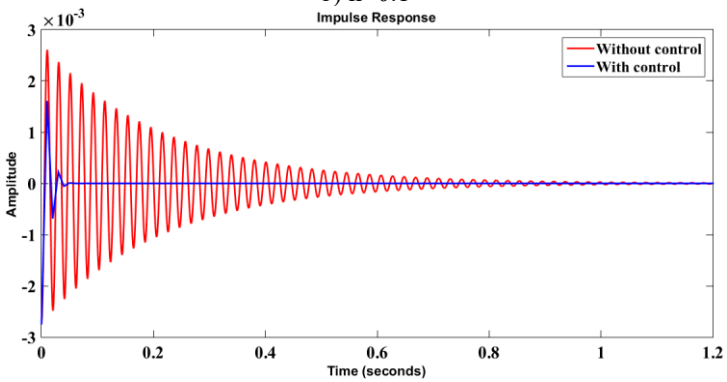
Figure 1 indicates that the vibration amplitude increases with the porosity index. The remark that an increase in the porosity index leads to higher vibration amplitudes is strongly supported by the data presented in Figure 1. The graph clearly shows a positive correlation between the two parameters. Specifically, as the porosity index increases from [n=0] to [n=0.2], the vibration amplitude rises from [1.5] to [3]. This trend is consistent across the observed range, indicating that the material's propensity to vibrate is directly influenced by its void content.



a) $n = 0$



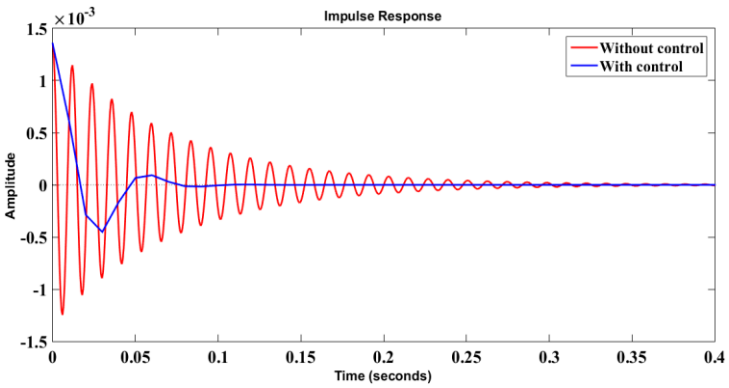
b) n=0.1



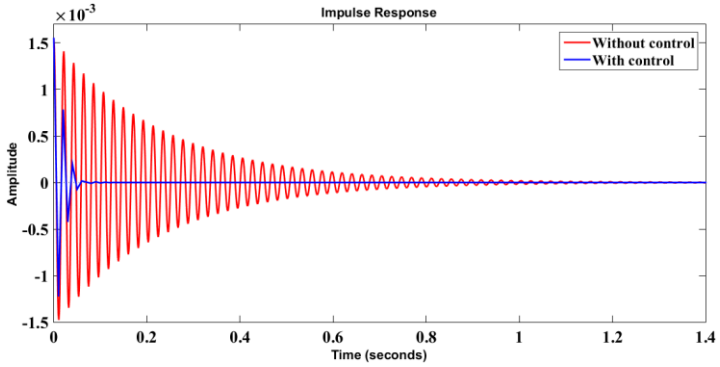
c) n=0.2

Figure 1. Variation of the Porosity İndex n ($b = 2.2$; $k = 0.2$)

Figure 2 depicts the relationship of the power index k for constant porosity index n and width b. Figure 2 demonstrates that the system's vibrational energy is directly driven by the power index. This is a logical outcome, as a higher power index supplies more energy, forcing the system to oscillate with greater amplitude.



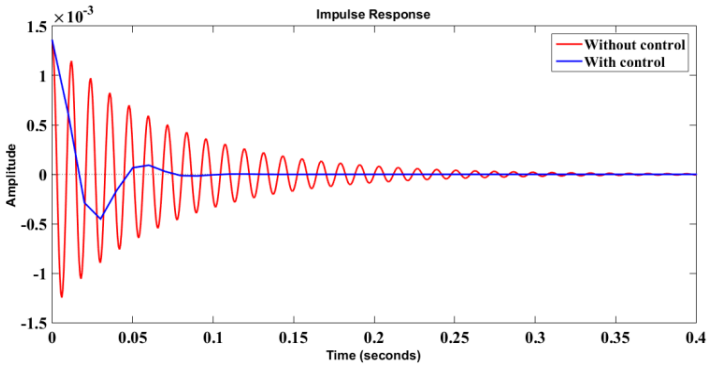
$k = 0.2$



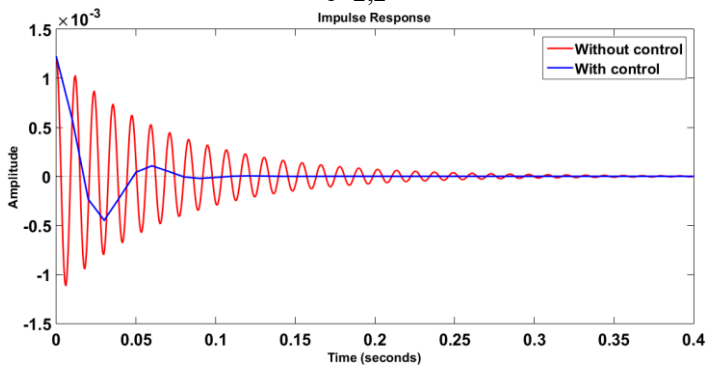
$k = 50$

Figure 2. Variation of power index $k(b = 2.2\,; n = 0)$

Figure 3 presents the variation in the width b, while the porosity index n and power index k are kept fixed. Figure 3 reveals a distinct inverse relationship between the width and the resulting vibration amplitudes. This trend can be physically justified by considering that an increase in width enhances the structural stiffness and inertia of the system. A stiffer structure is inherently more resistant to deformation, leading to a lower vibrational response for the same level of excitation. Consequently, width emerges as a key geometric parameter for controlling and dampening vibrations in this context.



b=2,2



b=2,8

Figure 3. Variation of the width b, $(k = 0.2; n = 0)$

Conclusion

This study has presented a comprehensive numerical investigation into the active vibration control of a cantilevered, functionally graded (FGM) beam with a tapered geometry and integrated piezoelectric sensor/actuator pairs. The developed model, grounded in Euler-Bernoulli beam theory and discretized via the Finite Element Method (FEM), successfully captured the complex dynamic behavior of the system under the coupled influences of material gradation, geometric taper, and inherent porosity.

The primary objective was to rigorously analyze the suppression of transient vibrations using an LQG control strategy, with a specific focus on quantifying the individual and synergistic effects of key parameters. The results and discussion yielded several critical insights:

- Porosity Impact: A strong positive correlation was established between the porosity index and vibration amplitudes. An increase in porosity, which effectively reduces the material's stiffness, was shown to significantly amplify the vibrational response, underscoring the detrimental effect of manufacturing imperfections on dynamic performance.
- Power-Law Index Influence: The power-law index, governing the material gradation profile, was confirmed as a direct driver of vibrational energy. Higher values of this index resulted in increased oscillation amplitudes, highlighting the critical role of the FGM composition in the system's dynamic characteristics.
- Geometric Stiffening via Width: In contrast, the beam's width was identified as a key geometric parameter for vibration mitigation. The analysis revealed a distinct inverse relationship, where an increase in width enhanced the structural stiffness and inertia, leading to a substantial reduction in vibration amplitudes.

In summary, this work elucidates the competing effects of material and geometric properties on the vibrational behavior of smart FGM structures. It demonstrates that while certain factors like porosity and material gradation can exacerbate vibrations, their negative impact can be effectively counteracted through strategic geometric design (e.g., increasing width) and the application of advanced active control systems using piezoelectric materials. The findings provide valuable guidelines for the optimal design and control of next-generation wind turbine blades and similar lightweight structures, where managing vibrations is paramount for structural integrity, longevity, and operational efficiency. Future work could explore the effects of different porosity distributions, more complex geometries, and nonlinear control strategies.

Scientific Ethics Declaration

* The authors declare that the scientific ethical and legal responsibility of this article published in EPSTEM journal belongs to the authors.

Conflict of Interest

* The authors declare that they have no conflicts of interest

Funding

* This research received no external funding

Acknowledgements or Notes

* This article was presented as an oral presentation at the International Conference on Technology, Engineering and Science (www.icontes.net) held in Antalya/Türkiye on November 12-15, 2025.

References

Boyere, E. (2011). Modélisation de l'amortissement en dynamique linéaire. *Manuel de référence, Code Aster, 40*(89), 130.

Mason, W. P. (1981). Piezoelectricity: Its history and applications. *The Journal of the Acoustical Society of America, 70*(6), 1561–1566.

Henderson, I. R. (2006). *Piezoelectric ceramics: Principles and applications*. APC International, Ltd.

Safaei, M., Sodano, H. A., & Anton, S. R. (2019). A review of energy harvesting using piezoelectric materials: State-of-the-art a decade later (2008–2018). *Smart Materials and Structures, 28*(11), 113001.

Mahapatra, S. D., Mohapatra, P. C., Aria, A. I., Christie, G., Mishra, Y. K., Hofmann, S., & Thakur, V. K. (2021). Piezoelectric materials for energy harvesting and sensing applications: Roadmap for future smart materials. *Advanced Science, 8*(17), 2100864.

Hu, W., Park, D., & Choi, D. (2013). Structural optimization procedure of a composite wind turbine blade for reducing both material cost and blade weight. *Engineering Optimization, 45*(12), 1469–1487.

ENGIE Innovation. (n.d.). *Wind turbine blade circularity*. Retrieved from https://innovation.engie.com

El Harti, K., Sanbi, M., Kadiri, I., & Rahmoune, M. (2022, May). Active vibration control of non-uniform section beam. In *International Moroccan Congress of Mechanics* (pp. 13–22). Springer Nature Switzerland.

Shabani, S., & Cunedioglu, Y. (2020). Free vibration analysis of cracked functionally graded non-uniform beams. *Materials Research Express, 7*(1), 015707.

El Harti, K., Rahmoune, M., Sanbi, M., Saadani, R., Bentaleb, M., & Rahmoune, M. (2020). Dynamic control of Euler–Bernoulli FG porous beam under thermal loading with bonded piezoelectric materials. *Ferroelectrics, 558*(1), 104–116.

El Harti, K., Saadani, R., & Rahmoune, M. (2022). Active vibration control of Timoshenko sigmoid functionally graded porous composite beam with distributed piezoelectric sensor/actuator in a thermal environment. *Designs, 7*(1), 2.

El Harti, K., Sanbi, M., Saadani, R., Bentaleb, M., & Rahmoune, M. (2021). Dynamic analysis and active control of distributed piezothermoelastic FGM composite beam with porosities modeled by the finite element method. *Composites: Mechanics, Computations, Applications: An International Journal, 12*(1), 1–21.

El Harti, K., Touil, M., Saadani, R., & Rahmoune, M. (2024). Vibration control of tapering E-FGM porous wind turbine blades using piezoelectric materials. *Solar Energy and Sustainable Development Journal*, 67–77.

Sanbi, M. (2010). *Contribution à l'étude de quelques structures mécatroniques: Dynamique, contrôle actif et propagation d'ondes* (Unpublished doctoral dissertation, Université Moulay Ismail).

Author(s) Information

Khalid El Harti
FS-EST, Moulay Ismail University of Meknes, Meknes, Morocco
Contact e-mail : *elhartikhalid@gmail.com*

Mohamed Touil
FS-EST, Moulay Ismail University of Meknes, Meknes, Morocco

Rachid Saadani
FS-EST, Moulay Ismail University of Meknes, Meknes, Morocco

Miloud Rahmoune
FS-EST, Moulay Ismail University of Meknes, Meknes, Morocco

To cite this article:

El Harti, K., Touil, M., Saadani, R., & Rahmoune, M. (2025). Smart control of vibrations in functionally graded porous wind turbine blades via piezoelectric materials. *The Eurasia Proceedings of Science, Technology, Engineering and Mathematics (EPSTEM), 38,* 912-920

The Eurasia Proceedings of Science, Technology, Engineering & Mathematics (EPSTEM)
ISSN: 2602-3199

The Eurasia Proceedings of Science, Technology, Engineering and Mathematics (EPSTEM), 2025

Volume 38, Pages 921-927

IConTES 2025: International Conference on Technology, Engineering and Science

Elaboration and Characterization of Transparent Conductive Oxide Thin Films and the Effect of Doping

Ahmed Hichem Yahi
Djilali Liabes University of Sidi Bel Abbes

Arslane Hatem Kacha
Djilali Liabes University of Sidi Bel Abbes

Abstract: This study presents the synthesis and characterization of Al-doped ZnO (AZO) thin films on glass substrates via spray pyrolysis. The influence of Al doping (3%, 5%, 7%) on structural, optical, and electrical properties was analyzed. XRD confirmed a polycrystalline wurtzite structure with a (002) orientation, ensuring successful Al incorporation. UV-Vis spectroscopy showed enhanced transparency (70% to 78%), with the bandgap widening from 3.23 eV to 3.32 eV due to the Burstein-Moss effect. Hall Effect measurements revealed improved conductivity (3.37×10^{-1} Ω^{-1} cm^{-1}) at 3% doping, though mobility saturation limited further gains at higher levels. These results highlight AZO as a cost-effective alternative to ITO for solar cells and optoelectronics.

Keywords: ZnO; Thin films; Al doping; Spray pyrolysis.

Introduction

Zinc oxide (ZnO) is a widely studied transparent conductive oxide (TCO) due to its excellent optical and electronic properties. With a direct bandgap of ~3.34 eV and high exciton binding energy (60 meV), it is ideal for optoelectronic applications such as solar cells, LEDs, and sensors (Fan et al., 2017; Ouhaibi et al., 2018; Pham, 2023). However, pure ZnO has low conductivity and suboptimal transparency due to limited carrier concentration (Van de Walle, 2009; Lee et al., 2023).

Doping, particularly with aluminum (Al), significantly enhances ZnO's electrical and optical properties. Al-doped ZnO (AZO) films offer improved conductivity, transparency, and stability, making them viable alternatives to indium tin oxide (ITO) for photovoltaic and optoelectronic devices (Liu et al., 2010; Petrov et al., 2023; Miloua et al., 2012; Amroun et al., 2020). Spray pyrolysis, a cost-effective and scalable deposition method, enables precise control over AZO film properties, making it suitable for large-area coatings (Otieno, 2023).

This study examines the impact of Al doping (3%, 5%, 7%) on ZnO thin films synthesized via spray pyrolysis. XRD, UV-Vis spectroscopy, Hall effect measurements, and XPS are used to analyze structural, optical, and electrical properties. The goal is to optimize doping concentration for superior conductivity and transparency, maximizing ZnO-based solar cell efficiency.

Method

Al-doped ZnO (AZO) thin films were deposited via spray pyrolysis at different doping concentrations (3%, 5%, 7%). Zinc acetate dihydrate (0.15 M) was dissolved in 75 mL of doubly distilled water and stirred at room

- This is an Open Access article distributed under the terms of the Creative Commons Attribution-Noncommercial 4.0 Unported License, permitting all non-commercial use, distribution, and reproduction in any medium, provided the original work is properly cited.

- Selection and peer-review under responsibility of the Organizing Committee of the Conference

© 2025 Published by ISRES Publishing: www.isres.org

temperature. Aluminum nitrate nonahydrate was then added, and the solution was homogenized before deposition.

The deposition was performed at 375 ± 10°C, with a solution flow rate of 1.75 mL/min and a nozzle-to-substrate distance of 28 cm to ensure uniform film formation. The estimated thickness values were 289 nm (ZnO), 281 nm (AlZO-3.00), 285 nm (AlZO-5.00), and 280 nm (AlZO-7.00), determined using the Seed Preprocessing Pattern Search (spPS) technique. The spray pyrolysis system used for the deposition process is schematically illustrated in Figure 1.

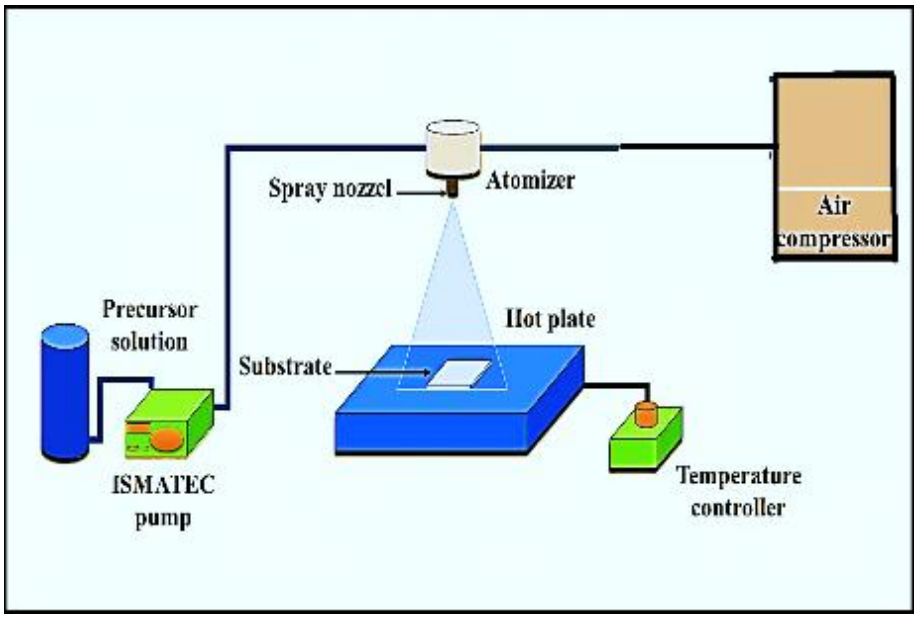


Figure 1. Schematic diagram of spray pyrolysis system used for the preparation of ZnO thin films.

The structural, morphological, optical, and electrical properties were analyzed using:

- X-ray Diffraction (XRD): Bruker D2 Phaser with CuKα radiation (λ = 1.5406 Å) for crystalline structure and phase analysis.
- Scanning Electron Microscopy (SEM) & Energy-Dispersive X-ray Spectroscopy (EDX): Jeol JSM 5800 and IXRF Model 550i for surface morphology and elemental composition.
- Optical Transmittance: JASCO 570 UV–Vis-NIR spectrophotometer (200–2500 nm).
- Electrical Properties: Hall effect measurements (ECOPIA HMS-5000) for conductivity, carrier concentration, and mobility.
- X-ray Photoelectron Spectroscopy (XPS): Kratos Axis Ultra with Al Kα (1486.6 eV) radiation, using C 1s at 284.5 eV for charge correction.

Results and Discussion

Structural Properties and Morphology

The X-ray diffraction (XRD) spectra of undoped and Al-doped ZnO thin films with different concentrations are illustrated in Figure 2 The XRD analysis confirms the *polycrystalline nature* of the films, with all peaks matching the *wurtzite ZnO structure* (JCPDS No. 36-1451). No secondary phases of aluminum or aluminum oxide were detected, indicating the *successful Al incorporation***.** The films exhibit a *preferred (002) orientation***,** with the *c-axis perpendicular* to the substrate, consistent with previous studies.

To determine the crystallite size (D) of the films, the Scherrer formula **(Eq.1)** is applied, which relies on measuring the full width at half maximum (FWHM) of the diffraction peaks b.

$$D = \frac{0.9\lambda}{\beta cos\theta} \quad (1)$$

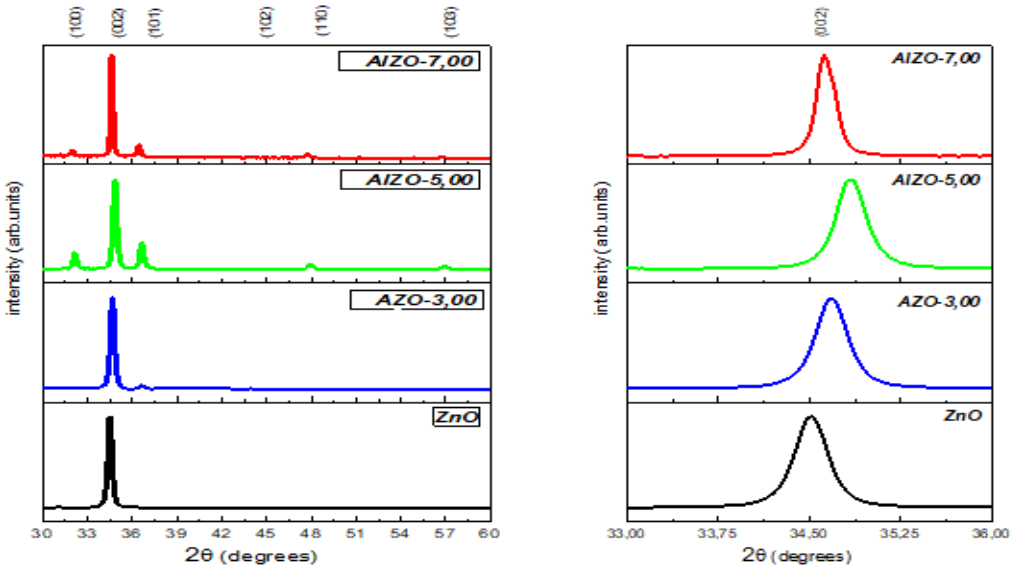


Figure 2. XRD of thin layers of ZnO and AlZO different concentrations of aluminum and Magnified and higher solution XRD pattern.

The chemical composition of pure ZnO and Al-doped ZnO thin films (3.00%, 5.00%, and 7.00%) deposited on glass substrates via the spray pyrolysis technique was analyzed using energy-dispersive X-ray spectroscopy (EDX), as shown in Figure 3.

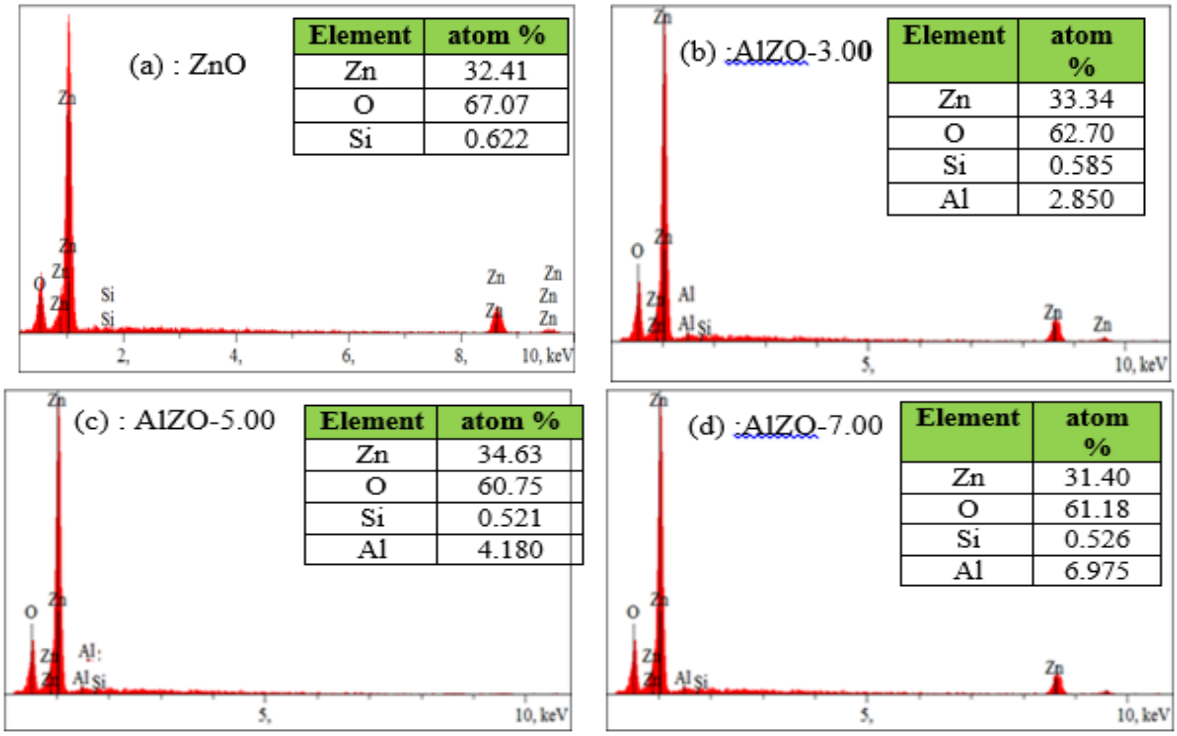


Figure 3. Energy dispersive X-ray (EDX) spectra of the obtained films, (a) ZnO, (b) AlZO-3.00, (c) AlZO-5.00 and (d) AlZO-7.00.

Fig.3a confirms the presence of Zn and O in pure ZnO films, while Fig.3b–3d validate the incorporation of Al in AlZO-3.00, AlZO-5.00, and AlZO-7.00 films. The absence of additional peaks supports the successful Al doping, consistent with XRD results. Si traces originate from the glass substrate. The atomic percentages in Fig.3 align with the intended doping levels, confirming the doping process's effectiveness. X-ray photoelectron spectroscopy (XPS) was performed to analyze the chemical states of elements present in the thin films. The XPS survey spectrum of the AlZO-5.00 sample is shown in Fig.4, revealing the presence of zinc (Zn), oxygen (O), and aluminum (Al).

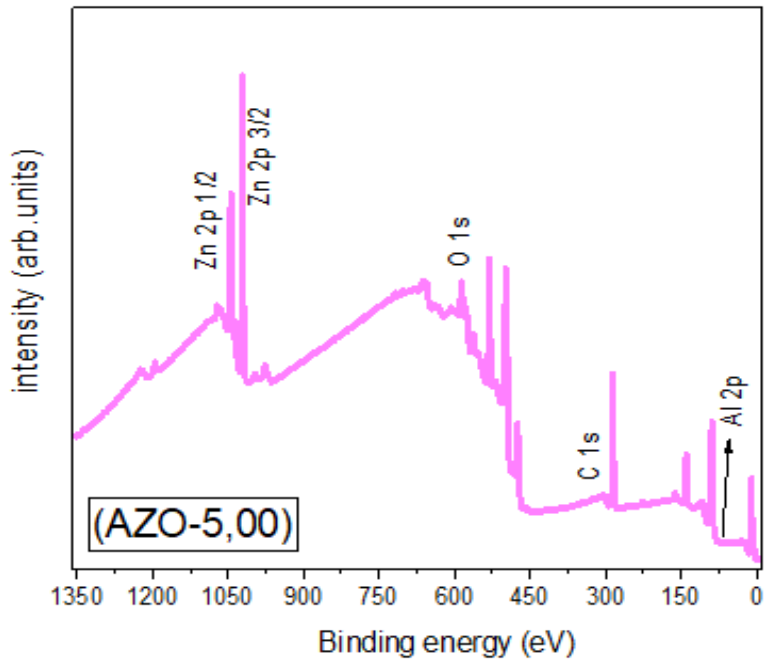


Figure 4. XPS full survey scans of AlZO-1.00 thin films.

Optical Properties

The optical transmittance spectra of ZnO, AlZO-3.00, AlZO-5.00, and AlZO-7.00 thin films are presented in Figure 5.

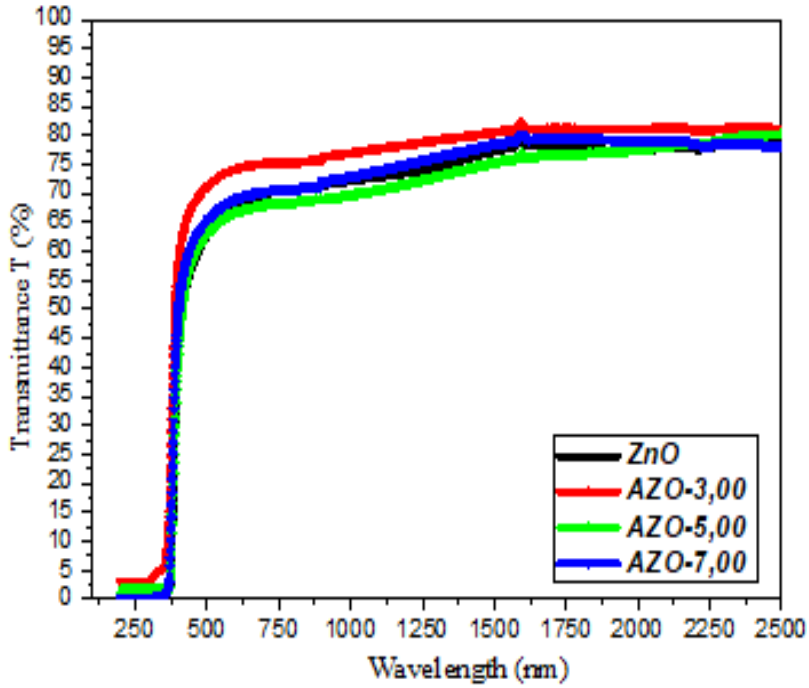


Figure 5. Transmittance spectra of the obtained films.

The curves indicate a clear increase in optical transparency with Al doping. The transmittance improves from 70% in the undoped ZnO film to 78% in the AlZO-3.00 thin film, reflecting an 8% enhancement in the visible range (380–550 nm). This improvement is due to the incorporation of Al, which alters the electronic structure and minimizes light scattering. ZnO is classified as a direct bandgap semiconductor, n = 2 is used in the optical bandgap calculations. $(\alpha h\upsilon)^2$ curves are plotted in Figure 6.

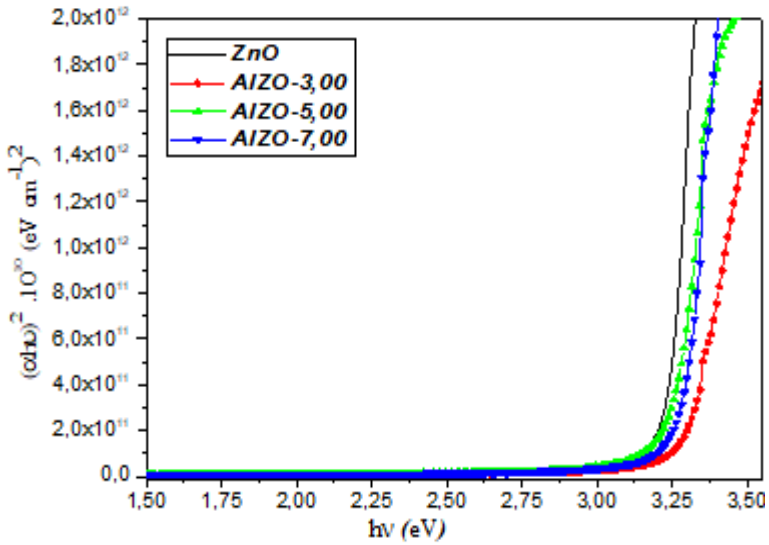


Figure 6. Variation of $(\alpha h\nu)^2$ versus energy of the obtained films.

As illustrated in Fig.7, the optical bandgap expands from 3.23 eV in the undoped ZnO film to 3.32 eV in the 3% Al-doped ZnO film. This increase is due to the Burstein-Moss effect, where a higher carrier concentration shifts the Fermi level, causing an apparent widening of the bandgap.

Electrical Properties

The electrical properties of Al-doped ZnO thin films were analyzed via Hall Effect measurements, with the results summarized in Table 3.

Table 3. Electrical parameters of ZnO and Al-doped ZnO thin films with different concentrations.

Doping level (wt.%)	Mobility (cm^2/V_s)	Carrier concentration (cm^{-3})	Conductivity $(\Omega.cm)^{-1}$
0% – ZnO	2.55×10^{-1}	-6.85×10^{16}	3.95×10^{-3}
3% – AlZO-3.00	5.89×10^{-1}	-4.02×10^{18}	3.37×10^{-1}
5% – AlZO-5.00	3.56×10^{-1}	-3.78×10^{18}	2.89×10^{-1}
7% – AlZO-7.00	4.78×10^{-1}	-1.60×10^{18}	2.98×10^{-2}

The conductivity and carrier concentration of ZnO and Al-doped ZnO thin films with varying doping .concentrations are presented in Figure 7

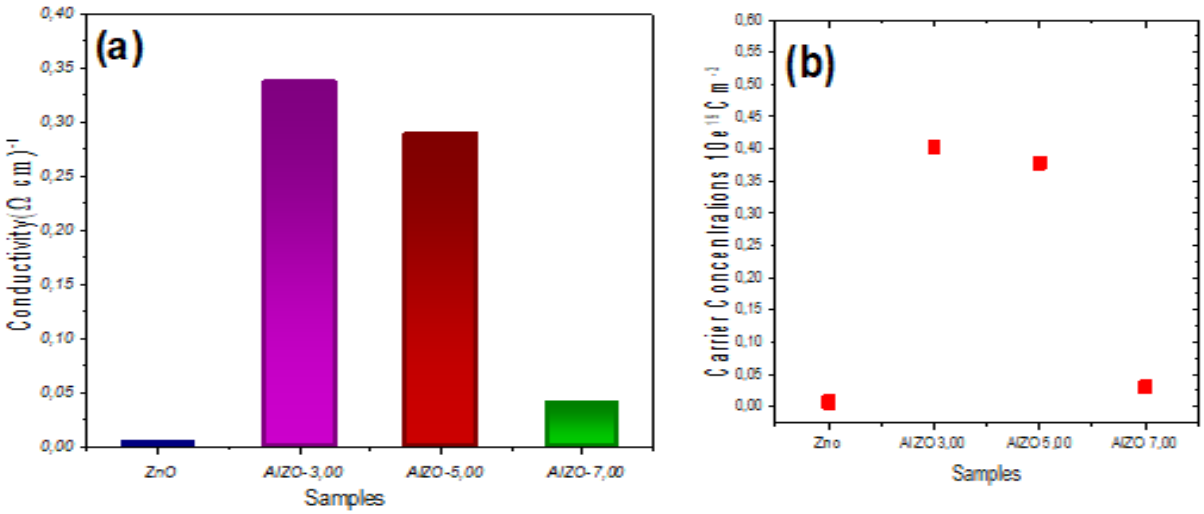


Figure 7. The functional properties of ZnO thin films

Conclusion

In this study, Al-doped ZnO (AZO) thin films were successfully synthesized on glass substrates using the spray pyrolysis technique. Structural analysis confirmed the formation of a polycrystalline wurtzite ZnO phase with strong (002) orientation, demonstrating effective aluminum incorporation without secondary phases. The crystallinity slightly improved at low doping concentrations, while excessive Al content induced lattice strain. Optical investigations revealed a significant increase in transmittance up to 78% and a widening of the optical bandgap from 3.23 eV to 3.32 eV due to the Burstein–Moss effect. Electrical measurements indicated that 3% Al doping yielded the highest conductivity and carrier concentration, whereas higher doping caused mobility reduction. These findings confirm that moderate Al doping effectively enhances both transparency and electrical performance. Therefore, AZO thin films are promising candidates to replace indium tin oxide (ITO) in low-cost, transparent electrodes for solar cells and optoelectronic applications. Future work will focus on optimizing deposition parameters and exploring other dopants to further improve film uniformity and long-term stability.

Scientific Ethics Declaration

* The authors declare that the scientific ethical and legal responsibility of this article published in EPSTEM journal belongs to the authors.

Conflict of Interest

* The authors declare that they have no conflicts of interest

Funding

* This research received no external funding

Acknowledgements or Notes

* This article was presented as an oral presentation at the International Conference on Technology, Engineering and Science (www.icontes.net) held in Antalya/Türkiye on November 12-15, 2025.

References

Amroun, M. N., Salim, K., Kacha, A. H., & Khadraoui, M. (2020). TCO thin films grown by spray pyrolysis technique for window layer of solar cell application: A comparative study. *International Journal of Thin Film Science and Technology, 9*(2), 103–110.

Fan, R., Lu, F., & Li, K. (2017). Single-mode channel waveguide at 1540 nm in Er-doped ZnO thin film. *Journal of Luminescence, 192*, 410–413.

Lee, J. W. N., Jo, C. H., … & Lee, G. (2023). Advancing Al-doped ZnO thin films: Structural, optical, and electrical properties of low-temperature PET substrates via flash lamp annealing. *Journal of Semiconductors, 44*(7), 070005.

Liu, H., Avrutin, V., Izyumskaya, N., Özgür, Ü., & Morkoç, H. (2010). Transparent conducting oxides for electrode applications in light-emitting and absorbing devices. *Superlattices and Microstructures, 48*, 458–484.

Miloua, R., Kebbab, Z., Chiker, F., Sahraoui, K., Khadraoui, M., & Benramdane, N. (2012). Determination of layer thickness and optical constants of thin films by using a modified pattern search method. *Optics Letters, 37*, 449–451.

Otieno, C. O. (2023). Second-order nonlinear optical properties of zinc oxide and aluminum-doped zinc oxide thin films grown by atomic layer deposition. *arXiv preprint*, arXiv:2304.14234.

Ouhaibi, A., Ghamnia, M., Dahamni, M. A., Heresanu, V., Fauquet, C., & Tonneau, D. (2018). The effect of strontium doping on structural and morphological properties of ZnO nanofilms synthesized by ultrasonic spray pyrolysis method. *Journal of Science: Advanced Materials and Devices, 3*, 29–36.

Petrov, V. V., Ignatieva, I. O., … & Volkova, M. G. (2023). Polycrystalline transparent Al-doped ZnO thin films for photosensitivity and optoelectronic applications. *Nanomaterials, 13*(16), 2348.

Pham, V. V. (2023). The preparation of Al-doped ZnO thin films by spray pyrolysis technique for alcohol vapor sensor. *HNUE Journal of Science, 68*(3), 165–172.

Van de Walle, C. G. (2009). Fundamentals of zinc oxide as a semiconductor. *Reports on Progress in Physics, 72*, 126501–126529.

Author(s) Information

Ahmed Hichem Yahi
Djilali Liabes University of Sidi Bel Abbes, Materials Development and Characterization Laboratory, Department of Electronics, Bp 89 Sidi Bel Abbes, Algeria
Contact e-mail: *hichem-y22@hotmail.com*

Arslane Hatem Kacha
Djilali Liabes University of Sidi Bel Abbes, Applied Microelectronics Laboratory, Department of Electronics, BP89, Sidi Bel Abbes, 22000 Algeria

Yahi, A. H., & Kacha, A. H. (2025). Elaboration and characterization of transparent conductive oxide thin films and the effect of doping. *The Eurasia Proceedings of Science, Technology, Engineering and Mathematics (EPSTEM), 38,* 921-927.

The Eurasia Proceedings of Science, Technology, Engineering & Mathematics (EPSTEM)
ISSN: 2602-3199

The Eurasia Proceedings of Science, Technology, Engineering and Mathematics (EPSTEM), 2025

Volume 38, Pages 928-934

IConTES 2025: International Conference on Technology, Engineering and Science

C-V and G-V Characteristics of Nitridated GaAs (100) Structures as Function of Frequency-Effect of Series Resistance

Benamara Mekki Abdelkader
Djillali Liabes University of Sidi Bel Abbès

Talbi Abbassia
Djillali Liabes University of Sidi Bel Abbès

Toumi Hayet
Djillali Liabes University of Sidi Bel Abbès

Benamara Zineb
Djillali Liabes University of Sidi Bel Abbès

Benamara Fatima Yasmine Maroua
Djillali Liabes University of Sidi Bel Abbès

Abstract: Different works show that the nitridation of the GaAs surface improves the electrical quality of the Schottky diodes based on gallium arsenic. In order to observe this improvement, capacitance/conductance – voltage characteristics were watched at three frequencies (50, 100 and 500 kHz). These characteristics were corrected by eliminating the effect of the series resistance. First, values of the series resistance were determined and plotted at different frequencies. R_s versus voltage curves show significant values of the series resistance. A peak was observed in these curves at about -0.5 V for the 50 and 100 kHz frequencies and at 0.25 V for the 500 kHz. These peaks are caused by the ohmic back contact and the surface states density. Then the real electrical parameters of the fabricated Schottky diode were calculated and the surface states density of the Schottky diode was estimated with and without the effect of series resistance. Surface states density was highly reduced after the elimination of the series resistance effect. Electrical parameters show an improvement of the electrical quality of the fabricated Au/GaN/GaAs Schottky diode.

Keywords: GaN, GaAs, Schottky diode, Series resistance, Interface states

Introduction

Semiconductors containing element N offer interesting opportunities for microelectronic and optoelectronics devices. Gallium nitride is the ideal material for the manufacture of high frequency devices, blue emitters and detectors operating in the UV spectral range. The preparation of the well cleaned surfaces arranged and passivated is of paramount importance for the growth of GaN and development of devices based on this material. Several methods have been developed for the growth of gallium nitride. The characterization of the devices based on this material is extensively studied in recent years, especially the study of the Schottky diodes parameters (Akkal, 2000;Rabehi, 2015). The analysis of the electrical characteristics of the Schottky diode only at one frequency by using (C–V and G–V) measurements cannot give detailed information on the conduction mechanisms and the formation of barrier height at the M/S interface. Therefore, the investigation of these measurements, especially at low frequencies, can supply more information both on conduction mechanism and formation of barrier height at the M/S interface (Demirezen, 2015). The electrical characteristics of the

- This is an Open Access article distributed under the terms of the Creative Commons Attribution-Noncommercial 4.0 Unported License, permitting all non-commercial use, distribution, and reproduction in any medium, provided the original work is properly cited.

- Selection and peer-review under responsibility of the Organizing Committee of the Conference

© 2025 Published by ISRES Publishing: www.isres.org

Au/GaN/GaAs are dependent on many parameters such as the process of elaboration, the density of interface states, series resistance of the diode and applied bias voltage.

The C-V and G-V characteristics are usually frequency independent at high frequencies, on the other side, at low and moderate frequencies the depletion and accumulation regions depend on the contribution of interface states density, interfacial layer and series resistance of the device. In this work, we investigated the effect of the series resistance on the parameters of the Au/GaN/GaAs diode extracted from C-V and the G-V measurements such as doping concentration N_d, barrier height Φ_b the diffusion potential V_d and the interface states density N_{ss} at three frequencies (50, 100 and 500 kHz) at room temperature.

Experimental Part

The Au/GaN/GaAs Schottky diode (Figure 1) was fabricated by the nitridation of n-GaAs (100) substrate using a glow discharge source (GDS) (Matolin, 2004). Details of the fabrication of the Au/GaN/GaAs Shottky diode have been given in detail in the previous works (Rabehi,2015; Kacha, 2015).

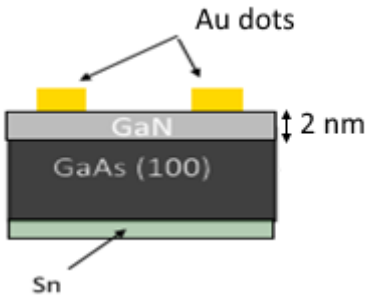


Figure 1. Au/GaN/GaAs Schottky diode

The C-V and G-V measurements were realized in three frequencies (50, 100, 500 kHz) at room temperature using an Impedance Analyzer.

Results and Discussion

C-V curves presented in Figure 2 show an inversion, depletion and accumulation regions such as MIS type Schottky diodes. The C-V plots show a higher capacitance value at low frequencies. This additive capacitance can be explained by the existence of the interface states and traps.

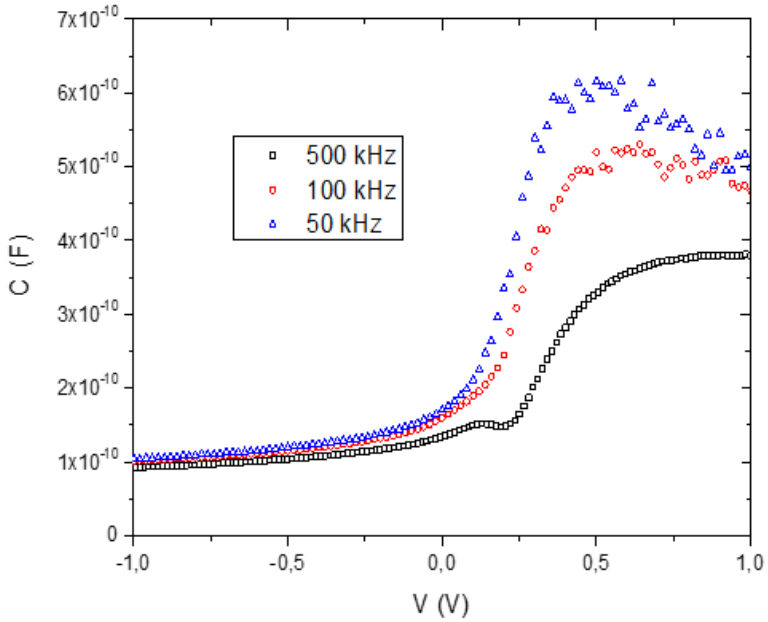


Figure 2. Capacitance – voltage characteristics of the Au/GaN/GaAs Schottky diode at different frequencies.

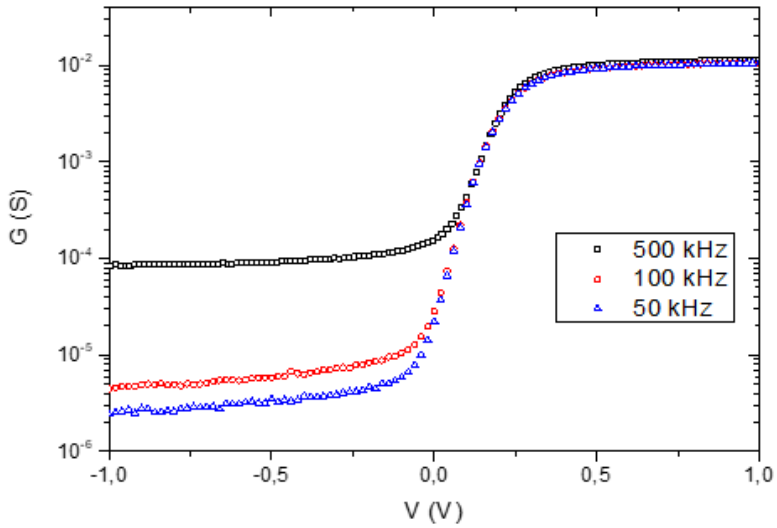


Figure 3. Conductance – voltage characteristics of the Au/GaN/GaAs Schottky diode at different frequencies.

At a high frequency, the N_{ss} cannot follow the ac signal and the contribution of these interface states capacitance to the total capacitance is negligible. In the other side, one can clearly distinct a peak in the accumulation zone especially for low frequencies, this behavior car be explained by the effect of the series resistance of the Schotty diode which causes ohmic back contact S (Demirezen,2012,2014; Tsormpatzoglou, 2005).

G-V curves presented in Figure 3 show a frequency dependence especially at the inverse region. The conductance values increase with decreasing frequency. This can be explained by the distribution of the interface states and traps which follow easily the ac signal. The real value of the series resistance R_s of a Schottky diode can be determined from measured capacitance at accumulation zone C_{ma} and conductance G_{ma} by Nicollian (1982):

$$R_s = \frac{G_{ma}}{G_{ma}^2 + \omega^2 C_{ma}^2} \tag{1}$$

The voltage dependent resistivity R_i of the diode can be also determined using equation (1) for any measured capacitance and conductance for any applied bias voltage. The voltage dependent resistivity calculated from equation (1) for three frequencies (50, 100 and 500 kHz) are plotted in Figure 4.

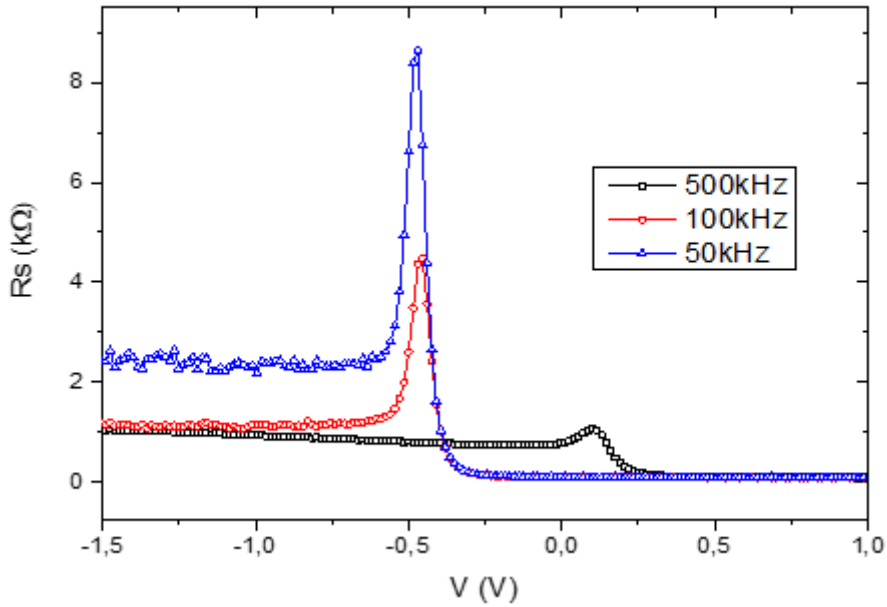


Figure 4. Series resistance vs. applied bias voltage at different frequencies

Rs plots in Figure 4 show a very significant values of the series resistance. These plots give a peak at about -0.5 V for 50 and 100 kHz and a peak at about 0.25 V for 500 kHz. Rs seems to be the most important parameter which causes non-ideality of the C-V and G-V characteristics. Demirezen (2014) have observed two peaks in the R_s plots for an Au/GaAs, they deduced that one of the peaks was caused by the existence of N_{ss} and their particular distribution in semiconductor band gap and the other one was caused by the native interfacial layer.
To obtain the real C-V and G-V characteristics of the Au/GaN/GaAs Schottky diode, the measured capacitance C_m and conductance G_m values were corrected by eliminating the effect of the series resistance R_s using (Nicollian, 1982):

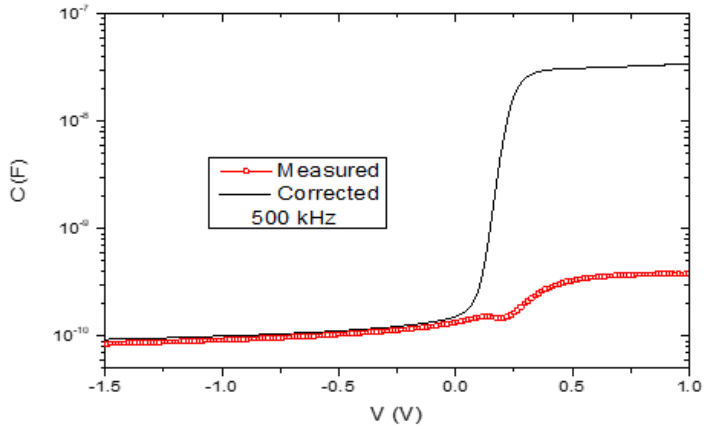
$$C_c = \frac{[G_m^2+(\omega C_m)^2]C_m}{a^2+(\omega C_m)^2} \tag{2}$$

$$G_c = \frac{G_m^2+(\omega C_m)^2 a}{a^2+(\omega C_m)^2} \tag{3}$$

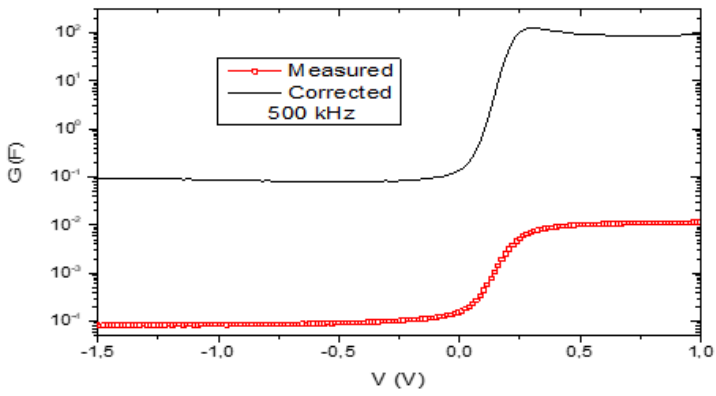
Where:

$$a = C_m - [G_m^2 + (\omega C_m)^2]R_s \tag{4}$$

Capacitance and conductance of the Au/GaN/GaAs Schottky diode for 500 kHz were corrected using equation (2) and (3) and plotted in Figure 5. After correction, values of the C_c and G_c increase in all the range of applied voltage (Figure 5). The corrected C_c shows considerable increase with increasing voltage in the depletion and accumulation zones. It's clearly shown that both change in C-V and G-v characteristics can be affected by R_s especially in accumulation region at high frequencies. So R_s causes errors in the extraction of the electrical parameters. The other more effective parameter on both C and G measurements is the interface states and particular distribution in the semiconductor band gap.



(a)



(b)

Figure 5. Voltage dependent corrected (a) C_c –V and (b) G_c –V plots of the Au/GaN/GaAs Schottky diode for 500 kHz

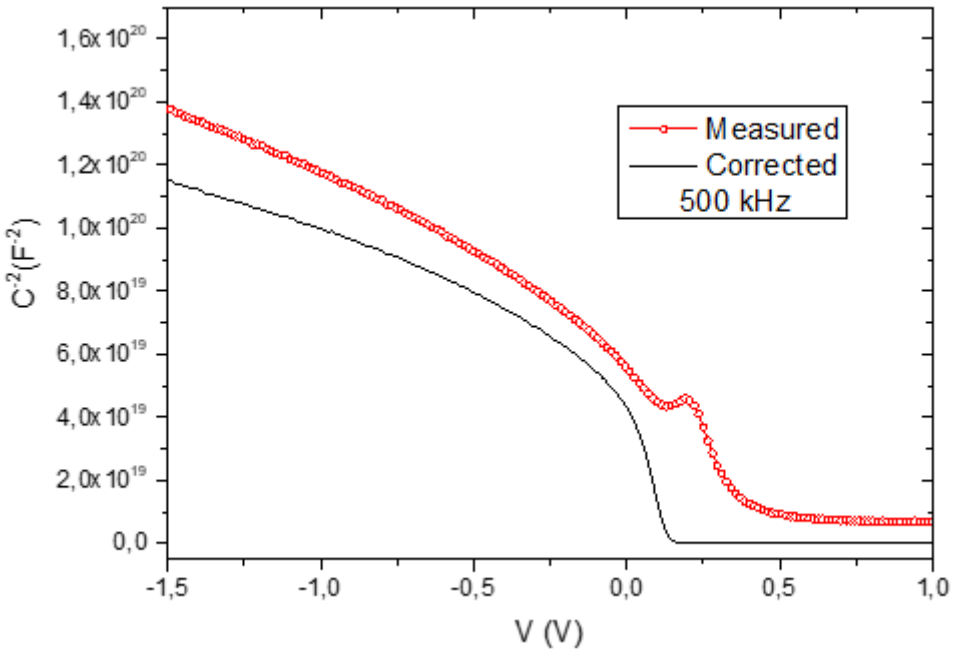


Figure 6. Measured and corrected C^{-2}-V plots of the Au/GaN/GaAs Schottky diode at 500 kHz

The electrical parameters of the Au/GaN/GaAs such as the diffusion potential V_d, the doping concentration N_d and the barrier height Φ_b. The diffusion potential is obtained by the extrapolation of the linear region of the C^{-2}-V characteristic. The doping concentration can be calculated from the slope of the linear region of the C^{-2}-V characteristic using:

$$\frac{dC^{-2}}{dV} = \frac{2}{q\varepsilon_S S^2 N_d} \tag{5}$$

Where ε_s is the substrate permittivity and S the surface of the Schottky contact. The barrier height can be calculated from:

$$\Phi_b = V_d + \frac{kT}{q} ln \frac{N_C}{N_d} \tag{6}$$

The electrical parameters of the Au/GaN/GaAs Schottky diode extracted from the corrected C-V characteristics are regrouped in table 1.

Table 1. Electrical parameters obtained after the elimination of the series resistance effect

V_d (V)	N_d (cm^{-3})	Φ_b (eV)
0.42	5.48×10^{15}	0.54

Electrical parameters shown in table 1 are different than those obtained in our previous works for the same sample (Kacha, 2015). Parameters obtained in this study seem to be the real parameters of the studied Au/GaN/GaAs Schottky diode. The doping concentration obtained with this method is the same concentration of the n-GaAs substrate given by constructor.

The N_{ss} can be extracted from its capacitance contribution to the measured C-V plot by the high-low frequency capacitance method (Nicollian, 1982) with and without the effect of the series resistance. The interface states capacitance C_{ss} can be determined by subtracting the depletion layer capacitance (extracted from the measured high frequency capacitance C_{HF}) from the depletion layer capacitance in parallel with interface states capacitance (extracted from the measured low frequency capacitance C_{LF}). The interface states density is calculated using:

$$qSN_{ss} = C_{ss} = \left[\frac{1}{C_{LF}} - \frac{1}{C_{ox}}\right]^{-1} - \left[\frac{1}{C_{HF}} - \frac{1}{C_{ox}}\right]^{-1} \tag{7}$$

The N_{ss} calculated from equation (7) for the Au/GaN/GaAs Schottky diode before and after correction of the C-V curves are plotted in Figure 7.

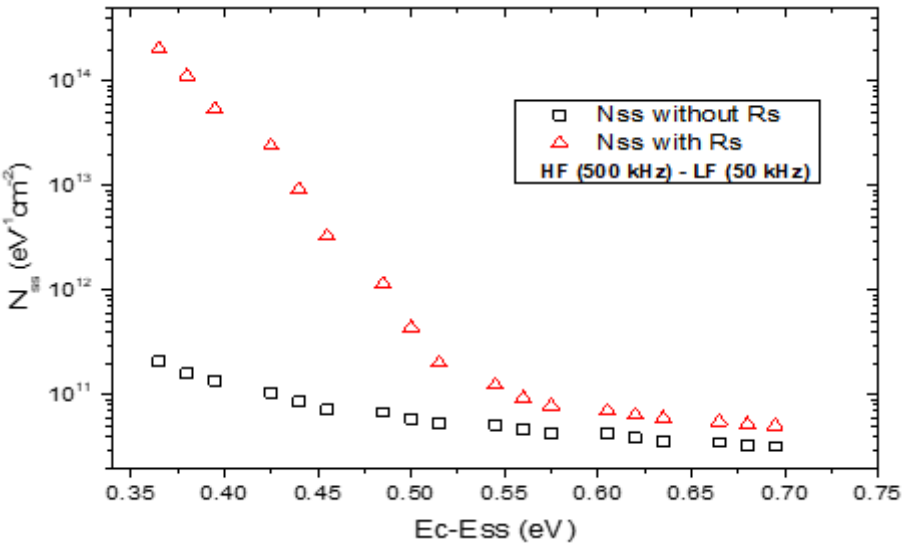


Figure 7. The interface states density distribution in the band gap

The N_{ss} values calculated by elimination of the series resistance R_s are lower than those calculated with R_s. By eliminating R_s effect, the electrical parameters of the Au/GaN/GaAs Schottky diode extracted from C-V measurements are much better than those obtained in our previous study (Kacha, 2015).

Conclusion

The C-V and G-V characteristics of the Au/GaN/GaAs Schottky diode have been investigated for three frequencies (50, 100, 500 kHz). Series resistance influences on the electrical parameters of the Schottky diode. In order to obtain the real parameters, the value of the series resistance was calculated. Then C-V and G-V curves were corrected by eliminating the series resistance which is generally caused by ohmic back contact and surface states. Surface states density was plotted with and within taken in consideration the effect of the series resistance. The surface states density was highly reduced which confirms that the series resistance is a major factor in the fabrication of a Schottky diode. Series resistance can be reduced by improving the ohmic back contact and the conditions of the surface cleaning process and metal deposition on the front side of the diode. Results in this study show an improvement of the electrical quality of the Au/n-GaAs (A. Rabehi, 2015) by the nitridation process. The thin layer of the GaN protects the GaAs surface and improves the quality of the Schottky contact.

Scientific Ethics Declaration

* The authors declare that the scientific ethical and legal responsibility of this article published in EPSTEM journal belongs to the authors.

Conflict of Interest

* The authors declare that they have no conflicts of interest

Funding

* This research received no external funding

Acknowledgements or Notes

* This article was presented as an oral presentation at the International Conference on Technology, Engineering and Science (www.icontes.net) held in Antalya/Türkiye on November 12-15, 2025.

References

Akkal, B., Benamara, Z., Abid, H., Talbi, A., & Gruzza, B. (2004). Electrical characterization of metal–semiconductor structures. *Materials Chemistry and Physics, 85*(1), 27–31.

Benamara, Z., Akkal, B., Talbi, A., & Gruzza, B. (2006). Electrical properties of Schottky contacts. *Materials Science and Engineering: C, 26*(2–3), 519–522.

Ebeoğlu, M. A. (2008). Electrical and interface properties of Schottky barrier diodes. *Physica B: Condensed Matter, 403*(1), 61–66.

Rabehi, A., Amrani, M., Benamara, Z., Akkal, B., Kacha, A. H., Robert-Goumet, C., Monier, G., & Gruzza, B. (2015). Electrical characterization of semiconductor interfaces. *The European Physical Journal Applied Physics, 72*, 10102.

Demirezen, S., Özavcı, E., & Altındal, Ş. (2014). Interface state analysis of Schottky diodes. *Materials Science in Semiconductor Processing, 23*, 1–6.

Matolín, V., Fabík, S., Glošik, J., Bideux, L., Ould-Metidji, Y., & Gruzza, B. (2004). Surface and interface studies of metal–semiconductor systems. *Vacuum, 76*(4), 471–475.

Kacha, A. H., Akkal, B., Benamara, Z., Amrani, M., Rabhi, A., Monier, G., Robert-Goumet, C., Bideux, L., & Gruzza, B. (2015). Electrical properties of multilayer semiconductor structures. *Superlattices and Microstructures, 83*, 827–833.

Tsormpatzoglou, A., Hastas, N. A., Tassis, D. H., Dimitriadis, C. A., Kamarinos, G., Frigeri, P., Franchi, S., Gambia, E., & Mosca, R. (2005). Electrical characterization of MOS structures. *Applied Physics Letters, 87*(16), 163109.

Demirezen, S., Sönmez, Z., Aydemir, U., & Altındal, Ş. (2012). Electrical analysis of metal–semiconductor contacts. *Current Applied Physics, 12*(1), 266–272.

Nicollian, E. H., & Brews, J. R. (1982). *Metal–oxide–semiconductor (MOS) physics and technology*. John Wiley & Sons.

Author(s) Information

Benamara Mekki Abdelkader
Djillali Liabes University of Sidi Bel Abbès, Applied Microelectronic Laboratory, 22000, Sidi Bel Abbes. Algeria.
Contact e-mail: *Mekki_2007@yahoo.fr*

Talbi Abbassia
Djillali Liabes University of Sidi Bel Abbès, Applied Microelectronic Laboratory, 22000, Sidi Bel Abbes. Algeria.

Toumi Hayet
Djillali Liabes University of Sidi Bel Abbès, Applied Microelectronic Laboratory, 22000, Sidi Bel Abbes. Algeria.

Benamara Zineb
Djillali Liabes University of Sidi Bel Abbès, Applied Microelectronic Laboratory, 22000, Sidi Bel Abbes. Algeria.

Benamara Fatima Yasmine Maroua
Djillali Liabes University of Sidi Bel Abbès, Faculty of Exact Sciences, 22000. Sidi Bel Abbes. Algeria.

To cite this article:

Abdelkader, B. M., Abbassia, T., Hayet, T., Zineb, B., & Maroua, B. F. Y. (2025). C-V and G-V characteristics of nitridated GaAs (100) structures as function of frequency-effect of series resistance. *The Eurasia Proceedings of Science, Technology, Engineering and Mathematics (EPSTEM), 38,* 928-934.